AD-A286 753

75 10

DTIC
SELECTE
APR 1 3 1994
S D
F

(792) MD
95-01205
Seven Hundred Ninety Two

AMERICAN
INSTITUTE
PHYSICS

Best
Available
Copy

JOURNAL OF APPLIED PHYSICS

CODEN: JAPIAU
ISSN: 0021-8979

Editor

Steven J. Rothman
Argonne National Laboratory
Argonne, IL

Associate Editors at Argonne National Laboratory

Robert C. Birtcher
Gian P. Felcher
R. E. Holland
John N. Mundy
Simon R. Phillpot

Editorial Board

Term ending 31 December 1994
William R. Frensley (Univ. of Texas at Dallas)
Julia M. Phillips (AT&T Bell Labs, Murray Hill, NJ)
Paul M. Solomon (IBM, Yorktown Heights, NY)

Term ending 31 December 1995
Ulrich Gösele (Max Planck Inst., Halle, Germany)
William L. Johnson (Caltech, Pasadena, CA)
William F. Krupke (Lawrence Livermore Lab, CA)

Term ending 31 December 1996
Gene F. Dresselhaus (MIT, Cambridge, MA)
Allen M. Goldman (Univ. Minnesota, Minneapolis)
Klaus H. Ploog (Paul Drude Inst., Berlin, Germany)
Robert Sinclair (Stanford Univ., Stanford, CA)

Editorial Office
Diane M. Kurtz, *Editorial Supervisor*

Editorial Staff: Catherine M. Dial, *Assistant to the Editor*; Jennifer A. Smeets, *Secretary*

AIP Editorial Operations
John T. Scott, *Manager*

AIP Production
Deborah McHone, *Editorial Supervisor*
Elizabeth Belmont, *Journal Coordinator*
Julie Macklin, *Chief Production Editor*
Cindy Klingensmith, *Senior Production Editor*
Joan Elgo, *Production Editor*

The *Journal of Applied Physics* (ISSN: 0021-8979) is published semimonthly by the American Institute of Physics, 500 Sunnyside Blvd., Woodbury, NY 11797-2999. Second-class postage paid at Woodbury, NY, and additional mailing offices. POSTMASTER: Send address changes to *Journal of Applied Physics*, AIP, 500 Sunnyside Blvd., Woodbury, NY 11797-2999.

© 1994 by the American Institute of Physics.

The *Journal of Applied Physics* is the American Institute of Physics' (AIP) archival journal for significant new results in applied physics. The journal publishes articles that emphasize understanding of the physics underlying modern technology. There are two issues per month. The subject coverage includes, but is not limited to, experimental or theoretical physics applied to all aspects of materials: for example, charge and mass transport, superconductivity, magnetism; surfaces, interfaces, thin films, crystal lattice defects; electrical, optical, magnetic, and structural properties; processing; ion implantation. Materials covered include semiconductors, superconductors, metals and alloys, amorphous materials, and oxides. Other important topics are: electrical, optical, and magnetic devices; optics and lasers; nonlinear optics; electrical discharges; acoustics. The Proceedings of the Annual Conference on Magnetism and Magnetic Materials is a regular feature. *Applied Physics Reviews* is a series of occasional review articles on similar subjects.

Submit manuscripts (3 copies) to Editor, *Journal of Applied Physics*, Argonne National Laboratory, Bldg. 203, Room R-127, 9700 South Cass Avenue, P.O. Box 8296, Argonne, IL 60439-8296.

Subscription Prices* (1994)	U.S.A. & Poss.	Can., Mex., Central & S. Amer. & Caribbean	Foreign Surface Mail	Air Freight Europe, Asia, Africa & Oceania	Optional Air Freight
Members†	$190	$270	$270	——	$380
Nonmembers	$1655	$1735	——	$1845‡	——

*The journal is available on microfiche at $190 per year to members and $1655 per year at the nonmember rate.
†AIP Member and Affiliated Societies. ‡Includes air freight service.

Back-Number Prices: 1994 single copies: $80. Prior to 1994 single copies: $24 for members; $80 for nonmembers. Prices for conference supplements available on request.

Subscription, renewals, and address changes should be addressed to *AIP Circulation and Fulfillment Division (CFD), 500 Sunnyside Blvd., Woodbury, NY 11797-2999.* Allow at least six weeks advance notice. For address changes please send both old and new addresses and, if possible, include a mailing label from a recent issue.

Claims, Single Copy Replacement and Back Volumes: Missing issue requests will be honored only if received within six months of publication date (nine months for Australia and Asia). Single copies of a journal may be ordered and back volumes are available in print or microform. Members—contact AIP Member Services at (516) 576-2288; (800) 344-6901. Nonmember subscribers—contact AIP Subscriber Services at (516) 576-2270; (800) 344-6902.

Page Charge and Reprint Billing: Contact: AIP Publication Page Charge and Reprints—CFD, 500 Sunnyside Blvd., Woodbury, NY 11797-2999; (516) 576-2234; (800) 576-6909.

Copying Fees: Copying of articles beyond that permitted by the Fair Use provisions (Sections 107 and 108) of the U.S. Copyright Law requires payment of fees. The code at the bottom of the first page of each article gives the fee for each copy of the article. Fees should be paid through the *Copyright Clearance Center (CCC), 222 Rosewood Drive, Danvers, MA 01923.* Persons desiring to photocopy materials for classroom use should contact CCC's Academic Permissions Service.

The item-fee code for this publication is 0021-8979/94 $6.00.

Permission For Other Use: Permission is granted to quote from the journal with the customary acknowledgment of the source. To reprint a figure, table, or other excerpt requires in addition the consent of one of the original authors and notification to AIP. Reproduction for advertising or promotional purposes, or republication in any form, is permitted only under license from AIP, which will normally require that the permission of one of the authors also be obtained. Direct inquiries to: Office of Rights and Permissions, American Institute of Physics, 500 Sunnyside Blvd., Woodbury, NY 11797-2999.

Document Delivery: For information on obtaining copies of individual articles, contact AIP Circulation and Fulfillment Division, 500 Sunnyside Blvd., Woodbury, NY 11797-2999; phone: (516) 576-2277; (800) 344-6908; fax: (516) 394-9704; E-mail: *elecprod@pinet.aip.org.*

Online Availability: Abstracts of journal articles published by the AIP and its Member Societies are available in bibliographic databases on major online hosts. The abstracts are also available in the SPIN database via the AIP online service, PINET (Physics Information Network). PINET also offers Advance Abstracts, a current awareness service with abstracts of research papers up to three months prior to their publication in AIP or Member Society Journals. Call (800) 874-6383 or (516) 576-2262 for further information.

PROCEEDINGS OF THE THIRTY-EIGHTH ANNUAL CONFERENCE ON MAGNETISM AND MAGNETIC MATERIALS

PART A

November 15–18, 1993
Minneapolis, Minnesota

DTIC
ELECTE
MAR 01 1995
S D
G

Edited by W. B. Yelon, J. L. Nix,
F. E. Pinkerton, W. M. Saslow, and R. H. Victora

DTIC QUALITY INSPECTED 4

Journal of Applied Physics
Volume 75, Number 10, Part II, 1994

DISTRIBUTION STATEMENT A
Approved for public release;
Distribution Unlimited

Library of Congress Catalog Card Number: 94-70649
International Standard Book Number: 1-56396-337-X
CONF-931133—Vol. 1
Copyright © 1994 by the American Institute of Physics
Published by the American Institute of Physics
500 Sunnyside Blvd., Woodbury, New York 11797-2999
Printed in the United States of America

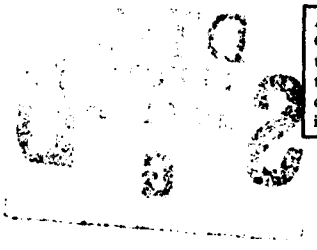

All papers in this volume, and in previous Proceedings Conference on Magnetism and Magnetic Materials published this series, have been reviewed for technical content. The selection of referees, review guidelines, and all other editorial procedures are in accordance with standards prescribed by the American Institute of Physics.

THIRTY-EIGHTH ANNUAL CONFERENCE ON MAGNETISM AND MAGNETIC MATERIALS

November 15–18, 1993

Minneapolis, Minnesota

Accesion For	
NTIS CRA&I	☒
DTIC TAB	☐
Unannounced	☐
Justification	
By	
Distribution /	
Availability Codes	
Dist	Avail and / or Special
A-1	

Sponsored by

The American Institute of Physics
The Magnetics Society
of the
Institute of Electrical and Electronics Engineers

In Cooperation with

The Minerals, Metals, and Materials Society
The American Society for Testing and Materials
The Office of Naval Research
The American Ceramic Society

The Conference is especially grateful to

THE OFFICE OF NAVAL RESEARCH
for its support of the expenses of foreign and interdisciplinary speakers

CONTRIBUTORS TO THE 38TH ANNUAL CONFERENCE ON MAGNETISM AND MAGNETIC MATERIALS

The 38th Annual Conference on Magnetism and Magnetic Materials wishes to express appreciation to the following Corporations for their generous support.

Allegheny Ludlum Corporation
AlliedSignal, Inc.
Applied Magnetics Corporation
BASF Magnetics GmbH
Eastman Kodak Company
F. G. Jones Associates, Ltd.
Fuji Photo Film Company, Ltd.
Fujitsu Limited
General Electric Company
Hitachi, Ltd.
Hitachi Magnetics Corporation
Hitachi Maxell, Ltd.
Craig D. Hubler
IBM
Innovative Instrumentation Incorporated
Magnetic Materials Producers Association
Magnetics Division of Spang & Company
NEC Corporation
Nortronics
The Permanent Magnet Company, Inc.
Quantum Corporation
Seagate Technology
TDK Corporation
3M
Toda Kogyo Corporation
UGIMAG, Inc.

Conference Organization

38th Conference on Magnetism and Magnetic Materials

General Conference Chairman

D. L. Huber

Program Committee

E. D. Dahlberg and D. N. Lambeth, *Co-Chairmen*

C. Brucker
F. Cadieu
W. Cain
M. Chen
G. Dionne
W. Doyle
J. Florczak
P. George
K. Hathaway
F. Hellman
Y. Idzerda
H. Jansen
J. Krebs
D. Landau
B. Maple
I. Mayergoyz
W. Mitchell
D. Naugle
L. Nix
F. Pinkerton
G. Prinz
M. Re
M. Sharrock
P. Trouilloud
R. Victora
W. B. Yelon
J.-G. Zhu

Publications Chairmen

W. B. Yelon
J. L. Nix
F. E. Pinkerton
W. Saslow
R. H. Victora

Secretary

D. L. Huber

Treasurer

D. R. Krahn

Publicity

J. Nyenhuis

Industrial Support

M. P. Sharrock

Local Chairman

D. P. Stubbs

Chairman Elect

S. H. Charap

Magnetism Conference Advisory Committee

G. E. Fish, *Chairman*
D. L. Huber, *Secretary*

Term Expires 1993	Term Expires 1994	Term Expires 1995
J. C. Bonner	I. A. Beardsley	R. J. Celotta
R. L. Carlin	J. E. Crow	W. D. Doyle
S. H. Charap	E. D. Dahlberg	G. E. Fish
C. L. Chien	E. Della Torre	K. B. Hathaway
R. E. Fontana, Jr.	A. J. Freeman	R. R. Katti
D. L. Huber	F. B. Hagedorn	D. R. Krahn
T. M. Jagielinski	I. S. Jacobs	J. W. Lynn
D. N. Lambeth	J. E. Opfer	G. A. Prinz
A. Smith	F. E. Pinkerton	B. J. Shula
R. M. White	D. D. Stancil	

Sponsoring Society Representatives

American Institute of Physics
J. T. Scott

IEEE Magnetics Society
C. D. Graham

Cooperating Society Representatives

The Minerals, Metals, and Materials Society
M. Hong

ASTM Comm. A-6
K. H. Moyer

Office of Naval Research
K. B. Hathaway

American Ceramic Society
B. B. Ghate

PREFACE

MMM '93, the 38th Annual Conference on Magnetism and Magnetic Materials, was held in Minneapolis at the Hyatt Regency Hotel, November 15–18, 1993. Despite a slowdown in the economy and competition from other meetings, there was a total of 586 full registrants and 202 student/retiree registrants. 1018 abstracts were submitted to the Program Committee. The final program was made up of 858 papers, of which 33 were invited papers, 10 contributed papers that had been promoted to invited paper status, 478 poster papers, and 332 contributed oral presentations. The Conference Proceedings is subdivided into 59 sections and contains 30 invited papers, 479 contributed papers, and 153 abstracts.

The meeting began with a well-attended Sunday evening tutorial where informal talks were given on theory of magnetism, magnetic measurements, magnetic force microscopy and other imaging techniques, and materials science: deposition and characterization. In the four-day program, there were symposia on magnetic circular dichroism, novel time-resolved probes of dynamical magnetism, and perpendicular transport in layered structures, along with evening symposia on environmental magnetism and national user facilities. Although there were reports from virtually all areas of magnetics research, studies relating to the magnetic properties of surfaces and artificially structured magnetic materials were especially prominent in the program. Also noteworthy were the large numbers of graduate and post-doctoral students in attendance, which will help ensure the vitality of the field for years to come. Another welcome trend is the growing international character of the meeting as reflected in the fact that 60% of the abstracts accepted for presentation came from outside the United States.

A meeting the size of MMM requires the dedicated efforts of a large number of people. I would especially like to thank the members of the Steering Committee, the Local Committee, the Program Committee, and the Conference Editors as well as staff from the American Institute of Physics and Courtesy Associates for their help in organizing and running the meeting. In addition to the corporate sponsors, who are listed on the third page of the Proceedings, the Conference received financial support for invited speakers from the Office of Naval Research.

David L. Huber
General Chairman
MMM '93

JOURNAL OF APPLIED PHYSICS

Vol. 75, No. 10, 15 May 1994

CODEN: JAPIAU ISSN: 0021-8979

Micromagnetics and Hysteresis

5475	Monte Carlo simulations of remanent magnetization decay driven by interactions	M. E. Matson, D. K. Lottis, E. Dan Dahlberg
5478	The Preisach model with stochastic input as a model for aftereffect	Isaak D. Mayergoyz, Can E. Korman
5481	The measurement of irreversible magnetization and activation volumes	R. Cammarano, P. G. McCormick, R. Street
5484	A phenomenological differential-relation-based vector hysteresis model	A. Bergqvist, G. Engdahl
5487	Master equation approach to anhysteresis of noninteracting particles	Ivo Klik, Ching-Ray Chang, J. Lee
5490	Scaling aspects of domain wall dynamics and Barkhausen effect in ferromagnetic materials	G. Bertotti, G. Durin, A. Magni
5493	Monte Carlo simulations of the magnetocaloric effect in superferromagnetic clusters having uniaxial magnetic anisotropy	L. H. Bennett, R. D. McMichael, H. C. Tang, R. E. Watson
5496	A phenomenological magnetomechanical hysteresis model	A. Bergqvist, G. Engdahl
5499	Reversible transverse susceptibility of particulate recording media	Jing Ju Lu, Huei Li Huang, Ching-Ray Chang, Ivo Klik
5502	Efficient Preisach demagnetization algorithm and its experimental testing	A. A. Adly, Y. J. Zhao
5505	Interpreting logarithmic decay	Ivo Klik, Ching-Ray Chang, J. Lee
5508	Magnetization processes in Co–Cr submicron samples: Hall measurements and micromagnetic simulations	M. van Kooten, S. de Haan, J. C. Lodder, Th. J. A. Popma
5511	Frequency dependence of hysteresis curves in conducting magnetic materials (abstract)	D. C. Jiles

Spin Glasses and Other Disordered Systems

5512	Hierarchical scaling: An analytical approach to slow relaxations in spin glasses, glasses, and other correlated systems (invited)	J. Souletie
5517	Exchange stiffness of Ca-doped YIG	I. Avgin, D. L. Huber
5520	Random-exchange to random-field crossover breaking in $Mn_{0.35}Zn_{0.65}F_2$	F. C. Montenegro, J. C. O. de Jesus, A. Rosales-Rivera
5523	Order by disorder in an anisotropic pyrochlore lattice antiferromagnet	S. T. Bramwell, M. J. P. Gingras, J. N. Reimers
5526	A new scheme to percolation thresholds	Serge Galam, Alain Mauger
5529	Heat capacity and magnetic properties of $CoCl_2 \cdot H_2O$	J. A. Lukin, S. A. Friedberg, S. Chardarlapaty, W. W. Brubaker, C. C. Cinquina, G. C. DeFotis
5532	Perturbative approximation scheme for isolated impurity bonds in the two-dimensional spin-$\frac{1}{2}$ Heisenberg antiferromagnet	P. Schlottmann
5535	Magnetic properties of a new amorphous magnet	C. P. Landee, C. M. Wynn, A. S. Albrecht, W. Zhang, G. B. Vunni, J. L. Parent, C. Navas, M. M. Turnbull
5538	The influence of heat treatments on order–disorder phenomena in a naturally occurring manganese-ferrite	Cherie R. Bluncson, B. J. Evans
5541	Remanent magnetization in the diluted Ising antiferromagnet $Fe_{0.6}Zn_{0.4}F_2$	C. Djurberg, J. Mattsson, P. Nordblad
5544	Freezing transition in the Z_3 gauge glass	Ronald Fisch

(Continued)

Particulate Recording Media

5547	Reptation and viscosity in particulate recording media in the time-limited switching regime	W. D. Doyle, L. Varga, L. He, P. J. Flanders
5550	Ferromagnetic resonance spectra of oriented barium ferrite tapes	Yuwu Yu, J. W. Harrell, W. D. Doyle
5553	Angular dependence measurement of individual barium ferrite recording particles near the single domain size	Thomas Chang, Jian Gang Zhu
5556	Co-Sn substituted barium ferrite particles	X. Z. Zhou, A. H. Morrish, Zheng Yang, Hua-Xian Zeng
5559	Magnetic properties of modified Ba-ferrite particles	H. Sadamura, N. Sugita, M. Maekawa, N. Nagai
5562	H_c enhancement of Co-adsorbed γ-Fe_2O_3 particles via surface treatment with sodium polyphosphate	F. E. Spada, F. T. Parker, A. E. Berkowitz, T. J. Cox
5565	Coercivity enhancement in γ-Fe_2O_3 by surface treatment with phosphate ions	David E. Nikles, Martin R. Parker, Elizabeth M. Crook, Terry M. Self
5568	Electrochemical evaluation of the effect of binder additives on iron corrosion	J. Carlos Arroyo, Hassan M. Saffarian, Garry W. Warren
5571	Molecular dynamics of magnetic particulate dispersions	P. A. Deymier, C. Jung, S. Raghavan
5574	A computer simulation of the microstructure of a particulate dispersion	G. N. Coverdale, R. W. Chantrell, A. Hart, D. Parker
5577	The effect of dc bias fields on the switching speed in magnetic particulate media (abstract)	W. D. Doyle, L. He
5577	Preparation and magnetic properties of Al-modified acicular α-Fe particles (abstract)	C. H. Lin, P. C. Kuo, S. C. Chen, C. S. Hsih
5578	Studies into the use of waterborne coating formulations for the preparation of magnetic tape (abstract)	Stacy Barrom, Ashley Bray, Song Cheng, John Elike, Hong Fan, Alan M. Lane, David E. Nikles
5579	Rheo-optical measurements on suspensions of magnetic recording particles (abstract)	Hyoung J. Choi, Yoon D. Park, Paul L. Frattini, Myung S. Jhon

Thin and Ultrathin Films

5580	Growth and magnetic dynamic scaling of ultrathin ferromagnetic films: Fe/Au(001)	Y.-L. He, Y.-F. Liew, G.-C. Wang
5583	Mössbauer investigation of the magnetic hyperfine field distribution in Fe(100)/Ag(100) structures	P. J. Schurer, Z. Celinski, B. Heinrich
5586	Magnetization reversal processes in epitaxial Fe/GaAs(001) films	C. Daboo, R. J. Hicken, D. E. P. Eley, M. Gester, S. J. Gray, A. J. R. Ives, J. A. C. Bland
5589	Surface magnetization processes investigated by the combined surface magneto-optical Kerr effects in Fe/Cu(100) thin films	Z. J. Yang, S. D. Healy, K. R. Heim, J. S. Drucker, G. G. Hembree, M. R. Scheinfein
5592	The initial phases of epitaxy of fcc Fe/Cu(100): Supersurface and subsurface island formation	S. D. Healy, K. R. Heim, Z. J. Yang, G. G. Hembree, J. S. Drucker, M. R. Scheinfein
5595	Effect of surface layers on ferromagnetic resonance in thin Fe films: Ni, Co, Si, and $YBa_2Cu_3O_{7-\delta}$	P. Lubitz, M. Rubinstein, D. B. Chrisey, J. S. Horwitz, P. R. Broussard
5598	Magneto-optical Kerr effect study of ac susceptibilities in ultrathin cobalt films	A. Berger, S. Knappmann, H. P. Oepen
5601	Ferromagnetic resonance determination of fcc→hcp structural change in epitaxial Co/Mn superlattices	K. Ounadjela, Y. Henry, M. Farle, P. Vennegues
5604	Magnetization of thin Gd films on W(110) near the Curie temperature	M. Farle, W. A. Lewis

(Continued)

High Frequency and Nonlinear Phenomena

5607	Origin of the fine structure of subsidiary absorption in tangentially magnetized YIG films	A. V. Pomyalov, I. Laulicht
5610	Instability mechanism of collective spin wave oscillations in finite-size ferrite samples	A. N. Slavin, G. Srinivasan, S. S. Cordone, V. B. Cherepanov
5613	Controlling spin-wave chaos	S. M. Rezende, F. M. de Aguiar, A. Azevedo
5616	Spin-wave chaotic transients	F. M. de Aguiar, S. M. Rezende, F. C. S. da Silva
5619	Magnetoelastic interaction in yttrium iron garnet films with magnetic inhomogeneities through the film thickness	Yu. V. Gulyaev, A. G. Temiryazev, M. P. Tikhomirova, P. E. Zil'berman
5622	Nonlinear statics and dynamics of highly anisotropic magnets	V. S. Ostrovskii
5625	Applications of ferrites and ferromagnets in tuning rf cavities for accelerators	S. M. Hanna
5628	Forward volume wave microwave envelope solitons in yttrium iron garnet thin films: Peak profiles and multisoliton signatures (abstract)	M. A. Tsankov, M. Chen, C. E. Patton
5629	Microwave magnetic envelope solitons: Threshold powers and soliton numbers (abstract)	J. M. Nash, M. Chen, M. A. Tsankov, C. E. Patton
5630	Self-channeling of magnetostatic waves in ferromagnetic film (abstract)	J. Boyle, S. A. Nikitov, A. D. Boardman, A. Moghadam, K. M. Booth, J. G. Booth
5631	Spin wave solitons in an antiferromagnetic film (abstract)	A. D. Boardman, S. A. Nikitov, N. A. Waby
5632	Brillouin light scattering study of spin wave instability magnon distributions in yttrium iron garnet thin films (abstract)	P. Kabos, G. Wiese, C. E. Patton
5633	Nonlinear surface spin waves (abstract)	A. L. Sukstanskii, S. V. Tarasenko

Magnetic Properties: Tunneling

5634	Thermal equilibrium noise with 1/f spectrum and temperature-dependent magnetic viscosity in the amorphous alloy DyNi	B. Barbara, A. Ratnam, A. Cavalleri, M. Cerdonio, S. Vitale
5637	Time-dependent phenomena at low temperature in magnetic digital compact cassette tape	X. X. Zhang, J. Tejada
5639	Low-temperature magnetic relaxation of organic coated $NiFe_2O_4$ particles	R. H. Kodama, C. L. Seaman, A. E. Berkowitz, M. B. Maple
5642	Quantum tunneling across a domain wall junction (abstract)	Bernard Barbara, Leon Gunther
5642	Macroscopic quantum tunneling in antiferromagnetic horse-spleen ferritin particles (abstract)	J. Tejada, X. X. Zhang
5643	Magnetism of thin magnetic layers with strong anisotropy and quantum tunneling (abstract)	P. Perera, M. J. O'Shea

Magnetoelastic Behavior of Films and Crystals

5644	Magnetic and structural modifications in Fe and Ni films prepared by ion-assisted deposition	William A. Lewis, Michael Farle, Bruce M. Clemens, Robert L. White
5647	Magnetostrictive hysteresis in nickel polycrystalline thick films	Isabelle Brard, Roland Georges, Gilles Le Blevennec
5650	Method for determining both magnetostriction and elastic modulus by ferromagnetic resonance	R. D. McMichael
5653	Multitarget sputtering of high magnetostrictive Tb-Dy-Fe films	E. Quandt
5656	Magnetostriction, elastic moduli, and coupling factors of composite Terfenol-D	L. Sandlund, M. Fahlander, T. Cedell, A. E. Clark, J. B. Restorff, M. Wun-Fogle
5659	Structure and magnetic properties of mechanically alloyed $SmFe_2$	Clive D. Milham

(Continued)

5662 High pulsed field magnetostriction in RMn_2 (R=Gd, Tb, Nd, and Y) — M. R. Ibarra, C. Marquina, L. Garcia-Orza, Z. Arnold, A. del Moral

5665 An ultrasonic study of the Néel transition in dilute Cr-Al alloy single crystals — H. L. Alberts

5667 Magnetostriction of polycrystalline Co-Pd alloys — S. U. Jen, B. L. Chao

5670 Hysteretic and other relationships between technical magnetostriction and magnetization — I. J. Garshelis

5673 Micromagnetic model for the influence of biaxial stress on hysteretic magnetic properties — M. J. Sablik, L. A. Riley, G. L. Burkhardt, H. Kwun, P. Y. Cannell, K. T. Watts, R. A. Langman

5676 Modeling the effects of stress on magnetization in ferromagnetic materials (abstract) — D. C. Jiles

Hysteresis and Micromagnetics

5677 Interpretation of hysteresis curves and Henkel plots by the Preisach model (invited) — V. Basso, M. Lo Bue, G. Bertotti

5683 Experimental testing of applicability of the Preisach hysteresis model to superconductors — G. Friedman, L. Liu, J. S. Kouvel

5686 2D vector Preisach models and rotational hysteretic losses — I. D. Mayergoyz

5689 Demagnetized-state dependence of Henkel plots. I. The Preisach model — Ferenc Vajda, Edward Della Torre, R. D. McMichael

5692 Demagnetized-state dependence of Henkel plots. II. Domain wall motion — R. D. McMichael, Ferenc Vajda, Edward Della Torre

5695 Model calculations of rotational hysteresis for ferromagnetic particles with competing anisotropies — Y. Yoshida, T. L. Templeton, A. S. Arrott

5698 A hysteresis model with interactions — J. Planès

5701 Simulation of magnetization reversal in two-phase exchange coupled nanocrystalline materials — E. H. Feutrill, P. G. McCormick, R. Street

5704 Activation volume of a pair of magnetostatically coupled particles — A. Lyberatos

5707 Parameter template in local magnetic measurements — R. Kaczmarek, M. Dautain, S. Defoug

5710 3-D micromagnetic modeling of domain configurations in soft magnetic materials — Zhenzhou Guo, Edward Della Torre

5713 Magnetization in current carrying iron whiskers (abstract) — A. S. Arrott, J.-G. Lee

Magnetic Semiconductor

5714 Spin-dependent confinement in DMS-based heterostructures (invited) — A. Petrou, L. P. Fu, W. Y. Yu, S. T. Lee, B. T. Jonker, J. Warnock

5719 Optical transitions in (ZnCo)Se and (ZnFe)Se: Role of an effective $p-d$ exchange (invited) — Chee-leung Mak, J. Bak, R. Sooryakumar, M. M. Steiner, B. T. Jonker

5725 Coexistence of Brillouin and Van Vleck spin exchange in $Zn_{1-x}Mn_xSe/Zn_{1-y}Fe_ySe$ spin superlattice structures — B. T. Jonker, H. Abad, L. P. Fu, W. Y. Yu, A. Petrou, J. Warnock

5728 Magnetic study of the diluted magnetic semiconductor $Sn_{1-x}Mn_xTe$ — P. J. T. Eggenkamp, C. W. H. M. Vennix, T. Story, H. J. M. Swagten, C. H. W. Swüste, W. J. M. de Jonge

5731 Magnetic behavior of $(CuIn)_{1-x}Mn_{2x}Te_2$ — P. M. Shand, P. A. Polstra, I. Miotkowski, B. C. Crooker

5734 Relaxation of magnetization in $Cd_{1-x}Mn_xTe$ diluted magnetic semiconductors under illumination — M. Smith, A. Dissanayake, H. X. Jiang, L. X. Li

5737 Theory of magnetization in IV–VI based diluted magnetic semiconductors — R. L. Hota, G. S. Tripathi, P. K. Misra

(Continued)

5740 Effects of oxygen vacancies on magnetic properties of Ca-substituted yttrium iron garnet (abstract) — Y. J. Song, R. E. Bornfreund, G. B. Turpin, P. E. Wigen

Magnetic Recording: Frequency, Spatial, and Tribological Effects

5741 Tribological studies of silicon for magnetic recording applications (invited) — Bharat Bhushan, Vilas N. Koinkar

5747 Mathematical modeling of lubrication for the head-disk interface using incompressible fluids — Paul R. Peck, Myung S. Jhon, Ralph F. Simmons, Jr., Thomas J. Janstrom

5750 Wear and stiction regimes of thin-film magnetic disks — Arlen Bowen

5753 Recording medium properties and capacity bounds — J. A. O'Sullivan, D. G. Porter, R. S. Indeck, M. W. Muller

5756 Direct imaging of track edge fringing fields on recorded media — R. D. Gomez, I. D. Mayergoyz, E. R. Burke

5759 Computation of magnetic fields from recording surfaces with multiple tracks — E. R. Burke, R. D. Gomez, R. Madabhushi, I. D. Mayergoyz

5762 Micromagnetic modeling and experimental study of transition noise correlation in thin-film media — Jian-Gang Zhu, Haiyun Wang, Thomas C. Arnoldussen

5765 Noise correlations in dibit recording — Gang Herbert Lin, H. Neal Bertram, Ralph Simmons

5768 Magnetic viscosity in high-density recording — Pu-Ling Lu, Stanley H. Charap

5771 Friction and wear of ultrahigh-density magnetic tapes — Bharat Bhushan, Steven T. Patton

5774 Analysis of write and read spacing loss for perpendicular recording (abstract) — Yoichiro Tanaka, Tomoko Komai, Takashi Hikosaka

5775 Experimental Preisach analysis of the Wohlfarth relation (abstract) — Ferenc Vajda, Edward Della Torre

Soft Magnetic Materials and Applications I

5776 Magnetic fine structure of domain walls in iron films observed with a magnetic force microscope — Roger Proksch, Sheryl Foss, E. Dan Dahlberg, Gary Prinz

5779 Influence of rf magnetron sputtering conditions on the magnetic, crystalline, and electrical properties of thin nickel films — M. S. Miller, F. E. Stageberg, Y. M. Chow, K. Rook, L. A. Heuer

5782 Molecular magnets V(tetracyanoethylene)$_x \cdot y$(solvent): Applications to magnetic shielding — B. G. Morin, C. Hahm, Joel S. Miller, A. J. Epstein

5785 Soft magnetic properties of nanocrystalline Fe-Hf-C-N films — J. O. Choi, J. J. Lee, S. H. Han, H. J. Kim, I. K. Kang

5788 Electrical characteristics of spiral coil planar inductors using amorphous alloy ribbons as magnetic layers — K. Tanigawa, H. Hirano, T. Sato, N. Tanaka

5791 Bending stresses and bistable behavior in Fe-rich amorphous wire — M. Vázquez, C. Gómez Polo, J. Velázquez, A. Hernando

5794 Relaxation in magnetic continua — V. L. Sobolev, I. Klik, C. R. Chang, H. L. Huang

5797 Generalized equations for domain wall dynamics — Vladimir L. Sobolev, Huei Li Huang, Shoan Chung Chen

5800 Magnetic induced uniaxial anisotropy in NiFe and NiFeCr films (abstract) — Terry Torng, Simon H. Liao

5800 Structural and magnetic properties of rf-sputtered iron nitrides using NH_3 (abstract) — John Q. Xiao, C. L. Chien

5801 Nucleation of the nanocrystalline phase in $Fe_{73.5}Cu_1Nb_3Si_{13.5}B_9$ (abstract) — J. D. Ayers, V. G. Harris, J. A. Sprague, W. T. Elam

Symposium: Magnetic Circular Dichroism

5802 Validity and the applicablity of magnetic-circular-dichroism sum rules for transition metals (invited) — Ruqian Wu, Dingsheng Wang, A. J. Freeman

(Continued)

5807	X-ray magnetic circular dichroism studies of multilayered thin films of 3d transition metals (invited) (abstract)	D. Weller, M. G. Samant, J. Stöhr, Y. Wu, B. D. Hermsmeier, G. Held, C. Chappert
5807	Physical information in polarized x-ray absorption spectroscopy and x-ray photoemission spectroscopy (invited) (abstract)	Bernard Theodoor Thole
5808	Element specific magnetic hysteresis curves of Fe/Cu/Co multilayers (invited) (abstract)	Y. U. Idzerda, H.-J. Lin, G. Ho, G. Meigs, A. Chaiken, G. A. Prinz, C. T. Chen
5809	Core-level magnetic circular dichroism in 3*d* and 4*f* magnetic systems (invited) (abstract)	T. Koide
5810	Soft x-ray magneto-optical Kerr effect (invited) (abstract)	C. C. Kao, C. T. Chen, E. D. Johnson, Y. U. Idzerda, J. B. Hastings

Cooperative Phenomena: Critical Phenomena and Disordered Systems

5811	Application of the spreading of damage technique to the $S=1/2$ Ising thin film	I. V. Rojdestvenski, U. M. S. Costa
5814	Quantum renormalization of the XY model	Alessandro Cuccoli, Valerio Tognetti, Paola Verrucchi, Ruggero Vaia
5817	Magnetization and static structure factor behavior in a first-order helix-fan phase transition	E. Rastelli, S. Sedazzari, A. Tassi
5820	Magnetic properties in the Ising mixed spin-1/2–spin-1 superlattice	E. F. Sarmento, J. C. Cressoni, R. J. V. dos Santos
5823	Monte Carlo calculation of the correlation range for the $S=\frac{1}{2}$ isotropic Heisenberg ferromagnetic thin film	I. V. Rojdestvenski, M. G. Cottam, I. A. Favorski
5826	Static critical properties of disordered ferromagnets studied by superconducting quantum interference device magnetometry and small-angle neutron-scattering techniques	S. Pouget, M. Alba, M. Nogues
5829	Thermodynamical properties of a Heisenberg model with Dzyaloshinski–Moriya interactions	F. Lacerda, J. Ricardo de Sousa, I. P. Fittipaldi
5832	A unified effective-field renormalization-group framework approach for the quenched diluted Ising models	Douglas F. de Albuquerque, I. P. Fittipaldi
5835	Critical behavior of the anisotropic Heisenberg model by effective-field renormalization group	J. Ricardo de Sousa, I. P. Fittipaldi
5838	Random decorated antiferromagnetic Ising model with mixed spins	Vanêssa M. Correia, Roberto J. V. dos Santos
5841	Phase diagrams of diluted ferromagnetic Ising films in a transverse field	J. C. Cressoni, J. W. Tucker, E. F. Sarmento
5844	Relaxation dynamics in a reentrant (FeNi)Mn ferromagnet: A percolation analysis	D. Li, R. M. Roshko, G. Yang
5847	Spin glasses with cubic anisotropy	Z. Domański, T. K. Kopeć, F. Pázmándi, P. Erdős
5850	Macroscopic random magnetic anisotropy constant in crystalline $Dy_xY_{1-x}Al_2$ ($x=0.3$, 0.4)	A. del Moral, M. Ciria, J. I. Arnaudas, J. S. Abell, Y. Bi
5853	Temperature dependence of the hyperfine field distributions in the $Fe_{93.5-x}Nd_xZr_{6.5}$ ($x=0$, 2) amorphous alloys	G. K. Nicolaides, M. Pissas, D. Niarchos, R. D. Taylor, K. V. Rao
5856	Blocking of logarithmic temporal relaxation of magnetic remanence by piezomagnetically induced domains in $Fe_{1-x}Zn_xF_2$	J. Kushauer, C. Binek, W. Kleemann
5859	One-dimensional antiferromagnetic behavior in $AVOPO_4$ ($A=NH_4$, Na) prepared from hydrothermal conditions	Charles J. O'Connor, Victoria Soghomonian, Robert C. Haushalter, Zhanwen Wang, Jon Zubieta
5862	ac susceptibility on the dilute antiferromagnet $Mn_xZn_{1-x}F_2$ close to the percolation threshold (abstract)	F. L. A. Machado, F. C. Montenegro, E. Montarroyos, J. C. O. de Jesus, A. Rosales-Rivera, S. M. Rezende

(Continued)

5862 The frequency dependence of the ferro-to-spinglass transition of amorphous Fe-rich Fe-Zr (abstract) — J. Nogués, K. V. Rao

5863 Cooperative spin-crossover transition: Effects of the antiferro- and ferri-ordered phase (abstract) — Benjamin G. Veldster

Small Particles

5864 Nanocomposite formation in the Fe_3O_4-Zn system by reaction milling — Laszlo Takacs, Martha Pardavi-Horvath

5867 Fe-Al_2O_3 nanocomposites prepared by high-energy ball milling — Søren Linderoth, Michael S. Pedersen

5870 Synthesis and properties of α''-$Fe_{16}N_2$ in magnetic particles — Xiaohua Bao, Robert M. Metzger, Massimo Carbucicchio

5873 Magnetism and spin dynamics of nanoscale FeOOH particles — M. M. Ibrahim, G. Edwards, M. S. Seehra, B. Ganguly, G. P. Huffman

5876 Magnetic properties of microemulsion synthesized cobalt fine particles — J. P. Chen, K. M. Lee, C. M. Sorensen, K. J. Klabunde, G. C. Hadjipanayis

5879 Magnetic properties of carbon-coated rare-earth carbide nanocrystallites produced by a carbon arc method — B. Diggs, A. Zhou, C. Silva, S. Kirkpatrick, N. T. Nuhfer, M. E. McHenry, D. Petasis, S. A. Majetich, B. Brunett, J. O. Artman, S. W. Staley

5882 Magnetic properties of carbon-coated, ferromagnetic nanoparticles produced by a carbon-arc method — E. M. Brunsman, R. Sutton, E. Bortz, S. Kirkpatrick, K. Midelfort, J. Williams, P. Smith, M. E. McHenry, S. A. Majetich, J. O. Artman, M. De Graef, S. W. Staley

5885 Structural and magnetic properties of ultrafine Fe-Pd particles — L. Yiping, G. C. Hadjipanayis, C. M. Sorensen, K. J. Klabunde

5888 Fine structure and magnetic properties of Mn- and Co-doped nanocrystalline γ-Fe_2O_3 — Ming-Cheng Deng, Tsung-Shune Chin, F. R. Chen

5891 Elongated superparamagnetic particles — Amikam Aharoni

5894 Interactions between single domain particles — Roger Proksch, Bruce Moskowitz

5897 Temperature dependence of switching field distribution — Jiang-Ching Lin, I. Klik, C. J. Chen, Ching-Ray Chang

5900 Dynamics of fine particles observed in zero-field neutron scattering — M. Hennion, C. Bellouard, I. Mirebeau, J. L. Dormann, R. Ober

5903 Magnetic properties of fine Ni particles coated with Pd (abstract) — Makoto Yamaguchi, Yoshichika Otani, Hideki Miyajima

5903 Nuclear magnetic resonance studies on the surface magnetism of vanadium ultrafine particles (abstract) — Yukihiro Hirayama, Tomoki Erata, Eiji Kita, Akira Tasaki

New Instrumentation and Measurement Techniques

5904 Polyphase eddy current testing — I. Marinova, S. Hayano, N. Ishida, Y. Saito, Y. Hirama, M. Yamamoto

5907 Defect recognition in conductive materials by local magnetic-field measurement — T. Doi, S. Hayano, I. Marinova, N. Ishida, Y. Saito

5910 Component-resolved imaging of surface magnetic fields — R. D. Gomez, E. R. Burke, I. D. Mayergoyz

5913 Measurement of Young's moduli for film and substrate by the mechanical resonance method — Y. H. Lee, Y. D. Shin, K. H. Lee, J. R. Rhee

5916 A new structure of torque sensors using thin pickup head—Use of mutual coupling modulation — I. Sasada, F. Koga

5919 A microwave transmission spectrometer — Carlo Waldfried, Scott Wadewitz, G. Dewar

(Continued)

5922	Measurements of intrinsic magnetic properties of materials from surface inspection (abstract)	Z. J. Chen, D. C. Jiles
5922	Three component magnetic field measurements using cubic anisotropy in (111) YIG films (abstract)	A. Ya. Perlov, A. I. Voronko, P. M. Vetoshko, V. B. Volkovoy
5923	Magnetoresistive characterization of thin-film structures by a gradient-field method (abstract)	P. L. Trouilloud, F. Suits, C. V. Jahnes, M. A. Russak, E. J. Spada, J. W. Chang
5924	Dispersivity measurement of magnetic powders using the magnetic noise method (abstract)	V. M. Vasilyev
	Symposium: Environmental Magnetism	
5925	Contributions of fine-particle magnetism to reading the global paleoclimate record (invited)	Subir K. Banerjee
5931	Collection, measurement, and analysis of airborne magnetic particulates from pollution in the environment (invited)	Philip J. Flanders
	Critical Phenomena	
5937	Dynamics of the one-dimensional spin-1 Heisenberg antiferromagnet with exchange and single-site anisotropy	Shu Zhang, Yongmin Yu, V. S. Viswanath, Joachim Stolze, Gerhard Müller
5940	Ferromagnetism of single crystal $Fe[S_2CN(C_2D_5)_2]_2Cl$	G. C. DeFotis, W. W. Brubaker, S. Chandarlapaty, K. L. Beers, G Coffey
5943	Spin-1/2 Heisenberg antiferromagnet on the square and triangular lattices: A comparison of finite temperature properties	N. Elstner, R. R. P. Singh, A. P. Young
5946	Disorder-driven first-order phase transformations: A model for hysteresis	Karin Dahmen, Sivan Kartha, James A. Krumhansl, Bruce W. Roberts, James P. Sethna, Joel D. Shore
5949	Magnetic properties of the two-dimensional "triangles-in-triangles" Kagomé lattice $Cu_9X_2(cpa)_6$ (X=F,Cl,Br)	Sanchit Maruti, Leonard W. ter Haar
5952	Magnetic properties of two copper (II)-halide layered perovskites	N. Sivron, T. E. Grigereit, John E. Drumheller, K. Emerson, R. D. Willett
5955	Can the universal jump be observed in two-dimensional XY magnets?	S. T. Bramwell, P. C. W. Holdsworth
5958	Strong thermal fluctuation effects on the dynamics of Bloch walls (abstract)	M. Hartl, D. Garanin, J. Koetzler
5959	Depth-dependent magnetic correlation length in terbium (abstract)	P. M. Gehring, K. Hirota, C. F. Majkrzak, G. Shirane
	Thin Film Recording Media I	
5960	Ba-ferrite thin-film media for high-density longitudinal recording (invited)	T. L. Hylton, M. A. Parker, M. Ullah, K. R. Coffey, R. Umphress, J. K. Howard
5966	Microstructural investigations of barium ferrite longitudinal thin-film media	B. Y. Wong, X. Sui, D. E. Laughlin, M. H. Kryder
5969	Low-temperature deposition of hexagonal ferrite films by sputtering	Akimitsu Morisako, Hiroaki Nakanishi, Mitsunori Matsumoto, Masahiko Naoe
5972	Surface roughness and magnetic properties of *in situ* heated and postannealed thin films of perpendicular barium ferrite	Kyusik Sin, John M. Sivertsen, Jack H. Judy
5975	Preparation of Co-Zn ferrite films at low substrate temperature by plasma-free dc sputtering for magnetic recording media	N. Matsushita, K. Noma, S. Nakagawa, M. Naoe
5978	Magnetic and crystallographic properties of Co-Cr-(Ta,Pt)/Cr films deposited by excimer laser ablation	A. Ishikawa, K. Tanahashi, Y. Yahisa, Y. Hosoe, Y. Shiroishi
5981	Transverse susceptibility and ferromagnetic resonance of Hi-8 metal-evaporated tape	C. Sürig, G. Zimmermann, K. A. Hempel

(Continued)

5984 Low-temperature sputter deposition of high-coercivity Co-Cr films for perpendicular recording — Naoki Honda, Kazuhiro Ouchi, Shun-ichi Iwasaki

5987 Improvement of anisotropy of perpendicular magnetic recording tape by Ta addition and Kr sputtering gas (abstract) — Kiyoshi Kuga, Hideaki Yoshimoto, Yoshiro Yoneda, Junji Numazawa, Masahiko Naoe

Emerging Hard Magnets Based on Interstitials

5988 High field magnetization measurements of Sm_2Fe_{17}, $Sm_2Fe_{17}N_3$, $Sm_2Fe_{17}D_5$, and Pr_2Fe_{17}, $Pr_2Fe_{17}N_3$ (invited) — O. Isnard, S. Miraglia, M. Guillot, D. Fruchart

5994 Comparative Mössbauer effect study of several R_2Fe_{17} and $R_2Fe_{17}N_x$ compounds — Gary J. Long, S. Mishra, O. A. Pringle, F. Grandjean, K. H. J. Buschow

5997 The effects of group IV B/V B/VI B additions on the magnetic properties of $Sm_{2+\delta}Fe_{17}$ carbonitrides — X. Chen, Er. Girt, Z. Altounian

6000 Phase transformation induced by gas phase reaction in $RFe_{10}SiC_x$ alloys — E. W. Singleton, G. C. Hadjipanayis, V. Papaefthymiou, Z. Hu, W. B. Yelon

6003 A detailed study of nitride precipitates in Nd_2Fe_{17} — C. C. Colucci, S. Gama, C. A. Ribeiro, L. P. Cardoso

6006 Aligned high anisotropy $Pr(Fe,Co,Mo)_{12}N$ film samples — R. Rani, H. Hegde, A. Navarathna, F. J. Cadieu

6009 Anisotropy and flux density enhancement in aligned $ThMn_{12}$-type $NdFe_{11}Co_{1-y}Mo_yN$ film samples — A. Navarathna, H. Hegde, R. Rani, F. J. Cadieu

6012 Hydrogenation decomposition desorption recombination magnets based on $Sm_{2+\delta}Fe_{17}M_{0.4}$ carbonitrides (M=IVB/VB/VIB group elements) — X. Chen, Z. Altounian

6015 Nitriding of melt-spun Nd-Fe-Mo alloys — F. E. Pinkerton, C. D. Fuerst, J. F. Herbst

6018 Effect of milling on the magnetic and microstructural properties of $Sm_2Fe_{17}N_x$ permanent magnets — P. A. P. Wendhausen, B. Gebel, D. Eckert, K.-H. Müller

6021 Magnetic properties of $Y(Fe,Co)_{10}Mo_2$ alloys — Xie Xu, Roy Tucker, S. A. Shaheen

Field Computations

6024 Magnetic thin-film media response in presence of displacement eddy currents — A. Geri, A. Salvini, G. M. Veca

6027 On finite element implementation of impedance boundary conditions — I. D. Mayergoyz, G. Bedrosian

6030 Three-dimensional iterative solution for the multiconductor eddy current and free surface calculations — M. Ramadan Ahmed, K. F. Ali, Ibrahim Moustafa

6033 Modeling and analysis of electric and magnetic coupled problems under nonlinear conditions — A. Geri, M. La Rosa, G. M. Veca

6036 Transformation methods in computational electromagnetism — A. Nicolet, J.-F. Remacle, B. Meys, A. Genon, W. Legros

6039 The effects of various magnetic materials on lamination design for stator–rotor diecasting of induction motors for electric vehicle applications — N. M. Elkasabgy, C. Di Pietro

6042 An improved method for magnetic flux density visualization using three-dimensional edge finite element method — Vlatko Čingoski, Hideo Yamashita

6045 Optimum design of voice coil motor with constant torque coefficients using evolution strategy — Chang Seop Koh, Osama A. Mohammed, Jun-o Kim, Song-yop Hahn

6048 Three-dimensional eddy current solution of a polyphase machine test model (abstract) — Uwe Pahner, Ronnie Belmans, Vlado Ostovic

6049 Numerical methods and measurement systems for nonlinear magnetic circuits (abstract) — Axel Heitbrink, Hans Dieter Storzer, Adalbert Beyer

6050 Comparative analysis of two methods for time-harmonic solution of the steady state in induction motors (abstract) — Robrecht DeWeerdt, Kostadin Brandisky, Uwe Pahner, Ronnie Belmans

(Continued)

Spin Waves, Hyperfine Fields, and Resonance

6051 Selection of the ground state in $CsCuCl_3$ by quantum fluctuations — E. Rastelli, A. Tassi

6054 Scaling behavior of the homogeneous magnetization dynamics in the ferromagnetic state of EuS — R. Dombrowski, D. Görlitz, J. Kötzler, Chr. Marx

6057 Dynamical properties of quantum spin systems in magnetically ordered product ground states — V. S. Viswanath, Joachim Stolze, Gerhard Müller

6060 Magnons in ferromagnetic terbium under high pressure — S. Kawano, J. A. Fernandez-Baca, R. M. Nicklow

6063 Polarization analysis of magnons in $CsMnI_3$ — Z. Tun, T. C. Hsu, J-G. Lussier

6066 Orientation dependence of dipole gaps in the magnetostatic wave spectrum of Bi-substituted iron garnets — Ana K. Chamakova, Andrew Cash, Jose Peruyero, Daniel D. Stancil

6069 Polarization analysis of the magnetic excitations in $Fe_{65}Ni_{35}$ Invar — J. W. Lynn, N. Rosov, M. Acet, H. Bach

6072 Temperature dependence of the magnetic excitations in ordered and disordered $Fe_{72}Pt_{28}$ — N. Rosov, J. W. Lynn, J. Kästner, E. F. Wassermann, T. Chattopadhyay, H. Bach

6075 Theory of ferromagnetic resonance relaxation in very small solids — J. B. Sokoloff

6078 Crystallographic and magnetic properties of $Co_xFe_{1-x}Cr_2S_4$ — Chul Sung Kim, Min Yong Ha, Heung Moon Ko, Young Jei Oh, Heung Soo Lee, Sang Youl Lee, Jung Chul Sur, Jae Yun Park

6081 The effect of Co doping on spin cluster resonance in the one-dimensional Ising ferromagnet FeTAC — R. S. Rubins, T. D. Black, K. Ravindran, John E. Drumheller

6084 New perspective on the Green's function dipole-exchange spin wave theory for thin films (abstract) — Ming Chen, Carl E. Patton

6085 Ground state and spin dynamics in hexagonal antiferromagnet $CsCuCl_3$ (abstract) — E. P. Stefanovskii, A. L. Sukstanskii

Magnetic Bubble and VBL Memories

6086 Successive Bloch line write operation in a 1-μM bubble material — K. Matsuyama, T. Ohyama, H. Asada, K. Taniguchi

6089 Micromagnetic computation for wall and Bloch line coercivity in thin films with perpendicular anisotropy — H. Asada, K. Matsuyama, M. Gamachi, K. Taniguchi

6092 Phase transitions in bubble lattice under temperature lowering (abstract) — V. S. Gerasimchuk, Yu. I. Gorobets, K. De Ville

6093 An adaptive computational method for domain wall dynamics (abstract) — Sergey G. Osipov

Soft Magnetic Materials: Ferrites

6094 Wet-process preparation of amorphous Y-Fe oxide films ferromagnetic at room temperature — Q. Zhang, T. Itoh, M. Abe, M. J. Zhang

6097 Magnetic anomalies in single crystal Fe_3O_4 thin films — D. T. Margulies, F. T. Parker, A. E. Berkowitz

6100 An analysis of the high-temperature relaxation in polycrystalline magnetite — J. Castro, D. Martinez, J. Rivas, H. J. Blythe

6103 $Dy_3Fe_5O_{12}$ garnet thin films grown from sputtering of metallic targets — J. Ostoréro, M. Escorne, A. Pecheron-Guegan, F. Soulette, H. Le Gall

6106 Enhanced coercivity due to a local anisotropy increase — J. A. Jatau, M. Pardavi-Horváth, E. Della Torre

6109 The microwave absorbing and resonance phenomena of Y-type hexagonal ferrite microwave absorbers — H. J. Kwon, J. Y. Shin, J. H. Oh

6112 Effect of Er_2O_3 addition on microstructure and physical properties of Mn–Zn ferrites for high-power use — C. S. Liu, J. M. Wu, C. J. Chen, M. J. Tung

(Continued)

6115	Dispersion observed in electrical properties of titanium-substituted lithium ferrites	Bijoy Kumar Kuanr, G. P. Srivastava
6118	Electrical conductivity of Mn–Zn ferrites	D. Ravinder, K. Latha
6121	Composition dependence of the elastic moduli of mixed lithium–cadmium ferrites	D. Ravinder
6124	Deposition and properties of $NiFe_2O_4$ thin films (abstract)	R. B. van Dover, E. M. Gyorgy, J. M. Phillips, J. H. Marshall, R. J. Felder, R. M. Fleming, H. O'Bryan, Jr.
6124	Studies of stoichiometric variations of epitaxially grown $Fe_{3-\delta}O_4$ (abstract)	E. Lochner, K. A. Shaw, R. C. DiBari, D. Hilton, D. M. Lind, S. D. Berry
6125	Cation distribution of Li-Ti mixed ferrites (abstract)	M. Bhagavantha Reddy, P. Venugopal Reddy

Thin Film Recording Media II

6126	Magnetic and microstructural properties of CoCrPt/CoCrPtSi dual-layered magnetic recording media	N. Inaba, Y. Matsuda, M. Suzuki, A. Nakamura, M. Futamoto
6129	Bicrystal advanced thin-film media for high density recording	Tai Min, Jian-Gang Zhu
6132	AFM structure and media noise of SmCo/Cr thin films and hard disks	E. M. T. Velu, D. N. Lambeth, J. T. Thornton, P. E. Russell
6135	Modeling of thin-film media with advanced microstructure for ultrahigh density recording	Xiao-Guang Ye, Jian-Gang Zhu
6138	Evaluation of the CoCrTaPt alloy for longitudinal magnetic recording	Yuanda Cheng, Mojtaba Sedighi, Irene Lam, Richard A. Gardner, ZhiJun Yang, Michael R. Scheinfein
6141	Analysis of the electronic properties of CoCrPt thin films using parallel electron energy loss spectroscopy (PEELS)	Pawel Glijer, John M. Sivertsen, Jack H. Judy
6144	Noise properties and microstructure of oriented CoCrTa/Cr media	R. Ranjan, W. R. Bennett, G. J. Tarnopolsky, T. Yamashita, T. Nolan, R. Sinclair
6147	Effects of oxide addition on magnetic and structural properties of CoNiPt alloy films	A. Murayama, S. Kondoh, M. Miyamura
6150	Comparison of reproduce signal and noise of conventional and keepered CoCrTa/Cr thin film media	Kyusik Sin, Juren Ding, Pawel Glijer, John M. Sivertsen, Jack H. Judy, Jian-Gang Zhu
6153	Process temperature dependence of ∂M plots on Co alloy media on amorphous carbon substrates	Masago Kuwabara, Haydee Saffari, Mark R. Visokay, Hidetaka Hayashi, Motoharu Sato
6156	Friction and wear of ion-implanted diamondlike carbon and fullerene films for thin-film rigid disks	Bharat Bhushan, B. K. Gupta
6159	Thin film disks for high density recording with textured underlayers (abstract)	Mohammad Mirzamaani, Michael A. Russak, Christopher V. Jahnes
6160	A study of the structural properties of sputtered CoCrPt based on x-ray diffraction, small angle x-ray scattering, XAFS, and transmission electron microscopy measurements (abstract)	S. Yumoto, N. Ohshima
6161	Multinuclear nonmagnetic resonance studies of perfluoro poly ether lubricants (abstract)	K. V. Viswanathan
6162	The durability of new rigid disks by molded plastic substrates (abstract)	Osamu Morita, T Sano, Yasuyuki Imai, Naoko Hisayama, Hiroshi Takino

Coupling Through Nonmagnetic Layers

6163	Temperature-dependent non-Heisenberg exchange coupling of ferromagnetic layers (invited)	R. P. Erickson

(Continued)

6169	Photo-induced antiferromagnetic interlayer coupling in Fe superlattices with iron silicide spacers (invited)	J. E. Mattson, Eric E. Fullerton, Sudha Kumar, S. R. Lee, C. H. Sowers, M. Grimsditch, S. D. Bader, F. T. Parker
6174	An alternate route to giant magnetoresistance in MBE-grown Co–Cu superlattices (invited)	Roy Clarke, Darryl Barlett, Frank Tsui, Baoxing Chen, Clirad Uher
6178	Magnetic profile as a function of structural disorder in Fe/Cr superlattices	Michael J. Pechan, J. F. Ankner, C. F. Majkrazk, David M. Kelly, Ivan K. Schuller
6181	Temperature dependence of the exchange coupling in the Fe(001) whisker/ 11 ML Cr/20 ML Fe structure	M. From, L. X. Liao, J. F. Cochran, B. Heinrich
6184	Anisotropy studies of AFM coupled MBE grown Co/Cu(001) superlattices	K. Bröhl, S. Di Nunzio, F. Schreiber, Th. Zeidler, H. Zabel
6187	"Loose spins" in Fe/Cu/Fe(001) structures	B. Heinrich, Z. Celinski, L. X. Liao, M. From, J. F. Cochran
6190	Interlayer coupling and spin polarization of the nonmagnetic layers in Fe/Cu and Fe/Ag CMFs	Y. B. Xu, M. Lu, Q. Y. Jin, C. Hu, Y. Z. Miao, Y. Zhai, Q. S. Bie, H. R. Zhai, G. L. Dunifer, R. Naik, M. Ahmad
6193	Growth temperature dependence of biquadratic coupling in Fe/Cr(100) superlattices studied by polarized neutron reflectivity and x-ray diffraction (abstract)	M. Schäfer, J. A. Wolf, P. Grünberg, J. F. Ankner, A. Schreyer, H. Zabel, C. F. Majkrzak
	Symposium: Novel Time-Resolved Probes of Dynamical Magnetism	
6194	Picosecond pulsed-field probes of magnetic systems (invited)	M. R. Freeman
6199	Femtosecond Faraday rotation in spin-engineered heterostructures (invited)	J. J. Baumberg, D. D. Awschalom, N. Samarth
6205	Time-resolved scanning probe microscopy: Investigations and applications of dynamic magnetostriction (invited)	G. Nunes, Jr., M. R. Freeman
6211	Magnetic resonance detection and imaging using force microscope techniques (invited)	O. Züger, D. Rugar
6217	Measurement of thermal switching of the magnetization of single domain particles (invited)	M. Lederman, D. R. Fredkin, R. O'Barr, S. Schultz, M. Ozaki
	Hard Magnets III: Substitutional Alloys and Novel Materials	
6223	Magnetic phase diagram of $(Tb_{1-x}Gd_x)Fe_{11}Ti$ alloys	L. C. C. M. Nagamine, H. R. Rechenberg, P. A. Algarabel, M. R. Ibarra
6226	Magnetic phase diagram of $Nd(Fe,Mo)_{12}$ alloys	Y. Z. Wang, B. P. Hu, X. L. Rao, G. C. Liu, L. Song, L. Yin, W. Y. Lai
6229	Magnetic anisotropies in $RFe_{10-x}Co_xMo_2$ compounds (R=Dy, Er)	Roy Tucker, Xie Xu, S. A. Shaheen
6232	Magnetic properties of $Nd(Fe,Ti)_{12}$ and $Nd(Fe,Ti)_{12}N_x$ films of perpendicular texture	D. Wang, D. J. Sellmyer, I. Panagiotopoulos, D. Niarchos
6235	^{57}Fe Mössbauer studies of $Nd(Fe_{12-x}Mo_x)$ and $Nd(Fe_{12-x}Mo_x)N_{0.9}$ (x=1.25 and 1.50)	Qi-Nian Qi, Bo-Ping Hu, J. M. D. Coey
6238	Magnetic properties of $(Er,R)_2Fe_{17}N_y$ compounds (R=Y,Gd)	J. L. Wang, W. G. Lin, N. Tang, W. Z. Li, Y. H. Gao, F. M. Yang
6241	Magnetic properties of $Er_2Fe_{17-x}Al_xN_y$ compounds	F. M. Yang, N. Tang, J. L. Wang, X. P. Zhong, R. W. Zhao, W. G. Lin
6244	Electrical and magnetic studies of (Cu/Zn)-bonded $Sm_2Fe_{17}M_xN_y$ magnets (M=B or C)	Y. D. Yao, P. C. Kuo, W. C. Chang, C. J. Liu

(Continued)

6247	Structure and magnetic properties of interstitial compounds of the series $Dy_2Fe_{17-x}Al_xZ_y$ (Z=N or H)	J. P. Liu, D. C. Zang, N. Tang, A. J. M. Winkelman, F. R. de Boer, K. H. J. Buschow
6250	High-coercivity Sm–Fe–Ga–C compounds with Th_2Zn_{17} structure by melt spinning	Lin-Shu Kong, Bao-gen Shen, Fang-wei Wang, Lei Cao, Hui-qun Guo, Tai-shan Ning
6253	A novel hard magnetic material for sintering permanent magnets	Bao-gen Shen, Fang-wei Wang, Lin-shu Kong, Lei Cao, Wen-shan Zhan
6256	Effect of Sm substitution on structure and magnetic properties of high-carbon $Er_2Fe_{17}C_y$ compounds	Bao-gen Shen, Lei Cao, Lin-shu Kong, Tai-shan Ning, Ming Hu
6259	Structure and magnetic properties of $Gd_2Fe_{17-x}Ga_xC_2$ compounds	Bao-gen Shen, Fang-wei Wang, Lin-shu Kong, Lei Cao, Bo Zhang, Jian-gao Zhao
6262	Effect of cobalt substitution on magnetic properties of R_2Fe_{17} silicides (R=Y, Gd, Tb, Er, and Tm)	F. Pourarian, R. T. Obermyer, S. G. Sankar
6265	A contribution to the knowledge of phase equilibria and the magnetic properties of the Nd–Fe–B–X systems (X=Al,Co,V)	Anders Micaki, Björn Uhrenius
6268	Investigations of magnetic properties and microstructure of 40Cedidymium–Fe–B based magnets	S. X. Zhou, Y. G. Wang, R. Hèier
6271	Investigation of interaction mechanisms in melt-quenched NdFeB	L. Folks, R. Street, R. Woodward
6274	Crystal structure and low-temperature magnetic properties of melt-spun $Sm_2Co_7B_3$ compounds	C. J. Yang, W. Y. Lee, S. D. Choi
6277	Saturation magnetization and anisotropy fields in the $Sm(Co_{1-x}Cu_x)_5$ phases	E. Lectard, C. H. Allibert, R. Ballou
6280	SmCo (2:17-type) magnets with high contents of Fe and light rare earths	M. Q. Huang, Y. Zheng, W. E. Wallace
6283	Effect of Dy substitution on the magnetocrystalline anisotropy of $GdCo_4B$	T. Ito, H. Asano, H. Ido, G. Kido
6286	Permanent magnet film magneto-optic waveguide isolator	M. Levy, R. Scarmozzino, R. M. Osgood, Jr., R. Wolfe, F. J. Cadieu, H. Hedge, C. J. Gutierrez, G. A. Prinz
6289	Investigation of Pr-Fe-B magnets with high performance (abstract)	F. Z. Lian, F. Pourarian, S. Simizu, S. G. Sankar, W. E. Wallance
6289	*In situ* and dynamic observation of NdFeCoB magnet by high voltage transmission electron microscope (abstract)	Pan Shuming, Liu Jinfang, Xu Yinfan
	Magnetic Ordering and Magnetic Structure	
6290	Influence of electron damping and reservoir on the magnetic phase diagram of chromium alloys	R. S. Fishman, S. H. Liu
6293	Spin fluctuation effect in the ordered Fe_2N alloy	Guan-mian Chen, Ming-xi Lin, Ji-wu Ling
6296	Isoelectronic early *n-d* impurities in Fe: Magnetic and hyperfine field properties	N. A. de Oliveira, A. A. Gomes, A. Troper
6298	Electronic structure and the Stoner *I* parameter for RPd_3 compounds (*R*=La, Ce, Pr, and Nd)	T. Nautiyal, A. Kashyap, S. Auluck, M. S. S. Brooks
6301	Band structure calculations of heavy fermion YbSbPd and YbSbNi	A. K. Solanki, Arti Kashyap, S. Auluck, M. S. S. Brooks
6303	Electronic structure and Curie temperature of $YFe_{12-x}Mo_xN_y$ compounds	A. S. Fernando, J. P. Woods, S. S. Jaswal, D. Welipitiya, B. M. Patterson, D. J. Sellmyer
6306	The percolation limit for the disappearance of ferromagnetism in melt spun Co-B-C amorphous alloys	G. K. Nicolaides, A. Inoue, K. V. Rao
6309	High-field magnetization behavior in random anisotropy amorphous Co-Er alloys	H. Lassri, L. Driouch, R. Krishnan

(Continued)

6312 Magnetic properties and crystallization of amorphous Fe-Nd-B alloys at constant Nd concentration — Bao-gen Shen, Lin-yuan Yang, Hui-qun Guo, Jian-gao Zhao

6315 Influence of applied torsion on the bistable behavior of CoSiB amorphous wire — J. M. Blanco, P. Aragoneses, E. Iruretа, J. González, K. Kulakowski

6318 Details of the magnetic phase diagram of holmium from neutron diffraction in *b*-axis fields — D. A. Tindall, C. P. Adams, M. O. Steinitz, T. M. Holden

6321 Critical magnetic neutron scattering above T_N in Cr+0.18 at. % Re (abstract) — D. R. Noakes, E. Fawcett, B. J. Sternlieb, G. Shirane, J. Jankowska

6321 Photoinduced disaccommodation of magnetic permeability in yttrium iron garnet (abstract) — I. Matsubara, K. Hisatake, K. Maeda

High T_c Superconductivity: Experiment and Theory

6322 Unidirectional pinning in irradiated $Bi_2Sr_2CaCu_2O_8$ (invited) — L. Klein, E. R. Yacoby, A. Tsameret, Y. Yeshurun, K. Kishio

6328 Unusual transport and magnetic properties of Tb-doped $YBa_2Cu_3O_7$ single crystals and epitaxial thin films — G. Cao, J. W. O'Reilly, J. E. Crow, R. J. Kennedy, D. H. Nichols

6331 Magnetic order of Pr ions in related perovskite-type Pr123 compounds — M. Guillaume, P. Fischer, B. Roessli, A. Podlesnyak, J. Schefer, A. Furrer

6334 Collective magnetic excitations of Ho^{3+} ions in grain-aligned $HoBa_2Cu_3O_7$ — U. Staub, F. Fauth, M. Guillaume, J. Mesot, A. Furrer, P. Dosanjh, H. Zhou, P. Vorderwisch

6337 Combined electronic-nuclear magnetic ordering of the Ho^{3+} ions and magnetic stacking faults in $HoBa_2Cu_3O_x$ (x=7.0,6.8,6.3) — B. Roessli, P. Fischer, U. Staub, M. Zolliker, A. Furrer

6340 Raman spectra of two-dimensional spin-$\frac{1}{2}$ Heisenberg antiferromagnets — Stephan Haas, Elbio Dagotto, Jose Riera, Roberto Merlin, Franco Nori

6343 Vortex flux creep and magnetic hysteresis in a type-II superconductor (abstract) — M. K. Hasan, S. J. Park, J. S. Kouvel

6343 Interactions with the Dy^{3+} sublattice observed in high resistance ultrathin $DyBa_2Cu_3O_{7-x}$ films (abstract) — K. M. Beauchamp, G. C. Spalding, W. H. Huber, A. M. Goldman

6344 Probing of the pairing state of HTSCs utilizing *a*-*b* plane magnetization anisotropy (abstract) — J. Buan, N. E. Israeloff, C. C. Huang, A. M. Goldman, J. Z. Liu, R. N. Shelton

6345 *Theory of two-dimensional antiferromagnets with a nearly critical ground state (abstract)* — *Andrey V. Chubukov, Subir Sachdev*

Magneto-optics

6346 Electronic structure and magneto-optical properties of MnBi and MnBiAl — S. S. Jaswal, J. X. Shen, R. D. Kirby, D. J. Sellmyer

6348 Low-temperature characterization of the magnetic properties of MnBiAl thin films — K. W. Wierman, J. X. Shen, R. D. Kirby, D. J. Sellmyer

6351 The functions of Al in MnBiAlSi magneto-optical films — D. Huang, X. W. Zhang, C. P. Luo, H. S. Yang, Y. J. Wang

6354 Magnetic and magneto-optical properties of $Mn_5(Ge_{1-x}M_x)_3$ alloys with M=Sn, Pb — Y. Zhang, A. P. Runge, Z. S. Shan, D. J. Sellmyer

6357 Magnetic and optical characteristics of bilayered films composed of Tb-Fe-Co layer with overlayers of Co-Cr, Ni-Fe, Ta, and C — Kibong Song, Masahiko Naoe

6360 Change of magneto-optical Kerr rotation due to interlayer thickness in magnetically coupled films with noble-metal wedge — T. Katayama, Y. Suzuki, M. Hayashi, W. Geerts

6363 Chemical modification of magneto-optic garnet film properties — Roger F. Belt, John B. Ings, Jonathan B. Whitlock

6366 Circular magnetic x-ray dichroism in rare-earth magnets — Xindong Wang, V. P. Antropov, B. N. Harmon, J. C. Lang, A. I. Goldman

6369 Resonant photoemission and magnetic x-ray circular dichroism in the *M* shell of ultrathin films of Fe — J. G. Tobin, G. D. Waddill

(Continued)

6372	Molecular-orbital analysis of magneto-optical Bi-O-Fe hybrid excited states	Gerald F. Dionne, Gary A. Allen
6375	A new Faraday rotation glass with a large Verdet constant	Sui hua Yuan, Xiao Zhou Shu
6378	Experimental investigation of the magnetic circular dichroism sum rules (abstract)	C. T. Chen, Y. U. Idzerda, H.-J. Lin, G. Meigs, G. Ho, N. V. Smith
	Magnetic Recording Heads: Materials, Structures, and Micromagnetics	
6379	Linearity and hysteresis in the magnetoresistive response of (NiFe,NiFeCo)/Cu and Co/Cu/NiFe multilayers in patterned stripes	K. Noguchi, S. Araki, T. Chou, D. Miyauchi, Y. Honda, A. Kamijima, Ø. Shinoura, Y. Narumiya
6382	Microstructural origin of giant magnetoresistance in a new sensor structure based on NiFe/Ag discontinuous multilayer thin films	M. A. Parker, T. L. Hylton, K. R. Coffey, J. K. Howard
6385	Micromagnetics of GMR spin-valve heads	Samuel W. Yuan, H. Neal Bertram
6388	Micromagnetic study of narrow track orthogonal giant magnetoresistive heads	Yimin Guo, Jian-Gang Zhu
6391	Dynamic domain instability and popcorn noise in thin-film heads	F. H. Liu, M. H. Kryder
6394	Dynamic response of domain walls on the air-bearing surface of thin-film heads	X. Shi, F. H. Liu, Yuet Li, M. H. Kryder
6397	Omega head—an experimental 120-turn inductive head	D. D. Tang, R. E. Lee, J. L. Su, F. Chu, J. Lo, H. Santini, L. Lane, N. Robertson, M. Ponce, P. Cisneroz, G. Guthmiller
6400	Local magnetoresistance and point-source excitation of Ni-Fe thin films (abstract)	R. W. Cross, A. B. Kos
6400	Sensitivity distribution asymmetries in magnetoresistive heads with domain control films (abstract)	N. Koyama, C. Ishikawa, Y. Suzuki, H. Aoi, K. Yoshida
	Anisotropy of Films and Interfaces	
6401	Overlayer-induced perpendicular anisotropy in ultrathin Co films (invited)	Brad N. Engel, Michael H. Wiedmann, Charles M. Falco
6406	Interfacial anisotropy and magnetic transition of cobalt films on Cu(111)	F. Huang, G. J. Mankey, R. F. Willis
6409	Local spin-density theory of interface and surface magnetocrystalline anisotropy: Pd/Co/Pd(001) and Cu/Co/Cu(001) sandwiches	Ding-sheng Wang, Ruqian Wu, A. J. Freeman
6412	Perpendicular magnetic anisotropy in Co_xPd_{1-x} alloy films grown by molecular beam epitaxy	J. R. Childress, J. L. Duvail, S. Jasmin, A. Barthélémy, A. Fert, A. Schuhl, O. Durand, P. Galtier
6415	*In situ* measurement of stress and surface morphology for Co/Pd multilayer films fabricated by rf sputtering	H. Takeshita, K. Hattori, Y. Fujiwara, K. Nakagawa, A. Itoh
6418	Temperature-dependent interface magnetism and magnetization reversal in Co/Pt multilayers	Z. S. Shan, J. X. Shen, R. D. Kirby, D. J. Sellmyer, Y. J. Wang
6421	Structural and magnetic properties of Co/Cr(001) superlattices	W. Donner, T. Zeidler, F. Schreiber, N. Metoki, H. Zabel
6424	Orientational and structural dependence of magnetic anisotropy of Cu/Ni/Cu sandwiches: Misfit interface anisotropy	R. Jungblut, M. T. Johnson, J. aan de Stegge, A. Reinders, F. J. A. den Broeder
6427	Magnetic anisotropy in ultrathin films grown on vicinal surfaces (abstract)	D. S. Chuang, C. A. Ballentine, R. C. O'Handley
6428	Theoretical predictions for magnetic anisotropy of superlattice defects (abstract)	R. H. Victora, J. M. MacLaren
6429	Magnetoelastic coefficients at tetragonal surfaces (abstract)	Oh Sung Song, C. A. Ballentine, R. C. O'Handley
6430	Magnetic anisotropy in epitaxial Ni/Cu(001) thin films: Effects of misfit strain on perpendicular magnetic anisotropy (abstract)	G. Bochi, C. A. Balentine, H. E. Inglefield, S. S. Bogomolov, C. V. Thompson, R. C. O'Handley

(Continued)

Interlayered Exchange

6431	Spin-wave study of the magnetic excitations in a layered structure with bilinear and biquadratic interlayer exchange	M. Macciò, M. G. Pini, P. Politi, A. Rettori
6434	Temperature dependence of interlayer exchange coupling in Co/Ru/Co trilayer structures	Z. Zhang, L. Zhou, P. E. Wigen, K. Ounadjela
6437	Oscillatory exchange coupling in Fe/Au/Fe(100)	J. Unguris, R. J. Celotta, D. T. Pierce
6440	Oscillation of the interlayer coupling in Co/Au(111)/Co	J. J. de Vries, W. J. M. de Jonge, M. T. Johnson, J. aan de Stegge, A. Reinders
6443	Theory of Brillouin light scattering from dipole-exchange spin waves in magnetic double layers with interlayer exchange coupling	A. N. Slavin, I. V. Rojdestvenski, M. G. Cottam
6446	Self-stabilization of domain walls in antiferromagnetically coupled multilayered magnetic films	Hideo Fujiwara, Tomohiro Ishikawa, W. D. Doyle
6449	Short period oscillation of the interlayer exchange coupling in sputtered Co-Re superlattices	J. L. Leal, P. P. Freitas
6452	Hot electron spin-valve effect in coupled magnetic layers	R. J. Celotta, J. Unguris, D. T. Pierce
6455	Magnetothermopower of $Co/Cu_{1-x}Ni_x$ multilayers	Jing Shi, E. Kita, S. S. P. Parkin, M. B. Salamon
6458	High-field polar MOKE magnetometry as a probe of interlayer exchange coupling in MBE-grown Co/Cu/Co(111) and Fe/Cr/Fe(001) wedged trilayers	A. J. R. Ives, R. J. Hicken, J. A. C. Bland, C. Daboo, M. Gester, S. J. Gray
6461	Orientationally independent antiferromagnetic coupling in epitaxial Fe/Cr (211) and (100) superlattices	Eric E. Fullerton, M. J. Conover, J. E. Mattson, C. H. Sowers, S. D. Bader
6464	Oscillatory interlayer coupling through (111) oriented noble metal spacers	D. J. Keavney, D. F. Storm, J. W. Freeland, J. C. Walker, M. G. Pini, P. Politi, A. Rettori
6467	*Ab initio* study of the interlayer magnetic couplings in Fe/Pd(001) superlattices and of the polarization induced in the Fe and Pd layers	D. Stoeffler, K. Ounadjela, J. Sticht, F. Gautier
6470	Induced spin polarization on Fe/nonmagnetic metal interfaces	J. L. Pérez-Díaz, M. C. Muñoz
6473	The temperature dependence of the bilinear and biquadratic exchange coupling in Fe/Cu, Ag/Fe(001) structures (abstract)	Z. Celinski, B. Heinrich, J. F. Cochran
6474	Exchange coupling through ferromagnetic bridges in magnetic multilayers (abstract)	J. C. Slonczewski
6475	Exchange coupling between ferromagnetic layers: Effect of quantum well states (abstract)	James R. Cullen, Kristi B. Hathaway
6476	Ferromagnetic resonance studies of Py bilayers for the system (Permalloy/Al_2O_3) (abstract)	H. Hurdequint, N. Bouterfas, A. Vaurés

Magnetic Multilayers

6477	Exchange coupling in [Dy|Er] metallic superlattices	W. T. Lee, H. Kaiser, J. J. Rhyne, K. Dumesnil, C. Dufour, Ph. Mangin, G. Marchal, R. W. Erwin, J. A. Borchers
6480	Spin-valve structures exchange biased with a-$Tb_{0.23}Co_{0.77}$ layers	P. P. Freitas, J. L. Leal, T. S. Plaskett, L. V. Melo, J. C. Soares
6483	^{151}Eu Mössbauer study on Fe/Eu multilayers	E. Baggio-Saitovitch, E. C. Passamani, K. Mibu, T. Shinjo
6486	Phase transitions in coupled double-layer systems	Xiao Hu, Yoshiyuki Kawazoe
6489	Comparison of the electron-spin-resonance linewidth in multilayered CuMn spin glasses with insulating versus conducting interlayers	D. L. Leslie-Pelecky, F. VanWijland, C. N. Hoff, J. A. Cowen, A. Gavrin, C.-L. Chien

(Continued)

6492 Anisotropy studies of molecular-beam-epitaxy-grown Co(111) thin films by ferromagnetic resonance — F. Schreiber, A. Soliman, P. Bödeker, R. Meckenstock, K. Bröhl, J. Pelzl, I. A. Garifullin

6495 Magnetic and magneto-optic properties of sputtered Co/Ni multilayers — Y. B. Zhang, P. He, J. A. Woollam, J. X. Shen, R. D. Kirby, D. J. Sellmyer

6498 Spatial modulation of the magnetic moment in Co/Pd superlattices observed by polarized neutron reflectivity — J. A. Borchers, J. F. Ankner, C. F. Majkrzak, B. N. Engel, M. H. Wiedmann, R. A. Van Leeuwen, C. M. Falco

6501 Electron-energy-loss spectroscopy of Fe thin films on GaAs(001) — J. Yuan, E. Gu, M. Gester, J. A. C. Bland, L. M. Brown

6504 Effect of interface on the properties of Ti/NiFe thin films — Shuxiang Li, Minglang Yan, Chengtao Yu, Wuyan Lai

6507 Magnetization reversal in compositionally modulated Tb/Fe multilayers (abstract) — Roger D. Kirby, J. X. Shen, D. J. Sellmyer

6507 Remanence and coercivity in exchange coupled amorphous R-TM/Fe bilayers and multilayers (abstract) — Hong Wan, A. Tsoukatos, G. C. Hadjipanayis

6508 *Paramagnetic/ferromagnetic transition of Co/Cu(001) films during growth* (abstract) — F. O. Schumann, M. E. Buckley, J. A. C. Bland

6508 Photothermally modulated ferromagnetic resonance investigations of epitaxially grown thin films (abstract) — R. Meckenstock, F. Schreiber, O. von Geisau, J. Pelzl

6509 Structural and magnetic characteristics of $Co_{81}Cr_{19}$/Al multilayers deposited by plasma-free sputtering with Kr gas (abstract) — Takakazu Takahashi, Masahiko Naoe

Magnetotransport and Giant Magnetoresistance

6510 Effects of exchange bond disorder on transport measurements — P. A. Stampe, H. Ma, H. P. Kunkel, G. Williams

6513 Electrical resistivity and local magnetic order in random anisotropy amorphous ferromagnets — V. S. Amaral, J. B. Sousa, J. M. Moreira, B. Barbara, J. Filippi

6516 *In situ* magnetic and structural analysis of epitaxial $Ni_{80}Fe_{20}$ thin films for spin-valve heterostructures — I. Hashim, H. A. Atwater

6519 Magnetic and magnetoresistive properties of inhomogeneous magnetic dual-layer films — John O. Oti, Stephen E. Russek, Steven C. Sanders

6522 Comparison of giant magnetoresistance in multilayer systems and uranium compounds — H. Nakotte, K. Prokeš, E. Brück, P. F. de Châtel, F. R. de Boer, V. Sechovsky, L. Havela, H. Fujii

6525 Preparation of Ni–Fe/Cu multilayers with low coercivity and GMR effect by ion beam sputtering — Masahiko Naoe, Yasuyoshi Miyamoto, Shigeki Nakagawa

6528 Novel magnetoresistance behavior in single trilayer spin valves — M. Patel, T. Fujimoto, E. Gu, C. Daboo, J. A. C. Bland

6531 *1/f noise in giant magnetoresistive materials* — H. T. Hardner, S. S. P. Parkin, M. B. Weissman, M. B. Salamon, E. Kita

6534 Effect of annealing on the giant magnetoresistance of sputtered Co/Cu multilayers — H. Zhang, R. W. Cochrane, Y. Huai, Ming Mao, X. Bian, W. B. Muir

6537 Magnetoresistance and exchange effects of NiCo/Cu sandwich films with oxide overlayer — T. R. McGuire, T. S. Plaskett

6540 Effect of oxygen incorporation on magnetoresistance in Co/Cu multilayers — K. Kagawa, H. Kano, A. Okabe, A. Suzuki, K. Hayashi

6543 Giant magnetoresistance in electrodeposited Co–Ni–Cu/Cu superlattices — M. Alper, K. Attenborough, V. Baryshev, R. Hart, D. S. Lashmore, W. Schwarzacher

(Continued)

6546 Giant magnetoresistance in melt-spun $Cu_{87}Co_{13}$ — M. A. Howson, S. O. Musa, M. J. Walker, B. J. Hickey, R. Cochrane, R. Stevens

6548 Temperature effect on magnetoresistance in Co/Ru sandwiches — A. Dinia, S. Zoll, K. Ounadjela

6551 Magnetothermopower in antiferromagnetically coupled Co-Re superlattices — J. B. Sousa, R. P. Pinto, B. Almeida, M. E. Braga, P. P. Freitas, L. V. Melo, I. G. Trindade

6554 Structural and magnetotransport properties of Co/Re superlattices — Y. Huai, R. W. Cochrane, X. Bian, M. Sutton

6557 Magnetic properties of an Fe/Cu granular multilayer — Mark Rubinstein, J. Tejada, X. X. Zhang

6560 *Structural and magnetoresistance studies in granular* $(Ni_{81}Fe_{19},Ni_{80}Co_{20})$/Ag synthesized from annealed multilayers — X. Bian, Z. Altounian, J. O. Stöm-Olsen, A. Zaluska, Y. Huai, R. W. Cochrane

6563 Giant ac magnetoresistance in the soft ferromagnet $Co_{70.4}Fe_{4.6}Si_{15}B_{10}$ — F. L. A. Machado, B. L. da Silva, S. M. Rezende, C. S. Martins

6566 On the resistivity minimum in amorphous metallic spin-glasses (abstract) — J. Koetzler, G. Thummes

6567 Dependence of the anisotropic magnetoresistance on aspect ratio in cobalt films (abstract) — Mark Tondra, B. H. Miller, E. Dan Dahlberg

6567 Nonoscillatory behavior in the magnetoresistance of Cu/Ni superlattice (abstract) — W. Abdul-Razzaq

Magnetic Alloys and Compounds

6568 Preparation and magnetic properties of Mn_4N films by reactive facing targets sputtering — Shigeki Nakagawa, Masahiko Naoe

6571 Magnetovolume effects in strong paramagnets — E. G. Moroni, T. Jarlborg

6574 Synthesis and characterization of $Fe_{16}N_2$ in bulk form — M. Q. Huang, W. E. Wallace, S. Simizu, A. T. Pedziwiatr, R. T. Obermyer, S. G. Sankar

6577 Magnetic properties of FeRhP: Influence of metallic clusters on ferromagnetism — M. Guillot, M. Artigas, M. Bacman, D. Fruchart, D. Boursier, R. Fruchart

6580 Magnetism in metastable bcc and fcc iron-copper alloys — P. A. Serena, N. García

6583 On spin-canting in maghemite particles — S. Linderoth, P. V. Hendriksen, F. Bødker, S. Wells, K. Davies, S. W. Charles, S. Mørup

6586 Metamagnetism and spin arrangement in $Nd_6Fe_{13}Sn$ — M. Rosenberg, R. J. Zhou, M. Velicescu, P. Schrey, G. Filoti

6589 Temperature dependence of magnetic order in single-crystalline UPdSn — R. A. Robinson, J. W. Lynn, A. C. Lawson, H. Nakotte

6592 Magnetic properties of Dy-Lu alloys — B. A. Everitt, M. B. Salamon, C. P. Flynn, B. J. Park, J. A. Borchers, R. W. Erwin, F. Tsui

6595 Magnetic ordering and electric polarizability of Zn-doped $La_2CuO_{4+\delta}$ single crystals — G. Cao, J. W. O'Reilly, J. E. Crow, L. R. Testardi

6598 Two-dimensional magnetic order in $Pb_2Sr_2TbCu_3O_8$ — S. Y. Wu, W. T. Hsieh, W-H. Li, K. C. Lee, J. W. Lynn, H. D. Yang

6601 Structure of the modulated magnetic phase of Mn_3Sn (abstract) — J. W. Cable, N. Wakabayashi, P. Radhakrishna

6602 Magnetic structure of $NdCu_2$ (abstract) — R. R. Arons, M. Loewenhaupt, E. Gratz

6603 Easy-axis transition in $SmMn_2Ge_2$ (abstract) — R. B. van Dover, E. M. Gyorgy, R. J. Cava, J. E. Krajewski, W. F. Peck, Jr., R. J. Felder

(Continued)

6603 Neutron diffraction study of the magnetic ordering of $BaCuO_{2+x}$ (abstract) — Xun-Li Wang, J. A. Fernandez-Baca, Z. R. Wang, D. Vaknin, D. C. Johnston

Granular Films

6604 Magnetic properties of metallic Co- and Fe-based granular alloys — Gang Xiao, Jian-Qing Wang

6607 Magnetic and ferromagnetic resonance studies in Co-Cu composite films — R. Krishnan, H. Lassri, M. Seddat, M. Tessier, Sivaraman Guruswamy, Satyam Sahay

6610 Structure and magnetism of heat-treated nanocrystalline $Cu_{80}Co_{20}$ powders prepared via chemical means — V. G. Harris, F. H. Kaatz, V. Browning, D. J. Gillespie, R. K. Everett, A. M. Ervin, W. T. Elam, A. S. Edelstein

6613 Relaxation measurements and particle size determination in Co–Ag heterogeneous alloy films — S. B. Slade, F. T. Parker, A. E. Berkowitz

6616 Studies of magnetic interactions between Gd granules in copper matrix — J. H. Hsu, Y. H. Huang

6619 Magnetic reversal in small structures — D. I. Paul, A. Cresswell

6622 Exchange interactions among ferromagnetic clusters in Cu-Co heterogeneous alloy films (abstract) — A. E. Berkowitz, F. T. Parker, D. Rao

6622 Ferromagnetic resonance studies of granular materials (abstract) — Mark Rubinstein, Badri Das, D. B. Chrisey, J. Horwitz, N. C. Koon

6623 Magnetic properties of cobalt clusters deposited on MgO substrates by molecular beam epitaxy (abstract) — R. Morel, A. Barthélémy, F. Charrière, J. R. Childress, A. Fert, B. Bellamy, A. Masson

6623 Particle interactions in granular Co films (abstract) — A. Tsoukatos, H. Wan, G. C. Hadjipanayis

6624 Investigation of the microstructure of granular Ag-Fe and Ag-Co thin films by TEM and STEM (abstract) — Z. G. Li, H. Wan, J. Liu, T. Tsoukatos, G. C. Hadjipanayis

Hard Magnets II: 2-14-1 and Other Hard Magnets

6625 Resonant ultrasound measurements of elastic constants in melt-spun $R_2Fe_{14}B$ compounds (R=Ce, Pr, Nd, Er) — C. D. Fuerst, J. F. Herbst, J. L. Sarrao, A. Migliori

6628 Comparison of the improvement of thermal stability of NdFeB sintered magnets: Intrinsic and/or microstructural — B. M. Ma, W. L. Liu, Y. L. Liang, D. W. Scott, C. O. Bounds

6631 *Mechanical properties of hot-rolled Pr-Fe-B-Cu magnets* — A. Arai, O. Kobayashi, F. Takagi, K. Akioka, T. Shimoda

6634 Magnetocaloric dependence of magnetic viscosity measurements in NdFeB — L. Folks, R. Street, R. Woodward, P. G. McCormick

6637 Die-upset $PrCo_5$-type magnets: Enhanced coercivities — C. D. Fuerst, E. G. Brewer

6640 Nonepitaxial sputter synthesis of aligned strontium hexaferrite, $SrO{\cdot}6(Fe_2O_3)$, films — H. Hegde, P. Samarasekara, F. J. Cadieu

6643 Order-disorder and magnetic exchange interactions in substituted strontium hexaferrite $SrA_xFe_{12-x}O_{19}$(A=Ga, In) — G. K. Thompson, B. J. Evans

6646 Enhanced remanence in isotropic Fe-rich melt-spun Nd-Fe-B ribbons — L. Withanawasam, G. C. Hadjipanayis, R. F. Krause

6649 Mechanically alloyed nanocomposite magnets — Wei Gong, G. C. Hadjipanayis, R. F. Krause

6652 Microstructure of high-remanence Nd-Fe-B alloys with low-rare-earth content — Raja K. Mishra, V. Panchanathan

6655 Magnetic properties of sintered Alnico 5 magnet via rapid solidification technology — C. J. Yang, W. Y. Lee, S. D. Choi

6658 Effect of additives on thermal stability of Nd-Fe-B bonded magnets *(abstract)* — T. Nishio, H. Yagi, T. Furuya, Y. Kasai

(Continued)

6658 Coercivity in hard magnets based on Sm_2Co_{17} (abstract) — Eric Lectard, Claire Maury, Colette H. Allibert, Lew Rabenberg

Exchange Biasing and Oxides

6659 Orientational dependence of the exchange biasing in molecular-beam-epitaxy-grown $Ni_{80}Fe_{20}/Fe_{50}Mn_{50}$ bilayers (invited) — R. Jungblut, R. Coehoorn, M. T. Johnson, J. aan de Stegge, A. Reinders

6665 Magnetic properties of epitaxial MnAl/NiAl magnetic multilayers grown on GaAs heterostructures (invited) — T. L. Cheeks, J. P. Harbison, M. Tanaka, D. M. Hwang, T. Sands, V. G. Keramidas

6670 Magneto-optical and structural properties of BiAlDyIG/Fe multilayers — J. X. Shen, K. W. Wierman, Y. B. Zhang, R. D. Kirby, J. A. Woollam, D. J. Sellmyer

6673 Inverted hysteresis in magnetic systems with interface exchange — M. J. O'Shea, A.-L. Al-Sharif

6676 Magnetic and structural properties of Co/CoO bilayers — X. Lin, G. C. Hadjipanayis, S. I. Shah

6679 Resistivity anomaly in nonmagnetic metals with ferromagnetic insulator proximity layers — G. M. Roesler, Jr., Y. U. Idzerda, P. R. Broussard, M. S. Osofsky

6682 Complex magnetization processes of exchange coupled trilayers — S. Wüchner, J. Voiron, D. Givord, D. Boursier, J. J. Préjean

6685 Magnetic properties of antiferromagnetic superlattices — Shufeng Zhang, Guihua Zhang

6688 Magnetic and crystallographic properties of molecular beam epitaxially grown Fe_3O_4/NiO superlattices and Fe_3O_4 films — J. J. Krebs, D. M. Lind, E. Lochner, K. A. Shaw, W. Portwine, S. D. Berry

6691 Studies of the Verwey transition in Fe_3O_4/NiO superlattices by SQUID magnetometry and neutron diffraction techniques (abstract) — S. D. Berry, J. A. Borchers, R. W. Erwin, D. M. Lind, K. A. Shaw, E. Lochner

6692 Magnetic structure determination for Fe_3O_4/NiO superlattices by neutron diffraction techniques (abstract) — J. A. Borchers, R. W. Erwin, J. F. Ankner, S. D. Berry, D. M. Lind, E. Lochner, K. A. Shaw

Symposium: Perpendicular Transport in Layered Structures

6693 Perpendicular magnetoresistance in magnetic multilayers: Theoretical model and discussion (invited) — Albert Fert, Thierry Valet, Jozef Barnas

6699 How to isolate effects of spin-flip scattering on giant magnetoresistance in magnetic multilayers (invited) — J. Bass, Q. Yang, S. F. Lee, P. Holody, R. Loloee, P. A. Schroeder, W. P. Pratt, Jr.

6704 Scattering theory of perpendicular transport in metallic multilayers (invited) — Gerrit E. W. Bauer, Arne Brataas, Kees M. Schep, Paul J. Kelly

6709 Perpendicular giant magnetoresistance of microstructures in Fe/Cr and Co/Cu multilayers (invited) — M. A. M. Gijs, J. B. Giesbers, M. T. Johnson, J. B. F. aan de Stegge, H. H. J. M. Janssen, S. K. J. Lenczowski, R. J. M. van de Veerdonk, W. J. M. de Jonge

6714 Spin polarization of gold films via transported (invited) — Mark Johnson

High T_c Superconductivity: Experiment and Theory

6720 Transport and magnetic properties of polycrystalline $Sm_{2-x}Ce_xCuO_{4-y}$ — R. F. Jardim, C. H. Westphal, C. H. Cohenca, L. Ben-Dor, M. B. Maple

6723 Relationship between weak ferromagnetism, superconductivity, and lattice parameter in the $A_{2-x-y}B_xCe_yCuO_4$ (A,B=La, Pr, Nd, Sm, Eu, Gd, Y) compounds — T. Schultz, R. Smith, A. Fondado, C. Maley, T. Beacom, P. Tinklenberg, J. Gross, C. Saylor, S. Oseroff, Z. Fisk, S.-W. Cheong, T. E. Jones

6726 Alkali metals impurities influence on the magnetic and electrical properties of YBCO — I. Nedkov, A. Veneva

(Continued)

6729	Kinematical pairing and magnetism in layered systems	Valery A. Ivanov, Michail Ye. Zhuravlev, Pavel B. Z'ubin
6731	Ground-state properties and excitations of an integrable one-dimensional model with δ-function interaction involving several bands	P. Schlottmann
6734	Two-band model for Kondo insulators: Thermodynamic and scaling properties	M. A. Continentino, G. M. Japiassu, A. Troper
6737	Local magnetic moments and intermediate valence state of cerium impurities in ferromagnetic rare-earth metals	C. E. Leal, A. Troper
6740	Thermoelectric power studies of a $Nd_{1.82-x}Sr_xCe_{0.18}CuO_y$ superconducting system (abstract)	Okram G. Singh, B. D. Padalia, Om Prakash, V. N. Moorthy, Anant V. Narlikar
6740	The magnetic and superconducting properties of $Pb_2Sr_2(R/Ca)Cu_3O_8$, R=Pr, Ce, and Cm (abstract)	J. Simon Xue, C. W. Williams, L. Soderholm
6741	^{57}Fe and ^{119}Sn Mössbauer studies on $La_{1.25}Nd_{0.6}Sr_{0.15}CuO_4$: Evidence for local magnetic ordering below ≈32 K (abstract)	M. Breuer, B. Büchner, H. Micklitz, E. Baggio-Saitovitch, I. Souza Azevedo, R. B. Scorzelli, M. M. Abd-Elmeguid
6741	Peculiarities of inelastic neutron scattering on magnons in high-T_c materials of stoichiometrical composition Nd_2CuO_4, La_2CuO_4, and $YBa_2Cu_3O_6$ (abstract)	Yu. Pashkevich, M. Larionov
6742	The sign reversal of the acoustoelectric effect in anisotropic superconductors (abstract)	A. V. Goltsev
6743	Four-spin exchange in Bi_2CuO_4 (abstract)	G. Petrakovskii, V. Val'kov, K. Sablina, B. Fedoseev, A. Furrer, B. Roessli, P. Fischer
6744	Antiferromagnetic spin correlation suppression and superconducting characteristics improvement in $YBa_2Cu_3O_{6+\delta}$ films under light illumination (abstract)	V. Eremenko, V. Fomin, I. Kachur, V. Piryatinskaya, O. Prikhod'ko
6744	ac susceptibility of $Pb_xBi_{2-x}Sr_2Ca_2Cu_3O_{10}$ high T_c superconductors sintered for different durations (abstract)	S. C. Mathur, D. C. Dube, Urvija Sinha, P. K. N. Raghavan
6745	Spin magnetic moment of conduction quasiparticle (abstract)	Vladimir L. Safonov
6745	Restoration of the continuous phase transition in the vortex state due to the lattice translational symmetry: Large-N limit (abstract)	Boris N. Shalaev, Sergey A. Ktitorov
6746	Damping of spin waves in a square-lattice quantum antiferromagnet due to spin-phonon interaction (abstract)	Dirk Uwe Saenger
6746	The superconducting transition temperature of layered $S_i - J_{ij} - S_j$ superconductors (abstract)	Valery A. Cherenkov
6747	Magnetism and superconductivity in heavy-fermion compounds (abstract)	A. V. Goltsev

Magneto-optic and Other Magnetic Properties

6748	Magnetic properties of an isolated ferromagnetic bond embedded in Heisenberg antiferromagnets	S. T. Ting, S. Haas, J. E. Crow
6751	Spin diffusion in classical Heisenberg magnets with uniform, alternating, and random exchange	Niraj Srivastava, Jian-Min Liu, V. S. Viswanath, Gerhard Müller
6754	Theoretical study of magnetostriction in FeTaN thin films	James C. Cates, Chester Alexander, Jr.
6757	Dependence of the magnetic properties $Gd_{2-x}Ce_xCuO_4$, $0 \leq x \leq 0.15$, on their particle size	J. Mahia, C. Vázquez-Vázquez, J. Mira, M. A. López-Quintela, J. Rivas, T. E. Jones, S. B. Oseroff
6760	Magnetic properties of materials in the $CaO-P_2O_5-Fe_2O_3$ system	Binod Kumar, Christina H. Chen
6763	Magnetic properties of $Y_{3-x-y}Pr_xLu_yFe_5O_{12}$ garnet films	A. Azevedo, C. Cinbis, M. H. Kryder
6766	Magnetic properties of amorphous Cr–Fe alloys prepared by thermal evaporation and mechanical milling	S. K. Xia, E. Baggio-Saitovitch, C. Larica, B. V. B. Sarkissian, S. F. Cunha, J. L. Tholence

(Continued)

6769 Magnetostriction in RE-Co amorphous alloy films (abstract) — S. Uchiyama, S. Yoshino, H. Takahashi, K. Tomi-ita, T. Mori, A. Itakura, S. Iwata, S. Tsunashima

6769 A model for the Barkhausen noise power as a function of applied field and stress (abstract) — M. J. Sablik

Recording Head and System Modeling and Phenomena

6770 The effects of closure domains on flux conduction in thin film recording head — Zhenzhou Guo, Edward Della Torre

6773 Effect of recorded transition shape on spatial noise distributions and correlations — T. C. Arnoldussen, J. G. Zhu

6776 Mean interaction field in magnetic recording media — Ikuya Tagawa, Akihiko Takeo, Yoshihisa Nakamura

6779 Micromagnetic studies of medium noise mechanisms — Xiaodong Che, H. Neal Bertram

6782 Improving ferrite MIG head read-back distortions caused by domain walls and granularity (abstract) — B. E. Argyle, R. Schäfer, P. L. Trouilloud, M. E. Re, A. P. Praino, S. Takayama, D. Dingley

Magneto-optics

6783 MO polar Kerr studies of Co rich molecular beam epitaxy grown Au/Co multilayers — S. Višňovský, M. Nývlt, V. Prosser, R. Atkinson, W. R. Hendren, I. W. Salter, M. J. Walker

6786 Magneto-optical properties and magnetization processes in superlattices — Ron Atkinson, Nikolai F. Kubrakov, Sergey N. Utochkin, Anatoley K. Zvezdin

6789 The magnetic and magneto-optical properties of Co, Cr, Mn, and Ni substituted barium ferrite films — R. Carey, P. A. Gago-Sandoval, D. M. Newman, B. W. J. Thomas

6792 Anisotropy of the magnetic and magnetooptic properties of HoIG:Al single crystals (low and high magnetic field) — J. Ostoréro, M. Guillot

6795 Measurement of the Faraday effect of garnet film in alternating magnetic fields — Jia Ouyang, Ying Zhang, Huahui He

6798 An investigation on the magneto-optic and magnetic properties of Tb:YIG — Jie Hui Yang, You Xu, Guo Ying Zhang

6801 Magneto-optical properties of $(BiGdY)_3Fe_5O_{12}$ for optical magnetic field sensors — O. Kamada, H. Minemoto, N. Itoh

6804 Magneto-optical properties of Al and In-substituted CeYIG epitaxial films grown by sputtering (abstract) — M. Gomi, M. Abe

6804 Enhancement of the magneto-optical quality of YIG films in a structure containing a thin metal film (abstract) — A. D. Boardman, A. I. Voronko, P. M. Vetoshko, V. B. Volkovoy, A. Yu. Toporov

6805 Magnetic Davydov splitting in 2D AFM $(CH_2)_2(NH_3)_2MnCl_4$ (abstract) — V. Eremenko, I. Kachur, V. Piryatinskaya, V. Shapiro

Symposium: User Facilities in Magnetism

6806 Magnetic neutron scattering (invited) — J. W. Lynn

6811 Soft x-ray synchrotron radiation facilities for the study of magnetic materials (invited) (abstract) — Brian Tonner, W. O'Brien, M. A. Green, H. Höchst, R. Reininger

6812 High magnetic field research: Overview of facilities and science and technology opportunities (invited) (abstract) — J. E. Crow, H. J. Schneider-Muntau, D. M. Parkin, N. Sullivan

Magnetic Structure

6813 $LiNiO_2$: Quantum liquid or concentrated spin glass? — M. Rosenberg, P. Stelmaszyk, V. Klein, S. Kemmler-Sack, G. Filoti

6816 Disappearance of three-dimensional magnetic ordering in Gd_2CuO_4 — T. Chattopadhyay, P. J. Brown, B. Roessli

(Continued)

6819 Spin-Peierls transition in $CuGeO_3$: Electron paramagnetic resonance study — S. Oseroff, S-W. Cheong, A. Fondado, B. Aktas, Z. Fisk

6822 Observations of magnetization reversal and magnetic clusters in copper ferrite films — M. M. Ibrahim, M. S. Seehra, G. Srinivasan

6825 The structure and spin dynamics of lanthanide-bearing silicate glasses — A. J. G. Ellison, C.-K. Loong, J. Wagner

6828 Magnetization and ferromagnetic resonance studies on amorphous films of Fe_2O_3-Bi_2O_3-Li_2O — J. Chen, S. Cheney, G. Srinivasan

6831 Hysteresis and magnetic aftereffect in amorphous CoZrDy films: Trends and variations versus Dy content — G. Suran, K. Roky

6834 First-principles calculation of orbital moment distribution in amorphous Fe — Xue-Fu Zhong, W. Y. Ching

6837 A magnetocalorimetric study of spin fluctuations in amorphous Fe_xZr_{100-x} — A. LeR. Dawson, D. H. Ryan

6840 Magnetic properties of colloidal silica: Potassium silicate gel/iron nanocomposites — R. D. Shull, H. M. Kerch, J. J. Ritter

Magneto-optic Recording

6843 Origin of high coercive force in rare-earth–transmission-metal thin film — D. Roy Callaby, Robert D. Lorentz, Shigeki Yatsuya

6846 Study of the effect of defect sizes and their distribution on the coercivity of magnetic media — James A. Jatau, Edward Della Torre

6849 Reversal mechanisms in Tb/Fe multilayers — K. O'Grady, T. Thomson, S. J. Greaves, G. Bayreuther

6852 Write/erase cyclability of TbFeCo for mark edge recording — Hiroyuki Awano, Masahiro Ojima, Katsusuke Shimazaki, Satoru Ohnuki, Norio Ohta

6855 Recording characteristics of Kr-sputtered Tb/FeCo multilayer magneto-optical disks — Hiro Karube, Kunihiko Matsumura, Masafumi Nakada, Osamu Okada

6858 Double compensation point media for direct overwrite — T. K. Hatwar, D. J. Genova, R. H. Victora

6861 Design and performance of magneto-optic enhanced Co/Pt-based trilayers having zero Kerr ellipticity — R. Atkinson, P. J. Grundy, C. M. Hanratty, R. J. Pollard, I. W. Salter

6864 Effect of substrate roughness on microstructure, uniaxial anisotropy, and coercivity of Co/Pt multilayer thin films — Chung-Hee Chang, Mark H. Kryder

6867 Depth distribution of birefringence in magneto-optical recording disk substrates — Raymond-Noel Kono, Myung S. Jhon, Thomas E. Karis

6870 Growth and subsequent relaxation of the anisotropic structure of amorphous Tb-Fe (abstract) — F. Hellman, M. C. Robson, M. T. Messer

6871 Macroscopic ferrimagnets as magneto-optic media (abstract) — Richard J. Gambino, Ralph R. Ruf, Nestor Bojarczuk

Magnetic Imaging and Measuring Techniques

6872 High-resolution magneto-optic measurements with a Sagnac interferometer (invited) — A. Kapitulnik, J. S. Dodge, M. M. Fejer

6878 dc magnetic force microscopy imaging of thin-film recording head — Paul Rice, John Moreland, Andrzej Wadas

6881 Proposed antiferromagnetically coupled dual-layer magnetic force microscope tips — John O. Oti, Paul Rice, Stephen E. Russek

6884 Anisotropy and magnetostriction measurement by interferometry — Peter S. Hartlee III, George H. Bellesis, David N. Lambeth

6887 New complex permeability measurement device for thin magnetic films — S. Hayano, I. Marinova, Y. Saito

6890 Element specific magnetic microscopy with x rays (invited) (abstract) — B. Hermsmeier, J. Stöhr, Y. Wu, M. Samant, G. Harp, S. Koranda, D. Dunham, B. P. Tonner

(Continued)

6890	High spatial resolution spin-polarized scanning electron microscopy (abstract)	H. Matsuyama, K. Koike, F. Tomiyama, H. Aoi, Y. Shiroishi, A. Ishikawa
6891	An analysis of magnetization patterns measured using a magnetic force scanning tunneling microscope (abstract)	E. R. Burke, R. D. Gomez, I. D. Mayergoyz
6892	Magnetic force microscopy of single crystal magnetite (Fe_3O_4) (abstract)	R. Proksch, S. Foss, C. Orme, S. Sahu, B. Moskowitz
6893	Interpretation of magnetic force microscopic images (abstract)	Atsushi Kikukawa, Hiroyuki Awano, Sumio Hosaka, Yukio Honda, Ryo Imura

Giant Magnetoresistance in Granular Materials

6894	Determination of para- and ferromagnetic components of magnetization and magnetoresistance of granular Co/Ag films (invited)	Mary Beth Stearns, Yuanda Cheng
6900	Giant magnetoresistance and microstructural characteristics of epitaxial Fe-Ag and Co-Ag granular thin films	N. Thangaraj, C. Echer, Kannan M. Krishnan, R. F. C. Farrow, R. F. Marks, S. S. P. Parkin
6903	Giant magnetoresistance and its dependence on processing conditions in magnetic granular alloys	Jian-Qing Wang, Edward Price, Gang Xiao
6906	Theory of magnetotransport in inhomogeneous magnetic structures	Horacio E. Camblong, Shufeng Zhang, Peter M. Levy
6909	Giant magnetoresistance of dilute Cu(Co) granular films	R. J. Gambino, T. R. McGuire, J. M. E. Harper, Cyril Cabral, Jr.
6912	Dependence of giant magnetoresistance on film thickness in heterogeneous Co-Ag alloys	J. R. Mitchell, A. E. Berkowitz
6915	Modulation-induced giant magnetoresistance in a spinodally decomposed Cu-Ni-Fe alloy	S. Jin, L. H. Chen, T. H. Tiefel, M. Eibechutz, R. Ramesh
6918	Magnetoresistance in a granular Fe–Mg system	Kevin Pettit, E. Kita, K. Araga, A. Tasaki, M. B. Salamon
6921	Giant magnetoresistance and induced exchange anisotropy in mechanically alloyed $Co_{30}Ag_{70}$	K. Ounadjela, A. Herr, R. Poinsot, J. M. D. Coey, A. Fagan, C. R. Staddon, D. Daniel, J. F. Gregg, S. M. Thompson, K. O'Grady, S. Grieves
6924	Correlation of x-ray diffraction and Mössbauer effect measurements with magnetic properties of heat-treated $Cu_{80}Co_{15}Fe_5$ ribbons	V. G. Harris, M. Rubinstein, B. N. Das, N. C. Koon
6927	Giant magnetoresistance in $Ag_{1-x}Ni_{x-y}Fe_y$ heterogeneous alloy films	M. L. Watson, V. G. Lewis, K. O'Grady
6930	Giant and anisotropic magnetoresistance in single layer $Ni_{66}Fe_{16}Co_{18}$–Ag films	A. Waknis, J. A. Barnard, M. R. Parker
6933	Giant magnetoresistance in heterogeneous $(CoFe)_xAg_{1-x}$ films (abstract)	R. S. Beech, D. Rao, M. J. Carey, F. T. Parker, A. E. Berkowitz

Soft Magnetic Materials and Applications II

6934	The effects of film geometry on the properties of FeTaN films	Gan Qiu, J. A. Barnard
6937	Relationship between ac and dc magnetic properties of a Co-based amorphous alloy	S. H. Lim, Y. S. Choi, T. H. Noh, I. K. Kang
6940	Effects of nanocrystallization upon the soft magnetic properties of Co-based amorphous alloys	P. Quintana, E. Amano, R. Valenzuela, J. T. S. Irvine
6943	Magnetic properties behaviors in $Fe_{88}Zr_7B_4Cu_1$ nanocrystalline alloy prepared by different postanneal cooling rates	K. Y. Kim, J. S. Lee, T. H. Noh, I. K. Kang, T. Kang
6946	Soft-magnetic properties of amorphous tapes after dynamic current annealing	M. A. Escobar, J. C. Perron, R. Barrué, A. R. Yavari
6949	Magnetic behavior of the amorphous wires covered by glass	Horia Chiriac, Gheorghe Pop, Firuta Barariu, Manuel Vázquez

(Continued)

6952 Tensor components of the magnetization in a twisted Fe-rich amorphous wire — L. Kraus, S. N. Kane, M. Vázquez, G. Rivero, E. Fraga, A. Hernando, J. M. Barandiarán

6955 A metastable ternary Nd-Fe-B compound — B. X. Gu, B. G. Shen, H. R. Zhai

6958 Helical anisotropy and Matteucci effect in Co-Si-B amorphous wires with negative magnetostriction (abstract) — J. Yamasaki, M. Takajo, F. B. Humphrey

6959 The rf permeability of dc planar magnetron sputtered FeNi multilayer films (abstract) — Craig A. Grimes, Catherine C. Ballantyne

Applied Superconductivity

6960 *Phase transitions in the one-dimensional frustrated quantum XY model* and Josephson-junction ladders — *Enzo Granato*

6963 *Penetration of circularly polarized electromagnetic fields into* superconductors with gradual resistive transitions — I. D. Mayergoyz

6966 *Magnetic shielding from alternating magnetic field by NbTi/Nb/Cu* superconducting multilayer composite cylinder — Hiroaki Otsuka, Ikuo Itoh

6969 A method of increasing magnetic energy of superconducting magnetic energy storage — T. Morisue, T. Yajima

6972 Synthesis of high-temperature superconducting thin films in microwave field — Victor I. Kojuharoff

Applied Magnetics

6975 Estimation of fatigue exposure from magnetic coercivity — Z. J. Chen, D. C. Jiles, J. Kameda

6978 Overview of applications of micromagnetic Barkhausen emissions as noninvasive material characterization technique — L. B. Sipahi

6981 Monitoring neutron embrittlement in nuclear pressure vessel steels using micromagnetic Barkhausen emissions — L. B. Sipahi, M. R. Govindaraju, D. C. Jiles

6984 Experimental study on opening compensation for magnetic shields by current superposition — I. Sasada, Y. Oonaka

6987 Effects of pole flux distribution in a homopolar linear synchronous machine — M. J. Balchin, J. F. Eastham, P. C. Coles

6990 Compensation of field distortion with ferromagnetic materials and permanent magnets — Manlio G. Abele, Henry Rusinek, Franco Bertora, Alessandro Trequattrini

6993 Equivalent structures of permanent magnets and electric currents designed to generate uniform fields — M. G. Abele

6996 Thermal magnetic noise due to eddy currents in a strip wound ferromagnetic core at 4.2 K (abstract) — Yu. V. Maslennikov, O. Snigirev, M. Cerdonio, G. A. Prodi, S. Vitale

6996 Design of fast acting actuators for cryogenic valve applications in the ARIANE5-program (abstract) — Peter Schiebener, Alfred Pfeiffer, Karl Smirra

Magnetic Domains in Soft Magnetic Materials

6997 Barkhausen transitions in single layer and bilayer thin permalloy films — G. P. Farrell, E. W. Hill

7000 Equation of motion of domain walls and equivalent circuits in soft ferromagnetic materials — G. Aguilar-Sahagun, P. Quintana, E. Amano, J. T. S. Irvine, R. Valenzuela

7003 Pinned domain-wall structure in magnetic field — Chai Tak Teh, Huei Li Huang, Vladimir L. Sobolev

7006 Susceptibility of current-carrying iron whiskers — J. -G. Lee, A. S. Arrott

7009 The effects of demagnetizing and stray fields on magnetoacoustic emission — D. H. L. Ng, C. C. H. Lo, J. P. Jakubovics

Magnetic and Electronic Structure

7012 IR spectroscopy on FeNi and FePt Invar alloys — B. Buchholtz, E. F. Wassermann, W. Pepperhoff, M. Acet

(Continued)

7015 Anti-Invar in Fe-Ni — M. Acet, T. Schneider, H. Zähres, E. F. Wassermann, W. Pepperhoff

7018 X-ray-absorption fine structure of selected R_2Fe_{17} nitrides — T. W. Capehart, R. K. Mishra, F. E. Pinkerton

7021 Exchange stiffness and magnetic anisotropies in bcc $Fe_{1-x}Co_x$ alloys — X. Liu, R. Sooryakumar, C. J. Gutierrez, G. A. Prinz

7024 Approach to the electronic structure of antiferromagnets — J. Callaway, D. G. Kanhere, A. Kolchin

7027 Magnetization density in URu_2Si_2 and URh_2Si_2 — Alessandra Continenza, Patrizia Monacheei

7030 Spectroscopic studies of magnetic transitions in $TbPO_4$ — G. K. Liu, C.-K. Loong, F. Trouw, M. M. Abraham, L. A. Boatner

7033 Magnetic structures of itinerant electron systems (abstract) — J. Kübler, L. Sandratskii, M. Uhl

7034 Electronic structure and spin-density distribution in Y_2Fe_{17} (abstract) — Ming-Zhu Huang, W. Y. Ching

7034 Energetics of bcc-fcc lattice in Fe-Co-Ni compounds (abstract) — E. G. Moroni, T. Jarlborg

Correlated *f*-Electron Phenomena

7035 Prediction of pressure-induced changes in magnetic ordering of correlated-electron uranium systems (invited) — Q. G. Sheng, Bernard R. Cooper

7041 Magnetic properties of the lattice Anderson model — H. Q. Lin, H. Chen, J. Callaway

7044 Effects of doping in Kondo insulators (invited) — P. Schlottmann

7050 Structural and magnetic ordering in the cerium hydride (abstract) — R. R. Arons, J. K. Cockcroft, E. Ressouche

7051 Recent developments in multi-channel Kondo physics (invited) (abstract) — Kevin Ingersent, Barbara A. Jones

Giant Magnetoresistance in Multilayers

7052 Giant magnetoresistance in $Fe_{0.95}Cr_{0.05}$/Cr multilayer films — L. H. Chen, S. Jin, T. H. Tiefel, R. B. Van Dover, E. M. Gyorgy, R. M. Fleming

7055 The effect of Au impurities at the interfaces on the magnetoresistance of MBE-grown Co/Cu multilayers — K. P. Wellock, B. J. Hickey, D. Greig, M. J. Walker, J. Xu, N. Wiser

7058 Low field giant magnetoresistance in discontinuous magnetic multilayers — T. L. Hylton, K. R. Coffey, M. A. Parker, J. K. Howard

7061 Epitaxial spin-valve structures for ultra-low-field detection — A. Schuhl, O. Durand, J. R. Childress, J.-M. George, L. G. Pereira

7064 Giant magnetoresistance with low saturation field in (Ni_xCo_{100-x}/Cu) multilayers — X. Bian, J. O. Ström-Olsen, Z. Altounian, Y. Huai, R. W. Cochrane

7067 Hysteresis reduction in NiFeCo/Cu multilayers exhibiting large low-field giant magnetoresistance — S. Hossain, D. Seale, G. Qiu, J. Jarratt, J. A. Barnard, H. Fujiwara, M. R. Parker

7070 Calculation of the temperature dependence of the giant MR and application to Co/Cu multilayers — J. L. Duvail, A. Fert, L. G. Pereira, D. K. Lottis

7073 Magnetization reversal in CoFe/Ag/Fe/ZnSe thin layer sandwiches — D. Bilic, E. Dan Dahlberg, A. Chaiken, C. Gutierrez, P. Lubitz, J. J. Krebs, M. Z. Harford, G. A. Prinz

7076 Effective internal fields and magnetization buildup for magnetotransport in magnetic multilayered structures — Peter M. Levy, Horacio E. Camblong, Shufeng Zhang

7079 Structure and giant magnetoresistance in sputtered and MBE grown Fe/Cr superlattices (invited) (abstract) — Ivan K. Schuller, David M. Kelly, R. Schad, M. Potter, Y. Bruynseraede

(Continued)

7079	Direct measurement of spin dependent mean free paths in metals (abstract)	Bruce A. Gurney, Virgil S. Speriosu, Harry Lefakis, Dennis R. Wilhoit, Omar U. Need
7080	Giant magetoresistance in epitaxial sputtered Fe/Cr(211) superlattices (abstract)	M. J. Conover, Eric E. Fullerton, J. E. Mattson, C. H. Sowers, S. D. Bader
	Magneto-optic Recording	
7081	Compositional dependence of the structural and magnetic properties of PtMnSb films	R. Carey, H. Jenniches, D. M. Newman, B. W. J. Thomas
7084	Secondary ion bombardment effects on the magnetic properties and microstructures of ion-beam-deposited TbFe thin films	S. Yatsuya, M. B. Hintz
7087	Optical and magneto-optical constants of Pr substituted TbFeCo films	R. Carey, D. M. Newman, J. P. Snelling, B. W. J. Thomas
7090	Thermal stability of NdGd/FeCo multilayers	X. Y. Yu, T. Suganuma, H. Watabe, S. Iwata, S. Tsunashima, S. Uchiyama
7093	Physical and magnetic microstructure of rapid thermally annealed thin film bismuth-doped garnets	W. R. Eppler, B. K. Cheong, D. E. Laughlin, M. H. Kryder
7096	Uniaxial anisotropy of double-layered garnet films and magneto-optical recording characteristics	Katsuji Nakagawa, Seiji Kurashina, Akiyoshi Itoh
7099	Anisotropy and Faraday effect in Co spinel ferrite films	H. Y. Zhang, B. X. Gu, H. R. Zhai, M. Lu, Y. Z. Miao, S. Y. Zhang, H. B. Huang
7102	Magnetic and magneto-optical properties of (Tb,Dy)Nd/FeCo multilayers (abstract)	X. Y. Yu, Y. Fujiwara, H. Watabe, S. Iwata, S. Tsunashima, S. Uchiyama
7102	Magnetization reversal dynamics in CoPt alloys and Co/Pt multilayers (abstract)	J. Valentin, Th. Kleinefeld, D. Weller
7103	Amorphous to polycrystalline transformation of (BiDy)IG films (abstract)	H. Y. Zhang, B. X. Gu, H. R. Zhai, Y. Z. Miao, M. Lu, T. Tang, H. B. Huang
7104	Epitaxial Bi-content ferrite-garnet film memory (abstract)	E. I. Il'yashenko, V. P. Klin, A. D. Nickolsky, A. G. Solovjov
	Magnetic Alloys and Compounds	
7105	Ferromagnetism of YFe_2H_x	Kazuo Kanematsu
7108	Longitudinal and transverse magnetoresistance and magnetoresistive anisotropy in ternary $(Pd_{1-x}Fe_x)_{95}Mn_5$ alloys	Z. Wang, H. P. Kunkel, Gwyn Williams
7111	Formation and magnetic properties of $Y_2(Fe_{0.8}Ga_{0.2})_{17}C_x$ compounds	Fang-Wei Wang, Lin-Shu Kong, Lei Cao, Ming Hu, Bao-Gen Shen, Jian-Gao Zhao
7114	Structural and magnetic properties of $Nd_2(Fe,Ti)_{19}$	J. M. Cadogan, Hong-Shuo Li, R. L. Davis, A. Margarian, S. J. Collocott, J. B. Dunlop, P. B. Gwan
7117	Possible ferrimagnetic coupling in light-rare-earth transition-metal intermetallic compounds	Z. G. Zhao, F. R. de Boer, V. H. M. Duijn, K. H. J. Buschow, Y. C. Chuang
7120	Magnetic properties of a novel Pr-Fe-Ti phase	Hong-Shuo Li Suharyana, J. M. Cadogan, G. J. Bowden, Jian-Min Xu, S. X. Dou, H. K. Liu
7122	Magnetic properties of $Gd(Fe_{1-x}Co_x)_9Ti_2$ alloys	Suharyana, J. M. Cadogan, Hong-Shuo Li, G. J. Bowden
7125	Magnetic resonance in PdFe alloys near T_c	A. N. Medina, V. S. Oliveira, F. G. Gandra, A. A. Gomes

(Continued)

7128	Effects of Co and Y substitution on magnetic properties of $CeFe_2$	Xianfeng Zhang, Naushad Ali
7131	Preparation and magnetic properties of BaM films with excellent crystallinity by Xe sputtering	N. Matsushita, K. Noma, S. Nakagawa, M. Naoe
7134	Magnetic ordering in $UCoNiSi_2$ and $UCoCuSi_2$ studied by ac-susceptibility and neutron-diffraction measurements	Moshe Kuznietz, Haim Pinto, Mordechai Melamud
7137	Ferromagnetic ordering in dilute *Pd*Co alloys	R. E. Parra, A. C. Gonzalez
7140	Magnetic susceptibility of RCo_3B_2 (R=Y, Sm, Gd, and Dy)	H. Ido, M. Nanjo, M. Yamada
7143	^{139}La nuclear quadrupole resonance and relaxation in Zn-doped La_2CuO_4	M. Corti, A. Lascialfari, A. Rigamonti, F. Tabak, F. Licci, L. Raffo
7146	^{35}Cl nuclear-magnetic-resonance study of magnetic ordering in $Sr_2CuO_2Cl_2$ single crystal	M. Corti, F. Borsa, L. L. Miller, A. Rigamonti
7149	Magnetic effects in Cr-Mn alloy single crystals containing 0.05 and 0.1 at. % Mn	P. Smit, H. L. Alberts
7152	Antiferromagnetism of metastable Cr-rich Cr-Gd alloys	Jen Hwa Hsu, Y. W. Fu
7155	Magnetic properties of two new compounds: $Gd_2Ni_3Si_5$ and $Sm_2Ni_3Si_5$	Chandan Mazumdar, R. Nagarajan, L. C. Gupta, R. Vijayaraghavan, C. Godart, B. D. Padalia
7158	Low-field ac magnetic susceptibility under pressure in $GdMn_2$ and $TbMn_2$ intermetallics	M. R. Ibarra, Z. Arnold, C. Marquina, L. García-Orza, A. del Moral
7161	Time evolution of magnetization in the FeRh system near antiferromagnetic-ferromagnetic transition temperature (abstract)	Shinji Yuasa, Yoshichika Otani, Hideki Miyajima
7161	Unusual magnetic properties and time dependent magnetization in $ErCo_3Ga_2$ (abstract)	Naushad Ali, Xianfeng Zhang

Biomagnetism, Magnetochemistry, and Magnetic Separation

7162	Effects of magnetic fields on fibrinolysis	M. Iwasaka, S. Ueno, H. Tsuda
7165	Early embryonic development of frogs under intense magnetic fields up to 8 T	S. Ueno, M. Iwasaka, K. Shiokawa
7168	Influence of spreading neuronal electric sources on spatio-temporal neuromagnetic fields	K. Iramina, K. Ueno, S. Ueno
7171	Magnetite coating prepared by ferrite plating on expanded polytetrafluoroethylene membrane for medical use	Q. Zhang, T. Itoh, M. Abe
7174	Redistribution of dissolved oxygen concentration under magnetic fields up to 8 T	S. Ueno, M. Iwasaka, T. Kitajima
7177	Properties of diamagnetic fluid in high gradient magnetic fields	S. Ueno, M. Iwasaka
7180	Influence of ultraworking frequency alternating weaking magnetic field on the microvasculture of mice (abstract)	Ningjiang Yang, Changmin Zhang
7181	Enzymatic oxidation-reduction processes under magnetic fields up to 8 T (abstract)	M. Iwasaka, S. Ueno
7181	Induction of mutati[illegible]oy magnetic field for the improvement of sunflower (abstract)	V. Kiranmai
7182	The magnetic transformation of iron hydroxides under the action of micro-organism (Azotobacter vinelandii) (abstract)	Nadezda V. Verkhovtseva, Irina V. Shpilkina, Vyacheslav F. Babanin
7182	Magnetic properties of heterotrophic bacteria (abstract)	Nadezda V. Verkhovceva, Irina N. Glebova, Anatoly V. Romanuk
7183	Spin-glass structures in biological systems (abstract)	Alexandre I. Tsapin, L. A. Blumenfeld

(Continued)

7183	The testing of action of chemical extracts on soils by magnetic methods (abstract)	Vyacheslav F. Babanin, Irina V. Shpilkina, Alexandr V. Ivanov
7184	The magnetic diagnostics of cosmic and industrial silt in humus horizons of soils (abstract)	Vyacheslav F. Babanin, Irina V. Shpilkina, Sergei A. Shoba, Alexander V. Ivanov
7185	Dislocation etching of flux grown strontium hexaferrite single crystals (abstract)	Urvashi Raina, Sushma Bhat, P. N. Kotru, F. Licci
7186	Dipole-dipole interactions in $KEr(MoO_4)_2$ (abstract)	A. G. Anders, S. V. Volotskii, O. E. Zubkov
7186	Database of magnetochemistry in solutions (abstract)	O. Ju. Tarasov, A. G. Vinogradov
7187	The magnetodynamic filters in monitoring the contaminants from polluted water systems (abstract)	R. Swarup, Bharat Singh

AUTHOR INDEX

A publication of the American Institute of Physics, 500 Sunnyside Blvd., Woodbury, NY 11797-2999

PREFACE

MMM '93, the 38th Annual Conference on Magnetism and Magnetic Materials, was held in Minneapolis at the Hyatt Regency Hotel, November 15–18, 1993. Despite a slowdown in the economy and competition from other meetings, there was a total of 586 full registrants and 202 student/retiree registrants. 1018 abstracts were submitted to the Program Committee. The final program was made up of 858 papers, of which 33 were invited papers, 10 contributed papers that had been promoted to invited paper status, 478 poster papers, and 332 contributed oral presentations. The Conference Proceedings is subdivided into 59 sections and contains 30 invited papers, 479 contributed papers, and 153 abstracts.

The meeting began with a well-attended Sunday evening tutorial where informal talks were given on theory of magnetism, magnetic measurements, magnetic force microscopy and other imaging techniques, and materials science: deposition and characterization. In the four-day program, there were symposia on magnetic circular dichroism, novel time-resolved probes of dynamical magnetism, and perpendicular transport in layered structures, along with evening symposia on environmental magnetism and national user facilities. Although there were reports from virtually all areas of magnetics research, studies relating to the magnetic properties of surfaces and artificially structured magnetic materials were especially prominent in the program. Also noteworthy were the large numbers of graduate and post-doctoral students in attendance, which will help ensure the vitality of the field for years to come. Another welcome trend is the growing international character of the meeting as reflected in the fact that 60% of the abstracts accepted for presentation came from outside the United States.

A meeting the size of MMM requires the dedicated efforts of a large number of people. I would especially like to thank the members of the Steering Committee, the Local Committee, the Program Committee, and the Conference Editors as well as staff from the American Institute of Physics and Courtesy Associates for their help in organizing and running the meeting. In addition to the corporate sponsors, who are listed on the third page of the Proceedings, the Conference received financial support for invited speakers from the Office of Naval Research.

David L. Huber
General Chairman
MMM '93

Monte Carlo simulations of remanent magnetization decay driven by interactions

M. E. Matson, D. K. Lottis, and E. Dan Dahlberg
School of Physics and Astronomy, University of Minnesota, Minneapolis, Minnesota 55455

Many physical systems, including ferromagnets, exhibit slow relaxation behavior. The usual explanation of this time dependence is to assume a distribution of energy barriers, i.e., disorder. A recent model [Phys. Rev. Lett. 67, 362 (1991)] relies on a mean field approximation of magnetostatic interactions to be the driving force responsible for the decay. Following this work, we have simulated the dynamics interacting Ising spin system key features found in the original model. In addition, it is shown that the interaction driven relaxation results in a faster decay of the magnetization; a result reflecting the model system is being driven towards its equilibrium state by the interactions.

Many magnetic systems exhibit the magnetic aftereffect[1,2] which is identified as a slow, nonexponential, or quasilogarithmic decay of the remanent magnetization. A typical equation used to characterize this slow decay is

$$M(t)=M_1+S\ \ln(t), \tag{1}$$

where M is the remnant magnetization at $t=1$ unit, and S is constant for any given temperature.[2] The traditional model used to obtain this relationship involves the presence of a distribution (disorder) of barrier heights which must be thermally overcome for a given grain of magnetic material to reverse its magnetic orientation.

After the first suggestion that interactions were responsible for the slow relaxation,[3] a model was developed[1,4] to account for the slow dynamics and the nonmonotonic decay slope of this system. In this model one considers a plane of spins or magnetic moments that may only point up or down and are coupled by their dipole–dipole interactions. Based on this earlier work and through private communications, other researchers have used Monte Carlo techniques to include interactions,[5] and have modeled the dynamics of other systems dominated by couplings[6] in a similar fashion.

In the present work, we use this model as the basis for Monte Carlo simulations of the decay of a coupled or interacting spin system on a 200×200 spin lattice. The solution of the model system by the Monte Carlo technique required a modification of the algorithm to include an energy barrier. Included is some discussion to justify the simple conclusion that the probability of a spin flipping to a different energy state, separated from the first by an energy barrier ΔE_b, is simply $P_b=Pe^{-\Delta Eb}$, where P is the properly normalized probability of the spin flipping without this barrier. This modified algorithm is different from that previously used,[5] and therefore there are distinct differences in the results of the present work with that done previously.

The model system consists of a plane of spins or magnetic moments with an anisotropy energy such that the energy minima are with the moments perpendicular to the plane, i.e., the energy minima states are up and down states that are perpendicular to the plane. These spins interact through dipole–dipole interactions that are treated in a mean-field approximation. In the ground state this system contains no net magnetization, with one spin up for every spin down. When the system is saturated along the positive z axis, the demagnetizing field of the system will be along the negative z axis, driving the system back to equilibrium. Because the remnant field decreases as equilibrium is approached, the energy needed to overcome the energy barrier increases. This slows the relaxation process over time, leading to quasilogarithmic relaxation. As will be shown later, if there were no interactions the system would still relax, but since the barriers remain at their maximum height, the decay, although exponential, will take a much longer time.

In this model each spin has an anisotropy energy of the form $-K_u v\cos^2(\varnothing)$, where v is the volume of the spin grain, $\varnothing$ is the angle between the spin vector and the positive z axis, and K_u is a positive constant. The energy due to an external field has the form $M_s Hv\cos(\varnothing)$, where M_s is the saturation magnetization of the spin grain and H is an applied field along the *negative* z axis. This gives a total energy per grain of

$$E=-K_u v\ \cos^2(\varnothing)+M_s Hv\ \cos(\varnothing). \tag{2}$$

If one differentiates Eq. (2) by $\varnothing$ and sets the result to 0, one obtains the values of $\varnothing$ corresponding to the energy minima and maxima. The maximum value for the energy, which we call E_b, is the energy maximum separating the minima E_1 (spin up, $\varnothing=0$) and E_2 (spin down, $\varnothing=\pi$). Of course, it is the relative energies that are important for the dynamics of the system. Defining $E_{1(2)}$ as the energy with $\varnothing=0(\pi)$, the up (down) state energy, we can determine the energy from a particular state to the barrier maximum as

$$E_{b1(b2)}=E_b-E_{1(2)}=\frac{v}{4K_u}\ [M_s H-(+)2K_u]^2. \tag{3}$$

Any dynamics or change in the relative populations of the spins is then given by

 0021-8979/94/75(10)/5475/3/$6.00 © 1994 American Institute of Physics

$$\frac{dN_1}{dt} = -w_1 N_1 e^{-\beta E_{b1}} + w_2 N_2 e^{-\beta E_{b2}}, \tag{4}$$

where N_1 is the number of spins pointing up, N_2 is the number of spins pointing down, w_1 and w_2 are the attempt frequencies, and $\beta = 1/K_b T$. The attempt frequencies are assumed to be equal and constant.

The inclusion of interactions is straightforward by identifying the magnetic field H with the demagnetization field. This corresponds to using a mean-field approximation for the dipolar couplings. For the limiting case of planar symmetry with the magnetization perpendicular to the plane, this gives a magnetic field of $-4\pi M$, where $M = M_s(N_1 - N_2)/N$, where N is the total number of spins. Defining ΔN such that $N_{1(2)} = \frac{N}{2} + (-)\Delta N/2$ (so $\Delta N = N_1 - N_2$), one obtains

$$\frac{d\Delta N}{dt} = -w_+ \left(\frac{N}{2} + \frac{\Delta N}{2}\right) \exp\left[-\frac{\beta v}{K_u}\left(\frac{2\pi M_s^2 \Delta N}{N} - K_u\right)^2\right] + w_- \left(\frac{N}{2} - \frac{\Delta N}{2}\right) \times \exp\left[-\frac{\beta v}{K_u}\left(\frac{2\pi M s^2 \Delta N}{N} + K_u\right)^2\right]. \tag{5}$$

For a number of applications, such as including the effects of disorder, it is easiest to use an Ising model and perform Monte Carlo (MC) computer simulations of the decay to equilibrium[7] rather than include these effects in Eq. (5). Usually in MC simulations, the algorithm used to flip the spins is the Metropolis algorithm.[7] This algorithm calculates the probability of the spin flipping to be

$$P = \frac{e^{\Delta E \beta}}{1 + e^{\Delta E \beta}}, \tag{6}$$

where the ΔE is the energy difference and $\beta = 1/K_b T$ (often $P = e^{\Delta E \beta}$ is used, which gives the same equilibrium statistics, but arrives at equilibrium faster. While this is a desirable property for most uses, it shows a less accurate time dependence.)

Equation (6) does not include the effects of the energy barrier or maximum on the dynamics. Previous efforts[5] to incorporate the energy barriers altered the probabilities for both spin up and spin down, and then proceeded to use the same Metropolis algorithm for flipping spins. The following is the development of a different technique to incorporate the barriers.

Given a system of spins where each spin is allowed to occupy one of two states with energies E_1 and E_2 (representing spin up and spin down, respectively) and an additional energy level, E_b, which is not a state the spin is allowed to occupy. This energy level is larger than E_1 or E_2 and acts as a barrier between the two levels. Without loss of generality, one can assume that $E_1 > E_2$ (this reflects the fact that the demagnetization field is in the $-z$ direction) and define $\Delta E = E_1 - E_2$, $\Delta E_b = E_b - E_1$, as before. If $\Delta E_b = 0$ then we use the usual Boltzmann distribution to calculate P_{12}, the probability spin flips from the E_1 to E_2 (E_2 to E_1) state given by

$$P_{12(21)} = \frac{e^{-E_{2(1)}\beta}}{e^{(-)E_1\beta} + e^{-E_2\beta}} = \frac{e^{(-)\Delta E \beta}}{1 + e^{\Delta E \beta}}, \tag{7}$$

with $\beta = 1/K_b T$.

To verify that these probabilities will work, consider the system to be in equilibrium. Then, if N_1 and N_2 are the number of spins in the up and down states, with energies E_1 and E_2, we expect the average spin, $\langle S \rangle$, to be

$$\frac{N_1 - N_2}{N_1 + N_2} = \langle S \rangle = \frac{\Sigma_{i=1}^2 S_i e^{-E_i\beta}}{\Sigma_{i=1}^2 e^{-E_i\beta}} = \frac{e^{-E_1\beta} - e^{-E_2\beta}}{e^{-E_1\beta} + e^{-E_2\beta}}. \tag{8}$$

In the Monte Carlo program equilibrium will be achieved when $N_1 P_{12} = N_2 P_{21}$. So we expect the average spin to be

$$\frac{N_1 - N_2}{N_1 + N_2} = \frac{N_1/N_2 - 1}{N_1/N_2 + 1} = \frac{P_{21}/P_{12} - 1}{P_{21}/P_{12} + 1} = \frac{e^{-E_1\beta}/e^{-E_2\beta} - 1}{e^{-E_1\beta}/e^{-E_2\beta} + 1}, \tag{9}$$

which is the same as Eq. (9).

The more difficult question is how to deal with the energy barrier E_b. For this, three logical conditions which must be satisfied are: (1) P_{1b2} (the probability a spin will flip from E_1 to E_2 with an energy barrier E_b) must be equal to P_{12} when $E_b = E_1$; (2) P_{2b1} (the probability a spin will flip from E_2 to E_1 with an energy barrier E_b) will be proportional to $e^{-E_b\beta}$ when written in the first form of Eqs. (7) and (3) the partition function $e^{-E_1\beta} + e^{-E_2\beta}$ should remain unchanged, i.e., Eq. (8) must remain true. The equations that accomplish this are

$$P_{1b2} = \frac{e^{-(E_2\beta + E_b\beta - E_1\beta)}}{e^{-E_1\beta} + e^{-E_2\beta}} = \frac{e^{\Delta E \beta}}{1 + e^{\Delta E \beta}} e^{-\Delta E_b \beta} = P_{12} e^{-\Delta E_b \beta} \tag{10}$$

and

$$P_{2b1} = \frac{e^{-E_b\beta}}{e^{-E_1\beta} + e^{-E_2\beta}} = \frac{e^{-\Delta E \beta}}{1 + e^{-\Delta E \beta}} e^{-\Delta E_b \beta} = P_{21} e^{-\Delta E_b \beta}. \tag{11}$$

This gives the very simple result that the energy barrier reduces the probability of a spin flipping by a factor $e^{-\Delta E_b \beta}$. Note also that the final equilibrium value will not change due to this barrier, only the rate of decay to equilibrium.

The results obtained from Monte Carlo simulations using the above analysis are shown in Fig. 1, plot of the normalized remnant magnetization Mn/Mo versus log (time) (actually the nth Monte Carlo step). For the upper data in this plot the interactions have been turned off and the plot is that expected for an exponential decay. In this same figure are the data generated with the same initial values, but with the dipolar couplings or interactions included. These data give a somewhat straight line until they reach a value of around 0.2 of the normalized remnant magnetization. At the lower values of Mn/Mo the energy ΔE approaches zero, changing very little from one Monte Carlo step to the next. For this reason it is not surprising to see an end to slow relaxation in this region.[8]

An important feature to note in this figure is the relative values of the magnetization with and without interactions. As

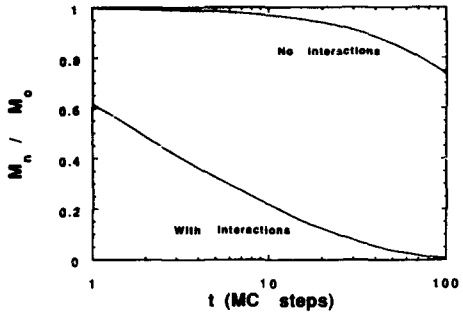

FIG. 1. A simulated decay when the dipole–dipole couplings are omitted, i.e., no interactions (upper curve) and with dipolar couplings (lower curve). For these data, $M_s=0.0005$, $K_u=0.1$, and the temperature is 200 K. Mn/Mo is the reduced magnetization at the nth Monte Carlo step. The time is in units of Monte Carlo steps. One should note the quasilogarithmic time dependence of the dipolar coupled simulation. Also, as can be seen, the coupling drives the system to its equilibrium faster than the zero coupling case.

stated before, this figure shows that the slow relaxation curve actually reaches equilibrium faster than the exponential decay curve. This is merely the consequence of the system decaying to equilibrium faster when there is a magnetic field, the demagnetization field, helping it along.

Figure 2 shows the magnetization decay at several temperatures. In actual measurements, the decay rate or slope is measured at a fixed time or over a narrow time window. This experimental limitation is the origin of the nonmonotonic temperature dependence, as discussed previously.[2,4,5] To show this, one can consider the temperature-dependent slopes at different times for these data. For example, if one

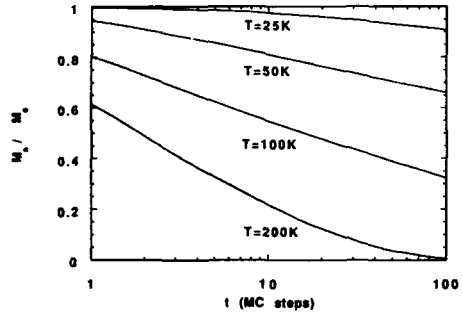

FIG. 2. Decays of the magnetization with couplings present at four different temperatures. The decay slope, although not constant for a given temperature, can be determined for each temperature at any fixed time.

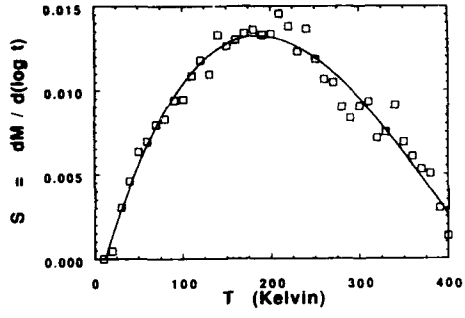

FIG. 3. The decay slope of the magnetization between log t values of 0.5 and 1 at each temperature of data similar to that in Fig. 2 are plotted against temperature. The nonmonotonic behavior of the decay slope is similar to that measured experimentally and found in the model referred to in the text.

considers the slope at a t value of 2, the slope of the curve increases (in absolute value) as the temperature increases. On the other hand, if the t is 20 when the slope is measured, the decay slope passes through a maximum at 100 K. This latter case is shown in Fig. 3. In Fig. 3 the decay slope determined between two fixed times or numbers of Monte Carlo steps is plotted versus temperature. The nonmonotonic behavior is clearly seen. A comparison of this figure with a similar plot in Ref. 5 shows the differences in the two approaches.

In summary, this work has shown that, with the proper choice for the probability defining equation, the Monte Carlo routine replicates the previous experimental and theoretical data. Although the particular algorithm developed is different from that used by other workers,[5] the results are similar. One feature of the general model[4] explicitly pointed out here is that although the model system with interactions or couplings relaxes quasilogarithmically with time, it is actually a faster relaxation than the same system without interactions.

One of the authors, EDD, would like to thank Professors Chandan Dasgupta and Oriol Valls for a number of interesting and useful conversations. This work was suported by a grant from the AFOSR (AF/FA9620-92-J-0185/P00001).

[1] D. K. Lottis, E. Dan Dahlberg, J. Christner, J. I. Lee, R. Peterson, and R. White, J. Appl. Phys. **63**, 2920 (1988).
[2] R. Street and J. C. Woolley, Proc R. Soc. London Ser. B **62**, 562 (1949).
[3] D. K. Lottis, E. D. Dahlberg, J. A. Christner, J. I. Lee, R. L. Peterson, and R. M. White, J. Phys. C **8**, 407 (1988).
[4] D. K. Lottis, R. M. White, and E. Dan Dahlberg, Phys. Rev. Lett. **67**, 362 (1991).
[5] R. W. Chantrell, A. Lyberatos, and A. Hoare, IEEE Trans. Magn. MAG-**26**, 222 (1990).
[6] A. Lyberatos, R. W. Chantrell, E. R. Sterringa, and J. C. Lodder, J. Appl. Phys. **70**, 4431 (1991).
[7] *Monte Carlo Methods in Statistical Physics*, edited by K. Binder (Springer, Berlin, 1986).
[8] J. Shore (private communication).

The Preisach model with stochastic input as a model for aftereffect

Isaak D. Mayergoyz
Department of Electrical Engineering and Institute for Advanced Computer Studies, University of Maryland, College Park, Maryland 20742

Can E. Korman
Department of Electrical Engineering and Computer Science, The George Washington University, Washington, DC 20052

In previous papers, we have suggested to use the Preisach model driven by stochastic inputs as a model for aftereffect. However, in these papers the stochastic inputs have been modeled by discrete time I.I.D. (independent identically distributed) random processes. Here, we further extend the aforementioned approach by modeling the stochastic inputs by continuous time diffusion processes. It is shown that the mathematical machinery of the "exit problem" is instrumental for calculations of time evolutions of the expected value of the output of the Preisach model.

It is well known that the physical origin of hysteresis is due to the multiplicity of metastable states. At equilibrium, large deviations of random thermal perturbations may cause a hysteretic system to move gradually from higher- to lower-energy metastable states. This phenomenon is generally referred to in the literature as "aftereffect," "viscosity," or "creep."

Traditionally, the modeling of hysteresis and viscosity has been pursued along two quite distinct lines. In phenomenological modeling of hysteresis, the Preisach approach has been prominent, while the viscosity phenomenon has been studied by using thermal activation-type models. It is desirable to develop the uniform approach to the modeling of both hysteresis and viscosity. Recently, it has been suggested to use the Preisach model driven by stochastic inputs as a model for aftereffect (see Refs. 1–3). However, in these publications, the stochastic inputs have been modeled by discrete time I.I.D. (independent identically distributed) random processes. Below, this approach is further extended by modeling the stochastic inputs by continuous time diffusion processes. From the mathematical point of view, it makes the problem much more complicated. It is shown below that these difficulties can be largely overcome by using the mathematical machinery of the "exit problem."

Consider a deterministic input $u(t)$ of the Preisach model that at time $t=0$ assumes some value u_0 and remains constant thereafter. In a purely deterministic situation, the output would remain constant for $t\geq 0$ as well. To model the aftereffect, we assume that some noise is superimposed on the constant input. In other words, we assume that the Preisach model is driven by the process

$$x_t = u_0 + X_t, \quad \bar{X}_t = 0. \tag{1}$$

The noise X_t will be modeled by a (continuous time and continuous samples) diffusion process, which is a solution to the Ito stochastic differential equation:

$$dX_t = b(X_t)dt + \sigma(X_t)dW_t. \tag{2}$$

The output f_t of the Preisach model,

$$f_t = \iint_{\alpha\geq\beta} \mu(\alpha,\beta)\hat{\gamma}_{\alpha,\beta}x_t \, d\alpha \, d\beta, \tag{3}$$

will be a random process as well, and we shall be interested in the time evolution of the expected value, $\bar{f}_t$, of this output process.

Since integration is a linear operation, from (3) we derive

$$\bar{f}_t = \iint_{\alpha\geq\beta} \mu(\alpha,\beta)E\{\hat{\gamma}_{\alpha,\beta}x_t\}d\alpha \, d\beta. \tag{4}$$

Thus, the problem is reduced to the evaluation of the expected value, $E\{\hat{\gamma}_{\alpha,\beta}x_t\}$.

Let

$$q_{\alpha,\beta}(t) = \text{Prob}\{\hat{\gamma}_{\alpha,\beta}x_t = +1\}. \tag{5}$$

Since $\hat{\gamma}_{\alpha,\beta}x_t$ may assume only two values $+1$ and -1, we find

$$E\{\hat{\gamma}_{\alpha,\beta}x_t\} = 2q_{\alpha,\beta}(t) - 1. \tag{6}$$

In this way, the problem is reduced to the calculation of $q_{\alpha,\beta}(t)$. The last quantity can be expressed in terms of switching probabilities $P_k^+(t)$ and $P_k^-(t)$, which are defined as follows:

$$P_k^+(t) = \text{Prob}\left\{\begin{matrix} k \text{ switchings of } \hat{\gamma}_{\alpha,\beta} \text{ during} \\ \text{time interval } (0,t) \end{matrix} \middle| \, \hat{\gamma}_{\alpha,\beta}x_0 = +1, \right\} \tag{7}$$

$$P_k^-(t) = \text{Prob}\left\{\begin{matrix} k \text{ switchings of } \hat{\gamma}_{\alpha,\beta} \text{ during} \\ \text{time interval } (0,t) \end{matrix} \middle| \, \hat{\gamma}_{\alpha,\beta}x_0 = -1. \right\} \tag{8}$$

By using the above switching probabilities, we derive

$$q_{\alpha,\beta}(t) = \begin{cases} \sum_{k=0}^{\infty} P_{2k}^+(t), & \text{if } \hat{\gamma}_{\alpha,\beta}x_0 = +1, \\ \sum_{k=0}^{\infty} P_{2k+1}^-(t), & \text{if } \hat{\gamma}_{\alpha,\beta}x_0 = -1. \end{cases} \tag{9}$$

The last expression is valid because occurrences of different numbers of switchings are nonintersecting (disjoint) events.

Next, we shall discuss the mechanism of switching. It is clear from Fig. 1 that the first switching occurs at the moment when the stochastic process x_t starting from the point x_0 exits the semi-infinite interval (β,∞). Then, the second switching occurs at the moment, when the process x_t starting from the point $x=\beta$ exits the semi-infinite interval $(-\infty,\alpha)$.

 0021-8979/94/75(10)/5478/3/$6.00 © 1994 American Institute of Physics

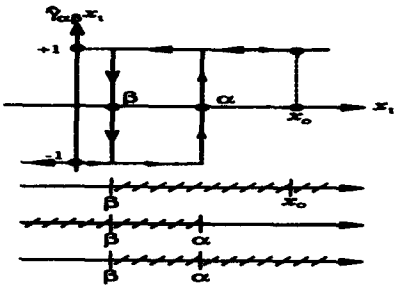

FIG. 1. Mechanism of switching.

The third switching takes place at the moment when the process x_t starting from the point $x=\alpha$ exits the semi-infinite interval (β,∞). It is apparent that the mechanism of all subsequent even switchings is identical to the mechanism of the second switching, while all subsequent odd switchings occur in the same manner as the third switching. Thus, switchings of rectangular loops $\hat{\gamma}_{\alpha,\beta}$ are closely related to the exit problems for stochastic process x_t, which can be translated into the exit problems for process X_t. This problem is one of the most studied problems in the theory of diffusion processes and the mathematical machinery developed for the solution of this problem will be utilized in the calculation of probabilities $P_k^{\pm}(t)$.

The exit problems described above can be characterized by exit times $\tau_x^{\pm}$, which are random variables. In the above notation for the exit times, subscript "x" means that process X_t starts from point x, while superscripts "$\pm$" correspond to the exits of this process at points $\alpha-u_0$ and $\beta-u_0$, respectively. Next, we introduce the functions

$$v^{\pm}(t,x)=\text{Prob}\{\tau_x^{\pm}\geq t\}, \tag{10}$$

$$V^{\pm}(t,x)=e(t)-v^{\pm}(t,x), \tag{11}$$

where $e(t)$ is a unit step function. It is clear that

$$V^{\pm}(t,x)=\text{Prob}\{\tau_x^{\pm}\leq t\}, \tag{12}$$

which means that $V^{\pm}(t,x)$ has the meaning of a cumulative distribution function for the random variable $\tau_x^{\pm}$. This, in turn, implies that

$$\rho^{\pm}(t,x)=\frac{\partial V^{\pm}(t,x)}{\partial t} \tag{13}$$

is the probability density function for the random variable $\tau_x^{\pm}$.

It is apparent from (11)–(13) that $\rho^{\pm}(t,x)$ can be easily computed if $v^{\pm}(t,x)$ are somehow found. It turns out (and this is a well-known result from the theory of stochastic processes) that $v^{\pm}(t,x)$ is the solution to the following initial-boundary value problem for the backward Kolmogorov equation:

$$\frac{\partial v^{\pm}}{\partial t}=\frac{\sigma^2(x)}{2}\frac{\partial^2 v^{\pm}}{\partial x^2}+b(x)\frac{\partial v^{\pm}}{\partial x}, \tag{14}$$

$$v(0,x)=1, \quad v(t,c^{\pm})=0, \tag{15}$$

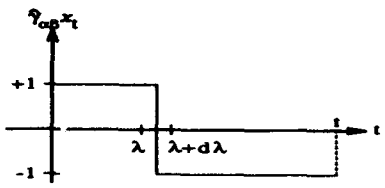

FIG. 2. Occurrence of exactly one downward switching.

where $c^{\pm}$ are the exit points for the process X_t, which are equal to $\alpha-u_0$ and $\beta-u_0$, respectively.

Next, we shall show that switching probabilities $P_k^{\pm}(t)$ can be expressed in terms of $v^{\pm}(t,x)$ and $\rho^{\pm}(t,x)$. Note that, according to (11)–(13), $\rho^{\pm}(t,x)$ are related to $v^{\pm}(t,x)$ as follows:

$$\rho^{\pm}(t,x)=\frac{\partial}{\partial t}\,[e(t)-v^{\pm}(t,x)]. \tag{16}$$

It is clear from the very definition of $v^{\pm}(t,x)$ that

$$P_0^{\pm}(t)=v^{\pm}(t,0). \tag{17}$$

It is apparent from Fig. 2 that the occurrence of exactly one downward switching is the union of the following disjoint elementary events: downward switching occurs in the time interval $(\lambda,\lambda+d\lambda)$, and then no upward switching occurs up to the time t. Due to the strong Markov property of X_t, the probability of the above elementary event is given by

$$\rho^{-}(\lambda,0)v^{+}(t-\lambda,\beta-u_0)d\lambda. \tag{18}$$

Now, the probability $P_1^{+}(t)$ of exactly one downward switching can be found by integrating (18) from 0 to t:

$$P_1^{+}(t)=\int_0^t \rho^{-}(\lambda,0)v^{+}(t-\lambda,\beta-u_0)d\lambda. \tag{19}$$

In other words, $P_1^{+}(t)$ is the convolution of $\rho^{-}(t,0)$ and $v^{+}(t,\beta-u_0)$:

$$P_1^{+}(t)=\rho^{-}(t,0)*v^{+}(t,\beta-u_0). \tag{20}$$

By using similar reasoning, we can derive

$$P_1^{-}(t)=\rho^{+}(t,0)*v^{-}(t,\alpha-u_0). \tag{21}$$

Next, consider the probability $P_2^{+}(t)$ of the occurrence of exactly two switchings, starting from the initial state $\hat{\gamma}_{\alpha\beta}x_0=1$. According to Fig. 3, this occurrence can be considered as the union of the following disjoint elementary

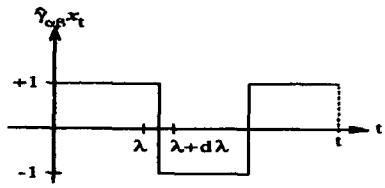

FIG. 3. Occurrence of exactly two switchings.

events: downward switching occurs in the time interval $(\lambda,\lambda+d\lambda)$, and then exactly one upward switching occurs up to the time t. The probability of these elementary events is given by

$$\rho^-(\lambda,0)P_1^-(t-\lambda)d\lambda. \tag{22}$$

Now, by integrating (22), we find

$$P_2^+(t)=\int_0^t \rho^-(\lambda,0)P_1^-(t-\lambda)d\lambda. \tag{23}$$

From (21) and (23), we obtain

$$P_2^+(t)=\rho^-(t,0)*\rho^+(t,\beta-u_0)*v^-(t,\alpha-u_0). \tag{24}$$

By using the same line of reasoning, we derive

$$P_2^-(t)=\rho^+(t,0)*\rho^-(t,\alpha-u_0)*v^+(t,\beta-u_0). \tag{25}$$

For the sake of conciseness, we introduce the notations

$$\rho^\pm(t,0)=\rho_0^\pm(t),\quad \rho^+(t,\beta-u_0)=\rho^+(t),$$
$$\rho^-(t,\alpha-u_0)=\rho^-(t), \tag{26}$$

$$v^\pm(t,0)=v_0^\pm(t),\quad v^+(t,\beta-u_0)=v^+(t),$$
$$v^-(t,\alpha-u_0)=v^-(t). \tag{27}$$

Now, by using the same line of reasoning as before and the induction argument, we can easily derive the following expressions for the switching probabilities:

$$P_{2k}^+(t,u_0)=\rho_0^-(t)*\rho^+(t)*\overbrace{\rho^-(t)*\cdots*\rho^-(t)*\rho^+(t)}^{2k-2\ \text{terms}}*v^-(t), \tag{28}$$

$$P_{2k+1}^-(t,u_0)$$
$$=\rho_0^+(t)*\overbrace{\rho^-(t)*\rho^+(t)*\cdots*\rho^-(t)*\rho^+(t)}^{2k\ \text{terms}}*v^-(t). \tag{29}$$

By substituting (28) and (29) into (9), we obtain the expression for $q_{\alpha\beta}(t)$ in terms of an infinite series of iterated convolutions. These series can be reduced to geometric ones by employing Laplace transforms:

$$\tilde\rho(s)=\int_0^\infty \rho(t)e^{-st}\,dt \quad (\mathrm{Re}\ s>0), \tag{30}$$

$$\tilde v(s)=\int_0^\infty v(s)e^{-st}\,dt. \tag{31}$$

It is clear that

$$|\tilde\rho(s)|<1. \tag{32}$$

By using these Laplace transforms, from (17), (28), and (29), we obtain

$$\tilde P_0^\pm(s)=\tilde v_0^\pm(s), \tag{33}$$

$$\tilde P_{2k}^+(s)=\tilde\rho_0^-(s)\tilde\rho^+(s)\tilde v^-(s)[\tilde\rho^-(s)\tilde\rho^+(s)]^{k-1}, \tag{34}$$

$$\tilde P_{2k+1}^-(s)=\tilde\rho_0^+(s)\tilde v^-(s)[\tilde\rho^-(s)\tilde\rho^+(s)]^k. \tag{35}$$

From (35) and (9), we derive

$$\tilde q_{\alpha\beta}(s)=\frac{\tilde\rho_0^+(s)\tilde v^-(s)}{1-\tilde\rho^-(s)\tilde\rho^+(s)},\quad \text{if } \hat\gamma_{\alpha\beta}x_0=-1. \tag{36}$$

A similar expression can be derived for the case $\hat\gamma_{\alpha\beta}x_0=+1$.

According to (16),

$$\tilde\rho^\pm(s)=1-s\tilde v^\pm(s). \tag{37}$$

Thus, the problem of computing $\tilde q_{\alpha\beta}$ is reduced to the problem of determining $\tilde v^\pm(s)$. This can be accomplished by using the initial-boundary value problem (14)–(15). The complexity of this task will depend on the nature of the stochastic process X_t that models the noise in hysteretic systems. It is natural to require that the stochastic process that models the noise must be a stationary Gaussian Markov process. According to the Doob theorem, the only process that satisfies these requirements is the Ornstein–Uhlenbeck process. This process is the solution to the following Ito stochastic differential equation:

$$dX_t=-bX_t\,dt+\sigma\,dW_t, \tag{38}$$

where $1/b$ has the meaning of the correlation time. (This means that X_t and $X_{t'}$ are only significantly correlated if $|t-t'|\leq 1/b$.)

The backward Kolmogorov equation for the Ornstein–Uhlenbeck process has the form

$$\frac{\partial v^\pm}{\partial t}=\frac{\sigma^2}{2}\frac{\partial^2 v^\pm}{\partial x^2}-bx\frac{\partial v^\pm}{\partial x}. \tag{39}$$

This equation should be considered jointly with initial and boundary conditions (15). By applying the Laplace transform to (39) and (15), we arrive at the following boundary value problem for $\tilde v^\pm(s)$:

$$\frac{\sigma^2}{2}\frac{d^2\tilde v^\pm(s,x)}{dx^2}-bx\frac{d\tilde v^\pm(s,x)}{dx}-s\tilde v^\pm(s,x)=-1, \tag{40}$$

$$\tilde v^\pm(s,c^\pm)=0,\quad v^\pm(s,\infty)=1/s. \tag{41}$$

The solution to the boundary value problem (40)–(41) can be written in the form

$$\tilde v^\pm(s,x)=\frac{1}{s}\left(1-e^{[x^2-(c^\pm)^2]/4\lambda^2}\frac{\mathscr{D}_{-s/b}(x/\lambda)}{\mathscr{D}_{-s/b}(c^\pm/\lambda)}\right), \tag{42}$$

where $\mathscr{D}_{-s/b}(x/\lambda)$ are parabolic cylinder functions, while

$$\lambda=\sigma/\sqrt{2b}.$$

Expressions (36), (37), and (42) jointly with (4) and (6) outline the main steps of the solution of the problem posed in this paper.

ACKNOWLEDGMENT

This work was supported by the U.S. Department of Energy, Engineering Research Program.

[1] I. D. Mayergoyz and C. E. Korman, J. Appl. Phys. **69**, 2128 (1991).
[2] I. D. Mayergoyz and C. E. Korman, IEEE Trans. Magn. **27**, 4766 (1991).
[3] I. D. Mayergoyz, *Mathematical Models of Hysteresis* (Springer, New York, 1991).

The measurement of irreversible magnetization and activation volumes

R. Cammarano
Department of Mechanical and Materials Engineering, University of Western Australia, Nedlands 6009, W. A. Australia

P. G. McCormick
Department of Mechanical and Materials Engineering, University of Western Australia, Nedlands 6009, W. A. Australia

R. Street
Department of Physics, University of Western Australia, Nedlands 6009, W. A. Australia

The phenomenological model of magnetization kinetics developed by Estrin *et al.* [J. Phys. 1, 4845 (1989)] yields a macroscopic magnetic equation of state or magnetic constitutive equation of functional form $\mu_0 H = f(J_{irr}, \dot{J}_{irr})$, where, $\mu_0 H$ is the internal magnetic field, J_{irr} is the irreversible magnetic polarization and $\dot{J}_{irr}$ its time derivative. In differential form the relation takes the form $dH = (1/\chi_{irr})dJ_{irr} + \Lambda d(\ln \dot{J}_{irr})$. The quantity Λ is related to the activation volume involved in the process of irreversible magnetization. To obtain Λ, three different experimental techniques are used. One involves the traversal of hysteresis loops at constant $\dot{J}_{irr}$, from which both χ_{irr} and Λ can be obtained most directly, using a modified version of a technique previously described.[2] The second method involves traversing the hysteresis loop at constant $\mu_0 H$, and subsequently separating the reversible and irreversible components of magnetization. In the third method, the parameter Λ is obtained from magnetic viscosity measurements, which is the technique most commonly used. Results are presented for all three experimental techniques for measurements performed on Alnico-type permanent magnets. The limitations of each method will be reviewed in relation to materials properties.

I. INTRODUCTION

The magnetic state of a ferromagnet may be described by a constitutive equation of functional form $\mu_0 H = f(\dot{J}, J)$, where $\mu_0 H$ is the internal magnetic field intensity. In differential notation the relation takes the form $\mu_0 H = (1/\chi_{irr})dJ_{irr} + \Lambda d(\ln \dot{J}_{irr})$. J_{irr} is the irreversible magnetic polarization, $\dot{J}_{irr}$ is its time derivative, and χ_{irr} is the irreversible susceptibility given by $1/\chi_{irr} = \mu_0(\partial H/\partial J_{irr})|_{\dot{J}_{irr}}$ and Λ is related to the activation volume involved in the process of irreversible magnetization,[1] defined by

$$\Lambda = \mu_0 \left(\frac{\partial H}{\partial(\ln \dot{J}_{irr})} \right) \Bigg|_{J_{irr}} . \tag{1}$$

Various techniques and models used to describe irreversible and reversible magnetization (and susceptibility) have been discussed in the literature.[2] In this work, a general experimental technique for the separation of reversible and irreversible magnetization has been developed. The technique is phenomenologically based, with no specific assumptions about magnetization processes. The measurement techniques described below have been developed in order to verify the validity of the magnetic constitutive equation, and in particular to determine and compare the values of Λ obtained using different methods.

II. EXPERIMENT

A permeameter system was developed to enable the majority of a hysteresis loop to be traversed while maintaining $\dot{J}_{irr}$ constant.[2,3] Two Alnico permanent magnet materials were examined. Sample 1 (S1) was an isotropic specimen of Alnico 7. Sample 2 (S2) was an anisotropic specimen of Alnico 5DG measured along its easy axis.

For the constant $\dot{J}_{irr}$ experiments, several assumptions were made about the relative proportions of J_{rev} and J_{irr} and about the measurement of J_{rev}; (i) For S2, the approximation $J_{irr} \sim J$ (and $\dot{J}_{irr} \sim \dot{J}$) was made, due to the relatively small proportion of J_{rev} compared to J over the majority of the hysteresis loop; (ii) assumption (i) could not be applied to S1 because of the relatively large proportion of J_{rev} compared to J. A simple estimate of J_{rev} was used. In this method it is postulated that the reversible susceptibility χ_{rev}, and therefore J_{rev}, is a function of only the magnetic field at which χ_{rev} is measured. By measuring χ_{rev} around a major hysteresis loop, J_{rev} at a given value of $\mu_0 H$ could be obtained by

$$J_{rev}(\mu_0 H) = J_{rev}(\mu_0 H_0) + \mu_0 \int_{\mu_0 H_0}^{\mu_0 H} \chi_{rev}\, dH, \tag{2}$$

where $J_{rev}(\mu_0 H_0)$ is usually (arbitrarily) chosen to be identically zero at the maximum applied field, $\mu_0 H_0 = -\mu_0 H_{max}$. It is therefore possible to separate J_{irr} from J through $J = J_{irr} + J_{rev}$, which facilitates the measurement of hysteresis loops while maintaining $\dot{J}_{irr}$ constant.

In general, the reversible magnetization is not only dependent on the applied field, but also on the domain configuration. The reversible magnetization may be expressed phenomenologically as[2] $J_{rev} = J_{rev}(\mu_0 H, J_{irr})$ or, in differential form, $dJ_{rev} = \chi^*_{rev}\mu_0\, dH + \eta\, dJ_{irr}$, where $\chi^*_{rev} = (\partial J_{rev}/\mu_0\, \partial H)|_{J_{irr}}$ and $\eta = (\partial J_{rev}/\partial J_{irr})|_{\mu_0 H}$. In most studies of reversible magnetization, the η term is neglected, since it cannot be measured directly from a single hysteresis loop. The measurements are fully described by Cammarano.[2]

 0021-8979/94/75(10)/5481/3/$6.00 © 1994 American Institute of Physics

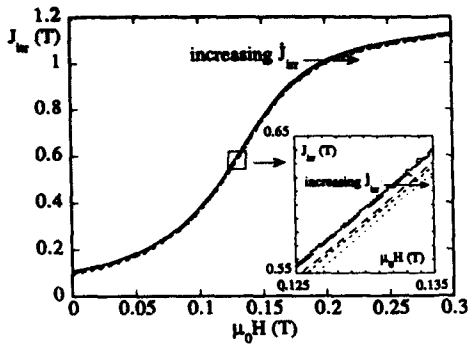

FIG. 1. J_{irr} vs $\mu_0 H$ magnetization curves for S1 measured with $\dot{J}_{irr}$=0.0317, 0.0635, 0.159, 0.317, and 0.635 T/s, from constant $\dot{J}_{irr}$ experiments. The inset shows detail around the coercive point, taken as J_{irr}=0.58 T.

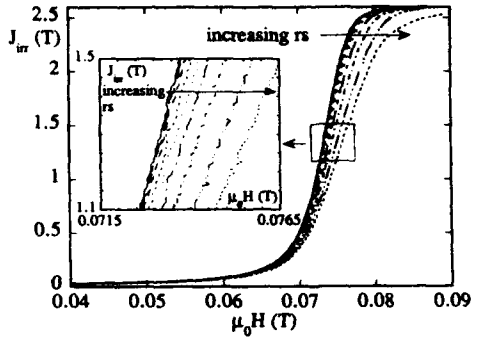

FIG. 2. J_{irr} vs $\mu_0 H$ magnetization curves for S2, derived from ramped field experiments, with rs=0.0005, 0.001, 0.002, 0.004, 0.008, 0.015, 0.03, 0.06, and 0.1 T/s. The inset shows detail around the coercive point, taken as J_{irr}=1.4 T.

With a functional form for $J_{rev}=J_{rev}(\mu_0 H,J_{irr})$, it was possible to extract $(J_{irr},\mu_0 H)$ data from experimental $(J,\mu_0 H)$ data for any major hysteresis loop measured with an arbitrary monotonic magnetic field waveform. For simplicity, the hysteresis loop was measured by using different slopes (rs) for a linear ramp. For $-\mu_0 H_{max}\leq\mu_0 H\leq 0$ (experiments always commenced at $-\mu_0 H_{max}$), (2) was used to obtain $(J_{irr},\mu_0 H)$ data, simply, in a closed form solution. For $0<\mu_0 H\leq\mu_0 H_{max}$, an iterative procedure was devised,[2] since J_{irr} was not known *a priori* to calculate $J_{rev}=J_{rev}(\mu_0 H,J_{irr})$. With a set of $(J_{irr},\mu_0 H)$ magnetization curves measured at different rates (either constant J_{irr} or constant rs) it is then possible to plot graphs of $\mu_0 H$ vs $\ln \dot{J}_{irr}$ taken at constant J_{irr}, for different values of J_{irr}. The slope of these curves is then equivalent to Λ (1). In the case of the constant rs experiments, the value of $\dot{J}_{irr}$ was calculated by performing a linear extrapolation about the given value of J_{irr}.

The third method of calculating the parameter Λ is based on the magnetic viscosity experiment.[4] Magnetization curves of $(J_{irr},\mu_0 H)$ at constant $\dot{J}_{irr}$ can be derived from the magnetic viscosity data, as explained by Street *et al.*,[5] from which Λ is calculated. The tests were conducted on polished spheres of 5 mm diam using a computer controlled Vibrating Sample Magnetometer (VSM) with a 5 T superconducting solenoid.

III. RESULTS

Examples of irreversible magnetization curves are shown in Figs. 1 and 2 for S1 and S2, respectively. Note that only half the hysteresis loops are shown and that J_{irr} was arbitrarily set to zero at $-\mu_0 H_{max}$. Also, if the intrinsic coercivity ${}_JH_c$ is defined as the value of field at which J_{irr} is half the maximum value, the intrinsic coercivity of S1 occurs at $J_{irr}\approx$0.58 T and for S2 at $J_{irr}\approx$1.4 T. ${}_JH_c$ increases with increasing magnetization rate, as would be expected. Figure 1 shows data taken from constant $\dot{J}_{irr}$ experiments for S1. In Fig. 2 results from ramped field experiments on S2 are shown. In both cases, the results are consistent, showing increased hysteresis with increasing magnetization rate.

An example of a graph of $\mu_0 H$ as a function of $\ln \dot{J}_{irr}$ at constant J_{irr} is shown in Fig. 3, taken from constant $\dot{J}_{irr}$ experiments performed on S2. The majority of results showed a similar nonlinear functional form. Similar plots taken from magnetic viscosity experiments showed a definite linear relationship between $\mu_0 H$ and $\ln \dot{J}_{irr}$ at constant J_{irr}. It was for this reason that Λ was estimated as the slope of the straight line fit using the lower values of $\ln \dot{J}_{irr}$. For the constant $\dot{J}_{irr}$ experiments on S1, Λ was estimated as the slope of the line of best fit using the whole range of $\dot{J}_{irr}$ shown in Fig. 1 [Fig. 4(a)]. Figures 4(b) and 4(c) show the Λ calculated from ramped field experiments using, respectively, the five and four lowest values of $\ln \dot{J}_{irr}$. A similar range in $\ln \dot{J}_{irr}$ was used in calculating Figs. 4(a) and 4(b).

The quantity Λ derived for S2 is shown in Fig. 5(a) for the constant $\dot{J}_{irr}$ experiments and Fig. 5(b) for the ramped field experiments. A similar range in $\ln \dot{J}_{irr}$ was used to determine Λ for both sets of results. Λ was calculated using, respectively, the four and three lowest values of $\ln \dot{J}_{irr}$ for

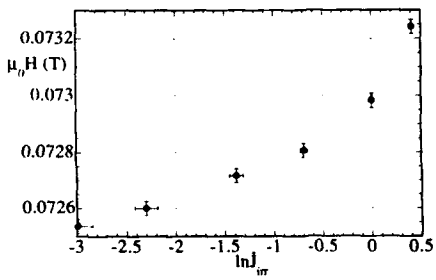

FIG. 3. $\mu_0 H$ vs $\ln \dot{J}_{irr}$ at constant J_{irr} from constant $\dot{J}_{irr}$ experiments for the anisotropic Alnico (S2) at J_{irr}=1.208 T, close to the coercive point. Error bars are shown.

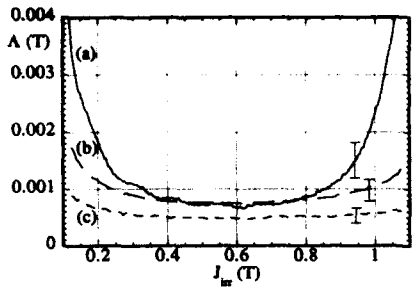

FIG. 4. Λ vs J_{irr} for S1 from (a) constant $\dot{J}_{irr}$ experiments, using the whole range of $\ln \dot{J}_{irr}$ shown in Fig. 1, (b) and (c) ramped field experiments using, respectively, the five and four lowest values of $\ln \dot{J}_{irr}$ to calculate Λ. Average error bars are shown.

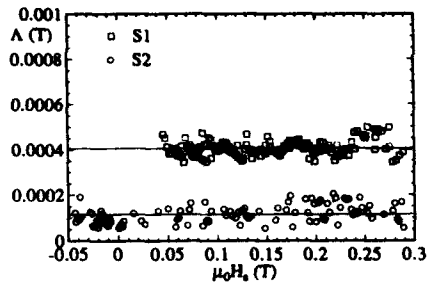

FIG. 6. Λ vs $\mu_0 H_a$, the external applied field at which a magnetic viscosity test was conducted, for both S1 and S2. The line drawn through each set of data represents the average value of Λ.

Figs. 5(a) and 5(b). Figure 6 shows Λ obtained from magnetic viscosity experiments. It should be noted that Λ is plotted as a function of the external applied field $\mu_0 H_a$, at which the viscosity test was performed, for convenience. The −0.05–0.3 T span in $\mu_0 H_a$ corresponds to a range in $\mu_0 H$ of about 0–0.18 T for S1 and about 0.066–0.086 T for S2.

IV. DISCUSSION

From Fig. 4(c), for S1 over the majority of the magnetization curve, Λ is almost constant with an average value of 0.55 mT.

The greatest deviation from constancy occurs at both high [also note Figs. 4(a) and 4(b)] and low values of J_{irr}, regions in which reversible magnetization processes predominate, and thus errors in J_{irr} (and $\dot{J}_{irr}$) are the greatest. This should be compared to the average value obtained from magnetic viscosity experiments of 0.41 mT (Fig. 6). The values of $\dot{J}_{irr}$ used for the calculation of Λ from magnetic viscosity experiments were three to six orders of magnitude lower than those used for the calculation of Λ from either constant $\dot{J}_{irr}$ or ramped field experiments. It is likely that extrapolation of the latter data to lower values of $\dot{J}_{irr}$ would result in a lower value of Λ. In any case, considering the scatter in both sets of results, there is reasonable agreement between the two values of Λ obtained from the two totally disparate experimental techniques, reinforcing the validity of using the magnetic constitutive relation for analyzing time-dependent magnetization. Also, the greatest errors in the estimation of Λ will occur in materials in which the reversible component of magnetization is a relatively large proportion of the total magnetization, as was the case for the isotropic S1.[2]

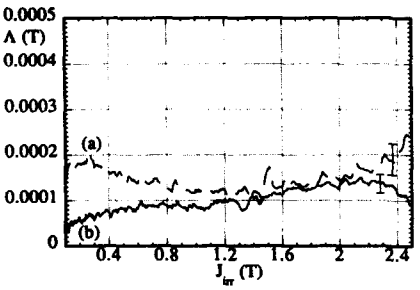

FIG. 5. Λ vs J_{irr} for S2 from (a) constant $\dot{J}_{irr}$ experiments, using the four lowest values of $\ln \dot{J}_{irr}$ to calculate Λ and (b) ramped field experiments, using the three lowest values of $\ln \dot{J}_{irr}$ of the data shown in Fig. 2. Average error bars are shown.

For S2, Fig. 5(b) shows a median value of Λ of about 0.10 mT. Comparing this value of Λ with that obtained from magnetic viscosity experiments (see Fig. 6, noting the scatter in the results) and from constant $\dot{J}_{irr}$ experiments [Fig. 5(a)] of 0.12 mT, the agreement is good. These values of Λ are in excellent agreement with previously published results on similar Alnico permanent magnet materials.[4]

The experimentally derived estimate of Λ will, in general, be dependent on the range and magnitude of $\ln \dot{J}_{irr}$ used to calculate the slope of the $\mu_0 H$ vs $\ln \dot{J}_{irr}$ curve at constant J_{irr}, which is equivalent to Λ. This study has emphasized the need for examining plots of $\mu_0 H$ vs $\ln \dot{J}_{irr}$ at constant J_{irr} to obtain Λ. In general, Λ is a function of both $\mu_0 H$ and J_{irr}. The magnetic constitutive relation suggests that it is more appropriate to analyze Λ as a function of J_{irr}, where Λ is determined over a limited range of $\dot{J}_{irr}$, than to plot Λ vs $\mu_0 H$. This is particularly significant if the plot of $\mu_0 H$ vs $\ln \dot{J}_{irr}$ at constant J_{irr} is nonlinear, as was the case in this work.

ACKNOWLEDGMENTS

One of the authors (R.C.) would like to thank Jody Simpson for all her support, Tony Cammarano, Director, Better Mobile Mechanics, and Professor D. Kepert, Director, RCAMMP for providing partial funding for this work.

[1] Y. Estrin, P. G. McCormick, and R. Street, J. Phys. I, 4845 (1989).
[2] R. Cammarano, Ph.D. thesis, University of Western Australia, 1993.
[3] R. Cammarano, R. Street, P. G. McCormick, and M. E. Evans, J. Appl. Phys. 69, 5100 (1991).
[4] R. Street and J. C. Woolley, Proc. Phys. Soc. A 62, 562 (1949).
[5] R. Street, P. G. McCormick, and L. Folks, J. Magn. Magn. Mater. 104–107, 368 (1992).

A phenomenological differential-relation-based vector hysteresis model

A. Bergqvist
Electric Power Engineering, Royal Institute of Technology, S-10044, Stockholm, Sweden

G. Engdahl
Power Engineering, ABB Corporate Research, S-72178, Västerås, Sweden

A phenomenological inherently vector hysteresis model employing simple differentials as a means of keeping track of the past history of the magnetic field is proposed. This results in a simple and computationally fairly efficient formulation for vector hysteresis of any dimension. An expression for determining model parameters from experimental data or from the Preisach function is given. The model exhibits rotational hysteresis and reduction of remanent magnetization by an orthogonal field and reduces to the classical Preisach model in one dimension. Details concerning the numerical implementation are discussed and computational examples demonstrating model properties are presented.

I. INTRODUCTION

Magnetic vector hysteresis models are usually constructed as superpositions of what is sometimes called relay hysteresis operators. A relay operator here means an operator that changes its value reversibly, unless the input field leaves a given region at which point irreversible discontinuous switching may occur, depending on the present state of the operator. Examples are the Stoner–Wohlfarth model[1] and various types of vector Preisach models; see Refs. 2–5, among others. This work is concerned with representing a complex hysteresis operator by using a set of simple hysteresis operators that are instead defined by an irreversible differential relation.

II. MODEL FORMULATION

As the starting point for the model we use the irreversible differential relation,

$$d\boldsymbol{\eta}=\begin{cases}(1/r^2)[(\mathbf{H}-\boldsymbol{\eta})\cdot d\mathbf{H}](\mathbf{H}-\boldsymbol{\eta}), & \text{if } (\mathbf{H}-\boldsymbol{\eta})\cdot d\mathbf{H}>0 \text{ and } (\mathbf{H}-\boldsymbol{\eta})^2=r^2,\\ 0, & \text{otherwise,}\end{cases} \tag{1}$$

where we also require that initially $|\mathbf{H}-\boldsymbol{\eta}|\leq r$. Here $\mathbf{H}$ is the vector magnetic field, r is some positive scalar constant, and $\boldsymbol{\eta}$ is an output vector.

Differential relations similar to (1), but usually more complex, are often used in solid mechanics to describe plastic stress–strain relations (where they are not usually referred to as hysteresis models; in mechanics, the convention is to reserve the term hysteresis for cyclic processes). More precisely, (1) is mathematically equivalent to a simple case of classical plasticity theory with linear kinematic hardening and a von Mieses yield criterion; cf. Ref. 6.

The relation between $\mathbf{H}$ and $\boldsymbol{\eta}$ can be interpreted as follows: If $\mathbf{H}$ lies at a distance r from $\boldsymbol{\eta}$ and moves in a direction away from $\boldsymbol{\eta}$, $\boldsymbol{\eta}$ will be dragged toward $\mathbf{H}$ and remain at a distance r. Otherwise $\boldsymbol{\eta}$ will not change. To visualize this, we can imagine $\mathbf{H}$ and $\boldsymbol{\eta}$ as being connected by a string of length r. Thus, $\boldsymbol{\eta}$ is quite literally lagging behind $\mathbf{H}$ and depends on the past history of $\mathbf{H}(t)$. From this analogy it is obvious that we always have $|\mathbf{H}(t)-\boldsymbol{\eta}(t)|\leq r$. In one dimension, this is identical to the so-called "play" operator P_r illustrated in Fig. 1. The full vector relation will be referred to as a "lag" operator and denoted L_r, i.e.,

$$\boldsymbol{\eta}(t)=L_r[\mathbf{H}](t), \tag{2}$$

is by definition equivalent to (1).

This simple case of vector hysteresis has some interesting properties. For instance, if $\mathbf{H}$ at some time is restrained to vary along one arbitrary direction and increases indefinitely, then the orthogonal component of $L_r[\mathbf{H}](t)$ will be asymptotically reduced to zero. This recalls the well-known fact that, if $\mathbf{H}$ increases indefinitely along an easy axis, the orthogonal component of the magnetization will be reduced to zero.[2,3,5] If, on the other hand, $\mathbf{H}$ is uniformly rotating, then $L_r[\mathbf{H}](t)$ will asymptotically approach a uniformly rotating vector lagging behind $\mathbf{H}$, provided the field magnitude is larger than r. The lag angle goes to zero if the field magni-

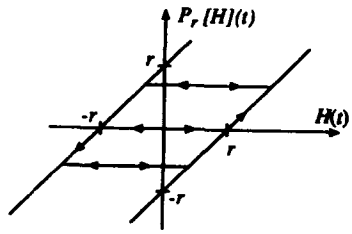

FIG. 1. Illustration of the play hysteresis operator.

 0021-8979/94/75(10)/5484/3/$6.00 © 1994 American Institute of Physics

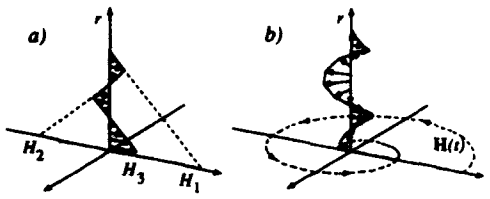

FIG. 2. Illustration of L_r operator states for two types of field variation.

tude goes to infinity. Thus the operator exhibits rotational hysteresis. Both these properties can be shown by solving (1) analytically which takes some work, and they are also intuitively quite natural.

To evaluate the magnetization M, we postulate, relating it to the set of all lag operators, $r \geq 0$, through the formula

$$\mathbf{M}(t)=\int_0^\infty \mathbf{q}(L_r[\mathbf{H}](t),r)dr. \tag{3}$$

Here the function q depends on the material and should be adjusted to fit experimental data. One reason for this particular choice of expression for the magnetization is that for fields restrained to one direction, the model will be equivalent to the classical Preisach model (CPM). This can be shown by representing the CPM with play operators as[7]

$$M(t)=\int_0^\infty q(P_r[H](t),r)dr. \tag{4}$$

Here $q(\eta,r)$ is given by

$$q(\eta,r)=4\int_0^\eta \mu(R+r,R-r)dR, \tag{5}$$

where $\mu(\alpha,\beta)$ is the Preisach distribution function used in the conventional representation of the CPM,[2] and α and β are up and down switching values of elementary rectangular loops. Since L_r reduces to P_r in one dimension, it is obvious that (3) is equivalent to (4) in the one-dimensional case.

The CPM is associated with a well-known geometric interpretation of how the past history is accumulated.[2] Here it similarly holds for fields restrained to one direction that the state of the lag operators can be collectively illustrated by a staircase function with the individual links corresponding to local field extrema; see Fig. 2(a). A case where instead the field is rotating with a decreasing amplitude is shown in Fig. 2(b). The past history of H is reflected in some manner in the collective state of the lag operators; however, it is, at present, uncertain exactly what information can be extracted from such a diagram.

The expression for the magnetization inherits some basic properties of the individual operators. If a remanent magnetization has been induced by a past field value in one direction y, it can be reduced by applying a large field in the orthogonal direction x. This result follows readily from the fact that under such circumstances, the y component of all operator values will be asymptotically reduced to zero, regardless of past history. If for an isotropic material, H is uniformly rotating, then M will asymptotically approach a state, where it can be separated into two components; one that is constant and depends on the history of H prior to the rotation, and one that is uniformly rotating and lagging behind H. This is very similar to the behavior proved for some vector Preisach models,[2] except that in those models the output becomes periodic in finite time. The fact that in this model M, like the individual lag operators, may become periodic only asymptotically for a periodic input, makes it hard to see how the model could be expressed by relay operators. It is remarkable that the lag operator, despite being a very simple and mundane case of vector hysteresis, cannot be represented by vector Preisach models.

A procedure for determining the function $\mathbf{q}(\boldsymbol{\eta},r)$ from experimental data will be given. The reduction to the CPM for fields restrained to one direction, permits us to draw on what is known concerning the identification problem in that model. Let $\hat{\mathbf{v}}$ denote the unity vector in some arbitrary direction and define $\mathbf{M}^-(H_1,H_2,\hat{\mathbf{v}}), H_1 \geq H_2$, as the magnetization value we get, if the field is restrained to vary along direction $\hat{\mathbf{v}}$ and goes from negative saturation to H_1 and then to H_2. In analogy with the standard formula for the Preisach function,[2] we define a function $\boldsymbol{\mu}(\alpha,\beta,\hat{\mathbf{v}})$ from

$$\boldsymbol{\mu}(H_1,H_2,\hat{\mathbf{v}})=\frac{1}{2}\frac{\partial^2\mathbf{M}^-(H_1,H_2,\hat{\mathbf{v}})}{\partial H_1\,\partial H_2}. \tag{6}$$

This is the function that would be used for a scalar CPM restrained to direction $\hat{\mathbf{v}}$, except that here it is vector valued to account for nonaligned H and M due to anisotropy. In analogy with (4), $\mathbf{q}(\boldsymbol{\eta},r)$ is given by

$$\mathbf{q}(\boldsymbol{\eta},r)=4\int_0^{|\boldsymbol{\eta}|}\boldsymbol{\mu}(R+r,R-r,\boldsymbol{\eta}/|\boldsymbol{\eta}|)dR. \tag{7}$$

Thus $\mathbf{q}(\boldsymbol{\eta},r)$ can be determined by measuring first-order reversal curves in all directions, evaluating $\boldsymbol{\mu}(\alpha,\beta,\hat{\mathbf{v}})$ from (6) and then using (7). For isotropic materials, one can show that $\mathbf{q}(\boldsymbol{\eta},r)=(\boldsymbol{\eta}/|\boldsymbol{\eta}|)\times|\mathbf{q}(|\boldsymbol{\eta}|,r)|$ and, of course, in such a case, measurements only have to be taken in one direction.

Of special interest is the factorization $\mathbf{q}(\boldsymbol{\eta},r)=\mathbf{p}(\boldsymbol{\eta})z(r)$. The anhysteretic state for a given H is often assumed to be achieved by superimposing a symmetrical AC field with slowly decreasing amplitude. It can be shown, by, for instance, using conventional Preisach diagrams, that at this

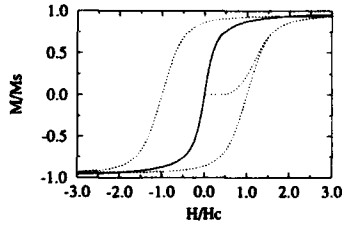

FIG. 3. Anhysteretic curve (solid), virgin curve, and major loop (dotted) for the computational example.

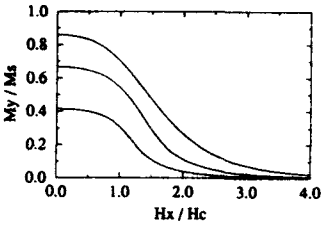

FIG. 4. Reduction of remanent magnetization by orthogonal field. The remanence was caused by applying and removing a field of $1.2H_c$, $1.5H_c$, and $3H_c$, respectively.

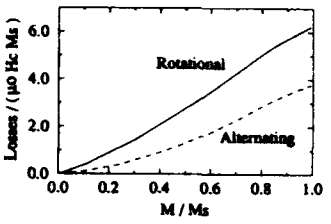

FIG. 5. Normalized rotational and alternating losses vs flux density amplitude.

state $L_r[\mathbf{H}](t)=\mathbf{H}(t)$ for all r. Substitution into (3) yields that $\mathbf{p}(\mathbf{H})$ is equal to the anhysteretic magnetization if $z(r)$ is normalized.

In a numerical implementation we use a finite number N of lag operators and approximate (3) by

$$\mathbf{M}(t_k)=\sum_{j=1}^{N} \mathbf{q}(\boldsymbol{\eta}_{j,k},r_j)\Delta r_j, \tag{8}$$

where $\boldsymbol{\eta}_{j,k}\equiv L_{r_j}[\mathbf{H}](t_k)$. Equation (1) involves an integration in time for each operator. Due to the irregular nature of (1), conventional time-stepping schemes, such as Euler forward or Euler backward, have been found inaccurate or unstable. Instead, the following algorithm has proved effective: Suppose that $\boldsymbol{\eta}_{j,k-1}$ and $\mathbf{H}_k\equiv\mathbf{H}(t_k)$ are known, and that $\boldsymbol{\eta}_{j,k}$ is sought. If for a given r_j, $|\mathbf{H}_k-\boldsymbol{\eta}_{j,k-1}]\leqslant r_j$, then the operator value has not changed since t_{k-1}. If, on the other hand, $|\mathbf{H}_k-\boldsymbol{\eta}_{j,k-1}]>r_j$, it means that $\boldsymbol{\eta}_j$ has been dragged toward $\mathbf{H}$ during (t_{k-1},t_k) and should lie at a distance r_j from $\mathbf{H}_k$, i.e., $|\mathbf{H}_k-\boldsymbol{\eta}_{j,k}|=r_j$. As an approximation for the direction the operator has been moved in, we use $(\mathbf{H}_k-\boldsymbol{\eta}_{j,k-1})$. This yields

$$\boldsymbol{\eta}_{j,k}=\begin{cases}\boldsymbol{\eta}_{j,k-1}+(1-r_j/c_j)(\mathbf{H}_k-\boldsymbol{\eta}_{j,k-1}), & \text{if } c_j>r_j,\\ \boldsymbol{\eta}_{j,k-1}, & \text{otherwise,}\end{cases} \tag{9}$$

where $c_j=|\mathbf{H}_k-\boldsymbol{\eta}_{j,k-1}|$. This is simple, stable, and fast, and can be used to keep track of past history for any kind of field variation in any number of dimensions. It is clear that the computational speed, complexity, and storage requirements only marginally depend on the number of dimensions. The speed is of the same order as for two-dimensional vector Preisach models composed of angularly distributed scalar models as in both cases a single integral is approximated by a sum.

III. COMPUTATIONAL EXAMPLES

Some computational results illustrating model properties are given. For the sake of illustration we use an isotropic function, $q(\eta,r)=(2M_s/\pi)\arctan(\eta/k)\,(\sigma\sqrt{\pi})^{-1}\exp\{-[(r-H_c)/\sigma]^2\}$ with $k=0.2H_c$ and $\sigma=0.4H_c$. Some scalar properties for this function are illustrated in Fig 3. Figure 4 shows three examples of how a remanent magnetization caused by applying and removing a field in the y direction can be reduced by a field in the x direction. The results are qualitatively consistent with experimental literature results.[2,3,5] Figure 5 shows losses for a uniformly rotating field and a field alternating along one axis, respectively, versus the magnetization amplitude. It is seen that the rotational losses are in the order of twice as large, which agrees reasonably well with published experiments for moderate fields. However, it is generally agreed that the rotational losses decrease near saturation, cf. Ref. 8, which is not reflected in the model. This could be tentatively attributed to the fact that near saturation reversible processes begin to dominate while the model is fully irreversible. It is therefore possible that in order to accurately describe a nearly saturated state, reversibility must be integrated in the model. Several *ad hoc* ways of doing this and make the rotational losses decrease near saturation can be conceived, but this topic needs further investigation.

IV. CONCLUSIONS

A new type of phenomenological, inherently vectorial hysteresis model based on a simple hysteresis operator defined by a differential relation has been presented. The model is found to be simple and computationally quite efficient in any number of dimensions, and exhibits major features of vector hysteresis.

ACKNOWLEDGMENT

The authors wish to thank Professor I. D. Mayergoyz for valuable discussions.

[1] E. C. Stoner and E. P. Wohlfarth, Trans. R. Soc. London **240**, 599 (1948).
[2] I. D. Mayergoyz, *Mathematical Models of Hysteresis* (Springer, New York, 1991).
[3] K. Wiesen and S. H. Charap, J. Appl. Phys. **61**, 4019 (1987).
[4] J. Oti and E. Della Torre, J. Appl. Phys. **67**, 5364 (1990).
[5] A. A. Adly and I. D. Mayergoyz, J. Appl. Phys. **73**, 5824 (1993).
[6] I. H. Shames and F. A. Cozzarelli, *Elastic and Inelastic Stress Analysis* (Prentice–Hall, Englewood Cliffs, NJ, 1992).
[7] P. Krejči, Appl. Mat. **34**, 364 (1989).
[8] F. Fiorillo and A. M. Rietto, J. Appl. Phys. **73**, 6615 (1993).

Master equation approach to anhysteresis of noninteracting particles

Ivo Klik and Ching-Ray Chang
Department of Physics, National Taiwan University, Taipei, Taiwan, Republic of China

J. Lee
Department of Electrical Engineering, Chang Gung College of Medicine and Technology, Kwei-San, Tao-Yuan, Taiwan, Republic of China

Hysteresis in an array of thermally relaxing, aligned, noninteracting uniaxial particles driven by a periodic applied field with an attenuating amplitude and a dc bias is studied. The asymptotic state reached after the ac component attenuated to zero has the characteristics of anhysteretic magnetization. The convergence of the solution is studied, the anhysteresis curve is shown to lie below the curve of the equilibrium magnetization, a heuristic formula for the initial anhysteretic susceptibility is proposed, and the effects of interparticle interactions is discussed.

I. INTRODUCTION

We consider here a thermally relaxing bistable system driven by a periodic applied field H_{app} with attenuating amplitude and constant dc bias H. This model is applied to an array of noninteracting single domain particles and we calculate the asymptotic ($t\to\infty$) value $M_a(H)$ of the mean magnetization $\langle M\rangle$. It has the linear characteristics of anhysteretic magnetization[1] whose frequency[2] (ω) and temperature[3] (T) properties are studied. A discussion of the role of particle interactions conclude this work.

Let the energy of a single domain uniaxial particle aligned with applied field H_{app} be $E=V[K(1-\alpha_3^2)-M_sH_{app}\alpha_3]$ where V is the activation volume, K the anisotropy constant, M_s the saturation magnetization, and α_3 a direction cosine. The nucleation field is $H_n=2K/M_s$ and we write $h_{app}=H_{app}/H_n$. The system is bistable[4] if $|h_{app}|<1$ and at small T it may be regarded as having two levels with occupation numbers n_1 and $n_2=1-n_1$ satisfying the master equation

$$\dot{n}_i=-\kappa_{ij}n_i+\kappa_{ji}n_j. \tag{1}$$

Here $i\neq j=1,2$, $\dot{n}_i=dn_i/dt$, and $\kappa_{12}(h_{app})=\kappa_{1\to2}=f_0\times\exp[-q(h_{app})]$ and $\kappa_{21}(h_{app})=\kappa_{12}(-h_{app})$ are the thermal transition rates between the two levels. The prefactor is f_0 and $q(h_{app})=Q(1-h_{app})^2$ is a reduced barrier height where $Q=KV/T$ ($k_B\equiv1$). The reduced mean magnetization of the ensemble is $\langle m(t)\rangle=\langle M(t)\rangle/M_s=[n_2(t)-n_1(t)]$.

II. THE HYSTERESIS PROCESS

We address first the rather trivial yet instructive case of a piecewise *constant* applied field

$$h_{app}(k)=h+(-1)^kA(1-k/2N), \tag{2}$$

where the variable $k=2\omega t$ takes on only the integer values $0,1,2,\ldots,2N$, and h is the dc component. The amplitude $A(1-k/2N)$ vanishes after $2N$ half periods of duration $\tau=1/2\omega$, ($h_{app}=h$ for $k>2N$) its initial value A is chosen as follows: In our system bistability exists only for fields $|h_{app}|<1$. Accordingly, $n_1=0$ if $h_{app}\geq1$ and $n_2=0$ if $h_{app}\leq1$ and we set $A=1-h$ so that $h_{app}(0)=1$ and $|h_{app}(t)|\leq1$ during the interval on which the ac component attenuates. On the kth half period, in constant field, the solution of Eqs. (1) is

$$n_1[h_{app}(k)|t]=n_1[h_{app}(k-1)|\tau]e^{-\Gamma(k)t}+\kappa_{21}(k)\Gamma^{-1}(k)(1-e^{-\Gamma(k)t}), \tag{3}$$

where $\kappa_{ij}(k)=\kappa_{ij}[h_{app}(k)]$ for brevity and $\Gamma(k)=\kappa_{12}(k)+\kappa_{21}(k)$. Further, $t\in\langle0,\tau\rangle$ and $n_1[h_{app}(k-1)|\tau]=n_1[h_{app}(k)|0]$ is the population of the first well at the beginning of the kth half period; with our choice of the field $n_1[h_{app}(0)|0]=n_1[h_{app}(0)|\tau]=0$. Successive iterations of Eq. (3) yield the final population after N periods of duration 2τ

$$n_1[h|\tau]=n_1[h_{app}(0)|\tau]\exp\left\{-\tau\sum_{l=1}^{2N}\Gamma(l)\right\}+\frac{\kappa_{21}(2N)}{\Gamma(2N)}+S_N(\omega,f_0|Q,h), \tag{4}$$

$$S_N(\omega,f_0|Q,h)=\sum_{l=0}^{2N-2}\left[\frac{\kappa_{21}(2N-l-1)}{\Gamma(2N-l-1)}-\frac{\kappa_{21}(2N-l)}{\Gamma(2N-l)}\right]\times\exp\left\{-\tau\sum_{l'=0}^{l}\Gamma(2N-l')\right\}. \tag{5}$$

This equation has the form of our previous result for the nonequilibrium probability distribution[5] integrated over the domain of attraction of the first well.

According to Eq. (4) an arbitrary initial state is destroyed and the final state consists of the thermal equilibrium distribution $\kappa_{21}(2N)/\Gamma(2N)$ at constant bias h and of the sum $S_N(\omega,f_0|Q,h)$. To study its dependence on N and ω we shall consider first the $h=0$ case where it is known[6] that the anhysteretic magnetization is zero so that $n_1[h|\tau]|_{h=0}=\kappa_{21}(2N)/\Gamma(2N)|_{h=0}=1/2$. The first term in the sum S_N is $2^{-1}\tanh(Q/N)\cdot\exp(-f_0\omega^{-1}e^{-Q})$ and the series itself is estimated by the integral

$$|S_N(\omega,f_0|Q,0)|\leq\frac{Q}{2N}\int_0^{2N}dy\;y\exp\left(-\frac{f_0}{\omega}\;ye^{-Q}\right)\sim\frac{Q}{2N}\left(\frac{\omega}{f_0}\right)^2e^{2Q}. \tag{6}$$

Certainly, to every Q, f_0, and ω there exists N such that the integral (8) is arbitrarily small (the sum is identically zero if the system remains in thermal equilibrium, $\omega=0$), neverthe-

 0021-8979/94/75(10)/5487/3/$6.00 © 1994 American Institute of Physics

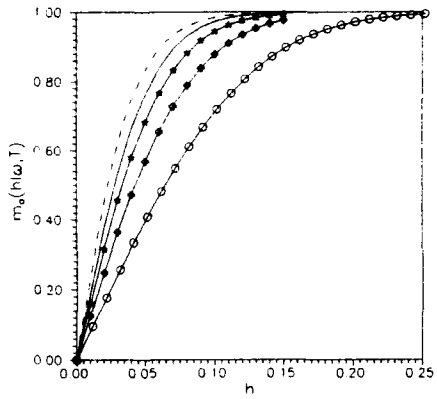

FIG. 1. A sample plot of anhysteresis curves obtained as limiting values of Eq. (8) for the field (7). To improve convergence we used the unrealistic system values $Q=12$ and $f_0=e^{10}$ Hz. Sweep rates are $\omega=e^1$ Hz (unmarked), e^2 Hz (star), e^3 Hz (cross) and e^4 Hz (circle). Number of sweeps $N<10^4$. The dashed line denotes $m_{eq}(h) \geq m_a(h)$.

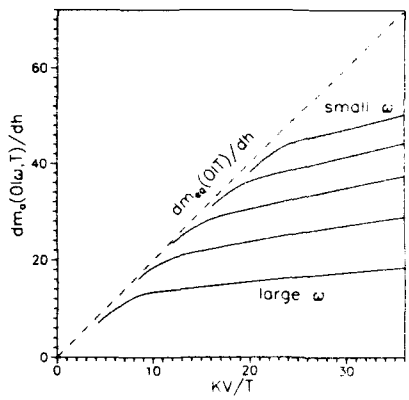

FIG. 2. The derivatives $dm_a(0)/dh \sim [m_a(dh)-m_a(0)]/dh$ calculated from Eq. (8) vs field (7) with realistic prefactor $f_0=e^{25}$ Hz and realistic values of the reduced barrier height $Q=KV/T$. Because of convergence problems these results are qualitative only and we refrain from identifying the sweep rates ω equally spaced on a logarithmic scale. The high T section of dm_a/dh approaches the equilibrium value, the low T section is described by Eq. (9).

less, this estimate bodes ill for numerical calculations based on the system (1) since while $f_0 \sim e^{25}$ Hz one also has $Q \sim 40-50$ for commercial particles at room temperature and many sweeps are required to satisfy the condition $|S_N(\omega,f_0|Q,0)| \to 0$. Numerical tabulations show that as a function of N the sum $|S_N(\omega,f_0,|Q,0)|$ decreases initially fairly rapidly to values ~ 0.025 corresponding to $|m_a(0)| \sim 0.05$ but unless $\omega e^Q/f_0 \sim 1$ further approach to zero is exceedingly slow. This convergence problem is known from numerical simulations[7] and, as Eq. (6) shows, becomes ever more intractable as ω and Q grow; a nonzero bias, $q(h) < Q$, improves the convergence.[8]

A *quantitative* calculation of the anhysteresis curve for realistic values of f_0 and Q is thus hardly practicable. Nevertheless, any solution of the set (1) tends *ipso facto* to thermal equilibrium, regardless of the choice of Q and f_0, and this property makes it suitable for studying the *qualitative* features of anhysteresis using some smaller values of f_0 and Q. The improved convergence then allows one to study not only process (2) but also the smooth field

$$h_{app}(t)=h+(1-h)(1-\omega t/N)\cos 2\pi\omega t \tag{7}$$

for which the solution of Eqs. (1) becomes

$$n_1[h|t]=n_1[h_{app}(0)|0]\exp\left\{-\int_0^t dt'\ \Gamma(t')\right\} + \int_0^t dt'\ \kappa_{21}(t')\exp\left\{-\int_{t'}^t dt''\ \Gamma(t'')\right\}. \tag{8}$$

A sample plot of anhysteretic curves $m_a(h)$ calculated from Eq. (8) is compared, in Fig. 1, with equilibrium magnetization $m_{eq}(h)=\tanh 2Qh$. There is always $m_a(h) \leq m_{eq}(h)$ [because $dq(h)/dh \leq 0$] and the initial slope $dm_a(0)/dh$ decreases with increasing sweep rate ω. For sufficiently large bias $m_a(h)$ approaches, as expected, $m_{eq}(h)$ again. The initial slope $dm_a(0|\omega,T)/dh$ may either be calculated for the unrealistic small values of Q, f_0, and ω as was done above or (approximately) also for the much larger physical values. The derivative namely, $dm_a(0)/dh \sim [m_a(dh)-m_a(0)]/dh$, changes very little after a sufficiently large number of periods, i.e., the curve $m_a(h)$ shifts almost rigidly in the $h-m_a$ plane. The derivative is therefore far easier to calculate than $m_a(h)$ proper.

The functions $dm_a(0|\omega,T)/dh$, shown in Fig. 2, obviously consist of two linear segments separated by a transition region. Both Eqs. (4) and (8) yield essentially the same results and we shall refer here to Eq. (4) where the state of thermal equilibrium is explicitly singled out. The high temperature linear section of dm_a/dh corresponds obviously to states close to the thermal equilibrium where $\tau\Gamma(k)$ is very large, be it on account of the small sweep rate or high temperature. This regime is reached for slow sweeps at lower temperatures than for fast ones. The low temperature linear region, on the other hand, is ω dependent and deviates strongly from the equilibrium curve. An analysis of numerical data suggests for this region a heuristic formula

$$\frac{dm_a(0|\omega,T)}{dh} \sim \mathscr{A}\ln^2\frac{f_0}{\omega}+\frac{\mathscr{B}}{T}\ln\frac{f_0}{\omega}, \tag{9}$$

where $\mathscr{A}$ and $\mathscr{B}$ are (possibly amplitude[6] dependent) empirical constants to be determined experimentally.

III. CONCLUSION

We wish yet to discuss the *possible* effects which interparticle interactions have on anhysteretic magnetization and of the means by which these effects may be studied. Interactions introduce a spectrum of local fields such as are employed by the Preissach model.[9] The spectrum is determined

by sample geometry but the relative intensity of the local fields depends on the immediate configuration of the ensemble, i.e., on time. The *mean* interaction field, estimated[10] as proportional to the sample magnetization, $h_{int} = \alpha\langle m\rangle$, enhances the transition probabilities κ_{ij}. We used [11] our probabilistic method to calculate the coercivity $h_c(\omega,T|\alpha)$ and found it to be decreasing approximately linearly with α. The mean field model is immediately applicable to the set (1) but no qualitatively new features are introduced. These are encountered in the system formed by a pair of magnetostatically coupled identical uniaxial particles.[12] This system is at most tristable ristable and its evolution may be described by the occupation numbers n_1, n_2 and $n_3 = 1 - n_1 - n_2$ corresponding to the physically distinct configurations $\uparrow\uparrow$, $\uparrow\downarrow$, and $\downarrow\downarrow$. The magnetization $\langle m\rangle = 2(n_1 - n_3)$ in the field (2) is easily found but its interpretation is rendered difficult by the presence of the intermediate state $\uparrow\downarrow$ whose occupation number n_2 constitutes a new degree of freedom. Clearly, the hysteresis properties of this system must be mastered first, before the far more complicated anhysteretic effects can be addressed. A favorable geometric arrangement of the two particles may again enhance the rate of thermal reversals which then take place even at temperatures at which the individual components are stable. Within the bistable model of noninteracting particles anhysteretic magnetization satisfies the inequality $0 \leq m_a \leq m_{eq}$ and this property is retained also within the mean field theory.[10] At small h the equilibrium magnetization of an interacting system may be (depending on geometry) much smaller than the equilibrium magnetization of the individual components and the variation of anhysteretic magnetization is therefore constrained to a narrower interval. We therefore conjecture that interparticle interactions also extend the field range over which $m_a(h)$ is approximately linear in the dc bias h.

To sum up, we have shown that anhysteretic effects follow quite naturally from the theory of thermal relaxation. For realistic *noninteracting* particles, however, an anhysteretic curve distinct from $m_{eq}(h)$ could only be observed in practice at extremely high sweep rates ω (compare Fig. 1). It is interparticle interactions which enhance the relaxation rates and make anhysteresis observable also at lower frequencies; moreover, by the conjecture of the preceding paragraph, they also extend the range of the desirable linear dependence of $m_a(h)$ on h.

ACKNOWLEDGMENT

This research was in part sponsored by the National Research Council of the Republic of China under Grant No. NSC-82-0208-M002-035.

[1] E. Della Torre, IEEE Trans. Audio AU-13, 61 (1965); H. N. Bertram, J. Phys. (Paris) Colloq. C2–3, 684 (1971).
[2] E. Kneller, J. Appl. Phys. 39, 945 (1968).
[3] W. F. Jaep, J. Appl. Phys. 40, 1297 (1969); 41, 2790 (1971); A. E. Berkowitz and W. H. Meiklejohn, IEEE Trans. Magn. MAG-11, 996 (1975).
[4] I. Klik and L. Gunther, J. Appl. Phys. 67, 4505 (1990).
[5] I. Klik, C. R. Chang, and H. L. Huang, Phys. Rev. B 47, 8605 (1993).
[6] D. K. Middleton, in *Magnetic Recording*, edited by C. D. Mee and E. D. Daniel (McGraw-Hill, New York, 1987), Vol. 1.
[7] B. W. Chantrell, A. Lyberatos, and E. P. Wohlfarth, J. Magn. Magn. Mater. 54–57, 1693 (1986).
[8] Our estimate (8) breaks down for $h > 0$ where S_N is nonpositive.
[9] I. D. Mayergoyz and C. E. Korman, J. Appl. Phys. 69, 2128 (1991).
[10] D. C. Jiles and D. L. Atherton, J. Magn. Magn. Mater. 61, 48 (1986); D. L. Atherton and J. R. Beattie, IEEE Trans. Magn. MAG-26, 3059 (1990). A similar mean field theory of equilibrium states was proposed by Jaepe (Ref. 3) on a purely thermodynamic basis.
[11] I. Klik and C. R. Chang (unpublished).
[12] W. Chen, S. Zhang, and H. N. Bertram, J. Appl. Phys. 71, 5579 (1992).

Scaling aspects of domain wall dynamics and Barkhausen effect in ferromagnetic materials

G. Bertotti, G. Durin, and A. Magni
Istituto Elettrotecnico Nazionale Galileo Ferraris and GNSM-INFM, Corso M. d'Azeglio 42, I-10125, Torino, Italy

It is shown through theoretical considerations on stochastic domain wall motion in a perturbed medium with quenched-in disorder that the Barkhausen signal v, as well as the size Δx and duration Δu of Barkhausen jumps follow scaling distributions of the form $v^{-\alpha}$, $\Delta x^{-\beta}$, $\Delta u^{-\gamma}$, where $\alpha=1-c$, $\beta=3/2-c/2$, $\gamma=2-c$, and c is proportional to the magnetization rate. In order to test these predictions, Barkhausen effect experiments were performed on polycrystalline SiFe alloys. Preliminary experiments to determine both the absolute value and the c dependence of the measured exponents are in agreement with the theoretical predictions.

I. INTRODUCTION

There have been widespread attempts in the past to describe the most evident feature of the Barkhausen Effect (BE), the existence of Barkhausen jumps (BJ), in terms of clustering of elementary domain wall (DW) displacements triggered by some local instability.[1,2] More recently, there has been renewed interest in BE scaling properties,[3] and in their connection with so-called self-organized criticality.[4] These studies have led to experimental estimates of the scaling exponents describing the distribution of BJ size and duration, but the derivation of these exponents from physical models is still at a preliminary stage.

In this paper we discuss BE scaling properties in the frame of the Langevin approach developed in Ref. 5, where the BE is associated with stochastic DW dynamics in a medium with quenched-in disorder. This description leads to two basic results: (i) there exists a dimensionless parameter c, such that the DW motion has a jerky character and proceeds by BJs when $c<1$, whereas it is continuous when $c>1$; (ii) when $c<1$, there exist BJs widely distributed in size and duration, and characterized by self-similar properties. In this paper, we show that, in the $c<1$ regime, the distributions of BJ size Δx and duration Δu follow scaling laws of the form $(\Delta x)^{-\beta}$ and $(\Delta u)^{-\gamma}$, with $\beta=3/2-c/2$ and $\gamma=2-c$.

These predictions, which are in qualitative agreement with recent data,[3,4] were tested through BE measurements under controlled values of permeability and magnetization rate, whereby independent estimates of β, γ, and c could be obtained. This permitted a test of the theory with no adjustable parameters.

II. MODEL

In Refs. 5 and 6, DW dynamics is described in terms of a single degree of freedom subject to viscous-like friction (i.e., Joule dissipation through eddy currents). This leads to an equation of the form $v_{DW} \propto H_a - k x_{DW} - H_p(x_{DW})$, where v_{DW} is the DW velocity, x_{DW} is the DW position, H_a is the applied field, $k x_{DW}$ is the restoring force due to magnetostatic effects, and $H_p(x_{DW})$, describing DW pinning interactions, is a random function of the DW position. By taking the time derivative of the previous relation and by assuming, as is commonly the case in BE experiments, that the applied field increases in time at a constant rate, we obtain, in terms of convenient dimensionless variables [u for time, x and $v=dx/du$ for the DW position and velocity, $h_p(x)$ for applied and pinning fields], the equation

$$\frac{dv}{du} + (v-c) = -\frac{dh_p}{du}. \tag{1}$$

Quantitative predictions are worked out by making specific assumptions on the random process $h_p(x)$. The properties of $h_p(x)$ have been experimentally investigated[7] for some special systems containing a single active DW. It was found that $h_p(x)$ can be approximately described by the Wiener–Lévy (WL) process, i.e., $h_p(x)$ is a process with independent increments dh_p characterized by $\langle dh_p \rangle = 0$, $\langle |dh_p|^2 \rangle = 2\,dx = 2v\,du$. Under this assumption, the problem can be solved considering the Fokker–Planck equation for the conditional probability density $P(v,u|v_0)$:[5]

$$\frac{\partial P}{\partial u} - \frac{\partial}{\partial v}\left[(v-c+1)P + v\frac{\partial P}{\partial v}\right] = 0. \tag{2}$$

In particular, the stationary amplitude distribution $P_u(v)$ is given by

$$P_u(v) = \frac{1}{\Gamma(c)}\, v^{c-1} \exp(-v) \tag{3}$$

According to Eq. (3), the behavior of $v(u)$ changes drastically when c crosses the value $c=1$. Computer simulations[5] show that, for $c<1$, $v(u)$ is made of a random sequence of BJs widely distributed in size and duration. The power-law divergence in $P_u(v)$ suggests the existence of scaling properties in the distribution of such BJs. In order to clarify this point, let us consider the region $v \ll 1$, where the v term in the expression $(v-c+1)$ of Eq. (2) is negligible and Eq. (3) becomes $P_u(v) \sim v^{c-1}$. This also corresponds to neglecting the v term of Eq. (1), i.e., $dv/du - c \cong -dh_p/du$. This approximate equation describes a self-similar process, because it is invariant with respect to a change of both v and u by the same scale factor k. In fact, when $v \to kv$ and $u \to ku$, $x = \int v\,du \to k^2 x$ and $\langle |dh_p|^2 \rangle = 2\,dx \to k^2 \langle |dh_p|^2 \rangle$, i.e., $h_p \to k h_p$.

In order to apply these results to the analysis of BJ scaling properties, we need to clarify how Barkhausen jumps can

 0021-8979/94/75(10)/5490/3/$6.00 © 1994 American Institute of Physics

be detected for a self-similar process like $v(u)$. In fact, deciding whether the DW is jumping ($v>0$) or not ($v\cong 0$) depends on one's ability to resolve fine $v(u)$ details. This can be dealt with through the introducion of the resolution coefficient $r\ll 1$ in u and v estimates, i.e., by assuming that we are able to measure u and v in units 0, r, $2r$,..., only, so that $u\cong 0$ or $v\cong 0$ whenever $u<r$ or $v<r$. Given the resolution r, the mean BJ duration $\langle \Delta u\rangle$ is proportional to the probability that $v>r$, estimated from Eq. (3). With $r\ll 1$ and $c\ll 1$, we obtain

$$\langle \Delta u\rangle \propto \mathrm{Prob}(v>r)\simeq 1-\int_0^r dv\ P_u(v)\simeq 1-r^c. \tag{4}$$

Let us now consider the distribution $P(\Delta u;r)$ of BJ durations. Given the self-similar nature of the process, $P(\Delta u;r)$ is a function of $\Delta u/r$ only, of the form $P(\Delta u/r)\sim(\Delta u/r)^{-\gamma}$. The resolution r allows us to detect jumps of minimum duration $\Delta u\sim r$. On the other hand, the characteristic relaxation time of Eq. (1), equal to unity, forbids jump durations $\Delta u\gg 1$. This means that

$$\langle \Delta u\rangle \propto \int_r^1 d(\Delta u)\ \Delta u\left(\frac{\Delta u}{r}\right)^{-\gamma}\propto 1-r^{2-\gamma}. \tag{5}$$

By comparing Eqs. (4) and (5), we obtain $\gamma=2-c$.

Similar considerations can be made for the distribution $P(\Delta x;r)$ of BJ sizes. The first point is to redefine Eq. (3) when we consider the probability of finding a given v value at a random position x rather than at a random time u. It is easily checked that this introduces an extra v factor in Eq. (3), which thus becomes $P_x(v)=v^c\exp(-v)/\Gamma(c+1)$. The mean BJ size $\langle \Delta x\rangle$ can be estimated from this expression in the same way $\langle \Delta u\rangle$ was estimated from Eq. (3):

$$\langle \Delta x\rangle \propto 1-\int_0^r dv\ P_x(v)\simeq 1-r^{c+1}. \tag{6}$$

Since x scales like $\int v\ du$, the distribution $P(\Delta x;r)$ of BJ sizes is a function of $\Delta x/r^2$ only, of the form $P(\Delta x/r^2)\sim(\Delta x/r^2)^{-\beta}$. Under the resolution r, the minimum detectable jump size is $\Delta x\sim r^2$, and the cutoff at $\Delta u=1$ and $v=1$ forbids jump sizes $\Delta x\gg 1$. This means that

$$\langle \Delta x\rangle \propto \int_{r^2}^1 d\ (\Delta x)\ \Delta x\left(\frac{\Delta x}{r^2}\right)^{-\beta}\propto 1-r^{4-2\beta}. \tag{7}$$

By comparing Eqs. (6) and (7), we obtain $\beta=3/2-c/2$. Finally, it is worth remarking that Eq. (3) also has a scaling structure, with a scaling exponent, say α, equal to $1-c$. In conclusion, we have the following result:

DW velocity:	$P(v)\sim v^{-\alpha}$,	$\alpha=1-c$;
BJ size:	$P(\Delta x)\sim(\Delta x)^{-\beta}$,	$\beta=3/2-c/2$;
BJ duration:	$P(\Delta u)\sim(\Delta u)^{-\gamma}$,	$\gamma=2-c$.

III. EXPERIMENTAL RESULTS

The BE experiments were performed on polycrystalline Si–Fe alloys. Single strips (length 20 cm, width 1 cm, and thickness 0.18 mm) of 1.8 wt % Si–Fe (electrical conductivity $\sigma=2.76\times10^6\ \Omega^{-1}\ \mathrm{m}^{-1}$) were placed in a solenoid and magnetized by a triangular primary current waveform of variable frequency. A flux-closing NiFe yoke was used to reduce the reluctance of the magnetic circuit. The specimen was placed in a double mu-metal box and all measurements were performed in a shielded room in order to prevent electromagnetic disturbances. The BE signal was detected by a narrow 50 turn coil placed in the middle of the strip. The noise analysis was restricted to a magnetization interval of 0.3 T around the central part of the saturation hysteresis loop. In this region, the differential permeability $\mu=dB/dH_a$ is fairly constant, and the application of a constant external field rate $\dot{H}_a$ gives a stationary BE process associated with well-defined values of μ ($\mu/\mu_0=14\,300$ in the present experiments) and of the magnetization rate $\dot{I}=\mu\dot{H}_a$ (for a more complete description of the experimental setup see Ref. 5).

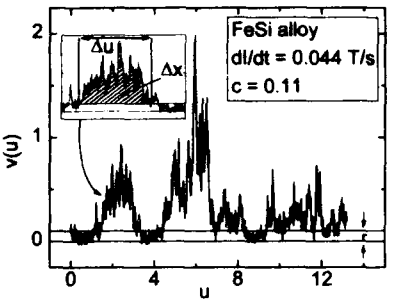

FIG. 1. Time behavior of BE flux rate $\dot{\Phi}$. Dimensionless quantities $u=t/\sigma GS\mu$ and $v=(\sigma G/AS\mu)\dot{\Phi}$ are shown. $r=0.1$ is the resolution parameter used in the determination of BJ distributions. Definition of BJ duration Δu and BJ size Δx is shown in the inset.

According to the theory,[5] the dimensionless quantities u, v, and x appearing in Eqs. (1)–(7) are defined as $u=t/\tau$, $v=(\sigma G/AS\mu)\dot{\Phi}$, $x=\int v\ du$, where t is the time, $\dot{\Phi}$ is the induced flux rate per coil turn, $\tau=\sigma GS\mu$ is the time constant controlling the decay of magnetostatic fields, S is the specimen cross-sectional area ($S=1.8\times10^{-6}\ \mathrm{m}^2$), $G=0.1357$, and A is a microstructural parameter measuring the strength of local pinning interactions. The parameter $c=\langle v\rangle=(\sigma G/AS\mu)S\dot{I}$ is proportional to the average magnetization rate $\dot{I}$. Therefore, varying c values were simply obtained by controlling the applied field rate $\dot{H}_a=\dot{I}/\mu$. The value of A was determined through measurements of the BE power spectrum.[5] For the present material $A=8\times10^6\ \mathrm{A^2\ m^{-2}\ Wb^{-1}}$, which implies $c=2.6\dot{I}$.

Figure 1 shows the typical measured time behavior of $v(u)$. As discussed in the previous section, given a threshold r, the BJ duration Δu is defined as the time interval between the two successive points for which the signal $[v(u)>r]$ crosses the threshold. Correspondingly, the BJ size Δx is the area of the signal between the two points. The log–log histograms of the relative frequency of occurrence of different v, Δu, and Δx values ($c=0.11$) are shown in Fig. 2. $P(\Delta x)$ and $P(\Delta u)$ exhibited a similar well-defined slope in all cases, which permitted a reliable determination of the exponents β and γ (broken lines). This was not the case for

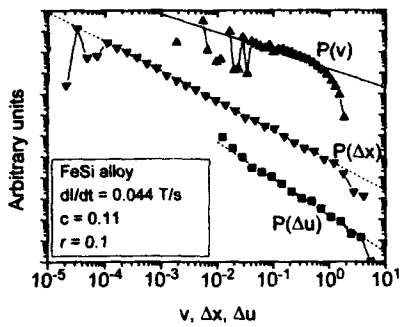

FIG. 2. Log–log plot of v distribution $P_u(v)$, BJ duration distribution $P(\Delta u)$, and size distribution $P(\Delta x)$. Broken lines are best fit lines, giving exponents β and γ. The continuous line of slope $c-1$ is shown for comparison.

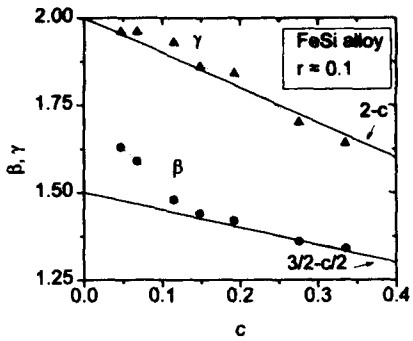

FIG. 3. Measured behavior of β and γ vs $c=2.6I$. Continuous lines are theoretical predictions. No adjustable parameter is involved in the comparison.

$P_u(v)$, where the presence of large fluctuations in the distribution at low v and the dominant role of the exponential cutoff at large v made the determination of α quite unreliable. The continuous line in the figure shows that these data are, at least, consistent with the expected law $P_u(v)\sim v^{c-1}$.

The symbols in Fig. 3 show the behavior of β and γ vs c (i.e., vs I) obtained from this analysis. The continuous lines are the theoretical predictions previously discussed. Both the absolute value and the c dependence of the exponents are well described by the theory. It is worth remarking that this comparison does not involve any adjustable parameter.

IV. DISCUSSION AND CONCLUSIONS

BE scaling properties have recently been the subject of several investigations.[3,4,8,9] Interesting results were obtained[8] by applying the methods of fractal geometry to the analysis of the BE signal. These authors find that BE behaves like a self-affine process describable in terms of fractional Brownian motion processes, with fractal dimensions in the range 1.5–1.7 (the standard random walk process corresponds to the value 1.5). The analysis presented in our paper is based on the assumption that the local pinning field experienced by the DW can indeed be described as a space random-walk process. This is reflected by the fact that the distribution of BJ sizes in the limit $c\to 0$ has a scaling exponent of 1.5. In fact, in this limit the BJ sizes correspond to the segments obtained by cutting the $H_p(x)$ function with a line of constant height H_a (the time variation of H_a in a BJ can be neglected if c is small), and it is known[10] that this gives a distribution of segment lengths with exponent 1.5.

The results obtained in Ref. 8 suggest a generalization of the present approach, where, in the equation $v\propto h_a(u)-x-h_p(x)$, $h_p(x)$ is a fractional Brownian motion process, spanning a continuous range of fractal dimensions. Future work will be devoted to the study of the scaling properties of this class of stochastic processes.

[1] H. Bittel, IEEE Trans. Magn. MAG-5, 359 (1969).
[2] G. Montalenti, Z. Angew. Phys. 28, 295 (1970).
[3] R. D. McMichael, L. J. Swartzendruber, and L. H. Bennett, J. Appl. Phys. 73, 5848 (1993).
[4] P. J. Cote and L. V. Meisel, Phys. Rev. Lett. 67, 1334 (1991); L. V. Meisel and P. J. Cote, Phys. Rev. B 46, 10 882 (1992).
[5] B. Alessandro, C. Beatrice, G. Bertotti, and A. Montorsi, J. Appl. Phys. 68, 2901, 2908 (1990).
[6] G. Bertotti, in *Models of Hysteresis, Pitman Research Notes in Mathematics*, edited by A. Visintin, (Longman, London, 1993), pp. 1–9.
[7] R. Vergne, J. C. Cotillard, and J. L. Porteseil, Rev. Phys. Appl. 16, 449 (1981).
[8] O. Geoffroy and J. L. Porteseil, J. Magn. Magn. Mat. 97, 198, 205 (1991).
[9] H. Yamazaki, Y. Iwamoto, and H. Maruyama, J. Phys. Paris 49-C8, 1929 (1988).
[10] M. Schroeder, *Fractals Power Laws and Correlation* (Freeman, New York, 1991), p. 153.

Monte Carlo simulations of the magnetocaloric effect in superferromagnetic clusters having uniaxial magnetic anisotropy

L. H. Bennett, R. D. McMichael, and H. C. Tang
NIST, Gaithersburg, Maryland 20899

R. E. Watson
Brookhaven National Laboratory, Upton, New York 11973

The magnetic entropy change, ΔS (hence the heating or cooling) of ferromagnetically coupled magnetic clusters induced by an application of a magnetic field is substantial and occurs over a broad temperature range. This behavior contrasts with a ferromagnetic material, where larger entropy changes can be obtained, but only over small temperature ranges close to the Curie point. Monte Carlo simulations have been carried out to obtain ΔS when the spins are subjected to uniaxial anisotropy fields. While previous calculations for interacting spins showed increases in the Curie temperature and enhancements of ΔS in the vicinity of the Curie point with increasing anisotropy, the present results for interacting clusters show similar increases in the temperature of ΔS peaks accompanied by *decreases* in the peak values of ΔS. These results show that the flattening of the ΔS peaks, which make superferromagnetic materials valuable for magnetic refrigeration is assisted by the presence of uniaxial anisotropy. Some effects on ΔS of placing the spins on fixed BCC, FCC, and sc lattices are reported.

I. INTRODUCTION

The magnetocaloric effect is the adiabatic temperature shift induced in a magnetic material due to the change in an externally applied magnetic field. The changing field induces a change in the material's magnetic entropy, and this can be quite substantial in the immediate vicinity of the Curie temperature of a ferromagnet. The phenomenon has potential for specialized applications as a refrigerator, air conditioner, or heat pump.[1,2] For utilization, it is desirable to have a device that operates with modest applied magnetic fields and over temperature ranges greater than just a few degrees of a Curie point. As we have discussed previously,[3,4] one possibility is to employ samples consisting of ferromagnetically interacting superparamagnetic clusters. Anisotropy inevitably occurs in such systems and the main purpose of the present work is to consider, for the first time, Monte Carlo results for the effects of uniaxial anisotropy on an array of superparamagnetic particles with the sign and the axis of the anisotropy term such that the spins are aligned parallel to the applied magnetic field. The effects of anisotropy on a FCC system of ferromagnetically coupled individual spins were reported previously. They differ in an important way from the present results, and in order to see this, results will be reported here for both individual and superparamagnetic clusters of spins both with and without anisotropy terms. The effect on ΔS of going from BCC to FCC and, in turn, simple cubic arrays of spins will also be included.

It will be seen that the *combination* of having superparamagnetic particles and a suitably orientated anisotropic term contribute to broadening the temperature range over which significant magnetic entropy changes may be made.

II. CALCULATIONS AND RESULTS

Monte Carlo simulations are carried out using the Hamiltonian,

$$E=\sum_i \left(\frac{1}{2}\sum_j J\mathbf{s}_i\cdot\mathbf{s}_j-\mu\mathbf{s}_i\cdot\mathbf{H}-\mu A s_{zi}^2\right), \tag{1}$$

to obtain the magnetization as a function of H and T. For a cluster of "p" spins, $\mu=p\cdot\mu_B$. The exchange constant, J, which represents the interaction between clusters, does not depend on cluster size. The interaction is limited to near neighbors, an appropriate approximation when dealing with interactions between clusters of spins. (Extending the interaction to longer range would bring the simulation closer to a mean field description.[5]) When the uniaxial anisotropy, $A>0$, magnetization is favored in a direction parallel to the applied magnetic field, H. The entropy change associated with changing the magnetic field is[3,4,6]

$$\Delta S=\int_0^H\left(\frac{\partial M}{\partial T}\right)_H dH. \tag{2}$$

From the magnetization data, the entropy is calculated by integrating Eq. (2) over finite elements.

The Monte Carlo calculations employ a $20\times20\times20$ lattice with periodic boundary conditions. In the sampling, Heisenberg spins are chosen at random and flipped to a random orientation, and the Metropolis criterion is used to determine whether the new spin array is kept. For each value of field and temperature, every spin is reoriented an average of 2×10^4 times. Variations in cell size and run length are used to assure that the essential features of the results reported are not overly sensitive to the choice of these parameters, as discussed earlier.[3]

The results of Monte Carlo simulations of the entropy change, ΔS, induced by removal of a 1 T magnetic field for the simple cubic (SC), body-centered-cubic (BCC), and face-centered-cubic lattices are shown in Fig. 1. A value of $p=1$ and an exchange value of $J/k=1$ K (where k=the Boltzmann constant) are used in all three lattices. The small value of J/k is responsible for the small Curie points, T_C, in the

 0021-8979/94/75(10)/5493/3/$6.00 © 1994 American Institute of Physics

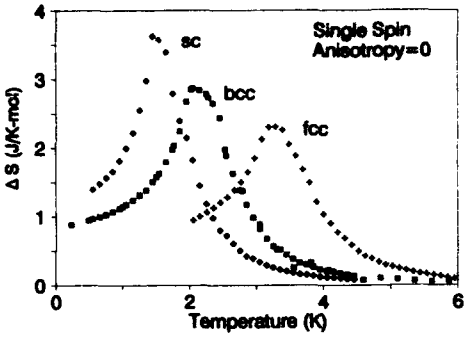

FIG. 1. Monte Carlo simulations of the entropy change ΔS induced by removal of a 1 T magnetic field for systems of classical Heisenberg spins for three lattices without anisotropy.

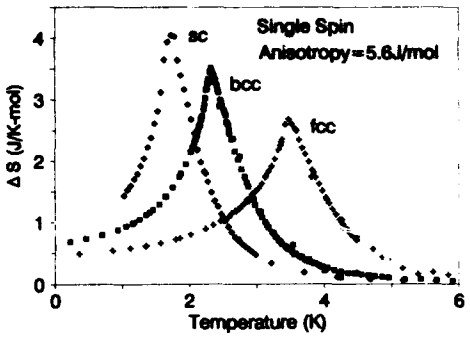

FIG. 3. Monte Carlo simulations of the entropy change ΔS induced by removal of a 1 T magnetic field for systems of classical Heisenberg spins for three lattices with an anisotropy coefficient of 5.6 J/mol.

figure, which occurs near the ΔS peaks. The use of a larger J/k value would not qualitatively affect the results to come in this paper. If the Rushbrooke and Wood[7] values for J/k (0.346 for SC, 0.2425 for BCC, and 0.1572 for FCC) were used, all three peaks would fall at the same value of T_C. The saturation magnetization per atom is 1 μ_B for all three spin lattices, and a sum rule[6] states that the areas under the three curves must be equal. The most significant feature of the ΔS is their strong peaking near T_c, which arises because a given applied field has its largest effect on the magnetization (hence the spin disorder entropy) in this regime.

As emphasized before,[3,4] the formation of magnetic clusters tends to create a lowered and broadened ΔS peak near the ordering temperature, because pinning groups of spins together reduces the reordering entropy available near T_c. This effect can be seen for the three lattices by comparing Fig. 1, which is for ferromagnetic materials comprised of single atomic moments, with Fig. 2, which is for superferromagnetic materials incorporating 100-atom clusters, each

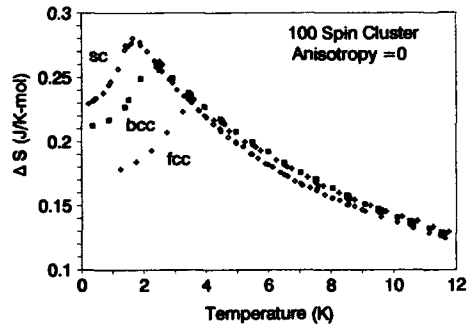

FIG. 2. Monte Carlo simulations of the entropy change ΔS induced by removal of a 1 T magnetic field for superferromagnetic clusters of 100 atoms in three lattices without anisotropy. Note that the ΔS scale does not start at zero.

atom having the magnetic moment of the single atom in the ferromagnet. Note the order of magnitude reduction in the ΔS scale on going to Fig. 2. As the cluster size increases from that of a single spin, the Monte Carlo calculations show a decrease in the entropy change at T_c for a given applied field, constant magnetic moment per atom, and constant number of atoms, and an increase in the entropy change well above T_c. The sum rule[6] indicates that the areas, $\int(\Delta S)dT$, of the three curves of Fig. 2, are equal to each other and to those of Fig. 1. For the two BCC curves shown in the two figures, there is a crossover at ≈4 K, where the value of ΔS for the superferromagnet becomes larger than ΔS for the ferromagnet. The effects of going from the single spin ferromagnetics to the clusters have been discussed extensively elsewhere.[3,4]

The effect on ΔS of subjecting the single spin magnets to an aligning uniaxial anisotropy field is illustrated in Fig. 3 for all three spin lattices. As was discussed previously[4,8] for the FCC lattice, an anisotropy term that encourages alignment causes a sharpening (see Fig. 1 of Ref. 4) i.e., an increase in the critical exponent of the magnetization curve at zero applied field, as well as a small increase in the ordering temperature.[9] This narrows the temperature range over which a given applied field has a large effect on the spin disorder, and this results in a concomitant sharpening and shift in the ΔS peaks on going from Fig. 1 to Fig. 3. Again the sum rule applies and the sharpening is attended by a small increase in ΔS peak height and small increases in ΔS at high temperatures.

The effects on ΔS due to varying strengths of the anisotropy term for a BCC array of 100-spin clusters are illustrated in Fig. 4. These anisotropy field strengths are characteristic of what are encountered in permanent magnets. For the sake of comparison, the exchange coupling between clusters here and in Fig. 2 has been kept equal to that used for the single spins of Figs. 1 and 3. Also, the 5.6 J/mol curve employs the same value of A, i.e., the same strength anisotropy per *single* spin 1 site, as used in Fig. 3. Unlike the cases of single spins, the 100-spin $H=0$ magnetization curves do not sharpen upon

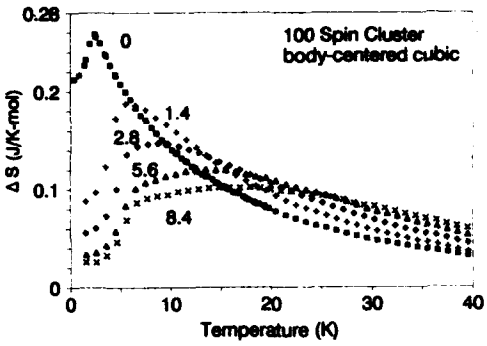

FIG. 4. Monte Carlo simulations of the entropy change ΔS induced by removal of a 1 T magnetic field for superferromagnetic clusters of 100 atoms in a body-centered-cubic lattice with varying anisotropy coefficients, A, in J/mol.

introduction of the anisotropy, and neither do the ΔS curves. (Again, due to the sum rule, these curves have equal areas under them.) These curves each have a sharp initial rise, followed by a break in slope (most visible in the 5.6 and 8.4 curves) to a broadened peak. In the 8.4 curve, the peak has broadened to a flat curve with almost constant ΔS over a broad temperature range. The breaks (e.g., at ≈6 K for the 8.4 curve) correspond to the T_c's of these systems at their respective anisotropies.

III. DISCUSSION AND SUMMARY

The present results have been limited to the case of the easy axis of the anisotropy being parallel to the applied magnetic field. Previously, we reported some results for single spins, where the easy anisotropy direction was also normal to the magnetic field. Mørup and Christiansen[10] have reported molecular field results for the zero-field magnetizations for varying anisotropy, displaying the T_c shifts encountered here. They also considered the case where the anisotropy and magnetization were constrained to have different axes. Except for very small angles, Mørup and Christiansen showed that this depresses T_c for some given strength anisotropy constant—something seen for the single spin Monte Carlo results. The issue of noncollinear anisotropy and applied field terms requires further investigation.

We have obtained results for both individual spins and spin clusters on SC, BCC, and FCC lattices. The peak values of the ΔS are largest for the lattice having the lowest T_c. The heights of the peaks for the single spin ΔS of Fig. 1 (and to a lesser degree, Fig. 3) scale approximately as the square root of the Rushbrooke–Wood J/k factors [i.e., as $\sim(1/T_c)^{1/2}$]. The variation in relative peaks is reduced for the 100-spin cluster represented in Fig. 4. The relationship of this reduction to the suppression of the cluster peak heights and to the associated peak broadenings (relative to those of the single spin) requires further elucidation.

There is an interplay between the anisotropy and the clustering of the spins. In Fig. 4, the "action" in the ΔS behavior occurs above the ordering temperature, arising because one key variable, namely $\mu H/kT$, can be substantial for the clusters. If ΔS of modest magnitude are of interest, these can be obtained over broad temperature ranges by employing superferromagnetic clusters having suitable anisotropy.

ACKNOWLEDGMENTS

The assistance of H. J. Brown in organizing the data is gratefully acknowledged. Work at Brookhaven National Laboratory is supported by the Division of Materials Sciences, U.S. Department of Energy, under Contract No. DE-AC02-76CH00016.

[1] J. A. Barclay, Adv. Cryo. Eng. Mat. **33**, 719 (1988).
[2] R. D. Shull, L. J. Swartzendruber, and L. H. Bennett, *Proceedings of the 6th International Cryocooler Conference*, edited by G. Green and M. Knox, David Taylor Research Center Publication No. DTRC-91/002, Annapolis, MD, 1991, p. 231.
[3] L. H. Bennett, R. D. McMichael, L. J. Swartzendruber, R. D. Shull, and R. E. Watson, J. Magn. Magn. Mat. **104–107**, 1094 (1992).
[4] L. H. Bennett, R. D. McMichael, R. D. Shull, L. J. Swartzendruber, and R. E. Watson, J. Appl. Phys. **73**, 6507 (1993).
[5] See, e.g., K. K. Mon and K. Binder, Phys. Rev. E, **48**, 2498 (1993), and references therein.
[6] R. D. McMichael, R. D. Shull, L. J. Swartzendruber, L. H. Bennett, and R. E. Watson, J. Appl. Phys. J. Magn. Magn. Mat. **111**, 29 (1992).
[7] G. S. Rushbrooke and P. J. Wood, Mol. Phys. **1**, 257 (1958); P. J. Wood and G. S. Rushbrooke, Phys. Rev. Lett. **17**, 307 (1966).
[8] The FCC lattice results of Figs. 1 and 3 of the present paper are much less noisy than their counterparts in Fig. 2 of Ref. 4. This improvement is due to improved efficiencies in the Monte Carlo samplings, thus allowing better samplings to be made. One improvement involves employing variable temperature steps, proportional to $(dM/dt)_H^{-1}$, and another, eliminating the repetitive generation of indexing.
[9] The single-site anisotropy appearing in Eq. (1) is different than the spin–spin anisotropy operators in A. Margaritsis, G. Odor, and A. Patkós, J. Phys. A **20**, 1917 (1987), and references therein, for which no such sharpening is obtained.
[10] S. Mørup and G. Christiansen, J. Appl. Phys. **73**, 6955 (1993).

A phenomenological magnetomechanical hysteresis model

A. Bergqvist
Electric Power Engineering, Royal Institute of Technology, S-10044, Stockholm, Sweden

G. Engdahl
Power Engineering, ABB Corporate Research, S-72178, Västerås, Sweden

To obtain accurate design tools for applications involving giant magnetostrictive materials, magnetomechanical hysteresis effects should be taken into account. The problem consists of determining the magnetization and mechanical strain from the combined past history of magnetic field and mechanical stress. In this work, coupled magnetomechanical hysteresis has been modeled by using simple path-dependent differentials to accumulate the past history in functions related to the magnetization and strain through material-dependent parameters. By using anhysteretic curves and a few additional parameters to characterize a material, major, and minor loops with respect to both field and stress have been calculated for Terfenol-D and have shown good agreement with experiments.

I. INTRODUCTION

To design actuators based on highly magnetostrictive materials such as Terfenol-D, it is important to have reliable computational tools. The behavior of such a material is, in addition to Maxwell's and Newton's equations, governed by a constitutive law relating the magnetization M and the mechanical strain S to the independent parameters magnetic field H and mechanical stress T. To obtain a high degree of accuracy, it should be taken into account that this relation is hysteretic. More specificially, there is hysteresis in both M and S with respect to both H and T, and these hysteresis effects are coupled so that the response to a change in one independent parameter is affected by the past history of the other, and the influence of the past history of one independent parameter can be erased by a large value of the other.

There are some models in existence for treating this problem. Adly *et al.*[1] proposed a Preisach model with two inputs, which can be expressed as the sum of two components, in this case one depending on the past history of H and the momentary value of T and one depending on the past history of T and the momentary value of H. The main problem with this model is that because there is no coupling between the past histories of the two inputs, there is erratic correspondence between the past history accumulated by the model and that relevant to the situation. As a result the model can give notable qualitative disagreement from experiments.

Another generalization of the classical Preisach model (CPM) in which H is replaced by a function of H,T and the up and down switching values of the elementary rectangular loops[2] takes into account the coupling between H and T, and has shown good agreement with experiments, but has other problems. First, the identification problem is very hard to solve, involving nonrobust nonlinear equation systems. Second, it has turned out to be rather more difficult to model S than M. Third, it is hard to see how the model could be generalized to account for fields and/or stresses with more than one component. Therefore the model may not be entirely sound.

The fact that if one independent material is fixed, the system will behave as ordinary scalar hysteresis and that all past history can be erased if one parameter becomes sufficiently large recalls the behavior of vector hysteresis and suggests that a similar formalism can be used for magnetomechanical hysteresis as for vector hysteresis. In this work, coupled magnetomechanical hysteresis has been modeled by employing the formalism of a recent phenomenological approach to vector hysteresis.[3] By using simple path-dependent differentials, the past history is accumulated in functions that are related to the magnetization and strain through material-dependent parameters.

II. MODEL FORMULATION

In analogy with the expression for the vector magnetization given in Ref. 3 here we propose to calculate magnetization and strain for arbitrary variations of field and stress by taking

$$M(t)=\int_0^\infty q_M[\eta(r,t),\tau(r,t),r]dr, \tag{1a}$$

$$S(t)=\int_0^\infty q_S[\eta(r,t),\tau(r,t),r]dr, \tag{1b}$$

where q_M and q_S are material-dependent functions that should be determined from experiments. $\eta(r,t)$ and $\tau(r,t)$ are functions of the dimension magnetic field and mechanical stress, respectively, and depend on the combined past history of H and T. Their values are given by

$$\begin{pmatrix}\eta(r,t)\\ \tau(r,t)\end{pmatrix}=C^{-1}L_r\left[C\begin{pmatrix}H\\ T\end{pmatrix}\right](t), \tag{2}$$

where C is a diagonal matrix and L_r denotes a hysteresis operator associated with a simple static irreversible differential relation between its argument and its value, as described in Ref. 3. In this manner the model is formally equivalent to the vector model with $C(H,T)^T$ as the input vector. It is straightforward to show that one of the nonzero elements in C can be fixed to some arbitrary value. Therefore we choose to set

$$C=\begin{pmatrix}1 & 0\\ 0 & c\end{pmatrix}, \tag{3}$$

 0021-8979/94/75(10)/5496/3/$6.00 © 1994 American Institute of Physics

where the parameter c should be determined from experiments. It will be seen later that it controls the proportions of hysteresis with respect to T and to H. Combining (2), (3), and the definition of L_r, the path-dependent differential relations for η and τ can be explicitly written as

$$(d\eta,d\tau)=\begin{cases}(H-\eta,T-\tau)dK, & \text{if } dK>0 \text{ and } f=0,\\ (0,0), & \text{otherwise,}\end{cases} \tag{4}$$

where $dK=(H-\eta)dH+c^2(T-\tau)dT$ and $f=(H-\eta)^2+c^2(T-\tau)^2-r^2$.

In Ref. 3 it was shown that the vector hysteresis model discussed was equivalent to the CPM for fields restrained to one direction. Here it similarly holds that if either one of H or T is fixed while the other varies, the model behaves like the CPM, which means it exhibits the congruency property and the wiping-out property.[4] As an example of the coupling between magnetic and mechanical quantities, we can consider the following case: Let T be fixed in time and H go to infinity. Then it can be found from (4) that $[\eta(r,t),\tau(r,t)]\rightarrow(H-r,T)$ for all r, regardless of the initial values of $\eta(r,t)$ and $\tau(r,t)$. A similar result holds if instead H is fixed and T goes to infinity. This means that all past history can be erased by a large value of either H or T.

There is no reversibility in the model unless q_M and q_S are Dirac-type singularities for $r=0$. A way to incorporate reversibility and keep q_M and q_S finite is to replace (1) by

$$M(t)=\int_0^\infty q_M[\lambda H(t)+(1-\lambda)\eta(r,t),\lambda T(t)+(1-\lambda)\tau(r,t),r]dr, \tag{5a}$$

$$S(t)=\int_0^\infty q_S[\lambda H(t)+(1-\lambda)\eta(r,t),\lambda T(t)+(1-\lambda)\tau(r,t),r]dr, \tag{5b}$$

where λ is a dimensionless constant between 0 and 1 to be determined from experiments. If $\lambda=0$, we end up with (1) and if $\lambda=1$ there is no dependence on $\eta(r,t)$ or $\tau(r,t)$, and therefore full reversibility, i.e., no hysteresis. In the case of constant stress or field this also relaxes the congruency property of the CPM. It can be shown that the model will in such a case instead have the more general equal-chords property of the input-dependent Preisach model.[4]

III. DETERMINATION OF PARAMETERS

The model parameters that should be determined are λ, c, and the functions q_M and q_S. A method for doing this will be outlined. Due to space limitations proofs will be omitted.

The reversibility ratio λ can be determined in the following manner: Define the differential susceptibility $\chi_{\text{diff}}(T,H)$ as the slope of the ascending branch of a major M,H loop at constant stress T and the incremental susceptibility $\chi_{\text{inc}}(T,H)$ as the slope of a small minor M,H loops excursion from such a major loop. It is then possible to show that

$$\lambda=\chi_{\text{inc}}(T,H)/\chi_{\text{diff}}(T,H), \tag{6}$$

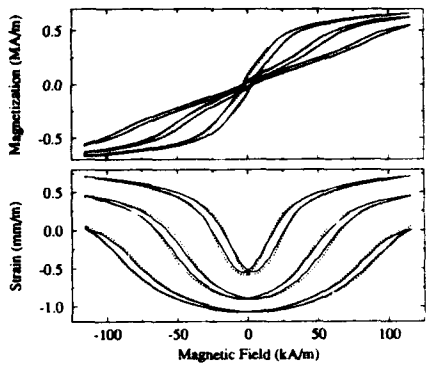

FIG. 1. Measured (dotted) and calculated (solid) major loops vs H for $T=-8.8$, -23.3, and -37.7 MPa.

for any choice of (T,H). Instead of M,H loops, we could equally well use S,H,M,T or S,T loops. This is in agreement with the recent observation that the magnetomechanical coupling factor is independent of whether it is determined from differential or incremental measurements.[5]

The functions q_M and q_S can, in principle, be determined from experimentally measured first-order reversal curves in the standard fashion of the Preisach model.[4] However this would involve taking second derivatives of experimentally measured scattered points, which is numerically difficult, and, for the material investigated, we failed to find a method that produced smooth results without undue distortion. To get around this difficulty we used the separation of variables,

$$q_M(\eta,\tau,r)=p_M(\eta,\tau)z(r), \tag{7a}$$

$$q_S(\eta,\tau,r)=p_S(\eta,\tau)z(r). \tag{7b}$$

By analogy with what was stated in Ref. 3, p_M and p_S can be shown to be equal to the anhysteretic magnetization and

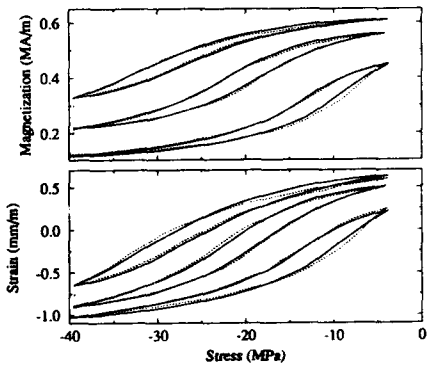

FIG. 2. Measured (dotted) and calculated (solid) major loops vs T for $H=23$, 46, and 70 kA/m.

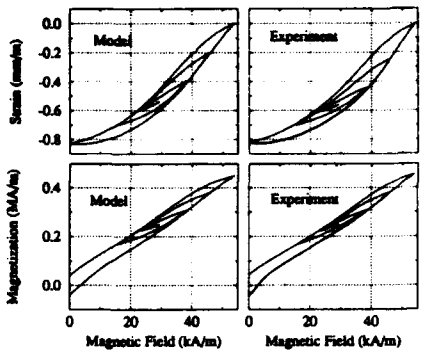

FIG. 3. S and M vs H for fixed $T=-19.4$ MPa.

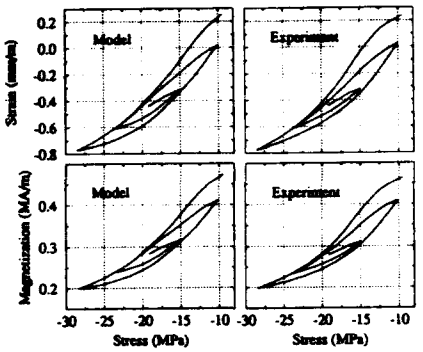

FIG. 4. S and M vs T for fixed $H=31$ kA/m.

strain, respectively, if $z(r)$ is normalized. In addition, we assume $z(r)$ to be a Gaussian with a material specified parameter r_0, to get

$$q_M(\eta,\tau,r)=M_{an}(\eta,\tau)A\ \exp[-(r/r_0-\tfrac{1}{2})^2], \tag{8a}$$

$$q_S(\eta,\tau,r)=S_{an}(\eta,\tau)A\ \exp[-(r/r_0-\tfrac{1}{2})^2], \tag{8b}$$

where $M_{an}(\eta,\tau)$ and $S_{an}(\eta,\tau)$ are the anhysteretic magnetization and strain, respectively, and A is given by normalization of $z(r)$.

We should then determine experimentally the anhysteretic curves and the parameter r_0. Strictly measuring the anhysteretic curves is a difficult and time-consuming procedure, since for every single point on the curves the field or the stress should be cycled with a slowly decreasing amplitude. Fortunately for Terfenol-D with its low squareness ratio, a good approximation is provided by taking the average of the upper and lower branches of major loops with respect to H. Some care should be observed for the strain curves at low values of H, as the anhysteretic in this case lies below both branches of the major loops.[6] The value of r_0 is directly related to the width of major loops with respect to H. This width clearly depends on both the stress and the location on the loop but, except near saturation, it does not change much. If we define H_w as a "representative" value of this width, such as twice the coercivity, then we can use

$$r_0 \approx H_w/(1-\lambda). \tag{9}$$

This value can be iteratively improved by employing the model with this r_0 value to calculate major loops and comparing their width to experiments and properly adjusting r_0.

Finally, c should be determined. If we define T_w as the width of a major loop with respect to T for a constant H, we can get a good match by setting

$$c=H_w/T_w. \tag{10}$$

This value can be iteratively improved in the same fashion as r_0.

IV. EXPERIMENTAL RESULTS

Computations have been compared to experiments done on a sample of Terfenol-D. The experimental equipment has been described in Ref. 7. We used parameter values $\lambda=0.40$, $r_0=3.83$ kA/m, and $c=1.99$ kA/m/MPa. In Figs 1 and 2, all four types of major loops are shown. Figures 3 and 4 show typical examples of what happens if either one of H or T is constant while the other is oscillating with decreasing amplitude. The accuracy is seen to be generally good and does not greatly exceed the error range of the measurements. However, while the calculated M,H and S,H loops have almost exactly the same width, experiments exhibit more hysteresis in the latter. This could be due to an experimental error, especially as Restorff *et al.*[8] have reported experimental results that better agree with the model in this respect.

V. CONCLUSIONS

A phenomenological magnetomechanical hysteresis model has been presented. The model is simple to use, computationally fairly efficient, and has been found to give good agreement with experimental results for Terfenol-D when three parameters are used to characterize hysteresis properties. In addition, the formal generalization to multidimensional fields and stresses appears straightforward. What this amounts to is that expanding a nonhysteretic representation of material properties to an inclusion of hysteresis can be done with a rather modest effort. The method is therefore useful as a design tool.

[1] A. A. Adly, I. D. Mayergoyz, and A. Bergqvist, J. Appl. Phys. **69**, 5777 (1991).
[2] A. Bergqvist and G. Engdahl, IEEE Trans. Magn. **MAG-27**, 4796 (1991).
[3] A. Bergqvist and G. Engdahl, J. Appl. Phys. (in press)
[4] I. D. Mayergoyz, *Mathematical Models of Hysteresis* (Springer, New York, 1991).
[5] L. Kvarnsjö and G. Engdahl, presented at the 1st MEA'93, Paper No. 0P2.13.
[6] D. C. Jiles and S. Hariharan, J. Appl. Phys. **67**, 5013 (1990).
[7] L. Kvarnsjö and G. Engdahl, IEEE Trans. Magn. **MAG-27**, 5349 (1991).
[8] J. B. Restorff, H. T. Savage, A. E. Clark, and M. Wun-Fogle, J. Appl. Phys. **67**, 5016 (1990).

Reversible transverse susceptibility of particulate recording media

Jing Ju Lu, Huei Li Huang, Ching-Ray Chang, and Ivo Klik
Department of Physics, National Taiwan University, Taipei, Taiwan, Republic of China

The response of a system to an infinitesimal perturbation becomes singular if the system changes its degree of metastability, i.e., if it has an inflection point. This theory is used to calculate the reversible transverse susceptibility χ_t of a single domain particle executing a major hysteresis loop under the influence of a field $\mathbf{H}(t)$ applied at an angle β to the easy axis. Thermal relaxation is taken into account and the response of the nonequilibrium system to the infinitesimal field $h(t)=h\sin\omega t$, $\mathbf{h}\perp\mathbf{H}$, is found. The resultant χ_t is studied as a function of β, temperature, and of the frequency Ω of the biasing field H.

In a recent article, Hoare *et al.*,[1] using the theory of Aharoni *et al.*,[2] analyzed their measurements of the reversible transverse susceptibility (RTS) of particulate recording media. Coherent rotation of magnetization within the Stoner–Wohlfarth limit was assumed.[3] The role of the ubiquitous thermal switching effects is considered here.

For definiteness of discussion we shall first derive a general expression for the response of a system with energy $E(x^{(i)}|h)$, $x^{(i)}$ are its internal degrees of freedom, to an infinitesimal applied field h. The extremal points $x_j^{(i)}[h]$ satisfy the set of equations $E_{x^{(k)}}(x_j^{(i)}[h]|h)=0$, $E_{x^{(k)}}=\partial E/\partial x^{(k)}$, and we shall now determine the functions $x_j^{(i)}[h]$ to the first order in h. To this end we write $x_j^{(i)}[h]=x_j^{(i)}[0]+h\,\delta x_j^{(i)}[0]+o(h)$ and demand that the extremal condition,

$$0=E_{x^{(k)}}(x_j^{(i)}[0]|0)+h\left(E_{h,x^{(k)}}(x_j^{(i)}[0]|0)+\sum_i \delta x_j^{(i)}[0]E_{x^{(k)},x^{(i)}}(x_j^{(i)}[0]|0)\right)+o(h), \tag{1}$$

be satisfied separately in every order of h. The zeroth-order term yields the location of the unperturbed extremum $x_j^{(i)}[0]$ and the first-order term constitutes a set of linear equations for the perturbation $\delta x_j^{(i)}[0]$. The discriminant of this system, $\det(E_{x^{(k)},x^{(i)}})$, is the Hessian of the energy function $E(x^{(i)}|0)$ at the local extremum $x_j^{(i)}[0]$, which vanishes if this extremum becomes an inflection point. The set of linear equations for $\delta x_j^{(i)}[0]$ thus becomes singular whenever the degree of metastability of the system $E(x^{(i)}|0)$ changes.

We apply Eq. (1) to a uniaxial single domain particle with volume V, anisotropy constant K, and saturation magnetization M_s. Its easy axis is in the $[\sin\beta,0,\cos\beta]$ direction and it is driven by two periodic biasing fields, $\mathbf{H}(t)$ and $\mathbf{h}(t)$, applied perpendicular to each other: $\mathbf{H}=H(t)[0,0,1]$ and $\mathbf{h}=h(t)[\cos\gamma,\sin\gamma,0]$. Their frequencies are Ω and ω, respectively. We shall assume that the field $H(t)$ varies slowly (hours, say) and that it drives a major hysteresis loop, i.e., that its amplitude $H\geqslant H_a(\beta)$, where $H_a(\beta)$ is the particle's nucleation field.[4] The field $h(t)=h\sin\omega t$, by contrast, is assumed to vary rapidly ($\omega\sim10^1$–10^2 Hz), but with infinitesimal amplitude $h\to0$. We shall determine the linear response of the nonequilibrium system, executing a hysteresis loop to the small transverse perturbing field $h(t)$. The (scaled) energy is

$$E(\alpha_i|h)=1-(\sin\beta\alpha_1+\cos\beta\alpha_3)^2-H(t)\alpha_3-h(t)\cos\gamma\alpha_1-h(t)\sin\gamma\alpha_2, \tag{2}$$

where we introduced the notation $E\to E/KV$, $H\to HM_s/K$, and $h\to hM_s/K$. The direction cosines $\alpha=[\sin\theta\cos\phi,\sin\theta\sin\phi,\cos\theta]$ refer to the magnetization direction and $\phi\in(0,2\pi)$ and $\theta\in(0,\pi)$.

The singularities of Eq. (1) can only be observed if the system finds itself at one of the vanishing minima. We shall assume that the dynamics of the particle (2) are fully determined by thermally activated jump processes. Then for fields smaller than $H_a(\beta)$, the system (2) is bistable, and we shall treat it as having two levels with occupation numbers n_1 and $n_2=1-n_1$. The rates of thermally activated transitions between them are $\kappa_{12}=\kappa_{1\to2}=f_0\exp[-KV(E_3-E_1)/T]$ and $\kappa_{21}=f_0\exp[-KV(E_3-E_2)/T]$. For the prefactor we take the customary value[5,6] $f_0=e^{25}$ Hz; E_1 and E_2 are the energies of the two local minima, E_3 is the energy of the saddle point separating them, and T is temperature ($k_B\equiv1$). The mean time evolution of the particle (2) is given by the equations[6]

$$\dot n_1=-\kappa_{12}n_1+\kappa_{21}n_2=-\dot n_2, \tag{3}$$

where $\dot n_i=dn_i/dt$ and $\kappa_{ij}=\kappa_{ij}[H(t),h(t)]$. Now let $\mathbf{m}=\mathbf{M}/M_s$ be the reduced magnetization; we shall be concerned with its projections $m_H=(\mathbf{m}\cdot\mathbf{H})/H$ and $m_h=(\mathbf{m}\cdot\mathbf{h})/h$, where $\mathbf{m}$, in the two level approximation, is given by the vector

$$\mathbf{m}=\sum_{i=1}^{2} n_i[\sin\theta_i\cos\phi_i,\sin\theta_i\sin\phi_i,\cos\theta_i], \tag{4}$$

and $\theta_i=\theta_i[H(t),h(t)]$, $\phi_i=\phi_i[H(t),h(t)]$ are the locations of the two local minima. We define the (reduced) longitudinal and transverse reversible susceptibilities as $\chi_l\sin\omega t=\lim_{h\to0}\partial m_H/\partial h$ and $\chi_t\sin\omega t=\lim_{h\to0}\partial m_h/\partial h$, respectively, with the limits referring to the amplitude of $h(t)$. In the spirit of linear response theory, we shall now treat h as a small perturbation and expand, following Eq. (1), all variables to the first order in h, e.g., $\theta[H,h]\to\theta[H]+h(t)\delta\theta[H]$, etc. The extrema are at the point $(\phi+h\,\delta\phi,\theta+h\,\delta\theta)$, where[7]

$$0=\pm\sin2(\theta-\beta)+H\sin\theta, \tag{5}$$

$$0=[2\cos2(\theta\mp\beta)+H\cos\theta]\delta\theta\mp\cos\theta\cos\gamma, \tag{6}$$

 0021-8979/94/75(10)/5499/3/$6.00 © 1994 American Institute of Physics

$$0 = \pm 2 \sin\beta \sin\theta \cos(\theta \mp \beta)\delta\phi \mp \sin\theta \sin\gamma. \quad (7)$$

The upper signs refer to the equilibrium direction $\phi=0$, the lower ones to $\phi=\pi$. Further, $E \to E + h(t)\delta E$, where $E = \sin^2(\theta \mp \beta) - H\cos\theta$ and $\delta E = \mp \sin\theta\cos\gamma$. The roots of $\partial E/\partial\theta = 0$, Eq. (5), are then used to calculate the extremal values of $\delta\theta$, $\delta\phi$, E, and δE.

Now let $n_1 = 1 - n_2 \to n_1 + h\ \delta n_1$ and $\kappa_{ij} \to \kappa_{ij} + h\ \delta\kappa_{ij}$, where $\delta\kappa_{ij} = -\kappa_{ij}(\delta E_3 - \delta E_i)/T$ by the definition of κ_{ij}. From Eq. (4), we obtain

$$\chi_t[H(t)|\omega] = \sum_{i=1}^{2} \{[\cos\theta_i \cos\gamma\ \delta\theta_i + \sin\theta_i \sin\gamma\ \delta\phi_i]n_i(t) + \cos\gamma \sin\theta_i\ \delta n_i(t)\}, \quad (8)$$

where all variables are defined by the state of the hysteresis loop driven by $H(t)$. In the plane geometry of the unperturbed system, we have set $\phi=0$ and extended the range of θ: $\theta \in (0, 2\pi)$. By Eq. (3), $\dot{n}_1 = -\kappa n_1 + \kappa_{21}$, $\kappa = \kappa_{12} + \kappa_{21}$, so that

$$n_1(t) = n_1(0)\mathscr{K}(t,0) + \int_0^t dt' \kappa_{21}(t')\mathscr{K}(t,t'), \quad (9)$$

where $\mathscr{K}(t_2,t_1) = \exp\left[-\int_{t_1}^{t_2} dt\ \kappa(t)\right]$. This equation determines the unperturbed hysteresis loop. The rapidly oscillating infinitesimal field $h(t)$ also alters the instantaneous relaxation rates κ_{ij} and the stationary state toward which the system, at a given moment, relaxes. Expanding thus Eq. (3) to the first order in h, we obtain the corrections $\delta n_1(t) = -\delta n_2(t)$ from the equation $\delta\dot{n}_1 = -\kappa\ \delta n_1 + [\delta\kappa_{21} - \delta\kappa\ n_1]$. Assuming $\omega \gg \Omega$, we may regard n_1 here as a constant, characterizing the immediate state of the slow nonequilibrium system at time t and write, with $\delta n_1(0) \approx 0$,

$$\delta n_1(t) = \tilde{\omega}^{-1}(\omega e^{-\kappa t} + \kappa \sin\omega t - \omega\cos\omega t), \quad (10)$$

where $\tilde{\omega}^{-1} = (\delta\kappa_{21} + \delta\kappa\, n_1)/(\kappa^2 + \omega^2)$. Resonances of the minima with $h(t)$ are neglected as occurring only at frequencies comparable to the prefactor f_0. Equation (8) for χ_t thus consists of an ω-independent part and of the incoherent term (10), which is small ($\sim\delta\kappa$) compared to the (potentially singular) coherent term. At room temperature, as a rule, $\kappa \ll \omega$, so that $\delta n_1 \sim \omega^{-1}$.

In the following analysis of the hysteresis process determining $n_i(t)$ we shall, for simplicity, first assume that $\gamma=0$. Let $n_1(t)$ refer to the well (local minimum) that exists at applied fields $H > -H_n(\beta)$, and that vanishes (turns into an inflection point) at $H = -H_n(\beta)$. We see that $n_1[H(t)] \equiv 0$ if $H \leqslant -H_n$ (the well does not exist) and $n_1[H(t)] \equiv 1$ if $H \geqslant H_n$, where this well is the sole local minimum. By the same token, the function $\delta\theta_1[H(t)]$ is defined by Eqs. (5) and (6) on the interval $(-H_n, \infty)$ on whose left edge it is singular. Similarly, $n_2[H(t)] \equiv 1$ if $H \leqslant -H_n$ and $n_2[H(t)] \equiv 0$ if $H \geqslant H_n$, and the function $\delta\theta_2[H(t)]$ is singular on the right edge of the interval $(-\infty, H_n)$. We thus detect two competing mechanisms in Eq. (8), since $n_i[H]$ identically vanishes as $\delta\theta_i[H]$ becomes singular. The position and height of the peak of $n_i\ \delta\theta_i$ therefore depend on the state of the nonequilibrium system: In the Stoner–Wohlfarth limit $n_1[H(t)] \equiv 1$ for $H > -H_n$ on a sweep from H_n to $-H_n$ and the vanishing well is fully populated arbitrarily close to the singular point $-H_n$ of $\delta\theta_1[H]$. In the reverse sweep, similarly, $n_2[H(t)] \equiv 1$ for $H < H_n$. If, however, thermal relaxation is taken into account and coercivity $H_c < H_n$, then only particles that have not reversed close to the nucleation field contribute to the singular behavior of χ_t. The occupation number of the vanishing minimum is trivially tabulated from Eq. (9), it depends on β, T, and also[6,8] on Ω.

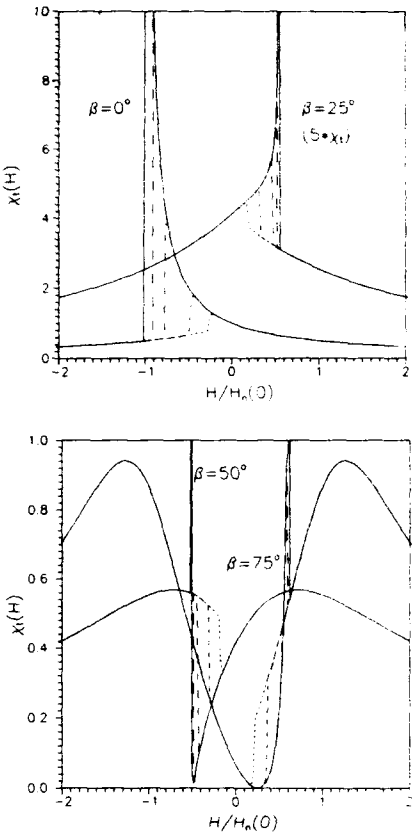

FIG. 1. The coherent part of the RTS χ_t for inclination angles, $\beta=0°$, 25° (here we plot $5\chi_t$ for better clarity), 50°, and 75°. The $\beta=0°$ and 50° curves are plotted for sweep $H_n \to -H_n$, and the remaining two curves for a reverse sweep. The solid line corresponds to the Stoner–Wohlfarth limit ($KV/T \to \infty$), to finite temperatures ($KV/T = 3000$, 500, 100, and 50) there correspond progressively shorter dashes. The finite-temperature coercivities at $\beta=0°$ are $H_c/H_n(0) \approx 0.82$, 0.75, 0.44, and 0.20 at $\Omega = 10^{-3}$ Hz.

The results of these calculations are shown in Fig. 1. It is seen that in the Stoner–Wohlfarth limit, the RTS peak width decreases with increasing inclination angle β. If relaxation effects are taken into account, then the broad peak corresponding to small β decreases in height and shifts to lower fields; our calculations show that it lies close to coercivity.

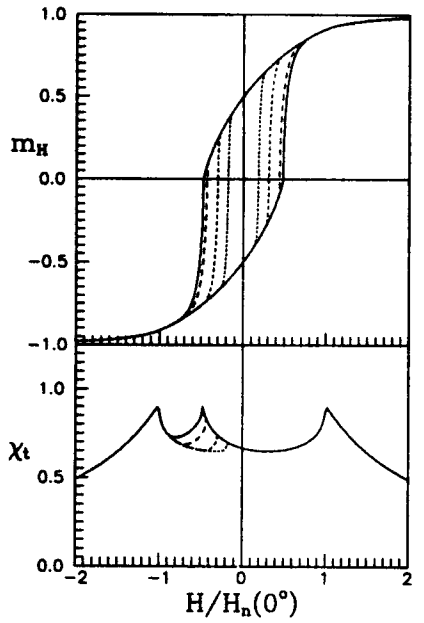

FIG. 2. A particle array with totally random orientation of easy axes. The upper plot shows mean hysteresis loops measured in the direction of the field H (sweeps $H_n \leftrightarrow -H_n$) for the four finite temperatures of Fig. 1 (here the solid line denotes $KV/T=3000$). The lower portion shows the corresponding RTS χ_t (on sweep $H_n \rightarrow -H_n$). Note, in particular, the vanishing peak close to coercivity.

On the other hand, the very narrow peak corresponding to large β is easily obliterated by thermal effects altogether. Exceptional is the case of β very close to $\pi/2$, where both minima are equally occupied[6] at all times so that the RTS peak at $H_n(\pi/2)=H_n(0)$, is insensitive to temperature. In Fig. 2 we present the hysteresis loops of an ensemble of randomly distributed[9] particles, together with their RTS plots. In accordance with the forgoing analysis, the peaks at $\pm H_n(\pi/2)$ remain unaffected by temperature variations, while the peak at the (T-dependent) coercivity is rapidly suppressed. This identification of the temperature-dependent and temperature-independent parts of RTS constitutes our main result.

Let it yet be remarked that our hysteresis calculations are based on a field-independent prefactor f_0, but, in fact,[10] $f_0=f_0(H)$ and $\lim_{H\rightarrow\pm H_n(\beta)} f_0(H) = 0$, so that thermal relaxation slows down at large applied fields and *high* coercivity is thus enhanced. The Stoner–Wohlfarth limit is accordingly reached at temperatures significantly lower than predicted by a theory with constant prefactor, and our figures overestimate the influence of thermal relaxation at low temperatures [whenever coercivity is about 75% of $H_n(\beta)$ or more].

ACKNOWLEDGMENT

This research was in part sponsored by the National Research Council of the R.O.C. under Grant No. NSC-83-0405-E02-001.

[1] A. Hoare, R. W. Chantrell, W. Schmitt, and A. Eiling, J. Phys. D Appl. Phys. **26**, 461 (1993).
[2] A. Aharoni, E. H. Frei, S. Shtrikman, and D. Treves, Bull. Res. Council Israel **5A**, 80 (1955).
[3] S. Nieber and H. Kronmüler, Phys. Status Solidi b **165**, 503 (1991).
[4] C. R. Chang, J. Appl. Phys. **69**, 2431 (1991).
[5] P. D. E. Dickson, N. M. K. Reid, C. Hunt, H. D. Williams, M. El-Hilo, and K. O'Grady, J. Magn. Magn. Mat. **125**, 345 (1993).
[6] I. Klik, C. R. Chang, and H. L. Huang, Phys. Rev. B **47**, 8605 (1993).
[7] The singularity of $\delta\phi$ at $\beta=\theta=0$ is unphysical and has its origin in the singular nature of the spherical coordinates. See I. Klik and L. Gunther, J. Stat. Phys. **60**, 473 (1990) and J. Appl. Phys. **67**, 4505 (1990).
[8] J. C. Lin, I. Klik, C. J. Chen, and C. R. Chang (these proceedings).
[9] I. Klik, H. L. Huang, and C. R. Chang, J. Appl. Phys. **73**, 6662 (1993).
[10] I. Klik, C. R. Chang, and H. L. Huang, Phys. Rev. B **48**, 15823 (1993).

Efficient Preisach demagnetization algorithm and its experimental testing

A. A. Adly and Y. J. Zhao
LDJ Electronics Inc., Troy, Michigan 48099

The topic of demagnetization has always been considered important to the area of magnetics in general. Whether it is required to characterize the initial permeability of a premagnetized sample or to erase, nondestructively, previously recorded data on disks or tapes, demagnetization processes are indispensable. Theoretically, demagnetization can be achieved by applying infinite ac field cycles with slowly decaying amplitudes. In practice, however, only a finite subset of this sequence may be applied. As a result, achieving the demagnetized state, or even a zero residual magnetization state, becomes uncertain. The purpose of this paper is to present an efficient Preisach-type demagnetization algorithm that can lead to a zero residual magnetization state within few field cycles. While this state might not fully match the demagnetized state, it can be regarded as a good approximation especially for data erasure applications. The algorithm has been experimentally tested and compared to particular demagnetization techniques employing finite ac field cycles with decaying amplitudes. Some sample results of this experimental testing are reported in the paper.

I. INTRODUCTION

The capability to carry out demagnetization processes has always been a topic of wide interest. For instance, when the characterization of initial permeability of a premagnetized sample is required, demagnetization becomes an obvious prerequisite. In the field of magnetic recording, bulk ac erasure, which is a typical demagnetization process, is frequently used to, nondestructively, remove previously recorded data (see, e.g., Refs. 1–4).

Theoretically, the demagnetized state can be achieved by applying an infinite sequence of alternating fields having slowly decaying amplitudes. In practice, however, only a finite subset of this sequence may be applied. Typical conventional demagnetization techniques employ such a finite sequence in the form of an ac field having a linearly decaying amplitude.[3] In such cases, the ability to achieve demagnetization, or even a zero residual magnetization state, becomes dependent on several factors such as the rate of the ac field amplitude decay. The smaller the rate of field decay (i.e., the larger the number of applied field cycles), the better demagnetization results are obtained. More generally, it can be stated that the selection of the number as well as the magnitudes of applied field extrema becomes crucial to the demagnetization process.

In this paper, an efficient algorithm based on the classical Preisach model of hysteresis[5,6] is introduced. This algorithm can lead to a zero residual magnetization state within few applied field cycles through the appropriate selection of field extrema. While this state might not fully match the demagnetized state, and thus corresponding initial permeabilities might not be identical, it can be regarded as a good approximation for the demagnetized state especially for data erasure applications. The algorithm has been developed and numerically implemented. Verification of this algorithm and comparisons with demagnetization approaches employing finite ac field cycles with linearly decaying amplitudes have been carried out experimentally, on various magnetic samples, by means of a computer controlled vibrating sample magnetometer (VSM). Some sample results of the experimental testing are reported in the paper.

II. THEORY AND NUMERICAL IMPLEMENTATION

It has been shown in Ref. 6 that the output (magnetization) of the classical Preisach model $f_1(t)$, while the input (field) $u(t)$ is being monotonically increased, can be expressed as follows:

$$f_1(t)=f_+ + \sum_{j=1}^{n(t)-1} (f_{mj,Mj}+f_{mj,M(j-1)}) + f_{m(n-1),u(t)} - f_{u(t),u(t)}, \tag{1}$$

where, $f_{\beta,\alpha}$ is the model output at the input value α along the increasing first-order reversal curve initiated from the major descending branch at the input value β, $n(t)$ is the number of local maxima stored by the model at time t, and f_+ is the model output corresponding to the state of positive saturation (i.e., when $u(t)\geq H_{sat}$).

In the particular case when $n(t)=1$, expression (1) will give the model output $f_1(t)$ corresponding to the input field sequence $\{H_{sat},m_1,u(t)\}$. If $u(t)=0$, this input sequence can be regarded as a one-cycle demagnetization sequence initiated from the input field value H_{sat}. For convenience, $f_1(t)$ will be denoted by f_{res1} since this output represents a residual value. Thus, Eq. (1) will reduce to the form

$$f_{res1}=f_{m_1,0}. \tag{2}$$

Similarly, the model output f_{res2} corresponding to the input field sequence $\{H_{sat},m_2,0\}$ can be given by

$$f_{res2}=f_{m_2,0}. \tag{3}$$

In Ref. 6, it has been shown that global linearization of output increments computed by the classical Preisach model, and corresponding to two different input sequences, can be performed if one sequence is considered as a perturbation of

 0021-8979/94/75(10)/5502/3/$6.00 © 1994 American Institute of Physics

the other. This approach has demonstrated considerable accuracy for output-dependent models[7] and can, as well, be applied on expressions (2) and (3).

By assuming that the input minimum m_2 is a perturbation of m_1, and by using only the first two terms of Taylor expansion, f_{res2} can be evaluated in terms of f_{res1} as follows:

$$f_{res2} \approx f_{res1} + (m_2 - m_1) \left. \frac{\partial f_{\beta,0}}{\partial \beta} \right|_{\beta = m_1} . \tag{4}$$

The partial derivative in Eq. (4) can be linearly approximated by the expression,

$$\left. \frac{\partial f_{\beta,0}}{\partial \beta} \right|_{\beta = m_1} \approx \frac{(f_{res1} - f_{res0})}{(m_1 - m_0)} , \tag{5}$$

where, f_{res0} is the residual output corresponding to the demagnetization cycle whose extrema are given by $\{H_{sat}, m_0, 0\}$.

Substituting Eq. (5) into Eq. (4), and solving for the only unknown variable m_2 in the input sequence $\{H_{sat}, m_2, 0\}$ that would result in a zero residual output (i.e., $f_{res2} \approx 0$), we get,

$$m_2 \approx m_1 - f_{res1} \frac{(m_1 - m_0)}{(f_{res1} - f_{res0})} . \tag{6}$$

Equation (6) suggests that sufficient information can be drawn from the results of two preliminary demagnetization cycles to come up with a possible set of input extrema for an additional cycle that would lead to a zero residual magnetization value. These two preliminary cycles can be considered as some partial identification process required to be performed on the sample. It may, thus, be expected that the results obtained by using this algorithm would be independent of the material characteristics. Practically, however, achieving a zero residual magnetization state within three cycles might not be possible because of the inherent approximations in Eq. (6) which are introduced by Eqs. (4) and (5).

In the case when the residual magnetization value is not satisfactory after three cycles, the algorithm may be reapplied, in a recursive manner, by first performing the following mathematical steps, in the given order:

$$f_{res0} = f_{res1} \text{ and } m_0 = m_1 ,$$

$$\text{then } f_{res1} = f_{res2} \text{ and } m_1 = m_2 . \tag{7}$$

According to these steps, the two most recent cycles will be regarded as the two preliminary ones from the model's point of view. In other words, it updates the identification process. The new value m_2 can then be dynamically calculated using Eq. (6) and an additional demagnetization cycle may be initiated. This dynamic recursive approach can be carried out for any number of cycles $N \geq 3$ until the desired residual magnetization level is achieved. It will be shown, however, in Sec. III that remarkable residual magnetization values have been reached within less than five cycles. It should be pointed out that convergence to the zero residual magnetization value is guaranteed by the fact that first-order reversal curves are nonintersecting.

In order to utilize and verify this recursive algorithm, the digital code implementing it has been developed, using Test Development Language (TDL), on an IBM PC controller of a (VSM). A TDL digital code implementing particular demagnetization techniques employing finite ac field cycles with linearly decaying amplitudes has also been developed to perform comparisons between both approaches.

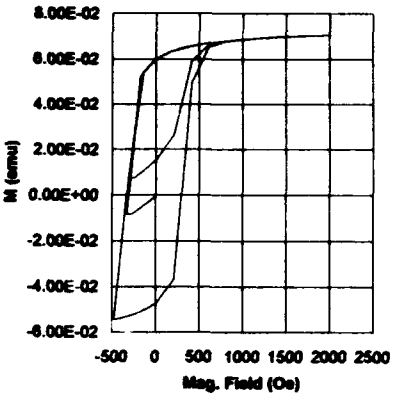

FIG. 1. Demagnetization performed by using the new algorithm on a disk sample cut from the magnetic strip of a commercially available calling card (3 cycles).

III. EXPERIMENTAL TESTING

Experimental testing has been carried out on various samples having different applications. All experiments have been performed by using a PC controlled VSM (LDJ VSM model 9500) at the LDJ Magnetic Measurement Services Laboratory. Throughout the tests, minimum values m_0 and m_1 of the first two cycles (i.e., the original identification cycles) were set to about $-1.5H_c$ and $-H_c$, respectively, where H_c is the sample coercivity. These coercivity values were determined by tracing the major hysteresis loops prior

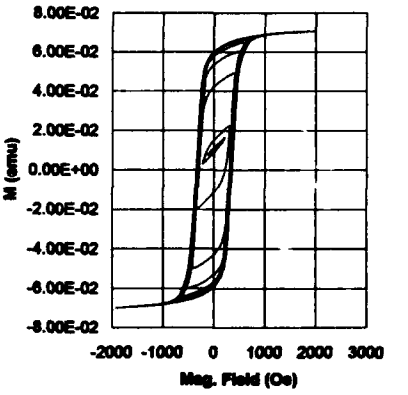

FIG. 2. Demagnetization performed by using the conventional algorithm on the same sample shown in Fig. 1 (20 cycles).

TABLE I. Some of the tested samples and results of demagnetization experiments.

Sample	Barium ferrite	BASF floppy	Cred. card mag. strip	Securi[illegible] tape
Geom. dimens.	Disk $d=5.9$ mm $t=1.5$ mm	Disk $d=6.5$ mm	Disk $d=6.5$ mm	Disk $d=6.5$ mm
H_c	3724 Oe	633 Oe	209 Oe	505 Oe
SR	0.59	0.68	0.32	0.55
M_r	3.321	$4.55E-03$	4.966	$1.059E-03$
$f_{res\,(4)}$	$2.557E-02$	$2.501E-04$	$1.564E-03$	$2.439E-05$
$f^*_{res\,(20)}$	1.031	$1.002E-03$	$2.794E-03$	$4.199E-04$
M units	emu	emu	emu	emu

to starting the demagnetization process. For tape and floppy disk samples, fields were applied along their intended longitudinal recording directions. Bulk samples of the unoriented type, on the other hand, were appropriately positioned to minimize demagnetization effects. Figure 1 shows the result of applying a total of three demagnetization cycles utilizing the presented algorithm on a sample of high squareness ratio (SR=0.83), having a diameter $d=6.5$ mm, and cut from the magnetic strip of a commercially available calling card. The effect of demagnetizing the same sample by an ac field that linearly decays over 20 cycles is demonstrated in Fig. 2.

Data concerning some of the other magnetic samples chosen for experimental testing are given in Table I. In Table I, M_r denotes the remanent magnetization of the major loop, SR is the squareness ratio, while, $f_{res(4)}$ and $f^*_{res(20)}$ represent the residual magnetization achieved after four cycles of the new algorithm and 20 cycles of the aforementioned conventional one, respectively. In Fig. 3, the result of applying the new demagnetization algorithm on the bulk barium ferrite sample (i.e., the first samples in Table I) is given. Because of the space limitation, other results are not included in graphical form. Nevertheless, the effectiveness of both algorithms on demagnetizing various samples can be easily extracted from the residual and remanent magnetization values given in Table I.

It can be concluded from these experimental results that the residual magnetization levels achieved within four cycles by using the introduced algorithm are significantly less than those achieved by the aforementioned conventional algorithm after 20 demagnetization cycles. In other words, the new algorithm is more efficient than the particular conventional one discussed in this paper. Results in Table I also suggest that the new algorithm leads to, somewhat, consistent favorable results irrespective of the sample involved in the demagnetization process. This can be mainly attributed to the fact that material characteristics are taken into account during the demagnetization procedure through the identification process performed by the algorithm. Conventional ac algorithms discussed in this paper, on the other hand, do not involve material characteristics in the demagnetization process and, for this reason, their performance may widely vary depending on the material as shown in Table I as well as Fig. 2.

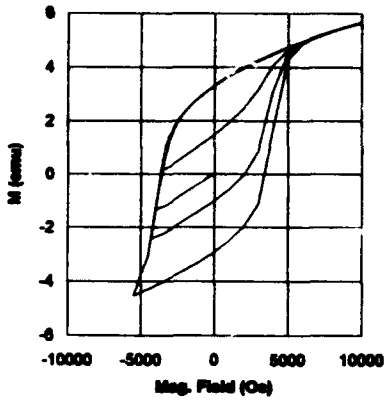

FIG. 3. Demagnetization performed by using the new algorithm on a bulk barium ferrite sample in the form of a disk (four cycles).

[1] E. R. Burke and D. R. Sanders, IEEE Trans. Magn. **MAG-21**, 1374 (1985).
[2] E. R. Christensen and B. I. Finkerstein, IEEE Trans. Magn. **MAG-21**, 1377 (1985).
[3] R. R. Katti, F. Servan-Schreiber, and M. H. Kryder, J. Appl. Phys. **61**, 4037 (1987).
[4] K. C. Wiesen, R. R. Katti, S. H. Charap, and M. H. Kryder, J. Appl. Phys. **63**, 3378 (1988).
[5] I. D. Mayergoyz, Phys. Rev. Lett. **56**, 1518 (1988).
[6] I. D. Mayergoyz, *Mathematical Models of Hysteresis* (Springer, New York, 1991).
[7] I. D. Mayergoyz and A. A. Adly, IEEE Trans. Magn. **MAG-28**, 2605 (1992).

Interpreting logarithmic decay

Ivo Klik and Ching-Ray Chang
Department of Physics, National Taiwan University, Taipei, Taiwan, Republic of China

J. Lee
Department of Electrical Engineering, Chang Gung College of Medicine and Technology, Kwei-San, Tao-Yuan, Taiwan, Republic of China

We consider an array of thermally relaxing single domain particles with lognormal distribution of nucleation fields. At a constant applied field we calculate the mean magnetization and the magnetic viscosity and irreversible susceptibility due to thermal activation, and analyze the existence conditions of logarithmic decay and the time interval on which it can be observed. For very narrow distributions multiexponential decay is obtained. An approximate relation between magnetic viscosity and irreversible susceptibility is proposed and the influence of activation volume distribution is included.

I. INTRODUCTION

This work is a sequel to a previous publication[1] in which, following Aharoni's suggestion,[2] we studied, from a purely mathematical point of view, the mean magnetization of an ensemble of thermally relaxing single domain uniaxial particles with energy,

$$E=V[K(1-\alpha_3^2)-HM_s\alpha_3]=VK(1-\alpha_3^2-2h\alpha_3), \quad (1)$$

and lognormally distributed activation volumes, $P(V)=(\xi V)^{-1}(2\pi)^{-1/2}\exp[-(2\xi^2)^{-1}\ln^2 v]$, $v=V/V_0$. Further, α_3 is a direction cosine, K is the anisotropy constant, M_s is the saturation magnetization, and $h=H/H_n$ is the applied field scaled by the nucleation field $H_n=2K/M_s$. Here we carry out this program for an ensemble in which the nucleation fields H_n are lognormally distributed, $P(H_n)=(\sigma H_n)^{-1}(2\pi)^{-1/2}\exp[-(2\sigma^2)^{-1}\ln^2 h_n]$, $h_n=H_n/H_{n0}$. Such distribution[3] arises, e.g., due to variation in demagnetizing fields (dependent on shape, inclusions, interparticle interactions, etc.), which randomly modify the nucleation fields of individual particles. We analyze and tabulate the integral expressions for the mean magnetization and the corresponding thermal activation-type magnetic viscosity and irreversible susceptibility, and then propose a simple approximate relation between the latter two quantities.

II. THE MASTER EQUATION

For fields $|h|<1$ at sufficiently low temperature T, the system (1) may be treated as having two levels with occupation numbers $n_1(t)$ and $n_2(t)=1-n_1(t)$ and thermal jump probabilities $\kappa_{ij}\equiv\kappa_{i\to j}$. Its evolution is given by the master equation

$$\frac{d}{dt}\begin{pmatrix}n_1\\ n_2\end{pmatrix}=\begin{pmatrix}-\kappa_{12} & \kappa_{21}\\ \kappa_{12} & -\kappa_{21}\end{pmatrix}\begin{pmatrix}n_1\\ n_2\end{pmatrix}. \quad (2)$$

The reduced magnetization $m(t)=M(t)/M_s=n_2(t)-n_1(t)$ is

$$m(t)=m_{eq}-2[n_1(0)-\mu]\exp[-(\kappa_{12}+\kappa_{21})t], \quad (3)$$

where $m_{eq}=(\kappa_{12}-\kappa_{21})/(\kappa_{12}+\kappa_{21})$ and $\mu=\kappa_{21}/(\kappa_{12}+\kappa_{21})$. It should be noted that as opposed to a Fokker–Planck equation, which goes to thermal equilibrium by construction,[4] the stationary state m_{eq} of Eq. (3) yields the correct (quadratic approximation) result only if κ_{ij} are calculated within the transition state theory,[5] $\kappa_{ij}\sim\omega_i\exp(-Q_i/T)$, where ω_i is the frequency at the bottom of the ith well of depth Q_i (we set $k_B=1$). A dissipative constant dependent prefactor[4,5] would introduce unphysical terms into m_{eq}.

Let us set $m(0)=-1$. For $h>0$ and $T\to 0$, Eq. (3) then takes on the simple form $m(t)=1-2e^{-\kappa t}$, since $\kappa_{21}\ll\kappa_{12}=\kappa(H_n,H)=\omega_1\exp[-Q_1(H_n,H)/T]$, where $2Q_1(h,H_n)=M_sVH_n(1-h)^2\ll 2Q_2$. For the prefactor[1] we may set here $\omega_1=e^{25}$ Hz.

Yet, for brevity, we introduce the notation $Q=M_sVH_{n0}/2$.

III. THE MEAN EVOLUTION

The most probable nucleation field within the ensemble is $H_{np}=H_{n0}\exp(-\sigma^2)$; we shall assume (in order to define a convenient time scale) that the applied reversing field H satisfies the condition $0<H<H_{np}$ and write $\beta_p=H/H_{np}<1$. The number of particles with nucleation fields $H_n\leq H$ is

$$n_<(H)=[1+\mathrm{Erf}(\ln\beta/\sqrt{2}\sigma)]/2, \quad (4)$$

where $\beta=H/H_{n0}$ and $\mathrm{Erf}(x)$ is the error function. These particles reverse, by assumption, immediately while the remaining $n_>(H)=1-n_<(H)$ particles switch thermally, each with its particular decay rate $\kappa(H_n,H)$. On averaging the thermal decay law over the lognormal distribution of nucleation fields, we obtain the expectation value of the net system magnetization in the form

$$\langle m(\tau,\beta)\rangle=1-2n_>(H)I_1(\tau,\beta|\sigma), \quad (5)$$

where the integral I_1 is defined as

$$I_1(\tau,\beta|\sigma)=\sigma^{-1}(2\pi)^{-1/2}\int_\beta^\infty dx\ g_1(x)\times\exp[-\tau g_2(x)]\quad\left(x=\frac{H_n}{H_{n0}}\right), \quad (6)$$

with $g_1(x)=x^{-1}\exp[-(2\sigma^2)^{-1}\ln^2 x]$ and $g_2(x)=\exp[-Qx(1-\beta/x)^2+q]$. Here we also introduced the reduced time $\tau=t\kappa(H_{np},H)$, where $\kappa(H_{np},H)=\exp(25-q)$ is the relaxation rate associated with the *most probable*

 0021-8979/94/75(10)/5505/3/$6.00 © 1994 American Institute of Physics

nucleation field H_{np} and $q=Q(1-\beta_p)^2\exp(-\sigma^2)$. The magnetic viscosity S is defined by means of the derivative

$$\frac{\partial\langle m(\tau,\beta)\rangle}{\partial \ln \tau}=\frac{2n_>}{\sigma(2\pi)^{1/2}}\int_\beta^\infty dx\; g_1(x)\tau g_2(x) \times\exp[-\tau g_2(x)]\equiv 2n_> I_2(\tau,\beta|\sigma), \quad (7)$$

and the irreversible susceptibility χ_{irr} by means of

$$\frac{\partial\langle m(\tau,\beta)\rangle}{\partial\beta}=-2\left(\frac{\partial n_>}{\partial\beta}\right)I_1-2n_>\left(\frac{\partial I_1}{\partial\beta}\right), \quad (8)$$

where, by virtue of Eqs. (4) and (6),

$$\frac{\partial n_>}{\partial\beta}=-(\beta\sigma)^{-1}(2\pi)^{-1/2} \times\exp[-(2\sigma^2)^{-1}\ln^2\beta], \quad (9)$$

$$\frac{\partial I_1}{\partial\beta}=-(\beta\sigma)^{-1}(2\pi)^{-1/2}\exp[-(2\sigma^2)^{-1}\ln^2\beta-\tau e^q] -I_3(\tau,\beta|\sigma), \quad (10)$$

$$I_3(\tau,\beta|\sigma)=\frac{2Q}{\sigma(2\pi)^{1/2}}\int_\beta^\infty dx\left(1-\frac{\beta}{x}\right)g_1(x)\tau g_2(x) \times\exp[-\tau g_2(x)]. \quad (11)$$

The integrand of I_2 in Eq. (7) is a product[1] of the peaked functions $g_1(x)$ and $g_2(x)e^{-\tau g_2(x)}$: The function $g_1(x)$ originates from the lognormal distribution of H_n, and has an immobile maximum at the point $x_{10}=\exp(-\sigma^2)$. The extremal properties of the function $g_2e^{-\tau g_2}$ are determined by the time-dependent factor

$$\Delta^2(\tau)=(2\beta Q+q+\ln\tau)^2-4\beta^2Q^2. \quad (12)$$

For sufficiently large times, $\Delta^2(\tau)>0$ and $g_2e^{-\tau g_2}$ has a movable peak at

$$x_{20}(\tau)=[2\beta Q+q+\ln\tau+\Delta(\tau)]/(2Q), \quad (13)$$

which shifts to the right with increasing time. If $\Delta^2(\tau)<0$, on the other hand, then $g_2e^{-\tau g_2}$ has only an immobile maximum at $x=\beta$ (the edge of integration domain). For $\Delta^2(\tau)>0$, this point becomes a local minimum and $x_{20}(\tau)$ of Eq. (13) gives the position of the movable peak, which has split from the point $x=\beta$ at time τ_0, $\Delta(\tau_0)=0$. In Fig. 1 we plot the integrals I_1 and I_2 versus the relaxation time $\kappa^{-1}(\langle H_n\rangle,H)=\exp[Q(1-\beta_a)^2\exp(\sigma^2/2)-25]$, $\beta_a=H/\langle H_n\rangle$, associated with the *average* nucleation field. The large initial slope of the function I_1 is easily understood: The fraction of particles with $H_n<\langle H_n\rangle=H_{n0}\exp(\sigma^2/2)$ increases with σ, and these particles switch rapidly on the time scale of $\kappa^{-1}(\langle H_n\rangle,H)$. The small σ curves, though exhibiting no logarithmic decay, cannot be approximated by a single exponent but very well by a sum[6] of exponential terms.

The overall structure of the functions I_1 and I_2 is remarkably insensitive to the magnitude of applied field; $I_2\approx$const at its *maximum* value, that is, on a time interval during which the movable peak $x_{20}(\tau)$ of Eq. (13) *overlaps* the immobile peak at $x_{10}=\exp(-\sigma^2)$. If $t=\rho\kappa^{-1}(\langle H_n\rangle,H)$ and Q is sufficiently large, then Eq. (13) becomes

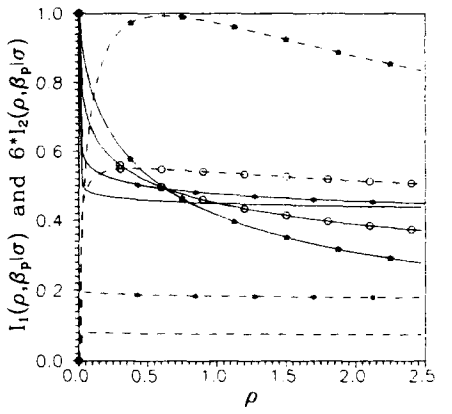

FIG. 1. The integrals $I_1(\rho,\beta_p|\sigma)$ (full lines) and $I_2(\rho,\beta_p|\sigma)$ (dashed lines, denote the scale) plotted versus the reduced time $\rho=t\kappa(\langle H_n\rangle,H)$. The applied field is $\beta_p=H/H_{np}=0.1$ and $\sigma=0.05$ (*), 0.1 (○), 0.3 (•), and 0.6 (unmarked). In all cases $\kappa^{-1}(H_{np},H)=1$ yr.

$$x_{20}(\tau)\approx\exp(\sigma^2/2)+Q^{-1}\ln\rho, \quad (14)$$

and logarithmic decay is observed if $x_{20}(\tau)\approx x_{10}$. For large σ the peak of $g_1(x)$ is very broad, and this overlapping condition is easily satisfied for long time intervals on which I_2 maintains its maximum value. With increasing σ, the peak value of $g_1(x)$ decreases, and so does the peak value of I_2 The result (14) was also obtained[1] by averaging with respect to V; in this case it is exact and $\rho=t\kappa(\langle V\rangle)$, where $\kappa(\langle V\rangle)$ is the decay rate associated with the average volume. The overlap of two peaks, which, here, happen to be of essentially equal height and width apparently disqualifies any attempts to expand $g_1(x)$ into a power series:[7] These expansions invariably result in linear dependence of I_2 on T, whereas $I_2\propto T^{1/2}$ according to Fig. 2; $I_2\propto T^{1/2}$ also holds for averages over V.

IV. THE VISCOSITY PARAMETER

In our study[1] of averages over activation volumes, we found that the relation

$$T\left(\frac{\partial\langle M\rangle}{\partial H}\right)=\langle V\rangle\left(\frac{\partial\mathcal{H}}{\partial H}\right)\cdot\left(\frac{-\partial\langle M\rangle}{\partial\ln\tau}\right), \quad (15)$$

defining the viscosity parameter $S_v=S/\chi_{irr}$, is well satisfied for lognormal distribution of V with $\xi\leq 0.6$. In the present case the activation energy density $\mathcal{H}(x,\beta)=Qx(1-\beta/x)^2/V$, $x=H_n/H_{n0}$, depends on the random nucleation field. We find that the best fit between the two derivatives (7) and (8) is obtained if one evaluates $\partial\mathcal{H}(x,\beta)/\partial\beta$ at the point $\langle x\rangle=\exp(\sigma^2/2)$, i.e., at the average nucleation field. In Fig. 3 we plot, for selected values of β and σ, the ratio of Eq. (8) to Eq. (7) scaled by the proposed factor:

$$\nu(\tau,\beta|\sigma)=\left(n_>\frac{\partial\mathcal{H}(\langle x\rangle,\beta)}{\partial\beta}\,I_2(\tau,\beta|\sigma)\right)^{-1}$$

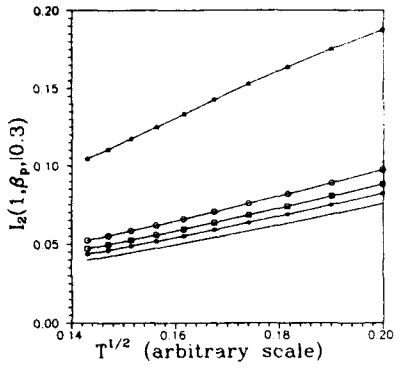

FIG. 2. The integral $I_2(1,\beta_p|0.3)$ plotted versus $T^{1/2}$. Applied field is $\beta_p=0$ (unmarked curve, valid as a limiting value only), 0.3 (*), 0.4 (□), 0.5 (○), and 0.8 (*). This graph and the structure of the Arrhenius factor suggest that $I_2 \propto T^{1/2}/(1-h)$. The highest temperature corresponds to $\kappa^{-1}(H_{np},0)=1$ s, the lowest one to $\kappa^{-1}(H_{np},0)=10^4$ yr.

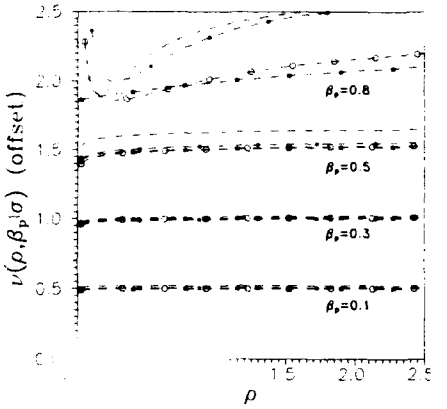

FIG. 3. The ratio $\nu(\rho,\beta_p|\sigma)$ plotted versus the reduced time $\rho=t\kappa(\langle H_n\rangle,H)$. The families of plots are offset by the values $\Delta\nu(\beta_p)=-0.5$ for $\beta_p=0.1$, by 0 for $\beta_p=0.3$, by 0.5 for $\beta_p=0.5$, and by 1 for $\beta_p=0.8$. Further, $\sigma=0.05$ (*), 0.1 (○), 0.3 (*), and 0.4 (unmarked). In all cases $\kappa^{-1}(H_{np},H)=1$ yr.

$$\cdot\left\{\frac{I_1(\tau,\beta|\sigma)}{\beta\sigma(2\pi)^{1/2}}\ \exp\left(-\frac{\ln^2\beta}{2\sigma^2}\right)\right.$$
$$+n_>\left[\frac{1}{\beta\sigma(2\pi)^{1/2}}\ \exp\left(-\frac{\ln^2\beta}{2\sigma^2}+\tau e^q\right)\right.$$
$$\left.\left.+I_3(\tau,\beta|\sigma)\right]\right\}. \tag{16}$$

We see that to a good approximation $\nu\approx 1$ for sufficiently small reversing field β and parameters σ. Deviations (on the order of unity) are observed only for large σ and/or large β. We therefore propose that the relation (15) be modified as

$$\frac{\partial\langle M\rangle}{\partial H}=\frac{\langle V\rangle}{T}\frac{\partial\mathcal{E}(\langle H_n\rangle,H)}{\partial H}\left(-\frac{\partial\langle M\rangle}{\partial\ln\tau}\right). \tag{17}$$

The existence of logarithmic decay has a sound analytic foundation in the overlapping condition and in the logarithmic t dependence of Eq. (14), both of which are independent of the specific distribution of H_n, which merely alters the peak value of I_2 and the time interval over which it is maintained. On the other hand, Eqs. (15) and (17) are empirical results of unclear mathematical origin. We have tested them for other distributions (e.g., xe^{-x^2/σ^2}) and obtained similar results as for the lognormal distribution: At very small σ, logarithic decay is *not* observed but $\nu\approx 1$ all the same. At large σ or large fields logarithmic decay is present, but $S\propto\chi_{\rm irr}$ only at very large times, and the constant of proportionality must be chosen differently (see Fig. 3). Clearly, analytic study of the integrals I_2 and I_3 is required to clarify their relation.

ACKNOWLEDGMENT

One of us (IK) acknowledges support by the National Science Council of the Republic of China under Grant No. NSC-82-0208-M002-035.

[1] I. Klik and C. R. Chang, Phys. Rev. B **47**, 9091 (1993).
[2] A. Aharoni, J. Appl. Phys. **57**, 4702 (1985).
[3] M. el-Hilo, S. H. Uren, K. O'Grady, J. Popplewell, and R. W. Chantrell, IEEE Trans. Magn. **MAG-26**, 244 (1990).
[4] I. Klik, J. Stat. Phys. **66**, 635 (1992).
[5] I. Klik and L. Gunther, J. Stat. Phys. **60**, 473 (1990); I. Klik and L. Gunther, J. Appl. Phys. **67**, 4505 (1990).
[6] R. M. Kloepper, B. Finkelstein, and D. P. Braunstein, IEEE Trans. Magn. **MAG-20**, 757 (1984)
[7] P. Gaunt, J. Appl. Phys. **59**, 4219 (1986); L. Gunther and B. Barbara, J. Magn. Magn. Mat. **128**, 35 (1993).

Magnetization processes in Co–Cr submicron samples: Hall measurements and micromagnetic simulations

M. van Kooten, S. de Haan, J. C. Lodder, and Th. J. A. Popma
Mesa Research Institute, University of Twente P.O. Box 217, NL-7500 AE, Enschede, The Netherlands

The magnetization reversal of Co–Cr with perpendicular anisotropy is studied by anomalous Hall effect measurements and by micromagnetic simulations. In a measured hysteresis loop of a 300 nm×300 nm sample (consisting of approximately 40 columns of Co–Cr), discrete jumps are observed, together with a more or less continuous change in magnetization, the latter with both positive and negative sign. The continuous and discrete parts of the hysteresis loop are separated to extract micromagnetic information from the anomalous Hall measurement. The discrete jumps are attributed to parts of columns that switch irreversibly, the continuous magnetization change is attributed to reversible rotation, partly of volumes with in-plane anisotropy. These assumptions are checked by means of a micromagnetic model.

I. INTRODUCTION

The magnetization reversal mechanism of Co–Cr for perpendicular recording is still not entirely understood. Neither domain wall motion nor incoherent reversal are able to explain the behavior, especially for the high coercivity films. Anomalous Hall effect measurements are applied on Co–Cr. With suitable lithography and etching, the measurement area can be as small as (300 nm)^2.[1] With this technique, the reversal can be clearified up to a great extent. For this purpose, we used the step size distribution in the measured hysteresis loop.[1] To interpret the measured hysteresis loops, simulations are neccesary to check whether intuitive models are correct or need extension. Micromagnetic simulations are believed to be most suitable for this task, because they start with first principles (exchange, magnetization, anisotropy, and morphology) and yield hysteresis loops and magnetization patterns. The morphology, the texture, and the composition are incorporated into the model by varying the exchange, the magnetization, and the anisotropy locally.

II. ANOMALOUS HALL MEASUREMENTS

A Co–Cr sample with a Cr content of 23 at. % is sputtered on Si covered with thin layer of SiO_2. The unetched sample has an M_s of 321 kA/m and a perpendicular coercivity H_c of 93 kA/m. The film thickness is 200 nm and the average column size at the surface is 60 nm. The samples are etched to a Hall cross geometry with a central area of (300 nm)^2.[2] The measurement area contains approximately 40 columns. At least 70% of the contribution to the Hall voltage comes from the central area of the sample of (300 nm)^2.[3]

In the anomalous Hall effect measurement setup, a current is sent through the sample, and the voltage perpendicular to the current, is measured. The hysteresis loop of an etched sample is shown in Fig. 1.[1] The loop shows many more large discrete magnetization changes (steps) as there are columns and a more or less continuous magnetization change between the steps. Further, changes with a negative ΔM can be seen. Five steps corresponding to the switching of one column are found, but most steps are smaller than 2% of M_s, corresponding to less than half a column. The Johnson noise of the sample is the main source of noise and is estimated to correspond with $0.001M_s$ in the Hall loop. This threshold is indicated in Fig. 1.

The measured hysteresis loops are decomposed as follows: The changes in magnetization ΔM after each field step (see Fig. 1) are categorized into five different classes:

I. $\Delta M > 0.003M_s$ [equivalent to > (30 nm)^3];
II. $0.003M_s > \Delta M > 0.001M_s$;
III. $0.001M_s > \Delta M > 0$;
IV. $0 > \Delta M > -0.001M_s$; and V. $-0.001M_s > \Delta M$.

The steps of the different classes are put together to a hysteresis loop again (see Fig. 2 for a clarification of the method). Since one extracted hysteresis loop consists only of magnetization changes of one class, we will call these loops Stepsize-distinguished Partial Hysteresis loops (SPH). The superposition of the SPHs from class (I), (II), and (III) yield a loop with a "saturation magnetization" of $1.3M_s$.

The Hall loop, together with the SPHs, are shown in Fig. 3. The shapes of the SPHs are very different. Loop I in Fig.

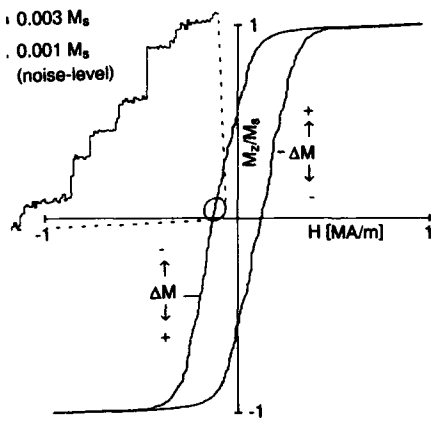

FIG. 1. The hysteresis loop of the etched sample[3] with the definition of ΔM for both the descending and the ascending branch. Inset: enlarged part of the loop with clearly visible steps and the thresholds (see the text).

 0021-8979/94/75(10)/5508/3/$6.00 © 1994 American Institute of Physics

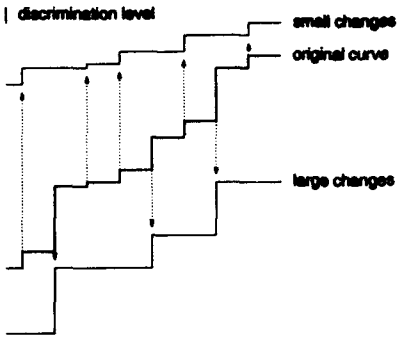

FIG. 2. Example of the extraction of two step size-distinguished partial hysteresis loops (SPHs). Changes smaller than the discrimination level (upper curve) and changes larger than the discrimination level (lower curve) are separated.

3(a), consisting of ΔMs from class I, is an almost ideal hysteresis loop of a particulate medium with perpendicular anisotropy. The loop shows the usual shearing due to demagnetization, a sharp onset of magnetization reversal, and only a small "tail," a decrease of the slope at the end of magnetization reversal. The coercivity is 10% higher than the coercivity of the original hysteresis loop. Loop II, consisting of ΔMs from class II, is clearly different. It shows a gradual onset of magnetization reversal, no tail, and a coercivity that is about half of the film coercivity. The loop consisting of negative changes above the noise level [V in Fig. 3(b)] has the same properties as loop II, except for the lower saturation value. The loops consisting of magnetization changes below the noise level (III and IV) show hysteresis and saturation. We tend to attribute this, at least partly, to magnetization reversal.

The number of magnetization changes of class I is 155, much larger than the number of columns in the measurement area. This indicates that the column is not the smallest magnetic unit in this particular Co–Cr film. A microstructure that could explain this is the CP structure,[4] where small Co-rich platelets are embedded in a Cr-rich matrix inside the column. The small changes can be explained by reversible rotation of regions with in-plane anisotropy,[5] which have no perpendicular anisotropy. The negative ΔMs might indicate the presence of magnetic volumes at the limit of superparamagnetism. According to the step size, their volume could be around $(20\ \text{nm})^3$. When using the Néel–Arrhenius law for time decay in particle assemblies $1/\tau = 10^{-9} \exp(K_1 V/kT)$[6] the estimated superparamagnetic limit of Co–Cr is $(8\ \text{nm})^3$ when using a relaxation time τ of 100 s and an anisotropy constant K_1 of $1.6\times10^5\ \text{J/m}^3$. For particulate media, it is also observed that the mentioned formula does predict the so-called activation volume, which is much smaller than the particle volume.[7] The magnitude of the SPH of class V can be an indication for the volume fraction of magnetic units at the superparamagnetic limit. With a micromagnetic model,

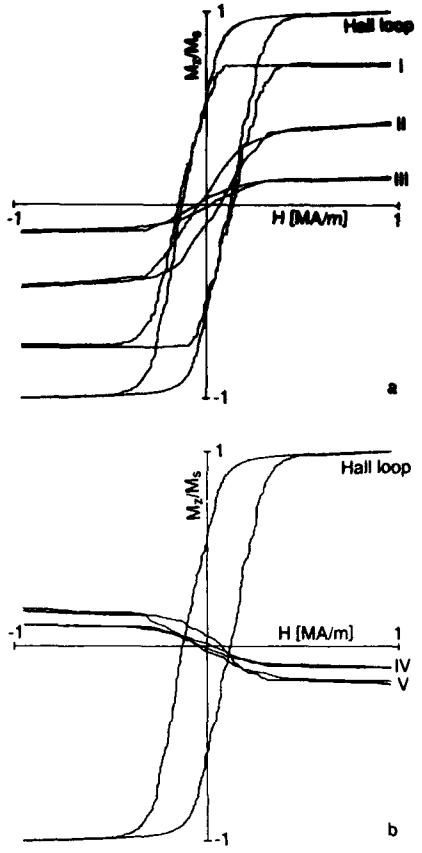

FIG. 3. The original Hall loop and the various step size-distinguished partial hysteresis loops (SPHs).

the influence of some microstructural parameters on the observed magnetic behavior are investigated.

III. MICROMAGNETIC SIMULATIONS

The used micromagnetic model[8] consists of particles in the shape of cubes of $(50\ \text{nm})^3$, which are subdivided into cubic elements of $(5\ \text{nm})^3$ with uniform magnetization. Exchange between the particles is modeled by assigning an exchange to a few randomly chosen element pairs, which are on the particle boundaries. The initial layer, as present in our Co–Cr, is modeled by assigning an in-plane easy axis to cubes of eight elements on the bottom two rows of elements in the model. These cubes are exchange coupled to the particle to which they belong.

A typical simulated hysteresis loop of a 25 particle cluster with the SPH containing magnetization changes smaller than $0.003\ M_s$ is shown in Fig. 4. These changes are due to reversible magnetization rotation. Like in the measurement, the coercivity of the SPH is about half the coercivity of the

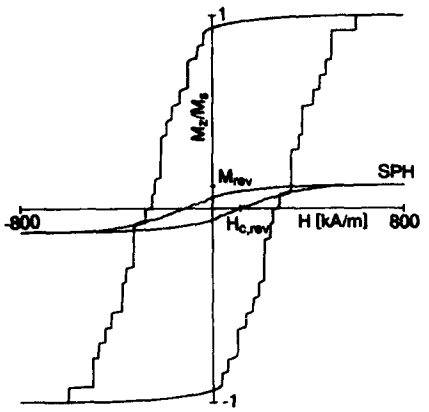

FIG. 4. A typical simulated hysteresis loop and the SPH containing the reversible rotation. The volume with in-plane anisotropy is 2%, the exchange coupling between the particles is 20%, and the spread of the easy axes of the particles is 7°.

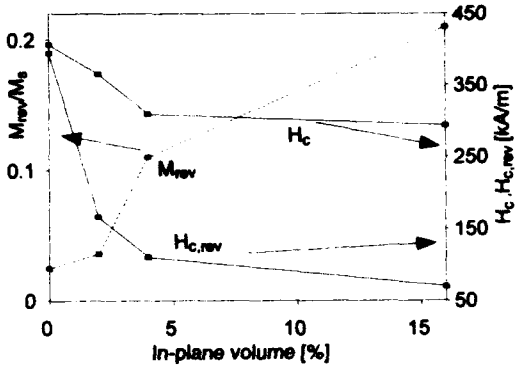

FIG. 5. The magnitude of the SPH (M_{rev}) and the coercivities of the original loops (H_c) and of the SPH ($H_{c,rev}$) as a function of the volume fraction of the initial layer.

whole system. Immediately observable and comparable quantities of the simulations are the coercivity of the major loop H_c, the coercivity of the SPH $H_{c,rev}$, and the contribution of the SPH to the total hysteresis loop M_{rev}, which are indicated in Fig. 4.

A moderate spread of the easy axes of the particles (up to 15°) only influence H_c, $H_{c,rev}$, and M_s by a few percent. The initial layer volume affects, as expected, M_{rev} considerably (Fig. 5). On the basis of this quantity, an estimate of the total volume with in-plane anisotropy can be made. In Fig. 5, H_c and $H_{c,rev}$ are shown as a function of the initial layer volume. The sharp decrease of H_c with increasing initial layer volume can partly be attributed to the artificially high switching field of micromagnetically modeled particles (Brown's paradox[9]), the reversal of the initial layer facilitates nucleation of particle reversal. $H_{c,rev}$ can, like M_{rev}, be used to estimate the volume fraction of the initial layer of the investigated Co–Cr sample, since reversible rotation in the regions with perpendicular anisotropy yields a $H_{c,rev}$ almost equal to H_c, as can be concluded from the simulation with no initial layer. With increasing initial layer volume, $H_{c,rev}$ decreases rapidly. Simulations show further, in agreement with Ref. 10, that exchange interaction between the particles lowers H_c considerably (20% exchange lowers H_c by 25%). Exchange interaction does not affect $H_{c,rev}$ and M_{rev}.

IV. CONCLUSIONS

We showed that the analysis of hysteresis loops of submicron Co–Cr samples on the basis of the measured magnetization changes yields information on distinguishable magnetic volumes in the sample. The size of the measured discrete magnetization changes shows that the average magnetic unit in Co–Cr is considerably smaller than one column. We observed five steps of approximately one column, the rest of the steps is smaller. From the presence of negative ΔMs and their distribution along the hysteresis loop, we conclude that magnetic units on the limit of superparamagnetism could be present in Co–Cr. Magnetic viscosity measurements and temperature-dependent hysteresis measurements will have to give more information about this.

Simulations show that the initial layer has a large effect on the magnetization processes in the film. Its magnetization process is reversible rotation. Simulations show further that the exchange coupling of the initial layer with the columns facilitates their magnetic reversal.

ACKNOWLEDGMENTS

This work was sponsored by the Stichting Nationale Computerfaciliteiten (NCF) for the use of supercomputer facilities. The E.C. CAMST-initiative is also acknowledged for financial support. We thank Dr. Vladimir Kambersky for many helpful discussions.

[1] S. de Haan *et al.* (to be published).
[2] S. de Haan, J. C. Lodder, and Th. J. A. Popma, J. Magn. Soc. Jpn. **15**, 349 (1991).
[3] B. C. Webb and S. Schultz, IEEE Trans. Magn. **24**, 3006 (1988).
[4] Y. Maeda and M. Asahi, J. Appl. Phys. **61**, 1972 (1987).
[5] J. C. Lodder, T. Wielinga, and J. Worst, Thin Solid Films **101**, 61 (1982).
[6] L. Néel, Adv. Phys. **4**, 191 (1955).
[7] A. M. de Witte, K. O'Grady, G. N. Coverdale, and R. W. Chantrell, J. Magn. Magn. Mat. **88**, 183 (1990).
[8] M. van Kooten, S. de Haan, J. C. Lodder, A. Lyberatos, R. W. Chantrell, and J. J. Miles, J. Magn. Magn. Mat. **120**, 145 (1993).
[9] W. F. Brown, Jr., Rev. Mod. Phys. **17**, 15 (1945).
[10] J.-G. Zhu and H. N. Bertram, J. Appl. Phys. **66**, 1291 (1988).

Frequency dependence of hysteresis curves in conducting magnetic materials (abstract)

D. C. Jiles
Ames Laboratory, Iowa State University, Ames, Iowa 50011

An extension of the differential equation for hysteresis has been developed, which takes into account the effects of eddy currents on the hysteresis curves in electrically conducting media. In the derivation presented, it is assumed that the frequency of the applied field is low enough (or the thickness of the material medium small enough) that the skin effect can be ignored. In this case, the DC hysteresis equation is extended by the addition of a term depending on (i) the rate of change of magnetization with time, (ii) the resistivity of the material, and (iii) the shape of the specimen. In the limit, as the frequency of the exciting field tends to zero, the frequency-dependent hysteresis curve approaches the DC curve.

This work was supported by the U.S. Department of Energy, Office of Basic Energy Science, under Contract No. W-7405-ENG-82.

 0021-8979/94/75(10)/5511/1/$6.00 © 1994 American Institute of Physics

Hierarchical scaling: An analytical approach to slow relaxations in spin glasses, glasses, and other correlated systems (invited)

J. Souletie
Centre de Recherches sur les Très Basses Températures, Laboratoire associé à l'Université Joseph Fourier, CNRS, BP 166, 38042 Grenoble-Cédex 9, France

A model has been developed that associates a hierarchical criterion to the usual renormalization of the distances near a phase transition. At times t smaller than $\tau_\alpha \propto (1-T_c/T)^{-z\nu}$, which diverges at T_c, it is found that the relaxation develops at a scale $s(t)$, which is a power law of the time elapsed: $s \propto t^{T/zT_c}$. If one sits in the ergodic regime $T>T_c$, the system abruptly reaches an equilibrium at $s(\tau_\alpha)=\xi(T)=\tau_\alpha^{1/z}$. If $T<T_c$, by contrast, it deviates to logarithmic behavior. The α relaxation is well approximated by a stretched exponential $\exp(-t/\tau_\alpha)^{\beta(T)}$, which traduces the effect of underlying lognormal statistics. The exponent $\beta(T)\propto[1-b\ln(1-T_c/T)]^{-1/2}$ would cancel at T_c if it was possible to wait for the sample to equilibrate at this temperature. The model has the necessary ingredients to describe effects that have been reported in both the "activated" nonergodic regime and in the critical regime of spin glasses, and of other correlated systems like orientational glasses, glass-forming liquids, and vortex glasses. A possible extension of the model is discussed to describe the "macroscopic quantum effects."

I. LOGNORMAL STATISTICS

Usual scaling accounts for the static properties of correlated systems by referring to a renormalized characteristic scale $\xi(T)$ different from the natural atomic length ξ_0, where the interaction sits. The assumption is

$$\frac{\xi(T)}{\xi_0}=\left(1-\frac{T_c}{T}\right)^{-\nu}=1+\frac{\theta}{T_c}+\cdots=\left(1-\frac{T_c}{T}\right)^{-\theta/T_c}, \quad (1)$$

where $\theta=\nu T_c$ is a natural energy scale to measure the temperature. Then through renormalization the different thermodynamic quantities can be expressed in terms of powers of the $\xi(T)$ dependence. Comparing two equilibrium situations ξ_n and $\xi_{n+1}=2^a\xi_n$ suppose we observe that their relaxation times are τ_n and $\tau_{n+1}=2^\mu\tau_n$. (In these statistical systems, some event at scale $n+1$ always comes in coincidence with the relaxation of one object at scale n): We call hierarchical scaling the situation where we have a given μ for a given a[1] as it associates a hierarchical criterion with the usual renormalization of distances (say Palmer *et al.*[2] with Kadanoff). Iterating n times, we find

$$\xi_n \sim 2^a\xi_{n-1}=2^{na}\xi_0,$$

when

$$\tau_n=2^\mu\tau_{n-1}=2^{n\mu}\tau_0, \quad (2)$$

which leads to the so-called dynamic scaling hypothesis,

$$\frac{\tau}{\tau_0}\sim\left(\frac{\xi}{\xi_0}\right)^z, \quad \text{where } z\sim\frac{\mu}{a}, \quad (3)$$

and critical slowing down follows if we use Eq. (1).

In the presence of disorder on μ, then $\ln(\tau/\tau_0)=\Sigma\mu$ is a sum of random variable. From the central limit theorem, after many steps the variance σ^2 and the most probable value $\ln(\tau_\alpha/\tau_0)$ are proportional to the number of renormalization steps hence to each other. This leads to

$$\ln\frac{\tau_\alpha}{\tau_0}\propto\sigma^2\propto -z\nu\ln\left(1-\frac{T_c}{T}\right)\propto z\frac{\theta}{T}+\frac{z\theta T_c}{T^2}\cdots. \quad (4)$$

A log-normal distribution is found as in other cases, where a recipe [Eq. (2)] is applied and repeated again and again: this is how nature proceeds, hence the importance of log-normal distributions in physics.[1,3]

The response of many individual relaxations $s(t/\tau)$ is

$$m=\int P(\ln\tau)s\left(\frac{t}{\tau}\right)d\ln\tau. \quad (5)$$

The usual exponential form of $s(t/\tau)$ would correspond to a sharp cutoff in the $\ln\tau$ scale, where $P(\ln\tau)$ is a Gaussian. Then

$$m\sim\int^{\ln t}P(\ln\tau)d\ln\tau\propto 1-\mathrm{erf}\left(\ln\frac{t}{\tau_\alpha}\right),$$
$$\overline{\frac{\partial m}{\partial\ln t}}\propto P\left(\ln\frac{t}{\tau_\alpha}\right). \quad (6)$$

An error function of $\ln(t/\tau_\alpha)$ can be fitted with a stretched exponential $\exp(-t/\tau_\alpha)^{\beta(T)}$ around $\tau=\tau_\alpha$, provided $\beta=\sigma^{-1}$.[1,3] Indeed, Ogielski has calculated relaxations for the Ising spin glass in dimension three, which he fitted with a stretched exponential.[4] $\beta^{-2}(T)$, which he determined, increases like $\log\tau_\alpha$, which is itself described by Eq. (1), in agreement with our Eq. (4) (Fig. 1).

These results are surprisingly similar to those of σ^2 vs $\ln\tau_\alpha$ in salol, which we deduced from the dielectric data of Dixon *et al.*[5] In these data, σ is directly determined. The

 0021-8979/94/75(10)/5512/5/$6.00 © 1994 American Institute of Physics

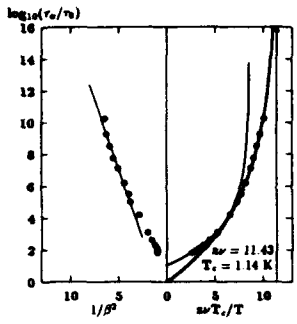

FIG. 1. The right-hand side is an Arrhenius plot of $\log(\tau_\alpha/\tau_0)$ vs $z\theta/T$ with the data of Ref. 4 for the $3d$ Ising spin glass. The energy $z\theta$ is the coefficient of the first term in the expansion of $\ln(\tau_\alpha/\tau_0)$ vs $1/T$ and a natural unit to scale the temperature. The continuous curve is a fit of the data to the power law $\tau_\alpha = \tau_0(1-T_c/T)^{-z\nu}$, which diverges when $z\theta/T = z\nu$. On the left-hand side we show $\beta^{-2}(T)$ vs $\log \tau_\alpha$, where $\beta(T)$ is the exponent of the stretched exponential $\exp(-t/\tau_\alpha)^{\beta(T)}$, which better fits the $m(t)$ relaxation in Ref. 4. A linear dependence is expected in our model, which is based on a lognormal distribution, whose width σ is related with β^{-1}. Notice that, in this frustrated system, the uncertainty σ on $\log \tau_\alpha$ is of the order of $\log \tau_\alpha$ itself when the temperature is of the order of $z\theta$.

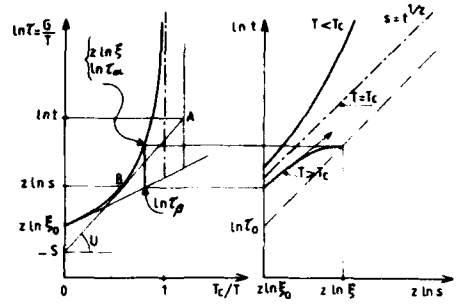

FIG. 3. To each point $A(T)$ in the nonergodic regime $t < \tau_\alpha(T)$ a Legendre construction associates on the left-hand side of the figure, a point $B(T_t)$ of the equilibrium $\ln \tau_\alpha = G/T = z \ln \xi$ curve, which has the same phase space $[S(T_t), U(T_t)]$ characterized by the same length $\xi(T_t) = s(t,T)$. As shown on the right-hand side of the figure, near T_c, $s(t)$ is a power of time $s(t) \sim t^{-T_c/zT_c}$, which deviates toward logarithmic behavior at long times below T_c or abruptly reaches an arrest at $s(t) = \xi(T)$ over T_c when $t/\tau_0 = \tau_\alpha/\tau_0 = [\xi(T)/\xi_0]^z = (1-T_c/T)^{-z\nu}$.

change of slope in salol (Fig. 2) corresponds to a change of regime, which is also observed on the $\log \tau_\alpha$ vs θ/T dependence; this change of regime is confirmed by many other experiments in salol and in other "fragile" glass forming liquids, and is currently the object of much attention,[6] being often considered as the mark of a transition that has been predicted by mode coupling theory:[7] Beyond this particular interpretation (we propose another one[8]), it is striking that two calculations based on very different microscopical hypotheses (the mode coupling starts from a hydrodynamical point of view) end up in both describing the same physics.

Consideration of the data (Figs. 1 and 2) shows that at temperatures of the order of $z\theta$, where, from Eq. 4, $\tau \sim \tau_0 \times e$, we also have $\beta \sim \sigma \sim 1$. This tells us that disorder also affects $\ln \tau_0$. We have $\Delta \ln \tau_0 \sim \ln \tau_0$ in these frustrated systems, and $z\theta$ therefore is presumably the center of a distribution whose smallest value is zero and largest $2z\theta$. The situation would be different in a ferromagnet, where we expect $z\theta$ to be of the order of $z\theta_{max}$ and no distribution to start with. With these initial conditions fixed the renormalization then takes on and β^{-2} increases like $\ln \tau$, as predicted.

The model as such, however, has several shortcomings. At times shorter than τ_α there is a tail in the relaxations that neither our error function nor the stretched exponential, despite an inherent asymmetry of the latter, are capable to describe. Also, our model would preclude any type of relaxation below T_c, in contradiction with the evidence.

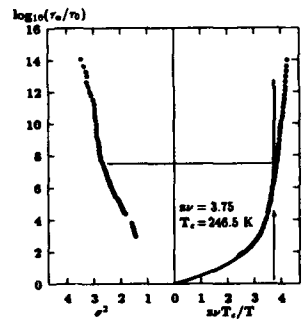

FIG. 2. The right-hand side is a plot of $\log(\tau_\alpha/\tau_0)$ vs $z\theta/T$, with the data of Ref. 5 for the dielectric susceptibility of salol. $z\theta$ has been defined in Fig. 1. We interpret as a crossover the deviation from one to another power law regime on approaching T_c. Observe on the left-hand side of the figure that σ^2 is a linear function of $\ln \tau_\alpha$ in each of these two regimes.

II. A QUASIEQUILIBRIUM APPROACH TO THE RELAXATION IN THE NONERGODIC REGIME

We will hereafter assume that the system at times $t < \tau_\alpha$ is already characterized by one length $s(t) < \xi(T)$. We propose[9] to measure this length at the contact point B of the tangent, which we can draw from the current point $A(\ln t, T)$ to the equilibrium $\ln \tau_\alpha \sim z \ln \xi$ vs θ/T curve (see Fig. 3). If we write

$$\ln \frac{\tau_\alpha}{\tau_0} \sim \frac{G}{T} = -S(T) + \frac{U(T)}{T} = z \ln \frac{\xi}{\xi_0}, \tag{7}$$

all points on this tangent have the same entropy, $S(T_t) = -\{\partial[G(T)]/\partial T\}$, and the same potential $U(T_t) = \partial(G/T)/\partial(1/T)$, which characterize the system at equilibrium at point $B(T_t)$. Therefore they picture the same phase space, where $S(T_t)$ is the degeneracy of the different paths to equilibrium, and $U(T_t)$ is a typical barrier height on these paths. With this Legendre construction, we find $z \ln(s/s_0) = -S(T_t) + [U(T_t)/T]$, which leads to

$$t^{-1/z\nu}\times e = s^{-1/\nu}\exp\frac{1-T_c/T}{s^{-1/\nu}}. \tag{8}$$

It is the time elapsed $t<\tau(T)$ that determines the scale $s(t)$ of the relaxation. The latter initiates at atomic size $s(t)=\xi_0$ on the $\tau_\beta=\tau_0\exp(z\theta/T)$ line. Then, depending on the conditions, we can identify different regimes. In the whole B domain $\tau_\beta<\tau<\tau_{a\pm}$, where

$$\tau_{a\pm}=\tau_0\left|1-\frac{T_c}{T}\right|^{-1/z\nu}, \tag{9}$$

$s(t)$ is well represented by the power law

$$s(t)^{-1/\nu}\sim t^{-T/z\theta}\times e=\exp\left(1-\frac{T}{z\theta}\ln\frac{t}{\tau_0}\right), \tag{10}$$

which is an exact result at T_c.

Below T_c, the relaxation deviates toward logarithmic decays in the C domain at times larger than τ_{a^-},

$$s(t)^{-1/\nu}\sim\frac{z\theta}{T}\frac{1}{\ln(t/\tau_0)}. \tag{11}$$

Over T_c, by contrast after many renormalizations, $s(t)$ jumps from $\sim\xi(T)\times e$ to $\xi(T)$ on the τ_a line,

$$\left(\frac{s(t)}{\xi(T)}\right)^{-1/\nu}\sim e-\frac{eT}{z\theta}\ln\frac{t}{\tau_a}, \quad \text{for } t<\tau_a,$$
$$=1, \quad \text{for } t\gg\tau_a. \tag{12}$$

As a result,

$$\frac{\partial[s(t)^{-1/\nu}]}{\partial\ln t}\propto(e-1)\delta(t=\tau_a)+\frac{T}{z\nu T_c}h(t=\tau_a), \tag{13}$$

where $\delta(x)$ and $h(x)$ are the delta function and the stepfunction, respectively.

These are the $s(t/\tau)$ values that we have to substitute to the $\exp(t/\tau)$ in Eq. (5). At short range, on the τ_β line, $P(\ln\tau)$ is not yet the renormalized Gaussian, which we discussed in Eq. (5). Taking

$$P\left(\ln\frac{\tau_\beta}{\tau_0}\right)=\frac{T}{z\theta_{\max}}, \quad \text{for } \ln\frac{\tau_\beta}{\tau_0}<\frac{z\theta_{\max}}{T}=0,$$
$$\text{for } \frac{z\theta_{\max}}{T}<\ln\left(\frac{\tau_\beta}{\tau_0}\right),$$

we found, using Eqs. (9) and (11) in the B and C domains, respectively,

For $0<T\ln(t/\tau_0)<z\theta_{\max}$,

$$\overline{s^{-1/\nu}}\sim\begin{cases}1-[1-eE_2(1)]\dfrac{T}{z\theta_{\max}}\ln\dfrac{t}{\tau_0}, & \text{in B domain for } t<\tau_{a\pm},\\[2ex] 1-\dfrac{T}{2z\theta_{\max}}\ln\dfrac{t}{\tau_0}, & \text{in C domain for } t\gg\tau_{a^-};\end{cases} \tag{14}$$

and for $\theta_{\max}<T\ln(t/\tau_0)$,

$$\overline{s^{-1/\nu}}\sim\begin{cases}eE_2\left(\dfrac{T}{z\theta_{\max}}\ln\dfrac{t}{\tau_0}\right), & \text{in B domain for } t<\tau_{a\pm},\\[2ex] \dfrac{z\theta_{\max}}{2T}\dfrac{1}{\ln(t/\tau_0)}, & \text{in C domain for } t\gg\tau_{a^-},\end{cases} \tag{14'}$$

where $E_2(x)$ is the exponential integral of order 2.

Over T_c we deduce, from Eq. (13) around τ_a,

$$\frac{\partial[s(t)^{-1/\nu}]}{\partial\ln t}\propto(e-1)P(\ln\tau_a)+\frac{T}{z\nu T_c}\int_t P(\ln\tau_a). \tag{15}$$

For $\tau_a\gg\tau_\beta$, $P(\ln\tau_a)$ is now the Gaussian distribution, which is obtained after many renormalizations. The additional error function introduces a skewness that was not present in Eq. (6), and has the shape and magnitude requested, to account for the observed asymmetry in the relaxation of the magnetization.

III. GENERALIZATION TO DIFFERENT CURVATURES OF THE $\ln(\tau/\tau_0)(\theta/T)$ CURVE

All these features proceed from the hierarchical structure of the response: the latter results from the necessity to establish a cascade between the physical scale $\xi(T)$ by which the system is in equilibrium with the thermal bath if $T>T_c$ and the atomic scale, where the interaction sits and where the energy has to be introduced or evacuated. For this reason the same type of solutions are found in many problems unrelated *a priori*: for example, the problem of spin glasses and its modelization by Ogielski and the problem of the glass transition and the mode-coupling theory. For these reasons, we observe, with no surprise, $(t/\tau)^{-aT}$ or $(T\ln t)^{-a}$ dependencies in spin glasses[10,11] or vortex glasses,[12,13] depending on the external conditions, as well as in dipolar or structural glasses (Fig. 4). What else could justify that the same word of glass is indifferently applied to so different systems?

In the cases that we considered so far, the system constructs larger effective barriers $U=\partial\ln\tau/\partial(1/T)$ for larger scales. Damage therefore first hits the system at atomic range and then spreads out toward larger scales. This, with our

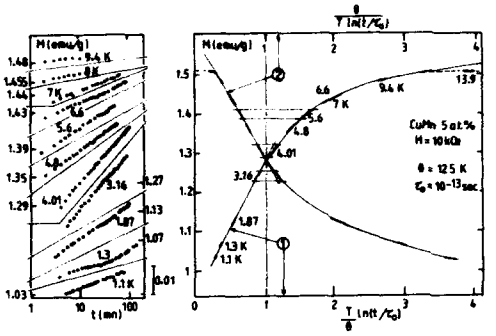

FIG. 4. In Ref. 10, the relaxations over 10^4 s in a constant field at different temperatures below T_c of a CuMn 5 at. % spin glass have been rescaled onto a unique master curve of $(T/\theta)\ln(t/\tau_0)$. The present representation in terms of $(T/\theta)\ln(t/\tau_0)$ (curve 1) and of $\theta[T\ln(t/\tau_0)]$ (curve 2) shows that the master curve is well described by Eq. (14) in the C version, which predicts $1-T\ln t$ dependence at small times and $(T\ln t)^{-1}$ at longer times.

Legendre construction, is obviously associated with the curvature of the equilibrium $\ln(\tau/\tau_0)$ vs $z\theta/T$ curve. With Eq. (1), where we impose that θ exists and is finite, we have

$$\ln\frac{\tau_\alpha(T)}{\tau_0}=-\frac{z\theta}{T_c}\ln\left(1-\frac{T_c}{T}\right)\sim\frac{z\theta}{T}+\frac{z\theta T_c}{T^2}+\cdots . \quad (16)$$

The sign of T_c fixes the sign of the curvature.

For $T_c=0$, we are in the marginal situation where the system is just capable to build up the same U_{eff} for each new range. As a result, there is only one time scale:

$$\ln(\tau_\alpha/\tau_0)=\ln(\tau_\beta/\tau_0)=z\theta/T,$$

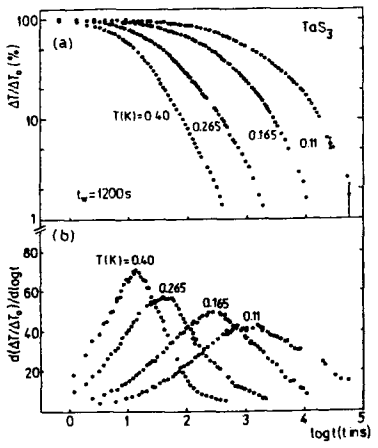

FIG. 5. A one step relaxation is observed on an activated time scale in the charge density wave system TaS_3 (Ref. 14). The relaxation ΔT becomes closer to an error function and $d\Delta/d\log t$ closer to a Gaussian of the $\log t$ variable at lower temperatures. This suggests a larger phase space and a transition at $T_c=0$.

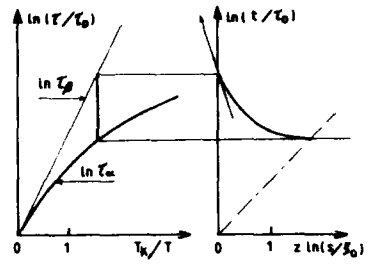

FIG. 6. The left-hand side is an Arrhenius representation of $\log(1-T_c/T)^{-\theta T_c}$ vs θ/T for T_c negative. T_c fixes the sign of the curvature, with the consequence that, with our Legendre construction of Fig. 3, the relaxation time decreases with s if $T_c=-T_K$. Damage therefore spreads out from large toward atomic ranges. On the right-hand side, we show a schematic shape of the relaxation. A large initial variation followed by a logarithmic decay is expected, contrary to what is predicted for T_c positive.

and all ranges respond simultaneously. The shape of the relaxation is fixed by the distribution $P[\ln(\tau/\tau_0)]$. The latter is closer to a Gaussian and the relaxation closer to a symmetrical error function of $(T/z\theta)\ln(t/\tau_0)$ if the temperature is decreased, as averages are less sensitive to the conditions of local disorder, being performed over larger ξ/ξ_0 ratios. This feature, we believe, contrasts a true transition at $T_c=0$, as it is observed in TaS_3[14] or in "strong" glass formers from an average over a fixed distribution of potential barriers, where always the same phase space is explored and the shape of the relaxation remains the same in terms of $T\ln(t/\tau_0)$ (Fig. 5).

Finally for T_c negative, Eq. (16) provides solutions of curvature opposite to those previously discussed. This with our Legendre construction (Fig. 3) would mean that the system builds up energy barriers that are smaller at larger ranges, so that $\tau_\alpha<\tau_\beta$, and damage spreads out from the larger ranges toward the smaller (Fig. 6). We want to stress here that the legitimacy of parameter T_c is entirely determined by the aptitude that Eq. (1), where it is defined, has to describe a given physical situation. Thus, although the idea of a negative T_c may appear unusual, we have shown previously that it permits to account extremely well for the static properties of systems like heavy fermions,[15] where it is agreed that we are close to a phase transition, but not enough to observe a divergence of a correlation at a finite temperature. Equation (1), with $T_c<0$, leads to power laws of the temperature, which describe well what is observed. The temperature dependence of the relaxation time τ_α would correspondingly flatten to a power law much slower than an Arrhenius behavior, and we would expect that $\tau_\alpha<\tau_\beta$. These features when they are observed are currently interpreted in terms of macroscopic quantum effects. In other words, concepts completely different are called for, in order to account for a change of sign in the curvature of experimental evidence gathered in systems sometimes very close to one another. We obtain the same effect by changing the sign of parameter T_c. An implication is that the information that flows from ξ_0 toward $\xi(T)$ in the case where we have a transition flows from $\xi(T)$ toward ξ_0 in these cases that per-

tain to superparamagnetism, where we have no singularity at finite temperature of the $\xi(T)$ dependence.

We observe in Eq. (17) that all the information that we need, i.e., the energy scale $z\theta$ and the curvature $z\theta/T_c$, is contained in the first two terms of the expansion of $\ln(\xi/\xi_0)$ in terms of $z\theta/T$, i.e., at small scales. We need a microscopical description to extract this information. The microscopical theory therefore acts as a kind of boundary condition in the time domain from which we are directed toward a limited number of universal scenarios, whose evolution is entirely determined by scaling considerations. Some of these scenarios lead to an equilibrium. Equilibrium, in this context, can be seen as the termination of a dynamical process.

ACKNOWLEDGMENTS

The author is grateful to D. Bertrand and J. Le G. Gilchrist for their help.

[1] B. Castaing and J. Souletie, J. Phys. I France **1**, 403 (1991).
[2] R. G. Palmer, D. L. Stein, E. Abrahams, and P. W. Anderson, Phys. Rev. Lett. **53**, 958 (1984).
[3] E. W. Montroll and J. T. Bendler, J. Stat. Phys. **34**, 129 (1984).
[4] A. T. Ogielski, Phys. Rev. B **32**, 7384 (1985).
[5] P. K. Dixon, L. Wu, S. R. Nagel, B. D. Williams, and J. P. Carini, Phys. Rev. Lett. **65**, 1108 (1990).
[6] F. Mezei, W. Knaak, and B. Farago, Phys. Rev. Lett. **58**, 571 (1987). M. Z. Cummins, G. Li, W. M. Du, X. K. Chen, N. J. Tao, and A. Saka, in *Slow Dynamics in Condensed Matter*, edited by K. Kawasaki, T. Kawaratsu, and M. Tokuyama, AIP Conf. Proc. **256**, 1992, p. 40.
[7] U. Bengtzelius, W. Götze, and A. Sjölander, J. Phys. C **17**, 5915 (1984).
[8] J. Souletie, J. Phys. France **51**, 883 (1990); J. Souletie and D. Bertrand, J. Phys. I **1**, 1627 (1991).
[9] J. Souletie, Philos. Mag. **65**, 1311 (1992), Physica A (in press); J. Non-Cryst. Sol. **131–133** (in press).
[10] R. Omari, J. J. Prejean, and J. Souletie, J. Phys. Paris **45**, 1809 (1984).
[11] K. Ilio, A. Kitazawa, and K. Nagata, in Ref. 6, p. 421.
[12] J. J. Prejean and J. Souletie, Phys. Rev. Lett. **60**, 1884 (1988).
[13] A. Gurevich and K. Kupler, Phys. Rev. B **48**, 6477 (1993).
[14] K. Biljaković, J. C. Lasjaunias, P. Monceau, and F. Levy, Phys. Rev. Lett. **67**, 1902 (1991).
[15] J. Souletie, J. Phys. (France) **49**, 1211 (1988).

Exchange stiffness of Ca-doped YIG

I. Avgin[a] and D. L. Huber
Department of Physics, University of Wisconsin—Madison, Madison, Wisconsin 53706

An effective medium theory for the zero-temperature exchange stiffness of uncompensated Ca-doped YIG is presented. The theory is based on the assumption that the effect of the Ca impurities is to produce strong, random ferromagnetic interactions between spins on the *a* and *d* sublattices. In the simplest version of the theory, a fraction, x, of the *ad* exchange integrals are large and positive, x being related to the Ca concentration. The stiffness is calculated as function of x for arbitrary perturbed *ad* exchange integral, J_{ad}^{x}. For $J_{ad}^{x}>(\frac{1}{5})|8J_{aa}+3J_{dd}|$, with J_{aa} and J_{dd} denoting the *aa* and *dd* exchange integrals, respectively, there is a critical concentration, X_c, such that when $x>X_c$, the stiffness is complex. It is suggested that X_c delineates the region where there are significant departures from colinearity in the ground state of the Fe spins. Extension of the theory to a model where the Ca doping is assumed to generate Fe^{4+} ions on the tetrahedral sites is discussed. Possible experimental tests of the theory are mentioned.

I. INTRODUCTION

Recently, there has been a growing interest in the effect of uncompensated Ca doping on the magnetic and other properties of YIG (yttrium iron garnet, $Y_3Fe_5O_{12}$) and related compounds.[1] There appears to be a general consensus that the addition of Ca introduces strong ferromagnetic interactions between Fe ions on the tetrahedral and octahedral sites. Two models have been proposed to explain how this might come about. The first of these assumes that the extra hole arising from the Ca^{2+} substitution resides on the tetrahedral site, so that the Ca doping leads to a random distribution of Fe^{4+} ions with ferromagnetic interactions with neighboring Fe ions on the *a* and *d* sublattices.[2] In the second model, it is assumed that the excess hole is located on the oxygen ion, bridging a tetrahedral and octahedral site. The presence of the O^- ion leads to a strong ferromagnetic *ad* exchange interaction.[3] Studies of the spectral and temporal dependence of the Faraday rotation and x-ray photoemission spectroscopy suggest that the Fe^{4+} model is appropriate for Ca concentrations less than 0.16 per formula unit, while at higher concentrations, there is evidence indicating the existence of O^- ions.[4]

The purpose of this paper is to outline a theoretical analysis of the effects of Ca doping on the exchange stiffness of YIG that is based on the effective medium approximation (EMA). The theory is developed in detail for the O^- model, and then extended, with additional approximations, to the Fe^{4+} picture. In addition to predicting the variation of the stiffness constant with Ca doping, the theory also provides information about the onset of significant departures from colinearity in the ground state of the spin system.

II. THEORY

The effective medium approximation exploits the formal connection between the zero-temperature exchange stiffness and the conductivity of an equivalent network of resistors.[5] In the EMA, the effective exchange stiffness, $A_{\rm eff}$, is given as the solution to the equation[6]

$$\int P(A)(A-A_{\rm eff})(2A_{\rm eff}+A)^{-1}\,dA=0, \tag{1}$$

where $P(A)$ denotes the probability distribution for the stiffness, A. In order to calculate $P(A)$ for the O^- model, we note that the stiffness of YIG is proportional to the sum $8J_{aa}-5J_{ad}+3J_{dd}$, where J_{aa}, J_{ad}, and J_{dd} denote the nearest-neighbor octahedral–octahedral, tetrahedral–octahedral, and tetrahedral–tetrahedral exchange integrals, respectively.[7] Since the doping is hypothesized to affect only the *ad* interactions, $P(A)$ is given by an expression of the form

$$P(A)=x\,\delta(A-uJ_{ad}^{x}-v)+(1-x)\,\delta(A-uJ_{ad}-v), \tag{2}$$

where J_{ad}^{x} is the interaction between Fe ions on *a* and *d* sites bridged by an O^- ion. The fraction of perturbed *ad* interactions is denoted by x, and u and v are constants.

After inserting (2) into (1), it becomes convenient to rewrite the solution in terms of $A_{\rm eff}/A_0$, the ratio of $A_{\rm eff}$ to the stiffness of pure YIG, A_0, and the parameter R, defined by

$$R=(5J_{ad}^{x}-8J_{aa}-3J_{dd})/(8J_{aa}-5J_{ad}+3J_{dd}), \tag{3}$$

which is seen to be the negative of the ratio of the stiffness of YIG with J_{ad} replaced by J_{ad}^{x} to the stiffness of pure YIG. The resulting solution for $A_{\rm eff}/A_0$ takes the form

$$2A_{\rm eff}/A_0=1+(\tfrac{1}{2})R-(\tfrac{3}{2})x(1+R)$$
$$\times\{[1+(\tfrac{1}{2})\,R-(\tfrac{3}{2})x(1+R)]^2-2R\}^{1/2}. \tag{4}$$

Because of the radical in Eq. (4), $A_{\rm eff}$ becomes complex for $x>X_c$ (assuming $R>0$), where X_c is given by

$$X_c=(\tfrac{2}{3})[1-(R/2)^{1/2}]^2/(1+R). \tag{5}$$

It is useful to define two other functions of R, $X_1(>X_c)$, which denotes the concentration where the real and imagi-

[a]Current address: Department of Physics, West Virginia University, Morgantown, West Virginia 26506.

 0021-8979/94/75(10)/5517/3/$6.00 © 1994 American Institute of Physics

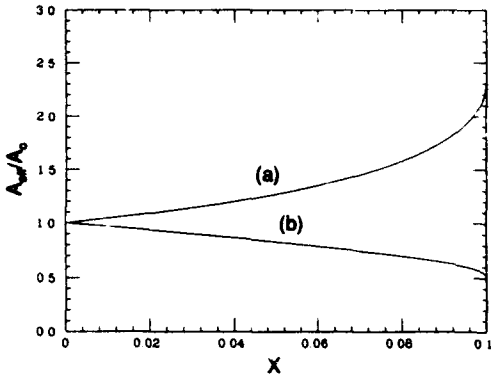

FIG. 1. A_{eff}/A_0 vs x for $0 \leq x \leq 0.1$. (a) $R=11$; (b) $R=0.54$. A_{eff} is the effective exchange stiffness of Ca-doped YIG [cf. Eq. (1)], and A_0 is the stiffness of pure YIG; x is the fraction of perturbed *ad* exchange integrals and R is defined by Eq. (3). These two values of R correspond to $X_c=0.1$.

nary parts of A_{eff} are equal, and $X_2(>X_1)$, where the real part of A_{eff} is zero. From Eq. (3), we obtain the results

$$X_1=(\tfrac{2}{3})(1+R/2-R^{1/2})/(1+R) \tag{6}$$

and

$$X_2=(\tfrac{2}{3})(1+R/2)/(1+R). \tag{7}$$

Figure 1 shows the variation of the ratio A_{eff}/A_0 with x for two values of R corresponding to the physically plausible value $X_c=0.1$, while Fig. 2 displays the variation of X_c, X_1, and X_2 with R, which are obtained from Eqs. (5), (6), and (7), respectively, over the interval $0 \leq R \leq 11$.

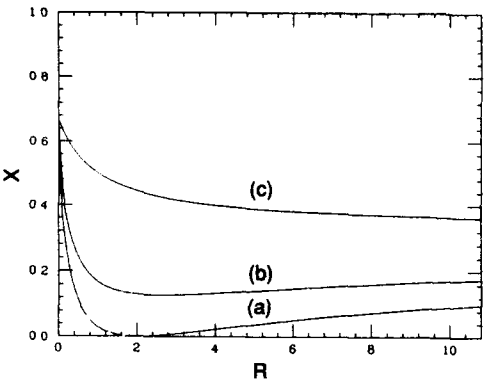

FIG. 2. (a) X_c, (b) X_1, and (c) X_2 vs R. X_c denotes the concentration, marking the boundary between real and complex values of A_{eff}; for $x>X_c$, A_{eff} has a finite imaginary part. X_1 denotes the concentration at which the real and imaginary parts of A_{eff} are equal, and X_2 is the concentration at which the real part of A_{eff} equals zero.

III. DISCUSSION

According to the interpretation of Vannimenus *et al.*,[8] the presence of an imaginary part in the EMA approximation for the exchange stiffness signals the breakdown of the collinear approximation for the ground state that underlies the EMA. That is, for $x>X_c$ (fixed R), one expects significant noncolinearity among the spins. The results for the O^- model indicate a breakdown of the colinear approximation with increasing Ca doping for all $R>0$, i.e., for $J^x_{ad}>-|8J_{aa}+3J_{dd}|$. The connection between x, the fraction of perturbed *ad* interactions, and the Ca concentration is made explicit by the fact that each formula unit of YIG corresponds to 12 *ad* interactions. As a consequence, if c denotes the number of Ca^{2+} ions per formula unit, $x=c/12$, since the excess hole can be located on any one of 12 bonds.

As mentioned in the Introduction, the theory can also be applied to the Fe^{4+} model, albeit with further approximations. The essential assumption is that the interaction between the Fe^{4+} ion on the tetrahedral site and the Fe^{3+} ion on the nearest-neighbor octahedral site is much greater than the interaction between the Fe^{4+} and the Fe^{4+} and Fe^{3+} ions on the nearest-neighbor tetrahedral sites. Assuming this to be the case (and neglecting the difference between the spins of the Fe^{3+} and Fe^{4+} ions), Eqs. (4)–(7) are applicable, with R defined as $(8J^x_{ad}-5J_{aa})/(5J_{aa}-8J_{ad}+3J_{dd})$ and x, identified as the fraction of tetrahedral sites occupied by Fe^{4+} ions. Since there are three tetrahedral sites per formula unit, $x=c/3$.

It should be noted that the theory outlined in this paper pertains to the exchange stiffness, which is related to the spin wave dispersion constant, D, through the equation $D=A/M$, where M is the magnetization. Since M is real, a complex value for A translates into a complex value for D, which is indicative of strong spin wave damping. Measurements of the spin wave dispersion constant, along with the magnetization, should provide information about the renormalization and damping of the spin wave modes that can be compared with the predictions of the EMA. Also, measurements of the local fields using NMR and Mössbauer techniques may provide information about the breakdown of colinearity in the ground state with increasing Ca doping, thus leading to an estimate of R and hence J^x_{ad}.

Finally, we should emphasize that our approach is based on the assumption that the holes are localized and immobile. If the holes are delocalized or can hop from site to site, our theory is not applicable, and alternative approaches must be relied upon.[9]

ACKNOWLEDGMENTS

D. L. H. would like to thank Dr. A. Lehmann-Szweykowska for stimulating his interest in the problem of Ca-doped YIG. The research was supported in part by the National Science Foundation.

[1] A. Lehmann-Szweykowska, R. Wojciechowski, L. Pust, P. E. Wigen, and S. Batra, Phys. Rev. B **43**, 3500 (1991), and references therein.
[2] S. Batra, A. Lehmann-Szweykowska, and P. E. Wigen, J. Appl. Phys. **61**, 3274 (1987).
[3] M. Maryško, P. Novak, L. Pust, J. Paces, J. Šimšova, M. Neriva, S.

Krupička, and V. V. Volkov, J. Phys. Paris Colloq. **49**, C8-981 (1988).
[4]Z. Šimša, J. Šimšová, J. Zemek, P. E. Wigen, and M. Pardavi-Horvath, J. Phys. (Paris) Colloq. **49**, C8-975 (1988).
[5]A. B. Harris and S. Kirkpatrick, Phys. Rev. B **16**, 542 (1977).
[6]S. Kirkpatrick, Rev. Mod. Phys. **45**, 570 (1973).
[7]B. Dreyfus, J. Phys. Chem. Solids **23**, 287 (1962).
[8]J. Vannimenus, S. Kirkpatrick, F. D. M. Haldane, and C. Jayaprakash, Phys. Rev. B **39**, 4634 (1989).
[9]A. Lehmann-Szweykowska, A. Koper, R. Wojciechowski, and T. Tomalak, J. Magn. Magn. Mat. **104–107**, 447 (1992).

Random-exchange to random-field crossover breaking in $Mn_{0.35}Zn_{0.65}F_2$

F. C. Montenegro, J. C. O. de Jesus, and A. Rosales-Rivera[a)]
Departamento de Física, Universidade Federal de Pernambuco 50670-901 Recife-PE, Brazil

The critical phase boundary $T_c(H)$ of $Mn_{0.35}Zn_{0.65}F_2$ has been mapped in a (H,T) phase diagram using dc magnetization measurements. Our data show that $T_c(H)$ is governed by a scaling law $T_N - T_c(H) \sim H^{2/\phi}$, with $\phi = 3.4 \pm 0.2$. This value of ϕ exponent is in clear departure with the universal random-exchange Ising model to random-field Ising model (REIM-RFIM) crossover exponent $\phi \cong 1.4$, found in weakly diluted samples of $Mn_xZn_{1-x}F_2$ and $Fe_xZn_{1-x}F_2$. This observation and results from previous birefringence studies for samples of $Mn_xZn_{1-x}F_2$ with $x \geq 0.4$ suggest that a REIM-RFIM crossover breaking occurs somewhere in the interval $0.35 < x < 0.4$.

I. INTRODUCTION

The weakly anisotropic dilute antiferromagnetic (DAF) compound $Mn_xZn_{1-x}F_2$ has its critical phase boundary $T_c(H)$ determined for a number of values of $x (x > 0.4)$, from different experimental techniques.[1-6] Under a weak magnetic field H applied along the easy [001] direction $T_c(H)$ is governed by a random-exchange Ising model (REIM) to random-field Ising model (RFIM) crossover scaling. This crossover scaling stipulates[7] that $T_N - T_c(H) \sim H^{2/\phi}$, where T_N is the Néel temperature and $\phi \cong 1.4$ is the universal REIM-RFIM crossover exponent. For $x < 0.4$, the magnetic behavior of $Mn_xZn_{1-x}F_2$ has been studied using magnetization and ac susceptibility measurements by Bazhan and Petrov.[8] They claim that for $H = 0$ and near the percolation concentration ($x_p = 0.24$) this compound converts into a state of a time-varying spin glass at low temperatures. However, for $H = 0$, neutron scattering data close to x_p showed[9] that long-range antiferromagnetic order (AF LRO) is maintained for all $x > x_p$. This apparent controversy motivated the present study. Moreover, little attention has been given to the critical behavior in $Mn_xZn_{1-x}F_2$ for $x < 0.4$. It is a major purpose of this paper to map the critical phase boundary of $Mn_{0.35}Zn_{0.65}F_2$ in a (H,T) phase diagram.

II. EXPERIMENTAL RESULTS AND DISCUSSION

The experiments were performed on a single crystal of $Mn_{0.35}Zn_{0.65}F_2$. The concentration of magnetic ions was determined using density measurements. We have measured the magnetization M in $Mn_{0.35}Zn_{0.65}F_2$ with a vibrating sample magnetometer. The temperature and applied field were varied in the ranges $4.2 < T < 20$ K and $0 < H < 20$ kOe, respectively. The temperature of the sample was controlled within 1 mK using an almost field-insensitive carbon glass thermometer. H was applied parallel to the easy [001] direction. The temperature (T) dependence of M was measured using temperature cycling (H fixed), following the usual zero-field-cooling (ZFC) and field-cooling (FC) procedures.

In Figs. 1 and 2 we show the measured temperature dependence of the susceptibility (M/H) for applied field in the interval $3.5 \leq H \leq 20$ and $0.5 \leq H \leq 1.5$ kOe, respectively, using ZFC and FC procedures. For $0.5 \leq H < 7.5$ kOe the ZFC curves of Figs. 1 and 2 are those typical of a predominant AF order taking place at low temperatures. For $H = 0$ AF LRO in $Mn_xZn_{1-x}F_2$ is supported by neutron scattering investigations for $x > 0.4$ (Ref. 10) and also close to x_p.[9] In presence of a uniform field parallel to the easy axis and following the ZFC procedure, neutron scattering studies also support AF LRO under weak H for $x > 0.4$.[4,11,12] However, no neutron scattering data is available for values of x close to the one used in the present work. $(M/H) \times T$ curves of Fig. 1 also show that for $H > 8$ kOe the ZFC data are no longer compatible with AF ordering, however, no clear signature of a first-order AF to spin-flop (SF) transition is seen in the $(M/H) \times T$ curves (see Ref. 6).

Another low-temperature feature evidenced in Figs. 1 and 2 is the presence of an excess of magnetization ($\Delta M \equiv M_{FC} - M_{ZFC}$) in the FC curves as compared with the ZFC ones, in the field range $0.5 \leq H \leq 12.5$ kOe. For $2 \leq H \leq 10$ kOe, ΔM increases with increasing H (see Fig. 1), as expected[13-15] from the nucleation of field aligned domains on cooling diluted uniaxial antiferromagnets from the paramagnetic (P) phase under an applied field parallel to the easy axis. No significant time dependence has been observed in the time scale of acquisition of M_{FC} data (typically 5 min per point). However, dynamic effects were not explored in the present work in a long-time basis. For $0.5 \leq H < 2$ kOe, ΔM undergo a striking reversal of its H dependence (compare the ZFC-FC irreversibilities of Fig. 1 with corresponding ones in Fig. 2), i.e., ΔM decreases as H increases for this low-H range. This behavior does not follow the current theoretical predictions for the field dependence of the excess of magnetization in $d = 3$ DAF realizations of the RFIM problem.[13,14]

The ZFC temperature dependence of $d(M/H)/dT$ in the vicinity of $T_c(H)$ is shown in Fig. 3 for values of H in the range $0.5 \leq H \leq 7.5$ kOe. The position of the $d(M/H)/dT$ peaks indicates[16-18] the critical temperature $T_c(H)$ in DAF compounds. As seen in Fig. 3, $d(M/H)/dT$ peaks become drastically rounded and shift to lower T upon increasing H. The excessive rounding of the peaks here is possibly not entirely due to concentration gradients and RFIM critical slowing down as experimentally observed[5,6] for $x > 0.4$ in $Mn_xZn_{1-x}F_2$. If so, $T_c(H)$ represents only a virtual line of destroyed (rounded) phase transitions. Neutron scattering measurements in samples with x values in the range of the

a)Permanent address: Departamento de Física, Universidad Nacional de Colombia, A.A. 127, Manizales, Colombia.

 0021-8979/94/75(10)/5520/3/$6.00 © 1994 American Institute of Physics

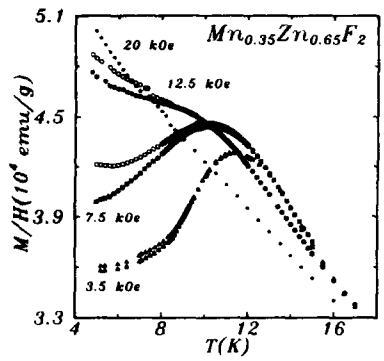

FIG. 1. Temperature dependence of the dc susceptibility (M/H) of $Mn_{0.35}Zn_{0.65}F_2$, in the ZFC (full symbols) and FC (open symbols) procedures for $3.5 \leq H \leq 20$ kOe.

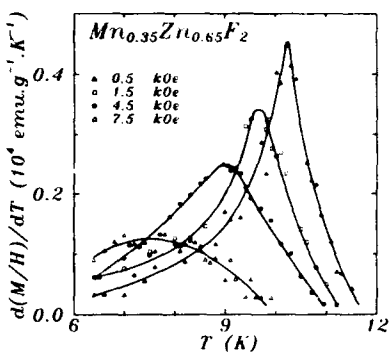

FIG. 3. ZFC temperature dependence of $d(M/H)/dT$ in $Mn_{0.35}Zn_{0.65}F_2$, for $0.5 \leq H \leq 7.5$ kOe. The solid lines are guides to the eye.

one used in the present work are requested to clarify this point.

The mapping of the critical phase boundary $T_c(H)$, obtained from data in Fig. 3, in a (H,T) phase diagram is presented for $0<H\leq 5$ kOe in Fig. 4. As well known, in presence of a *weak* uniform field parallel to the easy axis, the peak position at $T_c(H)$ in DAF systems is generally governed by a scaling law $T_N - T_c(H) \sim H^{2/\phi}$, after mean-field correction,[7] where $\phi \cong 1.4$ is the universal REIM-RFIM crossover exponent. However, by using the above scaling law to fit data of Fig. 4, we get $\phi = 3.4 \pm 0.2$, where $T_N = 10.8 \pm 0.1$ K was obtained from peaks in the ac susceptibility measured[19] at zero field in the same sample used in the present work (see Fig. 5). The position of T_N coincides with the extrapolation of the $T_c(H)$ data to $H=0$. As no frequency dependence was found in the close vicinity of T_N in the ac suceptibility data and the temperature sensors used in both experiments have been previously calibrated, we can conclude that the convex "$\phi \cong 3.4$ regime" extends to $H=0$ in $Mn_{0.35}Zn_{0.75}F_2$. The $T_c(H)$ phase boundary is also shown in the inset of Fig. 4, but plotted as $H^{2/\phi}$ vs T, with $\phi \cong 3.4$. This is in contrast with the standard $\phi \cong 1.4$ REIM-RFIM crossover behavior, found at *weak* applied fields in all measured samples of $Mn_xZn_{1-x}F_2$ for $x \geq 0.4$.[5,6] These studies suggest that the REIM-RFIM crossover breaking occurs somewhere in the interval $0.35<x<0.4$. It can be also observed from Fig. 3 that the amplitudes of the $d(M/H)/dT$ peaks decrease as H increases, and then they also do not follow a REIM-RFIM crossover scaling.[17,18]

One would expect the $Mn_{0.35}Zn_{0.65}F_2$ sample to behave in a qualitatively similar way to highly diluted samples of the isostructural system $Fe_xZn_{1-x}F_2$,[20-22] but with smaller limits for the high-H regime with Mn than with Fe, due to the smaller anisotropy of the former. However, the experimental results do not confirm this expectation. In the Fe system, it

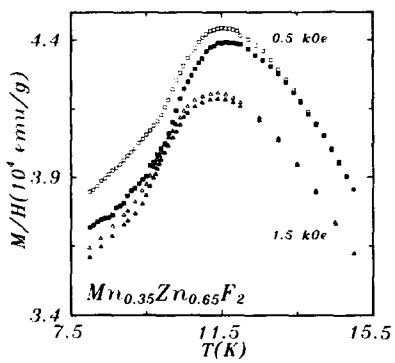

FIG. 2. Temperature dependence of the dc susceptibility (M/H) of $Mn_{0.35}Zn_{0.65}F_2$, in the ZFC (full symbols) and FC (open symbols) procedures for $0.5 \leq H \leq 1.5$ kOe.

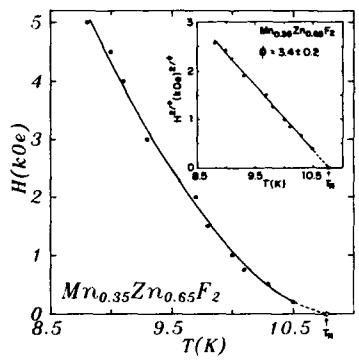

FIG. 4. (H,T) phase diagram of $Mn_{0.35}Zn_{0.65}F_2$ for $0<H\leq 5$ kOe. The inset shows the same data in a $H^{2/\phi}$ vs T plot. The solid lines are best fitted to the data using the scaling law $T_N - T_c(H) \sim H^{2/\phi}$ with $\phi = 3.4 \pm 0.2$. T_N was obtained from ac susceptibility measurements at $H=0$ (see Fig. 5) and coincides with the extrapolation of the $T_c(H)$ data to $H=0$.

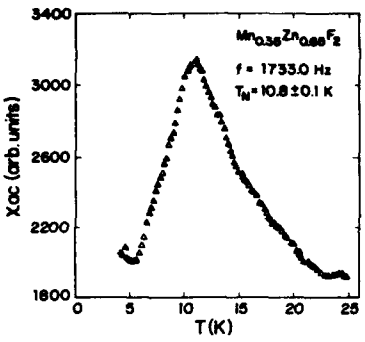

FIG. 5. χ_{ac} vs T curve of $Mn_{0.35}Zn_{0.65}F_2$ at $H=0$, using a driven field of magnitude $H_{ac}\cong 1.0$ Oe (adapted from Ref. 19).

has been found for a sample with $x=0.31$ (Ref. 21) a standard low-H REIM-RFIM regime, characterized by an exponent $\phi\cong 1.4$ governing both the *critical* and *equilibrium* phase boundaries, where the stable long-range ordered AF ground state is accessed by the ZFC procedure. As the magnitude of the external field increases, a different "high-H regime" takes place where the equilibrium phase boundary is now governed by an exponent $\phi\cong 3.4$ and the AF long-range ordered state becomes unstable against the presence of strong random fields. A glassy phase sets in below the convex equilibrium line ($\phi\cong 3.4$) and the critical AF-paramagnetic phase boundary is, of course, no longer present. For a sample with $x=0.25$ this equilibrium line with $\phi\cong 3.4$ is the sole feature (see Ref. 22). The situation in $Mn_{0.35}Zn_{0.65}F_2$ is somewhat different: the exponent $\phi\cong 3.4$ governs a line of critical points (or probably destroyed phase transitions) starting at $H=0$, and this convex line is not accompanied by any detectable time dependence in the ZFC data. The above features make evident the different magnetic behavior of these isostructural DAF systems for $x<0.4$.

Finally, we anticipate here that ac susceptibility data[19] at $H=0$ in the same sample used in this work indicate the presence of frozen and spatially oriented clusters at low temperatures. Bazhan and Petrov[8] have already observed a change in the relaxation time of highly diluted samples of $Mn_xZn_{1-x}F_2$ as T is lowered at $H=0$, which they call a "state of a time-varying spin glass." As H is increased, they found that the system converts into a *stable* state in which the magnetic moments are oriented randomly with respect to the direction of H. Their conclusions fit in with data presented in this work. However, a careful study on the stability of the long-range AF order as a function of x is necessary for a better understanding of the magnetic properties of this system close to the percolation threshold.

ACKNOWLEDGMENTS

The authors acknowledge U. A. Leitão, J. R. L. de Almeida, C. C. Becerra, S. M. Rezende, and F. L. A. Machado for fruitful discussions and suggestions. This work is supported by CAPES, CNPq, FACEPE, and FINEP (Brazilian agencies). One of us (A.R.R.) also acknowledges the support of COLCIENCIAS (Colombian agency).

[1] Y. Shapira, N. F. Oliveira, Jr., and S. Foner, Phys. Rev. B **30**, 6639 (1984), and references therein.
[2] D. P. Belanger, A. R. King, and V. Jaccarino, Phys. Rev. Lett. **48**, 1050 (1982).
[3] H. Ikeda and K. Kikuta, J. Phys. C **16**, L445 (1983); **17**, 1221 (1984); H. Ikeda, *ibid.* **19**, L811 (1986).
[4] J. P. Hill, T. R. Thurston, R. W. Erwin, M. J. Ramstad, and R. J. Birgeneau, Phys. Rev. Lett. **66**, 3281 (1991), and references therein.
[5] C. A. Ramos, A. R. King, and V. Jaccarino, Phys. Rev. B **37**, 5483 (1988).
[6] F. C. Montenegro, J. C. O. de Jesus, F. L. A. Machado, E. Montarroyos, and S. M. Rezende, J. Magn. Magn. Mater. **104**, 277 (1992).
[7] S. Fishman and A. Aharony, J. Phys. C **12**, L729 (1979).
[8] A. N. Bazhan and S. V. Petrov, Sov. Phys. JETP **53**, 337 (1981); **59**, 1269 (1984).
[9] R. A. Cowley, G. Shirane, R. J. Birgeneau, and E. C. Svenson, Phys. Rev. Lett. **39**, 894 (1977).
[10] P. W. Mitchell, R. A. Cowley, H. Yoshizawa, P. Böni, Y. J. Uemura, and R. J. Birgeneau, Phys. Rev. B **34**, 4719 (1986).
[11] R. A. Cowley and W. J. L. Buyers, J. Phys. C **15**, L1209 (1982).
[12] R. J. Birgeneau, R. A. Cowley, G. Shirane, and H. Yoshizawa, Phys. Rev. Lett. **54**, 2147 (1985).
[13] J. Villain, Phys. Rev. Lett. **52**, 1543 (1984); R. Bruinsma and G. Aeppli, *ibid.* **52**, 1547 (1984).
[14] H. Yoshizawa and D. P. Belanger, Phys. Rev. B **30**, 5220 (1984); U. Nowak and K. D. Usadel, *ibid.* **39**, 2516 (1989).
[15] U. A. Leitão and W. Kleemann, Phys. Rev. B **35**, 8696 (1987).
[16] M. E. Fisher, Philos. Mag. **7**, 1731 (1962).
[17] W. Kleemann, A. R. King, and V. Jaccarino, Phys. Rev. B **34**, 479 (1986).
[18] W. Kleemann, B. Igel, and U. A. Leitão, in *New Trends in Magnetism*, edited by M. D. Coutinho-Filho and S. M. Rezende (World Scientific, Singapore, 1989), p. 85.
[19] F. C. Montenegro, A. Rosales-Rivera, J. C. O. de Jesus, F. L. A. Machado, and E. Montarroyos (unpublished work).
[20] I. B. Ferreira, A. R. King, and V. Jaccarino, Phys. Rev. B **43**, 10797 (1991), and references therein.
[21] F. C. Montenegro, A. R. King, V. Jaccarino, S-J. Han, and D. P. Belanger, Phys. Rev. B **44**, 2155 (1991); D. P. Belanger, Wm. E. Murray, Jr., F. C. Montenegro, A. R. King, V. Jaccarino, and R. W. Erwin, *ibid.* **44**, 2161 (1991).
[22] F. C. Montenegro, M. D. Coutinho-Filho, and S. M. Rezende, Europhys. Lett. **8**, 383 (1989).

Order by disorder in an anisotropic pyrochlore lattice antiferromagnet

S. T. Bramwell
Institut Laue-Langevin, 156X-38042 Grenoble, France, and TRIUMF, 4004 Wesbrook Mall, Vancouver, British Columbia V6T 2A3, Canada

M. J. P. Gingras
TRIUMF, 4004 Wesbrook Mall, Vancouver, British Columbia V6T 2A3, Canada

J. N. Reimers
Department of Physics, Simon Fraser University, Burnaby, British Columbia V5A 1S6, Canada

The properties of the classical Heisenberg pyrochlore lattice antiferromagnet with local planar single ion anisotropy are discussed. The zero temperature ground state is found to be macroscopically degenerate and without long range order. Monte Carlo simulations are used to investigate the properties of the system at finite temperature. We find that thermal fluctuations select a subset of the ground state manifold, and induce a first-order phase transition to a conventional Néel ground state.

In recent years, there has been increasing interest in spin models which show the phenomenon of "order by disorder."[1] The phenomenon is generally associated with frustrated systems, in which the classical ground state manifold is highly degenerate, and includes both ordered and disordered states. However, the degeneracy of the ground state may be lifted by thermal fluctuations in the following way. At a small but finite temperature, $T=0^+$, there are usually a greater number of softer and more easily excitable states associated with the ordered, than with the disordered ground states, and so entropy prefers the ordered states. Usually one state is selected, apart from the trivial global symmetry operations, with the ironic result that thermal *disorder* has induced *order* in the system. In a quantum system, zero point fluctuations can achieve the same effect.

In this paper we present a spin model in which order by thermal disorder occurs in a rather spectacular fashion, via a discontinuous phase transition, as in the type-I face centered cubic Heisenberg antiferromagnet.[2] The system we consider is the Heisenberg pyrochlore lattice antiferromagnet with local easy-plane anisotropy. The pyrochlore lattice[3] is illustrated in Fig. 1. Its near neighbor bonds form a three-dimensional array of corner-linked regular tetrahedra, with overall cubic symmetry. It can be regarded as the three-dimensional analog of the better-known kagomé lattice, which is a corner-linked array of equilateral triangles. In both systems, with antiferromagnetic near neighbor Heisenberg exchange, the elementary tetrahedral or triangular plaquettes are highly frustrated, and the ground state is determined only by the rather unrestrictive condition $\Sigma_{\text{plaquette}}\ \mathbf{S}_i=0$ on *each* individual plaquette, where $\mathbf{S}_i$ are classical spins. Because of this, the ground state manifold is highly degenerate. Thermal selection of a long range magnetically ordered state in the Heisenberg pyrochlore lattice antiferromagnet is not observed down to $T\approx O(J/100)$, where J is the antiferromagnetic exchange.[4] Whether or not it occurs in the Heisenberg kagomé lattice antiferromagnet is not yet firmly established and is the subject of current investigation.[5]

The pyrochlore lattice is particularly common in nature, occurring in several extensive series of compounds. In the cubic pyrochlores, of general formula $A_2B_2O_7$ (e.g., $Hg_2Nb_2O_7$[3]), the metallic A^{n+} and $B^{(7-n)+}$ ions lie on separate interpenetrating pyrochlore lattices; in the spinels AB_2O_4 (e.g., $MgCr_2O_4$),[6] the B sites form a pyrochlore lattice; in intermetallics of general formula AB_2 with the "C15" structure (e.g., YMn_2[7]), the B atoms occupy a pyrochlore lattice. Another example is the Fe^{3+} lattice in FeF_3,[8] which can be represented as a cubic pyrochlore structure with vacancies. In most of these compounds the magnetic interactions are predominantly antiferromagnetic; however, few appear to be simple Heisenberg systems. They display a particularly rich variety of magnetic phenomena, including helical structures,[7] first-order phase transitions,[6] irreversibilities,[8] and—most intriguing of all—spin glass behavior, in compounds such as $M_2Mo_2O_7$ (M=Y, Tb).[9] These materials have apparently negligible disorder, and are possibly the closest thing we know to a nondisordered spin glass.[10]

In order to begin to understand the properties, and, in particular, the spin glass behavior of the real materials, we are currently investigating the effect of perturbations to the basic Heisenberg Hamiltonian. In this paper we treat the case of local easy-plane single-ion anisotropy, and use the Hamiltonian

$$H=-J\sum_{\langle i,j\rangle}\mathbf{S}_i\cdot\mathbf{S}_j-D\sum_i(\mathbf{S}_i\cdot\hat{n}_i)^2, \tag{1}$$

where $J<0$ is the near neighbor antiferromagnetic exchange coupling and $D<0$ an anisotropy constant.[11] The $\hat{n}_i$ axes for each spin are parallel to the four threefold axes of the elementary bond tetrahedra, as illustrated in Fig. 2(a). These

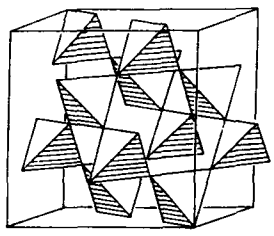

FIG. 1. Pyrochlore lattice, showing the cubic unit cell.

 0021-8979/94/75(10)/5523/3/$6.00 © 1994 American Institute of Physics

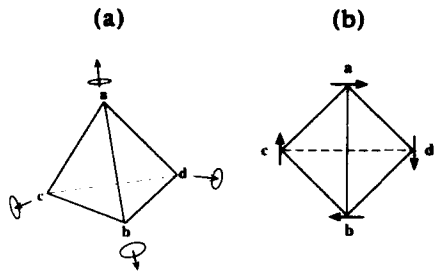

FIG. 2. (a) Elementary tetrahedral bond plaquette *abcd*, indicating the local anisotropy axes (arrows) and corresponding easy spin planes. (b) Elementary tetrahedron viewed down a two-fold axis, showing one of the 12 degenerate ground state spin arrangements.

local axes are dictated by the space group symmetry of the cubic pyrochlore lattice, and are parallel to the four ⟨111⟩ directions (see Fig. 1).

The ground state of the elementary tetrahedron can be found by the following argument. Consider the tetrahedron $a-b-c-d$ illustrated in Fig. 2(a), with spins $\mathbf{S}_a$, etc. situated at each vertex. The anisotropy energy of $\mathbf{S}_a$ is minimized when $\mathbf{S}_a$ lies in a plane parallel to $b-c-d$; and similar relationships hold for the other spins. Now introduce the two antiferromagnetic bonds $a-b$ and $c-d$, and temporally ignore the other four bonds. Minimization of the energy of each spin pair occurs when the two spins are antiferromagnetically aligned parallel to the direction of intersection of their two easy planes. $\mathbf{S}_a$, $\mathbf{S}_b$ therefore lie parallel to the bond $c-d$, and $\mathbf{S}_c$, $\mathbf{S}_d$ lie parallel to the bond $a-b$. This can be seen by viewing the tetrahedron down one of its twofold axes, as shown in Fig. 2(b). The configuration is fourfold degenerate, with the states related by flips of the spin pairs. These configurations actually obey the condition $\Sigma \mathbf{S}_i = 0$, which minimizes the total exchange energy of the tetrahedron. The ground state manifold of the tetrahedron therefore comprises the three symmetry-related sets of such configurations, which are generated by the three twofold axes of the tetrahedron. It should be noted that the anisotropy introduces no extra frustration, but selects only 12 of the originally infinite set of ground states.

The energy of the whole lattice is minimized if each tetrahedron of spins can adopt a configuration such as that shown in Fig. 2(b). Referring to Fig. 1, the bonds of the pyrochlore lattice, when viewed perpendicular to the cube face of the unit cell, form two sets of infinite rods that are mutually perpendicular. These rods can be labeled as $a-b-a-b-a\ldots$ or $c-d-c-d-c\ldots$, where any permutation of ($abcd$) defines an elementary tetrahedron. It can be seen that the ground state of the whole system is such that each rod has a perfectly antiferromagnetic spin arrangement. There is no correlation between rods, but all the spins in the system are coplanar. The ground state manifold is thus divided into three symmetry-related subsets, in which the spins lie in the (1 0 0) (0,1,0) or (0,0,1) planes; and in each subset there are approximately $2^{N^{1/3}}$ states related by flipping the spin direction of each rod (N is the number of spins). It is seen that the ground state has broken symmetry with a unique spin plane, but no conventional spin order, and may thus be described as a "uniaxial nematic." The entropy per spin approaches zero in the thermodynamic limit as $N^{-2/3}$, but the spins remain disordered.

At first sight the system presently studied would appear to be a good candidate for intrinsic spin glass behavior, as observed in several real materials. However, we have investigated the finite temperature properties using Monte Carlo simulations, and discovered that thermal fluctuations induce an antiferromagnetic ground state, at least in our finite lattice simulations. We now give a brief summary of our results.

Monte Carlo simulations were carried out using the conventional Metropolis spin flipping algorithm in the temperature range $0.05 \leq T/J \leq 1$. Lattice sizes ranging from $L^3 = 2^3 - 6^3$ were used, where L^3 is the number of unit cells (see Fig. 1). These correspond to $16L^3$ spins ranging from 128 to 3456, respectively. The strongly anisotropic case with $D = 5J$ has been studied, in order to clearly reveal the effect of the anisotropy. All thermodynamic quantities were calculated using multiple histogram methods.[12] All simulation runs were started with a random spin configuration at a high temperature above T_N, and were systematically annealed in such a way that histograms for neighboring temperatures overlapped. Equilibrium spin configurations for one temperature were used as starting configurations for the next simulation at a slightly lower temperature. At least 1000 Monte Carlo steps were allowed for equilibration at each temperature, and at least 10 000 steps were used for generation of thermodynamic data. Long range order was detected by calculating the four-sublattice magnetization:

$$m_s = \tfrac{1}{4}(m_a^2 + m_b^2 + m_c^2 + m_d^2)^{1/2}, \tag{2}$$

where, for example m_a is the net moment on sublattice a:

$$\mathbf{m}_a = \left(\frac{4}{N}\right) \sum_i \mathbf{S}_i . \tag{3}$$

The four sublattices are labeled in Fig. 2. The ordering susceptibility,

$$\chi_s = (N/T)(\langle m_s^2 \rangle - \langle m_s \rangle^2), \tag{4}$$

was also measured. Figure 3 shows the behavior of the sublattice magnetization, m_s, and indicates that long range order occurs below $T_N/J = 0.1$, with an ordering wave vector $\mathbf{q} = 0$. The very sharp rise in m_s indicates that the transition is strongly first order. A small degree of rounding of any thermodynamic quantity is always expected in finite systems at a first-order transition. The inset shows the lattice size dependence of the maximum in the heat capacity, indicating a divergence $C_{\max} \propto L^3$, as expected, at a first-order transition.[13] The maximum in χ_s also shows similar behavior. This is a new example[1,2] of thermal selection of a long range ordered state. A rapid quench from $T = \infty$ to below T_N, $T/J = 0.06$, resulted in formation of the ordered phase after about 10^5 Monte Carlo steps, indicating that slow annealing is not re-

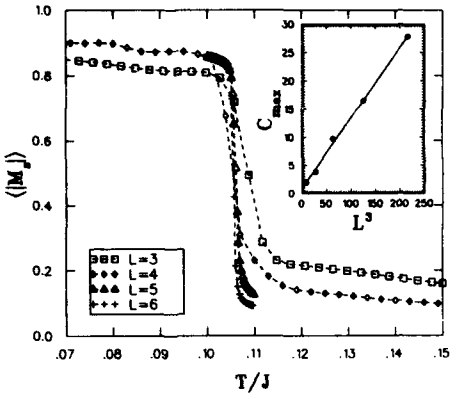

FIG. 3. Sublattice magnetization versus temperature for different lattice sizes, with $16L^3$ spins. Inset: linear dependence of maximum in specific heat on L^3.

quired for developing long range order, at least for these small lattice sizes. A number of questions still remain regarding the phase transition:

(1) Is the thermal selection of an ordered phase only a result of the finite extent of the lattice studied here? Perhaps larger systems will have either (a) lower ordering temperatures or (b) smaller ordered moments, both of which may vanish as $L \to \infty$.

(2) Is there any hysteresis near T_N? Long range order may survive to temperatures above $T/J = 0.1$ when warming from the ordered phase.

(3) How does T_N and the nature of the transition vary with the anisotropy strength in the range $0 \leq D/J \leq 5$?

We hope to answer these questions in a future publication.

In conclusion, we have studied the pyrochlore lattice Heisenberg antiferromagnet with a physically realistic anisotropy allowed by symmetry (the easy plane case). The system has a disordered $T=0$ ground state with nematic order, consisting of randomly oriented antiferromagnetic "rods" of spins. Monte Carlo simulations suggest $\mathbf{q}=0$ ordering via a strongly first-order phase transition. This can be understood as resulting from a thermally-induced effective coupling between the spin rods, and constitutes a remarkable example of "order by disorder."

It is a pleasure to thank P. C. W. Holdsworth for useful comments on the manuscript, and J. Dahn for supplying the computer facilities.

[1] J. Villain, R. Bidaux, J.-P. Carton, and R. Conie, J. Phys. **41**, 1263 (1980).
[2] H. T. Diep and H. Kawamura, Phys. Rev. B **40**, 7019 (1989); M. T. Heinilä and A. S. Oja, Phys. Rev. B (to be published).
[3] A. W. Sleight, Inorg. Chem. **7**, 1704 (1968).
[4] J. N. Reimers, Phys. Rev. B **45**, 7287 (1992).
[5] See, for example, J. T. Chalker, P. C. W. Holdsworth, and E. F. Shender, Phys. Rev. Lett. **68**, 855 (1992); P. Chandra, P. Coleman, and I. Ritchey J. Phys. I (France) **3**, 591 (1993); A. Chubukov, Phys. Rev. Lett. **69**, 832 (1992); J. N. Reimers and A. J. Berlinsky, to appear in Phys. Rev. B; E. F. Shender and P. C. W. Holdsworth, in *Fluctuations and Order, The New Synthesis*, edited by M. M. Millonas (MIT Press, Cambridge, MA) (to be published).
[6] H. Shaked, J. M. Hastings, and L. M. Corless, Phys. Rev. B **1**, 3116 (1970).
[7] R. Ballou *et al.*, J. Magn. Magn. Mat. **70**, 129 (1987).
[8] G. Ferey *et al.*, Rev. Chim. Min. **23**, 474 (1986); J. N. Reimers *et al.*, Phys. Rev. B **43**, 5692 (1991).
[9] J. E. Greedan *et al.*, Phys. Rev. B **43**, 5682 (1991); B. D. Gaulin *et al.*, Phys. Rev. Lett. **69**, 3244 (1993).
[10] J. Villain, Z. Phys. B **33**, 31 (1979) has suggested that a vanishingly small concentration of impurities can give rise to spin glass behavior in tetragonal Hesienberg spinels. His argument could also apply to the present system with local easy-plane anisotropy.
[11] The alternate case of easy-axis anisotropy ($D>0$) is less relevant to the spin glass problem, as it gives rise to a nondegenerate four-sublattice ground state, as observed experimentally in FeF_3.[8]
[12] See Ref. 30, in J. N. Reimers and A. J. Berlinsky, Ref. 5.
[13] K. Binder and D. P. Landau, Phys. Rev. B **30**, 1477 (1984).

A new scheme to percolation thresholds

Serge Galam and Alain Mauger
Groupe de Physique des Solides,[a] Tour 23, 2 place Jussieu, 75251 Paris Cedex 05, France

Using a ferromagnetic Ising model, a new lattice homogeneity breaking approach (HBA) for two-dimensional site dilution is presented. The critical temperature is stated to result from an energetic balance between the cluster center and its surface. This definition produces a breaking in the homogeneity of the system between the fluctuating cluster magnetization and the mean bulk counterpart. Site dilution is then found to generate additional breaking of the system homogeneity, with the introduction of a generalized surface effect which makes our procedure qualitatively different from the Bethe one. The HBA results in a simple new analytic expression for site percolation thresholds, which reproduces the exact values or numerical estimates for all lattice topologies in dimension two, within few percent.

I. INTRODUCTION

The relevance of percolation phenomena to describe physical systems in analogy to phase transitions has been understood for decades.[1,2] Since then, much effort has been expended to determine values for critical thresholds according to the symmetry classification of all existing lattices (for reviews, see Refs. 3–6).

Percolation is associated with two kinds of dilution, which are attached, respectively, to bond and site. Exact results for percolation thresholds are very hard to obtain analytically. Most difficult is the site percolation problem. In this case, only the two-dimensional triangular and Kagomé cases are solved exactly.[4] Not a single exact result has been obtained for three dimensions. It is also worth noting that each exact result has been derived by itself and not as an outcome of some general approach. Last, but not least is the Scher and Zallen proposal[7] to have a constant product $p_c f$, where f is the lattice filling factor. However, this idea, although general, does not yield good results. It needs an ad hoc choice of the constant, which varies with the dimension, and has a 15% error bar.

For more than 50 years the Bethe scheme has been a well-known approch to go beyond the mean-field treatment of many-body problems. In the present work, we extend it to calculate percolation thresholds analytically using a new cluster-like scheme in a ferromagnetic Ising system. The mean-field expression for the critical temperature $kT_c = qJ$ is postulated to hold beyond the inclusion of fluctuations within a nearest-neighbors cluster, in the form $kT_c = qJ_{\text{eff}}$. The effective coupling constant J_{eff} is calculated from an energetic balance between the center and the surface of the cluster. The homogeneity is thus broken, which results in three distinct magnetizations: at the cluster center, the cluster surface, and the bulk. That is why we call this model the homogeneity breaking approach (HBA), which differs from the Bethe scheme, where the magnetizations at the cluster center and the surface are forced to be equal. The HBA yields all two-dimensional site thresholds within a few percent. Moreover, a simple average of our general result with the Bethe one is found to produce, surprisingly, all three-dimensional site thresholds within a few percent.

II. THE FERROMAGNETIC ISING PROBLEM

Let us consider a ferromagnetic Ising system on a q-nearest-neighbor lattice. The Hamiltonian is

$$H = -J \sum_{(i,j)} S_i S_j , \tag{1}$$

where $S_i = \pm 1$ is an Ising variable, and the interactions J are restricted to nearest neighbors (nn's). To go beyond the molecular field approximation, it is necessary to distinguish the local environment of any magnetic site from the more remote part of the crystal. To achieve such a goal, we start from one site labeled i, to which we refer as an A site. Then we label the set of its nn by the index j and call them B sites. Last, the nn of j sites, except the i site, are labeled by the index k and are called C sites. The A site plus these B and C shells constitute a supercell for the lattice. This supercell is then used to pave the space and reproduce the whole lattice. The lattice is thus divided into three distinct sublattices denoted respectively A, B, and C. The scheme is easily visualized in the square case. In this scheme, Eq. (1) can be written in the equivalent form,

$$H = -J \sum_{i \in A} \left(S_i \sum_{j \in B, j=1}^{q} S_j^i + \sum_{j \in B, j \neq i}^{q} S_j^i \left\{ \sum_{k \in C}^{\prime} S_k^{i,j} \right\} \right). \tag{2}$$

The prime means that the summation over k j-nn sites does not include the i site. The first step beyond the mean-field approach amounts to treat exactly both S_i and nn spins S_j^i, while more remote $S_k^{i,j}$ spins are treated within mean field. These remote spins belonging to the C sublattice are replaced by their thermal average $\langle S_k^{i,j} \rangle \equiv m_C$ in the Hamiltonian. We are left with three unknown magnetizations which are respectively, $m_A \equiv \langle S_i \rangle$, $m_B \equiv \langle S_j^i \rangle$, and $m' \equiv m_C$. Equation (2) reduces to $H = \Sigma_{i \in A} H_i$, where H_i is given by

$$H_i = -JS_i \sum_{j=1}^{q} S_j^i - h \sum_{j=1}^{q} S_j^i ; \quad h \equiv J \sum_{k=1}^{q-1} \langle S_k^{i,j} \rangle . \tag{3}$$

[a]Laboratoire associé au C.N.R.S. (U.A. No. 17) et aux Universités Paris VII et Paris VI.

 0021-8979/94/75(10)/5526/3/$6.00 © 1994 American Institute of Physics

where the set k runs for all $(q-1)$ nearest neighbors of, respectively, each site j, site i being excluded. The molecular field h takes the form

$$h=J(q-1)m', \tag{4}$$

We now introduce spin dilution on the lattice. At each site l is associated a random variable ϵ_l with the probability distribution function, $p(\epsilon_l)=x\delta(\epsilon_l-1)+(1-x)\delta(\epsilon_l)$, where x is the occupied site density. From Eq. (3) the partition function Z can be written $Z=Z_+ + Z_-$, where the suffix corresponds to, respectively, $S_i=+1$ and $S_i=-1$. Under this form the mean value $\langle \epsilon_i S_i\rangle$ is obtained as equal to $\epsilon_i(Z_+ - Z_-)/(Z_+ + Z_-)$. The derivative of Z with respect to $\alpha \equiv \beta h$, divided by $(q-1)Z$ is just $\langle \epsilon_j^i S_j^i\rangle$. At order one in α, the following two mean-value equations are obtained:

$$\overline{\langle \epsilon_i S_i\rangle}=x^2 q \tanh(\gamma)\tilde{\alpha}, \tag{5}$$

and

$$\overline{\langle \epsilon_j^i S_j^i\rangle}=[x+x^3(q-1)\tanh^2(\gamma)]\tilde{\alpha}, \tag{6}$$

where $\overline{\langle \ldots\rangle}$ denotes a configurational average over site disorder variables $\{\epsilon_l\}$ and $\gamma \equiv \beta J$.

A. The Bethe approach

The requirement $\overline{\langle \epsilon_i S_i\rangle} = \overline{\langle \epsilon_j^i S_j^i\rangle}$ produces a Bethe version of the usual self-consistent mean-field equation of state. The associated critical temperature is

$$\tanh\left(\frac{J}{k_B T_c^B}\right)=\frac{1}{x(q-1)}. \tag{7}$$

The critical threshold for percolation is then obtained at $T_c^B=0$ giving

$$x_c^B=\frac{1}{(q-1)}, \tag{8}$$

which is the exact percolation threshold derived on a Caylee tree.

B. The homogeneity breaking approach

We assume that the T_c functional is universal under the form

$$k_B T_c = q J_{\text{eff}}, \tag{9}$$

where J_{eff} is an effective coupling. At the mean-field level $J_{\text{eff}}=J$. To go beyond this result we now determine J_{eff} from the expression for $\tilde{\alpha}$ accounting for the interaction with $x(q-1)$ site magnetizations, after Eq. (4):

$$J_{\text{eff}}^d=\frac{\tilde{h}}{x(q-1)\overline{\langle \epsilon_i S_i\rangle}}. \tag{10}$$

Using Eq. (5) the critical temperature T_c^N becomes

$$\tanh\left(\frac{J}{k_B T_c^N}\right)=\frac{1}{x^2(q-1)}. \tag{11}$$

The associated percolation threshold is

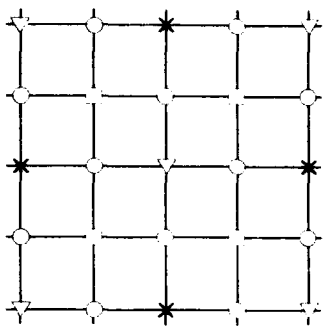

FIG. 1. Multilattice view of the two-dimensional square lattice. Symbols (▽), (○), (□), and (×) denote respectively A, B, C, and D lattice sites.

$$x_c^N=\frac{1}{\sqrt{(q-1)}}. \tag{12}$$

Note that $T_c^N=T_c^B$ for $x=1$, since Eq. (11) matches Eq. (7), with the consequence that $\langle S_i\rangle=\langle S_j^i\rangle$. The HBA approach is at this stage equivalent to the Bethe model. However, in the Bethe scheme, it is usually stated that the common mean-value magnetization $m\equiv\langle S_i\rangle=\langle S_j^i\rangle$ is the magnetization in the bulk, i.e., $m=m'$. Nevertheless, substitution of Eq. (4) into Eq. (5) results in

$$m=q\tanh(\gamma)\beta J(q-1)m', \tag{13}$$

which obviously shows that $m\neq m'$, thus proving wrong the above homogeneity assumption. To get $m=m'$ at any temperature would require a temperature dependent coupling in Eq. (4) instead of J. The lattice homogeneity has thus been already broken within the Bethe model. Though opposite to what is usually assumed in all textbooks, this result is fully consistent with the cluster character of the Bethe scheme which is enhanced by the symmetry-lattice view.

As soon as $x\neq 1$, our model differs from the Bethe one. In particular, at $T=T_c^N$, we now have $\overline{\langle \epsilon_i S_i\rangle} \neq \overline{\langle \epsilon_j^i S_j^i\rangle}$ in contradistinction to the pure situation. Dilution is thus found to produce an additional breaking in homogeneity through a surface effect which results in three different magnetizations at respectively, the center, the surface, and the bulk. Such a *multibreaking in homogeneity is indeed consistent with the* site hierarchy we have built. The treatment is fully exact for the central site, partly exact for its nearest neighbors, and mean field for next nearest neighbors. Equation (3) corresponds to such a cluster which covers the whole space by translational invariance (see Fig. 1). On the opposite Eq. (8) is associated to a perfect mean-field lattice realized only in the Caylee tree.

III. RESULTS AND CONCLUSION

At this stage, to check our procedure it is worth comparing various lattices exact estimate percolation thresholds to those obtained, respectively, from Eqs. (8) and (12). Results are shown in Table I. From the table it is clearly seen that x_c^N

TABLE I. Percolation thresholds in the Bethe model x_c^B, and in the present work x_c^N, compared with exact or numerical estimates p_c after Ref. 3. The * means frustrated lattice and $\delta=2$, otherwise, $\delta=1$.

d	Lattice	q	x_c^B	x_c^N	p_c
$d=2$	Square	4	0.333	0.577	0.593
	Honeycomb	3	0.500	0.707	0.698
	Triangular*	6	0.200	0.500	0.500
	Kagomé*	4	0.333	0.707	0.653
$d=3$	Diamond	4	0.333	0.577	0.428
	sc	6	0.200	0.447	0.311
	bcc	8	0.143	0.378	0.245
	fcc*	12	0.091	0.316	0.198
$d=\infty$	Caylee tree	q	$\frac{1}{(q-1)}$	$\frac{1}{\sqrt{(q-\delta)}}$	$\frac{1}{(q-1)}$

gives rather good results for two dimensions. However, for three dimension the data do not fit very well. It is worth noticing that while the usual Bethe scheme underestimates fluctuations, giving lower threshold values, our own scheme overestimates them with higher thresholds. At this stage it turns out that making a simple average of the respective two values gives rather good three-dimensional data x_c^{av} with, in respective order, 0.455, 0.323, 0.260, and 0.196. This average does not hold either at two or four dimensions.

Looking more precisely at two-dimensional results in Table I, a rather good agreement, within a few percent, is found to hold for the square and honeycomb lattices. For the triangular and Kagomé lattices the error is of order 10%. This discrepancy results indeed from a topological pathology. Equation (3) does not hold for all lattices. It can be seen that in the particular cases of triangular and Kagomé lattices, a site k is simultaneously a mean-field nearest neighbor of a site j and an exact nearest neighbor of the central site i. In other words some sites k are also sites j. In such a case, the distinction between the subsets j and l is irrelevant, and so are Eqs. (2) and (3). Such a topology is characteristic of frustrated lattices, so-called because the sequence $(+-)$ cannot be fulfilled simultaneously for all nearest neighbors in case the interaction is antiferromagnetic. Accounting exactly for all interactions among first nearest neighbors yields, in the Kagomé case the expression $x_c^N = 1/\sqrt{(q-2)}$ instead of Eq. (12), giving $x_c^N=0.707$ which is closer to $p_c=0.653$ than $x_c^N=0.577$. Extending the formula to the triangular case gives the exact result $x_c^N=0.500$.

In conclusion, this new approach to tackle two-dimensional lattice problems goes beyond the usual Bethe scheme, and yields the first analytic formula for all two-dimensional percolation thesholds, in agreement (within a few percent) with exact results. In a field where most results are either numerical or specific to a given lattice, our general analytical result should shed new light on the actual state of understanding.

ACKNOWLEDGMENT

The authors would like to thank A. Jaganathan for discussions at an early stage of this work.

[1] J. M. Hammersley, Proc. Cambridge Phil. Soc. **53**, 642 (1957).
[2] C. Domb, Nature **184**, 509 (1959).
[3] D. Stauffer, Phys. Rep. **54**, 1 (1979)
[4] J. W. Essam, in *Phase Transitions and Critical Phenomena*, edited by C. Domb and M. S. Green (Academic, New York, 1972), Vol. 2, p. 197.
[5] R. Zallen, *The Physics of Amorphous Solids* (Wiley, New York, 1983).
[6] D. Stauffer and A. Aharony, *Introduction to Percolation Theory* (Taylor and Francis, London, 1992).
[7] H. Scher and R. Zallen, J. Chem. Phys. **53**, 3759 (1970).

Heat capacity and magnetic properties of $CoCl_2 \cdot H_2O$

J. A. Lukin and S. A. Friedberg
Department of Physics, Carnegie Mellon University, Pittsburgh, Pennsylvania 15213

S. Chardarlapaty, W. W. Brubaker, C. C. Cinquina, and G. C. DeFotis
Department of Chemistry, College of William and Mary, Williamsburg, Virginia 23187

Recent magnetic studies of polycrystalline $CoCl_2 \cdot H_2O$ showed an antiferromagnetic ordering transition at $T_N \sim 14$ K and an apparent spin glass transition at ~7 K. We now have extended the magnetic susceptibility measurements up to 300 K. The results above T_N can be well described if the lowest electronic states of Co^{2+} in this salt are two Kramers doublets separated by $\Delta E/k = 230$ K, and if a predominantly ferromagnetic mean field interaction is introduced. The heat capacity of $CoCl_2 \cdot H_2O$ over the range 0.6–80 K has also been measured. Below ~10 K, $C_p \approx aT^{-2} + bT^3$. The first term is the hyperfine contribution of the $^{59}Co^{2+}$ nuclei. The second is the sum of lattice vibrational and electronic spin parts. C_p exhibits a λ-type peak at $T_{N1} \approx 15.0 \pm 0.05$ K, and a second λ anomaly of comparable size at $T_{N2} = 13.9 \pm 0.05$ K, which appears to be associated with a spin reorientation transition. Correcting the observed C_p data for the nuclear spin contribution, one may calculate the sum of lattice vibration and electron spin entropies, and thus obtain at T_{N1} an upper limit to the critical magnetic entropy. This amounts to 0.38 R ln 2, suggesting that a substantial part of the spin ordering in this system is of short-range and lower dimensionality. C_p also exhibits an inflection point near 4.5 K, where an unusual feature in the temperature dependence of the spin glass thermoremanent magnetization was found.

I. INTRODUCTION

Recent magnetic measurements[1] on polycrystalline samples of $CoCl_2 \cdot H_2O$, a previously unexamined member of an otherwise familiar family of Co^{2+} salts, show a rounded maximum in χ_p near 16 K, with a distinct maximum in $d\chi/dT$ at 14.0±0.1 K. These features suggest an antiferromagnetic ordering transition at $T_N \approx 14$ K. Comparison of field-cooled and zero-field-cooled susceptibilities reveals an apparent spin glass transition with a freezing temperature T_g in the 6–7 K range. $CoCl_2 \cdot H_2O$ is prepared by the partial removal at elevated temperature of water from $CoCl_2 \cdot 2H_2O$, a well-known metamagnet composed of antiferromagnetically coupled chains of ferromagnetically aligned Co^{2+} spins.[2] While the structure of the monohydrate is as yet unknown, the nature of the starting material and mode of preparation suggest that $CoCl_2 \cdot H_2O$ may well exhibit significant magnetic ion site randomness or defect concentration as well as frustration and low dimensionality of magnetic interactions.

In this paper we present (1) the extension of powder susceptibility measurements up to 300 K and (2) the determination of the equilibrium heat capacity of $CoCl_2 \cdot H_2O$ between 0.6 and 80 K. The new χ_p data establish the presence of important ferromagnetic as well as antiferromagnetic interactions in this system. The C_p results suggest that these competing interactions and anisotropy effects produce several phase transitions, and that the system has a low-dimensional character.

II. EXPERIMENTAL DETAILS

Fine-grained polycrystalline samples of $CoCl_2 \cdot H_2O$ were prepared as described in Ref. 1. Magnetic susceptibility measurements were made on a 123.68 mg polycrystalline sample using a low-temperature vibrating sample magnetometer. Susceptibilities reported here have been corrected for diamagnetism ($\chi_{dia} = -77 \times 10^{-6}$ emu/mol) and demagnetization. The heat capacity $C_p(H=0)$ was measured in a vacuum calorimeter using a mechanical heat switch and cooled with liquid ^3He or ^4He. The data reported here were obtained with a specimen consisting of 28.068 g (0.1898 mol) of powdered $CoCl_2 \cdot H_2O$ by the method previously described.[3]

III. RESULTS AND DISCUSSION

Figure 1 shows the molar magnetic susceptibility vs temperature of $CoCl_2 \cdot H_2O$ as χ vs T and χ^{-1} vs T. The antiferromagnetic maximum at 16.2 K and lower χ vs T data are not shown here, but appear in Ref. 1. It is fairly evident from Fig. 1 that χ^{-1} vs T is not acceptably linear in any significant temperature range above ~60 K. A Curie–Weiss fit

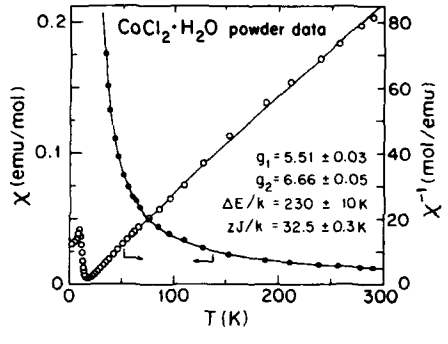

FIG. 1. Magnetic susceptibility χ_{mol} and $1/\chi_{mol}$ of powdered $CoCl_2 \cdot H_2O$ with the model curve described in the text and the parameters shown.

 0021-8979/94/75(10)/5529/3/$6.00 © 1994 American Institute of Physics

$[\chi_M = C/(T-\theta)]$ to data in the rather linear 29–70 K range yields $C = 2.99 \pm 0.02$ emu K/mol and $\theta = 14.8 \pm 0.3$ K. The θ value is positive and much larger than that reported for $CoCl_2 \cdot 2H_2O$, suggesting that ferromagnetic exchange is more predominant in the monohydrate than the dihydrate.

For weak octahedral coordination the crystal field ground term of Co^{2+} is a $^4T_{1g}$ level. The effects of crystal field distortions and spin-orbit coupling lead to a splitting of this level into six Kramers doublets, typically separated by more than kT, even for $T = 300$ K. Under such circumstances, Curie(–Weiss) behavior over a fairly broad temperature range below 300 K is expected. Only the ground Kramers doublet is significantly populated and the system is describable on an effective $S' = \frac{1}{2}$ basis. For $CoCl_2 \cdot 2H_2O$, the corresponding average g value[2] is 4.83. The value of C reported above for $CoCl_2 \cdot H_2O$ in a much more restricted temperature range leads to $g = 5.65 \pm 0.02$ on the same $S' = \frac{1}{2}$ basis.

The substantial curvature in our $\chi^{-1}(T)$ data suggests that in $CoCl_2 \cdot H_2O$, assuming a somewhat analogous pattern of states, the separation between ground and first excited doublets is not large with respect to kT. In order to account for these data, we adopt a model in which a lower doublet, characterized by g_1, is ΔE below a first excited doublet, characterized by g_2. Application of the Van Vleck equation gives

$$\chi = 0.0938 \text{ emu K/mol } \frac{g_1^2 + g_2^2 e^{-\Delta E/kT}}{T(1+e^{-\Delta E/kT})}. \quad (1)$$

Exchange interactions are evidently substantial in $CoCl_2 \cdot H_2O$, and are accounted for using the mean field expression[4]

$$\chi_{ex} = \chi/[1-(2zJ/N_0 g^2 \mu_B^2)\chi], \quad (2)$$

where J is a mean exchange interaction over z neighbors.

Equations (1) and (2) are used to fit χ_p between 40 and 300 K in Fig. 1 with RMS deviation 1.5%; the agreement is satisfactory. The fitted parameters are shown in the figure. The energy separation between ground and first excited doublets $\Delta E/k = 230$ K is, as anticipated, not large compared to kT for much of the fitted range. This separation was reported as 196 K for $CoCl_2 \cdot 2H_2O$.[2] The g values, though perhaps a bit larger than might be expected, are plausible. The zJ/k value agrees well with the 29–70 K Curie–Weiss fit θ *via* the familiar mean field relation $\theta = 2S(S+1)zJ/3k$.

While the exchange interaction deduced from data in the paramagnetic region is predominantly ferromagnetic, a weaker antiferromagnetic interaction must also be present, to account for the maximum in χ_p and the onset of antiferromagnetic long-range order below T_{N1}. The $1/\chi_p$ vs T behavior of Fig. 1 is similar to that seen in a number of systems shown to consist of chains (or planes) of ferromagnetically coupled ions with weaker antiferromagnetic interactions between the chains (or planes). Application of a large enough magnetic field to such a system below T_N can cause the magnetization to rise rapidly from the low value of the antiferromagnetic ordered state to a large value corresponding to near-ferromagnetic saturation. $CoCl_2 \cdot 2H_2O$ is such a metamagnet.[2]

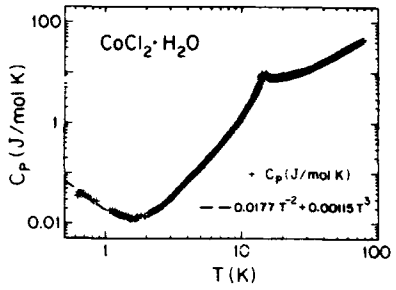

FIG. 2. Log–log plot of $C_p(T)$ of $CoCl_2 \cdot H_2O$, with a fitted nuclear contribution.

The heat capacity C_p of powdered $CoCl_2 \cdot H_2O$ measured between 0.6 and 80 K is shown on a log–log plot in Fig. 2. C_p passes through a minimum near 2 K, and can be well described in the range $0.6\text{ K} \leq T \leq 4$ K by an equation of the form $C_p = aT^{-2} + bT^3$, with $a = 0.0177 \pm 0.0013$ J K mol and $b = 0.001\,15 \pm 0.000\,10$ J/mol K^4, as indicated by the dashed curve. The first term may be interpreted as arising from the hyperfine interaction of the spin $(I = \frac{7}{2})$ of the $^{59}Co^{2+}$ nucleus with the spin $(S' = \frac{1}{2})$ of the electronic ground state according to the Hamiltonian $\mathbf{S'} \cdot \mathbf{A} \cdot \mathbf{I}$. The resultant splitting makes a contribution to the heat capacity, which in the high temperature limit may be shown[5] to be $CT^2/R = (\frac{21}{16})(A_x^2 + A_y^2 + A_z^2)/k^2$. Equating experimental and theoretical coefficients of T^{-2}, one finds for the hyperfine coupling constants $\sqrt{A_x^2 + A_y^2 + A_z^2}/k = 0.040 \pm 0.013$ K, a value very close to those found by a variety of methods for $^{59}Co^{2+}$ in a number of different solids.

The T^3 term in C_p at low temperatures is probably a superposition of two contributions varying as T^3, one due to lattice vibrations, the other to excitations of the coupled spin system, e.g., three-dimensional (3-D) antiferromagnetic spin waves. The spin contribution grows more rapidly as T exceeds ~9 K, C_p eventually exhibiting a succession of two sharp λ anomalies of comparable size at $T_{N2} = 13.9 \pm 0.05$ K and $T_{N1} = 15.0 \pm 0.05$ K. The data, after subtraction of the hyperfine contribution, are shown enlarged on a linear plot in Fig. 3. These anomalies lie well below 17.2 K, the Néel temperature of $CoCl_2 \cdot 2H_2O$, where a strong single λ peak has been observed.[6] The absence of such a peak and others at the ordering temperatures of $CoCl_2$ and its other hydrates is good evidence that our sample consists of single-phase $CoCl_2 \cdot H_2O$. While T_{N2} in the C_p data agrees well with the temperature of maximum $d\chi/dT$, a corresponding anomaly in χ at T_{N1} has not yet been resolved.

Twin C_p peaks such as those in Figs. 2 and 3 are not common, but several cases have been studied, among them $CsNiCl_3$[7] and $NiCl_2 \cdot 2H_2O$.[8] $CsNiCl_3$ is a quasi-one-dimensional antiferromagnet[9] on a stacked triangular (simple hexagonal) lattice with weak antiferromagnetic interchain coupling. The effects of anisotropy and frustration produce a complicated phase diagram, which in zero field yields the observed succession of transitions. $NiCl_2 \cdot 2H_2O$, on the other

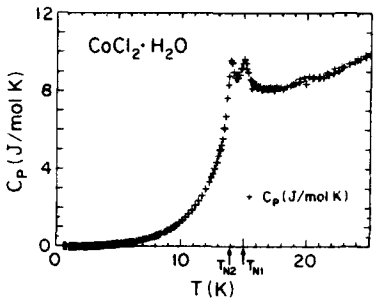

FIG. 3. Linear plot of $C_p(T)$ of $CoCl_2 \cdot H_2O$ corrected for the nuclear contribution.

hand, is effectively a system of ferromagnetic chains weakly coupled by antiferromagnetic exchange, producing net antiferromagnetism and the characteristic behavior of a metamagnet. The transition from the upper ordered phase to the lower is one of spin reorientation, and has been attributed[10] to a competition of different anisotropy mechanisms with different temperature dependences. As shown by our susceptibility results, interactions of both signs occur in $CoCl_2 \cdot H_2O$ with the ferromagnetic coupling dominant. In this respect it resembles $NiCl_2 \cdot 2H_2O$.

There is also evidence of low-dimensional character in the coupled spin system. To see this we calculate the entropy by computing the integral $\int_0^T (C_p/T)\, dT = S - S_0$ and setting $S_0 = 0$. We use the C_p data corrected only by subtracting the nuclear contribution, a/T^2, determined above. The result is the sum of electronic and lattice vibrational entropies. At T_{N1}, it amounts to $0.263R = 0.38R \ln 2$ and represents an upper limit to the critical entropy of the electronic spins. Note that the entropy difference between the fully ordered and totally disordered states of a system of N_0 ions with effective spin $S' = \frac{1}{2}$ is $R \ln 2$. While the critical entropy of a typical 3-D model magnet with $S' = \frac{1}{2}$ ranges from $\sim 0.6R \ln 2$ to $\sim 0.85R \ln 2$, that of a 2-D Ising model is only $0.44R \ln 2$. The critical entropy of the electron spin system in $CoCl_2 \cdot H_2O$ is substantially less than this, suggesting that its dominant interactions are of a low-dimensional nature.

To improve the estimate of the critical spin entropy, it is necessary to correct the C_p data for the contribution of lattice vibrations. In the absence of a diamagnetic isomorph of $CoCl_2 \cdot H_2O$, one might hope to obtain this contribution with the help of a theoretical model,[11] much as we were able to do[3] in the case of $MnCl_2 \cdot H_2O$ ($T_N = 2.18$ K). However, for $CoCl_2 \cdot H_2O$, the magnetic anomalies in C_p occur at relatively high temperatures, and it is much more difficult to estimate the parameters of such a model. A crude attempt employing a scaled version of the same model used for $MnCl_2 \cdot H_2O$ suggests that at T_{N1} the lattice vibrational entropy might amount to $\sim 0.13R \ln 2$, thus reducing the critical entropy of the electron spins to $\sim 0.25R \ln 2$. In any event, as $CoCl_2 \cdot H_2O$ is cooled below 100 K, much of the reduction in its spin entropy occurs through the development of short-range order in lower-dimensional spin arrays, presumably spin chains. This is seen directly in the large tail, which C_p exhibits above T_{N1} in Fig. 2, and the fact that the peaks at the long-range ordering transitions T_{N1} and T_{N2} are rather small.

One other feature of Fig. 2 deserves mention. The C_p data show a distinct inflection point at ~ 4.5 K, where an unusual feature also occurs in the T dependence of the thermoremanent magnetization. This and other spin glass characteristics of $CoCl_2 \cdot H_2O$ will be discussed elsewhere.

ACKNOWLEDGMENTS

The contribution of one of us (G. C. D) to this work was supported by the National Science Foundation Solid State Chemistry Grant No. DMR-9213198. We should like to thank D. Petasis for his assistance with some of the measurements.

[1] G. C. DeFotis, R. V. Chamberlain, W. R. A. Jarvis, and D. J. Krovich, J. Magn. Magn. Mat. **104–107**, 1603 (1992).
[2] A. Narath, Phys. Rev. A **136**, 776 (1964); **140**, 552 (1965).
[3] J. A. Lukin, S. A. Friedberg, and G. C. DeFotis, J. Appl. Phys. **69**, 5807 (1991).
[4] J. W. Stout and W. B. Hadley, J. Chem. Phys. **40**, 55 (1964).
[5] B. Bleaney, Phys. Rev. **78**, 214 (1950).
[6] T. Shinoda, H. Chihara, and S. Seki, J. Phys. Soc. Jpn. **19**, 1637 (1964).
[7] K. Adachi and M. Mekata, J. Phys. Soc. Jpn. **34**, 269 (1973).
[8] L. G. Polgar, A. Herweijer, and W. J. M. de Jonge, Phys. Rev. B **5**, 1953 (1972).
[9] See, for example, M. L. Plumer, K. Hood, and A. Caillé, Phys. Rev. Lett. **60**, 4' (1987).
[10] T. de Neef and W. J. M. de Jonge, Phys. Rev. B **10**, 1059 (1974).
[11] K. Kopinga, P. van der Leeden, and W. J. M. de Jonge, Phys. Rev. B **14**, 1519 (1976).

Perturbative approximation scheme for isolated impurity bonds in the two-dimensional spin-½ Heisenberg antiferromagnet

P. Schlottmann
Department of Physics, Florida State University, Tallahassee, Florida 32306

An isolated impurity bond of coupling $-K$ replacing a link J in the spin-½ Heisenberg antiferromagnet on a square lattice is considered. A simple perturbative approximation scheme is deviced, in which the two-site cluster formed by the spins linked by the impurity bond is embedded into the linearized spin wave approximation for the antiferromagnet. The resolvent for the local states of the cluster is calculated in three successive levels of approximation. The ground state wave function, the magnetization at the impurity link, and the transverse correlation across the impurity link as a function of the coupling K are discussed.

Several mechanisms for high temperature superconductivity invoke the strong antiferromagnetic correlations within the CuO planes. Properties of the high-T_c compounds are believed to be related to defects in the planes, e.g., static vacancies,[1,2] mobile holes,[3,4] and ferromagnetic bonds.[5,7] For instance, the addition of holes in La_2CuO_4 (e.g., by doping with Sr) introduces a local effective ferromagnetic exchange coupling between the Cu spins.[8] The resulting frustration affects the antiferromagnetic correlations in the neighborhood of the ferromagnetic link, and could be the origin of the spin-glass phase, and is possibly related to the superconductivity.[8]

Isolated ferromagnetic impurity bonds in an otherwise antiferromagnetic square lattice have been studied numerically by diagonalization of clusters,[6,7] and within the simple linearized spin wave approximation (LSWA).[5] The LSWA provides a reasonable description of the pure quantum antiferromagnet at $T=0$. The ground state has a broken symmetry (Néel state), and quantum fluctuations reduce the sublattice magnetization to an ordered moment of about 0.3. Since the scattering potential arising from the impurity link is factorizable, the problem of one isolated ferromagnetic bond embedded in an antiferromagnetic lattice can be solved exactly within the LSWA.[1,2,5] With increasing strength of the ferromagnetic coupling, the staggered magnetization is gradually suppressed close to the impurity link, and the two spins joined by the ferromagnetic bond tend to form a triplet state (with spin projection perpendicular to the Néel staggered magnetization). Since the LSWA only takes into account the leading terms of a $1/S$ expansion about the Néel state, a strongly ferromagnetic link then eventually leads to the breakdown of the LSWA.[5]

To overcome the artificial singularities that lead to the breakdown of the LSWA,[5] the local correlations at the isolated ferromagnetic link have to be treated properly. Here we consider three successive approximations for the two-site cluster formed by the spins joined by the impurity bond of arbitrary coupling K embedded into the antiferromagnet of coupling J described within the LSWA.

The *first approximation* consists of the two site Hamiltonian (the impurity link joins sites 1 and 2) coupled to the static staggered magnetization of the antiferromagnet, m,

$$H_0=-K\mathbf{S}_1\mathbf{S}_2+3mJ(S_1^z-S_2^z). \tag{1}$$

Note that each of the spins is coupled to three sites of the lattice, and within the LSWA $m=0.3034$. The Hamiltonian (1) has four eigenstates, which we denote $|T+\rangle=|\uparrow\uparrow\rangle$, $|T-\rangle=|\downarrow\downarrow\rangle$, $|G\rangle=\cos\theta|\downarrow\uparrow\rangle+\sin\theta|\uparrow\downarrow\rangle$, and $|E\rangle=-\sin\theta|\downarrow\uparrow\rangle+\cos\theta|\uparrow\downarrow\rangle$. Here θ is a mixing angle given by

$$\tan\theta=(K/2)/\{3mJ+[(K/2)^2+(3mJ)^2]^{1/2}\}, \tag{2}$$

and the energies are $E_{T\pm}=-K/4$, $E_G=K/4-[(K/2)^2+(3mJ)^2]^{1/2}$, and $E_E=K/4+[(K/2)^2+(3mJ)^2]^{1/2}$. The sites 1 and 2 have opposite magnetizations, the one of site 2 being $m_0=(\frac{1}{2})\cos(2\theta)$, and the transversal correlation across the impurity link is given by $\langle S_1^xS_2^x\rangle=(\frac{1}{4})\sin(2\theta)$. The angle θ varies from $-\pi/2$ for a strong antiferromagnetic link to $\pi/2$ for a strong ferromagnetic coupling, and vanishes for the missing link, $K=0$. Within this simple approximation the magnetization then tends to zero as $|K|\to\infty$ and is maximum, $m_0=0.5$, for $K=0$. The transversal correlation, on the other hand, is maximum for $|K|\to\infty$ (the spins are parallel or antiparallel) and vanishes for the missing link (the two spins are independent). m_0 and $\langle S_1^xS_2^x\rangle$ are displayed in Figs. 1(a) and 1(b) (dotted line), and the angle θ is shown in Fig. 1(c).

In principle, we could equate m_0 with m for $K=-J$ (i.e., the impurity link is just one more bond in the lattice) and search for a self-consistent solution. This yields $m_0=m=0.471$, which is a strong overestimation of the true sublattice magnetization. This result is not unexpected, since the quantum fluctuations of the lattice have been neglected. The quantum fluctuations admix the states $|T\pm\rangle$ and $|E\rangle$ into the ground state. Since the spins are parallel in the states $|T\pm\rangle$, they do not contribute to the antiferromagnetic order nor to the transverse correlations (the matrix elements vanish), but they reduce the spectral weight of the states $|G\rangle$ and $|E\rangle$. These admixtures are considered below.

Within the LSWA, the pure $S=\frac{1}{2}$ antiferromagnet is described by spin waves,[9,10]

$$H_{sw}=-6NJ+\sum_{\mathbf{k}}\omega_{\mathbf{k}}(\alpha_{\mathbf{k}}^\dagger\alpha_{\mathbf{k}}+\beta_{\mathbf{k}}^\dagger\beta_{\mathbf{k}}+1), \tag{3}$$

where $\omega_{\mathbf{k}}=4J(1-\gamma_{\mathbf{k}}^2)^{1/2}$ with $\gamma_{\mathbf{k}}=(\frac{1}{2})(\cos k_x+\cos k_y)$, the lattice parameter is equal to unity, N is the number of sites of one sublattice, and the $\mathbf{k}$ summation is over the reduced Brillouin zone. The operators $\alpha_{\mathbf{k}}^\dagger$ and $\beta_{\mathbf{k}}^\dagger$ create the two branches of spin wave excitations. The coupling of the cluster (sites 1 and 2) to the antiferromagnet is $H_1=H_{1\perp}+H_{1\parallel}$.

 0021-8979/94/75(10)/5532/3/$6.00 © 1994 American Institute of Physics

$$H_{1\perp}=\frac{J}{2\sqrt{N}}\sum_{\mathbf{k}}\left[S_1^{\dagger}z_{\mathbf{k}}^{*}(u_{\mathbf{k}}\alpha_{\mathbf{k}}^{\dagger}+v_{\mathbf{k}}\beta_{\mathbf{k}})+S_1^{-}z_{\mathbf{k}}(u_{\mathbf{k}}\alpha_{\mathbf{k}}+v_{\mathbf{k}}\beta_{\mathbf{k}}^{\dagger})+S_2^{\dagger}z_{\mathbf{k}}e^{ik_x}(v_{\mathbf{k}}\alpha_{\mathbf{k}}^{\dagger}+u_{\mathbf{k}}\beta_{\mathbf{k}})+S_2^{-}z_{\mathbf{k}}^{*}e^{-ik_x}(v_{\mathbf{k}}\alpha_{\mathbf{k}}+u_{\mathbf{k}}\beta_{\mathbf{k}}^{\dagger})\right], \quad (4a)$$

$$H_{1\parallel}=JS_1^z\left(\frac{3}{2}-3m+\frac{1}{N}\sum_{\mathbf{kk}'}z_{\mathbf{k}-\mathbf{k}'}^{*}(u_{\mathbf{k}}\alpha_{\mathbf{k}}^{\dagger}+v_{\mathbf{k}}\beta_{\mathbf{k}})(u_{\mathbf{k}'}\alpha_{\mathbf{k}'}+v_{\mathbf{k}'}\beta_{\mathbf{k}'}^{\dagger})\right)$$

$$+JS_2^z\left(-\frac{3}{2}+3m-\frac{1}{N}\sum_{\mathbf{kk}'}z_{\mathbf{k}-\mathbf{k}'}^{*}e^{-i(k_x-k_x')}(v_{\mathbf{k}}\alpha_{\mathbf{k}}+u_{\mathbf{k}}\beta_{\mathbf{k}}^{\dagger})(v_{\mathbf{k}'}\alpha_{\mathbf{k}'}^{\dagger}+u_{\mathbf{k}'}\beta_{\mathbf{k}'})\right), \quad (4b)$$

where $z_{\mathbf{k}}=4\gamma_{\mathbf{k}}-e^{-ik_x}$, $u_{\mathbf{k}}=\cosh(\kappa_{\mathbf{k}})$, $v_{\mathbf{k}}=\sinh(\kappa_{\mathbf{k}})$ and $\tanh(2\kappa_{\mathbf{k}})=-\gamma_{\mathbf{k}}$. Finally, the seven bonds corresponding to the impurity link and its connections to the lattice have to be projected out from the spin wave description of the lattice, H_{sw}, to avoid double counting. This gives rise to an additional term in the Hamiltonian, H_2, which, however, within our approximation schemes enters the calculation in a higher order, and can be neglected. The Hamiltonian of the system is then $H=H_0+H_{sw}+H_1+H_2$.

Within our *second approximation* we admix the $|T\pm\rangle$ states into the ground state, by keeping only one intermediate spin wave state to be consistent with the LSWA, but we neglect the admixture of the $|E\rangle$ state. Note that the expectation value of $H_{1\parallel}$ vanishes if m is chosen adequately, i.e., neglecting the feedback of the cluster on the lattice, this corresponds to $m=0.3034$. Perturbative admixtures involving matrix elements of $H_{1\parallel}$ can then contribute only if more than one spin wave is excited in an intermediate state, and will be neglected. This is equivalent to neglecting longitudinal spin fluctuations, which are as well disregarded in the LSWA. The $|T\pm\rangle$ states are hybridized with $|G\rangle$ to first order through matrix elements of $H_{1\perp}$. Since matrix elements of the staggered magnetization and the transversal spin correlation involving the $|T\pm\rangle$ states vanish identically, the main action of the admixture is to reduce the spectral weight of $|G\rangle$.

To calculate the spectral weight of $|G\rangle$ in the ground state, we consider the resolvant matrix element $\langle G|(\omega-H)^{-1}|G\rangle$, where ω is a complex frequency. The hybridization with $|T\pm\rangle$ introduces a self-energy,

$$\Sigma_{GG}(\omega)=F_1(\omega)+\cos(2\theta)F_2(\omega)-\sin(2\theta)F_3(\omega), \quad (5)$$

where $F_j(\omega)$ are the following functions:

$$F_1(\omega)=\frac{J^2}{4N}\sum_{\mathbf{k}}\frac{1+8\gamma_{\mathbf{k}}^2}{\omega-E_T+E_G-\omega_{\mathbf{k}}}(1-\gamma_{\mathbf{k}}^2)^{-1/2},$$

$$F_2(\omega)=\frac{J^2}{4N}\sum_{\mathbf{k}}\frac{1+8\gamma_{\mathbf{k}}^2}{\omega-E_T+E_G-\omega_{\mathbf{k}}},$$

$$F_3(\omega)=\frac{J^2}{4N}\sum_{\mathbf{k}}\frac{16\gamma_{\mathbf{k}}^4-7\gamma_{\mathbf{k}}^2}{\omega-E_T+E_G-\omega_{\mathbf{k}}}(1-\gamma_{\mathbf{k}}^2)^{-1/2}. \quad (6)$$

Note that the energy denominator only involves one spin wave energy $\omega_{\mathbf{k}}$. The summations over $\mathbf{k}$ are converted into a two-dimensional integral, which is straightforwardly performed numerically (good convergence is reached with a few hundred points in each of the k_x and k_y directions). In the absence of admixture, the energy of the state $|G\rangle$ corresponds to $\omega=0$. The self-energy reduces the ground state energy, which is now given by the lowest solution of $\omega=\Sigma_{GG}(\omega)$, which we call Ω. The residue of this state yields the spectral weight of $|G\rangle$, i.e., $sw=(1-d\Sigma_{GG}/d\omega|_{\Omega})^{-1}$. The magnetization of the spins of the cluster is now $m_0=(sw/2)\cos(2\theta)$, and the transversal correlation across the impurity link is $\langle S_1^xS_2^x\rangle=(sw/4)\sin(2\theta)$. Their θ or K dependence is then still similar, but their amplitude is reduced. The magnetization and $\langle S_1^xS_2^x\rangle$ as a function of K within this second approximation are the dashed curves in Figs. 1(a) and 1(b), respectively. The K dependence of the

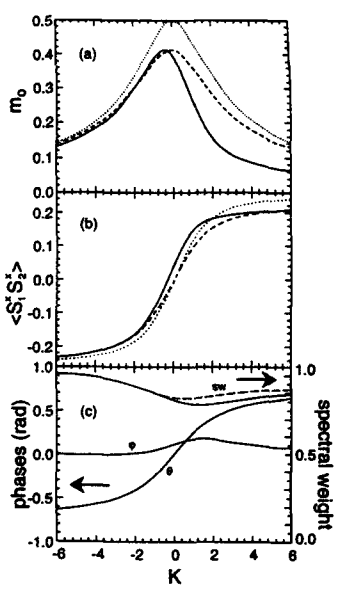

FIG. 1. (a) Magnetization at the sites adjacent to the impurity link and (b) transversal correlation across the impurity link as a function of the coupling K ($J=1$). The dotted, dashed, and solid curves correspond to the first, second, and third approximations discussed in the text. (c) Admixture angles θ and φ and spectral weights as a function of K. The dashed and solid lines correspond to the second and third approximations, respectively.

spectral weight introduces a weak asymmetry in the antiferro- versus ferromagnetic coupling. The spectral weight is given by the dashed curve in Fig. 1(c).

There are two major contributions that have been neglected in the second approximation: (i) the admixture of the $|E\rangle$ state into the ground state, and (ii) the self-energy dressing of the $|T\pm\rangle$ states. The latter further reduces the spectral weight, sw, since it lowers the energy of the $|T\pm\rangle$ states and enhances in this way the hybridization matrix element. On the other hand, the admixture of the $|E\rangle$ state introduces further asymmetries, i.e., a qualitative change. We consider the effect of (i) in our third approximation.

Our *third approximation* consists of calculating the resolvent matrix for the two states, $|G\rangle$ and $|E\rangle$. This matrix is diagonal in the absence of mixing, i.e., $\langle G|(\omega-H_0)^{-1}|G\rangle=\omega^{-1}$ and $\langle E|(\omega-H_0)^{-1}|E\rangle=(\omega-E_E+E_G)^{-1}$. Spin flips create spin waves and transitions to the $|T\pm\rangle$ states, giving rise to a self-energy matrix. This matrix is nondiagonal and symmetric, i.e., $\Sigma_{GE}(\omega)=\Sigma_{EG}(\omega)$. Keeping only intermediate states involving one spin wave, we obtain

$$\Sigma_{EE}(\omega)=F_1(\omega)-\cos(2\theta)F_2(\omega)+\sin(2\theta)F_3(\omega), \quad (5')$$

$$\Sigma_{GE}(\omega)=-\sin(2\theta)F_2(\omega)-\cos(2\theta)F_3(\omega), \quad (5'')$$

and $\Sigma_{GG}(\omega)$ is still given by (5). To obtain the ground state within this approximation, we have to find the lowest value of ω (denoted by Ω), satisfying

$$\det(\omega)=[\omega-\Sigma_{GG}(\omega)][\omega-E_E+E_G-\Sigma_{EE}(\omega)] -[\Sigma_{GE}(\omega)]^2=0. \quad (7)$$

The condition (7) corresponds to the determinant of the inverse of the resolvent matrix equated to zero. For $\omega=\Omega$, the matrix has two real eigenvalues; one of them is zero, since the determinant is zero. Hence, only the nonvanishing eigenvalue gives rise to a state of nonzero spectral weight, namely the ground state, which is given by

$$sw=-[E_E-E_G+\Sigma_{EE}(\Omega)+\Sigma_{GG}(\Omega)-2\Omega]/[d\ \det(\omega)/d\omega|_\Omega]. \quad (8)$$

The corresponding eigenstate can be written as $\psi=\cos\varphi|G\rangle+\sin\varphi|E\rangle$, where the mixing angle φ is determined via

$$\tan(2\varphi)=2\Sigma_{GE}(\Omega)/[E_E+\Sigma_{EE}(\Omega)-E_G-\Sigma_{GG}(\Omega)]. \quad (9)$$

The angle φ adds to the prediagonalization angle θ, i.e., $\psi=\cos(\theta+\varphi)|\downarrow\uparrow\rangle+\sin(\theta+\varphi)|\uparrow\downarrow\rangle$, so that now $m_0=(sw/2)\times\cos[2(\theta+\varphi)]$ and $\langle S_1^z S_2^z\rangle=(sw/4)\sin[2(\theta+\varphi)]$. Our numerical results for the third approximation are shown as the solid curves in Figs. 1(a) and 2(b). The spectral weight (solid line) and the angle φ are displayed in Fig. 1(c).

Note that almost everywhere φ is small compared to θ. This means that the prediagonalization of the two-site cluster already contains the dominant admixture of the states $|\downarrow\uparrow\rangle$ and $|\uparrow\downarrow\rangle$. φ is only significant in the neighborhood of $K=J$. Similarly, the spectral weight of the third approximation does not differ significantly from that of the second approximation if K is antiferromagnetic. The renormalization is only important for ferromagnetic K. Here the low energy of the $|T\pm\rangle$ states for $K\gg 0$ competes with the strength of the mixing matrix elements, which are large when K is not too big. This competition is most clearly seen in the magnetization m_0, which is dramatically suppressed at about $K\approx J$. For $K>J$, the ground state is predominantly the triplet state with zero spin projection. The LSWA (without prediagonalizing, the two-site cluster) is based on the Néel state, and cannot overcome the crossover, leading, in this way, to an unphysical breakdown,[5] which is the consequence of an artificial infrared singularity.

The general dependence of m_0 on K for $K<1$ is similar to that obtained within the LSWA.[5] m_0 has a maximum for slightly antiferromagnetic K and the magnetization for the missing link is larger than the one of the pure antiferromagnet. The overall magnetization obtained here is too large, since we neglected to include the self-energy for the $|T\pm\rangle$ states. This self-energy (which is $\mathbf{k}$ dependent) has the effect of reducing the energy denominators in (6), and hence to suppress the spectral weight in Eq. (8). The effect of the self-energy of the $|T\pm\rangle$ states is of the same order as contributions from the Hamiltonian H_2, which would also reduce m locally, and hence also m_0.

The support of the U.S. Department of Energy under Grant No. DE-FG05-91ER45443 is acknowledged.

[1] N. Bulut, D. Hone, D. J. Scalapino, and E. Y. Loh, Phys. Rev. Lett. **62**, 2192 (1989).
[2] N. Nagaosa, Y. Hatsugai, and M. Imada, J. Phys. Soc. Jpn. **58**, 978 (1989).
[3] C. L. Kane, P. A. Lee, and N. Read, Phys. Rev. B **39**, 6880 (1989).
[4] Z. Liu and E. Manousakis, Phys. Rev. B **44**, 2414 (1991).
[5] K. Lee and P. Schlottmann, Phys. Rev. B **42**, 4426 (1990).
[6] R. E. Camley, W. von der Linden, and V. Zevin, Phys. Rev. B **40**, 119 (1989).
[7] J. Oitmaa and D. D. Betts, Physica A **177**, 509 (1991).
[8] A. Aharony, R. J. Birgeneau, A. Coniglio, M. A. Kastner, and H. E. Stanley, Phys. Rev. Lett. **60**, 1330 (1988).
[9] P. W. Anderson, Phys. Rev. **86**, 694 (1952).
[10] T. Nagamiya, K. Yosida, and R. Kubo, Adv. Phys. **4**, 97 (1955).

Magnetic properties of a new amorphous magnet

C. P. Landee, C. M. Wynn, A. S. Albrecht, W. Zhang, G. B. Vunni, J. L. Parent, C. Navas, and M. M. Turnbull
Departments of Physics and Chemistry, Clark University, Worcester, Massachusetts 01610

An amorphous phase of $Co_3BTCA_2(H_2O)_6$ has been prepared (BTCA=1,3,5-benzenetricarboxylate). The static properties (dc susceptibility, hysteresis) of $Co_3BTCA_2(H_2O)_6$ are similar to those of other "glassy" magnetic systems, but the dynamics of $Co_3BTCA_2(H_2O)_6$ (absence of long relaxation times, disappearance of frequency dependence at low temperatures) are unusual. The amorphous phase is characterized by a narrow hysteresis loop at low temperature. For the hysteresis curve at 4.2 K, the coercive field is several hundred Oersted and the remnant magnetization is on the order of $10^{-2} M_{sat}$. The temperature dependence of the dc magnetic susceptibility shows an unusual field dependence below 30 K, with the largest effective moments being obtained in the smallest applied fields. The freezing temperature, T_f, in zero field, as determined by both dc and ac susceptibilities, has been found to be $T_f=23$ K. The ac susceptibility shows the characteristic spin glass frequency dependence, yet loses all frequency dependence for temperatures below 9 K.

I. INTRODUCTION

The magnetic behavior of disordered systems has been widely studied during the past two decades.[1] The classical spin glasses (transition metal atoms lightly doped into a noble metal matrix, such as iron in gold) show a variety of behaviors which are now generally referred to as "glassy." These include the existence of distinctly different remnant moments for samples cooled below the "freezing temperature," T_f, by either the "field cooled" or "zero-field cooled" sequences. Hysteresis is also commonly found below T_f, as are remnant moments, the values of which depend on the sequence in which field and temperature were changed. It is also characteristic of spin glasses that the magnetization changes logarithmically with time below T_f. These long relaxation times manifest themselves in ac susceptibility measurements, which characteristically reveal a peak or a cusp at a temperature T_{max} which is typically a function of the measuring frequency. This set of glassy behaviors has been shown[2] to arise from models which contain both randomness and frustration, i.e., the inability to satisfy all magnetic interactions simultaneously. In the classical spin glasses, these two conditions are the consequence of randomly placed moments interacting through the oscillatory Ruderman–Kittel–Kasuya–Yosida (RKKY) interaction.

The above set of magnetic behaviors is not unique to spin glasses. Systems in which the exchange is uniform but either random fields[3] or random anisotropies[4] are also present can show the same features. Even model systems of periodic frustrated lattices can show the same pattern of behavior provided some disorder is introduced. Recent experiments[5] on a physical representation of the highly frustrated Kagomé lattice show the onset of glassy behavior at low temperatures.

The present work grows out of a research program in the development of new, highly frustrated magnetic systems. Ligands are selected for the appropriate symmetry and connectivity to provide the superexchange pathways called for by the Kagomé lattice. One such ligand is BTCA (1,3,5-benzenetricarboxylic acid). Initial attempts[6] to prepare the metal salts of the deprotonated BTCA trianion from aqueous solutions showed that water molecules occupied many of the coordination sites around the metal ions, preventing the formation of the desired lattice. When the crystalline cobalt analog was partially dehydrated, the resulting compound, $Co_3BTCA_2(H_2O)_6$ was amorphous. This paper reports on the glassy magnetic properties of the amorphous phase.

II. EXPERIMENT

The amorphous hexahydrate phase of $Co_3BTCA_2(H_2O)_6$ was obtained by an azeotropic dehydration of the crystalline dodecahydrate phase. The synthesis of the previously unreported crystalline dodecahydrate phase was carried out by dissolving cobalt (II) perchlorate (2.764 g, 7.6 mmol) in 20 ml of water. A solution consisting of BTCA (1.065 g, 5 mmol) and potassium hydroxide (0.95 g, 17 mmol), which had been dissolved in 26 ml of water, was added to the metal solution. A pink precipitate formed immediately. The solution was filtered, and the recovered precipitate was air dried and washed with acetone. This precipitate was heated in refluxing toluene in a Dean–Stark apparatus for 18 h. The resulting material was a deep purple powder which x-ray studies showed to be amorphous. Elemental analysis indicates the presence of only six waters in this phase.

Magnetic measurements were performed on a vibrating sample magnetometer (VSM), a SQUID magnetometer, and an alternating current susceptometer. Magnetization studies showed the moments to be linear with the field up 10 000 Oe at temperatures as low as 4.2 K. The dc susceptibilities were obtained by dividing the measured moments by the applied magnetic field. Corrections for diamagnetism were made.

III. RESULTS AND DISCUSSION

The product of the molar susceptibility and temperature, $\chi_m T$, is plotted as a function of temperature in Fig. 1. Data were collected in several different magnetic fields, ranging from 1 to 10 000 Oe. The measurements were made by cooling the sample in zero magnetic field to 5.8 K, turning on the applied field, and measuring the moment while warming the sample to 100 K. The general shape of the curves is similar for all but the highest magnetic field. An upward curvature in

 0021-8979/94/75(10)/5535/3/$6.00 © 1994 American Institute of Physics

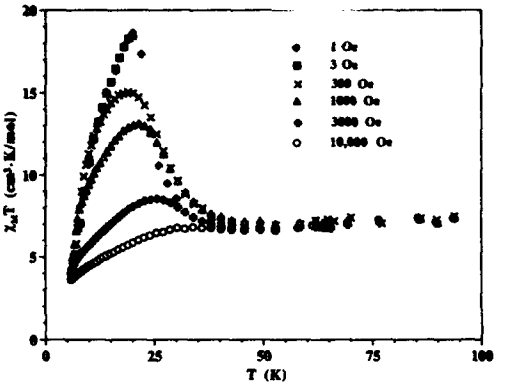

FIG. 1. The product of the molar susceptibility and temperature, $\chi_m T$, is plotted as a function of temperature for size values of the applied field. Data were collected upon warming after cooling in zero field.

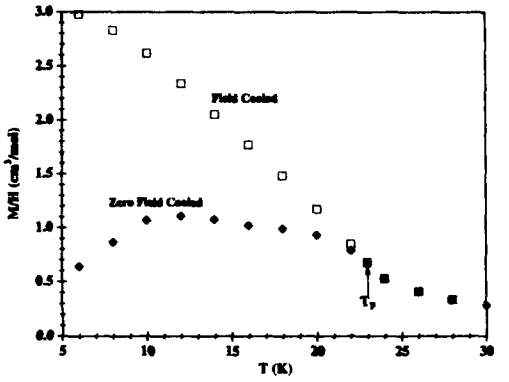

FIG. 2. Field cooled and zero field cooled dc susceptibilities for $Co_3BTCA_2(H_2O)_6$ in an applied field of 1 Oe.

the $\chi_m T$ product is observed in the neighborhood of 35 K, indicating the existence of ferromagnetic interactions. The curves reach a maximum and then decrease as the temperature is lowered. In a uniform, nonfrustrated lattice this decrease would indicate the presence of antiferromagnetic interactions. It is interesting to note that as the magnetic field is decreased, the $\chi_m T$ product actually increases, with the maximum response being observed in the smallest applied fields. In the highest field, 10 000 Oe, the peak is no longer visible. Varying the magnetic field also tends to shift the temperature at which the maximum in $\chi_m T$ occurs. Behavior of this type is rare, but has also been observed[7] in the two-dimensional "triangles within triangles" Kagomé lattice compound $Cu_9X_2(cpa)_6$.

To illustrate the history dependent behavior of the system, measurements were made of the field cooled (FC) and zero field cooled (ZFC) dc susceptibilities. The ZFC measurements were made in an identical manner to those discussed above while for the field cooled measurements the sample was cooled in an applied field and the moment measured as the sample was rewarmed in the same field. Again, data was collected in various applied fields. SQUID data taken in a field of 1 Oe is shown in Fig. 2. The freezing transition temperature T_f is taken as the temperature at which the FC and ZFC curves separate; in a field of 1 Oe, T_f=23 K. For larger fields it was observed that T_f drops rapidly; for example, when H=300 Oe, T_f=12 K. As was true for all applied fields, the FC susceptibility did not exhibit a maxima, but instead continued to increase as the temperature was lowered. This is in contrast to the ZFC susceptibility which always showed field dependent maxima.

Hysteresis has also been observed at low temperature. A hysteresis curve obtained at 4.6 K showed a coercive field of 700 Oe and a remnant magnetization of about 500 cgs G/mol.

Figure 3 shows the thermoremnant magnetization, TRM, and isothermoremnant magnetization, IRM, at 5.8 K for applied fields from 0 to 10 000 Oe. The TRM was obtained cooling the sample in an applied field from a temperature well above T_f to the measurement temperature. The field was then turned off and, after the moment had decayed *rapidly* to its equilibrium value, its value was recorded. Between measurements, the sample was warmed to more than 50 K and the process was repeated at each different measuring field. The IRM was measured by cooling the sample to 5.8 K in a zero field, turning the field on and allowing the sample to come into equilibrium then turning the field off and recording the remnant moment. The shapes of the TRM and IRM curves (Fig. 3) are typical to those found in other spin glasses,[8] but the magnitude of H_{sat} is large. While the TRM and IRM curves for CoTAC:Mn converge[8] for fields in excess of 70 Oe, the IRM and TRM curves for $Co_3BTCA_2(H_2O)_6$ approach one another only for a saturation field H_{sat} somewhat larger than 10 kOe.

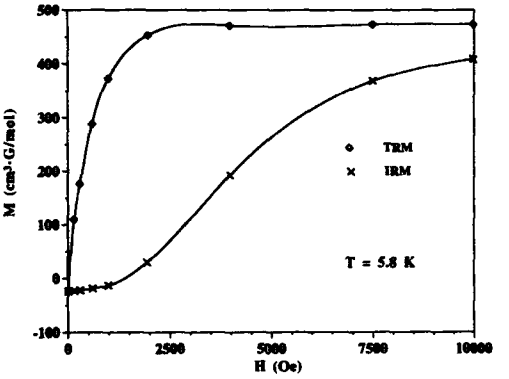

FIG. 3. The remnant magnetizations (TRM and IRM) for $Co_3BTCA_2(H_2O)_6$ as determined at 5.8 K. The slight negative moments obtained in small applied fields are reproducible.

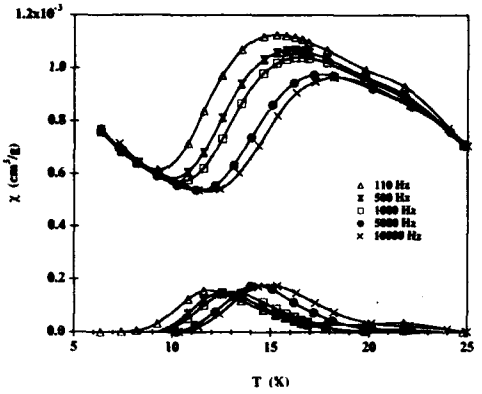

FIG. 4. Complex ac susceptibilities of $Co_3BTCA_2(H_2O)_6$ as a function of temperature for five different frequencies between 110 Hz and 10 kHz. The upper set of data points correspond to the in-phase susceptibilities, χ', while the lower set corresponds to the out-of-phase susceptibilities, χ''. The solid lines are guides to the eye only.

While the curves in Fig. 3 display qualitative behavior typical of a spin glass, the equilibrium times of $Co_3BTCA_2(H_2O)_6$ are decidedly abnormal. Standard spin glass materials possess extremely long relaxation times (on the order of hours or days) when below T_f. However, the relaxation times for $Co_3BTCA_2(H_2O)_6$ were no longer than the instrumental time constant (several minutes) when working at 5.8 K, a temperature well below the transition temperature for this compound. This absence of long equilibrium times below T_f is one of the most notable features of this compound.

Although the absence of long relaxation times is atypical spin glass behavior, the ac frequency dependence is similar to that found for other spin glass systems. The complex ac susceptibility of $Co_3BTCA_2(H_2O)_6$ has been determined in a 1 G ac field and a zero dc field over a range of frequency from 5 Hz to 10 kHz. In Fig. 4, both the in-phase (χ') and out-of-phase (χ'') susceptibilities are shown as a function of temperature. The onset of frequency dependent behavior occurs slightly below 25 K, nearly the same as the value for T_f=23 K as determined by the FC and ZFC dc susceptibilities (Fig. 2). As the temperature is lowered, the in-phase susceptibility reaches the frequency dependent maximum typical of spin glasses. As the frequency is lowered, the magnitude of the susceptibility at the maximum increases, while the temperature at which it occurs decreases. The out-of-phase susceptibilities are vanishingly small above 25 K but grow in magnitude below T_f, reaching a broad maximum before vanishing at still lower temperatures. The maxima of both χ' and χ'' do not occur at the same temperature; rather the maximum in χ'' occurs at the same temperature where occurs an inflection point in the temperature dependence of χ'.

It should be noted that the susceptibility of $Co_3BTCA_2(H_2O)_6$ is much more rounded and displays less of a cusp than many typical spin glasses.[9] It is also interesting to note the behavior as the temperature is lowered well below T_f. As noted above, the χ'' susceptibilities vanish while the in-phase susceptibilities go through a minimum before increasing again in a frequency independent manner. This absence of frequency dependence at low temperatures is a second notable feature of this compound.

In summary, the static properties (dc susceptibility, hysteresis) of $Co_3BTCA_2(H_2)O_6$ are similar to those of other glassy magnetic systems but the dynamics of $Co_3BTCA_2(H_2O)_6$ (absence of long relaxation times, disappearance of frequency dependence at low temperatures) are unusual. The ultimate explanation for this set of behavior must surely lie in the preparation and structure of the compound. We recall that the ligand binding the metals, BTCA, has the correct structure to bind the metal ions into the highly frustrated Kagomé lattice. This is certainly one origin of the observed frustration. However, it has been learned previously[6] that the BTCA ligands can bind to metal ions in several different ways (chelating, monodentate, bridging), each of which yields a different exchange constant. If BTCA is coordinated to the cobalt ions in several different ways in the amorphous phase, there will be some random exchange present as well. In addition, the metal ion involved is the highly anisotropic Co^{2+} ion, in which a large amount of unquenched orbital angular moment is tied to the lattice through spin–orbit coupling. Since the material is amorphous, the local easy axes of the metal ions are randomly oriented, creating a situation in which random anisotropy is also present. The amorphous phase of $Co_3BTCA_2(H_2O)_6$ therefore represents an extremely disordered magnetic system.

ACKNOWLEDGMENTS

This research was supported in part by the National Science Foundation, Division of Materials Research, through Grant No. DMR-9006470. We thank our colleagues at SUNY-Albany and Tufts University for instrument time on the ac susceptometer and SQUID magnetometer, respectively. The equipment in the magnetometry facility at Tufts University was made available by the Keck Foundation.

[1] D. S. Fisher, G. M. Grinstein, and A. Khurana, Phys. Today **41**, 56 (1988).
[2] K. Binder and A. P. Young, Rev. Mod. Phys. **58**, 801 (1986).
[3] D. P. Belanger and A. P. Young, J. Magn. Magn. Mat. **100**, 272 (1991).
[4] K. Moorjani and J. M. D. Coey, *Magnetic Glasses* (Elsevier, New York, 1984), Chap. 6.
[5] A. P. Ramirez, G. P. Espinosa, and A. S. Cooper, Phys. Rev. Lett. **64**, 2070 (1990); C. G. Broholm, G. Aeppli, G. P. Espinosa, and A S. Cooper, J. Appl. Phys. **69**, 4968 (1991).
[6] J. L. Parent, M. M. Turnbull, W. Zhang, and C. P. Landee (in preparation).
[7] M. Gonzalez, F. Cervantes-Lee, and L. W. Ter Haar, Mol. Cryst. Liq. Cryst. **233**, 317 (1993); S. Maruti and L. W. ter Haar (these proceedings).
[8] A. Cheikhrouhou, C. Dupas, J. P. Renard, and P. Veillet, J. Magn. Magn. Mat. **49**, 201 (1985).
[9] C. A. M. Mulder, A. J. van Duyneveldt, and J. A. Mydosh, Phys. Rev. B **23**, 1384 (1981).

The influence of heat treatments on order–disorder phenomena in a naturally occurring manganese-ferrite

Cherie R. Bluncson and B. J. Evans
University of Michigan, Department of Chemistry, Ann Arbor, Michigan 48109-1055

Naturally occurring samples of iwakiite, $Mn_{1.1}Fe_{1.9}O_4$, have been annealed for 17 and 77 h at 1000 K in an investigation of order–disorder phenomena in Mn–Fe oxide spinels. Two distinct magnetic hyperfine patterns, which correspond to Fe- and Mn-rich phases, were observed in the ^{57}Fe Mössbauer spectra for the two annealed samples. While the spectrum of the Fe-rich phase corresponds to a magnetically and crystallographically highly ordered α-Fe_2O_3-like phase, the Mn-rich phase exhibits considerable disorder, as indicated by very broad linewidths and a low value for H_{eff}. Annealing for longer periods of times leads to a considerable increase in the ordering of the Mn-rich spinel phase, as evidenced by the considerable narrowing of the lines, from $\Gamma = 2.40$ mm s^{-1} to $\Gamma = 1.17$ mm s^{-1}, and an increase in H_{eff} from 318 to 417 kOe at 298 K. The Fe-rich, α-Fe_2O_3-like phase is not affected by further annealing, as expected. At 85 K, the ^{57}Fe Mössbauer spectrum of the Mn-rich, spinel phase continues to exhibit rather broad lines, indicating the presence of significant cation disorder.

I. INTRODUCTION

The $Mn_xFe_{3-x}O_4$ system continues to present challenges concerning structure–property relationships, cation distributions, oxidation states, crystallographic order–disorder, and the electric and magnetic properties of oxide spinels exhibiting both variable cation distributions and mixed valence states.[1–4]

Previous investigations of an iwakiite sample with the composition, $Mn_{1.7}Fe_{1.3}O_4$,[4] a naturally occurring mineral in the Mn_3O_4–Fe_3O_4 solid solution series, have demonstrated the existence of an unusually high degree of long-range order, as evidenced by a tetragonal distortion at a manganese content well below the limiting concentration observed in synthetic samples. In addition, results of ^{57}Fe Mössbauer spectroscopic measurements on this sample at 92 K in an applied field of 30 kG have shown that Fe^{3+} occupies exclusively the octahedral sites.[5] The occurrence of Mn^{3+} clustering and the resulting Mn-rich and Mn-poor (or Fe-rich) regions, have been suggested, on the basis of the observation of two Fe^{3+} species on a single magnetic sublattice. It was proposed that the two Fe^{3+} species correspond to those occupying Mn-rich and Mn-poor (or Fe-rich) regions of the crystal.[5]

Further confirmation and delineation of the characteristics of the clustering suggested above has been sought in the study reported here by investigating the thermal stability of the naturally equilibrated iwakiite and monitoring the local and long-range crystal/chemical structures as a function of laboratory-based heat treatments. It is expected that the degree of order observed in iwakiite does not correspond to thermodynamically stable structures at temperatures at which ionic motion is observable on laboratory time scales, and that mild heat treatments will bring about significant changes in both the local and long-range crystal/chemical structures.

II. EXPERIMENT

Pure iwakiite samples from the Gozaisho Mine, Iwaki City, Japan, were prepared by pulverizing whole-rock, hand specimens and grinding them with an agate mortar and pestle to a fine powder that passed a 400 mesh standard sieve. Iwakiite was isolated from the associated minerals by suspending the powder in organic liquids and separating the iwakiite by means of a manually manipulated rare-earth permanent magnet. This process was repeated until a pure spinel phase was obtained, as determined by x-ray diffractometry.

The chemical composition of the separated sample was determined by means of electron microprobe analysis.

The iwakiite sample was separated into two fractions; one fraction was annealed in an evacuated quartz ampoule for 17 h at 1000 K, and the remaining fraction was annealed under the same conditions for 77 h. Both samples were cooled rapidly to 298 K following the heat treatments.

TABLE I. ^{57}Fe hyperfine parameters at 298 K for iwakiite samples.

Sample	Subpattern	H_{eff} (kOe)	ΔE_Q (mm s^{-1})	δ (mm s^{-1})	Γ (mm s^{-1})	Area (%)
Iwakiite Unannealed	···	388	−0.007	0.392	0.920	100
Annealed 17 h	Fe rich	500	−0.109	0.390	0.458	38
Annealed 17 h	Mn rich	318	−0.020	0.347	2.400	62
Annealed 77 h	Fe rich	513	−0.104	0.373	0.343	30
Annealed 77 h	Mn rich	417	−0.009	0.383	1.17	70

[a]Isomer shifts are relative to Fe metal.

TABLE II. ^{57}Fe hyperfine parameters at 85 K for iwakiite samples.

Sample	Subpattern	H_{eff} (kOe)	ΔE_Q (mm s^{-1})	δ (mm s^{-1})	Γ (mm s^{-1})	Area (%)
Iwakiite Unannealed	···	503	0.011	0.500	0.623	100
Annealed 17 h	Fe rich	525	−0.097	0.486	0.449	41
Annealed 17 h	Mn rich	496	−0.003	0.492	0.817	59
Annealed 77 h	Fe rich	529	−0.050	0.460	0.384	24
Annealed 77 h	Mn rich	500	−0.005	0.476	0.731	76

[a]Isomer shifts are relative to Fe metal.

 0021-8979/94/75(10)/5538/3/$6.00 © 1994 American Institute of Physics

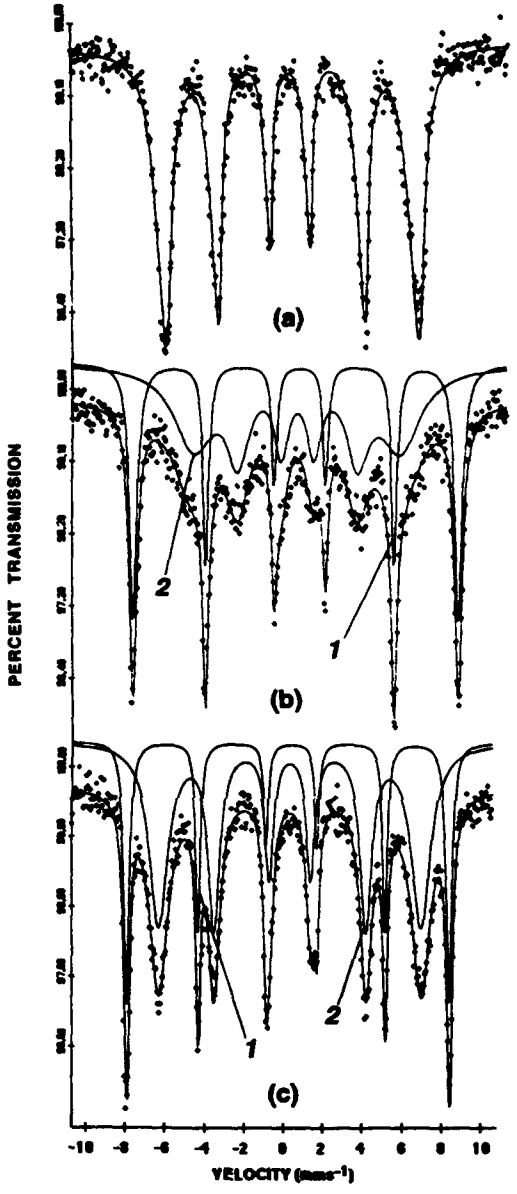

FIG. 1. ^{57}Fe Mössbauer spectra (298 K) of (a) unannealed iwakiite, (b) iwakiite annealed for 17 h at 1000 K, (c) iwakiite annealed for 77 h at 1000 K Fe-rich and Mn-rich regions are represented by 1 and 2, respectively.

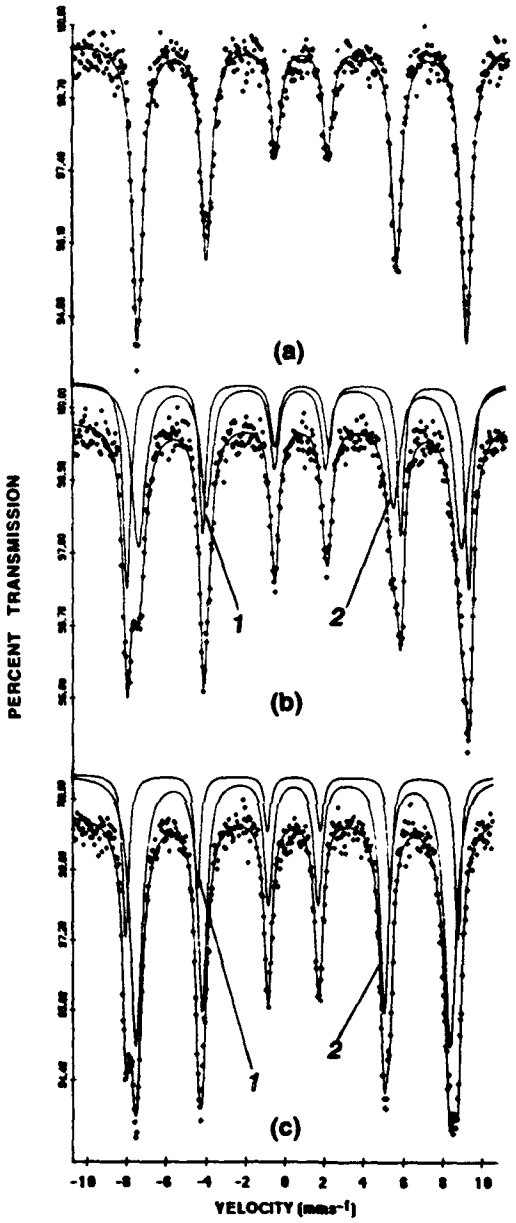

FIG. 2. ^{57}Fe Mössbauer spectra (85 K) of (a) unannealed iwakiite, (b) iwakiite annealed for 17 h at 1000 K, (c) iwakiite annealed for 77 h at 1000 K Fe-rich and Mn-rich regions are represented by 1 and 2, respectively.

^{57}Fe Mössbauer spectra were obtained in a transmission geometry using a 512 channel, microcomputer-configured multichannel scaler and a constant acceleration electromechanical drive. Spectra were obtained with the absorber at 298 and 85 K in a vacuum cryostat. (See Tables I and II.) The source was always maintained at 298 K. The spectra were analyzed by means of a previously described least-mean-squares fitting procedure.[6] The filled dots in the spectra

are the experimental data and the solid lines are the results of the fitting procedure.

III. RESULTS AND DISCUSSION

The chemical composition of the iwakiite sample used in this investigation was found to be $Mn_{1.1}Fe_{1.9}O_4$. The manganese content is considerably lower than that of the previously studied sample, which had the composition $Mn_{1.7}Fe_{1.3}O_4$.[4,5]

The ^{57}Fe Mössbauer spectrum at 298 K for the unannealed sample shown in Fig. 1 was fitted to one six line pattern corresponding to a magnetic hyperfine field, H_{eff}, of 388 kOe. The samples annealed for 17 and 77 h were fitted to two six line patterns, where subpattern 1 with $H_{eff}=500$ kOe in Fig. 1(b), would be derived from the Fe-rich regions of the untreated iwakiite and subpattern 2, with $H_{eff}=318$ kOe, results from the Mn-rich regions of the untreated iwakiite. The parameters corresponding to these fits are given in Tables I and II.

The spectrum in Fig. 1(b), representing the sample annealed for 17 h can be understood as consisting of two components: subpattern 2, which is attributed to a poorly crystalline Mn-rich phase, as indicated by the large linewidths, $\Gamma=2.40$ mm s^{-1}, which has undergone phase separation from the unannealed iwakiite, and subpattern 1, which would correspond to a Fe-rich phase. From both the x-ray diffraction data and the ^{57}Fe Mössbauer parameters, it is clear that the phase giving rise to subpattern 1 is hematite, α-Fe_2O_3. Upon further heating, as in the case of the 77 h anneal, there is considerable recrystallization and growth of the Mn-rich phase, giving rise to well-defined, long-range crystal/chemical structures characteristic of the spinel structure. Clear evidence is provided for this by the remarkable decrease in the linewidths of subpattern 2 and the increase in the magnitude of H_{eff} from 318 to 417 kOe (cf. Table I). The width of the (404) line in the x-ray powder diffraction patterns undergoes a remarkable narrowing, in support of a decrease in the crystallographic disorder following the 77 h anneal at 1000 K.

Spectra of the iwakiite samples at 85 K exhibit similar trends to those obtained at 298 K, with the linewidths of subpattern 2, representing the Mn-rich phase, being broader for the sample annealed for 17 h than for the sample annealed for 77 h (cf. Table II).

A somewhat similar behavior has been observed for naturally occurring jacobsite, $MnFe_2O_4$, samples following heat treatments between 675 and 1175 K.[7] The findings of this investigation are quite similar to those reported for jacobsite,[7] inasmuch as there is a facile separation of a highly ordered hematite-like phase. The phase-separated spinel phase in the annealed jacobsite exhibits considerably less crystallinity and magnetic order than observed in the case of annealed iwakiites. We believe this difference is due to the greater degree of clustering in the iwakiite samples than in the jacobsites; there was no evidence for clustering in the unannealed jacobsites.[7]

IV. CONCLUSION

Evidence for cation clustering and the occurrence of Mn-rich and Mn-poor regions in naturally occurring $Mn_xFe_{3-x}O_4$ phases exhibiting high degrees of thermal equilibration has been provided by the ease with which such specimens undergo facile phase separations at temperatures well below those required for traditional solid state reactions. It is remarkable that the phase-separated, Fe-rich, α-Fe_2O_3-like phase is well ordered, even for short periods of thermal annealing; long-range order is well established for both the crystal and magnetic structures, as indicated by the close agreement between the hyperfine parameters of this pattern at 298 K and those for a pure hematite. By way of contrast, the Mn-rich spinel phase exhibits considerable cation disorder, even for very long annealing periods, and, as a consequence, has values of H_{eff} that are much lower than those seen in synthetic $MnFe_2O_4$. The persistence of this disorder is due, most likely, to insufficient thermal energy and or time for the Mn and Fe ions to achieve a narrow range of local cation configurations. The relative magnitude of the magnetic hyperfine fields are consistent with this interpretation.

[1] F. K. Lotgering and A. M. Van Diepen, J. Phys. Chem. Solids **34**, 1369 (1973).
[2] T. Yamanaka and M. Nakahira, Min. J. **7**, 202 (1973).
[3] V. A. M. Brabers, Y. G. Proykova, N. Salerno, and T. E. Whall, J. Appl. Phys. **61**, 4390 (1987).
[4] S. Matsubura, A. Kato, and K. Nagashima, Min. J. **9**, 383 (1979).
[5] B. J. Evans, W. R. Dunham, C. Porter, S. M. Abernathy, and C. Bluncson, J. Appl. Phys. **63**, 4133 (1988).
[6] H. N. Ok and B. J. Evans, Phys. Rev. B **14**, 2956 (1976).
[7] M. A. B. de Araujo, T. V. V. Costa, M. C. A. Lima, H. A. Maia, and V. W. Vieira, Phys. Scr. **40**, 682 (1989).

Remanent magnetization in the diluted Ising antiferromagnet $Fe_{0.6}Zn_{0.4}F_2$

C. Djurberg, J. Mattsson, and P. Nordblad
Department of Technology, Uppsala University, Box 534, S-751 21 Uppsala, Sweden

The field, $H \leq 5$ T, and temperature, $T \geq 2$ K, dependence of the remanent magnetization μ of the diluted Ising antiferromagnet $Fe_{0.6}Zn_{0.4}F_2$ has been investigated utilizing a superconducting quantum interference device magnetometer. The results at low temperatures, where there is no growth of random field domains after the field removal, are analyzed according to $\mu = AH^x(T \ln t/t_0)^{-\Psi} + B$, where the two terms are domain wall and volume contributions to the remanent magnetization, respectively. It is found that Ψ decreases continuously with decreasing temperature, and reaches a value of ~ 0.15 at 3 K. The field exponent x is found to decrease with increasing temperature, attaining values between 2 and 3. The results show a more complex behavior of the low-temperature remanent magnetization than a model proposed by Nattermann and Vilfan which predicts constant values of the exponents: $\Psi \approx 0.4$ and $x \approx 2$.

When a dilute Ising antiferromagnet is cooled in a magnetic field a metastable domain state is reached, even though the ground state in $3d$ systems has long-range antiferromagnetic order.[1] The domain formation is caused by pinning due to random fields (RF). At low temperatures these domains are very stable and it has been shown by neutron scattering that if the field is switched off at a low enough temperature the typical domain size remains virtually constant.[2] This observation indicates that the domain walls are effectively pinned by the vacancies on large length scales (in zero field there is no RF pinning) and that the only observable dynamics at low temperature arises from rearrangements of the domain walls on a local scale. Nattermann and Vilfan (NV) have developed a model for the relaxation of the remanent magnetization, μ, based on scaling arguments and the above physical picture.[3] The NV model, expected to be valid at low temperature and low fields, yields

$$\mu(H,T) \propto AH^2(T \ln /t_0)^{-\Psi} + \mu_v(H,T), \qquad (1)$$

where A is a constant, H is the field in which the sample is cooled, t_0 the microscopic spin flip time ($\approx 10^{-12}$ s), and Ψ is an exponent that should attain a value ≈ 0.4 for a $3d$ diluted Ising antiferromagnet. The first term in Eq. (1) represents the magnetization stored in the domain walls μ_w which decays through wall adjustments on a local scale. The second term μ_v is a volume contribution to the magnetization, which originates from a statistical imbalance of up and down spins within the domains.

During the last several years properties of the remanent magnetization of the diluted antiferromagnets $Fe_{0.7}Mg_{0.3}Cl_2$ (Refs. 4 and 5) and $Fe_{0.47}Zn_{0.53}F_2$ (Refs. 6 and 7) have been reported. When Eq. (1) has been used to analyze the decay of μ,[4-7] a systematic decrease of Ψ with decreasing temperatures has been observed and only at the lowest temperatures measured, a value $\Psi \sim 0.4$ has been extracted.[5,7] Thus, the applicability of the NV model to these systems is not evident.

In this paper we present results on the field and temperature dependence of the remanent magnetization in $Fe_{0.6}Zn_{0.4}E_2$ and the applicability of the NV model is tested. Previous studies of the remanent magnetization of $Fe_xZn_{1-x}F_2$ have been time-dependent relaxation measurements. In this study the remanent magnetization is measured as a function of temperature at constant observation time.

A single crystal of $Fe_{0.6}Zn_{0.4}F_2$ was investigated utilizing a commercial superconducting quantum interference device (SQUID) magnetometer. The sample was mounted with the c axis parallel to the applied field. From the maximum in dM/dT in low-field zero-field-cooled magnetization measurements the Néel temperature T_N was estimated to 46.4 K.

The remanent magnetization measurements were conducted by cooling the sample in a magnetic field, $H \leq 5$ T, to $T = 2$ K. At this temperature the field was switched off and the remanent magnetization was measured as a function of increasing temperature in steps of 0.2 K for $2 \leq T \leq 6$, 0.5 K for $6 < T \leq 10$ and 1 K for $10 < T \leq 60$ K. The heating rate was ~ 0.3 K/min in the whole temperature range. This procedure yields the remanent magnetization as a function of temperature at a constant observation time [cf. Eq. (1)].[8]

In Fig. 1, μ is plotted as a function of temperature after cooling in $H = 1$, 2, 2.5, 3, 3.5, 4, 4.5, and 5 T. For fields $0.001 \leq H \leq 1$ T the remanent magnetization is virtually field independent[9] and its temperature dependence looks similar to the temperature dependence of an order parameter. This is

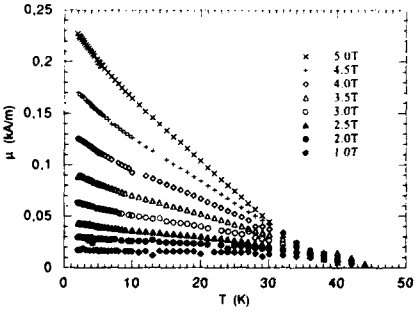

FIG. 1. Remanent magnetization μ vs temperature T at fields $H = 1$, 2, 2.5, 3, 3.5, 4, 4.5, 5 T.

 0021-8979/94/75(10)/5541/3/$6.00 © 1994 American Institute of Physics

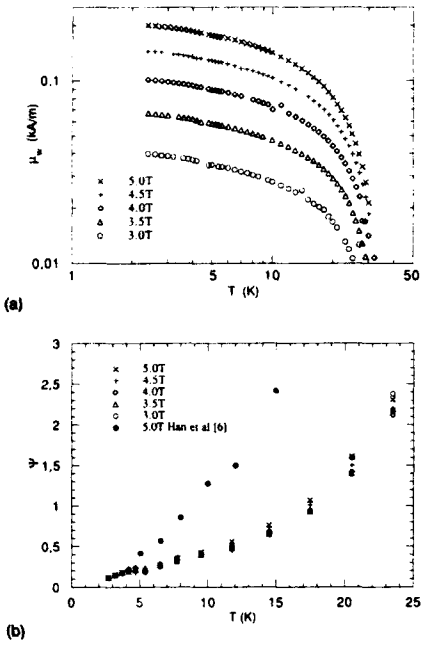

FIG. 2. (a) $\log \mu_w$ vs $\log T$ at fields $H=3$, 3.5, 4, 4.5, 5 T. (b) $\Psi=d \log(\mu_w)/d \log(T)$ vs temperature for fields $H=3$, 3.5, 4, 4.5, 5 T. The filled dots are data from Ref. 6 on $Fe_{0.47}Zn_{0.53}F_2$.

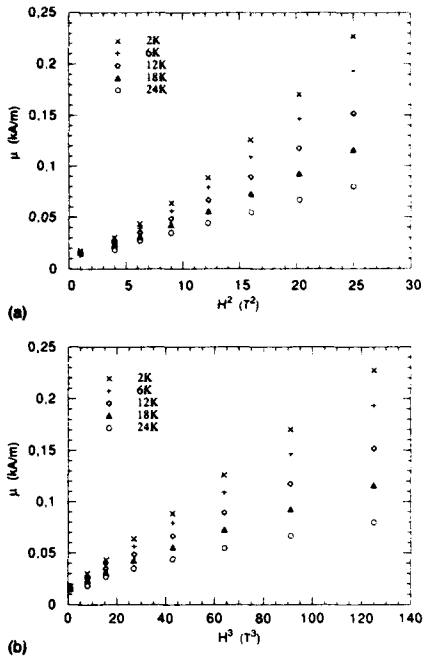

FIG. 3. (a) Remanent magnetization μ vs H^2 for $T=2$, 6, 12, 18, 24 K. (b) Remanent magnetization μ vs H^3 for $T=2$, 6, 12, 18, 24 K.

typical for a volume contribution to the remanent magnetization. For higher fields a second field-dependent contribution to the remanent magnetization appears which has a strikingly different temperature dependence. This contribution is attributed to the excess magnetization in the domain walls and for $H \geq 3$ T it is clearly dominant at low temperatures.

In Fig. 2(a), $\log \mu_w$ is plotted versus $\log T$ for $H=3$, 3.5, 4, 4.5, and 5 T. μ_w has here been determined by subtracting a small susceptibility contribution due to the remanence in the superconducting magnet (<1 mT) and an estimated value of μ_v from the measured μ. μ_v cannot be determined separately but was taken as the constant remanent magnetization observed for $H \leq 1$ T.

In Fig. 2(b), $\Psi=d \log(\mu_w)/d \log(T)$ is plotted versus temperature for $H=3$, 3.5, 4, 4.5, and 5 T. It is seen that Ψ decreases with decreasing temperature and that it reaches a value of ≈ 0.15 at $T=3$ K. A value $\Psi \leq 0.15$ is to low to be accounted for by the NV model. We note that Eq. (1) cannot hold as $T \rightarrow 0$ K with $\Psi > 0$, since the remanent magnetization cannot diverge. In the figure we have included data from Han *et al.*[6] extracted from time-dependent relaxation measurements of the remanent magnetization in $Fe_{0.47}Zn_{0.53}F_2$. The general behavior of the Ψ reported by Han *et al.* is similar to our results. The shift in temperature with respect to our data may be attributed to the difference in concentration between the samples.

At low temperatures, μ_v is virtually temperature independent and it has been claimed from experiments[10] that the field dependent part of μ_v is negligible in a field and temperature interval similar to ours. However, even if μ_v is treated as a free parameter in our analysis it is not possible to find a temperature interval where Ψ becomes a constant as proposed in the NV model.

We now turn to the field dependence of the remanent magnetization. If the domain walls are nonfractal on longer length scales, the proportion of domain walls in the sample is proportional to R^{-1}, where R is the typical size of a domain. Assuming that the magnetization of a domain wall is independent of the cooling field, μ_w is also proportional to R^{-1}. Since $R \propto H^{-\nu_H} H$ with $\nu_H = 2$, is predicted for the random field Ising model one therefore expects: $\mu_w \propto H^2$, at low temperatures where the domain size does not change with temperature. This is also the field dependence in the NV model.

We have analyzed our data according to

$$\mu_w \propto H^x, \tag{2}$$

where x is an effective exponent which may vary with temperature. In Fig. 3(a), μ is plotted versus H^2 and in Fig. 3(b), μ is plotted versus H^3 for $T=2$, 6, 12, 18, and 24 K. At $T=2$ K, the data are well described by Eq. (2) with $x=3$. At 24 K, the data are well described by $x=2$. At intermediate temperatures there is a gradual change of curvature. Neutron scattering studies of $Fe_{0.6}Zn_{0.4}F_2$ (Ref. 2) have shown that the domain size does not change when the field is removed at

$T < T_N/2 (\sim 23$ K). The change in curvature of $\mu(H)$, or equivalently a change in the effective exponent x, at temperatures without any domain growth is surprising.

For a comparison we have measured the temperature dependence of $\Delta M(H) = M_{fc}(H) - M_{zfc}(H)$, where M_{fc} is the field cooled magnetization and M_{zfc} is the zero-field-cooled magnetization. At all temperatures $T \leq 24$ K, $\Delta M(H)$ was found to be well described by $\Delta M \propto H^3$,[11] the exponent x is constant and has a value similar to the value found for $\mu(H)$ at $T = 2$ K.

We conclude that for $H \leq 5$ T the NV model is not a good description of the low-temperature remanent magnetization in $Fe_{0.6}Zn_{0.4}F_2$. The results show a more complicated behavior of the remanent magnetization. When analyzed according to the functional form $\mu(H,T) = AH^x(T \ln t)^{\Psi} + \mu_r(H,T)$ both Ψ and x turn out to be temperature dependent even at low temperatures where the domain size is constant.

Financial support from the Swedish Natural Science Research Council (NFR) is gratefully acknowledged.

[1] For a recent review of diluted Ising antiferromagnets, see e.g., D. P. Belanger and A. P. Young, J. Magn. Magn. Mater. **100**, 272 (1991).
[2] D. P. Belanger, A. R. King, and V. Jaccarino, Solid State Commun. **54**, 79 (1985).
[3] T. Nattermann and I. Vilfan, Phys. Rev. Lett. **61**, 223 (1988).
[4] U. A. Leitao, W. Kleemann, and I. B. Ferreira, Phys. Rev. B **38**, 4765 (1988).
[5] U. A. Leitao, W. Kleemann, and I. B. Ferreira, J. Phys. (Paris) Colloq. **49**, C8-1217 (1988).
[6] S-J. Han, D. P. Belanger, W. Kleemann, and U. Nowak, Phys. Rev. B **45**, 9728 (1992).
[7] J. Kushauer, W. Kleemann, J. Mattsson, and P. Nordblad, Phys. Rev. B (in press).
[8] The equivalence between this experimental procedure and a procedure where the field is switched off at the measurement temperature and the data are taken after a specific time has been experimentally verified in Ref. 4.
[9] A similar virtually field independent remanent magnetization at low fields has earlier been found in $Fe_{0.47}Zn_{0.53}F_2$, Ref. 7 and in $Fe_{0.7}Mg_{0.3}Cl_2$, Nordblad (unpublished).
[10] P. Pollak, W. Kleemann, and D. P. Belanger, Phys. Rev. B **38**, 4773 (1988).
[11] An exponent of 3.2 ± 0.3 was found for $Fe_{0.46}Zn_{0.54}F_2$; M. Ledeman, J. V. Selinger, R. Bruinsma, R. Orbach, and J. Hammann, Phys. Rev. B **48**, 3810 (1993).

Freezing transition in the Z_3 gauge glass

Ronald Fisch
Department of Physics, Washington University, St. Louis, Missouri 63130

A Monte Carlo algorithm has been used to study the Z_3 gauge glass model on simple cubic lattices. The glass transition temperature, T_g, for this model is $0.760 \pm 0.010 J$. There is an anomaly in the temperature derivative of the specific heat at T_g. The freezing transition appears to be describable by a picture in which localized "nuggets" organize themselves into a state of long-range order, leading to an extended state of the inverse susceptibility matrix with eigenvalue zero. The spatial decay of the spin-glass-type gauge-invariant correlation function at T_g seems to be a power law, whose exponent, η, is estimated to be 0.5 ± 0.2.

The XY gauge glass has been studied for a number of reasons[1-5] over the last 15 years. The Hamiltonian may be written as

$$H_{XY} = -J \sum_{\langle ij \rangle} \cos(\theta_i - \theta_j - \phi_{ij}), \tag{1}$$

where $\langle ij \rangle$ indicates a sum over nearest neighbors on some lattice. The θ_i are the dynamical variables. The ϕ_{ij} are taken to be independent quenched random variables, which have a probability distribution $P(\phi)$. $P(\phi)$ is usually assumed to be uniformly distributed on the interval $[-\pi, \pi]$. There have been a number of recent Monte Carlo simulations of this model on the simple cubic lattice.[6-9]

Instead of allowing the θ_i variables to be continuous, we can restrict them to take on values of the form $2\pi l_i/p$, where p is some fixed positive integer and l_i belongs to Z_p, the integers between 0 and $p-1$. With this substitution we rewrite Eq. (1) in the form

$$H_p = -J \sum_{\langle ij \rangle} \cos\left(\frac{2\pi}{p}(l_i - l_j) - \phi_{ij}\right). \tag{2}$$

The $p=3$ case, with a general $P(\phi)$, was introduced by Nishimori and Stephen.[10] Equation (1) can be recovered as the $p \to \infty$ limit of Eq. (2). The author has previously published a Monte Carlo study[11] of this $p=3$ model. Here we will give more detailed results for the case of a uniform $P(\phi)$, which we will call the Z_3 gauge glass. The reader may think of this model either as an approximation to an orientational glass[11] or as a discretization of Eq. (1), which preserves the universality class of the freezing transition. Note that for $p=2$, Eq. (2) becomes a form of the Ising spin glass.[12]

The Monte Carlo simulations[6-9] of Eq. (1) have provided evidence for a true thermodynamic phase transition in the three-dimensional XY gauge glass. The reason why the lower critical dimension of the XY gauge glass is less than that of the XY spin glass has been discussed by Gingras.[13] For the same reason, it turns out[11] that the lower critical dimension of the Z_3 gauge glass is less than that of the $p=3$ Potts glass.[14] It is much easier to simulate a model with discrete dynamical variables than a model with continuous variables. Therefore, it is very advantageous to learn about the universal parameters of the XY gauge glass phase transition by studying the Z_3 version of the model. Of course, the low temperature behavior of the two models is very different.

The model was studied on $L \times L \times L$ simple cubic lattices with periodic boundary conditions. More details of the procedures used may be found in Ref. 11. It was found that for $L=16$, the sample-to-sample variations of the dynamic freezing temperature ranged from about 0.60 to 0.75 J. This wide variation indicates that one cannot obtain valid results for the properties of large lattices by doing an extrapolation from the average properties of many small lattices, because the small lattices are not large enough to be in the asymptotic scaling region.

The freezing process in these systems is highly inhomogeneous. Since we are using a continuous probability distribution for $P(\phi)$, there are no regions of any significant size in which the bonds are perfectly ferromagnetic (or can be made perfectly ferromagnetic by a local gauge transformation). There are, however, a few isolated regions, of perhaps 100 spins each, that are only weakly frustrated. The spins in these regions, which will henceforth be called nuggets, relax much more slowly than average, because they are coherently correlated. The nuggets comprise about 1% of an $L=32$ sample. The relaxation times of the nuggets increase rapidly as the temperature is lowered from 0.85 to 0.80 J. In this temperature range, the correlation length in "typical" regions of the sample remains rather short. The "diameter" (they are not very spherical) of a nugget seems to be about five lattice units, and the distances between them are about two or three times this. Thus, it is not surprising that the sample-to-sample variations of the properties of $L=16$ lattices are quite large.

The nuggets can be identified as the localized eigenvectors of the susceptibility matrix, χ. As argued by Hertz, Fleishman, and Anderson[15] (HFA), a true phase transition occurs if the nuggets become locked together in a coherent fashion, so that χ^{-1} has an extended eigenvector with eigenvalue zero. A more subtle alternative possibility is that this eigenvector becomes power-law localized, rather than truly extended. The spreading of order in this model is not a simple process, since the interactions between the nuggets are highly frustrated. One could imagine carrying out a real-space renormalization group transformation in which the nuggets became sites, with effective interactions between them. Then one would look for "supernuggets" on the renormalized lattice, and iterate the transformation.

The inhomogeneity of the freezing process, and the inadequacy of a single relaxation time analysis, are graphically

 0021-8979/94/75(10)/5544/3/$6.00 © 1994 American Institute of Physics

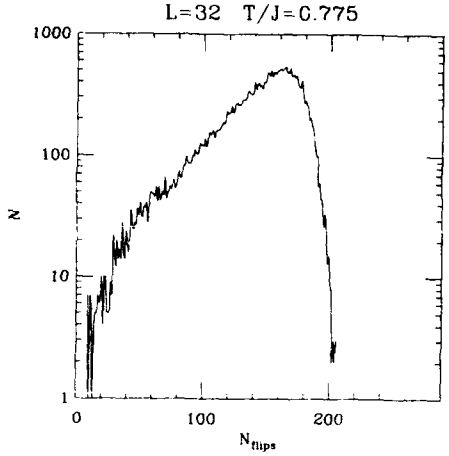

FIG. 1. Histogram of the spin-flip frequency for individual spins of the Z_3 gauge glass model on a simple cubic lattice. The data were obtained from a sequence of 288 states of a single $L=32$ lattice with $T=0.775$, using a time of 2560 Monte Carlo steps per spin between states. The y axis is scaled logarithmically.

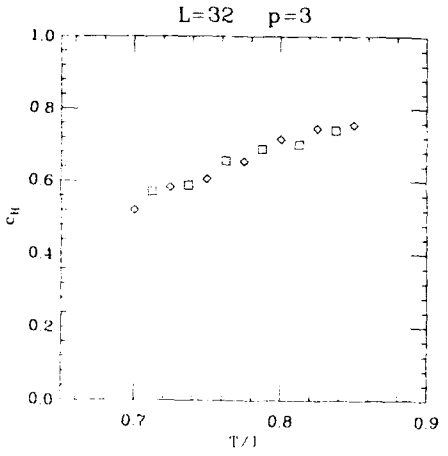

FIG. 2. Specific heat vs temperature for the Z_3 gauge glass model on a simple cubic lattice. The data are from the same lattice as those of Fig. 1. The diamonds were obtained from the fluctuations of the energy at a single T, and the squares were obtained by numerical differentiation of the energy.

illustrated in Fig. 1. This figure shows the distribution of single-spin-flip rates in an $L=32$ sample at $T=0.775\,J$, just above T_g. The tail on the fast side of the peak is Gaussian, and most of its observed width is due to finite time statistical noise. On the slow side, we see a broad tail that appears to be exponential over a significant range. This long-time tail is not consistent with a simple finite-size scaling analysis, but it is expected in the HFA picture. The slow spins are indeed clustered into nuggets, and at this temperature each nugget is able to polarize a large number of spins in its neighborhood.

The fact that the increase of relaxation times as T is reduced is too rapid to be consistent with an Arrhenius law does not prove the existence of a finite temperature phase transition. An analytic crossover from weak coupling to strong coupling, such as the Kondo effect, may also have this property. What evidence is there that the freezing transition seen in this model is a true phase transition? To some extent, the observation that the dynamical freezing appears to occur at a higher temperature, on the average, as L is increased supports this. It appears that as T is lowered to T_g, the effective sizes of the nuggets grow, and they become correlated with each other. The inhomogeneity of the freezing makes it difficult to quantify the growth of long-range spatial correlations as T is lowered through T_g, but the idea seems to be qualitatively correct. Because the freezing process is so inhomogeneous, it cannot be adequately characterized by a single number. It is more appropriate to speak of a distribution function for the local spin polarization. This should remind the reader of Parisi's spin-glass order parameter function[16] to which it is naturally related.

If T_g is a true thermodynamic phase transition, associated with a divergence of spin correlations, then one might expect to see some anomaly in the specific heat, c_H, at this temperature. The data from one $L=32$ lattice are shown in Fig. 2. The points shown as diamonds were obtained from the fluctuations in the energy at a fixed temperature, and the points shown as squares were obtained from the differences in the average energy at successive temperatures. The two methods agree fairly well, with no apparent systematic differences between them. Although c_H appears to be a monotonically increasing function in the temperature region of interest, the data suggest a weak maximum in dc_H/dT at $T=0.760\pm0.010\,J$. This is the same range of T in which the relaxation time of the nuggets becomes unobservably long. We identify this temperature as T_g.

We may define a spin-glass-type[12] two-point correlation function, $Q(i,j)$ for this model by

$$Q(i,j)=\sum_{n=0}^{2} P[l_i-l_j=n(\mathrm{mod}\ 3)]^2-\tfrac{1}{3}. \tag{3}$$

The results of calculating a spatial average of Q as a function of the distance, r_{ij}, between i and j, with $\mathbf{r}_{ij}$ along the cubic axes for an $L=32$ sample, and temperature near T_g are displayed in Fig. 3. The flattening out of the $T=0.775\,J$ data for large r_{ij} is a finite time statistical noise effect. At T_g, the range of spin correlations is clearly becoming larger than the size of the $L=32$ samples that have been simulated. The majority of the spins are still rather fluid at this temperature. They freeze out gradually as T is lowered further. The nuggets, however, are essentially rigid on accessible time scales (about 7.5×10^5 Monte Carlo steps per spin) for all $T\leq T_g$. From Fig. 3, it appears that Q decays like $(1/r_{ij})^{1+\eta}$ at T_g, with $\eta=0.5\pm0.2$.

The author believes that the flattening out of Q at large r_{ij} for $T=0.75\,J$ is an equilibrium effect, indicating the presence of true long range order for $T<T_g$. Thus, the dis-

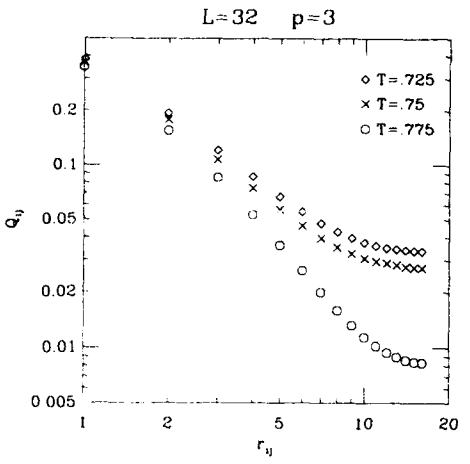

FIG. 3. Log–log plot of the glass correlation function vs distance for the Z_3 gauge glass model on a simple cubic lattice, at three different temperatures. The data sets are of the same type, and from the same lattice, as used in Fig. 1.

tribution of correlations for pairs of spins separated by the same large distance becomes broad for $T \leq T_g$. In Parisi's mean-field theory all spins are treated as equivalent, so the order-parameter distribution has been interpreted in terms of multiple minima[17,18] of the free energy. In a system with only short-range interactions, it is natural for the order-parameter distribution to represent the probability distribution of the polarizations of individual spins.

Since we find only two or three nuggets in an $L=32$ sample, we are just reaching the point where the true large distance behavior should become visible. For $L=32$, the relative orientations of the nuggets in the equilibrium frozen state of the sample appears to be essentially unique, except for rare fluctuations. From the arguments of HFA,[15] one would predict that in significantly larger three-dimensional samples, with many nuggets, this would not continue to be true. A meaningful test for the importance of frustration effects in the relative orientations of the nuggets, and therefore of the thermodynamical significance of multiple metastable minima of the free energy, would require the careful study of $L=64$ systems.

The data of Figs. 1–3 appear to indicate the existence of a true phase transition at T_g. If the study of an $L=64$ sample out to times of at least 10^6 Monte Carlo steps per spin were to give essentially similar results, the author would consider this to be convincing evidence for a phase transition. (Note that this represents an order of magnitude increase in computing effort.) HFA point out that this could occur, due to the behavior of topological structures such as vortex lines. A similar effect is seen in three-dimensional XY-type random anisotropy magnets.[19,20] As evidenced by these examples, the low temperature phase could have either true long-range order[20] or only a slower-than-exponential decay[19] of Q to zero as r_{ij} goes to infinity.

[1] J. A. Hertz, Phys. Rev. B **18**, 4875 (1978).
[2] M. Rubinstein, B. Shraiman, and D. R. Nelson, Phys. Rev. B **27**, 1800 (1983).
[3] W. Y. Shih, C. Ebner, and D. Stroud, Phys. Rev. B **30**, 134 (1984).
[4] S. John and T. C. Lubensky, Phys. Rev. B **34**, 4815 (1986).
[5] M. P. A. Fisher, Phys. Rev. Lett. **62**, 1415 (1989).
[6] D. A. Huse and H. S. Seung, Phys. Rev. B **42**, 1059 (1990).
[7] J. D. Reger, T. A. Tokuyasu, A. P. Young, and M. P. A. Fisher, Phys. Rev. B **44**, 7147 (1991).
[8] K. H. Lee and D. Stroud, Phys. Rev. B **44**, 9780 (1991).
[9] M. Cieplak, J. R. Banavar, and A. Khurana, J. Phys. A **24**, L145 (1991).
[10] H. Nishimori and M. J. Stephen, Phys. Rev. B **27**, 5644 (1983).
[11] R. Fisch, Phys. Rev. B **46**, 11 310 (1992).
[12] K. Binder and A. P. Young, Rev. Mod. Phys. **58**, 801 (1986).
[13] M. J. P. Gingras, Phys. Rev. B **44**, 7139 (1991).
[14] M. Scheucher, J. D. Reger, K. Binder, and A. P. Young, Phys. Rev. B **42**, 6881 (1990).
[15] J. A. Hertz, L. Fleishman, and P. W. Anderson, Phys. Rev. Lett. **43**, 942 (1979).
[16] G. Parisi, J. Phys. A **13**, 1101 (1980); 1887 (1980).
[17] G. Parisi, Phys. Rev. Lett. **50**, 1946 (1983).
[18] A. P. Young, Phys. Rev. Lett. **51**, 1206 (1983).
[19] R. Fisch, Phys. Rev. Lett. **66**, 2041 (1991).
[20] R. Fisch, Phys. Rev. B **46**, 242 (1992).

Reptation and viscosity in particulate recording media in the time-limited switching regime

W. D. Doyle, L. Varga, and L. He
Center for Materials for Information Technology and Department of Physics, The University of Alabama, Tuscaloosa, Alabama 35487-0209

P. J. Flanders
Department of Physics, University of Pennsylvania, Philadelphia, Pennsylvania 19104-63906

Measurement of P, the percentage reduction in remanence after the application of $1 \leqslant n \leqslant 10^4$ reverse field pulses of width 0.6 ns $\leqslant \tau \leqslant$ 9 ns, are reported for five particulate tape samples including γ-Fe_2O_3, Co-γFe_2O_3, Fe, and two different barium ferrites. For $\tau > \tau_c$, P depended only on $n\tau$. It increases quite rapidly at small values of $n\tau$ depending on the media and then at higher values of $n\tau$ approximately linearly with $\log(n\tau)$. In the linear regime, the decrements δ (% change/decade) agree within experimental error with the quasistatic values obtained from viscosity measurements between 10 and 100 s. Considering the arbitrariness of the logarithmic assumption, it is remarkable that the decrement is the same over eleven orders of magnitude. The reduction in P at $\tau < \tau_c$ is evidence for time-limited switching as reported previously. However, the dependence of P on $n\tau$ for small $n\tau$ cannot be explained by the usual viscosity model but is consistent with reptation, a phenomenon suggested by Néel.

I. INTRODUCTION

More than 35 years ago, Néel,[1,2] suggested that the repetitive application of a reverse field to a magnetic particulate system could result in a statistical fluctuation of the internal interaction fields which would cause a decrease in the remanence after each field cycle. No clear evidence for this effect has been obtained although it could be argued that phenomena such as domain wall creep[3] in thin films are a form of reptation. Earlier, Neél[4] also suggested and it is well documented[5] that the remanence in a magnetized particulate system subject to a constant reverse field will decrease monotonically with time at a rate characterized by a parameter of the material called the magnetic viscosity. The exact dependence on time t is still being discussed theoretically[6] but for an assembly of nonuniform particles is usually taken to be of the form $\log(f_0 t)$ where $(f_0 t) \gg 1$ and f_0 is a constant assumed to be $\sim 10^9$ s^{-1}. In any case, all the experimental data for assemblies of particles, usually measured in the range 10–1000 s, are well described[7] by a linear dependence on $\log t$ although it has been suggested[8] that $(\log t)^{1/2}$ is even better. Thus, assuming a $\log t$ dependence, the decay can be characterized conveniently by a decrement δ equal to the percentage change per decade. In 1986, Flanders[9] carried out reptation and viscosity measurements and showed that the decrease in the remanence could be explained completely by viscosity, i.e., by taking into account only the total time the reverse field was applied and not the number of field cycles. Within experimental error, reptation effects could not be detected. Recently, it was again suggested that reptation effects were observed[10] but extensive theoretical[11] and experimental[12] analysis resulted in further support for Flanders' earlier conclusion. For quasistatic measurements, viscosity effects occurring during the time required to make the reptation measurement dominate the process.

The function $\log t$ can only be an approximate description, since it diverges at very short and at very long times. Until now, the need to address this has not been compelling since measurements did not exist at either limit. We have the capability[13] to measure reversal after the application of very short pulses with widths <1 ns and rise times <0.3 ns such that $(f_0 t)$ should approach unity. To better understand this limit, an investigation of reptation and viscosity was undertaken on several magnetic tapes and the results compared to quasi-static measurements.

II. EXPERIMENTAL RESULTS AND DISCUSSION

The apparatus and measurement techniques have been described elsewhere.[13] For these experiments, the sample was initially saturated and then n pulses of width τ and current amplitude I were applied at a low repetition rate of ~1 Hz. After each pulse sequence, a field proportional to the remanence was measured and the percent switched $P = (\Delta M / 2M_R)100$ calculated. Here ΔM is the change in the remanence and M_R is the saturation remanence. For com-

TABLE I. Coercivity H_c and squareness SQ, measured with a VSM.

Media	H_c (Oe)	SQ	δ_z (% decade)	δ_p (%/decade)
γ-Fe_2O_3	330	0.82	1.3	1.8±0.5
Co-γFe_2O_3	880	0.77	2.3	1 ±0.5
MP (Fe)	1590	0.77	1.7	2 ±0.5
BaFe-1	1010	0.74	9.2	8 ±0.5
BaFe-2	1180	0.65	5.0	4 ±0.5

 0021-8979/94/75(10)/5547/3/$6.00 © 1994 American Institute of Physics

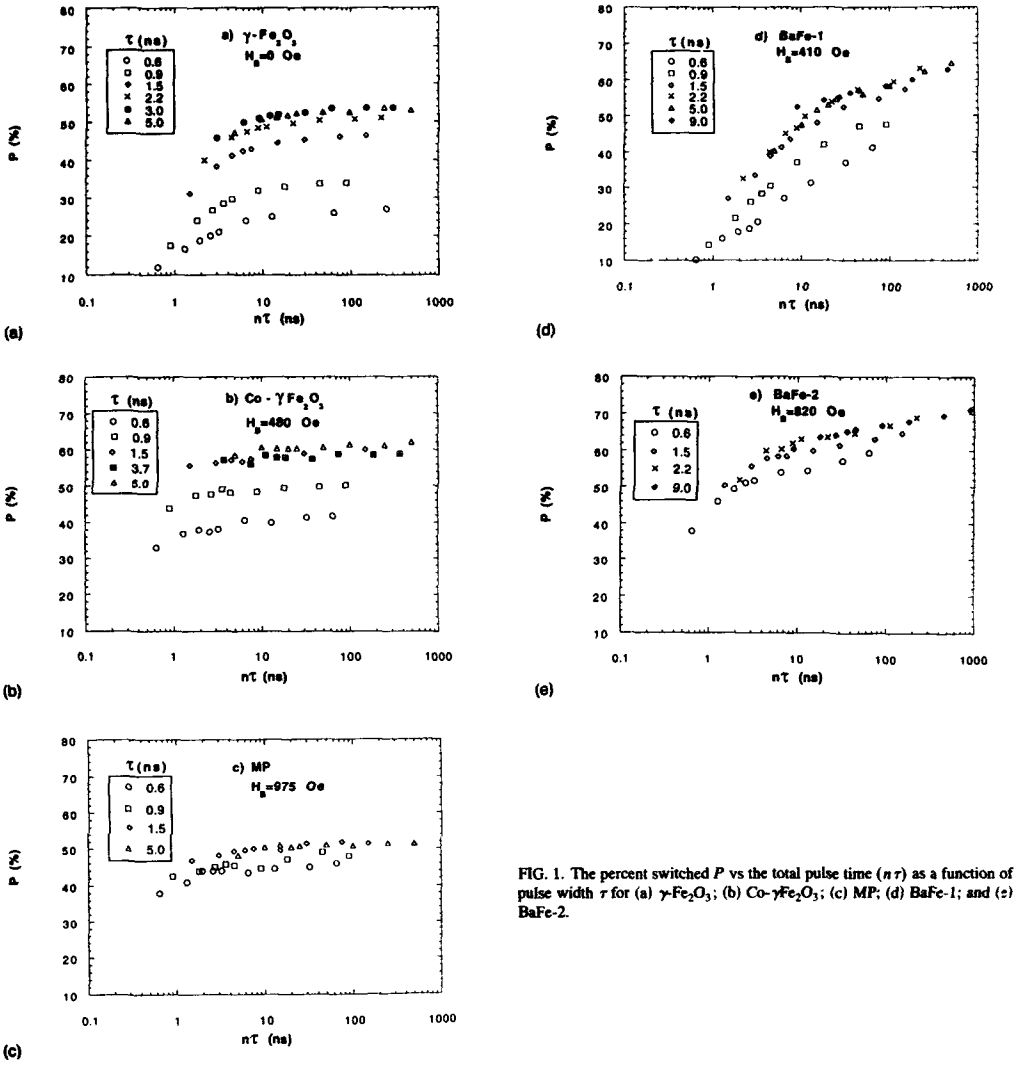

FIG. 1. The percent switched P vs the total pulse time ($n\tau$) as a function of pulse width τ for (a) γ-Fe_2O_3; (b) Co-γFe_2O_3; (c) MP; (d) BaFe-1; and (e) BaFe-2.

parison between samples, the current was adjusted to set P between 40% and 60% for $n=1$ and $\tau>5$ ns. For the higher coercivity samples, a dc bias field H_B was applied to the sample to allow $P=50\%$ to be reached at a convenient pulse current.[13,14] The coercivity H_c and the squareness SQ, measured with a *VSM* for the five tapes studied are listed in Table I.

The measured values of P are plotted in Figs. 1(a)–1(e) versus $\log(n\tau)$ for several τ. For all the media, there is an approximate value of $\tau=\tau_c$ such that for $\tau>\tau_c$, P depends only on $n\tau$. For $\tau<\tau_c$ at constant $n\tau$, P decreases rapidly with decreasing $n\tau$ although the functional dependence on τ remains about the same. P increases monotonically with $n\tau$; quite rapidly at small values of $n\tau$ depending on the media, and then more slowly at higher $n\tau$ at which point the increase of P against $\log(n\tau)$ becomes approximately linear. This can be visualized more easily if we plot P vs $\log(n\tau)$ for $\tau>\tau_c$ for all the media on one graph (Fig. 2). The linear dependence for $n\tau>10$ and the rapid change in slope for all the samples except Co-γFe_2O_3 below $n\tau=10$ are clearly evident. It is also obvious that P increases much more rapidly with $n\tau$ in the BaFe tapes than in the oxide or MP tapes.

For the γ-Fe_2O_3 sample, we carried out the measurements over four orders of magnitude. For large $\tau>\tau_c$, the linearity on $\log(n)$ [or $\log(n\tau)$] is quite good for three orders of magnitude from $n=10$ to 10^4. This data also showed clearly that the deviation from linearity occurs at larger values of n as $\tau<\tau_c$ decreases, from $n=10$ at $t=5$ ns to $n=100$ at $t=0.6$ ns.

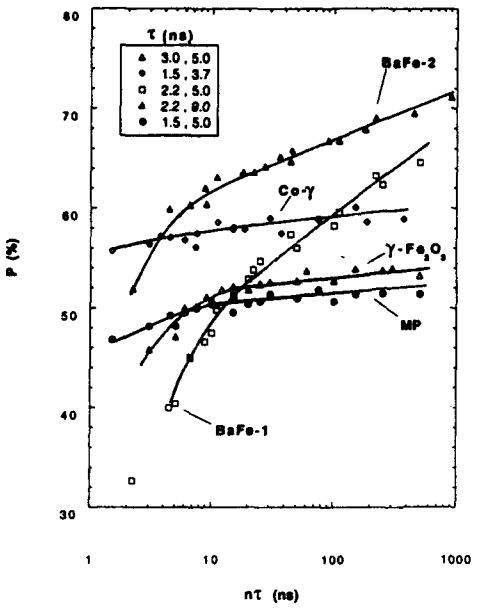

FIG. 2. The percent switched P vs the total pulse time ($n\tau$) at large pulse widths for several media. The curves are guides for the eye.

The linear behavior with $\log(n\tau)$ and the larger decrements in BaFe immediately suggest viscosity effects. The value of the quasi-static decrement δ_s and the pulsed decrement δ_p estimated from the linear region (Fig. 2) are listed in Table I. The measurement of δ_s was made on a Princeton Measurement Corp. alternating gradient magnetometer in which the field was switched from positive saturation to the negative coercive field in <1 s, thus eliminating sweep time effects and closely emulating the pulse measurement. Within experimental error, δ_p and δ_s agree. The large values of δ_s and δ_p in the BaFe compared to the oxides and MP are in agreement with previous reports.[5,15] The larger value in BaFe-1 is consistent with the differences in their particle diameter which is ~300 Å in BaFe-1 and ~500 Å in BaFe-2. We call attention to the arbitrariness of the logarithmic assumption[6] and only emphasize that over 11 orders of magnitude, remarkably, the decrement near the coercivity is the same.

The decrease in P for fixed $n\tau$ as τ decreases is evidence of the finite switching speed[13] in the tapes and depends on the material. Curiously, even for very short τ in the time-limited regime, P increases at large n linearly with $\log(n\tau)$ although the decrement decreases from ~2.2% at τ=0.6 ns to ~1.5% at τ=5.0 ns. This suggests that viscosity is still operative even in the region where dynamic effects dominate.

We have also measured δ_p at different values of I, i.e., for different values of P at constant $n\tau$ in γ-Fe_2O_3. From 20%<P<80%, δ_p is constant within experimental error. Quasistatic measurement[5] show greater sensitivity to the applied field as expected from straightforward physical arguments. The difference may be due only to the lack of precision in the pulse technique.

The data in Figs. 1 and 2 show that for each medium there is a value of $n\tau$ depending on τ above which P increases more or less linearly with $\log(n\tau)$ and below which it does not. The simple theories of viscosity assume that $(f_0 t) \gg 1$ and if $f_0 \sim 10^9\ s^{-1}$, our experiments surely violate that assumption. Therefore, deviation from the usual $\log(t)$ dependence should not be unexpected. However, recent measurements[16] suggest f_0 may be as large as 10^{12}–$10^{13}\ s^{-1}$ in which case the explanation for the deviation must be sought elsewhere. P surely increases rapidly with n for n<10 and this could be explained by reptation. We have not taken into account the demagnetizing field of ~100 Oe at maximum remanence[13] which adds to the switching field. However, this is greatly reduced after the first pulse which would therefore reduce switching for subsequent pulses, leading to an underestimate of the nonlinear behavior for small n.

It is possible that an improved theory of viscosity could explain the results for small n and $n\tau$, again negating the need to involve reptation. Until that happens, our data are consistent with that phenomenon.

ACKNOWLEDGMENTS

The research reported here was partially supported by a grant from a Commerce Department Advanced Technology Program administered by NSIC. We would also like to acknowledge the assistance of Princeton Measurement Corp. in making the viscosity measurements and helpful discussions with J. W. Harrell and H. Fujiwara.

[1] L. Neél, C. R. Acad. Sci. **244**, 2668 (1957).
[2] L. Neél, J Phys. Rad. **20**, 215 (1959).
[3] W. Kayser, IEEE Trans. Magn. **MAG-3**, 141 (1967).
[4] L. Neél, Am. G'eophys. **5**, 99 (1949).
[5] M. P. Sharrock, IEEE Trans. Magn. **MAG-26**, 193 (1990).
[6] A. Aharoni, *Studies of Magnetic Properties of Fine Particles*, edited by J. L. Dormann and D. Fiorani (Elsevier Science, Amsterdam, 1992).
[7] R. Street and J. L. Woolley, Proc. Phys. Soc. A **62**, 562 (1949).
[8] P. J. Flanders and M. P. Sharrock, J. Appl. Phys. **62**, 2918 (1987).
[9] P. J. Flanders, IEEE Trans. Magn. **MAG-22**, 145 (1986).
[10] G. Bottoni, D. Candolfo, A. Cecchetti, A. R. Corradi, and F. Masoli, IEEE Trans. Magn. **MAG-26**, 1885 (1990).
[11] M. El-Hilo, K. O'Grady, and R. W. Chantrell J. Appl. Phys. **73**, 6653 (1993).
[12] V. G. Lewis, P. I. Mayo, and K. O'Grady, J. Appl. Phys. **73**, 6656 (1993).
[13] W. D. Doyle, L. He, and P. J. Flanders, IEEE Trans. Magn. **MAG-29**, 3634 (1993).
[14] W. D. Doyle, L. He, and L. Varga (to be published).
[15] K. Song, M. R. Parker, and J. W. Harrell, J. Magn. Magn. Mater. **120**, 180 (1993).
[16] D. P. E. Dickson, N. M. K. Reid, C. Hunt, H. D. Williams, M. El-Hilo, and K. O'Grady, J. Magn. Magn. Mater. **125**, 345 (1993).

Ferromagnetic resonance spectra of oriented barium ferrite tapes

Yuwu Yu, J. W. Harrell, and W. D. Doyle
Center for Materials for Information Technology and Department of Physics and Astronomy, The University of Alabama, Tuscaloosa, Alabama 35487

Ferromagnetic resonance spectra have been measured for three barium ferrite tapes at 34.5 GHz for two different orientations of the tapes with respect to the static and microwave fields. The orientation distributions in the tapes have been measured using x-ray diffraction, and these distributions have been used to calculate the spectra using the Landau–Lifshitz equation. The anisotropy energy, damping constant, and volume packing fraction have been used as adjustable parameters in the calculations. Calculated spectra were in good agreement with measurements. Anisotropy constants and damping constants determined from the fits are consistent with results reported for fine particle assemblies.

I. INTRODUCTION

Ferromagnetic resonance (FMR) has been used by a number of investigators to study linewidths in single-crystal samples of barium ferrite.[1–4] Very little work, however, has been done on fine particle assemblies. For a random distribution of fine particles, FMR spectra were measured and spectra were calculated based on the Landau–Lifshitz equation assuming no interparticle interactions.[5] Excellent agreement was obtained between measurements and calculations, which enabled accurate determination of the magnetic parameters, in particular, the anisotropy constant and the damping constant. The FMR spectra for partially oriented samples is much more difficult to interpret, especially if interparticle interactions are strong. Netzelmann recently measured and calculated FMR spectra for a commercial oriented barium ferrite tape.[6] The spectrum in a tape sample depends on a number of parameters which Netzelmann used as inputs in his calculations, including the orientation distribution. Although Netzelmann obtained qualitative fits at 35 GHz, the widths of the calculated and measured spectra differed significantly.

We have measured and calculated FMR spectra for barium ferrite tapes with three different squarenesses and coercivities (Table I). In order to reduce the number of parameters in the calculation and improve the fits, we have measured the orientation distributions of the single-crystal barium ferrite particles using x-ray diffraction, and we have used these distributions in our calculations.

II. EXPERIMENTAL RESULTS

A. Orientation distributions

X-ray diffraction measurements were made on the tapes using a Rigaku diffractometer operating in the θ–2θ mode. The relative integrated intensities of the diffraction peaks depend on the orientation distribution of the c axis of the barium ferrite particles within the tapes. Figure 1 shows spectra for the three tapes which include the (110), (107), and (114) peaks. BaFe-1 has the highest degree of orientation and BaFe-3 has the lowest as measured by the squareness of the hysteresis loop (Table I).

The relative intensities of the three peaks were calculated using an equation of the form[7]

$$I=|F|^2 jLDe^{-2Q}, \tag{1}$$

where F is the structure factor, j the multiplicity factor, L a Lorentz–Polarization factor, D an orientation distribution factor, and e^{-2Q} a temperature factor (assumed constant). The orientation distribution factor is proportional to the number of particles which have a c axis such that the diffraction plane is in the plane of the tape and is given by

$$D=\int f(\theta)\,d\psi, \tag{2}$$

where $f(\theta)$ is the distribution function and θ is the angle between the c axis of a particle and the aligned direction of the tape. The integration is taken around the perimeter of a cone formed by all possible c axes oriented such that the diffraction plane is parallel with the tape plane.

In Eq. (2) an orientation distribution function of the form

$$f(\theta)=A\,\exp[-(\theta/\sigma)^n] \tag{3}$$

was assumed, where σ and n were chosen for best agreement with the measured intensities and A was chosen for normalization. Figure 2 shows the relative intensities of the diffraction peaks as a function of σ for $n=2$ (Gaussian) and for $n=4$, along with the measured intensities. For tapes BaFe-2 and BaFe-3, a Gaussian function gave a good fit, with σ values of 56° and 59°. For BaFe-1 the very low intensity of the (107) peak suggested a more nearly square type of distribution, and a good fit was obtained for $n=4$ and $\sigma=45°$.

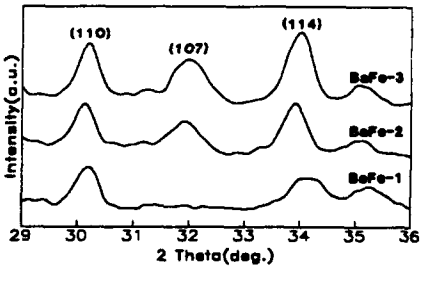

FIG. 1. X-ray diffraction spectra.

 0021-8979/94/75(10)/5550/3/$6.00 © 1994 American Institute of Physics

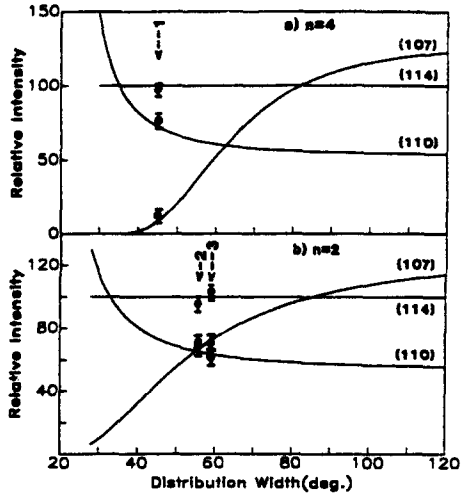

FIG. 2. Calculated relative intensities as a function of distribution width. Points show measured intensities.

For all three tapes, the parameters n and σ were such that all of the measured and calculated intensities agreed to within $\pm 5\%$ of the intensity of the strongest peak.

Orientation distributions were also determined using the angular dependence of remanence method.[8] The results, however, were not in satisfactory agreement with the x-ray results for all the tapes. This disagreement may be due in part to interactions, which do not affect the x-ray results.

B. Ferromagnetic resonance

First derivative absorption FMR spectra were measured at 34.5 GHz over the field range from 0.2 to 1.8 T. These spectra were numerically integrated in order to compare with the absorption spectra which were reported for randomly and partially oriented barium ferrite.[5,6] Figure 3 shows absorption spectra which were recorded for two orientations (B and C, as per Netzelmann[6]) of the tape with respect to the static field, $\mathbf{B}_0$, and the microwave field. For orientation B, $\mathbf{B}_0$ was perpendicular to the aligned direction of the tape and in the plane of the tape. For orientation C, $\mathbf{B}_0$ was perpendicular to the tape plane. For each orientation, the microwave field was in the aligned direction of the tape.

FMR spectra were calculated from the Landau–Lifshitz equation using the method of Netzelmann.[6] The energy density is given as

$$F = F_B + F_K + F_N, \tag{4}$$

where

$$F_B = -(1/\mu_0)\mathbf{M}\cdot\mathbf{B}_0, \tag{5}$$

$$F_K = K_1 \sin^2 \psi, \tag{6}$$

and

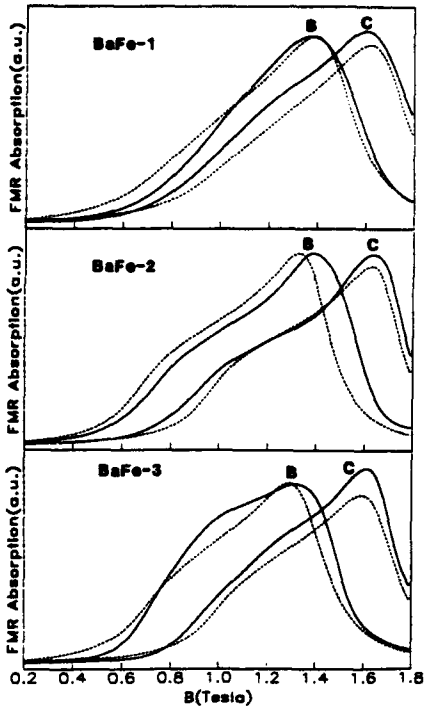

FIG. 3. Calculated and measured FMR spectra.

$$F_N = (1/2\mu_0)(1-p)\mathbf{M}\cdot\underline{\mathbf{N}}\cdot\mathbf{M} + (1/2\mu_0)p\mathbf{M}\cdot\underline{\mathbf{N}}_t\cdot\mathbf{M}. \tag{7}$$

In the above equations, $\mathbf{M}$ is the particle magnetization, K_1 the crystalline anisotropy energy density, p the volumetric packing fraction, $\underline{\mathbf{N}}$ the demagnetization tensor for the particle, and $\underline{\mathbf{N}}_t$ the demagnetization tensor for the tape. The second term in Eq. (7) is due to the demagnetization field of the tape, whereas the first term includes both the demagnetization energy of the particle, which depends on the aspect ratio and orientation of the particle, and a term with p to account for the local interactions between particles. Equation (7) has the correct limits for an isolated particle ($p=0$) and for a continuous medium ($p=1$); however, for arbitrary values of p the interaction term is only an approximation.

The breadth of the FMR spectra in Fig. 3 is due primarily to the orientation distribution of the particles, with the aligned particles contributing only to the high-field part of the spectrum. In both orientations B and C, the position of the high-field peak is determined primarily by K_{eff} and, to a lesser extent, by p, where

$$K_{\text{eff}} = K_1 + (1/2\mu_0)(1-p)M^2\Delta N, \tag{8}$$

and $\Delta N = N_b - N_a$, where a is the symmetry axis of the particle. (Orientation and relaxation broadening will slightly shift the peak positions.) Thus, K_{eff} and p can be determined

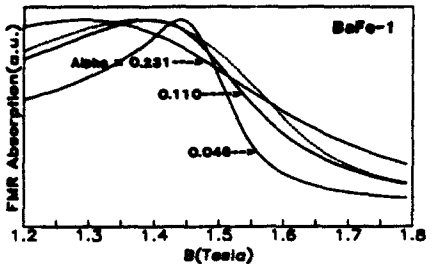

FIG. 4. Effect of α on calculated FMR spectrum for BaFe-1. (All calculations are normalized to the measured peak value.)

with reasonable accuracy by matching the calculated and measured positions of the high-field peak for the two orientations.

The high- and low-field tails of the spectra depend primarily on α. Figure 4 shows the high-field part of the calculated spectra for three different values of α along with the measured spectrum for BaFe-1, which gives an indication of the accuracy with which α can be determined.

Table I summarizes the parameters which were used to determine the calculated spectra in Fig. 3. The values of d/t and M_s are nominal values for a Toshiba Hi-8 tape (BaFe-3).[9] Although these parameters were not known for the other tapes, these same values were used for all the tapes to calculate K_1 from Eq. (8). The values of K_1 in Table I are consistent with values reported in the literature for both bulk crystal and fine particle assemblies of Co/Ti-doped barium ferrite.[5,6,10] The damping constants of the three tapes are similar to previously reported values for fine barium ferrite particles;[5,6,11] however, they are as much as two orders of magnitude larger than values estimated from linewidth measurements for single crystal samples.[1–4]

TABLE I. Tape parameters.

	BaFe-1	BaFe-2	BaFe-3
K_{eff} (10^5 J/m^3)	0.93	0.78	0.72
K_1 (10^5 J/m^3)	1.14	0.95	0.89
p	0.39	0.50	0.50
α	0.110	0.087	0.103
M_s (kA/m, emu/cm^3)	326	326	326
d/t	3.5	3.5	3.5
H_c	82 kA/m (1,030 Oe)	97 kA/m (1,220 Oe)	94 kA/m (1,180 Oe)
SQ	0.73	0.66	0.62
n	4	2	2
σ (deg)	45	56	59

III. SUMMARY

Particle orientation distributions in barium ferrite tapes determined by x-ray diffraction have allowed FMR spectra to be calculated which are in good agreement with measurements. Best-fit values of K_1 are in good agreement with bulk data, but α is considerably larger. This is consistent with previous work, although the reason for the large α values is not well understood.

ACKNOWLEDGMENT

This work was supported in part by a grant from a Commerce Department Advanced Technology Program administered by NSIC.

[1] W. A. Kaczmarek, J. Magn. Magn. Mater. **86**, 391 (1990).
[2] W. D. Wilber and L. M. Silber, J. Appl. Phys. **63**, 3353 (1988).
[3] L. M. Silber, E. Tsantes, and W. D. Wilber, J. Magn. Magn. Mater. **54–57**, 1141 (1986).
[4] M. Labeyrie, J. C. Mage, W. Simonet, J. M. Desvignes, and H. Le Gall, IEEE Trans. Magn. **MAG-20**, 1224 (1984), and references therein.
[5] C. Sürig, K. A. Hempel, and F. Schumacher, J. Magn. Magn. Mater. **117**, 441 (1992).
[6] U. Netzelmann, J. Appl. Phys. **68**, 1800 (1990).
[7] B. D. Cullity, *Elements of X-Ray Diffraction* (Addison–Wesley, Reading, MA, 1978).
[8] S. Strikman and D. Treves, J. Appl. Phys. **31**, 58S (1960).
[9] T. Suzuki (personal communication).
[10] D. J. de Bitetto, J. Appl. Phys. **35**, 3482 (1964).
[11] F. Schumacher, K. A. Hempel, and W. Salz, J. Magn. Magn. Mater. **83**, 219 (1990).

Angular dependence measurement of individual barium ferrite recording particles near the single domain size

Thomas Chang
IBM AdSTaR, 5600 Cottle Rd., San Jose, California 95193

Jian Gang Zhu
Electrical Engineering Department, University of Minnesota, 200 Union St., Minneapolis, Minnesota 55455

The switching field angular dependence measurement of individual barium ferrite recording particles with sizes ranging from 55 to 75 nm in diameter were measured via magnetic force microscopy technique. These experimental measurements were then used as a basis to investigate their nucleation mechanism and intrinsic switching modes. Our findings indicate that the effects nonuniform doping of Co-Ti can significantly affect the easy axis nucleation field and the switching mode.

I. INTRODUCTION

Recording particle such as barium ferrite has attracted much attention because of its exceptional recording properties. In past investigations, angular dependence switching field measurements were utilized to study the switching modes of Co-Ti doped barium ferrite particles.[1,2] These measurements of barium ferrite powder samples showed a switching field that increased monotonically with an increase in the applied field angle. It is uncertain whether the large anisotropy field, which is typically 4–5 times the easy axis switching field value, is due to incoherent switching of individual particles or whether the observed behavior is the result of strongly coupled particle clusters.[3]

Recently, a new method that allows direct measurement the switching fields of individual recording particles has been demonstrated.[4] This technique utilized an in-house-built magnetic force microscope (MFM) as an ultrasensitive magnetometer to measure the remanent magnetization state of individual particles. The measurement technique also combines the use of a high resolution scanning electron microscopy (SEM) imaging and atomic force microscopy (AFM) profilometry to quantify the geometric shape and the size of the particle specimens.

In this paper, the switching field angular dependence measurements of three particles were measured utilizing this MFM based technique. These experimental switching field measurements are used as a basis to investigate the intrinsic reversal modes and the switching mechanisms of individual barium ferrite recording particles [$BaFe_{12-2x}(CoTi)_xO_{19}$, $x=0.7$]. Micromagnetic modeling is used in the final analysis to gain a quantitative understanding of our experimental findings.

II. METHOD AND RESULTS

The switching field measurement technique used in this study has been described in a previously published article.[3] The switching field angular dependence of three barium ferrite particles (55, 57, and 75 nm in diameter, and aspect ratio equal to 2.4:1, 4.1:1, and 2.7:1 respectively) was measured at various applied field angles between 0° and 90° with respect to their easy axis directions.

Figure 1(a) shows a schematic of the particle orientation with respect to the applied field direction. Figure 1(b) shows the switching field angular dependence measurement of the 55 nm diameter particle. The angular dependence curve closely follows the Stoner–Wohlfarth behavior indicated by the large easy axis switching field (3150 Oe), with a minimum switching field value near 45°. With further increase in the applied field angle beyond 45°, the switching field again increases. Extrapolating the data points to 90°, gives the anisotropy field $H_a \sim 4100$ Oe. Such behavior has never been observed in macroscopic measurements. Figure 1(c), shows the angular dependence curve for the slightly larger 57 nm diameter particle. Although the particle size is similar, its angular dependence curve shows a near-inverse-cosine dependence suggesting incoherent switching. At small angles, the switching field is approximately 900 Oe, than increases sharply as the field angle increase beyond 70° ($H_a \sim 2500$ Oe). The angular dependence curve for the large diameter particle (75 nm) shows similar incoherent characteristics as shown in Fig. 1(d). The easy axis switching field is ~1300 Oe. The switching field at 65° dips slightly then sharply increases with further increase in the applied field angle ($H_a \sim 3100$ Oe).

III. DISCUSSION

It is interesting to note the large difference in the easy axis switching field between the two nearly identical size particles (55 and 57 nm diam). Even though they have different aspect ratios, this still does not explain the full magnitude of the easy axis switching field difference. Furthermore, a calculation of the particle's crystalline anisotropy field, calculated from the measured anisotropy field [$H_{sw}(90°)$] and the known thicknesses of these particles, was found to be nearly identical for all three particles. This indicates that the variations in the switching fields are not due to differences in the doping level among the particles. The source of the peculiar differences in the angular dependence behavior remain unclear.

To better understand this observed phenomenon, a micromagnetic simulation study was conducted using the calculation method that has been described in a previous article.[5] The previous calculation showed that a uniformly doped particle could not account for the measured switching

 0021-8979/94/75(10)/5553/3/$6.00 © 1994 American Institute of Physics

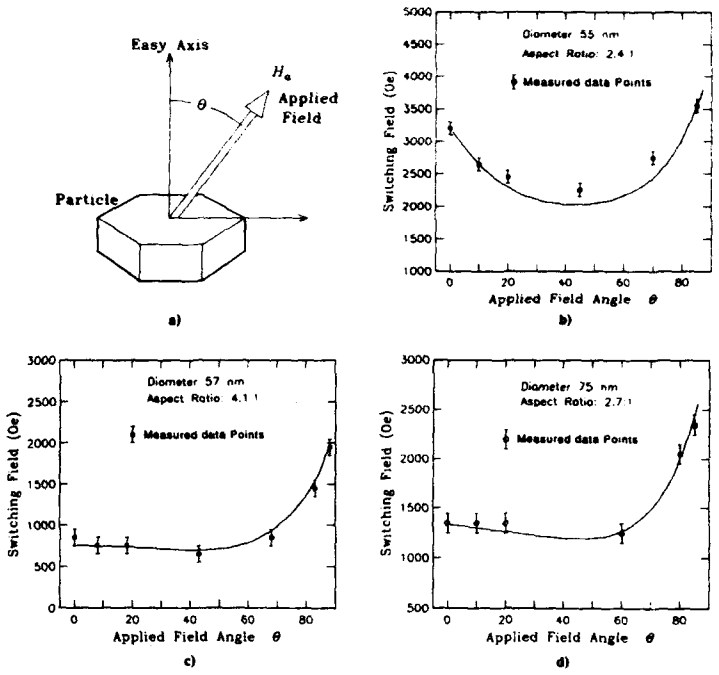

FIG. 1. (a) Schematic of the particle orientation with respect to the applied field direction. (b) Experimental switching field angular dependence curves for the 55 nm diam particle, (c) 57 nm diam particle, and (d) 75 nm diam particle. The micromagnetic simulation switching field values are shown by the solid lines.

field values. In this case, we assume that the doping of Co-Ti is spatially inhomogeneous. In other words, the particle is modeled as having small regions of excessive doping and other regions in the particle having less doping compared to the volume average doping level. The result is a particle that has random dispersion and a random spatial distribution of the local crystalline anisotropy constant. The switching field angular dependence simulation results are shown by the solid lines in Figs. 1(b), 1(c), and 1(d) corresponding to the 55, 57, and 75 nm diam particles, respectively. The simulation results closely predict both the magnitudes and the shape of their angular dependence curves. For each particle model, a different spatial distribution, generated by using different random seed numbers were used. Even though each set has the same volume average anisotropy value, each set gave a different angular dependence curves. This suggests that the reversal mechanism strongly depends on the specific spatial details of the anisotropy distribution. To understand this in

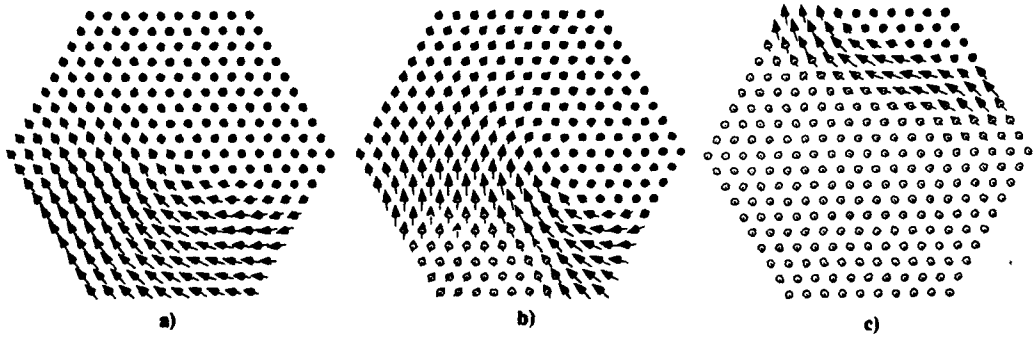

FIG. 2. The transient magnetization configuration at various stages during the switching process for the 57 nm diam particle. The small arrows represent each segment's magnetization vector which initially points up. The applied field direction is down into the page. The normalized average magnetization values for the four states are; (a) m_z=0.8, (b) m_z=0.4, (c) m_z=0.2, (d) m_z=0.2.

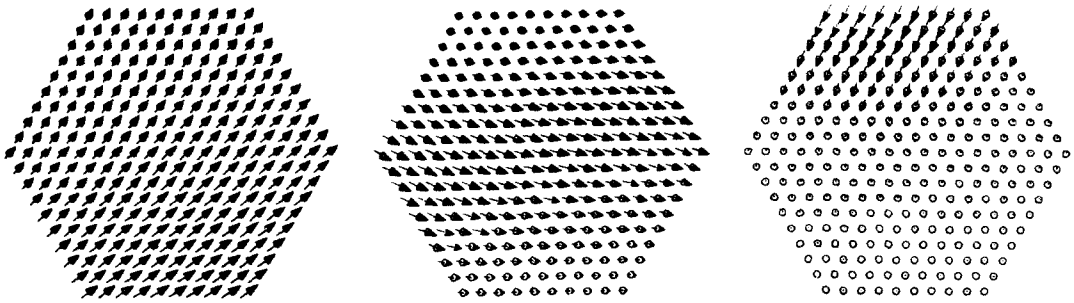

FIG. 3. The transient magnetization configuration during the switching process for the 55 nm diam particle. The normalized average magnetization values for the four states are; (a) $m_x=0.8$, (b) $m_x=0.6$, (c) $m_x=0.2$.

more detail, we examined the easy axis transient magnetization configurations. Figures 2 and 3 display the magnetization configuration for the 57 and 55 nm diam particle at various stages during the irreversible switching process respectively. In each case, nucleation initiates along an edge boundary of the particle [Figs. 2(a) and 3(a)]. The spacial anisotropy distribution for the 57 nm diam particle model shows that the nucleation site is a region of reduced crystalline anisotropy. Because of this local anisotropy reduction, the edge region nucleated at applied field value that is much less than its anisotropy field. Once the edge region switches, it forms a reverse domain as shown in Fig. 2(b). The reversed region expands and switches completely by the propagation of a domain wall [Fig. 2(c)]. This incoherent switching mode is consistent with the approximate inverse-cosine angular dependence behavior measured experimentally [refer to Fig. 1(b)]. The magnetization configuration for the 55 nm diam particle shown in Fig. 3, shows a switching configuration that is nearly coherent. The crystalline anisotropy distribution for this particle shows that there were only moderate degree of anisotropy dispersion along the edge of the particle while most of doping variation occurred in the interior regions of the particle. This indicates that large anisotropy dispersion at the interior regions does not significantly affect the switching process. Therefore, once the onset of nucleation occurs along an edge, the rest of the particle also begins to switch because the applied field value is close to the anisotropy field value [Figs. 3(b)–3(d)]. This quasicoherent switching mode is consistent with the near-Stoner–Wohlfarth switching field angular dependence curve observed experimentally [refer to Fig. 1(b)].

The transient magnetization configuration for the large diameter (75 nm) particle also shows a highly incoherent edge nucleation, domain wall propagation mode. Quasicoherent switching mode was never observed in any of the simulations for any given anisotropy distribution in the large size particle.

IV. CONCLUSION

The switching field angular dependence of individual barium ferrite recording particles has been experimentally measured for the first time.

Measurements of three particles 55, 57, and 75 nm diam particles revealed significant differences in their angular dependence behavior from a near-Stoner–Wohlfarth to an near-inverse cosine. Micromagnetic simulation could accurately predict the experimental observations when the effects due to nonuniform doping of Co-Ti were included. The specific nature of the switching mode and the nucleation field are significantly affected by the detail spatial doping distribution within the particle. Inhomogeneous doping of Co-Ti can form small local regions of reduced crystalline anisotropy. These small regions spawn nucleation sites along the edge boundaries of the particle, where switching initiates at very small easy axis field values. In such cases, the reversal occurs by a highly incoherent edge nucleation, domain wall propagation mode. Inhomogeneous doping that occurs primarily in the interior regions does not significantly influence the switching process. When the anisotropy dispersion occurs in this fashion, then irreversible switching occurs at field values nearly equal to its anisotropy field. In these cases, switching occurs by a quasicoherent mode.

In the larger size particles, incoherent reversal becomes the preferred switching configuration independent of the detail spatial anisotropy distribution.

ACKNOWLEDGMENTS

The authors would like to thank National Media Laboratory and Dr. Denis Mee for their support.

[1] A. R. Corradi, D. E. Speliotis, A. H. Morrish, Q. A. Pankhurst, X. Z. Zhou, G. Bottoni, D. Candolfo, A. Cecchetti, and F. Masoli, IEEE Trans. Magn. MAG-24, 2864 (1988).
[2] T. Ido, O. Kubo, and H. Yokoyama, IEEE Trans. Magn. MAG-22, 704 (1986).
[3] T. Chang and J. G. Zhu, J. Appl. Phys. 73, 6716 (1993).
[4] M. P. Sharrock, IEEE Trans. Magn. MAG-26, 255 (1990).
[5] T. Chang and J. G. Zhu, Intermag '93 [IEEE Trans. Magn. (to be published)].

Co-Sn substituted barium ferrite particles

X. Z. Zhou and A. H. Morrish
Department of Physics, University of Manitoba, Winnipeg R3T 2N2, Canada

Zheng Yang and Hua-Xian Zeng
Research Institute of Magnetic Materials, Lanzhou University, Lanzhou, China

Co-Sn substituted barium ferrite particles, $BaFe_{12-2x}Co_xSn_xO_{19}$ ($0 \leq x \leq 1.4$), have been investigated using x-ray, VSM, and Mössbauer spectroscopy. The magnetocrystalline-anisotropy constant has been determined as a function of x from an analysis of the approach to magnetic saturation. Mössbauer spectra indicate that Co^{2+} and Sn^{4+} ions have a strong preference for the $2b$, $4f_{VI}$, and $12k$ sites. The reduced anisotropy constants $k = K_1(x)/K_1(0)$ have been calculated based on the single-ion model and the site preferences and agree well with the measured values. The origin of the magnetic changes caused by Co^{2+} and Sn^{4+} substitution can be attributed to the site preferences.

I. INTRODUCTION

M-type barium ferrites, because of their large intrinsic uniaxial anisotropy and high coercive force, have been widely used as permanent magnets and microwave devices. When various combinations, such as Co-Ti or Co-Sn, are substituted for some iron in *M*-type barium ferrite particles, the coercivity is substantially reduced with only a little change in the saturation magnetization.[1,2] Recently it has been realized that these substituted materials are suitable for use in high density and perpendicular recording media.[3–5] However, the Co-Ti substituted barium ferrite particles have a larger temperature coefficient of coercive force, dH_c/dT, as compared to acicular particles of $\gamma-Fe_2O_3$, and it can be improved by a third element, Sn, substitution.[6] On the other hand, it was reported that Co-Sn substituted barium ferrite particles, $BaFe_{12-2x}Co_xSn_xO_{19}$ with $x=1.10-1.40$, had a small temperature coefficient for H_c and were suitable for magnetic recording.[2]

In an attempt to shed more light on the origin of the magnetic changes when the substitutions are made, the family of compounds, $BaFe_{12-2x}Co_xSn_xO_{19}$, where x ranges from 0 to 1.4, has been prepared and investigated using x-ray diffraction, a vibrating sample magnetometer (VSM), and Mössbauer spectroscopy. The number of iron ions at each of the crystallographic sites as a function of x has been inferred from the Mössbauer spectra. It was found that the Co^{2+} and Sn^{4+} ions have a strong preference for $2b$, $4f_{VI}$, and $12k$ sites. The Fe contributions to the anisotropy from each site have been calculated on the basis of the single-ion model and compared to the experimental results; they agree remarkably well.

II. EXPERIMENTAL

The samples $BaFe_{12-2x}Co_xSn_xO_{19}$ with $x=0-1.4$ in steps of 0.2 were prepared using the chemical coprecipitation technique. After the coprecipitation products were filtered out, no Sn^{4+} ions were detected in the remaining solution. The details of the sample preparation have been published elsewhere.[7] The structure and lattice parameters of all samples were determined using x-ray diffraction. The specific magnetization, σ_m and the coercive force, H_c, were measured with a VSM (Vibrating Sample Magnetometer) with a maximum field of 16 kOe. The law of approach to saturation was applied to determine the anisotropy fields, H_K, and the anisotropy constants K_1. Mössbauer spectra were taken using a constant acceleration spectrometer with a triangular drive and a 30 mCi source of ^{57}Co in a Rh matrix. A proportional counter made by Harwell and a multichannel analyzer CMCA 1000 with 512 channels were used to collect the spectra. The velocity of the spectrometer was calibrated using the six-line spectrum of an α-Fe foil. All Mössbauer spectra were folded and fitted with a least-squares computer program.

III. RESULTS AND DISCUSSION

The x-ray diffraction patterns show that all the $BaFe_{12-2x}Co_xSn_xO_{19}$ ($0 \leq x \leq 1.4$) have the magnetoplumbite structure; no trace of other phases was detected. Although the lattice constant a does not change significantly with x, the constant c does increases monotonically from 23.272 to 23.402 Å as x increases from 0 to 1.4. This may be attributed to the larger radius of Sn^{4+} (0.71 Å) as compared to that of Fe^{3+} (0.63 Å).

The specific magnetization, σ_m, the remanence, σ_r, the anisotropy constant K_1 and the coercive force H_c, are listed in Table I for various x. Clearly, although the anisotropy constant K_1 and coercivity H_c substantially decrease as x increases, the specific magnetization σ_m only decreases by a

TABLE I. Magnetic properties of $BaFe_{12-2x}Co_xSn_xO_{19}$ with $0 \leq x \leq 1.4$; the specific magnetization σ_m, remanence σ_r, crystalline anisotropy constant K_1, and coercive force H_c.

x	σ_m (emu/g)	σ_r (emu/g)	$K_1(10^6$ erg/cm$^3)$	H_c (Oe)
0.00	63.6	33.12	2.84	4800
0.20	61.5	32.82	2.53	3875
0.40	61.2	32.13	2.30	2925
0.60	59.6	30.31	1.89	1965
0.80	59.6	29.21	1.62	1560
0.95	58.5	28.22	1.43	1180
1.10	58.7	27.58	1.23	996
1.20	57.9	25.28	1.12	762
1.40	56.2	22.19	0.94	529

 0021-8979/94/75(10)/5556/3/$6.00 © 1994 American Institute of Physics

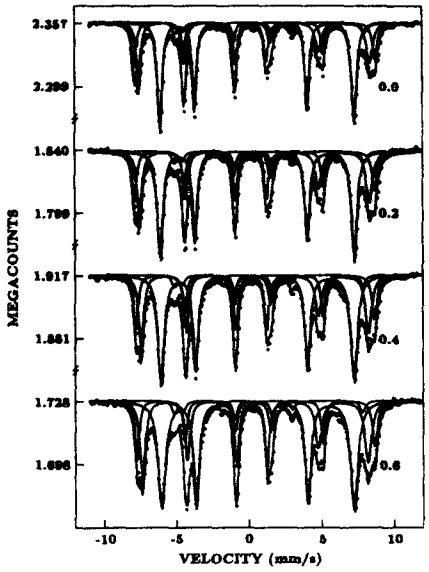

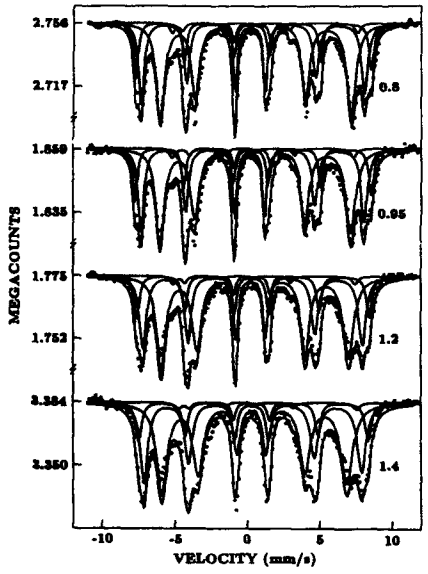

FIG. 1. Room temperature Mössbauer spectra for $BaFe_{12-2x}Co_xSn_xO_{19}$ (a) with $0 \leq x \leq 0.6$ and (b) with $0.8 \leq x \leq 1.4$.

relatively small percentage. The H_c value for the unsubstituted sample is too high for magnetic recording applications. When $x=1.1-1.4$ it is suitable for magnetic recording media.

Room-temperature Mössbauer spectra for $BaFe_{12-2x}Co_xSn_xO_{19}$ ($0 \leq x \leq 1.4$) are shown in Fig. 1. All spectra were fitted with four six-line subpatterns that were assigned to the $4f_{IV}$-$2a$ (which are not resolvable), $2b$, $4f_{VI}$, and $12k$ sites of the hexagonal crystal structure. The relative areas of the four subpatterns were assumed to correspond to the number, N, of iron ions on the corresponding sites. By comparing the relative spectral areas of the substituted to the unsubstituted samples the number N is obtained for each site as shown versus x in Fig. 2. The number of iron ions does not change much for the $4f_{IV}$-$2a$ site, but decreases for the $2b$, $4f_{VI}$, and $12k$ sites with increasing x. In other words, the Co^{2+}-Sn^{4+} ions have a strong preference for the $2b$, $4f_{VI}$, and $12k$ sites.

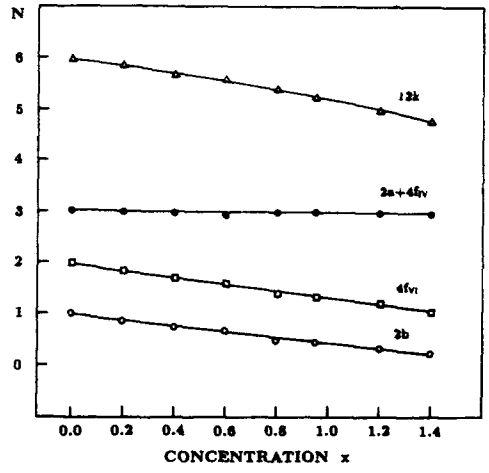

FIG. 2. The number, N, of iron ions at each site as a function of concentration x.

The hyperfine fields for each site deduced from computer fitting as a function of x are listed in Table II. For all sites the hyperfine fields decreased only slightly with increasing x. Usually the magnetization is proportional to the hyperfine field. This result is in a good agreement with magnetic measurements.

The single-ion model predicts that the largest contribution to the magnetocrystalline anisotropy is from the $2b$ site. However, the contributions from the other sites cannot be neglected; the $12k$ site has a negative value.[8] The contribu-

TABLE II. The hyperfine fields of $BaFe_{12-2x}Co_xSn_xO_{19}$ with $0 \leq x \leq 1.4$, deduced from computer fitted Mössbauer spectra for each site as a function of x.

x	$4f_{VI}$ (kOe)	$4f_{IV}+2a$ (kOe)	$12k$ (kOe)	$2b$ (kOe)
0.00	516.4	494.5	415.3	404.1
0.20	514.7	492.3	415.2	402.2
0.40	512.4	487.7	414.7	401.2
0.60	509.3	484.7	413.6	400.7
0.80	506.2	479.0	410.6	394.1
0.95	504.8	476.9	410.6	392.5
1.20	501.9	470.1	405.6	392.5
1.40	493.1	466.0	400.0	386.6

TABLE III. The values of K_1 for a single Fe^{3+} ion at each barium ferrite site at 0 K.

Site	$2a$	$2b$	$4f_{IV}$	$4f_{VI}$	$12k$
K_1 (cm^{-1}/ion)	0.23	1.40	0.18	0.51	−0.18

tions to the anisotropy constant, K_1, of a single iron ion at each site can be found in Ref. 8; for convenience these values are given in Table III. The higher-order anisotropy constants are zero for all sites.

Based on the number of iron ions at each site obtained from the Mössbauer results and the values of K_1 for each site the total value of K_1 for Co-Sn substituted barium ferrite as a function of x obtained is listed in Table IV. For comparison purposes a reduced anisotropy constant k is defined as the ratio of the anisotropy constant $K_1(x)$ for the substituted to that for the unsubstituted barium ferrites $K_1(0)$ [$k = K_1(x)/K_1(0)$]; these are also listed in Table IV. Lack of information precluded taking the Co^{2+} contributions into account. The measured $k(x)_m$ and calculated $k(x)_c$ agree well as shown in Fig. 3. It is important to note that Co^{2+} is a magnetic ion and usually makes a large contribution to the anisotropy constant in the ferrites, for example, in γ-Fe_2O_3. In this experiment the good agreement between the measured $k(x)_m$ and calculated $k(x)_c$ values without taking into account any Co^{2+} contribution may be because the Co^{2+} contributions at the different sites cancel or because the Co^{2+} moment is quenched. The contribution made by Co^{2+} ions requires further clarification.

The Mössbauer spectra show that the Co^{2+} and Sn^{4+} ions prefer the $2b$, $4f_{VI}$, and $12k$ sites. It is of interest to consider various distributions of the Co^{2+} and Sn^{4+} ions over these sites. If, for example, the Co^{2+} and Sn^{4+} ions occupy the $2b$, $4f_{VI}$, and $12k$ sites randomly, that is, 1/9 occupy the $2b$ site, 2/9 the $4f_{VI}$ site, and 6/9 the $12k$ site, then the calculated $k(x)_c$ decreases with increasing x much more slowly than the experimental data. Hence, this is unlikely. If relatively more Co^{2+} and Sn^{4+} ions occupy the $2b$ and $4f_{VI}$ sites than the $12k$ sites, for example, if 3/12, 4/12, and 5/12 occupy the $2b$, $4f_{VI}$, and $12k$ sites, respectively, then the calculated value of $k_1(x)_c$ agrees well with experimental data. This particular distribution is consistent with the Mössbauer results. It also predicts that when $x=2.4$ the uniaxial anisotropy will vanish, i.e., $k(2.4)=0$; then $BaFe_{12-2x}Co_xSn_xO_{19}$ with $x \geq 2.4$ will have planar anisotropy.

TABLE IV. The uniaxial anisotropy constant K_1 calculated from the single-ion model, the calculated reduced anisotropy constant, $k(x)_c$, and the measured reduced anisotropy constant $k(x)_m$ for $BaFe_{12-2x}Co_xSn_xO_{19}$ with $0 \leq x \leq 1.4$.

x	K_1 (cm^{-1}/ion)	$k(x)_c$	$k(x)_m$
0.00	1.93	1.00	1.00
0.20	1.68	0.87	0.89
0.40	1.48	0.77	0.81
0.60	1.33	0.69	0.67
0.80	1.10	0.57	0.57
0.95	1.02	0.53	0.51
1.20	0.84	0.44	0.39
1.40	0.72	0.37	0.34

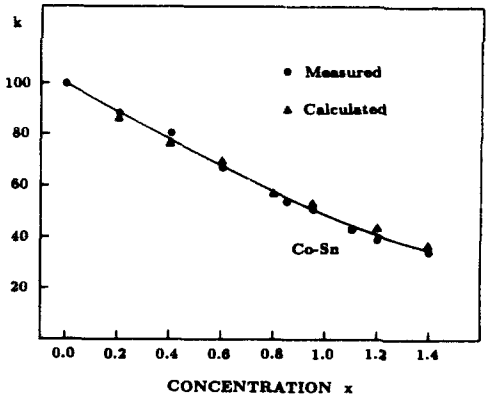

FIG. 3. Reduced magnetic anisotropy constant, k, as measured and as calculated from the single-ion model as a function of concentration x.

The agreement between the calculated and measured reduced anisotropy constants, $k(x)$, leads to the conclusion that the Co^{2+} and Sn^{4+} ions prefer the $2b$, $4f_{VI}$, and $12k$ sites with the probability 3/12, 4/12, and 5/12, respectively. The single-ion model for the magnetic anisotropy agrees with the experimental results. The origin of the magnetic changes caused by the substitution can be accounted for by considering only the site preferences of the Co^{2+} and Sn^{4+} ions.

ACKNOWLEDGMENTS

The work at the Manitoba was supported by the National Sciences and Engineering Research Council of Canada. The work at the Lanzhou University was supported by the foundation of Chinese National Educational Committee.

[1] X. Z. Zhou, A. H. Morrish, Z. W. Li, and Y. K. Hong, IEEE Trans. MAG-27, 4654 (1991).
[2] Z. Yang, H.-X. Zang, D.-H. Han, J.-Z. Liu, and S.-L. Geng, J. Magn. Magn. Mater. 115, 77 (1992).
[3] O. Kubo, T. Ido, and H. Yokoyama, IEEE Trans. Magn. MAG-18, 1122 (1982).
[4] T. Fujiwara, IEEE Trans. Magn. MAG-23, 3125 (1987).
[5] Yang Zheng, Liu Jian-Zhong, Zheng De, Geng Sheng-Li, and Chen Zi-Yu, IEEE Trans. Magn. MAG-23, 3131 (1987).
[6] O. Kubo, T. Nomura, T. Ido, and H. Yokoyama, IEEE Trans. Magn. MAG-24, 2859 (1988).
[7] Yang Zheng, Zeng Hua-Xian, Yan Ming-Long, and Geng Sheng-Li, J. Magn. Soc. Jpn. 13, 363 (1989)
[8] Xu You, Chu Daping, Yang Guiling, and Zhai Hongru, *Proceedings ICF-5 1989*, India, "Advances in Ferrites," edited by C. M. Srivastava and M. J. Patni (Oxford and IBH, PVT. Ltd., Bombay, 1990), p. 485.

Magnetic properties of modified Ba-ferrite particles

H. Sadamura, N. Sugita, M. Maekawa, and N. Nagai
R&D Division, Toda Kogyo Corporation, 4-1-2 Funairi-minami, Naka-ku, Hiroshima-shi, Hiroshima 730, Japan

Modification with magnetite on Ba-ferrite particles was carried out by heating alkaline suspension including Ba-ferrite particles and Fe^{2+} hydroxides as described by Kiyama *et al.* [J. Solid State Chem. **99**, 329 (1992)] to get higher magnetization. As a result of x-ray powder diffraction measurements, reflection intensity of magnetoplumbite phase decreases and that of spinel phase increases with increase of Fe^{2+} quantity added, simultaneously. Coercive force goes down and magnetization increases as Fe^{2+} quantity added increases. The differential hysteresis loop of the mixed samples (Ba-ferrite particles and magnetite particles) has two peaks. And that of the modified samples has only one peak. From these results, it becomes clear that there exists strong magnetic interaction between Ba-ferrite core and magnetite shell. The measurements of temperature dependence of magnetization at the applied field of about 16.5 kA/m shows that the Hopkinson peak shifts toward higher temperature with increase of the modified amount. It also indicates the strong magnetic interaction between core and shell materials.

I. INTRODUCTION

Magnetic recording media will be classified into thin film type and coating type. And most commercially available media are coating type made by coating the support material with a dispersion of magnetic particles in an organic binder.[1] In magnetic materials for coating type, the research and development on Ba-ferrite particles and its application on the high density recording becomes activated recently,[2–4] since Ba-ferrite tapes have the perpendicular anisotropy and small switching field distribution.[5] If the magnetization of Ba-ferrite could be increased, the possibility will become higher. Therefore the modification with magnetite or Co-ferrite on Ba-ferrite particles have been investigated to increase magnetization.[6] It was also investigated that the easy axis was deviated from c-axis in such modified Ba-ferrite particles.[6]

As mentioned above, switching field distribution (SFD) is very important specially in the field of high density magnetic recording. The SFD can be evaluated from the differential hysteresis loop. Therefore, it is the purpose to show the differences between the mixed samples and the modified samples by measuring the differential hysteresis loop and temperature dependence of magnetization.

II. EXPERIMENTAL

The platelet Ba-ferrite particles (sample No. A-0) substituted by Ni, Ti, and Zn were used as a core material,[7] which had a specific surface area of 50 m^2/g, an average diameter of 0.05 μm, an aspect ratio of 5 to 6, a coercive force of 130 kA/m and a saturation magnetization of 57 A m^2/kg.

First, the particles were dispersed in alkaline suspension (NaOH concentration of 2.5 mol/ℓ). The modification of core particles was performed with Fe^{2+} of 5, 10, and 20 wt % with respect to core material. The source of Fe^{2+} was $FeSO_4 7H_2O$ aqueous solution. Then this well-mixed suspension was heated to boiling and stirred for 5 h with N_2 bubbling. The modified particles in alkaline suspension were filtered, well-washed and dried at 50 °C in air. The modified samples with Fe^{2+} of 5, 10, and 20 wt % is corresponding to A-1, A-2 and A-3, respectively.

Furthermore, the mixed samples between above-mentioned Ba-ferrite particles and spherical magnetite particles having a coercive force of 12 kA/m and a saturation magnetization of 85 A m^2/kg were prepared. The mixed ratios of magnetite particles to Ba-ferrite particles were 0, 10, 30, 50, and 100 wt %.

Fe^{2+} content in the modified samples was quantitatively analyzed with the oxidation-reduction titration. Magnetic properties were measured with vibrating sample magnetometer up to 796 kA/m at 298 K. Temperature dependence of magnetization was measured with magnetic balance up to 873 K at the applied field of approximately 16.5 kA/m. X-ray powder diffraction patterns of core Ba-ferrite and the modified samples were taken with Fe $K\alpha$ radiation. $BaSO_4$ content in the sample was measured by gravimetric analysis, after it had been dissolved into HCl by heating. And the relative content of Fe_3O_4 in each sample was estimated from the corrected saturation magnetizations of the modified samples, using a saturation magnetization of 57 and 85 A m^2/kg for Ba-ferrite and magnetite, respectively, as already described by Kiyama *et al.* [8]

III. RESULTS AND DISCUSSIONS

A. Mechanism of the modification of Ba-ferrite with magnetite

Figure 1 shows the results of powder x-ray diffraction measurements of the core Ba-ferrite sample (A-0) and the modified samples (A-1 to A-3). Reflection intensity of spinel phase increases and that of magnetoplumbite phase decreases with increase of Fe^{2+} quantity added, and reflections of $BaSO_4$ come out at the same time.

These results mean that Ba ions are extracted from Ba-ferrite particles during the modification process, and that Fe^{3+} ions which are necessary for the formation of Fe_3O_4 is supplied from Ba-ferrite particles. Therefore, the mechanism of this reaction is almost same as that of Co-treatment as described in Ref. 9.

 0021-8979/94/75(10)/5559/3/$6.00 © 1994 American Institute of Physics

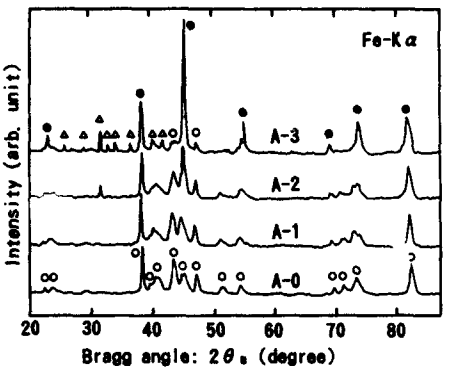

FIG. 1. X-ray diffraction patterns of the Ba-ferrite particles and the modified samples; Ba-ferrite core (A-0) and those modified with magnetite of 17 wt % (A-1), 34 wt % (A-2), and 78 wt % (A-3). And peaks are denoted as follows; ○: Ba-ferrite, ●: Fe_3O_4, △: $BaSO_4$.

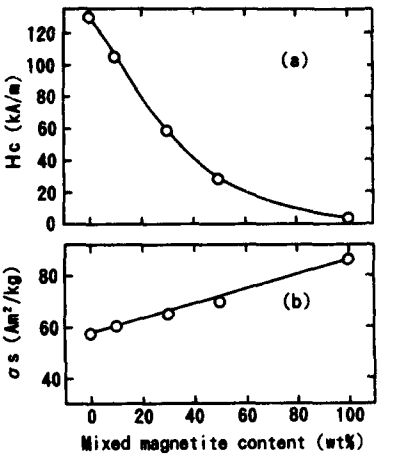

FIG. 2. Coercive force (a) and magnetization (b) as a function of magnetite content mixed to Ba-ferrite particles.

Specific surface area and magnetic properties of these samples are shown in Table I. The coercive force, H_c, decreases and magnetization, σs, increases with increase of Fe^{2+} added. They are attributed to the formation of magnetite layer on Ba-ferrite particles.

B. Difference between modified sample and mixed sample

In the mixed samples, magnetization increases linearly and coercive force decreases monotonically with increase of magnetite content as shown in Fig. 2. The hysteresis loop of these samples is distorted, because two kinds of magnetic particles those have different magnetization and coercive force exist. On the other hand, that of the modified samples is not distorted. These situations are clearly indicated by the differential curve of hysteresis loop.

Figure 3 shows dM/dH as a function of applied field in the reversing process. In Fig. 3, H_p is defined as the field with maximum dM/dH. In case of the mixed samples, there are two peaks and their positions do not vary with the magnetite content as shown in Fig. 3(b). And H_{p_1} and H_{p_2} are corresponding to that of magnetite and Ba-ferrite, respectively. That is, magnetite particles and Ba-ferrite particles are magnetically independent in the mixed samples.

However, there is only one H_p, and that decreases with increase of magnetite content in the modified samples, as shown in Fig. 3(a).

Therefore in the modified sample, there is the magnetic interaction between the Ba-ferrite core and magnetite shell.

TABLE I. Analytical results, specific surface area, and magnetic properties of the modified samples. Magnetization values are corrected using the estimated $BaSO_4$ content.

Sample No.	A-0	A-1	A-2	A-3
Analytical Fe^{2+} content: wt %	0	2.5	5.7	11.8
Estimated Fe_3O_4 content: wt %	0	17	34	78
Estimated $BaSO_4$ content: wt %	0	3.0	7.5	15.0
Specific surface area: m^2/g	50.0	44.5	38.5	30.0
Coercive force, H_c: kA/m	130.0	95.5	63.7	26.3
Magnetization, σ_s: A m^2/kg	57.0	61.8	66.5	78.2
σ_r/σ_s: ···	0.488	0.464	0.434	0.312

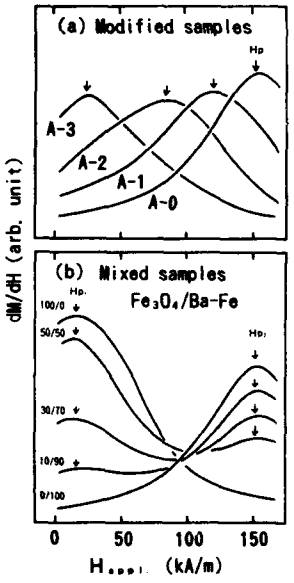

FIG. 3. dM/dH curves as a function of applied field in the reversing process, for (a) modified samples and (b) mixed samples.

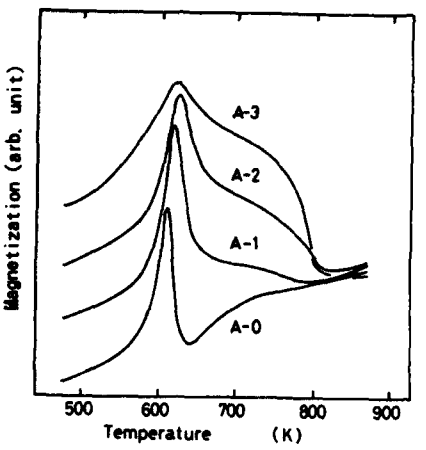

FIG. 4. Temperature dependence of low field magnetization for the modified samples of A-0 to A-3.

C. Magnetism of the modified particle

Temperature dependence of magnetization of Ba-ferrite particles used as core material and the modified samples were measured with magnetic balance at the applied field of approximately 16.5 kA/m as shown in Fig. 4. Curie temperature of core Ba-ferrite (*A-0*) is about 606 K, just below which there is the Hopkinson peak.[10] And that of magnetite is about 800 K.

For all samples, there is a peak at around 600 K, which is attributed to the Hopkinson effect. The peak shifts toward higher temperature and becomes broader as the modified amount increases. This change does not occur in simply mixed samples of Ba-ferrite and magnetite particles.

As described in Sec. III B, these results also indicate that the core Ba-ferrite particles have strong magnetic interaction with the modified layer of magnetite.

ACKNOWLEDGMENT

The authors wish to thank Toda Kogyo Corporation for encouragement throughout this study.

[1] M. P. Sharrock and R. E. Bodnar, J. Appl. Phys. **57**, 3919 (1985).
[2] M. Noda, Y. Okazaki, K. Hara, and K. Ogisu, IEEE Trans. Magn. **MAG-26**, 81 (1990).
[3] E. F. Wollack, R. M. Erkkila, and T. C. Mitchell, IEEE Trans. Magn. **MAG-25**, 4054 (1989).
[4] D. E. Speliotis, IEEE Trans. Magn. **MAG-23**, 3143 (1987).
[5] D. E. Speliotis, J. Appl. Phys. **61**, 3878 (1987).
[6] S. Kitahata and M. Kishimoto, Ferrite Proceedings of The Sixth International Conference on Ferrite ICF **6**, 972 (1992).
[7] N. Nagai, N. Sugita, and M. Maekawa, J. Magn. Magn. Mater. **120**, 33 (1993).
[8] M. Kiyama, T. Honmyo, N. Nakayama, and T. Shinjo, J. Solid State Chem. **99**, 329 (1992).
[9] H. Sadamura, K. Yamashita, and N. Nagai, J. Appl. Phys. **73**, 6731 (1993).
[10] M. Kersten, Z. f. Angew. Phys. **7**, 313 (1956); **8**, 382, 496 (1956).

H_c enhancement of Co-adsorbed γ-Fe_2O_3 particles via surface treatment with sodium polyphosphate

F. E. Spada, F. T. Parker, A. E. Berkowitz, and T. J. Cox
Center for Magnetic Recording Research-0401 University of California, San Diego, La Jolla, California 92093-0401

The coercive force H_C of partially reduced, acicular γ-Fe_2O_3 particles having an adsorbed Co layer (4 wt % Co; Fe^{+2}/Fe^{+3}~0.09; 2000 Å×240 Å particle dimensions; 36 m^2/g specific surface area) increases substantially following surface treatment with $(NaPO_3)_{n\sim14}\cdot Na_2O$. The maximum observed effect occurs at a polyphosphate-to-iron oxide weight ratio P/Fe near 0.5, denoted $(P/Fe)_{max}$, where H_C of the Co-adsorbed oxide increases from 687 to 1096 Oe immediately following treatment. The latter value increased to 1215 Oe after a four month storage in an argon environment containing less than 1 ppm H_2O and O_2, suggesting that the polyphosphate-oxide interaction is sensitive to moisture or oxygen. Co-adsorbed particles containing no Fe^{+2} in the oxide core also exhibit H_C enhancement following surface treatment, but the change in H_C is substantially less than that of particles containing Fe^{+2}. The general behavior of polyphosphate-treated Co-adsorbed particles is observed to be similar to that of treated berthollide particles having no adsorbed Co layer: (i) the magnitude and sign of change in H_C varies with P/Fe, reaching a peak value at $(P/Fe)_{max}$, (ii) the magnitude of increase in H_C at $(P/Fe)_{max}$ depends on the Fe^{+2} content of the particle core, (iii) saturation magnetization of the particles treated at $(P/Fe)_{max}$ is essentially unchanged from that of the untreated precursor, (iv) H_C of specimens treated at $(P/Fe)_{max}$ returns to the value of the untreated precursor when the polyphosphate coating is removed via washing with water, and (v) particle dissolution occurs when $P/Fe \gg (P/Fe)_{max}$. Studies of anisotropy field distributions show that there is no obvious bimodal character to the very broad distribution of anisotropy fields found in randomly oriented specimens of surface-treated particles.

I. INTRODUCTION

Very large increases in the coercive force of acicular, partially reduced γ-Fe_2O_3 particles have been observed following treatment with $(NaPO_3)_n\cdot Na_2O$, where $n>7$.[1-7] The origin of this phenomenon is still unknown, but the large change in the coercive force following treatment and its reversible nature suggest that the increased anisotropy emanates from an interaction at the surface of the oxide particle with the polyphosphate molecule. The strong affinity of polyphosphate molecules for certain metal cations has led to suggestions that the phosphate groups in the polymer molecule either interact directly with Fe^{+2} ions,[5] or influence the iron cation distribution near the particle surface,[6,8] thereby producing a large surface anisotropy. However, Mössbauer investigations[7] of partially reduced γ-Fe_2O_3 particles having surfaces enriched with ^{57}Fe indicated that polyphosphate treatments result in no observable changes of the iron cation distribution at the polyphosphate-particle interface.

Since the polyphosphate molecule also has a strong affinity for Co^{+2},[9] it seems logical to question whether γ-Fe_2O_3 particles having an adsorbed layer of Co also can exhibit H_c enhancement following polyphosphate treatment. Our preliminary studies[7] have indeed demonstrated that Co-adsorbed γ-Fe_2O_3 particles do respond to polyphosphate surface treatment. We have extended these latter studies of Co-adsorbed particles and have found much larger H_C enhancement than previously reported.

II. EXPERIMENT

Details of the method used for the polyphosphate surface treatment are described elsewhere.[7] All specimens were saturated in a 24 kOe applied field prior to obtaining the M vs H curves using a vibrating sample magnetometer, where M is magnetization and H is applied field. All resulting values for the coercive force, H_c, and magnetization in 20 kOe applied field, defined here as the saturation magnetization M_s, were corrected for the weight and diamagnetism of the polyphosphate matrix as well as the diamagnetism of the sample holder. Anisotropy field distributions were measured using the technique described earlier by Sharrock.[10]

The iron oxide specimen used as the precursor material for this study consisted of acicular particles having approximately 2000 Å length and 240 Å diam with 36 m^2/g specific surface area (SSA). The particle surface contained a 4 wt % adsorbed Co layer. The Fe^{+2}/Fe^{+3} cation ratio, obtained from analysis[7] of the Mössbauer spectrum of the precursor, was approximately 0.09. The room temperature M_s and H_c values for randomly oriented precursor particles were 78.1 emu/g and 687 Oe, respectively. Earlier studies[2,3,5,7] have shown that the Fe^{+2} content of the particle core influences the magnitude of the coercive force enhancement in polyphosphate-treated berthollides. In order to determine if the Fe^{+2} cation had a similar influence in iron oxides having an adsorbed Co layer, a specimen containing only Fe^{+3} was prepared by heating the precursor at 125 °C for 24 h under a flowing stream of oxygen saturated with water. The x-ray powder diffraction pattern of the oxide produced by this treatment was identical to that of the precursor, with no detectable quantities of α-Fe_2O_3 present. Mössbauer spectroscopy confirmed that the oxidized specimen contained no Fe^{+2}. The room temperature M_s value for the oxidized precursor was 72.4 emu/g and H_c was 623 Oe.

 0021-8979/94/75(10)/5562/3/$6.00 © 1994 American Institute of Physics

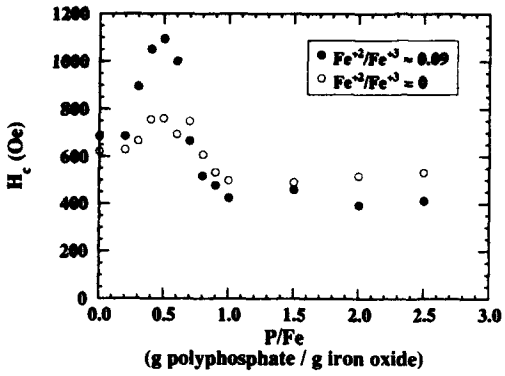

FIG. 1. Dependence of the room temperature coercive force on the sodium polyphosphate-to-iron oxide weight ratio P/Fe for Co-adsorbed precursor (solid circles), and oxidized Co-adsorbed precursor (open circles).

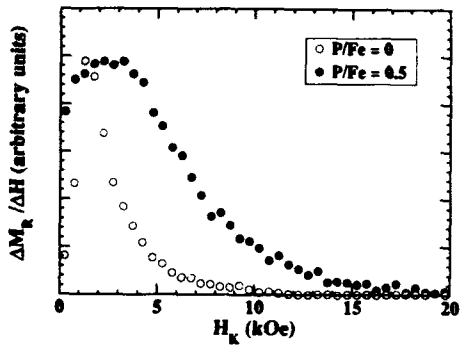

FIG. 2. Anisotropy field distributions for Co-adsorbed precursor before (open circles) and after polyphosphate surface treatment at P/Fe=0.5 (solid circles).

III. RESULTS

The influence of various polyphosphate treatments on the coercive force of Co-adsorbed iron oxide particles is shown in Fig. 1, where H_c is plotted as a function of the sodium polyphosphate-to-iron oxide weight ratio P/Fe. H_c reaches a maximum at P/Fe=0.5 [denoted $(P/Fe)_{max}$] for both the precursor (Fe^{+2}/Fe^{+3}=0.09) and the oxidized specimen (Fe^{+2}/Fe^{+3}=0), but the coercive force enhancement for the latter specimen is about one third that observed for the precursor oxide. H_c of the precursor was 1096 Oe immediately following treatment at $(P/Fe)_{max}$, but increased to 1215 Oe after a 4 month storage in a glove box filled with an argon atmosphere containing less than 1 ppm H_2O and O_2. For specimens treated at P/Fe<0.7, the values of M_S and remanence ratio did not appreciably change from those of the untreated powders. Furthermore, after several rinses in ultrasonically agitated water, the H_C and M_S of the polyphosphate-treated (P/Fe=0.5) precursor were 716 Oe and 78.6 emu/g, respectively. These values are essentially the same as before treatment and demonstrate that the adsorbed Co layer remains intact when treatment ratios do not exceed P/Fe=0.7. However, when P/Fe>0.7, values of both M_S and remanence ratio were substantially reduced relative to the values for the untreated materials. Paramagnetic Mössbauer subspectra confirm that particle dissolution occurs in this latter P/Fe range. These results are similar to those reported earlier[7] for iron oxide particles having no adsorbed Co layer.

Our previous studies[7] of the anisotropy field (H_K) distributions of polyphosphate-treated berthollides were based on fits of the first quadrant magnetization data to log-normal distributions. These studies demonstrated that polyphosphate surface treatments at $(P/Fe)_{max}$ resulted in large increases in mean anisotropy fields, as well as very broad distributions, the latter possibly due to the presence of bimodal anisotropy distributions in the treated powders. No such bimodal character is observed in the anisotropy field distribution of the polyphosphate-treated Co-adsorbed precursor (Fig. 2), determined by the more direct technique described in Ref 10. This latter method determines the remanent magnetization M_R (measured at a 90° angle from the direction in which the sample was previously saturated) that results after application of successively larger positive fields applied at a small angle θ from the saturation direction. The derivative of the resulting remanence vs applied field curve gives the H_K distribution of the sample. In the studies described here, the saturating field was 24 kOe, θ=5°, and the field increments were in the range 100–500 Oe. The anisotropy field distributions shown in Fig. 2 were obtained from the derivatives of the smooth curves drawn through the remanence vs applied field data for randomly distributed specimens of Co-adsorbed precursor before and after polyphosphate treatment at P/Fe=0.5. The distribution for the polyphosphate-treated material shows a single peak in the H_K range 2000–3000 Oe with a long broad tail extending to higher fields. Qualitative measurements of the distribution width were precluded by the presence of a small fraction of sample that switches near zero applied field. The origin of this behavior is currently unknown, but it should be noted that inspection of the M vs H curve for this specimen revealed no anomalous decrease in moment near zero field. The distribution for the untreated precursor exhibits a peak at about 1260 Oe and a full-width-at-half-maximum of about 2000 Oe.

IV. DISCUSSION

Itoh and co-workers[11] have postulated that partially reduced γ-Fe_2O_3 particles contain a thin surface layer having a Fe^{+2}/Fe^{+3} ratio different from that found in the particle core, and that this layer is necessary for interacting with the polyphosphate molecule to produce increases in the anisotropy. Mössbauer studies[7] of particles having surfaces enriched with ^{57}Fe, however, show no evidence of Fe^{+2} on the surface. A remarkable feature of the current results is that the additional adsorbed Co layer (about a monolayer) on the particle surface does not interfere with whatever interaction may exist between the polyphosphate molecule and the Fe^{+2} present in the particle core. The magnitude of the change in coercive force in the Co-adsorbed precursor is about the

same as that of berthollide specimens without adsorbed Co, so that the polyphosphate treatment has an additive effect on particle anisotropy. For the oxidized Co-adsorbed precursor, the change in H_C is greater than that observed for γ-Fe_2O_3 containing no Co^{+2} or Fe^{+2}, but much reduced from that of the Co-adsorbed precursor material. This may due to an affinity of the polyphosphate molecule for specific sites on the particle surface, such as the spinel B site which contains divalent Fe^{+2} and Co^{+2} cations. If this is the case, it is reasonable to expect that the available preferred sites on the particle surface will be saturated with polyphosphate molecules at the peak treatment ratio $(P/Fe)_{max}$. Using 36 m^2/g for the specific surface area of the Co-adsorbed precursor, $(P/Fe)_{max}=0.5$, and 1489 g/mol for the formula weight of the sodium polyphosphate ($n\sim14$ chain length) used in these studies, we find that there are six polyphosphate molecules per 100 $Å^2$ of available oxide surface when coercivity reaches a maximum. The same value is obtained for precursors 1 and 2 of our earlier studies.[7] This reasoning suggests that the value of $(P/Fe)_{max}$ should scale with the specific surface area of the particle specimen. Therefore, if the six molecules/100 $Å^2$ value is typical for all polyphosphate-treated γ-Fe_2O_3 particles, precursor 3 (SSA=26 m^2/g, see Table I, Ref. 7) should exhibit a peak in the H_c vs P/Fe curve at $(P/Fe)_{max}=0.4$. This value is exactly where the peak enhancement was observed.[6,7]

The computed polyphosphate surface density corresponds closely to the number density of cation A or B sites in the (110) plane of the spinel structure. Fukumoto *et al.*[12] have shown that there are 6.8×10^{22} A sites on the (110) surface planes of a 400 g specimen of γ-Fe_2O_3 powder with SSA=33 m^2/g. Using these numbers, and the fact that the number of A and B sites in the spinel (110) plane is the same, the density of A or B sites in this plane is calculated to be 5 sites/100 $Å^2$. Thus, one possible explanation for the variation of H_C with P/Fe (Fig. 1) may be that the polyphosphate molecule interacts with only one of the two metal cation sites when $P/Fe\leq(P/Fe)_{max}$. When $P/Fe>(P/Fe)_{max}$ polyphosphate begins to interact with the other site, the latter providing a deleterious effect on anisotropy. H_C then falls to near the original value when all available A and B sites are saturated with polyphosphate molecules. Direct interaction with the A and B sites may not be necessary but may instead occur via adjacent surface active moeities. In fact, Sugihara and co-workers[13] present evidence that surface OH^- groups (having densities between 3 $OH^-/100$ $Å^2$ for γ-Fe_2O_3 and 6 $OH^-/100$ $Å^2$ for Fe_3O_4) bond with oleic acid surfactant molecules. The one-to-one relationship between the number of adsorbed oleic acid molecules and available OH^- groups[13] suggests that these intermediates may play a role in bonding with surfactant molecules such as polyphosphate.

The surface density of polyphosphate implies that these chainlike molecules tend to orient themselves perpendicular to the particle surface. Computations based on published[14] interatomic distances and angles for long chain polyphosphates show that a polyphosphate chain with $n\sim14$ would require 104 $Å^2$ of an adjacent surface if the chain axis was aligned parallel to it, but only 5 $Å^2$ if aligned perpendicular to the surface. At $(P/Fe)_{max}$ we find that the perpendicular orientation of the polyphosphate chain covers only 40% of the available surface, whereas the parallel orientation would hypothetically cover 790% of the particulate surface. These results are entirely consistent with the conclusions of Itoh *et al.*,[15] who reported that the interaction between the polyphosphate chain and oxide surface occurs via the chain terminal groups. Thus, the circumstantial evidence presented here seems to suggest that the enhanced anisotropy is due to polyphosphate molecule association with either the A or B metal sites, or surface functional groups that have the same density as these sites, and that the interaction occurs with the terminal phosphate groups of the polyphosphate chain.

In conclusion, we find that polyphosphate surface treatments of Co-adsorbed γ-Fe_2O_3 particles result in substantial H_C enhancement, as observed in berthollide particles having no adsorbed Co surface layer. H_C enhancement via polyphosphate treatments appears to be additive, because the *changes* in H_C at $(P/Fe)_{max}$ have approximately the same magnitude for both types of particles. The *change* in H_C for oxidized Co-adsorbed precursor, however, is about double that observed[7] for γ-Fe_2O_3 containing no Fe^{+2}, implying that the divalent Co^{+2} ion has some role in the interaction between polyphosphate and the iron oxide core. The correlation between the surface densities of polyphosphate and the A or B metal sites implies that polyphosphate interacts sequentially with specific sites.

ACKNOWLEDGMENTS

This work was supported by a National Media Laboratory contract.

[1] F. Itoh and M. Satou, Jpn. J. Appl. Phys. **14**, 2091 (1975).
[2] F. Itoh and M. Satou, Nippon Kagaku Kaishi, No. 6, 853 (1976).
[3] F. Itoh, T. Kaneko and M. Satou, Nippon Kagaku Kaishi, No. 8, 1319 (1976).
[4] F. Itoh and M. Satou, Nippon Kagaku Kaishi, No. 4, 581 (1977).
[5] F. Itoh, M. Satou and Y. Yamazaki, IEEE Trans. Magn. **MAG-13**, 1385 (1977).
[6] F. E. Spada, A. E. Berkowitz, and N. T. Prokey, J. Appl. Phys. **69**, 4475 (1991).
[7] F. E. Spada, F. T. Parker, C. Y. Nakakura, and A. E. Berkowitz, J. Magn. Magn. Mater. **120**, 129 (1993).
[8] J. C. Slonczewski, J. Magn. Magn. Mater. **117**, 368 (1992).
[9] J. R. Van Wazer and D. A. Campanella, J. Am. Chem. Soc. **72**, 655 (1950).
[10] M. P. Sharrock, IEEE Trans. Magn. **26**, 225 (1990).
[11] F. Itoh, T. Namikawa, and M. Satou, in *Ferrites: Proceedings of the 3rd International Conference, 1980*, edited by H. Watanabe, S. Iida, and M. Sugimoto (Center for Academic Publications, Tokyo, 1981), p. 537.
[12] Y. Fukumoto, K. Matsumoto, and Y. Matsui, J. Appl. Phys. **69**, 4469 (1991).
[13] H. Sugihara, Y. Taketomi, T. Uehori, and Y. Imaoka, in Ref. 11, p. 545.
[14] D. E. C. Corbridge, *Phosphorous, An Outline of Its Chemistry, Biochemistry and Technology*, 4th ed. (Elsevier, Amsterdam, 1990).
[15] F. Itoh and M. Satou, Nippon Kagaku Kaishi, No. 8, 1281 (1982).

Coercivity enhancement in γ-Fe_2O_3 by surface treatment with phosphate ions

David E. Nikles, Martin R. Parker, Elizabeth M. Crook, and Terry M. Self
Center for Materials for Information Technology, University of Alabama, Tuscaloosa, Alabama 35487-0209

Significant increases in coercivity were observed for stoichiometric γ-Fe_2O_3 pigments that were treated with different phosphate ions. The objectives of this investigation were to determine if the effect was specific to the phosphate anions as well as establishing the influence, if any, of induced compressive stress in coercivity enhancement. Stoichiometric γ-Fe_2O_3 pigments were treated with aqueous solutions containing the sodium salts of different anions and the changes in coercivity measured by vibrating sample magnetometry. The surface treatments were done in an aqueous suspension, followed by water evaporation, and vacuum treatment at 150–160 °C. Sodium phosphate, sodium pyrophosphate, sodium tripolyphosphate, sodium metaphosphate, poly(sodium acrylate), and sodium *p*-toluenesulfonate were used and the weight ratio of salt to pigment was fixed at 1.5. Within the range of anions in this work, the coercivity enhancement was specific to the polyphosphate anions. The coercivity for pigments treated with sodium *p*-toluenesulfonate (273 Oe) or poly(sodium acrylate) (280 Oe) was only slightly higher than 265 Oe for the as-received pigments. For the phosphate anions, the coercivity enhancement increased in the order sodium phosphate (268 Oe), sodium pyrophosphate (287 Oe), sodium tripolyphosphate (316 Oe), sodium polyphosphate (336 Oe). To evaluate the effect of stress on the coercivity, samples treated with sodium polyphosphate were ground to a powder and then pressed into pellets. The coercivity for the samples decreased linearly with increasing applied pressure during pellet formation. Therefore applied stress does not account for the coercivity increase.

I. INTRODUCTION

The increase in coercivity of γ-Fe_2O_3 pigments by surface treatment has been the subject of ongoing scientific and technological interest. The magnetic tape industry has taken great commercial advantage of higher coercivity enhancement arising from surface treatment with cobalt(II) ions.[1] There have been reports of significant coercivity increases when γ-Fe_2O_3 was treated with polyphosphate anions.[2–8] This effect depended on the ratio of Fe^{2+} to Fe^{3+} in the pigments and on the weight ratio of polyphosphate to pigment. Slonczewski[9] has proposed a model where polyphosphate binding caused a subsurface oxidation of Fe^{2+} to Fe^{3+}, presumably pinning the Fe^{2+} state to the pigment surface. However, Mossbauer studies of non-stoichiometric pigments containing ^{57}Fe doped in the surface did not show significant increases in surface Fe^{2+} upon polyphosphate binding.[8]

The treatment of γ-Fe_2O_3 may be considered in the realm of surface coordination chemistry. The polyphosphate anion displaces coordinated water from the surface of γ-Fe_2O_3. The new ligand would modify the energy levels of the *d*-states on the surface iron. If γ-Fe_2O_3 is considered to be a heavily doped semiconductor,[10] the *d* states for the surface iron would be partially filled and would have an energy somewhere between the valence band and the conduction band. Modification of the *d* states at the surface would lead to a modification of the space charge region extending from the surface into the bulk.[11,12] If ligand binding lowers the energy of an empty *d* state, then electrons may migrate from the bulk to the surface iron. Alternatively, if ligand binding raises the level of filled *d* states, then electrons may migrate from the surface iron into the bulk. Thus, surface treatment may pin a valence state, either Fe^{2+} or Fe^{3+}, to the surface of the γ-Fe_2O_3 pigments. The pigments are acicular cylinders with a length to diameter aspect ratio greater than 5. The sides of the pigment provide a much greater surface area than the ends of the pigments, therefore there are more binding sites along the sides. If coordination of surface iron site leads to changes in electronic structure that extends into the bulk of the pigment, then the changes would be greater along the sides of the pigments. This would enhance the electronic anisotropy of the pigments and consequently the magnetic anisotropy, leading to coercivity enhancements.

In this paper we determine whether the coercivity enhancement is specific to surface treatment by polyphosphate anions. Stoichiometric γ-Fe_2O_3 pigments were treated with aqueous solution containing the sodium salts of different anions. The different anions were chosen because of their different affinity for binding to Fe^{2+} and Fe^{3+} ions. The anions were phosphate, pyrophosphate, tripolyphosphate, metaphosphate, *p*-toluenesulfonate, and polyacrylate. The polyphosphate anions present similar ligands, while the *p*-toluenesulfonate and polyacrylate are different and would present a difference in the binding constants with surface iron ions and differences in changes in electronic structure upon binding. These differences may lead to differences in coercivity enhancement for pigments treated with these different salts.

II. EXPERIMENTAL SECTION

The γ-Fe_2O_3 pigments, *K*-300, were a gift from Magnox Pulaski, Inc., Pulaski, VA. The pigments had a coercivity of 265 Oe and a specific surface area of 13.5 m^2/g. The FeO content was 0.25%, corresponding to a Fe^{2+}/Fe^{3+} ratio of 1/180.[13] The surface treatments were done in aqueous sus-

 0021-8979/94/75(10)/5565/3/$6.00 © 1994 American Institute of Physics

TABLE I. Coercivities for surface treated γ-Fe_2O_3 pigments.

Sample, surface treatment	Vacuum treatment	H_c (Oe)
As-received, no treatment	No	265
Distilled water only	Yes	270
Sodium *p*-toluenesulfonate	Yes	273
Poly(sodium acrylate)	Yes	280
Sodium phosphate	Yes	268
Sodium pyrophosphate	Yes	278
Sodium tripolyphosphate	Yes	316
Sodium metaphosphate	No	263
Sodium metaphosphate	Yes	338

pension in a manner similar to that described by Spada *et al.*[7] Sodium phosphate, sodium pyrophosphate, sodium tripolyphosphate, sodium metaphosphate, poly(sodium acrylate), and sodium *p*-toluenesulfonate were used as surface treatment agents. For all samples the weight ratio of salt to pigment was fixed to 1.5. A 1.00 g sample of γ-Fe_2O_3 was stirred with a solution containing 1.50 g of the salt dissolved in 10.00 g distilled water. The suspension was evaporated to dryness and then heat treated at 150–160 °C under 0.200 Torr vacuum for 1.0 h. A control sample was treated with distilled water only, the water evaporated, and then heat treated at 150–160 °C under 0.200 Torr vacuum for 1.0 h. A sample was treated with sodium metaphosphate, the water evaporated off, but was not subjected to hot vacuum treatment. A sample was treated with sodium metaphosphate solution, the water evaporated off, heat treated under vacuum, ground to a powder in a mortar and pestle, and then pressed into pellets at room temperature. Magnetic hysteresis loops were measured by vibrating sample magnetometry using a 10 kOe saturating field. Measurements on replicate samples gave a standard deviation in the coercivity value of 2%.

III. RESULTS

The data in Table I shows the effect of various surface treatments on the coercivity of the γ-Fe_2O_3 pigments. As-received, the pigments had a coercivity of 265 Oe. Pigments simply treated with water, dried and then heated to 150 °C under vacuum showed no increase in coercivity. Within the range of anions used in this study only the higher polyphosphate anions showed a significant increase in coercivity. There was little or no increase in coercivity for pigments treated with sodium *p*-toluenesulfonate poly(sodium acrylate), or sodium pyrophosphate. Only pigments treated with sodium tripolyphosphate and sodium metaphosphate showed a significant increase in coercivity. This coercivity enhancement required the 150 °C vacuum treatment and without this treatment, there was no coercivity increase. Pigments treated with sodium tripolyphosphate had a coercivity of 316 Oe, an increase of 15%. The largest increase in coercivity was seen for pigments treated with sodium metaphosphate, 338 Oe, a 28% increase. This increase was comparable to that reported by Spada *et al.* for stoichiometric γ-Fe_2O_3 pigments.[8]

In the course of this study it was observed that the samples, displaying coercivity enhancement, consisted of γ-Fe_2O_3 pigments fused together in a glassy matrix. However, the samples with no coercivity enhancement were fine powders. It was speculated that sodium tripolyphosphate and sodium metaphosphate treated samples consisted of γ-Fe_2O_3 pigments in a phosphate glass matrix. After heating to 150 °C and cooling the phosphate glass put the pigments under compressive stress, giving rise to a change in coercivity. To test this hypothesis samples of sodium metaphosphate treated γ-Fe_2O_3 pigments were pressed into pellets with different applied pressures. The purpose was to obtain a series of pellets where the pigments experienced different and somewhat controlled degrees of compressive stress. It was supposed that the amount of compressive stress retained in the pellets increased with increasing applied pressure. The pellets were composites of γ-Fe_2O_3 in a glassy matrix. The data in Fig. 1 shows that the coercivity decreased linearly with increasing applied pressure. Clearly increasing the compressive stress decreased the coercivity γ-Fe_2O_3 pigments and compressive stress was not responsible for the observed coercivity enhancements. Spada and co-workers[7] contended that if the coercivity enhancement has a magnetostrictive origin, then compressive stress would decrease the coercivity, a contention in agreement with our experiments. An alternative explaination is that as the applied pressure increases, the packing fraction of the pigments increases. It has been demonstrated that increasing the packing fraction of γ-Fe_2O_3 pigments, leads to a decrease in coercivity.[14]

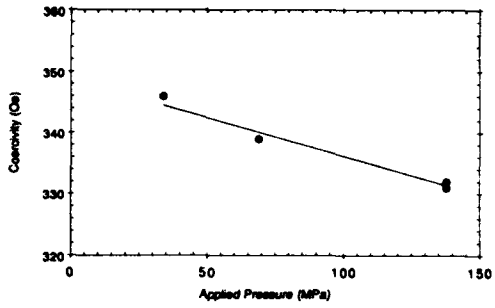

FIG. 1. Plot of coercivity as a function of applied pressure for pellets containing γ-Fe_2O_3 and sodium metaphosphate.

IV. DISCUSSION

Experimental evidence presented here and elsewhere[2–8] leads to the conclusion that coordination of certain species to iron ions the surface of γ-Fe_2O_3 pigments gave rise to changes in surface electronic states which ultimately changes the coercivity. When γ-Fe_2O_3 pigments are exposed to aqueous salt solutions, the anions must compete with water for coordination sites on the surface of the pigments. Clearly, water had a higher affinity for these surface sites than the other ions present. Only after heat treatment in vacuum, which removed the surface moisture, did the higher polyphosphate anions give rise to a coercivity enhancement. Some anions, *p*-toluenesulfonate and poly(acrylate) ions, either did not have a high enough affinity for the pigment

TABLE II. Binding constants for phosphate anion to Fe^{2+} and Fe^{3+} in aqueous solution.

Polyphosphate	anion	Fe^{2+}, log K	Fe^{3+}, log K
Phosphate	$(HPO_4)^{2-}$	7.03[a]	9.35[d]
Pyrophosphate	$(H_2P_2O_7)^{4-}$		6.62[a]
Tripolyphosphate	$(H_2P_3O_{10})^{3-}$	2.54[b]	7.03[f]
Metaphosphate	$(P_nO_{3n+1})^{(n+2)-}$ $n\sim5$	3.0[c]	6.5[c]

[a]Reference 15.
[b]Reference 18.
[c]Reference 20.
[d]Reference 16.
[e]Reference 17.
[f]Reference 19.

surface or, if they did have an adequate affinity, binding did not lead to significant coercivity enhancement. It is intriguing that the phosphate anions did not all show the same degree of coercivity enhancement. They all present a similar ligand to the iron and one would expect similar changes in surface iron electronic states upon binding. However, coordination of phosphate anion to iron is thermodynamically reversible and water may rapidly displace the surface bound phosphate ions. The chelating of the higher polyphosphate anions to multiple sites on the surface of the pigments slows down the kinetics for water displacement and therefore allows one to observe coercivity enhancement with the higher phosphate anions.

There is little information about the coordination chemistry of surface iron sites on γ-Fe_2O_3 pigments. However, the coordination behavior of Fe^{2+} and Fe^{3+} in aqueous solution has been well characterized and may provide some insight into possible reactions on the surface of γ-Fe_2O_3. Coordination of a phosphate anion to an iron ion involves displacement of a water ligand, as indicated in Eq. (1). The data in

$$[Fe^{n+}(OH_2)_6]+L\rightarrow[Fe^{n+}L(OH_2)_5]+H_2O \quad (1)$$

Table II show the binding constants for coordination of different phosphate species to Fe^{2+} or Fe^{3+}. Each different phosphate anion has a higher binding constant, therefore a higher affinity, for Fe^{3+} than for Fe^{2+}. This leads to the conclusion that the phosphate anion would preferentially bind to surface Fe^{3+} sites on the pigments. In the coordination chemistry literature it is well-known that the reduction potential for a transition metal ion in solution greatly depends on the ligands coordinated to that ion. In aqueous solution $[Fe^{3+}(OH_2)_6]^{3+}$ has a one-electron reduction potential of +0.77 V.[21] When coordinated with phosphate ion, the resultant complex ion has a one-electron reduction potential of +0.61 V. Clearly, in aqueous solution, phosphate binding somewhat stabilizes the Fe^{3+} state. One could conclude that the polyphosphate anions would preferentially coordinate to Fe^{3+} sites on the pigment surface and that polyphosphate coordination would stabilize the Fe^{3+} state at the surface. However, such extrapolations from properties in aqueous solution to solid state surface properties are hazardous. These observations clearly point to the need to fully characterize the surface coordination chemistry of iron in γ-Fe_2O_3 pigments.

[1] E. Koster and T. C. Arnoldussen, *Magnetic Recording*, edited by C. D. Mee and E. D. Daniel, Technology, Vol I (McGraw–Hill, New York, 1987), p. 98.
[2] F. Itoh and M. Satou, Jpn. J. Appl. Phys. **14**, 2091 (1975).
[3] F. Itoh and M. Satou, J. Chem. Soc. Jpn. **1976**, 853.
[4] F. Itoh, T. Kaneko, and M. Satou, J. Chem. Soc. Jpn. **1976**, 1319.
[5] F. Itoh and M. Satou, J. Chem. Soc. Jpn. **1977**, 581.
[6] F. Itoh, M. Satou, and Y. Yamazaki, IEEE Trans. Magn. **MAG-13**, 1385 (1977).
[7] F. E. Spada, A. E. Berkowitz, and N. T. Prokey, J. Appl. Phys. **69**, 4475 (1991).
[8] F. E. Spada, F. T. Parker, C. Y. Nakamura, and A. E. Berkowitz, J. Magn. Magn. Mater. **120**, 129 (1993).
[9] J. C. Slonczewski, J. Magn. Magn. Mater. **117**, 368 (1992).
[10] J. P. Suchet, *Crystal Chemistry and Semiconduction in Transition Metal Binary Compounds* (Academic, New York, 1971).
[11] A. Many, Y. Goldstein, and N. B. Grove, *Semiconductor Surfaces* (North-Holland, Amsterdam, 1965).
[12] D. R. Frankl, *Electrical Properties of Semiconductor Surfaces* (Pergamon, New York, 1967).
[13] Information taken from product specifications sheet and from private communication.
[14] S. Umeki, H. Sugohara, Y. Taketomi, and Y. Imaoka, IEEE Trans. Magn. **MAG-17**, 3014 (1981).
[15] S. C. Lahiri and S. Aditya, Ind. J. Chem. **41**, 517 (1964).
[16] O. E. Lanford and S. J. Kiehl, J. Am. Chem. Soc. **64**, 291 (1942).
[17] L. P. Andrusenko, Z. A. Sheka, and I. A. Sheka, Zhur. Neorg. Khim. **11**, 1266 (1966).
[18] C. F. Wells and M. A. Salam, J. Chem. Soc. A **1968**, 308.
[19] L. P. Andrusenko and I. A. Sheka, Zhur. Neorg. Khim. **13**, 2645 (1968).
[20] J. R. Van Wazer and D. A. Campanella, J. Am. Chem. Soc. **72**, 655 (1950).
[21] F. Basolo and R. G. Pearson, *Mechanisms of Inorganic Reactions* (Wiley, New York, 1958), p. 61.

Electrochemical evaluation of the effect of binder additives on iron corrosion

J. Carlos Arroyo, Hassan M. Saffarian, and Garry W. Warren
Center for Materials for Information Technology and Department of Metallurgical and Materials Engineering, University of Alabama, Tuscaloosa, Alabama 35487

Recent research efforts have emphasized the archivability of metal particle media which utilizes "passivated" iron particles as the magnetic material. Two fundamental processes limit the archival lifetime of such media (1) corrosion of metal particles, and (2) degradation of polymer binder. This paper addresses the first process by quantifying the effect of *p*H and various binder additives (lubricant, dispersant, polymer degradation products, etc.) on the corrosion of pure iron in aqueous 0.05 M K_2SO_4. This study is unique in its use of electrochemical techniques to adequately quantify the corrosion process. Both ac [electrochemical impedance spectroscopy, (EIS)] and dc polarization techniques have been used. Experimental data showed that the addition of stearic acid (a lubricant) and lecithin (a dispersant) resulted in a decrease in the corrosion rate of iron in K_2SO_4. Five different carboxylic acids of various chain lengths were investigated since such compounds can be viewed as simple models for binder additives, or as polymer degradation products. Except for stearic acid, all of the carboxylic acids significantly accelerated iron dissolution at the corrosion potential. The corrosion rate increased as chain length or *p*H decreased and as acid concentration increased. The charge involved in passive film formation increased as the solution becomes more acidic, indicating that the passive film was less stable or more difficult to form. In the passive region the corrosion rate was lower than that of the base electrolyte for high concentrations of carboxylic acids.

I. INTRODUCTION

High density metal particle (MP) tape used in various formats (e.g., D-2, R-dat, 8 mm), is a leading candidate for mass storage systems. With regard to an evaluation of the archivability of MP tape, two important aspects which must be considered are (1) corrosion of the metal particles and (2) degradation of the polymer binder. The first is unique to metallic media, e.g., MP, metal evaporated, and the second is common to many forms of flexible media. In addition, degradation of the polymer binder may well affect the corrosion of metal particles. Reports of corrosion failure for MP tape under conditions of environmental stress are conflicting. For example, in one study,[1] exposure at 60 °C and 90% RH resulted in relatively small changes in bulk magnetic properties (M_s, M_r, and H_c). In another study,[2] exposure of MP tape to 60 °C and 90% RH resulted in large changes in bulk magnetic properties.

The nature of much of the previous work has involved measurement of magnetic properties or recording performance of MP tape before and after exposure to elevated temperature and humidity. In many cases this was done with no attempt to control pollutant gases.[1,3,4] In others, pollutant gases were carefully controlled through the Battelle class II environment (30 °C, 70% RH, 10 ppb Cl_2, 10 ppb H_2S and 100 ppb NO_2).[2,5] The degradation of passivated metal particles, separate from tape, were also examined as a function of RH and temperature.[6] Very little research has been reported where electrochemical techniques have been employed.

This paper reports the results of a basic research project aimed at understanding the role which binder components and additives, and *p*H play in the corrosion of iron in MP media. Since it is difficult to directly examine iron particles electrochemically, an iron rod was used as a model electrode. Both ac and dc electrochemical techniques have been used to examine the effects of various organic materials, i.e., carboxylic acids and lecithin, on iron corrosion. Depending on chain length, these materials may be viewed as either model binder additives or binder degradation products.

II. EXPERIMENTAL

An iron electrode with a cross sectional area of 0.20 cm^2 was prepared from a 5 mm diam rod (Johnson Matthey 99.9985%) imbedded in epoxy. Surface preparation of the Fe electrode consisted of mechanical polishing with 600 grit SiC paper, ultrasonic cleaning in water and drying in air. Aqueous solutions of various organic materials including a model lubricant and dispersant, stearic acid and lecithin, were prepared in 0.05 M K_2SO_4 by dissolving reagent grade chemicals in deionized water. Solutions were deaerated by purging with nitrogen for ~1 h prior to the experiments, and a nitrogen blanket was maintained over the solutions during the measurements. Solution *p*H was adjusted to the desired value before deaeration. Experiments were performed in a glass cell with a three electrode system: (a) iron working electrode, (b) platinum (2.5×1.2 cm) counter electrode, and (c) a saturated calomel reference electrode (SCE).

The corrosion potential of the iron samples was allowed to reach steady state prior to all experiments. Both ac and dc electrochemical experiments were performed. Impedance measurements were conducted at the open circuit potential using a Solartron 1255 frequency response analyzer and 1286 potentiostat with associated computer and ZPLOT software. dc potentiodynamic anodic polarization curves were obtained with an EG&G 273A potentiostat and M352 corrosion software, by sweeping the potential at 1 mV/s from the open circuit value to about 1.5 V vs SCE and measuring the current response.

 0021-8979/94/75(10)/5568/3/$6.00 © 1994 American Institute of Physics

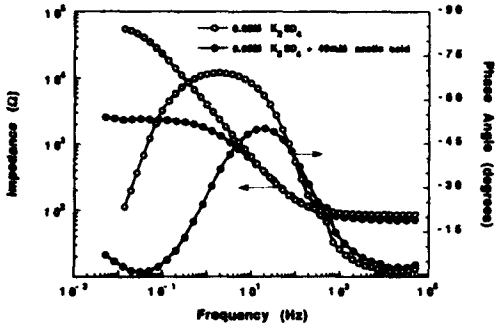

FIG. 1. Bode plots showing the impedance magnitude and phase angle behavior of iron in 0.05 M K_2SO_4 measured at E_{corr} in the presence and absence of acetic acid, pH=6.0.

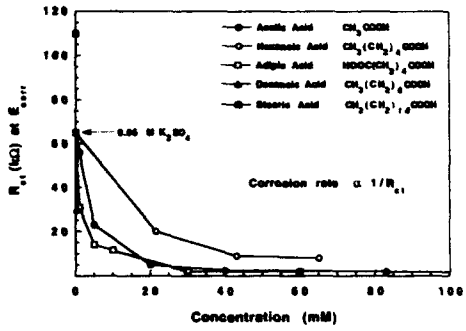

FIG. 3. Effect of different carboxylic acids on the charge transfer resistance of iron in 0.05 M K_2SO_4, pH=6.0.

III. RESULTS AND DISCUSSION

A. ac impedance results

The effect of various carboxylic acids, used as both model binder additives and polymer binder degradation products on iron corrosion was investigated by the impedance technique at the open circuit or corrosion potential, E_{corr}. Since the addition of carboxylic acids lowers the pH, all solutions were adjusted to a constant pH of 6, the natural pH of the 0.05 M K_2SO_4 base electrolyte. Impedance data can be displayed several different ways. For example, Fig. 1 shows the impedance and phase angle data for iron in 0.05 M K_2SO_4 in the presence and absence of 40 mM acetic acid. A significant decrease in impedance in the presence of 40 mM acetic acid relative to the base electrolyte is indicative of a decrease in corrosion resistance. Impedance data for a series of acetic acid concentrations are also shown in Fig. 2 in a typical complex impedance format or Nyquist plot. Fitting each set of data in Fig. 2 to a semicircle yields the value of charge transfer resistance, R_{ct}, which is inversely proportional to corrosion rate.

Data similar to that shown in Figs. 1 and 2, were also collected for other carboxylic acids, and a summary of the R_{ct} values thus obtained is shown in Fig. 3, as a function of concentration and chain length of each acid. In general, the iron corrosion rate in 0.05 M K_2SO_4, measured at E_{corr} and pH=6, increases with increasing concentration and with decreasing chain length for carboxylic acids containing 2–10 carbons. However, in the presence of stearic acid (18 carbons), often used as a lubricant in the formulation of metal particle tape, a significant increase in R_{ct} was observed, indicating a higher resistance to corrosion.

The corrosion rate of iron was also affected by the number of acidic groups in the molecule. As shown in Fig. 3, R_{ct} values, at constant concentration and pH are consistently higher in hexanoic (a monocarboxylic acid) than in adipic (a dicarboxylic acid) while both contain six carbons. Similar to stearic acid, lecithin was also observed to have an inhibiting effect on corrosion as shown in Table I. The inhibitive effect of lecithin on iron corrosion was a linear function of concentration in the range of 0%–0.005% w/v (aqueous solubility limit).

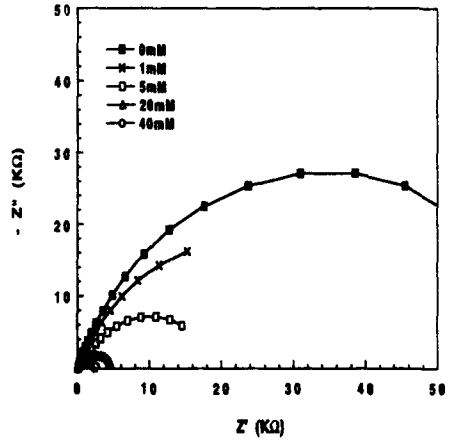

FIG. 2. Nyquist plots for iron at E_{corr} in 0.05 M K_2SO_4 for various concentrations of acetic acid, pH=6.0.

B. dc results

Potentiodynamic polarization curves for iron in various concentrations of acetic acid are shown in Fig. 4. The corrosion behavior of iron in the "active region," at potentials below ≈−0.2 V (vs SCE), is similar to that observed during

TABLE I. Charge transfer resistance, R_{ct}, of iron in 0.05 M K_2SO_4 as a function of lecithin concentration.

Conc. lecithin (wt/vol%)	R_{ct} (KΩ)
0	65
0.0025	100
0.0050	130

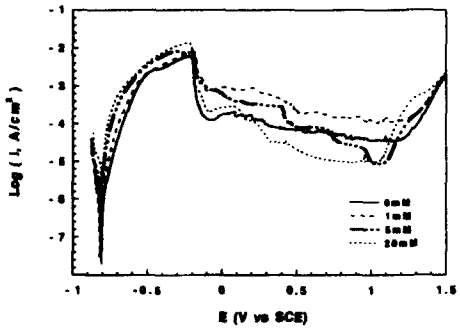

FIG. 4. Potentiodynamic polarization curves for iron in 0.05 M K_2SO_4 for various concentrations of acetic acid at $pH=6.0$. Scan rate 1 mV/s.

TABLE II. Effect of carboxylic acid concentration and pH on the charge involved in the passivation of iron in 0.05 M K_2SO_4.

Carboxylic acid	Conc. (mM)	pH	Charge (Coul)
None	0	3.5	3.30
	0	6.0	0.29
	0	9.5	0.22
Acetic	1	6.0	0.38
	5	6.0	0.51
	20	6.0	0.66
	20	3.5	9.7
Adipic	1	6.0	0.31
	5	6.0	0.43
	20	6.0	0.3
	20	4.0	7.9
	20	10.0	0.002

impedance measurements, i.e., increasing acetic acid concentration results in higher currents or higher corrosion rates. This behavior is probably associated with the formation of soluble corrosion products (iron salts and/or complexes) which allow continuous dissolution of iron. Since the solubility of iron carboxylates decreases with increasing the chain length, a reduction in corrosion rate is expected for acids with longer chain length such as stearic acid.

At more anodic potentials, in the passive region, passivation or oxide formation prevails, and the currents are decreased significantly. In this potential range, current depends on the carboxylic acid concentration and becomes even lower than that of the base electrolyte at higher concentrations. This behavior may be due to the formation of a salt film at the interface. The charge involved in the formation of the passive film on iron was affected by solution pH and acid concentration as shown in Table II.

As pH decreased, the charge involved in the formation of the passive film increased and the passivation potential was also observed to shift to more anodic values. In other words, the passive film is less stable or more difficult to form as the solution pH is lowered. The passivation charge also increased with increasing acid concentration but the effect was not as pronounced as in the case of pH, see Table II.

IV. CONCLUSIONS

The effect of various additives on the corrosion of iron in 0.05 M K_2SO_4 has been studied by electrochemical impedance spectroscopy and dc polarization techniques. At the corrosion potential, all carboxylic acids except stearic acid (a lubricant) accelerate corrosion. Stearic acid even at a concentration ≤ 2 ppm resulted in a marked reduction in corrosion rate. The corrosion rate increased as the acid concentration increased and as the hydrocarbon chain length or pH decreased. In the presence of lecithin (a dispersant), iron corrosion was significantly decreased and the inhibitive effect was a linear function of lecithin concentration.

When the electrode was polarized in the anodic direction, the charge involved in the formation of the passive film increased as pH decreased and as acid concentration increased, but pH seems to be the dominant factor. In the passive region, however, a different behavior was observed and the corrosion rate was lower than that of the base electrolyte for high concentrations of carboxylic acids. These results indicate that carboxylic acids accelerate the corrosion of unpassivated iron, but might inhibit the corrosion of passivated iron particles.

[1] Y. Yamamoto, K. Sumiya, A. Miyake, M. Kishimoto, and T. Taniguchi, IEEE Trans. Magn. MAG-26, 2098 (1990).
[2] D. Speliotis, IEEE Trans. Magn. MAG-26, 124 (1990).
[3] M. Mathur, G. Hudson, and L. Hackett, IEEE Trans. Magn. MAG-28, 2362 (1992).
[4] Y. Okazaki, K. Hara, T. Kawashima, A. Sato, and T. Hirano, IEEE Trans. Magn. MAG-28, 2365 (1992).
[5] A. Djalali, D. Seng, W. Glatfelter, H. Lambropoulos, J. Judge, and D. Speliotis, J. Electrochem. Soc. 138, 2504 (1991).
[6] M. Mathur, G. Hudson, R. Martin, W. McKinley, and L. Hackett, IEEE Trans. Magn. MAG-27, 4675 (1991).

Molecular dynamics of magnetic particulate dispersions

P. A. Deymier, C. Jung, and S. Raghavan
Department of Materials Science and Engineering, University of Arizona, Tucson, Arizona 85721

A computational investigation using the method of molecular dynamics was undertaken to characterize the state of magnetic particle dispersions. The simulations revealed that the microstructure of spherical particulate dispersions consists of chainlike clusters resulting from magnetic dipole alignment. Acicular particles formed clusters such as dimers, chains, and rings. The effect of fluid viscosity on the dispersion quality and the response of the magnetic dispersions to an external DC magnetic field are also reported.

I. INTRODUCTION

The dispersion quality and stability of magnetic particle dispersions (magnetic inks) is controlled by the balance between attractive and repulsive forces between particles in a dispersion medium of a specific chemistry. The attractive forces arise from van der Waals and magnetic interactions whilst the electrostatic and steric interactions give rise to repulsive forces between particles. Calculations have shown that van der Waals and electrostatic contributions to the total energy of interaction between particles are much smaller than the other two forces.[1,2]

The classical energy of interaction–distance plots found in colloid chemical literature are useful in predicting whether a dispersion is stable or not but do not yield information on the dispersion quality (i.e., presence of magnetic agglomerates), especially as a function of time. One computational method which can yield information on the dispersion quality of a magnetic particulate dispersion is molecular dynamics (MD). In this method, the state of a system of interacting particles is simulated by solving the classical equations governing the motion of each individual particle.

II. METHOD AND MODEL

The total energy for a system containing N interacting magnetic particles is the sum of a kinetic energy and a potential contribution. The kinetic energy consists of two parts: translational and rotational. In our model, the potential energy includes only magnetic attractive and steric repulsive energies.

The magnetic interaction energy for spherical particles is based on the magnetic dipole–dipole interaction and is given by

$$U_{\text{mag}}=\sum_{j>i}^{N}\sum_{i=1}^{N-1}\frac{\mu_0}{4\pi}\frac{1}{|\mathbf{r}_{ij}|}\left(\mathbf{m}_i\cdot\mathbf{m}_j-\frac{3}{r_{ij}^2}(\mathbf{m}_i\cdot\mathbf{r}_{ij})(\mathbf{m}_j\cdot\mathbf{r}_{ij})\right), \tag{1}$$

where $\mathbf{m}$ is the magnetic moment, μ_0 is the permeability, and $\mathbf{r}_{ij}$ is the separation vector between spherical particles. For the calculation of the magnetic interaction energy between cylindrical particles, a pole–pole interaction approach is used and the resulting expression is as follows:

$$U_{\text{mag}}=\sum_{k=1}^{2}\sum_{l=1}^{2}\sum_{j>i}^{N}\sum_{i=1}^{N-1}\frac{\mu_0}{4\pi}\frac{P_i(k)P_j(l)}{r_{ij}(k,l)}, \tag{2}$$

where $r_{ij}(k,l)$ is the separation distance between poles of two different particles i and j, and P is the pole strength. Signs of the magnetic energy for cylindrical particles is determined by the signs of the interacting poles.

Available expressions for the calculation of steric repulsion energy between dispersant coated spherical particles are rather complex and require quantities that are not easily measured. Hence, a simple form of steric repulsion energy is employed in this simulation and is given by a truncated parabola:

$$U_{\text{st}}=\sum_{j>i}^{N}\sum_{i>1}^{N-1}\Phi_{ij}^{s}=\sum_{j>i}^{N}\sum_{i>1}^{N-1}A(r_1-r_{ij})^2,\quad\text{if}\quad r_{ij}\leq r_1. \tag{3}$$

The parameters A and r_1 are chosen such that the equilibrium center-to-center distance between two particles is no less than $2.3a$, where a is the radius of a particle.

The steric interaction energy between two cylindrical particles, i and j, is also represented by a truncated parabola

$$\Phi_{ij}^{s}=A\cdot(r_1-r_s)^2,\quad\text{if}\quad r_s\leq r_1, \tag{4}$$

where r_s is the minimum distance of separation between the longitudinal axis of the particles. The parameters A and r_1 are also chosen to simulate a steric layer of thickness $0.15a$.

The equations of motion of each particle have two forms: (1) translational ($M d^2\mathbf{r}_i/dt^2=\mathbf{F}_i$) and (2) rotational ($I d\boldsymbol{\omega}_i/dt=\mathbf{T}_i$), where $\mathbf{F}_i$ is the force on particle i, I is the moment of inertia, $\boldsymbol{\omega}_i$ is the angular velocity, and $\mathbf{T}_i$ is the torque. In the case of spherical particles, the torque arises from the magnetic interactions, whereas for cylindrical particles, both magnetic and steric contributions to the torque have to be taken into account. For spherical particles a drag term can be included in the translational equation of motion by adding to the force a term in the form $-6\pi a\eta\mathbf{V}_i$, where η is the viscosity of the fluid and $\mathbf{V}_i$ is the translational velocity of particle i. At this stage, rotational motion in a viscous fluid is not accounted for.

To study the dynamical and structural response of the magnetic dispersions containing spherical particles to an external dc field, we include the contribution of an external torque, $\mathbf{T}_{\text{ext}}$ ($=\mathbf{m}_i\times\mathbf{B}$, where $\mathbf{B}$ is the applied dc field), to the rotational equation of motion.

For both spherical and cylindrical geometries, the dipole moment is assumed to be attached physically to the particle. In the latter case the moment is parallel to the long axis of the cylindrical particle. Instead of Euler angles, the orientation of the particles is described by a set of four parameters

 0021-8979/94/75(10)/5571/3/$6.00 © 1994 American Institute of Physics

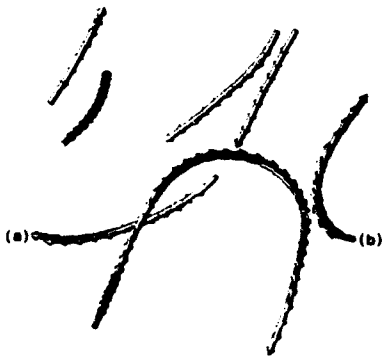

FIG. 1. Relaxing configuration of a suspension of spherical particles after 4000 integration time steps in absence of fluid viscosity and external field. (a) and (b) mark two ends of chains linked through periodic boundary conditions.

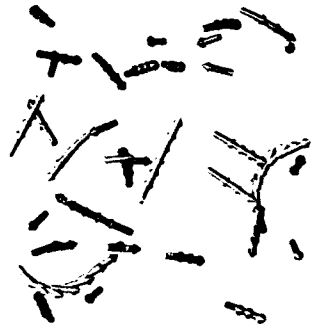

FIG. 2. Suspension of spherical particles at step 6000 in a fluid with a viscosity of 0.001 P.

(quaternions) developed by Evans *et al.*[3] Contrary to Euler angles, these parameters lead to equations of motion without singularity.[4]

Our simulation system is a three dimensional box with an edge length of $50a$ containing 100 particles ($N=100$). A periodic boundary condition is used. The physical and magnetic properties of magnetic particles are $M=3\times10^{-18}$ kg, $a=500$ Å, $m=380$ emu/cm^3 ($=4.75\times10^{-16}$ A m^2), and adsorbed polymer layer thickness=75 Å. In the case of cylindrical particles, the radii of the hemispheric tip and of the cylindrical body are assumed to be 500 Å with an aspect ratio of 2:1. The equations of motion are solved numerically using a finite difference approximation for the time derivatives. The time integration step in these simulations is 6.76×10^{-9} s. All simulations were carried out under the constraint of a constant kinetic energy of 1.66×10^{-22} J/particle.

III. RESULTS AND DISCUSSION

In all the simulations reported in this article, the same initial set of positions and magnetic moment orientations were used. The orientations were generated at random according to a normal distribution. Random numbers were also used for the positions of each particle. However, random positions leading to overlapping pairs of particles were excluded.

A. Spherical particles

Three simulations were conducted under the following conditions: (A) time=4000 integration steps, no fluid viscosity, and no external magnetic field; (B) time=6000 integration steps, viscosity=0.001 P, and no external field; and (C) time=4000 integration steps, zero fluid viscosity, an external magnetic field of 300 Oe applied after 2000 time steps.

Figure 1 shows the structure of the magnetic dispersion at the final stage in simulation A. In the case of spherical particles, minimization of energy takes place by alignment of magnetic moments. Here the particles form chains with nearly aligned dipole moments. Obviously, the lowest energy state corresponds to a single infinite chain. In our simulation such a state can be approached at large time steps. It may be noted that the periodic boundary condition imposed on the simulation cell permits a chain from exiting the cell from one side and reentering it on the other side. This feature is clearly seen in Fig. 1.

Simulation B was run to test the effect of fluid viscosity on the state of the dispersion. An increase in viscosity of the dispersion medium augments the time for relaxation. Minimization of energy is achieved by the formation of chains of particles in the initial stage of the calculation. However, since the motion of chains is more sluggish than that of single particles, further energy minimization by attachment of pieces of chains is strongly impeded by the fluid viscosity. The resulting suspension is therefore only composed of short pieces of chains as shown in Fig. 2, this despite the longer simulation time.

In Fig. 3 we illustrate the final structure of a suspension subjected to an external magnetic field (simulation C). The stimulation of the suspension with a magnetic field results in a strong structural anisotropy. Here, upon application of the field after 2000 time steps, those long chains of spherical particles which were perpendicular to the field break off into pieces which subsequently align with the field. All other

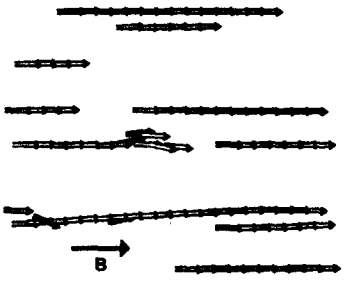

FIG. 3. Orientation of chains of spherical particles in an external magnetic field, B, of 300 Oe.

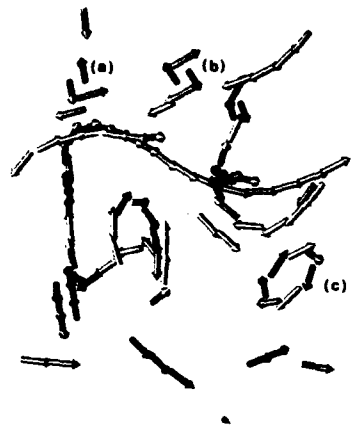

FIG. 4. Suspension of acicular particles after 4000 integration time steps (see text for details).

chains respond to the stimulus by directly aligning in the direction of the external field. Attachment of chains to form longer chains is also observed.

B. Acicular particles

The lowest energy state formed by two acicular particles interacting through pole–pole interactions can be shown to be a dimer with magnetic moments in opposite directions. A configuration composed of aligned particles constitutes only a metastable state. Moreover, rings of three, four,..., particles with opposite poles in contact are more stable than linear chain configurations. A simulation of 100 acicular particles with an aspect ratio of 2:1 was run for a period of 4000 integration steps. The final configuration of the suspension of acicular particles is shown in Fig. 4. As expected, stable dimers and rings are observed. For instance, a dimer, a four-particle ring, and a seven-particle ring are labeled on the figure as (a), (b), and (c), respectively. Similar ring configurations have already been observed in Monte Carlo calculations of dispersion of acicular magnetic particles with an aspect ratio of 10:1.[5] In addition to the observation of stable ring configurations, metastable pieces of chains are also seen. The structure of the suspension of acicular particles also shows aggregated configurations involving dimers, rings, and pieces of chains.

IV. CONCLUSION

We have developed a computational tool to understand at the microscopic level the dynamical behavior of dispersions of magnetic particles. The preliminary results reported in this article show the potential of the MD method to simulate the structure and behavior of dispersions of magnetic particles. Of particular interest are the relationships between particle geometry, steric repulsion, and the stability of the suspension. Further refinement of the model such as the inclusion of the translational and rotational motion of acicular particles in a viscous medium will lead to future progress in the understanding of the complex rheology of magnetic suspensions.

ACKNOWLEDGMENTS

We would like to gratefully acknowledge M. Landis of the Computer Center and Information Technology at the University of Arizona for his assistance in data visualization. Partial financial support from the IBM Corp. is also gratefully acknowledged.

[1] V. Novotny, Colloids Surf. **24**, 361 (1987).
[2] M. C. A. Mathur, S. Raghavan, and C. Jung, Adv. Info. Storage Syst. **1**, 337 (1991).
[3] D. J. Evans and S. Murad, Mol. Phys. **34**, 327 (1977).
[4] H. Goldstein, *Classical Mechanics* (Addison–Wesley, Reading, MA, 1971), Chap. 4.
[5] G. N. Coverdale, R. W. Chantrell, A. Hart, and D. Parker, J. Magn. Magn. Mater. **120**, 210 (1993).

A computer simulation of the microstructure of a particulate dispersion

G. N. Coverdale and R. W. Chantrell
Keele University, Keele, Staffordshire, ST5 5GB, United Kingdom

A. Hart and D. Parker
University of Central Lancashire, Preston PR1 2TQ, United Kingdom

A computational simulation of a dispersion of iron particles undertaken to study the influence of the magnetostatic interactions on the microstructure of a particle ensemble is reported herein. The simulation considers an equilibrium state derived from an initial random state by the force-bias Monte Carlo technique. This method favors particle moves in the direction of the magnetostatic forces. A three dimensional ensemble in zero field and a saturating field are studied. An approach which takes into account the magnetostatic interactions between clusters by allowing Monte Carlo moves of whole clusters has been developed. This approach leads to the formation of extended networks consisting of particles in strongly bound clusters which themselves interact and give rise to an extended network. This is similar to the long-range order observed in practical dispersions. The structure analysis is found to characterize the local order, being especially sensitive to anisotropy in the order produced by an aligning field.

I. INTRODUCTION

Little is known at present about the microstructure of a magnetic dispersion and its influence in determining the characteristics that reflect the quality of particulate recording media.[1] We have undertaken a computational study[2] designed to investigate the influence of the magnetostatic interaction on the equilibrium configuration of an assembly of 1000 elongated iron particles. The particles have a length of 0.25 μm and aspect ratio 10:1, exhibiting a bulk magnetization of 1700 emu/cc, and are modeled as spherocylinders. The magnetostatic properties are approximated by a magnetic pole sited at the center of each hemisphere since the $\approx$10% volume packing fraction does not lend itself to the usual dipole approximation. The computation cell is extended using periodic boundary conditions.

We have employed a short-range surface potential to simulate the surfactant layer. This potential acts as a nonrigid barrier to surface–surface contact, effective when the separation distance falls below 50 Å.

The combination of the magnetostatic and the surface potential determines the energetic behavior of the particle. It can be seen, Fig. 1, that the interaction is effectively magnetostatic and attractive until the particle separation decreases to 0.025, $\approx$60 Å. Then surface potential begins to take effect, providing an effective barrier to particle overlap. At equilibrium, the position of the particle will tend to fluctuate about the minimum of the potential well at $\approx$50 Å.

The behavior of the system appears to be determined, to a first approximation, by the near particle interactions and for this computation we have employed a magnetostatic potential with a spherical cutoff.

The particles are placed in the three-dimensional (3D) computation cell by an algorithm which ensures a random spatial and angular distribution. The force-bias Monte Carlo[3] scheme is used to derive an equilibrium configuration. The scheme employs the forces and torques derived from the magnetostatic and surface potentials to influence the path of the particle in the computation cell.

During the computation, particles are found to associate due to magnetostatic attraction and form groups that are energetically bound. If we consider two such bound particles, it is clear that the action of external forces will result in some form of cooperative behavior. Thus, for a short time at least, the two particles will migrate within the dispersion as a pair. The cooperative behavior of particles on a larger scale will contribute to the physical and magnetic properties of the dispersion. Thus from a physical perspective, it is important to take this effect into account during the simulation.

For this reason, we subject the particle ensemble to a cluster analysis which allocates particles with a low mutual magnetostatic energy to a cluster. A cluster is then treated as a rigid body which may undergo small displacements and rotations in the computation cell under the Monte Carlo scheme.

This approach gives rise to the concept of a mutual magnetostatic energy of a cluster and the interaction energy of a cluster with another cluster or particle.

II. RESULTS

The recognition of the importance of clusters forms the basis for investigating the equilibrium configuration.

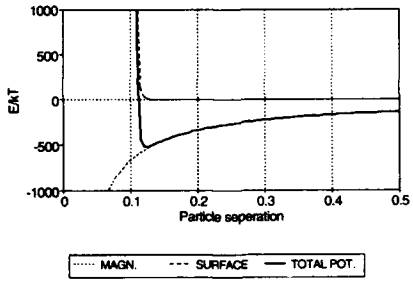

FIG. 1. The pole–pole and surface interaction potential with pole separation in units of one particle length.

 0021-8979/94/75(10)/5574/3/$6.00 © 1994 American Institute of Physics

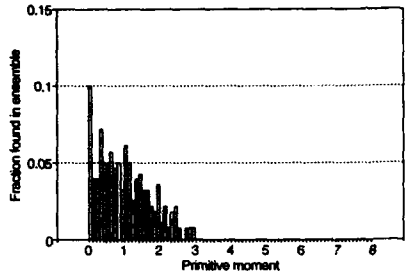

FIG. 2. The frequency distribution of cluster moments derived in zero field.

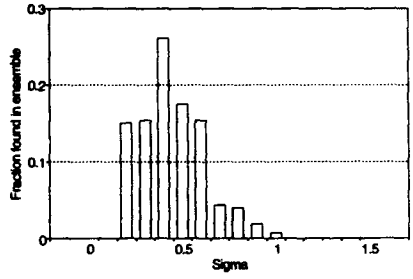

FIG. 4. The frequency distribution of the structure parameter Σ for the clusters derived in zero field.

As a simple parameter characterizing a cluster, we have defined a primitive magnetic moment calculated as the vector sum of the moments of individual particles normalized with respect to (w.r.t.) a single particle moment.

In an equilibrium configuration with no external field, Fig. 2, we find that clusters with a low primitive moment tend to be the most common, suggesting that the particles tend to cluster with particle orientations that yield a low net cluster moment. This is probably due to flux closure which alows a minimization of the magnetostatic energy in zero field.

The effect of particle alignment is clearly seen in an ensemble subject to a saturating applied field. The distribution of the cluster moments is strongly discretised at values corresponding to whole multiples of a single particle moment. Clearly the primitive moment is a useful parameter characterizing the form and extent of clustering.

The relative size and shape of a cluster has also been investigated with a function devised to compare its geometry with a straight chain. Consider a cluster of N particles 1,2,...,N where the distance between the center of particle n and particle m is denoted r_{nm}. We ascribe a correlation parameter σ to the cluster with N members, where

$$\sigma=\sum_{\text{all } n}\sum_{m>n} r_{nm}. \tag{1}$$

σ can be calculated for any arbitrary geometry. A measure of the compactness of the cluster is obtained by normalizing this value w.r.t. σ_N defined as σ for N particles arranged as a chain. Thus

$$\Sigma=\frac{\sigma}{\sigma_N}, \tag{2}$$

which may be interpreted as a measure of the extension of the cluster. A true chain will yield $\Sigma=1$ whilst a cluster with particle centers in close proximity will yield a smaller Σ; e.g., $\Sigma=0.375$ for a closed triangle of particles. It should be emphasised that Σ does not yield specific information about cluster geometry but is a useful measure for the concept of "compactness," particularly when considered in conjunction with other data such as the cluster moment distributions of Fig. 2 and Fig. 3. The normalized distribution of Σ values for the ensemble of Fig. 2 are shown in Fig. 4. The ensemble is shown to exhibit few chain clusters and the more compact configurations predominate. A similar analysis for the ensemble of Fig. 3 is shown in Fig. 5. Here the large number of straight chains is indicated by the peak at $\Sigma=1$.

A different type of analysis on the ensemble has been made by a simulated stereological technique. The method we have employed may also be used to analyze micrograph sections taken of particulate media. A series of parallel lines are drawn across the surface of the micrograph. A filament

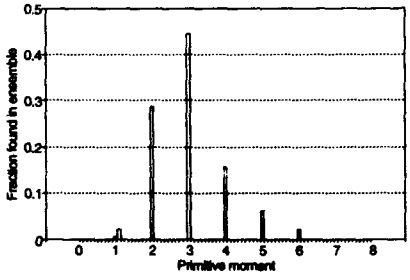

FIG. 3. The frequency distribution of cluster moments derived in a saturating field.

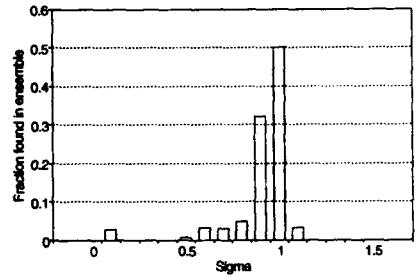

FIG. 5. The frequency distribution of the structure parameter Σ for the clusters derived in a saturating field.

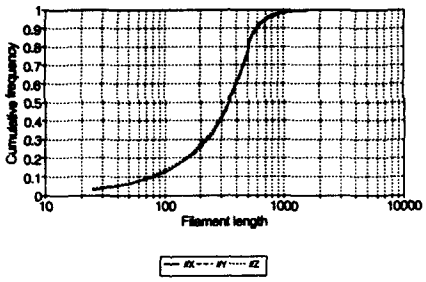

FIG. 6. The cumulative frequency distribution of filament length in zero field, sampling parallel to the X, Y, and Z axes of the computational cell. (Unit of length=Å).

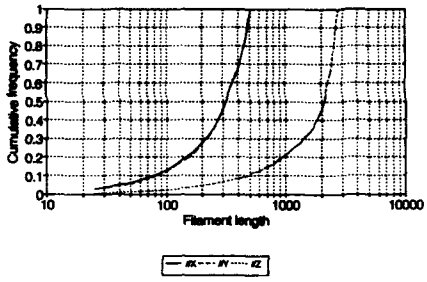

FIG. 7. The cumulative frequency distribution of filaments in a saturating field. (Unit of length=Å.)

length is obtained by measuring a section of a line where it intersects a particle. Three distributions of filament length may be obtained for the 3D ensemble by taking lines parallel to the X, Y, and Z axis. In zero field, Fig. 6, little variation is to be seen for the three directions, confirming the isotropic nature of the particle spatial and angular distribution.

In experimental dispersions, the application of a saturating field produces anisotropic chainlike structures. This feature is also reproduced by the simulation. In Fig. 7, the anisotropy is indicated by the different stereology in the Z direction. Consideration of Figs. 3 and 5 suggests that the anisotropy is due to the formation of chainlike structures in the field direction. The stereology distributions in the X and Y directions are found to be similar as may be expected from symmetry considerations.

III. CONCLUSION

The dispersion simulation was influenced by the cooperative behavior of small groups of particles resulting from the strong magnetostatic interactions. We were able to take account of this behavior by using a cluster analysis technique to identify clusters of particles exhibiting low mutual interaction energy. These clusters were then integrated into the Monte Carlo scheme for a few trial moves together with the usual single particle trial moves. It was found to be important to maintain an ongoing cluster reallocation by regular use of the cluster analysis algorithm.

Characterization of the microstructure of the equilibrium configuration is also assisted by recognizing the presence of clusters. The dispersion has been analyzed in terms of the primitive magnetic moment and the geometry of each cluster. Cluster analysis is therefore an important step in the simulation process for strongly interacting systems.

Finally we have analyzed the microstructure by means of stereological techniques. In principle the techniques are also applicable to experimental microscopy. Consequently, such techniques may provide an important future means of comparison between theory and experiment.

ACKNOWLEDGMENTS

The authors wish to acknowledge helpful discussions with R. G. Gilson on the analysis of the particle configurations. The financial support of the SERC and BRITE/EURAM Project No. BE 5132 is also gratefully acknowledged.

[1] K. O'Grady, R. G. Gilson, and P. C. Hobby, J. Magn. Magn. Mater. **95**, 341 (1991).
[2] G. N. Coverdale, R. W. Chantrell, A. Hart, and D. Parker, J. Magn. Magn. Mater. **120**, 210 (1993).
[3] C. Pangali, M. Rao, and B. J. Berne, Chem. Phys. Lett. **55**, 413 (1978).

The effect of dc bias fields on the switching speed in magnetic particulate media (abstract)

W. D. Doyle and L. He
Center for Materials for Information Technology and Department of Physics, The University of Alabama, Tuscaloosa, Alabama 35487

New results on the switching speed limit in high coercivity particulate magnetic media have recently been reported[1] using pulse fields with widths $t<1$ ns. Because the pulse amplitude is presently limited to <950 Oe, switching measurements on media with higher coercivities were carried out in the presence of a dc bias field H_B and the switching constant S_w[1] at zero bias field estimated by extrapolating the data at several high bias fields to $H_B=0$. The sensitivity of S_w to H_B was significant particularly in barium ferrite so it is prudent to examine this dependency more carefully in a lower coercivity system in which S_w can be measured from $0 \leqslant H_B \leqslant H_{CR}$ and H_{CR} is the remanent coercivity. The results (Fig. 1) for a standard γ-Fe_2O_3 iron oxide tape with $H_{CR}=375$ Oe show a nearly linear dependence of S_w on H_B except for $H_B/H_{CR} \geqslant 0.7$ and validate our earlier speculation that switching in barium ferrite particles is significantly slower than in metal particles. The experimental results will be compared to the calculated switching time[2] as a function of H_B expected for an appropriate distribution of uniaxial, single domain particles.

Research supported in part by the National Storage Industry Consortium and ARPA.

[1] W. D. Doyle, L. He, and P. J. Flanders, IEEE Trans. Mag. **29**, 3634 (1993).
[2] P. R. Gillette and K. Oshima, J. Appl. Phys. **29**, 529 (1958).

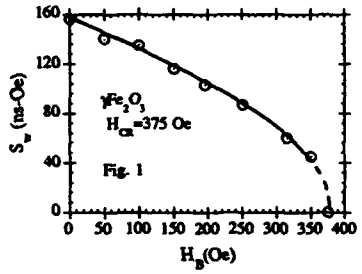

FIG. 1. The switching constant S_w as a function of bias field H_B.

 0021-8979/94/75(10)/5577/1/$6.00 © 1994 American Institute of Physics

Studies into the use of waterborne coating formulations for the preparation of magnetic tape (abstract)

Stacy Barrom, Ashley Bray, Song Cheng, John Elike, Hong Fan, Alan M. Lane, and David E. Nikles
Center for Materials for Information Technology, University of Alabama, Tuscaloosa, Alabama 35487-0209

The objective of this research project is to replace the organic solvents used in modern tape manufacture with water, thereby eliminating the potential for solvent emissions. This has led to a search to identify tape components compatible with a waterborne coating process. The pigments were either cobalt-modified γ-Fe_2O_3 or barium ferrite, with the majority of the research focused on cobalt-modified γ-Fe_2O_3 formulations. A combination of sodium polyphosphate and Surfynol CT-136, a pigment grinding aid, were used as dispersing agents. The binders included commercial water-dispersed polyurethanes and a commercial ethylene-vinylchloride copolymer emulsion. A commercial waterborne melamine-formaldehyde was used as a cross-linking agent. Addition of the ethylene-vinylchloride copolymer to the polyurethane increased the tensile strength and Young's modulus of the unpigmented binder films. The melamine-formaldehyde cross-linker further enhanced the mechanical properties and increased the adhesion between the pigmented binder films and the polyester base film. In a 180° peel test, the adhesion easily exceeded the ITO specification for 8 mm helical scan magnetic tape.[1] Rheological studies of the waterborne dispersions revealed that the viscosity was too low. Hydroxyethylcellulose, a water soluble polymer, was added as a thickener and this gave rise to a desirable thixotropic behavior in the dispersion. Waterborne dispersions were cast onto polyester base film, oriented in a 2000 G longitudinal magnetic field, and cured in a convection oven at 60 °C. Magnetic hysteresis loops showed a squareness of 0.875 and a switching field distribution of 0.324 for films containing cobalt-modified γ-Fe_2O_3.

Sponsored by the U.S. Environmental Protection Agency through the Gulf Coast Hazardous Substances Research Center, Beaumount, Texas.

[1] ISO/IEC DIS 10779—8 mm Wide Magnetic Tape Cartridge for Information Interchange—Helical Scan Recording.

 0021-8979/94/75(10)/5578/1/$6.00 © 1994 American Institute of Physics

Rheo-optical measurements on suspensions of magnetic recording particles (abstract)

Hyoung J. Choi, Yoon D. Park, Paul L. Frattini,[a)] and Myung S. Jhon
Department of Chemical Engineering, Carnegie Mellon University, Pittsburgh, Pennsylvania 15213

New rheo-optic measurements of the orientation of magnetic particles (used in particulate recording media) in suspension under imposed external fields (hydrodynamic and/or magnetic) are presented. The apparatus consists of a rheo-optical device[1] employing polarization modulation technology, and the external magnetic and flow field generating equipment (plane Poiseuille flow cell and quadrupole electromagnet). The polarization modulation dichroism measurement technique, which has the advantage of improved sensitivity and precision over conventional optical measurements, is able to characterize uniaxial single domain magnetic particle suspensions under external magnetic and hydrodynamic fields. Linear dichroism measurements, which reflect the degree of particle alignment about the field axis, are shown to be sensitive indicators of particle magnetic interactions, of effects of particle intrinsic magnetic properties, and of effects of particle shape. In this paper we focus on the comparison between effects of imposed magnetic and hydrodynamic fields on particle orientation for rodlike γ-Fe_2O_3, CrO_2, and plate-like Ba ferrites. Relationships between the particle orientation due to the two external fields are established through dimensional analysis, and the "equivalent magnetic field," which yields the same magnitude of dichroism obtained under a given flow field, is measured. The flow field and the equivalent magnetic field show a nearly linear relationship. Once the equivalent magnetic field plot is obtained experimentally, one can conveniently transform hydrodynamic field to applied magnetic field and then determine the particle orientation. Preliminary results indicate that this device represents the best technique for systematic investigation of magnetic particle orientation during simultaneous imposition of magnetic and hydrodynamic fields.

[a)]Eifle, Inc., c/o 11465 Clayton Road, San Jose, CA 95127.

[1]P. L. Fratini, E. S. G. Shaqfeh, J. L. Levy, and D. L. Koch, Phys. Fluids A 3, 2516 (1991).

 0021-8979/94/75(10)/5579/1/$6.00 © 1994 American Institute of Physics

Growth and magnetic dynamic scaling of ultrathin ferromagnetic films: Fe/Au(001)

Y.-L. He,[a] Y.-F. Liew,[b] and G.-C. Wang
Department of Physics, Rensselaer Polytechnic Institute, Troy, New York 12180-3590

Dynamic responses of the magnetic hysteresis of a few monolayer thick smooth Fe films on a Au(001) surface were measured by the surface magneto-optic Kerr effect technique. The Fe films were prepared by molecular beam epitaxy technique and their growth and structures were characterized *in situ* by high resolution low energy electron diffraction with angular profile measurement. The shape of the hysteresis loop changes with the frequency Ω and the amplitude H_0 of the applied periodic magnetic field. Over a range of frequency (<225 Hz) at a fixed amplitude and at room temperature, the area of the hysteresis loops follows a scaling form. The best fit of a scaling function to the frequency-dependent area gives exponents $a=0.58\pm0.03$ and $b=0.24\pm0.02$. For low values of frequency (<25 Hz) and amplitude (<400 Oe), the area of hysteresis loops measured at room temperature reduces to a power law $A\propto H_0^a\Omega^b$ with $a=0.59\pm0.07$ and $b=0.26\pm0.05$. Our measured exponents and the scaling function are consistent with recent results of theory and Monte Carlo simulations.

I. INTRODUCTION

Advances in sample preparation techniques and in methods of characterization for ferromagnetic ultrathin films and superlattices have led to the discovery of many exciting new phenomena in the last decade.[1] Examples are surface anisotropy, giant magnetoresistance, and magnetic couplings. Most studies have concentrated on the equilibrium properties of samples. In this article, we present experimental results on the growth of ultra thin Fe films on the same Au(001) surface and the dynamic responses of those films over a range of frequencies and amplitudes of external time-varying magnetic fields.

In the few monolayers (ML) regime, the Fe films are grown in a layer-by-layer mode with subsurface inversion.[2] Using these well characterized ultrathin ferromagnetic Fe/Au(001) films, we found that, for a fixed field amplitude, the frequency-dependent hysteresis loss first increases, reaches a maximum, and then decreases with increasing field frequency. For the first time, we have compared these data for a wide range of frequencies with a scaling form predicted recently[3] to extract the scaling exponents. For low frequency and amplitude, this scaling form reduces to a power law.[4,5] We have previously reported our determination of this power.[6]

II. EXPERIMENT

The experiment was performed in an ultrahigh vacuum (UHV) chamber equipped with high resolution low energy electron diffraction (HRLEED), surface magneto-optic Kerr effect (SMOKE), Auger-electron spectroscopy (AES), and a sputter ion gun. The ultrathin Fe films were deposited on a Au(001) surface from an Fe foil heated by electron bombardment from the back. The lattice mismatch between Fe and Au(001) is ~0.4%. Details related to the growth and morphology of films have been presented elsewhere[7] and will not be described here. However, the calibration of the effective magnetic field in the surface magneto-optic Kerr effect (SMOKE) measurement will be described below.

The Kerr signals from the ultrathin Fe films were measured by the SMOKE technique in situ.[8] The magnetic field in the gap of a C-shape cast iron core was produced by passing a sawtooth time-varying current through the Cu coil wound around the core. The AC field in the gap of the electromagnet was calibrated using either a homemade pickup coil or a commercial Hall sensor. This calibration is necessary because a time-varying magnetizing field generates eddy currents in the core resulting in a counter field that reduces the magnitude of the applied field. The effective magnetic field was measured by positioning either the Hall sensor or the pickup coil at the center of the gap (to replace the sample) and measuring the output voltage. We have plotted the normalized peak-to-peak voltage, which is proportional to the effective magnetic field, as a function of frequency at a fixed coil current. All the data[9] show that the most rapid drop in field amplitude occurs at low frequency (below 20 Hz). At 20 Hz, the field amplitude has dropped by about 40% of the DC magnetic field. The decrease of the field gradually slows down after 20 Hz and almost reaches a constant (about 50%) around 50 Hz and beyond. (We have measured the voltage which stays constant up to 1000 Hz.) This frequency-dependent effective magnetic field has been included in the calculation of loop areas.

Another calibration is needed for the phase difference between the effective magnetic field and the driving current

[a]Present address: Physics Department, University of Nebraska, Lincoln, NE 68588-0113.
[b]Present address: Center for Magnetic Recording Research, U. C.–San Diego, La Jolla, CA 92093.

 0021-8979/94/75(10)/5680/3/$6.00 © 1994 American Institute of Physics

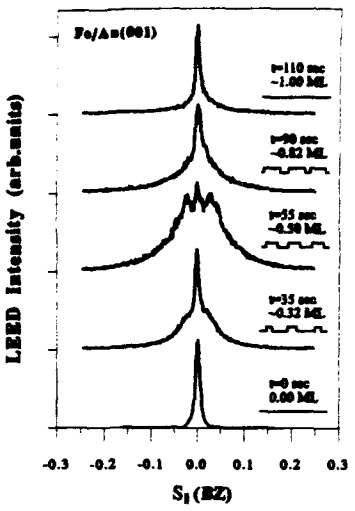

FIG. 1. Coverage evolution of the (00) beam angular profiles taken at the near out-of-phase condition (~25.5 eV) during Fe deposition on a Au(001) surface. The profiles correspond to coverages equal and less than 1 ML. The insets below the coverages are schematics of the two level islands and spacings.

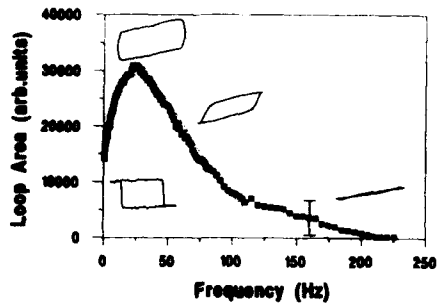

FIG. 2. Frequency-dependent hysteresis loop shapes and area for ~3 ML thick smooth Fe film at room temperature. The field amplitude is ~75 Oe. The solid curve is the fit using the scaling function $g(x)$ given by Eq. (2). Note that the lowest frequency used in the area measurement is ~0.8 Hz.

in the coil. This information is needed because the Kerr signal is measured as a function of the output of a bipolar power supply which provides the AC current in the coil. The phase shift of the effective magnetic field relative to the driving current in the coil, measured by comparing the output of the Hall sensor to the output of the bipolar power supply, shows a lag of ~10°–15° for 10–100 Hz and ~20° at ~250 Hz. This phase shift may distort the shape of the hysteresis loop slightly and affects the accuracy of the area calculation by a few percent.[9] This phase shift was used to correct the area of hysteresis loops by proper programming.

III. RESULTS AND DISCUSSIONS

A. Growth and characterization of a few ML thick Fe films

The growth of submonolayer and a few monolayer thick Fe films can be monitored by the angular profile of the (00) diffraction beam near the out-of-phase condition where the line shape change is most dramatic.[10] Figure 1 shows the evolution of the (00) beam profiles as a function of Fe coverage (≤1 ML). The profile at zero coverage, which corresponds to that from the clean Au(001) surface, is a convolution of the scattered electron intensity distribution from ordered terraces with the instrument response function (~0.006 $Å^{-1}$). The inverse of the full width at half maximum intensity of the deconvoluted profile indicates ordered terraces of ~400 Å. As the Fe coverage increases, the profile changes into a narrow spike on a shouldered structure and then a triple peak structure at ~0.5 ML. Beyond this coverage, the trend of the profile reverses, with the last profile returning to almost the shape of that from a clean Au surface. We define the coverage as 1 ML when we observe this clean-surfacelike profile. The profile at ~0.5 ML is consistent with a two level system with about equal island size and spacing between islands.[10] The profiles at ~0.32 ML are consistent with a two level system with different preferred island size and spacing. At ~0.82 ML, following the particle–hole symmetry argument, the preferred island size and spacing switch.

The changes in profile beyond 1 ML basically follow a similar trend but less dramatic than that of the first ML. This is because the first layer of deposited film is less perfect than the clean Au surface. After the deposition of a second layer, we measured the angular profiles of the (00) beam as a function of energy. Most profiles show a high spike intensity on a low intensity diffuse shoulder. We find the width of the spikes associated with all the profiles almost a constant, an indication of a smooth film. For films thicker than 2 ML the same procedure for growth of the Fe films and their profile analysis were used.[7] Therefore, we know the surface morphology of the Fe films (whether it is a two-dimensional (2D) smooth film or a 3D isolated island film) before our measurement of the hysteresis loops. The magnetic measurement presented here is for a smooth Fe/Au(001) film of ~3 ML thick.

B. Hysteresis loop areas as a function of frequency of magnetic field

Figure 2 shows the loop area versus frequency at a fixed magnetic field of ~75 Oe when the Fe film is held at room temperature, and also shows the corresponding loop shapes. A square loop was observed at low frequency (~5 Hz). As the frequency increases, the loop rounds off at the corners (~23 Hz) and forms a parallelogram (~79 Hz). Eventually the loop collapses to a straight line with zero area (~225 Hz). This shape evolution[6] is consistent with the Rao–Krishnamurthy–Pandit (RKP) prediction.[4] The centroid of the loop, i.e., the time-averaged magnetization $\langle M(t)\rangle$, has also moved away from zero.[6] This indicates that a dynamic phase transition has occurred[4–6] from a zero time-averaged symmetric state, $\langle M(t)\rangle=0$, to a nonzero time-averaged

magnetization, $\langle M(t)\rangle \neq 0$. The area calculated from these loops increases with frequency and reaches a maximum, depending on H_0, and then decreases at high frequencies. It is important to note that the absolute value of loop areas also depends on the temperature of the sample. However, this temperature dependence does not affect the scaling behavior of the loop areas over the frequency (and amplitude) of magnetic field.[4,6,11] At low frequency, the sample magnetization has a finite response delay and a finite area loop is observed. On the other extreme, at high frequency, the delay of the magnetization response of the sample with respect to the time-varying field is reduced[3] and the loop area decreases and eventually reduces to zero. Data taken at higher field (~105 Oe) shows a similar frequency dependence except the whole curve is higher and the peak is shifted towards higher frequency (not shown here).

C. Scaling of hysteresis loop areas

Recently, Acharyya *et al.*[3] have proposed a scaling form for the area of hysteresis loops

$$A \sim H_0^{\alpha} T^{-\beta} g(\Omega / H_0^{\gamma} T^{\delta}), \tag{1}$$

with a scaling function

$$g(x) \sim x^{\epsilon} \exp(-x^2/\sigma) \tag{2}$$

by Monte Carlo simulations of a 2D Ising ferromagnet system with nearest neighbor interactions. The values of those exponents calculated by Acharyya *et al.* are $\alpha=1.00$, $\beta=0.60$, $\gamma=1.75$, and $\delta=1.00$. In the limit of $\Omega \to 0$ for fixed temperature, the scaling form reduces to a power law

$$A \sim H_0^{a} \Omega^{b}, \tag{3}$$

where $a=\alpha-\epsilon\gamma$ and $b=\epsilon$. (4)

The power law behavior was proposed in RKP's theory[4] and also was obtained in the model simulations for 2D Ising spins.[4,5]

We have fitted the frequency-dependent loop area to the above scaling function, Eq. (2). The best fit is shown as a solid curve in Fig. 2. The solid curve peaks at ~25 Hz and decays faster than the data at high frequency. The error in the data at high frequency is large due to the small area of the loop and large noise level in the measurement. The best fit gives a value for the exponent $\epsilon=0.24\pm0.02$ which equals b [according to Eq. (4)].

In order to obtain the value of a, one should scale other frequency-dependent area curves at different H_0 to the one shown in Fig. 2. Unfortunately, we only have a set of data covering a limited range of frequency (<225 Hz) at ~105 Oe and room temperature. Using this limited frequency-dependent area curve, we were able to superpose it on the curve taken at ~75 Oe by using the scaled frequency Ω/H_0^{γ} ($\gamma=1.75$) in the horizontal axis and the scaled amplitude H/H_0^{α} ($\alpha=1.0$) in the vertical scale. For higher scaled frequency (>60 Hz) the measured area decays slower than the fitted curve (not shown here). We believe the range of frequency, magnetic field amplitude, and temperature for scaling may be very limited. Substituting these values of γ and α into Eq. (4), we obtain $a=0.58\pm0.03$.

The values of a and b are in agreement with our previously measured exponents 0.59 and 0.26, respectively, obtained from the low frequency and low field alone.[6,9,12] Our value of b (0.24) is comparable to 0.36 obtained by Monte Carlo simulation but the value of a (0.58) is larger than 0.37 of the Monte Carlo result.[3] We also tried other functional forms for $g(x)$ such as Gaussian, Lorentzian, and exponential modified Gaussian, to fit the frequency-dependent area. None of them gave a better fit than the function of Eq. (2).

One should be cautious when comparing the measured exponents with the modeling results. In theoretical simulations, the system is assumed to be free of defects, free standing, and have no dipolar interaction, with low magnetic anisotropy and low magnetoelastic coupling. In reality, our molecular beam epitaxy (MBE) grown Fe/Au(001) ultrathin film contains many defects and domains and is not free standing. There is also dipolar interactions in the Fe film. In spite of these complications, we obtained measured exponents[6,9,12] in qualitative agreement with the models.[3-5]

IV. SUMMARY

Using the angular profile measurement of HRLEED, we have monitored the growth of ultrathin Fe films and characterized their morphology. The hysteresis response of these characterized films was measured by the SMOKE technique. For low values of the magnetic field amplitude the area is frequency dependent. The frequency-dependent area can be fitted by a recently predicted scaling function. The exponents a and b extracted from the fit are consistent with recent theory and simulations. We believe the scaling behavior, and even possibly universality classes, may exist in other ferromagnetic ultrathin films. More systematic measurements of hysteresis responses of ultrathin films are needed.

ACKNOWLEDGMENT

This work was supported by ONR.

[1] For reviews, see L. M. Falicov, D. T. Pierce, S. D. Bader, R. Gronsky, K. B. Hathaway, H. J. Hopster, D. N. Lambeth, S. S. P. Parkin, G. Prinz, M. Salamon, I. K. Schuller, and R. H. Victora, J. Mater. Res. **5**, 1299 (1990); L. M. Falicov, *Thin Solid Films* **216**, 169 (1992).

[2] Y.-L. He and G.-C. Wang, Phys. Rev. Lett. **71**, 3834 (1993); Mater. Res. Soc. Symp. Proc. **237**, 429 (1992).

[3] M. Acharyya and B. K. Chakrabarti, Physica A **192**, 471 (1993); M. Acharyya, B. K. Chakrabarti, and A. K. Sen, Physica A **186**, 231 (1992).

[4] M. Rao, H. R. Krishnamurthy, and R. Pandit, Phys. Rev. B **42**, 856 (1990); J. Phys. **1**, 9061 (1989); M. Rao and R. Pandit, Phys. Rev. B **43**, 3373 (1991).

[5] W. S. Lo and R. A. Pelcovits, Phys. Rev. A **42**, 7471 (1990); S. Sengupta, Y. Marathe, and S. Puri, Phys. Rev. B **45**, 7828 (1992).

[6] Y.-L. He and G.-C. Wang, Phys. Rev. Lett. **70**, 2336 (1993).

[7] Q. Jiang, Y.-L. He, and G.-C. Wang, Surf. Sci. **295**, 197 (1993).

[8] E. R. Moog and S. D. Bader, Superlattices Microstruct. **1**, 543 (1985); J.-P. Qian and G.-C. Wang, J. Vac. Sci. Technol. A **8**, 4117 (1990); C. A. Ballentine, R. L. Fink, J. Araya-Pochet, and J. L. Erskine, Phys. Rev. B **41**, 2631 (1990).

[9] Y.-L. He, Ph.D. thesis, Rensselaer Polytechnic Institute, Troy, NY, 1993.

[10] J. M. Pimbley and T.-M. Lu, J. Appl. Phys. **57**, 1121 (1985).

[11] D. Dhar and P. B. Thomas, J. Phys. A **25**, 4967 (1992); D. Dhar and P. B. Thomas, Europhys. Lett. **21**, 965 (1993).

[12] Y.-F. Liew, Ph.D. thesis, Rensselaer Polytechnic Institute, Troy, NY, 1992.

Mössbauer investigation of the magnetic hyperfine field distribution in Fe(100)/Ag(100) structures

P. J. Schurer
Royal Roads Military College, F.M.O. Victoria, B.C., Canada, V0S 1B0

Z. Celinski and B. Heinrich
Surface Physics Laboratory, Physics Department, Simon Fraser University, Burnaby, B.C., Canada, V5A 1S6

A monolayer of ^{57}Fe is used as a probe layer in Ag/9Fe(001)/10Ag(001) structures grown by the molecular beam epitaxy technique. Different Fe sites can be resolved in the spectrum. From the analysis of the isomer shift values, ^{57}Fe deposited at the Fe/Ag interface can be distinguished from ^{57}Fe atoms that are deposited one or more atomic layers removed from the interface. The variation of the magnetic hyperfine field H_{hf} with distance from the Fe/Ag interface agrees qualitatively with values calculated previously.

I. INTRODUCTION

Mössbauer effect spectroscopy (MES) studies can in principle obtain information with atomic scale resolution on the individual Fe monolayers (ML) in iron based molecular beam epitaxy (MBE) grown structures. Such a resolution can be obtained in Fe(100)/Ag(100) structures only if just one ^{57}Fe ML is used as a probe layer in the iron multilayer.[1,2] By using this technique different components can be resolved in the Mössbauer spectrum.[1–3] MES studies where two or more atomic layers are sampled at the same time in the iron multilayer show only broadened structureless peaks.[4–6]

Conversion electron Mössbauer studies (CEMS) of the iron multilayer in MBE grown Ag/Fe(100)/Ag(100) structures using one ^{57}Fe ML as probe layer clearly show the existence of different components in the Mössbauer spectra.[2,3] These components can be associated with different Fe sites in the iron multilayer mainly from an analysis of the isomer shift (i.s.) and quadrupole splitting values (QS). The values of these parameters are significantly different for ^{57}Fe at the Fe/Ag interface (sites I, I_t, and I_b) compared to those for ^{57}Fe atoms that do not make contact with the Ag atoms (sites II, III, etc.) (Fig. 1).

The identification of different Fe sites in MES studies makes it possible to compare experimental and theoretical values of the magnetic hyperfine field H_{hf} at different locations in the iron multilayer. Ohnishi *et al.* determined the values of H_{hf} for the three different monolayers in Ag/5Fe/Ag(100) from self-consistent spin-polarized local-spin-density calculations.[7] Liu and Gradmann used the single ^{57}Fe probe layer technique for a MES study of a series of Ag/40Fe/Ag structures.[1] They conclude from this study that the H_{hf} variation with ^{57}Fe ML location does not agree with the predictions of Ohnishi. However at least a qualitative agreement may be possible if a different interpretation[2] of these spectra is accepted. The purpose of the present article is to compare H_{hf} values obtained for MBE grown Ag/6.7Fe/Ag and Ag/9Fe/Ag structures with the values calculated by Ohnishi *et al.*[7] The comparison is not strictly straightforward because the theoretical values are for the ground state H_{hf} and our values are obtained at room temperature. However, previous measurements suggest that the temperature dependences of the H_{hf} values vary only slightly between neighboring iron layers.[1,4]

II. EXPERIMENT

The preparation of MBE structures of multilayers of Fe(001) and Ag(100) has been described in previous articles.[8,9] For the present CEMS study two samples have been prepared:

sample 1: Ag/7.8Fe/1 ^{57}Fe/10Ag/9Au,

sample 2: Ag/4.7Fe/1 ^{57}Fe/4Fe/10Ag/9Au. The last three layers of Fe for sample 1 were grown at 390 K. All of sample 2 was grown at room temperature.

III. RESULTS AND DISCUSSION

The Mössbauer spectra of sample 1 and 2 are presented in Fig. 2. The spectrum obtained for sample 1 was least squares fitted with three sextet components (Table I). The broadened linewidths, especially for component 1, can be explained from the presence of components corresponding to sites I_t and I_b that were not included in the fit. The results are in agreement with those of a sample of almost the same composition that was produced by growing the last three iron layers at 420 K.[2]

Charge-density calculations have shown that the s charge density at the ^{57}Fe nucleus is expected to be smaller at the Fe/Ag boundary than at locations one or more atomic layers removed from the Fe/Ag interface.[7] Furthermore, systematic studies have shown that the i.s. values in binary Fe-X alloys vary proportional to the surface-weighted concentration of the X-atom nearest neighbors of a central Fe atom.[10] The i.s. value of a central ^{57}Fe atom increases with an increasing number of Ag nearest neighbors. For instance, in

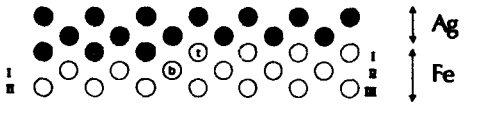

FIG. 1. Different Fe positions I, I_t, I_b, II, and III close to a terraced Fe/Ag(001) interface.

 0021-8979/94/75(10)/5583/3/$6.00 © 1994 American Institute of Physics

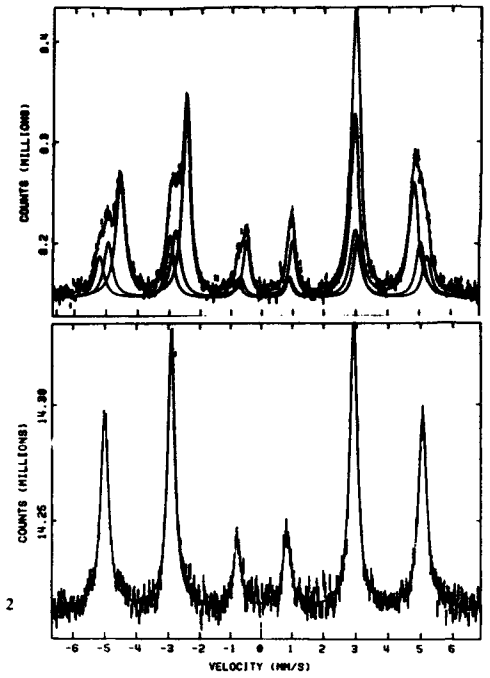

FIG. 2. CEMS spectra for Ag/4Fe/1 ^{57}Fe/4Fe/10Ag/9Au (bottom) and Ag/7.8Fe/1 ^{57}Fe/10Ag/9Au (top).

disordered $Fe_{1-x}Ag_x$ the i.s. value has increased to i.s.~0.2 mm/s for $x=0.5$.[11,12] The same value is observed for site I Fe atoms at the top Ag/Fe interface where the ^{57}Fe atoms have four Fe and four Ag nearest neighbors.[2]

Based on these considerations, we conclude that component 1 in the spectrum of sample 1 is associated with Fe sites I at the Fe/Ag interface. Components 2 and 3 correspond to ^{57}Fe atoms that do not make contact with Ag atoms at the Fe/Ag interface. Because we expect a smaller area for the component that is associated with Fe site III, we will identify components 2 and 3 with Fe sites II and III, respectively.

TABLE I. Values of the magnetic hyperfine fields H_{hf}, the quadrupole splittings QS, and the isomer shifts i.s. measured with respect to natural iron. The linewidth Γ is shown for the outside lines of the sextets.

Component	Rel. area	H_{hf} (kOe)	i.s. (mm/s)	QS (mm/s)	Γ (mm/s)
		Ag/7.8Fe/1^{57}Fe/10Ag/9Au			
1	0.57	292	0.20	−0.11	0.36
2	0.25	311	0.08	−0.05	0.32
3	0.19	325	0.03	−0.03	0.32
		Ag/4.7Fe/1^{57}Fe/4Fe/10Ag/9Au			
1	1.00	313	0.02	−0.01	0.30

TABLE II. Theoretical and experimental values of $\Delta H_{hf}=H_{hf}(n)-H_{hf}(I)$ (kOe) for different positions n of an ^{57}Fe monolayer in the Fe multilayer of MBE grown Ag/Fe/Ag structures. The theoretical values in the second column are for 0 K, the experimental values are determined at 300 K. The uncertainties are given in parentheses.

Site n	Ag/5Fe/Ag[a]	Ag/6.7Fe/Ag[b]	Ag/9.7Fe/Ag[c]
II	4	14(3)	19(2)
III	24	25(3)	33(2)
IV			
V			21(2)

[a]Ohnoshi *et al.*[7]
[b]Schurer *et al.*[3]
[c]Present study.

The spectrum obtained for sample 2 can be well fitted with only one sextet component (Table I). The ^{57}Fe in this sample is deposited in Fe sites IV and V, about four to five atomic layers removed from the Fe/Ag interface. The presence of ^{57}Fe in two adjacent atomic layers and the 2% abundance of ^{57}Fe in the natural iron layers is probably the main cause for the slightly broadened linewidth of the sextet. The i.s. value shown in Table I confirms the previous correlation of Fe sites and MES components, i.e., the i.s. value is close to zero for ^{57}Fe atoms that do not make contact with Ag atoms at the interface. This result is also consistent with the calculations of the charge density at the nucleus.[7]

Table II shows the differences between the H_{hf} value of the iron ML at the interface (site I) and that of subsequent layers below the interface (site II, III, and V). Our results agree fairly well with those of Liu and Gradmann if the components 1a and 1b in their spectrum are identified as approximately Fe sites I and II. In that case the experimental *data qualitatively supports* the calculations of Ohnishi *et al.*[7] which show that the H_{hf} value should increase from site I to site II positions. Our results also agree with the calculations in that H_{hf} for site III is larger than for site I Fe atoms in a 5 ML Fe film. The results of Liu and Gradman for a 40 ML Fe film suggest that the H_{hf} values steadily decrease towards the center of the Fe film for Fe layers more than 2 layers removed from the Fe/Ag interface. This is in agreement with our results for a 9 ML Fe film where the decrease in H_{hf} starts at least at 5 ML away from the interface. It would be useful to extend the calculations to thicker iron multilayers. This would make it possible to make a more complete comparison between theoretical and experimental results.

ACKNOWLEDGMENTS

This work was financially supported by the Department of National Defence Canada and the National Research Council of Canada.

[1] G. Liu and U. Gradmann, J. Magn. Magn. Mater. **118**, 99 (1993).
[2] P. J. Schurer, Z. Celinski, and B. Heinrich. Phys. Rev. B **48**, 2577 (1993).
[3] P. J. Schurer, Z. Celinski, and B. Heinrich (to be published).
[4] N. C. Koon, B. T. Jonker, F. A. Volkening, J. J. Krebs, and G. A. Prinz, Phys. Rev. Lett. **59**, 2463 (1987).
[5] G. T. Gutierrez, M. D. Wieczorek, H. Tang, Z. Q. Oiu, and T. C. Walker, J. Magn. Magn. Mater. **99**, 215 (1991).

[6]D. J. Keavney, M. D. Wieczorek, D. F. Storm, and J. C. Walker, J. Magn. Magn. Mater. 121, 49 (1993).
[7]S. Onoshi, M. Weinert, and A. J. Freeman. Phys. Rev. B 30, 36 (1984).
[8]B. Heinrich, A. S. Arrott, J. F. Cochran, Z. Celinski, and K. Myrtle, *Science and Technology of Nanostructure Magnetic Materials*, edited by G. C. Hadgepanayis and G. A. Prinz (Plenum, New York, 1991), p. 15.
[9]B. Heinrich, Z. Celinski, A. S. Arrott, and K. Myrtle, Phys. Rev. B 47, 5077 (1993).
[10]A. R. Miedema and F. Van der Woude, Phys. B 100, 145 (1980).
[11]C. Larica, E. M. Baggio-Soitovitch, and S. K. Xia. J. Magn Magn. Mater. 110, 106 (1992).
[12]C. L. Chien and K. M. Aaruah, Phys. Rev. B 28, 1214 (1983).

Magnetization reversal processes in epitaxial Fe/GaAs(001) films

C. Daboo, R. J. Hicken, D. E. P. Eley, M. Gester, S. J. Gray, A. J. R. Ives, and J. A. C. Bland
Cavendish Laboratory, University of Cambridge, Madingley Road, Cambridge CB3 0HE, United Kingdom

In this article we present the results of a detailed study of the switching behavior observed in epitaxial single Fe films of thickness between 30 and 450 Å, and a wedge shaped Fe film with a thickness range of 10–60 Å grown on GaAs (001). These films have cubic and uniaxial anisotropies which change with film thickness. For the fixed thickness films the values of the anisotropy constants were accurately determined by Brillouin light scattering (BLS) measurements together with polar magneto-optic Kerr effect (MOKE) measurements that gave the value of the magnetization. The switching behavior of these samples was observed with in-plane MOKE magnetometry as a function of the angle between the applied field and the in-plane crystallographic axes. Measurements of the component of magnetization perpendicular to the applied field allow a precise determination of the relative orientation of the hard and easy in-plane anisotropy axes. This can be used to accurately determine the ratio of uniaxial to cubic anisotropy constants, when this ratio is less than one. The ratios obtained from MOKE agree well with those obtained from BLS. Minimum energy calculations predict that the reversal process should proceed by a continuous rotation of the magnetization vector with either one or two irreversible jumps, depending on the applied field orientation and the nature of the anisotropy of the film. The calculations provide a good qualitative description of the observed reversal process, although the magnetic microstructure influences the exact values of the switching fields.

I. INTRODUCTION

A number of groups have reported magneto-optic Kerr effect (MOKE) M-H loops for the component of magnetization parallel to the applied field ($M_\parallel$) which show "overshoots" which depend on the analyzer setting chosen to observe the MOKE signal.[1] This has been explained as an additional optical effect caused by "mixing in" a contribution caused by the component of magnetization perpendicular to the applied field ($M_\perp$).[1] It is the different *magnetic* switching behavior observed in $M_\parallel$ and $M_\perp$ that produces the overshoots in the $M_\parallel$-H MOKE loops.[2,3] Here we extend the previous studies of this system[2–4] to show how the detailed switching behavior is expected to vary with precise orientation of the applied field and the exact ratio r of uniaxial to cubic anisotropy constants ($r=K_u/K_1$), which are known to be present in such samples.[4]

II. EXPERIMENTAL PROCEDURES

The samples were grown under ultrahigh vacuum (UHV) conditions (pressure during evaporation less than $\sim 5\times10^{-10}$ mbar) on GaAs (001) substrates and studied by low-energy electron diffraction LEED, Auger spectroscopy, and *in situ* MOKE. The substrates were held at 150 °C during Fe growth at ~ 1 Å min^{-1} from the e-beam evaporator. A series of samples with thickness between 30 and 450 Å were grown, together with a wedge shaped Fe film in the thickness range of 10–60 Å. Each was capped with ~ 20 Å of Cr. The *in situ* MOKE was used to study the evolution of the magnetic anisotropy as the Fe films were grown[5] so that films with different final anisotropy strengths could be produced.

The fixed thickness samples were characterized *ex situ* using Brillouin light scattering (BLS) and polar MOKE to determine the anisotropy constants K_1 and K_u of each sample. By fitting the BLS data as a function of the angle ϕ between the applied field direction and the hard uniaxial anisotropy axis it was possible to determine the quantities $2K_1/M$ and $2K_u/M$. The saturation field determined from the polar MOKE gave the value of the magnetization M in the samples, ignoring any surface anisotropy, thus allowing the anisotropy constants to be determined from the combined measurements. The thickness dependence of the anisotropy is reported elsewhere,[5] but in general it was found that thinner Fe layers had a larger anisotropy ratio r, and a reduced average magnetization. Due to the uniaxial anisotropy which was found to be parallel to a $\langle 110\rangle$ direction, the two $\langle 110\rangle$ directions in the sample are inequivalent as one is a hard cubic axis and hard uniaxial axis (the hard–hard axis) while the other is a hard cubic axis and easy uniaxial axis (the hard–easy axis).

For the MOKE measurements the sample and an electromagnet were separately mounted on two concentric precision (0.001° step) rotary stepper drives, so that they could each be turned independently to any desired orientation over the full 0°–360° range under computer control. The MOKE technique used here measures MOKE M-H loops for two orientations of the applied field, namely, parallel and perpendicular to the plane of incidence of the light. By using the same optical geometry for each measurement it was possible to determine $M_\parallel$ and $M_\perp$ directly from the resulting loops.[6,7]

III. RESULTS

In general it was found that the magnitude of the magnetization vector remained virtually constant during the reversal process indicating that the sample behaved as a single domain, except very close to a switching field value. Figure 1 shows three typical sets of MOKE loops illustrating the different switching behavior observed in our samples. These loops were taken from the wedge shaped Fe film for an an-

 0021-8979/94/75(10)/5586/3/$6.00 © 1994 American Institute of Physics

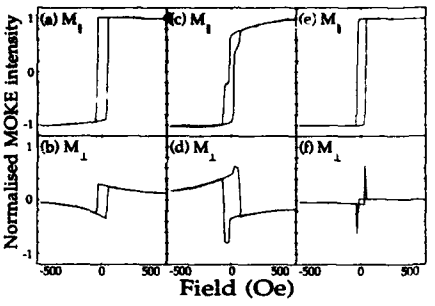

FIG. 1. Typical MOKE loops for the Fe wedged film for $r=0.4\pm0.02$. (a) $M_{\parallel}$-H and (b) $M_{\perp}$-H loops at $\phi=75°$. (c) $M_{\parallel}$-H and (d) $M_{\perp}$-H loops at $\phi=20°$. (e) $M_{\parallel}$-H and (f) $M_{\perp}$-H loops at $\phi=60°$.

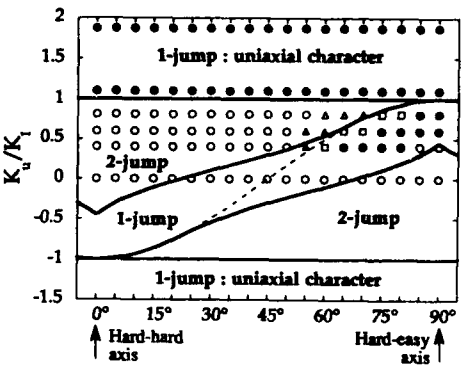

FIG. 2. Calculated and experimental phase diagram of one- and two-jump switching as a function of applied field orientation ϕ and anisotropy ratio r. The solid lines indicate the calculated boundary between one- and two-jump switching, while the dashed line shows the calculated position of the easy axis. Experimental switching is indicated by the symbols: ●—one-jump switching; ○—normal two-jump switching; □—reverse two-jump switching; △—cannot discriminate between one- or two-jump switching.

isotropy ratio $r=0.4\pm0.02$. Figures 1(a) and 1(b) show $M_{\parallel}$-H and $M_{\perp}$-H loops, respectively, for $\phi=75°$. Both loops show one irreversible jump at the *same* field of ~50 Oe as the field is reversed, corresponding to "one-jump" switching. Figures 1(c) and 1(d) show $M_{\parallel}$-H and $M_{\perp}$-H loops, respectively, for $\phi=20°$. Here both loops show *two* irreversible jumps as the field is reversed, corresponding to "two-jump" switching. These two jumps each occur when the magnetization traverses each of the two hard axis directions that exist in a sample with $|r|<1$. This implies that when the uniaxial anisotropy dominates over the cubic anisotropy (i.e., $|r|>1$) only one-jump switching should occur, and this behavior is indeed observed. Figures 1(e) and 1(f) show $M_{\parallel}$-H and $M_{\perp}$-H loops, respectively, for $\phi=60°$. In this case a "reversed" two-jump switch occurs since the magnetization initially rotates away from the field direction in a clockwise sense, say, but switches back over the field direction in an anticlockwise sense.

In order to study the magnetic switching behavior in more detail we used a coherent rotation model[8] to calculate the shape of the $M_{\parallel}$-H and $M_{\perp}$-H loops, for various values of ϕ and r. These calculations indicated that the reversal process can proceed either by one or two jumps depending on the exact values of ϕ and r. It is possible to understand the calculated switching behavior by tracking local energy minima as a function of applied field strength. The reversal process starts off with the magnetization sitting in the positive saturation energy minimum with an orientation close to the applied field direction. As the field reverses this minimum becomes shallower and eventually disappears. At this point the magnetization undergoes an irreversible jump and falls into a different energy minimum. In the one-jump switching process this second minimum is the negative saturation energy minimum, and the magnetization remains in this minimum as the applied field is taken towards negative saturation. In the two-jump switching process, there is a third intermediate energy minimum that exists when the positive saturation minimum disappears, with the result that the magnetization falls into this minimum in preference to the negative saturation minimum. However, as the field is further reversed this intermediate minimum also disappears and the magnetization eventually ends up in the negative saturation energy minimum. For one-jump switching it is also possible that the intermediate minimum is initially present, but disappears just before the positive saturation minimum disappears. However, in real magnetic films the magnetization can switch via domain wall sweeping *before* the positive saturation minimum has disappeared, and *before* the intermediate minimum has disappeared with the result that a two-jump switch occurs when the calculations predict a one-jump switch, and in this case two possibilities occur. When ϕ is on the hard–hard axis side of the easy axis, normal two-jump switching is seen to occur [Figs. 1(c) and 1(d)]. When ϕ is on the hard–easy axis side of the easy axis a reverse two-jump switch is seen [Figs. 1(e) and 1(f)].

The switching processes are illustrated in Fig. 2, which shows the calculated phase diagram for one- and two-jump switching as a function of ϕ and r. The boundary between the one- and two-jump switching regimes is shown by a solid line, and is defined as the point at which the intermediate and positive saturation minima both disappear at the same applied field. A simple expression for the angle θ between the hard–hard axis and the easy axis, shown by the dashed line on Fig. 2, is given by

$$\cos 2\theta=-r, \quad \text{for} \quad |r|\leq 1,$$
$$\theta=90°, \quad \text{for} \quad |r|\geq 1. \tag{1}$$

Experimental results for three samples with anisotropy ratios of ~0 (sample 1—almost completely cubic), 0.4, 0.6, 0.8, and 1.1 (sample 2—various positions along the wedge shaped sample), and 1.8 (sample 3—strongly uniaxial) are also shown at 5° intervals with different symbols to indicate different switching behavior. For $|r|>1$ the calculations show that only one-jump switching can occur, and this is confirmed by the experimental results for sample 3 and sample 2 (with $r=1.1$). The results for sample 2 (with

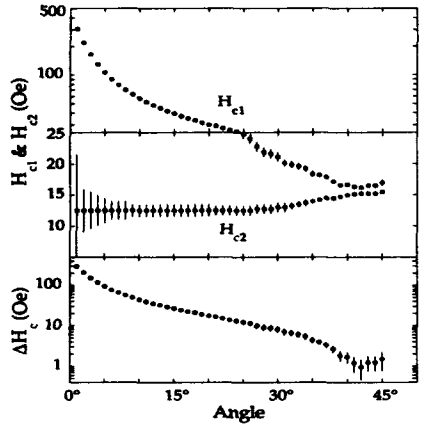

FIG. 3. The two-jump switching fields H_{c1} and H_{c2} (top panels), and their difference ΔH_c (bottom panel) as a function of applied field orientation ϕ.

$r=0.4$, 0.6, and 0.8) are in good agreement with the calculations, though close to the easy axis it is difficult to discriminate between one- and two-jump switching. Reverse two-jump loops are only seen on the hard–easy axis side of the easy axis. For sample 1, the observed switching behavior conflicts with that predicted by the calculations since two-jump switching is always present indicating that domain wall sweeping can be more easily induced when r is close to zero.

For two-jump switching, as ϕ approaches an easy axis the difference ΔH_c between the two switching fields H_{c1}, defined as the larger switching field, and H_{c2} is reduced, and very close to the easy axis ΔH_c can be ~2 Oe. The dependence of H_{c1}, H_{c2}, and ΔH_c on ϕ is shown in Fig. 3 for sample 1, as ϕ varies between 0° (hard axis) and 45° (easy axis). H_{c2} is seen to remain almost constant at ~12 Oe up to $\phi\sim30°$, beyond which it gradually increases to ~15 Oe at $\phi=45°$. However, H_{c1} changes rapidly from ~300 Oe down to ~25 Oe at $\phi\approx30°$, and then gradually decreases to ~17 Oe at $\phi=45°$. Thus ΔH_c changes from ~300 Oe at $\phi=0°$ to ~2 Oe at $\phi=45°$, providing a tuneable switching behavior that may be of use in device applications.

When the applied field direction is close to a hard or easy axis, the magnetization vector moves, respectively, away from or towards the axis as the field is reduced. Therefore, depending on which side of the anisotropy axis the field is applied, the magnetization will move either in a clockwise or anticlockwise sense. A change in the clockwise or anticlockwise motion of the magnetization can be clearly seen in $M_\perp$-H MOKE loops, and by using high precision rotary stepper drives to turn the sample and align the magnet, it is possible to accurately determine the angles of the hard and easy axes in the sample plane. Since the angle between the easy axis and the hard–hard axis varies with r, as given by Eq. (1), it is possible to determine r when $|r|<1$ from MOKE measurements, and these values agree well with those determined by BLS. However, for the case of $|r|\geq1$ MOKE cannot be used to determine r directly.

IV. SUMMARY

We have studied the switching behavior of Fe/GaAs samples for various values of uniaxial and cubic anisotropy constants using in-plane MOKE magnetometry. Coherent rotation calculations showed that the switching mechanism depends on ϕ and r. In general, the observed switching behavior agreed well with the switching mechanism predicted by the calculations, though in some cases domain wall sweeping caused two-jump switching where one-jump switching was expected from the calculation. The two-jump switching fields were found to depend on r, and for a field applied close to the cubic easy axis the difference in the switching fields could be as little as 2 Oe. It was found that r could be accurately found from the MOKE data by determining the angles at which the magnetization switched between a clockwise or anticlockwise motion. A simple analytical expression for this angle was given, and the experimental results for r determined from MOKE agreed well with that found from the BLS measurements. Since the sample behaves mostly as a single domain and the switching process is controllable, this behavior is of interest for device applications.

ACKNOWLEDGMENTS

The financial support of the SERC, the Toshiba Corporation, and the Newton Trust, Cambridge for this work is gratefully acknowledged. M. G. would like to thank the EC for a bursary (Contract No. BREU-900293). S. J. G. would like to thank the DRA, UK for support.

[1] J. M. Florczak and E. D. Dahlberg, J. Appl. Phys. **67**, 7520 (1990).
[2] J. M. Florczak and E. D. Dahlberg, Phys. Rev. B **44**, 9338 (1991).
[3] J. M. Florczak and E. D. Dahlberg, J. Magn. Magn. Mater. **104**, 399 (1992).
[4] J. J. Krebs, B. T. Jonker, and G. A. Prinz, J. Appl. Phys. **61**, 2596 (1987).
[5] C. Daboo *et al.* (to be published).
[6] C. Daboo, J. A. C. Bland, R. J. Hicken, A. J. R. Ives, M. J. Baird, and M. J. Walker, Phys. Rev. B **47**, 11852 (1993).
[7] C. Daboo, J. A. C. Bland, R. J. Hicken, A. J. R. Ives, M. J. Baird, and M. J. Walker, J. Appl. Phys. **73**, 6368 (1993).
[8] B. Dieny, J. P. Gavigan, and J. P. Rebouillat, J. Phys. C **2**, 159 (1990).

Surface magnetization processes investigated by the combined surface magneto-optical Kerr effects in Fe/Cu(100) thin films

Z. J. Yang, S. D. Healy, K. R. Heim, J. S. Drucker, G. G. Hembree, and M. R. Scheinfein
Department of Physics and the Center for Solid State Science, Arizona State University, Tempe, Arizona 85287-1504

Surface and ultrathin-film anisotropies in epitaxial fcc Fe thin films grown on room temperature Cu(100) single crystals in an ultrahigh vacuum has been investigated, *in situ*, by the combined surface magneto-optical Kerr effects (SMOKE). When the applied field is perpendicular to the film surface, rotation processes occurring between out-of-plane and in-plane directions suggest the presence of an induced uniaxial (canted) anisotropy directed out of the plane of the film. This hypothesis is tested with a simple coherent rotation model.

I. INTRODUCTION

The low-dimensional properties predicted for ultrathin ferromagnetic films has stimulated considerable interest in exploring epitaxial metal/metal systems.[1] The most studied, and perhaps the most complex metal/metal epitaxial system, is fcc Fe/Cu(100). Interpretation of data from the fcc Fe/Cu(100) system is complicated by a rich physical structure, which includes bilayer growth during initial phases of epitaxy,[2–6] strain relief at intermediate thicknesses, weak surface reconstructions,[7] and fcc to bcc transitions.[8] Behavior of growth-temperature and film-thickness correlations with the magnetic spin orientations have also been intensively studied.[2,9,10] Our results for room temperature epitaxial Fe/Cu(100) thin films[11,12] indicate that subsurface Fe islands can form during the initial phases of epitaxy. For films thicker than 2 ML, nearly continuous Fe films have been observed, consistent with the onset of ferromagnetic ordering. Polar and longitudinal Kerr-effect measurements show that the easy axis transition from out of plane to in plane (of the film) occurs near a thickness of 4.7 ML. Here, we describe a unique implementation of a combined three-axis magneto-optical Kerr effect apparatus that is used to explore mixed in-plane/out-of-plane rotation modes in ultrathin film Fe/Cu(100).

II. THE COMBINED THREE-AXIS SURFACE MAGNETO-OPTICAL KERR EFFECTS

Three magneto-optical Kerr effects (polar, longitudinal, and transverse effects are shown in Fig. 1) are classified according to the direction of the magnetization with respect to the plane of the incidence. Since the Kerr effect exists for any arbitrary direction of the magnetization (relative to the scattering plane), for non-normal incidence, magnetization loops obtained from any of the three Kerr effects may contribute to the detected signal. With different orientations of polarizer, modulator, and analyzer, SMOKE can detect either all three magnetization components or any one of them. Thus, thin-film anisotropies and switching modes can be studied by comparing Kerr-effect magnetization loops.[13,14] The normalized light intensity of the combined three-axis surface magneto-optical Kerr effects for our SMOKE measurements can be expressed as[13]

$$I = m_p^2 (r_{ps}^p)^2 + m_l^2 (r_{ps}^l)^2 + 2 m_p m_l r_{ps}^p r_{ps}^l \cos(\delta_{ps}^p - \delta_{ps}^l) + 0.2 r_{pp}^l m_p r_{ps}^p \sin(\delta_{pp}^l - \delta_{ps}^p) \sin \omega t + 0.2 r_{pp}^l m_l r_{ps}^l \sin(\delta_{pp}^l - \delta_{ps}^l) \sin \omega t, \quad (1)$$

where m_l and m_p are the direction cosines of the magnetization axes along the applied field direction (projection of M onto H) for longitudinal and polar Kerr effects, respectively. r_{ps}^l and δ_{ps}^l are the absolute magnitude and the phase angle of the Fresnel reflection coefficients [superscripts indicate (p) polar or (l) longitudinal Kerr effects], and ω is the angular frequency of the modulator.[13] The expression for the intensity is independent of the transverse Kerr effect, regardless of the direction of the applied magnetic field in our SMOKE arrangement. It includes the contributions from both polar and longitudinal Kerr effects, which allows us to investigate magnetization reorientations between out-of-plane and in-plane directions simultaneously.

III. EXPERIMENTAL RESULTS

The specimen preparation chamber of an UHV scanning transmission electron microscope (STEM),[2] a Vacuum Generators HB501-S, operating at base pressures of 5×10^{-11} mbar, has been equipped with an *in situ* SMOKE characterization system.

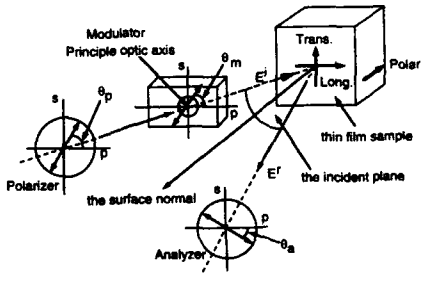

FIG. 1. A schematic diagram of a SMOKE experiment. The polarizer, modulator, and analyzer angles are θ_p, θ_m, and θ_a, respectively, relative to the scattering plane. The longitudinal, transverse, and polar Kerr effect directions are also shown.

 0021-8979/94/75(10)/5589/3/$6.00 © 1994 American Institute of Physics

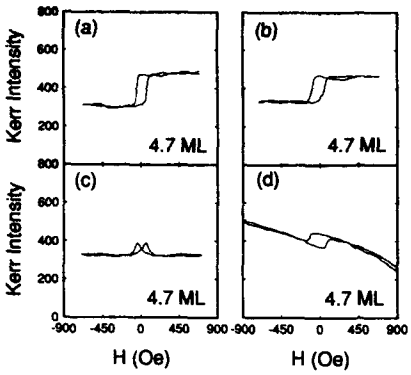

FIG. 2. SMOKE loops are shown for applied fields along the (a) longitudinal, (b) 45° from longitudinal (in the plane of the film surface), (c) transverse, and (d) normal to the film surface (polar) directions, respectively. Applied fields in (a)–(c) are in the film plane.

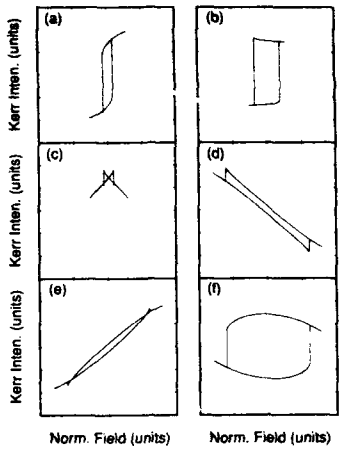

FIG. 3. Computed SMOKE loops are shown for applied fields along the (a) longitudinal (b) 45° from longitudinal (in the plane of the film surface), (c) transverse, and (d) normal to the film surface (polar) directions, respectively. Since the polar Kerr signal contains both longitudinal and polar components (e) and (f) show the polar and longitudinal components [to Fig. 3(d)], respectively. All loops are displayed on the same scale.

Longitudinal, polar, and transverse hysteresis loops were recorded by scattering modulated (polarized), He–Ne (632.8 nm) laser light from magnetic surfaces at an angle of incidence of 45°.[13] Nanometer lateral spatial resolution surface microanalysis, using secondary electron or Auger electron spectroscopy and imaging allows for epitaxial film microstructure to be correlated with magnetic properties.

Single crystal Cu(100) substrates, were electropolished, cyclically sputtered at 330 °C with 600 eV Ar ions at 45° incident angles, then annealed at 600 °C. The thickness dependence of SMOKE hysteresis loops of as-grown fcc Fe on room temperature Cu(100) substrates has been given elsewhere.[2] In summary, for Fe film thicknesses below 2ML, no magnetic response was observed, The initial magnetic response is observed as a zero-remanence, linear hysteresis loop in the polar direction, with no magnetization in-plane. At intermediate thicknesses, 3.5 ML, remanent polar and longitudinal SMOKE loops are observed. While the in-plane loop is square, the tilted polar loop displays the effects of shape anisotropy indicating a canted easy axis. SMOKE loops from thicker films, 4.7 ML, loose polar remanence, but retain square in-plane loops characteristic of an in-plane easy axis.

We examined the magnetization switching process for the as-deposited 4.7 ML thick Fe. In Figs. 2(a)–2(d), SMOKE loops are shown for applied fields along the longitudinal, 45° from longitudinal (in the plane of the film surface), transverse, and normal to the film surface (polar) directions, respectively. Applied fields in Figs. 2(a)–2(c) are in the film plane. A coherent rotation[14,15] model was employed to interpret these results. The normalized energy functional is given in Eq. (2), where K_{in} and K_{out} are the in-plane and out-of-plane anisotropies, M_s is the saturation magnetization, H_l, H_t, and H_p are the longitudinal, transverse and polar applied magnetic fields, θ is the polar angle (from the polar direction, (ϕ is the azimuthal angle (from the longitudinal direction), α defines the out-of-plane easy-axis angle, β defines the direction of the easy axis in the film plane, and c is a constant whose value is 1 (2) for uniaxial (cubic) in-plane anisotropy. External fields include the ramping field and any residual external stray fields. This expression was minimized using a conjugate gradient method. The results of this minimization are shown in Figs. 3(a)–3(f). The computed loops are meant to indicate gross structure as a means of interpreting the SMOKE results, and discrepancies between the computed loops and the measurements are due to the crudeness of the model (i.e., no domain walls or domain wall motion):

$$E=\frac{1}{2}\sin^2(\theta-\alpha)+\frac{1}{2c}\frac{K_{in}}{K_{out}}\sin^2[c(\phi-\beta)]\sin^2\theta + \frac{2\pi M_s}{(2K_{out}/M_s)}\cos^2\theta-\left(\frac{H_l}{(2K_{out}/M_s)}\sin\theta\cos\varphi + \frac{H_t}{(2K_{out}/M_s)}\sin\theta\sin\varphi+\frac{H_p}{(2K_{out}/M_s)}\cos\theta\right). \quad (2)$$

The in-plane anisotropy is cubic, and oriented at 45° from the longitudinal direction (in the plane of the film surface). The perpendicular anisotropy is uniaxial and oriented 10° out of the film surface. The out-of-plane anisotropy was twice as large as the in-plane component, and equal to $2\pi M_s$. Figs. 3(a)–3(d) show SMOKE hysteresis loops computed for the identical conditions described for Figs. 2(a)–2(d). Since the polar Kerr signal contains both longitudinal and polar components [Eq. (1)], Figs. 3(e) and 3(f) show the polar and longitudinal components, respectively. The polar signal is five times as large and of opposite sign than the longitudinal signal.[13] The general features are the asymmetrical structure on the corners of the loops in Figs. 2(b) and

3(b), the twin peak structures in Figs. 2(c) and 3(c), and the canted/inverted loops in Figs. 2(d) and 3(d). When the field is applied in the transverse direction, a small stray field forces the loops to close in the same direction, thus not completing a 360° rotation in plane. This is strong evidence for in-plane biaxial anisotropy.[13] When the field is applied along the polar direction, the magnetization rotates from a direction perpendicular to the plane into the plane as the field is reduced. As the field changes sign, the magnetization rotates in the plane of the surface first, aligning itself with the projection of the easy magnetization direction in the plane of the film. As the field is further increased, the linear magnetization curve is once again observed. Upon return, the magnetization rotates within the film plane thus completing at least a 180° rotation within the film plane during the switching process. These observations provide direct evidence for a canted induced uniaxial anisotropy.

IV. CONCLUSION

Three axis SMOKE measurements were used to determine the switching mode of intermediate thickness fcc Fe/Cu(100) epitaxial thin films. SMOKE loops observed with polar applied fields indicate a canted induced uniaxial anisotropy.

ACKNOWLEDGMENTS

This work was supported by the Office of Naval Research under Grant No. N00014-93-1-0099.

[1] U. Gradmann, J. Magn. Magn. Mat. **100**, 481 (1991).
[2] G. G. Hembree, J. Drucker, S. D. Healy, K. R. Heim, Z. J. Yang, and M. R. Scheinfein, Appl. Phys. Lett. (in press).
[3] S. A. Chambers, T. J. Wagener, and J. H. Weaver, Phys. Rev. B **36**, 8982 (1987).
[4] D. A. Steigerwald and W. F. Egelhoff, Jr., Surf. Sci. **192** L887 (1987); D. A. Steigerwald, F. Jacob, and W. F. Egelhoff Jr., Surf. Sci. **202**, 472 (1988).
[5] H. Glatzel, Th. Farster, B. M. U. Scherzer, and V. Dose, Surf. Sci. **254**, 58 (1991).
[6] A. Brodde and H. Neddermeyer, Ultramicr. **42–44**, 556 (1991).
[7] P. Xhonneux and E. Courtens, Phys. Rev. B **46**, 5561 (1992).
[8] J. Thomassen, F. May, B. Feldmann, M. Wuttig, and H. Ibach, Phys. Rev. Lett. **69**, 3831 (1992).
[9] L. M. Falicov, D. T. Pierce, S. D. Bader, R. Gronsky, Kristl B. Hathaway, H. J. Hopster, D. N. Lambeth, S. S. P. Parkin, G. Prinz, M. Salamon, I. K. Schuller, and R. H. Victora, J. Mat. Res. **5**, 1299 (1990).
[10] C. Liu, E. R. Moog, and S. D. Bader, Phys. Rev. Lett. **60**, 2422 (1988).
[11] K. R. Heim, S. D. Healy, Z. J. Yang, G. G. Hembree, J. S. Drucker, and M. R. Scheinfein, J. Appl. Phys. (in press).
[12] S. D. Healy, K. R. Heim, Z. J. Yang, J. S.Drucker, G. G. Hembree, and M. R. Scheinfein, J. Appl. Phys. (in press).
[13] Z. J. Yang, and M. R. Scheinfein, J. Appl. Phys. **74**, 6810 (1993).
[14] J. M. Florczak, E. D. Dahlberg, J. N. Kuznia, A. M. Wowchak, and P. I. Cohen, J. Appl. Phys. **69**, 4997 (1991).
[15] E. C. Stoner and E. P. Wohlfarth, Philos. Trans. R. Soc. London Ser. A **240**, 74 (1948).

The initial phases of epitaxy of fcc Fe/Cu(100): Supersurface and subsurface island formation

S. D. Healy, K. R. Heim, Z. J. Yang, G. G. Hembree, J. S. Drucker,[a)] and M. R. Scheinfein
Department of Physics and Astronomy, Arizona State University, Tempe, Arizona 85287-1504

Nanometer transverse resolved real space observations of the initial phases of room-temperature heteroepitaxy of fcc Fe/Cu(100) indicate that vertical atomic site exchange occurs locally. The formation of two-dimensional supersurface and subsurface islands has been characterized by secondary and Auger electron imaging. The persistence of vertical site exchange during the deposition of the first two monolayers is not inconsistent with the lack of observed ferromagnetism for the room-temperature grown fcc Fe/Cu(100) at these coverages.

Ferromagnetic ultrathin epitaxial films grown on single crystal metal substrates display unusual properties characteristic of two-dimensional ferromagnetism stabilized by magnetic (surface) anisotropy.[1] Extensive work has been devoted to correlating film microstructure with magnetic properties of the metastable[2] epitaxial fcc Fe/Cu(100) system. This has been stimulated by observations of rich structural properties present during various phases of film growth,[3–10] including bilayer growth during initial phases of epitaxy,[6,7] weak surface reconstructions,[3] strain-relief and fcc to bcc transitions for thicknesses greater than 11 ML (monolayer) (e.g., 4). Vertical site exchange during the initial phases of epitaxy have been observed by high-resolution low-energy electron diffraction,[11] x-ray photoelectron forward scattering,[12] and scanning tunneling microscopy.[13] In this article, we report not only on the supersurface Fe island formation, but also on real space, chemically specific, nanometer resolved observations of what appears to be subsurface island formation during the initial phases of room-temperature epitaxial growth of fcc Fe/Cu(100).

The specimen preparation chamber of an ultrahigh vacuum (UHV) scanning transmission electron microscope (STEM),[14] a Vacuum Generators HB501-S, operating at a base pressure of 5×10^{-11} mbar, has been equipped for the *in situ* preparation and characterization of ultrathin magnetic films. This instrumentation includes an ion sputtering gun, a broad beam Auger electron spectrometer, a reflection high-energy electron diffraction (RHEED) analysis system, a specimen heating stage ($T<800$ °C), and an electron beam evaporator. Magnetic properties are characterized using a novel three-axis implementation of the surface magneto-optic Kerr effect (SMOKE).[15] Nanometer lateral spatial resolution surface microanalysis, using secondary electron (SE) and Auger electron (AE) spectroscopy and imaging,[14] was performed in the magnetic field of the STEM objective lens using the parallelizer principle.[14,16] This instrumentation allows for the epitaxial film microstructure to be correlated with magnetic properties and is described in detail elsewhere.[17]

Single crystal Cu(100) substrates, 1 mm thick and 3 mm in diameter, were electropolished,[18] sputtered at 330 °C with 225 nA of 600 eV Ar ions at 45° incident angles, then annealed at 600 °C. Samples were observed in the electron microscope with biased SE imaging after the surface oxygen concentration had been depleted below the minimum detectable limits of our broad beam AE spectrometer. These surfaces often displayed small copper-oxide islands[17] at coverages of less than 0.01% of a monolayer which can be imaged in the microscope. Fe films were grown with an electron beam Fe source on clean, room-temperature ($T<40$ °C) Cu(100) surfaces. Room-temperature growth ensures longer (surface) diffusion lengths and films with lower defect densities. Evaporation rates of 0.14 ML/min were calibrated using Auger electron spectroscopy, Rutherford backscattering, and a quartz-crystal microbalance. The pressure during evaporation was normally below 2×10^{-9} mbar.

The thickness dependence of the SMOKE hysteresis loops of as-grown fcc Fe/Cu(100) films, and the observation of a field induced, metastable state has been correlated with the film microstructure.[19] Here, we focus on the characterization of films during the initial phases of epitaxy which are observed to be nonmagnetic. Figure 1 illustrates the surface structure of clean Cu(100) as observed, *in situ*, using nm resolution UHV SE microscopy. The surface has terraces with an average width between 25 and 75 nm (although some regions of the surface have extremely broad terraces), separated by steps (step bands) seen as white lines. The

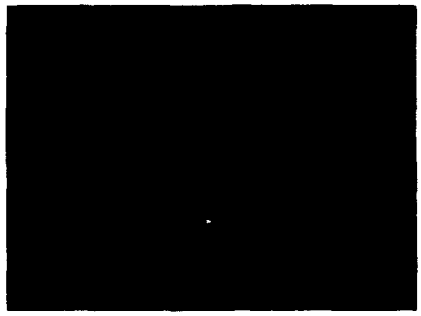

FIG. 1. High-resolution secondary electron micrographs of a clean Cu(100) surface. The white lines are steps (step bands) between terraces. The terraces have an average width of 25 to 75 nm.

[a)]Address: Center for Solid State Science, Arizona State University, Tempe, Arizona 85287-1504.

 0021-8979/94/75(10)/5592/3/$6.00 © 1994 American Institute of Physics

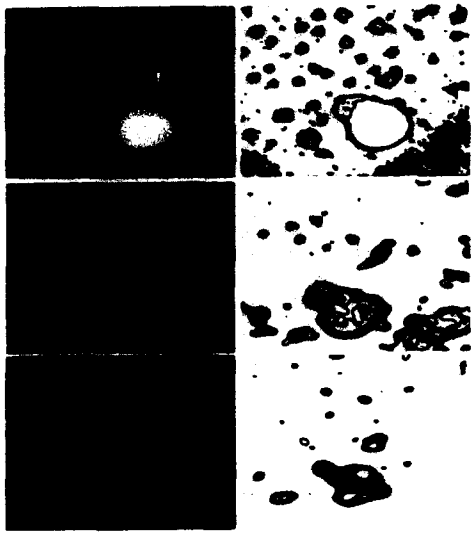

FIG. 2. After deposition of 0.33 ML of Fe at room temperature supersurface islands are observed: (a) secondary electron (SE) image, (b) contour map of SE image indicating island positions, (c) Cu LMM Auger electron (AE) image indicating Cu depletion (black) regions, (d) corresponding contour map of the Cu AE image, (e) Fe LMM AE image indicating Fe (white) islands, and (f) the corresponding contour map of the Fe AE image. The correlation of these three signals indicates that the islands have formed upon the Cu surface. These three images have identical scale factors.

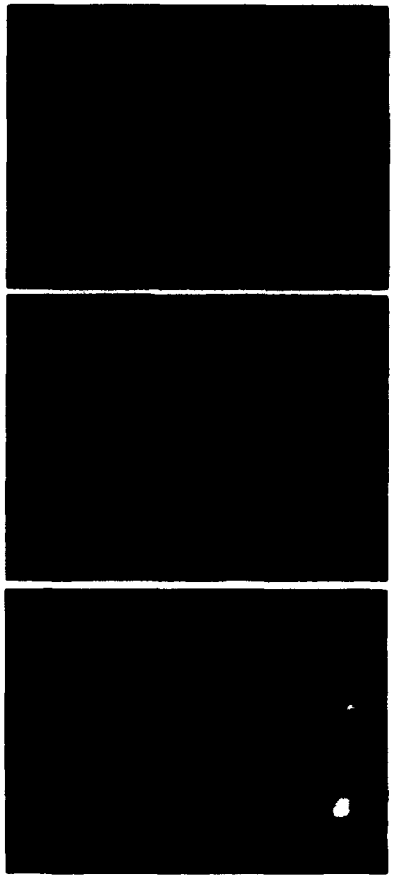

FIG. 3. After deposition of 1.7 ML of Fe at room temperature, subsurface islands are observed: (a) secondary electron image, (b) Cu LMM Auger electron (AE) image indicating Cu depletion regions (black), and (c) Fe LMM AE image indicating Fe rich regions (white). The correlation of the structure in (b) and (c) and the lack of any contrast in (a) indicates that these islands are within the surface of the substrate. These three images have identical scale factors.

widely separated nodules are copper-oxide contamination remaining after surface preparation. After Fe deposition, RHEED analysis indicated an fcc film structure with the in-plane lattice constant of the substrate (3.61 Å) for all films thinner than 10 ML. (Our RHEED measurements permit an evaluation of the in-plane lattice constant to within ±4%.)

At low film coverages, supersurface island formation can be observed locally by correlating the SE images with the Cu and Fe AE images. One such set of spatially correlated images is displayed in Fig. 2 for a 0.33 ML thick Fe film. SE images are sensitive to both the work function and topography of the surface.[20] The SE image in Fig. 2(a) illustrates supersurface Fe islands with the corresponding contour plot shown in Fig. 2(b). The large island (~45 nm in diameter) has intensity contours near its upper left quadrant indicating that this island is composed of more than 1 ML of Fe within the bulk of the island. The contrast of the smaller islands is identical to the contrast of the tip of the larger island (within the signal-to-noise limits of these measurements) indicating identical Fe island thicknesses. AE images and contour maps derived from the Cu [Figs. 2(c) and 2(d)] and Fe [Figs. 2(e) and 2(f)] Auger electron signals can be directly correlated with the SE image of the Fe islands. The AE images are produced by rastering the finely focused 100 keV incident electron beam across the sample surface and collecting most of the Fe (Cu) LMM peak Auger electrons using a spectrometer with a 1.5 eV window which is selected to pass electrons with the respective energy thus generating a two-dimensional surface map. A background map for each Auger map is subsequently acquired by selecting the passband of the spectrometer to lie 20 eV higher than the Auger peak energy. The images shown in Figs. 2(c) and 2(e) result from subtracting the background map from the peak map, such that the intensity within each pixel of the image is proportional to the number of counts within a particular Auger peak, and, therefore, proportional to the number of atoms probed by the incident beam[14] (the sensitivity factors for the Cu and Fe LMM peaks are almost identical). The black areas in Fig. 2(c) indicate the lack of a Cu signal, while the white areas in Fig. 2(e) indicate the presence of Fe. It is evident by correlating the contrast in the images and contour maps that the large island and several smaller islands are composed of Fe. Since

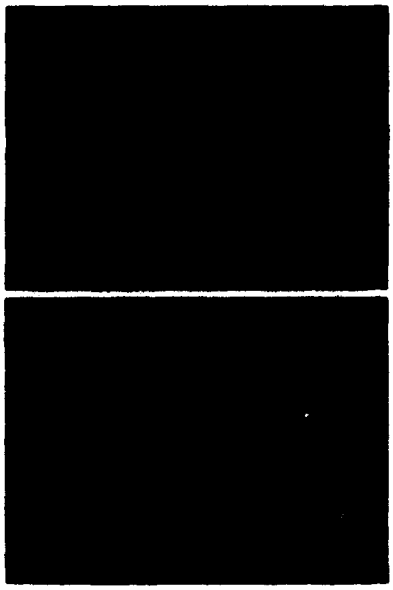

FIG. 4. The same surface as depicted in Fig. 3: (a) Cu LMM Auger electron (AE) image indicating Cu depletion regions (black) with superimposed subsurface island contour lines and (b) Fe LMM AE image indicating Fe rich regions (white) with superimposed subsurface island contour lines. These two images have identical scale factors.

the signal-to-noise ratio is much better in the SE image, the island density pictured in Fig. 2(a) likely characterizes the surface.

Figures 3(a)–3(c) display SE, Cu AE, and Fe AE images, respectively, all in registry for a Cu substrate with 1.7 ML of Fe deposited at room temperature. The bright regions in the SE image are not correlated with any structure in the Cu [Fig. 3(b)] or Fe [Fig. 3(c)] AE images. However, these same Cu and Fe AE images with superimposed contour plots, shown in Figs. 4(a) and 4(b), respectively, indicate that the regions depleted of Cu are rich in Fe. Since there is no contrast in the SE image, and the SE yield for fcc Fe and Cu are practically identical ($\delta_{Fe}=\delta_{Cu}=0.38$ at 20 keV),[21] we conclude that there is no topographic structure on the surface in this region, indicating that the contrast observed in the AE images is a result of two-dimensional subsurface island formation. This conclusion is consistent with the work of others.[11–13] We have also observed both types of island growth as well as layer-by-layer growth in the same film at different positions along the film. This indicates that these phenomena are controlled by locally varying template surface conditions.

Our observations suggest that in the regions where subsurface islands occur, a vertical Fe-Cu atomic site exchange occurs. This process continues until the driving force causing the exchange diminishes. We observed this Fe coverage to be thicker than 2 ML, beyond which continuous Fe films grew.

The lack of ferromagnetic ordering observed in this sub-2 ML regime is not inconsistent with the observed growth process. In order for the moment of an Fe island to be stable against thermal fluctuations, it must have a minimum size. Assuming a Boltzmann-type probability distribution, it is straightforward to show that most of the Fe islands, which are ~4 nm in diameter [Figs. 2(a) and 2(b)], are too small for the moments to be unaffected by thermal energy.

In summary, we have observed both supersurface islanding and subsurface islanding through vertical atomic site exchange in room-temperature grown films of fcc Fe/Cu(100) in the 0–2 ML regime. We observed no long range order to either the sub- or supersurface islands. These observations are not inconsistent with the lack of ferromagnetism observed in room-temperature grown sub-2 ML fcc Fe/Cu(100) ultrathin films.

ACKNOWLEDGMENTS

We would like to acknowledge stimulating discussions with K. Schmidt, S. Bader, and M. Hart. We acknowledge G.-C. Wang for sending prepublication results. This work is supported by the Office of Naval Research under Grant No. N00014-93-1-0099. The microscopy was performed at the National Science Foundation supported Center for High-Resolution Electron Microscopy at Arizona State University, Grant No. DMR-91-15680.

[1] N. D. Mermin and H. Wagner, Phys. Rev. Lett. **17**, 1133 (1966).
[2] T. B. Massalski, *Binary Alloy Phase Diagrams* (ASM International, Metals Park, OH, 1990), Vol. 2.
[3] P. Xhonneux and E. Courtens, Phys. Rev. B **46**, 556 (1992).
[4] J. Thomassen, F. May, B. Feldmann, M. Wuttig, and H. Ibach, Phys. Rev. Lett. **69**, 3831 (1992); J. Thomassen, B. Feldmann, and M. Wuttig, Surf. Sci. **264**, 406 (1992); H. Landskron, G. Schmidt, K. Heinz, K. Müller, C. Stuhlmann, U. Beckers, M. Wuttig, and H. Ibach, *ibid.* **256**, 115 (1991).
[5] W. A. Jesser and J. W. Matthews, Philos. Mag. **15**, 1097 (1967); **17**, 461 (1968).
[6] S. A. Chambers, T. J. Wagener, and J. H. Weaver, Phys. Rev. B **36**, 8992 (1987); H. Glatzel, Th. Fauster, B. M. U. Scherzer, and V. Dose, Surf. Sci. **254**, 58 (1991).
[7] D. A. Steigerwald and W. F. Egelhoff, Jr., Surf. Sci. **192**, L887 (1987); D. A. Steigerwald, I. Jacob, and W. F. Egelhoff, Jr., *ibid.* **202**, 472 (1988).
[8] S. H. Lu, J. Quinn, D. Tian, F. Jona, and P. M. Marcus, Surf. Sci. **209**, 364 (1989).
[9] A. Brodde and H. Neddermeyer, Ultramicroscopy **42–44**, 556 (1991).
[10] H. Magnan, D. Chandesris, B. Villette, D. Heckmann, and J. Lecante, Phys. Rev. Lett. **67**, 859 (1991).
[11] Y.-L. He and G.-C. Wang, Phys. Rev. Lett. (in press).
[12] W. F. Egelhoff, Jr., Mater. Res. Soc. Symp. Proc. **229**, 27 (1991).
[13] S. Rousset, S. Chiang, D. E. Fowler, and D. D. Chambliss, Phys. Rev. Lett. **69**, 3200 (1992); A. Brodde and H. Neddermeyer, Ultramicrosc. **42–44**, 556 (1991).
[14] G. G. Hembree, P. A. Crozier, J. S. Drucker, M. Krishnamurthy, J. A. Venables, and J. M. Cowley, Ultramicroscopy **31**, 111 (1989).
[15] Z. J. Yang and M. R. Scheinfein, J. Appl. Phys. **74**, 6810 (1993).
[16] A. J. Bleeker, Ph.D. thesis, Technische Universiteit Delft, 1991; A. Bleeker and P. Kruit, Nucl. Instrum. Methods A **298**, 269 (1990); P. Kruit and J. A. Venables, Ultramicroscopy **25**, 183 (1988).
[17] K. R. Heim, S. D. Healy, Z. J. Yang, G. G. Hembree, J. S. Drucker, and M. R. Scheinfein, J. Appl. Phys. **74**, 7422 (1993).
[18] Crystals were custom fabricated by Virgil Straughn, Monocrystals Inc. Cleveland, OH.
[19] G. G. Hembree, Jeff Drucker, S. D. Healy, K. R. Heim, Z. J. Yang, and M. R. Scheinfein, Appl. Phys. Lett. (in press).
[20] L. Reimer, *Scanning Electron Microscopy* (Springer-Verlag, Berlin, 1985).
[21] H. Seiler, J. Appl. Phys. **54**, R1 (1983).

Effect of surface layers on ferromagnetic resonance in thin Fe films: Ni, Co, Si, and $YBa_2Cu_3O_{7-\delta}$

P. Lubitz, M. Rubinstein, D. B. Chrisey, J. S. Horwitz, and P. R. Broussard
Naval Research Laboratory, Washington, DC 20375

The results of ferromagnetic resonance experiments on 10 nm polycrystalline films of Fe with very thin surface layers of Ni and Co, using Si and a high temperature superconductor (YBCO) as substrates is reported herein. An earlier fmr investigation of Fe films on YBCO showed strongly temperature dependent linewidths and resonance fields but only small effects in Fe on Si. In this work, the resonance of Fe on Si is found to be significantly narrower when the Fe film has thin (0.5 to 1.0 nm) Ni surface layers, compared to uncoated Fe; linewidths are as narrow as 15 Oe at 9 GHz. However, when YBCO substrates are used, the iron resonance properties are nearly the same as in the case where no Ni was used. This indicates that the effects seen in earlier work were not the result of an oxide layer on the Fe but may indicate a magnetically active surface layer in the YBCO. Co surface layers have the effect of producing strongly temperature dependent anisotropies and linewidths on all substrates used, with the strongest temperature dependence near 160 K, possibly caused by the ordering of an antiferromagnetic surface layer.

I. INTRODUCTION

In an earlier article[1] we described some dramatic effects occuring in the ferromagnetic resonance (fmr) of thin films of polycrystalline Fe deposited on the surface of the high temperature superconductor, $YBa_2Cu_3O_{7-\delta}$ (YBCO). Fe of about 10 nm thickness was chosen because under those conditions it grows as a fine grained polycrystalline film with a narrow linewidth. For Fe on YBCO, as the temperature was reduced below 300 K, we observed that the resonances broadened considerably, and shifted towards lower applied fields in a manner that can be characterized by an effective anisotropy field acting along the applied field with temperature dependence approximately $H_a \exp(-T/T_0)$, where T_0 is about 70 K, and H_a is on the order of 1 kOe and varies inversely with the Fe layer thickness. Similar iron films grown on Si showed a much smaller temperature dependence of their properties. Evidently, some property of the YBCO or of the YBCO–Fe interface region is transferred via interatomic exchange to the bulk of the iron; by analogy with microwave magnetic resonance data observed in spin glasses,[2] we suggested that the unknown system acting on the Fe may be a spin glass. No indications of a change in the superconducting properties of the YBCO, or of the Fe properties at the superconducting transition were seen, indicating a lack of any electronic effects. The temperature dependence of some properties of oxygen deficient YBCO (Ref. 3) suggested that it might be the magnetic system coupling to the Fe.

In this article we report an attempt to determine whether the strong anisotropy arises from the Fe, from the YBCO, or from a mixed interface region; we investigated the effects of placing very thin layers of another magnetic material at the interface between the Fe and the YBCO. About 1 nm of Ni or Co was deposited on both sides of the Fe; the literature indicates that thin layers of Ni and Co at the surfaces of Fe are ferromagnetic and are strongly exchange coupled to the Fe.[4] We have also made 10 and 20 nm pure Ni and Co films to help separate surface effects from those occuring in the bulk. Because the depositions are done at ambient temperatures, we expect negligible interdiffusion at the interfaces; however, the layers cannot be expected to be atomically flat under our growth conditions. To some degree, the width of the fmr is a probe of the magnetic layer roughness,[5] indicating that the YBCO has a rather rough surfaces,[6] and that Si is much smoother.

II. EXPERIMENT

High purity Fe, Ni, and Co were electron beam evaporated onto either YBCO, which was grown epitaxially on MgO, as described in Ref. 1, or onto polished Si (100). The deposition system uses independently controlled electron beams with shuttering to control the species and duration of the layer being deposited. The substrates were unheated during the deposition and no attempt was made to remove the native oxide on the Si. Total pressure in the vacuum system was about 10^{-7} Torr during deposition; however, since the system was cryopumped and is "gettered" by the deposition of the transition elements inside the chamber, the reactive gases are preferentially removed. Rates of evaporation were 0.1 nm/s for the thin layers of Co and Ni and 0.2 nm/s for the Fe. Rates were controlled and thicknesses monitored using quartz crystal thickness gauges. An indication of the affinity of the evaporated metals to reactive gases in the system was given by the reduction in background pressure caused by "gettering" as each electron beam was turned on. Ni has little effect on the pressure, but evaporation of Fe and Co reduced the system pressure by about an order of magnitude indicating that the free surfaces of these elements are oxidized rapidly in our system.

The fmr data were taken using a standard x-band absorption spectrometer operating at about 9.25 GHz; data at low temperatures were obtained using a He flow system with a nominal temperature accuracy of 0.5 K.

III. RESULTS

Detailed results are described below and in Figs. 1 and 2 for four samples:

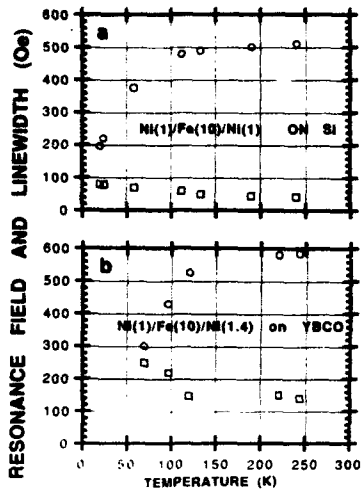

FIG. 1. Temperature dependence of the 9.2 GHz fmr position (O) and linewidth (□) for a Ni/Fe/Ni sandwich on (a) Si and (b) YBCO, described as samples A and B, respectively, in the text.

(A) Ni(0.5 nm)/Fe(1.0 nm)/Ni(0.5 nm) deposited on Si,
(B) Ni(0.5 nm)/Fe(1.0 nm)/Ni(0.5 nm) deposited on YBCO,
(C) Co(1.0 nm)/Fe(1.0 nm)/Co(1.4 nm) deposited on Si,
(D) Co(1.0 nm)/Fe(1.0 nm)/Co(1.4 nm) deposited on YBCO.

The linewidths of some of the Ni/Fe/Ni films we have made are as narrow as 15 Oe (derivitive peak to peak) at x-band frequencies, and are, we believe, the narrowest reported linewidths for any metallic ferromagnets at that frequency. The narrowest linewidths are seen in films made with elevated substrate temperatures, however, and were therefore not investigated in this study.

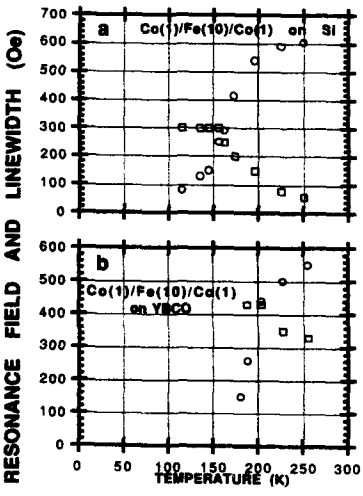

FIG. 2. Temperature dependence of the 9.2 GHz fmr position (O) and linewidth (□) for a Co/Fe/Co sandwich on (a) Si and (b) YBCO, described as samples C and D, respectively, in the text.

The temperature dependences of the resonance field and of the linewidth of sample A are shown in Fig. 1(a). The temperature dependence differs significantly from that reported in Ref. 1 in which no Ni layers were present. With the surface layers of Ni, sample A has narrower linewidths at all temperatures and shifts only slightly for temperatures down to 100 K; at the lowest temperatures the resonance shifts rapidly and broadens. The resonance properties of a sample with identical transition metal layers, but evaporated onto YBCO, sample B, are shown in Fig. 1(b). This sample has a broader linewidth, and its temperature dependence is similar to that described in Ref. 1 for a similar sample without the Ni.

We also note that the properties of our pure 20 nm thick Ni film are quite temperature dependent from 300 down to about 100 K, i.e., at temperatures where bulk properties such as magnetization, magnetostriction, and magnetic anisotropy change. Thus the bulk effects seen in Ni are not prominent in the fmr of thin layers of Ni on Fe, as seen in Fig. 1, for this temperature range.

In Fig. 2(a) we see the effects of thin surface layers of Co, sample C, on the resonance properties. The results are very different from those seen in Ref. 1 or in samples A and B in that the onset of broadening and downward shift occur at about 200 K and the changes occur most rapidly at about 160 K. Similar results were seen in all samples containing substantial Co, including pure Co layers and Ni/Co/Ni sandwiches, except for variations of about 20 K in the temperature at which changes are most rapid.

Finally we see in Fig. 2(b) the results for sample D, which is the same as C except that YBCO is used as the substrate. As before, the linewidths are broader for the YBCO than the Si substrate; the downward shifts are larger than those seen in sample C, perhaps indicating a combination of the processes occuring in Ref. 1 for Fe on YBCO, and in sample C. The onset of the rapid changes occurs at about 200 K, at which point the mechanism described in Ref. 1 produces only a slight shift.

IV. DISCUSSION

The addition of very thin layers of Ni or Co at the surface of the 10 nm Fe layers is seen to have significant effects on the low temperature fmr of the system, and to modify strongly the temperature dependences noted in Ref. 1. Some of these effects appear to be similar to the exchange anisotropy phenomena seen for permalloy films on NiO/CoO multilayers.[7]

Ni surface layers reduce the linewidth and the temperature dependence of the resonance field when the Fe is deposited on Si. However the strong temperature dependences noted in Ref. 1 for Fe on YBCO are not altered by the intervening Ni layer. Thus, we still consider it likely that a spin-glasslike state exists in the surface of the YBCO which is coupled by interatomic exchange to the Ni and Fe overlay-

ers. We attribute the difference in linewidth for the two substrates as being caused by their different roughness, rather than any electronic effects.

Ni may reduce the Fe linewidth by protecting the Fe from surface oxidation, which is known to have significant effects on the fmr at low temperatures. Patton and Wilts[8] found, at least for permalloy, that oxidation increased linewidth, with greater effects at low temperatures (the effect on the resonant field was not reported).

When the Ni layers are present the effects at the lowest temperatures may be caused by the presence of NiO. A recent study[7] of 2.1 nm NiO layers showed that the Neel temperature was reduced by about 70 K from the bulk value of 520 K. A greater reduction in our case is plausible because NiO layers in our sample would be even thinner.

The presence of spin-glass-like effects even when Ni layers are interposed between the Fe and the YBCO substrates suggests that these effects do not arise from some interaction of Fe and one or more constituents of the surface of the YBCO. The literature suggests that thin Ni layers on Fe have essentially their full moment and are strongly coupled to adjacent Fe,[4,9] so that information about the magnetic state of a YBCO surface layer could be communicated through the Ni to the Fe.

For the case of Co layers on Fe, it is unlikely that the temperature dependence of any of the parameters of bulk Co which affect the position, such as magnetization, magnetostriction, and magnetocrystalline anisotropy, could produce effects such as we observe, since these properties all vary slowly with temperature below about 200 K.[10] We do observe that Co has a strong affinity for reactive gases in our system; bulk CoO is antiferromagnetic, ordering near room temperature. Strong pinning at below room temperature in 20 nm cobalt particles with oxidized surfaces has been reported.[11] While the nominal ordering temperature of bulk CoO is 293 K, the ordering may occur at lower temperatures than reported for the bulk oxide, as is the case for NiO.[12] Both bulk Co and Ni metals do show strong increases in linewidth below 100 K which have been attributed[10] to intrinsic effects but could also be caused by temperature dependent properties of thin surface oxide layers.

We related the effects of pinning at the Fe surface to the surface energy using the calculation of Bailey and Vittoria.[13] The presence of shifts to negative fields suggests a modification allowing the form of the surface energy to be uniaxial with the axis along the applied field direction; the planar form given in Ref. 13 does not allow the resonance field to approach zero in a continuous manner. To explain the large shifts seen in Fe on YBCO or Co or Ni on Fe at the lowest temperatures, the magnitude of the surface energy is found to be about 0.5 erg/cm^2 or about 10^8 erg/atomic layer, suggesting surface fields of about 10^5 Oe. This is of the order of magnitude of the anisotropy fields in antiferromagnetic Co oxide.

V. CONCLUSIONS

Based on fmr, we observe several kinds of surface phenomena caused by the substrates, by surface layers which we deposit on the Fe, and by oxide layers. We observe that a previously suspected spin-glasslike layer occuring at the interface of Fe and YBCO thin films is not affected when a few monolayers of Ni are interposed; and infer that an oxide layer on thin Co layers becomes magnetically ordered at about 160 K, with the ordered phase possessing very large anisotropy which is felt by the Fe.

[1] M. Rubinstein, P. Lubitz, W. E. Carlos, P. R. Broussard, D. B. Chrisey, J. Horwitz, and J. J. Krebs, Phys. Rev. B **47**, 15 352 (1993).
[2] M. A. Manheimer, S. M. Bhagat, and D. J. Wolf, J. Appl. Phys. **51**, 3476 (1985).
[3] H. Alloul, T. Ohno, and P. Mendels, Phys. Rev. Lett. **63**, 1700 (1989).
[4] Y. Nagai, M. Senda, and T. Toshima, J. Appl. Phys. **63**, 1136 (1988).
[5] L. L. Hirst, unpublished Ph.D. thesis, University of Maryland, 1965.
[6] C. C. Chang, X. D. We, R. Ramesh, X. X. Xi, T. S. Ravi, T. Venkatesan, D. M. Hwang, R. E. Muenchausen, S. Foltyn, and N. S. Nogar, Appl. Phys. Lett. **57**, 1814 (1990).
[7] M. J. Carey and A. E. Berkowitz, J. Appl. Phys. **73**, 6892 (1993).
[8] C. E. Patton and C. H. Wilts, J. Appl. Phys. **38**, 3537 (1967).
[9] B. Heinrich S. T. Purcell, J. R. Dutcher, K. B. Urquhart, J. R. Cochran, and A. S. Arrott, Phys. Rev. B **38**, 12879 (1988).
[10] S. M. Bhagat and P. Lubitz, Phys. Rev. B **10**, 179 (1974).
[11] W. H. Meiklejohn and C. P. Bean, Phys. Rev. **105**, 904 (1957).
[12] J. A. Borchers, M. J. Carey, R. W. Erwin, C. F. Majkrzak, and A. E. Berkowitz, Phys. Rev. Lett. **70**, 1878 (1993).
[13] G. C. Bailey and C. Vittoria, Phys. Rev. B **8**, 3247 (1973).

Magneto-optical Kerr effect study of ac susceptibilities in ultrathin cobalt films

A. Berger,[a] S. Knappmann, and H. P. Oepen
Institut für Grenzflächenforschung und Vakuumphysik, Forschungszentrum Jülich, Postfach 1913, D-52425 Jülich, Germany

The ac susceptibility of ultrathin Co/Cu(100) films has been investigated *in situ* under ultrahigh vacuum conditions using the magneto-optical Kerr effect. A conventional Kerr effect setup was combined with an ac-field modulation technique to improve the experimental detection limit. A sensitivity in the range of 10^{-8} rad for the Kerr ellipticity has been achieved in the present study. The ac susceptibility χ_{ac} of the investigated cobalt films is mainly characterized by a pronounced and sharp maximum as a function of the temperature T. This $\chi_{ac}(T)$ dependency corresponds to the ferromagnetic-paramagnetic phase transition occurring at the Curie temperature T_c of the cobalt films, which is also confirmed by experimental observation of the hysteresis behavior. Besides the measurement of Curie temperatures, the experimental technique presented here allows the determination of magnetic properties for ultrathin films even in the paramagnetic regime far above T_c.

I. INTRODUCTION

In recent years, the magneto-optical Kerr effect has been proven to be a powerful tool for studying ferromagnetic properties of ultrathin films *in situ* under ultrahigh vacuum (UHV) conditions.[1] Many studies have demonstrated that even the critical behavior of ferromagnetic films in the monolayer thickness range can be investigated by using this technique.[2–4] Despite its successful application to various problems in the field of thin film magnetism, all these studies have been based on the observation of $M(H)$-hysteresis loops only. For the investigation of the critical behavior and the determination of Curie temperatures, however, this technique has the disadvantage that a vanishing quantity, i.e., the remanent magnetization, is measured as a function of temperature.

Just the opposite is true for the ac susceptibility χ_{ac} of ferromagnets. The susceptibility χ_{ac} is characterized by a sharp and pronounced maximum at the Curie temperature.[5] Moreover, χ_{ac} follows a certain power law in the paramagnetic temperature range, which provides additional information about the critical behavior of the ferromagnetic system.[6] Therefore, it is very promising to have an experimental tool which is able to measure the susceptibility χ_{ac} of ultrathin ferromagnetic films. Recently, conventional ac-susceptibility measurements for ultrathin gadolinium films have been reported.[7]

In this study, we have experimentally determined the ac susceptibility of cobalt monolayer films by means of the magneto-optical Kerr effect.

II. EXPERIMENT

The magnetic properties as well as the growth behavior of ultrathin cobalt films grown on Cu(100) have been extensively studied in the past.[8] It has been demonstrated, that this system exhibits layer-by-layer growth for substrate temperatures between 300 and 450 K, although double layer growth is present to a certain extent below film thicknesses of 2 monolayers.[8–10] Cobalt films grown under these conditions show ferromagnetic order at room temperature already for thicknesses below 2 monolayers.[8,11] The ⟨110⟩ directions in the film plane have been determined as the easy axes of magnetization.[11,12] In the present study, cobalt films were grown under UHV conditions ($p<2\times10^{-10}$ mbar during evaporation) by means of an *e*-beam evaporator onto a Cu(100) single crystal with typical deposition rates of 0.5 ML/min. The Cu crystal was previously cleaned by ion etching (Argon, $E_{kin}=800$ eV) and annealing ($T=900$ K). The substrate temperature during evaporation was held at $T=330$ K. After deposition, no contamination like carbon or oxygen was detectable via Auger spectroscopy.

The magnetic properties of the films were investigated by means of the longitudinal Kerr effect *in situ* under UHV conditions. The experimental setup is similar to the one used by Bader *et al.*[1] and is schematically shown in Fig. 1. With a polarizer ($P1$) HeNe-laser light is polarized perpendicular to the scattering plane. In the reflected light beam the polarization is slightly changed due to the magneto-optical Kerr effect, caused by the long range ferromagnetic order of the sample.[13] Using a quarter wave plate and a second polarizer ($P2$) with its orientation nearly perpendicular to $P1$, this polarization change in the reflected light beam can easily be

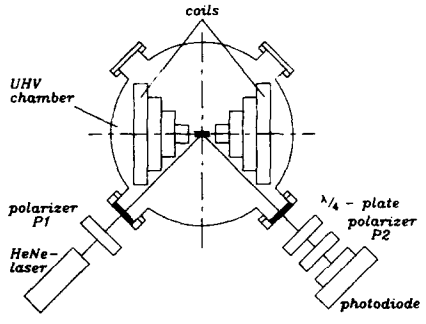

FIG. 1. Schematic of the experimental Kerr effect setup.

[a]Current address: University of California, Department of Physics, Irvine, CA 92717-4575.

 0021-8979/94/75(10)/5598/3/$6.00 © 1994 American Institute of Physics

observed as a change in light intensity with a photodiode. In the conventional mode the light intensity is measured as a function of the externally applied magnetic field strength produced by a Helmholtz coil arrangement inside the UHV. This technique is used to monitor the $M(H)$ dependency of the sample. For measurements of the ac susceptibility χ_{ac}, a small ac current of fixed frequency and amplitude is applied to the Helmholtz coils producing a small ac-magnetic field. The response of the magnetic film to this ac field is measured via the longitudinal Kerr effect as an ac voltage at the photodiode. Using a lock-in technique, the signal-to-noise ratio for this ac voltage is strongly improved and a much higher sensitivity for the susceptibility is achieved. Details of the experimental setup are described elsewhere.[14]

Utilizing the magneto-optical Kerr effect for susceptibility measurements, one has to keep in mind what quantity is actually measured. The phase sensitive signal we obtain in our experiment is proportional to the difference of the Kerr ellipticity ϵ at $\pm H_{max}$ of the ac field, i.e., a quantity proportional to the slope of $\epsilon(H)$. Assuming a constant magneto-optical coupling factor Q for the films investigated, this $\epsilon(H)$ dependency is proportional to $M(H)$. Therefore, despite a constant factor, we probe the susceptibility χ_{ac} in our experiment.[14]

III. EXPERIMENTAL RESULTS

Figure 2 shows an example for the field dependency of the Kerr ellipticity, representing the $M(H)$ behavior of a 2.2 $\pm$0.2 monolayer thick Co/Cu(100) film, which was measured with the conventional Kerr effect setup for four different temperatures. Figure 2(a), measured at $T=328$ K, shows the typical hysteresis effect that one expects for a ferromagnetic film. The nearly rectangular shape of the hysteresis loop suggests, that the film magnetization switches between two single domain states, at least within the area of the light spot (1 mm diameter). The Kerr ellipticity, i.e., the magnetization, does not depend on the field strength except for the very small region around the switching fields. This behavior is typical for temperatures far below the Curie temperature. In Fig. 2(b) ($T=383$ K) it is clearly observable that the remanent magnetization is already reduced compared to Fig. 2(a), although a hysteresis loop is still present. This demonstrates, that the temperature $T=383$ K is still below the Curie temperature of the film. It is also obvious from Fig. 2(b), that there is now a field dependence of the magnetization even apart from the immediate vicinity of the switching fields. The experimental data shown in Fig. 2(c) are obtained with the sample at $T=509$ K. Remanence cannot be observed anymore, i.e., the Kerr ellipticity is represented by a single line as a function of the magnetic field strength H. Despite of the absent remanent magnetization, i.e., long range ferromagnetic order, a steep increase of the Kerr ellipticity with the field strength at $H=0$ is found. This behavior corresponds to a large susceptibility value at zero field, which means that the temperature is slightly above T_c. The strong nonlinear field dependency seen in Fig. 2(c) confirms the immediate vicinity of T_c. Figure 2(d) shows results for an even higher temperature ($T=563$ K). As the susceptibility drops off very strongly with increasing temperature in the paramagnetic

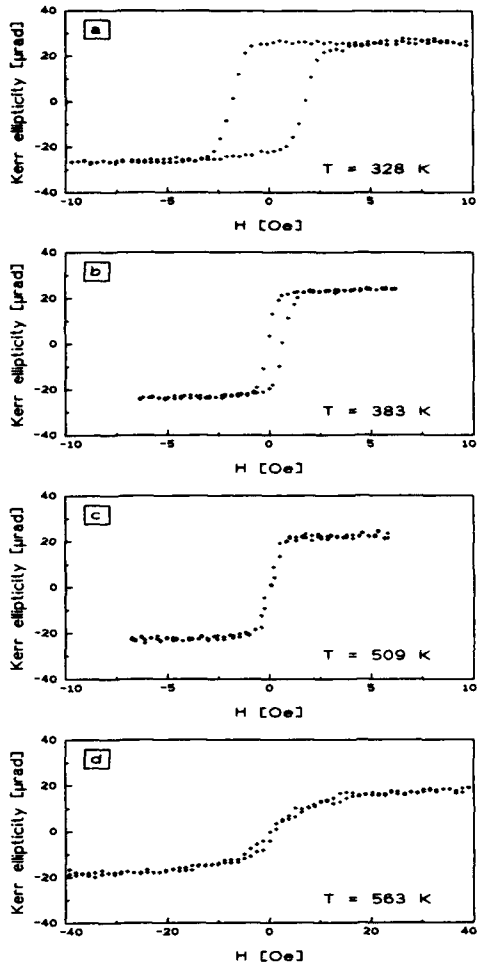

FIG. 2. Measured Kerr ellipticity as a function of the applied field strength H (conventional Kerr effect measurement) for a 2.2 monolayer Co/Cu(100) film. Temperatures as indicated.

state, the field necessary to obtain the same magnetization value as in Fig. 2(c) is considerably higher. Thus, it is obvious from Fig. 2(d) that this kind of magneto-optical Kerr effect experiment enables us to study the paramagnetic behavior of ultrathin films but is limited to the vicinity of the critical temperature, at least with reasonable field strength. With an increase of sensitivity, however, the range accessible for studies in the paramagnetic state can be extended to temperatures far above T_c.

Figure 3 shows experimental data that have been measured with the ac-field modulation technique. Here, the measured Kerr ellipticity amplitude is shown as a function of the sample temperature for the same film as in Fig. 2. The two

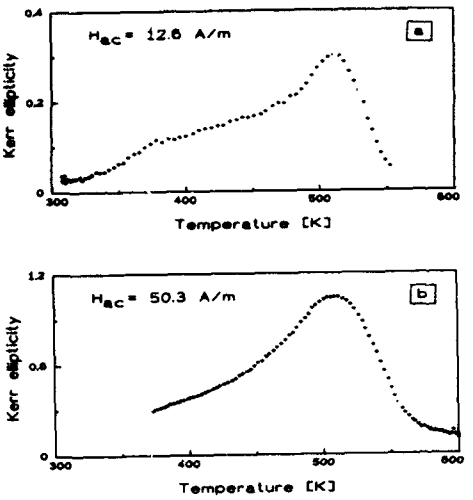

FIG. 3. Measured Kerr ellipticity response [in μrad] to an applied ac field as a function of temperature (ac-modulation technique). Experimental data were taken for a 2.2 monolayer Co/Cu(100) film with modulation field strengths H_{ac} as indicated. The measured quantity corresponds to the ac susceptibility of the film.

curves presented in Fig. 3 differ only by the field strength H_{ac} which is applied to the sample. Both curves are mainly characterized by a pronounced maximum of the Kerr ellipticity as a function of temperature, which corresponds to the maximum of the ac susceptibility at the Curie temperature. This maximum evidently represents the ferromagnetic-paramagnetic phase transition of the cobalt film and demonstrates the feasibility for an exact determination of T_c by this technique. The varying value of the Kerr ellipticity for the two different curves in Fig. 3 is due to the different modulation amplitudes used. The different shape of the curves, especially the broadening in the ferromagnetic regime in Fig. 3(b) is also caused by the increased ac-field strength. This can easily be understood by considering the temperature dependence of the coercivity which is characterized by a strong increase of the coercive field with decreasing temperature. As long as the modulation field strength H_{ac} is larger than the coercive field H_c, the magnetic field is able to reverse the sample magnetization resulting in a large value for the Kerr ellipticity. Therefore, an increased field strength H_{ac} corresponds to a larger temperature range in which $H_c < H_{ac}$ and results in a broadening of the $\chi_{ac}(T)$ peak as seen in Fig. 3. But also with the smaller field strength [Fig. 3(a)], the $\chi_{ac}(T)$ peak has a finite width which might be attributed to thickness variations in the cobalt film. In ultrathin films, the Curie temperature increases with increasing film thickness.[15] Thus, the roughness present in monolayer films results in a distribution of Curie temperatures. This explains that for ultrathin films one has to expect a finite width of the $\chi_{ac}(T)$ maximum even if a very small ac-field strength is applied. Taking the strong thickness dependence of T_c for Co/Cu(100) films into account,[8] one might take the small peak width of Fig. 3(a) as an indication for high film quality regarding its thickness homogeneity.

Figure 3(a) demonstrates that the field modulation technique is able to reach an extremely high sensitivity for Kerr ellipticity or rotation with an detection limit in the range of 10^{-8} rad in this study. This high sensitivity makes it possible to extend the temperature range which is accessible for Kerr effect investigations on monolayer films far into the paramagnetic regime. As the slope of the $M(H)$ curves around zero field decreases [see Fig. 2(d)] with increasing temperature ($T > T_c$) the modulation amplitude might be increased. Hence, paramagnetic properties are detectable far beyond the Curie temperature, e.g., 100 K above T_c in Fig. 3(b). In other words, the data presented in Fig. 3(b) reflect the paramagnetic film behavior for the highest temperatures very well while the modulation amplitude is too large to observe the susceptibility around T_c correctly. It should be mentioned that Fig. 3(b) does not represent the limit of the accessible temperature range concerning the sensitivity of the susceptibility measurement. The temperatures have not been raised further because of severe problems of Co-Cu intermixing.[8]

IV. CONCLUSIONS

In this article, we have demonstrated that the ac susceptibility χ_{ac} of ultrathin films can be determined by means of the longitudinal magneto-optical Kerr effect. The extremely high sensitivity of the modulation technique used in our experimental approach enables us to measure χ_{ac} of a 2.2 monolayer Co/Cu(100) film for temperatures even far above the Curie temperature. Therefore, this technique is most promising to detect magnetic ordering in overlayers on nonmagnetic materials, which might have very low Curie temperatures and have been proposed recently.[16]

ACKNOWLEDGMENT

One of us (A.B.) would like to thank the Alexander von Humboldt Foundation for their financial support.

[1] See S. D. Bader, J. Magn. Magn. Mater. **100**, 440 (1991) and references therein.
[2] C. A. Ballentine, R. L. Fink, J. Araya-Pochet, and J. L. Erskine, Phys. Rev. B **41**, 2631 (1990).
[3] C. Liu and S. D. Bader, J. Appl. Phys. **67**, 5758 (1990).
[4] Z. Q. Qiu, J. Pearson, and S. D. Bader, Phys. Rev. Lett. **67**, 1646 (1991).
[5] E. Kneller, *Ferromagnetismus* (Springer, Berlin, 1962).
[6] D. C. Mattis, *The Theory of Magnetism II*, Springer Series in Solid-State Science Vol. 55 (Springer, Berlin, 1985).
[7] M. Farle, K. Baberschke, U. Stetter, A. Aspelmeier, and F. Gerhardter, Phys. Rev. B **47**, 11571 (1993).
[8] C. M. Schneider, P. Bressler, P. Schuster, J. Kirschner, J. J. de Miguel, and R. Miranda, Phys. Rev. Lett. **64**, 1059 (1990).
[9] H. Li and B. P. Tonner, Surf. Sci. **237**, 141 (1990).
[10] A. K. Schmidt and J. Kirschner, Ultramicroscopy **42–44**, 483 (1992).
[11] D. Kerkmann, Appl. Phys. A **49**, 523 (1989).
[12] H. P. Oepen, M. Benning, H. Ibach, C. M. Schneider, and J. Kirschner, J. Magn. Magn. Mater. **86**, L137 (1990).
[13] P. N. Argyres, Phys. Rev. **97**, 334 (1955).
[14] A. Berger and H. P. Oepen (unpublished).
[15] See D. L. Mills, J. Magn. Magn. Mater. **100**, 515 (1991) and references therein.
[16] See A. J. Freeman and R. Q. Wu, J. Magn. Magn. Mater. **100**, 497 (1991) and references therein.

Ferromagnetic resonance determination of fcc→hcp structural change in epitaxial Co/Mn superlattices

K. Ounadjela, Y. Henry, M. Farle, and P. Vennegues
IPCMS, CNRS, UMR46 Université Louis-Pasteur, 67070 Strasbourg, France

A series of epitaxial $[Co_{24\ Å}Mn_{t_{Mn}}]_{12}$ superlattices (3.2 Å$\leq t_{Mn}\leq$32 Å) was grown on hcp(0001) Ru buffer layers by ultrahigh vacuum *e*-beam evaporation. Ferromagnetic resonance has shown that for samples with 3.2 Å$\leq t_{Mn}\leq$12 Å, the cobalt layers are predominantly fcc and almost perfectly fcc for the sample having the thinnest Mn thickness $[Co_{24\ Å}/Mn_{3.2\ Å}]_{12}$. For samples with greater Mn thickness (t_{Mn}>12 Å), the cobalt layers are predominantly hcp with structural defects corresponding either to large inclusions of fcc Co or stacking faults.

The growth of epitaxial thin films of ferromagnetic materials on single-crystalline substrates under ultrahigh vacuum conditions offers the possibility of producing materials that do not exist in nature. Indeed, if coherent growth on a substrate is achieved, the in-plane lattice parameter of the epitaxial phase is constrained which may lead to the stabilization of new structures. Such a new phase may be a forced stable structure, supported by interfacial interactions that favor registry with the substrate. There is then a critical thickness beyond which this forced structure should relax This point is reached when the bulk strain energetic cost of maintaining the forced structure overcomes the interfacial energy. Moreover, the epitaxial phase may be metastable, corresponding to a local minimum of the free energy.

In order to understand the above mentioned mechanisms, we studied the growth of single-crystalline epitaxial Co/Mn superlattices on a (0001) Ru buffer layer.

Reflection high energy electron diffraction (RHEED) and x-ray analysis[1] on a series of $[Co_{24\ Å}/Mn_{t_{Mn}}]_{12}$ superlattices (3.2 Å$\leq t_{Mn}\leq$32 Å), have shown that a phase change occurs within both Mn and Co sublayers at a critical Mn thickness of 12 Å. Up to six Mn monolayers, the Mn layers are highly strained. Co and Mn are stabilized in nonequilibrium pseudomorphic fcc lattices. As the thickness of the Mn layers is increased, there is a trade-off between strain relaxation in the Mn and a larger density of epitaxial dislocations, which reduces the coherence between the Mn and Co layers. Eventually, for a Mn layer thickness of 6 ML (monolayer), the dislocation density at the interfaces is maximum with very little strain in either layer. Consequently, the cobalt reverts to its normal bulk hcp structure. In parallel, the manganese also tends to approach its Mn-α stable bulk structure by adopting the $MgCu_2$-type lattice.[1,2]

The aim of this contribution is to use ferromagnetic resonance (FMR) experiments to distinguish fcc and hcp components in the crystalline structure of the cobalt layers and to obtain a quantitative measure of their associated structural defects in the $[Co_{24\ Å}/Mn_{t_{Mn}}]_{12}$ series.

Epitaxial Co/Mn superlattices with fixed Co layers (t_{Co}=24 Å) and Mn layer thicknesses ranging from 3.2 and 32 Å have been grown on mica substrates by *e*-beam evaporation. The high crystalline quality of these samples deposited on a 150 Å thick (0001) hcp Ru buffer layer has been verified by RHEED and x-ray diffraction analysis as described in detail elsewhere.[1] For complementary information on the magnetic anisotropies, we also prepared Co/Mn/Co trilayers with, respectively, 4, 10, and 16 Å fixed Mn thickness and cobalt layer thicknesses ranging from 5 to 40 Å under the same growth conditions the superlattices.

Ferromagnetic resonance (FMR) is a well established method for a quantitative determination of magnetic anisotropies and inhomogeneities in magnetic superlattices.[3,4] As hcp and fcc cobalt bulk structures display very different magnetocrystalline (MC) anisotropies, FMR turns out to be particularly useful to quantify the crystallographic structure within the cobalt layers (fcc, hcp, or in between) and the density of stacking faults.

FMR was measured at room temperature (RT) and at 9.8 GHz in a TE_{011} cavity that allowed to vary the angle Θ_H of the applied field with respect to the film normal. The FMR data were analyzed using the standard theory which involves solving the Landau–Lifshitz equation of motion for the magnetization **M**.[3,4] The in-plane magnetization curves at RT of the all Co/Mn samples are fully saturated for a field of about 100 Oe which indicates that adjacent cobalt layers are not antiparallel coupled. In this case, the calculation of the FMR dispersion relation for this system can be simplified by the the standard single layer model.[3,4]

The energy density due to the effective anisotropy is given by

$$E_K=K_{\rm eff}\times\cos^2\Theta,\quad K_{\rm eff}=2\pi M^2+K_{\rm MC}+2\times\frac{K_s}{t_{\rm Co}},\quad (1)$$

where Θ is the angle between **M** and the surface normal, $2\pi M^2$ corresponds to the demagnetizing energy density, K_{MC} to the magnetocrystalline anisotropy which reflects the symmetry of the crystal, and $2\times(K_s/t_{Co})$ to the anisotropy arising from the two interfaces for each Co layers. Here, we have neglected (i) the magnetoelastic anisotropy which is small, since the cobalt layers are fully relaxed as deduced from RHEED and x-ray results,[1] (ii) the small six-order in-plane anisotropy present in these samples.

The standard equilibrium and FMR conditions for the magnetization give a direct determination of the effective anisotropy field $H_{eff}=2\times(K_{eff}/M_s)$.

We have determined K_{MC} of the cobalt layers for each of the $[Co_{24\ Å}/Mn_{t_{Mn}}]_{12}$ samples by deducing independently:

(a) The demagnetizing anisotropy term $K_{shape}=2\pi M^2$, from direct magnetization measurements. The same saturation magnetization (about 16 kOe) is found for all samples of

 0021-8979/94/75(10)/5601/3/$6.00 © 1994 American Institute of Physics

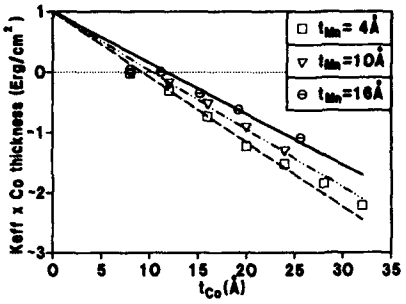

FIG. 1. Dependence of the measured effective anisotropy per surface unit of Co, $K_{eff}\times t_{Co}=(K_{MC}+K_{shape})\times t_{Co}+2\times K_s$ on the Co thickness t_{Co} for the three sets of trilayers: $[Co_{t_{Co}}Mn_4\ Å]_2$, open squares; $[Co_{t_{Co}}Mn_{10}\ Å]_2$, open triangles; $[Co_{t_{Co}}Mn_{16}\ Å]_2$, open circles. K_{eff} has been determined from the value of H_{eff} and M_s measured, by FMR and AGFM experiments, respectively. We note a slight decrease of the measured magnetization as the Co layer decreases from 1350 emu/cm^3 for $t_{Co}=32$ Å to 1200 emu/cm^3 for $t_{Co}=8$ Å which indicates a reduced diffusion at the interfaces.

the $[Co_{24\ Å}/Mn_{t_{Mn}}]_{12}$ series with a slight dispersion of about 5% within the experimental error bars.

(b) The interfacial magnetic anisotropy from FMR measurements on three $[Co_{t_{Co}}/Mn_{t_{Mn}}]_2$ series with constant Mn layer thicknesses (t_{Mn}=4, 10, 16 Å) and varying Co layer thicknesses. According to Eq. (1), $K_{eff}\times t_{Co}$ is a linear function of t_{Co}, and $(K_{MC}+K_{shape})$ is obtained from the slope and $2\times K_s$ from the intercept with the y axis. Several studies on Co/Pd (Ref. 5), Co/Ni (Ref. 6), have been reported in the literature to determine the value of the interfacial anisotropy and its origin using the same method. Figure 1 shows the experimental results, $K_{eff}\times t_{Co}$ versus t_{Co}, for the three sets of trilayers.

(i) For Co layers thicker than 10 Å, the $K_{eff}\times t_{Co}$ values are negative and follow the expected linear function. $K_{MC}\times t_{Co}+2\times K_s$ is smaller than the shape anisotropy term and the easy axis remains in the film plane. The slope $(K_{MC}+K_{shape})$ becomes more positive with increasing Mn thickness. This corresponds to an increase of K_{MC} only, since $K_{shape}=2\pi M^2$ is constant. This indicates a change of the crystalline structure of the cobalt layers for different Mn thicknesses. On the other hand, the extrapolation of K_s from the intercept with the y axis of the linear fits is valid only for $t_{Co}>10$ Å, for which the cobalt layers are fully relaxed as shown by x ray and RHEED experiments.[1] This gives an interfacial anisotropy $2\times K_s\simeq 1$ erg/cm^2, which does not show a significant change for the three series of samples. This result suggests that the mechanism responsible for the interfacial anisotropy is due to Néel-type interactions. Indeed, for a free $(111)_{fcc}$ or $(0001)_{hcp}$ surface, the nearest neighbor atom distribution is exactly the same for a fcc or hcp structure with a c/a ratio equal to $\sqrt{8/3}=1.63$. In our sample, the c/a ratio for the hcp Co layer is very close to this value, $c/a=1.622$, which results in a very close distribution of the nearest neighbors for the $(111)_{fcc}$ and $(0001)_{hcp}$ Co surface. If we consider that the interfacial anisotropy is described by pseudodipolar interactions between magnetic moments of all pairs of atoms and limited to the nearest neighbors as in the Néel model, we should not expect any change in the value of K_s even if the stacking within the Co layers changed from fcc to hcp in our samples. Consequently, we conclude that the interfacial anisotropy $2\times K_s=1$ erg/cm^2 should remain constant for all samples of the $[Co_{24\ Å}/Mn_{t_{Mn}}]_{12}$ series.

(ii) Below a cobalt thickness of 10 Å, $K_{eff}\times t_{Co}$ deviates clearly from the linear fits shown in Fig. 1. One finds a small and positive value of K_{eff} which results in a perpendicular easy axis of the magnetization. A possible explanation for such a kink in $K_{eff}\times t_{Co}$ versus t_{Co} is related to the presence of misfit strains within the cobalt layers. As shown from RHEED and x-ray experiments,[1] the cobalt layers becomes highly strained for such thin thicknesses with an exponential decrease of their elastic strains when the Co layers increase from 0 to 10 Å. This gives an apparent interface contribution—the magnetoelastic interface anisotropy—that is certainly negative and which contributes to the decrease of the effective anisotropy, K_{eff}.

Figure 2(a) is a plot of the magnetocrystalline anisotropy field $H_{MC}=2\times(K_{MC}/M_s)$ versus t_{Mn} for the $[Co_{24\ Å}/Mn_{t_{Mn}}]_{12}$ series. The strong variation of H_{MC} with the Mn thickness can be interpreted in the following way.

If our samples had ideal hcp and fcc structures, the magnetocrystalline anisotropy field should be $H_{MC}^{hcp}\simeq 6.7$ kOe and $H_{MC}^{fcc}\simeq 0.35$ kOe, respectively, as calculated from Co bulk anisotropy constants[7] including $4\pi M_s=16$ kOe. First, for the $[Co_{24\ Å}/Mn_{3.2\ Å}]_{12}$ superlattice, we measure H_{MC} (0.5 kOe) close to H_{MC}^{fcc}. This confirms the presence of the almost perfect Co fcc structure of the cobalt layers observed by x rays.[1] Then, for samples with intermediate Mn thicknesses, 3.2 Å$<t_{Mn}<$12 Å, the anisotropy field reaches a plateau with $H_{MC}=1.6\pm0.3$ kOe which is closer to H_{MC}^{fcc} than to H_{MC}^{hcp}. This result suggests that in this Mn thickness range, the structure of the cobalt layers is predominantly fcc with no indication of an increasing hcp Co component. Finally, for samples with $t_{Mn}>12$ Å, the magnetocrystalline anisotropy field increases with a large spread of values. This indicates that the Co layers have a predominant hcp structure, but with some inclusions of the fcc Co phase.

In order to determine the structural quality of the samples in terms of the perfection of the fcc or hcp phase, we studied the FMR linewidth, ΔH, of the absorption peaks in both perpendicular ($\Theta_H=90°$) and parallel ($\Theta_H=0°$) orientations of the external applied field with respect to the film plane. ΔH most likely originates from only two sources besides the intrinsic damping mechanism. The first contribution is the distribution of the orientation of the c axis for different crystallites. The other one is the internal effective field inhomogeneity which arises from the presence of both fcc and hcp phases within the cobalt layers. The resonance linewidth ($\Delta H_\perp$ and $\Delta H_\parallel$ for Θ_H equal to, respectively, 0° and 90°) is plotted in Fig. 2(b) as a function of t_{Mn} for the $[Co_{24\ Å}/Mn_{t_{Mn}}]_{12}$ superlattices. The results are complementary to the previous observations: (i) for the $[Co_{24\ Å}/Mn_{3.2\ Å}]_{12}$ sample, the small values of $\Delta H_\parallel$ (48 Oe)

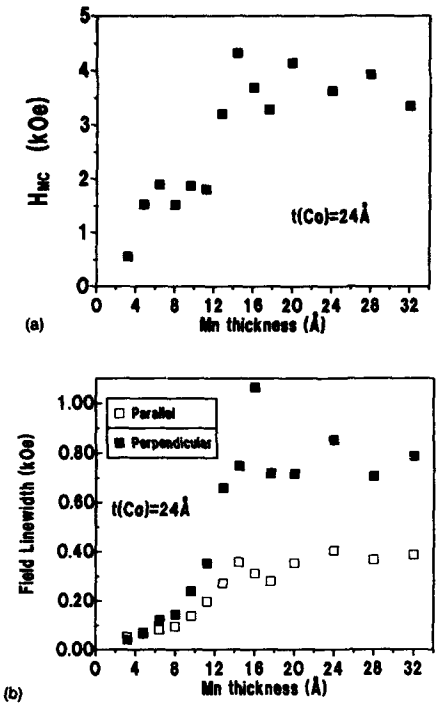

FIG. 2. (a) Magnetocrystalline anisotropy field H_{MC} as a function of the Mn thickness for the $[Co_{24}\,Å/Mn_{t_{Mn}}]_{12}$ series. H_{MC} has been determined from the effective anisotropy field H_{eff} measured by FMR. Linewidths of the resonance field ΔH in perpendicular (full square) and parallel (empty square) orientations of the external field, as a function of the Mn thickness for the $[Co_{24}\,Å/Mn_{t_{Mn}}]_{12}$ series.

and $\Delta H_\perp$ (38 Oe) show that there are only a very small number of defects. In fact, this sample compares favorably with the narrowest lines observed in ultrathin films and superlattices.[8] This result is compelling evidence that this sample possesses an excellent structure. Moreover, the possible spread of the internal fields due to the presence of hcp grains is very small and confirms the high purity of the fcc phase. RHEED and x-ray results[1] also confirmed the high crystalline quality of the whole set of the $[Co_{24}\,Å/Mn_{t_{Mn}}]_{12}$ samples with an angular distribution of the c axis of only 1.5°. Since the latter is found for all samples, we conclude that ΔH is not broadened by this effect to the extent reported below. (ii) For thicker Mn layers, ($t_{Mn}>6$ Å), the resonance linewidth and also the difference between $\Delta H_\parallel$ and $\Delta H_\perp$ increases with t_{Mn}. This can be understood if the main contribution to the FMR absorption linewidth is due to the inhomogeneous line broadening as discussed by Chappert *et al.*[4] Their idea is that the specimen can be considered as a collection of independent domains: each region is supposed to be subject to a different anisotropy field due to the presence of stacking faults or grains having different structures, and therefore different resonance fields. Indeed, the FMR fields of perfect hcp and fcc grains are respectively, $H_\parallel^{fcc}\simeq 0.75$ kOe, $H_\parallel^{hcp}\simeq 1.4$ kOe for $\Theta_H=0°$ and $H_\perp^{fcc}\simeq 14$ kOe, $H_\perp^{hcp}\simeq 7.9$ kOe for $\Theta_H=90°$. Therefore the internal field distribution broadens the absorption line at all angles, but the maximum broadening occurs when the field is applied perpendicular to the film plane. Indeed, for $\Theta_H=90°$, the difference between the hcp and fcc FMR fields is the largest ($H_\perp^{fcc}-H_\perp^{hcp}\simeq 6$ kOe) and $\Delta H_\perp$ provides a measure of the [illegible] field distribution and consequently, the partition [illegible]d fcc phases within the cobalt sublayers. How[illegible] for $\Theta_H=0$, the FMR field is much less sensitive to the variations of the anisotropy fields ($H_\parallel^{fcc}-H_\parallel^{hcp}\simeq 0.6$ kOe) yielding a smaller linewidth. Farle *et al.*[9] have reported a fit of the field linewidth for the $[Co_{24}\,Å/Mn_{t_{Mn}}]_{12}$ series assuming that the anisotropy is distributed around its mean value [defined in Fig. 2(a)] according to a Gaussian distribution. They show that a fluctuation smaller than ±2% of the magnetocrystalline anisotropy is sufficient to explain both line broadenings ($\Delta H_\perp$ and $\Delta H_\parallel$) for samples with Mn thickness $t_{Mn}<12$ Å. Such a variation can be attributed to the small density of stacking faults which strongly affect the MC anisotropy. In a predominantly fcc Co structure, it is clear that a stacking fault like *ABCABABC*... would strongly affect two adjacent atomic layers where the involved atoms are in a hcp nearest neighbor environment. In the presence of such stacking faults in the cobalt sublayers, the average value of H_{MC} is expected to increase and the linewidth to broaden. However, for larger Mn thicknesses, for which the Co sublayers have now a predominant hcp structure ($t_{Mn}>12$ Å), the sudden jump in $\Delta H_\perp$ up to about 0.8 kOe [Fig. 2(b)] indicates a larger spread of the internal field than in the previous case (corresponding to ±8% fluctuations in the MC anisotropy[9]). This is considerable if compared to other very clean hcp cobalt structures. For example Co/Ru superlattices[10] prepared under the same conditions present $\Delta H_\parallel\simeq\Delta H_\perp\simeq 0.2$ kOe. This larger spread should be related to more stacking faults which tend to increase the cubic environment of the cobalt atoms within the Co sublayers. Most striking is the fact that the linewidth does not change for larger Mn thicknesses up to $t_{Mn}\simeq 32$ Å, as shown in Fig. 2(b), suggesting that the number of stacking faults remains approximately the same.

[1] K. Ounadjela, P. Vennegues, Y. Henry, A. Michel, V. Pierron, and J. Arabski, Phys. Rev. B (in press).
[2] B. Heinrich, A. S. Arrott, C. Liu, and S. T. Purcell, J. Vac. Sci. Technol. A **5**, 1935 (1988); Y. Henry, V. Pierron, P. Vennegues, and K. Ounadjela (unpublished).
[3] A. Berghaus, M. Farle, Y. Li, and K. Baberschke, Springer Proc. Phys. **50**, 61 (1990).
[4] C. Chappert, K. Le Dang, P. Beauvillain, H. Hurdequint, and D. Renard, Phys. Rev. B **34**, 3192 (1986).
[5] B. N. Engel, C. D. England, R. A. van Leeuwen, M. H. Wiedmann, and C. M. Falco, Phys. Rev. Lett. **67**, 1910 (1991).
[6] G. H. O. Daalderop, P. J. Kelly, and F. J. A. den Broeder, Phys. Rev. Lett. **68**, 682 (1992).
[7] W. Sucksmith and J. E. Thompson, Proc. R. Soc. London A **255**, 362 (1954).
[8] B. Heinrich and Z. Celinski, J. Appl. Phys. **70**, 5769 (1991).
[9] M. Farle, V. Pierron, P. Vennegues, and K. Ounadjela (unpublished).
[10] K. Ounadjela, D. Muller, A. Dinia, A. Arbaoui, G. Suran, and P. Panissod, Phys. Rev. B **45**, 7768 (1992).

Magnetization of thin Gd films on W(110) near the Curie temperature

M. Farle
IPCMS-GEMME, 4, rue Blaise Pascal, F-67070 Strasbourg, France

W. A. Lewis
Department of Materials Science and Engineering, Stanford University, Stanford, California 94305-2205

In situ temperature dependent magneto-optic Kerr effect measurements in ultrahigh vacuum are presented for 80 and 300 Å thick Gd(0001) films. Films were deposited at 300 K and stepwise annealed to 820 K. It was found that the remanent magnetization $M_r(T)$ depends on the annealing temperature. The as-deposited films have a reduced Curie temperature T_c, e.g., T_c(80 Å)=273 K, which gradually shifts up to the bulk T_c of Gd upon annealing. The changes in $M_r(T)$ are correlated with a sharpening of the Gd low energy electron diffraction pattern. The best magnetic homogeneity and structural coherence is found for films annealed to 620 K. At higher temperatures the films break up into large three-dimensional islands with nearly uncovered W areas in between (W Auger is observed). The magnetic behavior was simulated with a model which assumes a Gaussian distribution of T_c values. From these simulations and the known bulk pressure dependence of T_c we estimate the mean strain and the strain distribution within the films.

I. INTRODUCTION

Reports of epitaxially prepared Gd films in ultrahigh vacuum have shown many interesting and sometimes contradictory magnetic results.[1–10] In earlier studies Weller *et al.* found an enhanced Curie temperature T_{cs}=322 K and a possible antiferromagnetic alignment of the surface magnetization.[5] The monolayer Curie temperature T_c was determined to be only 10% smaller than the bulk value.[1] In both studies films were grown at 450 °C on W(110). At that substrate temperature Gd forms three-dimensional islands (Stransky–Krastanov growth mode). More recently, Gd films were studied which were deposited at room temperature. They grow layer by layer and when properly annealed[6,11] form smooth and magnetically homogeneous layers. For films prepared in this manner, a perpendicular component of the surface magnetization was reported with a T_{cs}=370 K.[8] Also, the Curie temperature of a five monolayer film was now found to be reduced by more than 50% from bulk T_c.[11] The latter result was obtained by an *in situ* ac-susceptibility technique, which was also used to measure the annealing dependence of the susceptibility.[6,11] In these experiments, however, one did not find any evidence for an enhanced T_{cs} or a magnetic surface reconstruction.

In the present contribution, we will report $M_r(T)$ as a function of temperature near T_c and study its changes with thermal treatment of the film. The data is obtained by *in situ* magneto-optic Kerr effect in ultrahigh vacuum (UHV). We find a strong dependence of the magnetization on the annealing procedure in agreement with previous results.[6,11] We find T_c=272 and 285 K for the as-deposited 80 and 300 Å Gd film, which shifts to 289 and 290 K, respectively, upon a 5 min anneal at 620 K. Furthermore, we find evidence of a perpendicular component of the magnetization within the film, which may be located at the Gd surface, at the Gd/W interface, or in bubble domains within the film. An enhancement of the surface Curie temperature, however, could not be unambiguously resolved.

II. SAMPLE PREPARATION

Gd films were evaporated from a precleaned Ta crucible in a vacuum better than 4×10^{-10} mbar at rates of 1 to 2 monolayers per minute. The 10 mm^2 W(110) substrate was prepared carbon- and oxygen-free in the usual manner[1,5,6,12] and held at a maximum of 310±10 K during deposition. Low energy electron diffraction (LEED) and Auger electron spectroscopy (AES) was performed at different stages of the growth. The contamination level of oxygen was always below 1/20 of a monolayer. Films thicker than 2 monolayers have a barely distinguishable Gd(0001) LEED pattern on a bright background. This does not change up to 300 Å. When the films are annealed to 620 K for about 5 min the LEED pattern sharpens considerably and the background becomes as dark as for the clean W(110). The Gd spots, however, are on the order of 2 to 3 times broader than the sharp W spots. Longer anneals (20 min) improved the sharpness only negligibly. Neither changes in the geometry of the LEED pattern nor in the Gd Auger line shapes are observed. The Gd(1120) direction is always found to lie parallel to the W(001) axis in the surface plane. When the films are heated to 820 K, a considerable difference is found immediately. The W Auger signal reappears with a ratio Gd(108 eV)/W(163/169 eV) =120 (for the 300 Å film!) and the Gd LEED spots become very sharp. The appearance of the W Auger signal indicates that the film has formed large three-dimensional (3D) islands with open areas in between covered by at most three atomic Gd layers.

Magnetic hysteresis loops were recorded *in situ* by the magneto-optic Kerr effect in the longitudinal geometry as described elsewhere.[7] S-polarized light of a He-Ne laser is incident at 40° from the film normal. The sampling depth of the Kerr effect for Gd at this wavelength is 400 Å.[13] The signal of a 80 Å film is calculated to be 50% of the 300 Å signal.

III. RESULTS AND DISCUSSION

Temperature dependent magnetization data between 260 and 300 K was recorded by sampling the easy-axis in-plane hysteresis loop at ±200 Oe and at ±0 Oe. The difference at 0 Oe measures the remanent magnetization $M_r(T)$, and the difference at ±200 Oe is the field dependent magnetization M(200 Oe, T). The in-plane anisotropy was studied approxi-

 0021-8979/94/75(10)/5604/3/$6.00 © 1994 American Institute of Physics

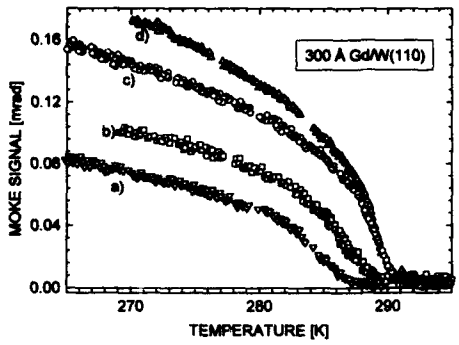

FIG. 1. Remanent magnetization of 300 Å Gd(0001) on W(110) for different annealing steps: (a) as-deposited 310 K, (b) 410 K, (c) 620 K, (d) 820 K. Each anneal took at most 10 min.

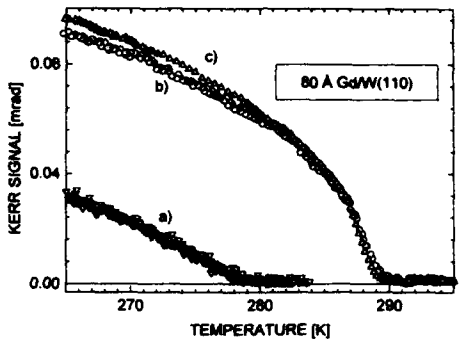

FIG. 2. Remanent magnetization of 80 Å Gd(0001) on W(110) for different annealing steps: (a) as-deposited 310 K, (b) 620 K, (c) 820 K.

mately every 5 K for both films. Temperature dependent measurements were always taken with the field applied along the easy in-plane direction. In Fig. 1 we show $M_r(T)$ of the 300 Å film for different annealing stages. The as-deposited film (a) has a smaller magnetization which vanishes at a temperature $T_v=287$ K. Annealing at 370 K for ~2 min results in the magnetization curve (b). $M_r(T)$ vanishes at $T_v=289$ K and the initial slope of the magnetization is steeper. Further annealing to 620 K shifts T_v to 291 K and increases the magnitude of $M_r(T)$ and the slope of the curve. Interestingly, annealing to 820 K increases the magnetization by a few percent, but does not shift $T_v=291$ K any higher. The initial slope near T_v, however, becomes steeper, or in other words the transition becomes sharper. In Fig. 2, we show the results for the 80 Å thin film. The as-deposited film (a) has only a weak signal which vanishes with a quasilinear temperature dependence at 279 K. Annealing yields qualitatively the same results as for the 300 Å film. The magnetization increases and T_v shifts close to the bulk T_c.

For both films the coercive fields H_c are typically 50 to 70 Oe at 260 K. Neither an angular dependence of H_c nor shape of the rectangular hysteresis loops is observed. Only a weak, angular independent linear signal of Gd is superimposed on the squarish hysteresis within −200 to +200 Oe. We will come back to this later. Annealing to 820 K decreases H_c to 10–15 Oe. And a weak in-plane anisotropy is found, which can be modeled by a superposition of the Gd threefold magnetocrystalline anisotropy and a lattice-mismatch induced uniaxial in-plane stress anisotropy.

To accurately determine the ordering temperature and to quantify the observed changes of $M_r(T)$ (Fig. 1 and Fig. 2) we simulate our experimental data with the convolution of the theoretical power law for the spontaneous magnetization and a Gaussian distribution

$$M_{\rm sim}(T)=\frac{1}{s\sqrt{2\pi}}\int_{-\infty}^{\infty}M(0)(1-T/T_{ci})^{\beta}\times e^{-(1/2s^2)(T_{ci}-\langle T_c\rangle)^2}\,dT_{ci}. \quad (1)$$

In analogy to other studies[6,14] this model assumes that the film consists of homogeneous regions in each of which the magnetization is described by a 3D Heisenberg-like power law with a different regional T_{ci}. For simplicity we assume a Gaussian distribution of T_{ci} around a mean value $\langle T_c\rangle$. The different T_{ci} may originate from locally varying strains which arise due to defects and from the thickness dependent strain accommodation. Using the well-known pressure dependence of bulk T_c of Gd and considering the large bulk lattice mismatch (about 15%) of W(110) and Gd(0001), a distribution of several degrees kelvin within the film is reasonable. The result of the simulation is shown in Fig. 3. We chose $M(0)=0.21$ and $\beta=0.365$ (3D Heisenberg) and left $\langle T_c\rangle$ be fixed at 290 K to clearly show the effect of broadening the T_c distribution. For a width $s=0.2$ K (b) one already obtains a deviation of about half a kelvin from the uniform spontaneous magnetization (a) and a decrease of the slope near T_c. For the larger distribution of $s=1$ K (c) one finds **quantitatively** the same form as for the experimental 300 Å data annealed at 620 K. The zero field tail of approximately 2 K and the curvature of $M_r(T)$ is reproduced. We also show a distribution of $s=6$ K (d) since it reproduces the weak slope and the reduced magnetization of the as-deposited 80 Å data. For this distribution $\langle T_c\rangle$ lies 6 K below T_v. By comparison with our simulations we determine $\langle T_c\rangle=273$ K for the unannealed 80 Å film. Similar simulations for all the curves shown in Fig. 1 and Fig. 2 yield the ordering temperatures and their distributions given in Table I. To obtain the best possible fits for all curves a variation of 20% had to be allowed for $M(0)$. The detailed presentation of these simulations, the critical behavior, and the effective critical exponent β is beyond the scope of this publication and will be presented elsewhere. We would like to point out, however, that a determination of the transition temperature based on a double logarithmic plot of $M_r(T)$ versus the reduced temperature would yield erroneous results, since T_c is used as a fit parameter to maximize the linear region of such a presentation. Furthermore, we find that the effective β of the data which includes a distribution of T_c [curves (b), (c), and (d) in Fig. 3] is reduced in comparison to the pure power

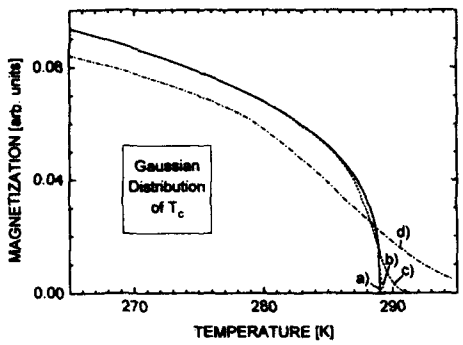

FIG. 3. Simulation of the magnetization according to Eq. (1). The width s of the distribution used is (a) 0 K, (b) 0.2 K, (c) 1 K, (d) 6 K.

law [curve (a) in Fig. 3]. This is evident from the smaller slope of $M_r(T)$ near T_c (Fig. 3). In addition, we estimate an average strain $\epsilon=2.8\%$ and a strain distribution $\Delta\epsilon=1\%$ for the annealed 80 Å film. This is calculated assuming the known pressure dependence $\Delta T_c/\Delta p=-14$ K/GPa (Refs. 15 and 16) of T_c and elasticity constants[17] of bulk Gd.

Now we will comment briefly on the shape of the hysteresis loops as mentioned before. In general, the magneto-optic Kerr effect (MOKE) signal at remanence was only about 80%–90% of the one at 200 Oe. From the hysteresis it is evident that a linear background signal [not present for the clean W(110) substrate] is added to the squarish in-plane loop. This signal is angular independent. The difference between $M_r(T)$ and $M(200\text{ Oe}, T)$ decreases when the films are annealed to 820 K or contaminated for several hours in vacuum. We suppose that the origin of the linear background signal is due to a perpendicular component of the magnetization within the film. This would show up as a hard-axis loop in our geometry. However, we cannot distinguish a surface from a bulk contribution, since MOKE samples the total film thickness. We suppose that the signal arises from a surface layer and possibly from the Gd bottom layer. The perpendicular component at the interface may be strain induced. This would be consistent with the observation that upon annealing the signal difference decreases (strain relaxation) and that the difference for the 80 Å film it is about a factor of 2 larger than for the 300 Å film (sampling depth). Comparison with a calculation for the thickness dependence of the MOKE signal[13] yields an interface/surface layer thickness of about eight atomic layers.

TABLE I. Average Curie temperature and its spread s for different annealing steps as obtained by fitting the experimental data to Eq. (1).

Film	Annealing temperature (K)	$\langle T_c\rangle$ (K)	s (K)
300 Å	300	285	2
	400	287.5	1.5
	619	290	1
	850	290	0.6
80 Å	300	272	6
	619	288	1.2
	850	289	0.7

We do not find clear evidence for an enhanced T_{cs}. For a few cases a weak $M(200,T)$ signal was observed up to 310 K, but we never see an signal up to 370 K.[8] However, it seems possible that in the longitudinal MOKE configuration the sensitivity is not sufficient to detect a hard axis loop of a few layers only. Studies using the polar Kerr geometry would be required to give a clear answer to the existence of a perpendicular component.

IV. SUMMARY

We have presented the first detailed study of the magnetization of 80 and 300 Å Gd(0001) films on W(110) near the Curie temperature and its dependence on the heat treatment of the film. The temperature dependence is modeled by a Gaussian distribution of Curie temperatures. From this we determine the average $\langle T_c\rangle$ and the width of the T_c distribution within the film. With the known pressure dependence of the bulk T_c, we estimate the average strain within the film and its relaxation as a function of heat treatment. We also present evidence for a perpendicular component of the magnetization within the film.

ACKNOWLEDGMENTS

We acknowledge helpful discussions with K. Baberschke and R. L. White. We thank E. Kay for use of his UHV chamber and the Deutsche Volkswagenstiftung and the IBM Almaden Research Center for financial support. M.F. acknowledges the hospitality of the Department of Materials Science and Engineering, and support through a stipend from the Deutsche Forschungsgemeinschaft.

[1] M. Farle, and K. Baberschke, Phys. Rev. Lett. **58**, 511 (1987).
[2] M. Farle, A. Berghaus, and K. Baberschke, Phys. Rev. B **39**, 4838 (1989).
[3] D. Li, J. Zhang, P. A. Dowben, and M. Onellion, Phys. Rev. B **45**, 7272 (1992).
[4] G. A. Mulhollan, K. Garrison, and J. L. Erskine, Phys. Rev. Lett. **69**, 3240 (1992).
[5] D. Weller, S. F. Alvarado, W. Gudat, K. Schroeder, and M. Campagna, Phys. Rev. Lett. **54**, 1555 (1985).
[6] U. Stetter, M. Farle, K. Baberschke, and W. G. Clark, Phys. Rev. B **45**, 503 (1992).
[7] M. Farle, W. A. Lewis, and K. Baberschke, Appl. Phys. Lett. **62**, 2728 (1993).
[8] H. Tang, D. Weller, T. G. Walker, J. C. Scott, C. Chappert, H. Hopster, A. W. Pang, D. S. Dessau, and D. P. Pappas, Phys. Rev. Lett. **71**, 444 (1993).
[9] F. Tsui, P. D. Han, and C. P. Flynn, Phys. Rev. B **47**, 13648 (1993).
[10] E. Vescovo, O. Rader, T. Kachel, U. Alkemper, and C. Carbone, Phys. Rev. B **47**, 13899 (1993).
[11] M. Farle, K. Baberschke, U. Stetter, A. Aspelmeier, and F. Gerhardter, Phys. Rev. **47**, 11571 (1993).
[12] J. Kolaczkiewicz and E. Bauer, Surf. Sci. **175**, 487 (1986).
[13] The complex Kerr signal was calculated using the optical constants of bulk Gd within the formalism given in S. D. Bader, J. Magn. Magn. Mater. **100**, 440 (1991).
[14] U. Stetter, A. Aspelmeier, and K. Baberschke, J. Magn. Magn. Mater. **116**, 183 (1992).
[15] H. Bartholin, J. Beille, D. Bloch, P. Boutron, and J. L. Ferou, J. Appl. Phys. **42**, 1679 (1971).
[16] R. G. Chapman and N. H. March, J. Magn. Magn. Mater. **61**, 81 (1986).
[17] B. Coqblin, *The Electronic Structure of Rare-Earth Metals and Alloys: The Magnetic Heavy Rare Earths* (Academic, London, 1977).

Origin of the fine structure of subsidiary absorption in tangentially magnetized YIG films

A. V. Pomyalov
Jack and Pearl Resnick Institute of Advanced Technology, Department of Physics, Bar-Ilan University, Ramat Gan 52900, Israel

I. Laulicht
Department of Physics, Bar-Ilan University, Ramat Gan 52900, Israel

Parametric excitation of spin waves (SWs) under conditions of perpendicular pumping was investigated in epitaxial films of yttrium iron garnet (YIG). The related microwave power absorption was measured at the frequency 9.1 GHz in the magnetic field range 1200–1600 Oe. A series of absorption peaks closely spaced on the magnetic field scale were observed near the threshold of first-order Suhl instability of spin waves. The peaks spaced by 0.2–0.7 Oe originate from the shallow ripple of the butterfly curve. This is the first observation of the fine structure at subsidiary absorption in YIG films. The peak spacing was measured as a function of dc magnetic field H, film thickness d, and in-plane sample dimensions L for square samples. In the field range 1300–1400 Oe the spacing did not depend on H and was inversely proportional to L in the range of 0.6–3 mm. No thickness dependence was found in the range $d=3$–45 μm. Explanation is given in terms of standing spin waves set in the film plane and related to the exchange part of SW dispersion curves in ferrite film.

I. INTRODUCTION

The phenomenon of first-order Suhl instability of spin waves (SWs) is known since the early experimental work of Wang and Blombergen[1] and theoretical treatment given by Suhl.[2] The two basic techniques to detect this type of instability are perpendicular pumping and parallel pumping, when a ferrite sample, placed in a dc magnetic field, is subjected to a microwave magnetic field directed either perpendicularly or parallel to a dc magnetic field. The SW instability results in energy absorption taking place above the certain threshold level of pumping power which is due to the parametric excitation of spin waves at half a pumping frequency. A dc magnetic field dependence of the threshold power is very similar for both perpendicular and parallel pumping geometrics and is usually called a butterfly curve. The perpendicular pumping technique is also regarded as that of subsidiary absorption.

In the seventies Jantz and Schneider observed the fine structure of the absorption in YIG spheres both for parallel and perpendicular pumping (see, e.g., Ref. 3). The structure resulted from the ripple of the butterfly curves and looked like a series of narrow absorption peaks closely spaced on a dc magnetic field scale. The authors[3] ascribed the structure to the parametric excitation of single exchange SW modes associated with standing waves set in over the diameter of the sphere. This model was in good correlation with the experiment for parallel pumping but did not give a satisfactory explanation for the case of subsidiary absorption. Later Berezin *et al.*[4] and Kalinikos *et al.*[5] observed a similar effect at parallel pumping in thin YIG films and found the dips of the butterfly curve corresponding to SW resonances over the film thickness at half the pumping frequency. Recently Wiese *et al.*[6] reported on the same effect in relatively thick YIG films at parallel pumping.

The fine structure at perpendicular pumping was not yet reported in YIG film experiments and its explanation for spheres remained uncertain. Lately Wiese[7] has made the exact theoretical calculations of unstable SW modes in sphere both for perpendicular and parallel pumping and used the obtained selection rules to identify the modes responsible for the structure of subsidiary absorption in experiments of Jantz and Schneider.[3] Despite a good agreement with the previously reported experimental data this identification is somewhat ambiguous because it needs additional assumptions on the relaxation mechanism of SWs. The difficulty of unambiguous identification is due to the high degeneracy of the SW spectrum in spheres as well as to the lack of more definite experimental data than that of Ref. 3.

In the present work we report on the first observation of the fine structure of subsidiary absorption in YIG films. In contrast to spheres the thin film samples feature the SW spectrum descreteness due to quantization of SW wave number over the film thickness. A tangentially magnetized film also has anisotropic dispersion law of SWs. These two factors make it easier to single out the SW modes responsible for the fine structure on the basic of experimental data without any assumptions on the relaxation mechanism of the SWs. We investigated the fine structure dependence on the film thickness, in-plane sample dimensions on the dc mag-

 0021-8979/94/75(10)/5607/3/$6.00 © 1994 American Institute of Physics

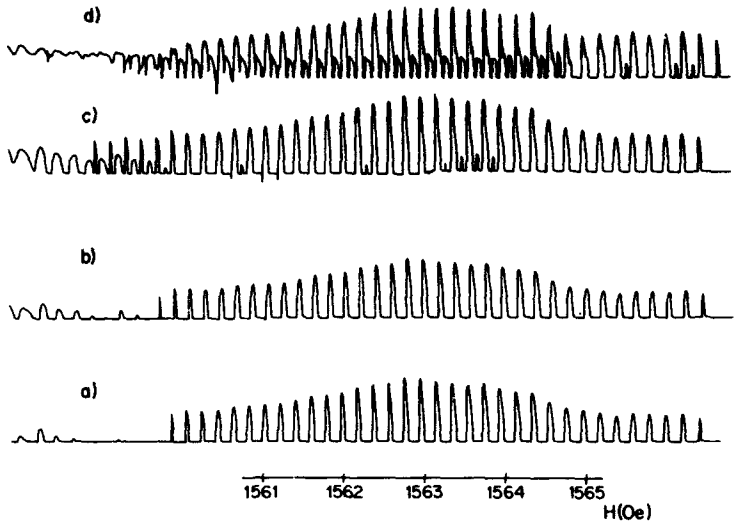

FIG. 1. The example of the subsidiary absorption fine structure observed in YIG film. Film thickness is 29.1 μm, tangentially magnetized square sample with in-plane dimensions of 1.5×1.5 mm. The microwave pumping power increases from a to d being equal to 42 mW for a and 42.5 mW for d. The appearance of the second series of peaks and its overlapping with the first one can be easily seen.

netic field and associated it with in-plane resonances of standing exchange SWs.

II. EXPERIMENT

The measurements were performed at 9.1 GHz, the microwave and dc magnetic fields being oriented in the film plane perpendicular to each other. We used the conventional electron spin resonance spectrometer (Varian E12) with dc field modulation at 100 kHz. The 100 kHz signal from the lock-in amplifier was used to record the fine structure and to measure the fine structure spacing. Along with the 100 kHz signal the dc signal from the microwave detector was monitored with an oscilloscope to avoid possible artefacts related to dc field modulation. The details of the measuring procedure are described elsewhere.[8] The investigated samples were rectangulars cut from YIG films epitaxially grown on (111) oriented GGG substrates. The film thickness ranged from 2.95 to 45 μm, the in-plane dimensions from 0.6 to 2.9 mm, the sample edge being parallel to the dc magnetic field. The fine structure (Fig. 1) looked like a series of narrow peaks well separated on the magnetic field scale with no absorption between peaks. The structure was usually observed at the flat parts of the butterfly curve—mainly near the bottom of the broad minimum of the butterfly curve typical of subsidiary absorption in YIG.[9] The local flatness of the curve is a necessary condition for the structure observation because the structure originates from the shallow ripple of the butterfly curve, each absorption peak in Fig. 1 corresponding to the dip on the butterfly curve. When the pumping power level is increased (Fig. 1 from a to d), the additional peaks appear forming another series. Finally the peaks merge into the continuous absorption band when the pumping power exceeds the amplitude of the ripple. The small changes $d\omega_p$ of pumping frequency ω_p (up to 20 MHz) resulted in the shift dH of the peaks position on magnetic field scale, the ratio $d\omega/dH$ being equal to $\gamma/2$, where γ is the gyromagnetic ratio of YIG. This definitely indicates that the observed peaks and related ripple of the butterfly curve originate from some resonances at half a pumping frequency $\omega_p/2$ rather than from probable variations of the pumping field amplitude at ω_p. These amplitude variations might result from microwave absorption related to the excitation of high order SW modes. With changing dc magnetic field, this absorption causes the small changes of microwave magnetic field inside the spectrometer cavity. Being rather small these changes might however trigger the subsidiary absorption—if the pumping power level is close to the threshold. Using the above measurements of $d\omega/dH$ we made ourselves confident that this sort of artefact was not the case in our experiments and that we dealt with "true" first-order instability of SWs.

To further test the origin of these resonances we measured the peaks spacing δH as a function of the dc field position and of the in-plane dimensions of the sample (Fig. 2). In the range 1300–1400 Oe the spacing did not change substantially for a given sample but was inversly proportional to the in-plane dimensions. The thickness dependence of δH showed no substantial variations of the spacing despite the change of the thickness by a factor more than 15 (Fig. 3).

The additional information on the structure was obtained by the roughening of the sample in-plane edges with 50 μm sandpaper and by putting the 100 Å conducting layer (60

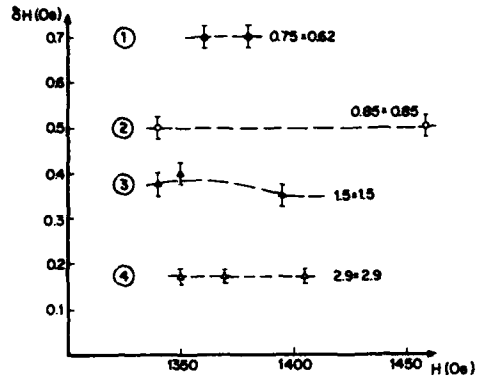

FIG. 2. The fine structure spacing δH as a function of magnetic field H for different sample dimensions. The film thickness is 29.1 μm for all the samples. The dashed lines are a guide for the eye and connect the points related to the same sample. The sample dimensions (in mm) are given near the corresponding lines.

Ω/□) adjacent to the film plane. The roughening was used to eliminate the fine structure and increased the threshold of the subsidiary absorption. The metal did not influence the fine structure but gave rise to the increase of the linewidth of the dipole (magnetostatic modes) in linear spectrum. For the 1.5 ×1.5 mm sample from Fig. 2 the magnetostatic resonance lines observed in the dc field range 2.5–3.1 kOe were broadened by factor from 2 at 3.1 kOe to 15 at 2.5 (kOe). Nonetheless no effect was found in the field range 1200–1600 Oe corresponding to subsidiary absorption. The dipole magnetostatic modes at 3.1 kOe had in-plane resonance numbers

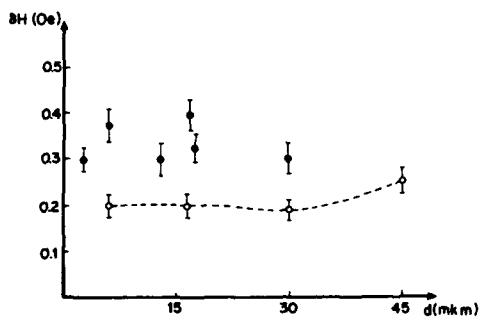

FIG. 3. The fine structure spacing δH as a function of YIG film thickness d. The samples are rectangular with in-plane dimensions varying from 1 to 2.5 mm. The open circles correspond to the data scaled to the sample size 2.5×2.5 for square samples. The dashed line is a guide for the eye.

about 65 which corresponded to the value of an in-plane wave number q about 1500 cm^{-1}, the total wave number being about 2000 cm^{-1}.

III. DISCUSSION

The above results show that the observed structure is related to resonances taking place at half a pumping frequency. Unlike the results obtained at parallel pumping[4–6] the structure is not associated with standing SWs over the film thickness d because in our case the peaks spacing depends on in-plane dimensions of the samples rather than on their thickness. In-plane SWs eligible to go unstable at half a pumping frequency $\omega_p/2$ may belong either to dipole (magnetostatic) or to the exchange part of the dispersion curves of SWs in thin tangentially magnetized films.[10] The slope of the dispersion curves in the dipole (low q) region strongly depends on the film thickness—the well-known result of Damon and Eshbach. For this reason the dipole modes spacing should strongly depend on the film thickness which was not observed in experiment. Therefore in-plane standing SWs that could be responsible for the structure in our case cannot be of dipole origin. Also the metal-induced broadening of the dipole magnetostatic resonances did not influence the fine structure which indicates the structure relation with a SW having a wave number much more than 2000 cm^{-1}. Bearing in mind the above considerations we would explain the structure as originating from the in-plane standing SWs related to the upgoing exchange parts of SW dispersion curves in tangentially magnetized ferrite films. However this simple model cannot quantitatively explain the measured values of peaks spacing δH in the fine structure (Fig. 2). The maximum value of δH that can result from π/L quantization of in-plane wave vector of exchange in-plane SW modes corresponds to SWs propagating along the dc magnetic field. This value for the samples listed in Fig. 2 is by a factor of 7 less than the experimental one. The possible cause for such a discrepancy might be the interaction of spin and elastic waves. This point can be testified via measurements of the exact proportion of the in-plane wave number components for these modes as well as on their thickness number. The work on this problem is in progress.

ACKNOWLEDGMENT

This work has been done with the partial support of the Israeli Ministry of Absorption.

[1] N. Blombergen and S. Wang, Phys. Rev. **93**, 72 (1954).
[2] H. Suhl, J. Phys. Chem. Solids. **1**, 209 (1957).
[3] W. Jantz and J. Schneider, Phys. Status Solidi **31**, 595 (1975).
[4] I. Z. Berezin, B. A. Kalinikos, N. G. Kovshikov, S. P. Orobinskii, and D. N. Chartorizhskii, Sov. Phys. Solid State **20**, 1214 (1978).
[5] B. A. Kalinikos, N. G. Kovshikov, and N. V. Kozhus, Sov. Phys. Solid State **26**, 1735 (1984).
[6] G. Wiese, L. Buxman, P. Kabos, and C. E. Patton, J. Appl. Phys. (in press).
[7] G. Wiese, Z. Phys. B-Condens. Matter **82**, 453 (1991).
[8] A. V. Pomyalov, I. Laulicht, and J. Barak, Physica A **200**, 267 (1993).
[9] C. E. Patton, Phys. Rep. **103**, 251 (1984).
[10] B. A. Kalinikos and A. N. Slavin, J. Phys. C **19**, 7013 (1986); IEEE Trans. Magn. **MAG-27**, 5444 (1991).

Instability mechanism of collective spin wave oscillations in finite-size ferrite samples

A. N. Slavin, G. Srinivasan, and S. S. Cordone
Department of Physics, Oakland University, Rochester, Michigan 48309

V. B. Cherepanov
Department of Physics, University of Manitoba, Winnipeg, Manitoba R3T 2N2, Canada

A sample-size effect on spin wave auto-oscillations under parallel pumping is studied experimentally in tangentially magnetized rectangular samples of yttrium-iron garnet (YIG) films where one of the in-plane sizes is varied. A previously developed one-dimensional theoretical model of unstable collective oscillations in the system of parametrically excited spin waves is used to describe the mechanism of spin wave auto-oscillations observed in YIG films. Our results show that the one-dimensional model (that works well for YIG spheres) gives only qualitative description of the sample-size effect in YIG films and the incorporation of the second finite size (film thickness) in this model is needed to achieve quantitative agreement with experiment in the film geometry.

Spin wave auto-oscillations in ferrites above the threshold of parametric excitation of spin waves discovered in Ref. 1 were studied intensively during the last decade mostly because of interesting chaotic dynamics they demonstrate in a strongly nonlinear regime (see, e.g., Refs. 2–5).

Although a lot of experimental and theoretical work has been done in this field some features of spin wave auto-oscillations even in a weakly nonlinear regime (near the threshold of spin wave auto-oscillations) were not well understood. In particular, experiments performed by Rezende *et al.*[6,7] demonstrate a pronounced sample-size dependence of auto-oscillation frequency and threshold that was not explained by the traditional theory.[8,9]

In our previous work[10,11] we developed a one-dimensional model of spin wave auto-oscillations under parallel pumping in finite-size ferromagnetic samples taking into account the boundary conditions for the envelope of the packet of parametrically excited spin waves at the boundaries of a magnetic sample. This model explains the sample-size dependence of auto-oscillation frequencies and thresholds observed in YIG spheres in Refs. 6 and 7. In our present paper we describe our own experiments on sample-size dependence of auto-oscillations performed in tangentially magnetized rectangular YIG film samples, and discuss the applications of our theoretical model to the case of films.

The theoretical model[10,11] that we are using to describe the sample-size effect in spin wave auto-oscillations is an extension of the S theory of auto-oscillations in infinite ferromagnetic medium.[8] In the framework of this theory spin wave auto-oscillations are interpreted as unstable collective oscillations in the system of parametrically excited spin waves. These oscillations are originated from the four-wave interaction between parametric spin waves. The criterion of instability of collective oscillations can be formulated as (see Ref. 8)

$$2R+1<0, \tag{1}$$

where $R=T/S$, and S and T are the coefficients of four-wave interaction between spin waves defined in Ref. 8.

In the case of a finite magnetic sample we assume that the collective oscillations in the system of parametrically excited spin waves can be spatially inhomogeneous (i.e., can propagate in the sample) and the amplitudes A_k of these oscillations (or secondary waves) must satisfy certain boundary conditions at the sample boundaries. For simplicity we assume that only one size of the sample is relevant—the size in the direction of propagation of parametric spin waves excited at the threshold. In the case when the mean free path $l=v_g/\gamma_k$ of spin waves in a sample is much smaller than the sample size $D(l\ll D)$ the boundary conditions for the oscillation amplitudes must be the conditions of "no reflection" at the boundary ($A_k=0$). Under these conditions the model[10,11] yields the following expressions for the auto-oscillation threshold h_{osc} and the auto-oscillation frequency ω_{osc} at this threshold:

$$\frac{h_{osc}^2}{h_{th}^2}-1=\frac{1}{2}\left(\frac{\pi v_g}{D\gamma_k}\right)^2\frac{1}{|2R+1|}, \tag{2}$$

$$\frac{\omega_{osc}}{\gamma_k}=\frac{1}{2}\left(\frac{\pi v_g}{D\gamma_k}\right)^2\left(\frac{5R+1}{2R+1}\right)^{1/2}, \tag{3}$$

where

$$h_{th}=\frac{2\omega_p\gamma_k}{\gamma\omega_M} \tag{4}$$

is the threshold of parametric excitation of spin waves under parallel pumping, $v_g=\partial\omega_k/\partial k$ is the group velocity of parametric spin waves ($\theta_k=\pi/2$),

$$\omega_k^2=(\omega_H-N_Z\omega_M+\alpha\omega_M k^2)(\omega_H-N_Z\omega_M+\alpha\omega_M k^2+\omega_M) \tag{5}$$

is the spin wave eigenfrequency, k is the wave number, $\omega_H=\gamma H_0$, H_0 is the external bias magnetic field, $\omega_M=\gamma 4\pi M_0$, M_0 is the saturation magnetization, α is the exchange constant, ω_p is the pumping frequency, γ_k is the spin wave relaxation parameter, and γ is the modulus of the gyromagnetic ratio for electron spin. The four-wave interaction coefficients T and S (and their ratio $R=T/S$) can be calculated from the general expressions presented in Ref. 12 [see Eqs. (3.1.24)–(3.1.25) in Ref. 12].

In our present paper we apply the model Eqs. (2) and (3) to the case of a tangentially magnetized film. In this case the

 0021-8979/94/75(10)/5610/3/$6.00 © 1994 American Institute of Physics

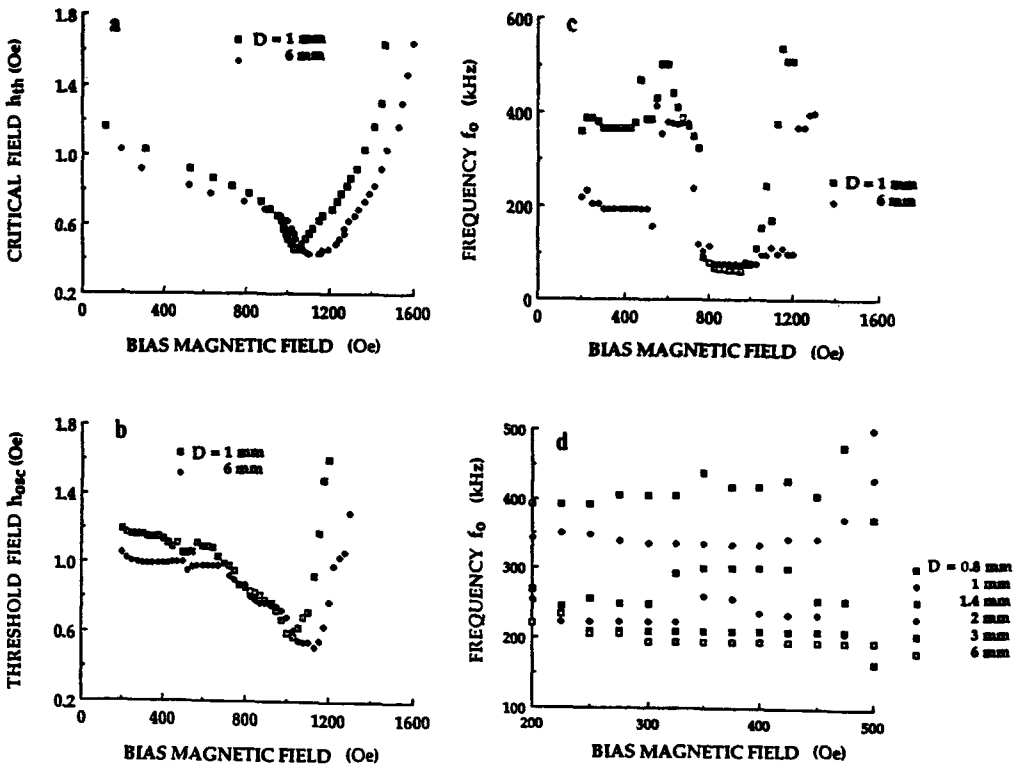

FIG. 1. Experimental characteristics of spin wave auto-oscillations in tangentially magnetized YIG film samples [thickness $L=110$ μm, width $W=2$ mm, orientation (111)] of different lengths 0.8 mm$<D<$6 mm: (a) threshold of parametric excitation h_{th}; (b) threshold of spin wave auto-oscillations h_{osc}; (c) frequency of spin wave auto-oscillations; (d) frequency of spin wave auto-oscillations for several intermediate sample lengths D in the bias field region ($H_0<700$ Oe) where the sample-size effect was observed.

spin wave distribution lacks axial symmetry and both S and T are dependent on the difference H_0-H_c between the bias magnetic field H_0 and its critical value H_c corresponding to the minimum of the "butterfly" curve:

$$S=\frac{3\omega_M}{2\omega_p}\left[1+\left(\frac{\omega_M}{\omega_p}\right)^2\right]^{1/2}+\left(\frac{\omega_M}{\omega_p}\right)^2\left(2N_z-\frac{3}{2}\right)+N_z-1+\beta\frac{\omega_a}{\omega_M}\left[3\left(\frac{\omega_M}{\omega_p}\right)^2+2\right]+\frac{H_c-H_0}{4\pi M_0}\left[\left(\frac{\omega_M}{\omega_p}\right)^2+2\right], \quad (6)$$

$$T=\frac{3\omega_M}{2\omega_p}\left[1+\left(\frac{\omega_M}{\omega_p}\right)^2\right]^{1/2}+\left(\frac{\omega_M}{\omega_p}\right)^2\left(2N_z-\frac{3}{2}\right)+\frac{3}{2}N_z-1+\beta\frac{\omega_a}{\omega_M}\left[3\left(\frac{\omega_M}{\omega_p}\right)^2+2\right]+\frac{H_c-H_0}{4\pi M_0}\left(\frac{\omega_M}{\omega_p}\right)^2. \quad (7)$$

Here and above N_z is the demagnetization factor of the magnetic sample in the direction of the bias magnetic field ($N_z=1/3$ for a sphere and $N_z=0$ for a tangentially magnetized film), $\omega_a=\gamma H_a$, $H_a=2K_1/M_0$ is the effective anisotropy field ($H_a=-84$ Oe for YIG at a room temperature), K_1 is the constant of cubic crystallographic anisotropy, and β is a coefficient dependent on the orientation of the saturation magnetization $\mathbf{M}_0$ relative to the crystallographic axes of the sample (see Refs. 12 and 13 for details).

The model (2), (3) takes into account only one finite size D of the sample and is applicable when parametric spin waves with wave numbers $k>0$ ($H_0<H_c$) are excited in the sample by parallel pumping.

We performed a series of experiments on rectangular YIG film samples magnetized in the film plane along the sample width ($W=2$ mm). The idea of these experiments was to change the length of the sample ($D=0.8-6$ mm) and to see how it affects the frequency of spin wave auto-oscillations. The samples were cut from an epitaxial YIG film (thickness $L=110$ μm) of the orientation (111) to get the minimum crystallographic anisotropy in the film plane. The spin waves were excited by parallel pumping in a TE_{102} reflection type cavity at the frequency $\omega_p/2\pi=9.24$ GHz.[14]

The microwave pumping field was parallel to the bias magnetic field (and to the width W of the sample), so the effective sizes of the sample for parametrically excited spin waves (at the angle $\theta=\pi/2$ to the bias field) were the length D and the thickness L. The experimental results for the threshold of parametric excitation of spin waves h_{th}, the threshold of spin wave auto-oscillations h_{osc}, and the auto-oscillations frequency f_0 as functions of a bias magnetic field H_0 in tangentially magnetized YIG film samples of different lengths D are presented in Figs. 1(a)–1(d). It is easy to see, that in films the sample-size effect is observed only for sufficiently small values of the bias field $H_0<700$ Oe (or for sufficiently large values of a spin wave wave number $k>3\times10^5$ cm^{-1}).

Our theory of a size effect in auto-oscillations,[10,11] was developed for a one-dimensional case where only one size of the sample (e.g., D) was relevant. To apply our model to the case of a tangentially magnetized film sample we made a naive assumption that the auto-oscillation frequency in this sample can be represented in the form of a sum

$$\omega_{osc}(L,D)=\omega_{osc}(D)+\Omega_{osc}(L), \tag{8}$$

where the first term depends on the sample length D and is given by the above presented Eq. (3), while the second term is determined by the film thickness L and by small effects like scattering of auto-oscillations on each other and on random inhomogeneities of the medium. These effects are described in detail in Ref. 15 and were not taken into account in the simple S theory of auto-oscillations.[8,10,11] When D is increasing $\omega_{osc}(D)\to0$ and for relatively large values of D we get $\omega_{osc}(L,D)\to\Omega_{osc}(L)$. We did not calculate $\Omega_{osc}(L)$ here and assumed that this term is equal to the auto-oscillation frequency $\Omega_{osc}(L)=190$ kHz in the sample having the largest length $D=6$ mm (see Figs. 1(c) and 1(d).

It is clear from Figs. 1(b) and 1(c) that the sample-size effect in films manifests itself only for $H_0<700$ Oe. (The nature of auto-oscillations observed in the bias field region $H_0>700$ Oe will be discussed elsewhere.[16]) To explain this fact we assumed that for $H_0\geq700$ Oe the instability criterion Eq. (1) is broken and the coefficient $S(H_0)$ Eq. (6) changes its sign from positive to negative at $H_0=700$ Oe. Using this assumption we determined the parameter β in Eqs. (6) and (7) ($\beta=-0.65$ for YIG film where $H_c=1150$ Oe, $4\pi M_0=1760$ Oe, and $H_a=-84$ Oe) and calculated theoretical dependencies of auto-oscillation frequency $f_0=\omega_{osc}(L,D)/2\pi$ on the sample length D (at a fixed $H_0=300$ Oe) and on the bias field H_0 (at two fixed lengths $D_1=0.8$ mm and $D_2=2$ mm) from Eqs. (3) and (8). The results of comparison of these theoretical calculations with the experimental results from Figs. 1(c) and 1(d) are presented in Figs. 2(a) and 2(b). It can be seen that in films our theoretical model demonstrates qualitative (and in the modified form (8) even reasonable quantitative) agreement with the experimental results for auto-oscillation frequencies. The calculations done for the auto-oscillation threshold using Eq. (2) demonstrate, however, only limited qualitative agreement with the experiment in this case.

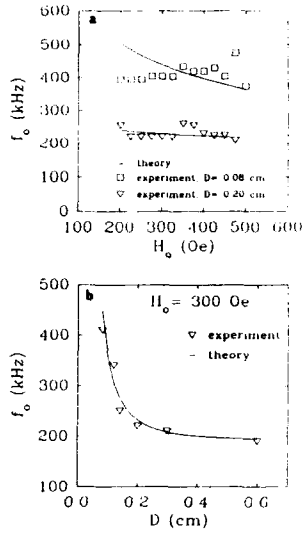

FIG. 2. Comparison of theoretical and experimental results for frequency of spin wave auto-oscillations in tangentially magnetized YIG film samples.

This work was supported by Grant No. C-3401 from the Research Corporation.

[1] T. S. Hartwick, E. R. Peressini, and M. T. Weiss, J. Appl. Phys. **32**, 223 (1961).
[2] G. Gibson and C. Jeffries, Phys. Rev. A **19**, 811 (1984).
[3] F. M. de Aguiar and S. M. Rezende, Phys. Rev. Lett. **56**, 1070 (1986).
[4] C. D. Jeffries, P. H. Bryant, and K. Nakamura, J. Appl. Phys. **64**, 5382 (1988).
[5] H. Yamazaki, J. Appl. Phys. **64**, 5391 (1988).
[6] S. M. Rezende and A. Azevedo, Phys. Rev. B **45**, 10 387 (1992).
[7] S. M. Rezende, F. M. de Aguiar, and A. Azevedo, J. Appl. Phys. **67**, 5624 (1990); **73**, 6805 (1993).
[8] V. S. L'vov, S. L. Musher, and S. S. Starobinets, Sov. Phys. JETP **37**, 546 (1973).
[9] X. Zhang and H. Suhl, Phys. Rev. B **38**, 4893 (1988).
[10] V. B. Cherepanov and A. N. Slavin, Phys. Rev. B **47**, 5874 (1993).
[11] V. B. Cherepanov and A. N. Slavin, J. Appl. Phys. **73**, 6811 (1993).
[12] V. S. L'vov, *Wave Turbulence under Parametric Excitation* (Springer, Berlin, 1993).
[13] V. E. Zakharov, V. S. L'vov, and S. S. Starobinets, Sov. Phys. Usp. **17**, 896 (1975).
[14] G. Srinivasan, Solid State Commun. **80**, 5 (1991).
[15] V. S. L'vov and V. B. Cherepanov, Sov. Phys. JETP **48**, 822 (1978).
[16] V. B. Cherepanov and A. N. Slavin (to be published).

Controlling spin-wave chaos

S. M. Rezende, F. M. de Aguiar, and A. Azevedo
Departamento de Física, Universidade Federal de Pernambuco, 50670-901 Recife-PE, Brazil

Microwave pumped spin-wave instabilities in YIG spheres were one of the first experimental systems used to demonstrate that chaos can be suppressed by small periodic modulations in an accessible system parameter. Here we show that the equations describing two interacting spin-wave modes account satisfactorily for the experimental results, as long as the field modulation is appropriately introduced in the model. The finite detuning parameters expressing the boundary conditions of the sample provide a natural way for introducing the field modulation. Thus the present results constitute additional evidence of the validity of the two-mode model with momentum-nonconserving driving Hamiltonian used to explain the sample size dependence of the self-oscillations.

I. INTRODUCTION

Microwave pumped spin-wave instabilities in YIG spheres were one of the first experimental systems used to demonstrate[1] that chaos can be suppressed by small time-dependent variations in an accessible system parameter. This method of controlling chaos is based on the fact that a chaotic attractor usually has embedded within it an infinite number of unstable periodic orbits. As shown by Ott, Grebogi, and Yorke[2] (OGY) it is possible to tailor the time dependence of a relevant parameter so as to stabilize a chosen unstable orbit. In systems with relatively slow dynamics, the parameter variation necessary to stabilize the orbit can be determined at each cycle according to the prescription of OGY and the result fedback into the system.[3,4] In the case of spin-wave instabilities, where the self-oscillation frequencies lie in the range of 100 kHz–10 MHz, a closed-loop feedback experiment is difficult to implement.[5] So the stabilization of the orbits has been achieved[1] with a periodic modulation signal provided by an independent oscillator. In general terms the parametric perturbation scheme of Lima and Pettini[6] accounts for the observed suppression of chaos, however there is no specific model for the spin-wave case.

In this paper we show that the control of chaos in the spin-wave experiments can be explained satisfactorily by the two-mode model employed to describe spin-wave nonlinear dynamics. The field modulation used in experiments to control the chaotic state is naturally introduced in the model through the detuning parameters expressing the boundary conditions which have been shown to account for the sample size dependence of the self-oscillations.[7,8]

II. EXPERIMENTS

The experiments have been previously described[1] in detail and we only present here some of their main features and results. They were carried out with a polished sphere (diameter 1.0 mm) of the prototype ferromagnet yttrium iron garnet (YIG) at room temperature pumped with X-band radiation in the "subsidiary-resonance" configuration. The experimental arrangement is the same used in spin-wave pumping experiments[7,11] except for a loop placed inside the microwave cavity to allow the modulation of the sample biasing field $H=H_0+\delta H\cos(2\pi f_m t)$ over a broad frequency range 0–10 MHz, typically with $\delta H/H_0\sim 10^{-4}$.

The usual experiment to study spin-wave phenomena is done with fixed values of H_0 and varying microwave power. At low power levels the steady-state reflection from the critically coupled cavity is negligible. As the microwave driving field h is increased, an abrupt change in reflection occurs at the Suhl threshold h_c, due to parametric excitation of a magnon pair with frequency $\omega_k\simeq\omega_p/2$ and wave vector $\mathbf{k}$ and $-\mathbf{k}$. The value of k is determined by the frequency ω_p, the field H_0, and the condition for minimum threshold, which depends on the pumping configuration.

The suppression of chaos has been observed at many points of the $h\times H_0$ diagram. The results presented here were observed after the system has been driven to a full chaotic regime with $h=1.1$ Oe and $H_0=1750$ Oe, with the field applied in the [110] crystal direction. Figure 1(a) shows the power spectrum of a chaotic auto-oscillation for $\delta H=0$, displaying a characteristic broadband feature. By increasing δH, the spectrum becomes progressively cleaner, with sharp

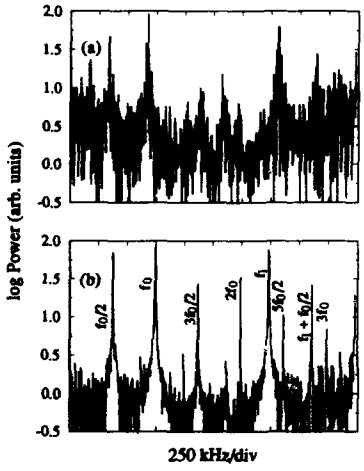

FIG. 1. Power spectra of observed auto-oscillations for different values of the amplitude δH of the field modulation. (a) Chaos for $\delta H=0$. (b) Chaos under control with $\delta H=0.435$ Oe and $f_m=1480$ kHz (Ref. 1).

 0021-8979/94/75(10)/5613/3/$6.00 © 1994 American Institute of Physics

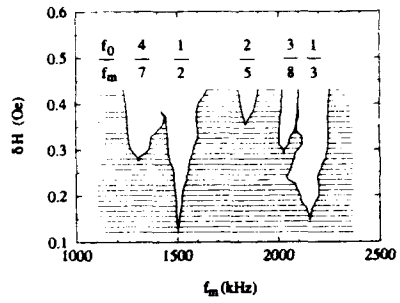

FIG. 2. Critical modulation amplitude δH^* vs modulation frequency f_m. The boundaries between the chaotic and controlled regions have minima at values of f_m commensurate with the fundamental frequency f_0 at ratios indicated at the top (Ref. 1).

lines characteristic of a periodic signal. Figure 1(b) shows the result for $\delta H=0.435$ Oe and $f_m=1480$ kHz. The spectrum in this case corresponds to a quasiperiodic signal with fundamental frequencies $f_0=740$ kHz and $f_1=1975$ kHz, and a subharmonic component at $f_0/2$. In Fig. 2 we show the variation of the critical amplitude δH^* necessary to control chaos with the modulation frequency f_m. Notice that δH^* has minima at values commensurate with the fundamental frequency f_0, i.e., $f_0/f_m=p/q$, where p and q are integers. In addition, for the f_m range shown in Fig. 2, the minima are strikingly ordered according to the devil's staircase, i.e., the values between p/q and p'/q' are characterized by the ratio $(p+p')/(q+q')$. The suppression of chaos in the shaded regions of Fig. 2 was also confirmed by the behavior of the information dimension D_1 and the metric entropy K of the attractor. As δH increases at fixed f_m and crosses the boundaries in the $\delta H\times f_m$ diagram, D_1 and K approach the values 1 and 0, respectively, characteristic of a periodic orbit.[1]

III. THEORETICAL MODEL AND RESULTS

The usual two-mode model[9–11] for describing the nonlinear dynamics considers that the interacting spin-wave system is driven by a uniform microwave field in an infinite medium, so that the driving Hamiltonian $\mathcal{H}'(t)$ preserves momentum. However, in a finite medium, $\mathcal{H}'(t)$ can be nonzero for pairs $\mathbf{k},-\mathbf{k}'$ for which k and k' differ by an amount of the order of the reciprocal of the sample size L. In this case, it can be shown[7] that a new driving term is introduced in the spin-wave equations, having magnitude proportional to a factor $\alpha_{\Delta k}$ which depends on the wave-vector mismatch $\Delta\mathbf{k}=\mathbf{k}-\mathbf{k}'$. For instance, for two neighboring standing waves along x with $\Delta k_x=\pi/L_x$, $\alpha_{\Delta k}$ attains its maximum value $2/\pi\simeq 0.64$. In an infinite medium, $\alpha_{\Delta k}=0$. With this new momentum nonconserving driving term, the equations of motion for the slowly varying spin-wave variables c_k for two neighboring modes become[7]

$$\dot{c}_1=-(\gamma_1+i\Delta\omega_1)c_1-ih\rho_1(c_1^*+\alpha e^{i\beta/2}c_2^*) -i2(S_1c_1^2c_1^*+S_{12}c_1^*c_2^2+2T_{12}c_2c_2^*c_1), \quad (1)$$

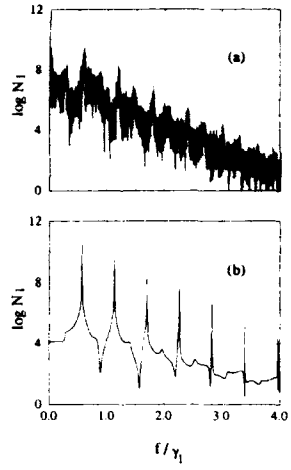

FIG. 3. Fourier transform of mode 1 amplitude without (a) and with field modulation (b) $\delta H=0.4\ \gamma_1/\gamma$, $f_m=0.56\ \gamma_1$. The clean spectrum in (b) demonstrates suppression of chaos with the two-mode model.

$$\dot{c}_2=-(\gamma_2+i\Delta\omega_2)c_2-ih\rho_2(c_2^*+\alpha e^{-i\beta/2}c_1^*) -i2(S_2c_2^2c_2^*+S_{12}c_2^*c_1^2+2T_{12}c_1c_1^*c_2). \quad (2)$$

where $\Delta\omega_k=\omega_k-\omega_p/2$, $\alpha\equiv\alpha_{\Delta k}$, $\beta\equiv\beta_{12}$ is the phase difference between modes 1 and 2, γ_k is the relaxation rate, ρ_k the coupling factor between mode k and the pumping field h, and the S_s and T_s are the nonlinear coupling parameters.[7]

The presence of one mode in the pumping term of the other represents a modulation with the frequency difference $\Delta\omega=\omega_1-\omega_2$ leading to self-oscillations with frequency that depends not only on the relaxation rate but also on $\Delta\omega$. For two neighboring modes in k space, $\Delta\omega\simeq\pi/L$, which accounts for the observed size dependence of the spin-wave self-oscillations. When a small ac field variation is superimposed to the static field, the spin-wave detuning parameters become

$$\Delta\omega_k=\omega_k-\frac{\omega_p}{2}+\gamma\delta H\cos(2\pi f_m t). \quad (3)$$

Equations (1) and (2) with the time-dependent detunings (3) constitute our model to explain the suppression of chaos. Those equations have been integrated numerically in a SUN Sparc 2 workstation with a Runge–Kutta subroutine. Chaotic dynamics and control of chaos with field modulation are observed with many sets of parameters. The results described below were obtained with[12] $\gamma_1=\gamma_2$, $\rho_1=\rho_2$, $\Delta\omega_1/\gamma_1=0.2$, $\Delta\omega_2/\gamma_1=-0.5$, $S_1/\gamma_1=S_2/\gamma_1=0.5$, $S_{12}/\gamma_1=-0.2$, $T_{12}/\gamma_1=-0.4$, $\alpha=0.65$ and $\beta=\pi$. With these parameters, auto-oscillations with frequency $f_0\simeq 0.49\gamma_1$ (with no field modulation, $\delta H=0$) develop at a normalized microwave amplitude $R\equiv h\rho_1/\gamma_1=1.32$ (the Suhl threshold is $R=1.0$) and chaos sets in at $R=1.808$. Figure 3(a) shows the power spectrum of mode 1 amplitude, $n_1=c_1^*c_1$, for $R=1.83$ and $\delta H=0$,

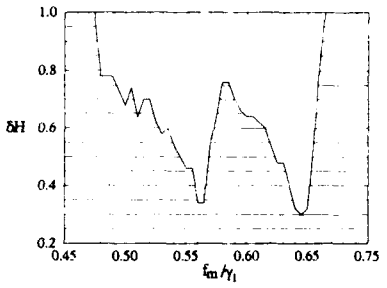

FIG. 4. Critical amplitude δH^* in units of γ_1/γ vs frequency f_m γ_1 obtained with the model and parameters described in the text.

characterizing a chaotic state. With the modulation turned on at some frequency values, if δH exceeds a critical amplitude δH^*, chaos is suppressed after a transient time. Figure 3(b) shows the power spectrum for $f_m=0.56\gamma_1$ and $\delta H=0.4\gamma_1/\gamma$ (γ is the gyromagnetic ratio), demonstrating that the signal has become periodic with frequency 0.56 γ_1. The boundaries of the stability regions in the modulation-amplitude ×frequency plane, shown in Fig. 4, display tongues like the experimental results of Fig. 2.

The results shown in Figs. 3 and 4 were obtained by integrating the equations of motion with the field modulation on for a length of time on the order of 200 cycles of the oscillation, so that the response has reached steady state. Actually, the stable orbit resulting from the field modulation is preceded by a chaotic transient in which orbits similar to those of the uncontrolled chaotic attractor dominate.[2] The duration τ of such chaotic transient depends sensitively on the initial conditions. For a given modulation, we calculate the average duration $\langle\tau\rangle$ for 256 randomly chosen initial conditions. For $f_m=0.56\gamma_1$ this average time is found to scale with the modulation amplitude as $\langle\tau\rangle\sim(\delta H-\delta H^*)^{-\nu}$, where $\nu\approx0.287$. A scaling relation of this type was predicted by OGY, though with a different value for the critical exponent.

IV. CONCLUSIONS

The experimental observations on controlling chaos in spin-wave instabilities driven by microwave radiation in YIG spheres, by means of a small periodic variation in the applied magnetic field, are explained by a two-mode model. The field modulation is introduced in the model through the same detuning parameters used to explain the sample size dependence of the self-oscillations. Hence, the present results provide additional evidence of the validity of the two-mode model with momentum-nonconserving driving Hamiltonian for describing spin-wave dynamics.

ACKNOWLEDGMENTS

This work was supported by FINEP, CNPq, PADCT, CAPES, and FACEPE.

[1] A. Azevedo and S. M. Rezende, Phys. Rev. Lett. **66**, 1342 (1991).
[2] E. Ott, C. Grebogi, and J. A. Yorke, Phys. Rev. Lett. **64**, 1196 (1990).
[3] W. L. Ditto, S. N. Rauseo, and M. L. Spano, Phys. Rev. Lett. **65**, 3211 (1990).
[4] E. R. Hunt, Phys. Rev. Lett. **67**, 1953 (1992).
[5] M. Ye, D. E. Jones, and P. E. Wigen, J. Appl. Phys. **73**, 6822 (1993).
[6] R. Lima and M. Pettini, Phys. Rev. A **41**, 726 (1990).
[7] S. M. Rezende and A. Azevedo, Phys. Rev. B **45**, 10387 (1992).
[8] S. M. Rezende, F. M. de Aguiar, and A. Azevedo, J. Appl. Phys. **73**, 6805 (1993).
[9] K. Nakamura, S. Ohta, and K. Kawasaki, J. Phys. C **15**, L143 (1982).
[10] P. H. Bryant, C. D. Jeffries, and K. Nakamura, Phys. Rev. A **38**, 4223 (1988).
[11] S. M. Rezende and F. M. de Aguiar, Proc. IEEE **78**, 893 (1990).
[12] Energy should be conserved within an uncertainty on the order of the relaxation rate (or linewidth). It is well known that one can pump one spin-wave mode with frequency differing from $\omega_p/2$ by some detuning $\Delta\omega_k$. The only consequence is that the threshold increases with $\Delta\omega_k$. The reason for the choice of our values is that, in general, the value of $\omega_p/2$ will not coincide with the mean value of the frequencies of the two modes. Since the sum of the two detunings is smaller than the relaxation rate γ, there is no violation of energy conservation. The best proof of this is the very fact that the two modes we choose are indeed pumped and produce chaotic dynamics.

Spin-wave chaotic transients

F. M. de Aguiar, S. M. Rezende, and F. C. S. da Silva
Departamento de Física, Universidade Federal de Pernambuco, 50732-910 Recife, Brazil

We report the observation of transient chaotic spin-wave auto-oscillations in X-band pulsed subsidiary-resonance experiments in a YIG sphere. Chaotic transients to a periodic attractor have been observed near a critical microwave power $p_c \sim 10$ dB relative to the Suhl instability threshold. By an averaging of 100 randomly chosen initial conditions at each power, we estimate a critical exponent $\gamma \sim 0.57$. In addition, we demonstrate that the results can be qualitatively understood within the framework of the standard two-mode model. Numerical simulations yield, for a particular set of parameters, chaotic transients obeying the predicted scaling law with a critical exponent $\gamma \sim 0.54$.

I. INTRODUCTION

The transition to sustained chaotic behavior via chaotic transients was discovered by Yorke and Yorke in the Lorenz model in the late 1970s.[1] Several years later, Grebogi, Ott, and Yorke[2] identified transient chaos as a particular manifestation of a rather general phenomenon that occurs in dissipative dynamical systems, the so-called *crisis*. Three types of crisis have been characterized,[2] namely, attractor *destruction*, attractor *merging*, and attractor *widening*. A chaotic attractor is destroyed when, as a system parameter p reaches a critical value p_c, it collides with the stable manifold of an unstable periodic orbit. The characteristic behavior in this case is the existence of chaotic transients suddenly followed by periodic orbits. The duration of a chaotic transient depends sensitively on the initial conditions and can be remarkably long. The average lifetime depends upon the system control parameter as $\langle T \rangle \sim |p - p_c|^{-\gamma}$, where γ is the critical exponent of the chaotic transient.

Finite-time chaotic behavior has been observed in a number of physical systems.[3] However, only a few experiments have been analyzed in detail. As far as spin waves are concerned, the only results available on such transients were obtained by Carroll, Pecora and Rachford[4] a few years ago, in subsidiary-resonance experiments in a YIG sphere. At driving frequencies between 2.0 and 3.4 GHz, their experimental findings suggested the existence of "multiple attractors," while numerical simulations suggested the need of more than three interacting spin-wave modes to explain the long-lived transients they had observed in the experiments.

In this paper we report on transient chaos in YIG spheres at higher driving frequencies (8.0–10.0 GHz) at room temperature. Pulsed experiments have revealed the existence of long-lived chaotic transients involving "single attractors" in the spin-wave auto-oscillations (~1 MHz), 9–10 dB beyond the Suhl instability threshold. In addition, we present numerical results of a two-spin-wave-mode calculation in good qualitative agreement with the experiments. By an averaging of N randomly chosen initial conditions at each power, we estimate a critical exponent in the range $0.5 < \gamma < 0.6$ both in the experiments ($N = 100$) and in the numerical simulations ($N = 400$).

II. EXPERIMENTAL RESULTS

Our experiments were carried out with single-crystal samples of yttrium iron garnet (YIG) at room temperature. Here we present results in a 1-mm YIG sphere, which is placed at the center of a critically coupled rectangular TE_{102} microwave cavity ($Q \sim 2000$). An electromagnet provides the static magnetic field $\mathbf{H}_0$ perpendicular to the microwave magnetic field $\mathbf{h}$, in the subsidiary resonance region. The power is provided by a 10-W traveling-wave-tube (TWT) amplifier fed by a solid-state tunable YIG oscillator. The frequency ($f_p = 8.9$ GHz) is stabilized by an external crystal oscillator and manually adjusted to the center of the cavity resonance. The radiation power is controlled with a variable precision attenuator and directed by a circulator to the cavity, where it drives spin waves in the sample. The reflected microwave signal is then detected with a sensitive Schottky-barrier diode at the output port of the circulator and recorded at intervals of 0.1 μs using a commercial digitizer. In order to study the transient response, the microwave is pulsed by a *p-i-n* modulator placed before the TWT amplifier. Pulses up to 800 μs long were comfortably used with no detectable heating effects. The results presented here were observed at a fixed magnetic field $H_0 = 1830$ Oe, parallel to the [100] crystal axis. At low-power levels the pulse reflected from the cavity has essentially the same shape as the incoming microwave pulse. As the power is increased, abrupt changes in the pulse shape occur due to spin-wave instabilities at subsequent thresholds, namely, the Suhl instability threshold (SIT), h_c, the spin-wave auto-oscillation threshold, h_c', and a sequence of bifurcations that lead to spin-wave chaos.[5] Henceforth we will consider $R \equiv h/h_c$ as our control parameter. Well above the SIT ($R = 1$), we have observed the destruction of the strange attractor due to the collision between the chaotic attractor and a coexisting unstable periodic orbit. This collision occurs at the critical value $R_c = 2.88$. For $R > R_c$ we observe an intermittent signal with laminar (periodic) regions interrupted by chaotic bursts. For $2.82 < R < R_c$, the steady-state response is periodic after a chaotic transient whose duration swings intermittently, as we observe on the screen of an oscilloscope. Figure 1 shows a frozen digitized version of a chaotic transient with duration $T \sim 618$ μs, with $R = 2.84$. The measured average duration

 0021-8979/94/75(10)/5616/3/$6.00 © 1994 American Institute of Physics

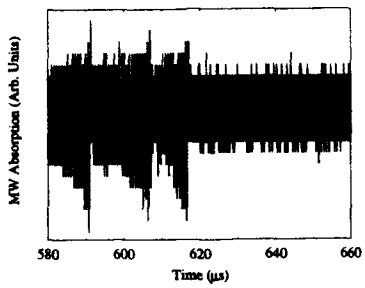

FIG. 1. Detected microwave absorption vs time in a YIG sphere at subsidiary resonance with $H_0=1830$ Oe, $R=2.84$, and $f_p=8.9$ GHz.

as a function of the control parameter is shown in the log-log plot of Fig. 2 (solid circles). From a linear regression (solid line) we estimate a critical exponent $\gamma=0.57$.

III. NUMERICAL SIMULATIONS AND DISCUSSION

The efforts in modeling the instabilities observed in high-power ferromagnetic resonance experiments are based on a theory introduced by Suhl[6] in the mid 1950s, and have been phrased in terms of the excitation and the nonlinear interaction of spin waves in the sample. The number and the nature of the excited modes are essentially the hitherto unsolved problems in this longstanding subject. We have recently provided experimental results that strongly support the two-mode model (TMM),[6] at least for the interval $h_c<h<h_c'$. In this section we present numerical results with the TMM in good qualitative agreement with the transient experiments described above. The particular set of parameters are the same we have originally used to explain the unusual spectra observed in parallel-pumping experiments.[7] In this case, the model gives higher values for the autooscillation frequency and threshold, but shares interesting qualitative features with the experiments. We refer to Ref. 5 for a detailed description on the microscopic approach with the TMM. Figure 3(a) shows a chaotic transient in the phase plane n_1 vs n_2, where n_1 and n_2 are the populations of the

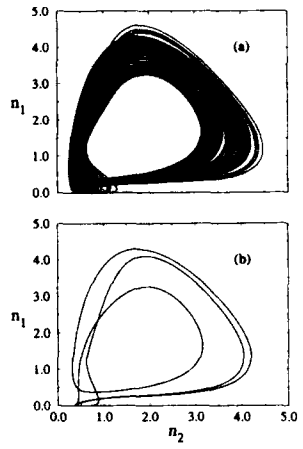

FIG. 3. Phase plane n_1 vs n_2 showing numerical solutions of the two-mode model, as described in Ref. 7, with $R=8.100\,005\,06$: (a) transient strange attractor for $0<\gamma_1 t<88.0$ and (b) period-3 limit cycle for $90.0<\gamma_1 t<3000.0$.

two excited spin-wave modes, for $R=8.100\,005\,06$. We have chosen an initial condition inside the strange attractor for which the solutions are attracted during a time interval $\gamma_1 T\sim 87.7$, where γ_1 is the phenomenological relaxation rate of mode 1. The steady-state solution is the period-3 attractor shown in Fig. 3(b) for $90.0<\gamma_1 t<3000.0$. This scenario is quite similar to the experiments: By decreasing R, an intermittent (chaos↔period-3) solution is destroyed at the critical value $R_c=8.100\,055\cdots$ below which there is a sharp period-3 window. Within this window the chaotic bursts no longer exist and the steady-state solution is reached after a chaotic transient, whose duration is very sensitive to the initial conditions. By an averaging of 400 randomly chosen initial conditions within a small volume on the strange attractor at each value of the control parameter, we have obtained the results shown in Fig. 4 (solid circles). The straight line is a fit from which we estimate a critical exponent $\gamma=0.54$. One might guess at first that we are, in both experiment and

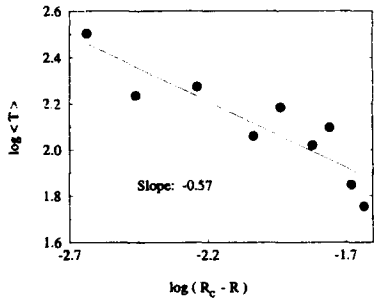

FIG. 2. Measured average duration of chaotic transients as a function of the control parameter. The straight line is a fit with a slope $\gamma=-0.57$.

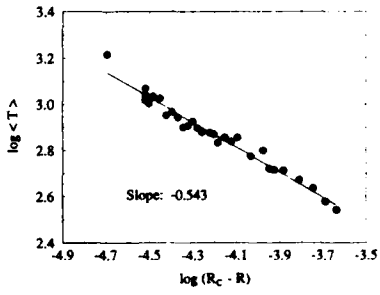

FIG. 4. Calculated average duration of chaotic transients as a function of the control parameter. The straight line is a fit with a slope $\gamma=-0.543$.

simulation, close to a situation where the system could be described by a one-dimensional map with a quadratic extremum, since in this case γ has the universal value 0.5. However, we stress that preliminary studies with return maps do not point in this direction and further investigations are under way.

ACKNOWLEDGMENTS

This work has been supported by the Brazilian agencies CNPq, FINEP, and FACEPE.

[1] J. A. Yorke and E. D. Yorke, J. Stat. Phys. **21**, 263 (1979).
[2] C. Grebogi, E. Ott, and J. A. Yorke, Physica D7, 181 (1983); Phys. Rev. Lett. **57**, 1284 (1986); Phys. Rev. A **36**, 5365 (1987).
[3] T. Tél, in *Directions in Chaos*, edited by H. Bai-lin (World Scientific, Singapore, 1990), Vol. 3, pp. 149–211.
[4] T. L. Carroll, L. M. Pecora, and F. J. Rachford, Phys. Rev. Lett. **59**, 2891 (1987); Phys. Rev. A **40**, 377 (1989).
[5] For a review, see: S. M. Rezende, F. M. de Aguiar, and A. Azevedo, J. Appl. Phys. **73**, 6805 (1993); Braz. J. Phys. **22**, 301 (1992).
[6] H. Suhl, J. Phys. Chem. Solids **1**, 209 (1957).
[7] F. M. de Aguiar and S. M. Rezende, Phys. Rev. Lett. **56**, 1070 (1986).

Magnetoelastic interaction in yttrium iron garnet films with magnetic inhomogeneities through the film thickness

Yu. V. Gulyaev, A. G. Temiryazev, M. P. Tikhomirova, and P. E. Zil'berman
Institute of Radioengineering & Electronics, Russian Academy of Sciences, Fryazino, Moscow Region, 141120, Russia

Experimental study of the spin-wave resonance (SWR) spectrum of a nonuniform yttrium iron garnet (YIG) film has revealed an existence of sharp disturbances inside the spectrum. The experiments were carried out at frequency range 4–12 GHz. The observation has been attributed to excitation of acoustic waves. The interpretation follows from the facts that (1) nonuniformity of magnetic parameters across the thickness of the tested film results in effective excitation of spin waves; and (2) coincidence of phase velocities of the spin waves and the transverse acoustic waves leads to partial power, transforming from the magnetic into the elastic system.

It is well known that the magnetoelastic interaction can be used for the generation of acoustic waves (AW) in solids at microwave frequencies. The interaction is the most strongly pronounced when phase velocities of spin waves (SW) and acoustic waves (AW) are coincident. At the point of synchronism, where the phase velocities and hence the wave lengths of SW and AW are equal, an effective transformation of magnetic oscillations energy into the elastic system can occur. Since both the spin waves and the acoustic waves in the yttrium iron garnets (YIG) have rather small losses, this material is very attractive for realization of the mentioned way of AW generation. Since the AWs have a small wavelength at microwave frequencies, it is necessary to excite very short spin waves in order to obtain an effective magnetoelastic coupling. This itself is a rather complicated problem because of the weak coupling between the short SW and electromagnetic wave. At microwave frequencies up to 4 GHz the observation of magnetoelastic interaction has been reported in Refs. 1–7, where the propagation of magnetostatic waves (MSW) in YIG films was studied. MSW propagated in the plane of the film and only in-plane components of MSW and AW coincided. It was found[4,5,8] that better coupling at frequencies above 2.5 GHz arose when spins at the surfaces were pinned, which resulted in excitation of spin wave resonance (SWR) modes.

Another way that was proposed for the excitation of the AW is to use spatially nonuniform media for the generation of the short spin waves and further acoustic waves.[9,10] In experiments,[11–13] an inhomogeneity arose due to demagnetization fields existing at the end of the longitudinal magnetized rod, and led to a gradual decrease in the SW wave number q from $q\sim 0$, giving coupling with electromagnetic waves, up to $q\sim 10^4$ cm^{-1} that was large enough to excite acoustic waves at frequency of 500 MHz.

The aim of the present paper is to show that experiments on SWR in nonuniform YIG films demonstrate excitation of acoustic waves at frequencies 3–12 GHz. Moreover, there are possibilities for further increasing the operating frequency.

We studied experimentally the microwave absorption spectra of the yttrium iron garnet (YIG) film magnetized normal to its plane. The film of thickness $L=15$ μm was epitaxially grown on a gadolinium gallium garnet (GGG) substrate with the (111) orientation. Figure 1(a) shows a plot of microwave power P absorbed by the film as the strength of the external magnetic field H was varied, and the driving frequency ω was fixed. It can be seen that the experimental spectra exhibits a large number of strongly excited modes. Since the mode spacing does not fit a quadratic law expected for a uniform film,[14] one can assume that the film has a variation of magnetic parameters through the film thickness. Our experiments[15] have verified that assumption. We shall now highlight that there are two different regions in the dependence $P(H)$. The regions are separated by an attenuation band shown by arrows, where oscillations of the absorbed power are weakened. The absorption notches look rather regular on the right side of the arrows, whereas there are disturbances of the absorption spectrum on the left side. We will show that both the disturbances observed and the existence of the attenuation band are caused by the magnetoelastic interaction, and indicate the excitation of the acoustic waves.

At first, we note that the relative position of the attenuation band inside the SWR spectrum depends on frequency. The two spectra in Fig. 1 have been measured at different frequencies, and hence at different magnetic fields. The magnetic field corresponding to the right-hand boundary of the

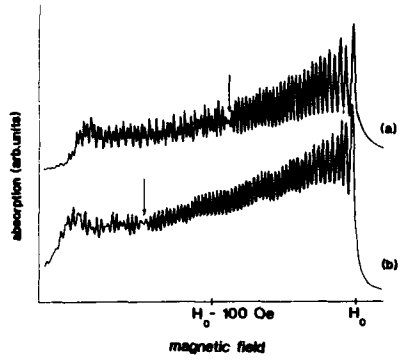

FIG. 1. Absorbed power versus the magnetic field. (a) $\omega/2\pi=7854$ MHz, $H_0=4814$ Oe; (b) $\omega/2\pi=10\,300$ MHz, $H_0=5587$ Oe.

 0021-8979/94/75(10)/5619/3/$6.00 © 1994 American Institute of Physics

absorption zone is designated as H_0. Denote the spacing between the pointer and H_0 by ΔH. Contrast the spectrum in Fig. 1(a) with that in Fig. 1(b) One can see that ΔH grows as the frequency increases.

Consider a magnetic film of thickness L placed in the bias magnetic field **H**, so that **H** is directed along the x axis perpendicular to the plane of the film. We introduce an effective magnetization M that will be defined as $4\pi M(x)=4\pi M_s(x)-H_A(x)$, where $M_s(x)$ is the saturation magnetization and $H_A(x)$ is the uniaxial anisotropy field. Suppose that M varies along the film thickness but other parameters of the film are constants. Denote the maximum value of $M(x)$ by M_{MAX} and the minimum value by M_{MIN}. An effective wave number $q(x)$ of the spin wave propagating in the x direction depends on x, and can be found from the spin wave dispersion formula,

$$\omega/\gamma=H-4\pi M(x)+D\cdot q(x)^2, \tag{1}$$

where γ is the gyromagnetic ratio and D is the exchange constant (5.6×10^{-9} Oe cm^2). The condition for the effective excitation of the SW is the existence of a layer inside the film where $q(x)\sim0$, and conversion from the electromagnetic waves into the spin waves takes place. It can be seen from Eq. (1) that this condition will be satisfied inside the magnetic field band,

$$H_1<H<H_2,$$
$$H_1=\omega/\gamma+4\pi M_{\mathrm{MIN}}, \tag{2}$$
$$H_2=\omega/\gamma+4\pi M_{\mathrm{MAX}}.$$

Note that the bandwidth is independent of frequency ω, since $H_2-H_1=4\pi\,\Delta M$, where $4\pi\,\Delta M$ is the maximum variation of the effective magnetization: $4\pi\,\Delta M=4\pi M_{\mathrm{MAX}}-4\pi M_{\mathrm{MIN}}$.

Strong coupling between spin waves and acoustic waves can be the case in the layer in which the wave numbers of those waves coincide. The wave number of the AW q_{AW} is equal to ω/V, where V is the acoustic wave velocity. Then we obtain from Eq. (1) a condition for the existence of such a layer,

$$H_1-D\cdot(\omega/V)^2<H<H_2-D\cdot(\omega/V)^2. \tag{3}$$

Thus, the spin waves can be excited over a band defined by condition (2), but the region of coupling with AW [condition (3)] is shifted by

$$\delta H=D\cdot(\omega/V)^2. \tag{4}$$

If $\delta H>4\pi\,\Delta M$, these bands will be separated. Hence, it follows that the maximum frequency of the acoustic wave that can be excited by this way is equal to

$$\omega_{\max}=V\cdot\sqrt{\frac{4\pi\,\Delta M}{D}}. \tag{5}$$

On the other hand, the value of δH represents the width of part of the SWR spectrum where no strong coupling between SW and AW can be expected. Compare the calculated dependence $\Delta H(\omega)$ with experimental values of ΔH that represent the width of the regular part of the absorption spectrum. We have found that good agreement can be obtained (Fig. 2) if

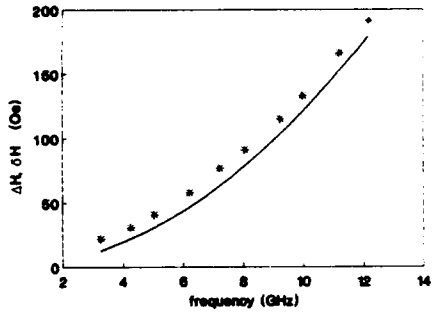

FIG. 2. Experimental points $\Delta H(\omega)$ and calculated dependence $\delta H(\omega)$.

$V=3.85\times10^5$ cm/s. Since this is the velocity of transverse acoustic waves, this is evidence that just this type of acoustic wave is generated under the experimental conditions.

We can assume that the attenuation band emerges if conditions for the most effective coupling between SW and AW arise. Such can be the case if the waves are coupled inside a spatially wide layer. To check this hypothesis we shall find the variation of $q(x)$ for the tested film. Figure 3 shows a profile of effective magnetization across the thickness of the film under investigation. The profile has been obtained using the procedure reported in Ref. 15. One can see that $M(x)$ varies monotonically and $M_{\mathrm{MAX}}=M(0)$. The experimental points are in a good agreement with a parabolic dependence $4\pi M(x)=4\pi M(0)-4\pi\,\Delta M\cdot(x/L)^2$, where $4\pi\,\Delta M=198$ G. We can calculate from Eq. (1) that if $M(x)$ varies parabolically, the dependence $q(x)$ is given by an ellipse equation,

$$\frac{q^2}{a^2}+\frac{x^2}{b^2}=1,$$
$$a^2=\frac{\delta H^*}{D},\quad b^2=\frac{L^2\cdot\delta H^*}{4\pi\,\Delta M}, \tag{6}$$
$$\delta H^*=\omega/\gamma-H+4\pi M(0).$$

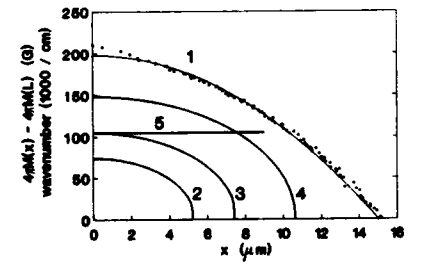

FIG. 3. Profile of the effective magnetization and the variation of the wave number across the thickness of the film. Points: the experimental data of $4\pi M(x)-4\pi M(L)$; (1) profile of magnetization $4\pi M(x)=4\pi M(0)-4\pi\,\Delta M\cdot(x/L)^2$ at $4\pi\,\Delta M=198$ G; (2)–(4) wave number of spin wave at (2)–$\delta H^*<\delta H$ ($\delta H^*=25$ Oe); (3) $\delta H^*=\delta H$ ($\delta H^*=50$ Oe); (4) $\delta H^*>\delta H$ ($\delta H^*=100$ Oe); and (5) wave number of acoustic wave at $\omega/2\pi=6400$ MHz.

When H decreases, the value of δH^* grows, thus the dimensions of the ellipse also grow (Fig. 3). From Eqs. (1), (4), and (6) we obtain that the point of synchronism appears first at $x=0$ if $\delta H^* = \delta H$. When $\delta H < \delta H^* < \delta H + 4\pi\,\Delta M$, the point of synchronism also exists, but the most effective coupling between SW and AW is to be expected at $\delta H^* \simeq \delta H$, since then the equality $q \simeq q_{AW}$ is fulfilled in a spatially wide layer. The value of δH represents the spacing between the right-hand edge of the SWR spectrum and the boundary of the coupling region. That is why we observe the attenuation band just near this boundary. A constant shift of the experimental data toward the bigger values of ΔH in Fig. 2 can be explained by the real profile deviation from the parabolic dependence used in our model.

It is worth noting that the absorption spectrum pattern depends strongly on the operating frequency everywhere over the disturbance region. The spectrum pattern varies periodically as ω changes. The period equals to approximately 3.5 MHz, which corresponds to the spacing between acoustic modes of the film–substrate structure. That shows the acoustic wave excited within the YIG film propagates into the substrate.

Thus, experimental results show that the use of nonuniform magnetic films, having the magnitude of variation $4\pi\,\Delta M \simeq 200$ G, offers the possibility for effective excitation of acoustic waves at frequencies as high as 12 GHz. The frequency range of excitation can be expanded, since films with a larger value of $4\pi\,\Delta M$ exist.[15] In this respect the described way of AW generation appears to be very promising.

[1] Yu. V. Gulyaev, P. E. Zil'berman, G. T. Kazakov, V. G. Sisoev, V. V. Tikhonov, Yu. A. Filimonov, B. P. Nam, and A. S. Khe, Pisma Zhur. Exp. Teor. Fiz. **39**, 500 (1981).
[2] G. T. Kazakov, V. V. Tikhonov, and P. E. Zil'berman, Fiz. Tverd. Tela **25**, 2307 (1983).
[3] W. S. Ishak, IEEE Trans. Magn. **MAG-19**, 1880 (1983).
[4] A. S. Andreev, Yu. V. Gulyaev, P. E. Zil'berman, V. B. Kravchenko, Yu. F. Ogrin, A. G. Temiryazev, and L. V. Filimonova, Pisma Zhur. Tekh. Fiz. **10**, 90 (1984).
[5] A. S. Andreev, Yu. V. Gulyaev, P. E. Zil'berman, V. B. Kravchenko, Yu. F. Ogrin, A. G. Temiryazev, and L. V. Filimonova, Radiotek. Elektron. **30**, 991 (1985).
[6] J. D. Adam, M. R. Daniel, and S. H. Talisa, *1988 IEEE MTT-S Digest*, IEEE Catalog No. 88CH2489-3, 1988, p. 879.
[7] N. Bilaniuk and D. D. Stancil, J. Appl. Phys. **67**, 4790 (1990).
[8] V. B. Gorskii and A. V. Pomyalov, Pisma Zhur. Tekh. Fiz. **15**, 61 (1989).
[9] E. Schlömann, J. Appl. Phys. **35**, 159 (1964).
[10] E. Schlömann and R. I. Joseph, J. Appl. Phys. **36**, 875 (1965).
[11] E. G. Spencer, R. T. Denton, and R. P. Chambers, Phys. Rev. **125**, 1950 (1962).
[12] W. Strauss, J. Appl. Phys. **35**, 1022 (1964).
[13] T. Kohane, E. Schlömann, and R. J. Joseph, J. Appl. Phys. **36**, 1267 (1965).
[14] C. Kittel, Phys. Rev. B **110**, 1295 (1958).
[15] A. G. Temiryazev, M. P. Tikhomirova, and P. E. Zil'berman (these proceedings).

Nonlinear statics and dynamics of highly anisotropic magnets

V. S. Ostrovskii[a)]
Institute of Physics, Ukrainian Academy of Sciences, Kiev, Ukraine

It is shown that an adequate description of static and dynamic properties of highly anisotropic magnets in circumstances, where the violation of their initial symmetry induced by external fields or dynamic perturbations is not small, can be achieved by making use of the generalized coherent states. A complete set of equations governing coupled dipole and quadrupole degrees of freedom is presented for a system of spins $S=1$. The solutions obtained for uni- and biaxial ferromagnets and antiferromagnets make it apparent that the strong anisotropy qualitatively affects the behavior of such systems in external magnetic fields; in particular, it can change the nature of phase transition and give rise to the new ones. The complete set of equations makes it possible to derive solutions, corresponding to crucially new nonlinear objects such as domain walls, vortices, etc. whose treatment cannot be approached from the classical theory.

I. INTRODUCTION

As early as in the 1960s and 1970s, Moriya and Lines brought forth the problem of an appropriate description of the magnets exhibiting the single-ion anisotropy (SIA) and biquadratic exchange, comparable with the bilinear one. They elucidated the fundamental importance of the competition between the "transversal" SIA and exchange field that resulted in a quantum mechanical reduction of the average spin $\Delta\langle S\rangle\sim(\mathrm{SIA/EX})^2$. On the other hand, in specifying a spin configuration in a strong magnetic field which breaks the initial high symmetry of the system, one usually reduces this problem to determination of the spin orientations assuming $|\langle\mathbf{S}\rangle|=\mathrm{const}$ and thus starting from the quasiclassical approximation. Nonlinear phenomena (domain walls, solitons, and highly excited states) occurring in magnets are considered in much the same way. Here, theoretical studies usually start from equations of the Landau–Lifshits type (LLE) which apply, strictly speaking, only to small SIA.

Nevertheless, the LLE framework can be extended to the case of arbitrary values of spins without any limitations on the strength of allowed interactions. With this aim in view, it is important to point out that the parameters specifying the orientations of the local magnetization refer to a coherent state of the SU(2) group, which represents the dynamical symmetry group for the spin $S=1/2$ or the classical spin $S\to\infty$.[1] In the general case of the spin $S>1/2$, a physical state can be described in terms of a generalized coherent state of the group $G_{\mathrm{dyn}}=SU(2S+1)$, with the dynamics being interpreted as the motion of a $4S(S+1)$-dimensional vector on the orbit $SU(2S+1)/H$ in the space of a complete set of the generators of the $SU(2S+1)$ algebra; e.g., such a state can be given by a set of the tensors O_{kq} $(k,q=1,\ldots,2S)$ or by that of the Hubbard operators x_{nm} $(n,m=1,\ldots,S)$. The stationary subgroup H determines all kinematic properties of the system. For the particular case of a pure state, we get $H=SU(2S)\times U(1)$ and the motion takes place in the $4S$-dimensional subspace CP^{2S}, i.e., it is a local motion on the sphere S^{4S}.[2] Thus, the description of the dynamics in terms of the ($4S$ parametric) generalized coherent states enables one to allow automatically for $4S^2$ integrals of motion and to remove the troubles associated with the introduction and account of the so-called "kinematic interactions." From the above discussion it follows that the magnetization vector is just a component of the $4S(S+1)$-dimensional vector of the "generalized spin" (the "coherence vector")[3] on the three-dimensional subspace, thus the magnetization alone cannot provide an adequate description of the spin system. It can be shown, however, that a consistent quantum mechanical approach to the case, when the perturbation theory with respect to the small parameter (SIA/EX) does apply, results in the LLE-set obtained as the first approximation.

II. EQUATIONS OF MOTION FOR THE CASE $S=1$

For a system of spins $S=1$, we can parametrize a generalized coherent state of the $SU(3)$ group in such a way that its physical meaning becomes manifestly evident, and the equations of motion can be presented in a form very close to that of the well-known LLE set. In so doing we take, as two of the four independent parameters, two Euler angles ϑ, φ which specify the magnetization direction. For classical spins, the other two independent parameters have no physical sense because the third parameter is nothing but the third Euler angle γ, which specifies the rotation of the principal axes of the quadrupolar tensor $Q^{ij}=1/2(S^iS^j+S^jS^i)$ about the magnetization, and the fourth parameter $q=\langle Q^{xx}-Q^{yy}\rangle$ is the value of the transversal component of this tensor or the magnetization magnitude $s=[(1-q^2)]^{1/2}$.

In the reference frame given by these angles, the dynamics is described by the following nonlinear system:

$$\dot{s}-2q\tilde{A}^{xy}=0, \tag{1}$$

$$\dot{\Phi}^z+\tilde{h}^z-(s/2q)(\tilde{A}^{xx}-\tilde{A}^{yy})=0, \tag{2}$$

$$\dot{\Phi}^y+\tilde{h}^y+(s/1-q)\tilde{A}^{yz}=0, \tag{3}$$

$$\dot{\Phi}^x+\tilde{h}^x+(s/1+q)\tilde{A}^{xz}=0, \tag{4}$$

where $\dot{\Phi}^\alpha$ are components of the angular velocity, and $\tilde{h}^\alpha$, $\tilde{A}^{\alpha\beta}$ are the effective magnetic and quadrupole fields which comprise, apart from the usual inhomogeneous terms, such contributions as $\epsilon_{z\nu\mu}(\nabla\Phi^\mu)(\nabla s)$, $\delta_{\nu z}\Delta s$, etc.

a)Present address: 1959 East 17th St., Brooklyn, NY 11229.

 0021-8979/94/75(10)/5622/3/$6.00 © 1994 American Institute of Physics

In the cases when the pairs of the variables (ϑ,φ) and (γ,s) can be separated, Eqs. (1) and (2) describe a wave of the coupled oscillations of the magnetization magnitude and axes of the quadrupolar tensor; by linearizing these equations we arrive at the dispersion of the longitudinal $(\Delta S^z=2)$ magnons, whereas from Eqs. (3) and (4) we can arrive at the ordinary "transversal" magnons, e.g., see Fig. 1(b). In the $\tilde{A}^{\alpha\beta}\ll\tilde{h}^z$ limit, the pair (3) and (4) transforms into LLE.

III. THE EQUILIBRIUM STATE IN STRONG MAGNETIC FIELDS

In the static limit $(d/dt=0)$, Eqs. (1)–(4) determine the selfconsistent equilibrium state of the system. The fact that the value of q is an independent variable reflects the existence of nonlinear coupling of the dipole and quadrupole degrees of freedom which affects drastically the behavior of a magnet in external magnetic fields. Consider two examples to illustrate this statement.

A. Biaxial antiferromagnet (AFM) in a longitudinal field

The classical solution for the AFM governed by the Hamiltonian

$$\mathcal{H}=-\sum_{n\alpha}\left[H_z S^z_{n\alpha}+AQ^{zz}_{n\alpha}+B(Q^{xx}_{n\alpha}-Q^{yy}_{n\alpha})\right]$$

$$+\sum_{nm} I_{n1m2}\mathbf{S}_{n1}\mathbf{S}_{m2} \tag{5}$$

(sublattices $\alpha=1, 2$, $A>B$) is well known: if $(A-B)<I$, where $I=\Sigma_m I_{oam\beta}$, etc., a spin-flop transition takes place, in the opposite case, for a field $H_z=I$ we should observe a metamagnetic transition from the state $s^z_1=-s^z_2=1$ into that with $s^z_1=s^z_2=1$. The suggested approach invites solution of the set of two equations of the form (2) for $\alpha=1$ and 2. Fortunately, these equations can be solved exactly, and the calculated functions $s_{1,2}(H_z)$ are shown in Fig. 1(a). Such behavior may manifest itself in the experimental observation of resonance frequencies and optical spectra,[4] Figs. 1(b) and 1(c).

B. Easy-plane ferromagnet in longitudinal field

Figure 2(a) presents the phase diagram for a FM described by

$$\mathcal{H}=\sum_n\left(-H_\parallel S^z_n+AQ^{zz}_n\right)$$

$$-\frac{1}{2}\sum_{nm}\left(J_{nm}\mathbf{S}_n\mathbf{S}_m+J'_{nm}S^z_nS^z_m\right), \tag{6}$$

where $J>0$; the solid and dashed curves correspond to the phase transitions of the first and second kind, respectively, between easy-axis (EA), easy-plane (EP), and singlet-magnet (SM) phases. The classical EA–EP boundary is shown by a dash–dotted line. The states with nonzero magnetization $s=[(1-q^2)]^{1/2}$, making an angle ϑ with the Z axis, are given by the equations

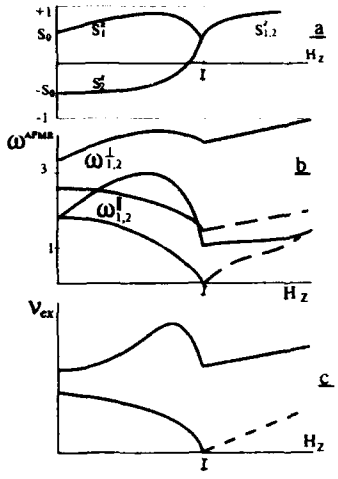

FIG. 1. The metamagnetic transition in highly anisotropic biaxial AFM (a) sublattice magnetization $s^z_{1,2}(H_z)$; (b) frequencies of transversal $\omega^{\perp}_{1,2}$ and longitudinal $\omega^{\parallel}_{1,2}$ spin excitations, (c) frequencies of exciton absorption lines.

$$\cos\vartheta=H_\parallel(1+q)/s[A-(1+q)J'], \tag{7}$$

$$AH^2_\parallel=[A-(1+q)J']^2(A+2qJ). \tag{8}$$

Note, that in the SM phase (for $A>2J$) the magnetization arises only in field $H_\parallel>H'$: $s\sim(H_\parallel-H')$, where $H'=[A(A-2J)]^{1/2}$. The dotted lines in Fig. 2(a) separate the regions of different behavior of the system in $\mathbf{H}_\parallel$. So, in the parameter region 1, the vector $\langle\mathbf{s}\rangle$ continuously turns to the $\mathbf{H}$ direction and the second-order transition take place at $H_f=A-J'$. In region 2 the angular phase loses its stability at $\vartheta(H_0)\neq 0$, see the insert in Fig. 2; the angle discontinuity $\Delta\vartheta$ at the first-order transition to the state $\vartheta=0$ increases

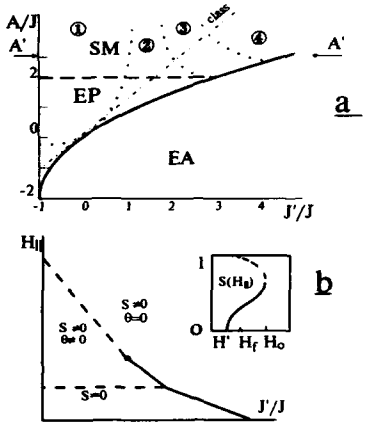

FIG. 2. (a) The (A,J') Phase diagram for a uniaxial FM in a longitudinal field; (b) the (H,J') Phase diagram plotted for a specific value $A'>2J$.

from 0 to $\pi/2$ with increase of J'. In regions 3 and 4 $\Delta\vartheta = \pi/2$, but in 3 the angular phase may exist as a metastable one. Figure 2(b) presents the $(H_\parallel - J')$ phase diagram corresponding to some specific value of $A' > 2J$.

IV. SPATIALLY INHOMOGENEOUS SOLUTIONS

With additional active degrees of freedom introduced into Eqs. (1)–(4), the scope of possible nonlinear effects greatly widens in excess of that described by the LLE set. Here we will not dwell upon the problems connected with the interference of dipole and quadrupole variables and confine ourselves to some special results referring to the quadrupole variables.

A. Domain wall in a biaxial FM

At $(A-B) > J$, the Bloch-type domain wall (DW) is very unlikely to arise, much as in a highly anisotropic AFM (5) the spin-flop phase dies out. The static solution to Eqs. (1)–(4), satisfying the boundary conditions $s(\pm\infty) = \pm s_0$, where $s_0 = [(1-b^2)]^{1/2}$, $b = B/J$, is a spatial area with the width $L = 2/[(1-b)]^{1/2}$ inside which only the magnetization magnitude varies. In contrast with the classical Ising DW ($s_n = \pm 1$), such DW is a mobile excitation and its motion along the y axis with the velocity V is accompanied by a rotation wave of the tensor $Q^{\alpha\beta}$:[5]

$$\frac{\sqrt{2}\cdot(y-Vt)}{[1-(v/v_c)^2]^{1/2}} = \frac{b}{s_0}\ \mathrm{arcsinh}\left\{\frac{ss_0}{\sqrt{(1-s^2)-b}}\right\} + \arcsin s, \tag{9}$$

$$\sin 2\gamma = \frac{v}{v_c}\frac{s_0}{1+b\cosh[s_0(y-vt)\sqrt{2}]}, \quad v_c = \sqrt{2}B/\hbar. \tag{10}$$

In a magnetic field $\mathbf{H} \| OZ$, this DW moves like a particle with the mass $m_0 = \sqrt{2}\hbar^2 J s_0^3/6B^2$. It must be emphasized that the derived expressions (9) and (10) refer to a pure quantum mechanical state for $T=0$. Here, as in biaxial AFMs (Fig. 1), the reduction "quenching" and vanishing of the magnetization are related to changes of the component of the eight-dimensional "generalized spin" vector on the three-dimensional subspace (s_x, s_y, s_z). Figure 3 shows how for a static DW the orientation of this vector varies in the subspace (s_x, s_z, q) in weakly (curve 1) and highly anisotropic (curve 2) FMs; the dashed line corresponds to a classical DW of the Bloch type.

B. Magnetic vortex

In the frame of the classical approach, the energy minimum of the magnetic vortex is provided by a deflection of the magnetization from the easy plane at the vortex core. Yet, Eqs. (1)–(4) admit an alternative solution where spins are left in the plane and the energy remains finite due to variations of the s (r) modulus and to the magnetization vanishing at the vortex axis. In the cylindric coordinate system (r, λ), the solution for $r < r_\nu$ is

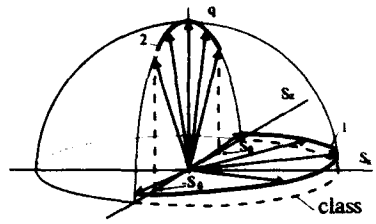

FIG. 3. The orientation of the "generalized spin" vector in domain walls for weakly (curve 1) and highly (curve 2) anisotropic FMs. The parameter varied along curves 1 and 2 is the spatial coordinate y.

$$s(r) = s_\infty J_\nu(rs_\infty) \sim s_\infty (r/r_\nu)^\nu, \tag{11}$$

where $\nu = 1,2,\ldots$, $s_\infty = [1-(A/2J)^2]^{1/2}$ and $r_\nu = 2(\nu!)^{1/\nu}/S_\infty$ is a characteristic scale, equal to the vortex core radius.

V. CONCLUDING REMARKS

In the foregoing we have surveyed just a small part of the results related to rather simple examples of the nonlinear behavior of highly anisotropic magnets in strong magnetic fields. Further progress is rich with prospects in studying more complicated systems[6,7] and allowing for corrections to the solutions of the self-consistent problem.[8,9]

Furthermore, the avenue of the research pertaining to nonlinear dynamics, in particular to solitonlike objects, remains almost unexplored. As shown above, even in the systems with spins $S=1$ there may exist novel objects associated with quadrupole degrees of freedom. It is also likely that interactions between dipole and quadrupole variables (or even those of a higher multiplicity for $S>1$) will not only modify the related solutions[10] but also result in the revelation of novel mixed objects with additional internal structure. Naturally, the suggested theoretical investigations invite further target-oriented experiments.

[1] A. M. Perelomov, Sov. Phys. Usp. **20**, 703 (1977).
[2] Thus, for the mixed state described by the density matrix $H = \otimes U(1)$ we have $2S$ integrals of motion.
[3] F. T. Hioe and J. H. Eberly, Phys. Rev. Lett. **47**, 838 (1981).
[4] A. F. Prikhot'ko, V. S. Ostrovskii, Yu. G. Pikus, and L. I. Shanskii, Sov. J. Low Temp. Phys. **6**, 518 (1980).
[5] V. S. Ostrovskii, Sov. Phys. JETP **64**, 999 (1986).
[6] V. S. Ostrovskii and Yu. G. Pogorelov, Sov. Phys. Solid State **32**, 1626 (1990).
[7] V. S. Ostrovskii, Sov. J. Low Temp. Phys. **16**, 689 (1990).
[8] V. V. Valkov, A. N. Matsuleva, Sov. Phys. Solid State **33** (No. 4) (1991).
[9] F. P. Onufrieva, Sov. Phys. JETP **89** (6) (1985).
[10] V. I. Butrin, B. A. Ivanov, A. N. Kichizhiev, and Y. N. Mitsai, Sov. J. Low Temp. **17** (1) (1991).

Applications of ferrites and ferromagnets in tuning rf cavities for accelerators

S. M. Hanna
Brookhaven National Laboratory, Upton, New York 11973

Traditionally ferrites have been used in accelerators for tuning rf cavities and in nonreciprocal devices controlling the power flow in rf accelerating systems. Recently, the development of cavity tuners based on perpendicularly biased ferrites has shown good progress. Yttrium iron garnet (YIG) is gradually replacing the traditional Ni Zn ferrites. The use of conventional parallel-biased Ni Zn ferrites for varying the frequency of accelerating cavities has the disadvantage of high saturation magnetization ($4\pi M_s$). This precludes practical operation in low magnetic loss regions. Different substitutions have been used with YIG to reduce its $4\pi M_s$, making it a practical candidate for perpendicular biasing operating in the saturation region. In addition, YIG is known for its low dielectric and magnetic losses. In this paper we give a short review of development in accelerator cavity tuners based on perpendicularly biased iron garnet ferrites. We use the operation of a 52 MHz stripline-based YIG tuner which we have tested at BNL as an example to demonstrate the advantages of using YIG in cavity tuners. We also discuss magnetic tuning techniques based on magnetostriction of Ni.

I. INTRODUCTION

Some of the well known characteristics of ferrites that have been exploited in accelerators are the ease of changing the permeability, the nonreciprocal properties, and dependence of magnetic losses on the biasing field (or operating frequency). Low-loss ferrites have found applications such as tuners and circulators. More recently the inclusion of ferrite absorbers in the inside walls of beam pipes for selectively damping of undesirable modes has been under investigation. Tuning of radio-frequency (rf) cavities in storage rings is needed to maintain accelerating gap voltage under varying beam load conditions. Conventionally, this has been done using motor-driven capacitive posts or inductive loops. Under conditions of fast injection, the need exists for a different type of tuner in which the mechanical movements of the tuning elements are eliminated. In this paper we present a short review of the application of ferrites in tuning accelerating cavities. We use a stripline-based garnet tuner which was tested at the Brookhaven Laboratory as an example for the new directions for ferrite tuners. We also discuss briefly the magnetostrictive ferromagnetic tuners used with superconducting accelerating cavities.

II. NEED FOR TUNERS IN ACCELERATORS

The effect of the passage of a bunch of charges (e.g., electrons) in a cavity is to excite an additional field in the cavity. These induced fields can be described in terms of beam image current induced in the cavity walls. To the accelerating cavity, the generator current i_g and the beam image current i_b are indistinguishable, and the net cavity driving current is their phasor sum i_t. In the vicinity of resonance the cavity can be presented by a parallel RLC circuit (seen from the accelerating gap). In the phasor diagram shown in Fig. 1, V is the gap voltage, ϕ_s is phase difference between the gap voltage and the harmonic component of the beam current at the cavity resonance frequency.[1] The total current flowing through the resonator, i_t is related to V through the cavity admittance:

$$i_t = YV = (1/R + jB)V, \tag{1}$$

where R is the shunt resistance of the cavity which is constant. The susceptance B can be varied by adjusting the tuning angle of the resonator. As a consequence, i_t follows the locus shown in Fig. 1 (dotted line) depending on the cavity tuning. The minimum value of $|i_g|$ is obtained when i_g and V are in phase. This is the best operating condition for the power generator. Usually there is a servo tuner which measures the phase difference between the rf drive and gap voltage, and controls the cavity tuning through the motion of a mechanical tuner or the change of the magnetic biasing field on a ferrite (or a magnetostrictive) tuner to minimize the required rf power.

III. FERRITE CAVITY TUNERS

The idea of using ferrites to tune rf and microwave cavities is almost four decades old.[2–4] These early x-band (around 10 GHz) experiments were successful in demonstrating the potential of ferrite tuning of cavities. Practical applications in tuning accelerator cavities followed the improvement in the quality of ferrites available. Conventional ferrite-tuned particle accelerator cavities,[5] used nickel-zinc ferrites rings loading short-circuited coaxial transmission lines. The resulting variable inductance was used to resonate the accelerating gap capacitance. The accelerating voltage is kept in tune with the required accelerating frequency by changing the biasing magnetic field. A simplified basic structure is illustrated in Fig. 2. In the early designs the ferrite rings encircled the beam pipe.[6] In later machines, the ferrite was moved from around the beam pipe, thus making the tuners demountable and several turns of bias current were used to reduce the current requirement. An example of that is the Fermi National Laboratory (FNL) booster cavity,[7] providing a tuning range of 30.3–52.8 MHz.

 0021-8979/94/75(10)/5625/3/$6.00 © 1994 American Institute of Physics

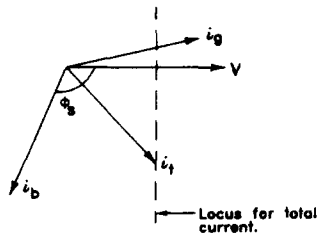

FIG. 1. Phasor diagram for cavity currents and gap voltage.

A. Effect of biasing orientation

Two approaches have been implemented for biasing the ferrite for varying its permeability. In the parallel biased tuners nickel-zinc ferrite was the material of choice. Because of their high saturation magnetization ($4\pi M_s$), it was not practically possible to bias the ferrite to saturation avoiding domain wall loss. Thus, low magnetic Q's were typical of these cavities. Additional Q degradation occurred at low bias fields resulting from domain wall motion accompanying rapid change in bias field. This dynamic loss was found to seriously affect the accelerator performance when low-frequency biasing was required for frequency sweeping.[8] Recently, substituted yttrium iron garnet (YIG) was used in ferrite cavity tuners using perpendicular biasing.[9–14] With different substitutions, the $4\pi M_s$ was reduced enough to allow for biasing above saturation. Thus, low-loss operation was achieved, exploiting the high magnetic Q of the YIG. In addition, YIG offers high electric Q. We review here the main characteristic of a garnet tuner by discussing a garnet tuner[12,13] of the stripline configuration.

B. BNL stripline garnet tuner

A new type of ferrite tuner has been tested at the BNL. The ferrite tuner uses garnet slabs partially filling a stripline. One of the important features of the tuner is that the ferrite is perpendicularly biased and the dc magnetic field is set for operation above FMR, thus reducing the magnetic losses in the ferrite. A unique design was adopted to achieve efficient cooling.

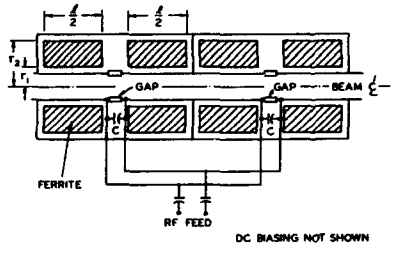

FIG. 2. AGS ferrite cavity, schematic representation.

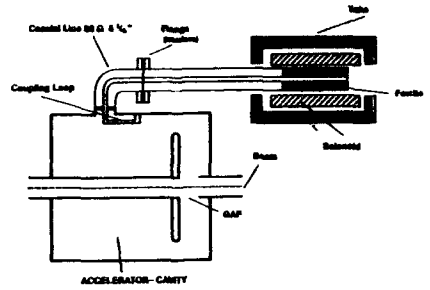

FIG. 3. Configuration for YIG stripline tuner.

1. Basic concept

A loop-coupled transmission line is used to tune a 52 MHz cavity. The transmission line is partially loaded by ferrite. By changing the bias field, the permeability of the ferrite can be changed. This results in a change in the circulating current in the coupling loop, which in turn changes the magnetic field in the region around the loop. Thus, the ratio of the magnetic to electric stored energy in the cavity is changed with the accompanying change in the cavity's resonant frequency. A schematic for the ferrite tuner and the rf cavity is shown in Fig. 3.

2. Circuit model

The ferrite tuner can be modeled as a short-circuited transmission line whose effective length varies as a function of the bias current, $l(I)$ as shown in Fig. 4. From the tuner equivalent circuit shown in Fig. 5(a), one can deduce the coupled impedance reflected into the cavity. This is shown in Fig. 5(b).

$$Z_c=\frac{(\omega M)^2}{Z_s+Z_t} \tag{2}$$

giving

$$Z_c=\frac{K^2(\omega L_p)(\omega L_s)}{Z_s+Z_t}=\frac{-K^2Z_pZ_s}{Z_s+Z_t}, \tag{3}$$

where $K^2=M^2/L_pL_s$. Since the resistive part of Z_s is negligible, then

$$Z_s=j\omega L_s.$$

The resonance frequency of the cavity is

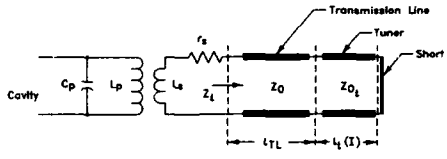

FIG. 4. Transmission line model for the ferrite tuner.

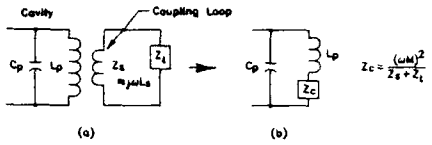

FIG. 5. Equivalent circuit for the cavity/tuner coupling structure.

$$2\pi f = \frac{1}{\sqrt{L_{\text{eff}} C_p}},$$

where

$$L_{\text{eff}} = L_p\left(1 - \frac{K^2}{1 + Z_l/Z_s}\right).$$

If the capacitance is fixed, then we have

$$\frac{\Delta f}{f} = -\frac{\Delta L_{\text{eff}}}{L_{\text{eff}}}. \tag{4}$$

3. Tunability

We have optimized the coupling between the tuner and the cavity as well as the length of the connecting transmission line to obtain the required tunability. A length of $l = 56.5''$ gave a linear tuning characteristics as shown in Fig. 6. The cavity frequency is plotted against the tuner biasing current I. The maximum frequency shift obtained is 78 kHz, which exceeds the design goal of 50 kHz.

VI. MAGNETOSTRICTIVE TUNERS FOR SUPERCONDUCTING CAVITIES

Superconducting (SC) cavities normally require two tuning systems.[15] The slow tuning system has to compensate for frequency fluctuations due to changes in the operating pressure of the liquid-helium (LHe) bath or variations from one cooling cycle to another. Fast tuning system has to cope with fast frequency changes resulting from cavity vibration (typically 10–500 Hz) produced by external sources (such as vacuum pumps) or by fast pressure changes in LHe bath.

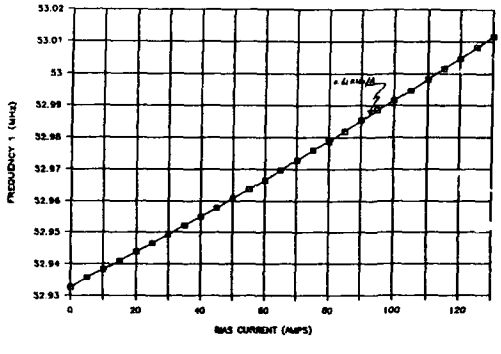

FIG. 6. Tuning characteristics of the YIG tuner.

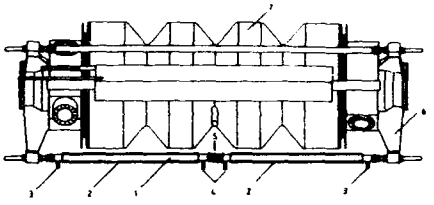

FIG. 7. Tuning system of LEP cavities: (1) Ni tube, (2) coil for magnetostriction, (3) cold [illegible] gas inlet, (4) cold He gas outlet, (5) heater, (6) supporting frame, and (7) cavity with welded He vessel.

Magnetostrictive tuning system is based on changing the cavity length by applying mechanical forces resulting from the magnetostriction of ferromagnetic bars supporting the cavity. Pure nickel (Ni) is chosen over other magnetostrictive materials because of its proven cryogenic properties. This approach for fast tuning has been used in the niobium cavities at the large electron positron (LEP) collider at European Organization for Nuclear Research (CERN). The four-cell 350 MHz LEP cavity is shown in Fig. 7.[16] Three Ni tubes (anchored to the cavity end flanges) sustain the cavity and He vessel. Each tube is surrounded by two coils providing the magnetic field needed for the magnetostrictive effect. The sensitivity of tuning is 40 kHz/mm at a speed of 20 Hz/ms covering a tuning range of 2000 Hz at a maximum exciting field of 4400 A/m. The same system is used for slow tuning exploiting the thermal expansion of the Ni bars by varying their temperature by electrical heating coils. The tuning range is 50 kHz with tuning speed of 8 Hz/s.

ACKNOWLEDGMENT

This work was performed under the auspices of the U.S. Department of Energy, under contract No. DE-AC02-76CH00016.

[1] D. Boussard, IEEE Trans. Nucl. Sci. **NS-32**, 1852 (1985).
[2] G. R. Jones and J. C. Morrison, Proc. IRE **44**, 1431 (1956).
[3] C. E. Fay, Proc. IRE **44**, 1446 (1956).
[4] C. E. Nelson, Proc. IRE **44**, 1449 (1956).
[5] I. S. K. Gardner, CERN Report No. 92-03, 1992, pp. 349–369.
[6] G. Rakowsky, IEEE Trans. Nucl. Sci. **NS-14**, 315 (1967).
[7] Q. A. Kerns *et al.*, IEEE Trans. Nucl. Sci. **NS-12**, 185 (1965).
[8] J. E. Griffin and G. Nicholls, IEEE Trans. Nucl. Sci. **NS-26**, 3965 (1979).
[9] W. R. Smythe *et al.*, IEEE Trans. Nucl. Sci. **NS-32**, 2951 (1985).
[10] L. M. Earley *et al.*, 1982 IEEE MTT-S Int. Microwave Symposium, 1982, pp. 246–248.
[11] R. M. Hutcheon, Proceedings of the 1987 IEEE Particle Accelerator Conference, Washington, D.C., 1987, Vol. 3, pp. 1543–1545.
[12] E. Pivit, S M. Hanna, and J. Keane, Proceedings of the 1991 IEEE Particle Accelerator Conference, 1991, Vol. 2, pp. 774–776.
[13] S. M. Hanna, E. Pivit, and J. Keane, IEEE Trans. Magn. **MAG-28**, 3210 (1992).
[14] R. L. Poirier, 1993 IEEE Particle Accelerator Conference, Washington, D.C., May 17–20, 1993.
[15] H. Lengeler, in Proceeding of CAS-Superconductivity in Particle Accelerators, edited by S. Turner, CERN Report No. CERN 89-04, 1989, pp. 197–229.
[16] G. Cavallari *et al.*, in Proceedings of the 3rd Workshop on rf Superconductivity, edited by K. W. Shepard, ANL-PHY-88-1, 1988, Vol. 2, pp. 625–638.

Forward volume wave microwave envelope solitons in yttrium iron garnet thin films: Peak profiles and multisoliton signatures (abstract)

M. A. Tsankov, M. Chen, and C. E. Patton
Department of Physics, Colorado State University, Fort Collins, Colorado 80523

Microwave envelope solitons have been observed in yttrium iron garnet (YIG) films for different field configurations and surface pinning conditions. Earlier work on magnetostatic forward volume wave (MSFVW) solitons in YIG films has focused on the break from the low power linear dependence of the output pulse peak power P_{out} on input pulse power P_{in},[1] or on the evolution of the shape of the microwave pulse envelope with increasing power.[2] In this work, both (1) the nonlinear dependence of P_{out} on P_{in} and (2) the shape of the output pulses for MSFVW solitons have been examined over a wide range of power levels and pulse widths. The experiments used 7.2-μm-thick single crystal YIG films with unpinned surface spins. A field of 3744 Oe was applied perpendicular to the plane of a 15×2 mm film sample. Microwave pulses at 5.4–6 GHz, with a width τ of 5–50 ns and peak powers up to 3 W, were launched by a microstrip antenna about 5 mm from one end and picked up by a second, parallel antenna about 5 mm from the other end. Data were processed with a microwave transition analyzer operated in a time domain mode. For a given pulse width, the initial break and nonlinear increase in P_{out} relative to P_{in} noted in Ref. 1 is followed by a gradual leveling off in P_{out} at high power. For a given pulse power above soliton threshold, the P_{out} versus τ profiles show an initial linear increase which is followed by a decrease and an oscillatory response as multiple solitons are formed. These profiles are directly correlated with the formation of a single soliton pulse which evolves into multiple soliton wave packets with increasing either power or pulse length.

This work was supported by the National Science Foundation, Grant DMR-8921761, and the U.S. Army Research Office, Grant DAAL03-91-G-0327. The films were provided by Dr. J. D. Adam, Westinghouse Research Laboratory, Pittsburgh, PA.

[1] P. De Gasperis, R. Marcelli, and G. Miccoli, Phys. Rev. Lett. **59**, 481 (1987).
[2] B. A. Kalinikos, N. G. Kovshikov, and A. N. Slavin, IEEE Trans. Magn. **26**, 1477 (1990).

 0021-8979/94/75(10)/5628/1/$6.00 © 1994 American Institute of Physics

Microwave magnetic envelope solitons: Threshold powers and soliton numbers (abstract)

J. M. Nash, M. Chen, M. A. Tsankov, and C. E. Patton
Department of Physics, Colorado State University, Fort Collins, Colorado 80523

Microwave envelope solitons may be generated in thin yttrium iron garnet (YIG) films by microwave pulses if the input power is above some threshold power P_{th}. Above P_{th}, single solitons or multiple solitons may be generated. De Gasperis and co-workers have examined P_{th} versus input microwave pulse length τ without regard to the number of solitons actually generated.[1] Kalinikos and co-workers have extracted a soliton number from actual profiles.[2] Collectively, these works demonstrate that both the number of solitons and the threshold power for the generation of those solitons depends on τ. In this work, P_{th} vs τ data are analyzed to obtain a soliton number index N. This index has a quantitative basis in soliton theory and represents a significant improvement over a qualitative profile based determination. Measurements were made on a 7.2 μm YIG film in a microstrip delay line structure. Microwave pulses 5–50 ns wide and at a carrier frequency of 5.78 GHz were used to generate backward volume wave solitons. Deviations from a linear response of the measured peak output power were observed above some P_{th} for each τ value. Plots of P_{th} vs $1/\tau^2$ show three linear regimes that correspond to three distinct values of N, $N=1$ for 5 ns$<\tau<$10 ns, $N=2$ for 20 ns$<\tau<$30 ns, and $N=3-4$ for 30 ns$<\tau<$50 ns. Even when experimental conditions mask the number of distinguishable peaks in a given profile, the threshold power may be used to determine the number of solitons present.

This work was supported in part by the National Science Foundation, Grant No. DMR-8921761 and by the U.S. Army Research Office, Grant No. DAAL03-91-G-0327. The YIG films were provided by Dr. J. D. Adam, Westinghouse Research Laboratory, Pittsburgh, PA.

[1] P. De Gasperis, R. Marcelli, and G. Miccoli, Phys. Rev. Lett. **59**, 481 (1987).
[2] B. A. Kalinikos, N. G. Kovshikov, and A. N. Slavin, Sov. Phys. Solid State **27**, 135 (1984).

 0021-8979/94/75(10)/5629/1/$6.00 © 1994 American Institute of Physics

Self-channeling of magnetostatic waves in ferromagnetic film (abstract)

J. Boyle
Physics Department, Salford University, Salford M5 4WT, England

S. A. Nikitov
Institute of Radioengineering and Electronics, Russian Academy of Sciences, 103907 Moscow, Russia

A. D. Boardman, A. Moghadam, K. M. Booth, and J. G. Booth
Physics Department, Salford University, Salford M5 4WT, England

Low power magnetostatic wave (MSW) experiments reporting beam formation and propagation inside ferromagnetic films have been carried out .[1,2] In this work, we report the first observation of self channeling of MSW and the formation of the spatial solitons of MSW for an in-plane magnetized YIG film and waves propagating perpendicularly to the direction of magnetization. The experiments were conducted using YIG film of 4.9 μm thickness magnetized in-plane by a permanent magnetic field of 1094 Oe. A cw signal was launched into the film through a microstrip antenna. A Brillouin scattering system consisting of a tandem Fabry–Perot interferometer has been used to observe the profile of a MSW beam. Self-channeling MSW beam propagation occurring as a result of an interplay between diffraction of the beam and self-modulation was observed for various magnitudes of input power and initial frequency. At low power levels the formed MSW beam broadens and weakens during the propagation. As the input power increases, the intensity of the peak power of the beam also increases and a narrow channel of the MSW beam is formed. The power threshold depends on the wavelength of MSW and the width of the excitation microstrip. A theory describing the spatial MSW self-channeling is developed. The necessary and sufficient conditions are analyzed and numerical calculations are provided. The experimental data are in a semi-quantitative agreement with theory.

[1]A. V. Vashkovskii *et al.*, Sov. Phys. J. **31**, 908 (1988).
[2]N. P. Vlannes, J. Appl. Phys. **62**, 972 (1987).

 0021-8979/94/75(10)/5630/1/$6.00 © 1994 American Institute of Physics

Spin wave solitons in an antiferromagnetic film (abstract)

A. D. Boardman
Department of Physics, University of Salford, Salford M5 4WT, England

S. A. Nikitov
Institute of Radioengineering and Electronics, Russian Academy of Sciences, 103907 Moscow, Russia

N. A. Waby
Department of Physics, University of Salford, Salford M5 4WT, England

The propagation of nonlinear dipole spin waves in a film consisting of a two sublattice, uniaxial, antiferromagnetic material has been investigated. The system when the external magnetic field is assumed to be parallel to the anisotropy axis of the antiferromagnetic film and is directed parallel, or perpendicular, to the film surface is considered. For the first case, surface and volume waves can propagate in the film, and for the second case, volume waves can propagate in the film for a rather weak external magnetic field when the magnetization of the sublattices are counter parallel to each other and are perpendicular to the film surface. The *linear* dispersion relations for all three types of waves are analyzed and their group velocity dispersion is calculated. The *nonlinear* shift of the frequency, due to the finite power of the wave, is also obtained for the three types of dipole waves for the case of a thin antiferromagnetic film, when $kd \ll 1$ (k is the wave number and d is the thickness of the film). The nonlinear Schrödinger equation governing the propagation of the nonlinear spin wave in the film is investigated. It is shown that the criterion for the existence of spin wave solitons is fulfilled, for parallel magnetization, which permits the existence of surface waves (one branch) and volume waves (both branches), but the criterion is not fulfilled for perpendicular magnetization. The power threshold for soliton creation is also calculated and estimates are given for the data appropriate to a MnF_2 crystal.

 0021-8979/94/75(10)/5631/1/$6.00 © 1994 American Institute of Physics

Brillouin light scattering study of spi ve instability magnon distributions in yttrium iron garnet thin films (abs)

P. Kabos, G. Wiese, and C. E. Patton
Department of Physics, Colorado State University, Fort Collins, Colorado 80523

There has been increased interest recently in nonlinear microwave phenomena in bulk and thin film single crystal ferrite materials. These nonlinear phenomena show a variety of novel effects such as spin wave instability, auto-oscillation, multistability, period multiplication, intermittency, and chaos. Emerging theories to explain these phenomena have generally been based on simple two mode models. It is clear that an experimental determination of the number and distribution of the modes excited at and above the spin wave instability threshold could play a key role in the refinement of these theories. This work is concerned with a Brillouin light scattering (BLS) experimental study of the wave vector distribution of the parametric spin wave modes excited at and above the subsidiary absorption spin wave instability threshold in yttrium iron garnet (YIG) films. The in-plane magnetized 4.15-μm-thick films were transverse pumped at 8.47 GHz, with the microwave field also in-plane. The BLS data were obtained with a tandem, multipassed, high contrast Sandercock Fabry–Perot interferometer. The data show a complicated wave vector distribution for the excited modes. The spin wave propagation direction is sharply peaked at the value expected from standard instability theory. However, the wave number distribution is quite broad, even at threshold. For power levels above threshold, this distribution evolves in a complicated manner that depends on field and propagation direction. These results show that simple two mode models are inadequate to deal with high frequency nonlinear processes in ferrite thin films.

This work was supported by the U.S. Office of Naval Research, Grant No. N00014-90-J-4078, the National Science Foundation, Grant No. DMR-8921761, and the U.S. Army Research Office, Grant No. DAAL03-91-G-0327. The films were provided by Dr. J. D. Adam, Westinghouse Research Laboratory, Pittsburgh, PA.

 0021-8979/94/75(10)/5632/1/$6.00 © 1994 American Institute of Physics

Nonlinear surface spin waves (abstract)

A. L. Sukstanskii and S. V. Tarasenko
Physico-Technical Institute, Donetsk 340114, Ukraine

There has been extensive theoretical and experimental work devoted to investigations of surface spin waves in magnets. However, such excitations have usually been studied in the linear approximation, whereas large-scale dynamic excitations (magnetic solitons, nonlinear spin waves of different types) were discussed in infinite media only. The purpose of this work is to investigate a new type of surface excitation: nonlinear surface spin waves (surface solitons) in semi-infinite magnets. We analyzed the simplest model of a one-sublattice ferromagnet taking into account the nonhomogeneous exchange interaction and the easy-axis magnetic anisotropy. In addition, the boundary conditions on the surface describing uniaxial surface anisotropy were used. Linear surface spin waves in such a model are known to exist when the latter is of the easy-plane type only whereas nonlinear solutions of the equations of motion satisfying the boundary conditions are proved to exist whatever surface anisotropy takes place. These solutions describe nonlinear surface spin waves traveling along the surface. Moreover, for some values of precession frequency and surface anisotropy constant there are two or even three such soliton-like solutions. It should be noted that localization of these excitations near the surface is entirely due to nonlinearity, and the surface solitons under consideration have no linear analogy. We also proved the existence of so-called internal nonlinear spin waves describing soliton-like magnetic excitations localized on the interface between two semi-infinite magnets. In addition, the generalization of all results mentioned above was obtained for more complicated two- and many-sublattice magnets.

 0021-8979/94/75(10)/5633/1/$6.00 © 1994 American Institute of Physics

Thermal equilibrium noise with $1/f$ spectrum and temperature-dependent magnetic viscosity in the amorphous alloy DyNi

B. Barbara and A. Ratnam
Laboratoire L. Néel, CNRS-UJF, 38042 Grenoble Cedex, France

A. Cavalleri, M. Cerdonio, and S. Vitale
Department of Physics, University of Trento and Centro di Fisica degli Stati, Aggregati ITC-CNR, I-38050, Povo, Trento, Italy

We report on the magnetization noise and the imaginary susceptibility for the random anisotropy amorphous alloy $DyNi_{1.32}$ for frequencies $f<10$ Hz, temperatures $1.2<T<4.2$ K, and excitation field amplitudes <150 μA/m (1.9 μOe). The noise spectra agree, without any adjustable parameter, with the fluctuation dissipation formula and the measured imaginary susceptibility of the material. The spectra show a $1/f$ shape coming from a frequency-independent imaginary susceptibility that it is found to be temperature-dependent extrapolating to zero at zero temperature. We discuss the connection between this approach and the usual relaxation experiments.

I. INTRODUCTION

Thermal equilibrium noise with $1/f$ power spectrum has been reported at low temperature for soft ferromagnetic alloys,[1] spin glasses,[2] and high-T_c superconductors.[3] The noise, when purely $1/f$, originates from the existence of a frequency-independent imaginary susceptibility χ_0'' that gives origin, via the standard fluctuation dissipation formula, to a magnetization noise with spectrum $S_M(\omega) = (2k_BT/\mu_0) \times(\chi_0''/V\omega)$, with T, V, and ω the temperature, the sample volume, and the angular frequency, respectively.

A constant, or weakly frequency-dependent, imaginary susceptibility translates, via standard Fourier transform, to a logarithmic relaxation of the magnetization after a field step excitation.[4] Thus, though this behavior is a property of the sample at thermal equilibrium and in a fully linear response regime, it is a remainder of the analogous behavior shown by magnetic systems in relaxation experiments and often referred to as magnetic viscosity. To be specific the magnetization M of a sample having a fully frequency-independent imaginary susceptibility χ_0'', would relax,[4] after a field step of very small amplitude ΔH, with a logarithmic rate $s = dM/d\ \ln(t) = \Delta H(2/\pi)\chi_0''$.

Magnetic viscosity is commonly assigned to the existence of a collection of incoherent exponential relaxation processes with a distribution of time constants spanning many orders of magnitude. Hopping of the system between nearby free-energy minima with different values of the magnetization would, for instance, provide such a collection of relaxation phenomena if the energy barriers between the minima have a distribution spanning a range $\gg k_BT$. If the lifetime of each minimum is regulated by thermal activation, and if the energy differences Δ between the minima are in turn distributed from zero to a value much higher than k_BT, then (see Sec. IV below) χ_0'' is also a function of T.

Both temperature-dependent[5] and temperature-independent[6] χ_0'' have been reported for soft ferromagnetic alloys. A temperature-independent χ_0'' suggests a nonthermal hopping mechanism like, for instance, the quantum tunnelling of the magnetization.[7] This last possibility should, however, involve a crossover from a temperature-independent regime to a temperature-dependent one at a crossover temperature T_c. Extrapolating the results of the theoretical models developed for relaxation experiments, T_c should strongly depend on the kind of material considered and should fall in the 1 K range for high anisotropy materials.

In view of these considerations we have initiated a study on the imaginary susceptibility and the thermal equilibrium noise of hard magnetic alloys. Here we report some results for the random anisotropy[8] alloy DyNi.

II. EXPERIMENT

The sample studied consists of 13 stacked $\approx$5 mm$\times$5 mm, 20-μm-thick DyNi foils, obtained by sputtering. X-ray analysis and atomic absorption measurements showed that the chemical composition is $DyNi_{1.32}$ and that the upper limit to the dimensions of a possible microcrystal is $\approx$15 Å.

Imaginary susceptibility measurements have been performed as described in detail elsewhere.[1,6,9] Here we only remind that they are based on the measurement of the complex self-inductance $L = L' - iL''$ of a superconducting transformer coupled to the sample on one side and to a commercial rf superconducting quantum interference device (SQUID) on the other. The ac field amplitudes used to measure the complex susceptibility are always less than 150 μA/m and the sample behaves for such small signals as a linear device.[1,9]

The data for the phase Φ_L of the transformer inductance result from the subtraction of a proper blank measurement obtained by substituting the pickup coil coupled to the sample with a test coil with the same value of self-inductance. In the 0.1–10 Hz frequency range the method achieves an accuracy for Φ_L of $\approx 10^{-3}$ deg, while the modu-

 0021-8979/94/75(10)/5634/3/$6.00 © 1994 American Institute of Physics

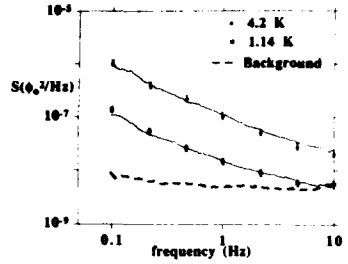

FIG. 1. Spectral noise density at the SQUID output for the two extreme temperatures 1.14 and 4.2 K. The continuous noisy lines are the experimental spectral densities. The broken line is the SQUID background noise. The symbols represent the noise calculated from Eq. (1) using the measured values of the imaginary susceptibility.

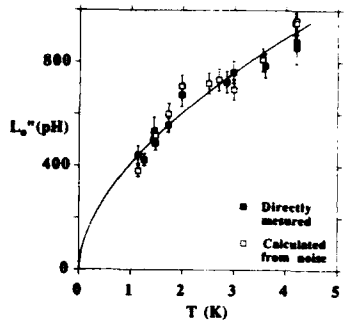

FIG. 2. The imaginary inductance below 10 Hz L_0'', as a function of the temperature. Closed symbols represent the values as directly measured. Open symbols are the values calculated from noise using fluctuation dissipation formula without any adjustable parameter. The solid line is a linear least-squares fit to data with a power law.

lus $|L|$ is measured with a ≈0.5% relative precision. Above 10 Hz, due to the need to use a less precise A/D converter, the accuracy for Φ_L drops to $\approx 10^{-2}$ deg.

The data for L can be converted to a complex susceptibility $\chi = \chi' - i\chi''$, using standard formulas for coils and transformer cores. For the present very low permeability sample, this conversion cannot be better than an estimate of the order of magnitude. In fact we notice that the insertion of the sample into the pickup coil does not change $|L|$ by a measurable quantity and only Φ_L is affected by the sample. However, we stress that any inaccuracy in the conversion is of no consequence when calculating the thermal noise. In fact the flux noise at the SQUID output S depends only on L according to[9]

$$S = 2k_B T \frac{M^2}{|L|^2} \frac{L}{\omega} + S_0, \tag{1}$$

where S_0 is the SQUID background noise and M is the mutual inductance between the SQUID and the transformer.

Because of the large inaccuracy of the conversion between L and χ, we have chosen to report in the following the values of L'' which, we notice again, are just proportional to χ''.

The spectral density S is measured by standard FFT methods.[1,6] The background noise S_0 is measured by substituting the sample coil with the above-mentioned test coil and has been found to be frequency independent down to a $1/f$ corner at about 0.3 Hz.

The sample temperature was adjusted by regulating the pressure above the liquid-Helium bath and was measured by a calibrated germanium resistor.

III. RESULTS

The imaginary inductance L'' has been found to be frequency independent in the 0.1–10 Hz range. The precision sets an upper limit for the logarithmic slope $a = |d \log(L'')/d \log(\omega)|$ of $a < 0.1$. Above 10 Hz, due to the much lower accuracy of the measurements, L'' is significantly different from zero only above ≈2.5 K.

In Fig. 1 we report the noise spectral density S as a function of the frequency, for frequencies between 0.1 and 10 Hz and for the two extreme temperatures 1.14 and 4.2 K. The noisy continuous line are the (smoothed) experimental spectra, while the broken one is the measured background SQUID noise S_0 at 1.14 K. The symbols represent the noise calculated via Eq. (1) using the measured values of L and S_0 without any adjustable parameter. It can be seen that the experimental spectra and the calculated ones agree within their precision.

In Fig. 2 the average value of L'' in the 0.1–10 Hz range L_0'' is reported as a function of the temperature. Also reported are the values of L_0'' calculated from the measured noise spectra by inverting Eq. (1). Again the agreement between the two sets of data is obtained without any adjustable parameter.

The reported error bars also include a slight lack of reproducibility, observed for this sample, of the values of L_0'' obtained by both methods but in different experimental runs. Between two successive runs the helium dewar is refilled and the sample warms up at a temperature above ≈20 K.

A fit of the data in Fig. 2 to a simple straight line gives an intercept of 260±30 pH. The fit is rather poor, the chi-square test giving a probability of random occurence of ≈7%. A good fit, with ≈50% random occurrence probability, is obtained by the power law $L_0'' = AT^{\delta}$. The best fitting curve, shown in Fig. 2, corresponds to an exponent $\delta = 0.56 \pm 0.04$. We notice in addition that the data below 2 K can be alternatively well fitted to a straight line with zero intercept. The above-mentioned slight lack of reproducibility from run to run does not allow to consider as significant the change in slope between 2 and 3 K that suggests the beginning of a plateau.

IV. DISCUSSION

The agreement between the measured value of the noise and that calculated from Eq. (1) shows that the sample acts as a linear device at thermal quasi equilibrium. This is consistent with the observation that the values of the applied

field variation δH are $\delta H < 150$ μA/m, a value much less than any field scale at which irreversible effects are displayed.[8]

As already stated in the introduction, the logarithmic relaxation of the magnetisation is commonly explained in terms of a collection of exponential relaxation processes with time constants τ distributed over many orders of magnitude. This picture, however, has been developed in connection with relaxation experiments, where large field steps are applied to the sample. As a consequence the model assumes that in each relaxation process the applied field forces some magnetic subsystem, initially trapped in a free-energy minimum, to overcome the energy barrier and to begin to evolve in a fully irreversible way.

To translate this popular picture, that successfully explains much of the results[10] from relaxation experiments, to the present, linear response, thermal equilibrium case, one needs to rephrase it in terms of equilibrium between nearby metastable minima. Let us consider then a system flipping between two nearby free-energy minima, with different values of magnetization. It is well known that such a system has an equilibrium susceptibility

$$\chi \propto \frac{1}{k_B T} \cosh(\Delta/2k_B T)^{-2} \frac{1}{1+i\omega t}, \tag{2}$$

where Δ is the free-energy difference between the minima. The time constant τ is $\tau = \tau_+/(1 + e^{-\Delta/k_B T})$, where τ_+ is the mean lifetime of the minimum with the largest energy. Equation (3) again represents a simple exponential relaxation but with a temperature-dependent prefactor. However, by integrating over a uniform distribution of Δ up to a value much larger than $k_B T$, one easily calculate that χ'' can be approximated as $\chi'' \simeq \hat{\chi}[\omega\tau_e/1+(\omega\tau_e)^2]$, with $\tau_e \simeq 0.74\tau_+$ and $\hat{\chi}$ a temperature-independent factor.

Let's now assume that τ_e is distributed over many orders of magnitude and let's call $g(x)$ the density distribution of $\ln \tau_e$. The imaginary susceptibility is then

$$\chi'' = \hat{\chi} \int_0^\infty \frac{g(\ln \tau_e)}{1+(\omega\tau_e)^2} \, d\omega\tau_e. \tag{3}$$

A frequency-independent χ'' is then obtained by assuming, for instance, that $\ln \tau_e$ is uniformly distributed between two values $\ln \tau_1$ and $\ln \tau_2$ such that the angular frequency of the measurements ω is $1/\tau_1 \ll \omega \ll 1/\tau_2$. In this case $\chi'' \simeq (\pi/2)\hat{\chi}/[\ln(\tau_1/\tau_2)]$ and is indeed frequency independent.

The temperature dependence of χ'' can then be explained, in close analogy to what is done for magnetic viscosity in relaxation experiments,[10] by assuming that the hopping of the magnetization between the two free-energy minima occurs by thermal activation above the intervening energy barrier. In this case $\tau_+ = \tau_0 e^{E/k_B T}$, with E the barrier height, and a uniform density distribution of $\ln \tau_e$ reduces to a uniform density distribution of E. In this case χ'' is proportional to T,

$$\chi'' \simeq k_B T \frac{\pi}{2} \frac{\hat{\chi}}{E_2 - E_1}, \tag{4}$$

with E_1 and E_2 the extrema of the energy density distribution.

It is important to notice that, even if the density distribution of E $g(E)$ is not exactly a uniform one, χ'' can still be a very weak function of ω. On the contrary the temperature dependence in this case can significantly differ from the simple proportionality above. For instance a power law distribution $g(E) \propto E^{-\delta}$, gives origin to an approximately logarithmic dependance of χ'' on ω while χ'' depends on the temperature[11] as $T^{1-\delta}$. Such a distribution, with $\delta \simeq 0.5$, would clearly fit our data.

A transition from thermal activation to quantum tunneling would make τ_e, and then χ'', temperature independent. Our data indicate that such a crossover, if any, has to take place at $T_c < 1.14$ K.

Experiments below 1 K, as well as with samples with expected crossover temperatures above 1 K, are now planned to help clarifying this problem.

[1] G. A. Prodi, S. Vitale, M. Cerdonio, and P. Falferi, J. Appl. Phys. **66**, 5984 (1989).
[2] M. Ocio, H. Bouchiat, and P. Monod, J. Physique Lett. **46**, L-647 (1985).
[3] F. C. Wellstood *et al.*, Phys. Rev. Lett. **70**, 89 (1993).
[4] M. Cerdonio *et al.*, Physica B **165&166**, 65 (1990).
[5] S. Vitale, A. Cavalleri, M. Cerdonio, and G. A. Prodi (unpublished).
[6] S. Vitale *et al.*, J. Appl. Phys. **72**, 4820 (1992).
[7] See for instance the review papers, P. C. E. Stamp, E. M. Chudnovsky, and B. Barbara, Int. J. Mod. Phys. B **6**, 1355 (1992); D. D. Awshalom, D. P. DiVincenzo, and J. F. Smyth, Science **258**, 414 (1992); B. Barbara *et al.*, J. Appl. Phys. **73**, 6703 (1993).
[8] J. Filippi, B. Barbara, and B. Dieny, Solid State Commun. **53**, 523 (1985).
[9] S. Vitale, G A Prodi, and M. Cerdonio, J. Appl. Phys. **65**, 2130 (1989).
[10] R. Street and J. C. Woolley, Proc. Phys. Soc. London Sect. A **62**, 562 (1956).
[11] B. Barbara *et al.*, *Proceedings of the International Workshop on Magnetic properties of fine particles Roma 1990*, edited by Fiorani and Dormann (Elsevier, Amsterdam, 1990).

Time-dependent phenomena at low temperature in magnetic digital compact cassette tape

X. X. Zhang and J. Tejada
Facultat de Física, Universitat de Barcelona, Diagonal 647, 08028 Barcelona, Spain

In this paper we report on the low-temperature magnetic relaxation of CrO_2 particles of digital compact cassette tapes. The observed temperature dependence of the magnetic viscosity, $S \equiv \partial M / \partial \ln t$, shows three different regimes below room temperature. The most remarkable is that for $T \leq 5$ K, $S(T)$ remains constant, suggesting the occurrence of macroscopic quantum tunneling of magnetization.

I. INTRODUCTION

Magnetic relaxation phenomena is a natural consequence of the existence of metastable states having a lifetime comparable to the observation time 10^1–10^4 s. The change in the magnetization which follows the change in the applied magnetic field at temperature $T \ll T_B$ is given.[1]

$$M(t) = M(t_0)\left[1 - \frac{K_B T}{\langle U \rangle} \ln\left(\frac{t}{t_0}\right)\right], \quad (1)$$

where $\langle U \rangle$ is the average energy barrier which determines the blocking temperature T_B in the static $M(T,H)$ measurements: T_B corresponds to the temperature at which appears a peak in the zero-field cooled magnetization data as due to random orientations of the anisotropy directions; t_0 is a constant, and the magnetic viscosity $S(T)$ is defined[1] as $S(T) \equiv K_B T / \langle U \rangle$.

The $\ln(t)$ dependence of the remanent magnetization is expected for a complex system like these of recording media which are formed by small particles with a broad distribution of barrier heights.[2,3]

As the temperature goes down the stability of the magnetic system increases as a consequence of the supression of thermal decay of the metastable states. However, in some cases, at low temperature the magnetic relaxation is quantum underbarrier decay[4,5] and the relaxation law is independent of temperature.[1,6,7] Therefore, in some cases, at very low temperatures quantum effects constitute the most important sources of instability of small particles used in recording media.

II. EXPERIMENTAL AND RESULTS

The materials studied in this work are commercial magnetic tapes containing CrO_2 particles. The electron microscope study has shown that these particles have an elongated shape with the average short semiaxis about 300 Å and the long semiaxis about 1500 Å. The x-ray study revealed the crystalline structure on a scale not exceeding 400 Å.

The magnetic measurements were carried out using a SHE-SQUID magnetometer. Hysteresis measurements at different temperatures were performed in order to get the variation with temperature of the coercive field H_C, the anisotropy field H_K, the remanence magnetization M_r, and switching field distribution (SFD). In Fig. 1 we show the $M(H)$ data at $T=2$ K and in Table I we give the values of H_C, H_K, $R=M_r/M_s$, and SFD at 2 K. The H_K value listed in Table I corresponds to the field at which appears a cusp in the second differential of the hysteresis loop. The energy barrier values involved in the low-temperature relaxation experiments are those corresponding to particles with coercive field larger than the applied field. Therefore the SFD is fully related to the density of energy barriers.

Before commenting our relaxation experiments, we would like to stress that our experiments have been in part suggested by reading very interesting papers of Oseroff *et al.*,[8,9] Charap,[10] Chantrell,[11] and Sharrock[12] who have discussed in detail many questions existing in the relaxation of recording media. The main point of the papers of Oseroff *et al.*[8,9] and Charap[10] was to try to explain the apparent extrapolation of their data for S to a finite value at $T=0$. As we show later, our results are in qualitive agreement with their data, but in our case the appearance of the plateau for the viscosity is much more clear because we have recorded data below 4 K. In any case, only those $S(T)$ data corresponding to temperatures $T \ll T_B$ can be extrapolated to $T=0$ K to estimate $S(0)$.

The relaxation experiments were done by applying a field H_2 (−500, −800, −900 Oe) after saturating the sample at $H_1=5000$ Oe. The first measurement of the magnetization was taken 100 s after the change of the field. In Fig. 2 we show, in logarithmic scale, the variation with time of the remanent magnetization, at different temperatures and in Fig. 3 we plot the magnetic viscosity $S(T) \equiv (1/M_0)\partial M/\partial \ln t$ as a function of temperature. The relaxation of the remanent magnetization follows the $\log(t)$ law, as we expected in the case of a broad distribution of energy barriers.

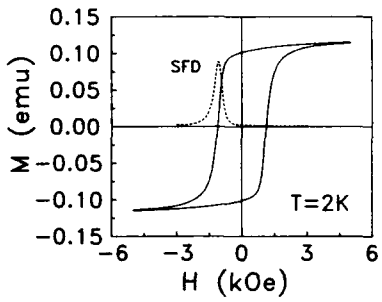

FIG. 1. Hysteresis curve obtained at $T=2$ K.

 0021-8979/94/75(10)/5637/2/$6.00 © 1994 American Institute of Physics

TABLE I. Values of H_C, H_K, $R=M_r/M_s$, and SFD AT 2 K.

T (K)	H_K (Oe)	H_C (Oe)	R	SFD
2	12 000	1125	0.878	0.400

The magnetic viscosity data show the following features:

(1) $S(T)$ presents a maximum at T_B which corresponds to the blocking of the average barrier of the relaxing particles. This maximum shifts to lower temperatures as the field H_2 increases from -500 to -900 Oe. The maximum of S at $T \approx T_B$ reflects the fact that for temperatures $T > T_B$, the major parts of barriers are overcome with a switching time smaller than the experimental time and consequently the magnetic viscosity decreases. This is in agreement with results obtained in computer simulation studies of magnetic relaxation in anisotropic magnetic systems.[13]

(2) The values $S(T)$ increase when increasing H_2 as a consequence of the reduction of the average energy barrier [see Eq. (1)].

(3) At temperature $T < T_B$, the relaxing fraction of the total magnetization is still large and the magnetic viscosity does not depend linearly on temperature.

(4) At temperature $T \ll T_B$ the relaxing fraction of the total magnetization is very small and $S(T)$ is almost proportional to temperature indicating that the magnetic viscosity goes via statistically independent individual events occuring rather far from each other.

(5) $S(T)$ presents an almost flat behavior at low temperature with a nonzero intercept of its extrapolation to 0 K which in our opinion, constitutes the evidence of quantum magnetic relaxation. The temperature T_C at which appears the plateau for the $S(T)$ values decreases as the value of H_2 increases; $T_C \approx 4.5$ K when $H_2 = -800$ Oe and $T_C \approx 3$ K when $H_2 = -900$ Oe. Concerning the physical mechanism of the relaxation, we believe that the most plausible one is the uniform rotation of the magnetic moment in single-domain particles. In this case and assuming that our particles have uniaxial anisotropy barriers, the crossover temperature from classical to quantum is[2] $k_B T_C \approx \mu_B H_K \epsilon^{1/2}$, where $H_K \approx 12\,000$ Oe, and $\epsilon = 1 - H_2/H_K$. We have found the experimental value of T_C agrees qualitatively with the theoretical expectation.

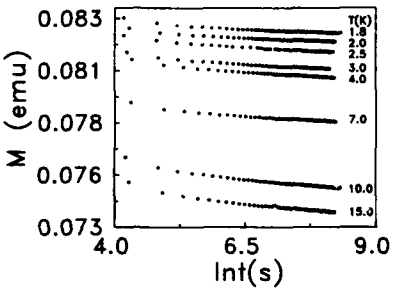

FIG. 2. Variation of remanent magnetization with time at different temperatures ($H_2 = -800$ Oe).

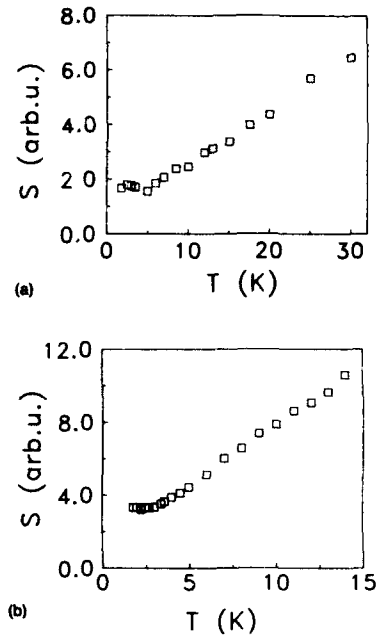

FIG. 3. Low-temperature $S(T)$ curves for the relaxation processes when (a) $H_2 = -800$ Oe and (b) $H_2 = -900$ Oe.

ACKNOWLEDGMENTS

JT and XXZ thank "Fundación Domingo Martínez" for financial support. XXZ thanks "DGICYT" for financial support.

[1] J. Tejada, X. X. Zhang, and E. M. Chudnovsky, Phys. Rev. B **47**, 14977 (1993).
[2] R. Streat and J. C. Wooly, Proc. Phys. Soc. London Sect. A **62**, 562 (1949).
[3] M. Uehara and B. Barbara, J. Phys. (Paris) **47**, 235 (1986), and references threrein.
[4] E. M. Chudnovsky and L. Gunther, Phys. Rev. Lett. **60**, 661 (1988).
[5] E. M. Chudnovsky and L. Gunther, Phys. Rev. B **37**, 9455 (1988).
[6] J. Tejada, X. X. Zhang, and Ll. Balcells, J. Appl. Phys. **73**, 6709 (1993).
[7] X. X. Zhang, Ll. Balcells, J. M. Ruiz, O. Iglesias, J. Tejada, and B. Barbara, J. Phys. Condens. Matter **4**, L163 (1992). J. Tejada, X. X. Zhang, Ll. Balcells, O. Iglesias, and B. Barbara, Europhys. Lett. **22**, 211 (1993).
[8] S. B. Oseroff, D. Franks, V. M. Tobin, and S. Schultz, IEEE Trans. Magn. **MAG-23**, 2871 (1987).
[9] S. B. Oseroff, D. Clark, S. Schultz, and S. Shtrikman, IEEE Trans. Mag. **MAG-21**, 1495 (1985)
[10] S. H. Charap, J. Appl. Phys. **63**, 2054 (1988).
[11] R. W. Chantrell, J. Magn. Magn. Mater. **95**, 365 (1991).
[12] M. P. Sharrock, IEEE Trans. Magn. **MAG-26**, 193 (1990).
[13] J. Gonzalez and J. Tejada, Phys. Rev. B (to be published).

Low-temperature magnetic relaxation of organic coated $NiFe_2O_4$ particles

R. H. Kodama
Physics Department and Center for Magnetic Recording Research, University of California, San Diego, La Jolla, California 92093

C. L. Seaman
Institute for Pure and Applied Physical Sciences, University of California, San Diego, La Jolla, California 92093

A. E. Berkowitz
Physics Department and Center for Magnetic Recording Research, University of California, San Diego, La Jolla, California 92093

M. B. Maple
Physics Department and Institute for Pure and Applied Physical Sciences, University of California, San Diego, La Jolla, California 92093

We report measurements of relaxation rate of the remanent magnetization versus temperature for $NiFe_2O_4$ particles coated with the surfactant oleic acid. It has been reported that the organic coating induces a strong surface anisotropy resulting in surface spin canting and anomalous hysteresis properties at low temperature as compared to the bulk material. We have measured, at temperatures down to 400 mK, relaxation of remanent magnetization which extrapolates to a nonzero value at zero temperature. Macroscopic quantum tunneling at these temperatures has been predicted and observed only for materials with high magnetocrystalline anisotropy, so it is particularly interesting to observe it in $NiFe_2O_4$, which has a relatively low bulk anisotropy. It is suggested that the strong surface anisotropy induced by the organic coating may be responsible for tunneling in these particles.

I. INTRODUCTION

The possibility of a macroscopic ensemble of atomic magnetic moments collectively passing through an effective energy barrier much larger than the thermal energy, i.e., macroscopic quantum tunneling (MQT), has recently been developed theoretically by a number of authors.[1–3] The canonical experiment for observation of MQT is a relaxation measurement on a collection of magnetic grains or particles, where a field is applied and reversed or removed and the magnetization decay with time is measured. The theory of thermally activated decay[4,5] predicts a relaxation rate proportional to temperature at low temperatures. The signatures of MQT in such an experiment are a nonzero relaxation rate at zero-temperature and a low-temperature regime with temperature-independent relaxation rate. It is predicted theoretically[3] that the crossover temperature from thermal activation regime to quantum tunneling regime scales with the component of magnetic anisotropy normal to the easy axis, so tunneling should be observable at experimentally accessible temperatures only for materials with high anisotropies.

There have been a number of reports of low-temperature relaxation measurements consistent with MQT in particulate systems such as $Tb_{0.5}Ce_{0.5}Fe_2$,[6] $CoFe_2O_4$, and FeC.[7] These materials exhibit fairly high bulk magnetocrystalline anisotropies, so the observation of tunneling is consistent with the requirement of high anisotropy. We report measurements on $NiFe_2O_4$, which has a relatively low bulk anisotropy, but exhibits very high effective anisotropy fields in surfactant coated particle form. These high anisotropy fields may be due to the strong interaction of the surface spins with the organic surfactant coating, or may be an intrinsic property of the particle surface. The modeling of tunneling in this material may require consideration of surface anisotropies in addition to crystalline anisotropies.

II. EXPERIMENT

The fine particle samples were produced by grinding coarse powder (1–2 μm) of high-purity $NiFe_2O_4$ in a ball mill containing an equal mass of the surfactant oleic acid, and a kerosene carrier liquid.[8,9] The milling was carried out for 1000 h, and the fine particle component was extracted by centrifugation. It was determined by transmission electron microscopy (TEM) studies and x-ray diffraction line widths that the average particle size is 70 Å, with a dispersion of about 50%. High-resolution TEM studies on an identically prepared $CoFe_2O_4$ sample showed that the cubic spinel structure was preserved, and that the particles are for the most part equiaxed single crystals.[10] The samples were washed of excess surfactant and dried. A monolayer of surfactant remains strongly bonded to the particle surfaces, and has been proposed to cause a surface spin canting which reduces the net magnetization of the material.[8,9] The powders were pressed in silver foil to immobilize them.

Magnetization measurements were performed using a commercial Quantum Design superconducting quantum interference device (SQUID) magnetometer down to 3 K, and a Faraday balance magnetometer, equipped with a ^{3}He refrigerator, down to 400 mK. In the SQUID magnetometer, temperature was measured by a germanium resistance thermometer calibrated for magnetoresistive shifts. In the Faraday magnetometer, the temperature was measured at zero field by a pair of germanium resistance thermometers and controlled during field sweeps by carbon thermometers.

 0021-8979/94/75(10)/5639/3/$6.00 © 1994 American Institute of Physics

The SQUID is coupled to a second derivative coil set through which the sample is moved and the resultant signal is integrated over the scan. The measured moment is a weighted average of the actual moment during the 30 s scan. The time we associated with each data point was a simple average of the start and end of each scan. The Faraday magnetometer was operated in a differential mode, with the 300 Oe/cm gradient field being reversed for each data point, thus minimizing long term drift. Similarly, the time we associated with each data point was an average of the times of positive and negative readings.

Before relaxation measurements, the samples were demagnetized at room temperature and cooled in zero field to the measurement temperature. A field of 60 kOe was applied and then brought to zero. The magnetization was measured for 6000–60 000 s following removal of the field. Two different methods were used to bring the field to zero. One was to ramp the current to zero in a period of 5–10 min, the other was to quench the superconducting magnet from high field in a controlled manner, which takes 6 s. The quench method was only possible with the SQUID magnetometer, and the time required for the quench to occur was determined by a magnetoresistive sensor. The time $t=0$ was defined as the time at which the field reached zero. In most cases, runs at several temperatures were performed during a single cooldown. In these cases we always cooled to the lowest temperature before applying any fields and warmed monotonically in zero field between runs. This produces an initial state similar to a zero-field cooled state for subsequent temperatures.

Low-field magnetization versus temperature measurements in field cooled and zero-field cooled states were made in the following way. The sample was demagnetized at 300 K, then cooled to 5 K in 20 Oe and zero field, respectively. Then the magnetization was measured in 20 Oe at each temperature up to 300 K.

III. RESULTS AND DISCUSSION

A. dc magnetization

Figure 1 shows a magnetization hysteresis loop taken at 0.6 K for the nickel ferrite sample. It is interesting to note that the loop remains open up to the highest field (60 kOe), indicating the presence of anisotropy fields higher than 60 kOe. Figure 2 shows 20 Oe field cooled and zero-field cooled magnetization as a function of temperature measured in 20 Oe. The peak in the zero-field cooled curve is generally associated with the mean superparamagnetic blocking temperature. The temperature at which the curves meet is the maximum blocking temperature, so that above this temperature the magnetization relaxes to its thermodynamic equilibrium value in the time scale of the measurement. The particles show a broad range of blocking temperatures consistent with the observed particle size distribution.

B. Time dependence

The time dependence of the remanent magnetization was fitted to the logarithmic function

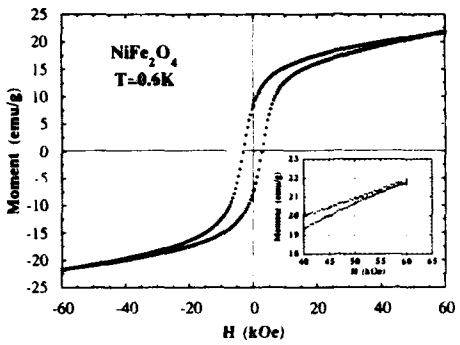

FIG. 1. Magnetization hysteresis loop for organic coated $NiFe_2O_4$ measured at 0.6 K. Inset is the high-field region, showing that the loop is not closed.

$$M(t)=M_0(t=\tau_0)[1-S(T)\ln(t/\tau_0)], \tag{1}$$

which was proposed by Néel[5] to describe the magnetization of an ensemble of ferromagnetic grains in fields far from the coercive field, where the "magnetic viscosity" is given by

$$S(T)\propto T\times f(t,T), \tag{2}$$

where f is a slowly varying function of time and temperature. Equation (1) is clearly not a universal law for all time scales; in fact, some authors[11] claim this is not an appropriate expression for any time scale. However, it is a reasonable fit to our measurements on the time scale of 100–60 000 s, and contains only two adjustable parameters.

Figure 3 shows magnetization versus time for nickel ferrite measured at 5 K in the SQUID magnetometer after quenching to zero field. The curvature in the data for low times could be fit by a shift in the zero time by ~30 s, or a real deviation from logarithmic dependence. The low-temperature relaxation data taken on the Faraday magnetometer is shown in Fig. 4. Data taken on both magnetometers

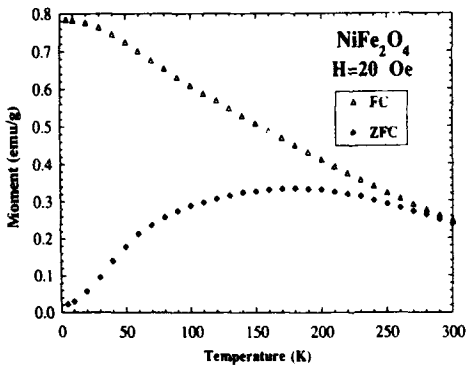

FIG. 2. Low-field moment vs temperature for field cooled and zero-field cooled states.

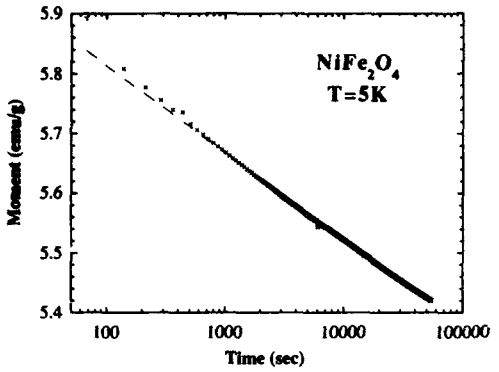

FIG. 3. Time decay of the remanent magnetization at 5 K after a 6 s quench from high field to zero, measured with the SQUID magnetometer.

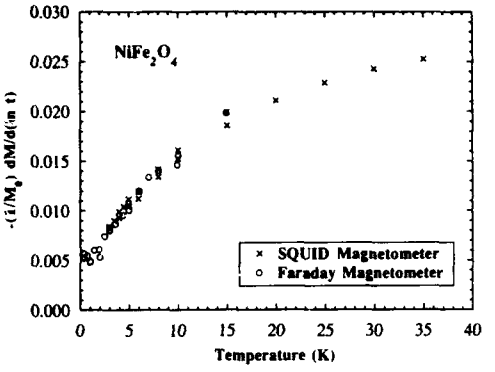

FIG. 5. Temperature dependence of the magnetic viscosity $(1/M_0)dM/d(\ln t)$ obtained from fits of the $M(t)$ data to Eq. (1).

are summarized in Fig. 5, where we have plotted fitted values for the viscosity $S(T)$. There is good agreement between the two sets of data where they overlap, and they indicate a nonzero extrapolation to zero temperature, inconsistent with thermal relaxation. At temperatures below 2 K, the viscosity is roughly constant.

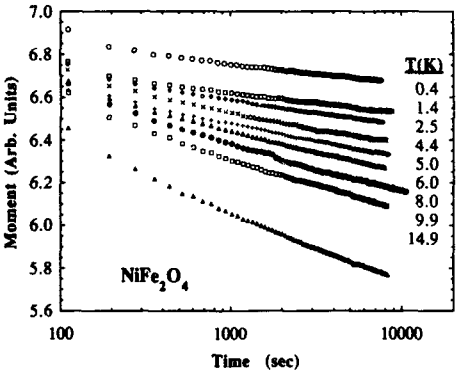

FIG. 4. Time decay of remanent magnetization after a 450 s linear ramp from 60 kOe to zero, measured at various (constant) temperatures with the Faraday magnetometer. Some curves were shifted vertically for clarity.

IV. SUMMARY

We have reported dc magnetization and magnetic relaxation data in the temperature range 0.4–35 K on a $NiFe_2O_4$ particulate sample coated with an organic surfactant. These data show a nonzero extrapolation of the magnetic viscosity $(1/M_0)dM/d(\ln t)$ to zero temperature, indicating a nonthermal relaxation mechanism. If the mechanism is macroscopic quantum tunneling, the bulk magnetocrystalline anisotropy is not high enough to account for the observability of this tunneling. A high crossover temperature could be explained by a large surface anisotropy due to interaction of surface spins with the surfactant, or an intrinsic surface anisotropy.

ACKNOWLEDGMENTS

This work is supported by NSF Grants ECS-9119005, DMR-9107698, and DMR-9010908.

[1] E. M. Chudnovsky and L. Gunther Phys. Rev. Lett. **60**, 661 (1988).
[2] A. Garg and G.-H. Kim, Phys. Rev. Lett. **63**, 2512 (1989).
[3] P. C. E. Stamp, E. M. Chudnovsky, and B. Barbara, Int. J. Mod. Phys. B **6**, 1355 (1992).
[4] R. Street and J. C. Woolley, Proc. Phys. Soc. London Ser. A **62**, 562 (1949).
[5] L. Néel, J. Physique **11**, 49 (1950).
[6] C. Paulsen, L. C. Sampaio, R. Tachoueres, B. Barbara, D. Fruchart, A. Marchand, J. L. Tholence, and M. Uehara, J. Magn. Magn. Mater. **116**, 67 (1992).
[7] J. Tejada, L. Balcells. S. Linderoth, R. Perzynski, B. Rigau, B. Barbara, and J. C. Bacri, J. Appl. Phys. **73**, 6952 (1993).
[8] A. E. Berkowitz, J. A. Lahut, I. S. Jacobs. L. M. Levinson, and D. W. Forester, Phys. Rev. Lett. **34**, 594 (1975).
[9] A. E. Berkowitz, J. A. Lahut, and C. E. Van Buren, IEEE Trans. Magn. **16**, 184 (1980).
[10] A. C. Nunes, E. L. Hall, and A. E. Berkowitz, J. Appl. Phys. **63**, 5181 (1988).
[11] A. Aharoni, Phys. Rev. B **46**, 5434 (1992).

Quantum tunneling across a domain wall junction (abstract)

Bernard Barbara
Laboratoire de Magnétisme Louis Néel, CNRS, B.P. 166-Cedex 09, 38100-Grenoble-cedex, France

Leon Gunther
Department of Physics, Tufts University, Medford, Massachusetts 02155

In this paper, we discuss a system that is appropriately called a "domain wall junction" (DWJ). The DWJ is a close analog of the Josephson junction with respect to the usefulness of both systems in studying switching by thermal activation (TA) and by quantum tunneling (QT). What makes this system especially attractive for experimental and theoretical studies is that it is a single system, with a single set of parameters that characterizes its behavior. The essential nature and behavior of a DWJ has been elucidated by numerous authors.[1-6] We show through theoretical analysis that it is within our means to fabricate a DWJ that should exhibit switching via quantum tunneling of magnetization. We further provide experimental procedures for looking for quantum tunneling of magnetization in a DWJ; these are based upon those that have been used in observing macroscopic quantum tunneling in Josephson junctions. Two examples of DWJs have been recently made that apparently show a crossover from TA to QT. Results of these experiments will be summarized.

[1] T. G. Egami, Phys. Status Solidi B **57**, 211 (1973); *ibid.* A **20**, 157 (1973).
[2] P. C. E. Stamp, Phys. Rev. Lett. **61**, 2905 (1988).
[3] E. M. Chudnovsky, O. Iglesias, and P. C. E. Stamp, Phys. Rev. **46**, 5392 (1992).
[4] L. Gunther, reported at the Madrid Workshop on Nanomagnetic Devices (1992).
[5] B. Barbara *et al.*, reported at the 37th Annual Conference on Magnetism and Magnetic Materials (Houston, TX, 1992).
[6] L. Gunther and B. Barbara (unpublished).

Macroscopic quantum tunneling in antiferromagnetic horse-spleen ferritin particles (abstract)

J. Tejada and X. X. Zhang
Facultad de Fisica, Universita de Barcelona, Diagonal 647, 08028 Barcelona, Spain

In this paper we report a comprehensive study of the low temperature magnetic relaxation of nanometer-scale antiferromagnetic horse-spleen ferritin particles. First we report on the static magnetic characterization of the sample at low and high field in the temperature interval between 4 and 300 K. Secondly, we present experimental results on the magnetic relaxation of the remanent magnetization $M_r(t)$ associated with the uncompensated surface spins on such small particles. The magnetic viscosity $S \equiv 1/M_r[dM/d\ \ln(t)]$ is proportional to temperatures above 3 K. At lower temperatures, the viscosity is independent of temperature, providing evidence to quantum tunneling of the Néel vector.

 0021-8979/94/75(10)/5642/1/$6.00 © 1994 American Institute of Physics

Magnetism of thin magnetic layers with strong anisotropy and quantum tunneling (abstract)

P. Perera and M. J. O'Shea
Department of Physics, 116 Cardwell Hall, Kansas State University, Manhattan, Kansas 66506-2601

We report on the magnetic properties of Dy(t Å)/Mo(d Å), DyCo(t Å)/Mo(d Å), and Gd(t Å)/Mo(d Å) multilayers where $d=180$ Å and t ranges from 10 to 3000 Å. We find a decrease in T_c with decreasing t, with the most rapid decrease occurring for the Gd system where the anisotropy is the weakest. We have looked at the time dependence of magnetization in the anisotropic systems (Dy based). At long times (5×10^4 s) the magnetization shows a stretched exponential dependence on time as is found in other magnetically disordered systems. We have also looked at the rate of magnetic relaxation at short times (<1000 s) and find that it becomes independent of temperature below a temperature in the range 3–6 K depending on the magnetic layer thickness t. We shall consider the possibility of macroscopic quantum tunneling here and estimate the temperature, T^*, below which a system is expected to cross over from thermally activated to quantum tunneling.[1,2] We shall also compare our results to previous work on Dy/Cu.[3]

[1] A. J. Leggett, Rev. Mod. Phys. **59**, 1 (1987); E. M. Chudnovsky and L. Gunther, Phys. Rev. Lett. **60**, 661 (1988).
[2] B. Barbara and E. M. Chudnovsky, Phys. Lett. A **145**, 205 (1990).
[3] L. L. Balcells *et al.*, J. Magn. Magn. Mater. **109**, L159 (1992).

 0021-8979/94/75(10)/5643/1/$6.00 © 1994 American Institute of Physics

Magnetic and structural modifications in Fe and Ni films prepared by ion-assisted deposition

William A. Lewis
Department of Materials Science and Engineering, Stanford University, Stanford, California 94305-2205

Michael Farle
I.P.C.M.S., Universite Louis Pasteur, 4 rue Blaise Pascal, F-67070 Strasbourg, France

Bruce M. Clemens and Robert L. White
Department of Materials Science and Engineering, Stanford University, Stanford, California 94305-2205

We summarize our observations of in-plane uniaxial magnetic anisotropy induced in 1000 Å Ni and Fe thin films by 100 eV Xe^+ ion bombardment during deposition. The anisotropy was measured by means of the magneto-optic Kerr effect and full angular scan ferromagnetic resonance. The maximum in-plane anisotropy field was 150 Oe for Ni and 80 Oe for Fe. The hard direction of magnetization lies parallel to the plane of incidence for Ni and perpendicular to it for Fe. An expansion of the lattice of up to 0.6% normal to the film and an enhancement of the fiber texture are found in both cases. This out-of-plane expansion is accompanied by an in-plane compression. In addition, a small in-plane difference in lattice spacings (<0.2%) is found between directions parallel and perpendicular to the plane of incidence of the ions. The in-plane uniaxial magnetic anisotropy is attributed to the in-plane anisotropic strain using a simple magnetoelastic model.

I. INTRODUCTION

It has been found that in-plane uniaxial magnetic anisotropies can be induced in magnetic thin films by techniques ranging from deposition in a magnetic field to deposition at an oblique angle of incidence.[1] We have also shown that such an anisotropy can be generated by ion-beam-assisted deposition of Ni films.[2,3] This technique involves bombarding the growing film with low-energy ions (50–500 eV) that arrive at an angle relative to the sample normal. For 1000 Å Ni films we reported uniaxial magnetic anisotropies, with the hard direction parallel to the plane of incidence of the secondary ions, having saturation fields as large as 150 Oe. The present work is intended to gain insight into the mechanism for this anisotropy. We report here further magnetic characterization of our Ni samples by ferromagnetic resonance (FMR), and investigate the influence of ion bombardment on Fe films. By studying the magnetic differences between Ni and Fe in combination with in-plane structural properties we will attempt to correlate microstructural modifications with the magnetic properties.

II. EXPERIMENT

1000 Å Fe and Ni films were deposited by ion-beam-assisted deposition as described in detail elsewhere.[2,4] High-purity Xe gas was used for the ion bombardment and was incident upon the growing film at a 60° angle with respect to the sample normal. The Xe^+ ion energy was held at 100 eV while varying the incident flux. We define the relative flux ratio R as the number of Xe^+ ions arriving at the sample per deposited atom. Magnetic characterization was performed *ex situ* using a magneto-optic Kerr effect (MOKE) apparatus operating in longitudinal mode, and a 9 GHz FMR system. Structural characterization was performed by x-ray diffraction in both radial Bragg θ-2θ and grazing incidence x-ray scattering (GIXS) geometries in order to obtain lattice spacings and texture information.

III. RESULTS

Hysteresis curves were obtained for both Fe and Ni samples at different in-plane angles. Figure 1 shows the Kerr rotation for an Fe sample deposited with $R=0.22$. The square loop was obtained when the field was applied in a direction that lies in the plane of incidence of the ions. The second curve is indicative of a hard axis of magnetization and was obtained when the magnetic field was applied perpendicular to the plane of incidence. Samples prepared without ion bombardment are magnetically isotropic in the plane. The magnitude of this in-plane uniaxial magnetic anisotropy is given by the field required to saturate the magnetization in the hard direction H_a. The sample in Fig. 1 exhibited the largest anisotropy for Fe with $H_a=80$ Oe. This value is only half as large as for Ni, and, in contrast, the hard axis is oriented perpendicular to the bombardment direction. It is this difference in magnitude and orientation that will provide some keys to discerning the mechanism of the anisotropy.

We carefully investigated the variation of the anisotropy and coercivity with R as shown in Fig. 2. For R values greater than 0.12 we see an increasing anisotropy up to a maximum at 0.22 and then a decrease for larger values. For values below 0.06 and from 0.35 and above, we observe

 0021-8979/94/75(10)/5644/3/$6.00 © 1994 American Institute of Physics

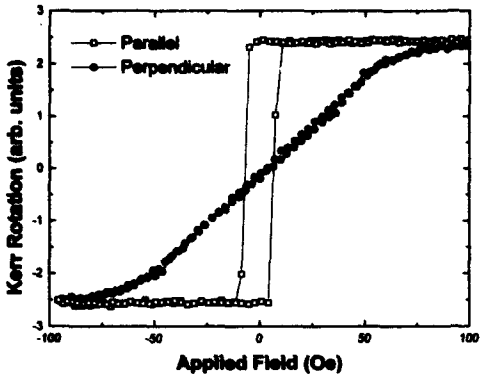

FIG. 1. Magneto-optic Kerr effect hysteresis loops for a 1000 Å Fe film obtained with the magnetic field applied parallel and perpendicular to the plane of incidence of the Xe^+ ions for $R=0.22$.

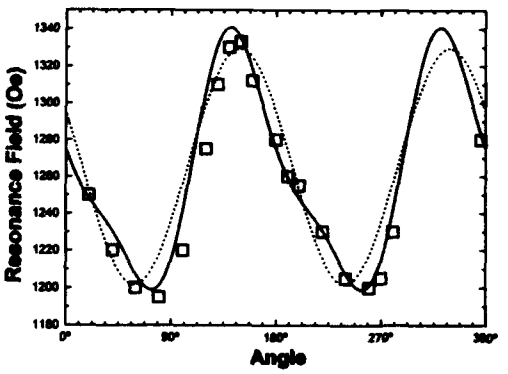

FIG. 3. In-plane 9 GHz FMR measurement for a 1000 Å Ni film with $R=0.12$. The solid line is a fit according to Eq. (1) with $M=493$ G, $g=2.2$, $\mu=9.3$ GHz, $K_u^{\perp}=-5\times10^4$ ergs/cm^3, $K_u^{\parallel}=1.7\times10^4$ ergs/cm^3, $K_1=5\times10^3$ ergs/cm^3, and $\phi_u=30°$. The dotted line is the best possible fit with $K_1=0$.

isotropic in-plane magnetic behavior as evidenced by the coincidence of the data points.

FMR measurements were performed on selected Ni films reported earlier.[2,3] The magnetic field could be rotated in the sample plane or in a plane normal to the film plane. It is well known that this type of measurement[5,6] yields complete information on the magnetic anisotropies of a magnetic thin film. To fit the experimental data of the in-plane measurement for a 1000 Å Ni film (Fig. 3) we use the resonance condition[6] appropriate to our film structure

$$\left[\frac{\omega}{\gamma}\right]^2=\left[H_{\parallel}+4\pi M_{\text{eff}}+\frac{K_1}{M}\ (2-\sin^2 2\phi)-\frac{2K_u^{\parallel}}{M}\ \cos^2(\phi-\phi_u)\right]\left[H_{\parallel}+\frac{2K_1}{M}\ \cos 4\phi-\frac{2K_u^{\parallel}}{M}\ \cos 2(\phi-\phi_u)\right], \tag{1}$$

$$4\pi M_{\text{eff}}=4\pi M+\frac{2K_u^{\perp}}{M},$$

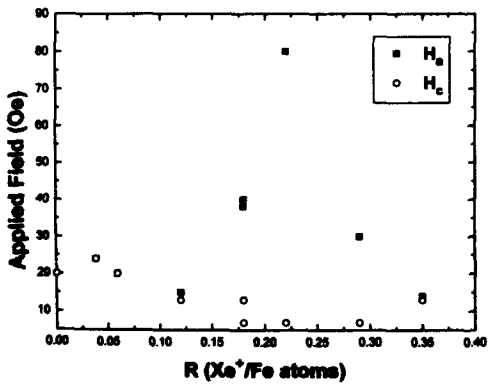

FIG. 2. In-plane uniaxial anisotropy field and coercivity as functions of the relative flux ratio R for 1000 Å Fe films.

which includes cubic K_1, and in-plane uniaxial $K_u^{\parallel}$ contributions, and the out-of-plane anisotropy $K_u^{\perp}$. The axis of the uniaxial in-plane anisotropy and the cubic axis are permitted to differ by an angle ϕ_u. In Fig. 3 we show the best fit (solid line) to the experimental data. As a result we find a weak cubic anisotropy superimposed on the strong in-plane uniaxial anisotropy, which corresponds to our earlier MOKE measurements. However, hysteresis loops recorded by MOKE could not resolve the weak cubic contribution.

Investigations into the microstructure of the Fe samples were conducted, and symmetric Bragg scans yielded out-of-plane results similar to those found for Ni.[2] We found that the spacing of (110) planes increases rapidly from its bulk value at $R=0$ to a maximum of 0.6% strain for $R>0.15$. There is also an enhancement of (110) texture as measured by the intensity of (110) planes as compared to (100) planes under ion bombardment. In-plane lattice spacings and crystallite orientation were determined by GIXS.[7] Radial scans were performed near the critical angle for Ni and Fe samples with the scattering vector q in directions both parallel and perpendicular to the plane of incidence of the Xe^+ ions. Values for the average difference in the in-plane strain between parallel and perpendicular $\Delta\epsilon_{\text{avg}}$, are obtained from the measurement of three in-plane diffraction peaks [for Ni: (111), (200), and (220); for Fe: (110), (200), and (211)]. In units of percent strain these values are 0.05 ± 0.02 for Ni and 0.2 ± 0.1 for Fe. It is important to note that while there appears to be a considerable variation in the magnitude of the strain for different planes, as reflected in the error, there is a consistency in sign. That is, both Fe and Ni have a expanded lattice spacing in the plane of incidence of the ions relative to perpendicular for all diffraction peaks. There is also evidence for some in-plane crystallographic ordering which we report as the ratio of (111):(200) integrated peak intensities for Ni and (110):(200) for Fe. This ratio parallel to the plane of incidence is larger than it is perpendicular by about a factor of 2 for both Fe and Ni. Samples prepared without ion bom-

bardment show no evidence of either in-plane anisotropic strain or crystallographic ordering.

IV. DISCUSSION

The two potential mechanisms for the observed uniaxial magnetic anisotropy that are possible based on our previous results are that the ion bombardment: (a) produces in-plane preferential orientation of the crystallites which contributes through the magnetocrystalline anisotropy of the material or (b) generates an anisotropic in-plane strain that produces a magnetic anisotropy through inverse magnetostriction.

While there is evidence of some preferred in-plane crystallographic orientation, we argue that the first mechanism cannot account for our observations. The leading cubic anisotropy term K_1 is equal to 4.8×10^5 ergs/cm^3 for Fe and -0.45×10^5 ergs/cm^3 for Ni.[8] We would expect *a priori* that the anisotropy in Fe films should be much larger, perhaps ten times larger, than in Ni. Using bulk magnetization values[8] and the maximum observed anisotropy field we calculate that the uniaxial anisotropy constant K_u is 0.68×10^5 ergs/cm^3 for Fe films and 0.36×10^5 ergs/cm^3 for Ni. This difference of only a factor of 2 means that there must be a fivefold greater in-plane orientation in Ni as compared to Fe. Furthermore, since the magnitude of the induced anisotropy for Ni is comparable to the bulk K_1 value, the film would need to be nearly perfectly ordered in the plane. Such an extreme degree of orientation is not possible based on our structural data. Therefore, we find that magnetocrystalline anisotropy cannot be the primary mechanism for producing the uniaxial anisotropy.

It is therefore very probable that the uniaxial anisotropy is a consequence of an inverse magnetostrictive effect. An anisotropic in-plane stress state can generate a uniaxial in-plane anisotropy with the magnitude given by

$$H_a(\text{stress}) = 3\lambda \frac{\Delta\sigma}{M_s}, \tag{2}$$

where λ is the appropriate magnetostriction constant, M_s is the saturation magnetization, and $\Delta\sigma$ is the stress differential between two orthogonal in-plane directions. From the average anisotropic in-plane strain measured by GIXS we calculate an average anisotropic in-plane stress $\Delta\sigma_{\text{ave}}$ for Ni using bulk elastic constants[9] in the (111) plane. For this orientation we use $\lambda_{111}=-24\times10^{-6}$, and the bulk magnetization and obtain an anisotropy field of 150 Oe. This result is in excellent agreement with our experimental observation. Also, the orientation of the hard axis agrees with our results. Since λ is always negative for Ni, the hard direction should lie parallel to the plane of incidence of the ions because this direction is expanded relative to perpendicular. Calculations made using isotropic elastic and polycrystalline magnetostriction constants ($E=200$ GPa and $\lambda_p=-33\times10^{-6}$) yield similar results [H_a(stress)=200 Oe]. The results are comparable because the two magnetostriction constants for Ni have the same sign and the (111) plane is elastically isotropic.

The calculation for Fe, however, is complicated by the equal magnitude but different sign of the two magnetostriction constants[8] ($\lambda_{100}=+21\times10^{-6}$, $\lambda_{111}=-21\times10^{-6}$) and the elastically anisotropic nature of the (110) plane. Therefore, the form of the solution is more complicated than Eq. (2) and has been detailed elsewhere.[10] Using bulk elastic constants and our in-plane structural data, we again calculate H_a(stress) and find that the orientation of the easy axis is independent of the direction of the ion bombardment within the (110) plane. Therefore, crystallites of this orientation will not contribute to the uniaxial anisotropy that we observe. If we instead calculate the anisotropy due to an in-plane anisotropic strain in a (100) plane we find that

$$H_a(\text{stress}) = 3\lambda_{100} \frac{(C_{11}-C_{12})\Delta\epsilon_{\text{ave}}}{M_s}, \tag{3}$$

where c_{ij} are the bulk elastic constants for Fe. This crystal orientation yields an anisotropy field of 70 Oe. This result agrees quantitatively with our magnetic observations and also produces the correct orientation of the uniaxial anisotropy. Since λ_{100} is positive, and all other terms have the same sign as for Ni, the hard direction of magnetization lies perpendicular to the plane of incidence. Although we have found an increased (110) texture for Fe films prepared under ion bombardment, it is possible that the minority (100) grains are responsible for the anisotropy. Considering how sensitive the calculation of the anisotropy due to magnetostriction is to the microstructure, further attempts to fully characterize the structure of these films are necessary. Nonetheless, we are able to reproduce the correct magnitude and orientation for the uniaxial in-plane magnetic anisotropy in Ni and Fe through inverse magnetostriction, and we therefore conclude that it is the most probable mechanism.

ACKNOWLEDGMENTS

This research was supported by the IBM Almaden Research Center (W.A.L.), Stiftung Volkswagenwerk (M.F.), and the National Science Foundation (B.M.C., R.L.W). GIXS measurements were performed at the Stanford Synchrotron Radiation Laboratory and were supported by the Department of Energy, Division of Chemical Science. We also thank K. Baberschke, Freie Universität Berlin, for use of his FMR equipment.

[1] K. Itoh, J. Magn. Magn. Mater. **95**, 237 (1991).
[2] W. A. Lewis, H. Saffari, M. Farle, E. Kay, and S. B. Hagstrom, Mater. Res. Soc. Symp. Proc. **268**, 161 (1992).
[3] M. Farle, H. Saffari, W. A. Lewis, E. Kay, and S. B. Hagstrom, IEEE Trans. Magn. MAG-28, 2940 (1992).
[4] F. Parmigiani, E. Kay, T. C. Huang, J. Perrin, M. Jurich, and J. D. Swalen, Phys. Rev. B 33, 879 (1985).
[5] A. Berghaus, M. Farle, Y. Li, and K. Baberschke, Springer Proc. Phys. **50**, 61 (1990).
[6] B. Heinrich, A. S. Arrott, Y. F. Cochran, K. B. Urquhart, K. Myrtle, Z. Celinski, and Q. M. Zhong, Mater. Res. Soc. Symp. Proc. **151**, 177 (1989).
[7] P. H. Fuoss and S. Brennan, Annu. Rev. Mater. Sci. **20**, 365 (1990).
[8] B. D. Cullity, *Introduction to Magnetic Materials* (Addison–Wesley, Reading, MA, 1972).
[9] R. F. S. Hearmon, *An Introduction to Applied Anisotropic Elasticity* (Oxford University, London, 1961), p. 216.
[10] B. M. Clemens, R. Osgood, A. P. Payne, B. M. Lairson, S. Brennan, R. L. White, and W. D. Nix, J. Magn. Magn. Mater. **121**, 37 (1993).

Magnetostrictive hysteresis in nickel polycrystalline thick films

Isabelle Brard
Commissariat à l'énergie atomique, B.P No 2, 33114 Le Barp, France

Roland Georges
Laboratoire de Chimie de Solide du C.N.R.S, 351 Cours de la libération, 33405 Talence, France

Gilles Le Blevennec
Commissariat à l'énergie atomique, B.P. No. 2, 33114 Le Barp, France

Simultaneous magnetization and linear magnetostriction measurements have been performed on a 0.1-mm-thick polycrystalline nickel film. First magnetization and hysteresis loop type experiments are reported. The magnetostriction versus magnetization behavior appears to follow an approximate M^4 law, and to exhibit a weak but clear-cut hysteresis. Moreover, the film shape is changed by the applied magnetic field as the saturation magnetization is approached. Magnetostriction has also been measured as a function of the applied field direction for both saturation and intermediate magnetization states. Hysteresis effects appear in the second case. These results are interpreted in terms of domain wall motion and magnetization reorientation mechanisms within each domain.

I. INTRODUCTION

Discrepancies between magnetic measurements and theoretical models are sometimes attributed to magnetostrictive coupling between crystallites. In order to clarify this point and to estimate the amplitude and effectiveness of such couplings, we have undertaken an experimental and theoretical work dealing with interfilm magnetostrictive effects. The present article reports part of this work, dealing with the magnetostriction effects in a single sample. The experiments have been performed on a nickel sample, since this metal exhibits relatively large magnetostriction effects. Moreover, the sample has been given a sheet form, since it will be used later on for coupling studies.

II. EXPERIMENTAL CONSIDERATIONS

Experiments have been performed on a very high-purity nickel sample (Johnson–Matthey, Grade 1-m4N7). The circular sample (diameter: 18 mm, thickness: 0.1 mm) is cut from a foil obtained by cold rolling, without annealing. As a result of cold rolling, the polycrystalline structure exhibits a significant structure. A Bragg diffractogram obtained with Co $K_{\alpha 1}$ x radiations has given the following relative line intensities (111): 10.4, (200): 60.7, (220): 100.0, (311): 21.3, instead of 100, 42, 21, and 20 respectively for the isotropic random crystallite distribution.[1] The anomalous large relative intensity of the (110) ray indicates that the proportion of crystallites with their (110) planes parallel to the film surface is much larger than in a purely random distribution. This preferential orientation may be attributed to the cold rolling to which the sample has been submitted. However, since the line widths estimation leads to an approximate crystallite size 0.06 μm, this could affect the crystallites close to the surface only. Moreover, hysteresis loops determined with the magnetic field applied along various directions parallel to the sample surface may be fully superimposed to within experimental errors. Thus, the sample seems to exhibit no in-plane crystallite distribution anisotropy.

The experimental work essentially consists in the simultaneous determination of the magnetization and the relative magnetostriction $\delta_\parallel$ or $\delta_\perp$ measured parallel or normal to the applied field. Due to the uncertainties of the relation between the applied and internal magnetic field, in a sample which is not limited by an exactly quadric surface, it is better, and of more fundamental significance to relate the magnetostrictive effects to the magnetization itself instead of to the applied field. Since the sample is initially demagnetized, and due to the in-plane isotropic crystallite distribution, magnetization should lie along the applied field. The magnetization measurements have been performed using an EG&G 4500 vibrating sample magnetometer. The magnetostriction effects are deduced from the relative resistance variations of a strain gauge. In order to avoid direct magnetic field effects, we have used specific field insensitive strain gauges (Vishay–Micromesures, H06A-AC1-125-700). Direct field influence estimation shows that it is more than 1% of the order of magnitude of the pertinent observed effects. In order to eliminate thermal effects due to Joule heating of the 700 Ω strain gauge on the sample, an additional strain gauge was similarly cemented on to the surface of an identical sample not subjected to the magnetic field. These two strain gauges formed adjacent legs of a Wheastone bridge. The remaining legs are two nearly 700 Ω resistors, one of them being adjustable in order to balance the bridge. Practically, the bridge is balanced at the beginning of each experiment, and the strain variations are considered to be directly proportional to the bridge unbalanced voltage.

III. EXPERIMENTAL RESULTS

The behavior of the parallel magnetostriction $\delta_\parallel$ versus the reduced magnetization M/M_s (referred to the saturation magnetization M_s) is shown in Fig. 1 for the first magnetization process and the hysteresis loop. A slight but well defined and symmetrical hysteresis is observed. Moreover, the $\delta_\parallel$ vs $(M/M_s)^4$ plot (Fig. 2) suggests that a M^α law, with α close to 4 very conveniently describes the phenomenon at least for M larger than $M_s/2$, i.e., when the hysteresis effects are significantly smaller.

 0021-8979/94/75(10)/5847/3/$6.00 © 1994 American Institute of Physics

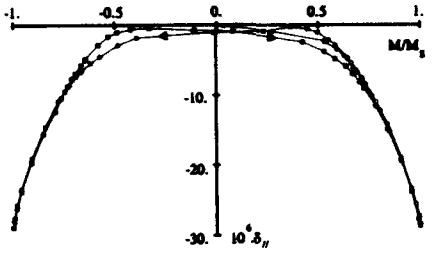

FIG. 1. Dependence of the parallel magnetostrictive strain $\delta_{\parallel}$ on the relative magnetization M/M_s. White points: first magnetization curve. Black points: hysteresis loop (see arrows).

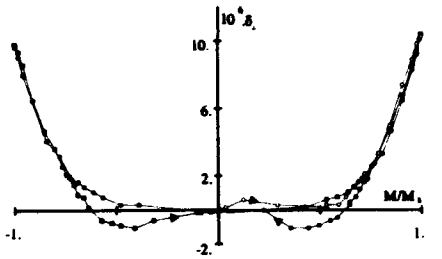

FIG. 3. Dependence of the normal magnetostrictive strain $\delta_{\perp}$ on the relative magnetization M/M_s. White points: first magnetization curve. Black points: hysteresis loop (see arrow).

Similarly, the behavior of the magnetostriction $\delta_{\perp}$, normal to the magnetization is shown in Fig. 3 as a function of the reduced magnetization. A $\delta_{\perp}$ vs $(M/M_s)^4$ plot (not reported here) also supports a M^4 law for M larger than $M_s/2$. It must also be noticed that apart from a well-defined symmetrical hysteresis effect, which may be correlated to the previous one, the normal strain does not exhibit a constant sign when the applied field is reduced from the maximum down to the coercive value. A sign change occurs when the magnetization is reduced to nearly $0.63M_s$. Finally, it must be underlined that the maximum parallel and normal strains ($-28.7\pm0.5\times10^{-6}$ and $11.3\pm0.5\times10^{-6}$) are in a ratio close to -2.5 instead of -2 as expected for a polycrystalline sample exhibiting an isotropic distribution of the crystal axes.

In order to clear up the hysteresis effects, we have determined the strain variations along a definite direction of the sample, as a function of the applied field direction for a field large enough for saturating the sample (2000 Oe), and an intermediate one (60 Oe) which corresponds to a relative magnetization 0.45, associated with the maximum hysteresis in both the parallel and normal determinations. The sample is first demagnetized using an alternating decreasing field applied along the strain gauge measurement direction. The applied field is increased until the magnetization reaches the desired value without rotating the sample. Then, the sample is rotated step by step forward, up to a complete turn, and then backward. The strain is measured for each angle θ between the initial and current field orientation. The results are shown in Figs. 4 and 5 for the saturation and intermediate magnetization case, respectively. In the saturation case, a Fourier analysis of the experimental results indicates well-defined $a+b\sin[2(\theta+\phi)]$ laws, with $a=-6.56\times10^{-6}$, $b=19.53\times10^{-6}$, $\phi=-43.9°$; and $a=-6.77\times10^{-6}$, $b=19.23\times10^{-6}$, $\phi=-44.3°$, for the forward and backward rotation experiments, respectively. These differences are definitely within the measurement errors. Thus, as expected, no strain versus magnetization orientation hysteresis is detectable when the sample is saturated. In the so-called intermediate magnetization case, the magnetization appears to keep a nearly constant value along the applied field, in agreement with the fact that the magnetization direction lies at a constant angle with respect to the applied field, except in the first rotation steps, where the magnetic torque is too weak. On the other hand, the results are not so clear for the strain measurements, essentially due to the smallness of the values we deal with. However, the experimental results may be again Fourier analyzed, in order to extract the significant effects from the noise. The results of this analysis are $a=-2.14\times10^{-6}$, $b=0.66\times10^{-6}$, $\phi=-26.6°$; and $a=-1.85\times10^{-6}$, $b=0.64\times10^{-6}$, $\phi=58.6°$, for the forward and backward rotations. Despite the relative importance of the noise, the close b values, and the fact that the ϕ angles are roughly opposite, are indications that we are dealing with a definite hysteresis effect.

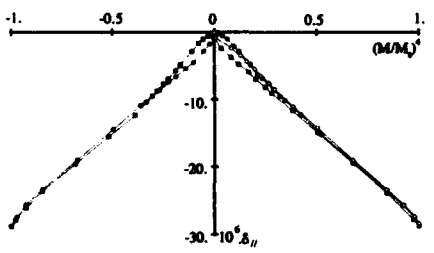

FIG. 2. Dependence of the parallel magnetostrictive strain $\delta_{\parallel}$ on $(M/M_s)^4$. White points: first magnetization curve. Black points: hysteresis loop.

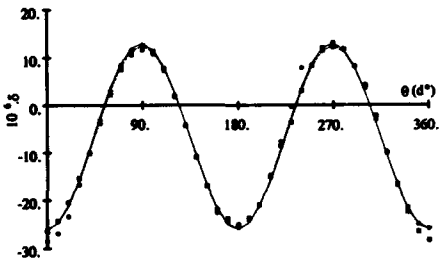

FIG. 4. Angular dependence of the parallel magnetostrictive strain $\delta_{\parallel}$ for $M=M_s$. Round points: forward run. Square points: backward.

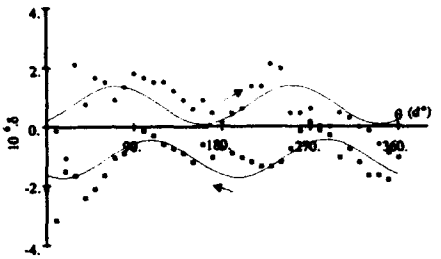

FIG. 5. Angular dependence of the parallel magnetostrictive strain $\delta_\parallel$ for $M=0.45M_s$. Round points: forward run. Square points: backward.

IV. DISCUSSION

Assuming a uniform distribution of the magnetization directions in the demagnetized state, the isotropic saturation strain λ_s is given by the $\delta_\parallel$ value in the saturation experiments, i.e., $-28.7\pm0.5\times10^{-6}$. This value lies within the ones usually reported[2–4] for polycrystalline samples (-25×10^{-6} to -47×10^{-6}). However, it must be noticed that the $\delta_\parallel/\delta_\perp$ ratio, which is close to -2.5, is not consistent with such an assumption. We assume, as a very crude description, that the moments in the crystallites may only lie along the x, y, or z axis (x and y being the sample plane, and z being normal) and that in the demagnetized state, the corresponding volume proportions are p, p', and $1-p-p'$, it is easily shown that the $\delta_\parallel/\delta_\perp$ ratio, when the saturation is performed along the x direction, is linked to p and p' by Eq. (1).

$$\delta_\parallel/\delta_\perp=(p-1)/p'. \tag{1}$$

Assuming $p=p'$ in the demagnetized state, as suggested by the mentioned in-plane isotropy, the experimental ratio is accounted for by the values $p=p'=0.29$. This is an indication that the moments lie closer to the direction normal to the plane than to in-plane directions. Actually, since the crystallites are significantly smaller than the sample thickness, one could at most imagine that the moments, despite demagnetizing field effects, are equally distributed along all the available directions. On the other hand, the cold rolling which induces at least surface crystallite orientations may induce some kind of surface anisotropy, which, in its turn, may favor normal magnetization.

The next point to discuss is the quasi-M^4 strain behavior. Heisenberg[5] considering that the domain distribution is governed by probability considerations consistent with the observed magnetization along the applied field predicts a rather regular strain-magnetization behavior. Akulov[6] suggests that, in iron single crystals, the first magnetization changes, as the field increases, take place by 180° reversal on the domains oriented opposite to the field. Bozorth[7] emphasizes that this may be a consequence of weak internal strains, which as we have shown may be present in our sample. Such a reversal does not affect the magnetostriction state. As a result, most of the field-induced strain is delayed to larger values of the magnetization, when 90° (or nearly so for nickel) wall motions set on. Then the deformation must vary more rapidly in order to catch up to its ultimate value. This evolution of the process results in an original strain versus magnetization behavior. Although it appears to remain conveniently described by a M^α law, α is significantly larger than 2 (actually close to 4).

This may be consistent with the strain-magnetization observed hysteresis. As the field is reduced from its maximum value, nearly 90° wall motion first occurs, giving rise to a relatively rapid algebraic increase of the parallel strain $\delta_\parallel$. Then, due to the coercive field, the magnetization is reversed in the domains magnetized opposite to the field direction, whereas the moment rotation which begins to take place in the other domains is now accompanied by a parallel strain decrease. The complementary phenomenon is observed on the perpendicular strain $\delta_\perp$. It must be noticed that the observed butterfly shape of these hysteresis curves results from the quadratic magnetization dependence of the strains.

V. CONCLUSIONS

We have evidenced various strain-magnetization hysteresis effects in the polycrystalline nickel sample under investigation. It has been shown that the observed relations between strain and magnetization variations may be explained on the basis of statistical uniaxial anisotropy, probably induced by cold rolling the polycrystalline sample. Further experiments including simultaneous normal and parallel strain and magnetization measurements are presently in progress, as well as an analysis on the basis of recent works on magnetization processes and magnetostriction in polycrystalline materials.[8,9]

[1] J.C.P.D.S. File 4-850, A.S.T.M.
[2] A. Schulze, Ann. Physik **5**, 937 (1931).
[3] H. Masumoto and S. Nara, Sci. Rept. Tohoku Imp. Univ. **16**, 333 (1941).
[4] A. Hernando, M. Vasquez, G. Rivero, J. M. Barandiaran, O. V. Nielsen, and A. Garcia-Escorial, J. Phys. Cond. Mater. **2**, 1885 (1990).
[5] W. Heisenberg, Z. Physik **69**, 287 (1931).
[6] N. Akulov, Z. Physik **69**, 78 (1931).
[7] R. M. Bozorth, *Ferromagnetism* (Van Nostrand, 1961), p. 653.
[8] M. Le Floc'h, J. Appl. Phys. **67**, 405 (1990).
[9] J. Furthmüller, M. Fähnle, and G. Herzer, J. Magn. Magn. Mater. **69**, 79 (1989); **69**, 89 (1989).

Method for determining both magnetostriction and elastic modulus by ferromagnetic resonance

R. D. McMichael
National Institute of Standards and Technology, Gaithersburg, Maryland 20899

The magnetostriction constant λ_s includes a combination of both elastic constants c_{ij} and magnetoelastic coupling constants B_i. To provide information on both c_{ij} and B_i, a method for measurement of both λ_s and the elastic modulus Y of thin films has been developed using ferromagnetic resonance (FMR). As in prior FMR schemes for measuring λ_s, a strain is produced in the film by bending the substrate, and the resulting anisotropy field is measured. However, by using a triangular polymer beam as a substrate, three important advantages are obtained (i) the triangular beam shape has uniform strain along its surface, (ii) the polymer material supports large strains ($>10^{-3}$) without breaking, and (iii) the low elastic modulus of the beam allows measurement of the sample elastic modulus through variation of the sample aspect ratio. Measurements on Ni foils yield values of λ_s and Y which fall within the scatter of literature data.

I. INTRODUCTION

For a known tensile stress σ in a polycrystalline cubic material, the magnetoelastic energy density is given by[1] $E=-(3/2)\lambda_s\sigma\cos^2\theta_\sigma$, where θ_σ is the angle between the magnetization and the stress axis. The magnetostriction constant is $\lambda_s=2\lambda_{100}/5+3\lambda_{111}/5$, where

$$\lambda_{100}=-\frac{2}{3}\frac{B_1}{c_{11}-c_{12}},\quad \lambda_{111}=-\frac{B_2}{3c_{44}}, \tag{1}$$

B_1 and B_2 are the magnetoelastic coupling constants and c_{11}, c_{12}, and c_{44} are the elastic constants.[1] Because the magnetostriction is a combination of both the magnetoelastic coupling constants and the elastic constants, a detailed description of the magnetomechanical properties requires knowledge of both elastic and magnetoelastic properties.

The magnetoelastic energy is a stress/strain-induced magnetic anisotropy energy which is detectable through ferromagnetic resonance (FMR). A variety of experimental schemes for measuring stress/strain anisotropies using FMR have been developed in which either a known stress is generated in the sample by direct application of force[2,3] or a known strain is developed by bending the substrate.[4–7] The stress in the sample (and therefore, the resonance field) may be also modulated by incorporating the sample into an acoustic resonator in strain modulated FMR (SMFMR).[8,9] However, these schemes measure only the magnetostriction constants or the magnetoelastic coupling constants. For a complete understanding of magnetostriction in complex systems such as multilayers, the ability to separate the contributions of the elastic and magnetoelastic coupling constants is of value. This paper describes the first FMR technique that allows such a separation to be made.

II. THEORY

The FMR resonance condition is given by[10]

$$\frac{\omega}{\gamma}=\frac{1}{M\sin\theta}\left[\frac{\partial^2F}{\partial\theta^2}\frac{\partial^2F}{\partial\phi^2}-\left(\frac{\partial^2F}{\partial\theta\partial\phi}\right)\right]^{1/2}, \tag{2}$$

where $\omega/2\pi$ is the resonance frequency, M is the saturation magnetization of the material, and F is the free energy given by

$$F=-\mu_0MH\sin\theta\cos\phi+\left(\frac{\mu_0}{2}M^2+K_u^2\right)\sin^2\theta\sin^2\phi-\frac{3}{2}\lambda_s\sigma_z\cos^2\theta-\frac{3}{2}\lambda_s\sigma_x\sin^2\theta\cos^2\phi. \tag{3}$$

In Eqs. (2) and (3), the angles θ and ϕ are the polar coordinates of the magnetization direction as shown in Fig. 1, H is the applied field and K_u is a uniaxial anisotropy energy. The final terms are the anisotropy energies produced by a tensile stresses σ_z and σ_x directed along z and x axes, respectively. Using the expression for F given by Eq. (3), it can be shown from Eq. (2) that, to first order, for constant ω the resonance field is modified by the application of stresses in the z and x directions by an amount δH given by

$$\mu_0\delta H=\frac{3\lambda_s}{M}\sigma_z\left[1+\left(\frac{\mu_0H_0}{\omega/\gamma}\right)^2\right]^{-1}-\frac{3\lambda_s}{M}\sigma_x, \tag{4}$$

where H_0 is the resonance field with zero applied strain.

Application of strain to the sample is accomplished by bonding the sample to the surface of a cantilever beam and bending the beam. A triangular beam is used so that when it is loaded at its tip in a direction perpendicular to the triangular faces, it will have uniform curvature as shown in Fig. 1. In this configuration, the strain in the z direction at the

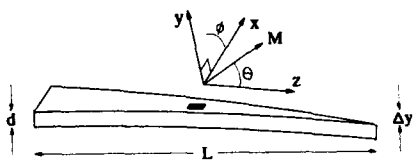

FIG. 1. Configuration of cantilever beam used to induce strains in the sample.

 0021-8979/94/75(10)/5650/3/$6.00 © 1994 American Institute of Physics

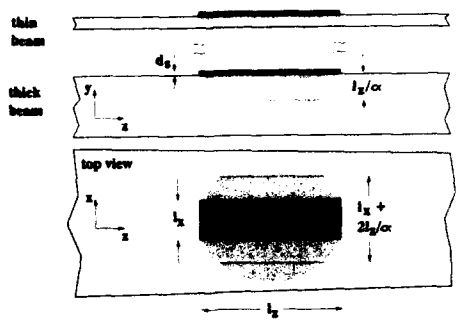

FIG. 2. Illustration of nonuniform strain in the beam. Black regions represent the sample and shaded regions represent the region of nonuniform strain.

surface of the beam, ϵ_{z0} is given by $\epsilon_{z0}=\Delta y d/L^2$, where Δy is the deflection of the tip of the beam, d is the beam thickness, and L is the distance from the beam tip to the clamping point. The strain in the x direction ϵ_{x0} is then $-\nu\epsilon_{z0}$, where ν is Poisson's ratio for the beam.

To estimate the strain in the film, we first consider the case of a thin film with cross-sectional area A_s and elastic modulus Y_s on a beam of cross-sectional area A_b and elastic modulus Y_b carrying a strain ϵ_0 far away from the sample. The lateral dimensions of the film are assumed to be much greater than the thickness of the beam. This "thin beam" configuration is illustrated in Fig. 2. The force carried by the beam far away from the sample must also be carried by the film and beam under the sample such that $Y_bA_b\epsilon_0 = Y_bA_b\epsilon+Y_sA_s\epsilon$, and therefore $\epsilon=\epsilon_0/(1+\beta)$, where $\beta=Y_sA_s/Y_bA_b$.

When the lateral dimensions of the beam are smaller than the thickness of the beam, the region of perturbed strain is not expected to extend completely through the beam, but would extend into the beam a distance which depends on the lateral dimensions of the sample ("thick beam" illustrated in Fig. 2). In this case, the effective cross section of the beam is $A_{bz}^{\text{eff}} = (l_x + 2l_z/\alpha)l_z/\alpha$ for strains in the x direction and $A_{bx}^{\text{eff}} = (l_z + 2l_x/\alpha)l_x/\alpha$ for strains in the y direction, where α describes the ratio of lateral sample dimensions to effective beam thickness. Under these assumptions, two β parameters can be defined to be

$$\beta_z=\alpha\frac{Y_s}{Y_b}\frac{l_xd_s}{l_z(l_x+2l_z/\alpha)};\quad \beta_x=\alpha\frac{Y_s}{Y_b}\frac{l_zd_s}{l_x(l_z+2l_x/\alpha)}. \tag{5}$$

Simple solutions for the strains in the film can be obtained for three limiting cases of the sample dimensions: (1) $l_z\gg l_x$, (2) $l_x\gg l_z$, and (3) $l_z=l_x=l_s$.

In case (1), $\beta_z\to 0$ and $\beta_x\to\infty$. Because $\beta_x\to\infty$, the beam is unable to exert significant force on the sample in the x direction, and $\sigma_x\to 0$. Because the cross section of the sample normal to the z axis is small, the z component of the sample strain will match that of the beam. The sample stress is completely in the z direction and is given by $\sigma_z=Y\epsilon_{z0}$, and the resonance field shift is given by the first term in Eq. (4).

In case (2), $\beta_z\to\infty$ and $\beta_x\to 0$. Because $\beta_z\to\infty$, the beam is unable to exert significant force on the sample in the z direction, and $\sigma_z\to 0$. Because the cross section of the sample normal to the x axis is small, the x component of the sample strain will match that of the beam. The sample stress is completely in the x direction and is given by $\sigma_x=-\nu Y\epsilon_{z0}$, and the resonance field shift is given by the second term in Eq. (4).

In case (3), the case of a symmetric sample, $\beta_z=\beta_x=\beta=\alpha^2(Y_s/Y_b)(d_s/l_s)/(\alpha+2)$. When the sample aspect ratio, d_s/l_s, is very small ($\beta\to 0$), the strains in the film are identical to the strains in the beam surface where $\epsilon_{sx}=-\nu\epsilon_{0z}$. The stress in the sample is only in the z direction, and is given by $\sigma_z=Y_s\epsilon_{0z}$. When the sample aspect ratio is increased by reducing the lateral dimensions of the sample, the strains will be attenuated by the factor $1/(1+\beta)$ and the FMR field shift, which is proportional to the stress, is therefore also proportional to $1/(1+\beta)$. The inverse of the field shift per unit strain, $(\mu_0\delta H/\epsilon_{z0})^{-1}$ becomes a linear function of the sample aspect ratio, d_s/l_s

$$\left(\frac{\mu_0\delta H}{\epsilon_{z0}}\right)^{-1}=\frac{M}{3\lambda_sY_s}\left[1+\left(\frac{\mu_0H_0}{\omega/\gamma}\right)^2\right]^{-1}\left(1+\frac{\alpha^2}{\alpha+2}\frac{Y_s}{Y_b}\frac{d_s}{l_s}\right). \tag{6}$$

If the geometrical factor α is known, the slope and intercept of the line described by Eq. (6) can provide independent measurements of λ_s and Y_s.

III. EXPERIMENTAL

The FMR setup consists of a TE_{102} cavity with a clamping mechanism for the cantilever beam on one side and the free end of the cantilever beam extending through the cavity. Beams were cut from 3.1-mm-thick acrylic sheet and 3.3-mm-thick bakelite sheet. Values of the elastic moduli of the beams Y_b were calculated from measurements of the deflection of the beam tip created by forces at the beam tip. The beam orientation in the cavity is such that the applied field remains in the plane of the film when the beam is bent. The free end of the cantilever beam is displaced by a screw mechanism driven by a stepper motor. Typically, ten spectra are used to determine the ratio $\delta H/\epsilon_{z0}$. A typical plot of resonance field versus ϵ_{z0} is shown in Fig. 3 with the resonance linewidth, which remains essentially constant as ϵ_{z0}, is varied.

In Fig. 4 $(\mu_0\delta H/\epsilon_{z0})^{-1}$ is plotted versus the sample aspect ratio for d_s=4.4-μm-thick rolled Ni foils. Starting with a nominally square piece of foil, the aspect ratio was modified by trimming the edges of the sample. To approach the limit represented by case (1) above, only l_x was reduced and the aspect ratio is taken to be d_s/l_x. To approach the limit represented by case (2) above, only l_z was reduced and the aspect ratio was taken to be d_s/l_z. The square samples were produced by reducing l_z and l_x by nominally equal amounts.

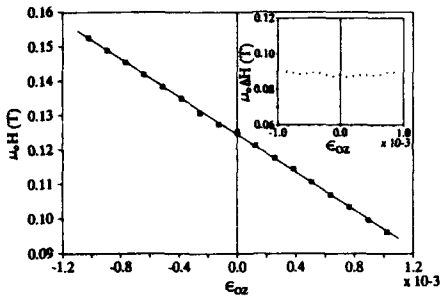

FIG. 3. Resonance field as a function of ϵ_{0z} for a nominally square 2.8 mm×4.4 μm thick Ni foil on an acrylic beam. Inset: peak-to-peak linewidth of the resonance as a function of ϵ_{0z}.

IV. DISCUSSION

To evaluate the results of these measurements by comparison with published values, a search of the literature was made for values of λ_s and Y for Ni. Values of λ_s ranged from -30×10^{-6} (Ref. 11) to -38×10^{-6} (Ref. 12) and values of Y ranged from 191 GPa[13] to 217 GPa.[14] For narrow strips oriented along the z direction, calculated values of $(\mu_0\delta H/\epsilon_{z0})^{-1}$ then range from -0.023 to -0.034 T^{-1} for $\mu_0 H_0=0.136$ T and $\omega/\gamma=0.320$ T. For narrow strips oriented along the x direction, calculated values of $(\mu_0\delta H/\epsilon_{z0})^{-1}$ range from -0.57 to -0.081 T^{-1}, assuming a value of $\nu=.35$ for the beam.

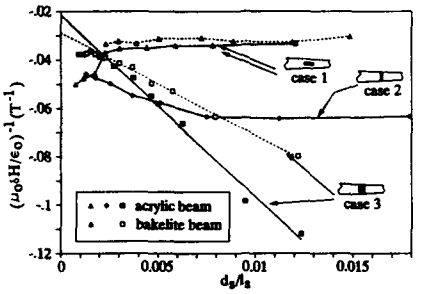

FIG. 4. Plots of $(\mu_0\delta H/\epsilon_{z0})^{-1}$ vs sample aspect ratio for three different sample configurations and two beam materials. The upper and lower horizontal shaded bands represent the range of calculated values of $(\mu_0\delta H/\epsilon_{z0})^{-1}$ for stresses in the z and x directions, respectively. The straight lines are least-squares fits to the data for square samples.

The dependence of $(\mu_0\delta H/\epsilon_{z0})^{-1}$ on the sample aspect ratio for square samples follows the linear relation given by Eq. (6) for small sample sizes. For larger sample sizes, Eq. (6) is not expected to hold since the lateral sample dimensions become larger than the beam thickness. Least-squares fits to the square sample data have intercepts that fall within the range of calculated values. Since the elastic modulus of Ni is available, values of α rather than Y_s were calculated from the slopes of the fit lines. The values are $\alpha=7.1$ for the acrylic beam and $\alpha=8.3$ for the bakelite beam, indicating that the region of nonuniform strain lies close to the sample surface.

The sensitivity of this technique for measurements of λ_s can be estimated from Eq. (4). Conservatively estimating that a 1 mT (10 G) field shift is detectable for a maximum strain of 10^{-3}, and using values of M and Y for Ni, the λ_s sensitivity is estimated to be $\sim10^{-6}$. Important advantages of this technique are the availability of large strains (up to 1.5×10^{-3} in the current setup) and the ability to measure elastic properties through the dependence of the resonant field shift on the sample aspect ratio.

[1] Soshin Chickazumi, *Physics of Magnetism* (Wiley, New York, 1964).
[2] A. B. Smith and R. V. Jones, J. Appl. Phys. **34**, 1283 (1963).
[3] A. B. Smith, Rev. Sci. Instrum. **39**, 378 (1968).
[4] B. Hoekstra, F. van Doveren, and J. M. Robertson, Appl. Phys. **12**, 261 (1977).
[5] X. Wang, C. S. Kraft, and M. H. Kryder, IEEE Trans. Magn. **MAG-18**, 1295 (1982).
[6] L. Pust and Z. Frait, Phys. Status Solidi A **85**, 179 (1984).
[7] S. E. Bushnell, W. B. Nowak, S. A. Oliver, and C. Vittoria, Rev. Sci. Instrum. **63**, 2021 (1992).
[8] J. C. M. Henning and J. H. den Boef, Appl. Phys. **16**, 353 (1978).
[9] R. Zuberek, H. Szymczak, R. Krishnan, and M. Tessier, J. Phys. C **8**, 1761 (1988).
[10] J. Smit and H. G. Beljers, Philips Res. Rept. **10**, 113 (1955); H. Suhl, Phys. Rev. **97**, (1955).
[11] M. Kaneko, S. Hashimoto, M. Hayakawa, and K. Aso, J. Phys. E **21**, 487 (1988).
[12] E. Klokholm and J. Aboaf, J. Appl. Phys. **53**, 2661 (1982).
[13] E. W. Lee, Rept. Prog. Phys. **18**, 184 (1955).
[14] D. I. Bower, E. Claridge, and I. S. Tsong, Phys. Status Solidi **29**, 617 (1968).

Multitarget sputtering of high magnetostrictive Tb-Dy-Fe films

E. Quandt
Institute of Materials Research I, Kernforschungszentrum Karlsruhe GmbH, D-76021 Karlsruhe, Germany

Giant magnetostrictive thin films of both the binary compound Tb_xFe_{1-x} and the ternary compound $(Tb_yDy_{1-y})_xFe_{1-x}$ have been prepared by multitarget magnetron sputtering in wide compositional ranges. In view of their potential use as actuators in microsystem technology the research was focused on low-field magnetostrictive properties in connection with low coercivity. Giant magnetostriction was found for a range of compositions with Tb contents higher than those of the crystalline Tb-Fe compounds. Depending on the composition, amorphous films with a magnetostriction as large as $\lambda \approx 450 \times 10^{-6}$ at an applied field of 6 kOe and a coercive field $H_c < 10$ Oe could be prepared. The improvement of the low-field magnetostriction of the ternary alloy Tb-Dy-Fe in comparison to Tb-Fe was found to be less distinct than for crystalline materials, probably because all reported films showed a perpendicular easy axis. The amorphous state of the films are stable at least up to 300 °C.

I. INTRODUCTION

Magnetostrictive thin films are promising candidates for integrated actuating mechanisms in membrane-type microsystem components. The development of highly magnetostrictive thin films is based on the rare-earth iron Laves phases, in particular on $(Tb_{0.3}Dy_{0.7})Fe_2$ which is, under the name of Terfenol-D, well known to exhibit giant magnetostriction in combination with reduced magnetocrystalline anisotropy.[1] Recently, the preparation of amorphous films having the Terfenol-D[2] and Tb-Fe[3] compositions by sputtering from mosaic targets has been reported.

The present paper describes the preparation of highly magnetostrictive Tb-Fe and Tb-Dy-Fe films using multitarget magnetron sputtering, a technique which allows film preparation over a wide range of compositions. The purpose of this work is to study the effect of both the total rare-earth content and the Tb/Dy ratio on the soft magnetic properties in films with giant magnetostriction. In addition, the degradation of the magnetic properties due to crystallization of the amorphous films will be discussed. The results will be compared to reported data obtained with alternative preparation methods.

II. EXPERIMENTAL

Both TbFe and TbDyFe thin films were dc magnetron cosputtered from a multiple target arrangement with pure element targets onto unheated Si, SiO_2, different metals, and carbon-coated Cu grids for direct transmission electron microscopy (TEM) observation. This technique allows the wide adjustment of the composition, for each element between 10 and 90 at %, by varying the sputtering power of the targets. The film thicknesses, except for the TEM samples, were about 2.5 μm. The sputtering argon pressure was typically 0.4 Pa with a base pressure of 4×10^{-5} Pa.

Compositions were measured by wavelength dispersive x-ray microanalysis (WDX), and depth profiles were obtained using Auger electron spectroscopy (AES). TEM, electron, and x-ray diffraction were used to determine the crystallographic structure of the films. Magnetostriction was measured in a field of 6 kOe by the cantilevered substrate technique[4] sensing the deflection of the free end of the cantilever by laser beam reflection. Polarization at room temperature was determined using a vibration-sample magnetometer (VSM) at 8 kOe. Thermal stability was investigated by *in situ* annealing experiments in a TEM.

III. RESULTS AND DISCUSSION

A. Composition and structure

The cosputtered rare-earth Fe films were found by x ray to be amorphous. Scanning electron microscopy (SEM) observation of the fracture surface (Fig. 1) showed dense growth, in contrast to the columnar growth obtained with an alternative method of film preparation.[2] The surface of the films was found to oxidize immediately upon exposure to air, but once formed the oxide layer showed a high stability and a slow further growth.

The residual film stress is compressive at a sputtering pressure of 0.4 Pa Ar; a stress-free deposition, important for thin-film actuator devices, can be achieved by increasing the Ar pressure to about 1 Pa Ar. Further increase in the Ar

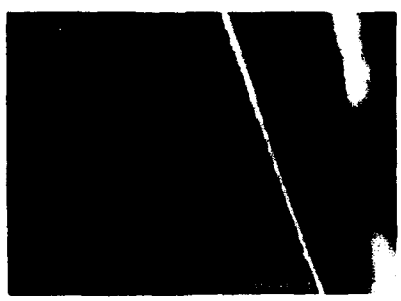

FIG. 1. SEM micrograph of the fracture surface of a TbDyFe film onto Si substrate.

 0021-8979/94/75(10)/5653/3/$6.00 © 1994 American Institute of Physics

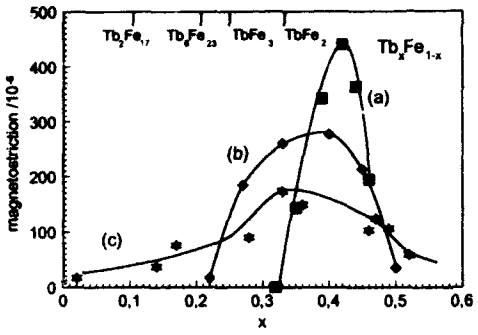

FIG. 2. Magnetostriction vs Tb content for amorphous Tb_xFe_{1-x} films. The data of multiple dc-magnetron sputtered films (a) at $H=6$ kOe are compared with evaporated films (Ref. 5) (b) at 15 kOe and hf-magnetron sputtered films (Ref. 3) at 16 kOe.

pressure results in a tensile residual film stress which is assumed to be helpful in obtaining an inplane magnetic easy axis. However, the correlated tremendous increase in the oxygen content from less than 0.5 to about 24 at % destroys the magnetic properties at high Ar pressures. An improved process technique is required to overcome this effect.

B. Magnetic properties

Compared to the crystalline magnetostrictive TbFe compounds—Tb_2Fe_{17}, Tb_6Fe_{23}, $TbFe_3$. $TbFe_2$—magnetostrictive properties of amorphous Tb_xFe_{1-x} films have only been observed for compositions with higher Tb contents. The largest magnetostriction has been measured for the $x=0.42$ sample. Its value of 450×10^{-6} at a magnetic field of 6 kOe applied in the film plane is significantly higher than values obtained with alternative preparation methods for Tb-Fe films (Fig. 2).[3,5] Comparison of the polarization curves for the $x=0.37$ and $x=0.44$ samples (Fig. 3) shows that both the strong perpendicular easy axis and the hysteresis decrease with higher Tb content, resulting in a coercivity of <10 Oe for the $x=0.44$ sample; this is the lowest coercivity reported for magnetostrictive amorphous rare-earth Fe films. Nevertheless, the applied magnetic field of 6 kOe saturates neither the magnetostriction nor the polarization of these films.

The ternary $(Tb_yDy_{1-y})_xFe_{1-x}$ compound has been investigated to examine the effect of the Tb/Dy ratio y and the rare-earth/Fe ratio x. Figure 4 shows the optimum magnetostriction curves obtained for different ratios y. Out of a large number of different compositions two effects were identified. In the case of $y=0.7$ the anisotropy reduction by Dy seems to work even in amorphous materials, leading to improved low-field but reduced high-field magnetostriction. Preliminary results show that the total rare-earth content has to be reduced from 42 at % for the Tb-Fe film ($y=1.0$) to 33 at % for the Tb-Dy-Fe film with the room-temperature anisotropy compensation composition ($y=0.3$). However, according to the Tb-Fe film results this total rare-earth reduction in the

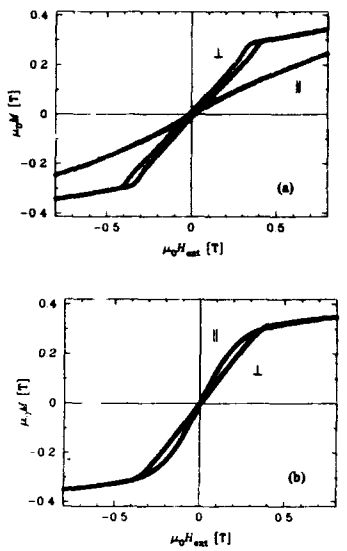

FIG. 3. Polarization vs external field applied parallel (∥) and perpendicular (⊥) to the film plane for (a) a $Tb_{0.37}Fe_{0.63}$ and (b) a $Tb_{0.44}Fe_{0.56}$ sample.

films counteracts the low-field improvement of the Dy alloying observed for the $y=0.7$ composition.

It is obvious that the low-field magnetostriction is strongly influenced by the orientation of the magnetic easy axis, which in the present experiments is always perpendicular to the film plane. The orientation might be changed in future experiments by the adjustment of the residual film stress as already discussed.

C. Thermal stability

The electron diffraction patterns of a carbon sandwiched $(Tb_{0.3}Dy_{0.7})Fe_2$ sample recorded at different temperatures show good stability of the amorphous films (Fig. 5) up to 300 °C. At 350 °C the amorphous halo is resolved, at 400 °C

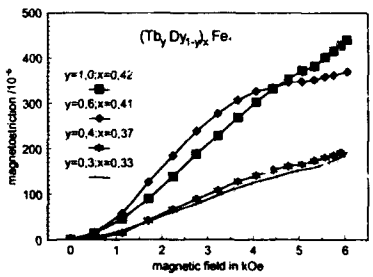

FIG. 4. Magnetostriction vs external field applied parallel to the film plane for different $(Tb_yDy_{1-y})_xFe_{1-x}$ samples showing the optimum curves for different Tb-Dy ratios y.

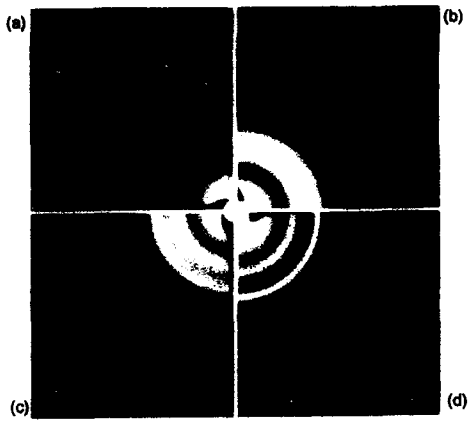

FIG. 5. Electron diffraction patterns of an *in situ* annealing experiment from a $(Tb_{0.3}Dy_{0.7})_{0.33}Fe_{0.67}$ film covered with amorphous carbon layers on both sides at annealing temperatures of (a) 300 °C, (b) 350 °C, (c) 400 °C, and (d) 450 °C.

the Laves phase has begun to crystallize, and at 450 °C a complete nanocrystalline structure is observed. Up to 600 °C the growth of only very few larger crystals in the nanocrystalline matrix could be found. These results are in good agreement to data reported elsewhere,[6] although we find the amorphous phase to be more stable. Preliminary data on TbFe films indicate that this crystallization point is transferred to an even higher temperature.

IV. CONCLUSIONS

Multitarget magnetron sputtering has been proved to be a powerful tool for preparing giant magnetostrictive films with low coercivity. Annealing experiments have shown the amorphous structure to be very stable. As discussed a further improvement of the low-field magnetostriction should be attainable by altering some preparation conditions in order to prepare films with in-plane magnetic easy axis.

ACKNOWLEDGMENTS

I would like to thank Professor H. Holleck for helpful discussions and F. Schatz (MPI für Metallforschung, Stuttgart) for the VSM measurements.

[1] A. E. Clark, in *Ferromagnetic Materials*, edited by E. P. Wohlfarth (North Holland, Amsterdam, 1980), Vol. 1, p. 531.
[2] F. Schatz, M. Hirscher, G. Flik, and H. Kronmüller, Phys. Status Solidi A **137**, 197 (1993).
[3] Y. Hayashi, T. Honda, K. I Arai, K. Ishiyama, and M. Yamaguchi, IEEE Trans. Magn. **MAG-29**, 3129 (1993).
[4] E. Klokholm, IEEE Trans. Magn. **MAG-12**, 819 (1976).
[5] D. W. Forester, C. Vittoria, J. Schelleng, and P. Lubitz, J. Appl. Phys. **49**, 1966 (1978).
[6] E. T. M. Lacey, D. G. Lord, and P. J. Grundy, IEEE Trans. Magn. **MAG-24**, 1713 (1988).

Magnetostriction, elastic moduli, and coupling factors of composite Terfenol-D

L. Sandlund and M. Fahlander
Feredyn Europe, Seminariegatan 30, S-752 28 Uppsala, Sweden

T. Cedell
Department of Production and Materials Engineering, Lund Institute of Technology, Box 118, S-221 00 Lund, Sweden

A. E. Clark, J. B. Restorff, and M. Wun-Fogle
Naval Surface Warfare Center, Silver Spring, Maryland 20903-5640

Recently it was discovered that composites of Terfenol-D alloys with an insulating binder produce very large magnetostrictions. Resistivities of these composites reach high values, making them attractive for high-frequency applications which require small eddy current losses. In this paper the magnetostriction, magnetization, and Young's moduli measurements made under constant magnetic field conditions and under constant flux conditions are reported. From these measurements, magnetomechanical coupling factors are calculated. The properties are compared to those of ordinary metallic Terfenol-D and nickel. Two different types of composites were investigated. In the first type the composite has an isotropic structure and in the second type, anisotropic. It is shown that the anisotropic type is more desirable since it possesses both higher magnetostriction and higher coupling factors. It is also clearly shown that the magnetization process for the anisotropic type can be explained by a 180° domain wall motion followed by a magnetization rotation.

I. INTRODUCTION

Terfenol-D alloys of type $Tb_{0.27-0.30}Dy_{0.73-0.70}Fe_{1.90-1.95}$ have been known since the 1970's[1] and have been commercially available since the mid 1980's in the U.S. and in Sweden. This material, which has outstanding elongation and energy density at room temperature, has shown great potential in applications up to ~10 kHz.[2] At higher frequencies eddy current losses limit its use.

To create a complement to ordinary Terfenol-D for higher-frequency applications, a new magnetostrictive material has been developed.[3] This material is based on Terfenol-D powder and is formed together with a nonmetallic binder into a composite. The binder creates an insulating layer between the particles which increases the resistivity and strongly reduces eddy current losses at high frequencies. Consequently this material broadens the useful range of the giant magnetostrictive materials into the ultrasonic regime. Further, this material has a rather high tensile strength (~ four times higher than the tensile strength in metallic Terfenol-D) which makes it suitable for applications in which tensile strengths larger than those of Terfenol-D are required, such as resonant applications. In this paper we present the magnetomechanical properties of composites prepared by two techniques. In the first technique, the Terfenol-D particles are randomly oriented (density, δ=7.5×10^3 kg/m^3; resistivity, $\rho\cong$300 $\mu\Omega$ m); in the second technique, the particles are magnetically oriented (δ=6.75×10^3 kg/m^3, $\rho\cong$600 $\mu\Omega$ m). Of particular importance is the field dependence of the magnetostriction, the elastic moduli and the permeability. To determine the magnetomechanical coupling, Young's modulus was measured under constant magnetic field conditions (Y^H). The modulus under constant magnetic induction (Y^B) was also measured.

II. EXPERIMENT

Rod-shaped samples of Terfenol-D composites (0.9 cm diam×4.33 cm), fitted with two resistive strain gages and an induction pick-up coil, were inserted into a 1.2 cm i.d. solenoid. Longitudinal compressive stresses were applied by adding fixed weights to a platform attached to the upper surface of the rods. Large soft iron end pieces were fastened at the ends of the samples to reduce the demagnetization factors and to homogenize the magnetic fields generated by the solenoid. A computer-controlled feedback circuit was used to keep the magnetization constant for the Y^B measurements. Magnetization and permeability were measured under constant stress (σ) conditions for stresses up to 16.3 MPa and magnetic fields up to ~160 kA/m.

III. MAGNETOSTRICTION

In this section, we discuss the field dependence of the magnetization and magnetostriction for composites composed of (a) randomly oriented particles and (b) magnetic field oriented particles and note how these results compare with those of the fully dense Terfenol-D metal reported previously.[4] From Fig. 1 we can compare the magnetization (M) versus magnetic field (H) and magnetostriction (λ) versus magnetic field for composites of randomly oriented particles and magnetically oriented particles at a prestress of 16.3 MPa. Magnetostrictions at 160 kA/m reach ~0.8×10^{-3} for the oriented particulate composite and ~0.5×10^{-3} for the randomly oriented particulate composite. Note, that for the fully dense metallic Terfenol-D at room temperature, the single-crystal saturation magnetostriction $(3/2)\lambda_{111}$ $\cong$2.4×10^{-3} and the saturation magnetization is 1.0 T.[5,6] From the measured densities of the compacted particulate samples, we calculate the volume fraction of Terfenol-D in the composites to be 80% for the composite of randomly

 0021-8979/94/75(10)/5656/3/$6.00 © 1994 American Institute of Physics

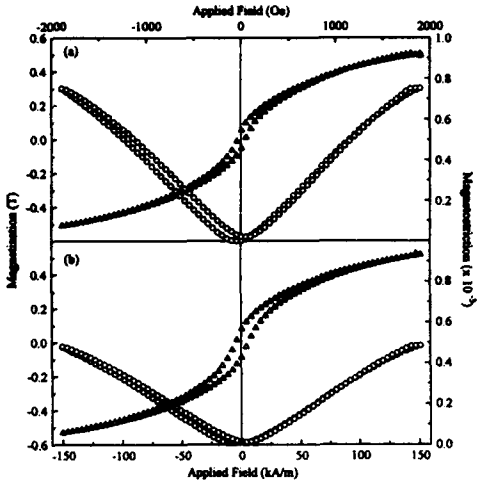

FIG. 1. Magnetization (triangles) and magnetostriction (circles) vs applied field for (a) the Terfenol-D composite with magnetically oriented particles and (b) the Terfenol-D composite with randomly oriented particles at a prestress of 16.3 MPa.

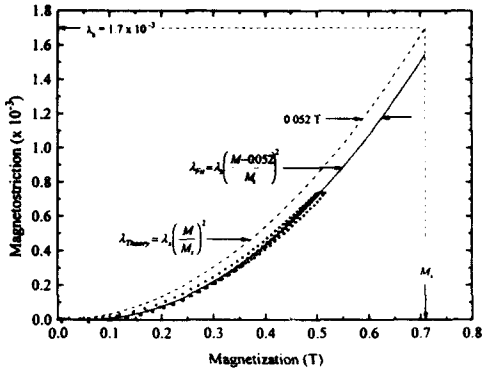

FIG. 2. Magnetostriction vs magnetization for the magnetically oriented Terfenol-D composite at a prestress of 16.3 MPa. The dotted line is the theoretical magnetostriction for a fully magnetization rotation process.

oriented particles and 71% for the composite of oriented particles. With the magnetic fields applied in this study, the maximum magnetization achieved is ~0.5 T (~50% of the saturation magnetization of the metallic Terfenol-D) and maximum magnetostrictions are ~1/5–1/3 of the saturation magnetostriction of the fully dense Terfenol-D single crystal. Hysteresis is ~5 kA/m for the composite of oriented particles.

In the sample of oriented particles, we find that ~0.05 T or 7% of the saturation magnetization is accounted for by nonmagnetostrictive 180° domain wall motion. Figure 2 shows the magnetostriction versus magnetization for a stress of 16.3 MPa. With a volume density of 71% for this composite, we calculate the saturation magnetization M_s to be 0.71 T and the magnetostriction (λ_s) based upon fully oriented [111] single-crystal particles of Terfenol-D to be $0.71(3/2)\lambda_{111}=1.7\times10^{-3}$. The dotted line in this figure illustrates the theoretical magnetostriction which would arise from a fully magnetization rotation process, $\lambda=\lambda_s(M/M_s)^2$. The data agree well with a λ vs M^2 curve having a magnetization displacement of 0.052 T which can be accounted for by 180° domain wall motion. Thus, using the available preparation method, a magnetostriction (λ_s) of 1.53×10^{-3} is predicted for full saturation. For this composite the magnetization process can be clearly separated into two regions: a 180° domain wall motion followed by a rotation process.

Measurements were taken on two samples with oriented particles and stresses of 9.5, 12.9, and 16.3 MPa. The upper curve of Fig. 3 is a composite from two such samples with three stresses each. The breadth of the line is an indication of the uncertainity in the value of the magnetostriction. These data are compared with the λ vs M curve for the sample containing randomly oriented particles. Clearly orientation is significant. Since $\lambda_{111}\gg\lambda_{100}$, nonaligned particles will substantially reduce the magnetostriction from the total available strain. At $M=0.5$ T, the strain in the sample of randomly oriented particles is only 60% of the strain in the sample of oriented particles. In the sample of randomly oriented particles the magnetization due to 180° wall motion is 0.084 T and the hysteresis is larger (~10 kA/m) (see Fig. 1). Also we find a small dependence of the magnetization and magnetostriction upon stress, especially for the sample with randomly oriented particles.

IV. ELASTIC MODULI AND COUPLING FACTORS

The magnitude of the forces generated by a magnetostrictive material depends upon its elastic moduli. In this section we report Young's moduli for the composite Terfenol-D samples measured under fixed magnetic field

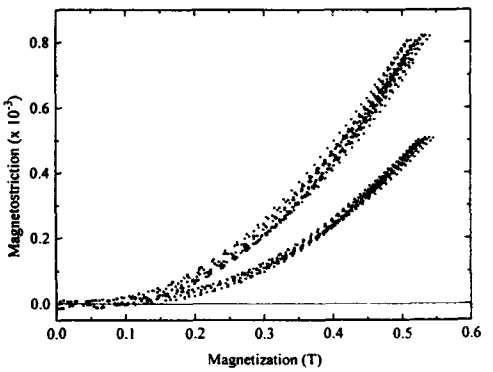

FIG. 3. Magnetostriction vs magnetization for the two oriented Terfenol-D composites (upper curve) and the randomly oriented Terfenol-D composite (lower curve) for three different prestresses (9.5, 12.9, and 16.3 MPa).

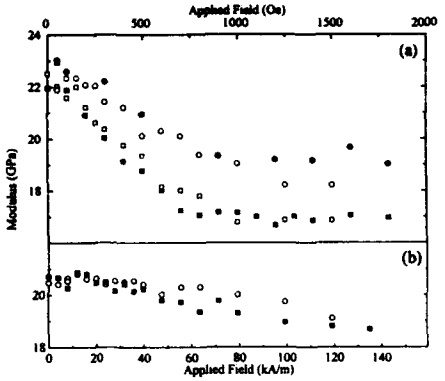

FIG. 4. Elastic moduli at a prestress of 15.5 MPa for (a) the two oriented Terfenol-D composites at constant magnetic field [(■) sample 1, (□) sample 2] and constant magnetic induction [(●) sample 1, (○) sample 2] and (b) the randomly oriented Terfenol-D composite at constant magnetic field (■) and constant magnetic induction (○).

conditions (Y^H) and under fixed magnetic induction (Y^B). From Y^H it is possible to calculate the material coupling factor $k_{33}^2 \equiv (d^2/\mu^\sigma)Y^H$. Here d is the piezomagnetic constant defined by $\delta\lambda/\delta H$ and μ^σ is the permeability at fixed stress (σ) defined by $\mu_{\rm rel}\mu_0 = \mu_0 + \delta M/\delta H$, where $\mu_{\rm rel}$ is the relative permeability, μ_0 is the permeability of free space, M is in units of Teslas, and H is in units of A/m. Alternatively, the coupling can be determined from $1 - k_{33}^2 = Y^H/Y^B$. (The former calculation is generally more accurate whenever $k_{33} < 0.7$ and is employed here.) In Fig. 4 we plot the field dependences of Young's moduli for both composites at 15.5 MPa. The moduli are almost independent of compressive stress ($\sigma < 16.3$ MPa). In Table I are compared the values of $\mu_{\rm rel}$, d, and k_{33} for both composites. Clearly the coupling is much larger for the sample with aligned particles. Both samples have slight maxima near $H = 80$ kA/m.

In Table II we compare the resistivity, density, and some magnetic properties of nickel and Terfenol-D in metallic form and with nonmetallic binders. The density of the

TABLE I. Piezomagnetic properties of composite Terfenol-D.

	H (kA/m)	$\mu_{\rm rel}$	d (nm/A)	Y^H (GPa)	k_{33}
Isotropic composite	40	4.1	3.8	20.2	0.24
	80	2.8	3.7	19.7	0.28
	120	2.2	3.1	19.2	0.26
Anisotropic composite	40	4.0	5.8	19.5	0.36
	80	2.9	5.9	17.0	0.40
	120	2.2	4.8	17.0	0.38

TABLE II. Some physical, electrical, and magnetic properties of nickel, Terfenol-D, and Terfenol-D composites.

	$\delta\times10^{-3}$ (kg/m^3)	$\rho\times10^8$ (Ω m)	T_c (°C)	M_s (T)	$\lambda\times10^6$ at 120 kA/m
Nickel	8.8	7.8	358	0.61	50
Isotropic composite	7.5	30 000	380	0.80	400
Anisotropic composite	6.8	60 000	380	0.71	620
Terfenol-D	9.2	60	380	1.0	1100–1400[a]

[a]Depending on composition.

Terfenol-D composites is ~75% of the densities of nickel and metallic Terfenol-D. The saturation magnetizations are large, having values between those of nickel and metallic Terfenol-D. Most importantly, the magnetostrictions of the composite samples greatly exceed that of nickel by an order of magnitude (~40% of metallic Terfenol-D) while at the same time the electrical resistivity is three orders of magnitude larger. We believe that for the first time giant magnetostrictions can be achieved for frequencies greater than 100 kHz.

V. CONCLUSION

The magnetomechanical properties of these new composite materials, plus their high resistivity make them attractive for high-frequency applications. In spite of a lower density, the anisotropic composite exhibits higher magnetostriction and coupling factor and is therefore preferable for most purposes. This shows the need for magnetic alignment of the Terfenol-D particles. However, there is a considerable potential for improvement of the magnetostriction and the coupling factors since the density, which is rather low, might be increased. But, on the other hand, an increase in the density might give a decrease in the resistivity which can limit the high-frequency performance.

ACKNOWLEDGMENTS

The Swedish part of this work was performed under the sponsorship of NUTEK's New Industrial Metal program. The American part was performed under the Independent Research Program of the U.S. Naval Surface Warfare Center. The Swedish authors thank J.-E. Ståhl for his continued support and A. Maanikhah for his help during sample preparation.

[1] A. E. Clark, AIP Conf. Proc. **18**, 1015 (1974).
[2] M. Fahlander and M. Richardson, Proceedings of the 10th International Workshop on Rare Earth Magnets and Their Applications, Kyoto, Part 1, 1989, p. 289.
[3] L. Sandlund and T. Cedell, in *Transducers for Sonics and Ultrasonics*, edited by M. D. McCollum, B. F. Hamonic, and O. B. Wilson (Technomic, Orlando, 1992), p. 113.
[4] See, for example, A. E. Clark, M. L. Spano, and H. T. Savage, IEEE Trans. Magn. **MAG-19**, 1964 (1983).
[5] R. Abbundi and A. E. Clark, IEEE Trans. Magn. **MAG-13**, 1519 (1977).
[6] A. E. Clark, R. Abbundi, and W. R. Gillmor, IEEE Trans. Magn. **MAG-14**, 542 (1978).

Structure and magnetic properties of mechanically alloyed $SmFe_2$

Clive D. Mitham
Research Centre for Advanced Mineral and Materials Processing, The University of Western Australia, Nedlands WA 6009, Australia

Mechanical alloying has been used to prepare $SmFe_2$ from powdered Sm and Fe. A maximum remanence M_{r_i} of 40.9 emu/g and a maximum coercivity ${}_MH_c$ of 3.09 kOe were measured for samples annealed at 500 and 600 °C, respectively. Above these temperatures both M_{r_i} and ${}_MH_c$ decrease monotonically with increasing grain size. Annealing at temperatures between 500 and 800 °C lead to the formation of second-phase $SmFe_3$ affecting saturation magnetization M_s, which ranges from 55.7 to 61.9 emu/g, and resulted in constriction of the hysteresis curves. Activation volumes v were determined from the results of magnetic viscosity measurements and range from 3.3×10^{-18} to 10.5×10^{-18} cm^3 for samples annealed at 500 and 800 °C, respectively. An estimate of the anisotropy energy coefficient K of 5.6×10^6 ergs/cm for mechanically alloyed $SmFe_2$ was calculated using an estimate of the exchange energy coefficient A and the experimentally determined value of v.

I. INTRODUCTION

Mechanical alloying has been extensively investigated as a method for the synthesis of permanent magnetic materials.[1,2] Research into the production of rare-earth transition metal alloys indicates that not only is mechanical alloying a useful method for materials preparation due to the small number of total production steps compared with other techniques, it also has a pronounced effect on the magnetic properties of such materials. Very high coercivities, remanence enhancement effects, and large energy products have been reported.[3,4]

$SmFe_2$ is one of the highly magnetostrictive RE-Fe_2 compounds which have attracted considerable research interest.[5] Like commercially available anisotropic magnetostrictive alloys, $SmFe_2$ is usually prepared by conventional melting and solidification techniques. In comparison, the mechanical alloying process may prove to be a useful and cost effective method for the production of isotropic polycrystalline magnetostrictive materials. To this end, the effect of post-milling heat treatment on the structure and magnetic properties of mechanically alloyed $SmFe_2$ is reported here.

II. EXPERIMENTAL

Starting materials Sm (99.9%, −40 mesh) and Fe (99.9%, −325 mesh) were sealed in a cylindrical hardened steel vial under an argon atmosphere with ten 12.7-mm-diam hardened steel balls. A 10% excess of Sm was added to limit the formation of phases more iron rich than $SmFe_2$ and a ball to powder mass ratio of 10 was used. The powders were milled for 24 h in a Spex 8000 mixer/mill and after completion toluene was added and the mixture was milled for a further 5 min to increase recovery. As-milled powders were annealed in vacuum-sealed silica tubes for 2 h at temperatures T_a in the range 500–800 °C.

Samples were studied using a Siemens D5000 x-ray diffractometer with monochromatic Cu $K\alpha$ radiation. Magnetic measurements were made at 298 K using a vibrating sample magnetometer in conjunction with a 5 T superconducting solenoid.

Measurement of magnetic viscosity was carried out and the magnetic viscosity coefficient Λ was determined according to a phenomenological theory of magnetization kinetics.[6] Magnetic viscosity is due to thermal activation of domain processes which are responsible for irreversible changes in magnetization. The activation energy barriers over which thermal activation occurs are functions of field and the activation volume v is the fundamental volume swept out as the activation barrier is overcome. v can be related to Λ by the following equation:

$$\Lambda=\frac{kT}{vM_{sp}},$$

where k=Boltzmann's constant and M_{sp}=spontaneous magnetization. Values of v were determined for samples annealed at 500, 600, 700, and 800 °C.

III. RESULTS AND DISCUSSION

The x-ray diffraction (XRD) patterns for the as-milled and heat-treated powders are shown in Fig. 1. The as-milled

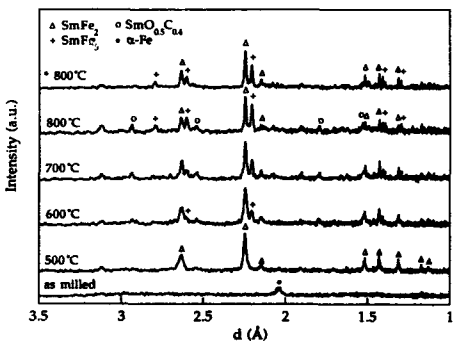

FIG. 1. X-ray diffraction patterns of mechanically alloyed and heat treated $SmFe_2$. (* Sample not milled in toluene.)

 0021-8979/94/75(10)/5659/3/$6.00 © 1994 American Institute of Physics

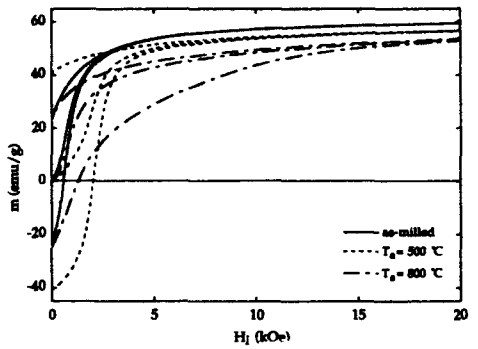

FIG. 2. Hysteresis loops and initial magnetization curves of as-milled and annealed samples.

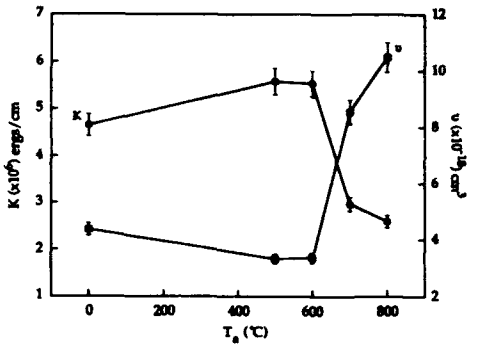

FIG. 4. Average activation volume v and anisotropy energy coefficient K of as-milled (T_a=0 °C) and annealed samples.

powder shows a broad peak corresponding to the major diffraction line of α-Fe. No other phases are present in the diffraction pattern. Annealing for 2 h at 500 °C crystallized the $SmFe_2$ phase and produced large changes in the material's magnetic properties which can be seen in Figs. 2 and 3. Coercivity ${}_M H_c$ was found to more than double from 0.58 to 2.1 kOe with an associated increase in remanence M_{r_i} from 23.5 emu/g to a maximum value of 40.9 emu/g.

Saturation magnetization M_s remains relatively unaffected by the annealing treatment and ranges from a maximum value of 61.9 emu/g for the as-milled powder to a minimum of 55.7 emu/g for the sample annealed at 700 °C. This compares favorably with the value of M_s=59.7 emu/g reported for $SmFe_2$ by Dublon *et al.*[7] While the variation in M_s is slight, the effect of annealing on phase formation is significant. Annealing enables the free α-Fe present in the as-milled powder to combine to form the $SmFe_2$ phase thereby lowering M_s slightly. Loss of Sm by vaporization for $T_a \geq 600$ °C leads to the formation of $SmFe_3$ as a second phase. $SmFe_3$ possesses an M_{sp} much larger than that of $SmFe_2$ (Ref. 8) and consequently M_s increases with increasing $SmFe_3$ concentration as T_a is raised to 800 °C.

Annealing at 600 °C produced the largest coercivity, ${}_M H_c$=3.09 kOe. ${}_M H_c$ was found to then decrease monotonically with increasing T_a and this can be attributed to the increase in grain size. As a result ${}_M H_c$ decreases with the decreasing density of centers impeding magnetization reversal. This is evident in the changing shape of the initial magnetization curves in Fig. 2.

The XRD pattern indicates that a small proportion of SmO-C phase[9] formed as a result of the brief milling in toluene. The diffraction pattern of a sample mechanically alloyed without toluene and annealed at 800 °C showed the same crystalline structure without the presence of the SmO-C phase. Magnetic properties were not significantly affected by its presence nor did its inclusion affect magnetization mechanisms.

When the as-milled material containing a 10% excess of Sm is annealed above its eutectic temperature of 720 °C (Ref. 10) liquid Sm is expected to form. The high concentration of $SmFe_3$ indicated by XRD did not result in a large change in the saturation magnetization of the bulk material indicating that the 1:3 phase tends to form at the surface of the sample where preferential loss of Sm results from vaporization. While the amount of $SmFe_3$ in the bulk material remains small, complex two phase magnetic behavior results and the hysteresis loops become increasingly constricted as T_a increases. Two phase magnetic behavior was also indicated by a second maxima in the intrinsic irreversible susceptibility χ^i_{irr} at an applied field of ~ -10 kOe which is close to the reported coercivity of mechanically alloyed $SmFe_3$.[11] Demagnetization processes become less reversible with increasing $SmFe_3$ concentration and remanence decreases accordingly.

Activation volumes determined from magnetic viscosity measurements are plotted against T_a in Fig. 4. The activation volume for the as-milled material is 4.4×10^{-18} cm^3. Annealing at 500 °C decreases v to 3.3×10^{-18} cm^3. This may be due to microstructural changes in the bulk material which cannot be confirmed without detailed microstructural infor-

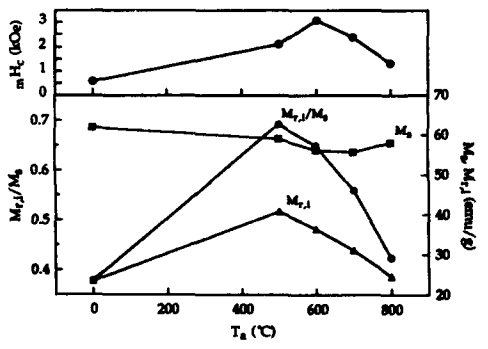

FIG. 3. Magnetic properties of as-milled (T_a=0 °C) and annealed samples.

mation. v changes little for $T_a \leq 600$ °C but as the amount of second-phase $SmFe_3$ is increased by annealing at higher temperatures, v increases considerably to a value of 10.5×10^{-18} cm^3 at 800 °C. The magnitude of v is very similar to that reported for $DyFe_2$ prepared by mechanochemical reduction[12] and is estimated to be an order of magnitude less than that of bulk $Tb_{0.27}Dy_{0.73}Fe_2$ at room temperature.[13] This suggests that the microstructure arising from preparation by mechanical alloying may have a considerable effect on the mechanisms responsible for magnetization in these materials. Further study is required to confirm this.

The activation volume of a ferromagnetic material can be related to the domain wall thickness δ by $\delta^3 = v$.[14] This relationship and the expression for δ of a ferromagnetic material with a simple cubic crystal structure $\delta \sim \pi\sqrt{A/K}$ were used to provide an estimate of the first anisotropy energy coefficient K for $SmFe_2$. A value for the exchange energy coefficient $A = 1.26\times10^{-6}$ erg/cm was estimated from the Curie temperature $T_c = 675$ K and lattice parameter $a = 7.417$ Å (Ref. 9) using the expression $A = (kT_c)/a$. The estimated variation in anisotropy energy for the samples studied is plotted in Fig. 4 which gives an estimate of $K = 5.6\times10^6$ ergs/cm for mechanically alloyed and heat treated $SmFe_2$. The estimated domain wall thickness for a sample annealed at 500 °C is ~15 nm which, when compared to an average crystallite size determined by transmission electron microscopy (TEM) of 80 nm, indicates that these materials are multidomain.

IV. CONCLUSIONS

The preparation of single-phase $SmFe_2$ by mechanical alloying is dependent upon post-milling annealing conditions. Some $SmFe_3$ crystallizes in the material and is thought to form by preferential loss of Sm at the sample surface despite the addition of Sm in excess of stoichiometric requirements. M_s remains unaffected by the formation of $SmFe_3$ indicating that it is only present as a minor phase. The concentration of $SmFe_3$ increases with annealing temperature and gives rise to two phase magnetic behavior which manifests itself in constriction of the hysteresis loop and a second maxima in χ^i_{irr} at a field corresponding to the coercivity of the harder $SmFe_3$ phase. Annealing at 600 °C produces a maximum ${}_M H_c = 3.09$ kOe which then decreases monotonically with increasing annealing temperature. This decrease in ${}_M H_c$ correlates with the increase in grain size brought about by annealing at higher temperatures. Annealing at 500 °C produced a maximum value of $M_{r,i} = 40.9$ emu/g with a corresponding $M_{r,i}/M_s = 0.69$. Demagnetization was found to become less reversible with increasing $SmFe_3$ concentration and as a result $M_{r,i}$ decreases with increasing T_a.

Activation volumes ranging from 3.3×10^{-18} cm^3 for a sample annealed at 500 °C to 10.5×10^{-18} cm^3 for a sample annealed at 800 °C were determined from the results of magnetic viscosity tests. The magnitude of v is similar to that of $DyFe_2$ prepared by mechanochemical reaction and an order of magnitude less than that of bulk $Tb_{0.27}Dy_{0.73}Fe_2$. This suggests that similar magnetization mechanisms develop in Laves phase rare-earth iron alloys prepared by mechanical alloying. The anisotropy energy coefficient K of $SmFe_2$ prepared by mechanical alloying is estimated to be of the order of 5.6×10^6 ergs/cm.

Measurement of the magnetostriction of mechanically alloyed materials is currently in progress.

ACKNOWLEDGMENT

I would like to thank L. Folks for use of the software developed to analyze the results of magnetic viscosity tests.

[1] L. Schultz, K. Schnitzke, and J. Wecker, J. Magn. Magn. Mater. **80**, 115 (1989).
[2] J. Ding, P. G. McCormick, and R. Street, J. Alloys Comp. **191**, 197 (1993).
[3] Yinong Liu, M. P. Dallimore, P. G. McCormick, and T. Alonso, J. Magn. Magn. Mater. **116**, L320 (1992).
[4] J. Ding, P. G. McCormick, and R. Street, J. Magn. Magn. Mater. **124**, L1 (1993).
[5] A. E. Clark, in *Ferromagnetic Materials*, edited by E. P. Wohlfarth (North Holland, Amsterdam, 1980), Vol. 1, p. 531.
[6] Y. Estrin, P. G. McCormick, and R. Street, J. Phys. **1**, 4845 (1989).
[7] G. Dublon, M. P. Dariel, and U. Atzmony, Phys. Lett. **51A**, 262 (1975).
[8] K. H. J. Buschow, in *Ferromagnetic Materials*, edited by E. P. Wohlfarth (North Holland, Amsterdam, 1980), Vol. 1, p. 297.
[9] J. M. Haschke, Inorg. Chem. **19**, 527 (1980).
[10] K. H. J. Buschow, J. Less Common Met. **25**, 131 (1971).
[11] J. Wecker, M. Katter, K. Schnitzke, and L. Schultz, J. Appl. Phys. **69**, 5847 (1991).
[12] C. D. Milham, First International Conference on Processing Materials for Properties, Honolulu, Hawaii 1993, TMS (to be published).
[13] L. Folks, C. D. Milham, and R. Street, Proceedings of the 7th International Symposium on Magn. Anisotropy and Coercivity in Rare-Earth Transition Metal Alloys, Canberra, 1992, p. 274.
[14] D. Givord, P. Tenaud, T. Viadieu, and G. Hadjipanayis, J. Appl. Phys. **61**, 3454 (1987).

High pulsed field magnetostriction in RMn_2 (R=Gd, Tb, Nd, and Y)

M. R. Ibarra, C. Marquina, L. Garcia-Orza, Z. Arnold,[a] and A. del Moral
Departamento de Física de la Materia Condensada c, Instituto de Ciencia de Materiales de Aragón, Universidad de Zaragoza-CSIC, 50009-Zaragoza, Spain

We have performed thermal expansion and magnetostriction experiments on several compounds of the series RMn_2 and $R(Mn_{1-x}Ni_x)_2$ (R=Nd, Gd, Tb, and Y) using high pulsed magnetic field up to 15 T in the temperature range 4–300 K. A giant volume magnetostriction of $\omega=-17\times10^{-3}$ was observed in $TbMn_2$ at 15 T and 4 K. A negligible forced volume magnetostriction was observed in YMn_2. In $GdMn_2$ paramagnetic magnetostrictive behavior was found below T_N. Magnetostriction experiments were confirmed as a powerful tool in order to determine the stability of the magnetic moment on Mn in this series of compounds.

The compounds RMn_2 crystallize in the Laves phases structures. Either in the hexagonal $C14$ phase or in the cubic $C15$ depending of the rare-earth ion. Large jumps observed in the thermal expansion are associated with the appearance of a local magnetic moment on the manganese atoms (μ_{Mn})[1] at T_N for R=Pr, Nd, Sm, Gd, Tb, and Y. Recent studies using neutron diffraction techniques established the existence of two magnetic phases below T_N in $TbMn_2$ (Ref. 2) and the nonhomogeneous destabilization of the μ_{Mn} under pressure.[3] Low-field ac susceptibility measurements under pressure and magnetostriction in $GdMn_2$ (Ref. 4) indicated a paramagnetic behavior of the Gd ion below T_N. The observed magnetic and magnetostrictive behaviors could be explained on the hypothesis of the coexistence of two phases below T_N. A transformed phase (TP), which transforms at T_N, is responsible for the large spontaneous magnetovolume effect. In this phase $\mu_{Mn}\neq0$. The other phase no-transformed phase (NTP) does not present a structural transformation at T_N. In this phase μ_{Mn} is either zero or it is induced in some crystallographic sites on the Mn by the molecular field produced by the ordered R sublattice as observed in $DyMn_2$.[5] A further systematic study of the magnetic susceptibility under pressure on $GdMn_2$ and $TbMn_2$ (Ref. 6) gave support to this hypothesis in order to explain the experimental results. In the present paper we report magnetostriction measurements up to 15 T and thermal expansion measurements either under applied magnetic field or under induced chemical pressure.

We have studied the compounds RMn_2 with R=Gd, Tb, Nd, and Y, and the pseudobinary $R(Mn_{1-x}Ni_x)_2$ for (R=Y and Gd). The samples were prepared by the standard arc melting technique as explained in these proceedings (Ibarra *et al.*[6]). Thermal expansion and magnetostriction were measured in the range of temperature 4–300 K using the strain gage technique and either steady magnetic field up to 12 T or pulsed magnetic field up to 15 T. The anisotropic ($\lambda_t=\lambda_\parallel-\lambda_\perp$) and volume ($\omega=\lambda_\parallel+2\lambda_\perp$) magnetostrictions were obtained from the measurement of the parallel ($\lambda_\parallel$) and perpendicular ($\lambda_\perp$) magnetostrictions.

There is a well-established large magnetovolume effect at T_N~60–90 K on cooling with a large thermal hysteresis (~10–30 K depending on the sample internal stress and method of measurement). Either the applied or chemical pressures have a strong influence on the magnetic and structural properties of this compound. In fact, an applied pressure of 3 kbar can completely suppress the structural transformation in this compound. We performed thermal expansion measurements in YMn_2 under a steady magnetic field of 12 T and the sample was destroyed at T_N as a consequence of the large spontaneous magnetovolume effect, which is not affected by the existence of the high applied magnetic field. In Fig. 1 we display the spontaneous thermal expansion of the pseudobinary $Y(Mn_{0.99}Ni_{0.01})_2$ and also under an applied field of 12 T. The observed forced volume magnetostriction was negligible ($\omega<10^{-6}$).[7] This result constitutes a clear evidence that the μ_{Mn} is stable under such a field and also the absence of any contribution to the magnetostriction from the Mn ordered sublattice.

Thermal expansion measurements in this compound under an applied magnetic field up to 1.5 T and in the pseudobinary compounds $Gd(Mn_{1-x}Ni_x)_2$ were performed in order to determine the effect of the chemical pressure on T_N and also to test the influence either of the pressure or the applied magnetic field on the low-temperature magnetic phase (within the NTP phase[4,6]). In Fig. 2 we display the thermal expansion results on the substituted compounds for different Ni concentrations. From these results we can observe for x=0 a large volume anomaly associated with the first order transition at T_N~104 K and an other small anomaly at T_c~35–40 K which can be associated with the magnetic

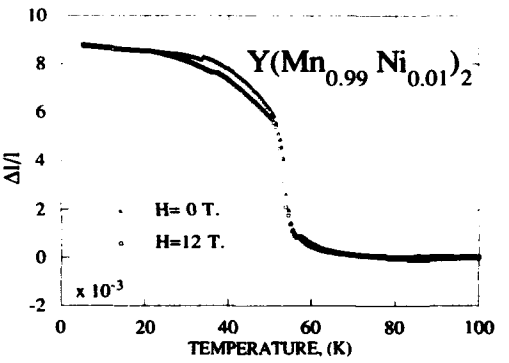

FIG. 1. Thermal expansion of $Y(Mn_{0.09}Ni_{0.01})_2$ without and under and applied magnetic field of 12 T.

[a]Permanent address: Institute of Physics, Czech Academy of Sciences, Cukrovarnicka 10, 162 00 Praha 6, Czech Republic.

 0021-8979/94/75(10)/5662/3/$6.00 © 1994 American Institute of Physics

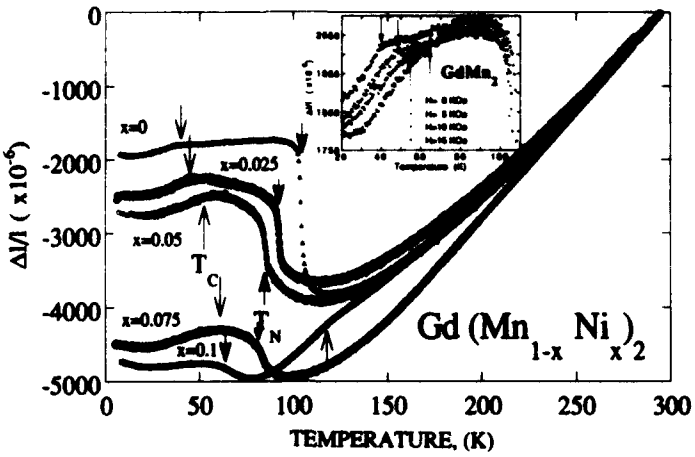

FIG. 2. Thermal expansion in $Gd(Mn_{1-x}Ni_x)_2$. Inset: field dependence of thermal expansion in $GdMn_2$ at low temperatures.

ordering within the NTP. The increase of the Ni concentration is considered only as an increase of chemical pressure due to the different atomic radii of the Mn and Ni atoms. In fact, we observed a decrease of the T_N for increase x values in good agreement with the pressure effect on magnetization.[8] We also observed an increase of T_c with concentration as it was observed in ac susceptibility under pressure experiments.[4] These experiments confirmed the localization of the μ_{Mn} in the ordered regime ($T_N < T_c$ for $x=0.1$). The decreasing value of the anomaly associated with T_N as x increases can be understood considering the effect of pressure which can limit the volume of the TP below the first order transformation occurring at T_N.

The study of the thermal expansion under an applied magnetic field up to 1.5 T revealed that T_N was not affected by this field. However, T_c increases with field (see inset Fig. 2). These results confirmed that the effect of the applied magnetic field on T_c is similar to that found under applied pressure.[4,6]

The obtained forced volume magnetostriction ω ($=3\lambda_{\parallel}=3\lambda_{\perp}$) is represented in Fig. 3 at several selected temperatures. A large increase of ω is observed in the neighborhood of T_N. This behavior was attributed to the anomalous behavior of the elastic constant due to the softening of the phonon modes that we can expect at the first order structural transformation at T_N (Ref. 4 for more details). In the tem-

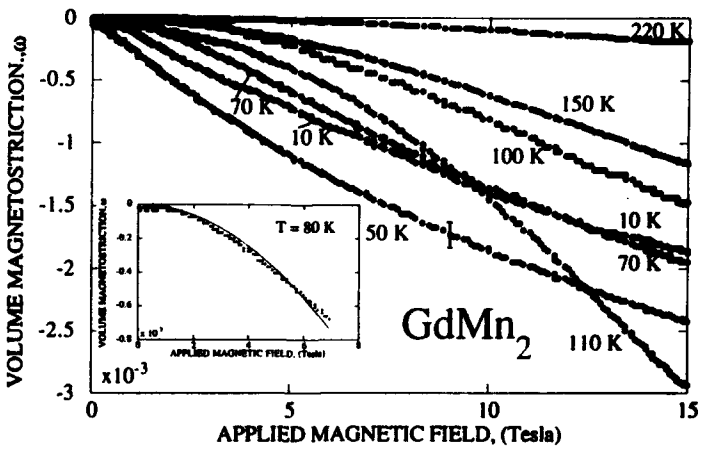

FIG. 3. Forced volume magnetostriction in $GdMn_2$. Inset: quadratic field fit of ω at 80 K (see text).

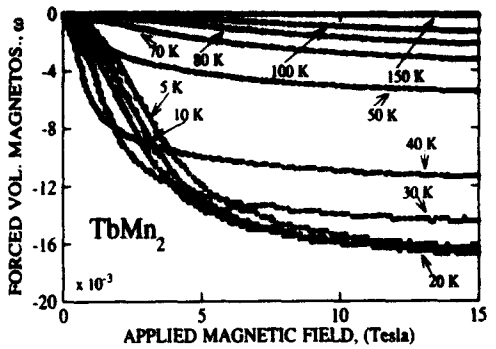

FIG. 4. Forced volume magnetostriction in $TbMn_2$.

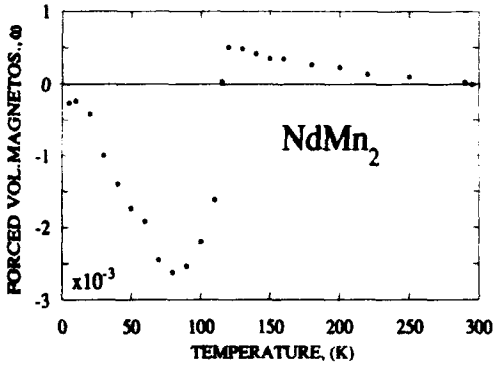

FIG. 5. Thermal dependence of ω at 15 T in $NdMn_2$.

perature range 50–100 K we can observe a quadratic behavior of the magnetostriction up to 6 T (see inset Fig. 3). This magnetostriction is attributed to the paramagnetic Gd ions in the NTP.[4] We cannot expect a magnetostrictive contribution from the TP phase on the basis of an antiferromagnetic ordering and the lack of magnetostriction in YMn_2 up to 15 T.

A detailed study of the magnetostrictive behavior of this compound was given by Ibarra *et al.*[9] A large thermal expansion anomaly was observed at $T_N \sim 45$ K. Below this temperature a local μ_{Mn} appears. Neutron diffraction experiments revealed the existence of two magnetic phases, which coexist at low temperatures.[2] The collinear antiferromagnetic S_1 phase in which $\mu_{Mn} \neq 0$ and the S_2 ($DyMn_2$ like structure) in which $\mu_{Mn} = 0$ (except some Mn atoms, which present a induced magnetic moment).[5] A large anomaly was found in thermal expansion at T_N. The volume magnetostriction of this compound is represented in Fig. 4. The high-field low-temperature value is the largest ever observed magnetostriction ($\omega = -17 \times 10^{-3}$ at 4 K and 15 T). This large magnetovolume effect can be explained on the basis of the instability of the TP under an applied magnetic field. These results confirmed the destabilization of the μ_{Mn} under field observed in neutron diffraction experiments.[2] The magnetostriction measurements show that the TP is transformed into the NTP when the magnetic field increases; as a consequence, the sample volume is reduced resulting in a huge volume magnetostriction. The equivalent value of ω at high field and the observed spontaneous distortion $[\omega_0 = 3 \times (\Delta l/l) = -\omega]$ confirmed the former conclusion. We also performed thermal expansion measurements under a high steady magnetic field.[10] These results showed the absence of the structural transformation under field higher than 5 T and made magnetostriction an excellent tool in order to test the stability of the TP under an applied magnetic field in $TbMn_2$.

Thermal expansion measurements performed on this compound showed a large volume expansion of 0.9% at $T_N \sim 104$ K. We performed magnetostriction measurements up to 15 T in the temperature range 4–300 K. In Fig. 5 we display the thermal dependence of ω at 15 T. A large increase of the negative value of ω is observed at T_N. However, the field dependence of the ω isotherms was observed to be the same above and below T_N. We attribute, as in the case of the $GdMn_2$, this large increase to an anomalous behavior of the elastic constants as a consequence of the possible softening of the phonon modes at T_N. A more detailed report of these results will be published elsewhere.[11] As a general result we should mention the large hysteresis observed in the magnetostriction isotherms at temperatures below the structural transformation. The effect of the field is transduced in a remanent magnetostriction which results in a reduction of 0.4% in the volume of the sample. Increasing the temperature we observed a spontaneous contraction of 0.5% instead of the 0.9% observed when the sample is not subjected to the action of an applied magnetic field. As a consequence of these results we cannot exclude the effect of the magnetic field on the stability of μ_{Mn} in this compound.

We can conclude that magnetostriction measurements are quite valuable in order to obtain information on the nature of the different magnetic phases in $R\,Mn_2$ and constitute the best and easiest test for the stability of the μ_{Mn} under an applied magnetic field in these compounds.

[1] M. Shiga, Physica B **149**, 293 (1988).
[2] P. J. Brown, B. Ouladdiaf, R. Ballou, J. Deportes, and A. S. Markosyan, J. Phys. **4**, 1103 (1992).
[3] S. Moudal, R. Ciwinsky, S. H. Kilcoyne, B. D. Rainford, and C. Ritter, Physica B **180-181**, 108 (1992).
[4] M. R. Ibarra, C. Marquina, L. García-Orza, Z. Arnold, and A. del Moral, J. Magn. Magn. Mater. **228**, L249 (1993).
[5] C. Ritter, S. H. Kilcoyne, and R. Ciwinski, J. Phys. **3**, 727 (1991).
[6] M. R. Ibarra, Z. Arnold, C. Marquina, L. Garciá-Orza, and A. del Moral (these proceedings).
[7] M. R. Ibarra, L. Garcia-Orza, and A. del Moral, Solid State Commun. **84**, 875 (1992).
[8] J. Voiron, R. Ballou, J. Deportes, R. M. Galera, and E. Lelievre, J. Appl. Phys. **69**, 5678 (1991).
[9] M. R. Ibarra, C. Marquina, L. García-Orza, and A. del Moral, Solid State Commun. **87**, 695 (1993).
[10] M. R. Ibarra, C. Marquina, C. de la Puente, and del Moral (unpublished).
[11] C. Marquina, M. R. Ibarra, L. Garcia-Orza, and A. del Moral (unpublished).

An ultrasonic study of the Néel transition in dilute Cr-Al alloy single crystals

H. L. Alberts
Department of Physics, Rand Afrikaans University, P. O. Box 524, Auckland Park, Johannesburg 2006, South Africa

Measurements are reported of the temperature variation of the sound velocity and ultrasonic attenuation coefficient of Cr-Al alloy single crystals containing 1.2, 1.9, and 2.6 at % Al. The results close to the Néel temperature are not satisfied by existing theories for the critical behavior of itinerant electron antiferromagnets.

I. INTRODUCTION

The incommensurate (I) spin density wave (SDW) to paramagnetic (P) transition at the Néel temperature (T_N) of pure Cr is weakly first order, making the application of existing theories for the critical behaviour near T_N strictly speaking not valid. The order as well as the nature of the transition at T_N are, however, modified by alloying Cr with other elements to form dilute solid solutions. For some impurities the first-order transition is changed to a second-order one and the ISDW-P transition to a commensurate (C) SDW-P transition. It was recently observed,[1] using neutron diffraction techniques, that the transition at T_N in Cr-Al alloys containing 1.2, 1.9, and 2.6 at % Al is of the second order, being an ISDW-P transition in the first two alloys and a CSDW-P transition in the 2.6 at % Al alloy. Cr-Al alloys with these Al concentrations are therefore ideally suited to test theoretical predictions for the contributions of critical fluctuations to the ultrasonic attenuation coefficient (α) and the longitudinal velocity of sound (v_L) near T_N for both types of transitions. We report here measurements of α and v_L as a function of temperature through T_N for Cr-Al alloy single crystals, containing 1.2, 1.9, and 2.6 at % Al. The data are analyzed in terms of the theoretical predictions of Maki and Nakanishi[2] and Sato and Maki[3] that are valid for second-order CSDW-P and ISDW-P transitions.

II. EXPERIMENTAL

The single crystals, containing 1.2, 1.9, and 2.6 at % Al, are the same crystals previously used[1] in magnetoelastic and neutron diffraction studies. In the present study the pulse-echo-overlap technique[4] has been used to obtain ultrasonic velocities and ultrasonic attenuation coefficients. The phase comparison method used in the previous study[1] on the magnetoelastic properties of these crystals, do not allow for attenuation measurements and has a sensitivity of only 1 in 10^3 for velocity changes with temperature, compared to 1 in 10^5 for the pulse-echo-overlap technique. X-cut 10 MHz quarts transducers were bonded to the crystals with Araldite epoxy resin to generate longitudinal waves propagating along the [100] or [110] crystallographic directions.

III. RESULTS AND DISCUSSION

Figure 1 shows the temperature dependence of v_L for the three crystals and Fig. 2 that of α for Cr+1.2 at % Al. The ISDW-P transition in the Cr+1.2 at % Al crystal is characterized by a sharp attenuation peak of width at half amplitude of about 3 K, occurring at 217.4 K (Fig. 2). We do not know the reason for the small shoulder on the α-T curve observed in Fig. 2 at 214 K for this crystal, but note that it is not reflected on the v_L-T curve of this alloy [Fig. 1(a)]. Difficulties were encountered near T_N in measuring α for the other two crystals and we do not give α-T graphs for them. Away from the transition region the pulse-echo trains of the two crystals containing 1.9 and 2.6 at % Al showed normal exponential decay. However, the pulse-echo train developed a distinctive interference pattern in the transition region close to T_N. This interference pattern is temperature dependent, making α measurements close to T_N in these two crystals to a certain extent unreliable. Similar effects were previously also encountered[5] in a Cr-Ru single crystal and may be at-

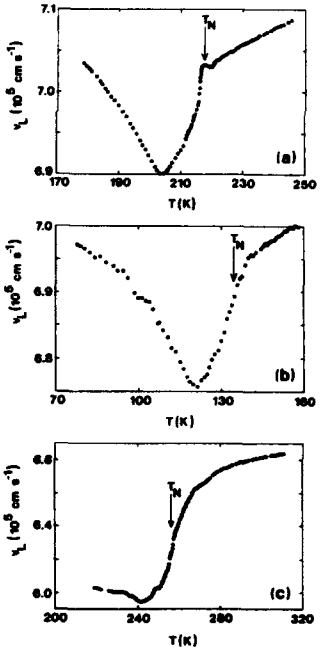

FIG. 1. Temperature dependence of the longitudinal sound velocity (v_L) for (a) Cr+1.2 at % Al along [100], (b) Cr+1.9 at % Al along [100], and (c) Cr+2.6 at % Al along [110].

 0021-8979/94/75(10)/5665/2/$6.00 © 1994 American Institute of Physics

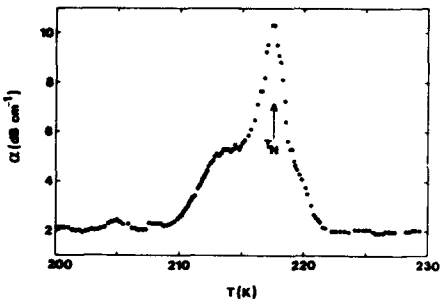

FIG. 2. Temperature dependence of the ultrasonic attenuation coefficient (α) for Cr+1.2 at % Al for wave propagation along [100].

tributed to macroscopic ISDW and P domains, due to slight sample inhomogeneities, that coexist near T_N in Cr+1.9 at % Al and Cr+2.6 at % Al. Notwithstanding the difficulties with interference effects near T_N, the following observations could, however, be made for these two crystals: Firstly, α shows a peak centered around (132±4) K for Cr+1.9 at % Al and around (255±5) K for Cr+2.6 at % Al. Secondly, for both Cr+1.9 at % Al and Cr+2.6 at % Al, α is larger in the SDW state than in the P state away from the transition where the interference effects are absent. For Cr+1.9 at % Al, for which the transition at T_N is an ISDW-P transition, α(ISDW) $\sim 6\alpha$(P) and for Cr+2.6 at % Al with a CSDW phase at $T<T_N$, α(CSDW)$\sim 2\alpha$(P). The intereference effects were absent for Cr+1.2 at % Al.

The α-T curves show peaks at (217.6±0.3) K, (132±4) K, and (255±5) K, respectively, for Cr+1.2 at % Al, Cr+1.9 at % Al, and Cr+2.6 at % Al. These temperatures correspond well with values of T_N equal to 219, 134, and 256 K, determined[1] respectively for these three crystals using neutron diffraction techniques. The temperatures at the peak in α is thus taken as T_N. T_N is about 13 K above the temperature of the deep minimum observed on the v_L-T curves for Cr +1.2 at % Al and Cr+1.9 at % Al and also about 13 K above the weaker minimum at 242 K for Cr+2.6 at % Al. For the Cr+1.2 at % Al crystal the peak on the α-T curve coincides nearly exactly with the temperature 217.6 K at the small peak on the v_L-T curve (see Figs. 1 and 2). In the case of the other two crystals, T_N lies at the inflection point occurring above the minimum of their v_L-T curves. The small peak at T_N on the v_L-T curve of Cr+1.2 at % Al was not observed in the previous[1] magnetoelastic measurements. This is probably due to the fact that data were recorded previously[1] only every 2–3 K, compared to the present study in which data were recorded at about 0.3 K intervals near T_N. Furthermore, the v_L-T curve of Fig. 1 for Cr+1.2 at % Al does not show the discontinuous jump previously observed[1] for the elastic constant c_{11} at T_N. Instead, the present measurements show a continuous transition at T_N for this crystal as is also observed in the neutron diffraction measurements.[1]

Maki and Nakanishi[2] used a two-band model in which the electron and hole Fermi surface sheets are spherical but of different sizes, to calculate the effects of critical fluctuations on α and v_L for itinerant electron antiferromagnets like Cr and its dilute alloys. They further assumed $ql \gg 1$, where q is the wave vector of the sound wave and l the electronic mean-free path, and found that α for longitudinal sound waves diverges near T_N as $\eta^{-3/2}$, where $\eta = |1 - T/T_N|$, for a transition from the P phase to the CSDW phase (as in Cr +2.6 at % Al) and like $\eta^{-5/2}$ for a P-ISDW transition (as in Cr+1.2 at % Al and Cr+1.9 at % Al).

For v_L they predicted a sharp dip at T_N diverging as $\eta^{-1/2}$ for a P-CSDW transition and as $\eta^{-3/2}$ for a P-ISDW one. Sato and Maki[3] did the same type of calculations but considered the electron and hole Fermi surface sheets to be octahedral in shape instead of spherical. In the limit $ql \ll 1$, which should correspond better[3] with the experimental situation, they obtained a $\eta^{-1/2}$ divergence near T_N for α in a P-ISDW transition while the divergence is negligible for a P-CSDW transition. In the case of v_L they found no divergence for both the P-CSDW and P-ISDW transitions at T_N.

The predictions of Sato and Maki[3] do not satisfy the experimental observations for the v_L-T curves of Fig. 1. This is also the case for the predictions of the theory by Maki and Nakanishi,[2] who predict a dip in the v_L-T curve at T_N with the divergences as described above. Although the experiment does indeed give a dip in the v_L-T curves, it only appears about 13 K below T_N. There is no $\eta^{-1/2}$ or $\eta^{-3/2}$ divergence near the observed T_N.

Plots of $\ln(\alpha/\alpha_0 - 1)$ vs $\ln|(1 - T/T_N)|$ for the Cr+1.2 at % Al crystal were found to be straight lines for $T > T_N$ (from 217.6 to 220.6 K) and $T < T_N$ (from 212.1 to 217.1 K), suggesting that $\alpha = \alpha_0 + b|(1 - T/T_N)|^{\gamma}$ with α_0 and b constants, fits the experimental results well close to T_N. For this crystal we obtain $\gamma_- = -(0.34 \pm 0.03)$ for $T < T_N$ and $\gamma_+ = -(1.1 \pm 0.1)$ for $T > T_N$. The value of γ_- is very similar to the value $\gamma_- = -(0.28 \pm 0.05)$ obtained by de Camargo *et al.*[6] for a Cr+0.5 at % V crystal that also has an ISDW state at $T < T_N$. The value of γ_+ do not compare too well with $\gamma_+ = -2.5$ predicted by Maki and Nakanishi[2] and also not with the value $\gamma_+ = -0.5$ predicted by Sato and Maki[3] for this transition.

In conclusion, the temperature dependences of the velocity of sound and ultrasonic attenuation coefficient near T_N of Cr-Al alloy single crystals are not satisfied by existing theories. The measurements reported here were done on poly-Q single crystals, consisting each of three possible Q domains, where the SDW Q vector is along a different cube axis in each domain. To resolve the discrepancy between experiment and theory found above, measurements should also be done on single-Q Cr-Al crystals, containing only one Q domain with the SDW Q vector directed along a chosen cubic axis. It is, however, presently not known how to prepare such a state in the Cr-Al alloys. This is a problem for future study.

[1] A. Baran, H. L. Alberts, A. M. Strydom, and P. de V. du Plessis, Phys. Rev. B **45**, 10473 (1992).
[2] K. Maki and K. Nakanishi, J. Low-Temp. Phys. **6**, 141 (1972).
[3] H. Sato and K. Maki, Int. J. Magn. **4**, 163 (1973).
[4] E. P. Papadakis, in *Physical Acoustics*, Vol. XII, edited by W. P. Mason and R. N. Thurston (Academic, New York, 1976).
[5] M. Cankurtaran, G. A. Saunders, Q. Wang, P. J. Ford, and H. L. Alberts, Phys. Rev. B **46**, 14370 (1992).
[6] P. C. de Camargo, E. Fawcett, and J. M. Perz, J. Appl. Phys. **67**, 5265 (1990).

Magnetostriction of polycrystalline Co-Pd alloys

S. U. Jen and B. L. Chao
Institute of Physics, Academia Sinica, Taipei, Taiwan 11529, China

Magnetostriction of polycrystalline $Co_{100-x}Pd_x$ alloys was measured by the strain gauge method from 4 to 300 K. The saturation magnetostriction $\lambda_s=(2/3)[(\Delta L/L)_{\parallel}^s-(\Delta L/L)_{\perp}^s]$, where $(\Delta L/L)_{\parallel}^s$ and $(\Delta L/L)_{\perp}^s$ are the saturated values (when $H_E>5$ kG) of $\Delta L/L$ in fields parallel and perpendicular to sample's length (L). λ_s at 4 K is found to change sign from positive to negative value as x is increased from below $x_0=50$ at. % Pd to above. This phenomenon can be understood from the split-band theory for Co-Pd alloy. However, since some experimental facts indicate that unquenched orbital moments may exist in the $x>50$ at. % Pd alloys it is necessary to consider $\lambda_s=\lambda_s^{band}+\lambda_s^{ion}$, where λ_s^{band} is due to the split-band theory and λ_s^{ion} is from the one-ion mechanism. Under this proposal, it is possible to explain why λ_s(4 K) is not antisymmetric with respect to x_0. Finally, two different origins of temperature dependence of λ_s are discussed.

I. INTRODUCTION

In the past, magnetocrystalline anisotropy and magnetostriction of Co-Pd single crystals have been measured along the ⟨100⟩ and ⟨111⟩ axes.[1–3] The temperature range of the measurements was from 77 to 300 K. By plotting $h_1=3/2\lambda_{100}$ and $h_2=3/2\lambda_{111}$ as a function of the reduced temperature T/T_C, where T_C is the Curie temperature, they obtained h_1 and h_2 values at 0 K by extrapolation method.

In this paper, we report saturation magnetostriction data λ_s of polycrystalline $Co_{100-x}Pd_x$ samples as a function of x at 4 K, and their temperature dependence from 4 to 300 K. In addition, since λ_{100} and λ_{111} are known, it is possible to test the empirical formula for averaged $\bar{\lambda}_s$ (Ref. 4)

$$\bar{\lambda}_s=\alpha\lambda_{100}+(1-\alpha)\lambda_{111} \tag{1}$$

and to see whether α is equal to 2/5. In Eq. (1), a polycrystalline aggregate of cubic materials is assumed.

II. EXPERIMENTS

A series of $Co_{100-x}Pd_x$ alloys have been made previously.[5] In order to fit the sizes of strain gauges used, each sample was cut in the form of $1.0\times0.4\times0.06$ cm^3 from an ingot. No further heat treatment was made. We have checked the room temperature resistivities of these samples, and they agree with our earlier results quite well.

Magnetostriction was measured with a Karma-alloy type strain gauge (WK-06-062AP-350), purchased from Measurements Group company. This kind of gauge is best suited for the strain measurements in the low-temperature and high magnetic-field environment. The gauge was glued to each sample along the long axis with an M-600 bond. The glue was cured at $T=110$ °C for 2 h. Then, the sample was glued to the tips of two phosphorus-bronze strips with Duco Cement. The strips are flexible to move in the direction of longitudinal magnetic field, but at the same time they minimize other motions, including rotations, of the sample in magnetic field; the other ends of the strips are simply bolted on the tip of a sample holder. The sample-holder rod is inserted into a CF1200 cryostat, which is fitted in the gap of a 7 in. electromagnet. The temperature can be varied from 4 to 300 K by using an ITC4 temperature controller. On the sample holder, very near to the sample, we have placed another "identical" dummy gauge with the same orientation as that of the active gauge. The active and the dummy gauges form two arms of a half-bridge circuit. Then, with an excitation voltage of 2–3 V applied to the bridge, we can read the strain value directly from the model 3800 strain indicator.

An uniform strain cantilever beam was made to check the gauge factor F of the WK gauge at room temperature.[6] By setting $F=2.02$, supplied by the manufacturer, we find that the ratio of calculated strain $\epsilon=(\Delta y)t/l^2$, where Δy is the deflection of the free end, t is the thickness, and l is the length of the beam, to measured strain $\Delta L/L$ is about 95%. We did not investigate the temperature variation of gauge factor. However, Ref. 6 has already plotted the temperature dependence curve of F for the Karma type strain gauges. The maximal percentage change in F is only about 4% from 300 down to 4 K. With the characteristic F-factor curve known, it is possible to determine the gauge factor value at any temperature between 4 and 300 K.

The sample was first cooled down all the way to 4 K. When temperature reaches a steady value, we started to measure the changes of strain, $(\Delta L/L)_{\parallel}$ and $(\Delta L/L)_{\perp}$, with the fields in sample's plane, and parallel and perpendicular to the sample's long axis, respectively. Two typical $(\Delta L/L)_{\parallel}$ and $(\Delta L/L)_{\perp}$ curves as a function of external magnetic field H_E are plotted in Fig. 1. When $H_E>5$ kG, $(\Delta L/L)_{\parallel}$ and $(\Delta L/L)_{\perp}$ will approach the saturated values $(\Delta L/L)_{\parallel}^s$ and $(\Delta L/L)_{\perp}^s$, respectively. By definition, the linear magnetostriction at saturation for polycrystalline samples is[7]

$$\lambda_s=(2/3)[(\Delta L/L)_{\parallel}^s-(\Delta L/L)_{\perp}^s]. \tag{2}$$

Then, the sample's temperature was raised in 50 K increments, and the $(\Delta L/L)_{\parallel}$ and $(\Delta L/L)_{\perp}$ measurements were repeated. It was found that after cycling between low temperature and room temperatures, λ_s may show some thermal hysteresis. If we cycle the temperature again, the degree of thermal hysteresis decreases. Here, we only present λ_s data from the first run. Note, the thermal hysteresis does not change the sign of λ_s. In addition, a piece of brass, the same construction material for sample holder, was substituted for the sample. By measuring λ_s of brass, we found that the noise is smaller than 2×10^{-7} up to 7 kG. The magnitude of

 0021-8979/94/75(10)/5667/3/$6.00 © 1994 American Institute of Physics

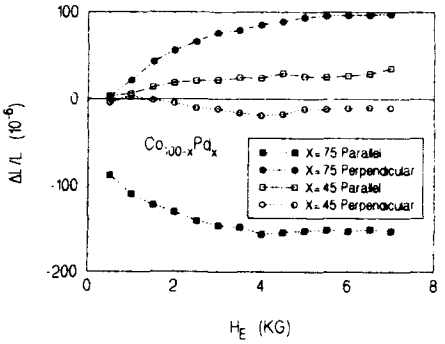

FIG. 1. The linear magnetostriction $\Delta L/L$ in parallel and perpendicular external fields H_E for $Co_{55}Pd_{45}$ and $Co_{25}Pd_{75}$ at 4 K.

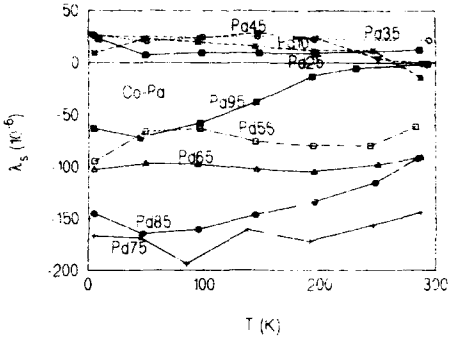

FIG. 3. The temperature dependences of $Co_{100-x}Pd_x$ alloys as a function of temperature. Pd75 means $Co_{25}Pd_{75}$ sample.

λ_s in Co-Pd is about 1×10^{-5} or more. The polycrystalline nature of each sample was checked by x ray.

III. RESULTS AND DISCUSSION

The open circles in Fig. 2 represent the linear saturation magnetostriction λ_s data as a function of x at $T=4$ K. λ_s changes its sign, from positive to negative, near $x_0=50$ at. % Pd. This finding coincides with our earlier discovery that the anisotropic magnetoresistance of Co-Pd has a maximum at $x_0=55$ at. % Pd.[5] The same things also happen in Co-Ni alloys with $x_0=65$ at. % Ni.[8] From the split-band model, these phenomena are associated with the Fermi level crossing the boundary between the Co and Pd subbands or the near degeneracy caused by the spin-orbit interaction. Since the shift in energy $\langle\delta\epsilon_l\rangle_{av}$ above the degeneracy is the same but opposite in sign to that below the degeneracy. We think that magnetostriction due to split-band term λ_s^{band} should be antisymmetric with respect to x_0. In other words, as x is near x_0, $\lambda_s^{band}(x_> - x_0) = -\lambda_s^{band}(x_0 - x_<)$, where $x_>>x_0$, $x_<<x_0$ and $x_>-x_0=x_0-x_<$. Looking at λ_s data for Co-Ni,[8] we know the above statement is true, provided x is not far from x_0. However, in Fig. 2 λ_s of Co-Pd behaves slightly different; although $\lambda_s(x_>)<0$ and $\lambda_s(x_<)>0$, $|\lambda_s(x_>)|$ is much larger than $|\lambda_s(x_<)|$. To resolve this difference, it is first noted that Co-Pd may have an unquenched orbital (or localized) moment in the Pd-rich ($x_>$) region. Then, aside from the band contribution, there is also the one-ion contribution to λ_s. Mathematically, we write

$$\lambda_s(x_>)=\lambda_s^{ion}(x_>)+\lambda_s^{band}(x_>)=\lambda_s^{ion}(x_>)-\lambda_s^{band}(x_<)$$
$$\lambda_s^{ion}(x_<)=0, \tag{3}$$

where the antisymmetric nature of λ_s^{band} has been assumed. The dashed line in Fig. 2 indicates the split band term, and the connected solid squares indicate the one-ion term for $x>x_0$. Clearly, $|\lambda_s^{ion}(x_>)| \gg |\lambda_s^{band}(x_>)|$ and $\lambda_s^{ion}(x_>)$ has a peak at $x_>=75$ at. %. This agrees with the finding on crystalline anisotropy energy of Co-Pd that it peaks at $x_>=85$ at. % Pd.[1]

This negative value of λ_s^{ion} is understood from Refs. 9 and 10

$$\lambda_s^{ion}=-(\eta/Y)[A_{av}f_l(R)+R(\partial f_l/\partial R)], \tag{4}$$

where η is a constant, Y is the Young's modulus, R is the distance between the nearest neighbors, $f_l(R)\propto(1/R)^{l+1}>0$ is the interaction between the local moment and the neighboring ions, l is the angular momentum, and $A_{av}>6(2/5)+2(3/5)=3.6$ for polycrystalline fcc alloys (usually for most fcc elements, $C_{11}-C_{12}\leq C_{44}$, where C_{ij} is the elastic stiffness constant). Since l is usually set equal to 2, from Eq. (4), it is easy to show that $\lambda_s^{ion}<0$.

Considering Eq. (1) and taking λ_{100} and λ_{111} data[1-3] with $\alpha=2/5$, we find $\bar{\lambda}_s$ does not necessarily equal the λ_s found here. Perhaps, as stated in Ref. 4, α differs from 2/5, depending on the measure $C\equiv 2C_{44}/(C_{11}-C_{12})$ of the elastic anisotripy of the crystals.

Figure 3 shows λ_s of $Co_{100-x}Pd_x$ alloys as a function of temperature. Grossly speaking, in the temperature range 4–300 K, it is observed that (1) if $x<x_0$, λ_s is mostly posi-

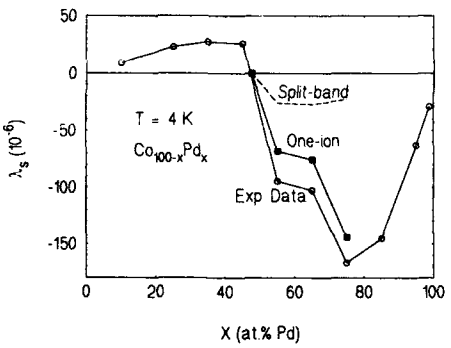

FIG. 2. The saturation magnetostriction λ_s plotted vs the Pd concentration x at 4 K.

tive and the temperature dependence of λ_s is flat, and (2) if $x>x_0$, λ_s is mostly negative and the temperature dependence of λ_s is steeper.

As discussed in Ref. 8, $\lambda_s^{band} \propto G/Y$, where G is a measure of magnetostriction, proportional to the shift $\langle \delta\epsilon_1 \rangle_{av}$. This shift is related to orbital angular momentum $L_z(\epsilon_F)$ by $\langle \delta\epsilon_1 \rangle_{av} = \zeta L_z(\epsilon_F)$, where ζ is the spin-orbit interaction parameter in the solid state.[8,11] ζ or the energy gap is of the order of 0.15 eV$\simeq O$(1000 K), though it may be reduced to one-half due to the nonsphericity of the Fermi surface. Then, ζ or G is less likely to be affected by the rising temperature ($T \leqslant 300$ K). Here, since both λ_s^{band} and λ_s^{ion} contain the temperature dependent Young's modulus term, the effect of Y is left out when considering the temperature dependence of λ_s^{band} and λ_s^{ion}. For λ_s^{ion}, from Eq. (4), the angular component contained in η is also temperature dependent. According to Callen's theory,[12] because of changes of populations among quantized states when temperature is raised, $\lambda_s^{ion}(T)/\lambda_s^{ion}(0) = \langle \eta \rangle_T / \langle \eta \rangle_0 \propto [M_s(T)/M_s(0)]^{l(l+1)/2}$, where M_s is the saturation magnetization and $l=2$.[13] Usually, the level splitting due to the exchange molecular field H_m in metal or nonmetal is $2\mu_B H_m \simeq 0.02$ eV, where μ_B is Bohr magneton.[14] Since $2\mu_B H_m < \zeta$, it is believed that the λ_s^{ion} is more easily affected by temperature than λ_s^{band}. For example, for $Co_{25}Pd_{75}$, its $M_s(300\text{ K}) = 0.58T$, $M_s(5\text{ K}) = 0.68T$, and $(T=300\text{ K})/T_C \simeq 0.72$ from this measurement. Then, by taking $l \simeq 2$ we have $[M_s(300\text{ K})/M_s(5\text{ K})]^3 = 0.62$. But $\lambda_s(300\text{ K})/\lambda_s(4\text{ K}) \simeq 0.82$. The slower temperature dependence of $\lambda_s(T)$, since $0.82>0.62$, indicates that besides $\lambda_s^{ion}(T)$, there is a less temperature dependent $\lambda_s^{band}(T)$ term contributing to $\lambda_s(T)$. This point is also reflected from the observation in Fig. 3 that for $Co_{90}Pd_{10}$ - $Co_{55}Pd_{45}$ samples, the changes in $\lambda_s(T)$ from 4 to 300 K are smaller than that for $Co_{45}Pd_{55}$ - Co_5Pd_{95} samples in general.

IV. CONCLUSION

We have disscussed the linear satureation magnetostriction λ_s of Co-Pd alloys. λ_s changes its sign near $x_0=50$ at. %Pd as predicted from the split-band model. For $x>x_0$, we find that in addition to the band mechanism the one-ion mechanism, due to the unquenched orbital moment, gives second contribution to λ_s. The order of λ_s^{ion} in the range $x>x_0$ is estimated. Finally, the temperature dependence of λ_s is so discussed that $\lambda_s^{band}(T)$ could be separated form $\lambda_s^{ion}(T)$.

ACKNOWLEDGMENT

We are thankful for the financial support from the National Science Council under Grant No. NSC82-0208-M001-092.

[1] H. Fujiwara, H. Kadomatsu, and T. Tokunaga, J. Magn. Magn. Mater. **31–34**, 809 (1983).
[2] H. Kadomatsu, T. Kamimori, T. Tokunaga, and H. Fujiwara, J. Phys. Soc. Jpn. **49**, 1189 (1980).
[3] T. Tokunaga, M. Kohri, H. Kadomatsu, and H. Fujiwara, J. Phys. Soc. Jpn. **50**, 1411 (1981).
[4] H. B. Callen and N. Goldberg, J. Appl. Phys. **36**, 976 (1965).
[5] S. U. Jen, Phys. Rev. B **45**, 9819 (1992).
[6] R. D. Greenough and C. Underhill, J. Phys. E **9**, 451 (1976).
[7] E. W. Lee, Rep. Pro. Phys. **18**, 184 (1955).
[8] L. Berger, Phys. Rev. **138**, A 1083 (1965).
[9] S. Chikazumi, *Physics of Magnetism* (Wiley, New York, 1964).
[10] Y. Suzuki and T. Egami, J. Magn. Magn. Mater. **31–34**, 1549 (1983).
[11] L. Berger, Physica **91B**, 31 (1977); L. Hodges, D. R. Stone, and A. V. Gold, Phys. Rev. Lett. **19**, 655 (1967).
[12] E. Callen, J. Appl, Phys. **39**, 519 (1968).
[13] R. C. O'Handley, Phys. Rev. B **18**, 930 (1978).
[14] J. C. Slonczewski, Phys. Rev. **122**, 1367 (1961); S. U. Jen, Y. R. Huang, and T. P. Chen, J. Magn. Magn. Mater. **109**, 91 (1992).

Hysteretic and other relationships between technical magnetostriction and magnetization

I. J. Garshelis
Magnetoelastic Devices, Inc., P. O. Box 625, Pittsfield, Massachusetts 01202

The appearance of functional relationships between magnetostrictive strain, $\epsilon=\Delta l/l$, and magnetization, M, is critically examined. Correlations between ϵ and M are found to derive entirely from the dependence of each on the orientation of the spin vector relative to a common measurement direction. In single uniaxial domains, or in equivalent bulk bodies, with isotropic magnetostrictions λ_s, the simple $\epsilon \propto M^2$ relationship arises from the closely related trigonometric functions involved in their respective measurements. To be hysteretic it is shown that it is at least necessary for λ_s to be anisotropic in a single domain or for there to be two or more domains distinguished by their orientations or other factors affecting their switching fields. It is concluded from this study that ϵ has no direct dependence on M nor are there physical sources in their hysteretic relationships that are not already manifest in M vs H.

INTRODUCTION

The generally nonlinear and hysteretic dependence of magnetization, M, on applied field, H, is the quintessential feature of ferromagnetic behavior. In most ferromagnetic materials, the application of stress, σ, markedly alters the slopes and intercepts characterizing this M-H relationship; only the material-dependent saturation magnetization, M_s, is unaffected. The dimensions of a body made from such stress-sensitive ferromagnetic materials also vary with H in a generally nonlinear and hysteretic manner. The change in any dimension l is characterized by a magnetostrictive strain $\epsilon(=\Delta l/l)$. The slopes and intercepts characterizing the ϵ-H relationship are also markedly affected by σ, although there again exists a material-dependent saturation magnetostriction, λ_s, which is reached at the same field as M_s. These remarkable similarities in the dependencies of M and ϵ on H and σ lead naturally to the idea that some systematic relationship exists between M and ϵ. Observations of ϵ varying with M^2, e.g., in nickel under tension,[1] 68 permalloy heat treated in a transverse field,[2] and terfenol under compression,[3] suggest that ϵ is in fact more dependent on M than on H. The notably reduced hysteresis[4] often seen in plots of ϵ vs M, compared to ϵ vs H, adds to this view.

Still, there are circumstances where ϵ and M are just as clearly unrelated. For example, ϵ varies with σ even in an unmagnetized body (when $M=0$). This is manifested as an elastic modulus defect (ΔE effect) and in magnetomechanical damping.[5] Also, magnetization changes in square loop materials take place with no concomitant change in ϵ.

In order to clarify these various and inconsistent appearances of a functional relationship between ϵ and M, we examine the physical bases of the manifestation of each and critically appraise the circumstances under which they can be related by an analytical function as well as the requirements for hysteresis to appear in their relationship.

THEORY

It is instructive to first examine the relationship between M and ϵ for a single domain particle. For convenience we consider a small particle, schematically illustrated in Fig. 1(a), that is fixed in space and spherical in shape in its paramagnetic state at some elevated temperature. When cooled to an equilibrium temperature below its Curie point [Fig. 1(b)], the particle develops a spontaneous magnetic moment of volume density M_s orientated within the particle by some anisotropic influence generally associated with some regularity in the composition or microstructure. Orbital alignments related to the spins also act to alter the interatomic spacing differently in spin versus nonspin directions. The cumulative effect is a spontaneous elongation or contraction of the dimensions of the particle in a manner dependent on the *measurement direction* relative to the anisotropy axis. When measured in the moment direction, this spontaneous magnetoelastic strain (which can be >0 or <0) defines λ_s. For the example illustrated in Fig. 1, $\lambda_s>0$.

Ignoring the actual physical source, for the present the anisotropy is assumed to be uniaxial, of energy density K_u. At this stage λ_s is also assumed to be isotropic, i.e., the magnetoelastic strain in the direction of the moment is independent of the orientation of the moment relative to the prime (easy) axis established by the anisotropy source.

Using a simple approximation to the new shape of the particle, and assuming that its volume is unchanged by the presence of its moment, the strain measured in a direction inclined at angle ϕ to the moment can be found from[6]

$$\epsilon=3\lambda_s(\cos^2\phi-1/3)/2. \tag{1}$$

The measured magnetization in this same direction is

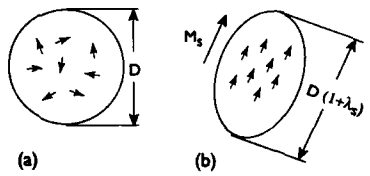

FIG. 1. (a) A small spherical particle above its Curie temperature (T_C). (b) Below T_C, magnetization M_s and magnetostriction λ_s develop in a direction associated with structural or compositional anisotropy.

 0021-8979/94/75(10)/5670/3/$6.00 © 1994 American Institute of Physics

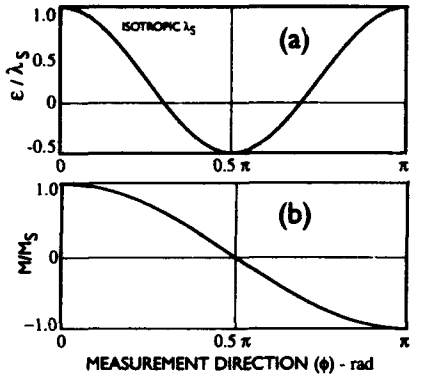

FIG. 2. (a) Variation of ϵ in a single domain with inclination (ϕ) of measurement axis to moment direction. (b) Corresponding variation of M.

$$M = M_s \cos \phi. \tag{2}$$

The manner and extent of the variations in ϵ and M with direction relative to M_s are seen in the (reduced form) plots of Eqs. (1) and (2) shown in Figs. 2(a) and 2(b), respectively.

The *measurement direction* of interest is not casually selected but is most usually associated with (e.g., coincident with) the direction of an applied field or stress. Under the condition where H is applied at some angle ψ to the K_u axis, the moment rotates from its quiescent alignment with K_u, towards H, through such an angle θ as to minimize the sum (E) of the magnetostatic (E_H) and anisotropy (E_K) energies. This is illustrated by the vector diagram in Fig. 3(a). At some critical value[7] of a reversed polarity field, the stable orientation of M_s jumps from the position shown in Fig. 3(b) to that shown in Fig. 3(c). By minimization of E and recognizing $\psi-\theta$ in Figs. 3(a)–(c) and $\pi-(\psi+\theta)$ in Fig. 3(b) as ϕ, the *measurement direction* of interest, we can find

$$\sin \phi = \sin \theta \cos \theta / h \tag{3}$$

with the field expressed in reduced form as $h = HM_s/2K_u$.

Plots of ϕ against h from Eq. (3) for ψ=0°, 30°, 60°, and 90° are shown in Fig. 4. Points on the plots (ψ<90°), where the M_s vector position jumps, are indicated.

If M is continuously measured as the field undergoes sufficiently large, bipolar ($|-h_{peak}|=h_{peak}>1$) excursions, M vs H will follow one of the many familiar loop shapes, from

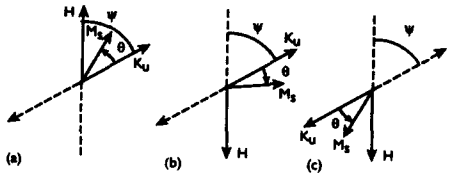

FIG. 3. Reorientation of M_s vector by fields of positive polarity (a) and negative polarity (b). M_s jumps from position shown in (b) to position shown in (c) when E for ($\psi-\theta$) is smaller than for $\pi-(\psi+\theta)$.

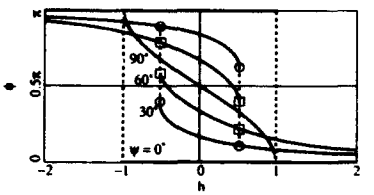

FIG. 4. Variation in effective measurement direction with field applied at 0°, 30°, 60°, and 90° to the easy axis of a single domain.

the straight line (ψ=90°, $-1 \leq h \leq 1$) to the square loop (ψ =0°). At the critical fields where there are jumps from one value of ϕ to another at constant h, there will obviously be corresponding jumps in M from one value to another at constant H. Thus, although there are for ψ<90°, some "forbidden" values of ϕ, for each stable value of ϕ the corresponding value of M will be found on the line shown in Fig. 2(b). Similarly, if λ_s is isotropic, for each stable value of ϕ, there is from Eq. (1) only one value of ϵ and thus, although there may be gaps, all corresponding values of ϕ and ϵ will be found on the line shown in Fig. 2(a).

As illustrated in the vector diagrams of Fig. 5 to minimize the total free energy the M_s vector will also be rotated by stress. Now however, θ is restricted such that $0 \leq \phi \leq \pi/2$, and except for ψ=0° and ψ=90°, ϕ varies continuously with σ. Once again, for each value of ϕ there are unique values of M and ϵ with corresponding pairs (M,ϕ) and (ϵ,ϕ) always falling on the lines plotted in Figs. 2(b) and 2(a). Stress simply alters the effective value of K_u and the orientation of the easy axis. Thus in a single domain with isotropic λ_s, there is a unique functional relationship between M and ϵ for any conditions of ψ, H, and σ. This is found by substituting cos ϕ, obtained from Eq. (2), into Eq. (1)

$$\epsilon = 3\lambda_s[(M/M_s)^2 - 1/3]/2. \tag{4}$$

If λ_s is not independent of the orientation of M_s relative to K_u, i.e., if $\lambda_s = f(\theta)$, ϵ and M are no longer constrained to a unique relationship. In particular, it can be seen in Fig. 4 for ψ=60° that, within small ranges near $|h|$=0.5, there are two stable values of h (one on each limb of the curve) corresponding to one value of ϕ. Consequently, in this range, for each value of ϕ (hence M) there are two values of θ [from Eq. (3)], and therefore, [depending on $f(\theta)$], possibly two values of λ_s (hence ϵ). The resulting occurrence of hys-

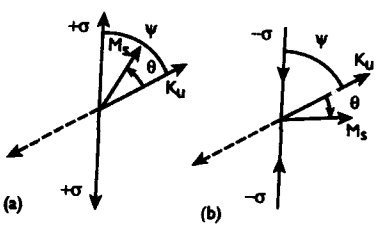

FIG. 5. Reorientation of M_s by tensile (a) and compressive stress (b).

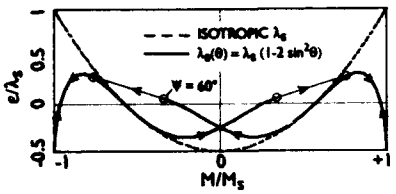

FIG. 6. Universal anhysteretic ϵ vs M relationship in a single domain with isotropic λ_s. Anisotropic λ_s can produce hysteresis as shown.

teresis in ϵ vs M in a single domain as a consequence of anisotropic λ_s is clearly shown by the plot in Fig. 6 for a hypothetical $f(\theta)=\lambda_0(1-2\sin^2\theta)$. The anhysteretic plot of Eq. (4) with isotropic λ_s is also shown.

While no hysteresis between ϵ and M is possible for a single domain particle if λ_s is isotropic, the situation can be different in a multidomain body. This can be demonstrated by considering a composite body comprised of just two noninteracting single domain particles having unequal and sufficiently large easy axis orientations (i.e., $90°>\psi_1>\psi_2>64°$). In this range of ψ, the critical switching angles[7] $[\theta_c=\tan^{-1}(\tan^{1/3}\psi)]$ are such that the limiting stable magnetization on the ascending limb of the M-H loop will exceed the remanent value, i.e., $M_r/M_s=\cos\psi<\cos[\pi-(\theta_c+\psi)]$, a feature illustrated in Fig. 7. These conditions ensure that a point exists on the ascending limb of the composite body's M-H loop where $M_a=M_r$. Since M of the composite body is the average, $(M_1+M_2)/2$, of the two domains, $\cos\phi_{1a}+\cos\phi_{2a}=\cos\psi_1+\cos\psi_2$. But this disallows (except the singularity: $\psi_1=\phi_{2a}$ and $\psi_2=\phi_{1a}$) the equality of $(\cos^2\phi_{1a}+\cos^2\phi_{2a})$ and $(\cos^2\psi_1+\cos^2\psi_2)$. Thus, $\epsilon_a\neq\epsilon_r$; the average strains are unequal at the two values of H for which the magnetizations are the same; therefore, ϵ vs M for a body comprised of just two domains can be hysteretic even if λ_s is isotropic. Hysteresis in ϵ vs M arising from the more extensive averaging of $\cos\phi$ and $\cos^2\phi$ over a randomly oriented assembly of single domain particles with isotropic λ_s has already[8] been demonstrated.

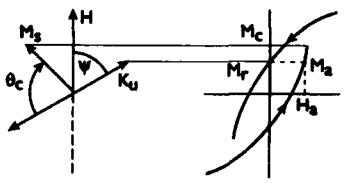

FIG. 7. Domains with $90°>\psi>64°$ orientations have loops with $M_c>M_r$. Composite body with only two such domains will have a hysteretic ϵ vs M.

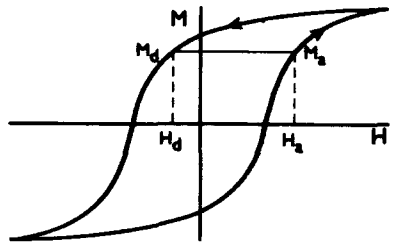

FIG. 8. Typical M-H loop. Differences in the detailed domain structure at H_a and H_d (although $M_a=M_d$) portend hysteresis in ϵ vs M.

The more general nature of hysteresis in ϵ vs M should now be recognized. In the classic M-H loop for a multidomain body shown in Fig. 8, regions are seen in which there are two values of H, H_a, and H_d, for which $M_a=M_d\neq 0$. Since H affects both the orientations, and via wall motion, the volumes of domains having particular orientations, details of the domain structures at H_a will differ from that at H_d. While the volumetrically weighted $(\overline{\cos}\,\phi)_a=(\overline{\cos}\,\phi)_d$, corresponding averages of $\cos^2\phi$ will generally differ, resulting in dual values of ϵ, ϵ_a, and ϵ_d, and this duality in ϵ will be manifested by a hysteretic relationship with M.

CONCLUSION

Correlations between ϵ and M derive entirely from the dependence of each on the orientation of the spin vector relative to a *common measurement direction*. In single uniaxial domains with isotropic λ_s, a simple analytical relationship arises from the closely related trigonometric functions involved in their respective measurements. With anisotropic λ_s this relationship can become hysteretic, since ϵ, but not M, is also dependent on the orientation of M_s relative to the anisotropy axes. In multidomain bodies the independence of ϵ, but not of M, to reversals of individual domain magnetizations introduces another source of hysteresis. Hysteresis in M vs ϵ has no physical source not already manifest in M vs H but arises only as an artifact of the peculiarities of averaging $\cos\phi$ and $\cos^2\phi$.

[1] H. Kirchner, Ann. Physik **27**, 49 (1936).
[2] R. M. Bozorth, *Ferromagnetism* (Van Nostrand, Princeton, 1951), p. 638.
[3] A. E. Clark, H. T. Savage, and M. L. Spano, IEEE Trans. Magn. **MAG-20**, 1443 (1984).
[4] D. L. Atherton, T. Sudersena Rao, V. De Sa, and M. Schönbächler, IEEE Trans. Magn. **MAG-24**, 2177 (1988).
[5] A. Cochardt, in *Magnetic Properties of Metals and Alloys* (American Society of Metals, Cleveland, 1959), p. 251.
[6] R. M. Bozorth, in Ref. 5, p. 812.
[7] B. D. Cullity, *Introduction to Magnetic Materials* (Addison–Wesley, Reading, MA, 1972), p. 336.
[8] E. W. Lee and J. E. L. Bishop, Proc. Phys. Soc. **89**, 661 (1966).

Micromagnetic model for the influence of biaxial stress on hysteretic magnetic properties

M. J. Sablik, L. A. Riley, G. L. Burkhardt, and H. Kwun
Southwest Research Institute, P.O. Drawer 28510, San Antonio, Texas 78228-0510

P. Y. Cannell and K. T. Watts
Naval Surface Warfare Center, Annapolis, Maryland 21402

R. A. Langman
University of Tasmania, Hobart, Tasmania, 7001, Australia

A micromagnetic formulation has been developed for modeling the effect of biaxial stress on magnetoelastic proce[illegible] in polycrystalline steels. In particular, the formulation employs the Schneider–Cannell[illegible] model and involves substitution of an effective stress equal to one of the deviatoric (i.e., di[illegible]l) normal stress components, depending on whether the field is parallel to a tensile or compres[illegible]e axis or to the third axis perpendicular to the plane of biaxial stress. Computer results are compared to experimental results on the effects of biaxial stress on magnetic properties in mild steel and in SAE-4130 steel. Good qualitative agreement is found in almost all cases, in that in going from one biaxial stress case to the next, the same kinds of changes are seen magnetically. It is also shown from the model and the data that a method can be formulated to nondestructively determine the difference in biaxial stresses.

I. INTRODUCTION

To model magnetoelasticity in steels under uniaxial stress conditions, the works of Schneider *et al.*[1,2] and Sablik *et al.*[3,4] have been employed. Most real physical situations however involve biaxial and triaxial stresses acting along mutually perpendicular axes. The magnetoelastic behavior under such conditions is different.[5–7] Models for the effect of biaxial stress on magnetic properties have been published by Schneider and Richardson[1] and Kashiwaya.[8]

In this paper, additional data are presented on magnetic properties under biaxial stress conditions. The data were taken by R.A.L. on mild steel and by G.L.B. and H.K. on SAE-4130 steel. An improved micromagnetic model, which qualitatively explains the magnetic behavior, is additionally described. Finally, a nondestructive method for determining the difference in biaxial stresses is described.

II. THEORETICAL MODEL

The micromagnetic model used by Schneider *et al.* is found in Ref. 2. In that model, the change in magnetization ΔM at the end of a process in which magnetic field H or stress σ varies is

$$\Delta M = \sum_i \int f_i \chi(H_i) dH_i, \tag{1}$$

where the sum i is over domain wall types i. In single crystal iron, there are three domain wall types–180°, +90°, −90°. In polycrystals, because of the varying angle θ_i between stress axis and local magnetization, a much larger number of domain wall types must be considered in the sum, indexed by angle. The weight factor f_i is an appropriate weight factor for each domain wall type. The $\chi(H_i)$ is the magnetic susceptibility dM/dH_i associated with change dH_i in internal field H_i, which is computed from

$$H_i = H - (3\lambda_s \sigma \cos\theta_i / B_s) - D_\sigma M, \tag{2}$$

where the middle term is the stress contribution H_σ to the internal field and $-D_\sigma M$ is the stress demagnetization contribution. D_σ is a function of stress which behaves as in Fig. 1 of Ref. 2. In Eq. (2), λ_s is the saturation magnetostriction, B_s is the saturation flux density, and D_σ is the stress demagnetization factor.

In Eq. (1), the susceptibility $\chi(H_i) = dM/dH_i$ satisfies

$$\chi^{-1}(H_i) = \chi^{-1}(H) - D_\sigma, \tag{3}$$

which is derived by differentiating Eq. (2) with respect to M, and the change dH_i is

$$dH_i = dH/[1 + \chi(H_i) D_\sigma] \tag{4}$$

for processes in which H varies while σ is held constant, or

$$dH_i = -d\sigma[3(\lambda_s/B_s)\cos\theta_i]/[1 + \chi(H_i) D_\sigma] \tag{5}$$

for processes in which σ varies while H is constant.

Schneider and Richardson,[1] in treating biaxial stress effects, asserted that the above model may be still used, but with σ replaced by $\sigma_{\text{eff}} = \sigma_1 - \sigma_2$ and $d\sigma$ by $d\sigma_{\text{eff}} = d\sigma_1 - d\sigma_2$ in the case where H is parallel to the σ_1 axis, and by $\sigma_2 - \sigma_1$ and $d\sigma_2 - d\sigma_1$, respectively, when H is parallel to the σ_2 axis. This however, does not prove to be satisfactory. One major reason is that stresses combine tensorially and do not superpose like vectors.

In a new approach, we invoke a three-dimensional stress model[9,10] noting that the spherical part[9] of the three-dimensional stress does not actually contribute to the part of the energy involving linear magnetostriction, and thus the effective components of stress in the three principal directions have the form[10]

$$s_1 = \sigma_1 - \sigma_0 = (2\sigma_1 - \sigma_2 - \sigma_3)/3, \tag{6a}$$

$$s_2 = \sigma_2 - \sigma_0 = (2\sigma_2 - \sigma_3 - \sigma_1)/3, \tag{6b}$$

$$s_3 = \sigma_3 - \sigma_0 = (2\sigma_3 - \sigma_1 - \sigma_2)/3, \tag{6c}$$

where σ_0 is the spherical stress, given as

 0021-8979/94/75(10)/5673/3/$6.00 © 1994 American Institute of Physics

$$\sigma_0=(\sigma_1+\sigma_2+\sigma_3)/3. \tag{7}$$

This spherical stress is also called the hydrostatic stress.[10] The stress components s_1, s_2, s_3 are known as normal deviatoric stress components and also normal distortional stress components.[10] They each represent the effective stress leading to distortion in each of the principal directions.

Since the magnetic effect is coupled to linear magnetostriction, it must be coupled to these deviatoric stresses. If an effective field H_σ due to stress is to develop along some axis in the material, it must be because there is a difference between the stresses in the principal directions. This is why the spherical part of the stress does not contribute to the magnetic effect.

In this paper, we consider the magnetic field acting only along the stress axes in order to simplify considerations. Also, we consider stress σ_3 to be zero, so that only biaxial stresses act.

We also note that when the external field acts along an axis of compression, the magnetic effect is different than when the field acts along an axis of tension. Physically, compression tends to push moments away from axes of compression, and tension tends to pull moments toward axes of tension.

Thus, for biaxial stresses, when the field is parallel to an axis of compression, the effective stress contributing to the magnetic effect is proposed to be $\sigma=s_1$, whereas when the field is parallel to an axis of tension, the effective stress is proposed to be $\sigma=-s_2$. The effective stress is therefore modeled as

$$\sigma=\begin{cases}\frac{1}{3}[(\sigma_1-\sigma_2)+\sigma_1] & \text{for } \sigma_1<0\ , \\ \frac{1}{3}[(\sigma_1-\sigma_2)-\sigma_2] & \text{for } \sigma_1>0\ , \end{cases} \tag{8}$$

assuming that H is parallel to the σ_1 axis. Physically, these may be viewed in terms of relative stresses $\sigma_i-\sigma_j$ with respect to the three principal axes, including that for which the applied stress is $\sigma_3=0$. In the case of compression, the effective stress is the sum of the relative stresses associated with axis 1. In the case of tension, the effective stress is the negative of the sum of the relative stresses associated with axis 2.

Equation (8) applies only if σ_1 and σ_2 are nonzero. If either σ_1 or σ_2 is zero, then the effective stress is the appropriate uniaxial stress. An expression similar to Eq. (8) for change $d\sigma$, due to changes $d\sigma_1$ and $d\sigma_2$, can also be obtained.

III. COMPARISON TO EXPERIMENTAL RESULTS

Experimental results in mild steel on the effect of constant biaxial stress on hysteresis loop parameters were presented recently by Langman.[6] However, discussion was restricted to equal biaxial stresses. We here compare model predictions to additional data from Langman on a more complete range of biaxial stresses.

The experimental setup for this wider range of data is the same as in Ref. 6. It utilizes a surface method of magnetization with a C core placed on the steel specimen, rather than a more accurate permeameter method. There are as a result systematic errors in the hysteresis loops caused by the C-core material, due to the fact that the flux sensing coil is wrapped around the C core rather than the sample. However, the errors are not felt to be significant when a qualitative comparison of trends is involved.

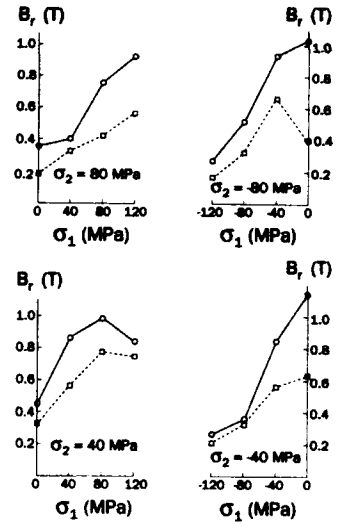

FIG. 1. Remanence B_r as a function of stress σ_1 for (a) $\sigma_2=80$ MPa, (b) $\sigma_2=-80$ MPa, (c) $\sigma_2=40$ MPa, and (d) $\sigma_2=-40$ MPa. Experimental values are denoted by ○ and are joined by solid lines; computed values, by □ and dashed lines. Field H is along axis 1.

Figure 1 shows the behavior of B_r (obtained from the computed hysteresis loop) as a function of stress σ_1 for values of $\sigma_2=+80$, $+40$, -40, and -80 MPa. The experimental values of B_r for the various cases are also plotted. Because the trends qualitatively match so closely between experimental and computed plots, one can have confidence in the general physical correctness of the model.

Measurements were also made on an annealed cruciform (cross-shaped) SAE-4130 steel specimen. Details concerning the apparatus and specimen dimensions in the case of the SAE-4130 steel may be found in Ref. 11.

Figure 2 shows experimental results (open circles joined by solid lines) compared to theoretical results (diamonds joined by dashed lines) for the case of remanence B_r. In this case, the data were normalized by the value of B_r when $\sigma_1=\sigma_2=0$. The theoretical points were extracted from the hysteresis loop computed from Eqs. (1)–(5) and (8), with the variation of D_σ with stress scaled by constant factor 2.1. Trends seen in the experimental results again are qualitatively in agreement with the trends predicted by the model.

Figure 3 exhibits an interesting result. When the difference in values B_r/B_r (0,0) between when the field is parallel to the σ_1 axis and when the field is parallel to the σ_2 axis are plotted against the stress difference $\sigma_1-\sigma_2$, a straight line band is found, both for theory and experiment. However, bandwidths and slopes differ slightly, with experimental

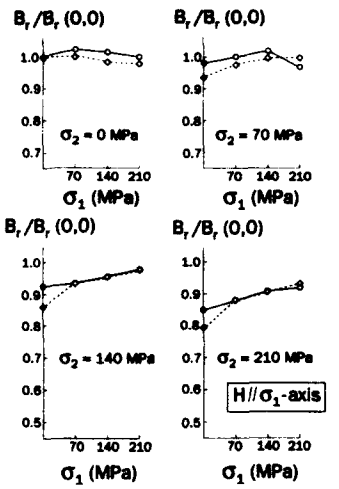

FIG. 2. Comparison between model and experiment of normalized remanence values in SAE-4130 steel. H is along the σ_1 axis.

bandwidths being larger possibly because of lift-off variation of the probe.

IV. CONCLUSIONS

We have presented a new physical model for the effects of biaxial stress on magnetic properties. The model is a micromagnetic model, which improves upon the model of Schneider and Richardson[1] and which takes into account the tensorial relationship between stress and magnetic field. The model also improves on the Kashiwaya model,[8] which requires an oversimplified zero effect when the field is aligned with the axis of largest stress. The computed results from the new model were compared to new experimental data on the effect of a range of unequal biaxial stresses on magnetic properties. In almost all cases, computed results behave qualitatively the same way as the experimental results and show the same types of magnetization changes with changes in biaxial stresses.

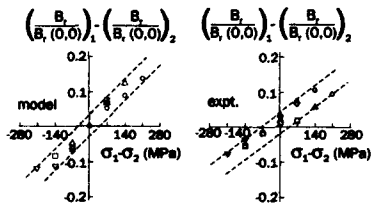

FIG. 3. Differences between normalized remanence values for $H\|\sigma_1$ axis and $H\|\sigma_2$ axis plotted against $\sigma_1-\sigma_2$. Results for both model and experiment are shown. Data points are: ○, σ_2=0; △, σ_2=70 MPa; □, σ_2=140 MPa; ▽, σ_2=210 MPa.

That a straight-line correlation can be found between $\sigma_1-\sigma_2$ and algebraically manipulated values for magnetic properties is quite useful. It means that a nondestructive evaluation magnetic technique can be constructed for obtaining the biaxial stress difference $\sigma_1-\sigma_2$ to within a certain band of error. In particular, the difference between normalized values for remanence when field is parallel to one axis and then the other can be used to determine $\sigma_1-\sigma_2$ to within a certain error range [in this case, 15 ksi (105 MPa) based on experiment and 10 ksi (70 MPa) based on the model]. It remains to be seen whether these error ranges can be reduced both experimentally and theoretically, or whether other magnetic properties might exhibit smaller error ranges when the same procedure is used for them.

In the future, it is anticipated that modifications will be made to the Sablik–Jiles model,[3,4] which will enable the Villari effect to be taken into account. At that point, a synthesis of the two models—micromagnetic and macromagnetic—should be possible.

ACKNOWLEDGMENTS

Support for this work was provided by DOE Project No. DOE/ER/14180 and by the Office of Naval Research through NSWC Annapolis Contract No. N6153392M2117. The Australian National Railway provided support for R.A.L.

[1] C. S. Schneider and J. M. Richardson, J. Appl. Phys. **53**, 8136 (1982).
[2] C. S. Schneider, P. Y. Cannell, and K. T. Watts, IEEE Trans. Magn. **MAG-28**, 2626 (1992).
[3] M. J. Sablik and D. C. Jiles, IEEE Trans. Magn. **MAG-29**, 2113 (1993).
[4] M. J. Sablik, S. W. Rubin, L. A. Riley, D. C. Jiles, D. A. Kaminski, and S. B. Biner, J. Appl. Phys. **74**, 480 (1993).
[5] K. Kashiwaya, H. Sakamoto, and Y. Inoue, in *Proceedings of the VI International Congress on Experimental Mechanics* [Society for Experimental Mechanics (SEM), Bethel, CT, 1988], Vol. 1, pp. 30–35.
[6] R. A. Langman, IEEE Trans. Magn. **MAG-26**, 1246 (1990).
[7] D. J. Buttle, W. Dalzell, C. B. Scruby, and R. A. Langman, in *Review of Progress in Quantitative Nondestructive Evaluation*, edited by D. O. Thompson and D. E. Chimenti (Plenum, New York, 1990), pp. 1879–1885.
[8] K. Kashiwaya, Jpn. J. Appl. Phys. **30**, 2932 (1991).
[9] R. W. Little, *Elasticity* (Prentice-Hall, Englewood Cliffs, NJ, 1973), pp. 52–54.
[10] J. Chakrabarty, *Theory of Plasticity* (McGraw-Hill, New York, 1987), p. 18.
[11] M. J. Sablik, G. L. Burkhardt, and H. Kwun, in *Proceedings of the 11th DOE Basic Engineering Sciences Symposium*, Argonne, IL, 1993 (U.S. G.P.O., Washington, DC), Conf.-9305134, pp. 213–220.

Modeling the effects of stress on magnetization in ferromagnetic materials (abstract)

D. C. Jiles
Ames Laboratory, Iowa State University, Ames, Iowa 50011

In previous papers, it has been shown how stress affects the magnetic properties of materials.[1,2] Although a model theory has been developed for the case of changing H field under constant stress, so far no attempts have been made to quantitatively model the effects of changing stress under constant field. The main principle in this case is the approach of the magnetization to the anhysteretic.[1] The anhysteretic is itself stress dependent, and therefore presents a moving target for the bulk magnetization. The displacement of the bulk magnetization in isotropic media is determined by the elastic energy supplied $\Delta W=(1/E)(\Delta\sigma)^2$, where E is the elastic modulus, and $\Delta\sigma$ the change in stress. The displacement of the magnetization $D=M_{an}(H,\sigma)-M(H,\sigma)$ decays with W according to $dD/dW=-\xi D$, where ξ is the decay coefficient. Solving this equation gives, $M_{an}(H,\sigma)-M(H,\sigma)=[(M_{an}(H,\sigma)-M(H,\sigma_0)]\exp[(-\xi/E)(\Delta\sigma)^2]$, which can be rewritten in terms of the change in magnetization with stress $\Delta M(H,\sigma,\sigma_0)$ the magnetomechanical effect, $\Delta M(H,\sigma,\sigma_0)=[M_{an}(H,\sigma)-M(H,\sigma)]\{1-\exp[(-\xi/E)(\Delta\sigma)^2]\}$. The stress dependent anhysteretic $M_{an}(H,\sigma)$ can then be determined from the unstressed anhysteretic through the addition of the extra effective field term H_σ: $H_\sigma=(3/2)(\sigma/\mu_0)(d\lambda/dM)$ so that $M_{an}(H,\sigma)=M_{an}(H+H_\sigma)$. Through the use of the last three equations it is possible to describe the changes in magnetization of the material arising from changing stress.

[1] D. C. Jiles and D. Atherton, J. Phys. D (Appl. Phys.) 17, 1265 (1984).
[2] D. Kaminski, D. C. Jiles, and M. Sablik, J. Magn. Magn. Mater. 104, 382 (1992).

 0021-8979/94/75(10)/5676/1/$6.00 © 1994 American Institute of Physics

Interpretation of hysteresis curves and Henkel plots by the Preisach model (invited)

V. Basso, M. Lo Bue,[a] and G. Bertotti
Istituto Elettrotecnico Nazionale Galileo Ferraris and INFM-GNSM, corso M. d'Azeglio 42, I-10125 Torino, Italy

We discuss some properties of the scalar moving Preisach model (MPM) in relation to the description of magnetic interactions. MPM predictions for the behavior of Henkel plots are worked out. The role of the factorization properties of the Preisach distribution and the consequences of the joint presence of mean-field effects and local random interactions are discussed. Literature data are analyzed in the frame of this description, with particular attention to thin-film media with perpendicular magnetization, where mean-field effects are particularly strong. Some of the theoretical predictions are directly tested by hysteresis and Henkel plot measurements performed on SiFe soft alloys. A good agreement, in some cases involving no adjustable parameters, is found.
75.60.Ej 75.50.Bb

I. INTRODUCTION

In recent years, there have been a number of important results clarifying the role of the Preisach model (PM) as a general mathematical tool for the description of hysteresis phenomena.[1] In spite of these achievements, however, the connection between the PM mathematical structure and the physical mechanisms responsible for hysteresis in ferromagnets still raises several intriguing problems. Much of this stems from the drastically simplified PM treatment of magnetic interactions. In PM, hysteresis is described in terms of a collection of elementary rectangular loops with various up and down switching fields α and β. The switching field distribution $p(\alpha,\beta)$ is *a priori* given, which would seem to imply that the elementary switching events are independent and do not interfere. On the other hand, in all cases where it is not concentrated along the $\alpha=-\beta$ line, $p(\alpha,\beta)$ describes elementary loops shifted from their symmetric position, a fact which is usually attributed to the presence of interactions creating a local field which adds to the external field. This interaction field will inevitably depend on the state of the sorrounding switching elements and will thus randomly fluctuate as the magnetization process proceeds. The applicability of PM as a physical model rests then on the existence, for a given system, of some class of Preisach distributions $p(\alpha,\beta)$ statistically stable against such fluctuations. The conceptual difficulties associated with this requirement have raised attention since a long time ago.[2] A simple but important advancement came with the so-called moving Preisach model (MPM),[3,4] in which it is shown that the lack of stability of the Preisach distribution results in its shifting as a whole during the magnetization process. The distribution approximately becomes a function $p(\alpha+ki,\beta+ki)$, where k is a constant and i is the macroscopic magnetization. In terms of interaction effects, this description is equivalent to assuming that each elementary PM loop is no longer subject to the applied field h_a only, but to the effective field $h=h_a+ki$.

According to recent suggestions,[5–8] some insight into the physical nature of MPM could come from a class of models suggested by the theory of spin glasses. In these models, the athermal behavior of a set of N bistable objects (say spins) $s_i=\pm 1$, interacting through random coupling constants J_{ij}, is considered. The evolution of the system is controlled by the local field h_i experienced by each s_i, $h_i=\Sigma_j J_{ij}s_j+h_i^c+h_a$, where h_a is the applied field and h_i^c is some random local pinning field.[6,7] The magnetization process consists of bursts of spin-flip events taking place when the stability condition $s_i=\mathrm{sign}(h_i)$ is destroyed for some spin by the time variation of the applied field. This description contains the same basic ingredients of MPM, but with an explicit description of interactions, given by J_{ij}. Its study can thus significantly contribute to clarifying the physical meaning of the Preisach distribution $p(\alpha,\beta)$ and its stability properties against the random shuffling produced by subsequent spin-flip events. In addition, the mean-field effects characteristic of MPM have here a direct counterpart in the mean value, say J_0, of the coupling constants J_{ij}, considering that $h_i=\Sigma_j J_{ij}s_j+h_i^c+h_a=\Sigma_j(J_{ij}-J_0)s_j+J_0\Sigma_i s_i+h_i^c+h_a$, and $\Sigma_i s_i$ is just the macroscopic magnetization of the system.

This spin-glass approach represents quite an idealized attempt in the direction of what would really be a breakthrough in Preisach modeling, that is the (approximate) derivation of the Preisach distribution from some microscopic description of magnetization processes. Perhaps, the most important result in this respect is still Néel's proof[9] that domain wall (DW) motion in a random potential under small applied fields is equivalent to PM with a constant switching field distribution. In order to achieve further progress, a detailed analysis of the description of interactions built in MPM seems mandatory. In this connection, really revealing results are obtained by considering the so-called Henkel plot of remanences.[10,11] In the Henkel plot construction, one mea-

[a]Dipartimento di Fisica, Politecnico di Torino, corso Duca degli Abbruzzi, I-10129 Torino, Italy.

 0021-8979/94/75(10)/5677/6/$6.00 © 1994 American Institute of Physics

sures the remanence i_r, obtained after application and removal of the field h to the demagnetized state, and the remanence i_d, obtained after application and removal of the field $-h$ to the saturation remanence i_∞, and plots i_d vs i_r. For a set of single-domain, noninteracting particles, the linear Wohlfarth relation $i_d=i_\infty-2i_r$ holds,[12] so that deviations from linearity appear as a natural indication of the presence of interaction effects. Yet, the interpretation of such deviations often remains at a qualitative stage and sometimes merely reduces to the statement that Henkel plots lying below (above) the Wohlfarth line describe demagnetizing-like (magnetizing-like) interactions. The aim of the present paper is to show that a deeper insight is obtained when Henkel plots are considered in the frame of MPM. MPM predicts in fact that, for any arbitrary Preisach distribution, the Henkel plot will always lie in the region $-i_r \leq i_d \leq i_\infty-2i_r$. This means that demagnetizing-like Henkel plots are generally expected as a consequence of the intrinsic disorder of ordinary materials. This conclusion has little to do with the existence of demagnetizing fields, since the Preisach distribution describes an equal amount of demagnetizing-like and magnetizing-like local interactions. In addition, the Henkel plot will follow the law $i_d/i_\infty=1-2\sqrt{i_r/i_\infty}$ whenever $p(\alpha,\beta)$ takes the factorized form $p(\alpha,\beta)=f(\alpha)f(-\beta)$. This result, completely independent of $f(\alpha)$, is the direct universal consequence of the assumed $p(\alpha,\beta)$ factorization. Finally, the Henkel plot phenomenology predicted by MPM becomes extremely rich and complex when mean-field interactions are present. In particular, oscillating Henkel plots are a certain indication of the joint presence of random local interactions and magnetizing-like mean-field effects. We will give some examples of the value of MPM in the interpretation of Henkel plot literature data on superconductors, permanent magnets, magnetic recording media.

In addition to these comparisons, we made direct tests of MPM predictions on soft metallic materials, for which relatively few studies on the characterization of magnetic interactions have been carried out. Henkel plot measurements on SiFe are reported by Bissell *et al.*[13] Evidence of mean-field magnetizing-like interactions in crystalline and amorphous soft alloys was found in Refs. 11 and 14. A particularly appealing property of soft materials is that mean-field internal effects can easily be compensated by adjusting the demagnetizing field associated with the geometry of the magnetic circuit. This permitted us to generate a set of hysteresis conditions associated with a fixed Preisach distribution and a mean-field parameter k continuously varying from definitely positive values, when only internal mean-field interactions were active, to large negative values, when demagnetizing effects were dominating. The variation of k could be accurately monitored by MPM fittings of the Henkel plots associated with each experimental condition. The obtained results show that MPM is indeed able to provide a physically sound description of the hysteresis behavior of soft materials and of the associated Henkel plots, through theoretical expressions that in some cases involve no adjustable parameters.

II. PREISACH MODEL DESCRIPTION OF INTERACTIONS

In this section, the basic properties of PM for what concerns the description of magnetic interactions are discussed. We will consider the scalar PM only. The extension of the results presented here to vector models is outside the scope of this article and will be discussed elsewhere.

The basic PM equation is

$$i(h)=\int_{-\infty}^{+\infty} d\alpha \int_{-\infty}^{\alpha} d\beta p(\alpha,\beta)\Phi(\alpha,\beta;[h(t)]), \tag{1}$$

where small letters indicate dimensionless quantities, i.e., measured in units of the saturation magnetization I_s, (i), and of some characteristic field H_c, (h,α,β), typically of the order of the static coercive field. $\Phi(\alpha,\beta;[h(t)])=\pm 1$ describes the state of each elementary PM loop resulting from the past field history $[h(t)]$. A well-known graphical representation shows that the boundary between the regions, where $\Phi=1$ and $\Phi=-1$ is a staircase line with slopes either 0 or $-\infty$.[1] It is often useful to employ the coordinates $h_c=(\alpha-\beta)/2$ and $h_u=(\alpha+\beta)/2$, representing the half width of each elementary loop and its shift from the symmetric position. h_c plays the role of a local coercive field, and h_u of (minus) a local interaction field.

Of particular importance for the physical interpretation of MPM are the factorization properties of $p(\alpha,\beta)$. Two factorizations consistent with the basic symmetry $p(\alpha,\beta)=p(-\beta,-\alpha)$ [or equivalently, $p(h_c,h_u)=p(h_c,-h_u)$] are of special interest: $p(h_c,h_u)=f(h_c)g(h_u)$ and $p(\alpha,\beta)=f(\alpha)f(-\beta)$. The former is usually considered in the description of magnetic particle assemblies. In particular, we will often make use of the lognormal-Gaussian distribution

$$p(h_c,h_u)=\frac{1}{4\pi\sigma_c\sigma_u h_c}\exp\left[-\frac{(\log h_c)^2}{2\sigma_c^2}\right]\exp\left[-\frac{h_u^2}{2\sigma_u^2}\right]. \tag{2}$$

The latter, first proposed by Biorci and Pescetti,[15] is the one expected when DW motion in a random potential is the basic magnetization process.[11] We will show that this factorization has far-reaching consequences, which can be directly tested by suitable experiments.

The final feature to be added to this description is the presence of mean-field effects, according to the equation

$$h=h_a+ki(h), \tag{3}$$

where h is the effective field acting on each PM elementary loop, h_a is the applied field and k measures mean-field effects. Interestingly enough, Eq. (3) does not imply any modification of the PM algorithm. In order to obtain $i(h_a)$ vs h_a from a given PM curve $i(h)$, we have simply to represent that curve under nonorthogonal axes, with the new magnetization axis tilted by an angle θ such that $\tan(\theta)=k$. The existence of this skew transformation permits one to extend several general properties of PM to MPM as well.

The calculation of Henkel plots by PM is not difficult when $k=0$. What one has to do is to construct the Φ boundary describing the state of the system at the remanences i_∞, i_r, i_d and to evaluate the corresponding PM integrals through Eq. (1). The demagnetized state, achieved by the application

of an ac field of amplitude slowly decreasing to zero, is described by the boundary $h_u=0$. The various remanences can all be expressed in terms of the three integrals

$$q(h)=\int_0^h d\alpha\int_{-h}^{0} d\beta p(\alpha,\beta), \tag{4a}$$

$$Q(h)=\int_h^{\infty} d\alpha\int_{-\infty}^{-h} d\beta p(\alpha,\beta), \tag{4b}$$

$$R(h)=\int_0^h d\alpha\int_{-\infty}^{0} d\beta p(\alpha,\beta), \tag{4c}$$

as

$$i_r(h)=q(h), \quad i_d(h)=Q(h)-q(h)=Q(0)-2R(h),$$

$$i_\infty=Q(0)=q(\infty). \tag{5}$$

The detailed analysis of these relations[11,16] leads to several interesting conclusions.

(P-i) For any arbitrary Preisach distribution,

$$-\frac{i_r}{i_\infty}\leq\frac{i_d}{i_\infty}\leq 1-2\,\frac{i_r}{i_\infty}. \tag{6}$$

In addition, it is found that the upper boundary of this region, $i_d=i_\infty-2i_r$ (i. e., the Wohlfarth relation) is attained when $p(h_c,h_u)=f(h_c)\delta(h_u)$, which is just the case of absence of interactions. On the other hand, the lower boundary, $i_d=-i_r$, corresponds to a class of distributions that includes, in particular, $p(h_c,h_u)=\delta(h_c-h_0)g(h_u)$, i. e., a distribution of interacting loops of fixed half-width h_0. Equation (6) shows that demagnetizing-like Henkel plots are inevitably expected whenever the Preisach distribution has a nonzero width along the h_u axis. In this sense, they are the natural consequence of the intrinsic disorder of ordinary materials. This conclusion applies in spite of the fact that $p(h_c,h_u)$ is symmetric with respect to h_u, that is it describes an equal amount of demagnetizing-like and magnetizing-like local interactions.

(P-ii) If there exists some field h_0 such that $p(h_c,h_u)=0$ for $h_c<h_0$, then the Henkel plot will exhibit a downward step of finite amplitude at $i_r=0$. On the other hand, if there exists some field h_0 such that $p(h_c,h_u)=0$ for $h_c>h_0$ then the Henkel plot will exhibit a finite part up to $i_r=i_\infty$, where $i_d=-i_r$. In addition, for distributions of the form $f(h_c)g(h_u)$, the slope di_d/di_r for $i_r\to i_\infty$ will change in between -1 and -2 depending on how fast is the decay of $f(h_c)$ with respect to that of $g(h_u)$.

(P-iii) When p obeys the factorization $p(\alpha,\beta)=f(\alpha)f(-\beta)$, the Henkel plot takes the form

$$i_d/i_\infty=1-2\sqrt{i_r/i_\infty}. \tag{7}$$

This result is fully independent of $f(\alpha)$. It is the direct, universal consequence of the assumed factorization.

All these results pertain to the *PM* with $k=0$. The introduction of mean-field effects, described by Eq. (3), leads to quite a richer structure.

(MP-i) As a consequence of the skew transformation connecting PM and MPM, the line $i_d=-i_r$ keeps on being a lower boundary for Henkel plots under any arbitrary k. On the contrary, the Henkel plot will generally invade the magnetizing-like region under sufficiently positive k.

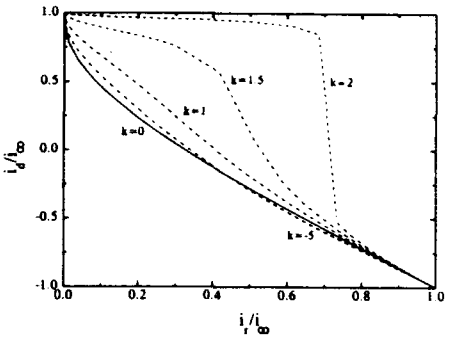

FIG. 1. MPM Henkel plots calculated from Eqs. (2) and (3), with $\sigma_c=1$, $\sigma_u=1$, and variable $k=-5$, 0, 1, 1.5, 2.

(MP-ii) When $p(h_c,h_u)=f(h_c)\delta(h_u)$ and interactions derive from mean-field effects only, the Henkel plot has the commonly expected behavior: A positive k (magnetizing-like interactions) gives a Henkel plot all above the Wohlfarth line, and the opposite for negative k. In the limit of strong negative k, however, the Henkel plot may not simply approach the boundary $i_d=-i_r$, but it may acquire a more complex behavior, in dependence of the shape of the coercive field distribution $f(h_c)$. This can be shown in analytic terms when $f(h_c)$ is a box-like distribution, different from zero in some field interval from h_0 to h_1.[16] It is found that, in the limit $k\to-\infty$, the Henkel plot will exhibit a downward jump at the point $i_r/i_\infty=2h_0/(h_0+h_1)$. An example is given below, in connection with the discussion of Alumite systems. This peculiar behavior is destroyed by the presence of a sufficiently wide h_u distribution and offers then an interesting opportunity to test the simultaneous presence of random interactions $[g(h_u)]$ and strong demagnetizing-like mean-field effects.

(MP-iii) The situation of greater physical interest is when both local random interactions and mean-field effects are present. We know from Eq. (6) that random interactions give rise to a demagnetizing-like Henkel plot, so that it is natural to consider whether it might be possible to compensate such effect by some positive mean-field contribution capable of reducing the Henkel plot to the noninteraction line. It results that this is in general not possible. Positive mean fields have a strong influence on the Henkel plot at low i_r, but quite a weak one around $i_r\sim i_\infty$. As a consequence, the joint presence of random interactions and magnetizing-like mean-fields will result in oscillating Henkel plots, crossing the noninteraction line (see Fig. 1).

(MP-iv) Equation (7) is strongly modified (in a way similar to Fig. 1) under positive k, but it is weakly affected by a negative k. This gives further support to its universal character.

III. APPLICATIONS

The Wohlfarth relation is expected to apply to assemblies of noninteracting single-domain particles,[12] as well as

to DWs in continuous media interacting with a fixed distribution of pinning sites.[17] Henkel plot nonlinearities should thus reveal magnetic interactions in a vast class of magnetic systems. There have been in fact numerous attempts to apply Henkel plots and related delta-I plots to superconductors, hard magnets, magnetic recording media, thin films and multilayers, soft materials. If we look at these results having in mind the conclusions of our previous analysis, we realize that many of the observed features can find a natural interpretation in the frame of MPM.

A first interesting case is the study of hysteresis in type-II and high-T_c superconductors. A direct application of our results is made possible by the equivalence[18] between PM and the critical state Bean model[19] for the description of flux penetration in the presence of fluxoid pinning effects. Recent investigations[20,21] show that the Henkel plot lies within the region described by Eq. (6). The Preisach density associated with the Bean model is easily evaluated[18] and the corresponding Henkel plot can be analytically calculated. In this way, the interpretation by MPM of the deviations of experimental Henkel plots from the Bean model prediction can be exploited to extract information on the fluxoid density profile inside the system. Studies on permanent magnets[22,23] give Henkel plots all lying in the magnetizing-like region. This is a certain indication of the presence of magnetizing-like mean-field effects of dominant intensity with respect to local interactions. In fact, an accurate fit of Henkel plots can be obtained from Eqs. (2) and (3), with $\sigma_u \sim 0$ and positive k.[16] Wide interest is currently devoted to the study of systems for high-density magnetic recording. BaFe media with different amounts of doping exhibit oscillating Henkel plots of rich and complex structure.[24] Interestingly enough, the observed behavior is basically that illustrated by Fig. 1. In fact, it is shown in Ref. 25 that the experimental data can be naturally described through MPM, by making the mean-field parameter k dependent on doping, probably as a consequence of different correlated particle arrangements in the doped media.

Dipolar interactions in thin-film media for perpendicular recording raise intriguing problems. The description in terms of the macroscopic demagnetizing field associated with the slab geometry of the problem is usually oversimplified, because it completely disregards the random deviations of local fields from the mean-field value, related to the magnetic moment orientations in neighboring switching elements. As an example, let us consider the behavior of Alumite,[26] a system which, although not yet of direct practical interest, is most interesting as a model material for perpendicular magnetization processes. A typical Alumite system consists of a thin layer of porous aluminum oxide, whose pores are filled in by electrodeposition with a magnetic material (Fe in the case considered here). The result is an exagonal array of Fe columns, switching from up to down magnetization under the external field action. In addition, reversible magnetization processes are found to have a minor role with respect to irreversible switching. The situation thus very much resembles the one assumed in MPM. The value of the mean-field parameter k is expected to be controlled by the thin-film demagnetizing factor, i. e., $kH_c/I_s \sim -1/\mu_0$ [see Eq. (3)].

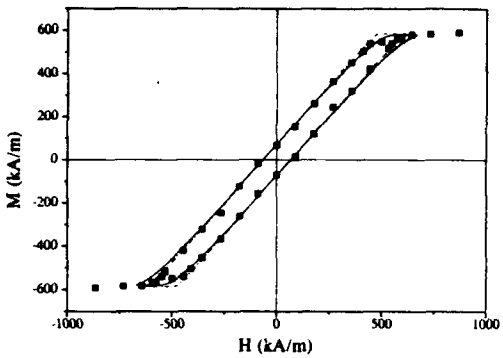

FIG. 2. Hysteresis loop for Alumite. Solid squares: experimental data after Ref. 26. Lines: MPM prediction obtained from Eqs. (2) and (3), with $H_c=65$ kA/m, $I_s/\mu_0=580$ kA/m, $\sigma_c=0.2$, and $\sigma_u=1$, $k=-7$ (continuous), $\sigma_u=0.01$, $k=-8$ (broken).

With the parameter values reported in Fig. 2 ($H_c=65$ kA/m, $I_s/\mu_0=580$ kA/m) we obtain $k \sim -9$. More detailed calculations of the magnetostatic energy of the columns array[27] show that an approximate 10% reduction of this value is expected, which gives $k \sim -8$. To this estimate, some description of random local field deviations from the mean-field value must be added. The authors in Ref. 26 claim that Henkel plots can provide but poor information in this respect when demagnetizing fields are dominating. In the frame of MPM, however, a certain number of considerations of potential physical interest can be worked out. A typical hysteresis loop measured on Alumite and the associated Henkel plot are shown in Figs. 2 and 3. According to what was said in (P-ii), the downward jump in i_d at $i_r=0$ indicates that the distribution $f(h_c)$ of individual column coercivities is rather narrow, with no contribution for $h_c \sim 0$. This is reasonable, since one does not expect large differences in the morphology of individual columns. In terms of the lognormal distribution of Eq. (2), this is described by values $\sigma_c \ll 1$. In our analysis, we assumed $\sigma_c=0.2$. The overall Henkel plot shape, on the other

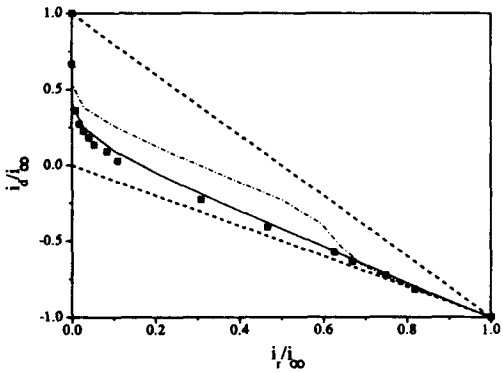

FIG. 3. Henkel plot for Alumite. Meaning of symbols and lines is the same as in Fig. 2. The broken straight lines indicate the region described by Eq. (6).

hand, indicates the presence of a substantial distribution of random interactions $g(h_u)$. In fact, as discussed in (MP-ii), if random interactions were not present [i.e., $p(h_c,h_u)\sim f(h_c)\delta(h_u)$], the Henkel plot would tend to become discontinuous under strong negative mean fields, which is not observed in measurements. Figures 2 and 3 illustrate this conclusion. The two theoretical hysteresis loops were calculated under different combinations of σ_u and k values. A reasonable fit is obtained in both cases, but the Henkel plot under small σ_u is in definite disagreement with experiments. A more detailed analysis of this type should in principle permit one to estimate a lower bound for the random interaction variance, to be compared with the predictions of models connecting the statistical distribution of local dipolar fields with the correlation properties of magnetic moment orientations in neighboring switching elements.

IV. SOFT MATERIALS

We tested MPM predictions for soft materials by performing specific hysteresis and Henkel plot measurements on single strips (length 200 mm, width 10 mm, thickness 0.18 mm) of 1.8 wt % Si-Fe polycrystalline alloys (grain size ~50 μm). The magnetization $i(h)$ associated with various field histories was measured by a computer-driven low-drift fluxmetric setup. The virgin magnetization curve, the saturation and minor hysteresis loops as well as the first-order reversal curves associated with i_r and i_d were measured. The degree of flux closure at the strip ends was varied by adjusting the air gap between the strip and a flux-closing permalloy yoke. In this way, it was possible to change the apparent permeability of the system by more than one order of magnitude, in order to make an accurate study of mean-field effects. The demagnetized state was generated by applying an ac field of amplitude slowly decreasing to zero. Some test measurements of i_r were performed, in which the curve $i_r(h_a)$ was first measured by demagnetizing the system before each field application and removal, and then by demagnetizing the system only once, before the first field application. It was checked that the results given by the two methods were coincident within experimental errors, after which only the much quicker latter method was employed. It is worth remarking that the coincidence of the two measurement methods is expected for any system described by PM. It corresponds to the so-called wiping out property.[1] In the Henkel plot construction, The $i_d(h_a)$ and $i_r(h_a)$ datasets were conveniently interpolated in order to evaluate the remanences at exactly the same field values.

In the interpretation of experiments, it was necessary to include some treatment of reversible processes (coherent magnetization rotations inside domains, reversible DW motion in a single potential well) which play an important role in soft materials. In Fe-based alloys, coherent rotations become important at fields much higher than the coercive field. This permitted us to take due account of rotations by properly reducing the value of the saturation magnetization I_s and by assuming that I_s was associated with DW processes only. The contribution to I_s coming from reversible DW motion was described in terms of the permeability $\mu_{rev}=\mu_i \exp(-|H|/H_{rev})$, dependent on the field H only. This

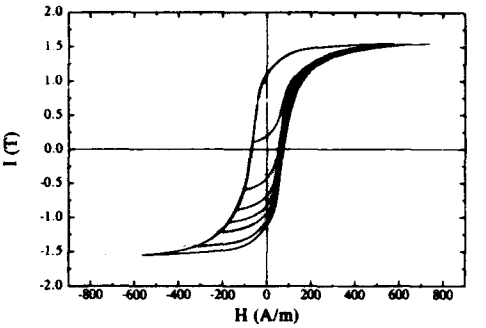

FIG. 4. Hysteresis loop and reversal curves for Si-Fe. The air gap between the strip and the yoke was adjusted in order to approach zero-mean-field conditions. Continuous lines: experimental data. Broken lines: MPM prediction calculated from Eqs. (8) and (3), with $H_c=55$ A/m, $I_s=1.65$ T, $d=1.2$, and $k=0$.

is a strong approximation which disregards the dependence of μ_{rev} on the actual state of the system at a given field. In the literature there are much more refined and detailed treatments of this problem.[28] Yet, this simple description was sufficient for our purposes. We point out that a reversible contribution of this form modifies magnetization curves but has no influence on Henkel plots. The parameters μ_i and H_{rev} were determined by measuring $\mu_{rev}(H)$ at various points along the virgin magnetization curve. A reasonable fit of the data was obtained by setting $\mu_i/\mu_0=800$ and $H_{rev}=200$ A/m, which corresponds to a contribution $\Delta I_{rev}\approx 0.2$ T to I_s. The magnetization $(I_s-\Delta I_{rev})$ associated with irreversible DW motion (Barkhausen jumps) was described by MPM, assuming a Preisach distribution of the form

$$p(\alpha,\beta)=f(\alpha)f(-\beta), \quad f(\alpha)\propto \frac{1}{[1+(\alpha/d)^2]}. \tag{8}$$

As mentioned in the introduction, the factorization $p(\alpha,\beta)=f(\alpha)f(-\beta)$ is expected when DW motion in a random potential is the dominant magnetization mechanism.[11] The Lorentzian character of $f(x)$ is suggested by previous results[29] and was confirmed by the present experiments. A good fit of all hysteresis loops and reversal curves was in fact obtained by choosing $d=1.2$. An example is given in Fig. 4. Several sets of measurements under varying degree of flux closure were performed. We found that all the data could be reproduced by the same Preisach distribution, and that only the mean-field parameter k had to be adjusted in the range from $k=-3.5$ (open strip) to $k=1$ (yoke in full contact with the strip). The Henkel plots of Fig. 5 give revealing evidence of the nature of the interactions present in the system. The Henkel plot for the open strip is close to the universal law given by Eq. (7). We recall that this law is expected when the Preisach distribution takes the form $p(\alpha,\beta)=f(\alpha)f(-\beta)$, and that this factorization is expected when stochastic DW motion is the dominant magnetization mechanism.[11] The deviation from this behavior for the closed circuit measurement is accurately reproduced by MPM under positive k and is thus a clear indication of the presence of magnetizing-like

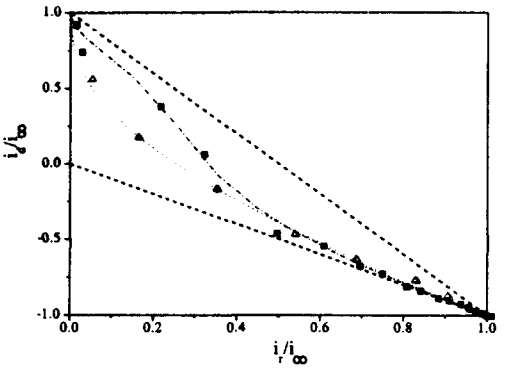

FIG. 5. Henkel plots for SiFe. Symbols: experimental data for open strip (triangles) and yoke in full contact with the strip (squares). Lines: MPM prediction calculated from Eqs. (8) and (3), with $d=1.2$ and $k=-3.5$ (dotted), $k=1$ (dashed dotted). The broken straight lines indicate the region described by Eq. (6).

mean-field interactions. Such mean-field effects, also observed in loss measurements on amorphous materials,[14] should be strictly related to the mechanisms controlling the longitudinal propagation of Barkhausen avalanches.

These results suggest that it should be possible to compensate the internal magnetizing-like interactions by a demagnetizing field of convenient intensity. Figures 4 and 6 show what we obtained by properly adjusting the air gap between the strip and the yoke in order to approach as much as possible zero-mean-field conditions. The PM predictions were calculated as before from Eqs. (8) and (3), with $d=1.2$ and $k=0$. We stress that the remarkable agreement of experimental Henkel plot data with Eq. (7) does not involve any adjustable parameter. It is the direct consequence of the Preisach distribution factorization properties and of the fact that

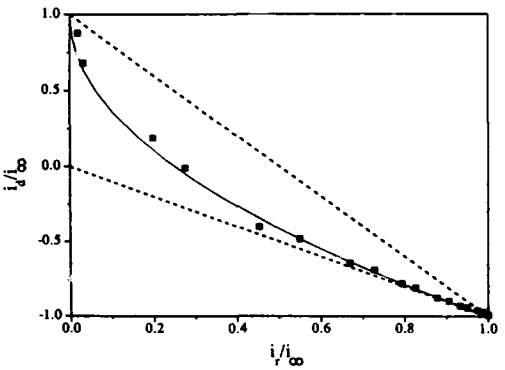

FIG. 6. Henkel plot for SiFe under the same conditions of Fig. 4. The continuous line represents Eq. (7). No adjustable parameter is involved in the comparison.

magnetizing-like internal interactions and macroscopic demagnetizing fields, having the same physical nature, can be balanced out to zero.

V. CONCLUSIONS

The analysis presented in this paper shows that MPM can be a useful tool in the characterization and interpretation of interaction effects and Henkel plots in magnetic systems. This mainly comes from the ability of MPM to deal in a unified way with local pinning, local random interactions and mean-field effects. The joint presence of these contributions gives rise to a rich and complex phenomenology (e.g., oscillating Henkel plots) which is in remarkable agreement with experimental findings. We tested some of these predictions by hysteresis measurements on soft materials, for which there are relatively few Henkel plot studies in the literature. Our measurements are accurately reproduced by MPM, in some cases with no adjustable parameters. These results greatly support the value of MPM as a physical model for the description of ferromagnetic hysteresis and call for additional studies aiming at deriving the basic properties of the Preisach distribution (factorization, Lorentzian or Gaussian or lognormal shape, etc.) from microscopic models of magnetization processes.

[1] I. D. Mayergoyz, *Mathematical Models of Hysteresis* (Springer, New York, 1991).
[2] L. Néel, J. Phys. Radiat. **20**, 215 (1959).
[3] E. Della Torre, IEEE Trans. Audio **14**, 86 (1966).
[4] F. Vajda and E. Della Torre, IEEE Trans. Magn. **27**, 4757 (1991).
[5] G. Bertotti and M. Pasquale, J. Appl. Phys. **67**, 5255 (1990).
[6] G. Bertotti and M. Pasquale, J. Appl. Phys. **69**, 5066 (1991).
[7] J. P. Sethna, K. Dahmen, S. Kartha, J. A. Krumhansl, B. W. Roberts, and J. D. Shore, Phys. Rev. Lett. **70**, 3347 (1993); this conference, paper CA-07.
[8] V. Basso, M. Lo Bue, A. Magni, G. Ummarino, and G. Bertotti, SMM-11, Venezia, Italy, 1993, Paper S1-35, *to be published in* J. Magn. Magn. Mater.
[9] L. Néel, Cahiers de Physique **12**, 1 (1942).
[10] O. Henkel, Phys. Status Solidi **7**, 919 (1964).
[11] G. Bertotti and V. Basso, J. Appl. Phys. **73**, 5827 (1993).
[12] E. P. Wohlfarth, J. Appl. Phys. **29**, 595 (1958).
[13] P. R. Bissell, R. W. Chantrell, H. J. Lutke-Stetzkamp, S. Methfessel, G. W. Spratt, and E. P. Wohlfarth, J. Phys. (Paris) **49-C8**, 1925 (1988).
[14] G. Bertotti, F. Fiorillo, and M. Pasquale, Proceedings of the Intermag '93, Stockholm, Sweden, 1993, IEEE Trans. Magn. **29**, (1993).
[15] G. Biorci and D. Pescetti, Il Nuovo Cimento **7**, 829 (1958).
[16] V. Basso and G. Bertotti, IEEE Trans. Magn. (in press).
[17] R. A. McCurrie and P. Gaunt, *Proceedings of ICM '64* (The Institute of Physics, London, 1964), p. 780.
[18] I. D. Mayergoyz and T. A. Keim, J. Appl. Phys. **67**, 5466 (1990).
[19] C. P. Bean, Rev. Mod. Phys. **36**, 31 (1964).
[20] K. Moloni and E. D. Dahlberg, J. Appl. Phys. **73**, 5842 (1993).
[21] K. Moloni and E. D. Dahlberg, J. Appl. Phys. **73**, 5868 (1993).
[22] P. Gaunt, G. Hadijpanayis, and D. Ng, J. Magn. Magn. Mater. **54–57**, 841 (1986).
[23] G. J. Tomka, P. R. Bissell, K. O'Grady, and R. W. Chantrell, IEEE Trans. Magn. **26**, 2655 (1990).
[24] P. I. Mayo, A. Bradbury, R. W. Chantrell, P. E. Kelly, H. E. Jones, and P. R. Bissell, IEEE Trans. Magn. **26**, 228 (1990).
[25] G. Bertotti, V. Basso, and M. Pasquale, EMMA '93, Kosice, Slovakia 1993, Paper I-1-02, to be published in IEEE Trans. Magn.
[26] E. O. Samwel, P. R. Bissell, and J. C. Lodder, J. Appl. Phys. **73**, 1353 (1993).
[27] E. O. Samwel, P. R. Bissell, and J. C. Lodder, J. Magn. Magn. Mater. **115**, 327 (1992).
[28] F. Vajda and E. Della Torre, J. Appl. Phys. **73**, 5833 (1993).
[29] G. Bertotti, F. Fiorillo, and G. P. Soardo, J. Phys. (Paris) **49-C8**, 1915 (1988).

Experimental testing of applicability of the Preisach hysteresis model to superconductors

G. Friedman and L. Liu
Electrical Engineering and Computer Science Department, University of Illinois at Chicago, Chicago, Illinois 60657

J. S. Kouvel
Physics Department, University of Illinois at Chicago, Chicago, Illinois 60657

Applicability of the Preisach hysteresis model to superconductive hysteresis is tested on two types of materials using a vibrating sample magnetometer. The experiments are set up to check if the hysteresis displayed by the two samples satisfies the necessary and sufficient conditions for the applicability of the Preisach model. These conditions are wiping out of some field history by certain subsequent field extrema and congruency of minor hysteresis loops corresponding to the same field cycles, but having different histories. Observation of the measured minor hysteresis loops indicates that the two conditions are satisfied for the two samples tested. For this reason, it can be concluded that the Preisach model is a very accurate representation of superconductive hysteresis, at least for some superconducting materials.

It is well known that changes of the magnetic flux distribution in type-II superconducting samples can be hindered by defects and inhomogeneities in the material. This phenomenon is referred to as flux pinning. On the one hand, flux pinning leads to higher critical currents in type-II superconductors. On the other hand, it is also responsible for hysteresis between the applied magnetic field and the persistent currents in the sample (or, equivalently, sample magnetization). Models of superconducting hysteresis are needed to predict the persistent currents for arbitrary variations of the applied field. A phenomenological model[1] was proposed by Bean. Bean's model is based on an idealized step-like constitutive law between the persistent current density and the electric field. As a result, magnitude of the persistent current density within the material is taken to be constant and equal to a critical current density J_c, which can be viewed as a model parameter. In some generalizations of the Bean model[2] the critical current density parameter is a function of the flux density, $J_c(B)$.

An important limitation of the critical state models is the following. Distribution of persistent currents have been found analytically for those samples which are shaped like plane slabs and circular cylinders. Computing persistent currents in samples of arbitrary shapes requires numerical implementation of the critical state models which is complicated by the need to resolve rapid variations of the persistent current density. This problem is compounded by the fact that locations of such rapid variations within the sample depend on history and are not known *a priori*. In addition, questions regarding the applicability of the critical state models to superconductors remain largely unanswered.

In a recent work,[3] Mayergoyz has shown that the critical state models are very particular cases of a more general phenomenological hysteresis model known as the Preisach model. These cases correspond to a particular choice of parameters of the Preisach model (Preisach function). This article will focus on the applicability of the Preisach model to superconductive hysteresis. The experiments were performed on two different superconducting materials using a vibrating sample magnetometer and results indicate that the Preisach model gives a very accurate description of superconductive hysteresis. Before the discussion of the experiments and their results, a brief review of the Preisach model will be presented.

From a control theory point of view, the original Preisach model[5] can be regarded as a mathematical operator relating a scalar input, $u(t)$, to an output, $f(t)$. This operator, in turn, is assembled from many elementary operators which are bistable relays with different switching thresholds. The output of each relay, denoted by $\hat{\gamma}_{\alpha\beta}u(t)$, can take on the value of either 1 or -1. The relay remains in one of the two possible output states until the input forces it to switch to the other state by increasing above an upper threshold α or decreasing below a lower threshold β. Thus, a pair of thresholds (α,β) such that $\alpha \geq \beta$ uniquely defines the behavior of each relay.

The output of the Preisach model is obtained by weighting the output of each relay and summing the results over all possible threshold pairs. Mathematically, this statement can be expressed as follows:

$$f(t)=\iint_{\alpha\geq\beta} \mu(\alpha,\beta)\hat{\gamma}_{\alpha\beta}u(t)d\alpha\, d\beta, \tag{1}$$

where $\mu(\alpha,\beta)$ is the weight function called the Preisach function. This function constitutes a set of parameters for the model and has to be identified by matching the model output to experimental data for specific variations of the input.

The technique suggested for the parameter identification[4] is based on obtaining a set of first-order transition curves experimentally. A first-order transition curve is obtained when, after saturation is reached, the input (magnetic field) is increased to some value x and then reversed back to reach material saturation. Let f_{xy} denote the value of the output (magnetization) when the input value is y and a reversal at value x has taken place. The following function is easily computed from a set of first-order transition curves:

$$F(x,y)=\tfrac{1}{2}(f_{xx}-f_{xy}). \tag{2}$$

Input variation used to obtain the first-order transition curves can also be applied to the Preisach model. Matching the out-

 0021-8979/94/75(10)/5683/3/$6.00 © 1994 American Institute of Physics

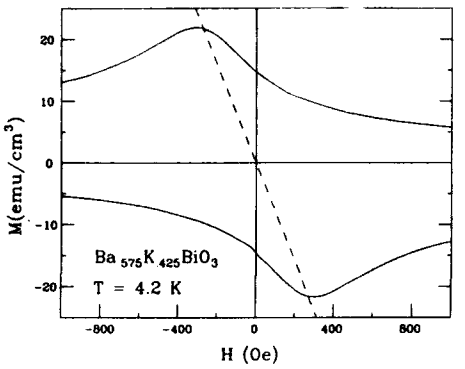

FIG. 1. Major hysteresis loop for the $BaKBiO_3$ sample.

put of the model to the output of the experiment, it can be shown that[4]

$$\mu(x,y) = -\frac{\partial^2 F(x,y)}{\partial x \partial y}. \tag{3}$$

Thus, it is possible to find such model parameters that the output of the model matches experimental observations for a specific type of input variation. The question arises: Does there exist a set of model parameters (Preisach function) such that the model output matches experimental observations for arbitrary input variations? If the answer is affirmative, the model is fully applicable to a given hysteresis nonlinearity. Otherwise, the applicability of the Preisach model is limited to some specific input variations such as those producing first-order transition curves.

Mayergoyz's representation theorem[4] helps to determine the extent of applicability of the Preisach model. The theorem states that an arbitrary hysteresis nonlinearity can be represented by the Preisach model if and only if this nonlinearity satisfies two conditions: wiping out of some field history by certain subsequent field extrema and congruency of

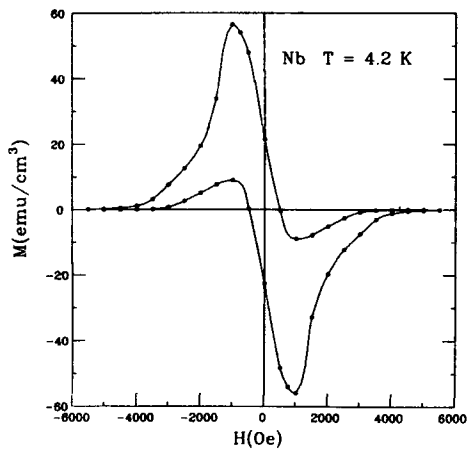

FIG. 2. Major hysteresis loop for the Nb sample.

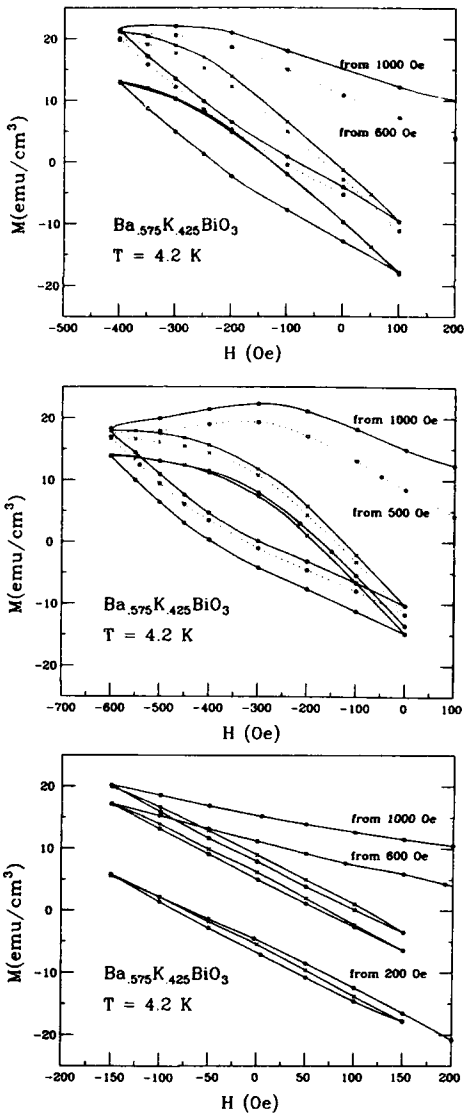

FIG. 3. Minor hysteresis loops corresponding to the same field cycles and different histories for the $BaKBiO_3$ sample.

all minor hysteresis loops formed by cycling of the field between the same extrema. These two conditions will be discussed next.

For a hysteresis nonlinearity, field history consists of past field extrema. Wiping out occurs if a field maximum and following it minima are erased from history when a greater maximum is encountered. Similarly, wiping out occurs if a field minimum and following it maxima are erased when a smaller minimum is encountered. An important consequence

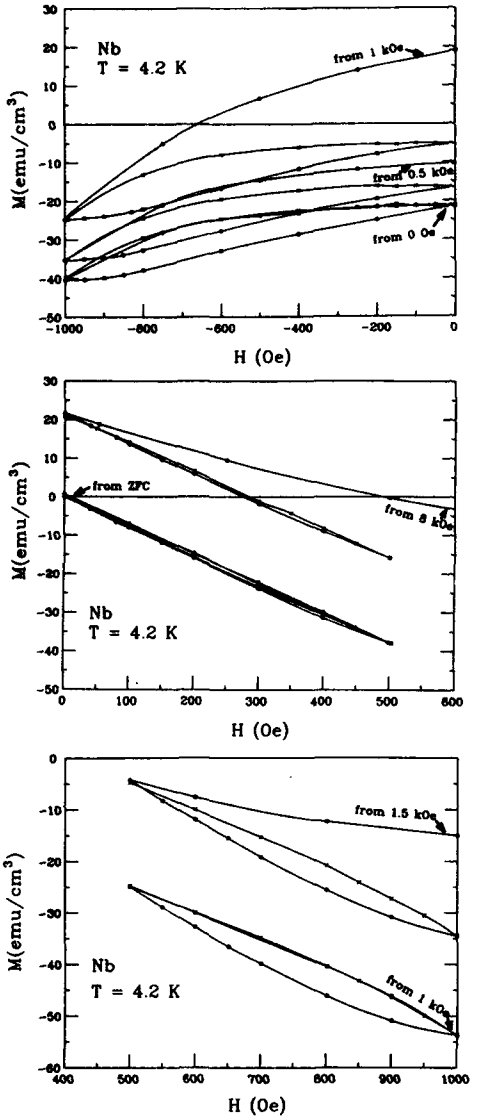

FIG. 4. Minor hysteresis loops corresponding to the same field cycles and different histories for the Nb sample.

of the wiping-out condition is closure of minor hysteresis loops at the end of the first cycle in field variation. The existence of a major hysteresis loop in many materials indicates that wiping out does occur to some extent. However, for minor hysteresis loops, reptations[6] (nonclosure) are often observed in many magnetic materials.

If the wiping-out condition occurs, minor hysteresis loops are formed. Different loops will result from different field histories even if the cycles of the field which form the loop are the same (have the same extrema). The second condition is satisfied if all loops which can be formed by the same field cycles are congruent. It is worth noting that in many magnetic materials, congruency has not been observed.[6]

Experiments were carried out to test the extent of applicability of the Preisach model to superconductive hysteresis. Two superconducting samples were used. One is a high-temperature superconductor $Ba_{0.575}K_{0.425}BiO_3$. The other is niobium (Nb). $BaKBiO_3$ material was prepared in the form of sintered powder. Individual crystallites of the material ranged in size between few microns and one hundred microns when viewed under a microscope. The H_{c2} field for this material was much larger than 15 kOe, which is the highest magnetic fields attainable with the magnet of our vibrating sample magnetometer. It was, however, possible to come close to the major hysteresis loop for this material. The increasing and decreasing branches of hysteresis loops obtained by cycling the field between extrema greater than 8 kOe coincided, except for a portion where transitions between the loop branches occurred. For this reason, it can be concluded that branches of the major loop are close to those shown in Fig. 1. Nb sample was prepared from a Nb powder and held together by an epoxy. The major loop for this sample is shown in Fig. 2. The samples of each material were made in the shape of a disc of about 1 mm thick and 5 mm in diameter. All the experiments were conducted at 4.2 K to avoid flux creep.

The wiping-out property of the superconductive hysteresis was checked by observing closure of minor hysteresis loops at the end of the first cycle of the magnetic field. To observe the congruency property, minor hysteresis loops were formed by cycling the magnetic field. Before cycling, a large negative value of the magnetic field was applied in order to reach the major hysteresis loop. After the major loop was reached, the magnetic field was increased to some value and reversed. After the reversal, magnetic field was cycled between two extrema. The resulting hysteresis loops corresponding to the same field cycles and to different field reversals prior to cycling are shown in Fig. 3 for the $BaKBiO_3$ sample. Minor hysteresis loops for different field histories prior to field cycling for the Nb sample are shown in Fig. 4. The number of hysteresis loops presented here is limited by constraints on the length of this article. However, many hysteresis loops were observed and show similar behavior. These observations indicate that the Preisach model is a very accurate representation of the hysteresis phenomenon in these superconductors.

[1] C. P. Bean, Phys. Rev. Lett. **8**, 250 (1962).
[2] Y. B. Kim, C. F. Hempstead, and A. R. Strnad, Phys. Rev. Lett. **9**, 306 (1962).
[3] I. D. Mayergoyz, *Mathematical Models of Hysteresis* (Springer, New York, 1991).
[4] I. D. Mayergoyz, Phys. Rev. Lett. **56**, 1518 (1986).
[5] F. Preisach, Z. Phys. **94**, 277 (1935).
[6] C. Salling and S. Schultz, J. Appl. Phys. **61**, 4010 (1987).

2D vector Preisach models and rotational hysteretic losses

I. D. Mayergoyz
Electrical Engineering Department and Institute for Advanced Computer Studies, University of Maryland, College Park, Maryland 20742

Depending on the physical nature of hysteresis, rotational hysteretic losses in isotropic materials may decrease to zero or even continuously increase with the increase in the magnitude of uniformly rotating magnetic fields. It is shown in the paper that recently developed 2D Preisach models of vector hysteresis accommodate this broad spectrum of behavior of rotational hysteretic losses.

It is well known that in the case of isotropic hysteresis a uniformly rotating magnetic field results in uniformly rotating magnetization. This magnetization lags behind the magnetic field due to hysteretic losses. Depending on the physical nature of hysteresis, these losses may decrease to zero or even continuously increase as the magnitude of the uniformly rotating magnetic field is increased. It is the generally held opinion that the former case is realized for magnetic hysteresis,[1–3] while there is some credible evidence that the latter case is true for superconducting hysteresis.[4] Successful Preisach models of vector hysteresis should be able to accommodate this broad spectrum of behavior of rotational hysteretic losses. The purpose of this work is to demonstrate that this is true for 2D isotropic vector Preisach models recently proposed in Refs. 5 and 6.

These models can be mathematically formulated as follows:

$$\mathbf{f}(t) = \int_{-\pi/2}^{\pi/2} \mathbf{e}_\varphi \left(\iint_T \nu(\alpha,\beta)\hat{\gamma}_{\alpha\beta}\,|\mathbf{u}(t)|\,g(\theta(t)-\varphi)\,d\alpha\,d\beta \right) d\varphi, \tag{1}$$

where $\mathbf{f}(t)$ is the model output (magnetization) at time t, $\theta(t)$ is the polar angle which defines the orientation of the input (magnetic field) $\mathbf{u}(t)$ at time t, $\mathbf{e}_\varphi$ is a unit vector along the direction specified by a polar angle φ, and $\hat{\gamma}_{\alpha\beta}$ are elementary hysteresis operators represented by rectangular loops with α and β being "up" and "down" switching values, respectively, while T is the triangle $\{-\alpha_0 \leq \beta \leq \alpha \leq \alpha_0\}$ which contains the support of $\nu(\alpha,\beta)$. Further details concerning the notations used here can be found in Ref. 7.

In the above models, functions $\nu(\alpha,\beta)$ and $g(\varphi)$ are not specified in advance but rather should be determined by fitting these models to some experimental data. This is an identification problem. This problem together with experimental testing of these models was first discussed in Ref. 5 for a particular case of $g(\varphi)=\cos^{1/n}\varphi$, $(n>1)$. Then, the identification problem was studied in Ref. 6 for a general case of $g(\varphi)$ subject to the natural constraints

$$g'(\varphi)\leq 0, \quad g(0)=1, \quad g(\pi/2)=0,$$

$$g(\pi)=-1, \quad g(\pi-\varphi)=-g(\varphi). \tag{2}$$

It will be shown below that with appropriate choice of function $g(\varphi)$ [within the constraints (2)] the model (1) is able to replicate various asymptotic behavior of rotational hysteretic losses.

Consider a uniformly rotating input (that is one of constant magnitude and angular velocity)

$$\mathbf{u}(t)=\{u_x(t)=u_m\cos\omega t, \quad u_y(t)=u_m\sin\omega t\}. \tag{3}$$

Then, by literally repeating the same line of reasoning as in Ref. 7 (pp. 161–165), it can be shown that the output of model (1) can be represented as

$$\mathbf{f}(t)=\mathbf{f}_0+\mathbf{f}_1(t), \tag{4}$$

where $\mathbf{f}_0$ is a history-dependent constant component of $\mathbf{f}(t)$,

$$\mathbf{f}_0=\text{const}, \tag{5}$$

while $\mathbf{f}_1(t)$ is a uniformly rotating vector:

$$\mathbf{f}_1(t) = \{f_{1x}(t)=f_m\cos(\omega t-\delta), \quad f_{1y}(t)=f_m\sin(\omega t-\delta)\}. \tag{6}$$

By using Eqs. (3)–(6) it can be easily shown that the following expression is valid for rotational hysteretic losses per one cycle:

$$L=\oint \mathbf{u}\cdot d\mathbf{f}=2\pi u_m f_m\sin\delta. \tag{7}$$

Now, by using exactly the same way of reasoning as in Ref. 7 (pp. 161–166), the following formula can be derived:

$$B=f_m\sin\delta = 2P(u_m,-u_m)-2\int_0^\pi \sin\theta P(u_m,u_m g(\theta))\,d\theta, \tag{8}$$

where the function $P(\alpha,\beta)$ is defined by (see Fig. 1)

 0021-8979/94/75(10)/5686/3/$6.00 © 1994 American Institute of Physics

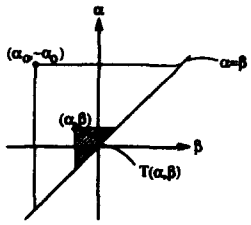

FIG. 1. Geometric illustration of $P(\alpha,\beta)$.

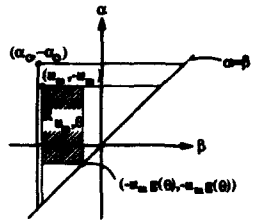

FIG. 2. Geometric illustration of $F(u_m,\theta)$.

$$P(\alpha,\beta)=\int\int_{T(\alpha,\beta)} \nu(\alpha',\beta')d\alpha'\,d\beta'. \tag{9}$$

The subsequent analysis of rotational hysteretic losses is based on a special transformation of expression (8). This transformation proceeds as follows:

$$f_m \sin\delta=\int_0^{\pi/2} \sin\theta[P(u_m,-u_m)-2P(u_m,u_m g(\theta))]d\theta$$

$$+\int_{\pi/2}^{\pi} \sin\theta[P(u_m,-u_m)-2P(u_m,u_m g(\theta))]d\theta. \tag{10}$$

Next, the following change of variables is used in the second integral in Eq. (10):

$$\theta'=\pi-\theta. \tag{11}$$

From Eqs. (11) and (2), we find

$$d\theta=-d\theta',\quad \sin\theta=\sin\theta',\quad g(\theta)=-g(\theta'). \tag{12}$$

By using Eq. (12), the last integral in Eq. (10) can be transformed as follows:

$$\int_{\pi/2}^{\pi} \sin\theta[P(u_m,-u_m)-2P(u_m,u_m g(\theta))]d\theta$$

$$=\int_0^{\pi/2} \sin\theta'[P(u_m,-u_m)-2P(u_m,-u_m g(\theta'))]d\theta'. \tag{13}$$

By substituting Eq. (13) into Eq. (10) and by changing θ' to θ, we obtain

$$f_m \sin\delta$$

$$=2\int_0^{\pi/2} \sin\theta[P(u_m,-u_m)-P(u_m,u_m g(\theta))$$

$$-P(u_m,-u_m g(\theta))]d\theta. \tag{14}$$

We shall next introduce the function

$$F(u_m,\theta)=P(u_m,-u_m)-P(u_m,u_m g(\theta))$$

$$-P(u_m,-u_m g(\theta)). \tag{15}$$

By using definition (9), the fact that $P(u_m,u_m g(\theta))=P(-u_m g(\theta),-u_m)$ and Fig. 2, it is easy to conclude that function $F(u_m,\theta)$ is equal to the integral of $\nu(\alpha,\beta)$ over the shaded rectangle $R_{u_m,\theta}$:

$$F(u_m,\theta)=\int_{R_{u_m,\theta}}\int \nu(\alpha,\beta)d\alpha\,d\beta. \tag{16}$$

By using Eq. (15) in Eq. (14), we find.

$$f_m \sin\delta=2\int_0^{\pi/2} F(u_m,\theta)\sin\theta\,d\theta. \tag{17}$$

It is clear from Eq. (16) and Fig. 2 that

$$F(u_m,\theta)=0, \tag{18}$$

if

$$u_m g(\theta)\geqslant\alpha_0. \tag{19}$$

This means that for sufficiently large magnitude u_m expression (17) can be transformed as follows:

$$f_m \sin\delta=2\int_{\theta_0}^{\pi/2} F(u_m,\theta)\sin\theta\,d\theta, \tag{20}$$

where

$$\theta_0=g^{-1}(\alpha_0/u_m),$$

and $\theta=g^{-1}(x)$ is the function inverse to $x=g(\theta)$.

According to (2), we have

$$\lim_{u_m\uparrow\infty} g^{-1}\left(\frac{\alpha_0}{u_m}\right)=g^{-1}(0)=\frac{\pi}{2}. \tag{21}$$

In connection with Eq. (20), this implies that

$$\lim_{u_m\uparrow\infty} f_m \sin\delta=0. \tag{22}$$

Expression (22) does not necessarily mean that rotational hysteretic losses tend to zero. The asymptotic behavior of these losses depends on how fast $f_m \sin\delta$ approaches zero. This, in turn, depends on asymptotic behavior of $g^{-1}(x)$ for small x. We shall characterize this behavior by expression

$$\pi/2-g^{-1}(x)\simeq cx^{\lambda}. \tag{23}$$

From Eqs. (23), (20), and (7), we then derive

$$L=c_1 u_m^{1-\lambda}. \tag{24}$$

From Eq. (24) we conclude that the rotational hysteretic losses approach zero if $\lambda>1$; these losses approach some constant nonzero value if $\lambda=1$ and they continuously increase if $\lambda<1$.

We shall illustrate the above conclusion with two examples.

Example 1

$$x=g(\theta)=\cos^{1/n}\theta, \quad (n>1). \tag{25}$$

This choice of function g was used in Ref. 5, where the corresponding vector Preisach model has been successfully experimentally tested. For small x, from Eq. (25) we obtain

$$g^{-1}(x)=\cos^{-1}x^n\simeq\pi/2-x^n. \tag{26}$$

By comparing Eqs. (26) and (23), we find that $\lambda=n>1$ and the rotational hysteresis losses approach zero as u_m is increased.

Example 2

$$x=g(\theta)=\cos\theta. \tag{27}$$

This choice of g leads to the vector Preisach models which were extensively studied in Ref. 7. For small x, from Eq. (27) we have

$$\pi/2-g^{-1}(x)=x. \tag{28}$$

This means that $\lambda=1$ and the rotational hysteresis losses approach some nonzero value as u_m is increased.

In conclusion, it is hoped that this paper will clarify the ongoing discussion concerning the ability of vector Preisach-type models to adequately describe the rotational hysteretic losses.

This research is supported by the U.S. Department of Energy, Engineering Research Program.

[1] S. H. Charap and A. Kteza, J. Appl. Phys. 73, 5818 (1993).
[2] H. A. J. Cramer, J. Magn. Magn. Matter 88, 194 (1990).
[3] M. A. Pinto, J. Magn. Magn. Matter 98, 221 (1991).
[4] C. P. Bean, J. Appl. Phys. 41, 2482 (1970).
[5] A. A. Adly and I. D. Mayergoyz, J. Appl. Phys. 73, 5824 (1993).
[6] I. D. Mayergoyz and A. A. Adly, IEEE Trans. Magn. (to be published).
[7] I. D. Mayergoyz, *Mathematical Models of Hysteresis* (Springer, New York, 1991).

Demagnetized-state dependence of Henkel plots. I. The Preisach model

Ferenc Vajda and Edward Della Torre
Institute for Magnetics Research, George Washington University, Washington, D. C. 20052

R. D. McMichael
National Institute of Standards and Technology, Gaithersburg, Maryland 20899

The interpretation of interaction through Henkel plots and Δm plots has become popular in recent years; however, the demagnetized state is often not specified. In this paper, the demagnetized state dependence of Henkel plots is calculated using the classical Preisach model, the moving model, and the complete-moving-hysteresis model. In the calculation of the virgin remanence curve, ac, dc+, and dc− demagnetized states were used. The resulting collection of Henkel plots contains examples of "up" and "down" deviations from the Wohlfarth line by changing the demagnetized state only.

I. INTRODUCTION

A technique that has been gaining popularity in recent years is to use the virgin remanent magnetization curve, $m_r(H)$, and the remanent major hysteresis curve, $m_D(H)$, to characterize interaction in recording media. The virgin remanent magnetization curve starts at a demagnetized state, and traces the remanence as a function of an increasing applied field, H. The major remanent curve starts at positive saturation, and measures the remanence as a function of a decreasing negative field, $-H$. Unless otherwise stated, all magnetization values are normalized to the saturation remanence. The Wohlfarth relation[1] states that, for noninteracting particles, the remanence major loop, $m_D(H)$ is twice the virgin remanent magnetization curve, $m_r(H)$, shifted down by the saturation remanence, that is,

$$m_D(H)=1-2m_r(H). \tag{1}$$

Plots of m_D vs m_r have come to be known as Henkel plots.[2] The difference between the curves can be measured by

$$\Delta m=1-2m_r(H)-m_D(H). \tag{2}$$

Plots of Δm vs H or Δm vs m_D have come to be known as Δm plots.[3] Deviations of the measured Henkel plots from the straight line representing Eq. (1) have been interpreted as indications of "positive" and "negative" interactions depending on whether the measured variation is "above" or "below" the line representing the Wohlfarth relation. In Ref. 4 it is shown that Henkel plots and Δm plots measure a combination of effects, not simply the effect of interaction.

Although $m_r(H)$ depends on the method of demagnetization, in much of the literature the nature of the demagnetization is often not specified, including Wohlfarth's paper.[1] In fact, using the classical Preisach model with no interaction, one can easily show[4,5] that the Wohlfarth relation holds if the virgin state is the ac demagnetized state, but does not hold in case of dc demagnetized states. An experimental analysis of ΔM curves corresponding to different demagnetized states has been presented.[6]

This paper discusses the demagnetized-state dependence of Henkel plots using the classical Preisach model, the moving Preisach model,[7] and the complete-moving-hysteresis (CMH) model.[8] A companion paper[9] discusses the demagnetized-state dependence of Henkel plots using a domain wall motion model. Three demagnetized states have been used in our calculations. The ac demagnetized state is obtained by applying an oscillating field with a slowly decaying amplitude whose initial amplitude is sufficient to saturate. The dc− demagnetized state is obtained by first applying a positive saturating field followed by a negative field that brings the remanence to zero and then removing this field. The dc+ demagnetized state is obtained by first applying a negative saturating field followed by a positive field that brings the remanence to zero and then removing this field.

II. THE CLASSICAL PREISACH MODEL

In the following analysis, it is assumed that the Preisach function is Gaussian in both the critical field distribution and the interaction field distribution, that is,

$$P_{ic}(h_i,h_c)=\frac{1}{2\pi\sigma_c\sigma_i}\exp-\left[\frac{(h_i)^2}{2\sigma_i^2}+\frac{(h_c-h_{ci})^2}{2\sigma_c^2}\right], \tag{3}$$

where σ_c and σ_i are the standard deviation in the critical field and the interaction field, respectively, and h_{ci} is the remanent coercivity. It has been shown that this form of the Preisach function is in agreement with experimental results for a variety of recording media.[10]

The computed Henkel plots for dc+, dc−, and ac demagnetization are shown in Fig. 1. Since the dc+ demagnetization curve is identically zero if $h<h_{ci}$ and is identical to the major remanence curve if $h\geq h_{ci}$, the Henkel plot corresponding to this initial state consists of two straight lines whose coordinates are (0,1) (0,0) and (0,0) (1,−1), respectively. The Henkel plot corresponding to the ac demagnetized state is shown by the solid line. It is noted that, since the Preisach function for recording media given by Eq. (3) is not generally factorizable in the coordinate system of the "up" and "down" switching fields, this curve does not follow the general square root law[5] for ac demagnetized Henkel plots. It can be shown that the virgin curve corresponding to the ac demagnetized state will always lie above that of the dc+ demagnetized state and below that of the dc− demagnetized state;[11] therefore, as seen in Fig. 1, the Henkel plot of the dc− demagnetized state lies above that of the ac demagnetized state for any choice of model parameters. In the limiting case of $\sigma_c=0$, the three demagnetized states, and therefore the three Henkel plots become identical.

 0021-8979/94/75(10)/5689/3/$6.00 © 1994 American Institute of Physics

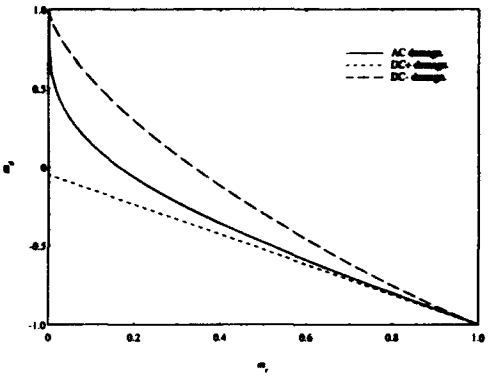

FIG. 1. Henkel plots computed by the classical Preisach model, $h_{ci}=8$, $\sigma_c=20\%$, $\sigma_i=35\%$ of h_{ci}.

III. THE MOVING MODEL

The physical applicability of the moving model[7] to accurately characterize recording media and a robust identification of the moving parameter, α, have been discussed in Refs. 12 and 10, respectively. The Henkel plots computed by the moving model are shown by the dashed curves in Fig. 2 using $\alpha=3.2$ in normalized units. It is noted that the Preisach parameters in this simulation are identical to that of Fig. 1. The ac demagnetized Henkel plot deviates down from the Wohlfarth line, but the variation is significantly different from the corresponding classical model variation. The dc+ demagnetized Henkel plot deviates "up" from the Wohlfarth line showing that it is possible to deviate up or down from the Wohlfarth line using the same model parameters and varying the demagnetized state only.

Using an analogous method to the classical case, it can be shown that the virgin curve of the moving model corresponding to the ac demagnetized state will always lie above that of the dc+ demagnetized state and below that of the dc− demagnetized state; therefore as seen in Fig. 2, the Henkel plot of the dc−demagnetized state lies above that of the ac demagnetized state, for any choice of model parameters. Furthermore, it has also been shown[4] that the moving model computes ac demagnetized Δm plots that deviate down from the Wohlfarth line if α is small and deviate up if α is large. Figure 2 illustrates the case where the moving parameter is such that the ac demagnetized Henkel plot is below the Wohlfarth line and the dc− demagnetized Henkel plot is above the Wohlfarth line.

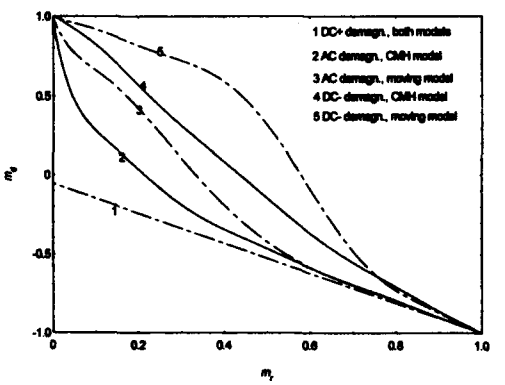

FIG. 2. Henkel plots computed by the moving model and the CMH model.

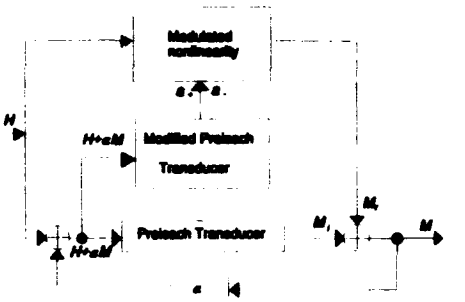

FIG. 3. Block diagram of the CMH model.

IV. THE COMPLETE-MOVING-HYSTERESIS MODEL

The CMH model is a seven-parameter model that accurately computes both the reversible and the irreversible magnetization components and the relationship between these components. The block diagram of the model is shown in Fig. 3, and Fig. 4 shows how the elementary particle hysteresis loops are mathematically decomposed into the sum of an irreversible and a locally reversible component.[13] An identification algorithm for the model has been developed and experimentally tested for various recording materials.[14] The Henkel plots of the CMH model corresponding to the various

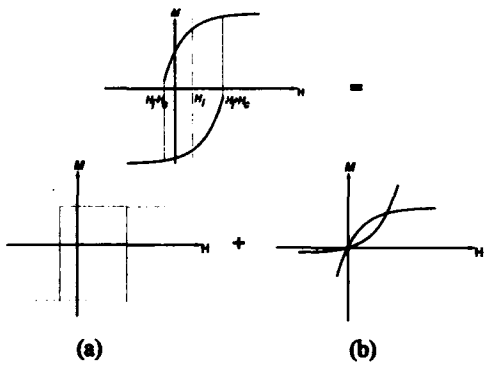

FIG. 4. Decomposition of the CMH model particle hysteresis loop into the sum of an irreversible (a) and a state-dependent locally reversible component (b).

demagnetized states are shown by the solid curves in Fig. 2. The same model parameters were used as for the moving model and the squareness was chosen to be 0.7. The ac demagnetized Henkel plot deviates down from the Wohlfarth line to a greater extent than the corresponding moving model variation. The dc− demagnetized variation deviates up from the Wohlfarth line to a smaller extent than the corresponding moving model variation. These results also show that, although Δm plots and Henkel plots use remanence curves, the computed curves are effected by the state-dependent reversible magnetization that is coupled to the irreversible component through the feedback parameter, α.

V. CONCLUSIONS

A Preisach model based analysis of the Wohlfarth relation shows that the computed Henkel plots are dependent on the demagnetized state. It was shown that the Wohlfarth relation for noninteracting particles holds only if the demagnetized state is ac demagnetization. The effect of demagnetized states was investigated using the classical Preisach model, the moving model, and the CMH model. Using the robust identification technique of the CMH model an experimental analysis of the demagnetized-state dependence of Henkel plots and Δm plots needs to be performed to validate these calculations.

[1] E. P. Wohlfarth, J. Appl. Phys. **29**, 595 (1958).
[2] O. Henkel, Phys. Status Solidi **7**, 919 (1964).
[3] P. E. Kelly *et al.*, IEEE Trans. Magn. **MAG-25**, 3881 (1989); K. O'Grady, *ibid.* **MAG-26**, 1870 (1990); P. R. Bissel and A. Lyberatos, J. Magn. Magn. Mater. **95**, 27 (1991); G. Bottoni *et al.*, *ibid.* **104–107**, 975 (1992).
[4] F. Vajda and E. Della Torre, these proceedings.
[5] G. Bertotti and V. Basso, J. Appl. Phys. **73**, 5827 (1993).
[6] P. R. Bissell, R. W. Chantrell, G. Tomka, J. E. Knowles, and M. P. Sharrock, IEEE Trans. Magn. **MAG-25**, 3650 (1989); M. Fearon, R. W. Chantrell, and E. P. Wohlfarth, J. Magn. Magn. Mater. **86**, 197 (1990).
[7] E. Della Torre, IEEE Trans. Audio Electroacoust. **14**, 86 (1965).
[8] F. Vajda and E. Della Torre, J. Magn. Magn. Mater. **115**, 187 (1992).
[9] R. D. McMichael, F. Vajda, and E. Della Torre, these proceedings.
[10] F. Vajda and E. Della Torre, IEEE Trans. Magn. **MAG-29**, 3658 (1993).
[11] F. Vajda and E. Della Torre, IEEE Trans. Magn. **MAG-28**, 2611 (1992).
[12] F. Vajda and E. Della Torre, IEEE Trans. Magn. **MAG-27**, 4757 (1991).
[13] F. Vajda and E. Della Torre, IEEE Trans. Magn. **MAG-28**, 2611 (1992).
[14] F. Vajda, E. Della Torre, and M. Pardavi-Horvath, J. Magn. Magn. Mater. **120**, 289 (1993).

Demagnetized-state dependence of Henkel plots. II. Domain wall motion

R. D. McMichael
National Institute of Standards and Technology, Gaithersburg, Maryland 20899

Ferenc Vajda and Edward Della Torre
Institute for Magnetics Research, George Washington University, Washington, D.C. 20052

The interpretation of various magnetization curves through Henkel plots and Δm plots has become popular in recent years for characterization of interactions in hysteresis. To investigate this approach, we have calculated Henkel plots using a hysteresis model based on independently moving domain walls. A variety of demagnetized states produced by ac, dc+, and dc− demagnetization methods as well as microscopically and randomly demagnetized states are used to calculate $m_r(H)$. The resulting collection of Henkel plots contains examples of both "positive" and "negative" deviations from the Wohlfarth relation which depend on the demagnetization method. Also, the Henkel plot calculated for the ac demagnetized state deviates from the square-root law previously calculated for domain wall pinning using a classical Preisach model.

I. INTRODUCTION

A technique that has been gaining popularity in recent years is to use the irreversible remanent magnetization curve, $m_r(H)$ and the remanent demagnetization curve $m_d(H)$ to characterize magnetic media. The $m_r(H)$ curve is obtained by starting from a demagnetized state, increasing the field to a value H, and measuring or calculating the magnetization at zero field. The $m_r(H)$ curve depends on the method by which the demagnetized state is produced,[1,2] but often the nature of the demagnetized state has not been specified in the literature. The $m_d(H)$ curve is generated in a similar manner except that the sample is intially saturated in a positive field and the remanent magnetization is measured or calculated after applying a field $-H$. Both the $m_r(H)$ and $m_d(H)$ curves are normalized to the saturation remanence. For noninteracting particles, such as in a Stoner–Wohlfarth (SW) model, the Wohlfarth relation[3] states that

$$m_d(H)=1-2m_r(H), \tag{1}$$

and plots of m_d vs m_r have come to be known as Henkel plots.[4]

Deviations of Henkel plots from the straight line described by Eq. (1) have been interpreted as indications of interactions between particles or magnetic regions.[5–8] If $m_d>1-2m_r$, the interaction is said to be positive (magnetizations in interacting regions tend to align parallel), and if $m_d<1-2m_r$, the interaction is said to be negative (magnetizations tend to align antiparallel).

For cases where magnetization proceeds by domain wall motion and where the coercivity (perhaps dominated by domain wall nucleation) is greater than the field required to sweep a domain wall through a grain, the Wohlfarth relation is expected to hold.[9] However, Bertotti and Basso have recently calculated Henkel plots representing domain wall motion using the classical Preisach model.[10] To represent hysteresis due to domain wall motion, it was assumed that upswitching fields α of magnetization elements are independent of down-switching fields β, and therefore the Preisach distribution function, $p(\alpha,\beta)$ can be factorized as $p(\alpha,\beta)=f(\alpha)\cdot f(-\beta)$. Starting from the ac demagnetized state, the Henkel plot was shown to follow a square-root law

$$m_d=1-2\sqrt{m_r}, \tag{2}$$

for any factorizable Preisach function.[10]

The hysteresis model used in this paper is based on a domain wall potential model first introduced by Neél[11] to describe hysteresis loops in the Raleigh region. In this model, domain wall elements move through a fluctuating pinning field $h_c(x)$ which is proportional to the gradient of the domain wall energy and is assumed to be described by a Langevin equation,[12]

$$\frac{dh_c}{dx}=-\frac{h_c}{\xi}+\frac{dW}{dx}, \tag{3}$$

where ξ is a material correlation length and W is a Gaussian random function such that the expectation values $\langle dW\rangle=0$ and $\langle(dW)^2\rangle=2A\,dx$, where A is a parameter describing the amplitude of W. In addition to the pinning field, the domain wall element is subjected to an applied field, H. For $H>h_c(x)$, the position of the domain wall x will increase, and for $H<h_c(x)$, x will decrease. The motion of each domain wall element continues until it reaches a stable equilibrium at point such that $H=h_c(x)$, and $dh_c/dx>0$ as illustrated in Fig. 1.

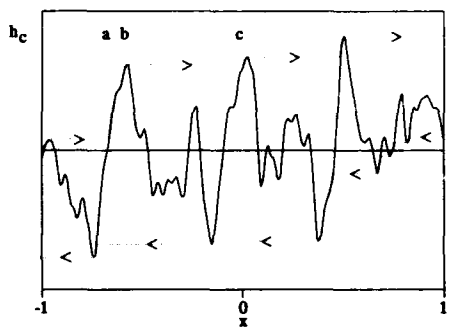

FIG. 1. Example of $h_c(x)$. The trajectory of the domain wall element is shown by the dotted lines.

 0021-8979/94/75(10)/5892/3/$6.00 © 1994 American Institute of Physics

The magnetization M is taken to be the ensemble average value of the domain wall positions, and is limited to saturation values of ± 1 by limiting the domain wall paths to $-1<x<1$. This simple model of domain wall motion results in a hysteretic model of magnetization, complete with minor loops and a combination of reversible and irreversible magnetization processes.[13]

In this paper, we investigate the validity of using Henkel plots for the characterization of interactions in cases where domain wall pinning and motion are the dominant magnetization mechanisms. Henkel plots are calculated using the domain wall model of hysteresis for a variety of demagnetization methods and a variety of correlation length values ξ. In a companion paper, similar results are described for Henkel plots calculated using the classical Preisach model, the moving Preisach model and the complete-moving-hysteresis model.[14]

II. COMPUTATIONAL PROCEDURE

Magnetization values were calculated for 2×10^4 noninteracting domain wall elements propagating between $-1\leq x\leq 1$, with pinning fields $h_c(x)$ generated for each domain wall element by finite differences using Eq. (3) for 1000 values of x. To simplify the comparison between loops calculated with different values of ξ, the parameter A in the random function W is chosen to be $A=1/\xi$ so that $\langle(h_c)^2\rangle=1$.

A number of distinct demagnetization methods were used for the calculations of $m_r(H)$ and the resulting Henkel plots. The "microscopically demagnetized" state was prepared by starting each domain wall at $x=0$ and then allowing each domain wall to propagate to a stable position, and the "randomly demagnetized" state was prepared by placing the domain walls at uniformly distributed random initial positions between -1 and 1 and then allowing the domain walls to propagate to nearby stable positions.

The ac demagnetized state was obtained by applying an oscillating field with a slowly decaying amplitude with an initial amplitude sufficient to saturate M.

The dc− demagnetized state was obtained by first saturating the magnetization in the positive direction, applying a remanent coercive field in the negative direction and then returning the field to $H=0$, yielding $M=0$. The dc+ demagnetized state was obtained by applying a negative saturation field followed by a positive remanent coercive field, and then reducing the field to $H=0$, yielding $M=0$.

Plots of $m_r(H)$ from microscopic, random, ac and dc− demagnetization states and $m_d(H)$ are shown in Fig. 2 for $\xi=0.2$.

III. HENKEL PLOTS

Henkel plots were calculated using the domain wall model for values of ξ ranging from 0.02 to 2.0, and a portion of the results are shown in Fig. 3. In all examined cases, the curves generated using the microscopic, random, and dc− demagnetized states were found to be grouped together, and the curve generated using the ac demagnetized state followed a curve distinctly below the others. Also, in all cases, the

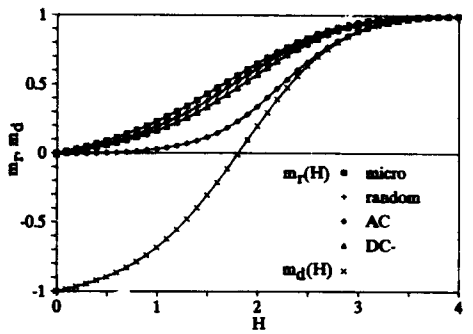

FIG. 2. Remanent magnetization curves, $m_r(H)$ for microscopic, random, dc−, and ac demagnetization states with $m_d(H)$ for $\xi=0.2$.

Henkel plot obtained from the dc+ demagnetized state (not shown) is made up of two straight line segments from (0,1) to (0,0) and from (0,0) to (1,−1).

For short correlation lengths, the microscopic, random, and dc− demagnetized Henkel plots follow trajectories with $m_d(H)>1-2m_r(H)$, and initial slopes of ≈ -1. The ac demagnetized Henkel plot follows a trajectory with $m_d(H)<1-2m_r(H)$ and an initial slope of ≈ -5.

For the longest correlation length calculated, $\xi=2$, the microscopic, random, and dc− demagnetized states produced Henkel plots which follow trajectories slightly below $m_d(H)=1-2m_r(H)$, and the ac demagnetized state produced a Henkel plot which has a very large negative initial slope and a final slope of ≈ -1 in close agreement with the *square-root law* described by Eq. (2) but falling slightly below it.

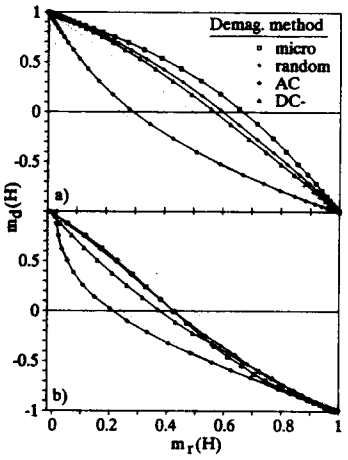

FIG. 3. Henkel plots, $m_d(H)$ vs $m_r(H)$, for noninteracting domain walls starting from four demagnetized states for (a) $\xi=0.02$ and (b) $\xi=2.0$. The dotted lines are plots of Eq. (1) and Eq. (2).

IV. DISCUSSION OF RESULTS

From the ac demagnetized state, the slow rise of the $m_r(H)$ curve and the associated strong "negative" deviation from the Wohlfarth condition are both consistent with the physical interpretation that ac demagnetization places domain walls in the energy wells with the steepest sides. In the ac demagnetized state, the initial stable points of the domain walls are not arbitrary, but are selected by the demagnetization process. Starting with a large amplitude applied ac field, at first the domain wall elements will propagate back and forth between $x=-1$ and $x=1$ in each cycle, but as the field amplitude decreases, the highest maxima and the lowest minima in $h_c(x)$ will begin to impede the domain wall motion, and then as the field amplitude is further reduced, the domain wall motion will become caught between successively less extreme maxima and minima. In terms of the domain wall energy, rather than the energy gradient [which is proportional to $h_c(x)$] the ac method preferentially places the domain wall elements in the local energy wells with the steepest sides. It is interesting that, although no such physical interpretation is made for ac demagnetization in the Preisach model, the square-root law derived from the factorizable Preisach model[10] also describes a strong "negative" deviation from the Preisach model.

For correlation lengths which are short in comparison with the total domain wall path length, the domain wall model produces Henkel plots which differ significantly from both the Wohlfarth relation and the square-root law. None of the Henkel plots follow the straight line given by Eq. (1), and in particular, the Henkel plot for the ac demagnetized state does not follow the square-root law given by Eq. (2).

The disagreement with the square-root law when ξ is small could be due to the existence of multiple stable points distributed between $x=-1$ and $x=1$ which a domain wall must pass in sequence, in contrast to the classical Preisach model in which there are only two stable points at -1 and 1 for each magnetization element. When ξ is large, $h_c(x)$ is correlated along its entire length, and the assumption used in the derivation of the square-root law, that up-switching fields and down-switching fields are independent, may break down.

From the variety of Henkel plots that were obtained from the domain wall model it is clear that the magnetization curves due to domain wall motion depend sensitively on the demagnetization method, and in particular that the demagnetization method should be specified if any conclusions can be drawn from a Henkel plot. From a practical point of view, when experimental Henkel plots deviate from the Wohlfarth relation (1) one may *not* safely draw conclusions about interactions since when domain wall motion is involved in magnetic hysteresis, both positive and negative deviations from $m_d(H)=1-2m_r(H)$ can be generated by domain wall elements without interactions.

[1] M. Fearon, R. W. Chantrell, and E. P. Wohlfarth, J. Magn. Magn. Mater. **86**, 197 (1990).
[2] M. Pardavi-Horvath, J. Oti, G. Vertesy, L. H. Bennett, and L. J. Swartzendruber, J. Magn. Magn. Mater. **104**, 313 (1992).
[3] E. P. Wohlfarth, J. Appl. Phys. **29**, 595 (1958).
[4] O. Henkel, Phys. Status Solidi **7**, 919 (1964).
[5] P. E. Kelley, K. O'Grady, P. I. Mayo, and R. W. Chantrell, IEEE Trans. Magn. **MAG-25**, 3881 (1989).
[6] D. E. Speliotis, and W. Lynch, J. Appl. Phys. **69**, 4496 (1991).
[7] X. He, C. Alexander, Jr., and M. R. Parker, IEEE Trans. Magn. **MAG-26**, 1876 (1992).
[8] K. O'Grady, R. W. Chantrell, and I. L. Sanders, IEEE Trans. Magn. **MAG-29**, 286 (1993).
[9] R. A. McCurrie and P. Gaunt, Proceedings of the International Conference on Magnetism, Nottingham, 1964, p. 780.
[10] G. Bertotti and V. Basso, J. Appl. Phys. **73**, 5827 (1993).
[11] L. Neél, Cahiers Phys. **12**, 1 (1942).
[12] B. Alessandro, C. Beatrice, G. Bertotti, and A. Montorsi, J. Appl. Phys. **68**, 2901 (1990).
[13] R. D. McMichael, L. J. Swartzendruber, and L. H. Bennett, J. Appl. Phys. **73**, 5848 (1993).
[14] F. Vajda, E. Della Torre, and R. D. McMichael, presented at this conference.

Model calculations of rotational hysteresis for ferromagnetic particles with competing anisotropies

Y. Yoshida,[a] T. L. Templeton, and A. S. Arrott
Physics Department, Simon Fraser University, Burnaby, British Columbia V5A 1S6, Canada

The net work $W_r(360°)$ on rotating a particle through 360° about an axis perpendicular to an applied field is called the rotational hysteresis. Its dependence on field is calculated for model particles with large surface anisotropies that compete with the bulk anisotropies. Both anisotropies are uniaxial and twofold but acting along different axes. If the axes are separated by any angle except 0° or 90°, $W_r(360°)$ is quite different for clockwise and counterclockwise rotations, for the range of fields where it is not zero. Because the magnetization is nonuniform, the results depend upon the exchange interaction and the particle size. The results are given for a range of particle sizes from small to large compared to a domain wall width. The results for particles with uniform anisotropy and magnetization are given for comparison.

The starting point for discussion of the magnetism of small particles is the Stoner–Wolhfarth (SW) model. The behaviors of single domain particles with uniaxial anisotropy are best known for the cases where a variable magnetic field is applied along a given axis to produce a hysteresis loop with remanence, coercivity and irreversible rotations of the magnetization vector. The behavior when the particle is rotated with respect to a fixed field has been known for a long time, also, but not so widely. In low fields the magnetization is trapped by the anisotropy and rotates with the particle. In high fields the magnetization follows the applied field. In both limits the process is reversible. No net work is done in rotating the particle through 180° about an axis perpendicular to the plane formed by the field and the anisotropy axis. For intermediate fields the magnetization jumps irreversibly from staying near the anisotropy axis to following the field axis as the particle is rotated. This is rotational hysteresis. The purpose of this communication is to discuss rotational hysteresis for small particles where competing anisotropies in different regions of the particle result in nonuniform magnetization patterns.

Rotational hysteresis for SW particles where the anisotropy is more complicated than uniaxial are not well known, partially because there are so many different possibilities. Some of these were considered in our recent review.[1] A restricted class of anisotropies is that with two axes at angles θ_a and θ_b. A further restriction on that class is that the field and the magnetization are confined to the plane formed by the two axes. The confinement of the magnetization to the plane implies the presence of a strong negative anisotropy perpendicular to the plane, as occurs for thin films. If the anisotropy energies E_K for both axes are twofold; that is, $E_K=-K_a\cos^2(\theta-\theta_a)$ and $E_K=-K_b\cos^2(\theta-\theta_b)$, the behavior is the same as for a uniaxial twofold anisotropy along another axis. There are quite different rotational hysteresis effects to be seen if at least one axis is fourfold; for example, $E_K=K_b\cos^2(\theta-\theta_b)\sin^2(\theta-\theta_b)$. In particular, the hysteresis for rotation about an axis perpendicular to the plane containing the field and the anisotropy axes depends on whether the rotation is clockwise (CW) or counterclockwise (CCW). This requires that (1) the angle between the two axes is neither 0° nor 90°, (2) the anisotropies are distinguishable from each other, and (3) at least one is more complicated than twofold anisotropy.

Here we treat uniaxial anisotropies along two axes, both of which are twofold, but now they act on different parts of the same particle. The competing torques produce nonuniform magnetization patterns. This increases the exchange energy. We have studied, previously, the ordinary hysteresis of one such system. The angle between the bulk and surface anisotropy axes was 65°. The surface anisotropy was much larger than the bulk anisotropy. Small and large particles for this system resembled SW particles with twofold axes.[2] For intermediate sizes resemblance to a SW particle required a particular combination of one twofold and one fourfold axis.[1] As such a SW particle shows difference in hysteresis for CW and CCW rotations, one would anticipate correctly this effect for our noncollinear model.

Rotational hysteresis in noncollinear spin systems is demonstrated for the same conditions for which earlier we calculated the ordinary hysteresis.[2] We emphasize that we are not calculating the properties of real particles. These are model calculations in which the problem is reduced to a one-dimensional chain of atoms or of atomic planes. There is an implied strong negative anisotropy perpendicular to the plane of the two axes. The field is restricted to that plane. Yet this is sufficient to demonstrate that the net work for full rotation can be different for the two senses of rotation in the plane.

There is at least one experimental paper in which a collection of fine particles of CrO_2 exhibits this effect.[3] To establish a sense of rotation there had to be at least two axes, defined for the system of particles as a whole. If it were shown that both of these axes were twofold axes, then the implication would be that the magnetization processes in the individual particles were nonuniform.

The model has a line of n moments with one uniaxial twofold anisotropy acting on all the moments and another larger twofold anisotropy acting only on the moments at the ends of the line. This models a particle with pinning from large surface anisotropy. The length of the line λ is an addi-

[a]Permanent address: R & D Division, Daido Steel Co., Ltd., 2-30 Daido-cho, Minami-ku, Nagoya 457, Japan.

 0021-8979/94/75(10)/5695/3/$6.00 © 1994 American Institute of Physics

tional parameter that enters with the exchange constant A in the energy expression $E_{ex}=A(\text{curl } M)^2$. We have given, previously, the full equations and the method of their solution for the calculation of the ordinary hysteresis.[2] Here the sequence is that of repeated solutions for a series of angles of the field at fixed magnitude rather than a series of fields at fixed angle. For each field angle we calculate the angles that the moments make with the field axis. We determine the net moment of the system along that axis and the net torque exerted by the field on the system. If the field is neither too high nor too low, there are critical angles at which the magnetization and the torque change abruptly and irreversibly. These are different for CW and CCW rotation.

We have considered a range of length scales from very small to large particles. In small particles the exchange effects couple the moments into almost collinear patterns. In large particles there is uniform rotation against the bulk anisotropy except close to the ends where the surface anisotropy pins the magnetization. Both limits approach SW behavior with an effective anisotropy that depends on the two anisotropies and the number of units in the line. For particle sizes comparable to domain wall dimensions the effects of competing anisotropies and the deviations from SW behavior are most noticeable.

First we consider the minimum field H_{c1} for the onset of rotational hysteresis. The rotational hysteresis at H_{c1} is large. For the SW limit, it is a maximum at H_{c1}. For the noncollinear system, it is the same for both senses of rotation right at H_{c1}. For higher fields, it increases for CCW and decreases for CW. The sense of rotation is defined below. When the particle is small, H_{c1} will be high, because the surface anisotropy is greater than the bulk anisotropy. We normalize the field to the effective anisotropy what would apply for infinite exchange coupling

$$K_{\text{eff}}=\frac{1}{n}\,[4K_s^2+4(n-2)K_sK_b\cos\alpha+(n-2)^2K_b^2]^{1/2}, \tag{1}$$

where α is the angle between the anisotropy axes with anisotropy constants K_s and K_b for the surface and bulk, respectively. We take the bulk anisotropy axis as the reference angle. We have chosen the constants such that $\alpha=65°$ and $2K_s=(n-2)K_b$ for $n=52$.

The reduced critical field for the onset of hysteresis is

$$h_{c1}=\frac{M_sH_{c1}}{2K_{\text{eff}}}, \tag{2}$$

where M_s is the moment per unit volume. This goes to the SW value $h_{c1}=1/2$ in both size limits. The deviations of h_{c1} from 1/2 are in the opposite sense for small and large particles as shown in Fig. 1. The length of the particles is normalized to the domain wall parameter $\delta_w=\pi(A/K_b)^{1/2}$. For smaller particles, the noncollinearity of the spin system reduces the actual effective anisotropy below that used for normalization, K_{eff}. For larger particles, the field acts primarily on the bulk moments rotating them against the bulk anisotropy, but there is a residual anisotropy effect from the exchange coupling to the end moments which act as pins in the low fields needed to rotate the bulk. The residual effect accounts for the almost constant offset seen for large λ in Fig. 1. For much larger particles, h_{c1} returns to 1/2.

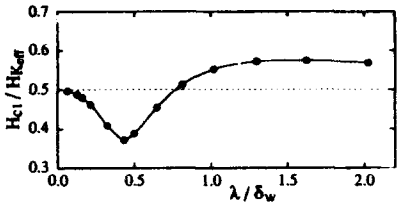

FIG. 1. The onset of rotational hysteresis for a one-dimensional model of a particle with large surface anisotropy. The minimum field H_{c1} depends on the size λ of the particle. $H_{K_{\text{eff}}}=2K_{\text{eff}}/M_s$, where K_{eff} is defined in Eq. (1) and δ_w is the domain wall parameter.

Next we consider in detail the rotational hysteresis for a particular example with $\lambda/\delta_w=0.65$ and $h=M_sH/(2K_{\text{eff}})=0.6>h_{c1}$. There are strong differences for CW and CCW rotations; see Fig. 2. The magnetization and torque repeat with a periodicity of 180° in either direction. (There are other cases where the minimum periodicity is 360° in one or the other or both directions.) The presentation in Fig. 2(a) sacrifices some clarity for the sake of compactness. The right side of the diagram shows the response to angle changes for CW rotation. The left side describes rotation in the CCW sense. The field is along the bulk anisotropy axis at the origin. At 0° the torques from the end moments rotate the magnetization slightly clockwise from alignment with the field. At +65° and −115° the field is along the axis of the end moments. The net moment along the field axis is a local maximum when the field is near 30°. This almost bisects the acute angle between the anisotropy axes. This condition can be achieved starting with the field along the bulk anisotropy axis and rotating the particle so that the field angle is closer to the axis of the pinned ends at 65°. This is the meaning of CW clockwise rotation of the field.

If the particle is rotated in the opposite sense (CCW rotation of the field) the moment remains near to the bulk anisotropy axis, in the initial direction, until the magnetization is at a negative maximum with respect to the field. This happens at an angle of −160° where the field and the magnetization are again near the middle of the acute angle between the two anisotropy axes, but now in opposite directions. On continued CCW rotation, the magnetization rotates further from the bulk axis and closer to the pinning axis until there is sufficient torque from the field to pull all the moments close to the field direction at −172°. This is the transition from e to f in Fig. 2(a). We show the configuration of the spins before and after this transition in Fig. 2(b). Note that all the moments switch with respect to their local anisotropy axes, but the end moments rotate the most in this transition

As the field is rotated CW, starting from along the bulk axis, the magnetization aligns more closely with the field, but then starts to lag behind until at 119° it rotates irreversibly toward the field. This is the transition from a to b in Fig. 2(a). The field and the magnetization are near the middle of

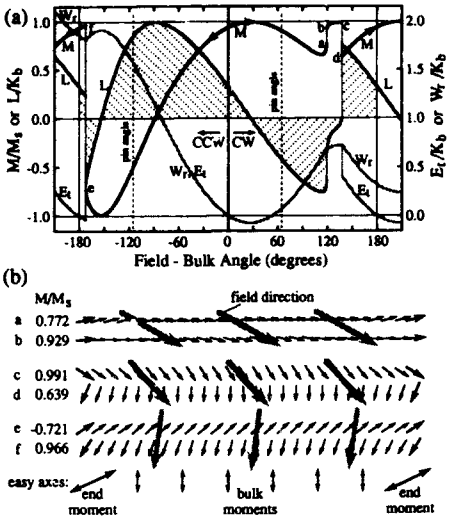

FIG. 2. Rotation of a model particle, $\lambda/\delta_w=0.65$, with large surface anisotropy in an applied field, $h=M_sH/(2K_{eff})=0.6$. (a) Magnetization M, torque L, energy E_t, and work W_r for clockwise CW and counterclockwise CCW rotation. (b) Moment configurations, showing a fraction of the moments, before and after the irreversible changes as noted in (a).

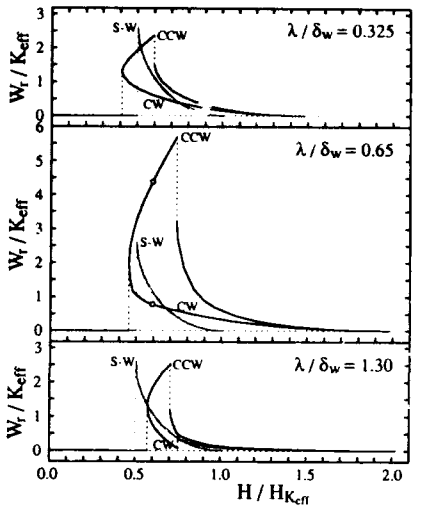

FIG. 3. The field dependence of $W_r(360°)$, the net work done on rotation CW and CCW through 360°, for three sizes of model particles. The curves labeled SW describe $W_r(360°)$ for the same particles in the limit of very strong coupling of the moments.

the obtuse angle between the anisotropy axes. The slight changes in the spin configuration are shown in Fig. 2(b). Only the bulk moments switch with respect to their anisotropy axis. For calculations at lower fields the rotation in this region of angles is reversible.

As the field angle is increased further to 138° in the CW direction, another irreversible transition goes from c to d in Fig. 2(a). Only the end moments switch with respect to their anisotropy axis, as shown in Fig. 2(b). For calculations at lower fields all the moments switch at the equivalent angle.

For fields between $-172°$ and $+119°$ the magnetization can rotate back and forth reversibly. On rotation CW beyond 138° the behavior is the same as starting at $-42°$ and rotating CW. On rotation CCW beyond $-172°$ the behavior is the same as starting at 8° and rotating CCW.

The torques at each field are shown in Fig. 2(a). Note that the torque can jump from being large in one direction to being large in the opposite direction. The shaded regions in Fig. 2(a) show the positive and negative work done for each rotation direction through 180°.

There are two equivalent measures of the net work done on rotation through 360°. The integral of the torque, shown as W_r in Fig. 2(a), is measured starting with the field along the bulk axis. W_r increases for CCW rotation from 0 to $-160°$. Then, just as some of that energy is beginning to be recovered, the big jump at $-172°$ dissipates the energy as heat. For CW and for CCW rotations, the sum of all the drops in energy is equal and opposite to the net work done by the torque in a complete cycle. The energy of the particle as a function of field angle is shown as E_t in Fig. 2(a). The net work $W_r(360°)$ for CW and CCW for this case $[h=M_sH/(2K_{eff})=0.6,\lambda/\delta_w=0.65]$ is shown as two open circles on the middle panel in Fig. 3. If each point in Fig. 3 were discussed in the same detail given for these two points, there would be many different stories to be told.

Extensive calculations for a series of fields produce the results that are summarized in Fig. 3. The field dependence of $W_r(360°)$ for CW and CCW rotations is shown for three particles that can be considered as small, intermediate and large in the sense of Fig. 1. The net work for each size particle is compared with the behavior of a SW particle with the effective anisotropy given by Eq. (1).

These calculations used a single choice of the angle between the two anisotropy axes. This is but a small look at the behavior of these model particles.

[1] A. S. Arrott, T. L. Templeton, and Y. Yoshida, in *Nanophase Materials: Synthesis, Properties, Applications*, edited by R. D. Siegel and G. C. Hadjipanayis (Plenum, New York, in press).
[2] A. S. Arrott, T. L. Templeton, and Y. Yoshida, IEEE Trans. Magn. **MAG-29**, 2622 (1993).
[3] S. R. Hoon and J. Lowe, IEEE Trans. Magn. **MAG-26**, 1813 (1990).

A hysteresis model with interactions

J. Planès
Office National d'Etudes et de Recherches Aérospatiales, Direction des Matériaux, B.P. 72, F-92322 Châtillon Cedex, France

The magnetic properties of an assembly of monodomain ferromagnetic particles are computed, considering the whole set of dipolar interactions in competition with magnetocrystalline anisotropy. Coercive field, remanent magnetization, initial susceptibility, are studied as a function of the ratio p of competing energies, and also of geometrical parameters such as density. $p \simeq 1$ corresponds to a crossover region, separating an anisotropy-dominated regime from a coupling-dominated regime. An example of a possible experimental realization is presented, for which the magnetization curve and hysteresis loop present strong similarities with calculated ones; a numerical discrepancy, however, remains.

I. INTRODUCTION

The hysteretic behavior of magnetic material still remains a complicated problem, whose computation often relies on phenomenological concepts. Numerous models have been developed, depending on the considered magnetization processes. For ferromagnetic particulate media, the role of dipolar interactions is known to be of great importance (recent contributions can be found in Ref. 1). But their long-range character is a major drawback for them to be taken into account. Most techniques either use a mean-field approach[2] or set a cutoff or else only deal with special configurations like aligned easy axes.[3]

We are guided in this work by experimental results on very fine particles which exhibit rather high coercivity (40–80 kA m^{-1}) but low remanence (15%–25% of the saturation value). It is believed that strong interactions are responsible for those values, clearly departing from Stoner–Wohlfarth (SW) values. Transmission electron microscopy (TEM) observations[4] clearly show the particle aggregation.

Let us also mention two very recent works on the field of interacting particles. In Ref. 5, Westwood *et al.* analyze hysteresis loops and remanence curves of a cluster of Fe_3O_4 particles extracted from a magnetic ink, which are described as 20–200 nm single-domain crystallites. Coercivity (6.4 kA m^{-1}) and remanence (0.1) are quite low, in even stronger contrast to "bulk" magnetite than our ferromagnets. The second contribution[6] is an attempt to explain observed departures of the properties of Fe_3O_4 microcrystallites to spin-glass behavior through a mean-field approach of our problem: competition of random anisotropy with dipolar forces. Calculated hysteresis loops qualitatively resemble ours, and a comparison between MFA and "exact" calculation should be fruitful.

The model described below is designed to calculate some properties of a finite cluster of particles whose dynamics is driven by an intrinsic anisotropy competing with the dipolar coupling to all the other particles, providing that (i) their magnetic structure is monodomain (rotation susceptibility only), (ii) the thermal relaxation of magnetization can be neglected. The major point of those calculations compared to previous ones is to be found in the quantitative description of the influence of interactions on the magnetic properties of ferromagnetic particles, exhibiting two well-defined regimes: magnetostatic and anisotropic.

II. THE MODEL

In the following we consider an assembly of spherical particles whose intrinsic properties are identical (saturation magnetization M_s, uniaxial anisotropy constant K), the anisotropy direction being uniformly distributed in the $3d$ space. Two kind of geometries are considered: (i) particles, of identical radii but possibly surrounded by a nonmagnetic spherical layer, lie on a cubic lattice with a certain amount of empty sites randomly chosen; (ii) particles, whose radii are distributed according to a predefined statistical law, are aggregated following a cluster-cluster aggregation model. Results for this geometry will not be given here. Each particle is supposed to act as a giant moment, whose intensity is frozen by the exchange interaction. The torque acting on each moment $\mathbf{M}_n$ is $\mathbf{\Gamma}_n = \mathbf{M}_n \times \mathbf{B}_n$, where the local field $\mathbf{B}_n$ is defined by

$$\mathbf{B}_n = -\nabla_n \mathcal{H}, \tag{1}$$

where ∇_n is the vector whose components are $\partial/\partial M_n^{x,y,z}$ and $\mathcal{H}$ is the total energy of the system:

$$\mathcal{H} = -\mu_0 \mathbf{H}_{\text{ext}} \cdot \sum_n \mathbf{M}_n + \sum_n K v_n \left(1 - \frac{(\mathbf{M}_n \cdot \mathbf{u}_n)^2}{(M_s v_n)^2}\right) - \frac{1}{2}\frac{\mu_0}{4\pi} \sum_{n,p} \left(\frac{3(\mathbf{M}_n \cdot \mathbf{r}_{np})(\mathbf{M}_p \cdot \mathbf{r}_{np})}{r_{np}^5} - \frac{\mathbf{M}_n \cdot \mathbf{M}_p}{r_{np}^3}\right), \tag{2}$$

v_n being the volume of particle n ($\|\mathbf{M}_n\| = M_s v_n$), $\mathbf{u}_n$ a unitary vector along the anisotropy direction, and $\mathbf{r}_{np}$ the vector joining particles n and p. No thermal relaxation is considered; the system is taken below its blocking temperature. At equilibrium the torques vanish, resulting in a distribution of local fields which are colinear with the moments.[7] From Eqs. (1) and (2)

 0021-8979/94/75(10)/5698/3/$6.00 © 1994 American Institute of Physics

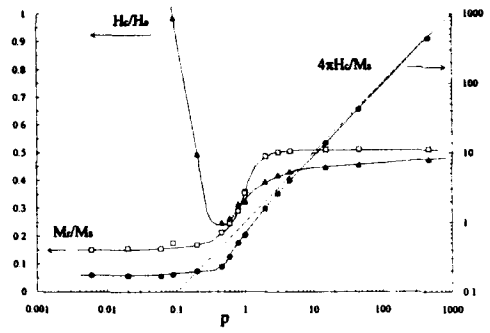

FIG. 1. Evolution of remanent magnetization and coercive field with p, for 400 particles on a 1000 sites cubic lattice. Relative remanence M_r/M_s (squares) has to be compared with SW value (dotted line). B_c is plotted in units of "anisotropy field" $H_a=2K/\mu_0 M_s$ (triangles) and "magnetostatic field" M_s (disks); for the latter, the dashed line correspond to SW value $0.98K/\mu_0 M_s$. Solid lines are only guides to the eye.

$$\frac{4\pi}{\mu_0 M_s}(\mathbf{B}_n-\mu_0\mathbf{H}_{\text{ext}})=\frac{4\pi K}{\mu_0 M_s^2}\frac{2\mathbf{m}_n\cdot\mathbf{u}_n}{v_n}\mathbf{u}_n+\sum_p\left(\frac{3\mathbf{m}_p\cdot\mathbf{r}_{np}}{r_{np}^5}\mathbf{r}_{np}-\frac{\mathbf{m}_p}{r_{np}^3}\right), \tag{3}$$

where $\mathbf{M}_n=M_s\mathbf{m}_n$. Apart from the geometry (distributions of $\mathbf{u}_n$, $\mathbf{r}_{np}$, and v_n) the distribution of local fields $\mathbf{B}_n$ does not depend separately on M_s and K, but on the dimensionless *ratio*

$$p=\frac{4\pi K}{\mu_0 M_s^2} \tag{4}$$

which measures the relative strength of magnetocrystalline anisotropy energy versus dipolar energy. Because of couplings, an iterative method is necessary to solve the system of equilibrium equations $\Gamma_n=0$. The algorithm is as follows: (i) choose a starting distribution of $\mathbf{M}_n$; (ii) calculate the local fields and the total energy; (iii) if the change in energy compared to the previous iteration is greater than a predefined threshold, rotate the moments towards the local fields and return to step (ii), else end.

Apart from the very beginning, the starting distribution is the equilibrium distribution of the previous calculation (for hysteresis loops, magnetization or remanence curves).

III. RESULTS

Hysteresis loops. Influence of the parameters of the model are presented through the variation of the coercive field H_c and remanent magnetization M_r/M_s. This is obviously not sufficient to correctly describe the loop but essential features are present. More details will be published in a longer paper.[4] Figure 1 shows the influence of p in a large range of values (from very soft to very hard materials), for a cubic lattice of 400 particles distributed over 1000 sites, without dead layer. It can be seen that sensitivity to p is maximum for $0.2<p<2$. Outside those bounds is the system entirely driven by geometry (lower bound) or by anisotropy (upper bound).

We have verified that the size of the cluster was not a prominent parameter for a given configuration, by varying the number of particles at constant density 0.4 on a lattice. Error bars are estimated for three cases by changing the disorder in the configuration (the location of empty sites). One finds for M_r/M_s and H_c/H_a, respectively: 0.212 ± 0.024 and 0.275 ± 0.039 for 200 particles, 0.213 ± 0.016 and 0.266 ± 0.023 for 400 particles, 0.209 ± 0.008 and 0.286 ± 0.013 for 800 particles. The choice of 400 particles for most examples here results from a compro[illegible]mputing time and statistical reliability, inclu[illegible]opy.

The influence of density has been tested: the system exhibits a monotonic decrease of H_c and M_r with increasing density, which is consistant with a globally demagnetizing effect of the dipolar interactions.

Initial susceptibility. The slope $s=(M/M_s)/(H/H_a)$ at origin is extracted from magnetization curves. The dimensionless $\chi_i=dM/dH|_{H=0}$ is then equal to $(2\pi/p)s$, the prefactor being the SW value when the field is perpendicular to the anisotropy axis. For an assembly of SW particles with a uniform distribution of anisotropy direction, this value is lowered by a factor 2/3.[8] Figure 2 shows the variation of χ_i with p for the same assembly of 400 particles on a 1000 sites cubic lattice. Attention have been paid to chose a field direction perpendicular to the spontaneous magnetization of the cluster, whose typical intensity is less than $0.05M_s$. The susceptibility is measured for an applied field equal to $0.05H_a$.

Experimental comparison. The material which is thought to fulfill the assumptions of this model is an iron-cobalt powder prepared by a physical process.[9] Its main properties are (i) a spherical shape with an asymmetric size distribution ($\varnothing$ from 15 to 150 nm), (ii) no domain wall contribution to the susceptibility, constant ($\simeq 4$) from dc to 1 GHz. The magnetization curve and hysteresis loops are superimposed in Fig. 3 to calculated ones with $p=0.45$ and a lattice density of 0.4. However, the agreement is only apparent, because one of the axes has to be rescaled. In fact, since M_s is known, the field scale is fixed by p. Thus, in this case, fields of the simulation data have to be doubled, or equivalently, the (M_s,K) couple has to be changed to $(2M_s,4K)$, giving exactly the same curve in a $(M/M_s,H)$ plot.[10] Despite this unexplained numerical disagreement, these plots show that the nontrivial shape of the experimental curves could be recovered. Other choices for p or geometry do not lead to similar shapes. Note also that the aggregation process in the real material is not known, and can be reasonably thought to be driven by magnetostatic forces, resulting in a special distribution of anisotropy axes. This effect will be examined.

Remanence curves. These curves are extensively used in the field of recording materials to characterize their performances in terms of switching field distribution (SFD) or signal-to-noise ratio for instance. The reversible and irreversible parts of the remanence (IRrev and IRM) and demagnetization (IDrev and DCD) curves are defined as in Ref. 11. Figure 4 shows the predicted remanence curves for the pa-

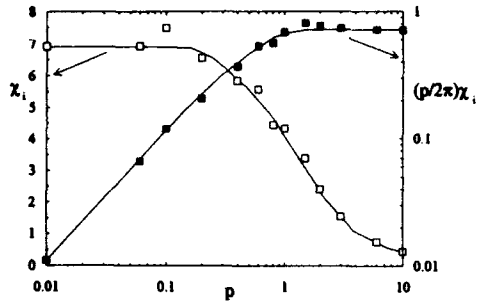

FIG. 2. Initial susceptibility as a function of p for 400 particles on a 1000 sites cubic lattice. Saturation of χ_i for "soft" materials ($p \ll 1$), which is currently observed for particulate media, is recovered. When couplings vanish ($p \to +\infty$), $(p/2\pi)\chi_i$ tends to the SW value 2/3.

rameters estimated for the experimental case. It can be seen that reversible components superimpose on each other and do not present peaks around the remanent coercivity as other systems or SW calculations.[12] This effect, as well as the slow variations of the irreversible components, denotes the enlarging contribution of interactions on the local field distribution in general, and the SFD in particular.

IV. DISCUSSION

The most difficult question to answer about this model concerns its validity range. Despite the fact that M_s and K are dimensioned input parameters, the whole problem is dimensionless, including lengths. Results of micromagnetic calculations should idealy indicate for which sizes and which p values the assumptions of single-domain and coherent rotation are relevant.

Numerous extensions of this model are straightforward: rotational hysteresis, anhysteretic susceptibility,..., as well as modifications like considering magnetostatic instead of magnetocrystalline anisotropy (spheroidal particles). Relations

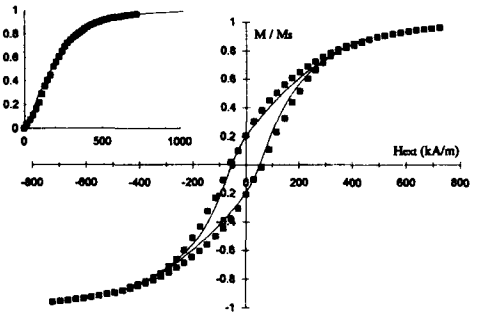

FIG. 3. Comparison of experimental (solid line) magnetization curve (inset) and hysteresis loop of an iron-cobalt powder with simulated data (squares) for a 1000 sites lattice with density 0.4 and $p=0.45$. The field values of simulated data have been rescaled as explained in the text.

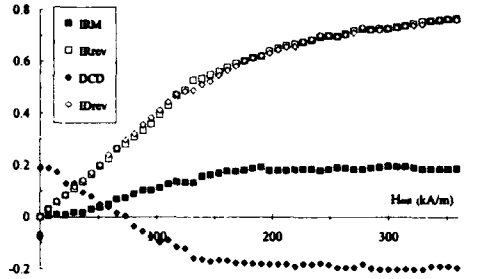

FIG. 4. Remanence curves with irreversible (filled symbols) and reversible (empty symbols) parts predicted for the same set of "fitting" parameters as Fig. 3.

and/or equivalences between geometrical and physical parameters are also to be studied in order to lower the number of relevant parameters.

The central point in this model is the computation of the equilibrium distribution. Because of geometrical disorder, the energy landscape must be quite complicated and convergence to (metastable) equilibrium states should be carefully studied.[13]

Finally, as stated in the introduction, it would be of great interest to compare those "exact" calculations with a mean-field approach, or a generalized MFA in which only nearest neighbors interactions would be calculated, the remaining of the sample acting through a mean field.

ACKNOWLEDGMENTS

Fruitful discussions with F. Boust are acknowledged. This work was supported by the French Ministry of defense, under contract DRET No. 89/34/001, and by C.P.R "Matériaux Absorbant le Rayonnement Hyperfréquence."

[1] *Magnetism of Fine Particles*, edited by J. L. Dormann and D. Fiorani (North-Holland, Delta Series, Amsterdam, 1992).
[2] D. L. Atherton and J. R. Beattie, IEEE Trans. Magn. **MAG-26**, 3059 (1990).
[3] A. Lyberatos, E. P. Wohlfarth, and R. W. Chantrell, IEEE Trans. Magn. **MAG-21**, 1277 (1985); M. Fearon, R. W. Chantrell, and E. P. Wohlfarth, J. Magn. Magn. Mater. **86**, 197 (1990).
[4] J. Planès (unpublished).
[5] S. M. Westwood, V. G. Lewis, K. O'Grady, and B. Tanner, J. Magn. Magn. Mater. **125**, 27 (1993).
[6] M. A. Załuska-Kotur and M. Cieplak, Europhys. Lett. **43**, 85 (1993).
[7] To see that it corresponds to an energy extremum, one should write the energy as a function of $2N$ independent variables (say $M_n^{x,y}$) and consider the constrained gradient $\vec{\nabla}_n$ whose components are $\partial/\partial M_n^{x,y} - (M_n^{x,y}/M_n^z)\partial/\partial M_n^z$. Thus $\vec{\nabla}_n \mathcal{H}|_{M^{eq}} = 0$.
[8] S. Chikazumi, *Physics of Magnetism* (Wiley, New York, 1964), pp. 260–264.
[9] Y. H. Zhou, M. Harmelin, and J. Bigot, Scr. Metall. **23**, 1391 (1989).
[10] Though an error of 2 is unrealistic, it should be kept in mind that only the mass magnetization is correctly measured; due to the difficult measurement of the powder density, the volume M_s is subjected to some uncertainty.
[11] K. O'Grady, IEEE Trans. Magn. **MAG-26**, 1870 (1990).
[12] P. R. Bissel and A. Lyberatos, J. Magn. Magn. Mater. **95**, 27 (1991).
[13] J. Planès and A. Finel (unpublished).

Simulation of magnetization reversal in two-phase exchange coupled nanocrystalline materials

E. H. Feutrill, P. G. McCormick, and R. Street
Research Centre for Advanced Mineral and Materials Processing, The University of Western Australia, Nedlands 6009, Australia

A nanoscale two-phase uniaxially anisotropic material has been numerically modeled using a two-dimensional array of micromagnetic moments to represent the material on an atomic scale. Demagnetization curves are calculated by minimizing the total energy of the system which includes a component due to exchange interactions between nearest neighbors, as well as magnetocrystalline and magnetostatic energies. Magnetization reversal is shown to be initiated in the soft magnetic phase and to proceed by reversible rotation until a critical field, coercivity, at which the magnetization of the system switches irreversibly. As the dimension of the soft magnetic phase increases, coercivity approaches a lower limit and there is a transition from single- to two-phase magnetic behavior.

I. INTRODUCTION

The magnetic behavior of nanocrystalline rare earth-transition metal permanent magnet materials synthesized by rapid solidification and mechanical alloying techniques has received increased attention in recent years. Of particular interest has been the observation of high values of remanent magnetization in both single-phase and two-phase materials.[1–3] This behavior has been attributed to exchange coupling at intercrystalline interfaces and the increasing influence of such interaction effects as crystal sizes decrease.[4] Remanence-enhanced materials offer potential for attaining high energy products in crystalline isotropic permanent magnets.

In this paper we present results of a numerical study of the demagnetization process using a two-dimensional model of a material comprising small particles of a hard magnetic phase in a soft magnetic matrix. The results illustrate the important effects of particle and matrix size on the magnetic behavior.

II. THE MODEL

A two-dimensional array of micromagnetic moments is used to represent a material on an atomic scale. Different magnetic phases of varying sizes are modeled by specifying the same magnetocrystalline anisotropy (first order only), easy axis of magnetization (uniaxial), and magnitude of magnetic moment for groups of neighboring elements.

For a given field, the equilibrium configuration of the moments is determined by minimizing the total energy of the system, where the energy at each site is expressed as the sum of magnetostatic, magnetocrystalline, and exchange energy components.[5] The effects of demagnetizing fields have not been taken into account. Previous modeling studies on fine structure materials suggest that exchange interactions dominate in nanoscale materials.[6,7]

The results presented in this paper are for materials comprising a uniform distribution of particles of a hard magnetic phase in a matrix of a soft magnetic phase. Figure 1 is a schematic diagram of the corresponding array of micromagnetic moments. The easy direction of magnetization of the hard magnetic phase is aligned with the field so that remanence is maximised. That of the soft magnetic phase is at $\pi/4$ to the field direction. Material properties of $Nd_2Fe_{14}B$ and α-Fe have been used for the hard and soft magnetic phase, respectively. The lattice dimension is assumed to be 3 Å.

II. RESULTS AND DISCUSSION

Simulation of magnetization reversal suggests that the properties are critically dependent on the size of the soft magnetic phase. In zero field the soft magnetic moments, which in the absence of exchange coupling would lie along their easy axis of magnetization at $\pi/4$ to the field direction, align with the hard magnetic phase. As the reverse field increases those soft magnetic moments furthest from the interface begin to rotate first. For a given field, the amount of rotation depends on the size of the phase. Figure 2 compares the equilibrium distribution of moments at the same field in systems with the same size of the hard magnetic phase and different dimensions of the soft magnetic phase. In the smallest system all the soft magnetic moments are relatively proximate to the hard magnetic phase and rotation is suppressed. For larger sizes there is more rotation in the center of the soft magnetic phase with an associated increase in the nonuniformity of magnetization in the system. Demagnetization proceeds by reversible rotation until a critical field, the

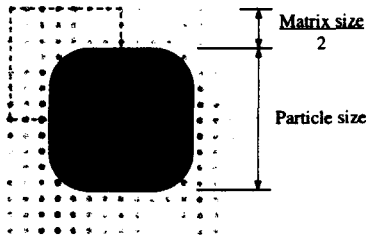

FIG. 1. Two-dimensional array of micromagnetic moments used to model a two-phase material comprising a uniform distribution of identical particles in a matrix of a different phase.

 0021-8979/94/75(10)/5701/3/$6.00 © 1994 American Institute of Physics

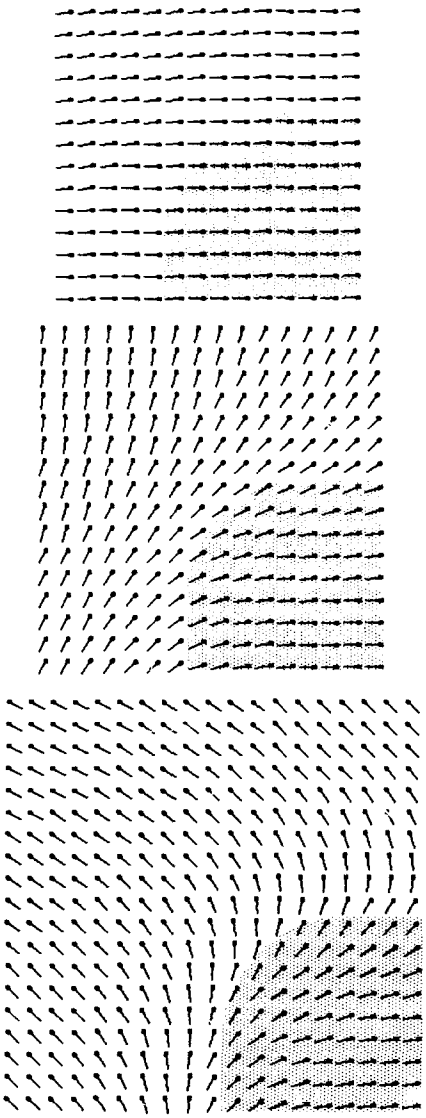

FIG. 2. Comparison of the distribution of orientations of the micromagnetic moments in materials with the same particle size of hard magnetic phase =5.1 nm and minimum dimensions of the soft magnetic matrix phase=2.7, 3.9, and 5.7 nm. The field is just less than the coercivity of the largest system and the corresponding values of magnetization as a fraction of saturation M/M_{sat}=1.0, 0.6, ~0.3. Note that these configurations are for the top left-hand quarter of the array as indicated in Fig. 1. Refer to Fig. 3 for the complete demagnetization curves.

coercivity, is reached at which the system becomes unstable and all the moments flip irreversibly. The field corresponding to the configurations in Fig. 2 is close to the coercivity of the largest system for which it can be seen that all the hard

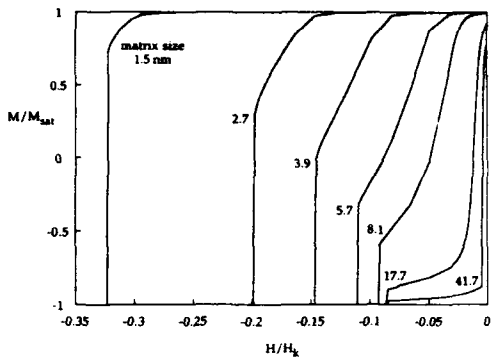

FIG. 3. Demagnetization curves for a particle size of hard magnetic phase =5.1 nm and a range of minimum dimensions of the soft magnetic phase. The magnetic field H is plotted as a fraction of the anisotropy field of the hard magnetic phase H_k. Note that the ratio of the anisotropy fields is 0.005.

magnetic moments have been disturbed from their easy direction of magnetization because of the extent of the rotation in the soft magnetic phase.

Demagnetization curves for a range of sizes of the soft magnetic phase are shown in Fig. 3. The change in shape of the curves indicates a transition from single- to two-phase magnetic behavior with increasing size of the soft magnetic phase. For systems with small matrix dimensions the curves are approximately square and there is little change in magnetization due to reversible rotation prior to coercivity. As the size of the soft magnetic phase increases and there is more rotation at the center of the phase, the systems become unstable in lower fields. After coercivity all the systems are approximately saturated in the reverse direction because the easy axis of magnetization of the hard magnetic phase is aligned with the field such that there is no subsequent rotation.

Figure 4 shows the reduction in coercivity with increas-

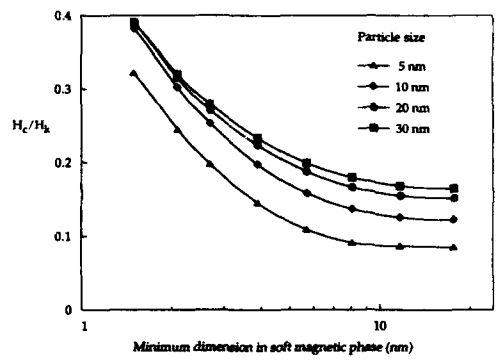

FIG. 4. Decrease in coercivity H_c with increasing minimum dimension of the soft magnetic phase for particle sizes of the hard magnetic phase=5, 10, 20, and 30 nm.

ing minimum dimension of the soft phase for a range of sizes of the hard magnetic phase. The highest coercivity is achieved in the system with the largest particle size and smallest matrix dimension. As the amount of soft magnetic phase increases there is an initially rapid decrease in coercivity. For larger dimensions of this phase, coercivity is approximately constant reflecting the fact that there is little further increase in the amount of nonuniform magnetization in the system. Above a critical dimension a second discontinuity is observed because the soft magnetic moments sufficiently far from the interface behave independently of the presence of the hard magnetic phase and flip irreversibly in a field which, for the easy axis of magnetization of the soft magnetic phase at $\pi/4$ to the field, is approximately half the anisotropy field of the phase.

There is a lesser dependence of coercivity on the size of the hard magnetic phase and again this is only significant for small sizes. The increase in coercivity with increasing particle size in the context of this model is a result of the lower proportion of material in the interfacial region that is experiencing maximum nonuniformity of magnetization due to rotation in the center of the soft magnetic phase.

IV. CONCLUSIONS

An atomic scale model has been used to demonstrate the mechanism of magnetization reversal in an exchange coupled nanoscale mixture of a hard and soft magnetic phase. The results suggest that coercivity and enhancement of magnetization, and hence maximum energy product, depend significantly on the size of the soft magnetic phase.

[1] R. Coehoorn, D. B. de Mooij, J. P. W. B. Duchateau, and K. H. J. Buschow, J. Phys. C **8**, 669 (1988).
[2] R. W. McCallum, A. M. Kadim, G. B. Clemente, and J. E. Keem, J. Appl. Phys. **64**, 5299 (1988).
[3] J. Ding, P. G. McCormick, and R. Street, J. Magn. Magn. Mater. **124**, 1 (1993).
[4] E. F. Kneller and R. Hawig, IEEE Trans. Magn. **MAG-27**, 3588 (1991).
[5] E. Feutrill, J. Ding, R. Street, and P. G. McCormick, Proceedings of IUMRS-ICAM-93, Tokyo, 31 August–4 September 1993.
[6] T. Schrefl, H. F. Schmidts, J. Fidler, and H. Kronmüller, J. Magn. Magn. Mater. (in press).
[7] H. Fukunaga and H. Inoue, Jpn. J. Appl. Phys. **31**, 1347 (1992).

Activation volume of a pair of magnetostatically coupled particles

A. Lyberatos
Physics Department, Keele University, Keele, ST5 5BG, United Kingdom

The activation volume of an interacting pair of uniaxially anisotropic fine ferromagnetic particles is studied assuming a dipole approximation, for the case of the applied field parallel to the bond direction and the common anisotropy axis. Using an analytical treatment, it is shown that the activation volume depends primarily on activation energy and to a smaller extent on the location of the saddle point of the transition. The incoherent reversal by "fanning" and the collective thermal excitations of the magnetization result in a reduction of the activation volume. The dependence on coupling strength is also discussed. Numerical calculations using the Langevin formalism provide a correction to the theory that is significant in the limit of very short relaxation times.

I. INTRODUCTION

The magnetic viscosity observed in fine particle media arises from the thermal activation of the magnetization over energy barriers that arise primarily from the shape or crystal anisotropy. The time dependence is quasilogarithmic and the decay constant S is relate ' to the irreversible susceptibility χ_{irr} (Ref. 1)

$$V_{act}=\frac{kT}{M_s}\frac{\chi_{irr}}{S}, \tag{1}$$

where V_{act} is the activation volume. If the magnetic reversal is coherent, V_{act} is related to the change of the magnetization required to attain the direction of maximum energy and initiate the activation (discussed in a recent review[2]). Theoretical studies have so far been confined to the case of noninteracting particles and coherent reversal.[3] There is experimental evidence, however, that interactions may result in enhancement of the activation volume.[4] Incoherent reversal is probably also of importance since the measured activation volume of elongated particles is a small fraction of the particle size.[3]

In the present study, the activation volume is calculated for the simplest case of an interacting pair of particles. The energy surface of this system has been mapped[5] and the analysis represents the basis of the treatment in Sec. II. The validity of the approximations is then tested by comparison with numerical calculations in Sec. III. The approach used considers the thermal forces as white Gaussian "noise" and a set of stochastic equations of motion for the magnetization is derived and integrated numerically.[6]

II. ANALYTIC TREATMENT

We consider first an aligned ensemble of noninteracting particles. The mean switching time τ of any moment in the direction of an applied field H is given by the Néel–Arrhenius law, $\tau^{-1}=f_0e^{-E_B/kT}$, where E_B is the energy barrier of the reversal and f_0 is a frequency factor that is dependent on applied field, temperature, and anisotropy.[7] Transitions against the field are ignored. It is convenient to define f_0 as a constant, for example, $f_0'=\alpha|\gamma_0|H_K$, where $H_K=2K/M_s$ is the anisotropy field and α, γ_0 are the damping and gyromagnetic parameters in the Landau–Lifshitz equation of motion of the magnetization, and express τ as

$$\tau^{-1}=f_0'e^{-E_B^{eff}/kT}. \tag{2}$$

The activation volume of the ensemble is derived from Eqs. (1) and (2) (Ref. 8)

$$V_{act}=\frac{(dE_B^{eff}/dH)|E_B^{eff}=E'}{M_s}, \tag{3}$$

where $E'=kT\ln(f_0't')$ is the activation energy dependent on the characteristic time t' of measurement. The activation volume of individual particles is obtained from Eqs. (2) and (3) as

$$V_{act}=\frac{kT}{M_s}\frac{d}{dH}\left[\ln(f_0'\tau)\right]|_{\tau=t'}. \tag{4}$$

The theory is next applied to the case of an interacting pair of particles of uniaxial anisotropy. If the bond direction and the easy axes are parallel to the applied field, the magnetization reverses by fanning and the energy barrier E_B was evaluated by Chen *et al.*[5] assuming a dipole approximation.

Analytic expressions for the activation volume of the dipole pair can be obtained for some special cases.

Case A. In the asymptotic limit $kT/E_B\to 0$, $E_B^{eff}=E_B-kT\ln(f_0/f_0')\to E_B$, since the T dependence of f_0 is relatively weak. The activation volume is then obtained from Eq. (3).

$$\frac{V_{act}}{V}=2\left(1-\frac{h}{(1+k)}\right)\Bigg|_{h=h'}=\sqrt{2E'/[KV(1+k)]}$$

$$\text{if } k>\tfrac{1}{3} \text{ or else } h>h_{cr}$$

$$=2-h-\sqrt{(1-k)(1-3k)}|_{h=h'}$$

$$=\sqrt{4[1-2k-\sqrt{(1-k)(1-3k)}]+E'/KV}, \quad \text{otherwise,} \tag{5}$$

where $h=-H/H_K$ is the reverse field, h' is the field when $E_B=E'$, $k=M_sV/(H_KR^3)$ is a measure of the coupling strength, R is the dipole pair separation, and $h_{cr}=(1+k)\sqrt{(1-3k)/(1-k)}$ is the critical field associated with the transition between symmetric ($h>h_{cr}$) and asymmetric ($h<h_{cr}$) fanning.[5]

It can be shown that

 0021-8979/94/75(10)/5704/3/$6.00 © 1994 American Institute of Physics

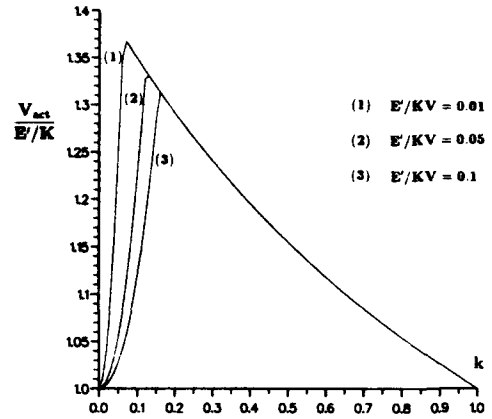

FIG. 1. The activation volume dependence on coupling strength k for different values of the ratio E'/KV.

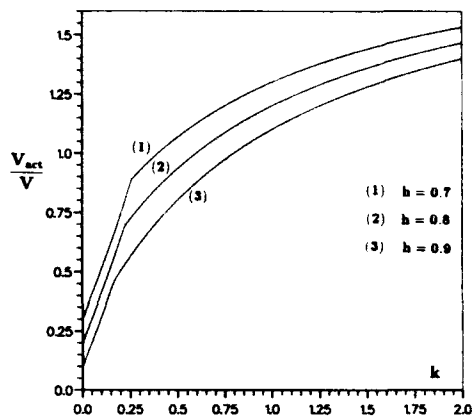

FIG. 2. The activation volume dependence on coupling strength k for different values of the applied field h.

$$V_{act}=\frac{\Delta m_H}{M_s}, \tag{6}$$

where Δm_H is the variation in the component of the magnetic moment of the pair (in the direction of the field) involved in the rotation from the configuration of locally minimum energy to the saddle point of the transition. Equation (6) is consistent with the definition Eq. (3) and should not therefore be dependent on the reversal mechanism. For coherent reversal, we obtain $V_{act}/V=\Delta m_H/M_sV=2[1-h/(1+3k)]$, a value larger than the expression for symmetric or asymmetric fanning [Eq. (5)]. Incoherent reversal therefore reduces the activation volume of the pair.

The activation volume of the pair is shown in Fig. 1 as a function of the coupling strength k. The field h' is chosen so that the activation energy $E'(\equiv E_B)$ is invariant in the calculation. The activation volume of the pair scales with the activation energy E' and depends to second order on the strength of the interaction k which determines the shape of the energy surface. Initially, when $k=0$, $h'=1-\sqrt{E'/KV}<h_{cr}=1$. As k increases, h' increases until $h'=h_{cr}$ and the activation volume acquires a maximum value, since the change Δm_H is largest at that point.

The dependence of the ratio V_{act}/V on coupling strength k at constant field h is shown in Fig. 2. The enhancement of the activation volume of the pair with interaction strength results primarily from the increased energy of activation E'.

Consider the activation volume of an ensemble of noninteracting pairs of particles characterized by a dispersion in sizes V. The activation volume in this case is dependent on the energy of activation $E'(T,t')$ and does not become temperature independent in the limit of low T. By expressing V as a function of (E',h,k) and substituting in Eq. (5), the activation volume of the ensemble is

$$V_{act}=\frac{E'/K}{1+k-h}$$

$$\text{if } k>\tfrac{1}{3} \text{ or else } h>h_{cr}$$

$$=\frac{[2-h-\sqrt{(1-k)(1-3k)}]E'/K}{1+4k+3k^2+h^2-4h+2h\sqrt{(1-k)(1-3k)}} \quad \text{else.} \tag{7}$$

Of particular interest is the case when the activation energy E' is fixed, for example by an experimental setup. An increase in interaction strength then results according to Eq. (7) to a reduction of the activation volume of the ensemble.

Case B. In the absence of interactions ($k=0$), it is possible to use the "high-energy barrier" approximation for f_0

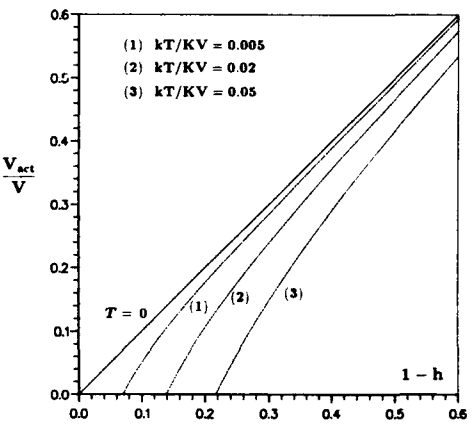

FIG. 3. The field dependence of the activation volume of a single-domain particle for different values of the ratio kT/KV.

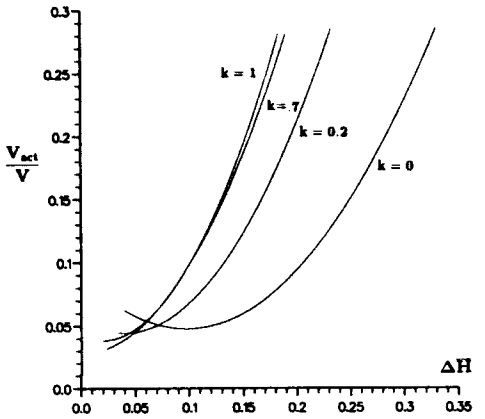

FIG. 4. Computed V_{act}/V vs $\Delta\tilde{H} = (H_K^{eff} - H)/H_K^{eff}$ for different values of coupling strength k ($KV/kT=50$).

derived by Brown,[7] valid for $E_B/kT>1$, to obtain an expression for the activation volume of a single particle

$$\frac{V_{act}}{V} = 1 - h - \frac{kT}{2KV}\frac{1+3h}{1-h^2}. \tag{8}$$

The equilibrium thermal fluctuations of the magnetization result in the reduction of the activation volume as shown in Fig. 3. Equation (8) is valid for $KV(1-h)^2/kT>1$ but this condition is not satisfied close to the switching field ($h\to 1$). The energy surface in this case becomes flat and the thermal fluctuations can not adequately be described by a second-order energy expansion.[7]

Case C. In the limit of strong coupling ($k>1/3$), low temperatures ($E_B \gg kT$) and strong fields [$H \to H_K^{eff} = H_K(1+k)$, the switching field at $T=0$], reversal occurs by near symmetric fanning.[6] In this case, it can be shown using Kramer's rate theory[9] that f_0 is given by Brown's high-energy barrier approximation with the substitution $H_K \to H_K^{eff}$. The activation volume in this case is given by

$$\frac{V_{act}}{V} = 2(1-h_r) - \frac{kT}{2K^{eff}V}\frac{1+3h_r}{1-h_r^2}, \tag{9}$$

where $h_r = H_K/H_K^{eff} = h/(1+k)$. In the asymptotic limit $T\to 0$, Eq. (9) is consistent with the previous approximation [Eq. (5)].

III. NUMERICAL TREATMENT

The numerical method described in Ref. 6 was used to evaluate the relaxation time. The activation volume was then evaluated from Eq. (4) using weighted Chebyshev-series polynomial approximations to the numerical data.

The main features of Figs. 1,2,3 are reproduced by the numerical data. The dependence of the activation volume on reduced field $\Delta\tilde{H} = (H_K^{eff} - H_K)/H_K^{eff}$ is shown in Fig. 4. At constant $\Delta\tilde{H}$, the activation volume increases with coupling strength to a constant value as is predicted by the theory [Eq. (5)]. In the limit $\Delta\tilde{H}\to 0$, the magnetic reversal is nearly spontaneous and the behavior is more complex since the dependence of the prefactor f_0 on $(k,h,KV/kT)$ becomes significant.[6,9]

IV. CONCLUSIONS

The activation volume in fine particles is not the volume that reverses magnetically or any part as it is often assumed. In the asymptotic limit $E_B \gg kT$, the activation volume of an interacting pair is related to the physical process of rotation of the magnetization to the saddle point of the transition through relation (6). This relation should also be valid for more complex collective activation processes provided they can be described by a single energy barrier. In this case, the energy barrier of lowest height and hence the activation volume can be evaluated by the Ridge method,[10] an efficient technique for finding saddle points in energy surfaces.

ACKNOWLEDGMENT

This work was supported by the SERC.

[1] E. P. Wohlfarth, J. Phys. F **14**, L155 (1984).
[2] A. Lyberatos, R. W. Chantrell, and K. O'Grady, NATO ASI Nanophase Materials, Corfu, 1993.
[3] A. M. de Witte, K. O'Grady, G. N. Coverdale, and R. W. Chantrell, JMMM **88**, 183 (1990).
[4] M. El-Hilo, K. O'Grady, and R. W. Chantrell, IEEE Trans. Magn. MAG-**27**, 4666 (1991).
[5] W. Chen, S. Zhang, and H. N. Bertram, J. Appl. Phys. **71**, 5579 (1992).
[6] A. Lyberatos and R. W. Chantrell, J. Appl. Phys. **73**, 6501 (1993).
[7] W. F. Brown, Jr., Phys. Rev. **130**, 1677 (1963).
[8] P. Gaunt, Philos. Mag. **34**, 775 (1976).
[9] A. Lyberatos (unpublished).
[10] I. V. Ionova and E. A. Carter, J. Chem. Phys. **98**, 6377 (1993).

Parameter template in local magnetic measurements

R. Kaczmarek, M. Dautain, and S. Defoug
Service Electrotechnique et Electronique Industrielle, Ecole Supérieure d'Electricité, 91192 Gif sur Yvette cedex, France

Surface Kerr-effect hysteresis loops used to determine loop parameters such as coercive field and remanence in the percent of saturation, may be obtained with video detection via uniform illumination but without invoking multiple image summation, averaging and subtraction as previously used to overcome poor signal to noise when investigating weak Kerr-contrast materials. The approach taken here applied to power ferrite surfaces is to calculate for each applied field in the repetitive field excitation cycle, an accurate number representing the average of all pixels over a grain area. The grain under study had 20–50 microns across. Results stabilize after 20 cycles, within a parameter range that may be qualified as the parameter template. For small grains the template values become more important, which seems to be in accord with theories of the H_c fluctuations and the nature of hysteresis losses.

INTRODUCTION

The arrival of powerful imaging technologies and the enhancement of the Kerr effect (KE) performances in the 1980s and the 1990s resulted in a substantial resurgence in surface imagery. Schaefer *et al.*[1–3] have recently studied the domain movements in MnZn recording heads in order to find relations between the magnetic response and the material structure. But researchers were primarily interested in examining the materials as used in recording devices. As far as the authors know nobody had observed the domains on power ferrites (PF). There are two major reasons for this fact. First, the benefit of observing the bulk ferrites' surface seemed very uncertain, especially when looking for global core losses or permeability. Second, the technical difficulties are high in PF, as its porosity, texture, and grain disorientation are particularly hostile to observations in polarized reflected light.

Specific for PF is the demand for the highest saturation possible and low losses. In 1992, Goeffroy and Porteseil found[4] that the quasistatic losses were a direct consequence of the fluctuations of the coercive field. This followed numerous studies on one wall movements,[5,6] where the interaction fields between different domain walls may eventually be treated in terms of the local fields H and H_c, acting on a single domain.[6] The measurements of the spatial H_c fluctuations in the case of the polycristalline materials would provide verification data for the theoretical multidomain H_c analysis.

To visualize the magnetic domains in PF,[7] we constructed a classical longitudinal KE setup, giving particular attention to the light stability and the numerical treatment (Fig. 1). Fig. 2 shows an example of the domains, which we called the differential domains, obtained by the subtractions of images taken at consecutive field values. The domains are adjacent, proving a regular wall progression. Their contrast is very weak, two or three numerical levels, on the scale of 256.

When measuring the spatial H_c fluctuations, we record the parameter variations due to nonrepetitivity. To repeat the acquisition a sufficient number of times, with the image averaging as a rule, we had to acquire images for six, seven, or more hours. Whereupon the problem of optical and mechanical stability becomes delicate. To diminish the acquisition time, it is necessary to automate the process and to limit the number of acquisitions, possibly by giving up the image averaging. The averaging being a problem in static measurements is also a hindrance to the application of the stroboscopy in a dynamic regime, because we average the noncorrelated noise together with the nonrepetitive magnetic contrast itself.

AUTOMATION

The automation of acquisition on power ferrites is a tiresome problem, because the differential domains are irregular in form and weak in contrast. The problem is then an efficient integrating method.

To plot the local hysteresis loop, we combine the longitudinal magnetization variations ΔM_l^i with the field variations. There are two methods used in the case of directly visible domains: first, the surface method, as used by Knowles in 1959,[8] and the second one, the average brightness method as used by Minvehchi in 1990.[9] In a paper presented recently,[10] we proposed a generalization of these methods to be applied in the case of the differential domains. Here we apply the average brightness method, where the magnetization increment equals the mean pixel value over the whole grain:

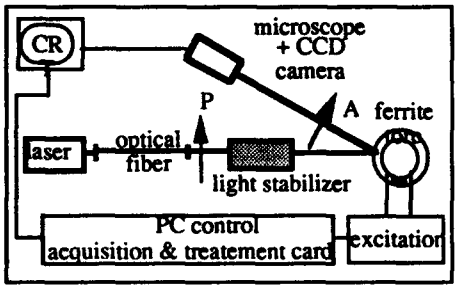

FIG. 1. The longitudinal Kerr effect setup.

 0021-8979/94/75(10)/5707/3/$6.00 © 1994 American Institute of Physics

FIG. 2. An example of differential domains on the surface of power ferrite.

$$\Delta M_f^g = \frac{\Sigma \Delta n_i}{P},$$

where P is the pixel number on one frame and $\Delta n_i = n_i^{(1)} - n_i^{(2)}$ is the contrast increment of the ith pixel under the field variation from $H^{(1)}$ to $H^{(2)}$.

Once we have linked ΔM_f^g with the entire grain area, the automation becomes a much simpler task because the grain surface is delimited once and for all, which permits us to not look for the identification of irregular and weak domains on each acquired image.

AVERAGING AND SUBTRACTION

The problem of automation being resolved, there still exists the problem of averaging the images. However, the averaging may not be imperative for a numerical analysis.

We have examined the pixel value distribution over one nonaveraged frame, such as the first image on Fig. 3. Any pixel value is composed of three contributions: a nonmagnetic background, a magnetic information, and a noise. The pixel value distribution is quasi-Gaussian, and if we average them over a frame we eliminate the noise. Thus, the work of eliminating the noncorrelated noise is shifted from frames averaging to pixels averaging in one image.

On the other hand, in the adopted average brightness method the longitudinal magnetization variation is given as a difference of two numbers:

$$\{H^{(1)}, H^{(2)}\} \rightarrow \Delta M_f^g = \frac{\Sigma_i \Delta n_i}{P} = \frac{\Sigma_i n_i^{(1)}}{P} - \frac{\Sigma_i n_i^{(2)}}{P},$$

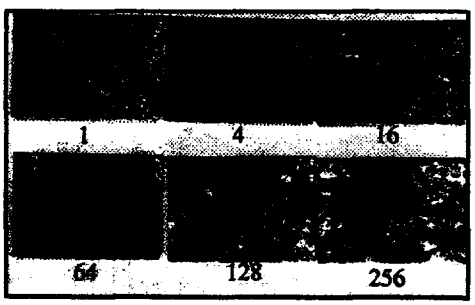

FIG. 3. Differential domains with 1, 4, 16, 64, 128, and 256 images averaged before subtraction.

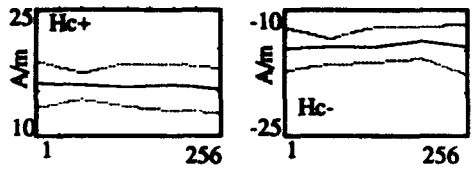

FIG. 4. Local coercive field measured for the different number of the images averaged before subtraction (the mean value and dispersion).

and the work of the nonmagnetic background elimination is shifted from image subtraction to numbers subtraction.

When we measure the local parameters for different numbers of averaged images, we find that their values vary only slightly (Fig. 4). We may then obtain the magnetic information from a nonaveraged image, where the magnetic contrast is optically absent.

PARAMETER TEMPLATE

Once the problem of the acquisition time and automation is resolved, we may proceed to a multiacquisition that will furnish informations relative to the H_c fluctuations due to the nonrepetitivity. When repeating the measurements, we found that the results stabilize after about 20 acquisitions. Figure 5 shows a plot of 30 local hysteresis loops. From this ensemble of loops, we retrieved data to determine the local parameter template that we defined as the parameter range and their mean value (Table I).

When the measurements are brought about on large grains—of about 50 μ—then the loop parameters of the whole acquisition series present a reasonable relationship with the global measurements, the latter giving the following values: the coercive field $H_c = 17$ A/m, the remanent magnetic induction $B_r = 93\%\ B_{sa}$, the saturation induction being 0.35 T.

GRAIN SIZE IMPACT

The measurements of 20 grains have given the mean local Hc and its dispersion growing when the grain size becomes smaller. As the smaller grains are favorable to larger hysteresis losses, these measurements might confirm the theoretical formula of Porteseil,[4] for whom the hysteresis losses grow with more important Hc fluctuations. However, the experimental results are too few for the moment.

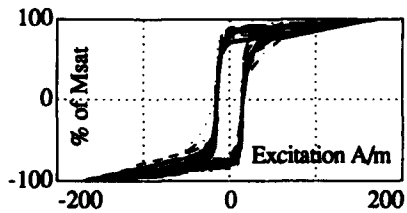

FIG. 5. Thirty local hysteresis taken in one automatic acquisition

TABLE I. Local parameter template retrieved from 30 cycles.

	Template	Mean
H_c^+ (A/m)	14,2,...,16,4	15,3
H_c^- (A/m)	−15,7,...,−13,3	−14,5
M_r^+ (%)	75,...,87	81
M_r^- (%)	73,...,81	77

CONCLUSION

The application of the average brightness method to the measurements of the local hysteresis loop permits the automation of repetitive acquisition, because the pictures may be acquired without the image averaging or subtraction. The individual measurements are nonrepetitive, but they remain within a limited range that may be quantified by the notion of template. This template gives the measure of the spatial Hc fluctuations in multidomain materials. On the other hand, the elimination of the image averaging from the acquisition procedure makes possible the application of stroboscopy in PF surface observations. The template variations with frequency may provide informations concerning the H_c fluctuations in a dynamic regime, possibly permitting certain correlation between local and global measurements in power ferrites.

ACKNOWLEDGMENTS

This work was supported in part by the Ministère de l'Industrie et du Commerce Exterieur. The samples have been supplied by the LCC Thomson Beaune and LCR Thompson Corbeville. The authors also thank M. Don White for help.

[1] R. Schaefer, B. E. Argyle, and P. L. Trouilloud, IEEE Trans. Magn. **26**, 2394 (1992).
[2] R. Schaefer, B. E. Argyle, and D. Dingley, Paper GP-07, INTERMAG '93, Stockholm.
[3] B. E. Argyle, R. Schaefer, P. L. Trouilloud, M. E. Re, A. P. Praino, S Takayama, and D. Dingley (these proceedings).
[4] O. Geoffroy and J. L. Porteseil, J. Magn. Magn. Mater. **104–107**, 379 (1992).
[5] R. Vergne, J. C. Cotillard, and J. L. Porteseil, Rev. Phys. Appl. **16**, 449 (1981).
[6] B. Alessandro, C. Beatrice, G. Bertotti, and A. Montorsi, J. Appl. Phys. **64**, 5355–5360 (1988).
[7] R. Kaczmarek, M. Dautain, and T. Barradi-Ismail, Proceedings of the ICF6, Tokyo, 1992.
[8] J. E. Knowles, Proceedings of the Physics Society LXXV, 1959, p. 6.
[9] E. Mivenchi, P. Beckley, and D. H. Horrocks, SMM, 1990, p. 10.
[10] R. Kaczmarek and M. Dautain, Paper SP-07, SMM, 1993, p. 11.

3-D micromagnetic modeling of domain configurations in soft magnetic materials

Zhenzhou Guo and Edward Della Torre
Institute for Magnetics Research, George Washington University, Washington, D.C. 20052

This paper describes a micromagnetic model that computes the vector magnetization in a three-dimensional geometry. Since the magnitude of the magnetization is constant, the energy minimization is performed with respect to polar and azimuthal angles. This generates a pair of coupled nonlinear partial differential equations solved numerically in spherical coordinates. The demagnetizing field, on the other hand, is not constrained in magnitude and therefore requires three variables at each point to fully describe it. Applying this to a Permalloy film whose thickness is equal to one mesh unit permits direct comparison to our 2-D study that only permitted pure Neél walls to form. The extra degree of freedom allows the magnetic spins to have an out-of-plane component, which is especially noticeable in the region where a vortex formed in the 2-D model. This numerical model is being used to study and optimize the flux conduction in a pipe whose cross section permits the elimination of closure domains, thus improving both the magnetic susceptibility and the magnetic stability of the recording head.

I. INTRODUCTION

Early micromagnetic models of domains[1,2] were essentially analytic. More recently some two-dimensional solutions[3,4] were carried out using numerical techniques. In a previous paper,[5] we used a micromagnetic model, defined upon a 2-D lattice, to obtain the magnetization pattern in a soft magnetic thin film. In all these cases the spin angle was allowed to rotate only in a plane. The magnetization, whose magnitude is constant for quantum mechanical reasons, can be defined by a single variable, the angle that it makes with respect to a given axis. Based on this model, we examined the effects of closure domains on the performance of thin film recording heads.[6]

Although 1-D and 2-D models have been useful in analyzing magnetic materials, they introduce an error since the magnetization structure is really three dimensional. Though the major component of the magnetization lies in the plane in thin films, such as those widely used in recording heads, under certain circumstance some magnetic flux may leak out of plane. This paper addresses the question of under what circumstances the 2-D assumption is valid.

It was pointed out elsewhere[6] that the closure domains may negatively affect the performance of the recording head. A laminated structure has been suggested as a way to eliminate the closure domains.[7] To optimize this geometry and to solve similar problems we developed a 3-D numerical model, presented here, in which there are no constraints placed on the direction of magnetization and the bodies considered are three dimensional.

To compare our new 3-D program with our 2-D work,[5] we first examined the same films. We saw that when increasing the magnitude of the magnetization the 2-D approximation improved, since the larger demagnetizing field tends to constrain the magnetization to lie in the plane. In general, a pure Néel wall is not observed, as in the 2-D case. As the thickness increased, the walls in the center of the film are more Bloch type while at the surfaces they are more Néel type. The vortices in the thin film are also discussed in detail in this paper.

II. FORMULATION

The sample is discretized into a 3-D array of cubes, and the magnetic moment of each cube is represented by a dipole $\mathbf{m}_i$ at the center of that cube equal to the average of the moment of the atomic spins in the cube. Corrections for this approximation have been discussed elsewhere.[8] The total magnetic energy is the sum of the exchange, anisotropy, demagnetization, and Zeeman energies.[9] The exchange energy E_e due to the coupling of spins $\mathbf{S}_i$ and $\mathbf{S}_j$ is given by

$$E_e = 2A \sum \sum \sum \mathbf{S}_i \cdot \mathbf{S}_j , \tag{1}$$

where the sums are carried out over the nearest-neighbor atoms. When the cubes are small enough, the direc... variations between the neighbors can also be small. Then the above dot product can be expressed in a threefold integral in terms of polar and azimuthal angles as illustrated in Fig. 1 and given by

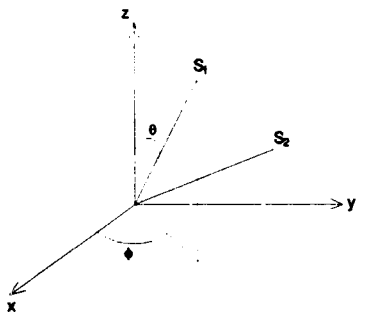

FIG. 1. Magnetization vectors.

 0021-8979/94/75(10)/5710/3/$6.00 © 1994 American Institute of Physics

$$E_e = A \int\int\int \left[\frac{\partial^2 \theta_x}{\partial x^2} + \frac{\partial^2 \theta_y}{\partial y^2} + \frac{\partial^2 \theta_z}{\partial z^2} + \left(\frac{\partial^2 \phi_x}{\partial x^2} + \frac{\partial^2 \phi_y}{\partial y^2} + \frac{\partial^2 \phi_z}{\partial z^2} \right) \sin^2 \theta \right] dx\, dy\, dz. \quad (2)$$

The coordinate system is oriented so that the easy axis of the uniaxial crystalline anisotropy is the x axis. Then the anisotropy energy is given by

$$E_k = K \int\int\int \sin^2 \theta \cos^2 \phi dx\, dy\, dz. \quad (3)$$

The sum of demagnetization and Zeeman energies is given by

$$E_k = \mu_0 \int\int\int (\mathbf{M}\cdot\mathbf{H}_0 - \tfrac{1}{2}\mathbf{M}\cdot\mathbf{H}_d) dx\, dy\, dz. \quad (4)$$

The equilibrium state is determined by finding the local minimum of the sum of (1), (2), and (3). The Euler–Lagrange variation method is used to minimize this integral with respect to both $\theta(x,y,z)$ and $\phi(x,y,z)$, thus automatically satisfying the restriction of keeping the magnitude of magnetization constant. This results in the following two coupled partial differential equations:

$$\sum_{i=x,y,z} \theta_{ii} = \frac{1}{2} \sin 2\theta \sum \left(\frac{\partial \phi}{\partial x_i} \right)^2 - \frac{K}{2A} \sin 2\theta \cos^2 \phi - \frac{\mu_0 M_s}{2A} (H_x \cos \theta \cos \phi + H_y \cos \theta \sin \phi - H_z \sin \theta) \quad (5)$$

and

$$\sum_{i=x,y,z} \phi_{ii} = \frac{K}{A} \sin 2\phi + \frac{\mu_0 M_s}{2A \sin \theta} \times (H_x \sin \phi - H_y \cos \phi). \quad (6)$$

These equations are solved numerically using the Gauss–Seidel method, and the acceleration and stabilization techniques that we adopted in our 2-D model.[5] The calculation of the demagnetizing field was discussed elsewhere.[10]

It is noted that in Eq. (6) there is a singularity at $\theta=0$; however, at this point the direction is the unique polar axis whatever the value of ϕ. Thus, whenever θ falls below an arbitrarily chosen small angle, we let the program solve Eq. (5) only and instead of solving Eq. (6) we leave ϕ unchanged. The errors introduced are acceptable since the direction is not sensitive to ϕ value around polar axis.

III. RESULTS

Using the same saturation magnetization, anisotropy constant, and exchange constant of permalloy, as we used in our previous paper,[5] we first considered a film discretized into a single layer of mesh cubes, i.e., the thickness of the film is equal to the thickness of a cube. Thus, a film whose size is 2 μm×1 μm×100 nm consisted of 200 such cubes. The initial state of the calculation was taken to be the pattern of two antiparallel domains with all the magnetization in the plane, which resulted in the equilibrium state shown in Fig. 2. The closure domains formed as in our 2-D work; however, at the center of the horizontal wall, the magnetization came out of the plane and formed a Bloch point. Due to the abrupt change of the magnetization direction, the energy at this point is extremely high. In the 2-D model, which only allows the magnetization to rotate in the plane, a vortex appeared in the same place. The size of the vortex was reduced so that it did not effect the minimization of the total energy of the whole sample by increasing the number of mesh points; however, this vortex could not be completely eliminated. By comparison of our 2-D and 3-D modeling, we concluded that the energy of the Bloch point was lower than that of the vortex.

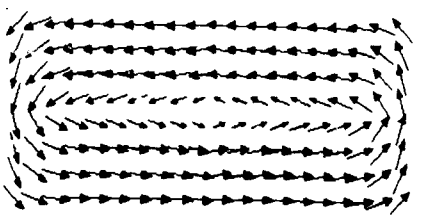

FIG. 2. Projection of a three-dimensional sample 20×10×1 on x-y plane. The length of the arrows represents the in-plane magnetization component.

The leakage of the magnetization out of the plane was then studied for various saturation magnetizations. The absolute value of the z component was integrated over the film as a measure of this leakage. Figure 3 shows that the leakage decreases rapidly, to avoid the surface poles with increasing saturation magnetization. Thus, the 2-D approximation would be better for materials with higher magnetic moment.

We then discretized a bulk permalloy material with dimensions of 2 μm×2 μm×500 nm into a 20×20×5 array of cubes (Fig. 4). Again, we used the two antiparallel domain configuration as the starting point of the calculation. By viewing the inner layer of the ground state, shown in Fig. 5, and the outer layer shown in Fig. 6, we saw that the surface

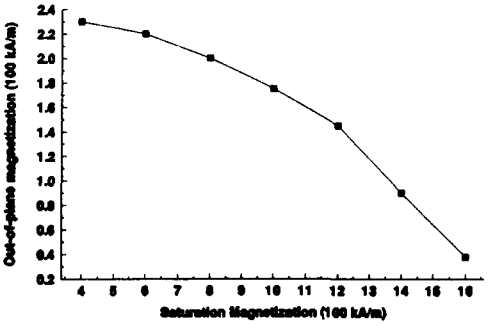

FIG. 3. Out-of-plane magnetization vs saturation magnetization.

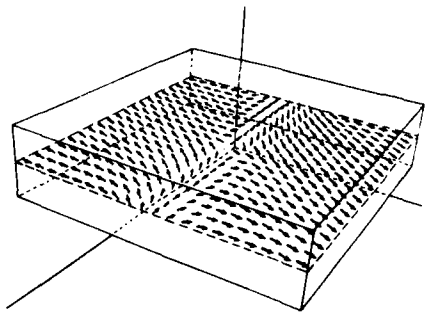

FIG. 4. Bulk material.

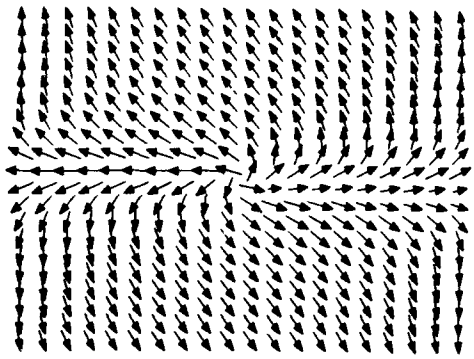

FIG. 6. The outer layer of the bulk material.

wall approximates a Néel wall while the center it approximates Bloch wall. Thus, in free space the Bloch wall has lower energy than the Néel wall.

IV. DISCUSSION

The above analysis demonstrates that the magnetization behavior is always 3-D even in thin films. Although it can get more accurate results, 3-D modeling takes much more computer time to compute and requires more memory allocation due to larger discretization arrays and more complicated function evaluations. Since new recording head material, such as Fe-NiO_2, have larger magnetic moments, the difference between 2-D and 3-D may not be important for some heads. Thus, 2-D model which computes faster and has smaller memory requirements may still be adequate in many circumstances; however, to analyze laminated head cores, such as the head suggested by Slonczewski in Ref. 7 it is still necessary to do 3-D calculations.

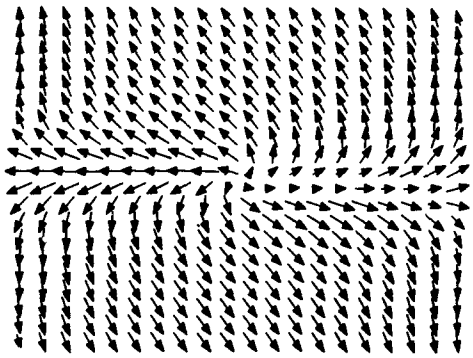

FIG. 5. The inner layer of the bulk material.

ACKNOWLEDGMENTS

The authors would like to acknowledge the use of the CRAY Y-MP2 supercomputer of the National Institute of Standards and Technology, Gaithersburg, Maryland, and would particularly like to thank Dr. L. H. Bennett and Dr. R. D. McMichael for their assistance. We would also like to thank F. Vajda and J. Jatau for helpful discussions. This work was supported by an ATP grant though the National Storage Industries Consortium.

[1] L. D. Landau and E. M. Lifshitz, Phys. Z. Sowjet. **8**, 153 (1935).
[2] C. Kittel, Phys. Rev. **70**, 965 (1946).
[3] A. Aharoni and J. P. Jakubovics, Philos. Mag. B **53**, 133 (1986).
[4] J. G. Zhu and H. N. Bertram, J. Appl. **63**, 3248 (1988).
[5] Z. Guo and E. Della Torre, IEEE Trans. Magn. **MAG-29**, 2521 (1993).
[6] Z. Guo and E. Della Torre, MMM '93.
[7] J. C. Slonczewski, IEEE Trans. Magn. **MAG-26**, 1322 (1990).
[8] Y. D. Yan and E. Della Torre, IEEE Trans. Magn. **MAG-24**, 2368 (1988).
[9] W. F. Brown, *Micromagnetics* (Krieger, New York, 1978).
[10] Y. D. Yan and E. Della Torre, IEEE Trans Magn. **MAG-25**, 2919 (1989).

Magnetization in current carrying iron whiskers (abstract)

A. S. Arrott and J.-G. Lee
Simon Fraser University, Burnaby V5A 1S6, Canada

The structure deduced for a ⟨100⟩ iron whisker carrying a current along its axis in the presence of a magnetic field is shown in Fig. 1. An analytic model of the ac response is obtained by considering the competition of exchange, anisotropy and magnetostatic energies. For the analytic model the magnetization is assumed to point either along an easy axis in the plane or out of the plane everywhere except in the walls where the energies of the walls per unit area are assumed to be independent of field. It is argued that the energy scales with that of the central cross section subjected to demagnetizing fields that depend on the magnetization along the axis in that cross section. The model is shown to account for the ac susceptibility of a current carrying whisker. The calculation is refined by considering a pattern that is divergenceless. The pattern is generated by taking the curl of a vector potential to produce the components in the plane and adding a component perpendicular to the plane to conserve the magnitude. The vector potential has a single component given by $A_z = M_s q \coth^{B/q}[(1/\sqrt{2})\ (q/\{a \ln[\cosh(x/a)\cosh(y/a)]\})^{q/B} - A_c[(x/a), (y/a)]$, where the parameter q determines the size of the central region of Fig. 1, the constant a sets the scale for the 90° domain walls between the four outer domains, and B sets the scale for the 90° domain wall between the central region and the outer domains. The term A_c is added to turn the magnetization along the axis of the whisker in each corner of the central cross section. The only parameter in A_c is a. The total energy is minimized for parameters q, B, and a. The field dependence of q accounts for the magnetic behavior.

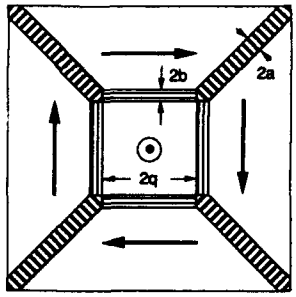

FIG. 1. Magnetization in the central cross section of an iron whisker carrying a current.

 0021-8979/94/75(10)/5713/1/$6.00 © 1994 American Institute of Physics

Spin-dependent confinement in DMS-based heterostructures (Invited)

A. Petrou, L. P. Fu,[a] W. Y. Yu, and S. T. Lee
Department of Physics and Center for Electronic and Electro-Optic Materials, State University of New York at Buffalo, Buffalo, New York 14260

B. T. Jonker
Naval Research Laboratory, Washington, D.C. 20375-5343

J. Warnock
IBM Research Division, T. J. Watson Research Center, P. O. Box 218, Yorktown Heights New York 10598

We describe the results of a magneto-optical study of a class of semiconductor heterostructures in which one of the constituent layers is a diluted magnetic semiconductor (DMS). The large magnetic band splittings of DMS materials result in spin-dependent confining potentials for electrons and holes which can be changed externally by varying the applied magnetic field. The modifications in the band alignment result in changes, sometimes dramatic, of the optical properties in the vicinity of the band gap.

I. INTRODUCTION

It is highly desirable to induce changes in the band structure of semiconductor quantum wells via the application of an external perturbation such as an electric field.[1,2] These changes can form the basis of operation of these systems as optical modulators. Even more dramatic modifications of the band alignment, and thus the strength of the interband optical transitions, can be achieved in semiconductor heterostructures which consist of alternating nonmagnetic and magnetic (DMS) II–VI materials. When a fraction of the group II cation in a II–VI semiconductor (such as ZnSe, CdTe, etc.) is randomly substituted by a transition metal ion (such as Fe^{+2}, Mn^{+2}, Co^{+2}, etc.) the resulting alloy is known as a diluted magnetic semiconductor (DMS).[3] The most dramatic difference between the parent nonmagnetic II–VI compound and the corresponding DMS material is the very large spin splitting (several meV) in the conduction and valence band of the latter. The splittings which are due to an exchange interaction between the spins of the electrons and those of the transition metal ions form the basis of the spin-dependent confining potentials for the carriers in structures that incorporate DMS layers.

In this paper we present the results of a magneto-optical study of two types of ZnSe-based heterostructures: The first group consists of $ZnSe/Zn_{0.9}Fe_{0.1}Se$ quantum wells; in this system the confinement of heavy holes ($j=3/2$) is controlled by the externally applied magnetic field. The second system is $ZnSe/Zn_{0.99}Fe_{0.01}Se$ heterostructures (also known as "spin superlattices") in which the confinement of the heavy holes as well as that of the electrons can be tuned by varying the magnetic field. The experimental results are modeled using a variational calculation that describes systems with zero or very weak confinement.

[a]Present address: Physics Department, Emory University, Atlanta, GA 30322.

II. EXPERIMENTAL

The samples were grown by molecular-beam epitaxy (MBE) from elemental Knudsen cell-style sources of Zn, Se, and Fe on GaAs (001) semi-insulating device grade wafers. The substrate surface exhibited a well-ordered 4×3 reconstruction as observed by reflection high-energy electron diffraction (RHEED) with the shuttered Se source at operating temperature. All samples were grown in (001) orientation at a substrate temperature of 300 °C and growth rates of 20–40 Å/min, with a Se:Zn beam equivalent pressure ratio >2:1. RHEED was used to monitor the growth, and showed a well-ordered 2×1 surface reconstruction. The thickness and composition of the samples were confirmed by x-ray fluorescence following growth. Some relevant parameters of the samples used in this work are listed in Table I. The magnetic spin splitting of the excitons in these structures was studied

TABLE I. Sample parameters.

Sample	ZnSe layer thickness (Å)	$Zn_{1-x}Fe_xSe$ layer thickness (Å)	x	Structure type
1	100	100	0.1	Single quantum well
2	150	100	0.1	Single quantum well
3	200	100	0.1	Single quantum well
4	100	100	0.01	Single quantum well
5	96	96	0.01	Multiple quantum well

 0021-8979/94/75(10)/5714/5/$6.00 © 1994 American Institute of Physics

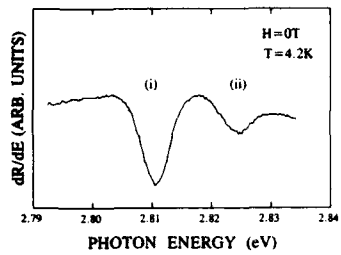

FIG. 1. Zero-field reflectance derivative spectrum (dR/dE) from sample 1. Features (i) and (ii) are identified as the heavy- and light-hole excitons, respectively.

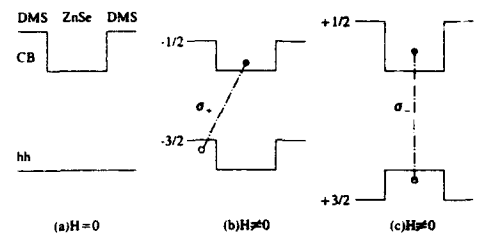

FIG. 2. Schematic diagram of the conduction and valence band alignment in $ZnSe/Zn_{0.9}Fe_{0.1}Se$ quantum well structures. (a) $H=0$; (b) $H\neq 0$, $m_j=-1/2$ electrons, $m_j=-3/2$ holes; (c) $H\neq 0$, $m_j=+1/2$ electrons, $m_j=+3/2$ holes. The dot–dashed lines indicate the allowed heavy-hole exciton transitions in the Faraday geometry.

using direct magnetoreflectance spectroscopy. A monochromatic beam, produced by the combination of a 250-W tungsten–halogen lamp and a grating spectrometer, was reflected from the sample surface. The intensity of the reflected beam was synchronously detected by a photomultiplier tube. The spectra were stored on disk and derivative spectra were taken numerically. The samples were placed in an optical cryostat equipped with an 8-T superconducting coil.

III. RESULTS AND DISCUSSIONS

Our samples fall into two broad categories: The first class consists of $ZnSe/Zn_{0.9}Fe_{0.1}Se$ quantum wells in which the heavy-hole ($j=3/2$) confinement is controlled by the externally applied magnetic field. The second type are $ZnSe/Zn_{0.99}Fe_{0.01}Se$ structures where both the electron and hole confinement depends on magnetic field.

A. $ZnSe/Zn_{0.9}Fe_{0.1}Se$ quantum wells

The zero-field reflectance derivative spectrum from sample 1 is shown in Fig. 1. It contains two features marked (i) and (ii) at 2.811 and 2.825 eV. They are identified as the heavy- ($j=3/2$) and light- ($j=1/2$) hole excitons, respectively. All the structures discussed in this paper were grown on GaAs substrates with a total thickness below the critical value for which the strain imposed by the thick substrate can be released via the formation of dislocations. The compressive strain removes the heavy–light hole degeneracy at the Brillouin zone center and is responsible for the splitting of the corresponding excitons. A schematic diagram of the zero-field band alignment of a $ZnSe/Zn_{0.9}Fe_{0.1}Se$ quantum well structure is shown in Fig. 2(a). Most of the offset appears in the conduction band, while the valence band offset is small. In Fig. 2(a) the heavy-hole offset is shown to be zero for simplicity. The exact band offset values will be discussed later. When a magnetic field is applied along the growth axis, the $Zn_{0.9}Fe_{0.1}Se$ layers exhibit large band splittings which are characteristic of DMS materials. The ZnSe layers on the other hand have a negligible splitting. The relative positions of the $m_j=-1/2$ ($m_j=+1/2$) conduction and $m_j=-3/2$ ($m_j=+3/2$) heavy-hole bands in the presence of a magnetic field are shown in Fig. 2(b) [Fig. 2(c)]. The zero-field conduction band offset is large enough so that the externally applied field only modifies the electron confinement; the electron potential increases for the $m_j=+1/2$ and decreases for the $m_j=-1/2$ spin state. In both cases the electrons remain confined in the ZnSe wells. The situation for the $j=3/2$ heavy-hole band is quite different. The zero-field offset in this case is small and is overwhelmed by the large magnetic spin splitting of the heavy-hole band. As a result, the confinement of the $m_j=\pm 3/2$ holes is controlled by the applied field. The $m_j=-3/2$ holes are confined in the $Zn_{0.9}Fe_{0.1}Se$ layers while the $m_j=+3/2$ holes are localized in the ZnSe wells. The energy of the σ_+ $(-1/2,-3/2)$ exciton component exhibits a large red shift as function of a magnetic field H while that of the σ_- $(+1/2,+3/2)$ component is almost field independent for $H>2$ T. Here the first (second) number in the parentheses gives the magnetic quantum number m_j of the electron (hole). The pronounced asymmetry of the heavy-hole exciton spin splitting is illustrated in Fig. 3 for sample 1 (circles), sample 2 (diamonds), and sample 3 (triangles). The σ_+ and σ_- excitonic transitions are indicated by the dot–

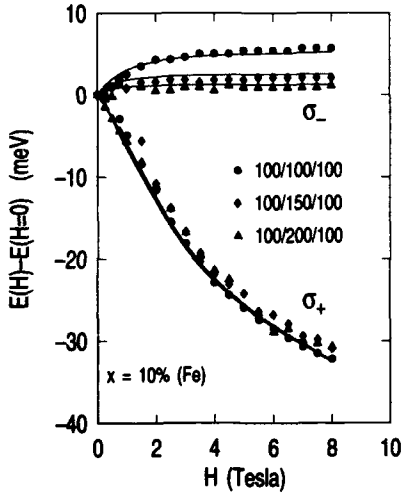

FIG. 3. Energy shifts of the σ_+ and σ_- heavy-hole exciton components plotted vs magnetic field for samples 1, 2, and 3. Circles: sample 1; diamonds: sample 2; triangles: sample 3.

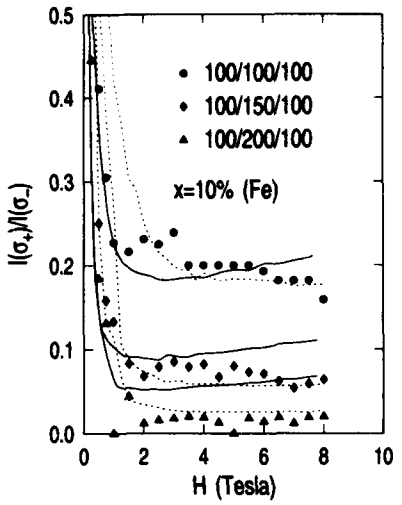

FIG. 4. Intensity ratio $I(\sigma_+)/I(\sigma_-)$ of the lower and upper heavy-hole exciton spin components plotted as a function of applied magnetic field for samples 1, 2, and 3.

dashed lines in Figs. 2(b) and 2(c), respectively. The σ_- transitions involve electrons ($m_j=+1/2$) and holes ($m_j=+3/2$) which are confined in the ZnSe wells, i.e., they are spatially direct (type I). The σ_+ component on the other hand is spatially indirect (type II) because it involves the $m_j=-1/2$ electrons which are confined in the ZnSe wells and the $m_j=-3/2$ holes that are localized in the $Zn_{0.9}Fe_{0.1}Se$ barriers. The intensity ratio $I(\sigma_+)/I(\sigma_-)$ of the lower to the upper exciton component dependence is plotted vs magnetic field in Fig. 4. The ratio drops monotonically with H and saturates at a value which decreases with increasing ZnSe well width. The latter represents the average electron-hole separation for the σ_+ component. The type-I→type-II field induced transition for the lower σ_+ exciton component[4,5] has been observed in ZnSe/ZnMnSe[6] and CdTe/CdMnTe[7] quantum wells. The work of Refs. 6 and 7 confirmed that there is nothing special about the ZnSe/ZnFeSe system and that the external control of the hole confinement is connected with the general properties of the DMS layers. Further confirmation came from studies of the magnetic field value H_0 at which the σ_- component becomes nonmagnetic as a function of temperature in ZnSe/ZnFeSe[8] and CdTe/CdMnTe[9] quantum wells. In both studies H_0 increases with increasing T because the DMS layer magnetization, and thus the band splittings, decrease.

The above discussion is rather oversimplified and incomplete because it does not take into account the electron-hole Coulomb attraction responsible for the formation of the exciton. Below we describe a variational calculation suitable for the modeling of excitons in systems with zero or very weak confinement.

The Hamiltonian of the exciton is given by the expression

$$H=\frac{p_{ze}^2}{2m_e}+\frac{p_{zh}^2}{2m_h}+\frac{p_x^2+p_y^2}{2\mu}-\frac{e^2}{\epsilon r}+V_e+V_h. \tag{1}$$

Here m_e, $\mathbf{r}_e$, and p_{ze} are the electron effective mass, the position vector, and momentum component in the direction perpendicular to the layers (z axis). Similarly, m_h, $\mathbf{r}_h$, and p_{zh} are the corresponding symbols for the $j=3/2$ hole; $\mathbf{r}=\mathbf{r}_e-\mathbf{r}_h$ is the relative electron-hole displacement, μ is the electron-hole reduced mass in the xy plane, and ϵ is the dielectric constant. $V_e(z_e)$ and $V_h(z_h)$ are the electron and hole confining potentials due to the band offset. Both functions depend strongly on magnetic field. The variational wave function which is used to describe the exciton has the form

$$\psi=\varphi_e(z_e)\varphi_h(z_h)\varphi_{eh}(z_e-z_h,r_\perp). \tag{2}$$

We choose $\varphi_{eh}\propto\exp(-r/\lambda a_0)$, where λ is a variational parameter and a_0 is the bulk exciton Bohr radius. The chosen form of φ_{eh} is appropriate for the situation where the electron and hole confining potentials are shallow and ensures that the solution extrapolates correctly to the bulk limit when V_e and V_h vanish. For a particular value of λ it is possible to determine a self-consistent set of functions $\varphi_e(z_e)$ and $\varphi_h(z_h)$ which minimize the exciton energy using an iterative method. We start with a trial electron wave function φ_{1e} which can be chosen as the single particle ground state wave function for the potential V_e. The hole wave function φ_{1h} is then found by numerically solving the equation

$$\langle\varphi_{1e}\varphi_{eh}|H|\varphi_{1e}\varphi_{eh}\rangle\varphi_{1h}=\langle\varphi_{1e}\varphi_{eh}|E|\varphi_{1e}\varphi_{eh}\rangle\varphi_{1h}. \tag{3}$$

The function φ_{1h} minimizes the overall exciton energy for a particular value of λ. To improve the estimate of the excitonic energy a new electron wave function φ_{2e} is calculated using φ_{1h} by numerically solving the equation

$$\langle\varphi_{1h}\varphi_{eh}|H|\varphi_{1h}\varphi_{eh}\rangle\varphi_{2e}=\langle\varphi_{1h}\varphi_{eh}|E|\varphi_{1h}\varphi_{eh}\rangle\varphi_{2e}. \tag{4}$$

The procedure is repeated until a close enough convergence is obtained. In most situations four to five iterations were sufficient. Physically the iteration is analogous to a process of mutual adjustment where the hole minimizes the exciton energy E by adjusting to the presence of the electron; then the electron minimizes E by adjusting to the hole-induced potential, and the process continues until a self-consistent energy minimum is obtained for a given value of λ. The parameter λ is then varied to find the overall energy minimum. The results of the variational calculation for samples 1, 2, and 3 are shown in Fig. 3 using the solid lines. The fitting parameter is the conduction and valence band offset ratio. The best fit was obtained with zero-field offsets of 20 and -12.5 meV for the conduction and valence band, respectively. This means that the band alignment is weakly type II, but the exciton binding energy is large enough so that both electron and hole wave functions are mainly in the ZnSe wells and the exciton itself is type I in character. As the magnetic field increases the Coulomb attraction can keep the exciton together for small valence band splittings. At high enough magnetic field the σ_+ exciton component is literally

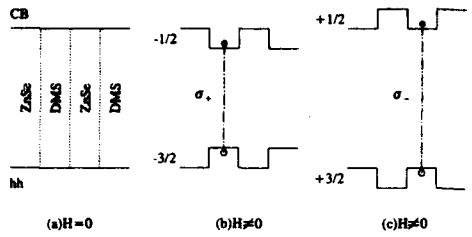

FIG. 5. Schematic diagram of the conduction and valence band alignment in $ZnSe/Zn_{0.99}Fe_{0.01}Se$ spin superlattices. (a) $H=0$; (b) $H\neq 0$, $m_j=-1/2$ electrons, $m_j=-3/2$ holes; (c) $H\neq 0$, $m_j=+1/2$ electrons, $m_j=+3/2$ holes. The vertical dot–dashed lines represent the allowed heavy-hole exciton transitions in the Faraday geometry.

pulled apart and the transition becomes type II. The results of the calculation for the intensity ratio $I(\sigma_+)/I(\sigma_-)$ for samples 1, 2, and 3 are shown in Fig. 4 using solid lines. The dashed lines represent a fit to the data assuming that each well is 25 Å narrower than its nominal value in order to show the sensitivity of the fit to the well width. The intensity ratios were found to be quite sensitive to the conduction band offset. Conduction and valence band offsets of 27 and −9 meV were obtained from the fit of Fig. 4. The variational calculation yields an interesting result for the lower type-II σ_+ exciton component. In addition to the type-II exciton wave function which exhibits an absolute energy minimum, the calculation also yields a metastable excitonic state associated with a shallower local energy minimum. The wave function of the latter is more bulk-like with the electron and hole both confined in the ZnSe layers.

B. $ZnSe/Zn_{0.99}Fe_{0.01}Se$ spin superlattices

More than ten years ago von Ortenberg[10] theoretically described a system which consists of alternating magnetic and nonmagnetic layers that have approximately the same band gap. The first such system to be studied consisted of $ZnSe/Zn_{0.99}Fe_{0.01}Se$ quantum well structures.[11,12] The zero-field band alignment of these structures for which von Ortenberg introduced the term spin superlattice is shown in Fig. 5(a). The conduction and valence band offsets are approximately equal to zero and the confinement of both electrons and holes is controlled by the magnetic splittings of the DMS layers. The band alignment for the $m_j=-1/2$ ($m_j=+1/2$) electrons and the $m_j=-3/2$ ($m_j=+3/2$) holes is shown in Fig. 5(b) [Fig. 5(c)]. The spin-dependent confining potentials are such that they localize the $m_j=+1/2$ ($m_j=-1/2$) electrons and the $m_j=+3/2$ ($m_j=-3/2$) holes in the ZnSe ($Zn_{0.99}Fe_{0.01}Se$) layers. In this system we have spatial segregation of the carriers according to their spin state. The corresponding σ_+ (−1/2,−3/2) and σ_- (+1/2,+3/2) transitions are indicated in Figs. 5(b) and 5(c) using vertical dot–dashed lines. The electrons and holes involved in the lower σ_+ (upper σ_-) transitions are confined in the DMS (ZnSe) layers. As a result, the energy of the lower exciton component exhibits the characteristic red shift as function of magnetic

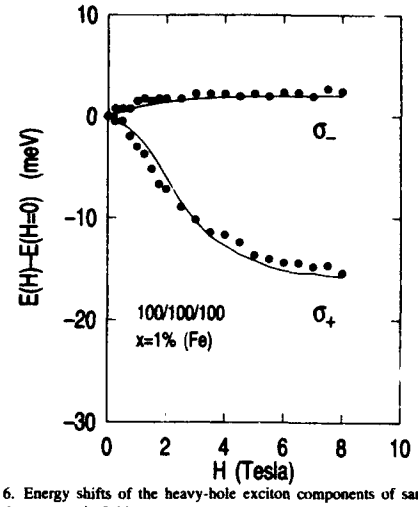

FIG. 6. Energy shifts of the heavy-hole exciton components of sample 4 plotted vs magnetic field.

field, while the upper component shows a nonmagnetic behavior. The energy shifts of the heavy-hole exciton components for sample 4 are plotted as a function of applied field in Fig. 6. The solid line represents the results of a variational calculation which yields conduction and valence band offsets of 5 and 0 meV, respectively. The large asymmetry of the exciton components of spin superlattices is similar to that observed in the $ZnSe/Zn_{0.9}Fe_{0.1}Se$ structures discussed in the previous section. What differentiates the former from the latter heterostructures is the fact that both exciton components of a spin superlattice are type I and thus have comparable intensity. As a matter of fact this property constitutes the

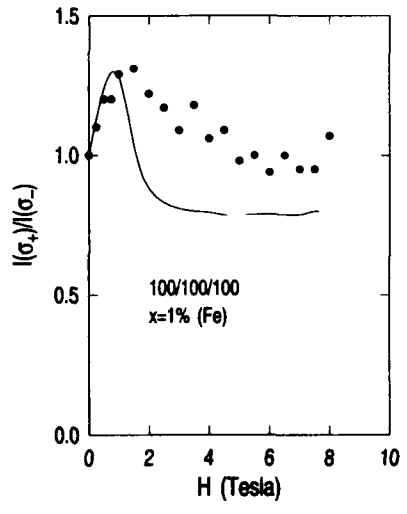

FIG. 7. Intensity ratio $I(\sigma_+)/I(\sigma_-)$ of the lower and upper heavy-hole exciton spin components of sample 4 plotted as a function of applied magnetic field.

"signature" of a spin superlattice.[11,12] The intensity ratio $I(\sigma_+)/I(\sigma_-)$ for sample 4 is plotted in Fig. 7 as a function of applied magnetic field. The ratio increases initially for low field values and then saturates at a value close to unity. Spin superlattice behavior has also been observed in ZnSe/ZnMnSe structures.[13,14] More recently spin superlattices of the form ZnMnSe/ZnFeSe which incorporate two different types of DMS materials have been reported.[15]

IV. CONCLUSIONS

We have discussed the results of a magneto-optical study of semiconductor heterostructures which have the form $ZnSe/Zn_{1-x}Fe_xSe$ grown by molecular beam epitaxy (MBE). The large spin splittings of the $Zn_{1-x}Fe_xSe$ layers produced by an external magnetic field H create spin-dependent potentials that can be modified continuously by changing H. Depending on the zero-field band offset and its distribution among the conduction and the valence bands we can have a system in which both electron and hole confinement depend on H ($x=0.01$) or one in which the external field controls only the hole confinement ($x=0.1$). Excitons in both types of structures have been modeled using a variational calculation which describes systems that have zero or very weak confinement. The model yields exciton energies, wave functions, and transition probabilities that quantitatively describe the magneto-optical properties of these novel systems.

ACKNOWLEDGMENTS

The work at SUNY was supported by NSF Grant No. DMR9223054 and by DoD/ONR under the MFEL program; at NRL work was supported by ONR.

[1] D. S. Chemla, Helv. Phys. Acta **56**, 607 (1983).
[2] E. E. Mendez, F. Argulo-Rueda, and J. M. Hong, Phys. Rev. Lett. **60**, 2426 (1988).
[3] J. K. Furdyna, J. Appl. Phys. **64**, R29 (1988).
[4] X. Liu, A. Petrou, J. Warnock, B. T. Jonker, G. A. Prinz, and J. J. Krebs, Phys. Rev. Lett. **63**, 2280 (1989).
[5] B. T. Jonker, X. Liu, W. C. Chou, A. Petrou, J. Warnock, J. J. Krebs, and G. A. Prinz, J. Appl. Phys. **69**, 6097 (1991).
[6] X. Liu, W. C. Chou, A. Petrou, J. Warnock, B. T. Jonker, G. A. Prinz, and J. J. Krebs, *Proceedings of the 20th ICPS*, edited by E. M. Anastassakis and J. K. Joannopoulos (World Scientific, Singapore, 1990), pp. 621–624.
[7] E. Deleporte, J. M. Berroir, G. Bastard, C. Delalande, J. M. Hong, and L. L. Chang, Phys. Rev. B **42**, 5891 (1990).
[8] X. Liu, A. Petrou, J. Warnock, B. T. Jonker, G. A. Prinz, J. J. Krebs, and L. R. Cooper, Bull. Am. Phys. Soc. **35**, 672 (1990).
[9] G. Peter, E. Deleporte, J. M. Berroir, C. Delalande, J. M. Hong, and L. L. Chang, Phys. Rev. B **44**, 11,302 (1991).
[10] M. von Ortenberg, Phys. Rev. Lett. **49**, 1041 (1982).
[11] W. C. Chou, A. Petrou, J. Warnock, and B. T. Jonker, Phys. Rev. Lett. **67**, 3820 (1991).
[12] B. T. Jonker, W. C. Chou, A. Petrou, and J. Warnock, J. Vac. Sci. Technol. A **10**, 1458 (1992).
[13] N. Dai, H. Luo, F. C. Zhang, N. Samarth, M. Dobrowolska, and J. K. Furdyna, Phys. Rev. Lett. **67**, 3824 (1991).
[14] W. C. Chou, A. Petrou, J. Warnock, and B. T. Jonker, Phys. Rev. B **46**, 4316 (1992).
[15] L. P. Fu, W. Y. Yu, A. Petrou, J. Warnock, and B. T. Jonker, Phys. Rev. B **48**, 18 272 (1993).

Optical transitions in (ZnCo)Se and (ZnFe)Se: Role of an effective $p-d$ exchange (invited)

Chee-leung Mak, J. Bak, R. Sooryakumar, and M. M. Steiner
Department of Physics, The Ohio State University, Columbus, Ohio 43210

B. T. Jonker
Naval Research Laboratory, Washington, D.C. 20375

In this paper we discuss photoluminescence (PL) and Raman excitations in the diluted magnetic semiconductors $Zn_{1-x}Co_xSe$ and $Zn_{1-x}Fe_xSe$. The PL spectra associated with isolated crystal field d levels are found to rapidly weaken and/or broaden as the transition metal ion concentration approaches and increases beyond a critical value. In addition a Raman continuum, that overlaps with the optical phonon, is observed to develop when the PL features are modified. In the corresponding $Zn_{1-x}Co_xSe$ samples the optical phonons acquire a characteristic Fano line shape suggestive of its coupling to the Raman continuum. It is proposed that these changes to the optical transitions arise from the enhancement of an *effective* $p-d$ hybridization between low-lying d levels and band electrons with increasing x—an effect largely due to the proximity of the Co^{2+} and Fe^{2+} crystal field ground levels to the valence band maximum.

I. INTRODUCTION

Diluted magnetic semiconductors (DMS), which are typically solid solutions formed by alloying a nonmagnetic semiconductor compound with a $3d$ transition metal ion, have attracted much attention in the recent past.[1,2] Among their interesting properties are pronounced magneto-optic and magneto-transport behavior whose source is the exchange interaction between the host carriers and substitutional magnetic ions. Such interactions also play a major role in the magnetic properties of other insulating transition-metal and rare-earth compounds that exhibit localized moments. For instance, the character of the magnetic order of these substances and their related ordering temperatures are determined by various exchange and superexchange mechanisms. Enhancements in the exchange interactions, achieved, e.g., through doping or hydrostatic pressure, can result in delocalization of the tightly bound d or f electronic wave function and thus to dramatic changes to their electronic, magnetic, or optical properties. It is well known from rare-earth and actinide physics that if the band hybridization becomes large, the impurity level very rapidly loses its localized nature and becomes extended.[3–5] For example, the low-temperature specific heat of $UAs_{1-x}Sb_x$ is found to be extremely sensitive to subtle changes in the $5f$ conduction band hybridization,[3] while modifications in the hybridization on going from UPt_3 to UPd_3 dramatically affects the XPS spectrum.[4] Another example of the importance of exchange couplings is the observation of pressure-induced metallization accompanied by the spontaneous collapse of magnetic order in NiI_2 that has been accounted for in terms of the hybridization between the $5p$ iodine band and the nickel $3d$ states,[6] which lie just above the $5p$ band maximum.

In this paper we focus on the optical and vibrational properties of the DMSs $Zn_{1-x}Co_xSe$ and $Zn_{1-x}Fe_xSe$, where significantly larger $sp-d$ and $d-d$ exchange interactions are found relative to their more widely studied Mn counterpart.[7] Introduction of Fe and Co to the ZnSe lattice is a relatively recent advance[8] and it has been demonstrated that up to 10% Co and 100% Fe can be incorporated into ZnSe. As the $3d$ ion concentration increases we find dramatic changes in the optical emission spectra associated with isolated crystal field (CF) split $3d$ levels. As x increases, intra-$3d$–ion transitions within the CF manifold weaken and/or broaden rather rapidly beyond a critical concentration. It is proposed[9] that the increase in the transition metal ion concentration leads to an increase in the $p-d$ hybridization between low-lying CF d levels and the band electrons. The hybridization effects are more pronounced in (ZnCo)Se where the ground Co^{2+}CF ground state is only 0.25 eV above the host valence band maximum. Concomitant with the broadening of the optical transitions, we observe a Raman continuum that overlaps with the longitudinal optical phonon which acquires an asymmetric line shape. The continuum likely arises from intraband excitations within the newly formed impurity band while the renormalization of the phonon self-energy indicates a continuum-phonon coupling.

II. EXPERIMENTAL DETAILS

The $Zn_{1-x}Co_xSe$ and $Zn_{1-x}Fe_xSe$ samples were single-crystal epilayers grown by molecular-beam epitaxy (MBE) on (001) GaAs substrates and were all stabilized in the zinc blende phase.[10] The Co and Fe concentrations were determined through x-ray fluorescence. The epilayer thickness ranged from about 0.25 to 2.6 μm with $x<0.094$ for Co and about 0.04 to 2 μm with $0<x<0.75$ for Fe. The Co-doped films with $x\geq 0.03$ were all of the order of 0.25-μm thick while the $Zn_{1-x}Fe_xSe$ films with $x>0.3$ were about 1000-Å thick. X-ray double crystal rocking curve linewidths for $Zn_{1-x}Co_xSe$ films thinner than 0.3 μm are found to be significantly narrower than those of the thicker samples, particularly for the higher concentrations.[8] The thinner films therefore accommodate the lattice mismatch via strain and hence do not support a significant density of misfit dislocations. The thicker films, which were of lower Co and Fe concentrations, had a smaller lattice mismatch strain and therefore also displayed relatively narrow x-ray double rock-

 0021-8979/94/75(10)/5719/6/$6.00 © 1994 American Institute of Physics

ing curves. Further these data showed that there were no abrupt changes in the microscopic quality of the films used in this study with increasing Co and Fe concentrations. The photoluminescence (PL) and Raman spectra were excited and recorded in backscattering using about 100-mW incident power using the 457-, 488-, 514-, and 530-nm laser lines from an Ar–ion laser. Standard four terminal Hall measurements showed that all epilayers were highly resistive with nominal macroscopic carrier concentration below 10^{-14} cm^{-3}.

III. EXPERIMENTAL RESULTS

Figure 1 shows PL and Raman spectra at 10 K in the vicinity of the intra-Co ion transitions in $Zn_{1-x}Co_xSe$. In the absence of Co, i.e., nominally pure ZnSe, luminescence bands centered at 2.60 (Y), 2.57 (Y–LO), 2.53 (S_0), 2.24 (SA_1), 2.09 (SA_2), and 1.92 eV (SA_3) are observed when excited at 457.9 nm. Since the excitation energy is less than the band gap, band-edge PL is not observed. With the addition of Co, the emission from ZnSe is quenched and three luminesecence bands labeled I, II, and III are evident with a strong, very sharp (0.37-meV) zero-phonon line L at 2.361 eV. The structure on the low-energy side of L has been shown,[11] for $x<0.01$, to approximately replicate the phonon density of states of ZnSe. Luminescence II and III at 1.82 and 1.62 eV are relatively broad with a full width at half-maximum (FWHM) of ~60 meV that is hence much larger than that of peak L.

As the Co concentration increases to 3.7%, PL I and II weaken drastically and are not evident beyond $x=0.037$. While some emission associated with band III is similarly reduced, a few weak peaks associated with band III remain relatively sharp until $x\sim0.09$. Concomitant with the weakening and broadening of the main PL bands at $x=0.037$, a broad peak emerges. This broad excitation has a significant Raman component and likely also includes contributions from photoluminescence. The estimated inelastic scattering, shown as hatched regions in Fig. 1, overlaps with the optical phonon P. The Raman component of this broad excitation is confirmed by its observation at 457.9-, 488.0-, and 514.5-nm exciting radiation as shown in the top of Fig. 1. Figure 2 further illustrates the Raman nature of the excitation for the $x=3.7\%$ film. In this case Fig. 2 shows the peak of the broad Raman excitation around 1900 cm^{-1} when excited at four different laser wavelengths of 457, 488, 514, and 530 nm. The continuum extends to low energies and overlaps with the optical phonon P around 260 cm^{-1}.

Figure 3 shows PL and Raman spectra of $Zn_{1-x}Fe_xSe$. For $x\leq0.22$, the main feature is a peak at ~1.89 eV with a FWHM~70 meV. For $x\geq0.22$, this PL broadens and the peak position shifts to 1.94 eV and FWHM~150 meV at $x=0.34$; as x increases further this emission weakens and continues to broaden. A broad Raman mode is observed beyond $x=0.34$ that displays characteristics similar to the continuum observed in the Co-doped samples. These common features include the general location of the continuum peak position, its width, and appearance only when the PLs associated with the $3d$ ions begin to broaden. The most striking difference between the continua in the two series of samples

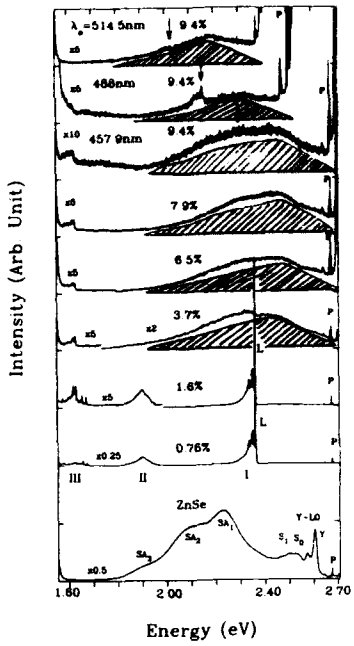

FIG. 1. Photoluminescence (PL) and Raman spectra at 10 K from $Zn_{1-x}Co_xSe$ films for x up to 0.094. All spectra, except the top two, were recorded with 457.9-nm excitation wavelength. Features labeled I, II, and III identify PL, with peak L being the strongest emission for the lower Co concentrations. The hatched regions for $x\geq0.037$ highlight the estimated continuum of Raman excitations, while the sharp peaks P are first-order Raman phonons. The peak identified by the arrow in the 488.0-nm spectrum is impurity related.

is that it turns on only at a much higher Fe concentration ($x\sim0.3$) in comparison to that for Co ($x\sim0.03$) doping.

Polarized and depolarized Raman spectra excited at 514 nm in the vicinity of the optical-phonon frequencies of ZnSe and several $Zn_{1-x}Co_xSe$ ($x<0.094$) films and two $Zn_{1-x}Fe_xSe$ ($x=0.08$ and 0.22) epilayers are shown in Fig. 4. The solid lines are fits to the data based on the Fano analysis[12] for a continuum-discrete excitation coupling. In the depolarized geometry $z(xy)\bar{z}$, where $z\|[001]$, $y\|[010]$, and $x\|[100]$, the optical phonon (LO_1) in ZnSe is Raman allowed and observed as a symmetric peak and remains symmetric up to the highest Co concentration ($x=0.094$). As illustrated in the top of Fig. 4(a), the corresponding phonon in $Zn_{1-x}Fe_xSe$ also remains symmetric for $x\leq0.22$. In addition to LO_1 a weak peak, labeled LO_2, arises from the mixed mode behavior of the $Zn_{1-x}Co_xSe$ alloy. It is identified by an arrow in Fig. 4. In agreement with previous work,[13] LO_2 occurs at a slightly lower frequency in $Zn_{1-x}Fe_xSe$ in comparison to its value in $Zn_{1-x}Co_xSe$.

In the polarized geometry $z(xx)\bar{z}$, the LO phonon in ZnSe is Raman forbidden and not observed. At $x=0.7\%$ a symmetric peak is observed in this scattering geometry at the LO_1 phonon frequency of $Zn_{1-x}Co_xSe$ [Fig. 4(b)]. As x in-

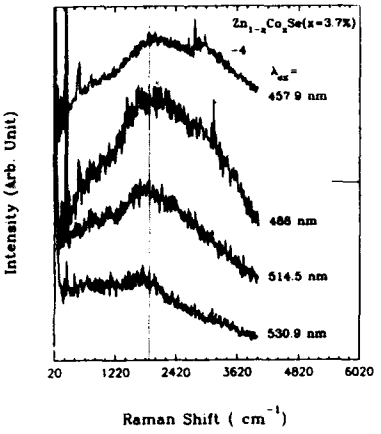

FIG. 2. Spectra recorded at 10 K from $Zn_{1-x}Co_xSe$ ($x=0.037$) showing resonant Raman character of continuum. Four different excitation wavelengths λ_{ex}=457.9, 488.0, 514.5, and 530.9 nm were utilized. The base line for the spectra recorded at 457.9 nm is indicated by the horizontal line on the right-hand side while that for the other three spectra is the x axis. The peak in the Raman continuum is around 1900 cm^{-1} as indicated by the dotted line.

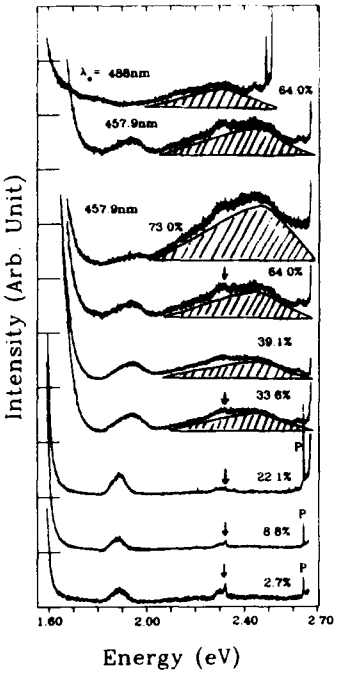

FIG. 3. Photoluminescence (PL) and Raman spectra at 10 K from several $Zn_{1-x}Fe_xSe$ films for $0.027<x<0.75$. All spectra, except the top one was recorded with 457.9-nm excitation wavelength. The peak around 1.9 eV is PL. The hatched regions for $x \geq 0.33$ highlight the estimated continuum of Raman excitations. P are Raman phonons, while the peak identified by an arrow is extrinsic as in $Zn_{1-x}Co_xSe$ (Fig. 1).

creases to 3.7% the line shape of LO_1 becomes strongly skewed on the low-energy side and its peak position down shifted by ~ 1 cm^{-1} relative to that for depolarized scattering. Beyond $x=3.7\%$ the asymmetry of LO_1 in polarized scattering continues to be present to the highest Co concentrations utilized in our study. In fitting the $z(xx)\bar{z}$ spectra, the linewidth and frequency characterizing the Lorentzian profile of LO_2 that may emerge in Fig. 4(b) was directly determined from corresponding fits to depolarized spectra. In addition, the intensity of the contribution of peak LO_2 (which is over an order of magnitude weaker than LO_1) to $z(xx)\bar{z}$ was deduced by scaling the intensity ratio I_{LO_2}/I_{LO_1} in the $z(xy)\bar{z}$ spectrum to the LO_1 intensity in the polarized spectrum. Thus the parameters required for fitting the contributions of LO_2 to Fig. 4(b) were known. It was found that no satisfactory fits to the data of Fig. 4(b) from $Zn_{1-x}Co_xSe$ ($x>0.03$) were obtained with a Lorentzian description of LO_1 in the polarized spectrum. Mode LO_1 in the polarized Raman spectra from $Zn_{1-x}Fe_xSe$ remains symmetric with no frequency difference from that in the $z(xy)\bar{z}$ geometry up to $x=0.22$.

IV. DISCUSSION

A. Luminescence: $Zn_{1-x}Co_xSe$ and $Zn_{1-x}Fe_xSe$

The luminescence bands in undoped ZnSe are similar to those reported earlier.[14] The peaks at 2.24 (SA_1), 2.09 (SA_2), and 1.92 (SA_3) arise from zinc vacancies and impurities in the ZnSe lattice, while S_0 and S_1 are related to donor–acceptor pairs involving shallow donors and deep traps.[14] The Y transition has been associated with electronic states on dislocations while Y–LO is the optical phonon replica.[14] As the Co concentration increases to 0.76%, the PL bands of ZnSe are quenched. This suggests that in addition to substituting for Zn the Co ions fill Zn vacancies. It is thus clear that the new transitions observed with Co doping concentrations greater than 0.7% are of a totally different nature than those associated with Zn vacancies. We identify these new emissions to be associated with intra-Co d level transitions. A similar conclusion is applicable to the Fe-doped ZnSe samples.

The relevant multiplet energy structure of Co^{2+} and Fe^{2+} in ZnSe are reproduced in Figs. 5(a) and 5(b) from Ref. 15. While electric dipole transitions between states constructed of pure d functions are forbidden, spin–orbit interaction and lack of inversion symmetry in the zinc blende structure, however, allow such transitions. Our assignment of the observed PL transitions in $Zn_{1-x}Co_xSe$ are identified by arrows in Fig. 5(a) where I, II, and III correspond to the transitions yielding bands I, II, and III in Fig. 1.

We identify the transition $^2T_1 \rightarrow {}^4A_2$ with the narrow emission peak L. The initial state associated with L has been previously associated as either the $^2T_1$ excited multiplet level of the Co^{2+} ion,[16] or the exciton state $[Co^{3+}\cdot e]$.[11] Our recent high pressure measurements[17] confirm that the energy of peak L decreases with pressure at a rate (~ 1.4 cm^{-1}/kbar) in

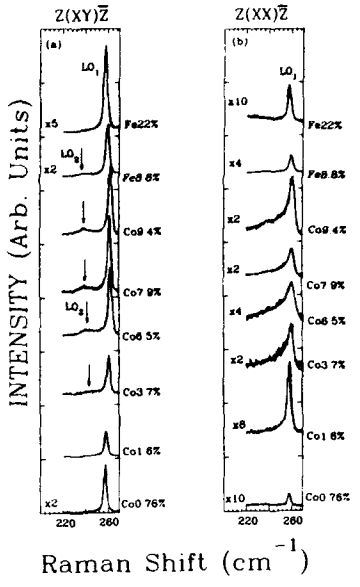

FIG. 4. Raman spectra at 10 K in the vicinity of the LO phonon in several $Zn_{1-x}Co_xSe$ and $Zn_{1-x}Fe_xSe$ films. (a) Depolarized backscattering; (b) polarized backscattering. The solid lines are fits to the data based on a Fano analysis. The spectra were recorded with 514.5-nm laser radiation.

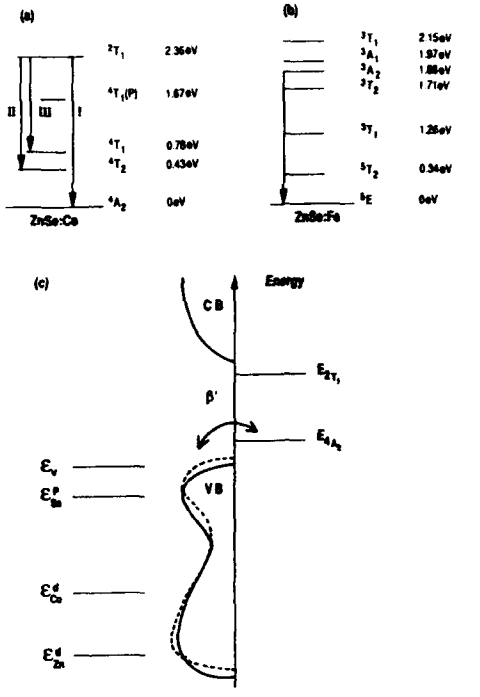

FIG. 5. (a) Crystal field split manifold of Co^{2+} in ZnSe from Ref. 15 (spin–orbit effects have not been included). Transitions I, II, and III relate to the photoluminescence bands shown in Fig. 1. (b) Crystal field split manifold of Fe^{2+} in ZnSe from Ref. 15. The transition identified relates to the photoluminescence at ~1.9 eV in Fig. 2. (c) To the left of the energy axis schematically represents the one-electron conduction and valence bands (solid line) in ZnSe. The one-electron energies ϵ^d_{Zn}, ϵ^d_{Co}, and ϵ^p_{Se} are the Zn-d, Co-d, and Se-p one-electron levels, respectively, and ϵ_v is the valence band maximum. The dashed line is the slightly shifted valence band due to the replacement of Zn by Co. As in Fig. 4(a) the $^2T_1$ and $^4A_2$ states are discrete many-body levels. The effective exchange β' couples the host with the impurity.

contrast to the increase of ~56-cm^{-1}/kbar pressure dependence of the ZnSe band gap.[18] This would hence make the excitonic state unlikely to be associated with L.

We assign luminescence II and III as transitions from $^2T_1$ that terminate at the intermediate spin-quartet excited states of Co^{2+}, i.e., $^2T_1 \rightarrow {}^4T_2(F)$ and $^2T_1 \rightarrow {}^4T_1(F)$, respectively. The spectral linewidth of bands I and II differ significantly. Transitions between different configurations (with different m and n in $e^m t^n$ configuration) are broadened due to fluctuations of the cubic field arising from nuclear relaxation.[19] This is consistent with our assignment of the initial state ($^2T_1$) to a e^4t^3 configuration. In this case L is narrow since the final state $^4A_2$, characterized by an e^4t^3 configuration, does not involve changes in m and n. In contrast, luminescence II is broad since the final state $^4T_2(F)$ is of e^3t^4 configuration. The transition associated with PL III, $^2T_1 \rightarrow {}^4T_1(F)$, should be weak since optical transitions are forbidden between $e^n t^m$ and $e^{n+k}t^{m-k}$ levels for $|k| \geq 2$.[20] It is likely that this transition is observed due to an admixture of $^4T_1(F)$ with either a e^3t^4 or e^4t^3 level. From Fig. 5(b), we assign the 1.89-eV PL peak in $Zn_{1-x}Fe_xSe$ to connect the $^3A_2 \rightarrow {}^5E$ transition. The ^5E and $^3A_2$ states have configurations e^3t^3 and e^2t^4, respectively; thus the luminescence is expected to be broad. This assignment of the optical transition in (ZnFe)Se is consistent with absorption data[21] of ZnS:F where the oscillator strength is strongest for the $^5E \rightarrow {}^3A_2$ transition compared to other spin-forbidden transitions.

On the left-hand side of the energy axis of Fig. 5(c) we schematically represent the ZnSe valence separated by 2.8 eV from the conduction bands (CB). The valence bands arise predominantly from the hybridization of Zn 3d orbitals and Se-4p orbitals. It is not in general obvious how to place the many-electron atomic levels shown in Figs. 5(a) and 5(b) with respect to the one-electron valence band maximum ϵ_v. However, from electroabsorption[20] and photoluminescence excitation data,[11] the ground state ($^4A_2$) of Co^{2+} is known to lie ~2.56 eV below the conduction band. Since L occurs at 2.361 eV, it follows that the initial state associated with this optical transition is ~200 meV below the conduction band.

We propose that the very rapid broadening of PL emissions I and II for Co concentrations beyond 1.6% reflects the proximity of the lowest Co configuration to the valence band maximum. We denote the quantity which determines to what extent valence band states mix into the localized levels as β',

which can also be viewed as the rate at which electrons hop from and to the ground state of the impurity site into the valence band. So the effective exchange interaction β' has the form

$$\beta'(x) \sim (V_{pA_2})^2 \times \frac{1}{E_{A_2} - \epsilon_v(x)} .$$

It is well known from rare-earth and actinide physics that if the fluctuation rate becomes too large, the impurity level very rapidly loses its localized nature and becomes extended.[3–5] Analogously we expect the extent of delocalization of the many-electron state of Co-impurities atoms to be very sensitive to β'. While there are many reasons why β' could depend on x, we propose that the dependence comes predominantly from an upwards shift in the valence band maximum on doping, i.e., the replacement of Zn by Co introduces a dependence of ϵ_v on x.

While a theoretical treatment of the shifts of the valence band edge for $Zn_{1-x}Co_xSe$ does not exist, an analysis for $Cd_{1-x}Mn_xTe$ shows that the valence band maximum increases steadily by about 0.5 eV as the Mn concentration increases from zero to 60%.[22] This dependence (~1 eV per Cd atom replaced by Mn) is rather weak. However, on alloying Co into ZnSe, we expect a larger shift as the *one-electron* Co d levels, ϵ^d_{Co}, lie higher above *one-electron* Zn levels, ϵ^d_{Zn}, than do the majority Mn levels. (We also point out that as well as the upwards shift, one should expect a broadening of the valence band states due to extra scattering from the random potential. This can also be viewed as an upwards shift of the "effective" valence band maximum, and indeed might well dominate the shift in the case of 30% Fe substitution.) Since the location of many-body crystal field split Co d levels are, to a good approximation, independent of x and the spacing $(E_A - \epsilon_v)$ at $x < 0.01$ is only 0.25 eV, the valence band edge will approach the low-lying $^4A_2$ state as x increases. It thus follows that β' will increase rapidly with increasing Co concentration. These effects are not seen in Mn-doped systems, where E_A lies well below ϵ_v $[(E_A - \epsilon_v) \sim -2$ eV$]$[23] and therefore the effect of shifting ϵ_v is very small. On the other hand, as the Fe^{2+} ground state ^5E initially lies over 1 eV from the valence band edge,[24] the same effect is seen. But, a larger doping concentration will be required prior to the occurrence of significant enhancement in the effective exchange interaction in these alloys.

These concentration dependencies of β' are consistent with the observed broadening of the PL transitions involving the low-lying d levels in the two alloys. At a given Co concentration the exchange interaction will be greatest for the $^4A_2$ ground state with the exchange decreasing progressively for the higher-lying $^4T_2$ and $^4T_1$ Co d levels. This level interaction hence gives rise to the broadening and eventual weakening of the PL associated with transitions connecting to the $^4A_2$ state in the optical emission. At $x = 0.037$ and beyond PL bands I and II both appear to have been broadened or quenched. This would argue for the ground state as well as the first excited state $^4T_2$ being broadened through exchange at this concentration. On the other hand, it is evident from Fig. 1 that PL III $[^2T_1 \rightarrow {}^4T_1(F)]$ remains well defined until x approaches 9.4%, the highest Co concentration used in this study. This is consistent with the location of the final state ($^4T_1$) being initially over 1 eV from the valence band edge and therefore a higher Co concentration is required prior to being broadened through the $p-d$ exchange.

B. Raman continuum

We propose that the broad Raman continuum in Figs. 1 and 2 is associated with excitations within the broadened CF $3d$ manifold. As proposed, the broadening of the CF levels with increasing x primarily occurs through enhanced exchange with the band electrons. As evident from Fig. 5, at low Co and Fe concentrations the separations between the first few low-lying crystal field states of Co^{2+} and Fe^{2+} are about 0.35 eV. Thus as these levels broaden and overlap, one expects the resulting band to be few tenths of an eV wide. The Raman continuum observed in both alloys extends beyond 3000 cm^{-1} and is thus consistent with our model that the inelastic scattering events occur within the strongly hybridized d levels.

Our identification of the nature of the continuum is also consistent with the following findings: (1) The continuum distinctly appears only in $Zn_{1-x}Co_xSe$ and $Zn_{1-x}Fe_xSe$ when the discrete PL bands have broadened. (2) The Raman continuum in $Zn_{1-x}Co_xSe$ occurs at a critical concentration ($x \sim 0.03$) much smaller than that in $Zn_{1-x}Fe_xSe$ ($x \sim 0.3$). These differences are related to the distinct dependencies of β' on x in the two alloys. (3) Dopant induced structural disorder is eliminated as the source of the Raman continuum since the continuum is not observed in $Zn_{1-x}Fe_xSe$ at similar x values as in $Zn_{1-x}Co_xSe$ where the same degree of disorder would be present. (4) It is likely that continuum-discrete phonon coupling leads to the asymmetric line shape of the LO phonon in $Zn_{1-x}Co_xSe$ for $x > 0.03$ [Fig. 4(b)]. The asymmetric phonon line profile occurs only beyond the critical concentration when the continuum is observed. Consistent with the *absence* of the continuum for x up to 0.22, the optical phonon in $Zn_{1-x}Fe_xSe$ ($x \leq 0.22$) does not show any evidence of Fano-type interactions.

Finally we note that the proposed model related to the enhancement in the effective $p-d$ hybridization and its influence on the PL transitions is consistent with the data associated with the intra-d-level transitions presented here. These optical spectra were excited with laser radiation that was at most about 0.3 eV above the energy of PL I. Further experiments with even higher energy laser radiation including those *above* the fundamental band gap are being planned. These experiments would ascertain if the observed modifications to the optical transitions with increasing Co and Fe concentrations are affected by any subtle effects in populating the initial state associated with the PL emission. A tunable dye laser operating in the 410–470-nm spectral region is being set up for this purpose. Furthermore a study of the role, if any, of structural defects that may introduce deep levels around 2.4 eV in these ZnSe-based systems and their possible effect on the optical transitions connecting isolated crystal field d levels should be useful. Such studies could, e.g., include deep level transient spectroscopy studies of these diluted magnetic semiconductors to identify specific deep levels.

V. CONCLUSIONS

In summary we have reported on the photoluminescence and Raman excitations associated with $3d$ levels in $Zn_{1-x}Co_xSe$ and $Zn_{1-x}Fe_xSe$. The striking changes in the PL spectra with x are discussed in terms of an increase in the exchange between d levels and band electrons with transition metal ion concentration that leads to the broadening of the ground and lower excited CF split d levels. The enhancement in the exchange coupling with concentration x arises primarily due to the proximity of the Co^{2+} and Fe^{2+} crystal field ground levels to the valence band maximum. Beyond the critical concentration, a broad Raman continuum is observed. Evidence for this continuum is also derived from the fact that the optical phonon self-energies in $Zn_{1-x}Co_xSe$ are modified in a manner consistent with a continuum-discrete interaction leading to the asymmetric LO line shape when the PL transitions have broadened in $Zn_{1-x}Co_xSe$. It is proposed that the continuum arises from excitations within the broadened crystal field $3d$ manifold.

ACKNOWLEDGMENTS

Work at the Ohio State University was supported by the NSF and that at the NRL by the Office of Naval Research. Partial support of M.M.S. was provided by the DOE Basic Energy Sciences, Division of Materials Science. We also acknowledge useful correspondence with Dr. K. Hass.

[1] *Diluted Magnetic Semiconductors*, edited by J. K. Furdyna and J. Kossut, Vol. 25 of *Semiconductors and Semimetals*, edited by R. K. Willardson and A. C. Beer (Academic, San Diego, 1988).

[2] *Diluted Magnetic Semiconductors*, edited by M. Jain (World Scientific, Singapore, 1991).

[3] H. Rudigier, H. R. Ott, and O. Vogt, J. Magn. Magn. Mater. **63 & 64**, 159 (1987).

[4] J. M. Imer, D. Malterre, M. Grioni, P. Weibel, B. Dardel, and Y. Baer, Phys. Rev. B **44**, 10,455 (1991).

[5] B. R. Cooper, R. Siemann, D. Yang, P. Thayamballi, and A. Banerjea, in *Handbook on Physics and Chemistry of the Actinides*, edited by A. J. Freeman and G. H. Lander (North-Holland, Amsterdam, 1985), Vol. 2, Chap. 6, pp. 435–500.

[6] M. P. Pasternak, R. D. Taylor, A. Chen, C. Meade, L. M. Falicov, A. Gieskus, R. Jeanlos, and P. Y. Yu, Phys. Rev. Lett. **65**, 790 (1990).

[7] X. Liu, A. Petrou, B. T. Jonker, G. A. Prinz, J. J. Kerbs, and J. Warnock, Appl. Phys. Lett. **55**, 1023 (1989); T. M. Giebultowicz, P. Klosowski, J. J. Rhyne, T. J. Udovic, J. K. Furdyna, and W. Giriat, Phys. Rev. B **41**, 504 (1990); J. P. Lascaray, F. Hamdani, D. Coquillat, and A. K. Bhattacharjee, J. Magn. Magn. Mater. **104–107**, 995 (1992); A. Lewicki, A. I. Schindler, P. M. Shand, B. C. Crooker, and J. K. Furdyna, Phys. Rev. B **44**, 6137 (1991).

[8] *Growth, Characterization and Properties of Ultrathin Magnetic Films and Multilayers*, Vol. 151 of *Materials Research Society Symposium Proceedings*, edited by B. T. Jonker, E. E. Marinero, and J. P. Heremans (MRS, Pittsburgh, 1989); B. T. Jonker, S. B. Qadri, J. J. Krebs, G. A. Prinz, and L. Salamanra-Young, J. Vac. Sci. Technol. A **7**, 1360 (1989).

[9] C. L. Mak, R. Sooryakumar, M. M. Steiner, and B. T. Jonker, Phys. Rev. B **48**, 11 743 (1993).

[10] B. T. Jonker, S. B. Qadri, J. J. Kerbs, and G. A. Prinz, J. Vac. Sci. Technol. A **6**, 1946 (1988); B. T. Jonker, S. B. Qadri, J. J. Kerbs, G. A. Prinz, and L. Salamanca-Young, *ibid.* **7**, 1360 (1989).

[11] D. J. Robbins, P. J. Deans, C. L. West, and W. Hayes, Philos. Trans. R. Soc. London Ser. A **304**, 499 (1982); D. J. Robbins, J. Lumin. **24 & 25**, 137 (1981).

[12] U. Fano, Phys. Rev. B **124**, 1866 (1961).

[13] C. L. Mak, R. Sooryakumar, B. T. Jonker, and G. A. Prinz, Phys. Rev. B **45**, 3344 (1992).

[14] J. C. Bouley, P. Blanconnier, A. Herman, Ph. Ged, P. Henoc, and J. P. Noblanc, J. Appl. Phys. **46**, 3549 (1979); P. J. Dean, Phys. Status Solidi A **81**, 625 (1984).

[15] A. Fazzio, M. J. Caldas, and A. Zunger, Phys. Rev. B **30**, 3430 (1984). Electronic levels of Co^{2+} and Fe^{2+} in DMSs are also discussed in M. Villeret, S. Rodriguez, and E. Kartheuser, Physica B **162**, 89 (1990).

[16] J. M. Noras, H. R. Szawelska, and J. W. Allen, J. Phys. C **14**, 3255 (1981); E. M. Wray and J. W. Allen, *ibid.* **4**, 512 (1971).

[17] U. D. Venkateswaran, C. L. Mak, R. Sooryakumar, and B. T. Jonker, Bull. Am. Phys. Soc. **38**, 797 (1993), C. L. Mak, U. D. Venkateswaran, R. Sooryakumar, and B. T. Jonker (to be published).

[18] P. Jaszczyn-Kopec, B. Canny, G. Syfosse, and H. Hammel, Solid State Commun. **49**, 795 (1984).

[19] S. Sugano, Y. Tanabe, and H. Kamimura, *Multiplets of Transition Metal Ions in Crystals*, Vol. 33 of *Pure and Applied Physics*, edited by H. S. W. Massey and K. A. Brueckner (Academic, New York, 1970).

[20] V. I. Sokolov, T. P. Surkova, M. P. Kulakov, and A. V. Fadeev, Phys. Status Solidi B **130**, 267 (1985); V. I. Sokolov, A. N. Mamedov, T. P. Surkova, M. V. Chukichev, and M. P. Kulakov, Opt. Spectrosc. (USSR) **62**, 480 (1987); T. Dietl, in *Semimagnetic Semiconductors and Diluted Magnetic Semiconductors*, edited by M. Averous and M. Balkanski (Plenum, New York, 1991).

[21] M. Skowronski and Z. Liro, J. Phys. C **15**, 137 (1982).

[22] K. C. Hass and H. Ehrenreich, Physica Polonica Sect. A **73**, 933 (1988).

[23] V. I. Sokolov, A. N. Mamedov, V. V. Chernyaev, E. Z. Kurmaev, V. R. Galakhov, S. N. Nemnonov, M. P. Kulakov, and A. V. Fadeev, Sov. Phys. Solid State **27**, 1268 (1985).

[24] K. P. O'Donnell, K. M. Lee, and G. D. Watkins, J. Phys. C **16**, 728 (1983).

Coexistence of Brillouin and Van Vleck spin exchange in $Zn_{1-x}Mn_xSe/Zn_{1-y}Fe_ySe$ spin superlattice structures

B. T. Jonker and H. Abad[a)]
Naval Research Laboratory, Washington, D.C. 20375

L. P. Fu, W. Y. Yu, and A. Petrou
State University of New York at Buffalo, Buffalo, New York 14260

J. Warnock
IBM Watson Research Center, Yorktown Heights, New York 10598

We have studied a new type of semiconductor quantum well system in which the carrier-ion exchange interactions are determined by the spin of the carrier. The samples consist of alternating layers of $Zn_{1-x}Mn_xSe$ and $Zn_{1-y}Fe_ySe$ grown by molecular-beam epitaxy (MBE). At zero field, the carriers initially interact randomly with both transition metal species. When a magnetic field is applied, the excitonic wave functions are increasingly localized in one or the other of the magnetic layers according to their spin state as the competing spin exchange interactions define the confining potential. The spin components of the heavy hole exciton are subsequently dominated by different exchange interactions as revealed by their temperature and field dependence: the behavior of the spin-down component $(-3/2,-1/2)$ is described by exchange interactions of the carriers with the Mn^{2+} ions and exhibits Brillouin paramagnetic behavior, while the spin-up component $(+3/2,+1/2)$ is dominated by interactions with Fe^{2+} ions and exhibits Van Vleck paramagnetism. These structures are thus characterized by an initial competition and eventual coexistence of Brillouin- and Van Vleck-like paramagnetic behavior for the exciton.

An increasing amount of study has focused on spin-dependent effects in semiconductor heterostructures and associated spin relaxation mechanisms and lifetimes. These effects are especially manifest in diluted magnetic semiconductor (DMS) compounds (e.g., $Zn_{1-x}Mn_xSe$), in which strong spin-exchange interactions between the band carriers and the *d* electrons localized on the substitutional magnetic ions strongly modify the band structure in the presence of an applied magnetic field.[1] This has been vividly demonstrated in the recent realization of spin superlattice structures,[2–4] which consisted of alternating layers of magnetic and nonmagnetic semiconductors chosen to have very small band offsets. As a magnetic field is applied, the giant spin splitting of the DMS band edges produces a spin-dependent confining potential resulting in localization of the carriers according to their spin: spin-down carriers become confined to the DMS layers, while the spin-up carriers are localized in the non-DMS layers.

We report here an initial study of a new type of spin superlattice (SSL), in which both constituent materials of the structure are DMS compounds, but with very different magnetic and spin-exchange character: $Zn_{1-x}Mn_xSe$ is a classic Brillouin paramagnet, while $Zn_{1-y}Fe_ySe$ exhibits Van Vleck paramagnetic behavior. The application of a magnetic field again produces a SSL potential which localizes the two spin components of the excitonic wave functions in alternating layers of the structure. In these new structures, however, the two spin components are dominated by different exchange interactions as revealed by their temperature and field dependence. This behavior can be directly observed using polarization and field dependent reflectance and photoluminescence spectroscopies. These new structures thus simultaneously exhibit both Brillouin and Van Vleck paramagnetic behavior, and open many opportunities for studying spin-exchange phenomena.

The samples were grown by molecular beam epitaxy on GaAs(001) substrates, and consist of multiple quantum well structures of the form $(Zn_{1-x}Mn_xSe/Zn_{1-y}Fe_ySe)_4$, with $0.01 \leq x,y \leq 0.04$. Details of the growth have been given elsewhere.[4] The total thickness of each sample was kept below ~1000 Å to insure that each layer was under compressive strain imposed by the substrate, thereby removing the heavy-hole/light-hole degeneracy at the zone center, so that the heavy-hole states define the valence band edge. Magnetoreflectance (MR) and photoluminescence (PL) were used to study the behavior of the heavy-hole excitons, with the two spin components distinguished through their polarization dependence.

The zero field PL and reflectance spectra from a (100-Å $Zn_{0.96}Mn_{0.04}Se$/138-Å $Zn_{0.99}Fe_{0.01}Se)_4$ SSL sample are shown in Fig. 1. The PL spectrum shows a large peak (*X*) at 2.802 eV identified as the heavy-hole free exciton (hh), with a linewidth of only 2.5 meV demonstrating high sample quality. The lower-energy feature (*BX*) is identified as a donor bound exciton, while the small high-energy feature is believed to be associated with the air interface. The reflectivity spectrum exhibits these same features (with the exception of *BX*), as well as the light-hole free exciton (lh) which is shifted by strain to higher energy. These features split into spin components with applied magnetic field, and in the remaining discussion we focus on the behavior of the hh exciton peak.

The hh exciton splits into two spin components according to the electric dipole selection rules, corresponding to a transition involving "spin-up" carriers ($m_j = +1/2$ electrons

[a)]National Research Council Postdoctoral Associate.

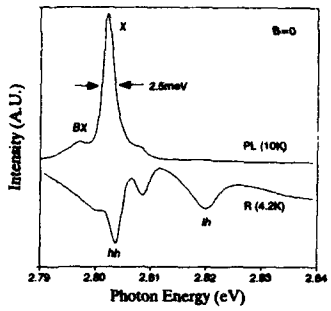

FIG. 1. Zero field photoluminescence (PL) and derivative reflectance (R) spectra from a (100-Å $Zn_{0.96}Mn_{0.04}Se$/138-Å $Zn_{0.99}Fe_{0.01}Se)_4$ sample (PL with Kr 4067-Å excitation).

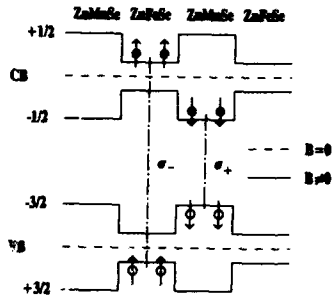

FIG. 3. Diagram illustrating the conduction and valence band splitting, and resultant spin-dependent carrier confinement with applied magnetic field. The allowed hh transitions and their polarizations are indicated.

and $m_j=+3/2$ holes) and a transition involving "spin-down" carriers $(-1/2,-3/2)$, which are distinguished by their circular polarization character $\sigma-$ and $\sigma+$, respectively. The field dependence of these features is summarized in Fig. 2(b) for

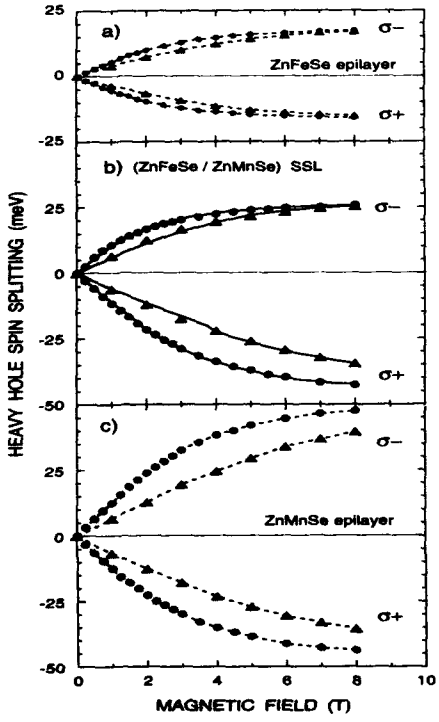

FIG. 2. Plots of the hh exciton spin splitting obtained from MR spectra (4.2 K) for (a) 540-Å $Zn_{0.99}Fe_{0.01}Se$ epilayer; (b) (100-Å $Zn_{0.96}Mn_{0.04}Se$/138-Å $Zn_{0.99}Fe_{0.01}Se)_4$ SSL; and (c) 520-Å $Zn_{0.96}Mn_{0.04}Se$ epilayer samples. Circles: 4.2 K; triangles: 10-K data. The solid lines in (b) are the calculated exciton splittings.

temperatures of 4.2 and 10 K. Note that the $\sigma-$ and $\sigma+$ components exhibit very different field and temperature dependence. The $\sigma+$ component exhibits a larger spin splitting and the strong temperature dependence characteristic of Brillouin paramagnetic behavior, indicating that the spin-down carriers are dominated by the spin-exchange interactions of the ZnMnSe layers. The behavior of the $\sigma+$ component is identical to that obtained from a uniform $Zn_{0.96}Mn_{0.04}Se$ epilayer, as shown in Fig. 2(c). Conversely, the behavior of the $\sigma-$ component of this SSL is identical to that obtained from a uniform epilayer of $Zn_{0.99}Fe_{0.01}Se$, as shown in Fig. 2(a). The $\sigma-$ component exhibits a smaller spin splitting due to the lower magnetic ion concentration, and a weak temperature dependence characteristic of Van Vleck paramagnetic behavior, indicating that the spin-up carriers are strongly effected by spin-exchange interactions with the ZnFeSe layers.

The band diagram derived from this behavior is shown in Fig. 3. At zero field, the band offsets are small relative to the exciton binding energy, and the carriers interact randomly with both transition metal species in the absence of a confining potential. When a magnetic field is applied, the conduction and valence band edges split into spin levels, with the splitting larger in the ZnMnSe than in the ZnFeSe, primarily due to the larger Mn concentration. As the band-edge splittings define the spin-dependent confining potential, the excitonic wave functions are localized in one or the other of the magnetic layers according to spin state: the spin-up carriers forming the spin up $(\sigma-)$ hh exciton are localized in the ZnFeSe layers, while the spin-down carriers $(\sigma+)$ become confined to the ZnMnSe layers. The spin components of the hh exciton are subsequently dominated by different exchange interactions resulting in the very different temperature and field dependence observed experimentally.

The system can be quantitatively described by an analytical model appropriate for describing excitons in shallow quantum wells.[5] The results of the calculations are plotted as solid lines in Fig. 2(b), and provide good agreement with the temperature and field dependence of the data. The exciton wave functions derived from the model show separate localization of the spin-up and spin-down excitons in the respective layers as indicated in Fig. 3.

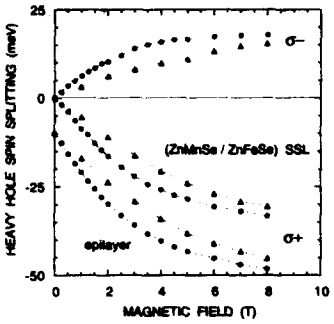

FIG. 4. Summary plot of the hh spin splitting obtained from MR spectra (4.2 K) for a (100-Å $Zn_{0.99}Mn_{0.01}Se$/104-Å $Zn_{0.96}Fe_{0.04}Se)_4$ SSL and a 500-Å $Zn_{0.96}Fe_{0.04}Se$ epilayer. The epilayer data has been displaced by −10 MeV for clarity. Circles: 4.2 K; triangles: 10-K data.

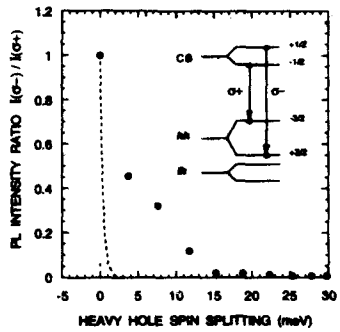

FIG. 5. Ratio of the intensity of the PL peaks (Kr 4067-Å excitation, $T=4.2$ K) corresponding to the $\sigma-$ $(+1/2,+3/2)$ and $\sigma+$ $(-1/2,-3/2)$ hh transitions as a function of net hh spin splitting for a (100-Å $Zn_{0.98}Mn_{0.02}Se$/105-Å $Zn_{0.99}Fe_{0.01}Se)_4$ SSL. The dashed line shows the expected ratio $\exp(-ss/kT)$, where ss is the spin splitting.

This interpretation may be readily tested by simply reversing the concentrations of the Fe and Mn, in which case the behavior of the $\sigma-$ and $\sigma+$ hh components should be reversed, with the $\sigma-$ component now exhibiting the stronger Brillouin-like temperature dependence due to localization of the spin-up hh exciton in the ZnMnSe rather than in the ZnFeSe. MR data for a (100-Å $Zn_{0.99}Mn_{0.01}Se$/104-Å $Zn_{0.96}Fe_{0.04}Se)_4$ SSL sample are summarized for the hh spin splitting in Fig. 4. The $\sigma-$ component indeed shows a smaller spin splitting due to the low Mn concentration and the strong temperature dependence expected. The $\sigma+$ component exhibits behavior identical to that obtained from a uniform $Zn_{0.96}Fe_{0.04}Se$ epilayer, also shown in Fig. 4 for comparison. Note that the temperature dependence for the $\sigma+$ component (ZnFeSe) appears more pronounced in these samples than those of Fig. 2 because the net spin splitting is larger due to the higher Fe concentration.

Photoluminescence data obtained from these SSL samples show the same behavior for the hh spin splitting as presented above. Additional information regarding carrier lifetimes may be inferred from the relative intensities of the spin split components using rate equation modeling, as discussed previously for magnetic/nonmagnetic SSL structures.[6,7] The PL intensity ratio $I-/I+$ of the spin-up $(\sigma-)$ to spin-down $(\sigma+)$ hh components is shown in Fig. 5 for a (100-Å $Zn_{0.98}Mn_{0.02}Se$/103-Å $Zn_{0.99}Fe_{0.01}Se)_4$ sample. It is interesting to note that the higher energy $\sigma-$ component due to recombination of the spin-up carriers is clearly visible in a static PL measurement up to substantial values of the net spin splitting, even though it would be much more energetically favorable for these carriers to first spin relax to the spin-down state before radiative recombination. The persistence of this feature indicates that the carrier spin relaxation time is comparable to the radiative lifetime, and that the spin relaxation process which is so clearly favored from an energetic standpoint is significantly impeded in these strained layer structures. This has been attributed to the strain induced splitting of the light- and heavy-hole bands, which inhibits heavy-hole $(m_j=\pm 3/2)$ spin flip processes which would otherwise occur via interaction with the light-hole states $(m_j=\pm 1/2)$.[7–9] Rate equation modeling of the data in Fig. 5 yields electron- and heavy-hole spin lifetimes in good agreement with those derived earlier,[7] with $\tau_{hs}/\tau_{es}\sim 50$.

In summary, we have studied a new type of semiconductor quantum well system in which the carrier-ion exchange interactions are determined by the spin of the exciton. These structures are characterized by an initial competition and eventual coexistence of Brillouin- and Van Vleck-like paramagnetic behavior for the exciton, and open many opportunities for studying spin-exchange phenomena.

The work at NRL was supported by the Office of Naval Research, and at SUNY by ONR and NSF.

[1] *Diluted Magnetic Semiconductors*, edited by M. Jain (World Scientific, Singapore, 1991).
[2] W. C. Chou, A. Petrou, J. Warnock, and B. T. Jonker, Phys. Rev. Lett. **67**, 3820 (1991).
[3] N. Dai, H. Luo, F. C. Zhang, N. Samarth, M. Dobrowolska, and J. K. Furdyna, Phys. Rev. Lett. **67**, 3824 (1991).
[4] B. T. Jonker, W. C. Chou, A. Petrou, and J. Warnock, J. Vac. Sci. Technol. A **10**, 1458 (1992).
[5] J. Warnock, B. T. Jonker, A. Petrou, W. C. Chou, and X. Liu, Phys. Rev. B **48**, 17 321 (1993).
[6] W. C. Chou, A. Petrou, J. Warnock, and B. T. Jonker, Phys. Rev. B **46**, 4316 (1992).
[7] B. T. Jonker, J. Warnock, L. P. Fu, W. Y. Yu, W. C. Chou, and A. Petrou, J. Vac. Sci. Technol. A **11**, 1033 (1993).
[8] T. Uenoyama and L. J. Sham, Phys. Rev. Lett. **64**, 3070 (1990).
[9] R. Ferreira and G. Bastard, Phys. Rev. B **43**, 9687 (1991).

Magnetic study of the diluted magnetic semiconductor $Sn_{1-x}Mn_xTe$

P. J. T. Eggenkamp
Department of Physics, Eindhoven University of Technology, P.O. Box 513, NL-5600 MB Eindhoven, The Netherlands

C. W. H. M. Vennix
Netherlands Energy Research Foundation ECN, P.O. Box 1, NL-1755 ZG Petten, The Netherlands

T. Story
Institute of Physics, Polish Academy of Sciences, Al. Lotników 32/46, PL-02-668 Warsaw, Poland

H. J. M. Swagten, C. H. W. Swüste, and W. J. M. de Jonge
Department of Physics, Eindhoven University of Technology, P.O. Box 513, NL-5600 MB Eindhoven, The Netherlands

New measurements of the magnetic carrier-induced properties of $Sn_{1-x}Mn_xTe$ for $x \leq 0.10$ are presented. The results of these and previously reported measurements for other compositions and carrier concentrations will be compared to model calculations of the low-temperature magnetic state. A magnetic phase diagram will be presented.

$Sn_{1-x}Mn_xTe$ is a diluted magnetic semiconductor, in which a small amount of the nonmagnetic cation Sn^{2+} is replaced by the magnetic ion Mn^{2+}. It has been shown that the magnetic properties of $Sn_{1-x}Mn_xTe$ not only depend on the manganese concentration, but also on the free carrier (hole) concentration.[1–4] For manganese concentrations below $x=0.04$ it was observed that at relatively low carrier concentrations ($p=5–7\times10^{20}$ cm^{-3}) the system is ferromagnetic at liquid helium temperatures. At slightly higher carrier concentrations ($p=9–12\times10^{20}$ cm^{-3}) the ferromagnetic nature of the material weakens and a reentrant spin-glass phase is observed. At high carrier concentrations ($p=20–23\times10^{20}$ cm^{-3}) the ferromagnetism has vanished and a spin-glass phase is observed. The nature of these phases was established using magnetization, specific heat, (frequency dependent) ac susceptibility,[1–3] and neutron diffraction[4] measurements. These results are used to compile a phase diagram, in which the magnetic phase of the material is indicated for various carrier and manganese concentrations (see Fig. 1). In this figure the data of samples of $Pb_{0.28-x}Sn_{0.72}Mn_xTe$ are also included, which show a similar transition from ferromagnetism to a spin-glass state upon increasing the carrier concentration.[1]

In this paper we will concentrate on the location of the ferromagnetic to spin-glass transition in the phase diagram. We have performed calculations of this boundary using three different models. These calculations will be confronted with the experimental data. Below we will first present some new measurements, which are already included in Fig. 1.

In Fig. 2 the ac susceptibility is shown for four samples with $p\approx20\times10^{20}$ cm^{-3} and $x=0.04$, 0.06, 0.08, and 0.10, respectively. For $x=0.04$ and 0.06 a clear cusp in the susceptibility is present, indicating a transition to a spin-glass state. For $x=0.08$ two maxima are observed. The first maximum, at $T=10.8$ K, results from a transition from the paramagnetic state to a ferromagnetic state, and the second maximum, at $T=2.3$ K, from a transition from a ferromagnetic state to a spin-glass state. This is interpreted as a reentrant spin-glass phase. The sample with $x=0.10$ displays a ferromagnetic transition at $T=15.5$ K, and no other transition at $T>1.3$ K. However, the flattening of the curve below 3 K may indicate the presence of a second transition below 1.3 K, similar to that for $x=0.08$. The measurements indicate that at higher manganese concentrations the transition to the spin-glass state occurs at a higher carrier concentration.

The explanation of the results is based on the RKKY interaction, which is dominant in these compounds (see Fig. 3).[1] This interaction is an oscillating function with argument $2k_FR_{ij}$, where k_F is the wave number at the Fermi level and R_{ij} is the distance between two ions. The most elementary

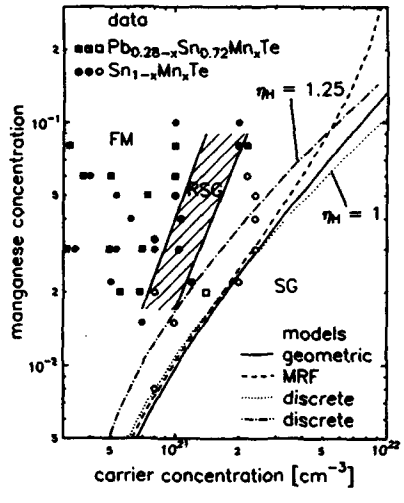

FIG. 1. Magnetic phase diagram of the compounds $Pb_{0.28-x}Sn_{0.72}Mn_xTe$ (squares) and $Sn_{1-x}Mn_xTe$ (circles). Filled symbols indicate ferromagnetic (FM) samples, half-filled symbols reentrant spin-glass (RSG) samples, and open symbols spin-glass (SG) samples. The hatched region indicates the experimentally observed reentrant spin-glass regime. Calculated phase boundaries are also included: full line: geometric model; dashed line: MRF model ($\eta_H=1$); dotted line: discrete model ($\eta_H=1$); and dash–dotted line: discrete model.

 0021-8979/94/75(10)/5728/3/$6.00 © 1994 American Institute of Physics

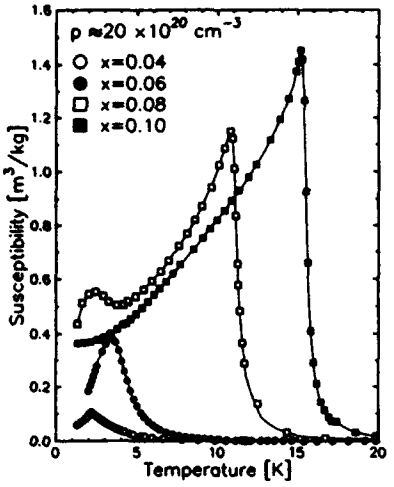

FIG. 2. Real part of the ac susceptibility vs temperature for four samples of $Sn_{1-x}Mn_xTe$ with hole concentration $p \approx 20\times10^{20}$ cm^{-3}. Open circles: $x=0.04$; filled circles: $x=0.06$; open squares: $x=0.08$; and filled squares: $x=0.10$. The full lines are a guide to the eye.

way to describe the transition between the ferromagnetic and spin-glass states is based on simple geometrical arguments. For this we will define two characteristic distances. First, R_0, which is the minimal distance at which the RKKY interaction changes from ferromagnetic to antiferromagnetic. R_0 is proportional to $k_F^{-1} \propto p^{-1/3}$. Second, R_{Mn-Mn} is the average

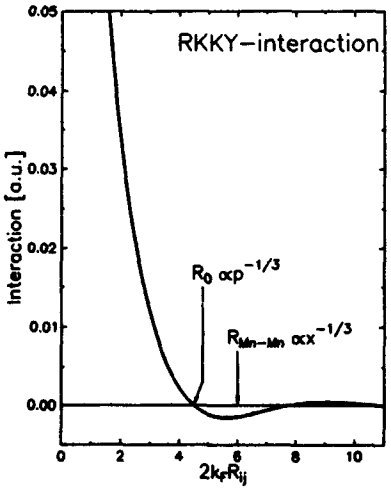

FIG. 3. Strength of the RKKY interaction. R_0 is the distance at which the interaction changes from ferromagnetic to antiferromagnetic. R_{Mn-Mn} indicates a possible average Mn–Mn distance.

distance between the Mn ions. R_{Mn-Mn} is proportional to $x^{-1/3}$. Whenever $R_0 \gg R_{Mn-Mn}$ many ions will be coupled by the first ferromagnetic part of the interaction, resulting in a ferromagnetic phase in the material. If $R_0 \ll R_{Mn-Mn}$ only few ions will be coupled by this ferromagnetic part and many will sense the oscillating tail of the interaction, inducing frustration and competition which will lead to a spin-glass state. We now conjecture that the transition from ferromagnetism to spin-glass behavior will take place when $R_0 = R_{Mn-Mn}$. This leads to the relation x/p=constant. In Fig. 1 this phase boundary is represented by the full curve. In spite of the crudeness of the model, the slope of the experimental phase boundary is reproduced quite accurately. The actual position of the line is not so well described.

A more sophisticated calculation of the phase boundary can be obtained with the mean random field (MRF) model,[5] which has been used to describe spin glasses before. In this model the probability $P(H)dH$ is calculated that a spin senses an internal field between H and $H+dH$, produced by the other spins. Using this probability distribution the mean internal field $\langle H \rangle$, and its variance ΔH, can be calculated. The parameter $\eta_H = \langle H \rangle / \Delta H$, comparable to the Sherrington–Kirkpatrick order parameter[6,7] then determines the magnetic phase in the system: a spin-glass phase for $\eta_H < 1$, a reentrant spin-glass phase for $1 < \eta_H < 1.25$, and a ferromagnetic phase for $\eta_H > 1.25$. We have calculated the distribution of internal fields using an isotropic, damped RKKY interaction at $T=0$ K:

$$J_{RKKY}(R_{ij}) = \frac{m^* J_{sd}^2 a_0^6 k_F^4}{32\pi^3\hbar^2} \left(\frac{\sin(2k_F R_{ij}) - (2k_F R_{ij})\cos(2k_F R_{ij})}{(2k_F R_{ij})^4} \right) \times \exp(-R_{ij}/\lambda), \quad (1)$$

where m^* is the effective mass of carriers ($m^* = 1.7 m_e$), J_{sd} is the exchange integral (J_{sd}=100 meV), a_0 is the lattice constant (a_0=6.33 Å), and λ is the mean free path. In the calculation we have only taken the contribution from the second valence band into account.[8] As an example some distributions for $p = 13\times10^{20}$ cm^{-3} and λ=40 Å are displayed in Fig. 4(a). For increasing manganese concentration the distribution shifts to higher fields and broadens considerably. This is to be expected, as for higher manganese concentrations, the probability of finding one or more ions near the reference ion increases considerably, and therefore the internal field will rise. From these distributions it is possible to obtain the phase boundary by calculating $P(H)$ for a number of combinations of x and p. For $\lambda=\infty$, however, the phase boundary can be calculated analytically, and the latter curve (for $\eta_H=1$) is shown in the phase diagram (dashed curve in Fig. 1). This line is comparable to the line of the geometrical model. However, at high carrier concentrations the line diverges, indicating a breakdown of the validity of the model.

The MRF model has two major disadvantages. First, it is a continuum model, not taking the discreteness of the lattice into account, and second, it is only valid for small concentrations of manganese.[5] These disadvantages are not present in the last model that we will present, where we have

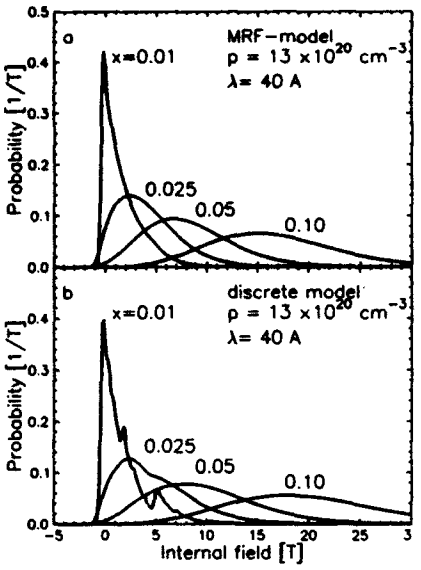

FIG. 4. Calculation of internal fields for $p=13\times10^{20}$ cm^{-3} and $\lambda=40$ Å using the MRF model (a) and the discrete model (b).

summed the fields from all ions situated at discrete lattice positions around a reference ion:

$$H=\sum_{j=1}^{N} n_j h_j, \tag{2}$$

$$h_j=\frac{2S}{g\mu_B}\, J_{\mathrm{RKKY}}(R_{ij}), \tag{3}$$

where n_j is the number of ions present in shell number j, S is the spin of the ion ($S=5/2$), μ_B is the Bohr magneton, g is the Landé factor ($g=2$), and N is the number of shells taken in the calculation ($N=10\,000$). The spins were distributed randomly over the lattice and all possible configurations of Mn ions within those shells were taken into account. This model can in principle be considered as a discrete analog of the MRF model. As an example the calculated distributions, for the same set of parameters as used with the MRF model, are shown in Fig. 4(b). As expected, these results are similar to those obtained with the MRF model. In Fig. 4(b) the effect of the discreteness is visible for small manganese concentrations. The curves for the higher manganese concentrations are shifted toward higher fields. This indicates that in the MRF model, which is not valid for higher manganese concentrations, the nearby ions are not correctly taken into account. For the discrete model the phase boundary can also be calculated analytically, as

$$\langle H\rangle = x\sum_{j=1}^{N} z_j h_j, \tag{4}$$

$$(\Delta H)^2=(x-x^2)\sum_{j=1}^{N} z_j h_j^2, \tag{5}$$

where z_j is the number of lattice sites in shell j. In the phase diagram the phase boundaries for $\lambda=\infty$ are represented by the dotted ($\eta_H=1$) and dash–dotted ($\eta_H=1.25$) line, respectively.

At this point we will discuss the influence of the mean free path in our system. Results from experiments on transport properties indicate that the mean free path is at least smaller than 100 Å.[8] The value of 40 Å was taken rather arbitrarily, but λ may well be as small as 10 Å. The effect of a decrease of λ is to suppress the oscillating tail of the interaction. The calculated distributions will then narrow and shift toward lower fields. η_H is oppositely affected by these two effects. It turns out that at high values of p the phase boundary shifts towards lower values of x, whereas at low values of p it shifts toward higher values of x. For $\lambda>40$ Å the effect is quite small, as the difference in η_H between $\lambda=\infty$ and $\lambda=40$ Å is only a few percent. However, when the value of λ is very small the effect is much larger. The simple exponential damping of the interaction is then not valid anymore.[9]

To conclude, our new magnetic measurements on $Sn_{1-x}Mn_xTe$ samples with $0.04<x<0.10$ show a gradual change from spin-glass behavior to ferromagnetism as x increases at fixed p. We have calculated the phase boundary between these regimes using three different models, namely a geometrical model, the mean random field, and a discrete model in which a summation of internal fields over lattice positions is performed. All three models describe the slope of the phase boundary reasonably well, but the actual position is not recovered.

The authors wish to thank A. J. M. Gielen for his help with the calculations, and A. H. Menting and C. van der Steen for their help with the measurements. One of us (H.J. M.S.) acknowledges a grant from the Royal Netherlands Academy of Arts and Sciences.

[1] W. J. M. de Jonge, T. Story, H. J. M. Swagten, and P. J. T. Eggenkamp, Europhys. Lett. 17, 631 (1992).
[2] P. J. T. Eggenkamp, T. Story, H. J. M. Swagten, C. W. H. M. Vennix, C. H. W. Swüste, and W. J. M. de Jonge, Semiconduct. Sci. Technol. 8, S152 (1993).
[3] P. J. T. Eggenkamp, C. W. H. M. Vennix, H. J. M. Swagten, and W. J. M. de Jonge (unpublished).
[4] C. W. H. M. Vennix, E. Frikkee, P. J. T. Eggenkamp, H. J. M. Swagten, K. Kopinga, and W. J. M. de Jonge, Phys. Rev. B 48, 3770 (1993).
[5] M. W. Klein, Phys. Rev. 173, 552 (1968).
[6] D. Sherrington and S. Kirkpatrick, Phys. Rev. Lett. 35, 1792 (1975).
[7] M. W. Klein, Phys. Rev. B 14, 5008 (1976).
[8] H. J. M. Swagten, W. J. M. de Jonge, R. R. Gałązka, P. Warmenbol, and J. T. Devreese, Phys. Rev. B 37, 9907 (1988).
[9] P. G. de Gennes, J. Phys. Radium 23, 630 (1962).

Magnetic behavior of $(CuIn)_{1-x}Mn_{2x}Te_2$

P. M. Shand
Physics Department, University of Northern Iowa, Cedar Falls, Iowa 50614

P. A. Poistra, I. Miotkowski, and B. C. Crooker
Physics Department, Purdue University, West Lafayette, Indiana 47907

Magnetic susceptibility measurements have been made on the chalcopyrite diluted magnetic semiconductor $(CuIn)_{1-x}Mn_{2x}Te_2$ for concentrations $0.01 \leq x \leq 0.101$ and temperatures 33 mK$\leq T \leq$300 K. Samples with $x > 0.05$ had similar values of the effective nearest-neighbor exchange constant, with $J_{eff}/k_B \sim -18.5$ K. The strength of J_{eff} fell sharply in samples with lower x, a characteristic not seen in wide band gap II–VI based alloys. Low-field ac susceptibility measurements showed spin-glass behavior. Analysis of freezing temperature T_f vs x data showed a possible crossover between different modes of exchange, coincident with the sharp drop in J_{eff}. Preliminary carrier concentration data suggests that the crossover may be driven by increased numbers of free holes in some samples.

I. INTRODUCTION

The properties of the exchange interaction and spin-glass behavior in pseudobinary diluted magnetic semiconductors (DMSs) have been subjects of considerable interest for some time.[1–4] Recently, DMS alloys based on ternary chalcopyrite hosts have become available. These materials present a good opportunity to gain more insight into the nature of exchange interactions and spin freezing by studying the behavior of magnetic ions distributed in a different host system.

$(CuIn)_{1-x}Mn_{2x}Te_2$ is produced by randomly diluting the chalcopyrite host semiconductor $CuInTe_2$ with Mn. On average, one Cu atom and one In atom are replaced by two Mn atoms in the cation sublattice. For $x<0.5$, $(CuIn)_{1-x}Mn_{2x}Te_2$ retains the chalcopyrite crystal structure, with a tetragonal unit cell. The unit cell of the parent $CuInTe_2$ has a c/a value exactly equal to the ideal value of 2. Thus, at low x, one expects little tetragonal distortion in $(CuIn)_{1-x}Mn_{2x}Te_2$. The cation sites are surrounded by tetrahedrally distributed Te ions. However, the bonds are distorted in chalcopyrite materials because each anion is bonded to dissimilar cations of different sizes and electronegativities. The ^6S ground multiplet of a substitutional Mn^{2+} ion is split by the S_4 symmetric field at the cation sites into three Kramers doublets.[5] The splitting is, however, very small (~100 mK) as in the case of the $II_{1-x}Mn_xVI$ alloys. The ground state of Mn^{2+} ions in $(CuIn)_{1-x}Mn_{2x}Te_2$ for temperatures above 5 K can therefore also be taken as the sixfold degenerate spin-only ^6S state.

Another parameter which comes into play in $(CuIn)_{1-x}Mn_{2x}Te_2$ is electrical conductivity. Unlike the wide band gap $II_{1-x}Mn_xVI$ materials, as-grown $(CuIn)_{1-x}Mn_{2x}Te_2$ alloys have significant conductivities, with typical hole concentrations between 10^{17} and 10^{19} cm^{-3}. The presence of mobile carriers could influence the exchange processes between the Mn ions, thereby affecting exchange constants and the temperature dependence of spin-glass transitions.

The similarities and differences between $(CuIn)_{1-x}Mn_{2x}Te_2$ and the wide band gap $II_{1-x}Mn_xVI$ alloys make the former an inviting prospect for further study. In order to glean more information about exchange and spin freezing in these DMS systems, we have measured the magnetic susceptibility of $(CuIn)_{1-x}Mn_{2x}Te_2$ for concentrations $0.01 \leq x \leq 0.101$ and temperatures 33 mK$\leq T \leq$300 K.

II. EXPERIMENTAL DETAILS

The $(CuIn)_{1-x}Mn_{2x}Te_2$ samples used in our experiments were prepared by means of the Bridgman method. All samples were polycrystalline and consisted of a single chalcopyrite phase, as determined by x-ray powder diffraction. Concentrations of Mn ions were determined by electron microprobe for four samples and by magnetic measurements in the others. In all cases, the experimentally determined x values were very close to the nominal values. Further, the microprobe measurements also determined the concentrations of Cu, In, and Te. This confirmed that Mn did replace both In and Cu in the host lattice.

For the dc susceptibility measurements above 4.2 K, a Cryogenic Consultants superconducting quantum interference device (SQUID) magnetometer was used. The diamagnetic susceptibility of the undoped host $CuInTe_2$ was found to be -2.7×10^{-7} emu/g. This value was subtracted from all susceptibility data. For 33 mK$\leq T \leq$4.2 K, ac susceptibility data were obtained by using a dilution refrigerator fitted with a SQUID susceptometer running at 26 Hz.

To determine carrier concentrations (p), the samples were cooled to 77 K and the Hall voltages were measured in magnetic fields up to 1.8 T. For the higher p values, a Linear Research LR 400 ac resistance bridge was used to obtain the Hall voltages, and for the lower p values, a Keithley Model 225 current source and a Keithley Model 181 nanovoltmeter were used.

III. RESULTS AND DISCUSSION

The susceptibility χ of DMS materials has been found to show Curie–Weiss behavior at high temperatures:

$$\chi = C(x)/[T+\Theta(x)]. \quad (1)$$

For $(CuIn)_{1-x}Mn_{2x}Te_2$, the Curie constant per mole $C(x)$ is given by

$$C(x) = 2xN_A(g\mu_B)^2S(S+1)/3k_B, \quad (2)$$

 0021-8979/94/75(10)/5731/3/$6.00 © 1994 American Institute of Physics

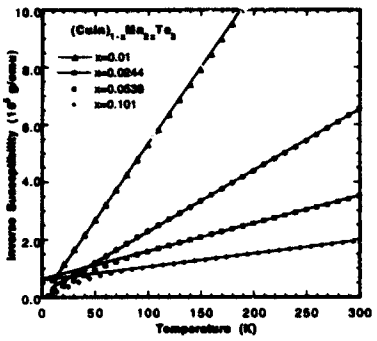

FIG. 1. Inverse susceptibility vs temperature for $(CuIn)_{1-x}Mn_{2x}Te_2$ samples with $x=0.01$, 0.0244, 0.0538, and 0.101. The straight lines are Curie–Weiss fits to the data.

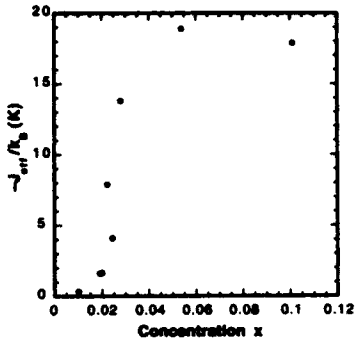

FIG. 2. Effective nearest-neighbor exchange interaction J_{eff} vs x for several $(CuIn)_{1-x}Mn_{2x}Te_2$ samples.

where N_A and k_B are Avogadro's and Boltzmann's constants, μ_B is the Bohr magneton, g is the electron g factor, and S is the spin of the Mn^{2+} ion.

Assuming a random distribution of spins, the Weiss temperature $\Theta(x)$ is given by

$$\Theta(x)=2xS(S+1)\sum_p z_p J_p/3k_B, \tag{3}$$

where the summation index p designates pth neighbor atoms, z_p is the number of such neighbors, and J_p is the corresponding exchange parameter. The effective nearest-neighbor (NN) exchange parameter J_{eff} is defined by

$$z_1 J_{eff}=\sum_p z_p J_p, \tag{4}$$

where z_1 is the number of nearest neighbors. J_{eff} is a good approximation of the NN exchange integral J_1 only if further neighbor interaction strengths are very small in comparison to J_1.

Figure 1 depicts inverse dc susceptibility vs temperature data for the four samples of $(CuIn)_{1-x}Mn_{2x}Te_2$ for which x was determined by microprobe. Curie–Weiss behavior is clearly observed for $x=0.0538$ and 0.101, giving Θ values of -66 and -131 K, respectively. Thus, the dominant exchange interaction between Mn ions in these samples is antiferromagnetic. At low temperatures, there is a downturn in the inverse susceptibility, indicative of the formation of antiferromagnetically bonded clusters. This behavior was also seen in $Cu_{1-x}Mn_xInTe_2$ for $x=0.09$ and 0.12 (Ref. 6) and in standard II-VI DMS materials.

For the $x=0.01$ and 0.0244 samples, there is no discernible deviation from linearity down to the lowest temperatures (~7 K), and very small Θ values (-0.2 and -6.5 K) are obtained. Clearly, total exchange strengths in these samples are very small. This weak exchange coupling at lower x values was also seen in $Cu_{1-x}Mn_xInTe_2$.[6] It should also be mentioned that values of S for the Mn^{2+} ion were calculated for each of the four samples using Eq. (2), with $g=2.02$ (Ref. 7). The average value of S was 2.42 ± 0.09, which is very close to the free ion value of 5/2.

In order to better illustrate the behavior of the exchange strength as x is varied, we have plotted in Fig. 2 J_{eff} vs x for the samples used in Fig. 1, as well as several other samples. J_{eff} was calculated by using Eq. (3). For $x=0.101$ and 0.0538, we obtained J_{eff}/k_B values of -18 and -19 K, respectively. Thus, for these samples, J_{eff} is independent of x which is characteristic of randomly dilute magnetic systems. However, the magnitude of J_{eff} in this case is significantly larger than J_1 values in the Mn-based pseudobinary tellurides ($6.3\ \text{K} \leqslant -J_1/k_B \leqslant 10.0$ K). Of course, J_{eff} includes further *neighbor* interactions, which could be stronger in $(CuIn)_{1-x}Mn_{2x}Te_2$ than in the $II_{1-x}Mn_xTe$ alloys. Further, different valence-band-edge characteristics[8,9] and greater distortion in the tetrahedral bonds in $(CuIn)_{1-x}Mn_{2x}Te_2$ may lead to a higher J_1 (and hence J_{eff}) value.

At lower concentrations, J_{eff}/k_B falls off rapidly to values close to zero in a manner reminiscent of a "threshold" effect. This effect was not exhibited by $II_{1-x}Mn_xVI$ materials, as shown by an extensive study of their high-temperature susceptibilities.[10] The rapid drop in J_{eff} could be the result of the introduction of a ferromagnetic component to the total exchange at low x.

The RKKY interaction is a possible vehicle for such a ferromagnetic coupling. Shown in Fig. 3 are preliminary data for J_{eff} vs as-grown hole concentration p for the four microprobed samples. One sees that the sharp reduction in J_{eff} occurs at $p \sim 2.5\times10^{19}$ cm^{-3}. Materials such as $Sn_{1-x}Mn_xTe$ display carrier-induced transitions from paramagnetism to ferromagnetism due to the RKKY interaction, albeit at somewhat higher p.[11] In order to better establish the effect of carriers on exchange in $(CuIn)_{1-x}Mn_{2x}Te_2$, experiments involving the variation of the carrier concentration in a single sample are planned.

Low-temperature measurements of ac susceptibility for the same four samples reveal cusps which are interpreted as spin-glass transitions. The behavior of the spin-freezing temperature T_f as a function of x gives information about the

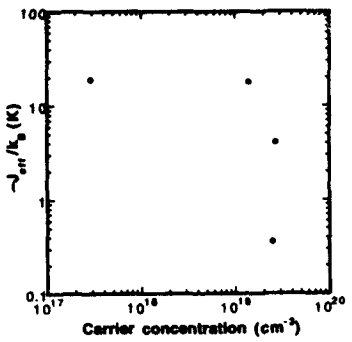

FIG. 3. J_{eff} vs as-grown carrier concentration for four samples of $(CuIn)_{1-x}Mn_{2x}Te_2$.

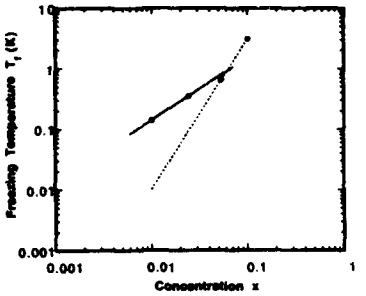

FIG. 4. Freezing temperature T_f vs concentration x for $(CuIn)_{1-x}Mn_{2x}Te_2$. The different slopes of the lines signify a possible crossover to longer-range exchange (shallower slope) at lower concentrations.

spatial dependence of the exchange interaction $J(R)$.[1-3] In II–VI based alloys, it is found that $J(R) \sim R^{-n}$, with $n \sim 7$. Figure 4 shows a log–log plot of T_f vs x. The dashed line passing through the higher concentration points corresponds to $n=7.4$. The fact that the lower concentration points lie on a line of significantly smaller slope ($n=3.1$) suggests that there is a crossover to longer-ranged exchange, consistent with the RKKY interaction. Additional samples will be measured to establish if there is indeed a crossover to a longer-ranged exchange interaction at low x, and if this crossover is coincident with the apparent transition in J_{eff}.

Summarizing, we have measured the magnetic susceptibility as a function of temperature of $(CuIn)_{1-x}Mn_{2x}Te_2$ for several concentration values. For $x>0.05$, $J_{eff}/k_B \sim -18.5$ K and is independent of x. In the vicinity of $x=0.025$, the magnitude of J_{eff} decreases sharply, indicating a sudden transition to much smaller exchange strengths. All samples exhibit spin-glass behavior, and an analysis of the T_f vs x plot indicates a possible crossover in the spatial dependence of the exchange interaction from $R^{-7.4}$ to $R^{-3.1}$ behavior at low x. Preliminary Hall effect data also indicate that the behavior of J_{eff} may have been induced by an increase in the free hole concentration.

[1] A. Twardowski, C. J. M. Denissen, W. J. M. de Jonge, A. T. A. M. de Waele, M. Demianiuk, and R. Triboulet, Solid State Commun. **59**, 199 (1986).
[2] A. Twardowski, H. J. M. Swagten, W. J. M. de Jonge, and M. Demianiuk, Phys. Rev. B **36**, 7013 (1987).
[3] P. M. Shand, A. Lewicki, I. Miotkowski, B. C. Crooker, and J. K. Furdyna, Phys. Rev. B **44**, 6152 (1991-II).
[4] A. Lewicki, A. I. Schindler, P. M. Shand, B. C. Crooker, and J. K. Furdyna, Phys. Rev. B **44**, 6137 (1991-II).
[5] G. L. Troeger, R. N. Rogers, and H. M. Kasper, J. Phys. C **9**, L73 (1976).
[6] L.-J. Lin, J. H. Wernick, N. Tabatabaie, G. W. Hull, and B. Meagher, Appl. Phys. Lett. **51**, 2051 (1987).
[7] H. J. M. Swagten (unpublished).
[8] J. E. Jaffe and A. Zunger, Phys. Rev. B **29**, 1882 (1984).
[9] K. Takarabe, K. Kawai, S. Minomura, T. Irie, and M. Taniguchi, J. Appl. Phys. **71**, 441 (1992).
[10] J. Spalek, A. Lewicki, Z. Tarnawski, J. K. Furdyna, R. R. Galazka, and Z. Obuszko, Phys. Rev. B **33**, 3407 (1986).
[11] T. Story, P. J. T. Eggenkamp, C. H. W. Swüste, H. J. M. Swagten, W. J. M. de Jonge, and L. F. Lemmens, Phys. Rev. B **45**, 1660 (1992), and references therein.

Relaxation of magnetization in $Cd_{1-x}Mn_xTe$ diluted magnetic semiconductors under illumination

M. Smith, A. Dissanayake, and H. X. Jiang
Department of Physics, Kansas State University, Manhattan, Kansas 66506-2601

L. X. Li
Cleveland Crystals, Inc., Cleveland, Ohio 44110

Relaxation of thermoremanent magnetization (TRM) of $Cd_{1-x}Mn_xTe$ diluted magnetic semiconductors (DMS) in the spin-glass state have been studied under light illumination. The relaxation of TRM can be described well by a power law decay, $M(t)=M(t_0)t^{-\alpha}$ ($t>t_0$, $t_0\sim2$ s). The variations of the decay parameter α with the illumination light intensity has been measured and a relation which indicates that α is proportional to the photogenerated carrier concentration n has been observed.

The diluted magnetic semiconductors (DMS) are a group of materials which have attracted a great deal of attention for many years because of their unique properties for understanding many fundamental physics as well as their promising practical applications.[1,2] The magnetic behavior of different kinds of DMS show many common characteristics, which can be understood on the basis of a random array of localized magnetic moments coupled by isotropic antiferromagnetic interaction.[3] Many aspects of this interaction between magnetic ions are still under investigation. One of the interesting and important subjects in the DMS is the spin-glass (SG) state at low temperatures. It is well established in DMS that there exists a paramagnetic to a SG transition at low temperatures because of randomness of magnetic ion distribution and spin–spin interactions. The transition temperature or freezing temperature T_f depends on magnetic ion composition,[4,5] magnetic field,[6] and history of the system. Although some work has been devoted to study SG dynamics in the DMS previously,[7–10] the understandings of the dynamic process of SG formation and transformation, as well as the relaxation in the SG state are still far from complete.

In this paper, we report the studies of the relaxation of thermoremanent magnetization (TRM) of $Cd_{1-x}Mn_xTe$ in the SG state under light illumination. A power law time dependence of TRM relaxation has been observed and the decay parameter at different excitation light intensities has been measured. The main results reported in this paper are the investigations of the spin–spin interaction of the magnetic ions in the SG state as affected by photogenerated electrons and holes. We have measured TRM under light illumination at different conditions and the results have been compared to those obtained in the dark.

The sample used for this study was a $Cd_{0.74}Mn_{0.26}Te$ single crystal provided by Cleveland Crystal, Inc. It was grown by temperature gradient technique and nominally undoped. However, photoluminescence measurements of a bound exciton transition indicated a low concentration of impurities in the samples. The size of the sample was a few cubic millimeters. The magnetization was measured by a superconducting quantum interference device (SQUID) magnetometer (Quantum Design MPMS5). In order to study the effects of photoexcitation to the relaxation of TRM, a quartz fiber optic probe was used with the SQUID. The fiber optic probe was made of an optic fiber bundle with a diameter of about 2 mm. One end of the fiber optic probe was in the sample chamber within a few mm from the sample and the other end was outside the SQUID. A mercury lamp with a set of neutral density filters was used as an excitation source.

We have measured the susceptibility of a $Cd_{0.74}Mn_{0.26}Te$ sample under the field-cooled (FC) and zero-field-cooled (ZFC) conditions to determine the freezing temperatures T_f of the SG state. The data show that T_f is about 4.2 ± 0.2 K, which is consistent with previous measurements.[5–7,11] In this paper, we only report relaxation of TRM in the SG state, or at temperatures below T_f. We did not observe any remanent magnetization above T_f.

Figure 1 is the plot of relaxation of magnetization at $T=1.7$ K and measured at $B=100$ Oe. The experiment was performed by cooling down the system with the magnetic field on ($B=1$ T), i.e., under FC condition, then by reducing the field to $B=100$ Oe after the temperature has reached 1.7

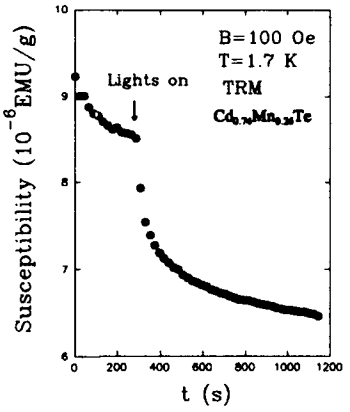

FIG. 1. Decay of magnetic susceptibility of TRM of a $Cd_{0.74}Mn_{0.26}Te$ sample in the dark and under illumination in the spin-glass state at $T=1.7$ K measured at a magnetic field of $B=100$ Oe. The arrow indicates the moment the light illumination was turned on. The applied magnetic field during the cooling down was 1 T.

 0021-8979/94/75(10)/5734/3/$6.00 © 1994 American Institute of Physics

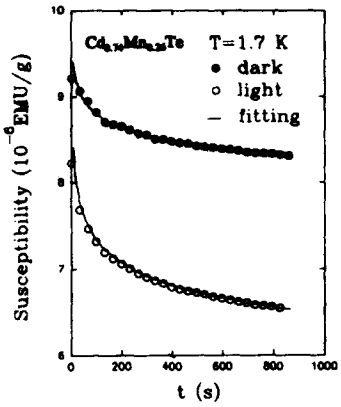

FIG. 2. Decay of magnetic susceptibility of TRM of a $Cd_{0.74}Mn_{0.26}Te$ sample in the dark (●●●) and under illumination (○○○) at $T=1.7$ K measured at a magnetic field of $B=100$ Oe. The solid lines are the least-squares fit by the power law decay of Eq. (1).

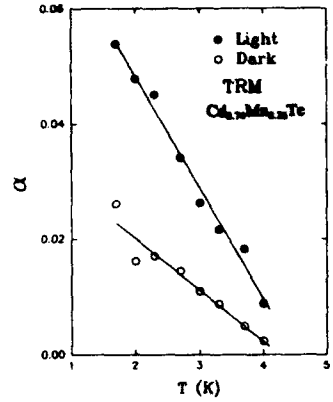

FIG. 3. The decay parameter α as a function of temperature in the dark (○○○) and under the illumination (●●●) for a $Cd_{0.74}Mn_{0.26}Te$ sample. The solid lines are the least-squares fit using $\alpha=a-bT$, where a is 3.8×10^{-2} and 8.7×10^{-2} and b is 9.0×10^{-3} and 1.9×10^{-2}/K in the dark and under illumination, respectively. Extrapolate these two lines to $\alpha=0$ gives $T_f=4.2\pm0.2$ and 4.5 ± 0.2 K for the dark and under illumination, respectively.

K. Shown in Fig. 1 is an initial decay measured in the dark for about 300 s and a subsequent decay measured after the moment the light excitation was turned on as indicated by an arrow in the figure. As we can see from Fig. 1, the decay of the magnetization under illumination proceeds faster compared to that in the dark.

Figure 2 shows the results of relaxation of magnetization measured at 100 Oe in the dark (●●●) and under illumination (○○○) at $T=1.7$ K for a $Cd_{0.74}Mn_{0.26}Te$ sample together with a least-squares fit using a power law decay (solid lines). We have to point out that the initial condition for the relaxation depends on the waiting period before the measurement. In order to minimize the difference in the initial condition, we begin to collect the relaxation data under illumination and in the dark at the same time so that direct comparison between two cases can be made here. Previously, a power law decay of magnetization in DMS has been observed.[12] Here, we also find that the experimental results shown in Fig. 2 can be described quite well by a power law decay,

$$M(t)=M_0t^{-\alpha}(t>t_0,t_0\sim2\ \text{s}), \tag{1}$$

both in the dark and under illumination, where α is the decay parameter. The fitted values in Fig. 2 are $\alpha=2.6\times10^{-2}$ and 5.4×10^{-2} and $M_0=9.9\times10^{-6}$ and 9.4×10^{-6} emu/g for the conditions in the dark and under illumination, respectively. The decay parameter α is directly correlated with the decay rate. Therefore, the experimental results indicates that the decay rate is about a factor of 2 larger under illumination than that in the dark.

Figure 3 are the plots of decay parameter α as a function of temperature in the dark (○○○) and under illumination (●●●) for $Cd_{0.74}Mn_{0.26}Te$. The decay parameter α decreases linearly with increasing of temperature for both cases. At all temperatures, the magnetization relaxes faster under illumination compared to that in the dark. The difference between α under illumination and in the dark becomes smaller as temperature approaches to T_f. Eventually, α approaches to zero at the freezing temperature T_f. Dependence of α on temperature T can be described by a linear relation, $\alpha=a-bT$ ($T<T_f$). Extrapolating from $\alpha=0$, we obtain T_f to be 4.2 ± 0.2 and 4.5 ± 0.2 K in the dark and under illumination, respectively. We have also measured the magnetization of ZFC vs temperature under illumination and in the dark, we cannot determine whether or not T_f has been changed under illumination because the difference between the values of T_f in the dark and under illumination is within the experimental uncertainty. However, the values of T_f extrapolated from $\alpha=0$ in Fig. 3 are consistent with the freezing temperature $T_f(=4.2\pm0.2$ K) obtained from the FC susceptibility measurement within the experimental uncertainty. The results in Fig. 3 tells us that we can also determine the freezing temperature T_f of the SG state by measuring the temperature dependence of the relaxation parameters of magnetization.

We have also measured the decay parameter α of TRM at a fixed temperature ($T=2$ K) under photoexcitation with different light intensities. Figure 4 shows a plot of α vs the square root of excitation light intensity, $I^{1/2}$. The magnetic field for the measurements was 100 Oe and the field applied during the cooling down was 1 T. As we expected, the exponent α increases as light intensity increases. Relaxation of magnetization obtained under illumination with different light intensities can be described quite well by the power law decay. We see that α increases linearly with the square root of light intensity, $\alpha\propto I^{1/2}$. The insert of Fig. 4 shows α vs light intensity I.

One obvious mechanism which may be responsible for

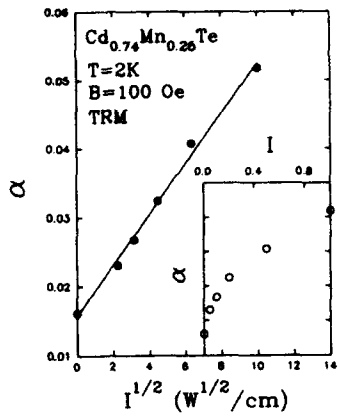

FIG. 4. Dependence of the decay parameter α of TRM on the square root of excitation light intensity $I^{1/2}$ for a $Cd_{0.74}Mn_{0.26}Te$ sample at $T=2$ K. Here $I=0$ corresponds to the dark. The solid line in the figure is the linear fit of α with $I^{1/2}$ according to Eq. (4) with fitted values $B_0(=1.57\times10^{-2})$ and $B_1(=3.68\times10^{-3})$. The insert is the plot of α vs light intensity I. The unit of the light intensity I in the inset is in 0.25 W/cm^2 and of $I^{1/2}$ in the main figure is in 0.05 W$^{1/2}$/cm. The scales of α are the same for both the main figure and the inset.

the observed light intensity dependence of α is the heating effect under light excitation. However, the systematic dependence of α on the excitation intensity cannot be explained by considering the heating effects. Furthermore, from Fig. 3, we see that the decay parameter α decreases as temperature increases in the temperature region investigated here. If the changes of α under light excitation is due to heating, we should expect that α decreases as light intensity increases, which has never been observed. These observations preclude the possibility of heating effects. Therefore we can conclude that the observed decay rate increasing under light excitation is due to photoexcited carriers. It is clear from our experimental results that the mechanism responsible for manganese–ion coupling in DMS is carrier concentration sensitive.

Under photoexcitation, free or localized carriers (electrons and holes) are generated and subsequently recombined radiatively or nonradiatively. Photoluminescence due to carrier recombination in DMS has been observed in many experiments.[13,14] The electron concentration under illumination can be written as

$$\frac{dn}{dt}=G-Cnp/\tau, \tag{2}$$

where τ is the carrier recombination lifetime, n and p the electron and hole concentrations, and C a proportionality constant in units of cm^3. Here G is the carrier generation rate writing as $G=\alpha_a\eta I/\hbar\omega$, with $\hbar\omega$ being the excitation photon energy, I the light intensity in units of W/cm^2, α_a the absorption coefficient, and η the quantum efficiency—number of electrons generated per each absorbed photon. Under continuous and constant intensity light illumination, the photogenerated electrons and holes will be under equilibrium and so we have $dn/dt=0$. We should also have the condition $n=p$ since our samples are undoped. Then we have

$$n=(G\tau/C)^{1/2}=AI^{1/2}, \tag{3}$$

with $A=(\tau\alpha_a/C\hbar\omega)^{1/2}$. From the fact that the relaxation of magnetization proceeds faster under illumination, we can assume that the relaxation rate of magnetization is proportional to the carrier concentration through the carrier–manganese ion interactions,[14] $\alpha\propto n$. From Eq. (3), we have

$$\alpha=B_0+B_1I^{1/2}, \tag{4}$$

where B_0 is the decay parameter α in the dark ($I=0$), and B_1 (in units of cm/W$^{1/2}$) is a proportionality constant. In Fig. 4, we have plotted the least-squares fit of data to Eq. (4) as a solid line.

In conclusion, effects of carriers, which are generated by photoexcitation, to the relaxation of TRM of SG in $Cd_{0.74}Mn_{0.26}Te$ DMS have been studied. A power law decay both in the dark and under illumination has been observed. The decay parameter α as a function of light intensity has been measured at different temperatures. We found that the decay parameter under illumination increases linearly with the photogenerated carrier concentration. More detailed experimental results and discussions, including the results for different Mn concentrations, will be reported elsewhere.

We acknowledge many helpful discussions with J. Y. Lin, G. Wysin, M. O'Shea, and C. Sorensen. This work is supported by the National Science Foundation under Grant No. DMR 91-18818 and OSR 92-55223.

[1] *Semiconductors and Semimetals*, edited by J. K. Furdyna and J. Kossut (Academic, New York, 1988), Vol. 25.
[2] *Diluted Magnetic Semiconductors*, edited by M. Jain (World Scientific, Singapore, 1991).
[3] J. Spalek, A. Lewicki, Z. Tarnawski, J. K. Furdyna, R. R. Galazak, and Z. Obuszko, Phys. Rev. B 33, 3407 (1986).
[4] S. Oseroff and P. H. Keesom, in Ref. 1, pp. 73–123.
[5] R. R. Galazka, S. Nagata, and P. H. Keesom, Phys. Rev. B 22, 3344 (1980).
[6] S. B. Oseroff, Phys. Rev. 25, 6584 (1982).
[7] S. B. Oseroff and F. Gandra, J. Appl. Phys. 57, 3421 (1985).
[8] M. Escorne and A. Mauger, Phys. Rev. B 25, 4674 (1982).
[9] W. Kinzel, Phys. Rev. B 19, 4595 (1979).
[10] C. Dasgupta, S. Ma, and C. Hu, Phys. Rev. B 20, 3837 (1979).
[11] M. A. Novak, O. G. Symko, D. J. Zheng, and S. Oseroff, Physica B 126, 469 (1984).
[12] W. Kinzel, Phys. Rev. B 19, 4595 (1979).
[13] A. Golnik, J. Ginter, and J. A. Gej, J. Phys. C 16, 6073 (1983).
[14] K. H. Fisher and J. A. Hertz, *Spin Glasses* (Cambridge University, New York, 1991).

Theory of magnetization in IV–VI based diluted magnetic semiconductors

R. L. Hota and G. S. Tripathi
Department of Physics, Berhampur University, Berhampur 760007, Orissa, India

P. K. Misra
Department of Physics, Mesa State College, Grand Junction, Colorado 81502

The magnetization (M) in IV–VI based diluted magnetic semiconductors is expressed as a sum of contributions due to isolated impurities, pair interactions, lattice diamagnetism, and spin density due to carriers. We calculate the contribution of each of these mechanisms for p-type $Pb_{1-x}Mn_xTe$ for different x and magnetic field (H) and compare the results with experiment.

Diluted magnetic semiconductors (DMS) have attracted considerable attention in recent years due to the interplay of magnetism and semiconductor physics as well as the fact that these materials are technologically important.[1–3] While a considerable amount of work has been done on the DMS based on II–VI compounds, only recently has attention been drawn to IV–VI based DMS. The interesting properties exhibited by these systems include carrier-induced ferromagnetism,[4–7] anisotropic g factors,[8] and magnetization (M).[9–12] Hitherto, the theoretical effort to calculate M of IV–VI DMS has been restricted to empirical formulas. For example, the only known calculation of M of $Pb_{1-x}Mn_xTe$ has been done by Anderson *et al.*[12] They have used three fitting parameters in the two-spin cluster model of Bastard and Lewiner[13] to calculate the contributions due to isolated impurities (M_s) and pair interactions (M_p). They have ignored the contribution of spin density of carriers (M_c) and calculated the diamagnetic contribution (M_d) from the experimental value of diamagnetic susceptibility (χ_{dia}) of Pb Te thereby neglecting the compositional dependence.

In the present work, we have calculated M_s, M_p, M_d, and M_c of $Pb_{1-x}Mn_xTe$ from first principles without using any adjustable parameters. We have analyzed the relative contributions of the four mechanisms with the variation of the Mn concentration (x) and the magnetic field strength (H).

A system of randomly distributed spins in the presence of an external magnetic field H is described by the Hamiltonian

$$H=-g\mu_B\Sigma_i\mathbf{H}\cdot\mathbf{S}_i-\Sigma'_{i,j}J_{ij}\mathbf{S}_i\cdot\mathbf{S}_j, \tag{1}$$

where g is the g factor of the impurity atom, μ_B is the Bohr magneton, and J_{ij} is the strength of the coupling between spins on sites i and j. Assuming the spins to be identical and neglecting quadratic terms in fluctuations, Eq. (1) can be written in the form

$$H=-g\mu_B\Sigma_i H_{\text{eff},i}S_{iz}+\Sigma'_{i,j}J_{ij}\langle S_{iz}\rangle\langle S_{jz}\rangle, \tag{2}$$

where

$$H_{\text{eff},i}=H+2/(g\mu_B)\Sigma'_j J_{ij}\langle S_{jz}\rangle. \tag{3}$$

In the molecular field approximation, the Hamiltonian for a single impurity spin is given by

$$H_s=-g\mu_B S_z H_{\text{eff}}. \tag{4}$$

In the virtual crystal approximation, H_{eff} is independent of position. The average spin has to be chosen self-consistently from

$$\langle S_z\rangle_s=P_s(x)\left[\sum_{s=-S}^{S}\{\exp(\beta g\mu_B S_z H_{\text{eff}})s\}/\sum_{s=-S}^{S}\exp(\beta g\mu_B S_z H_{\text{eff}})\right], \tag{5}$$

where we have used the relation $S_z|s\rangle=s|s\rangle$, and $P_s(x)$ is the probability of finding an isolated spin, which for a fcc lattice is $(1-x)^{12}$. M_s is obtained from the expression $M_s=xN_0g\mu_B\langle S_z\rangle_s$, where N_0 is the number of unit cells in the crystal. After some algebra, we obtain

$$M_s=M_0Sx(1-x)^{12}B_s(\xi), \tag{6}$$

where $M_0=g\mu_BN_0$, $\beta=(k_BT)^{-1}$, $\xi=g\mu_BHS/(T+T_0)$, $T_0=-2TJ\langle S_z\rangle/g\mu_BH$, and $B_s(\xi)=(2S+1)/(2S)\coth\{(2S+1)/(2S)\xi\}-1/(2S)\coth\{\xi/(2S)\}$.

It was shown by Bastard and Lewiner[13] that even for small x in $Hg_{1-x}Mn_xTe$, the contribution from pairs of closely spaced Mn ions are important. We shall use their model, which is a self-consistent two-spin cluster approximation, for $Pb_{1-x}Mn_xTe$. The Hamiltonian describing the correlated motion of the pair is

$$H_p=-g\mu_B(S_{iz}+S_{jz})H_{\text{eff}}-\Sigma'_{ij}J_{ij}\mathbf{S}_i\cdot\mathbf{S}_j. \tag{7}$$

By following a procedure similar to that used in Ref. 13, it can be easily shown that

$$M_p=M_0\left\{\sum_{S=0}^{2S_{\max}}\exp[\beta J_pS(S+1)]SB_s(\xi)\sinh[(2S+1)/(2S)\xi]\right\}\left\{\sum_{S=0}^{2S_{\max}}\exp[\beta J_pS(S+1)]\times\sinh[(2S+1)/(2S)\xi]\right\}^{-1}6x^2(1-x)^{18}. \tag{8}$$

The contribution due to lattice diamagnetism is obtained from the expression $M_d=\chi_dH$, where χ_d is the diamagnetic susceptibility. We have obtained χ_d by using the general formula for magnetic susceptibility of Bloch electrons derived by Misra and co-workers.[14–16] Since we are interested in

 0021-8979/94/75(10)/5737/3/$6.00 © 1994 American Institute of Physics

calculating the magnetization of $Pb_{1-x}Mn_xTe$, we consider the host crystal PbTe which is a direct band gap semiconductor with the minimum energy gap occuring at the L point of the Brillouin zone. We use Mitchell–Wallis[17] basis functions and Bernick–Kleinman ordering[18] for the six levels near the minimum energy gap. We first assume a two-band model and consider the Brillouin zone as consisting of four spheres located at four inequivalent L points. The radius of each sphere is determined from the formula[19] $k_0=[2(m_c+m_v)E_g]^{1/2}$, where m_c and m_v are the effective masses of the conduction and valence band edges, respectively, and E_g is the energy gap. The band-edge states are diagonalized exactly and the other states are obtained within the framework of a $\mathbf{k}\cdot\boldsymbol{\pi}$ model developed by us[20–24] summarized here. We consider the eigenvalue equation

$$(H_0+H')\psi=E\psi, \tag{9}$$

where $H_0=\pi^2/2m+V(r)$, $H'=(\hbar/m)\mathbf{k}\cdot\boldsymbol{\pi}+\hbar^2k^2/2m$, and ψ stands for the perturbed band-edge states. We diagonalize the Hamiltonian for the conduction and valence band-edge states to obtain

$$\begin{aligned}
\psi_1&=\left(\frac{1+W}{2W}\right)^{1/2}L_{62}^{-}\alpha-\frac{2^{1/2}(\hbar/m)sk_z}{E_G[W(1+W)]^{1/2}}\,L_{61}^{+}\alpha\\
&\quad+\frac{2^{1/2}(\hbar/m)tk_+}{E_G[W(1+W)]^{1/2}}\,L_{61}^{+}\beta,\\
\psi_2&=\left(\frac{1+W}{2W}\right)^{1/2}L_{62}^{-}\beta+\frac{2^{1/2}(\hbar/m)sk_z}{E_G[W(1+W)]^{1/2}}\,L_{61}^{+}\beta\\
&\quad+\frac{2^{1/2}(\hbar/m)tk_-}{E_G[W(1+W)]^{1/2}}\,L_{61}^{+}\alpha,\\
\psi_3&=\left(\frac{1+W}{2W}\right)^{1/2}L_{61}^{+}\alpha+\frac{2^{1/2}(\hbar/m)sk_z}{E_G[W(1+W)]^{1/2}}\,L_{62}^{-}\alpha\\
&\quad-\frac{2^{1/2}(\hbar/m)tk_+}{E_G[W(1+W)]^{1/2}}\,L_{62}^{-}\beta,\\
\psi_4&=\left(\frac{1+W}{2W}\right)^{1/2}L_{61}^{+}\beta-\frac{2^{1/2}(\hbar/m)sk_z}{E_G[W(1+W)]^{1/2}}\,L_{62}^{-}\beta\\
&\quad-\frac{2^{1/2}(\hbar/m)tk_-}{E_G[W(1+W)]^{1/2}}\,L_{62}^{-}\alpha,
\end{aligned} \tag{10}$$

where

$$W=[1+(2\hbar^2s^2/m^2E_G^2)k_p^2+(4t^2\hbar^2/m^2E_G^2)k_z^2]^{1/2}$$

and $L_{62}^{-}(\alpha,\beta)$ and $L_{61}^{+}(\alpha,\beta)$ are the Kramer's pairs for the conduction and the valence band-edges respectively. The interaction of the ψ's with the far bands are treated up to second order in a $\mathbf{k}\cdot\boldsymbol{\pi}$ perturbation theory.[21]

The effect of Mn atoms is considered through the modified energy gap as a function of Mn concentration.[25] χ_d for different concentrations of Mn was calculated by using these $\mathbf{k}\cdot\boldsymbol{\pi}$ parameters in the general theory of Misra *et al.*[14,15,21] For PbTe, we obtained $\chi_d=-2.6\times10^{-7}$ emu/g which compares favorably with the experimental results.[26]

The contribution to the magnetization due to the spin density of carriers is

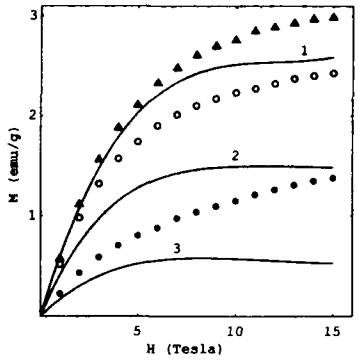

FIG. 1. Magnetization vs external magnetic field for $Pb_{1-x}Mn_xTe$ for different values of x and for a hole concentration of $5\times10^{18}/cm^3$ at 4.2 K. The closed circles (●), open circles (○), and closed triangles (▲) represent the experimental results of Anderson *et al.* (Ref. 12) and the solid curves 3, 2, and 1 represent our theoretical results for $x=0.01$, 0.022, and 0.04, respectively.

$$M_c=(n_\alpha-n_\beta)\mu_B, \tag{11}$$

and $(n_\alpha-n_\beta)$ is the spin density. In order to calculate the spin density due to holes, we consider the splitting of the valence band by an exchange interaction of the type[8]

$$H_{ex}=1/2xN_0\langle S^\mu\rangle\sigma^\mu J(r), \tag{12}$$

where μ represents Cartesian components, J is the exchange interaction strength, σ is the Pauli spin matrix, and repeated indices imply summation. The spin density is evaluated self-consistently, using a cylindrical Fermi surface for the holes.[21]

We have used the values of J_p and T_0 from Ref. 12. The energy levels and amplitudes of double group functions[17] were used from Ref. 18. The momentum matrix elements between the single group wave functions were obtained from Ref. 24. The matrix elements involving exchange interaction $J(r)$ between the band-edge states were obtained from Ref. 27. Our results for the total magnetization vs external magnetic field as a function of Mn composition are plotted in Fig. 1. The corresponding experimental results[12] are also shown in Fig. 1. The relative contributions to M in p-type $Pb_{1-x}Mn_xTe$ for different values of x and for a hole density of 5×10^{18} cm^{-3} are given in Table I. We notice that while M_s is the dominant term, M_d and M_p are equally important. However, M_c is relatively small.

The most significant aspect of our results is that the theoretical values of M, which have been calculated from first principles without any adjustable parameters, do not agree with the experimental values when either the concentration of Mn ions is very small or the magnetic field is high. Surprisingly, our results agree quite well for $x=0.04$ up to large magnetic fields. The general trend of our results follow the same pattern as the experimental results. However, the disagreement for $x=0.01$ and $x=0.02$ for high magnetic fields is quite large. It is interesting to note that similar pronounced

TABLE I. Relative strengths of different contributions to the magnetization (emu/g) in p-type $Pb_{1-x}Mn_xTe$ (hole concentration $=5\times10^{18}/cm^3$ at 4.2 K) as a function of x and magnetic field (H in T).

x	H	M_s	M_p	M_d	M_c	M_{total}	M_{exp}[a]
0.01	1	0.184	0.003	−0.018	0.000 31	0.169	0.225
	5	0.594	0.019	−0.093	0.000 79	0.521	0.803
	10	0.702	0.046	−0.181	0.000 87	0.568	1.148
	15	0.727	0.068	−0.271	0.000 88	0.525	1.389
0.022	1	0.393	0.031	−0.015	0.000 74	0.410	0.515
	5	1.178	0.174	−0.075	0.001 90	1.279	1.739
	10	1.353	0.286	−0.149	0.002 08	1.492	2.231
	15	1.390	0.314	−0.224	0.002 11	1.482	2.428
0.04	1	0.526	0.078	−0.012	0.001 49	0.594	0.583
	5	1.663	0.420	−0.058	0.003 82	2.029	2.121
	10	1.949	0.674	−0.116	0.004 18	2.511	2.769
	15	2.015	0.741	−0.174	0.004 24	2.586	2.998

[a]Reference 12.

disagreement between theory and experiment was repeatedly observed for II–VI DMS[13] even for $x=0.008$ and higher concentrations.

It may be noted that the number of paired spins is very small at low concentrations of Mn and the pairs are essentially frozen. Therefore $M_p \ll M_s$ until either the concentration increases or the magnetic field becomes substantially high. However, the long-range interaction between localized spins arises from the virtual transitions between the filled valence band and the empty conduction band. The energy levels in these bands become quantized (Landau levels) in high magnetic fields and there is also a first-order exchange shift. These will strongly affect the results of M_p when the magnetic field increases even when the Mn concentration is low.

We further note that M_p has been calculated in a two-cluster spin approximation which contributes very little at small x and low H. However, if there are a few larger clusters formed during the processing of the IV–VI DMS, their contribution to M would be very significant. We believe that the statistical mechanics of random spins[28] should be considered for a more rigorous calculation of M_s and M_p.

[1] J. K. Furdyana, J. Appl. Phys. **64**, R29 (1988).
[2] J. K. Furdyna and J. Kossut, in *Semiconductors and Semimetals*, edited by R. K. Willardson and A. C. Beer (Academic, New York, 1988), Vol. 25.
[3] G. Bauer, H. Pascher, and W. Zawadzki, Semiconduct. Sci. Technol. **7**, 703 (1992).
[4] T. Story, R. R. Galazka, R. B. Frankel, and P. A. Wolff, Phys. Rev. Lett. **56**, 777 (1986).
[5] H. J. M. Swagten, W. J. M. deJonge, R. R. Galazka, P. Warmenbol, and J. T. Devreese, Phys. Rev. B **37**, 9907 (1988).
[6] W. J. M. de Jonge, H. J. M. Swagten, S. J. E. A. Eltnik, and N. M. J. Stoffels, Semiconduct. Sci. Technol. **5**, S131 (1990).
[7] C. W. H. M. Vennix, E. Frikee, H. J. M. Swagten, K. Kopinga, and W. J. M. de Jonge, J. Appl. Phys. **69**, 6025 (1991).
[8] R. L. Hota, G. S. Tripathi, and J. N. Mohanty, Phys. Rev. B **47**, 1913 (1993).
[9] J. R. Anderson and M. Gorska, Solid State Commun. **52**, 601 (1984).
[10] M. Gorska and J. R. Anderson, Solid State Commun. **63**, 1055 (1987).
[11] G. Karczewski, M. von. Orteaberg, Z. Wilamowski, W. Dobrowolski, and J. Niewodniczanska-Zawadzka, Solid State Commun. **55**, 249 (1985).
[12] J. R. Anderson, G. Kido, Y. Nishina, M. Gorska, L. Kowalczyk, and Z. Golacki, Phys. Rev. B **41**, 1014 (1990).
[13] G. Bastard and C. Lewiner, J. Phys. C **13**, 1469 (1980).
[14] P. K. Misra and L. Kleinman, Phys. Rev. B **5**, 4581 (1972).
[15] S. K. Misra, P. K. Misra, and S. D. Mahanti, Solid State Commun. **39**, 51 (1981); Phys. Rev. B **26**, 1903 (1982).
[16] G. S. Tripathi, Phys. Lett. A **115**, 169 (1986); Phys. Rev. B **35**, 5237 (1987).
[17] D. L. Mitchell and R. F. Wallis, Phys. Rev. **151**, 581 (1966).
[18] R. L. Bernick and L. Kleinman, Solid State Commun. **8**, 569 (1970).
[19] L. Liu, Phys. Rev. B **26**, 975 (1982).
[20] G. S. Tripathi, L. K. Das, P. K. Misra, and S. D. Mahanti, Solid State Commun. **38**, 1207 (1981); Phys. Rev. B **25**, 3209 (1982).
[21] S. Misra, G. S. Tripathi, and P. K. Misra, J. Phys. C **17**, 869 (1984).
[22] C. M. Misra and G. S. Tripathi, Phys. Rev. B **40**, 11 168 (1989).
[23] R. L. Hota and G. S. Tripathi, Phys. Rev. B **44**, 1918 (1991).
[24] R. L. Hota, C. M. Misra, and G. S. Tripathi, Phys. Rev. B **45**, 10 783 (1992).
[25] N. B. Brandt and V. V. Moshchalkov, Adv. Phys. **33**, 193 (1984).
[26] S. N. Lykov and I. A. Chernic, Sov. Phys. Semiconduct. **14**, 1112 (1980).
[27] J. Niewodniczanska-Zawadazka, J. Kossut, A. Sandauer, and W. Dowrolowski, *Lecture Notes in Physics*, edited by W. Zawadzki (Springer, Berlin, 1982), Vol. 152, p. 326.
[28] M. W. Klein and R. Brout, Phys. Rev. **132**, 2412 (1963).

Effects of oxygen vacancies on magnetic properties of Ca-substituted yttrium iron garnet (abstract)

Y. J. Song, R. E. Bornfreund, G. B. Turpin, and P. E. Wigen
Department of Physics, Ohio State University, Columbus, Ohio 43210

Ca-substituted YIG samples, $Y_{3-x}Ca_xFe_5O_{12-0.5x-z}$ for $0.14 \leqslant x \leqslant 0.23$ were annealed for 6–8 h at various temperatures between 600 °C and 1000 °C in N_2 atmosphere. The magnetization barely shows any change by annealing under 900 °C but by annealing between 900 °C and 1000 °C a significant change over the temperature range from 4.2 K to the Curie temperature is observed. The lattice constant is also observed to change. The magnetization and the lattice constant of the samples did not change within experimental error by annealing in O_2 atmosphere at 1000 °C. For the sample with $x=0.23$, annealing at 1000 °C in N_2 resulted in a decrease of $4\pi M$ at 4.2 K by 560 G and a decrease of the lattice constant by 0.031 Å. The Curie temperature also changes from 531 K in the as-grown sample to 508 K for this annealing condition. The change in $4\pi M$ for various annealing conditions is linear with the change in the lattice constant. For the samples tested, the oxygen vacancies, z, in the as-grown state shows $z>0$ and that z did not change by annealing in O_2 atmosphere. A microscopic molecular field model based on the Heisenberg Hamiltonian in which a singly charged oxygen vacancy, $V_{\dot{O}}$, mediates a ferromagnetic superexchange between the iron ions at adjacent sites is proposed. The model explains the temperature dependence of $4\pi M$, the magnitude of superexchange constant mediated by $V_{\dot{O}}$ and the variation of the Curie temperature with annealing conditions. This model also explains the positive slope of $4\pi M$ at low temperature for Ca-substituted YIG.

This research is supported by ARO Grant No. DAAL03-91-G-0068.

 0021-8979/94/75(10)/5740/1/$6.00 © 1994 American Institute of Physics

Tribological studies of silicon for magnetic recording applications (Invited)

Bharat Bhushan and Vilas N. Koinkar
Computer Microtribology and Contamination Laboratory, Department of Mechanical Engineering, The Ohio State University, Columbus, Ohio 43210-1107

In the present study our objective is to investigate whether the friction and wear performance of bare silicon is adequate for disk drive application or whether certain coatings/treatments are necessary for low friction and wear. Macrotribological experiments have been performed with various pin/slider materials and magnetic disks in a modified disk drive. Microtribological studies have also been conducted on silicon using a friction force microscope. Based on macrotests, we found that the friction and wear performance of bare silicon is not adequate. With single and polycrystalline silicon, transfer of amorphous carbon from the disk to the pin/slider and oxidation-enhanced fracture of pin/slider material followed by oxidation of the transfer coating (tribochemical oxidation) is responsible for degradation of the sliding interface and consequent friction increase in ambient air. With dry-oxidized or plasma-enhanced chemical-vapor deposition-SiO_2-coated silicon, no significant friction increase or interfacial degradation was observed in ambient air. In the absence of an oxidizing environment (in dry nitrogen), the coefficient of friction decreased from 0.2 to 0.05 following amorphous carbon transfer for the materials tested. Nanoscratching/nanowear and nanoindentation studies also indicate that coated silicon is superior to bare silicon. Macro- and microcoefficient of friction values of all samples is found to be about the same with the microvalues lower than the macrovalues. Based on this study, we conclude that coated silicon is an excellent candidate for the construction of magnetic head sliders.

I. INTRODUCTION

The advantages of miniaturization and low cost are resulting in an increasing use of silicon (Si) as a mechanical material.[1,2] Read-write sliders made of silicon have been fabricated using integrated circuit technology.[3,4] Integrated circuit technology offers the advantages of low cost and high volume production. However, limited data exist on the tribological behavior of Si as to be used in the disk drives.[4–9] In the present study our objective is to evaluate the friction and wear performance of Si with and without coatings and surface treatments, in sliding contact with lubricated and unlubricated amorphous carbon coated thin-film disks for potential use as a slider material.[10] Results from experiments performed with commonly used slider materials (Al_2O_3-TiC and Mn-Zn ferrite) are also presented for comparison.

To further understand the tribological properties of Si material, microtribological tests were conducted on the bare and treated Si. Nanoscratching/wear, nanoindentation, and microfriction measurements have been made using a friction force microscope.[11–13] Results of macro- and microtribological studies are the subject of this paper.

II. EXPERIMENTAL

Macrotribological experiments have been performed with various pin/slider materials and magnetic disks in a modified disk drive.[5] The normal load used in the experiments was 0.15 N and the sliding speeds at track radii ranging from 45 to 55 mm varied from 0.9 to 1.2 m/s. At these speeds the pin remained in contact throughout the period of testing to simulate start/stop conditions.[10]

Microtribological experiments have been performed using a friction force microscope (FFM), to conduct studies of scratching, wear, indentation, and friction.[11,13] Simultaneous measurements of friction force and surface roughness can be made using this instrument. A single-crystal natural diamond tip was used for nanoscratch, nanowear, and nanoindentation measurements at relatively higher loads (10–150 μN). The tip was ground to the shape of a three-sided pyramid with an apex angle of 80° whose point was sharpened to a radius of about 100 nm. The tip was mounted on a stainless steel beam with a normal stiffness of about 25 N/m.[12,13] A microfabricated Si_3N_4 tip on a beam with a stiffness of 0.4 N/m (at a normal load 10–150 nN) was used for topographic imaging and friction force measurements. The tip was square pyramidal with a tip radius of about 30 nm.

For scratching and wear, the sample was scanned in a direction orthogonal to the long axis of the cantilever beam at a scanning speed of 1 μm/s. For wear, an area of 2 μm×2 μm was scanned. The operation procedures for nanoindentation were similar to those used for nanowear except that the scan size was set to zero in the case of nanoindentation, in order for the tip to continuously press the sample surface for about 2 s. Sample surfaces were scanned before and after the scratch, wear or indentation to obtain the initial and the final surface topography at a load of about 0.5 μN, over an area larger than the affected region to observe the scratch or wear scars or indents. Nanohardness was calculated by dividing the indentation load by the projected residual area. For measurement of friction force, the sample was scanned over 500 nm×500 nm area in a direction orthogonal to the long axis

 0021-8979/94/75(10)/5741/6/$6.00 © 1994 American Institute of Physics

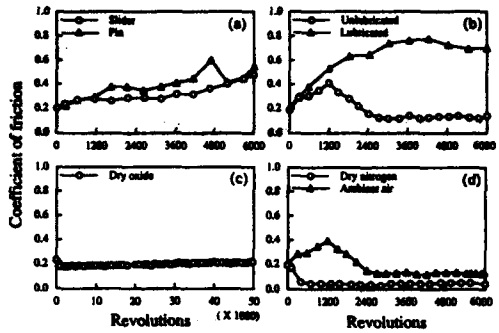

FIG. 1. Variation of the coefficient of friction with number of sliding cycles in ambient air (a) Al_2O_3-TiC pin and slider against a lubricated disk, (b) Si (111) pin against a lubricated and unlubricated disk, (c) dry-oxidized Si pin against a lubricated disk, (d) Si (111) against a lubricated disk in ambient air and dry nitrogen.

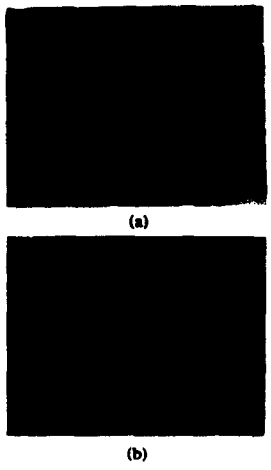

FIG. 2. Scanning electron microscopy micrographs of Si (111) after sliding against a lubricated disk in (a) ambient air for 6000 cycles, and (b) in dry nitrogen after 15 000 cycles.

of the cantilever beam with a scan rate of 5 Hz (scanning speed of 5 μm/s).

The disks used in the macroexperiments were commercially available 130-mm-diam thin-film rigid disks.[5] The unlubricated disks did not contain the lubricant coating. The pins and wafers used in the macroexperiments were made of single and polycrystalline Si, Mn-Zn ferrite, and Al_2O_3-TiC.[5] Single-crystal Si of (111), (110), and (100) orientations were tested. The grain size of the polycrystalline Si samples was about 5 mm. Commercial full size sliders (rail dimensions: 3.6 mm×0.4 mm) were also used in the experiments.[10] Besides virgin silicon pins, thermally oxidized (under both wet and dry conditions), plasma-enhanced chemical-vapor deposition (PECVD) oxide coated and ion implanted Si (111) were also tested.[5] The thickness of the thermal oxide on the silicon pins used in the present investigation was about 0.5 μm for dry oxidation and about 1 μm for wet oxidation. The oxide on the PECVD coated pins was about 5 μm thick and the film surface was polished using a lapping tape. Single-crystal Si pins of orientation (111) ion implanted with C^+ ions at 2–4 mA cm^{-2} current densities, 100 keV accelerating voltage, and at a fluence of 1×10^{17} ions cm^{-2} were also tested. Si pins used for macrotribological studies were also used for microtribological studies.

TABLE I. Macro friction data for various pin materials sliding against thin-film rigid disks in ambient air. Normal load=0.5 N; sliding speed=0.9–1.2 m/s; ambient air (R.H. 45±5%).

Pin material	Initial coeff. of friction		Cycles to friction increase by factor of 2		Max. or ending value of coeff. of friction	
A_2O_3-TiC	0.20	lubed	~2 200	lubed	0.78	lubed
	0.25	unlubed	~200	unlubed	0.78	unlubed
Mn-Zn ferrite	0.22	lubed	~5 500	lubed	0.45	lubed
	0.22	unlubed	~600	unlubed	0.68	unlubed
Single-crystal	0.20	lubed	~1 200	lubed	0.40	lubed
silicon	0.20	unlubed	~500	unlubed	0.70	unlubed
Polysilicon	0.20	lubed	~3 000	lubed	0.60	lubed
	0.22	unlubed	~1 000	unlubed	0.50	unlubed
PECVD-oxide-	0.28	lubed	>50 000	lubed	0.23–0.28	lubed
coated Si (111)	0.28	unlubed	~500	unlubed	0.72	unlubed
Dry-oxidized	0.22	lubed	>50 000	lubed	0.20	lubed
Si (111)	0.22	unlubed	~1 600	unlubed	0.56	unlubed
Wet-oxidized	0.26	lubed	>50 000	lubed	0.26–0.40	lubed
Si (111)	0.26	unlubed	~1 000	unlubed	0.60	unlubed
C^+-implanted	0.16	lubed	~1 000	lubed	0.60	lubed
Si (111)	0.25	unlubed	~1 000	unlubed	0.50	unlubed

III. RESULTS AND DISCUSSION

A. Macrotribological studies

Sliders are expensive to produce compared to pins and hence it would be advantageous to conduct tribotesting with pins. This requires that pin and slider tribological behavior be similar, so that results from tribotesting with pins can serve as a useful guide in the choice of slider material. The variation of the coefficient of friction (μ) with number of sliding cycles for an alumina/titanium-carbide pin and slider tested under the same load-speed-environment conditions is shown in Fig. 1(a). The results suggest that the frictional

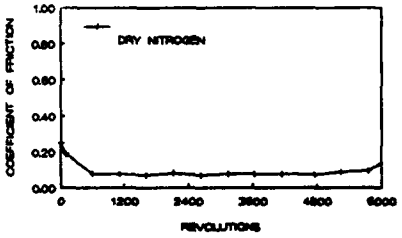

FIG. 3. Variation of the coefficient of friction with number of sliding cycles in dry nitrogen for a DLC coated silicon pin sliding against a lubricated disk.

TABLE II. rms, microfriction, nanoscratching/nanowear, and nanoindentation hardness data for various virgin coated and treated silicon samples.

Material	Rms roughness, scan size; 500 nm × 500 nm	Coeff. of friction	Scratch depth at 40 μN (nm)	Wear depth at 40 μN (nm)	Hardness at 100 μN (GPa)
Si (111)	0.11	0.03	20	27	11.7
Si (110)	0.09	0.04	20		
Si (100)	0.12	0.03	25		
Polysilicon	1.07	0.04	18		
Polysilicon (lapped)	0.16	0.05	18	25	12.5
PECVD-oxide-coated Si (111)	1.50	0.01	8	5	18.0
Dry-oxidized Si (111)	0.11	0.04	16	14	17.0
Wet-oxidized Si (111)	0.25	0.04	17	18	14.4
C^+-implanted Si (111)	0.33	0.02	20	23	18.6

behavior of pins is reasonably similar to that of sliders.

The objective of this study was to evaluate the potential of using Si as a slider material. A failure criteria was established which was that a significant increase in friction with number of revolutions was considered a failure since an increase in friction implies some degradation of the interface. In the present investigation it was observed that for Si sliding against lubricated thin-film disks, μ was 0.2 at the start of sliding and increased to 0.4 before decreasing to a steady state value of 0.1. Using this as a standard for comparison the number of revolutions before the friction increased by a factor of 2 was taken to be indicative of the contact life or durability of the slider-disk interface for the various tests

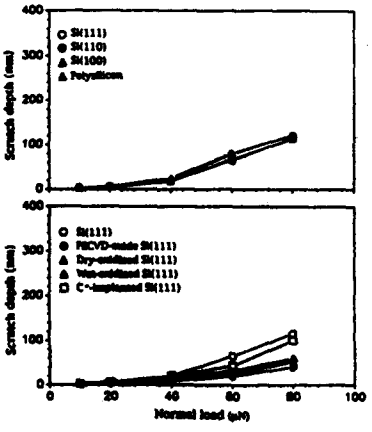

FIG. 4. Scratch depth as a function of load after ten cycles for virgin, treated, and coated Si surfaces.

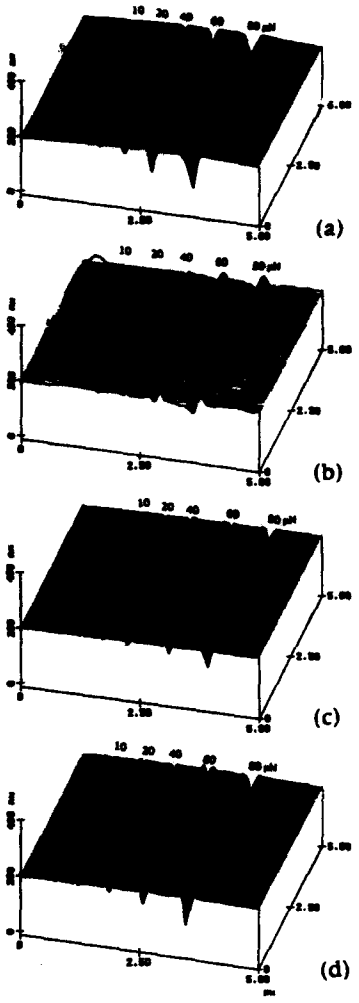

FIG. 5. Surface profiles for scratched (a) Si (111), (b) PECVD-oxide coated Si (111), (c) dry-oxidized Si (111), and (d) C^+-implanted Si (111). The loads used for various scratches at ten cycles are indicated in the plot.

conducted. For quick reference, friction data obtained from the various tests conducted in ambient air in terms of the initial μ, the contact life, i.e., the number of revolutions before the μ increased by a factor of 2, the maximum value of the μ for cases when the increase was more than by a factor of 2 are presented in Table I. For the case of oxidized samples a significant increase (by a factor of 2 or more) was not observed and so the range of variation of the μ for the duration of 50 000 cycles is indicated.

The variation of the coefficient of friction with sliding cycles for Si(111) sliding against lubricated and unlubricated disks in air is shown in Fig. 1(b). Crystalline orientation of Si has no effect on friction and wear. Scanning electron micros-

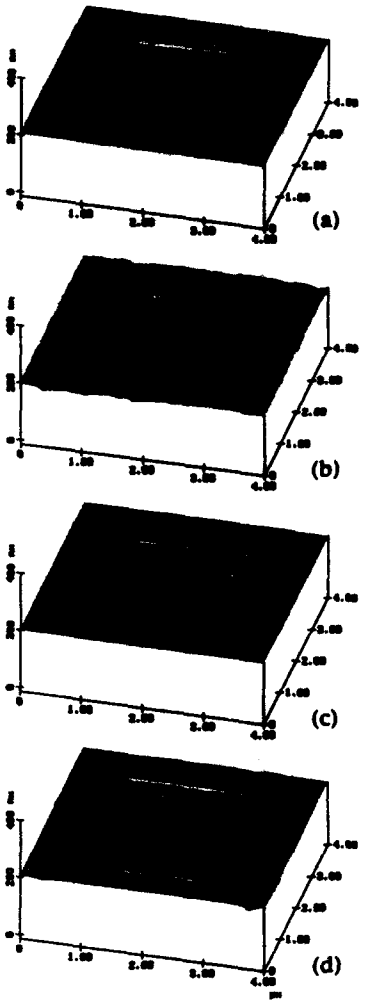

FIG. 6. Surface profiles showing the worn region (center 2 μm×2μm) after one cycle of wear at 40 μN load (a) Si (111), (b) PECVD-oxide coated Si (111), (c) dry-oxidized Si (111), and (d) C^+-implanted Si (111).

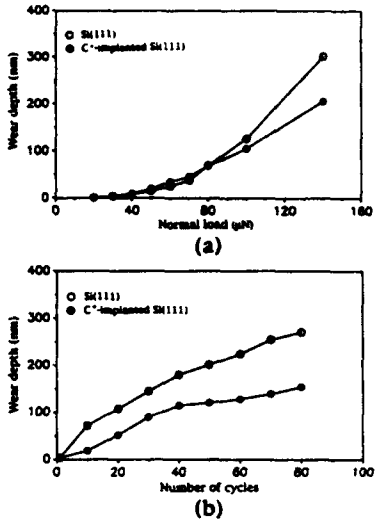

FIG. 7. Wear depth as a function of (a) load (after one cycle), and (b) cycles (normal load=40 μN) for Si (111) and C^+-implanted Si (111).

copy (SEM) and chemical analysis using energy dispersive analysis of x rays suggested that the rise in the μ and damage on the pin surface for Si(111) is associated with the transfer of amorphous carbon from the disk to the pin, oxidation-enhanced fracture of pin material followed by tribochemical oxidation of the transfer film. Against lubricated disks the μ drops to a steady state value of 0.1 following the increase as seen in Fig. 1(b). This is associated with the formation of a transfer coating on the pin, Fig. 2(a). The mechanism of transfer and tribochemical oxidation was seen to be operative for the friction increase for Al_2O_3-TiC and Mn-Zn ferrite pin/slider materials tested in ambient air. As seen in Table I and Fig. 1(c), dry oxidized Si(111) exhibits excellent characteristics in lubricated sliding and this behavior has been attributed to the chemical passivity of the oxide and lack of transfer of diamondlike carbon (DLC) from the disk to the pin. The behavior of PECVD was comparable to that of dry oxide but for the wet oxide there was some variation in the μ (0.26–0.4). The difference between dry and wet oxide has been attributed to increased porosity of the wet oxide.[5,14]

Since tribochemical oxidation was determined to be a significant factor, experiments were conducted in dry nitrogen. The variation of the μ for a Si pin sliding against a lubricated thin-film disk is shown in Fig. 1(d). For comparison the behavior in ambient is also shown. It is seen that in a dry nitrogen environment the μ of Si(111) sliding against lubricated disks decreased from an initial value of about 0.2 to 0.05 with continued sliding. Similar behavior was also observed while testing with Al_2O_3-TiC and Mn-Zn ferrite pins and sliders. With unlubricated disks though the friction decrease was not observed. Based on SEM and chemical analysis this behavior has been attributed to the formation of a smooth amorphous-carbon/lubricant transfer patch and suppression of oxidation in a dry nitrogen environment, Fig. 2(b).

The experiments in dry nitrogen indicated that low friction conditions can be achieved in dry nitrogen although transfer of carbon from the disk to the pin occurs. An experiment was performed with a hydrogenated amorphous carbon coated (~18 nm thick) Si pin sliding against a lubricated thin-film disk in dry nitrogen. The friction variation with sliding for this experiment is shown in Fig. 3. No damage for the pin and disk surfaces could be detected after this experiment.

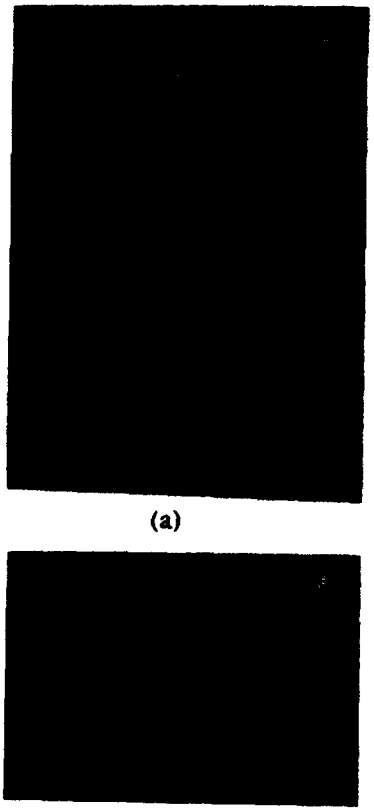

FIG. 8. Gray-scale plot and line plot of the *inverted* nanoindentation mark on (a) Si (111) at 70 μN (hardness~15.8 GPa), and (b) gray-scale plot of indentation mark on C^+-implanted Si (111) at 70 μN (hardness~19.5 GPa). The indentation depth of indent was about 3 nm.

B. Microtribological studies

A summary of rms, microscale friction, nanoscratching, nanowear, and nanohardness data for various samples is presented in Table II. Virgin and modified Si surfaces could be scratched at 10 μN load, see Figs. 4 and 5 and Table II. Scratch depth increased with an increase in load. We note that crystalline orientation of Si has little influence on the scratch depth, similar to observations made in macrotribological tests. PECVD-oxide samples had the largest scratch resistance followed by dry-oxidized, wet-oxidized, and ion-implanted samples. Ion implantation showed no improvements on the scratch resistance. By scanning the sample (in two dimension) while scratching, wear scars were generated on the sample surface. Wear data on selected samples are presented in Table II and the wear profiles at 40 μN of load are shown in Fig. 6. PECVD-oxide samples had the largest wear resistance followed by dry-oxidized, wet-oxidized, and ion-implanted samples. These results are consistent with the macrotribological data. We observed wear debris in the wear zone just after the wear test which could be easily removed by scanning the worn region. It suggests that wear debris is loose.

We further studied the wear resistance of ion-implanted samples, Fig. 7. For tests conducted at various loads on Si (111) and C^+-implanted Si (111), we find that wear resistance of implanted sample is slightly poorer than that of virgin Si up to about 80 μN. Above 80 μN, the wear resis-

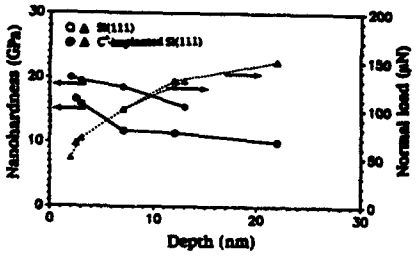

FIG. 9. Nanohardness and normal load as function of indentation depth for virgin and C^+-implanted Si (111).

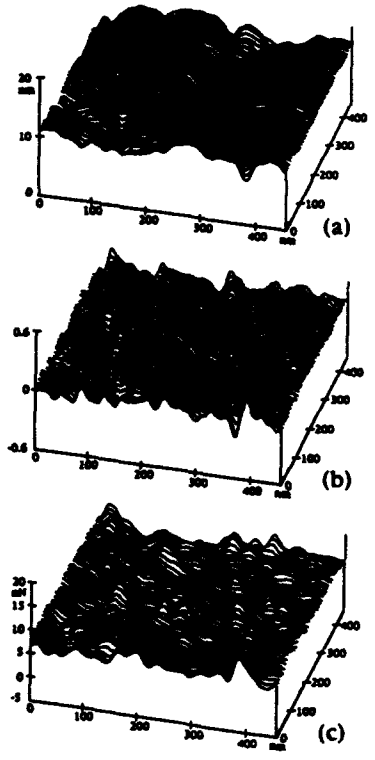

FIG. 10. Surface roughness profile (σ=1.07 nm), (b) slope of the roughness profile along the sample sliding direction (the horizontal axis) (mean=−0.02, σ=0.05), and friction profile (mean=5.8 nN, σ=1.3 nN) of rough polysilicon for a normal load of 140 nN.

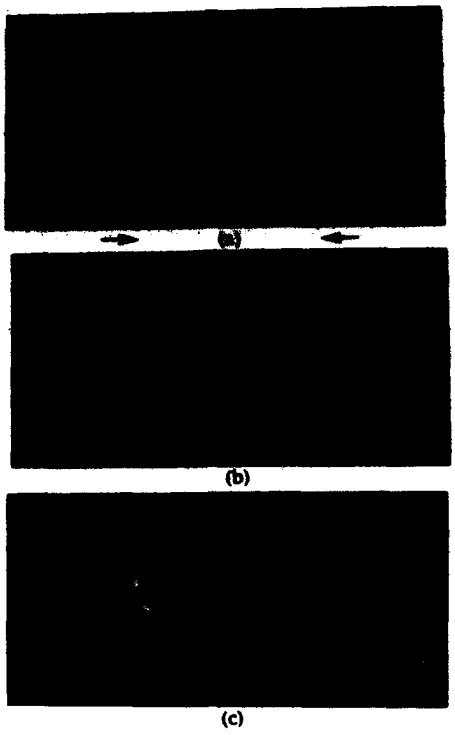

FIG. 11. Gray-scale plots of (a) the slope of the surface roughness, (b) the friction, and (c) the friction (with sign reversed in the right-hand side profile) of a Si (111). The left-hand side of the figure corresponds the sample sliding from left to right. Higher points are shown by lighter color.

tance of implanted Si improves. As we continue to run tests at 40 μN for larger number of cycles, the implanted sample exhibits higher wear resistance than the unimplanted sample. Miyamoto *et al.*[15] have also reported that damage from the implantation in the top layer results in poorer wear resistance, however, the implanted zone at the subsurface is more wear resistant than the virgin Si.

We measured nanoindentation hardness of all samples, Table II. Coatings and treatments improved nanohardness of Si. We note that dry-oxidized and PECVD films are harder than wet-oxidized films as these films may be porous.[5] High hardness of oxidized films may be responsible for measured low wear on macro- and microscale. Figure 8 shows the indentation marks generated on virgin and C^+-implanted Si (111) at a normal load of 70 μN with a depth of indentation about 3 nm and hardness values of 15.8 and 19.5 GPa, respectively. Hardness values of virgin and C^+-implanted Si (111) at various indentation depths (normal loads) are presented in Fig. 9. Hardness value of C^+-implanted Si (111) at a normal load of 50 μN is 20.0 GPa with an indentation depth of about 2 nm which is comparable to the hardness value of 19.5 GPa at 70 μN. Measured hardness value for virgin Si at an indentation depth of about 7 nm (normal load of 100 μN) is about 11.7 GPa, comparable to nanohardness values reported by others.[16] We note that the surface layer of the implanted zone is much harder compared to the subsurface, and may be brittle leading to higher wear on the surface. Subsurface of the implanted zone is harder than the virgin silicon, resulting in higher wear resistance.

From the data presented in Tables I and II, we note that macro- and microcoefficient of friction values of all samples are about the same with the microvalues lower than the macrovalues. Roughness effects on the friction of polysilicon can be clearly observed. Next we examine the relationships between friction and roughness profiles, Fig. 10. We find that there is no resemblance between the μ profiles and the corresponding roughness profiles, e.g., high or low points on the friction profile do not correspond to high or low points on the roughness profiles. We calculated the slope of the roughness profile in the tip sliding direction. By comparing the resulting slope profile and corresponding friction profiles, we observe a strong correlation between the two. Surface slope and friction profiles obtained with sample sliding in either direction are shown in Fig. 11. We again note the resemblance between local variations in the surface slope and local variations in friction. We further note the *directionality* in friction. Bhushan and Ruan[12] have shown that the local variation in friction arises from a "ratchet" mechanism. According to this mechanism, friction increases as the FFM tip slides over the leading (ascending) edge of asperity because of a positive surface slope. Friction decreases during sliding over the trailing (descending) edge of the asperity as the slope is negative. The ratchet mechanism thus explains the correlation between the slopes of the roughness profiles and friction profiles observed in Fig. 10. Since the local friction is a function of the local slope of sample surface, the local variation in friction should be of the opposite sign as the scanning direction is reversed. In Fig. 11(c), the sign of friction in one direction is reversed, but we still see some difference in the two friction profiles which may result from the asymmetrical asperities.

[1] K. E. Petersen, Proc. IEEE **70**, 420 (1982).
[2] B. Bhushan and S. Venkatesan, Adv. Info. Storage Systems **5**, 211 (1993).
[3] J. P. Lazzari and P. Deroux-Dauphin, IEEE Trans. Magn. **MAG-25**, 3190 (1989).
[4] B. Bhushan, M. Dominiak, and J. P. Lazzari, IEEE Trans. Magn. **MAG-28**, 2874 (1992).
[5] B. Bhushan and S. Venkatesan, J. Mater. Res. **8**, 1611 (1993).
[5] S. Venkatesan and B. Bhushan, Adv. Info. Storage Systems **5**, 243 (1993).
[7] S. Venkatesan and B. Bhushan, Wear **171**, 25 (1994).
[8] B. K. Gupta, J. Chevallier, and B. Bhushan, J. Trib. Trans. ASME **115**, 392 (1993).
[9] B. K. Gupta, J. Chevallier, and B. Bhushan, Trib. Trans. (*in press*).
[10] B. Bhushan, *Tribology and Mechanics of Magnetic Storage Devices* (Springer, New York, 1990).
[11] J. Ruan and B. Bhushan, J. Trib. Trans. ASME (in press).
[12] B. Bhushan and J. Ruan, J. Trib. Trans. ASME (in press).
[13] B. Bhushan, V. N. Koinkar, and J. Ruan, J. Eng. Trib. Proc. J Mech. E **208**, 17 (1994).
[14] W. A. Pliskin, J. Vac. Sci. Technol. **14**, 1064 (1977).
[15] T. Miyamoto, S. Miyake, and R. Kaneko, Wear **162–163**, 733-738 (1993).
[16] G. M. Pharr, W. C. Oliver, and D. R. Clarke, J. Electron. Mater. **19**, 881 (1990).

Mathematical modeling of lubrication for the head-disk interface using incompressible fluids

Paul R. Peck and Myung S. Jhon
Department of Chemical Engineering, Carnegie Mellon University, Pittsburgh, Pennsylvania 15213

Ralph F. Simmons, Jr. and Thomas J. Janstrom
Disk Memory Division, Hewlett-Packard Co., Boise, Idaho 83707

In order to keep pace with the demand for higher storage densities in magnetic recording disk drives, new technology must be developed to reduce the tribological problems associated with ultralow flying. Non-Newtonian liquid bearings may become a feasible alternative to slider miniaturization due to the decrease in slider-disk contacts. Issues pertaining to modeling the head-disk interface are presented, and non-Newtonian effects are described. Generalized Newtonian fluid models describe the dependence of the apparent viscosity on the shear rate for bulk fluids, but the extremely high shear rate and the confined geometry at ultralow flying heights complicate conventional non-Newtonian rheological models. Equations are developed for generalized Newtonian fluids which can determine the flying characteristics of recording sliders in viscoelastic drives. Order-of-magnitude analyses are performed in order to determine the effect of drive parameters and fluid properties on the load bearing capacity of the slider and power consumption due to frictional forces. The results obtained are new and may become important in providing design criteria for VISqUS drives or to related design engineers.

I. INTRODUCTION

As high-density recording becomes a major headline for disk drive manufacturers, the technology of ultralow flying (less than two microinches in head-disk separation) becomes critically important. Decreasing the flying height increases the storage density, but it also increases the tribological problems at the head-disk interface (HDI). The current generation of drives operates in almost a full flying mode with limited intermittent contacts between the slider and the disk surface. In order to achieve the demanded storage densities, however, the next generation drives will most likely operate in a region of mixed flying and/or sliding. This mixed region will produce significantly more wear during normal operation unless technologies are implemented to decrease the number and severity of head-disk contacts.

There are many possible technologies being developed which could achieve high-density recording while reducing the tribological problems of wear. Miniaturization of current air-bearing sliders produces lower-flying heights while minimizing the impact force of head-disk collisions.[1] The limitation of miniaturization seems to be the tooling costs and precision of fabricating extremely small sliders (less than 20% of a full 3370-type slider) and integration problems associated with the suspension and electrical leads. An alternative to this approach is to use an incompressible liquid film as the lubrication layer instead of a conventional air bearing.[2,3] The main advantage of using a viscoelastic liquid bearing (VLB) is the absence of contacts with the disk, which limits the severity of the tribological and tribochemical problems. This VLB technology, known commercially as VISqUS, could be advantageous for small form factor devices containing a single disk, and a high-performance 500 megabyte drive operating at less than 1 W power consumption could be feasible. Integration problems will be a major hurdle to overcome in order for this technology to be commercially feasible. In contrast to conventional air-bearing technology, however, there are very few theoretical tools available for designing ultralow incompressible film drives. The objective of this article is to develop qualitative models and to discuss issues relating to VLB drives, rather than developing full-scale numerical simulation capabilities.

II. THEORETICAL DEVELOPMENT

The governing equation for the stress distribution underneath the bearing surface of a slider is derived from the equation of motion (Navier–Stokes equation for Newtonian fluids) using the lubrication approximation and conservation of mass. Conventional bearings operate in an ambient air environment and are well established,[4] while VISqUS-type drives use a non-Newtonian liquid for the lubrication layer. Equations are developed below to describe the characteristics of the HDI that are applicable to these viscoelastic fluids. The local velocity profile, v_x and v_y, can be expressed in terms of the normalized nth moment of fluidity, $\Gamma_n(z)$ which is defined as

$$\Gamma_n(z)=\frac{\int_0^z \xi^n/\eta(\xi)\,d\xi}{\int_0^h \xi^n/\eta(\xi)\,d\xi}. \tag{1}$$

Here η is the position-dependent apparent viscosity and h is the film thickness. By neglecting inertial and external forces in the equation of motion, (i.e., $\nabla P=-\nabla\cdot\tau(\dot\gamma)$, where P is the fluid pressure and τ is the deviatoric stress tensor which is a function of the shear rate $\dot\gamma$),[5] the resulting velocity profile is obtained:

$$v_x=\frac{\partial P}{\partial x}\,[\Gamma_1(z)-\Gamma_0(z)]\int_0^z\frac{\xi}{\eta(\xi)}\,d\xi+V_x[1-\Gamma_0(z)],$$

and

$$v_y=\frac{\partial P}{\partial y}\,[\Gamma_1(z)-\Gamma_0(z)]\int_0^z\frac{\xi}{\eta(\xi)}\,d\xi+V_y[1-\Gamma_0(z)], \tag{2}$$

 0021-8979/94/75(10)/5747/3/$6.00 © 1994 American Institute of Physics

where V_x and V_y are the x and y components of the relative disk velocity. This velocity profile can be integrated across the film thickness to yield an equation which determines the pressure (related to the density ρ) or normal stress component

$$\int_0^h \left(\frac{\partial \rho}{\partial t} + \frac{\partial(\rho v_x)}{\partial x} + \frac{\partial(\rho v_y)}{\partial y} \right) dz = 0. \tag{3}$$

For Newtonian fluids (such as nonconfined air), the apparent viscosity is homogeneous over the entire film, and the classical Reynolds equation is obtained (assuming isothermal conditions) from Eqs. (1)–(3). For non-Newtonian fluids, the apparent viscosity depends on the shear rate, which is a function of position and velocity. Therefore, Eqs. (1) and (2) should be included in mathematical models in order to capture the spatial variation of η. This adds extra complexity to the formulation of a closed-form Reynolds type of equation.[5] Note that for air bearings, η can also be thought of as position dependent, since the apparent slip[6] at the surfaces (originating from gaseous rarefaction effects) modifies the bulk or continuum viscosity.

Due to the nonlinearity of Eqs. (2) and (3) and the complicated shape of the slider rails, numerical solutions are required to solve for the pressure distribution. For the air-bearing case, a large number of numerical simulations have been reported.[7–11] For the VLB case, we discuss qualitative aspects of the mathematical models. Once the pressure (or normal stress) distribution is obtained, a load bearing capacity W defined as

$$W = \int\int (\pi_{zz} - P_{amb}) dA \tag{4}$$

can be calculated, where π_{zz} is the normal component of the total stress tensor $[\pi_{zz} = P + \tau_{zz}(\dot{\gamma})]$ of the fluid and P_{amb} is the ambient pressure. Note that for generalized Newtonian fluids, $\tau_{zz} = 0$. This value determines the force that the slider can support while operating at a given height. In addition to W, the frictional drag force on the slider F is also an important design variable in order to minimize power consumption P_c in liquid bearing drives. F of the fluid can be obtained from,

$$\mathbf{F} = \int\int \tau(\dot{\gamma}) \cdot d\mathbf{A}, \tag{5}$$

and P_c due to the fluid may be computed as

$$P_c = \int\int [\tau(\dot{\gamma}) \cdot \mathbf{v}] \cdot d\mathbf{A}. \tag{6}$$

These additional quantities, F and P_c, are usually not studied in air-bearing modeling but are especially important in designing VLB drives.

Although numerical solutions to Eqs. (2) and (3) are possible, a simple order-of-magnitude analysis on Eqs. (4) and (6) can capture most of the essential dependencies of the load-bearing capacity and power consumption on the operating parameters and fluid properties. For a generalized Newtonian fluid, by replacing the pressure difference in Eq. (4) by an integrated pressure derivative, one can obtain

$$W \propto R_f^3 \frac{\partial \dot{\gamma}}{\partial z} \eta(\dot{\gamma}) \left(\frac{d[\log \eta(\dot{\gamma})]}{d(\log \dot{\gamma})} + 1 \right), \tag{7}$$

where R_f is a reduction factor for the slider (i.e., $R_f = 0.5$ corresponds to a 50% slider). The dependence of the load-bearing capacity on molecular or operating variables can be determined using Eq. (7) and either rheological measurement data (usually expressed in log η vs log $\dot{\gamma}$ form) or a constitutive equation describing the functionality of these quantities (e.g., power-law model of Ostwald[12] and de Waele[12] or Carreau–Yasuda's five-parameter model[13]). An order-of-magnitude equation can also be obtained for the power consumption,

$$P_c \propto R_f^2 v_x \eta(\dot{\gamma}) \dot{\gamma}. \tag{8}$$

Equations (7) and (8) constitute the primary results obtained so far to predict drive performance. Even though the results appear simple, they may provide qualitative design criteria for VLB.

III. NON-NEWTONIAN CONSTITUTIVE MODELS

To illustrate the essence and utility of Eqs. (7) and (8), the two-parameter (m and n) power-law model,[12] $\eta = m\dot{\gamma}^{n-1}$, can be used for the viscosity, shear rate relationship. When $n = 1$, the Newtonian fluid model is recovered (applicable to air bearings). If $n < 1$, the fluid is described as "pseudoplastic" or "shear thinning" (applicable to VLB technology), and if $n > 1$, the fluid is described as "dilatant" or "shear thickening" (not useful for drive applications). Applying Eq. (7) to the power-law fluid, recognizing the order-of-magnitude approximation, $\dot{\gamma} \propto v/h$ and $\partial\dot{\gamma}/\partial z \propto v/h^2$, a scaling equation is derived as

$$W(m,n) \propto \frac{R_f^3 m n (v/h)^n}{h}. \tag{9}$$

This result was compared with a finite-element simulation code for Newtonian fluids, and showed excellent agreement.[14] Equation (9) relates the load-bearing capacity to the disk velocity v, film thickness h, and the rheological properties of the film (through the parameters m and n). In a similar manner, the dependence of P_c on the operating and molecular parameters can be derived as

$$P_c(m,n) \propto R_f^2 m v (v/h)^n. \tag{10}$$

Figure 1 shows the dependence of W and P_c, normalized to a Newtonian fluid, on n for differing values of the shear rate (v/h). As the fluid has more shear thinning behavior (decreasing n) the load-bearing capacity for a given film thickness and disk velocity decreases. There is also a corresponding increase in the power consumption as n is decreased. These phenomena increase in magnitude as the shear rate is increased.

For a given fluid, the order of magnitude equations can be used to determine the effect of operating parameters on drive performance. Figure 2 shows an increase in power consumption, as expected, when the disk velocity is increased. The increase, however, is not as severe as the fluid becomes more shear thinning. This is a major advantage of using non-Newtonian fluids for the lubricating layer. Equation (9) can

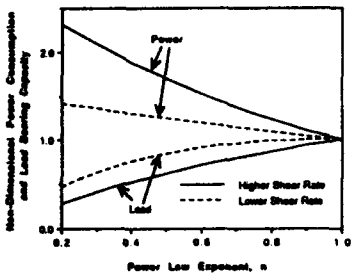

FIG. 1. W and P_c as a function of the power-law exponent n for two different shear rates. Values are normalized with respect to a Newtonian fluid.

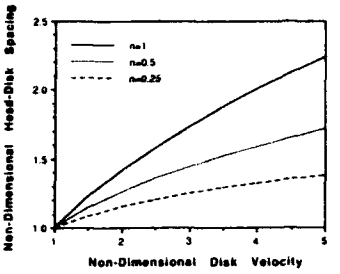

FIG. 3. Nondimensional head-disk spacing as a function of nondimensional relative disk velocity at constant normal load for three different values of n.

also capture relationships between drive operating parameters, such as the dependence of the film thickness on disk velocity as shown in Fig. 3.

IV. DISCUSSION AND SUMMARY

Mathematical modeling capabilities are critical for designing a VLB disk drive. Valuable time and effort could be saved if simulations are accurate enough to predict the performance of the HDI before test drives are constructed. In order for the simulations to be accurate, the physics of a thin film of non-Newtonian fluid undergoing high shear rates must be incorporated correctly. The order-of-magnitude approximations presented above were based on the simplest generalized Newtonian fluid model, namely the power-law model. Rigorous constitutive stress-strain relationships should include normal stress, stress overshoot phenomena, surface tension, and the effect of a confined geometry.

There is great concern about the applicability of bulk rheological equations of state in accurately describing the physics occurring in a confined geometry.[15] The apparent viscosity in bulk fluids is only a function of $\dot{\gamma}$. When a fluid is confined to an ultralow spacing h, the apparent viscosity will take a functional form of $\eta(\dot{\gamma},h)$. One possible form of η in a confined geometry can be modeled by separating the shear rate and geometric effects, $\eta(\dot{\gamma},h)=\eta_b(\dot{\gamma})f(h)$, where

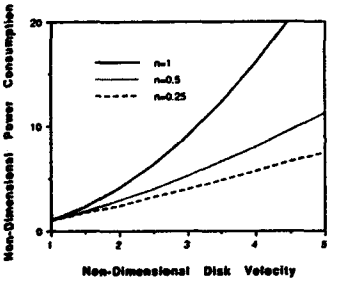

FIG. 2. Nondimensional power consumption P_c as a function of nondimensional relative disk velocity at constant normal load for three different values of n.

$f(h)$ is a function which could be determined experimentally. Models for $\eta_b(\dot{\gamma})$, such as various generalized Newtonian models,[12,13,16] may be used for the bulk viscosity in this functional form.

Many polymer films exhibit normal stress effects under high shear rate conditions due to stretching of the polymer chains. Under extremely high shear, polymers may also degrade. Fluids also exhibit an overshoot phenomena, implying that the stress is dependent on time or its history of deformation. These microrheological effects have not yet been thoroughly studied and applied to VLB applications.

With a combination of order-of-magnitude analyses and numerical simulations using a physically realistic viscoelastic constitutive equation, accurate predictions on VLB drive performance could be obtained. The new results presented [Eqs. (7) and (8)] provide qualitative insight into the behavior of VLB drives. A state-of-the-art finite-element algorithm[7] can be used to numerically evaluate Eqs. (2) and (3) for comparisons with drive performance.

ACKNOWLEDGMENT

This work was supported in part by the National Science Foundation under grant # ECD-8907068.

[1] M S. Jhon, P. R. Peck, R. F. Simmons, Jr., and T. J. Janstrom, IEEE Trans. Magn. (to be published).
[2] J. U. Lemke and W. W. Peach, U.S. Patent No. 5,193,046 (1993).
[3] J. S. Foster and A. M. Homola, European Patent No. 0522714A2 (1993).
[4] R. M. Crone, M. S. Jhon, T. E. Karis, and B. Bhushan, Adv. Info. Storage Syst. 4, 105 (1992).
[5] P. Yang and S. Wen, ASME J. Trib. 114, 81 (1992).
[6] A. Burgdorfer, ASME J. Basic Eng. 81, 94 (1959).
[7] R. M. Crone, Ph.D. thesis, Carnegie Mellon University, Pittsburgh, PA, 1992.
[8] S. Fukui and R. Kaneko, ASME J. Trib. 110, 253 (1988).
[9] O. J. Ruiz and D. B. Bogy, ASME J. Trib. 112, 593 (1990).
[10] Y. Mitsuya, ASME J. Trib. 115, 289 (1993).
[11] J. White and A. Nigam, ASME J. Lub. Tech. 102 (1980).
[12] W. Ostwald, Kolloid-Z. 36, 99 (1925); A. de Waele, Oil Color Chem. Assoc. J. 6, 33 (1923).
[13] P. J. Carreau, Ph.D. thesis, University of Wisconsin, Madison, WI, 1968; K. Yasuda, Ph.D. thesis, Massachusetts Institute of Technology, Cambridge, MA, 1979.
[14] R. M. Crone, P. R. Peck, M. S. Jhon, and T. E. Karis, ASME J. Trib. 115 566 (1993).
[15] S. Granick, Science 253, 1374 (1991).
[16] R. B. Bird, R. C. Armstrong, and O. Hassager, *Dynamics of Polymeric Liquids*, Vol. 1, Fluid Mechanics (Wiley, New York, 1987).

Wear and stiction regimes of thin-film magnetic disks

Arlen Bowen
Disk Engineering, IBM Adstar, Rochester, Minnesota 55901

The mechanical integrity of a thin-film disk drive is determined by contact start-stop (CSS) testing. Poor results in CSS testing are called either a wear or a stiction failure. Ambiguities are identified between wear and stiction observations and properties of the head/disk interface that caused the failure. The CSS test results are categorized into five wear and stiction regimes that are related to the physical properties of the head/disk interface.

I. INTRODUCTION

The trend in magnetic hard disk drives is toward smaller sizes. The spindle motor starting torque available in the smaller drives requires that the static coefficient of friction (SCOF) be less than 1.0 at each head/disk interface. This requirement on the SCOF is the dominant failure mode in small drives rather than the historic failure mode of visual wear. For completeness, visual wear is included in this study, but it is only one of five regimes that will be addressed. Stiction is defined as a SCOF response to contact start-stop (CSS) wear cycles when visual wear is not present. Tribology models, which include why high stiction occurs at low lubricant thickness, are discussed.

II. SCOF WITHOUT CSS CYCLING

Thin-film disks with the same surface roughness are lubricated to give four different thicknesses. A polar perfluoropolyether lubricant is applied on top of the outer carbon layer. The disk's thin-film structure is common in the magnetic recording industry.[1] The lubricant thickness is measured using an optical ellipsometer and categorized in order of increasing thickness as follows: underlubricated (UL), nominally lubricated (NL), overlubricated (OL), and excessively lubricated.

Each of the four types of disks are built into three identical hard files modified to measure SCOF. All measurements are done with less than one revolution of the spindle and for this study that is considered a "no CSS cycling" situation. The excessively lubricated disks have large stiction values (SCOF>4.0) and are not tested further. The remaining three types (UL, NL, and OL) are placed in 5% and 80% relative humidity (RH) environments for various rest times. Rest times are measured after the inside of the drive is acclimated to the ambient RH condition. The rest time is the time the magnetic head is in contact at one location on the disk prior to the SCOF measurement. The SCOF values are averaged for the three drives in each category and given in Figs. 1, 2, and 3. The rest times and RH conditions are taken in random order. The linearity of the data indicates that the SCOF of the head/disk interface is reversible prior to CSS cycling. The three figures show that high stiction occurs at lubricant thicknesses that are both less (UL) and greater (OL) than the nominal thickness (NL).

III. WEAR AND STICTION REGIMES AFTER CSS CYCLING

The effects of lubricant thickness and surface roughness on the SCOF are measured after CSS cycling. The texturing and lubrication process parameters are different for each disk type. The disk roughness is measured using a contact stylus profilometer. Prior to CSS testing, all disk types in this section behave like those of type NL of the previous section. The measured SCOF values at 80% RH and any observed wear are given in Fig. 4. Visual wear is defined as any continuous wear scar visible on the disk surface at 50 times magnification. The wear and stiction values of Fig. 4 indicate that five regimes can be identified. The five regimes are summarized in Table I. Data from Figs. 1, 2, and 3, along with the investigation below, support the identification of the five regimes in Fig. 4.

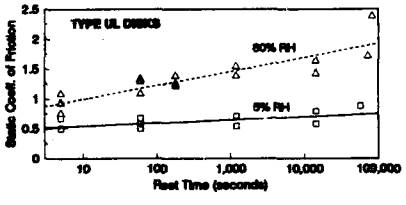

FIG. 1. SCOF for type UL disks without CSS cycling.

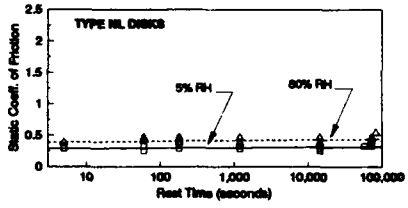

FIG. 2. SCOF for type NL disks without CSS cycling.

 0021-8979/94/75(10)/5750/3/$6.00 © 1994 American Institute of Physics

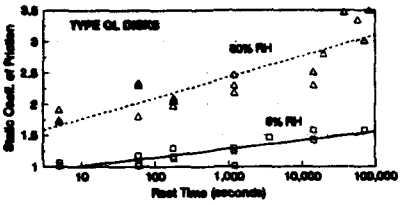

FIG. 3. SCOF for type OL disks without CSS cycling

TABLE I. Summary of five wear and stiction regimes.

Regime	CSS cycles	Visual wear	Stiction
1	yes	yes	high or low
2	yes	no	high or low
3	yes	no	low
4	yes	no	high
5	no/yes	no	very high

IV. FURTHER INVESTIGATIONS

All the data in Fig. 4 are taken after the same number of CSS cycles and the same rest time at 80% RH. The effect of the number of CSS cycles on the SCOF for different regimes is investigated in this section. Experimentation is done with a single head in a special drive so the onset of visual wear can be determined. Disks from regimes one and two are used to measure the SCOF versus the number of CSS cycles. A typical result is given in Fig. 5. This particular test is terminated at 16 000 cycles when wear is first observed. High and low stiction are noted on these low lubricant thicknesses disks before visual wear.

Figure 6 shows typical SCOF values for disks from regime four with up to 30 000 CSS cycles. CSS cycling is terminated at 30 000 cycles since the SCOF is no longer increasing rapidly. No visual wear is detected. The SCOF recovery after CSS cycling is measured for 1 week following the termination of cycling. The insert in Fig. 6 shows the SCOF values over 1 week for equal intervals of time between measurements. Significant, but not total, recovery is observed.

V. DISCUSSION

The reversibility of SCOF values without CSS cycling indicates that measurements are made without significantly disturbing the surface distribution of lubricant or without reducing the disk's peak heights. After CSS cycling, the SCOF measurements are irreversible and dependent on initial lubricant thickness and roughness values (or regimes).

The observing of high SCOF values caused by high lubricant thickness is well documented.[2,3] The rest time dependency for thick lubricant layers is explained by the "microdescent" of the head into the lubricant layer.[4] For thick lubricant layers (Fig. 3), the increased SCOF values with RH are caused by the interaction of water vapor with oxygen on the backbone of the lubricant molecule. Scanning tunneling microscopy is used to detect the presence of water on lubricant molecules.[5] A lubricant molecule with water vapor is attracted to both the hydrophilic head and disk.

The increase in SCOF by CSS cycling of regime four disks is due, in part, to a change in the lubricant's surface distribution. The CSS cycling appears to micropool the lubricant around regions of head/disk contact. The recovery seen in the Fig. 6 insert suggests the pooled lubricant areas need about 1 week to equilibrate. Recovery is not total as some run-in of the high contact summits occurs and not all pooled lubricant will uniformly redistribute itself due to the immobilizing effect of the functional end groups on the lubricant.[6]

Visual wear caused by low lubricant thickness is well known.[3,7] High and low values of SCOF prior to observing wear are shown in Fig. 5. The cause of the initial increase in SCOF in Fig. 5 is the same as for type UL disks of Fig. 1. The lubricant in these two cases does not form a complete monolayer and this allows water vapor to form a meniscus at the head/disk interface.[8] Very small wear particles are formed from the unlubricated contacts during CSS cycling. The small particles cause the SCOF to drop as they become

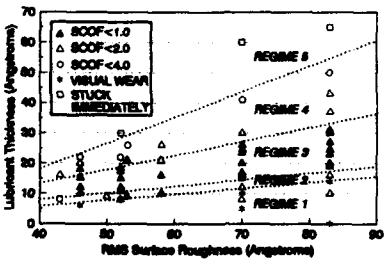

FIG. 4. Stiction and wear regimes after CSS cycling.

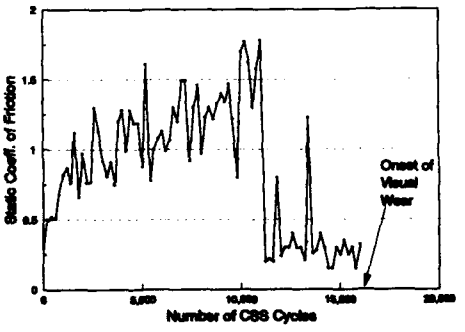

FIG. 5. Typical SCOF vs CSS for regime one or two disks.

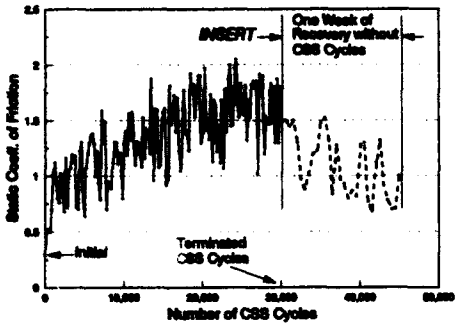

FIG. 6. Typical SCOF vs CSS for regime four disks.

a rolling third body in the interface. A sudden drop in the SCOF is regularly seen prior to the onset of visual wear. Generation of small particles continues to the point that wear can be observed.

Table I summarizes the five regimes shown in Fig. 4. The table shows that stiction measurements alone cannot be used to determine the regime of an unknown disk. The difficulty comes from the unexpected possibility of high stiction at low lubricant thicknesses. Efforts to determine the regime belonging to an unknown disk are further complicated by the disappearance of regime three at very large CSS cycles.[9]

ACKNOWLEDGMENTS

Dave Erickson, Doug Piltingsrud, Kevin Schulz, and Ken Johnson are thanked for providing critical support and discussion.

[1] L. Chen and T. T. Yamashita, U.S. Patent No. 4,786,564 (1988).
[2] B. Bhushan and M. T. Dugger, ASME J. Tribol. 112, 217 (1990).
[3] T. Kita, STLE Tribol. Trans. 35, 551 (1992).
[4] N. V. Gitis and R. Sonnenfeld, Trans. ASME 115, 214 (1993).
[5] Y. Andoh, S. Oguchi, and R. Kaneko, in ASME/STLE Tribology Conference, 1992.
[6] A. M. Scarati and G. Caporiccio, IEEE Trans. Magn. MAG-23, 106 (1987).
[7] T. Ginnai, A. Harrington, V. Rodov, M. Matsuno, and K. Saito, Thin Solid Films 180, 277 (1989).
[8] K. Miyoshi, D. H. Buckley, T. Kusata, C. Maeda, and B. Bhushan, STLE Tribol. Mech. Magn. Storage Syst. 5, 12 (1988).
[9] A. Bowen, ASME J. Tribol. 115, 376 (1993).

Recording medium properties and capacity bounds

J. A. O'Sullivan, D. G. Porter, R. S. Indeck, and M. W. Muller
Department of Electrical Engineering, Washington University, St. Louis, Missouri 63130-4899

The effect of such medium properties as magnetic unit size, film thickness, and strength of anisotropy, dipolar, and exchange interactions on the storage capacity limit of a thin-film recording medium is investigated. Relationships are derived for media with different properties that have equivalent capacity. The physically realizable range of material properties and their effect on the capacity bound are explored. Results on edge effects for capacity bound computations are presented. The results indicate that media for which anisotropy is the dominant source of magnetic energy have the greatest potential for information storage.

I. INTRODUCTION

Recent measurements have shown that medium noise is largely repeatable, suggesting that it is generated by a permanent magnetic microstructure of the recording medium.[1,2] These measurements motivate a model of the recording medium comprising fixed magnetic structures. We have devised such a model.[3] It has many features of other micromagnetic medium tessellation models,[4–6] but requires less computation. We model a variety of media by varying parameters which represent the physical properties of recording media. These parameters include tile size, film thickness, and strength of anisotropy, dipolar, and exchange interactions. A tile represents a single-domain microstructural entity, and may correspond to a single grain, a part of a grain, or a cluster of grains.

Bounds on storage capacity of magnetic recording systems have been computed based on models of their physical operation.[7–9] We have presented a method to compute upper bounds on the capacity of an ensemble of media and a single medium, irrespective of the read and write transducers.[10] The bound on the capacity of a single recording medium serves as a bound on the capacity of any recording system using that medium for storage. The inclusion of read/write transducers will reduce this capacity. The capacity bound is based on an argument that only stable states of the model may be used to store information. Thus, an estimate of the number of stable states of the model provides a fundamental upper limit to the capacity of information storage possible for a given medium. The capacity bound is computed in units of information bits per single domain magnetic tile. This capacity can be transformed into the more usual capacity measure of bits per unit of medium area based on the tile size.

II. EQUIVALENT MEDIA

Table I displays the parameters of the medium model. The interactions of the tiles which make up the medium depend on these parameters. Through this dependence, the parameters determine the medium storage capacity.

The energy of a tile is determined by the normalized effective magnetic field $\mathbf{h}$ at the tile. The field is normalized to the anisotropy field, as in Prutton,[11]

$$\mathbf{h}=\mathbf{H}/H_a, \quad \text{where } H_a=2K_a/M. \tag{1}$$

The magnetic field $\mathbf{H}$ is the sum of two component effective fields, due to exchange and dipolar interactions respectively, in dimensional and normalized form,

$$\mathbf{H}=\mathbf{H}_e+\mathbf{H}_d, \quad \mathbf{h}=\mathbf{h}_e+\mathbf{h}_d. \tag{2}$$

The exchange field $\mathbf{H}_e$ is generated by the neighboring tiles. Using i to index the set of neighbor tiles, and $\mathbf{M}_i$ to denote the corresponding magnetizations, we may write

$$\mathbf{H}_e=\sum_i K_e\mathbf{M}_i. \tag{3}$$

The dipolar field $\mathbf{H}_d$ is generated by the magnetic dipole moments of all other tiles in the medium. These dipole moments are the product of the tiles' magnetizations with their volumes. Using similar notation, we may write

$$\mathbf{H}_d=\sum_i \mathbf{A}_i(d^2\,\delta\mathbf{M}_i), \tag{4}$$

where $\mathbf{A}_i$ represents the appropriate linear operation to generate the magnetostatic field at the tile under examination due to the ith tile in the sum. The dependence of $\mathbf{A}_i$ on the parameters from Table I is

$$\mathbf{A}_i\propto 1/d^3. \tag{5}$$

This proportion represents the inverse relationship of field magnitude with the cube of the distance between the source dipole and the test point. Equations (1)–(5) imply that the field components vary according to[12]

$$\mathbf{h}_e\propto K_eM^2/K_a, \quad \mathbf{h}_d\propto \delta M^2/dK_a. \tag{6}$$

When the model parameters are varied, the total magnetic field at a tile is unchanged if both proportionality factors of Eq. (6) are unchanged.

TABLE I. Medium model parameters.

Symbol	Description	Units
K_e	exchange strength	H/m
δ	film thickness	m
d	tile spacing	m
K_a	anisotropy energy density	J/m^3
M	magnetization magnitude	A/m

 0021-8979/94/75(10)/5753/3/$6.00 © 1994 American Institute of Physics

TABLE II. Physical parameter ranges.

Symbol	Low	High
K_e	10^{-10}	10^{-7}
δ	3×10^{-8}	2×10^{-7}
d	10^{-8}	10^{-7}
K_a	10^{6}	10^{5}
M	5×10^{5}	2×10^{6}

If we represent a medium by a quintuple of its parameters, and use the symbol $\equiv$ to indicate that two media generate the same normalized field values, we conclude for any positive values of the medium parameters

$$(K_e,\delta,d,K_a,M)\equiv(K_eM^2/K_a,\delta M^2/dK_a,1,1,1). \quad (7)$$

Thus, two parameters suffice to describe the influence of all five parameters on the behavior of the medium model. We may represent a medium by a quintuple, $(K_e'\delta',1,1,1)$, or equivalently by the pair (K_e',δ'). The parameters (K_e',δ') in our model are similar to the parameters h_e, h_m in the numerical simulation work of Zhu and Bertram.[13]

Our method for computing capacity bounds depends on the normalized field values. According to the model, a state of the medium is stable if each tile in the medium has a magnetization stable against reversal. That is, the normalized field at each tile does not force the tile's magnetization to reverse direction. This reversal test does not consider thermal effects. Effectively, the model represents a medium at absolute zero. Furthermore, rotations of magnetization off the easy axis are not permitted. Reversals of direction along the easy axis are the only variations of tile magnetization accounted for by this model. The easy axes of the tiles are independently generated from a uniform distribution. The results depend on the choice of distribution for the easy axes; other distributions have been investigated.[2,14] This model constrains each tile to two magnetic states. If a medium has N stable states, the information storage capacity of that medium is bounded above by $\log_2 N$.[10] The constraint of two states per tile implies an absolute maximum possible storage capacity (when all states of a medium are stable) of 1 bit per tile.

Thus, we conclude that two media which produce the same proportionality factors in Eq. (6) share the same capacity bound in bits per tile. Varying the tile size yields different capacities in bits per unit area among what we call equivalent media.

III. PARAMETER AND CAPACITY VALUES

Table II displays ranges of parameter values which include physically realizable media. When these parameter ranges are transformed into the two-variable parameter space (K_e',δ'), a bounding rectangle may be drawn around the set of physically realizable parameters, yielding transformed parameter ranges,

$$10^{-4}\leq K_e'\leq 10^{2}, \quad 10^{5}\leq\delta'\leq 10^{10}. \quad (8)$$

To estimate the variation of the capacity bound over these parameter ranges, the capacity bound was computed for a set of grid points within the parameter ranges. The largest square medium patch for which a direct count of stable states may be used to exactly compute the capacity bound in reasonable time using our simulations and computing resources is a 5×5 medium. Figure 1 displays the capacity bounds computed for a single 4×4 medium in bits per tile as a function of the base 10 logarithms of its transformed parameters K_e' and δ'. The use of a slightly smaller patch allows a large number of simulations to be run. A plot of the average of the capacity bounds for 50 consecutive media has a similar shape. Note by comparison of the definitions of K_e' and δ' with Eq. (6) that the parameters K_e' and δ' correspond to the relative magnitudes of the exchange and dipolar field components.

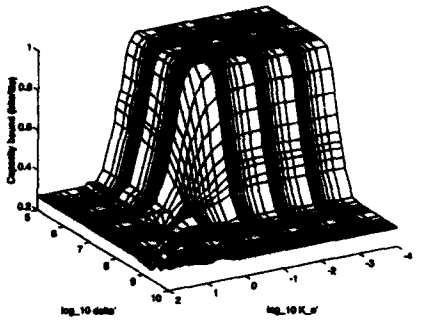

FIG. 1. Capacity bound as a function of parameters K_e' and δ'.

Larger patches require statistical analysis to estimate the number of stable states N. As the patch size increases N decreases as a fraction of the total number of states. Estimating N by a Monte Carlo simulation corresponds to estimating the probability of a stable state assuming a uniform distribution on possible states. This event grows rarer as the patch size increases, and Monte Carlo simulation fails to estimate the probability of such a rare event in reasonable time. More powerful computational methods are needed.

One strategy to increase computational power is to implement simulations on a massively parallel architecture. Such an implementation has been developed, and it does improve computational efficiency. As an example, the massively parallel implementation can sample and evaluate states of a 32×32 medium approximately 12 times faster than a single processor implementation. At present, this improvement is not sufficient to generate reliable estimates for large patches in reasonable time, although improved sampling methods are being studied.

IV. EDGE EFFECTS

Although full computation of capacity bounds for large numbers of tiles is not feasible at present, we can characterize the edge effects resulting from model simulations of small numbers of tiles. We study the set of equivalent media represented by transformed medium parameters $(K_e',\delta')=(0.15,7.8\times10^{7})$, a medium near the middle of our parameter ranges. A simulation was run to illustrate the effect

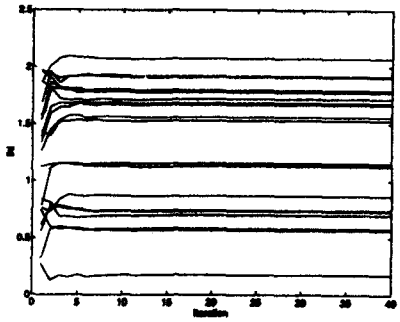

FIG. 2. Field magnitude vs patch size.

of small patch size on the magnetic fields of randomly generated media. A medium was constructed in steps, beginning with a 3×3 medium, and adding a new square ring of tiles at each step (making a 5×5, 7×7, etc.). The magnetic field of the center tile was examined at each step. This simulation was run several times to collect results for several randomly generated media.

Figure 2 plots the magnitude of the magnetic field versus the step in the construction for several runs of the simulation. Similar plots were generated for the magnetic-field direction. The plots indicate that after about eight steps, the magnetic field changes relatively little. This indicates that the field at a tile at the center of a randomly generated 17×17 medium serves as a good representation for the field at a tile in the interior of a larger randomly generated medium. Similar experiments may be run with other choices of medium parameters.

For these parameters, it appears that an 8-tile-wide border around a small patch will produce small patch capacity bounds with reduced dependence on the patch size. For example, we randomly generate and evaluate the stability of the center 5×5 collection of tiles within a randomly generated 25×25 media. The capacity bound estimated for an ensemble of isolated 5×5 media based on 10^6 samples is 0.44 ±0.02 bits per tile. The capacity bound estimated for an ensemble of 5×5 cores in a 25×25 medium based on 10^6 samples is 0.30±0.05 bits per tile. As expected, the latter capacity is smaller due to the increase in the effective field magnitudes in the core due to the effect of the outer ring. The large difference between the two motivates further study of larger media.

V. CONCLUSION AND FUTURE WORK

We have investigated the dependence of the fundamental limit of storage capacity of a medium on its physical properties. Our analysis has shown that there are media with different parameter values which have the same storage capacity. Media may be grouped into equivalence classes by this analysis, and each class may be represented by a parameter pair (K_e', δ'). Large values of K_e lead to small values of both K_e' and δ', which correspond to a capacity bound of 1 bit per tile, the largest possible capacity consistent with the medium model used. This indicates that media for which anisotropy is the dominant source of magnetic energy have the greatest potential for information storage. The value of K_e necessary to achieve such a medium given other medium properties can be computed using Eq. (7) and Fig. 1.

The computed capacity bounds do not decrease monotonically with large values of K_e' and δ' as might be expected on physical grounds, but reach nonzero plateaus. This effect may be an artifact caused by the constraint precluding magnetization rotation; it will be removed in future work.

ACKNOWLEDGMENT

This work was supported in part by NSF Grant No. ECS91-00157.

[1] J. R. Hoinville, R. S. Indeck, and M. W. Muller, IEEE Trans. Magn. MAG-28, 3398 (1992).
[2] J. R. Hoinville, Ph.D. thesis, Department of Electrical Engineering, Washington University, December 1991.
[3] J. A. O'Sullivan, D. G. Porter, R. S. Indeck, and M. W. Muller, in Proceedings of the 30th Allerton Conference on Comm., Cont., and Comp., 1992, p. 792.
[4] M. Mansuripur and R. Giles, Comput. Phys. 4, 291 (1990).
[5] J.-G. Zhu and H. N. Bertram, J. Appl. Phys. 69, 6084 (1991).
[6] J.-G. Zhu and H. N. Bertram, J. Appl. Phys. 69, 4709 (1991).
[7] C. A. Frosch and J. K. Wolf, IEEE Trans. Magn. MAG-24, 2247 (1988).
[8] C. D. Heegard, A. Duel-Hallen, and R. Krishnamoorthy, IEEE Trans. Inform. Theory IT-37, 712 (1991).
[9] S. W. McLaughlin and D. L. Neuhoff, IEEE Trans. Magn. MAG-29, 59 (1993).
[10] J. A. O'Sullivan, D. G. Porter, R. S. Indeck, and M. W. Muller, IEEE Trans. Magn. MAG-29, 4036 (1993).
[11] M. Prutton, *Thin Ferromagnetic Films* (Butterworths, London, 1964), p. 56.
[12] D. G. Porter, J. A. O'Sullivan, R. S. Indeck, and M. W. Muller, Tech. Rep. WUEE-93-147, Washington University, 1993.
[13] J.-G. Zhu and H. N. Bertram, IEEE Trans. Magn. MAG-27, 3553 (1991).
[14] X. Che and H. N. Bertram, IEEE Trans. Magn. MAG-29, 317 (1993).

Direct imaging of track edge fringing fields on recorded media

R. D. Gomez and I. D. Mayergoyz
Department of Electrical Engineering, University of Maryland at College Park, Maryland 20742

E. R. Burke
Laboratory for Physical Sciences, 8050 Greenmead Drive, College Park, Maryland 20740

The capability to image individual vector components of surface magnetic fields locally has been developed recently, and this component-selective technique has been applied to understand the field distribution of recorded patterns. Apart from the commonly measured in-plane component in the direction of the track H_x, a cross-track component H_y has been observed along the edges. While the H_x field images show side written patterns extending laterally from the edges, the H_y field images reveal localized bright and dark spots on both sides of the track. This suggests that pairs of mutually opposite magnetic dipole layers persist on both edges which are oriented transverse to the track direction. A systematic investigation was made of these side fringing fields to understand their behavior as a function of recording wavelength.

I. INTRODUCTION

One of the main consequences in the trend toward narrower track recording is the disproportionate increase in the area occupied by the edges relative to the main track. This is responsible for the growing attention given in recent years to high resolution imaging of track edges, particularly by Lorentz transmission electron microscopy. Arnoldussen *et al.* studied side writing with emphasis on establishing the differences between isotropic and strongly oriented media,[1] while Byun *et al.* compared the differences in magnetic domain structure for high- and low-noise media and illustrated the effect of head pole geometry on the bit-cell shape.[2] Most recently, Kawabe and Judy focused on the micromagnetic structures which exhibited clockwise and counterclockwise magnetic vortices and showed that the transitions were larger at the track edges than at the centers.[3] We extend those magnetization-sensitive measurements by imaging the distribution of specific magnetic-field vector components of recorded patterns at a fixed distance from the surface. We point out that the present method responds to the field-producing (curl-free) component of the magnetization and is therefore a natural complement to the above electron microscopies which measures the non-field-producing (divergence-free) component of the magnetization.[4]

In this article we first discuss some intriguing features of side writing, as observed principally by using two distinct component imaging schemes, namely, on-track (H_x) sensitive and cross-track (H_y) sensitive imaging modes. We then discuss their behavior as a function of recording wavelength.

II. EXPERIMENT

Images of the surface fields were obtained by magnetic force scanning tunneling microscopy.[5,6] Basically, this method generates a 2D mapping of magnetic-induced deflection of a probe as a function of its position on the surface. The deflection of the probe Δz which provides the contrast mechanism, is related to the local field by the relation[5,7]

$$\Delta z \propto \sin\theta(\cos\theta\cos\phi H_x + \cos\theta\sin\phi H_y + \sin\theta H_z), \quad (1)$$

where H_x and H_y refer to the in-plane components along the track and cross-track directions, respectively, while H_z is the vertical component of the field. The angle θ is the inclination of the probe relative to the surface normal and ϕ defines its azimuthal orientation relative to the sample magnetization direction. By varying the probe inclination, we can set the relative sensitivity between the in-plane and out-of-plane magnetic-field components; while by varying ϕ, we can select the in-plane component to be preferentially imaged.

In these experiments, the probe was fixed at an inclination of $\theta \sim 30°$, and the angle ϕ was varied between 0° and 90°. The patterns which we studied were recorded on thin-film isotropic rigid disk media with $H_c = 957$ Oe and $M_r = 1.4$ memu/cm^2. An 18 turn inductive thin-film head with 14 μm leading and 11.5 μm trailing pole widths was used to create these patterns at fixed current. The bit size was adjusted by varying the head field frequency while keeping the linear velocity constant.

III. RESULTS AND DISCUSSION

A. H_x and H_y images: Edge effects

The difference between the orthogonal in-plane surface field components for a single recorded track is shown in Fig. 1. In Fig. 1(a), the azimuthal orientation of the probe magnetization was nominally aligned parallel to the track so that the contrast is due to the component in this direction (H_x). This is distinguished from Fig. 1(b), where the probe was oriented 90° with respect to the track direction and the image contrast is mainly from the field component along the cross-track direction (H_y). A long-wavelength pattern ($\lambda \sim 20$ μm) was deliberately used to yield strong contrast and to render the features more prominently.

Figure 1(a) shows the usual bright and dark pattern corresponding to a periodic alternating magnetization along the x direction.[5] Besides the central track region, we see substantial field extension from the edges whose intensity gradually diminishes with increasing distance from the edge. In this specific case, the side pattern can be detected up to a lateral distance of 4 μm from the edge, which is a significant fraction of the pole width. We point out, however, that this num-

 0021-8979/94/75(10)/5786/3/$6.00 © 1994 American Institute of Physics

FIG. 1. Component-resolved images of a 20 μm wavelength magnetic pattern along the (a) track direction and (b) cross-track directions. Head pole outline is shown on top and dashed lines mark track and edge patterns. Inset: uneven magnetization pattern showing reduced vertical field component and enhanced transverse edge component. Arrows shows areas along the edges where subtle bright/dark contrast, characteristic of transverse dipole layer, is most visible.

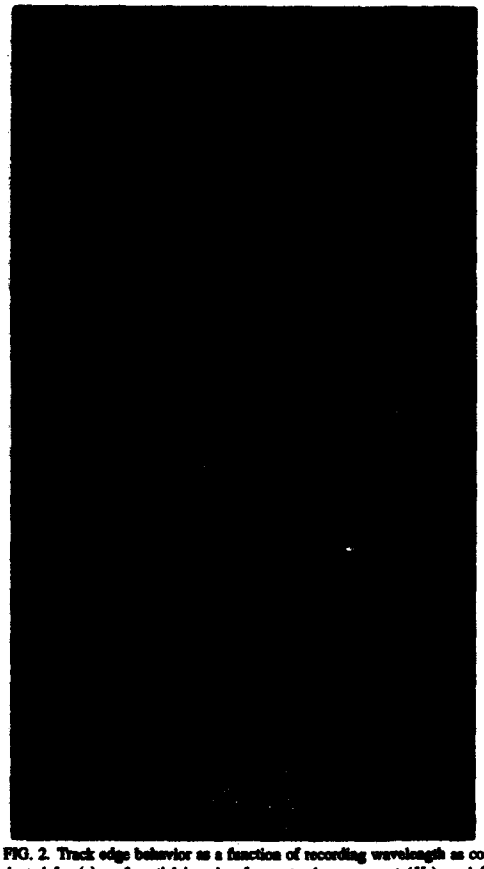

FIG. 2. Track edge behavior as a function of recording wavelength as conducted for (a) preferential imaging for on-track component (H_x), and (b) cross-track or transverse field imaging.

ber was not corrected for our instrumental broadening, and the actual distance may be somewhat shorter.[8,9] The side patterns appear to make an oblique angle of roughly 45° with the track direction and in the direction of head motion. This suggests the presence of an ancillary edge magnetization which was presumably created by the side fringing field of the recording head. The characteristic shape of the side pattern, i.e., the slant in the direction of head motion, may be attributed to the motion of the media in a varying head field[1,10] and may have been further aggravated by the uneven pole geometry of the recording head. The cross-track component image in Fig. 1(b) shows a markedly different feature of the side patterns. Instead of the side extensions, we find a series of alternating bright and dark strips which are localized along the edges. The cross-track distance separating two associated strips is about 16 μm, which is 2 μm longer than the leading pole width of the head. These field patterns, which occur pair-wise on both sides of the track in mutually opposite directions, were clearly produced by a component of magnetization transversely oriented with respect to the track. We infer that this cross-track magnetization was created by the y component of the recording head field which is concentrated mainly near the edges of its poles.

It is interesting to note that since these edge strips are correlated with the magnetization pattern of the main track, then the same information contained in the main pattern can, in principle, be obtained by reading the side strips, instead. Employing these edges either as tracking servo or data channels may be appealing since these edge strips are intrinsically localized, having widths of less than a micron. A system using these edges as recording channel may be able to achieve a much larger track density in comparison with conventional systems requiring the full track width for signal detection.

We now focus on the subtleties of these observations. Note that the variations in the interior of the track in Fig. 1(b) are not due to the H_y component persisting at these regions since there is negligibly small H_y field at the centers of the track. Rather, these are due to residual contribution from the vertical field component H_z which, as given in Eq. (1), mixes with the nominally H_y-sensitive imaging scheme. This point becomes clear if we consider the image of a track with the same wavelength but uneven magnetization pattern shown in the inset. In this case when the bit size is small, the z component is greatly reduced which causes the edge strips to appear more pronounced. The degree of differentiation into individual components is dependent upon the specific pattern and field components other than the preferential component can similarly interact with the imaging probe.[7] Nevertheless, this feature of the technique has also allowed us to observe some interesting features of the side band. Close examination of Fig. 1(b) reveals that each indi-

vidual edge strip is actually composed of a pair of adjacent bright and dark strips. (The arrows show where this is most noticeable.) This is the characteristic image of a magnetic dipole layer, where the vertical field is more or less enhanced at the positions of the charges.[11] Thus, we can create a picture of the track as being composed of an alternating series of magnetization along the track direction and pairs of magnetic dipole layers along the edges oriented in the transverse or cross track direction.

With this in mind, we examine the situation when two magnetic edge dipoles of opposite orientations meet at the corners formed by transition regions and the edges, to form a quadrupole charge distribution.[1] From Fig. 1(b), these areas show very little contrast indicating that to the extent of our sensitivity and resolution, no definite magnetization exists there. We suspect that a distinct quadrupole charge distribution cannot persist at these areas since this would require the media to be able to sustain very sharp discontinuities in the magnetization distribution. Certain processes, such as curling of the magnetization near the transition, may be energetically more favorable than the formation of distinct quadrupole charge distributions.

B. Edge effects and recording wavelength

We now characterize these edge effects as the wavelength is reduced to values closer to real recording systems, and understand how the edge patterns and the effective trackwidth behave as the recording wavelength is decreased. We define the effective trackwidth as the sum of the main track plus the width of both side patterns; and we define the boundary between the main track edge and side written region in H_x imaging as the intersection of an imaginary line drawn across the track with a similar line across the side recorded region as illustrated in dashed lines in Fig. 1(a).

Figure 2 shows some representative component-resolved images for various pattern wavelengths ranging from 10 to 2.2 μm. In Fig. 2(a), we find that the lateral extent of the side written areas diminish more or less proportional to the recorded wavelength, reduced from 3 μm at $\lambda=10$ μm, 1 μm for $\lambda=3$ μm, and imperceptible at $\lambda=2$ μm. By considering a large number of images similar to those in Fig. 2, we established some characteristic trends in the behavior of the main track width. From the longest wavelength ($\lambda=20$ μm) down to about $\lambda=3$ μm, the width is more or less constant at 15 μm (1 μm greater than the head pole width), but diminishes gradually at shorter wavelengths up to about 13 μm. Thus, the effective trackwidth shortening is a two step process: First, occurring from long to intermediate recording wavelengths, the side pattern contribution contracts while the main track remains at about 1 μm wider than the leading pole. Then, at extremely short wavelengths, the main track width decreases likewise and approaches a value closer to the average pole width. We speculate that since the magnitude of the head field diminishes with increasing frequency,[12] then the locus of points on the media such that $H_x > H_c$ correspondingly affects a much smaller area.[13] At the highest recording frequencies, the recorded pattern are truncated abruptly in the areas where the field gradients are high, namely, at the ends of the poles and midway between them. These results are consistent with the H_y edge structures shown in Fig. 2(b). The characteristic shortening of the width of the main track is identical for both imaging schemes. In the present case, while the imaging mode was preferential to H_y, the patterns appear to have large H_x field content as well because at these wavelengths H_x is much stronger than the H_y edge field. Nevertheless, we observe that the edge structures get more localized and the intensity weakens much more rapidly with wavelength in comparison with edge the structures in Fig. 2(a). Similarly, the cross-track separation between the edge bands, measured from center to center, is fixed at 15 μm at intermediate wavelengths and is reduced by a micron at the shortest wavelengths. These observations imply that the ability of the record head to produce cross-track magnetization declines quickly with frequency, and that the cross-track head field is more or less concentrated in the areas beyond the physical extent of the recording head poles.

In summary, recording artifacts depend very strongly on the specific recording parameters and it is difficult to predict the outcome of a particular head and field combination. This work was done on isotropic media and it would be interesting to compare our observations with highly oriented media. Nevertheless, it is clear that simultaneous imaging of the on-track and cross-track field components reveal significant insights on recording characteristics.

ACKNOWLEDGMENTS

We are grateful to J. Gorczyca and Professor M. H. Kryder at Data Storage Systems Center, Carnegie Mellon University, for helpful discussions and for preparing the samples used in this experiment.

[1] T. C. Arnoldussen, L. L. Nunnelley, F. J. Martin, and R. P. Ferrier, J. Appl. Phys. 69, 4718 (1991).
[2] C. Byun, G. C. Rauch, J. Greggi, Jr., C. Mesinger, and P. Ng, J. Appl. Phys. 69, 5886 (1991).
[3] T. Kawabe and J. Judy, IEEE Trans. Magn. MAG-28, 2470 (1992).
[4] I. A. Beardsley, IEEE Trans. Magn. MAG-25, 671 (1989).
[5] R. D. Gomez, E. R. Burke, A. A. Adly, and I. D. Mayergoyz, Appl. Phys. Lett. 60, 906 (1992).
[6] R. D. Gomez, E. R. Burke, A. A. Adly, and I. D. Mayergoyz, IEEE Trans. Magn. MAG-29, 2494 (1993).
[7] R. D. Gomez, I. D. Mayergoyz, and E. R. Burke (these proceedings).
[8] G. F. Hughes and D. S. Bloomberg, IEEE Trans. Magn. MAG-13, 1457 (1977).
[9] D. Lindholm, IEEE Trans. Magn. MAG-13, 1460 (1977).
[10] I. A. Beardsley, IEEE Trans. Magn. MAG-22, 361 (1986).
[11] I. D. Mayergoyz, A. A. Adly, R. D. Gomez, and E. R. Burke, J. Appl. Phys. 73, 5796 (1993).
[12] T. Lin, J. A. Christner, T. B. Mitchell, J.-S. Gau, and P. K. George, IEEE Trans. Magn. MAG-25, 710 (1989).
[13] C. D. Mee and E. D. Daniel, *Magnetic Recording: Vol. I: Technology* (McGraw-Hill, 1987), p. 255 and references therein.

Computation of magnetic fields from recording surfaces with multiple tracks

E. R. Burke
Laboratory for Physical Sciences, 8050 Greenmead Drive, College Park, Maryland 20740

R. D. Gomez, R. Madabhushi, and I. D. Mayergoyz
Department of Electrical Engineering, Institute for Advanced Computer Studies, University of Maryland, College Park, Maryland 20742

Calculations of the magnetic fields emanating from a recorded surface that contains an infinite number of identical tracks are presented. The solutions are obtained by assuming that the magnetization is uniform through the thickness of the film and can be represented by Fourier series in the other two dimensions. Solutions are obtained for both longitudinal and vertical recording. To make these calculations useful Fourier distributions are obtained with arctan transitions that are both representative and easy to use. These magnetic fields are then used to calculate the voltage from an idealized reproduce head. Effects on the output voltage caused by track width, track separation, head registration, and transition lengths can then be calculated. Examples are given and it is shown that the effects can be large, compared to the usual *infinite* track width calculations, when the track width or the track separation become comparable to the recorded wavelength.

I. INTRODUCTION

In the seminal article by Wallace,[1] the magnetic fields from a recording surface were calculated assuming an infinite track width. Since then there have been numerous articles in the literature[2] that have examined the effects of finite track widths, but they have always been for isolated tracks. To our knowledge, the problem has never been attacked in its entirety, for multiple tracks.

In order to determine the effects of finite track widths, we have calculated the magnetic fields from a recorded surface containing an infinite number of identical tracks. Once the magnetic fields are determined, measurable quantities such as the voltage from a magnetic recording head can be calculated. We have performed numerous such calculations and the results can be compared to the same quantities calculated for an infinite track width. For the read head voltages we show the effects of track widths and track separations on the output voltages. We show that these effects can become significant when the wavelength of the signal approaches the width of the track.

II. THEORY

The magnetic medium is a thin film of thickness δ in the z direction and infinite extent in the x and y directions. We assume that the magnetization is uniform through the thickness of the medium and can be represented by Fourier series in the other two dimensions. The magnetic field H in the absence of any currents, can be written as the gradient of a scalar potential, $H=-\nabla\Phi$. The scalar potential must satisfy the equation $\nabla^2\Phi=4\pi\nabla\cdot M$, where M is the magnetization in the thin-film medium. This latter equation comes from the constitutive equation $B=H+4\pi M$, and the Maxwell's equation, $\nabla\cdot B=0$. We have performed the calculations for the more realistic constitutive equation,[3] $B=\mu H+4\pi M$, but for the sake of simplicity we will present here the case where $\mu=1$ in the thin-film medium.

The first magnetization pattern we will consider is in the x direction. This would correspond to longitudinal recording and can be written as

$$M_x=M_s\sum_{n,m} L_{n,m}\sin k_x x\cos k_y y, \tag{1}$$

where M_s is the saturation magnetization, $L_{n,m}$ are the normalized Fourier coefficients, and k_x and k_y are the wave numbers in the x and y directions ($k_x=2\pi n/\lambda_x$, $k_y=2\pi m/\lambda_y$) while λ_x and λ_y are the wavelengths. This representation is for a magnetization that is symmetric and repetitive. We could, of course, further generalize this by including phase angles for a nonsymmetric case or Fourier integrals for a nonrepetitive case.

We will obtain solutions for Φ in three regions: (I) above the film; (II) in the film; and (III) below the film. The three solutions are

$$\text{(I)}\quad \Phi^{(\mathrm{I})}=\sum_{n,m}\Phi^{(\mathrm{I})}_{n,m}e^{-kz}\cos k_x x\cos k_y y, \tag{2}$$

$$\text{(II)}\quad \Phi^{(\mathrm{II})}=\sum_{n,m}\left(\Phi^{(\mathrm{II}-)}_{n,m}e^{-kz}+\Phi^{(\mathrm{II}+)}_{n,m}e^{kz}-\frac{4\pi M_s L_{n,m}k_x}{k^2}\right)\cos k_x x\cos k_y y, \tag{3}$$

$$\text{(III)}\quad \Phi^{(\mathrm{III})}=\sum_{n,m}\Phi^{(\mathrm{III})}_{n,m}e^{kz}\cos k_x x\cos k_y y, \tag{4}$$

where $k=\sqrt{k_x^2+k_y^2}$. These solutions were obtained by using: (i) the symmetry of the problem; (ii) the fact that Φ must vanish at $z=\pm\infty$; (iii) the method of separation of variables; and (iv) the fact that the trigonometric functions form a complete orthogonal set.

The coefficients in Eqs. (2)–(4) may be determined by requiring the continuity of the normal B and the transverse H at the surfaces of the film ($z=0,-\delta$). The results are

 0021-8979/94/75(10)/5759/3/$6.00 © 1994 American Institute of Physics

$$\Phi^{(I)}_{n,m} = -2\pi M_z L_{n,m}(1-e^{-k\delta})k_x/k^2, \tag{5}$$

$$\Phi^{(II-)}_{n,m} = 2\pi M_z L_{n,m} e^{-k\delta} k_x/k^2, \tag{6}$$

$$\Phi^{(II+)}_{n,m} = 2\pi M_z L_{n,m} k_x/k^2, \tag{7}$$

$$\Phi^{(III)}_{n,m} = 2\pi M_z L_{n,m}(1-e^{k\delta})k_x/k^2, \tag{8}$$

where again we have used the orthogonality of the trigonometric functions. The magnetic fields can now be completely determined by putting the coefficients from Eqs. (5)–(8) into the solutions, Eqs. (2)–(4), and calculating the magnetic-field components.

For perpendicular recording the magnetization will be in the z direction, and can be written as

$$M_z = -M_z \sum_{n,m} P_{n,m} \cos k_x x \cos k_y y. \tag{9}$$

The solutions will be the same as for the longitudinal case except for the last term in Eq. (3) which will now vanish since $\nabla \cdot M = 0$ in all three regions. The coefficients can now be calculated as before, with the result for the (I) region given by

$$\Phi^{(I)}_{n,m} = -2\pi M_z P_{n,m}(1-e^{-k\delta})/k. \tag{10}$$

We have chosen the relative phases for the magnetization distributions in Eqs. (1) and (9) to be the same as Wallace. The fields that we have calculated reduce to those found by Wallace, who used completely different techniques, in the limit of one Fourier component ($k_x \to k$, $k_y \to 0$). Wallace showed that the fields above the medium are identical for longitudinal and vertical recording. Our results show that this is no longer true if $k_y \neq 0$.

Wallace also calculated the fields inside a high-permeability head by using the method of images. In our case, this would correspond to adding a fourth region above the recording medium where $B = \mu H$ and μ is the permeability of the head. We would then have to add an exponentially increasing solution in the region between the head and the film and then proceed as before. The modifications are the same as those found by Wallace and, in particular, the field inside the head is found to be the same as the field previously found above the film except multiplied by the factor $2\mu/(\mu+1)$.

III. FOURIER DISTRIBUTIONS

For these techniques to be useful, we must find Fourier series that are both representative and easy to use. To this end, we have made an extensive study of numerous Fourier series[4] and have found that the most useful ones are series with arctan transitions where a is the transition length. The Fourier series that we use can be shown to be identical to the series that would be constructed from the linear superposition principle.[5] The Fourier coefficients that would correspond to a magnetization variation in the x direction are given by

$$X_n = 4e^{-2\pi a(2n+1)/\lambda}/\pi(2n+1). \tag{11}$$

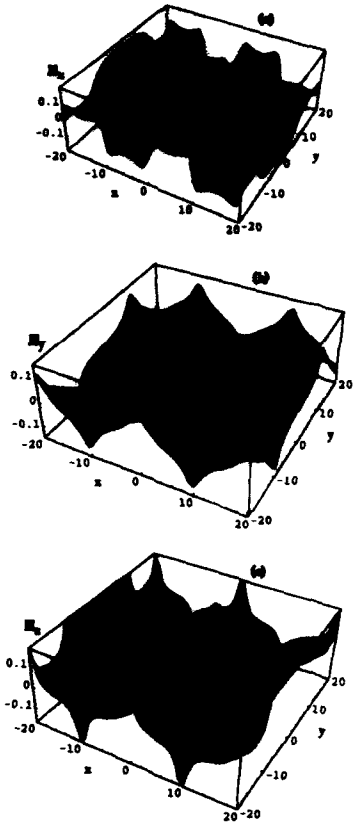

FIG. 1. 3D calculations of the magnetic-field components: (a) $H_x(x,y)$, (b) $H_y(x,y)$, and (c) $H_z(x,y)$.

The coefficients that would represent the magnetization distribution in the y or track width direction are given by

$$Y_m = \frac{2e-[2\pi ma/(W+b)]}{\pi m} \sin\frac{\pi m W}{W+b}, \quad m>0,$$
$$Y_m = \frac{W}{W+b}, \quad m=0, \tag{12}$$

where W is the track width, b is the track separation, and a is the arctan transition length in the y direction. The coefficients in Eq. (1) would now be simply $L_{n,m} = X_n Y_m$. The coefficients for vertical recording would be constructed similarly. With the use of Eqs. (11) and (12) we are now in the position to calculate the magnetic-field components.

IV. MAGNETIC-FIELD CALCULATIONS

Examples of the calculated field components are shown in Fig. 1. These fields were calculated for the case of longitudinal recording with the following values: $M_z = 1$, $z = 0$, $\lambda = 20$, $W = 20$, $b = 10$, $\delta = 0.1$, and $a = 1$ (arbitrary units).

These values were chosen for illustration. The profiles of the H_x and the H_z fields along the center of the tracks are similar to those found in the literature[6] for single pulses, but now we have a complete description of the fields everywhere, including the space between the tracks. The H_y field is new.

V. HEAD VOLTAGE

We now calculate the voltage from an idealized reproducing head by finding the time rate of change of the magnetic flux through the head. In this case we have to integrate H_x over the head area in both the z and y directions with the result

$$V=\frac{\mu}{\mu+1}4\pi M_s \nu N W_h \sum_{n,m} X_n Y_m \left(\frac{k_x}{k}\right)^3 \frac{\sin k_y W_h/2}{k_y W_h/2} \times e^{-kz}(1-e^{-k\delta})\cos k_x x \cos k_y y, \quad (13)$$

where ν is the velocity of the head relative to the medium, N is the number of head turns, W_h is the width of the head, and the point (x,y,z) is now at the center of the head. The same calculation can be performed for perpendicular recording with the identical result except that the factor $(k_x/k)^3$ is replaced by the factor $(k_x/k)^2$.

Equation (13) is an extremely useful equation. When combined with Eqs. (11) and (12) it allows the calculation of the usual losses (spacing, thickness, and frequency losses), but it also allows the calculation of effects due to the track width, the track separation, the location of the head relative to the track, and the effects of the transition lengths on the output voltage. The effects of a finite head gap can be included in Eq. (13) by multiplying each term by the factor, $\sin(k_x g/2)/(k_x g/2)$, where g is the width of the head gap.

We will use Eq. (13) to calculate the peak output voltage in the Wallace case (one harmonic in the x direction); divide the result by the Wallace voltage; and then plot the result as a function of the track separation b. The result is shown in Fig. 2 (dashed curve), where the other parameters are: $z=0$, $W/\lambda=1$, $\delta/\lambda=0.01$, and $a/\lambda=0.02$. It can be seen that the relative output first decreases and then levels off. These results are not unreasonable since we have shown that our result reduces to that of Wallace when $b\to 0$, and when b becomes finite the output will decrease until there is no longer any interaction between the tracks. Figure 2 thus contains two important results: (i) it shows how far the tracks have to be separated to prevent interaction (about one wavelength); and (ii) it shows the magnitude of the loss due to the track separation (about 20% in this case).

We can now keep the separation constant ($b/\lambda=0.5$) and see how this loss changes as the width W is varied. The result is also shown in Fig. 2, and it can be seen that the loss

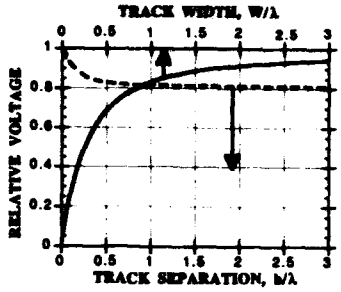

FIG. 2. Relative output voltage as a function of b/λ (dashed curve), and W/λ (solid curve).

can be considerable for small W ($W<\lambda$). This is due to the fact that the Wallace voltage is linear in W while our result is proportional to W^2 for small W and constant b.

The results shown in Fig. 2 are just a sampling of the type of calculation that can be performed using Eq. (13). Another measurable quantity that can be calculated from the magnetic fields is the displacement of the probe tip of a magnetic force scanning tunneling microscope[7] (MFSTM). We have shown previously how the probe tip deflections are related to the magnetic fields and how the different components of the fields can be isolated by the orientation of the probe. These calculations can now be repeated for the magnetic fields that we have calculated here. It can be shown that the different components of the fields can still be isolated for the case of a rigid triangular probe that is constrained to rotate in only one direction. These isolation effects have been confirmed experimentally.[8] The calculations become quite complicated when the H_y component is included and space precludes their presentation here. We do, however, intend to pursue these studies, both theoretically and experimentally.

ACKNOWLEDGMENT

The authors wish to thank Shannon Keehn for invaluable assistance with the computer calculations.

[1] R. L. Wallace, Bell Syst. Tech. J. 30, 1145 (1951).
[2] See, for instance, C. D Mee and E. D. Daniel, *Magnetic Recording* (McGraw-Hill, New York, 1987), and the many references therein.
[3] I. D. Mayergoyz, E. P. Furlani, and S. Reznik, J. Appl. Phys. 73, 5440 (1993).
[4] R. D. Gomez, E. R. Burke, A. A. Adly, I. D. Mayergoyz, J. A. Gorczyca, and M. H. Kryder, J. Appl. Phys. 73, 6181 (1993).
[5] J. C. Mallinson, IEEE Trans. Magn. MAG-10, 69 (1974).
[6] R. I. Potter, J. Appl. Phys. 41, 1647 (1970).
[7] E. R. Burke, R. D. Gomez, A. A. Adly, and I. D. Mayergoyz, IEEE Trans. Magn. MAG-28, 3135 (1992).
[8] R. D. Gomez, E. R. Burke, and I. D. Mayergoyz (these proceedings).

Micromagnetic modeling and experimental study of transition noise correlation in thin-film media

Jian-Gang Zhu and Haiyun Wang
The Center for Micromagnetics and Information Technologies, Department of Electrical Engineering, University of Minnesota, Minneapolis, Minnesota 55455

Thomas C. Arnoldussen
IBM Corporation, Storage Systems Division, 5600 Cottle Road, San Jose, California 95193

Micromagnetic modeling and time-domain experimental measurements are combined to study spatial noise correlations between two closely recorded transitions in oriented longitudinal thin-film media. The Karhunen–Loeve expansion method is utilized to characterize the noise correlations. The analysis shows that the noise correlation of the dipulses exhibits three principle modes: amplitude variation, shift in unison, and breathing. The supralinear increase of noise at small bit intervals in well-oriented longitudinal film media is dominated by the amplitude variation, which arises from large variation of the degree of percolation between adjacent transition boundaries. The results from the micromagnetic modeling shows excellent agreement with the results obtained from the experimental time-domain noise measurements.

I. INTRODUCTION

Not only is transition noise in thin-film media nonstationary, noise of closely recorded transitions at high recording densities is also correlated due to intertransition interactions.[1] Understanding noise behavior should help advanced recording system design. With the introduction of more advanced data recovering channels, knowledge of noise correlation between adjacent transitions becomes extremely important.

Micromagnetic modeling can clarify the relationship of medium noise behavior to film microstructure and magnetic properties. Our previous modeling studies on di-bit transitions have characterized the nonlinear noise enhancement at high recording densities in the presence of intertransition interactions. In this article, we present an analysis of film medium noise at high recording densities based on a combined micromagnetic modeling and experimental measurements of di-bit transition pairs.

II. METHOD OF NOISE ANALYSIS

Noise of a closely recorded di-bit transition pair represents the simpliest case of intertransition interactions.[1,2] In this article, we focus on noise correlation in such di-bits. However, the method for the noise correlation analysis presented can be applied to any multiple transition patterns.

Suppose that we have an assembly of voltage dipulses, read back from an assembly of dibit transition pairs. By subtracting the ensemble mean from each dipulse, one obtains an assembly of noise voltage wave forms,

$$\Delta V_k(x)=V_k(x)-\bar{V}(x), \quad k=1,2,\ldots,N, \tag{1}$$

where

$$\bar{V}(x)=\frac{1}{N}\sum_{k=1}^{N} V_k(x) \tag{2}$$

is the mean voltage wave form. The autocovariance of noise voltage,

$$A_v(x_1,x_2)=\frac{1}{N}\sum_{k=1}^{N}\Delta V_k(x_1)\Delta V_k(x_2), \tag{3}$$

contains noise correlations between the two adjacent transitions in the di-bit. To characterize noise correlations, the Karhunen–Loéve (KL) expansion, used previously in analyzing noise properties of isolated voltage pulses,[3] is used to obtain the noise correlation in the dipulse here. In the KL expansion, the kth noise voltage wave form in the assembly [Eq. (1)] can be expressed by

$$\Delta V_k(x)=\sum_{i=1}^{m}\alpha_i(k)\phi_i(x), \tag{4}$$

where $\alpha_i(k)$ are random variables with zero mean and $\{\phi_i(x),\ i=1,\ldots,m\}$ are the eigenfunctions of $A_v(x_1,x_2)$,

$$\frac{1}{L}\int_0^L A_v(x,s)\phi_i(s)ds=\lambda_i\phi_i(x). \tag{5}$$

Note that α_i and α_j are statistically independent provided that $i\neq j$,

$$\frac{1}{N}\sum_{k=1}^{N}\alpha_i(k)\alpha_j(k)=\lambda_i\delta_{i,j}. \tag{6}$$

Thus, $\phi_i(x)$ and $\phi_j(x)$ will be referred to as different noise modes, provided $i\neq j$. The total noise power and weighting of each noise mode can be defined respectively as

$$\mathrm{NP}=\sum_{i=1}^{N}\lambda_i, \tag{7}$$

and

$$\mathrm{Wt}_i=\frac{\lambda_i}{\mathrm{NP}}. \tag{8}$$

 0021-8979/94/75(10)/5762/3/$6.00 © 1994 American Institute of Physics

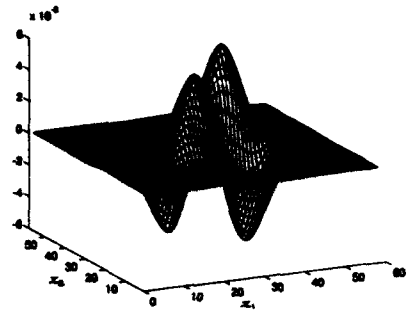

FIG. 1. Autocovariance of voltage noise $A_v(x_1,x_2)$ from micromagnetic simulation at $B=0.36$ μm. The unit of the axis is the diameter of a grain in the modeled thin film, $D=0.03$ μm.

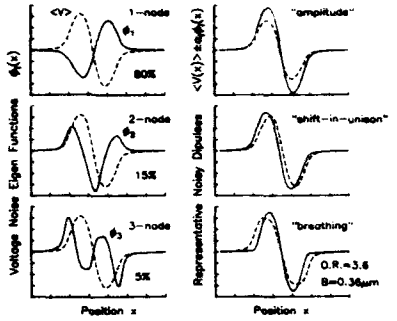

FIG. 2. Significant eigenfunctions ϕ_i of the autocovariance shown in Fig. 1 and the representative noisy dipulses: $\langle V(x)\rangle \pm \alpha_i \phi_i$, demonstrating the corresponding dipulse variation of each noise mode. The percentage numbers represent weightings of each noise mode over the total noise power.

III. RESULTS OF MICROMAGNETIC MODELING

A micromagnetic model, developed previously, is used to simulate di-bit transition pairs in a highly oriented thin-film medium. The angles between the magnetocrystalline easy axes of the grains in the modeled film are assumed to follow a Gaussian distribution in the film plane with standard deviation $\Delta\theta=30°$. The calculated orientation ratio through simulation of hysteresis loops is 3.6.[4] Zero intergranular exchange coupling and $M_s/H_k=0.2$ were assumed in the calculation.

Recording of di-bit transition pairs is simulated using the Karlqvist head field function. A gap length $g=0.36$ μm and a head medium spacing $d=0.06$ μm are assumed. The read-back voltage wave form is calculated from the simulated magnetization pattern by reciprocity theorem. $N=60$ di-bit transition pairs are simulated with different random distribution of the grain easy axis orientation to mimic recording at different locations of a film medium. The write interval between the two transitions in a dibit, B, is varied from $B=1.08$ μm to $B=0.24$ μm. Detailed noise analysis will be given only for $B=0.36$ μm where the integrated noise power reaches the maximum.[4]

Figure 1 shows the autocovariance of the read-back noise voltage, $A_v(x_1,x_2)$. Along the diagonal line $(x_1=x_2)$, the profile represents the variance of the voltage dipulses which exhibits two peaks at dipulse peak positions. Off the diagonal line, the autocovariance shows two well-pronounced negative peaks.

The left-hand-side column in Fig. 2 shows the three most significant eigenfunctions with the mean voltage dipulse plotted as dashed curves. According to the number of zero crossings, the eigenmodes have been named one-node, two-node, and three-node modes. On the right-hand-side column, corresponding noisy voltage wave forms, $\langle V(x)\rangle \pm \alpha\phi_i(x)$, are plotted. The figure clearly shows that the one-node mode corresponds to coherent magnitude fluctuation of the two peaks in the dipulse, thereby referred to as the amplitude mode. Note that at this bit interval, this mode dominates the total noise power with 80% weighting. The two-node mode here represents the two voltage pulses essentially shifting together, thereby referred to as shift-in-unison mode which is 15% of the total noise power. The three-node mode constitutes only weights 5% of the total noise power with the two pulses moving toward or away from each other.

Analysis of the corresponding magnetization transition assembly, $\{M_k(x),k=1,\ldots,N\}$, provides understanding of the voltage noise modes since the eigenmodes of the magnetization transition noise and the eigenmodes of the voltage noise have approximate one-to-one correspondence. Figure 3 shows the three magnetization transition noise eigenmodes, corresponding to the three voltage noise modes shown in Fig. 2. The eigenfunctions are plotted in the left-hand-side column with average magnetization transition profile shown as dashed curve. On the right-hand-side column, the corresponding two noise di-bit transitions are plotted. Note at this interbit interval that the two adjacent transitions are significantly overlapped and transition boundaries have percolated.[4] The voltage noise amplitude mode is caused by the variation of the degree of the percolation, as the first

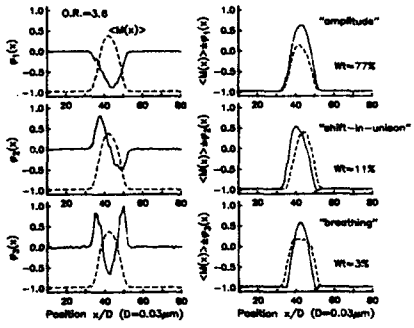

FIG. 3. The eigenfunctions of magnetization transition noise autocovariance corresponding to the voltage noise eigenfunctions shown in Fig. 2. The curves in the right-hand-side column are the representative noisy transition profiles.

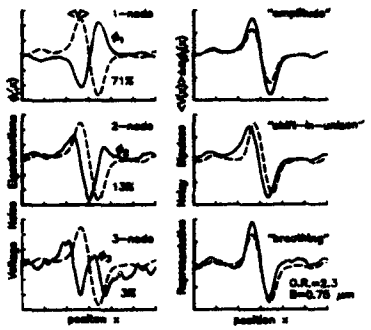

FIG. 4. Three significant eigenfunctions of autocovariance calculated from the experimental dipulse noise measurement.

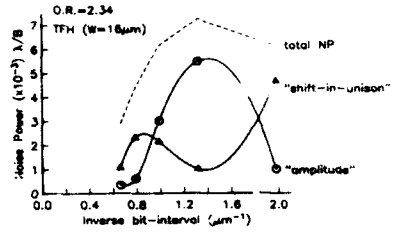

FIG. 5. Noise power, eigenvalues normalized by interbit interval B, of the first two significant noise modes, obtained from experimental measurements, are plotted as a function of interbit interval B. The dashed curve in the figure represents the measured total noise power.

magnetization transition noise mode shows. The fact that the weighting of this transition noise mode is slightly less than that of the voltage is due to the slight intermode mixing between the magnetization transition and read-back voltage noise. The voltage shift-in-unison mode arises from a shift in unison of the transition pair. This is likely caused by local variation of the magnetic reversal properties due to local variation of the grains' easy-axis orientation. The voltage noise breathing mode corresponds to another type of percolation variation: If the transition boundaries become more severely percolated, the residual transitions become broader.

IV. EXPERIMENTAL MEASUREMENT

A time-domain measurement of medium di-bit noise was performed on an air-bearing spin-stand tester. A thin-film head with a track width $W=10$ μm and a flying height $d\sim4$ μin. was used for recording and read back. A sequence of 100 dibit transition pairs with an index single transition were recorded on a previously dc saturated track in a longitudinal thin-film medium with orientation ratio 2.34.[5] A Tektronix digitizer, model RTD720A, is used to capture the entire di-pulse sequence waveform in a single record repeatedly for 30 times. The electronic noise in the wave form is eliminated by averaging the multiple read backs using the index pulse for alignment. The 100 dipulses in the electronic noise-free wave form forms the dipulse assembly and the analysis of noise autocovariance is then performed.

Figure 4 shows the eigenfunctions corresponding to the largest three eigenvalues for interbit interval $B=0.75$ μm, where the total noise power reaches its maximum, chosen for a fair comparison with simulation results. The three modes show exactly the same characteristic shape as the simulation results (Fig. 2) and similar noise power weightings for each mode.

Figure 5 shows the noise power values for both the amplitude mode and shift-in-unison mode versus inverse interbit interval $1/B$. At large bit intervals, the shift-in-unison mode constitutes the main noise power while the contribution from the amplitude mode is small. At small bit intervals where the total noise power increase sharply with decreasing bit interval, the amplitude mode starts to dominate the transition noise, just as the micromagnetic simulation results showed.

V. CONCLUSION

Utilizing the KL expansion method, noise correlation of a pair of interacting transitions in a well-oriented longitudinal thin film is characterized mainly by three correlation modes: amplitude mode where the amplitude of the two pulses increase, or decrease, together; shift-in-unison mode where the dipulse shifts its position while maintaining the essential functional shape; and breathing mode where the two pulses move toward or away from each other. At interbit intervals before transition boundaries become percolated, the noise is dominated by shift-in-unison mode. At small bit intervals where the percolation occurs, the amplitude variation mode becomes greatly pronounced, yielding a supralinear noise increase at high recording densities, while the shift-in-unison fluctuation reduces its magnitude. Excellent agreement on the noise characteristics between the micromagnetic simulation and time-domain experimental measurements has been obtained. Understanding of these noise characteristics should help to guide an improved recording system design.

ACKNOWLEDGMENTS

The authors would like to thank Dr. C. D. Mee for his continued support. This research is supported in part by the NSF Young Investigator Award under Grant No. ECS 9358309 and the IBM Faculty Development Award. San Diego Supercomputer Center and Minnesota Supercomputer Institute have provided grants for performing these studies.

[1] J.-G. Zhu, IEEE Trans. Magn. MAG-27, 5040 (1991).
[2] T. C Arnoldussen, M. A. Burleson, L. L. Nunnelley, and D. S. Parker, IEEE Trans. Magn. MAG-29, 3703 (1993).
[3] S. W. Yuan and H. N. Bertram, IEEE Trans. Magn. MAG-28, 84 (1992).
[4] J.-G. Zhu, X.-G. Ye, and T. C. Arnoldussen, IEEE Trans. Magn. MAG-29, 324 (1993).
[5] H. Takano, T. T. Lam, J.-G. Zhu, and J. H. Judy, IEEE Trans. Magn. MAG-29, 3709 (1993).

Noise correlations in dibit recording

Gang Herbert Lin and H. Neal Bertram
Center for Magnetic Recording Research, University of California, San Diego, La Jolla, California 93093-0401

Ralph Simmons
Hewlett-Packard Corporation, 11413 Chinden Boulevard, Boise, Idaho 83707

Medium noise correlations in dibit data patterns have been studied experimentally in thin film disk/head recording systems. An empirical eigenfunction expansion was utilized to identify the dominant noise modes and possible associated physical mechanisms. At large bit separation where noise power adds linearly, dibit in-phase jitter and out-of-phase jitter were found to be the leading noise modes. The noise waveform shape associated with out-of-phase jitter approaches that of the dibit signals (i.e., this mode of noise becomes amplitude-like) as the bit separation is reduced. In addition, dibit amplitude variation due to the interaction between the two pulses generates the same amplitude-like noise for a small dibit separation. Amplitude mode noise increases as the bit separation is reduced, causing the supralinear noise increase in high recording density. Results from nonlinear amplitude reduction measurement in dibit recording indicate a close correlation between the nonlinearities and the supralinear noise enhancement at high recording density.

Earlier studies have shown that the integrated noise power in thin film longitudinal recording media increases with signal frequency, indicating the nonstationary nature of the noise.[1] For new drives operating at higher density, especially when MR heads are integrated into the system resulting in a high playback gain, the importance of medium noise increases. The understanding of medium noise correlation is especially crucial for the PRML channel. The time domain noise autocorrelation function is particularly suitable for characterizing the nonstationary noise.[2]

One of the difficulties in time domain noise measurement is to generate a stable timing reference. Any fluctuation in the timing reference appears in the measurements as data pattern position fluctuation. The time domain medium noise correlation function was first measured by Tang[3] using a delayed trigger technique. A new measurement technique that does not require special hardware trigger was recently introduced.[4] In this paper, an improved version of this technique is extended to the dibit noise correlation study.

The data pattern used in this study is illustrated in Fig. 1. A dibit pattern is placed between two well-separated isolated pulses, which are captured for alignment purposes. Ensembles of data patterns, each composed of 200–400 waveforms, were collected for each dibit separation. The energy median of the first pulse, defined as the temporal point, where energy to the left equals energy to the right, is calculated for each ensemble member. Each data pattern is then shifted in order to align the energy median of the first isolated pulses of all the data patterns. After alignment, the center dibits were averaged and the noise associated with each waveform was determined by subtracting the average. The two-dimensional noise correlation function for an ensemble of waveforms was calculated by

$$C(t_1,t_2)=\frac{1}{N}\sum_{i=1}^{N} n_i(t_1)n_i(t_2), \tag{1}$$

where N is the number of waveforms in the ensemble, $n_i(t)$ is the noise waveform for the ith waveform, and t_1 and t_2 are two temple points. Since the energy median locations are affected by the noise in the channel, this alignment introduces an extra amount of position jitter to the noise correlation function of the center dibit, i.e., the noise correlation calculated after the alignment is composed of both the intrinsic noise of the dibit pattern and the alignment jitter introduced in the alignment process. The alignment jitter, namely the energy median fluctuation of the first isolated pulse in Fig. 1, can be determined by measuring the fluctuation of the energy median separation of the first and second isolated pulses. Since the two isolated pulses are well separated, and the fluctuations of the two energy medians are assumed to be independent and identical, the alignment jitter is determined by the energy median separation fluctuation divided by $\sqrt{2}$. The energy median is chosen as an alignment reference because it is relatively insensitive to white Gaussian noise. The alignment jitter is removed from the total jitter embedded in $C(t_1,t_2)$, which is determined by empirical eigenfunction expansion.[5]

The experimental parameters utilized in this study are listed in Table I. For both setups, a two stage trigger tech-

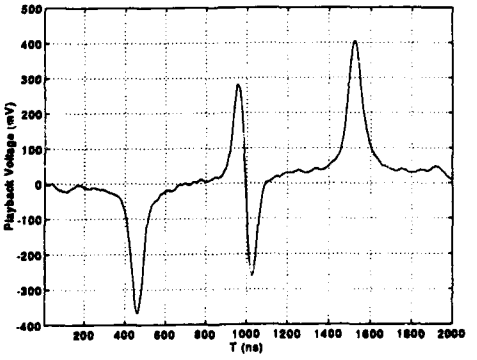

FIG. 1. Waveform used in the study.

 0021-8979/94/75(10)/5765/3/$6.00 © 1994 American Institute of Physics

TABLE I. Experimental parameters for the noise correlation measurements.

	Head			Disk		Head/Disk	
	g (nm)	$p1/p2$ (μm)	N	Hc (Oe)	Mrt (m emu/cm^2)	FH (nm)	V (m/s)
Setup 1	70	3.7/3.7	23	650	5.4	195	20.3
Setup 2	35	7.5/9.5	42	1450	3.0	93	8.1

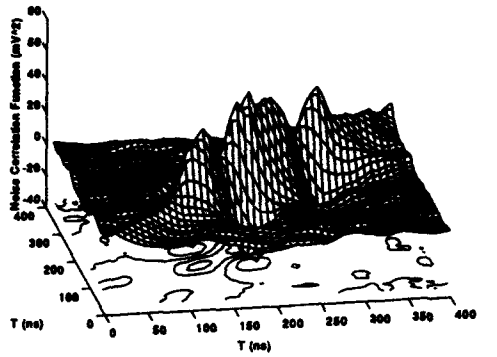

FIG. 2. Noise correlation function for a well-separated dibit pattern. Data of dibit with 838 nm bit separation in setup 2 were used.

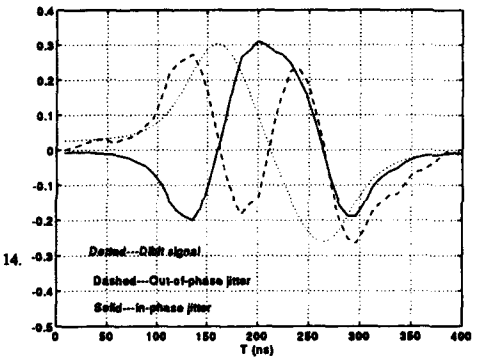

FIG. 3. The leading two eigenfunctions for the noise correlation matrix shown in Fig. 2.

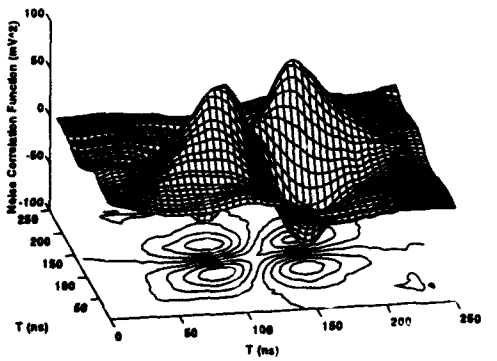

FIG. 4. The noise correlation function for a closely spaced dibit. Data of dibit with 287 nm bit separation in setup 2 were plotted.

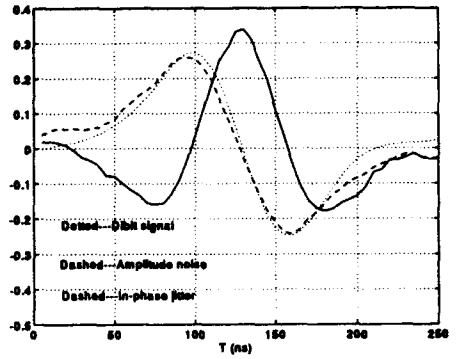

FIG. 5. The leading two eigenfunction for the noise correlation function shown in Fig. 4.

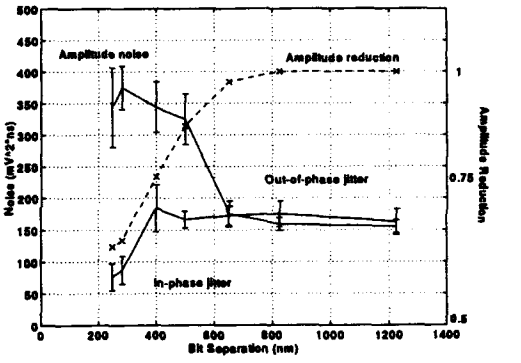

FIG. 6. The noise power associated with the two leading noise modes and dibit amplitude reduction vs bit separation.

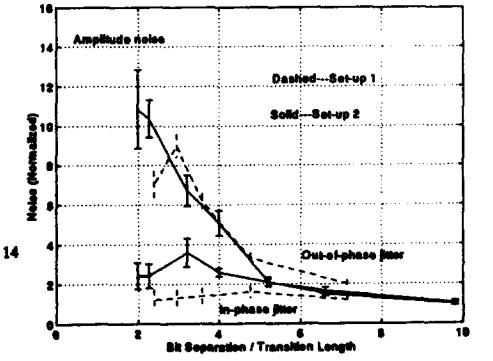

FIG. 7. The ratio of noise power for the two leading modes to bit separation vs the ratio of bit separation to transition parameters for both setups. The data are normalized to that of low density.

nique was used with a digital oscilloscope. The primary trigger was the index of the spindle to ensure a once per revolution data capture, the second trigger source in the delay-by-event mode was the repeating data pattern. Each waveform was averaged up to 64 times to remove the stationary electronic noise. After data collection, the trigger delay event number was advanced for the next waveform capture. This process was repeated until the desired number of waveforms was stored. Dibit with different bit separations were measured. The waveforms were sampled at 2 GSamples/s by using a Tektronix DSA 602A scope for setup 1. The sample rate for setup 2 was 400 MSamples/s by using a HP54112D digital scope. The empirical eigenfunction expansion was applied to the correlation function $C(t_1,t_2)$.[5] The noise modes and associated mechanisms are discussed in the following section. The nonlinear amplitude loss for each bit separation was also measured. This loss is defined as the ratio of measured dibit peak-to-peak amplitude to that expected from measured isolated pulse based on linear superposition.

The measured noise correlation function (after removing alignment jitter) for a well-separated dibit is shown in Fig. 2. The data from setup 2 are used. It is clearly seen that the dibit noise correlation can be determined from linear superposition of the noise correlation of the isolated pulse[3,4] at large bit separations. The leading two normalized eigenfunctions for the noise correlation function shown in Fig. 2 are plotted in Fig. 3. The dibit signal is also shown for comparison. The eigenvalue associated with the first two eigenfunctions is much larger than the other eigenvalues in the expansion. This is true for the entire range of the dibit separations used in this study, indicating the dominance of the two noise modes in dibit recording. The first eigenfunction, almost identical to the first-order derivative of the signal, is identified as the dibit position fluctuation, i.e., the locations of both pulses in the dibit move in the same direction (in-phase jitter). The second eigenfunction results from the fluctuations of the locations of the two pulses in the dibit in the opposite direction (out-of-phase jitter) and resembles the first-order derivative of the positive and negative isolated pulses placed in the locations of the two pulses in the dibit.

The measured dibit noise correlation function for a small bit separation is shown in Fig. 4. The correlation function exhibits two separated peaks. Noise power in the center of the dibit is very low similar to Ref. 8. The associated two leading eigenfunctions are plotted in Fig. 5. The dibit signal is also shown. The in-phase jitter remains and an amplitude-like noise emerges as the leading noise mode. This mode of noise originates from two possible physical mechanisms: First, the out-of-phase jitter (the shape of the out-of-phase jitter approaches that of the dibit signal as the bit separation is reduced); and second, the amplitude variation of the dibit. The latter may be caused by the nonlinear interaction between the two pulses in the dibit (e.g., the percolation fluctuation). The noises resulting from these two mechanisms are almost identical (in vector space, the two noise vectors are nearly parallel) for small bit separations.

The noise power in the two leading noise modes is plotted versus bit separation for setup 2 in Fig. 6. The errors are the spread of the result from multiple data collections. The noise associated with in-phase jitter decreases slightly at small bit separation. The noise associated with the amplitude mode (out-of-phase jitter for large bit separations) increases and hence becomes the dominant noise source as the bit separation is reduced. The two separate peaks of the noise correlation function are the direct result of the dominance of the amplitude mode noise. The amplitude reduction of dibits is also plotted versus bit separation in the same figure. It is seen that the increase in the amplitude mode noise and the amplitude reduction occur approximately at the same bit separation, as noted previously by Melas *et al.*[7] Comparison for setup 1 shows the same result. In Fig. 7, the ratio of noise power to bit separation for the two leading eigenfunctions are plotted versus the ratios of bit separation to transition parameter for both setups. The data are normalized to that at low density. The transition parameters were calculated by using the Williams–Comstock Model (343 and 127 nm are used for each setup, respectively). The supralinear increase in the amplitude noise results in the supralinear noise enhancement for a high-frequency recording, as observed in frequency domain measurements.[1]

Noise correlation functions were measured for dibit patterns with varying bit separations. An empirical eigenfunction expansion was used to identify the leading noise modes. For large bit separation, in-phase and out-of-phase jitter were found to be the leading noise sources. The shape of the eigenfunction associated with the out-of-phase jitter approaches that of the dibit signal, resulting in an amplitude-like noise mode, almost identical to the noise generated by amplitude fluctuation of the dibit. As the effects of the two physical mechanisms combine, the amplitude noise increases dramatically for a reduced bit separation, corresponding to the supralinear noise enhancement in a high-frequency data pattern. The comparison of nonlinear amplitude loss and noise measurement shows the supralinear increase in noise, and the amplitude reduction occurs at about the same bit separation.

[1] R. A. Baugh, E. S. Murdock, and B. R. Natarajan, IEEE Trans. Magn. **19**, 1722 (1983).
[2] H. N. Bertram and X. Che, IEEE Trans. Magn. **29**, 201 (1993).
[3] Y. S. Tang, IEEE Trans. Magn. **21**, 1389 (1985).
[4] G. H. Lin and H. N. Bertram, IEEE Trans. Magn. **29**, 3697 (1993).
[5] S. Yuan and H. N. Bertram, IEEE Trans. Magn. **28**, 84 (1992).
[6] M. Melas, P. Arnett, and J. Moon, IEEE Trans. Magn. **24**, 2712 (1983).
[7] L. Nunnelly, T. Arnoldussen, M. Burleson, and D. Parker, IEEE Trans. Magn. **29**, 3703 (1993).

Magnetic viscosity in high-density recording

Pu-Ling Lu and Stanley H. Charap
Data Storage Systems Center, Department of Electrical and Computer Engineering, Carnegie Mellon University, Pittsburgh, Pennsylvania 15213

For future ultrahigh-density magnetic recording, the magnetic viscosity in thin-film media will become an issue due to the drastic reduction in grain size. An algorithm combining a Monte Carlo method and molecular dynamics was employed to study the thermal effects in thin-film media. The component of the field perpendicular to the plane defined by the axes of shape anisotropy and uniaxial crystalline anisotropy makes it necessary to use the three-dimensional energy surface to find the minimum energy barrier. This barrier is used to sample the reversal rate and the elapsed time. Hysteresis loops for various $K_u V/kT$ ratios and sweep times are simulated. Isolated and di-bit transitions are written, taking into account thermally assisted switching. After the head field is turned off, the subsequent thermal decay is computed for time spans as long as 6 months. Significant aftereffect is found for grain volumes about twice that for ordinary superparamagnetism.

I. INTRODUCTION

With the assistance of thermal energy, the magnetization of a particle can surmount an energy barrier and switch from one stable direction to another. This process will take a certain time compared with the quick approach of the particle magnetization to a local minimum when subjected a large external field. This phenomenon is an inherent behavior of ferromagnets and is well known as the magnetic aftereffect or viscosity.[1] The ratio of the energy barrier to the thermal energy kT (k is the Boltzmann's constant, T is the absolute temperature) determines the magnitude of the aftereffect. A comprehensive treatment of thermal fluctuations was given by Brown.[2] In magnetic recording, the media must be adequately resistant to thermal fluctuations. To maintain a certain amount of written signal so as to have adequate signal-to-noise ratio (SNR) after thermal decay, generally requires a $K_u V/kT$ much higher than the commonly known superparamagnetic limit of about 25.[3] Studies of the magnetic aftereffect have been widely reported for particulate recording media.[3–6] In their work on granular Fe-(SiO_2), Kanai and Charap[6] first implemented an algorithm combining a molecular dynamics method and a Monte Carlo method to study the aftereffect and transition broadening in the media. This algorithm was introduced to treat an ensemble of spherically shaped uniaxial particles with a distribution of easy-axis directions and with particle magnetizations free to orient in three dimensions. Good agreement with vibrating sample magnetometer (VSM) experimental results was found. While no significant thermal effect is expected for current thin-film media, which typically have $K_u V/kT$ values of more than 1000, it will be an important issue for future ultrahigh-density magnetic recording media due to the dramatic reduction in grain size in order to maintain reasonable jitter performance. In this investigation, an algorithm was introduced to study the magnetic viscosity in thin-film media under conditions of ultrahigh-density recording.

II. MODEL

A computer simulation model has been developed on DEC 3100 and 5000 workstations, based on a combined molecular-dynamics model and the Monte Carlo simulation of aftereffect.

The molecular-dynamics part of the model is similar to the micromagnetic model of Zhu and Bertram.[7] In the model, the film is considered to consist of a planar array of hexagonally shaped grains. The grains are hexagonal close packed and every grain is assumed to be a single-domain particle with a nonmagnetic boundary; within each grain only coherent rotation is assumed. Crystalline uniaxial anisotropy, magnetostatic interactions, and the self-demagnetizing field of each grain are included in the calculation. Intergranular exchange interaction across the boundaries is not included in this study. All grains have the same anisotropy energy constant K_u and saturation magnetization M_s. We have chosen arrays of grains with random distribution of easy-axis orientations, confined to the plane.

The Landau–Lifshitz equation with Gilbert damping is employed to describe the time development of the magnetization of each grain,

$$\frac{d\hat{\mathbf{M}}}{d\tau} = -\frac{1}{1+\alpha^2}\,(\hat{\mathbf{M}}\times\mathbf{H}) - \frac{\alpha}{1+\alpha^2}\,[\hat{\mathbf{M}}\times(\hat{\mathbf{M}}\times\mathbf{H})]. \quad (1)$$

Here $\hat{\mathbf{M}}$ is the unit vector in the direction of the magnetization of the grain, γ is the gyromagnetic ratio, τ is the time normalized to the period $(\gamma H_k)^{-1}$, and α is the damping constant, which is chosen to be 1 for numerical convenience in all calculations. Previous studies[7] have found that the macroproperties such as coercivity and remanence are insensitive to the damping constant. Although the precession time does depend on its value, this time is usually of the order of nanoseconds which is very short compared with the elapsed time in the Monte Carlo simulations. $\mathbf{H}$ is the effective field acting on the grain, normalized to H_k. H_k is the crystalline anisotropy field, $H_k = 2K_u/M_s$, and M_s is the saturation magnetization. It is through $\mathbf{H}$ that the equations for the individual grains are coupled. The integration of the Landau–Lifshitz equations is conducted by a fourth-order Runge–Kutta method.

In this Monte Carlo method,[8] the energy barriers ΔE for all grains are calculated first. The probability per unit time for reversal of each grain can be obtained by utilizing Néel's formalism: $r_i = 1/\tau = f_0 \exp(-\Delta E_i/kT)$. Here τ is the time constant, ΔE_i is the energy barrier for the ith grain, and f_0 is

 0021-8979/94/75(10)/5768/3/$6.00 © 1994 American Institute of Physics

a frequency constant chosen to be 10^9 s^{-1} as an approximation.[2] The reversal rate R of the assembly can be found by summing all the reversal probabilities,

$$R=\sum_{i=1}^{N} r_i.$$

According to the probability r_i/R, one of the magnetizations is selected to reverse. The time Δt needed for this reversal to happen can be sampled from the exponential probability density function $R\exp(-tR)$, i.e., $\Delta t=-\ln(\xi)/R$, where ξ is a random number uniformly distributed from 0 to 1.

This algorithm uses, as the time increment, the average time between successful reversals instead of the constant amount of simulation time increment in the conventional Monte Carlo method. For the latter method, the number of time increments yielding a successful reversal may be but a small fraction of the increments tested. For this method, the time increment will tend to increase as the total activity decreases, reflecting the increased time between successful magnetization reversals. This method eliminates the unsuccessful switching attempts *a priori* and makes the simulation practical for any time length of interest although it starts slower than the conventional Monte Carlo method.

Generally, a grain has two forms of anisotropy. One is the crystalline uniaxial anisotropy and the other is the shape anisotropy which is also uniaxial if an ellipsoid approximation of the grain shape is assumed. The latter one can vary from zero to comparable, or even larger than the former, and can be in the film plane or out of the plane, both depending on the ratio of grain height to its in-plane dimension and M_s. The combined effects of these two anisotropies defines a plane; for magnetizations confined to that plane the anisotropy is effectively uniaxial; but, thin-film media usually have a distribution of the crystalline easy-axis orientations. The magnetizations, and so the interaction fields, are free to orient in the film plane or space. The effective field on each grain, including the applied field and the interaction field, is usually not in the plane defined by the crystalline easy axis and the easy axis from shape anisotropy. The grains are no longer uniaxial. In general, a three-dimensional energy surface must be used in order to find the minimum energy barrier which is the difference between the energy at a saddle point on the surface and the energy at the local minimum. A two-dimensional secant method is employed to search for this barrier.

The molecular dynamics and Monte Carlo method are used alternately. The former is employed first to find the local equilibrium configuration and then, by the Monte Carlo method, one grain magnetization is chosen to reverse and the elapsed time for this step is sampled. The total elapsed time equals the accumulated Δt for all steps. This process is repeated till the desired simulation time is reached.

III. RESULTS AND DISCUSSIONS

The system we used for calculation was a 60×60×1 array of hcp grains. Easy axes were randomly distributed in the film plane. The boundary conditions in the track direction for di-bit transitions and across a track were set to be periodic, while an antiperiodic boundary condition was employed in track direction for isolated transitions. The head field used to write transitions was a Karlquist field produced by a head with a gap length $g=120$ nm and a head media separation $d=38.5$ nm. The thermal effect during the writing process was included. The 3D energy surface was used to find the minimum energy barriers. The subsequent thermal decay was observed for as long as 6 months. The temperature was always 300 K.

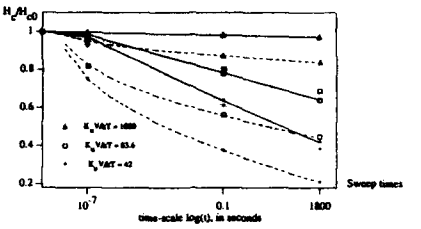

FIG. 1. The simulated coercivity H_c (solid), normalized by the coercivity without thermal effect H_{c0}, against logarithmic time scale for $K_uV/kT=42$, $K_uV/kT=83$, $K_uV/kT=1000$. The dashed curves are calculated from Eq. (2). The dotted curves are a linear dependence on log(t).

Figure 1 shows coercivities normalized to the value H_{c0} in the limit of zero sweep time for $K_uV/kT=1000$, 83, 42, corresponding to grains with both diameters D and film thicknesses δ of 23, 10, and 8 nm and sweep times of 10^{-7} s, 0.1 s, and 30 min, corresponding to recording, MH loop, and VSM measurements. Here D is the diameter of the circle inscribed within the hexagonal grain. For all cases, K_u was 4×10^6 erg/cm^3, $M_s\delta/H_kD=0.1$ ($M_s/H_k=0.1$), and there was no exchange interaction between grains. The step size of the applied field was chosen as that in a VSM measurement: a small one of about 90 Oe in the vicinity of coercivity and a big one of about 900 Oe for the remaining range. At zero sweep time, or without thermal effect, the coercivities for three cases are all equal to a same value: $H_{c0}=0.435H_k$. For $K_uV/kT=1000$, no significant thermal effect on coercivity is observed. However, when $K_uV/kT=83$, which is very near the value of the likely ratios for the future single layer media, the coercivity has pronounced time dependence. The H_c obtained from the simulated VSM measurement is about 65% of that without thermal effect. For $K_uV/kT=42$, the value is further reduced to less than half of H_{c0}. The remanence squareness and the coercivity squareness, however, show little change for all cases. In his article,[3] Sharrock derived the following time dependence formula of coercivity for particulate media without interactions among particles:

$$\frac{H_c(t)}{H_0}=1-\left[\frac{kT}{KV}\ln\left(\frac{f_0t}{0.693}\right)\right]^{1/2}, \tag{2}$$

This formula instead of the linear dependence on log(time) was found to fit experimental data well; but, our simulation results for thin-film media fit with the log(time) curve for $\tau>1/f_0$. Interactions among grains and lack of orientation may contribute to the difference.

Figure 2 shows the thermal effect on (a) an isolated transition and (b) a di-bit transition for a single-layer film with

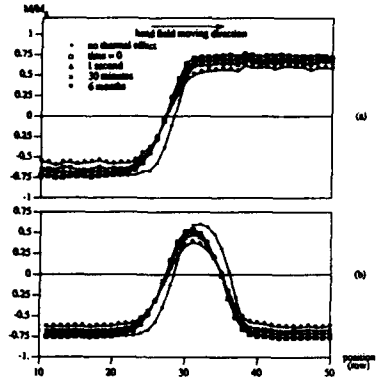

FIG. 2. (a) An isolated transition and (b) a di-bit transition in a single-layer film for cases without thermal effect, with thermally assisted switches during writing, and after 1 s, 30 min, and 6 month decay. Here $K_u V/kT \simeq 60$ and magnetostatic interaction parameter $M_s\delta/H_k D = 0.1$ ($M_s/H_k = 0.1$).

$D = \delta = 9$ nm, and $M_s\delta/H_k D = 0.1$. These dimensions lead to $K_u V/kT \simeq 60$. This value is more than twice that for ordinary superparamagnetism. In the figure, the horizontal axis is the position represented by the number of the row along the track direction and vertical axis is the magnetization component along the recording track direction averaged across the track and normalized by M_s. A writing head moves from left- to right-hand side. Head fields are reversed at row 40 for the isolated transition and at rows 40 and 48 for the di-bit transition, respectively. There are usually 60 rows in our model, and the magnetizations from rows 1 to 9 and from 51 to 60 are not shown here. The bit length, i.e., the distance between two transitions in the di-bit transition, is about 62 nm (8 rows). The positions of transition centers shift about one row, corresponding to about 8 nm, due to the thermally assisted switches during writing. The magnitude of the magnetization away from a transition decreases from around $0.74M_s$ to about $0.61M_s$ after 6 months of decay. The decay in the region between two transitions of a di-bit becomes worse when they become closer and interact with each other. The magnetization at the bit center is reduced from about $0.6M_s$ without thermal aftereffect to $0.54M_s$ when including the thermally assisted switches during writing. It further decays to about $0.38M_s$ after 6 months. The magnetostatic interaction from the magnetization beyond the two transitions tends to reverse the recorded magnetization between them with the help of thermal energy. Some of the first transition is erased by the head field while writing the second one.

IV. CONCLUSIONS

A combined molecular-dynamics and Monte Carlo computer simulation method has been developed to study the thermal effect in magnetic thin-film recording media. The crystalline anisotropy, shape anisotropy, applied field, and magnetostatic interaction field are included in the model. A three-dimensional energy surface is used to find the minimum energy barrier in general. The writing process was simulated with thermally assisted switches taken into consideration and subsequent thermal decay was observed for long time spans. Significant aftereffect was found both in hysteresis loop simulations and transition decays for grain volumes more than twice that for ordinary superparamagnetism.

ACKNOWLEDGMENTS

The authors would like to express their gratitude to Dr. Yasuhisa Kanai for discussions. This material is based (in part) upon work supported by the National Science Foundation under Grant No. ECD-8907068. The government has certain rights in this material.

[1] S. Chikazumi and S. Charap, *Physics of Magnetism* (Krieger, Malabar, FL, 1964), Chap. 15.
[2] W. F. Brown, IEEE Trans. Magn. **MAG-15**, 1196 (1979).
[3] M. P. Sharrock, IEEE Trans. Magn. **MAG-26**, 193 (1990).
[4] S. B. Oseroff, D. Clark, S. Schultz, and S. Shtrikman, IEEE Trans. Magn. **MAG-21**, 1495 (1985).
[5] S. H. Charap, J. Appl. Phys. **63**, 2054 (1988).
[6] Y. Kanai and S. H. Charap, IEEE Trans. Magn. **MAG-27**, 4972 (1991).
[7] J. Zhu and N. Bertram, J. Appl. Phys. **63**, 3248 (1988).
[8] K. Binder, *Monte Carlo Method in Statistical Physics* (Springer, Berlin, 1986), Chap. 1, p. 32.

Friction and wear of ultrahigh-density magnetic tapes

Bharat Bhushan and Steven T. Patton
Computer Microtribology and Contamination Laboratory, Department of Mechanical Engineering, The Ohio State University, Columbus, Ohio 43210

The objective of this study was to identify any differences in the friction and wear characteristics of particulate tapes produced with various magnetic particles and metal-evaporated (ME) tapes. Accelerated friction and wear experiments were conducted with a tape reciprocated in a shoeshine mode over an aluminum drum. We have found that barium ferrite and Co-γFe_2O_3 tapes exhibit the least damage to themselves and the mating drum. The ME tape exhibited the least durability among all tapes. The effect of tape roughness on friction was found to be dependent on the hardness of the mating material. Friction increased with an increase in the roughness during the tests with a soft aluminum drum due to severe plowing of the aluminum. However, friction decreased with an increase in the roughness with a hard ferrite surface which is consistent with the asperity contacts being elastic in nature (with no appreciable plowing contribution to the friction).

I. INTRODUCTION

Particulate tapes with γFe_2O_3, Co-γFe_2O_3, and CrO_2 magnetic particles are most commonly used for audio, video, and data processing applications. In order to achieve ever increasing higher recording densities, metal particle (MP) and metal-evaporated (ME) tapes with high smoothness have been introduced. Particulate tapes with barium ferrite (BaFe) particles may be introduced in the future for ultrahigh-density applications. Most of the research to date related to the tribology of the head-tape interface has been conducted on tapes with γFe_2O_3 and CrO_2 particles in contact with ceramic heads, and little understanding exists on the other tapes. Barium ferrite particles are smaller in size than other magnetic particles which may affect the friction and wear of the interface. High surface energy, high ductility, and high reactivity of the metal particles and the ME films compared to oxide particles are expected to affect the tribological performance of the metal tapes. ME tapes are expected to differ in tribological performance when compared to the particulate tapes.

The objective of this study was to identify any differences in the friction and wear characteristics of the various tapes (Table I) when they were mated with an aluminum drum used in video cassette recorders (VCR), camcorders, and instrumentation and data recorders. An Al drum (with trace amounts of Si and Cu and a microhardness of ~160 kg/mm^2) was chosen as the mating surface for the following reasons: in rotary head recorders there is continuous contact of the magnetic layer with a stationary lower Al drum, contact can also occur with the high speed rotating upper drum, and finally little is known about the tribology of magnetic tapes in contact with materials other than those commonly used for magnetic heads. The effect of tape roughness (for identical composition tapes) was also investigated for the cases of mating the tapes against both a soft Al drum and a hard Ni-Zn ferrite head (microhardness ~700 kg/mm^2).

TABLE I. Summary of friction and wear data using various magnetic tapes against an aluminum drum (24.6 nm rms) for 7 k passes.

Tape Mag. part./HCA/rms (nm)	$\mu_s/\mu_p/\mu_{max}$	Drum damage	Tape damage
CrO_2/none/21.9	0.33/0.28/0.34	Large	Large
Co-γFe_2O_3/Al_2O_3/35.3	0.30/0.30/0.46	Small	Small
MP/Al_2O_3, Cr_2O_3/5.7	0.23/0.16/0.23	Medium	Medium
BaFe/Al_2O_3/8.5	0.24/0.21/0.25	Small	Small
ME (Co-Ni)/9.5	0.20/0.38[a]/0.38	Small	Medium

[a]ME tape failed after 4 k passes.

II. EXPERIMENTAL PROCEDURE

The experiments were performed using a portable reciprocating friction test apparatus.[1] In this apparatus a tape reciprocates in a shoeshine mode using a motorized linear stage over a cylindrical mating surface of interest. One end of the tape is secured to a dead weight, and the other end is attached to a load cell. The coefficient of friction is then calculated using the belt equation.[1] Tests were conducted at the following conditions: wrap angle=0.52 rad (30°), tape length=150 mm, average tape speed=60 mm/s, and a contact pressure of about 0.5 kPa. The tests were performed in a class 10 000 laboratory at a temperature of 22±1 °C and 50±5% RH. Each wear test was stopped when either the number of tape passes (one tape pass is tape motion over drum in either direction) was 7000 (test duration ~6 h) or the coefficient of friction attained a value of twice its initial value. The tapes and the Al samples were subjected to materials analyses.

III. RESULTS AND DISCUSSION

A. Friction and wear of magnetic tapes mated with an Al surface

Table I gives a summary of the results of our experimental observations along with tape compositions, surface roughnesses, and the initial, maximum, and final coefficients of friction. We also describe the extent of drum and tape damage in a relative manner. We find that uniaxial scratching (via an abrasive mechanism) and rolling particle impact wear (rolling particles are large Al asperities sheared by the test tapes) are the primary wear mechanisms for the drum. For each mating tape used in these experiments we find that material from the magnetic layer is transferred to the drum sur-

 0021-8979/94/75(10)/5771/3/$6.00 © 1994 American Institute of Physics

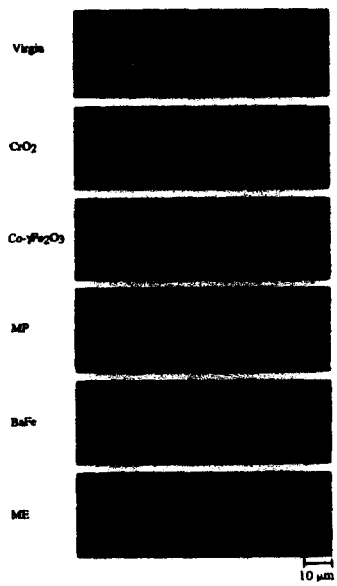

FIG. 1. Optical micrographs of a virgin and worn Al drum surfaces used in wear tests against various tapes

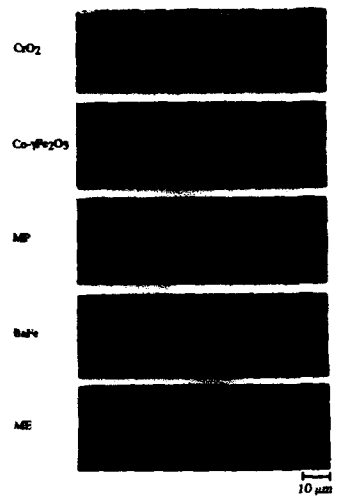

FIG. 2. Optical micrographs of worn tape surfaces used in wear tests with a mating surface of Al.

face. This material is either loosely adhered binder uniaxially transferred to the drum (particulate tapes) or strongly adhered tape coating material that is locally transferred to the drum (particulate and thin film tapes). Figure 1 presents optical micrographs of the worn drum surfaces and the virgin drum surface is given for comparison. The drum surface mated with the CrO_2 shows evidence of excessive uniaxial scratching, clearly the CrO_2 tape has severely damaged the drum surface.[1] In the case of Co-γFe_2O_3, the drum scratching is relatively mild when compared to the CrO_2. The MP tape is observed to scratch the drum more than the Co-γFe_2O_3 tape but slightly less than the CrO_2 tape, this severity of damage is somewhat surprising and unexpected since the metal particles have lower hardness and higher ductility than the oxide magnetic particles. This observation can be explained however when one considers that abrasive head cleaning agents normally added in the tape construction could contribute excessively to the drum damage in the case of MP tape and that the metal particles are oxidized prior to tape loading for corrosion resistance. The BaFe tape is found to scratch the drum only mildly (comparable in severity to Co-γFe_2O_3) and the scratches appear to be inflicted by very small sharp particles, this is consistent with the fact that BaFe particles are the smallest magnetic particles used in these experiments.[1] The ME tape inflicts no abrasive scratching to the drum surface, however we do see evidence of impact wear due to rolling Al particles in the interface and unique to the ME tape the presence of adhesive-type wear scars are seen on the drum surface.

The tape damage is found to be proportional (except in the case of ME tape) to the drum damage in each experiment. This suggests that Al debris plays an important role in the tape wearing process. Several wear mechanisms for the tape surfaces have been identified. We find that pull out (via a pull-out mechanism triggered by embedded Al debris), rolling particle impact wear (as described earlier), and three-body abrasion (the third-body particle being Al) are the primary wear mechanisms. Figure 2 presents optical micrographs of the worn tape surfaces. The CrO_2 tape is severely damaged by pull out and the worn area is found to have a large concentration of Al debris. In the case of Co-γFe_2O_3 tape, pull out is also the primary wear mechanism but the severity of the wear is much less than the case of the CrO_2 tape. The MP tape is found to have pull out wear (in a teardrop-shaped Al-rich region) as well as three-body abrasive wear scars (note Al debris in the wear tracks). The BaFe tape is found to be only mildly damaged and the type of damage is rollover particle impact wear and the formation of teardrop-shaped flat regions on the tape surface (due to a sandpaper-type abrasion of very fine Al particles). The wear mechanisms for the ME tape are adhesive wear and rollover particle impact wear. The adhesive wear of the ME tape is consistent with the observations of drum wear. We found that the ME tape is particularly susceptible to impact wear, this may be a result of the fact that ME tape does not easily embed large Al asperities that are sheared from the drum surface.

The coefficient of friction for each tape as measured during the wear test is given in Fig. 3. The trends in the frictional behavior of the tapes can be explained assuming an elastic contact between the tapes and drum.[1] In an elastic contact regime, the surface roughness of each mating surface

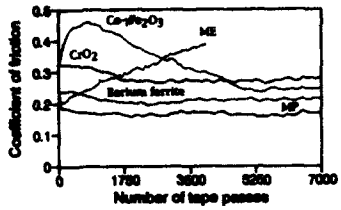

FIG. 3. Friction plot of CrO_2, Co-γFe_2O_3, MP, BaFe, and ME magnetic tapes during wear tests with an Al mating surface.

FIG. 5. Optical micrographs of Al drum and 11.6 nm rms MP tape after a single pass of the tape over the drum surface.

plays an important role in determining the coefficient of friction.[1] The CrO_2 and the MP tapes both inflict severe damage to the drum surface which increases the surface roughness; thus we expect the coefficient of friction to decrease. This is exactly what we see for these two tapes (Fig. 3). This also confirms that in this particular case the roughness of the tapes plays no significant role in the trend in the coefficient of friction (CrO_2 being rough and MP being smooth, Table I). Also notice that this effect seems to saturate after about 2000 passes, this suggests that the roughness of the drum becomes saturated at this stage of the wear test. The Co-γFe_2O_3 and BaFe tapes inflict only mild damage to the drum surface, this suggests that the effect of tape roughness may play a significant role in determining the trends in the coefficient of friction for these two tapes. The Co-γFe_2O_3 tape has higher roughness than the BaFe tape (Table I) and we expect the Co-γFe_2O_3 tape to first be smoothened by the drum surface to saturation and will only then begin to roughen as it is damaged in the wear process. Hence for Co-γFe_2O_3 tape, we expect the coefficient of friction to increase to saturation and then decrease until the tape roughness saturates at a high value. This is exactly what we see for the Co-γFe_2O_3 tape (Fig. 3). The BaFe tape (being smooth) should only be roughened by the wear process and hence we expect its coefficient of friction to only decrease during the wear test. This is exactly what we see (Fig. 3) for the BaFe tape. Notice that the coefficient of friction saturates at a minimum after about 1000 passes. The ME tape clearly gave the worst frictional performance of all the tapes. Its coefficient of friction increased with a nearly linear dependence on the number of passes (Fig. 3). This could be a result of topical lubricant starvation and/or degradation which leads to excessive metal on metal contact and consequently a high adhesive contribution to the frictional force.

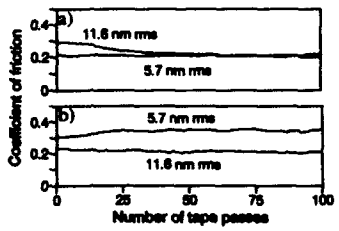

FIG. 4. Friction plot of 5.7 and 11.6 nm rms MP tapes with a mating surface of (a) Al drum and (b) Ni-Zn ferrite head.

B. The effect of surface roughness on friction and wear of magnetic tapes mated with a soft Al drum and a hard Ni-Zn ferrite head

Figure 4 shows the coefficients of friction for a smooth (5.7 nm rms) and an uncalendered rough (11.6 nm rms) MP tape that were reciprocated against both a soft Al drum and a hard Ni-Zn ferrite head. We found that in the case of an Al mating surface that the rough tape gives a higher coefficient of friction throughout the test [Fig. 4(a)], this result was attributed to excessive plowing of the Al by the rough tape. This was proven by passing both the smooth and rough tape over the drum only one time. We then observed the drum for both cases looking for signs of excessive plowing in the case of the rough tape compared to the smooth tape case. Figure 5 shows the evidence of plowing of the drum and severe damage by three-body abrasion to the rough tape. We also found that in the case of a Ni-Zn ferrite mating surface that the rougher tape gives a lower coefficient of friction than the smooth tape [Fig. 4(b)]. This is completely consistent with the expected result if the contact between the tapes and head is elastic with no appreciable plowing occurring at the interface.[1] Analogous experiments were performed using both rough (32.4 nm rms) and smooth (16.6 nm rms) CrO_2 tapes and the same trends were obtained in these experiments.

IV. CONCLUSIONS

Among the four particulate tapes studied here, Co-γFe_2O_3 and BaFe tapes inflicted the least damage to the mating surface and to itself with the BaFe exhibiting a low and stable coefficient of friction. The ME tape succumbed to a severe adhesive wear mechanism and the coefficient of friction attained a value of twice its initial value in only 4000 passes. The effect of tape roughness (for tapes with identical composition) was found to be dependent on the hardness of the mating material.

[1] B. Bhushan, *Tribology and Mechanics of Magnetic Storage Devices* (Springer, New York, 1990).

Analysis of write and read spacing loss for perpendicular recording (abstract)

Yoichiro Tanaka, Tomoko Komai, and Takashi Hikosaka
Communication and Information Systems Research Laboratories, Toshiba R&D Center, Komukai, Kawasaki 210, Japan

Spacing loss phenomena for perpendicular recording have been experimentally investigated but are yet analytically unclear. This paper provides an analytical model of the write and read processes for perpendicular recording to study spacing loss. In the write process, the magnetic transition length is determined mainly by the head field gradient and demagnetizing field gradient at transition assuming perfectly square M-H loops of the perpendicular media.[1] An arctangent transition is a reasonable approximation just in the process of creating transitions under a single-pole-type write head field. Decreased magnetization, however, between transitions due to a strong demagnetizing field has to be involved to simulate the write process more accurately. A double arctangent transition model is newly proposed to represent both a sharp transition and magnetization decay away from transition which is supposed to change the transition length after writing. Magnetization decay is characterized by a maximum demagnetization limit ($H_d < H_c$) near the transition. Write spacing loss ($=K_w\ d/\lambda$ [dB]) is derived from the derivative of double arctangent transition length in terms of spacing. Read spacing loss ($=K_r\ d/\lambda$ [dB]) is characterized by both $\exp(-2\pi d/\lambda)$ and the head-to-media magnetic interaction parameter η as a function of spacing.[2] Experimental proof is shown with double-layer perpendicular media and single-pole-type flying heads. Write and read spacing is independently controlled by the air pressure of the vacuum chamber enclosing the spinstand. It has been found that the write spacing loss factor K_w depends on the head field distribution and wavelength. Measured K_w values showed a maximum value of -110 [dB] at short wavelength where magnetization decay is considered to give little effect. K_w decreased with wavelength as the calculated loss factor behaved. The wavelength dependence of the read spacing loss factor K_r has been found to quantify the strength of the head-to-media magnetic interaction.

[1] D. J. Bromley, IEEE Trans. Magn. **19**, 2239 (1983).
[2] Y. Nakamura *et al.*, IEEE Trans. Magn. **22**, 376 (1986)

 0021-8979/94/75(10)/5774/1/$6.00 © 1994 American Institute of Physics

Experimental Preisach analysis of the Wohlfarth relation (abstract)

Ferenc Vajda and Edward Della Torre
Institute for Magnetics Research, George Washington University, Washington, DC 20052

The Wohlfarth relation[1] states that, for noninteracting particles, the ascending normalized remanent major loop, $m_D(H)$, is twice the shifted normalized virgin remanent magnetization. Researchers[2] claim to measure the interaction field and characterize it as "positive" and "negative" depending on whether it is "above" or "below" the axis on a Henkel plot or a ΔM plot. It has been shown[3] that the moving Preisach model can compute all observed types of ΔM plots by varying only the moving parameter, α, and over only positive values. This type of behavior is characterized by the ratio of α to the standard deviation of the interaction field. In this paper the measured ΔM plot for two commercial recording media, namely longitudinal BaFe and γ-Fe_2O_3, is presented and the positive moving parameter of each sample is identified. Let us define the operative field of the system by $H_{op}=H+\alpha M$, where M is the total magnetization. It is then shown that, when plotted as a function of H_{op}, all samples deviate from the Wohlfarth relation in the same way, even though they exhibit "positive" and "negative" ΔM when plotted as a function of the applied field, H, as seen in Fig. 1. It will also be shown that deviations from the Wohlfarth relation are due to a combination of parameters, not only the interaction field. The model and the identification algorithm has been used to simulate all the observed ΔM plots.

[1] E. P. Wohlfarth, J. Appl. Phys. **29**, 595 (1958).
[2] P. E. Kelly *et al.*, IEEE Trans. Magn. **25**, 3888 (1989); P. R. Bissel and A. Lyberatos, J. Magn. Magn. Mater. **95**, 27 (1991).
[3] F. Vajda and E. Della Torre (unpublished).

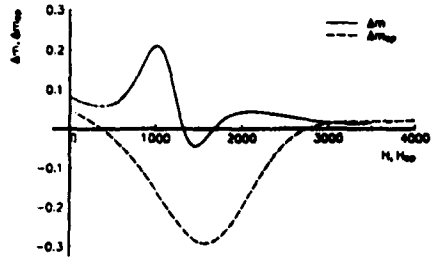

FIG. 1. ΔM plot (solid line) and operative ΔM plot (dashed line) of the BaFe sample.

 0021-8979/94/75(10)/5775/1/$6.00 © 1994 American Institute of Physics

Magnetic fine structure of domain walls in iron films observed with a magnetic force microscope

Roger Proksch,[a] Sheryl Foss, and E. Dan Dahlberg
School of Physics and Astronomy, University of Minnesota, Minneapolis, Minnesota 55455

Gary Prinz
Naval Research Laboratory, Washington, D.C. 20375

The submicron magnetic structure of domain walls in a single-crystal iron film has been studied using a magnetic force microscope (MFM). The MFM tip was sensitized to the component of the field perpendicular to the film plane. The sample examined was a 500-nm-thick single-crystal film of iron, grown by molecular-beam epitaxy (MBE). Before it was imaged, the film was magnetized along its (in-plane) easy axis in a 2000-Oe field. Studies of the domain structure at numerous locations on the film surface revealed a rich variety of micromagnetic phenomena. Parallel domain walls, determined to be Bloch walls with a width of 70–100 nm, were seen along the easy axis, spaced roughly 30 μm apart. These appeared to be Bloch walls. Bloch lines were also observed in the walls with an average periodicity of 1.5 μm. This is a value smaller than that predicted for Bloch wall-line structures. In addition, a pronounced zig–zag structure was observed, as expected from previous Fe whisker observations.

The sample examined in this work was an epitaxially grown single crystal of iron, grown in the (110) plane.[1] It is a bcc, α-Fe crystal with unit cell $a=2.866$ Å, grown on a fcc (110) GaAs substrate. The single-crystal nature of the film has been verified by x-ray analysis and magnetic measurements. In the images presented here, the vertical axis corresponds to the [001] axis of the film. The hard axes are the [111] body diagonals, 55° away from the [001], and the intermediate [110] axis is oriented 90° from the [100].

Representative high-resolution images of the (110) surface of a 0.5-μm-thick, epitaxially grown iron film are shown in Figs. 1 and 2. The images were acquired using a Nanoscope III scanning probe microscope from Digital Instruments. The microscope was operated in the tapping/lift™ mode. This technique allows the separation of the topography from the long-range, magnetic forces. A good example of this is shown in Fig. 1 where the magnetic signal from a domain wall is shown on the left and the associated surface topography is shown on the right. For this work, the noncontact scan height was maintained at 50 nm.

The MFM probes used in this study were microfabricated Si cantilevers coated with 30 nm of a CoCr alloy. This coating was optimized for best response and resolution of the MFM. When imaging with an MFM, one concern is that stray fields from the magnetic tip can modify the micromagnetic structure of the sample.[2] An experimental test for this can be made by observing the dependence of the micromagnetic structure on the MFM tip scan height.[3] For the iron samples studied in this work, there was no variation of the sample micromagnetic structure when the tip scan height was varied between 20 and 250 nm. Accordingly, for the remainder of this work, we will assume that modification of the micromagnetic sample structure by the tip is negligible.

The importance of being able to separate topography and magnetism is especially apparent when examining the 15-μm-square scan above part of the iron film shown in Fig. 1. In this figure, the vertical axis corresponds to the [001] magnetic easy axis of the film, and the horizontal axis to the [110] intermediate axis. The [111] hard axis is oriented 55° away from the vertical [001] axis.

Because the MFM is sensitive to the stray field gradients and not the magnetization itself, it is not possible to determine the magnetization in regions where it is constant (e.g., in the middle of a domain). In the case of this sample, however, we are "fortunate" enough to have a number of scratches in the film surface. Where the magnetization intersects these imperfections, magnetostatic charge builds up, resulting in stray magnetic fields that can be detected with the MFM. By observing the polarity of the stray fields from a scratch, it is possible to get an idea of the projection of the magnetization onto the line of the scratch. Thus, the presence of normally unwanted flaws in the sample allow statements about the magnetization that would otherwise be impossible to make.

Using this, we can return to Fig. 1 and immediately observe several "scratch signatures" in the magnetic image. These can be used to verify the presence of a domain wall and assign directions to the magnetization of the two identifiable domains in the image. Specifically, there is a deep scratch running horizontally along the upper quarter of the topographical image of Fig. 1. An examination of the corresponding section of the magnetic image shows stray fields above the scratch. On the left of the bright vertical line in the magnetic image, the contrast is bright (attractive interaction) on the top and dark (repulsive interaction) on the bottom. When the scratch crosses the vertical line, this flips to dark

[a]Present address: Dept. of Physics, St. Olaf College, Northfield, MN.

 0021-8979/94/75(10)/5776/3/$6.00 © 1994 American Institute of Physics

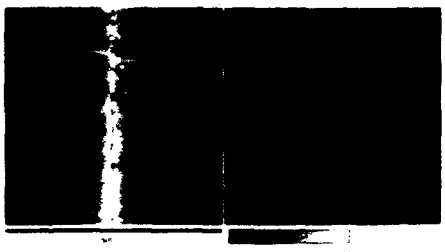

FIG. 1. A 15-μm-square scan of a domain wall. The left image is the magnetic signal and the right is the associated topographical image. In the magnetic image, the direction of the magnetization is clearly visible from the stray fields above the scratches running horizontally through the image. On the left-hand side of the domain wall, the stray fields above the scratches are attractive (bright) on the top and repulsive (dark) on the bottom. The situation is reversed on the right-hand side of the domain wall. Also clearly visible is a wide, bright envelope superimposed on the narrow Bloch line structure. The scale bar is for the topographical image on the right.

FIG. 2. The gray scale image on the left is a 2.5-μm zoom onto a section of the domain wall of Fig. 1. The three traces on the right-hand side of the figure are average wall profiles obtained by averaging roughly 50 line scans made across each of the two dark and center bright wall segments in the gray scale image.

on the top and bright on the bottom. Thus, we can infer that the [100] component of the magnetization flips across the vertical line, i.e., the vertical line is a domain wall. This effect is visible to a lesser extent in a horizontal scratch near the bottom of the figure.

The Bloch wall seen in Fig. 1 contains many remarkable features. Figure 2 is a 2.5-μm-square high-resolution image of a section of the domain wall in Fig. 1. Also shown in Fig. 2 are three traces which are averaged wall profiles for the two dark and middle bright wall segments shown in the magnetic image. There are a number of observations that can be made of both of these figures. These include:

(i) Alternating dark and bright segments indicative of Bloch lines in the domain wall. Alternating wall segments are visible in all the images.

(ii) Zig–zag structure, where the joints of the zig–zag are the points where the dark and bright segments connect. This zig–zag effect is visible in every image.

A qualitative explanation of features (i) and (ii) follows from simple magnetostatic energy considerations and was provided by Shtrikman and Treves.[4] When a Bloch wall encounters a surface, there is a buildup of magnetostatic charge on the surface. By alternating the sense of the wall rotation, the sign of the charge on the surface also alternates, reducing the magnetostatic energy. The loss of magnetostatic energy is offset by a gain in wall energy associated with the transition regions between the wall segments with opposite rotation senses. Through a simple energy approximation method, Shtrikman and Treves predicted the relationship between the period of the segmented wall T and the thickness of the film L to be $T/L \sim 0.38$ for iron. For the sample studied here we observed an average of $T/L = 1.1$, significantly larger than the predicted. Shtrikman and Treves also explained that the magnetostatic energy could be further reduced if the Bloch wall becomes canted along the line of the wall, resulting in a surface zig–zag structure.

(iii) The sharp, Bloch wall-like section of the wall is always 70–100 nm wide.

(iv) Diffuse, overall bright (or dark) signal superimposed on the wall that is at least three to four times as wide as the alternating segments of the wall. This sort of structure is visible in all the images.

These observations [(iii) and (iv)] can be compared to a number of predictive calculations. First, both Hubert[5] and Scheinfein *et al.*[6] have predicted a Néel-type structure near the surface which caps the bulk Bloch wall. The film modeled in Scheinfein and co-workers was a 0.5-μm-thick single crystal of iron. Their work makes testable predictions and leads to a qualitative understanding of at least some of the features observed here. Their calculations predict that within the bulk of the sample, the transition takes the form of a Bloch wall. The width of the calculated wall in the bulk was within 5% of the classical uniaxial result of $\delta = \kappa(A/K)^{1/2}$. For a magnetic crystal with uniaxial anisotropy, $\kappa = \pi$, and the calculation gives $\delta = 70$ nm. At the surface, the Bloch walls curl in response to demagnetizing fields to form Néel walls. In this calculation the Néel "cap" of the wall is at least 300-nm wide, more than three times the bulk Bloch wall value. According to Lilley,[7] cubic anisotropy has the effect of changing the prefactor κ. Following Lilley, for a domain wall where the direction of the normal to the boundary is along the [110] axis, the prefactor becomes $\kappa = 5.6$. Thus, by including the cubic nature of the anisotropy, the domain wall width is predicted to be $\delta = 125$ nm. This is a value roughly 25–50 nm larger than that observed. Hartmann[8] extended some of these calculations to include surface demagnetizing effects. For iron at room temperature, Hartmann calculated $\kappa = 9.03$ for a domain wall well below the surface. At the surface, the wall narrows considerably to $\kappa = 0.7$. Translated into distances, this implies the bulk wall is $\delta^{(\text{bulk})} = 200$ nm and the surface wall is $\delta^{(\text{surface})} = 15$ nm. This calculation is based on the spatial extent of the vertical component of the magnetization and does not preclude the Néel cap effect predicted by Hubert and Scheinfein *et al.* Given the large range of predictions, the measured wall widths are reasonable. A final note concerning the wall widths is that the CoCr film on the cantilever was on the order of 50 nm, so we would expect the magnetic resolution of the cantilever to be on that scale or larger.

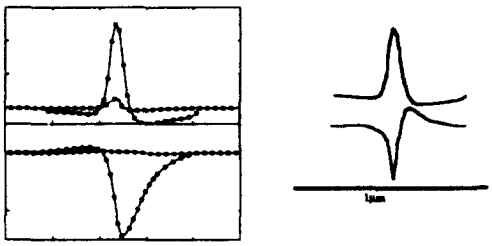

FIG. 3. (a) The results of the micromagnetic calculation of Scheinfein *et al.* for a 0.5-μm-thick iron film. The magnetization as a function of position in a domain wall is shown at the surface of the film (denoted "surface") and in the middle of the film (denoted "bulk"). At the top, the vertical component of the magnetization in both regions is plotted and the bottom two curves show the component perpendicular to the wall plane. (b) The magnetostatic charge densities obtained from the magnetization curves in (a).

The MFM is sensitive to stray fields arising from magnetostatic charge from the divergence of the magnetization ($\rho_M = -\nabla \cdot \mathbf{M}$). In the following analysis, we will hypothesize that the MFM responds to a combination of magnetostatic charges at and below the sample surface. To qualitatively calculate the magnetostatic charge, we will use the two-dimensional wall calculation of Scheinfein *et al.* The magnetization as a function of position resulting from this model is plotted in Fig. 3(a). For this model, there are two divergence terms that contribute to the charge, $\rho_x = -\partial M_x/\partial x$ and $\rho_z = -\partial M_z/\partial z$. Referring to Fig. 3(a), we can see that at the surface there is only a very small vertical component of the magnetization. Thus, between the middle of the crystal (we will refer to this as the "bulk") and the surface there is a significant amount of magnetostatic charge originating from the divergence of the z component of the magnetization. Although a quantitative statement about the magnitude of this charge cannot be made from observations of the differences between the M_x surface and bulk curves in Fig. 3(a), we can see that the distribution of ρ_z is symmetric about the center of the wall and is roughly 150-nm wide. Thus, for qualitative purposes, we will assume it has the form of the M_z curve [see Fig. 3(b)]. If we extend this result to three dimensions, this should be the charge responsible for the Bloch lines observed in the MFM images.

Returning to the surface [Fig. 3(a)], we also see that the x component of the magnetization has significant divergence. The charge density from the x divergence of the magnetization ρ_x, where $\rho_x = -\partial M_x/\partial x$ at the surface is plotted qualitatively in Fig. 3(b). It is this contribution to the charge which may lead to the wide, diffuse signal surrounding the narrow Bloch line structure of the walls. The total magnetostatic charge which results in the stray fields measured by an MFM should be the sum of these two curves. Plots of the charge density from the bulk ρ_z and the surface ρ_x and the three traces from Fig. 2 are plotted in Fig. 4.

A qualitative comparison of the calculated charge densities to the observed wall profiles (Fig. 4) shows a number of disparities. In particular, although the width of the narrow

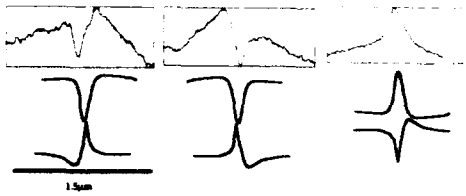

FIG. 4. From symmetry arguments, the wall structure resulting from the model of Scheinfein *et al.* can take on four possible permutations. Three of them were chosen as "best fits" for the averaged wall profiles shown in Fig. 2. Although there is rough qualitative agreement between the experimental averages and a combination of the charge distributions, there are some important disparities. The most obvious is the long wavelength signal in the experimental data that is not present in the charge distributions.

portion of the domain walls agrees with the models, there is an overall curve superposed on each of the walls which, if originating from ρ_x, is much larger than expected. This is the bright, diffuse structure observed in almost all of the magnetic images. An explanation for this large scale structure is still needed from micromagnetic models. In addition, the length scales of the asymmetries observed in the experimental traces do not match the predicted charge distribution very well. Thus, while interpretation of the MFM response to stray fields above the iron film in terms of the micromagnetic model of Scheinfein *et al.* shows some agreement, there are troublesome length scale questions that must still be addressed.

The technique of magnetic force microscopy has been applied to domain wall structures in a 500-nm-thick ferromagnetic single crystal of iron. A wide variety of phenomena was observed in the sample, including Bloch walls, Bloch lines, and zig–zag walls. The structure of the Bloch walls has been discussed in terms of a two-dimensional micromagnetic model. Although the results presented are qualitative, several inconsistencies between modeled and measured data were determined. Work is in progress on more sophisticated, quantitative modeling of the MFM response to domain walls in iron, taking into account the extended nature of the tip, tip domain structure, and topographical effects between the tip and the sample surface.

This work was partially supported by the ONR, Grant No. N0014-89-J-1355. This is contribution 9309 of the Institute for Rock Magnetism. The Institute for Rock Magnetism is supported by grants from the Keck Foundation and the NSF.

[1] G. A. Prinz and J. J. Krebs, Appl. Phys, Lett. **39** (1981).
[2] U. Hartmann, J. Appl. Phys. **64**, 1561 (1988).
[3] H. J. Mamin, D. Rugar, J. E. Stern, R. E. Fontana, Jr., and P. Kasiraj, Appl. Phys. Lett. **55**, 318 (1989).
[4] S. Shtrikman and D. Treves, J. Appl. Phys. **31**, 147S (1960).
[5] A. Hubert, *Theorie der Domanenwande in Geordneten Medien* (Springer, Berlin, 1974), p. 246.
[6] M. R. Scheinfein, J. L. Blue, K. J. Coakley, D. T. Pierce, R. J. Celotta, and P. J. Ryan, Phys. Rev. B **43**, 3395 (1991); M. R. Scheinfein, R. J. Celotta, and D. T. Pierce, Phys. Rev. Lett. **63**, 668 (1989); M. R. Scheinfein, D. T. Pierce, and R. J. Celotta, J. Appl. Phys. **67**, 5932 (1990).
[7] B. A. Lilley, Philos. Mag. **41**, 792 (1950).
[8] U. Hartmann, Phys. Status Solidi A **101**, 227 (1987).

Influence of rf magnetron sputtering conditions on the magnetic, crystalline, and electrical properties of thin nickel films

M. S. Miller, F. E. Stageberg, Y. M. Chow, K. Rook, and L. A. Heuer
Seagate Technology, 7801 Computer Avenue South, Minneapolis, Minnesota 55435

Thin nickel films with thicknesses ranging from 30 to 150 nm were deposited via radio frequency (rf) magnetron sputtering. The influence of argon pressure, film thickness, rf input power, and deposition rate on the magnetic, crystalline, and electrical properties of the films was evaluated. Depending on deposition conditions, film coercivity could be varied from 2 to 290 Oe while saturation magnetization could be varied from 280 to 500 emu/cm^3. Higher argon pressures produced lower coercivity films. The films exhibited a dominant fcc(111) orientation. Lower argon pressures and higher rf input powers increased nickel grain sizes. Classical models based on domain wall energy considerations and film microstructure are used to intrepret the observed experimental results.

I. INTRODUCTION

Nickel is a simple ferromagnetic material with an fcc crystalline structure. The magnetic properties of evaporated[1] and electrodeposited[2] thin nickel films have been studied as a function of film thickness, grain size, and substrate material.[3]

The goal of this study was to evaluate the influence of rf magnetron deposition conditions on the magnetic, crystalline, and electrical properties of thin nickel films.

II. EXPERIMENTAL PROCEDURE

Nickel films were rf magnetron sputtered onto 3-in.-diam silicon wafers. A deposition matrix was conducted whereby both the argon pressure and rf input power were systematically varied. An rf input power of 250 W produced a 0.2-nm/s deposition rate while a 2000-W input power corresponded to a 1.3-nm/s deposition rate. The silicon substrate was held directly above the sputtering target and simultaneously rotated about its center during deposition. Film thickness was varied from 30 to 150 nm.

Film thickness was determined via a profilometer step height measurement at five different locations on the wafer. Film resistance was determined via a standard four-point probe measurement.

The magnetic properties of the samples were measured with a vibrating sample magnetometer (VSM) and a low-field $B-H$ looper. The maximum field of the VSM was 12.5 kG.

An x-ray diffractometer using Cu$K\alpha$ radiation was used to provide x-ray diffraction data.

III. EXPERIMENTAL RESULTS

Figures 1 through 3 exhibit the influence of thickness on nickel coercivity for films deposited at various argon pressures and rf input powers. With the exception of the films deposited above 500-W input power at 4-μm argon, the coercivity of the nickel films show a similar behavior with increasing film thickness. As the film thickness increases, the nickel coercivity rapidly rises and reaches a maximum value between 55 and 80 nm. At thicknesses greater than 100 nm, nickel coercivity tends to level off at a value roughly equal to two-thirds of the peak coercivity value. Similar behavior has recently been reported for thin sputtered iron films.[4]

For a specific input power, Figs. 1–3 also show that the peak nickel coercivity tended to decrease with increasing argon pressure. The magnetic properties of the nickel films were isotropic.

Figure 4 shows that lower argon pressures can significantly increase the saturation magnetization of nominally 65-nm thick nickel films. For argon pressures above 8 μm, higher rf powers also tended to increase film saturation magnetization.

X-ray diffraction analysis of nominally 65-nm-thick nickel films revealed a dominant fcc (111) orientation with a lattice parameter of 3.51 Å. A weak fcc (200) orientation was also noted in the films.

By using the Scherrer equation[5] and the full width at half-maximum (FWHM) values of the (111) diffraction peaks, the crystalline grain sizes in the nickel films can be estimated.

Figure 5 shows that lower pressures and higher rf input powers increased the grain sizes of the nickel films. Higher input powers increase the amount of substrate heating which, in turn, promotes lateral grain growth.

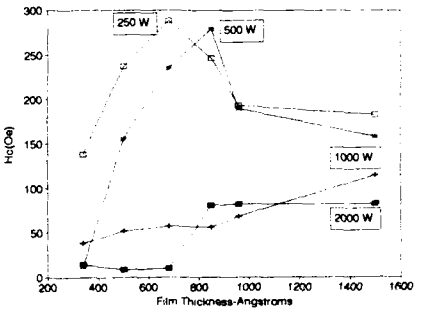

FIG. 1. Nickel coercivity as a function of film thickess for films deposited at 4-μm pressure and various rf input powers.

 0021-8979/94/75(10)/5779/3/$6.00 © 1994 American Institute of Physics

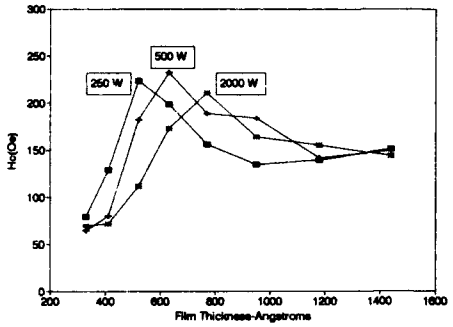

FIG. 2. Nickel coercivity as a function of film thickness for films deposited at 10-μm pressure and various rf input powers.

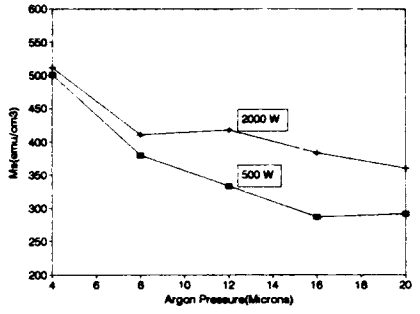

FIG. 4. Nickel saturation magnetization vs argon pressure for films deposited with 500- and 2000-W rf input powers.

IV. DISCUSSION

The variations in nickel properties with changes in the deposition variables are quite interesting. The general behavior of nickel coercivity with film thickness and the variations in film saturation magnetization can be explained by consideration of classical models of domain wall energetics and film microstructure.

The large variations in nickel saturation magnetization are most easily understood by considering the influence of argon pressure and substrate temperature on film microstructure.

In general, lower argon pressures and higher substrate temperatures produce films with a denser microstructure.[6,7]

Denser films typically exhibit less intergranular voiding and are more resistant to oxidation effects. In the case of magnetic films, such microstructurally dense films should exhibit lower resistivity and higher saturation magnetizations. This precise behavior is exhibited in Figs. 4 and 6.

Higher argon pressures can also influence film coercivity. Scanning electron microscopy (SEM) and atomic force microscope (AFM) analysis have revealed that the high resistivity, low M_s films may have void contents as high as 10%–15%. These voids may promote increased oxidation in the film.[4] Nonmagnetic inclusions will also serve as local sites for domain wall pinning.

The general behavior of nickel coercivity with thickness can be understood by considering domain wall energetics. Domain wall energetics will dictate the amount of field necessary to saturate the film magnetization in a particular direction.

For film thicknesses greater than 100 nm, Bloch wall formation is favored. The total wall energy density for a Bloch wall[8] can be expressed by

$$E_{\text{Bloch}}=A\left(\frac{\pi}{w}\right)^2 w+\frac{1}{2}\ wK+\frac{\pi w^2 M_s^2}{w+t}, \tag{1}$$

where A is the exchange stiffness, w the wall width, K the anisotropy constant, M_s film saturation magnetization, and t is the film thickness.

For film thicknesses below 100 nm, the magnetostatic energy per unit area of a domain wall becomes appreciable relative to the usual exchange and anisotropy energies. At thicknesses below 50 nm, the total wall energy is almost entirely magnetostatic and is best approximated in an expression derived by Néel,[9]

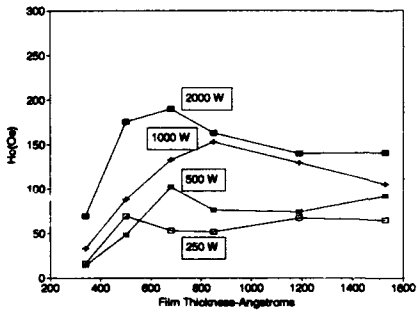

FIG. 3. Nickel coercivity as a function of film thickness for films deposited at 20-μm pressure and various rf input powers.

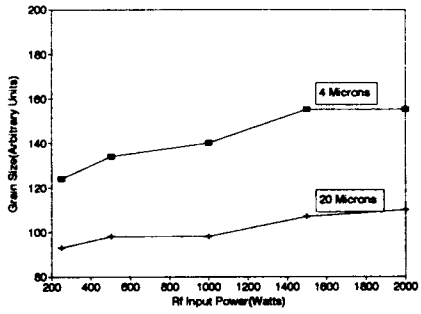

FIG. 5. Relative nickel grain sizes as a function of argon pressure and rf input power.

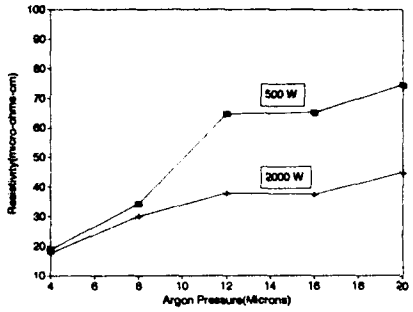

FIG. 6. Resistivity of nominal 65-nm-thick nickel films vs argon pressure for films deposited at various rf input powers.

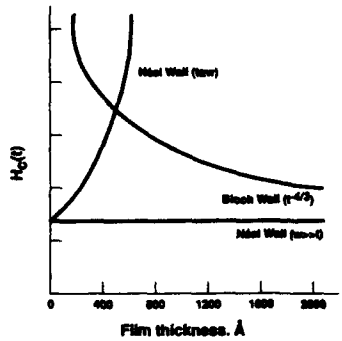

FIG. 7. Theoretical dependence of nickel coercivity with film thickness for Bloch- and Néel-type walls.

$$E_{\text{Néel}}=\frac{\pi t w M_s^2}{t+w}. \tag{2}$$

Film coercivity H_c is related to the variation of the wall energy along the direction s of wall motion via[8]

$$H_c(t)=\frac{1}{2M_s}\left[\frac{\partial E}{\partial t}+\frac{E}{t}\right]\frac{dt}{ds}. \tag{3}$$

For thin films with Bloch or cross tie walls, with thicknesses t, such that $t>w$, Eqs. (1) and (3) yield the well known "4/3 law" of Néel:

$$H_c(t)_{\text{Bloch}}=4.2\left(\frac{A^2}{M_s}\right)^{1/3}\frac{dt}{ds}\ t^{-4/3}=ct^{-4/3}, \tag{4}$$

where dt/ds is assumed to be a nonzero constant.

Similarly for Néel walls, Eqs. (2) and (3) yield

$$H_c(t)_{\text{Néel}}=\frac{\pi M_s}{2}\left[2+\left(\frac{t}{w}\right)^2\frac{\partial w}{\partial t}\right]\frac{dt}{ds}=aM_s. \tag{5}$$

Thus, for Néel wall widths such that $w\gg t$, there should be no first-order dependence of coercivity on film thickness.

This result provides an explanation for the lack of observed coercivity variation with film thickness for the films deposited at 4-μm argon pressure and high input power. Figures 4 and 6 indicate that low argon pressures and high powers produce films with dense oxide-free microstructures. This type of microstructure is likely to produce a high degree of intergranular exchange and magnetostatic coupling.[10] Such highly coupled films would be expected to have relatively wide, $w\gg t$, domain walls.

Conversely, voids in the films or oxidized grain boundaries reduce intergranular magnetic coupling and produce domain wall pinning sites. These effects, which occur as argon pressure increases and or as process temperature (rf power) decreases, are likely to reduce the width of the Néel domain walls. For Néel wall widths where $t\simeq w$, Eq. (5) shows that coercivity will vary quadratically with film thickness.

Equation (5) also exhibits a linear dependence of coercivity on M_s. This relation can be used to account for the observed increase in film peak coercivity with reduced argon pressures, since lower pressures produce higher M_s nickel films.

Finally, Fig. 7 employs Eqs. (4) and (5) to exhibit the theoretical dependence of coercivity on film thickness for Bloch and Néel walls. The theoretical curves of Fig. 7 appear quite similar to the experimental data of Figs. 1–3.

[1] L. Reimer, Z. Naturforsch. Teil A **11**, 649 (1956).
[2] W. Ruske, Ann. Phys. (Leipzig) **2**, 274 (1958).
[3] M. Prutton, *Thin Ferromagnetic Films* (Butterworths, London, 1964).
[4] Y. K. Kim and M. Oliveria, J. Appl. Phys. **74**, 1233 (1993).
[5] B. D. Cullity, *Elements of X-ray Diffraction* (Addison-Wesley, Reading, MA, 1978), p. 102.
[6] B. A. Movchan and A. V. Demchishin, Phys. Met. Metallogr. (USSR) **28**, 83 (1969).
[7] J. A. Thornton, J. Vac. Sci. Technol. **11**, 666 (1974).
[8] S. Middelhock, *Ferromagnetic Domains in Thin NiFe Films* (Drukkerji Wed. G. Van Soest, N. V. Amsterdam, 1961).
[9] L. Néel, C. R. Acad. Sci. **241**, 533 (1955).
[10] J. G. Zhu and H. N. Bertram, J. Appl. Phys. **63**, 3248 (1988).

Molecular magnets V(tetracyanoethylene)$_x \cdot y$(solvent): Applications to magnetic shielding

B. G. Morin and C. Hahn
Department of Physics, The Ohio State University, Columbus, Ohio 43210-1106

Joel S. Miller
Department of Chemistry, The University of Utah, Salt Lake City, Utah 84112

A. J. Epstein
Department of Physics and Department of Chemistry, The Ohio State University, Columbus, Ohio 43210-1106

The specific advantages and limitations of a new class of polymer based magnets [exemplified by V(TCNE)$_x \cdot y$(solvent) (TCNE=tetracyanoethylene)] for static and low frequency magnetic shielding and inductive applications are evaluated using results of dc superconducting quantum interference device magnetization and ac permeability measurements. Present materials have very low density ($\rho \sim 1$ g/cm^3), relatively high resistivity ($\sim 10^4$ Ω cm), and low power loss (as low as ~ 2 erg cm^{-3} cycle^{-1}). The highest initial room temperature permeability observed to date (for solvent=CH_2Cl_2) of $\mu_i = 13$ is modest for practical applications. Flexible processing methods are suggested for optimization of magnetic properties important for shielding applications.

Molecular based magnets present opportunities for developing a new class of lightweight materials for magnetic shielding and inductive applications, that are processible at room temperature using conventional organic chemistry. The field of molecular magnetism is in its infancy compared with other classes of soft magnetic materials. The discovery in the mid 1980's of ferromagnetism at 4.8 K in the linear chain electron transfer salt [$FeCp_2^*$][TCNE] (TCNE=tetracyanoethylene) marked the birth of molecular magnetism as a class of magnetic materials.[1,2] The report[3] in 1991 of room temperature ferrimagnetism in the polymeric material V(TCNE)$_x \cdot y(CH_2Cl_2)$ ($x \sim 2, y \sim 0.5$) was the first indication that this class may be of technological use.

Magnetic shielding of low frequency magnetic fields is accomplished with soft magnetic materials.[4] Current soft magnetic materials suitable for magnetic shielding include transition metal alloys and ferrite ceramics.[4] Transition metal alloys may be tailored to have very high initial permeabilities ($\mu_i \sim 20\,000$) and low coercive fields ($H_c = 0.006$ Oe) through choice of the transition metal concentrations, and annealing procedure to increase crystalline order. Cold working and machining reduce the shielding effectiveness of these materials to near that of high purity iron ($\mu_i \sim 200$). Ferrite materials also require an anneal to reach their maximum permeabilities ($\mu_i \sim 3000$).

Results of dc superconducting quantum interference device (SQUID) magnetization and ac permeability studies of V(TCNE)$_x \cdot y$(solvent) molecule based magnets are presented. The specific advantages and limitations of V(TCNE)$_x \cdot y$(solvent) and other molecular based magnets for static and low frequency magnetic shielding and inductive applications are identified. Although no members of this class are immediately suitable for these applications, their density, low power loss, and flexible low temperature processibility are promising for the development of lightweight shielding materials.

Samples of V(TCNE)$_x \cdot y$(solvent) are prepared by adding a solution of $V(C_6H_6)_2$ in solvent X dropwise to a solution of TCNE in solvent Y, resulting in a black powder precipitate. Examples of solvents are: (i) V(TCNE)$_x \cdot y(CH_2Cl_2)$ (X=Y=CH_2Cl_2); (ii) V(TCNE)$_x \cdot y(CH_3CN/C_6H_6)$ (X=C_6H_6, Y=CH_3CN); (iii) V(TCNE)$_x \cdot y(CH_3CN)$ (X=Y=CH_3CN). IR spectra showed an absence of C_6H_6 in the precipitate. Samples of V/TCNE based magnets also were prepared using an alternate procedure.[5] All samples are very reactive towards oxygen. Measurements were performed on powdered samples which were sealed under vacuum in quartz tubes. Elemental analyses yield significant uncertainties in x and y.[3]

The complex ac permeability was measured using the mutual inductance technique for 10–10^4 Hz.[6] The results presented in Fig. 1 were measured on powder samples at 400 Hz with an exciting field of 220 mOe. For V(TCNE)$_x \cdot y(CH_2Cl_2)$ (both preparations) and V(TCNE)$_x \cdot y(CH_3CN/C_6H_6)$, the permeability was measured by cooling to 2.0 K and stabilizing at each temperature before the ac permeability measurement. The ac permeability of

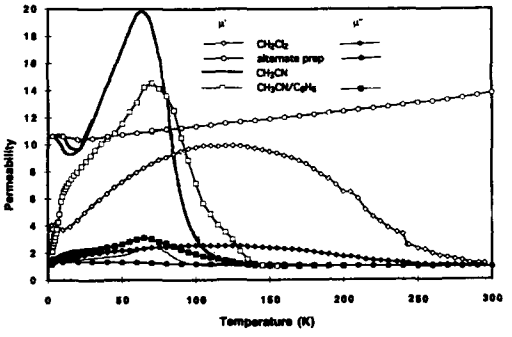

FIG. 1. Real and imaginary permeability of V(TCNE)$_x \cdot y(CH_2Cl_2)$, V/TCNE (alternate preparation), V(TCNE)$_x \cdot y(CH_3CN/C_6H_6)$, and V(TCNE)$_x \cdot y(CH_3CN)$. Uncalibrated χ' for V(TCNE)$_x \cdot y(CH_3CN/C_6H_6)$, and V(TCNE)$_x \cdot y(CH_2Cl_2)$ were previously published in Ref. 7.

 0021-8979/94/75(10)/5782/3/$6.00 © 1994 American Institute of Physics

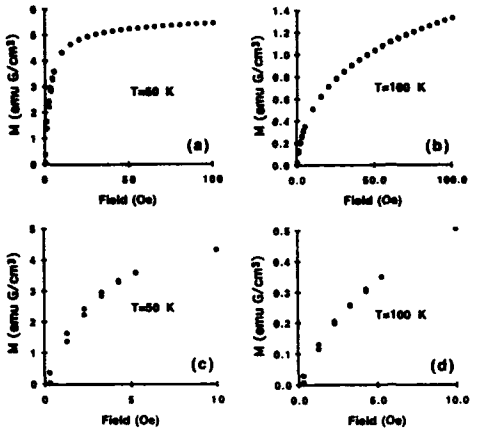

FIG. 2. Half hysteresis loops of $V(TCNE)_x \cdot y(CH_3CN)$ at 50 K [(a) and (c)] and 100 K [(b) and (d)]. Lower figures [(c) and (d)] have expanded axes.

$V(TCNE)_x \cdot y(CH_3CN)$ was measured as the sample was cooled from 30 to 5 K at a rate of 0.5 K/min, and then held at 5 K for 2 min before sweeping up to 150 K at the same rate.

Magnetic hysteresis was measured at 50 and 100 K with a Quantum Design MPMS SQUID magnetometer by cooling in zero field from 150 K to the measurement temperature, and then measuring the magnetization as the field is ramped up to 100 Oe, down to −100 Oe, and then back up to 100 Oe (at~0.33 Oe/s). The density of 1.0±0.2 g/cm^3 for both $V(TCNE)_x \cdot y(CH_2Cl_2)$ and $V(TCNE)_x \cdot y(CH_3CN)$ was determined in a glove box by pressing a pellet (1.3 cm diameter), and measuring its dimensions and mass. The demonstration shown in Fig. 3 was performed by suspending soft iron rods (common staples) above a $SmCo_5$ permanent magnet [Fig. 3(a)], and then placing a pressed pellet (1.3 cm diameter) of $V(TCNE)_x \cdot y(CH_2Cl_2)$ above the magnet [Fig. 3(b)] at room temperature under argon.

The ordering temperature T_c is above 350 K for $V(TCNE)_x \cdot y(CH_2Cl_2)$[3,5] (its decomposition temperature) 130–140 K for $V(TCNE)_x \cdot y(CH_3CN/C_6H_6)$,[7,8] and 80–120 K for $V(TCNE)_x \cdot y(CH_3CN)$ from both ac permeability and dc magnetization measurements. Initial permeability for $V(TCNE)_x \cdot y$(solvent) is independent of frequency from 10 Hz to 10 kHz, except near the spin glass freezing temperature T_f in $V(TCNE)_x \cdot y(CH_3CN/C_6H_6)$ and $V(TCNE)_x \cdot y(CH_3CN)$, where strong frequency dependence is seen.[9] Microwave experiments at 6 GHz show very small (~1) initial permeability for $V(TCNE)_x \cdot y(CH_2Cl_2)$ and $V(TCNE)_x \cdot y(CH_3CN/C_6H_6)$ at all temperatures in this frequency range.[10] The real and imaginary parts of the 400 Hz ac permeability, μ' and μ'', Fig. 1, do not follow the dc magnetization curves[7] for these materials.

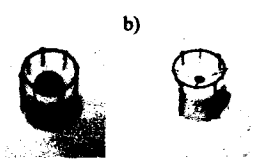

FIG. 3. (a) Folded soft iron rods (staples) are shown attracted to a $SmCo_5$ permanent magnet. (b) With a pellet (r=6.5 mm, t=1.7 mm) of $V(TCNE)_x \cdot y(CH_2Cl_2)$ at room temperature shielding the magnetic field, the soft iron rods hang freely.

The μ' indicated that the energy loss is greatest for $V(TCNE)_x \cdot y(CH_3CN/C_6H_6)$, and lowest for $V(TCNE)_x \cdot y(CH_3CN)$. $V(TCNE)_x \cdot y(CH_3CN/C_6H_6)$ has a re-entrant spin glass phase below 10 K.[7] For $V(TCNE)_x \cdot y(CH_3CN)$, warming and cooling ac permeabilities, Fig. 1, show irreversibility below $T_f \sim 18$ K.

The half hysteresis loops, Fig. 2, show low energy loss for $V(TCNE)_x \cdot y(CH_3CN)$ of 2 erg cm^{-3} cycle^{-1} at 50 K and 0.1 erg cm^{-3} cycle^{-1} at 100 K. This compares favorably with the losses for technological materials presented in Table I. Room temperature hysteresis for $V(TCNE)_x \cdot y(CH_2Cl_2)$ indicates a remanant magnetic induction $4\pi M = 10$ G, coercive field 60 Oe, and hysteresis loss of 5000 erg cm^{-3} cycle^{-1}. The coercive field for an alternately prepared V/TCNE based magnet is two orders of magnitude lower.

Figure 4 presents the calculated static magnetic shielding factor,[11] defined as $S = -20 \log(H_i/H_0)$, where H_0 is an applied static uniform magnetic field and H_i is the static magnetic field inside the sphere. Results are shown for a 10 cm outer radius spherical shield of mass 1 kg. Shielding factors $S > 10$ are for materials that have undergone extensive purification and annealing treatments, which have not yet been developed for $V(TCNE)_x \cdot y$(solvent) based magnets.

Table I gives a comparison of present molecular magnets (including a variant prepared using solvent=C_4H_8O[11]) with other magnetic materials used in shielding applications. Transition metal alloys offer high initial permeabilities (μ_i) and high saturation induction (B_s), at the cost of having large densities (ρ_d), large hysteresis losses (W), and large eddy current losses caused by low resistivities (ρ_r). Ferrite materials have smaller saturation induction and smaller initial permeabilities, but have lower eddy current and hysteresis power loss. $V(TCNE)_x \cdot y$(solvent) based magnets as yet have lower permeabilities [largest room temperature value to date being $\mu_i = 13$ for $V(TCNE)_x \cdot y(CH_2Cl_2)$, Fig. 2] and low saturation induction, but have the advantage of being an order of magnitude less dense than transition metal materials and having low eddy current and hysteresis losses. For comparison, μ_i for the linear chain molecular magnets $[FeCp_2^*][TCNE]$[1] and $[CrCp_2^*][TCNE]$[13] are 3.1 (4.7 K) and 3.6 (2.0 K), respectively, determined from their dc susceptibilities. With increases in permeability, molecular magnetic materials analogous to $V(TCNE)_x \cdot y$(solvent) can be applied to lightweight shielding of dc magnetic fields, and also to lightweight, low loss inductive applications such as transformer, inductor, and motor cores. Figure 3 demonstrates the effectiveness of $V(TCNE)_x \cdot y(CH_2Cl_2)$ in attenuating the magnetic force exerted by a $SmCo_5$ magnet on soft iron.

Though significant shielding is obtained for molecular based magnets such as $V(TCNE)_x \cdot y(CH_3CN)$, the effectiveness is much lower than that of currently used materials

TABLE I. Magnetic materials properties for shielding applications. Measurements are at room temperature, except where a footnote reference appears. Saturation induction (B_s) for V/TCNE based magnets is taken at 100 G field, which represents induction outside of the hysteresis loop; saturation magnetization is much higher. MF and LF ferrites are MnZnFe ferrites for medium frequency (MF, 0.1–2 MHz) and low frequency (LF, <0.2 MHz) applications. Information from References 3, 4, 7, 13, and 16.

Material	B_s (G)	B_r (G)	H_c (Oe)	μ_i	μ_i/ρ_d	ρ_r (Ω cm)	W (erg/cm^3)	ρ_d (g/cm^3)
Fe (99.8%)	20 500	8600	1.4	10	1.3	3×10^{-5}	30 000	7.9
Fe (99.9%)	21 500	···	1.0	200	25	1×10^{-5}	5000	7.9
Fe (99.95%)	21 500	···	0.05	10 000	1300	1×10^{-5}	5000	7.9
Mumetal	6500	3000	0.05	20 000	2300	6×10^{-5}	300	8.7
MF Ferrite	4000	1500–2000	0.05–1.2	500–1000	100–200	3.3×10^{6}	250	5
LF Ferrite	3500–5000	800–1400	0.12–0.38	800–2500	160–500	50–700	45–130	5
V(TCNE)$_x\cdot y$(CH_2Cl_2)	140 (320[b]) (315[a,b])	10 (19[a,c])	20–60, (0.5[a,c])	2 (14[d]) (13[a])	2 (13[a])	1×10^{4}	5000 (13[a,c])	~1
V(TCNE)$_x\cdot y$(C_4H_8O)	210[b]	···	···	10[e]	~10[e]	···	···	~1
V(TCNE)$_x\cdot y$(CH_3CN/C_6H_6)	180[b]	···	···	15[f]	~15[f]	1×10^{5}	···	~1
V(TCNE)$_x\cdot y$(CH_3CN)	190[b]	0.3[e]	0.15[e]	20[g]	20[g]	···	2[e]	~1

[a]Alternate preparation technique (Ref. 5); [b]20 K; [c]250 K; [d]150 K; [e]50 K; [f]75 K; [g]60 K.

($\mu_i^{V(TCNE)_x\cdot y(CH_3CN)} \approx 0.01\ \mu_i^{ferrite}$; $\mu_i/\rho_d^{V(TCNE)_x\cdot y(CH_3CN)} \approx 0.05\ \mu_i/\rho_d^{ferrite}$). Disorder may be added to V(TCNE)$_x\cdot y$(solvent) based magnets during preparation through the presence of additional reactants, present either as solvent or solute, creating molecular "alloy" materials. In V(TCNE)$_x\cdot y$(CH_2Cl_2), dichloromethane is suggested to be present primarily as a *spinless interstitial dopant*. As such, it will add disorder weakly to the exchange through superexchange and through van der Waals interactions with the unpaired-spin orbitals. It will also perturb the anisotropy by changing the local symmetry.

The role of acetonitrile in V(TCNE)$_x\cdot y$(CH_3CN), and V(TCNE)$_x\cdot y$(CH_3CN/C_6H_6) is much stronger, and is that of a *spinless substitutional* as well as *interstitial dopant*. Its effects on the exchange are through coordinating with the V, directly changing the occupancies of the unpaired-spin orbitals. Also, T_c is reduced through dilution. Replacement of a TCNE by an acetonitrile molecule breaks the local symmetry, inducing random anisotropy.[8] Though the acetonitrile content cannot be measured accurately it is suggested that T_c is a measure of the relative concentration. Reduction of $T_c\sim140$ K in V(TCNE)$_x\cdot y$(CH_3CN/C_6H_6) to $T_c\sim100$ K in V(TCNE)$_x\cdot y$(CH_3CN) indicates that the level of "solvent doping" can be controlled by the relative concentration of reactants, both solvent and solute.

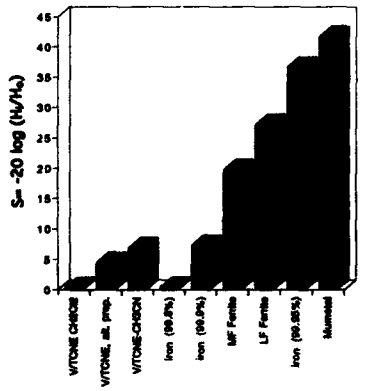

FIG. 4. Calculated magnetic shielding factor of various materials for a 1 kg spherical shield with a 10 cm outer radius. Values for ferrites, Fe (99.9%) and Mumetal are for materials that have undergone detailed annealing and purification processes to obtain high permeability. (Values from Ref. 3, 4, 7, and 13.)

It is suggested that through the fabrication of high purity molecular magnet "alloys," materials may be produced which are suitable for magnetic shielding and inductive applications at room temperature and above.

We thank C. Vasquez (DuPont) for sample preparation. This project was supported in part by the Department of Energy Division of Materials Sciences under Grant No. DE-FG-02-86BR456271.

[1] S. Chittipeddi, K. R. Cromack, J. S. Miller, and A. J. Epstein, Phys. Rev. Lett. **58**, 2695 (1987); for references, see also J. S. Miller, A. J. Epstein, and W. M. Reiff, Chem. Rev. **88**, 201 (1988); J. S. Miller and A. J. Epstein, Angew. Chem. **33**, xxx (1994).

[2] W. E. Broderick, J. A. Thompson, E. P. Day, and B. M. Hoffman, Science **249**, 401 (1990); G. T. Yee, J. M. Manriquez, D. A. Dixon, R. S. McLean, D. M. Groski, R. B. Flippen, K. S. Narayan, A. J. Epstein, and J. S. Miller, Adv. Mater. **3**, 309 (1991); W. E. Broderick, and B. M. Hoffman, J. Am. Chem. Soc. **113**, 6334 (1991); J. S. Miller, R. S. McLean, C. Vasquez, J. C. Calabrese, F. Zuo, and A. J. Epstein, J. Mater. Chem. **3**, 215 (1993).

[3] J. M. Manriquez, G. T. Yee, R. S. McLean, A. J. Epstein, and J. S. Miller, Science **252**, 1415 (1991); J. S. Miller, J. M. Manriquez, G. T. Yee, and A. J. Epstein, *Proceedings of the Novel Symposium*, #NS-81, edited by W. R. Salaneck, I. Lundström, and B. Ranby (Oxford University, New York, 1993), p. 461.

[4] C. W. Chen, *Magnetism and Metallurgy of Soft Magnetic Materials* (Dover, New York, 1977); E. C. Snelling, *Soft Ferrites* (Iliffe, London, 1969).

[5] J. S. Miller *et al.* (to be published).

[6] B. G. Morin, dissertation, The Ohio State University, 1994.

[7] B. G. Morin, P. Zhou, C. Hahm, A. J. Epstein, and J. S. Miller, J. Appl. Phys. **73**, 5648 (1993).

[8] P. Zhou, B. G. Morin, J. S. Miller, and A. J. Epstein, Phys. Rev. B **48**, 1325 (1993).

[9] J. Joo, J. S. Miller, and A. J. Epstein (private communication).

[10] See J. D. Jackson, *Classical Electrodynamics* (Wiley, New York, 1975), p. 199.

[11] P. Zhou, S. M. Long, J. S. Miller, and A. J. Epstein, Phys. Lett. A **181**, 71 (1993).

[12] F. Zuo, S. Zane, P. Zhou, A. J. Epstein, R. S. McLean, and J. S. Miller, J. Appl. Phys. **73**, 5476 (1993).

[13] G. Du, J. Joo, J. S. Miller, and A. J. Epstein, J. Appl. Phys. **73**, 6566 (1993).

Soft magnetic properties of nanocrystalline Fe-Hf-C-N films

J. O. Choi and J. J. Lee
Department of Metallurgical Engineering, Seoul National University, Shilim, Kwanak, 151-742 Seoul, Korea

S. H. Han, H. J. Kim, and I. K. Kang
Magnetic Alloys Laboratory, Korea Institute of Science and Technology, P.O. Box 131, Cheongryang, 130-650 Seoul, Korea

Fe-Hf-C-N films with excellent soft magnetic properties were fabricated by $Ar+N_2$ reactive sputtering for the first time. The newly developed films were found to have better soft magnetic properties than those of Fe-Hf-C or Fe-Hf-N films. The best magnetic properties achieved in this work are H_c of 0.15 Oe, μ_{eff} of 8200, and $4\pi M_s$ of 17 kG. The thermal stability of the Fe-Hf-C-N films was also found to be excellent, e.g., H_c was less than 0.3 Oe and μ_{eff} was about 4000 for the films annealed up to 700 °C. It was observed by transmission electron microscopy that the films consisted of two phases: a fine crystalline α-Fe phase whose grain size is about 6 nm, and Hf(C,N) precipitates with a size of less than 2 nm. The fine grained α-Fe structures, together with finely dispersed Hf(C,N) precipitates, is considered to be one of the main factors for the excellent magnetic properties and thermal stability.

I. INTRODUCTION

Fe-M-C (M: early transition metals such as Hf, Ta, Zr, etc.) and Fe-M-N nanocrystalline films are reported to have good soft magnetic properties together with high thermal stability.[1,2] The nanocrystalline films can be obtained by the crystallization of precursor amorphous films. M-carbides or M-nitrides formed during the heat treatment are considered to act as nucleation or pinning sites of grain growth, resulting in nanoscale α-Fe grains. The fine grains of α-Fe is regarded as one of the essential factors for magnetic softness.

In this article we first study the magnetic properties of Fe-Hf-C-N films, in order to examine the effect of the simultaneous addition of C and N. The magnitude of the free energy of formation of M-nitrides is generally larger than that of M-carbides.[3] Therefore it would be of interest to examine how the process for the formation of nanocrystallites and the resultant magnetic properties change with the C and N content in Fe-M alloys.

II. EXPERIMENT

Fe-Hf-C-N films were fabricated in $Ar+N_2$ plasma by an rf magnetron sputtering apparatus. The target consisted of an Fe disc with small pieces of Hf and C. The partial pressure of N_2 gas (P_{N_2}) was controlled in the range of 0–10% keeping the total gas pressure of 1×10^{-3} Torr constant. The fabricated films which were deposited onto Corning 7059 glass substrates were disc shaped with 10 mm diameter and 1 μm thickness. The deposition rate was 470–620 Å/min, mainly depending on P_{N_2} at the power density of 3.82 W/cm^2. The composition of films was analyzed by Auger electron spectroscopy (AES), and some of films also by Rutherford backscattering spectroscopy (RBS). When analyzed by AES, the composition was calibrated with the standard sample analyzed by RBS. The films were annealed at 350–700 °C for 30 min in vacuum. The saturation magnetization ($4\pi M_s$) and coercive force (H_c) were measured by a vibrating sample magnetometer (VSM). Thermomagnetic analysis was performed in the temperature range of liquid nitrogen temperature to 800 °C under an external field of 10 kOe using the VSM. The effective permeability (μ_{eff}) was measured at 1 MHz by an impedance analyzer using a horse-shoe shaped ferrite core. The microstructure was investigated by transmission electron microscopy (TEM) and x-ray diffractometry (XRD).

III. RESULTS AND DISCUSSION

Magnetic properties of Fe-Hf-C-N films produced by $Ar+N_2$ reactive sputtering showed strong dependence on P_{N_2}. Figure 1 shows the dependence of H_c on P_{N_2} for the films annealed at 550 °C. In this figure the film with 0% P_{N_2} indicates the Fe-Hf-C film deposited in the pure Ar plasma. H_c decreases abruptly with P_{N_2}, reaching the minimum value of about 0.17 Oe at 2% P_{N_2}, and then increases with a further increase of P_{N_2}. The content of nitrogen incorporated in the films was almost linearly increased with increasing P_{N_2}. The typical compositions of the films were $Fe_{81.4}Hf_{8.2}C_{6.7}N_{3.7}$, $Fe_{78.1}Hf_{6.8}C_{5.9}N_{9.2}$, and $Fe_{72.3}Hf_{5.7}C_{5.6}N_{16.4}$ at 2%, 5%, and 10% P_{N_2}, respectively. In this figure μ_{eff} is also shown. μ_{eff} shows the peak value of more than 7500. In the high P_{N_2} region exceeding 5% P_{N_2}, μ_{eff} shows a relatively low value corresponding to high H_c.

Figure 2 shows the variation of $4\pi M_s$, H_c, and μ_{eff} with annealing temperature for the films prepared at various P_{N_2}. In N-free Fe-Hf-C films, $4\pi M_s$ showed a rapid increase at around 550 °C, which is commonly observed during the crystallization of Fe-M based amorphous alloys.[1,4,5] It is to be noted that as P_{N_2} increases, $4\pi M_s$ of as-deposited Fe-Hf-C-N films increases and the increments in $4\pi M_s$ with temperature become low. In Fe-M based alloys, $4\pi M_s$ is a structure-dependent property which increases as the structure changes from amorphous to crystalline α-Fe, combined with Curie temperature (T_c).[5] Therefore

 0021-8979/94/75(10)/5785/3/$6.00 © 1994 American Institute of Physics

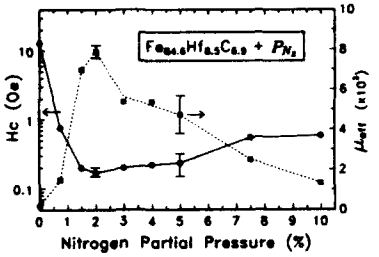

FIG. 1. Coercive force and effective permeability as a function of P_{N_2} for the films annealed at 550 °C.

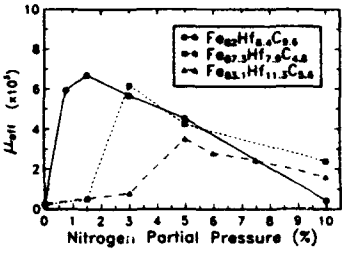

FIG. 3. Effective permeability as a function of P_{N_2} for the films where the ratios of [C]/[Hf] are 1.1, 0.6, 0.5.

the increase in $4\pi M_s$ with P_{N_2} in the as-deposited films implies that crystallinity changes with P_{N_2} as well as annealing temperature. As is also shown in this figure, the films with P_{N_2} ranging 2%–5% show excellent thermal stability, H_c being less than 0.3 Oe and μ_{eff} being 4000 for the films annealed up to 700 °C. However magnetic softness of the films with 0% or a P_{N_2} of 10% and over is not good in the entire temperature range.

In order to understand the nitrogen effect, the P_{N_2} at which μ_{eff} exhibits its peak value were determined at varying ratios of [C]/[Hf] in Fe-Hf-C alloys. Figure 3 shows the P_{N_2} dependence of μ_{eff} for the Fe-Hf-C-N films annealed at 550 °C. The ratios of [C]/[Hf] are 1.1, 0.6, and 0.5 which correspond to $Fe_{82}Hf_{8.4}C_{9.6}$, $Fe_{87.3}Hf_{7.9}C_{4.8}$, and $Fe_{83.1}Hf_{11.3}C_{5.6}$, respectively. It is seen that the higher the ratio of [C]/[Hf], the lower the P_{N_2} showing peak permeability. This suggests that the critical total amount of C and N depends on the Hf content in order to obtain good soft magnetic properties. The reason for this is explained as follows. In the Fe-Hf-C-N alloys, it is expected that Hf has a strong tendency to form nitrides and/or carbides. These compounds are likely to play an important role in the microstructure.

Figure 4 shows x-ray diffraction patterns of as-deposited Fe-Hf-C-N films as a function of P_{N_2}. The structural changes with P_{N_2} are somewhat peculiar. As P_{N_2} increases the structure of the as-deposited film changes from an amorphouslike to a crystalline phase and again returns to an amorphous phase. It could be divided into two regions: region I in which crystallinity improved and region II in which amorphization occurred again. In region I, the microstructure changed from an amorphouslike phase and HfC to a crystalline one and Hf(C,N). On the contrary, in region II exceeding 5% P_{N_2} the structure returned to an amorphouslike one again. In region I, the origin of the microstructural change with P_{N_2} is considered to be due to the fact that N reacts more readily with Hf than C owing to a larger magnitude of free energy of formation of HfN than HfC. As P_{N_2} increases,

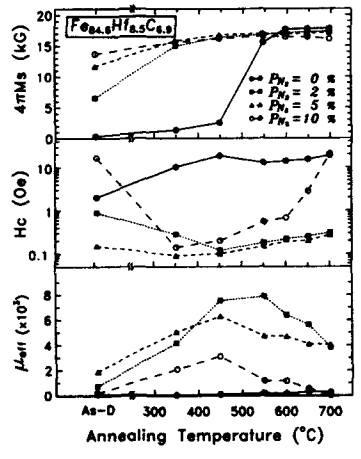

FIG. 2. Saturation magnetization, coercive force, and effective permeability as a function of annealing temperature for the films with various P_{N_2}.

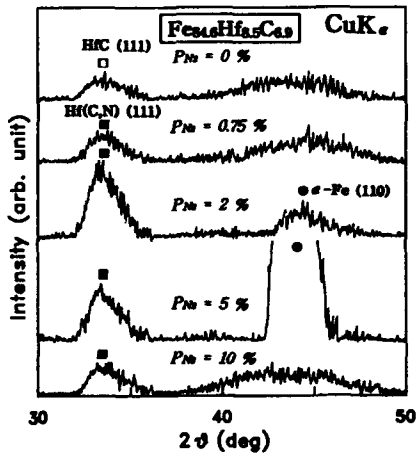

FIG. 4. XRD patterns of as-deposited films as a function of P_{N_2}.

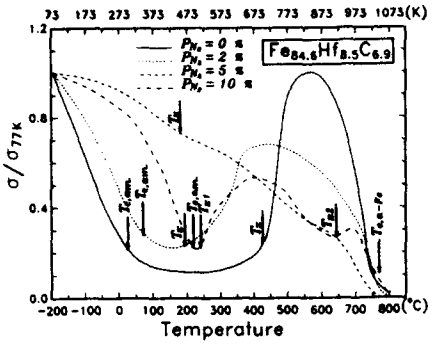

FIG. 5. Thermomagnetic diagrams as a function of P_{N_2}.

the Fe-Hf-C-N amorphous matrix becomes deficient in Hf content owing to the precipitation of Hf(C,N) from the matrix. This lowers the crystallization temperature of the remaining amorphous phase, with some parts of the matrix being crystallized. In region II, however, it is expected that excessive N would be solutionized into an α-Fe lattice and thereby the structure transformed to an amorphouslike one, which may be driven by accumulated strain induced from the incorporation of N into the α-Fe lattice.[6,7]

The above suggestion can be verified indirectly by the crystallization behavior of the remaining amorphous phase in the as-deposited films through thermomagnetic analysis. The results are shown in Fig. 5. As P_{N_2} increases in region I, the Curie temperature of amorphous phase ($T_{c,am}$) increases and the crystallization temperature (T_x) of the amorphous phase decreases and the shape of the change in the reduced magnetization ($\sigma/\sigma_{77\ K}$) near T_x becomes shallow. This means that the fraction of the remaining amorphous phase was decreased and crystallinity improved. In region II, on the contrary, the shape of change in $\sigma/\sigma_{77\ K}$ near T_x becomes deeper again, which means that the fraction of the amorphous phase increases. As for the crystallization behavior, the amorphous precursor of Fe-Hf-C-N is different from that of N-free Fe-Hf-C. The former has higher T_c and lower T_x compared to the latter, and the former is crystallized into α-Fe through two steps.

Figure 6 shows TEM images and the diffraction pattern of the $Fe_{81.4}Hf_{8.2}C_{6.7}N_{3.7}$ film produced in region I with 2% P_{N_2} and subsequently annealed at 550 °C. The films consisted of two phases: a fine crystalline α-Fe phase whose grain size is about 6 nm and Hf(C,N) precipitates with a size of less than 2 nm. Although not shown here due to space limitation, it was also observed by TEM that the N-Free Fe-Hf-C films consisted of large grains of both α-Fe and HfC precipitates, with sizes of 10–20 nm and about 3 nm, respectively. In region II, however, a diffraction pattern similar to γ'-Fe_4N was observed by both TEM and XRD. This phase may cause the deterioration of the magnetic properties of the annealed films as shown in Fig. 2. As seen from the above results, more refined nanocrystalline structures and precipitates can be obtained by annealing the Fe-Hf-C-N films with phase mixtures of amorphous, bcc α-Fe and Hf(C,N) precipitates rather than by using N-free films with a fully amorphous phase.

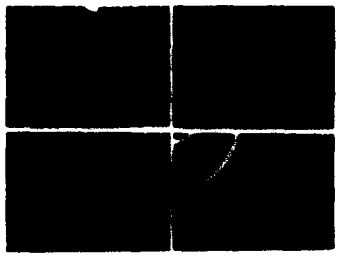

FIG. 6. TEM micrographs and diffraction pattern of Fe-Hf-C-N films annealed at 550 °C: (a) bright field image; (b) α-Fe (110) dark field image; (c) Hf(C,N) (111)+(200) dark field image; (d) diffraction pattern.

In conclusion, we were able to fabricate Fe-Hf-C-N films with excellent magnetic and thermal properties. The excellent properties are believed to result from the very fine grains of the α-Fe phase, together with finely dispersed Hf(C,N) precipitates.

[1] N. Hasegawa, M. Saito, A. Kojima, A. Makino, Y. Misaki, and T. Watanabe, J. Mag. Soc. Jpn. **14**, 319 (1990).
[2] K. Nakanishi, O. Shimizu, and S. Yoshida, J. Mag. Soc. Jpn. **15**, 371 (1991).
[3] I. Barin, *Thermochemical Data of Pure Substances* (VCH, Weinheim, 1989).
[4] K. Suzuki, N. Kataoka, A. Inoue, A. Makino, and T. Masumoto, Mater. Trans. JIM **31**, 743 (1990).
[5] M. Naoe, M. Kodaira, Y. Hoshi, and S. Yamanaka, IEEE Trans. Magn. **MAG-17**, 3062 (1981).
[6] T. Egami and Y. Waseda, J. Non-Cryst. Solids **64**, 113 (1984).
[7] A. Seidel, G. Linker, and O. Meyer, J. Less-Common Metals **145**, 89 (1988).

Electrical characteristics of spiral coil planar inductors using amorphous alloy ribbons as magnetic layers

K. Tanigawa, H. Hirano, and T. Sato
Advanced Materials and Technology Research Laboratories, Nippon Steel Corporation, Kawasaki 211, Japan

N. Tanaka
Yutaka Electric Mfg. Co., Ltd., Kawasaki 211, Japan

Various types of planar inductors have been proposed for reducing the volume of switching converters. Planar inductors using amorphous alloy ribbons as magnetic layers are also studied. The purpose of this study is to clarify the relation between the electrical performance of the inductor, and the properties and composition of amorphous ribbon. The experimental results show that superimposed dc current, I_{80}, increases linearly with the product of B_m and ribbon thickness t, where I_{80} is defined as the dc current corresponding to an inductance which decreases to 80% of an initial value. In the case of stacking amorphous alloy ribbons, I_{80} increases with gradual approach to saturation, as the stack thickness increases regardless of ribbon thickness. However, the saturation value of I_{80} depends on ribbon thickness. The saturation value increases with increasing ribbon thickness. The above results suggest that from a practical viewpoint the use of thick ribbons is preferable. With respect to alloy composition, the Fe-based alloy is more favorable compared with the Co-based alloy because of its higher stored magnetic energy.

I. INTRODUCTION

For the purpose of reducing the volume of switching converters, efforts have so far been made to miniaturize magnetic devices. However, there are limitations in further miniaturizing conventional cores because of difficulties in core fabrication and coil winding.

Recently various types of planar inductors have been proposed,[1–4] which are laminations composed of a planar coil, magnetic layers, and insulating layers. These planar type devices are promising in view of their flat shape and capability of high frequency use.

In this article we study planar inductors using amorphous alloy ribbons as magnetic layers. The effects of the composition, ribbon thickness, and stack thickness of amorphous alloys on electrical characteristics are examined in order to optimize the constitution of magnetic layers. The results are analyzed using the finite element method.

II. EXPERIMENTAL PROCEDURES

The structure of planar inductors studied in this article is shown in Fig. 1. The amorphous alloy ribbons were prepared by a rapidly quenching method[5] and annealed after cutting a 14 mm square. The composition of amorphous alloys were $Co_{69}Fe_4Si_{16}B_9Mo_2$ (Co-based for short) and $Fe_{75}B_{12}C_4Ni_5Mo_4$ (Fe-based for short). One to ten sheets of them were stacked on each side of the planar coil of a spiral type, which gives larger inductance.[1] The planar spiral coil with 38 spiral turns was formed on both sides of an alumina substrate, and connected electrically through a hole. The spiral coil pattern and the direction of electric current flow are the same on each side. The planar coil and the insulating layers were annealed in a N_2 atmosphere after screen-printing treatment.

Inductance was measured at a frequency of 500 kHz and a current, I_{ac}, of 1 mA with an impedance meter. Its superimposed dc current characteristics were examined by means of superimposing a dc current, I_{dc}, of 50–300 mA with a dc bias circuit.

In order to analyze the results of the above electrical characteristics, amplitude relative permeability, μ_a, and maximum magnetic flux density, B_m, of the amorphous alloy

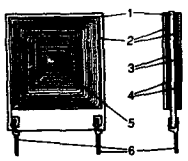

FIG. 1. Structure of planar inductor: (1) substrate (alumina); (2) planar spiral coil (Cu); (3) insulating layers (glass); (4) magnetic layers (amorphous alloy ribbons); (5) through hole; (6) lead terminals.

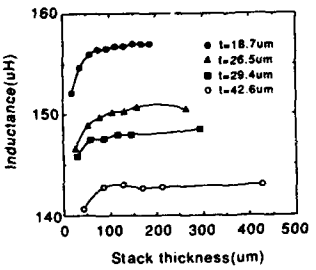

FIG. 2. Stack thickness dependences of inductance measured at a frequency of 500 kHz for Co-based amorphous alloy ribbons of different thicknesses.

 0021-8979/94/75(10)/5788/3/$6.00 © 1994 American Institute of Physics

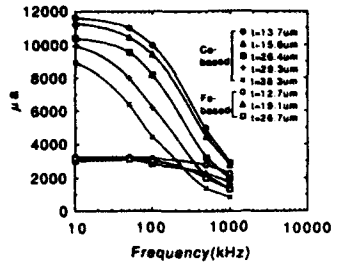

FIG. 3. Frequency dependences of amplitude relative permeability, μ_a, for amorphous alloy ribbons of different thicknesses.

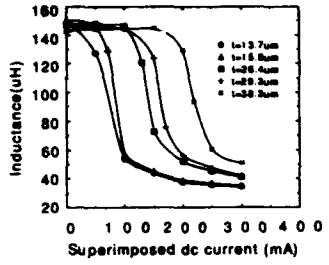

FIG. 5. Superimposed dc current characteristics measured at a frequency of 500 kHz for Co-based amorphous alloy ribbons of different thicknesses.

ribbons were measured on toroidal cores. Amplitude relative permeability, μ_a, was measured at a maximum magnetic field, Hm, of 0.4 A/m with a B-H analyzer (SY-8232). B_m was measured with a dc B-H tracer.

III. RESULTS AND DISCUSSION

The inductance initially increases rapidly, and then gradually approaches saturation as the stack thickness increases as shown in Fig. 2. The saturation value of the inductance increases with decreasing ribbon thickness. This tendency is attributable to a ribbon thickness dependence of μ_a.

The μ_a increases with decreasing ribbon thickness as shown in Fig. 3. Also, the μ_a increases with decreasing frequencies. These behaviors are related to eddy current loss. It is noted that the composition dependence of μ_a is small at 500 kHz.

In order to analyze the results, we calculated the inductance using the finite element method, where an axis-symmetrical model was assumed.

The calculated inductances increase with gradual approach to saturation with an increase in the product of relative permeability, μ_a, and the thickness of the magnetic layers, t, as the solid curve shows in Fig. 4, where n denotes stack numbers of amorphous alloy ribbons. This behavior probably results from a demagnetizing field effect within the plane of the magnetic layers. The plotted data coincide with the solid curve. The μ_a used for plotting are data from amorphous alloy ribbons wound on a toroidal core, which apparently contain the effect of eddy current loss at high frequencies. When stacking 18.7 μm thick Co-based ribbons, the data are a little lower than the calculated values. This difference is probably related to the stacking factor.

A dc current is superimposed on an ac current when the inductor is used as a choke coil for storing magnetic energy. Figure 5 shows the superimposed dc current characteristics of inductance at 500 kHz in the case of stacking a sheet of different thicknesses on each side of the planar coil. The superimposed dc current, at which the inductance begins to decrease, increases with increasing ribbon thickness.

Now, I_{80} is defined as the superimposed dc current corresponding to an inductance L_{80} which decreases to 80% of an initial value. The inductance L_{80} is generally used in the safety design of switching converters. I_{80} increases linearly with increasing ribbon thickness for Co-based and Fe-based alloys but with different slopes as shown in Fig. 6. These linearities result from the dependence of the dc current characteristics on magnetic fluxes within the plane, namely, the cross section of the magnetic pass, with a constant ribbon size.

The stored magnetic energy of the inductor is calculated from $(1/2)L_{80}I_{80}^2$. The inductor using Fe-based ribbons can store greater energy than that using Co-based ribbons.

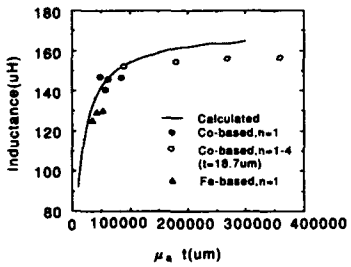

FIG. 4. Dependence of inductance on the product of amplitude relative permeability, μ_a, and ribbon thickness, t.

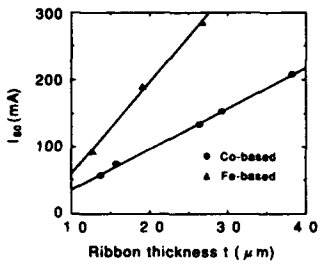

FIG. 6. Ribbon thickness dependences of I_{80} measured at a frequency of 500 kHz.

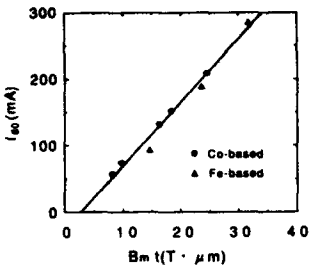

FIG. 7. Dependence of I_{80} on the product of maximum magnetic flux density, B_m, and ribbon thickness, t.

The superimposed dc current characteristics are generally known to depend on the magnetic saturation effect. We plotted the results of I_{80} versus the product of the maximum magnetic flux density, B_m, and ribbon thickness, t, as shown in Fig. 7. The I_{80} increases linearly with increasing $B_m t$. I_{80} can be predicted from this linearity. B_m of the Co-based alloy is approximately 0.6 T, and that of the Fe-based is approximately 1.2 T. Magnetization of the magnetic layers exhibits a minor loop under the dc current superimposed condition. Strictly speaking, the superimposed dc current characteristics depend on the permeability of the minor loop, but macroscopically depend on $B_m t$.

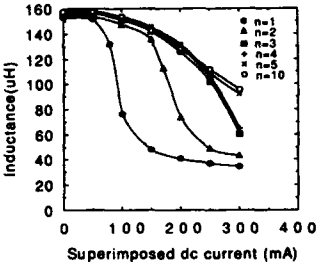

FIG. 8. Superimposed dc current characteristics measured at a frequency of 500 kHz for different stack numbers, n, of 18.7 μm thick Co-based amorphous alloy ribbons.

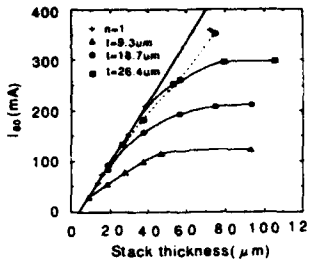

FIG. 9. Stack thickness dependences of I_{80} measured at frequencies of 500 kHz (—) and 50 kHz (---) for Co-based amorphous alloy ribbons of different thicknesses.

When increasing the stack number n of amorphous alloy ribbons, the superimposed dc current characteristics can be improved as shown in Fig. 8. But the improvement diminishes when the stack number is over 3.

I_{80} increases with the gradual approach to saturation, as the stack thickness increases at a frequency 500 kHz as shown in Fig. 9. The saturation value of I_{80} increases with increasing ribbon thickness, and also with decreasing frequency. The dependence of I_{80} on thickness and frequency is mainly related to eddy current loss and the stacking factor.

The above results suggest that from a practical viewpoint the use of thick ribbons as magnetic layers is preferable, particularly at high frequencies.

IV. CONCLUSIONS

We have clarified the relation between the electrical performance of inductors and the properties of amorphous ribbon. We suggest that a stack of thick ribbons should be used. With respect to alloy composition, an Fe-based alloy is more favorable.

[1] K. Kawabe, H. Koyama, and K. Shirae, IEEE Trans. Magn. **MAG-20**, 1804 (1984).
[2] T. Sato, M. Hasegawa, T. Mizoguti, and M. Sahashi, IEEE Trans. Magn. **MAG-27**, 5277 (1991).
[3] M. Mino, T. Yachi, A. Tago, K. Yanagisawa, and K. Sakakibara, IEEE Trans. Magn. **MAG-28**, 1969 (1992).
[4] S. Arakawa, M. Yamaguchi, H. Ohzeki, and K. I. Arai, Tech. Rep. IEE Jpn. **MAG-92** (1992).
[5] T. Sato, T. Ozawa, and T. Yamada, An. Fis. Ser. B **86**, 148 (1990).

Bending stresses and bistable behavior in Fe-rich amorphous wire

M. Vázquez,[a] C. Gómez Polo, J. Velázquez, and A. Hernando
Instituto de Magnetismo Aplicado. Laboratorio Salvador, Velayos. RENFE-Complutense Univ. Apartado de Correos 155, 28230 Las Rozas. Madrid. Spain

The aim of this work is to analyze for the first time the changes in magnetic properties of an Fe-rich amorphous wire ($Fe_{77.5}Si_{7.5}B_{15}$) when it is submitted to bending stresses. Upon a reduction of the radius of curvature, R_c, of the wire (i.e., increasing bending stresses), the main changes in the magnetic properties are summarized as follows: (a) Bistable behavior disappears when reducing R_c below about 11 cm but it is again observed for R_c less than about 2.5 cm. This latter effect is also obtained for short wires (less than around 7 cm) which do not show spontaneous bistability. (b) For the case when bending stresses make bistability disappear, the susceptibility increases more than one order of magnitude with regards to the case of bistable wire, and parallel to the increase of susceptibility, a reduction of remanent magnetization is observed. The disappearance and later occurrence of the bistable behavior with increasing bending stresses are discussed in terms of the tensile and compressive stresses induced when the sample is bent. The possibility of having bistable wires with toroidal symmetry is also discussed owing to its interest for particular applications as pulse generators with reduced size and magnetic switches.

The magnetic bistability observed in highly magnetostrictive Fe-rich amorphous wires is a consequence of the particular distribution of internal stresses frozen in during the fabrication by the in-rotating-water quenching technique. Such stresses coupled to magnetization via the magnetostriction constant determine two regions within the wire, namely, a cylindrical core and an internal sheath having axial and radial easy axes, respectively. This domain structure is responsible for the square loops observed when magnetization reverses its direction inside the core upon application of an ac axial field.[1]

The influence on bistability of tensile, compressive, and torsional stresses has been analyzed in previous reports.[2–5] The aim of this work has been to present the first results concerning the influence of bending stresses on the phenomenon of bistability in amorphous wires.

Amorphous wire with nominal composition $Fe_{77.5}Si_{7.5}B_{15}$ and 125 μm diameter was kindly provided by UNITIKA Inc. Pieces of different length (from 3 to 10 cm) were taken for magnetic measurements. In order to measure the axial hysteresis loops, the wire was inserted into a plastic tube 12 cm long with a 2 mm outer diameter. A primary coil wounded on the tube supplied the ac axial field (18 Hz in frequency) while a pickup coil 2 mm wide and wound around the exciting coil at its center position allowed the detection of axial magnetization by the conventional induction technique. A second primary-secondary set of coils was taken to compensate the changes of flux from the air. The set consisting of flexible tube with primary and pickup coils and the amorphous wire can be fitted into a ring-shaped holed piece having the possibility of taking different radius of curvature. In this way, the axial hysteresis loops were measured as a function of the radius of curvature.

Figure 1 shows the hysteresis loops for a 10 cm long bent wire for different radius of curvature, R_c. For the larger radii of curvature, bistability starts being modified in the sense of reducing the switching field and remanence (equivalent to the fractional volume of the core or fractional magnetization involved in the switching process). For a radius of curvature less than around 11 cm, bistability is lost. But finally, for R_c around 2 cm this phenomenon is again recovered. The same experiments were performed on short wires which do not show magnetic bistability before bending. Nevertheless, after reduction of the radius of curvature, bistability can be recovered. It is noteworthy to remind that nonbistable short wires also recover bistability under large enough applied tensile stress.[5]

Figure 2 shows the dependence of a coercive field on the radius of curvature for two wires 6 and 10 cm long, respectively. It should be noted that bistable behavior is not observed for intermediate radius of curvature as mentioned previously. In fact, coercive fields larger than 3 $A\,m^{-1}$ correspond to switching fields typical of squared loops.

Figure 3 shows the dependence of susceptibility χ, around the remanence, on the radius of curvature. Susceptibility takes larger values for the range of bending stresses for which bistability is lost. The observed decrease of susceptibility in bistable loops should be related to its reduced number of domain walls and to the stronger forces that pin those walls. Parallel to the increase of χ, a drastic reduction of the remanence is observed which is associated to the disappearance of bistability.

The modification of the magnetic parameters shown in the preceding section has to be related to the magnetoelastic anisotropy induced by bending stresses. In order to analyze more quantitatively that modification, we have calculated bending stresses according to the classical theory of elasticity.[6] When a cylinder is bent, a shear stress, σ_{xz}, and the stresses σ_θ, σ_z, and σ_x are induced where the θ axis is parallel to the axis of the wire, the x axis is perpendicular to θ axis within the plane of bending, and the z axis is perpendicular to this plane. These stresses are

[a]Present address: Instituto de Ciencia de Materiales. Serrano, 144, 28006 Madrid. Spain.

 0021-8979/94/75(10)/5791/3/$6.00 © 1994 American Institute of Physics

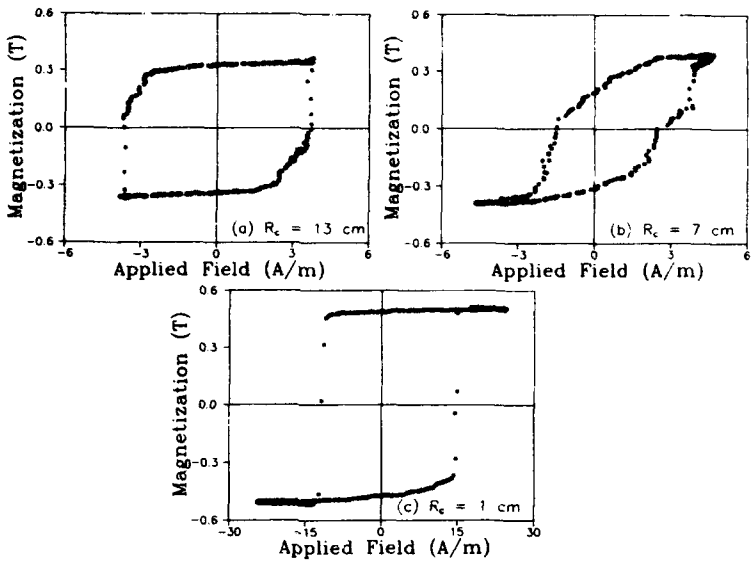

FIG. 1. Axial hysteresis loops for a 10 cm long wire under different radii of curvature: (a) 13 cm, (b) 7 cm, (c) 1 cm.

$$\sigma_x(x,z)=\frac{E(r^*)^2}{8R_c^2(1+\nu)}\,[(7+6\nu)(x^2-1)(5+2\nu)z^2], \tag{1}$$

$$\sigma_z(x,z)=\frac{-(1+2\nu)E(r^*)^2}{8R_c^2(1+\nu)}\,[3x^2+z^2-1], \tag{2}$$

$$\sigma_\phi(x,z)=-\left[\frac{x}{r^*}+\frac{1}{8(1+\nu)R_c}\,[(8+10\nu+4\nu^2)x^2 -(6\nu+4\nu^2)z^2-(2+\nu)]\right]\frac{2E(r^*)^2}{R_c}, \tag{3}$$

$$\sigma_{xz}(x,z)=\frac{E(r^*)^2(1+2\nu)}{4R_c^2(1+\nu)}\,zx, \tag{4}$$

where r^* and R_c are the radius of the wire and that of the curvature, respectively, and E and ν are the moduli of Young ($E=1.62\times10^{11}$ Pa) and Poisson ($\nu=0.3$). The coordinates $x=(R_c-\rho)/r^*$ and $z=\xi/r^*$ are dimensionless being ρ and ξ, the radial and axial coordinates, respectively, in a system with the reference placed in the center of curvature with the ξ axis perpendicular to the plane of bending (in such a system the axis of the wire has coordinates $x=0$ and $z=0$).

Figure 4(a) shows the dependence of σ_ϕ with the distance to the neutral fiber for $z=0$ (i.e., the plane parallel to that of bending and containing the axis of the wire). As known, positive (tensile) and negative (compressive) stresses are obtained. Similar behavior is found for z different from zero. In Fig. 4(b), the variation of the rest of the stresses is

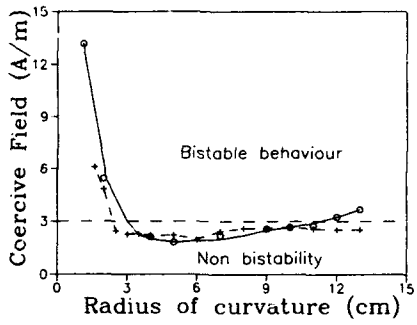

FIG. 2. Coercive field as a function of the radius of curvature for wires with different lengths: (O) 10 cm and (+) 6 cm.

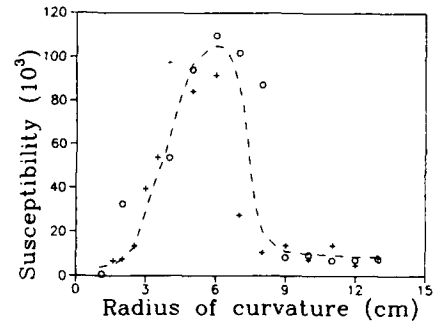

FIG. 3. Dependence of susceptibility at the remanence on the radius of curvature for wires with different lengths: (O) 10 cm and (+) 6 cm.

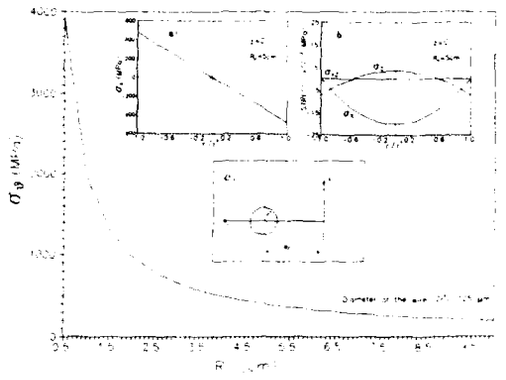

FIG. 4. Dependence of the axial stress σ_θ in the surface of the wire on the radius of curvature. (a) Shows the dependence of σ_θ on the distance to the neutral fiber in a plane parallel to that of bending and containing the axis of the wire, for a radius of curvature $R_c=5$ cm, being $r=R_c-\rho$ (see text). (b) Shows, for the same parameters, the dependence of σ_{rz}, σ_r, and σ_z on the distance to the neutral fiber. (c) Shows the coordinate system considered.

also plotted. Comparison of results from both insets indicates that only in a small region close to the neutral fiber does σ_θ takes values comparable to those of the other stresses. Consequently, only σ_θ stresses will be considered in the following. In Fig. 4 the maximum σ_θ values (obtained at the surface of the wire, $r/r^*=-1$ being $r=R_c-\rho$) for the plane $z=0$, are plotted as a function of the radius of curvature.

According to Fig. 4, we can consider, only in a first approximation, that the bent wire is subjected exclusively to the tensile and compressive axial stresses for the regions of the wire with convex and concave curvatures, respectively. The induced magnetoelastic anisotropy exhibits easy axis which is either parallel or transverse to the axis of the wire depending on the curvature.

Bistable magnetic behavior is a consequence of the particular distribution of the intrinsic magnetoelastic anisotropies in magnetostrictive wires which give rise to the coaxial core with axial easy axis and the shell with radial easy axis for Fe-rich wires.[7] Upon application of bending stresses, each half cross section of the wire is submitted to tensile and compressive axial stresses, respectively, so that there will be a competition between intrinsic and applied stresses. As a consequence of that, for increasing bending stresses (decreasing radius of curvature), the initial core will decrease its volume or even disappear and a multidomain structure will be present. On the other hand, a part of the shell will reinforce its transverse easy axis, while in the other half, there will be a counterbalance between compressive and tensile stresses. Accordingly, for a relatively large radius of curvature, the initial coaxial core is probably destroyed and half of the shell decreases its magnetoelastic energy constant with both effects inducing a magnetic softening of the material. This is the origin for the observed increase of the initial susceptibility and decrease of the coercivity.

For the largest bending stresses obtained when the radius of curvature is decreased below 3 cm, bistable behavior is observed again and susceptibility drops very quickly. In this case, bistability should be ascribed to the appearance of an eccentric core with axial easy axis generated by the tensile stress of the convex region of the wire. In the residual volume of the wire, magnetization would lie transversely as a consequence of the compressive bending stresses.

The appearance of magnetic bistability in Fe-rich bent wires for short enough radii of curvature, allows the design of reduced size pulse generator elements. In such devices the exciting circular field that causes the magnetization reversal within the wire can be generated by an electrical current flowing through a conductor wire perpendicularly placed across the plane formed by the bent sample. In this way, a sharp voltage pulse is detected in a pickup coil wound around a certain point of the bent sample, when a critical current flows through the conductor wire. Therefore, this configuration can be used to build sharp pulse generator devices and magnetic switches of reduced size.

This work has been supported by the Spanish C.I.C.Y.T. (Project No. MAT-92/0156) and IBERDROLA, S.A.

[1] F. B. Humphrey, K. Mohri, J. Yamasaki, H. Kawamura, R. Malmhäll, and I. Ogasawara, *Proceedings of the Symposium on Magnetic Properties of Amorphous Metals*, edited by A. Hernando *et al.* (Elsevier, Amsterdam, 1987), pp. 110–115.
[2] F. Kinosita, R. Malmhäll, K. Mohri, F. B. Humphrey, and J. Yamasaki, IEEE Trans. Magn. **22**, 445 (1986).
[3] M. Wun-Fogle, H. T. Savage, L. T. Kabacoff, M. L. Spano, J. R. Cullen, G. A. Jones, and D. G. Lord, IEEE Trans. Magn. **25**, 3617 (1989).
[4] M. Vázquez, J. González, J. M. Blanco, J. M. Barandiarán, G. Rivero, and A. Hernando, J. Magn. Magn. Mater. **96**, 321 (1991).
[5] A. M. Severino, C. Gómez-Polo, P. María, and M. Vázquez, J. Magn. Magn. Mater. **103**, 117 (1992).
[6] S. Timoshenko and J. N. Goodier, *Theory of Elasticity*, edited by Urmo (Bilbao, 1968), Chap. 13, Sec. 131.
[7] J. Velázquez, M. Vázquez, H. T. Savage, A. Hernando, and M. Wun-Fogle, J. Appl. Phys. **70**, 6525 (1991).

Relaxation in magnetic continua

V. L. Sobolev, I. Klik, C. R. Chang, and H. L. Huang
Department of Physics, National Taiwan University, Taipei, Taiwan, Republic of China

Within a recently developed axiomatic formalism for construction of stochastic field equations of motion a new form of the equation for damped dynamics of magnetization in ferromagnets is proposed. It takes into account spatially inhomogeneous dissipation due to exchange interactions and replaces the customary dissipation constant (due to relativistic effects) by a dissipation operator. This operator is constructed here by comparison of the resultant phenomenological spin wave spectra with results of microscopic calculations. Dynamic description of relaxation of the modulus of magnetization is discussed.

A consistent description of the damped dynamics of the magnetization vector $\mathbf{M}(\mathbf{r},t)$ in magnetic continua is a problem of considerable theoretical and practical interest, yet, to date, possibly due to the difficulty of solving the resultant equations, relatively little effort has been devoted to a generalization of the original Landau–Lifschitz–Gilbert[1,2] (LLG) theory which is distinguished by the presence of a single dissipation constant ϵ. In a recent significant development,[3] however, Bar'yakhtar (Ref. 4 provides a summary of his theory) argued that the observed discrepancy between the value of ϵ deduced experimentally from domain-wall drag and from ferromagnetic resonance (ϵ is here much smaller) is due to spatially inhomogeneous dissipative processes. He derived an equation of motion for magnetization in which dissipative strength depends not only on the vector $\mathbf{M}$ proper, but also on its spatial derivatives and then recovered the exchange approximation expression for spin wave damping which cannot be obtained from the LLG theory.

Dissipative forces, however, are invariably associated with randomly fluctuating thermal fields whose combined action drives the system in question towards the stationary state of thermal equilibrium. The existence of this stationary state, neglected by Bar'yakhtar, can only be included in the phenomenological theory within the framework of stochastic differential equations (SDE, see, e.g. Ref. 5). To every SDE one may then construct a (Stratonovich) Fokker–Planck operator and one demands that its stationary state is thermal equilibrium.

We have recently derived[6] such a phenomenological SDE for damped magnetization dynamics in continua using a real time modification of the celebrated Caldeira–Leggett formalism.[7] In this stochastic field theory the dissipation constant is replaced by a dissipation operator constructed in such a way as to satisfy a generalized fluctuation-dissipation (FD) theorem which guarantees that thermal equilibrium is the stationary state of the corresponding Fokker–Planck equation. It is easy to write down a phenomenological equation of motion which has a given spatial symmetry, but the dissipative operator is not *a priori* known and must be reconstructed *a posteriori* by comparison with microscopic theory and experimental data on spin wave dispersion. Here we carry out this program for the special case of an easy axis ferromagnet and then also discuss the more complicated easy plane model of high degeneracy.

In Ref. 6 we proposed that the damped dynamics of magnetization be described by the equation

$$\mathbf{M}_t = \gamma_0 \mathbf{M} \times [-H_{\mathbf{M}} - \Delta^2_{\epsilon,\eta} \mathbf{M}_t], \tag{1}$$

where, for simplicity, we omitted the stochastic (noise) terms irrelevant to the present analysis of damped dynamics. In this equation $\mathbf{M}_t = \partial \mathbf{M}/\partial t$, $H_{\mathbf{M}} = \delta \mathcal{H}/\delta \mathbf{M}$ ($\mathcal{H}$ is the Hamiltonian), γ_0 is the gyromagnetic ratio, and $\Delta^2_{\epsilon,\eta}$ is the above mentioned dissipation operator which replaces here the familiar Gilbert's dissipation constant ϵ_g. In general $\Delta^2_{\epsilon,\eta}$ may be an operator in both the magnetization components M_i and the spatial variable $\mathbf{r}$. In our previous study[6] we used the simple form $\Delta_{\epsilon,\eta} = \epsilon_g^{1/2} - \eta_g \Delta$ where Δ is the Laplacian and η_g is a newly introduced dissipation constant associated with propagation of inhomogeneities through the medium. By construction the magnitude of magnetization remains conserved. This assumption is not altogether justified and we shall return to it in our concluding remarks. Equation (1), however, is but a special case of a more general class of equations, to wit

$$\mathbf{M}_t = \gamma_0 \mathbf{M} \times [-H_{\mathbf{M}} - \hat{\Delta}^2_{\epsilon,\eta} \mathbf{f}_t], \tag{2}$$

where $\hat{\Delta}_{\epsilon,\eta}$ is a symmetric tensor (a 3×3 matrix) and the components of the vector $\mathbf{f}$ are polynomials in $M^{(i)}$ of desired spatial symmetry. It can be shown[6,8] that the stochastic version of Eq. (2) describes evolution towards thermal equilibrium, however, in the underdamped limit only. The general form of this equation, valid for any dissipation strength remains unknown.

We shall assume here that $\mathbf{f} \equiv \mathbf{M}$ and find a scalar operator $\Delta_{\epsilon,\eta}$ such that the damped system described by Eq. (1) not only goes to thermal equilibrium (which must be the stationary value of the Fokker–Planck operator associated with the stochastic equations of motion) but also yields the correct dispersion relation for damped spin waves in a uniaxial ferromagnet.

Let us first consider the simplest microscopic model of a ferromagnet with uniaxial anisotropy. The Hamiltonian may be written in the following form:

$$\mathcal{H} = -\frac{1}{2}\sum_{l,m} J(R_{l,m})(\mathbf{S}_l \cdot \mathbf{S}_m) - \frac{1}{2} K \sum_l (S_l^{(z)})^2 - g\mu_B \mathbf{H}_0 \cdot \sum_l \mathbf{S}_l, \tag{3}$$

 0021-8979/94/75(10)/5794/3/$6.00 © 1994 American Institute of Physics

where $J(R_{l,m})$ is an exchange integral, K is the anisotropy constant, g is the g-factor, μ_B is the Bohr magneton, and the sum is taken over all lattice sites. The quantization procedure for this Hamiltonian is described, for example, in Ref. 9. Within this model, in the case of the so-called easy axis type of magnetic anisotropy (i.e., if in the absence of external magnetic field magnetization is parallel to the easy axis) the expression for the spin wave spectrum has the simple form

$$E_{sw}(\mathbf{k})=E_0+Dk^2, \tag{4}$$

where $k=|\mathbf{k}|$ is the wave vector modulus. Further, $E_0=E_A+E_H$ with $E_A=SK=\gamma_0 H_A$ ($\gamma_0=g\mu_B$ and $\hbar=1$) and $E_H=\gamma_0 H_0$ being the anisotropy and Zeeman energy terms, respectively. The exchange stiffness constant is $D=SJ_0a^2$ where S is the spin of an ion, a is lattice constant, and $J(0)-J(\mathbf{k})\sim J_0(ak)^2$ in the long wavelength approximation $ak\ll 1$. It is common practice to consider also the limiting exchange approximation in which one sets $E_A\to 0$ and $E_H\to 0$ so that the spin wave spectrum (4) takes on the form $\epsilon_{sw}(\mathbf{k})=Dk^2$. Spin wave damping[10] may then be represented as

$$\gamma_{sw}(\mathbf{k})=(ak)^4\,\frac{3\theta_c}{(2\pi)^3S^2}\left(\frac{T}{\theta_c}\right)^2\ln^2\left[\frac{T}{\theta_c(ak)^2}\right], \tag{5}$$

where $\theta_c=SJ_0$ for brevity. Thus, in the long wavelength limit the k dependence of the spin wave spectrum and damping should be $\gamma_{sw}(\mathbf{k})\propto k^4$ and $E_{sw}(\mathbf{k})\propto k^2$, respectively. These results are of primary importance to test the correct choice of the relaxation term in the phenomenological equations for damped dynamics of magnetization. Let us again recall that we also demand that the stochastic form of these equations[6] leads to the state of thermal equilibrium. In the case of an easy axis ferromagnet, for example, our Eq. (3), the spin wave damping is determined by a process of four magnon interaction. It may be described by the Hamiltonian (see, e.g., Refs. 9 and 11)

$$H_{int}=\sum_{1,2,3,4}\Psi(1,2;3,4)c_1^+c_2^+c_3c_4\Delta(\mathbf{k}_1+\mathbf{k}_2-\mathbf{k}_3-\mathbf{k}_4)+\text{H.c.} \tag{6}$$

in which $i\equiv\mathbf{k}_i$, the summation is carried out over the wave vectors of individual magnons, and

$$\Psi(1,2;3,4)=-\frac{1}{2SN}\left\{\frac{1}{2}\,D(\mathbf{k}_1\cdot\mathbf{k}_2+\mathbf{k}_3\cdot\mathbf{k}_4)+E_A\right\}. \tag{7}$$

The resultant expression for spin wave damping within this model (assuming $k\to 0$) has the simple form

$$\gamma_{sw}\sim\frac{E_A^2T^2}{S^2\theta_c^3}. \tag{8}$$

Dipole–dipole, magnetoelastic, and other interactions are neglected.

The problem now is to find such a tensorial operator $\hat{\Delta}^2_{\epsilon,\eta}$ and vector $\mathbf{f}$ in Eq. (2) such that the resultant phenomenological equations of motion are compatible with Eqs. (4), (5), and (8) derived microscopically. For simplicity we consider here Eq. (1) only, i.e., we assume that $\mathbf{f}=\mathbf{M}$ and that the dissipation operator is a scalar quantity. The phenomenological counterpart of Eqs. (4) and (5) is then obtained if one sets

$$\Delta^2_{\epsilon,\eta}=M^{-1}\gamma_0^{-1}\kappa^2_{r,ex}=M^{-1}\gamma_0^{-1}(\kappa_r-\kappa_{ex}a^2\Delta), \tag{9}$$

where $M=|\mathbf{M}(\mathbf{r},t)|=\text{const}$. The dimensionless operator $\kappa_{r,ex}$ combines the relativistic and exchange contributions to dissipation and yields

$$\gamma^{(ph)}_{sw}(\mathbf{k})=(E_0+Dk^2)(\kappa_r+\kappa_{ex}a^2k^2), \tag{10}$$

where $E_0=E_A+E_H$. for the dissipative part of the spin wave spectrum. Co[illegible]omenological expression (10), in which, in t[illegible]roximation, we must set $\kappa_r=0$, with the microscopic result (5) we identify

$$\kappa_{ex}\sim\frac{3}{(2\pi)^3S^2}\left(\frac{T}{\theta_c}\right)^2\ln^2\left[\frac{T}{\theta_c(ak)^2}\right]. \tag{11}$$

Beyond the exchange approximation, with $E_A\neq 0$, a comparison of Eqs. (10) and Eq. (8) yields

$$\kappa_r\sim\frac{E_A^2T^2}{S^2E_0\theta_c^3}. \tag{12}$$

The foregoing results show that for an easy axis ferromagnet it is possible to reconcile the demands of microscopic and phenomenological, thermodynamic theories. So far, however, we have not succeeded in carrying out this program for the highly degenerate case of an easy plane ferromagnet.[4] In this case, namely, the dissipative operator and the vector $\mathbf{f}$ cannot be chosen to be isotropic, as was conveniently done here, but their choice must reflect the easy plane symmetry. This is a somewhat intractable problem since the theory then contains two nontrivial quantities to be determined *ad hoc*, the vector $\mathbf{f}$ and the dissipation operator $\Delta^2_{\epsilon,\eta}$. We have little doubt, however, that a consistent theory of a uniaxial (both easy plane and easy axis) ferromagnet is feasible within the proposed formalism of Eq. (2) which should, in principle, also allow to develop phenomenological models of even more complicated dissipative couplings.[8]

In deriving Eqs. (1) and (2) we assumed that $|\mathbf{M}(\mathbf{r},t)|=M=\text{const}$. This assumtion allowed us to introduce a conjugate pair of action angle variables[6] and to write down canonical equations of motion. Problems arise if the above condition is violated and the rapid relaxation of M towards its equilibrium value is incorporated into a theory which then contains three dynamical variables (the components M_i), rendering the canonical formalism inapplicable. By the study of Callen[12] the relaxation of the magnetization modulus is related to the number of magnons with nonzero k vector and we expect that the missing dynamical variable is related to a collective effect in this system.

This research was sponsored by the National Science Council of Republic of China under Grant No. NSC-83-0405-E02-001.

[1] L. D. Landau, *Collected Papers*, edited by D. ter Haar (Pergamon, Oxford, 1965).
[2] T. L. Gilbert, Phys. Rev. **100**, 1243 (1955).
[3] V. G. Bar'yakhtar, Sov. Phys. JETP **60**, 863 (1984).
[4] V. G. Bar'yakhtar, Physica B **159**, 20 (1989).

[5] C. W. Gardiner, *Handbook of Stochastic Methods*, 2nd ed. (Springer, Berlin, 1985), Chaps. 4 and 5.
[6] I. Klik and C. R. Chang, Phys. Rev. E **48**, 607 (1993).
[7] A. O. Caldeira and A. J. Leggett, Ann. Phys. **149**, 374 (1983).
[8] I. Klik, J. Stat. Phys. **66**, 635 (1992).
[9] A. I. Akhiezer, V. G. Bar'yakhtar, and S. V. Peletminskii, *Spin Waves* (North-Holland, Amsterdam, 1968), Chap. 7.
[10] F. Dyson, Phys. Rev. **102**, 1217 (1956).
[11] V. Kashcheev and M. Krivoglaz, Fiz. Tverd. Tela **3**, 1541 (1961).
[12] H. B. Callen, J. Phys. Chem. Solids **4**, 256 (1958).

Generalized equations for domain wall dynamics

Vladimir L. Sobolev,[a] Huei Li Huang, and Shoan Chung Chen
Department of Physics, National Taiwan University, Taipei, Taiwan, Republic of China

Generalized domain wall dynamic equations have been derived. The influence of the external magnetic field normal to the anisotropy axis on the critical parameters of the domain wall motion has been studied and illustrated.

I. INTRODUCTION

The phenomenological analysis of domain wall (DW) dynamics is typically based on the Landau–Lifshitz–Gilbert (LLG) equation which enables to consider different types of magnets and take into account various interaction both between the internal subsystems of the crystal and with the external field.[1–8] Rigorous mathematical analysis is limited to the simplest models[4] which of course do not provide a complete description of real situations, while the approximate approaches have proved to be fruitful for the investigation of the DW dynamics.[1–3,6–8] The approximation for theoretical investigations of the DW dynamics in ferromagnets usually is to assume high values of the material quality factor $Q \gg 1 (Q = K/2\pi M^2$; K is the uniaxial anisotropy constant, and M is the spontaneous magnetization). This approximation allows to neglect any change of the DW structure during its movement. However, the account of these changes is of principal importance especially for the case of $Q \geqslant 1$ and the investigation of the DW movement under the action of magnetic field normal to the anisotropy axis.

In this article, generalized Slonczewski-type equations describing the movement of an isolated DW in the presence of an external magnetic field normal to the anisotropy axis are obtained. For symmetric orientations of the in-plane field, namely, parallel and normal to the DW plane, the equations are applicable to any materials with $Q \geqslant 1$. For arbitrary orientations of the in-plane field, the equations are limited to $Q \gg 1$ materials only. Using these equations the analysis of the in-plane field influence on the DW dynamics and its critical parameters has been carried out.

II. DERIVATION OF THE EQUATIONS

Consider an isolated DW wall in a ferromagnet with a uniaxial anisotropy along the z axis. The DW plane coincides with the $x-z$ plane and the y axis is along the DW movement direction. The energy density of the system may be written as follows:[1]

$$W_{\mathrm{DW}} = 2\pi M^2\{\Delta_B^2 Q[\vartheta'^2 + \sin^2\vartheta\,\varphi'^2] + Q\sin^2\vartheta + -2h_t\sin\vartheta\cos(\varphi-\psi_H)\} + W_{\mathrm{md}} + W_{\mathrm{dr}}. \quad (1)$$

Here Δ_B is the Bloch DW width; ϑ and φ are the polar and azimuthal angles of the magnetization vector $\mathbf{M} = M\{\sin\vartheta\cos\varphi, \sin\vartheta\sin\varphi, \cos\vartheta\}$, the anisotropy axis is taken to be the polar one. In the one-dimensional problem under consideration the ϑ and φ angles depend only on time and coordinate y normal to the DW; $h_t = H_t/4\pi M$ is the dimensionless external field applied in the $x-y$ plane, $\mathbf{H}_t = H_t(\cos\psi_H, \sin\psi_H, 0)$; W_{dr} is the energy density describing the interaction of the system with the drive field applied along the anisotropy axis

$$W_{\mathrm{dr}} = -2\pi M^2\{2h_\parallel\cos\vartheta\},$$

where $h_\parallel = H_z/4\pi M$; W_{md} is the demagnetization energy density. Following Slonczewski[1] we will consider W_{md} in the form

$$W_{\mathrm{md}} = \frac{1}{8\pi}\mathbf{H}_m^2,$$

where the demagnetization field $\mathbf{H}_m$ satisfies the equations

$$\mathrm{curl}\,\mathbf{H}_m = 0, \quad \mathrm{div}(\mathbf{H}_m + 4\pi\mathbf{M}) = 0.$$

In our case of the infinite medium the sample surface is not important.[3] In order to solve these equations we restrict ourselves to the DW on the surface of which the condition of the continuity of the normal component of magnetization is satisfied

$$(\mathbf{M}_1\cdot\mathbf{n}) = (\mathbf{M}_2\cdot\mathbf{n}),$$

where $\mathbf{n}$ is the normal to the DW, and $\mathbf{M}_1$, $\mathbf{M}_2$ are the magnetization vectors of neighboring domains. The expression for the magnetic-dipole energy density may be represented as follows:

$$W_{\mathrm{md}} = 2\pi M^2(\sin\vartheta\sin\varphi - \sin\vartheta_0\sin\psi_H)^2.$$

Here ϑ_0 is the polar angle of the magnetization inside the domain. The equations for the determination of the magnetization angles inside domains obtained via the variation of the corresponding energy density have the form

$$\begin{aligned} &Q\sin\vartheta_0\cos\vartheta_0 - h_t\cos\vartheta_0 + h_\parallel\sin\vartheta_0 = 0, \\ &\varphi_0 = \psi_H. \end{aligned} \quad (2)$$

In the DW dynamic problems H_z, as a rule, is much smaller than $4\pi M$ ($h_\parallel \ll 1$) and, as a result, the asymmetry of the solutions of Eq. (2) inside domains will also be small. The static DW structure can be obtained via the variation of Eq. (1). The boundary conditions for the equations describing the distribution of the magnetization in the DW are as follows:

$$\vartheta(y) = \begin{cases} \vartheta_0, & \text{at} \quad y \to -\infty \\ \pi - \vartheta_0, & \text{at} \quad y \to +\infty, \end{cases}$$

$$\varphi(y) = \psi_H \quad \text{as} \quad y \to \pm\infty.$$

[a]Permanent address: Institute for Single Crystals of the Academy of Sciences of Ukraine, Kharkov, 310001 Ukraine.

 0021-8979/94/75(10)/5797/3/$6.00 © 1994 American Institute of Physics

For the two symmetric orientations of the in-plane field, $\psi_H=0$ (parallel to the DW) and $\psi_H=\pi/2$ (normal to the DW), the static DW structure has the form[8]

$$\sin\vartheta=\sin\vartheta_0+\frac{\cos^2\vartheta_0}{\cosh\xi+\sin\vartheta_0},\quad \xi=y/\Delta_0 \tag{3}$$

in which for $\psi_H=0$ the DW width is $\Delta_0=\Delta_B/\cos\vartheta_0$, and for $\psi_H=\pi/2$, $\Delta_0=\Delta_N/\cos\vartheta_0$, where $\Delta_N^2=Q\Delta_B^2/(Q+1)$. Note that in the case of the in-plane field normal to the DW, $\psi_H=\pi/2$, the solution (3) is realized for $H_x>8M$. It is necessary to emphasize that these solutions are *exact*, in the sense that they are obtained without making any approximations for arbitrary values of the Q parameter. In the case of the arbitrarily oriented in-plane field one can use Eq. (3) for the static DW structure relying on the approximation $Q\gg1$.

We express the LLG equation in spherical coordinates and assume that the moving DW centered at $q(t)$ has the same DW structure as described by Eq. (3) in which it is necessary to substitute $\xi\to u=[y-q(t)]/\Delta(t)$ and for azimuthal angle

$$\varphi(y,t)=\psi_H+\psi(t)\{U(u+\pi/2)-U(u-\pi/2)\}. \tag{4}$$

Here $\Delta(t)$ is the time dependent DW width which now has to be determined from the minima condition for the DW energy; $U(u)$ is a symmetric step function. The distinction of our choice of $\varphi(y,t)$ from the one used in Ref. 6 for the approximate analysis of the DW motion is that we consider the angle $\varphi(y,t)$ as coordinate dependent within the interval $-(\pi/2)\Delta\leqslant y-q(t)\leqslant(\pi/2)\Delta$, corresponding to an effective DW width $\pi\Delta$. The choice Eq. (4) can be regarded as justified if at the same time for self-consistency sake we demand that

$$\vartheta(u=-\pi/2,t)=\vartheta_0,\quad \vartheta(u=\pi/2,t)=\pi-\vartheta_0.$$

The prescription given above fulfills of the inequalities $|\dot\psi\cdot\psi^{-1}|\gg|\dot\Delta\cdot\Delta^{-1}|$ and $|\dot\Delta|\ll|\dot q|$ during the wall movement.

The equations for the DW motion, derived in the same way as in Ref. 1, now have the form

$$\dot q-\alpha\Delta\dot\psi=\Delta\omega_M\{f(\vartheta_0)\sin(\psi+\psi_H)\cos(\psi+\psi_H)+g(\vartheta_0)\times[h_t\sin\psi-\sin\vartheta_0\sin\psi_H\cos(\psi+\psi_H)]\}, \tag{5}$$

$$\dot\psi\Delta+\alpha\dot q r(\vartheta_0)=\Delta\omega_M h_\parallel, \tag{6}$$

where $\omega_M=4\pi\gamma M$, α is the Gilbert phenomenological parameter describing the viscous damping, and $f(\vartheta_0)$, $g(\vartheta_0)$, and $r(\vartheta_0)$ are given by

$$\begin{aligned}f(\vartheta_0)&=[\pi\sin^2\vartheta_0+2\cos^2\vartheta_0-\sin\vartheta_0\cos\vartheta_0\times(\pi-2\vartheta_0)]/2\cos\vartheta_0,\\ g(\vartheta_0)&=[\pi\sin\vartheta_0+\cos\vartheta_0(\pi-2\vartheta_0)]/2\cos\vartheta_0,\\ r(\vartheta_0)&=[2\cos\vartheta_0-\sin\vartheta_0(\pi-2\vartheta_0)]/2\cos^2\vartheta_0.\end{aligned} \tag{7}$$

The time dependent DW width $\Delta(t)$ is determined by the expression

$$\Delta^2=\Delta_B^2Qr(\vartheta_0)/n[\vartheta_0,\psi(t)], \tag{8}$$

where

$$\begin{aligned}n[\vartheta_0,\psi(t)]&=[Q+\sin^2(\psi+\psi_H)]f(\vartheta_0)-2g(\vartheta_0)\\&\times[h_t\cos\psi+\sin\vartheta_0\sin\psi_H\sin(\psi+\psi_H)]\\&-\pi t_g\vartheta_0[Q\sin\vartheta_0-2h_t+\sin\vartheta_0\sin^2\psi_H]/2.\end{aligned} \tag{9}$$

These equations allow to consider the DW movement under the action of an in-plane field varied from zero up to the anisotropy field.

III. INFLUENCE OF THE IN-PLANE FIELD ON THE DW MOVEMENT

The influence of an in-plane field on the steady state DW movement has been already considered.[8] Here we will consider the DW movement under the action of the drive field exceeding the Walker critical field $H_W=2\pi\alpha M$ and for a particular case in which the in-plane field is parallel to the DW ($\psi_H=0$). From Eqs. (5) and (6) we have

$$\dot q=\frac{\omega_M\Delta}{1+\alpha^2f(\vartheta_0)r(\vartheta_0)}\{\alpha h_\parallel f(\vartheta_0)+g(\vartheta_0)h_t\sin\psi+f(\vartheta_0)\sin\psi\cos\psi\}, \tag{10}$$

$$\dot\psi=\frac{\omega_M\Delta}{1+\alpha^2f(\vartheta_0)r(\vartheta_0)}\{h_\parallel-\alpha r(\vartheta_0)g(\vartheta_0)h\sin\psi-\alpha r(\vartheta_0)f(\vartheta_0)\sin\psi\cos\psi\}. \tag{11}$$

As was already done in Ref. 8 let us take the data from a uniaxial ferromagnet with the composition $(Eu_{1.7}Yb_{1.3})Fe_5O_{12}$ for numerical analysis. This material has the following parameters:[9]

$$4\pi M=1450\ \text{G};\quad K_u=0.176\times10^6\ \text{erg cm}^{-3};$$

$$Q=2.1;\quad l=0.062\ \mu\text{m};$$

$$\gamma=1.64\times10^7\ \text{Oe}^{-1}\,\text{s}^{-1};\quad \alpha=0.061.$$

Here $l=\sigma_{DW}/4\pi M^2$ is the material characteristic length and σ_{DW} is the DW energy density $\sigma_{DW}=4\sqrt{AK_u}$. The values of the anisotropy field and the Walker critical field are $H_K=3.45$ kOe and $H_W=44.2$ Oe, respectively.

The analysis shows that the DW motion has an oscillatory character. The time intervals during which the DW moves with a positive value of the velocity increase with increasing the in-plane field. As a result the average DW velocity increases with the in-plane field. At certain value of the in-plane field this regime of the DW movement changes from the oscillatory state to the steady state. For example, take an initial drive field $H_x=50$ Oe, the change in the regime of the DW motion takes place at $H_x=88$ Oe. For higher starting values of the drive field the changes in the regime of the DW motion take place at still higher values of the in-plane field. Thus, the presence of an in-plane field leads to the increase of the Walker critical field. To study the situation more detailedly, we carried out a numerical experiment. We chose one particular value of the in-plane field and carried out the numerical calculations of the time dependence of the DW velocities for different drive fields, looking for the mo-

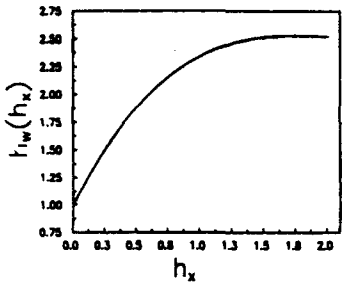

FIG. 1. The dependence of the reduced Walker critical field, h_W, on the in-plane field, h_x.

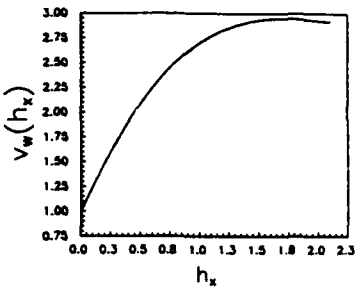

FIG. 2. The dependence of the reduced Walker critical velocity $v_W(h_x)$, on the in-plane field, h_x.

ment at which the change in the regime of the motion takes place. Doing so we obtained the different values of the critical drive field (Walker critical fields) for the different values of the in-plane field h_x parallel to the DW, varying in a small interval from 0 to 0.3. The result shows that the dependence of the Walker critical field on the in-plane field is practically linear over the small in-plane field interval examined.

Our equations allow to obtain the dependencies of the critical parameters of the DW movement over a wide interval of the in-plane field variation. To illustrate, it is necessary first to determine the critical value of the azimuthal angle, ψ_{cr}, corresponding to the moment of the change in the regime of the DW motion. As was shown in Ref. 5, the critical value of the azimuthal angle of the magnetization ($\psi_{cr}=\pi/4$ at $h_t=0$) corresponds to $H_z=H_W$, and that the derivative of the azimuthal angle with respect to the drive field tends to infinity at $H_z=H_W$. We use the condition to obtain the dependence of $\psi_{cr}(h_t)$. The derivative of the azimuthal angle of the magnetization with respect to the drive field may be obtained from Eq. (11) in which $\dot{\psi}=0$ (steady state DW motion). The condition that $d\psi_{cr}(h_t)/dh_{\parallel}\to\infty$ is equivalent to the relation

$$f(\vartheta_0)\cos 2\psi_{cr}+g(\vartheta_0)h_t\cos\psi_{cr}=0. \tag{12}$$

To obtain the dependence of the critical azimuthal angle on the in-plane field, $\psi_{cr}(h_t)$, one has to solve the above equation together with Eq. (2) in which $h_{\parallel}=\alpha h_W(h_t,\vartheta_0)/2$, where $h_W(\vartheta_0,h_t)=H_W(h_t,\vartheta_0)/H_W$ is reduced Walker critical field. The expression for $h_W(\vartheta_0,h_t)$ may be easily obtained from Eq. (11)

$$\frac{h_W(\vartheta_0,h_t)}{2r(\vartheta_0)}=[f(\vartheta_0)\cos\psi_{cr}+g(\vartheta_0)h_t]\sin\psi_{cr}, \tag{13}$$

and, as a result, we get

$$\begin{aligned}Q\sin\vartheta_0\cos\vartheta_0-h_t\cos\vartheta_0&\\ =-\alpha r(\vartheta_0)\sin\vartheta_0[f(\vartheta_0)\sin\psi_{cr}\cos\psi_{cr}&\\ +g(\vartheta_0)h_t\sin\psi_{cr}].&\end{aligned} \tag{14}$$

From the substitution of the (numerical) solutions for $\psi_{cr}(h_t)$ and $\vartheta_0(h_t)$ from the system of Eqs. (12) and (14) into (13) we are ready to obtain the in-plane field dependence of Walker critical field $h_W(h_t)$. A salient feature of the dependence is shown in Fig. 1. Note that h_W varies linearly with h_t at small h_t (in agreement with the above numerical experimental results), but saturates at large values of h_t. The in-plane field dependence of the Walker critical velocity may be obtained in conjunction with Eq. (10) and is given by

$$v_W(h_t)=\frac{\sqrt{(2(2Q+1)r(\theta_0)}}{\sqrt{n(\theta_0,\psi_{cr})}}\times[f(\theta_0)\cos\psi_{cr}+g(\theta_0)h_t]\sin\psi_{cr}, \tag{15}$$

where $v_W(h_t)=V_W(h_t)/V_W$ is the reduced Walker critical velocity, and the critical velocity at the zero in-plane field[5] is $V_W=\omega_M\Delta_B\sqrt{Q}/\sqrt{2(2Q+1)}$. A plot of Eq. (15) showing the in-plane field dependence of the Walker critical velocity is presented in Fig. 2.

Briefly summarizing, we have derived in this article the generalized DW dynamic equation taking into account the in-plane field influence on the DW structure. As an illustration, the dependence of the Walker critical field and velocity over a wide range of the magnetic field normal to the anisotropy axis was calculated.

ACKNOWLEDGMENTS

This research was supported by contracts from the National Science Council, ROC through: NSC-82-0212-M-002-172 and 82-0405-E02-124.

[1] A. P. Molozemoff and J. C. Slonczewski, *Magnetic Domain Walls in Bubble Materials* (Academic, New York, 1979).
[2] F. W. de Leeuw, R. Van der Doel, and U. Enz, Rep. Prog. Phys. **43**, 690 (1980).
[3] A. Hubert, *Teorie der Domanenwande in Geordneten Medien* (Springer, Berlin, 1974) (in German).
[4] A. M. Kosevich, B. A. Ivanov, and A. S. Kovalev, Phys. Rep. **194**, 117 (1990).
[5] N. L. Schryer and L. R. Walker, J. Appl. Phys. **45**, 5406 (1974).
[6] T. Fujii, T. Shinoda, S. Shiomi, and S. Uchiyama, Jpn. J. Appl. Phys. **17**, 1197 (1978).
[7] H. L. Huang and S. C. Chen, Jpn. J. Appl. Phys. **32**, 1962 (1993).
[8] V. L. Sobolev, S. C. Chen, and H. L. Huang, Chin. J. Phys. (Taipei) **31**, 403 (1993).
[9] H. L. Hu and E. A. Giess, AIP Conf. Proc. **24**, 605 (1975).

Magnetic induced uniaxial anisotropy in NiFe and NiFeCr films (abstract)

Terry Torng and Simon H. Liao
Applied Magnetic Corporation, Goleta, California 93117

We report the experimental results of magnetic uniaxial anisotropy induced during sputtering (K_1) and annealing (K_2) of NiFe and NiFeCr films. The NiFe and NiFeCr films of around 30 nm thickness were deposited using dc magnetron sputtering. Glass and Ta (20 nm) coated glass were used as substrates. The magnetic properties were determined using a B-H looper at 10 Hz. The crystal orientation was determined using x-ray diffraction. The results show that the predictions from a two-component anisotropy model[1] (that is $K_2/[K_1+K_2]$) for a 3 h 310 °C anneal are in good agreement with experimental data for both NiFe/glass and NiFeCr/glass, but not for NiFe/Ta/glass and NiFeCr/Ta/glass. This can be explained by the orientation effect[2] from x-ray diffraction studies. The NiFe and NiFeCr have higher (111) preferred orientation when deposited on Ta coated glass as compared to samples deposited on glass only. The effects of annealing temperature and Ta underlayer will be discussed. The activation energy for magnetic annealing induced anisotropy will also be discussed.

[1] W. Metzdorf, Z. Angew. Phys. 18, 534 (1965).
[2] K. Nishimoto and T. Furuoya, Jpn. J. Appl. Phys. 12, 80 (1973).

Structural and magnetic properties of rf-sputtered iron nitrides using NH_3 (abstract)

John Q. Xiao and C. L. Chien
Department of Physics and Astronomy, The John Hopkins University, Baltimore, Maryland 21218

Thin films of iron nitrides have attracted much attention due to their superior magnetic properties. Conventional rf reactive sputtering using N_2 gas encounters a number of difficulties, including mixed phases, which are alleviated by the use of NH_3 gas. By controlling the partial pressure of NH_3, we have been able to fabricate all stable Fe nitrides of ζ-Fe_2N, ϵ-$Fe_{2-3}N$, and γ'-Fe_4N in single-phase films. The structure has been determined using an x-ray diffractometer. The magnetic properties have been investigated using VSM, SQUID magnetometers, and Mössbauer spectroscopy. All nitrides except Fe_2N have high saturation moments with a large in-plane anisotropy. The saturation moment decreases with increasing nitrogen concentration. The Mössbauer results, in excellent agreement with those from bulk samples, are consistent with structural results and magnetization measurements.

Supported by ONR Grant No. N00014-91-J-1633.

 0021-8979/94/75(10)/5800/1/$6.00 © 1994 American Institute of Physics

Nucleation of the nanocrystalline phase in $Fe_{73.5}Cu_1Nb_3Si_{13.5}B_9$ (abstract)

J. D. Ayers, V. G. Harris, J. A. Sprague, and W. T. Elam
Naval Research Laboratory, Washington, DC 20375-5000

A new class of soft magnetic alloys derive their attractive properties from the fact that they contain a high volume fraction of iron rich, nanometer scale, DO_3 structure precipitates. These precipitates are imbedded within, and separated from one another by, a portion of the amorphous phase from which they formed. In an effort to determine the mechanism by which the addition of modest amounts of Cu and Nb to Fe-Si-B amorphous alloys induce the formation of the metastable nanocrystalline structure, melt-spun samples of $Fe_{73.5}Cu_1Nb_3Si_{13.5}B_9$, $Fe_{76.5}Cu_1Si_{13.5}B_9$, and $Fe_{74.5}Nb_3Si_{13.5}B_9$ were heat treated at 550 °C for times ranging from 2 to 60 min and studied by means of transmission electron microscopy (TEM), x-ray diffraction, and extended x-ray absorption fine structure (EXAFS) analysis. EXAFS spectra from the Cu absorption edge in the $Fe_{73.5}Cu_1Nb_3Si_{13.5}B_9$ alloy show that tiny clusters of a Cu rich phase are present even in the amorphous, as-melt-spun ribbon, and that these clusters have close atomic packing. These clusters are found to coarsen and increase in number during the first few minutes of heat treatment. TEM observations show that a high proportion of the precipitates are nucleated within this same short time, supporting the belief that the clusters catalyze nucleation of the DO_3 precipitates. Examination of the alloys without Cu or Nb indicate that the Nb is important both for stabilizing the amorphous phase component and for inducing formation of the Cu clusters.

 0021-8979/94/75(10)/5801/1/$6.00 © 1994 American Institute of Physics

Validity and the applicability of magnetic-circular-dichroism sum rules for transition metals (invited)

Ruqian Wu, Dingsheng Wang,[a] and A. J. Freeman
Department of Physics and Astronomy, Northwestern University, Evanston, Illinois 60208

X-ray magnetic-circular-dichroism (MCD) spectra are calculated using the thin film full potential linearized augmented plane wave energy band method for transition metal surfaces. Together with a model analysis, a clear physical insight is provided for this new and exciting phenomenon. The MCD sum rule for the orbital moments originally derived from a single ion model are found to be valid to within 5–10% even in the band approach which treats the strongly hybridized multiband structure. However, the spin sum rule may result in a larger error due to the effects of $s,p-d$ hybridization. In addition, the magnetic dipole term is very important in the spin sum rule, especially for atoms with lower local symmetry.

I. INTRODUCTION

Recently, x-ray magnetic circular dichroism (MCD), has become an exciting new powerful tool for investigating the magnetism of transition and rare-earth metal systems based on recent advancements in the sophisticated use of synchrotron radiation facilities.[1–8] Its unique properties, e.g., its high element selectivity, offer a strong potential for magnetic materials characterization and visualization.[9]

Physically, MCD measures the difference in absorption between left- (with cross section, σ_+) and right-circularly (with cross section, σ_-) polarized incident light during the process of electric transitions from core states ($2p$ for $3d$ transition metals) to the unoccupied valence states. Due to the strong spin–orbit coupling (SOC), the $2p_{1/2}$ and $2p_{3/2}$ core states are no longer degenerate and thus the absorption peaks from these components are separated in energy (L_2 denotes the transition from $2p_{1/2}$ and L_3 denotes the transition from $2p_{3/2}$).

Based on a single ion model analysis, Carra *et al.*[10–12] established a direct relationship for the MCD and total adsorption cross sections, i.e., σ_m $(=\sigma_+-\sigma_-)$ and $\sigma_t(=\sigma_++\sigma_-+\sigma_z)$, with the average spin and orbital moments, i.e., $\langle S_z\rangle$ $(S_z=\pm 1)$ and $\langle L_z\rangle$ as

$$\frac{I_m=\int_{L_3+L_2}\sigma_m\,dE}{I_t=\int_{L_3+L_2}\sigma_t\,dE}=\frac{C\langle L_z\rangle}{N_h=\int\rho(E)dE} \tag{1}$$

and

$$\frac{I_s=\int\sigma_s=\{\sigma_{m,L_3}+[(c+1)/c]\sigma_{m,L_2}\}dE}{I_t=\int_{L_3+L_2}\sigma_t\,dE}$$

$$=\frac{\langle S_e\rangle=(A\langle S_z\rangle+B\langle T_z\rangle)}{N_h}, \tag{2}$$

where $A=[l(l+1)-2-c(c+1)]/6c$, $B=\{l(l+1)[l(l+1)+2c(c+1)+4]-3(c-1)^2(c+2)^2\}/6cl(l+1)$, and $C=[l(l+1)+2-c(c+1)]/2l(l+1)$. For L adsorption edges in Fe, the core and valence angular-momenta c and l are equal to 1 and 2, respectively, and thus we have $A=1/3$, $B=7/3$, and $C=1/2$. The number of valence holes, N_h, can be obtained from the integration over the density of states, $\rho(E)$. In Eq. (2), $\mathbf{T}$ is the magnetic dipole operator $\{\mathbf{T}=\frac{1}{2}[\mathbf{S}-3\hat{r}(\hat{r}\cdot\mathbf{S})]$, and $T_z=S_z(1-3\cos^2\theta)/2$ for $\mathbf{S}$ aligned along the z direction$\}$.

There are two major assumptions in the derivation of the sum rule:[10–12] (i) the radial matrix elements are a constant for all transitions, (ii) no hybridization exists between different l shells (i.e., l is a good quantum number). In addition, $\langle T_z\rangle$ has to be negligible for the determination of $\langle S_z\rangle$ directly from the MCD spectra. However, as is well known, assumptions (i) and (ii) fail in real materials and $\langle T_z\rangle$ is small only for atoms with cubic local symmetry. Therefore, it is obviously necessary to verify the validity of these sum rules and provide solutions for the possible problems in applying them to real materials from a first principles energy band approach in which all the complexities (such as a strongly hybridized multiband structure) are accounted for.

To this end, we developed our full potential linearized augmented plane wave (FLAPW) method to directly calculate MCD spectra, $\langle L_z\rangle$, $\langle S_z\rangle$, and $\langle T_z\rangle$ in order to provide a deeper understanding of these new exciting phenomena and give guidance for the analysis and interpretation of MCD spectra. We found that the MCD orbital sum rules are valid in the band approach to within 5–10%.[13,14] For the spin sum rule the error bar becomes larger [14% for surface Fe(001)], and, the $\langle T_z\rangle$ term is very important especially for atoms at surfaces and interfaces.[14]

II. METHODOLOGY

We employ a second-variational procedure to account for the spin–orbit coupling (SOC) in the valence band. In this procedure, the wave functions of the unperturbed states, namely, $\psi_i=\Sigma_j\,c_j^i\phi_j$, where ϕ_j is the augmented plane wave

[a]Institute of Physics, Academia Sinica, Beijing 100080, People's Republic of China.

 0021-8979/94/75(10)/5802/5/$6.00 © 1994 American Institute of Physics

basis in semirelativistic calculations, are used as a basis set to expand the SOC Hamiltonian. Therefore, we have a diagonalized non-SOC Hamiltonian H_0 and a traceless SOC matrix as the perturbation. Since the off-diagonal matrix elements of SOC are very small (usually a few meV in practical calculations) compared to the bandwidth, a much smaller energy cutoff (e.g., 0.5 Ry above E_F) can be adopted in the diagonalization of the new eigenvalue equation

$$(H_0+\xi\boldsymbol{\sigma}\cdot\mathbf{L})|C_j\rangle=\lambda|C_j\rangle \tag{3}$$

to obtain the perturbed wave functions $\psi_i' = \Sigma_j C_j^i \psi^j$.

For dipole-excited transitions, the cross section for absorption of incident light can be expressed as

$$\sigma_n(E)=\int_k |\langle\psi_c|p_n|\psi_v'\rangle|^2\delta[E-(E_v-E_c)]dk, \quad n=\pm,z, \tag{4}$$

where p_n stands for the momentum operators corresponding to the polarization of the light. In the second-variational procedure described above, the matrix elements can be obtained from integrations of $\langle\psi_c|p_n|\phi_j\rangle$ as

$$\langle\psi_c|p_n|\psi_v'\rangle=\sum_{j,k} C_k^i c_j^k\langle\psi_c|p_n|\phi_j\rangle. \tag{5}$$

A seven layer slab is used to simulate the bcc Fe(001) surface with the lattice constant chosen as $a=5.4168$ a.u. An energy cutoff of 12 Ry is used for the variational plane wave basis set. Within the muffin-tin (MT) spheres, lattice harmonics with angular-momentum l up to 8 are employed to expand the charge density, potential, and wave functions. Convergence is assumed when the average root mean square distance between the input and output charge and spin densities is less than 2.5×10^{-4} e/(a.u.)^3.

III. RESULTS AND DISCUSSION

Before describing the first principles results, a simple but helpful physical insight can be obtained from a perturbative model discussion. We calculated σ_t, σ_s, σ_m, L_z, T_z, and s_z analytically up to first order in ξ for the Slater–Koster d and s basis with minority spin ($S_z=-1$).[14] For d states (with R_d representing the radial integration), independent of their angular wave function characters, we found the relations (i) $\sigma_t=4R_d/5$, (ii) $\Sigma_{L_2,L_3}\sigma_m = (4R_d/5)(L_z/2)$, and (iii) $\sigma_s = \sigma_{m,L_3} - 2\sigma_{m,L_3} = (4R_d/5)S_e$. From (i) and (ii), we obtain the MCD orbital moment sum rule[10] if only the d states are involed. Interestingly, the s state contributes to neither σ_m nor L_z, and thus the proportionality between these two quantities is expected to hold well even for real transition metal systems.[13,14] Obviously, (i) and (iii) denote the proportionalities between the numerators and the denominators on the left and the right sides of Eq. (2) for each d states and thus the MCD spin sum rule is also a natural result of this simple single atom model.

A. The orbital sum rule

In real materials, the angular-momentum l is not a good quantum number, and the real wave function usually contains

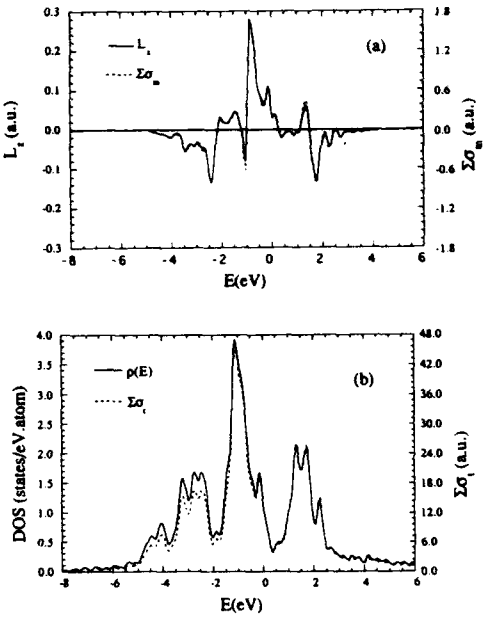

FIG. 1. The energy distributions of (a) L_z and $\Sigma_{L_3,L_2}\sigma_m$, (b) the density of states and $\Sigma_{L_3,L_2}\sigma_t$ for bulk Fe.

contributions from all the l values (mainly s, p, and d in $3d$ metals). Thus we expect the sum rule to hold only in the region where the d states dominate (i.e., in the d band range for $3d$ transition metals) since the quantities in Eq. (1) depend differently on the wave functions (i.e., $\langle L_z\rangle$ depends on p and d components, σ_m and σ_t relate to s and d components while N_h is independent of the wave function character).

As discussed above, the s,p contributions to σ_m and L_z are canceled due to either the summation over the two adsorption edges (s states to σ_m) or the small exchange splitting (p states to L_z). As a result, we found that the calculated L_z and σ_m, as shown in Fig. 1(a), track each other very well in the whole energy range shown. Therefore, the assumption that the radial matrix is a constant for each transition to the d state is a good approximation. Comparatively, the denominators, i.e., $\rho(E)$ and σ_t, track each other less well in Fig. 1(b), especially in the bottom region of the d band because the s,p contributions do not cancel.[14] Thus, neglect of the multishell hybridization is a good approximation for the numerators in Eq. (1), but leads to some errors for the denominators.

Beyond the d band range, especially in the higher energy region (6 eV above E_F), the deviation between $\rho(E)$ and σ_t becomes more important because they will accumulate during the energy integration and result in a large error for the quantities in Eq. (1) and thus the failure of the sum rule. To solve this problem, an upper energy limit has to be set for the integrals in Eq. (1) to stay in the d band range. However, since different choices of this upper energy limit can introduce uncertainties for N_h and I_t, we propose to use the MCD

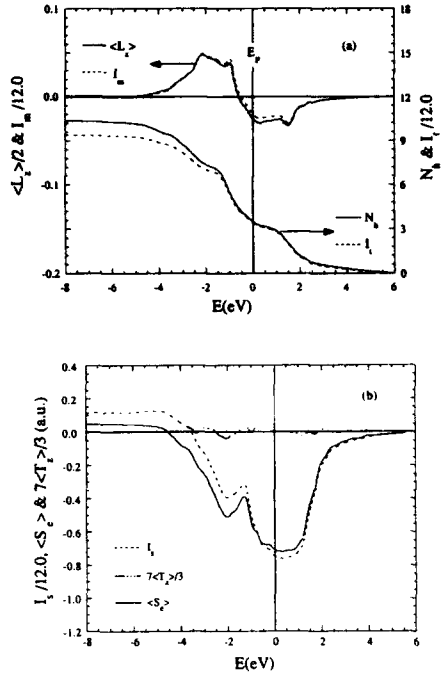

FIG. 2. The dependence of the integrated quantities on the band filling for (a) $\langle L_z \rangle$ (solid line, left scale), I_m (dashed line, left scale), N_h (solid line, right scale), and I_t (dashed line, right scale) and (b) $\langle S_z \rangle$ (solid line), $\langle I_z \rangle$ (dashed line), and $\langle T_z \rangle$ (dashed-dotted line) for bulk Fe. $E=0$ corresponds to the position of the physical Fermi level.

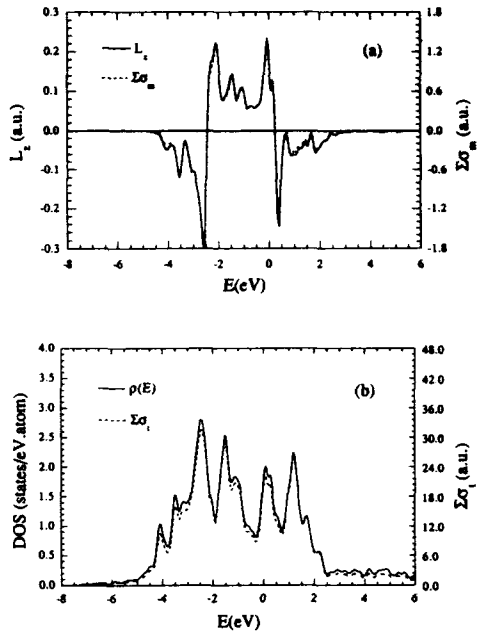

FIG. 3. The energy distributions of (a) L_z and $\Sigma_{L_3,L_2}\,\sigma_m$, (b) the density of states and $\Sigma_{L_3,L_2}\,\sigma_t$ for surface Fe.

(or equally the $\langle L_z \rangle$) curves as a criterion to determine the range of the d bands for the integrations: thus we terminate the integrations for I_t and N_h where the MCD counterparts become acceptably close to zero for both L_3 and L_2. In fact, this criterion has already been used in experiments[8] by determining the energy cutoff for I_t according to the MCD spectrum using a spline fit and a step function subtraction.[8] Now we know that this procedure serves to eliminate the contributions from high lying s and p states (or continuum states) and thus ensures the validity of the sum rule.

For $3d$ transition metal systems, we found that it is suitable to cut the integrations at 6 eV above the Fermi level. To give a clear physical insight, we plot the four integrated quantities [i.e., the numerators and the denominators of Eq. (1)] as functions of the band filling (by varying E_F from the bottom of the d band to the upper limit of 6 eV) in Fig. 2(a) for bulk Fe. Good proportionality between both numerators and both denominators can be found, especially in the physically interesting region ($E_F=0$)—hence the sum rule holds to within 5–10%. Quantitatively, for example, we can determine $\langle L_z \rangle$ from Eq. (1). $\langle L_z \rangle$ obtained in this way is 0.05 μ_B, which is very close to the directly calculated value 0.055 μ_B for bulk Fe.

Note that in Fig. 2(a), the slope of N_h and I_t is obviously not zero at the arbitrary energy cutoff of 6 eV. This again suggests the importance of the energy cutoff for the validity of the sum rule. In addition, the deviation between N_h and I_t becomes larger and larger at the bottom of the d band because of the accumulation of the s,p influence in the integrals. However, the effects of s,p states on $\langle L_z \rangle$ and I_m are truely small since both of them quickly approach zero with an almost zero slope above 4 eV. This may hint a possibility to determine $\langle L_z \rangle$ solely from the proportionality between the denominators without the uncertainties involved in obtaining the normalization factors, I_t and N_h, if (i) the scaling factor (6.0 for Fe) between I_m and $\langle L_z \rangle$ remains constant in different environments and (ii) I_m can be measured absolutely (not a relative value as in the present experiments).

Indeed, as plotted in Figs. 3(a) and 3(b) for surface Fe, we see that the two pairs of functions [i.e., L_z vs $\Sigma_{L_3,L_2}\,\sigma_m$, and $\rho(E)$ vs $\Sigma_{L_3,L_2}\,\sigma_t$] also track each other very well; more importantly, they do so with the same scaling factor for bulk Fe (cf. Fig. 1). Since the wave functions of the surface Fe atom contain larger s,p components, the deviation between N_h and I_t even start from the begining (6 eV) of the integration, as shown in Fig. 4(a). However, the sum rule still holds if a 5%–10% error bar is allowed. The $\langle L_z \rangle$ for the surface Fe determined from the sum rule, 0.09 μ_B, is also very close to that (0.095 μ_B) evaluated directly. By contrast, it is quite striking how the I_m values track the $\langle L_z \rangle$ curve even for this large a change in shape and value of

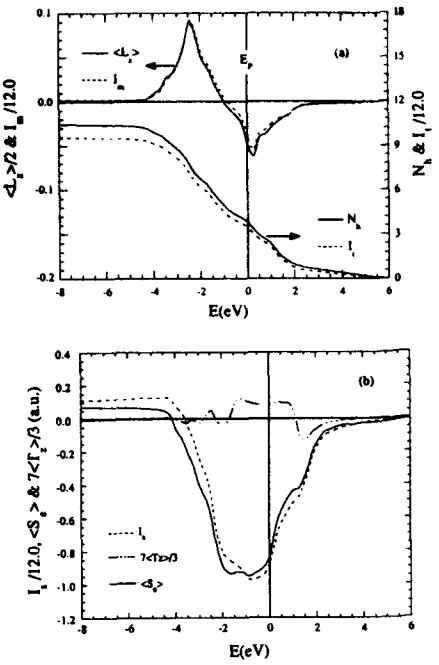

FIG. 4. The dependence of the integrated quantities on the band filling for (a) $\langle L_z \rangle$ (solid line, left scale), I_m (dashed line, left scale), N_h (solid line, right scale), and I_t (dashed line, right scale) and (b) $\langle S_e \rangle$ (solid line), $\langle I_s \rangle$ (dashed line), and $\langle T_z \rangle$ (dashed-dotted line) for surface Fe. $E=0$ corresponds to the position of the physical Fermi level.

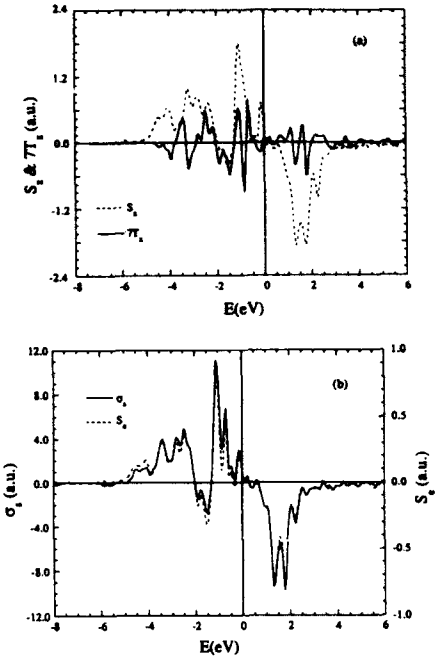

FIG. 5. The energy distributions of (a) S_z and $7T_z$, (b) S_e and σ_s for bulk Fe.

$\langle L_z \rangle$ from the surface to the bulk. In fact, this good proportionality and the constant scaling factor hold very well for Fe systems we studied so far [the Fe(001) monolayer, Fe surfaces, and the Fe/Pd(001) interface, etc.].

B. The spin sum rule

Unlike the case for the MCD orbital sum rule, all the quantities in Eq. (2) are independent of SOC in the valence band (up to ξ^2). The s state contributes even to the numerators such as S_z and σ_s. As a result, the sum rule is expected to work less well than the orbital sum rule does in real materials. As seen from the single atom model,[14] the contribution of T_z to the MCD spin moment sum rule is large for each d state although the sum of T_z over the whole d band or over the t_{2g} and e_g sets (degenerate separately in the O_h symmetry) is zero.

Indeed, as shown in Fig. 5(a) by the first principles results for S_z and T_z for bulk Fe, T_z strongly oscillates in the d band region—even up to several times within the unoccupied minority spin peak. The magnitude of $7T_z/3$ is comparable to that of $S_z/3$, especially in the occupied part. It is the dipole term which ensures the proportinality between the numerators in Eq. (2), i.e., σ_s vs S_e in Fig. 5(b). Due to the contributions of s states (to both σ_s and S_e) and p states (to S_z), some evident deviations can be found between the two curves in Fig. 5(b) in the region of the majority (-6 to -4 eV) and minority (-2 to 0 eV) spin band bottoms. Therefore, we expect that a proper energy cutoff for the integrations in Eq. (2) is even more important for Eq. (1).

In Fig. 2(b), calculated results for I_s and $\langle S_e \rangle$ are plotted for bulk Fe. Together with I_t and N_h shown in Fig. 2(a), we found that the spin sum rule also holds with an error bar of 5%–10%. Interestingly, the curve of $7\langle T_z \rangle/3$ shows a very small magnitude in the whole energy range shown in Fig. 2(b), corresponding to its strong oscillatory behavior [cf. Fig. 5(a)]. Thus for atoms with high symmetry, the MCD spin sum rule can be applied to measure the spin moment directly by neglecting the $\langle T_z \rangle$ term.

By contrast, the $\langle T_z \rangle$ term becomes important for the Fe surface atom due to the lowered symmetry. As shown in Fig. 6(a), the magnitude of $7T_z/3$ is even larger than that of $S_z/3$. At 1.2 eV, the S_z peak is almost entirely compensated by that of T_z—resulting in a very small S_e at this energy in Fig. 6(b). Dramatically, the proportionality between σ_s and S_e still holds for the surface Fe atom with the same scaling factor for the center layer Fe atom, after such drastic cancellations between T_z and S_z. Therefore, the MCD spin sum rule also works for and surface atoms but with larger error (14%). As shown in Fig. 4(b), the deviation between I_s and $\langle S_e \rangle$ starts even from the very beginning of the integration.

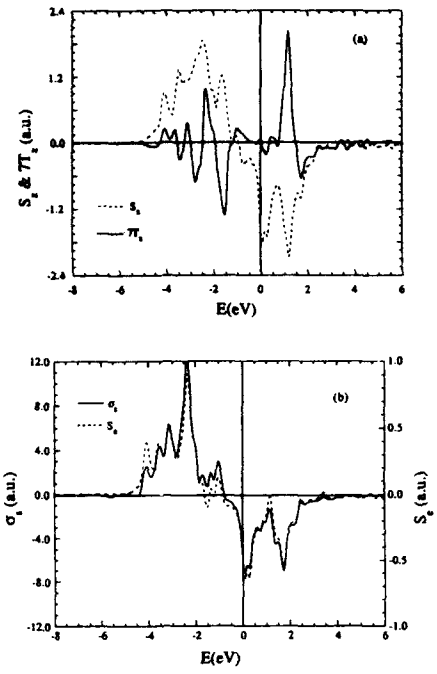

FIG. 6. The energy distributions of (a) S_z and $7T_z$, (b) S_z and σ_z for surface Fe.

Obviously, as shown in Fig. 4(b), the $\langle T_z \rangle$ term is no longer negligible for the surface Fe. Without $\langle T_z \rangle$, the difference between S_z and S_z can reach as much as 50% at 1.5 eV (and 12% at E_F). Evn larger $\langle T_z \rangle$ at E_F are found for Fe atoms at interfaces.[15] Therefore, the knowledge of T_z is extremely significant for the application of the MCD spin sum rule to transition metal surfaces and especially to interfaces. For these systems, highly precise first principles determinations for both the MCD spectra and ground state properties (e.g., S_z and T_z, etc.) are essential for interpreting experimental results.

IV. CONCLUSIONS

From local density energy band studies, we have checked the validity and applicability of the MCD sum rules aimed at direct measurements of $\langle L_z \rangle$ and $\langle S_z \rangle$ for Fe(001). We found that while the orbital sum rule derived from a single ion model still hold in the solid state to within 5%–10%, the spin sum rule may result in a larger error, in addition, they must be applied with caution since: (i) the s,p contributions should be excluded by using an appropriate upper energy limit for the integrations; and (ii) the magnetic dipole term must be included in the spin sum rule.

ACKNOWLEDGMENTS

Work supported by the Office of Naval Research and by a grant of computer time at the Pittsburgh Supercomputing Center. We thank G. Prinz and Y. Idzerda for stimulating discussions.

[1] B. T. Thole, G. van der Laan, and G. A. Sawatzky, Phys. Rev. Lett. **55**, 2086 (1985); G. van der Laan, B. T. Thole, G. A. Sawatzky, J. B. Goedkoop, J. Fuggle, J. M. Esteva, R. Karnatak, J. P. Remeika, and H. A. Dabkowska, Phys. Rev. B **34**, 6529 (1986).
[2] G. Schütz, W. Wagner, W. Wilhelm, P. Kienle, R. Zeller, and G. Materlik, Phys. Rev. Lett. **58**, 737 (1987); G. Schütz, M. Knülle, R. Wienke, W. Wilhelm, W. Wagner, P. Kienle, and R. Frahm, Z. Phys. B **73**, 67 (1988); G. Schütz, R. Wienke, W. Wilhelm, P. Kienle, R. Zeller, and R. Frahm, *ibid.* B **75**, 495 (1989).
[3] C. T. Chen, F. Sette, Y. Ma, and S. Modesti, Phys. Rev. B **42**, 7262 (1990); C. T. Chen, N. V. Smith, and F. Sette, Phys. Rev. B **43**, 6785 (1991).
[4] L. Baumgarten, C. M. Schneider, H. Petersen, F. Schäfers, and J. Kirschner, Phys. Rev. Lett. **65**, 492 (1990).
[5] J. G. Tobin, G. D. Waddill, and D. P. Pappas, Phys. Rev. Lett. **68**, 3642 (1992); G. D. Waddill, J. G. Ton'bin, and D. P. Pappas, Phys. Rev. B **46**, 552 (1992).
[6] Y. U. Idzerda, L. H. Tjeng, H. J. Lin, C. J. Gutierrez, G. Meigs, and C. T. Chen, Phys. Rev. B **48**, 642 (1993).
[7] G. van der Laan, M. A. Hoyland, M. Surman, C. F. J. Flipse, and B. T. Thole, Phys. Rev. Lett. **69**, 3827 (1992).
[8] Y. Wu, J. Stöhr, B. D. Hermsmeier, M. G. Samant, and D. Weller, Phys. Rev. Lett. **69**, 2307 (1992).
[9] J. Stöhr *et al.*, Science **259**, 658 (1993).
[10] B. T. Thole, P. Carra, F. Sette, and G. van der Laan, Phys. Rev. Lett. **61**, 1943 (1992); P. Carra, Synch. Rad. News **5**, 21 (1992).
[11] M. Altarelli, Phys. Rev. B **47**, 597 (1993).
[12] P. Carra, B. T. Thole, M. Altarelli, and X-D. Wang, Phys. Rev. Lett. **70**, 694 (1993).
[13] R. Wu, D. Wang, and A. J. Freeman, Phys. Rev. Lett. **71**, 3581 (1993).
[14] R. Wu, D. Wang, and A. J. Freeman, J. Magn. Magn. Mater. (in press).
[15] R. Wu and A. J. Freeman (unpublished).

X-ray magnetic circular dichroism studies of multilayered thin films of 3d transition metals (invited) (abstract)

D. Weller, M. G. Samant, J. Stöhr, and Y. Wu
IBM Research Division, Almaden Research Center, 650 Harry Road, San Jose, California 95120-6099

B. D. Hermsmeier
IBM San Jose, 5600 Cottle Road, San Jose, California 95153

G. Held
IBM Research Division, T. J. Watson Research Center, Route 134, Yorktown Heights, New York 10598

C. Chappert
Institut d'Électronique Fondamentale, Université Paris Sud, 91405 Orsay, France

X-ray magnetic circular dichroism (XMCD) is used to probe both the spin and orbital d moments of Co in Co/Pd, Co/Pt, and Co/Ni multilayers, and in a Au/Co-wedge/Pd structure. While the spin moment per Co atom is found to be constant within the experimental error, the orbital moment shows a strong dependence both on the chemical environment and on the thickness of the Co layer. In particular, we find an orbital moment enhancement of up to a factor of three for a Co layer thickness of four atomic layers in the present Au/Co/Pd sandwich structure. This enhancement decays to the bulk Co value, roughly following a $1/d_{Co}$ dependence, thus confirming its interfacial origin. The relevance of these observations with respect to the perpendicular magnetic anisotropy in these samples will be discussed.

Physical information in polarized x-ray absorption spectroscopy and x-ray photoemission spectroscopy (invited) (abstract)

Bernard Theodoor Thole
Materials Science Center, 9747AG Groningen, The Netherlands

Core level and localized level x-ray absorption spectroscopy and x-ray photoemission spectroscopy contain information that can be extracted in a way independent of the theory used for the valence band. The sum rule method essentially integrates over core hole effects, which average to zero, leaving only one-particle effects. The results present interesting problems for both localized and band structure theory. In particular, more information on orbital moments has already become available, which needs a correct treatment of spin-orbit coupling. On the other hand, the multiplet structure is for a large part due to interactions in the final state and therefore gives only indirect information on the ground state. The interpretation is more complex and theory dependent.

 0021-8979/94/75(10)/5807/1/$6.00 © 1994 American Institute of Physics

Element specific magnetic hysteresis curves of Fe/Cu/Co multilayers (invited) (abstract)

Y. U. Idzerda
Naval Research Laboratory, Washington, DC 20375

H.-J. Lin
AT&T Bell Laboratories, 600 Mountain Avenue, Murray Hill, New Jersey 07974

G. Ho
Department of Physics, University of Pennsylvania, Philadelphia, Pennsylvania 19104

G. Meigs
AT&T Bell Laboratories, 600 Mountain Avenue, Murray Hill, New Jersey 07974

A. Chaiken and G. A. Prinz
Naval Research Laboratory, Washington, DC 20375

C. T. Chen
AT&T Bell Laboratories, 600 Mountain Avenue, Murray Hill, New Jersey 07974

We report the first results employing a new technique for studying heteromagnetic multilayers by element specific magnetic hysteresis measurements. Dramatically different Fe and Co hysteresis curves of Fe/Cu/Co trilayers were obtained by recording the soft x-ray magnetic dichroism[1] at their respective L_3 absorption edges as a function of the applied magnetic field. The complicated conventional hysteresis curves, obtained by a vibrating sample magnetometer, were resolved into linear combinations of the two individual elemental hysteresis curves, thus determining the average atomic magnetic moments of each element within the multilayer structure (Fe is 2.0 ± 0.08 μ_B and Co is 1.1 ± 0.04 μ_B). Furthermore, fine hysteresis features associated with one element, imperceptible in the conventional curves, were also observed, and demonstrate a new and powerful means for studying heteromagnetic multilayer systems.

[1]See, for example, C. T. Chen *et al.*, Phys. Rev. B **42**, 7262 (1990).

 0021-8979/94/75(10)/5808/1/$6.00 © 1994 American Institute of Physics

Core-level magnetic circular dichroism in 3*d* and 4*f* magnetic systems (invited) (abstract)

T. Koide
Photon Factory, National Laboratory for High Energy Physics, 1-1 Oho, Tsukuba, Ibaraki 305, Japan

With the recent availability of circulary polarized synchrotron radiation over a wide photon energy range from VUV to hard X rays, the magnetic circular dichroism (MCD) in core-level photoabsorption has rapidly attracted growing interest, both experimentally and theoretically. This novel technique can provide element-specific and site-selective information about the magnetic and the electronic states in various magnetic substances because the core-level MCD process involves optical transitions in which the one-electron initial states are well localized and have well-defined angular momenta. In order to get insight into the local magnetic states in 3*d* and 4*f* magnetic systems, we have studied MCD of ferrites, $Fe_{1-x}Pt_x$ alloys, and mixed-valence $CeRh_3B_2$ at the core-absorption edges in the VUV~soft x-ray region. The experiments were performed by utilizing directly characterized, circularly polarized undulator radiation and off-plane synchrotron radiation[1] in conjunction with an ultrahigh vacuum compatible superconducting magnet of special design.[2] Clear MCD signals were observed for $CeRh_3B_2$ in the prethreshold region of the Ce $4d \rightarrow 4f$ ($N_{4,5}$) edges. A comparison of the experimental MCD spectrum with theoretical ones[3] for uniaxial crystal fields of $\Delta_c=0$ and 0.2 eV shows that the experimental spectrum qualitatively agrees with the theoretical one for $\Delta_c=0$ eV. Theory predicts that the MCD pattern for $\Delta_c<0.14$ eV will be essentially the same as that for $\Delta_c=0$ eV. Considering a Δ_c value of 0.1–0.2 eV, which was determined from the linear dichroism measurement,[4] the present result leads to the conclusion that $\Delta_c \sim 0.1$ eV. With a model based on the strong hybridization between the neighboring Ce $4f_0(l_z=0)$ and Ce $5d_0(l_z=0)$ orbitals together with the value of $\Delta_c \sim 0.1$ eV, we can successfully explain many of the extraordinary magnetic properties of $CeRh_3B_2$. We will also present the MCD data in the $M_{2,3}$ core-absorption region for ferrites (Fe_3O_4 and $CoFe_2O_4$) and $Fe_{1-x}Pt_x$ alloys, discussing the results.

[1] T. Koide *et al.*, Nucl. Instrum. Methods A **308**, 635 (1991).
[2] T. Koide *et al.*, Rev. Sci. Instrum. **63**, 1462 (1992).
[3] T. Jo and S. Imada, J. Phys. Soc. Jpn. **59**, 1421 (1990).
[4] K. Yamaguchi *et al.*, Phys. Rev. B **46**, 9845 (1992).

 0021-8979/94/75(10)/5809/1/$6.00 © 1994 American Institute of Physics

Soft x-ray magneto-optical Kerr effect (invited) (abstract)

C. C. Kao
National Synchrotron Light Source, Brookhaven National Laboratory, Upton, New York 11973

C. T. Chen
AT&T Bell Laboratories, Murray Hill, New Jersey 07974

E. D. Johnson
National Synchrotron Light Source, Brookhaven National Laboratory, Upton, New York 11973

Y. U. Idzerda
Naval Research Laboratory, Washington, DC 20375

J. B. Hastings
National Synchrotron Light Source, Brookhaven National Laboratory, Upton, New York 11973

Recently, there has been a great deal of interest in x-ray magnetic circular dichroism (MCD) and its applications to the study of magnetic thin films and multilayers due to the dramatically enhanced dichroic effect and its element specific nature. In this work, the soft x-ray magneto-optical Kerr effect, an effect closely related to MCD, is investigated. Detailed comparison between MCD and the Kerr effect is discussed. As an example, recent results from a thin bcc Co film will be presented. In the Kerr effect measurement, specular reflectivity as a function of incident angle and photon energy was measured using both linearly polarized and circularly polarized x rays. To give the largest effect, in the case of linearly polarized light, specular reflectivity was measured in the transverse configuration, while in the case of circularly polarized light, the measurement was carried out in the longitudinal configuration. In both cases very large changes in reflectivity, up to 40% in the linearly polarized case and 75% in the circularly polarized case, were observed near the Co L_{II} and L_{III} absorption edges upon reversal of the direction of the magnetic field. These results agree very well with a macroscopic model calculation.

 0021-8979/94/75(10)/5810/1/$6.00 © 1994 American Institute of Physics

Application of the spreading of damage technique to the $S=1/2$ Ising thin film

I. V. Rojdestvenski[a] and U. M. S. Costa[b]
Department of Physics, University of Western Ontario, London, Ontario N6A 3K7, Canada

We apply the spreading of the damage technique to a $S=1/2$ Ising ferromagnetic thin film. We use Metropolis dynamics to calculate the temperature dependence of the Hamming distance as well as the Hamming distance distributions along the Markov chain. We suggest a modification of the algorithm for calculating the Hamming distance in the case of Metropolis dynamics and we discuss the results for the two-dimensional model obtained by the modified approach. For a film with three layers we present the thermal dependences of the above quantities. We also suggest a new way to introduce damage to the system as the difference in the boundary conditions. We discuss the results of this new approach for the two-dimensional model.

I. INTRODUCTION

Recently a certain amount of research work has been done studying how a single perturbation spreads in a cooperative system. In genetics, for example, one can ask what effect a single mutation in a gene has on the whole animal. This study has been done in the case of cellular differentiation.[1] Another interesting problem is the study of the consequences of small "damage" in Ising and cellular-automata systems. This technique is known as "spreading of damage" and has already been applied to the three-dimensional[2] and two-dimensional[3] ferromagnetic Ising model as well as to the Ising spin glass.[4,5]

The spreading of damage algorithm in Ising models is an investigation of the temporal evolution of two configurations which differ initially by the spin values in 1, 2, or up to one-half of the lattice sites. As the Ising model does not have an intrinsic dynamics, one has to use an "external" dynamics. The dynamics usually utilized are the Metropolis, the Glauber, and the "heat bath" ones. All these dynamics imply flipping a spin with a given probability. An important feature of the technique is that the results depend strongly on the dynamics chosen and, particularly for the heat bath dynamics, on the type of initial configurations. This is contrary to the case of usual statistical Monte Carlo modeling, where all the dynamics give the same values for the magnetization, susceptibility, and specific heat, differing only in the convergence rate.[4]

Generally, the spreading of damage simulation is done in the following manner. (i) Take a configuration A in thermal equilibrium at a given temperature T. (ii) Make a copy B of that configuration and introduce a damage by changing the state of the spin at one or more sites. (iii) Treat both configurations in exactly the same manner by applying the same algorithm, the same dynamics, and the same random numbers. (iv) Take the configurational average by repeating the process for several different initial configurations. (v) The quantities that are usually being calculated are the Hamming distance, i.e., the fraction of sites which are different in the two lattices at a given time, and the total damage time, i.e., the time for all the spins to be damaged at least once.

For a given nonzero initial damage, after a long period of time, one of the two following distinct regimes can be found, depending on the value of the temperature: (a) "chaotic" regime, when the damage propagates and the two configurations remain apart in phase space (average Hamming distance being equal to 0.5 then), and (b) a "frozen" regime when the damage heals and after some time the Hamming distance will be zero. The sharp frontier between these two regimes characterizes a phase transition at a given spreading temperature T_s. There is some controversy concerning the correlation between these transitions and the usual phase transition in statistical models. For the two-dimensional ferromagnetic Ising model, the spreading temperature T_s coincides with the Curie temperature[3,6] T_c, while for the three-dimensional Ising model, T_s is different[2] from T_c. Another interesting feature of the spreading of damage technique is that, if the Glauber or the Metropolis dynamics[2,3] are applied below T_s, the frozen phase appear while for the heat bath dynamics[5] there is the chaotic phase.

The aim of the present paper is to discuss some modifications of the spreading of the damage algorithm and to apply the modified technique to the two-dimensional $S=\frac{1}{2}$ Ising model and the three-layer thin film. We suggest calculating the Hamming distance distributions along the Markov chain and show that they might be useful in understanding the details of the damage spreading process. We introduce a new concept of "limited" spreading of damage and discuss how to identify this phenomenon by analyzing the Hamming distance distributions. We also suggest a new type of damage

[a]Permanent address: Dept. of Physics, St. Petersburg Marine University, 190008, St. Petersburg, Russia.
[b]Permanent address: Departamento de Física, Universidade Federal de Alagoas, 57060 000 Maceio, Alagoas, Brazil.

 0021-8979/94/75(10)/5811/3/$6.00 © 1994 American Institute of Physics

introduction through the difference in the boundary conditions for the two configurations, and we discuss the results of our simulation of the two-dimensional model with the damage introduced in this way. For the three-monolayer film with different exchange parameters in different layers and between the layers we show the presence of the limited spreading of damage phenomenon. Further results and discussion will be published elsewhere.[7]

II. THE MODEL OF A THIN MONOCRYSTALLINE FILM AND THE SPREADING OF THE DAMAGE ALGORITHM

We represent the thin ferromagnetic film as a $S=\frac{1}{2}$ Ising ferromagnet on a simple cubic lattice with the nearest-neighbor interactions having two equivalent surfaces in one direction and being infinite in the others. The Hamiltonian thus can be written in the following general form:

$$H=-\sum_{\lambda=1}^{N-2}\sum_{(ij)} J^B S_{i\lambda}^z S_{j\lambda}^z-\sum_{\alpha=1}^{2}\sum_{(lm)} J^S S_{l\alpha}^z S_{m\alpha}^z$$
$$-\sum_{\nu=1}^{N-1}\sum_{p} J^T S_{p\nu}^z S_{p\nu+1}^z, \tag{1}$$

where N is the number of monolayers, the first sum corresponds to the interactions of the spins within the inner layers, the second to the surface-spin interactions, and the third to the interactions between the layers. All the sums are taken over pairs of nearest neighbors.

We use an algorithm for calculating the average Hamming distance $\langle D\rangle$ that differs slightly from the standard one. To explain the difference, we note that, if the Hamming distance becomes equal to zero at a certain step, then, in the case of Metropolis dynamics, the two configurations eventually will remain identical for the rest of the run as the same random numbers are applied. Hence it is logical to reintroduce the damage again every time it is suppressed. The same situation occurs if the Hamming distance becomes equal to 1 and both configurations become exactly opposed. Again, they remain so as they have the same thermodynamic weights and the damage is being suppressed. The algorithm presented below is free from the above-stated problems. (i) At each step we calculate the fraction F of the sites with spin values different for both configurations. (ii) If $F\leqslant 0.5$ we define $D=F$, otherwise $D=1-F$. (iii) If $D=0$ (that means that F equals either 0 or 1) then the damage is suppressed and we reintroduce it, e.g., flipping one spin in one of the configurations and putting $D=1/M$, M being the total number of the sites. (iv) To obtain $\langle D\rangle$ we average D along the Markov chain.

We discuss the properties of this algorithm elsewhere.[7]

III. NUMERICAL RESULTS AND DISCUSSION

A. Two-dimensional model

The described algorithm has been applied to the two-dimensional square lattice that corresponds to a film with a single monolayer. The results of the calculation of the average Hamming distance are presented in the insert to Fig. 1,

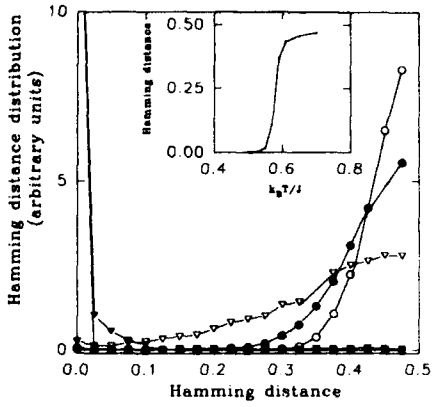

FIG. 1. The Hamming distance distributions for the 2D Ising model on a square lattice. $kT/J^B=$: ○ 0.65; ● 0.61; ▽ 0.59; ▼ 0.55; □ 0.50. *Insert*: The temperature dependence of the average Hamming distance (see Ref.5 for the details).

the dependence coinciding very well with the results obtained by Stanley.[3]

Together with the calculation of $\langle D\rangle$, we studied the histograms of the Hamming distance distribution along the Markov chain. This characteristic of the process of the damage spreading displayed an interesting temperature dependence. The Hamming distance distribution along the Markov chain is presented in Fig. 1. For the temperatures above[3] $T_s=T_c\cong 0.56$, the distribution has a pronounced maximum near $D=0.5$. When approaching T_c from above, the maximum becomes more and more flat. Below T_s we have a rapid crossover of the distribution to the shape with the pronounced maximum around $D=0$; that means suppression of the damage. The critical regime in the vicinity of T_s is characterized by strong fluctuations of D. The larger the system is, the more narrow this interval becomes and, hence, the more rapid is the crossover to the regime $T<T_s$.

B. Damage introduced through the boundary conditions

The spreading of damage algorithm can be used as well to study the influence of the boundary conditions on the critical properties of the system. To illustrate this, we make the calculations of $\langle D\rangle$ and the Hamming distance distributions in the same model and with the same dynamics, but now one sample of the lattice has periodic boundary conditions and the second has the free boundary. From the results in Fig. 2 we can conclude that the distribution function of D now has pronounced maxima between $D=0$ and $D=0.5$ for the temperatures below T_s. We should note that, contrary to the case of the traditional introduction of damage, the values of $\langle D\rangle$ are well defined even close to T_s. This phenomenon can be called *limited spreading of damage* and has been observed before for the heat bath dynamics procedures below T_s.[5] We have a simple physical explanation for this fact. In both con-

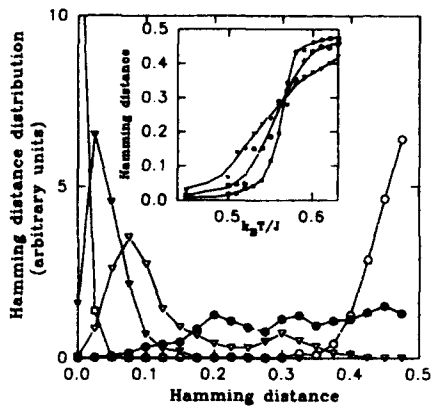

FIG. 2. The Hamming distance distributions for the 2D Ising model on a square lattice, the perturbation being in boundary conditions. $kT/J^B =$: ○ 0.65; ● 0.58; ▽ 0.54; ▼ 0.52; □ 0.45. *Insert*: The temperature dependence of the average Hamming distance: linear size $L =$: ▽ 20; ○ 40; □ 80.

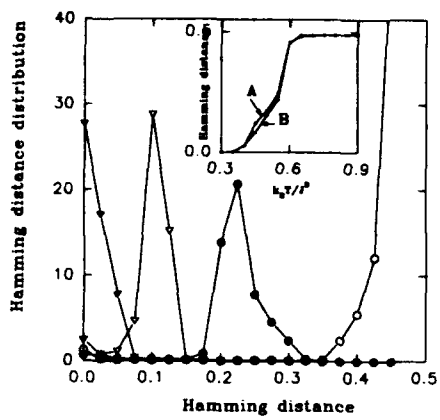

FIG. 3. The Hamming distance distributions for the *three-layer* film, $J^T = 0.2J^B$, $J^S = 0.3J^B$, the perturbation being localized in the *middle* layer. $kT/J^B =$: ○ 0.60; ● 0.55; ▽ 0.45; ▼ 0.40. *Insert*: The temperature dependencies of the average Hamming distance for the *three-layer* film, $J^T = 0.2J^B$, $J^S = 0.3J^B$; (A) perturbation is localized in the *surface* layer, (B) in the *middle* layer.

figurations the areas far from the boundaries, taken separately, display the same type of behavior as in the case of the standard way of damage introduction, e.g., $\langle D \rangle = 0.5$ above T_s and $\langle D \rangle = 0$ below. However, different boundary conditions produce differences in the values of those spins in both configurations that are situated near the boundaries and, hence, outside the correlation region of the central spins. The wider the correlation region is, the smaller is the overall $\langle D \rangle$ value. We can conclude that the accomplished calculations might give us an opportunity to investigate indirectly the spin correlations.

C. The spreading of damage in the three-monolayer film

We investigated the spreading of damage in the ferromagnetic film consisting of three monolayers. We used different exchange parameters for the interaction in the inner layer (J^B), in the surface layers (J^S) and between the layers (J^T). In Fig. 3 we present our results for the $\langle D \rangle$ temperature dependence (in the insert) and the Hamming distance distribution histograms for one set of parameters (see the figure caption for the numerical values). We interpret our results as evidence of a certain kind of crossover in the slope of the temperature dependence of $\langle D \rangle$ from two-dimensional to three-dimensional type. At the same time the Hamming distance distributions display a similar type of limited spreading of damage phenomenon, having maxima for $0 \leqslant \langle D \rangle \leqslant 0.5$. In our opinion this is evidence of partial ordering in different layers at different temperatures. Further investigations of the model in question may include the calculation of $\langle D \rangle$ (or some analogous quantity) for each layer separately and thus a study of the geometrical properties of the process of ferromagnetic ordering.

D. Conclusions

In the present paper we applied the spreading of the damage technique to the investigation of the critical properties of the Ising thin ferromagnetic films. We suggested some modifications of the standard algorithm and showed how to use the Hamming distance distributions along the Markov chain to interpret the thermal dependencies of the average Hamming distance $\langle D \rangle$. We discussed a way of introducing the damage through boundary conditions and the limited spreading of damage concept. We applied the technique in question to the three-monolayer ferromagnetic Ising film.

ACKNOWLEDGMENTS

The authors gratefully thank Professor M. G. Cottam, Dept. of Physics, University of Western Ontario, Canada for a useful discussion of the results. One of the authors (U. C.) is grateful to the CNPq of Brazil for financial support.

[1] S. A. Kauffmann, J. Theoret. Biol. **22**, 437 (1969).
[2] U. M. S. Costa, J. Phys. A. **20**, L583 (1987).
[3] H. E. Stanley, D. Stauffer, J. Kertesz, and H. J. Herrmann, Phys. Rev. Lett. **59**, 2326 (1987).
[4] U. M. S. Costa, H. R. da Cruz, and E. M. F. Curado, in *Proceedings of the Workshop on Computational Physics and Cellular Automata*, edited by A. Pires, D. P. Landau, and H. Herrmann (World Scientific, Singapore, 1990), pp. 48–58.
[5] B. Derrida and G. Weisbuch, Europhys. Lett. **4**, 657 (1987).
[6] G. Le Caer, J. Phys. A. **22**, L647 (1989).
[7] I. V. Rozhdestvensky and U. M. S. Costa (to be published).

Quantum renormalization of the *XY* model

Alessandro Cuccoli, Valerio Tognetti, and Paola Verrucchi
Dipartimento di Fisica dell'Università di Firenze, Largo E. Fermi 2, I-50125 Firenze, Italy

Ruggero Vaia
Istituto di Elettronica Quantistica del Consiglio Nazionale delle Ricerche, Via Panciatichi 56/30, I-50127 Firenze, Italy

The statistical mechanics of the two-dimensional ferromagnetic model with easy-plane anisotropy is approached by the pure-quantum self-consistent harmonic approximation (PQSCHA), that reduces the calculation of thermodynamic averages to effective classical expressions. In the PQSCHA, the quantum corrections to the classical thermodynamics are reduced to suitable (temperature-dependent) renormalizations of the interaction parameters, so that the full role of the nonlinear excitations is preserved. A particular case is the *XX*0 model (also known as the quantum *XY* model), which undergoes a Kosterlitz–Thouless phase transition at some finite temperature T_c. Since it is possible to calculate how much the effective exchange interaction is weakened by quantum fluctuations, we can predict, for instance, the corresponding amount of reduction of T_c for any value of the spin. Even in the extreme quantum case of the spin-1/2 model, our result is compatible with the estimates of T_c obtained by other authors.

The system considered in this paper is the 2D easy-plane ferromagnet, described by the Hamiltonian

$$\hat{\mathcal{H}}=-\frac{1}{2}\,J\sum_{\mathbf{i},\mathbf{d}}\left[(\hat{S}_{\mathbf{i}}^{x}\hat{S}_{\mathbf{i}+\mathbf{d}}^{x}+\hat{S}_{\mathbf{i}}^{y}\hat{S}_{\mathbf{i}+\mathbf{d}}^{y})+\lambda\hat{S}_{\mathbf{i}}^{z}\hat{S}_{\mathbf{i}+\mathbf{d}}^{z}\right]$$

$$+\sum_{\mathbf{i}}\left[D(\hat{S}_{\mathbf{i}}^{z})^{2}-\mu H\hat{S}_{\mathbf{i}}^{x}\right], \tag{1}$$

where the index $\mathbf{i}\equiv(i_1,i_2)$ runs over the sites of a two-dimensional Bravais lattice, and $\mathbf{d}\equiv(d_1,d_2)$ represents the displacements of the z nearest neighbors of each site.

The first sum describes an anisotropic exchange interaction between nearest-neighbor spins, with an easy-plane anisotropy λ ($0<\lambda<1$), whereas the second sum contains a single-site easy-plane anisotropy $D\geq 0$, and the interaction with an applied in-plane magnetic field H, where $\mu=g\mu_B$ is the gyromagnetic factor times the Bohr magneton. The quantum mechanical spin operators $\hat{\mathbf{S}}_{\mathbf{i}}$ belong to the spin-S representation, $|\hat{\mathbf{S}}_{\mathbf{i}}|^2=S(S+1)$. For $\lambda=0$, $D=0$, and $H=0$, the above Hamiltonian describes the *XX*0 model, often also called the quantum *XY* model:

$$\hat{\mathcal{H}}=-\frac{1}{2}\,J\sum_{\mathbf{i},\mathbf{d}}\left(\hat{S}_{\mathbf{i}}^{x}\hat{S}_{\mathbf{i}+\mathbf{d}}^{x}+\hat{S}_{\mathbf{i}}^{y}\hat{S}_{\mathbf{i}+\mathbf{d}}^{y}\right). \tag{2}$$

If Eq. (1) is considered as a classical Hamiltonian (i.e., the spins are taken as classical vectors with some fixed length $\tilde{S}$), in the limit of very strong easy-plane anisotropy $D\to\infty$ the z components of the spins are suppressed, and one obtains the so-called *planar* model,

$$\mathcal{H}=-\frac{1}{2}\,J\tilde{S}^{2}\sum_{\mathbf{i},\mathbf{d}}\cos(\varphi_{\mathbf{i}}-\varphi_{\mathbf{i}+\mathbf{d}})-\mu H\tilde{S}\sum_{\mathbf{i}}\cos\varphi_{\mathbf{i}}. \tag{3}$$

This model is also referred to as the *XY* model, for which Berezinskii,[1] Kosterlitz and Thouless[2] (BKT) characterized the phase transition, named after them, that occurs for $H=0$ at a finite temperature $T_c/(J\tilde{S}^2)\simeq 0.89$.[3,4] The transition has a topological character, being driven by the unbinding of vortex pairs.[5] For $T<T_c$ the correlation function $\langle\cos(\varphi_{\mathbf{i}}-\varphi_{\mathbf{j}})\rangle$ displays a power law decay, $\sim|\mathbf{i}-\mathbf{j}|^{-\eta(T)}$, whereas for $T>T_c$ the behavior is exponential; moreover, the susceptibility has an exponential divergence for $T\to T_c^{+}$, although long-range order is absent also in the low temperature phase, i.e., $\langle\cos\varphi_{\mathbf{i}}\rangle=0$ for all T.

A different classical model is found for $D=0$. In this case the out-of-plane components $s_{\mathbf{i}}^{z}$ of the spins are involved in the dynamics of the system, but still a BKT transition is expected for $H=0$ at a finite temperature $T_c(\lambda)$, which vanishes logarithmically[6,7] when the easy-plane anisotropy $\lambda\to 1$. This system has been numerically simulated on the square lattice by Kawabata and Bishop,[8,9] who (despite the use of relatively small lattices) have observed the crossover from power-law to exponential behavior of the in-plane correlations and obtained estimates of the transition temperature that confirm the theoretical asymptotic dependence of $T_c(\lambda\sim 1)$, whereas their result in the *XX*0 limit is $T_c(\lambda=0)/(J\tilde{S}^2)=0.78\pm 0.02$.

For $H=0$ the quantum system (1) preserves the rotational symmetry around the z axis, and, from universality arguments, should display the same qualitative features of a BKT system as its classical analogue, with only quantitative modifications of the critical parameters due to quantum fluctuations. Such an assumption has been confirmed by recent extensive quantum Monte Carlo simulations of the spin-1/2 quantum *XY* model (2),[10,11] which showed clear signatures of a phase transition at $T/(J\tilde{S}^2)\simeq 0.35$ having a BKT character. The work by Ding and Makivić[10–12] hints that the quantum effects mainly contribute to a renormalization of the interaction parameters; moreover their analysis of the temperature dependence of energy and specific heat reveals that the excitation spectrum of the system is dominated by spin waves up to temperatures very near the critical one.

The aim of this work is to take advantage of a recent theoretical approach, the *pure-quantum self-consistent harmonic approximation* (PQSCHA),[13] in order to simplify the

 0021-8979/94/75(10)/5814/3/$6.00 © 1994 American Institute of Physics

treatment of the general quantum model (1). By means of the PQSCHA, the thermodynamics of the quantum model can indeed be reduced to an *effective* classical problem, with the effects of quantum fluctuations (which are treated exactly up to the harmonic level) embodied in the temperature-dependent renormalized interaction parameters.

Let us consider a canonical quantum system with momentum and coordinate operators $(\hat{\mathbf{p}},\hat{\mathbf{q}})\equiv\{\hat{p}_1,\hat{q}_1\}$ (the indexes i corresponding to the N sites of some Bravais lattice) such that $[\hat{q}_i,\hat{p}_j]=i\hbar\delta_{ij}$, and with Hamiltonian $\hat{\mathcal{H}}(\hat{\mathbf{p}},\hat{\mathbf{q}})$. The PQSCHA,[13] is most conveniently worked out in terms of Weyl symbols,[14,15] i.e., the phase-space functions $\mathcal{O}(\mathbf{p},\mathbf{q}) \equiv \int d\boldsymbol{\xi} e^{-i\mathbf{p}\cdot\boldsymbol{\xi}}\langle\mathbf{q}+\frac{1}{2}\boldsymbol{\xi}|\hat{\mathcal{O}}|\mathbf{q}-\frac{1}{2}\boldsymbol{\xi}\rangle$ associated with any operator $\hat{\mathcal{O}}$. The main result of the PQSCHA is that one can write the quantum thermal average of an observable $\hat{\mathcal{O}}$ as a classical-like phase-space integral

$$\langle\hat{\mathcal{O}}\rangle=\frac{1}{\mathcal{Z}}\int\frac{d\mathbf{p}\,d\mathbf{q}}{(2\pi)^N}\,[e^{\Delta}\mathcal{O}(\mathbf{p},\mathbf{q})]e^{-\beta\mathcal{H}_{\rm eff}(\mathbf{p},\mathbf{q})}, \tag{4}$$

with the effective Hamiltonian

$$\mathcal{H}_{\rm eff}(\mathbf{p},\mathbf{q})=e^{\Delta}\mathcal{H}(\mathbf{p},\mathbf{q})-\Delta e^{\Delta}\mathcal{H}(\mathbf{p}_0,\mathbf{q}_0) + \beta^{-1}\sum_{\mathbf{k}}\ln(\sinh f_{\mathbf{k}}/f_{\mathbf{k}}), \tag{5}$$

where $(\mathbf{p}_0,\mathbf{q}_0)$ is the *minimum configuration* of $\mathcal{H}_{\rm eff}(\mathbf{p},\mathbf{q})$ (we will assume it to be translation invariant) and Δ is the second-order differential operator $\Delta\equiv\sum_{ij}[\frac{1}{2}\mathcal{J}_{ij}^{(pp)}\partial_{p_i}\partial_{p_j}+\mathcal{J}_{ij}^{(pq)}\partial_{p_i}\partial_{q_j}+\frac{1}{2}\mathcal{J}_{ij}^{(qq)}\partial_{q_i}\partial_{q_j}]$, where $\mathcal{J}_{ij}^{(pp)}=N^{-1}\sum_{\mathbf{k}}e^{i\mathbf{k}\cdot(\mathbf{i}-\mathbf{j})}m_{\mathbf{k}}(\omega_{\mathbf{k}}^2+\sigma_{\mathbf{k}}^2)\alpha_{\mathbf{k}}$, $\mathcal{J}_{ij}^{(pq)}=-N^{-1}\sum_{\mathbf{k}}e^{i\mathbf{k}\cdot(\mathbf{i}-\mathbf{j})}\sigma_{\mathbf{k}}\alpha_{\mathbf{k}}$, and $\mathcal{J}_{ij}^{(qq)}=N^{-1}\sum_{\mathbf{k}}e^{i\mathbf{k}\cdot(\mathbf{i}-\mathbf{j})}m_{\mathbf{k}}^{-1}\alpha_{\mathbf{k}}$, are the *renormalization parameters*. The Fourier index $\mathbf{k}$ runs over N values in the first Brillouin zone, $f_{\mathbf{k}}=\frac{1}{2}\beta\hbar\omega_{\mathbf{k}}$ and $\alpha_{\mathbf{k}}=(\hbar/2\omega_{\mathbf{k}})(\coth f_{\mathbf{k}}-f_{\mathbf{k}}^{-1})$. Finally, the quantities $m_{\mathbf{k}}$, $\sigma_{\mathbf{k}}$, and $\omega_{\mathbf{k}}$ are self-consistently determined by

$$\begin{aligned}
m_{\mathbf{k}}^{-1}&=\sum_{ij}e^{i\mathbf{k}\cdot(\mathbf{i}-\mathbf{j})}e^{\Delta}\partial_{p_i}\partial_{p_j}\mathcal{H}(\mathbf{p}_0,\mathbf{q}_0),\\
\sigma_{\mathbf{k}}&=\sum_{ij}e^{i\mathbf{k}\cdot(\mathbf{i}-\mathbf{j})}e^{\Delta}\partial_{p_i}\partial_{q_j}\mathcal{H}(\mathbf{p}_0,\mathbf{q}_0),\\
m_{\mathbf{k}}(\omega_{\mathbf{k}}^2+\sigma_{\mathbf{k}}^2)&=\sum_{ij}e^{i\mathbf{k}\cdot(\mathbf{i}-\mathbf{j})}e^{\Delta}\partial_{q_i}\partial_{q_j}\mathcal{H}(\mathbf{p}_0,\mathbf{q}_0).
\end{aligned} \tag{6}$$

The parameters $\alpha_{\mathbf{k}}$ are equal to the difference between the quantum and the classical (i.e., the *pure-quantum*) mean square coordinate fluctuations of a harmonic oscillator with unit mass and frequency $\omega_{\mathbf{k}}$; they decrease with T, and, for $\beta\hbar\omega_{\mathbf{k}}\ll1$, $\alpha_{\mathbf{k}}\simeq\frac{1}{12}\hbar^2\beta$. Then, as T increases, the $\mathcal{J}_{ij}^{(\cdots)}$'s tend to zero, and $\mathcal{H}_{\rm eff}(\mathbf{p},\mathbf{q})$ reduces to the bare Weyl symbol $\mathcal{H}(\mathbf{p},\mathbf{q})$. Actually, it can be shown that Eq. (4) shares the high-T behavior of the Wigner expansion.[15,16] The operator e^{Δ} yields a Gaussian smoothing of the phase-space functions on a scale given by the $\mathcal{J}_{ij}^{(\cdots)}$'s, i.e., the pure-quantum fluctuations of the canonical variables. Physically, this means that the system is not able to test a definite phase-space configuration, but only averages over neighborhoods of finite size, according to the uncertainty principle. On the other hand, the classical thermal fluctuations are embodied in the canonical ensemble phase-space integral (4).

One can make use of the PQSCHA also for the quantum spin Hamiltonian (1), as it can be expressed in terms of canonical operators. Thanks to its easy-plane character, it indeed makes sense to apply the *Villain transformation*,[17] i.e., $\hat{S}_i^+=\tilde{S}e^{i\hat{q}_i}\{1-(\hat{p}_i+1/2\tilde{S})^2\}^{1/2}\equiv(\hat{S}_i^-)^\dagger$ and $\hat{S}_i^z=\tilde{S}\hat{p}_i$, to canonical operators $\hat{q}_i$ and $\hat{p}_i$ with $[\hat{q}_i,\hat{p}_j]=i\tilde{S}^{-1}\delta_{ij}$, where $\tilde{S}\equiv S+\frac{1}{2}$ plays the role of $\hbar^{-1}$. Remarkably, the Weyl symbol for $\hat{S}^+$ is $S_i^+(\mathbf{p},\mathbf{q})=\tilde{S}\sqrt{1-p_i^2}e^{iq_i}$, so that for the Hamiltonian (1) one immediately finds (see also Ref. 18 for the one-dimensional case)

$$\begin{aligned}
\mathcal{H}(\mathbf{p},\mathbf{q})=-\epsilon\sum_{i,\mathbf{d}}&[\sqrt{1-p_i^2}\sqrt{1-p_{i+\mathbf{d}}^2}\cos(q_i-q_{i+\mathbf{d}})\\
&+\lambda p_i p_{i+\mathbf{d}}]+\epsilon\sum_i(dp_i^2-h\sqrt{1-p_i^2}\cos q_i),
\end{aligned} \tag{7}$$

where $\epsilon=J\tilde{S}^2$ sets the energy scale, and we have defined the *reduced field* $h=\mu H/(J\tilde{S})$, as well as the dimensionless anisotropy parameter $d=D/J$. For symmetry reasons, the minimum configuration is $\{p_{0,i}=0,q_{0,i}=0\}$, and the coefficients $\sigma_{\mathbf{k}}$ and $\mathcal{J}_{ij}^{(pq)}$ are vanishing, so that the operator Δ acts separately on the momenta and on the coordinates. The relevant renormalization parameters are finally found to be three, describing the pure-quantum square fluctuations of p_i, q_i, and $\delta q_{i,i+\mathbf{d}}=q_i-q_{i+\mathbf{d}}$, namely $\mathcal{J}_p\equiv\mathcal{J}_{ii}^{(pp)}$, $\mathcal{J}_q\equiv\mathcal{J}_{ii}^{(qq)}$, and $\mathcal{J}_{\delta q}\equiv 2(\mathcal{J}_{ii}^{(qq)}-\mathcal{J}_{i,i+\mathbf{d}}^{(qq)})=2N^{-1}\sum_{\mathbf{k}}\gamma_{\mathbf{k}}m_{\mathbf{k}}^{-1}\alpha_{\mathbf{k}}$, with $z\gamma_{\mathbf{k}}=\sum_{\mathbf{d}}(1-\cos\mathbf{k}\cdot\mathbf{d})$. With a procedure similar to that of Ref. 18 the effective Hamiltonian can be rewritten in terms of (effective) classical spin variables, i.e., normalized vectors $\mathbf{s}_i=(s_i^x,s_i^y,s_i^z)$, $|\mathbf{s}_i|=1$. It has the same form of the original quantum Hamiltonian (1), with suitably renormalized interaction parameters:

$$\begin{aligned}
\mathcal{H}_{\rm eff}=\epsilon\theta^2\Bigg(-\frac{1}{2}\sum_{i,\mathbf{d}}&[\tau(s_i^x s_{i+\mathbf{d}}^x+s_i^y s_{i+\mathbf{d}}^y)+\lambda s_i^z s_{i+\mathbf{d}}^z]\\
&+\sum_i[d(s_i^z)^2-\tilde{h}s_i^x]\Bigg)+NG(T),
\end{aligned} \tag{8}$$

where $\tilde{h}=he^{-\mathcal{J}_q/2}$, $\theta^2=1-\mathcal{J}_p/2$, $\tau=\theta^2e^{-\mathcal{J}_{\delta q}/2}$, and $G(T)$ is an additive correction that does not enter the calculation of operator averages. The $\mathcal{J}$'s are evaluated self-consistently using

$$\begin{aligned}
m_{\mathbf{k}}^{-1}&=\epsilon\{2d+\tilde{h}+z[\tau-\lambda(1-\gamma_{\mathbf{k}})]\},\\
m_{\mathbf{k}}\omega_{\mathbf{k}}^2&=\epsilon\theta^2(\tilde{h}+\tau z\gamma_{\mathbf{k}}).
\end{aligned} \tag{9}$$

In the effective Hamiltonian the renormalized energy scale ($\epsilon\to\epsilon\theta^2$) arises from the quantum fluctuations of the z component of the spins, whereas the renormalization of the in-plane magnetic field ($h\to\tilde{h}$) comes from the azimuthal quantum fluctuations; the exchange easy-plane anisotropy is made weaker by the factor $\tau<1$, due to the combined effect of both types of fluctuations.

Using Eq. (4) one can then calculate averages and correlations by means of classical expressions involving the ef-

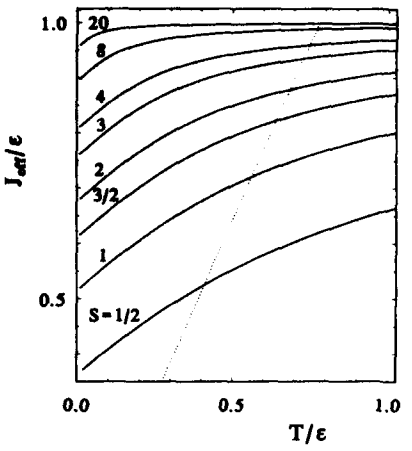

FIG. 1. The effective exchange coupling for the $XX0$ model vs temperature and for different values of the spin S (solid lines). The energy scale is $\epsilon = J\tilde{S}^2 = J(S+\frac{1}{2})^2$. The dotted line represents the relation that gives the critical temperature in terms of the effective exchange, $T_c(J_{eff}) = 0.78 J_{eff}$, as found in the classical MC simulations in Ref. 9.

fective Hamiltonian. Generalizing the derivation made in Ref. 18, and defining the classical average with the effective Hamiltonian

$$\langle \cdots \rangle_{eff} = \mathcal{Z}^{-1} \left(\Pi_{\mathbf{i}} \int ds_{\mathbf{i}} \right) (\cdots) e^{-\beta \mathcal{H}_{eff}}, \tag{10}$$

the magnetization can be expressed as $\langle \hat{S}_{\mathbf{i}}^x \rangle = \tilde{S}\theta^2 e^{-\mathcal{C}_q/2} \langle s_{\mathbf{i}}^x \rangle_{eff}$. Similarly, the in-plane correlations take the form $\langle \hat{S}_{\mathbf{i}}^x \hat{S}_{\mathbf{j}}^x \rangle = \tilde{S}^2 \theta^4 e^{-\mathcal{C}_q} (\cosh \mathcal{D}_{\mathbf{ij}}^{(qq)} \langle s_{\mathbf{i}}^x s_{\mathbf{j}}^x \rangle_{eff} + \sinh \mathcal{D}_{\mathbf{ij}}^{(qq)} \langle s_{\mathbf{i}}^y s_{\mathbf{j}}^y \rangle_{eff})$ (and the same with $x \leftrightarrow y$). Noting that $\mathcal{D}_{\mathbf{ij}}^{(\cdots)} \to 0$ for $|\mathbf{i}-\mathbf{j}| \to \infty$, the asymptotic behavior is just that obtained for the effective classical model.

For the quantum $XX0$ model (2) the effective Hamiltonian takes again the $XX0$ form, but with the effective exchange interaction $J_{eff}(T) = J\tilde{S}^2\theta^2\tau$. As a consequence, there will be a critical temperature T_c, where the in-plane correlations change from power-law to exponential decay. After the classical simulations of Ref. 9, T_c is implicitly defined by $T_c \simeq 0.78 J_{eff}(T_c)$. Figure 1 reports a graphical solution of this implicit equation. The curves represent $J_{eff}(T)$ for different spin values, numerically computed from the above formulas. Of course, the quantum effects are weaker the larger the spin and the larger the temperature. The intersections with the dotted line give the expected BKT critical temperatures, which depend upon the spin, namely $T_c/(J\tilde{S}^2) \simeq 0.41$, 0.56, 0.64, 0.68,..., 0.78, for $S = \frac{1}{2}$, 1, $\frac{3}{2}$, 2,..., ∞, respectively.

In the extreme case of $S = \frac{1}{2}$ the solution $T_c/J \simeq 0.41$ can be compared with the values found by high temperature expansions[19] (0.39), by real-space renormalization group techniques[20] (0.40), and by quantum Monte Carlo simulations[10,11] (0.35). We do not believe that our result could solve the controversy between these different outcomes, also because our procedure to estimate the critical temperature uses as an input the result found in Ref. 9 with rather small simulated lattices, and a more accurate MC simulation is in order to get a more reliable estimate of T_c for the classical $XX0$ model.

The problem of the very existence of a BKT transition in the $S = \frac{1}{2}$ two-dimensional $XX0$ model cannot be firmly answered by the PQSCHA, which essentially is a semiclassical approach. Nevertheless, the breakup of the BKT scenario should be accompanied by the breakup of the renormalization scheme of the PQSCHA, as it happens when the out-of-plane fluctuations become so strong that the assumed dominant easy-plane character (justifying the use of the Villain transformation) becomes meaningless. Actually, such a breakup does not occur for the $XX0$ model. This instability shows up when finite values of λ are considered, as it can be understood from Eqs. (9), for small enough temperatures, which are however less than the estimated critical temperature for $\lambda < 0.5$. As a matter of fact, also the quantum MC simulations of Refs. 11 and 12 show the typical classical BKT scaling behavior, leading us to conclude that quantum effects do modify the quantitative prefactors, but not the universality class of the transition, that is determined by symmetries and dimensionality. Indeed, quantum fluctuations are basically short ranged, and—in a renormalization group scheme—they are to be integrated out, resulting just in renormalized interaction parameters.

[1] V. L. Berezinskii, Zh. Eksp. Teor. Fiz. **59**, 907 (1970).
[2] J. M. Kosterlitz and D. J. Thouless, J. Phys. C **6**, 1181 (1973).
[3] J. Tobochnik and G. V. Chester, Phys. Rev. B **20**, 3761 (1979).
[4] R. Gupta and C. F. Baillie, Phys. Rev. B **45**, 2883 (1992).
[5] J. Villain, J. Phys. (Paris) **36**, 581 (1975).
[6] S. B. Khokhlachev, Zh. Exp. Teor. Fiz. **70**, 265 (1976).
[7] S. Hikami and T. Tsuneto, Progr. Theor. Phys. **63**, 387 (1980)
[8] C. Kawabata and A. R. Bishop, Solid State Commun. **42**, 595 (1982).
[9] C. Kawabata and A. R. Bishop, Solid State Commun. **60**, 169 (1986).
[10] H.-Q. Ding and M. S. Makivić, Phys. Rev. B **42**, 6827 (1990).
[11] H.-Q. Ding, Phys. Rev. B **45**, 230 (1992).
[12] M. S. Makivić, Phys. Rev. B **46**, 3167 (1992).
[13] A. Cuccoli, V. Tognetti, P. Verrucchi, and R. Vaia, Phys. Rev. A **45**, 8418 (1992).
[14] F. A. Berezin, Sov. Phys. Usp. **23**, 763 (1980).
[15] M. Hillery, R. F. O'Connell, M. O. Scully, and E. P. Wigner, Phys. Rep. **106**, 122 (1984).
[16] K. Imre, E. Ozizmir, M. Rosenbaum, and P. Zweifel, J. Math. Phys. **8**, 1097 (1967).
[17] J. Villain, J. Phys. (Paris) **35**, 27 (1974).
[18] A. Cuccoli, V. Tognetti, P. Verrucchi, and R. Vaia, Phys. Rev. B **46**, 11601 (1992).
[19] J. Rogiers, E. W. Grundke, and D. D. Betts, Can. J. Phys. **57**, 1719 (1979).
[20] A. Drzewiński and J. Sznajd, Phys. Lett. **138**, 143 (1989).

Magnetization and static structure factor behavior in a first-order helix-fan phase transition

F. Rastelli, S. Sedazzari, and A. Tassi
Dipartimento di Fisica, Università di Parma, 43100 Parma, Italy

The behavior of noncollinear spin patterns when an external magnetic field is applied in the plane of the spins can be successfully studied by analytic approaches for helix configurations commensurated with the underlying lattice. Here we study the magnetization and static structure factor as a function of temperature and field for a planar square lattice with exchange coupling up to third neighbor. It has been limited to spin–spin couplings that stabilize a helix characterized by a spin–spin turn angle $Q=2\pi/5$ and $Q=4\pi/5$ in a zero magnetic field. Analytic calculations in harmonic approximation and Monte Carlo simulations are performed on finite size samples. At low temperature, the static structure factor for $Q=2\pi/5$ shows an abrupt transfer of weight from the satellite peak at the helix wave vector to the central peak for a critical field, which is weakly temperature dependent. Above a critical temperature the evolution of the low field helix configuration into the fan configuration occurs in a continuous way. Even richer is the phenomenology found when $Q=4\pi/5$, since a spin-flop phase intervenes for intermediate fields, yielding two first-order phase transitions between distorted helix–spin-flop, and spin-flop–fan phases.

The influence of an external magnetic field on helix spin patterns was currently believed to yield a simple distortion of the helix at low field, with a first-order phase transition to a fan phase, where no spin components opposite to the field exist, for a field about half the saturation field.[1] This scenario was sketched on the basis of zero temperature low field–high field expansion of the energy of classical spin models with continuous symmetry by an extrapolation in the intermediate field range.

However, this picture does not exhaust all possibilities. For instance, low temperature expansion[2,3] and Monte Carlo simulation[2,4] prove that in the planar and Heisenberg antiferromagnet on a triangular lattice, where the zero field zero temperature minimum energy configuration is the 120° three sublattice configuration, an additional collinear phase with two spin parallel and one spin antiparallel to the field intervenes at intermediate fields.

Exact expansion of the energy of models with continuous symmetry and exchange competition supporting helix configuration proves[5] that commensurate phases are locked, owing to nonanalytic contributions proportional to h^p, where h is the reduced magnetic field and p is the number of spins per magnetic cell.

At zero temperature the minimization of the energy of commensurate helices supported by suitable exchange competition leads to a first-order helix–fan phase transition, only for the spin–spin turn angle $Q<\pi/2$, otherwise a continuous distortion occurs.[6] This result is based on the hypothesis that the zero field magnetic cell is unchanged under the application of an external magnetic field. Notice that this hypothesis is well grounded in low magnetic fields,[5] but its validity is not assured at intermediate and high fields.

Here we study the finite temperature behavior of these models by low temperature expansion and Monte Carlo simulation on samples of 25×25 and 50×10 spins when periodic boundary conditions are assumed. We focus on a planar square lattice with spins interacting via competing exchange up to third neighbors. The zero temperature phase diagram is shown in Fig. 2 of Ref. 7. In particular, we consider exchange competition giving helix configurations characterized by a spin–spin turn angle $Q=2\pi/5$ and $Q=4\pi/5$ at zero field, where the spin modulation appears in the ⟨10⟩ direction. Let us define the nearest neighbor (NN), next nearest neighbor (NNN), and third nearest neighbor (TNN) exchange interactions as J_1, J_2, J_3, and the reduced quantities $j_2=J_2/J_1$, $j_3=J_3/J_1$. $Q=2\pi/5$ is achieved in the parameter space on the line $1+2j_2=-j_3(\sqrt{5}-1)$ with $-1/(3+\sqrt{5})<j_3<0$ and $Q=4\pi/5$ on the line $1+2j_2=j_3(\sqrt{5}+1)$ with $-1/(3-\sqrt{5})<j_3<0$.

Here we give only a summary of our main results. The low temperature expansion we perform is the harmonic approximation for a generic external field under the hypothesis that the five spin cell is preserved, even in the external magnetic field. This assumption is supported by the locking of commensurate helices in low external magnetic fields.[5]

In Fig. 1 we show the reduced magnetization as a function of the external magnetic field for selected temperatures for Hamiltonian parameters that give a zero field turn angle $Q=2\pi/5$. For instance, we have chosen $j_2=-0.422\,75$ and $j_3=-0.125$. As one can see, the evidence of a first-order phase transition is obtained for $Q=2\pi/5$ at zero temperature. An analogous trend is obtained at low temperature within the harmonic approximation. Obviously Monte Carlo simulation cannot yield a genuine discontinuity, owing to the finite size of the sample, but a kink is observed at $t=k_BT/2J_1=0.05$, whereas a smooth behavior is found at $t=0.2$.

In Fig. 2 we give the static structure factor $S(q_x,0)$ for $t=0.05$ and $h=0.08$ and $h=0.1$, where $h=\mu H/2J_1$, μ is the magnetic moment per site, and H is the applied magnetic field. Monte Carlo simulation shows a substantial transfer of weight from the satellite to the central peak for a small change of the magnetic field in the neighborhood of the

 0021-8979/94/75(10)/5817/3/$6.00 © 1994 American Institute of Physics

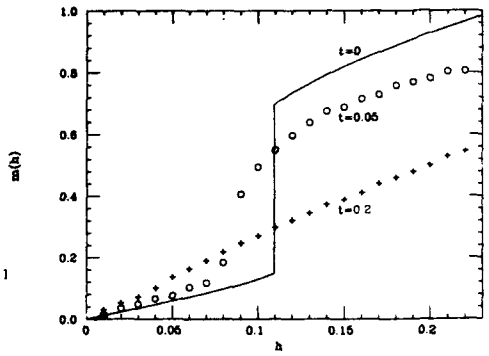

FIG. 1. Reduced magnetization $m=M(H,T)/\mu SN$ versus reduced magnetic field of the model with $j_2=-0.422\,75$, $j_3=-0.125$ ($Q=2\pi/5$) for selected temperatures: $t=0$ (continuous curve) $t=0.05$ (dots), and $t=0.2$ (crosses).

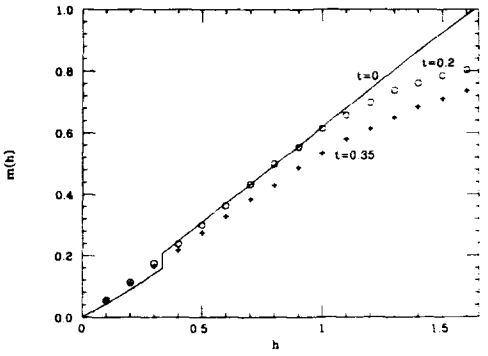

FIG. 3. Reduced magnetization versus reduced magnetic field of the model with $j_2=-0.702\,25$, $j_3=-0.125$ ($Q=4\pi/5$) for selected temperatures: $t=0$ (continuous curve) $t=0.2$ (dots), and $t=0.35$ (crosses).

change of the spin configuration, that is consistent with the analytic harmonic result. The analytic harmonic expansion and Monte Carlo simulation gives a coherent picture for $Q=2\pi/5$. On the contrary, unexpected instabilities are found in harmonic approximation at intermediate fields when the case $Q=4\pi/5$ is considered.

Indeed, the elementary excitation energies that one finds by diagonalization of the energy expansion keeping terms containing, at most, two fluctuation angles with respect to the minimum energy configuration, are well defined for the minimum energy configuration when $Q=2\pi/5$ at zero field, but become negative about $q_x=\pi$ for a substantial range of intermediate fields ($0.7<h<1.3$) when $Q=4\pi/5$. This is the signature of a phase transition induced by the field involving a configuration that differs from both a distorted helix and a symmetric fan, which are the phases one finds minimizing the energy of the model under the assumption of a magnetic cell of five spins. The softening of the elementary excitation energy at $q_x=\pi$ suggests the onset of a new phase of two spins per unit cell. So we have compared the zero temperature energy of the spin-flop configuration with those of the distorted helix and the symmetric fan with five spins per cell. We have found that the stable configuration is the distorted helix for $0<h<h_1=0.334$, the spin-flop phase for $h_1<h<h_2=1.419$, the fan phase for $h>h_2$. In Fig. 3 we show the zero temperature magnetization, where two first-order phase transitions occur at $h=h_1=0.334$ and $h=h_2=1.419$, respectively. The magnetization jumps are very small ($\Delta m=0.049$ at h_1 and $\Delta m=0.010$ at h_2), so that they are expected to be easily rounded off by thermal effects. Indeed, Monte Carlo simulations for $t=0.2$ and 0.35 provide a smooth behavior apparently consistent with the guess based on the hypothesis of five spins per unit cell.[6]

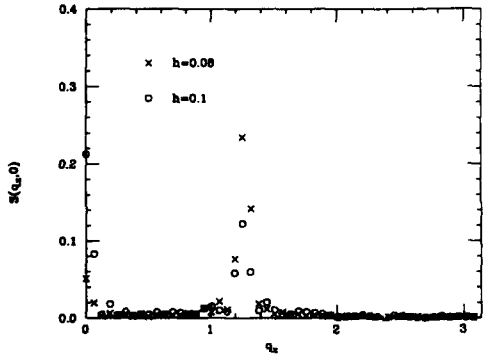

FIG. 2. Static structure factor $S(q_x,0)$ for Hamiltonian parameters as in Fig. 1 at $t=0.05$ with $h=0.08$ (crosses) and $h=0.1$ (dots).

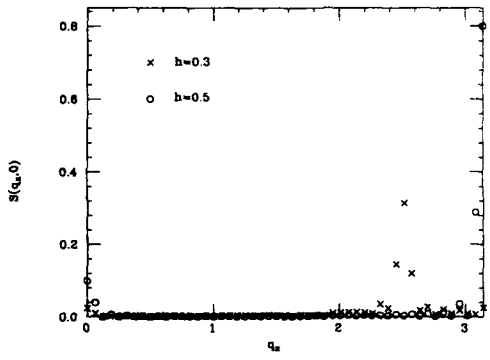

FIG. 4. Static structure factor $S(q_x,0)$ for Hamiltonian parameters as in Fig. 3 at $t=0.05$ with $h=0.3$ (crosses) and $h=0.5$ (dots).

However, the static structure $S(q_x,0)$ is expected to show the occurrence of a new peak at $q_x=\pi$ when $h=h_1$, the disappearance of the peak at $q_x=Q=4\pi/5$ in the range $h_1<h<h_2$, and vice versa at $h\geq h_2$. Figure 4 shows $S(q_x,0)$, as obtained by Monte Carlo simulation at $t=0.05$ for $h=0.3$ and $h=0.5$, where the two peaks at $q_x=4\pi/5$ and $q_x=\pi$ are clearly seen.

The results we have obtained raise various questions, since the possibility of first-order phase transitions from a commensurate spin configuration to another configuration with a different magnetic cell is a novel feature for spin models with continuous symmetry. An interesting question is about the existence of a critical point for the helix–spin-flop phase transition. Moreover, it is not clear for the moment what the regions of the parameter space are, where similar phase transitions occur.

This research was supported in part by INFM.

[1] T. Nagamiya, Solid State Phys. Acad. NY **20**, 346 (1967).
[2] H. Kawamura, J. Phys. Soc. Jpn. **53**, 2452 (1984); H. Kawamura and S. Miyashita, J. Phys. Soc. Jpn. **54**, 4530 (1985).
[3] E. Rastelli, A. Tassi, A. Pimpinelli, and S. Sedazzari, Phys. Rev. B **45**, 7936 (1992).
[4] D. H. Lee, J. D. Joannopoulos, J. W. Negele, and D. P. Landau, Phys. Rev. Lett. **52**, 433 (1984); Phys. Rev. B 33, 450 (1986).
[5] A. B. Harris, E. Rastelli, and A. Tassi, Phys. Rev. B **44**, 2624 (1991).
[6] E. Rastelli, A. Tassi, G. Melegari, and A. Pimpinelli, J. Magn. Magn. Mat. **104-107**, 173 (1992).
[7] E. Rastelli, A. Tassi, and L. Reatto, Physica B **97**, 1 (1979).

Magnetic properties in the Ising mixed spin-1/2–spin-1 superlattice

E. F. Sarmento, J. C. Cressoni, and R. J. V. dos Santos
Departamento de Física, Universidade Federal de Alagoas, 57072-340, Maceió, Brazil

An effective-field theory that accounts for the self-spin correlation function is used to derive the phase diagrams and magnetization curves of a magnetic superlattice, consisting of a mixed spin-1/2–spin-1 (with a single-ion anisotropy D) alternate monolayers of ferromagnetic material. It is found that the phase diagrams exhibit a number of interesting phenomena resulting from the dependence of the crystal-field interaction. Both limit cases for very large positive and very large negative D reproduce respectively the $T(3D)\simeq 5.07$ and the $T(2D)=3.08$ Ising critical temperatures which are in agreement with earlier results. On the other hand, in particular, no tricritical point could be found. The magnetization curves are presented for a range of interaction strengths and D, respectively.

I. INTRODUCTION

The recent advances of modern vacuum science, and in particular epitaxial growth techniques, have made possible the preparation of a large variety of magnetic layered structures, whose properties can differ drastically from the bulk ones. One can envisage a superlattice in which the magnetic films are in direct contact, namely, they are bound together by an exchange interaction between the interface atoms. Phase diagrams in a ultrathin Ising films,[1] two-component magnetic superlattice,[2] and infinite dilute Ising superlattice[3] have been studied. More recently,[4] a spin-1/2 Ising model of an alternating magnetic superlattice was studied. In this article we examine a magnetic superlattice consisting of spin-1/2–spin-1 alternating monolayers of ferromagnetic material. Our aim is to present a discussion of the phase diagrams and magnetization curves in such systems.

II. MODEL AND FORMULATION

We consider an infinite simple cubic superlattice in which spin-1/2 layers of material 1 alternate with spin-1 layers of material 2. The system is described by the following Hamiltonian:

$$\mathcal{H}=-\sum_{\langle i,j\rangle}J_{ij}S_i^zS_j^z-\sum_{\langle m,n\rangle}J_{mn}\mu_m^z\mu_n^z-\sum_{\langle i,m\rangle}J_{im}S_i^z\mu_m^z-\sum_i D_i(S_i^z)^2, \tag{1}$$

where $S_i^z=\pm 1$ and 0, $\mu_m^z=\pm 1$, and the summations are carried out only over nearest-neighbor (n.n.) pair of spins. J_{ij} is the exchange interaction between spins on the spin-1 layers, which is assumed to be J_1. $J_{im}=J_2$ is the interaction between spins at the material 1 and its n.n. in the material 2, and $J_{mn}=J_3$ is the interaction between spins on the spin-1/2 layers. D_i is the single-ion anisotropy parameter at the spin-1 layers.

The starting point to discuss the statistic of our system is the evaluation of the mean values of $\langle\mu_m^z\rangle$, $\langle S_i^z\rangle$ and $\langle(S_i^z)^2\rangle$. For the spin-1/2 layers the expectation value is given by

$$\langle\mu_m^z\rangle=\langle\tanh(\beta E_m)\rangle, \tag{2}$$

with $\beta=1/k_BT$ and $E_m=\Sigma_n J_{mn}\mu_n^z+\Sigma_i J_{im}S_i^z$. As has been discussed,[5] we can obtain the exact spin correlation function for the spin-1 layers as follows:

$$\langle S_i^z\rangle=\left\langle\frac{2\sinh(\beta E_i)}{2\cosh(\beta E_i)+\exp(-\beta D)}\right\rangle, \tag{3}$$

$$\langle(S_i^z)^2\rangle=\left\langle\frac{2\cosh(\beta E_i)}{2\cosh(\beta E_i)+\exp(-\beta D)}\right\rangle, \tag{4}$$

where $E_i=\Sigma_j J_{ij}S_j^z+\Sigma_m J_{im}\mu_m^z$. Introducing a differential operator $\nabla=\partial/\partial x$, we may rewrite Eqs. (2), (3), and (4) as

$$\langle\mu_m^z\rangle=\langle\Pi_n\exp(\nabla J_{mn}S_n^z)\Pi_i\exp(\nabla J_{im}S_i^z)\rangle f(x)|_{x=0}, \tag{5}$$

$$\langle S_i^z\rangle=\langle\Pi_j\exp(\nabla J_{ij}S_j^z)\Pi_m\exp(\nabla J_{im}\mu_m^z)\rangle F(x)|_{x=0}, \tag{6}$$

$$\langle(S_i^z)\rangle^2=\langle\Pi_j\exp(\nabla J_{ij}S_j^z)\times\Pi_m\exp(\nabla J_{im}\mu_m^z)\rangle G(x)|_{x=0}, \tag{7}$$

where $f(x)=\tanh(\beta x)$, and the functions $F(x)$ and $G(x)$ are defined by

$$F(x)=\frac{2\sinh(\beta x)}{2\cosh(\beta x)+\exp(-\beta D)}, \tag{8}$$

$$G(x)=\frac{2\cosh(\beta x)}{2\cosh(\beta x)+\exp(-\beta D)}. \tag{9}$$

The exact equations (5), (6), and (7) yield a set of relations between $\sigma=\langle\mu_m^z\rangle$, $m=\langle S_i^z\rangle$, $q=\langle(S_i^z)^2\rangle$, and the associated thermal multiple correlation functions occurring on the right-hand side, and will be used here as the basis for the present formalism. However, it is clear that if we try to treat exactly all the spin-spin correlations which appear through the expansions of these equations, the problem quickly becomes mathematically untractable. Therefore, we restrict ourselves to the simplest approximation in which all high-order spin correlations are neglected.

III. PHASE DIAGRAMS AND MAGNETIZATION

Within the present framework the magnetizations σ, m, and the quadrupolar moment q for our layered simple cubic superlattice are given by

 0021-8979/94/75(10)/5820/3/$6.00 © 1994 American Institute of Physics

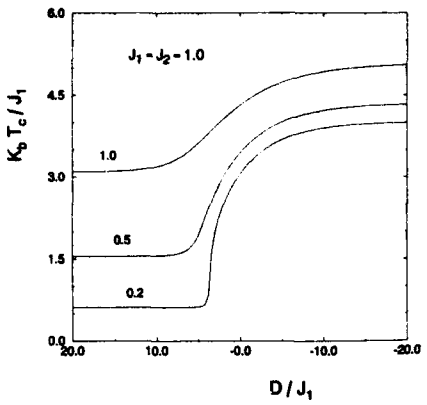

FIG. 1. Phase diagram on the $(t_c\Delta)$ plane for different values of J_3.

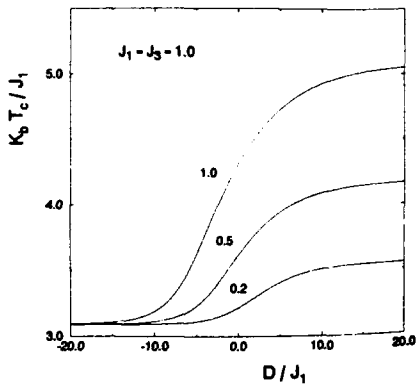

FIG. 2. Phase diagram on the $(t_c\Delta)$ plane for different values of J_2.

$$\sigma=(c_3+\sigma s_3)^4(qc_2+ms_2+1-q)^2 f(x)|_{x=0}, \tag{10}$$

$$\begin{Bmatrix} m \\ q \end{Bmatrix} = (qc_1+ms_1+1-q)^4(c_2+\sigma s_2)^2 \begin{Bmatrix} F(x)|_{x=0} \\ G(x)|_{x=0} \end{Bmatrix}, \tag{11,12}$$

where $s_i=\sinh(J_i\nabla)$, $c_i=\cosh(J_i\nabla)$ $(i=1-3)$. In order to examine not only the phase diagrams but also the possibility of tricritical point, let us first substitute

$$q=q_0+q_1m^2+q_2m\sigma+q_3\sigma^2 \tag{13}$$

into Eq. (12) to obtain the q's coefficients. Replacing q in Eqs. (10) and (11) we obtain.

$$\sigma=b_1m+b_2\sigma+b_3m\sigma^2+b_4m^2\sigma+b_5m^3+b_6\sigma^3, \tag{14}$$

$$m=a_1m+a_2\sigma+a_3m\sigma^2+a_4m^2\sigma+a_5m^3+a_6\sigma^3, \tag{15}$$

where a's and b's are coefficients not given here. By doing successives substitutions of σ [Eq. (14)] into m [Eq. (15)] and by retain only terms in m and $\mathcal{O}(m^3)$ we obtain

$$m=d_1m+d_2m^3. \tag{16}$$

The second-order phase transition is determined by $d_1=1$, or

$$(1-a_1)(1-b_2)=a_2b_1. \tag{17}$$

In the vicinity of second-order phase transition line, the right-hand side of Eq. (16) must be positive. If this is not the case, the transition is of the first order. Thus, the tricritical point is determined from $d_1=1$ and $d_2=0$, simultaneously. However, our model did not present tricritical points.

IV. NUMERICAL RESULTS

By solving Eq. (17) numerically, we discuss the effect of the crystal-field interaction $\Delta=D/J_1$ on the Curie temperature $t_c=k_BT_c/J_1$. In Fig. 1 we show the transition lines or the plane $(t_c\Delta)$ for $J_1=J_2=1.0$ and different values of J_3. For positive increasing values of Δ the transition temperatures tend to that of a corresponding 3D $\mu=1/2$ Ising model in which one has alternate sheets with J_1 or J_3 in-plane interactions and J_2 interplane interaction. For negative decreasing values of Δ the behavior is that of a 2D $\mu=1/2$ Ising model with exchange interaction J_3, as the magnetization of the spin-1 plane vanishes.

In Fig. 2 is shown the $(t_c\Delta)$ phase diagram for $J_1=J_3=1.0$ and different values of J_2. In the limit of $\Delta\to\infty$ one obtains the 3D Ising critical temperature. However, when $\Delta\to-\infty$ the coupling between the sheets plays no role and the critical temperature is that of a 2D $\mu=1/2$ $J_3=1.0$ Ising model. Both limit cases reproduces $t_c(2D)=3.08$ and $t_c(3D)=5.07$ which are in agreement with earlier results.

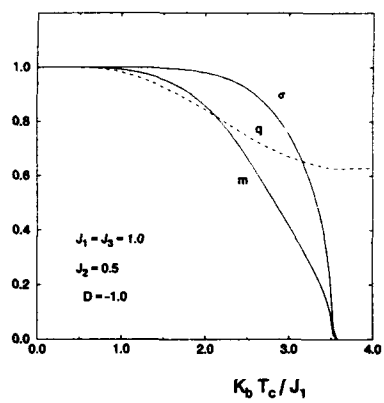

FIG. 3. Magnetizations and quadrupolar moment vs temperature $(D=-1.0)$.

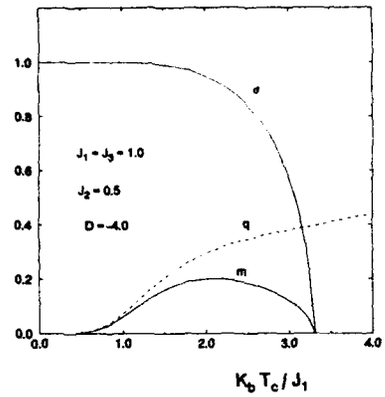

FIG. 4. Magnetizations and quadrupolar moment vs temperature ($D=-4.0$).

In Figs. 3 and 4 we present the behaviors of the order parameters σ, m, and q of the model for two different values of $D<0$. We notice the existence of two regimes for the magnetization m of the spin-1 sheet. In the first one (small absolute value of D) the magnetization m at low temperature is driven by the magnetization σ of the spin-1/2 sheets, both starting at the saturation limit and going down to zero at the same critical temperature. In the second one (large absolute value of D) the anisotropy field is strong enough to retain the spins of the spin-1 sheet in the eigenstate $S=0$, at low temperature. At higher temperatures the thermal fluctuations of S are biased by the magnetization σ and so m initially increases and afterward goes to zero at the same critical temperature as σ. The behavior of q is explained by the same reasoning.

ACKNOWLEDGMENTS

The work of E.F.S. and R.J.V.S. was partially supported by CNPQ (Brazilian financial agency).

[1] F. Aguilera-Granja and J. L. Moran-López, Solid State Commun. **74**, 155 (1990).
[2] W. Figueiredo and J. A. Plascak, Solid State Commun. **69**, 403 (1989).
[3] P. Tomczak, J. Magn. Magn. Mater. **78**, 403 (1989).
[4] H. K. Sy and M. H. Ow, J. Phys. Condensed Matter **4**, 5891 (1992).
[5] T. Kaneyoshi, Physica A **178**, 389 (1991).

Monte Carlo calculation of the correlation range for the $S=\frac{1}{2}$ isotropic Heisenberg ferromagnetic thin film

I. V. Rojdestvenski and M. G. Cottam
Department of Physics, University of Western Ontario, London, Ontario, Canada N6A 3K7

I. A. Favorski[a)]
Faculty of Physics, Leningrad State University, Russia

The Handscomb Monte Carlo technique is used to investigate the critical properties of $S=\frac{1}{2}$ isotropic Heisenberg ferromagnetic films with nearest-neighbor interactions. We study a simple-cubic lattice with the number of monolayers $L=1,2$ as done previously, but we now include the effects of different values for interlayer and intralayer exchange parameters. We calculate numerically the temperature dependences of the correlation range. For the two-monolayer film, for the investigated temperature interval these results confirm our previous conclusions about the two-dimensional type of critical behavior of the system with a renormalized (modified) exchange parameter. Numerical data on the behavior of the surface-surface spin correlation function are also presented.

I. INTRODUCTION

Recently some experimental work[1,2] has been done to investigate the magnetic properties of quasi-two-dimensional ferromagnetic systems. For example, $[C_6H_5(CH_2)_nNH_3]_2CuBr_4$ is interpreted as a quasi-two-dimensional Heisenberg nearly isotropic ferromagnet[3] with the ratio of the intralayer exchange to the interlayer interaction parameter being as low as 0.04. The temperature of the second-order phase transition was found from the susceptibility data to be around 10 K depending on the structural index n.

Also the magnetization and longitudinal susceptibility of 2.5 monoatomic layers of ^{3}He adsorbed on graphite are reported to be well described by the high-temperature expansions and other present theories of the two-dimensional Heisenberg ferromagnet.[2] It is well established that the $S=\frac{1}{2}$ Heisenberg ferromagnet with the nearest-neighbor interaction displays no phase transition in two dimensions[3,4] at finite temperatures, as expected from the Mermin-Wagner theorem.[5] According to the results of the momentum-shell renormalization-group theory confirmed by quantum Monte Carlo calculations, the susceptibility and the correlation range for $S=\frac{1}{2}$ have the following dependences[4] on the temperature in the critical regime $J/T \gg 1$:

$$\chi T = C_\chi \left(\frac{C_\xi}{2\pi}\right)^2 2^7 \left(\frac{T}{2J}\right)^3 \exp\left(\frac{2\eta_\chi \pi J}{T}\right), \tag{1}$$

$$\xi \sim (T/J)^{1/2} \exp\left(\frac{\eta_\chi \pi J}{T}\right) \tag{2}$$

with $\eta_\chi = 1$. We note here that the quoted expressions differ slightly from those in Ref. 4 because of differences in our notations. Some expressions similar to Eqs. (1) and (2), but with different powers of T before the exponential, were subsequently derived in Ref. 3.

In our previous paper[6] we investigated the thermal dependences of the uniform longitudinal susceptibility for films with one, two, and three monolayers by means of the Handscomb Monte Carlo technique. Our results provide evidence that, in a certain temperature interval, the temperature dependences of the susceptibility and the correlation range of the L-layer film obey the two-dimensional expressions [Eqs. (1) and (2)] with the single exchange parameter J replaced by LJ. This result may provide for an explanation of the fact that the direct nuclear exchange parameter $J=2.1$ mK, quoted in Ref. 2 as a result of fitting to the analytical expressions for the two-dimensional model, is the highest ever reported. In the discussion of the results of experiment,[2] the authors assumed that only one of two completed monolayers of ^{3}He was magnetized, thus forming the two-dimensional Heisenberg system. However, if we assume both monolayers to be magnetized, we fit the same two-dimensional temperature dependences of the susceptibility and the correlation range, but now the fitting exchange parameter corresponds to $2J$; hence J should be half the value quoted in Ref. 2.

The aim of the present paper is to continue the numerical investigation of the critical properties of ultrathin monocrystalline films with the $S=\frac{1}{2}$ isotropic Heisenberg ferromagnetic Hamiltonian on the simple-cubic lattice and the number of monolayers $L=1,2$. By applying the numerical technique described in our previous paper,[6] we calculate the temperature dependences of the correlation range, incorporating the effects of the modified exchange parameter.

II. THE HAMILTONIAN AND THE PROCEDURE OF CALCULATION OF THE CORRELATION RANGE

As before,[6] we take the thin film to be finite in one dimension with two equal surfaces and infinite in the other two dimensions. The Hamiltonian thus has the following form:

[a)]Deceased.

 0021-8979/94/75(10)/5823/3/$6.00 © 1994 American Institute of Physics

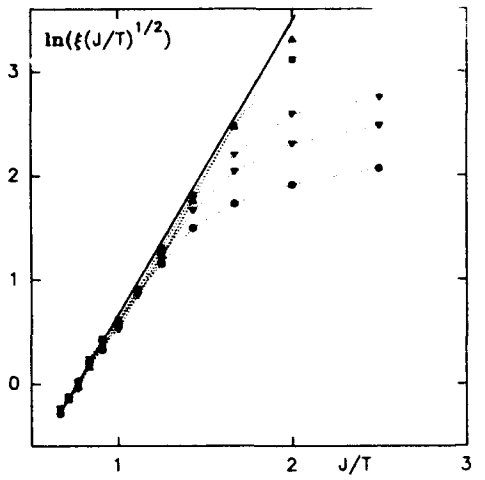

FIG. 1. The temperature dependence of the correlation range ξ for the one-layer film. N=○, 20; v, 30; v,40; ■, 80; △, 120; —, fit to the function $2.8J/T-2.1$.

$$H=-2\sum_{(ij)} J^{bb}\mathbf{S}_i\mathbf{S}_j-2\sum_{(pq)} J^{sb}\mathbf{S}_p\mathbf{S}_q$$

$$-2\sum_{(lm)} J^{ss}\mathbf{S}_l\mathbf{S}_m, \tag{3}$$

where the three sums, corresponding to the interactions of spins within the bulk layers, and the interlayer interactions between the surface and bulk layers and within the surface layers, respectively, are taken over the pairs of the nearest neighbors. In our previous paper[6] we ignored the effect of the modified exchange, i.e., we took $J^{ss}=J^{bb}=J^{sb}$.

The procedure of approximation of an infinite thin film by a finite spin system has already been discussed in Ref. 6.

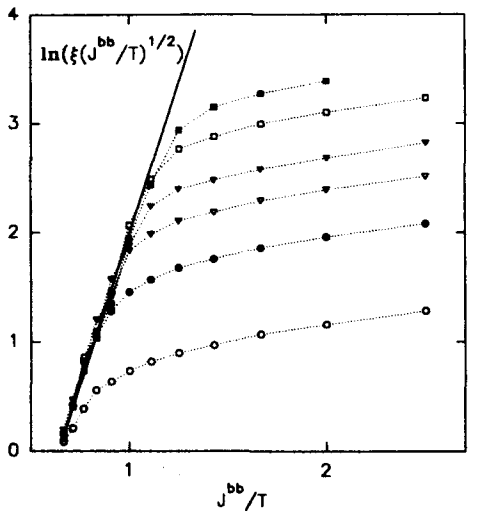

FIG. 2. The temperature dependence of the correlation range ξ for the two-layer film, $J^{sb}=J^{bb}$. N=○, 10; ⊗, 20; v, 30; v,40; □, 60; ■, 80; —, fit to the function $5.8J/T-3.8$.

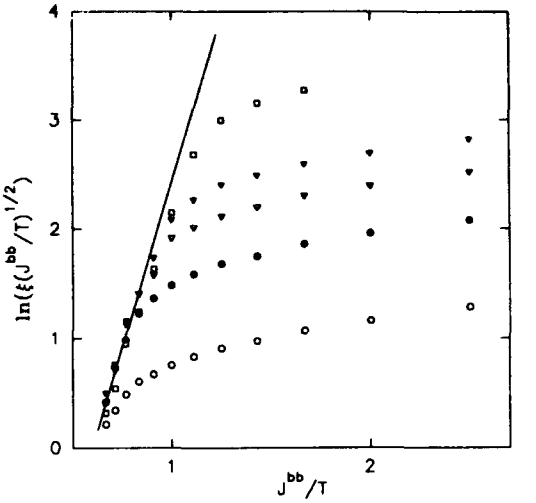

FIG. 3. The temperature dependence of the correlation range ξ for the two-layer film, $J^{sb}=2J^{bb}$. N=○, 20; ⊗, 20; v, 30; v, 40; □, 60; —, fit to the function $5.9J/T-3.6$.

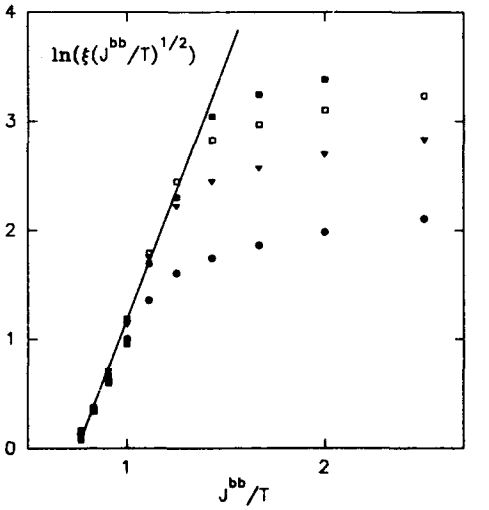

FIG. 4. The temperature dependence of the correlation range ξ for the two-layer film, $J^{sb}=0.3J^{bb}$. N=⊗, 20; v, 40; □, 60; ■, 80; —, fit to the function $4.4\,J/T-3.2$.

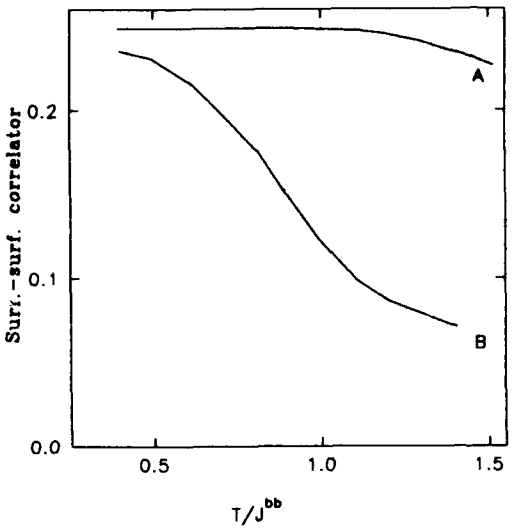

FIG. 5. The temperature dependence of the surface-surface correlator for the two-layer film. A, $J^{sb}=2J^{bb}$; B, $J^{sb}=0.3J^{bb}$.

We apply the standard Handscomb procedure for the $S=\frac{1}{2}$ isotropic Heisenberg ferromagnet (see, e.g., Ref. 4 and references therein). To obtain the expression for the estimator of the in-plane correlation range, ξ, we first calculate the in-plane correlation function $g(\mathbf{r})=\langle \mathbf{S}(\mathbf{r})\mathbf{S}(0)\rangle$. However, when calculating this function we take into account only the pairs of spins that belong to the same monolayer and the spatial radius vector $\mathbf{r}$ lying within the film plane and co-directed with the sides of the elementary plaquette. Within this assumption the spins are separated by a distance equal to an integer multiple of the lattice constant. The procedure of evaluation of $g(\mathbf{r})$ is as follows:

(1) At each step of the Markov chain we make a random choice of the lattice site i.

(2) We choose randomly the distance $|\mathbf{r}|$ so that it does not exceed $N/2$, N being the linear size of the system.

(3) We define the second lattice site j as having one of the two in-plane coordinates equal to that of i and the second in-plane coordinate shifted by $|\mathbf{r}|$ with respect to in-plane periodic boundary conditions.

(4) We calculate the quantity $0.25\Delta_{ij}$ for the pair of sites i and j, with $\Delta_{ij}=1$ when i and j belong to the same cycle of the current permutation $P(C_r)$ and $\Delta_{ij}=0$ otherwise.

(5) We average this quantity along the Markov chain.

Having calculated the described correlation function we then calculate the correlation range as

$$\xi=\left[\left(\sum_i r_i^2 g(r_i)\right) \Big/ \left(\sum_i g(r_i)\right)\right]^{1/2}. \tag{3}$$

III. NUMERICAL RESULTS AND DISCUSSION

A. One-layer film (the two-dimensional model)

We calculated the thermal dependences of the correlation range ξ for the systems with the numbers of sites $N\times N$, $N=10$, 15, 20, 30, 40, 60, 80, and 120 within the temperature interval $0.4\leq T/J\leq 1.3$. Markov chains varied from 200 Monte Carlo (MC) steps/spin for $T/J\geq 1.0$ to 500 MC steps/spin for $0.4\leq T/J\leq 1.0$. The averaging was made over the second half of Markov chain, the first half being left for the relaxation. A comparison between our results and the theoretical expression for ξ in Eq. (2) is shown in Fig. 1. The slope of the straight line approximating the obtained dependence of $\ln[\xi(J/T)^{1/2}]$ vs J/T is 2.8, which is close to the theoretical value π for $S=\frac{1}{2}$. The difference between our results for ξ and those of Ref. 4 can be possibly explained by differences in the definitions of ξ in the two cases.

B. Two-layer film

In this case we introduce different constants of the exchange interactions in the surfaces and inside the film. Under consideration were the systems with the linear size $N=10$, 20, 30, 40, 60, and 80 spins. Our results for ξ (see Fig. 2) in the case $J^{sb}=J^{bb}$ fit the expression in Eq. (2) with the exponential power 5.8, i.e., approximately twice our value 2.8 for the two-dimensional system. We previously employed simple theoretical arguments[6] to support this kind of behavior based on the fact that the transverse correlations (see Fig. 5 of Ref. 6) are saturated in the critical regime, providing for an effective two-dimensional Hamiltonian.

Similar conclusions can be done for the case of $J^{sb}=2J^{bb}$ (see Fig. 3). For the exponential power in Eq. (2) we get the value of 5.9, which is close to the above value of 5.8. The surface-surface correlations for this case are stronger than those for the previous one (e.g., see Fig. 4, curve A).

Next, we studied the same system with $J^{sb}=0.3J^{bb}$. The results of our calculations for the temperature dependence of ξ are presented in Fig. 4 and the temperature dependence of the surface-surface correlator is shown in Fig. 5, curve B (see Ref. 6 for the details of its definition). Because the correlations between the surfaces are much weaker now, we expect the two-dimensional behavior of the modeled system to be less apparent. To test this we tried to fit our results to the same two-dimensional dependence, Eq. (2). The exponential power (i.e., the slope of the straight line approximant in Fig. 4) appeared to be 4.4, which is much smaller than in the two previous cases.

[1] P. Zhou, J. E. Drumheller, B. Patyal, and R. D. Willett, Phys. Rev. B **45**, 12 365 (1992).
[2] H. Godfrin, R. R. Ruel, and D. D. Osheroff, Phys. Rev. Lett. **60**, 305 (1988).
[3] M. Takahashi, Prog. Theor. Phys. **83**, 815 (1990).
[4] P. Kopietz and S. Chakravarty, Phys. Rev B **40**, 4858 (1989).
[5] N. D. Mermin and H. Wagner, Phys. Rev. Lett. **17**, 1133 (1966).
[6] I. V. Rojdestvensky and I. A. Favorski J. Phys. Condens. Matter **5**, L279 (1993).

Static critical properties of disordered ferromagnets studied by superconducting quantum interference device magnetometry and small-angle neutron-scattering techniques

S. Pouget
Laboratoire de Physique des Solides, INSA, Avenue de Rangueil, 31077, Toulouse Cedex, France, and I.L.L., BP 156X, 38042, Grenoble cedex, France

M. Alba
I.L.L., BP 156X, 38042, Grenoble Cedex, France, and CEA/DRECAM, 91191 Gif sur Yvette Cedex, France

M. Nogues
Laboratoire de Magnetisme, CNRS, 92195 Meudon Cedex, France

$CdCr_{(2-2x)}In_{(2x)}S_4$ is a highly frustrated magnetic system based on $CdCr_2S_4$, a well-known Heisenberg 3D ferromagnet. A study is presented of its static critical properties as a function of concentration, performed by low-field superconducting quantum interference device SQUID magnetometry and small-angle neutron-scattering SANS techniques. Samples were prepared from isotopic cadmium ^{114}Cd with a low absorption cross section for thermal neutrons. Magnetic measurements performed with low dc fields in the temperature range 5–300 K allow one to determine the magnetic state of the samples, the reentrant temperature T_G, the Curie temperature T_C, and the critical exponent γ of the susceptibility above T_C as a function of dilution in the domain $0<x<0.15$. By directly measuring the critical magnetic fluctuations in zero field in SANS experiments, access is gained to the magnetic correlation length ξ, its exponent ν above T_C, and another independent determination of γ. Whereas the pure compound exhibits exponents ($\gamma=1.37$, $\nu=0.70$) compatible with a 3D Heisenberg ferromagnetic model, a pronounced increase of measured exponents with dilution was found, namely $\gamma=1.97$, $\nu=1.03$. The results are compared to the ones of similar studies in the related system $Eu_{(1-x)}Sr_{(x)}S$ and to the renormalization group treatment of strongly random ferromagnets, and possible mechanisms to explain how a small dilution can provoke large alterations in the critical behavior and move the system in the strong disorder region are discussed.

I. INTRODUCTION

Disordered magnetic systems with competing interactions usually display a very specific phase diagram characterized by reentrance phenomena: With decreasing temperature, the system first undergoes a paramagnetic-ferromagnetic transition (PM-FM) at T_C, then at a lower temperature T_G reenters a magnetic state with spin-glass-like properties.

Despite a prolonged interest shown in the study of these systems, no general consensus regarding the exact nature of the different phases has emerged so far and even the occurrence of a real PM-FM transition at T_C is still questioned.[1] Most experiments on amorphous metallic alloys[2] tend to confirm theoretical predictions of an unchanged critical behavior at T_C but recent experiments in insulating systems[3] appeared to be consistent with renormalization group predictions[4] that effective critical exponents should change in the limit of strong disorder.

The above considerations prompted us to undertake a detailed low-field magnetization study in conjunction with small-angle neutron-scattering (SANS) experiments of the alterations with dilution in the critical behavior observed along the PM-FM transition line of an insulating system,[5] namely $CdCr_{2-2x}In_{2x}S_4$.

II. SUPERCONDUCTING QUANTUM INTERFERENCE DEVICE MEASUREMENTS

We carried out low-field magnetization with a commercial superconducting quantum interference device (SQUID) magnetometer from Cryogenic Consultants, Ltd. Measurements were done in very small dc fields ($H\leq 40$ Oe) by an extraction method throughout a second-order gradiometer. A calibrated flux attenuator is automatically switched on for huge signals, e.g., in ferromagnetic phases. Residual magnetic fields ($H\leq 1$ Oe) were carefully taken in account. Powder samples ($m\leq 0.04$ g) enclosed in a plastic capsule and placed in a variable temperature insert were thermalized by a regulated helium gas flow. Temperature was controlled by two thermometers and the gradient along the 6 cm extraction path was always kept lower than 0.2%.

We present in Fig. 1 initial susceptibilities of all four measured samples. The three more concentrated samples saturate at 0.4 emu/cm^3, corresponding to the inverse demagnetizing factor for 2:1 cylinders.[5] Only the two $x=0.00$ and $x=0.05$ samples present a well-defined PM-FM transition; the following sample with $x=0.10$ has a very high susceptibility but reaches the demagnetizing factor over a very small temperature range and no clear divergence of the susceptibility is observed; the last sample with $x=0.15$ behaves like a good spin glass. The small slope in the $x=0.00$ sample susceptibility below T_C may indicate a slightly in homogeneous demagnetizing field in this powdered sample

 0021-8979/94/75(10)/5826/3/$6.00 © 1994 American Institute of Physics

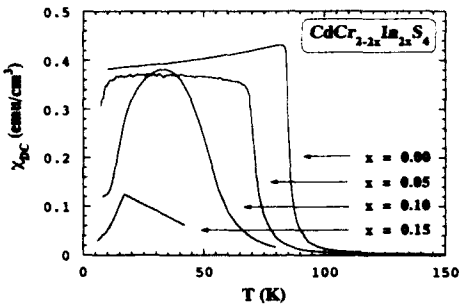

FIG. 1. Initial magnetic susceptibility of $CdCr_{2-2x}In_{2x}S_4$ for $0.00<x<0.15$ measured in low dc fields.

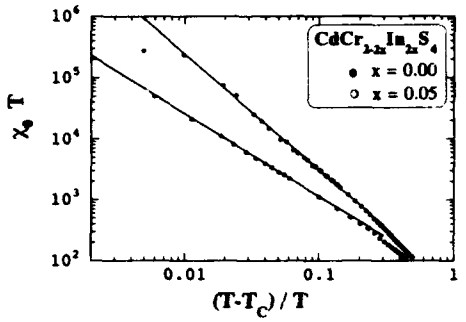

FIG. 2. Critical behavior of $CdCr_{2-2x}In_{2x}S_4$. Solid symbols for $x=0.00$, open symbols for $x=0.05$. Solid lines are fits of the γ exponent: $\gamma=1.36$ for $x=0.00$ and $\gamma=1.9$ for $x=0.05$.

but the pronounced decrease in the $x=0.05$ and $x=0.10$ susceptibility at low temperature comes from a reentrant disordered phase. We list in Table I characteristic temperatures: T_G deduced from thermoremanent magnetization and T_C deduced from the divergence of the true susceptibility. The true susceptibility χ_0 is obtained from the measured one χ_m after corrections of the demagnetizing field, using the standard formula: $1/\chi_m=1/\chi_0+N$. We restricted our analysis to the temperature domain where uncertainties on the demagnetizing factor N yield errors less than 5%, i.e., for a reduced temperature range $\tau>8\times10^{-3}$. Data for the two ferromagnetic samples were analyzed above T_C according to new scaling arguments[6] involving the nonlinear reduced temperature $\tau=1-T_C/T$. Following this approach, we looked for the divergence of the product $\chi_0 T$ against the reduced temperature τ. We display in Fig. 2 the critical behavior of the two ferromagnetic samples: Fitted values of the effective exponent measured in the range $8\times10^{-3}<\tau<2\times10^{-1}$ are $\gamma=1.36\pm0.02$ for the pure compound, $\gamma=1.9\pm0.1$ for the $x=0.05$ compound.

Our measurements on the pure compound compare well with ac susceptibility results[7] giving $\gamma=1.38$ and to the theoretical prediction[8] for 3D Heisenberg ferromagnet $\gamma=1.386$. The effective exponent found in the $x=0.05$ sample is very close to the limiting value $\gamma=2$ of the theory for strong disorder.[4] This striking variation of critical behavior with a dilution as small as 5% is, however, consistent with the proximity of the critical concentration. Deviations at smaller reduced temperatures, as seen in the pure compound ac susceptibility[7] or predicted by the theory for dilute samples, are beyond the precision of our measurements at the moment. However, we can see in Fig. 2 that in both samples the effective exponent $\gamma(\tau)=-\Delta \ln \chi_0 T/\Delta \ln(\tau)$ increases with temperature. Such a behavior has also been observed in amorphous metallic alloys.[6]

TABLE I. Characteristic temperatures T_G (reentrant or spin glass) and T_C (ferromagnetic) of $CdCr_{2-2x}In_{2x}S_4$ as a function of the dilution x.

x	T_G (K)	T_C (K)
0.00	...	84.3±0.2
0.05	10.8±0.2	68.5±0.5
0.10	18.2±0.3	(35)[a]
0.15	16.9±0.1	...

[a]Temperature where the dc susceptibility reaches its maximum.

III. SANS EXPERIMENTS

SANS experiments were performed at the Orphée reactor of the "Laboratoire Léon Brillouin" (Paris, France) on the PAXY and PAXE spectrometers, with a neutron wavelength at 6 Å (±5%), 64×64 cm^2 multidetector, and a detector-sample distance of 5 m giving a Q range of 0.008–0.08 Å^{-1}. Samples were placed in an ILL standard "orange" cryostat with sapphire windows and the sample temperature was regulated by an ILL controller with an accuracy better than 0.01 K. Inelastic scattering measurements performed on triple-axis spectrometers (to be described in a forthcoming article), justify the quasielastic approximation in the SANS experiments on all measured samples. Data reported below are averages of the observed intensities over rings concentric with the incident beam. A room-temperature background ($T>3T_C$) was subtracted in order to obtain the magnetic intensity after standard corrections for multidetector efficiency. Keeping a balance between limited neutron beam time, good transmission of samples ($T\sim0.80-0.95$), and the rapid decrease of the magnetic signal with temperature, we have restricted our study to the reduced temperature range $8\times10^{-3}<\tau<10^{-1}$.

The principal finding was that for each temperature the magnetic scattering integrated over all inelastic processes at all Q is very well described by a single Lorentzian as can be seen for the $x=0.05$ sample in Fig. 3. This result enables us to extract easily from the spectra the isothermal susceptibility χ_0 (without any demagnetizing corrections) and the inverse correlation range κ ($\xi=1/\kappa$ being the correlation length). Whereas the $x=0.0$ and $x=0.05$ samples have a similar behavior compatible with a divergence of χ_0 and κ, for the $x=0.10$ sample χ_0 does not diverge and κ does not reach a resolution-limited value. These findings corroborate the SQUID results and establish that the critical concentration x_C for the disappearance of a true ferromagnetic order must be slightly smaller than 0.10; for this concentration

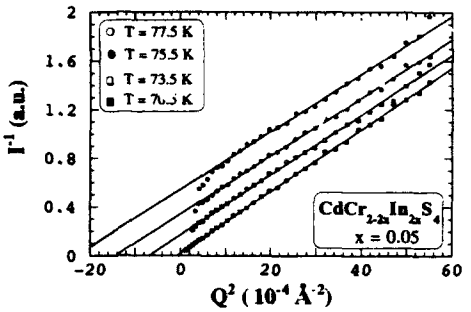

FIG. 3. Inverse magnetic intensity of SANS spectra for the $x=0.05$ sample at different temperatures close to T_C. Solid lines display Lorentzian fits to the data.

ferromagnetic correlations are very large but do not diverge.

We analyzed the critical behavior in a similar way as for the SQUID results, i.e., looking for the divergence of $\chi_0 T$ and κ against the reduced temperature $\tau=1-T_C/T$. Apart from a slight shift (0.3 K) in critical temperatures indicating some mismatch in the thermometer calibrations, extracted values of the γ exponent are fully compatible with the SQUID finding of a strong increase with dilution: $\gamma=1.37\pm0.02$ for the pure compound, $\gamma=1.97\pm0.09$ for the $x=0.05$ compound.

As pictured in Fig. 4, the inverse correlation length κ obeys the standard scaling law: $\kappa=\kappa_0\tau^{-\nu}$. We obtained from least-square fits to the data $\nu=0.70\pm0.01$, $\kappa_0=0.361\pm0.015$ Å^{-1} for the pure sample, and $\nu=1.03\pm0.03$, $\kappa_0=0.452\pm0.010$ Å^{-1} for the $x=0.05$ sample. The pure sample exponent corresponds nicely to the predicted value[8] for a 3D Heisenberg ferromagnet and dilute sample exponent being equal to the limiting case of the theory can be viewed in this framework as if the sample has already been pushed in the strong disorder limit. The critical amplitude κ_0 decreases with dilution, this variation being compensated in Fig. 4 by

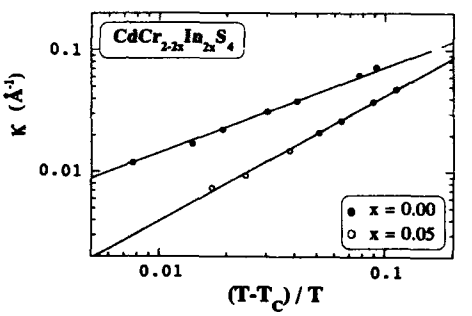

FIG. 4. Critical behavior of the correlation length in $CdCr_{2-2x}In_{2x}S_4$. Solid symbols for $x=0.00$, open symbols for $x=0.05$. Solid lines are fits of the ν exponent: $\nu=0.70$ for $x=0.00$ and $\nu=1.03$ for $x=0.05$.

the exponent increase. In the end, at each reduced temperature, the correlation length in the dilute sample is markedly larger than in the pure sample.

IV. DISCUSSION

We have determined that the critical concentration for ferromagnetic order in the $CdCr_{2-2x}In_{2x}S_4$ system is close to 0.10 and we measured the critical behavior for ferromagnetic samples by SQUID and SANS techniques. Critical exponents γ and ν change as predicted by the theory from approximately their pure values toward $\gamma=2$ and $\nu=1$ when going from the pure compound to the critical concentration. As for the correlation lengths we can add that they behave on a reduced temperature scale like in the AuFe metallic system:[9] Close to the critical concentration, ferromagnetic correlations in disordered systems are much larger than in the pure system, inducing a wider critical region and a larger number of correlated magnetic atoms despite the dilution. This feature common to a metallic and an insulating system must be characteristic of disordered frustrated systems, regardless of details of magnetic interactions. Few studies have been made on insulating compounds, mainly on the $Eu_{1-x}Sr_xS$ and $Eu_{1-x}Sr_xS_ySe_{1-y}$ systems[3] where a high degree of frustration can be obtained by tuning the sulfur concentration y close to a critical value $y_C=0.10$. For example, the system with $y=0.20$ displays a phase diagram and a critical behavior very similar to ours; but, in $CdCr_{2-2x}In_{2x}S_4$ frustration enhancement goes with dilution, In^{3+} ions playing a double role: topological disorder of the Cr^{3+} magnetic network and increase of antiferromagnetic next-nearest-neighbor interactions, as seen in nuclear-magnetic-resonance spectra.[10] We end up with a site and bond disorder, which becomes relevant even at dilution as small as 5% and destabilizes very rapidly the ferromagnetic order. The enhanced frustration lowers the transition temperature allowing ferromagnetic correlations to develop on larger scales and forcing them to diverge more abruptly at T_C, as seen in the increase of critical exponents.

ACKNOWLEDGMENTS

We are indebted to J. Souletie and J. Hammann for valuable discussions and to F. Boué for invaluable help during the SANS experiments at the Orphée reactor in Paris.

[1] D. Boumazouza, Ph. Mangin, B. George, P. Louis, R. A. Brand, J. J. Rhyne, and R. W. Erwin, Phys. Rev. B **39**, 749 (1989), and Refs. therein.
[2] M. Fähnle, P. Braun, R. Reisser, and H. Kronmüller, J. Phys. (Paris) Colloq. **49**, 1201 (1988).
[3] J. Wosnitza and H. v. Löhneysen, Europhys. Lett. **10**, 381 (1989); K. Westerholt, J. Magn. Magn. Mater. **54-57**, 721 (1986).
[4] H.-O. Heuer and D. Wagner, Phys. Rev. B **40**, 2502 (1989); K. Westerholt and G. Sobotta, J. Phys. F **13**, 2371 (1983).
[5] S. Pouget, M. Alba, N. Fanjat, and M. Nogues, Physica B **180&181**, 244 (1992); M. Alba, J. Hammann, and M. Nogues, J. Phys. C **15**, 5441 (1982).
[6] J. Souletie, J. Phys. (Paris) **49**, 2111 (1983); J. Souletie and J. L. Tholence, Solid State Commun. **48**, 407 (1983).
[7] I. D. Luzyanin and V. P. Khavronin, Sov. Phys. JETP **60**, 1229 (1984).
[8] J. C. Le Guillou and J. Zinn-Justin, J. Phys. (Paris) Lett. **46**, L137 (1985).
[9] C. Lartigue, F. Mezei, C. Pappas, and M. Alba, Physica B **180&181**, 359 (1992).
[10] M. C. Méry, P. Veillet, and K. Le Dang, Phys. Rev. B **31**, 2656 (1985).

Thermodynamical properties of a Heisenberg model with Dzyaloshinski–Moriya interactions

F. Lacerda, J. Ricardo de Sousa, and I. P. Fittipaldi
Departamento de Física, Universidade Federal de Pernambuco, 50670-901 Recife-PE, Brasil

Within the framework of a new correlated effective-field theory (CEF) the effects of the Dzyaloshinski–Moriya (DM) interactions on magnetic properties of the spin-$\frac{1}{2}$ anisotropic Heisenberg model are discussed. The CEF theory is based on a generalized but approximate Callen–Suzuki spin relation for cluster with two spins, and makes use of the Honmura–Kaneyoshi exponential operator technique. The phase diagram and the thermal behavior of magnetization are analyzed for the simple cubic lattice, and compared with the corresponding two-spin cluster mean-field (MFA) predictions. It is shown that for the easy direction ($\mathbf{D}=D\mathbf{z}$; where $\mathbf{D}$ is the DM vector coupling), the model exhibit a tricritical point (TCP), at which the phase transition changes from second to first order. The TCP is explicitly obtained, and the tricritical temperature, T_t, is independent of the exchange anisotropy parameter Δ ($\Delta=0$ and $\Delta=1$, correspond the isotropic Heisenberg and Ising models, respectively), while the tricritical parameter, D_t, has dependence on Δ. In spite of its simplicity, the present CEF formalism yields results, which represent a remarkable improvement on the usual MFA treatment.

Recently, models with Dzyaloshinski–Moriya (DM) interactions have been studied in the literature, for describing a certain class of insulators[1] and reentrant spin glass.[2] Some qualitative aspects of the phase diagram of the spin-$\frac{1}{2}$ anisotropic Heisenberg model with DM interactions have recently been analyzed by Cordeiro *et al.*[3] by using renormalization group technique. On the other hand, only very recently a complete study—including *all* regions of interest in the parameter space—of the phase diagram of this model has been made within an appropriated version of mean-field (MFA) treatment.[4] As a new find, it was shown in Ref. 4 that the corresponding MFA scheme, although analytically simple, leads to the prediction of a tricritical point (TCP) in the anisotropic Heisenberg model with DM interactions, which has improperly been overlooked in *all* previous calculations.

The main purpose of the present paper is to employ the same approximate procedure of Ref. 5 to study an extended spin-$\frac{1}{2}$ anisotropic Heisenberg model described by a Hamiltonian, which consists of anisotropic dipolar exchange and DM interactions, and examine the existence of TCP in the phase diagram (see, for instance Ref. 6). The Hamiltonian in study is given by

$$H=-J\sum_{\langle ij\rangle}\left[(1-\Delta)(S_i^xS_j^x+S_i^yS_j^y)+S_i^zS_j^z\right]-\sum_{ij}\mathbf{D}\cdot(\mathbf{S}_i\times\mathbf{S}_j), \tag{1}$$

where the coupling constant $J>0$ is restricted to the nearest-neighbors pairs of spins, $\Delta\in[0,1]$ is the exchange anisotropy parameter and $\mathbf{D}$ is the DM interaction parameter.

The determination of the average magnetization per sites, defined by $m=\langle(1/N)\,\Sigma_{i=1}^{N}S_i^z\rangle$ (where N is the number of sites of the cluster), is obtained from the approximate Callen–Suzuki relation derived in Ref. 7, that for $N=2$ is given by

$$m=\left\langle\frac{\mathrm{Tr}_{\{1,2\}}(\frac{1}{2})(S_1^z+S_2^z)e^{-\beta H_{\{1,2\}}^z}}{\mathrm{Tr}_{\{1,2\}}e^{-\beta H_{\{1,2\}}^z}}\right\rangle, \tag{2}$$

with

$$H_{\{1,2\}}^z=-J[(1-\Delta)(S_1^xS_2^x+S_1^yS_2^y)+S_1^zS_2^z]-\mathbf{D}\cdot(\mathbf{S}_1\times\mathbf{S}_2)-(a_1S_1^z+a_2S_2^z), \tag{3}$$

where a_i $(i=1,2)=\Sigma_\delta JS_{i+\delta}^z$ with δ denoting an elementary lattice vector and $\beta=(k_BT)^{-1}$. Here $\langle\cdots\rangle$ indicates the usual canonical thermal average and $\mathrm{Tr}_{\{1,2\}}$ is the partial trace over the set $\{1,2\}$ of spin variables.

Using Eqs. (3) and (2), and $\mathbf{D}=D\hat{z}$, the average magnetization is given by

$$m=\left\langle\frac{\sinh(u+v)}{\cosh(u+v)+e^{-2K}\cosh\sqrt{(u-v)^2+w}}\right\rangle, \tag{4}$$

where $u=\beta a_1=\Sigma_\delta KS_{1+\delta}^z$, $v=\beta a_2=\Sigma_\delta KS_{2+\delta}^z$, and $w=4K^2[(1-\Delta)^2+D_0^2]$, with $D_0=D/J$ and $K=\beta J$.

By using the exponential operator technique introduced by Honmura and Kaneyoshi,[8] namely $\exp(aD_x+bD_y)g(x,y)=g(x+a,y+b)$, where $D_\lambda\equiv(\partial/\partial\lambda)$ $(\lambda=x,y)$ are the differential operators, and also using the van der Waerden identity for the two-state spin system [i.e., $\exp(\lambda S_i^z)=\cosh\lambda+S_i^z\sinh\lambda$) and, finally, using a decoupling procedure that ignores all high-order spin correlations (i.e., $\langle S_i^zS_j^z\cdots S_n^z\rangle\simeq\langle S_i^z\rangle\cdots\langle S_n^z\rangle$, $i\neq j\neq\cdots\neq n$), Eq. (4) may be written as

$$m=\left\langle\prod_{\delta_1}^{z-1}(c_x+ms_x)\prod_{\delta_2}^{z-1}(c_y+ms_y)\right\rangle g(x,y)|_{x,y=0}, \tag{5}$$

where $c_\nu=\cosh KD_\nu$ and $s_\nu=\sinh KD_\nu$ with $(\nu=x,y)$, and the function $g(x,y)$, defined by

 0021-8979/94/75(10)/5829/3/$6.00 © 1994 American Institute of Physics

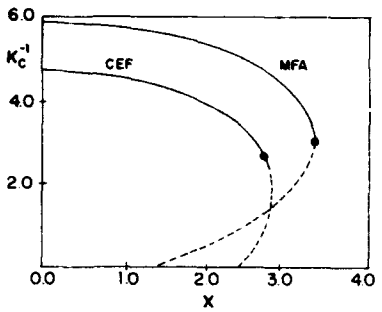

FIG. 1. The variation of K_c^{-1} as a function of $X=\sqrt{D_0^2+(1-\Delta)^2}$ for a simple cubic lattice ($z=6$), obtained in the present CEF and in the MFA[4] treatments. The black point denotes the TCP. Continuous and dashed lines represent, respectively, stable and unstable solutions of Eq. (7).

$$g(x,y)=\frac{\sinh(x+y)}{\cosh(x+y)+e^{-2K}\cosh\sqrt{(x-y)^2+w}}. \quad (6)$$

In Eq. (5), z is the lattice coordination number.

Utilizing the fact that $\Phi_{even}(D_x,D_y)g(x,y)|_{x,y=0}$, valid for any *even* functional $\Phi(D_x,D_y)$, and by expanding the right-hand side of Eq. (5), one obtains the following equation for m:

$$m=A_1m+A_3m^3+A_5m^5+A_7m^7+A_9m^9, \quad (7)$$

where the coefficients A_n ($n=1,3,5,7,9$), which are not explicitly present here, are temperature dependent and also functions of the parameters Δ and D_0. The equation (7) with $D_0=0$ reduced to the equation obtained in Ref. 5.

According to Eq. (7) the second-order critical transition temperature (K_c^{-1}) is obtained from the condition $A_1=1$ with $A_3<0$ (stable solution), and, when $A_3>0$ an unstable solution appear. The point at which $A_1=1$ and $A_3=0$ (with $A_5<0$), separating the stable ($A_3<0$) and the unstable ($A_3>0$) solutions, is the tricritical point (TCP), at which the system undergoes a first-order phase transition. An analogous expression like Eq. (7) were obtained in Ref. 4 within a two-spin cluster mean-field treatment.

At this point, it is worth mentioning that the reduced transition temperature in the absence of the DM interaction [i.e., $K_c^{-1}(\Delta;D=0)$], obtained within the present CEF procedure, for the limit cases of $\Delta=1$ (Ising) and $\Delta=0$ (Heisenberg) are given by $K_c^{-1}(\Delta=1)=5.039$ and $K_c^{-1}(\Delta=0)=4.891$, in complete contrast with the single value of 6.0 predicted by the one-spin cluster MFA for the case of $z=6$. On the other hand, the estimated values predicted by the two-spin cluster MFA scheme of Ref. 4 are $K_c^{-1}(\Delta=1)=5.847$ and $K_c^{-1}(\Delta=0)=5.719$. We recall that the series expansions results are, respectively, 4.511 and 3.360.[9] Hence, such a comparison between these results gives to the present CEF treatment[5] some qualitative, and, to a certain extent, quantitative confidence.

In Fig. 1, the variation of the transition temperature K_c^{-1} in the case of $z=6$, is plotted as a function of a convenient reduced parameter X, defined by $X=\sqrt{(1-\Delta)^2+D_0^2}$, obtained in both the MFA[4] and the present correlated effective-field approximations (CEF). In the figure, the solid and dashed lines represent the stable ($A_3<0$) and unstable ($A_3>0$) solutions of (7), respectively, and the black points denote the TCP. As can be seen in the figure, when X increases from zero, the critical second-order phase transitions lines decreases from its values in the absence of the DM interaction, reaching the TCP at (T_t,D_t). The tricritical point, T_t, is found to be independent of the exchange anisotropy parameter Δ, with the constant value of $T_t^{CEF}=2.68$. This value should be compared with the result $T_t^{MFA}=3.33$ predicted by MFA[4] [i.e., $T_t^{MFA}=2(z-1)/3$]. On the other hand, the tricritical parameter, D_t, is found to be Δ dependent, given by $D_t^{CEF}=\sqrt{7.29-(1-\Delta)^2}$, which should be compared with $D_t^{MFA}=\sqrt{10.75-(1-\Delta)^2}$.[4] We should note that in both approximations one obtains the interesting result $D_t(\Delta=0)<D_t(\Delta=1)$, indicating a possible universal behavior, since it is independent of the approximations. This tricritical behavior of the system may be interpreted as resulting from a competition between the exchange interaction that tries to align the spins in the same direction and the effect of the DM anisotropy, which has the tendency to destroy this alignment. Also, one should note that by imposing the Ising limit $\Delta=1$, the system Hamiltonian in (1) reduces to a two-state (spin-$\frac{1}{2}$) Ising Hamiltonian, in which the DM interactions play the same rule as the single-ion uniaxial crystal field anisotropy term does [i.e., $-D\sum_i(S_i^z)^2$], in the Blume–Capel models for $D<0$ (see, for instance, Ref. 10, and references therein). It is well known that, for some values of this uniaxial anisotropy parameter, the Blume–Capel Hamiltonian may exhibit tricritical behavior.

The polynomial equation (7) can easily be solved numerically in order to get m as functions of the reduced tem-

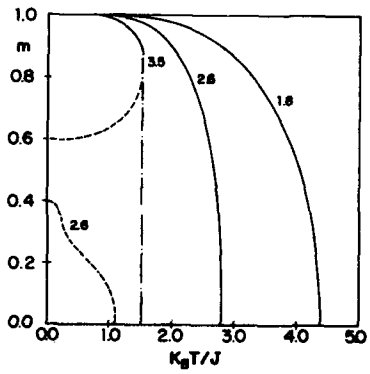

FIG. 2. Temperature dependences of m in the present CEF approximation, for the Ising limit (i.e., $\Delta=1$), and for selected values of $D_0=D/J$ (numbers on the curves), on a simple cubic lattice ($z=6$). Solid and dashed lines refer to the stable and unstable solutions of (7), while the dashed–dotted line in the curve labeled 3.5 is to stress the discontinuousity of the magnetization for $D_0\geq D_t$ ($\Delta=1$), in which region the first-order phase transitions appear.

perature k_BT/J, as well as its dependence with the other parameters Δ and D_0. Figure 2 shows the results for the temperature dependence of m in the case $\Delta=1$ (Ising limit), for some typical values of D_0 (the numbers associated with each curve). The continuous lines represent physically stable solutions of (7), while the dashed lines are the unstable ones. As one can see from Fig. 2 for values $D_0=1.8$ and 2.6, the magnetization falls smoothly to zero when the temperature increases from zero to T_c, characterizing a second-order phase transition. Note that for the case $D_0=2.6$, we also find unphysically unstable solutions of (7), which are described by the dashed curve labeled 2.6 in Fig. 2. These unphysical solutions of (7) are also represented by the dashed regions of the curves in Fig. 1. On the other hand, we also find that for $D_0=3.5>D_t$ ($\Delta=1$) [note that $D_t^{\mathrm{CEF}}(\Delta=1)=2.7$], the magnetization jumps discontinuously from a certain value m_c^* to zero, at a temperature T_c^* (see the curve marked 3.5 in Fig. 2), which characterize a first-order phase transition.

In conclusion, all these results are also qualitatively predicted by our previous MFA calculations,[4] and so, although with some quantitative differences, the present CEF treatment provides a subsequent corroboration (beyond the usual MFA) of the occurrence of a TCP in the model under consideration.

ACKNOWLEDGMENT

This work was partially supported by CNPq and FINEP (Brazilian Agencies).

[1] V. Bindilatti, T. Q. Vu, Y. Shapira, C. C. Agosta, E. J. McNiff, R. Kershaw, K. Dwight, and A. Wold, Phys. Rev. B **45**, 5328 (1992).
[2] L. Yi, G. Büttner, and K. D. Usadel, Phys. Rev. B **47**, 254 (1993), and references therein.
[3] C. E. Cordeiro, E. V. de Mello, and M. A. Continentino, Z. Phys. B Cond. Matter. **85**, 307 (1991).
[4] J. Ricardo de Sousa, D. F. de Albuquerque, and I. P. Fittipaldi, submitted to Phys. Lett. A.
[5] T. Idogaki and N. Uryû, Physica A **181**, 173 (1992).
[6] M. Kaufman, R. B. Griffiths, J. M. Yeomans, and M. E. Fisher, Phys. Rev. B **23**, 3448 (1981).
[7] F. C. Sá Barreto and I. P. Fittipaldi, Physica A **129**, 360 (1985).
[8] R. Honmura and T. Kaneyoshi, J. Phys. C **12**, 3979 (1979).
[9] C. Domb, in *Phase Transitions and Critical Phenomena*, edited by C. Domb and M. S. Green (Academic, London, 1974), Vol. 3.
[10] A. F. Siqueira and I. P. Fittipaldi, Physica A **138**, 592 (1986).

A unified effective-field renormalization-group framework approach for the quenched diluted Ising models

Douglas F. de Albuquerque and I. P. Fittipaldi
Departamento de Física, Universidade Federal de Pernambuco, 50670-901 Recife-PE, Brazil

A unified effective-field renormalization-group framework (EFRG) for both quenched *bond*- and *site*-diluted Ising models is herein developed by extending recent works. The method, as in the previous works, follows up the same strategy of the mean-field renormalization-group scheme (MFRG), and is achieved by introducing an alternative way for constructing classical effective-field equations of state, based on rigorous Ising spin identities. The concentration dependence of the critical temperature, $T_c(p)$, and the critical concentrations of magnetic atoms, p_c, at which the transition temperature goes to zero, are evaluated for several two- and three-dimensional lattice structures. The obtained values of T_c and p_c and the resulting phase diagrams for both *bond* and *site* cases are much more accurate than those estimated by the standard MFRG approach. Although preserving the same level of simplicity as the MFRG, it is shown that the present EFRG method, even by considering its simplest size-cluster version, provides results that correctly distinguishes those lattices that have the same coordination number, but differ in dimensionality or geometry.

Over the last several years the real-space mean-field renormalization-group (MFRG) method, introduced by Indekeu *et al.*,[1] has been used to provide useful qualitative and quantitative insights into the critical behavior of a wide variety of classical and quantum lattice spin systems.[2] One of the most severe limitations of the standard MFRG is the inefficacy of the method to distinguish lattice structures. It is clear that within the scope of the usual mean-field classical equation of state, on which MFRG is based, the lattice symmetry is lost, and the real dimensionality of the system is only partially incorporated through the coordination number of the lattice.

In this work a new unified effective-field renormalization-group framework (EFRG) for both quenched *bond*- and *site*-diluted Ising models is presented by extending recent works on pure[3] and disordered[4] Ising systems. The scheme, which follows up the same strategy of the usual MFRG approach,[1,2] is based on an alternative way for constructing classical effective-field equations of state, by using rigorous Ising spin identities as a starting point. The method is achieved by treating the effects of the surrounding spins of each of the clusters through a convenient differential operator expansion technique introduced by Honmura and Kaneyoshi,[5] by which all the relevant self-spin correlations are taken exactly into account. In order to illustrate the EFRG procedure for diluted Ising spin systems,[6] we discuss the concentration dependence of the critical temperature, $T_c(p)$, and the critical concentrations of magnetic atoms, p_c, at which the transition temperature goes to zero, for several two- and three-dimensional lattice structures. Here we are particularly concerned with the efficiency of the EFRG method versus lattice structure when working with the smallest possible clusters sizes; namely, clusters with one and two spins. Thus, we perform calculations by looking especially at those lattices having the same coordination number, but differing in geometry or space dimensionality.

Our prototype reduced Hamiltonian is the spin-$\frac{1}{2}$ ferromagnetic Ising model,

$$H=\sum_{(i,j)} K_{ij}\sigma_i\sigma_j, \quad (\sigma_i,\sigma_j=\pm 1), \tag{1}$$

where for each nearest neighbor coupling $K_{ij}(\equiv J_{ij}/k_BT)$ are assumed to be independent random variables with quenched probability distribution. The bond- and site-diluted versions of (1) are conceptually realized by assuming the parametrization $K_{ij}=\epsilon_{ij}K$ (bond problem) and $K_{ij}=\epsilon_i\epsilon_jK$ (site problem), in which the ϵ_{ij} and ϵ_i are random variables governed by the following quenched probability distributions: $P^{(B)}(\epsilon_{ij})=p^{(B)}\delta(\epsilon_{ij}-1)+(1-p^{(B)})\delta(\epsilon_{ij})$ and $P^{(S)}(\epsilon_i)=p^{(S)}\delta(\epsilon_i-1)+(1-p^{(S)})\delta(\epsilon_i)$, respectively, for the *bond* and *site* problems, in which $p^{(B)}(p^{(S)})$ are the bond (site) concentrations of magnetic atoms.

We shall consider two finite cluster with $N'=1(\sigma_1)$ and $N=2(\sigma_1$ and $\sigma_2)$ spins each of them characterized by coupling constants K' and K, respectively. According to the ex-

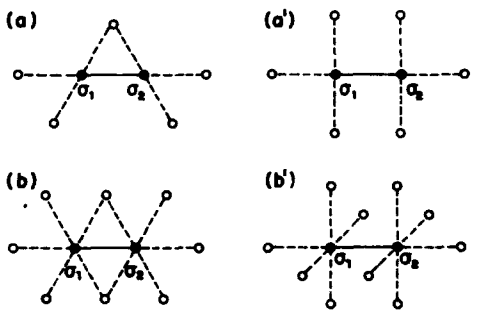

FIG. 1. Two-spin clusters geometry on the following lattices: $z=4$(a) square (a') Kagomé; $z=6$ (b) plane triangular and (b') simple cubic.

 0021-8979/94/75(10)/5832/3/$6.00 © 1994 American Institute of Physics

act Callen relations,[7] the average magnetizations $m_{N'(N)}$ associated to $N'=1$ and $N=2$ clusters, are given by[3]

$$m_{N'}=\langle \Pi_j e^{K'_{1j}\sigma'_j D_x}\rangle \tanh x|_{x=0} \quad (N'=1), \tag{2}$$

$$m_N=\langle \Pi'_j e^{K_{1j}\sigma_j D_x}\Pi'_l e^{K_{2l}\sigma_l D_y}\ \Pi'_k e^{\sigma_k(K_{1k}D_x+K_{2k}D_y)}\rangle \times f(x,y)|_{x=0;y=0} \quad (N=2), \tag{3}$$

where $f(x,y)=\sinh(x+y)/[\cosh(x+y)+\exp(-2K_{12})\times\cosh(x-y)]$, and $D_\lambda=\partial/\partial\lambda(\lambda=x,y)$ are the differential operators. The products Π' over j and l are, respectively, over the isolated nearest-neighbors spins of sites 1 and 2, whereas the product Π' over k is restricted to the sites, which are, simultaneously, nearest neighbors of both σ_1 and σ_2 spins. A schematic illustration showing the geometric structures of the two-spin clusters on lattices analyzed herein, is depicted in Fig. 1.

Equations (2) and (3) are exact and will be used here as the basis of the present formalism. By using the van der Waerden identity [i.e., $\exp(\lambda\sigma_i)=\cosh\lambda+\sigma_i\sinh\lambda$; $\forall\lambda$) for the exponential factors appearing in (2) and (3), these equations yield a set of formal exact relations between the clusters magnetizations $m_{N'}$ and m_N and corresponding multispin correlation functions associated to the various sites for each cluster under consideration. Here, in the effective-field approximation, we shall proceed as follows: we take, on both sides of these equations the thermal and spin configurational averages (denoted by $\langle\langle\cdots\rangle\rangle_c$), then completely decouple the multispin correlation functions, namely $\langle\langle\sigma_i\sigma_j\cdots\sigma_n\rangle\rangle_c \simeq\langle\langle\sigma_i\rangle\rangle_c\langle\langle\sigma_j\rangle\rangle_c\cdots\langle\langle\sigma_n\rangle\rangle_c$, with $i\neq j\neq\cdots\neq n$. Based on this approximation and replacing each boundary configurational spin average $\langle\langle\sigma'_j\rangle\rangle_c$ ($\langle\langle\sigma_j\rangle\rangle_c$) by the symmetric breaking mean-field parameters $b'_j(b_j)$, one obtains two equations of states for $\tilde{m}_{N'}=\langle m_{N'}\rangle_c$ and $\tilde{m}_N\equiv\langle m_N\rangle_c$, which by expanding up to first order in these parameters and assuming translational invariance, we have[4]

$$\tilde{m}_{N'}(K',p';b')=A_{N'}^{(z)}(K',p')b'+O(b'^3) \quad (N'=1), \tag{4}$$

$$\tilde{m}_N(K,p;b)=A_N^{(\tilde{z})}(K,p)b+O(b^3) \quad (N=2). \tag{5}$$

The coefficients of $A_{N'}^{(z)}$ and $A_N^{(\tilde{z})}$ depend on dilution studied, either bond or site dilution. By simplicity, the coefficients are given by

$$A_{N'}^{(z)}(K',p')=z\langle\cosh(K'_1D_x)\rangle_c^{z-1}\tanh x|_{x=0}, \tag{6}$$

$$A_N^{(\tilde{z})}(K,p)=\{2z'\langle\sinh(K_1D_x)\rangle_c\langle\cosh(K_1D_x)\rangle_c^{z'-1}\langle\cosh(K_2D_y)\rangle_c^{z'}\langle\cosh[K_1D_x+K_2D_y]\rangle_c^{z''}+z''\langle\cosh(K_1D_x)\rangle_c^{z'} \times\langle\cosh(K_2D_y)\rangle_c^{z}\langle\sinh[K_1D_x+K_2D_y]\rangle_c\langle\cosh(K_1D_x+K_2D_y)\rangle_c^{z''-1}\}\ \tilde{f}(x,y)|_{x=0}, \tag{7}$$

where $\tilde{f}(x,y)$ means the configurational average of $f(x,y)$. Here, z is the lattice coordination number, z' denotes the number of sites that are nearest neighbors of σ_1 (or σ_2), but no neighboring σ_2 (or σ_1), and z'' denotes the number of sites that are, simultaneously, nearest neighbor of both σ_1 and σ_2. Hence, $\tilde{z}=2z'+z''$ is the total number of nearest-neighbors sites of the two-spin cluster (see Fig. 1). Now, by imposing the same scaling relation between the average magnetizations $\tilde{m}_{N'}$ and $\tilde{m}_N$, and between the parameters b and b', one finds the following recursion relation:

$$A_{N'}^{(z)}(K',p')=A_N^{(\tilde{z})}(K,p) \quad (N'=1,N=2), \tag{8}$$

which is independent of the rescaling factor. Although from Eq. (8) alone one cannot determine the complete renormalization flow diagram in the parameter space (K,p), however, it is reasonable to consider the solution of the fixed-point equation obtained from (8) by setting $p=p'$ as critical points $K_c(p)$ of the system.

Equations (6) and (7) are valid for any kind of lattice structure characterized by numbers z and $\tilde{z}$. It is clear from (7) that the coefficient $A_N^{(\tilde{z})}(K,p)$associated to the two-spin

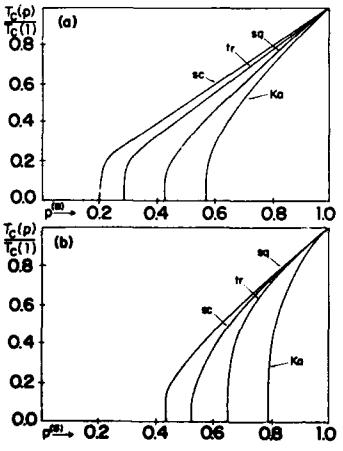

FIG. 2. Concentration dependences of the reduced critical temperature $T_c(p)/T_c(1)$ for the (a) bond and (b) site problems, on the following lattices: sq, Ka, tr, and sc.

TABLE I. Values of the critical percolation concentrations $p_c^{(\nu)}$ in the bond ($\nu=B$) and site ($\nu=S$) problems for several lattice structures obtained in the present EFRG and MFRG (the numbers in parentheses). The exact/series values are taken from Ref. 7.

	sq	Ka	tr	sc
$p_c^{(B)}$	0.43(0.33)	0.57(0.33)	0.28(0.17)	0.20(0.17)
Exact/Series	0.500	0.449	0.347	0.247
$p_c^{(s)}$	0.43(0.57)	0.79(0.57)	0.64(0.41)	0.52(0.41)
Exact/Series	0.590	0.652	0.500	0.307

cluster, incorporate details of the geometry of the lattice beyond its coordination number z, through the numbers z' and z''. In order to exemplify the use of Eqs. (6) and (7) we have obtained numerically the nontrivial fixed point $K'=K=K^*=K_c$ solutions of Eq. (8) (with $p=p'$) for the square (sq), Kagomé (Ka), triangular (tr), and simple cubic (sc) lattices. Note that the square and Kagomé are lattices having the same dimensionality ($d=2$) and common coordination number ($z=4$), but differing in geometry, while the triangular and the simple cubic are lattices with same $z=6$ but differing in space dimensionality (see Fig. 1). The values obtained by EFRG for the reduced critical temperature have distinct values of K_c^{-1} (sq)=2.794, K_c^{-1} (Ka)=2.083, K_c^{-1} (tr)=4.101, K_c^{-1}(sc)=4.993 in contrast with the unique values predicted by MFRG, i.e., K_c^{-1} (sq,Ka)=2.885 and K_c^{-1} (tr,sc)=4.926; we recall that the exact/series values are K_c^{-1} (sq)=2.269, K_c^{-1} (Ka)=2.143, K_c^{-1}(tr)=3.641 and K_c^{-1}(sc)=4.511.[8]

The critical frontiers associated to the bond- and site-diluted Ising model are presented in Fig. 2 for the sq, Ka, tr, and sc lattices, respectively. The bond (B) and site (S) critical percolation concentrations p_c, at which K_c^{-1} $(p_c)=0$ obtained with this method, are given in Table I.

The results presented in Table I reveal that, in contrast with the MFRG predictions, the present EFRG correctly distinguishes the geometry of the lattice structure. We should also remark that the present EFRG framework provides the exact asymptotic forms for the critical lines simultaneously in both limits $T_c \to 0$ and $p \to 1$.

We conclude by saying that the satisfactory comparison here presented, supports the belief that the results provided by the EFRG method can be given qualitative, and, to a certain extent, quantitative confidence.

This work was partially supported by CnPq and FINEP (Brazilian Agencies).

[1] J. O. Indekeu, A. Maritan, and A. L. Stella, Phys. A **15**, L291 (1982).
[2] See, for instance, J. O. Indekeu, A. Maritan, and A. L. Stella, Phys. Rev. B **35**, 305 (1987), and references therein.
[3] I. P. Fittipaldi, Abstract communicated at the STATPHYS 17, Rio de Janeiro, Brazil (1989); also see I. P. Fittipaldi, J. Magn. Magn. Mat. (in press).
[4] I. P. Fittipaldi and D. F. de Albuquerque, J. Magn. Magn. Mat. **104–107**, 236 (1992).
[5] R. Honmura and T. Kaneyoshi, J. Phys. C **12**, 3979 (1979).
[6] See, for a brief discussion, C. Jayaprakash, E. K. Riedel, and M. Wortis, Phys. Rev. B **18**, 2244 (1978); and also S. R. McKay and A. N. Berker, J. Appl. Phys. **64**, 5785 (1988); and references therein.
[7] H. B. Callen, Phys. Lett. **4**, 161 (1963).
[8] C. Domb, in *Phase Transitions and Critical Phenomena*, edited by C. Domb and M. S. Green (Academic, London, 1974), Vol. 3.

Critical behavior of the anisotropic Heisenberg model by effective-field renormalization group

J. Ricardo de Sousa and I. P. Fittipaldi
Departamento de Física, Universidade Federal de Pernambuco, 50670-901 Recife-PE, Brazil

A real-space effective-field renormalization-group method (ERFG) recently derived for computing critical properties of Ising spins is extended to treat the quantum spin-1/2 anisotropic Heisenberg model. The formalism is based on a generalized but approximate Callen–Suzuki spin relation and utilizes a convenient differential operator expansion technique. The method is illustrated in several lattice structures by employing its simplest approximation version in which clusters with one ($N'=1$) and two ($N=2$) spins are used. The results are compared with those obtained from the standard mean-field (MFRG) and Migdal–Kadanoff (MKRG) renormalization-group treatments and it is shown that this technique leads to rather accurate results. It is shown that, in contrast with the MFRG and MKRG predictions, the EFRG, besides correctly distinguishing the geometries of different lattice structures, also provides a vanishing critical temperature for *all* two-dimensional lattices in the isotropic Heisenberg limit. For the simple cubic lattice, the dependence of the transition temperature T_c with the exchange anisotropy parameter Δ [i.e., $T_c(\Delta)$], and the resulting value for the critical thermal crossover exponent ϕ [i.e., $T_c \simeq T_c(0)+A\Delta^{1/\phi}$] are in quite good agreement with results available in the literature in which more sophisticated treatments are used.

In a series of studies, several authors have generated the real-space renormalization-group (RSRG) approach to quantum-spin systems such as Heisenberg, xy, and transverse Ising models.[1–4] In particular, one is interested in the effects caused by the noncommutation aspects of the Hamiltonian. In the absence of exact solutions for the RSRG scheme, any of a number of approximations have been proposed in the literature. Recently a new RSRG approach [denoted effective-field renormalization group (EFRG)][4–6] has been introduced in the literature for the Ising model. The scheme, which follows the same strategy of the usual mean-field renormalization group (MFRG),[3] is based on an alternative way for constructing classical effective-field equations of state,[5] and provides results which represent a remarkable improvement on those obtained by the MFRG method.

The purpose of this work is to generalize the new idea of the EFRG approach to treat the quantum anisotropic Heisenberg model with spin 1/2. The method is illustrated for several lattice structures in which clusters with one ($N'=1$) and two ($N=2$) spins are used. We obtain the critical temperature as a function of anisotropy parameter and the crossover exponent for the simple cubic lattice.

The anisotropic Heisenberg model has the Hamiltonian given by

$$H=-J\sum_{\langle ij\rangle}[(1-\Delta)(S_i^xS_j^x+S_i^yS_j^y)+S_i^zS_j^z], \tag{1}$$

where $J>0$ is the nearest-neighbor exchange interaction, S_i^ν ($\nu=x,y,z$) are components of a spin-1/2 operator at site i, and Δ is the exchange anisotropy ($\Delta=0$ and $\Delta=1$ correspond the isotropic Heisenberg and Ising model, respectively). The critical temperature T_c, for $\Delta=0$ in two-dimensional lattices has been proved to vanish.[7]

The Hamiltonian (1) for clusters with one ($N'=1$) and two ($N=2$) spins, can be written in the axial approximation[8] as

$$H'_{\{1\}}=-J'a'_1S_1^{z'} \tag{2}$$

and

$$H_{\{1,2\}}=-J[(1-\Delta)(S_1^xS_2^x+S_1^yS_2^y)+S_1^zS_2^z] -J(a_1S_1^z+a_2S_2^z), \tag{3}$$

where $a'_1=\Sigma_\delta^z S_{1+\delta}^{z'}$ and $a_n(n=1,2)=\Sigma_\delta^{z-1}S_{n+\delta}^z$, with δ denoting an elementary vector of the lattice and z the lattice coordination number.

According to the approximate Callen–Suzuki relation derived in Ref. 9, the average magnetizations $m_{N'}=\langle S_1^{z'}\rangle$ and $m_N=\langle\frac{1}{2}(S_1^z+S_2^z)\rangle$ are given by

$$m_{N'}=\left\langle\prod_\delta^z[c'_x+S'^z_{1+\delta}s'_x]\right\rangle\tanh x|_{=0} \tag{4}$$

and

$$m_N=\left\langle\prod_{\delta_1}^{z-1}(c_x+S^z_{1+\delta}s_x)\prod_{\delta_2}^{z-1}(c_y+S^z_{2+\delta_2}s_y)\right\rangle \times g(x,y)|_{x,y=0}, \tag{5}$$

where $c_\nu=\cosh K\,D_\nu$, $s_\nu=\sinh KD_\nu$ ($\nu=x,y$), $D_\nu=\partial/\partial\nu$, and $g(x,y)$ is given by

$$g(x,y)=\frac{\sinh(x+y)}{\cosh(x+y)+e^{-2K}\cosh u}, \tag{6}$$

where $u=\sqrt{(x-y)^2+4K^2(1-\Delta)^2}$ and $K=J/k_BT$.

Equations (4) and (5) are approximate and will be used here as the basis of the present formalism. In the limit $\Delta=1$ (Ising model) both equations are exact, and have been studied in Refs. 5 and 6. Here, we use a decoupling procedure which ignores all high-order spin correlations on both right-hand sides of Eqs. (4) and (5), i.e.,

 0021-8979/94/75(10)/5835/3/$6.00 © 1994 American Institute of Physics

$$\langle S_i^z S_j^z \cdots S_N^z \rangle \simeq \langle S_i^z \rangle \langle S_j^z \rangle \cdots \langle S_n^z \rangle,$$

with $i \neq j \neq \cdots n$, and we adopt $\langle S_i^z \rangle = b$ and $\langle S_i^{z'} \rangle = b'$ for the clusters with N and N' spins, respectively (where b and b' are the symmetric breaking effective fields). Before applying the decoupling, we should observe that in Eq. (5) sites 1 and 2 of the two-spin cluster may exhibit a set of common nearest-neighbors sites. Thus, Eq. (5) can be recast in the following form;

$$m_N = \left\langle \prod_{\delta_1}^{z-z'-1} (c_x + S_{1+\delta_1}^z s_x) \prod_{\delta_2}^{z-z'-1} (c_y + S_{2+\delta_2}^z s_y) \times \prod_{\delta}^{z'} (c_{x+y} + S_{\delta}^z s_{x+y}) \right\rangle g(x,y)|_{x,y=0}, \quad (7)$$

where $c_{x+y} = \cosh K(D_x + D_y)$, $s_{x+y} = \sinh K(D_x + D_y)$, and z' is the number of sites that are, simultaneously, nearest neighbors of both S_1 and S_2. Now, expanding Eqs. (4) and (7) up to first order in the parameters b and b' one finds

$$m_N(K',b') \simeq A_{N'}^{(z)}(K') b' \quad (N'=1) \quad (8)$$

and

$$m_N(K,\Delta,b) \simeq A_N^{(z,z')}(K,\Delta) b \quad (N=2), \quad (9)$$

where the coefficients $A_{N'}^{(z)}(K')$ and $A_N^{(z,z')}(K,\Delta)$ are given by

$$A_{N'}^{(z)}(K') = z s_x c_x^{z-1} \tanh x|_{x=0} \quad (10)$$

and

$$A_N^{(z,z')}(K,\Delta) = \{[2(z-z'-1) s_x c_x^{z-z'-2} c_y^{z-z'-1} c_{x+y}^{z'} + z' c_x^{z-z'-1} c_y^{z-z'-1} s_{x+y} c_{x+y}^{z'-1}\}] \times g(x,y)|_{x,y=0}. \quad (11)$$

By imposing the same scaling relations between the average magnetizations $m_{N'}$ and m_N, and between the fields b and b', one finds the following recursion relation:

$$A_{N'}^{(z)}(K') = A_N^{(z,z')}(K,\Delta), \quad (12)$$

which is independent of the scaling factor.

The reduced critical temperature K_c^{-1} is the nontrivial fixed-point solutions of Eq. (12), $K' = K = K^* = K_c$. For the isotropic model ($\Delta = 0$), we find for the reduced critical temperature $K_c^{-1} = 0$ for all bidimensional lattices [such as, square ($z=4$, $z'=0$), Kagomé ($z=4$, $z'=1$), triangular ($z=6$, $z'=2$) and honeycomb ($z=3$, $z'=0$)] which is the exact result.[7] Other renormalization-group treatments[1-3] do not correctly distinguish the geometry and the dimensionality of the lattice structure, and as a consequence this leads to K_c^{-1} values which remain finite for the triangular and Kagomé lattices in contrast with the exact result $K_c^{-1} = 0$.[7] In Fig. 1 the dependence of transition temperature K_c^{-1} with the exchange anisotropy parameter Δ is presented for a triangular lattice for EFRG (this work) and MFRG.[3]

For the simple cubic lattice ($z=6$, $z'=0$) and $\Delta=0$, we obtain $K_c^{-1} = 3.69$, which should be compared with the results by Suzuki and Takano ($K_c^{-1} = 2.91$),[1] Mariz *et al.* ($K_c^{-1} = 4.18$),[2] and Plascak ($K_c^{-1} = 3.64$).[3] We recall that the series expansions result[10] is $K_c^{-1} = 3.360$.

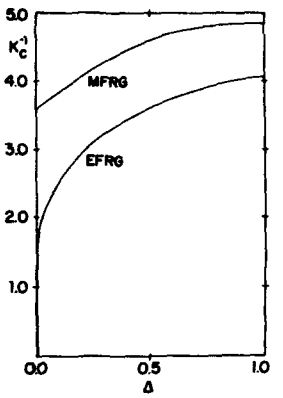

FIG. 1. Critical temperature K_c^{-1} as a function of Δ obtained in MFRG (Ref. 3) and EFRG (this work) for the two-dimensional triangular lattice anisotropic Heisenberg model.

Near the isotropic limit [i.e., $\Delta \to 0$], Eq. (12) may be expanded, giving the following expression for the critical temperature:

$$K_c^{-1}(\Delta) \simeq K_c^{-1}(\Delta=0) + A\Delta^{1/\phi}, \quad (13)$$

where A is a constant and ϕ is the crossover exponent; the value predicted here of $\phi = 1.43$ is to be compared with the results of Suzuki and Takano ($\phi = 1.56$),[1] Mariz *et al.* ($\phi = 1.27$),[2] and series expansions ($\phi = 1.25$).[10]

In Fig. 2 we show the critical temperature K_c^{-1} as function of the anisotropy parameter Δ for the simple cubic lat-

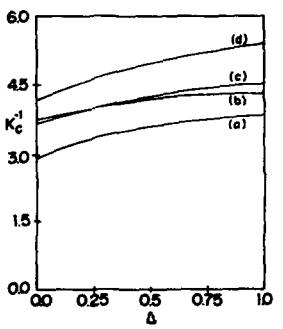

FIG. 2. Dependence of the critical temperature K_c^{-1} with respect to the exchange anisotropy parameter Δ for the simple cubic lattice, obtained by (a) MKRG (Ref. 1), (b) EFRG (present work), (c) MFRG (Ref. 3), and (d) Mariz *et al.* (Ref. 2).

tice, using the present EFRG, MFRG,[3] Migdal–Kadanoff (MKRG),[1] and the Mariz *et al.*[2] methods.

We observe that, even for the smallest possible clusters, the dependence of the transition temperature K_c^{-1} on the exchange anisotropy Δ (see Fig. 2) and the resulting value for the critical thermal exponent ϕ predicted by the present EFRG are in quite good agreement with the others RSRG approximations and series expansion results. In particular, we have obtained critical temperatures T_c which reflect the details of the lattice geometry beyond its coordination number. For example, in contrast with the MFRG (Ref. 3) and MKRG (Ref. 1) predictions, the present EFRG provides in the isotropic Heisenberg limit ($\Delta=0$) a correctly vanishing critical temperature for all two-dimensional lattices.

Finally, let us conclude by saying that owing to its simplicity, the paradigm used in this article can be extended and generalized to others interacting quantum spin systems.

This work partially supported by FACEPE, CAPES, CNPq, and FINEP (Brazilian Agencies).

[1] M. Suzuki and H. Takano, Phys. Lett. A **69**, 426 (1979).
[2] A. M. Mariz, R. M. Z. dos Santos, C. Tsallis, and R. R. dos Santos, Phys. Lett. A **108**, 95 (1985).
[3] J. A. Plascak, J. Phys. A **17**, 597 (1984), and refereaces therein; see also J. O. Indekeu, A. Maritan, and A. L. Stella, *ibid.* **15**, 291 (1982).
[4] Q. Jiang and Z. Y. Li, Phys. Rev. B **40**, 11264 (1989); Z. Y. Li and C. Z. Yang, *ibid.* **37**, 5744 (1988).
[5] I. P. Fittipaldi, abstract communicated at the STATPHYS '17, Rio de Janeiro, Brazil, 1989; see also, I. P. Fittipaldi, J. Magn. Magn. Mater. (1994) (to be published).
[6] I. P. Fittipaldi and D. F. de Albuquerque, J. Magn. Magn. Mater. **104-107**, 236 (1992).
[7] N. D. Mermin and H. Wagner, Phys. Rev. Lett. **17**, 1133 (1966).
[8] T. Idogaki and N. Uryû, Physica A **181**, 173 (1992).
[9] F. C. Sá Barreto and I. P. Fittipaldi, Physica A **129**, 360 (1985).
[10] C. Domb, in *Phase Transitions and Critical Phenomena*, edited by C. Domb and M. S. Green (Academic, London, 1974), Vol. 3.

Random decorated antiferromagnetic Ising model with mixed spins

Vanêssa M. Correia and Roberto J. V. dos Santos
Departamento de Física, CCEN, Universidade Federal de Alagoas, Cidade Universitária, Maceió, Alagoas, Brazil

A new approach to studying random quenched decorated models is introduced, which after an approximation on the decoration transformation equation makes use of the exact solution of the partition function of the host lattice. The method is applied to study the phase diagram of an antiferromagnetic Ising square lattice randomly decorated with spins $S_1=\pm 1;0$ with probability p or $S_2=\pm 1$ with probability $1-p$, in the isotropic case, in which all the bonds are decorated. Several phase diagrams are obtained spanning the various parameter spaces of the model.

I. INTRODUCTION

Decorated spin models were introduced by Syozi[1] in connection with the determination of the transition temperature of an Ising spin model on a Kagomé lattice, starting from its value on a honeycomb lattice. Lately, the random annealled antiferromagnetic Ising model on a square lattice was used in the study of the phase diagram of CuO_2 sheets of high-Tc superconductors.[2] The quenched version of the decorated antiferromagnetic Ising square lattice was also studied, using an effective field theory to obtain the phase diagram.[3] For a recent review on the literature and other applications of decorated models, the reader is referred to the paper of Coutinho *et al.*[4]

In this paper we propose a new approach to study random quenched decorated models, which combine an effective treatment with the exact solution of Onsager for the square lattice.[5]

II. GENERAL FORMALISM

The Hamiltonian of the decorated system may be written as

$$H=\sum_b H_b, \tag{1}$$

where H_b is the bond Hamiltonian and the summation runs over all the bonds of the lattice. If $\{S\}$ is the set of all the variables associated with the decorating system on the bond b that connects the lattice spins σ and σ', one defines the decoration transformation as follows:

$$A\,\exp(K_{\text{eff}}\sigma\sigma')=\operatorname{Tr}_{\{S\}}\exp[-\beta H_b(\{S\},\sigma,\sigma')]$$
$$=F(\sigma,\sigma'), \tag{2}$$

where $\beta=1/k_BT$, and the trace operation is taken over all the configurations of the decorating variables; K_{eff} is the effective coupling between the spins σ and σ' and A is an analytic function of the temperature and of the parameters of the decorating system (this may affect the extensive variables of the model but not the intensive ones as, for example, the critical temperature).

It is straightforward to show that

$$K_{\text{eff}}=\frac{1}{2}\ln\left(\frac{F(1,1)}{F(1,-1)}\right) \tag{3}$$

and

$$A=[F(1,1)F(1,-1)]^{1/2},$$

so that the partition function of the effective square lattice is

$$Z=A^N Z_0(K_{\text{eff}}), \tag{4}$$

where N is the number of the bonds and Z_0 is the partition function of the ordinary square lattice Ising model with coupling factor K_{eff}.

From the Onsager solution,[5] the critical temperature of the model is given by the equation

$$\sinh(2K_{\text{eff}})=\pm 1, \tag{5}$$

where the signs on the right-hand side are for the ferromagnetic (+) or the antiferromagnetic (−) cases.

If the decorating spins are random variables, however, H_b will be a random function, since it depends on the kind of decorating spin on the bond. In that case the previous results are not valid any more. The approach proposed in this paper is to substitute Eq. (2) by

$$A\,\exp(K_{\text{eff}}\sigma\sigma')=\operatorname{Tr}'_{\{S\}}\exp(-\beta\langle H_b\rangle), \tag{6}$$

where $\langle H_b\rangle$ is the average functional form of H_b and Tr′ is a restrict trace that is to be taken on the appropriate spin variable. The remaining formalism is exactly as before, making use of the exact Onsager solution.

III. THE MODEL

We consider an antiferromagnetic Ising $\sigma=\pm 1$ square lattice with nearest neighbor exchange interaction J_A, and with all the bonds decorated with spins $S=S_1=\pm 1;0$ with probability p or $S=S_2=\pm 1$ with probability $1-p$. For each kind of decorating spin the bond Hamiltonian is given by

$$H_b^1=-J_A\sigma\sigma'-JS_1(\sigma+\sigma')-DS_1^2 \tag{7}$$

or

$$H_b^2=-J_A\sigma\sigma'-JS_2(\sigma+\sigma'), \tag{8}$$

where J is a ferromagnetic exchange constant and D is a single ion anisotropy field. The functional probability distribution for the Hamiltonian is, in this case,

$$P(H_b)=p\,\delta(H_b-H_b^1)+(1-p)\,\delta(H_b-H_b^2), \tag{9}$$

where $\delta(x-a)$ is the function delta of Dirac. Thus, we have for the average form of H_b,

 0021-8979/94/75(10)/5838/3/$6.00 © 1994 American Institute of Physics

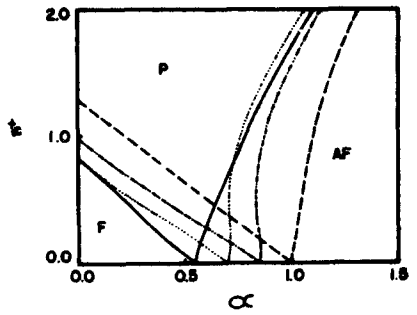

FIG. 1. Phase diagram on the $(t_c-\alpha)$ plane for $\delta=-1.0$. (- - -) $p=0.0$; (- · · -) $p=0.3$; (···) $p=0.6$; (—) $p=0.9$.

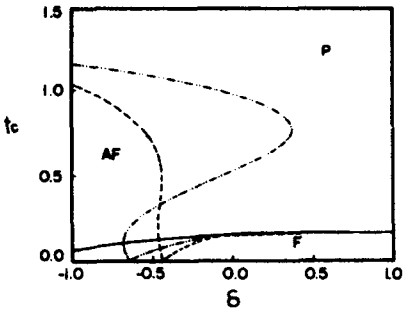

FIG. 3. Phase diagram on the $(t_c-\delta)$ plane for $\alpha=0.8$. (—) $p=0.3$; (- · · -) $p=0.6$; (- - -) $p=0.9$.

$$\langle H_b\rangle = pH_b^1 + (1-p)H_b^2, \tag{10}$$

so that Eq. (6) becomes

$$A\exp(K_{\text{eff}}\sigma\sigma') = \operatorname{Tr}_{\{S_1\}}\exp(-\beta pH_b^1)\operatorname{Tr}_{\{S_2\}} \times \exp[-\beta(1-p)H_b^2], \tag{11}$$

after performing the traces, we finally obtain

$$K_{\text{eff}} = -\alpha K + \tfrac{1}{2}\ln(X/Y), \tag{12}$$

with

$$X = \cosh[2K(1-p)][1+2\exp(p\ \delta K)\cosh 2pK], \tag{13}$$

$$Y = 1+2\exp(p\ \delta K), \tag{14}$$

where $\alpha=-J_A/J$, $\delta=D/J$, and $K=\beta J$.

It is now a matter of little algebra to get the analytic expressions for the critical transition lines, connecting the parameters of the model:

$$\alpha(K_c,p,\delta) = (1/2K_c)\ln[(X/Y)(\sqrt{2}\pm 1)] \tag{15}$$

$$\delta(K_c,p,\alpha) = (1/pK_c)\ln[\tfrac{1}{2}(X_1/Y_1)], \tag{16}$$

where

$$X_1 = \exp(2\alpha K_c) - \cosh[2K_c(1-p)](\sqrt{2}\pm 1), \tag{17}$$

$$Y_1 = \cosh(2pK_c)\cosh[2K_c(1-p)](\sqrt{2}\pm 1) - \exp(2\alpha K_c), \tag{18}$$

where $K_c=J/k_BT_c$ and the signs are (+) for the antiferromagnetic transition line and (−) for the ferromagnetic one. It is not possible to obtain analytically the expression for $p(K_c,\alpha,\delta)$ except for the ground state, and so this must be obtained numerically.

IV. RESULTS AND CONCLUSIONS

In Fig. 1 we show the phase diagram on the $(t_c=1/K_c-\alpha)$ plane for different values of p and for $\delta=-1.0$. We notice the existence of a ferromagnetic (F), an antiferromagnetic (AF), and a paramagnetic (P) phase, and the existence of a multiphase point in the ground state, where the three phases coexist. The multiphase point is given by the equation $\alpha=1+p\delta/2$, for $0>\delta>-2/p$, $\alpha=0$ for $\delta<-2/p$, and $\alpha=1$ for $\delta>0$. As p increases from zero, the antiferromagnetic ground state becomes more stable, and we see the appearance of a reentrance. This is in accord with Ueno's[6] hypothesis that the ordered phase appears as one increases the temperature by lessening the free energy due to

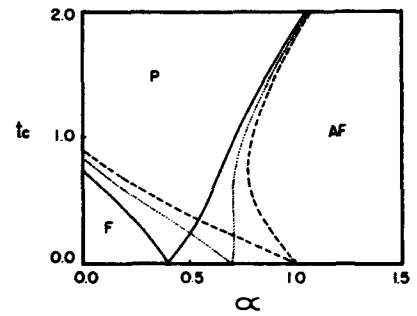

FIG. 2. Phase diagram on the $(t_c-\alpha)$ plane for $p=0.6$. (- - -) $\delta=0.0$; (···) $\delta=-1.0$; (—) $\delta=-2.0$.

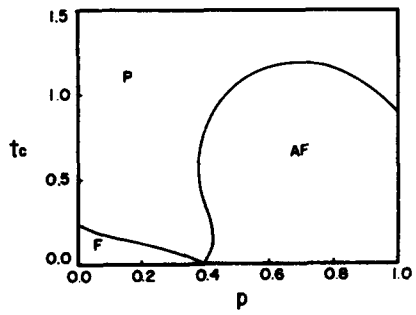

FIG. 4. Phase diagram on the (t_c-p) plane for $\alpha=0.8$ and $\delta=-1.0$.

entropy gains. This is clearly so, since increasing p means to increase the number of states of the decorating spin variable. However, as one also notices from Fig. 1, a further increase of p eliminates the reentrance and makes the antiferromagnetic phase less stable at high temperatures. This can be explained by the fact that although the number of spins states increases with p, the number of possible lattice configurations of random decorated bonds decreases with p as one gets closer to saturation. Figures 2, 3, and 4 show typical aspects of the phase diagram on the $(t_c-\alpha)$, $(t_c-\delta)$, and (t_c-p) planes for a fixed value of p and different values of δ, a fixed value of α, and different values of p and fixed values of α and δ, respectively.

In conclusion, we have introduced a new approach to study random quenched decorated models, which preserves the use of the exact solution of the partition function of the host lattice, by making an approximation on the decoration transformation equations. The present method may be applied to also study any kind of random distribution of the parameters of the decorating system. This is presently under investigation.

ACKNOWLEDGMENTS

One of us (RJVS) acknowledges Dr. F. C. Sá Barreto for clarifying discussions on the present approach. This work was partially supported by CNPq and FAPEAL (Brasilian Agencies).

[1] I. Syozi, Prog. Theor. Phys. **6**, 306 (1951).
[2] R. J. Vasconcelos dos Santos, I. P. Fittipaldi, P. Alstrøm, and H. E. Stanley, Phys. Rev. B **40**, 4522 (1989).
[3] I. P. Fittipaldi, J. R. de Souza, and R. J. Vasconcelos dos Santos, J. Magn. Magn. Mat. **104–107**, 279 (1992).
[4] S. Coutinho, F. C. Sá Barreto, and R. J. Vasconcelos dos Santos, Physica A **96**, 461 (1993).
[5] L. Onsager, Phys. Rev. **65**, 117 (1944).
[6] Y. Ueno, J. Phys. Soc. Jpn. **55**, 2586 (1986).

Phase diagrams of diluted ferromagnetic Ising films in a transverse field

J. C. Cressoni
Departmento de Fisica, Universidade Federal de Alagoas, 57072-340 Maceio, Brazil

J. W. Tucker
Department of Physics, The University of Sheffield, Sheffield S3 7RH, United Kingdom

E. F. Sarmento
Departmento de Fisica, Universidade Federal de Alagoas, 57072-340 Maceio, Brazil

An effective-field theory that accounts for the self-spin correlation function is used to study the effect of surface dilution on the critical behavior of a ferromagnetic Ising film in transverse surface and bulk fields. Surface exchange enhancement (or reduction) is considered. It is shown that the surface and bulk fields affect the critical ratio of surface to bulk interactions, at which the surface orders before the bulk, in opposite ways. Although it is found that for the undiluted film this leads to a critical ratio that is practically insensitive to field for common bulk and surface field strengths, this feature is relaxed to a certain degree with surface dilution. The thickness dependence of the critical temperature, and phase diagrams in the fields, interaction strength ratio, and dilution parameter space, are presented.

I. INTRODUCTION

The development of the molecular-beam-epitaxy technique and its application to the growth of thin metallic films has stimulated renewed interest in both experimental and theoretical thin-film magnetism. Part of this theoretical activity has been devoted to the study of Ising thin films. Among the more recent investigations has been the study of thin magnetic films having enhanced (or reduced) surface exchange, both by mean-field theory[1,2] and within an effective field treatment that accounts for the self-spin correlations.[3,4] Both the thickness dependence of the critical temperature[1–4] and the magnetization profiles[4] have been studied. More recently, the influence of surface and bulk transverse fields on the critical behavior of Ising thin films has been studied in depth by Sarmento and Tucker.[5] Other studies on this problem have been reported[6,7] but only for the situation where the surface and bulk transverse fields are equal.

In real situations, the film surfaces are unlikely to be regular on an atomic scale. It is therefore of interest to study the influences of surface irregularities on the magnetic properties. In this article we examine one such aspect, namely, the influence of surface dilution on the critical behavior. A limited study of the effects of this dilution has already been made in Ref. 3 for an Ising film, but only in the absence of transverse fields. However, even for that situation our results are new because we have treated the configurational averaging of the surface disorder in an improved way.

II. MODEL AND FORMULATION

The system to be treated is an Ising magnetic film having a simple cubic structure with L atomic layers in the z direction, similar to that studied in Ref. 5, but with the addition of surface dilution. The modified Hamiltonian is

$$H=-\frac{1}{2}\sum_{i,j} J_{ij}\xi_i\xi_j S_i^z S_j^z-\sum_i \Omega_i\xi_i S_i^x, \tag{1}$$

where ξ_i is a site occupancy number that is 1 or 0 depending whether the site is occupied or not. Thus, since only the surface is diluted, $\xi_i=1$ or 0 when i refers to a surface site, and unity for the bulk. J_{ij} is the nearest-neighbor exchange interaction between spins at sites i and j, that takes the value J_s if both spins lie on the surface of the thin film and J_b otherwise. $\Omega_i=\Omega_b$ and Ω_s represent transverse fields in the bulk and on the surface of the film, respectively.

The method we use is the single-site cluster theory, fully described in Ref. 5, that employed the differential operator technique and the Van der Waerden identities to account for the single-site spin correlations. Following that procedure, we find in the current situation that for a fixed configuration of surface atoms the thermal average $\langle\sigma_i^z\rangle\equiv 2\langle S_i^z\rangle$ is given by

$$\langle\sigma_i^z\rangle=\xi_i\prod_j [1-\xi_j+\xi_j\cosh(J_{ij}\nabla) + \xi_j\langle\sigma_j^z\rangle\sinh(J_{ij}\nabla)]f_i(x)|_{x\to 0}, \tag{2}$$

where

$$f_i(x)=\frac{x}{[x^2+4\Omega_i^2]^{1/2}}\tanh\left(\frac{\beta}{4}(x^2+4\Omega_i^2)^{1/2}\right), \tag{3}$$

and $\nabla\equiv\partial/\partial x$. In deriving this result, use of the identity $\exp(\lambda\xi_j)=1-\xi_j+\xi_j\exp(\lambda)$ has been made, and the multispin correlation functions decoupled in the Zernike-type approximation, as used in Ref. 5.

The next step is to carry out the spatial configurational averaging, to be denoted by $\langle\cdots\rangle_r$. To make progress, the simplest approximation as used for the thermal averaging of neglecting the correlations between quantities pertaining to different sites will be made. That is,

$$\langle X_iX_jX_k\cdots\rangle_r=\langle X_i\rangle_r\langle X_j\rangle_r\langle X_k\rangle_r\cdots,$$

whence it follows that

$$m_i\equiv\langle\langle\sigma_i^z\rangle\rangle_r=\langle\xi_i\rangle_r\prod_j [1-\langle\xi_j\rangle_r+\langle\xi_j\rangle_r\cosh(J_{ij}\nabla) + m_j^z\sinh(J_{ij}\nabla)]f_i(x)|_{x\to 0}, \tag{4}$$

 0021-8979/94/75(10)/5841/3/$6.00 © 1994 American Institute of Physics

where $\langle \xi_i \rangle_r$ is unity when i refers to a bulk site, and is equal to the surface atom concentration p for a surface site. The improvement between the configuration averaging adopted here and that employed by some other authors (including Hai and Li) has been fully discussed by one of us in Ref. 8. The essential point is that the method we use includes correlations between the spatial disorder and the local ...nfigurational-dependent thermal averages of the spin ...iables—in particular, the exact identity $\langle\langle \xi_i \sigma_i \rangle\rangle_r = \langle\langle \sigma_i \rangle\rangle_r$ ...satisfied.

III. PHASE DIAGRAMS

Allowing for the site magnetizations to take different values in each atomic layer parallel to the surface of the film, and labeling them in accordance with the layer number in which they are situated, the application of Eq. (4) to the film in question leads to the following set of equations:

$$m_1 = p(p\alpha_s + m_1\beta_s + 1 - p)^4(\alpha_b + m_2\beta_b) f_s(x)|_{x\to 0}, \tag{5}$$

$$m_2 = p(p\alpha_b + m_1\beta_b + 1 - p)(\alpha_b + m_2\beta_b)^4 \times (\alpha_b + m_3\beta_b) f_b(x)|_{x\to 0}, \tag{6}$$

$$m_\nu = (\alpha_b + \beta_b m_{\nu-1})(\alpha_b + \beta_b m_\nu)^4 \times (\alpha_b + \beta_b m_{\nu+1}) f_b(x)|_{x\to 0} \quad \text{for } \nu = 3, \ldots L-2, \tag{7}$$

$$m_{L-1} = (\alpha_b + m_{L-2}\beta_b)(\alpha_b + m_{L-1}\beta_b)^4 \times [p(p\alpha_b + m_L\beta_b + 1 - p)] f_b(x)|_{x\to 0}, \tag{8}$$

$$m_L = (\alpha_b + m_{L-1}\beta_b)[p(p\alpha_s + m_L\beta_s + 1 - p)^4] f_s(x)|_{x\to 0}, \tag{9}$$

where $\alpha_s = \cosh(J_s\nabla)$, $\beta_s = \sinh(J_s\nabla)$, $\alpha_b = \cosh(J_b\nabla)$, and $\beta_b = \sinh(J_b\nabla)$. It is noted that the concentration dependence in these equations is different from that reported earlier by Hai and Li[3] because of our use of the improved decoupling procedure in the configurational averaging alluded to above. Linearization of these equations for small m_i leads to the following $L \times L$ determinant:

$$|\mathbf{M}| = \begin{vmatrix} a & -1 & & & & & \\ c & b & -1 & & & & \\ & -1 & d & -1 & & & \\ \cdots & \cdots & \cdots & \cdots & \cdots & \cdots & \cdots \\ & & -1 & d & -1 & & \\ \cdots & \cdots & \cdots & \cdots & \cdots & \cdots & \cdots \\ & & & -1 & d & -1 & \\ & & & & -1 & b & c \\ & & & & & -1 & a \end{vmatrix}_L , \tag{10}$$

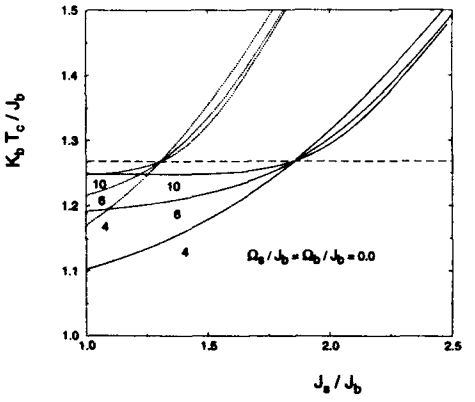

FIG. 1. Variation of the critical temperature with surface exchange enhancement for a surface dilution of $p = 0.8$ (solid curves). The dotted curves refer to the undiluted film. The number accompanying each curve denotes the film thickness L. The broken line is the infinite bulk transition temperature.

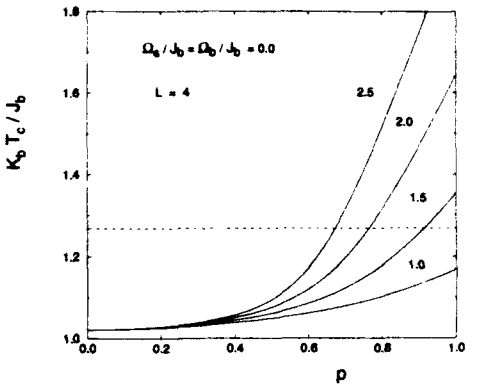

FIG. 2. Variation of the critical temperature with surface dilution. The broken line is the infinite bulk transition temperature. The numbers accompanying each curve denote the value of J_s/J_b.

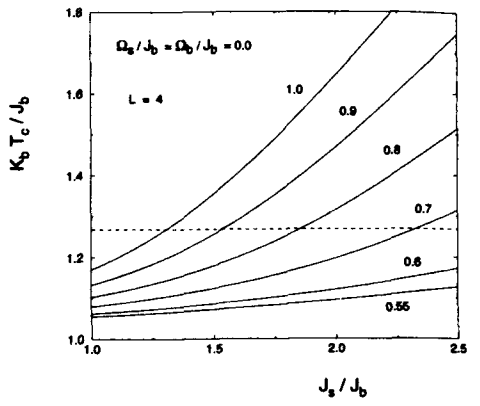

FIG. 3. Variation of the critical temperature with surface exchange enhancement. The number accompanying each curve is the value of p. The broken line is the infinite bulk transition temperature.

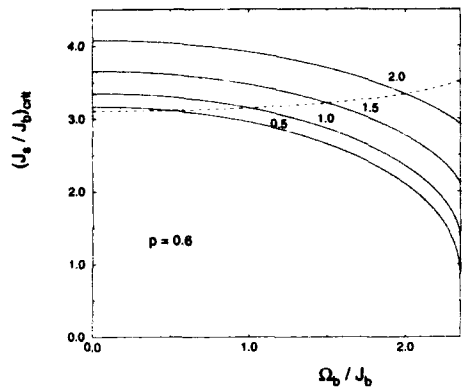

FIG. 4. Variation of $(J_s/J_b)_{crit}$ with the bulk transverse field strength. The number accompanying each curve denotes the value of Ω_s/J_b. The broken line is the locus $\Omega_b=\Omega_s$.

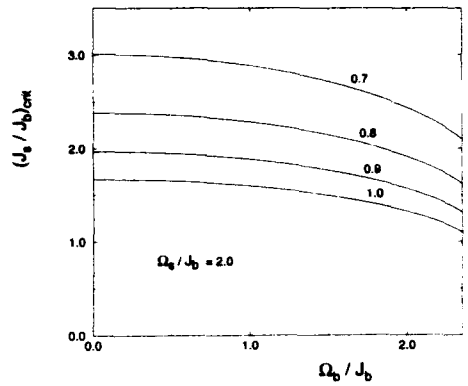

FIG. 5. Variation of $(J_s/J_b)_{crit}$ with the bulk transverse field strength. The number accompanying each curve denotes the value of p.

whose elements are

$$a=(1-X_1)/X_2, \quad b=(1-4X_3)/X_3,$$
$$c=-X_4/X_3, \quad d=(1-4K_1)/K_1, \tag{11}$$

with

$$X_1=4p^4A_1+12p^3(1-p)A_2+12p^2(1-p)^2A_3 + 4p(1-p)^3A_4,$$
$$X_2=p^5A_5+4p^4(1-p)A_6+6p^3(1-p)^2A_7+4p^2(1-p)^3A_8 + p(1-p)^4A_9,$$
$$X_3=pK_1+(1-p)K_2, \quad X_4=K_1, \tag{12}$$

and

$$A_1=\alpha_s^3\alpha_b\beta_s f_s(x)|_{x\to 0}, \quad A_2=\alpha_s^2\alpha_b\beta_s f_s(x)|_{x\to 0},$$
$$A_3=\alpha_s\alpha_b\beta_s f_s|_{x\to 0}, \quad A_4=\alpha_b\beta_s f_s(x)|_{x\to 0},$$
$$A_5=\alpha_s^4\beta_b f_s(x)|_{x\to 0}, \quad A_6=\alpha_s^3\beta_b f_s(x)|_{x\to 0},$$
$$A_7=\alpha_s^2\beta_b f_s(x)|_{x\to 0}, \quad A_8=\alpha_s\beta_b f_s(x)|_{x\to 0}, \tag{13}$$
$$A_9=\beta_b f_s(x)|_{x\to 0},$$
$$K_1=\alpha_b^5\beta_b f_b(x)|_{x\to 0}, \quad K_2=\alpha_b^4\beta_b f_b(x)|_{x\to 0}.$$

The phase transition temperature T_c in (J_i,L,p,Ω_i) parameter space is derived from the highest eigenvalue of $|\mathbf{M}|=0$, which can be put into a more convenient form for computation by use of appropriate reduction formulas, as in Ref. 5.

To illustrate how the thickness dependence of the critical temperature varies with surface dilution, we present in Fig. 1 our results for $p=0.8$. Comparison with the pure case (Fig. 1 of Ref. 5) shows that, as expected, the critical temperature falls with dilution, the fall being greater the thinner the film. This variation of the critical temperature with concentration is shown more clearly in Fig. 2 for a four-layer film. For large dilutions T_c tends to a value independent of the surface exchange enhancement. Figure 1 also shows that the critical ratio of the surface to bulk exchange, at which the surface orders before the bulk, moves to a higher value with dilution of the surface. This variation is shown more comprehensively in Fig. 3 for the case $L=4$.

Whereas, in Ref. 5, it was observed that the surface and bulk fields act on $(J_s/J_b)_{crit}$ in opposite ways such that in the presence of a common field strength $(\Omega_s=\Omega_b)$ the crossover value of T_c for films of different thicknesses is almost insensitive to Ω, this feature is relaxed to a certain extent with surface dilution, as can be seen in Fig. 4 for the case when $p=0.6$. As the minimum value of $(J_s/J_b)_{crit}$ is reached when the infinite bulk transition temperature is reduced to zero, this occurs at a value of Ω_b (right-hand extremity of Figs. 4 and 5) independent of surface concentration. The value of this minimum will, of course, depend on the surface dilution, as can be seen in Fig. 5.

[1] Q. Hong, Phys. Rev. B **41**, 9621 (1990).
[2] F. Aguilera-Granja and J. L. Morán-López, Solid State Commun. **74**, 155 (1990).
[3] T. Hai and Z. Y. Li, Phys. Status Solidi B **156**, 641 (1989).
[4] G. Wiatrowski, J. Mielnicki, and T. Balcerzak, Phys. Status Solidi B **164**, 299 (1991).
[5] E. F. Sarmento and J. W. Tucker, J. Magn. Magn. Mater. **118**, 133 (1993).
[6] X.-Z. Wang, X.-Y. Jiao, and J.-J. Wang, J. Phys. Condensed Matter **4**, 3651 (1992).
[7] X.-Z. Wang and Y. Zhao, Physica A **193**, 133 (1993).
[8] J. W. Tucker, J. Magn. Magn. Mater. **102**, 144 (1991).

Relaxation dynamics in a reentrant (FeNi)Mn ferromagnet: A percolation analysis

D. Li, R. M. Roshko, and G. Yang
Department of Physics, University of Manitoba, Winnipeg, Manitoba, Canada R3T 2N2

Measurements of the low-field thermoremanent relaxation in a reentrant $(Fe_{0.65}Ni_{0.35})_{1-x}Mn_x$ ferromagnet with $x=0.117$ reveal a crossover, in the vicinity of the reentrant transition, from equilibrium dynamics in the ferromagnetic phase to age-dependent, nonequilibrium dynamics in the reentrant phase. Least-squares fits to two mesoscopically exact relaxation functions show that both dynamic regimes can be described within a common theoretical framework of magnon relaxation on a percolation distribution of fixed, finite domains of dynamically correlated spins.

I. INTRODUCTION

The relaxation dynamics of "glassy" systems continues to be the focus of intense theoretical and experimental effort. Materials as diverse as ordinary glass, amorphous polymers, random magnets, and dielectrics all exhibit anomalously slow relaxation[1] in response to a sudden change in a system variable, and some, most notably spin glasses and polymers, show an age-dependent behavior indicative of nonequilibrium dynamics. While the ubiquitous stretched exponential $q(t)\sim\exp[-(t/\tau)^{\beta}]$ has emerged as probably the best two-parameter, empirical description of a wide range of glassy materials, systematic deviations indicate that its applicability may be limited to a particular regime of observation times. Furthermore, neither the stretched exponential representation, nor any other class of empirical functions (such as logarithm, simple power law, "enhanced" power law, power-law stretched exponential product) appears to be universal, and all lack a sound microscopic basis.

Recently, Chamberlin and Haines have proposed a phenomenological model[2] of relaxation dynamics in random systems which, although not a microscopic theory, may nevertheless provide the physical basis for the prevalence of this anomalous behavior. The model describes the relaxation of isotropic, low-energy dispersive excitations (magnons) within a fixed distribution of finite, dynamically correlated clusters of spins (domains). Each cluster relaxes independently with a relaxation rate which is assumed to vary exponentially with inverse cluster size s as $\omega_s\sim\exp(C/s)$, which is a characteristic of finite-size quantization of elementary excitations. Percolation theory[3] provides the distribution of cluster sizes, $n_s\sim s^{-\theta}\exp(-s^{\delta})$ with $\theta=-1/9$ and $\delta=2/3$, which, when combined with the exponential decay typical of thermally activated dynamics, yields two mesoscopically exact relaxation functions,

$$M_{\pm}(t)=M_i\int_0^{\infty}x^{10/9}\exp(-x^{2/3})\exp(-t\omega_{\infty}^{\pm}e^{\pm C/x})dx, \quad (1)$$

for domains aligned $(-)$ or antialigned $(+)$ with the applied field, where $\omega_{\infty}^{\pm}$ is the relaxation rate of an infinite cluster. Thus, this model transcends the details of specific systems while offering a common link to fundamental excitations.

In this article the predictions of this percolation theory are compared with measurements of the low-field thermoremanent relaxation on a reentrant $(Fe_{0.65}Ni_{0.35})_{1-x}Mn_x$ ferromagnet, with $x=0.117$. This system is shown to exhibit a dynamic crossover between a high-temperature regime of equilibrium dynamics and a low-temperature regime of age-dependent, nonequilibrium dynamics, and fits to the model relaxation functions (1) indicate that this behavior may be related to a change from aligned to antialigned cluster dominance.

II. EXPERIMENTAL DETAILS

An alloy of $(Fe_{0.65}Ni_{0.35})_{1-x}Mn_x$ with $x=0.117$ was fabricated by mixing appropriate amounts of 99.999% pure Fe (Johnson-Matthey Chemicals), 99.99% pure Ni (Johnson-Matthey), and 99.98% pure Mn flake (Aldrich Chemical Co.) on the water-cooled copper hearth of a titanium-gettered argon arc furnace, using a tungsten electrode. The ingot was repeatedly inverted and remelted in order to achieve a homogeneous consistency. The ingot was cold rolled into a thin sheet, and a long, needle-shaped sample with dimensions $8.14\times0.36\times0.24$ mm^3 was spark cut from the sheet. The sample was encapsulated in a quartz tube under a partial pressure of argon gas, annealed for 4 days at 920 °C, and then quenched rapidly into water. The magnetization and viscosity measurements were performed with a variable-temperature, variable-frequency superconducting quantum interference device susceptometer described in detail elsewhere in the literature.[4]

III. ANALYSIS AND DISCUSSION

Figure 1 shows the temperature dependence of the static magnetization of the $(Fe_{0.65}Ni_{0.35})_{0.883}Mn_{0.117}$ sample, measured under both field-cooled (FC) and zero-field-cooled (ZFC) conditions in an applied field $H_a=1.0$ Oe. The profile is consistent with that observed in other studies of similar compositions,[5] and with the magnetic phase diagram,[6] which predicts a Curie temperature $T_c\cong170$ K and a reentrant temperature $T_R\cong70$ K for this alloy. For all temperatures $T<170$ K, $M_{FC}(T)>M_{ZFC}(T)$, indicating significant irreversibility everywhere below T_c.

Figures 2 and 3 summarize the essential features of the thermoremanent relaxation at several representative measurement temperatures T_m, and for various wait times t_w. The isotherms were obtained by cooling the sample in a field $H_c=5.0$ Oe from a reference temperature $T_{ref}=170$ K, where relaxation effects were negligible, to the measurement

 0021-8979/94/75(10)/5844/3/$6.00 © 1994 American Institute of Physics

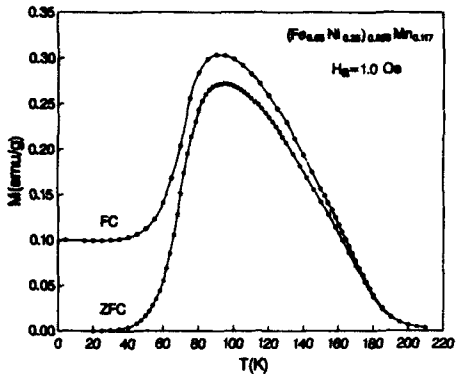

FIG. 1. Temperature dependence of the field-cooled (FC) and zero-field-cooled (ZFC) static magnetization of $(Fe_{0.65}Ni_{0.35})_{0.883}Mn_{0.117}$ measured in $H_a = 1.0$ Oe.

temperature T_m (cooling times were typically $t_c \cong 900$ s), aging the system for a time t_w at a constant temperature T_m, and then abruptly reducing the field to zero and recording the decay over an observation time interval 2 s$\leq t \leq 10^4$ s. The system possesses two distinct thermal relaxation regimes.

(a) One is a high-temperature regime of equilibrium dynamics, for $T_m \geq 65$ K, which corresponds closely with the ferromagnetic phase, where the curvature of the isotherms is uniformly concave up (see the $T_m = 70$ and 85 K isotherms in Fig. 3), and where there is no measurable dependence on

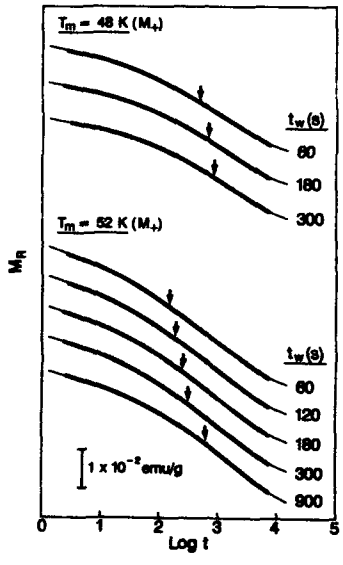

FIG. 2. Thermoremanent relaxation at $T_m = 48$ and 52 K for various wait times t_w. The solid curves are best fits and the vertical arrows mark the average relaxation times $\tilde{\tau}_+$.

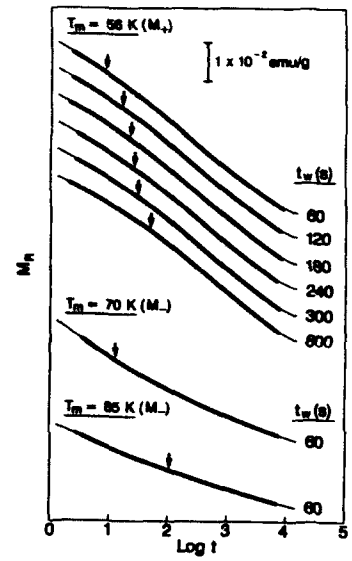

FIG. 3. Thermoremanent relaxation at $T_m = 56$, 70, and 85 K for various wait times t_w. The solid curves are best fits and the vertical arrows mark the average relaxation times $\tilde{\tau}_+$ and $\tilde{\tau}_-$.

system age, for all wait times $t_w \leq 10^4$ s. The simplest empirical description of these "ferromagnetic" isotherms consists of the superposition of a weak power law and a constant, $M_R(t) = M_0 + M_i t^{-m}$, with $m \cong 0.06$.

(b) The other is a low-temperature regime of nonequilibrium dynamics, for $T_m \leq 60$ K, which is essentially coincident with the reentrant phase, where the isotherms exhibit a crossover from positive to negative curvature, through an age-dependent inflection point which propagates systematically toward longer observation times with increasing wait time t_w (see the $T_m = 48$, 52, and 56 K isotherms in Figs. 2 and 3). The shape of these "reentrant" isotherms is replicated with considerable accuracy by the empirical superposition of a stretched exponential and a constant, $M_R(t) = M_0 + M_i \exp(-t/\tau)^{1-n}$, with values of n and τ typical of pure spin glasses.

Since weak power-law decay is a characteristic of "good" random ferromagnets such as $Pd_{0.986}Fe_{0.014}$,[7] which has ideal critical exponents and no reentrant phase, while age-dependent, stretched exponential dynamics is one of the defining features of the spin-glass state, a thermally driven crossover from equilibrium to nonequilibrium behavior of the type described above is clearly consistent with a physical picture of orientational collapse from parallel to random spin alignment below $T \cong 60-65$ K. However, the physical mechanism underlying the dynamic response is not well understood in either regime, and while phenomenological models[8,9] of domain growth, pinned to the disorder and limited by an overlap length scale, are able to simulate much of the experimental systematics in the spin-glass/reentrant

TABLE I. Best-fit parameters to $M_-(t)+M_0$.

T_m (K)	t_w (s)	M_0 (10^{-3} emu/g)	M_i (10^{-3} emu/g)	ω_∞^- (s^{-1})	C
70	60	57.1±0.8	27.9±1.7	$(4.6\pm1.0)\times10^4$	61.7±0.3
85	60	65.7±1.2	20.2±1.4	$(1.2\pm0.5)\times10^4$	79.1±1.8

TABLE II. Best-fit parameters to $M_+(t)+M_0$.

T_m (K)	t_w (s)	M_0 (10^{-3} emu/g)	M_i (10^{-3} emu/g)	ω_∞^+ (s^{-1})	C
48	60	113.5 ± 0.1	10.6 ± 0.1	$(21.6 \pm 0.5) \times 10^{-6}$	25.7 ± 0.1
48	180	113.6 ± 0.1	9.8 ± 0.1	$(26.5 \pm 0.5) \times 10^{-6}$	22.8 ± 0.1
48	300	114.2 ± 0.1	9.6 ± 0.1	$(24.9 \pm 0.5) \times 10^{-6}$	21.8 ± 0.1
52	60	103.7 ± 0.1	16.2 ± 0.1	$(12.6 \pm 0.3) \times 10^{-6}$	35.4 ± 0.2
52	120	102.4 ± 0.1	15.6 ± 0.1	$(14.5 \pm 0.3) \times 10^{-6}$	33.2 ± 0.2
52	180	103.8 ± 0.1	15.0 ± 0.1	$(15.3 \pm 0.3) \times 10^{-6}$	31.5 ± 0.1
52	300	104.0 ± 0.1	14.5 ± 0.1	$(16.2 \pm 0.3) \times 10^{-6}$	29.9 ± 0.1
52	900	104.1 ± 0.1	13.6 ± 0.1	$(13.9 \pm 0.3) \times 10^{-6}$	26.9 ± 0.1
56	60	93.2 ± 0.1	27.4 ± 0.1	$(3.09 \pm 0.09) \times 10^{-6}$	59.4 ± 0.3
56	120	92.2 ± 0.1	25.4 ± 0.1	$(3.93 \pm 0.11) \times 10^{-6}$	54.5 ± 0.3
56	180	95.3 ± 0.1	24.7 ± 0.1	$(4.14 \pm 0.10) \times 10^{-6}$	52.4 ± 0.2
56	240	92.5 ± 0.1	23.7 ± 0.1	$(5.28 \pm 0.14) \times 10^{-6}$	50.1 ± 0.2
56	300	92.5 ± 0.1	23.7 ± 0.1	$(4.71 \pm 0.12) \times 10^{-6}$	49.8 ± 0.2
56	600	92.5 ± 0.1	22.6 ± 0.1	$(4.46 \pm 0.12) \times 10^{-6}$	47.5 ± 0.2

phase, the specific analytical forms predicted for the decay do not appear to be relevant to real systems. On the other hand, the two mesoscopic relaxation functions in Eq. (1), based on a model of activated dynamics within a percolating system of fixed domains, are able to reproduce both the empirical power law and stretched exponential in appropriate limits,[2] suggesting that many of the apparently diverse relaxation effects in disordered materials may have a common physical origin in quantized dispersive excitations. In fact, least-squares fits of the isotherms in Figs. 2 and 3 to the functions $M_+(t)$ and $M_-(t)$, individually and in superposition, ultimately favored the following representations.

(a) In the high-temperature ferromagnetic phase, the best description was achieved by superposing the aligned function on a constant baseline, $M_-(t)+M_0$, as shown by the solid curves through the $T_m=70$ and 85 K isotherms in Fig. 3, and the vertical arrows mark the characteristic relaxation times of the average-size aligned domains, $\tilde{\tau}_-\equiv[\omega_\infty^- \exp(-C/\tilde{x})]^{-1}$, where $\tilde{x}=(19/6)^{3/2}$. The fits were indistinguishable in quality from the empirical power-law fits, and the best-fit parameters, listed in Table I, satisfy the condition $C\omega_\infty^- t\gg1$, for which $M_-(t)$ reduces to a simple power law.[2]

(b) In the low-temperature, reentrant phase, the most consistent results were obtained with a simple superposition of the antialigned function and a constant baseline, $M_+(t)+M_0$. However, the quality of the fits was clearly dependent on the age of the system: for relatively short wait times ($t_w\leqslant300$ s), the fits were measurably inferior to the stretched exponential fits, but improved systematically with increasing age until, for $t_w>300$ s, the two representations became essentially interchangeable. The solid curves through the $T_m=48$, 52, and 56 K isotherms in Figs. 2 and 3 show the best fits, and the vertical arrows mark the characteristic relaxation times of the average-size antialigned domains $\tilde{\tau}_+\equiv[\omega_\infty^+ \exp(+C/\tilde{x})]^{-1}$. The corresponding fitting parameters in Table II satisfy the condition $C\omega_\infty^+ t\leqslant1$ for $M_+(t)$ to reduce to a stretched exponential.[2]

The preceding analysis shows that the relaxation dynamics of (FeNi)Mn are generally consistent with a model of quantized magnon relaxation within a system of fixed domains (or clusters) of dynamically correlated spins, and that the dynamics in the ferromagnetic phase are dominated by domains which are aligned with field, presumably because the reorientation of antialigned domains on field cooling is relatively unhindered in this phase, while, in the reentrant phase, such reorientation is inhibited, and the decay is due predominantly to slowly relaxing, higher-energy antialigned domains. However, the wait-time dependence of the fits in the reentrant phase may reflect the inadequacy of a single, fixed domain size distribution, due to possible domain growth in the early stages of aging, and the microscopic origins of the aging process have yet to be resolved within this formalism.

ACKNOWLEDGMENT

This work was supported in part by a grant from the Natural Sciences and Engineering Research Council of Canada.

[1] R. G. Palmer, in *Heidelberg Colloquium on Glassy Dynamics*, Proceedings, Heidelberg, 1986 (Springer, Berlin, 1987).
[2] R. V. Chamberlin and D. N. Haines, Phys. Rev. Lett. **65**, 2197 (1990).
[3] T. C. Lubensky and A. J. McKane, J. Phys. A **14**, L157 (1981).
[4] H. P. Kunkel, R. M. Roshko, W. Ruan, and G. Williams, Philos. Mag. B **63**, 1213 (1991).
[5] R. D. Barnard, Ch. Böttger, S. Thamm, and J. Hesse, J. Phys. Condensed Matter **4**, 7219 (1992).
[6] A. Wulfes, Ch. Bottger, J. Hesse, J. Sievert, and H. Ahlers, J. Magn. Magn. Mater. **104-107**, 2069 (1992).
[7] P. D. Mitchler, R. M. Roshko, and W. Ruan, Philos. Mag. B **68**, 539 (1993).
[8] D. S. Fisher and D. A. Huse, Phys. Rev. B **38**, 373 (1988).
[9] G. J. M. Koper and H. J. Hilhorst, J. Phys. (Paris) **49**, 429 (1988).

Spin glasses with cubic anisotropy

Z. Domański, T. K. Kopeć,[a] F. Pázmándi, and P. Erdös
Institute of Theoretical Physics, University of Lausanne, CH-1015 Lausanne, Switzerland

The infinite-range quantum spin glasses with cubic anisotropy (K) are studied using a combination of the imaginary-time representation with the n-replica approach and the thermofield dynamic method. Mean-field theory phase diagrams in the temperature-anisotropy plane (T,K) are presented for quantum spin numbers S ranging from 2 to 9/2. At $T=0$, the ground state is nonmagnetic and the spin-glass order is absent for integer spin and large cubic anisotropy, the sign of which depends on S. For half-integer S and sufficiently low temperatures the spin-glass phase persists for arbitrary K.

In recent years it has been found that many properties of spin glasses are strongly influenced by various types of anisotropies. Examples are anisotropies due to the crystal field of the host[1] or nonmagnetic impurities which affect the spin interaction symmetries.[2]

Experimentally, strong uniaxial anisotropy of the magnetic susceptibility has been observed in a number of hexagonal metallic spin-glass systems.[1,3] From the theoretical point of view, anisotropy brings about several new features which have been investigated for classical spin models with or without a magnetic field, and a multiplicity of phases has been found.[4] The corresponding quantum spin problem can yield results which are qualitatively different from their classical counterparts.[5,6] For example, for large negative uniaxial anisotropy one expects, for integer spins at low temperatures, a condensation in the state resulting in a nonmagnetic spin phase accompanied by the destruction of the spin-glass character.[6]

In the present paper we look at the effect of the single-ion cubic anisotropy on a spin glass. This problem has not been treated extensively in the literature: only a few studies of the spin glass in the presence of cubic anisotropy have been made for the classical[7] and for quantum Ising[8] spin models. We analyze the quantum version of the vector spin-glass model for the spin cases ranging from $S=2$ to $S=9/2$, and present the corresponding phase diagrams.

The Hamiltonian of the model is given by

$$H=-\frac{1}{2}\sum_{i,j=1}^{N}\sum_{m=1}^{d}J_{ij}S_{mi}S_{mj}-K\sum_{i=1}^{N}(S_{xi}^4+S_{yi}^4+S_{zi}^4). \tag{1}$$

Here $\mathbf{S}_i=(S_{xi},S_{yi},S_{zi})$ is the quantum spin operator referring to the ith member of an ensemble of N local moments S. An index $m=1,2,3$ stands for x, y, and z. For $d=1$ we have the Ising model. Cases $d=2$ and $d=3$ correspond to the XY and the Heisenberg models, respectively. The J_{ij} ($J_{ij}=J_{ji}$) are quenched random exchange interactions governed by independent symmetric Gaussian distributions with mean zero and variance $J/\sqrt{N}$. The second term in the Hamiltonian (1) describes the cubic anisotropy field of strength K favoring spin alignment along the edges ($K>0$) or diagonals ($K<0$) of a three-dimensional cube with edges along the respective coordinate axes. The model described by Eq. (1) undergoes a transition between the paramagnetic (P) and the spin-glass (SG) phases as a function of the temperature T and the anisotropy strength K. To our knowledge the boundary between these phases has not been calculated previously even in the classical case. The purpose of this work is to use available approaches from which the phase boundary can be calculated.

We present the results of two alternative investigations of this model. One is the Matsubara imaginary-time representation combined with the n-replica approach and the other is the thermofield dynamic method[9] (a real-time finite-temperature quantum field theory). Here we restrict ourselves to the simplest approximations. Within the Matsubara time formalism we employ the static approximation (SA) which neglects the imaginary time dependence of the so-called dynamic self-interaction of the spins created by the quantum fluctuations. In the latter approach, we derive the results using the instantaneous approximation (IA) for the dynamic self-interaction, i.e., we approximate its real-time part by an instantaneous term.

For both approaches the derivation of the critical line equations follows closely that for the quantum Ising model discussed in detail elsewhere.[8] Here we report only the most important results referring to the location of the phase transition line. Thus, for the spin-glass freezing temperature from the Matsubara time formalism we obtain

$$\left(\prod_m\int_{-\infty}^{+\infty}d\xi_m e^{-\xi_m^2}\right)\times\left(d-\sum_m\xi_m^2\right)\mathrm{Tr}\exp[H_{\mathrm{eff}}^{\mathrm{SA}}(\xi_1,\ldots,\xi_d)]=0. \tag{2}$$

The effective single-ion Hamiltonian is equal to

$$H_{\mathrm{eff}}^{\mathrm{SA}}=\sqrt{2\beta J}\sum_m\xi_m S_m+\beta K(S_x^4+S_y^4+S_z^4),\quad \beta=1/k_BT. \tag{3}$$

In the second approach which relies on the thermofield dynamic method the phase boundary is given by

$$1=J\chi_0, \tag{4}$$

where χ_0 is the local static susceptibility related to the single-site effective Hamiltonian:

[a]Permanent address: Institute for Low Temperature and Structure Research, Polish Academy of Sciences, P.O. Box 937, 50-950 Wrocław 2, Poland.

 0021-8979/94/75(10)/5847/3/$6.00 © 1994 American Institute of Physics

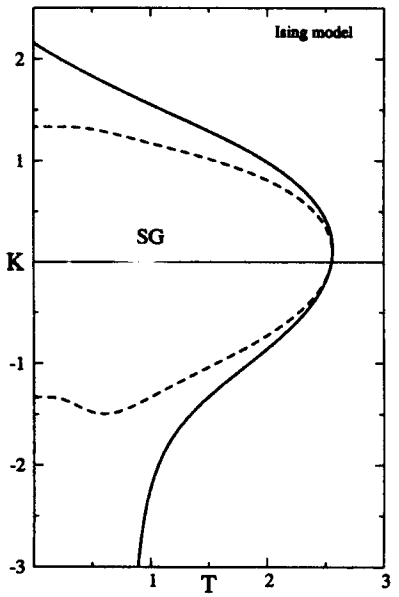

FIG. 1. The anisotropy-temperature phase diagram for the Ising model with $S=2$: imaginary-time approach SA (solid line); thermofield dynamic method IA (broken line). The lines separate the SG phase from the paramagnetic region. T: temperature in units of $J=(\langle J_{ij}^2\rangle \cdot N)^{1/2}$; K: anisotropy in units of J.

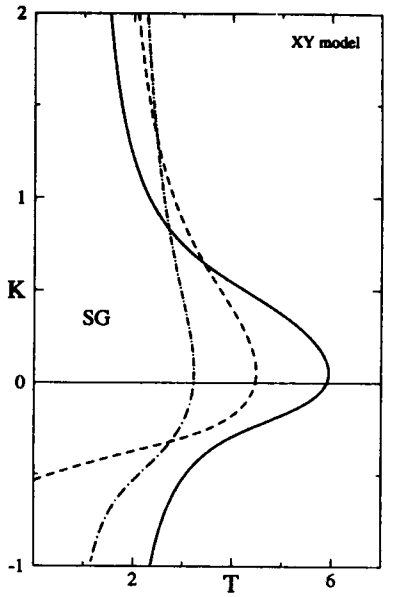

FIG. 2. The anisotropy-temperature phase diagram for the XY model (SA) with $S=5/2$ (dash-dotted line), $S=3$ (dashed line), and $S=7/2$ (solid line). The lines separate the SG phase from the paramagnetic region. Temperature (T) and anisotropy (K) are in units of J.

$$H_{\text{eff}}^{\text{IA}}=-\frac{1}{2}\,J^2\chi_0\sum_m S_m^2-K(S_x^4+S_y^4+S_z^4). \tag{5}$$

We calculated the phase-separation lines for the Ising, the XY, and the Heisenberg models for a few relevant low spin values, i.e., for $2\leqslant S\leqslant 9/2$. A qualitative difference between the imaginary-time static approximation and the thermofield dynamics instantaneous approximation is found for $S=2$ for the Ising and the XY models. For large negative anisotropy ($K<0$) the former method predicts an asymptotic behavior, whereas the latter yields a finite critical value $K_c(T=0)$ (see Fig. 1). For $S>2$ in all models, both approximations used give the same qualitative behavior, although quantitative differences are present. Figures 1–3 show examples of the resulting phase diagrams for the Ising, the XY, and the Heisenberg models. In the models studied for integer spins and sufficiently large anisotropy ($K>0$ for even S and $K<0$ for odd S) the phase transition between the SG and paramagnetic phases occurs at all temperatures. For half-integer S the spin-glass phase persists for arbitrary K.

Similar behavior, though in a different context, was observed in the model described by Eq. (1) when the random long-range interactions J_{ij} were replaced by ferromagnetic short-range ones.[10] In the integer spin case a condensation in the nonmagnetic spin state results, whereas for noninteger spin one observes an asymptotic behavior for negative and positive values of K. It is interesting to note that, in the

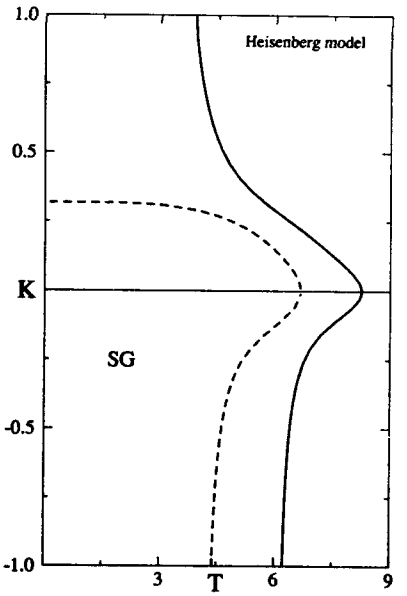

FIG. 3. The anisotropy-temperature phase diagram for the Heisenberg model (IA) with $S=4$ (broken line) and $S=9/2$ (solid line). The lines separate the SG phase from the paramagnetic region. Temperature (T) and anisotropy (K) are in units of J.

systems with integer spins also, uniaxial anisotropy leads to a destruction of the magnetic order. This destruction occurs in the presence of both the long-range (random[6]) as well as the short-range (antiferromagnetic[11]) interactions.

The support of the Swiss National Science Foundation and of the Foundation Herbette is gratefully acknowledged.

[1] S. Murayama, K. Yokosawa, Y. Miyako, and E. F. Wassermann, Phys. Rev. Lett. **57**, 1785 (1986).
[2] P. M. Levy and A. Fert, Phys. Rev. B **23**, 4667 (1981); T. K. Kopeć, *ibid.* **43**, 10853 (1991).
[3] H. Albrecht, E. F. Wassermann, F. T. Hedgcock, and P. Monod, Phys. Rev. Lett. **48**, 819 (1982); A. Fert, P. Pureur, F. Hippert, K. Baberschke, and F. Bruss, Phys. Rev. B **26**, 5300 (1982).
[4] D. J. Elderfield and D. Sherrington, J. Phys. A **15**, L513 (1982); J. Phys. C **15**, 783 (1982); J. Phys. A **15**, L437 (1982); J. Phys. C **16**, 4865 (1983); D. M. Cragg, D. Sherrington, and M. Gabay, Phys. Rev. Lett. **49**, 158 (1982).
[5] G. Brieskorn and K. D. Usadel, J. Phys. C **19**, 3413 (1986); K. D. Usadel, K. Bien, and H.-J. Sommers, Phys. Rev. B **27**, 6957 (1983).
[6] T. K. Kopeć, G. Büttner, and K. D. Usadel, Phys. Rev. B **41**, 9221 (1990); G. Büttner and K. D. Usadel, Europhys. Lett. **14**, 165 (1991).
[7] S. A. Roberts, J. Phys. C **15**, 4155 (1982).
[8] Z. Domański, T. K. Kopeć, and F. Pázmándi, Phys. Rev. B (in press).
[9] H. Umezawa, H. Matsumoto, and M. Tachiki, *Thermo Field Dynamics and Condensed States* (North-Holland, Amsterdam, 1982).
[10] Z. Domański and J. Sznajd, Phys. Status Solidi B **129**, 135 (1985); A. I. Mitsek, K. Yu. Guslienko, and S. V. Pavlovski, *ibid.* **135**, 173 (1986); V. V. Valkov and T. A. Valkova, Theor. mat. Fiz. **59**, 453 (1984).
[11] T. Moriya, Phys. Rev. **117**, 635 (1960).

Macroscopic random magnetic anisotropy constant in crystalline $Dy_xY_{1-x}Al_2$ ($x=0.3$, 0.4)

A. del Moral, M. Ciria, and J. I. Arnaudas
Laboratorio de Magnetismo, Dipartimento Física de Materia Condensada and ICMA, Universidad de Zaragoza and CSIC, 50009 Zaragoza, Spain

J. S. Abell and Y. J.Bi
School of Metallurgy and Materials, University of Birmingham, Birmingham B15 2TT, United Kingdom

Cooling in a weak magnetic field the random magnetic anisotropy (RMA) spin glasses $Dy_xY_{1-x}Al_2$ ($x=0.3$, 0.4) induces unidirectional and uniaxial anisotropies, on top of the cubic coherent one. The unidirectional anisotropy constant K^u_{RMA} has been determined at 3.8 K, amounting at zero applied field 127 and 255 J/m^3 for $x=0.3$ and 0.4, respectively. The predicted model ratio between K^u_{RMA} and the uniaxial constant K^a_{RMA}, i.e., $K^a_{RMA}=2K^u_{RMA}$, has been confirmed. As by-product the relevant RMA parameter D^2/J, where D is the RMA crystal field strength and J, the exchange constant has been determined, as well as separate estimates of D and J.

I. INTRODUCTION AND EXPERIMENTAL DETAILS

The intermetallics $Dy_xY_{1-x}Al_2$ crystallize in the cubic Laves phases structure. Extensive magnetic measurements: low field ac susceptibility,[1,2] low field FC and ZFC magnetizations,[3,4] Arrott plots,[4] hysteresis,[3,5] ferromagnetic-like critical scaling,[3] critical scaling of the nonlinear susceptibility,[1,4] law of magnetization approach to saturation,[3,6] small angle neutron scattering (SANS),[7] observation of Gabay Toulouse transition lines,[4] and Bragg neutron scattering,[8] point out the existence of a weak random magnetic anisotropy (RMA), induced by the yttrium substitution and, in part, of magnetoelastic origin,[3] superposed to the cubic coherent one. The magnetic phase diagram,[1,3,6] encompasses paramagnetic (P), spin glass (SG), correlated spin glass (CSG), random-ferromagnetic (RFM), and ferromagnetic (FM) phases, with a triple point at $x_t=0.31$ and $T_t=5.9$ K. The predicted[9] low-temperature first-order phase transition from CSG to FM, driven by the cubic coherent anisotropy, was observed[6,8] by the first time. Estimates of the RMA crystal field strength parameter D and of the ferromagnetic exchange constant J yield ratios $D/J\sim0.05$.[3] A determination of $(D/J)^2(R_a/a)^3$, where a is the lattice constant and R_a the structural correlation length, shows an increase of $\Delta=(D/J)^2$ with decreasing x.

We have now focused on the determination of the macroscopic field-cooled-induced anisotropy of RMA origin, with the determination of the corresponding anisotropy constant K_{RMA}, the system exhibiting, at the lower fields of measurement ($H\leq0.7$ kOe), both unidirectional and uniaxial RMA origin anisotropies. Most anisotropy measurements up to now have been done either in canonical SG, polycrystalline,[10] or crystalline uniaxial,[11] and where the anisotropy is of Dzialoshinsky–Moriya (DM) type, or in rare earth-transition metal amorphous alloys, where the anisotropy is of RMA character only.[12] In our present $Dy_xY_{1-x}Al_2$ crystals we have the additional complication of the cubic coherent (CC) anisotropy, three orders of magnitude larger than the induced weak of RMA origin, making the determination of the latter considerably more difficult.

Single crystals with Dy concentrations $x=0.3$, 0.4 were grown by the Czochralski technique, the samples being discs, with their base parallel to the (110) plane, containing the ⟨100⟩ easy axis, for the CC anisotropy. The RMA origin easy axis was induced by cooling the samples from the PM phase in the presence of the measuring magnetic field (0.3–20 kOe), down to 3.8 K, both compounds being in the SG regime.[1,3,4] The FC direction was ⟨100⟩, to have the CC and macroscopic RMA easy axes coincident. The magnetic anisotropy was measured from the perpendicular to the field H, magnetization component $M_\perp$, inasmuch as the anisotropy torque is $L_k=M_\perp H$. The sample was rotated within the field and in the (110) plane, and $M_\perp$ recorded versus the angle of rotation Ψ formed by $\mathbf{H}$ with ⟨100⟩ direction. Corrections were made to determine the angle θ formed by the magnetization vector $\mathbf{M}$ with the ⟨100⟩ initial direction. $M_\perp$ was measured using an induction-extraction magnetometer. The magnetic field was accurately monitored with a calibrated Hall probe.

II. OUTLINE OF MODEL OF MACROSCOPIC RMA

Two models have been proposed which predict the existence of unidirectional and uniaxial anisotropy contributions in RMA and DM spin glasses and ferromagnets with RMA. One is the anisotropy triad model of Saslow,[13] the other the model proposed by Henley *et al.*[14] (HSH). We will adhere to the HSH model, with specific application to our problem of weak RMA crystalline systems. We start with the usual RMA Hamiltonian,

$$H=J\sum_{i,j}\sum_{\alpha,\beta}S_i^\alpha S_j^\alpha+D\sum_{i\alpha}(p_i^\alpha S_i^\alpha)^2, \tag{1}$$

where $\hat{p}_i$ are the local RMA easy axis (EA) direction. i,j stand for the sites and α,β for the spin components. We assume uncorrelated EAs, i.e., $(p_i^\alpha p_j^\beta)_{av}=\frac{1}{3}\delta_{ij}\delta_{\alpha,\beta}$, where $(...)_{av}$ stands for the spatial average. In our situation of *weak* RMA (D/J small), in any metastable state of the SG system in zero applied field, spins will try to remain aligned due to the strong exchange, tilting away from the local EAs. Then, from the situation of perfect alignment of spin and EA

 0021-8979/94/75(10)/5850/3/$6.00 © 1994 American Institute of Physics

direction *components*, exchange energy will increase on average, $\Delta E_{ex} = J(S_i^\alpha S_j^\beta - p_i^\alpha p_j^\beta)_{av} = J(S_i^\alpha S_j^\beta - \frac{1}{3}\delta_{ij}\delta_{\alpha\beta})_{av}$. From the point of view of the weak anisotropy, spins will appear perfectly aligned by the strong exchange, so that $(S_i^\alpha S_j^\beta) = \frac{1}{3}\delta_{\alpha\beta}$, the decrease in anisotropy energy being, for a single-ion i,

$$\Delta E_a = -D(\tfrac{1}{3}\delta_{\alpha\beta} - p_i^\alpha p_i^\beta).$$

In equilibrium $\Delta E_{ex} + \Delta E_a = 0$, obtaining $(S_i^\alpha S_j^\beta)_{av} \cong -(D/J)p_i^\alpha p_i^\beta$, which introduced in Eq. (1) yields for the average RMA energy, per spin,

$$E_a^0 = -\frac{D^2}{J}\sum_{i\alpha,\beta}(p_i^\alpha p_i^\beta)(p_i^\alpha p_i^\beta)_s. \tag{2}$$

Performing now a uniform or bodily rigid rotation, $\tilde{R}(\theta)$, of the *spin* system part in Eq. (2), i.e., of $(p_i^\alpha p_i^\beta)_s$, where $\tilde{R}(\theta)$ is the $S03$ matrix, the average anisotropy energy cost becoming from Eq. (2) is

$$\Delta E_{RMA} = \frac{D^2}{J}\sum_{i\alpha,\beta}\{(p_i^\alpha p_i^\beta)[(\tilde{R}p_i)^\alpha(\tilde{R}p_i)^\beta] - (p_i^\alpha p_i^\beta)^2\}. \tag{3}$$

Introducing a reference frame system fixed to the sample and averaging ΔE_{RMA} over the local EA disorder, one obtains a macroscopic anisotropy energy for the metastable state of the form (except for a constant term),

$$E_{an}^{RMA} = -K_{RMA}\cos\theta - 2K_{RMA}\cos^2\theta, \tag{4}$$

where

$$K_{RMA} = \frac{4}{15}N\frac{D^2}{J}, \tag{5}$$

N being the ion number per volume unit. The total anisotropy energy is E_{an}^{RMA} plus the CC one E_{an}^{cc}, the torque acting upon the magnetization vector, $\Gamma_{an} = -[\partial(E_{an}^{RMA} + E_{an}^{cc})/\partial\theta]$, becoming

$$\Gamma_{an}(\theta) = -K_{RMA}(\sin\theta + 2\sin 2\theta) - \left(\frac{K_1}{4} + \frac{K_1}{64}\right)\sin 2\theta$$

$$-\left(\frac{3K_1}{8} + \frac{K_2}{16}\right)\sin 4\theta + \frac{3K_2}{64}\sin 6\theta, \tag{6}$$

where K_1 and K_2 are the CC anisotropy constants. Therefore, the uniaxial RMA torque is contaminated by the CC anisotropy one, one of the main difficulties for the determination of K_{RMA}.

III. EXPERIMENTAL RESULTS AND INTERPRETATION

The CC anisotropy constants K_1 and K_2 are (see below) around three orders of magnitude larger than K_{RMA}. Then, high-field measurements where the sample is likely a single domain are useless to determine K_{RMA}. To perform such a determination we need to average out the CC anisotropy. This has been realized by decreasing the measuring field below a experimentally determined level where the crystal becomes decomposed, in the $H=0$ limit, in six systems of magnetic domains, along ⟨100⟩ directions, giving an average spontaneous magnetization $\langle M_s\rangle = 0$, the only magnetization

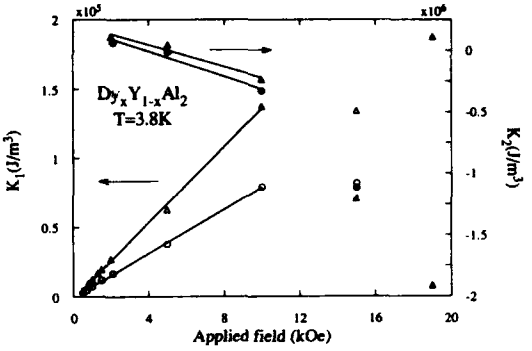

FIG. 1. Field dependence of the cubic anisotropy constants K_1 and K_2 at 3.8 K, for $Dy_{0.3}Y_{0.7}Al_2$ (○,●) and $Dy_{0.4}Y_{0.6}Al_2$ (△,▲).

being the induced thermoremanent one (TRM), due to the RMA. At finite but low enough fields, the magnetization vector will be $\mathbf{M} = \chi\mathbf{H} + \mathbf{M}_r$, where χ is the first-order cubic susceptibility (isotropic) and M_r, the TRM. We have traced $\Gamma_{an}(\theta)$ torques for decreasing fields, between ≅20 and ≅0.25 kOe. In Fig. 1 we present the field dependences of K_1 and K_2 for both compounds, and we can observe how both constants decrease with decreasing field, the RMA torque dominating at low enough fields. At high fields, torque curves show in fact clearly sin 4θ and sin 6θ components (see Fig. 2).

In Fig. 3 we present the measured torques at the fields of measurement $H = 0.30$ and 0.25 kOe for $x = 0.3$ and 0.4, respectively, together with fits including *only* sin θ and sin 2θ components. Notice, for $x = 0.4$, the strong unidirectional character of the torque. The θ dependent torque is superimposed on a constant one, responsible for the rotational "hysteresis" observed when performing a 2π rotation, not considered in Eq. (6). The origin of this torque could be ascribed to a magnetization component rotating in phase with **H**, cast by spins with short relaxation times.

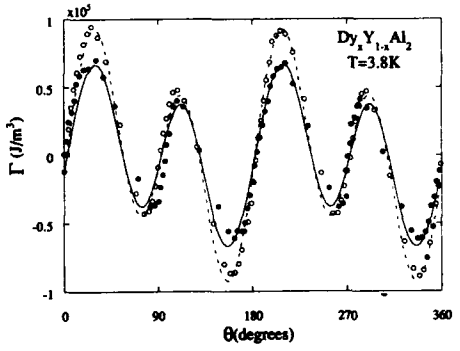

FIG. 2. High-field ($H = 10$ kOe) torques at 3.8 K vs the angle θ of the magnetization vector with the [100] direction and within the (110) plane, for the $x = 0.3$ (●) and $x = 0.4$ (○) compounds. The curves are Fourier fits including sin θ, sin 2θ, sin 4θ, and sin 6θ components. The coefficient of sin θ is irrelevant.

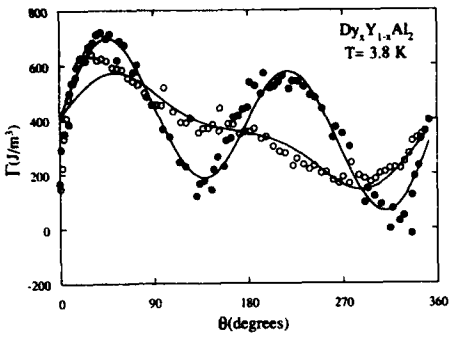

FIG. 3. Same as Fig. 2 with applied field $H=0.25$ kOe. (●) $x=0.3$, (○) $x=0.4$. The curves are the fits with the theoretical torque obtained from Eq. (4). The constant torque background is $\Gamma_0=381$ and 357 J/m^3, for $x=0.3$ and $x=0.4$, respectively.

In Fig. 4 we show the field dependence of K_{RMA} obtained from the sin θ component of Γ_{an}, not contaminated by the CC torque. The linear variation allows to determine, by extrapolation to $H=0$, K_{RMA} at the zero-field spin-glass metastable state. The values so obtained, at $T=3.8$ K, were K_{RMA} $(H=0)=127$ and 255 J/m^3 for $x=0.3$ and $x=0.4$, respectively. We notice that the Fourier coefficient of sin 2θ, Γ_2

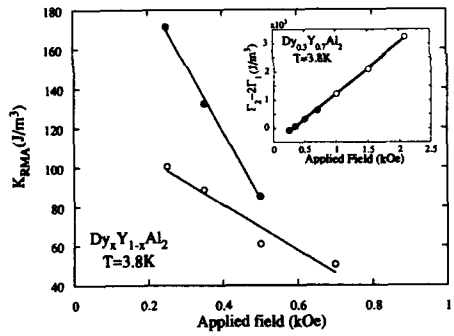

FIG. 4. Field variation of the induced unidirectional anisotropy constant K_{RMA}, at $T=3.8$ K, for $x=0.3$ (●) and $x=0.4$ (○). Insert: Field variation of $(K_1/4+K_2/64)$, at 3.8 K, for $x=0.3$ (○). Difference $(\Gamma_2-2\Gamma_1)$ (●) for the low-field coefficients of sin $\theta(\Gamma_1)$ and sin $2\theta(\Gamma_2)$ according to the model Eq. (6).

was not $\Gamma_2=2\Gamma_1$ [Γ_1 is the coefficient for sin θ as in Eq. (6)] for the RMA contribution. This should be the effect of the CC anisotropy contamination, as demonstrated in the Fig. 4 insert where we plot $(\Gamma_2-2\Gamma_1)$ below ≅0.7 kOe (points ●) and $[(K_1/4)+(K_2/64)]$, determined from the coefficient of the sin 2θ torque component for higher fields (points ○), for $x=0.3$. The merging of both lines probes the point. Therefore the model Eq. (4) for the induced macroscopic RMA origin anisotropy has been plainly confirmed.

Our final task is to determine D^2/J, from the model expression (5), using the $H=0$, K_{RMA} values. We obtain $D^2/J=0.007$ and 0.01 in K, for $x=0.3$ and 0.4, respectively. This parameter is quite relevant inasmuch as it determines the magnon gap δ in weak RMA systems,[6] i.e., $\delta=(2/15)(D^2/J)(R_a/a)^{-1}$. We can also separately estimate the D and J values. It was shown [6] that for $x=0.4$, $D/J\cong 0.045$, assuming $R_a\cong 10a$. Therefore from the D^2/J value we obtain $D\cong 0.23$ K/ion and $J\cong 5.11$ K.

ACKNOWLEDGMENT

We acknowledge the financial help of the Spanish DGICYT through Grants. No. PB90-1014 and No. PB91-0936.

[1] A. del Moral and J. I. Arnaudas, J. Magn. Magn. Mater. **62**, 71 (1986).
[2] A. del Moral, P. M. Gehring, J. I. Arnaudas, and M. B. Salamon, J. Phys. (France), **49** C8-1233 (1988).
[3] P. M. Gehring, M. B. Salamon, A. del Moral, and J. I. Arnaudas, Phys. Rev. B **13**, 9134 (1990).
[4] A. del Moral, P. M. Gehring, and J. I. Arnaudas (unpublished).
[5] J. I. Arnaudas, A. del Moral, and J. S. Abell, J. Magn. Magn. Mater. **61**, 370 (1986).
[6] A. del Moral, J. I. Arnaudas, P. M. Gehring, M. B. Salamon, C. Ritter, E. Joven, and J. Cullen, Phys. Rev. B **47**, 7892 (1993).
[7] A. del Moral, J. I. Arnaudas, M. R. Ibarra, P. A. Algarabel, and J. Schweizer, J. Magn. Magn. Mater. **83**, 160 (1990); A. del Moral, J. I. Arnaudas, P. A. Algarabel, and M. R. Ibarra, *Spanish Science Research using Neutron Scattering Techniques*, edited by J. Gomez-Sal *et al.* (Serv. Pub. Univ. Cantabria, Santander, 1991).
[8] A. del Moral, J. Schweizer, J. I. Arnaudas, M. B. Salamon, C. Ritter, E. Joven, P. M. Gehring, P. A. Algarabel, and J. Cullen, J. Magn. Magn. Mater. **104-107**, 243 (1992).
[9] A. Aharony, Solid State Commun. **28**, 667 (1978); A. Aharony and E. Pytte, Phys. Rev. Lett. **45**, 1583 (1980); Y. Y. Goldschmidt and A. Aharony, Phys. Rev. B **32**, 264 (1985).
[10] A. Fert and F. Hippert, Phys. Rev. Lett. **49**, 1508 (1982); A. Fert, D. Avarnaitis, and F. Hippert, J. Appl. Phys. **55**, 1640 (1984); Y. Yeshurun and J. Felner, J. Magn. Magn. Mater. **54-57**, 215 (1986).
[11] Y. Yeshurun, J. Felner, and B. Wanklyn, Phys. Rev. Lett. **53**, 620 (1984).
[12] B. Dieny, B. Barbara, G. Fillion, M. Maeder, and B. Michelutti, J. Phys. (France) **48**, 1741 (1987); M. J. O'Shea, K. M. Lee, and A. Fert, J. Appl. Phys. **67**, 5769 (1990).
[13] W. M. Saslow, Phys. Rev. Lett. **17**, 1320 (1983); Phys. Rev. B **27**, 6873 (1983); W. M. Saslow, Phys. Rev. **35**, 3454 (1987).
[14] C. L. Henley, H. Sompolinsky, and B. I. Halperin, Phys. Rev. B **25**, 5849 (1982).

Temperature dependence of the hyperfine field distributions in the $Fe_{93.5-x}Nd_xZr_{6.5}$ ($x=0$, 2) amorphous alloys

G. K. Nicolaides, M. Pissas, D. Niarchos, R. D. Taylor,[a] and K. V. Rao[b]
National Center for Scientific Research "Demokritos," Institute of Materials Science Aghia Paraskevi, Attikis 153 10, Greece

The 112 K spin-glass $Fe_{93.5}Zr_{6.5}$ and the reentrant $Fe_{91.5}Nd_2Zr_{6.5}$ amorphous alloys have been studied at various temperatures with Mössbauer spectroscopy technique. At around $T=135$ K for the $Fe_{93.5}Zr_{6.5}$ and at around $T=255$ K for the $Fe_{91.5}Nd_2Zr_{6.5}$, six broad lines appear, which are not well resolved. This broadening is ascribed to the magnitude distribution of the magnetic moments of the Fe atoms. From the fitting of the Mössbauer spectra at $T=4.2$ K, the mean hyperfine field $\langle H\rangle$ and the Ecart-type standard deviation σ_H were estimated, and are (i) for the $Fe_{93.5}Zr_{6.5}$ sample, $\langle H\rangle\sim 205$ kOe, and $\sigma_H\sim 77$ kOe; (ii) for the $Fe_{91.5}Nd_2Zr_{6.5}$ sample, $\langle H\rangle\sim 228$ kOe and $\sigma_H\sim 70$ kOe. These values are found to be relatively consistent with the expected degree of magnetic frustration of the correspondingly Fe moments, according to the Fe content of these alloys.

I. INTRODUCTION

It is known that the Fe-rich Fe–Zr amorphous alloys exhibit interesting magnetic properties at cryogenic temperatures.[1] Especially when the Zr content is 8–12 at. % ac susceptibility measurements have shown a double transition (reentrant) behavior below room temperature. That is, as the temperature is lowered, a first transition occurs at $T=T_c$, which presumably is a paramagnetic to ferromagnetic state transition. When the temperature is lowered further, a second transition is encountered at $T=T_{sf}$ bearing the characteristics of a ferromagnetic to a "spin-glass-like" transition. The mechanism responsible for the phenomenon at the lower temperature transition has been for the last decade the topic of controversial results and discussions.[2–6] However this behavior can be explained[7–9] in terms of the statistical fluctuations of the coexisting and competing ferromagnetic (FM) and antiferromagnetic (AFM) exchange interactions, where the Gabay–Toulouse[10] magnetic phase diagram would apply. Various recent experimental studies indicated that the coexistence of FM and AFM interactions (which is due to the amorphization of these alloys) leads to a frustration of the magnetic moments and consequently to the "collapse" of the collinear (ideal) ferromagnetic order. The degree of collapse depends on the relative amount of the AFM interactions involved. In the case where the concentration of the AFM interactions is low (i.e., Fe content 88 at. %–93 at. %), a noncollinear ferromagnetic state results,[11] while in the opposite case (Fe content >93 at. %), a totally disordered magnetic state (spin-glass) would be expected below some temperature T_{sg}.

In our recent work,[12] we investigated the magnetic properties of the amorphous $Fe_{93.5-x}Nd_xZr_{6.5}$ alloys, where $x=0$, 1, 2, and 3. It was found that the $x=0$ sample undergoes a single transition from a paramagnetic to a spin-glass state at $T_{sg}=112$ K, and was suggested that this alloy could represent the percolation limit of the long-range ferromagnetic interactions. The Nd substituted samples exhibit a double transition behavior, where the width of the ferromagnetic plateau increases with increasing Nd content. This behavior of the Nd substituted samples was rather expected, since Nd couples ferromagnetically with Fe atoms, and this results in an increase of the amount of the FM interactions. In order to have a better picture of the magnetic states of the amorphous alloys $Fe_{93.5-x}Nd_xZr_{6.5}$ on a microscopic level, we carried out detailed Mössbauer studies of the samples with $x=0$ and 2 at. % of Nd content, at various temperatures.

II. EXPERIMENTAL

Ingots of nominal composition $Fe_{93.5-x}Nd_xZr_6$ with $x=0$ and 2 were prepared in a arc-melting furnace under a continuous flow of argon gas, and subsequently melt spun under a relatively low pressure of argon atmosphere. The obtained ribbons were 5–60 cm in length, 20 μ thick, 1.5 mm wide, and shiny. The amorphicity, chemical composition, and the quality of the samples has been verified using x-ray diffraction and Inductively Coupled Plasma absorption. ac susceptibility measurements were performed using a calibrated and balanced mutual inductance bridge, employing a two phase PAR lock-in signal analyzer, so we were able to measure both components of χ_{AC}, the real χ', and the imaginary χ'' simultaneously. The ac results were also corrected for demagnetizing effects. For the dc magnetic studies we employed a Quantum Design SQUID magnetometer and a PAR VSM. The Mössbauer measurements were obtained with a constant acceleration spectrometer using a ^{57}Co–Rh source.

III. RESULTS AND DISCUSSION

A. $Fe_{93.5}Zr_{6.5}$

In Fig. 1(a) are shown the Mössbauer spectra of the amorphous $Fe_{93.5}Zr_{6.5}$ at various temperatures, starting at RT down to 4.2 K. The observed spectra were analyzed using the *Le Caer program*,[13] and the distribution of the magnetic hyperfine fields $P(H)$ was obtained for each spectrum. The RT spectra show a paramagnetic behavior with broad absorption lines indicating the existence of some distribution of quadru-

[a]Also at the Los Alamos National Laboratory.
[b]Also at the Royal Institute of Technology, Department of Condensed Matter, S-10044 Stockholm, Sweden.

 0021-8979/94/75(10)/5853/3/$6.00 © 1994 American Institute of Physics

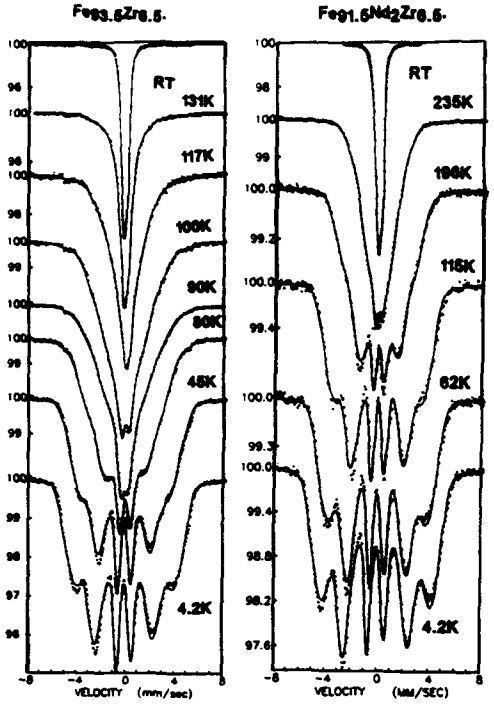

FIG. 1. Mössbauer spectra at (a) RT, 131, 117, 100, 90, 80, 45, and 4.2 K for $Fe_{93.5}Zr_{6.5}$ (b) and at RT, 235, 196, 115, 62, and 4.2 K for $Fe_{91.5}Nd_2Zr_{6.5}$.

pole interactions. In addition, the low velocity absorption part is deeper and slightly sharper than the high velocity one. This might have been caused from a correlation between the isomer shift and the quadrupole interactions.[14] The mean quadrupole splitting was found to be $\langle \Delta E_Q \rangle = 0.3$ mm/s and the $\sigma_{\Delta E_Q} = 0.1$ mm/s. Between RT and 150 K, the spectra do not indicate any change. Down to 135 K the evolution of the whole spectrum is characterized by a sharp increase of the line broadening with decreasing temperature. Between 135 and 45 K there is no longer any resolved structure in the lineshape. In addition, it can be seen in Fig. 1 that the spectra exhibit a magnetic character down to 90 K, but the lines are broad and not well resolved. A major part of the spectra is due to the Fe atoms in the paramagnetic state. The distribution of H [Fig. 2(a)] down to 90 K exhibits a tail on the right side of its maximum, while at temperatures lower than 80 K, where the sextet gradually appears, this tail moves to the left side of the maximum. At 4.2 K the fitting of these spectra gave the following results: $\langle H \rangle = 205$ kOe and $\sigma_H = 77$ kOe. Using the conversion factor 150 kG/μ_B, $\langle H \rangle$ corresponds to an Fe moment of $1.36\mu_B$. Here, also, it has to be noted that the paramagnetic character at 4.2 K is reduced substantially. In Fig. 3 the thermal evolution of mean hyperfine field $\langle H \rangle$ versus temperature for $Fe_{93.5}Zr_{6.5}$ and $Fe_{91.5}Nd_2Zr_{6.5}$ is presented.

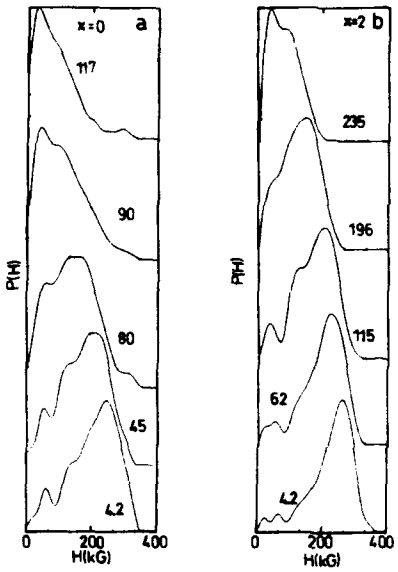

FIG. 2. Hyperfine magnetic field distributions of (a) $Fe_{93.5}Zr_{6.5}$ and (b) $Fe_{91.5}Nd_2Zr_{6.5}$ (b), at different temperatures.

B. $Fe_{91.5}Nd_2Zr_{6.5}$

The substitution of Fe by Nd results in an increase of the temperature, where the Mössbauer spectra show a magnetic character. In Fig. 1(b) and Fig. 2(b) are also shown the Mössbauer spectra and the hyperfine field distributions, respectively, of the $Fe_{91.5}Nd_2Zr_{6.5}$ amorphous alloy for some temperatures in the range of 300–4.2 K. At $T = 300$ K, the spectrum is similar to the one of $Fe_{93.5}Zr_{6.5}$ alloy, and the average quadrupole splitting according to the fitting results is found to be the same as in the case of $Fe_{93.5}Zr_{6.5}$. As the temperature is lowered at $T = 255$ K the magnetic structure

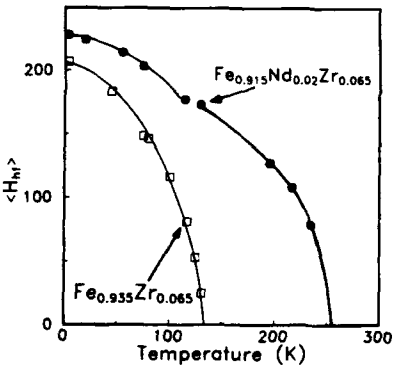

FIG. 3. Variation of $\langle H \rangle$ for $Fe_{93.5}Zr_{6.5}$ and $Fe_{91.5}Nd_2Zr_{6.5}$ (full line curves are eye guides).

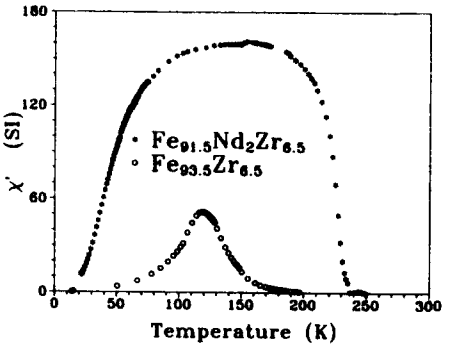

FIG. 4. Real part $\chi'(T)$ for $Fe_{93.5}Zr_{6.5}$ (○) and $Fe_{91.5}Nd_2Zr_{6.5}$ (•).

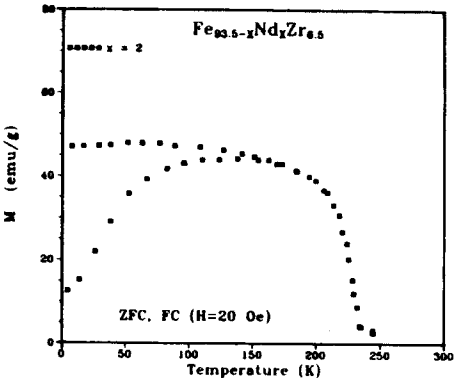

FIG. 6. Magnetization vs temperature for $Fe_{91.5}Nd_2Zr_{6.5}$.

starts appearing, but the absorption lines show a strong overlapping. At this temperature, the mean field from the fitting procedure was found to be $\langle H\rangle = 79$ kOe and $\sigma_H = 47$ kOe. In addition, the H distribution exhibits a tail on the right side of its maximum value, and this behavior reverses as the temperature is reduced to $T = 196$ K, while σ_H varies from 50 to 70 kOe. The behavior of the $\langle H\rangle$ field demonstrates that a significant portion of Fe exhibits a paramagnetic character. As temperature is lowered further, the magnetic hyperfine lines progressively separate out as the overall splitting increases. At $T = 4.2$ K it is found that $\langle H\rangle = 228$ kOe or $1.52\mu_B$ and $\sigma_H = 70$ kOe. Interpolating the results of Fig. 3, the temperature above which $\langle H\rangle = 0$ is found to be $T_M = 255$ K for $Fe_{91.5}Nd_2Zr_{6.5}$ and $T_M = 135$ K for $Fe_{93.5}Zr_{6.5}$. For the $x = 2$ sample, there is a break in slope in the temperature dependence of $\langle H\rangle$ at 110 K, which can be attributed to the reentrant spin-glass transition.

The above temperatures (T_M) are about 20 K higher than the corresponding transition temperatures extracted from the ac and dc susceptibility data seen in Figs. 4–6. It has to be noted that in the case of the dc susceptibility data for the $Fe_{93.5}Zr_{6.5}$, the transition temperature has to be taken as the temperature, for which the irreversibility between the ZFC and FC data occurs. The $\chi'(T)$ data for $Fe_{93.5}Zr_{6.5}$ show a single transition at $T \equiv T_{sg} = 112$ K, while for $Fe_{91.5}Nd_2Zr_{6.5}$, $T_c = 235$ K. Following Meyer *et al.*,[15] at $T = T_{sg}$ a spin glass system stays essentially within one well,[16] but there are numerous rapid transitions between excited states of the system within this well. The Mössbauer spectra appear static in this temperature range, because these intrawell effects occur on a very short time scale, as with magnons in a ferromagnet. In the spin glasses, there are interwell relaxation processes that accelerate rapidly as the temperature is raised. If the system is jumping rapidly between wells on the time scale of some particular experiment, it will appear to be paramagnetic. For $T < T_{sg}$, the samples possess a static behavior, while between T_{sg} and T_M there might be jumps between different wells at less than the Mössbauer frequency.

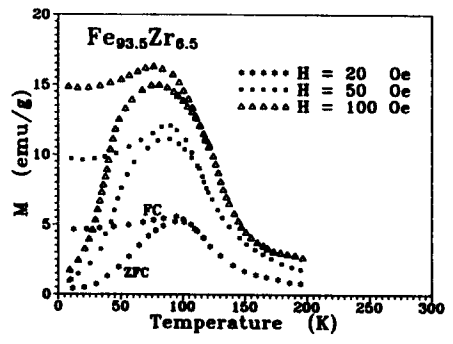

FIG. 5. Magnetization vs temperature for $Fe_{93.5}Zr_{6.5}$.

[1] H. Hiroyoshi and K. Fukamichi, Phys. Lett. A **85**, 242 (1981).
[2] H. Hiroyoshi and K. Fukamichi, J. Appl. Phys. **53**, 2226 (1982).
[3] Z. Wronski, A. J. Janicki, and H. Matyja, J. Mat. Sci. Lett. **2**, 50 (1983).
[4] J. J. Rhyne and G. E. Fish, J. Appl. Phys. **57**, 3407 (1985).
[5] G. K. Nicolaides, G. Wei, G. C. Hadjipanayis, and K. V. Rao, Mat. Sci. Eng. **99**, 69 (1988).
[6] N. Saito, H. Hiroyoshi, K. Fukamichi, and Y. Nakagawa, J. Phys. F: Met. Phys. **16**, 911 (1986).
[7] D. H. Ryan, J. O. Strom-Olsen, R. Provencer, and M. Townsend, J. Appl. Phys. **64**, 5787 (1988).
[8] D. H. Ryan, J. M. D. Coey, E. Batalla, Z. Altounian, and J. O. Strom-Olsen, Phys. Rev. B **35**, 8630 (1987).
[9] K. Moorjani and J. M. D. Coey, in *Magnetic Glasses* (Elsevier, Amsterdam, 1984).
[10] M. Gabay and G. Toulouse, Phys. Rev. Lett. **47**, 201 (1981).
[11] G. K. Nicolaides, G. C. Hadjipanayis, and K. V. Rao, Phys. Rev. B **48**, 12 759 (1993).
[12] G. K. Nicolaides and K. V. Rao, J. Appl. Phys. **69**, 5081 (1991); G. K. Nicolaides and K. V. Rao, J. Magn. Magn. Mater. **125**, 195 (1993).
[13] G. Le Caer, J. M. Dubois, H. Fischer, U. Gonser, and H. G. Wagner, Nucl. Instrum. Methods Phys. Res. B **5**, 25 (1984).
[14] G. Le Caer, J. M. Cadogan, R. A. Brand, J. M. Dubois, and H. J. Guntherodt, J. Phys. F. Meteorol. Phys. **14**, L73 (1984).
[15] C. Meyer, F. Hartmann-Boutron, Y. Gros, and I. A. Campbell, J. Magn. Magn. Mat. **46**, 254 (1985).
[16] K. Binder and A. P. Young, Rev. Mod. Phys. **58**, 801 (1986).

Blocking of logarithmic temporal relaxation of magnetic remanence by piezomagnetically induced domains in $Fe_{1-x}Zn_xF_2$

J. Kushauer, C. Binek, and W. Kleemann
Angewandte Physik, University of Duisburg, 47048 Duisburg, Germany

Faraday rotation and superconducting quantum interference device magnetometry were used to investigate the relaxation of the weak-field induced remanence, μ, of the random-field Ising model system $Fe_{1-x}Zn_xF_2$. The stretched logarithmic decay law, as predicted by Nattermann and Vilfan for the case of compact domains with fractal surfaces, was confirmed for freezing fields of $3 \leq B \leq 5$ T. Virtually constant remanence, μ, was found at low fields, $0.0002 \leq B \leq 1.5$ T. This ferrimagnetic moment is due to the piezomagnetic effect acting on random-stress induced immobile domains. Chemical etching, which removes surface stress originating from the sample preparation, proves to decrease the remanence by about 50%, part of which is restored after renewed optical polishing.

I. INTRODUCTION

Diluted uniaxial antiferromagnets (AFs) exposed to a uniform external magnetic field, B, are well known to exhibit the critical behavior of the random-field Ising model (RFIM).[1,2] Recently, considerable interest has been focused onto their nonequilibrium behavior after field cooling (FC) to below $T_{eq} \gtrsim T_c(B)$. Metastable domain states[3] arise, which are characterized by finite correlation lengths of the AF order parameter[4] and excess magnetization, ΔM, which is primarily concentrated on the domain walls.[3] After removing B a small portion of about 10% remains as long-lived thermoremanent magnetization (TRM), μ. In the absence of random-field (RF) pinning at $B=0$, μ evolves with time via random-exchange Ising model (REIM) dynamics.[5] This was demonstrated on prototypical systems like $Fe_{0.7}Mg_{0.3}Cl_2$[6] and $Fe_{0.47}Zn_{0.53}F_2$[7] as well as in Monte Carlo simulations.[8] It was noticed that no significant growth of the correlation length, after removing B, is visible in neutron scattering experiments.[4] This means that the reduction of the long-lived TRM arises merely from local rearrangements of the spins on the AF domain boundaries. For this situation stretched logarithmic decay with time, t,

$$\mu(t) = a[\ln(t/\tau)]^{-\psi}, \tag{1}$$

was predicted by Nattermann and Vilfan (NV)[5] and confirmed by measurements on $Fe_{0.7}Mg_{0.3}Cl_2$[6] and $Fe_{0.47}Zn_{0.53}F_2$[9] after FC in weak fields, $B/|J| \approx 0.1$, to low temperatures, $T/T_N \approx 0.1$. J, T_N, and τ are the leading exchange constant, the Néel temperature, and a microscopic relaxation time, respectively. In accordance with theory[5] exponents $\psi = 0.4 \cdots 0.55$ were observed. At larger fields, $B/|J| \lesssim 1$, and higher temperatures, $T/T_N \lesssim 1$, however, the polydispersivity of the TRM decay function is better described by ordinary or generalized power laws.[7] This is related to volume relaxation processes of interpenetrating fractal domains, which render the system spin-glass like.[3]

Surprisingly, recent TRM experiments on $Fe_{0.47}Zn_{0.53}F_2$[9] did not reveal better agreement with the NV prediction, Eq. (1), in the very low B range. On the contrary, constant weak TRM emerges, which is virtually independent of $B < 1.5$ T and t. Its temperature dependence approximately follows that of the AF order parameter. It was argued[9] that this unexpected effect is due to the formation of random shear-stress induced AF domains. They are expected to carry weak ferrimagnetic moments owing to symmetry-allowed piezomagnetism of the rutile-type crystal structure.[10] In fact, the formation of surface-stress induced AF domains was evidenced previously[11] on MnF_2 via neutron topography. On the other hand, residual magnetization persisting in poling fields as low as $B = 10^{-3}$ mT were recently observed.[12] Very probably, this hitherto unexplained[12] ferrimagnetism is related to residual stress originating from sample growth and preparation.

This idea will be pursued in the present paper. First, we recall[9] the crossover from logarithmically relaxing to piezomagnetically frozen TRM on a sample of $Fe_{0.47}Zn_{0.53}F_2$ when decreasing B from 4.86 to 0.001 T. Second, on a sample of $Fe_{0.6}Zn_{0.4}F_2$ with smaller stress-induced TRM, a weak B dependence, $\mu \propto B^{0.05}$, is found for $B < 0.1$ T. This is explained by the inhomogeneity of the built-in stress fields. Furthermore, by chemical etching of the surface the TRM is asymptotically reduced to its bulk value. Subsequent mechanical polishing partially restores the surface-stress induced TRM. Its time independence is demonstrated.

II. EXPERIMENTAL

Relaxation of the field-induced TRM was observed[9] on the same diluted sample of $Fe_{0.47}Zn_{0.53}F_2$ used previously.[7] In a longitudinal magnetic field, parallel to the crystallographic c direction, the Faraday rotation (FR) angle θ, $\propto M$, was measured with light of wavelength $\lambda = 442$ nm using a compensation circuit with a resolution of $\Delta\theta \sim 5 \times 10^{-4}$ deg and previously described modulation techniques.[6] The data were taken after FC from $T = 2T_N (\sim 80$ K) to $T = 2.8$ K. After stabilizing the temperature T to within $\Delta T = 1$ mK, the field was switched off. The switch-off time was properly[7] taken into account when fitting to the different decay laws.

Commercial superconducting quantum interference device (SQUID) magnetometers (Quantum Design MPMS2 and MPMS5S) were used to determine the TRM of two samples, $Fe_{0.47}Zn_{0.53}F_2$[9] and $Fe_{0.6}Zn_{0.4}F_2$, after FC in a constant field, $0.00024 \leq B \leq 5$ T, from $T \sim 2T_N$ to $T = 10$ and (for obtaining the paramagnetic response) 55 K. Furthermore, the low-field TRM, $\mu(0.24$ mT), of the $Fe_{0.6}Zn_{0.4}F_2$ sample was repeatedly measured both at $T = 10$ and 55 K after stepwise etching with diluted nitric acid (4 vol % HNO_3 in H_2O at

 0021-8979/94/75(10)/5856/3/$6.00 © 1994 American Institute of Physics

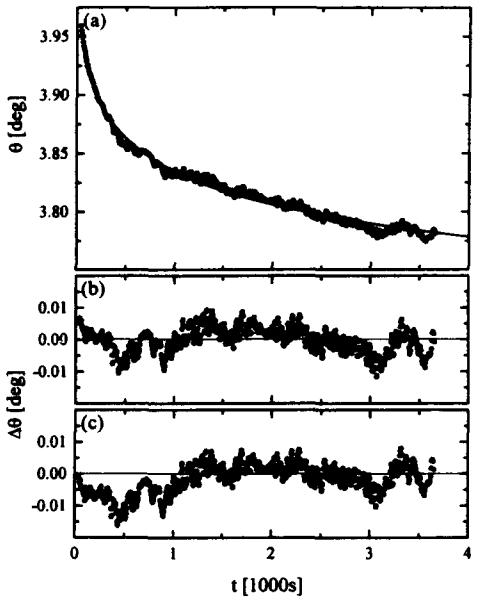

FIG. 1. Remnant Faraday rotation angle, θ, vs time, t, (a) measured on $Fe_{0.47}Zn_{0.53}F_2$ with $\lambda=442$ nm at $T=2.8$ K after FC with $B=4$ T (Ref. 9). The solid line is a best fit to the NV function, Eq. (1). Deviations of the experimental data, θ vs t (a), from the best-fitted NV function and the power law approximation, $\theta \propto t^{-x}$, are shown as $\Delta\theta$ vs t [(b) and (c), respectively].

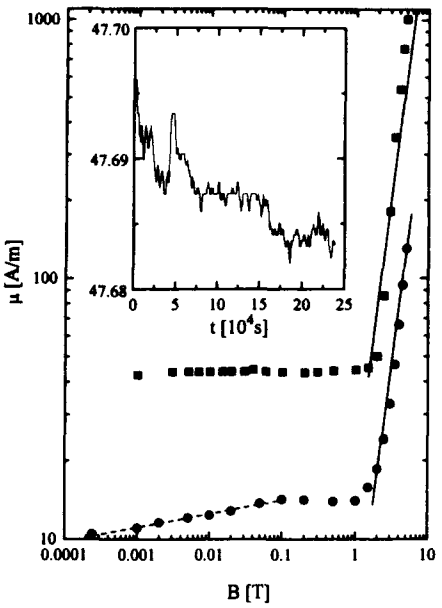

FIG. 2. Log–log plots of the TRM, μ, of $Fe_{1-x}Zn_xFe_2$ [$x=0.53$: squares (Ref. 9); $x=0.4$: circles] vs freezing field at $T=10$ K. The solid and dashed lines represent B^2 and $B^{0.05}$ dependences (see the text). The inset shows the t dependence of μ for the $x=0.53$ sample in zero field after FC with $B=0.8$ T to $T=10$ K.

$T=293$ K). After 5 h total etching time the sample was repolished with 7 and 1 μm diamond abrasive in order to demonstrate the surface stress induced ferrimagnetic moment. The loss of weight of the sample due to etching and polishing was monitored at each step.

III. RESULTS AND DISCUSSION

Figure 1(a) shows the time dependence of TRM measured by FR angle, θ, in zero field, after cooling in a magnetic field of $B=4.0$ T down to $T=2.8$ K. On the experimental time scale up to 3500 s the magnetization drops by about 0.5°, while the scattering of the data is in the order of 5 mdeg and does not affect the resulting shape of the relaxation curve. Among the different fitting functions, NV, pure (PP), and generalized power law (GP), NV turns out to be the best choice.[9] This becomes evident from χ^2 tests[9] and from direct comparison of the deviations $\Delta\theta$ between experimental data and model functions. This is shown in Fig. 1, where $\Delta\theta$ clearly yields smaller rms values for NV (b) than for PP (c). Although the GP yields similar χ^2 numbers as NV, it does not qualify as the best fit function since an additional fitting parameter is involved. Another crucial argument in favor of the NV theory is the appearance of the predicted exponent, $\psi\sim0.4$ [$\psi=0.38$ in the case of Fig. 1(a)]. This holds for intermediate freezing fields, $3\leq B\leq5$ T, at low temperatures.[9] At larger fields, $B>5$ T, the system crosses over into the spin-glass-like domain state,[3] where the PP or the GP are found to be valid.[7] At lower fields, $B<3$ T, perturbations due to piezomagnetic domain formation become important as will be discussed below.

Figure 2 shows the remnant magnetic moment, μ, in zero field ($B<0.2$ mT) as a function of the freezing field after FC to $T=10$ K for $Fe_{0.47}Zn_{0.53}F_2$ (squares)[9] and $Fe_{0.6}Zn_{0.4}F_2$ (circles). Straight interpolated lines in the range $1.5\leq B\leq5$ T are best fits to $\mu=bB^2-c$ with adjustable parameters b and c. These parabolas indicate RF-like behavior corrected for relaxation loss in the vicinity of $T_c(B)$.[3,9] In the low-field range the μ vs B data level off to become virtually constant, $\mu_0\sim44$ A/m for $x=0.53$ within $0.001\leq B\leq1.5$ T and $\mu_0\sim15$ A/m for $x=0.4$ within $0.1\leq B\leq1.1$ T. These remanences are attributed[9] to piezomagnetic moments, $m_z\propto\lambda_2\sigma_{xy}l_z/|l_z|$. They are generated by accidental built-in shear stress, σ_{xy}, and controlled by the external field, B_z, via minimization of the magnetostatic energy, $E_m=-m_zB_z$. As argued previously,[9] randomly distributed shear stress fields with alternating signs of the σ_{xy} components give rise to antiferromagnetic domains with alternating signs of the AF order parameter, $l_z/|l_z|$, while cooling through $T_c(B)$ with $B\|[001]$. All domains contribute to m_z with the sign of B_z. Only at very low or really vanishing freezing field $\mu=0$ will be achieved,[12] where nonvanishing stress fields might still create piezomagnetic moments with zero average, $\langle m_z\rangle=0$. The different μ_0 values found for both samples seem to re-

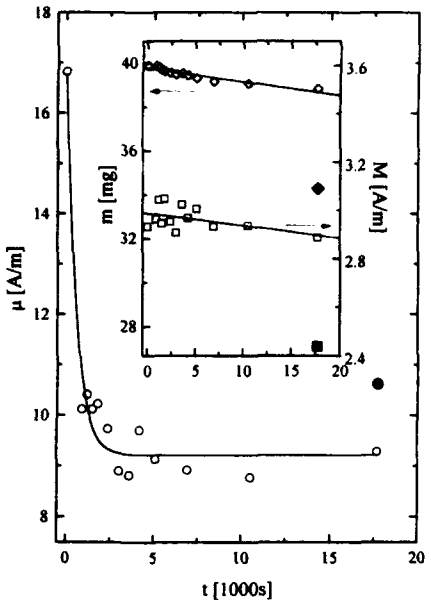

FIG. 3. Magnetization at $T=10$ K (μ; circles) and 55 K (M; squares) and mass (m; diamonds) of a sample with $x=0.4$, field cooled and measured in $B_0=0.24$ mT, as a function of etching time up to $t=1.6\times10^4$ s (open symbols) and after subsequent optical polishing (solid symbols).

flect different average stress fields, $\langle\sigma_{xy}\rangle$. The lower stress in the $x=0.4$ sample—about 1/3 of that of the $x=0.53$ sample—gives rise to a marked field dependence, $\mu_0\propto B^{0.05}$, at very low fields, $0.0002\leq B\leq0.1$ T, where the thermal energy comes close to the magnetostatic one, $\langle E_m\rangle$. Hence, thermal disorder will destroy the complete alignment of the domains and thus decrease $\langle m_z\rangle$.

It will be interesting to study the change of the TRM from relaxational to static behavior when decreasing B to below 1.5 T. Very weak time dependence is found in the crossover region. The inset of Fig. 2 shows the decrease of the TRM in the $x=0.53$ sample after FC to $T=10$ K with $B=0.8$ T. The rate, $-(d\mu/dt)/\mu\sim8\times10^{-10}\,\mathrm{s}^{-1}$, as measured over a period of 2.5×10^5 s is clearly above the noise level of the MPMS5S SQUID apparatus. Tentatively it is ascribed to NV-type relaxation of magnetized AF domain walls, which are preferentially formed at unstrained sample regions, where σ_{xy} and, hence, $l_z/|l_z|$ change sign from one domain to the other.

Figure 3 shows the total magnetization, μ, of the $x=0.4$ sample obtained after FC with $B_0=0.24$ mT (=remanence of the supraconducting coil) to $T=10$ K versus etching time, t (open circles). In parallel, both the paramagnetic magnetization, M, induced by B_0 at $T=55$ K and the mass, m, of the sample have been determined as functions of t (inset: open squares and diamonds). It is seen that these quantities decrease linearly with t by about 3% within the total etching time of 1.6×10^4 s. This is a consequence of the loss of mass during the chemical attack. Far greater effects are found with the low-T magnetization (open circles), which is primarily due to stress induced piezomagnetic moments beside a nearly negligible unperturbed AF contribution [M^{AF}(10 K)~M^{PM}(55 K)/6~0.5 A/m].[13] Within 10^4 s nearly 50% of the initial magnetization are removed. The μ vs t data are best fitted to an exponential decay law, $\mu=\mu_s e^{-t/\tau}+\mu_v$ with volume and surface contributions $\mu_v=9.2$ A/m and $\mu_s=8.0$ A/m, respectively, and a time constant $\tau=580$ s. Obviously, a large amount of stress centers is very efficiently removed from the surface by a first-order chemical reaction, $-d\mu/dt\propto\mu$. Very probably these stress fields are due to the surface treatment of the sample, which was optically polished at the beginning, $t=0$. In fact, repolishing of the slightly roughened surfaces after the etching procedure at $t=1.6\times10^4$ s recovers about 20% of μ_s (Fig. 3: full circle) despite a volume loss due to abrasion of about 12% (inset of Fig. 3: solid symbols).

IV. CONCLUSION

The field-induced thermoremanence of the prototypical domain state system $Fe_{1-x}Zn_xF_2$ ($x=0.53$) is confirmed to follow the stretched logarithmic temporal decay law of Nattermann and Vilfan.[5] At weak fields, $B\leq1.5$ T, the relaxation rate drops to nearly unmeasurable values. About 50% of the virtually constant residual magnetic moment of an $x=0.4$ sample is demonstrated to be due to surface stress by virtue of the longitudinal piezomagnetic effect.[10] Revision of results obtained previously[2,3] in the critical regime with fairly weak fields, $1\leq B\leq2$ T, appears desirable.

ACKNOWLEDGMENTS

Thanks are due to V. Jaccarino for the high quality crystals. Work supported by Deutsche Forschungsgemeinschaft through Sonderforschungsbereich 166.

[1] S. Fishman and A. Aharony, J. Phys. C **12**, L729 (1979).
[2] For a review see D. Belanger and P. Young, J. Magn. Magn. Mater. **100**, 272 (1991).
[3] For a review see W. Kleemann, Int. J. Mod. Phys. B **7**, 2469 (1993).
[4] R. A. Cowley, H. Yoshizawa, G. Shirane, and R. J. Birgeneau, Z. Phys. B **58**, 15 (1984).
[5] T. Nattermann and I. Vilfan, Phys. Rev. Lett. **61**, 223 (1988).
[6] U. A. Leitão and W. Kleemann, Phys. Rev. B **35**, 8696 (1987).
[7] S.-J. Han, D. P. Belanger, W. Kleemann, and U. Nowak, Phys. Rev. B **45**, 9728 (1992).
[8] U. Nowak and K. D. Usadel, Phys. Rev. B **39**, 2516 (1989).
[9] J. Kushauer, W. Kleemann, J. Mattsson, and P. Nordblad, Phys. Rev. B (in press).
[10] A. S. Borovik-Romanov, Sov. Phys. JETP **11**, 786 (1960).
[11] M. Schlenker and J. Baruchel, J. Appl. Phys. **49**, 1996 (1978); Acta Cryst. A **34**, S 255 (1978); J. Baruchel, M. Schlenker, and B. Barbara, J. Magn. Magn. Mater. **15–18**, 1510 (1980).
[12] T. Fries, Y. Shapira, A. Paduan-Filho, C. C. Becerra, and F. Palacio, J. Phys. Cond. Matt. **5**, L 107 (1993); M. Lederman, J. Hammann, and R. Orbach, Physica B **165 & 166**, 179 (1990).
[13] W. Kleemann, A. R. King, and V. Jaccarino, Phys. Rev. B **34**, 479 (1986).

One-dimensional antiferromagnetic behavior in $AVOPO_4$ ($A = NH_4$, Na) prepared from hydrothermal conditions

Charles J. O'Connor
Department of Chemistry, University of New Orleans, New Orleans, Louisiana 70148

Victoria Soghomonian and Robert C. Haushalter
NEC Research Institute, Princeton, New Jersey 08540

Zhanwen Wang and Jon Zubieta
Department of Chemistry, Syracuse University, Syracuse, New York 13244

Two vanadyl phosphates have recently been prepared in superheated aqueous solutions. These materials crystallize as infinite chains of corner sharing VO_6 octahedra. The magnetic susceptibility of $NaVOPO_4$ and NH_4VOPO_4 has been recorded over the 2–300 K temperature region. At higher temperatures, both compounds exhibit Curie–Weiss paramagnetism, where $C = 0.416$ emu K/mole, $\theta = -31$ K; $C = 0.417$ emu K/mole, $\theta = -4.7$ K, for $NaVOPO_4$ and NH_4VOPO_4, respectively. At lower temperatures, there is a maximum in the temperature-dependent magnetic susceptibility of each compound. The data for the two compounds have been successfully analyzed following the Bonner–Fisher numerical calculations that describe the magnetic behavior of antiferromagnetically coupled $S = 1/2$ one-dimensional chains. The results of the Bonner–Fisher analysis of the magnetic data are $g = 2.00$, $J/k = -18.6$ for $NaVOPO_4$; and $g = 2.1$, $J/k = -3.26$ K, for NH_4VOPO_4. The theoretical analysis of the NH_4VOPO_4 analog also required the addition of a molecular field correction ($zJ'/k = -2.1$ K) to the Bonner–Fisher calculation in order to adequately fit the data. The trans crosslinking via phosphate bridges of the magnetic chains in NH_4VOPO_4 gives rise to the onset of long-range antiferromagnetic ordering at $T_{AF} = 3.71$ K.

I. INTRODUCTION

The use of hydrothermal synthetic techniques has proven to be an extremely valuable procedure in the chemistry of microporous solids.[1] Several interesting and intricate structures have been isolated and some unusual magnetic properties have been observed when magnetic ions are incorporated into the solid.[2]

Several vanadium phosphates of the formula $AVOPO_4$ have recently been reported, where $A = Li$,[3] Na,[4] K,[5] and NH_4.[6] Lii and co-workers have recently reported the crystal structure and Curie–Weiss magnetic fit of $NaVOPO_4$[2] and have reported a negative Weiss constant. Haushalter and coworkers have also observed antiferromagnetism and determined the crystal structure for NH_4VOPO_4.[6] In this report, we examine the magnetic susceptibility of $NaVOPO_4$ and NH_4VOPO_4 over the 2–300 K temperature region and successfully model the magnetic data with the Heisenberg $S = 1/2$ antiferromagnetic linear chain interaction.

II. EXPERIMENT

A. Synthesis

$NaVOPO_4$: A mixture of 1.5 g $Na_4V_2O_3$ and 0.75 g V_2O_3 was added to 10 ml of 7.5 M H_3PO_4 in a 25 ml Teflon lined vessel and heated to 200 °C for three days. The original product contained several transparent light blue crystals, but these were readily separated from the bulk polycrystalline green solid by manual separation.

NH_4VOPO_4: A mixture of $CsVO_3$:V:$CH_3PO_3H_2$:$(NH_4)_2HPO_4$:$(C_2H_5)_3CH_3NBr$:H_2O in the mole ratio 3.96:1:4.88:11.97:4.96:1498 was heated in a Teflon lined vessel at 200 °C for four days.

B. Magnetism

The magnetic susceptibility data were recorded on 155 and 81.8 mg polycrystalline sample of $NaVOPO_4$ and NH_4VOPO_4, respectively. Data were recorded over the 2–300 K temperature region using a Quantum Design MPMS superconducting quantum interference device (SQUID) susceptometer. Measurement and calibration techniques have been reported elsewhere.[7] The magnetic data are shown in Figs. 1 and 2 (NH_4VOPO_4) as molar magnetic susceptibility plotted as a function of temperature.

III. RESULTS AND DISCUSSION

The two complexes crystallize as infinite chains of corner sharing VO_6 octahedra. The linear chain structures of the

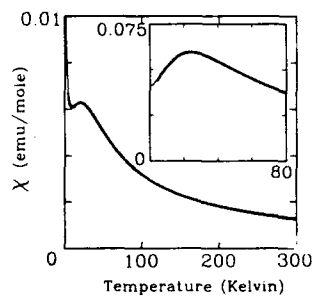

FIG. 1. The magnetic susceptibility of $NaVOPO_4$ plotted as a function of temperature over the 2–300 temperature region. The inset shows an expansion of the magnetic susceptibility data corrected for a 2.1% paramagnetic impurity and plotted over the 2–80 K temperature region. The curves through the data are the fits to $S = 1/2$ Heisenberg antiferromagnetic linear chain model as described in the text.

 0021-8979/94/75(10)/5859/3/$6.00 © 1994 American Institute of Physics

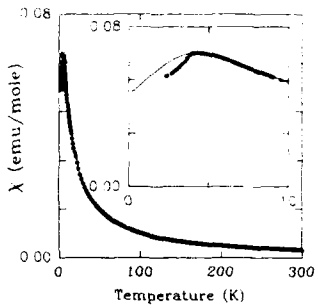

FIG. 2. The magnetic susceptibility of NH_4VOPO_4 plotted as a function of temperature over the 2.3–300 temperature region. The inset shows an expansion of the 2.3–10 temperature region. The curves through the data are the fits to the theoretical models as described in the text.

two materials are illustrated in Fig. 3 ($NaVOPO_4^5$ chain 1 and $NH_4VOPO_4^7$ chain 2). Note that 1 exhibits only trans coordination within the chain while 2 exhibits alternating cis-trans coordination along the chain. Figure 4 illustrates the cross linking of 2. The presence of transcoordinated cross linking in 2 is important to understand the interchain magnetic interactions that lead to an antiferromagnetic transition.

The high-temperature magnetic susceptibility data ($T>100$ K) for $NaVOPO_4$ (1) and ($T>25$ K) NH_4VOPO_4 (2) exhibit Curie–Weiss paramagnetism

$$\chi=\frac{C}{T-\theta}=\frac{Ng^2\mu_B^2S(S+1)}{3k(T-\theta)}, \tag{1}$$

with $C=0.416$ emu K/mole and $\theta=-31$ K and $C=0.417$ emu K/mole and $\theta=-4.72$ K for (1) and (2), respectively.

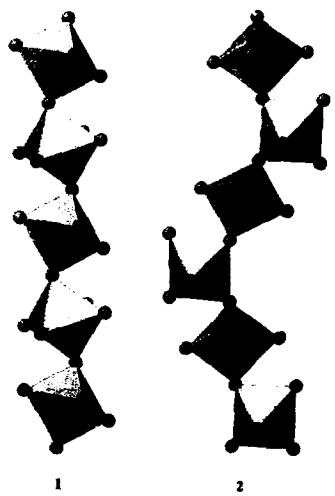

FIG. 3. The coordinating pattern of the linear chains in (1) $NaVOPO_4$ and (2) NH_4VOPO_4.

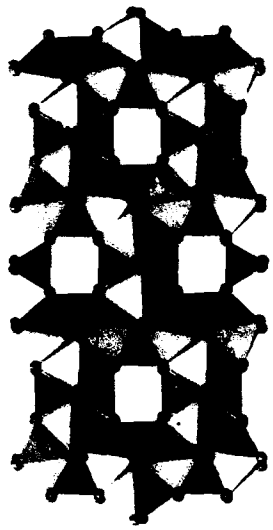

FIG. 4. The crystal packing of NH_4VOPO_4 showing the linear chain arrangement of cis-trans-corner sharing VO_6 octahedra. Extensive crosslinking with coordination trans- to chain propagation via phosphate bridges is also evident.

The electron structure of both complexes corresponds to one unpaired electron per VO formula unit. This results in a Curie–Weiss g value of $g=2.1$ for the V(IV) ion in each analog.

At lower temperatures an anomaly is observed in the temperature dependence of the magnetic susceptibility data of both samples. Both materials are structural linear chains that are propagated along corner sharing VO_6 bonding pathway. As the temperature is lowered to around 20 K (for sample 1), the magnetic susceptibility of the sample passes through a maximum and begins to decrease at lower temperatures. This behavior is expected for short-range antiferromagnetic exchange in the crystal lattice.

The magnetic exchange that is expected in a d^1 vanadium (IV) with spin $S=1/2$ is represented by the isotropic Heisenberg spin Hamiltonian.

$$\mathcal{H}=-2J\sum_{i,j}S_iS_j. \tag{2}$$

Within the context of the crystal structure of these materials, the magnetic exchange is expected to be propagated via a one-dimensional magnetic exchange interaction along the structural chain axis.

The behavior of a one-dimensional Heisenberg linear chain has been described by Bonner and Fisher.[8] The Bonner–Fisher Heisenberg linear chain calculation was applied to the magnetic susceptibility data of these complexes to determine if the short-range order can be theoretically explained by the one-dimensional magnetic interaction. The magnetic susceptibility data of 1 were fit over the entire re-

gion including the maximum to the Bonner–Fisher numerical calculation corrected for the presence of a paramagnetic impurity. The fitted parameters for 1 are $g=2.00$, $J/k=-18.6$, $TIP=0.00009$ emu/mole, and 2.7% paramagnetic impurity. The smooth line drawn through the data points in Fig. 1 is the theoretical curve with the parameters indicated. The paramagnetic impurity was subtracted from the magnetic susceptibility data and the result is plotted in the inset of Fig. 1 along with the fitted curve calculated from the linear chain model. The magnetic analysis of $NaVOPO_4$ required no additional interaction term to fit the data, consistent with well insulated one dimensional magnetic behavior.

The same procedure was used to analyze the magnetic susceptibility data of 2. For this compound, it was observed that the Bonner–Fisher calculation did not satisfactorily fit the temperature region in the vicinity of the maximum. Moreover, at a temperature of about 3.71 K, there is an abrupt deviation of the magnetic susceptibility data from the broad maximum. Since there is enhancement of crosslinking through transphosphate bridging in 2, a molecular field correction to the linear chain model was used to approximate the effect of interchain magnetic interactions.

The equation that describes the effect of a molecular exchange field is shown below:[7]

$$\chi=\frac{\chi'}{1-(zJ'/Ng^2\mu_B^2)\chi'}+TIP, \tag{3}$$

where χ' is the magnetic susceptibility of the linear chains in the absence of the exchange field and χ is the molecular exchange field influenced magnetic susceptibility that is actually measured. The exchange field coupling parameter is zJ', where z is the number of exchange coupled neighbors.

The result of the fit of the molecular field corrected Bonner–Fisher calculation to the magnetic data, neglecting the data at temperatures below 4.0 K, is illustrated as the smooth curve in the inset of Fig. 2. The parameters used in the fit were $g=2.10$, $J/k=-3.26$, $zJ'/k=-2.1$ K. The need for a large interchain coupling parameter (zJ') is consistent with the onset of the three-dimensional phase transition. The magnitude of this parameter requires that it be viewed with caution; however, the model shows excellent agreement with the measured magnetic susceptibility data until the onset of long-range order at $T=3.71$ K.

There are several other examples of phosphate bridged V (IV) structural linear chains reported in the literature.[9–11] In general, the previous reports of low-dimensional behavior have required significant interchain interactions, for example, dimeric interactions[9,10] or alternating chains.[11]

IV. CONCLUSION

Two crystalline solids of the formula $AVOPO_4$ ($A=Na,NH_4$) have been prepared from hydrothermal synthetic techniques. These materials crystallize as infinite chains of corner sharing VO_6 octahedra. In the high-temperature region, both complexes exhibit Curie–Weiss paramagnetism with antiferromagnetic Weiss constants. The lower-temperature magnetic susceptibility of the two complexes exhibits a broad maximum and the data are successfully analyzed with the numerical predictions calculated by Bonner and Fisher using the Heisenberg $S=1/2$ antiferromagnetic linear chain model. The ammonium analog requires a correction for interchain magnetic coupling and exhibits an antiferromagnetic phase transition at $T=3.71$ K.

[1] R. M. Barrer, *Hydrothermal Chemistry of Zeolites* (Academic, New York, 1982); R. C. Haushalter and L. A. Mundi, Chem. Mater. **4**, 31 (1992).
[2] V. Soghomonian, Q. Chen, R. C. Haushalter, J. Zubieta, and C. J. O'Connor, Science **259**, 1596 (1993); K.-H. Lii, R. C. Haushalter, and C. J. O'Connor, Angew. Chem. **99**, 576 (1987); Angew. Chim., Int. Ed. (Engl.) **26**, 549 (1987).
[3] A. V. Lavrov, V. P. Nickolaev, G. G. Sadikov, and M. A. Porai-Koshits, Sov. Phys. Dokl. **27**, 680 (1982).
[4] K. H. Lii, C. H. Li, T. M. Chen, and S. L. Wang, Z. Krist, **197**, 67 (1991).
[5] M. L. F. Phillips, W. T. Harrison, T. E. Gier, G. D. Stucky, G. V. Kulkarni, and J. K. Burdett, Inorg. Chem. **29**, 2158 (1990).
[6] R. C. Haushalter, J. Zubieta, and C. J. O'Connor (unpublished).
[7] C. J. O'Connor, Prog. Inorg. Chem. **29**, 203 (1982).
[8] J. C. Bonner and M. E. Fisher, Phys. Rev. A **135**, 640 (1964).
[9] G. Villanaeuve, K. S. Suh, P. Amords, N. Casa-Pastor, and D. Beltran-Porter, Chem. Mater. **4**, 108 (1992); G. Huan, J. W. Johnson, A. J. Jacobson, and D. P. Goshorn, *ibid.*, **3**, 539 (1991).
[10] J. W. Johnson, D. C. Johnston, H. E. King, T. R. Halbert, J. F. Brody, and D. P. Goshorn, Inorg. Chem. **27**, 1646 (1988).
[11] D. C. Johnston, J. W. Johnson, D. P. Goshorn, and A. J. Jacobson, Phys. Rev. B **35**, 219 (1987).

ac susceptibility on the dilute antiferromagnet $Mn_xZn_{1-x}F_2$ close to the percolation threshold (abstract)

F. L. A. Machado, F. C. Montenegro, E. Montarroyos, J. C. O. de Jesus, A. Rosales-Rivera,[a] and S. M. Rezende
Departamento de Física, Universidade Federal de Pernambuco, 50732-910 Recife-PE, Brazil

ac susceptibility measurements have been performed on the dilute antiferromagnet $Mn_{0.35}Zn_{0.65}F_2$ in the absence of an external uniform field. For a driving field of amplitude $H_{ac}\sim 1.0$ Oe applied parallel to the easy [001] direction, a frequency-dependent susceptibility has been observed at low temperatures. When the driving field is applied perpendicular to this direction, a departure from the Curie–Weiss behavior indicates that some spin clusters are spatially oriented at low temperatures. The presence of these randomly oriented magnetic moments may cause the random-exchange Ising model to be inappropriate[1] in explaining the zero-field behavior near to the percolation concentration x_p. A random-anisotropy model may be useful to explain the magnetic features of $Mn_xZn_{1-x}F_2$ close to x_p.

This work was partially supported by FINEP (PADCT), CNPq, and FACEPE (Brazilian agencies).

[a]Permanent address: Departamento de Fisica, Universidad Nacional de Colombia, A. A. 127, Manizales, Colombia.

[1] F. C. Montenegro, J. C. O. de Jesus, and A. Rosales-Rivera (unpublished).

The frequency dependence of the ferro-to-spinglass transition of amorphous Fe-rich Fe-Zr (abstract)

J. Nogués and K. V. Rao
Department of Condensed Matter Physics, Royal Institute of Technology, 10044 Stockholm, Sweden

It is well known that competing magnetic interactions in amorphous Fe-rich Fe-Zr alloys result in a ferromagnetic-like transition below room temperature (for example, $T_c\approx 235$ K for a $Fe_{90}Zr_{10}$ alloy). The field dependence of the ac response of such a system with competing interactions is thus complex, with the possible coexistence of ferromagnetic domains and spin freezing processes. One consequence of this is the observed[1] Hopkinson peak in ac susceptibility and its strong field dependence when measured at ordinary fields (>80 A/m). The existence of such a complex Hopkinson peak, which arises from the contribution of domain wall motion and hysteretic effects, makes it very difficult to identify, unambiguously, a spin freezing temperature. The purpose of this paper is to clarify this point. Complex ac susceptibility [$\chi'(T)$, $\chi''(T)$] measurements have been carried out over an extended range of field amplitude (0.08–8000 A/m) and three decades of frequency (1–1000 Hz) along the axis of a single sample of melt spun $Fe_{90}Zr_{10}$ ribbon. We find that, below the threshold field, there is a unique spin freezing temperature with almost no frequency or field dependence. At higher fields (>80 A/m) the viscous susceptibility, $\chi''(T)$, peak at low temperatures shows a strong temperature, frequency, and field dependence, indicating a superposition of the effects of "induced" long range order with the spinglass state. The ferro-to-spin glass transition temperature using this approach has been found to be $T_{sf}=25$ K.

[1] J. Nogués and K. V. Rao, IEEE Trans. Magn. 29, 3246 (1993).

 0021-8979/94/75(10)/5862/1/$6.00 © 1994 American Institute of Physics

Cooperative spin-crossover transition: Effects of the antiferro- and ferri-ordered phase (abstract)

Benjamin G. Vekhter
Chemistry Department, Northwestern University, Evanston, Illinois 60208-3113

The considerable increase of magnetic moment M with increasing temperature T [the spin-crossover (SC) effect] in some transition metal complexes is caused by a predominant occupation of the excited high-spin (HS) state which has a larger statistical weight than the low-spin (LS) ground one. Rather unusual experimentally observed $M(T)$ behavior that provides for molecular electronics applications with such compounds, gives evidence of the importance of cooperative intermolecular interactions. The microscopic theory of cooperative SC transitions is developed. This is based on the phonon-mediated ion-ion interaction and accounts for the possibility of a phase with antiferro-ordered local distortions around the magnetic ions, in addition to the homogeneous ferro-phase that was the only one considered previously. If the parameter $|J|$ of the antiferro-coupling ($J<0$) is greater than the energy gap Δ between the LS and HS states, then at $T=0$ one-half of the ions are in the "excited" HS state while the other half reside in the LS state. A temperature increase causes a $M(\mathrm{HS})/2 \rightarrow M(\mathrm{HS})$ transition to the phase where all the ions are in the HS states. The larger is the value of $|J|$, the higher is the transition temperature. If $|J|<\Delta$, then at $T=0$ all the ions are in the LS state because the intermolecular correlations are too small to lead to antiferro-ordering. However, if $|J|$ is close enough to Δ, then the intermediate ferri-ordered phase appears, resulting in two $[M(\mathrm{LS}) \rightarrow M(\mathrm{HS})/2 \rightarrow M(\mathrm{HS})]$ consecutive transitions (two-step SC change). The closer $|J|$ is to Δ, the lower the temperature of the first transition is and the wider the temperature interval of the ferri-phase existence is. Hysteresis phenomena and effects of magnetic dilution and external pressure, examined within the framework of the developed microscopic approach, are in a good agreement with experiment.

 0021-8979/94/75(10)/5863/1/$6.00 © 1994 American Institute of Physics

Nanocomposite formation in the Fe_3O_4-Zn system by reaction milling

Laszlo Takacs
Department of Physics, University of Maryland, Baltimore County, Baltimore, Maryland 21228

Martha Pardavi-Horvath
Institute for Magnetics Research, George Washington University, Washington, D.C. 20052

Magnetic nanocomposites of small iron particles embedded in nonmagnetic zinc oxide matrix have been prepared by ball milling, with an *in situ* displacement reaction between a metal oxide (Fe_3O_4) and a more reactive metal (Zn). The phase composition of the samples has been analyzed by x-ray diffraction. Metallic zinc disappears during the first 100 min of milling and the magnetization decreases to almost zero, indicating the formation of a nonmagnetic intermediate iron-zinc oxide phase. This intermediate phase decomposes into iron and ZnO upon further milling. The change in magnetic properties also reflects the decreasing size of the iron particles. The final particle size is about 9 nm, as estimated from x-ray diffraction linewidth measurements. The final product of the process is a semihard magnetic material with a room-temperature saturation magnetization of 40 emu/g and coercivity of 400 Oe. A significant fraction of the final Fe particles is superparamagnetic.

I. INTRODUCTION

The interest in the magnetic properties of small particles is driven by basic questions concerning superparamagnetism, interparticle interaction, magnetization processes, etc.[1] Potential applications in recording, pigments,[2] and magnetic refrigeration[3] are also considered. In this paper, we will restrict our attention to nanometer-size magnetic metal particles embedded in an oxide matrix. Conventionally, such systems are prepared by vacuum deposition[4] and chemical[5] methods. As it was shown recently, metal–metal-oxide nanocomposites can also be prepared by mechanical alloying. Intentional chemical changes induced by ball milling offer additional control of the preparation process.[6–8]

Our first attempt to prepare a magnetic nanocomposite by reaction milling involved the reduction of magnetite by aluminum metal in order to obtain a nanocomposite of iron particles in alumina.[6] This system was chosen because similar nanocomposites had been prepared by other methods and thoroughly studied.[4,5] Unfortunately, the reaction is highly exothermic, the impact of the milling balls can initiate self-supporting thermal combustion.[9] In order to obtain a nanocomposite, combustion had to be suppressed by inert additives.[6]

Higher magnetization can be achieved if a less exothermic chemical reaction is chosen, so that the dilution of the reaction mixture is not necessary. The reduction of magnetite by zinc is such a reaction: it releases 17 kcal during the exchange of one mole of oxygen atoms between iron and zinc, as opposed to 68 kcal when magnetite is reduced by aluminum.

The mechanochemical reduction of a metal oxide by a more reactive metal usually occurs through a complex series of overlapping reactions, forming several intermediate, metastable phases.[10] X-ray diffraction data suggest that the reduction of magnetite by zinc is a relatively simple, two-step process, involving one single intermediate phase. However, the diffraction results are quite ambiguous due to the broadening and overlap of the diffraction lines. More information on the reaction sequence is expected from the magnetic measurements.

II. EXPERIMENTAL

Reaction milling was performed using SPEX 8000 Mixer Mills with round bottom stainless-steel vials. The vials were filled in a glove box under argon. Each sample was prepared separately, without opening the vial at any intermediate stage. The composition of the starting powder mixture corresponded to the stoichiometry of the

$$Fe_3O_4+4Zn \rightarrow 3Fe+4ZnO$$

reaction with 10% extra zinc. Low (97%) purity starting materials were used, because a significant amount of contamination from the milling tools is unavoidable anyway. Zinc is a malleable metal, which can collect in a large, compacted chunk on the wall of the milling vial. This problem could be avoided by using a combination of large (45.5 g) and small (3.5 g) balls as milling tools.

The phase composition of the samples has been analyzed using a Philips x-ray diffractometer with vertical goniometer, Cu tube, and intrinsic Ge detector.

Hysteresis loops have been measured in a vibrating sample magnetometer at room temperature. Saturation magnetization (M_s), the remanent magnetization (M_r), and coercivity (H_c) have been determined from measurement of major loops. Samples were exposed to a saturating field of 9 kG before measuring the major loop. In fact, saturation has been achieved for all samples in less than 4 kG.

 0021-8979/94/75(10)/5864/3/$6.00 © 1994 American Institute of Physics

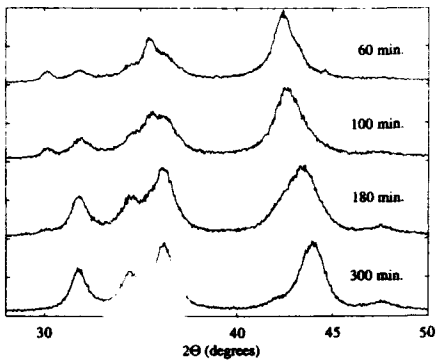

FIG. 1. X-ray diffraction patterns of ball-milled Fe_3O_4-Zn system for intermediate milling times. A more complete set of data has been published in Ref. 10.

III. RESULTS AND DISCUSSION

A preliminary understanding of the reduction of magnetite by zinc was based on x-ray diffraction data alone.[10] The diffraction patterns for intermediate milling times are reproduced on Fig. 1 for the most informative range of diffraction angles. Clearly, broadening and overlap of the diffraction lines makes the unambiguous interpretation of the results quite difficult.

The results of the magnetic measurements are shown in Figs. 2 and 3. The saturation magnetization M_s characterizes the amount of the magnetic phases present. The remanence M_r and coercivity H_c are typical of the magnetic hardness and particle size of the phases. The coercivity is independent of the amount of the phase present, changing characteristically with the size of the particles. In Fig. 2 room-temperature hysteresis loops, measured after 20, 100, and 540 min of milling show the change in saturation magnetization of the samples, illustrating the transformation from the initial magnetite phase to iron through a nonmagnetic intermediate phase. The similar shape of the major loops after 20 min mixing and 540 milling is due to the fact, that the original magnetite particles are magnetically harder with a higher coercivity, and after prolonged milling the size of the resulting iron particles is decreased near to the single domain size,

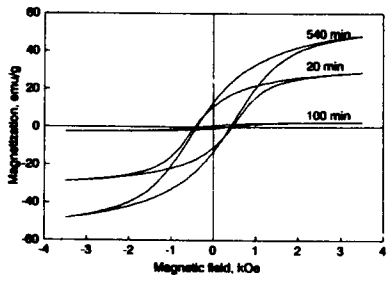

FIG. 2. Room-temperature hysteresis loops for Fe_3O_4-Zn system, measured after 20, 100, and 540 min of milling.

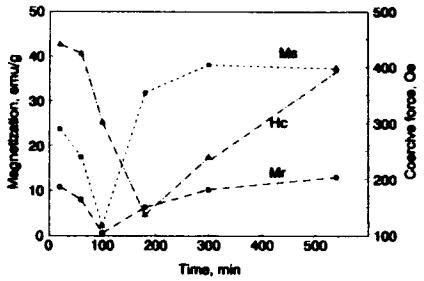

FIG. 3. Dependence of room-temperature magnetic properties of ball-milled Fe_3O_4+Zn system on the duration of milling. M_s saturation magnetization, M_r remanent magnetization, H_c coercivity.

with an increased coercivity and remanence. Figure 3 shows the dependence of M_s, M_r, and H_c upon the duration of ball milling.

The diffraction and magnetic data will be discussed simultaneously in order to achieve a better understanding of the sequence of changes.

A. First 60 min of milling

X-ray diffraction indicates that the amount of zinc decreases very quickly, only trace amounts remain after 60 min of milling. The most intense (101) line of zinc metal at 43.3° may be the source of the shoulder on the high-angle side of the largest peak and its well separated (100) peak (at about 39°) remains within statistical uncertainty. The amount of magnetite decreases more gradually. Both the presence of its diffraction lines [e.g., (220) at 30.1°] and the gradually decreasing saturation magnetization indicate that a significant amount of magnetite is still present after 60 min of milling. As seen in Figs. 2 and 3, the coercivity slowly decreases between 20 and 60 min of milling, suggesting that the magnetization originates from the same phase (magnetite) and the particle size and defect structure of that phase does not change significantly. Some ZnO appears immediately after the start of the milling, the intensity of its diffraction peaks increases gradually during the whole process [see, e.g., the well resolved (100) and (102) lines at 31.8° and 47.6°].

None of the above phases explain the most intense diffraction peak at about 42.4°. The intensity of the broad peak at about 36° is also too large to originate from overlapping peaks of magnetite and zinc oxide. We suggest that these lines originate from a nonmagnetic mixed Fe-Zn-O intermediate phase. Its structure may be related to the structure of wurtzite (with main peaks at 36.1° and 42°) or it may be noncrystalline. Preliminary transmission electron microscopy (TEM) results suggest the presence of a eutectic composite.[11] Similar intermediate mixed oxide phases were detected when reducing CuO by Fe (Ref. 7) and magnetite by Al.[6] However, in those cases the formation of the final metal phase begins simultaneously with the formation of intermediate phases, while in the present case the formation of α-Fe starts significantly later. (The small sharp diffraction peak at 44.7° may indicate impurity from the milling tools. It is not present in any of the other samples.)

B. 100 min of milling

The most astonishing property of this sample is the extremely low saturation magnetization. This, together with the x-ray diffraction pattern suggest that most of the sample consists of an intermediate Fe-Zn-O, a nonmagnetic mixed oxide phase. The small magnetization in Figs. 2 and 3 originates from the residual magnetite as indicated both by the diffraction pattern and the still quite high coercivity. Very little if any metallic iron is present.

This sample sharply separates the two steps of the mechanochemical process: the formation of a mixed Fe-Zn-O and its decomposition into ZnO and metallic iron. Such a strict separation of the two processes is not possible on the basis of the x-ray diffraction data alone, and only the magnetic data can confirm the process.

C. 180 min of milling

The main process between 100 and 180 min of milling is the decomposition of the intermediate mixed oxide into metallic iron and ZnO. This is suggested by the significant increase of the intensity of the ZnO diffraction lines. Also, the Fe-Zn-O peak at 42° reduces to a shoulder and a peak close to the (110) diffraction peak of α-Fe appears. Although this change could be viewed as a mere shift of the peak at 42°, it actually signals a major change in the phase composition.

The change of the magnetic parameters fully supports this interpretation. The large increase of the saturation magnetization corresponds to the formation of metallic iron. The low coercivity is consistent with freshly formed large magnetically soft iron particles.

D. Final stage of the process

The remaining mixed oxide decomposes upon further milling, and the last traces of magnetite disappear. The final product after 540 min of milling consists of bcc Fe and ZnO. A gradual shift of the (100) line of iron originates from the demixing process. The bcc phase contains a significant amount of Zn when formed, and the Zn content decreases upon further milling.[10] A particle size of about 9 nm can be estimated on the basis of the Sherrer equation.

The increasing coercivity suggests decreasing particle size toward single-domain size and increasing defect concentration. The saturation magnetization slightly decreases after very long milling, probably due to an increasing fraction of superparamagnetic particles. Based on x-ray data, the final product is bcc Fe. However, the amount of the saturation magnetization is only about 50% of the expected value calculated from the stoichiometry of the initial composition. The missing iron might be accounted for by a substantial superparamagnetic fraction, as is frequently the case in nanocomposites, like the case of Cu-Fe_3O_4.[12]

IV. CONCLUSIONS

The application of mechanical alloying to manufacturing technically useful materials requires detailed understanding of the mechanism of the process. The reduction of magnetite by zinc may be a useful model reaction due to its well-separated reaction steps. Although intermediate phases, similar to the mixed iron-zinc oxide form in most similar systems, the formation and decomposition of those phases occur concurrently.[6,7]

Magnetic measurements supported the characterization of the metal–metal-oxide displacement reactions between magnetite and aluminum[6] and iron and CuO.[11] The role of the magnetic data is more crucial in the present case, where the very sharp minimum of the saturation magnetization indicates the most clearly the separation of the two steps of the reaction.

The magnetic properties of the final Fe-ZnO nanocomposites are typical of a semihard magnetic material with a significant superparamagnetic fraction. Further work on determining the microstructure of the composite is in progress.

ACKNOWLEDGMENTS

The support of this work by the Designated Research Initiative Fund of the UMBC and the University Facilitating Fund of the GWU is gratefully acknowledged.

[1] E. F. Kneller and F. E. Luborsky, J. Appl. Phys. **34**, 656 (1963); K. Haneda, Can. J. Phys. **65**, 1233 (1987).
[2] G. Bottoni, D. Candolfo, A. Cecchetti, and F. Masoli, J. Magn. Magn. Mater. **116**, 285 (1992).
[3] R. D. Shull, R. D. McMichael, J. J. Ritter, and L. H. Bennett, in *Nanophase and Nanocomposite Materials*, edited by S. Komarnemi, J. C. Parker, and G. J. Thomas, Mater. Res. Soc. Symp. Proc. Vol. 286 (MRS, Pittsburgh, 1993), p. 449.
[4] C. L. Chien, in *Physical Phenomena in Granular Materials*, edited by G. D. Gody, T. H. Geballe, and Ping Sheng, Mater. Res. Soc. Symp. Proc. Vol. 195 (MRS, Pittsburgh, 1990), p. 411.
[5] R. D. Shull, J. J. Ritter, A. J. Shapiro, L. J. Swartzendruber, and L. H. Bennett, J. Appl. Phys. **67**, 4490 (1990).
[6] M. Pardavi-Horvath and L. Takacs, IEEE Trans. Magn. **MAG-28**, 3186 (1992).
[7] L. Takacs and M. Pardavi-Horvath, 121st TMS Annual Meeting, San Diego, CA, March 1–5, 1992 (in press).
[8] P. Matteazzi and G. Le Caer, J. Am. Ceramic Soc. **75**, 2749 (1991).
[9] L. Takacs, Mater. Lett. **13**, 119 (1992).
[10] L. Takacs, Nanostructured Mater. **2**, 241 (1993).
[11] Courtesy of F. Cser, Monash University, Australia.
[12] M. Pardavi-Horvath and L. Takacs, J. Appl. Phys. **73**, 6958 (1993).

Fe-Al_2O_3 nanocomposites prepared by high-energy ball milling

Søren Linderoth
Materials Department, Risø National Laboratory, DK-4000 Roskilde, Denmark

Michael S. Pedersen
Physics Department, Technical University of Denmark, DK-2800 Lyngby, Denmark

Nanocomposites of α-Fe and α-Al_2O_3, prepared by high-energy ball milling, exhibit coercivities which are enhanced by about two orders of magnitude with respect to the bulk value. The degree of enhancement depends on the volume fraction (x_v) of Fe, with a maximum for $x_v \approx 0.25$. The effect is ascribed to the production of single-domain magnetic grains. Mössbauer spectroscopy reveals the presence of iron oxide phases which could not be seen by x-ray and electron diffraction measurements.

I. INTRODUCTION

Magnetic particles in the size range below about 15 nm are single-domain particles. Such particles are of significant technological importance because single-domain particles exhibit superior magnetic properties compared to multidomain materials, e.g., single-domain particles can yield coercivities 100–1000 times higher than that of the bulk material.[1] Agglomeration of single-domain sized particles typically diminishes the otherwise enhanced magnetic properties. Separation of the magnetic particles by a nonmagnetic material may retain, or even improve, the superior magnetic properties, e.g., films of ultrafine magnetic particles embedded in a metal or ceramic matrix have resulted in large-coercivity materials.[2] Usually such films are prepared by cosputtering of two immiscible elements, e.g., Fe-Cu or Fe-Al_2O_3.[2,3] Here we report on the preparation of Fe-Al_2O_3 nanocomposite powders by high-energy ball milling.

II. EXPERIMENTAL

Ball milling of fine powders of α-Al_2O_3 and α-Fe (1–10 μm) was performed in a Fritsch (Pulverisette 5) planetary mill. Powder to ball weight ratio was 1:20 with a total of 9.6 g powder per vial. The ball and vial materials were tungsten carbide. The vial was sealed in an argon-filled glove box before milling the powder for 70 h. Samples with Fe volume fractions (x_v) in the range 0.1–0.5 were prepared and investigated.

The prepared samples were studied by a number of techniques: x-ray and electron diffraction, transmission and scanning electron microscopy, Mössbauer spectroscopy, and magnetization measurements.

X-ray diffraction measurements were obtained by using Cu K_α radiation from a Philips powder diffractometer equipped with a single-crystal monochromator in the diffracted beam.

Transmission electron microscopy and electron diffraction studies were performed by using a *JEOL* 2000× microscope operating at 200 kV.

Mössbauer spectroscopy spectra were obtained by using a constant acceleration spectrometer with a source of ^{57}Co in rhodium. The linewidth obtained for an α-Fe foil reference sample was smaller than 0.25 mm s^{-1} (FWHM), both at room temperature and at 80 K. The spectra were fitted with Lorentzian lines using a least-squares method.

Magnetization measurements were performed at room temperature employing a vibrating-sample magnetometer.

III. RESULTS AND DISCUSSION

Figure 1 shows the x-ray diffraction spectrum of the $Fe_{0.3}(Al_2O_3)_{0.7}$ sample. The peaks are significantly broadened with respect to the peaks in spectra obtained of μm-sized particles. Besides α-Fe and α-Al_2O_3 also WC is observed in the x-ray diffraction spectrum. From the excess broadening of the lines the crystallite size of the α-Fe is estimated to be about 9 nm. The x-ray diffraction spectra of the samples with different volume fraction of Fe indicated similar mean sizes. Dark-field transmission electron micrographs of the sample with $x_v = 0.1$ confirmed the presence of nanometer-sized crystallites, but indicated a wide distribution of crystallite sizes.

Neither the x-ray nor the electron diffraction patterns indicated any presence of iron oxides in the samples. However, Mössbauer spectra of the samples clearly showed the presence of iron oxide. Figure 2 shows Mössbauer spectra obtained at 80 K. The six-line pattern of α-Fe is easily recognized. The remaining spectrum is well described by a doublet ($\delta = 1.1$ mm s^{-1} and a quadrupole splitting of about 1.9 mm s^{-1}) due to Fe^{2+}. The linewidth of absorption lines due to α-Fe are broadened with respect to the intrinsic linewidth. This broadening is most probably due to a large fraction of the iron atoms being situated in interface regions, with modified hyperfine parameters due to lattice distortions in this region. Plastic strain may also be affecting the Mössbauer spectrum. Mössbauer spectra of assemblies of 5 nm nanoparticles of α-iron have previously been shown to exhibit broad absorption lines due to the presence of an interfacial component.[4]

The relative area of the component ascribed to iron oxide was, from the Mössbauer spectra, observed to increase with decreasing x_v. In Table I the relative number of oxidized iron atoms, obtained from fittings of the spectra in Fig. 2, are given as a function of x_v. Surely, this is the main reason for the observed decrease of the saturation magneti-

 0021-8979/94/75(10)/5867/3/$6.00 © 1994 American Institute of Physics

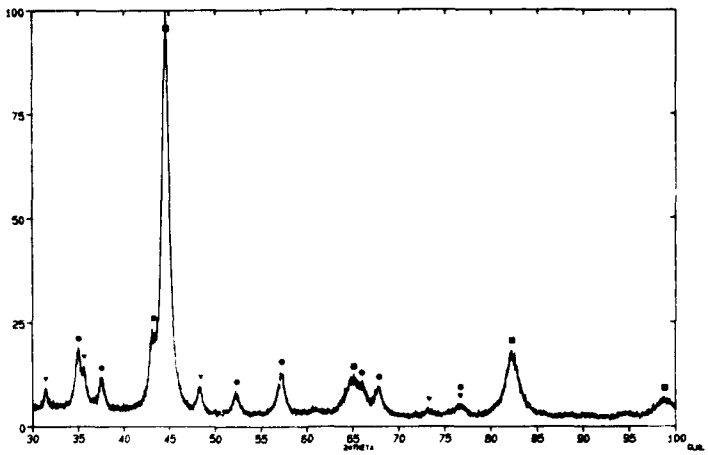

1. X-ray diffraction curve of ball-milled $Fe_{0.3}(Al_2O_3)_{0.7}$. Squares, balls, and triangles indicate the positions of the diffraction lines of α-Fe, α-Al_2O_3, and respectively.

zation (M_s) per iron atom for decreasing x_v. Table I shows M_s, as well as M_s^{corr}, where the latter is the saturation magnetization per iron atom corrected for the number of iron atoms in the oxide when these are assumed not to contribute to the magnetization of the samples. The presence of iron oxide may also affect other magnetic properties, e.g., the coercivity of iron particles have been found to be much influenced by surface oxide components.[5]

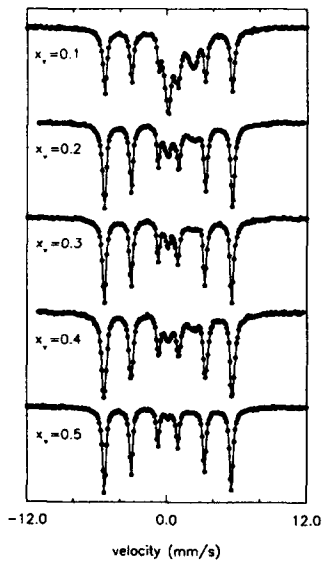

FIG. 2. Mössbauer spectra of ball-milled $Fe_x(Al_2O_3)_{1-x}$ samples, with x_v being the volume fraction of iron. The spectra were obtained at 80 K.

Figure 3 shows the coercivity, at room temperature, as a function of x_v. Maximum coercivity ($\approx 3\times10^4$ A m^{-1}) is found for $x_v \approx 0.25$. For comparison, the coercivity of bulk α-iron is about 2×10^2 A m^{-1}, i.e., about two orders of magnitude smaller. We ascribe this enhancement of the coercivity to be due to a reduction of the crystallite size to the size region of single-domain particles. If the crystallite size would be much less than the about 10 nm deduced for the crystallites of the presently investigated samples, superparamagnetic behavior would begin to cause very low coercivities.

When approaching the percolation limit ($x_p \approx 0.5$) the coercivity decreases. This is probably due to magnetic exchange interactions between the crystallites. Above the percolation threshold the particles may no longer be regarded as truly single domain. In Fig. 3 coercivities found by Ambrose

TABLE I. The relative number of oxidized Fe atoms are given as a function of the volume fraction (x_v) of Fe in the Fe-Al_2O_3 nanocomposites. The saturation magnetization (M_s^{Fe}) is per Fe atom in the sample. $M_s^{\text{Fe, corr}}$ is corrected for the amount of oxidized iron, assuming that oxidized iron atoms contribute insignificantly to the magnetization. The magnetization of bulk iron at 298 K is 217 J T^{-1} kg^{-1}.

x_v	Oxidized Fe (%)	M_s^{Fe} (J T^{-1} kg^{-1})	$M_s^{\text{Fe, corr}}$ (J T^{-1} kg^{-1})
0.1	49.5	91.6	181
0.2	23.2	157.3	205
0.3	19.4	172.2	214
0.4	17.0	176.0	212
0.5	8.6	188.8	207

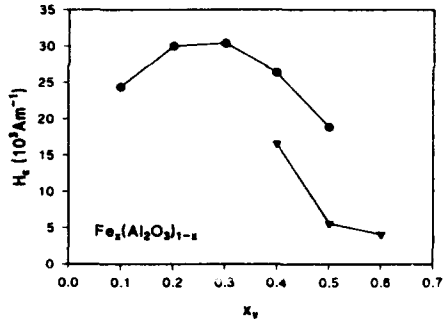

FIG. 3. Room-temperature coercivity as a function of x_v after 70 h of ball milling. Solid triangles are data from Ref. 6.

et al.[6] on similarly prepared samples are also shown. The coercivities obtained in the present work are found to be significantly larger. This may be an effect of different ball milling conditions (e.g., milling velocity and weight ratios between powder and balls).

Figure 4 shows the remanent magnetization for the different samples at room temperature. The remanent magnetization is seen to peak at $x_v=0.3$, which is about the composition region where also H_c has its maximum value. The decrease of M_r for x_v below 0.3 is due to the decreasing amount of iron in the samples. When the remanent magnetization is given relative to the saturation magnetization of the samples, maximum is obtained for the sample with the lowest content of iron, decreasing monotonically for increasing x_v.

IV. CONCLUSIONS

High-energy ball milling of mixtures of μm-sized particles of α-iron and α-Al_2O_3 was found to yield nanocomposite materials with an α-Fe crystallite size of about 9 nm. The coercivity of the ball milled samples was enhanced by about two orders of magnitude with respect to bulk α-iron. Mössbauer measurements revealed the presence of iron oxide phases, which were not seen in x-ray and electron diffraction patterns of the samples.

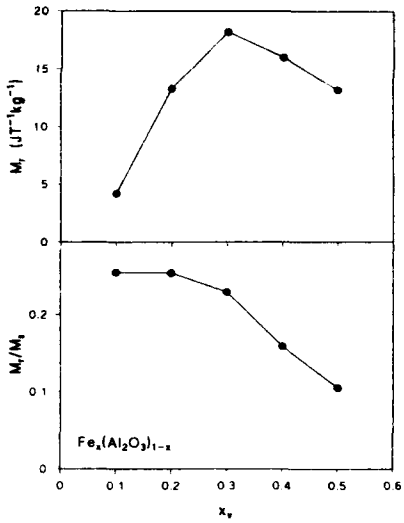

FIG. 4. The upper figure shows the remanent magnetization per mass unit of the sample. The lower figure shows the remanent magnetization, relative to the saturation magnetization, as a function of x_v. The values are obtained at room temperature.

ACKNOWLEDGMENT

O. V. Nielsen is acknowledged for the use of the magnetometer.

[1] G. Xiao and C. L. Chien, J. Appl. Phys. **63**, 4252 (1988).
[2] C. L. Chien, in *Science and Technology of Nanostructured Magnetic Materials*, edited by G. C. Hadjipanayis and G. A. Prinz (Plenum, New York, 1991), p. 477.
[3] J. L. Dormann, C. Djega-Mariadassou, and J. Jove, J. Magn. Magn. Mater. **104-107**, 1567 (1992).
[4] U. Herr, J. Jing, R. Birringer, U. Gonser, and H. Gleiter, Appl. Phys. Lett. **50**, 472 (1987).
[5] G. C. Hadjipanayis, S. Gangopadhyay, L. Yiping, C. M. Sorensen, and K. J. Klabunde, in *Science and Technology of Nanostructured Magnetic Materials*, edited by G. C. Hadjipanayis and G. A. Prinz (Plenum, New York, 1991), p. 497.
[6] T. Ambrose, A. Gavrin, and C. L. Chien, J. Magn. Magn. Mater. **116**, L311 (1992).

Synthesis and properties of α''-$Fe_{16}N_2$ in magnetic particles

Xiaohua Bao and Robert M. Metzger
Department of Chemistry and Center for Materials for Information Technology, University of Alabama, Tuscaloosa, Alabama 35487-0336

Massimo Carbucicchio
Department of Physics, Università di Parma, Viale delle Scienze, I-43100 Parma, Italy

The α''-$Fe_{16}N_2$ phase was synthesized by a nitriding, quenching, and tempering process starting from Fe_2O_3. Acicular γ-Fe_2O_3 was first reduced to α-Fe under H_2, then it was converted to γ-austenite at 650–700 °C by nitriding using a NH_3-H_2 mixed gas. A martensitic transformation to α'-martensite occurred when the sample was quenched in liquid nitrogen. Finally, the α''-$Fe_{16}N_2$ phase was formed from the α'-martensite by tempering in the temperature range 120–200 °C. In order to increase the extent of the martensitic transformation, acicular Fe_2O_3 particles with 10–15 at % MnO_2 were prepared by oxidizing Fe^{++} and Mn^{++} in alkaline aqueous solution. When a quenched sample, which contains martensite, α-Fe, and austenite, was tempered at 200 °C for different times, the magnetic moment first increased (transformation of α'-martensite to α''-$Fe_{16}N_2$); the highest magnetic moment was obtained at about 60 min of tempering. Using even longer tempering times, the magnetic moment decreased (decomposition of α''-$Fe_{16}N_2$ to α-Fe and γ'-Fe_4N). Only a very small amount of γ'-Fe_4N was formed after tempering at 120 °C for one week. The average coercivity of the samples nitrided at 650–700 °C is about 200–300 Oe; the sample magnetization is about 170 emu g^{-1}. Mössbauer spectroscopy and x-ray diffraction confirm the presence of α''-$Fe_{16}N_2$. The estimated mole fraction of α''-$Fe_{16}N_2$ (which should be called more simply Fe_8N) is 0.30–0.40. The low coercivity of the final product indicates that sintering of the acicular particles occurred, presumably because the silica protective coating of the particles did not resist the high temperatures needed to form austenite.

Because of the reported large saturation magnetization (>300 emu g^{-1}) of α''-$Fe_{16}N_2$, intensive efforts have been made to form this material in thin films by different methods.[1–3] α''-$Fe_{16}N_2$ was first reported by Jack[3] in his comprehensive study of the Fe-N phase diagram. In this phase diagram,[4] the α''-$Fe_{16}N_2$ phase has a body-centered tetragonal structure[3] (a=5.72 Å, c=6.29 Å, space group I4/mmm) and is *metastable* for Fe_xN, ($6<x<11$, 150 °C$<T$<300 °C). This compound was formed by a nitriding, quenching, and tempering process and was considered as an ordered form of nitrogen martensite. α''-$Fe_{16}N_2$ also precipitates at the strain boundaries of supersaturated "nitrogen ferrite" (Fe_xN).[5–7] (Incidentally, the historical name α''-$Fe_{16}N_2$ should be replaced by the simpler name Fe_8N, as has already been done elsewhere.[8])

Kim and Takahashi[1] first reported the high magnetic moment of α''-$Fe_{16}N_2$ (B_S=2.83 T) in polycrystalline Fe-N thin films deposited by evaporation. Komuro *et al.*[2] reported its formation by molecular beam epitaxy on Fe(100)/$In_{0.2}Ga_{0.8}As$(100) and $In_{0.2}Ga_{0.8}As$(001) substrates; the reported saturation magnetic flux density B_S was from 2.8 to 3.0 T (3.1μ_B to 3.3μ_B per Fe atom).[2] Nakajima and Okamoto[9] reported the formation of crystalline α''-$Fe_{16}N_2$ phase in nitrogen-implanted epitaxial iron films on MgO substrates. Implantation of N_2^+ ions transformed α-iron into partially ordered nitrogen martensite (α'-Fe_xN) and α''-$Fe_{16}N_2$ (the ordered form of martensite). The amount of α''-$Fe_{16}N_2$ was increased from 16 to 24 wt % by annealing in vacuum at 150 °C for 2 h. Gao and Doyle[10] recently reported powder x-ray diffraction evidence for the formation of α''-$Fe_{16}N_2$ on sputtered single-layer Fe-N films.

In our previous work,[11] we tried to both nitride α-Fe and denitride γ'-Fe_4N directly at temperatures close to the reported metastable existence region[4] for α''-$Fe_{16}N_2$ (about 300 °C): in neither case was a detectable amount of α''-$Fe_{16}N_2$ formed. Here we wish to report the formation of α''-$Fe_{16}N_2$ particles (mixed with α-Fe and γ-austenite) in a practical and economical procedure.

For unalloyed particles, the starting material, acicular γ-Fe_2O_3 (from Magnox), was coated with sodium silicate or sodium borate at pH<7, filtered, washed with deionized water, and dried. For alloyed particles, manganese-iron oxide (MnO_2-Fe_2O_3; 10–15 at % Mn/Mn+Fe) was prepared by oxidizing $FeSO_4$ and $MnSO_4$ in alkaline aqueous solution through which air was bubbled, and then coating the resulting particles (typical sizes: 0.3 μm×0.06 μm×0.06 μm) with sodium silicate or sodium borate to protect them from spontaneous combustion.

2.0 g of SiO_2-coated γ-Fe_2O_3 or MnO_2-Fe_2O_3 powder were loaded into a quartz reactor in a Fisher Isotemp controlled-temperature furnace, through which nitrogen gas was passed until the temperature increased to 450 °C, then

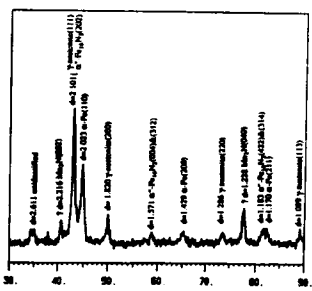

FIG. 1. X-ray diffraction spectrum for sample containing 15 at % Mn, treated with NH_3:H_2, tempered for 60 min at 200 °C.

 0021-8979/94/75(10)/5870/3/$6.00 © 1994 American Institute of Physics

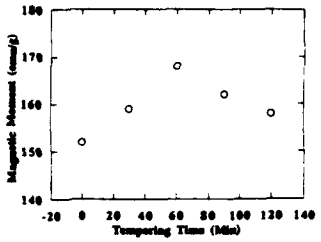

FIG. 2. Plot of saturation magnetic moment against tempering time at 200 °C for 15 at % Mn-Fe sample.

H_2 gas was passed at 450 °C for 2 h to reduce the oxides to Fe or Mn-Fe alloy powders. These powders were nitrided under a hydrogen-ammonia mixed gas (volume ratio 7:1–10:1) at 650–700 °C. After the nitriding, the reactor was quickly quenched into liquid nitrogen. The quenched sample was finally tempered under nitrogen at 120–200 °C for different periods of time.

The phases of the products were identified by powder x-ray diffraction (Rigaku DXG-2B) using Cu $K\alpha$ X radiation. The magnetic properties (magnetization, coercivity) were measured using a vibrating sample magnetometer (Digital Measurement Systems) with a maximum field of 14 kOe. The Mn content was known from the initial molar ratios, and also determined by an x-ray fluorescence spectroscopy attachment to a JEOL 8600 Super Probe scanning electron microscope. The presence and the contents of different Fe phases were evaluated by transmission Mössbauer spectroscopy. The absorption spectra were measured at room temperature using a 15 mCi ^{57}Co(Rh) source, and standard constant-acceleration techniques. A least-squares minimization routine was used to fit the spectra as a superposition of Lorentzian lines.

According to the Fe-N phase diagram,[4] iron particles, when nitrided under NH_3/H_2 mixed gas at temperatures

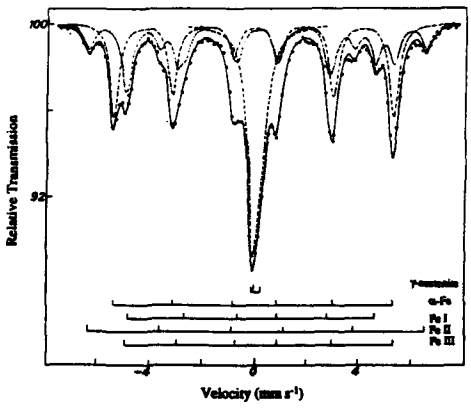

FIG. 3. Transmission Mössbauer spectrum for sample containing 15 at % Mn, treated with NH_3:H_2, tempered for 150 min at 200 °C.

TABLE I. Hyperfine magnetic fields, H_M (kOe), quadrupole splittings, ΔE_Q (mm s^{-1}), and isomer shifts against pure iron, IS (mm s^{-1}), for the contributions to the spectrum of Fig. 3.

Species	Site	H_M	ΔE_Q	IS
α''-$Fe_{16}N_2$	Fe I	292	−0.17	0.01
α''-$Fe_{16}N_2$	Fe II	397	−0.04	0.07
α''-$Fe_{16}N_2$	Fe III	317	0.15	0.10
α-Fe	···	330	0	0
γ-austenite	···	···	···	0.04
	···	···	0.37	0.07

above 600 °C, form nitrogen γ-austenite; when austenite is quenched to low temperature, it undergoes a "martensitic" transformation to α'-martensite (a solid solution of N in Fe): the conversion efficiency to martensite depends on the quenching temperature. In our work, the γ-Fe_xN particles were quenched at different temperatures by putting the quartz reactor into ice water, dry ice acetone, or liquid nitrogen. Powder x-ray diffraction data showed that, the lower the quenching temperature, the higher was the extent of martensitic transformation. This is because the speed of the temperature change in the sample determines the molar ratios of α'-martensite, α-iron, and retained γ-austenite; this is described by the time and temperature transformation (TTT) diagram for the martensitic transformation.[12] The extent of the martensitic transformation can also be increased by alloying manganese (10–15 at %)[4] into the particles.

The x-ray diffraction pattern showed that quenched samples were composed of α-Fe, α'-martensite and γ-austenite, while the tempered samples contained α-Fe, γ-austenite, and α''-$Fe_{16}N_2$. The x-ray diffraction powder pattern for a tempered sample (Fig. 1) shows peaks due to α-Fe [(110), (200), (211), a=2.86 Å]; α''-$Fe_{16}N_2$ [(202), (220), (004) and (312), (422), and (314)]; and γ-austenite [(111), (200), (220), (113); a=3.64 Å], two peaks that may possibly be due to Mn_2N [(002): d=2.216 Å, and (040): d=1.228 Å], plus one unassigned peak [d=2.611 Å]. The angular resolution of the x-ray diffraction pattern was not sufficient to detect the expected small lattice expansion due to the presence of Mn (whose single-bond metallic radius is 0.5% larger than that of Fe). The peaks due to α''-$Fe_{16}N_2$ are broad, and mostly overlap with peaks due to other species. The one nonoverlapped peak at d=1.571 Å is consistent with the (004) and (312) reflections of α''-$Fe_{16}N_2$. Estimates of the molar fractions of the several phases seen in Fig. 1 could not be made with certainty.

TABLE II. Relative population for 15 at % Mn alloyed particles tempered at 200 °C for different times (t/min).

		Population (%)			
Species	Site	t=45	t=60	t=150	t=210
α''-$Fe_{16}N_2$	Fe I	12.3	9.7	14.2	13.9
α''-$Fe_{16}N_2$	Fe II	12.3	9.7	8.4	10.3
α''-$Fe_{16}N_2$	Fe III	15.9	15.8	13.7	13.4
α-Fe	···	29.5	29.1	32.7	32.0
γ-austenite	···	30.0	35.7	31.0	30.4

Recent transmission electron microscopy has shown unambiguous evidence for the presence of the α''-$Fe_{16}N_2$ phase; this evidence will be discussed in a later publication.

The saturation magnetization for unalloyed Fe particles (no Mn) before tempering was about 170 emu g^{-1}, which is considerably lower than that of bulk α-Fe (210 emu g^{-1}), possibly due to the surface oxidation of the sample. Alloying manganese (15 at %) reduced the magnetic moment of the particles to about 150 emu g^{-1} before tempering. When the martensite-containing sample was tempered at 200 °C for different times, the magnetic moment at first increased, due to the transformation to α''-$Fe_{16}N_2$: the highest magnetic moments (σ_S=170 emu g^{-1} for 15 at % Mn alloyed particles) were obtained for tempering times of about 45–60 min (Fig. 2). For longer tempering times, the magnetic moment decreased, because the α''-$Fe_{16}N_2$ phase decomposed to α-Fe and γ'-Fe_4N; this decomposition was much slower at the lower tempering temperatures. After tempering at 120 °C for one week, only a very small amount of γ'-Fe_4N was detected by powder x-ray diffraction. Sintering was observed after the high-temperature nitriding above 600 °C: the coercivity of the final particles was only about 200 Oe (for both pure Fe and Mn-Fe particles), while the coercivity of the particles reduced and nitrided at 450 °C was about 600 Oe. The average final particle shape may have become less acicular when nitriding above 600 °C, and coating the acicular oxide particles with sodium silicate or sodium borate did not keep the particles from sintering.

The Mössbauer spectra for all samples (tempered for different times) are very similar. Figure 3 shows the Mössbauer spectrum of 15 at % Mn alloyed particles tempered at 200 °C for 150 min. It can be interpreted as a superposition of contributions from pure α-Fe (one sextet), from γ-austenite (the central peak and quadrupole doublet), and from α''-$Fe_{16}N_2$ (three sextets). These three sextets correspond to the three different sites Fe I, Fe II, and Fe III in the crystal structure[3] of α''-$Fe_{16}N_2$, i.e., they correspond, respectively, to Fe atoms which are first, second, and third nearest neighbors with respect to nitrogen atoms. Table I gives the hyperfine parameters for the contributions to the spectrum: hyperfine magnetic fields (H_{hf}) in kOe, quadrupolar splittings (ΔE_Q) and isomer shifts against pure iron (IS) in mm s^{-1}. Figure 2 and the H_{hf} data of Table I agree quantitatively with the Mössbauer results of Nakajima and Okamoto,[13] but disagree with the lower-resolution data of Sugita *et al.*;[14,15] note that Mn is absent in the samples of Refs. 13, 14, 15.

Sample tempering conditions do not affect substantially the hyperfine parameters. The relative populations (as estimated from the contributions to the Mössbauer spectra) for samples treated at different tempering times are given in Table II. The amount of α''-$Fe_{16}N_2$ in the samples is about 30%–40%. As the tempering time increased, the contents of α''-$Fe_{16}N_2$ decreased slowly. The averaged ratios for Fe I, Fe II, and Fe III are about 4.5:4.5:7 for the samples tempered 45 and 60 min, and 6:4:6 for the samples tempered 150 and 210 min (the ratios reported by Nakajima and Okamoto[13] were 4:3:9), while in the crystal structure of α''-$Fe_{16}N_2$ the occupancy ratios should be 4:8:4. The low occupancy of the Fe II site might be a consequence of some lattice irregularity. The amount of retained nitrogen γ-austenite varied from 31% to 36%, during the tempering process at 200 °C: this relatively high percentage is due to the stabilization of the γ-austenite phase due to Mn.

The amount of Mn/Fe estimated by x-ray fluorescence is 20 at %, while the mixing stoichiometry was 15 at %.

In the Fe-Mn binary alloy system,[16] the magnetic moment at first drops slowly as the Mn increases; when the Mn concentration is greater than 7 at %, the α phase transforms to the nonmagnetic γ phase, and the magnetic moment drops rapidly. In our samples, the α phase is still present (0.3 Fe atom fraction); the Mn atoms may be distributed very inhomogeneously, or the quenching from high temperature to liquid-nitrogen temperature may have stabilized the α phase.

We now estimate the contribution of Fe_8N to the measured magnetization. Put most simply, the addition of N to the (Fe,Mn) alloy increases the measured magnetization from 150 to 170 emu g^{-1}. For the 15 at % Mn alloyed sample with t=60 min tempering, by neglecting the possible presence of small amounts of other ferromagnetic phases (such as γ-Fe_2O_3 and γ'-Fe_4N), by neglecting differences in densities, by assuming 0.85 atom fraction Fe/(Fe+Mn), by using the measured 0.352 Fe atom fraction of Fe_8N with σ_S=310 emu g^{-1}, and 0.291 Fe atom fraction of α-Fe(Mn) with σ_S=210 emu g^{-1}, the calculated magnetic moment of the sample becomes 144 emu g^{-1}, in moderate agreement with measured value of 170 emu g^{-1}. If we do not correct for the presence of Mn, then the calculated moment becomes, fortuitously, 0.291×210+0.352×310=170 emu g^{-1}.

We have shown that in a particulate sample prepared under close to industrial conditions, up to 30 at % can be converted to Fe_8N, historically known as α''-$Fe_{16}N_2$. The measured moment is in agreement with estimates that Fe_8N should have a dramatically large bulk magnetization. The coercivity could not be raised above 200 Oe, because the acicular particles sintered at the high temperatures used. Further work on better coating procedures is in progress.

[1] T. K. Kim and M. Takahashi, Appl. Phys. Lett. **20**, 492 (1972).
[2] M. Komuro, Y. Kozono, M. Hanazono, and Y. Sugita, J. Appl. Phys. **67**, 5126 (1990).
[3] K. H. Jack, Proc. Roy. Soc. London Sect. A **208**, 216 (1951).
[4] K. H. Jack, Proc. Roy. Soc. London Sect. A **208**, 200 (1951).
[5] P. Ferguson and K. H. Jack, Philos. Mag. A **52**, 509 (1985).
[6] U. Dahmen, P. Ferguson, and K. H. Westmacott, Acta Metall. **35**, 1037 (1987).
[7] Y. Nakada, W. C. Leslie and T. P. Churay, Trans. ASM **60**, 223 (1967).
[8] W. Pies and A. Weis, in *Landolt–Börnstein Numerical Data and Functional Relationships in Science and Technology, New Series*, edited by K.-H. Hellwege, Vol. 7, Part c1 (Springer, Berlin, 1978), p. 78.
[9] K. Nakajima and S. Okamoto, Appl. Phys. Lett. **54**, 2536 (1989).
[10] C. Gao and W. D. Doyle, J. Appl. Phys. **73**, 6579 (1993).
[11] X. Bao, R. M. Metzger, and W. D. Doyle, J. Appl. Phys. **73**, 6734 (1993).
[12] D. A. Porter and K. E. Easterling, *Phase Transformations in Metals and Alloys* [Van Nostrand Reinhold (UK), Wokingham, Berkshire, 1981], p. 287.
[13] K. Nakajima and S. Okamoto, J. Appl. Phys. **65**, 4357 (1989).
[14] Y. Sugita, K. Mitsuoka, and M. Komuro, IEEE Trans. Magn. Jpn. **6**, 1061 (1991).
[15] Y. Sugita, K. Mitsuoka, M. Komuro, H. Hoshiya, Y. Kozono, and M. Hanazono, J. Appl. Phys. **70**, 5977 (1991).
[16] R. M. Bozorth, *Ferromagnetism* (Van Nostrand, New York, 1978), p. 235.

Magnetism and spin dynamics of nanoscale FeOOH particles

M. M. Ibrahim, G. Edwards, and M. S. Seehra[a)]
Physics Department, West Virginia University, P. O. Box 6315, Morgantown, West Virginia 26506-6315

B. Ganguly and G. P. Huffman
Consortium for Fossil Fuel Liquefaction Science, 233 Mining and Mineral Resources Building, University of Kentucky, Lexington, Kentucky 40506

The nature of magnetism and electron paramagnetic resonance (EPR) spin dynamics in 30 Å particles of FeOOH have been investigated in the range 5–350 K. X-ray diffraction shows that the particles are neither α-Fe_2O_3 nor α-FeOOH based and they convert to Fe_3O_4 (α-Fe_2O_3) on heating to 800 K in vacuum (air). Magnetization M vs T data show a blocking temperature T_B in the range 40 K$<T_B<$100 K so that for $T\geq 100$ K, scaling of M with H/T for H up to 50 kOe verifies superparamagnetism. In EPR, both the linewidth ΔH and the g value decreases upon increasing T so that near 300 K, $g\simeq 2.05$ (characteristic of Fe^{3+}). A model of motional narrowing is used to explain the ΔH vs T behavior. The dramatic changes in M, ΔH, g value, and the recoilless fraction of Mössbauer spectroscopy observed near 50 K are all related to the thermal motion of the superparamagnetic nanoscale particles.

I. INTRODUCTION

In this work, the nature of magnetism and spin dynamics of nanoscale (~30 Å) iron oxyhydroxide particles have been investigated by temperature dependent magnetization and electron paramagnetic resonance (EPR) spectroscopy, supplemented by Mössbauer, and x-ray diffraction (XRD) measurements. This sample, available commercially (called nanocat™ by Mach I, Inc.[1]), is used in rocket propellants and it is also a part of a group of iron-based oxides with potential applications in direct coal liquefaction.[2,3] In addition to the inherent interest in the properties of nanoscale particles vis-a-vis bulk materials, the structure of this material is also controversial. Whereas, the phase of this material is described as α-Fe_2O_3 by the manufacturer, a recent work by Zhao *et al.*,[4] using the extended x-ray fine structure (EXAFS) and the x-ray absorption near-edge structure (XANES) studies indicate the structure to be an iron oxyhydroxide (FeOOH), with the valence state of iron being Fe^{3+}. Bulk α-FeOOH is a known antiferromagnet with $T_N\simeq 358$ K (Ref. 5) so that an EPR signal from α-FeOOH is not expected for $T<T_N$. Initial room-temperature EPR of the nanocat yielded a strong signal with $g=2$, characteristic of Fe^{3+} indicating that either the structure is different from α-FeOOH and α-Fe_2O_3 or the $T_N<300$ K for the nanocat. Temperature variation of the EPR was then undertaken which yielded strong temperature variation of the g value and the linewidth. To further elucidate the nature of magnetism in this material, temperature and field variation of the magnetization were also investigated, supplemented by room-temperature XRD studies of the sample annealed under different conditions. Finally, the recent temperature-dependent Mössbauer studies of Ganguly *et al.*[6] are also considered in the interpretation of the data. Details of these results are presented below.

a)Address correspondence to this author.

II. EXPERIMENTAL PROCEDURES

A superconducting quantum interference device (SQUID) magnetometer (Quantum Design Model MPMS) was used for magnetic studies in the 5–350 K range and for fields up to 50 kOe. The EPR studies reported here on the as-received sample were carried out on a Brucker x-band spectrometer for the range 10–350 K. The linewidth ΔH reported here are the peak-to-peak field separations in the absorption derivative and for g-value measurements, the cavity frequency ν was measured at each temperature and the resonance field H_0 is determined by the location of the zero of the absorption derivative. Then, $g=0.71448\nu/H_0$, where ν is in GHz and H_0 in kOe. The XRD spectra were taken on a Rigaku D/Max diffractometer.

III. EXPERIMENTAL RESULTS AND DISCUSSION

Figure 1 shows the XRD 2θ scans of the as-received sample, a vacuum-sealed sample heated to 700 K, and a sample heated to 700 K in air. For comparison, stick diagrams of the expected diffractograms for α-FeOOH, α-Fe_2O_3, and Fe_3O_4 are also shown. From the broadened (due to small particle size) two-line diffractogram of the nanocat sample, it is not possible to identify its phase. However, it is quite clear that the material structure is not based on the structures of either α-FeOOH or α-Fe_2O_3 since some prominent lines of these structures are not present in the nanocat diffractogram. Rather, a case may be made that basic structure is based on Fe_3O_4, although severe broadening of the line due to small particle size[7] limits an accurate identification. Using the Scherrer equation[8] and half width of the two lines from the high-angle side where there is no interference from the other lines of Fe_3O_4, a particle diameter $\simeq 20$ Å is estimated. This is in good agreement with the results of transmission electron microscopy measurements[8] which yielded a near Gaussian distribution of particles with a mean diameter of about 30 Å and particle range from 15 to 45 Å. In Fig. 1, we also show XRD patterns of the sample heated to about 700 K both in vacuum and in air. These studies

 0021-8979/94/75(10)/5873/3/$6.00 © 1994 American Institute of Physics

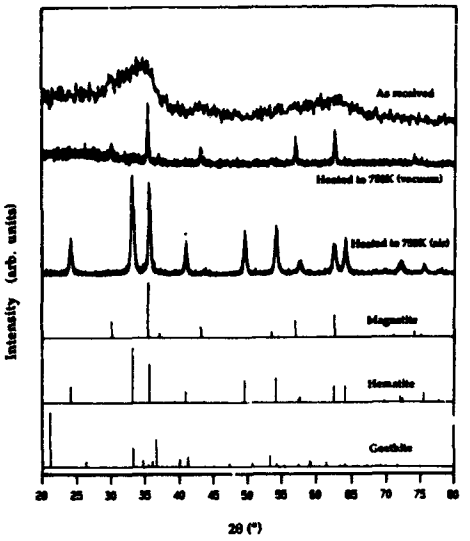

FIG. 1. X-ray diffractograms of the as-received nanocat, and nanocat heated to 750 K in vacuum and in air. Stick diagrams of magnetite, hematite, and goethite (α-FeOOH) are shown for comparison.

clearly show that heating in vacuum produces Fe_3O_4 whereas heating in air leads to α-Fe_2O_3. This result may provide some insight into the structure of the nanocat.[4]

The temperature variation of the magnetic susceptibility $\chi = M/H$, measured in $H = 100$ Oe, for the zero-field-cooled (zfc) and the field-cooled (fc) cases, is shown in Fig. 2, using the protocol described elsewhere.[9] The two curves begin to separate at temperatures as high as 200 K, although clear distinction is perhaps best evident only below about 100 K and there is a distinct peak in $d\chi/dT$ near 50 K. To verify whether $T_B \sim 100$ K is indeed the blocking temperature for superparamagnetism,[10] we measured M vs H at the selected

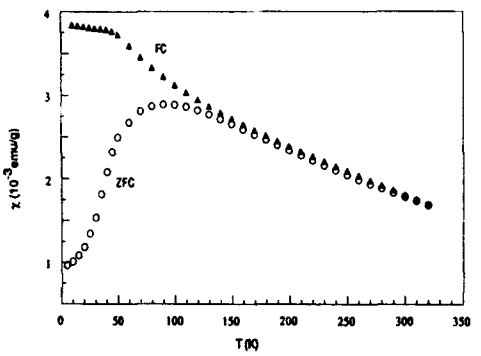

FIG. 2. Magnetic susceptibility $\chi = M/H$ vs temperature for the zero-field-cooled (zfc) and field-cooled (fc) nanocat in $H = 100$ Oe.

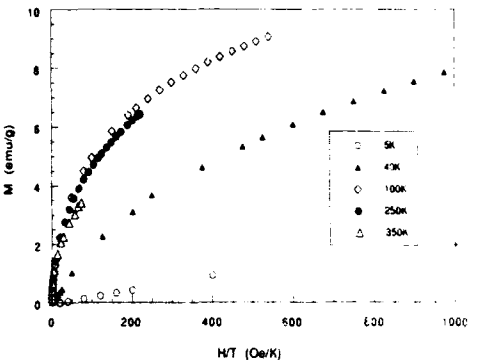

FIG. 3. Plots of measured magnetization M of the nanocat against H/T for several temperatures.

temperatures of 5, 40, 100, 250, and 350 K. Since for superparamagnetism, M should scale as H/T, we show in Fig. 3 plots of M vs H/T for the temperatures noted above. The data at 100, 250, 350 K collapse on to one curve as expected for superparamagnetism for $T \geq T_B$ (Refs. 8,10) so that T_B for this material is in the range 40 K $< T_B <$ 100 K, perhaps more closer to 100 than 40 K (Fig. 2).

Figure 4 shows the EPR spectra at 20, 70, and 310 K. It is clear that both the g value and the linewidth ΔH increase as T decreases. Also the line shape becomes quite asymmetric at the lower temperatures. Figure 5 shows the temperature variation of ΔH and the g value for the as-received sample.

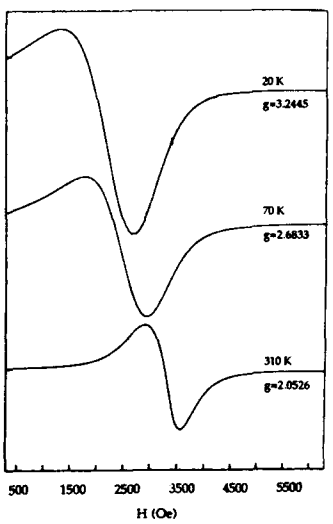

FIG. 4. Magnetic field scans of the EPR spectra of the nanocat at three temperatures.

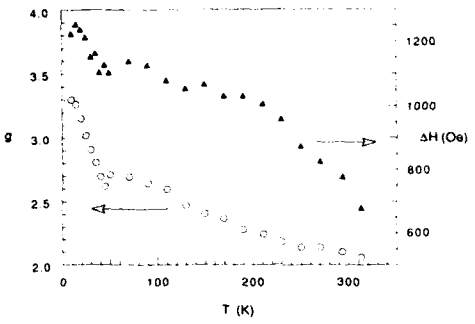

FIG. 5. Temperature dependence of the EPR linewidth ΔH and the g value for the nanocat.

Comparing the data in Fig. 2 and Fig. 5, it is evident that there are correlations of the temperatures at which significant changes in χ, g, and ΔH occur.

We consider the narrowing of the EPR line with increasing T as one of the most interesting results of this work. Sharma and Waldner[11] have discussed the superparamagnetic resonance of the ultrafine particles of Fe_3O_4 in ferrofluids in terms of the response time τ_{sp} of the magnetic moment to thermal forces and the Larmor precession time τ_L in a magnetic resonance field H_0. This analysis yields $f \equiv \tau_{sp}/\tau_L = M_s V H_0/2\pi k_B T$, where M_s is the saturation magnetization of a superparamagnetic particle of volume V_0 and k_B is the Boltzmann constant. If $f \ll 1$, i.e., $\tau_{sp} \ll \tau_L$, then motional narrowing of the superparamagnetic resonance is valid. Note that f decreases as T increases, thus increasing the motional narrowing effect, in agreement with the experimental observations of Fig. 5. Using the data of Fig. 3 and particle diameter of 30 Å, we find $f = 0.003$ at 300 K so that the condition $f \ll 1$ for motional narrowing is valid in this case. (For M_s, we have used the value of M at 50 kOe for this calculation. The lack of saturation of M even at 50 kOe may be due to pinning of the moments of the surface spins[12] of the nanocat.)

The g value of the EPR line at 310 K equals 2.05, characteristic of an ion with negligible spin-orbit contribution such as Fe^{3+}. This result is consistent with the conclusion of Zhao *et al.*[4] from the EXAFS and XANES studies of this material. Part of the g shift with lowering T (Fig. 5) may be due to the increase in the demagnetizing fields. A demagnetizing field ~100 Oe at 10 K is estimated from the data of Fig. 2. However, shifts in H_0 are ~1000 Oe at 10 K. Therefore the g shifts as well as the observed asymmetry of the line shapes at the lower temperatures is not understood at present.

The Mössbauer spectroscopy studies of this sample by Ganguly *et al.*[6] show that the recoilless fraction decreases dramatically with increasing T, becoming effectively zero near 50 K so that no Mössbauer spectra is observed above 50 K unless the sample is compacted or frozen in cornuba wax. One can therefore infer that dramatic changes in χ, ΔH, g, and the recoilless fraction of the nanocat observed near 50 K are all related to the same phenomenon, viz., thermal motion of the nanoscale superparamagnetic particles. The motional narrowing of the EPR line is a dramatic consequence of this thermal effect. Preliminary measurements at still higher temperatures have shown that this narrowing continues till about 550 K above which the sample begins to convert to Fe_3O_4 when heated under vacuum. Further studies in this interesting system are in progress.

ACKNOWLEDGMENTS

This work was supported in part by the U. S. Department of Energy, Grant Nos. DE-FC22-90PC90029 and DE-FC22-93PC93053. We thank Mach I, Inc. for supplying the samples used in these studies.

[1] Mach I, Inc., 340 East Church Road, King of Prussia, PA 19406.
[2] V. R. Pradhan, J. W. Tierney, I. Wender, and G. P. Huffman, Energy Fuels **5**, 497 (1991).
[3] G. P. Huffman, B. Ganguly, J. Zhao, K. R. P. M. Rao, N. Shah, Z. Feng, F. E. Huggins, M. M. Taghiei, F. Lu, I. Wender, V. R. Pradhan, J. W. Tierney, M. S. Seehra, M. M. Ibrahim, J. Shabtai, and E. M. Eyring, Energy Fuels **7**, 295 (1993).
[4] J. Zhao, F. E. Huggins, Z. Feng, F. Lu, N. Shah, and G. P. Huffman, J. Catal. **143**, 499 (1993).
[5] S. Bocquet and S. J. Kennedy, J. Magn. Magn. Mater. **109**, 260 (1992).
[6] B. Ganguly, F. E. Huggins, Z. Feng, and G. P. Huffman (unpublished).
[7] M. M. Ibrahim, J. Zhao, and M. S. Seehra, J. Mater. Res. **7**, 1856 (1992).
[8] Z. Feng, J. Zhao, F. E. Huggins, and G. P. Huffman, J. Catal. **143**, 510 (1993).
[9] Z. Feng and M. S. Seehra, Phys. Rev. B **45**, 2184 (1992-I).
[10] W. F. Brown, Phys. Rev. **130**, 1677 (1963).
[11] V. K. Sharma and F. Waldner, J. Appl. Phys. **48**, 4298 (1977).
[12] A. E. Berkowitz, J. A. Lahut, I. S. Jacobs, L. M. Levinson, and D. W. Forester, Phys. Rev. Lett. **34**, 594 (1975).

Magnetic properties of microemulsion synthesized cobalt fine particles

J. P. Chen, K. M. Lee, and C. M. Sorensen
Department of Physics, Kansas State University, Manhattan, Kansas 66506

K. J. Klabunde
Department of Chemistry, Kansas State University, Manhattan, Kansas 66506

G. C. Hadjipanayis
Department of Physics and Astronomy, University of Delaware, Newark, Delaware 19716

Two microemulsion systems, the ternary system H_2O/AOT/isooctane and the binary system DDAB/toluene, were used to prepare metallic cobalt particles by borohydride reduction of a cobalt salt. The particles prepared in the AOT system were extremely small and superparamagnetic with magnetic moment per particle of $11.5\mu_B$, a blocking temperature of 2 K, and $\sigma_s = 146$ emu/g at 1.7 K. The magnetic moment and σ_s combined imply a particle size of about 5.4 Å. However, the particles made in the DDAB system were relatively large, ~10 nm. They were ferromagnetic at room temperature but with no coercivity.

I. INTRODUCTION

Inversed micelles can be formed by dissolving surfactants in organic solvents either in the presence or in the absence of water. These micelles can solubilize inorganic reagents, and mixing of such solutions can be used to create very small particles. The particle size can be controlled by adjusting the water to surfactant molar ratio or reagent concentrations. Recently, the microemulsion synthesis technique has seen considerable use in preparing metallic particles,[1,2] semiconductor particles,[3] and metal boride particles.[4] Our goal is to study the magnetic properties of very small particles, and we are exploring the microemulsion synthesis technique as a possibly viable method of synthesis. In this work we describe two different microemulsion systems to prepare cobalt particles. One of the systems is the ternary system H_2O/AOT/isooctane with the precursors of the reaction confined in the micelles in the presence of water. The other is the binary system DDAB/toluene. The precursors are trapped in the empty cavity without water. Sodium borohydride is used as the reducing reagent. The synthetic methods and concomitant small size have considerable effect on the magnetic properties.

II. EXPERIMENTAL METHODS

All organic solvents and the distilled, deionized water were degassed with Ar. All the reactions were carried out under Ar to prevent the oxidation of the final products.

The first system we used to produce Co particles was the anionic surfactant system H_2O/AOT/isooctane. 11.2 ml of 0.27 M AOT (sodium di-2-ethyl hexylsulfosuccinate) in isooctane was mixed with either 0.6 ml of 0.3 M $CoCl_2$ or 0.6 M $NaBH_4$ aqueous solutions. They were stirred and sonicated until transparent. The molar ratio w of water to AOT in the water-in-oil microemulsion was 11. The ratio of Co^{2+} to BH_4^- was 1:2. When the two microemulsions of $CoCl_2$ and $NaBH_4$ were mixed together, the solution turned from light pink to black in a few seconds. This black colloid was stable for about ten days. Exposed to the air, the colloid turned from black to light brown in about an hour. The isooctane could be evaporated at room temperature to yield a *paste* sample of Co particles in AOT. *Powder* samples were obtained by flocculating the colloids with acetone and water, then filtering, and washing with water to remove the AOT. Some powder samples were heat treated at 550 °C for 2 h under Ar protection in order to make the particles grow and/or crystallize.[5]

The second system was the cationic surfactant/solvent system with didodecyldimethylammonium bromide (DDAB) at 10 wt % dissolved in toluene. $CoCl_2 \cdot H_2O$ was dissolved in the DDAB solution at concentrations of either 0.005 or 0.01 M. A 5 M $NaBH_4$ aqueous solution was added in excess and stirred vigorously. The solution turned from blue to black and formed a stable colloid. The colloids were stable for more than one month, which is more stable than those made with AOT. This is most likely due to the fact that the surfactant DDAB adheres irreversibly to the metal colloid particles.[2] Since DDAB is insoluble in hexadecane it was added to the colloid to force the DDAB out of the solution. This procedure leaves the surfactant coated particles unprecipitated. The remaining colloid particles were slightly flocculated and could be removed from the supernatant above the precipitated DDAB by gentle filtration.

III. RESULTS AND DISCUSSIONS

A. Co particles made from the H_2O/AOT/isooctane system

The as-prepared particles in both the paste and the powder showed no structure in the x-ray diffraction (XRD) spectra, suggesting the particles were either smaller than the resolution limit of the XRD (~3 nm) or amorphous. However, the XRD spectra of the powder samples heat treated at 550 °C for 2 h showed solely the presence of Co.

Transmission electron microscope (TEM) was used to size the particles in the paste and powder samples. The particle sizes in the powder were estimated at about 4 nm in diameter. In the paste sample the largest particles were ~3 nm or perhaps smaller, but our ability to measure this size became limited by our TEM resolution.

Magnetization is plotted in Fig. 1 as a function of the applied field for the as-prepared paste sample. We see the

 0021-8979/94/75(10)/5876/3/$6.00 © 1994 American Institute of Physics

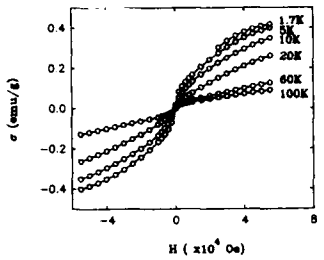

FIG. 1. Magnetization as a function of applied field for an AOT paste sample at different temperatures.

sample cannot be saturated even at 1.7 K and 55 kOe. This implies that the particles are very small. The saturation magnetization σ_s was found from a linear extrapolation of a σ vs $1/H$ graph. High-temperature curves of σ vs H show a kink at low field. When considered with the nonsaturability, this suggests that the sample consists of particles of two different sizes, a superparamagnetic and a ferromagnetic fraction. If we subtract the ferromagnetic fraction of magnetization and replot the data with H/T, the three curves for temperatures 20, 60, and 100 K superimpose as shown in Fig. 2, to imply superparamagnetism.

The low-field susceptibility χ was measured as a function of temperature and found to obey the Curie Law

$$\chi=\frac{\sigma_s\mu}{3kT}, \tag{1}$$

where μ is the magnetic moment per particle and k is Boltzmann's constant. From the slope of χ^{-1} vs T and the σ_s value, μ was obtained. The mass saturation magnetization and magnetic moment per particle are listed in Table I. The saturation magnetization of the Co particles is ~10% smaller than that of bulk Co (σ_{Co}=162.5 emu/g). From σ_s, μ, and the density of bulk Co, ρ=8.9 g/cm^3, we calculated the particle diameter to be 5.4 Å. We also cooled the sample in zero field, then measured the magnetization at 50 Oe while warming, to find a blocking temperature of T_B=2±2 K. If we make the assumption that these particles have the bulk anisotropy K=4.5×10^6 erg/cm^3, then the particle volume

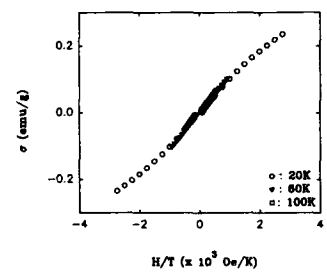

FIG. 2. Dependence of magnetization with the ferromagnetic fraction removed on H/T for the AOT paste sample at different temperatures.

TABLE I. Summary of σ_s and μ for samples made in the AOT system with w=11.

	σ_s (paste) (emu/g)	Co in 1 g paste (mg)	σ_s (Co) (emu/g)	μ (μ_B)
Sample 1	0.492	3.3	149	11.7
Sample 2	0.439	3.1	142	11.7
Sample 3	0.507	3.5	146	11.0

found from $V=25kT_B/K$ (Ref. 6) yields a diameter of 15 Å. Often small particles have order of magnitude larger anisotropy than the bulk.[7] If this were the case, the diameter would be 7 Å. These values are qualitatively consistent with the moment derived size.

The size calculated from the magnetic data is much smaller than that measured by TEM. One possible explanation is that each particle in the TEM pictures may consist of several 5 Å particles which are closely packed and could not be resolved by our TEM. High-resolution TEM study is necessary to determine if the substructure exists. Otherwise some unexplained and perhaps novel magnetic effect may have occurred.

B. Co particles prepared from the DDAB/toluene system

XRD of the as-prepared particles from the DDAB/toluene system showed the particles were metallic cobalt. Note that the products prepared from both systems were cobalt instead of Co_2B. Previous work[5] in nonmicelle aqueous solutions showed the product of the reaction to be Co_2B under anaerobic conditions, Co if in air. The difference might be related to the water structure in the water pool of the micelle. At low water content, water molecules bind at the micelle interface so that no free water can take part in the reaction. Pileni *et al.*[8] found the oxidation states of copper metallic cluster changed with the change of water content in the micelles.

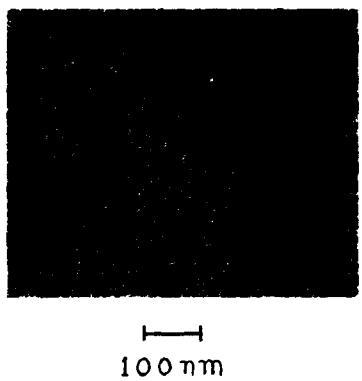

FIG. 3. TEM photograph of the cobalt particles made in the DDAB system with [Co^{2+}]=0.01 M.

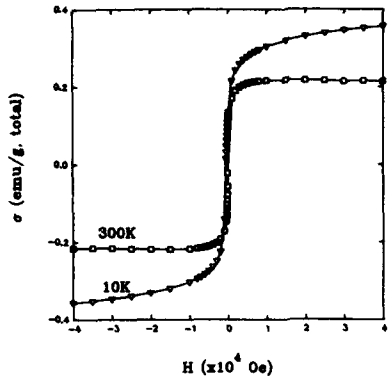

FIG. 4. Magnetization as a function of applied field at temperatures $T=10$ and 300 K for the cobalt particles made in the DDAB system with $[Co^{2+}]=0.01$ M.

TEM showed that as we changed the concentration of Co^{2+} ions from 0.005 to 0.01 M, the average particle size increased from 7.5 to 13 nm. An example TEM micrograph is given in Fig. 3. Many of the particles appear not to touch their neighbors, an indication of their thin surfactant coating.

Magnetic studies were carried with the superconducting quantum interference device (SQUID) magnetometer. After the samples were cooled in zero field, the magnetization was measured during warming. No obvious phase transition was observed from 10 to 350 K, implying the blocking temperature was >350 K. Hysteresis curves are given in Fig. 4. At $T=10$ K, both samples had a coercivity of several hundred oersted. At room temperature there was no coercivity, but the samples were saturated with an applied field of 5000 Oe. The reason why these ferromagnetic particles were so soft is not clear yet. Saturation magnetization per gram Co could not be measured because the Co concentration of these samples could not be determined. All the data are given in Table II.

The particle sizes were quite different with the two surfactant systems. Particles made from the AOT system were extremely small, 3 nm or smaller. Whereas the particles made from the DDAB system were relatively large, around 10 nm. This caused the particles to show quite different magnetic behavior: superparamagnetic as opposed to ferromagnetic.

TABLE II. Summary of magnetic data for the cobalt particles made in the DDAB system.

$(Co^{2+}=)$	0.005 M	0.01 M
TEM size	7.5±1 nm	13±2 nm
H_c (300 K)	0 Oe	0 Oe
H_c (10 K)	820 Oe	550 Oe
T_B	>350 K	>350 K

IV. CONCLUSIONS

We have made Co particles in both the H_2O/AOT/isooctane and DDAB/toluene microemulsion systems. We found the sizes of the particles to be quite different, which caused the different magnetic behavior. At room temperature the larger, ferromagnetic particles were very soft. The magnetic moment of the smaller superparamagnetic particles did not match well with the saturation magnetization and TEM determined particle size for undetermined reasons.

ACKNOWLEDGMENT

This work was supported by NSF Grant No. 9013930.

[1] M. Boutonnet, J. Kizling, P. Stenius, and G. Maire, Colloids Surf. **5**, 209 (1982).
[2] J. P. Wilcoxon and A. N. Mex, U. S. Patent No. 5 147 841 (1992).
[3] P. Lianos and J. K. Thomas, Chem. Phys. Lett. **125**, 299 (1986).
[4] I. Ravet, N. B. Lufimpadio, A. Gourgue, and J. B. Nagy, Acta Chim. Hung. **119**, 155 (1985).
[5] G. N. Glavee, K. J. Klabunde, C. M. Sorensen, and G. C. Hadjipanayis, Langmuir **8**, 771 (1992).
[6] B. D. Cullity, *Introduction to Magnetic Materials* (Addison–Wesley, New York, 1972).
[7] G. Xia, S. H. Liou, A. Levy, J. N. Taylor, and C. L. Chien, Phys. Rev. B **34**, 7573 (1986).
[8] M. P. Pileni, J. Phys. Chem. **97**, 6961 (1993).

Magnetic properties of carbon-coated rare-earth carbide nanocrystallites produced by a carbon arc method

B. Diggs and A. Zhou
Data Storage Systems Center NSF Research Experience for Undergraduate Participants, Carnegie Mellon University, Pittsburgh, Pennsylvania 15213

C. Silva, S. Kirkpatrick, N. T. Nuhfer, and M. E. McHenry
Department of Materials Science and Engineering, Carnegie Mellon University, Pittsburgh, Pennsylvania 15213

D. Petasis and S. A. Majetich[a)]
Department of Physics, Carnegie Mellon University, Pittsburgh, Pennsylvania 15213

B. Brunett and J. O. Artman
Department of Physics and Department of Electrical and Computer Engineering, Carnegie Mellon University, Pittsburgh, Pennsylvania 15213

S. W. Staley
Department of Chemistry, Carnegie Mellon University, Pittsburgh, Pennsylvania 15213

Carbon-coated gadolinum and holmium carbide nanocrystallites have been generated using a modification of the Huffman-Krätschmer carbon arc process. Bulk amounts of these particles were isolated from the other by-products using a magnetic field gradient. Transmission electron microscopy revealed the presence of 10–50 nm diameter crystallites coated with numerous graphitic layers. The nanocrystallite phases were identified as Gd_2C_3 and Ho_2C_3, respectively, by x-ray and electron diffraction. Magnetization measurements were performed using a superconducting quantum interference device magnetometer between ±5 T at temperatures ranging from 4 to 200 K. The magnetization curves were shown to scale as a function of H/T. The RE^{3+} sites in RE_2C_3 have C_3 site symmetry. For Gd_2C_3 the universal curve was fit with a Brillouin function consistent with the Gd^{3+} free-ion ground-state values of $J=7/2$ and $g=2$. The $^5I_8$ Ho^{3+} free-ion ground state is split, presumably due to a C_3 symmetry crystal field. Consequently, for Ho_2C_3 the Ho^{3+} free-ion parameters could not be used to fit the experimental data. Empirical fits to the Brillouin function yield a reduced moment of $7.5\mu_B$, compared to the free-ion value of $10.6\mu_B$. A similarly reduced moment was observed in holmium-containing endohedral fullerenes.

I. INTRODUCTION

A new area of fine particle magnetism arose when it was noted that carbon-coated nanocrystallites could be produced in a carbon arc;[1] subsequently this technique was applied to the generation of magnetic nanocrystallites.[2] Both para- and ferromagnetic nanocrystallites have been generated by this method; preparation details are discussed elsewhere.[2–4] Here we describe the magnetic behavior of the cubic rare-earth sesquicarbides, Gd_2C_3 and Ho_2C_3.

These nanocrystallites are one of several compounds produced in a modified Huffman Krätschmer carbon arc. One of the graphite electrodes is hollowed out and packed with a mixture of metal oxide and graphite cement. The magnetic nanoparticles are separated from nonmagnetic species by a magnetic field gradient. Though the separation from carbon components is incomplete, this process significantly enriches the magnetic fraction. The isolated black powder contained small magnetic nanocrystallites encased in larger amorphous carbon particles. A small amount of endohedral RE fullerenes was also produced.

II. STRUCTURAL CHARACTERIZATION

High-resolution transmission electron microscopy (HRTEM) revealed faceted nanocrystallites, roughly spherical and 10–50 nm in diameter. Surrounding each nanoparticle were multiple graphite layers with the characteristic spacing of 0.34 nm (Fig. 1). Energy dispersive x-ray fluorescence spectroscopy (EDS) indicated the presence of the rare-earth elements only within the nanocrystallites.

X-ray diffraction scans made with a Rigaku diffractometer were characterized by the presence of large graphitic peaks, with weaker, broadened peaks indexed to the rare-earth sesquicarbide phase, RE_2C_3. The rare-earth sesquicarbides are cubic, having the T_d^6 $I\bar{4}3d$ space group with eight sesquicarbide formula units per unit cell.[5,6] Each rare-earth ion in the sesquicarbide is at a site of C_3 symmetry with nine nearby carbon atoms and eleven nearby rare-earth ions.[7] Since the background contributions to x-ray diffraction in these samples were large, the lattice parameters of the nanocrystallites were obtained from electron microdiffraction (Fig. 2). For Gd_2C_3 the nanocrystallite and bulk lattice parameters are 0.8024 and 0.8330 nm, respectively.[2] Such lattice contractions (3.7%) have been associated with surface tension-induced excess strain frequently observed in nanocrystallites.[8,9]

a)Author to whom correspondence should be addressed.

 0021-8979/94/75(10)/5879/3/$6.00 © 1994 American Institute of Physics

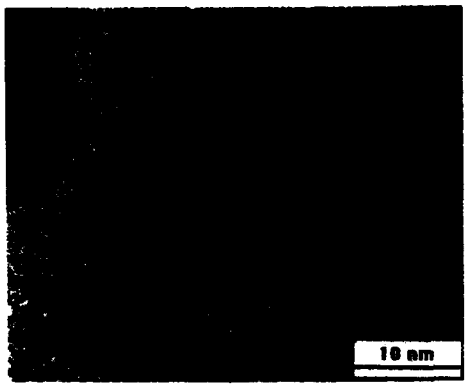

FIG. 1. Transmission electron micrograph of a gadolinium carbide nanocrystallite enclosed by several curved graphitic sheets, taken with a JEOL 4000 high-resolution TEM.

III. MAGNETIZATION

Magnetization curves were obtained at temperatures between 4 and 300 K, for fields between ±5 T, with a Quantum Design superconducting quantum interference device (SQUID) magnetometer. The samples were unoriented powders of Gd_2C_3 and Ho_2C_3 immobilized in epoxy.

A. Gd_2C_3

For Gd_2C_3 nanocrystallites the magnetization data, when scaled as a function of H/T, lie on a universal curve, indicating paramagnetic behavior (Fig. 3). Though bulk gadolinium metal is ferromagnetic, with a Curie temperature of 292 K, we detected no evidence of hysteresis. The magnetic behavior of bulk Gd_2C_3 is unknown, but bulk GdC_2 is paramagnetic with a moment slightly less than the free-ion value, and with an antiferromagnetic transition at 42 K.[10] β-Gd_3C is ferromagnetic at room temperature.[11]

The paramagnetic magnetization M as a function of H/T was fit with a Brillouin function, $B_J(x)$.

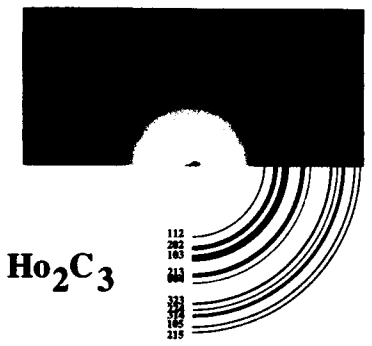

FIG. 2. Ho_2C_3 electron diffraction intensity, showing main reflections.

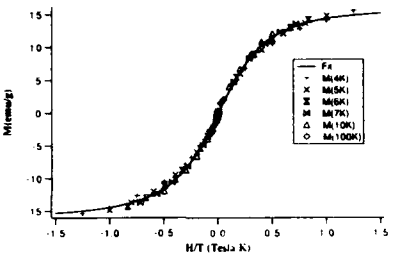

FIG. 3. Gd_2C_3 nanocrystallite magnetization (emu/g) vs H/T for data sets collected at 4, 5, 6, 7, 10, and 100 K exhibiting a characteristic paramagnetic scaling consistent with a Gd^{3+} ground state.

$$M = ngJ\mu_B B_J(x), \tag{1}$$

where

$$B_J(x) = (2J+1/J)\coth((2J+1)x/2J) - (1/2J)\coth(x/2J). \tag{2}$$

Here n is the number of magnetic atoms per unit volume, g is the Lande g factor, J is the total angular momentum, μ_B is the Bohr magneton, and $x = gJ\mu_B H/kT$. The ground electronic state of the Gd^{3+} free ion is $^8S_{7/2}$, and $g=2.00$ for an S state. The results of the fit to the magnetization data were $J=3.67$ ($\chi^2=0.000341$) using the theoretical $g=2.00$ value, compared with the theoretical value of $J=7/2$.

The inverse susceptibility, $1/(\chi-\chi_0)$, for the Gd_2C_3 nanocrystallites is plotted versus temperature in Fig. 4. The values of the Curie temperature, $\Theta=(-2.94\pm2.57)$ K and the Curie constant, $C=(0.113\pm0.025)\times10^{-2}$ emu K/gOe (per g of sample) were obtained by fitting the equation

$$(\chi-\chi_0)^{-1} = (T+\Theta)/C. \tag{3}$$

B. Ho_2C_3

The magnetization curves of carbon-coated Ho_2C_3 nanocrystallites also scale with H/T (Fig. 5). The ground electronic state of the Ho^{3+} free ion is $^5I_8$; $g=1.25$ and $J=8$. However, the best empirical fit to the susceptibility corre-

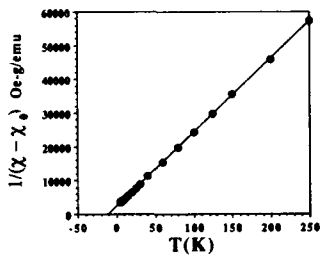

FIG. 4. Gd_2C_3 nanocrystallite Curie–Weiss fit to inverse susceptibility vs temperature data taken in a 5 T fixed field.

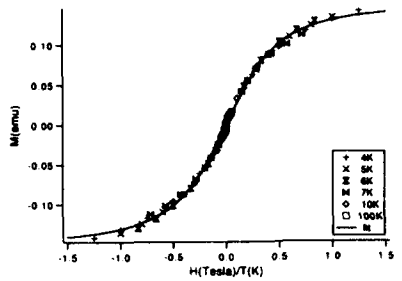

FIG. 5. Ho_2C_3 nanocrystallite magnetization (emu/g) vs H/T for data sets collected at 4, 5, 6, 7, 10, and 100 K, along with an empirical fit to a Brillouin function using the Ho^{3+} free-ion g value of 1.25.

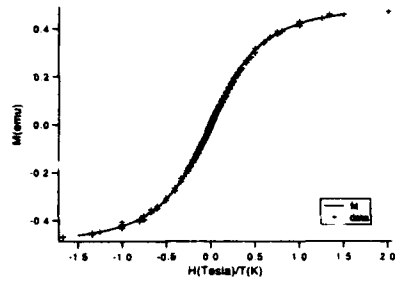

FIG. 6. Fit of low-temperature SQUID magnetometer data (2, 3, 4, and 5 K) for a sample containing holmium endohedral fullerenes. In this fit g was fixed at the Ho^{3+} free-ion value of 1.25, and the effective moment was found to be $6.41\mu_B$.

sponded to an effective magnetic moment magnitude of $g[J(J+1)]^{1/2}\sim 7.5$, with $\chi^2=0.00281$ for the fit, rather than 10.6 predicted for the free ion.

The neutron diffraction studies[7] have indicated that the value of the projected moment gJ for Ho^{3+} in Ho_2C_3 corresponds to 7.3 ± 0.2 instead of the free-ion value of 10.0. The saturation moment was essentially independent of moment direction. Detailed calculations of the crystal field splittings of the Ho^{3+} ions in the Ho_2C_3 C_3 site symmetry sites are in progress. Group theory predicts that the $J=8$ state will split into five singlets and six doublets. The latter are composed of mirror image combinations of $M_J=\pm8$, ±5, ±2, ∓1, ∓4, ∓7; the former are composed of combinations of $M_J=\pm6$, ±3, and 0.

C. Ho-containing fullerenes

The carbon arc process used to generate the Ho_2C_3 nanocrystallites also produced a small amount of endohedral fullerenes. The fullerenes were separated from the nanocrystallites by extraction in carbon disulfide and characterized by mass spectroscopy. The empty fullerenes were most abundant, but the mass peaks corresponding to Ho and HoO were at background levels, so the magnetic behavior was dominated by the endohedral components. The predominant endohedral species were identified as C_{82} clusters containing one, two, and three holmium atoms. SQUID magnetometry measurement of the magnetization revealed a similarly reduced moment ($\mu_{\text{eff}}=6.41\mu_B$ with $\chi^2=0.00514$ for the fit), compared to a Ho^{3+} free ion (Fig. 6). For Ho^{3+} a C_{82} paramagnetism would be associated both with the $4f^{10}$ configuration of the Ho^{3+} ion and with the electrons transferred to the carbon shell. We expect the holmium ion to occupy a site of C_3 symmetry. For Ho_3 a C_{82} the details of the paramagnetic behavior would be even more complex.

IV. CONCLUSIONS

Magnetic properties of carbon-coated gadolinium and holmium sesquicarbide nanocrystallites have been investigated by SQUID magnetometry. A fit of the H/T scaled data to a Brillouin function indicated free Gd^{3+} ion $^8S_{7/2}$ ground-state paramagnetic behavior in Gd_2C_3. In isostructural Ho_2C_3 the departure from free-ion behavior is attributed to crystal field splitting of the highly degenerate Ho^{3+} $^5I_8$ ground state.

ACKNOWLEDGMENTS

M. E. M. and S. A. M. would like to thank the National Science Foundation for support through NYI awards No. DMR-9258450 and No. DMR-9258308, respectively. This material is also based (in part) upon work supported by the National Science Foundation under Grant No. ECD-8907068. The assistance of the Carnegie Mellon University SURG program, the DSSC NSF REU program, and the participation of the CMU Buckyball Project members have been invaluable. In addition we would like to thank L. Berger, S. G. Sankar, S. Simizu, R. Sutton, E. Brunsman, and J. Amster for technical assistance.

[1] R. S. Ruoff, D. C. Lorents, B. Chan, R. Malhotra, and S. Subramoney, Science **259**, 346 (1993).
[2] S. A. Majetich, J. O. Artman, M. E. McHenry, N. T. Nuhfer, and S. W. Staley, Phys. Rev. B Phys. Rev. B **48**, 16 845 (1993).
[3] M. E. McHenry, S. A. Majetich, J. O. Artman, M. DeGraef, and S. W. Staley, Phys. Rev. B (in press).
[4] E. M. Brunsman, M. E. McHenry, S. A. Majetich, J. O. Artman, M. DeGraef, S. W. Staley, R. Sutton, E. Bortz, S. Kirkpatrick, K. Midelfort, J. Williams, and B. Brunett, J. Appl. Phys. (in press).
[5] K. A. Gschneider, Jr. and F. W. Calderwood, Bull. Alloy Phase Diagrams **7**, 421 (1986).
[6] R. W. G. Wyckoff, *Crystal Structures*, 2nd ed. (Wiley, New York, 1960), Vol. 2, p. 37*ff*.
[7] M. Atoji and Y. Tsunoda, J. Chem. Phys. **54**, 3510 (1971).
[8] A. N. Goldstein, C. M. Echer, and A. P. Alivisatos, Science **256**, 1425 (1992).
[9] J. K. Vassiliou, V. Mehrotra, M. W. Russell, E. P. Giannelis, R. D. McMichael, R. D. Shull, and R. F. Ziolo, J. Appl. Phys. **73**, 5109 (1993).
[10] T. Sakai, G. Adachi, T. Yoshida, and J. Shiokawa, J. Less-Common Metals **81**, 91 (1981).
[11] F. H. Spedding, K. Gschneider, Jr., and A. H. Daane, J. Am. Chem. Soc. **80**, 4499 (1958).

Magnetic properties of carbon-coated, ferromagnetic nanoparticles produced by a carbon-arc method

E. M. Brunsman, R. Sutton, E. Bortz, S. Kirkpatrick, K. Midelfort, J. Williams, P. Smith, M. E. McHenry, S. A. Majetich, J. O. Artman, M. De Graef, and S. W. Staley
Carnegie Mellon University, Pittsburgh, Pennsylvania 15213-3890

The Kratschmer–Huffman carbon-arc method of preparing fullerenes has been used to generate carbon-coated transition metal (TM) and TM-carbide nanocrystallites. The magnetic nanocrystallites were extracted from the soot with a magnetic gradient field technique. For TM=Co the majority of nanocrystals exist as nominally spherical particles, 0.5–5 nm in radius. Hysteretic and temperature-dependent magnetic response, in randomly and magnetically aligned powder samples frozen in epoxy, correspond to fine particle magnetism associated with monodomain TM particles. The magnetization exhibits a unique functional dependence on H/T, and hysteresis below a blocking temperature T_B. Below T_B, the temperature dependence of the coercivity can be expressed as $H_c=H_{c0}[1-(T/T_B)^{1/2}]$, where H_{c0} is the 0 K coercivity.

I. INTRODUCTION

We report here on the synthesis and separation of carbon-coated ferromagnetic transition metal (TM) and TM-carbide nanocrystallites.[1] These were produced by the Kratschmer *et al.*[2] carbon-arc process commonly used to synthesize fullerenes.[3] Endohedrally doped[4] fullerenes have been produced by modifying the carbon electrodes. It was subsequently found that carbon-coated metal or metal carbide nanocrystallites could also be generated with these modified electrodes. The first of these nanoparticles to be produced was LaC_2.[5,6] We have recently described the preparation of rare-earth carbide nanocrystallites[7] and their isolation.

The magnetic particles produced by our carbon-arc process are predominately monodomain. These nanocrystallites are of potential interest for applications for which ferromagnetic iron oxide particles are currently used, i.e., in data storage, for toner in xerography, in ferrofluids, and as contrast agents in magnetic resonance imaging. The carbon coating provides an effective oxidation barrier. We describe magnetic measurements on carbon-coated TM nanocrystals which have revealed interesting manifestations of fine particle magnetism, including superparamagnetic response. Our data provide the first link between fullerene-related nanocrystals and fine particle magnetism with the aim of producing materials interesting for magnetic applications.

II. EXPERIMENTAL

Graphite rods (0.25 in. diam) were drilled and packed with a mixture of transition metal oxide (TM=Fe, Co, and Ni) powder and a combination of graphite powder and graphite cement and baked to drive off water vapor and to cure the graphite cement. Our starting materials had an ~0.04 TM/C molar ratio, consistent the LaC_2 preparation scheme.[5,6] These rods were set in the upper electrode position of a dc carbon arc, with a disc-shaped graphite anode.[1] Rods were consumed under 100 A, 30 V arc conditions, in 125 Torr of He. In general, a metal oxide, Me_xO_y, is reduced in the plasma arc according to the reaction

$$Me_xO_y+yC \Leftrightarrow xMe+yCO, \quad (1)$$

which is favored at the high plasma temperature. The nature of the carbide or supersaturated metal present in the soot depends on the metal/carbon phase diagram. The raw soot is ground to a fine, μm-sized powder and passed through a magnetic field gradient to separate the magnetic from the nonmagnetic species. The shear action of the grinding process has not been seen to damage the nanoparticles. A ferromagnetic particle, with magnetization **M**, sees a force:

$$\mathbf{F}_M=(\mathbf{M}\cdot\nabla)\mathbf{H}. \quad (2)$$

In the first pass through the separator 95% by volume of TM-containing soot was retrieved; however, only a small fraction of this magnetically responding powder is ferromagnetic. Thus it appears that this "magnetic" powder contains ferromagnetic TM nanocrystallites embedded in larger carbon particles. Small amounts of fullerenes, including endohedral species, are also present. The nonmagnetic soot contains amorphous carbon, graphitic nanoparticles, and empty fullerenes. Most of the fullerenes were removed by extraction in carbon disulfide.[8] We have produced Fe (carbide), Co, and Ni nanocrystals by this procedure.

The structure and morphology of the magnetic powder were examined by x-ray diffraction and electron microscopy. X-ray diffraction revealed the fcc rather than hcp cobalt phase, typical of fine particles. Energy dispersive x-ray fluorescence spectroscopy (EDS) indicates the transition metal to be uniformly distributed. Scanning electron microscopy (SEM) reveals submicron-sized nominally spherical particles. Closer inspection was made with a JEOL 4000, 400 keV, high-resolution transmission electron microscope (HRTEM). The 0.5–5 nm range of radii observed for the encapsulated Co is about a fifth of the 5–25 nm range previously observed for Gd_2C_3 nanocrystallites. Our particle sizes are roughly equivalent to those observed by Bethune *et al.*[9] but without the spider web-like morphology of carbon nanotubes reported in their paper.

Magnetization data for the TM nanocrystallite powder samples have been obtained with a Quantum Design superconducting quantum interference device (SQUID) magnetometer. Powders containing nanocrystallites were stabilized by epoxy. Samples containing randomly aligned particles and

 0021-8979/94/75(10)/5882/3/$6.00 © 1994 American Institute of Physics

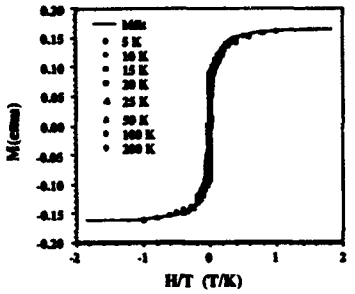

FIG. 1. Magnetization data plotted as a function of H/T at temperatures of 5, 10, 15, 20, 25, 50, 100, and 200 K for randomly oriented nanocrystalline Co/C particles immobilized by epoxy.

those aligned in the field provided by a pair of FeNdB permanent magnets were prepared for observation. $M(H,T)$ then was determined in solenoidal fields between ± 5 T at temperatures ranging from 4 to 300 K.

III. RESULTS AND DISCUSSION

We have synthesized nanocrystalline Gd_2C_3 (Ref. 7) and Ho_2C_3 paramagnets and nanocrystalline Fe, Co,[1] and Ni ferromagnets. The ferromagnets display textbook superparamagnetic response.[10–12] The hysteretic and temperature-dependent magnetization, *in* randomly and magnetically aligned powder samples frozen in epoxy, are characteristic of fine particle magnetism. As an example, we illustrate the behavior of monodomain Co particles. Magnetization data for the randomly aligned nanocrystalline Co/C particles are plotted versus H/T in Fig. 1. Data were taken at eight temperatures covering the range between 5 and 200 K. In Fig. 2(a) an expanded view of the 5 K curve is shown. In Fig. 2(b) the corresponding plot for the magnetically aligned specimen is given. Hysteresis is present in both .

The coercivity H_c present at the low temperatures was plotted versus T and fit to the expression

$$H_c = H_{c0}[1-(T/T_B)^{1/2}]. \tag{3}$$

See Fig. 3. The intrinsic H_{c0} was determined to be ~450 Oe and the blocking temperature T_B, to be ~160 K. Note that the coercivity data for both aligned and randomly oriented specimens lie on the same curve.

Direct observation of particles by TEM gives a sense of the distribution of particle sizes. These particle sizes can then be compared with those inferred independently from other types of magnetic measurements. The scaled magnetization data (e.g., Fig. 1) can be fit to a Langevin function L using the relation

$$\frac{M}{M_0} = L(a) = \coth(a) - \frac{1}{a}, \tag{4}$$

where M_0 is the 0 K saturation magnetization and $a = \mu H/kT$. The effective moment μ is given by the product $M_s\langle V\rangle$, where M_s is the saturation magnetization and $\langle V\rangle$ is the average particle volume. Assigning the bulk value to M_s we can infer a particle volume from the Langevin fit. Also coercivity data exists for elemental and other common magnets as a function of size.[13] Comparison of our magnetically determined coercivities H_c with these data offers another way of estimating mean particle radius. Finally, the blocking temperature T_B also offers information as to the magnetic particle size. T_B is the temperature at which metastable hysteretic response is lost for a particular experimental time frame.

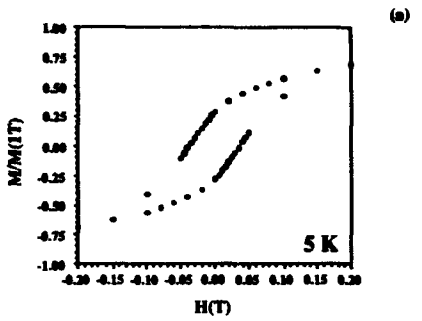

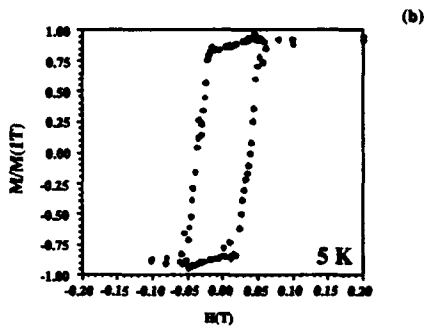

FIG. 2. Low field magnetization curves at 5 K for Co/C particles (a) randomly oriented and (b) magnetically aligned.

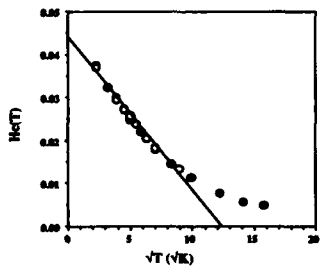

FIG. 3. $H_C(T)$ vs $\sqrt{T}$ for aligned and unaligned Co/C particles. The blocking temperature, T_B, is ~160 K.

TABLE I. Anisotropy, coercivity, and moment data for certain nanocrystallites.

	Crystalline anisotropy energy (K_1) (10^5 ergs/cm^3)	Blocking temp. T_B (K)	Coercivity H_{c0} (Oe)	Cluster moment (10^3 μ_B)
Co	−27[a] (4 K)	160	450	11
Fe	5.7[b] (77 K)	80	350	10
Ni	−6[c] (100 K)	150	260	25
γ-Fe_2O_3	−0.46[d] (RT)	80	370	6.7

[a]References 15, 16.
[b]Reference 17.
[c]Reference 18.
[d]Reference 19.

Below T_B, hysteretic response is observed since thermal activation is insufficient to allow the alignment of particle moments with the applied field in the time scale of the measurement. For spherical particles the rotational energy barrier to alignment is given by the magnetocrystalline anisotropy energy per unit volume K multiplied by the particle volume V. For hysteresis loops taken over ~1 h, the blocking temperature should roughly satisfy the relationship:

$$T_B = \frac{K\langle V\rangle}{30k_B}. \tag{5}$$

The factor of 30 represents $\ln(\omega_0/\omega)$, where ω is the inverse of the experimental time ($\sim 10^{-4}$ Hz) and ω_0 an attempt frequency (~1 GHz). If K can be estimated (i.e., from bulk values) and the value of T_B determined then the mean particle volume can be estimated. The error in T_B was ±30 K, yielding a particle radius of $(4.11\pm0.33)\times10^{-7}$ cm for cobalt. Radii determined this way were larger than estimated by other methods, suggesting an anisotropy greater than bulk .

We have characterized fine particle magnetism in Fe[carbide], Co, and Ni nanocrystals produced by the Krätschmer arc process. For comparison we also have made similar measurements on nanocrystalline γ-Fe_2O_3 nanocrystals[14] of a similar size, produced by a matrix-mediated synthesis route and provided by Xerox Corporation. In Table I we summarize the bulk K values for each of these materials as well as values of T_B and H_{c0} determined from fits to H_c [Eq. (3)]. We also include the cluster moment μ as determined Eq. (4). In Table II we summarize the mean-particle radius for our nanocrystalline samples as inferred from the Langevin function fits, T_B data analysis and comparison with previous coercivity measurements in fine particle magnets. Wherever possible these are compared with TEM observations of the particle size distribution. In most cases these are seen to be in excellent agreement. The discrepancy between radii determined by T_B analysis for γ-Fe_2O_3 suggests a smaller anisotropy constant but not by several orders of magnitude as has been previously suggested.[20]

TABLE II. Nanocrystallite particle radii (in nm) determined by various methods.

	Langevin fit	Blocking temp.	Coercivity (10)	TEM analysis
α-Co	2.5	3.9	1.5–2	0.5–5
Fe carbide	2.3	5.2	1–2	···
Ni	4.7	6.0	···	···
γ-Fe_2O_3	3.3	12	···	3.25–5.25

IV. CONCLUSIONS

The Krätschmer–Huffman carbon-arc method has been used to generate carbon-coated TM and TM-carbide nanocrystallites. These were collected by magnetic gradient separation. Particles have a spherical morphology with an ~0.5–5 nm radius (for Co) from TEM. These monodomain particles exhibit superparamagnetic response with hysteresis only at temperatures $T<T_B$. Analysis of the T_B data, as well as the Langevin fits, allows calculation of mean-particle radii for superparamagnetic particles. The radii so calculated are in agreement with TEM observations and with prior measurements of fine particle magnetism in TM particles.

ACKNOWLEDGMENTS

M.E.M. and S.A.M. thank the NSF for support through NYI awards No. DMR-9258450 and No. DMR-9258308. We are indebted for support from the CMU DSSC REU program. This material is also based (in part) upon work supported by the NSF under Grant No. ECD-8907068. The assistance of the CMU SURG program has been invaluable. Finally, we would also like to thank R. F. Ziolo of Xerox for providing γ-Fe_2O_3 nanocrystals.

[1] M. E. McHenry, S. A. Majetich, J. O. Artman, M. De Graef, and S. W. Staley, Phys. Rev. B (in press).
[2] W. Kratschmer, L. D. Lamb, K. Fostiropoulos, and D. R. Huffman, Nature **347**, 354 (1990).
[3] H. W. Kroto, J. R. Heath, S. C. O'Brien, R. F. Curl, and R. E. Smalley, Nature **318**, 162 (1985).
[4] Y. Chai, T. Guo, C. Jin, R. E. Haufler, L. P. F. Chibante, J. Fure, L. Wang, J. M. Alford, and R. E. Smalley, J. Phys. Chem. **95**, 7564 (1991).
[5] Rodney S. Ruoff, Donald C. Lorents, Bryan Chan, Ripudaman Malhotra, and Shekhar Subramoney, Science **259**, 346 (1993).
[6] M. Tomita, Y. Saito, and T. Hayashi, Jpn. J. Appl. Phys. **32**, L280 (1993).
[7] S. A. Majetich, J. O. Artman, M. E. McHenry, N. T. Nuhfer, and S. W. Staley, Phys. Rev. B (in press).
[8] R. S. Ruoff, R. Malhotra, D. L. Huestis, D. S. Tse, and D. C. Lorents, Nature **362**, 141 (1993).
[9] D. S. Bethune, C. H. Klang, M. S. de Vries, G. Gorman, R. Savoy, J. Vazquez, and R. Beyers, Nature **363**, 605 (1993).
[10] B. D. Cullity, *Introduction to Magnetic Materials* (Addison–Wesley, Reading, MA, 1972).
[11] C. P. Bean and J. D. Livingston, J. Appl. Phys. **30**, 120S (1959).
[12] I. S. Jacobs and C. P. Bean, in *Magnetism*, edited by G. T. Rado and H. Suhl (Academic, New York, 1963), Vol. 3.
[13] F. E. Luborsky, J. Appl. Phys. **32**, 171S (1961).
[14] R. F. Ziola, E. P. Giannelis, B. A. Weinstein, M. P. O'Horo, B. N. Ganguly, V. Mehrotra, M. W. Russell, and D. R. Huffman, Science **257**, 219 (1992).
[15] W. D. Doyle and P. J. Flanders, International Conference on Magnetism, Nottingham, 1964, p. 751, published in the Proc. of The Physical Society.
[16] W. A. Sucksmith and J. E. Thompson, Proc. R. Soc. London Sect. A **254**, 362 (1954).
[17] R. M. Bozorth, J. Appl. Phys. **8**, 575 (1937).
[18] G. Aubert, J. Appl. Phys. **39**, 504 (1968).
[19] *Magnetic Oxides*, edited by D. J. Craik (Wiley, London, 1975).
[20] J. K. Vassiliou, V. Mehotra, M. W. Russell, E. P. Giannelis, R. D. McMichael, R. D. Shull, and R. F. Ziolo, J. Appl. Phys. **73**, 5109 (1993).

Structural and magnetic properties of ultrafine Fe-Pd particles

L. Yiping and G. C. Hadjipanayis
Department of Physics and Astronomy, University of Delaware, Newark, Delaware 19716

C. M. Sorensen
Department of Physics, Kansas State University, Manhattan, Kansas 66506

K. J. Klabunde
Department of Chemistry, Kansas State University, Manhattan, Kansas 66506

The structural and magnetic properties of evaporated ultrafine Fe-Pd particles have been studied near the equiatomic composition. Particles with an average size in the range of 65–360 Å were obtained with the argon pressure varied between 0.5–40 Torr. All of the as-made particles had a face centered cubic (fcc) structure and they were magnetically soft. A fcc to face centered tetragonal (fct) phase transformation was observed after annealing the powders at 500 °C resulting in room-temperature coercivities up to 3.6 kOe and a magnetization (at 55 kOe) around 95 emu/g. An enhanced magnetic moment of about $3.0\mu_B$ per atom was found for Fe.

I. INTRODUCTION

Fe-Pd alloys have been of special scientific interest because the Fe atoms induce a large host polarization leading to an overall enhancement in the magnetic moment.[1,2] According to the equilibrium phase diagram of $Fe_{1-x}Pd_x$ alloys.[3] below 1000 °C an Fe-rich bcc phase is expected for $0<x<0.2$, a bcc-fcc mixed phase for $0.2<x<0.45$, and an fcc phase for $x>0.45$. There are two ordered-disordered phase transformations in these alloys; one to the FePd face centered tetragonal (fct) phase near the 50% Pd composition and another to $FePd_3$ face centered cubic (fcc) phase in the range of 62.8%–74.4% Pd. The ordered fct phase is a hard magnetic phase because of its high anisotropy.[4] In Fe-Pd thin films no superlattice structure was detected for the concentration regions around 50% Pd and 75% Pd.[5]

Magnetic ultrafine particles in the nanometer scale prepared by evaporation are very easy to burn and need a protective coating to resist oxidation when exposed to the ambient. The magnetic properties of ultrafine particles are mainly influenced by the size of the particles and by the surface layer of the properties.[6,7]

In this paper we studied the size effects on the magnetic and structural properties of Fe-Pd ultrafine particles with both the fcc and fct structures.

II. EXPERIMENTAL METHODS

Bulk Fe-Pd alloys were made by arc-melting high-purity Fe and Pd metals in an argon atmosphere. Ultrafine Fe-Pd particles (UFP) were produced by gas evaporation and condensation of a piece of bulk $Fe_{100-x}Pd_x$ in an argon atmosphere. A tungsten crucible was used as the heating element. Control of the particle size was obtained by varying the argon pressure from 0.5 to 40 Torr during evaporation. The particles were passivated with an Ar/air mixture before they were taken out from the evaporation chamber. Then they were annealed under vacuum (10^{-5} Torr) at temperatures in the range of 400–800 °C.

The composition of the particles was determined by ICP spectroscopy. The magnetic properties were measured by a superconducting quantum interference device (SQUID) and vibrating sample magnetometer (VSM) with applied fields up to 55 kOe. The particle structure and morphology were examined by x-ray diffraction (XRD) and transmission electron microscopy (TEM).

III. RESULTS AND DISCUSSION

The average particle size D was found to depend on the argon gas pressure during evaporation, increasing monotonically with increasing argon pressure. Because of the different vapor pressures of iron and palladium the particle composition was found to be slightly dependent on the evaporation pressure (Table I), with a lower Fe content obtained at higher Ar pressure. The Fe content of evaporated powders was in the range of 44–51 at % when a master ingot of $Fe_{45}Pd_{55}$ was used.

X-ray diffraction patterns showed that all the as-made particles have a face centered cubic (fcc) structure [Fig. 1(a)]. With increasing Ar pressure the (111) diffraction peak is shifted to smaller angles indicating an increase in the lattice parameters (Table II). This change of lattice parameter is the result of a composition change, where a larger lattice parameter means a higher percentage of palladium. However, ICP composition analysis data showed a lower Pd percentage in the smaller particles. These contradictory results are due to the fact that the ICP composition analysis data represent the entire particle composition while the x-ray diffraction shows only the structure of the fcc Fe-Pd major phase. We believe that a small amount of Fe-O forms on the particle surface leaving an Fe-Pd core with an Fe content below the equiatomic composition. The smaller particles have a larger surface area, which results in an inhomogeneous FePd composition distribution.

TABLE I. Composition as a function of Fe-Pd particle size.

Composition	Average particle size (Å)			
Ingot	65	135	230	360
$Fe_{45}Pd_{55}$	$Fe_{51.6}$ $Pd_{48.4}$	$Fe_{49.7}$ $Pd_{50.3}$	$Fe_{47.8}$ $Pd_{52.2}$	$Fe_{44.2}$ $Pd_{55.8}$

 0021-8979/94/75(10)/5885/3/$6.00 © 1994 American Institute of Physics

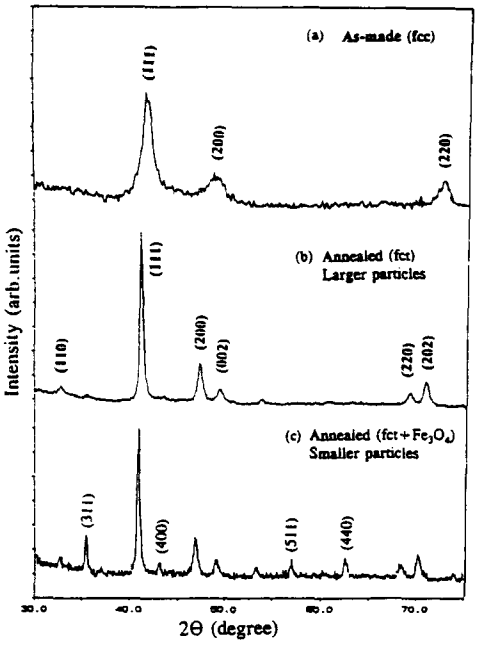

FIG. 1. X-ray diffraction patterns in Fe-Pd particles.

FIG. 2. Fe-Pd particle morphology, (a) as-made, (b) anncaled.

The x-ray diffraction peaks were weak and broad in the as-made samples and sharp in the annealed samples. The sharper peaks indicate larger particles. TEM pictures showed that the particle size is consistent with the x-ray diffraction results. The as-made spherical particles had an average size in the range of 65–360 Å corresponding to an Ar pressure between 0.5–40 Torr. After heat treatment the average particle size increased to 115–430 Å. The heat treatment also led to sintering of the smaller particles (Fig. 2).

The fcc to face centered tetragonal (fct) phase transformation was observed in the larger particles after a suitable heat treatment. X-ray diffraction patterns showed clearly the superlattice reflections of fct (002), (202), [Fig. 1(b)], with a trace of Fe_3O_4 present in the particles. The Fe_3O_4 x-ray diffraction peaks are stronger in the annealed smaller particles [Fig. 1(c)] indicating an increase in both the amount and grain size of the oxides. No phase transformation was observed in the as-made particles with a size below 100 Å. This result is consistent with the core-shell morphology picture where the composition of the Fe-Pd core in the smaller particles deviates from the equiatomic range. In order to obtain equiatomic FePd core in the smaller particles the composition of the master alloy had to be shifted toward the Fe-rich range. Table II(b) shows the lattice parameters of the smaller particles with a size below 100 Å. An attempt was made to eliminate the surface oxidation by sandwiching the smaller

TABLE II. Lattice parameters of Fe-Pd particles.

Composition of master ingot	Particle size (Å)	Lattice parameter a (Å)	Composition Fe (at %)
$Fe_{45}Pd_{55}$	360	3.822	44.2
	310	3.810	...
	230	3.806	47.8
	180	3.806	...
	135	3.804	49.7
	90	3.852	...
	65	3.881	51.6
$Fe_{55}Pd_{45}$	90	3.805	52.5
$Fe_{65}Pd_{35}$	75	3.801	59.14

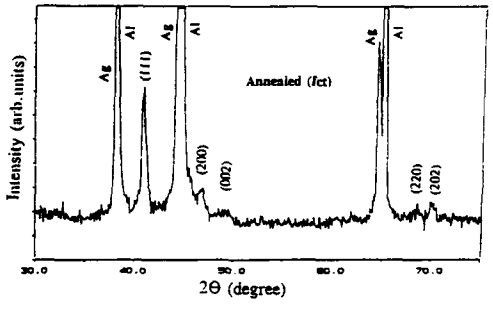

FIG. 3. X-ray diffraction pattern of Ag/FePd/Ag sandwiched particles (80 Å). The Al peaks come from the Al foil substrate.

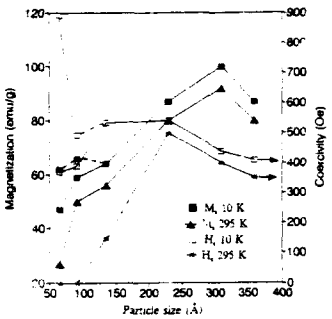

FIG. 4. Magnetic properties of as-made Fe-Pd particles, (—) nominal $Fe_{45}Pd_{55}$, (· · ·) with adjusted composition.

particles between two Ag thin films. After annealing, the sandwiched FePd particles with 80 Å size show the fct phase when an $Fe_{45}Pd_{55}$ master alloy was used (Fig. 3). This evidence supports the predicted particle morphology which influences the structural properties.

The magnetization of the as-made particles was found to be highly dependent on particle size (Fig. 4). The magnetization increases with particle size to the maximum value of 100 emu/g obtained in a sample with a size around 300 Å. The decrease in magnetization observed in the larger particles is due to a change in particle composition towards higher Pd content. The lower magnetization of smaller particles in the nominal $Fe_{45}Pd_{55}$ (solid line) and adjusted * composition samples (dashed line) is probably due to both surface oxidation and the Pd-rich core phase effects. The magnetization of annealed samples does not show much dependence on particle size (Fig. 5), and its value is close to that of Fe-Pd thin films.[5]

In fine Fe-Pd particles with both the fcc and fct phases, the magnetization value per Fe is obviously higher than 220 emu/g. Table III shows the magnetic moment of the samples. The samples with the asterisk (*) are those prepared from Fe-rich-Pd alloys. The moments decrease with decreasing particle size. The magnetization of the larger particles is

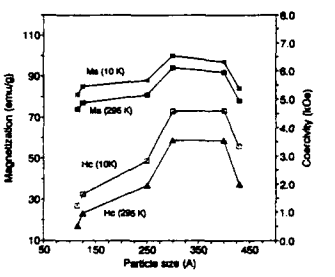

FIG. 5. Magnetic properties of annealed Fe-Pd particles (fct).

TABLE III. Magnetic moment of annealed Fe-Pd particles (fct) at 10 K.

As-made size (Å)	Fe (at %)	K (erg/cm^3) $\times 10^6$	μ_B (Fe) as-made	μ_B (fe) H.T.
360	44.2	2.3	2.97	2.86
230	47.8	3.65	2.68	3.08
135	49.7	2.59	1.87	2.58
90*	52.5	1.96	2.26	2.32
75*	59.14	1.69	1.46	1.88

close to that of bulk samples.[8] The moments are slightly different in the annealed samples and this is probably due to differences in the magnetization values of the fcc and fct phases and to a different Fe-O content in the samples.

The as-made powders had a coercivity in the range of 0–500 Oe which was dependent on particle size. The coercivity in the 65–90 Å particles was zero at room temperature, and increased with particle size reaching a maximum value of 500 Oe around 230 Å particles, and then it decreased again in larger particles. A different behavior has been observed at 10 K for particles with size below 200 Å. The largest coercivity has been obtained in the 75 Å particles and this behavior is similar to that of Fe/FeO and Fe-Cr particles and is believed to be the result of the FePd core/Fe-O shell particle morphology. After annealing, the samples with the fct structure had much higher coercivities (Fig. 5) with a maximum coercivity 3.56 kOe at 295 K corresponding to a particle size around 280 Å. The behavior of the coercivity as a function of size is similar to that of as-made powders. The estimated single domain particle size for equiatomic FePd is about 350 Å.

IV. SUMMARY

In the larger Fe-Pd particles the magnetic moments and the phase transformation behavior are close to those of bulk. The magnetization and coercivity of these particles are mainly governed by the FePd core phase (both fcc and fct). In the smaller particles, however, a larger lattice parameter and a trace of Fe_3O_4 indicate a particle morphology with an Fe-Pd-rich core surrounded by an Fe-O shell which we believe affects the fcc to fct phase transformation and the magnetization of the particles.

ACKNOWLEDGMENT

This work was supported by NSF CHE-9013930.

[1] A. Oswald, R. Zeller, and P. H. Dederichs, Phys. Rev. Lett. **56**, 1419 (1986).
[2] G. J. Nieuwenhuys, Adv. Phys. **24**, 515 (1975).
[3] M. Hansen and K. Anderko, *Constitution of Binary Alloys* (McGraw-Hill, New York, 1958), p. 696.
[4] R. A. McCurrie and P. Gaunt, Philos. Mag. **13**, 567 (1966).
[5] S. L. Zhang, K. Sumiyama, and Y. Nakamura, J. Magn. Magn. Mater. **73**, 58 (1988).
[6] S. Gangopadhyay, G. C. Hadjipanayis, B. Dale, C. M. Sorensen, K. J. Klabunde, V. Papaefthymiou, and A. Kostikas, Phys. Rev. B **45**, 9778 (1992).
[7] B. D. Cullity, *Introduction to Magnetic Materials* (Addision-Wesley, Reading, MA, 1972).
[8] J. W. Cable, E. O. Wollan, and W. C. Koehler, Phys. Rev. **138**, A755 (1965).

Fine structure and magnetic properties of Mn- and Co-doped nanocrystalline γ-Fe_2O_3

Ming-Cheng Deng and Tsung-Shune Chin
Department of Materials Science and Engineering, National Tsing Hua University, Hsinchu, 300 Taiwan, Republic of China

F. R. Chen
Materials Science Center, Tsing Hua University, Hsinchu, 300 Taiwan, Republic of China

High resolution TEM (HRTEM), Mössbauer spectroscopy and SQUID magnetometry were utilized to study the fine structure of equiaxed, Mn- and Co-doped γ-Fe_2O_3 nanocrystals with a particle size of 30–50 nm. The allocation of cation distribution, based on a redox mechanism and known cation site preferences is $(Mn^{2+}_{0.11}Fe^{3+}_{0.89})[Mn^{4+}_{0.07}Mn^{3+}_{0.16}Co^{2+}_{0.34}Fe^{3+}_{1.23}\square_{0.20}]O_4$, in which $\square$ is the vacancy, $(\cdots)$ is the A site, and $[\cdots]$ is the B site. This leads to an Fe occupancy ratio of B sites to A sites of 1.38, as verified by Mössbauer spectroscopy. The calculated saturation magnetic moment of $2.99\mu_B/MF$ is very close to the measured $2.84\mu_B/MF$. HRTEM micrographs of the air-cooled nanocrystals fits well with the simulated lattice images using the proposed cation distribution (without directional ordering). While the HRTEM micrograph of the core of an annealed nanocrystal are not in good agreement. This is thought to arise from directional ordering inside the annealed particles.

INTRODUCTION

Acicular γ-Fe_2O_3, CrO_2 with or without surface Co coating are ferrimagnetic or ferromagnetic nanoparticles well known as traditional magnetic recording media.[1] They owe their coercivity, 200–800 Oe, to shape anisotropy. Recently, high coercivity (1300–2150 Oe), equiaxed nanocrystalline (30–80 nm) γ-Fe_2O_3 particles doped with Mn and Co were reported to be obtainable by coprecipitation from an aqueous solution and heat treatments.[2–4]

The reason why the coercivity is much improved by the Mn and Co doping is speculated to arise from directional ordering.[2–5] The mechanism of the annealing and the role of Mn are thought to facilitate the migration of Co ions to a directional ordering manner. Tailhades *et al.* proposed a cation site occupancies by a reduction–oxidation (redox) model at different oxidation temperatures for Mn- and Co-doped acicular γ-Fe_2O_3 particles with coercivity of up to 1800 Oe.[5] There are, however, no studies on the equiaxed ones and no exploration on the directional ordering. These were the purposes of this study.

EXPERIMENTAL

The nanocrystalline particles were prepared by coprecipitation from an aqueous solution, containing 11.8 at. % Co^{2+}, 14.7 at. % Mn^{2+} and 73.5 at. % Fe^{2+}, by triethylamine and heat treatments, which included calcination (to α-Fe_2O_3), reduction (to Fe_3O_4) and oxidation (to γ-Fe_2O_3) then air cooling, or with further step annealings.[2,4]

Magnetic properties of the particulates were either measured by a VSM (maximum field 2 T) at room temperature or a SQUID (maximum field 4 T) from 10 K to 200 K. The lattice images of the particles were obtained by a Jeol 4000CX 400 kV HRTEM. Mössbauer spectra were obtained with a γ-ray source of Co^{57}.

RESULTS AND DISCUSSION

The air-cooled γ-(Fe, Mn, Co)$_2O_3$ (11.8 at. % Co, 14.7 at. % Mn) particles are equiaxed with a size of 30–80 nm (average 50 nm), and have a coercivity of 1380 Oe, a room temperature saturation magnetization of 71.1 emu/g and residual magnetization of 50.0 emu/g.[2] It is identified to be a pure spinel structure of which the lattice constant equal to 0.8353 nm from XRD analysis.

There are a great variety of possibilities of the cation distribution due to the oxidation extent of the species in γ-(Fe,Mn,Co)$_2O_3$, oxidizing from $Mn_xCo_yFe_{3-x-y}O_4$ (their corresponding magnetite precursors) and, in turn, depend upon oxidation temperature and oxidation time. Trials to solve exactly the true site occupancies is hardly possible. However, several rules of site preferences for Fe, Co, and Mn ions, respectively, in magnetite has been worked out by Hastings and Corliss:[6] (1) 80% Mn^{+2} occupies site A while 20% Mn^{+2} at site B as determined by neutron diffraction; (2) electron exchange appears between Mn^{+2} and Fe^{+3}, thus Mn^{+3} and Fe^{+2} exist at site B; (3) Co^{+3} is destabilized in the presence of Fe^{+2}, and it tends to be reduced to Co^{+2}.

Following the above criteria one knows that Mn^{+3}, Co^{+2}, and Fe^{+2} tend to occupy sites B, while Mn^{+2}, Mn^{+4}, and Fe^{+3} may occupy either sites A or B in the magnetite structure. While for the maghemite structure, a redox model has to be proposed to modify the cation distribution established in the corresponding magnetite precursor.

The cation distribution of the air-cooled γ-(Fe,Mn,Co)$_3O_4$ particles is proposed as

$$(Mn^{2+}_{0.8x}Fe^{3+}_{1-0.8x})[Mn^{3+}_{0.2x}Co^{2+}_{y}Fe^{2+}_{1-0.8x-y}Fe^{3+}_{1+0.6x}]O_4, \quad (1)$$

where those in $(\cdots)$ denoting sites A, while those in $[\cdots]$ denoting sites B, and $\square$ denoting cation vacancy. As Co 11.8 at. %, Mn 14.7 at. % is deduced to the magnetite formula, $x=0.44$ and $y=0.34$, substituting into formula (1):

$$(Mn^{2+}_{0.35}Fe^{3+}_{0.65})[Mn^{3+}_{0.09}Co^{2+}_{0.34}Fe^{2+}_{0.31}Fe^{3+}_{1.26}]O_4. \quad (2)$$

 0021-8979/94/75(10)/5888/3/$6.00 © 1994 American Institute of Physics

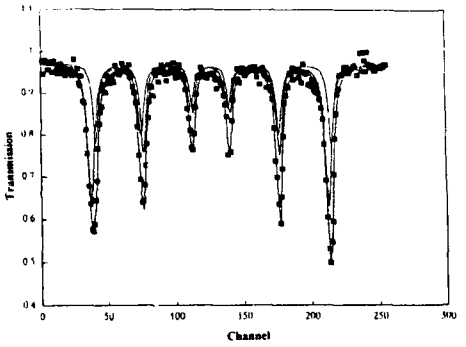

FIG. 1. A Mössbauer spectrum of the air-cooled γ-$(Fe,Mn,Co)_2O_3$ particles. The innermost curve denotes deconvoluted iron at site A, the intermediate curve that at site B, while the outermost curve outlines the datum points.

When they are oxidized at 270 to 360 °C, the redox mechanism proposed and verified in part by Tailhades[5] is adopted. Formula (2) can thus be deduced to be

$$(Mn^{2+}_{0.24x}Fe^{3+}_{1-0.24x})[Mn^{4+}_{0.15x}Mn^{3+}_{0.37x}Co^{2+}_{y}Fe^{3+}_{1.67-0.49x-0.67y} \times \square_{0.33-0.3x-0.33y}]O_4. \quad (3)$$

The net magnetic moment per formula is calculated as $3.33-0.52x-0.33y$ from the proposed cation distribution. It predicts that the saturation magnetization would decrease as the Mn content increases. This was experimentally verified.

The cation distribution of the air-cooled sample ($x=0.44$, $y=0.34$) was deduced from formula (3) to be

$$(Mn^{2+}_{0.11}Fe^{3+}_{0.89})[Mn^{4+}_{0.07}Mn^{3+}_{0.16}Co^{2+}_{0.34}Fe^{3+}_{1.23}\square_{0.20}]O_4. \quad (4)$$

Formula (4) does not tell the arrangement of cations in sites B, that is to say, those in sites B are random. Figure 1 shows a Mössbauer spectrum of the air-cooled particles. The calculation of Fig. 1 shows an Fe occupancy ratio of sites B to sites A as 1.38, in an exact match with the proposed one.

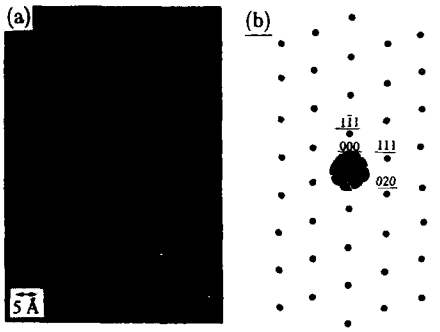

FIG. 2. (a) The $[10\bar{1}]$ lattice image of an air-cooled γ-$(Fe,Mn,Co)_2O_3$ particle; (b) the Fourier transformed diffraction pattern of (a).

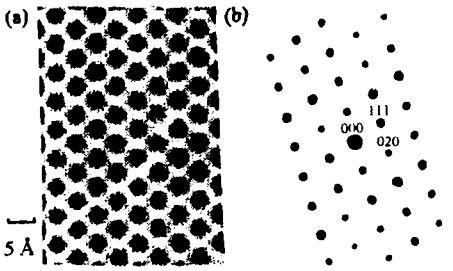

FIG. 3. (a) The simulated $[10\bar{1}]$ lattice image from the proposed cation distribution; (b) the simulated $[10\bar{1}]$ diffraction pattern of the same formula.

The magnetic moment per formula is calculated to be $2.99\mu_B/MF$. The magnetization in a field of 4 T at 10 K is measured to be 71.7 emu/g, corresponding to $2.84\mu_B/MF$, which is only 5% less than the calculated one from the proposed formula.

Figure 2(a) is the lattice image of an air-cooled γ-$(Fe,Mn,Co)_2O_3$ particle along $[10\bar{1}]$ direction. Figure 2(b) shows the Fourier transformed diffraction pattern of Fig. 2(a) by the Mac Tempas software,[7] and is indexed exactly with the [101] incident electron beam direction. The proposed cation distribution model was used to simulate the lattice image and diffraction pattern, as shown in Figs. 3(a) and 3(b), which are in good match with those in Fig. 2.

Figure 4 is the lattice image of an annealed γ-$(Fe,Mn,Co)_2O_3$ particle (with a coercivity of 1850 Oe) along the $[\bar{1}\bar{1}4]$ direction. Both the upper region (near the surface of the particle) and the lower region (near the core of the particle) is identified as the spinel structure by the Fourier transformed diffraction pattern. The lattice image of the upper region is in good match with the simulated lattice image, while that of the lower (core) region is not. This indicates that disordered cation distribution model is no longer suitable to explain the lattice image. This means that a kind of ordered cation arrangement, specifically those in sites B, exists in the core region. If so, the high resolution TEM micrographs provides, for the first time, direct proof for the

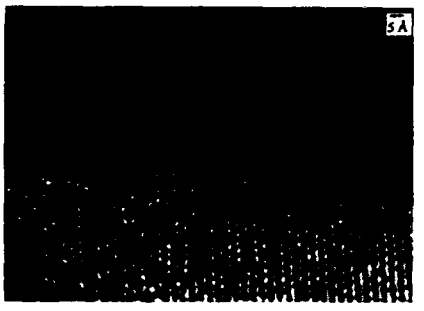

FIG. 4. The $[\bar{1}\bar{1}4]$ lattice image of an annealed γ-$(Fe,Mn,Co)_2O_3$ particle.

existence of directional ordering inside the core of the nanocrystalline particles. And the directional ordering seems to be destroyed for a few layers on the particle surface, this is also first disclosed.

CONCLUSION

The cation distribution of the air-cooled γ-$(Fe,Mn,Co)_2O_3$ (11.8 at. %Co, 14.7 at. %Mn) is proposed, based on a redox model and supported with saturation magnetization, Mössbauer spectrum, and HRTEM analyses to be most likely as

$$(Mn^{2+}_{0.11}Fe^{3+}_{0.89})[Mn^{4+}_{0.07}Mn^{3+}_{0.16}Co^{2+}_{0.34}Fe^{3+}_{1.23}\square_{0.20}]O_4.$$

The lattice images of the air-cooled and annealed particles are different due to the difference between disordered and ordered cation distribution within the B sites. It offers a possible evidence of the directional ordering, which is believed to be the main reason of a substantial increase in coercivity due to annealings.

ACKNOWLEDGMENTS

The authors are grateful to Professor B. K. Cheng for the Mössbauer spectroscopy. The sponsor of this research by the National Science Council of the Republic of China under the Contracts No. NSC82-0405-E007-091 and No. NSC81-0204-E007-08 is acknowledged.

[1] G. Bate, J. Magn. Magn. Mat. **100**, 413 (1991).
[2] M. C. Deng and T. S. Chin, Jpn. J. Appl. Phys. **30**, 1276 (1991).
[3] T. S. Chin and M. C. Deng, J. Appl. Phys. **71**, 821 (1992).
[4] M. C. Deng and T. S. Chin, J. Magn. Magn Mat. **120**, 37 (1993).
[5] Ph. Tailhades, P. Mollard, A. Rousset, and M. Gougeon, IEEE Trans. Magn. **26**, 1822 (1990).
[6] J. M. Hastings and L. M. Corliss, Phys. Rev. **106**, 865 (1957).
[7] Mac Tempas, a program for simulating high resolution TEM images and diffraction patterns, by Total Resolution Corporation, 1992.

Elongated superparamagnetic particles

Amikam Aharoni[a)]
Department of Electronics, Weizmann Institute of Science, 76100 Rehovoth, Israel

The relaxation time for superparamagnetic behavior is calculated for prolate spheroidal particles with a uniaxial, crystalline anisotropy superimposed on their shape anisotropy. Possible applications to the analysis of some experiments, in particular for the case of quantum tunneling, are discussed.

I. INTRODUCTION

All physical systems have a finite probability for jumping over an energy barrier, E_B, due to the thermal fluctuations at a finite temperature, T. This probability is usually expressed as being proportional to $\exp(-E_B/k_BT)$, where k_B is Boltzmann's constant. In the particular phenomenon of superparamagnetism the thermal fluctuations flip the direction of magnetization back and forth during the time of the measurement. Obviously, it is encountered only in small ferromagnetic particles for which the energy barrier (which is proportional to the volume of the particle) is not too large.

However, in this case it is customary[1] to speak of the *relaxation time*, τ, it takes the magnetization to flip, rather than in terms of the probability of flipping. The classical expression[1] for this τ is

$$\tau^{-1}=f_0\, e^{-\alpha}, \tag{1}$$

where f_0 is a constant, and where generally

$$\alpha=E_B/(k_BT). \tag{2}$$

Most theoretical studies of superparamagnetic relaxation were carried out for the case of a uniaxial anisotropy in *spherical* particles, for which the total energy is

$$E=K_uV\sin^2\theta, \tag{3}$$

where K_u is the anisotropy constant, V is the volume, and θ is the angle between the magnetization and the easy axis. In this case the energy minima are $E_{\min}=0$ for $\theta=0$ or π, the maximum is $E_{\max}=K_uV$ for $\theta=\pi/2$, and the energy barrier is

$$E_B=E_{\max}-E_{\min}=K_uV. \tag{4}$$

In this case, and only in this case, the more general expression in Eq. (2) becomes the more-commonly quoted

$$\alpha=K_uV/(k_BT). \tag{5}$$

For a cubic anisotropy, in ferromagnetic *spheres*, the expression is[1] only slightly different from that of Eq. (5), but for nonspherical particles there is no reason at all to use this relation. Nevertheless, in recent years it has been quoted, and used in analyzing experiments on quite elongated particles. It is the purpose of this paper to generalize Eq. (5) for the case of elongated particles with a magnetocrystalline, uniaxial anisotropy superimposed on their shape anisotropy, so that the energy barrier is *not* K_uV. The *correct* energy barrier that should be used in Eq. (2) for such particles with this combination of anisotropies will be calculated in the next section.

a)Electronic mail: a.aharoni@ieee.org.

II. PROLATE SPHEROIDS

The magnetostatic self-energy of a *saturated* general ellipsoid can be written[2] in the form:

$$E_m=\tfrac{1}{2}\ V(N_xM_x^2+ \tag{6}$$

where V is the volume of the particle, and $\mathbf{M}$ is the magnetization vector. The parameters N_x, N_y, N_z are called the demagnetizing factors. They depend on the ratios of ellipsoidal axes, a, b, and c, specific expressions for which have been given[2] in terms of elliptic integrals.

For the particular case of a prolate spheroid, namely an ellipsoid for which two axes are equal, say $a=b$ and $c>a$, two demagnetizing factors are the same, $N_x=N_y$. Obviously, Eq. (6) can be written in this case as

$$E_m=\tfrac{1}{2}\ V[(N_z-N_x)M_z^2+N_xM_s^2], \tag{7}$$

where the last term, with the saturation magnetization M_s, is a *constant*, and may be omitted. In this case, the expressions for the demagnetizing factors are also more elementary. Specifically, by using the notation

$$m=c/a\ (>1),\quad \xi=\sqrt{m^2-1}/m, \tag{8}$$

the equations of Osborn[2] become

$$N_z=\frac{4\pi}{m^2-1}\left[\frac{1}{2\xi}\ln\left(\frac{1+\xi}{1-\xi}\right)-1\right], \tag{9}$$

$$N_x=2\pi-\tfrac{1}{2}\ N_z. \tag{10}$$

Dropping an additive constant, and defining the angle θ from the z axis, Eq. (7) can be written in the form

$$E_m=K_mV\sin^2\theta, \tag{11}$$

where

$$K_m=\tfrac{1}{2}\,(N_x-N_z)M_s^2. \tag{12}$$

This energy is thus formally equivalent to a uniaxial anisotropy as in Eq. (3). Therefore, if a uniaxial, magnetocrystalline anisotropy is also present, and if its easy axis is also in the same x direction, the coefficients of these anisotropies simply add to each other.

Consider, however, a magnetocrystalline anisotropy of the same form as in Eq. (3), whose easy axis is at an angle ψ to the z axis. When added to the shape anisotropy of Eq. (11) the total energy per unit volume is

$$U=E/V=K_m\sin^2\theta+K_u\sin^2(\theta-\psi). \tag{13}$$

To within an additive constant Eq. (13) is the same as

$$2U=-K_m^*\cos(2\theta)-K_u\sin(2\psi)\sin(2\theta), \tag{14a}$$

$$K_m^*=K_m+K_u\cos(2\psi). \tag{14b}$$

 0021-8979/94/75(10)/5891/3/$6.00 © 1994 American Institute of Physics

Therefore, the solution of $\partial U/\partial\theta=0$ is

$$\tan(2\theta_m)=K_u \sin(2\psi)/K_m^*. \tag{15}$$

Hence,

$$\cos(2\theta_m)=\pm K_m^*/K_e^2, \tag{16a}$$

$$\sin(2\theta_m)=\pm K_u \sin(2\psi)/K_e^2, \tag{16b}$$

where

$$K_e=\sqrt{K_m^2+K_u^2+2K_mK_u\cos(2\psi)}. \tag{17}$$

The double solution, with $\pm$ in Eqs. (16), originates from the two possibilities of extracting the square root. It should be noted, however, that there are only two possibilities, and not four, in assigning signs to the expressions in Eqs. (16). The sign of one of them is the *same* as that of the other, due to the constraint imposed by Eq. (15).

Substituting from Eqs. (16) in the energy expression of Eqs. (14), the energy extrema are

$$U_{\max}=\tfrac{1}{2}K_e,\quad U_{\min}=-\tfrac{1}{2}K_e. \tag{18}$$

Hence, the energy barrier to be substituted in Eq. (2) is

$$E_B=K_eV, \tag{19}$$

with K_e of Eq. (17). This relation is similar to Eq. (4), and the expression which has to be substituted in Eqs. (1) and (2) is only *numerically* different from that of Eq. (5). The numerical value of K_e may be larger or smaller than K_u, depending on the value of the angle ψ.

A. Particular cases

(1) $\psi=0$. In this case the anisotropies are in the same direction, and just add up; and indeed Eq. (17) yields for this case

$$K_e=|K_m+K_u|. \tag{20}$$

(2) $\psi=\pi/2$. In this case the anisotropies are perpendicular and subtract from each other:

$$K_e=|K_m-K_u|. \tag{21}$$

(3) $K_m+K_u\cos(2\psi)=0$. This case needs a special attention, because formally the solution of Eq. (15) is not valid when the denominator vanishes. It is seen, however, that Eq. (17) yields for this case

$$K_e=K_u|\sin(2\psi)|. \tag{22}$$

If the value of ψ for this case is first substituted in Eqs. (14), the energy density is

$$2U=-K_u\sin(2\psi)\sin(2\theta). \tag{23}$$

The maxima and minima are thus those of $\sin(2\theta)$, namely $\pm$ 1, and the result is as in Eq. (22).

B. Magnetic field

It is not difficult to add the energy of interaction with an applied magnetic field to the energy density of Eq. (13) or Eqs. (14). Only in that case the solution of $\partial U/\partial\theta=0$ involves (for $H||z$) the roots of a fourth-order polynomial in $\sin\theta$ or $\cos\theta$. In principle this solution can be obtained analytically as well, but it is not as simply written in a closed form as in the case $H=0$. Therefore, in this case it is better to evaluate the energy barrier numerically.

C. Surface anisotropy

In the foregoing, an angle θ was defined for the whole ellipsoid, independent on the position within it, thus taking for granted a *coherent rotation* of the magnetization in the particle. This mode is assumed in almost all the calculations of superparamagnetism in the literature, except for one theoretical study[3] which allows a certain noncoherent reversal mode. It is most probably a good approximation for all small particles because exchange is so strong in them that all other forces are negligible in comparison. Superparamagnetism in a set of two dipoles[4] prefers noncoherent reversals, but in this case there is no exchange coupling between the two dipoles.

Generally, the surface anisotropy, in as much as it is not negligible, should enter the Micromagnetics calculations as a modification of the boundary conditions.[5] However, if there is no space-dependence of the magnetization, the angles on the surface are exactly the same as the angles inside the particle. Therefore, for the coherent rotation approximation, there is no difference between a bulk and a surface anisotropy, and the latter may just be added to the shape and magnetocrystalline anisotropies, in the same way as has been done in the foregoing. It is only an approximation, especially since the coherent rotation is *not*[6] an eigenmode of Brown's equations when there is a surface anisotropy. It is, however, a well-justified approximation, and one which is being used anyway for the *other* energy terms. It is particularly important to note this point because Awschalom *et al.*[7] mention that the particles in their experiment "are likely to be amorphous rather than crystalline, and their anisotropy is presumably dominated by surface and shape effects."

III. APPLICATIONS

A. Blocking temperature

Bocquet *et al.*[8] compared measurements of different samples of fine-particle goethite. The length-to-width ratio (m in the notation used here) varied[8] between 1.55 (for a length of 704 nm and a width of 455 nm) and 18.4 (for a length of 295 nm and a width of 16 nm). But in spite of this wide variation in m, Bocquet *et al.*[8] expect the blocking temperature for superparamagnetism to depend only on the particle *volume*, using a relation similar to Eq. (1), with Eq. (5) substituted in it. They[8] evaluated the anisotropy, K_u, for *one* of the samples, with $m=15.8$, for which this anisotropy was not very different from that of bulk goethite, and assumed that the same value should apply to all the other samples.

In view of the present results, the combination of shape and crystalline anisotropy at this particular m can be very different from that of the other samples. Therefore, the analysis of the data should be modified, and the conclusion of Bocquet *et al.*[8] about the possible onset of superparamagnetism in fine particles of goethite is not conclusive.

The present analysis *may* also change, if the assumption of a coherent magnetization rotation breaks down for ex-

tremely elongated particles. But it seems more likely that the coherent rotation will remain a good approximation for all small particles of a regular shape, because of the strong exchange interaction.

B. Quantum tunneling

The particles in the experiment of Awschalom *et al.*[7] may have been prolate spheroids, but they may also have had three unequal axes. For the more general ellipsoids one should use Eq. (6) which can also be written, to within an additive constant, in the form

$$E_m=\tfrac{1}{2}\ V[(N_x-N_y)M_x^2+(N_z-N_y)M_z^2]. \tag{24}$$

This form has been assumed in the model of Chudnovsky *et al.*[9] for quantum tunneling of the magnetization. Here, only the case $N_x=N_y$ is studied, for which the theory[9] does not apply. However, for calculating the *energy barrier* it is sufficient to consider a rotation in the y-z plane, with $M_x=0$. The foregoing is then a sufficiently good approximation for the case of two *nearly* equal axes, for which the demagnetizing factors are only slightly different from those in Eqs. (9) and (10). The use of Eq. (19), with K_e which depends on the axial ratio, m, could thus make a large difference to the analysis of Awschalom *et al.*,[7] who ignored the different m in their samples. They[7] measured a resonance at a frequency ω_c, and looked for a linear relation between $\log(\omega_c)$ and the volume, V, according to Eq. (1), as if all the samples had the same K_e in spite of the reported variation of m between them.

It should be noted, though, that this correction by itself is not likely to account for the wide discrepancies between theory and experiment. It is quite possible that this particular theoretical model[9] does not apply to this particular experiment.[7]

APPENDIX

It may be worth noting that for a small ξ, a power series expansion of the logarithm in Eq. (9) leads to

$$N_z=\frac{4\pi}{m^2}\left[\frac{1}{3}+\sum_{k=1}^{\infty}\frac{1}{2k+3}\left(\frac{m^2-1}{m^2}\right)^k\right]. \tag{A1}$$

[1] I. S. Jacobs and C. P. Bean, in *Magnetism*, edited by G. T. Rado and H. Suhl (Academic, New York, 1963), Vol. III, pp. 271–298.
[2] J. A. Osborn, Phys. Rev. **67**, 351 (1945).
[3] I. Eisenstein and A. Aharoni, Phys. Rev. B **14**, 2078 (1976).
[4] A. Lyberatos and R. W. Chantrell, J. Appl. Phys. **73**, 6501 (1993).
[5] A. Aharoni, J. Appl. Phys. **61**, 3302 (1987).
[6] A. Aharoni, J. Appl. Phys. **64**, 6434 (1988).
[7] D. D. Awschalom, M. A. McCord, and G. Grinstein, Phys. Rev. Lett. **65**, 783 (1990).
[8] S. Bocquet, R. J. Pollard, and J. D. Cashion, Phys. Rev. B **46**, 11 657 (1992).
[9] E. M. Chudnovsky and L. Gunther, Phys. Rev. Lett. **60**, 661 (1988); Phys. Rev. B **37**, 9455 (1988).

Interactions between single domain particles

Roger Proksch[a)]
School of Physics and Astronomy, University of Minnesota, Minneapolis, Minnesota 55455

Bruce Moskowitz
Department of Geology and Geophysics, Institute for Rock Magnetism, University of Minnesota, Minneapolis, Minnesota 55455

We present a variation of the Wohlfarth–Henkel technique for studying interactions in single domain particles (SDPs) in which samples are prepared in different remanent states before the remanent magnetization curves are measured. By analyzing the resulting series of switching field distributions (SFDs), it is possible to separate the effects of positive (magnetizing) and negative (demagnetizing) interactions, even when one type dominates the other. The method is applied to two types of samples consisting of uniform SPDs of magnetite produced by magnetotactic bacteria: (1) whole bacterial cells containing single, linear chains of SDPs; and (2) SDPs extracted from the cells and allowed to aggregate into clumps.

I. INTRODUCTION

One approach to understanding the effects of interactions in a remanent magnetic system has been a plot of the isothermal remanent magnetization $M_r(H)$ versus the dc-remanent demagnetization $M_d(H)$, where both parameters are normalized to the saturation remanence. These plots, referred to as "Henkel plots,"[1] are based on the work of Wohlfarth[2] who considered the magnetization reversal of a collection of noninteracting uniaxial single domain particles (SDPs). For this case, a Henkel plot is linear, with a slope of -2. When interactions are present, the Henkel plot will be nonlinear and the curvature will depend on whether the interactions are positive (magnetizing) or negative (demagnetizing). In general, a magnetic system can have both positive and negative interactions. Often, however, one type of interaction will be dominant. If a Henkel plot is made of such a system, the dominant interaction may obscure the effects of the other.

In this paper, we present a variation of the Henkel technique for studying interaction effects in which samples are prepared in different remanent states before the remanent magnetization curves are measured. The derivative of each of these remanent curves produces a switching field distribution, ρ_K. By analyzing the resulting series of switching field distributions, it is possible to separate the effects of positive and negative interactions as well as the dependence of the interactions on the remanent state of the system. This technique has been applied to two magnetic systems, each consisting of assemblies of uniform SDPs of magnetite (Fe_3O_4) produced by magnetotactic bacteria.[3] The first system was a collection of whole bacterial cells containing single, linear chains of SDPs. The chains are physically separated from each other by the cell bodies, resulting in a relatively noninteracting sample. The second system was a collection of the same uniform bacterial SDPs extracted from the cells and allowed to agglomerate, resulting in an interacting magnetic system.

II. EXPERIMENTAL METHOD

Samples were first given a saturation remanent magnetization by the application of a large positive field. The $M_d(H)$ curve was then measured to some negative field called the preparation field H_p. At this point, the sample had some net remanent magnetic moment M_p. Starting from this state, $M_r(H)$ was measured. Another large saturating field was again applied, bringing the sample back to its initial state and the process was repeated several times using increasingly larger negative values of H_p. The derivative of $M_r(H)$ with respect to the acquisition field was then ρ_K. All magnetic measurements were made at room temperature with an alternating gradient force magnetometer in fields up to 1000 Oe. The coercivity of the particle samples was always near 300 Oe. Henkel plots were made for comparison with the method outlined above. In this case, the initial state for the $M_r(H)$ curve was produced by dc demagnetization in a negative field equal to the remanent coercivity.

Samples used in this study consisted of a collection of SDPs produced by the magnetotactic bacteria strain MV1.[4] Bacterial SDPs are ideal for interaction studies because of their narrow size and shape distributions. Variations in the coercive fields of bacterial SDPs should be primarily due to interactions rather than a combination of interactions and particle size distribution effects. Magnetotactic bacteria synthesize intracellular membrane bounded magnetite particles called magnetosomes. Magnetosomes in MV1 are truncated hexahedral prisms with average dimensions of $53\times35\times35$ nm.[5] Inside the bacteria, the magnetosomes form a single linear chain of 10–20 particles per cell, with an average distance between magnetosomes of $\sim$10 nm. The magnetosomes are oriented with their magnetic easy axes aligned along the chain axis, forming an effective magnetic dipole. The bacterial dipoles are separated from each other by the cell bodies limiting interchain interaction distances to a few microns. Because of this configuration, negative chain-chain interactions should be small.

Magnetosomes are easily extracted from cells by dissolving the cell membranes in a hypochlorite solution and collecting the magnetic fraction with a magnet. This treatment disrupts the internal chain structure and produces an

a)Present address: Department of Physics, Saint Olaf College, Northfield, MN 55057.

 0021-8979/94/75(10)/5894/3/$6.00 © 1994 American Institute of Physics

agglomerated sample of SDPs. In such a system, one expects predominantly negative interactions from closed chain configurations.

Samples for remanence measurements were prepared by drying dilute suspensions of whole cells and extracted magnetosomes onto glass slides in the presence of the earth's magnetic field (0.5 Oe). Remanence ratios (M_r/M_s) of ≈0.5, measured from the full hysteresis loops, confirm that samples are randomly oriented and that the drying procedure produced little or no net particle orientation.

III. NONINTERACTING CASE

As a first step in the analysis, we will explore the case of a randomly oriented ensemble of completely noninteracting single domain particles. In this situation, the remanent behavior of the system has been described previously.[6] According to the Stoner–Wohlfarth model of a SDP, the particle coercivity is the same in both the positive and negative directions and depends only on the anisotropy and angle to the applied field. For a random, noninteracting collection of particles, two important points concerning the switching field distribution ρ_K are: The switching field distribution (ρ_K) for remanent acquisition should have a sharp cutoff at the preparation field H_p. Successive ρ_K curves should superpose for fields less than their respective cutoff points. These points are illustrated in Fig. 1(A) for two different preparation fields. Variations from these two ideal conditions indicate the presence of interactions.

IV. INTERACTION CASE

Positive interactions assist the magnetization process, whereas negative interactions hinder it. Therefore, interactions will modify the shape of the ideal noninteracting ρ_K curve in two distinct ways. First, positive interactions will shift ρ_K to lower fields, and for successive initial magnetization states, the ρ_K curves will no longer superpose for fields less than H_p. However, positive interactions should not affect the presence of a sharp cutoff of ρ_K at the preparation field H_p. The positive interaction case is schematically illustrated in Fig. 1(B). Secondly, negative interactions, on the other hand, will shift ρ_K to higher fields. Here, ρ_K curves for successive initial magnetization states will not superpose for fields larger than H_p. This is shown in Fig. 1(C). The more realistic case of both types of interactions is shown in Fig. 1(D).

Thus, the main advantage of our technique over the conventional Henkel plot is that it is possible to observe both positive and negative interactions in a sample with the same measurement. As we will show below, this is true even if one type of interaction dominates.

V. RESULTS

A family of ρ_K curves for an ensemble of whole cells is shown in Fig. 2. As expected, successive curves superimpose for low-field values, indicating minimal positive interactions. Magnetosomes arranged in a chain experience strong magnetic coupling resulting in collective magnetic response. In this case, the positive interactions are so strong that the chain

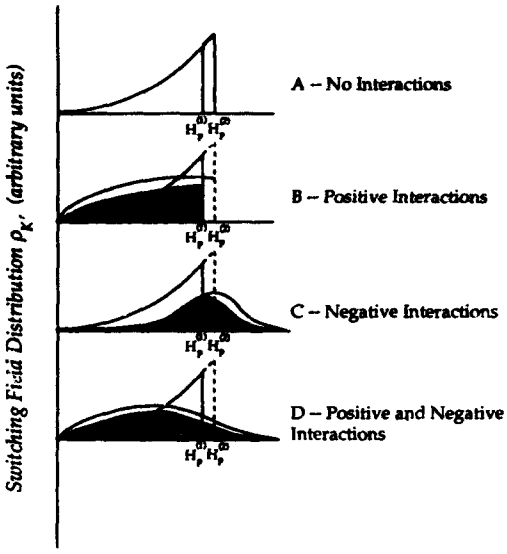

FIG. 1. A set of switching field distribution (ρ_K) curves for single domain particles. Each case [(A)–(D)] provides an example of the behavior of the ρ_K curve for successively increasing preparation field (H_p) values. (A) In the case of no interactions, successive ρ_K curves simply superpose. (B) If there are only positive (magnetizing) interactions present, the system will begin to switch at lower values of $H<H_p$, producing a larger ρ_K at small field values. The system will be completely switched by the time the preparation field is reached, resulting in a cutoff at that point as in the case of no interactions. (C) For the case in which the system exhibits only negative (demagnetizing) interactions, successive curves superpose until the initial preparation field value. Then successive curves will start to diverge as the negative interactions are overcome. To entirely switch the system, it may be necessary to apply a field significantly larger than the preparation field. (D) In the typical situation where both types of interactions are present, features of cases (B) and (C) are combined.

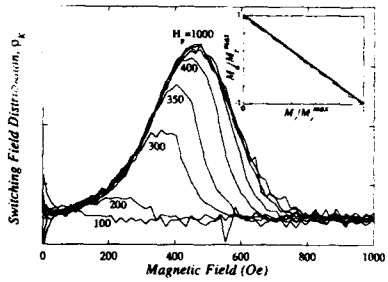

FIG. 2. A family of switching field distribution (ρ_K) curves for relatively noninteracting chains of single domain particles. The numbers on the curves correspond to the preparation field values (H_p). A Henkel plot for the same system is inset in the upper right corner. Whereas the Henkel plot suggests that this is a relatively noninteracting system, the behavior of the ρ_K curves is similar to that diagrammed in Fig. 1(C), indicating the presence of negative interactions.

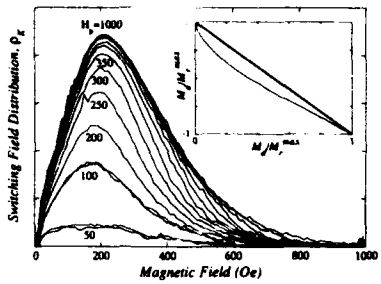

FIG. 3. A family of switching field distribution (ρ_K) curves for a system of highly interacting single domain particles. The numbers on the curves correspond to the preparation field values (H_p). The Henkel plot of this system (shown in the inset in the upper right corner) indicates the presence of negative interactions. This agrees with the family of ρ_K curves. However, the ρ_K curves also indicate the presence of significant positive interactions [see Figs. 1(B) and 1(D)].

of particles behave as a single magnetic particle, which is sufficient enough to maintain the superposition of the ρ_K curves for fields less than H_p. A Henkel plot for this sample (Fig. 2) is approximately linear with slope -2, suggesting no interactions (positive or negative). However, this type of Henkel plot is also similar to theoretical ones produced by aligned chains of particles with a narrow switching field distribution in a 1-D lattice geometry.[7] The ideal 1-D geometry may closely approximate the linear chain microstructure of the whole bacteria cells; however, in our case, the chains are randomly oriented.

Despite a linear Henkel plot for this sample (Fig. 2, inset), the lack of a sharp cutoff at H_p and tailing out at high fields in the ρ_K curves shown in the main part of Fig. 2, indicate the presence of negative interactions. Nevertheless, the shift of successive peaks towards higher fields [see Fig. 1(C)] suggests that the level of negative interactions is small, explaining the linear Henkel plot.

Results for extracted magnetosomes are shown in Fig. 3. Here, successive ρ_K curves do not superimpose, either at low- or high-field values. As expected, the ρ_K curves at high fields show the effects of large negative interactions. For example, a preparation field of 50 Oe requires a field greater than 600 Oe to fully remagnetize the sample (see Fig. 3). A Henkel plot for this sample (Fig. 3) shows the typical response for negative interactions, similar to results from some particulate recording media.[8]

Because this was a random collection of uniform SDPs, some of the particles are expected to interact positively. This is confirmed by nonsuperposition of the ρ_K curves at low fields. Thus, despite the high level of negative interactions, our method was able to pick out a small positive contribution.

VI. CONCLUSIONS

We have demonstrated the utility of examining the switching field distributions of families of remanent curves as a means of separating positive and negative dipolar interactions between single domain particles. In addition, this technique is sensitive to interactions, even when a conventional Henkel plot indicates the system is non-interacting. When interpreting the data shown in this paper, it is important to note that ρ_K depends on both the applied field and the micromagnetic state of the system. In an interacting system, it is possible to have the same bulk magnetization value for very different micromagnetic states. In general, the micromagnetic state is not possible to define, but some statements can be made about it by careful examination of the interactions. Further work is presently in progress in this area.

ACKNOWLEDGMENTS

We thank D. A. Bazylinski for supplying the magnetotactic bacteria samples, E. Dan Dahlberg for useful discussions, and Sheryl Foss for a critical reading of the manuscript. This work was partially supported by ONR Grant No. N0014-89-J-1355. This is contribution 9307 of the Institute for Rock Magnetism. The Institute for Rock Magnetism is supported by grants from the Keck Foundation and the National Science Foundation.

[1] O. Henkel, Phys. Status Solidi **7**, 919 (1964).
[2] E. P. Wohlfarth, J. Appl. Phys. **29**, 595 (1958).
[3] B. Moskowitz, R. Frankel, P. Flanders, R. P. Blakemore, and B. B. Schwartz, J. Magn. Magn. Mater. **72**, 273 (1988).
[4] B. Moskowitz, R. Frankel, D. Bazylinski, H. Jannasch, and D. Lovely, Geophys. Res. Lett. **16**, 665 (1989).
[5] N. H. C. Sparks, S. Mann, D. Bazylinski, D. Lovely, H. Jannasch, and R. Frankel, Earth Planet. Sci. Lett. **98**, 14 (1990).
[6] E. C. Stoner and E. P. Wohlfarth, Philos. Trans. R. Soc. London Ser. A **240**, 599 (1948).
...i. Fearon, R. Chantrell, and E. P. Wohlfarth, J. Magn. Magn. Mater. **86**, 197 (1990).
[8] G. W. D. Spratt, P. R. Bissell, R. W. Chantrell, and E. P. Wohlfarth, J. Magn. Magn. Mater. **75**, 309 (1988).

Temperature dependence of switching field distribution

Jiang-Ching Lin
Materials Research Laboratory, Industrial Technology Research Institute, Chutung, Hsinchu, 31015 Taiwan, Republic of China

I. Klik
Department of Physics, National Taiwan University, Taipei, Taiwan, Republic of China

C. J. Chen
Materials Research Laboratory, Industrial Technology Research Institute, Chutung, Hsinchu, 31015 Taiwan, Republic of China

Ching-Ray Chang
Department of Physics, National Taiwan University, Taipei, Taiwan, Republic of China

The peak value of switching field distribution χ_{max}, coercivity H_c, and saturation magnetization M_s are measured as functions of temperature T in Co-γ-Fe_2O_3 and γ-Fe_2O_3 powders. It is found that χ_{max} has a maximum at $T=T_p$ and evidence is presented also for the existence of a theoretically predicted minimum at $T=T_m<T_p$. Coercivity is decreasing with T. For Ba-ferrite platelets we find that H_c has a maximum at $T=\tilde{T}_p$ and a minimum at $T=\tilde{T}_m\approx T_p$, where χ_{max} has a local maximum. The possible origin of this unusual behavior is discussed.

Recently[1] we studied theoretically the response of an array of identical thermally relaxing noninteracting particles to time varying applied magnetic field $H(t)$. The particles were assumed to be uniaxial, with easy axes parallel to the direction of H so that their energy

$$E=K^{(2)}V(1-\alpha_3^2)-HM_sV\alpha_3. \tag{1}$$

Here $K^{(2)}$ is anisotropy constant, M_s saturation magnetization, V activation volume, α_i are direction cosines of magnetization, and we set $H(t)=H_a\cos\omega t$ for the biasing field. Its amplitude, $H_a=2K^{(2)}/M_s$, is the nucleation field and $H(t)$ drives a major hysteresis loop. At temperature T we tabulated the nonequilibrium magnetization $M[\omega,T|H(t)]$ and derived thence the coercivity $H_c(\omega,T)$ and the switching field distribution (SFD) $\chi[\omega,T|H(t)]\approx\Delta M[\omega,T|H(t)]/\Delta H(t)$. The SFD function χ was found to have a peak at, or close to, coercivity: $\chi_{max}(\omega,T)\approx\chi[\omega,T|H_c(\omega,T)]$. If $K^{(2)}$ and M_s are temperature independent then the model (1) yields $dH_c/dT<0$ for all T but, surprisingly, at a fixed sweep rate ω the function $\chi_{max}(\omega,T)$ has a local minimum at $T=T_m$ and a local maximum at $T=T_p>T_m$. For $0<T\ll T_m$ $\chi_{max}(\omega,T)\propto T^{-1/2}$ and coercivity is given by Sharrock's formula[1,2] while $\chi_{max}(\omega,T)\propto T^{-1}$ for very high temperatures $T_C>T\gg T_p$ as the system approaches thermal equilibrium. Obviously, in an infinitely slow sweep, $\omega\to 0$, this regime prevails throughout the entire temperature range while at very fast sweeps the system remains near thermal equilibrium only at high temperatures close to the Curie point T_C.

The two descending segments of $\chi_{max}(\omega,T)$ are separated by an ascending section at the intermediate temperatures $T_m<T<T_p$, where a transition between the low- and high-temperature switching regimes takes place. At present, however, there exists no analytic formula for χ_{max} which would bridge the gap between the two limits and the SFD function χ can only be studied through analysis of arrays of hysteresis loops.

The relation of χ_{max} to the SFD width was further discussed in Ref. 3 and the influence of easy axes misalignment in Ref. 4.

It appears that for particulate recording media the ascending section of χ_{max} falls squarely into the region of room temperatures and observations of $d\chi_{max}/dT>0$ have, indeed, been reported previously.[5] Here we plot our newly obtained experimental curves of the SFD peak value $\chi_{max}(\omega,T)$ for Co-γ-Fe_2O_3 and γ-Fe_2O_3 powders and for Ba-ferrite platelets. The coercivity and SFD of the first two materials behave in accordance with the theory of Ref. 1 while barrium ferrite, known for its exceptional T dependence of coercivity, cannot adequately be described by Eq. (1) alone. Its properties are discussed separately.

Commercial magnetic recording powders of acicular Co-γ-Fe_2O_3 (average length 0.3 μm and aspect ratio 8–10) and γ-Fe_2O_3 particles and barrium-ferrite platelets were mixed (separately, of course) in a resin polymer to form a slurry which was then deposited on a glass substrate and oriented in a magnetic field of 3000 Oe. The particle packing fraction was about 70% of weight and 30% of volume in all samples. A sequential program with identical measuring conditions over the whole temperature range was used to record the hysteresis loop of each sample as measured by a vibrating sample magnetometer (VSM). The oriented direction of the sample was parallel to the applied field in the in-plane measurement. The thickness of the magnetic coating could not be determined with sufficient precision and we present therefore the total measured magnetic moment I_s rather than the magnetization M_s.

From Figs. 1 and 2 we see that the coercivity of the Co-γ-Fe_2O_3 and γ-Fe_2O_3 powders decreases uniformly with temperature and, at the same time, that χ_{max} has a distinct peak at $T=T_p$. The thermal equilibrium region close to the Curie point $T_C>T_p$ is not shown in our graphs since large thermal fluctuations make experimental observations here too difficult. The experimental high T section of χ_{max} in Fig. 1 drops off faster than T^{-1} and, as the relatively high coercivity shows, the system is not in thermal equilibrium. At

 0021-8979/94/75(10)/5897/3/$6.00 © 1994 American Institute of Physics

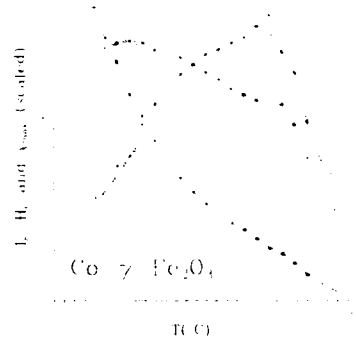

FIG. 1. Co-γ-Fe_2O_3 powder: Experimental dependence of the peak switching field distribution value χ_{max}, coercivity H_c and saturated magnetic moment I_s on temperature T. Units and markings: χ_{max} (arbitrary scale, full line), H_c (200 Oe, long dash), and I_s (arbitrary scale, short dash). The lines merely guide the eye. Three samples from the same production batch, distinguished by the symbols (○), (•), and (△).

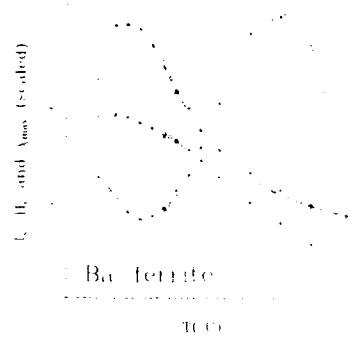

FIG. 3. Ba-ferrite platelets. Units and markings same as in Fig. 1 but with H_c (10^3 Oe). Three samples as in Fig. 1.

temperatures $T_m<T<T_p$ the experimental SFD function χ_{max} grows with T. On the other hand, if $T\to 0$ then the Stoner–Wohlfarth limit is reached in which $H_c\to H_n$. The SFD function is a δ function, $\chi\propto\delta(H-H_n)$, and $\chi_{max}\to\infty$. Obviously, there is therefore $d\chi_{max}/dT<0$ on some interval $T<T_m$ and the function χ_{max} must have a minimum at $T=T_m$. This low-temperature, almost irreversible[6] regime described by Sharrock's formula,[1,2] $\chi_{max}\propto T^{-1/2}$, could not be reached even at liquid-nitrogen temperatures though a trend towards a focal minimum in this region may be detected in Fig. 1. According to the theory of Ref. 1 the local minimum shifts to higher temperatures and, at the same time, becomes shallower with increasing sweep rate, which, however, is difficult to manipulate in VSM measurements.

It was shown in Ref. 1 that uniform *decrease* of $K^{(2)}(T)>0$ and $M_s(T)$ with temperature has, within the model (1), no effect on the overall behavior of H_c and χ_{max}: The two graphs $\chi_{max}(\omega,T)$ and $H_c(\omega,T)$ merely undergo a scaling transformation which is one-to-one, i.e., no new extrema can occur. In order to study the T dependence of magnetization we attempted to interpolate our data on the whole temperature range according to the simple formula

$$I_s(T)=I_s(0)(1-T/T_C)^{\sigma} \tag{2}$$

and found poor agreement between the interpolated values of T_C and those reported in literature.[7] Also the critical exponent σ deviated markedly from the theoretical bulk value[1] $\sigma=1/3$. We conclude that Eq. (2) is not adequate over large temperature intervals and propose that the experimental curve $M_s(T)$ be used if the theory based on Eq. (1) is to be matched with experiment. A separate measurement, currently in preparation, of the function $K^{(2)}(T)$ is also required. A fully consistent *quantitative* description of the powdered samples, however, is rendered difficult not only by the requirement that $M_s(T)$ and $K^{(2)}(T)$ be *a priori* known, but also by the intrinsically stochastic nature of thermal switching[4] (the thermal decay rate is only the *mean* value of the relaxation rate) and by the distribution of activation volumes within the sample which must be related to its magnetic viscosity.[8] Moreover, the thermal decay rate prefactor has a poorly understood temperature[9] and field[10] dependence which cannot be neglected on the large intervals studied.

The barrium ferrite data of Fig. 3 show that its coercivity has a minimum at $T=\tilde{T}_m$ and a maximum at $T=\tilde{T}_p>\tilde{T}_m$ and that H_c *increases*[11] with T at room temperatures, but decreases at very low and very high temperatures as has been reported previously.[12] The SFD function $\chi_{max}(\omega,T)$ behaves as in the previous two cases of Co-γ-Fe_2O_3 and γ-Fe_2O_3 but its peak at $T=T_p$ is at markedly low temperatures. It is certainly remarkable that $T_p\approx\tilde{T}_m$ where coercivity reaches its minimum and it should also be noticed that at the peak region of coercivity, for $T\approx\tilde{T}_p>T_p$, the function χ_{max} decreases very slowly. The peculiar increase of coercivity at room temperatures was explained by Kubo *et al.*[11] as a consequence of shape anisotropy which opposes alignment of

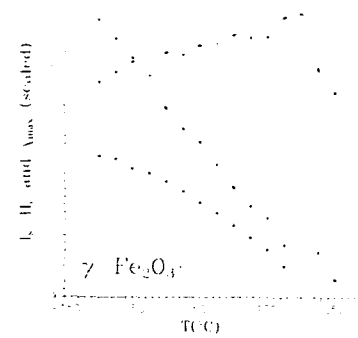

FIG. 2. γ-Fe_2O_3 powder. Units and markings same as in Fig. 1 but with H_c (20 Oe). One sample.

magnetization with the easy axis perpendicular to the platelet plane. In Eq. (1), then, $K^{(2)} \to \tilde{K}^{(2)} = K^{(2)} - NM_s^2$, and for the nucleation field one obtains $H_n = 2[K^{(2)}/M_s - NM_s]$. Assuming that the ratio[11] $K^{(2)}/M_s$ or $K^{(2)}$ alone[7,12] are temperature independent then the relation $H_c \propto H_n$ yields $dH_c/dT > 0$ since $dM_s/dT < 0$. This relation is certainly applicable locally, on a small temperature interval, but a theoretical model of Ba-ferrite coercivity valid for all T is, to date, lacking, in particular in regard of the prominent high-temperature peak at ~150 °C. The existence of an easy cone[13] rather than of an easy axis was assumed by Kubo and Ogawa;[14] this model includes also the quartic term

$$E = K^{(4)}V(1-\alpha_3^2)^2 + \tilde{K}^{(2)}V(1-\alpha_3^2) - HM_sV\alpha_3 \qquad (3)$$

and if $k = \tilde{K}^{(2)}/K^{(4)}$ then the nucleation field becomes[13]

$$H_n = \frac{K^{(4)}}{M_s} \begin{cases} [2k/3]^{3/2} & \text{if } 0 < k \leq 6 \\ 2k - 4 & \text{if } 6 < k \end{cases} \qquad (4)$$

Kubo and Ogawa[14] measured the temperature dependence of saturation magnetization and anisotropy constants and found Eq. (4) to give a good quantitative agreement with experiment. Unfortunately, however, their data did not include the high-temperature region of maximum coercivity and it remains an open question whether the model (3) is applicable also in this region. Similarly, it is unclear whether the SFD peak value $\chi_{max}(\omega,T)$ shown in Fig. 3 is compatible with Eq. (3); we recall yet that χ_{max} diverges in the limit $T \to 0$ so that there must exist also a low-temperature minimum. Measurements of anisotropy energy all the way to T_C are currently in preparation and shall be reported on in near future, together with hysteresis calculations based on Eq. (3) and the theory of Ref. 1.

[1] I. Klik, C. R. Chang, and H. L. Huang, Phys. Rev. B **47**, 8605 (1993); H. L. Huang, I. Klik, C. R. Chang, and K. K. Liang, J. Magn. Magn. Mater. **120**, 177 (1993).
[2] M. P. Sharrock, IEEE Trans. Magn. **MAG-26**, 193 (1990).
[3] I. Klik and C. R. Chang (unpublished).
[4] I. Klik, H. L. Huang, and C. R. Chang, J. Appl. Phys. **73**, 6662 (1993).
[5] K. O'Grady, IEEE Trans. Magn. **MAG-26**, 1870 (1990).
[6] A note on terminology: Thermally activated jumps over a barrier take place in both directions, though possibly with different probabilities. If the jump probability in one direction is zero we talk of a purely irreversible process (Stoner–Wohlfarth limit), if the jump probabilities in the two directions are equal (detailed balance) we talk of a purely reversible process.
[7] G. Bate, J. Magn. Magn. Mater. **100**, 413 (1991).
[8] I. Klik and C. R. Chang, Phys. Rev. B **47**, 9091 (1993); S. H. Charap, J. Appl. Phys. **63**, 2054 (1988).
[9] I. Klik, J. Appl. Phys. **73**, 6725 (1993).
[10] I. Klik, C. R. Chang, and H. L. Huang, Phys. Rev. B (to be published).
[11] O. Kubo, T. Ido, and H. Yokoyama, IEEE Trans. Magn. **MAG-18**, 1122 (1982).
[12] A. R. Corradi, D. E. Speliotis, G. Bottoni, D. Candolfo, A. Cachetti, and F. Masoli, IEEE Trans. Magn. **MAG-25**, 4066 (1989); M. Kishimoto and S.-I. Kitahata, *ibid.* 4063.
[13] C. R. Chang, J. Appl. Phys. **69**, 2431 (1991); G. Herzer, W. Fernengel, and E. Adler, J. Magn. Magn. Mater. **58**, 48 (1986).
[14] O. Kubo and F. Ogawa, IEEE Trans. Magn. **MAG-27**, 4657 (1991).

Dynamics of fine particles observed in zero-field neutron scattering

M. Hennion, C. Bellouard, and I. Mirebeau
Laboratoire Léon Brillouin (CEA-CNRS), CEN-Saclay, 91191 Gif-sur-Yvette Cedex, France

J. L. Dormann
Laboratoire de Magnétisme CNRS, 1 pl. A. Briand, 92125 Meudon Cedex, France

R. Ober
Laboratoire de Physique de la Matière Condensée ERA-CNRS College de France, 75231 Paris Cedex 05, France

We present here a dynamical study of Fe particles (Ø~50 Å) dispersed in an alumina matrix, performed by inelastic neutron scattering, in zero applied field. The line shape of the energy spectrum, quasielastic or inelastic, allows us to define three temperature ranges, attributed to three distinct regimes for the transverse fluctuations. At high temperature, the line shape is quasielastic with a nearly temperature independent energy linewidth. At intermediate temperature, one observes the expected precession mode with an inelastic line shape. At low temperature, a "reentrant" behavior occurs, which locates the disappearance of the precession mode, likely due to the effect of interparticle coupling.

Up to now, the magnetic properties of single domain particles have been extensively studied by susceptibility,[1] Mössbauer,[2] and ferromagnetic resonance,[3] namely, at frequency rates going up to 10^9 s^{-1}. Neutron experiments extend the frequency window to 10^{10}–10^{12} s^{-1}. Moreover, zero-field measurements provide direct information on the intrinsic properties of these systems which is of special interest for particles with random anisotropy axes. In a previous study[4] of very small Fe particles (Ø~25 Å) in an alumina matrix corresponding to about 20% Fe in volume, the observed energy spectra have shown the existence of a dual dynamics with two typical relaxation times for the particle magnetization. The large time, which is revealed by a resolution-limited component of the magnetic intensity, was attributed to the "longitudinal" fluctuations corresponding to the relaxation between the metastable states, defined by the particle anisotropy energy. The fast time was attributed to the transverse fluctuations of the magnetization trapped in one of its metastable states. Following theory,[5,6] the evolution in temperature of the dynamics is governed by the ratio E_B/kT, where E_B is the energy barrier between the metastable states. In a uniaxial assumption, usually justified by the existence of a shape anisotropy, one has $E_B=K^{\text{eff}}V$ (K^{eff} is the density of anisotropy energy and V the volume). For $E_B/kT\ll 1$, the two dynamics are expected to merge at high temperature in a single relaxation process which obeys the Debye law with a Curie susceptibility $\chi(T)\propto 1/T$ and a characteristic time $\tau\propto 1/T$. Experimentally, in the high T limit, the relaxation time deduced from the energy linewidth Γ ($\tau=1/2\pi\Gamma$) no more decreased with T but was found limited at some value, which could be related to the anisotropy energy of the particle. In the opposite limit $E_B/kT\ll 1$, one expects[6] to observe inelastic processes corresponding to the precession mode of the Landau–Lifshitz equation. Instead, down to 25 K, the fast dynamical component kept a quasielastic line shape. This could indicate that the condition $E_B/kT\gg 1$ was still not fulfilled in this sample, so that we were actually observing a transitory regime. To check this conjecture, we have studied a sample with larger particle sizes so that this limit could be easily reached. This new sample has been studied by magnetization, x-ray scattering, neutron diffraction at small angles, and inelastic neutron scattering. We present here the x-ray scattering experiment at small angles and some results obtained by inelastic neutron scattering.

Fe particles dispersed in an alumina matrix have been obtained by copulverization as in Ref. 1. Magnetization experiments allow the determination of a mean-particle diameter of about 50 Å. The x-ray scattering obtained at small q values is reported in Fig. 1. It consists of two parts: an increasing intensity at very small angle and a peak around $q=0.17$ Å^{-1}. This latter, very similar to the peak observed in the first studied sample, indicate the existence of a typical size of particles, and of a characteristic interparticle distance (25 and 46 Å, respectively within the same analysis as in Ref. 7). The very small q contribution indicates the existence of larger particles. Being out of the Guinier approximation, it cannot be analyzed quantitatively. Comparison between magnetization and x-ray scattering indicate therefore that the size distribution is likely more important in this sample than in the first one.

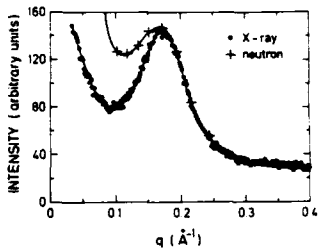

FIG. 1. Comparison between the q dependence of the x-ray scattering intensity and the q dependence of the resolution-limited peak C_1 measured at 300 K. The x ray and neutron intensities have been scaled at the peak position. We have omitted the neutron intensities at the smallest q values, being out of the scale (for $q=0.0775$ Å^{-1}, $I=295$ a.u.).

 0021-8979/94/75(10)/5900/3/$6.00 © 1994 American Institute of Physics

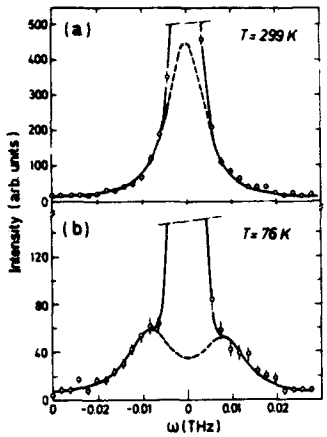

FIG. 2. Examples of fitted energy spectra using the single Lorentzian form ($T=300$ K) and the double Lorentzian one ($T=75$ K).

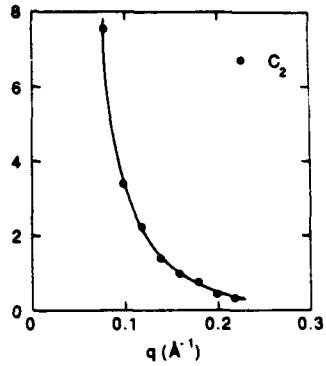

FIG. 3. q dependence of the energy-integrated intensity C_2 in arbitrary units measured at 300 K.

Inelastic neutron scattering experiments have been carried out at the Orphée reactor (Laboratoire Léon Brillouin) using the three-axis spectrometer 4F1 and the neutron cold source facilities. The collimations and the incident neutron wave vector ($K_i=1.05$ Å^{-1}) determine a resolution window (FWHM) of $2\Gamma_0=20$ μeV, corresponding to a characteristic time $\tau_0=1/2\pi\Gamma_0=6\times10^{-11}$ s. Three values of the momentum transfer q (0.045, 0.0775, 0.118 Å^{-1}) have been studied over the whole temperature range 10–480 K, whereas a more complete q range has been studied at 300 K. For each q, the energy spectra may be analyzed as the sum of a delta function of intensity C_1 and of an energy function corresponding to the inelastic cross section, both convoluted with the spectrometer resolution. The inelastic neutron cross section $I(q,\omega)$ where q and ω are the momentum and energy transfers, respectively, depends on the incident and final neutron wave vectors and of the spin correlation function $S(q,\omega)$ by $I(q,\omega)\propto(K_f/K_i)S(q,\omega)$. In the linear response theory, $S(q,\omega)$ is expressed as $S(q,\omega)=\omega[n(\omega)+1]\chi'(q,\omega=0)F(q,\omega)$. Here, $n(\omega)$ is the Bose factor, $\chi'(q,\omega=0)$ the static "transverse susceptibility" (as justified below) and $F(q,\omega)$ the spectral weight function. Depending on T, the better fits are obtained by using a spectral function $F(q,\omega)$ of either a single Lorentzian form (of linewidth Γ centered at $\omega=0$) or a double Lorentzian one (centered on $\pm\omega_0$ with a linewidth Γ). These two forms correspond respectively to the Debye model (high T limit) and to the Landau–Lifshitz model (low T limit) in Ref. 6. Examples of fits are reported in Fig. 2. In the approximation $\omega\ll kT$, valid here, the energy integrated intensity, $C_2(q)$, is directly related to $\chi'(q,\omega=0)$, by $C_2(q)\propto S'(q)=kT\chi'(q,\omega=0)$.

The delta function or "resolution-limited" peak C_1 consists of a nuclear contribution and possibly of a magnetic component with a characteristic fluctuation time τ larger than the time defined by the experimental resolution. Comparing the q dependence of C_1 (magnetic+nuclear contribution) with the q dependence of the x-ray profile (mere nuclear contribution) as in Fig. 1 for $T=300$ K, we conclude to the existence of a resolution-limited magnetic component ($\tau<6\times10^{-11}$ s) at this temperature. In Fig. 3, we have reported the q dependence of the energy-integrated intensity of the other magnetic component $C_2(q)$ at the same $T=300$ K value. The observed q dependence of this dynamic magnetic component is related to the spatial extension of the particle magnetization. The experimental energy range (some 1/100 of meV, therefore much smaller than the Fe-Fe exchange energy), as well as this q dependence, ensure that we are observing the dynamics of the particles, fluctuating as a whole. This dynamical component is described now.

In Fig. 4 we have reported the temperature dependence

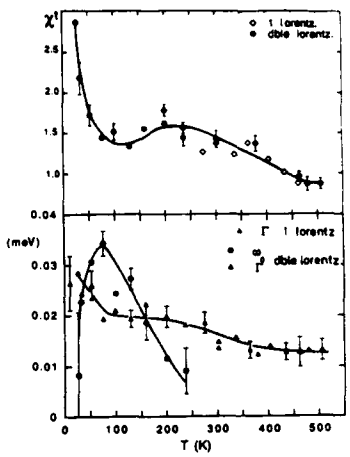

FIG. 4. Temperature dependences of the transverse susceptibility $\chi'(q,\omega=0)$, the Γ and ω_0 parameters deduced from the single Lorentzian or double Lorentzian analysis of the energy spectrum at $q=0.0775$ Å^{-1}.

of Γ, ω_0, and χ' for the intermediate $q=0.0775$ Å^{-1} value. The energy line shape of the spectrum allows us to define three distinct temperature regimes when decreasing T.

(i) In the first regime corresponding to 500 K$>T>$200 K, the energy spectrum is quasielastic (see Fig. 2 for $T=300$ K), namely, better described by one Lorentzian ($\omega_0 \ll \Gamma$). The linewidth Γ is roughly temperature independent down to 350 K and increases below whereas the susceptibility is close to $1/T$. (ii) In the second regime, 200 K$>T>$50 K, the signal appears weakly inelastic ($\omega_0 > \Gamma$) with heavily damped modes (see Fig. 2 for $T=75$ K). In this T range the transverse susceptibility exhibits a plateau. As T decreases further, ω_0 increases up to a maximum value and decreases beyond. In this same T range the damping Γ value is roughly constant and increases when ω_0 decreases. (iii) Finally, below 50 K, the energy spectrum appears again better fitted with a single Lorentzian ($\omega_0 \ll \Gamma$). The transverse susceptibility starts to increase steeply with a variation very close to $1/T$. The two other q values show the same three temperature regimes but one observes a significant shift of the transitions towards higher T for the smallest q and lower T for the larger q. Since one expects the change of regimes ruled by the KV/kT ratio, these shifts can be easily explained by a volume effect observed here through the q dependence. The evolution observed at the intermediate $q=0.0775$ Å^{-1} value appears therefore characteristic of the behavior of a particle with an intermediate size in the distribution.

As for the previous sample, one can attribute this dynamical magnetic component to the "transverse" fluctuations of the single particle magnetization. Accordingly, the slow dynamics revealed by the magnetic contribution in the resolution-limited peak, may correspond to the "longitudinal" fluctuations or relaxation between the metastable states. These definitions are meaningful locally, that is to say for a single particle anisotropy direction. In the high-temperature regime, the overall striking result is the similarity between these observations and those made in the previous sample, with essentially a strong shift towards higher temperatures in the present sample. From 350 K up to the highest T value (480 K), the Γ linewidth has reached a nearly temperature-independent value (0.013 meV) very close to the asymptotic one (~0.01 meV) measured above 100 K in the previous sample.[4] In particular, we never observe the increase of Γ with T predicted by theory. We are faced, therefore, with the same puzzling result as before. As already noticed, this asymptotical value, when converted in effective anisotropy field ($\Gamma=\gamma H^{\text{eff}}$, $H^{\text{eff}}=2K^{\text{eff}}/M_s$), yields a K^{eff} value ($K^{\text{eff}}=5\times10^5$ erg/cm^3) very close to that expected for Fe anisotropy. Whether this result is meaningful or not, remains to be checked by investigating other kinds of particles. Below 350 K, the increase of Γ as T decreases is very likely related to a preliminary effect of interparticle interaction. This is comforted by the occurrence of some short range interparticle order revealed by SANS experiment at these temperatures and which will be reported later. The quasielastic nature of the dynamical signal as well as the $1/T$ behavior of $\chi'(T)$, which were already observed in the previous sample, indicate that this regime is close to the "isotropic" one. Nevertheless, unlike the previous study, the isotropic regime is not completely reached even at 480 K since we still observe some magnetic intensity in the C_1 component at this T value.

Below 200 K, we observe an inelastic line shape in agreement with theory.[6] It corresponds to the evolution towards the precession mode of the Landau–Lifshitz equation. One expects χ' to obey a $1/\omega_0$ variation, which is in qualitative agreement with the observations. In the present case, this transition may be driven by temperature as well as by the interparticle coupling, this latter producing an enhancement of the effective anisotropy K^{eff} as discussed in Refs. 1 and 4. Therefore, down to 200 K, the transverse excitations can be described in terms of local modes, indicating that the interparticle interactions which are strongly temperature dependent, are still weak. Below 50 K, a kind of "reentrant" behavior occurs, revealed by the steep increase of the susceptibility whereas the energy spectrum turns back towards a quasielastic line shape. Clearly, in this new regime, the competing interparticle interactions have destroyed the local modes. It must be noticed that this new regime is observed in the transverse dynamics only, since no special changes occur in the short range interparticle ordering observed by SANS.

[1] J. L. Dormann, L. Bessais, and D. Fiorani, J. Phys. C **21**, 2015 (1988).
[2] S. Mörup, J. A. Dumesic, and H. Topsöe, in *Applications of Mössbauer Spectroscopy*, Vol. 2, edited by R. L. Cohen (Academic, New York, 1980).
[3] For instance, U. Netzelmann, J. Appl. Phys. **68**, 1800 (1990), and references herein.
[4] M. Hennion, C. Bellouard, I. Mirebeau, J. L. Dormann, and R. Ober, Europhys. Lett. **25**, 463 (1994); M. Hennion, C. Bellouard, I. Mirebeau, H. Blank, J. L. Dormann, and C. Djega-Mariadessou, in *Studies of Magnetic Properties of Fine Particles*, edited by J. L. Dormann and D. Fiorani (Elsevier, Amsterdam, 1992).
[5] W. F. Brown, Jr., Phys. Rev. **130**, 1677 (1963).
[6] Yu. L. Raikher and M. I. Shliomis, Sov. Phys. JETP **40**, 526 (1974).
[7] I. Mirebeau, C. Bellouard, M. Hennion, J. L. Dormann, C. Djega-Mariadessou, and M. Tessier, J. Magn. Magn. Mater. **104-107**, 1560 (1992).

Magnetic properties of fine Ni particles coated with Pd (abstract)

Makoto Yamaguchi, Yoshichika Otani, and Hideki Miyajima
Department of Physics, Faculty of Science and Technology, Keio University, Hiyoshi 3-14-1, Kohoku, Yokohama 223, Japan

Ni-Pd composite fine particle is an ideal system to study surface and interface magnetism because of its large surface area compared with the total volume. In this work, magnetic properties of Ni-Pd composite fine particles were studied in terms of the magnetic proximity effect and the effect of hydrogenation. The composite particle consists of Ni core and Pd shell. Five different particles with different Pd shell thicknesses, 50, 100, 150, 200, and 350 Å, were prepared. The average diameter of the Ni core is about 0.7 μm. The Curie temperatures of all the samples are lying around 630 K and are nearly equal to that of a bulk Ni. Unlike pure Ni, the samples exhibit a relatively large coercive force of a few hundred Oersted in the temperature range from 4.2 to 750 K. The magnetization of the Ni core is found to be somewhat lower than that of pure Ni. An enhanced interface anisotropy due to the Pd coating ($\sim -1.5\times10^5$ J/m^3) seems to impede saturation. Before hydrogenation, there appears quite a large thermal hysteresis. On heating, the isofield magnetization exhibits ferromagnetic behavior with a rise of magnetic moment below 30 K, suggesting that there is induced magnetization in the Pd shell. The change in magnetization follows the Curie–Weiss law, which gives a Curie temperature of 22 K. However, the steep rise of magnetization is not observed in the cooling process. After hydrogenation, this ferromagnetic behavior completely vanishes. There is also observed no lattice expansion, but this isovolumetric constraint seems to have little change on the saturation hydrogen loading.

Nuclear magnetic resonance studies on the surface magnetism of vanadium ultrafine particles (abstract)

Yukihiro Hirayama, Tomoki Erata, Eiji Kita, and Akira Tasaki
Institute of Applied Physics, University of Tsukuba, Tsukuba, Ibaraki, Japan

Nuclear magnetic resonance studies were carried out on the ultrafine particles of vanadium prepared by the gas evaporation method for making clear its Curie–Weiss like magnetism, which appeared besides the ordinary Pauli paramagnetism reported already.[1] The observed NMR signal was composed of two lines; one of those signals was identified as being from metal vanadium because of its Knight shift, 0.58%, and the other line with less intensity had a 0.7% Knight shift. Since the relative intensity of this low field shifted line was proportional to the inverse diameter of the particle and increased with the decrease of temperature, this line can be identified as being from the surface region of the particles. The spin-lattice relaxation time of the surface region has shown the Corringa's relaxation, which indicates that the surface electrons show metallic character. The resonance line with a 0.7% Knight shift originated from surface vanadium suggests the existence of the narrow band at its Fermi level and a rather localized character of the surface electrons, and this characteristic surface region increases with lower temperatures. The origin of the observed temperature dependent paramagnetism of vanadium ultrafine particles can be considered as the surface magnetism still having a metallic character.

[1] H. Akoh and A. Tasaki, J. Phys. Soc. Jpn. **42**, 791 (1977).

 0021-8979/94/75(10)/5903/1/$6.00 © 1994 American Institute of Physics

Polyphase eddy current testing

I. Marinova, S. Hayano, N. Ishida, and Y. Saito
College of Engineering, Hosei University, Kajino Koganei, Tokyo 184 Japan

Y. Hirama and M. Yamamoto
R&D Hitachi Building Systems Engineering and Service, 16-23 Nakagawa Adachi-ku, Tokyo 120 Japan

Polyphase eddy current testing is proposed. The operating principle of this system is as follows. The polyphase eddy current testing system may be regarded as one of the polyphase transformers. Primary balanced polyphase coils are star connected and secondary polyphase circuits are composed of the target. When balanced polyphase currents are fed into the primary coils, zero phase voltage is detected if the target has defects. No zero phase voltage is detected if the target has no defects. It is found that this method has a higher sensitivity compared with that of conventional eddy current testing.

I. INTRODUCTION

The search for cracks and defects is one of the most important elements of the nondestructive testing of many equipments, e.g., elevators, escalators, lifts, etc. Various testing methods, such as eddy current testing, electric potential method, ultrasonic wave imaging, and x-ray tomography, are currently utilized.[1-7] Among these methods, eddy current testing method does not require complex electronic circuits and direct contact to object. Further, objects of which major frame parts are composed of conductive metallic materials can be selectively inspected by eddy current sensors. In the present article, we propose a novel eddy current testing method utilizing polyphase alternating currents. The operating principle of this new method is as follows. First, the polyphase eddy current testing system may be regarded as a polyphase transformer. Primary balanced polyphase coils are star connected and secondary polyphase circuits are composed of the target. When balanced, polyphase currents are fed into the primary coils, zero phase voltage is detected if the target has defects, no zero phase voltage is detected if the target has no defects. Conventional eddy current testing method detects only the input impedance difference caused by the defects in the target. As an initial test, we measured a zero phase input impedance instead of zero phase voltage. It was found that our new method clarified a possibility to enhance the sensitivity of the eddy current testing compared with conventional eddy current testing.

II. POLYPHASE EDDY CURRENT TESTING

A. Conventional eddy current testing

As shown in Fig. 1 the conventional eddy current testing (ECT) system may be regarded as a single-phase transformer. The equivalent transformer is composed of the primary exciting coil having resistance R_1 and self-inductance L_1, and the secondary coil, being the metallic target having resistance R_2 and self-inductance L_2. Let us denote M as a mutual inductance between the primary and secondary circuits and k as a coupling factor defined by

$$k=\frac{M}{\sqrt{L_1L_2}}, \quad 0<k<1. \tag{1}$$

If there are no defects in the target, this would correspond to the secondary circuit short ($R_2\approx 0$) and input impedance Z becomes

$$Z=R_1+j\omega L_1(1-k^2). \tag{2}$$

If there are defects, then resistance of the secondary circuit becomes $R_2\approx\infty$, and the input impedance Z changes,

$$Z=R_1+j\omega L_1. \tag{3}$$

Analyzing Eqs. (2) and (3) it is obvious that the sensitivity of conventional ECT depends on the parameters ω, L_1, and k. Therefore, it is desirable that the inductance L_1 as well as coupling factor k are as large as possible, but due to the skin effect, it is not desirable to increase the angular velocity ω. To detect defects in axial as well as circular directions from the interior of cylindrical pipe, a multicoil ECT system, shown in Fig. 2 may be used. However each of the coils in multicoils is scanned by complex electronic circuits; also, the scanning speed is limited by the relaxion time of eddy current.

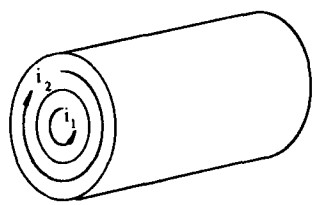

FIG. 1. Principle of conventional eddy current testing system.

 0021-8979/94/75(10)/5904/3/$6.00 © 1994 American Institute of Physics

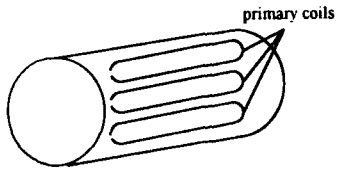

FIG. 2. Multicoil eddy current testing system.

B. Polyphase eddy current testing

In this article we propose a novel eddy current testing method utilizing polyphase alternating currents in order to increase the sensitivity of ECT system. The polyphase ECT system consists of polyphase coils and target. This system may be considered as a polyphase transformer. Primary balanced polyphase coils are star connected. Secondary polyphase circuits are composed of the target (see Fig. 3). For a star-connected system, with the time origin taken at the maximum positive point of the phase a voltage wave, the instantaneous voltages of the three phases are

$$V_a=\sqrt{2}V\cos(\omega t)=\sqrt{2}V\ \mathrm{Re}(e^{j\omega t}),$$

$$V_b=\sqrt{2}V\cos\left(\omega t-\frac{2\pi}{3}\right)=\sqrt{2}\ \mathrm{Re}(e^{j[\omega t-(2\pi/3)]}), \tag{4}$$

$$V_c=\sqrt{2}V\cos\left(\omega t+\frac{2\pi}{3}\right)=\sqrt{2}V\ \mathrm{Re}(e^{j[\omega t+(2\pi/3)]}),$$

where V is the rms value of the phase voltage. Considering a operator defined by

$$a=e^{-j(2\pi/3)}, \tag{5}$$

we can express

$$V_0=\tfrac{1}{3}(V_a+V_b+V_c),$$

$$V_P=\tfrac{1}{3}(V_a+a^2V_b+aV_c), \tag{6}$$

$$V_N=\tfrac{1}{3}(V_a+aV_b+a^2V_c),$$

where V_0, V_P and V_N are the zero sequence, positive sequence, and negative sequence. For the balanced three phase voltages, they become

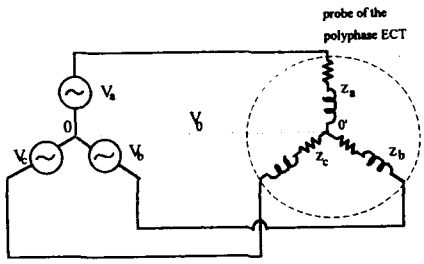

FIG. 3. Polyphase eddy current sensor.

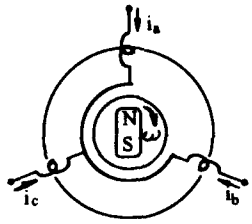

FIG. 4. The balanced polyphase current system used to scan the target.

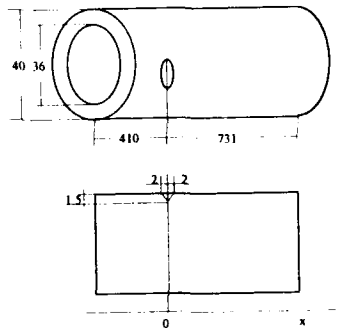

FIG. 5. Tested target tube with a defect (unit of mm).

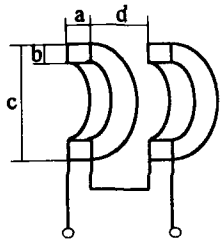

FIG. 6. Tested conventional eddy current sensor with $a=5$ mm, $b=5$ mm, $c=35$ mm, $d=10$ mm, and 50 turns.

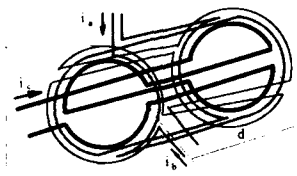

FIG. 7. Tested polyphase eddy current sensor with $d=20$ mm, $c=35$ mm. The number of turns is 50 or 80.

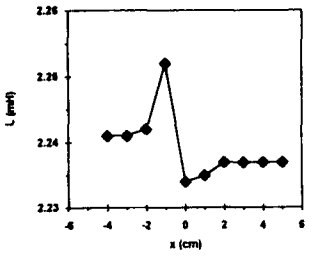

10p

FIG. 8. The change of the inductance in x direction using conventional eddy current testing.

$$V_0 = 0,$$
$$V_P = \sqrt{2}V\ \mathrm{Re}(e^{j\omega t}), \tag{7}$$
$$V_N = 0.$$

Figure 4 shows that with balanced polyphase currents, the primary coils generate a revolving magnetic field and this is used to scan the target.

To detect defects in the target, balanced polyphase currents are fed into the primary coils and the zero phase voltage V_0 is measured. If the target has defects then zero phase voltage V_0 is detected. If the target has no defects then zero phase voltage V_0 is not detected. Conventional eddy current testing method detects only the input impedance difference caused by defects in the target.

III. EXPERIMENTAL MODEL AND RESULTS

In order to investigate the efficiency of the proposed novel ECT system, a tube target with defect shown in Fig. 5 was examined. First, conventional ECT was applied to detect the defect. Figure 6 shows that a conventional eddy current sensor with two serial connected coils was used. The input impedance was measured by a resistance bridge. The experimental frequency was 1 kHz. Second, the polyphase eddy current sensor, as shown in Fig. 7, was employed to examine the target. Polyphase coils were star connected and supplied with balanced polyphase currents. In order to compare the sensitivity of this method with conventional ECT, the zero-phase impedance was measured instead of the zero-phase voltage.

Results showing the change of inductance in the x direction around the defects applying both conventional and polyphase ECTs are presented in Figs. 8 and 9, respectively. The polyphase eddy current sensors with 50 and 80 turns are used in Figs. 9(a) and 9(b), correspondingly.

The results of Fig. 8 show the change of inductance corresponding to the change of the field distribution in the coil volumes during movement in x direction. The changes of the field distribution are produced by the defect, which changes the impedance of the target, and the coupling between target and primary coils, respectively. Figures 9(a) and 9(b) show that the defect, increasing the impedance of the target (secondary circuits) caused a change of the impedances of the primary coils. This lead to an unbalanced polyphase current system. Near the defect the zero-phase voltage appeared and zero-phase impedance changed with position of the probe coils during the x direction. The inductance, corresponding to zero-phase impedance, began to increase around the defect. It reached a maximum when the middle of the polyphase coils was under the defect. After that, moving the polyphase coils in the x direction, the inductance decreases depending on the impedance of the secondary circuits. Figures 9(a) and 9(b) show that changing the number of turns it is possible to increase the sensitivity using the polyphase ECT. Thus, we succeeded to obtain 0.78% relative measured difference applying polyphase ECT with 50 turns while using polyphase ECT with 80 turns or conventional ECT it is 0.37% or 0.49%, respectively. Instead of zero-phase impedance, we measured a zero-phase voltage. This increases the sensitivity of our new polyphase ECT.

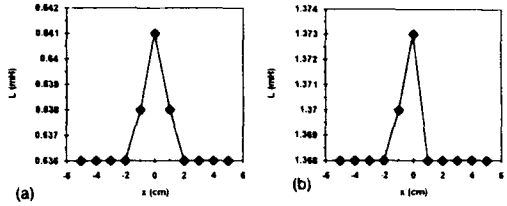

FIG. 9. The change of the inductance in x direction: (a) polyphase eddy current testing with 50 turns; (b) polyphase eddy current testing with 80 turns.

IV. CONCLUSION

We proposed a novel ECT to detect defects in targets. Experimental work concerning the ECT system utilizing polyphase alternating currents has been carried out. Star connection and balanced polyphase currents are used as primary coils. Examination of the zero phase voltage was proposed to detect the defects. Comparison with conventional ECT was made. It has been demonstrated that the new method enhances the sensitivity of the eddy current testing compared with conventional ECT.

[1] Y. Hirama and N. Sahoda, Paper on Technical Meeting of Magnetics in **MAG-92-73**, 143 (1992).
[2] T. Doi, H. Saotome, S. Hayano, and Y. Saito, *Applied Electromagnetics in Materials and Computational Technology* (Hokkaido University Press, Sapporo, 1992), 61.
[3] H. Saotome, T. Doi, S. Hayano, and Y. Saito, IEEE Trans. Magn. **MAG-29**, 1861 (1993).
[4] Y. Oohira, Y. Hirama, S. Hayano, and Y. Saito, in Proceedings of the ISEM, Sapporo, Jan. 1993.
[5] T. R. Schmidt. Mater. Eval. **42**, 225 (1984).
[6] W. Lord, S. Nath, Y. K. Shin, and Z. You, IEEE Trans. Magn. **MAG-25**, 3010 (1989).
[7] E. Cardelli, N. Esposito, and M. Raugi, IEEE Trans. Magn. **MAG-29**, 1849 (1993)

Defect recognition in conductive materials by local magnetic-field measurement

T. Doi, S. Hayano, I. Marinova, N. Ishida, and Y. Saito
College of Engineering, Hosei University, Kajino, Koganei, Tokyo 184, Japan

Among the various nondestructive testing methods, the electric potential method requires relatively simple device and measurement. However, because of the high electrical contact resistance, sometimes it is difficult to measure the correct local electric potentials by direct contact. In order to overcome this difficulty, method is proposed which involves substituting the local magnetic field for electric potential measurements. The comparison with the conventional electric potential method demonstrates the usefulness this method, especially for materials with low resistivity.

I. INTRODUCTION

In order to prevent accidents in aircraft, iron bridges, and nuclear reactors, crack or defect recognition is of paramount importance. Various nondestructive testing methodologies, e.g., eddy current testing, x-ray computed tomography, ultrasonic imaging, and the electric potential method, have been exploited and utilized. Among these methods, the electric potential method requires relatively simple instruments and techniques.[1-3] However, because of the high electrical contact resistance and relatively low resistance of the target, sometimes it is difficult to measure the correct local electric potentials by direct contact. In order to remove this difficulty, we propose a new method which substitutes the local magnetic field for electric potential measurements. This makes it possible to implement the electric potential method without requiring direct contact to measure potentials. Most of the defect recognition problems are, in essence, reduced to solving inverse problems. Previously, the current distributions in the human heart and brain have been successfully estimated from the local magnetic fields by the sampled pattern matching (SPM) method. The SPM method has been exploited for solving the inverse source problems, and this is applicable to defect recognition problems, i.e., medium parameter identification problems.[4-7] We apply this SPM method with some modifications to our new electric potential method. The comparison with the conventional electric potential method demonstrates the usefulness of our new method, especially for materials with low resistivity.

II. PROJECTIVE SAMPLED PATTERN MATCHING METHOD

A. Key Ideas

Let C, $\mathbf{X}$, $\mathbf{Y}_s$ be the system matrix, potential, and input current vectors, respectively. Then, it is possible to write

$$C\mathbf{X}=\mathbf{Y}_s, \tag{1}$$

as a discretized electric current flowing system equation of a conductive material having a defect or crack. This system equation can be modified into

$$C_0\mathbf{X}=(C_0-C)\mathbf{X}+\mathbf{Y}_s=\mathbf{Y}+\mathbf{Y}_s, \tag{2}$$

where C_0 is a system matrix without a defect or crack. This means that the potential vector $\mathbf{X}$ is composed of the two input vectors $\mathbf{Y}$ and $\mathbf{Y}_s$. The vector $\mathbf{Y}$ is the equivalent field source vector

$$\mathbf{Y}=(C_0-C)\mathbf{X}, \tag{3}$$

caused by the defect or crack. The vector $\mathbf{Y}_s$ is the externally impressed field source vector. Thus, the defect or crack recognition problems can be reduced into the equivalent source vector $\mathbf{Y}$ searching problems. Obviously, this equivalent source vector $\mathbf{Y}$ depends on the solution vector $\mathbf{X}$. Further, this solution vector $\mathbf{X}$ is a function of the externally impressed field source vector $\mathbf{Y}_s$. Thereby, the equivalent source vector $\mathbf{Y}$ can be expressed as a function of the impressed field source vector $\mathbf{Y}_s$. That is,

$$\mathbf{Y}=f(\mathbf{Y}_s). \tag{4}$$

Introducing this functional relationship into our SPM method leads to the following advantages. First, this method requires a quite low CPU resource compared with those of the original SPM method, because the SPM process has to be carried out only for the vectors satisfying the relationship (4). Second, relatively accurate solutions can be expected, because one of the characteristics of the solution vector $\mathbf{Y}$ is known. Finally, changing the direction of vector $\mathbf{Y}_s$ reaches the correct solution vector $\mathbf{Y}$ similar to the computed tomography. This new method is called the projective sampled pattern matching (PSPM) method, because the functional relationship (4) is the directional dependence of the known vector $\mathbf{Y}_s$. In the present article, we examine the characteristics of the PSPM method. As a result, we propose here the simple implementation techniques to improve the accuracy of PSPM method.

B. System equations

In Eq. (2), let us assume that C_0 is a square matrix of size m by m; $\mathbf{X}$, $\mathbf{Y}$, and $\mathbf{Y}_s$ are the mth-order column vectors, then taking the inverse matrix of C_0 and multiplying it to both sides of Eq. (2) yields

$$\mathbf{X}=C_0^{-1}\mathbf{Y}+C_0^{-1}\mathbf{Y}_s=C_0^{-1}\mathbf{Y}+\mathbf{X}_0, \tag{5}$$

where $\mathbf{X}_0\,(=C_0^{-1}\mathbf{Y}_s)$ is a potential vector without a defect or crack. Subtracting $\mathbf{X}_0$ from Eq. (5), we have

$$\mathbf{X}_d=\mathbf{X}-\mathbf{X}_0=C_0^{-1}\mathbf{Y}. \tag{6}$$

 0021-8979/94/75(10)/5907/3/$6.00 © 1994 American Institute of Physics

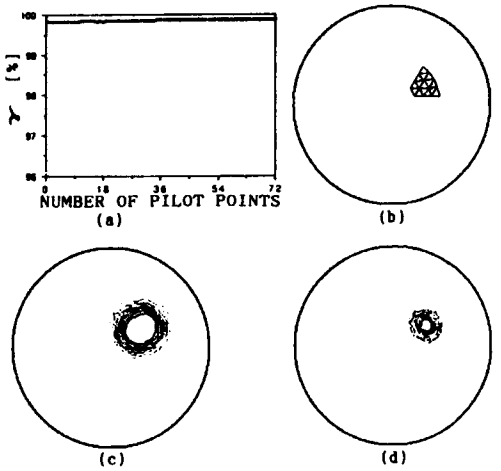

FIG. 1. Single defect recognition by measuring the electric potential around a target area. (a) γ vs number of the pilot points in the processes of electric potential method, (b) exact solution, (c) recognized defect by measuring the electrical potentials (d) recognized defect by measuring the magnetic fields. The number of subdivisions $m=1801$, and the number of measured points $n=72$. The direction of the externally impressed current input vector $\mathbf{Y}_s$ was changed 72 times with 5° subdivision.

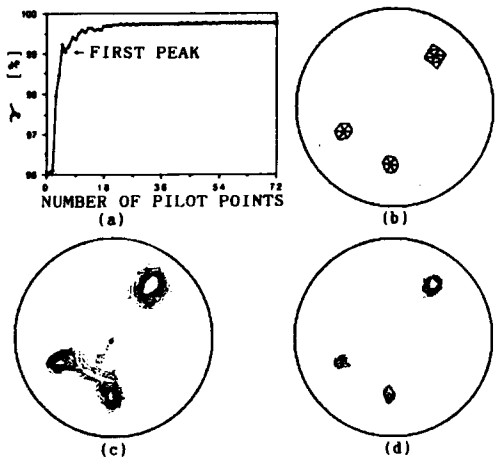

FIG. 2. Plural defects recognition by measuring the electric potential around a target area. (a) γ vs pilot points in the processes of electrical potential method, (b) exact solution, (c) recognized defect by measuring the electrical potentials (d) recognized defect by measuring the magnetic fields. The number of subdivisions $m=1801$, and the number of measured points $n=72$. The direction of the externally impressed current input vector $\mathbf{Y}_s$ was changed 72 times with 5° subdivision.

Generally, it is difficult to measure the entire difference vector $\mathbf{X}_d$ in Eq. (6) so that we can only obtain a part vector $\mathbf{X}_p$ of $\mathbf{X}_d$. This yields the system equations of the defect or crack recognition problem. Namely, denoting n as a number of measured points, we have

$$\mathbf{X}_p = D\mathbf{Y} = \sum_{i=1}^{m} y_i \mathbf{d}_i , \tag{7}$$

where D and $\mathbf{X}_p$ are the n by m partial matrix in C_0^{-1} and measured difference vector with order n, respectively. The y_i and $\mathbf{d}_i$ in Eq. (7) are the ith element of $\mathbf{Y}$ and ith column vector in D, respectively.

C. Sampled pattern matching SPM method

If a point h takes the maximum of

$$\gamma_i = \mathbf{X}_p^T \cdot \mathbf{d}_i / (|\mathbf{X}_p||\mathbf{d}_i|), \quad i=1,2,\ldots,m, \tag{8a}$$

then h is the first pilot point. If a point g takes the maximum of

$$\gamma_{hj} = \mathbf{X}_p^T \cdot (\mathbf{d}_h + \mathbf{d}_j) / (|\mathbf{X}_p||\mathbf{d}_h + \mathbf{d}_j|), \quad j=1,2,\ldots,m, j \neq h, \tag{8b}$$

then g is the second pilot point. A similar process to Eq. (8a) or (8b) is continued up to the first peak of γ.[5,6]

Thus, the pilot point solutions are given by the following.

If i is a pilot point, then:

$$y_i = 1,$$

if i is not a pilot point, then: (9)

$$y_i = 0.$$

Pilot point solutions of Eq. (7) mean that the magnitude of the solution is represented by the space occupying rate of unit input.

D. PSPM method

The SPM method is applicable to inverse problems where the solution vector $\mathbf{Y}$ is not a function of the known function $\mathbf{Y}_s$,

$$\mathbf{Y} \neq f(\mathbf{Y}_s). \tag{10}$$

However, if a relationship (4) is established, then the SPM processes are carried out only to the vectors $\mathbf{d}_i$ ($i=1,2,\ldots,m$) satisfying the relationship (4).

If medium parameter identification problems satisfy relationship (4), the SPM processes is continued up to the kth pilot point until the following condition is satisfied:

$$\frac{|\mathbf{X}_p|}{|\mathbf{X}_{0p}|} \leqslant \left| \sum_{j=1}^{k} \mathbf{d}_j \right| \left| \sum_{i=1}^{m} \mathbf{d}_i - \sum_{j=1}^{k} \mathbf{d}_j \right|^{-1}, \tag{11}$$

where the vector $\mathbf{X}_{0p}$ is composed of the measured potentials having a defect or crack.

This method is called the PSPM method. The PSPM method has the following advantages: (i) low CPU resource; (ii) relatively accurate solutions; (iii) changing the projective angles with $\mathbf{Y}_s$ and taking the average of entire solutions to reach the correct solution vector; (iv) the pilot point solutions are available if the known vector $\mathbf{X}_s$ encloses a target area.

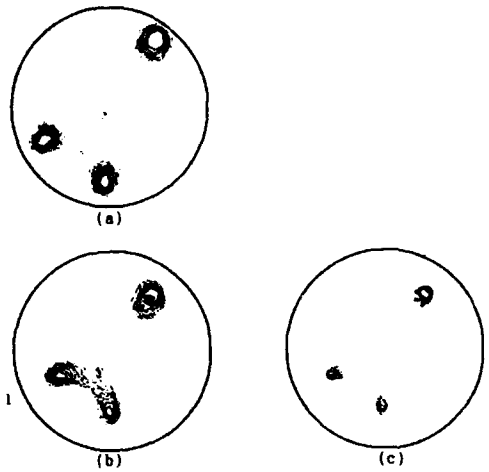

FIG. 3. Improved plural defects recognition: (a) Improvement by shrinking the target area, (b) and (c) show improved results by removing the pilot points up to the first peak for the electric potential and its modified methods, respectively.

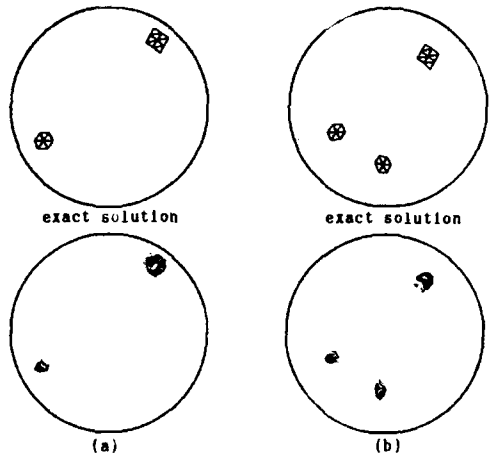

FIG. 4. The examples taking an average of the results obtained by electric potential and its modified methods (exact solution): (a) two defects, (b) three defects.

A curve obtained by plotting the pattern matching rate γ in Eq. (8a) or (8b) versus number of the pilot points reveals (i) if the curve continuously increases with addition of pilot points then the target area has a single defect or indistinguishable plural defects; (ii) if the curve has a deflection point then the object has plural defects. In this case, each of the plural defects can be distinguished by shrinking the target area or removing the pilot points up to the first peak value of γ. This is because the pilot points up to the first peak value of γ provide globally good pattern matching vectors common to the entire defects.

E. Examples

The two-dimensional electric potential method was chosen as the example. The electric potential method was carried out not only in the conventional way but also the modified way, which measured the magnetic fields instead of the electric potentials.

Figure 1(a) shows one of the γ versus number of pilot points curves in the processes of the electric potential method. Obviously, this curve continually increases with addition of pilot points, so that the target area has a single defect. In fact, results of PSPM method show the single defect as shown in Figs. 1(c) and 1(d).

Figure 2(a) shows one of the γ versus number of the pilot points curves. This curve has a deflection point, so that the target area must have the plural defects. In fact, the result of the PSPM method shows the plural defects as shown in Figs. 2(c) and 2(d).

Figure 3(a) shows improved plural defects recognition by shrinking the target area. Also, Figs. 3(b) and 3(c) show improved plural defects recognition by removing the pilot points up to the first peak of γ.

It must be noted here that the electric potential method always yields overestimated results in defect size. Conversely, the modified method yields underestimated results. Therefore, if it is possible to measure both electric potentials and magnetic field, the defect will stand midway between the results. Figure 4 shows examples of taking an average of both results.

Thus, the electric potential and its modified methods in combination with PSPM provide highly reliable results even if the plural defects are included in the target region.

III. CONCLUSION

As shown above, we have examined the PSPM method and proposed the methods of the improvement for the plural defects recognition problems. Examples have demonstrated that the plural defects recognition is improved by our method.

[1] S. Kubo, K. Ohji, and T. Sakagami, Int. J. Appl. Electromagn. Mater. **2**, 81 (1991).
[2] Y. Iwamura and K. Miya, IEEE Trans. Magn. **MAG-26**, 618 (1990).
[3] T. Miyoshi and S. Nakano, Trans. Jpn. Soc. Mech. Eng. A **52**, 1097 (1986).
[4] Y. Saito, E. Itagaki, and S. Hayano, J. Appl. Phys. **67**, 5830 (1990).
[5] H. Saotome, K. Kitsuta, S. Hayano, and Y. Saito, Int. J. Appl. Electromagn. Mater. **3**, 297 (1993).
[6] H. Saotome, T. Doi, S. Hayano, and Y. Saito, IEEE Trans. Magn. **MAG-29**, 1861 (1993).
[7] T. Doi, H. Saotome, S. Hayano, and Y. Saito, in *Proceedings of the 2nd Japan-Hungary Joint Seminar*, edited by T. Honma *et al.* (Hokkaido University Press, Sapporo, 1992), pp. 61–66.

Component-resolved imaging of surface magnetic fields

R. D. Gomez, E. R. Burke,[a] and I. D. Mayergoyz
Department of Electrical Engineering, University of Maryland at College Park, Maryland 20742

Successful imaging is demonstrated of the three individual Cartesian components of the vector magnetic field from a magnetized surface. This is accomplished by exploiting the capability of the magnetic force scanning tunneling microscope to generate two-dimensional mapping of definite combinations of orthogonal magnetic-field components. This method is applied to well-characterized patterns on thin-film longitudinal recording media and some peculiar characteristics of recorded magnetization patterns are found, including the presence of a significant cross-track magnetization component persisting along the track edges. The experimental approach and the unique physical insights acquired by simultaneously investigating individual magnetic-field components are discussed.

I. INTRODUCTION

Despite obvious fundamental impetus and potentially extensive technological applications, high-resolution imaging of individual components of the vector magnetic field near magnetic surfaces has not yet been accomplished. Lorentz transmission electron microscopy (TEM)[1] and spin-polarized scanning electron microscopy[2] yield images of minute magnetization structures, but not the field components exclusively. Electron-holographic interferometry[3] is capable of direct observations of magnetic-field lines in two dimensions, and it would be interesting to see its capability extended to differentiate components of the field along the surface plane as well. Other field sensing devices such as those based on the principles of Faraday induction, magnetoresistance, Kerr effect, Hall effect, superconducting quantum interference, and magnetostriction, at present, suffer from several inherent limitations. They either lack adequate sensitivity, have limited spatial resolution, or face formidable technical difficulties in detecting individual components separately.

One class of microscopy collectively called scanning probe microscopy offers the best promise in field-component detection. Spurred by the invention of the scanning tunneling (STM)[4] and the atomic force (AFM)[5] microscopes, the technique of magnetic force microscopy (MFM) has lead to the imaging of local variations in the gradient of the force between a probe and the magnetic field.[6] Experiments have shown that the MFM exhibits sensitivity to specific components of the field.[7] Thus far, notwithstanding a great deal of interest in the scientific community,[7–10] no systematic demonstration of three-dimensional field component imaging capability has been reported.

Over the last few years, we have been involved in the development of magnetic force scanning tunneling microscopy (MFSTM),[11] which is cognate to MFM, but fundamentally different since this method does not map contours of constant force[10] or force gradient,[9] but measures the field intensity at a fixed distance above the surface.[12] We have modeled the contrast mechanism,[11,13] developed special probes,[12] and experimentally demonstrated the images to be proportional to certain components of the surface field.[14] In this work, we extend this capability and demonstrate, for the first time, high-resolution imaging of the individual Cartesian field components of magnetic recording patterns.

II. EXPERIMENTAL TECHNIQUE

Details of our experimental apparatus and probe fabrication techniques have been reported elsewhere[11,12] and we merely reiterate the main points. A thin, flexible, triangular nickel film[15] is placed as a substitute to the usual rigid STM tip, and scanned across the surface as a conventional STM probe.[16] This probe geometry, which may yield somewhat lower resolution than sharply etched ferromagnetic wires,[17] has the advantage of confining the probe deflection only along its normal direction which greatly simplifies the interaction and corresponding analysis. The probe, biased at a small potential, is placed at about a nanometer from the surface to induce tunneling current while a feedback system adjusts the vertical height of the probe to keep the current constant. This height is recorded as a function of the probe's lateral position and displayed using computer graphics. The measurements reflect a combination of magnetic and topographic structures because momentary changes in the gap come as a result of magnetic-induced probe deflections as well as the surface texture. The probe's magnetic and mechanical properties were carefully selected to enhance the magnetic contribution over the topography[11] and to ensure that the probe interacts as a point magnetic charge at the apex.[14]

The samples were deliberately recorded patterns on otherwise ordinary commercial isotropic thin-film rigid disk media, and are identical to those in previous studies.[18–21] We concentrated on two pattern arrangements, namely: (i) a series of alternating magnetization with identically spaced 20 μm periodic transitions, and (ii) a series with the same wavelength but with one specific magnetization direction longer (17.5 μm) than the other (2.5 μm).

III. RESULTS AND DISCUSSION

The magnetic-induced variation in vertical displacement Δz and, hence, the contrast mechanism is governed by the relation[11]

$$\Delta z \propto H_x \sin\theta \cos\theta \cos\phi + H_z \sin^2 \cdot \theta, \qquad (1)$$

where H_x is the field component parallel to the surface plane and along the direction of magnetization, while H_z is the

[a]Laboratory for Physical Sciences, 8050 Greenmead Dr., College Park, MD 20740.

 0021-8979/94/75(10)/5910/3/$6.00 © 1994 American Institute of Physics

FIG. 1. Dependence of magnetic-field images on the probe orientation vector p, with enhanced detection of (a) H_x, (b) H_x and H_y, and (c) H_y and H_z components. The pattern is an evenly spaced alternating magnetization schematically shown in the bottom of (c).

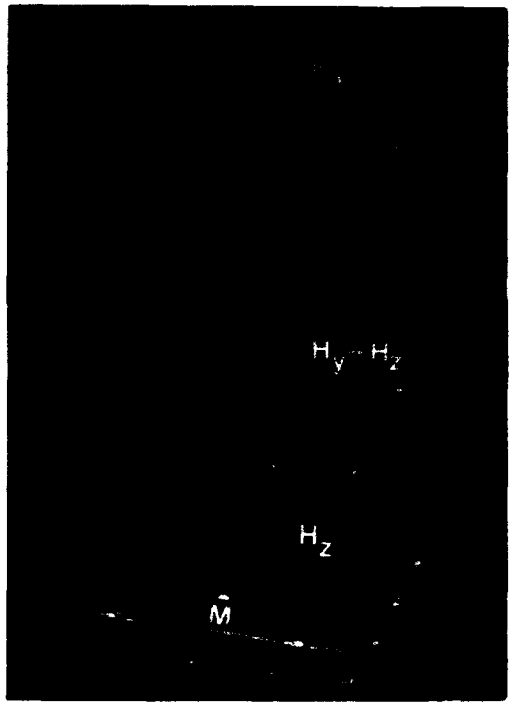

FIG. 2. Component-resolved surface field images of an unevenly spaced magnetization pattern. The most prominent component are (a) H_x, (b) H_z and H_y, and (c) H_z. The pattern is an evenly spaced alternating magnetization schematically shown in the bottom of (c).

field component in the normal direction. The angle θ defines the inclination of the probe measured relative to the surface normal, while ϕ is the angle made by the projection of the probe on the surface and the direction of magnetization.[13] The image then represents a two-dimensional mixture of the longitudinal and vertical field components, and the amount of relative contributions can be adjusted by changing the probe's orientation. Generalizing Eq. (1) to three dimensions, we obtain

$$\Delta z \propto (\hat{p}\cdot\mathbf{H}_{\parallel})\sin\theta\cos\theta + H_{\perp}\sin^2\theta, \tag{2}$$

where $\hat{p}$ is a unit vector in the direction of probe projection on the surface plane. In this form, we can interpret the contrast mechanism as the contributions of the vertical component $H_{\perp}$ plus the in-plane field $\mathbf{H}_{\parallel}$ in the direction of $\hat{p}$. The dependence of the image contrast on $\hat{p}$ is illustrated in Fig. 1. In these images, the probe was fixed as the sample was rotated about its normal axis. The coordinate system is defined such that the x and y axes coincide with the track (or magnetization) and cross-track directions, respectively.

In Fig. 1(a), $\hat{p}=\hat{x}$ and the image predominantly exhibits the in-plane component along the track (H_x) which appears as equally spaced bright and dark regions corresponding to the alternating magnetization pattern. The line shape made by a profile drawn along the track agrees quite well with the expected shape of the H_x component for this type of pattern.[7,22] As ϕ is increased to about 30°, we find a moderately dissimilar image in Fig. 1(b) where $\hat{p}=(\sqrt{3}/2)\hat{x}+\frac{1}{2}\hat{y}$. The H_x content is now reduced and combined with an appreciable H_y contribution. The presence of the H_y component is indicated by the faint appearance of bright and dark structures localized along the track edges. Close inspection reveals slight enhancements in contrast near the corners formed by the transition zones and the edges. This feature comes from the cross track component of the fringing field near the corners which arises even when the magnetization pattern is ideally oriented exclusively along the x axis.[23] In addition, since the edge structure is not merely confined at the corners but also forms extended bands along the edge, then the image of Fig. 1(b) suggests a significant magnetization along the edges and is oriented in the cross-track direction. This observation is further reinforced in Fig. 1(c) when the probe is aligned along the cross track direction or $\hat{p}=\hat{y}$. In this case, the side bands appear more prominently because of the drastic reduction in the H_x contribution. The bands occur as pairs in opposite directions in both edges, which clearly supports the contention that layers of transversely ori-

ented magnetization along the edges were inadvertently created. This behavior can be very important in magnetic recording technology, and we discuss the implications in a related article.[24] The enhancements at the corners previously evident in Fig. 1(b) are now less pronounced; this is because at distances close to the surface, the fields at the corners are oriented midway between the two orthogonal $\hat{x}$ and $\hat{y}$ directions; so that the effect is most conspicuous at intermediate probe orientations.

Note in Fig. 1(c), that what used to be an alternating series of broad H_x distributions in the interior of the track in Fig. 1(a) are now localized along the transition regions. This arises from the vertical field component $H_\perp$ (or H_z) as described in the second term of Eq. (2). The H_z component for this type of pattern is localized near the transition zones where $\nabla \cdot \mathbf{M}$ is largest.[22] Since the coefficient of $H_\perp$ depends only on the inclination angle θ, then $H_\perp$ contributes the same amount to the image contrast regardless of $\hat{p}$. Its effect, albeit, is masked by the dominant H_x component when $\hat{p}=\hat{x}$. When $\hat{p}=\hat{y}$, however, the H_x contribution declines, causing the H_z component to markedly emerge. Thus, by obtaining a set of images with judiciously chosen probe orientation angles θ and ϕ, we can reconstruct distinct pictures of all three individual field components. We further illustrate this idea in Fig. 2.

In contrast with Fig. 1, Fig. 2 is a series of patterns created with unequal bit cells, schematically shown in the bottom of the figure. The image in Fig. 2(a) was obtained with $\theta \sim 30°$ and $\hat{p}=\hat{x}$, and shows the H_x field component with slight hints of H_z at the transition regions. As expected, the contrast is much more intense in areas of narrow bit length in comparison with areas of long magnetization lengths. An important feature of Fig. 2(a) is the presence of peculiar side structures which extend obliquely beyond the track edges. These side structures presumably resulted from the motion of the recording head[25] and may have been further aggravated by the head's unequal pole-width geometry. These side effects, if present in actual recording systems, may lead to some noise and increase the effective trackwidth, both of which are of paramount concern in the technology.[24] The same track, imaged using the H_y sensitive scheme is shown in Fig. 2(b). In this case, $\hat{p}=\hat{y}$, and the side bands shown are reminiscent of those in Fig. 1(c), with the exception that they appear to be absent at the short bit length regions. It is easy to imagine that we arrive at Fig. 2(b) by progressively reducing the neighboring transitions in Fig. 1(c), while keeping the wavelength fixed. In other words, what used to be neighboring pairs of bright and dark regions at the transition regions separated by 10 μm ($\lambda/2$) in Fig. 1, have become bright-dark structures adjacent with each other. Finally, in Fig. 2(c) the sample was scanned in a manner similar to that used in Fig. 2(a), i.e., with $\hat{p}=\hat{x}$, but with the inclination angle set at about 70°. The vertical component ($H_\perp$) completely overrides the image, more or less obeying the prediction of Eq. (2). We point out, however, that this image was obtained by using a somewhat different probe which was specifically chosen to facilitate measurement of the angle θ and whose acquired images have been extensively analyzed.[21] Hence, we cannot directly compare absolute intensities between this image and the others since the mechanical properties and contrast sensitivity are different. Nevertheless, these images provide a plausible demonstration on selective high-resolution imaging of the three-dimensional components of the surface field.

In summary, by using the magnetic force scanning tunneling microscope (MFSTM), it is possible to generate images which enhance specific magnetic-field components to show unique manifestations of the individual field components. Admittedly, considerable sophistication in both the experimental methods and theory are needed to be able to completely untangle the individual Cartesian components of $\mathbf{H}=[H_x, H_y, H_z]$. We are confident, however, that with advances in analytical calculations of field distributions[23] combined with enhanced graphics capabilities, it will be possible in the near future to completely generate images of magnetic field distributions along any arbitrary spatial direction.

We would like to thank John Gorczyca and Professor M. H. Kryder at Data Storage Systems Center, Carnegie Mellon University, for helpful discussions and for providing recording samples, and to K. Ruybalid for her assistance in various aspects of this project.

[1] J. S. Suits, R. H. Geiss, C. J. Lin, D. Rugar, and A. E. Bell, Appl. Phys. Lett. **49**, 419 (1986); L. Reimer, *Transmission Electron Microscopy*, Springer Series in Optical Science, Vol. 36 (Springer, New York, 1984), and references therein.
[2] R. J. Cellota and D. T. Pierce, Science **234**, 333 (1986).
[3] T. Matsuda, A. Fukuhara, T. Yoshida, S. Hasegawa, and A. Tonomura, Phys. Rev. Lett. **66**, 457 (1991).
[4] G. Binnig, H. Rohrer, Ch. Gerber, and E. Weibel, Phys. Rev. Lett. **49**, 57 (1982).
[5] G. Binnig, C. F. Quate, and Ch. Gerber, Phys. Rev. Lett. **56**, 930 (1982).
[6] Y. Martin and H. K. Wickramasinghe, Appl. Phys. Lett. **50**, 1455 (1987).
[7] D. Rugar, H. J. Mamin, P. Guethner, S. E. Lambert, J. E. Stern, I. MacFadyen, and T. Yogi, J. Appl. Phys. **68**, 1169 (1990).
[8] P. Grutter, H. J. Mamin, and D. Rugar, in *Scanning Tunneling Microscopy II*, Springer Series in Surface Science Vol. 28, edited by H.-J. Guntherodt and R. Weisendanger (Springer, Berlin, 1992), p. 151 and references therein.
[9] U. Hartmann, T. Goddenhenrich, and C. Heiden, J. Magn. Magn. Mater. **101**, 263 (1991).
[10] C. Shoenenberger, S. F. Alvarado, S. E. Lambert, and I. L. Sanders, J. Appl. Phys. **67**, 7278 (1990).
[11] R. D. Gomez, E. R. Burke, A. A. Adly, and I. D. Mayergoyz, Appl. Phys. Lett. **60**, 976 (1992).
[12] R. D. Gomez, A. A. Adly, I. D. Mayergoyz, and E. R. Burke, IEEE Trans. Magn. **MAG-29**, 2494 (1993).
[13] E. R. Burke, E. R. Burke, R. D. Gomez, A. A. Adly, and I. D. Mayergoyz, IEEE Trans. Magn. **MAG-28**, 3135 (1992).
[14] I. D. Mayergoyz, A. A. Adly, R. D. Gomez, and E. R. Burke, J. Appl. Phys. **73**, 5796 (1993).
[15] P. Rice and J. Moreland, IEEE Trans. Magn. **MAG-27**, 3452 (1991).
[16] P. K. Hansma and J. Tersoff, J. Appl. Phys. **61**, R1 (1987).
[17] R. Wiesendanger, J. Appl. Phys. **73**, 5816 (1993).
[18] R. D. Gomez, E. R. Burke, A. A. Adly, I. D. Mayergoyz, J. A. Gorczyca, and M. H. Kryder, J. Appl. Phys. **73**, 6180 (1993).
[19] R. D. Gomez, E. R. Burke, A. A. Adly, I. D. Mayergoyz, J. A. Gorczyca, and M. H. Kryder, J. Appl. Phys. **73**, 6001 (1993).
[20] R. D. Gomez, A. A. Adly, I. D. Mayergoyz, and E. R. Burke, IEEE Trans. Magn. **MAG-28**, 3141 (1992)
[21] I. D. Mayergoyz, A. A. Adly, R. D. Gomez, and E. R. Burke, J. Appl. Phys. **73**, 5799 (1993).
[22] R. I. Potter, J. Appl. Phys. **41**, 1648 (1970).
[23] E. R. Burke, R. D. Gomez, and I. D. Mayergoyz (these proceedings).
[24] R. D. Gomez, E. R. Burke, and I. D. Mayergoyz (these proceedings).
[25] I. A. Beardsley, IEEE Trans. Magn. **MAG-22**, 361 (1986).

Measurement of Young's moduli for film and substrate by the mechanical resonance method

Y. H. Lee, Y. D. Shin, and K. H. Lee
Department of Physics, Jeonbuk National University, Jeonju 560-756, Korea

J. R. Rhee
Department of Physics, Sookmyung Women's University, Seoul 140-742, Korea

Young's moduli for films and substrates are obtained by measurement and theoretical analysis of the resonance frequencies for cantilevered substrates with and without films in the flexural vibration mode. Young's moduli of 7.1, 19.2, and 21.3×10^{10} Pa obtained for the glass substrate, Ni, and $Ni_{53}Fe_{47}$ films agree with the published values for bulk material within 10%. Decrease of the resonance curve Q value is observed for substrates with films, which implies an increase of internal friction.

I. INTRODUCTION

The conventional static method of bending a bar with weight in measuring Young's modulus[1] is hard to apply to thin films on a substrate, especially for very small samples. Young's moduli of thin film and substrate, needed for the study of magnetostriction in thin films, have used their bulk values.[2] Due to film thickness and interface effects, it is important to directly measure the Young's modulus of a thin film in contact with its substrate. To this end, the present work has been carried out.

II. EXPERIMENTAL SETUP

The schematic diagram of the apparatus used is shown in Fig. 1. An iron core C with a solenoid L acts as a small magnet. A signal generator (HP 3310B) is the power supply A for the magnet. The sample is a glass substrate S with or without a thin film F deposited on it. One end of the sample is held by support B and a small piece of iron M is attached to the free end. The ac current in the magnet makes M and hence the sample vibrate, and the resulting accoustic wave is detected with a nearby microphone E. The output signal of E is amplified by G and displayed on D, a voltmeter and oscilloscope. Mechanical resonance frequency is obtained by plotting the frequency-response curve of the sample. Young's moduli for film and substrate are calculated from the measured resonance frequencies with and without a film, as discussed in Sec. III.

The actuator (L and C) is made of iron core C (28 mm long with 2.5 mm diameter) wound 1000 turns with enamel wire of 0.2 mm diameter. A cover glass (0.15 mm thick, 7 mm wide, and 22 mm long) is used as substrate upon which Ni or $Ni_{53}Fe_{47}$ film of thickness 0.7–1.0 μm is deposited. The mass of the iron piece M is about 20 mg. Diameter of the microphone E is 10 mm, and the frequencies are measured with Fluke 1952B.

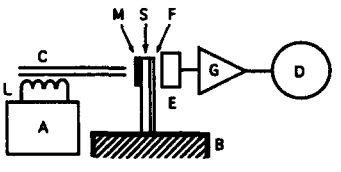

FIG. 1. Schematic diagram of measurement system. A: signal generator; L and C: actuator/electromagnet; M: iron piece; S: substrate; F: film; E: microphone; G: amplifier; D: voltmeter and oscilloscope

III. CALCULATION OF RESONANCE FREQUENCIES

In this section, the procedure for calculating Young's moduli from measured resonance frequencies is presented.

A. Simple cantilever (with S only in Fig. 1)

When a small periodic perpendicular force is applied to the free end, the cantilever (with length l, width b, thickness a, density ρ, and Young's modulus E) would look like Fig. 2. With x and y defined as indicated, the equation of motion is[3]

$$EI\left(\frac{\partial^4 y}{\partial x^4}\right)+\rho ab\left(\frac{\partial^2 y}{\partial t^2}\right)=0, \tag{1}$$

where $I=a^3b/12$ is the secondary moment of the cross section. With constants A and B, substitution of

$$y=Y(A\cos\omega t+B\sin\omega t), \quad \text{with } \beta^4=\omega^2\rho ab/EI, \tag{2}$$

into Eq. (1) leads to

$$(d^4Y/dx^4)-\beta^4Y=0. \tag{3}$$

The general solution of Eq. (3) is

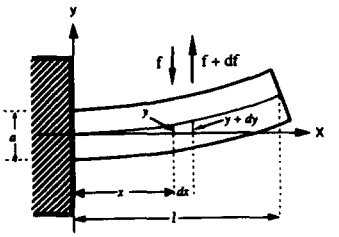

FIG. 2. Cantilevered sample geometry under flexural vibration.

 0021-8979/94/75(10)/5913/3/$6.00 © 1994 American Institute of Physics

TABLE I. Sample parameters. a: thickness in mm (with subscript s for substrate, f for film); b: width in mm; l: length in mm; m: mass in mg (with subscript i for iron piece); ρ: density in g/cm^3.

Film/substrate	a_s	a_f	b	l	m_s	m_f	m_i	ρ_s	ρ_f
Ni/glass	0.160	0.70	7.3	18	50.15	0.82	21.8	2.39	8.9
$Ni_{53}Fe_{47}$/glass	0.152	1.0	7.2	18	47.91	1.09	26.6	2.43	8.4

$$Y=C_1\cosh\beta x+C_2\sinh\beta x+C_3\cos\beta x+C_4\sin\beta x, \tag{4}$$

with constants C_1, C_2, C_3, and C_4 to be determined by the boundary condition.

B. Simple cantilever with end mass (with S and M in Fig. 1)

When an iron piece M of mass m_i is attached to the free end of the above simple cantilever of Sec. III A, the boundary condition for Y in Eq. (4) reads[4]

$$Y=\frac{dY}{dx}=0 \quad \text{at } x=0,$$

$$\frac{d^2Y}{dx^2}=0,$$

and

$$EI\left(\frac{d^3Y}{dx^3}\right)=-m_i\omega^2Y \quad \text{at } x=l. \tag{5}$$

Then the frequency equation becomes

$$1+\cosh\beta l-\mu\beta\, l(\cosh\beta l\sin\beta l-\sinh\beta l\cos\beta l)=0, \tag{6}$$

where $\mu=m_i/m_s$ with substrate mass $m_s=\rho_s a_s bl$.

With the given μ value, the root R_s of Eq. (6) for βl is obtained numerically and hence Young's modulus E_s for the substrate is expressed as

$$E_s=12(m_s/b)(l/a_s)^3(\omega_s/R_s^3)^2, \tag{7}$$

using the β-E relationship given in Eq. (2).

C. Filmed cantilever with end mass (with F/S and M in Fig. 1)

When a thin film (with thickness a_f, density ρ_f, and Young's modulus E_f) is deposited on the substrate described in Sec. III B, the frequency equation is of the form of Eq. (6) with replacement of some parameters as follows:

$$m_s=\rho_s a_s bl\rightarrow m_{sf}=(\rho_s a_s+\rho_f a_f)bl,$$
$$E_sI_s=a_s^3bE_s/12\rightarrow E_{sf}I_{sf}=(1+3\alpha\epsilon)E_sI_s, \tag{8}$$

with $\alpha=a_f/a_s$ ($\ll 1$) and $\epsilon=E_f/E_s$.

For a given $\mu_{sf}=m_i/m_{sf}$, with a procedure parallel to that in Sec. III B, the numerically obtained root R_{sf} of Eq. (6) is

$$R_{sf}^4=(\beta_{sf}l)^4=12\omega_{sf}^2m_{sf}l^3/(1+3\alpha\epsilon)a_s^3bE_s, \tag{9}$$

which leads to

$$E_f=[12(m_{sf}/b)(l/a_s)^3(\omega_{sf}/R_{sf}^2)^2-E_s]a_s/3a_f. \tag{10}$$

Thus, Young's modulus E_f of the film can be obtained by measuring the resonance frequency ω_{sf} (and ω_s) of a filmed substrate with end mass as shown in Fig. 1.

IV. EXPERIMENT AND DISCUSSION

The Ni film of 0.7 μm was deposited at a substrate temperature of 200 °C at 2×10^{-5} Torr with deposition rate of 1 Å/s. The $Ni_{53}Fe_{47}$ film of 1.0 μm is deposited at room temperature in 5×10^{-3} Torr argon environment with rate of 2 Å/s. The sample parameters are given in Table I.

The frequency response curves before and after film deposition are shown in Fig. 3 for the Ni film case. With a film on the substrate the resonance frequency is raised, but the Q value is lowered. This is attributed to internal friction of the thin film and the film-substrate interface. For the $Ni_{53}Fe_{47}$ film case, response curves similar to Fig. 3 were obtained.

Young's moduli were calculated using Eqs. (7)–(10) and results are given in Table II. One notes that the Young's modulus of the glass substrate is in the range of the Jena Crown bulk value; however, that for thin films shows some reduction from the bulk value.[5,6]

V. CONCLUSION

The mechanical resonance method, similar in principle to the vibrating-reed method for internal friction studies,[7] with a electromagnetic drive and accoustic detection system is used to measure Young's moduli of magnetic thin films and substrates with very small sample size. For Ni and

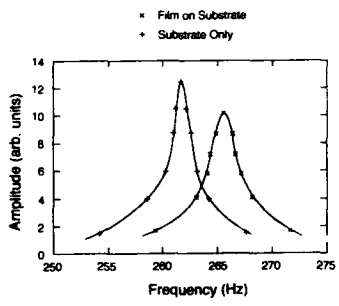

FIG. 3. Resonance curves for cantilevered sample with and without 0.7 μm Ni film.

TABLE II. Young's moduli and related sample parameters. f: measured resonance frequency in Hz (with subscript s for substrate only, sf for filmed substrate); R: root of the frequency Eq. (6); E: Young's modulus in 10^{10} Pa (with subscript f for film); Q: quality factor of resonance curve.

Film/substrate	f_s	f_{sf}	R_s	R_{sf}	E_s	E_f	Q_s	Q_{sf}
Ni/glass	251.6	265.5	1.453 12	1.456 92	7.1	19.2	164	115
$Ni_{53}Fe_{47}$/glass	224.9	230.8	1.394 67	1.400 12	7.0	21.3	173	121

$Ni_{53}Fe_{47}$ thin films, Young's moduli turn out to be somewhat smaller, but in the range of their bulk values. Since the Q value of the resonance curve is easily obtained by the procedure of this work, it would be useful for study of thin-film internal structures.

ACKNOWLEDGMENT

This work is supported in part by Korean Ministry of Education through Grant No. BS 93-213.

[1] See, for example, *Handbook of Chemistry and Physics*, 52nd ed., edited by R. C. Weast (Chemical Rubber Co., Cleveland, OH, 1971).
[2] M. Kaneko, S. Hashimoto, M. Hayakawa, and K. Aso, J. Phys. E **21**, 487 (1988).
[3] F. S. Tse, I. E. Morse, and R. T. Hinkle, *Mechanical Vibrations*, 2nd ed. (Allyn and Bacon, Boston, 1978), Chap. 7.
[4] T. Matsuhira, *Fundamentals of Vibration Analysis* (Kyoritsu, Tokyo, 1952), p. 229 (in Japanese).
[5] D. Halliday, R. Resnick, and J. Walker, *Fundamentals of Physics Extended*, 4th ed. (Wiley, New York, 1993), p. 368.
[6] W. J. M. Tegart, *Elements of Mechanical Metallurgy* (Macmillan, New York, 1966), p. 91.
[7] B. S. Berry and W. C. Pritchet, Rev. Sci. Instrum. **54**, 254 (1983); J. Appl. Phys. **67**, 3661 (1990), and references quoted therein.

A new structure of torque sensors using thin pickup head—Use of mutual coupling modulation

I. Sasada and F. Koga
Department of Electronics, Kyushu University 36, Fukuoka 812, Japan

A new structure is proposed for the magnetoelastic torque sensors using a pair of figure-eight coils as a pickup. Mutual coupling between two figure-eight coils is used as a measure of torque applied to a shaft. The mutual coupling is governed by torque-induced anisotropic permeability at the surface of the shaft. Basic characteristics of the torque sensor are examined using a tempered steel shaft of 25 mm in diameter and a pair of 25-turn figure-eight coils. Sensitivity was 16 μV/N m and hysteresis was 1.3% at the coil excitation condition of 60 kHz, 0.8 A (RMS). Exciting power needed to reduce hysteresis is much smaller with this structure than with previous methods using self-inductance as a measure of torque.

I. INTRODUCTION

Torque sensors are considered as one of the key elements needed to construct intelligent control scheme for systems such as robotic systems, machining tools, and automobiles. Torque sensors based on the magnetoelastic principle[1–3] are considered to be most suitable in those applications, because inductive coupling allows for noncontact structures and durability.

Miniaturization[4,5] is an important aspect of the torque sensors, so as to incorporate them into mechanical systems. We have proposed a new, thin pickup coil for magnetoelastic torque sensors, which consists of a pair of figure-eight coils stacked orthogonally each other. The above method was based on the measurements of the difference in self-inductance of both figure-eight coils while facing a steel shaft under torque. In this method, the coil exciting power necessary to reduce hysteresis was not low.[6]

In this paper, we propose a further simplified and low-power version of the torque sensor using a pickup coil of the same kind, in which mutual coupling between two figure-eight coils is used as a measure of torque instead of self-inductance. Similar characteristics are obtained as in the previous study[6] with much less exciting power.

II. NEW STRUCTURE OF THE TORQUE SENSOR

Figure 1 shows the operating principle of the torque sensor proposed in this paper. One of the figure-eight coils is placed on a shaft having a magnetoelastic effect with an air gap between them. One of the crossing parts of the coil is aligned along the circumferential direction of the shaft. When the shaft is free from applied torque, the magnetic flux in the shaft generated by the figure-eight coil is, in principle, parallel to the axis of the shaft, as shown in Fig. 1(a). On the other hand, when torque is applied, the exciting flux is skewed toward the direction of the easy magnetization axis. The direction of the easy magnetization axis is along the line of tension, as shown in Fig. 1(b), if the saturation magnetostriction constant of the shaft is positive. This means that a circumferential component of the flux appears upon applying torque to the shaft, and the polarity (or phase) of the flux can be uniquely determined. This component can be selectively picked up by putting a secondary figure-eight coil on the primary coil with its crossing parts along the axis direction of the shaft, as shown in Fig. 1(c). When the direction of the applied torque is reversed, the direction of the circumferential component is also reversed. In this manner, the mutual coupling of the two figure-eight coils is uniquely governed by the applied torque. The output of the torque sensor is easily obtained by an ordinary phase sensitive rectifier. The roles of the two figure-eight coils can be exchanged. As the primary side and the secondary side are electrically isolated by virtue of mutual coupling, it becomes easy to design a signal processing circuit afterward.

It should be noted that although the only difference between the new and the previous structure[6] is that the pickup coils are rotated in the coil plane by 45°, the operating principle is absolutely different.

III. EXPERIMENT

Because of the similarity in structure, the experimental setup used is the same as used previously.[6] A pickup coil consisting of a pair of figure-eight coils was prepared by stacking two copper wires of 0.2 mm in diameter in the form of a figure-eight. The two figure-eight coils were rotated 90° relative to each other. The number of turns for each figure-eight coil was 25. The outer diameter of the figure-eight coils

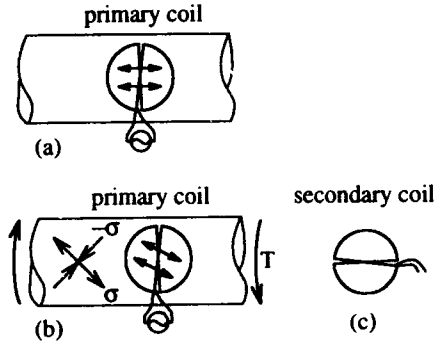

FIG. 1. Operating principle.

 0021-8979/94/75(10)/5916/3/$6.00 © 1994 American Institute of Physics

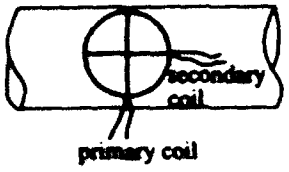

FIG. 2. Schematic view of the pickup coil and the shaft.

was 20 mm. The pickup coil was faced to a shaft of 25 mm in diameter with an air gap of 0.25 mm. A tempered chromium molybdenum steel shaft (SCM415, $Hv = 310$, $Hc = 18$ Oe) was used as a sample shaft, because chromium molybdenum steel is one of typical materials for shafts. Figure 2 shows schematic view of the arrangement. The pickup coil was backed by a magnetic yoke to enhance exciting flux. The magnetic yoke was made of 18 layers of Metglas 2705M amorphous ribbons (43 mm × 25 mm) with the magnetostriction constant close to zero. Pickup coil assembly is shown in Fig. 3. Schematic diagram of the experimental circuit is shown in Fig. 4, where a loosely coupled transformer consisting of a set of ring coils (20 turns, 15 mm in diameter) are incorporated to compensate a spurious component in the secondary voltage. Basic characteristics were measured as a function of exciting frequency and exciting current. Torque was applied statically using a lever and weights and was measured by strain gauges glued on the shaft under test.

IV. RESULTS AND DISCUSSION

All data points were scaled so that the total gain factor of the experimental system including a lock-in amplifier is unity. Sensitivity is shown in Fig. 5 for the exciting current, taking the exciting frequency as a parameter. Dependence of the sensitivity on the exciting frequency and the current is similar to that obtained previously using an inductance bridge configuration, where two pairs of figure-eight coils were used in the form a bridge circuit.[4] Output characteristics are shown in Fig. 6 for the exciting currents 0.4 and 0.8 A at the exciting frequency 60 kHz. Hysteresis in the input-output characteristics is 1.7% at 0.4 A and is 1.3% at 0.8 A. These values of hysteresis are small compared to 5.0% encountered previously, using an inductance bridge configuration for exciting current 0.8 A at 60 kHz.[4] The large hysteresis concerning an inductance bridge configuration was decreased to 1.8% by increasing the exciting current to 1.6 A. Exciting power at this condition was 9 W, which was dissipated at two pickup coils. In this case, sensitivity was 40 μV/N m. Power loss for the new structure, where a single pickup coil was used, was only 2 W for the exciting current 0.8 A at 60 kHz. It should be noted that smaller hysteresis was obtained at lower exciting power level with the new structure. The reason for this could be explained using a model for the exciting flux patterns shown in Fig. 7. The primary coil of the new structure carrying current i provides the exciting field all along the vertical branch of the figure-eight coil, on the other hand, figure-eight coils in an inductance bridge configuration, as used in our previous study, both carry the same current i and provide a localized exciting field, as shown in Fig. 7, which leaves the surfaces of the shaft under most of two quarter-areas at the top and the bottom unmagnetized, resulting in larger hysteresis. Or in other words, in order to reduce hysteresis, large exciting current is needed to magnetize those surfaces when pickup coils are used in an inductance bridge configuration.

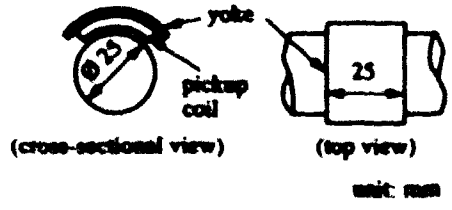

FIG. 3. Pickup coil assembly.

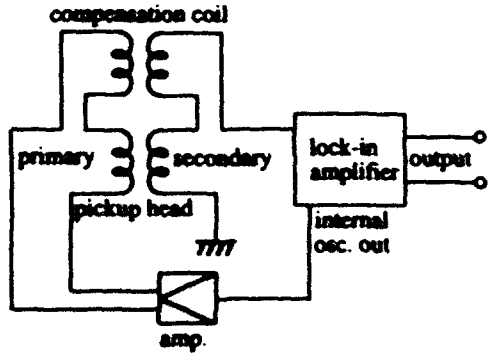

FIG. 4. Schematic diagram of the experimental circuit. Compensation coils are added for zero balance.

We also examined a case-hardened shaft and an unheat-treated shaft ($Hc = 6$ Oe) of the same material. Applied torque could not be detected from the case-hardened shaft.

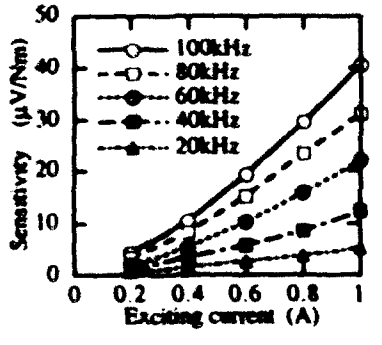

FIG. 5. Sensitivity of the torque sensor for the exciting current, taking frequency as a parameter.

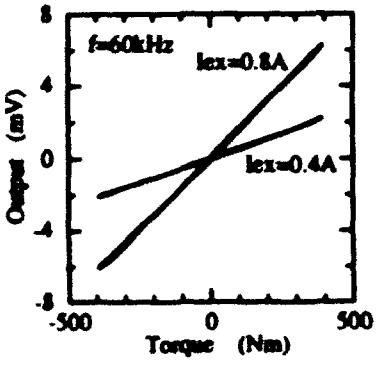

FIG. 6. Output characteristics of the torque sensor.

This could be due to large compressive stresses in the surface of the shaft resulting from case hardening. On the other hand, sensitivity was about 30 times higher for an unheat-treated shaft than for the tempered sample shaft at the cost of reduced dynamic range, ± 100 N m. However, the behavior of the hysteresis was rather complicated. Direction of the hysteresis loop in the *input–output plane* was *counterclockwise* for the exciting current less than 0.4 A and turned into clockwise for the exciting current larger than that.

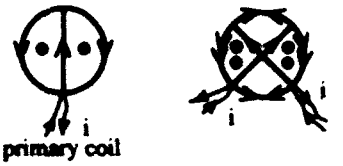

FIG. 7. A simple model for the exciting flux patterns.

V. CONCLUSION

We have proposed a new structure of magnetoelastic torque sensors using a pair of figure-eight coils as a pickup, where mutual coupling is a measure of torque. Due to the electrical isolation inherent in this structure, signal detection becomes easy. Low-profile, low-power torque sensors can be obtained by the proposed structure.

ACKNOWLEDGMENT

This work was supported by the Grant-in-Aid for Scientific Research from the Ministry of Education, Science, and Culture of Japan.

[1] R. A. Beth and W. W. Mosby, Rev. Sci. Instrum. 25, 603 (1954).
[2] O. Dahle, ASEA J. 33, 23 (1960).
[3] I. Sasada, A. Hiwatashi, and K. Harada, IEEE Trans. Magn. 20, 951 (1984).
[4] W. Fleming and P. W. Wood, SAE Paper No. 820308, 1982.
[5] Y. Hamamura, J. Sugiyama, K. Tsukada, M. Takeuchi, K. Itoh, and T. Kamiura, SAE Paper No. 870472, 1987.
[6] I. Sasada, F. Koga, and K. Harada, Intermag '93, BP-08, Stockholm, 1993.

A microwave transmission spectrometer

Carlo Waldfried, Scott Wadowitz, and G. Dewar
Physics Department, University of North Dakota, P.O. Box 7129, Grand Forks, North Dakota 58202-7129

The design and performance of a microwave transmission spectrometer operating in the 12.4–18 GHz frequency range is described. This spectrometer measures the microwave power passing through a magnetic, metallic sample as a function of temperature and applied magnetic field. Significant features of the apparatus are the use of a solid state microwave amplifier as the homodyne receiver's front end and the inclusion of a calibration signal which is injected into the receiver simultaneously with the signal to be measured. The excellent noise figure (<2 dB) and gain (>34 dB) of the amplifier yield a receiver sensitivity of $\sim 10^{-20}$ W in a 1 Hz bandwidth. The present microwave source is a dielectric resonant oscillator which generates 100 mW at 16.95 GHz, although the system can also operate with a klystron or microwave sweep oscillator locked to any frequency between 12.4 and 18 GHz. The first use of the system was to measure the transmission through the amorphous ferromagnet Metglas® 2605SC (Allied Chemical Corporation). A peak in the transmission was observed at ferromagnetic resonance. This transmission peak was contaminated by a signal going around, not through, the sample which we tentatively identify with surface acoustic waves.

I. INTRODUCTION

Measurement of the microwave transmission through a ferromagnetic metallic material complements the standard ferromagnetic resonance (FMR) reflection technique. The transmission experiment is particularly suitable for investigating weakly excited, but relatively unattenuated, transmission modes. For example, sound waves are responsible for a transmission peak which is slightly offset from the FMR absorption maximum.[1–3]

The transmission spectrometer described here has much in common with previous instruments.[4–6] The basic elements of the apparatus are a microwave source, a cavity pair which serve as impedance matching devices to the sample under study, a calibrated attenuator which may be substituted for the sample, and a homodyne microwave receiver. Two innovations in this apparatus' design result in an improvement of the signal-to-noise ratio over previous instruments by as much as 30 dB. First, this microwave receiver's front end is a low-noise solid-state microwave amplifier whereas other receivers use a mixer followed by a vacuum tube i.f. amplifier. Second, the calibrated attenuator which the sample is compared with is monitored by the receiver simultaneously with the sample; there is no need to switch the calibration line in and out of the signal path at 5–15 min intervals. This greatly reduces the $1/f$ noise of the system.

II. TRANSMISSION APPARATUS

A schematic of the apparatus is shown in Fig. 1. A MITEQ[7] dielectric resonant oscillator (model DRO-J-17000-SP) produces 100 mW of microwave power at 16.95 GHz. Most of this power is fed via the transmission line to a critically coupled transmitter cavity. The sample forms part of the common wall between this cavity and an identical receiver cavity, both operating in the TE_{102} mode. Indium gaskets are used to electrically seal the sample to the cavity walls and to minimize stress effects on the sample. Power passing through the sample and into the signal line is modulated at the 2.304 MHz intermediate frequency (i.f.) by an ARRA[8] pin diode reflective switch (model 62-115-1D) in the signal line. The modulated signal is routed to a MITEQ low-noise amplifier (AMF-6S-1218-30) having a gain of 34.5 dB and a noise figure of 1.83 dB at the system operating frequency. This amplified microwave signal (rf) is mixed (MITEQ model M1218M) with approximately 10 mW of unmodulated microwave local oscillator (LO) power coupled from the transmission line. The mixer's i.f. output is amplified by one of two different preamplifiers with gains of 6–22 dB and fed to detection electronics described below.

In addition to the signal through the sample a calibration signal is injected into the receiver via the calibration line which consists of a 40 dB directional coupler, a phase shifter, a precision variable attenuator, a modulator, a fixed attenuator, and a 20 dB directional coupler. The modulator is a reflective switch identical to the one in the signal line. The precision variable attenuator is a Hewlett-Packard[9] P382A. With the modulator switch open and the variable attenuator set to 0.0 dB, the calibration signal is 95.8 ± 0.6 dB down from the power in the transmission line. By comparison, the two isolators and modulator in the signal line as well as 3.6 in of waveguide attenuate the signal from the receiver cavity by 7.4 ± 0.5 dB.

The design of the system's electronics allowed the use of directional couplers to route the calibration signal into the receiver. This is unlike other spectrometers which use switches for this function.[4–6] The calibration signal and the sample's transmission signal go through the same rf/i.f. amplifier chain and are separated only at the final stage of the detection process. This separation is possible because the i.f. modulators have an additional square wave phase modulation of amplitude 180° impressed on the i.f. at the low frequency (LF) of 4.50 kHz for the calibration signal and of 1.125 kHz for the transmission signal. In addition, the two i.f. modulations are in quadrature. After the main i.f. amplifier (21 dB gain) the i.f. signal is split and mixed with 2.304 MHz local i.f. oscillators. The resulting LF signal pair is detected by PAR[10] phase-sensitive detectors: model HR-8 for the calibration signal and model 5104 for the transmission signal. The output of these detectors may be recorded sepa-

 0021-8979/94/75(10)/5919/3/$6.00 © 1994 American Institute of Physics

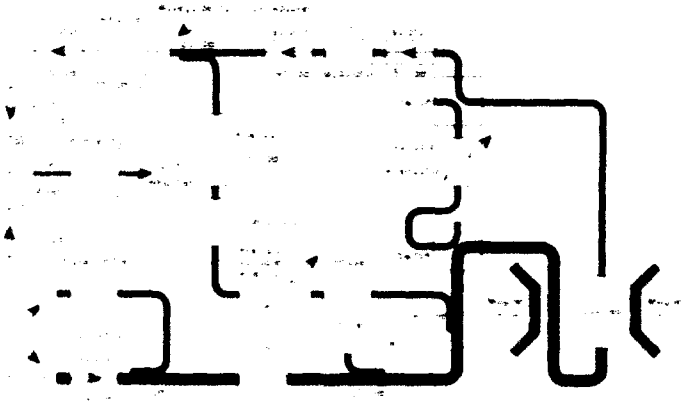

FIG. 1. Schematic outline of transmission apparatus.

rately or the 5104 may be connected so that the output is proportional to the ratio of transmission signal to the calibration signal measured by the HR-8.

The reference line provides the local oscillator power for the mixer. This power is tapped from the transmission line by a 10 dB directional coupler and passes through a Hewlett-Packard® precision phase shifter (model P885A), a waveguide-to-co-ax adapter, and a 22 dB isolator before reaching the mixer. The isolator eliminates any interaction between the mixer and the phase shifter and presents a well-matched 50 Ω load to the mixer.

More than 115 dB of isolation have been added to the components between the signal line modulator and the mixer. Along with the mixer's isolation of 36 dB and the amplifier's output-to-input isolation of more than 45 dB, this eliminates the possibility of a spurious signal arising from feedthrough of the microwave local oscillator reaching the modulator and being reflected back into the mixer.

The diode detector and two mechanical switches with attached variable attenuator are required in order to tune the cavities to the operating frequency of the system. With the switches set as shown in Fig. 1 the transmitter cavity may be tuned by observing the voltage on the diode and tuning the cavity for a minimum reflection. With both switches rotated clockwise 1/4 turn and the variable attenuator opened the receiver cavity may be similarly tuned. The switches were each measured to have more than 70 dB isolation and the variable attenuator to have a maximum insertion loss of 27 dB. No leakage through the switches from the transmission line to the signal line was detected.

The 30 dB isolator placed before the modulator in the signal line absorbs the power reflected from the modulator switch in its off state. The isolator and frequency meter in the transmission line are redundant when used with the dielectric resonant oscillator (DRO) source but are necessary when a klystron or sweep oscillator is substituted.

After construction of the apparatus a major difficulty with the electronics was encountered. The modulator switches have an integral driver which creates power supply line spikes lasting less than 10 ns and having an amplitude of 2–4 V. Microvolt level replicas of these spikes entered the detector between the i.f. preamplifier and the main i.f. amplifier. These spurious signals were eliminated with improved shielding.

III. EXPERIMENT

The highly magnetostrictive amorphous ferromagnet Metglas® 2605SC was the first material examined with this apparatus. Specimens obtained from a 5-cm-wide ribbon were cut into circular discs 2½ cm in diameter. Several samples of thickness 21.5±2.5 μm were mounted "as is" with indium O-ring seals. These samples were of nonuniform thickness and had a visible line pattern perpendicular to the roll direction imprinted in the surface. This surface relief had a characteristic length scale of 1 mm and was 2–5 μm in amplitude. The line pattern was ground (600 grit) from both sides of one sample. Its final thickness was 14±3 μm. The resistivity of the material was measured to be 150±15 μΩ cm.

Transmission data were recorded as a function of the magnetic field applied parallel to the plane of the sample but perpendicular to the microwave magnetic field. Since the receiver actually measures the component of the transmitted signal in phase with the local oscillator at the mixer, several data sets were obtained at different settings of the phase shifter in the reference line. From these data the transmission amplitude versus magnetic field, and relative transmission phase versus magnetic field, were obtained as described elsewhere.[5]

The as-is samples produced transmission signals which were characteristic of power going around, not through, the

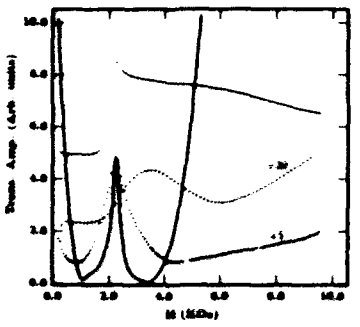

FIG. 2. Transmission vs applied magnetic field. Transmission through a 21.5-μm-thick sample without (⊕) and with (⊟) subtraction of signal going around the sample as shown; the latter has been magnified fivefold. The transmission through a 14-μm-thick sample (+) is shown demagnified 30-fold. The calculated transmission (line) has been normalized to the data. Parameters used in the calculation are: thickness of 21.5 μm, $4\pi M = 13.12$ kG, frequency of 16.95 GHz, density of 7.2 g/cm^3, g factor of 2.08, resistivity of 150.5 $\mu\Omega$ cm, shear modulus of 7.348×10^{11} erg/cm^3, exchange constant of 6.9×10^{-7} erg/cm, damping parameter of 6.0×10^8 s^{-1}, and magnetoelastic coupling of 6.7×10^7 erg/cm^3.

samples (see Fig. 2). This was verified by tightening the cavity/sample holder/sample sandwich, thus increased the width of the indium O-ring in contact with the sample from ~2 to ~3 mm and decreased the transmission amplitude by 20% to 50% for various samples. Under the assumption that tightening the seals only scaled the amplitude of the signal going around the sample, and rotated the phase by a field-independent increment, we were able to subtract most of this signal's effect. Figure 2 shows the result of this subtraction and, for comparison, the transmission through the polished, thinner sample. No signal was detected going around the polished sample.

The transmission signals observed with these samples were quite large and did not tax the capabilities of the transmission system. The system noise was measured by increasing the attenuation in the calibration line so that the 90 mW available was attenuated by 146 dB. Measurements of this small calibration signal indicate that the system noise is $\leq10^{-20}$ W in a 1 Hz bandwidth. This corresponds to a noise figure of ≤4 dB.

IV. COMPARISON WITH THEORY

The peak in the transmission data corresponds to transverse sound waves propagating through the sample.[7] These sound waves are coupled to the microwaves via magnetoelastic coupling and they are most strongly excited near FMR. The weakly field-dependent transmission at $H>5$ kOe is due to the electromagnetic wave penetrating the sample. The transmission calculation has been given by Heinrich and Cochran.[1] The solid line in Fig. 2 is the result of such a calculation using the material parameters listed in the caption. Note that transmission amplitude, not power, is plotted in this figure. A wave of unit amplitude corresponds to a receiver input of 8×10^{-14} W.

The experimental data are only qualitatively similar to the calculation. The transmission peak is stronger and broader than the calculated peak as well as shifted upfield. Reasonable modifications of the parameters used in the calculation cannot bring calculation and experiment into agreement. In fact, the as-is sample's nonuniform thickness should lead to partial destructive interference of the transmission near FMR since the sound wavelength of ~0.2 μm is less than the surface roughness of the sample. The electromagnetic wave is less affected by this nonuniformity since it is heavily attenuated and the thinnest parts of the sample dominate the transmission. Thus, one would expect the experimental ratio of peak height to high-field transmission to be much smaller than the calculated ratio; this is clearly not the case. The magnetic damping parameter used in the calculation normally controls the width of the transmission peak. However, the damping used in the calculation is so large that any attempt to increase it results in an increase of the acoustic attenuation and a severe decrease in the calculated transmission with only a small effect on the peak width. The calculated position of the peak is controlled by the value of the magnetization and g factor. Agreement between the calculated and measured peak position was forced by decreasing the magnetization ($4\pi M$) used in the calculation to 13.12 kG, the Metglas' true magnetization is close to 16 kG. The transmission peak for the polished sample is shifted to even higher fields. This is probably due to a decrease in the magnetization caused by the polishing process.

V. RESULTS AND CONCLUSIONS

A new low-noise and high-stability transmission spectrometer was used to measure the transmission through Metglas® 2605SC. This highly magnetostrictive amorphous ferromagnet exhibited the expected transmission peak due to the strong excitation of sound waves near FMR. This transmission peak was stronger, broader, and shifted to higher fields than calculations predicted.

The material in its as-is form allowed a signal to pass around, as well as through, the sample. Electromagnetic waves cannot be responsible for the signal going around the sample since the indium O rings used to seal the sample to the sample holder are an excellent barrier to these waves. Also, removal of the surface roughness resulted in at least an 80% reduction of the signal going around the sample. Thus we tentatively identify the source of this signal as a surface acoustic wave propagating along the Metglas-indium interface.

[1] B. Heinrich and J. F. Cochran, J. Appl. Phys. 50, 2440 (1979).
[2] G. C. Alexandrakis, J. W. Allen, and I. A. Privorotskii, J. Appl. Phys. 50, 2443 (1979).
[3] B. Heinrich and J. F. Cochran, J. Appl. Phys. 52, 1811 (1981).
[4] R. B. Lewis and T. R. Carver, Phys. Rev. 188, 309 (1969).
[5] J. F. Cochran, B. Heinrich, and G. Dewar, Can. J. Phys. 55, 834 (1977).
[6] J. B. Holmes and G. C. Alexandrakis, Phys. Rev. B 16, 404 (1977).
[7] MITEQ, 100 Davids Drive, Hauppauge, NY 11788.
[8] Antenna & Radome Research Associates, 15 Harold Court, Bay Shore, NY 11706.
[9] Hewlett-Packard Co., 1501 Page Mill Road, Palo Alto, CA.
[10] EG&G Princeton Applied Research, P.O. Box 2565, Princeton, NJ 08540.

Measurements of intrinsic magnetic properties of materials from surface inspection (abstract)

Z. J. Chen and D. C. Jiles
Ames Laboratory, Department of Electrical and Computer Engineering, and Center for NDE, Iowa State University, Ames, Iowa 50011

Surface inspection of magnetic properties with a sensor is a useful and practical technique because it gives a rapid and noninvasive measurement and requires minimum material preparation. However, this technique is handicapped by the practical problems of calculating inherent magnetic properties of the material from such a measurement. A transfer function based on the first approximation was developed previously[1] and it worked well when the dimension of the sample was comparable with the inspection head. However, the nonuniform distribution of the magnetic field is an inherent problem and gets more serious when the vertical and lateral dimensions of the test material become comparable with the pole length of inspection head. Therefore, it invalidates the application of first approximation. A more general and practical transfer function is derived in this paper, including the geometry effects of inspection head and test material. This transfer function is based on the surface magnetic charge model[1] and fits well in the situation when the test material has a large dimension. Test results on specimens by direct measurement and measurement from surface inspection will be presented.

Work supported by U.S. Nuclear Regulatory Commission under Grant No NRC-04091-098.

[1] Z. J. Chen, R. Govindaraju, and D. C. Jiles, J. Appl. Phys. 73, 6656 (1993).

Three component magnetic field measurements using cubic anisotropy in (111) YIG films (abstract)

A. Ya. Parlov, A. I. Voronko, P. M. Vetoshko, and V. B. Volkovoy
IMC Ltd., Technology House, Lansdale Street, Salford M6 6AP, United Kingdom

A magnetization behavior in YIG films with (111) orientation for a saturation in-plane magnetic field, taking into account the fourth ($K1$) and the sixth ($K2$) cubic anisotropy constants, is investigated theoretically and experimentally. Dependencies of a magnitude of the saturation field on material parameters were found. Different situations of a static and a rotating saturation magnetic field were considered. Analytical expressions for an induction signal caused by interference of in-plane magnetization homogeneous rotation with an ambient quasistatic magnetic field were obtained. It was shown that there exists a linear harmonic response to the ambient field both tangentially and perpendicularly to the film plane field orientations. Experimental results obtained for different kinds of YIG films were in good agreement with theory. Measured sensitivity was of the order of 10^{-7} Oe with a dynamic range of 80 dB. This, thereby, enables the design of a three component induction sensor with a high sensitivity and a large dynamic range.

 0021-8979/94/75(10)/5882/1/$6.00 © 1994 American Institute of Physics

Magnetoresistive characterization of thin-film structures by a gradient-field method (abstract)

P. L. Trouilloud, F. Suits, C. V. Jahnes, M. A. Russak, E. J. Spada, and J. W. Chang[a)]
IBM Research Division, T. J. Watson Research Center, Yorktown Heights, New York 10598

Magnetoresistance measurements can be used during manufacturing to characterize basic magnetic parameters at the device level. A fruitful approach is to take advantage of the gradient field generated by the current flowing through the sample. This method was employed by Smith *et al.*[1] in an elegant series of experiments that led to precise measurements of exchange constant in soft magnetic thin films. In the present paper, local coupling in bilayers, anisotropy, and interface quality are investigated using magnetoresistive response to gradient fields. Permalloy samples consisting of two sputtered layers (0.1 μm thick) separated by thin SiO_2 spacers were patterned in the form of long stripes parallel to the easy axis. Variation in resistance was measured as a function of external field applied in the easy-axis direction and of current density. For similar geometries, the samples have similar resistance. The curves display a sharp decrease in the resistance near zero field that is associated with the reversal of the magnetization in the stripe. Once the sample has switched, coupled layers have a flat response versus field: exchange coupling between the layers constrains the fanning of the magnetization, as previously described.[1] For uncoupled or weakly coupled samples, the curves show curvature at higher fields, and the curvature increases markedly with current density. The fanning within each layer is constrained by exchange, but the average magnetization in one layer rotates under the influence of the field generated by the current in the other layer.

a)Now at Daotek, 6580 Via del Oro, San Jose, CA 95119

[1] N. Smith, W. Doyle, D. Markham, and D. LaTourette, IEEE Trans. Magn. 23, 1248 (1987).

 0021-8979/94/75(10)/5923/1/$6.00 © 1994 American Institute of Physics

Dispersivity measurement of magnetic powders using the magnetic noise method (abstract)

V. M. Vasilyev
Department of Physics, Don State Technical University, Rostov-on-Don, 344010 Russia

In spite of the different nature of high coercivity in hexaferrites (Ba, Sr, Pb) and intermetallic compounds (Sm CO_5, Fe-Nd-B) the grain size distribution function in the powders is of a great importance for both types of sintered magnets.[1] The conventional techniques in many cases could not provide a reliable estimate of the powders' dispersion. The fine particles (particularly the single-domain ones) are magnetized almost to saturation and therefore are stretched together into the flocculas. These flocculas are taken by the various methods as a large particle, i.e., the methods fail. On the contrary, the jumplike domain wall motion parameters, obtained in BN spectrum study, let us analyze the distribution function of fine Ba-Sr hexaferrites powder particles by size.[2] Later it was found that such dependence of the BN spectrum $G(f)$ on the mean grain size dm is true for a wide variety of the powders whose dispersivity is far from a single-domain one. The stable dependences of BN parameters on a powder dispersity was observed for a wider range in Ba-Sr ferrite $0.5 < dm < 4$ mkm (since the single-domain size is about 1.3 mkm) and in Fe-Nd-B powders with $1.5 < dm < 20$ mkm, and in pulverized iron powders with $30 < dm < 400$ mkm and in fine electrolytic dendrite iron particles with a mean long axis size of $0.1 < lm < 0.2$ mkm. The applied field and $G(f)$ values are quite different in the above cases, but the main features remain the same. So the method may be widely used in various branches of magnetic powder and related technology for easy, fast, and reliable measurement and analysis of the distribution function of the powders' particle numbers and specific volumes by size. We have developed a complete range of devices for the SPDA (system for powders dispersion analysis) equipped with a PC and proper software for analyzing and displaying the information obtained.

[1] S. Chikazumi, J. Magn. Magn. Mater. 54–57, 1551 (1986).
[2] V. Vasilyev and G. Yagla, Dig. Intermag. '90 (JP 17, 1990).

 0021-8979/94/75(10)/5884/1/$6.00 © 1994 American Institute of Physics

Contributions of fine-particle magnetism to reading the global paleoclimate record (invited)

Subir K. Banerjee
Institute for Rock Magnetism, Department of Geology and Geophysics, University of Minnesota, 310 Pillsbury Drive, S.E., Minneapolis, Minnesota 55455

Paleoclimate changes are recorded by proxy as variations in concentration, composition, and grain size of magnetic minerals, principally magnetite (Fe_3O_4), in the sediments deposited in lakes, oceans, and continental eolian deposits. Cross-validated multiple-parameter magnetic measurements of such sediment cores provide global change data of high temporal resolution, useful for constructing a base-line record against which anthropogenic modifications may be discerned. Theories of superparamagnetism and magnetic domains are used to explain the physical basis of magnetic proxy recording. Examples of applications to validation of Milankovitch theory of climate change and delineation of the glacial and interglacial stages of the last 1 000 000 years are provided.

I. INTRODUCTION

Current interest in the possibility of rapid climatic changes in the future triggered by anthropogenic alterations in the global climate system has led geologists and geophysicists to delineate very long-term (1000–100 000 years) paleoclimate changes for establishing base-line records. Geological records of decadal to century-scale climate changes are "written" in long ice cores from the polar regions, rapidly deposited sediments from certain lakes, and offshore marine sediments, as well as in windblown (eolian) dust deposits on continental sites. Such records are usually "read" by determining changes in (a) elemental and isotopic chemistry of ice and sediment grains, (b) size, shape, and amount of eolian grains, and (c) the type and character of trapped pollen grains representing the different vegetations of the past. Careful synthesis of these multiple proxy records of climate change can yield paleorecords of humidity, temperature, wind direction, and wind intensity. Some of the above proxy records can and do provide quantitative data, but all of them consume a lot of time for data gathering. Compared to this, *magnetic proxies of climate change*, a newcomer to the field, can only be classified currently as semiquantitative or qualitative, and yet the magnetic methods are becoming increasingly popular because of their high speed and sensitivity.

Researchers in rock magnetism use all the instruments that are commonly used in fine particle magnetism research plus some others that are particularly useful for measuring the weak remanent magnetizations (RM) that remain in a sample after application of a steady (or dc) magnetic field, or an alternating magnetic field (af) or variable temperatures, either singly or in combinations thereof. For comprehensive discussions of remanent magnetizations we refer the reader to some recent publications.[1–3] Fuller[4] has recently reviewed rock magnetic instrumentation. When combined with steady fields on the order of 50–100 μT, the same af demagnetizer can impart anhysteretic remanent magnetizations (ARMs) to samples. Partial ARMs (PARMs) are given by activating the steady field for given af windows, and hence only to certain selected grain sizes in an ensemble.[5]

II. POPULAR ROCK MAGNETIC PARAMETERS FOR SAMPLE CHARACTERIZATION

In addition to a strong preference for studying RMs, the other special characteristic of rock magnetism is the need to study whole samples without always subjecting them to magnetic separation, since magnetic separation preferentially extracts the high-susceptibility (χ) grains that may or may not be the same as the high-coercivity (H_c) grains that give rise to lab-imparted or natural RMs. A large effort has, therefore, gone into the development of instruments and techniques that are sensitive enough for characterizing weakly magnetic whole sediments or rocks. Second, whether the intended application is to decipher climate change proxies or to determine the source of sediments in a stream, the rock magnetic parameters are chosen for their sensitivity to changes in concentration, composition, and grain size. For example, as humidity and temperature change from one climate regime to the other, the magnetic minerals undergo chemical and/or microstructural changes. We need to first recognize these subtle changes in the presence of a vast paramagnetic "noise," and then interpret them in terms of paleoenvironmental "signal."

A. Concentration-dependent parameters

Strongly magnetic (93 A m^2/kg) magnetite is usually the dominant magnetic mineral whose relative concentration (with depth, say) can be determined by measuring the variations in saturation magnetization J_s or low-field susceptibility χ, if the grains are only large multidomain (MD), say, above 10 μm and if no depth-dependent chemical change is present. If magnetite content falls below ten parts per million, as in organic-rich peat, saturation isothermal remanence (SIRM or J_{rs}) serves as a sensitive concentration-dependent

 0021-8979/94/75(10)/5823/6/$6.00 © 1994 American Institute of Physics

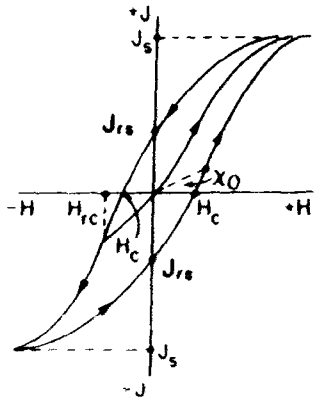

FIG. 1. A major (high-field) hysteresis loop (Ref. 1), showing saturation magnetization J_s, saturation isothermal remanent magnetization J_{rs}, coercivity of remanence H_{cr}, coercive force H_c, and low-field susceptibility χ_0.

parameter since the magnetite-free part of peat is paramagnetic or diamagnetic, unable to acquire remanence.

B. Composition-dependent parameters

The most intrinsic composition-dependent parameter is the Curie point, but it is frequently necessary to ascertain it from a mostly paramagnetic sample with a small (~0.1%) ferrimagnetic content, resulting in poor precision. Also, titanium (Ti^{4+}) ions can occur as a substitution for iron ions and lower the Curie point. Although calibration curves for titanium substitution are available,[1] in a totally "blind" situation a Curie point of 623 K could well signify the presence of pyrrhotite ($Fe_{1-x}S$), a titanomagnetite ($Fe_{3-x}Ti_xO_4$), a titanohematite ($Fe_{2-x}Ti_xO_3$), or a slightly cation-deficient titanomagnetite with appropriate titanium substitution.

X-ray diffraction or selected-area electron diffraction of the magnetic extract is usually attempted to confirm the composition, but, this too fails often due to low concentration or ultrafine grain size of the magnetic fraction. In such cases, Curie point data are combined with other composition-sensitive parameters, especially temperature dependence of magnetocrystalline anisotropy constant K or stepwise demagnetization of J_{rs} to determine H_{cr} (Fig. 1), the remanence coercivity, which is very different for magnetite and hematite.

Pyrrhotite, magnetite, and hematite all have characteristic temperatures for spin reorientation reflecting a change in sign of K.[1] Saturation isothermal remanent magnetization J_{rs} is given to pyrrhotite and magnetite at, say, 4.2 K in a field of 1.5 T and then the sample is warmed in the field-free space of a susceptometer to discover sharp drops in J_{rs} at the characteristic transition temperatures T_v, which are 34 and 120 K respectively, for pyrrhotite and magnetite. Hematite displays a T_v when room-temperature J_{rs} is cooled to 263 K.

For distinguishing magnetite from hematite at 300 K, the parameters S and HIRM (given below) have been defined[4,5] which take advantage of their large difference in H_{cr} (see Fig. 1 for H_{cr}),

$$S = -(\mathrm{IRM}_{-300\ \mathrm{mT}})/J_{rs},$$

$$\mathrm{HIRM} = (J_{rs} + \mathrm{IRM}_{-300\ \mathrm{mT}})/2.$$

The symbol $\mathrm{IRM}_{-300\ \mathrm{mT}}$ signifies the RM obtained by first saturating the sample in +1.5 T, and then applying −300 mT to demagnetize the magnetite component of J_{rs}. The remaining RM is due to the higher-coercivity hematite fraction, because while magnetite saturates at 300 mT, hematite requires 1000 mT or more. In the absence of hematite, $S=1$ whereas in the absence of magnetite HIRM=1.

C. Grain-size-dependent parameters

Although magnetic properties are not directly related to actual grain size, they do reflect the presence or absence of (i) magnetic relaxation phenomena and (ii) magnetic domains and their relative number in a sample. We list below the most popular parameters measured at room temperature by rock magnetists to find out where the mean or median value of a given size distribution occurs with respect to three critical size thresholds for magnetic transitions: (i) superparamagnetic (SP) to thermally stable d_1, (ii) single-domain (SD) to two-domain d_0, and (iii) pseudosingle-domain (PSD) to "true multidomain" (MD) transition d_m. Table I lists the threshold values for cubic magnetite determined by different authors either experimentally, or from theory of (i) *a priori* equilibrium domain states, or (ii) the more general nonequilibrium micromagnetic models.[2,15]

The notation d_{max} refers to the theoretical maximum size possible for SD state when the grain is only in a local energy minimum. For those interested in remanent magnetization, the pseudosingle-domain (PSD) range[16,17] of magnetite, 0.08 to ~10 μm, is a very useful empirical size window. PSD grains have RM values less than SD but their stability to alternating demagnetization and H_{cr} values is high like SD grains.

The critical volume V_p above which superparamagnetism (i.e., high χ but no RM) disappears was given by Bean and Livingston[18] as

$$V_p = 24kT \ln(f_0 t)/\mu_0 M_s H_c,$$

where k is Boltzmann's constant, attempt frequency $f_0 = 1 \times 10^{9}$ s^{-1}, t is measuring time, μ_0 is the free air permeability, M_s is saturation magnetization, and H_c is the microscopic coercive force. Lowering temperature T or mea-

TABLE I. Threshold values for cubic magnetite determined by different authors.

d_1 (μm)	d_0 (μm)	d_{max} (μm)	d_m (μm)
0.033 (range)[a]	0.05 (range)[a]	0.28 (all three)[a]	
0.025 (range)[b]	0.08 (three)[c]	0.11[d]	8.9 (three)
	0.12 (three)[b]	0.24[c]	
	0.10 (three)[c]	0.14[b]	

[a] From Ref. 8.
[b] From Ref. 9.
[c] From Refs. 10–12.
[d] From Ref. 13.
[e] From Ref. 14.
[f] From Ref. 11.
[g] From Ref. 12.
[h] From Ref. 15.

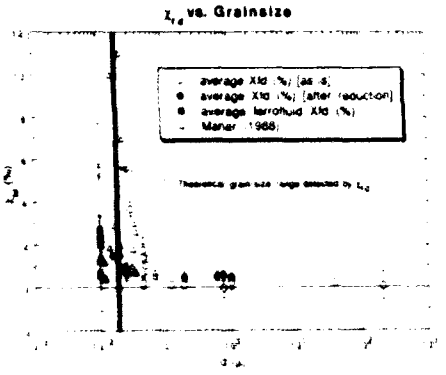

FIG. 2. Percentage change in χ when measured at 500 and 5000 Hz. It can only detect magnetite grains between 18 and 20 nm. Hollow circles denote cation-deficient magnetite.

surement time t leads to thermally stable SD behavior when RM becomes stable and low-field susceptibility χ is small. Therefore, a common technique at 300 K for detecting SP grains has been to measure the percentage decrease χ_{fd} in χ when measured at about 500 and 5000 Hz.[19] Thus, $\chi_{fd} = 100(\chi_{500} - \chi_{5000})/\chi_{500}$. It has been pointed out[20] that according to Neel's theory of magnetic relaxation χ_{fd} above reflects grains between 18 and 20 nm only, not all the SP grains at 300 K for magnetite, $(\sim 30$ nm. Hunt, Kletetschka, and Sun[21] have now shown (Fig. 2) that experimental data on χ_{fd} of synthetic magnetite confirms the above statement and a different approach (Fig. 6 below) is necessary to determine the complete SP fraction in a sample.

Next, we discuss the detection of grains larger than SP, i.e., SD, PSD, and MD. The most frequently used method[22] for relative grain-size determination for thermally stable grains is to plot hysteresis parameters J_{rs}/J_s vs H_{cr}/H_c [Fig. 3(a)], after cycling a magnetite bearing sample in a large saturating field, say, 900 mT. Uniaxial single-domain grains, in the absence of grain interactions, should display $J_{rs}/J_s = 0.5$ and $H_{cr}/H_c = 1.5$, while the largest or "true" multidomain samples have J_{rs}/J_s values < 0.10 and $H_{cr}/H_c < 3.5$. As seen in Fig. 3(a), there is no sharp transition in the magnetic parameters above the classical single-domain–to–two-domain threshold d_{sd}. Instead, there is a smooth transition spanning the pseudosingle-domain region, 0.1–10 μm. A major deficiency of Fig. 3(a) is that it cannot distinguish between (i) a mixture of sizes, say, 0.5 and 40 μm, and (ii) a homogeneous sample of 10 μm. Jackson, Worm, and Banerjee[23] find that Fourier analysis of the hysteresis loop can, however, accomplish that goal.

Figure 3(b) shows that ARM intensity J_{arm} vs χ data for magnetite[24] are useful for distinguishing grainsizes below 20 μm, which is the threshold for easy observation on an optical microscope. The slope J_{arm}/χ increases rapidly between 1.0 and 0.1 μm (near the SD threshold), and the apparent slight increase in χ is an artifact of unavoidable admixtures of SP grains in the experimental samples of small median size. Experimental data of J_{rs} and H_{cr} have also been used by Thompson and Oldfield[7] to construct Fig. 4, to identify the different magnetic domain states of magnetite, as well as to indicate the presence of hematite in a given mixture through its unusually high coercivity of remanence ($H_{cr} > 200$–300 μT).

III. MAGNETIC RECORDS OF PAST CLIMATE CHANGE

The most reliable magnetic proxies of climate change have come from concentration variation of magnetite in ma-

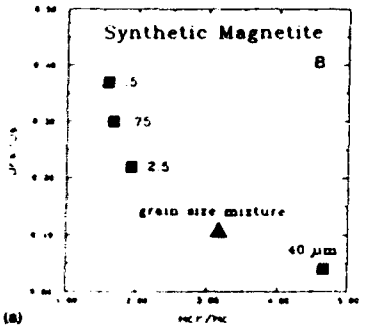

FIG. 3. (a) Jackson and co-workers' demonstration (Ref. 23) that mixtures of 0.5 and 40 mm grain appear like ~10 μm if characterized by J_{rs}/J_s vs H_{cr}/H_c plots. (b) King *et al.*'s calibration curve (Ref. 24) for magnetic grainsizes using ARM intensity J_{arm} and χ parameters. High slope denotes finer grain size.

rine sediments. Such magnetite owes its origin[7] to (i) distant volcanic eruptions and forest fires, or (ii) ice-rafted detritus during warm interglacial times, or (iii) monsoon winds blowing over arid land. Prior to our discovery of the magnetic proxies, much effort was spent in testing geologically the so-called Milankovitch theory of ice ages. This theory claims that variations in the (i) eccentricity of the Earth's orbit around the Sun, (ii) the obliquity or tilt of the Earth's rotation axis, and (iii) the precessional motion of the Earth's poles—all three contribute to variations in insolation from the Sun, and cause periodic cold glacial and warm interglacial times.[25] We discuss here three situations where the availability of high-precision and high-resolution magnetic susceptibility data have confirmed many details of the Milankovitch theory.

First, Blomendahl *et al.* have studied χ versus depth obtained from four widely separated cores of ocean sediments in the eastern Atlantic, next to west Africa.[26] They have shown that χ profiles correlate very well with variations in the glacial ice sheets that carry magnetite-bearing rock debris to lower latitudes during warmer times. Second, they have observed similar records of changes in wind-borne magnetite

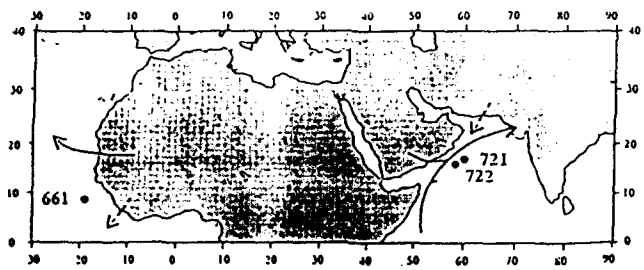

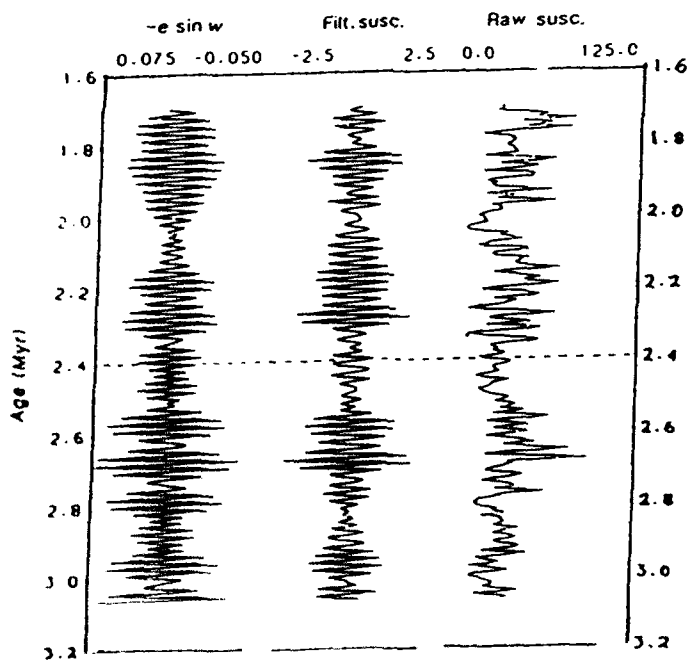

FIG. 4. Kukla *et al.*'s demonstration (Ref. 28) that oceanic temperatures (glacial/interglacial) from $\delta^{18}O$ data are reflected in the χ logs from two sites in central China. The arrows at the bottom of all profiles represent 730 000 years. Glacial/interglacial stages (even/odd) shown on the right-hand side.

in the Arabian sea as a proxy of changes in the intensity of paleomonsoons off the Arabian coast.[27]

Finally, we owe to magnetism our first attempts at a high-resolution comparison of oceanic and continental climates. Most of the reliable proxy data for global climate change over the last 1 000 000 years have come from the variations in oxygen isotopes ($\delta^{18}O$, which measures departures from a standard ratio of $^{18}O/^{16}O$) preserved in the $CaCO_3$ shells of fossil foraminifera in ocean sediments. Such globally averaged (or SPECMAP) $\delta^{18}O$ on the right-hand side of Fig. 4 was shown by Kukla *et al.*[28] to compare well in character with the χ versus depth data from Xifeng and Luochuan in the central Chinese loess plateau. It was claimed that during glacial times, strong winds from the desert bring nonmagnetic silicates which dilute the concentration of the worldwide "rain" of magnetite caused by volcanic eruptions and forest fires. Hence, Kukla *et al.* concluded that low temperatures in central China (low χ) have varied in phase with low temperatures recorded by the ocean sediments (high $\delta^{18}O$).

Hovan *et al.*[29] have now shown that the $\delta^{18}O$ record from a sediment core in the northwest Pacific follows the accepted globally averaged (SPECMAP) ice volume record. They then show that the eolian flux of separated sand grains in their core show signs of strong aridity and high wind speed (i.e., greater flux) during the colder glacial times (positive $\delta^{18}O$ values).

However, their correlations are only approximate, because when the Xifeng magnetic record is independently dated by the presence of a known geomagnetic polarity reversal, it does not match exactly the eolian flux record. Thus, the locations of interglacial S layers had to be "corrected" downward in order to match the oceanic climate record in eolian flux. I now believe that the lack of an exact fit is due to an incorrect model for χ variation, but this attempt by Hovan *et al.* was an important first step toward establishing a direct correlation between continental and oceanic climate records.

Maher and Thompson's work[30] shows that the problem above owes its origin, at least partly, to two sources of magnetite in the high susceptibility S layers. One source is indeed magnetite brought from elsewhere. The other is fine-grained superparamagnetic (SP) magnetite produced *in situ* by pedogenic alteration (soil forming) of paramagnetic silicate due to high humidity and temperature during summer monsoons. The magnetic proxy record thus contains both the global climate record and its regional modification. We have now developed a method[20] to estimate the total SP fraction from each horizon and contrasted this fraction for two nearby sites in China, Baicaoyuan and Xifeng, separated by Liupanshaan, a mountain range which causes a rain shadow in the arid site, Baicaoyuan.

Our method depends on warming a high-field (2.5 T) low-temperature (15 K) J_{rs} in zero field to separate the temperature-dependent loss of remanence by all grains that are SP at 300 K from the remanence carried by coarse-grained magnetite, distinguished by their sharp Verwey transition at ~120 K. Figure 5 shows the comparison of a glacial loess (L_{1a}) and its overlying interglacial soil (S_0) with a synthetic mixture of 50:50 SP and MD magnetite. Graphical methods of extrapolation of SP remanence to 15 K allow the estimation of the SP contribution which is then divided by the total J_{rs} at 15 K to obtain SP/total fractions shown in Fig. 6(a). This fraction, and not low-field χ, more accurately represents past changes in summer monsoon intensity.

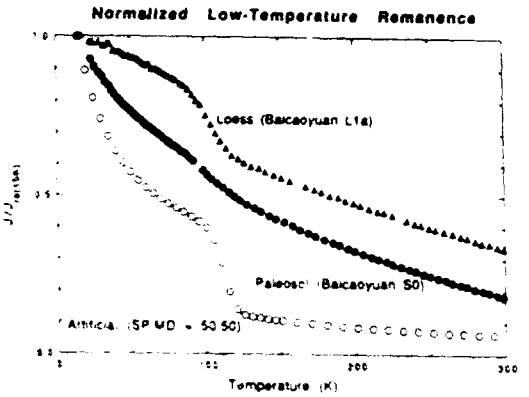

FIG. 5. Warming of 2.5 T J_{rs} (15 K) in zero field shows different characters for loess (less SP grains) and overlying soil (more SP) from Baicaoyuan. The temperature-dependent SP remanence is extrapolated to 15 K to obtain relative fraction, SP/total.

Our data show that during the coldest glacial periods, L_2 and L_{1c}, both sites show the expected minima in SP fraction, but, the more humid site, Xifeng, has a consistently higher fraction of SP grains due to greater local pedogenesis. The difference between the two profiles (arid Baicaoyuan, humid Xifeng) thus allows us to observe the regional variations in the impact of global climate changes. Even an unexpected observation, that during S_0 time (5–10 ka before present) both sites had similar pedogenesis has been confirmed independently. Figure 6(b) shows the bulk grain-size variation of whole sediments (magnetic and non-magnetic) of the S_0 horizons of the two sites. Both the magnetic and bulk grain-size data say that pedogenesis was the same during S_0 time. One possible interpretation is that at this time the summer monsoon came from South China Sea, parallel to the mountain range, thus removing the rain shadow. Future detailed work at these and other sites in the Chinese loess plateau are ongoing, both at our laboratory and elsewhere. The goal is to separate true global climate change signatures from the regional ones for Asia, so that we can finally attempt a valid comparison between global oceanic and continental climates and verify the validity of the current numerical paleoclimate models for predicting past temperatures for the whole Earth.

ACKNOWLEDGMENTS

This study was supported by NSF Grant No. EAR 9206024. The Institute for Rock Magnetism is funded by the Keck Foundation, the National Science Foundation, and the University of Minnesota. I thank Diana Jensen and Michelle

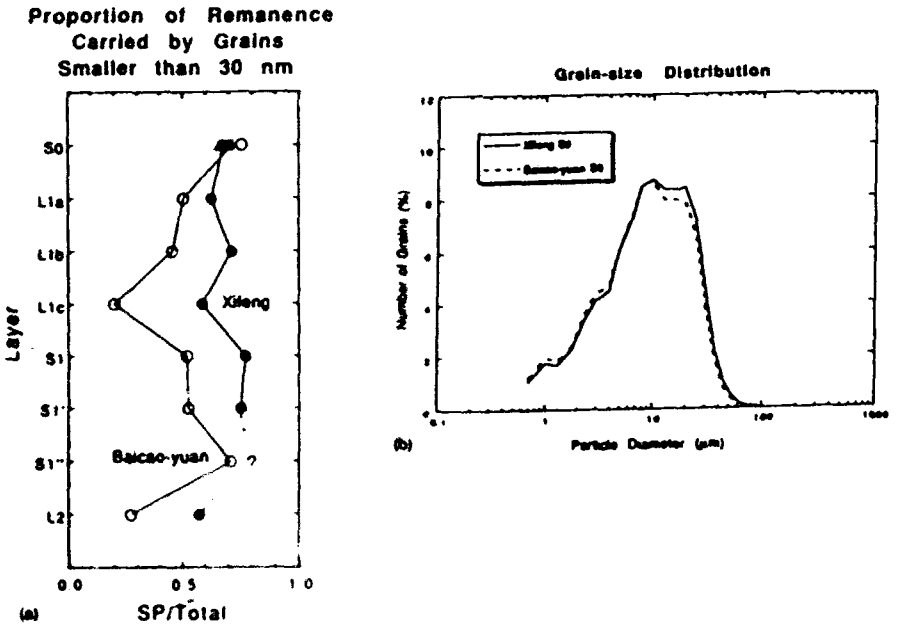

FIG. 6. (a) Left-hand side: variation of SP/total, i.e., summer monsoon intensity between arid Baicaoyuan and humid Xifeng (Ref. 20). The high rainfall at Xifeng produces high SP content. The difference between the two provides regional climate information. (b) Right-hand side: during formation of layer S, (9000–10 000 years ago) both sites enjoyed similar humidity to produce a similar amount of coarse and fine grains, as shown in the bulk grain-size variation. It would be possible if the summer monsoon was there from the south, rather than east.

Elston for help in preparing the manuscript. This is publication no. 9310 of the Institute for Rock Magnetism.

[1] C. P. Hunt, B. M. Moskowitz, and S. K. Banerjee, in *Handbook of Physical Constants*, edited by T. Ahrens (American Geophysical Union, Washington, D.C., in press).
[2] D. J. Dunlop, Rep. Prog. Phys. 53, 707 (1990).
[3] S. K. Banerjee, in *Geomagnetism*, edited by J. A. Jacobs (Academic, San Diego, 1989), Vol. 3, p. 1.
[4] M. D. Fuller, in *Methods of Experimental Physics*, 24A edited by C. G. Sammis and T. L. Henyey (Academic, Orlando, 1987), Vol. 24A, p. 101.
[5] M. J. Jackson, W. Gruber, J. Marvin, and S. K. Banerjee, Geophys. Res. Lett. 15, 440 (1988).
[6] R. Thompson and F. Oldfield, *Environmental Magnetism* (Allen and Unwin, London, 1986), p. 229.
[7] J. W. King and J. E. T. Channell, Rev. Geophys. 29 Suppl. 358 (1991).
[8] D. J. Dunlop, J. Geophys. Res. 78, 1780 (1973).
[9] D. J. Dunlop and M.-M. Blais, Geophys. J. R. Astron. Soc. 51, 121 (1977).
[10] B. M. Moskowitz and S. K. Banerjee, IEEE Trans. Magn. MAG-15, 1241 (1979).
[11] T. S. Moon and R. T. Merrill, Phys. Earth Planet. Inter. 37, 214 (1985).
[12] R. J. Enkin and D. J. Dunlop, J. Geophys. Res. 92, 12726 (1987).
[13] F. Heider and W. Williams, Geophys. Res. Lett. 15, 184 (1988).
[14] W. Williams and D. J. Dunlop, Nature 337, 634 (1989).
[15] V. P. Shcherbakov and B. E. Lamash, Geophys. Res. Lett. 15, 526 (1988).
[16] S. K. Banerjee, J. Geomagn. Geoelectr. 29, 319 (1977).
[17] D. J. Dunlop, J. Geomagn. Geoelectr. 29, 293 (1977).
[18] C. P. Bean and J. D. Livingston, J. Appl. Phys. 30, 120 (1959).
[19] F. Heller, X. M. Liu, T. S. Liu, and T. C. Xu, Earth Planet. Sci. Lett. 103, 301 (1991).
[20] S. K. Banerjee, C. P. Hunt, and X. M. Liu, Geophys. Res. Lett. 20, 843 (1993).
[21] C. P. Hunt, G. Kletetschka, and W. W. Sun (unpublished).
[22] R. Day, J. Geomagn. Geoelectr. 29, 233 (1977).
[23] M. J. Jackson, H. U. Worm, and S. K. Banerjee, Phys. Earth Planet. Inter. 65, 78 (1990).
[24] J. King, S. K. Banerjee, J. Marvin, and O. Özdemir, Earth Planet. Sci. Lett. 59, 404 (1982).
[25] J. Imbrie, in *Milankovitch and Climate: Understanding the response to Orbital forcing, Part 1*, edited by A. Berger, J. Imbrie, J. Hays, G. Kukla, and B. Saltzman (Reidel, Dordrecht, 1984), p. 269.
[26] J. Blomendal, B. Lamb, and J. King, Paleoceanography 3, 61 (1988).
[27] J. Blomendal and P. deMenocal, Nature 342, 897 (1989).
[28] G. Kukla, F. Heller, X. M. Liu, T. C. Xu, T. S. Liu, and Z. S. An, Geology 16, 811 (1988).
[29] S. A. Hovan, D. K. Rea, N. G. Pisias, and N. J. Shackleton, Nature 340, 296 (1989).
[30] B. A. Maher and R. Thompson, Geology 19, 3 (1991).

Collection, measurement, and analysis of airborne magnetic particulates from pollution in the environment (invited)

Philip J. Flanders
Department of Physics, University of Pennsylvania, Philadelphia, Pennsylvania 19104-6396

Magnetic particulates in the environment, collected from surfaces and directly from the atmosphere, are reported. A significant percentage of magnetic material in many air-borne samples consists of spherical magnetite from coal-burning utilities and from iron/steel manufacturing with particle diameters 2–10 μm which correspond to average coercive fields of ~100 Oe and remanence to saturation ratios of ~0.1. The amount of air-borne magnetic material that settles to the ground varies inversely with distance from its source.

I. INTRODUCTION

A common component of respirable magnetic particulates is magnetite, produced during the formation of dust compounds or by oxidation of Fe-containing dust (e.g., coal ash and particulates from iron/steel making[1]). A study which characterized the emissions from external combustion for electric power generation noted that adequate size distribution data for flue gas emissions of particulates is still lacking for bituminous coal-fired, lignite-fired, and residual oil-fired utility boilers.[2] Control of toxic emissions requires improved information about the spread and settling of air-borne particulates, since most heavy metals are found condensed on particles rather than present as vapor.[3] Particles from the iron/steel industry or coal combustion are relatively more hazardous than soil-derived particles.[4] In Utah County, deaths rose in proportion to air-borne particles less than 10 μm in size; a particle concentration of 100 μg/cm^3 increased the death rate by 16%.[5] There is little direct information about the expected rates of removal of atmospheric particulates as the result of deposition on trees, buildings, or other objects on the Earth's surface.[6]

This study examines the sources and transport of air-borne magnetic material, and describes methods to collect and measure magnetization of particulates found on plants, buildings, and other surfaces; in trains, upholstery, spider webs, beach sand, asbestos, volcanic ash, weld spatter, stack effluent from iron/steel mills, and from coal-burning utilities. Samples were collected by volunteers from a wide variety of locations in several countries.

II. SAMPLE COLLECTION

A. Wiping with tissues

Sufficient magnetic material for measuring magnetization, hysteresis loops, particle size and shape, and changes in magnetization with temperature can be obtained by wiping a smooth outdoor surface such as a tree trunk or wooden siding with a moist tissue of the kind called a towlette, which are sometimes distributed with airline meals. We have standardized a procedure by which particles are acquired from an area of about 1000 cm^2 using both sides of a moist tissue. The tissue is then placed in a beaker of water and agitated or stirred. Magnetic particles collect above a small permanent magnet placed under the bottom surface of the beaker. Most of the water, tissue fragments, and nonmagnetic particles are decanted, and the magnetic particles are transferred to a thin-walled plastic box. They follow a magnet moved beneath the surface of the box, and become concentrated into a circular compact about ~30 μm thick. If all the collected material has the same magnetization, the total moment of the collected sample is proportional to the circular area of the compact. In this way an approximate value of the total magnetic moment per unit area deposited on the original surface can be obtained without making any direct magnetic measurements on the sample. If similar surfaces (i.e., the same species of tree) can be found at varying distances from a source of particulates, the density of deposited magnetic particulates can be measured as a function of distance from the source.

B. Gummy surfaces and permanent magnets

To collect magnetic particulates directly from the atmosphere rather than from coated surfaces, we have used sticky tape, a cover glass coated with a gummy layer, or a permanent magnet. A magnet increases collection rates by a factor of ~25. The magnet is covered with a layer of weighing paper so that the magnetic particles can be easily removed. A magnet can also be used to remove particulates from sand, upholstery fiber, wooden tables, and benches, and many other sources that are too rough or porous for the moist tissues.

Magnetic material collects on permanent magnet disks at rates generally in the range of 5–100 μemu/cm^2/day, or on nonmagnetic sticky tape or grease-covered slides at rates of 0.2–4 μemu/cm^2/day. The higher depositions rates are often found near local iron/steel manufacturing or coal-burning power generation sites.

If appropriate natural or man-made surfaces are available, wiping with a moist tissue is a much more efficient way to collect samples than the use of magnets or sticky surfaces. The total magnetic moment of a sample collected by wiping 1000 cm^2 of a smoooth tree trunk would take 200 days to collect on a 1 cm^2 magnet, or 5000 days on a 1 cm^2 sticky surface (in the same location).

III. PARTICLE HANDLING AND EXAMINATION

When the samples are dry, magnetic particles can be at least partially separated from nonmagnetic material (if necessary) using a paper-covered permanent magnet. However, small magnetic particles collected or handled with a perma-

 0021-8979/94/75(10)/5931/6/$6.00 © 1994 American Institute of Physics

nent magnet become magnetized, and form into chains and clumps. To resolve individual particles in a micrograph, the clumps must be dispersed while maintaining a relatively high concentration of particles. One method is to transfer particles to a small sheet or foil by brushing it across the surface of the magnetic compact.

To study size and shape distributions of particles collected from various structures, magnetic material is concentrated onto a small flat surface. Magnification of at least 500× is required to resolve 1 μm spheres. When the particles are clumped, have broad size distributions, or lie in different planes, a scanning electron microscope (SEM) gives better resolution and greater depth of field than an optical microscope. An SEM equipped with an x-ray analytical apparatus also permits chemical analysis of the particles.

IV. MAGNETIC MEASUREMENTS

A high-sensitivity magnetometer is required to measure the magnetization of typical samples, such as 2–500 mg of diamagnetic leaf or bark material containing low concentrations of magnetic materials, 20 μm magnetite spheres from coal or oil combustion and iron/steel manufacturing, or fibers from spider webs and house dust. An alternating-gradient force magnetometer (AGFM)[7-9] with sensitivity of 10^{-8} emu/Hz$^{1/2}$ was chosen in preference to a superconducting quantum interference device (SQUID) because the AGFM is much faster (magnetic moment versus field curves in 30 s, moment at constant field from 77 to 300 K in 10 min), and can measure a moment up to the Curie temperature of magnetite, 574 °C.

V. PURE MAGNETITE

Since air-borne magnetic particles are often magnetite, it is useful to know how the structure-sensitive properties of pure magnetite depend on particle size and temperature. We prepared a series of Fe_3O_4 particles with progressively smaller size ranges by successive grinding of 0.5–1 mm natural grains (H_c=2–6 Oe) between etched microscope slides. The resultant coercive fields span two orders of magnitude. Low-temperature measurements permitted the preparation of plots of H_c (77 K)/H_c (300 K) vs H_c (300 K) [Fig. 1(a)]; these show a tenfold increase in H_c at 77 K for particles with the smallest H_c.

For the lower coercive field magnetite there is a large abrupt decrease in remanence M_r (W) near 120 K when warming from 77 K [Fig. 1(b)]. We express this change in M_r by the quantity δ, where

$$\delta=[M_r(77\ \text{K})-M_r(e)]/M_r(77\ \text{K}), \qquad (1)$$

$M_r(e)$ is found by extrapolating back to 77 K the remanence versus temperature measured on warming above the transition. A plot of δ vs H_c [Fig. 1(c)] shows a difference in low-temperature remanence behavior for magnetite with H_c above or below ~300 Oe.

VI. SOURCES OF AIR-BORNE PARTICULATES

The magnetic moment of most unburned fossil fuel is small, equivalent to ~10 ppm Fe_3O_4 by weight. Although fossil fuel is basically nonmagnetic, some produces magnetite when burned.[10] The magnetization of ash resulting from the burning of many fossil fuels and other combustible materials is equivalent to 500–10 000 ppm Fe_3O_4.

The magnetization of coal ash is much higher, ~160 000 ppm Fe_3O_4, due primarily to oxidation of iron in the FeS_2 (pyrite) component of coal. Low-sulfur coal is comparatively rare; ordinary bituminous coal has a sulfur content of 1.0%–4.5%. When FeS_2 is heated to ~1350 K in the absence of air it dissociates to form pyrrhotite (FeS) and sulfur gas. At higher temperatures, FeS decomposes into sulfur and iron. In

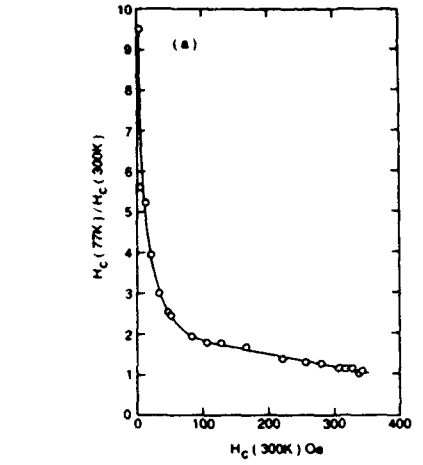

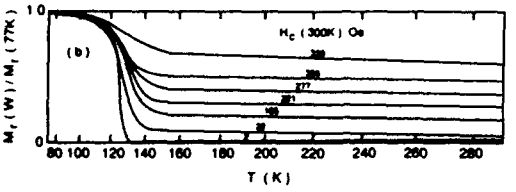

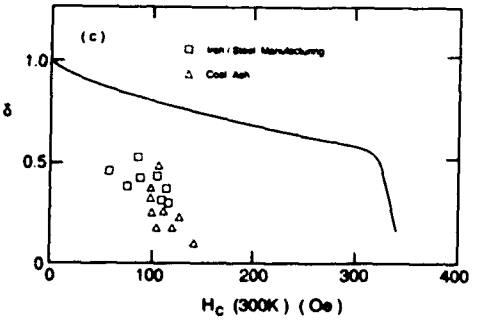

FIG. 1. (a) H_c (77 K)/H_c (300 K) vs H_c (300 K); (b) M_r (W)/M_r (77 K) vs T as a function of H_c (300 K); and (c) δ vs H_c (300 K). All for crushed natural Fe_3O_4, with data for particles from coal-burning and iron/steel manufacturing included in (c).

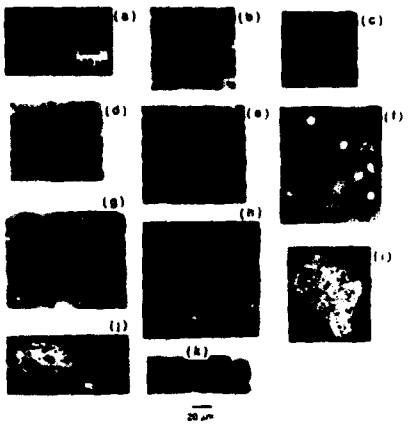

FIG. 2. Particulates collected from (a) bottom ash of a coal-burning steam plant; (b) stack fly ash from burning pulverized coal; (c) stack fly ash from burning no. 6 oil; (d) tree trunk 0.8 km from a coal-burning power plant; (e) a tree trunk 0.2 km from iron and steel manufacturing; (f) a welded angle iron; (g) an angle iron cut with a torch; (h) the water bath of a spark erosion apparatus; (i) an upholstered seat in a Southern Region British Rail train; (j) an upholstered seat in a London Underground train; (k) volcanic ash. Samples (a), (b), (c), (h), (i), (j), and (k) were collected using a paper-covered permanent magnet; samples (d), (e), (f), and (g) were collected by wiping with a moist tissue. Sample (a) uses 200 μm bar and (b)–(k) use 20 μm bar.

this process spherical particles of iron are formed and subsequently oxidized to magnetite (Fe_3O_4) [Figs. 2(a), 2(b), and 2(d)]. For every weight percent sulfur in coal there is approximately 7% of pyrite-originated iron oxide in the ash.[11] If coal-burning power plants in the U.S. were spread uniformly across the country, and one percent of the fly ash became air borne and settled to the ground, magnetization would accumulate at a rate of ~ 0.7 μemu/cm^2/day. This is in the range of measured values in many nonindustrial areas. Fly ash from oil combustion [Fig. 2(c)] contains less iron than ash from coal combustion.[12] Relatively large magnetic spheres, up to 200 μm, were found in this work in upholstery on oil-burning ferries, and on the ground and rooftops near oil-fired utilities.

X-ray-diffraction analysis shows that the crystalline portion of magnetic fly ash from coal combustion is composed primarily of magnetite.[13] The magnetite particles are spherical, with a characteristic "orange-peel" surface when viewed under the microscope.

The ferrous metallurgical industry contributes to particulate pollution of the atmosphere in a number of operations.[14] Levels of lung contamination are highest among blast furnace workers. Magnetic dust pollution from iron/steel mills is reported to vary with distance from a mill,[15] and much of the dust is spherical magnetite[16] [Fig. 2(e)].

VII. MEASUREMENTS

Dispersion patterns for dust from coal-burning utilities or from iron/steel manufacturing have been found by measuring magnetization as a function of distance from these sources. The magnetization M is generally found from the diameter of compacts collected by standardized wiping of an area A of relatively smooth tree trunk bark, as described above. To a first approximation, M/A from coal-burning utilities or from iron/steel manufacturing varies inversely with the distance X from the source:

$$M/A = C/X. \tag{2}$$

The constant C ranges from ~ 20 to 200 μemu km/cm^2, depending on source capacity and particulate emission controls. In samples from a localized source, the particle concentration is generally higher in the direction of the prevailing winds.

A high percentage of magnetic particles in many areas is spherical, regardless of magnetization level. Energy-dispersive x-ray analyses in the SEM show that the particles consist mainly of Fe and O. These spherical particles have been found in seven U.S. states ranging from industrial areas in Pennsylvania and New Jersey to rural areas in these states and in Maine and Vermont. As an example, a high percentage of spheres was found in central Philadelphia, where M/A ~ 20 μemu/cm^2, and also 55 km southeast downwind of Philadelphia in the rural pinelands at Batsto, NJ, where M/A ~ 1 μemu/cm^2. A smaller percentage of spherical magnetic particulates was found on the west coast in Seattle, WA (M/A ~ 10 μemu/cm^2), where there is less coal burning. There are almost no spherical particles 75 km to the west and upwind of Seattle in the Hoh Rain Forest of the Olympic National Park (M/A ~ 0.4 μemu/cm^2). Magnetic spheres were almost nonexistent in Israel (M/A ~ 0.3 μemu/cm^2), where there is minimal coal combustion or iron/steel industry.

When only a portion of the magnetic content in a sample is pure Fe_3O_4, δ falls below the curve in Fig. 1(c). Having measured the coercivity for each sample, the average value of δ for a collection of particles from iron/steel manufacturing is 0.4, and from coal-burning utilities is 0.25. The simplest interpretation of these results is that the collected particles are $\sim 40\%$ and 25% pure magnetite, respectively.

On this interpretation, measured values of δ indicate that the composition of magnetic particles from a single source can range from 0% to 100% pure Fe_3O_4.

Spherical iron oxide particles also come from weld spatter,[17] torch cutting, and from iron machined by spark erosion[18] [Figs. 2(f)–2(h)]. Large quantities of magnetic dust are found in the lungs of welders.[19]

Over 10^5 tons of extraterrestrial black metallic spheres, 10–80 μm in size, are reported to reach the Earth each year.[17] Micrometeorites are collected from deep-sea sediments, remote Arctic ice cores, high-altitude balloons, rockets, and manned Earth-orbiting satellites.[20] Even if these particles have the magnetic moment of magnetite and are distributed uniformly over the earth, magnetization would accumulate at a rate of $\sim 10^{-2}$ μemu/cm^2/day, several orders of magnitude below the lowest levels we have measured.

Flakelike magnetic particles given off by the braking system of rail vehicles are present in high concentrations in older coaches on Southern Region British Rail trains [Fig.

2(i)]. On these vehicles, cast-iron brake blocks are applied to steel train wheels using clasp-type actuators worked by compressed air. Similar dust found throughout the London Underground in large quantities is commonly referred to as "tunnel dust." The magnetic metal wear portion of the dust is generated primarily by erosion of wheels and rails [Fig. 2(j)]. This material is not spherical and is generally not magnetite. Its magnetic properties have not yet been extensively measured.

Iron occurs in volcanic ash as soluble salts, coatings of oxides and sulfides, as a constituent of glass, and in mineral phases.[21] 16% of ash particles collected from Mount St. Helens after its volcanic eruption contain some magnetic material, but they are not spherical [Fig. 2(k)].

Magnetite found imbedded in raw asbestos and in asbestos products has low coercive field. Low-temperature measurements on this material show a decrease in remanence of up to 90% when warming through 120 K, indicating that it is primarily slowly grown Fe_3O_4.

Micrographs of magnetic material removed from tail pipes of diesel and gasoline vehicles include only a few spherical particles.

VIII. DEPOSITION OF PARTICLES ON SURFACES

At the lower boundary of the atmosphere, particles may be removed permanently from the air by deposition on objects. Deposition may take place by one of three mechanisms: sedimentation, diffusion, or impaction.[22]

A. Plants

To check whether magnetization of plants is confined to their surfaces, we have examined cross sections of twigs and found the magnetization of the core to be almost two orders of magnitude below that of the surface. Magnetization on the surface of a twig is higher at leaf and bud scars than in clear areas. A scarred region is rough and at some stage gummy, enabling it to retain more airborne particulates.

Since magnetic material in plants is found mainly on the surface, we express magnetization of leaves and bark per unit area rather than per unit mass. Measured magnetization levels within a geographic region depend on the type of plant surface, its age, and its surface characteristics, as well as on local emission levels and distance from an emission source. Relative magnitudes of surface magnetization for green leaves, brown leaves, twig bark, and trunk bark are ~1, 2.5, 50, and 200, respectively (Fig. 3). These relative magnitudes are approximately the same at all locations studied.

An explanation for the difference in magnetization level for adjacent brown and green portions of a single leaf is that the brown surface is rougher, and covered with fungi which accumulate during senescence. Fungi collect air-borne particulates in the same way as a filter in an air-handling system.[23] Magnetization of leaves covered with a thick layer of fungi [Figs. 4(a) and 4(b)] shows a geographic distribution similar to that of fungus-free green leaves, but is an order of magnitude greater (Fig. 3). Fungi that grow on rotting logs [Fig. 4(c)] are often mechanically self-supporting and due to relatively long exposure times, the magnetization is an order of magnitude greater than for thick fungi on leaves (Fig. 3).

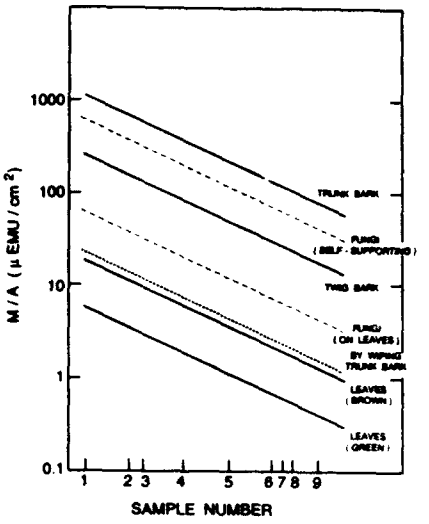

FIG. 3. Surface magnetization of bark, leaves, and fungi from nine different locations.

High-temperature measurements have been made on magnetic particles extracted from twigs. They show the Curie temperature of magnetite, 574 °C.

On average, the amount of material acquired by wiping smooth trunk bark is equivalent to a 5 day accumulation on a gummy surface exposed at the same site. This is much lower than the accumulation on thick or gummy bark, which incorporates particles into its structure.

B. Man-made structures

Up to five times as much magnetic dust is collected by wiping exposed house siding as by wiping smooth tree trunks. If the siding is protected from rain by an overhead structure, the magnetization levels are about five times higher than if the siding is exposed to the weather. These observations suggest that outdoor surfaces tend to reach an equilibrium concentration of magnetic particles, with old particles being washed away as new ones arrive.

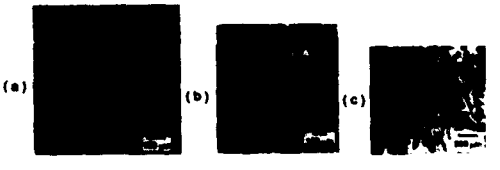

FIG. 4. (a) Powdery mildew (Microphaera alni) on a sycamore leaf, $M/A = 150$ μemu/cm^2; (b) mildew on a lilac leaf, $M/A = 75$ μemu/cm^2; and (c) Coriolus versicolor, $M/A = 1400$ μemu/cm^2.

C. Other structures

House dust and spider webs are highly efficient collectors of magnetic particles. Magnetic particulates are distributed throughout house dust (dust balls found under furniture). Magnetization per unit mass of dust at a given location is relatively independent of the size of the dust ball, implying that magnetic and nonmagnetic components of dust accumulate together. Spider webs have similar values of moment per unit mass: generally 2×10^4 and 2×10^5 μemu/g, although many spider webs have an average life of only 1 day. From measurements of magnetization and of particle diameter based on values of H_c, house dust and spider webs in some locations contain between 10^6 and 10^7 magnetic particles per gram.

Upholstery fiber is an effective medium for collecting particles, which can be easily removed with a paper-covered magnet. In a London Underground train, as much as 300 mg of magnetic dust can be removed in less than 1 min from a 1000 cm^2 area of a seat covered with closely woven fabric (~1 mm nap), using a 1-in.-diam permanent magnet disk. Similar amounts have been removed from seats in Southern Region British Rail trains.

D. Road dust

Magnetization deposited near the edge of a road has been measured by collecting particles on sticky tape wound circumferentially on a pole or tree. These particles are primarily nonspherical road dust, some of which comes from rust and attrition of vehicles, pipes, and other iron/steel surfaces. Accumulation rates are approximately eight times higher on the tape surface facing oncoming traffic, since road dust appears to be carried along in the wakes of moving vehicles. Rates at the edge of a roadway vary with elevation E in meters above ground level as

$$M_{\text{avg4}}/At = kE^{-1.5}, \tag{3}$$

where M_{avg4} is the magnetization averaged over four directions (N,S,E,W); k is as large as 100 μemu m$^{1.5}$/cm^2 day for heavy traffic. At distances of 100 m or more from many roadways, accumulations are much lower and there is no significant dependence on direction or elevation.

IX. COERCIVE FIELD OF PARTICULATES

Discounting road dust, magnetic particles from the environment fall into two general categories. A lower coercive field material found in asbestos, peat moss, soil, and some sand is slowly grown, unstrained Fe_3O_4 with relatively large particle size, not as readily transported through the air because of its size. Higher coercive field particles in the second class are small enough to be air borne and behave like crushed magnetite. They are primarily rapidly cooled, oxidized iron spheres from power-plant coal and oil combustion, and from iron/steel manufacturing. Locations at which these air-borne magnetic spheres are found span the globe (Fig. 5).

Heider, Dunlop, and Sugiura[24] found a relationship between particle diameter d and coercive field in magnetite.

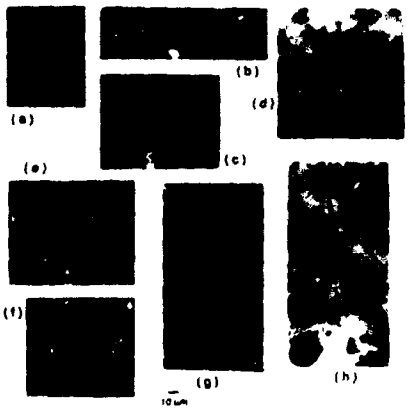

FIG. 5. Magnetic particles removed by wiping relatively smooth trunk bark with a tissue in (a),(b) England; (c) France; (d) Japan; (e) Czechoslovakia; (f) the Netherlands, and (g),(h) the U.S.

The relationship is different for crushed and for slowly grown magnetite. For crushed Fe_3O_4, d is related to H_c (Oe) by the expression

$$d\ (\mu\text{m}) = (H_c/C)^{-2.3}, \tag{4}$$

where C is 171 Oe μm$^{1/2.3}$.

Using Eq. (4) and experimental values of H_c, particle diameters for small diameter, high H_c spheres collected from the atmosphere are calculated to extend from ~2 μm (H_c=127 Oe) to ~10 μm (H_c=64 Oe), similar to the sizes we observe in micrographs [Figs. 2(a)–2(e) and Fig. 5].

Based on H_c, the average diameter of particles on trunk bark [Eq. (4)] is ~50% greater than on green leaves; particles removed from bark by wiping with tissues are more than twice the average diameter of the high percentage which remain imbedded.

When magnetic samples are measured as a function of distance from a coal-burning utility plant or from iron/steel manufacturing, we find a gradual reduction in H_c as well as the decrease in M/A described earlier. One reason for this behavior in H_c could be a background of lower coercive field magnetite from the soil which makes a relatively larger contribution at greater distances from the source. A reduction in H_c could also be due to an increase in particle size at greater distances from the source, although it would seem that larger particles should settle from the atmosphere faster and so be concentrated near the source. Using Eq. (4), the average particle diameter would have to double as the distance from the source increased by an order of magnitude in order to account for the decrease in H_c. It has been suggested that in the particle size range between 1 and 10 μm, the smaller particles which normally settle more slowly are removed from the lowest atmospheric layer by impaction on trees and buildings while those as large as 10 μm are kept air borne for extended time by turbulent diffusion.[21] Since there is a broad

distribution in particle size in virtually all our samples, it is difficult to get a reliable value for average particle size from examination of micrographs.

Estimates of d based on H_c indicate particles from iron/steel manufacturing are on average ~2.5 times larger than particles from coal-burning utilities.

X. FURTHER STUDY

Because coercive field depends on particle size in a known way for slowly grown and crushed magnetite, Fe_3O_4 should lend itself to controlled studies of air-borne particulate transport and deposition. More quantitative studies of size and shape distributions of magnetic particles need to be made, using the SEM. Since spherical iron oxide magnetic particulates are often generated in conjunction with sulfur dioxide, it seems likely that there should be a correlation between the deposition of magnetite particles and the occurrence of acid rain. Lastly, it should be useful to look for spherical magnetic particles in lung tissue of patients who die of respiratory-related illness, and to measure the magnetic properties of the particles if and when they are found.

ACKNOWLEDGMENTS

I thank C. D. Graham, Jr. for extensive editorial assistance and am indebted to the following for collecting specimens and for helpful suggestions and encouragement: Al Baltz; Charlotte Anne and Don Carver; Tony Cumbo; Ben Davies; Arnold Denenstein; Bob DeRoo; Jim and Lou Dietz; Bill Doyle; Betty Duke; Mike Finucane; Charles Fitti; Adrienne, Caroline, Jonathan, Melissa, and Nancy Flanders; Rachel Friedman; Millicent Gaskell; Fred Harrison; Jiri Jarnik; J. P. Jones; Richy Josephs; Lin Li; Janet McCoy; Brenda and Tony Moses; Bruce Moskowitz; N. Morito; Jim Mufalli; Kazunori Ozawa, Aage and Elsa Pederson; Robert Pollard; C. Arden Pope III; Charlotte Raffensperger; Harry Reichard; Bill Schuele; Mike Sharrock; Kyungho Shin; Mula Shtrikman; Eugene and Stephanie Sun; Dick Teale; Broese van Groenou; Gilbert White; David Wilson; and Foster Winters.

[1] G. Stroink, Med. Biol. Eng. Comput. **23**, Suppl 1, 44 (1985).
[2] C. C. Shih, R. A. Ornisi, D. G. Ackerman, R. Moreno, E. L. Moon, L. L. Scinto, and C. Yu, Emissions Assessment of Conventional Stationary Systems, Vol 3, EPA-600/S7-81-003a, April 1981, p. 8.
[3] R. C. Ritteahouse, Power Eng. **96**, 43 (1992).
[4] H. Ozkaynak and G. D. Thurston, Risk Anal. **7**, 449 (1987).
[5] C. A. Pope III, J. Schwartz, and M. R. Ransom, Arch. Environ. Health **47**, 211 (1992).
[6] S. I. Rasool, *Chemistry of the Lower Atmosphere* (Plenum, New York, 1973), p. 154.
[7] P. J. Flanders, J. Appl. Phys. **63**, 3940 (1988).
[8] P. J. Flanders, Rev. Sci. Instrum. **61**, 839 (1990).
[9] MicroMag™ 2900 AGM, Princeton Measurements Corp., 31 Air Park Road, Princeton, NJ 08540.
[10] C. E. Mullins, J. Soil Sci. **28**, 223 (1977).
[11] E. Raask, *Mineral Impurities in Coal Combustion* (Hemisphere, Washington, DC, 1988), Chap. 15.
[12] W. M. Henry and K. T. Knapp, Environ. Sci. Technol. **14**, 450 (1980).
[13] G. A. Norton, R. Markuszewski, and H. R. Shanks, Environ. Sci. Technol. **20**, 409 (1986).
[14] R. D. Cadle, *Particle Size* (Reinhold, New York, 1965), p. 262.
[15] R. J. K. Rinne and A. I. Makinen, Silva Fennica **22**, 89 (1988).
[16] P.-L. Kalliomaki, K. Aittoniemi, T. Gustafsson, K. Kalliomaki, M. Koponen, and V. Vaaranen, Ann. Occup. Hyg. **26**, 337 (1982).
[17] F. W. Wright, P. W. Hodge, and C. C. Langway, Jr., J. Geophys. Res. **68**, 5575 (1963).
[18] T. Yamaguchi and K. Narita, IEEE Trans. Magn. **MAG-13**, 1621 (1977).
[19] K. Kalliomaki, P. L. Kalliomaki, V. Kelha, and V. Vaaranin, Ann. Occup. Hyg. **23**, 175 (1980).
[20] *McGraw-Hill Encyclopedia of Science and Technology*, 5th ed. (McGraw-Hill, New York, 1982), Vol. 8, p. 496.
[21] C. S. Spirakis, Geology **17**, 599 (1989).
[22] A. H. Haagen-Smit and L. G. Wayne, *Air Pollution*, 3rd ed., edited by A. C. Stern (Academic, New York, 1976), Vol. 23, p. 284.
[23] *McGraw-Hill Encyclopedia of Science and Technolog*, 5th ed. (McGraw-Hill, New York, 1982), Vol. 1, p. 206.
[24] F. Heider, D. Dunlop, and N. Sugiura, Science **236**, 1287 (1987).

Dynamics of the one-dimensional spin-1 Heisenberg antiferromagnet with exchange and single-site anisotropy

Shu Zhang, Yongmin Yu, V. S. Viswanath, Joachim Stolze,[a] and Gerhard Müller
Department of Physics, The University of Rhode Island, Kingston, Rhode Island 02881-0817

The $T=0$ dynamical properties of the one-dimensional $s=1$ XXZ model with an additional single-site term are investigated by means of the recursion method. The dynamic structure factors $S_{\mu\mu}(q=\pi,\omega)$, $\mu=x,z$ bear the characteristic signatures of several different phase transitions. In the $s=1$ Heisenberg antiferromagnet, the intrinsic linewidth (at fixed q) of $S_{\mu\mu}(q,\omega)$ is larger for small q than for q near π, in contrast to well-established results for the corresponding $s=\frac{1}{2}$ model.

Spin chains with quantum number $s=1$ have been the object of sustained intense study ever since 1983, when Haldane[1] first predicted the existence of a nonmagnetic phase with an excitation gap for the isotropic Heisenberg antiferromagnet. That research activity has led to a broad consensus on the main features, and many intricate details of the $T=0$ phase diagrams pertaining to several model Hamiltonians involving spin-1 chains. The prototype among them is the Heisenberg antiferromagnet with exchange and single-site anisotropies,

$$H=\sum_{l=1}^{N}\{J(S_l^xS_{l+1}^x+S_l^yS_{l+1}^y)+J_zS_l^zS_{l+1}^z+D(S_l^z)^2\}. \quad (1)$$

Within the domain $0\leq J_z/J\leq 2$, $0\leq D/J\leq 2$ considered here for the two anisotropy parameters, a total of four distinct $T=0$ phases have been identified:[2-5] (i) A Néel phase (N) with antiferromagnetic long-range order in z direction is realized for sufficiently large J_z/J. (ii) A singlet phase (S) characterized by a nondegenerate ground state, and an excitation gap exists for large D/J. (iii) A critical phase (C) with algebraically decaying in-plane correlation function $\langle S_l^xS_{l+n}^x\rangle$ is present for sufficiently small J_z/J and D/J. (iv) Contiguous to these three phases is the phase (H)—the one first predicted by Haldane. Like (S), it is characterized by a nonmagnetic singlet ground state with an excitation gap.[6] The ground state is critical on the boundaries of (H). The (C/H) transition is of the Kosterlitz–Thouless type, and the (N/H) transition is of the 2D-Ising variety. Both transitions are specified by a single set of critical exponents for the entire phase boundary, except at the endpoints. The critical exponents of the (S/H) transition, by contrast, vary continuously along the phase boundary.

What is the characteristic signature of the four phases, and the impact of the three transitions on the $T=0$ dynamic structure factors $S_{\mu\mu}(q,\omega)$, defined as the Fourier transforms of the space-time correlation functions $\langle S_l^\mu(t)S_{l+n}^\mu\rangle$, $\mu=x,z$? The first goal of this study is to investigate this important question with an application of the recursion method. The second goal will be a study of line shapes of $S_{\mu\mu}(q,\omega)$ for an experimentally relevant situation.

The recursion method, which, in the present context, is based on an orthogonal expansion of the wave function $|\psi_q^\mu(t)\rangle=S_q^\mu(-t)|\phi_0\rangle$, $S_q^\mu=N^{-1/2}\Sigma_l e^{iql}S_l^\mu$, yields (after several intermediate steps)[7,8] a sequence of continued-fraction coefficients $\Delta_1^{\mu\mu}(q),\Delta_2^{\mu\mu}(q),\ldots$, for the relaxation function,

$$c_0^{\mu\mu}(q,z)=\cfrac{1}{z+\cfrac{\Delta_1^{\mu\mu}(q)}{z+\cfrac{\Delta_2^{\mu\mu}(q)}{z+\cdots}}}. \quad (2)$$

from which the $T=0$ dynamic structure factor can be inferred as

$$S_{\mu\mu}(q,\omega)=4\langle S_q^\mu S_{-q}^\mu\rangle\Theta(\omega)\lim_{\epsilon\to 0}\Re[c_0^{\mu\mu}(q,\epsilon-i\omega)]. \quad (3)$$

The finite-size ground-state wave function $|\phi_0\rangle$ must be computed up front. We use the conjugate-gradient method for that task.[9]

Despite the nontrivial N dependence of $|\phi_0\rangle$ in the present application, the first $K=N/2$ coefficients $\Delta_1^{\mu\mu}(q),\ldots,\Delta_K^{\mu\mu}(q)$ are, at most, *weakly* size dependent. They reflect key properties of $S_{\mu\mu}(q,\omega)$ for the *infinite* system more faithfully than the subsequent coefficients, which depend *strongly* on N. Our continued-fraction analysis uses the nearly size-independent coefficients (i) for the detection of dynamically relevant excitation gaps and (ii) for the determination of the spectral-weight distribution in $S_{\mu\mu}(q,\omega)$.

As is typical in quantum many-body dynamics, the nearly size-independent sequences $\Delta_k^{\mu\mu}(q)$, $k=1,\ldots,K$, obtained here grow linearly with k, on average, and exhibit one or several patterns that translate into specific properties of $S_{\mu\mu}(q,\omega)$ related to the type of ordering, the presence of excitation gaps, the size of bandwidths, and the exponents of infrared singularities. The techniques of analysis for these properties have been described in previous or concurrent ap-

[a]On leave from the Institut für Physik, Universität Dortmund, 44221 Dortmund, Germany.

 0021-8979/94/75(10)/5937/3/$6.00 © 1994 American Institute of Physics

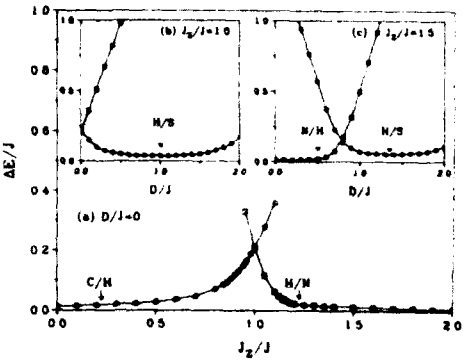

FIG. 1. Dynamically relevant excitation gaps for operators S^x_q (circles) and S^z_q (squares) along three lines in the parameter space of the Hamiltonian (1). The gaps are derived from $K=6$ nearly size-independent continued-fraction coefficients $\Delta^{\mu\mu}_k(\pi)$, $k=1,\ldots,K$ computed by means of the recursion method from the $N=12$ ground-state wave function. The vertical arrows indicate the locations where the three lines in parameter space cross phase boundaries.

plications of the recursion method to the 1D and 2D $s=\frac{1}{2}$ XXZ models[7,9] and the 1D spin-s XYZ model.[10]

For our first task, which is to map out the rather complex phase diagram of (1) in the given parameter range, we choose an operator (in our case S^μ_q with $q=\pi$ and $\mu=x,z$) which we know or expect to represent the critical fluctuations along a specified phase boundary. The method of determining the dynamically relevant excitation gap for that operator involves the matching of the nearly size-independent coefficients $\Delta^{\mu\mu}_1(q),\ldots,\Delta^{\mu\mu}_K(q)$, with the first K coefficients $\dot{\Delta}_1(\Omega),\ldots,\dot{\Delta}_K(\Omega)$ of a suitable model dynamic structure factor that has a gap of size Ω.[8] Since the matching criterion is not unique we cannot expect to obtain from that analysis accurate values for the gap sizes. Nevertheless, it proves to be a reliable indicator for the identification of phase boundaries and the dynamical variables that are subject to critical fluctuations.

For this short work, we have carried out the gap analysis along three lines in $(J_z/J, D/J)$ space. In Fig. 1(a) we have plotted the J_z/J dependence for fixed $D/J=0$ of the excitation gaps which are dynamically relevant for the operators S^x_q (circles) and S^z_q (squares). At $J_z/J=0$, our analysis yields a S^x_q gap very close to zero, and it remains near zero over some range of J_z/J values, reflecting the extended critical phase (C). The large S^z_q gap in that region indicates that the out-of-plane fluctuations are not critical. Even past the transition to the Haldane phase, marked (C/H) in Fig. 1(a), the S^x_q gap opens only very slowly, which is typical near a Kosterlitz–Thouless-type phase boundary. This is in marked contrast to the more rapid closing of the S^z_q gap at the other end of the Haldane phase. The (H/N) transition marks the onset of antiferromagnetic long-range order in the z direction. The large S^x_q gap near the phase boundary confirms Haldane's prediction[1] that the in-plane fluctuations have no part in that transition.

For the second line in parameter space [see Fig. 1(b)], we keep the exchange parameter fixed at $J_z/J=1$ and vary the single-site parameter D/J. At $D/J=0$, which is equivalent to the midpoint of line (a), the S^z_q gap starts out nonzero and grows with increasing D/J, which reflects the fact that low-frequency out-of-plane fluctuations are more and more suppressed as the easy-plane anisotropy becomes stronger. The S^x_q gap, by contrast, has a decreasing trend. Starting from the same value at $D/J=0$, it reaches a minimum near zero at $D/J\simeq 1.0$ and then grows again. The minimum marks the (H/S) transition between two nonmagnetic phases, where only the staggered in-plane fluctuations become critical.

Now we shift the line $0\leqslant D/J\leqslant 2$ in parameter space from $J_z/J=1$ [Fig. 1(b)] to $J_z/J=1.5$ [Fig. 1(c)]. At $D/J=0$ the system is in the Néel phase. Here the S^x_q gap is large, reflecting the transverse spin waves of a uniaxial antiferromagnet, whereas the S^z_q gap is effectively zero, reflecting the twofold degeneracy of the ground state associated with antiferromagnetic ordering. As D/J increases from zero, the S^z_q gap stays near zero up to the (N/H) phase boundary at $D/J\simeq 0.5$, where it starts to increase very rapidly with no further change in course. The S^x_q gap decreases from some large value as D/J increases from zero. It goes through a minimum near zero at $D/J\simeq 1.7$, marking, as in Fig. 1(b), the (H/S) transition, now shifted to a higher value of single-site anisotropy, in agreement with the broadly accepted picture.[2–6]

The significance of the results displayed in Fig. 1 is that they have been derived entirely from the ground-state wave function of a chain with just $N=12$ spins. It is certainly surprising that the spectral signatures of a rather complex phase diagram are so clearly encoded in that quantity and that this information is so easily retrievable.

The same type of gap analysis carried out for the q dependence of the operator S^μ_q yields the dispersion of the lowest branch of excitations which is dynamically relevant for $S_{\mu\mu}(q,\omega)$. Toward our second goal we reconstruct the dynamic structure factor itself via (3) from expression (2) with coefficients $\Delta^{\mu\mu}_1(q),\ldots,\Delta^{\mu\mu}_K(q)$ and a termination function tailored, such as to extrapolate the recognizable pattern of the first K coefficients. A detailed account of the reconstruction has been reported in Ref. 8. Here we must limit the discussion to a couple of specific issues: What is the main difference in line shape between the functions $S_{\mu\mu}(q,\omega)$ of the $s=1$ Heisenberg antiferromagnet and its $s=\frac{1}{2}$ counterpart, and what is the impact of a small easy-plane single-site anisotropy on the peak positions and line shapes in the $s=1$ case?

Figure 2(a) shows the reconstructed (normalized) dynamic structure factor $\tilde{S}_{\mu\mu}(q,\omega)=S_{\mu\mu}(q,\omega)/\langle S^\mu_q S^\mu_{-q}\rangle$ at $q=\pi/6$ and $q=5\pi/6$ for the 1D $s=1$ Heisenberg antiferromagnet. For both wave numbers, the function consists of a single peak with nonzero intrinsic linewidth. This is in strong contrast to the results obtained from truncated continued fractions[11] or equivalent procedures,[12] which are sums of δ functions, often broadened into Lorentzians for graphical representation.

We note two main differences between the results of Fig.

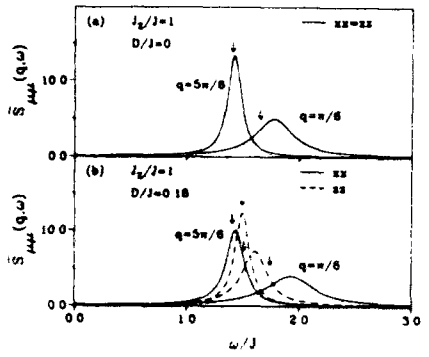

FIG. 2. Normalized dynamic structure factor $S_{\mu\mu}(q,\omega)/(S^{\mu\mu}_q S^{\mu\mu}_q)$ at $T=0$ of (a) the 1D $s=1$ Heisenberg antiferromagnet and (b) the same model with an additional easy-plane single-site anisotropy, $D/J=0.18$. We show results for $\mu=x,z$, and $q=\pi/6$, $5\pi/6$. They have been derived from $K=6$ continued-fraction coefficients $\Delta_k^{\mu\mu}(q), k=1,\ldots,K$ extracted from the $N=12$ ground-state wave function combined with the continued-fraction analysis described in Ref. 8. The arrow near the peak of each curve indicates the energy of the lowest excitation with nonzero matrix element in $S_{\mu\mu}(q,\omega)$ of the $N=12$ chain.

2(a) and the corresponding results of the $s=\frac{1}{2}$ model (see Ref. 8): (a) the peak positions at wave numbers q and $\pi-q$ are the same for $s=\frac{1}{2}$, but differ substantially for $s=1$. The symmetric dispersion of the $s=\frac{1}{2}$ chain is exactly known, and the asymmetric dispersion of the $s=1$ chain has been well established by extensive numerical diagonalizations.[11,12] (b) The linewidth is known to increase monotonically with increasing q in the $s=\frac{1}{2}$ case,[8,13] but in Fig. 2(a) the $s=1$ result at small q has a considerably larger linewidth than the one at q near π. Our $s=1$ results are consistent with the findings of Refs. 11 and 12 that the spectral weight in $S_{\mu\mu}(q,\omega)$ is dominated by a single δ function at q near π, but less so at small q. The opposite trends of line broadening in the $s=\frac{1}{2}$ and $s=1$ chains may be understood by interpreting the observable excitations as composites of different kinds of elementary states.

The presence of some easy-plane anisotropy, $D/J=0.18$, alters the functions $S_{\mu\mu}(\pi/6,\omega)$ and $S_{\mu\mu}(5\pi/6,\omega)$, as shown in Fig. 2(b). In-plane (xx) and out-of-plane (zz) fluctuations are now represented by separate peaks. At small q, the in-plane peak has moved up and the out-of-plane peak down. At small $\pi-q$, they have moved in opposite directions. the anisotropy causes an increase in in-plane linewidths. The peak positions of the reconstructed functions $S_{\mu\mu}(5\pi/6,\omega)$ shown in Fig. 2 are in good agreement with the energies of the lowest-lying dynamically relevant excitation of a chain with $N=12$ spins. The latter, quoted from Ref. 12, are indicated by arrows in Fig. 2. However, for $q=\pi/6$ the peaks lie significantly higher than the lowest $N=12$ excitation.

The significance of the point ($J_z/J=1$, $D/J=0.18$) in the parameter space of Hamiltonian (1) is its physical realization by the quasi-1D magnetic compound $Ni(C_2H_8N_2)_2NO_2ClO_4$ (NENP). A recent inelastic neutron scattering study on that compound[14] observes well-defined resonances for $0.3\pi \leq q \leq \pi$, including $q=5\pi/6$, where our result predicts a peak with small but nonzero linewidth. At smaller wave numbers including $q=\pi/6$, the resonance in the experiment has disappeared in a broad background intensity. Here our analysis predicts a broad signal, which, when multiplied by the very small integrated intensity, becomes indeed undetectable for all practical purposes.

ACKNOWLEDGMENTS

This work was supported by the U.S. National Science Foundation, Grant No. DMR-93-12252. Computations were carried out at the National Center for Supercomputing Applications, University of Illinois at Urbana–Champaign. J. S. gratefully acknowledges support by the Max Kade Foundation.

[1] F. D. M. Haldane, Phys. Rev. Lett. **50**, 1153 (1983); Phys. Lett. A **93**, 464 (1983).
[2] R. Botet, R. Jullien, and M. Kolb, Phys. Rev. B **28**, 3914 (1983).
[3] U. Glaus and T. Schneider, Phys. Rev. B **30**, 215 (1984).
[4] H. J. Schulz and T. Ziman, Phys. Rev. B **33**, 6545 (1986).
[5] H. J. Schulz, Phys. Rev. B **34**, 6372 (1986).
[6] For a detailed phase diagram, see Refs. 2–5 and J. C. Bonner, J. Appl. Phys. **61**, 3943 (1987).
[7] V. S. Viswanath and G. Müller, J. Appl. Phys. **67**, 5486 (1990); **70**, 6178 (1991).
[8] V. S. Viswanath, S. Zhang, J. Stolze, and G. Müller, Phys. Rev. B (in press).
[9] M. P. Nightingale, V. S. Viswanath, and G. Müller, Phys. Rev. B **48**, 7696 (1993).
[10] V. S. Viswanath, J. Stolze, and G. Müller (these proceedings).
[11] S. Haas, J. Riera, and E. Dagotto, Phys. Rev. B **48**, 3281 (1993).
[12] O. Golinelli, Th. Jolicoeur, and R. Lacaze, Phys. Rev. B **46**, 10854 (1992); J. Phys. C **5**, 1399 (1993).
[13] G. Müller, H. Thomas, H. Beck, and J. C. Bonner, Phys. Rev. B **24**, 1429 (1981).
[14] S. Ma, C. Broholm, D. H. Reich, B. J. Sternlieb, and R. W. Erwin, Phys. Rev. Lett. **69**, 3571 (1992).

Ferromagnetism of single crystal $Fe[S_2CN(C_2D_5)_2]_2Cl$

G. C. DeFotis, W. W. Brubaker, S. Chandarlapaty, K. L. Beers, and G. A. Coffey
Chemistry Department, College of William and Mary, Williamsburg, Virginia 23187-8795

The fully deuterated form of previously studied $Fe[S_2CN(C_2H_5)_2]_2Cl$, needed for neutron diffraction and scattering measurements, has been prepared for the first time and its magnetic behavior in single crystal form studied at low temperatures. Susceptibility and magnetization data show that $Fe[S_2CN(C_2D_5)_2]_2Cl$ has extremely similar magnetic anisotropy to the normal material: the monoclinic [101] direction is the only easy axis of ferromagnetism, with the orthogonal [010] and $(\bar{1}01)$ axes even showing antiferromagnetic-like maxima in their $\chi(T)$ near T_c. Only along [101] does M approach saturation at low fields. Analysis of $\chi(T)$ in the paramagnetic regime, assuming axial and rhombic crystal field distortions described by $H = D[\hat{S}_z^{32} - S(S+1)/3] + E[\hat{S}_x^{32} - \hat{S}_y^{32}]$ and including exchange interactions in a mean field approximation, leads to $D/k = -3.03(5)$ K, $E/k = -0.49(4)$ K, and $zJ/k = 0.99(3)$ K along with $g_x = 2.058(20)$, $g_y = 2.060(20)$, and $g_z = 2.080(20)$. These parameters are rather similar to those of the normal material, though zJ/k is significantly larger. The ordering temperature, obtained from a critical law fit to [101] data in a small field, i.e., $\chi_0 = \Gamma t^{-\gamma}$, is $T_c = 2.486(2)$ K, with $\gamma = 1.16(1)$ and $\Gamma = 1.07(5)$ emu/mol. The critical exponent γ is the same as in the normal material and corresponds to the theoretical value in Kawamura's $Z_2 \times S_1$ model. An ~1.2% enhancement in T_c over that of the normal material occurs, which may be due to slightly closer molecular packing. 75.30.Kz, 75.30.Cr, 75.30.Gw, 75.40.Cx

I. INTRODUCTION

Earlier studies[1-4] of the unusual pentacoordinate Fe^{3+} compound $Fe[S_2CN(C_2H_5)_2]_2Cl$ with $S = 3/2$, Fig. 1, demonstrated novel critical behavior at the 2.457 K ferromagnetic transition. Critical exponents $\gamma = 1.16(1)$, $\beta = 0.24(1)$, and $\delta = 5.65(15)$ were obtained, values consistent in light of the scaling relation $(\delta - 1)/\beta = \gamma$. Some sparse heat capacity data[5] led to a provisional estimate of $\alpha = 0.38(6)$,[3] also consistent with the above exponents in light of the scaling relation $\alpha = 2 - 2\beta - \gamma$. These exponents differ considerably from theoretical values for any conventional universality class, but are close to values found by Kawamura[6] for magnets with $Z_2 \times S_1$ symmetry (Ising chiral symmetry combined with XY rotational symmetry). Such symmetry may characterize a canted ferromagnet with Ising anisotropy, as $Fe[S_2CN(C_2H_5)_2]_2Cl$ is thought to be. Determination of the ordered spin arrangement by neutron diffraction is needed to confirm this hypothesis, while neutron scattering to further probe the critical behavior is also desirable. Because of the large incoherent scattering cross section of hydrogen, and the 20 hydrogens per molecule, deuterated material is needed in order to obtain satisfactory neutron data. We present here magnetization and susceptibility data on single crystals of deuterated $Fe[S_2CN(C_2D_5)_2]_2Cl$ and find that the behavior closely approximates that of the normal material, so that neutron data should be relevant to both.

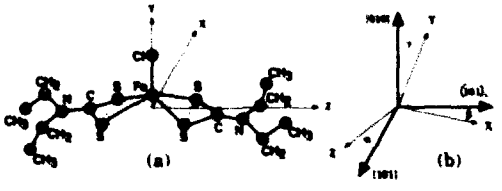

FIG. 1. (a) Molecular structure of $Fe[S_2CN(C_2H_5)_2]_2Cl$; (b) relation of molecular principal axes to principal axes of crystal susceptibility.

II. EXPERIMENTAL

Deuterated material was prepared by using $NH(C_2D_5)_2$, from Merck & Co., Inc., 98 at % D, as a starting material in place of normal ammine and following published procedures otherwise.[7] Polycrystalline $Fe[S_2CN(C_2D_5)_2]_2Cl$ thus obtained exhibited a melting point, 237–241 °C, essentially identical to that observed by us for the normal material. An IR spectrum (KBr pellet method) of the deuterated material showed significant shifts in several absorption peak positions compared to the normal material, but the patterns displayed many similarities in structure, and were easily distinguishable from IR spectra of the $Fe[S_2CN(C_2D(H)_5)_2]_3$ precursors.

Well formed single crystals of $Fe[S_2CN(C_2D_5)_2]_2Cl$, morphologically very similar to the normal material previously obtained in the same fashion, were grown from methylene chloride solution. The monoclinic [101] and [010] directions were readily located in the $(\bar{1}01)$ cleavage plane which characterizes these materials. Powder x-ray patterns of normal and deuterated material are virtually identical, implying a common structure.

Magnetic measurements were made with a vibrating sample magnetometer system using 36.02 and 26.68 mg single-crystal samples. Susceptibilities are corrected for diamagnetism ($\chi_{dia} = -0.000212$ emu/mol) and demagnetization. In the analysis of critical region data, with $H_{app} = 11.95(5)$ G, the demagnetization factor was inferred from the leveled value of the susceptibility below T_c in the usual way, leading to $N = 6.1_6$.

III. MEASUREMENTS AND ANALYSIS

Examination of the single-crystal susceptibility as a function of orientation revealed that, as for the normal ma-

 0021-8979/94/75(10)/6940/3/$6.00 © 1994 American Institute of Physics

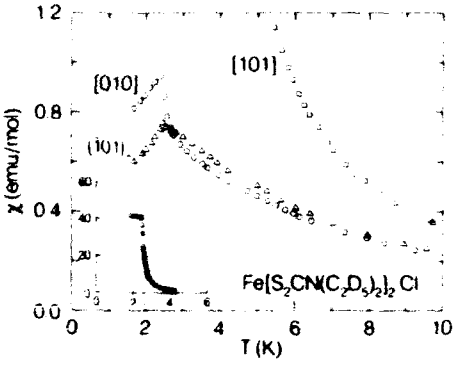

FIG. 2. Single-crystal magnetic susceptibility of $Fe[S_2CN(C_2D_5)_2]_2Cl$ vs temperature. Inset shows [101] data below 6 K in a small field.

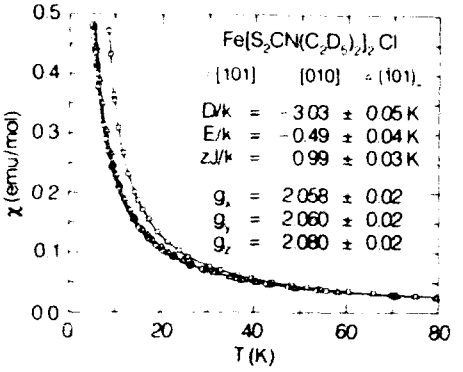

FIG. 4. Fit to single-crystal susceptibilities of $Fe[S_2CN(C_2D_5)_2]_2Cl$ with zero-field splitting and exchange parameters as described in text.

terial, the principal axes of susceptibility were along the monoclinic twofold axis [010], the [101] direction, and the direction perpendicular to the cleavage plane, $(\bar{1}01)_c$. Figure 2 shows the molar susceptibility versus T below 10 K along each principal axis. The [101] direction is evidently the ferromagnetic easy axis, and (inset) low-field data attain a demagnetization limited value below T_c, which is clearly ~2.5 K. Along the orthogonal [010] and $(\bar{1}01)_c$ directions the susceptibility has much smaller values and even exhibits antiferromagnetic-like maxima at 2.45(3) K, with $\chi_{max}=0.944(10)$ emu/mol, along [010] and at 2.49(1) K, with $\chi_{max}=0.758(10)$ emu/mol, along $(\bar{1}01)_c$. Rather similar behavior was observed[1] in the normal material, though there the susceptibility attained a higher value along $(\bar{1}01)_c$ than along [010]. Given the extremely large size of $\chi_{[101]}$ however, small misalignments could affect the relative values of $\chi_{[010]}$ and $\chi_{(\bar{1}01)_c}$ near the transition.

Figure 3 shows the magnetization versus applied field for each axis at various temperatures. An approach to satu-

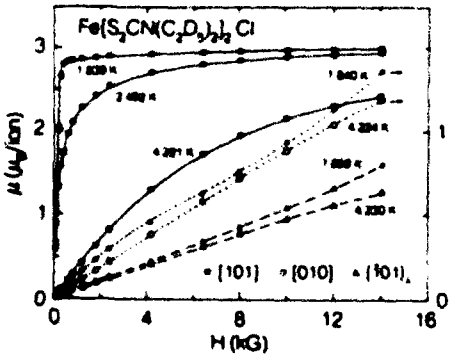

FIG. 3. Single-crystal magnetization of $Fe[S_2CN(C_2D_5)_2]_2Cl$ vs field and temperature, expressed on a per unit ion basis. Curves through data are only guides to the eye.

ration at relatively low field, if in excess of the demagnetizing field, is seen only for the [101] direction and is indicative of ferromagnetism. At 1.839 K (~74% of T_c) and 14 kG the magnetization is $2.99\mu_B$, just slightly below the saturation value of $3.00\mu_B$ for an $S=3/2$ system assuming $g=2.00$. Although this is about 3% less than seen under comparable conditions for the normal material[2] the difference is within experimental uncertainty. Some nonlinearity is apparent along [010] and $(\bar{1}01)_c$ directions at 4.2 K, and somewhat different degrees of low field curvature at 1.8 K. Also discernible is an upturn in magnetization along these two axes at 1.8 K for larger fields. This may be due to an incipient spin-reorientation transition. The behavior along [010] and $(\bar{1}01)_c$ is also similar to that in the normal material, though the lesser precision of the earlier data[2] made the curvatures less clear.

Well above T_c the susceptibility can be analyzed including the effects of axial and rhombic crystal field distortions, which produce a zero-field splitting δ of the ^4A ground term. The spin Hamiltonian is

$$\hat{H}=D[\hat{S}_z^2-S(S+1)/3]+E[\hat{S}_x^2-\hat{S}_y^2]+\mu_B[g_xH_x\hat{S}_x+g_yH_y\hat{S}_y+g_zH_z\hat{S}_z] \quad (1)$$

In zero field the eigenvalues correspond to a pair of Kramers doublets separated by $\delta=2(D^2+3E^2)^{1/2}$. If $D>0$ and $|E/D|$ is small, the ground doublet is essentially $|\pm 1/2\rangle$ and the upper doublet $|\pm 3/2\rangle$. If $D<0$ the levels are reversed. Single-ion susceptibilities χ_x, χ_y, and χ_z can be calculated,[1] and the crystal susceptibilities written in terms of these using relations between [101], [010], $(\bar{1}01)_c$, and x,y,z axes given by the structure. Based on the x-ray results we use here $\alpha=20.7°$, $\beta=4.05°$, and $\gamma=21.1°$ (Fig. 1) as earlier for $Fe[S_2CN(C_2H_5)_2]_2Cl$. The exchange interaction, $\hat{H}_{ex}=-2J\sum_{i,j}\hat{S}_i\cdot\hat{S}_j$, must also be accounted for, for which the mean-field approximation result is used[6]

$$\chi_i^{ex}=\chi_i/[1-(2zJ/Ng_i^2\mu_B^2)\chi_i]. \quad (2)$$

An average interaction J over z neighbors will be obtained.

In Fig. 4 appears the best fit (rms deviation 0.92%) ob-

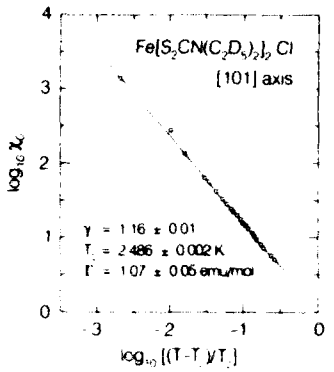

FIG. 5. Critical law fit to the initial susceptibility along [101] in $Fe[S_2CN(C_2D_5)_2]_2Cl$ as described in text.

tained to data between 7 K ($\sim 3T_c$) and 80 K, all three axes being fit simultaneously, with parameters indicated. The fitted parameters are only slightly sensitive to the minimum temperature fitted, and the uncertainties encompass values from $T_{min} = 6$ and 8 K fits. Using $T_{min} = 5$ K leads to D and E about 7% and 30% larger in magnitude (same signs) and zJ about 9% smaller, but a substantially worse fit. In view of the mean-field approximation employed, T_{min} as low as $2T_c$ is best avoided. The choice of x, y, and z axes in Fig. 1 is necessary in order to obtain, as required,[9] D and E satisfying $|E| \leq |D|/3$.

The initial susceptibility χ_0 along the ferromagnetic [101] axis was analyzed according to the critical law form

$$\chi_0 = \Gamma t^{-\gamma}, \tag{3}$$

where $t = (T - T_c)/T_c$. The best fit (rms deviation 1.7%) in the range 2.491–2.889 K ($0.0020 < t < 0.162$) is shown in Fig. 5, with parameters indicated. Data somewhat beyond 2.889 K, to $t = 0.260$, are also plotted and conform well to the fitted line; higher temperature data do not. The precision of the fitted parameters is better than the uncertainties indicated, which include effects of using slightly different T_{min} and T_{max} in the fit.

IV. DISCUSSION

The anisotropy in susceptibility and magnetization data reported here for $Fe[S_2CN(C_2D_5)_2]_2Cl$ is virtually the same as that in the normal material.[1] The zero-field splitting parameters previously reported for $Fe[S_2CN(C_2H_5)_2]_2Cl$ are[1] $D/k = -3.32(5)$ K and $E/k = -0.65(5)$ K, along with $zJ/k = 0.81(5)$ K, $g_z = 2.09(5)$, $g_y = 2.10(5)$, and $g_x = 2.12(5)$, from a 5–20 K fit. As noted earlier, if the present fit is extended to 5 K larger $|D|$ and $|E|$ emerge, ones which are almost exactly the same as for the normal material. However, zJ/k remains significantly larger (0.91 K) than for $Fe[S_2CN(C_2H_5)_2]_2Cl$. The g_i values in a 5–80 K fit are marginally enhanced but remain 1%–2% smaller than those of the normal material, differences which are within experimental uncertainty. Fitting normal material data with $T_{min} = 7$ K leads to only insignificant variations (0.05 K or less) in D/k, E/k, and zJ/k. We believe that only the zJ/k value shows a physically significant difference between the two materials, being 10%–20% larger in the deuterated system.

The critical exponent γ in $Fe[S_2CN(C_2D_5)_2]_2Cl$ is indistinguishable from that of the normal material. This universal parameter is characteristic of a magnetic model class, which is presumably then the same in the two materials. It is clear, however, that T_c is slightly enhanced in the deuterated material, by about 1.2%. This is consistent with the larger zJ value, though single-ion anisotropy also plays a major role in determining T_c. It is hypothesized that the heavier deuteron vibrates with a lesser amplitude than does hydrogen, making the deuterated molecule effectively smaller. If intermolecular separations are then also slightly smaller an enhanced exchange interaction, and enhanced T_c, are expected.

There is evidence in the literature for the suggested deuteration effect. For example, the molar volume of solid CD_4 is about 1.5% smaller at 70 K than that of solid CH_4.[10] Deuteration also leads to a decrease in unit cell size for $C_4H_8NO_4Br$[11] and HF.[12] The lesser zero-point energy of an X—D bond relative to an X—H bond is the common feature in these examples.

ACKNOWLEDGMENTS

This work was supported by National Science Foundation-Solid State Chemistry-Grant No. DMR-9213198. Support from the College of William and Mary is also acknowledged.

[1] G. C. DeFotis, F. Palacio, and R. L. Carlin, Physica B **95**, 380 (1978); Phys. Rev. B **20**, 2945 (1979).
[2] G. C. DeFotis and J. A. Cowen, J. Chem. Phys. **73**, 2120 (1980).
[3] G. C. DeFotis and S. A. Pugh, Phys. Rev. B **24**, 6497 (1981).
[4] G. C. DeFotis and J. R. Laughlin, J. Magn. Magn. Mater. **54-57**, 713 (1986); J. Chem. Phys. **84**, 3346 (1986).
[5] N. Arai, M. Sorai, H. Suga, and S. Seki, J. Phys. Chem. Solids **38**, 1341 (1977).
[6] H. Kawamura, J. Phys. Soc. Jpn. **55**, 2095 (1986); J. Appl. Phys. **61**, 3590 (1987).
[7] H. H. Wickman and A. M. Trozzolo, Inorg. Chem. **7**, 63 (1968).
[8] J. W. Stout and W. B. Hadley, J. Chem. Phys. **40**, 55 (1964).
[9] H. H. Wickman, M. P. Klein, and D. A. Shirley, J. Chem. Phys. **42**, 2113 (1965).
[10] S. C. Greer and L. Meyer, J. Chem. Phys. **52**, 468 (1970).
[11] A. Oskarsson, Acta Crystallogr. B **32**, 2163 (1976).
[12] M. W. Johnson, E. Sandor, and E. Arzi, Acta Crystallogr. B **31**, 1998 (1975).

Spin-1/2 Heisenberg antiferromagnet on the square and triangular lattices: A comparison of finite temperature properties

N. Elstner
Physics Department, University of California, Santa Cruz, California 95064

R. R. P. Singh
Physics Department, University of California, Davis, California 95616

A. P. Young
Physics Department, University of California, Santa Cruz, California 95064

We compare and contrast the behavior of the spin-half Heisenberg antiferromagnet on the square and triangular lattices. For both models, high temperature expansions are obtained for the structure factor at the ordering vector, the correlation length, the uniform susceptibility, and the entropy. We show that the antiferromagnetic correlations are significantly larger for the square lattice than for the triangular lattice. Analysis of the structure factor and the correlation length shows that the spin stiffness is an order of magnitude smaller in the triangular lattice than in the square lattice. These results indicate that the triangular lattice, although weakly ordered at $T=0$, is close to a quantum critical point. Thus, in contrast to the square lattice, a semiclassical spin-wave picture may not be sufficient to describe the ground state.

There has been considerable interest during the last years in the nature of the ground state of two-dimensional quantum spin systems. Most attention has been given to the spin-1/2 Heisenberg antiferromagnet (HAF) on the square and triangular lattices. Both systems show long range magnetic order (LRMO) in the classical case, but the behavior in the quantum regime has been a subject of long standing debate. Although there are still no mathematically rigorous arguments for the ground state of the square lattice, *there is overwhelming numerical*[1-4] *evidence supporting* LRMO. The numerical studies demonstrate that zero temperature properties of the system like the ground state energy, the sublattice magnetization, the spin-stiffness constant, and the spin-wave velocity are given quantitatively by the spin-wave theory truncated at order $1/S^2$.[5,6] *Furthermore*, finite temperature properties, such as temperature dependence of the correlation length, agree extremely well with a renormalized classical picture.[7]

In contrast to the square lattice, the HAF on the triangular lattice is a frustrated spin system. In the classical limit, this frustration is relieved by the neighboring spins pointing at 120° with respect to each other and ordering in the three sublattice pattern. For the quantum case, the spin-wave theory[8,9] predicts that the ground state remains ordered in the three sublattice pattern, with an order parameter comparable to the square lattice. However, many alternative propositions for disordered ground states have also been made. Most notable are the resonating valence bond theory of Anderson[10,11] and the variational mapping onto the quantum Hall state by Kalmeyer and Laughlin.[12]

Numerical studies of this model include variational studies,[13] exact diagonalization of small systems,[14,15] Ising expansions,[16] and recent high temperature expansions.[17] Monte Carlo simulations for this system are difficult due to sign problems. While most studies favor LRMO, there are considerable variations in the extent to which the system is predicted to be ordered. The exact diagonalization study of Bernu *et al.*[14] predicts a sublattice magnetization about 50% of the classical value, nearly the same as in spin-wave theory. They also find the low lying spectra to be consistent with LRMO. However, the similar data led Leung and Runge[15] to conclude the absence of LRMO. The Ising expansions,[16] extrapolated assuming long range order, suggest a sublattice magnetization of 20% the classical value. However, the extrapolations also suggested that the Heisenberg model at $T=0$ is very close to the critical point for antiferromagnetism. Thus, these zero temperature studies are unable to resolve the question of whether the ground state has long range order.

High temperature expansions present an unbiased method for studying the finite temperature thermodynamic properties of a physical system. We have recently calculated the high temperature series for various quantities (structure factor at the ordering wave vector, correlation length, uniform susceptibility, entropy) for the square and triangular lattices up to order 13 in $1/T$. Systematic Pade extrapolation of these series show that, while both lattices appear to have LRMO at $T=0$, there are striking quantitative differences in their low temperature behavior. The triangular lattice is much weakly ordered compared to the square lattice, and its ordering tendencies are not apparent until much lower temperatures.

The Heisenberg antiferromagnet is defined by the Hamiltonian

$$H = J \sum_{\langle i,j \rangle} \mathbf{S}_i \cdot \mathbf{S}_j, \quad J > 0. \tag{1}$$

The $\mathbf{S}_i$ are spin-1/2 operators and the sum is over all nearest-neighbor (NN) pairs of sites on the two lattices. From now on we set the exchange coupling J equal to unity. The classical ground state of the square lattice contains two sublattices with NN spins being antiparallel. On the triangular lattice the spins form three sublattices with a relative angle of 120° toward each other. Thus the ordering wave vector $\mathbf{Q}$ is given by

 0021-8979/94/75(10)/5943/3/$6.00 © 1994 American Institute of Physics

$$\mathbf{Q}=\pi(1,1)\text{(sq. lattice)}, \quad \mathbf{Q}=\frac{4\pi}{3}(1,0)\text{(tr. lattice)} \tag{2}$$

in units where the lattice spacing is one.

The antiferromagnetic structure factor is given by

$$S(\mathbf{Q})=\sum_j \exp[i\mathbf{Q}\cdot(\mathbf{R}_i-\mathbf{R}_j)]\langle S_i^z S_j^z\rangle. \tag{3}$$

The phase factors are unity if the two sites are on the same sublattice and -1 (square lattice) or $-1/2$ (triangular lattice) for different sublattices. A similar expression can be derived for the correlation length ξ giving

$$\xi^2=\frac{1}{4S(\mathbf{Q})}\sum_j (\mathbf{R}_i-\mathbf{R}_j)^2 \exp[i\mathbf{Q}\cdot(\mathbf{R}_i-\mathbf{R}_j)]\langle S_i^z S_j^z\rangle. \tag{4}$$

For wave vectors $\mathbf{q}$ near the ordering wave vector $\mathbf{Q}$, this agrees with the Ornstein–Zernicke form $S(\mathbf{q})\approx S(\mathbf{Q})/[1+\xi^2(\mathbf{q}-\mathbf{Q})^2]$. In addition to these two quantities we have generated the series for the logarithm of the partition function $\ln Z$ and the uniform structure factor $S(\mathbf{q}=0)$.

Before presenting the results of our extrapolations we discuss the expected behavior at low temperatures. For an ordered ground state the correlation length is expected to grow exponentially as

$$\xi=A_\xi T^x \exp[C/T][1+O(T)]. \tag{5}$$

The corresponding result for the structure factor at the ordering wave vector is

$$S(\mathbf{Q})=A_S T^y \exp[2C/T][1+O(T)]. \tag{6}$$

For the square lattice, there exist analytic results for the classical values of the parameters in these equations[7]

$$x=0, \quad y=2, \quad C=2\pi\rho_S \quad \text{with} \quad \rho_s=S^2. \tag{7}$$

Here ρ_s is the spin stiffness coefficient for twisting the spins. For the triangular lattice the situation is more complicated. The ground state is noncollinear resulting in two distinct stiffnesses. However, calculations by Azaria *et al.*[18] determined the parameters to be

$$x=-0.5, \quad y=3, \quad C=6.994S^2. \tag{8}$$

Thus, the classical values of C for the two lattices differ by less than 20%. Latest high precision quantum Monte Carlo simulations of the square lattice found the spin stiffness to be $\rho_S=0.186(4)$,[19] which is consistent with results from Ising expansions at $T=0$, $\rho_S=0.18\pm0.01$.[20] This is a reduction to roughly 70% of the bare (classical with spin-S) value of 0.25.

We analyzed the series for $T\log[4S(\mathbf{Q})]$ and $T\log[4T\xi^2/T_{mf}]$ as a function of temperature where T_{mf}, the mean field transition temperature has value $T_{mf}=1$ for the square lattice and $T_{mf}=0.75$ for the triangular lattice. Note that these quantities go toward $2C$ as $T\to0$. At infinite temperature $T\log[4S(\mathbf{Q})]$ goes to the mean field transition temperature T_{mf} and $T\log(4T\xi^2/T_{mf})$ to a constant given by the second coefficient of the series for ξ^2. The series were extended beyond their radius of convergence by the method of Pade approximants.

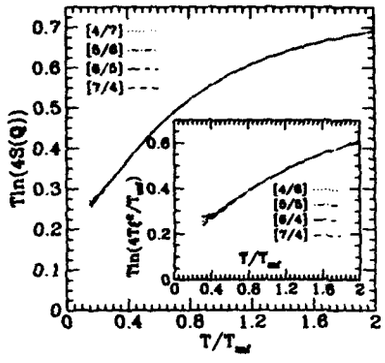

FIG. 1. Triangular lattice: $T\ln[4S(\mathbf{Q})]$ vs T/T_{mf}. The plots represent $[L,M]$ Padés in the Euler transformed variable $u=1/(T+0.08)$. The insert shows results for the correlation length. $T\ln[4T\xi^2/T_{mf}]$ vs T/T_{mf}; $u=1/(T+0.2)$.

In Figs. 1 and 2 we present our results for $T\log[4S(\mathbf{Q})]$ as function of temperature. Extrapolations of $T\log(4T\xi^2/T_{mf})$ are shown on the inserts. For these plots we first made an Euler transform to a new variable $u=1/(T+a)$ (values for a are given in the figure captions). The Pade analysis was then done in this variable. The main reason for this procedure is that the transformed series behaves better then the original one.

The plot for the square lattice shows an increase of $T\log[4S(\mathbf{Q})]$ and $T\log(4T\xi^2/T_{mf})$ with decreasing T tending toward the known zero temperature value of $4\pi\rho_S$. In the temperature regime $0.4<T<1$ our extrapolations for the correlation length are in excellent agreement with QMC results from Ding and Makivic,[2] although the latter define the correlation length through the exponential decay of the spin–spin correlation function. Our extrapolations break down below $T\sim0.3$, because at such low temperatures the correlation length is much larger (approximately 50 lattice spacings at $T=1/4$) than our largest system size (13th order).

The corresponding procedure for the triangular lattice reveals a different behavior. $T\log[4S(\mathbf{Q})]$ and $T\log[4T\xi^2/T_{mf}]$ both decrease. We are able to extrapolate our data down to $T=0.2T_{mf}$. Even at $T=0.25$, the correlation length is quite small (less than 2 lattice spacings). However, our data extrapolate to a value of $2C\sim0.2$ as $T\to0$, apparently nonzero but less than 10% of the bare value of 3.497!

One may argue that there could be a crossover to a different behavior at temperature lower than $T=0.15$. However, if this should be the case every method to determine the zero temperature behavior will run into problems.

Another interesting quantity revealing differences between the two lattices is the entropy. In Figs. 3 and 4 we present the extrapolations of the entropy per site, S/N, as

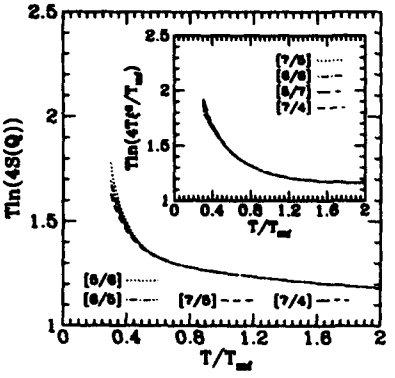

FIG. 2. Square lattice: $T \ln[4S(Q)]$ and $T \ln(4T\xi^2/T_{sf})$ (on the insert) vs T/T_{sf}; $u=1/(T+0.2)$.

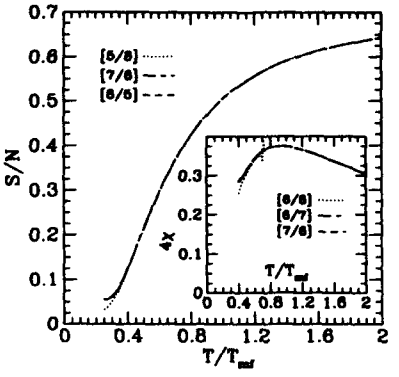

FIG. 4. Square lattice: entropy S/N and susceptibility 4χ vs T/T_{sf}; $u=1/(T+0.2)$.

function of temperature. The infinite temperature limit is given by ln(2). For the square lattice S/N is close to zero for $T=0.25$, but for the triangular lattice it is about one-third of the infinite temperature value. This again shows that the characteristic energy scale, i.e., the spin stiffness, is much smaller for the triangular lattice than for the square lattice.

The inserts of Figs. 3 and 4 show the results for the uniform susceptibility $\chi(0)=T^{-1}S(0)$, which is expected to go to a finite value as $T\to 0$ and to have a maximum at some intermediate temperature marking the onset of short-range antiferromagnetic order. Again this maximum occurs for the square lattice at significantly higher temperature ($T_{peak}\approx 0.9$) than for the triangular lattice ($T_{peak}\approx 0.3$).

To conclude, our results show that the triangular lattice has weak LRMO at zero temperature. However, we find striking quantitative differences between the square and the triangular lattices. While the factor C, which determines the strengh of the exponential, is similar for both systems in the classical limit, drastic differences occur in the quantum regime. For the square lattice C is reduced to roughly 70% of the bare value; a reduction that can be described quite well in a $1/S$ expansion. On the other hand the corresponding value for the triangular lattice is less than 10% of the classical limit, which seems to indicate that a semiclassical spin-wave picture may not be sufficient to describe the ground state properties of the Heisenberg antiferromagnet on the triangular lattice.

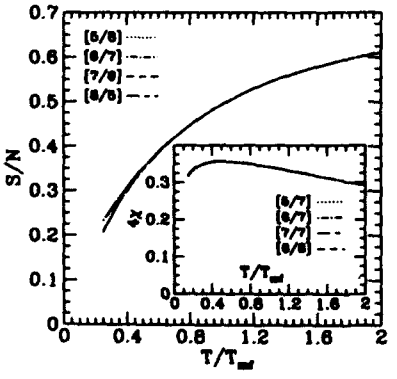

FIG. 3. Triangular lattice: entropy S/N vs T/T_{sf}; $u=1/(T+0.2)$; on the insert: susceptibility 4χ vs T/T_{sf}; $u=1/(T+0.08)$.

This work is supported by NSF Grant Nos. DMR 9111576 and DMR 9017361. One of us (N.E.) acknowledges support from the Deutsche Forschungsgemeinschaft.

[1] J. D. Reger and A. P. Young, Phys. Rev. B 37, 5978 (1988).
[2] M. S. Makivic and H.-Q. Ding, Phys. Rev. B 43, 3562 (1991).
[3] R. R. P. Singh, Phys. Rev. B 39, 9760 (1989).
[4] Z. Weihong, J. Oitmaa, and C. J. Hamer, Phys. Rev. B 43, 8321 (1991).
[5] C. M. Canali, S. M. Girvin, and M. Wallin, Phys. Rev. B 45, 10131 (1992).
[6] J. Igarashi and A. Watanabe, Phys. Rev. B 43, 13456 (1991).
[7] S. Chakravarty, B. I. Halperin and D. R. Nelson, Phys. Rev. Lett. 60, 1057 (1988); Phys. Rev. B 39, 2344 (1989).
[8] T. Jolicœur and J. C. Le Guillou, Phys. Rev. B 40, 2727 (1989).
[9] J. Miyake, J. Phys. Soc. Jpn. 61, 983 (1992).
[10] P. W. Anderson, Mater. Res. Bull. 8, 153 (1973).
[11] P. Fazekas and P. W. Anderson, Philos. Mag. 30, 432 (1974).
[12] V. Kalmeyer and R. B. Laughlin, Phys. Rev. Lett. 59, 2095 (1987).
[13] D. A. Huse and V. Elser, Phys. Rev. Lett. 60, 2531 (1988).
[14] B. Bernu, C. Lhuillier, and L. Pierre, Phys. Rev. Lett. 69, 2590 (1992).
[15] P. W. Leung and K. J. Runge, Phys. Rev. B 47, 5862 (1993).
[16] R. R. P. Singh and D. A. Huse, Phys. Rev. Lett. 68, 1766 (1992).
[17] N. Elstner, R. R. P. Singh, and A. P. Young, Phys. Rev. Lett. 71, 1629 (1993).
[18] P. Azaria, B. Delamotte, and D. Mouhanna, Phys. Rev. Lett. 68, 1762 (1992); P. Azaria, B. Delamotte, F. Delduc and T. Jolicœur, Saclay preprint T93/044.
[19] U.-J. Wiese and H.-P. Ying, Z. Phys. B 93, 147 (1994).
[20] R. R. P. Singh and D. A. Huse, Phys. Rev. B 40, 7247 (1989).

Disorder-driven first-order phase transformations: A model for hysteresis

Karin Dahmen, Sivan Kartha, James A. Krumhansl,[a] Bruce W. Roberts, James P. Sethna, and Joel D. Shore[b]
Laboratory of Atomic and Solid State Physics, Cornell University, Ithaca, New York 14853-2501

Hysteresis loops in some magnetic systems are composed of small avalanches (manifesting themselves as Barkhausen pulses). Hysteresis loops in other first-order phase transitions (including some magnetic systems) often occur via one large avalanche. The transition between these two limiting cases is studied, by varying the disorder in the zero-temperature random-field Ising model. Sweeping the external field through zero at weak disorder, we get one large avalanche with small precursors and aftershocks. At strong disorder, we get a distribution of small avalanches (small Barkhausen effect). At the critical value of disorder where a macroscopic jump in the magnetization first occurs, universal power-law behavior of the magnetization and of the distribution of (Barkhausen) avalanches is found. This transition is studied by mean-field theory, perturbative expansions, and numerical simulation in three dimensions.

The shapes of hysteresis curves in magnetic materials vary widely for different materials. This variation manifests itself in variation of parameters, such as the coercivity, remanence, and susceptibility. Of particular interest to us is the variation of the sizes of Barkhausen noise pulses.[1] These pulses are a manifestation of avalanches taking place in the magnetic system, with groups of domains (or spins) flipping over in one avalanche. One distinguishes between the small Barkhausen effect and large Barkhausen discontinuities. The small Barkhausen effect is the observation of small pulses representing small avalanches in the system. None of these pulses sweep through the entire system. Often, soft magnetic materials after annealing show mainly the small Barkhausen effect.[2] There are other materials that have hysteresis loops that are more square and have large jumps in the magnetization. These jumps are often called "large Barkhausen discontinuities"[2] in magnetic materials and "bursts" in a similar effect in Martensites.[3] These large jumps represent avalanches that sweep through a sizable fraction of the system. In the thermodynamic limit, we call avalanches that sweep a finite fraction of the system "infinite avalanches." There exist models like the Stoner–Wohlfarth model and the Preisach model,[2,4] that can describe both types of hysteresis loops. The Preisach model, and other models, break up the hysteresis loop into contributions from elementary hysteresis domains, each with their own value for remanence and coercivity, with no interactions between the domains.

We study hysteresis in the zero temperature random-field Ising model (RFIM), where *interaction* between hysteresis domains (spins) is implicit.[5] We note that we are not considering the equilibrium RFIM or any $T \to 0$ limit of that model. The dynamics of the approach to thermal equilibrium in that model has been well studied.[6] However, we are interested in a model with the same Hamiltonian as the equilibrium RFIM, but with a (very natural but nonequilibrium) specified dynamics.[5] By varying the randomness, we can use this RFIM to describe hysteresis loops, both with and without large Barkhausen discontinuities. The most interesting consequence, however, of introducing interactions between the magnetic domains, is that the transition from infinite avalanche to noninfinite avalanche hysteresis loops is accompanied by critical fluctuations and diverging correlation lengths. As one knows from the theory of phase transitions,[7] this allows one to write down scaling laws with universal exponents that are valid near the transition point. By "universal," we mean that the behavior is independent of many details of the system (and thus the same for theoretical models and real materials), and depends only on the dimension, the range of interaction, and the symmetries of the order parameter.

We consider a simple cubic lattice. Each site i in this lattice can represent an entire magnetic domain. The magnetization at site i is s_i. It can be pointing either up or down, i.e., $s_i = \pm 1$. The Hamiltonian of the RFIM is

$$\mathcal{H} = -\sum_{\langle ij \rangle} J s_i s_j - \sum_i (f_i s_i + H s_i), \tag{1}$$

where the first sum is over nearest-neighbor pairs. This term represents a ferromagnetic interaction of magnitude J between the domains. At each site in the crystal a random magnetic field f_i is added to model disorder (like defects, etc.) in the crystal. We assume a Gaussian distribution of width R for these random fields. H is the strength of the external, homogeneous magnetic field. As we change the external magnetic field H adiabatically, the system does not relax to its true equilibrium ground state. Instead, it stumbles from one metastable state to another in response to the changing field. For experimental systems with high enough barriers to relaxation for each elementary domain, such that thermal fluctuations can be ignored on experimental time scales, this assumption that the system does not relax to its true ground state is valid. This applies to most magnetic memory devices (by design), and also other systems, like athermal Martensites.[3]

A domain on a magnetic tape will flip over when the force from the external field exceeds the coupling forces due to the neighbors plus any forces from random anisotropies or random fields within the domain. Our model uses precisely this dynamics. To define a dynamics for this system, we as-

[a]Present address: 515 Station Road, Amherst, Massachusetts 01002.
[b]Present address: Department of Physics, Simon Fraser University, Burnaby, British Columbia, V5A 1S6, Canada.

 0021-8979/94/75(10)/5946/3/$6.00 © 1994 American Institute of Physics

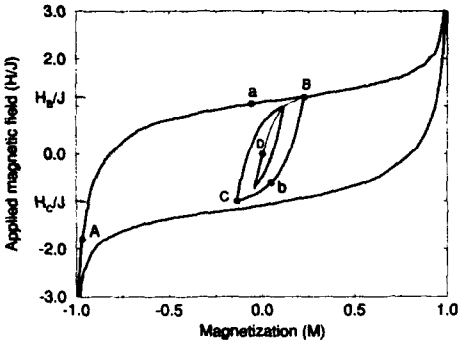

FIG. 1. Hysteresis loop showing return-point memory. The magnetization as a function of external field for a 30^3 system with disorder $R=3.5$ J. If the field H is made to backtrack from H_B to H_C, and swept up to H_B again, it returns to precisely the same state at H_B, from which it left the outer loop. It remembers this "return-point," even if it is forced to run through subcycles within cycles, and so on, as the figure shows. A simple proof for this "return-point memory" in certain systems is given elsewhere.[5]

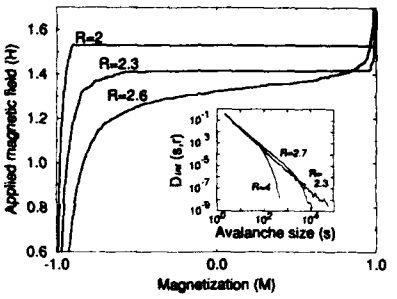

FIG. 2. Varying the disorder. Three $H(M)$ curves for different levels of disorder, for a 60^3 system. Our current estimate of the critical disorder is $R_c=2.23$ J (we set $J=1$). At $R=2<R_c$, there is an infinite avalanche that seems to appear abruptly. For $R=2.6>R_c$ the dynamics is macroscopically smooth, although, of course, microscopically it is a sequence of sizeable avalanches. At $R=2.3$, near the critical level of disorder, extremely large events become common. Inset: Log–log plot of the integrated avalanche-size distribution $D_{int}(s,r)$ vs avalanche size s. $D_{int}(s,r)$ is the integral of $D(s,r,h)$ (see the text) over one sweep of the magnetic field from $-\infty$ to $+\infty$, averaged here over five systems of size 120^3 and plotted at $R=2.3$, $R=2.7$, and $R=4.0$. Notice the power-law region $D_{int}(s)\sim s^{-(\tau+\sigma\beta\delta)}$ and the cutoff at $s_{max}\sim(R-R_c)^{-1/\sigma}$.

sume that as the external magnetic field is changed adiabatically, each domain will flip when the direction of its total local field,

$$F_i=\sum_j Js_j+f_i+H, \tag{2}$$

changes. Initially, all domains are pointing down at a sufficiently negative H. The system then transforms from negative to positive magnetization as the field is swept upward. Related approaches were discussed in Ref. 5. In addition, other related work has come to our attention.[8] The result of a simulation of this system for a width of the Gaussian distribution of random fields $R=3.5$ J in three dimensions is shown in Fig. 1. The outer loop shows the external magnetic field being slowly increased until all domains are pointing up and then decreased back to the initial value. Figure 2 shows the upper branch of three similar hysteresis loops at different disorders R. One sees that for increasing values of R the size of the jump or large Barkhausen effect goes to zero and the hysteresis loops look softer. In fact, one expects that for small R compared to the coupling J, one of the first domains to flip will push over its neighbors, which will cause their neighbors to flip and so on, until a finite fraction of the system is transformed in one "infinite avalanche," which manifests itself as a jump in the magnetization curve. The critical magnetic field $H_c^u(R)$ at which this jump occurs in the upper branch of the hysteresis loop, decreases monotonically with increasing disorder R, starting from $H_c^u(0)=zJ$, where z is the coordination number of the crystal. Experiments,[3] as well as our numerical simulation[5] and analytical calculations[9] suggest that the onset of the infinite avalanche at $H_c^u(R)$ seems to be abrupt for $R<R_c$ in three dimensions, as H is slowly changed.

In the other regime, where the disorder R is large compared to the coupling J, each domain will essentially flip on its own. There will be only small avalanches happening. Empirically, the coercivity decreases further for increasing R. There must be a critical disorder R_c separating these two regimes. In other words, the line of critical fields $H_c^u(R)$ at which an infinite avalanche occurs, ends at the point $H_c^u(R_c)$. For $R>R_c$ the magnetization curves do not show any infinite avalanches. This has been verified both experimentally[3] and in our simulation in three dimensions ($R_c=2.23$ J numerically). In two dimensions, the numerical results suggest that R_c is zero. We have found numerical[5] and analytical[5,9] evidence that the transition occurring at R_c from infinite avalanche to noninfinite avalanche hysteresis loops is continuous: One finds avalanches of all sizes at that point. As one approaches the critical end point at $[R_c,H_c^u(R_c)]$ in the (R,H) plane, we find diverging correlation lengths and presumably universal critical behavior. This transition between the two regimes has a natural parallel with ordinary equilibrium temperature-driven phase transitions. To make this parallel concrete, consider the pure equilibrium Ising model in three dimensions. In this model there is a transition at a certain temperature where the order parameter (which in this case is the magnetization) takes on a finite value. This transition occurs when the ordering tendency of the bonds between spins overcomes the disordering tendency of thermal fluctuations. In our model, the order parameter is the size of the infinite avalanche $\Delta M[H_c(R)]$. We have a finite value for our order parameter when the "ordering" tendency of the bonds between spins overcomes the disordering tendency of the random fields. For us, ordering is represented by the existence of an infinite avalanche, where a large number of domains flip at one field. We also note that the analog of the equilibrium correlation length for our model is the size of the largest finite avalanche.

From both mean-field approaches and renormalization

TABLE I. Universal exponents for critical behavior in hysteresis loops. The exponents β and δ tell how the magnetization scales with $r=(R_c-R)/R_c$ and $h=H-H_c$, respectively, for example, $\{M(H)-M[H_c^u(R_c)]\} \sim (H-H_c)^{(1/\beta)}$ at R_c. The correlation length exponent ν is measured (numerically) using finite-size scaling. The exponent σ tells how the cutoff of the avalanche size distribution scales with r, and τ is the exponent of the power-law decay of the differential avalanche size distribution $D(s,r,h)$ at the critical point ($r=0$ and $h=0$).

Exponent	ϵ expansion with $\epsilon=6-d$, at $\epsilon=3$	Simulation in three dimensions
$1/\nu$	$2-\epsilon/3=1$	1.0 ±0.1
β	$0.5-\epsilon/6=0$	0.17±0.07
$\beta\delta$	$1.5+O(\epsilon^2)\approx 1.5$	2.0 ±0.3
δ	$3+\epsilon=6$	(around 12)
$1/\sigma$	···	2.9 ±0.15
τ	···	1.35±0.2

group techniques, near R_c we expect universal scaling laws for the behavior of the magnetization M and the distribution D of sizes s of avalanches occurring upon increasing H by a differential amount dH. For $r\equiv(R_c-R)/R_c$ and $h\equiv[H-H_c^u(R_c)]$, we have $M(h,r)\sim|r|^\beta\mathscr{M}_\pm(h/|r|^{\beta\delta})$, and $D(s,r,h)\sim s^{-\tau}\mathscr{D}_\pm(s/|r|^{-1/\sigma},h/|r|^{\beta\delta})$, where $\pm$ refers to the sign of r and $\mathscr{M}_\pm$ and $\mathscr{D}_\pm$ are universal scaling functions. In mean-field theory, where we couple every domain with all N other domains with coupling J/N, we find $\delta=3$ and $\beta=\frac{1}{2}$. Near the end point, the jump in the magnetization ΔM due to the infinite avalanche scales like r^β. Furthermore, in mean-field theory, $\tau=\frac{3}{2}$ and $\sigma=\frac{1}{2}$. We expect these exponents to be accurate in six and all higher dimensions. We have performed an expansion around six dimensions to obtain an analytical prediction for these exponents in three dimensions, using renormalization group techniques.[9] Independently, we have determined the exponents from the numerical simulation in three dimensions.[5] Table I gives the results from both approaches.

Particularly interesting for comparison with experiments[1] is the avalanche size distribution integrated over a whole hysteresis loop (see the inset of Fig. 2). In fact, the distribution of avalanches, as it is measured in the Barkhausen effect, has been studied, and some preliminary fits to power laws were made.[1] These fits have been interpreted as an indication of self-organized criticality. The noticeable cutoff of the power law avalanche size distribution was thought to be due to finite size effects. In the view of our model, we would suggest that the power laws might be an indication of an ordinary critical point instead of self-organized criticality. We would expect the cutoff in the distribution to move to larger and larger avalanche sizes, as the critical point is approached by tuning the randomness R to its critical value R_c. We think that similar effects might be observed, for example, upon changing the distribution of random anisotropies. (Though the fact that random magnetic fields break time-reversal symmetry, whereas random anisotropies do not, could change the values of the critical exponents.) Furthermore, we expect this effect not only to be found in magnetic materials. Indeed, for a FeNi alloy, which is an athermal Martensite, an increase in grain sizes has been seen to lead to a crossover from noninfinite avalanche to infinite avalanche behavior.[3]

We acknowledge the support of the Department of Energy Grant No. DE-FG02-88-ER45364. BWR acknowledges support from the Hertz Foundation. SK acknowledges support from the Department of Education. We would like to thank J. Ortín, A. Planes, Llouis Mañosa, Teresa Castán, Oliver Penrose, Mark Robbins, and Po-zen Wong for helpful conversations.

[1] J. C. McClure, Jr. and K. Schröder, CRC Crit. Rev. Solid State Sci. **6**, 45 (1976); P. J. Cote and L. V. Meisel, Phys. Rev. Lett. **67**, 1334 (1991); L. V. Meisel and P. J. Cote, Phys. Rev. B **46**, 10 822 (1992); B. Alessandro, C. Beatrice, G. Bertotti, and A. Montorsi, J. Appl. Phys. **68**, 2908 (1990).

[2] E. C. Stoner and E. P. Wohlfarth, Philos. Trans. R. Soc. London Ser. A **240**, 599 (1948); J. Yamasaki, F. B. Humphrey, K. Mohri, H. Kawamura, H. Takamure, and R. Mälmhäll, J. Appl. Phys. **63**, 3949 (1988), and references therein.

[3] V. Raghavan in *Martensite*, edited by G. B. Olson and W. S. Owen (ASM International, Materials Park, OH, 1992), p. 197.

[4] F. Preisach, *Z. Phys.* **94**, 277 (1935); M. Krasnoselskii and A. Pokrovskii, *Systems With Hysteresis* (Nauka, Moscow, 1983), I. D. Mayergoyz, J. Appl. Phys. **57**, 3803 (1985); *Mathematical Models of Hysteresis* (Springer, New York, 1991); P. C. Clapp, Mat. Sci. Eng. A **127**, 189–95 (1990).

[5] J. P. Sethna, K. Dahmen, S. Kartha, J. A. Krumhansl, B. W. Roberts, and J. D. Shore, Phys. Rev. Lett. **70**, 3347 (1993).

[6] J. Villain, Phys. Rev. Lett. **29**, 6389 (1984); G. Grinstein and J. F. Fernandez, Phys. Rev. B **29**, 6389 (1984); A. J. Bray and M. A. Moore, J. Phys. C **18**, L927 (1985); D. S. Fisher, Phys. Rev. Lett. **56**, 416 (1986).

[7] N. Goldenfeld, *Lectures on Phase Transitions and the Renormalization Group*, (Addison–Wesley, New York, 1992), p. 383; K. G. Wilson and J. Kogut, Phys. Rep. C **12**, 76 (1974).

[8] C. M. Coram, A. E. Jacobs, N. Heinig, and K. B. Winterbon, Phys. Rev. B **40**, 6992 (1989); S. Maslov and Z. Olami, preprint.

[9] K. Dahmen and J. P. Sethna, Phys. Rev. Lett. **71**, 3222 (1993).

Magnetic properties of the two-dimensional "triangles-in-triangles" Kagomé lattice $Cu_9X_2(cpa)_6$ (X=F,Cl,Br)

Sanchit Maruti and Leonard W. ter Haar[a)]
Department of Chemistry, University of Texas, El Paso, Texas 79968

Magnetic properties of the isostructural series of compounds known as $Cu_9X_2(cpa)_6$ (cpa=carboxypentonic acid; X=F,Cl,Br) are reported as a function of the μ_3-halide ion. The interconnection topology within each layer is a hexagonal arrangement of trimeric units, i.e., a "triangles-in-triangles" Kagomé lattice. Magnetic field dependent susceptibility data in the range 1.7–250 K demonstrate that all three compounds have a magnetic ground state which is highly field dependent at lower temperatures, but that phase transitions to long-range order are not observed down to 1.7 K. Development of 2-D antiferromagnetic models appropriate for the chemical nature and symmetry of the $Cu_9X_2(cpa)_6$ lattice will require a two J-value solution (intratrimer and intertrimer), and although theoretical results for this type of lattice are as yet unknown, analogies can be clearly drawn to the Kagomé problem. The Curie–Weiss temperatures in the range of -250 K strongly suggest spin frustration in the absence of any traditional long-range order. Magnetization studies exhibit an intermediate saturation level corresponding to a ground state of one unpaired spin per unit cell at field values well below 1.0 kG, supporting the conclusion that the two J values are antiferromagnetic.

I. INTRODUCTION

The Heisenberg antiferromagnet on a square lattice is well accepted as having an ordered ground state.[1] Other more novel topologies for quantum (S=1/2) antiferromagnetic lattices are now of interest because of the unique ground-state properties that may derive from such features as next-nearest-neighbor exchange interactions and triangulation (which can lead to spin frustration). Ongoing theoretical studies in the literature focus on such exotic systems as the triangular, union-jack, honeycomb, and Kagomé antiferromagnets,[2] but known experimental examples are still limited. We recently reported[3] the synthesis and structure of $Cu_9F_2(cpa)_6 \cdot xH_2O$ and demonstrated that it is isomorphous with the Cl and Br congeners.[4] As part of our continued effort to understand and utilize these compounds in a guest-host chemical approach toward molecular-based magnetic materials, we now report that the magnetic properties of all three compounds are similar in nature and that the effect of the halogen substitution is minimal.

II. EXPERIMENT

$CuCl_2 \cdot 2H_2O$ was reacted with ascorbic acid (2:1 mol ratio). The mixture was heated and allowed to stir until the precipitation of CuCl was complete (~0.5 h), after which the CuCl was filtered off. CuX_2 (1 mmol) was added to the clear solution followed by the addition 0.10 M NaOH to raise the pH to a value of 6. Excess (25 mmol) KX was added. Blue hexagonal prisms were collected after two to three days. In all cases, materials were freshly prepared for immediate use, or frozen. Solvent water loss from within the channels of the structure can be rapid in our dry climate.

Magnetic susceptibility data were collected in the temperature range 1.7–250 K using a Quantum Design superconducting quantum interference device (SQUID)-based magnetometer utilizing modifications and procedures described elsewhere.[5] Data were corrected for temperature independent magnetism using Pascal's constants[6] for the diamagnetic components and a T.I.P./Cu(II) of 60×10^{-6} emu/mole.

III. RESULTS AND DISCUSSION

2-carboxypentonic acid is a polyhydroxypolycarboxylic acid obtained from the redox rearrangement reaction of ascorbic acid using Cu(II).[7] Its structure is conducive to a multitude of ligating possibilities in which interconnected high-nuclearity species are clearly possible. The structures of all three $Cu_9X_2(cpa)_6$ compounds are isomorphous; the preparation of products can be verified by powder x-ray diffraction.[3,4]

The crystal structures of all three products quite clearly suggest[3] the schematic of the magnetic lattice which can be used to correlate the magnetic properties to the chemical structure. Two unique environments are found for the Cu(II) ions. The copper designated $Cu_{trimer}(Cu_t)$ is in a square pyramidal coordination and near a crystallographic threefold axis, thereby generating a trimeric unit, as shown in Fig. 1. The basal coordination sites are oxygens from two different cpa anions, and the apical coordination site is filled by the common μ_3-halide ion located on the threefold axis. It is this bridging halide ion that is different among the three structures, and is the subject of this paper.

There are six Cu_t ions (i.e., two μ_3-halide trimers) per unit cell. $Cu_{monomer}(Cu_m)$ is located on a crystallographic twofold axis. It has four short Cu—O equatorial bonds and two longer Cu—O axial bonds; see Fig. 1. Two carboxylate groups (of a single cpa) bridge a Cu_m site to two Cu_t sites of two trimers. Three such Cu_m sites are connected to every Cu_t based trimer; two such trimers are connected to each Cu_m. To further develop the structure of the extended lattice, the fragment shown in Fig. 1 can be repeated so as to form a polymeric sheet in the ab plane. The layer shown in Fig. 2

a)Author to whom all correspondence should be addressed.

 0021-8979/94/75(10)/5949/3/$6.00 © 1994 American Institute of Physics

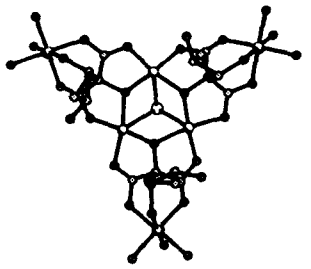

FIG. 1. Trimer of three square pyramidal Cu_i ions bridged to three octahedral Cu_m.

stacks in the c direction; the layers are held together hydrogen bonding. This stacking of the layers results in channels that are ~20 Å in diameter.

Representative 10 kG data are plotted in Fig. 3 for the bromo compound, as χ_m, $1/\chi_m$, and $\chi_m T$ using the molar basis of the unit cell formula, $Cu_9X_2(cpa)_6$. Both the chloro and the bromo compounds exhibit magnetic behavior similar to the fluoro[3] compound. χ_m diverges at low temperatures for all three compounds; it does not exhibit a maximum as a function of temperature for any of the compounds. Instead, $\chi_m T$ is very characteristic in that it reaches a *minimum* near 60 K and then rises toward a *maximum* near 6 K before falling again to lower values. This $\chi_m T$ maximum is field dependent in both magnitude and temperature.

For all three compounds the $1/\chi_m$ plot exhibits three distinct regions. For $T>150$ K, the data are linear as a function of temperature and can be fit by the Curie–Weiss law, $\chi_m = C/(T-\theta)$, with the best-fit parameters summarized in Table I. The line in Fig. 3 is drawn using these parameters. For $25<T<150$ K, the slope of the $1/\chi_m$ curve changes continuously and it is not appropriate to use a Curie–Weiss fit. Again, below 25 K the data become increasingly field dependent at progressively lower temperatures. For $T>125$ K, and using an average g value of 2.1 for Cu(II), the C values per unit formula are that expected for nine moles of noninteracting paramagnetic $S=1/2$ ions (~3.7 emu K/mol). But the $\chi_m T$ value at 250 K is clearly reduced with respect to such a C value. Coupled with the decreasing nature of $\chi_m T$ at lower temperatures, these results are indicative of the very strong antiferromagnetic exchange that is also suggested by the large negative θ values.

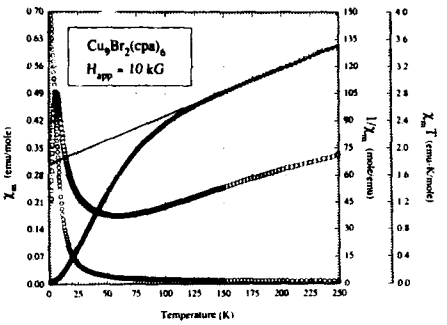

FIG. 3. Magnetic data [(○) χ_m, (▽) $1/\chi_m$, (□) $\chi_m T$], X=Br, H=10 kG.

At high fields (10 kG in Fig. 3), the $\chi_m T$ plot clearly indicates that a minimum effective spin value is reached before a rounded maximum occurs upon further cooling. The temperatures at which such rounded $\chi_m T$ maxima occur is highly dependent on the applied field; the maximum increases in magnitude and shifts to lower temperatures with smaller applied fields. The variable-field data in Fig. 4 clearly demonstrate this feature—note that $\chi_m T$ has not yet reached a maximum down to 1.7 K at 10 G.

The $Cu_9X_2(cpa)_6 \cdot xH_2O$ materials are clearly unique, particularly among two-dimensional magnetic materials. First, the chemical lattice shown in Fig. 2 corresponds to the magnetic schematic, or connectivity pattern, displayed in Fig. 5(d). Comparison to other triangulated lattices [Figs. 5(a)–5(c)] emphasizes a number of topological similarities and differences. Second, triangulated spin systems are notable for the spin frustration they may exhibit. Although a number of triangular molecular clusters are known,[8] $Cu_9X_2(cpa)_6 \cdot xH_2O$ lattice suggests a new direction for the design and synthesis of extended magnetic lattices. Third, triangulated magnetic lattices are of particular interest as experimental testing grounds for the physics associated with degenerate ground states and finite entropies (at $T=0$), as this relates to the order-from-disorder problem.[9]

Chemically, the $Cu_9X_2(cpa)_6 \cdot xH_2O$ lattice consists of two different spin sites and two exchange parameters (which are unlikely to be of equal magnitude). Topologically, the

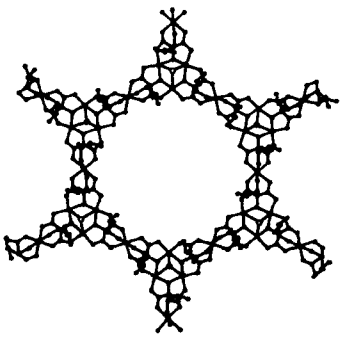

FIG. 2. Infinite layer structure where one columnar channel is evident.

TABLE I. Magnetic properties of $Cu_9X_2(cpa)_6$; $H=10\,000$ G.

Compound	C (emu K/mol)	Theta (K)	XT @250 K (emu K/mol)
$Cu_9F_2(cpa)_6$	3.84 (0.1)	−237 (5)	1.71
$Cu_9Cl_2(cpa)_6$	3.64 (0.1)	−226 (5)	1.88
$Cu_9Br_2(cpa)_6$	3.73 (0.1)	−243 (5)	1.90

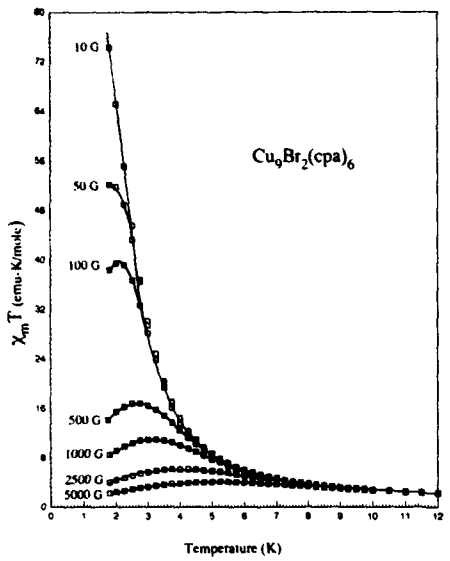

FIG. 4. Variable field data for $Cu_9Br_2(cpa)_6 \cdot xH_2O$. The $\chi_m T$ maximum increases in magnitude and shifts to lower-temperature values with decreased applied field strength. Curves serve as guides to the eye.

pairwise exchange interactions between Cu_t sites must be equal in value and we refer to it as the intratrimer exchange parameter. The trimeric units are interconnected to one another by way of four equivalent exchange interactions between four Cu_t sites (of two trimers), and the Cu_m site that interconnects two such trimers. We refer to these exchange interactions as the intertrimer parameter. The intratrimer exchange parameter is likely to be large in magnitude and antiferromagnetic in nature[10] because of the hydroxy bridging oxygens in the Cu_3O_3 "ring" and, to a much lesser extent, the tribridging halide whose effect is the subject of this paper.

Isothermal magnetization studies in the range 1.7–20 K demonstrate that the compound has a magnetic ground state which is highly field dependent. A saturation level of 1.1 B.M./unit formula (nine $S=1/2$ sites) is reached well below 1 kG at the lowest temperatures. Hysteresis is not observed. We conclude the intertrimer exchange parameter must therefore also be antiferromagnetic, and that the effective residual spin (nine spins coupled antiferromagnetically) results in a ferrimagnetic type of cooperative phenomena. Spontaneous magnetization, however, is not observed down to 1.7 K.

The $Cu_9X_2(cpa)_6$ compounds represent a unique extension [Fig. 5(d)] of the interconnection exhibited by the idealized Kagomé lattice [Fig. 5(c)]. It has been suggested[11] that the schematic of the lattice be refered to as a "triangles-in-triangles" Kagomé. Such interconnected triangulation suggests spin frustation, and clearly this could lead to an order-

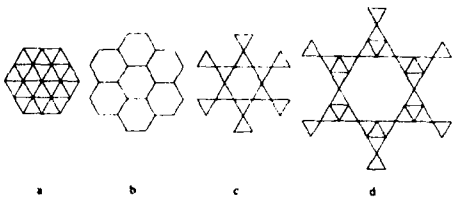

FIG. 5. (a) Triangular, (b) honeycomb, (c) Kagomé, (d) $Cu_9X_2(cpa)_6 \cdot xH_2O$.

from-disorder situation. Theoretical results for this type of lattice are unknown, but given (i) the topological arrangement of the triangles, (ii) that both J values are antiferromagnetic, and (iii) that there is an odd number of spins per unit cell; it is quite possible that a number of nonunique ground states exist due to frustration effects. Since there is presently interest in topologically frustrated systems,[12] in part from Anderson's RVB structure for superconductivity in doped cuprates[13] for which one feature of the liquidlike RVB state is the absence of long-range order in the ground state, it will be of interest to perform ac susceptibility and heat capacity experiments on the $Cu_9X_2(cpa)_6$ system. Theoretical studies on the $Cu_9X_2(cpa)_6$ ground state will be difficult since a large number of sites will be required to make any finite cluster calculation valid.[14] Nonetheless, we are pursuing work along these lines, as well as derivatives obtained through metal substitution and guest-host chemistry.

ACKNOWLEDGMENTS

This research was supported by the National Science Foundation, the R. A. Welch Foundation, and AT&T Bell Labs, as well as financial support from the DOD-DLA for the SQUID magnetometer.

[1] E. Manousakis, Rev. Mod. Phys. **63**, 1 (1991), and references therein.
[2] A. Chubukov, J. Appl. Phys. **73**, 5639 (1993), P. W. Leung and V. Elser, Phys. Rev. B **47**, 5459 (1993); P. W. Leung and K. J. Runge, *ibid.* **47**, 5861 (1993); I. Ritchey, P. Chandra, and P. Coleman, *ibid.* **47**, 15342 (1993).
[3] M. Gonzalez, F. Cervantes-Lee, and L. W. ter Haar, Mol. Cryst. Liq. Cryst. **233**, 317 (1993).
[4] R. E. Norman, N. J. Rose, and R. E. Stenkamp, J. Chem. Soc. Dalton Trans. 2905 (1987); R. E. Norman and R. E. Stenkamp, Acta Cryst. C **46**, 6 (1990).
[5] D. Nelson, and L. W. ter Haar, Inorg. Chem. **32**, 182 (1993).
[6] *Theory and Applications of Molecular Paramagnetism*, E. A. Boudreaux and L. N. Mulay (Wiley, New York, 1976).
[7] G. Wilkinson, *Comprehensive Coordination Chemistry* (Pergamon, New York, 1987), Vol. 5, 450ff.
[8] J. K. McCusker, H. G. Jang, S. Wang, G. Christou, and D. N. Hendrickson, Inorg. Chem. **31**, 1874 (1992), and references therein.
[9] See, e.g., D. A. Huse and V. Elser, Phys. Rev. Lett. **60**, 2531 (1988); V. Elser, *ibid.* **62**, 2405 (1989); X. Obradors, A. Labarta, A. Isalgué, J. Tejada, J. Rodriquez, and M. Pernet, Solid State Commun. **65**, 189 (1988); A. P. Ramirez, G. P. Espinosa, and A. S. Cooper, Phys. Rev. Lett. **64**, 2070 (1990).
[10] O. Kahn, Angew. Chem. Int. Ed. Engl. **24**, 834 (1985), and references therein.
[11] D. J. Klein (private communication).
[12] J. T. Chalker, P. C. W. Holdsworth, and E. F. Shender, Phys. Rev. Lett. **68**, 855 (1992); A. B. Harris, A. J. Berlinsky, and C. Bruder, J. Appl. Phys. **69**, 5200 (1991).
[13] P. W. Anderson, Science **235**, 1196 (1987).
[14] D. Gatteschi (private communication).

Magnetic properties of two copper (II)-halide layered perovskites

N. Sivron, T. E. Grigereit,[a] and John E. Drumheller
Department of Physics, Montana State University, Bozeman, Montana 59717

K. Emerson
Department of Chemistry, Montana State University, Bozeman, Montana 59717

R. D. Willett
Department of Chemistry, Washington State University, Pullman, Washington 99164

The magnetic properties of the powdered layered structures of 3-ammoniumpyridinium tetrabromocuprate(II) and 3-ammoniumpyridinium tetrachlorocuprate(II) have been studied from 4.2 to 150 K. The data were interpreted using both 1D and 2D series expansions for the Heisenberg model, combined with the appropriate mean-field corrections, yielding interlayer exchanges with J_{2h}/k values of (-11 ± 2) K for the chloride salt and (-52 ± 7) K for the bromide salt. The intralayer exchange (J_{1h}/k) values were found to be (14 ± 2) K and (20 ± 2.5) K for the chloride and bromide salts, respectively. The new results are compared with previous results for the eclipsed layered structure series $NH_3(CH_2)_nNH_3CuX_4$, where X=Br or Cl and $n=2$, 3, 4, or 5. As the halide-halide separation distance decreases the transition from magnetic isolation of the layers to a strong interlayer exchange is observed. The new study allows confirmation of the power dependence on the halide-halide separation.

Special interest has been shown in recent years in the magnetic properties of the $ACuX_4$ crystals, where A stands for a dication, and X stands for Cl or Br,[1–8] since variation of distances between the nearly planar CuX_4 layers of successive compounds in the group results in variation in the values of the interlayer exchange parameter J_{2h}, and makes it possible to investigate the magnetic insulation between layers. In spite of the fact that the interlayer exchange occurs through two intervening halides, a significant superexchange path was found,[2,3,5,7] resulting in some cases not only in quasi-2D systems, but also 3D,[3] and even 1D magnetism.[5,7] These results were reported for samples in which the Cu ions lay directly or nearly directly above one another (eclipsed structure).

An important factor affecting the interlayer exchange mechanism is the distance between the two intervening halides, denoted as the X···X bond length of the linkage Cu-X···X-Cu between the layers. The power dependence of the exchange parameter J_{2h} on the halide-halide separation was found[2] to be $J_{2h}\sim d^{\alpha}$, where $\alpha=-10\pm2$ for X=Br and -6 ± 2 for X=Cl, and d is the X···X bond length.

Since the 3-ammoniumpyridinium tetrabromocuprate(II) [(3AP)$CuBr_4$] and 3-ammoniumpyridinium tetrachlorocuprate(II) (3APCuCl_4) are examples of this structure they are appropriate to further investigate the dependence on the interlayer bond length. These monoclinic crystals have layers of $(CuX_4^2)_n$ arrays of tetrahedrally distorted anions, stacked in eclipsed conformation.[1] The $(CuX_4^2)_n$ arrays are approximately two dimensional, but some deviation from planarity within the layers has been found with an intralayer bridging angle Cu-X···Cu of 161.2° for chlorine and 157.6° for bromine.[1] It should be noted that the layers in these two compounds are noncentrosymmetric and that they have relatively short interlayer halide-halide distances (3.992 Å for X=Cl and 3.889 Å for X=Br). Therefore, predictions about their magnetization, made by comparison with other crystals, were limited, and subject to the fact that insufficient data existed to make satisfying correlations for the tetrahedrally distorted anions.[1]

Data were taken on a model 155 EG&G P.A.R. vibrating sample magnetometer. The crystals were grown according to the literature.[1,9,10] The magnetization was measured at 6000 Oe field over the temperature range 4.2–150 K. The data were interpreted using both 1D and 2D series expansions for the Heisenberg model, combined with the appropriate mean-field corrections.[11–14] Error values were obtained by comparing between results for different data sets. This procedure gave larger error values than the small statistical errors estimated by the computer program for each data set alone.

A fit of the chloride susceptibility data to the 2D model[11,12] is shown in Fig. 1. Error bars are smaller than the sizes of the markers in the low-temperature range. Both salts demonstrate antiferromagnetic exchange between the layers, $J_{2h}/k=-52\pm7$ for (3AP)$CuBr_4$ and -11 ± 2 for (3AP)$CuCl_4$. Both salts demonstrate ferromagnetic exchange within the layer, with positive $J_{1h}/k=14\pm2$ for the Cl salt and 20 ± 2.5 for the Br. Owing to the larger size both in-plane and out-of-plane couplings for bromide are found to be larger in magnitude than those for chloride, as expected. The Cu^{2+} g values are found to be 2.05 ± 0.06 for X=Cl and 2.12 ± 0.225 for X=Br.

These results are compared with those reported in previous work for similar crystals.[1] The graphs of J_{1h}/k values versus the Cu···X bond distance are shown in Fig. 2 for X=Br and X=Cl, adding the values of J_{1h}/k obtained for (3AP)CuX_4. Within the limits of error these new results agree with previous work and the assumption that the J_{1h}/k values of (3AP)$CuBr_4$ and (3AP)$CuCl_4$ would be strongly dependent upon the Cu···X bond distance[1] is confirmed,

[a]Current address: Center for Superconductivity Research, Department of Physics, University of Maryland, College Park, Maryland 20742, and Reactor Radiation Division, National Institute of Standards and Technology, Gaithersburg, Maryland 20899.

 0021-8979/94/75(10)/5952/3/$6.00 © 1994 American Institute of Physics

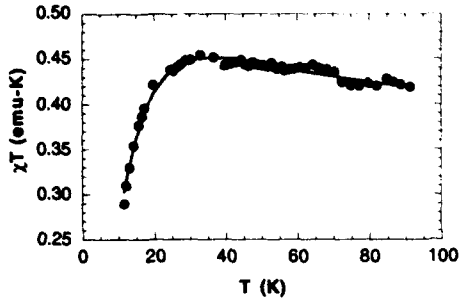

FIG. 1. Fits of the data of $(3AP)CuCl_4$. The experimental data points are marked as circles. The model calculated for the optimal values is marked as a solid line.

showing that longer bonds result in weaker interaction.

The natural logarithm of J_{2h}/k values versus the natural logarithm of X···X are shown in Fig. 3 adding the new values obtained for the $(3AP)CuX_4$ salts. The transition from a quasi-2D Heisenberg system to a 3D or 1D system is observed by comparing the relative strengths of the interlayer exchange parameters, which gradually become larger than those of the intralayer exchange parameters. From the slopes, the power dependence of J_{2h}, the interlayer exchange on the halide-halide distance can be calculated.[2] Assuming $J_{2h} \sim d^{\alpha}$ we find $\alpha = -10.9 \pm 2$ for X=Cl and $\alpha = -6 \pm 2$ for X=Br.

The chloride salt forms a 3D magnetic structure, since the absolute values of the inter- and intralayer exchange parameters are so similar. It is interesting that the interplanar exchange through the two-halide bridge is dominant in the case of $(3AP)CuBr_4$, indicating that the bromide salt with the stronger exchange may be described as a one-dimensional antiferromagnetic chain. Therefore, the values of J_{2h}/k were double checked with 1D models[13,14] yielding $J_{2h}/k = -57 \pm 3$ for X=Br and -9.5 ± 0.5 for X=Cl. Considering the short halide-halide distances these results are well understood and compare favorably with the magnetic structure of $(2DA)CuX_4$,[2,7,15] where 2DA stands for ethylenediammonium, and X=Cl or Br. Those were further investigated by growing a mixed sample, $(2DA)CuCl_2Br_2$, in which Cl anions substitute for the Br anions in the layer.[2] In this case the interlayer exchange parameter was reported to be $J_{2h}/k = -31$, almost half the value for the purely bromine case $(2DA)CuBr_4$,[7] in which $J_{2h}/k = -68.4$. Since the interlayer X···X bond lengths were very similar in both crystals (3.7 ± 0.2 Å for the mixed sample, 3.602 Å for the pure sample), it is not clear how the presence of the chlorides in the planes of the layers affected the interlayer exchange. This and other interesting examples found in the case of bromide[7] suggest that the exchange mechanism for these salts is not trivial and further investigations are needed, especially when the X···X bond lengths are very small. For further studies it may be interesting to repeat the process of growing a mixed sample for $(3AP)CuX_4$.

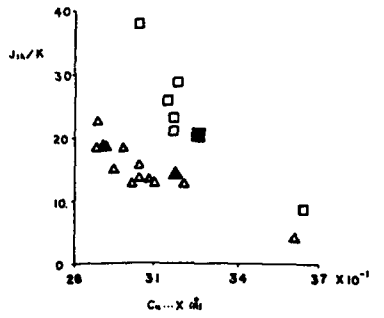

FIG. 2. J_{1h}/k values vs Cu···X bond lengths (Å) for $A'CuX_4$ and $A2CuX_4$. Previous data points obtained from Refs. 1 and 8 are marked as squares for X=Br, and the new result for the $(3AP)CuBr_4$ is marked as a solid square. For X=Cl previous data points are marked as triangles and the new result for $(3AP)CuCl_4$ is marked as a solid triangle.

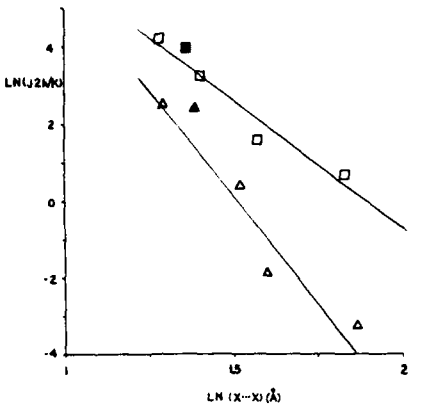

FIG. 3. The natural logarithm of J_{2h}/k vs the natural logarithm of X···X. Previous data points were obtained from Refs. 1–3, 5, 7, 8, and 13. For X=Br they are marked as squares, and the new result for $(3AP)CuBr_4$ is marked as a solid square. For X=Cl they are marked as triangles, and the new result for $(3AP)CuCl_4$ is marked as a solid triangle.

Special thanks to Dr. George Tuthill for his remarks and suggestions and to Ran Sivron for all the helpful comments. We thank Liu Ying for confirming the bromine data with ac susceptibility measurements. Research sponsored by NSF Grant No. DMR-9011072.

[1] R. D. Willett, H. Place, and M. Middleton, J. Am. Chem. Soc. **110**, 8639 (1988), and Refs. therein.
[2] L. O. Snively, G. F. Tuthill, and J. E. Drumheller, Phys. Rev. B **24**, 5349 (1981), and Refs. therein.
[3] L. O. Snively, P. L. Seifert, K. Emerson, and J. E. Drumheller, Phys. Rev. B **20**, 2101 (1979), and Refs. therein.
[4] P. Zhou, J. E. Drumheller, B. Patyal, and R. D. Willett, Phys. Rev. B **24**, (1992).
[5] T. M. Kite and J. E. Drumheller, J. Magn. Res. **54**, 253 (1983), and Refs. therein.
[6] R. D. Willett, F. H. Jardine, I. Rouse, R. J. Wong, C. P. Landee, and M. Numata, Phys. Rev. B **24**, 5372 (1981).

[7] G. V. Rubenacker, D. N. Haines, and J. E. Drumheller, J. Magn. Magn. Mater. **43**, 238 (1984), and Refs. therein.
[8] L. O. Snively, J. E. Drumheller, and K. Emerson, Phys. Rev. B **23**, 6013 (1981).
[9] J. Blanchette and R. D. Willett, Inorg. Chem. **27**, 843 (1988), and Refs. therein.
[10] N. Sivron, M.S. thesis, Montana State University, 1992.
[11] G. A. Baker, H. E. Gilbert, J. Eve, and G. S. Rushbrooke, Phys. Lett. A **25**, 207 (1967).
[12] G. S. Rushbrooke and P. J. Wood, Mol. Phys. **1**, 257 (1958).
[13] G. A. Baker, G. S. Rushbrooke, and H. E. Gilbert, Phys. Rev. **135**, A1272 (1964).
[14] M. Takahashi and M. Yamada, J. Phys. Soc. Jpn. **54**, 2808 (1985).
[15] H. Von Kanel, Physica (Utrecht) B **96**, 167 (1979).

Can the universal jump be observed in two-dimensional *XY* magnets?

S. T. Bramwell
Institut Laue-Langevin, 156-X, 38042 Grenoble, France

P. C. W. Holdsworth
Laboratoire de Physique, Ecole Normale Supérieure de Lyon, 69634 Lyon, France

The universal jump in the spin-wave stiffness is a characteristic property of the Kosterlitz–Thouless–Berezinskii phase transition in an infinitely large 2D-*XY* magnet. It has recently been demonstrated [S. T. Bramwell and P. C. W. Holdsworth, J. Phys. Condens. Matt. **5**, L53 (1993)] that finite-size rounding is much more important in two-dimensional than in three-dimensional systems. This is because the properties of the phase transition depend logarithmically, rather than algebraically, on the system size. Consequently, finite-size rounding will be dominant in any real, macroscopic 2D-*XY* magnet. How the rounded universal jump still exhibits observable universal properties is discussed.

The Mermin–Wagner theorem,[1] which predicts that two-dimensional systems with continuous symmetry of the Hamiltonian cannot sustain long-range order at finite temperature, has become part of the folklore of physics. However, although lost in the literature, it has been pointed out several times[2,3] that power-law decay of the low-temperature spatial correlations will result in long-range order on the length scale of any realizable laboratory system. Thus, these two-dimensional problems have the very interesting property that a macroscopic system is far from the thermodynamic limit.

We have recently given several illustrations of this[3,4] for the finite-size magnetization, $M(N,T)$, of a two-dimensional *XY* (2D-*XY*) model of N spins. One finds, using a harmonic approximation, that $M(N,T)=(2N)^{-1.8\pi K}$, where the "spin-wave stiffness" $K=J/T$, with T the temperature and J the coupling constant. For example, putting $T/J\sim 1$ and taking $N=10^{16}$, gives $M(N,T)\sim 0.2$. For an atomic spacing of 3 Å, this corresponds to a system about the size of a postage stamp.

Kosterlitz and Thouless, and Berezinskii (KTB)[5] showed that, although such systems cannot have a regular symmetry breaking phase transition, they do have a novel kind of phase transition mediated by the unbinding of pairs of topological defects, or vortices (KT theory). Below the transition temperature, T_{KT}, the correlations are critical, with power-law decay; above T_{KT} they are short ranged, with exponential decay. Renormalization group theory[6,7] predicts that $K=J/T$ is renormalized by the presence of vortex pairs to an effective value $K_{eff}=J_{eff}/T$. At the transition temperature there is a discontinuous jump in K_{eff} from the universal value $K_{eff}=2/\pi$ to zero.[8]

We investigated the finite-size behavior of KTB systems,[3,4] and used the renormalization group equations and Monte Carlo simulations to explain the magnetization observed in layered magnets, and more recently in ultrathin films.[9,10] These systems are clearly two dimensional up to a large length scale, and would be considered among the best realizations of the 2D-*XY* model, were it not for the observation of a magnetization in the two-dimensional critical regime. We approximately calculate the renormalized finite-size magnetization of the 2D-*XY* model, by replacing K in the harmonic expression with K_{eff},

$$M(N,T)=(2N)^{-1/8\pi K_{eff}}. \tag{1}$$

We find that the rounding of the KTB transition is abnormally large compared with that of a second-order phase transition, with T_{KT} being shifted logarithmically with system size. Our principal result is that this broadened transition region is characterized by a universal finite-size magnetization, with universal exponent $\beta=0.231\ldots$, the signature of vortex unbinding. This result is in excellent agreement with the many independent experiments.

It should be noted that $\beta=0.23$ occurs in any *XY* system in which 2D critical fluctuations are dominant regardless of the dimensionality of the magnetization itself. This is in keeping with the general conclusions of the renormalization group theory of phase transitions.[11] Thus, the 2D magnetization of ultrathin films, and the 3D magnetization of layered magnets, both show a broad region of $\beta=0.23$, just as analogous 2D-Ising-like systems show $\beta\sim 1/8$.[12,13] In the layered magnets the finite size, typically 10^4 spins, is an effective parameter determined by the interlayer coupling.[3]

In this article we discuss the spin-wave stiffness, and show that the universal jump cannot be seen in its purest form, but that its finite-size remnants have their own very universal character. The article is also relevant to work on superfluid helium films, where the equivalent of the spin-wave stiffness, the helicity modulus, has been measured with great precision,[14] and successfully fitted to dynamical theories of the 2D-*XY* model.[15]

In Ref. 4 we introduced a model which is described very precisely by KT theory, and which we refer to as the harmonic *XY* (H*XY*) model. We use the Hamiltonian

$$H=-J[1-(1/2)(\theta_i-\theta_j-2\pi n)^2],$$

where θ_i is periodic on 2π, and n is an integer ensuring that $(\theta_i-\theta_j-2\pi n)$ is bounded between $\pm\pi$. This model contains only harmonic spin waves and vortices, so renormalization of K_{eff} is due entirely to the vortex pairs. In the 2D-*XY* model, with pair interaction in the Hamiltonian, $\cos(\theta_i-\theta_j)$, there are in addition anharmonic, yet analytic corrections to spin-wave theory, which come from fourth-order and higher

 0021-8979/94/75(10)/5956/3/$6.00 © 1994 American Institute of Physics

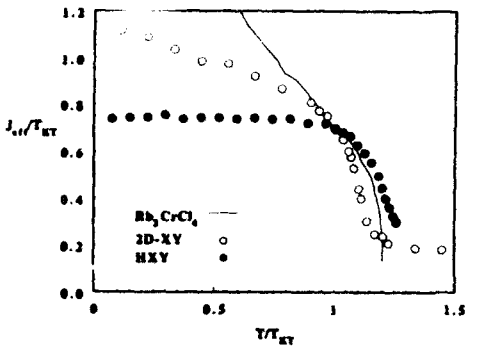

FIG. 1. J_{eff}/T_{KT} vs T/T_{KT} from experimental data and from Monte Carlo magnetization data for 10^4 spin systems, obtained by inverting Eq. (1). *HXY* refers to the harmonic *XY* model.

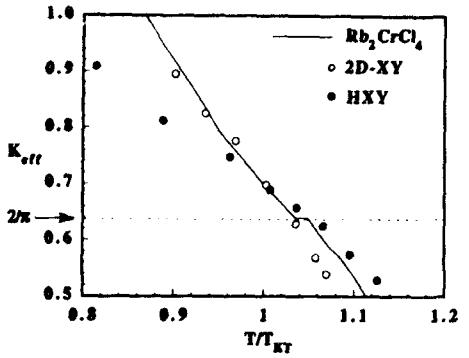

FIG. 2. K_{eff} vs T/T_{KT} from experimental data and from Monte Carlo magnetization data for 10^4 spin systems, obtained by inverting Eq. (1). The dashed line indicates the universal value $K_{eff}=2/\pi$.

terms in an expansion of the cosine function. These terms modify K_{eff} even in the absence of vortices.[4,16–18] In layered *XY* magnets, such as Rb_2CrCl_4,[19] $Ba(NiPO_4)_2$,[20] and K_2CuF_4,[21] the Hamiltonian is Heisenberg-like, with crystal field and other perturbation terms favoring a two-dimensional spin plane. In this case fluctuations out of the spin plane result in further corrections to harmonic spin-wave theory.[21]

Rb_2CrCl_4 was originally identified as an experimental realization of the 2D-*XY* ferromagnet by Hutchings *et al.*[22] The ratio of nearest neighbor to interlayer exchange J/J' is about 10^4. In our work[3,9] we propose that planar magnets have two-dimensional fluctuations on all length scales up to $L = L_{eff} \sim \sqrt{J/J'}$ in units of the lattice constant, and hence correspond to finite 2D-*XY* systems of this size ($\sim 10^4$ spins for Rb_2CrCl_4). The static magnetic behavior of Rb_2CrCl_4, in the two-dimensional temperature regime, has been explained completely and quantitatively by our model.[19] We can hence calculate K_{eff} and J_{eff} ($=TK_{eff}$) directly from the magnetization data of Ref. 19 by inverting Eq. (1).

In Fig. 1 we compare J_{eff}/T_{KT} vs T/T_{KT} for Rb_2CrCl_4, with that derived in the same way from the Monte Carlo data of the 10^4 spin *XY* and *HXY* systems of Refs. 3 and 4. $T_{KT}/J = 0.72$, 0.898, 1.351, respectively (J for Rb_2CrCl_4 is equivalent to $2JS^2$ in the notation of Refs. 19 and 22), showing clearly how anharmonic corrections reduce the transition temperature.[16] At low temperature J_{eff} is constant for the *HXY* model, indicating that the system contains harmonic spin waves only, whereas for the 2D-*XY* model and Rb_2CrCl_4, J_{eff} is renormalized strongly by the anharmonic corrections. Above a well-defined temperature near T_{KT},[4] vortex pairs cause a more rapid decrease in J_{eff}. The curves approach each other in this region, although they are not superimposed. This is to be compared with the findings of Ohta and Jasnow,[18] who showed that, for an infinite system, corrections to spin-wave theory become irrelevant in the limit $T \to T_{KT}$. Our Fig. 1 compares very favorably with their Fig. 2 for temperatures below T_{KT}, but differs in the critical region because of the considerable finite-size effects.

In Fig. 2 we plot K_{eff} vs T/T_{KT} for the same data. We see that the three curves cross the line indicating the universal value $2/\pi$ at different temperatures. This is to be expected, following the results of Ref. 3, where we show that K_{eff} takes its universal value $2/\pi$ at a shifted temperature

$$T^*(L)/J \sim T_{KT}/J + \pi^2/4c(\ln L)^2. \tag{2}$$

The constant c is nonuniversal, taking values 1.5, 3.3, and 3.1 for the HXY, 2D-*XY*, and Rb_2CrCl_4 data, respectively, which results in different values of T^* for each system. This difference is due to a reduction in the vortex core energy caused by the anharmonic contributions to the spin waves. On the present length scales, c can be considered to be constant, although it does evolve very slowly with system size.[4]

A remarkable feature of Fig. 2 is the intersection of all three curves at T_{KT}. This feature falls naturally out of our calculation. From the renormalization equation (4) of Ref. 3 we find

$$\Delta K = K_{eff}(T_{KT}) - 2/\pi \sim 1/\pi \ln(L). \tag{3}$$

Thus, the calculation predicts that $K_{eff}(T_{KT})$ is independent of c, and depends only on the size L. As all three systems considered have the same two-dimensional size, the curves should indeed intersect at this point. For $L = 100$ we predict $\Delta K = 0.069$, which is in excellent agreement with the value read from Fig. 2 of 0.064.

In the thermodynamic limit these results map onto those of Ohta and Jasnow.[18] In this case $T^* \to T_{KT}$, $\Delta K \to 0$, and the three curves intersect at the point of the universal jump. In this limit ΔK is predicted to approach zero as $\sqrt{T_{KT} - T}$.[6] Our results suggest that for real systems finite-size rounding will prevent the observation of this cusp.

As an independent test of our interpretation of layered magnets in terms of a finite-size 2D-*XY* model, we compare in Fig. 3 the spin-wave stiffness of Rb_2CrCl_4 found by inverting Eq. (1) with that determined by two other methods. In the first we derive K_{eff} directly from the spin-wave frequencies $\omega_{\ell=0.01}$ reported by Hutchings *et al.*,[22] assuming

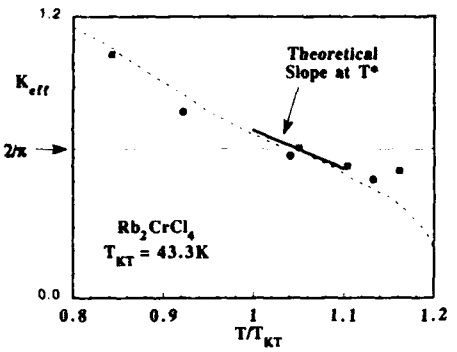

FIG. 3. K_{eff}/T_{KT} vs T/T_{KT} for Rb_2CrCl_4 determined by: (1) neutron inelastic scattering (circles, Ref. 22), (2) weak-field magnetization (squares, Ref. 23), and (3) magnetic Bragg scattering (dashed line, Ref. 19). The horizontal line indicates the universal value $K_{eff}=2/\pi$.

$$K_{eff}=\frac{2\tilde{J}S^2}{k_BT}\frac{\omega(T)}{\omega(0)}. \tag{4}$$

In the second we use the magnetization-field exponent $\delta(T)$ measured by Cornelius *et al.*,[23] and the relationship $\delta=8\pi K_{eff}-1$.[6] We also plot the theoretical slope $\partial K_{eff}/\partial T$ at T^*.[3] The agreement between the three curves and the theoretical prediction is impressive, considering the diversity of method involved, giving very strong evidence that our interpretation of these systems is correct.

This agreement brings up an interesting point concerning renormalization and the dynamics of the 2D-*XY* model. It can be argued[24] that the spin-wave frequency ω should renormalize as $\sqrt{JJ_{eff}}$, rather than as J_{eff}. Using semiclassical arguments one can show that, in the harmonic case, a spin wave corresponds to a harmonic oscillator with angular force constant J and moment of inertia $I\sim 1/J$,[25] which gives $\omega\sim\sqrt{J/I}\sim J$. On renormalization, a simple picture would be that one changes the length scale to a new system of oscillators, with modified force constant, but unchanged moment of inertia. This would give a new frequency $\omega_{ren}\sim\sqrt{JJ_{eff}}$. Coté and Griffin[24] put this argument on a more rigorous footing, after mapping the problem onto Maxwell's equations. However, the data of Fig. 3 suggests that this argument is not correct for real systems, as the best agreement between the static and dynamic measurements for K_{eff} is found by assuming that the frequencies renormalize linearly with J_{eff}.

Finally, it is worth noting that the curves of Fig. 1 are directly comparable to the reduced period shift versus temperature curves measured in the torsion balance experiments on helium films.[14] However, the shift T^*-T_{KT} for these systems is much smaller, indicating a much larger *XY* system size. In fact, the torsional oscillator probes a finite length scale, which according to fits to the dynamical theory of Ambegaokar *et al.*[15] is about 10^5 interparticle spacing: [14] The *XY* system size for the ultrathin superfluid films is presumably much larger still, and hence macroscopic. This contrasts with the situation in ultrathin magnetic films, where effective *XY* system sizes are limited by defects and weak interactions, and are unlikely to exceed about 10^3 lattice spacings.[4,10,13]

In conclusion, the universal jump cannot be observed in 2D-*XY* magnets, at least not in its purest form. The jump is rounded, but still has universal characteristics. As a result of the extreme finite-size broadening of the 2D critical regime, these characteristics are easily observed in both experiment and Monte Carlo simulation.

[1] N. D. Mermin and H. Wagner, Phys. Rev. Lett. **17**, 1133 (1966).
[2] See, for example, Y. Imry and L. Gunther, Phys. Rev. B **11**, 3939 (1971); M. M. Telo de Gama and P. Tarazona, Phys. Rev. A **41**, 1149 (1990); V. L. Berezinskii and A. Ya Blank, Sov. Phys. JETP **37**, 369 (1973).
[3] S. T. Bramwell and P. C. W. Holdsworth, J. Phys. Condensed Matter **5**, L53 (1993).
[4] S. T. Bramwell and P. C. W. Holdsworth, Phys. Rev. B (in press).
[5] J. M. Kosterlitz and D. J. Thouless, J. Phys. C **6**, 1181 (1973); V. L. Berezinskii, Sov. Phys. JETP **32**, 493 (1971).
[6] J. M. Kosterlitz, J. Phys. C **7**, 1046 (1974).
[7] J. V. José *et al.*, Phys. Rev. B **16**, 1217 (1977).
[8] D. R. Nelson and J. M. Kosterlitz, Phys. Rev. Lett. **39**, 1201 (1977).
[9] S. T. Bramwell and P. C. W. Holdsworth, J. Appl. Phys. **73**, 6096 (1993).
[10] W. Dürr *et al.*, Phys. Rev. Lett. **62**, 206 (1989).
[11] M. E. Fisher, Rev. Mod. Phys. **46**, 597 (1974).
[12] H. Ikeda and K. Hirakawa, Solid State Commun. **14**, 529 (1974).
[13] C. Liu and S. D. Bader, Springer Series in Physics **50**, 22 (1990).
[14] D. J. Bishop and J. D. Reppy, Phys. Rev. B **22**, 5171 (1980).
[15] V. Ambegaokar *et al.*, Phys. Rev. B **21**, 1980).
[16] J. Villain, J. Phys. (Paris) **36**, 581 (1975).
[17] T. Ohta and D. Jasnow, Phys. Rev. B **20**, 139 (1979).
[18] J. Als-Nielsen *et al.*, J. Phys. Condensed Matter **5**, 7875 (1993).
[19] L. P. Regnault *et al.*, J. Magn. Magn. Mater. **15-18**, 1021 (1980).
[20] K. Hirakawa, J. Appl. Phys. **53**, 1893 (1982).
[21] C. Kawabata and A. R. Bishop, Solid State Commun. **60**, 167 (1986).
[22] M. T. Hutchings *et al.*, J. Phys. C **14**, 5327 (1981); M. T. Hutchings *et al.*, J. Magn. Magn. Mater. **54-57**, 673 (1986).
[23] C. A. Cornelius *et al.*, J. Phys. C **19**, 909 (1986).
[24] R. Coté and A. Griffin, Phys. Rev. B **34**, 6240 (1986).
[25] F. J. Dyson, Phys. Rev. **102**, 1217 (1956).

Strong thermal fluctuation effects on the dynamics of Bloch walls (abstract)

M. Hartl, D. Garanin, and J. Koetzler
Institut fur Angewandte Physik, Universitaet Hamburg, D-20355 Hamburg, Germany

Approaching the Curie temperature of the uniaxial Ba and Sr hexaferrites from below in zero magnetic field, a rapid decrease of the domain wall relaxation rate Γ_w is observed which attains a minimum at $T^*=0.99\ T_c$. Above T^* the increase of the relaxation, $\Gamma_w \sim (T_c - T)^{-0.8}$, agrees with that observed previously on low-temperature ferromagnets[1] and is assigned to the presence of linear domain walls. Accordingly, the speeding-up of Γ_w towards T_c is associated with the divergence of the correlation length of a 3-dimensional Ising-magnet determining the width of the linear wall. The temperature T^* is found to be significantly larger than T_0^* predicted by mean field work of Bulaevskii and Ginzburg[2] for the second order transition from linear to Bloch domain walls, which is characterized by a continuously increasing transverse magnetization, $m_B \sim (T^* - T)^{\beta_B}$, in the wall. Adjusting the temperature variation of the relaxation rate below T^* to a recent kinetic theory for elliptic walls,[3] one finds $\beta_B=0.10$ to be close to the 2-dimensional Ising value. Along with the suppression of T^* this constitutes the first signature of severe fluctuation effects in domain walls.[4]

[1] M. Grahl and J. Koetzler, Z. Phys. B 75, 527 (1989); J. Koetzler *et al.*, Phys. Rev. Lett. 64, 2446 (1990).
[2] L. N. Bulaevskii and V. L. Ginzburg, Sov. Phys. JETP 18, 530 (1964).
[3] D. A. Garanin, Physica A 178, 467 (1991).
[4] J. Koetzler *et al.*, Phys. Rev. Lett. 71, 177 (1993).

 0021-8979/94/75(10)/5958/1/$6.00 © 1994 American Institute of Physics

Depth-dependent magnetic correlation length in terbium (abstract)

P. M. Gehring
Materials Science and Engineering Laboratory, National Institute of Standards and Technology, Gaithersburg, Maryland 20899

K. Hirota
Department of Physics,[a] Brookhaven National Laboratory, Upton, New York 11973

C. F. Majkrzak
Materials Science and Engineering Laboratory, National Institute of Standards and Technology, Gaithersburg, Maryland 20899

G. Shirane
Department of Physics,[a] Brookhaven National Laboratory, Upton, New York 11973

High q-resolution neutron-scattering measurements of the critical scattering in Tb above the magnetic-spiral phase transition temperature T_s exhibit a two-component line shape, as recently documented in Ho.[1] This implies the existence of a second length scale, which runs counter to our present understanding of second order phase transitions. By using a narrow beam only 300 μm wide, and then translating the crystal through the beam, we have established that the origin of the second length scale lies within the near surface volume or "skin" of the Tb crystal.[2] This is manifested by a large enhancement of the scattering intensity at the c-axis face of the cube-shaped crystal. In this context the meaning of skin is distinct from that of surface since the second component is spread over several hundred micrometers and not just one or two. In addition, we find that not all skins are equivalent. The intensity of the second component scattering is greatest in those faces that are orthogonal to the c-axis face. Such an anisotropy is easily motivated on physical grounds given that the spins in Tb are confined to the basal plane below T_s.

[a]Supported under DOE Contract No DE-AC0276CH00016.

[1]T. R. Thurston, G. Helgesen, D. Gibbs, J. P. Hill, B. D. Gaulin, and G. Shirane, Phys. Rev. Lett. **70**, 3151 (1993).
[2]P. M. Gehring, K. Hirota,C. F. Majkrzak, and G. Shirane, Phys. Rev. Lett. **71**, 1087 (1994).

 0021-8979/94/75(10)/5959/1/$6.00 © 1994 American Institute of Physics

Ba-ferrite thin-film media for high-density longitudinal recording (invited)

T. L. Hylton, M. A. Parker, M. Ullah, K. R. Coffey, R. Umphress, and J. K. Howard
IBM AdStar, San Jose, California 95193

Ba-ferrite is an attractive candidate for future high-density recording media because of its large coercivity, corrosion resistance, high hardness, and durability. In contrast to most recent work on Ba-ferrite thin film media, polycrystalline films with large in-plane remanence for longitudinal recording are emphasized. Films are prepared on a variety of substrates by on-axis sputtering at low temperatures from stoichiometric targets followed by a postdeposition anneal in a rapid thermal processor at ~850 °C to induce crystallization. Structural and chemical properties have been investigated by force microscopy, Rutherford backscattering, and other means. Stoichiometric films have large 5000 Å grains that are unsuitable for high-density recording. However, grain sizes as small as 200 Å have been produced by doping with small amounts of Cr_2O_3 and other additives. Compositional changes also influence crystallite orientation. Exceptional durability has been observed on disks without overcoats, presumably due to a fine-scale texturing that occurs during crystallization. Coercivities are greater than 4000 Oe even in small grain films. The effect of grain size on coercivity and signal-to-noise ratio of several Ba-ferrite disks is discussed. It is argued that the grains are magnetically decoupled based on the magnetic properties of these films.

I. INTRODUCTION

Barium ferrite ($BaFe_{12}O_{19}$) recording media in the form of particulates suspended in a binding material has been widely investigated as a recording layer on magnetic tape and flexible disks. Several investigations of the use of longitudinally oriented Ba-ferrite particulate media on rigid disks report that the performance of these disks is surprisingly close to that of Co-alloy thin-film disks with magnetic layers only 25% as thick as the Ba-ferrite particulate layer.[1,2] The exceptional performance of this particulate media has been attributed to the large anisotropy field and the magnetic decoupling of the particulates.[3] Also, over the past decade there has been substantial work by a few researchers in the development of Ba-ferrite thin-film media for perpendicular recording.[4–14] As the magnetic easy axis in this material is parallel to the c axis, a large effort has been made to develop processes for obtaining thin films with a high degree in c-axis perpendicular orientation. In contrast to the works just described, our effort has been directed toward the preparation of fine-grained, polycrystalline thin films with substantial in-plane remanence for use as a high-density, longitudinal recording media. We are motivated in this effort by the following properties of these Ba-ferrite thin films: (i) large anisotropy and coercivity; (ii) excellent durability and hardness; (iii) excellent corrosion resistance;[15] (iv) ease of preparation relative to the perpendicular Ba-ferrite thin film media; and (v) compatibility of longitudinal media with available magnetic recording heads. In this article we report on the preparation, microstructure, tribology, magnetic properties, and recording performance of Ba-ferrite thin-film, longitudinal recording media. In particular we discuss our efforts to reduce the grain size in these films and its impact on magnetic and recording properties.

II. EXPERIMENTAL PROCEDURE

A popular technique used to prepare the strongly c-axis textured films of interest as perpendicular recording media is to sputter Ba-ferrite from two facing, roughly stoichiometric targets with substrates oriented perpendicular to the targets at the periphery of the plasma.[5,7] This arrangement minimizes the bombardment of the film by energetic particles during growth, which is known to create problems in maintaining film stoichiometry. Substrate temperatures are typically 550–700 °C and crystallization proceeds during deposition. In contrast to this technique, we prepare our samples by S-gun magnetron sputtering in a conventional geometry with targets facing the substrates at a distance of about 10 cm. Substrates are unheated and move with continuous "planetary" motion over four different sputtering guns. Doping and alloying are accomplished by cosputtering two or more targets. Ba-ferrite targets are stoichiometric and typically sputtered with rf power; however, after several hours of rf sputtering the targets become conductive and dc sputtering is also possible. New targets require several hours of sputtering to achieve reproducible film properties. Presumably the stoichiometry of the surface of a new target changes during the first

TABLE I. Typical range of deposition parameters in the deposition of Ba-ferrite films.

Pressure	2–8 mTorr
% O_2 in Ar	5%–10%
Flow	40 sccm
Power	200–500 W dc or rf
Bias (negative)	0–80 V dc
Thickness	500–1100 Å
Rate	8.5–11 Å/min

 0021-8979/94/75(10)/5960/6/$6.00 © 1994 American Institute of Physics

TABLE II. A summary of our work on preparing Ba-ferrite films on a variety of substrates. Reactivity with the substrate was determined by the amount of film-substrate interdiffusion after high-temperature annealing. Samples with "small" reactivity have good magnetic properties and limited interdiffusion with a 1000-Å-thick film. The converse is true for samples with "large" reactivity. "Good" adhesion means films are resistant to scratching with stainless-steel tweezers.

Substrates	Description	Vendor	Reactivity	Adhesion
Fused si	O_2 glass	Valpey-Fisher	small	good
Fused qu	O_2 glass	Heraeus	small	good
7913 glass	96% SiO_2 glass	Corning	small	good
7059 glass	alkali-free glass	Corning	medium	good
0317 glass	soda glass	Corning	medium	good
Oxidized Si	SiO_2 glass		small	excellent
UDAC	C glass	Kobe precision	very large	very poor
Si	cubic, (100) (111)		large	good
Al_2O_3	hex., A,R,C plane	Insaco	small	good
MgO	cubic, (100)	Ceres	large	good
Y_2O_3-ZrO_2	cubic, (100)	Ceres	very small	poor
$LaAlO_3$	cubic, (100)	Ceres	very small	poor
$SrTiO_3$	cubic, (100)	Ceres	very small	very poor

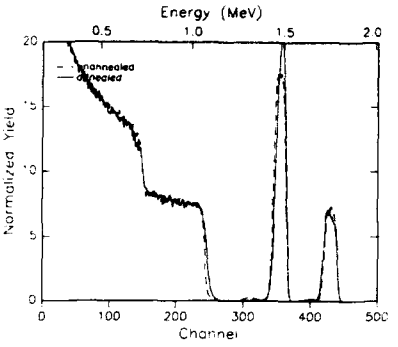

FIG. 1. The ^{4}He backscattering spectroscopy (RBS) of a 970-Å-thick Ba-ferrite film before and after crystallization by a high-temperature anneal clearly shows an interdiffused layer at the substrate surface nominally 310 Å thick. Also evident is a reduction in oxygen concentration and loss of trapped Ar after annealing. No significant change in the total number of counts under the Ba and Fe peaks is observed after annealing.

few hours of sputtering until a steady state is reached. Typical sputtering conditions are shown in Table I.

The films are nonmagnetic, insulating, and amorphous after deposition. Crystalline, magnetic films are obtained after removal from the vacuum system by annealing in a quartz-lamp-driven, rapid thermal processor. Similar processes using conventional furnaces have been reported by several authors previously.[16–19] A typical annealing condition is 850 °C for 10 min in 1 atm of O_2. Processing times as short as 10 s are possible for temperatures of 950 °C or more. Annealed films are polycrystalline with grain size and orientation that depend strongly on the composition of the film, which we describe in more detail below.

Table II summarizes our efforts to prepare Ba-ferrite thin films on a variety of substrates using the technique described above. The ideal substrate is inexpensive, mechanically robust, and compatible with high-temperature annealing, while providing limited interdiffusion and excellent adhesion with the Ba-ferrite film. The most promising substrates so far identified are oxidized Si, SiO_2 (fused silica or fused quartz glass), and Corning glass No. 7913 (Vycor 96% silica sheet glass). These substrates are quite similar and were used for all the results reported below. Unlike the pure silica or Vycor glasses, other glasses have failed as substrate materials primarily because their softening points are smaller than or comparable to the typical 850 °C annealing temperature. Very rapid annealing times (<15 s) have only been partially successful in crystallizing Ba-ferrite films on some of the lower-temperature glasses described in Table II. The amorphous carbon substrates have superb high-temperature capability, but are extremely reactive with Ba-ferrite and in oxygen atmospheres. We have achieved limited success growing Ba ferrite on a dual buffer layer structure of sputtered SiO_x/Si/C. Others have reported c-axis textured Ba-ferrite films crystallized during deposition at 580 °C on C substrates with SiO_2/Cr buffer layers.[20] Although expensive and unsuitable for use as a disk substrate, we have also investigated a variety of single-crystal, dielectric oxide substrates to examine the Ba-ferrite film morphology and reactivity on these materials. The table gives a qualitative description of the amount of interdiffusion observed between the substrate and Ba-ferrite film following a typical anneal at 850 °C as determined by Rutherford backscattering spectroscopy (RBS) and the film-substrate adhesion as determined by a crude scratch test with stainless-steel tweezers. Notable among these single-crystal substrates is sapphire in a variety of orientations. We observe strongly oriented, epitaxial growth of Ba-ferrite on these substrates[21] and coercivities in excess of 9 kOe for samples annealed at temperatures high enough to promote significant diffusion of Al into the Ba-ferrite film.[22]

III. RESULTS AND DISCUSSION

Figure 1 is a RBS spectrum of a Ba-ferrite film on SiO_2 sputtered from a stoichiometric $BaFe_{12}O_{19}$ target before and after annealing for 10 min at 850 °C in O_2. Analysis of the RBS data of the as-deposited film yields a composition $Ba_{1.07}Fe_{12}Ar_{0.4}O_{29}$. After annealing, the Ba peak shows an obvious diffusion of Ba into the substrate. A model assuming a single, homogeneously interdiffused layer of $Ba_{0.5}Fe_3Si_4O_{13}$ (310 Å) and a homogeneous ferrite layer $Ba_{0.83}Fe_{12}O_{21}$ (550 Å) provides a good fit to the data. Although this model is likely to be an oversimplification of the real structure, our reason for considering it will become more apparent below. Others have reported similar film-substrate reactions on samples crystallized *in situ* at temperatures of 650–750 °C.[19,23] After the anneal the small Ar peak present in the as-deposited film disappears, and the film is reduced to a more nearly stoichiometric oxygen concentration. The excess oxygen present in the films before annealing may be the result of energetic bombardment of the film by oxygen species during deposition. Consistent with observed loss of O and Ar, profilometer measurements reveal a 10%–15% reduction in film thickness after annealing, although this may

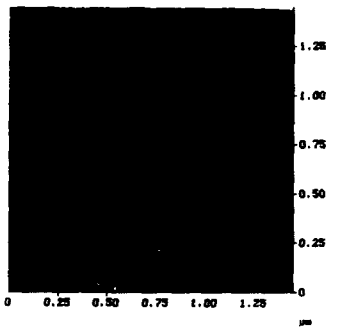

FIG. 2. AFM image the surface topography of an undoped Ba-ferrite film ($n=6$) with a deposited thickness of 1000 Å on a SiO_2 substrate after annealing. Light areas are higher than dark areas. Plate- and needlelike morphologies are apparent with needlelike grains having dimensions of roughly 3000×500 Å^2.

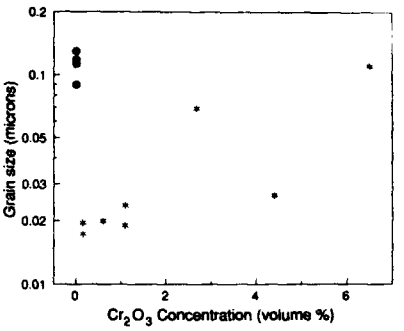

FIG. 3. Doping Ba-ferrite ($n=6$) thin films with Cr_2O_3 has a large impact on the average grain size. Averages were determined by measuring several grains with both needle and plate morphologies. Cr_2O_3 concentrations of 0.1–1 vol % yield an average grain size of order 200 Å, but larger concentrations result in increasing grain size. Asterisks denote doped films and circles undoped films.

also be a result of compaction during crystallization. As we describe below the interdiffusion between film and substrate strongly affects magnetic properties and suggests the need for a buffer layer between film and substrate. On the other hand, a structure without a buffer layer is simpler, and the interdiffused layer may promote adhesion. Also, the composition and thickness of the interdiffused layer changes insignificantly even for annealing temperatures as high as 1000 °C indicating that it is quite stable.

Figure 2 is an atomic force microscope (AFM) image of the surface topography of a typical Ba-ferrite thin film. Two distinct grain morphologies are readily apparent: (i) many needlelike grains with aspect ratios of about 6:1, and (ii) fewer platelike regions of larger area. Transmission electron microscopy (TEM) indicates that the grains are columnar and that the two different morphologies are the result of different orientations with respect to the substrate surface of the crystallites of the same shape. Namely, a range of orientations exist from c-axis normal to the substrate yielding large platelike grains to c axis in the substrate plane yielding needlelike grains. The needlelike grains are essentially plates viewed edge on, where the growth of the plates is interrupted at the film-substrate and film-vacuum interface. The relatively narrow size distribution of the grains implies that grain growth has proceeded normally, without discontinuous growth of large grains. These observations are consistent with the typical hexagonal platlet structures of Ba-ferrite grains in bulk ceramics, where abnormal grain growth occurs only at temperatures much higher than those reported here.[24,25] We have previously reported on the growth kinetics of these platelet-shaped grains on sapphire substrates.[26] Contrary to the acicular particles found in most particulate recording media, the easy axis in the Ba-ferrite needle-shaped grains is parallel to the short dimension, owing to the very large crystalline anisotropy of this material.

The grain sizes in Fig. 2, roughly 3000×500 Å for a typical needle-shaped grain, are too large to be useful in a high-density recording medium. Murdoch[27] has estimate that recording at densities of 10 Gbit/in.^{2} will require 100 Å grains that are magnetically decoupled from neighboring grains. In order to reduce the grain size in these thin films we have doped our Ba-ferrite films by cosputtering with other materials including ZrO_2, Cr_2O_3, Y_2O_3-stabilized ZrO_2, SiO_2, and Pt. With the exception of Pt, all of these materials were effective in reducing grain size to varying degrees. The most effective dopant in the range of compositions so far investigated is Cr_2O_3, deposited by reactive cosputtering of a Cr target under the conditions described in Table I. In Fig. 3 we show the change in grain size observed after addition of various amounts of Cr_2O_3 to a roughly stoichiometric $BaFe_{12}O_{19}$ host by cosputtering and annealing in the manner described above. A range of volumetric additions from approximately 0.1%–1%, determined by rate calibrations of the targets, produces a five-to-tenfold decrease in the average grain size as compared to undoped films and grain size increases again for higher levels of Cr_2O_3 addition. Some films show average in-plane grain dimensions as small as 200 Å, which approaches the grain sizes that will be required in future high-density recording media. Figure 4 is an AFM image of the surface topography of a Cr_2O_3-doped film with small grain size. The structure and magnetic properties of the doped and undoped films are discussed in more detail below. We point out that the small amounts of Cr_2O_3 used in these experiments should not have a significant impact on the intrinsic properties of the Ba ferrite, such as the saturation magnetization M_s and the magnetocrystalline anisotropy field H_k.[28]

The as-deposited films are extremely smooth, but a fine-scale roughness develops after crystallization. Figures 2 and 4 show that the needlelike grains protrude above the level of the platlets on the film surface. Hence, the Ba-ferrite surface has an intrinsic source of texture that may be beneficial in reducing friction forces between a head and a Ba-ferrite disk. As one might expect, the roughness of the Ba-ferrite film correlates well with the grain size. An undoped Ba-ferrite

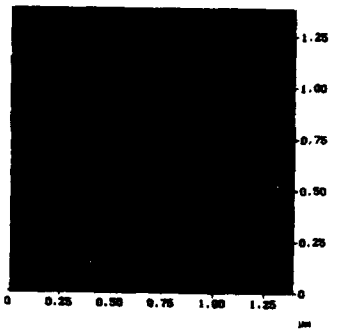

FIG. 4. AFM image of the surface topography of a Ba-ferrite film ($n=6$) doped with approximately 0.5 vol % Cr_2O_3 with a deposited thickness of 1000 Å on a SiO_2 substrate after annealing. The grain morphology is similar to that shown in Fig. 2, but the dimensions of a typical needlelike grain have been reduced to 375×750 Å^2.

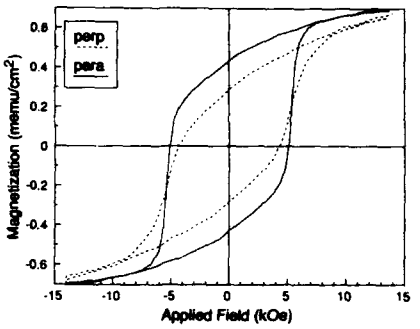

FIG. 5. Magnetization hysteresis of a Ba-ferrite film ($n=5$) doped with Cr_2O_3 with a deposited thickness of 500 Å for fields applied parallel and perpendicular to the film plane. This sample shows large $S=0.61$ for the field parallel, indicating a prefered in-plane orientation of the crystallites. Other parameters for the parallel field hysteresis loop are $H_c=5.1$ kOe and a coercive squareness $S^*=0.83$.

film with grains several thousand angstroms in size has a rms roughness of typically 200–300 Å, while a Cr_2O_3 doped film with 200 Å grain size has rms roughness of typically 20–30 Å. We frequently employ a stylus profilometer to obtain a crude estimate of the film roughness and, thereby, the grain size. Occasionally, other structures are observed that roughen the Ba ferrite surface. Figure 4 shows a weblike series of ridges about 0.5 μm apart. We have also observed hillocks in the form of blisters where the film detaches from the substrate over submicron areas, especially on thermally oxidized Si substrates. The origin of these additional structures is unclear.

The tribological performance of several Ba-ferrite disks without overcoats has been evaluated using a contact-start-stop (CSS) test. The disk substrates (SiO_2 and oxidized Si) are extremely smooth and the only texture to the disk surface is that provided during the crystallization process. Ba-ferrite disks lubricated with a conventional perflouropolyether and fabricated with and without dopants to reduce grain size have demonstrated excellent durability against Al_2O_3-TiC sliders. Several disks have shown no wear after 30 000 CSS cycles with stiction values from 3–10 g under ambient conditions. Conversely, several disks have also been observed to fail after several thousand cycles. While these results are mixed, they are also very encouraging because they suggest that this media may not require an overcoat, thereby reducing the spacing between head and disk and simplifying their manufacture. In fact, the disks that we describe in this article have only one thin-film layer—the Ba-ferrite itself. The distinction between the "good" and "bad" disks is unclear and the subject of ongoing investigation. In particular we seek to elucidate the role of lubricant thickness, grain size, and debris from the sputtering process on the tribological performance.

Figure 5 shows the magnetization hysteresis for a Cr_2O_3-doped and crystallized Ba-ferrite film, 500 Å thick as deposited. If bulk values for M_s are assumed (~375 emu/cm^3 at 20 °C), then we would expect an areal magnetization at saturation of 1.88 memu/cm^2 based on the deposition thickness, as compared to the 0.70 memu/cm^2 that we observe. Allowing a 10% shrinkage of the film after annealing, a possible explanation for this observation is a 190 Å Ba-ferrite layer with $M_s=375$ emu/cm^3 and a 260 Å nonmagnetic interdiffused layer at the film-substrate interface. A more complete analysis shows a roughly linear relationship between the magnetization and film thickness with $M_s \sim 0$ for deposited thicknesses in the range 250–300 Å. With few exceptions, the Ba-ferrite films on SiO_2 show no evidence of secondary magnetic phases, supporting the idea that the interdiffused layer is nonmagnetic and distinct from the Ba-ferrite crystallites on its surface. These results are consistent with the RBS data discussed above.

All our films exhibit a significant remanent moment M_r for fields applied both parallel and perpendicular to the plane of the sample. In all cases, a large in-plane squareness $S=M_r/M_s$ correlates well with a large number of needle- versus platelike grains in the microstructure, while for large out-of-plane S the reverse is true, consistent with our assignment of different crystallite orientations depending on the shape of the grain. In general, larger in-plane S results in larger read-back signals and is therefore desirable in longitudinal recording systems. The magnitude of in-plane S versus out-of-plane S varies depending on the film composition (and possibly other factors that remain unrecognized). In general, for compositions in the range $(BaO)\cdot n(Fe_2O_3)$ with $5<n<7$ we observe that samples with larger Ba concentrations show greater in-plane S, independent of Cr_2O_3 doping. We also observe that thicker films show a larger in-plane S. This may be related to the compositional effect just described; as the interdiffused layer forms while annealing, a thin ferrite film should be left relatively poor in Ba as compared to a thick ferrite film. The film thickness effect can be effectively compensated by using a Ba-rich composition for very thin films. The sample shown in Fig. 5 has the Ba-rich concentration $n=5$ and shows large in-plane $S=0.61$ for a 500 Å sputtered thickness (and a 190 Å magnetic thickness).

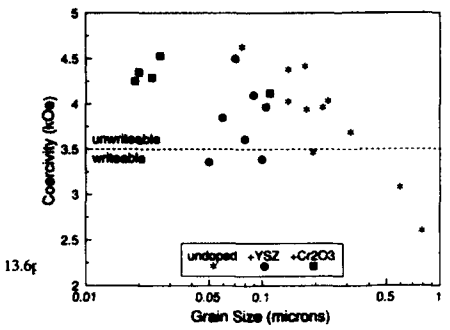

FIG. 6. Coercivity vs average grain size for a number doped and undoped Ba-ferrite films. Films with smaller grain size are generally observed to have larger H_c even down to average grain sizes of 200 Å. Coercivities of most films are slightly too large to be written with available heads.

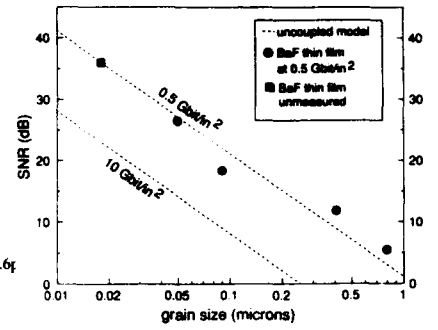

FIG. 7. Signal-to-noise ratio at 0.5 Gbit/in.^{2} of four Ba-ferrite disks with modest coercivity (see Fig. 6). The data show a reasonable correlation to a model that assumes magnetically decoupled grains. Also shown are the model's projected SNR of the 200 Å Ba-ferrite samples with large coercivity that we are unable to write. The model predicts a 13 dB drop in SNR when the density increases from 0.5 to 10 Gbit/in.^{2}

A typical film of the same thickness with $n=6$ is oriented preferentially out of plane with an in-plane $S\sim0.45$. Films of thickness >1000 Å with $n=6$, have typically in-plane $S\sim0.54$.

In Fig. 6 we show a plot of coercivity H_c versus grain size for a variety of undoped and doped Ba-ferrite films. We point out that the coercivity generally exceeds 3 kOe, a rough lower limit on the media coercivity required for 10 Gbit/in.^{2} recording. The general trend is that the coercivity increases as the grain size decreases down to the smallest grain size samples. To what degree the change in grain size actually determines the coercivity is unclear, but the trend is promising because there is no evidence of thermally assisted magnetization reversal, which decreases H_c and ultimately limits the maximum recording density. Currently available heads are unable to write films with coercivity in excess of approximately 3.5 kOe. Unfortunately most of our smallest grain samples, which would be expected to have the best recording noise performance, have coercivities well in excess of 3.5 kOe and cannot yet be evaluated. Sui and Kryder[29] have recently reported a reduction of both the grain size (down to 500 Å) and coercivity by doping Ba-ferrite with modest amounts of CoTi prepared in a manner similar to that described here. We are optimistic that future work will result in films with 100 Å grain sizes and a modest coercivity through some refined doping and/or preparation techniques.

In Fig. 7 we show a plot of the signal-to-noise ratio (SNR) versus grain size of several Ba-ferrite disks. The two smaller grain disks were measured at a recording density of 0.5 Gbit/in.^{2}, and the two larger grain disks were measured at 0.2 Gbit/in.^{2} In the latter case the SNR was scaled by a factor 0.2/0.5=0.4 to give an effective SNR at 0.5 Gbit/in.^{2} For comparison, a model[30] of the SNR assuming magnetically decoupled grains, SNR$=10\log(n_g/n_b)$ where n_g and n_b are the grain and bit densities, is superimposed on the data points for $n_b=0.5$ and 10 Gbit/in.^{2} We note that the measured SNR versus grain size shows a reasonable correlation to the uncoupled model, suggesting that the grains in the these films are also uncoupled. Also shown is the SNR at 0.5 Gbit/in.^{2} predicted by the uncoupled model of the 200 Å Ba-ferrite film with large coercivity that we are currently unable to write. As shown in the figure, the model predicts a 13 dB drop in SNR as the recording density increases from 0.5 to 10 Gbit/in.^{2} At grain sizes of 100 Å, however, the predicted SNR is a respectable 28 dB. Given the data presented here, we believe that Ba-ferrite is an excellent candidate to achieve such small, decoupled grains while maintaining a large coercivity.

Several other observations imply that very little intergranular coupling exists in these thin films. The magnetization hysteresis suggests that these samples may be well described as collections of decoupled magnetic particles with uniaxial anisotropy[31] having orientation distributions ranging from random in three dimensions ($S=0.5$) to random in the two dimensions defined by the substrate plane ($S=0.64$). Samples become more like the two-dimensional model as the concentration of needlelike grains versus platelike grains increases. Also, in the literature on Ba-ferrite particulates and ceramics, grain size is known to correlate with the coercivity. Typically, coercivity is observed to increase with decreasing grain size,[32] until grain sizes are so small that thermally activated reversal becomes important.[33] Figure 6 is qualitatively consistent with this picture, although we have observed a few films doped with large amounts of Cr_2O_3 having grain sizes of several thousand angstroms and coercivities of 5 kOe. Finally we comment that the superexchange mechanism, which is responsible for the ferrimagnetism in Ba-ferrite, depends strongly on the angle made by Fe—O—Fe bonds and, hence, the crystalline order. Therefore, it is not unreasonable to expect that the intergranular exchange interaction across high-angle grain boundaries in these thin films might be severely weakened as compared to the intragranular interaction and as compared to the intergranular interaction across high-angle boundaries in ferromagnetic metals, where the exchange interaction is mediated by conduction electrons.

IV. SUMMARY

We have prepared and characterized Ba-ferrite thin films on a variety of substrates in order to examine their potential as longitudinal magnetic recording media. Our work is distinct from other efforts to create Ba-ferrite media in that we emphasize unoriented, thin-film, longitudinal media, as compared to oriented, thin-film perpendicular media and oriented, particulate, longitudinal media. Samples were prepared by reactive sputtering from a stoichiometric target followed by a high-temperature anneal in a quartz lamp oven. A large but stable interdiffusion layer is observed on SiO_2 substrates after annealing, which may promote adhesion between film and substrate. An intrinsic texture is developed during the crystallization process with the result that disks without overcoats exhibit good durability and low friction against standard sliders. Grain size can be dramatically reduced to sizes of order 200 Å by the inclusion of Cr_2O_3 and other dopants, while maintaining coercivity in excess of 4 kOe. Magnetization and SNR measurements suggest that the intergranular magnetic coupling in these films is weak. With further work these Ba-ferrite thin films might yield a single-layer disk medium with the excellent durability and noise properties as required of future recording media.

ACKNOWLEDGMENTS

We gratefully acknowledge C. Corpuz and R. Ahlert for sample preparation and S. Lambert for SNR testing.

[1] D. E. Speliotis, IEEE Trans. Magn. **MAG-25**, 4048 (1989).
[2] R. G. Simmons, IEEE Trans. Magn. **MAG-25**, 4051 (1989).
[3] D. E. Speliotis, IEEE Trans. Magn. **MAG-26**, 141 (1990).
[4] M. Naoe, S. Hasunuma, Y. Hoshi, and S. Yamanaka, IEEE Trans. Magn. **MAG-17**, 3184 (1981).
[5] M. Matsuoka, Y. Hoshi, M. Naoe, and S. Yamanaka, IEEE Trans. Magn. **MAG-18**, 1119 (1982).
[6] A. Morisako and M. Naoe, IEEE Trans. Magn. **MAG-20**, 815 (1984).
[7] M. Matsuoka, Y. Hoshi, M. Naoe, and S. Yamanaka, IEEE Trans. Magn. **MAG-20**, 800 (1984).
[8] Y. Matsuda, M. Matsuoka, M. Naoe, and Y. Hoshi, IEEE Trans. J. Magn. Jpn. **JMJ-1**, 41 (1985).
[9] M. Matsuoka and M. Naoe, J. Appl. Phys. **57**, 4040 (1985).
[10] M. Matsuoka and M. Naoe, IEEE Trans. Magn. **MAG-21**, 1474 (1985).
[11] A. Morisako, M. Matsumoto, and M. Naoe, IEEE Trans. Magn. **MAG-23**, 56 (1987).
[12] A. Morisako, M. Matsumoto, and M. Naoe, IEEE Trans. Magn. **MAG-24**, 3024 (1988).
[13] K. Matsumoto, M. Yata, S. Nakagawa, and M. Naoe, in Proceedings of the Fifth International Conference on Ferrites, 1989, Vol. ICF-5, p. 507.
[14] J. Nakata, S. Iwata, and S. Uchiyama, IEEE Trans. J. Magn. Jpn **JMJ-3**, 816 (1988).
[15] D. E. Speliotis, IEEE Trans. Magn. **MAG-26**, 124 (1990).
[16] M. Matsumoto, A. Morisako, and T. Hae-iwa, in Proceedings of the Fifth International Conference on Ferrites 1989, Vol. ICF-5, p. 533.
[17] M. S. Yuan, H. L. Glass, and L. R. Adkins, Appl. Phys. Lett. **53**, 340 (1988).
[18] I. Zaquine, H. Benazizi, and J. C. Mage, J. Appl. Phys. **64**, 5822 (1988).
[19] E. Lacroix, P. Gerard, G. Marest, and M. Dupuy, J. Appl. Phys. **69**, 4770 (1991).
[20] K. Sin, J. M. Sivertsen, J. H. Judy, Y. Hoshi, and D. Speliotis, J. Appl. Phys. **73**, 6689 (1993).
[21] T. L. Hylton, M. A. Parker, K. R. Coffey, and J. K. Howard, J. Appl. Phys. **73**, 6257 (1993).
[22] T. L. Hylton, M. A. Parker, and J. K. Howard, Appl. Phys. Lett. **61**, 867 (1992).
[23] P. Gerard, E. Lacroix, G. Marest, M. Dupuy, G. Rolland, and B. Blanchard, J. Magn. Magn. Mater. **83**, 13 (1990).
[24] C. Lacour and M. Paulus, Phys. Status Solidi **27**, 441 (1975).
[25] F. Kools, Sci. Sintering **17**, 63 (1985).
[26] M. A. Parker, T. L. Hylton, K. R. Coffey, and J. K. Howard, Mater. Res. Soc. Symp. Proc. **280**, 625 (1993).
[27] E. S. Murdoch, IEEE Trans. Magn. **MAG-28**, 3078 (1992).
[28] H. Kojima, in *Ferromagnetic Materials*, edited by E. P. Wohlfarth (North-Holland, New York, 1982), Vol. 3.
[29] X. Sui and M. H. Kryder, Appl. Phys. Lett. **63**, 1582 (1993).
[30] We have used the model for wide-band signal-to-noise ratio by J. C. Mallinson, *The Foundations of Magnetic Recording* (Academic, San Diego, 1987).
[31] E. C. Stoner and E. P. Wohlfarth, Philos. Trans. R. Soc. London Ser. A **240**, 599 (1948).
[32] B. D. Cullity, *Introduction to Magnetic Materials* (Addison-Wesley, Reading, MA, 1972), p. 386.
[33] O. Kubo, T. Ido, H. Yokoyama, and Y. Koike, J. Appl. Phys. **57**, 4280 (1985).

Microstructural investigations of barium ferrite longitudinal thin-film media

B. Y. Wong, X. Sui, D. E. Laughlin, and M. H. Kryder
Data Storage System Center, Carnegie Mellon University, Pittsburgh, Pennsylvania 15213

Crystalline barium ferrite films with in-plane magnetic anisotropy have been obtained by postdeposition annealing of amorphous sputtered films. The magnetic properties, the crystallographic texture, and the microstructure are very sensitive to the sputtering and postdeposition annealing conditions. It was found that both H_c and the grain size decrease with the addition of Co and Ti ions. However, an excessive amount of dopants leads to a loss in the in-plane anisotropy. Barium ferrite films produced by this technique contain physical voids or channels separating the grains which help to decrease the exchange coupling between grains.

I. INTRODUCTION

Barium ferrite has been demonstrated, in the particulate form, to have excellent magnetic and recording characteristics for flexible media such as tape or flexible disks.[1–4] Recently, there has been interest in using thin-film barium ferrite for rigid disk media. The mechanical hardness and inert nature of barium ferrite ensure a long media lifetime and may enable a low flying height with no overcoat. Barium ferrite films sputtered under normal deposition conditions are amorphous in nature. Hence, crystalline barium ferrite films have to be obtained by either applying *in situ* substrate heating during deposition or through a postdeposition annealing process. By using the first technique, previous investigators have examined its usefulness as perpendicular rigid disk media.[5,6] Our recent works have explored the possibilities of utilizing it as thin-film vertical and longitudinal media by employing the latter approach.[7,8] In this study, we examined barium ferrite thin films with suitable magnetic properties and microstructures for high areal density recording. As in the case of flexible media, the in-plane coercivity H_c is adjusted by the incorporation of Co and Ti. The microstructure is controlled by the chemical composition, the sputtering, and the annealing conditions. The interplay between these entities is reported in this article.

II. EXPERIMENTAL PROCEDURE

Amorphous multilayer barium ferrite films were rf-diode sputtered onto thermally oxidized Si substrates in a Leybold Heraus Z-400 sputtering system. Two targets were used: $BaFe_{12}O_{19}$ and $Ba_{1.03}Co_{0.85}Ti_{1.17}Fe_{9.86}O_{19}$. Multilayer films with alternating layers sputtered from these two targets were made and the amount of Co and Ti in the films was adjusted by controlling the thicknesses of the respective layers. The total film thickness was between 130 and 200 nm. A forward sputtering power of 50 W was applied. A total sputtering gas (Ar/O_2) pressure of 5 mTorr with an O_2 partial pressure of 0.6 mTorr was used. The deposited films were first annealed in air at 600 °C to allow for composition homogenization within the film and this was followed by an annealing at 820 °C to induce crystallization. The annealed films were examined in plan view and cross section by transmission electron microscopy.

TABLE I. Chemical composition and magnetic characteristics of films A, B, and C.

Film	A	B	C
Chem. comp.	$BaFe_{12}O_{19}$	$Ba_{0.9}Co_{0.36}Ti_{0.5}Fe_{11}O_{19}$	$Ba_{0.78}Co_{0.85}Ti_{1.17}Fe_{9.86}O_{19}$
H_c (Oe)	4066	2201	758
M_s (emu/cm^3)	340	340	170
S	0.63	0.62	0.39
S^*	0.9	0.88	0.45

III. RESULTS AND DISCUSSION

The magnetic properties and the chemical composition of films A, B, and C are given in Table I. H_c of film A is similar to that found in particulate media[1,2] but the saturation magnetization M_s is slightly lower than the bulk value of 380 emu/cm^3. In film B, H_c falls with the addition of Co and Ti, which is most likely due to a decrease in the crystalline anisotropy.[9,10] The excessive amount of dopants in film C causes a sharp drop in M_s and also leads to a realignment of the magnetic easy axis from the crystallographic c axis into the hexagonal basal plane.[10] Hence, the easy axes are no longer in plane but are randomly distributed and this causes a drop in coercivity and S^*. It should be noted that the barium content in both film B and film C is less than in stoichiometric barium ferrite.

The x-ray spectra of these three films along with another film D, which was deposited with rf magnetron sputtering

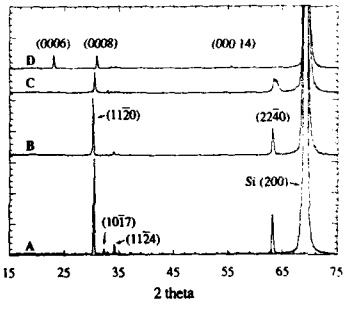

FIG. 1. X-ray diffraction spectra of films A–D.

 0021-8979/94/75(10)/5966/3/$6.00 © 1994 American Institute of Physics

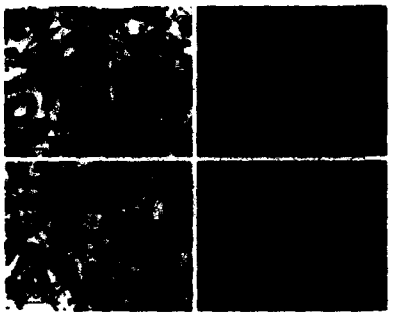

FIG. 2. Pure barium ferrite thin film: (a) and (c) plan-view bright-field (BF) images. (b) [11$\bar{2}$0] and (c) [10$\bar{1}$0] microdiffraction patterns of platelet 1 and grain 2 showing the in-plane easy-axis alignment.

and has a c axis perpendicular to the plane texture,[7] are shown in Fig. 1. A strong c-axis in-plane texture can be found in films A, B, and C. They were annealed at 600 °C for 10 h and then at 820 °C for 3 h. The degree of in-plane texture appears to be strengthened by the addition of Co and Ti, as indicated by the diminishing intensity ratio between (11$\bar{2}$0):(10$\bar{1}$7) and (11$\bar{2}$0):(11$\bar{2}$4) peaks.

The microstructures of films A, B, and C are shown in Figs. 2–4, respectively. The acicular grains are barium ferrite platelets observed from the edge[7] and they can be found readily in all the c-axis in-plane textured specimens. The majority of such grains in the films studied have their [11$\bar{2}$0] zone axis perpendicular to the plane of the film which means the c axis is in the film plane. Film A, which lacks doping, consists mainly of such acicular grains and the average plate length is approximately 380 nm with an aspect ratio of about 6.8 [Figs. 2(a) and 2(c)]. Figures 2(b) and 2(d) are microdiffraction patterns of platelet 1 and grain 2. The [11$\bar{2}$0] and [10$\bar{1}$0] zone axes reveal the c-axis in-plane alignment of these grains.

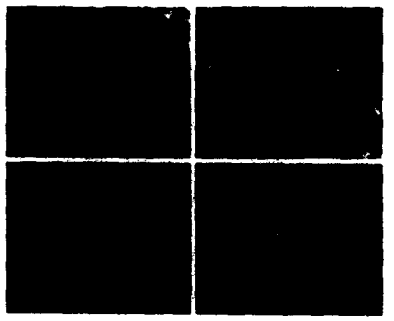

FIG. 3. Co-Ti barium ferrite thin film (multilayer): (a) and (b) plan-view BF images; (c) [10$\bar{1}$0] and (d) [11$\bar{2}$0] microdiffraction patterns of platelets 1 and 2 showing the in-plane easy-axis alignment.

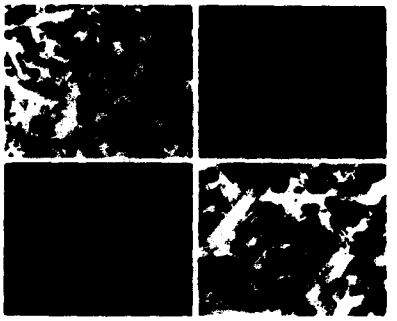

FIG. 4. Co-Ti barium ferrite thin film: (a) and (d) plan-view BF images; (b) [10$\bar{1}$0] and (c) [11$\bar{2}$0] microdiffraction patterns of platelets 1 and 2 showing the in-plane easy-axis alignment.

The incorporation of Co and Ti ions resulted in smaller grain size. In film B, the average plate length has been reduced to 150 nm with an aspect ratio of nearly 5 (Fig. 3). This decrease in aspect ratio should have a small positive effect on H_c since the c axis is perpendicular to the longer axis of these plates. The finer grain size is advantageous for increasing the signal-to-noise ratio in recording media. In film C, the high quantity of dopants leads to a reduction in the number of acicular grains and gives rise to a much finer grain size (Fig. 4). In addition to the acicular grains, an array of fine equiaxed grains with an average grain size of 16 nm can be seen. Fine defect structures [arrow, Fig. 4(d)] resembling stacking faults being observed edge on can be found within some of the grains. The stacking faults probably arise from the misstacking of the oxygen ions closest-packed planes due to excessive Co and Ti ions and a deficiency of Ba ions. The high Co-Ti content can also account for the loss of platelet shape anisotropy usually associated with barium ferrite. The reduction in grain size could be a result of an enhancement in nucleation sites through the addition of Co and Ti ions. The acicular grains can be completely eliminated by altering the annealing conditions as shown in Fig. 5. This film has the same composition as film C but was annealed at 600 °C for 5 h and then at 800 °C for 3 h. Only fine-equiaxed grains similar to those in film C are present.

From the bright-field (BF) and stereographic images, barium ferrite grains in these films are physically separated and the reasons are twofold. First, the inherent platelet morphology of barium ferrite particles does not favor a high packing density and thus results in physical voids between

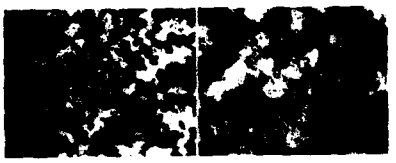

FIG. 5. Co-Ti barium ferrite thin film: (a) and (b) plan-view BF images.

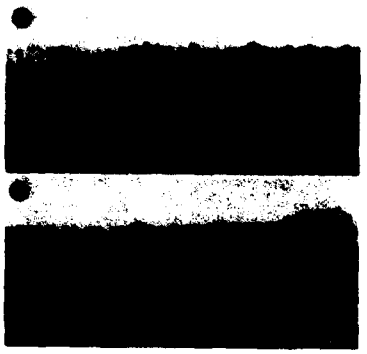

FIG. 6. Co-Ti barium ferrite thin film: (a) and (b) cross-section BF images.

the grains. Second, a volume reduction during the amorphous-to-crystalline phase transformation induces the formation of channels between grains. A cross section of film C is shown in Fig. 6. The rough surface reflects the low packing density, and physical channels can be observed between the grains. Such channels can also be found in Fig. 5(b) (arrow). These voids and channels can account for the slightly low measured M_s value. Moreover, such separation will lead to a reduction in the magnetic coupling between the barium ferrite grains, thus reducing the size of the basic magnetic units and encouraging magnetization reversal by individual particle rotation.

IV. CONCLUSIONS

The crystallographic texture and microstructure of barium ferrite films is very sensitive to the sputtering and postdeposition annealing conditions. The grain morphology and the grain size is controlled by the amount of Co and Ti present in the films and the annealing conditions. Furthermore, H_c can be adjusted by controlling the amount of dopants incorporated into the film. However, excess Co-Ti doping leads to the basal plane becoming a preferred orientation and causes a loss of in-plane anisotropy. Films fabricated with this technique have been found to have physical voids and channels separating the grains which should help decrease the exchange coupling between grains.

ACKNOWLEDGMENTS

This work is supported by National Science Foundation under Grant No. ECD-89007068. The United States Government has certain rights in this material.

[1] T. Fujiwara, IEEE Trans. Magn. **MAG-21**, 1480 (1985).
[2] T. Fujiwara, IEEE Trans. Magn. **MAG-23**, 3125 (1987).
[3] O. Kubo, T. Ido, and H. Yokoyama, IEEE Trans. Magn. **MAG-18**, 1122 (1982).
[4] D. E. Speliotis, IEEE Trans. Magn. **MAG-23**, 3143 (1987).
[5] M Matsuoka, Y. Hoshi, M. Naoe, and S. Yamada, IEEE Trans. Magn. **MAG-20**, 800 (1984).
[6] A. Morisako, M. Matsumoto, and M. Naoe, IEEE Trans. Magn. **MAG-22**, 1146 (1986).
[7] X. Sui, M. H. Kryder, B. Y. Wong, and D. E. Laughlin, IEEE Trans. Magn. **MAG-29**, 3751 (1993).
[8] X. Sui and M. H. Kryder, Appl. Phys. Lett. **63**, 1582 (1993).
[9] Z. Yang, J. Liu, P. Zheng, S. Geng, and Z. Chen, IEEE Trans. Magn. **MAG-23**, 3131 (1987).
[10] J. Smit and H. Wijn, *Ferrites: Physical Properties of Ferrimagnetic Oxides in Relation to Their Technical Applications* (Wiley, New York, 1959), p. 208.

Low-temperature deposition of hexagonal ferrite films by sputtering

Akimitsu Morisako, Hiroaki Nakanishi, and Mitsunori Matsumoto
Faculty of Engineering, Shinshu University, 500 Wakasato, Nagano 380, Japan

Masahiko Naoe
Department of Physical Electronics, Tokyo Institute of Technology, 2-12-1 O-okayama, Meguro-ku, Tokyo 152, Japan

Pb-substituted Ba-ferrite films were prepared at various substrate temperature T_s by dc magnetron sputtering and their crystallographic characteristics and magnetic properties were investigated. The substitution of Pb facilitates the crystallization and improves the crystallinity for hexagonal M phase. All of the films prepared at T_s above 460 °C exhibit a good c-axis orientation and the c-axis dispersion angle ($\Delta\theta_{50}$) for Pb-substituted Ba-ferrite films is as small as 1°. The coercivities ($H_{c\perp}$) and $H_{c\parallel}$) and saturation magnetization M_s of Pb-substituted Ba-ferrite films are 0.7–1.0 kOe, 0.2 kOe and 250–300 emu/cm^3, respectively.

INTRODUCTION

Many researchers have focused on perpendicular magnetic recording since it was proposed by Iwasaki and Nakamura.[1] Perpendicular recording is substantially preferable for high-density recording under the geometrical conditions of the head-medium configuration.

There are various candidates for the perpendicular recording materials such as Co-Cr thin films,[2] Fe- and Co-plated films on aluminum oxide substrate,[3] and Ba-ferrite particulate medium.[4]

Good chemical stability and mechanical durability as well as excellent magnetic properties are essential for recording medium. The authors have been studying a magnetoplumbite type of hexagonal Ba-ferrite (BaM) thin films prepared by sputtering[5] and sol-gel method[6] and reported that BaM sputtered rigid disks with small c-axis dispersion angle ($\Delta\theta_{50}$) possess excellent recording characteristics.[7] According to their reports, the recording density D_{50} depends on $\Delta\theta_{50}$ and the smaller $\Delta\theta_{50}$ results in the higher D_{50}.

There are some problems to be solved in a preparation of BaM films. One of the most important problems is that a high substrate temperature T_s is necessary to crystallize the hexagonal M phase. The T_s for preparing BaM films with $\Delta\theta_{50}$ as small as 2–3° is about 620 °C,[5] and such a high T_s limits the selection of substrate material. It is strongly recommended to reduce the T_s during deposition for the practical fabrication of the recording medium. Although the authors have already examined the low-temperature deposition and successive heat treatment, BaM films with c-axis orientation could not be prepared.[8]

It is known that there are some divalent ions such as Ba^{++}, Ca^{++}, Sr^{++}, and Pb^{++}, which have approximately the same ionic radii as that of the oxygen divalent ion and these elements are the constituents of the hexagonal M-type ferrites. Among them, Pb is the easiest to obtain as a pure metal and the melting point of PbM is 1315 °C, while that of SrM and BaM is 1500 and 1565 °C, respectively. Although it is expected that the low melting temperature leads to lowering the crystallization temperature of hexagonal ferrite, there are few studies on the PbM films.

In this study, Pb-substituted BaM [(Ba·Pb)M] films were prepared by dc magnetron sputtering system and the dependencies of their crystallographic characteristics and magnetic properties on T_s were investigated.

II. EXPERIMENT

BaM films had been prepared by means of rf diode sputtering in our previous studies. In order to compensate the lack of Ba content in the films and to obtain the films with a stoichiometric composition of BaM (i.e., $n=6$ in $BaO\cdot nFe_2O_3$), Ba content in the target was increased to 1.7 times ($BaO\cdot 3.5\ Fe_2O_3$) that of stoichiometric composition of BaM. The decrease of Ba content in the films was considered to be scattering loss mainly caused by the bombardment of high-energetic ions from the plasma.

In this study, the dc magnetron sputtering system was used to prepare Pb-substituted BaM[(Ba·Pb)M] films. The target is a sintered ferrite disk (8 cm diameter) with stoichiometric composition of BaM (i.e. $n=6$ in $BaO\cdot nFe_2O_3$) and Pb content was controlled by the number of Pb chips of 5 mm square on this disk. The substrate is a thermally oxidized silicon wafer and T_s is measured with a thermocouple in contact with the substrate surface. The discharge gas pressure P_{tot}, which is a sum of argon and oxygen partial gas pressure, was set at 2 mTorr. The partial oxygen gas pressure P_{O_2} was 0.03 mTorr and the thickness of (Ba·Pb)M films was about 1200 Å.

III. RESULTS AND DISCUSSION

The n for the stoichiometric composition of BaM is 6.0, where a molecular formula is $BaO\cdot nFe_2O_3$. The composition of films prepared in this study was about 5.5 in $(Ba\cdot Pb)O\cdot nFe_2O_x$ (i.e., $Pb_{0.55}Ba_{0.63}Fe_{12}O_x$) at 10 Pb chips.

Figure 1 shows the x-ray-diffraction diagrams for the films prepared at various T_s. The films prepared at T_s of 410 °C consisted of a spinel-like phase with the crystal orientation of the (111) plane which is the most closed-packed plane and those prepared at T_s of 460 °C consisted of a spinel-like phase and M phase without c-axis orientation. When T_s was elevated at 480 °C, the diffraction lines were only from both c plane of the hexagonal M phase and (111) plane of spinel-like ferrite. At T_s of 530 °C, the intensity of

 0021-8979/94/75(10)/5969/3/$6.00 © 1994 American Institute of Physics

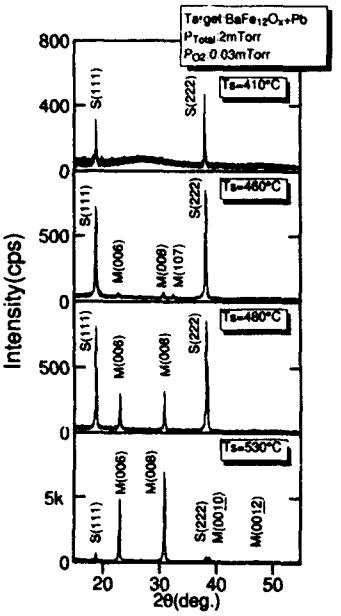

FIG. 1. X-ray-diffraction diagrams of (Ba·Pb)M films prepared at various T_s.

diffraction lines from the c plane of M phase becomes strong. This means that the M phase grows rapidly at about this temperature.

Figure 2 shows the dependence of a c-axis orientation factor f_c (Ref. 9) for M-phase crystallite on T_s. When the c axis is completely oriented perpendicularly to the film plane, f_c takes the value of 1.0 and when other planes of M-phase crystallite are detected together, f_c is less than 1.0. In order

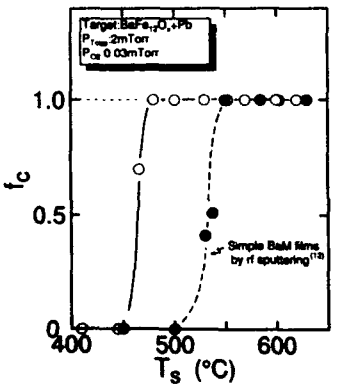

FIG. 2. Dependence of c-axis orientation factor f_c for (Ba·Pb)M films and BaM films on T_s.

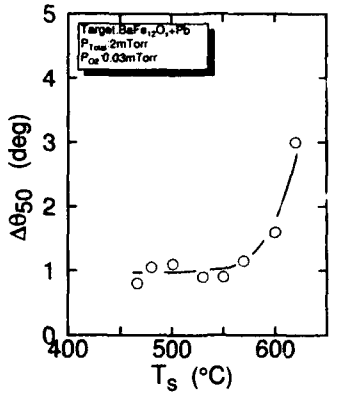

FIG. 3. Dependence of c-axis dispersion angle $\Delta\theta_{50}$ of (Ba·Pb)M films on T_s.

to clarify the effect of Pb substitution, f_c of the simple BaM films[10] prepared by rf diode sputtering is also included, shown by solid circles. The f_c reaches 1.0 at T_s of 480 °C for (Ba·Pb)M films, while that for simple BaM films reaches 1.0 at 550 °C. From these results, it is found that the substitution of Pb facilitates the crystallization and improves the orientation of c axis for hexagonal M phase.

Figure 3 shows the dependence of $\Delta\theta_{50}$, on T_s. $\Delta\theta_{50}$ for (Ba·Pb)M films below 550 °C is almost constant and as small as about 1°. Further increase of T_s results in slight increase of $\Delta\theta_{50}$. These small values of $\Delta\theta_{50}$ are suitable for the high-density recording media, where the ring-type head is used in perpendicular magnetic recording.[7]

Figure 4 shows the dependence of saturation magnetization M_s for (Ba·Pb)M films on T_s. The films prepared at T_s below 460 °C exhibit M_s of about 50 emu/cm^3. M_s increases rapidly with increase of T_s from 530 to 550 °C. This corre-

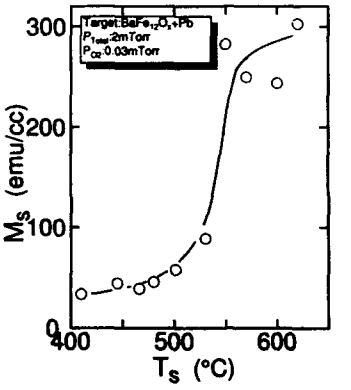

FIG. 4. Dependence of saturation magnetization M_s of (Ba·Pb)M films on T_s.

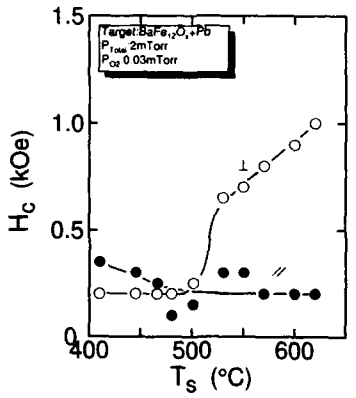

FIG. 5. Dependence of coercivities $H_{c\perp}$ and $H_{c\parallel}$ of (Ba·Pb)M films on T_s.

sponds to the growth of M phase, as shown in Fig. 1. M_s for the films prepared at T_s above 550 °C is in the range from 270 to 300 emu/cm^3.

Figure 5 shows the dependence of coercivities on T_s. The $H_{c\perp}$ is almost constant at T_s below 500 °C and increases rapidly at T_s above 530 °C, while $H_{c\parallel}$ decreases gradually with increase of T_s.

IV. CONCLUSION

(Ba·Pb)M films have been prepared by using a dc magnetron sputtering system and their crystallographic characteristics and magnetic properties were studied.

It is found that the substitution of Pb facilitates the crystallization and improves the crystallinity for hexagonal M phase. All of the films prepared at T_s above 460 °C exhibit a good c-axis orientation and the c-axis dispersion angle ($\Delta\theta_{50}$) for Pb-substituted Ba-ferrite films is as small as 1°. The coercivities $H_{c\perp}$ and $H_{c\parallel}$ and saturation magnetization M_s of Pb-substituted Ba-ferrite films are 0.7–1.0 kOe, 0.2 kOe, and 250–300 emu/cm^3, respectively.

ACKNOWLEDGMENTS

Research was sponsored in part by Hoso-Bunka Foundation and a Grant-in-Aid for General Scientific Research from the Ministry of Education, Science, and Culture of Japan.

[1] S. Iwasaki and Y. Nakamura, IEEE Trans. Magn. **MAG-13**, 1272 (1977).
[2] S. Iwasaki and K. Ouchi, IEEE Trans. Magn. **MAG-14**, 849 (1978).
[3] N. Tsuya, Y. Saito, H. Nakamura, S. Hayano, A. Furugohri, K. Ohta, Y. Wakui, and T. Tokushima, J. Magn. Magn. Mater. **54-57**, 1681 (1986).
[4] T. Fujiwara, IEEE Trans. Magn. **MAG-21**, 1480 (1985).
[5] A. Morisako, M. Matsumoto, and M. Naoe, IEEE Trans. Magn. **MAG-23**, 2359 (1987).
[6] M. Matsumoto, A. Morisako, and T. Haeiwa, in Proceedings of ICF-5, 1989, p. 533.
[7] A. Morisako, M. Matsumoto, and M. Naoe, IEEE Trans. Magn. **MAG-22**, 1146 (1986).
[8] A. Morisako, M. Matsumoto, and M. Naoe, in Proceedings of ICF-6, Tokyo and Kyoto, 1992, p. 436.
[9] F. K. Lotgering, J. Inorg. Nucl. Chem. **9**, 113 (1959).
[10] A. Morisako, M. Matsumoto, and M. Naoe, Trans. IEICE Part C **J69-C**, 902 (1986) (in Japanese).

Surface roughness and magnetic properties of *in situ* heated and postannealed thin films of perpendicular barium ferrite

Kyusik Sin and John M. Sivertsen
The Center for Micromagnetics and Information Technologies (MINT), Department of Chemical Engineering and Materials Science, University of Minnesota, Minneapolis, Minnesota 55455

Jack H. Judy
Department of Electrical Engineering, University of Minnesota, Minneapolis, Minnesota 55455

The surface roughness and magnetic properties of thin films of hexagonal barium ferrite (BaFe) deposited on SiO_2/Si and Si substrates by facing target sputtering were studied using *in situ* heating during deposition and postannealing after deposition. The perpendicular coercivity of the BaFe films varied between 775 and 1430 Oe with substrate temperature for both *in situ* heated (560–620 °C) and postannealed (800–1200 °C) films. The effect of temperature on the surface roughness of BaFe/Si was greater than that of BaFe/SiO_2/Si. The results of this study indicate that the mean surface roughness (R_a=11.4–27 nm) of BaFe films on Si substrates was greater than the roughness (R_a=3.9–17 nm) of BaFe films on amorphous SiO_2/Si substrates. This increase of surface roughness with increasing substrate temperature is due to the evolution of grain boundaries and step formation during deposition and annealing.

I. INTRODUCTION

Thin films of magnetoplumbite (M) type barium ferrite (BaFe) have potential for high-density contact or quasicontact recording because of high mechanical hardness and chemical stability. Either conventional or facing target sputtering (FTS) methods[1] can be used to prepare stoichiometric BaFe films which have good perpendicular magnetic properties.[2,3] Because high temperatures (550–600 °C) are required to grow hexagonal BaFe, the substrate heating during film growth or postannealing after deposition can have a significant effect on the surface roughness of the film. The surface roughness of magnetic recording media is one of the most important factors of the head/disk interface[4,5] for extremely low-flying heights or quasicontact recording.

The purpose of this research is to study the effects of high-substrate annealing temperatures during deposition and after deposition on the crystal structure and surface morphology of thin films of BaFe deposited on Si and thermally oxidized SiO_2/Si substrates.

II. EXPERIMENTAL PROCEDURE

Thin films of BaFe were prepared on thermally oxidized silicon (SiO_2/Si) and (001)-oriented bare silicon substrates using a dc magnetron FTS system. The thickness of the amorphous SiO_2 was 10 000 Å. Co- and Ti-doped barium ferrite (BaFe:$BaFe_{10.65}Co_{0.65}Ti_{0.7}O_{19}$) targets were used in this experiment. A gas mixture of argon and 5% oxygen was introduced after the chamber was evacuated to 2×10^{-6} Torr. The total pressure of the gas mixture was 0.5 mTorr. One set of samples was prepared using *in situ* heating during sputtering in the chamber and another set was prepared using postannealing after deposition without substrate heating. The thickness of the BaFe films was fixed at 2200 Å.

The magnetic properties were measured using a vibrating sample magnetometer. An x-ray diffractometer ($CuK\alpha$) was used to determine the crystallographic texture of the films.

An atomic force microscope (AFM) was used to measure the morphology and roughness of the BaFe film surface. The surface roughness was characterized by maximum height R_{max} and mean surface roughness R_a. R_a is defined by[6]

$$R_a=\frac{1}{L_xL_y}\int_0^{L_y}\int_0^{L_x}|f(x,y)|dx\,dy,$$

where $f(x,y)$ is surface position relative to the mean plane. L_x, L_y are the dimensions of the surface. R_{max} is the height difference between the highest and lowest position in the plane.

III. RESULTS AND DISCUSSION

Figures 1(a) and 1(b) show the perpendicular coercivity of the BaFe films deposited on SiO_2/Si and Si substrates at high substrate temperature (*in situ* heated) and annealed after deposition without substrate heating (postannealed), respectively. In the case of *in situ* heated samples from 560 to 620 °C, the perpendicular coercivity of BaFe/SiO_2/Si increased as the substrate temperature increased and showed a maximum value at 600 °C. It decreased to 906 Oe at 620 °C. The decrease of coercivity at 620 °C might be due to grain growth. The perpendicular coercivity of the BaFe/Si sample also has a maximum coercivity of 1050 Oe at 600 °C; however, the temperature dependence of the coercivity of BaFe/Si was lower than that of BaFe/SiO_2/Si. A higher coercivity of BaFe/Si than that of BaFe/SiO_2/Si at 560 °C might be due to a larger difference in the thermal-expansion coefficient between BaFe and Si than that between BaFe and amorphous SiO_2. The coercivity of postannealed BaFe/SiO_2/Si samples also increased with annealing temperature and showed maximum perpendicular coercivity of 1400 Oe at 950 °C. The coercivity of postannealed BaFe/Si samples showed maximum perpendicular coercivity of 1400 Oe at 900 °C and the temperature dependence of coercivity on the annealing temperature was also lower than that of

 0021-8979/94/75(10)/5972/3/$6.00 © 1994 American Institute of Physics

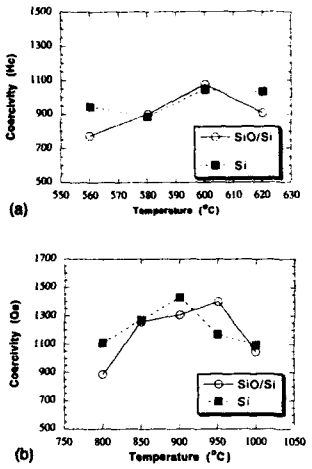

FIG. 1. Effect of (a) substrate temperature and (b) annealing temperature on perpendicular coercivity of thin films of BaFe on SiO_2/Si and Si substrates.

$BaFe/SiO_2/Si$. It decreased abruptly to 20 Oe at 1200 °C. This drastic reduction of coercivity might be due to the instability of BaFe phase at 1200 °C.

As shown in a previous report,[3] x-ray diffraction shows peaks from the basal plane of the hexagonal BaFe phase from both *in situ* heated and postannealed samples. Figure 2 shows the intensity of x-ray diffraction from the (00.8) plane for both *in situ* heated and postannealed samples. In the case of *in situ* heated samples, $BaFe/SiO_2/Si$ showed a much higher intensity than BaFe/Si samples. The reason might be the smaller difference in thermal-expansion coefficient between BaFe and SiO_2 than that between BaFe and Si. In the case of postannealed samples, both $BaFe/SiO_2/Si$ and BaFe/Si showed a smaller x-ray intensity than *in situ* heated $BaFe/SiO_2/Si$. This indicates that *in situ* heating is more efficient than the postannealing method.

Figures 3 and 4 show AFM micrographs and measurements of surface roughness of BaFe films on SiO_2/Si [Figs. 3(a) and 3(b)] and Si substrates [Figs. 3(c) and 3(d)] which were prepared with *in situ* heating during deposition. Figures 3(a) and 3(c) were prepared at the substrate temperature of

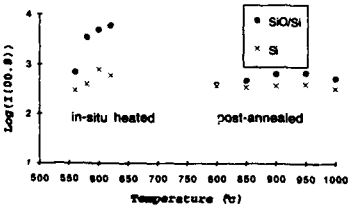

FIG. 2. Intensity of x-ray diffraction from (00.8) plane for *in situ* heated and postannealed BaFe on SiO_2/Si and Si substrates.

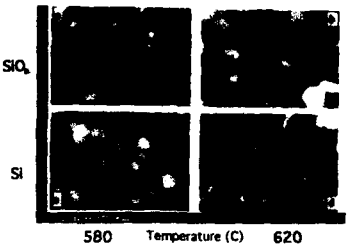

FIG. 3. AFM micrograph of BaFe *in situ* heated during deposition. Box size: (a)–(c) 2 μm; (d) 5 μm.

580 °C and Figs. 3(b) and 3(d) were prepared at the substrate temperature of 620 °C. The AFM micrograph shows an increase in grain size with increasing substrate temperature. One of the important features to note is that the film creates steps during the growth stage at high substrate temperature [Fig. 3(d)]. BaFe grains first grow as platelets and then a new platelet nucleates on the platelets so that overlapped platelets might be formed. The formation of overlapped platelets was also observed using transmission electron microscopy (TEM) and scanning electron microscopy (SEM).[3]

The surface roughness of BaFe films was characterized by R_a and R_{max} values where these values were obtained from a surface area of 2×2 μm^2 and 5×5 μm^2 for the films which have larger grain size. Without substrate heating, the R_a and R_{max} value of as-deposited $BaFe/SiO_2/Si$ was 0.4 and 3.6 nm, respectively. Such a smooth surface is one of the unique advantages of using a facing target sputtering system which deposits films without bombardment of gamma (γ) electrons and negative ions to the substrate surface. R_a values were slightly lower for BaFe films on a SiO_2/Si substrate

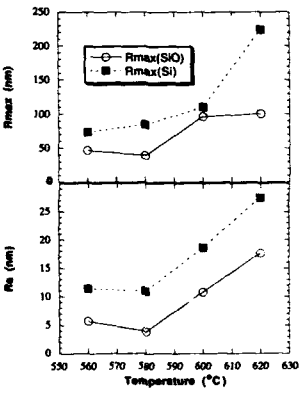

FIG. 4. Effect of substrate temperature (*in situ* heating) on roughness of thin films of BaFe on SiO_2/Si and Si substrates.

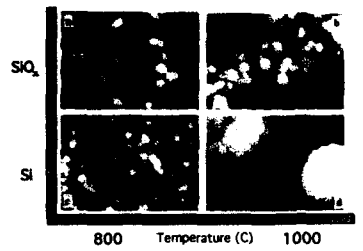

FIG. 5. AFM micrograph of BaFe postannealed after deposition. Box size: (a)–(c) 2 μm; (d) 5 μm.

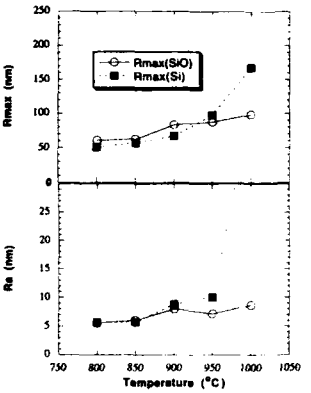

FIG. 6. Effect of annealing temperature on roughness of thin films of BaFe on SiO_2/Si and Si substrates.

for both *in situ* heated and postannealed samples because of the smoother surface of amorphous SiO_2/Si. The smallest measured R_a value was 3.9 nm for *in situ* heated and 5.6 nm for postannealed film; however, the R_a of postannealed BaFe/Si increased significantly at 1000 °C. The maximum height, which is an important parameter from the tribological point of view, increased from 46.6 to 100 nm for *in situ* heated BaFe films on SiO_2/Si substrate: BaFe films deposited on Si substrates showed much higher values of roughness. As the substrate temperature increased from 560 to 620 °C, the R_a increased from 11.4 to 27.5 nm as the R_{max} increased from 73.4 to 224.1 nm.

Figures 5 and 6 show AFM micrographs and surface roughness of postannealed BaFe films, respectively. These films were deposited at room temperature and annealed in air from 800 to 1000 °C for 4 h. The annealing temperature for samples in Figs. 5(a) and 5(c) was 800 °C, and 1000 °C for samples in Figs. 5(b) and 5(d). The grain size and surface roughness of BaFe/SiO_2/Si were similar to those of BaFe/Si at 800 °C; however, as the temperature increases, the difference becomes large. BaFe/Si shows large surface roughness which might be due to interaction between BaFe and Si or reconstruction of the (001) Si surface. The AFM micrographs show a large growth structure for both samples on SiO_2/Si [Fig. 5(b)] and Si substrates [Fig. 4(d)]. The average grain size was about 1500 Å for films annealed at 1000 °C and the surface structure became about 5 μm when annealed at 1200 °C. Hexagonal plates and growth steps were observed. These results indicate that postannealed BaFe films grow as platelets and they overlap during growth as in the case of *in situ* heating during deposition.

IV. CONCLUSION

The surface roughness and magnetic properties of *in situ* heated and postannealed thin films of hexagonal Barium ferrite deposited on SiO_2/Si and Si substrates by facing target sputtering were studied.

The coercivity of the BaFe films increased with increasing substrate temperature and showed maximum coercivity of 1050 Oe at 600 °C for *in situ* heated BaFe/Si film and 1430 Oe at 900 °C for postannealed BaFe/Si films. The surface roughness was higher for films on a Si substrate than on amorphous SiO_2/Si substrates. The smallest measured R_a value was 3.9 nm for *in situ* heated BaFe/SiO_2/Si and 5.6 nm for postannealed film. The effect of temperature on the surface roughness of BaFe/Si was greater than that of BaFe/SiO_2/Si. The increase of surface roughness with temperature is due to evolution of grain and step formation during deposition and annealing.

[1] M. Naoe, S. Hasunuma, Y. Hoshi, and S. Yamanaka, IEEE Trans. Magn. **MAG-17**, 3184 (1981).
[2] M. Matsuoka, Y. Hoshi, M. Naoe, and S. Yamanaka, IEEE Trans. Magn. **MAG-20**, 800 (1991).
[3] K. Sin, J. M. Sivertsen, J. H. Judy, Y. Hoshi, and D. Speliotis, J. Appl. Phys. **73**, 6689 (1993).
[4] H. Morita, K. Fukuda, and J. Ezaki, J. Magn. Soc. Jpn. **15**, Suppl. 2, 733 (1991).
[5] B. Bhushan, *Tribology and Mechanics of Magnetic Storage Devices* (Springer, Berlin, 1990).
[6] User's manual for Nanoscope III, version 2.3, Digital Instruments.

Preparation of Co-Zn ferrite films at low substrate temperature by plasma-free dc sputtering for magnetic recording media

N. Matsushita, K. Noma, S. Nakagawa, and M. Naoe
Department of Physical Electronics, Tokyo Institute of Technology, 2-12-1 O-okayama, Meguro, Tokyo 152, Japan

Co-Zn ferrite films with small grains for magnetic recording media at ultrahigh density were deposited "plasma free" on a substrate by using the dc facing targets sputtering apparatus without subsequent annealing process. The films deposited at a substrate temperature T_s as low as 90 °C were composed of crystallites with excellent (111) orientation and exhibited a saturation magnetization $4\pi M_s$ of 3.3 kG and an in-plane and perpendicular coercivity $H_{c\parallel}$ and $H_{c\perp}$ of 1.8 and 2.2 kOe, respectively. The films deposited at a T_s of 250 °C exhibited $4\pi M_s$ of 4.8 kG and possessed almost the same $H_{c\parallel}$ and $H_{c\perp}$ of 1.5 kOe.

I. INTRODUCTION

Since it has become difficult to attain high recording density using particulate media with fine particles of ferrite, such as γ-Fe_2O_3:Co and γ-Fe_2O_3:Os, the films of Co-based alloys such as Co-Cr,[1] Co-Cr/Cr,[2] and Co-Ni-Cr are mainly used for the magnetic layer in recording media. However, protective and lubricant layers are necessary on them because of their poor chemical stability and low corrosion resistance. In addition, it has been difficult for these alloy media to exhibit coercivity higher than 1.5 kOe which is necessary for ultrahigh-density recording media. On the contrary, since the sputtered films of ferrimagnetic oxide such as a spinel type of Co ferrite ($CoFe_2O_4$) and a magnetoplumbite type of Ba ferrite ($BaFe_{12}O_{19}$) exhibit moderate saturation magnetization $4\pi M_s$ and high coercivity H_c as well as a remarkable chemical stability and high corrosion resistance, they are expected to become applicable for high-density recording media.[3,4] Recently, films of a spinel type of Co-Zn ferrite have become attractive for recording media because of their capability of stably forming the smallest magnetic domains among all kinds of ferrites. However, it has been difficult to prepare ferrimagnetic oxide films with good crystallinity and sufficient magnetic characteristics using a conventional sputtering system, such as diode and magnetron, because of serious plasma damage and the low kinetic energy of adatoms. Therefore, $CoFe_2O_4$/ZnO double-layered films were deposited "plasma free" on substrates by using the facing targets sputtering (FTS) apparatus as shown in a previous article.[5] Although $CoFe_2O_4$/ZnO double-layered films had visible ⟨111⟩ orientation even at the substrate temperature T_s lower than 100 °C, the elevation of T_s above 500 °C was necessary to obtain sufficiently good magnetic characteristics; however, the deposition of these layers on low heat resistance substrates has to be achieved at low T_s for the entire process.

In this study, Zn substitution of Co ferrite was used for the purpose of increasing the $4\pi M_s$ (Ref. 6) and decreasing the H_c of the deposited films. Crystallographic and magnetic characteristics as well as surface texture and cross-section morphology of films deposited at low T_s were precisely investigated.

II. EXPERIMENTS

The specimen Co-Zn ferrite films were deposited using the FTS apparatus. A pair of $Co_{0.51}Zn_{0.45}Fe_{2.04}O_4$ plates 90 mm in diameter were used as targets. These targets were sintered from the starting mixture of $(CoO)_{0.5}$, $(ZnO)_{0.5}$, and $(\alpha$-$Fe_2O_3)_{1.0}$ powder at 1200 °C in air by a conventional dry ceramic technique. Since Co-Zn ferrite targets sintered by this process had too high a resistivity to sustain stable dc glow discharge, they were reduced in hydrogen atmosphere for 1 h to decrease their resistivity. Ar and O_2 gases were introduced individually into the sputtering and depositing chamber as working gases. The total gas pressure P_{tot} and the partial oxygen gas pressure P_{O_2} were set at 2.0 and 0.02 mTorr, respectively. The Co-Zn ferrite films were deposited on 15×15 mm^2 substrates of thermal oxidized Si wafers for 180 min. The substrate temperature T_s was varied in the range from 90 °C (without heating substrate) to 500 °C (with heating substrate) and the film thickness was in the range from 0.7 to 1.0 μm.

Film composition was determined by inductive coupled plasma analysis (ICPA). The surface texture and cross-section morphology was observed by scanning electron microscope (SEM). The crystallographic characteristics such as the crystallite size $\langle D \rangle$ and the full width of half-maximum of rocking profiles $\Delta\theta_{50}$ were estimated from x-ray-diffraction diagrams and magnetic characteristics such as $4\pi M_s$ and H_c were determined from the hysteresis loops measured by using a vibrating sample magnetometer (VSM).

III. RESULTS AND DISCUSSION

A. Film composition

Figure 1 shows the compositions of the target used in this study and films deposited at various T_s, in which the content of metallic ion is normalized for $C_{Co}+C_{Zn}+C_{Fe}=3.0$. The T_s without heating substrate was elevated to about 90 °C by the radiation from the plasma. While C_{Co} were constant in the target and all films, C_{Zn} of the films deposited at 90 °C (without heating substrate) was smaller than that of the target, decreased gradually with increasing of T_s up to 400 °C, and was almost zero at T_s of 400 °C. On the other hand, C_{Fe} increased with increasing of T_s as opposed to the decrease of C_{Zn}. As shown above, the

 0021-8979/94/75(10)/5975/3/$6.00 © 1994 American Institute of Physics

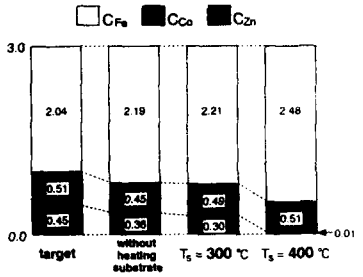

FIG. 1. Compositions of Co-Zn ferrite films determined by ICPA (content of metallic ions is normalized for $C_{Co}+C_{Zn}+C_{Fe}=3.0$).

substitution of Zn ions in the films became difficult with increasing T_s. It was found that the distribution of Zn and Fe ions had a close relationship to the crystallographic and magnetic characteristics.

B. SEM observation

The films deposited at T_s of 90 and 400 °C revealed completely different surface textures and cross-section morphologies as seen in Figs. 2(a) and 2(b), respectively. Although a uniform morphology as well as very flat surface were seen in Fig. 2(a), the film deposited at T_s of 400 °C revealed the excessive growth of crsytalline grains and a rough surface as seen in Fig. 2(b). The center-line average roughness R_a and the root-mean-square roughness R_{rms} for

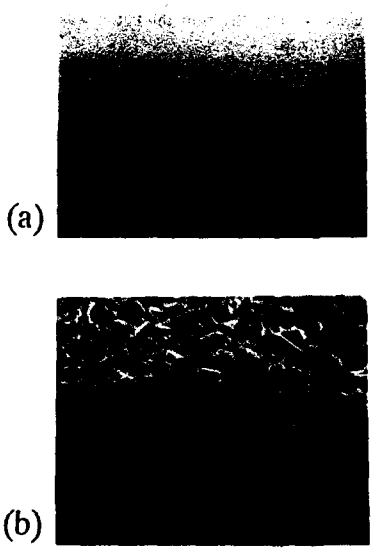

FIG. 2. SEM photographs of Co-Zn ferrite films deposited (a) at T_s of 90 °C (without heating substrate) and (b) at T_s of 400 °C (with heating substrate).

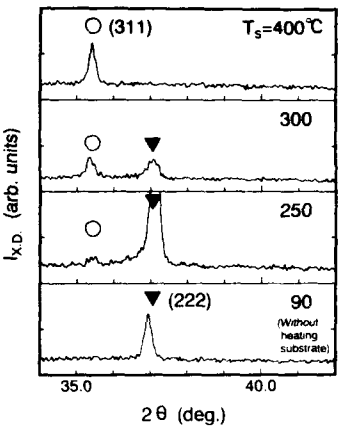

FIG. 3. X-ray diffraction diagrams at various T_s.

them were measured by using atomic force microscopy (AFM). R_a and R_{rms} of the film of Fig. 2(a) were 1.42 and 1.73 nm, and those of the film of Fig. 2(b) were 94.9 and 116.8 nm, respectively.

C. Crystal orientation and crystallographic characteristics

Figure 3 shows the x-ray-diffraction diagrams for the films deposited at various T_s. The film deposited at 90 °C was only composed of crystallites with excellent (111) orientation. However, for films deposited at T_s of 250 °C, although the x-ray-diffraction intensity I_{XRD} corresponding to (111) fairly increased, the (311) peak was also visible. I_{XRD} of (311) increased with increasing of T_s and the films deposited at T_s above 400 °C were composed of only crystallites with (311) orientation. This (311) peak is commonly visible and exhibits the largest I_{XRD} in powder-x-ray diffraction diagram of spinel ferrite. The Co ferrite ($CoFe_2O_4$) films depos-

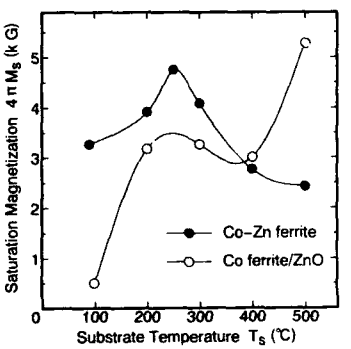

FIG. 4. Dependencies of saturation magnetization $4\pi M_s$ on substrate temperature T_s.

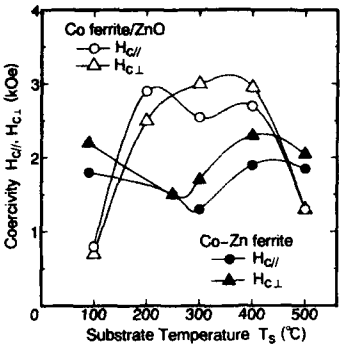

FIG. 5. Dependencies of in-plane and perpendicular coercivities $H_{c\parallel}$ and $H_{c\perp}$ on substrate temperature T_s.

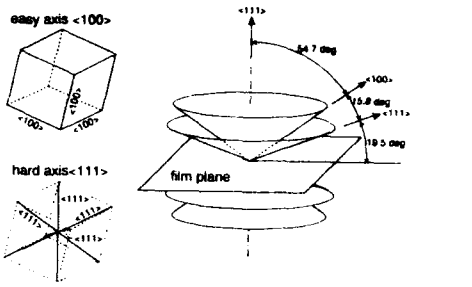

FIG. 6. Sketch of easy and hard axes, ⟨100⟩ and ⟨111⟩, of Co-Zn ferrite crystallite with (111) orientation.

ited under the same sputtering conditions, P_{tot} of 2 mTorr, P_{O_2} of 0.02 mTorr, and T_s of 90–600 °C, were mainly composed of crystallites with (311) orientation.[5] Therefore, the difference of the crystal structure between Co-Zn ferrite and Co ferrite films deposited at lower T_s below 300 °C seemed to be caused by the substitution of Zn ions in tetrahedral A site of spinel structure.

The crystallite sizes $\langle D\rangle_{(111)}$ calculated by Sherrer equations on the (111) peak were as large as 350 Å even at T_s of 90 °C. Although $\Delta\theta_{50(111)}$ took the minimum value of 2.5° at T_s of 250 °C, it was as small as about 5° even for the film deposited at T_s of 90 °C.

D. Magnetic characteristics: $4\pi M_s$ and H_c

Figures 4 and 5 show the T_s dependencies of $4\pi M_s$ and the in-plane coercivity and perpendicular coercivities $H_{c\parallel}$ and $H_{c\perp}$ of Co-Zn ferrite and $CoFe_2O_4$/ZnO films, respectively. It was confirmed that $4\pi M_s$ was increased by the substitution of Zn ions onto tetrahedral A site of Co-Zn ferrite at T_s up to 250 °C. It took the maximum value of 4.8 kG at T_s of 250 °C and then decreased with increasing of T_s above 250 °C. This seemed to be caused by the fact that the number of Fe^{3+} occupying the A site increased with decreasing the number of Zn^{2+} at T_s above 250 °C, as mentioned above and shown in Fig. 1. It should be noted that $4\pi M_s$ of Co-Zn ferrite film was as large as 3.3 kG even at T_s about 90 °C (without heating substrate), while that of $CoFe_2O_4$/ZnO film was as small as only 0.5 kG. On the other hand, although $H_{c\parallel}$ and $H_{c\perp}$ of $CoFe_2O_4$/ZnO films deposited at T_s of 100 °C were very low, those of the Co-Zn ferrite films deposited at T_s of 90 °C were as relatively large as 2.2 and 1.8 kOe, respectively, and those of ones at T_s of 250 °C took the same value of 1.5 kOe. Since the easy and hard axes of Co ferrite are ⟨100⟩ and ⟨111⟩, respectively, and ⟨100⟩ axes are distributed in a circular cone whose generation line canted at an angle of 35.3° to the film plane when films had (111) orientation as seen in Fig. 6, $H_{c\parallel}$ and $H_{c\perp}$ were both relatively high and they were not so different from each other. Therefore, these films may be applicable for isotropic media with ultrahigh density. Since Zn ions could substitute at T_s in this range as seen in Fig. 1, the substitution of Fe ions by Zn ones in tetrahedral A sites seemed to be useful not only for increasing $4\pi M_s$ and decreasing H_c but also for promoting the formation of the most closely packed plane of oxygen ions and decreasing the crystallization temperature of Co ferrite films.

IV. CONCLUSION

Co-Zn ferrite films were deposited by using the dc facing targets sputtering apparatus without subsequent annealing process. Films deposited at the substrate temperature T_s as low as 90 °C were composed of crystallites with excellent (111) orientation and the film surface texture exhibited excellent smoothness. They possessed the moderate saturation magnetization $4\pi M_s$ of 3.3 kG and the in-plane and perpendicular coercivity $H_{c\parallel}$ and $H_{c\perp}$ were 1.8 and 2.2 kOe, respectively. Since a very low-temperature process has been achieved in this study, Co-Zn ferrite films seemed to be applicable for flexible disk and tape with high recording density even if low heat resistance sheets such as polycarbonate (PC) disks and polyethylene terephthalate (PET) tapes are used as substrates.

[1] S. Yamamoto, Y. Nakamura, and S. Iwasaki, IEEE Trans. Magn. **MAG-23**, 2070 (1987).
[2] H. Suzuki, N. Goda, S. Nagaike, Y. Shiroishi, N. Shige, and N. Tsumita, IEEE Trans. Magn. **MAG-27**, 4718 (1991).
[3] H. Torii, E. Fujii, and M. Hattori, IEEE Trans. J. Magn. Jpn. **JMJ-6**, 765 (1991).
[4] M. Matsuoka, Y. Hoshi, M. Naoe, and S. Yamanaka, IEEE Trans. Magn. **MAG-18**, 1119 (1982).
[5] N. Matushita, S. Nakagawa, and M. Naoe, IEEE Trans. Magn. **MAG-28**, 3108 (1992).
[6] G. A. Petitt and D. W. Forester, Phys. Rev. B **4**, 3912 (1971).

Magnetic and crystallographic properties of Co-Cr-(Ta,Pt)/Cr films deposited by excimer laser ablation

A. Ishikawa, K. Tanahashi, Y. Yahisa, Y. Hosoe, and Y. Shiroishi
Central Research Laboratory, Hitachi, Ltd. 1-280, Higashi-koigakubo, Kokubunji-shi, Tokyo 185, Japan

The crystal structure and magnetic properties of Co-alloy films deposited by KrF excimer laser ablation were investigated. A pulsed laser beam with wavelength of 248 nm was focused onto the deposition targets which were fixed in the vacuum chamber. Cr underlayer and Co-alloy films were successively deposited at a rate of 0.012 nm/pulse. The film surface was microscopically smooth compared to the sputtered films. This may be due to the low shadowing effect during the laser deposition. The composition of the film was reproducibly controlled, though there was a slight difference between the composition of film and target material. The coercivities of Co-Cr-Pt/Cr films formed on the Si and Ni-P substrates at 250 °C were 130 and 220 Oe, which were about one-fifth of the coercivity of sputtered films. Crystallographic analyses showed that Cr underlayer had no crystal orientation, and Co-alloy film consisted of fine fcc-type crystal grains. Low coercivity of the laser-deposited film is probably due to the lack of hcp Co phase.

I. INTRODUCTION

Sputtered Co-alloy films formed on the Cr underlayer show high in-plane coercivity and have been widely developed for longitudinal magnetic recording media.[1–3] The sputtered film structure is granular owing to a shadowing effect which is caused by the Ar gas in the deposition chamber.[4] This grain structure is advantageous for the reduction of the media noise,[5] however, it is important to control the grain size of the magnetic film to be smaller than the recorded bit size.[6,7] Moreover, the microscopically smooth media surface is preferable to keep head-media spacing small.

Pulsed laser deposition[8–10] is one of the possible techniques to fabricate the fine-grain structure since the film can be formed in a vacuum. It has been also reported that this method is suited for control of the film composition. Thus, we evaluated the laser deposition method for the fabrication of Co-alloy thin-film media. There are several works concerning this method; however, little is known of the magnetic and crystallographic properties of such films.

II. EXPERIMENT

Figure 1 shows a schematic diagram of the experimental deposition apparatus. The pulsed KrF laser with wavelength of 248 nm and power of 500 mJ/pulse was focused by the quartz lens, and irradiated at an incident angle of 45° onto the deposition target which is fixed in the vacuum chamber. The irradiated area was scanned on the target surface to prevent local ablation. The deposition material was changed from Cr to Co alloy within 10 s by rotating the water-cooled target holder. A Ni-P–plated Al-Mg or Si substrate was placed on the heating block which faces the target at a distance of 40 mm. The base pressure of the chamber was 3×10^{-4} Pa, while the pressure raised to 3×10^{-3} Pa during the substrate heating and laser ablation. The sputtered Co-alloy/Cr film was also fabricated using the conventional dc magnetron sputtering apparatus to compare the film properties. The base pressure of the chamber and Ar gas pressure during deposition were 3×10^{-4} and 0.7 Pa. The composition of the Co-alloy film was determined by inductively coupled plasma spectroscopy (ICPS). Magnetic properties were measured by a vibrating sample magnetometer with a maximum applied field 13 kOe. The crystalline structure of the film was analyzed by scanning electron microscope (SEM) observation, x-ray diffraction, and transmission electron microscopy (TEM) micrograph.

III. RESULTS AND DISCUSSION

The energy density of the laser beam on the target surface was estimated as ~10 J/cm^2/pulse. The diameter of the deposition area where the relative thickness variation is less than ±5% was 17 mm. This shows that substrate rotation is necessary to obtain a uniform film thickness. Maximum deposition rate of the Co-alloy film at a laser repetition rate 10 Hz was 0.012 nm/pulse. The time-average deposition rate, which is defined by using the laser oscillation time, is 0.12 nm/s, which is defined by using the laser oscillation time, is 0.12 nm/s, which is one order lower than the conventional dc magnetron sputtering.

SEM photos of the surface structure of the laser-deposited and sputtered Co-Cr-Pt (30 nm)/Cr (50 nm) films are shown in Fig. 2. The surface of the laser-deposited film is microscopically smooth and no crystalline grain is observed, while grains of average diameter 30 nm can be seen for the

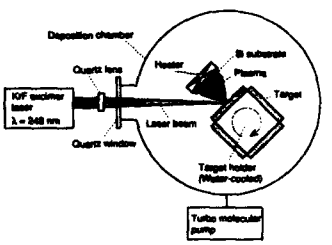

FIG. 1. Schematic diagram of the experimental laser deposition apparatus.

 0021-8979/94/75(10)/5978/3/$6.00 © 1994 American Institute of Physics

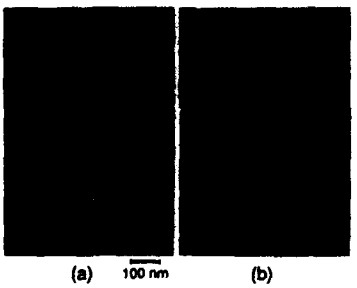

FIG. 2. SEM photos of the surface structure of the CoCrPt (30 nm)/Cr(50 nm) film deposited at 250 °C: (a) laser deposition, (b) sputter-deposition; Ar pressure: 0.7 Pa.

sputtered film. The flat surface of the laser-deposited film is probably formed owing to the low shadowing effect during the laser ablation.

The compositions of the Co-alloy films and corresponding target materials are shown in Table I. All data were reproducible and no local variation in the deposition area was observed. The relative difference between the film and target composition is less than 5% for the Co-Cr-Ta alloy. However, Cr concentration in the Co-Cr-Pt film is relatively 20%–30% lower than the target composition. The decrease of Cr content in the Co-Cr-Pt film might be due to the volatilization of Cr from the film during the high-energy deposition.[10]

Figure 3 shows the coercivities for the laser-deposited Co/Cr, Co-Cr-Ta/Cr, and Co-Cr-Pt/Cr films and the sputter-deposited Co-Cr-Pt/Cr film formed on Si substrate at a temperature of 250 °C. The coercivities for the laser-deposited film are as low as 20–150 Oe, which are roughly one-fifth of the value of the sputter-deposited film. The coercivities of the laser-deposited Co-Cr-Ta and Co-Cr-Pt films decrease as the Cr content in the films increases. Among the alloy compositions, the $CoCr_7Pt_4$ film showed the highest coercivity. Further, the coercivity raised up to 220 Oe by using Ni-P/Al-Mg as the substrate. Figure 4 shows the saturated flux

TABLE I. The composition of the Co-alloy films and corresponding target materials. The values in parentheses show the ratio of film composition to target composition.

Target composition (at. %)				Film composition (at. %)			
Co	Cr	Pt	Ta	Co	Cr	Pt	Ta
86.1	9.90	···	3.98	85.9 (1.00)	10.1 (1.02)	···	4.02 (1.01)
82.1	13.9	···	3.99	82.6 (1.01)	13.6 (0.98)	···	3.81 (0.96)
85.9	10.1	4.03	···	88.4 (1.03)	7.28 (0.72)	4.25 (1.05)	···
81.0	15.0	4.02	···	83.6 (1.03)	12.5 (0.83)	4.00 (1.00)	···

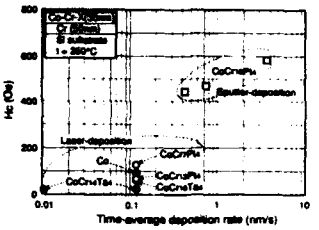

FIG. 3. Coercivity for the laser-deposited films and the sputter-deposited film vs the time-average deposition rate. Sputtering Ar pressure: 0.7 Pa.

density B_s for the same samples which are shown in Fig. 3. No remarkable change in the B_s by the deposition method is observed.

X-ray-diffraction spectra for the sputter-deposited and laser-deposited Co-alloy films formed on Si substrates with thickness of 200 nm are shown in Fig. 5(a). For the sputter-deposited film, a strong diffraction peak of hcp Co(002) and relatively weak diffraction of hcp Co(100), Co(101), and Co(110) are observed, while the laser-deposited films for various alloy compositions show the diffraction peaks of fcc Co(111) (d_{111}=0.2059 nm), Co(200), and Co(220). Weak diffraction of hcp Co(100) and Co(101) are also observed. Diffraction spectra for the Co-alloy(30 nm)/Cr(50 nm) films are shown in Fig. 5(b). Diffraction peaks of bcc Cr(110) and (200) are observed for the sputter-deposited film. However, the laser-deposited films show no diffraction from the Cr underlayer, and a broad diffraction peak of fcc Co(111) is observed for some alloy compositions. The diffraction of laser-deposited Co/Cr film could not be indexed. Figure 6 shows the dark-field image of a TEM micrograph for the laser-deposited $CoCr_7Pt_4$ (fcc)/Cr film. The crystalline grain size of the magnetic film is as small as 10–20 nm. The vague diffraction ring is attributed to the poor crystalline orientation of the fine grains. The low coercivity of the laser-deposited films is probably due to the lack of the hcp Co phase which is essential for a high magnetic anisotropy. The fcc Co of the high-temperature phase is possibly formed by the laser-depositing atom which has relatively high energy (~100 eV).[10]

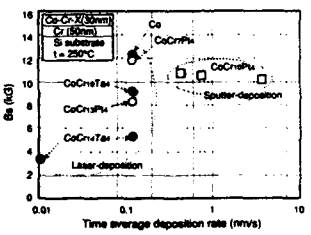

FIG. 4. Saturation flux density for the laser-deposited films and the sputter-deposited film vs the time-average deposition rate. Sputtering Ar pressure: 0.7 Pa.

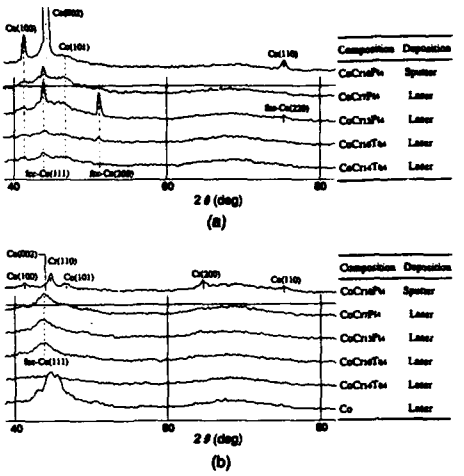

FIG. 5. X-ray-diffraction patterns for the sputter-deposited and laser-deposited films: (a) Co-alloy (200 nm)/Si, (b) Co alloy (30 nm)/Cr(50 nm)/Si; primary x ray: Cu$K\alpha$.

IV. CONCLUSIONS

Properties of the Co-alloy/Cr films deposited using KrF excimer laser ablation are evaluated. The film surface is microscopically smooth compared to the sputtered film. This is due to the low shadowing effect of the laser deposition. The composition of the Co alloy is reproducibly controlled, although there is a small difference between the film and the target. The coercivity of the Co-Cr-Pt/Cr film is as low as 220 Oe because the hcp Co phase is not formed in the magnetic film.

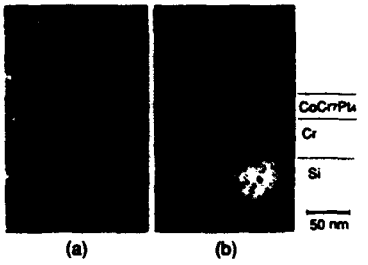

FIG. 6. Dark-field image of TEM micrograph for the laser-deposited $CoCr_7Pt_4$(fcc)/Cr film: (a) plan-view, (b) cross-sectional view.

ACKNOWLEDGMENTS

The authors would like to thank H. Okuhira, Dr. S. Yamamoto, T. Hukazawa, and Dr. M. Hiratani of Central Research Laboratory, Hitachi, Ltd., for discussions on the laser ablation, and T. Shimotsu of Hitachi Instrument Engineering Co. for the TEM observation.

[1] J. P. Lazzari, J. Melnick, and D. Randet, IEEE Trans. Magn. **MAG-3**, 205 (1967).
[2] T. Ohno, Y. Shiroishi, S. Hishiyama, H. Suzuki, and Y. Matsuda, IEEE Trans. Magn. **MAG-23**, 2809 (1987).
[3] I. Sanders, T. Yogi, J. Howard, S. Lambert, G. Gorman, and C. Hwang, IEEE Trans. Magn. **MAG-25**, 3869 (1989).
[4] J. Thornton, J. Vac. Sci. Technol. A **4**, 3059 (1986).
[5] T. Yogi, T. Nguyen, S. Lambert, G. Gorman, and G. Castillo, Mater. Res. Soc. Proc. **232**, 3 (1991).
[6] E. Murdock, R. Simmons, and R. Davidson, IEEE Trans. Magn. **28**, 3078 (1992).
[7] T. Yogi, T. Nguyen, IEEE Trans. Magn. **29**, 307 (1993).
[8] J. Cheung and H. Sankur, CRC Crit. Rev. Solid State Mater. Sci. **15**, 63 (1988).
[9] N. Cherief, D. Givord, A. Lienard, K. Mackay, O. McGrath, J. Rebouillat, F. Robaut, and Y. Souche, J. Magn. Magn. Mater. **121**, 94 (1993).
[10] N. Cherief, D. Givord, O. MacGrath, Y. Otani, and F. Robaut, J. Magn. Magn. Mater. **126**, 225 (1993).

Transverse susceptibility and ferromagnetic resonance of Hi-8 metal-evaporated tape

C. Sürig, G. Zimmermann, and K. A. Hempel
Institut für Werkstoffe der Elektrotechnik, Aachen University of Technology, Templergraben 55, 52056 Aachen, Germany

Transverse susceptibility (TS) and ferromagnetic resonance absorption (FMR) are measured on commercially available metal-evaporated video tape manufactured by the continuous varying incidence method, so that the columns are inclined at an angle ϑ_{int} with respect to the recording direction. Due to the demagnetization of the tape the magnetization vector is at an extrinsic inclination angle $\vartheta_{ext} < \vartheta_{int}$ with respect to the recording direction, which is determined to be 24° by analyzing angular remanence curves. The results of TS and FMR measurements on the dependence of the angle ϑ_N between applied field and tape normal are symmetrical to $\vartheta_N = \vartheta_{ext}$. In-plane TS measurements parallel and perpendicular to the recording direction lead to $H_A = 440$ kA/m and an intrinsic inclination angle $\vartheta_{int} = 44°$. Using these values, measured and calculated resonance field values H_{res} are in good agreement except for $0° < \vartheta_N < 50°$. The analysis of H_{res} in the vicinity of $\vartheta_N = 24°$ leads to $H_A = 640$ kA/m and $\vartheta_{int} = 37°$. Thus, Stoner–Wohlfarth behavior with lower anisotropy field strength as determined perpendicular to the preferential axis of magnetization is suggested. In contrast to TS measurements, no results can be found that fit the resonance field value both parallel and perpendicular to the film normal.

I. INTRODUCTION

Metal-evaporated (ME) recording tape is one of the most promising magnetic tapes because of its excellent magnetic properties. The measurements discussed in this article are performed on a commercially available metal-evaporated video tape, Sony Hi-8 metal-E. This tape is manufactured by oblique evaporation of $Co_{80}Ni_{20}$ in oxygen atmosphere in a roll-to-roll coater. As a result of the continuous varying incidence (CVI) method a curved columnar microstructure occurs: The columns are inclined at some average angle ϑ_{int} with respect to the recording direction.

The transverse susceptibility (TS) method was applied in the past in the field of magnetic recording[1,2] as well as to hard magnetic materials.[3] All measurements were performed on stacks of the tape material using an experimental setup described earlier.[3] Ferromagnetic resonance absorption (FMR) measurements have been carried out previously using particle assemblies with dominating magnetocrystalline anisotropy and magnetic recording media.[4,5] The absorption spectra are obtained using a cylindrical H_{011} microwave cavity with stacks of tape samples placed in the center of the cavity, where the applied static magnetic field and magnetic component of the microwave field are perpendicular.[6]

II. THEORY

In order to determine the theoretical TS and FMR curves, consider the coordinate system given in Fig. 1. The z axis is chosen parallel to the dc bias field direction perpendicular to which there is an additional ac excitation field $\mathbf{H}_e$. Furthermore, the curved anisotropy axis of the ME tape is approximated as a straight line with an angle ϑ_{int} to the recording direction and defines the x-z plane. The orientation of the film plane is indicated by the tape normal N or ϑ_N and φ_N, respectively. Characterizing the position of the magnetization vector by ϑ and φ the equilibrium state is determined by minimizing the free energy per unit volume G,

$$G/K_1 = -[\sin\vartheta\sin\vartheta_0\cos\varphi + \cos\vartheta\cos\vartheta_0]^2 - 2a\cos\vartheta + \beta[\sin\vartheta\sin\vartheta_N\cos(\varphi-\varphi_N) + \cos\vartheta\cos\vartheta_N]^2, \quad (1)$$

normalized by the first order anisotropy constant K_1. Abbreviations are $a = H/H_A$, $\beta = M_s/H_A$ and the anisotropy field strength $H_A = 2K_1/\mu_0 M_s$. M_s is the saturation magnetization of the tape taking the volumetric packing fraction into account.

For the determination of the transverse susceptibility a perturbation approach[2,7] is used, with the additional free-energy density in the excitation field

$$G_e/K_1 = 2a_e\sin\vartheta\cos(\varphi-\varphi_e) \quad \text{and} \quad a_e = H_e/H_A. \quad (2)$$

The resonance frequencies for the elliptical precession motion of the magnetization vector around its equilibrium posi-

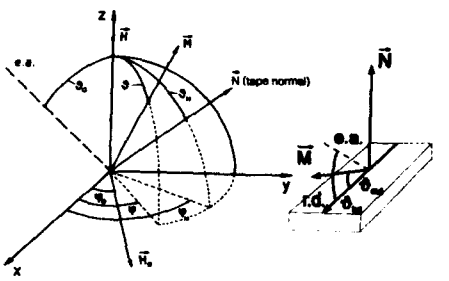

FIG. 1. Coordinate system: The crystallographic easy axis (e.a.) is indicated by a dashed line, N is the plane normal of the tape, and the intrinsic (extrinsic) inclination angle $\vartheta_{int}(\vartheta_{ext})$ with respect to the recording direction (r.d.) is shown in the inset.

 0021-8979/94/75(10)/5981/3/$6.00 © 1994 American Institute of Physics

tion are calculated[8] and the natural precession frequency ω_{nat}, which is the eigenfrequency for vanishing applied field, is determined to be

$$\omega_{nat} = \gamma\mu_0 H_A \sqrt{\cos^2(\vartheta_{int}-\vartheta_{ext}) - \beta \sin^2 \vartheta_{ext}} \times \sqrt{\cos 2(\vartheta_{int}-\vartheta_{ext}) + \beta \cos 2\vartheta_{ext}}, \quad (3)$$

with the gyromagnetic ratio γ and the angles ϑ_{int} and ϑ_{ext} [see Eq. (4) and Fig. 1].

Analyzing the theoretical results, ME tape behaves like a single-domain particle with an effective easy axis parallel to the equilibrium orientation of the magnetization vector in case of vanishing bias field. Therefore, the angle between recording direction and effective easy axis defines the extrinsic inclination angle ϑ_{ext}. Particularly, the magnetization vector always lies in the plane defined by **H** and the effective easy axis represented by ϑ_{ext}, which is related to ϑ_{int} and β by

$$\beta \sin 2\vartheta_{ext} = \sin[2(\vartheta_{int}-\vartheta_{ext})]. \quad (4)$$

III. MEASUREMENTS ON METAL-EVAPORATED TAPE

A. Transverse susceptibility

According to the calculation given above, the two significant curves for the TS of metal-evaporated tape are the out-of-plane measurement parallel to ϑ_{ext} and the in-plane measurement perpendicular to the recording direction.

In the out-of-plane case, the easy axis as well as the bias field is oriented perpendicular to the excitation field. The coincidence of the measuring angle with ϑ_{ext} can be confirmed by the largest field range of practically constant TS around $H=0$ and by the symmetry of the measuring results. For the ME tape investigated here, this procedure yields $\vartheta_{ext}=24°$ in accordance with the results of the angular remanence (AR) measurement.[9]

In case of in-plane measurement perpendicular to the recording direction, the easy axis and the excitation field are perpendicular to the bias field. The equilibrium state of magnetization becomes unstable at the transition into saturation, which is indicated by a theoretically infinite TS. Whereas in case of an ellipsoid of revolution with coinciding crystallographic and rotational axis the field strength H_p at this point is the effective anisotropy field,[10] it now depends on M_s, H_A and ϑ_{int}. Since the relation between β, ϑ_{int}, and ϑ_{ext} is already known [Eq. (4)], ϑ_{int} can be calculated to be

$$\tan \vartheta_{int} = (1+\beta/a_p)\tan \vartheta_{ext} \quad \text{with } a_p = H_p/H_A. \quad (5)$$

By use of the experimental results $H_p=320$ kA/m (Fig. 2), $\vartheta_{ext}=24°$ and $M_s=380$ kA/m,[11] ϑ_{int} is evaluated to 44°, corresponding to $H_A=440$ kA/m. If H_A is determined using a fit to the curve measured parallel to the recording direction,[3] the value $H_{A,0}$ obtained is about 5% higher.

B. Ferromagnetic resonance

Out-of-plane resonance spectra varying the angle ϑ_N between static magnetic field and tape normal are measured at 37.3 GHz. Due to the resonance behavior of single-domain particles the lowest (highest) resonance field strength for

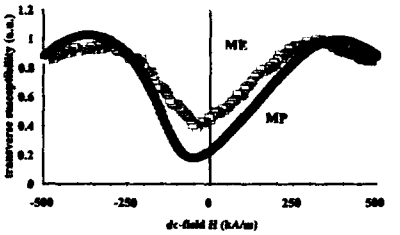

FIG. 2. Results of the in-plane TS measurement perpendicular to the recording direction for the ME and MP tape.

$\omega > \omega_{nat}$ can be detected if the external magnetic field is applied parallel (perpendicular) to the preferential direction of the magnetization vector. Taking into account the demagnetization due to the shape of the magnetic tape and an inclination angle ϑ_{int} between recording direction and the average crystal c axis, similar results can be observed by only considering the external inclination angle ϑ_{ext}: lowest (highest) resonance field strength occurs, if the external field is applied at ϑ_{ext} ($\vartheta_{ext}+90°$) with respect to the recording direction.

Figure 3 shows measured and calculated resonance field strength $H_{res}(\vartheta_N)$ of metal-evaporated tape in dependence on the angle between static magnetic field and film normal. In contrast to the measurements performed by Kohmoto and Alexander,[12] the shift of the maximum resonance field strength H^k to angles $\vartheta_N>0°$ for metal-evaporated tape is obvious. The external inclination angle ϑ_{ext} is determined to be 24° in accordance with AR and TS measurements. Using $\vartheta_{int}=44°$ and $H_A=440$ kA/m as obtained by the TS measurement (fit 1 in Fig. 3), the calculated resonance field strengths are in good agreement with the experimental results except for $|\vartheta_N-\vartheta_{ext}|<20°$.

In order to fit the out-of-plane measurements nearly perpendicular to the preferential axis of magnetization, the anisotropy field strength is determined to be $H_A=640$ kA/m (fit 2 in Fig. 3). So, the intrinsic inclination angle can be calculated to be $\vartheta_{int}=37°$ comparable to results of Richter.[11] Measured and calculated curves are fitted at a field strength $H^k=1650$ kA/m high above the switching field strength

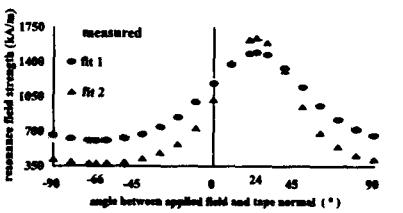

FIG. 3. Measured and calculated resonance field strength H_{res} for metal-evaporated tape. Using $H_A=440$ kA/m as obtained by TS measurements (fit 1), typical deviations occur for orientations nearly perpendicular to the effective easy axis. To fit these resonance field values $H_A=640$ kA/m is used (fit 2).

$$H_{sw} = H_A[\cos 2(\vartheta_{ext} - \vartheta_{int}) + \beta \cos 2\vartheta_{ext}]$$
$$= 830 \text{ kA/m},$$

so that incoherent switching behavior does not influence the determination of the anisotropy field. In order to analyze the switching behavior of the particles the measuring frequency must be lowered ($\omega < \omega_{nat}$), so that microwave hysteresis occurs. Using $\omega > \omega_{nat}$ FMR determines the anisotropy field strength considering the stiffness of the magnetization vector to its equilibrium position. The explanations due to the switching behavior and due to the stiffness are quite similar,[13] but the calculation is in contradiction to the experimental results for $|\vartheta_N - \vartheta_{ext}| > 20°$. Maximum resonance field strength H^h considering inclination is calculated approximately to be

$$H^h \approx 7H_A(\vartheta_{int}/\text{rad} - 0.278), \quad (6)$$

for $35° < \vartheta_{int} < 45°$, and that value of H_A yielding $\vartheta_{ext} = 24°$.

C. Comparison to measurements on metal-particle tape

Since in case of an ideally textured MP tape there is no inclination angle of the easy axes with respect to the film plane, in-plane measurements of the TS should be sufficient for the determination of the magnetic anisotropy. For the Sony MP tape investigated here, the measurement perpendicular to the recording direction yields a peak-field value of $H_p = 380$ kA/m (Fig. 2) whereas $H_{A,0}$ is evaluated to be 585 kA/m. According to the FMR measurements, $H_A = 585$ kA/m holds for the MP tape for all orientation angles ϑ_N, showing no deviations as mentioned in the measurements on ME tape.

IV. CONCLUSIONS

Considering TS measurement a misalignment of the easy axes influences the determination of $H_{A,0}$ (Ref. 3) but not H_p, so that the latter value is regarded as the real effective anisotropy field H_A. Thus, the reasonable agreement between both the values in case of ME tape on one hand indicates a very good orientational texture, on the other hand it shows that the bond of the magnetization vector to the equilibrium position can be described by the Stoner–Wohlfarth theory.[14] In case of MP tape the difference of about 50% corresponds to a standard deviation of about 30° if negligible inclination of the particles and an in-plane Gaussian distribution function is assumed. Since in this case the coercivity as well as the remanence of the out-of-plane magnetization curve perpendicular to the recording direction should vanish, which is not the case in practice, the consideration of a texture function with an out-of-plane distribution seems necessary.[1] If, therefore, a Gaussian distribution symmetrical to the recording direction is assumed at a rough estimate, the standard deviation amounts to 22° for the MP tape and to 6° for the ME tape. The latter results were obtained without considering the demagnetizing effect of the tape which in general reduces the observed inclination angle. Thus, these standard deviations may be regarded as concerning the angle ϑ_{ext}, whereas the correct value for ϑ_{int} should be higher.

Looking at the FMR results for ME tape, the deviation between experiment and calculation occurs for an applied field nearly perpendicular to the effective easy axis. An imperfect texture cannot affect this deviation, because misalignment of the particles causes a broader resonance spectrum, but maximum resonance field value is not influenced. Considering the demagnetization due to the particle shape and a volumetric packing fraction less than 1, the results of H_A have to be explained as the effective anisotropy field strength of the particles.

In contrast to the results performed on longitudinal and perpendicular recording media in case of ME tape no value of anisotropy field strength can be found to simultaneously fit resonance spectra parallel and perpendicular to the effective easy axis. Coherent rotation with lower anisotropy field strength as determined perpendicular to the preferential axis of magnetization is suggested to be a valid mechanism.

Summarizing, the equilibrium state of the magnetization vector can be described as predicted by Stoner and Wohlfarth,[14] whereas these results do not necessarily imply that irreversible switching occurs by uniform rotation.

[1] A. Hoare, R. W. Chantrell, W. Schmitt, and A. Eiling, J. Phys. D **26**, 461 (1993).
[2] R. W. Chantrell, A. Hoare, D. Melville, H. J. Lutke-Stetzkamp, and S. Methfessel, IEEE Trans. Magn. **MAG-25**, 4216 (1989).
[3] G. Zimmermann, J. Appl. Phys. **73**, 8436 (1993).
[4] K. A. Hempel, Z. Angew. Phys. **28**, 280 (1970).
[5] U. Netzelmann, J. Appl. Phys. **68**, 1800 (1990).
[6] F. Schumacher, Ph.D. thesis, RWTH Aachen, 1990.
[7] G. Zimmermann and K. A. Hempel, IEEE Trans. Magn. **28**, 3126 (1992).
[8] J. Smit and H. G. Beljers, Philips Res. Rep. **10**, 113 (1950).
[9] H. J. Richter and H. Hibst, J. Magn. Magn. Mater. **95**, 118 (1991).
[10] A. Aharoni, E. M. Frei, S. Shtrikman, and D. Treves, Bull. Res. Counc. Isr. Sect. A **6**, 215 (1957).
[11] H. J. Richter, IEEE Trans. Magn. **MAG-29**, 21 (1993).
[12] O. Kohmoto and C. Alexander, J. Magn. Magn. Mater. **116**, 405 (1992).
[13] K. Shinohara, H. Yoshida, M. Odagiri, and A. Tomago, IEEE Trans. Magn. **MAG-20**, 824 (1984).
[14] E. C. Stoner and E. P. Wohlfarth, Philos. Trans. R. Soc. London Ser. A **240**, 599 (1948).

Low-temperature sputter deposition of high-coercivity Co-Cr films for perpendicular recording

Naoki Honda and Kazuhiro Ouchi
Akita Research Institute of Advanced Technology, Akita 010-16, Japan

Shun-ichi Iwasaki
Tohoku Institute of Technology, Sendai 982, Japan

A low-temperature magnetron sputter-deposition method for Co-Cr medium has been developed. Films of 17 wt % Cr-Co were deposited to a thickness of 100–200 nm onto glass substrates over an extremely wide range of Ar gas pressures at room temperature. A high hcp c-axis orientation to the film normal ($\Delta\theta_{50}<6°$) could be obtained even at pressures over 50 Pa (375 mTorr) when the films were deposited onto a well-oriented c-axis Ti underlayer. Co-Cr films with a perpendicular coercivity as high as 1000 Oe with an anisotropy field of 5 kOe were obtained at extremely high Ar pressures; e.g., 70 Pa (525 mTorr). Scanning electron microscopy observations showed that the films had a fine columnar structure with distinct grain boundaries and the grain size was dramatically reduced with the introduction of the Ti underlayer. It was determined that the large anisotropy field for the Co-Cr films is attributed to crystalline anisotropy. The mechanism of magnetization reversal in the films is suggested to be rotational.

I. INTRODUCTION

Co-Cr films have been extensively investigated as ultrahigh-density recording media.[1–3] Such films require high perpendicular magnetic anisotropy and high coercivity. Sputter-deposited Co-Cr films with high anisotropy and coercivity have been thought to be attainable only under conditions of high temperature and low Ar gas pressure.[4] These conditions, however, impose difficulties in the design of production sputter systems for hard and flexible disk media and impose heat restrictions upon the substrates used. To avoid these problems, a new sputter-deposition method which enables low discharge voltage and low temperature for Co-Cr medium has been developed. An extremely wide range of Ar pressure together with underlayer effect was studied. The microstructure and magnetic properties of the films are also investigated.

II. EXPERIMENT

Films were deposited by dc magnetron sputtering using 3-in.-diam targets. A 17 wt % Cr-Co alloy target was used for Co-Cr films. Sputter-deposited Ti was used as the underlayer.[5] The target-substrate separation distance was 55 mm and the input power was 200 W for all cases. All depositions were made on slide glass substrates. The thicknesses of the films were 100 nm for the Ti underlayers and either 100 or 200 nm for the Co-Cr films. The deposition condition for the Ti underlayers was held constant at Ar pressure of 0.2 Pa and at room temperature. These conditions assure high c-axis orientation of the Ti film.[6] For Co-Cr depositions the Ar pressure ranged from 0.2 Pa up to 100 Pa and the substrate temperature was set at room temperature except for a reference film which was deposited at 250 °C.

Microstructure of the Co-Cr films was observed by a field-emission scanning electron microscope (FE SEM) for both the surface and the fractured cross section. Magnetic properties of the films were measured using a vibrating sample magnetometer (VSM). The perpendicular anisotropy field $H_k(\perp)$ for the films was evaluated from the area bounded by the initial magnetization curve and the saturation level in the first quadrant of the in-plane M-H curve. The temperature dependence of the magnetic properties and angular dependence of the coercivity of the films were measured as a means for investigating the origin of the magnetic anisotropy and the magnetization reversal mechanism. The hcp c-axis orientation of the films was evaluated by the half-width of the (002) x-ray-diffraction line using Cu$K\alpha$ radiation.

III. RESULTS AND DISCUSSION

A. Ar pressure dependence of coercivity

Figure 1 shows the Ar pressure dependence of perpendicular coercivity $H_c(\perp)$ for 100- and 200-nm-thick Co-Cr films deposited at room temperature onto well-oriented Ti underlayers. For Ar pressures greater than 50 Pa, the discharge voltage is reduced to as low as 300 V as compared to 500 V for Ar pressure of 0.2 Pa.[5] Using the Ti underlayer, the c-axis orientation of the Co-Cr films was improved ($\Delta\theta_{50}$ less than 6°) even at the highest Ar sputter pressure. The coercivity is very low at low Ar pressures as noted in earlier

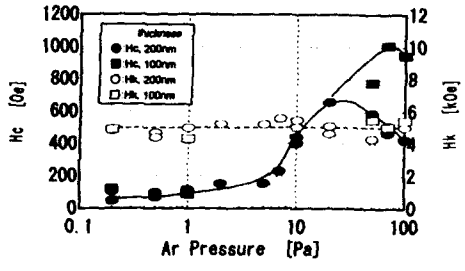

FIG. 1. Ar pressure dependence of $H_c(\perp)$ and $H_k(\perp)$ for Co-Cr films.

 0021-8979/94/75(10)/5984/3/$6.00 © 1994 American Institute of Physics

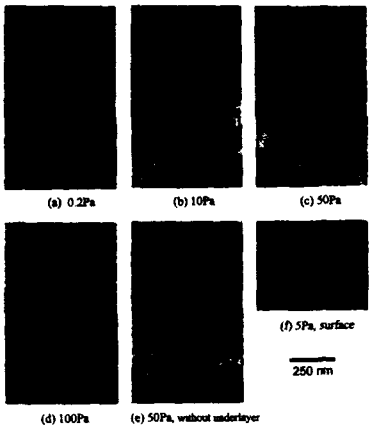

FIG. 2. SEM observation of surface and cross section of Co-Cr films deposited at Ar pressure of 0.2–100 Pa. (e) for Ti underlayer.

reports.[4,7] However, at pressures above 5 Pa, the coercivity increased significantly, showing a maximum value of 640 Oe for the 200-nm-thick films and 1030 Oe for the 100-nm-thick films at around 30 and 70 Pa, respectively. (The thickness dependence of coercivity will be presented elsewhere.) The perpendicular anisotropy field $H_k(\perp)$ for all films was about 5 kOe regardless of coercivity, as shown in Fig. 1. The Co-Cr films deposited without the Ti underlayer at high Ar pressures showed an increase in coercivity up to 600 Oe, but the films had low crystal orientation and low perpendicular anisotropy fields less than 2 kOe.

B. Microstructure

The microstructure was investigated for the films deposited over a wide Ar pressure range onto Ti underlayers. Figure 2 shows the surface and fractured cross section of the Co-Cr films 200 nm thick observed by SEM. The figure shows that at low Ar pressures, the grains are small with faint grain boundaries [Fig. 2(a)]. A transition region with fine grains is observed at around 5 Pa [Fig. 2(f)]. Then at about 10 Pa the grains become larger with increasing Ar pressure up to 50 Pa [Figs. 2(b) and 2(c)], whereupon a columnar structure with distinct grain boundaries is observed. The change of film morphologies is recognized as corresponding to the transition from zone T to zone 1 film structure as proposed by Thornton for thick sputter-deposited films.[8–10] It is also clear that the grain size is reduced by the Ti underlayer, especially at high Ar pressures (around 50 Pa) where the reduction is evident [compare Fig. 2(c) with Fig. 2(e)]. The grain diameter is reduced to about 35 nm from about 60 nm. The reduction was also confirmed by an atomic force microscope (AFM) observation of the film surface. Co-Cr depositions at these Ar pressures with the Ti underlayer exhibit a fine-grained columnar structure with distinct boundaries.

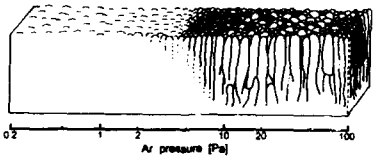

FIG. 3. Model for microstructure change of Co-Cr film with Ar pressure.

At higher Ar pressures (above 50 Pa), a reduction in grain size with Ar pressure was observed [Fig. 2(d)]. In the Thornton model,[8] the reduction in grain size is shown for low substrate temperatures below $T/T_m<0.1$, where T_m denotes the melting point of the material. However, $T/T_m=0.16$ for the Co-Cr alloy in this study, wherein the model predicts grain size growth. The deviation from Thornton's model may be explained by the decrease in migration energy for the deposited atoms due to collisions with Ar atoms at higher Ar pressures.

The microstructure change with Ar pressure is summarized in Fig. 3 as a schematic model for the present Co-Cr films deposited onto the Ti underlayer at wide Ar pressure range and at room temperature.

C. Magnetic properties

The M-H loops of three samples listed in Table I are shown in Figs. 4(a)–4(c). Sample no. 1 [Fig. 4(a)] was prepared by a high-temperature deposition as a typical conventional Co-Cr film with a high $H_c(\perp)$.[4] The perpendicular coercivity of sample no. 2 [Fig. 4(b)] is very small in spite of the large perpendicular anisotropy field. The M-H loop in the film normal shows a shoulder which suggests that the magnetization reversal of the film occurs primarily by domain-wall motion.[11,12] Sample no. 3 [Fig. 4(c)] has almost the same anisotropy field as sample no. 2 but exhibits a much higher coercivity [$H_c(\perp)>1000$ Oe]. The M-H loops are similar to those of sample no. 1 [Fig. 4(a)] suggesting that the magnetization reversal mechanism is rotational.[11] The dispersion of the crystal orientation of sample no. 3 is as

TABLE I. Sputtering conditions and magnetic properties of Co-Cr films.

Sample no.	Ar press. (Pa)	Temp. (°C)	$\delta_{Co\text{-}Cr}$ (nm)	$\Delta\theta_{50}$ (deg)	H_c (Oe)	H_k (kOe)	M_s (emu/cm^3)
1	0.2	250	180	3.9	1860	7	550
2	0.2	25	180	4.3	130	4.8	510
3	70	25	100	5.8	1030	5	550

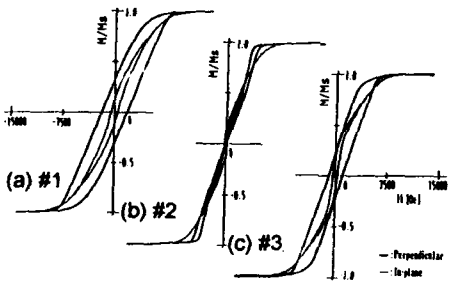

FIG. 4. M-H loops for Co-Cr films in Table I.

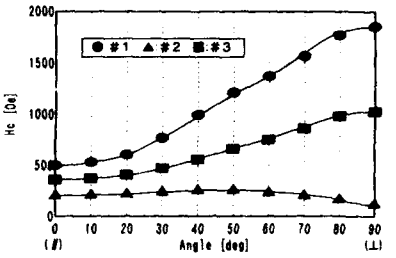

FIG. 6. Angular dependence of H_c for Co-Cr films in Table I.

small as samples no. 1 and no. 2 indicating that the large anisotropy also originates from crystalline anisotropy.

It is indicated above that the large anisotropy in the Co-Cr films deposited at high Ar pressures is derived from the film crystalline anisotropy. The SEM observation in Sec. III B, however, shows these films to have a fine columnar structure with distinct grain boundaries. This structure may also induce a large perpendicular anisotropy originating from the shape anisotropy. The temperature dependence of the anisotropy field was measured for the three samples and is shown in Fig. 5 together with temperature change of the saturation magnetization M_s for each sample. The temperature dependence of the anisotropy field for all three samples is almost the same and is larger than that of the saturation magnetization. These results suggest that shape anisotropy does not contribute to the overall perpendicular anisotropy for these films. Note that, the decrease in the anisotropy field for no. 3 is a little bit larger than that for no. 2 in which the contribution of shape anisotropy is negligible judged from its dense microstructure. It is concluded that crystalline anisotropy is the main contributor to perpendicular anisotropy for films deposited at high Ar pressures.

In order to clarify the magnetization reversal mechanism, the angular dependence of the coercivity of the films was investigated. The dependence for sample no. 3 qualitatively agreed with that for sample no. 1, as shown in Fig. 6. The dependence for no. 2 is entirely different from the other two and is a typical curve for films with magnetization reversal regulated by domain-wall motions; i.e., the angular dependence is concave near 90°. By contrast, the angular dependence for films no. 1 and no. 3 is convex at around 90° indicating the reversal to be regulated by a rotation mechanism.[11,13]

For film no. 3 the rotation magnetization reversal mechanism and the observation of a columnar microstructure with distinct grain boundaries strongly indicates that Co-Cr films deposited at high Ar pressures and at room temperature have magnetic separation between the grains. The magnetic isolation between grains could also be responsible for high coercivity of the films. The isolation in the films have been supported by a noise level decrease in the Co-Cr disk medium prepared at a high Ar pressure.[14] The Co-Cr films are likely candidates for high-density recording media.

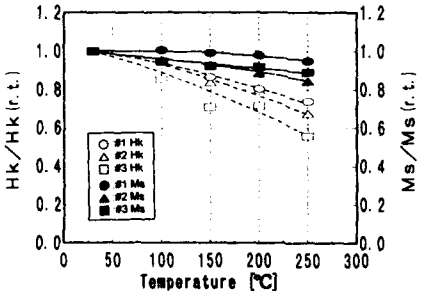

FIG. 5. Temperature dependence of $H_k(\perp)$ and M_s for films in Table I.

ACKNOWLEDGMENTS

The authors would like to express their thanks to J. Ariake, S. Okamoto, T. Chiba, and K. Harada of AIT for their assistance in the experiment.

[1] S. Yamamoto, Y. Nakamura, and S. Iwasaki, IEEE Trans. Magn. **MAG-23**, 2070 (1987).
[2] H. Uchiyama, E. Oyanagi, and N. Honda, J. Magn. Soc. Jpn. **15-S2**, 863 (1991).
[3] H. Wakamatsu, K. Kiuchi, M. Shinohara, and Y. Miura, J. Magn. Soc. Jpn. **15-S2**, 875 (1991).
[4] K. Ouchi, in *Perpendicular Magnetic Recording*, edited by S. Iwasaki and J. Hokkyo (Ohmusha, Tokyo, 1991), Chap. 7, p. 109.
[5] N. Honda, J. Ariake, K. Ouchi, and S. Iwasaki, J. Magn. Soc. Jpn. (to be published).
[6] N. Honda, J. Ariake, T. Chiba, K. Ouchi, and S. Iwasaki, J. Magn. Soc. Jpn. **17-S2**, 243 (1993) (in Japanese).
[7] S. Nakagawa, J. Park, and M. Naoe, J. Magn. Soc. Jpn. **13-S1**, 639 (1989).
[8] J. A. Thornton, J. Vac. Sci. Technol. **11**, 666 (1974).
[9] N. Honda, H. Awano, T. Samoto, and J. Hokkyo, J. Magn. Magn. Mater. **35**, 278 (1983).
[10] M. Sagoi, R. Nishikawa, and T. Suzuki, IEEE Trans. Magn. **MAG-20**, 2019 (1984) (with different notation for zone structures).
[11] K. Ouchi and S. Iwasaki, IEEE Trans. Magn. **MAG-23**, 180 (1987).
[12] T. Wielinga, J. C. Lodder, and J. Worst, IEEE Trans. Magn. **MAG-18**, 1107 (1982).
[13] S. Iwasaki, K. Ouchi, and N. Honda, IEEE Trans. Magn. **MAG-16**, 1111 (1980).
[14] N. Honda, J. Ariake, S. Okamoto, T. Komakine, S. Yanase, K. Ouchi, and S. Iwasaki, J. Magn. Soc. Jpn. **17-S2**, 40 (1993) (in Japanese).

Improvement of anisotropy of perpendicular magnetic recording tape by Ta addition and Kr sputtering gas (abstract)

Kiyoshi Kuga, Hideaki Yoshimoto, Yoshiro Yoneda, and Junji Numazawa
Science and Technical Research Labs., NHK (Japan Broadcasting Corpor... Kinuta, Setagaya-ku, Tokyo 157, Japan

Masahiko Naoe
Department of Physical Electronics, Tokyo Institute of Technology, 2-12-1 O-okayama, Meguro-ku, Tokyo 152, Japan

A perpendicular magnetic recording tape requires a high magnetic anisotropy field H_k and a small distribution of the perpendicular magnetic anisotropy field σ_{hk}/H_k. It can be expected that by the extension of the interplane distance of (002) plane $d_{(002)}$ in Co-Cr, a perpendicular magnetic anisotropy energy will be increased and H_k becomes higher. It can be also expected that the σ_{hk}/H_k becomes smaller by the improvement of the crystallinity of Co-Cr film. Therefore, in order to achieve the above, the following experiments were attempted. At first, a small amount of Ta was added to Co-Cr. This, as a result, extended the $d_{(002)}$ of the Co-Cr from 2.033 to 2.046 Å. Consequently, H_k was increased from 4.4 to 5.1 kOe and σ_{hk}/H_k was reduced from 0.14 to 0.11. Second, as a sputtering gas, Kr gas was used instead of Ar gas. The use of Kr resulted in greater crystallinity in the film, increasing the peak intensity $I_{(002)}$ of x-ray diffraction of the Co-Cr-Ta from 2090 to 2500 cps. Consequently, σ_{hk}/H_k was reduced up to 0.07. Last, a recording and reproducing experiment with the Co-Cr-Ta tape was attempted with the use of a hilical-scan VTR machine. As a result, a reproduced output of 56 $nV_{O\text{-}P}$ (μm T m/s) was obtained at the recording wavelength of 0.33 μm. This figure is equivalent to the output at the recording wavelength of 0.66 μm of metal-powder tape.

 0021-8979/94/75(10)/5987/1/$6.00 © 1994 American Institute of Physics

High field magnetization measurements of Sm_2Fe_{17}, $Sm_2Fe_{17}N_3$, $Sm_2Fe_{17}D_5$, and Pr_2Fe_{17}, $Pr_2Fe_{17}N_3$ (Invited)

O. Isnard
Institut Laue Langevin, BP 156, 38042 Grenoble Cedex, France

S. Miraglia
Laboratoire de Cristallographie, CNRS 166X, 38042 Grenoble Cedex, France

M. Guillot
Service National des Champs Intenses, CNRS 166X, 38042 Grenoble Cedex, France

D. Fruchart
Laboratoire de Cristallographie, CNRS 166X, 38042 Grenoble Cedex, France

We report high magnetic field magnetization measurements of the ferromagnetic compounds Sm_2Fe_{17}, $Sm_2Fe_{17}N_3$, $Sm_2Fe_{17}D_5$, and Pr_2Fe_{17}, $Pr_2Fe_{17}N_3$ performed up to 200 kOe in continuous field. We present isothermal magnetization curves measured at 4.2 and 300 K on oriented powder samples. The $M(H)$ curves show that the axial anisotropy fields obtained for the nitride are larger than those previously reported. The results are discussed in the light of neutron powder diffraction data. The magnetic anisotropy constants K_1 and K_2 have been determined, taking into account the angular distribution of the grain axis.

I. INTRODUCTION

Since the discovery of $Nd_2Fe_{14}B$ in 1983, the search for new hard magnetic materials has turned toward iron-rich compounds. Many works have been devoted to the study of the effect of hydrogen on the intrinsic properties of intermetallic phases. It has recently been found that hydrogen is not the only light element that can be inserted into intermetallic compounds. The discovery of new ternary magnetic materials based on rare earth element-transition metal and light elements, i.e., B, C, or N has triggered a renewed interest in permanent magnet materials. Among the new phases some have previously unknown structures such as $Nd_2Fe_{14}B$,[1,2] $Y_3Fe_{62}B_{14}$,[3] $Nd_2Fe_{23}B_3$,[4] and $R_6Fe_{13}Si$,[5] whereas others can be regarded as interstitial compounds whose crystal structure is closely related to that of a binary alloy: $ThFe_{11}C_x$,[6] $R_2Fe_{17}C_x$,[7,8] $R_2Fe_{17}H_x$,[9] $R_2Fe_{17}N_x$,[10] $R(FeM)_{12}N_x$,[11] $R(FeM)_{12}C_x$, and $R(FeM)_{12}H_x$[12] compounds. The most striking feature of these new interstitial compounds is the increase of Curie temperature (T_C) above that of the parent material. This effect is remarkably large in R_2Fe_{17}, where insertion of H, C, or N leads to an increase in T_c of about 200, 350, and 400 °C, respectively. Much attention has been paid to the $Sm_2Fe_{17}N_x$ and $Sm_2Fe_{17}C_x$ phases which have both an easy magnetization direction (EMD) parallel to the c axis of the Th_2Zn_{17} structure and a substantial anisotropy field. These two features make these compounds promising candidates for permanent magnet applications. The conventional figure of merit used to compare permanent magnetic materials is the energy product $(BH)_{max}$, which is proportional to the maximum energy that can be stored by the magnet in the field it creates. The theoretical maximum energy product is $(BH)_{max}=\mu_0 M_s^2/4$, where M_s is the saturation magnetization. It has been estimated to be about 470 kJ/m^3 for $Sm_2Fe_{17}N_{2.7}$, comparable to that of $Nd_2Fe_{14}B$ (512 kJ/m^3).[13–15] $Sm_2Fe_{17}N_{2.7}$ offers some intrinsic advantages such as a higher Curie temperature: 477 °C instead of 312 °C for $Nd_2Fe_{14}B$.

In addition, $R_2Fe_{17}Z_x$ compounds (Z=H, C, or N) are interesting from the fundamental point of view since light element insertion allows us to probe the physical properties of the compounds. Depending on the location of the interstitial in the crystal cell and its specific chemical properties (size, electronegativity, etc.), parameters such as Curie temperature, crystal electric field, magnetization, or magnetocrystalline anisotropy can be modified, leading to better knowledge of the magnetic interactions encountered in these structures.

We present high field magnetization measurements performed up to 200 kOe in continuous fields on Sm_2Fe_{17}, $Sm_2Fe_{17}N_3$, $Sm_2Fe_{17}D_5$, and on Pr_2Fe_{17}, $Pr_2Fe_{17}N_3$. The magnetic anisotropy constants K_1, K_2 are determined from the isothermal magnetization curves measured parallel and perpendicular to the EMD. The intrinsic magnetic properties of these compounds are discussed and compared. Emphasis is put on the influence of each interstitial element on the magnetocrystalline anisotropy. Results are discussed in light of previous neutron powder diffraction study, and the influence of the synthesis route on the properties of the nitride is also discussed.

II. SAMPLE PREPARATION

The starting alloys were prepared by induction melting in a cold crucible under an argon atmosphere. For the preparation of Sm_2Fe_{17}, a small excess of Sm was added in order to avoid α-Fe precipitation in the subsequent reactions that

 0021-8979/94/75(10)/5988/6/$6.00 © 1994 American Institute of Physics

lead to the hydride or nitride. We will now describe the preparation of hydrides and nitrides, respectively.

The main route that has been used to prepare these insertion compounds is a solid-gas reaction where the starting alloy is ground into a fine powder. The reactions have been performed at pressures ranging from 1 to 10 bar. Some samples needed a thermal activation at about 150 °C. If one disregards surface effects the hydrogenation process is rather well understood. It is a continuous process since pressure-composition isotherms show the typical solid solution shape with no absorption plateau.[16] Such a plateau would suggest the existence of a phase separation due to the formation of distinct stoichiometric phases. Surface effects prevent a clear analysis of the reaction kinetics; however, a rather reliable picture of the process can be derived from the lattice parameter behavior from in-beam hydrogenation as will be seen later.[17] The maximum amount of absorbed hydrogen estimated by gravimetric and volumetric methods was 5 hydrogen atoms per formula unit, which was subsequently confirmed by structure refinement.

The choice of nitrogen as a prospective interstitial was initiated by Coey's group. The early nitrogenation attempts were made using an ammonia flow at moderate pressures (≈1 bar).[10] This process led to the decomposition of ammonia into hydrogen and nitrogen with one or both of them being absorbed by the starting alloy. Later, most groups turned to nitrogen gas with a typical reaction temperature between 450 and 550 °C. The largest nitrogen concentration that can be accommodated in these compounds is 3 N atoms per formula unit. It is now established that the Sm_2Fe_{17} nitrides are metastable compounds which decompose into SmN and Fe or an Fe nitride in a thermally activated manner.[18,19] For this reason most low pressure nitrogenation routes lead to the formation of these coercivity-hindering products, because the reaction temperature has to be raised to values close to that of the decomposition temperature. The formation of iron particles during the process must be prevented since soft magnetic extra phases can act as nucleation sites for reverse magnetic domains and cause a decrease in coercivity.

We recently proposed a high pressure nitrogenation process[20] that permits a lower reaction temperature; by doing this, the diffusion of metal atoms and the disproportionation reaction are slowed down. This leads to cleaner samples with almost no α-Fe and with nitrogen compositions closer to 3.

The reaction kinetics and the nitrogen insertion scheme are a matter of controversy. It has to be known whether nitrides with intermediate compositions are stable or not. In order to understand the nitrogenation process, a sample of Nd_2Fe_{17} was heated under a constant N_2 gas flow at normal pressure in the beam of a neutron diffractometer and the diffraction patterns were recorded as a function of the reaction time.[18] This study showed that even at the beginning of the reaction the nitrogenated phase is highly charged, with a composition that remains constant during the course of the reaction. This picture is supported by Kerr microscopy experiments carried out by Mukai *et al.*[21] Colucci *et al.*[22–25] in a microanalysis study of the nitrogenation process reached the same conclusion.

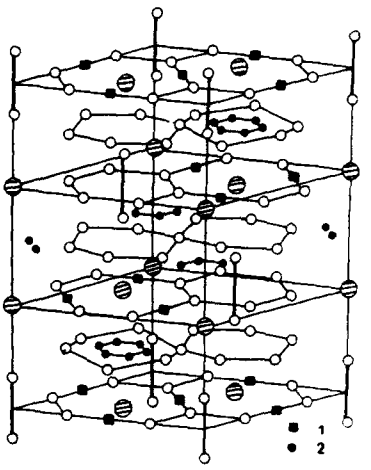

FIG. 1. R_2Fe_{17} crystal structure. Large and small circles refer to rare-earth and iron atoms, respectively. Octahedral and tetrahedral sites are labeled 1 and 2, respectively.

III. STRUCTURE

A significant increase of the unit cell volume is observed as well as a fairly anisotropic cell expansion which takes place in the basal plane rather than along the c axis of the hexagonal lattice. Neutron diffraction experiments have located H and N.[9,26,27] Mainly two kinds of available sites have been pointed out. The larger sites are six-coordinated holes that can be regarded as distorted octahedra with four iron atoms and two rare earth atoms at the corners (Fig. 1). Complete filling of these sites corresponds to the formulas $R_2Fe_{17}H_3$ and $R_2Fe_{17}N_3$, respectively. The other available sites are four-coordinated sites which can be considered as distorted tetrahedra with two iron atoms and two rare earth atoms at the corners. The latter sites can be additionally occupied by hydrogen but not nitrogen giving a final concentration $R_2Fe_{17}H_5$. A full occupancy of these sites is not possible owing to steric considerations and repulsion criteria. A time-resolved neutron diffraction experiment in which the in-beam desorption[17] of a hydride was followed has shown that the octahedral sites are filled first, up to the concentration $R_2Fe_{17}H_3$, after which the tetrahedral sites are filled. This filling scheme is nicely supported by the lattice parameter behavior as a function of the interstitial concentration.

An important structural result concerns the increase of certain interatomic distances induced by interstitial insertion. These distances are the so-called Fe-Fe dumbbells, which are very short in the host structure and are relaxed upon interstitial insertion. The relaxation of the local stressed parts of the structure is believed to favor positive Fe-Fe exchange interactions[28] and accounts for the spectacular increase of the Curie temperature that is observed upon insertion.

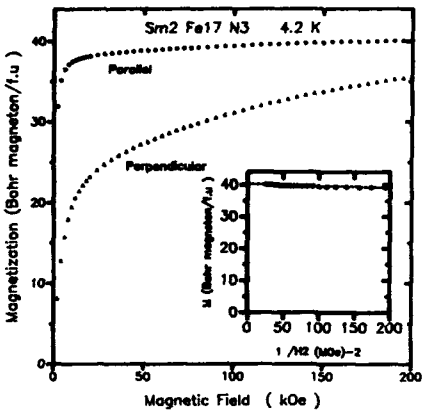

FIG. 2. $Sm_2Fe_{17}N_3$ magnetization curves at 4.2 K. Insert: $1/H^2$ extrapolation.

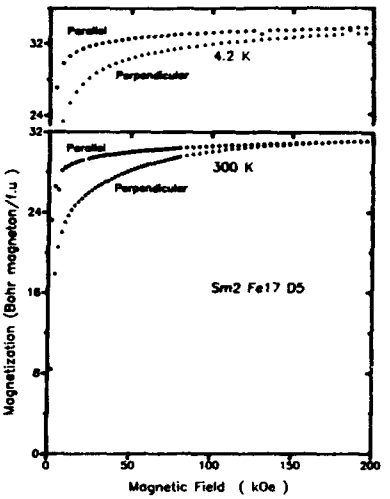

FIG. 4. $Sm_2Fe_{17}D_5$ magnetization curves at 4.2 and 300 K.

IV. EXPERIMENT

Magnetic measurements over the temperature range 4.2–300 K were performed using an automatic system provided with a cryostat associated with a calorimeter and described in Ref. 26. The extraction technique was used to measure the magnetization in continuous magnetic fields up to 200 kOe produced by a water-cooled Bitter magnet. No single crystals are available due to the high temperature instability of the nitrides. Thus, to distinguish between the easy plane and easy axis magnetocrystalline anisotropy, samples were made from oriented fine powders with a particle size smaller than 25 μm. The magnetic field was applied either parallel or perpendicular to the alignment direction. The powder was aligned at room temperature using an orientation field of typically 10 kOe and fixed in epoxy resin. Magnetization isotherm curves $M(H)$ obtained at 4.2 and 300 K are shown in Figs. 2, 3, 4, and 5 for $Sm_2Fe_{17}N_3$, $Sm_2Fe_{17}D_5$, and $Pr_2Fe_{17}N_3$ oriented samples, respectively. The experimental accuracy is estimated to be ±2%. The Curie temperature of the samples was determined using a homemade Faraday type device; the powder was sealed in silica tubes to avoid outgassing and oxidization at high temperature.

It can be seen that all the samples exhibit a high anisotropy. In a field higher than about 25 kOe, no hysteresis was detected when applying an increasing or decreasing field. No

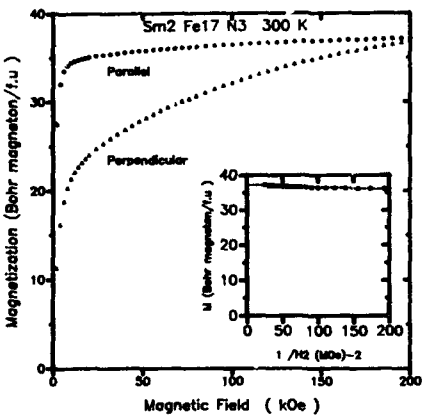

FIG. 3. $Sm_2Fe_{17}N_3$ magnetization curves at 300 K. Insert: $1/H^2$ extrapolation.

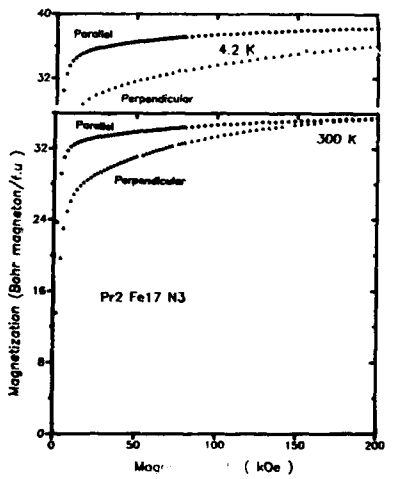

FIG. 5. $Pr_2Fe_{17}N_3$ magn... ...rves at 4.2 and 300 K.

TABLE I. Relevant magnetic features of the studied compounds.

		4.2 K			300 K		
	T_c (K)	M_s (μB/fu)	K_1 (MJ/m^3)	K_2 (MJ/m^3)	M_s (μB/fu)	K_1 (MJ/m^3)	K_2 (MJ/m^3)
Sm_2Fe_{17}	385	29.9	−3.0±0.4	$\|K_2\|$<0.1	26.3	−1.75±0.3	$\|K_2\|$<0.05
$Sm_2Fe_{17}D_5$	565	34.9	−3.8±0.25	0.55±0.3	31.5	−2.80±0.2	0.55±0.2
$Sm_2Fe_{17}N_3$	755	40.5	10.8±0.4	−4.1 ±0.4	37.8	10.4±0.4	−5±1
Pr_2Fe_{17}	293	35.2	−3.7±0.3	0.55±0.1	16.6[a]	...	...
$Pr_2Fe_{17}N_3$	731	38.5	−4.5±0.5	0.8 ±0.3	36	−4.0±0.5	0.5±0.2

[a]Values in applied field of 20 kOe.

change was found in any of our $M(H)$ curves when the cooling of the sample was made in the maximum field or without field. All the compounds display basal plane anisotropy, mainly determined by the Fe-sublattice anisotropy, except for $Sm_2Fe_{17}N_3$ where uniaxial anisotropy was found over the entire ferromagnetic temperature range. At 4.2 K the high field measurements on $Sm_2Fe_{17}N_3$ show that even in 200 kOe, the saturation magnetization is not achieved, although the anisotropy field is around 200 kOe at room temperature (Figs. 2 and 3).

V. DATA ANALYSIS

We discuss first the law of approach to saturation. In magnetic fields above 40 kOe the magnetization curves were found to be fitted by $M(H)=M_s+a/H^2$ with a goodness of fit better than 0.998. In Table I are reported the values of M_s per mole deduced from extrapolation of the $M(H)$ curves with H parallel to the alignment direction. The values of the Curie temperature have been listed as well. Nitrogenation or hydrogenation lead to a strong enhancement of the saturation magnetization and a large increase of the Curie temperature. This behavior originates from the crystal lattice expansion as discussed in previously published papers.

The magnetic anisotropy is the only parameter which affects the magnetization curve through a $1/H^2$ term for any crystal symmetry. Since in high fields domain wall processes are no longer active, any change in $M(H)$ results from a rotation of the magnetic moment.

Iron particles in the $R_2Fe_{17}N_3$ phase should result in a linear dependence of the magnetization with applied field which is a characteristic of the presence of a soft magnetic material. The good agreement with the $1/H^2$ saturation law (see the insert in Figs. 2 and 3) unambiguously witnesses the almost complete absence of elemental iron particles.

The determination of anisotropy constants K_j from magnetization curves of polycrystalline samples is not straightforward because imperfect alignment leads to erroneous values. It is quite difficult to deduce K_j even from the most general law of approach to saturation proposed by Néel[29]

$$M(H)=M_s+\sum_j \frac{a_j}{H^j} \tag{1}$$

because of the lack of explicit relationship between a_j and K_j.[30] In order to obtain accurate values of K_j from magnetization curves of partially oriented samples we start from the model proposed in Ref. 31 applied to Nd-Fe-B. The free energy of a single particle, i.e., a small single crystal, is given by

$$E_T=K_1 \sin^2\theta+K_2 \sin^4\theta-M_sH\cos(\phi-\theta), \tag{2}$$

where θ is the angle between the c axis and the magnetization M_s) and ϕ is the angle between the magnetic field H and the c axis. The first two terms represent the magnetocrystalline anisotropy for uniaxial crystals (anisotropy constants of higher order than K_2 were neglected). The magnetization resolved along the H direction is

$$M=M_s\cos[\phi-\theta(\phi,H)]. \tag{3}$$

Therefore we can obtain $M(H)$ if we know the distribution $f(\phi)$ which gives the probability that the angle between the EMD of a particular grain and the field H is equal to ϕ.

It seems reasonable to assume that the distribution of the EMD is a Gaussian function around the direction of the aligning field. To facilitate the numerical calculations, the distribution used was 40% of the grains for which ϕ=0, 28% (ϕ=5°), 18% (ϕ=10°), 9%, (ϕ=15°), 3% (ϕ=20°), and 1% (ϕ=25°). Within this approximation the component of the magnetization parallel to H at a given temperature can be expressed by

$$M=\frac{1}{N}M_s\sum_{i=1}^{N}\cos(\phi_i-\theta), \tag{4}$$

where the summation covers all N magnetic grains. For each set of parameters (M_s, K_1, K_2, ϕ_i, and H) the equilibrium angle is deduced by minimizing the free energy. Using M_s and ϕ_i values extracted from the approach to saturation and the Gaussian distribution, respectively, K_1, K_2, and θ were refined to fit the observed $M(H)$ curve in the range 30–200 kOe from

$$H=\frac{2K_1\sin\theta\cos\theta+4K_2\sin^3\theta\cos\theta}{-\frac{M_s}{N}\sum_{i=1}^{N}\sin(\theta-\phi_i)}. \tag{5}$$

In this procedure K_1 and K_2 were assumed to be field independent. Since for each studied compound, the values of M_s were found to be equal for both alignment directions, no anisotropy of M_s was taken into account.

A good control of the above distribution was obtained from the study of a magnetically aligned resin-bonded

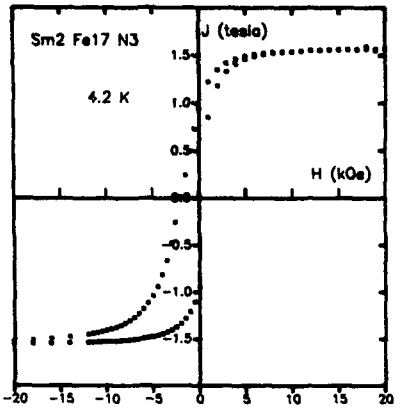

FIG. 6. $Sm_2Fe_{17}N_3$ hysteresis loop at 4.2 K.

Gd_2Fe_{17} powder sample, measured perpendicular to the alignment direction at 4.2 and 300 K. A satisfactory fit (better than 3%) to the magnetization curve in the 30–200 kOe range was obtained using the parameters M_s=0.955T, $K_1=-(2.0\pm0.1)$MJ/m^3, $K_2=-(0.1\pm0.05)$MJ/m^3 in reasonable agreement with a single crystal determination for Gd_2Fe_{17}:[32] $K_1=-(2.8\pm0.1)$MJ/m^3, $K_2=(0.14\pm0.05)$MJ/m^3 or for Y_2Fe_{17}: $K_1=-2.3$ MJ/m^3, $K_2=-0.11$ MJ/m^3.[33] Below 30 kOe the magnetization process is dominated by domain wall motion rather than by homogeneous rotation of magnetization as included in this model.

The intrinsic magnetic properties and the deduced anisotropy constants are summarized in Table I for the studied samples. Introduction of interstitial atoms produces a large increase in T_c: more than 400 K for $Pr_2Fe_{17}N_3$ but limited to 200 K in the hydride. The second salient feature is that while $Sm_2Fe_{17}N_3$ presents a strong uniaxial anisotropy, $Sm_2Fe_{17}D_5$ shows in-plane anisotropy at 4.2 and 300 K. Our results on $Sm_2Fe_{17}N_3$ can be compared to those of Katter *et al.*[34] obtained at 293 K. The values of the room temperature magnetic polarization 1.57 T are in good agreement; in contrast the anisotropy constants are rather different: a value of K_1 20% higher, and a large negative value for K_2. We suggest that in our compounds the nitrogen uptake attains its maximum value, which explains these large differences in K_i. This point of view is confirmed by the high T_C value of our samples.

At 4.2 K, the anisotropy constants and consequently the anisotropy fields are nearly the same in Sm_2Fe_{17} and $Sm_2Fe_{17}D_5$, the planar anisotropy of the hydride being slightly lower. This effect is explained as the result of a tendency of hydrogen to decrease the anisotropy of the rare earth as supported by Mössbauer experiments performed on $Gd_2Fe_{17}D_5$ compounds.[35] Note that, to our knowledge, this is the first determination of K_i for Sm_2Fe_{17} hydrides. For Pr_2Fe_{17} as the Curie temperature is at room temperature and no anisotropy was observed. The anisotropy constants obtained for $Pr_2Fe_{17}N_3$ reveal an enhancement of the planar anisotropy in comparison with Pr_2Fe_{17}. This demonstrates that N atoms increase the crystal electric field acting on the rare earth site.

Since $Sm_2Fe_{17}N_3$ offers a unique combination of high T_C, strong uniaxial anisotropy with little temperature dependence and large remanence, Fig. 6 shows half of the hysteresis cycle measured at 4.2 K for the parallel oriented powder. A very respectable saturation magnetization of $\mu_0M_s=1.57$ T is obtained above about 15 kOe; this corresponds to a theoretical maximum energy product $\mu_0M_s^2/4$ of 490 kJ/m^3. The remanent magnetization and the coercive field are found equal to 0.95 T and 2.1 kOe, respectively. The observed cycle corresponds to an estimated value of $(BH)_{max}$ of 5 MG Oe. This result is much smaller than previous determinations, but note that this is the hysteresis loop of untreated particles: no particular mechanical or thermal treatments were applied after the orientation of the grains to improve coercivity.

VI. DISCUSSION

Our contribution is mainly experimental, but some theoretical approach has recently arisen. The electronic structure calculation performed by Jaswal[36] on $R_2Fe_{17}N_x$ has shown that the tremendous increase of the Curie temperature can be understood theoretically using the spin fluctuation theory.[37] According to Jaswal, an increase in the magnetization and a substantial decrease in the density of states for the up (majority) spin are responsible for the T_C improvement. The increase in magnetization as well as T_C are mainly due to the cell expansion that occurs upon inserting light elements leading to a narrowing of the Fe-*d* band due to a reduction in overlap. This is a pure steric effect that is observed for C, N, as well as H. This is not the only effect of the interstitial on the magnetic properties. It has been shown[20] that the moments carried by the iron near neighbors of N are significantly lower than those on the other iron sites. This was confirmed by band structure calculation[36,38] and interpreted at the light of strong hybridization between the Fe and N electronic state.[20] This feature has been also observed on R_2Fe_{17} carbides.[39]

The influence of interstitial elements on the physical properties of $R_2Fe_{17}N_3$ can be divided into two classes.

(a) That induced by the volume expansion of the unit cell, such as the increase of Curie temperature and magnetization. These consequences of the interstitial insertion have steric origin and are not dependent on the chemical nature of the interstitials but only on their size.

(b) That related to the nature of the interstitial itself, such as the magnetocrystalline anisotropy. We have shown that insertion of H and N have opposite effects on the anisotropy of the rare-earth site. As discussed above, C or N have also a local effect on the magnetism. Forming strong bonds with their iron near neighbors, these light elements tend to limit the size of the magnetic moment carried by their iron near neighbors. This effect is also dependent upon the nature of the interstitial and has not been observed with hydrogen.

Our study shows that the energy product, the saturation magnetization, and the remanence of the interstitial compounds are comparable to those of the Nd-Fe-B compounds.

The $Sm_2Fe_{17}N_x$ samples have intrinsic advantages such as a higher Curie temperature 755 K instead of 593 K and a large anisotropy field at room temperature. Until now, the formation of iron particles during the nitrogenation process of R_2Fe_{17} was a significant drawback, decreasing the coercivity. The use of a high pressure synthesis technique overcomes these difficulties, producing iron-free $Sm_2Fe_{17}N_3$ compounds. Several studies have been undertaken in order to improve the coercive field of the Sm_2Fe_{17} nitrides.

Using mechanical alloying and a subsequent heat treatment, Schnitzke *et al.*[40] have obtained coercive field up to 30 kOe for isotropic microcrystalline $Sm_2Fe_{17}N_{\sim 2.7}$.

A similar treatment has been applied to $Sm_2Fe_{17}C_x$ compounds[41] but the coercivity and remanence at room temperature were 20% lower than that of the nitride.

Nitriding the Sm_2Fe_{17} samples obtained by hydrogenation-decomposition-desorption-recombination, Takeshita *et al.*[42] obtained an intrinsic coercivity of 8.2 kOe and a $(BH)_{max}$ of 14 MG Oe.

The synthesis of metal bonded $Sm_2Fe_{17}N_x$ type magnets[43,44] to improve coercivity. Using low-melting metals (Zn, Bi, Sn, In, or Al) as binder increases the coercive field. The best results were found for Zn. Such a treatment has led to a coercivity of 6 kOe in Ref. 44 whereas Huang *et al.*[43] obtained 10 –17 kOe.

Kuhrt *et al.*[45,46] have shown that the application of pressure can improve the synthesis of Zn bonded $Sm_2Fe_{17}N_x$, favoring Zn diffusion along the grain boundaries and optimizing the formation of the intergranular paramagnetic phase Zn_7Fe_3. They obtained a coercive field of ~44 kOe for their mechanically alloyed samples and about 21 kOe for melt-spun samples.

[1] J. F. Herbst, J. J. Croat, F. E. Pinkerton, and W. B. Yelon, Phys. Rev. B **29**, 4176 (1984).
[2] C. B. Shoemaker, D. P. Shoemaker, and R. Fruchart, Acta Cryst. C **40**, 1665 (1984).
[3] D. B. D. Mooij, J. L. C. Daams, and K. H. J. Buschow, Philips J. Res. **42**, 339 (1987).
[4] D. B. D. Mooij and K. H. J. Buschow, Philips Rep. **41**, 400 (1986).
[5] J. Allemand, A. Letant, J. M. Moreau, J. P. Nozières, and R. Perrier de la Bathie, J. Less. Comm. Met. **166**, 73 (1990).
[6] O. Isnard, J. L. Soubeyroux, D. Fruchart, T. H. Jacobs, and K. H. J. Buschow, J. Phys.: Conden. Matter. **4**, 6367 (1992)
[7] X. C. Kou, R. Grössinger, T. H. Jacobs, and K. H. J. Buschow, J. Magn. Magn. Mater. **88**, 1 (1990).
[8] X. P. Zhong, R. J. Radwanski, F. R. D. Boer, T. H. Jacobs, and K. H. J. Buschow, J. Magn. Magn. Mater. **86**, 333 (1990).
[9] O. Isnard, S. Miraglia, J. L. Soubeyroux, D. Fruchart, and A. Stergiou, J. Less-Comm. Met. **162**, 273 (1990).
[10] J. M. D. Coey and H. Sun, J. Magn. Magn. Mater. **87**, L251 (1990).
[11] Y.-C. Yang, X.-D. Zhang, S.-L. Ge, Q. Pan, L.-S. Kong, S.-L. Ge, H. Li, J.-L. Yang, B.-S. Zhang, Y.-F. Ding, and C.-T. Ye, J. Appl. Phys. **70**, 6001 (1991).
[12] L. Y. Zhang and W. E. Wallace, J. Less-Comm. Met. **149**, 371 (1989).
[13] J. M. D. Coey, Phys. Scr. T **39**, 21 (1991).
[14] Y. Otani, D. P. F. Hurley, H. Sun, and J. M. D. Coey, J. Appl. Phys. **69**, 5584 (1991).
[15] J. M. D. Coey, H. Sun, and D. P. F. Hurley, J. Magn. Magn. Mater. **101**, 310 (1991).
[16] B. Rupp and G. Wiesinger, J. Magn. Magn. Mater. **71**, 269 (1988).
[17] O. Isnard, J. L. Soubeyroux, S. Miraglia, D. Fruchart, L. M. Garcia, and J. Bartolomé, Physica B **180–181**, 629 (1992).
[18] O. Isnard, J. L. Soubeyroux, S. Miraglia, D. Fruchart, L. M. Garcia, and J. Bartolomé, Physica B **180–181**, 624 (1992).
[19] C. N. Christodoulou and T. Takeshita, J. Alloys Compounds **198**, 1 (1993).
[20] O. Isnard, S. Miraglia, J. L. Soubeyroux, and D. Fruchart, J. Alloys Compounds **198**, 129 (1992).
[21] T. Mukai and T. Fujimoto, J. Magn. Magn. Mater. **103**, 165 (1992).
[22] C. C. Colucci, S. Gama, and C. A. Ribeiro, J. Alloys Compounds **194**, 181 (1993).
[23] C. C. Colucci, S. Gama, and F. A. O. Cabral, IEEE Trans. Magn. **MAG-28**, 2578 (1992).
[24] C. C. Colucci, S. Gama, L. C. Labaki, and C. A. Ribeiro, J. Alloys Compounds **189**, 45 (1992).
[25] C. C. Colucci, S. Gama, L. C. Labaki, and C. A. Ribeiro, J. Mag. Magn. Mater. **125**, 161 (1993).
[26] S. Miragiia, J. L. Soubeyroux, C. Kolbeck, O. Isnard, D. Fruchart, and M. Guillot, J. Less-Common Met. **171**, 51 (1991).
[27] G. J. Long, O. A. Pringle, F. Grandjean, W. B. Yelon, and K. H. J. Buschow (these proceedings).
[28] O. Isnard, S. Miraglia, D. Fruchart, and J. Deportes, J. Magn. Magn. Mater. **103**, 157 (1991)
[29] L. Néel, J. Phys. Rad. **9**, 184 (1948).
[30] R. Grössinger, Phys. Status Solidi A **66**, 665 (1981).
[31] K. D. Durst and H. Kronmüller, J. Magn. Magn. Mater. **59**, 86 (1986).
[32] R. Verhoef, Thesis, University of Amsterdam, 1990.
[33] B. Kebe, Thesis, Université de Grenoble, France, 1983.
[34] M. Katter, J. Wecker, C. Kuhrt, L. Schultz, and R. Grössinger, J. Magn. Magn. Mater. **114**, 35 (1992).
[35] O. Isnard *et al.* (in press).
[36] S. S. Jaswal, IEEE Trans. Magn. **MAG-28**, 2322 (1992).
[37] P. Mohn and E. P. Wohlfarth, J. Phys. F: Met. Phys. **17**, 2421 (1987).
[38] L. P. Li, H.-S. Li, and J. M. D. Coey, Phys. Status Solidi B **166**, K107 (1991).
[39] Y. P. Li and J. M. D. Coey, Phys. Rev. B (*to be published*).
[40] K. Schnitzke, L. Schultz, J. Wecker, and M. Katter, Appl. Phys. Lett. **57**, 2853 (1990).
[41] C. Kuhrt, M. Katter, J. Wecker, K. Schnitzke, and L. Schultz, Appl. Phys. Lett. **60**, 2029 (1992).
[42] C. N. Christodoulou and T. Takeshita J. Alloys Compounds **196**, 155, (1993).
[43] M. Q. Huang, L. Y. Zhang, B. M. Ma, Y. Zheng, J. M. Elbicki, W. E. Wallace, and S. G. Sankar, J. Appl. Phys. **70**, 6027 (1991).
[44] Y. Otani, A. Moukarika, H. Sun, J. M. D. Coey, E. Devlin, and I. R. Harris, J. Appl. Phys. **69**, 6735 (1991).
[45] C. Kuhrt, K. O'Donnell, M. Katter, J. Wecker, K. Schnitzke, and L. Schultz, Appl. Phys. Lett. (to be published).
[46] L. Schultz, C. Kuhrt, J. Wecker, K. Schnitzke, and M. Katter (BREU-CT 91 private communication, 1991).

Comparative Mössbauer effect study of several R_2Fe_{17} and $R_2Fe_{17}N_x$ compounds

Gary J. Long, S. Mishra, and O. A. Pringle
Departments of Chemistry and Physics, University of Missouri-Rolla, Rolla, Missouri 65401

F. Grandjean
Institute of Physics, B5, University of Liege, B-4000 Sart-Tilman, Belgium

K. H. J. Buschow
Philips Research Laboratories, P.O. Box 80000, NL-5600 JA Eindhoven, The Netherlands

The Mössbauer spectra of Sm_2Fe_{17} and Ho_2Fe_{17} and their nitrides have been measured between 295 and 85 K and analyzed with a model which is consistent with our earlier work on R_2Fe_{17} and $R_2Fe_{17}N_x$ compounds, where R is Pr, Nd, and Th. This model is completely consistent throughout these rare-earth compounds and is in agreement with the crystallographic changes occurring upon nitrogenation and with the prediction of band structure calculations. The dramatic increase in Curie temperature in the nitrides results from the expansion of the crystallographic lattice, an expansion which is mainly centered on the $9d$ and $18h$ iron sites as is indicated by the increase of their Wigner–Seitz cell volumes upon nitrogenation. The $9d$ and $18h$ sites show a larger enhancement of their hyperfine fields as compared to the $6c$ and $18f$ sites as a result of improved ferromagnetic exchange between these sites and their near neighbors because of the lattice expansion and the consequent reduced iron $3d$-iron $3d$ overlap.

The R_2Fe_{17} compounds, where R is Pr, Nd, Sm, and Th, crystallize in the rhombohedral Th_2Zn_{17} structure[1] in which iron occupies four inequivalent crystallographic sites. Coey *et al.*[2,3] have shown that nitrogenation of these compounds induces a large lattice expansion and an ~400° increase in Curie temperature. We have recently analyzed the Mössbauer spectra of Nd_2Fe_{17}, Pr_2Fe_{17}, and Th_2Fe_{17}, and their nitrides with a model[4–6] based on the Wigner–Seitz cell volume. In this paper, we extend this analysis to Sm_2Fe_{17} and Ho_2Fe_{17} and their nitrides, and show that this model is consistent throughout the rare earths studied and is in agreement with both the crystallographic changes occurring upon nitrogenation and band structure calculations.[7–10]

The samples were prepared[11] and their spectra were measured and fit[4] as described previously. Between 2% and 7% of α-iron was found in the spectra of the R_2Fe_{17} compounds and between 5% and 20% of a nitrided iron phase was found in the $R_2Fe_{17}N_x$ compounds. The isomer shifts are given relative to α-iron and the estimated errors are at most ± 0.5 kOe for the hyperfine fields, ± 0.005 mm/s for the isomer shifts, and ± 0.01 mm/s for the quadrupole shifts.

Figure 1 shows the 85 K Mössbauer spectra of $R_2Fe_{17}N_x$, where R is Pr, Nd, Sm, and Ho. More extensive Mössbauer spectra have been published elsewhere.[4–6] Because the magnetization[3] is oriented along [001] in $Sm_2Fe_{17}N_x$, in the basal plane along [100] in Sm_2Fe_{17}, Nd_2Fe_{17}, Ho_2Fe_{17}, $Nd_2Fe_{17}N_x$, and $Ho_2Fe_{17}N_x$, along [010] in Pr_2Fe_{17}, $Pr_2Fe_{17}N_x$, and Th_2Fe_{17}, or along a general direction in $Th_2Fe_{17}N_x$, the Mössbauer spectra are analyzed with four, seven, or ten sextets representing the resulting inequivalent magnetic sites. In order to both reduce the number of adjustable parameters and to obtain a physically meaningful fit, we used the following constraints which are more restrictive than those used by other authors.[2,3,12–14] One linewidth was used for all lines in a given spectrum, the relative areas of the magnetically inequivalent iron sites were constrained equal to their relative crystallographic and magnetic degeneracies, and the isomer shifts were constrained equal for the two or three magnetically inequivalent sites originating from the same crystallographic site. The linewidths of all the spectra discussed in this paper are in the range of 0.25–0.28 mm/s. As a result of these narrow linewidths we observe more highly resolved spectra, an improvement which permits a more detailed spectral analysis, but places tighter restrictions on the model and the resulting hyperfine parameters.

In order to check the validity of our analysis for $Sm_2Fe_{17}N_x$, which shows uniaxial anisotropy, and to extend our work through the rare-earth series, we have extended earlier work[12–14] on Sm_2Fe_{17} and $Sm_2Fe_{17}N_x$ and analyzed the data as discussed[4–6] for the other R_2Fe_{17} compounds. The experimental results are similar to the earlier work but show linewidths of ~0.26 mm/s, a value which is substantially smaller than the values found by Hu and Coey[14] for Sm_2Fe_{17}, or by Chen *et al.*[13] for Sm_2Fe_{17} and $Sm_2Fe_{17}N_x$. The 85 K spectrum of $Sm_2Fe_{17}N_x$ is shown in Fig. 1 and the hyperfine parameters of Sm_2Fe_{17} and $Sm_2Fe_{17}N_x$, obtained at several temperatures, are given in Tables I and II.

The assignment of the sextets to the different crystallographic sites is based first upon the relative areas and then, for the $18f$ and $18h$ sextets, is based upon their isomer shifts, hyperfine fields, and Wigner–Seitz cell volumes. In general, the larger the Wigner–Seitz cell volume of a site, the larger its isomer shift. Further, the larger the number of iron near neighbors for a site, the larger its hyperfine field. Figure 2 shows the 85 K isomer shifts in Sm_2Fe_{17} and $Sm_2Fe_{17}N_x$ versus the Wigner–Seitz cell volumes for the four crystallographic sites.[1,15–17] This figure illustrates both the abovementioned correlation and the effect of nitrogenation upon the isomer shifts. All four isomer shifts increase upon nitrogenation, the $6c$ and $9d$ because of the lattice and Wigner–Seitz cell expansion, the $18f$ because of the presence of a nitrogen near neighbor, and the $18h$ because of both the Wigner–Seitz cell expansion and the presence of a nitrogen

 0021-8979/94/75(10)/5994/3/$6.00 © 1994 American Institute of Physics

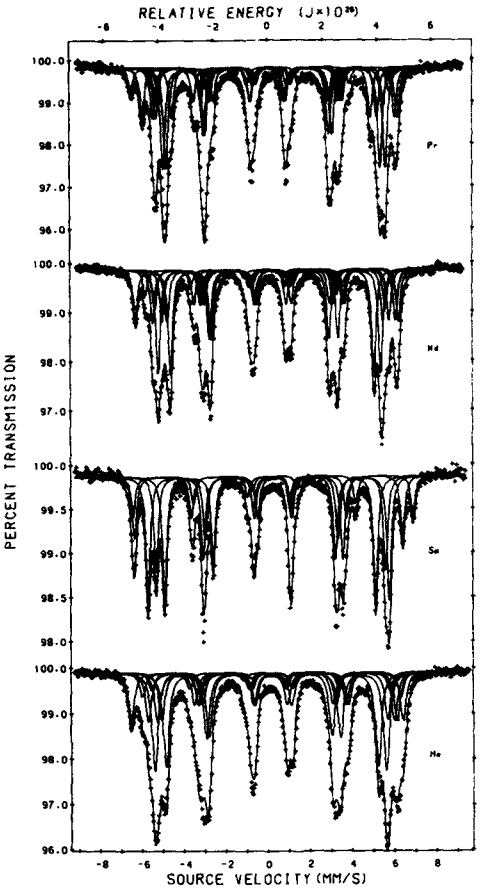

FIG. 1. The Mössbauer effect spectra of several $R_2Fe_{17}N_x$ compounds obtained at 85 K.

TABLE II. Mössbauer spectral hyperfine parameters for $Sm_2Fe_{17}N_{2.6}$.

	T, K	6c	9d	18f	18h	Wt. ave.
H,	85	413	395	355	311	353
(kOe)	155	411	395	354	310	352
	225	407	392	349	306	348
	295	394	378	337	297	337
δ,[a]	85	0.285	0.045	0.144	0.215	0.168
(mm/s)	155	0.255	0.030	0.130	0.210	0.155
	225	0.230	−0.010	0.100	0.180	0.124
	295	0.160	−0.070	0.040	0.120	0.063
QS,[b]	85	−0.09	−0.02	0.44	−0.21	···
(mm/s)	155	−0.09	−0.02	0.44	−0.21	···
	225	−0.09	−0.02	0.41	−0.21	···
	295	−0.07	−0.02	0.35	−0.21	···

[a]Relative to room temperature α-iron.
[b]The QS values are the quadrupole shift except for 6c site for which it is the quadrupole splitting for a θ value of 0°.

near neighbor. Very similar plots have been obtained for the other rare-earths compounds.[4–6] Figure 3 shows the 85 K isomer shifts in R_2Fe_{17} and $R_2Fe_{17}N_x$. The smooth variation of the isomer shifts, and their increase upon nitrogenation, for the different rare-earth compounds strongly support the model and our assignment of the sextets.

Figure 4 shows the 85 K weighted average hyperfine fields in R_2Fe_{17} and $R_2Fe_{17}N_x$ for the different rare-earth compounds and reveals small variations with the rare-earth atom. $Sm_2Fe_{17}N_x$ shows the largest field because of its uniaxial anisotropy. Th_2Fe_{17} shows the largest increase upon nitrogenation, in agreement with the large observed increases in its magnetic moment and unit cell volume. Pr_2Fe_{17}, Nd_2Fe_{17}, and Ho_2Fe_{17} show very similar increases of 40–50 kOe in their weighted average hyperfine fields upon nitrogenation.

Our model[4–6] for the analysis of the Mössbauer spectra of R_2Fe_{17} and $R_2Fe_{17}N_x$ is in excellent agreement with all available crystallographic data on these compounds and the resulting hyperfine parameters show both a smooth variation with the rare earth and the expected variation with temperature. Finally, the dramatic increase in Curie temperature in the nitrides results from the expansion of the crystallographic

TABLE I. Mössbauer spectral hyperfine parameters for Sm_2Fe_{17}.

	T, K	6c	$9d_6$	$9d_3$	$18f_{12}$	$18f_6$	$18h_{12}$	$18h_6$	Wt. ave.
H,	85	354	304	288	286	324	275	281	298
(kOe)	150	335	287	272	269	303	261	265	288
	225	307	257	246	244	277	238	238	255
	295	262	214	219	206	236	202	195	216
δ,[a]	85	0.245	−0.080	−0.080	0.050	0.050	0.060	0.060	0.054
(mm/s)	150	0.205	−0.115	−0.115	0.000	0.000	0.020	0.020	0.011
	225	0.160	−0.150	−0.150	−0.050	−0.050	−0.040	−0.040	−0.055
	295	0.090	−0.180	−0.180	−0.100	−0.100	−0.090	−0.090	−0.088
QS,[b]	85	−0.13	−0.34	0.06	0.42	−0.09	−0.33	0.69	···
(mm/s)	150	−0.11	−0.28	0.04	0.42	−0.08	−0.35	0.66	···
	225	−0.10	−0.18	0.04	0.42	−0.08	−0.39	0.63	···
	295	−0.08	−0.13	0.04	0.42	−0.05	−0.36	0.46	···

[a]Relative to room temperature α-iron.
[b]The QS values are the quadrupole shift except for 6c site for which it is the quadrupole splitting for a θ value of 90°.

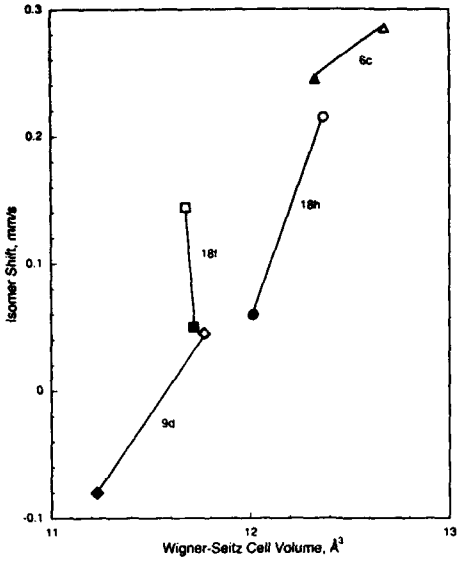

FIG. 2. The correlation between the Wigner–Seitz cell volume and the 85 K isomer shift for each site in going from Sm_2Fe_{17} (closed symbols) to $Sm_2Fe_{17}N_x$ (open symbols).

lattice, an expansion which is mainly centered on the $9d$ and $18h$ iron sites as indicated by the increase of their Wigner–Seitz cell volumes upon nitrogenation. In agreement with the predictions of band structure calculations,[8,10] the $9d$ and $18h$ sites show a larger enhancement of their hyperfine fields and magnetic moments as compared to the $6c$ and $18f$ sites because of improved ferromagnetic exchange between these sites and their near neighbors. Indeed, all the distances between the $9d$ and $18h$ sites and their iron near neighbors increase upon nitrogenation, an increase which results in a reduced iron $3d$-iron $3d$ overlap and hence improved ferromagnetic coupling. In contrast, the distances between the $6c$ and $18f$ sites and their near neighbors either increase or decrease upon nitrogenation, changes which yield a smaller improvement in the ferromagnetic exchange coupling for these two sites.

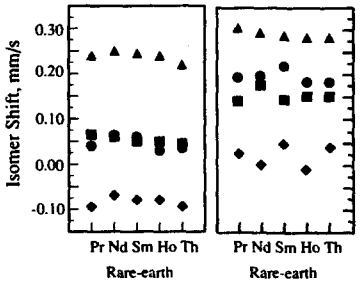

FIG. 3. Isomer shifts obtained at 85 K for the four crystallographic sites in R_2Fe_{17} (left) and $R_2Fe_{17}N_x$ (right) as a function of rare earth for the iron $6c$ site, ▲, for the iron $9d$ site, ◆, for the iron $18f$ site, ■, and for the iron $18h$ site, ●.

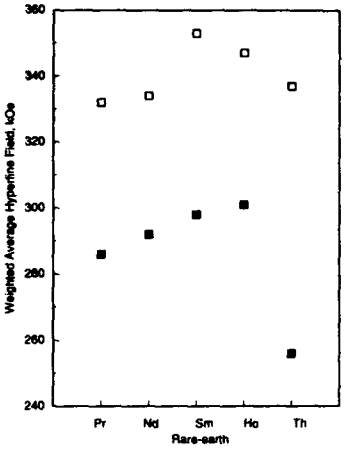

FIG. 4. The 85 K weighted average hyperfine fields in R_2Fe_{17} (solid symbols) and $R_2Fe_{17}N_x$ (open symbols) as a function of rare earth.

The authors acknowledge with thanks NATO for a cooperative scientific research Grant No. 92-1160, and the Division of Materials Research of the US National Science Foundation, for Grant No. DMR-9214271. G. J. L. would like to thank the Commission for Educational Exchange between the United States of America, Belgium, and Luxembourg for a Fulbright Research Fellowship during the 1993–1994 academic year.

[1] J. F. Herbst, J. J. Croat, R. W. Lee, and W. B. Yelon, J. Appl. Phys. **53**, 250 (1982).
[2] J. M. D. Coey and H. Sun, J. Magn. Magn. Mat. **87**, L251 (1990).
[3] H. Sun, J. M. D. Coey, Y. Otani, and D. P. F. Hurley, J. Phys. Condens. Matter **2**, 6465 (1990).
[4] G. J. Long, O. A. Pringle, F. Grandjean, and K. H. J. Buschow, J. Appl. Phys. **72**, 4845 (1992).
[5] G. J. Long, O. A. Pringle, F. Grandjean, and K. H. J. Buschow, J. Appl. Phys. **74**, 504 (1993).
[6] G. J. Long, O. A. Pringle, F. Grandjean, and K. H. J. Buschow, J. Appl. Phys. **75**, 2598 (1994).
[7] R. Coehoorn and G. H. O. Daalderop, J. Magn. Magn. Mater. **104–107**, 1081 (1992).
[8] S. S. Jaswal, IEEE Trans. Magn. **MAG-28**, 2322 (1992).
[9] T. Beuerle and M. Fähnle, Phys. Status Solidi B **174**, 257 (1992).
[10] Z. Gu and W. Lai, J. Appl. Phys. **71**, 3911 (1992).
[11] K. H. J. Buschow, R. Coehoorn, D. B. de Mooij, K. de Waard, and T. H. Jacobs, J. Magn. Magn. Mater. **92**, L35 (1990).
[12] M. Rosenberg, R. J. Zhou, M. Katter, L. Schultz, and G. Filoti, J. Appl. Phys. **73**, 6035 (1993).
[13] X. Chen, Z. Altounian, and D. H. Ryan, J. Appl. Phys. **73**, 6038 (1993).
[14] B. P. Hu and J. M. D. Coey, J. Less-Common Metals **171**, 33 (1991).
[15] In the absence of crystallographic positional parameters for the samarium compounds, the Wigner–Seitz cell volumes were calculated with the lattice parameters for Sm_2Fe_{17}, Ref. 16, and $Sm_2Fe_{17}N_x$, Ref. 17, and the positional parameters for Nd_2Fe_{17}, Ref. 1, and $Nd_2Fe_{17}N_{2.4}$, Ref. 16.
[16] S. Miraglia, J. L. Soubeyroux, C. Kolbeck, O. Isnard, and D. Fruchart, J. Less-Common Metals **171**, 51 (1991).
[17] T. H. Jacobs, Doctoral dissertation, University of Leiden, 1992.

The effects of group IV B/V B/VI B additions on the magnetic properties of $Sm_{2+\delta}Fe_{17}$ carbonitrides

X. Chen, Er. Girt, and Z. Altounian
Center for the Physics of Materials, Department of Physics, McGill University, 3600 University Street, Montréal, Québec, H3A 2T8, Canada

Curie temperature, anisotropy field, and lattice constants are measured for the $Sm_{2+\delta}Fe_{17}M_{0.4}$ ($\delta \leq 0.6$) carbonitrides for M=Ti, V, Cr, Zr, Nb, Mo, Hf, Ta, and W. It is found that minor additions of M reduce the Curie temperature, with the largest decrease of 28 K for M=Mo, and that the fluctuations in Curie temperature are not related to the changes in unit cell volumes. Compared with $Sm_{2+\delta}Fe_{17}N_xC_y$, most of the M additives reduce the anisotropy field with the largest decrease of about 10 kOe for M=Zr. The V addition has almost no effect on the anisotropy field and the Ti addition gives a 4–5 kOe enhancement of the anisotropy field.

I. INTRODUCTION

Sm_2Fe_{17} nitride, carbide and carbonitride have excellent magnetic properties, and are suitable for producing high performance magnets.[1–5] The techniques for manufacturing these magnets are mechanical alloying,[6,7] melt-spinning,[8] metal bonding,[9,10] and hydrogenation decomposition desorption recombination (HDDR).[11,12] A long homogenization process is often required to eliminate the α-Fe and other magnetic soft phases in the starting materials when metal bonding[9,10] and HDDR[11] methods are used. It has been reported[12] that minor additions (~2 at. %) of IV B/V B/VI B group elements significantly reduce the amount of the precipitated α-Fe in the starting materials, thus eliminating the need for a long homogenization process. For example, a permanent magnet, $Sm_{2+\delta}Fe_{17}Ti_{0.4}N_xC_y$ ($\delta \leq 0.6$) made by HDDR method, has an intrinsic coercivity of 18 kOe and an energy product of 9.8 MGOe at room temperature.[12] It is expected that such good performance is not only due to the reduction of α-Fe in the starting materials, but also due to the effects of these additives on the intrinsic magnetic properties. Endoh *et al.*[13] have investigated the effects of minor addition of impurities, including several refractory elements, on the intrinsic magnetic properties of Sm_2Fe_{17} nitrides. Their results show that Co addition increases the Curie temperature, T_c, and that Ti, V, or Co additions increase the anisotropy field, H_A. Since in their work, the anisotropy field was measured by VSM on aligned powder specimens, it is believed that the H_A values have been underestimated.[13,14] In the present work, the effects on the intrinsic magnetic properties have been investigated for the IV B/V B/VI B group additives. The H_A was measured by the singular point detection (SPD) technique[15] in an 18 T pulsed field over a temperature range between 480 and 590 K. In this temperature range, the SPD signals associated with H_A are very strong, so that the experimental errors are minimized.

II. EXPERIMENTAL METHODS

Elements (purity 99.9%) Sm, Fe, and M, where M=Ti, V, Cr, Zr, Nb, Mo, Hf, Ta, and W, were arc melted at least six times, followed by induction melting at least three times. Excess Sm was added to compensate for Sm loss during melting. The composition of the ingots was $Sm_{2+\delta}Fe_{17}M_{0.4}$ ($\delta \leq 0.6$). X-ray diffraction shows the main phases of the Th_2Zn_{17} rhombohedral structure and secondary phases of $SmFe_2$ in the starting materials. The ingots were ground into powder (<32 μm), annealed in N_2 at 480 °C for 9 h, and in C_2H_2 at the same temperature for 10 min. The resulting specimens were used for the H_A and T_c measurements. T_c was determined by making use of a thermogravimetric analyzer (Perkin–Elmer TGA-7) in a small field gradient. The SPD measurements were performed in a pulsed magnet of up to 180 kOe. Sample temperature was maintained to within ±1 K during the measurements.

III. RESULTS AND DISCUSSION

Figure 1 shows thermomagnetic scans of the $Sm_{2+\delta}Fe_{17}M_{0.4}$ (M=Ti and W) carbonitrides. For comparison, the curve for $Sm_{2+\delta}Fe_{17}N_xC_y$, which shows the highest T_c, is also plotted. It is obvious that the T_c depends on M. The decrease in T_c is also observed for other additives as shown in Table I. The largest decrease, about 28 K, in T_c is observed for M=Mo. For M=Ti and Nb, which show excellent performance as permanent magnets,[12] the decrease in T_c is 19 and 17 K, respectively.

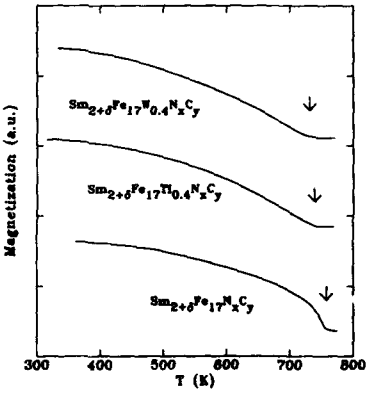

FIG. 1. Thermomagnetic scans of the $Sm_{2+\delta}Fe_{17}M_{0.4}$ carbonitrides for M=Ti, W, and Fe, showing that the T_c, denoted by arrows, varies with M.

 0021-8979/94/75(10)/5997/3/$6.00 © 1994 American Institute of Physics

TABLE I. Magnetic properties and lattice constants of $Sm_{2+\delta}Fe_{17}M_{0.4}N_xC_y$.

Temperature (K)	H_A (kOe) 480	500	520	550	590	T_c (K)	a (nm)	c (nm)	V (nm^3)
$Sm_{2+\delta}Fe_{17}N_xC_y$	87	78	70	59	50	758	0.875	1.265	0.839
$Sm_{2+\delta}Fe_{17}Ti_{0.4}N_xC_y$	91	83	74	64	47	739	0.873	1.266	0.836
$Sm_{2+\delta}Fe_{17}V_{0.4}N_xC_y$	88	78	70	62	47	741	0.873	1.267	0.836
$Sm_{2+\delta}Fe_{17}Cr_{0.4}N_xC_y$	81	74	67	56	46	746	0.872	1.268	0.835
$Sm_{2+\delta}Fe_{17}Zr_{0.4}N_xC_y$	75	69	63	51	42	750	0.871	1.270	0.834
$Sm_{2+\delta}Fe_{17}Nb_{0.4}N_xC_y$	85	75	67	57	44	741	0.873	1.267	0.836
$Sm_{2+\delta}Fe_{17}Mo_{0.4}N_xC_y$	80	72	65	55	41	730	0.873	1.268	0.837
$Sm_{2+\delta}Fe_{17}Hf_{0.4}N_xC_y$	77	71	64	52	43	757	0.872	1.267	0.834
$Sm_{2+\delta}Fe_{17}Ta_{0.4}N_xC_y$	86	76	69	59	47	751	0.873	1.267	0.836
$Sm_{2+\delta}Fe_{17}W_{0.4}N_xC_y$	80	72	64	53	43	731	0.872	1.269	0.836

Since the increase in T_c is mainly due to the volume expansion of the lattice for Sm_2Fe_{17} nitride, carbide, and carbonitride,[1–5,16] it is interesting to investigate the relationship between T_c and the lattice constants. Figure 2 shows the x-ray powder diffraction of $Sm_{2+\delta}Fe_{17}Mo_{0.4}$ carbonitride. The lattice constants obtained for all $Sm_{2+\delta}Fe_{17}M_{0.4}$ carbonitrides are shown in Table I. It is shown that the decreases in T_c are not accompanied by the decreases in unit cell volume. An example is the specimen for M=Mo, which has the lowest T_c but the largest unit cell volume among the specimens except $Sm_{2+\delta}Fe_{17}N_xC_y$. Therefore, the fluctuations in the T_c are not related to the changes in unit cell volumes.

The anisotropy field was measured over a temperature range between 480 and 590 K by the SPD method.[15] In this temperature range, the peak positions associated with H_A can be easily located, so that the uncertainty in the values of H_A is less than 2 kOe. Figure 3 shows an example of SPD signals, where the second derivative d^2M/dt^2 is plotted against the external field at various temperatures for the specimen with M=Cr. The values of H_A obtained by this technique are shown in Table I, where the H_A of $Sm_{2+\delta}Fe_{17}N_xC_y$ is also shown for comparison. It is worthwhile to mention that H_A of $Sm_{2+\delta}Fe_{17}N_xC_y$ obtained here is about 3 kOe higher than that reported in Ref. 5. This gain in H_A is due to the different carbonitriding conditions. As compared with those used in Ref. 5, the carbonitriding temperature used in the present work is lower and the time is much longer. In this condition, more nitrogen atoms are introduced into the specimens, resulting in a higher H_A. Similar results have been reported by Iriyama *et al.*[17] and Wei *et al.*[18] They observed that the H_A increases with the nitrogen content until the nitrogen content reaches 3.

As is shown in Table I, H_A varies with M. At 590 K, $Sm_{2+\delta}Fe_{17}N_xC_y$ has the highest H_A for its higher T_c. At other temperatures, most of the M additions reduce the H_A with the largest decrease of about 10 kOe for M=Zr. Compared with $Sm_{2+\delta}Fe_{17}N_xC_y$, the V addition has almost no effect on H_A and the Ti addition increases the H_A by about 4–5 kOe. Figure 4 shows the temperature dependence of H_A for $Sm_{2+\delta}Fe_{17}N_xC_y$ and $Sm_{2+\delta}Fe_{17}M_{0.4}N_xC_y$ (M=Ti and Zr). From these curves, a gain of several kOe in H_A by Ti addition is expected at room temperature.

Iriyama *et al.*[17] and Wei *et al.*[18] have studied the relationship between the H_A and nitrogen content of $Sm_2Fe_{17}N_x$ ($x=2$–6). They report that H_A increases and then decreases with nitrogen content, with the maximum at $x=3$. The lattice

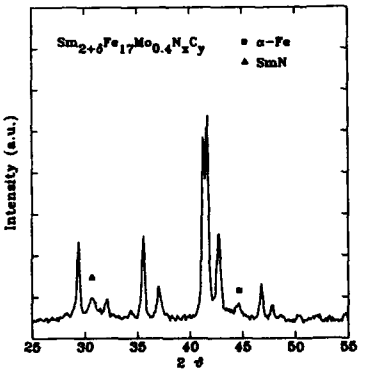

FIG. 2. X-ray (Cu $K\alpha$) powder diffraction of $Sm_{2+\delta}Fe_{17}Mo_{0.4}$ carbonitride.

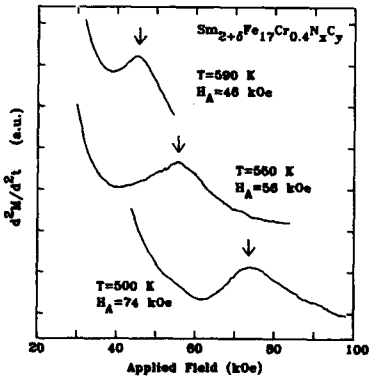

FIG. 3. Example of SPD signals: d^2M/dt^2 vs external magnetic field at various temperatures for $Sm_{2+\delta}Fe_{17}Cr_{0.4}$ carbonitride. The kinks are related to the anisotropy field.

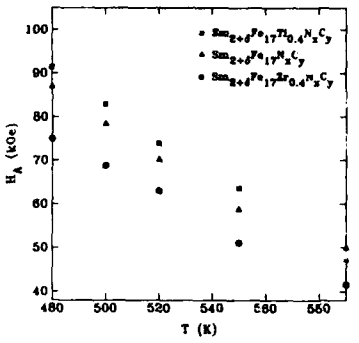

FIG. 4. Temperature dependence of anisotropy field of $Sm_{2+\delta}Fe_{17}M_{0.4}N_xC_y$ (M=Ti, Ar, and Fe). The values are not corrected for the demagnetizing field.

constant a remains almost constant when $x \geq 2$, while the lattice constant c always increases with x. Therefore, for $x \leq 3$, the increase in H_A is accompanied by an increase in the unit cell volume. This relationship is, however, not observed in the present work. The H_A of $Sm_{2+\delta}Fe_{17}M_{0.4}N_xC_y$ are randomly related to the unit cell volumes, indicating that the fluctuations in H_A are not related to the possible fluctuations of nitrogen and carbon contents caused by M.

In conclusion, minor additions of M slightly reduce T_c. Compared with the $Sm_{2+\delta}Fe_{17}N_xC_y$, introducing V, Nb, and Ta into the $Sm_{2+\delta}Fe_{17}N_xC_y$ has little effect on the H_A. The Ti addition increases H_A, and therefore improves the magnetic hardness for permanent magnet application.

ACKNOWLEDGMENTS

This research was supported by grants from the Natural Science and Engineering Research Council of Canada, Fonds pour la Formation de Chercheurs et l'aide à la Recherche, Québec.

[1] Y. Otani, D. P. F. Hurley, H. Sun, and J. M. D. Coey, J. Appl. Phys. **69**, 5584 (1991).
[2] J. M. D. Coey, H. Sun, Y. Otani, and D. P. F. Hurley, J. Magn. Magn. Mater. **98** 76 (1991).
[3] B. P. Hu and G.-C. Liu, Solid State Commun. **79**, 785 (1991).
[4] X. C. Kou, R. Grössinger, M. Katter, J. Wecker, L. Schultz, T. H. Jacobs, and K. H. J. Buschow, J. Appl. Phys. **70**, 2272 (1991).
[5] X. Chen, Z. Altounian, and D. H. Ryan, J. Magn. Magn. Mater. **125**, 169 (1993).
[6] L. Schultz, K. Schnizke, J. Wecker, M. Katter, and C. Kuhrt, J. Appl. Phys. **70**, 6339 (1991).
[7] J. Ding, P. G. McCormick, and R. Street, J. Alloys Compounds **189**, 83 (1992).
[8] F. E. Pinkerton and C. D. Fuerst, Appl. Phys. Lett. **60**, 2558 (1992).
[9] M. Q. Huang, L. Y. Zhang, B. M. Ma, Y. Zheng, J. M. Elbicki, W. E. Wallace, and S. G. Sankar, J. Appl. Phys. **70**, 6027 (1991).
[10] S. Suzuki and T. Miura, IEEE Trans. Magn. **MAG-28**, 994 (1992).
[11] C. N. Christodoulou and T. Takeshita, J. Alloys Compounds **196**, 155 (1993).
[12] X. Chen and Z. Altounian (these proceedings).
[13] M. Endoh, M. Iwata, and M. Tokunaga, J. Appl. Phys. **70**, 6030 (1991).
[14] M. Katter, J. Wecker, L. Schultz, and R. Grössinger, J. Magn. Magn. Mater. **92**, L14 (1990).
[15] G. Asti and S. Rinaldi, Phys. Rev. Lett. **28**, 1584 (1972).
[16] J. M. D. Coey and H. Sun, J. Magn. Magn. Mater. **87**, L251 (1990).
[17] T. Iriyama, K. Kobayashi, N. Imaoka, T. Fukuda, H. Kato, and Y. Nakagawa, IEEE Trans. Magn. **MAG-28**, 2326 (1992).
[18] Y.-N. Wei, K. Sun, Y.-B. Fen, J.-X. Zheng, B.-P. Hu, Y.-Z. Wang, X.-L. Rao, and G.-C. Liu, J. Alloys Compounds **194**, 9 (1993).

Phase transformation induced by gas phase reaction in $RFe_{10}SiC_x$ alloys

E. W. Singleton and G. C. Hadjipanayis
Department of Physics and Astronomy, University of Delaware, Newark, Delaware 19716

V. Papaefthymiou
Department of Physics, University of Ioannina, 45110 Ioannina, Greece

Z. Hu and W. B. Yelon
University of Missouri Research Reactor, Columbia, Missouri 65211

A new series of rare-earth iron intermetallic carbide compounds has been prepared by the reaction of powders with methane gas. The alloys prior to the methane heat treatment had the 2:17-type structure, $R_2(Fe,Si)_{17}$ (R=Y, Ce, Pr, Nd, and Sm). After heat treatment in temperatures up to 873 K the alloys absorb carbon and retain their original structure with a volume expansion over the carbon-free unit cell. For higher heat treatment temperatures (973–1073 K), a phase transformation occurs leading to the $BaCd_{11}$-type structure. These compounds have a lower Curie temperature than those with the Th_2Zn_{17}-type structure, in the range of 453–495 K. Rietveld analysis of neutron diffraction data on $NdFe_{10}SiC_x$ with the $BaCd_{11}$-type structure are reported. In addition, the average hyperfine parameters determined by Mössbauer spectroscopy are reported for the Nd compounds.

The gas interstitial modification (GIM) technique[1] has been used to improve the intrinsic magnetic properties of several iron-rich rare-earth iron alloys by introducing interstitial nitrogen or carbon. This discovery has led to work aimed at obtaining permanent magnet materials based predominately on $Sm_2Fe_{17}(N,C)_x$ and $Nd(Fe,M)_{12}(N,C)_x$ alloys.[2–4] In this paper, we report a novel technique for producing $BaCd_{11}$ (1:11) structure-type alloys from samples which initially had the $R_2(Fe,Si)_{17}$ (2:17) phase. The $BaCd_{11}$ phase is stable in rare-earth cobalt alloys[5] and rare-earth cobalt-iron alloys with the composition $RCo_{9-x}Fe_xSi_2$, $0<x\leq 0.55$.[6] The $BaCd_{11}$-type structure also forms from the melt in the series $RFe_{10}SiC_{0.5}$ with R=Ce, Pr, Nd, and Sm where small carbon additions stabilize the 1:11 phase.[7]

In this study GIM treatment in methane gas of the $R_2(Fe,Si)_{17}$ alloys lead to an expanded lattice due to interstitial carbon atoms and a corresponding increase in Curie temperature of up to 166 K. For methane heat treatment at high temperatures ($T>973$ K), a phase transformation to the $BaCd_{11}$-type structure occurs. Earlier we have reported the structural and intrinsic magnetic properties of this new series of alloys[8] and a summary of the results is shown in Table I. In this paper, we report the results of neutron powder diffraction studies on a $NdFe_{10}SiC_x$ sample, and standard ^{57}Fe Mössbauer spectroscopy for the Nd-Fe-Si-(C) samples.

Samples of nominal composition $RFe_{10}Si$ (R=Y, Ce, Pr, Nd, and Sm) were prepared by arc-melting high purity elements. The sample preparation, x-ray diffraction, and magnetic measurement techniques have been described previously.[8]

Conventional transmission mode ^{57}Fe Mössbauer spectroscopy was performed on a series of samples containing Nd. Room temperature spectra were obtained with a conventional constant acceleration spectrometer using a $^{57}Co(Rh)$ source. Isomer shifts are given relative to Fe metal at 295 K.

A powder sample (~1 g) of the Nd-containing sample having undergone methane heat treatment at 973 K for 3 h was prepared for neutron diffraction studies. The neutron diffraction data were collected at room temperature using the high resolution powder diffractometer at the University of Missouri Research Reactor (MURR). This instrument uses a linear position sensitive detector to collect data over a 20° angular span in 1° setting and measures the full diagram with 5° settings from 5° to 105°. The diffractometer uses a bent perfect Si (511) monochromator at 1.4683 Å. The data were analyzed using the Rietveld technique[9] as implemented in the FULLPROF program[10] which allows multiphase refinements and includes the magnetic refinements. Analysis showed two majority phases consisting of the $NdFe_{10}SiC_x$ phase and α-Fe. In addition, two small broad peaks from a third phase were observed and could not be identified. The regions corresponding to those peaks were excluded from the final refinements.

The x-ray diffraction data confirmed that the original alloys had the 2:17-type structure and those heat treated in methane in the temperature range of 450–650 °C retained their original structure with an expanded lattice, while those samples heat treated above 650 °C underwent a phase transformation to the 1:11-type structure. Figure 1 shows the lattice expansion and phase transformation seen in a typical sample. X-ray diffraction of the homogenized Pr-Fe-Si alloy is shown in Fig. 1(a) and is of the 2:17-type crystal structure, with the diffraction peaks labeled accordingly. Figure 1(b) shows the x-ray diffraction pattern of the same sample heat treated in methane gas at 500 °C for 3 h; the sample has the original crystal structure but with an expanded lattice. Figure 1(c) shows the formation of the 1:11-type crystal structure in a Pr-Fe-Si sample heat treated in methane gas at 700 °C for 3 h.

The T_C of the compounds was determined from low field thermomagnetic sweeps up to 800 °C. Upon carbon uptake in the low temperature carbonation range of 450–650 °C, the T_C increases dramatically corresponding to the formation of the expanded 2:17 phase. For methane heat treatments above 650 °C the 1:11 phase forms with a lower T_C. This Curie temperature is higher than those reported in Ref. 7 in alloys containing carbon content of $x=0.5$. The increased T_C over the carbon 0.5 alloys is in agreement with the larger lattice constant seen in the GIM-produced alloys

 0021-8979/94/75(10)/6000/3/$6.00 © 1994 American Institute of Physics

TABLE I. Summary of structural and magnetic properties of selected samples. For each rare earth, the first sample listed represents the homogenized sample. The remaining samples correspond to heat treatments in methane gas for the temperature and time indicated. Saturation magnetization and anisotropy field were determined at room temperature. *Values of M_s are corrected for α-Fe and determined using the law of approach to saturation.*

Rare earth	Heat treatment		Structure type	a (nm)	c (nm)	V (nm^3)	$\Delta V/V$ ($\times 10^2$)	T_c (K)	M_s (emu/g)	H_A (kOe)
	T (°C)	Time (h)								
Y	1100	48	Th_2Ni_{17}	0.768	0.827	0.422		476		
Y	600	3	Th_2Ni_{17}	0.790	0.841	0.454	7.6	642		
Y	700	3	$BaCd_{11}$	1.011	0.661	0.676		471		
Ce	1100	48	Th_2Zn_{17}	0.846	1.243	0.770		434	80	
Ce	500	3	Th_2Zn_{17}	0.869	1.308	0.856	11.2	523	85	
Ce	700	3	$BaCd_{11}$	1.016	0.662	0.683		461	97	
Pr	1100	48	Th_2Zn_{17}	0.854	1.247	0.788		475	104	
Pr	500	3	Th_2Zn_{17}	0.875	1.277	0.847	7.5	608	111	
Pr	700	3	$BaCd_{11}$	1.019	0.660	0.686		507	90	
Nd	1100	48	Th_2Zn_{17}	0.853	1.239	0.781		485	116	46
Nd	500	3	Th_2Zn_{17}	0.871	1.246	0.822	5.3	603	123	60
Nd	700	3	$BaCd_{11}$	1.012	0.662	0.678		505	93	···
Sm	1100	48	Th_2Zn_{17}	0.858	1.243	0.783		547	101	···
Sm	500	3	Th_2Zn_{17}	0.868	1.283	0.836	6.8	613	104	80
Sm	700	3	$BaCd_{11}$	1.013	0.660	0.677		495	96	45

which results in a larger Fe-Fe distance. Carbon content x was estimated by mass increase of the samples and $x>2$ was found in the 1:11-type samples. In the 1:11-type structure, carbon atoms are found to fill octahedral voids formed by two rare-earth atoms and four iron atoms. Full site occupancy would allow two carbon atoms per unit cell in the 1:11 compounds. This higher than expected carbon content could be the result of the formation of RC or some Fe-C phase. The magnetization seen in the 1:11-type compounds is higher than reported in Ref. 7. This is in agreement with the increased Curie temperature of the GIM-produced samples.

Figure 2 shows the ^{57}Fe Mössbauer spectra of a homogenized Nd-Fe-Si sample, and of Nd-Fe-Si-C heat treated in methane at 500 and 700 °C for 3 h. The theoretical fits to these spectra are given by the solid lines. The spectra were analyzed with an appropriate number of independent Zeeman

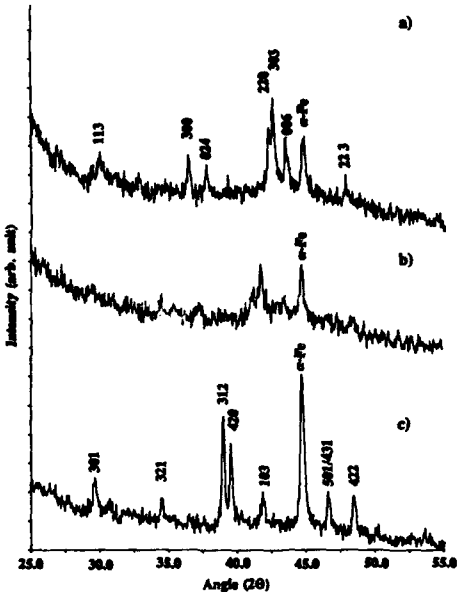

FIG. 1. X-ray diffraction pattern of (a) $PrFe_{10}Si$ homogenized sample; heat treated in CH_4 at (b) 500 °C for 3 h and (c) 700 °C for 3 h.

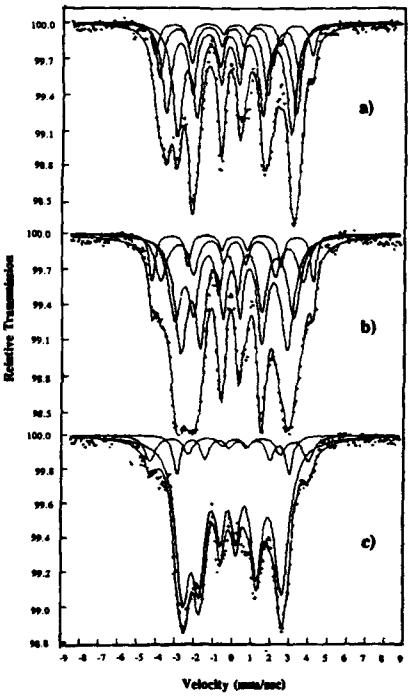

FIG. 2. Room temperature ^{57}Fe Mössbauer spectra of (a) $NdFe_{10}Si$ homogenized sample; heat treated in CH_4 at (b) 500 °C for 3 h and (c) 700 °C for 3 h. The solid line is a calculated fit to the data.

TABLE II. Hyperfine parameters determined by Mössbauer spectroscopy.

Sample (phase)	Site	δ (mm/s)	ΔE (mm/s)	H (kG)	ΔH (kG)	%	$\Gamma/2$ (mm/s)
$Nd_2Fe_{14}Si_3$ (2:17 type)	6c	0.11	−0.03	258	4.0	8	0.19
	9d	−0.06	−0.13	229	3.0	17	0.19
	18f	−0.09	0.07	212	5.0	32	0.19
	18h	−0.02	0.24	187	7.0	43	0.19
$Nd_2Fe_{14}Si_3C_x$ (2:17 type)	6c	0.11	−0.08	264	5.0	8	0.17
	9d	0.00	−0.14	233	11.0	17	0.17
	18f	0.01	0.25	195	13.0	32	0.17
	18h	0.08	0.14	174	14.0	43	0.17
$NdFe_{10}SiC_x$ (1:11 type)		0.07	−0.26	259	4.0	10	0.26
		0.10	−0.10	184	1.0	10	0.26
	32i	0.0	0.24	161	12.0	80	0.26

subspectra according to those reported previously[11] and assuming a distribution of hyperfine fields in each subcomponent. Results of the fit are reported in Table II. Because of the low resolution of the experimental spectra this analysis has an arbitrary character to some degree. All of the Mössbauer spectra contained about 37% of disordered alloy (Fe with 4.5% Si). The Mössbauer spectra in Fig. 2 are the result of proper subtraction of the impurities.[12] We could not assign all the sextets of the Mössbauer spectra obtained in the compound $NdFe_{10}SiC_{2-\delta}$. The most intense sextet corresponds to the 32*i* site.

From the analysis of the spectra, the first two compounds [Figs. 2(a) and 2(b)] have a 2:17-type structure and the third [Fig. 2(c)] is of the 1:11-type structure. Based on the area ratio of the independent subcomponents we can calculate the composition as $Nd_2Fe_{14}Si_3$ and $Nd_2Fe_{14}Si_3C_x$ for the 2:17-type compounds. Curie temperature and lattice parameters of the homogenized sample are in agreement with this analysis and those reported previously.[13] The hyperfine fields of the $Nd_2Fe_{14}Si_3$ at room temperature are larger than those of Nd_2Fe_{17}.[11] This is due to the increased Curie temperature over the nonsilicon-containing compound.[14] The average hyperfine field found in the 700 °C heat treated sample ($NdFe_{10}SiC_{2-\delta}$) is larger than that found previously in $NdFe_{10}SiC_{0.5}$.[15]

While the neutron refinement showed more than 30% α-Fe by volume, the refinement of the $NdFe_{10}SiC_x$ phase was stable and well behaved. The structure was refined in the space group I41/amd using the refinement of similar material by LeRoy *et al.*[7] as the starting point. The results of the neutron refinement are summarized in Table III. The Si atoms were found to occupy only the 8*d* site (0 0 $\frac{1}{2}$) as has previously been reported,[7] with a slightly greater than 50% fraction. The other Fe sites were consequently fixed to full occupancy as was the Nd site. The lattice parameters are significantly larger than previously reported for a sample containing approximately 25% C on the 8*c* site (0 0 0) and is consistent with a higher refined occupancy of that site. The lattice parameters found are also in good agreement with those found by x ray diffraction (Table I). We find nearly full occupancy of that site (95%) corresponding to a final stoichiometry of $NdFe_{9.85}Si_{1.15}C_{1.94}$. The position parameters for the Fe 32*i* site are also somewhat different from the previous report.[7]

TABLE III. Refinement results for $NdFe_{10}SiC_x$. The nuclear coordinates (in units of the cell constants *a* and *c*) are *x*, *y*, *z*; μ is the moment and are given in units of Bohr magnetons (μ_B); occupancy as a fraction of the full population of the site; R(wp) and R(mag) are quality-of-fit indices for the nuclear and magnetic scattering, respectively. Parentheses after the atom symbols in the first column enclose the occupancy factors and site symmetry designations; those following a numerical value contain the statistical uncertainty in the final digits.

Atom	*x*	*y*	*z*	Occup	μ
Nd(4*a*)	0.0	0.75	0.125	1	2.3(3)
Fe(4*b*)	0.0	0.25	0.375	1	1.7(3)
Fe(32*i*)	0.1277(2)	0.0470(2)	0.1952(3)	1	1.7(3)
Fe(8*d*)	0.0	0.0	0.5	0.424(16)	2.1(3)
Si(8*d*)	0.0	0.0	0.5	0.576(16)	
C(8*c*)	0.0	0.0	0.0	0.952(12)	
a=10.1601(3) Å		c=6.5134(3) Å			V=682.686 Å^3
μ(total)=18.49 μ_B/f.u.		α-Fe=32.7% (volume)			
R_{wp}=5.42		R_{mag}=12.4			

The magnetic moments were found to be aligned in the basal plane and are also given in Table III. The Fe moments are close to their saturation values around $2\mu_B$ and the bulk moment, found by summing the individual site moments is 18.5 μ_B/f.u., more than twice that refined by Le Roy *et al.*[7] for the $C_{0.5}$ compound. This is consistent with the increased Curie point found for the present compound (T_C=505 K). The total moment found by neutron diffraction is significantly greater than that found by magnetization measurements made with the VSM ($M_s \approx 12.6\mu_B$/f.u.). This difference could be due to non-saturation effects because of the relatively low field used to magnetize the sample with the VSM (20 kOe).

This work supported by DOE Grant No. DE-FG02-90ER45413.

[1] X. P. Zhong, R. J. Randwanski, F. R. DeBoer, T. H. Jacobs, and K. H. J. Buschow, J. Magn. Magn. Mater. **86**, 333 (1990).
[2] J. M. D. Coey and H. Sun, J. Magn. Magn. Mater. **87**, L251 (1990).
[3] Y. Z. Wang and G. C. Hadjipanayis, J. Appl. Phys. **70**, 6009 (1991).
[4] G. C. Hadjipanayis, Z. X. Tang, W. Gong, and E. W. Singleton, Proceedings of the 7th International Symposium on Magnetic Anisotropy and Coercivity in RE-TM Alloys, Canberra, Australia, July 1992 (unpublished), p. 403.
[5] O. I. Bodak and F. I. Gladyshevskii, Dopov. Akad. Nauk. Ukr. RSR, Ser A **5**, 452 (1969).
[6] Y. Berthier, B. Chevalier, J. Etoureau, H. R. Rechlenberg, and J. P. Sanchez, J. Magn. Magn. Mater. **75**, 19 (1988).
[7] J. Le Roy, J. M. Moreau, C. Bertrand, and M. A. Fremy, J. Less-Common Met. **136**, 19 (1987).
[8] E. W. Singleton and G. C. Hadjipanayis, J. Magn. Magn. Mater. **128**, L21 (1993).
[9] H. M. Rietveld, J. Appl. Cryst. **2**, 66 (1969).
[10] FULLPROF Reitveld refinement code. J. Rodriguez Carjaval, Institute Lane Langevin, Grenoble, France.
[11] B.-P. Hu, H.-S. Li, H. Son, and J. M. D. Coey, J. Phys. Condens. Matter **3**, 3983 (1991).
[12] M. B. Stearns, Phys. Rev. **129**, 1136 (1963).
[13] R. van Mens, J. Magn. Magn. Mater. **61**, 24 (1986).
[14] E. E. Alp, A. M. Umarji, S. K. Malik, G. K. Shenoy, M. Q. Huang, E. B. Boltich, and W. E. Wallace, J. Magn. Magn. Mater. **68**, 305 (1987).
[15] J. M. Cadogan, Hong-Shuo Li, M. A. Fremy, and J. M. D. Coey, in Ref. 4, p. 50.

A detailed study of nitride precipitates in Nd_2Fe_{17}

C. C. Colucci, S. Gama, C. A. Ribeiro, and L. P. Cardoso
Instituto de Fisica Gleb Wataghin, Universidade Estadual de Campinas-UNICAMP, Caixa Postal 6165, 13083-970, Campinas, SP, Brazil

We report electron microprobe measurements of the diffusion profile in partially nitrided samples of the $Fe_{17}Nd_2$ phase. The results are fully consistent with a step-like profile. This confirms that the nitrogenation process is one of precipitating a fully nitrided phase from a nitrogen-free phase. We report also x-ray diffraction patterns for the partially nitrided samples as a superposition of the pure and nitrided patterns, with displacements and broadenings of lines due to mutual stresses between the phases.

INTRODUCTION

As is now well known, the $Fe_{17}R_2$ (R=rare earths) phases can absorb up to three nitrogen atoms per formula unit (f.u.), increasing significantly the Curie temperature (T_c).[1,2] Regarding the nitrogenation mechanism, two models have been advanced. The first says that the nitrogen forms a solid solution, so that under partial nitrogenation of an isolated powder particle, a shell-core type diffusion profile with a smooth concentration gradient can be observed.[3] For a particle with 20 μm size and stoichiometry $Fe_{17}R_2N_{1.5}$, a concentration gradient about 5 μm thick is predicted.[3] The second model says that for the lighter rare earths the nitrogenation mechanism is such that, even for very small amounts of absorbed gas, a fully nitrided phase precipitates directly from the starting phase. The observed diffusion profile shows a step function concentration gradient.[4–6]

The objective of the present work is to present further evidence confirming the second model, through careful electron probe microanalysis (EPMA) and x-ray diffraction measurements on $Fe_{17}Nd_2$ samples.

EXPERIMENT

Samples were prepared from 99.99% Fe and 99.9% Nd through arc melting and annealing at 1000 °C for seven days. After this, the samples were crushed, milled, and sieved (200 mesh). The nitridation was performed in a Sieverts apparatus at 400 °C. For the x-ray diffraction measurements we used Fe $K\alpha$ radiation. For the EPMA the powders were hot embedded in conducting resin.[4] We used a wavelength dispersion spectrometer (WDS) with 18 kV as the accelerating voltage. The position of the electron beam was controlled by a microcomputer. The electron beam was first focused on a point in the interior of a nitrided grain and moved in 0.4 μm steps along a line perpendicular to the interface to an unnitrided region. For each step, the intensities of the Fe K_α and Nd L_α lines were measured for the sample and for a standard, in this case the pure 17:2 phase itself. After a data reduction procedure for quantitative EPMA,[7] the nitrogen content was obtained by difference. Based on the peak to background ratio of the signals we determined the minimum detectability limit (MDL) of our EPMA measurements, to be about 1.5 at. % N.

RESULTS AND DISCUSSION

Figure 1 shows typical EPMA results for our Nd based material. It is clear from this figure that on one side of the interface the signal is approximately at the saturation nitrogen concentration value and on the other side of the interface it is less than the MDL (the interface is defined by the fitting procedure described below). Even though we observe a great scatter of the nitrogen content in the nitrided region, it is clear that we have an interface between the two region with a width less than 1 μm. To interpret these data we modeled the lateral distribution of the x-ray generation by the electron probe as a Gaussian function with an effective width σ.[8] Convoluting this with a step concentration function to describe the interface, we obtain an expression for the EPMA signal proportional to $F(x)=AG(x/\sigma)$, where A is the saturated mean x-ray signal for nitrogen and

$$G(z)=\frac{1}{\sqrt{2\pi}}\int \exp\left(-\frac{t^2}{2}\right)dt, \quad -\infty<t<z. \tag{1}$$

For the experimental determination of σ we made an artificial sample with a step concentration profile by polishing one piece of nickel and another of cobalt, pressing the polished surfaces together and polishing the surface perpendicular to the interface. The WDS spectrometer was tuned to the Ni line and a 0.1 μm step scan was done crossing the

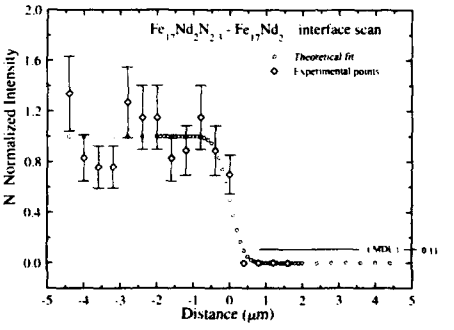

FIG. 1. EPMA results for the $Fe_{17}Nd_2N_{1.5}$ sample.

 0021-8979/94/75(10)/6003/3/$6.00 © 1994 American Institute of Physics

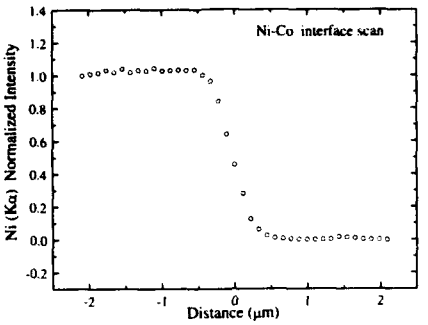

FIG. 2. Nickel EPMA signal for the Ni-Co sample.

interface. The results are shown in Fig. 2. To determine σ we numerically differentiated the data and fitted them to a Gaussian. For this we obtained $\sigma=0.31$ μm, so that we can consider that the thickness of the interface between the nitride and pure phases is less than or of the order of the probe size (see Fig. 1). This is strong evidence for the sharpness of the interface, confirming the step nature of the nitrogen concentration.

As stated in the Introduction, if the solid solution model were valid, we should expect a smooth variation of the nitrogen concentration over a distance of several μm (at the stoichiometry $x=1.5$, ≈ 5 μm). This smooth concentration variation would be easily measurable by our technique. Our observations, however, are fully consistent with results expected for a step concentration profile convoluted with a finite size function describing the electron probe. We can conclude, then, that the diffusion mechanism is really one of precipitation of a fully nitride phase in a matrix of the pure nitrogen-free phase.

We also performed x-ray diffraction measurements on our samples. The results are similar for all samples. Figure 3 shows the (113) diffraction lines for (a) the pure, (b) the $x=1.0$ intermediate, and (c) the saturated samples. It is clear that for the nitrogen-free and saturated samples the corresponding lines are narrower and stronger than the one for the intermediate sample, which clearly shows a double peak. This double line clearly is the superposition of two patterns, one for the pure and the other for the saturated sample, confirming again the coexistence of a fully nitrided phase and of a pure one.

Furthermore, the superposed lines are not as narrow as the ones for the phases, neither are they in the exact positions expected, but are broadened and displaced. Also the line corresponding to the pure phase is displaced in the opposite sense as the saturated one. These opposite line displacements originate in the fact that the pure phase is stretched while the saturated one is compressed. The broadening shows that these deformations are not homogeneous. This state of tension has already been observed by Mössbauer effect measurements in the Pr system.[5] The displacement of the line for the pure phase is $\Delta d/d_0 \approx 0.0081$, and using this as a maximum deformation, and a reasonable value for Young's modulus of the phase (we chose the value for Fe), we estimate the maximum tension in the system as $\sigma_{max} \approx 1600$ MPa. The pure phase line broadening was used to estimate the average inhomogeneous stress σ_{av}. Since $\Delta(2\theta) \approx 0.0035$ rad, we have $\Delta d/d_0 = \Delta(2\theta)/2 \tan(\theta) = 5.1 \times 10^{-3}$, and using the same value as above for the Young's modulus, we have $\sigma_{av} \approx 1000$ MPa, again a reasonable value.

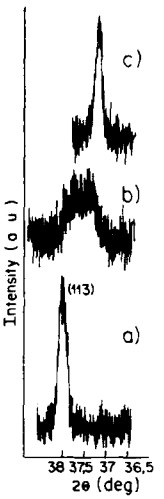

FIG. 3. (113) x-ray diffraction lines for the (a) pure, (b) $Fe_{17}Nd_2N_{1.0}$, and (c) saturated samples.

CONCLUSIONS

We can conclude that:

(1) the EPMA measurements confirm the step like nature of the nitrogen concentration diffusion profile, instead of a smooth one.

(2) the x-ray diffraction measurements show the diffraction pattern for intermediate nitrogen concentrations as the superposition of two patterns, one of the pure phase and the other of the saturated phase. The observed displacements and broadenings of the lines are attributed to the highly stressed condition of the sample under partial nitrogenation and allow an estimate of the maximum and average stresses in the samples.

ACKNOWLEDGMENTS

We acknowledge financial support from FAPESP-Fundação de Amparo à Pesquisa do Estado de São Paulo, and CNPq-Conselho Nacional de Desenvolvimento Científico e Tecnológico.

[1]J. M. D. Coey and H. Sun, J. Magn. Magn. Mater. **87**, L251 (1990).
[2]K. H. J. Buschow, R. Coehoorn, D. B. de Mooij, K. de Waard, and T. H. Jacobs, J. Magn. Magn. Mater. **92**, L35 (1990).
[3]J. M. D. Coey, R. Skomski, and S. Wirth, IEEE Trans. Magn. **28**, 2332 (1992).
[4]C. C. Colucci, S. Gama, and F. A. O. Cabral, IEEE Trans. Magn. **28**, 2578 (1992).
[5]J. D. Ardisson, M. Bogé, A. I. C. Persiano, C. C. Colucci, and S. Gama, IEEE Trans. Magn. **28**, 2584 (1992).
[6]O. Isnard, J. J. Soubeyroux, S. Miraglia, D. Fruchart, L. M. Garcia, and J. Bartolomé, Physica B **180&181**, Part B, 624 (1992).
[7]J. Colby, Adv. X-Ray Anal. **11**, 287 (1968).
[8]S. B. Reed, *IV International Congress on X-Ray Optics and Microanalysis*, edited by R. Castaing, P. Deschamps, and J. Philibert, Orasy, France (1965), pp. 339–349.

Aligned high anisotropy $Pr(Fe,Co,Mo)_{12}N$ film samples

R. Rani, H. Hegde, A. Navarathna, and F. J. Cadieu
Department of Physics, Queens College of CUNY, Flushing, New York 11367

Highly aligned (002) textured sputtered films of $Pr(Fe_{12-y-z}Co_yMo_z)N_x$, where $y=0-2.5$, and $z=0.4-1.0$ compounds have been successfully synthesized. Before nitriding, the films exhibited nonuniaxial soft magnetic properties with room temperature coercivities of 0.70 kOe. A profound change of magnetocrystalline anisotropy occurred on nitriding. X-ray diffraction traces showed that the $ThMn_{12}$-type tetragonal structure was retained with a saturating increase in cell volume over the first 15 min of nitriding time at 750 K. The coercivity, however, reached a maximum for a nitriding time of 25 min at 750 K. Samples nitrided for times greater than ≈25 min were taken as fully nitrided with ≈1 N per $ThMn_{12}$ formula unit. The samples slightly richer in Pr showed somewhat higher coercivity perpendicular to the film plane as compared to stochiometric $Pr(Fe,Co,Mo)_{12}N$ films. From high field measurements to 80 kOe, the maximum room temperature coercivity perpendicular to the film plane was 9.4 kOe, which rose to 22.0 kOe at 10 K. The $4\pi M_s$ value at 80 kOe measured perpendicular to the film plane was 11.6±0.5 kG at 293 K, 12.5 kG at 10 K, for $Pr_{1.04}Fe_{10.36}Co_{1.16}Mo_{0.44}N$ samples, and 10.5±0.5 kG at 293 K for $Pr_{1.05}Fe_{11.17}Mo_{0.78}N$ samples. After high field magnetization to 80 kOe, for measurements perpendicular to the film plane, the static energy product was 23.6 and 32.9 MG Oe at 293 and 10 K, respectively. The estimated anisotropy fields were 96 and 144 kOe at 293 and 10 K, respectively, for low cobalt film samples.

INTRODUCTION

In this paper we report that high anisotropy oriented sputtered film samples of $Pr(Fe_{12-y-z}Co_yMo_z)N_x$, where $y=0-2.5$, and $z=0.4-1.0$, compounds have been synthesized for as low as 10 min of *in situ* nitriding times. Yang *et al.*[1,2] recently reported the formation of arc melted $PrMo_{1.5}Fe_{10.5}$ compounds and their nitrides, with 2 kOe coercivities at room temperture for the nitrides. For our Pr $ThMn_{12}$-type nitrided films, room temperature coercivities of greater than 9 kOe have been measured. Before nitriding, the films exhibited nonuniaxial soft magnetic properties with room temperature coercivities of ≈0.70 kOe. The film synthesis procedures were similar to those previously used for the synthesis of other highly aligned $ThMn_{12}$-type systems.[3] In addition the deposited films were *in situ* nitrided as reported for other $ThMn_{12}$-type systems.[4,5] The increase in cell volume upon nitriding saturated before the coercivity reached a maximum as a function of nitriding time. The nitriding time required to reach a maximum coercivity was shorter for higher nitriding temperatures. For a nitriding temperature of 750 K the cell volume increase saturated after 15 min, but the coercivity did not reach the maximum value until a nitriding time of 25 min. Samples nitrided for times equal to or greater than that required to reach the maximum coercivity were taken to be fully nitrided with ≈1 N per $ThMn_{12}$ formula unit.[6,7]

EXPERIMENT

Oriented films of approximately 2–3 μm thickness were synthesized by the direct crystallization of the desired compositions through rf sputtering onto heated polycrystalline Al_2O_3 substrates in the temperature range of 675–800 K. Due to the relatively small thermal expansion coefficient of Al_2O_3 the films are under tension when cooled to room temperature from the deposition and nitriding temperatures. The sputtering targets used in these studies were made by arc melting in an inert atmosphere from pure elements of at least 99.9% pure. The sputtering deposition chamber had a base pressure of 5×10^{-8} mTorr. The sputtering gas pressure was 75 mTorr of argon. The deposition rate was ≈1.2 Å/s. These films were nitrided *in situ* at 570 Torr of N_2 for times ranging from 5 to 150 min. The nitriding temperatures were varied from 700 to 850 K. The magnetic data reported were measured using vibrating sample magnetometers. The x-ray diffraction data were collected with a digital system using Cu $K\alpha$ radiation.

RESULTS AND DISCUSSION

Figures 1 and 2, respectively, show $T=293$ K, and $T=10$ K, hysteresis loops for a $Pr_{1.04}Fe_{10.36}Co_{1.16}Mo_{0.44}N$ sample. This film exhibited an extreme degree of texturing such that the c axes of the grains were aligned perpendicular to the film plane. For $T=293$ K, the perpendicular to the film

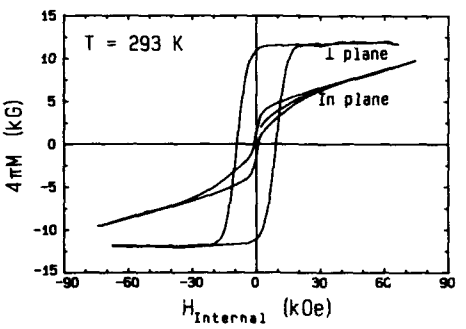

FIG. 1. Hysteresis loops are shown, $T=293$ K, for a $Pr_{1.04}Fe_{10.36}Co_{1.16}Mo_{0.44}N$ sample. For the flux density directed perpendicular to the surface, the $4\pi M_s$ was 11.6 kG, H_c was 9.4 kOe, and the static energy product was 23.6 MG Oe.

 0021-8979/94/75(10)/6006/3/$6.00 © 1994 American Institute of Physics

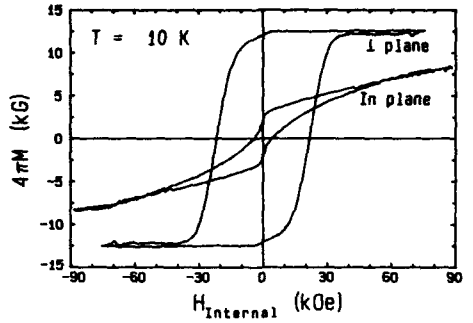

FIG. 2. Hysteresis loops are shown, $T=10$ K, for a $Pr_{1.04}Fe_{10.36}Co_{1.16}Mo_{0.44}N$ sample. For the flux density directed perpendicular to the surface, the $4\pi M_s$ was 12.5 kG, $_iH_c$ was 22.0 kOe, and the static energy product was 32.8 MG Oe.

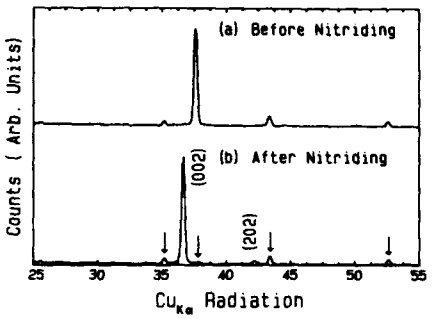

FIG. 4. (a) An x-ray diffractometer trace, $Cu_{K\alpha}$, for the sample of Fig. 3 is shown before nitriding. (b) An x-ray diffractometer trace for Figs. 1 and 2 is shown after nitriding. Arrows indicate the position of Al_2O_3 substrate lines. The volume increase upon nitriding was ≈6.9%.

plane saturation flux density, $4\pi M_s=11.6\pm0.5$ kG, intrinsic coercivity $_iH_c=9.40$ kOe, and maximum energy product $BH_{max}=23.6$ MG Oe. For the $T=10$ K curve, $4\pi M_s=12.5\pm0.5$ kG, $_iH_c=22.0$ kOe, and $BH_{max}=32.8$ MG Oe. As will be discussed shortly this film was *in situ* nitrided for a time long enough to maximize the coercivity. Such samples were taken as fully nitrided with ≈1 N per $ThMn_{12}$ formula unit. The nitrided tetragonal lattice cell parameters were $a=8.78$ Å, and $c=4.87$ Å. Note that measurements perpendicular to the film plane correspond to measurements parallel to the crystallite c axes. From these curves, the anisotropy fields of this $Pr_{1.04}Fe_{10.36}Co_{1.16}Mo_{0.44}N$ sample were estimated to be 144 and 96.5 kOe at 10 and 293 K, respectively. The anisotropy fields for $Pr(Fe,Mo,Co)_{12}N$ film samples did not differ significantly over a wide range of cobalt compositions, i.e., from 2.8 to 15.0 at. % metallic composition of the 1–12 phase.

Figure 3 shows hysterisis loops for an un-nitrided $Pr_{1.03}Fe_{10.44}Co_{1.13}Mo_{0.40}$ sample synthesized under similar sputter conditions before nitriding. It exhibited soft magnetic properties consistent with easy plane anisotropy. The room temperature flux density was higher in the film plane as compared to that perpendicular to the film plane. The field required to obtain saturation in the direction perpendicular to the film plane, obtained by extrapolation, was 34.8 kOe. The at. % of Pr was slightly higher as compared to the stochiometric composition for $Pr(Fe,Mo,Co)_{12}$ films.

Figure 4 shows the x-ray diffraction traces, $Cu_{K\alpha}$ radiation, after nitriding for the sample of Figs. 1 and 2, and before nitriding for the sample of Fig. 3. The direct synthesis of Pr-Fe-Mo-Co films into $ThMn_{12}$ phase with systematic control of deposition conditions allowed us to obtain an extreme degree of crystallographic texturing upon deposition. Following *in situ* nitriding the $ThMn_{12}$-type tetragonal structure was retained with an increase in cell volume which saturated for a nitriding temperature of 750 K after about the first 15 min of nitriding time at 6.9%. This behavior is shown in Fig. 5. The observed cell volume increase is larger than that observed in bulk samples because of film volume strain effects. The full width at half-maximum of the x-ray diffraction lines was unchanged after nitriding. The lines were fairly sharp before and after nitriding even for samples with very short nitriding times.

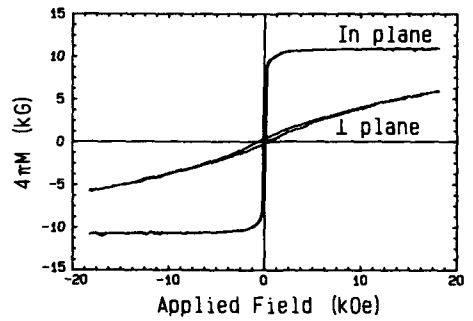

FIG. 3. Hysteresis loops measured at $T=293$ K, for an un-nitrided $Pr_{1.03}Fe_{10.44}Co_{1.13}Mo_{0.40}$ sample exhibiting easy plane anisotropy are shown. After nitriding the easy plane anisotropy behavior switched to uniaxial behavior as shown in Figs. 1 and 2.

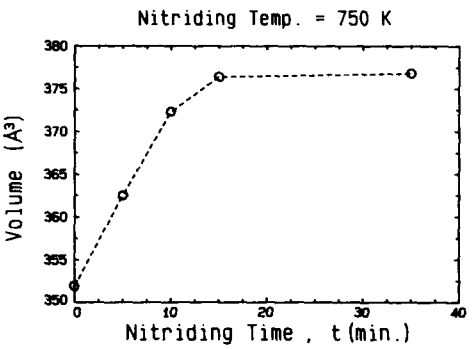

FIG. 5. The cell volume as a function of nitriding time at 750 K is shown for $Pr(Fe,Co,Mo)_{12}$ nitrided in 570 Torr N_2.

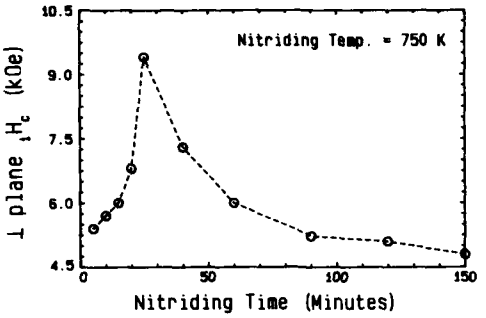

FIG. 6. The variation of room temperature coercivity, $_iH_c$, perpendicular to the film plane is shown as a function of nitriding time at 750 K, 570 Torr N_2, for film samples of nearly the same composition. All films were sputter synthesized under the same conditions except for the nitriding time.

The variation of $_iH_c$ was also studied as a function of nitriding time. A series of film samples were sputter synthesized under similar sputter conditions except for the nitriding time. As shown in Fig. 6, the maximum room temperature coercivity, $_iH_c$, perpendicular to the film plane was 9.4 kOe, for the film sample directly crystallized at 725 K and 75 mTorr of argon and nitrided at 750 K and 570 Torr of N_2 for 25 min. An attempt was made to determine the minimum nitriding time at various nitriding temperatures to optimize the coercivity. The nitriding time for the $Pr_{1.04}Fe_{10.36}Co_{1.16}Mo_{0.44}N$ sample at 750 K to maximum coercivity was 25 min. However, the minimum nitriding time to maximum coercivity was 10 min at 850 K, and the room temperature coercivity measured following low field magnetization to 18 kOe perpendicular to the film plane was 6.4 kOe for a similar composition sample.

Sputter deposition with systematic control of the deposition parameters allowed us to achieve an extremely high degree of c-axes texturing perpendicular to the film plane. For each nitriding temperature, the minimum nitriding time was determined to optimize the coercivity. It should be noted that perpendicular to the plane coercivity reached a maximum after the volume increase upon nitriding had saturated. This is consistent with the cell volume increase being due to N atoms occupying sites at the midpoint of the c-axes cell edges and the midpoint of the $a-b$ faces,[6,7] 2 N sites per tetragonal cell which contains two $ThMn_{12}$ formula units. Upon partial site filling the volume has to assume that saturated volume or else the cell would need to be distorted which is inconsistent with the x-ray data. The magnetic anisotropy and coercivity, however, continue to change until the N sites are filled. The maximum in coercivity has been taken as the indicator of full site occupancy rather than the cell volume saturtion time for that reason. It should also be noted that in spite of the larger cell volume expansion observed in the film samples due to additional strain effects, that the anisotropy values reached approximately the same values as have been observed in bulk samples. Longer than necessary nitriding times resulted in some phase deterioration with a lower than optimal coercivity. For higher nitriding temperatures less nitriding time was required to optimize the coercivity. For 850 K, the optimum nitriding time was found to be 10 min.

The room temperature easy plane anisotropy field of $Pr_{1.05}Fe_{11.20}Mo_{0.76}$, and $Pr_{1.03}Fe_{10.44}Co_{1.13}Mo_{0.40}$ samples, were 30 and 34.8 kOe, respectively. On nitriding a profound change of magnetocrystalline anisotropy occurred, the easy plane anisotropy switched to easy axis anisotropy. At room temperatures, the saturation flux density measured perpendicular to the film plane for high field measurements up to 90 kOe of applied fields was 10.5 ± 0.5 kG for $Pr_{1.05}Fe_{11.17}Mo_{0.78}N$, and 11.6 ± 0.5 kG for $Pr_{1.04}Fe_{10.36}Co_{1.16}Mo_{0.44}N$ samples. The available flux density and coercivity were both higher for Co-containing samples. The highest room temperature coercivity and energy product were obtained for a $Pr_{1.04}Fe_{10.36}Co_{1.16}Mo_{0.44}N_x$ sample. For this film at 293 K the perpendicular to the film plane saturation flux density, $4\pi M_s=11.6\pm0.5$ kG, the intrinsic coercivity $_iH_c=9.40$ kOe, and maximum energy product $BH_{max}=23.6$ MG Oe. At 10 K the corresponding $4\pi M_s$, $_iH_c$, and BH_{max}, were 12.5 ± 0.5 kG, 22.0 kOe, and $BH_{max}=32.8$ MG Oe, respectively. These are the highest values ever reported for $Pr(Fe,Mo,Co)_{12}N$ $ThMn_{12}$-type samples.

ACKNOWLEDGMENTS

We wish to acknowledge that some preliminary high field measurements to 55 kOe for $Pr(Fe,Co,Mo)_{12}N$ samples were made for us by Xie Xu at Florida State University. This work was supported by the Dept. of Energy.

[1] Y.-C. Yang, X.-D. Zhang, L.-S. Kong, Q. Pan, and S.-L. Ge., Appl. Phys. Lett. **58**, 2042 (1991).
[2] Y.-C. Yang, Q. Pan, X.-D. Zhang, J. Yang, and M.-H. Zhang, Appl. Phys. Lett. **61**, 2723 (1992).
[3] F. J. Cadieu, H. Hegde, A. Navarathna, R. Rani, and K. Chen, Appl. Phys. Lett. **59**, 875 (1991).
[4] A. Navarathna, H. Hegde, R. Rani, and F. J. Cadieu, J. Appl. Phys. **73**, 6242 (1993).
[5] H. Hegde, R. Rani, A. Navarathna, K. Chen, and F. J. Cadieu, J. Appl. Phys. **70**, 6345 (1991).
[6] Y. Yang *et al.*, Solid State Commun. **78**, 313 (1991).
[7] Z. W. Li, X. Z. Zhou, and A. H. Morrish, J. Phys.: Condens. Matter **4**, 10 409 (1992).

Anisotropy and flux density enhancement in aligned $ThMn_{12}$-type $NdFe_{11}Co_{1-y}Mo_yN$ film samples

A. Navarathna, H. Hegde, R. Rani, and F. J. Cadieu
Physics Department, Queens College of CUNY, Flushing, New York 11367

Highly aligned sputtered film samples of $ThMn_{12}$-type $NdFe_{12-y-z}Co_yMo_zN$, $y+z\approx 1$, have been synthesized. For low Co concentrations it has been possible to enhance the saturation flux densities, the coercivity, and the anisotropy field of the nitrided samples. Films which have a gradient along the substrate length in the Fe to Co ratio have been synthesized to determine the maximum coercivity and anisotropy values that can be obtained for the $Nd(Fe,Co,Mo)_{12}N$ nitrides. Maximum room temperature coercivities and anisotropies of 11.3 and 145 kOe were obtained for a $ThMn_{12}$-type $Nd_{8.9}Fe_{80.3}Co_{6.0}Mo_{4.8}N$ (002) textured film sample. At lower temperatures the coercivity and anistropy rose smoothly to 29.5 and ≈200 kOe, respectively by 10 K. Based on nitriding studies on similar films, all nitride sites should be occupied at ≈1 N per $ThMn_{12}$ formula unit for the high coercivity films reported.

INTRODUCTION

We have recently shown that highly aligned sputtered film samples of $ThMn_{12}$-type $NdFe_{11}Co_{0.5}Mo_{0.5}N$ can be synthesized to exhibit a room temperature static energy product of 46.3 MGOe with the flux density oriented perpendicular to the film plane.[1] The $Nd(Fe,Mo)_{12}$ compound was shown to be the most promising in film synthesized samples since highly aligned and α-Fe free samples could be made for T=Mo.[2] We have been able to synthesize the $NdFe_{11}Mo$ compound in film form with a high degree of crystallographic texture, where the c axis of the individual crystallites are highly aligned perpendicular to the film plane. We have been able to replace at least half of the Mo by Co and increase the saturation flux density as well as the anisotropy field of the nitrides.[1] The major problem of bulk $ThMn_{12}$ type samples is the common belief that large concentrations of a third nonmagnetic transition metal such as Mo, V, or Ti is required to allow the stabilization of the $ThMn_{12}$ phase.

Earlier it was shown for bulk samples that nitrided samples of $ThMn_{12}$-type $Nd(Fe,T)_{12}N$, T=Mo, Ti, or V exhibited potentially attractive properties as permanent magnets.[3] Anisotropy of 80 kOe at 300 K and 115 kOe at 1.5 K for $NdFe_{11}TiN_x$ bulk samples were reported.[3] The obstacles were those of lack of alignment, the formation of α-Fe, and the low-flux densities which resulted from the large concentrations of the nonmagnetic T element used to stabilize the $ThMn_{12}$ phase.

In this paper we report the magnetic properties of $NdFe_{12-y-z}Co_yMo_zN$, $y+z\approx 1$, aligned film samples to study the effects of anisotropy and coercivity enhancements upon the substitution of small amounts of Co for Fe. Such samples thus consist of approximately 88-at. % magnetic transition metal, 8-at. % Nd, and only 4-at. % Mo atoms in the $ThMn_{12}$ structure. It should be noted that it has not been possible to stabilize the $ThMn_{12}$ for such magnetic element concentrations by any other means. An added benefit of these magnetic element enhanced samples is that the anisotropy field and intrinsic coercivities have been increased across the range from room temperature to low temperatures. Room temperature $_iH_c$ values as high as 11.3 and 29.5 kOe at 10 K have been measured for the aligned nitrided samples. Based on nitride studies for analogous $Pr(Fe,Co,Mo)_{12}N$ films, all the nitride sites should be occupied at ≈1 N per $ThMn_{12}$ formula unit[4] for the nitriding times and temperatures used for these films.[5]

EXPERIMENT

The approximately $Nd(Fe_{1-y}Co_y)_{11.5}Mo_{0.5}N$ aligned film samples were synthesized by rf diode sputtering from a colinear arrangement of three targets with the compositions as indicated.

Target	A (at. %)	B (at. %)	C (at. %)
Nd	8	8	8
Fe	87.5	84	78.5
Co	0	4	9
Mo	4.5	4	4.5

The atomic fractions of Nd and Mo thus remained fairly constant across the length of a substrate while the relative amounts of Co to Fe increased along the substrate length from the side opposite target A to the side opposite target C. The Co atomic composition ranges from 1.3 to 6.3 at. % of the metallic elements across the substrate. Some Mo was retained in the samples since in our experience this aids in obtaining coercivity and suppressing α-Fe formation for stoichiometric samples. The samples were directly crystallized onto heated substrates so that the c axes of the $ThMn_{12}$-phase crystallites were oriented perpendicular to the film plane. The samples were nitrided after deposition by heating the samples in 500 Torr N_2 at 550 °C for 2 h. Based on studies of analogous Pr films, these nitriding conditions should result in essentially all the nitriding sites being occupied at 1 N per formula unit.[4] Results for only certain samples can be reported here. The resulting film compositions along the length of a substrate were determined by directly analyzing film regions with electron excited x-ray fluorescence in a scanning electron microscope (SEM). The magnetic properties were measured by two different vibrating sample magnetometers (VSM). A low-field VSM at applied fields up to 18

 0021-8979/94/75(10)/6009/3/$6.00 © 1994 American Institute of Physics

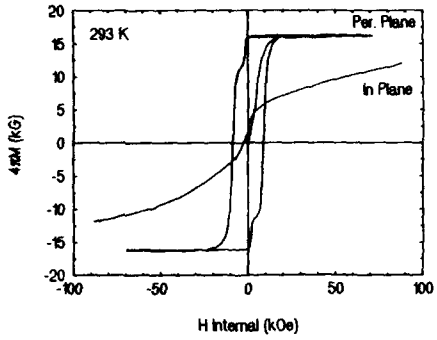

FIG. 1. Hysteresis loops are shown for a 2.5-μm-thick $Nd_{8.0}Fe_{85.8}Co_{1.8}Mo_{4.4}N$ sample as measured at 293 K, perpendicular to the film plane, the high flux density loop, the in plane demagnetization loop, and the initial flux density perpendicular to the film plane.

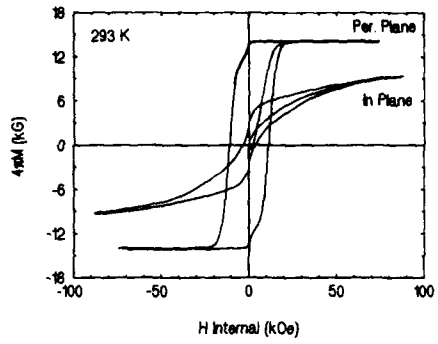

FIG. 3. Hysteresis loops as measured at 293 K are shown for a 1.5-μm-thick $Nd_{8.9}Fe_{80.3}Co_{6.0}Mo_{4.8}N$ predominantly (002) textured film sample.

kOe, and a high field one with applied fields to 90 kOe. The sample thicknesses were determined by SEM measurements. The x-ray diffraction traces were collected by a digital stepping motor system using $Cu_{K\alpha}$ radiation. Corresponding samples before and after nitriding were measured. A demagnetization factor of 4π was used to compute the flux densities as measured perpendicular to the film plane, and zero for the in plane measurements.

RESULTS AND DISCUSSION

Figure 1 shows hysteresis loops for a $Nd_{8.0}Fe_{85.8}Co_{1.8}Mo_{4.4}N$ sample as measured at 293 K, perpendicular to the film plane, the high flux density loop, the in plane magnetization loop, and the initial flux density perpendicular to the film plane. For this sample the room temperature remanent flux density was 16.2 kG and is essentially the same as the saturation value. The room temperature $_iH_c$ perpendicular to the plane was 8.7 kOe, and the static energy product was 30.4 MGOe. The large drop in flux density upon entering the demagnetization quadrant greatly lowers the possible energy product from that theoretically possible for such a high-remanent flux density. The drop in flux density as H internal reverses is expected because such samples contain a trace of α-Fe as indicated in the x-ray diffractometer data shown in Fig. 2. The x-ray diffraction traces yield a better estimate of α-Fe concentration than using one half the 2nd quadrant drop because the minimum wall reversal width for these aligned grains is unknown. This sample was strongly (002) textured, but not to the same extreme degree as previous films which were made to maintain uniform composition films. The room temperature magnetocrystalline anisotropy obtained by extrapolating the in plane flux density to the perpendicular value was 145 kOe.

Figure 3 shows hysteresis loops as measured at 293 K for a $Nd_{8.9}Fe_{80.3}Co_{6.0}Mo_{4.8}N$ predominantly (002) textured film sample. The main points of interest for this sample are that the room temperature coercivity has been increased to 11.3 kOe and the room temperature anisotropy field to an estimated 145 kOe. The room temperature static energy product perpendicular to the plane was also respectable at 30 MGOe. Figure 4 shows an x-ray diffraction trace for this sample after nitriding. Since this sample was only 1.5 μm thick, the characteristic polycrystalline Al_2O_3 substrate lines are clearly evident at 2Θ=35.13°, 37.78°, 43.36°, and 52.55°. Only a small α-Fe peak is evident at 44.70°. The second strongest $ThMn_{12}$ reflection is the (202). Hysteresis loops for this sample as measured at 10 K are shown in Fig. 5. By 10 K the magnetic properties had increased to $4\pi M_s$=16.5 kG, $_iH_c$=29.5 kOe, and BH_{max}=40.5 MGOe.

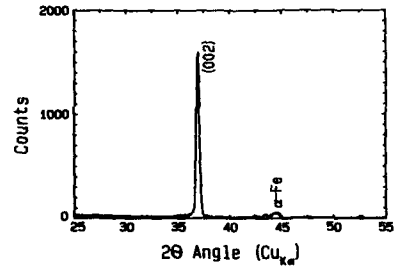

FIG. 2. An x-ray diffractometer trace, $Cu_{K\alpha}$ radiation, is shown for the nitrided sample of Fig. 1.

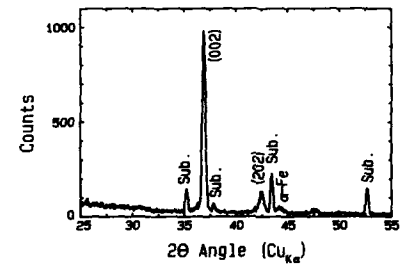

FIG. 4. An x-ray diffractometer trace, $Cu_{K\alpha}$ radiation, is shown for the nitrided sample of Fig. 3. The tetragonal nitrided lattice parameters were a=8.75, c=4.87 Å.

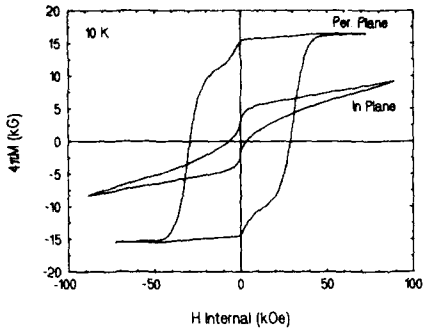

FIG. 5. Hysteresis loops for the sample of Fig. 3 are shown as measured at 10 K.

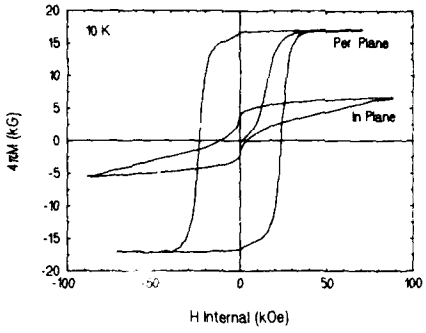

FIG. 6. Hysteresis loops as measured at 10 K are shown for a 2.31-μm-thick $Nd_{7.7}Fe_{84.6}Co_{3.8}Mo_{3.8}N$ (002) textured film sample.

The anisotropy field at 10 K can only be estimated to be a relatively high value of 200 kOe.

For comparison, hysteresis loops measured at 10 K for a $Nd_{7.7}Fe_{84.6}Co_{3.8}Mo_{3.8}N$ uniform composition film is shown in Fig. 6.[1] For such uniform composition films very high energy products were measured. At 10 K the $4\pi M_s$, $_iH_c$, and BH_{max} values were 17.0 kG, 24.0 kOe, and 59.6 MGOe. The corresponding values at 293 K were 15.5 kG, 8.7 kOe, and 46.3 MGOe.

In the present studies, exceptionally high values of intrinsic coercivity and anisotropy fields have been measured in film samples made with a gradient in the Fe to Co ratio along the substrate length. The highest intrinsic coercivity and anisotropy values obtained at 293 K were $_iH_c \approx 11.3$ kOe and $H_A \approx 145$ kOe. The corresponding values were 29.5 and 200 kOe at 10 K. The room temperature anisotropy field remained relatively high at ≈ 145 kOe across the range of Co substitutions reported. Despite the new high values of $_iH_c$ and H_A obtained for an Fe to Co ratio of 13.4 to 1, the room temperature BH_{max} value of 30 MGOe was comparatively low because of the partial decrease of the flux density for small demagnetizing fields. The high value of $_iH_c = 11.3$ kOe measured at 293 kOe is the highest value reported for $ThMn_{12}$-type systems.

ACKNOWLEDGMENT

F.J.C. was supported by the U. S. Department of Energy.

[1] A. Navarathna, H. Hegde, R. Rani, K. Chen, and F. J. Cadieu, IEEE Trans. Magn. **29**, 2812 (1993).
[2] A. Navarathna, H. Hegde, R. Rani, S. U. Jen, and F. J. Cadieu, IEEE Trans. Magn. **28**, 2838 (1993).
[3] Y. C. Yang, X.-D. Zhang, L-S Kong, and Q. Pan, Appl. Phys. Lett. **58**, 2042 (1991).
[4] Y.-c. Yang, *et al.*, Solid State Commun. **78**, 313 (1991).
[5] R. Rani, H. Hegde, A. Navarathna, and F. J. Cadieu (these proceedings).

Hydrogenation decomposition desorption recombination magnets based on $Sm_{2+\delta}Fe_{17}M_{0.4}$ carbonitrides (M=IVB/VB/VIB group elements)

X. Chen and Z. Altounian
Center for the Physics of Materials, Department of Physics, McGill University, 3600 University Street, Montréal, Québec H3A 2T8, Canada

The hydrogenation decomposition desorption recombination (HDDR) process is carried out to produce permanent magnets based on $Sm_{2+\delta}Fe_{17}M_{0.4}$ carbonitrides, where M=Ti, V, Cr, Zr, Nb, Mo, Hf, Ta, and W; and $\delta \leq 0.6$. It is found that minor additions of M significantly reduce the amounts of α-Fe and $SmFe_3$ in the starting materials. The best isotropic HDDR magnet obtained is for M=Ti, which has an intrinsic coercivity of 18 kOe and an energy product of 9.8 MGOe at room temperature.

I. INTRODUCTION

Since the discovery of Sm_2Fe_{17} nitride, carbide, and carbonitride,[1–5] a lot of efforts have been made to produce high performance magnets based on these materials. Some of these efforts include mechanical alloying,[6,7] melt spinning,[8] metal bonding,[9,10] and hydrogenation decomposition desorption recombination (HDDR).[11] The HDDR process has been successfully used to produce $Nd_2Fe_{14}B$-based magnets with high coercivity.[12,13] A coercivity, H_c, of about 12.6 kOe is reported for bonded magnets made of HDDR $Nd_{15}Fe_{77}B_8$-type alloys.[14] This is a very high value, as compared with the anisotropy field of about 80 kOe at room temperature.[15] In contrast, the coercivity so far reported for the HDDR Sm_2Fe_{17} nitride is rather low, less than 9 kOe,[11] in spite of the large anisotropy field of about 140 kOe[16] for this nitride. This relatively low coercivity is related to the secondary soft phases, mainly α-Fe, of the specimens. In order to have high performance magnets, these soft phases must be eliminated as much as possible. The present study is to investigate the effects of IVB/VB/VIB group additions on the coercivity of Sm_2Fe_{17} carbonitrides made by the HDDR process.

II. EXPERIMENTAL METHODS

Alloys consisting of elements (purity 99.9%) Sm, Fe, and M, where M=Ti, V, Cr, Zr, Nb, Mo, Hf, Ta, and W, were arc melted at least 6 times, followed by induction melting at least 3 times. Excess Sm was added to compensate for Sm loss during melting. The composition of the ingots after melting was $Sm_{2+\delta}Fe_{17}M_{0.4}$, where $\delta \leq 0.6$. X-ray (Cu-K_α) powder diffraction was used to check the presence of secondary phases.

The hydrogenation decomposition was carried out by heating the specimens in H_2 at 800 °C for up to 40 min. The desorption-recombination occurred simultaneously when the decomposed specimens were annealed in vacuum, produced by a mechanical pump, in a temperature range between 740 and 860 °C for up to 30 min. The resulting HDDR specimens were ground into powder (<32 μm), and then nitrided in N_2 at 460, 480, and 510 °C for up to 18 h, followed by carburizing in C_2H_2 at the same temperatures for up to 15 min. The carbonitrided powder was cold pressed. Hysteresis loop measurements were carried out in a pulsed magnet with a maximum field of 180 kOe. Sample temperature was maintained to within ±1 K during the measurements.

III. RESULTS AND DISCUSSION

The $Sm_{2+\delta}Fe_{17}M_{0.4}$ compounds prepared by arc melting and induction melting show very small amount of α-Fe and $SmFe_3$ phases for all values of δ under investigation ($0 \leq \delta \leq 0.6$). The x-ray diffractions show the main phase of Th_2Zn_{17} rhombohedral structure, and a secondary phase of $SmFe_2$. This is shown in Fig. 1(a) for $Sm_{2+\delta}Fe_{17}Ti_{0.4}$. Apparently, the minor addition of M has made α-Fe and $SmFe_3$ unstable in these alloys. Therefore, it is not necessary to carry out a long time homogenization process which is often required for Sm_2Fe_{17} to eliminate the α-Fe.

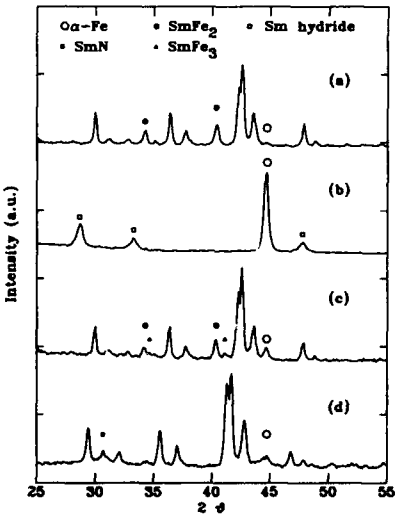

FIG. 1. X-ray (Cu-K_α) powder diffraction of $Sm_{2+\delta}Fe_{17}Ti_{0.4}$ (a) of the starting compound made by arc melting and induction melting; (b) after hydrogenation decomposition; (c) after HDDR, before carbonitriding; (d) after HDDR and carbonitriding. The secondary phases are indicated by the special symbols.

 0021-8979/94/75(10)/6012/3/$6.00 © 1994 American Institute of Physics

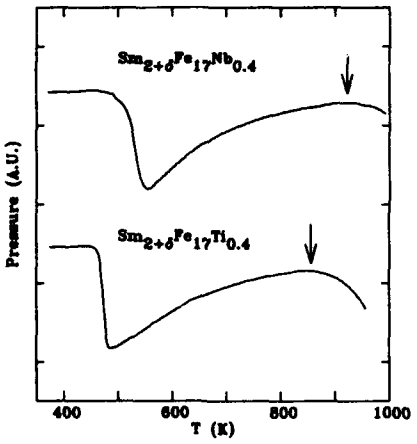

FIG. 2. Thermopiezic scans of $Sm_{2+\delta}Fe_{17}M_{0.4}$ (heating rate=5 K/min). The onset temperature of hydrogenation decomposition, indicated by arrows, depends on M.

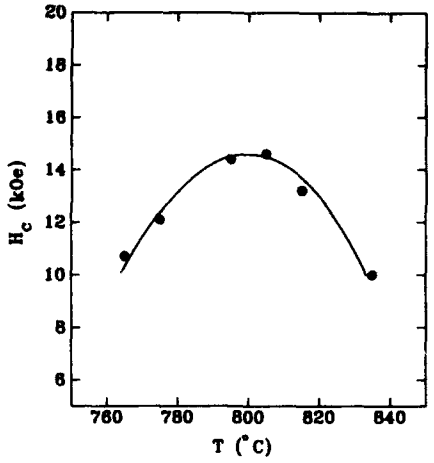

FIG. 3. Coercivity of $Sm_{2+\delta}Fe_{17}Ti_{0.4}N_xC_y$ as a function of temperature where the desorption recombination process is carried out for 10 min, followed by nitriding and carburizing the specimens at 510 °C for 120 and 15 min, respectively. The solid line is a guide to the eye.

Figure 2 shows a thermopiezic scan for M=Ti and Nb in hydrogen gas. The pressure decrease between 460 and 550 K is due to hydrogenation of the compounds. As is shown in Fig. 2 for M=Ti and Nb, the onset temperatures for hydrogenation decomposition, indicated by arrows, are related to M. At 1073 K, all $Sm_{2+\delta}Fe_{17}M_{0.4}$ decompose quickly. The time required to reach a complete decomposition was determined by the pressure change of H_2 gas. It ranges from 10 to 40 min, depending upon M. When decompostion is complete, only the α-Fe and Sm hydride are observed in x-ray diffraction, with no detectable trace of M. This is shown in Fig. 1(b) for M=Ti.

In order to obtain high coercivity, different conditions for the desorption recombination process have been tried. Figure 3 shows the coercivity as a function of temperature where the desorption recombination process was carried out for 10 min for the decomposed $Sm_{2+\delta}Fe_{17}Ti_{0.4}$. The nitriding and carbiding were carried out at 510 °C for 120 and 15 min, respectively, in this test. It will be shown later that other carbonitriding conditions will give higher coercivity. It is clear from Fig. 3 that the best recombination temperature is about 800 °C. At this temperature, several recombination times, up to 30 min, have been tried. From these tests, it is concluded that to obtain grain sizes favorable for high coercivity, the desorption recombination process should be carried out at 800 °C for 10–15 min. As is shown in Fig. 1(c) for $Sm_{2+\delta}Fe_{17}Ti_{0.4}$, the specimens after the whole HDDR process contain the main phase of Th_2Zn_{17} rhombohedral structure with small amounts of secondary phases of α-Fe, $SmFe_2$, and $SmFe_3$. The $SmFe_2$ and $SmFe_3$ phases disappear after carbonitriding, as is shown in Fig. 1(d). This is because the two phases decompose into SmN and α-Fe upon nitriding.[17,18] Comparing Figs. 1(c) with 1(d), it is found that the amount of α-Fe remains almost unchanged after carbonitriding, indicating that carbonitriding does not introduce more α-Fe into the specimens. This advantage is discussed in detail in Ref. 5.

Since Sm evaporates during the HDDR process due to its high vapor pressure, the near stoichiometric composition ($\delta \approx 0$) of the starting material leads to large amounts of α-Fe in the HDDR $Sm_2Fe_{17}M_{0.4}$ specimens. However, when δ is in the range of 0.5–0.6, the amount of α-Fe in the specimens after HDDR process is negligible. Further increase in δ has no effect on reducing α-Fe. For all specimens which will be reported later, the values of δ for the starting materials are

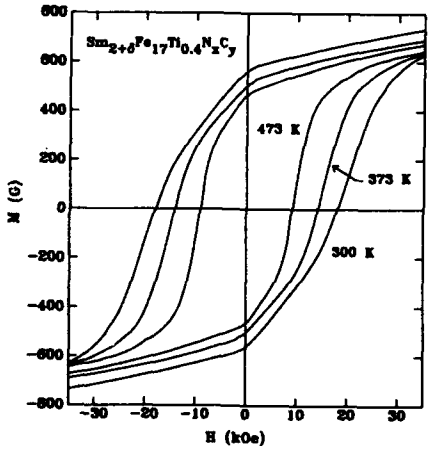

FIG. 4. Hysteresis loops of $Sm_{2+\delta}Fe_{17}Ti_{0.4}N_xC_y$ at 300, 373, and 473 K.

TABLE I. H_c and $(BH)_{max}$ of $Sm_{2+\delta}Fe_{17}M_{0.4}N_xC_y$ at 300 K.

M	Ti	V	Cr	Zr	Nb	Mo	Hf	Ta	W
H_c (kOe)	18	13	13	11	17	15	13	16	11
$(BH)_{max}$ (MGOe)	9.8	8.8	8.4	8.2	8.9	9.4	6.9	7.4	5.5

between 0.5 and 0.6. The actual values of δ of the final magnets are expected to be less than 0.6, because of the loss of Sm during the HDDR process.

Coey and Hurley[19] have shown that insufficient nitriding results in nitrogen-poor cores inside the particles, which reduce the coercivity. In order to eliminate these soft cores, two other carbonitriding conditions are investigated. Significant increase in coercivity, e.g., $\Delta H_c = +3.4$ kOe for M=Ti, was observed when nitriding was carried out at 480 °C for 9 h, followed by carbiding at the same temperature for 10 min. Compared with this carbonitriding condition, no significant increase in coercivity was obtained when nitriding was done at 460 °C for 18 h and carburizing for 15 min. These results suggest that carbonitriding at 480 °C for about 9 h is the best condition to eliminate the soft cores in a reasonably short time. The best magnet obtained is for M=Ti. Figure 4 shows the hysteresis loops of a $Sm_{2+\delta}Fe_{17}Ti_{0.4}N_xC_y$ magnet at three temperatures. Assuming full density, this magnet has the coercivity and the energy product of 18 kOe, 9.8 MGOe at 300 K, 14 kOe, 7.8 MGOe at 373 K and 9 kOe, 6.5 MGOe at 473 K. The coercivities and the energy products for other additives are listed in Table I. The good performance of the magnet with M=Ti can be, in part, explained by the enhancement of anisotropy field, which is about 4–5 kOe higher than that of Sm_2Fe_{17} carbonitride.[20]

In conclusion, by the HDDR process, high performance isotropic permanent magnets based on $Sm_{2+\delta}Fe_{17}M_{0.4}$ carbonitrides have been made for M=Ti, Nb, etc. Compared with the isotropic magnets based on Nd-Fe-B made by HDDR process, these magnets have superior magnetic properties, especially at elevated temperatures.

ACKNOWLEDGMENTS

The research was supported by grants from the Natural Sciences and Engineering Research Council of Canada, Fonds pour la Formation de Chercheurs et l'aide à la Recherche, Québec.

[1] Y. Otani, D. P. F. Hurley, H. Sun, and J. M. D. Coey, J. Appl. Phys. **69**, 5584 (1991).
[2] J. M. D. Coey, H. Sun, Y. Otani, and D. P. F. Hurley, J. Magn. Magn. Mater. **98**, 76 (1991).
[3] B.-P. Hu and G.-C. Liu, Solid State Commun. **79**, 785 (1991).
[4] X. C. Kou, R. Grössinger, M. Katter, J. Wecker, L. Schultz, T. H. Jacobs, and K. H. J. Buschow, J. Appl. Phys. **70**, 2272 (1991).
[5] X. Chen, Z. Altounian, and D. H. Ryan, J. Magn. Magn. Mater. **125**, 169 (1993).
[6] L. Schultz, K. Schnitzke, J. Wecker, M. Katter, and C. Kuhrt, J. Appl. Phys. **70**, 6339 (1991).
[7] J. Ding, P. G. McCormick, and R. Street, J. Alloys Compounds **189**, 83 (1992).
[8] F. E. Pinkerton and C. D. Fuerst, Appl. Phys. Lett. **60**, 2558 (1992).
[9] M. Q. Huang, L. Y. Zhang, B. M. Ma, Y. Zheng, J. M. Elbicki, W. E. Wallace, and S. G. Sankar, J. Appl. Phys. **70**, 6027 (1991).
[10] S. Suzuki and T. Miura, IEEE Trans. Magn. **MAG-28**, 994 (1992).
[11] C. N. Christodoulou and T. Takeshita, J. Alloys Compounds **196**, 155 (1993).
[12] P. J. McGuiness, X. J. Zhang, H. Forsyth, and I. R. Harris, J. Less-Common Met. **162**, 379 (1990).
[13] X. J. Zhang, P. J. McGuiness, and I. R. Harris, J. Appl. Phys. **69**, 5838 (1992).
[14] P. J. McGuiness, X. J. Zhang, X. J. Yin, and I. R. Harris, J. Less-Common Met. **158**, 359 (1990).
[15] R. Grössinger, R. Krewenka, R. Eibler, H. R. Kirchmayr, J. Ormerod, and K. A. J. Buschow, J. Less-Common Met. **118**, 167 (1986).
[16] M. Katter, J. Wecker, L. Schultz, and R. Grössinger, J. Magn. Magn. Mater. **92**, L14 (1990).
[17] C. N. Christodoulou and T. Takeshita, J. Alloys Compounds **194**, 31 (1993).
[18] C. N. Christodoulou and T. Takeshita, J. Alloys Compounds **191**, 279 (1993).
[19] J. M. D. Coey and D. P. F. Hurley, J. Magn. Magn. Mater. **104–107**, 1098 (1992).
[20] X. Chen, Er. Girt, and Z. Altounian (these proceedings).

Nitriding of melt-spun Nd-Fe-Mo alloys

F. E. Pinkerton, C. D. Fuerst, and J. F. Herbst
Physics Department, General Motors NAO Research and Development Center, 30500 Mound Road, Warren, Michigan 48090-9055

The hard magnetic properties of nitrided melt-spun Nd-Fe-Mo ribbons have been investigated as functions of composition, quench rate, and nitriding time. Ingots having the compositions $Nd_1Fe_{10}Mo_2$, $Nd_{1.15}Fe_{10}Mo_2$, $Nd_{1.3}Fe_{10}Mo_2$, and $Nd_{1.45}Fe_{10}Mo_2$ were melt spun over a range of quench rates specified by substrate wheel velocities v_s in the 5 m/s$\leq v_s \leq$40 m/s interval. Ribbons prepared with $v_s \leq 17.5$ m/s from the $Nd_{1.15}Fe_{10}Mo_2$ alloy consist only of stoichiometric $NdFe_{10}Mo_2$ with the $ThMn_{12}$ crystal structure; at higher quench rates the $ThMn_{12}$ structure is suppressed. It is found that all ribbons prior to nitriding are characterized by intrinsic coercivity $H_{ci}<0.4$ kOe. For ribbons direct quenched at wheel speeds between 12.5 and 17.5 m/s, nitriding produces technologically significant coercivity ($H_{ci}\sim 6$ kOe). The maxima in the technical magnetic properties as functions of v_s resemble those observed in direct-quenched Nd-Fe-B ribbons.

Since the discovery by Yang *et al.*[1] that nitrogen absorption can enhance the Curie temperature T_c, saturation magnetization M_s, and magnetocrystalline anisotropy of $RFe_{11}Ti$ (R denotes rare earth) compounds, nitrided $RFe_{12-x}T_x$ (T including Mo, Ti, and V) phases characterized by the tetragonal $ThMn_{12}$ structure have become of interest from the perspective of permanent magnet applications. In the case of the $NdFe_{12-x}Mo_x$ systems, which form for molybdenum contents in the $1.0 \leq x \leq 2.5$ range,[2–4] nitriding has been reported to improve T_c by 130–170 K, to increase M_s at 300 K by 7%–17%, and to change the easy magnetization direction from basal plane to c-axis orientation with a room-temperature anisotropy field $H_a \sim 70$ kOe.[4–8] Here we describe an effort to magnetically harden $NdFe_{10}Mo_2$ by nitriding direct-quenched melt-spun Nd-Fe-Mo ribbons, i.e., ribbons in which $ThMn_{12}$ grains having optimum size are formed directly on quenching from the melt. The technical magnetic properties have been examined as functions of composition, quench rate, and nitriding time.

Four starting compositions having fixed Mo and Fe but varying Nd concentration were chosen for this investigation: $Nd_1Fe_{10}Mo_2$, $Nd_{1.15}Fe_{10}Mo_2$, $Nd_{1.3}Fe_{10}Mo_2$, and $Nd_{1.45}Fe_{10}Mo_2$. Ingots were prepared by induction melting high-purity elemental constituents in an argon atmosphere. Each ingot was melt spun, again under argon, by ejecting molten alloy through an orifice (0.6 mm diam) in a quartz crucible onto the surface of a chrome-plated copper disk (25 cm diam). The quench rate was varied by changing the surface velocity v_s of the disk, with v_s in the range 5–40 m/s.

Nitriding was carried out on ground (<45 μm diam) powders of the melt-spun ribbons under a static 120 kPa pressure of N_2 gas. All samples in this work were nitrided at 740 K for times varying from 1 to 88 h. X-ray powder diffraction (Cu$K\alpha$ radiation) was used to identify phases in the ribbons before and after nitriding. Magnetic properties were measured using a vibrating sample magnetometer with a maximum applied field of 19 kOe after premagnetizing in a pulsed field of ~100 kOe. No demagnetization correction for the geometry of the samples was made, and a density of 8.2 (8.3) g/cm^3 was used for the nitrided (unnitrided) materials. T_c values were determined by differential scanning calorimetry.

From the x-ray analyses we found that the $Nd_{1.15}Fe_{10}Mo_2$ starting composition yielded essentially single-phase $NdFe_{10}Mo_2$ ribbons, but only for quench rates in the $v_s \leq 17.5$ m/s range. Figure 1 illustrates this point. A powder diagram calculated for $NdFe_{10}Mo_2$ using the nuclear coordinates and site occupancies determined via neutron diffraction by Yelon and Hadjipanayis[9] for $NdFe_{10}Mo_2N_x$ is displayed in Fig. 1(a), and Figs. 1(b), 1(c), and 1(d) are the patterns observed for ribbons melt spun from the $Nd_{1.15}Fe_{10}Mo_2$ ingot at v_s=15, 20, and 30 m/s. Lattice constants a=8.61 Å, c=4.81 Å, in excellent agreement with the values given in Ref. 3 for $NdFe_{10}Mo_2$, were inferred from the peak positions for the 15 m/s sample [Fig. 1(b)]; those parameters were employed in computing Fig. 1(a). Comparison of Figs. 1(a) and 1(b) demonstrates that only $NdFe_{10}Mo_2$ is detectable in the 15 m/s sample. This identification is consistent with quantitative elemental analysis of the 15 m/s ribbons by inductively coupled plasma atomic emission spectrometry, which indicated a slightly rare-earth-rich composition of $Nd_{1.08}Fe_{10.0}Mo_{2.01}$. The diffraction pattern for the v_s=20 m/s sample [Fig. 1(c)] shows line broadening indicative of decreasing particle size, perhaps combined with incipient deterioration of the $ThMn_{12}$ character through disordering of the transition-metal sublattices. At v_s=30 m/s [Fig. 1(d)] much of the fine structure has been eliminated; further particle size reduction associated with the higher quench rate cannot by itself account for the modification of the line pattern. Figure 1(d) suggests transformation to the disordered hexagonal $TbCu_7$ structure, evidence for which has also been reported for melt-spun Sm-Fe alloys.[10]

Results of nitriding the $Nd_{1.15}Fe_{10}Mo_2$ ribbons are summarized in Fig. 2, which displays B_r, $(BH)_{max}$, and H_{ci} as functions of nitriding time for five different quench rates corresponding to v_s=10, 12.5, 15, 17.5, and 30 m/s. Before nitriding the intrinsic coercivity is negligible, $H_{ci} \leq 0.2$ kOe, as is the energy product, but Fig. 2 makes it clear that the incorporation of nitrogen produces technologically significant magnetics. Values of H_{ci} and $(BH)_{max}$ exceeding 4.5 kOe and 2.0 MGOe, respectively, are observed for the v_s=12.5, 15, and 17.5 m/s ribbons over nitriding times extending from 16 to 64 h.

Figure 3 highlights the v_s dependence via plots of the

 0021-8979/94/75(10)/6015/3/$6.00 © 1994 American Institute of Physics

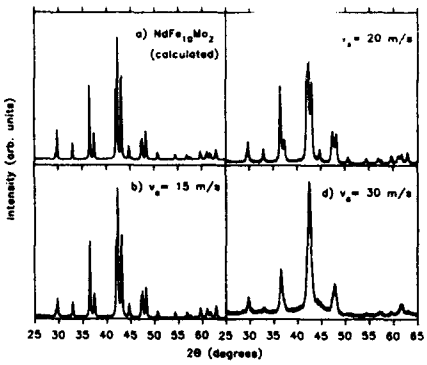

FIG. 1. (a) Calculated Cu$K\alpha$ x-ray powder-diffraction diagram for $NdFe_{10}Mo_2$, and observed patterns for $Nd_{1.15}Fe_{10}Mo_2$ ribbons melt spun at (b) v_s=15 m/s, (c) v_s=20 m/s, and (d) v_s=30 m/s.

three technical properties versus v_s for the $Nd_{1.15}Fe_{10}Mo_2$ ribbons nitrided for 16 h. The broad maxima, which all occur at v_s=15 m/s, resemble those observed in melt-spun Nd-Fe-B.[11] For these alloys, however, the property enhancement afforded by optimizing the quench rate is smaller. This is especially true of H_{ci}, which improves by as much as ~20 kOe in Nd-Fe-B,[11] as opposed to the ~2 kOe increase shown in Fig. 3. Since $Nd_2Fe_{14}B$ and $NdFe_{10}Mo_2$ have comparable

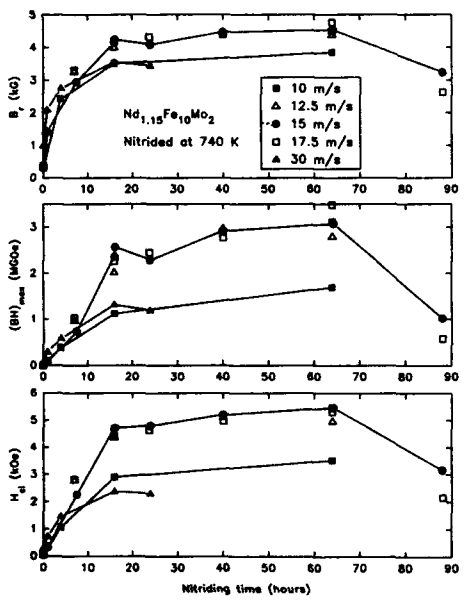

FIG. 2. Room-temperature remanence B_r, energy product $(BH)_{max}$, and intrinsic coercivity H_{ci} of $Nd_{1.15}Fe_{10}Mo_2$ ribbons melt spun at v_s=10, 12.5, 15, 17.5, and 30 m/s as functions of nitriding time.

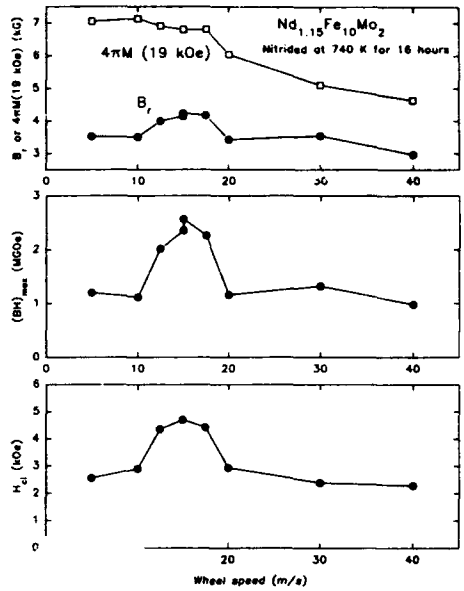

FIG. 3. B_r, $(BH)_{max}$, and H_{ci} of $Nd_{1.15}Fe_{10}Mo_2$ ribbons nitrided at 740 K for 16 h as functions of wheel speed v_s. The uppermost panel also includes values of $4\pi M$ measured in a 19 kOe external field.

anisotropy fields (H_a~70 kOe), the relatively small enhancement for the nitrided Nd-Fe-Mo ribbons underscores the challenge of realizing useful coercivity in these systems.

Despite also being comprised of essentially single-phase $NdFe_{10}Mo_2$, as revealed by the x-ray analyses, ribbons melt spun with $v_s \leq 10$ m/s do not develop properties equivalent to those of the 12.5 m/s$\leq v_s \leq$17.5 m/s ribbons on nitriding. Since grain size increases with diminishing v_s, it is our opinion that reduced H_{ci} associated with oversized grains, as observed in melt-spun Nd-Fe-B,[11] is responsible for this behavior. For the $v_s \geq 20$ m/s materials, on the other hand, we conclude that the inferior properties are due to the degradation of the $ThMn_{12}$ structure indicated by the x-ray work. Corroborative evidence for the transformation is provided by measurements of $4\pi M$ in the largest field applied, 19 kOe, shown as open squares in the top panel of Fig. 3. It is apparent that the progressive replacement of ordered $ThMn_{12}$-type material by a related but disordered phase for $v_s \geq 20$ m/s is accompanied by a substantial drop in magnetization.

Demagnetization curves for the $Nd_{1.15}Fe_{10}Mo_2$ (15 m/s) ribbons before and after nitriding (64 h) are presented in Fig. 4. While the coercivity is essentially zero in the as-spun state, the nitrided ribbons are characterized by H_{ci}=5.5 kOe, B_r=4.5 kG, and $(BH)_{max}$=3.1 MGOe. The remanence is near the 5 kG value to be expected for a random distribution of $NdFe_{10}Mo_2N_x$ crystallites whose saturation magnetization[4,5,7] is $4\pi M_s$~10 kG. The largest $(BH)_{max}$ attainable for such a distribution is approximately 6 MGOe, and our observation of half that limiting value is a conse-

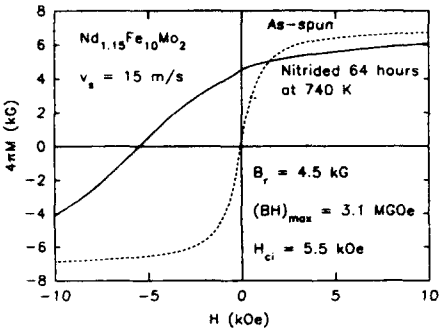

FIG. 4. Demagnetization curves for $Nd_{1.15}Fe_{10}Mo_2$ (v_s=15 m/s) ribbons in the as-spun state (dashed line) and after nitriding for 64 h at 740 K in N_2 gas at 120 kPa (solid line).

quence of the nonrectangular loop shape of the nitrided material in Fig. 4. Endoh and co-workers[4] observed H_{ci}~3 kOe and B_r~5 kG for nitrided melt-spun $Nd_{1.3}Fe_{10}Mo_2$. Working with *overquenched* $NdFe_{10}Mo_2$ ribbons melt spun at 40 m/s and which, in contrast to our work, were vacuum annealed prior to nitriding, Tang, Singleton, and Hadjipanayis[12] achieved H_{ci}~8.8 kOe and B_r~4.6 kG after optimizing the annealing and nitriding conditions. Coercivities and remanences of 8 kOe, 5 kG (Ref. 7) and 4 kOe, 7 kG (Ref. 4) have been reported for nitrided powders prepared from mechanically alloyed ingots much richer in rare-earth content than those investigated here.

We have determined T_c~365 K for the as-spun $Nd_{1.15}Fe_{10}Mo_2$ (15 m/s) ribbons and T_c~505 K for the same ribbons after nitriding, in reasonable agreement with the Curie temperatures reported in Ref. 4.[13] For the nitrided ribbons we find $ThMn_{12}$-type lattice constants a=8.69 Å and c=4.87 Å, implying a volume expansion of 3.3% on nitriding consistent with the results of others.[5,7,8,12]

Figure 5 compares the technical magnetic properties, again as functions of nitriding time as in Fig. 2, of nitrided v_s=15 m/s ribbons prepared from the four different starting compositions examined in this study. It amplifies our result that the $Nd_{1.15}Fe_{10}Mo_2$ formulation leads to the best magnetics. Together with the x-ray studies, the data of Fig. 5 afford two conclusions. First, some excess Nd facilitates development of the technical properties, but an overabundance of secondary phases is deleterious. The powder diagram of $Nd_1Fe_{10}Mo_2$ (15 m/s) material is indistinguishable from Fig. 1(b) for the $Nd_{1.15}Fe_{10}Mo_2$ (15 m/s) ribbons, so the markedly poorer properties of the former imply that some excess Nd is favorable, even though none is apparent in the diffraction pattern. In contrast, the x-ray diagrams of the $Nd_{1.3}Fe_{10}Mo_2$ and $Nd_{1.45}Fe_{10}Mo_2$ samples contain lines from secondary phases, which are evidently responsible for the reduced magnetics obtained from those compositions in Fig. 5. Second, nitriding for times longer than ~65 h disproportionates the $ThMn_{12}$-type component into NdN, α-Fe, and other phases; Fig. 5 shows that the magnetic properties deteriorate as well.

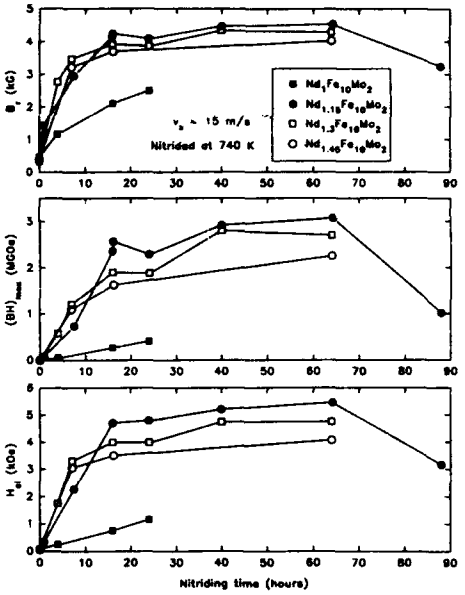

FIG. 5. Room temperature remanence B_r, energy product $(BH)_{max}$, and intrinsic coercivity H_{ci} of $Nd_1Fe_{10}Mo_2$, $Nd_{1.15}Fe_{10}Mo_2$, $Nd_{1.3}Fe_{10}Mo_2$, and $Nd_{1.45}Fe_{10}Mo_2$ ribbons melt spun at v_s=15 m/s as functions of nitriding time.

We are grateful to C. B. Murphy for expert technical assistance, to A. M. Wims for help with the x-ray work, to N. Potter for elemental analyses, and to T. S. Ellis for calorimetric measurements.

[1] Y.-C. Yang, X.-D. Zhang, L.-S. Kong, Q. Pan, and S.-L. Ge, Solid State Commun. **78**, 317 (1991).
[2] A. Müller, J. Appl. Phys. **64**, 249 (1988).
[3] K. H. J. Buschow and D. B. de Mooij, in *Concerted European Action on Magnets*, edited by I. V. Mitchell, J. M. D. Coey, D. Givord, I. R. Harris, and R. Hanitsch (Elsevier, London, 1989), p. 63.
[4] M. Endoh, K. Nakamura, and H. Mikami, IEEE Trans. Magn. **MAG-28**, 2560 (1992).
[5] M. Anagnostou, C. Christides, M. Pissas, and D. Niarchos, J. Appl. Phys. **70**, 6012 (1991).
[6] X. Chen, L. X. Liao, Z. Altounian, D. H. Ryan, and J. O. Ström-Olsen, J. Magn. Magn. Mater. **111**, 130 (1992).
[7] W. Gong and G. C. Hadjipanayis, IEEE Trans. Magn. **MAG-28**, 2563 (1992).
[8] Y. Z. Wang, G. C. Hadjipanayis, Z. X. Tang, W. B. Yelon, V. Papaefthymiou, A. Moukarika, and D. J. Sellmyer, J. Magn. Magn. Mater. **119**, 41 (1993).
[9] W. B. Yelon and G. C. Hadjipanayis, IEEE Trans. Magn. **MAG-28**, 2316 (1992).
[10] F. E. Pinkerton and C. D. Fuerst, Appl. Phys. Lett. **60**, 2558 (1992).
[11] J. J. Croat, J. F. Herbst, R. W. Lee, and F. E. Pinkerton, Appl. Phys. Lett. **44**, 148 (1984).
[12] Z. X. Tang, E. W. Singleton, and G. C. Hadjipanayis, J. Appl. Phys. **73**, 6254 (1993); Z. X. Tang, G. C. Hadjipanayis, and V. Papaefthymiou, J. Alloys Compounds **194**, 87 (1993).
[13] There is significant variation in the values of the intrinsic properties of these materials in the extant literature; most of the disparity likely arises from the rather broad homogeneity range over which the $ThMn_{12}$ structure forms.

Effect of milling on the magnetic and microstructural properties of $Sm_2Fe_{17}N_x$ permanent magnets

P. A. P. Wendhausen, B. Gebel, D. Eckert, and K.-H. Müller
Institut für Festkörper- und Werkstofforschung Dresden P.O. Box, 01171 Dresden, Germany

By ball milling $Sm_2Fe_{17}N_x$ the coercivity can be increased from 0.3 to 1.5 T. The coercivity increases continuously during milling up to a time of about 600 min, and then decreases for too intensive ball milling. This is connected to particle size reduction and other effects like the increase in oxygen content, introduction of mechanical stresses, formation of new grain boundaries, and amorphization of the material. Magnetic measurements, scanning electron microscopy, as well as domain wall observations indicate that long-time milled material is mainly constituted of single domain particles and isotropic polycrystalline particles with small grains.

I. INTRODUCTION

In the last three years much effort has been done to translate the excellent intrinsic magnetic properties of $Sm_2Fe_{17}N_x$ into essential permanent magnet properties like remanence and coercivity. A useful procedure is to regrind the powder after nitrogenation. In Ref. 1 a coercivity of 0.8 T was achieved by ball milling $Sm_2Fe_{17}N_x$ to a particle size of 2 to 4 μm. In Ref. 2 it was reported that below 5 μm these particles are single domain. Theoretical calculations derived from the domain width,[3,4] however, lead to values of 0.3 μm for the critical single-domain particle size. Despite of this fact it was found in Ref. 5 that magnets prepared from $Sm_2Fe_{17}N_x$ powders additionally milled after nitrogenation show lower initial susceptibilities and much higher coercivities compared to values obtained for magnets prepared from nitrogenated powder without additional milling. This fact might be related to a single-domain particle behavior or pinning of domain walls. In this work the effect of milling on microstructure and coercivity will be focused.

II. EXPERIMENT

The Sm_2Fe_{17} alloy was prepared by induction melting, starting from a Sm-rich alloy to which Fe was added to achieve the desired composition. The as-cast alloy was sealed in quartz tubes and homogenized at 1000 °C for seven days and then pulverized to a particle size less than 20 μm and nitrogenated at 450 °C for 5 h. The nitrogenated material was additionally milled in a vibration mill under toluene for different times varying up to 2000 min. Magnet samples were prepared by fixing the powders with resin or Zn bonding. The material was characterized by SEM (scanning electron microscopy) and x-ray diffractometry. Magnetic measurements were performed on a vibrating sample magnetometer with fields up to 8 T and domains were observed by Bitter technique.

III. RESULTS AND DISCUSSION

The decrease of particle size due to the additional milling is shown in Fig. 1. For the not additionally milled powder [Fig. 1(a)] big particles (5–20 μm) showing a smooth surface can be clearly seen. A few small particles are also present. The number of these small particles increases when the powder is milled for long times [Fig. 1(b)], but it is difficult to recognize all of them as single particles because

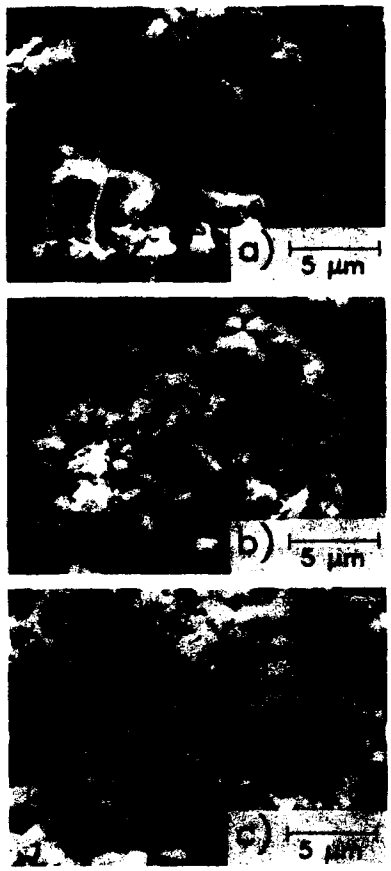

FIG. 1. SEM micrographs of $Sm_2Fe_{17}N_x$. (a) Not additionally milled, (b) additionally milled for 600 min, (c) agglomerate in the powder shown in (b).

 0021-8979/94/75(10)/6018/3/$6.00 © 1994 American Institute of Physics

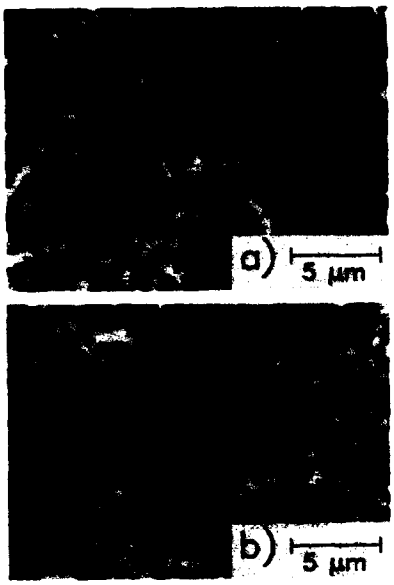

FIG. 2. SEM micrographs of resin mounted and polished powders from Fig. 1. (a) Not additionally milled, (b) additionally milled for 600 min.

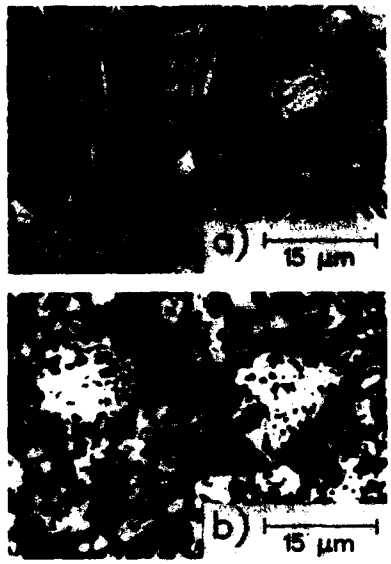

FIG. 3. Bitter patterns of $Sm_2Fe_{17}N_x$ powders (a) before and (b) after additionally milling for 600 min.

they form agglomerates. From the SEM micrographs it follows that most of the small particles are 3 μm or less in size. Sometimes they seem to be cold welded and tend to build particles as big as the original ones (5–20 μm) and show a rough surface [Fig. 1(c)]. SEM observations on polished powders show that the unmilled $Sm_2Fe_{17}N_x$ powder is constituted of particles with sharp edges and the polished surface is smooth and free of cracks [Fig. 2(a)]. The corresponding micrographs of 600 min milled powders [Fig. 2(b)] show besides many small particles, big ones (larger than 3 μm) with a round shape and cracklike defects on the polished surface. Probably these cracklike defects are boundaries between particles which are joined by magnetostatic forces or by cold welding. The existence of domain walls in $Sm_2Fe_{17}N_x$ particles of milled and unmilled powders was revealed by the Bitter technique (Fig. 3). Domain structures are clearly visible in particles of not additionally milled powders, but in the additionally milled state (600 min) they can hardly be seen. This indicates that the large particles in Fig. 3(b) as well as in 1(b), 1(c), and 2(b) are in reality agglomerated small particles without domain walls or cold-welded particles consisting of single-domain crystallites isotropically distributed.

Figure 4 shows the increase of oxygen content with milling time. The uptake of most of the oxygen occurs in the first 600 min of milling, connected with the creation of a larger specific surface as reported in Ref. 2. After that only a small change is observed up to 2000 min. By SEM observations it is difficult to distinguish a change in particles size after 600 min ball milling, because of the agglomeration effects. However, the small change in oxygen content after 600 min (see Fig. 4) indicates that the decrease of particle size might become less intensive after this milling time. The coercivity is very sensitive to the milling time as can be seen in Fig. 4. Values up to 1.5 T are achieved when $Sm_2Fe_{17}N_x$ is milled for about 600 min. After that a continuous decrease of coercivity is observed. A well known effect of milling regarding the enhancement in coercivity is the fragmentation of big particles into smaller ones. In this way the nucleation centers present on the surface of the particles, e.g., α-Fe, would be isolated in few subparticles, thereby confining their deleterious effect to a small fraction of volume. As a result of the

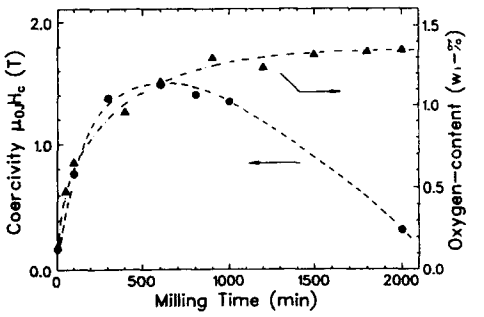

FIG. 4. Coercivity and oxygen content of additionally milled $Sm_2Fe_{17}N_x$ powder vs milling time.

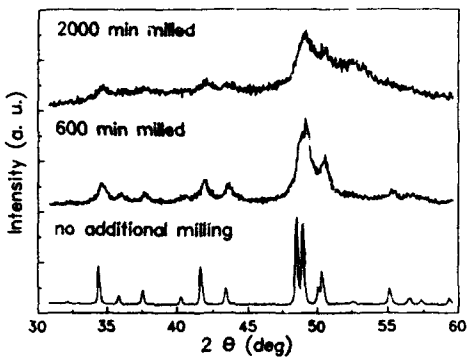

FIG. 5. X-ray diffraction patterns of $Sm_2Fe_{17}N_x$ powders before and after additional milling for different times.

milling, however, not only the particle size is reduced, but also the chemical composition, the surface state as well as the amount of phases may be changed and this can also affect the coercivity. The x-ray patterns of long time milled powders (600 min), show broadened x-ray lines (Fig. 5). This line broadening may be caused by microstresses and crystallite size reduction. Considering the line broadening to be caused by crystallite size reduction and applying the Scherrer formula a crystallite size of about 20 nm was estimated for the 600-min milled powder. In a further milling stage (2000 min) the x-ray peaks tend to disappear, indicating the formation of an amorphous structure. In Ref. 6 such an amorphization effect was also reported for nonnitrogenated Sm_2Fe_{17} which can be recrystallized by a heat treatment at 700 °C. At such high temperatures a recrystallization treatment of $Sm_2Fe_{17}N_x$ is not possible because of its decomposition into SmN and α-Fe. The decrease in coercivity observed for milling times longer than 600 min might be attributed to this formation of amorphous material.

From magnetic measurements on milled and unmilled $Sm_2Fe_{17}N_x$ additional information can be obtained which also hints to a refinement of the size and microstructure of the particles and formation of material with partial isotropic character by ball milling: First, there is a strong decrease of the initial susceptibility for magnets prepared with powders milled for very long time indicating pinning or single-domain particle behavior due to small crystallite or particle size.[5] Second, samples prepared from long time milled powders (600 min) by die pressing in a field of 2 T show a poor degree of texture ($B_r^{\perp}/B_r^{\parallel}=0.95$). Possible reasons are the small particle size which results in too low magnetic forces compared with the friction forces during pressing or the presence of isotropic particles formed by cold welding. To get more information about this we aligned well dispersed powders in low viscous epoxy resin in a field of 7.5 T. Some resulting texture parameters for different milling times are shown in Table I. The improvement of texture compared with the case of die pressing shows the presence of small particles which can be aligned. But the remarkable decrease of texture with increasing milling time points to the presence of particles with isotropic character as well.

TABLE I. Different texture parameters resulting from a numerical fit of demagnetization curves (assuming a Gaussian texture function with the half-width σ_g[7]). The $Sm_2Fe_{17}N_x$ powders were aligned in low viscous epoxy in a field of 7.5 T. For comparision the first and the last line show the texture parameters for the completely aligned and ideally isotropic cases.

Milling time (min)	σ_g (deg)	B_r/J_s	$B_r^{\perp}/B_r^{\parallel}$
...	0	1	0
0	13	0.95	0.19
300	31	0.76	0.47
600	40	0.69	0.59
...	∞	0.5	1

It should be noted that the enhancement of coercivity by additional milling, shown in Fig. 4, has the same order of magnitude as the increase of coercivity caused by Zn bonding.[4] As a surprising result, however, the combination of additional milling and Zn bonding gives no improvement compared to the coercivity of $Sm_2Fe_{17}N_x$ powder not additionally milled and not Zn bonded.[5]

[1] T. Iriyama, K. Kobayashi, N. Imaoka, T. Fukuda, H. Kato, and Y. Nakagawa, IEEE Trans. Magn. **28**, 2326 (1992).
[2] K. Kobayashi, T. Iriyama, T. Yamaguchi, H. Kato, and Y. Nakagawa, J. Alloys Comp. **193**, 235 (1993).
[3] T. Mukai and T. Fujimoto, J. Magn. Magn. Mater. **103**, 165 (1992).
[4] P. A. P. Wendhausen, D. Eckert, A. Handstein, K.-H. Müller, G. Leitner, and S. Skomski, J. Appl. Phys. **73**, 6044 (1993).
[5] P. A. P. Wendhausen, K.-H. Müller, A. Handstein, D. Eckert, W. Pitschke, and Bo-Ping Hu, INTERMAG'93, Stockholm, 1993, paper FC-05.
[6] J. Ding, P. G. McCormick, R. Street, and P. A. I. Smith, Proc. 12th Int. Workshop on RE Magnets and Their Applications, Canberra, 1992, p. 428.
[7] K.-H. Müller, D. Eckert, P. A. P. Wendhausen, A. Handstein, S. Wirth, M. Wolf, EMMA'93 Conf., Kosice, 1993, paper B-O-06.

Magnetic properties of $Y(Fe,Co)_{10}Mo_2$ alloys

Xie Xu, Roy Tucker, and S. A. Shaheen
Department of Physics and Center for Materials Research and Technology (MARTECH), Florida State University, Tallahassee, Florida 32306

The structural and magnetic properties of $YFe_{10-x}Co_xMo_2$ alloys ($0 \leqslant x \leqslant 10$) have been investigated by means of x-ray diffraction, thermomagnetic analysis, and magnetometry techniques. All the alloys exhibited the tetragonal $ThMn_{12}$ structure and were almost single phase materials. With the increase of Co content x, T_c increases initially, reaching a maximum at $x \sim 6$, followed by a decrease at higher x values. X-ray diffraction analyses on magnetically aligned samples indicate that $YFe_{10}Mo_2$ exhibits an axial easy direction of magnetization (EDM) at room temperature, and the addition of Co initially causes the EDM to deviate gradually from the c axis with increasing x ($x \leqslant 4$). On further increase of Co content ($x \geqslant 5$), the EDM of the $YFe_{10-x}Co_xMo_2$ compounds tends to become axial again, reaching a complete uniaxial behavior for the terminal compound $YCo_{10}Mo_2$.

I. INTRODUCTION

The compounds of type R (Fe, Co, TM)$_{12}$ (R=rare earth or yttrium, TM=Ti, V, Cr, Mo, Si, etc.)[1-3] have been a focus of numerous studies in recent years because of their potential applications as permanent magnets. They crystallize in the tetragonal $ThMn_{12}$ type structure with a space group of $I4/mmm$.[3] In a previous study,[4] we reported that the $ThMn_{12}$-type structure is retained in the $RCo_{10}Mo_2$ series; the $3d$ sublattice favors a uniaxial anisotropy, and the easy direction of magnetization (EDM) is along the c axis for R=Y, Ce, Pr, Nd, Gd, and Dy at room temperature. Our observations of uniaxial anisotropy behavior of $YCo_{10}Mo_2$ is at odds with the reported results on the $YFe_{10-x}Co_xMo_2$ series,[5] where it was claimed that the EDM of the $YFe_{10-x}Co_xMo_2$ compounds is along the c axis for $x \leqslant 6$, and deviates from the c axis for $x \geqslant 8$. In order to clarify this difference, we studied the $YFe_{10-x}Co_xMo_2$ ($0 \leqslant x \leqslant 10$) series and the structural and magnetic properties of the compounds are presented in this paper.

II. EXPERIMENT

$YFe_{10-x}Co_xMo_2$ alloys ($0 \leqslant x \leqslant 10$) were prepared by arc melting of stoichiometric amounts of the constituent elements under an argon atmosphere. After the melting, the samples were annealed at 1000 °C for a week and quenched in water. The crystal structures of these alloys were determined by x-ray diffraction using Cu$K\alpha$ radiation. For the magnetic anisotropy studies, the powdered samples were fixed in an epoxy resin in a magnetic field of 1 T. The EDM was deduced from the x-ray diffraction patterns of field-aligned samples at room temperature. A quantum design SQUID magnetometer with magnetic field up to 5.5 T was used for determination of the saturation magnetization and anisotropy field. The Curie temperatures were measured using a Faraday magnetometer.

III. RESULTS AND DISCUSSION

X-ray diffraction and thermomagnetic analyses showed that all compounds in the $YFe_{10-x}Co_xMo_2$ series crystallized in single phase with the $ThMn_{12}$-type structure. A weak impurity peak was observed for $YCo_{10}Mo_2$ sample, which is identified to be a Co_3Mo phase. Figure 1 shows the x-ray diffraction patterns of random and magnetically aligned powders at room temperature for $x=0$, 4, 10. The lattice parameter a and c decrease monotonically with the increase of Co content x, as shown in Fig. 2. This would indicate that the Co atoms are incorporated in the 1:12 phase and readily substitute for Fe atoms in the whole composition range.

The Curie temperature values as a function of Co content x are summarized in Table I and plotted in Fig. 3. With the increase of the Co content, T_c initially increases at the rate of ~45 K per substituted Co atom, reaching a maximum value of 610 K at $x \sim 6$, and then decreases almost linearly to 470 K at $x=10$. This behavior is similar to that observed in

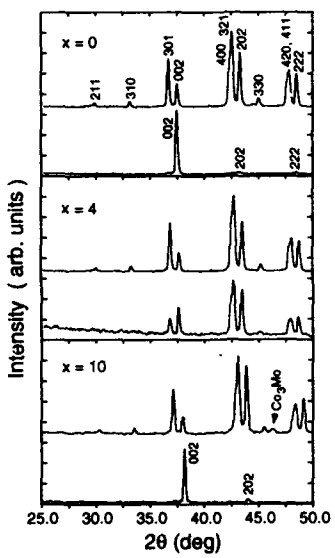

FIG. 1. Comparison of the x-ray spectra obtained on random and aligned powders for the $YFe_{10-x}Co_xMo_2$ series.

 0021-8979/94/75(10)/6021/3/$6.00 © 1994 American Institute of Physics

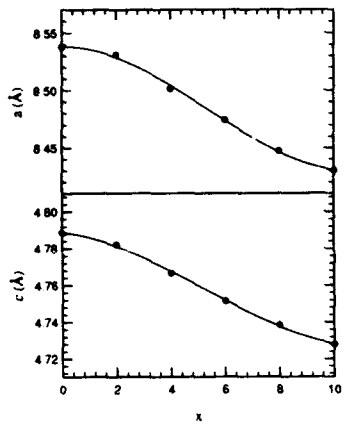

FIG. 2. The lattice parameters a and c across the $YFe_{10-x}Co_xMo_2$ series.

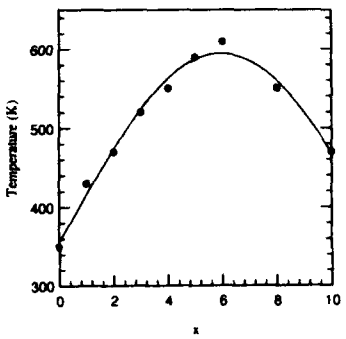

FIG. 3. Curie temperature as a function of x in the $YFe_{10-x}Co_xMo_2$ series.

the $YFe_{10-x}Co_xV_2$ series[6] but contrasts with that reported by Chin Lin *et al.*[5] for the $YFe_{10-x}Co_xMo_2$ series. The behavior of Curie temperature in the $YFe_{10-x}Co_xMo_2$ series also suggests that Co atoms probably substitute preferentially at the Fe sites, where a negative exchange interaction is involved in the $ThMn_{12}$ structure. It is interesting to note that the Curie temperatures of $YFe_{10-x}Co_xMo_2$ series are relatively low as compared to those of $YFe_{10-x}Co_xV_2$ series.[6]

The dependence of saturation magnetization σ_s on the Co fraction x in the $YFe_{10-x}Co_xMo_2$ series (at room temperature) is displayed in Fig. 4. Increasing the Co content leads initially to an increase in σ_s, giving a maximum at $x \approx 2$, followed by a subsequent decrease. The occurrence of a maximum in σ_s, which is well known for the Fe–Co binaries, appears to be a characteristic property of R–Fe–Co–M alloys as well. The values of saturation magnetization (σ_s) at 300 K are listed in Table I. Included in Table I are the values of the corresponding saturation moment (M_s) and the values of the corresponding moments per $3d$ atom (μ_{3d}). As shown in Table I, the average $3d$ moment decreases monotonically for $x>2$ as more Co is introduced into $YFe_{10-x}Co_xMo_2$. The $3d$ moment is $0.79\mu_B$ for $x=0$ (Fe moment) and $0.57\ \mu_B$ for $x=10$ (Co moment). The Co moment in this series is much lower than the corresponding values in Co metal, RCo_5, R_2Co_{17}, and $R_2Co_{14}B$.[7]

By comparing the intensity ratios of the (002) and (400) peaks in the x-ray diffraction patterns of random and aligned powders, the direction of easy magnetization (EDM) was determined at room temperature. As shown in Fig. 1 (top), the $YFe_{10}Mo_2$ ($x=0$) compound exhibits an axial EDM. This behavior is attributed to the uniaxial anisotropy of the Fe sublattice, since Y is a nonmagnetic element. With the addition of Co, the EDM of $YFe_{10-x}Co_xMo_2$ deviates gradually from the c axis. This is indicated by the increase of the intensity ratio, I_{400}/I_{002}, with increasing Co content in the aligned patterns for $x \leq 4$ (Fig. 5). With further increase of Co content ($x \geq 6$), the EDM of the $YFe_{10-x}Co_xMo_2$ compounds tends to change back to the c axis, as indicated by the decrease of the I_{400}/I_{002} ratio. The terminal compound $YCo_{10}Mo_2$ exhibits a complete uniaxial anisotropy, as seen in Fig. 1 (bottom). These results suggest that the Co sublattice exhibits a uniaxial magnetocrystalline anisotropy in $YCo_{10}Mo_2$. Sinha *et al.* observed a similar trend in the $GdFe_{11-x}Co_xTi$ series.[8] To understand the $3d$ anisotropy behavior in the $YFe_{10-x}Co_xMo_2$ system, one has to consider

TABLE I. Magnetic characteristics of $YFe_{10-x}Co_xMo_2$ compounds. The values of the saturation magnetization σ_s, magnetic moment M_s, and magnetic moment per $3d$ site μ_{3d} are taken at 300 K.

x	T_c (K)	σ_s (Am²/kg)	M_s (μ_B/f.u.)	μ_{3d} (μ_B/3d)
0	350	52.4	7.87	0.79
2	470	74.3	11.23	1.12
4	570	67.8	10.33	1.03
6	610	63.7	9.77	0.98
8	550	54.6	8.44	0.84
10	470	36.6	5.70	0.57

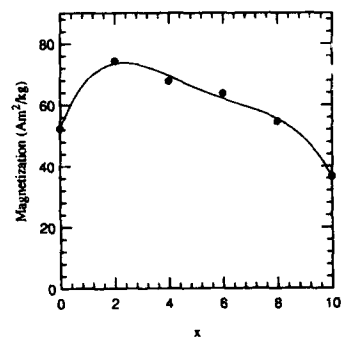

FIG. 4. Saturation magnetization at 300 K as a function of x in the $YFe_{10-x}Co_xMo_2$ series.

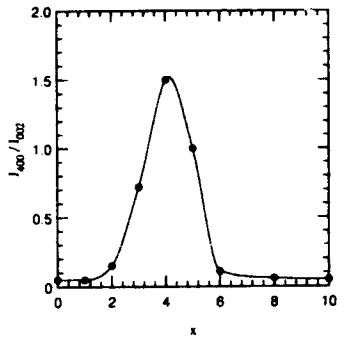

FIG. 5. Intensity ratio of (400) and (002) peaks in x-ray patterns of aligned powders as a function of x in the $YFe_{10-x}Co_xMo_2$ series.

the possibility of the preferential substitution of the Co atoms for the Fe atoms at different sites and the competition of the anisotropies among the different $3d$ sites ($8f$, $8i$, and $8j$). A study of such a preferential site occupation has been performed on the $YFe_{10-x}Co_xMo_2$ series using neutron diffraction technique.[9] This study confirms the preferential substitution of Co at various sites and is consistent with the uniaxial anisotropy behavior reported here for $YCo_{10}Mo_2$.

ACKNOWLEDGMENTS

We are grateful to H. Mathias for his technical assistance in x-ray measurements. This work was supported by the Florida High-Tech Council and the National High Magnetic Field Laboratory.

[1] D. B. De Mooij and K. H. J. Buschow, Philips J. Res. **42**, 246 (1987).
[2] K. Ohashi, Y. Tawara, R. Osugi, and M. Shimao, J. Appl. Phys. **64**, 5714 (1988).
[3] K. Ohashi, T. Yokoyama, R. Osugi, and Y. Tawara, IEEE Trans. Magn. **MAG-23**, 3101 (1987).
[4] Xie Xu and S. A. Shaheen, J. Magn. Magn. Mater. **118**, L6–L10 (1993).
[5] Chin Lin, Yun-Xi Sun, Zun-Xiao Liu, Gang Li, Ji-Lian Yang, Bai-Shen Zhang, Yong-Fan Ding, and Lan Jin, J. Appl. Phys. **69**, 5554 (1991).
[6] M. Jurczyk and O. D. Chistjakov, J. Magn. Magn. Mater. **82**, 239 (1989).
[7] K. H. J. Buschow, D. B. De Mooij, S. Sinnema, R. J. Radwanski, and J. J. M. Franse, J. Magn. Magn. Mater. **51**, 211 (1985).
[8] V. K. Sinha, S. F. Cheng, W. E. Wallace, and S. G. Sankar, J. Magn. Magn. Mater. **81**, 227 (1989).
[9] W. B. Yelon, Y. Y. Tang, X. Xu, R. Tucker, and S. A. Shaheen (unpublished).

Magnetic thin-film media response in presence of displacement eddy currents

A. Geri, A. Salvini, and G. M. Veca
Dipartimento di Ingegneria Elettrica, Università di Roma "La Sapienza," Via Eudossiana No. 18, 00184, Roma, Italy

Experimental tests have shown that macroscopic multilayer thin films excited by high-frequency magnetic field present permeance resonances. This unexpected behavior exists, even if the thickness of the magnetic films is smaller than the skin depth: in fact, for this condition, eddy currents within laminated magnetic sample should be inhibited. This phenomenon can be justified, observing that, for small thickness of the insulating interlayer, capacitive eddy currents across the dielectric layers begin to circulate between magnetic films. To predict the displacement eddy currents in macroscopic magnetic laminates some authors have provided various computational models based on different theoretical approaches. In particular, the computation of the effective complex permeability has been pointed out by means of coupled Maxwell's equations, both in differential form and in an integral one. In a previous work we have proposed and validated a circuit model able to simulate the behavior of magnetic samples in the frequency domain. In this paper we present an extensive comparative analysis between our model and the previous ones. The calculations provide the magnitude and the phase of the effective permeability of a laminate with 30 permalloy-ZrO_2 film pairs. The simulations have been performed over the frequency range of 1–100 MHz and for different geometries. The results of the simulations have been also compared with those provided by experimental tests available in literature. The main goal of this study is to evaluate the performance and reliability of each model.

INTRODUCTION

The magnetic sample of thin film, considered in this work, is shown in Fig. 1. The behavior of this laminate has been investigated by Webb *et al.* in Ref. 1. The experimental tests described in that paper have shown permeance resonances in the range 1–100 MHz, while electrical shorting at the film edges can cause the anomalies observed by Feng and Thompson in Ref. 2. The measurements seem to be reasonably acceptable, although, as supposed by the authors, both residual electrical shorting and interlayer optical thickness, smaller than assumed, have introduced some unforeseen behavior. In Ref. 1 the authors have simulated the responses of tested objects using an anisotropic effective medium. Assuming a two-dimensional (2D) approach and applying a mean-field approximation, the high-frequency performances of the magnetic samples have been numerically computed, solving the wave equation for anisotropic film by means of a Fourier series expansion. Then Walser *et al.* in Ref. 3 proposed a circuit model deduced from the coupled Maxwell's equations in integral form. The equivalent network excited by an ideal current source, representative of the external applied field, is solved using the loop analysis. The effective permeability is computed relating the average mesh current (including all displacement eddy currents) to the current source (proportional to the applied field). Recently we have introduced a new circuit model to evaluate the displacement eddy current effects in high-frequency devices.[4] The proposed model consists of an equivalent lumped parameter network defined as shown in Fig. 2. Applying the loop analysis in the frequency domain, the effective complex permeability can be determined relating the external magnetic field, $\bar{H}_0$, to the average total magnetic field, $\bar{H}_a$, as pointed out in the Appendix. The present version of our calculation code permits us to partition the magnetic objects along the Y axis (this capability is not yet actuated on the circuit model in Ref. 3). In addition, as it

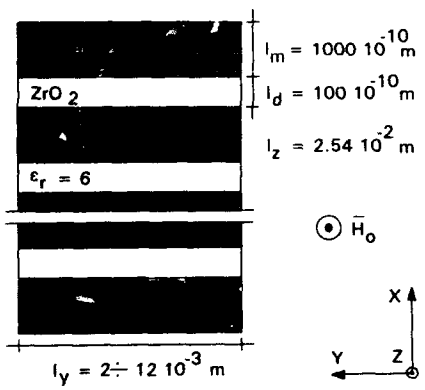

FIG. 1. Schematic view, geometry, and electromagnetic characteristics of the laminated object under analysis.

 0021-8979/94/75(10)/6024/3/$6.00 © 1994 American Institute of Physics

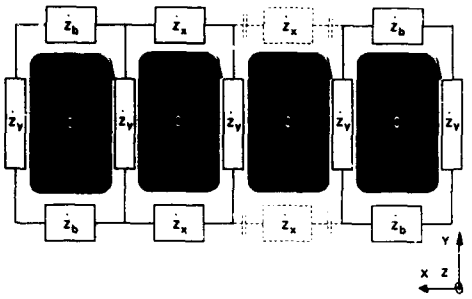

FIG. 2. Equivalent electrical network of the magnetic laminate. $\dot{Z}_y=\rho\cdot l_y/(l_z\cdot l_m)$, $\dot{Z}_b=[\rho\cdot 3\cdot l_m/(l_z\cdot l_y)]-j[2\cdot l_d/(\omega\cdot\epsilon\cdot l_z\cdot l_y)]$ and $\dot{Z}_x=[\rho\cdot 2\cdot l_m/(l_z\cdot l_y)]+j[2\cdot l_d/(\omega\cdot\epsilon\cdot l_z\cdot l_y)]$.

is possible to deduce from Fig. 2 the model can be easily extended to simulate shorting at the film edges.

COMPARATIVE ANALYSIS

Experimental data and responses of the anisotropic effective medium model have been drawn, referring to the plotted values in Ref. 2. While the results provided by the circuit model in Ref. 3 have been reproduced using a custom code developed by the authors. The reliability of the numeric results has been verified, comparing the calculations with the values in Ref. 3. Figures 3–6 show the results of the simulations executed. Both circuit models require the same memory resources and computing power. In addition, they present an equal degree of reliability with respect to the experimental data. The anisotropic effective medium model

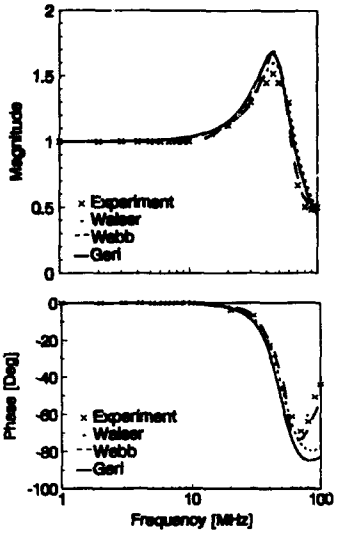

FIG. 4. Permeance resonance (magnitude and phase) for $l_y=3.0\times10^{-3}$ m.

presents more accurate results than the circuit ones. It is able to simulate multiple resonances even if it requires an appreciable time for code regulation and for computations. By partitioning the sample our code runs slower, but, at the same time, the results obtained using this improvement fit the experimental data in a more accurate way. Preliminary analysis, not reported here, provides very hopeful results: we have

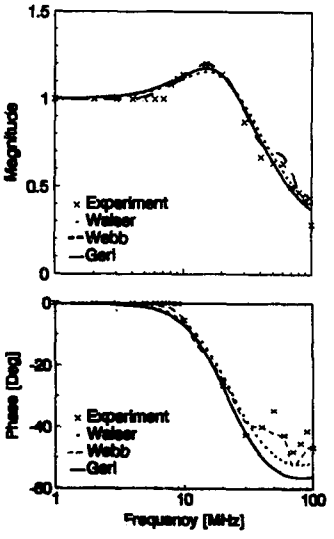

FIG. 3. Permeance resonance (magnitude and phase) for $l_y=2.0\times10^{-3}$ m.

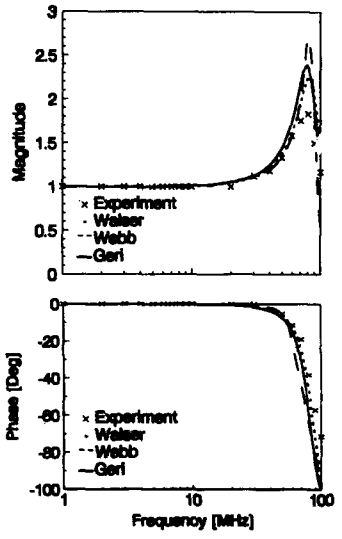

FIG. 5. Permeance resonance (magnitude and phase) for $l_y=5.0\times10^{-3}$ m.

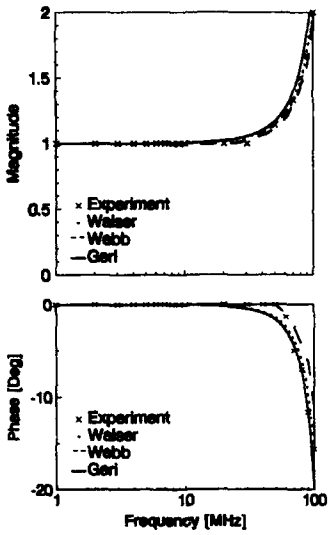

FIG. 6. Permeance resonance (magnitude and phase) for $l_y = 12.0 \times 10^{-3}$ m.

obtained multiple resonances, as in Ref. 2. The discussion about these results will be presented in a future work, after a more accurate test of the model to verify its sensibility to parameter variations.

CONCLUSIONS

The comparative analysis presented in this paper shows that all proposed models are in good agreement with experimental tests. The anisotropic effective medium model provides a best fitting of the measured values, in fact, it is able to simulate multiple resonance phenomena. In spite of this, we think that a circuit approach has the major advantage of being simple to implement in a flexible calculation code able to provide fast and reliable simulations of the magnetic laminates. As last remarks, we underline that our circuit model seems to be more intuitive and easier to implement than the other circuit model.

APPENDIX

The mesh equations are

$$[\dot{Z}_m][\tilde{I}_m]=[\tilde{E}_m], \tag{A1}$$

with $[\tilde{E}_m] = [\tilde{E}_{0_m}] + [\tilde{E}_{i_m}] = [\tilde{E}_{0_m}] - j\omega[A_m][\tilde{I}_m]$; and then

$$\{[\dot{Z}_m]+j\omega[A_m]\}[\tilde{I}_m]=[\tilde{E}_{0_m}], \tag{A2}$$

where $[\tilde{E}_{0_m}]$ are the electromotive forces due to $\tilde{H}_0$, $[\tilde{E}_{i_m}]$ are the electromotive forces induced by displacement eddy currents, $[A_m]$ is a diagonal matrix representative of induced effects. The mean value of the effective complex permeability is given by

$$\frac{\dot{\mu}_{ef}}{\mu_{DC}} = \frac{\tilde{H}_a}{\tilde{H}_0} = \frac{1}{N-1} \sum_{k=1}^{N-1} \left(1 + \frac{\tilde{I}_{m_k}/l_z}{\tilde{H}_0} \right). \tag{A3}$$

For more details about these equations, refer to the discussion proposed in Ref. 4.

[1] B. C. Webb, M. E. Re, M. A. Russak, and C. V. Jahnes, J. Appl. Phys. **68**, 4290 (1990).
[2] J. S. Y. Feng and D. A. Thompson, IEEE Trans. Magn. **MAG-13**, 1521 (1977).
[3] R. M. Walser and A. P. Valanju, IEEE Trans. Magn. **28**, 2280 (1992).
[4] A. Geri, A. Salvini, and G. M. Veca, IEEE Trans. Magn. (in press).

On finite element implementation of impedance boundary conditions

I. D. Mayergoyz
Electrical Engineering Department and Institute for Advanced Computer Studies, University of Maryland, College Park, Maryland 20742

G. Bedrosian
GE Corporate Research and Development, P.O. Box 8, Schenectady, New York 12301

In the paper, impedance boundary conditions are represented in terms of scalar magnetic potential. This leads to a scalar magnetic potential formulation of three-dimensional (3-D) eddy current problems with small skin depths. The scalar potential formulation is then reduced to a weak Galerkin form. The finite element discretization of this form results in two (volume and *surface*) "stiffness" matrices. This approach completely avoids vectorial calculations in 3-D eddy current analysis.

I. INTRODUCTION

Methods for the solution of three-dimensional (3-D) eddy current problems have been the focus of considerable research in past years.[1] It has been gradually realized that different approaches have to be exploited for the problems with very small skin depths and the problems with skin depths comparable to geometric dimensions of conductors. For the latter class of problems, a new iterative technique for computing 3-D eddy currents has been recently suggested.[2] As far as the first class of problems is concerned, the use of impedance boundary conditions has proved to be very attractive. These impedance boundary conditions can be expressed as follows:

$$\mathbf{n}\times\mathbf{E}=Z(\mathbf{n}\times\mathbf{H})\times\mathbf{n}, \tag{1}$$

where $\mathbf{E}$ and $\mathbf{H}$ are phasors of electric and magnetic fields, respectively, $\mathbf{n}$ is a unit vector of outward normal to the conductor boundary, and Z is a surface impedance.

In the case of small skin depths, electromagnetic fields within conductors are closely concentrated near conductor boundaries and can be construed as boundary layers. This suggests that eddy current problems with small skin depths belong to the class of singularly perturbed problems. For this reason, the impedance boundary conditions have long been justified by using the perturbation analysis. This approach can be traced back to the paper of Rytov.[3] The impedance boundary conditions have been widely used in field computations,[1] and their acceptance has reached the point that they are now presented in textbooks.[4]

By using impedance boundary conditions (1), one can completely avoid laborious calculations of electromagnetic fields within conductors. In this way, the 3-D eddy current problems can be reduced to the boundary value problems in regions that are exterior to conductors. The magnetic field in these regions can be characterized in terms of scalar magnetic potential. This makes it very desirable to represent the impedance boundary conditions in terms of the same potential. If this is accomplished, then the entire problem can be reduced to the calculation of scalar magnetic potential, and vectorial computations can be completely avoided. To this end, we shall next discuss the magnetic field formulation of impedance boundary conditions (1).

II. $\tilde{\mathbf{H}}$-FORMULATION OF IMPEDANCE BOUNDARY CONDITIONS

To arrive at this formulation, we introduce orthogonal curvilinear coordinates τ_1, τ_2, and n. These coordinates are such that τ_1- and τ_2-coordinate lines lie on the conductor boundary S, while n-coordinate lines are normal to S. Let $\mathbf{a}_1$, $\mathbf{a}_2$, and $\mathbf{a}_3$ be the triad of orthogonal unit vectors that are tangent to the τ_1-, τ_2-, and n-coordinate lines through any given point P and that form a right-handed set in this order. Also let h_1, h_2, and h_3 be the corresponding metrical coefficients. The introduced curvilinear coordinates will be extensively used in subsequent derivations. However, the final finite element formulation will contain no traces of these coordinates; in this sense it will be coordinate invariant.

By using the introduced curvilinear coordinates, the impedance boundary conditions (1) can be represented as follows:

$$E_{\tau_1}=-ZH_{\tau_2}, \quad E_{\tau_2}=ZH_{\tau_1}. \tag{2}$$

We shall next use the Maxwell equation,

$$\text{curl}\ \mathbf{E}=-j\omega\mu_0\mathbf{H}, \tag{3}$$

whose n component can be written as follows:

$$\frac{1}{h_1h_2}\left(\frac{\partial}{\partial\tau_1}(h_2E_{\tau_2})-\frac{\partial}{\partial\tau_2}(h_1E_{\tau_1})\right)=-j\omega\mu_0H_n. \tag{4}$$

By substituting (2) into (4), we derive

$$-j\omega\mu_0H_n=\frac{1}{h_1h_2}\left(\frac{\partial}{\partial\tau_1}(h_2ZH_{\tau_1})+\frac{\partial}{\partial\tau_2}(h_1ZH_{\tau_2})\right). \tag{5}$$

The last expression is the $\tilde{\mathbf{H}}$-representation of impedance boundary condition (1). To better understand the physical meaning of the right-hand side of (5), we shall need some machinery of the vector field theory on curvilinear surfaces (*manifolds*). This theory has already been used successfully for eddy current analysis.[5,6] To make this paper self-contained and easily readable, we shall present below some selected and relevant facts from this theory.

Consider some vector field $\mathbf{c}$ that is tangential to a curvilinear surface S. We shall next introduce the notion of divergence of vector field $\mathbf{c}$ on S. Consider an arbitrary point P on S and a closed path L on S that contains P. Let $\mathbf{p}$ be a

 0021-8979/94/75(10)/6027/3/$6.00 © 1994 American Institute of Physics

unit vector that is tangential to S and normal to L. Then, the divergence of c on S (i.e., div_S c) is defined as follows:

$$\mathrm{div}_S\,\mathbf{c}=\lim_{\Delta S\to 0}\frac{\oint_L c_\nu\,dl}{\Delta S}, \tag{6}$$

where ΔS is the area enclosed by L.

We shall next derive the expression for div_S c in terms of curvilinear coordinates τ_1 and τ_2. To this end, we consider integration path L formed by infinitesimally small portions of τ_1- and τ_2-coordinate lines (see Fig. 1). These coordinate lines are specified by coordinates τ_2', $\tau_2'+d\tau_2$, τ_1', and $\tau_1'+d\tau_1$, respectively. By using Fig. 1, the path integral in (6) can be evaluated as follows:

$$\oint_V c_\nu\,dl\approx\frac{\partial}{\partial\tau_1}\,(h_2c_{\tau_1})d\tau_1\,d\tau_2 + \frac{\partial}{\partial\tau_2}\,(h_1c_{\tau_2})d\tau_1\,d\tau_2. \tag{7}$$

On the other hand, the area enclosed by L can be evaluated as follows:

$$\Delta S\approx h_1h_2\,d\tau_1\,d\tau_2. \tag{8}$$

By substituting (7) and (8) into (6) and taking into account that expressions (7) and (8) become more and more accurate as ΔS goes to zero, we finally derive

$$\mathrm{div}_S\,\mathbf{c}=\frac{1}{h_1h_2}\left(\frac{\partial}{\partial\tau_1}\,(h_2c_{\tau_1})+\frac{\partial}{\partial\tau_2}\,(h_1c_{\tau_2})\right). \tag{9}$$

By comparing (9) and (5), we can represent the impedance boundary condition (5) in the form

$$H_n=\frac{j}{\omega\mu_0}\,\mathrm{div}_S(Z\mathbf{H}_\tau). \tag{10}$$

This form will be used in the development of finite element formulation. Before proceeding with this formulation, we shall state some other useful facts from the vector field theory on curvilinear manifolds. First, we point out the validity of the "divergence" theorem:

$$\oint_S \mathrm{div}_S\,\mathbf{c}\,dS=0. \tag{11}$$

This theorem can be proved by literally repeating the same line of reasoning that is used in the proof of the divergence theorem in 3-D space.

Then, by using expression (9) and the formula for a gradient of scalar function in curvilinear coordinates, it is easy to establish the following equality:

$$\mathrm{div}_S(\psi\mathbf{c})=\psi\,\mathrm{div}_S\,\mathbf{c}+\mathbf{c}\cdot\mathrm{grad}_S\,\psi. \tag{12}$$

From (11) and (12), we derive

$$\oint_S \psi\,\mathrm{div}_S\,\mathbf{c}\,ds=-\oint_S \mathbf{c}\cdot\mathrm{grad}_S\,\psi\,ds. \tag{13}$$

The last expression will be very instrumental in the forthcoming finite element formulation.

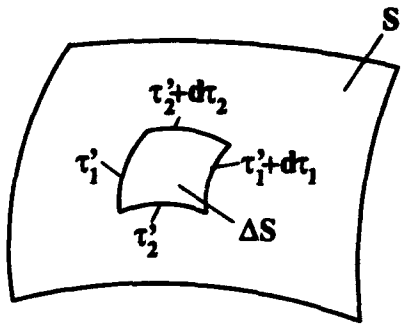

FIG. 1. Graphical illustration for the derivation of the expression for the divergence on curvilinear manifolds.

III. FINITE-ELEMENT FORMULATION

Consider the problem of calculation of 3-D electromagnetic field created by given time-harmonic currents j in coil V^j in the presence of conductor V^+ (see Fig. 2). It is assumed that the skin depth is much smaller than geometric dimensions of V^+. Thus, the impedance boundary conditions can be used on the boundary S of the conductor. The posed problem is a model one. However, the finite element formulation developed for this problem can be easily extended to more complex and realistic situations.

The posed problem can be reduced to the boundary value problem of finding the solution to equations

$$\mathrm{curl}\,\mathbf{H}=\begin{cases}\mathbf{j}, & \text{in } V^j,\\ 0, & \text{in } V^- - V^j,\end{cases} \tag{14}$$

$$\mathrm{div}\,\mathbf{H}=0, \quad \text{in } V^-, \tag{15}$$

subject to the boundary condition

$$H_n=\frac{j}{\omega\mu_0}\,\mathrm{div}_S(Z\mathbf{H}_\tau), \quad \text{on } S. \tag{16}$$

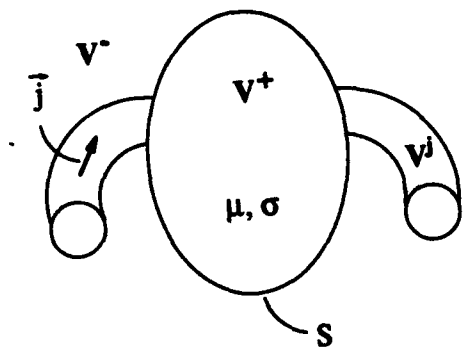

FIG. 2. A 3-D conductor subject to a time-harmonic magnetic field created by currents j.

It is evident from (14) that the magnetic field in V^- can be represented as follows:

$$\mathbf{H}=\mathbf{H}^0-\text{grad}\ \varphi, \tag{17}$$

where $\mathbf{H}^0$ is the magnetic field created by given currents under the assumption that the entire space is uniform and has magnetic permeability μ_0. It is clear that $\mathbf{H}^0$ can be computed by using the Biot–Savart law, although some other (computationally more efficient) choices of $\mathbf{H}^0$ can be developed for complicated current distributions.

By using (17), the boundary value problem (14)–(16) for $\mathbf{H}$ can be reduced to the following boundary value problem for scalar magnetic potential φ:

$$\nabla^2\varphi=0, \quad \text{in } V^-, \tag{18}$$

$$\frac{\partial\varphi}{\partial n}-\frac{j}{\omega\mu_0}\ \text{div}_S(Z\,\text{grad}_S\ \varphi)$$

$$=H_n^0-\frac{j}{\omega\mu_0}\ \text{div}_S(Z\mathbf{H}_\tau^0), \quad \text{on } S. \tag{19}$$

Next, we shall reduce this boundary value problem to the weak Galerkin form. To do this, we employ the Green's formula,

$$\iiint_{V^-}(\psi\nabla^2\varphi+\text{grad}\ \psi\cdot\text{grad}\ \varphi)dV=$$

$$-\oint_S \psi\frac{\partial\varphi}{\partial n}\,dS. \tag{20}$$

In (20), as well as in (19), $\partial/\partial n$ denotes differentiation with respect to inward normal with regard to V^-. By using Eq. (18) and boundary condition (19) in (20), we obtain

$$\iiint_{V^-}\nabla\psi\cdot\nabla\varphi\,dV+\frac{j}{\omega\mu_0}\oint_S \psi\,\text{div}_S(Z\ \text{grad}_S\ \varphi)dS$$

$$=\frac{j}{\omega\mu_0}\oint_S \psi\,\text{div}_S(Z\mathbf{H}_\tau^0)dS-\oint_S \psi H_n^0\,dS. \tag{21}$$

Now, we shall use the expression (13) in order to transform the surface integrals in (21). This leads us to the following weak Galerkin form:

$$\iiint_{V^-}\nabla\psi\cdot\nabla\varphi\,dV-\frac{j}{\omega\mu_0}\oint_S Z\,\nabla_S\psi\cdot\nabla_S\varphi\,dS$$

$$=-\oint_S\left(\psi H_n^0+\frac{j}{\omega\mu_0}\,Z\,\nabla_S\psi\cdot\mathbf{H}_\tau^0\right)ds. \tag{22}$$

If the conductor is homogeneous, then the surface impedance Z is constant along the boundary S, and the weak form (22) can be somewhat simplified:

$$\iiint_{V^-}\nabla\psi\cdot\nabla\varphi\,dV-\frac{jZ}{\omega\mu_0}\iint_S\nabla_S\psi\cdot\nabla_S\varphi\,dS$$

$$=-\oint_S\left(\psi H_n^0+\frac{j}{\omega\mu_0}\,Z\,\nabla_S\psi\cdot\mathbf{H}_\tau^0\right)dS. \tag{23}$$

The weak Galerkin form (23) [as well as (22)] can be used for the derivation of finite element equations. This derivation is quite straightforward and proceeds as follows. We look for the approximate solution in the form

$$\varphi=\sum_{k=1}^{N}\varphi_k\alpha_k, \tag{24}$$

where φ_k are the unknown values of φ in mesh points of some finite element mesh, while α_k are node-based finite element functions. By substituting (24) into (23), and by assuming

$$\psi=\alpha_i \quad (i=1,2,\ldots,N), \tag{25}$$

we end up with the following finite element equation:

$$\sum_{k=1}^{N}\varphi_k\left(\iiint_{V^-}\nabla\alpha_i\cdot\nabla\alpha_k\,dV-\frac{jZ}{\omega\mu_0}\oint_S\nabla_S\alpha_i\cdot\nabla_S\alpha_k\,dS\right)$$

$$=-\oint_S\left(\alpha_i H_n^0+\frac{j}{\omega\mu_0}\,Z\,\nabla_S\alpha_i\cdot\mathbf{H}_\tau^0\right)dS$$

$$(i=1,2,\ldots,N). \tag{26}$$

A remarkable feature of these equations is that the contribution of surface integrals into the overall matrix of finite element equations is very similar in the form to the contribution of volume integrals. For this reason, the submatrix formed by the surface integrals in (26) can be called "surface stiffness matrix." Its assembly will be very similar to the assembly of volume stiffness matrix. This suggests that the numerical implementation of the discussed technique may require very little new software development.

ACKNOWLEDGMENT

This research is supported in part by the U.S. Department of Energy, Engineering Research Program.

[1] S. R. H. Hoole, *Computer Aided Analysis and Design of Electromagnetic Devices* (Elsevier, New York, 1989).
[2] I. D. Mayergoyz and G. Bedrosian, IEEE Trans. Magn. 29, 2335 (1993).
[3] S. M. Rytov, USSR J. Tech. Phys. 10, 2058 (1940).
[4] A. Ishimaru, *Electromagnetic Wave Propagation, Radiation and Scattering* (Prentice–Hall, Englewood Cliffs, NJ, 1991).
[5] J. C. Nedelec, SIAM J. Num. Anal. 15, 580 (1978).
[6] P. R. Kotiuga, IEEE Trans. Magn. 25, 2925 (1989).

Three-dimensional iterative solution for the multiconductor eddy current and free surface calculations

M. Ramadan Ahmed
Faculty of Engineering & Technology in Helwan, Cairo, Egypt

K. F. Ali
Faculty of Engineering in Cairo, Cairo, Egypt

Ibrahim Moustafa
Egyptalum Company in Nag Hammady, Cairo, Egypt

In the three-dimensional (3-D) eddy current calculations, the obtaining of an accurate numerical solution with reasonable size and less computation efforts is still undertaken in many recent articles. Nowadays, such a solution becomes urgently required for designing and developing the electromagnetic confinement application, where the problem is not only 3-D but also involves more than one conducting region having a free boundary that is unknown *a priori*. For this class of applications, the present paper is devoted to discuss the developing of a 3-D iterative solution proposed for the analysis of an electromagnetic continuous casting (EMC) of an aluminum rectangular ingot installed in the Egyptalum Company. This solution is based on a derived 3-D Boundary Element (BE)—Impedance Boundary Condition (IBC) formulation, which leads to a significant reduction in the CPU time and the calculation efforts, as compared to the use of the regular BE formulation. In the present iterative solution, the IBC is applied to the resistively molten aluminum region, while the full BE formulation is used to present the field shaping screen. The validity of this iterative solution is tested by predicting the equilibrium meniscus shape of the free surface for an EMC mold having the size of 1050×280 mm for which experimental measurements for both the meniscus and the total active power supplied are available. Numerical results showing the magnetic flux density distributions over the boundaries of this mold are presented. The corresponding total surface power induced are estimated and compared with the corresponding actual (experimental) values. Also, the meniscus of the molten aluminum free surface is predicted and compared as well.

The basic concept of the electromagnetic casting (EMC) application is that the electromagnetic forces are used to confine a free-standing column of molten metal while a surface layer freezes. The analysis of this application is not a simple one, since, electromagnetically, it is a multiple-conducting regions problem and it cannot be solved unless the shape of the free boundary is reliably known. Very little work has been done to date in the field of simulating this class of problems. Lavers and Ramadan[1,2] introduced a 2-D iterative solution based on a Boundary Element–Impedance Boundary Condition formulation derived for the analysis of an electromagnetic caster producing billets. A variety of numerical results showing the effects of the supply frequency and the location of the electromagnetic screen, in the free space with respect to the induction coil, on the equilibrium free surface shape were presented. Li and Evans[3] presented a 3-D numerical solution based on the Surface Integral technique for the analysis of a CREM caster. The solution relied upon the introduction of imaginary magnetic surface charges to simplify the otherwise complicated calculation of the 3-D electromagnetic fields. Recently, a 3-D Finite Element method has been developed[4] to predict the free surface shape of molten metal in an electromagnetic melting system. This solution was applied to obtain the free surface shape of molten metal in a cold crucible.

In the present paper, a 3-D Boundary Element–Impedance Boundary Condition (BE–IBC) formulation is derived for the analysis of an EMC mold installed in the Egyptalum Company. The surface integral equations appearing in this formulation are given in the form of two-dimensional *Fredholm* integral equation of the second kind. A 3-D iterative solution based on this formulation is developed for the magnetic field calculations, as well as the free surface estimation. Numerical values for the total surface power induced and the corresponding free surface shape are given and discussed. The validity of this solution is tested by comparing these numerical values with the corresponding experimental values.

The basic configuration of the electromagnetic continuous casting considered is schematically illustrated in Fig. 1. It contains an electromagnetic mold, a metal feed system,

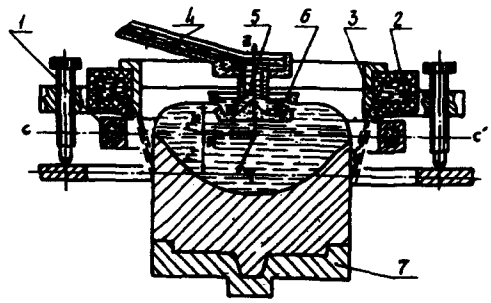

FIG. 1. Basic configuration of the present EMC as follows: (1) the inductor, (2) the ring-shaped cooler, (3) the screen, (4) the melt feed channel, (5) the distribution box, (6) the floating cup, (7) the pan.

 0021-8979/94/75(10)/6030/3/$6.00 © 1994 American Institute of Physics

and a casting machine with a pan. The electromagnetic mold consists of (1) an inductor carrying an alternating current to produce the required time-harmonic magnetic field; (2) a ring-shaped cooler to freeze the wall side of the melt: and (3) a field shaping turn (electromagnetic screen) for correcting the electromagnetic field distributions on the molten metal zone surface. The metal feed system contains (4) a channel through which the melt is fed into the distribution box: (5) a distribution box to control the flow of the melt; and (6) a floating cup for maintaining a constant level for the molten metal surface inside the EMC mold. The pan is usually used to form the bottom portion of the ingot, to stabilize the casting process in the instant of starting, and it is also considered as its support throughout the casting process.

In the last decade, the Boundary Element (BE) technique has been successfully used to obtain an accurate numerical solution for a relatively broad range of eddy current problems. As compared with either the Finite Element (FE) or the Finite Difference (FD), the BE approach has advantages in handling open boundary problems and eddy current applications where detailed field distributions are not required over the entire problem geometry. Also, the implementation of the Impedance Boundary Condition in the BE technique, when electromagnetic penetration depth is shallow wrt the geometry dimensions, will significantly reduce the computation time and the calculation efforts. Finally, the main advantage, though, is the ease with which the Integral Equation formulation then lends itself to numerical treatment.

In the present paper, a 3-D Boundary Element (BE)–Impedance Boundary Condition (IBC) formulation is derived for the free surface shape and magnetic field calculations of the EMC mold considered. In this formulation, the IBC is applied to the resistively molten aluminum region, where the electromagnetic penetration depth is shallow, while the full BE formulation is used to present the field shaping turn. The resulting BE–IBC formulation is obtained as follows:

$$\tfrac{1}{2}\mathbf{H}_m(\xi)\cdot\hat{\mathbf{c}}=\mathbf{H}_m^i(\xi)\cdot\mathbf{c}+\left(L_{m\Omega^-}^{(1)}\cdot\mathbf{H}_m(\eta)+\frac{Z_{Sm}}{Z_{\Omega^-}}\,L_{m\Omega^-}^{(2)}\cdot[\hat{\mathbf{n}}_\eta\times\mathbf{H}((\eta))]\right)+\frac{1}{Z_{\Omega^-}}\,L_{s\Omega^-}^{(2)}\cdot\tilde{E}_s(\eta)+L_{s\Omega^-}^{(1)}\cdot\mathbf{H}_s(\eta),\tag{1}$$

$$\mathbf{E}_s(\xi)\cdot\hat{\mathbf{c}}=\frac{2Y_{\Omega^-}}{Y_s+Y_{\Omega^-}}\,\mathbf{E}_s^i(\xi)\cdot\hat{\mathbf{c}}+\frac{2}{Y_s+Y_{\Omega^-}}\{Z_{Sm}Y_{\Omega^-}\cdot L_{m\Omega^-}^{(1)}\cdot\times[\mathbf{n}_m\times\mathbf{H}_m(\tilde{\eta})]+[L_{m\Omega^-}^{(2)}\cdot\mathbf{H}_m(\eta)]\}-\frac{2}{Y_s+Y_{\Omega^-}}\,(Y_sL_s^{(1)}-Y_{\Omega^-}L_{s\Omega^-}^{(1)})\mathbf{E}_s(\eta)-\frac{2}{Y_s+Y_{\Omega^-}}\,(L_s^{(2)}-L_{s\Omega^-}^{(2)})\mathbf{H}_s(\eta),\tag{2}$$

$$\mathbf{H}_s(\xi)\cdot\hat{\mathbf{c}}=\frac{2Z_{\Omega^-}}{Z_s+Z_{\Omega^-}}\,\mathbf{H}_s^i(\xi)\cdot\hat{\mathbf{c}}+\frac{2}{Z_s+Z_{\Omega^-}}\left(\frac{Z_{Sm}}{Z_{\Omega^-}}\,L_{m\Omega^-}^{(2)}\cdot[\mathbf{n}_m\times\mathbf{H}_m(\eta)]+L_{m\Omega^-}^{(1)}\cdot\mathbf{H}_m(\eta)\right)-\frac{2}{Z_s+Z_{\Omega^-}}\,(L_s^{(2)}-L_{s\Omega^-}^{(2)})\mathbf{E}_s(\eta)-\frac{2}{Z_s+Z_{\Omega^-}}\,(Z_sL_s^{(1)}-Z_{\Omega^-}L_{s\Omega^-}^{(1)})\mathbf{H}_s(\eta),\tag{3}$$

where the subscripts m and s stand for the aluminum and the field shaping turn regions, respectively, the superscript i stands for the incident values of H or E, the free space region is denoted by Ω-, $\tilde{\xi}$ and $\tilde{\eta}$ are position vectors at the observation and integration points, respectively, $\hat{c}$ is an arbitrary unit vector, and the integral operators are defined in terms of the vector Green's function $\tilde{G}$ as

$$L^{(1)}\mathbf{U}(\eta)=\int_s\{[\hat{\mathbf{n}}_\eta\times\mathbf{U}(\eta)]\cdot[\nabla_\eta\times\mathbf{G}(\xi,\eta)]\}ds_\eta$$

$$L^{(2)}U(\eta)=\int_s\{[\hat{\mathbf{n}}_\eta\times\mathbf{U}(\eta)]\cdot[\tilde{\nabla}_\eta\times\tilde{\nabla}\times\mathbf{G}(\xi,\eta)]\}ds_\eta.$$

Also, the parameters shown in these equations are defined as $Z=j\omega\mu$ and $Y=\delta-j\omega\epsilon$, while the surface impedance is defined as $Z_s=\omega\mu\delta(1-j)/2$.

As is well known, the shape of the free surface is governed primarily by the balance of the EM pressures against pressures due to gravity.[1,2] Therefore, at each point on the free surface, the equilibrium equation may be summarized as

$$P_m=\gamma gh,$$

where γ is the molten aluminum density, g is the gravitational force, h is the static head, and P_m is the EM pressure, which can be defined as

$$P_m=\frac{\mu}{4}\,(H_u^2+H_v^2).$$

This pressure can support a static head (e.g., as in a confinement application), but cannot do work (e.g., as in stirring the molten metal). It is important to note that in the round mold, the stirring force also contributes to the total electromagnetic pressure when the electromagnetic penetration depth is large relatively to the conductor dimensions; i.e., when there is full penetration of the magnetic flux.

As is well known, the shape of the meniscus has to be computed iteratively for the present EMC mold. For this purpose, an iterative procedure, based on the 3-D BE–IBC for-

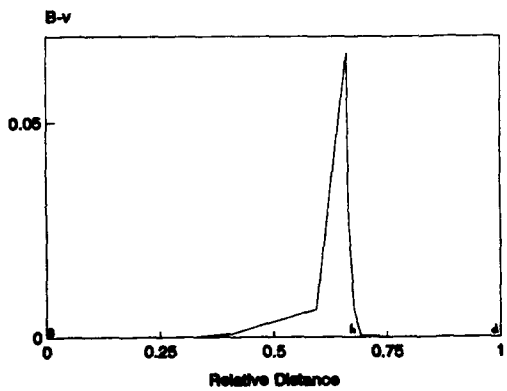

FIG. 2. The flux density distribution along the YZ contour.

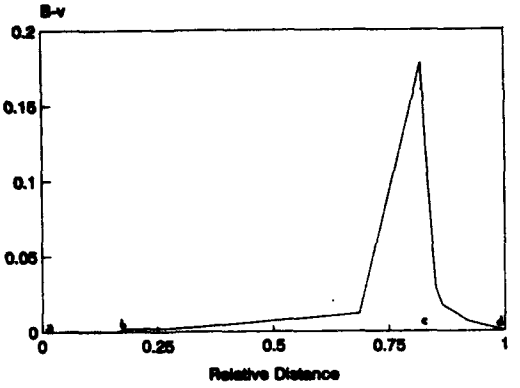

FIG. 3. The flux density distribution along the XZ contour.

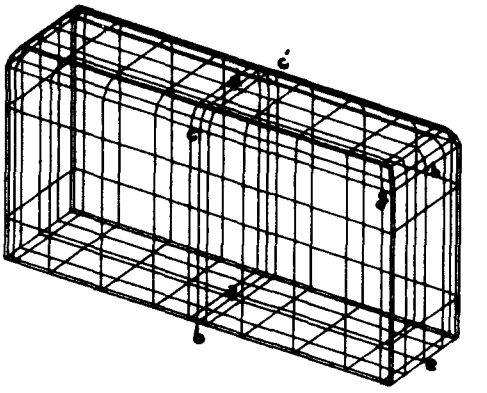

FIG. 5. The estimated ingot shape of the mold.

mulation, was developed. This procedure is applied to estimate the resulting free surface shape as well as the corresponding magnetic flux distributions and the total surface power induced over the boundaries of the EMC mold considered in Fig. 1.

In the present solution, the effect of the surface tension is neglected, where its value is comparably very small with respect to the resulting EM pressure value. The induction coil is supplied with an AC current of 13 500 at 1975 Hz. The casting ingot is dimensioned as 1050×280 mm and the electrical conductivity of the different parts are valued as follows: The melt region: $0.406\times10^{7}/\Omega$m; the ingot region: $0.12\times10^{8}/\Omega$m; the screen region: $0.1333\times10^{7}/\Omega$m.

The z component of the flux density distributions are predicted for the present EMC mold. The numerical results obtained are plotted on three different planes shown in Fig. 5 as the YZ plane, the XZ plane, and the Z plane, which are defined by the contours $aehd$, $abcd$, and cgh, respectively. Figures 2–4 show the flux density on these different planes.

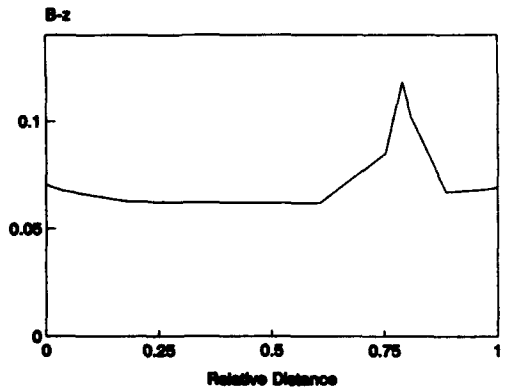

FIG. 4. The flux density distribution along the Z contour.

Figures 2 and 3 show that the peak value of the magnetic flux density, in the presence of the field shaping turn, still occurred at the center of the inductor, because the lower tip of this turn was placed at 5 mm above the center of the inductor. Figure 4 shows that the magnetic flux density at the sharp edge is comparably larger than its value at either sides of the ingot. The estimated free surface shape for this mold is shown in Fig. 5. It was found that four iterations were required to obtain the final meniscus shape. The height of the meniscus and the radius of curvature were 55 and 26 mm, compared with the corresponding measured values of 50 and 25 mm, respectively. Finally, the supplied total active power was calculated for the different parts of this mold and distributed as follows: Ingot and screen (calculated): 046.00 kW; inductor (calculated): 019.67 kW; transformer (calculated): 006.00 kW (copper only); and total: 071.70 kW. The total active power measured in the company for this parts was 76.5 kW.

A 3-D iterative solution was developed for the analysis of an electromagnetic caster producing an aluminum ingot of rectangular cross section. This solution was used for the magnetic field and free surface shape calculations of an EMC mold installed in the Egyptalum Company. The validity of this solution was tested by predicting the free surface shape and the corresponding numerical values for the total active power of this mold for which actual (experimental) values were available. The comparison between the predicted values and the corresponding experimental values showed that the accuracy of the solution is very satisfactory.

[1] J. D. Lavers and M. Ramadan Ahmed, "Mathematical modeling of electromagnetic confinement," *Casting of Near Net Shape Products*, The Metallurgical Society, 1988 pp. 395–410.
[2] M. Ramadn Ahmed and J. D. Lavers, "Boundary element analysis of the electromagnet casting mould," IEEE Trans. Magn. 25, 2843–2845, (1989).
[3] B. Q. Li and J. W. Evans, "Three-dimensional calculation of fields in electromagnetic casters," in Ref. 1, pp. 411–421.
[4] Y. Kawase, T. Yamaguchi, and N. Hayashi, "3D finite element analysis for molten metal shapes in an electromagnetic melting system," IEEE Trans. Magn. 29, (1993).

Modeling and analysis of electric and magnetic coupled problems under nonlinear conditions

A. Geri, M. La Rosa, and G. M. Veca
Dipartimento di Ingegneria Elettrica, Università di Roma, "La Sapienza" Via Eudossiana n. 18-00184 Roma, Italy

In this paper the authors define a numerical method to solve nonlinear combined magnetic and electric problems using reliable general purpose calculation codes. This method has been applied to analyze the behavior of a busbar system built with a saturable steel enclosure and connected with an arbitrary external circuit. The enclosure magnetic characteristics have been determined by means of experimental tests executed by the authors. To analyze this electrical system, the skin and proximity effects in the massive conductors, as well as the load conditions of the external circuit, must be taken into account. The present formulation permits us to solve the previously described coupled problems by means of an iterative procedure. Using this technique, it is possible to solve separately the field and the circuit equations by means of specific codes. In particular, an iterative procedure it is pointed out so defined: for each estimated load condition, a finite element code has been used to evaluate the relating busbar cross parameters, taking into account the nonlinear behavior of the steel enclosure, while, for each assigned set of the busbar cross parameters, a circuit simulator has been used to determine the relating load conditions of the busbar. In addition, a specialized post-processor has been developed to manage the data flow between the calculation codes. The originality of this work is linked to the use of general purpose commercial software to solve the nonlinear magnetic and electric coupled problems.

INTRODUCTION

In modern industrial electric plants, the qualification of economy and flexibility are becoming more and more important. This circumstance often leads to the use of busbar systems for supplying machine tools and nonlinear discontinuous devices, with severe electrical peak inputs, such as spot-welding machines. In order to verify the capability of busbar lines to supply loads, limiting the electromagnetic effects due to peak current, it is necessary to point out a method to solve the nonlinear electric and magnetic coupled problem.[1–10] We have approached this problem using an iterative procedure that solves separately the circuit equations and the field ones. The relating field and circuit solvers are fully independent, and specialized post-processors are needed in order to manage data files. This approach is based on the idea to represent each massive bar as a series branch, including a time varying ideal voltage generator linked to the Ohm's resistance of the conductor. The voltage generator represents all induced electromagnetic effects. The transient nonlinear behavior of busbar system starts estimating, by means of a network analysis, the voltage gradients in each conductor for null induced effects. These values are the initial conditions for finite element analysis (FEA). The field equations used in this work derive from those of Maxwell, for the case of a homogeneous material. In a two-dimensional (2-D) system and neglecting electromagnetic propagation phenomena, these relationships lead to the following equation:

$$\nabla\times(\nu\nabla\times\mathbf{A})=\mathbf{J}. \tag{1}$$

Using the "Coulomb gauge," $\nabla\cdot\mathbf{A}=0$, Eq. (1) becomes

$$-(\nabla\cdot\nu\nabla)\mathbf{A}=\mathbf{J}, \tag{2}$$

which can be rewritten as

$$-(\nabla\cdot\nu\nabla)\mathbf{A}+\sigma\nabla\cdot V+\sigma\frac{\partial\mathbf{A}}{\partial t}=0. \tag{3}$$

Imposing the estimated set of voltage gradient values, we have solved Eq. (3) by means of a FEA. Then, using an appropriated post-processor, we have evaluated the induced electromotive force (EMF) on the kth conductor as follows:

$$e_k=-\frac{l_k}{S_k}\int_{S_k}\frac{\partial\mathbf{A}}{\partial t}\,dS, \tag{4}$$

where l_k and S_k are, respectively, the length and the cross section of the conductor. From these values, it is possible to evaluate the voltage gradients for successive attempts using a circuit analysis. The FEA is restarted for each voltage gradient updating, until a fixed accuracy is reached. Then a subsequent time instant can be processed (see Fig. 1).

FIELD ANALYSIS

The field analysis refers to a busbar line with a saturable steel enclosure. The cross section of this system is shown in Fig. 2. The line electromagnetic field can be determined by solving an open boundary 2-D symmetrical problem. In order to do that the 2-D domain, corresponding to the busbar cross section and to its surrounding region, is divided in two subdomains (see Fig. 3): a central one, that is shaped by means of ordinary finite elements (FEs); and a peripheral one, that is framed by infinite boundary elements (IBEs).[12–14] This system can be studied by means of the ANSYS FEA software, using load conditions defined by external circuit (voltage gradients) and taking into account skin and proximity effects in massive conductors. The nonlinear magnetic characteristic of a busbar steel enclosure are defined by means of the first magnetization curve. Numerically,

 0021-8979/94/75(10)/6033/3/$6.00 © 1994 American Institute of Physics

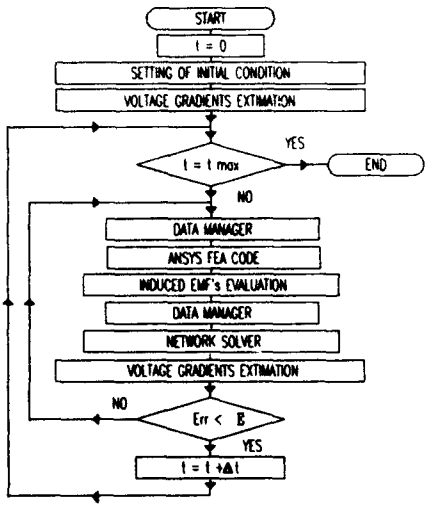

FIG. 1. Flow chart of the proposed procedure.

the nonlinear field problem is solved by means of the Newmark method, which is applied using the Newton–Raphson iterative procedure.[12]

CIRCUIT MODEL

The voltage gradients in each massive conductor can be estimated by means of a generic circuit simulator, such as SPICE (Simulation Program with Integrated Circuit Emphasis) or EMTP (ElectroMagnetic Transient Program). This is used to analyze the equivalent electrical network for the FEA fixed induced effects. For many simple circuit configurations, it is enough to use the ANSYS parametric design language (APDL) in order to simulate the electrical network using traditional algorithms.[11] The line-to-line or line-to-ground parameters can be included, if it is requested that their influence be evaluated. This can occur, for example, if one desires to analyze the system behavior during a fast transient.

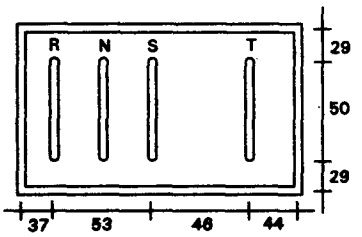

FIG. 2. Sketch of the busbar line cross section under analysis (dimensions in mm).

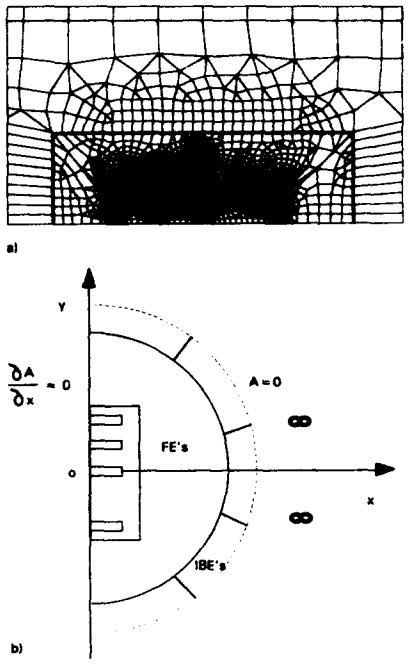

FIG. 3. Central region mesh near (a) the busbar system and (b) global arrangement used for FEA.

A DEMONSTRATIVE EXAMPLE

In order to show a numerical application of the described approach, the authors have used a typical industrial situation. In particular, we have studied the network in Fig. 4(a) during early time instants after welding firing. The one phase spot-welding machine is represented as an ideal EMF generator, because its supply voltage is controlled in order to generate a certain thermal power in the welding point. The connection

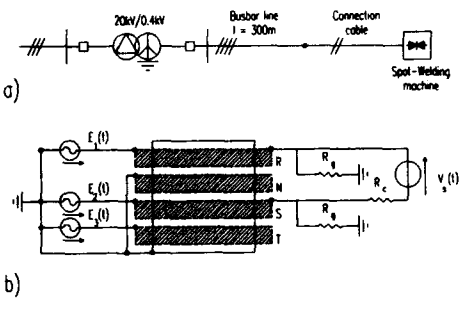

FIG. 4. Industrial plan under (a) analysis and (b) its equivalent electrical network, (b) where $R_c = 40 \times 10^{-5}$ Ω, $R_g = 1 \times 10^4$ Ω, $E_1 = 311.27 \sin(314.16 \cdot t - 2.62)$ (V), $E_2 = 311.27 \cdot \sin(314.16 \cdot t - 0.52)$ (V), and $V_s = 8267.71 \cdot (t + 0.04) \cdot \sin(314.16 \cdot t)[1(t) - 1(t - 0.1)]$ (V).

TABLE I. Geometrical and electrical data.

Section conductivity	Phase = 300 mm² Steel = 0.172 μΩ m	Neutral = 220 mm² Copper = 0.018 μΩ m	Enclosure = 650 mm²
H (As/m)	300	600	780	900	1200	1560	2280	2580	3000
B (T)	0.118	0.313	0.420	0.482	0.604	0.719	0.850	0.882	0.921

cable is linked between two phase bars and it can be represented by its resistance. This supply connection is required when the welding machine needs phase-to-phase voltage, even if a neutral conductor is available. The busbar line is in Fig. 2. A certain strain line-to-ground resistance will be represented by means of lumped resistors at the line load end. In this study we consider the supply network being an upstream transformer as an ideal 380 V three-phase system, while the line switch is regarded to be closed and ideal. With the above assumptions, the network in Fig. 4(a) is represented by the scheme in Fig. 4(b), where $E_1(t)$, $E_2(t)$, and $E_3(t)$ are sinusoidal EMFs, while $V_s(t)$ has been represented by a modulated amplitude sinusoid to take into account its dependence by the welding controller. Initial conditions are evaluated considering a rest state for the network and for the FEA model. Table I summarized the typical numerical values for the simulated industrial configuration. The system analysis is started at a zero passage of welding machine supply voltage. The computed load current is in Fig. 5, and it shows a good agreement with industrial reserved experimental data referred to similar configurations.

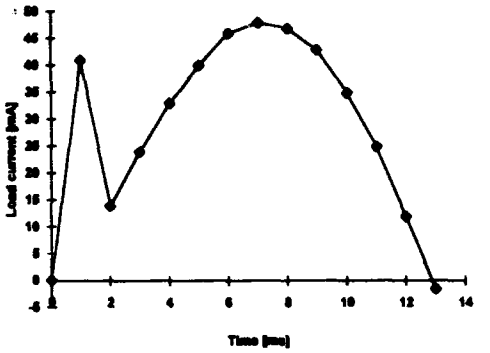

FIG. 5. Computed load current during the early 13 ms after welding machine firing.

CONCLUSIONS

This work has shown that the ANSYS industrial FEA code can be integrated usefully with network solvers, in order to analyze nonlinear systems. For industrial designers that are requested to front ever and ever new problems in short times, it is indispensable that FEA and network analysis software are very unfailing and flexible. The proposed approach permits to use general purpose codes, for different analysis phases. This circumstance makes the method easy to apply, even in an industrial context, where there is not a real interest to develop a specific and unfailing software for each particular problem.

[1] J. R. Brauer, IEEE Trans. Magn. **MAG-18**, 504 (1982).
[2] T. H. Fawzi, P. E. Burke, and T. C. H. Lau, IEEE Trans. Magn. **MAG-18**, 1061 (1982).
[3] P. Belforte, M. Chiampi, and M. Tartaglia, IEEE Trans. Magn. **MAG-21**, 2284 (1985).
[4] A. Konrad, IEEE Trans. Magn. **MAG-18**, 284 (1992).
[5] F. Piriou and A. Razek, IEEE Trans. Magn. **28**, 1295 (1992).
[6] I. A. Tsukerman, A. Konrad, and J. D. Lavers, IEEE Trans. Magn. **28**, 1299 (1992).
[7] P. Lombard and G. Meunier, IEEE Trans. Magn. **28**, 1291 (1992).
[8] I. A. Tsukerman, A. Konrad, G. Meunier, and J. C. Sabonnadière, IEEE Trans. Magn. **29**, 1701 (1993).
[9] A. Nicolet, F. Delincé, N. Bamps, A. Genon, and W. Legros, IEEE Trans. Magn. **29**, 1697 (1993).
[10] P. Lombard and G. Meunier, IEEE Trans. Magn. **29**, 1737 (1993).
[11] L. O. Chua and P. M. Lin, *Computer-Aided Analysis of Electronic Circuits* (Prentice-Hall, Inc., Englewood Cliffs, NJ, 1975).
[12] ANSYS, User's manual, Revision 4.4a, Swanson Analysis System, Inc.
[13] O. C. Zienkiewics, D. W. Kelley, and P. Bettes, Int. J. Num. Methods **11**, 355 (1977).
[14] Y. Kagawa, T. Yamabuchi, and S. Kitagami, "Infinite boundary element and its application to a combined finite-boundary element technique for unbounded field problems," *Boundary Elements VII* (Springer, New York, 1986).

Transformation methods in computational electromagnetism

A. Nicolet, J.-F. Remacle, B. Meys, A. Genon, and W. Legros
University of Liège Service d'Electricité Appliquée, Institut Montefiore—Sart Tilman Bât.B28 B-4000 Liège, Belgium

The representation of electromagnetic quantities by differential forms allows the use of nonorthogonal coordinate systems. A judicious choice of coordinate system facilitates the finite element modeling of infinite or very thin domains.

DIFFERENTIAL GEOMETRY

Because of the propagation of electromagnetic fields in free space (or in the air), electromagnetic problems are often open, i.e., characterized by the decay of the fields at infinity, the opposite to closed problems with boundary conditions at a finite distance. As the finite element computations can only involve a finite number of degrees of freedom, various methods have been proposed to overcome this difficulty. One of the most interesting ones is the transformation method: the infinite domain is transformed into a finite one used for the discretization and the resolution.[1] The problem has then to be formulated in this domain, where the coordinate system is not orthogonal. The differential geometry allows the use of any coordinate system and is the right tool to formulate the method clearly in a general way.

From a differential geometric point of view,[2–5] the vectors are the first-order linear differential operators on functions. They have a vector space structure, one basis of which is the set $\{\partial/\partial x^i\}$ of partial derivatives with respect to coordinates. The action of a vector v on a function f is noted $v(f)$. A 1-form α is a linear map from vectors v to real numbers $\alpha(v)$ (also noted $\langle\alpha,v\rangle$ to emphasize duality). A special 1-form associated to a function f is its differential df, defined such that $df(v)=v(f)$. One basis for the vector space of 1-forms is the set $\{dx^i\}$ of the differentials of the coordinates. A p-form ω is a multilinear totally skew symmetric map from p vectors $v_1,\ldots,v_p$ to real numbers $\omega(v_1,\ldots,v_p)$. Functions are identified with 0-forms. In three-space only 0-, 1-, 2-, and 3-forms are not identically equal to zero (because of skew symmetry). The 0- and 3-form spaces are one-dimensional vector spaces, while 1- and 2-forms are three-dimensional vector spaces. From this point of view, scalar from vector analysis are 0- or 3-forms, depending on their physical meaning: 0-forms are pointwise relevant functions, while 3-forms are densities to be integrated on volumes. The "vectors" from the vector analysis are 1-forms and 2-forms: 1-forms are integrands of line integrals, while 2-forms are flux densities. Operations on forms include the following.

(i) The exterior or wedge product $\wedge$ that maps pairs of a p-form ω_1 and a q-form ω_2 on the $(p+q)$-form $\omega_1\wedge\omega_2$, defined by

$$(\omega_1\wedge\omega_2)(v_1,\ldots,v_{p+q}) = \frac{1}{p!q!}\sum_{\pi\in S_{p+q}}[\mathrm{Sgn}(\pi)\omega_1(v_{\pi(1)},\ldots,v_{\pi(p)}) \times\omega_2(v_{\pi(p+1)},\ldots,v_{\pi(p+q)})], \quad (1)$$

where π runs over the set of permutations of $p+q$ indices. The set $\{dx^{i_1}\wedge\cdots\wedge dx^{i_p}\}$ of the linearly independent exterior products of p differentials of the coordinates is a basis for the $n!/[p!(n-p)!]$-dimensional vector space of p-forms. Any p-form can be expressed as a linear combination of such p-monomials.

(ii) The exterior derivative d that maps p-forms,

$$\omega=\frac{1}{p!}\sum_{i_1\cdots i_p=1}^{n}\omega_{i_1\cdots i_p}\,dx^{i_1}\wedge\cdots\wedge dx^{i_p}$$

on $(p+1)$-forms,

$$d\omega=\frac{1}{p!}\sum_{i_1\cdots i_p=1}^{n}(d\omega_{i_1\cdots i_p})\wedge dx^{i_1}\wedge\cdots\wedge dx^{i_p}.$$

From this definition it is obvious that the exterior derivative of a function is its differential df.

(iii) the integration of an n-form $\omega=f(x^1\cdots x^n)dx^1\wedge\cdots\wedge dx^n$ on a n-dimensional domain M is defined by

$$\int_M\omega=\int_{R^n}f(x^1\cdots x^n)dx^1\cdots dx^n, \quad (2)$$

where f is supposed to be zero outside M.

These objects and operations only involve the topology and the differential structure of the ambient space, i.e., they are independent of any notion of angle and/or distance. Those notions are introduced by giving a metric g, i.e., a symmetric bilinear map from two vectors v,w to real numbers $g(v,w)$. The metric allows the definition of the Hodge star operator $\star$, which maps p-forms on $(n-p)$-forms, where n is the dimension of the ambient space. In local coordinates, the star operator is defined for an exterior p-monomial by (using the Einstein summation convention on repeated indices)

$$\star dx^{i_1}\wedge\cdots\wedge dx^{i_p}=g^{i_1j_1}\cdots g^{i_pj_p}\,dx^{j_{p+1}}\wedge\cdots \wedge dx^{j_n}\,\epsilon_{j_1\cdots j_n}\frac{\sqrt{|g|}}{(n-p)!}, \quad (3)$$

where $\epsilon_{j_1\cdots j_n}$ is the Levi–Civita symbol. If the matrix, the elements of which are $g_{ij}=g(\partial/\partial x^i,\partial/\partial x^j)$ is considered, the g^{ij} are the components of its inverse and $g=\det(g_{ij})$ is its determinant. By linearity, the definition of the star operator may be extended to any form. In three-space, the Hodge star operator maps 0-forms on 3-forms, 1-forms on 2-forms, and conversely. This is why only functions and "vectors" are used in the vector analysis of the three-space with the Euclidean metric.

 0021-8979/94/75(10)/6036/3/$6.00 © 1994 American Institute of Physics

The interesting property of differential forms is their behavior under the mapping of domains. If ϕ is a differential map from a domain M to a domain N, a function f on N is mapped (pulled back) on a function $\phi^*(f)=f\circ\phi$ on M by composition with ϕ. Vectors on M are mapped (pushed forward) on vectors on N by considering their action on pulled-back functions. Since a vector v on M maps the pulled-back functions $\phi^*(f)$ to numbers $v[\phi^*(f)]$, it defines a linear differential operator for the functions f on N, i.e., a vector $\phi_*(v)$ on N, whose action on a function f on N is given by $\phi_*(v)(f)=v[\phi^*(f)]$. A 1-form on N is mapped (pulled back) on M by considering its action on pushed-forward vectors from M to N. The pull-back $\phi^*(\alpha)$ on M of a 1-form α on N is defined by $\langle\phi^*(\alpha),v\rangle=\langle\alpha,\phi_*(v)\rangle$. Any purely covariant object such as a p-form or the metric can be pulled back from M to N by the following definitions, for a p-form $\phi^*(\omega)(v_1,\ldots,v_p)=\omega[\phi_*(v_1),\ldots,\phi_*(v_p)]$, and for the metric $\phi^*(g)(v_1,v_2)=g[\phi_*(v_1),\phi_*(v_2)]$. As g allows the definition of the star operator $\star_g$ on N, $\phi^*(g)$ allows the definition of the star operator $\star_{\phi^*(g)}$ on M. In the preceding definitions, it is important to remark how the duality reverses maps leading to an alternation of push-forward and pull-back maps for the domains, the functions, the vectors, and the forms. The fundamental point for the setting of transformation methods is that the operations on forms previously defined commute with the pull-back. For forms α,β, one has

$$\phi^*(\alpha\wedge\beta)=\phi^*(\alpha)\wedge\phi^*(\beta), \tag{4}$$

$$\phi^*(d\alpha)=d\phi^*(\alpha), \tag{5}$$

$$\int_M\phi^*(\alpha)=\int_{N=\phi(M)}\alpha, \tag{6}$$

$$\star_{\phi^*(g)}\phi^*(\alpha)=\phi^*(\star_g\alpha). \tag{7}$$

The electromagnetic fields and sources may be represented by differential forms: the magnetic field H and the electric field E are 1-forms; the magnetic flux density B, the electric flux density D, and the current density J are 2-forms; and the charge density ρ is a 3-form. In this representation, Maxwell's equations are $dH=J+\partial_t D$, $dE=-\partial_t B$, $dB=0$, and $dD=\rho$, where ∂_t is for partial derivation with respect to time. The 1-form A and the 0-form V may be introduced as potentials, such that $B=dA$ and $E=-\partial_t A-dV$. All those equations are obviously independent of the metric. Nevertheless, this one is involved in the definition of the constitutive relations: the free space electromagnetic characteristics are, with $c=1$, $\mu_0=1$, and $\epsilon_0=1$, given by $D=\star E$ and $B=\star H$.

FINITE ELEMENTS AND TRANSFORMATION METHOD

In order to set up the finite element method, a variational form is introduced. For example, the magnetostatic Lagrangian is given by the integration of the 3-form L, the magnetostatic Lagrangian density, on the domain M^4 (the coefficient ν is the magnetic reluctivity):

$$\int_M L(A)=\int_M\left(-\frac{1}{2}\ dA\wedge\nu\star dA-A\wedge J\right). \tag{8}$$

The finite element method consists of approximating A by $\underline{A}=\Sigma A_i\omega_i$, where A_i are parameters and ω_i are 1-forms corresponding to "shape functions" obtained by assuming a simple behavior on elements from a meshing of M. The current density J is approximated by $\underline{J}=\Sigma J_i\star\omega_i$.

The equations for the parameters are found by expressing the extremum conditions for the discretized Lagrangian:

$$\frac{\partial}{\partial A_i}\int_M L(\underline{A})=0. \tag{9}$$

The first term of $L(\underline{A})$ leads to terms in the finite element equations, such that the unknowns are the A_j and the coefficients a_{ij} are the integrals of the discrete 3-forms $(-\nu/2)$ $d\omega_i\wedge\star d\omega_j$ on the elements. If a domain M^* is mapped on the domain M, the forms and the metric on M may be pulled-back on M^*, and the formulation of the problem on M^* is immediate. The transformation method is thus the following one: map the "transformed domain" M^* on the original domain M (and not the opposite!), pull-back the Lagrangian and apply the finite element method with the elements obtained by meshing M^*. It does not matter if the transformed domain no longer fits the geometry because it has only to be connected topologically with the rest of the problem.

In the case of a two-dimensional magnetostatic problem, invariant by translation along the z axis, the vector potential is the 1-form $A(x,y)dz$, and the geometry is described by its trace on the x-y plane. The shape 1-forms are $\omega_i=\alpha_i(x,y)dz$, where $\alpha_i(x,y)$ are the classical shape functions and $\star\omega_i=\alpha_i(x,y)\star dz=\alpha_i(x,y)dx\wedge dy$. With these Cartesian coordinates, it gives exactly the traditional method. The mapping of a domain M^* with coordinates $\{X,Y\}$ on the original domain M with coordinates $\{x,y\}$ is given by two functions, such that $\{X,Y\}\rightarrow\{x,y\}=\{f_1(X,Y),f_2(X,Y)\}$. The contribution of an element to the coefficient a_{ij} of A_j in the ith equation is the integral on the element of

$$-\nu\ (\partial_X\alpha_i\ \partial_Y\alpha_i)$$

$$\times\begin{bmatrix}\dfrac{\partial_Y f_1{}^2+\partial_Y f_2{}^2}{\partial_X f_1\,\partial_Y f_2-\partial_X f_2\,\partial_Y f_1} & -\dfrac{\partial_X f_1\,\partial_Y f_1+\partial_X f_2\,\partial_Y f_2}{\partial_X f_1\,\partial_Y f_2-\partial_X f_2\,\partial_Y f_1}\\ -\dfrac{\partial_X f_1\,\partial_Y f_1+\partial_X f_2\,\partial_Y f_2}{\partial_X f_1\,\partial_Y f_2-\partial_X f_2\,\partial_Y f_1} & \dfrac{\partial_X f_1{}^2+\partial_\lambda f_2{}^2}{\partial_X f_1\,\partial_Y f_2-\partial_X f_2\,\partial_Y f_1}\end{bmatrix}$$

$$\times\begin{pmatrix}\partial_X\alpha_j\\ \partial_Y\alpha_j\end{pmatrix}, \tag{10}$$

where ∂_X and ∂_Y indicate the partial derivative with respect to X and Y, respectively, and $\alpha_i(X,Y)$, $\alpha_j(X,Y)$ are the shape functions on the transformed element. This contribution of the transformed element is equal to the nontransformed one up to the central matrix. If the transformation is trivial $[f_1(X,Y)=X, f_2(X,Y)=Y]$ or corresponds to a conformal transformation $[f_1(X,Y)+if_2(X,Y)$ is analytic, i.e., $\partial_x f_1=\partial_y f_2$ and $\partial_x f_2=-\partial_y f_1]$, this matrix reduces to the unit matrix. As for the term involving the current density, the contribution to the ith equation of an element is the product of J_j by the integral of $\omega_i\wedge\star\omega_j=\alpha_i\alpha_j\theta$ on the element. θ is

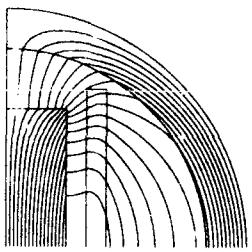

FIG. 1. Modeling of an infinite domain mapped on a corona.

the volume form associated to the metric, i.e., $*1=\theta=(\partial_X f_1\ \partial_Y f_2-\partial_X f_2\ \partial_Y f_1)dX\wedge dY$ and the integral transforms simply according to the formula for the change of coordinates in multiple integrals.

In the three-dimensional case, a family of discrete forms are the Whitney forms on tetrahedra.[6] They correspond to nodal elements for 0-forms (e.g., scalar magnetic potential ϕ) and to edge elements for 1-forms (e.g., A or H). Using such discretizations entirely based on differential forms allows a straightforward formulation of transformation methods by pull-back of the corresponding discrete Lagrangian density or weighted residuals.

NUMERICAL EXAMPLES

Infinite domain: The most obvious application of the transformation method is the case of open boundary problems. In the present example, the magnetic field around a coil with a ferromagnetic kernel is computed. A fictitious circular boundary of radius A is defined around the problem and the outside of this circle constitutes an infinite domain. The method consists of mapping a corona M^* on M.[1] The corona, a finite domain, has an inner radius A and an outer radius B, all the circles considered here having the same center. The Cartesian coordinates on M are x and y, and the coordinates on M^* are X and Y. The transformation is given by the two functions (with $R=\sqrt{X^2+Y^2}$):

$$x=f_1(X,Y)=X[A(B-A)]/[R(B-R)], \tag{11}$$

$$y=f_2(X,Y)=Y[A(B-A)]/[R(B-R)]. \tag{12}$$

Figure 1 shows the field lines computed by this method. Thanks to the symmetry of the problem, only one quarter has been computed.

Thin plate: Very thin objects and very small skin depths are other examples of problems difficult to model with finite elements. In this case it is interesting to stretch the geometry along the small dimension. The example considered here is a steel band heated by induction. The steel band is 1.2 mm thick and is heated by a one-turn rectangular coil (240 mm long and 3 mm thick), placed 28 mm above the band and fed by a 3490 A current. The thickness of the band is small with respect to the characteristic length of the problem, but the skin depth is even smaller: the frequency of the current is 275 kHz, the conductivity of the plate is 10^7 S/m, and the relative permeability is 405. In those conditions, the skin depth is equal to about 15 μm. To model the plate, surface layers of 45 μm are considered. Those layers are stretched by a factor 15 000 and then become layers of 675 mm in the transformed problem. Thus, the transformation used is simply $\{x=X,\ y=Y/15\ 000\}$. Although almost trivial, this transformation makes the problem more tractable. Moreover, the use of a general formalism allows the extension of this technique to curved plates or to nonlinear transformations, e.g., taking into account the exponential decay of the current density and field inside the plate. Figure 2 shows the field lines in the lower stretched layer at the phase-0 degree of the excitation current.

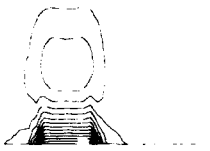

FIG. 2. Field lines in a stretched layer phase: 0 degree.

CONCLUSION

The use of the differential geometry in computational electromagnetics has been advocated by various authors.[5,7] It is the natural framework to set up the transformation method that becomes almost trivial in this context. Although the first examples of application of this method have been introduced with the help of the vector calculus more familiar to engineers, its formulation with the help of differential geometry allows a systematic generalization, and leads to a quasiautomatic implementation method, where all the steps are clearly defined.

[1] J.-F. Imhoff, G. Meunier, X. Brunotte, and J.-C. Sabonnadière, "An original solution for unbounded electromagnetic 2D- and 3D-problems throughout the finite element method," IEEE Trans. Magn. 26, 1659 (1990).

[2] P. Bamberg and S. Sternberg, *A Course in Mathematics for Students of Physics:* 2 (Cambridge U.P., Cambridge, 1990).

[3] S. W. Hawking and G. F. R. Ellis, *The Large Scale Structure of Space-Time* (Cambridge U.P., Cambridge, 1973), Chap. 2.

[4] W. Thirring, *A Course in Mathematical Physics: 2: Classical Field Theory* (Springer, New York, 1978).

[5] A. Bossavit, "Notions de géométrie différentielle pour l'étude des courants de Foucault et des méthodes numériques en électromagnétisme," *Méthodes Numériques en Électromagnétisme*, Coll. DEREdF, Eyrolles, Paris, 1991, pp. 1–141.

[6] A. Bossavit, "Whitney forms: a class of finite elements for three-dimensional computations in electromagnetism," IEEE Proc. 135, 493 (1988).

[7] P. R. Kotiuga, "Hodge decompositions and computational electromagnetics," Ph.D. dissertation, McGill University, Montreal, Canada, 1984.

The effects of various magnetic materials on lamination design for stator–rotor diecasting of induction motors for electric vehicle applications

N. M. Elkasabgy and C. Di Pietro
Westinghouse Motor Company Ltd., P.O. Box 2510, Hamilton, Ontario L8N 3K2, Canada

In this paper we describe a novel technique to model induction motors with a diecast stator and rotor and to examine the effects of various magnetic materials on the electrical performance of the motor. For electric vehicle applications, a high volume production operation of the electric motor requires the motor to be small and inexpensive. The expensive labor and material used to manufacture the motor encouraged the researchers to find new methods and techniques to reduce the cost and improve the performance. Diecast rotor and stator windings reduce motor cost and size. For diecasting induction motors, the motor laminations should be designed to optimize the electromagnetic field distribution over the cross section and along the axial direction. The magnetic material used for the laminations should also reduce losses and improve the overall efficiency. A 100 hp four-pole induction motor was modeled with finite elements, the field distribution, the magnetic flux density, and the mechanical performance of the motor were computed using nonlinear magnetostatic and complex steady-state eddy current techniques. The difference in the electrical and mechanical performance of the motor were evaluated for copper and aluminum diecasting. The results show that copper diecasting of the rotor and the stator of the induction motor with magnetic material properties and identified slotting shape is the way to achieve better motor performance and low cost operation.

I. INTRODUCTION

Interest in electric vehicles has grown markedly during the past few decades due to air quality concerns and due to uncertain petroleum imports. Also, due to the new legislation in the state of California, of all vehicles produced by the year 2000, 10% must be zero emission electric vehicles. Variable torque and speed control is the essential requirement for propulsion systems in electric vehicles. Several types of electrical motors may be used for electric vehicle propulsion purposes. Earlier traction motors were exclusively DC motors. Recently, more advanced AC drive systems have found applications in electric vehicle propulsion using induction motors.[1,2] The special features of electric vehicle application requires that the motor should be small in size, light in weight, and inexpensive with high constant power and efficiency over a wide range of speeds. Diecasting the rotor and the stator of the induction motor would reduce the labor intensive task of sizing the winding of the coils and eliminate the placing of the insulation material into the stator slots. In order to optimize the use of the diecasting process for induction motors, a special design for stator and rotor laminations should be developed to improve the overall electrical and mechanical performance of the motors.

In this paper we use field analysis[3,4] to provide an accurate evaluation of the magnetic field distribution and mechanical performance of the motor. The complex stator and rotor lamination geometry, the spatial distribution of the conductors in the stator slots, and the effect of the nonlinearity of the magnetic material must be taken into account. The finite element technique is an effective numerical tool to solve the electromagnetic field under these conditions. In this paper we present a finite element technique to find a better slot shape and high permeable magnetic material for diecasting the motor windings. The case under study is an induction motor used for an electric vehicles propulsion system.

II. FEATURES AND ASSUMPTIONS OF METHOD OF ANALYSIS

A 100 hp, four-pole, 115 V variable frequency induction motor drive was used for the analytical work. A two-dimensional cross section of the machine was modeled with finite elements to obtain a detailed representation of the stator slot and bar conductor shapes. In this paper, the nonlinear complex steady-state method for solving time varying problems in electric machines has been applied. The field variables, which are assumed to vary sinusoidally, are conveniently represented by phasors of the form $e^{j\omega t}$. Hence, the partial differential operator $(\partial/\partial t)$ may be replaced by the arithmetic factor $j\omega$. The magnetic field is assumed to lie in the cross-sectional (x,y) plane, to be excited by and induce only axial z-component currents, and to vary sinusoidally with time. The fundamental equation describing the space and time variation of the vector potential, A, over the region of analysis has the following form:

$$\frac{\partial}{\partial x}\left(\frac{1}{\mu}\right)\frac{\partial A}{\partial x}+\frac{\partial}{\partial y}\left(\frac{1}{\mu}\right)\frac{\partial A}{\partial y}-js\omega\sigma A+J=0, \tag{1}$$

where s is the slip at a specific operating condition, μ is the permeability of the ferromagnetic material, σ is the conductivity of the conducting media in the rotor, and ω is the angular frequency.

If we assume that three phase stator currents are

$$J_a=Je^{j\omega t},$$
$$J_b=Je^{j(\omega t+2\pi/3)}, \tag{2}$$
$$J_c=Je^{j(\omega t+4\pi/3)}$$

(where J is the stator current amplitude), then the magnetic vector potential at each nodal point in the machine discretization (Fig. 1) is likewise a sinusoidal function of time:

 0021-8979/94/75(10)/6039/3/$6.00 © 1994 American Institute of Physics

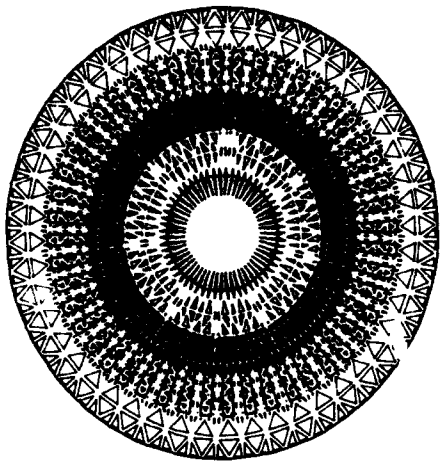

FIG. 1. Discretization of the full cross section of the motor.

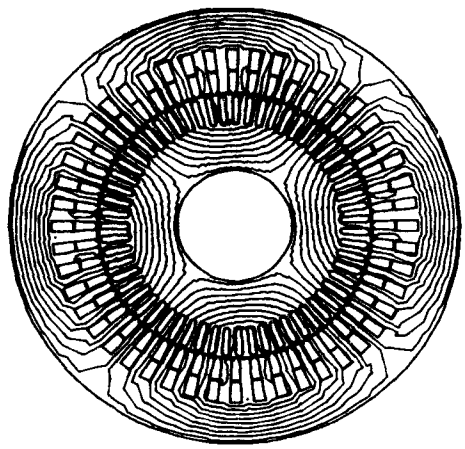

FIG. 3. Flux plots at the no-load condition.

$$A(x,y)=Ae^{j(\omega t+\phi)}, \tag{3}$$

where ϕ is the phase angle of the local magnetic vector potential A.

The assumptions and boundary conditions that have been used in finite element analysis to solve Eq. (1) are the following

(1) A is constant along the outside circumferential boundary.

(2) The relative positions of the stator and the rotor are assumed to be fixed.

(3) The magnetic field at any point in the machine varies sinusoidally at slip frequency, thus simulating the electromagnetic interaction of any particular slip condition.

The conductivity is zero outside any conducting region and the permeability is μ in nonmagnetic regions.

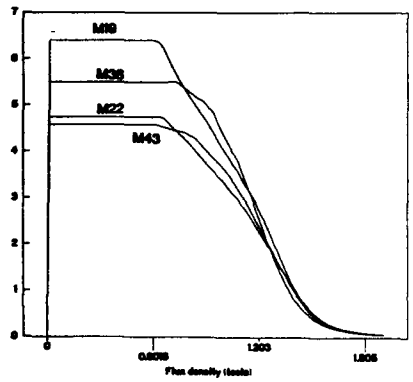

FIG. 2. Flux density versus permeability for various magnetic materials.

III. PRACTICAL EXAMPLE

The motor used for verifying the technique is a squirrel cage four-pole motor with 59 closed rotor slots and 48 semiclosed stator slots. The rotor slot shape is considered to be the most suitable shape for diecasting operations.[4] The stator slot shape is rather suitable for wound coils than diecasted windings. The coils are held by a wedge and separated by a divider. The analysis starts with pinpointing the proper magnetic material for the lamination; second, finding the proper stator slot shape for diecasting operation; and finally, examining the effect of using the copper and aluminum alloys on the mechanical performance of the motor.

A. Magnetic material

Four different typical magnetic materials namely M19, M22, M36, and M43 were used to model the motor laminations. The magnetic permeability versus the flux density for all four materials is shown in Fig. 2.

The magnetostatic state of the field presented by the no-load condition of the motor under three phase AC excitation was calculated. Typical field distribution is shown in Fig. 3. The magnetic field penetrates uniformly and deeply into the

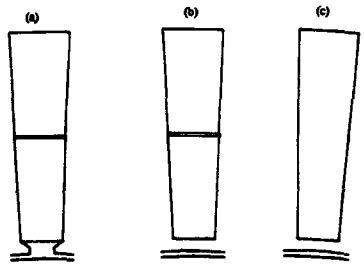

FIG. 4. Various stator slot shapes for diecasting operation. (a) One bridge at the middle of the slot. (b) Two bridges. (c) One bridge under the slot.

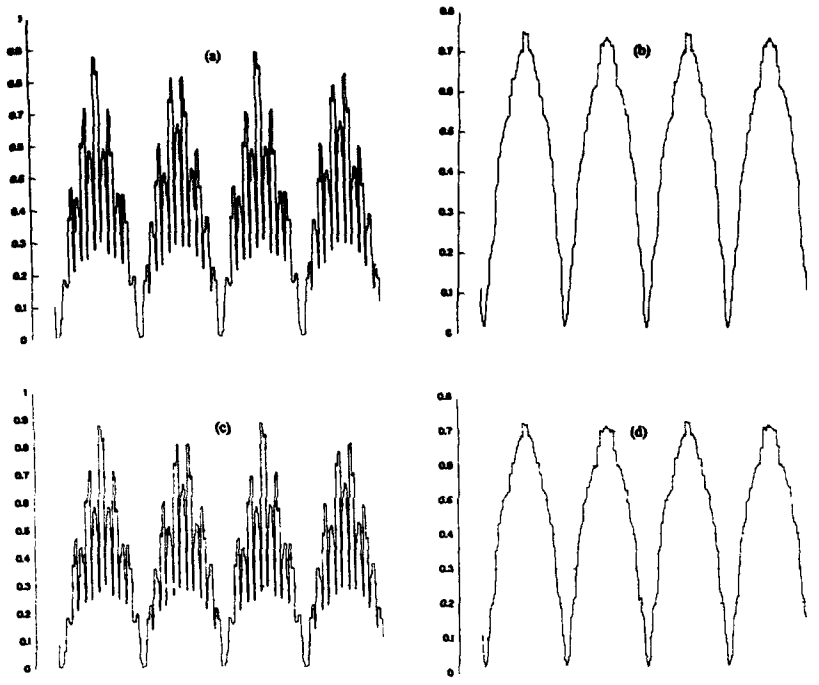

FIG. 5. Air gap flux plots for various stator slot shapes. (a) No bridges. (b) One bridge under the slot. (c) One bridge at the middle of the slot. (d) Two bridges.

rotor as the demagnetizing effect of the rotor is yet nonexistent. The magnetic flux density was calculated over a contour in the middle of the air gap. For the same applied field, M36 magnetic material shows more flux enclosure in the motor air gap of 0.90 T vs 0.89 T for M19, 0.88 T for M22, and 0.893 T for M43. M36 was chosen to model the motor laminations for any slot shape.

B. Stator slot shape

For diecasting operation, the windings are formed by solid coils rather than stranded coils. The insulation material, such as wedges and dividers, would be eliminated from the stator slots. The stator slot shape must be modified to accommodate the solid coils and the magnetic field distribution. Three cases of study are considered: (1) Semiclosed stator slot with one bridge in the middle of the slot; (2) closed stator slot with two bridges, one in the middle of the slot and one under the slot; and (3) closed stator slot with one bridge under the slot.

Figure 4 shows the stator slot outlines for the above three cases. Figure 5 shows the flux density in the airgap for all the above three cases and also for the regular slot shape. For cases (2) and (3), the magnetic field shows less harmonics superimposed on the sinusoidal field. Those harmonics are usually a source of losses. In case (1) the flux density follows the same regular pattern of flux density for a stator having a regular continuous slot shape with no bridges.

C. Rotor slot

Small size induction motors are usually rotor diecasted using aluminum alloys. Rotors with copper bars proved to have higher efficiency and lower losses, but more labor and cost. Recently, the copper bars have been replaced by diecasted rotor slots made in the same fashion as the aluminum diecast. A motor with a diecast stator and rotor would have the advantages of lower cost and high efficiency. Based on the analysis presented in the previous section, the stator with double bridges was chosen to be unified with a diecasted copper rotor.

This stator–rotor combination was examined for aluminium and copper alloys. For the same torque-speed condition, the results show that the copper rotor has 1.2% higher efficiency than its dual aluminum rotor.

[1] C. Bader and W. Stephan, IEEE Trans. Vehicular Technol. VT-26, 123 (1977).
[2] E. P. Cornell and R. H. Guss, IEEE Trans. Vehicular Technol. VT-26, 128 (1977).
[3] M. V. K. Chari and P. P. Silvester, *Finite Elements in Electric and Magnetic Field Problems* (Wiley, New York, 1980).
[4] N. M. Elkasabgy, A. R. Eastham, and G. E. Dawson, IEEE Trans. Ind. Appl. 28, 165 (1992).
[5] N. A. Demerdash and T. W. Nehl, IEEE Trans. Magn. MAG-15, 1482 (1979).

An improved method for magnetic flux density visualization using three-dimensional edge finite element method

Vlatko Čingoski and Hideo Yamashita
Electric Machinery Laboratory, Hiroshima University, Higashi-hiroshima, 724 Japan

Visualization of a magnetic flux density distribution in three-dimensional (3-D) finite element analysis (FEA) is very important in order to grasp the real behavior of the magnetic field, especially in the design process. In this paper, we present an improved method for visualizing magnetic flux density distributions calculated by 3-D first-order edge FEA. Compared with traditional methods, this method provides more accurate, smoother magnetic flux density distribution inside the analyzed region and satisfies the proper boundary conditions across intermaterial boundaries. The usefulness of our algorithm is demonstrated with several examples.

I. INTRODUCTION

In the analysis of various magnetic field problems, analysts are usually interested in the values of magnetic flux density at certain points, or its distribution over part or all of the analyzed domain. Therefore, the visualization of such a distributed physical quantity is very important in order to grasp the real behavior of the magnetic field, and correctly understand and evaluate the results of analysis.

Recently, first-order edge based FEA has become a very popular for a wide class of 3-D magnetic field and eddy current problems. The main reasons are its computational efficiency, small memory requirements, and most of all satisfaction of only proper boundary conditions on the material interfaces.[1] Unfortunately, due to the discrete character of the magnetic flux density in each finite element, good visualization of the magnetic flux density obtained by first-order edge FEA is not possible.

In this paper, we proposed an improved visualization algorithm, which provides more accurate, smoother visualization of the results obtained from the 3-D edge FEA. The algorithm for the 2-D nodal FEA already presented in Ref. 2, here is extended into a third dimension and applied to the 3-D data obtained from the edge FEA. That is, the proposed algorithm is a mixed approach in the visualization process, successfully combining edge and nodal FEA over the same 3-D mesh. In order to demonstrate the validity of the proposed algorithm, two simple models, with and without magnetic materials, are presented.

II. OUTLINE OF THE ALGORITHM

In the traditional method, the magnetic flux density vector **B** can be obtained as

$$\mathbf{B}=\text{rot}\,\mathbf{A}, \tag{1}$$

in the finite number of lattice points inside the display space. Since we use a first-order edge finite elements, the values for **B** obtained from (1) are equal at any point inside the element. That is, discontinuous visualization of magnetic flux density vector **B** can be observed. To overcome this problem we developed the following algorithm.

(i) Using the magnetic vector potential data obtained by the 3-D edge FEA, from (1) we compute the magnetic flux density vector **B** previously at each vertex of the tetrahedron.

(ii) Since one vertex P of a tetrahedron usually belongs to more than one finite element, we compute the values of all three components of magnetic flux density vector **B** as an average value from all contributions of magnetic flux density at vertex P from all elements that have P as a vertex (Fig. 1). Therefore

$$B_{pj}=\frac{1}{n}\sum_{i=1}^{n} B_{pji} \tag{2}$$

where j is an x, y, or z component, and n is the total number of elements that have P as a vertex.

This procedure does not have a large influence on the values of magnetic flux density vector **B** obtained by (1) directly from the edge FEA, because if the mesh is suitably dense, the values at each vertex computed from adjacent elements differ to a small degree. It is necessary to perform this procedure only to provide a linear distribution of magnetic flux density vector **B** between any two points inside the element.

(iii) If vertex P is on the boundary between different magnetic materials, a new vertex P' is constructed, an infinitesimally small distance removed from P. The averaging procedure is performed for each material, and the calculated values are associated with P and P', respectively.

(iv) The magnetic flux density inside each finite element is approximated by the average values of each component of the magnetic flux density vector **B** at the four tetrahedron vertices. For approximation, we use some low-order interpolation formulas, such as shape functions, for first-order nodal analysis:

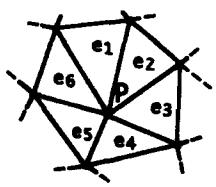

FIG. 1. Calculation of the magnetic flux density at vertex P.

 0021-8979/94/75(10)/6042/3/$6.00 © 1994 American Institute of Physics

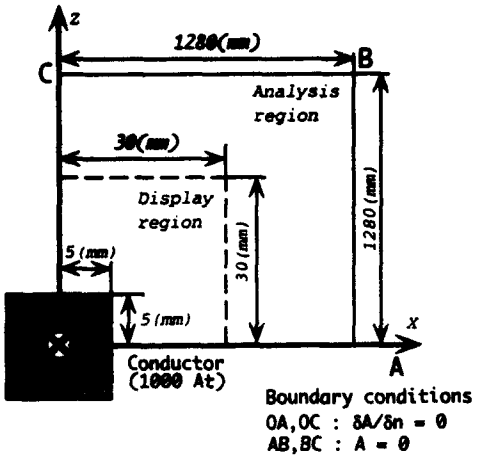

FIG. 2. Single-material model.

$$B_j = \sum_{i=1}^{4} N_i B_{ji}, \tag{3}$$

where j is the x, y, or z component of magnetic flux density. In this case, the distribution of magnetic flux density inside each finite element will be linear. Higher-order interpolation, e.g., quadratic, can be easily achieved using second-order

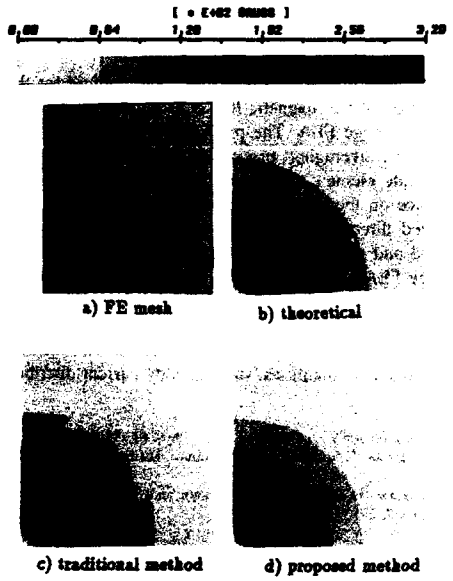

FIG. 3. Magnetic flux density distribution. (a) FE mesh, (b) theoretical (c) traditional method, and (d) proposed method.

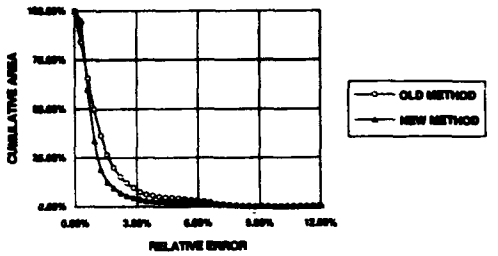

FIG. 4. Comparison of relative errors for traditional and proposed visualization methods.

nodal shape functions and six more values of magnetic flux density vector at midpoints of each edge of the element.

III. APPLICATION

In this section, we apply our method to the visualization of magnetic flux density for two models. One is a single-material model, of interest because of its known theoretical values, and the other is a multimaterial model, suitable for exploring the visualization on intermaterial boundaries.

A. Single-material region

Figure 2 shows the analysis and display region for the first model. Due to the symmetry of the model we performed analysis over only one quadrant. The calculated results are displayed in Fig. IV for theoretical, traditional, and our new visualization method using the same scale. Figure 3 also shows a division map used in the analysis. It is obvious that with no changing of the intensity of the magnetic flux density vector **B**, its distribution displayed by our method is almost identical with the theoretically obtained one, while the traditional visualization method results in a discontinuous distribution. In Fig. 4, the x axis represents relative error ϵ given as

$$\epsilon = \left| \frac{\mathbf{B}_t - \mathbf{B}_c}{\mathbf{B}_t} \right| \cdot 100, \tag{4}$$

where $\mathbf{B}_t$ and $\mathbf{B}_c$ are the theoretical and computed values for the magnetic flux density vector **B** at each lattice point inside the display space, respectively. In the same time, the y axis represents the cumulative area, given as

$$\text{cumulative area} = \frac{\text{display area with error over } \epsilon\ (\%)}{\text{total display area}} \cdot 100. \tag{5}$$

Figure 4 clearly shows that the relative error of the proposed method is smaller than that of the traditional one, therefore the accuracy of the results obtained by the proposed method is improved.

B. Multimaterial region

Figure 5 shows the analysis and display area for the multimaterial model. Here again we use the symmetry of the

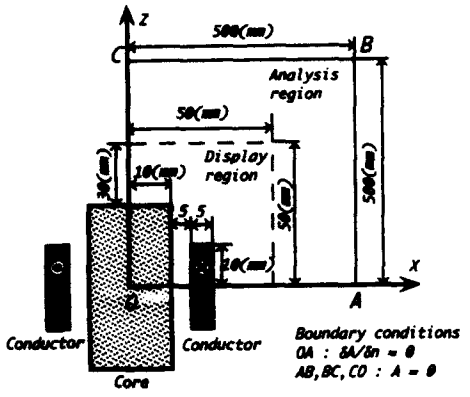

FIG. 5. Multimaterial model.

model and analyze only one quadrant. This model is quasi-3-D (a 2-D model extended into the third dimension); therefore 2-D analysis on the same model with an extremely dense finite element mesh is used as a standard value because

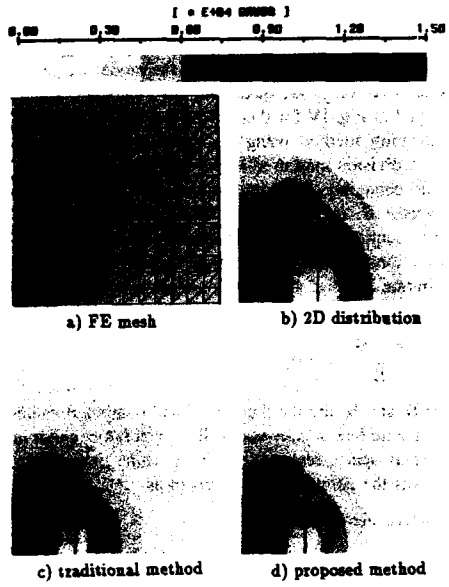

FIG. 6. Magnetic flux density distribution. (a) FE mesh, (b) 2-D distribution, (c) traditional method, and (d) proposed method.

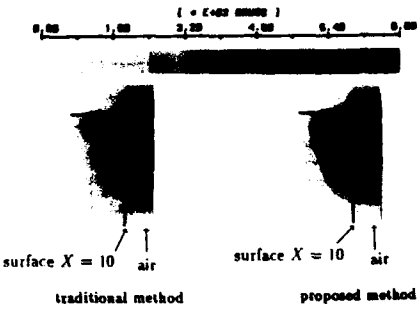

FIG. 7. The B_x distribution as a normal component on the intermaterial boundary.

no theoretical solution exists. This model is important to demonstrate the ability of our method to deal with multimaterial regions and their boundaries.

In Fig. 6, the visualization of 2-D and 3-D data using the traditional and our proposed visualization methods, again using the same scale and together with the part of interest of the finite element mesh used in the analysis are presented. It is clear that the proposed method provides a better visualization. In Fig. 7 the x component of magnetic flux density B_x as a normal component on the surface of material at $X=10$, for the traditional and the proposed visualization algorithms, is presented. The continuity of the normal components is apparent.

IV. CONCLUSION

We have presented a new, improved method for the visualization of the magnetic flux density obtained by the 3-D first-order edge FEA. The proposed method involves some algebraical averaging procedure and interpolation inside each finite element. These procedures do not have a large influence on the results of magnetic flux density vector B, obtained directly from the analysis, and are easily implemented and computationally efficient. Using the properties of edge FEA to satisfy only the proper boundary conditions on intermaterial boundaries, our method deals very well with them and provides smooth and highly accurate visualization. The method can be easily extended for the visualization of other magnetic quantities, such as eddy current distribution.

[1] M. L. Barton and Z. J. Cendes, J. Appl. Phys. 61, 3919 (1987).
[2] H. Yamashita, T. Yohkoh, and E. Nakamae, IEEE Trans. Magn. 26, 739 (1990).
[3] E. Nakamae, H. Yamashita, N. Kawano, and S. Nakano, Computer & Graphics 7, 295 (1983).

Optimum design of voice coil motor with constant torque coefficients using evolution strategy

Chang Seop Koh and Osama A. Mohammed
Department of Electrical & Computer Engineering, Florida International University, Miami, Florida 33199

Jun-o Kim and Song-yop Hahn
Department of Electrical Engineering, Seoul National University, Seoul 151-742, Korea

An effective optimum design method is presented. The method combines the three-dimensional boundary element method with the (1+1) evolution strategy. The reduced scalar potential formulation with the magnetic surface charge as the unknown variable is used under the assumption that the yokes are not saturated. It is found, through the numerical example, that the global optimum shape of the magnet can be easily found within a reasonable number of generations. More elaborate design can be achieved by increasing the number of design variables.

I. INTRODUCTION

The voice coil motor (VCM) is widely used in high speed and accurate position control actuators such as magnetic disk drives. In the design process of a VCM, the constant torque coefficient characteristic is very important.[1-3] The torque coefficient of a rotary-type VCM with flat coil changes along the positions of the rotor, which impairs high speed and accurate position control use. This fact comes from the uneven distribution of magnetic induction in the air gap. One possible solution is to optimize the shape of the permanent magnet of the VCM.

Several attempts have been made to offer a simulation and design tool for this purpose.[1-3] However, they are not sufficient to predict accurately the carriage motion in the disk drives because the VCM is either analyzed by the equivalent circuit model,[2,3] or by the two-dimensional finite element method,[1] although it has a full three-dimensional configuration. Furthermore, these previous attempts do not offer any guidance for the optimization of the dimension and shape of the VCM.

In this paper, an efficient optimum design algorithm, that combines the boundary element analysis and the (1+1) evolution strategy, is presented to find an optimum shape of a VCM that gives constant torque coefficients. The three-dimensional boundary element method is utilized to analyze the dynamic characteristics of a VCM.

II. CHARACTERISTICS ANALYSIS

The VCM is a kind of linear dc motor where the carriage reciprocates by the force induced by the interaction of the coil current and the magnetic flux generated by the permanent magnets in the air gap. Figure 1 shows the configuration of a VCM analyzed and designed in this paper. This is a rotary-type VCM with flat coil, where the two permanent magnets are magnetized upward and downward, respectively, and the magnetic flux passes through both yokes.

The VCM is excited by only the ferrite permanent magnet whose remanent magnetic flux density is 0.42 T. Hence, the pure steel yokes can be assumed to be unsaturated. Using this assumption, the reduced magnetic scalar potential formulation is utilized because the permanent magnets can be easily taken into consideration and the resultant system matrix becomes relatively small.[4] The unknown state variables are, in this case, equivalent magnetic surface charges defined as follows:

$$\rho(r)=-\frac{\partial\varphi(r)}{\partial n}+H_a(r)\cdot n, \tag{1}$$

where r is the position vector, $\varphi(r)$ is the reduced magnetic scalar potential, H_a is the incident magnetic field intensity created by the permanent magnets and given by

$$H_a(r_s)=\frac{1}{4\pi}\sum_{k=1}^{2}\int_{S_k}\frac{M(r)\cdot n(r)(r_s-r)}{|r_s-r|^3}\,ds, \tag{2}$$

where M is the magnetization vector, S_k is the surface of the kth magnet, and n is the outward unit normal vector.

The boundary integral equation is derived by using the scalar Green's identity from Maxwell's equations. If the condition of zero summation of the magnetic surface charges is

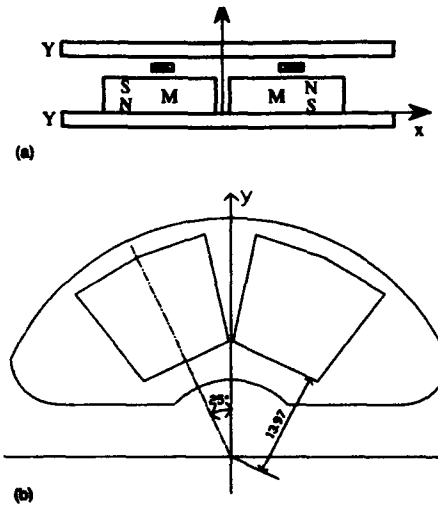

FIG. 1. The VCM configuration. Cross-sectional view (a) and top view (b).

 0021-8979/94/75(10)/6045/3/$6.00 © 1994 American Institute of Physics

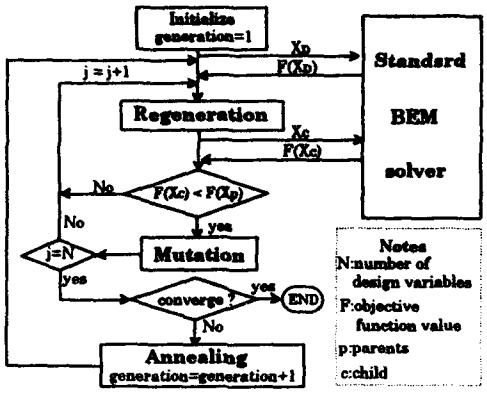

FIG. 2. Flow chart of the (1+1) evolution strategy.

introduced based on a penalty function method,[4] the constrained boundary integral equation can be obtained as follows:

$$\left[1-\left(1-\frac{1}{\mu}\right)\frac{\Omega}{4\pi}\right]\rho(r_p)-\left(1-\frac{1}{\mu}\right)\int_\Gamma \frac{(r_p-r)\cdot n}{4\pi|r_p-r|^3}\,\rho(r)ds$$

$$+\frac{1}{A}\int_\Gamma \rho(r)ds=H_a(r_p)n(r_p), \tag{3}$$

where Ω *is the interior* solid angle at r_p, μ and Γ are the relative magnetic permeability and the boundary surface of the yoke, respectively, and A is the area of Γ.

Discretizing the surface and applying the Galerkin formulation for Eq. (3) yield the following matrix equation:

$$[K]\{\rho\}=\{f\}. \tag{4}$$

Once Eq. (4) is solved, the magnetic induction in the air gap can be evaluated using the equation

$$B(r_p)=\mu_0 H_a(r_p)+\mu_0\left(1-\frac{1}{\mu}\right)\int_\Gamma \frac{(r_p-r)\cdot n}{4\pi|r_p-r|^3}\,\rho(r)ds. \tag{5}$$

All the integrals for Eqs. (4) and (5) are computed numerically using the Gauss–Radau or Gauss–Legendre integration formulas.

III. OPTIMIZATION ALGORITHM

In order to find an optimum shape for the magnets, the (1+1) evolution strategy is adapted. The method, which is one of the stochastic optimization algorithms, combines the genetic algorithm that copies the natural principles of mutation and selection with the simulated annealing process in thermodynamics.[5] The three major processes; regeneration, mutation, and annealing, are repeated until the optimum design is achieved as summarized in Fig. 2.

The new design variables vector X_c (child in a generation) are generated from the old design variables vector X_p (parent in a generation) by the rule;

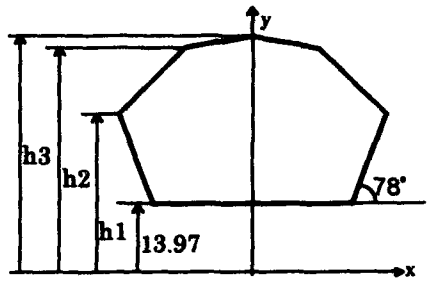

FIG. 3. Design variables.

$$X_{ci}=X_{pi}+\alpha R, \quad i=1,2,\ldots,N, \tag{6}$$

where N is the dimension of the design variables vector, α is the step length, and R is a random number with uniform distribution.

After computing the objective function values, $F(X_p)$ and $F(X_c)$, corresponding to the old and new design variable vectors, respectively, a new parent in the next generation is decided by the following rule to simulate the mutation:

$$X_p=\begin{cases} X_c & \text{if } F(X_c)<F(X_p) \\ X_p & \text{if } F(X_c)\geq F(X_p) \end{cases}. \tag{7}$$

The step length α is annealed by enlarging or reducing it by a factor of 0.85 according to the number of mutations for the previous ten generations, i.e.,

$$\alpha=\begin{cases} \alpha 0.85 & \text{if number of mutations} > 2N \\ \alpha/0.85 & \text{otherwise.} \end{cases} \tag{8}$$

IV. NUMERICAL EXAMPLE

The design target is to obtain the constant torque coefficients at the various positions of the rotor coil. The objective function to be minimized, hence, is defined as

$$F=\int_{\theta=-15^\circ}^{\theta=15^\circ}[T(\theta)-T_0]^2 d\theta \sim \sum_{k=1}^{N_T}(T_k-T_0)^2, \tag{9}$$

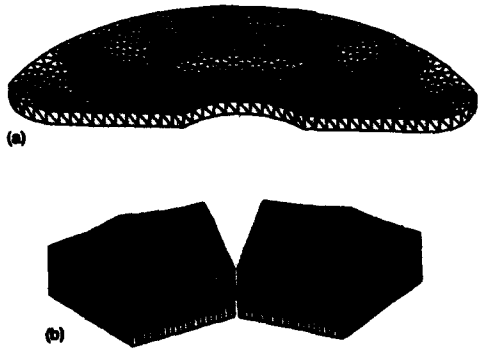

FIG. 4. Boundary element discretizations for yoke (a) and magnets (b).

TABLE I. Optimized design variables.

Case studies	Initial	Optimized	Generations
(h1,h3)	(28,30)	(28.90,29.398)	20
relative error	6.3%	0.62%	
(h1,h2,h3)	(28,29,30)	(28.16,28.68,29.31)	23
relative error	6.3%	0.54%	
(h1,h2,h3)	(28,28,28)	(28.19,28.70,29.31)	21
relative error	2.7%	0.54%	

where T_k and T_0 are the computed and target values of torque at kth coil position, respectively, and the torque generated can be expressed in vector form as

$$T(\theta)=\oint_l r\times[i\times B(\theta)]dl, \tag{10}$$

where i is the current in the coil and l is the current loop.

The upper shape of the magnet is represented as four straight lines and the three design variables (h1,h2,h3) are taken to modify the shape of the magnet as shown in Fig. 3.

In order to compute the magnetic induction in the air gap by using the boundary element method, the yoke and the permanent magnet are discretized into 6200 and 3520 linear triangular elements, respectively, as shown in Fig. 4.

The final optimized design variables are shown in Table I where the maximum relative error, E_r, is defined as

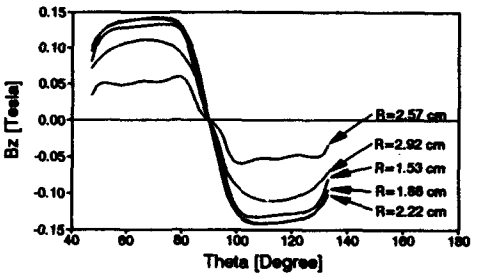

FIG. 5. Distribution of the magnetic induction in the air gap ($z=7.94$ mm).

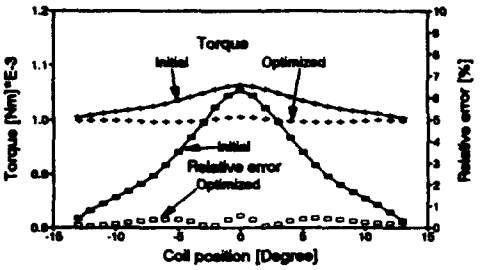

FIG. 6. Distribution of the torque coefficients.

$$E_r=\max_{1\le k\le N_T}\left(\frac{|T_k-T_0|}{T_0}\times 100\right)[\%]. \tag{11}$$

From Table I, it is found that more elaborate design is achieved with three design variables than with two design variables. In the case of two design variables, the mean value of h1 and h3 is taken for h2. Furthermore, final results are considered as a global optimum because different initial shapes converged into nearly the same shape. Figure 5 shows the distribution of the magnetic induction in the air gap at the final optimized shape. The torque coefficients are compared in Fig. 6 at the initial and final optimized shapes where the maximum relative error at the optimized shape is only 0.4[%].

V. CONCLUSION

An effective optimum design method is developed for the design of VCM by combining the three-dimensional boundary element method and the (1+1) evolution strategy. The method converges to a global optimum point from different initial points. It is found, through the numerical example, that the optimum shape of the magnet can be easily found within a reasonable number of iterations and more elaborate design can be achieved by increasing the number of design variables.

[1] C. Dong, IEEE Trans. Magn. MAG-19, 1689 (1983).
[2] J. Arthur Wagner, IEEE Trans. Magn. MAG-18, 1770 (1982).
[3] T. Nakata, Trans. IEE Jpn. 105B, 483 (1985).
[4] I. D. Mayergoyz, J. D'Angelo, and C. Crowely, J. Appl. Phys. 57, 3832 (1985).
[5] A. Gottvald, IEEE Trans. Magn. MAG-28, 1537 (1992).

Three-dimensional eddy current solution of a polyphase machine test model (abstract)

Uwe Pahner and Ronnie Belmans
Department EE, Labo EMA, KU Leuven, Belgium

Vlado Ostovic
ABB Mannheim, Kraftwerke AG, Abt.KW/DE, Germany

This abstract describes a three-dimensional (3D) finite element solution of a test model that has been reported in the literature. The model is a basis for calculating the current redistribution effects in the end windings of turbogenerators. The aim of the study is to see whether the analytical results of the test model can be found using a general purpose finite element package, thus indicating that the finite element model is accurate enough to treat real end winding problems. The real end winding problems cannot be solved analytically, as the geometry is far too complicated. The model consists of a polyphase coil set, containing 44 individual coils. This set generates a two pole mmf distribution on a cylindrical surface. The rotating field causes eddy currents to flow in the inner massive and conducting rotor. In the analytical solution a perfect sinusoidal mmf distribution is put forward. The finite element model contains 85824 tetrahedra and 16451 nodes. A complex single scalar potential representation is used in the nonconducting parts. The computation time required was 3 h and 42 min. The flux plots show that the field distribution is acceptable. Furthermore, the induced currents are calculated and compared with the values found from the analytical solution. The distribution of the eddy currents is very close to the distribution of the analytical solution. The most important results are the losses, both local and global. The value of the overall losses is less than 2% away from those of the analytical solution. Also the local distribution of the losses is at any given point less than 7% away from the analytical solution. The deviations of the results are acceptable and are partially due to the fact that the sinusoidal mmf distribution was not modeled perfectly in the finite element method.

 0021-8979/94/75(10)/6048/1/$6.00 © 1994 American Institute of Physics

Numerical methods and measurement systems for nonlinear magnetic circuits (abstract)

Axel Helbrink, Hans Dieter Storzer, and Adalbert Beyer
Institute of Electromagnetic Theory and Engineering, Duisburg University, Bismarckstrasse 81, 47048 Duisburg, Germany

In the past years an increasing interest in calculation methods of circuits containing magnetic nonlinearities could be observed. For this reason a new method was developed which makes it possible to calculate the steady state solution of such circuits by the help of an interactive CAD program. The modular concept of the software allows to separate the circuit into nonlinear and linear subnetworks. When regarding nonlinear magnetic elements one can choose between several numerical models for the description of the hysteresis loops or an inbuilt realtime measurement system can be activated to get the dynamic hysteresis loops. The measurement system is also helpful for the parameter extraction for the numerical hysteresis models. A modified harmonic-balance algorithm and a set of iteration schemes is used for solving the network function. The combination of the realtime measurement system and modern numerical methods brings up a productive total concept for the exact calculation of nonlinear magnetic circuits. A special application class will be discussed which is given by earth-leakage circuit breakers. These networks contain a toroidal high permeable NiFe alloy and a relay as nonlinear elements (cells) and some resistors, inductors, and capacitors as linear elements. As input dc signals at the primary winding of the core any curveform must be regarded, especially 135° phasecutted pulses. These signals with extreme higher frequency components make it impossible to use numerical models for the description of the nonlinear behavior of the core and the relays. So for both elements the realtime measurement system must be used during the iteration process. During each iteration step the actual magnetization current is sent to the measurement system, which measures the dynamic hysteresis loop at the probe. These values flow back into the iteration process. A graphic subsystem allows a look at the waveforms of all voltages and current when the iterations take place. One can determine how the steady state is reached, especially when one discusses different iteration methods. All parameters of interest, such as geometric data of the core, number of windings, and the linear elements can vary within the computer program and as a result all voltages and currents in the network stand can be used. With the help of this computer controlled measurement system and several iteration methods fast circuit design and optimization can be done.

 0021-8979/94/75(10)/6049/1/$6.00 © 1994 American Institute of Physics

Comparative analysis of two methods for time-harmonic solution of the steady state in induction motors (abstract)

Robrecht DeWeerdt, Kostadin Brandisky, Uwe Pahner, and Ronnie Belmans
Department EE, Labo EMA, K.U. Leuven, Belgium

The abstract presents two methods of solving induction motor problems using a time-harmonic approach, taking into account the saturation of the iron material. The first method uses the following algorithm. Initially, two static nonlinear problems are solved: one problem using the real part of the stator currents, and the other using the imaginary part. From both solutions, a reluctivity vector is generated. This reluctivity vector is then used in solving a time-harmonic problem to calculate the induced rotor currents. These currents are used to solve two new static problems. From the solution, a more accurate reluctivity vector can be generated. Convergence of this method occurs after 4 or 5 steps. The second method is an iterative method of solving nonlinear time-dependent problems by harmonic representation. It is assumed that $H(t)$ is a sinusoidal function of time. A new sinusoidal B_{eq} is introduced based on energy equivalence with the real nonsinusoidal B. This new B_{eq} is used to calculate the new B-H curve for the iron materials involved and after that an equivalent reluctivity. The nonlinear algorithm represents under-relaxation of the equivalent reluctivity, based on the formula: $\mathrm{RELUCT}_{new}=\mathrm{RELUCT}_{old}+\mathrm{ALPHA}*(\mathrm{RELUCT}_{crst}-\mathrm{RELUCT}_{old})$, where ALPHA is a relaxation factor usually chosen between 0 and 1. The algorithm shows a good convergence rate (from 10 to 20 steps) if the initial starting vector for reluctivities and the relaxation factor are chosen appropriately. Rules for this choice are given. Both methods are compared. The difference between the induced currents in both methods is about 1%, with a linear solution it is about 300%. Also stored energy, losses, reluctivities, and other quantities are compared.

 0021-8979/94/75(10)/6060/1/$6.00 © 1994 American Institute of Physics

Selection of the ground state in $CsCuCl_3$ by quantum fluctuations

E. Rastelli and A. Tassi
Dipartimento di Fisica, Universitá di Parma, 43100 Parma, Italy

The Heisenberg triangular antiferromagnet is a model widely studied by analytic low-temperature expansion and Monte Carlo simulation. The classical version of the model is characterized by infinitely many minimum energy configurations even if an in-plane external magnetic field is turned on. This degeneracy is lifted by thermal fluctuations and the same effect is found when quantum fluctuations are accounted for. We find an analogous scenario in the 3D hexagonal model where the intrachain coupling is ferromagnetic and the interchain one is antiferromagnetic. Such a model is suitable to describe some hexagonal ABX_3 compounds. We are interested, in particular, in $CsCuCl_3$, where our theoretical results compare favorably with magnetic resonance experimental data and with magnetization measurements as a function of the external magnetic field. The role of quantum and thermal fluctuations in the selection of a particular spin pattern out of the infinitely many configurations that minimize the classical energy of the model is discussed.

I. INTRODUCTION

The Heisenberg antiferromagnet on a triangular lattice is an interesting widely investigated model. The interest in this subject dates back to the exact solution of the Ising triangular antiferromagnet,[1] where long-range order fails both at zero and finite temperature.

An external magnetic field in the plane of the spins yields a very rich phenomenology in triangular antiferromagnets with continuous symmetry. Indeed, a continuous family of infinitely many spin configurations minimize the energy of such models in classical approximation so that quantum[2,3] and thermal fluctuations[4–6] are crucial to select the configuration observed in actual compounds.

Analytic expansion[2] for the isotropic triangular Heisenberg antiferromagnet suggests that zero-point motion fluctuations select a low-field three-sublattice configuration with one spin opposite to the field, followed by a collinear phase with two spins parallel and one spin antiparallel to the field at intermediate field. At higher fields an asymmetric fan appears until the saturated configuration is reached. The scenario is similar to that obtained in planar and classical models where the "up-up-down" phase is stabilized only by thermal fluctuations.[4–6]

Recently,[3] we have studied the behavior of the 2D triangular quantum Heisenberg model with a planar anisotropy. In particular, we have obtained the spin wave spectra and we have compared the uniform mode energies with magnetic resonance data of $CsCuCl_3$.[7,8] $CsCuCl_3$ is a hexagonal compound of the ABX_3 family, where A is an alkali element, B is a transition metal ion, and X can be Cl, Br, or I. $CsCuCl_3$ can be modeled as a lattice of linear ferromagnetic chains of spins $S=1/2$ forming a triangular lattice in the planes perpendicular to the c axis. In spite of the 2D nature of the model we have studied, the agreement with experiment as for the uniform mode energy in external magnetic field is suggestive.[3,8] Notice that this agreement is assured only if the in-plane spin configuration is the configuration selected by quantum fluctuations, whereas the fitting is impossible if one chooses as ground-state configuration the apparently more obvious spin configuration with a spin parallel to the field.[7,8]

However, the good fit between the uniform mode energies of a triangular antiferromagnet in an external magnetic field and the magnetic resonance data of $CsCuCl_3$ could appear to be an accident because one might expect that the 3D nature of the actual compound could be crucial, so that quantum fluctuations which are dominant in the 2D model might play a minor role in 3D.

For this reason we consider here a 3D model where the main features of $CsCuCl_3$ are taken into account.

II. UNIFORM MODES AND MAGNETIZATION

The Hamiltonian we consider is the Heisenberg Hamiltonian where the intrachain ferromagnetic interaction is J_0 and the interchain antiferromagnetic coupling between x and y spin components is $J<0$, whereas $J(1-\eta)$ is the interchain coupling between z spin components. An external magnetic field in the c plane is considered. The spin configurations we consider are characterized by three spins per unit cell. The in-plane and out-of-plane lattice constants will be assumed of unit length. Let us indicate by ϕ_1, ϕ_2, ϕ_3, the angles that the spins of the unit cell form with the magnetic field. In order to get the ground state configurations, the elementary excitation energies, and the low-temperature properties, we have performed the customary steps: introduction of local axis according to ϕ_1, ϕ_2, ϕ_3, and Holstein–Primakoff spin-boson transformation. The solution of the lin-

 0021-8979/94/75(10)/6061/3/$6.00 © 1994 American Institute of Physics

earized equations of motion for the spin components along the local reference axis, gives the following spin wave frequencies:

$$\hbar\omega_q^{(s)} = 4J_0 S\sqrt{x_q^{(s)}}, \qquad s=1,2,3, \tag{1}$$

where $x_q^{(s)}$ are the solutions of the following cubic equation:

$$x^3 - ax^2 + bx - c = 0, \tag{2}$$

where

$$a = 3(1-\cos q_z + j)^2 + 2j^2(1-\eta)s_1|\gamma_q|^2, \tag{3}$$

$$b = (1-\cos q_z + j)^2[3(1-\cos q_z + j)^2 - j^2 s_2|\gamma_q|^2] + j^2(1-\eta)(1-\cos q_z + j)[2(1-\cos q_z + j)s_1|\gamma_q|^2 + \tfrac{1}{2}j(s_2 - s_1^2)(\gamma_q^3 + \gamma_q^{*3})] + j^2(1-\eta)^2[j^2 s_1^2|\gamma_q|^4 - 3(1-\cos q_z + j)^2|\gamma_q|^2 - j(1-\cos q_z + j)s_1(\gamma_q^3 + \gamma_q^{*3})], \tag{4}$$

$$c = [(1-\cos q_z + j)^3 - j^2(1-\cos q_z + j)s_2|\gamma_q|^2 + \tfrac{1}{2}j^3(s_2 - 1)(\gamma_q^3 + \gamma_q^{*3})][(1-\cos q_z + j)^3 - 3j^2(1-\eta)^2(1-\cos q_z + j)|\gamma_q|^2 + j^3(1-\eta)^3(\gamma_q^3 + \gamma_q^{*3})] \tag{5}$$

with $j = 3|J|/2J_0$, $h = g\mu_B H/6|J|S$, and

$$s_1 = -\tfrac{3}{2} + \tfrac{1}{2}h^2, \tag{6}$$

$$s_2 = \cos^2(\phi_1 - \phi_2) + \cos^2(\phi_2 - \phi_3) + \cos^2(\phi_1 - \phi_3), \tag{7}$$

where the values of ϕ_1, ϕ_2, ϕ_3 are the same as given by Eqs. (3) and (4) of Ref. 4.

$$\gamma_q = \frac{1}{3}\left(e^{iq_z} + 2e^{-iq_z/2}\cos\frac{\sqrt{3}}{2}q_y\right). \tag{8}$$

We have evaluated the $T=0$ classical energy E_0

$$E_0 = -JNS^2(3+h^2) - 2J_0NS^2, \tag{9}$$

the zero-point motion energy ΔE

$$\Delta E = -3JNS - 2J_0NS + \frac{1}{2}\sum_{s=1}^{3}\sum_q \hbar\omega_q^{(s)}, \tag{10}$$

the free-energy F

$$F = E_0 + \Delta E + k_B T\sum_{s=1}^{3}\sum_q \ln(1 - e^{-\beta\hbar\omega_q^{(s)}}), \tag{11}$$

and the magnetization of the model M

$$M = -\frac{\partial F}{\partial H}. \tag{12}$$

Equations (10)–(12) are evaluated treating the model as a gas of noninteracting magnons.

We list only the main results we have obtained leaving the details to an extended paper which will appear elsewhere.

(a) In classical approximation the minimum energy configurations at $T=0$ are the same as in the triangular model, forming a continuous family of infinitely many ground states.

(b) The zero-point motion energy is minimized by the same in-plane configuration as the triangular model where the low-field configuration is characterized by a spin out of three antiparallel to the field.

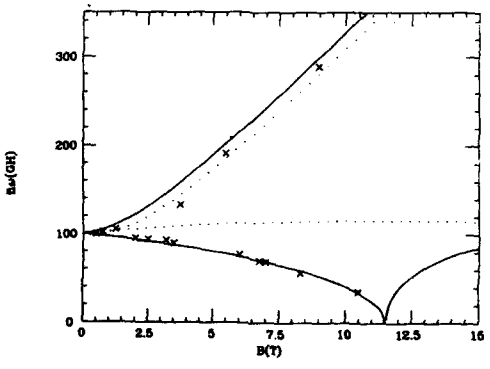

FIG. 1. Uniform modes of $CsCuCl_3$ vs magnetic field. Continuous and dotted curves are the theoretical results for the configuration with one spin opposite and parallel to the field, respectively. Crosses: magnetic resonance data (Ref. 8).

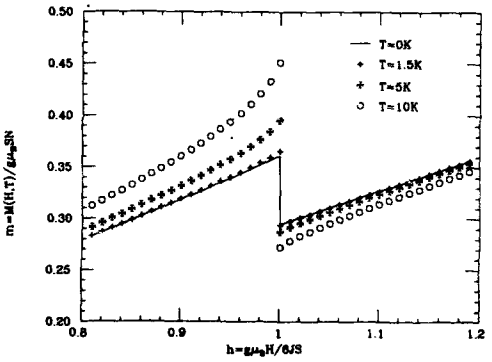

FIG. 2. Reduced magnetization as function of the magnetic field for $T=0$ K (continuous curve), $T=1.5$ K (crosses). $T=5$ K (fancy vertical crosses), $T=10$ K (circles).

(c) In the range of temperature and field we are interested to, thermal and quantum fluctuations support the same spin configuration. Only in the limit of vanishing field and temperature the thermal fluctuations favor the configuration with a spin parallel to the field, but the quantum fluctuations always dominate.

(d) The agreement between magnetic resonance data on $CsCuCl_3$ (Refs. 7,8) and the uniform mode energies as function of the field is very satisfactory as shown in Fig. 1 for Hamiltonian parameters $S=1/2$, $g=2.19$, $2J_0=64.5$ K, $j=0.2625$, $\eta=0.05364$, suggested by elastic neutron scattering in zero magnetic field.[9] Notice that dotted curves are the uniform mode energies one obtains starting from the configuration with one spin out of three parallel to the field. As one can see the selection of the spin configuration by quantum fluctuations is essential to explain experimental data.

(e) A first-order phase transition from the distorted helix to the asymmetric fan is induced by the zero-point motion. Notice that the reduced magnetization $m=M/g\mu_B NS$ in classical approximation at zero temperature is given by $m=h/3$ for $0<h<3$. In Fig. 2 the simultaneous effect of quantum and thermal fluctuations on the magnetization [see Eq. (12)] is shown for selected temperatures and the same Hamiltonian parameters quoted at point (d). Obviously the free energy in Eq. (11) is evaluated for the spin configurations selected by the quantum and thermal fluctuations as illustrated at points (b) and (c). Notice the unphysical decreasing of the magnetization at increasing magnetic field around $h=1$ ($H=11.5$ T) requiring an equal area Maxwell construction leading to a plateau in the curve $m(h)$. The size of the coexistence region is $\Delta H=2.1T$, $2.5T$, $3.6T$, for $T=1.5$, 5, 10 K, respectively. A plateau was actually observed in experiment[10] at $T\simeq 1.5$ K. An analogous plateau is found even in 2D model but it is related to the onset of the intermediate "up-up-down" phase supported by crucial nonlinear contributions which allow long-range order at finite temperature.[4] In the present 3D model long-range order is still found in harmonic approximation so that nonlinear contributions related to magnon-magnon interaction, can be neglected. Our result suggests that the plateau of the magnetization observed in $CsCuCl_3$ (Ref. 10) corresponds to coexistence of distorted helix and asymmetric fan, whereas in the triangular antiferromagnet the onset of the "up-up-down" phase is expected on the basis of analytic calculations[4] and Monte Carlo simulations.[6] Elastic neutron scattering experiment could unambiguously test the nature of this phase because the position of the Bragg peaks is the same in both cases, but the geometrical extinction of the Bragg peak could be fully achieved only if the spin configuration is collinear as it is the case of the "up-up-down" phase.

ACKNOWLEDGMENT

This research was supported in part by INFM.

[1] G. H. Wannier, Phys. Rev. **79**, 357 (1950); Phys. Rev. B **7**, 5017 (1973).
[2] A. V. Chubukov and D. I. Golosov, J. Phys. CM **3**, 69 (1991).
[3] E. Rastelli and A. Tassi, Z. Phys. B (in press).
[4] E. Rastelli, A. Tassi, A. Pimpinelli, and S. Sedazzari, Phys. Rev. B **45**, 7936 (1992).
[5] H. Kawamura, J. Phys. Soc. Jpn. **53**, 2452 (1984); H. Kawamura and S. Miyashita, *ibid.* **54**, 4530 (1985).
[6] D. H. Lee, J. D. Joannopoulos, J. W. Negele, and D. P. Landau, Phys. Rev. Lett. **52**, 433 (1984).
[7] W. Palme, F. Mertens, O. Born, B. Lüthi, and U. Schotte, Solid State Commun. **76**, 873 (1990).
[8] W. Palme, H. Kriegelstein, G. Gojkovic, and B. Lüthi, Transition Metal Conference ICPTM 92, Darmstadt, Germany.
[9] K. Adachi, N. Achiwa, and M. Mekata, J. Phys. Soc. Jpn. **49**, 545 (1980).
[10] H. Nojiri, Y. Tokunaga, and M. Motokawa, J. Phys. (Paris) **49**, C8-1459 (1988).

Scaling behavior of the homogeneous magnetization dynamics in the ferromagnetic state of EuS

R. Dombrowski, D. Görlitz, J. Kötzler, and Chr. Marx
Institut für Angewandte Physik, Universität Hamburg, Jungiusstrasse 11, D—20355 Hamburg, Germany

Using a broadband vectorial microwave reflectometer, we measured the longitudinal dynamic susceptibility of a EuS sphere between 0.1 and 20 GHz in the temperature interval 4.2 K$\ll T\ll T_c\approx$16.5 K. For low internal fields, the shape corresponds to a heavily overdamped Lorentzian resonance, $\chi_z^{-1}(\omega)=\chi_z^{-1}(0)i\omega/L_z-(\omega/\Omega_z)^2$ where $L_z\ll\Omega_z$. The field and temperature dependence of the intrinsic kinetic coefficient and resonance is fully explained by that of the static susceptibility $\chi_z(0)$. Surprisingly, the resulting scaling function, $L_z[\chi_z(0)]$, agrees exactly with that observed earlier above T_c, where $L_z[\chi_z(0)]$ could quantitatively be explained by a crossover from a van Hove behavior for large $\chi_z(0)$, due to dipolar anisotropic fluctuations, to a critical speeding-up for $\chi_z(0)<1$, where isotropic spin diffusion prevails. This finding suggests that the dipolar anisotropy dominates the magnetization dynamics also below T_c of EuS, which seems to be supported by the fact that the correlation frequency of the torques acting on the magnetization, $\omega_c=\Omega_z^2/L_z$, agrees with the relaxation rate of the longitudinal magnetization fluctuations, $\delta\mathbf{M}_\mathbf{q}\|\mathbf{q}$.

I. INTRODUCTION

Over almost two decades, the semiconducting europium sulphide serves as one of the preferred model ferromagnets for investigating the effects of fluctuations on the magnetization dynamics.[1–8] Whereas above the Curie temperature of EuS, $T_c=16.56$ K, all recent data on the homogeneous[6,8] and inhomogeneous ($\mathbf{q}\neq0$)[7] dynamics are now quantitatively explained by numerical solutions of the mode-coupling (MC) equation for a Heisenberg ferromagnet, including the inevitable dipole–dipole interaction,[9,10] the understanding is still unsatisfying below T_c. There the presence of the spontaneous magnetization, the spinwaves, the anisotropy field and of domains complicates the situation, and apart from results for some limiting cases,[9,11] a comprehensive theory on the magnetization dynamics for a real ferromagnet is still lacking.

The present communication extends a previous work on the homogeneous dynamics near T_c of EuS[8] to temperatures as low as 4.2 K and to higher magnetic fields required to remove the domains and to realize homogeneous internal fields within a crystalline sample spheroid $H_{\rm int}=H-N_zM(T,H)$, which should be larger than the anisotropy field of EuS, $H_A(T)=30$ Oe $[M_s(T)/M_s(0)]$[6,12] but also small enough to avoid the suppression of fluctuations. It is our aim to investigate how far the scaling property of the damping of the homogeneous magnetization observed near T_c[8] extends into the ferromagnetic regime and to finite internal fields. By increasing the maximum frequency from 1.5 to 20 GHz, we also search for intrinsic dynamical effects on the kinetic coefficient of the damping L_z of the longitudinal susceptibility defined by:[1]

$$\chi_z(\omega,T,H)=\left(\frac{1}{\chi_z(T,H)}+\frac{i\omega}{L_z(\omega,T,H)}\right)^{-1}, \tag{1}$$

which may help to elucidate the role of the fluctuations.

The results of this study should also provide a firmer basis to describe the dynamics of the magnetization at finite temperatures up to the Curie point,[13] within the domains and resulting from the wall motion, starting from the micromagnetic equations of motion.

II. RESULTS

The measurements have been performed on a sphere ($N_z=\frac{1}{3}$) by simultaneous recording of dispersion and absorption using a vectorial microwave reflectometer,[14] which recently was upgraded by a commercial *s-parameter test set* (hp-8516A). To investigate the longitudinal magnetization dynamics, the microwave field in the shorted end of a coaxial waveguide was aligned with the dc field supplied by a superconducting saddle coil up to 1.5 T. The amplitude was kept small enough to obtain linear-response signals. No hysteretic effects occurred in the present range of temperature and field. In the standard modes, we measured $\chi'-i\chi''$ sweeping field or temperature at fixed frequency and calibrated the signals using the absolute values available at T_c and lower frequencies.[8]

For some selected temperatures and fields, the frequency dependence of dispersion and absorption is shown in Fig. 1. An interesting feature we note is the significant deviation from pure relaxational dynamics, clearly evidenced by the negative dispersion. The dynamical shape can be well fitted by a Lorentzian,

$$\chi_z(\omega,T,H)=\left(\frac{1}{\chi_z(T,H)}+\frac{i\omega}{L_z(\omega,T,H)}-\frac{\omega^2}{\Omega_z^2(T,H)}\right)^{-1}. \tag{2}$$

In this form, the kinetic coefficient of the damping L_z and the resonance frequency Ω_z do not depend on the external susceptibility, $\chi_z^{-1}(T,H)$, but represent material constants reflecting the intrinsic dynamics. The effect of internal magnetic fields, larger than the maximum anisotropy field, $H_A(0)=30$ Oe,[12] on both parameters is illustrated by Fig. 2

 0021-8979/94/75(10)/6054/3/$6.00 © 1994 American Institute of Physics

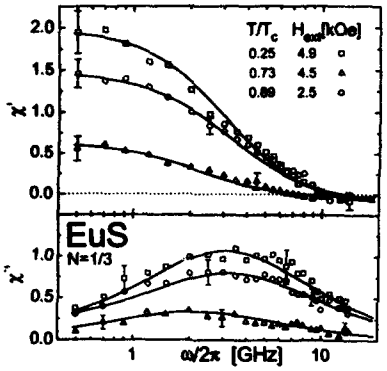

FIG. 1. (a) Dispersion and (b) absorption of the longitudinal dynamic susceptibility measured parallel to the applied field on a EuS sphere. Full lines represent fits to the Lorentzian shape, Eq. (2).

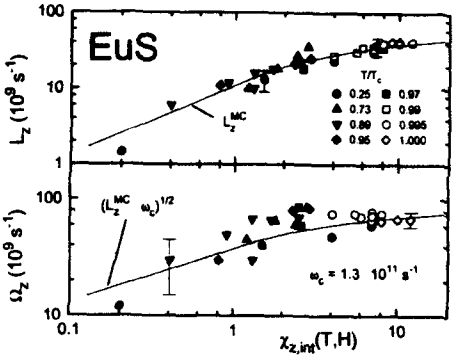

FIG. 3. Scaling behavior of (a) the kinetic coefficient and (b) the resonance frequency in terms of the internal susceptibility. The full line in (a) corresponds to solutions of the mode-coupling equations,[9] strictly valid above T_c and for $H=0$.

for various temperatures below T_c. Obviously, H_{int} is suppressing L_z and Ω_z more heavily at lower temperatures.

The most interesting phenomena are shown in Fig. 3. $L_z(T,H)$ and $\Omega_z(T,H)$ plotted against the static internal susceptibility $\chi_{z,int}=(\chi_z^{-1}-N_z)^{-1}$ [15] collapse on two single curves, and according to Fig. 3(a) the resulting scaling function agrees with that predicted (and confirmed[8]) for L_z for the *paramagnetic* critical regime and *zero applied field*.[9] This scaling behavior means that similar to the observation at elevated temperatures,[8] the intrinsic magnetization dynamics depends on temperature and field only via the internal susceptibility $\chi_z(T,H)$. Obviously, this scaling holds down to the lowest temperatures, where the spin-wave fluctuations dominate.

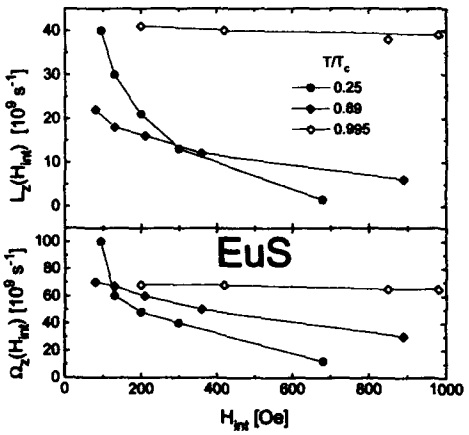

FIG. 2. (a) Kinetic coefficient and (b) resonance frequency, determined from fits exemplified by Fig. 1, versus the internal magnetic field for three different temperatures.

III. DISCUSSION

To discuss the results, let us first consider the Lorentzian shape of $\chi_z(\omega)$, since it can directly be associated to the general form, Eq. (1), by assuming a Debye spectrum for the frequency dependence of the kinetic coefficient,

$$L_z(\omega;T,H)=\frac{L_z(T,H)}{1+i\omega/\omega_c}\ . \tag{3}$$

Then the intrinsic resonance frequency is simply given by

$$\Omega_z(T,H)=[\omega_c\cdot L_z(T,H)]^{1/2}, \tag{4}$$

and the characteristic frequency ω_c is determined by the ratio Ω_z^2/L_z. Evaluating this quantity, we find it to be independent of temperature and field within the present accuracy, $\omega_c=1.3\times10^{11}\ s^{-1}$, which implies that the scaling property of $\Omega_z(T,H)$ shown in Fig. 3(b) arises from that of the "static" kinetic coefficient $L_z(T,H)$.

In order to find a possible origin for ω_c, we start from the general expression,

$$L_z(\omega;T,H)=\left(\frac{V}{kT}\right)\int_0^\infty dt[\dot{M}_z(t)\dot{M}_z(0)]e^{i\omega t}, \tag{5}$$

as given by the linear response theory,[16] where V is the sample volume and $\dot{M}_z(t)=i[\mathcal{H}(t),M_z]/\hbar$ are the torques acting on the longitudinal magnetization. Hence, the Debye shape in Eq. (3) implies that the correlation function of the torque decays exponentially, $[\dot{M}_z(t)\dot{M}_z(0)]\sim\exp(-\omega_c t)$. For ferromagnets, it has been demonstrated that regardless of their T_c the spin-flipping mechanism results from the dipole–dipole interaction $\mathcal{H}=\mathcal{H}_{dip}$.[6] We, therefore, refer to the MC theory for the Heisenberg ferromagnet with dipolar interaction[9] and extend the result for the "static" L_z to finite frequencies and fields in using:[17]

$$L_z^{Mc}(\omega;T,H)=\left(\frac{k_B\lambda_c}{\hbar}\right)^2\sum_{\mathbf{q}}\frac{\chi_l(\mathbf{q})\chi_t(\mathbf{q})}{\Gamma_l(\mathbf{q})+\Gamma_t(\mathbf{q})+i\omega}\ . \tag{6}$$

Here the static correlations between the longitudinal and transverse modes, $\delta\mathbf{M}(\mathbf{q})\|\mathbf{q}$, are given by $\chi_\alpha(\mathbf{q}) = [\chi_z^{-1}(T,H) + \delta_{\alpha,l} + (q/q_d)^2]^{-1}$, where q_d is the dipolar wave number[18] and $\Gamma_\alpha(\mathbf{q})$ are their relaxation rates ($\alpha = l,t$). Since the transverse correlations become critical at T_c, the sum in Eq. (6) is heavily weighted by the small-q contributions. Considering Eq. (6) at T_c, i.e., at the lowest temperature where the expression is valid, the relaxation rate of the transverse mode becomes extremely small, while that of the uncritical longitudinal modes attains a finite, q-independent value, $\hbar\Gamma_l(\mathbf{q}\to 0,T_c) = A q_d^{5/2}$.[9] Therefore, for the critical modes the denominators in Eq. (6) are dominated by Γ_l, which, after comparison of Eqs. (3) and (6), leads immediately to $\omega_c(T_c) \sim \Gamma_l(\mathbf{q}\to 0,T_c)$. Recently, the relaxation rate of these longitudinal modes has been determined by inelastic scattering of polarized neutrons,[7] resulting in $\Gamma_l(\mathbf{q}\to 0,T_c) = 98$ GHz, which is in good accord with ω_c following from the present analysis. Then the field and temperature independence of ω_c below T_c indicates that the dipolar anisotropy giving rise to this heavy damping still plays a dominant role in the ferromagnetic dynamics.

Finally, we discuss the key feature of the present work, i.e., the nearly constant kinetic coefficient at large static susceptibilities, crossing over to a slowing down of L_z with decreasing $\chi_{z,\mathrm{int}}(T,H)$, which agrees quantitatively with the scaling function $L_z[\chi_{z,\mathrm{int}}(T,H)]$ found above T_c of EuS, and also with the prediction of MC theory,

$$L_z^{\mathrm{MC}}(T \geqslant T_c, H\sim 0) = \frac{L_z(T_c, H\sim 0)}{[1+\chi_{z,\mathrm{int}}^{-1}(T,H)]^{(z+1)/2}}, \qquad (7)$$

indicated as a full line in Fig. 3(a). There is $L_z(T_c, H\to 0) = 58$ GHz, and the dynamical critical exponent z of the Heisenberg ferromagnet equals $\frac{5}{2}$. Qualitatively speaking, this feature indicates that the dipolar anisotropic scaling of the correlation functions $\chi_\alpha(\mathbf{q})$ below T_c is the same as above the Curie point. Accordingly, the strong dipolar force dictates the homogeneous magnetization dynamics also below T_c and minor energies, arising from the internal and anisotropy fields play no role. Apparently, this is due to the fact that the $q=0$ spin-wave gap is much smaller than the width of the spin-wave band, originating from the dipolar interaction. Then, the novel slowing down phenomenon of $L_z(T,H)$ observed here may be considered as an Anderson–Weiss exchange narrowing toward *low* temperatures, due to the dephasing of the spin-flipping dipolar interaction by the increasing dynamics of the magnetization modes. Of course, these rather crude arguments call for detailed theoretical considerations.

ACKNOWLEDGMENTS

We thank K. Fischer (Jülich) for supplying the EuS crystal and the Deutsche Forschungsgemeinschaft for financial support.

[1] J. Kötzler, G. Kamleiter, and G. Weber, J. Phys. C **9**, L361 (1976).
[2] O. W. Dietrich, J. Als-Nielsen, and L. Passell, Phys. Rev. B **14**, 4923 (1976).
[3] M. Shini and T. Hashimoto, Phys. Lett. A **68**, 241 (1978).
[4] S. C. Kondal and M. S. Seehra, J. Phys. C **15**, 2471 (1982).
[5] P. Böni, G. Shirane, H. G. Bohn, and W. Zinn, J. Appl. Phys. **61**, 3397 (1987); **63**, 3089 (1988).
[6] J. Kötzler, Phys. Rev. B **38**, 12 027 (1988).
[7] P. Böni, D. Görlitz, J. Kötzler, and J. L. Martinez, Phys. Rev. B **43**, 8755 (1991).
[8] J. Kötzler, E. Kaldis, G. Kamleiter, and G. Weber, Phys. Rev. B **43**, 11 280 (1991).
[9] E. Frey and F. Schwabl, Z. Phys. B **71**, 355 (1988).
[10] E. Frey, F. Schwabl, and S. Thoma, Phys. Rev. B **40**, 7199 (1989).
[11] R. Raghavan and D. L. Huber, Phys. Rev. B **14**, 1185 (1976).
[12] See, e.g., A. Kasuya and M. Tachiki, Phys. Rev. B **8**, 5298 (1973).
[13] D. Görlitz, J. Kötzler, and Chr. Marx (unpublished).
[14] D. Görlitz, J. Kapoor, and J. Kötzler, J. Phys. E **22**, 884 (1989).
[15] J. Kötzler, D. Görlitz, R. Dombrowski, and M. Pieper, Z. Phys. B (in press).
[16] E. Fick and G. Sauermann, *"The Quantum Statistics of Dynamic Processes," Springer Series in Solid State Sciences* (Springer, Berlin, 1990), Vol. 86.
[17] J. Kötzler, D. Görlitz, M. Hartl, and Chr. Marx, IEEE-MAG (in press).
[18] J. Kötzler, F. Mezei, D. Görlitz, and B. Farago, Europhys. Lett. **1**, 675 (1986).

Dynamical properties of quantum spin systems in magnetically ordered product ground states

V. S. Viswanath, Joachim Stolze,[a] and Gerhard Müller
Department of Physics, The University of Rhode Island, Kingston, Rhode Island 02881-0817

The one-dimensional spin-s XYZ model in a magnetic field of particular strength has a ferro- or antiferromagnetically ordered product ground state. The recursion method is employed to determine $T=0$ dynamic structure factors for systems with $s=\frac{1}{2}, 1, \frac{3}{2}$. The line shapes and peak positions differ significantly from the corresponding spin-wave results, but their development for increasing values of s suggests a smooth extrapolation to the spin-wave picture.

It necessarily the presence of strong quantum fluctuations in the ground state that is primarily responsible for turning the $T=0$ dynamics of a quantum many-body system into a challenging topic of condensed-matter theory. Even for systems with no correlated quantum fluctuations in their ground state, the dynamically relevant excitation spectrum may be exceedingly complex, and the spectral weight in dynamical quantities may be distributed over frequency bands of infinite width. This will be demonstrated for a system of localized spins with an exact ferro- or antiferromagnetic product ground state. The shortcomings of the *harmonic* alias *linear spin-wave* alias *single-mode* approximation are found to be considerable.

We consider the spin-s XYZ ferromagnet in a magnetic field,

$$H=-\sum_{l=1}^{N}\{J_x S_l^x S_{l+1}^x+J_y S_l^y S_{l+1}^y+J_z S_l^z S_{l+1}^z+hS_l^z\}, \quad (1)$$

for $J_x \geq J_y \geq J_z \geq 0$, even N, and periodic boundary conditions. If the magnetic field has a particular strength, $h=h_N=2s[(J_x-J_z)(J_y-J_z)]^{1/2}$, that system is known to have a product ground state wave function,

$$|G\rangle=\bigotimes_{l=1}^{N} U_l(\vartheta)|s\rangle_l, \quad (2)$$

where the unitary transformation represented by $U_l(\vartheta)$ describes a rotation of the spin direction at site l by an angle $\vartheta=\arccos\sqrt{(J_y-J_z)/(J_x-J_z)}$ away from the z axis into the xz plane.[1] $|G\rangle$ is a state of maximum ferromagnetic order, $\langle \mathbf{M}\rangle=\langle G|\mathbf{S}_l|G\rangle=(s\sin\vartheta, 0, s\cos\vartheta)$. The ground state energy is $E_G=-Ns^2(J_x+J_y-J_z)$.

Previous studies of this system, motivated by the search for new rigorous results in quantum many-body dynamics, led to two general conclusions:[2–4] (i) The conditions under which ferromagnetic spin waves are exact eigenstates of H are much more restrictive than those for the existence of the product ground state, namely $J_x=J_y$ or $q=\pi$ or $s\to\infty$, in addition to $h=h_N$. (ii) The realization of the product ground state $|G\rangle$ implies the following rigorous relations between the $T=0$ dynamic structure factors $S_{\mu\mu}(q,\omega)$:

$$S_{xx}(q,\omega)=S_{yy}(q,\omega)\cos^2\vartheta+4\pi^2 s^2\sin^2\vartheta\,\delta(\omega)\delta(q),$$

$$S_{zz}(q,\omega)=S_{yy}(q,\omega)\sin^2\vartheta+4\pi^2 s^2\cos^2\vartheta\,\delta(\omega)\delta(q). \quad (3)$$

The only known rigorous and explicit results pertain to the $s=\frac{1}{2}$ XY model ($J_x=1+\gamma$, $J_y=1-\gamma$, $J_z=0$), and can be evaluated in the form of a two-particle Green's function for free lattice fermions,[5] in combination with relations (3):[2–4]

$$S_{yy}(q,\omega)=\frac{\gamma}{2(1-\gamma)}\frac{\sqrt{4(1-\gamma^2)\cos^2(q/2)-(\omega-2)^2}}{[\omega-2\sin^2(q/2)]^2+\gamma^2\sin^2 q}\times\Theta[4(1-\gamma^2)\cos^2(q/2)-(\omega-2)^2]. \quad (4)$$

Whereas spin-wave theory predicts a single spectral line in $S_{\mu\mu}(q,\omega)$ at the frequency $\omega_{SW}=2s(J_x-J_y\cos q)$, expression (4) is represented by a spectral-weight distribution that consists of a peak shifted relative to ω_{SW} and with nonzero intrinsic width.[2] However, the result (4) does not yet fully reflect the generic structure of $S_{\mu\mu}(q,\omega)$ for this situation.

Our analysis of generic cases ($s>\frac{1}{2}$ XY or XYZ with arbitrary s) employs the recursion method. For this application, it is based on an orthogonal expansion of the wave function $|\Psi_q^\mu(t)\rangle=S_q^\mu(-t)|G\rangle$, where $S_q^\mu=N^{-1/2}\sum_l e^{iql}S_l^\mu$.[6–8] The recursion algorithm produces (after some intermediate steps) a sequence of continued-fraction coefficients $\Delta_1^{\mu\mu}(q)$, $\Delta_2^{\mu\mu}(q)$,..., for the relaxation function,

$$c_0^{\mu\mu}(q,z)=\cfrac{1}{z+\cfrac{\Delta_1^{\mu\mu}(q)}{z+\cfrac{\Delta_2^{\mu\mu}(q)}{z+\cdots}}}, \quad (5)$$

which is the Laplace transform of the symmetrized correlation function $\Re\langle S_q^\mu(t)S_{-q}^\mu\rangle/\langle S_q^\mu S_{-q}^\mu\rangle$. The dynamic structure factor $S_{\mu\mu}(q,\omega)$, which is the Fourier transform of $\langle S_q^\mu(t)S_{-q}^\mu\rangle$, can be obtained directly from (5) as follows (for $T=0$):

$$S_{\mu\mu}(q,\omega)=4\langle S_q^\mu S_{-q}^\mu\rangle\Theta(\omega)\lim_{\epsilon\to 0}\Re[c_0^{\mu\mu}(q,\epsilon-i\omega)]. \quad (6)$$

The simple dependence of the product wave function $|G\rangle$ on the size of the system offers the advantage that we can compute a significant number of size-independent coefficients $\Delta_l^{\mu\mu}(q)$.[9] In Fig. 1 we have plotted the sequences $\Delta_l^{\mu\mu}(q=0)$ for four different applications of the recursion method. Each one of the four qualitatively different patterns

[a]On leave from Institut für Physik, Universität Dortmund, 44221 Dortmund, Germany.

 0021-8979/94/75(10)/6057/3/$6.00 © 1994 American Institute of Physics

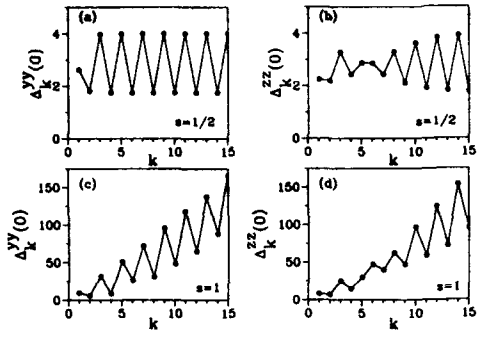

FIG. 1. Continued-fraction coefficients $\Delta_k^{yy}(0)$ and (rescaled) $\Delta_k^{zz}(0)$, as obtained from the recursion method for the determination of the $T=0$ dynamic structure factors $S_{\mu\mu}(q=0,\omega)$, $\mu=y,z$, of the 1D spin-s XY model ($J_x=1+\gamma$, $J_y=1-\gamma$, $J_z=0$, $h=h_N$) with $\gamma=\frac{3}{4}$, and the spin quantum number s, as specified in each of the four panels.

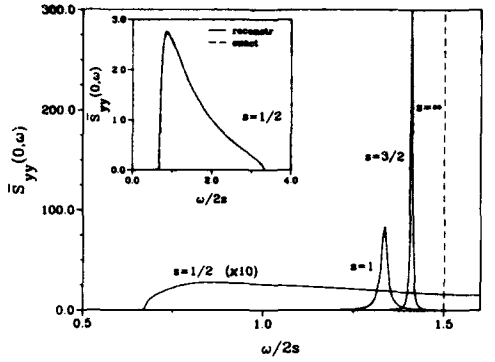

FIG. 2. Normalized dynamic structure factor $\tilde{S}_{yy}=S_{yy}(q,\omega)/\langle S_q^y S_{-q}^y\rangle$ (for $q=0$) at $T=0$ of the 1D XY model ($J_x=1+\gamma$, $J_y=1-\gamma$, $J_z=0$, $h=h_N$) with $\gamma=\frac{3}{4}$. The three curves in the main plot represent the results for $s=\frac{1}{2},1,\frac{3}{2}$, as obtained from the recursion method combined with the continued-fraction analysis outlined in the text. For better visibility, we have expanded the vertical scale by a factor of 10 for the spin-$\frac{1}{2}$ curve. The number of continued-fraction coefficients used is $K=16$. The vertical dashed line represents the classical spin-wave result for the same function. The inset shows again the spin-$\frac{1}{2}$ result (solid line) on different scales, now in comparison with the exact expression (4) (dashed line).

displayed by these sequences bears the signature of a characteristic property of the associated $S_{\mu\mu}(q=0,\omega)$.

In panels (a) and (b), the Δ_{2k-1} and the Δ_{2k} tend to converge to different (finite) values $\Delta_\infty^{(o)}$ and $\Delta_\infty^{(e)}$, respectively. If $\Delta_\infty^{(o)}>\Delta_\infty^{(e)}$ as in (a), the implication for the dynamic structure factor is that all its spectral weight is confined to the interval $\omega_{\min}\le\omega\le\omega_{\max}$, with $\omega_{\min}=|\sqrt{\Delta_\infty^{(e)}}-\sqrt{\Delta_\infty^{(o)}}|$, $\omega_{\max}=\sqrt{\Delta_\infty^{(e)}}+\sqrt{\Delta_\infty^{(o)}}$. If $\Delta_\infty^{(o)}<\Delta_\infty^{(e)}$ as indicated in (b) for $k>5$, the dynamic structure factor has a $\delta(\omega)$ contribution, in addition to the continuous part.[8] These are precisely the properties of the known functions $S_{yy}(0,\omega)$ and $S_{zz}(0,\omega)$ for the $s=\frac{1}{2}$ XY model, as inferred from (4) and (3).

In panels (c) and (d), the two subsequences Δ_{2k} and Δ_{2k-1} grow roughly linearly with k to infinity, but with different average slopes. The linear average growth of a Δ_k sequence implies that the associated dynamic structure factor has unbounded support and that the spectral weight tapers off by a Gaussian decay law, $\sim e^{-\omega^2}$, at high frequencies. If the Δ_{2k-1} grow more steeply than the Δ_{2k} as in (c), it can be concluded that the dynamic structure factor has a gap at $0<\omega<\Omega$. If that pattern is reversed asymptotically, as in (d) for $k>5$, it signals the presence of an additional $\delta(\omega)$ contribution in the dynamic structure factor. Our observations indicate that patterns (c) and (d) are generic for $S_{yy}(0,\omega)$ and $S_{zz}(0,\omega)$, $S_{xx}(0,\omega)$, respectively, of the spin-s XYZ model. The exception is the $s=\frac{1}{2}$ XY case, where patterns (a) and (b) obtain.

For fixed $q\neq 0$, the Δ_k sequences of all three functions $S_{\mu\mu}(q,\omega)$, $\mu=x,y,z$ are the same in consequence of (3). For $q=0$, by contrast, the additional $\delta(\omega)$ contributions in $S_{xx}(0,\omega)$ and $S_{zz}(0,\omega)$ lead to a pattern reversal from (a) to (b) or from (c) to (d), with two characteristic properties: (i) it leaves the sum of successive pairs of coefficients, $\Delta_{2k-1}^{\mu\mu}(0)+\Delta_{2k}^{\mu\mu}(0)$, invariant; (ii) the factor by which the first coefficient changes determines the weight of the $\delta(\omega)$ contribution: $\Delta_1^{xx}(0)/\Delta_1^{yy}(0)=\cos^2\theta$, $\Delta_1^{zz}(0)/\Delta_1^{yy}(0)=\sin^2\theta$.

For the reconstruction of the dynamic structure factor $S_{yy}(0,\omega)$ from the known coefficients $\Delta_1^{yy}(0),\ldots,\Delta_K^{yy}(0)$, such as is shown for two distinct cases in panels (a) and (c) of Fig. 1, we proceed according to the well-tested method outlined previously.[7,8,10] At first, we select a model spectral density $\bar{\Phi}_0(\omega)$, which is compatible with the general structure of $S_{yy}(0,\omega)$ identified above. For case (a) we choose the function

$$\bar{\Phi}_0(\omega)=\frac{\pi}{\omega_{\max}-\omega_{\min}}\Theta(|\omega|-\omega_{\min})\Theta(\omega_{\max}-|\omega|), \quad (7)$$

which has bounded support and a gap, and for the case (c) the function

$$\bar{\Phi}_0(\omega)=\frac{2\sqrt{\pi}}{\omega_0}\Theta(|\omega|-\Omega)e^{-(|\omega|-\Omega)^2/\omega_0^2}, \quad (8)$$

which has unbounded support and a gap. Each function has two parameters, whose values are determined by matching the coefficients $\Delta_k^{yy}(0)$ of panels (a) and (c) with the continued-fraction coefficients of the corresponding model relaxation function,

$$\bar{c}_0(z)=\frac{1}{2\pi i}\int_{-\infty}^{+\infty}d\omega\frac{\bar{\Phi}_0(\omega)}{\omega-iz}. \quad (9)$$

Next, we expand the model relaxation function into a continued fraction down to level K and replace its continued-fraction coefficients by those from panels (a) and (c) for the two situations, respectively. That yields an approximation of (5), which is of high precision, as we shall see. The dynamic structure factor $S_{yy}(0,\omega)$ is then obtained via (6). The practical aspects of this procedure have been described in previous applications to different physical situations.[7,10]

In order to demonstrate the degree of accuracy of our method, we first reconstruct the function $S_{yy}(0,\omega)$ for the $s=\frac{1}{2}$ XY model with $\gamma=\frac{1}{4}$, from the $\Delta_k^{\gamma\gamma}(0)$ of panel (a) and compare it with the exact expression (4). The two results are plotted in the inset to Fig. 2. The coefficients $\Delta_k^{\gamma\gamma}(0)$ of panel (c) pertain to spin quantum number $s=1$. The reconstructed dynamic structure factor $S_{yy}(0,\omega)$ is shown in the main plot of Fig. 2. Note the different vertical and horizontal scales. Also shown are the results for $s=\frac{1}{2}$ (the same as in the inset) and for $s=\frac{3}{2}$. The latter has been reconstructed from 16 coefficients $\Delta_k^{\gamma\gamma}(0)$, which also exhibit pattern (c). The spectral line shown dashed represents the spin-wave result $S_{yy}(0,\omega)=2\pi\delta(\omega-4s\gamma)$, which is exact in the classical limit $s=\infty$. We conclude that quantum effects are very significant. They produce nontrivial line shapes and move the peak positions by as much as a factor of 2.1 relative to the spin-wave prediction. Nevertheless, convergence of the quantum results for increasing s toward the classical result is indicated.

Our results thus expose the limitations of spin-wave theory in quantum spin dynamics very clearly. No matter how favorable the circumstances for the application of a harmonic analysis or single-mode approximation are, the generic structure of the functions $S_{\mu\mu}(q,\omega)$ for quantum spin systems at $T=0$ deviates considerably from the results produced on that basis, especially for small spin quantum numbers: The spectral weight is distributed over bands of infinite width (unbounded support),[11] and is dominated by lines with nonzero intrinsic width at frequencies that differ significantly from the spin-wave dispersion. Since these quantum effects cannot be attributed to the strongly fluctuating nature of typical 1D phenomena, there is no reason to assume that they are less pronounced in 2D and 3D magnetic systems.

All the conclusions reached in this study for the spin-s XYZ ferromagnet ($J_\mu \geq 0$) can be translated into similar conclusions for the same model with antiferromagnetic coupling ($J_\mu \leq 0$). That model has a spin-flop ground state at a particular strength of the magnetic field. Therefore, the order parameter causes a pattern reversal at $q=\pi$ in $S_{xx}(q,\omega)$ and at $q=0$ in $S_{zz}(q,\omega)$.

ACKNOWLEDGMENTS

This work was supported by the U.S. National Science Foundation, Grant No. DMR-93-12252. Computations were carried out on supercomputers at the National Center for Supercomputing Applications, University of Illinois at Urbana—Champaign. J.S. gratefully acknowledges support by the Max Kade Foundation.

[1] J. Kurmann, H. Thomas, and G. Müller, Physica A **112**, 235 (1982).
[2] J. H. Taylor and G. Müller, Phys. Rev. B **28**, 1529 (1983).
[3] G. Müller and R. E. Shrock, Phys. Rev. B **32**, 5845 (1985).
[4] G. Müller, Z. Phys. B **68**, 149 (1987).
[5] T. Niemeijer, Physica **36**, 377 (1967); S. Katsura, T. Horiguchi, and M. Suzuki, *ibid.* **46**, 67 (1970).
[6] E. R. Gagliano and C. A. Balseiro, Phys. Rev. Lett. **59**, 2999 (1987); M. H. Lee, Phys. Rev. B **26**, 2547 (1982).
[7] V. S. Viswanath and G. Müller, J. Appl. Phys. **67**, 5486 (1990); **70**, 6178 (1991).
[8] V. S. Viswanath and G. Müller, "The user-friendly recursion method" (unpublished).
[9] Since the functions $S_{xx}(0,\omega)$ and $S_{zz}(0,\omega)$ contain (for finite N) a strongly N-dependent contribution at $\omega=0$, which represents the (extensive) order parameter $N\langle M\rangle$, the corresponding coefficients $\Delta_k^{\mu\mu}(0)$, $\mu=x,z$ generated by the recursion method are not automatically N independent. However, they can be made N independent by a simple rescaling and then describe $S_{\mu\mu}(0,\omega)$ of the infinite system. For this study we have converted the $\Delta_k^{zz}(0)$ into frequency moments, multiplied those by $\langle S_q^z S_{-q}^z\rangle/\langle S_q^x S_{-q}^x\rangle$ (for $q=0$) and then converted them back to continued-fraction coefficients.
[10] V. S. Viswanath, S. Zhang, J. Stolze, and G. Müller, Phys. Rev. B (in press).
[11] The $s=\frac{1}{2}$ XY model, which yields finite bandwidths (bounded support), is an exception in that aspect.

Magnons in ferromagnetic terbium under high pressure

S. Kawano
Research Reactor Institute, Kyoto University, Kumatori, Sennan, Osaka 590-04, Japan

J. A. Fernandez-Baca and R. M. Nicklow
Solid State Division, Oak Ridge National Laboratory, Oak Ridge, Tennessee 37831-6393

We have performed an inelastic neutron scattering experiment in order to investigate the pressure dependence of the magnon dispersion of terbium in its ferromagnetic phase. Our measurements were performed along the crystal c axis at 90 K (well below the Curie temperature $T_c = 220$ K) at ambient pressure, and at 4.3 and 15.2 kbar of applied hydrostatic pressure. The difference between the magnon dispersion curves at ambient pressure and at 4.3 kbar is small, while at 15.2 kbar the dispersion curve shifts appreciably towards higher energies. The measured magnon dispersion curves have been analyzed using a Hamiltonian that includes Heisenberg exchange as well as single-ion anisotropy terms. For each dispersion curve we have calculated five exchange constants and two anisotropy terms. The energy gap at $q = 0$ due to the anisotropies is enhanced with pressure and exchange interactions acting between c planes appear to decrease with the application of high pressure.

I. INTRODUCTION

The magnetic properties of the rare earth (RE) metals under high pressure have been extensively studied in the past decades.[1] These studies have provided useful information on the nature of the magnetic interactions that cause the anisotropy and characteristic oscillatory spin configurations of these elements. These efforts, however, have been concentrated on magnetic static properties, and have included studies of the ordering temperatures from susceptibility and electrical resistivity measurements,[2,3] and studies of magnetic structures using neutron diffraction.[4,5] The study of the spin dynamics of these systems has been hampered by experimental difficulties, the requirement of relatively large samples (several mm^3) needed to perform neutron inelastic scattering measurements has been incompatible with the available high-pressure devices that could be used at low temperatures. Recently Onodera *et al.*[6] have developed a McWhan-(clamp) type high-pressure cell for neutron scattering that is capable of accommodating a relatively large sample, and achieving up to about 30 kbar at temperatures between 4 K and room temperature. In this paper, we present preliminary results of a recent inelastic neutron scattering experiment performed using this high-pressure device. In this experiment we have studied the magnon dispersion of ferromagnetic terbium under pressures of up to 15.2 kbar. The reason for the selection of Tb for this type of study is that this element has one of the lowest thermal neutron absorption cross sections among the RE, at the same time that it has a large magnetic moment ($9.3\mu_B$) in its ferromagnetic phase.

The nature of the magnetic excitations in the heavy RE metals is determined by the Hamiltonian:[7]

$$\mathcal{H} = \mathcal{H}_{ex} + \mathcal{H}_{cf}. \tag{1}$$

The first term in this equation, $\mathcal{H}_{ex}$, is the exchange energy due to a long-range RKKY exchange interaction between the RE highly localized 4f moments. This term is predominantly isotropic and has a Heisenberg form. The second term, $\mathcal{H}_{cf}$, is the crystal-field (CF) anisotropy energy. Other sources of anisotropy (magnetoelastic energy, etc.) are neglected in this Hamiltonian. It is frequently assumed that in the rare earth metals $\mathcal{H}_{ex} \gg \mathcal{H}_{cf}$ and that the only effect of the crystal-field anisotropy is to impose a preferred direction of the magnetization and to produce a gap in the magnon spectrum. The energy levels under this assumption are equally spaced J_z levels and the low-temperature elementary excitations of the system are magnons, or collective propagating excitations from the $\langle J_z \rangle = J$ ground state. In this model the magnon dispersion relation can be obtained by means of Holstein–Primakoff-type transformations followed by the proper diagonalization of the transformed Hamiltonian. This approach has been used successfully to describe the magnetic excitations of Gd, Tb, Dy, and Ho.[7] The magnetic excitations of ferromagnetic Tb at ambient pressure have been studied in detail some time ago.[8–10] It is of interest, therefore, to compare the magnon dispersion from our measurements with those performed under ambient pressure.

II. EXPERIMENT

The sample used in this experiment was a single crystal prepared by strain annealing an arc melted button of high-purity (99.9%) Tb. The sample was cut in an approximately cylindrical shape of about 8 mm length and 4 mm diameter. The sample was placed inside an aluminum microcell that contained a pressure-transmitting "incompressible" fluid, Fluorinert (a fluorocarbon manufactured by Sumitomo Chem. Co.). The aluminum microcell was placed in a high-pressure cell (described by Onodera *et al.*[6]), which was mounted in a closed cycle helium refrigerator. The pressure at the sample was hydrostatic and the magnitude of this pressure was monitored by *in situ* measurements of the lattice parameter of a NaCl single crystal, which was also mounted in the aluminum microcell, next to the Tb crystal. For the measurements at ambient pressure and at 4.3 kbar pressure, a sapphire (single crystal) cylinder was used as a pressure supporting device. The use of this cylinder resulted in a very favorable signal-to-background ratio in the magnon measurements. Unfortunately this sapphire cylinder could not stand

 0021-8979/94/75(10)/6080/3/$6.00 © 1994 American Institute of Physics

pressures higher than 7 kbar, and for the measurements of 15.2 kbar a polycrystalline Al_2O_3 pressure supporting cylinder was used instead. The use of this Al_2O_3 cylinder resulted in a poorer signal-to-background ratio. All the measurements were performed at 90 K, which is well below the Curie temperature (T_c=220 K).

The neutron scattering measurements were performed using conventional triple-axis spectrometers at the High Flux Isotope Reactor (HFIR) at Oak Ridge National Laboratory. The measurements were made in both the constant-wave-vector Q mode, at Q=(0,0,2+ξ) with $\xi \ll 1$, and the constant-energy mode. Pyrolitic graphite (PG) crystals were used as monochromator and analyzer. The final neutron energy was kept fixed at E_F=13.7 meV, and a PG filter was used in order to eliminate higher-order wavelength contaminations. Soller-slit collimators were utilized to obtain horizontal collimations of 60′-40′-40′-60′ (for the measurements at ambient pressure and at 4.3 kbar) and 60′-40′-40′-30′ (for the measurements at 15.2 kbar).

III. RESULTS AND DISCUSSION

In all our measurements at ambient pressure and at 4.3 kbar, well defined magnon peaks were observed at all wave vectors studied. At 15.2 kbar, on the other hand, well resolved peaks were observed only at the larger wave vectors while at the smaller wave vectors the observation of the magnon peaks was difficult due to the high background of neutrons scattered from the Al_2O_3 pressure supporting cylinder, and from the inevitable increase of the Tb crystal mosaic spread with applied pressure. Figure 1 shows an example of a magnon peak observed in a constant-Q=(0,0,2.7) scan at 90 K for the three pressures studied. In this figure the solid lines are the result of least-squares fits to Gaussian lineshapes. The magnon energies identified from scans along the (0,0,2+ξ) direction have been plotted versus ξ in Fig. 2 as filled circles (ambient pressure data), open circles (4.3 kbar data), and filled triangles (15.2 kbar data). In this figure it can be appreciated that the magnon energies at ambient pressure and at 4.3 kbar are very similar (within the errors of our experiment). These energies are in general agreement with the early (ambient pressure) results of Jensen *et al.*[8] In Fig. 2 it can also be seen that the dispersion curve of magnons at 15.2 kbar is evidently hardened at this pressure, i.e., the magnon energies shift toward higher energies at all wave vectors. The energy gap at q=0 due to the anisotropy also seems to be enhanced at this pressure, although a direct determination of this gap was not possible.

The magnon dispersion relation for Tb in its ferromagnetic phase, and for wave vectors q along the c-axis direction, can be approximated by:

$$E(\mathbf{q}) = \sqrt{[j(q)+D_x][j(q)+D_z]}, \tag{2}$$

where D_x and D_z are the planar and axial anisotropy parameters,

$$j(q) = \sum_n j_n[1-\cos(qnc)], \tag{3}$$

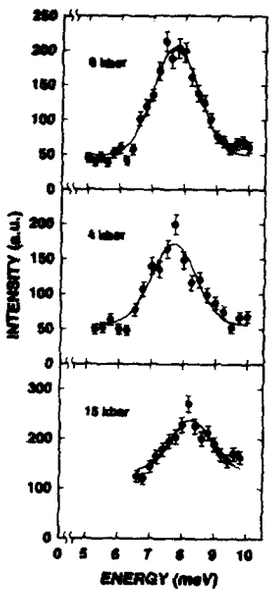

FIG. 1. Constant-Q scans at Q=(0,0,2+0.7) for ferromagnetic Tb at T=90 K under (a) ambient pressure, (b) 4.3 kbar, and (c) 15.2 kbar. The solid lines are from a fit to Gaussian lineshapes. The data sets (a) and (b) where collected using a sapphire cylinder and the data set (c) was collected using an Al_2O_3 cylinder.

$q \simeq |\mathbf{q}| = 2\pi\xi/c$, $\xi \ll 1$, and j_n is the effective exchange interaction between ions located in different planes that are normal to the c axis, and separated by a distance nc. In writing Eq. (2) we have neglected two-ion (i.e., q-dependent) anisotropy terms; this assumption seems to be reasonable at the temperature where our measurements were taken.[8] Note that in Ref. 7 $j(q)$ is written as $j(q)=J[\mathcal{J}(0)-\mathcal{J}(q)]$. Also note that $j(q)$ is, in general, temperature dependent, and we have assumed that its renormalization with temperature is not dependent on the wave-vector q. The energy gap of the dispersion relation of Eq. (2) is given by $\Delta=\sqrt{D_xD_z}$. We have performed a least-squares fit of our experimental data to the dispersion relation of Eq. (2). A reasonable fit to the data can be obtained when we include interactions of 5 or more neighboring planes [corresponding to 5 or more exchange constants in Eq. (3)], and two anisotropy constants (D_x and D_z). Houmann *et al.*[10] have shown that in Tb the axial anisotropy is considerably larger than the plane anisotropy and that $D_z/D_x \sim 20$ (at T=90 K). For this reason in our fits we have assumed that $D_z=20D_x$. The dispersion relations obtained from the fits using 5 exchange constants are shown in Fig. 2 as a solid line (for the ambient pressure and 4.3 kbar) which are indistinguishable for all practical purposes), and as a broken line (15.2 kbar data). These fits indicate that the energy gap Δ increases from ~1.44 meV (at ambient pressure and at 4.3 kbar) to ~2 meV at 15.2 kbar. We must reiterate, however, that in our measurements at this high

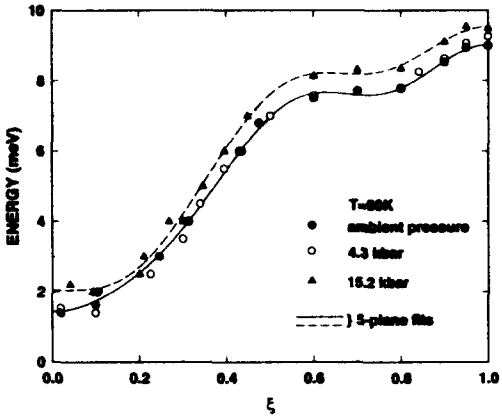

FIG. 2. Magnon dispersion relations for ferromagnetic Tb along the c axis at 90 K at ambient pressure and under 4.3 and 15.2 kbar. The solid and dotted lines shown in this figure represent the result of a least-squares fit.

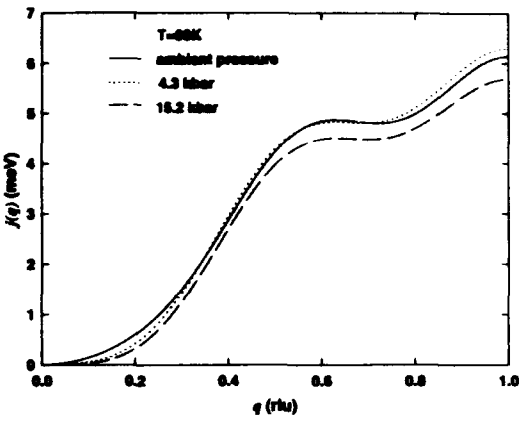

FIG. 3. The Fourier transformed exchange $j(q)=J[\vec{\jmath}(q)-\vec{\jmath}(0)]$ in the c direction deduced for ferromagnetic Tb from the magnon measurements at 90 K under (a) ambient pressure, (b) 4.3 kbar, and (c) 15.2 kbar. The lines shown represent the result of the least-squares fit. The values of q are expressed in reciprocal lattice units (rlu).

pressure we could not measure the magnitude of the energy gap directly due to the experimental difficulties mentioned above. Such a direct measurement would be highly desirable because in Eqs. (2) and (3) there is a correlation between the values of the D_x and D_z (which determine the energy gap Δ) and the values of j_n. The values of the j_n, D_x, and D_z obtained from our fits are shown in Table I. For comparison purposes in this table we have also listed the values of j_n of Jensen *et al.*[8] (calculated for $T=4.2$ K) renormalized by a q-independent factor of 0.9. The factor of 0.9 has been estimated from Refs. 9 and 10 to reflect the reduced magnetization at $T=90$ K. The discrepancies between our exchange constants and those from Jensen's at ambient temperature are most likely due to our assumption of q-independent renormalization of these constants. The corresponding values of $j(q)$ ($T=90$ K) have been plotted versus q in Fig. 3 for the three pressures studied. From this figure we conclude that the general features of $j(q)$ under applied pressure are qualitatively similar to the corresponding values at ambient pressure, and that $j(q)$ at 15.3 kbar is appreciably smaller than at ambient pressure or at 4.3 kbar. In order to obtain more detailed information that could be compared with the results of Jensen *et al.*[8] it might be necessary to account for a q-dependent renormalization of the exchange constants j_n. Further efforts in this direction are in progress.

TABLE I. Interplanar exchange and anisotropy parameters (in meV) obtained from the least-square fits of the $T=90$ K experimental results, to the dispersion relation of Eq. (2). The values shown in parentheses in the "ambient pressure" column correspond to the first five exchange constants of Jensen *et al.*[8] (for $T=4.2$ K) renormalized by a q-independent factor of 0.9.

	Ambient pressure	4.3 kbar	15.2 kbar
j_1	2.893 (2.883)	3.007	2.775
j_2	0.583 (0.761)	0.574	0.566
j_3	0.048 (0.013)	0.080	0.018
j_4	0.375 (−0.349)	−0.432	−0.398
j_5	0.129 (−0.016)	0.061	0.049
D_x	0.322	0.321	0.456
Δ	1.44	1.44	2.04

ACKNOWLEDGMENTS

The authors would like to acknowledge Dr. A. Onodera for kindly providing the sapphire cells used in these experiments. This work was performed under the auspices of the U.S.-Japan Cooperative Program in Neutron Scattering supported by the U.S. Department of Energy (DOE) and the Ministry of Education, Science and Culture, Japan. Oak Ridge National Laboratory (ORNL) is managed for the U.S. DOE by Martin Marietta Energy Systems, Inc. under Contract No. DE-AC05-84OR21400. One of authors (S.K.) would like to acknowledge the hospitality of the scientific and technical staff of the Oak Ridge National Laboratory during his visit to the laboratory.

[1] B. Coqblin, in *The Electronic Structure of Rare-Earth Metals and Alloys: The Magnetic Heavy Rare-Earths* (Academic, New York, 1977), p. 152.
[2] L. B. Robinson, S. Tan, and K. F. Sterrett, Phys. Rev. **141**, 548 (1966).
[3] J. E. Milton and T. A. Scott, Phys. Rev. **160**, 387 (1967).
[4] H. Umebayashi, G. Shirane, B. C. Frazer, and W. B. Daniels, Phys. Rev. **165**, 688 (1968).
[5] S. Kawano, B. Lebech, and N. Achiwa, J. Phys.: Condens. Matter **5**, 1535 (1993).
[6] A. Onodera *et al.*, Jpn. J. Appl. Phys. **26**, 152 (1987).
[7] A. R. Mackintosh and H. B. Møller, in *Magnetic Properties of Rare Earth Metals*, edited by R. J. Elliott (Plenum, New York, 1972), Chap. 5; J. Jensen and A. R. Mackintosh, in *Rare Earth Magnetism, Structures and Excitations* (Oxford, 1991).
[8] J. Jensen, J. W. Houmann, and H. B. Møller, Phys. Rev. B **12**, 303 (1975).
[9] J. Jensen and J. W. Houmann, Phys. Rev. B **12**, 320 (1975).
[10] J. W. Houmann, J. Jensen, and P. Touborg, Phys. Rev. B **12**, 332 (1975).

Polarization analysis of magnons in $CsMnI_3$

Z. Tun and T. C. Hsu
AECL Research, Chalk River Laboratories, Chalk River, Ontario K0J 1J0, Canada

J-G. Lussier
Department of Physics, McMaster University, Hamilton, Ontario L8S 4M1, Canada

A polarized neutron scattering experiment on $CsMnI_3$ shows previously unseen magnons at wave vectors (1/3,1/3,1) and (001), and also shows that the single-ion anisotropy for this material is substantially larger than previously reported. Linear spin wave theory can adequately describe the observed magnon frequencies.

Since the discovery of the Haldane gap[1] in $CsNiCl_3$, there has been continual activity[2] to investigate the spin-wave spectrum of Heisenberg antiferromagnetic (AFM) materials with the same hexagonal crystal structure. One such material recently examined by neutron scattering[3] is $CsMnI_3$. Its magnetic structure consists of AFM chains of Mn^{2+} ions (spin-only ions with $S=5/2$) parallel to the crystallographic c axis. The chains form a triangular lattice in the a-b plane. Due to a relatively short bridging through three halogen ions, the intrachain exchange J is much stronger than the interchain superexchange J'. At sufficiently high temperatures the chains are quasi-one-dimensional systems but a full three-dimensional order develops at $T_N=8.2$ K. In the fully ordered phase ($T \ll T_N$) the saturated moments of the Mn^{2+} ions form a planar 120° spin structure, with all the spins lying in the crystallographic a-c plane. Along a given chain the spins exhibit Néel order, but between nearest-neighbor chains they are canted from each other by approximately 120°. The primary ordering wave vector, Q_0, of this magnetic structure is (1/3,1/3,1).

The spin-wave spectrum of $CsMnI_3$ was measured by Harrison *et al.*[3] with inelastic neutron scattering. Constant-Q scans were performed along various symmetry directions in Q space and the observed magnon frequencies compared to the predictions of linear spin wave (LSW) theory obtained by adjusting the parameters in the Hamiltonian

$$H=J\sum_{i,j}\mathbf{S}_i\cdot\mathbf{S}_j+J'\sum_{i,j}\mathbf{S}_i\cdot\mathbf{S}_j+D\sum_i(S_i^z)^2,$$

where the first two sums are over nearest-neighbor intrachain and interchain pairs, while the last term represents single-ion anisotropy.

Harrison *et al.*[3] observed a small energy gap, <0.1 THz, at the AFM zone center Q_0 which they attributed to Ising-like anisotropy (i.e., negative D). They show that LSW theory with small $|D|$, merely 0.3% of the leading order interaction J, can adequately model the gap mode and most of the observed magnon frequencies. However, at the wave vector (001) the theory predicts three magnons, one nondegenerate mode at 0.44 THz and two degenerate modes at $0.44/\sqrt{2}$ or 0.32 THz, whereas only a single peak was observed experimentally. This led to speculation that LSW theory fails in the case of $CsMnI_3$, and that the observed peak actually consists of all three magnons at approximately the same frequency.

Another prediction of LSW theory[3] is, that the (001) magnons separated in frequency by the $\sqrt{2}$ ratio are due to excitations of Mn^{2+} spins in different directions. If so, it is possible to devise a polarized neutron experiment in which the nondegenerate mode appears in the non-spin-flip (NSF) scattering and the degenerate modes in the spin-flip (SF) scattering. Provided that the flipping ratio of the spectrometer, defined as (NSF intensity):(SF intensity) at a nuclear Bragg peak, is sufficiently high the two groups of excitations can be resolved into NSF and SF channels no matter how close they are in frequency.

A polarized neutron experiment as described above was recently reported by Tun *et al.*[4] A constant-Q scan at $Q\sim(001)$ showed peaks in both NSF and SF channels at approximately the same frequency. Additional observations were that the SF peak was 25% wider than the NSF peak, and that the SF and NSF peaks shifted oppositely in frequency when a magnetic field was applied. Hence, although the flipping ratio of the instrument was only 8:1, Tun *et al.*[4] concluded that the SF signal could not be dismissed as simply feedthrough of the stronger NSF signal. It then follows that the single peak observed by Harrison *et al.* must consist of both NSF and SF scattering, a feature that cannot be modeled by their small-$|D|$ LSW theory. However, as the authors[4] cautioned, a neutron scattering measurement made at a single point in Q space is not enough to reveal all the magnetic excitations at the corresponding reduced wave vector.

This paper reports further polarized neutron measurements on $CsMnI_3$ carried out at the NRU Reactor, Chalk River. The triple-axis spectrometer of the DUALSPEC facility was used with Cu_2MnAl Heusler alloy monochromator and analyzer, each with a mosaic spread of ~0.6°. The collimations of the reactor beam, monochromatic beam, scattered beam and the beam before the detector were 0.40°, 0.79°, 0.80°, and 2.6° respectively. A Mezei spin flipper before the analyzer was tuned to rotate the scattered neutron spin by π so that NSF and SF scattering processes could be measured alternately. The sample was mounted with its crystallographic a-c plane horizontal, and was cooled to 4 K in a vertical magnetic field so as to produce a single magnetic domain. We will denote the canting plane of the Mn^{2+} spins in this domain as the x-z plane, where x and z are unit vectors parallel to the a and c axes. The neutron polarization direction defined by the field is labeled y since it is normal to both x and z. Constant-Q inelastic scans were performed at

 0021-8979/94/75(10)/6063/3/$6.00 © 1994 American Institute of Physics

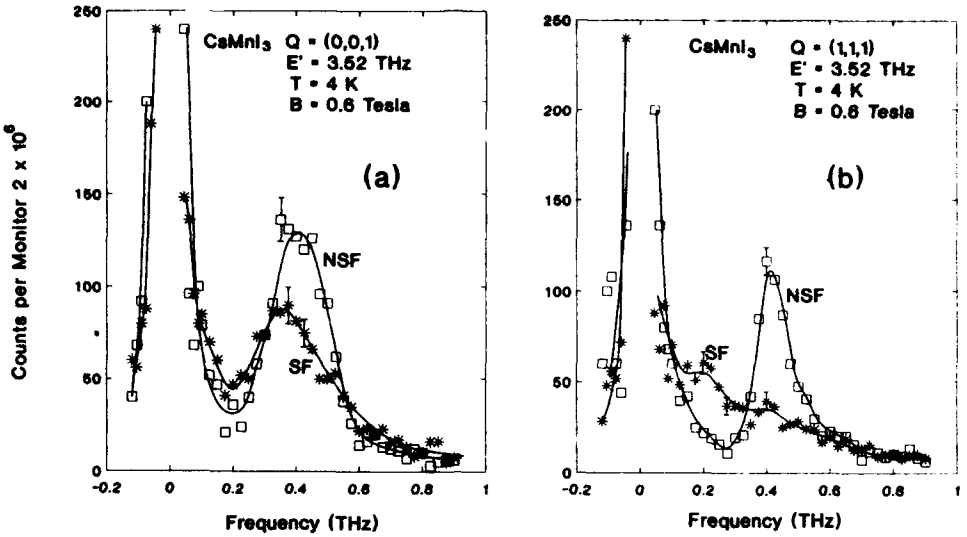

FIG. 1. Constant-Q scans at $Q=(001)$ and (111), measured with polarization analysis of the scattered neutrons. Typical counting errors are shown for selected points. The labels NSF and SF stand for non-spin-flip and spin-flip scattering.

(001) and (111), and also at $Q_0=(1/3,1/3,1)$ and nearby wave vectors. For the (001) and (111) measurements with a final neutron energy E' of 3.52 THz, a pyrolytic graphite filter was installed in the scattered beam to suppress $\lambda/2$ and $\lambda/3$ neutrons. This setup gave a flipping ratio of 24:1. No filter was used for the measurements around Q_0 with $E'=2.5$ THz. In this case the sample itself acts as a filter: (2/3,2/3,2) has zero intensity (an AFM reflection at the nuclear zone center $l=2$) while (113) is a systematically absent nuclear reflection. The inverse of the flipping ratio, measured on magnetic Bragg peaks, was 1:32.

The scans at (001) and the equivalent wave vector (111) are shown in Fig. 1. The scans show a NSF peak which arises from S^{yy} fluctuations of the Mn^{2+} spins. The frequency is 0.42 THz at both wave vectors but the peak is sharper at (111). The difference in peak width is well accounted for by how the spectrometer resolution ellipsoid is oriented with respect to the direction of grad(ω) in Q space. The integrated intensity, approximately given by (height ×FWHM), is ~50% lower at (111). This intensity variation is consistent with the decrease of the Mn^{2+} magnetic form factor at larger $|Q|$, combined with the increased neutron absorption by the sample at the (111) position (because of sample shape). In the SF channel, which detects S^{xx} and S^{zz} fluctuations, a peak with maximum intensity at 0.37 THz is observed at (001). The SF peak is wider than the NSF peak because of the asymmetric line shape with excess intensity on the high frequency side. The reason for this unusual line shape is not known. At (111) the 0.37 THz peak is greatly reduced in intensity and another peak appears at about 0.21 THz. The large differences in the SF peak intensities between (001) and (111) is understandable since magnetic scattering detects only those excitations normal to the scattering vector. For instance, at (001) the scattering vector is parallel to the c axis, and the spectrometer does not detect any S^{zz} fluctuations. The 0.21 THz peak at (111) is therefore identified as an S^{zz} mode and the 0.37 THz peak as an S^{xx} mode.

The results presented in Fig. 1, especially the newly observed 0.21 THz mode, lead us to conclusions significantly different from those of Tun *et al.*[4] The magnons at (001) can be modeled by LSW theory but the anisotropy $|D|$ required is larger than the value obtained by Harrison *et al.*,[3] 0.0005 THz. Based on the observed S^{xx} and S^{zz} frequencies we estimate that $|D|$ should be increased by about a factor of 4, i.e., $|D|=0.002$ THz.. The larger $|D|$ will of course require the anisotropy gap at the AFM zone center to be larger. It is therefore imperative to verify the size of the energy gap at Q_0.

Since Harrison *et al.*[3] identify the gap mode (at 0.07 THz)[5] as the second lowest S^{yy} mode at Q_0 (the lowest mode being the Goldstone mode), we expect to see it as NSF scattering. Constant-Q scans at Q_0 and at (1/3,1/3,1.02) are shown in Fig. 2. At the elastic position ($\nu=0$) of the Q_0 scan (see the peak scaled by 10^{-3}), (NSF intensity)≪(SF intensity) since the magnetic Bragg reflections from the single domain sample are entirely SF. However, there is a crossover in intensity between the two channels on the positive frequency side of the scan, leading to an excess NSF intensity at about 0.13 THz. We interpret this excess NSF scattering as the gap mode unresolved from the feedthrough $\nu=0$ peak. (Note that much less NSF scattering is observed on the negative frequency side, consistent with the factor of 4 reduction expected from detailed balance). In Fig. 2(b), with Q slightly shifted along c^*, a partially resolved peak is visible in the

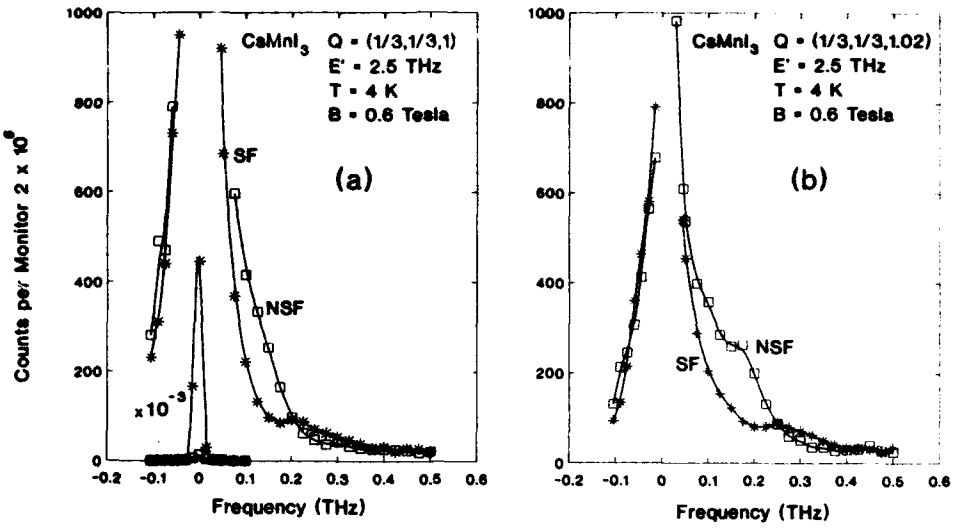

FIG. 2. Constant-Q scans at, panel (a), and near, panel (b), the three-dimensional ordering wave vector (1/3,1/3,1). Counting errors are smaller than the symbols. The scattering near zero frequency is shown reduced by a factor of 10^3 in panel (a).

NSF channel at 0.18±0.02 THz. Since this frequency is well above the Goldstone mode frequency, estimated to be 0.124 THz from the expression $|4JS|\sin[\pi(l-1)]$ with $|J|=0.198$ THz, this peak is identified as the gap mode. The scans presented in Fig. 2 thus show that the gap is indeed an S^{yy} mode as identified by Harrison *et al.*[3] However, its frequency deduced from Fig. 2 and other measurements (not shown) is larger, 0.13±0.02 THz. The corresponding $|D|$ given by LSW theory[5] is 0.0017±0.0006 THz, in essential agreement with the revised value of $|D|$ suggested by the S^{xx} and S^{zz} frequencies at (001).

Another feature visible in both panels of Fig. 2 is extra SF intensity well beyond the gap mode frequency, indicating a previously unseen[3] mode with a frequency of 0.21 THz at Q_0. The existence of this mode is indeed an expected result: Due to crystal symmetry the S^{xx} and S^{zz} modes at (001) are predicted to reappear at Q_0 with the same frequencies. The observation of a mode at 0.21 THz at Q_0 is therefore not a surprise. What is surprising is that the S^{xx} mode at 0.37 THz which is strong at (001) is not observed at Q_0.

We have shown in this paper that the anisotropy gap at the AFM zone center of $CsMnI_3$ is markedly larger than previously deduced by Harrison *et al.*[3] We have also reported the observation of previously unseen magnon modes. In contrast to the conclusions drawn in an earlier paper[4] the observed magnon modes in $CsMnI_3$ can be well represented by linear spin wave theory.

Comments and suggestions made by W. J. L. Buyers and E. C. Svensson are greatly appreciated. J-G. L. acknowledges the support of Natural Sciences and Engineering Research Council.

[1] R. M. Morra, W. J. L. Buyers, R. L. Armstrong, and K. Hirakawa, Phys. Rev. B **38**, 543 (1988).
[2] K. Kakurai, K. Nakajima, Y. Endoh, K. Iio, H. Tanaka, and M. Steiner, J. Magn. Magn. Mater. **104–107**, 857 (1992); M. Enderle, K. Kakurai, M. Steiner, and H. Weinfurter, *ibid.* **104–107**, 809 (1992); M. L. Plumer and A. Caillé, Phys. Rev. Lett. **68**, 1042 (1992).
[3] A. Harrison, M. F. Collins, J. Abu-Dayyeh, and C. V. Stager, Phys. Rev. B **43**, 679 (1991).
[4] Z. Tun, J-G. Lussier, R. W. Erwin, J. W. Lynn, and A. Harrison, Phys. Rev. B (in press).
[5] Provided J' is finite, the AFM zone center energy gap is given (Ref. 1) by $S\sqrt{8|JD|}$ where $S=5/2$ and $J=-0.198$ THz for $CsMnI_3$. For the value of $|D|$ reported by Harrison *et al.*, (Ref. 3), 0.0005 THz, the corresponding gap size is 0.07 THz.

Orientation dependence of dipole gaps in the magnetostatic wave spectrum of Bi-substituted iron garnets

Ana K. Chernakova, Andrew Cash, Jose Peruyero, and Daniel D. Stancil
Department of Electrical and Computer Engineering, Carnegie Mellon University, Pittsburgh, Pennsylvania 15213-3890

The orientation dependence of the dipole-exchange gaps in the magnetostatic forward volume wave spectrum of $Bi_{0.8}Lu_{2.2}Fe_5O_{12}$ thin films grown from a Bi-oxide flux has been studied. The spectrum is relatively insensitive to tilting the bias field toward the direction of propagation, but significant improvements are observed when the field is tilted toward a direction perpendicular to the propagation direction. Improvements include smoothing of the dipole-exchange gaps and a reduction of the insertion loss. These improvements are nonreciprocal; either reversing the direction of propagation or tilting the bias field in the opposite direction degrades the forward volume wave spectrum.

I. INTRODUCTION

Interactions between guided optical modes mediated by the presence of microwave magnetostatic waves are not only of intrinsic interest, but may lead to new microwave and optical signal processing devices.[1–8] Possible devices include microwave and optical tunable filters, multichannel filters, and optical frequency shifters.

The strength of this interaction is determined in large measure by the magnitude of the Faraday rotation in the film. Bismuth-substituted rare-earth iron garnet films exhibit large magneto-optical Faraday rotation, and are therefore promising for use in these devices. However, to qualify for optical-magnetostatic wave devices, these films should also possess low optical absorption and low magnetostatic wave (MSW) insertion loss. Significant progress toward these goals has been achieved with films grown from a Bi-oxide flux.[4,9] Nevertheless, the device applications of these films have been limited by the presence of large dipole-exchange gaps in the magnetostatic surface wave (MSSW) and magnetostatic forward volume wave (MSFVW) spectra. Kolodin, Rzhikhina, and Slavin[10] have shown that these gaps can be eliminated in the spectra of pure yttrium iron garnet by proper orientation of the bias field.

In this article, we report on the orientation dependence of the dipole-exchange gaps in $(Bi,Lu)_3Fe_5O_{12}$ films grown from a Bi-oxide flux. As in the case of yttrium iron garnet, we found that the dipole-exchange gaps can be significantly smoothed in the spectrum by proper bias field orientation. Further, tilting the bias field introduces nonreciprocal behavior in addition to smoothing the forward volume wave spectrum and reducing the insertion loss.

II. FILM GROWTH AND CHARACTERIZATION

The films used in this work were grown using the lead-free melt reported by Tamada and co-workers,[4] but with the addition of 4% Na_2O by weight to reduce the melt viscosity.[11] Although the effects reported here were seen in several samples, the specific data that follows were taken on the best sample (our number JPA15). The lattice parameter of this film measured by x-ray diffraction is 12.389 Å ($\Delta a = -0.006$ Å), and the composition was determined by x-ray fluorescence to be $Bi_{0.8}Lu_{2.2}Fe_5O_{12}$, neglecting sodium inclusion. Sodium is too light to be detected by x-ray fluorescence, so the amount of sodium incorporated in the film is unknown. From previous studies of sodium inclusion in YIG films,[11] the primary effect of sodium on MSW propagation is the introduction of a small (~200 Oe), negative growth-induced uniaxial anisotropy. This anisotropy can be removed by annealing. The thickness of the film was estimated to be 6 μm using the x-ray fluorescence areal density. The Faraday rotation was measured to be 0.95 deg/μm at an optical wavelength of 633 nm.

III. EXPERIMENTAL MAGNETOSTATIC WAVE SPECTRA

Magnetostatic waves were excited and detected using the experimental delay line shown in Fig. 1. The microstrip antennas are 50 μm wide, 10 mm long, and fed in the center by a 50 Ω microstrip line. The separation of the antennas is 3 mm, and the microstrip substrate is 254 μm thick. The delay line was mounted in a laboratory electromagnet with 6 in. poles and a 3 in. pole gap. The delay line was rotated so as to change the angles θ and ϕ shown in the figure, and the changes in the MSW transmission spectrum were noted. The sample used was irregular but roughly triangular in shape, with sides about 10 mm in length. The detailed shape of the transmission spectrum was very sensitive to the precise orientation of the sample on the microstrip owing to reflections from the sample edges.

The spectra were relatively insensitive to rotations that tilted the bias field parallel or antiparallel to the direction of

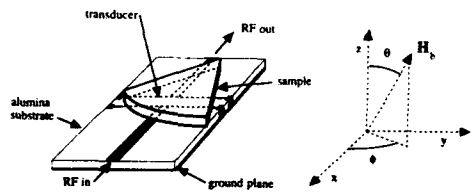

FIG. 1. Experimental geometry used to study the orientation dependence of the dipole-exchange gaps in $(Bi,Lu)_3Fe_5O_{12}$ films.

 0021-8979/94/75(10)/6066/3/$6.00 © 1994 American Institute of Physics

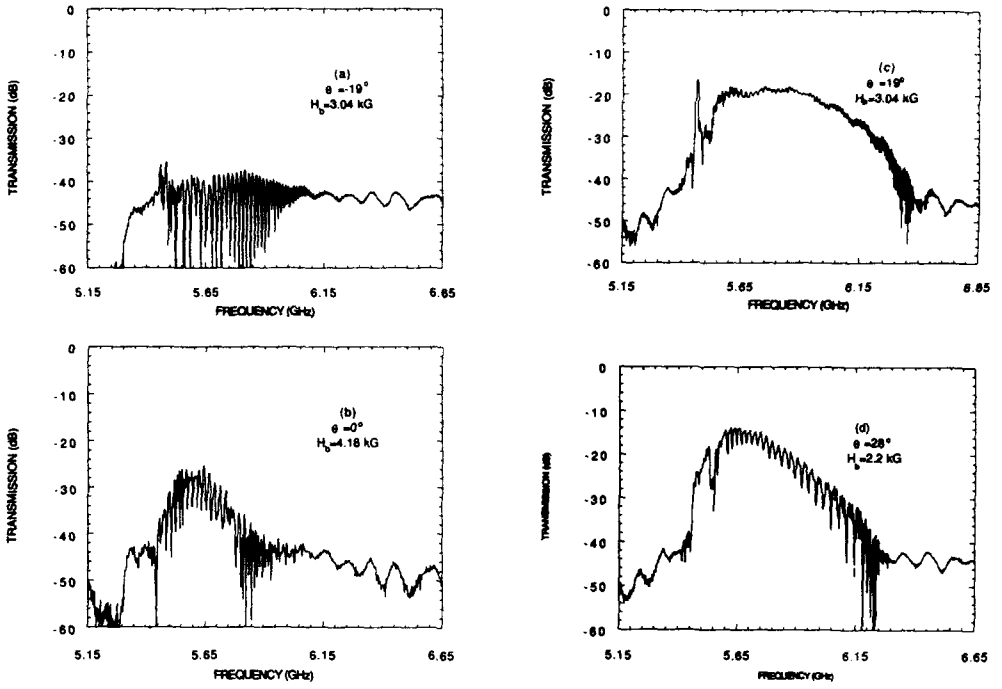

FIG. 2. MSW transmission spectra for different orientations of bias field for $Bi_{0.8}Lu_{2.2}Fe_5O_{12}$.

propagation (ϕ=0, 180°, θ>0). In contrast, significant improvements to the spectra were observed when the delay line was rotated so as to tilt the bias field parallel to the transducers (ϕ=90°, θ>0). The improvements included smoothing of the dipole-exchange gaps, and reduction of the insertion loss. Beyond an optimum rotation θ, the dipole-exchange gaps began to return and the insertion loss increased. In contrast, tilting the bias field in the opposite direction (ϕ=−90°, θ>0) resulted in the degradation of the transmission spectrum. These effects are illustrated in Fig. 2. Figure 2(b) shows the spectrum for perpendicular bias. The insertion loss is high (26 dB) and the dipole-exchange gaps in the spectrum would seriously degrade the performance of any MSW device. The optimum spectrum obtained by tilting in the direction ϕ=90°, θ=19° is shown in Fig. 2(c). Note that the insertion loss has been reduced to 18 dB, and the dipole-exchange gaps are no longer visible. The gaps reappear when the angle is further increased [Fig. 2(c)]. In contrast, Fig. 2(a) shows that tilting the bias field in the direction ϕ=−90°, θ=19° degrades the spectrum in comparison with the perpendicular orientation.

The angle necessary to obtain the best spectrum is not a strong function of the strength of the bias field, and was generally within a few degrees of θ=19°. Although best results were obtained near the frequency and field shown in Fig. 2, a bias field angle of 19° resulted in improved spectra over a tuning range of several GHz. The optimum angle was found to vary significantly from sample to sample. Measurements on a group of similar samples with slightly differing bismuth contents showed significant smoothing at angles from 2°–19°.

IV. DISCUSSION

The existence of dipole-exchange gaps in MSW spectra has been discussed by a number of authors.[12–15] Qualitatively, the origin of the gaps can be explained as follows. When the exchange interaction is neglected, the MSFVW modes with different variations through the film thickness are all degenerate at the k=0 band edge, and the dispersion relations do not cross. However, when exchange is taken into account, the frequency of the k=0 band edge increases quadratically with the number of oscillations through the film thickness. As a result, the dispersion curves of the higher-order-thickness modes cross the dispersion curve of the dominant, lowest-order mode. At the points where the curves cross, coupling between the modes occurs and the dispersion curves are split into separate branches. Near each crossing point, the splitting of the curves results in regions of unusually small group velocity. Since the attenuation of a MSW is a function of the propagation time, the waves are highly attenuated in these regions and attenuation notches appear in the transmission spectrum. These are the "dipole-exchange gaps" referred to earlier.

Kolodin and co-workers calculated the width of the dipole gaps as a function of the angle that the internal magne-

tization made with the film normal. They found that the width of the gaps could vary significantly with the angle of the magnetization with respect to the normal. Under certain conditions, the gap could become narrower than the relaxation frequency $\omega_r = -\gamma\mu_0\Delta H$, where γ is the gyromagnetic ratio, μ_0 is the permeability of free space, and ΔH is the full ferromagnetic resonance linewidth. When this occurs, the gaps will be smoothed out and will no longer be visible. The calculations showed that this only occurred when the pinning of the spins on one film surface was much stronger than the pinning on the other. In the case of symmetrical pinning, the width of the gaps increased monotonically with increasing angle of the magnetization and no smoothing would result. In light of this result, we interpret our experimental results as evidence of asymmetrical spin pinning. We believe the most likely situation is weakly pinned (or free) spins at the substrate-film interface, and strongly pinned spins at the film-air interface.

When the field is rotated from $\theta=0$ to $\theta=90°$, the mode undergoes a gradual change from volume to surface wave character.[16] The nonreciprocity results because of the introduction of surface wave character by tilting the field. The resulting field-displacement nonreciprocity then affects the coupling to the microstrip antennas when either the in-plane component of the field or the direction of propagation is reversed.

In summary, we have demonstrated an effective way to obtain MSW device quality transmission spectra in $(Bi,Lu)_3Fe_5O_{12}$ films grown from a lead-free melt. When combined with the techniques described by Tamada and coworkers for reducing optical attenuation, we believe these films show considerable promise for MSW optical device applications.

ACKNOWLEDGMENTS

We would like to acknowledge helpful discussions with N. Bilaniuk, B. Kalinikos, P. Kolodin, and A. Slavin. The work was supported in part by the National Science Foundation under Grant No. ECS-9206817.

[1] A. D. Fisher, J. N. Lee, E. S. Gaynor, and A. B. Tveten, Appl. Phys. Lett. **41**, 779 (1982).
[2] C. S. Tsai, D. Young, W. Chen, L. Adkins, C. C. Lee, and H. Glass, Appl. Phys. Lett. **47**, 651 (1985).
[3] A. D. Fisher, Circuits Syst. Signal Process. **4**, 265 (1985).
[4] H. Tamada, M. Kaneko, and T. Okamoto, J. Appl. Phys. **64**, 554 (1988).
[5] C. S. Tsai and D. Young, IEEE Trans. Microwave Theory Tech. **MTT-38**, 560 (1990).
[6] O. G. Rutkin, N. G. Kovshikov, A. A. Stashkevich, B. A. Kalinikos, A. N. Ageev, A. S. Trifonov, V. B. Kravchenko, and L. M. Filimonova, Pis'ma Zh. Tekh. Fiz. **11**, 933 (1985) [Sov. Tech. Phys. Lett. **11**, 386 (1985)].
[7] A. A. Klimov, V. L. Preobrazhenskii, and Yu. K. Fetisov, Pis'ma Zh. Tech. Fiz. **16**, 18 (1990) [Sov. Tech. Phys. Lett. **16**, 649 (1991)].
[8] N. Bilaniuk, D. D. Stancil, and S. H. Talisa, J. Appl. Phys. **67**, 508 (1990).
[9] H. Tamada, M. Saitoh, and M. Kaneko, J. Appl. Phys. **67**, 949 (1990).
[10] P. A. Kolodin, E. G. Rzhikhina, and A. N. Slavin, Zh. Tekh. Fiz. **60**, 132 (1990) [Sov. Phys. Tech. Phys. **35**, 951 (1991)].
[11] M. Ramesh, D. M. Gualtieri, S. D. Silliman, J. Peruyero, and D. D. Stancil, J. Appl. Phys. **70**, 6289 (1991).
[12] T. Wolfram and R. E. De Wames, Phys. Rev. B **4**, 3125 (1971).
[13] W. Schilz, Solid State Commun. **11**, 615 (1972).
[14] J. D. Adam, T. W. O'Keefe, and R. W. Patterson, J. Appl. Phys. **50**, 2446 (1979).
[15] B. A. Kalinikos and A. N. Slavin, J. Phys. C **19**, 7013 (1986).
[16] Yu. K. Fetisov, Zh. Tekh. Fiz. **57**, 2393 (1987) [Sov. Phys. Tech. Phys. **32**, 1451 (1988)].

Polarization analysis of the magnetic excitations in $Fe_{65}Ni_{35}$ Invar

J. W. Lynn[a] and N. Rosov
Reactor Radiation Division, National Institute of Standards and Technology, Gaithersburg, Maryland 20899

M. Acet
Tieftemperaturphysik, Universität Duisburg, W-4100 Duisburg, Germany

H. Bach
Experimentalphysik IV, Ruhr Universität Bochum, W-4630 Bochum, Germany

Triple-axis inelastic polarized neutron measurements have been performed as a function of temperature on a single crystal of the Invar alloy $Fe_{65}Ni_{35}$ to distinguish longitudinal from transverse magnetic excitations in the magnetically ordered phase. Well below the Curie temperature of 501 K the magnetic excitation spectrum is dominated by conventional transverse spin-wave excitations, which in fact follow the predictions of spin-wave theory very well. In particular, we find no evidence for propagating longitudinal excitations in this system, in sharp contrast to the behavior observed in the amorphous Invar $Fe_{86}B_{14}$ material as well as the non-Invar amorphous system $Fe_{40}Ni_{40}P_{14}B_6$.

For an isotropic ferromagnet the spin-wave dispersion relation in the long-wavelength (small-q) regime is given by[1] $E_{sw}=D(T)q^2$, where D is the spin-wave "stiffness" constant. The general form of the spin-wave dispersion relation, and hence the spin-wave density of states, is the same for all isotropic ferromagnets, while the numerical value of D depends on the details of the magnetic interactions and the nature of the magnetism. For the magnetization, the leading order temperature dependence is given by $M(T)=M(0)(1-BT^{3/2})$, where the coefficient B is simply related in spin-wave theory to D. A measurement of the spin-wave dispersion relation can then be directly related to the bulk magnetization and vice versa. These relationships, as well as many others provided by spin-wave theory, have been found to be in excellent accord with experimental observations for the vast majority of isotropic ferromagnetic materials, with the singular exception of Invar systems.[2–5] In all the Invar materials, whether they be amorphous or crystalline, the relationship between D and B is found to fail in a major way, with the observed stiffness constant D as much as a factor of 2 larger than inferred from magnetization measurements. We previously carried out extensive unpolarized neutron measurements on the amorphous Invar Fe-B system in order to make a detailed comparison between spin-wave theory and experiment.[4] With the exception of the discrepancy between D and B, conventional spin-wave theory was found to work very well in describing the long-wavelength spin dynamics of this system, and thus these unpolarized neutron measurements did not suggest an answer to this problem.

The conventional explanation for this Invar anomaly is that there are additional hidden excitations which participate in reducing the magnetization. If this explanation is correct, then the magnetization and neutron measurements already put stringent conditions on the form that such excitations might take, since there is no freedom to change the *form* of the theory (such as the $T^{3/2}$ behavior for the magnetization, for example). Hence we must have a density of hidden excitations which has precisely the same form as the conventional spin-wave excitations themselves. One possibility which has been suggested[6] is that the (transverse) spin-wave excitations couple to the longitudinal fluctuations, yielding propagating longitudinal excitations which peak at the transverse spin-wave energies. In an unpolarized beam experiment such transverse and longitudinal excitations cannot be distinguished. We therefore carried out inelastic polarized neutron measurements on the $Fe_{86}B_{14}$ Invar system to separate explicitly the longitudinal spin-fluctuation spectrum (S^z) from the usual spin-wave excitations represented by $S^{\pm}=S^x\pm iS^y$, and indeed we observed the presence of longitudinal excitations not only in the vicinity of T_c but substantially below the ordering temperature as well.[7] However, longitudinal excitations were also observed in the non-Invar amorphous ferromagnet $Fe_{40}Ni_{40}P_{14}B_6$, suggesting that these excitations might be related to the amorphous state rather than the Invar anomaly. In our present measurements we in fact do not observe any longitudinal propagating excitations in the crystalline Invar system, and a similar result has been recently obtained in the Fe_3Pt system.[8] Hence the longitudinal excitations observed in $Fe_{86}B_{14}$ are likely not related to the Invar properties but rather have the interesting interpretation that they are unique to the amorphous state. On the other hand, as the Curie temperature is approached from below we do observe longitudinal spin fluctuations, but these fluctuations are diffusive in nature (i.e., they peak at $\Delta E=0$) and appear to be similar to the longitudinal spin diffusion observed in other isotropic ferromagnets near T_c.

The experiments were carried out on the BT-2 triple-axis polarized beam spectrometer at the National Institute of Standards and Technology Research Reactor. Heusler alloy crystals in reflection geometry were employed for both monochromator/analyzer and polarizers. A pyrolytic graphite filter was used to suppress higher-order wavelengths. The sample was a single crystal weighing 22 g, in the shape of a cylinder 1 cm in diameter and 2 cm long. All the present data have been taken in the forward direction, around the (000) reciprocal-lattice point, even though the sample was a single crystal. We used this method so that we might directly compare this system with the data we obtained on amorphous

[a]Also at the University of Maryland.

 0021-8979/94/75(10)/6069/3/$6.00 © 1994 American Institute of Physics

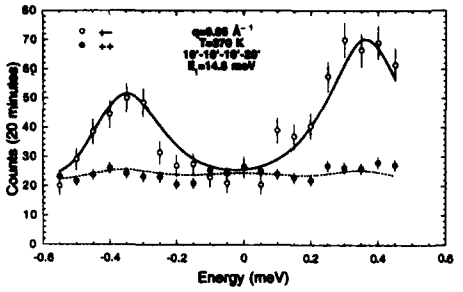

FIG. 1. Spin-flip (○) and non-spin-flip (●) scattering observed in a single crystal of $Fe_{65}Ni_{35}$ (Invar). Clear spin waves are observed in the spin-flip configuration for neutron energy gain ($E<0$) and energy loss ($E>0$), while the very weak inelastic scattering observed in the non-spin-flip configuration is a result of the finite flipping ratio of the instrument.

materials where (000) is the only reciprocal-lattice point, and also in order to be able to apply the field (of 0.6 T) along the cylinder axis to minimize demagnetization effects. In this small-angle regime tight collimation must be employed, and typically we used 20′-10′-10′-20′ (FWHM) in these experiments. We also took some data where the first (in-pile) collimation was 10′ to improve the resolution at smaller wave vectors. The flipping ratio measured through the ferromagnetic sample was between 7 and 13, depending principally on the temperature.

The polarization analysis technique as applied to this problem is in principle straightforward.[9] The (transverse) spin-wave scattering, represented in the Hamiltonian by the raising and lowering operators $S^{\pm}=S^{x}\pm iS^{y}$, causes a reversal of the neutron spin. These spin-flip cross sections are denoted by $(+-)$ and $(-+)$. For the results presented here the neutron polarization $\hat{P}$ is perpendicular to the momentum transfer $\mathbf{Q}$, $\hat{P}\perp\mathbf{Q}$, and we may then create a spin wave ($E>0$) or destroy a spin wave ($E<0$) with equal probability. Hence the $(+-)$ and the $(-+)$ cross sections are equal. The longitudinal (S_z) magnetic scattering, on the other hand, is directly related to the non-spin-flip $(++)$ or $(--)$ scattering.

Figure 1 shows the spin-flip and non-spin-flip scattering cross section observed at 375 K for a wave vector of 0.05 Å^{-1}. The scan at this wave vector is restricted in energy to $\sim\pm0.55$ meV due to kinematical constraints of the scattering process.[2] The asymmetry in the spin-wave intensities is due primarily to resolution effects, as discussed in detail in Ref. 10. The solid curve is a fit of the standard spin-wave cross section for isotropic spin waves, convoluted with the instrumental resolution.[10] We obtain excellent agreement with the observations, and for this temperature we have determined that $D=115$ meV Å^2. Also shown in the figure is the non-spin-flip scattering, which is clearly much weaker in strength than the spin-flip scattering. The dashed curve is again a fit, which contains three peaks. One is resolution limited and centered at $E=0$, and at this temperature originates from nuclear incoherent scattering (the scattering intensity of which is q-independent) as well as some magnetic disorder scattering. There are also weak peaks at the spin-wave positions, the intensities of which are approximately $\frac{1}{10}$ of the spin-flip peaks. However, some scattering intensity is expected here due to "leakage" from the imperfect polarization efficiency of the instrument and sample. Indeed the solid curve is the resulting calculated intensity based on the measured spin-flip spin-wave cross section, and clearly provides a complete explanation for this scattering. Thus we conclude that there are no observable longitudinal propagating excitations in this system. The absence of intrinsic peaks in the $(\pm\pm)$ inelastic scattering is in sharp contrast to the behavior observed in the amorphous systems,[7] where we found that the ratio of spin-wave to longitudinal scattering was 2.5:1. Hence it is clear that the longitudinal propagating excitations observed in those systems must have a different origin and are not related to the Invar anomaly.

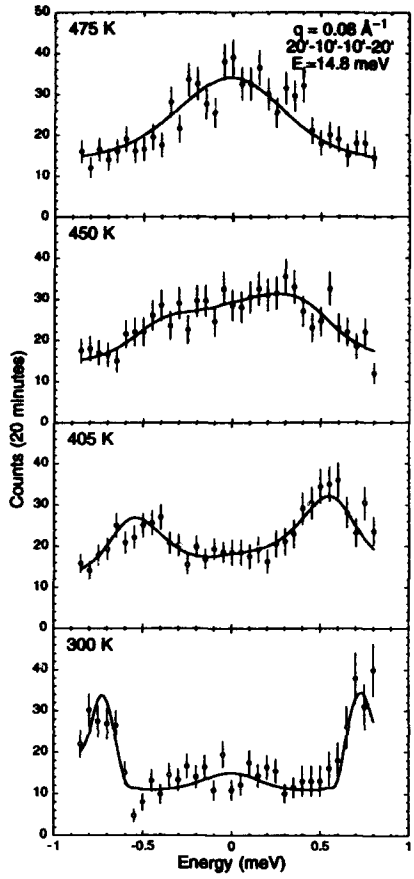

FIG. 2. Temperature evolution of the spin-flip scattering at a wave vector of 0.08 Å^{-1}. The spin waves are seen to renormalize to lower energies and broaden as T_c is approached, as expected.

The temperature evolution of the spin-flip (spin-wave) scattering for $q=0.08$ Å^{-1} is shown in Fig. 2. The solid

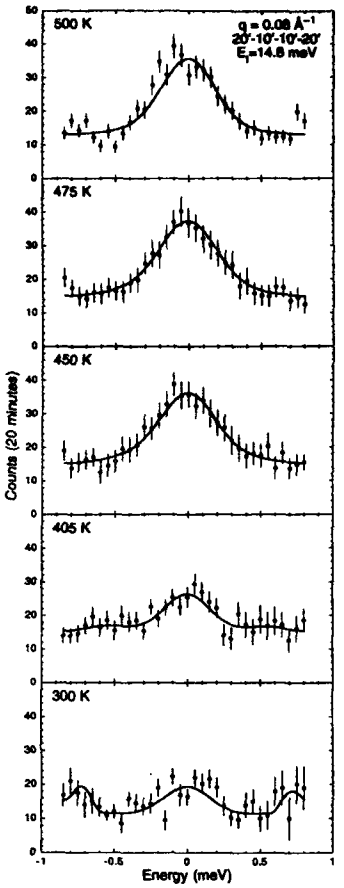

FIG. 3. Temperature evolution of the non-spin-flip scattering at the same wave vector as shown in Fig. 2. The intensity scales are the same so that the data may be directly compared. At room temperature the scattering consists of a resolution-limited elastic peak (nuclear incoherent plus magnetic disorder scattering) plus spin-wave "leakage" due to the imperfect polarization of the instrument and sample. As T_c is approached, a broadened quasielastic magnetic response is observed.

curves again represent the least-squares fits to the data of the spin-wave cross section convoluted with the instrumental resolution and polarization.[10] At room temperature we see two well-separated spin-wave peaks, and as T_c (501 K) is approached the spin waves renormalize to lower energy and broaden as expected. At 475 K we find that the spin waves are almost overdamped, and in fact after convolution with the instrumental resolution only a single broad peak is observed at this q. These data can be compared directly with the longitudinal (non-spin-flip) scattering as shown in Fig. 3. At room temperature the scattering consists of a resolution-limited elastic peak plus spin-wave peaks from "leakage." As the temperature is increased towards T_c the spin-wave peaks are diminished because of the improvement in the flipping ratio at higher temperatures and also because the spin waves are broadened. What is clear from these data is that a quasielastic peak develops as T_c is approached. With the assumption that the intrinsic cross section is a Lorentzian we obtain an intrinsic (half) width $\Gamma \approx 0.07$ meV at this q.

This quasielastic scattering originates from simple spin diffusion.[6] For $T \geq T_c$, x, y, and z are equivalent for an isotropic ferromagnet by definition, while below T_c this symmetry is broken and we have a transverse (x,y) and longitudinal (z) susceptibility. In the hydrodynamic regime above T_c only spin diffusion occurs, and it is reasonable to expect that the longitudinal response will remain diffusive below T_c.[11] Hence we do not believe that this scattering is related to the Invar effect but rather is the expected behavior for an isotropic ferromagnet for $T \lesssim T_c$. This still leaves the origin of the Invar anomaly as a mystery, and also implies that the longitudinal excitations observed in the amorphous ferromagnets are a new phenomenon. Both of these effects warrant further investigation.

The research at Maryland was supported by the NSF, Grant No. DMR 93-02380.

[1] F. Keffer, in *Handbuch der Physik*, edited by S. Flügge (Springer, Berlin, 1966), Vol. 18, Part 2, p. 1.
[2] A review is given by J. W. Lynn and J. J. Rhyne, in *Spin Waves and Magnetic Excitations*, edited by A. S. Borovik-Romanov and S. K. Sinha (North-Holland, Amsterdam, 1988), Chap. 4, p. 177.
[3] For a review of Invar systems see Y. Nakamura, IEEE Trans. Magn. MAG-12, 278 (1976).
[4] J. A. Fernandez-Baca, J. W. Lynn, J. J. Rhyne, and G. Fish, Phys. Rev. B 36, 8497 (1987), and references therein.
[5] Y. Ishikawa, K. Yamada, K. Tajima, and K. Fukamichi, J. Phys. Soc. Jpn. 50, 1958 (1981).
[6] See, for example, R. Raghavan and D. L. Huber, Phys. Rev. B 185 (1976); J. K. Bhattacharjee, *ibid.* 27, 3058 (1983); S. V. Malee Sci. Rev. A Phys. 8, 323 (1987).
[7] J. W. Lynn, N. Rosov, Q. Lin, C-H. Lee, and G. Fish, Physica B 180-181, 253 (1992); J. W. Lynn, N. Rosov, and G. Fish, J. Appl. Phys. 73, 5369 (1993).
[8] N. Rosov, J. W. Lynn, J. Kästner, E. F. Wassermann, T. Chattopadhyay, and H. Bach (these proceedings).
[9] R. M. Moon, T. Riste, and W. C. Koehler, Phys. Rev. 181, 920 (1969).
[10] N. Rosov, J. W. Lynn, and R. W. Erwin, Physica B 180-181, 1003 (1992).
[11] For experimental results see, for example, P. W. Mitchell, R. A. Cowley, and R. Pynn, J. Phys. C 17, L875 (1984).

Temperature dependence of the magnetic excitations in ordered and disordered $Fe_{72}Pt_{28}$

N. Rosov and J. W. Lynn[a)]
Reactor Radiation Division, National Institute of Standards and Technology, Gaithersburg, Maryland 20899

J. Kästner and E. F. Wassermann
Tieftemperaturphysik, Universität Duisburg, W-47057 Duisburg, Germany

T. Chattopadhyay
Institut Laue-Langevin, B.P. 156X, 38042 Grenoble Cedex, France

H. Bach
Experimentalphysik IV, Ruhr Universität Bochum, D-44780 Bochum, Germany

We have performed inelastic neutron scattering measurements of the long-wavelength spin wave excitations of both ordered and disordered $Fe_{72}Pt_{28}$ single crystals below their critical temperatures, $T_C = 510$ and 375 K, respectively. The spin waves followed the expected $E = Dq^2$ dependence, and the temperature-dependent spin stiffness D decreased as $(T/T_C)^{5/2}$, as expected for an isotropic ferromagnet. The extrapolated zero-temperature spin stiffness was $D = 98(4)$ meV Å^2 and 107(1) meV Å^2 for the disordered and ordered alloy, respectively. These values are significantly higher than the zero-temperature stiffness as determined by magnetization measurements.

INTRODUCTION

An understanding of the Invar effect has been suggested via recent band-structure calculations and experiments, which indicate that the magnetic moment of certain 3*d* alloys is unstable with respect to a change in volume.[1] The Invar effect originally referred to a magnetically induced suppression of the thermal contraction, first observed in disordered $Fe_{65}Ni_{35}$. Fe_3Pt alloys also display the Invar thermal expansion anomaly, with the added advantages that Fe is the sole magnetic component in the alloy, and that the Invar effect occurs in both atomically ordered and disordered Fe_3Pt (hereafter referred to as *o*-Fe_3Pt and *d*-Fe_3Pt, respectively). The thermal expansion anomaly associated with the magnetic ordering is much stronger than in $Fe_{65}Ni_{35}$, particularly for *d*-$Fe_{72}Pt_{28}$, where the thermal expansion coefficient changes from 1×10^{-5} K^{-1} at ≈40 K above T_C to -3.5×10^{-5} K^{-1} at ≈30 K below T_C.[2]

Another manifestation of the Invar effect is the discrepancy that exists between the magnetic excitation spectrum determined directly by neutron scattering and that inferred from magnetization measurements. For isotropic ferromagnets,[3] of which these cubic alloys are good examples, the dispersion relation is quadratic in the small-q regime, $E = Dq^2$, where D is the spin wave stiffness. The leading order temperature dependence of the magnetization is

$$M(T) = M(0)(1 - BT^{3/2}), \tag{1}$$

where in conventional spin wave theory

$$B = \frac{\zeta(3/2) g\mu_B}{M(0)} \left(\frac{k_B}{4\pi D} \right)^{3/2}. \tag{2}$$

The magnetization at $T = 0$ is $M(0)$; k_B is the Boltzmann constant; and ζ is the Riemann zeta function [$\zeta(3/2) \simeq 2.612$]. The dynamic interaction between spin waves, which arises from the fact that multiple spin waves are not eigenfunctions of the Heisenberg Hamiltonian, decreases the spin wave energies and lifetimes. As a result, the temperature dependence of the spin stiffness is predicted to decrease to leading order as $T^{5/2}$,

$$D(T) = D(0)(1 - AT^{5/2}). \tag{3}$$

It is thus possible to relate the spin wave stiffness to bulk magnetization measurements [using Eq. (1)]. In all Invar systems, there appears to be a substantial discrepancy between the spin wave stiffness as determined by bulk magnetization and by neutron scattering. In particular, the magnetization decreases more rapidly with increasing temperature than would be predicted by counting magnons as observed by neutron scattering. We have been studying a number of Invar and non-Invar systems in an effort to resolve this discrepancy.[4,5]

Previous inelastic neutron scattering work on *o*-$Fe_{72}Pt_{28}$ (Ref. 6) showed a 20% discrepancy between the decrease in magnetization calculated from applying spin-wave theory to the neutron data and the experimentally determined bulk magnetization. In this paper, we present the results of unpolarized inelastic neutron scattering measurements of the magnetic excitations in ordered and disordered $Fe_{72}Pt_{28}$. We find that there is indeed a significant difference between the spin wave stiffness as determined by bulk techniques and neutron scattering, for both the ordered and disordered alloy.

EXPERIMENT

The scattering measurements were performed at the BT-2 triple-axis spectrometer of the NIST Research Reactor with 21′–10′–10′–20′ collimation before and after the monochromator and analyzer, respectively, and a pyrolytic graphite (PG) filter before the monochromator to remove higher-order wavelength contamination. The incident neutron energy was fixed at 13.7 meV (2.444 Å). Both the

[a)]Also at the University of Maryland, College Park, M-

 0021-8979/94/75(10)/6072/3/$6.00 © 1994 American Institute of Physics

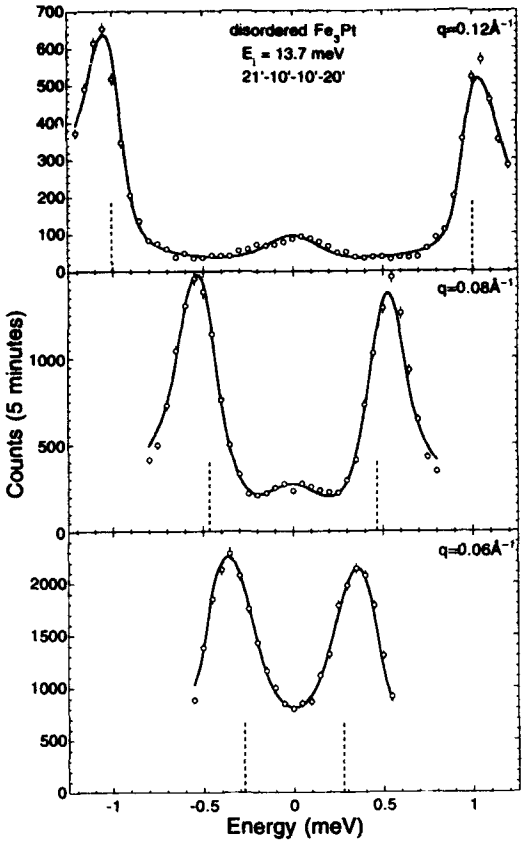

FIG. 1. Constant-q scans for disordered $Fe_{72}Pt_{28}$ about 000 at room temperature with momentum transfer $q=0.12$ Å^{-1} (top), 0.08 Å^{-1} (middle), and 0.06 Å^{-1} (bottom). The solid lines are best fits to the data of Lorentzian-broadened magnons and an elastic central peak convolved with the instrumental resolution function. The scans are limited in energy by the kinematic constraints on scattering about 000.

monochromator and the analyzer used the PG 002 reflection. In this configuration, the energy resolution is 0.33 meV, full width at half maximum (FWHM), the longitudinal q resolution in the scattering plane is $\sim$0.01 Å^{-1} FWHM, and the vertical resolution is $\sim$0.22 Å^{-1} FWHM.

The samples were approximately 20-g single crystals of $Fe_{72}Pt_{28}$. Atomically ordered and disordered $Fe_{72}Pt_{28}$ have Curie temperatures of $T_C=510$ and 375 K, respectively. The temperature was varied between 450 and 100 K using a closed-cycle He refrigerator. All the measurements were made well above the premartensitic transition that occurs in $Fe_{72}Pt_{28}$ below $T\sim70$ K.

We measured the energy dependence of the scattering cross-section at momentum transfers in the range $0.05\leq q\leq0.17$ Å^{-1}. The inelastic scans were made about the 000 position, which gives several advantages to the measurements. First, the magnetic excitations can be observed without a significant contribution from lattice excitations. Second, we have available the greatest possible intensity for the excitations around 000, where the magnetic form factor is unity. At the 111 reciprocal lattice point, for instance, the magnetic form factor for Fe is 0.4,[7] and thus the scattering intensity will be $\sim$ 16% of that observed about 000. Finally, we will be able to make a direct comparison of these results to planned polarized beam measurements about 000, which can be made on these samples only around 000 due to constraints on the orientation of the sample in the required applied magnetic field.[5] Nevertheless, there are several disadvantages to performing measurements about 000. First, the maximum achievable energy transfer increases linearly with momentum transfer, $E_\pm\sim\pm2k_iq$, whereas the spin wave energy increases quadratically with q. Thus, for a particular spin stiffness, we are limited in the range of momentum transfer for which we may observe excitations (see Fig. 1). Second, the requisite small scattering angles necessitate tight angular resolution, and with the combined constraint of a restrictive energy range we also require good energy resolution, thus reducing the signal considerably.

RESULTS AND DISCUSSION

At each temperature, we measured the energy-dependent scattering cross-section for several momentum transfers. Typical data, shown in Fig. 1 for the disordered sample, reveal several characteristic features. The two peaks at finite neutron energy gain and loss are the magnon annihilation and creation peaks. The central elastic peak is due mainly to magnetic disorder scattering. As discussed above, data cannot be taken over the full extent of the magnon peaks due to kinematic constraints. The data were fit to a double-

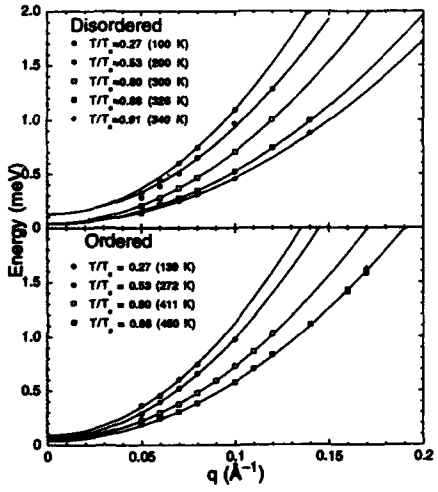

FIG. 2. Measured dispersion relations for magnons around 000 in disordered (top) and ordered (bottom) $Fe_{72}Pt_{28}$. The solid lines are the best fit of the data to a quadratic dispersion with a small gap, $E(q)=Dq^2+E_0$.

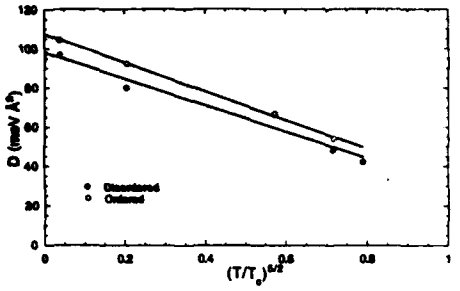

FIG. 3. The spin wave stiffness as a function of $(T/T_C)^{5/2}$ for disordered (●) and ordered (○) $Fe_{72}Pt_{28}$. The solid lines are linear best fits to the data; the slopes are the same, within experimental error, for both the ordered and disordered alloy.

Lorentzian spectral-weight function and an elastic central peak, which were numerically convolved with the triple-axis spectrometer resolution function.[8] For the purposes of the convolution, since the q-resolution is finite, the spin wave dispersion was assumed to be quadratic in q and the broadening was assumed to increase as q^4, according to spin wave theory; fits attempted with a quadratic dependence of the broadening on q were of poorer quality. In the data shown in Fig. 1, we obtained a spin stiffness $D(300\ \mathrm{K})=66.3(2)$ meV Å^2 and a line broadening $\Gamma(300\ \mathrm{K}, 0.08\ \text{Å}^{-1})=0.04$ meV HWHM. This intrinsic width is considerably smaller than the instrumental resolution.

From the fits to the measured scattering cross-sections, we have plotted the excitation energy versus momentum transfer for each temperature (see Fig. 2). The measured dispersions were then fit to a quadratic dispersion with a pseudo-gap that is due to dipolar interactions, $E(q,T)=D(T)q^2+E_0$. Obviously, from the quality of the fits, our assumptions in the fitting procedure of a quadratic dispersion are well founded. The temperature dependence of the spin-wave stiffness is shown in Fig. 3, plotted against $(T/T_C)^{5/2}$. The decrease in stiffness is consistent with a linear behavior over the range $0.27<T/T_C<0.91$, as indicated by the fit. The extrapolated zero-temperature spin stiffnesses are 98(4) meVÅ^2 and 107(1) meVÅ^2 for d-$Fe_{72}Pt_{28}$ and o-$Fe_{72}Pt_{28}$, respectively. The reduced temperature dependence of the spin stiffness scales with $D(0)$ for both alloys; the slopes of the fits in Fig. 3 are the same within experimental error. Thus, while the disorder causes a decrease in the magnetic ordering temperature, the spin dynamics of the alloys appears to follow the same Heisenberg-like behavior. The present $D(T)$ values for o-$Fe_{72}Pt_{28}$, as determined by neutron scattering, are in agreement with the room temperature neutron scattering spin stiffness [$D(300\ \mathrm{K})=85$ meVÅ^2][9] reported previously for o-$Fe_{72.7}Pt_{27.3}$. No previous results have been reported for the disordered system.

The zero-temperature spin stiffnesses for both the ordered and disordered alloys are significantly higher than the corresponding values determined from magnetization measurements, $D_m^{\mathrm{disord}}(0)=74$ meVÅ^2 and $D_m^{\mathrm{ord}}(0)=89$ meV Å^2. These values are about 20% less than the spin wave determinations, which is about the same relative difference as reported in previous measurements[6] on o-$Fe_{72}Pt_{28}$. The 20% discrepancy between the inelastic neutron and bulk magnetization spin stiffnesses is significantly less than the factor of two discrepancy that is observed for crystalline $Fe_{65}Ni_{35}$,[6] as well as other Invar systems such as amorphous $Fe_{86}B_{14}$,[3] despite the fact that the thermal expansion anomaly is much stronger in $Fe_{72}Pt_{28}$. Further work with polarized neutrons may allow us to characterize the nature of the excitations in these systems.[5]

ACKNOWLEDGMENTS

Research at Maryland is supported by the NSF, DMR 93-02380. Research at Bochum was supported by Deutsche Forschungsgemeinschaft within Sonderforschungsbereich (SFB)166.

[1] E. F. Wasserman, J. Magn. Magn. Mater. **100**, 346 (1991).
[2] K. Sumiyama, M. Shiga, M. Morioka, and Y. Nakamura, J. Phys. F **9**, 1665 (1979).
[3] See, for example, J. A. Fernandez-Baca, J. W. Lynn, J. J. Rhyne, and G. E. Fish, Phys. Rev. B **36**, 8497 (1987); J. W. Lynn and J. J. Rhyne, *in Spin Waves and Magnetic Excitations*, edited by A. S. Borovik-Romanov and S. K. Sinha (North-Holland, Amsterdam, 1988), Chap. 4, p. 177.
[4] J. W. Lynn, N. Rosov, and G. Fish, J. Appl. Phys. **73**, 5369 (1993).
[5] J. W. Lynn, N. Rosov, M. Acet, and H. Bach (these proceedings).
[6] Y. Ishikawa, S. Onodera, and K. Tajima, J. Magn. Magn. Mater. **10**, 183 (1979).
[7] R. M. Moon, Int. J. Magn. **1**, 219 (1971).
[8] M. J. Cooper and R. Nathans, Acta Crystallogr. **23**, 357 (1967).
[9] Y. Ishikawa, M. Kohgi, S. Onodera, B. H. Grier, and G. Shirane, Solid State Commun. **57**, 535 (1986).

Theory of ferromagnetic resonance relaxation in very small solids

J. B. Sokoloff
Northeastern University, Boston, Massachusetts 02115

Two models for ferromagnetic resonance (FMR) relaxation in magnetic solids which are sufficiently small for the discreteness of the magnon and phonon modes to be important are studied. The models exhibit a transition as a function of the number of atoms in the solid from a regime in which energy loss occurs, as evidenced by the fact that the energy of the solid increases as a function of time, to a regime in which there is no energy loss, as evidenced by the fact that the energy does not increase as a function of time on the average. It is shown that this phenomenon is due to a transition to chaotic behavior of the solid. These results open up the interesting possibility that sufficiently small magnetic solids could exhibit FMR with practically no energy loss.

In a ferrimagnetic resonance experiment (FMR), an electromagnetic field couples to a magnon mode (usually the zero wave vector or uniform magnon mode). The energy absorbed by this mode from the field is then transferred to other magnon and to phonon modes via various mechanisms,[1,2] which results in the uniform magnon being given a nonzero linewidth. The mechanism for this can be understood using Fermi's Golden rule perturbation theory, in which the uniform magnon is scattered into a continuum of other magnons of nearly the same frequency.[2] When one considers a finite size solid, however, the magnon and phonon modes do not form a continuum, and hence Fermi's Golden rule will not lead to a nonzero linewidth because in general the uniform mode will not be in resonance with any of the excitations of the solid. If the uniform magnon does not have a linewidth, the electromagnetic wave will only be able to impart energy to the uniform mode if it is exactly in resonance with it. Of course for larger solids there are other mechanisms that can damp the excitations. For example, interaction of the surface atoms with the surroundings will lead to a damping of the vibrational modes. Although the damping resulting from this is in general quite small,[3] it could be larger than the vibrational mode spacing if the solid is not too small. This would make the vibrational spectrum continuous, in which case Fermi's Golden rule would again give a nonzero linewidth. Nevertheless, for smaller samples, one must deal with the fact that the modes are discrete, and hence Fermi's Golden rule will predict zero linewidth.

A related problem was studied by Fermi *et al.*[4] They studied the question of whether a vibrating chain of atoms interacting with anharmonic interactions, with one of its vibrational normal modes excited, will exhibit equipartition of energy if one waits for a sufficiently long time. They found that in fact this does not occur. The energy in the mode that was originally excited alternately flows into other modes and then comes back to the original mode, with no net flow of energy to the other modes. Israelev and Chirakov[5] and Ford[6] studied this problem, concluding that the Fermi *et al.* result is a result of the Kolmogorov, Arnold, and Moser (KAM) theorem[7] in the sense that if the anharmonicity of the interatomic interaction is sufficiently small, the system moves on smooth trajectories (or more correctly, tori) in phase space, but if the anharmonicity were larger the atoms in the solid would move on chaotic trajectories, which would result in the equipartition of energy. In fact, since Chirikov has argued that the criterion for the onset of chaos is that the mode spacing must become smaller than the width of the (nonlinear) resonances,[5] this transition to chaotic behavior will also occur as a function of the size of the sample. In this article, it will be shown using simple models that a transition as a function of the size of the sample will occur from a regime in which there is an FMR linewidth to one in which there is not. Two models for dissipation in small magnetic solids will be studied to illustrate this phenomenon. The first will be a model for damping of the uniform magnon by the creation of lattice vibrations and the second will be a model for damping of the uniform magnon due to the creation of other magnons by nonlinearity (in the magnon operators) of the exchange and anisotropy. While there have been several studies of chaos in magnetic solids in recent years,[8] the possible connection between chaos and FMR relaxation in small solids has not been discussed before.

Classical dynamics will be used to describe the magnon and phonon systems in this article to study the dissipation due to lattice vibrations and magnons. The term in the classical Hamiltonian which couples the magnons and phonons will be assumed to be the expansion of the single ion anisotropy term to first order in the atomic displacement,

$$-\sum_{\alpha,j,\delta}(\partial D^{\alpha}/\partial X_{j,\delta})(S_j^{\alpha})^2 u_{j,\delta}, \tag{1}$$

where D^{α} is the anisotropy constant, $X_{j,\delta}$ is the δ component of the position of the atom on the jth lattice site, S_j^{α} is the α component of the spin on the jth lattice site, and $u_{j,\alpha}$ is the displacement of the atom on the jth lattice site.[9] Applying Hamilton's equations, we obtain the equations of motion for the atoms acted on by a force $-\Sigma_{\alpha,j,\delta}(\partial D^{\alpha}/\partial X_{j,\delta})(S_j^{\alpha})^2$ due to the anisotropy term given in Eq. (1).[8] If the uniform magnon is driven by the electromagnetic field, S_j^{α} will oscillate with the frequency of the electromagnetic field and hence this force will oscillate with twice that frequency. As a simple model, let us consider a chain of atoms with a nonlinear near-neighbor force given by $f(x)=-\alpha x+\beta x^2-\beta' x^3$ between them, where x is the difference between the separation of a neighboring pair of atoms and the lattice constant, with a magnetic atom placed at one site (let us take that site to be at one end of the chain). Then, the equation of motion becomes

 0021-8979/94/75(10)/6075/3/$6.00 © 1994 American Institute of Physics

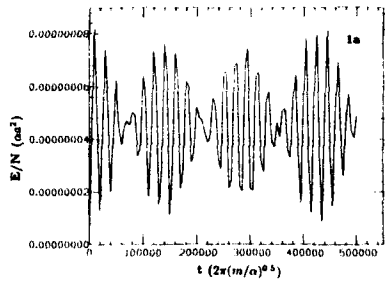

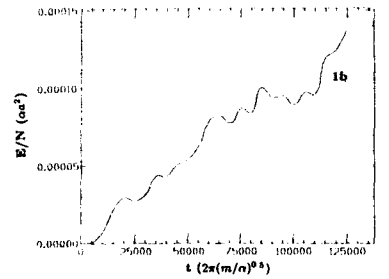

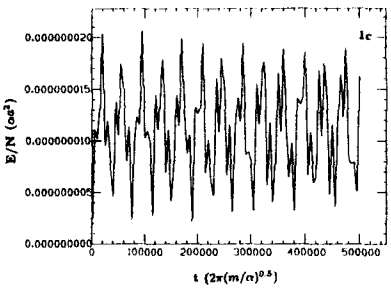

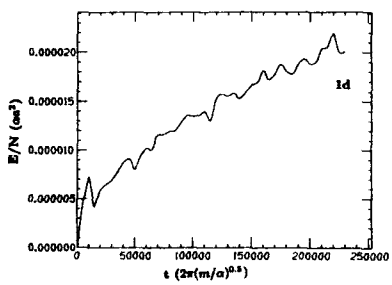

FIG. 1. The energy per atom (measured in units of αa^2) as a function of time [in units of $2\pi(m/\alpha)^{0.5}$], (a) for a 100 atom chain with $\omega=0.3(\alpha/m)^{0.5}$, (b) for a 100 atom chain with $\omega=0.6(\alpha/m)^{0.5}$, (c) for a 200 atom chain with $\omega=0.15(\alpha/m)^{0.5}$, (d) for a 200 atom chain with $\omega=0.3(\alpha/m)^{0.5}$.

$$m\ddot{x}_j=-\alpha(2x_j-x_{j-1}-x_{j+1})+\beta[(x_j-x_{j-1}-a)^2-(x_{j+1}-x_j-a)^2]-\beta'[(x_j-x_{j-1}-a)^3-(x_{j+1}-x_j-a)^3]+g(t)\delta_{j,N}, \quad (2)$$

where x_j is the location of the jth atom in the chain, a is the equilibrium lattice spacing, α, β, β' are parameters, m is the atomic mass, and $x_0=0$, and $g(t)=g_0\cos(\omega t)$, where N is the number of atoms in the chain and g_0 and ω are the amplitude and frequency of the force g on the end atom in the chain due to the anisotropy, which is made to oscillate by the uniform magnon mode. The parameters α, β, and β' were chosen to have the values corresponding to the coefficients in the expansion of the force calculated from the Lennard–Jones potential out to third order in the displacement from equilibrium. (This choice avoids the problem that one would encounter if one used only the second-order expansion, namely, that the assumed equilibrium state of such a model in which the atoms are equally spaced is not the ground state, leading to a possible instability if the system is driven hard enough.) This equation of motion was integrated by the fourth-order Runge–Kutta method and the vibrational energy was calculated as a function of time. The results for several system sizes are shown in Fig. 1. As can be seen, there is a transition from nondissipative to dissipative behavior as the size of the system increases beyond a critical value (in the sense that the internal energy of the 100 atom system of

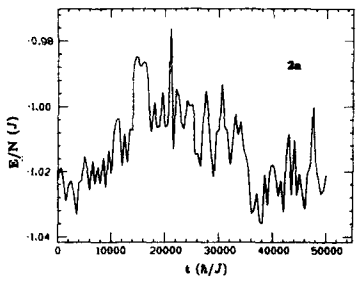

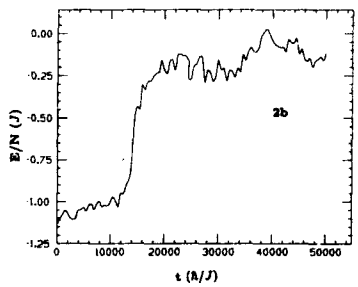

FIG. 2. The energy (in units of J, the exchange interaction for spin directions transverse to the c axis) is shown as a function of the time (in units of $\hbar/J$) for (a) a 6 atom chain and (b) a 10 atom chain. The ratio of the exchange along the c axis to J is 1.3, the magnetic moment of a site times the static field (which is along the c axis) is $0.1J$, and the product of the magnetic moment and the driving field is $0.1J$ and its frequency is equal to $J/\hbar$).

frequency $0.3\omega_1$, where $\omega_1=(\alpha/m)^{0.5}$, shown in Fig. 1 does not increase on the average as a function of time, whereas the energy of the 200 atom system of the same frequency does). The critical size also appears to depend strongly on the driving frequency. For example, the 100 atom system when driven at a frequency of $0.6\omega_1$ was ergotic, whereas when driven at $0.3\omega_1$ it was not. The critical driving frequency for a 64 atom chain was found to fall between 0.8 and $1.2\omega_1$. This apparent inverse proportionality of the critical value of N with ω implies that for lower values of ω, which are more realistic, the critical size will be considerably larger. Since the frequency scale in the present calculations ω_1 is of the order of 10^{13} rad/s, we would expect, on the basis of the apparent inverse proportionality of N with ω that the critical N would be about 10^5 for a driving frequency of about 1 GHz, which is a reasonable size for a mesoscopic system. This behavior can be understood qualitatively on the basis of Chirikov's overlap of resonances criterion because as the system size increases, the spacing of the vibrational modes decreases. The present calculations give a dependence which is an inverse proportionality of the critical N to ω, whereas a calculation based on Chirikov's overlap of resonance criterion gives a much stronger frequency dependence,[5] but Chirikov's method does predict the general result that the critical N decreases with increasing ω.

Next, let us consider a model for FMR relaxation in small magnetic systems due to decay of the uniform magnon into other magnons. For simplicity, let us consider a chain of spins, interacting with an anisotropic Heisenberg exchange interaction. The equation of motion for the spin on the lth lattice site is

$$\dot{\mathbf{S}}_l=\mathbf{H}_{\mathrm{eff}}\times\mathbf{S}_l, \tag{3}$$

where $H^{\alpha}_{\mathrm{eff}}=-(\partial H/\partial S^{\alpha}_l)+h(t)\delta_{\alpha,z}$, where $H=-\Sigma_{j,\alpha,\beta}J_{j,\alpha,\beta}S^{\alpha}_jS^{\beta}_{j+1}$ and $h(t)=h_0\cos(\omega t)$ is an applied external field due to the electromagnetic field. The equation of motion was solved and the energy of the magnetic system calculated as a function of time. The results are presented in Fig. 2. As in the previous model, if the energy increases, it means that the uniform mode is able to absorb energy from the external field, because it is damped by the interaction with the other spin waves by the nonlinearity of the anisotropic exchange interaction. We note that Fig. 2 shows a transition from dissipative to nondissipative behavior as a function of system size, like that found for the model for damping due to phonon excitation found earlier.

[1] T. Kasuya and R. C. Le Craw, Phys. Rev. Lett. **6**, 223 (1961).

[2] M. Sparks, *Ferromagnetic Relaxation Theory* (McGraw–Hill, New York, 1964), pp. 147–157.

[3] J. B. Sokoloff, Wear **167**, 59 (1993).

[4] E. Fermi, J. Pasta, and S. Ulam, *Collected Papers of Enrico Fermi* (Chicago University, Chicago, 1955), Vol. 2, p. 978.

[5] F. M. Israelev and B. V. Chirikov, Dokl. Akad. Nauk. USSR **166**, 57 (1966) [Sov. Phys. Dokl. **11**, 30 (1966)]; B. V. Chirikov, Phys. Rep. **52**, 263 (1979).

[6] J. Ford, Phys. Rep. **213**, 271 (1992); J. Ford and G. H. Lunsford, Phys. Rev. A **1**, 59 (1970); S. D. Stoddard and J. Ford, *ibid.* **8**, 1504 (1973); G. H. Walker and J. Ford, Phys. Rev. **188**, 416 (1969).

[7] A. N. Kolmogorov, Dokl. Akad. Nauk. USSR **98**, 527 (1954); V. I. Arnold, Usp. Mater. Nauk **18**, 91 (1963); V. I. Arnold and A. Avez, *Ergodic Problems of Classical Mechanics* (Benjamin, New York, 1968).

[8] For example, see the review by K. N. Alekseev, G. P. Berman, V. I. Tsifrinovich, and A. M. Frishman, Usp. Fiz. Nauk **162**, 81 (1992) [Sov. Phys. Usp.].

[9] S. P. Marshall, J. B. Sokoloff, and C. Vittoria, IEEE Trans. **25**, 3491 (1989).

Crystallographic and magnetic properties of $Co_xFe_{1-x}Cr_2S_4$

Chul Sung Kim, Min Yong Ha, and Heung Moon Ko
Department of Physics, Kookmin University, Seoul 136-702, Korea

Young Jei Oh
Division of Ceramics, Korea Institute of Science and Technology, Seoul 130-650, Korea

Heung Soo Lee
Microwave Group, Pohang Accelerator Laboratory, Pohang 790-600, Korea

Sang Youl Lee[a] and Jung Chul Sur
Department of Physics, Wonkwang University, Iri 570-749, Korea

Jae Yun Park
Department of Materials Science and Engineering, University of Incheon, Incheon 402-749, Korea

The mixed series $Co_xFe_{1-x}Cr_2S_4$ has been studied by x-ray, Mössbauer spectroscopy, and superconducting quantum-interference device (SQUID) magnetometry. The crystal structure is found to be a cubic spinel, and the lattice constant a_0 decreases linearly with increasing cobalt concentration. Mössbauer spectra of $Co_xFe_{1-x}Cr_2S_4$ have been taken at various temperatures ranging from 4.2 to 300 K. The iron ions are ferrous and occupy the tetrahedral sites. The Curie temperature increases linearly with cobalt concentration, suggesting that the superexchange interaction for the Co-S-Cr link is stronger than that for the Fe-S-Cr link. Magnetic hyperfine and quadrupole interactions in $Co_{0.9}Fe_{0.1}Cr_2S_4$ at 4.2 K have been studied, yielding the following results: $H_{hf}=80.8$ kOe, $\frac{1}{2}e^2qQ(1+\frac{1}{3}\eta^2)^{1/2}=2.65$ mm/s, $\theta=15°$, $\phi=75°$, and $\eta=1.0$. It is notable that, as the temperature decreases below the Curie temperature, quadrupole splitting increases with decreasing temperature, suggesting the presence of an electric field gradient and accompanying relaxation effects. Magnetic susceptibility measurements by SQUID magnetometry show that superexchange interactions between Fe^{2+} ions are ferrimagnetic.

I. INTRODUCTION

The ferrimagnetic materials[1,2] $CoCr_2S_4$ and $FeCr_2S_4$, both of which have normal spinel structure, have been studied in a large number of crystallographic, magnetic, and electric investigations as well as by Mössbauer spectroscopy.[3–5] The Curie point T_c is about 177 K for $FeCr_2S_4$ and 227 K for $CoCr_2S_4$.[1] As a result of the strong preference of the Cr^{3+} ions for the octahedral sites, the compounds become normal spinels with Fe^{2+} or Co^{2+} ions at the tetrahedral sites and Cr^{3+} ions at the octahedral sites.[6] The crystal structure of $FeCr_2S_4$ remained cubic down to 5 K.[7] $FeCr_2S_4$ undergoes a second-order phase transition at about 10 K that changes the local symmetry at the Fe^{2+} sites.[2] The most interesting feature of Mössbauer spectra is a quadrupole splitting below T_c which increases with decreasing temperature. Mössbauer studies of $Co_xFe_{1-x}Cr_2S_4$ which were done only in limited temperature ranges have been reported by several authors.[5,7] Above T_c, the spectra form a narrow singlet line, indicating a strictly cubic environment of the Fe^{2+} ion at tetrahedral sites. In the case of high-Co^{2+}-concentration samples, the strength of the hyperfine field H_{hf} decreases strongly while the values of the quadrupole splitting ΔE_Q increase strongly at low temperatures. The results are not complete for all the temperature regions so far. Moreover, Mössbauer spectra, which must result from the combined magnetic hyperfine and electric quadrupole interaction below T_c, have never been analyzed with constraint of linewidth.

Here we present the results of Mössbauer experiments which are analyzed under the consideration of H_{hf}, $\frac{1}{2}e^2qQ$, θ, ϕ, and η, and compare them with those of x-ray and superconducting quantum-interference device (SQUID) experiments.

II. EXPERIMENT

The mixed system $Co_xFe_{1-x}Cr_2S_4$ was prepared by direct reaction of the high-purity elements Co, Fe, Cr, and S in an evacuated quartz tube. The stoichiometric mixtures were sealed in evacuated quartz ampoules and heated at 500 °C for one day, at 800 °C for one day, and then at 1050 °C for three days. In order to obtain a homogeneous material, it was necessary to grind a sample after the first firing and to press it into a pellet for the second heating at 1050 °C for five days in evacuated and sealed quartz ampoules. The samples were ^{57}Fe enriched to 3.0 at. % of the metal atoms for Mössbauer measurements. The Mössbauer spectra were recorded using a conventional spectrometer of the electromechanical type with a ^{57}Co source in a rhodium matrix.

III. RESULTS AND DISCUSSION

The lattice constants were determined by using the Nelson-Riley function[8] and extrapolating to backward diffraction ($\theta=90°$). The results are shown in Table I. The lattice constant a_0 decreases linearly with increasing Co^{2+} concentration and follows Vegard's law approximately. This can be expected in view of the fact that the ionic radius of 0.71 Å for Co^{2+} ions is smaller than that of 0.77 Å for Fe^{2+} ions.

Mössbauer spectra of $Co_xFe_{1-x}Cr_2S_4$ were measured at various absorber temperatures from liquid-helium tempera-

[a]Present address: Department of Physics, Choseon University, Kwangjoo 501-795, Korea.

 0021-8979/94/75(10)/6078/3/$6.00 © 1994 American Institute of Physics

TABLE I. Lattice parameter (a_0), isomer shift (IS) for the metal iron at room temperature, and the Curie temperature T_c for $Co_xFe_{1-x}Cr_2S_4$.

x	a_0 (Å)	IS (mm/s)	T_c (K)
0.0	9.995	0.59	172
0.1	9.985	0.59	178
0.3	9.968	0.58	189
0.5	9.956	0.59	203
0.7	9.945	0.58	209
0.8	9.956	0.58	220
0.9	9.923	0.58	226

ture to room temperature. Some of them are shown in Figs. 1 and 2. The spectra below the Curie temperture T_c were fitted with eight Lorentzians by diagonalizing the 4×4 $\langle \frac{3}{2}M_I|\mathcal{H}|\frac{3}{2}M_I'\rangle$,[9] where $\mathcal{H}$ is the combined Hamiltonian of the magnetic hyperfine and electric quadrupole interaction, and $M_I, M_I' = \pm\frac{1}{2}, \pm\frac{3}{2}$. In the least-squares fitting of the data, the eight lines in a given spectrum were assumed to have an equal linewidth. The sum of the eight Lorentzians is drawn in the data points in Figs. 1 and 2. The magnetic hyperfine field H_{hf} and quadrupole splitting ΔE_Q of $x=0.9$ at 4.2 K have been fitted, yielding the following results:

$$H_{hf}=80.8 \text{ kOe}, \quad \Delta E_Q=\tfrac{1}{2}e^2qQ(1+\tfrac{1}{3}\eta^2)^{1/2}=2.65 \text{ mm/s},$$

$$\theta=15^\circ, \quad \phi=75^\circ, \quad \eta=1.0,$$

where θ and ϕ are the polar and azimuthal angles, respectively, of H_{hf} with respect to the principal axes of the EFG

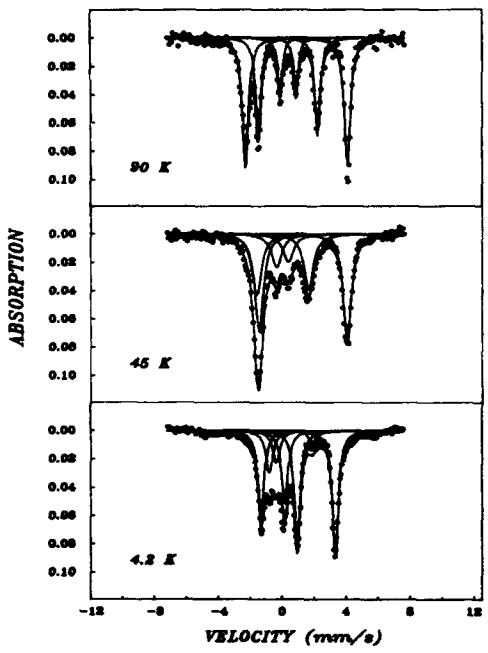

FIG. 1. Mössbauer spectra of $Co_{0.9}Fe_{0.1}Cr_2S_4$ at low temperature.

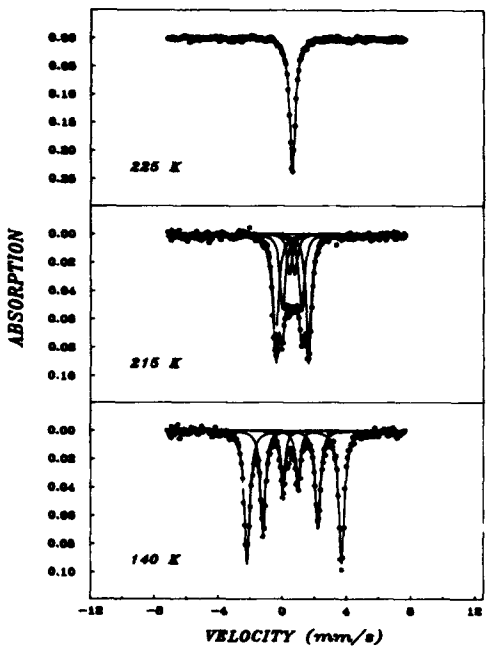

FIG. 2. Mössbauer spectra of $Co_{0.9}Fe_{0.1}Cr_2S_4$ near the magnetic ordering temperature.

tensor, and $\eta=(V_{x'x'}-V_{y'y'})/V_{z'z'}$ is the asymmetry parameter of the EFG. In the case of $x=0.9$, the value of θ is 15° below 8 K and with increasing temperature decreases linearly to 0° at 45 K. The calculated spectra were fairly insensitive to ϕ values above 35 K. The asymmetry parameter η remains at about 1.0, which means the EFG is not axially symmetric. This result is different from $\eta=0.0$ for $Co_{0.98}Fe_{0.02}Cr_2S_4$ by van Diepen and van Stapele.[7]

The spectra above T_c were fitted to a single Lorentzian. Some of them are shown in Table I and Fig. 2. The decrease in the isomer shift when Co^{2+} ions are substituted indicates that the electron density at the Fe^{2+} ion nucleus increases, which corresponds to the change in the Fe^{2+} ion electron configuration due to the greater covalence of Fe^{2+}—S^{2-} bonds with increasing Co^{2+} concentration. The increased covalence may also influence the dynamic Jahn-Teller effect, which gives rise to a change in the electric quadrupole interaction below T_c when there is a substitution of Co^{2+} ions.

Figure 3 shows the temperature dependence of the magnetic hyperfine fields H_{hf}. It is interesting that the magnetic hyperfine field has a maximum at about 90 K and decreases anomalously with decreasing temperature. This is similar to our former results[10] of the $Ni_xFe_{1-x}Cr_2S_4$ system in which the antiferromagnetic monoclinic structure, $NiCr_2S_4$, and the ferrimagnetic spinel structure, $FeCr_2S_4$, are mixed. This unusual reduction of the magnetic hyperfine field below 90 K can be explained in terms of the temperature dependence of the cancellation effect between the orbital current field term and Fermi contact term in H_{hf}.[10,11]

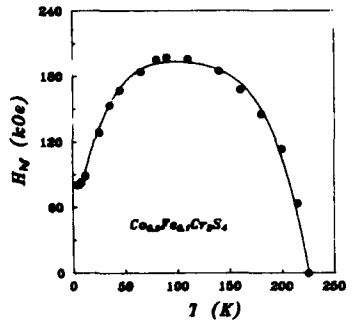

FIG. 3. Temperature dependence of the effective magnetic hyperfine field for $Co_{0.9}Fe_{0.1}Cr_2S_4$.

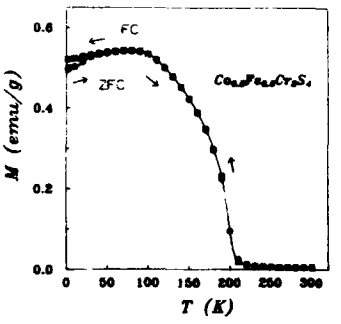

FIG. 5. Zero-field-cooled and field-cooled magnetic moment vs temperature curves for $Co_{0.5}Fe_{0.5}Cr_2S_4$.

As shown in Fig. 4, the quadrupole splitting ΔE_Q increases remarkably when the temperature goes down. The absence of quadrupole splitting above T_c suggests that the iron ions occupy tetrahedral sites in the spinel structure because the local symmetry of a tetrahedral site is cubic T_d while that of an octahedral site is trigonal D_{3d}. There are several views to explain this deviation below T_c from cubic symmetry at tetrahedral sites that are occupied by Fe^{2+} ions: for instance,[2] a magnetically induced EFG, small magnetostriction effects, and the concepts of both localized behavior and a dynamic Jahn-Teller effect.

It was recently known that of these views, the suggestion that the EFG arises from the dynamic Jahn-Teller stabilization of the ${}^5E_g(Fe^{2+})$ ground state is more plausible. Our results agree with this view too. It is notable that there is no abrupt change in the quadrupole splitting and magnetic hyperfine field in $Co_{0.9}Fe_{0.1}Cr_2S_4$, which means Co^{2+} is not active as part of a Jahn-Teller effect while the Fe^{2+} ion is a Jahn-Teller impurity instead of taking part in a cooperative Jahn-Teller effect.[12] The line-broadening effect was observed with a Co^{2+} concentration. Maximum line broadening was unexpectedly found to occur at $x=0.7$, not at $x=0.5$, which is most probable composition. It therefore means that this effect results not from the random distribution of Co^{2+} ions among tetrahedral sites[5] but from the Jahn-Teller effect.

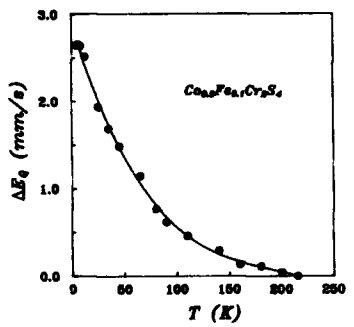

FIG. 4. Temperature dependence of the quadrupole splitting for $Co_{0.9}Fe_{0.1}Cr_2S_4$.

The Curie temperature T_c was determined from Mössbauer and SQUID measurements. Both are in fairly good agreement. As shown in Table I, the Curie temperature T_c increases linearly, suggesting that the superexchange interaction for the Co-S-Cr link is stronger than that for Fe-S-Cr link.

The temperature dependence of the magnetic moment for $Co_{0.5}Fe_{0.5}Cr_2S_4$ under an applied field $H_a=8$ kOe is shown in Fig. 5, in the zero-field-cooled (ZFC) and field-cooled (FC) modes. Below 80 K, the magnetic moment is not saturated but decreases with decreasing temperature. This is compatible with the tendency of the magnetic hyperfine field H_{hf} from Mössbauer data and may be explained in terms of differences in the temperature dependences of A and B sites.[2] Magnetic susceptibility measurements by SQUID magnetometry show that the shape of the susceptibility curve is typical of a Neél ferrimagnet.

ACKNOWLEDGMENTS

This paper was supported in part by the Nondirected Research Fund, Korea Research Foundation, 1993.

[1] P. Gibart, J. L. Dormann, and Y. Pellerin, Phys. Status Solidi **36**, 187 (1969).
[2] M. R. Spender and A. H. Morrish, Can. J. Phys. **49**, 2659 (1971); **50**, 1125 (1972); Solid State Commun. **11**, 1417 (1972).
[3] L. Treitinger, H. Göbel, and H. Pink, Mater. Res. Bull. **11**, 1375 (1976).
[4] H. N. Ok, K. S. Baek, and J. C. Sur, Solid State Commun. **60**, 955 (1986).
[5] Sh. Sh. Bashkirov, R. K. Gubaidullin, Sh. R. Safin, and V. N. Zaritskii, Sov. Phys. Solid State **27**, 451 (1985).
[6] G. Shirane and D. E. Cox, J. Appl. Phys. **35**, 954 (1964).
[7] A. M. Van Diepen and R. P. Van Stapele, Solid State Commun. **13**, 1651 (1973).
[8] J. B. Nelson and D. P. Riley, Proc. Phys. Soc. London **57**, 160 (1945).
[9] H. N. Ok and J. G. Mullen, Phys. Rev. **168**, 563 (1968); J. Y. Park, H. M. Ko, W. H. Lee, S. H. Ji, and C. S. Kim, J. Appl. Phys. **73**, 5739 (1993).
[10] C. S. Kim, D. Y. Kim, H. M. Ko, J. K. Kim, and J. Y. Park, J. Appl. Phys. **73**, 6986 (1993).
[11] H. Kondo, J. Phys. Soc. Jpn. **41**, 1247 (1976).
[12] L. F. Feiner, J. Phys. C **16**, 1515 (1982).

The effect of Co doping on spin cluster resonance in the one-dimensional Ising ferromagnet FeTAC

R. S. Rubins and T. D. Black
Department of Physics, University of Texas at Arlington, Box 19059, Arlington, Texas 76019

K. Ravindran
Department of Physics, University of Cincinnati, Cincinnati, Ohio 45221

John E. Drumheller
Department of Physics, Montana State University, Bozeman, Montana 59717

Electron paramagnetic resonance measurements at 36 GHz and in the range 12–18 GHz were made on a single crystal of the 1D Ising ferromagnet $[(CH_3)_3\ NH]\ FeCl_3 \cdot 2H_2O$, known as FeTAC, containing a nominal 10% of the isomorphous compound CoTAC. While the 4.2 K spectra obtained with the external field parallel to the chain axis were similar to the spin cluster resonance spectra previously identified in pure FeTAC, differences in the low-field satellite structure were observed, which are tentatively attributed to differences in the dipolar interaction and to shorter ferrous chains. An appreciable decrease in the strength of the demagnetizing field is associated with the tendency of the Co^{2+} moments to align perpendicularly to the chain axis.

The compound $[(CH_3)_3\ NH]\ FeCl_3\ 2H_2O$, known as FeTAC, is a member of a family which contains chains of bihalide-bridged metal ions extending along the b axis of the orthorhombic unit cell.[1] Magnetic and specific heat studies have shown FeTAC to be an almost ideal one-dimensional (1D) Ising ferromagnet in the range 6–20 K.[1,2] The phase diagram is metamagnetic with $T_c = 3.1$ K and $H_c(0) = 90$ Oe, and the b axis is the bulk easy axis. There are two inequivalent Fe^{2+} sites per unit cell, with significant spin canting in the a direction.

The Ising form of the exchange interaction in the $S = 1/2$ representation arises from the splitting of the free-ion ground level of Fe^{2+} ($3d^6$, $S = 2$) by the combined effects of the spin-orbit coupling and noncubic components of the crystal field, which produce a well-isolated $M_S = \pm 2$ pseudo-doublet ground state.[3] In the $S = 1/2$ representation, the Zeeman splitting of the $M_S = \pm 2$ doublet may be represented by a highly anisotropic g factor, with $g_z \approx 8$ and g_x, $g_y \approx 0$, where the z direction would correspond to the b axis of the crystal in the absence of the spin canting. The simplest spin Hamiltonian describing the magnetic behavior of this system when the external field is parallel to the easy axis ($H \| b$) may be written

$$\mathcal{H} = -2J \sum_i S_i^z S_{i+1}^z - g_z \mu_B H_{\text{eff}} \sum_i S_i^z, \tag{1}$$

where $H_{\text{eff}} = H - H_0$, H is the external field, and H_0 is the sum of the demagnetizing and interchain exchange fields.

The elementary excitations of the $S = 1/2$ Ising system given by Eq. (1) are localized spin reversals, known as spin clusters or magnon bound states.[4–6] Neglecting excitations in which there is a reversed spin at the end of a chain, the first set of excited states contains a single group of n neighboring reversed spins, known as an n-fold spin cluster. According to Eq. (1) the energy of such a cluster is given by

$$E_n = E_0 + 2J + n g_z \mu_B H_{\text{eff}}, \tag{2}$$

where E_0 is the energy of the ferromagnetic ground state in a field H_{eff}. The second set of excited spin cluster states consists of two separated spin clusters within a single chain. Here, the excitation is $4J$ for $H_{\text{eff}} = 0$. The value $2J/k_B = 35$ K, obtained from the magnetic susceptibility and specific heat measurements,[1,2] indicates that only single cluster excitations need be considered in the first approximation at liquid helium temperatures.

Electron paramagnetic resonance (EPR) spectra observed from single crystals of FeTAC showed the expected anisotropy.[7–9] In 9 GHz measurements below 10 K, Ravindran *et al.*[7,8] reported a strong resonance line with a maximum g value of roughly 8 in the $S = 1/2$ representation, together with a broad line at lower fields. Measurements at higher microwave frequencies by Rubins *et al.*[9] both confirmed Ravindran's suggestions that the strong line was caused by transitions between adjacent spin-cluster levels, given by $\Delta n = \pm 1$ in Eq. (2), and showed the broad line to be an unresolved satellite structure, which dominated the EPR spectrum at 35 GHz.

In a more complete investigation covering the range 10–36 GHz, Rubins *et al.*[10] showed that the $\Delta n = \pm 1$ transitions were responsible for both the strong line and major satellite lines, thus demonstrating unequivocally the existence of spin-cluster resonance (SCR), first proposed by Data and Motokawa[4] in 1966. Both the frequency dependence of this spectrum and the temperature variations of the line intensities were explained semiquantitatively by the addition to Eq. (1) of the term ΔS_x, where Δ is a fine-structure parameter in the $S = 1/2$ representation.[3] The best fit of the FeTAC data was obtained with the values $2J/k_B = 33$ K, $\Delta/k_B = 6.6$ K, $g_z = 8.2$, and $H_0 = 340$ Oe.[10]

In this work, we present results of an EPR investigation of a mixed crystal of FeTAC and CoTAC, grown from a solution containing 10% CoTAC. The measurements were made in the frequency range 12–18 GHz and at 36 GHz. EPR spectra obtained at 4.2 K with $H \| b$ are shown for the two ranges in Figs. 1 and 2, respectively.

The basic features of the EPR spectra observed from the

 0021-8979/94/75(10)/6081/3/$6.00 © 1994 American Institute of Physics

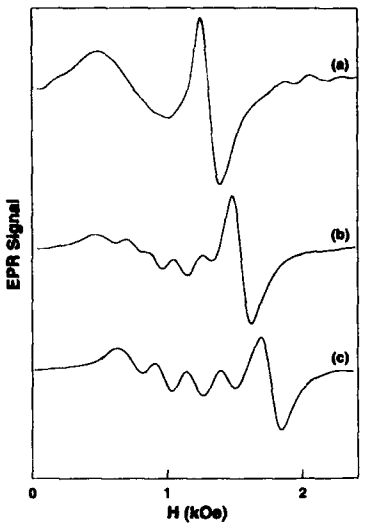

FIG. 1. EPR spectra at 4.2 K of a mixed (Fe, Co) TAC crystal with $H \| b$ and microwave frequency (a) 12.4 GHz, (b) 14.9 GHz, (c) 18.0 GHz.

mixed crystal, consisting of a main line and a lower-field satellite structure, are similar to those from pure FeTAC. Curve (a) of Fig. 1 shows that at sufficiently low microwave frequencies, the satellites appear as a single broad line, while curves (b) and (c) show that the satellites decrease in number, but increase in separation and relative intensity, as the frequency is increased. Figure 2 shows that these trends are continued at 36 GHz, except that the satellite structure becomes more complicated. Further evidence confirming a

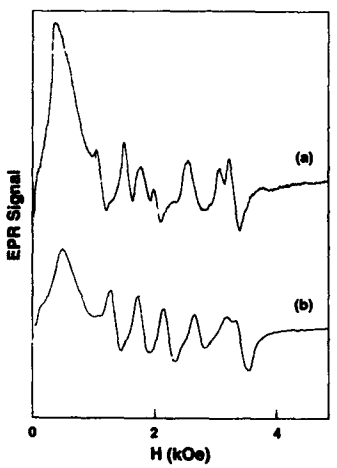

FIG. 2. EPR spectra at 4.2 K with $H \| b$ in (a) the mixed (Fe, Co) TAC crystal at 35.6 GHz (b) pure FeTAC at 35.6 GHz.

spin-cluster interpretation comes from the decrease in intensity of the spectra as the temperature is lowered, and the linear variation of the resonance field of the main line with frequency. From the latter, the values $g_z = 8.45 \pm 0.02$, $H_0 = (270 \pm 20)$ Oe were obtained.

The similarities mentioned above lead us to assume a spin-cluster interpretation for the mixed crystal spectra similar to that proposed for pure FeTAC. Interest then centers on the differences in the two sets of spectra, which are summarized below:

(i) The satellite structure of the mixed crystal, shown in the 36 GHz data of Fig. 2, has at least one more component, although fewer components were observed in the lower frequency data.

(ii) H_0, the sum of the demagnetizing and interchain exchange fields, is appreciably smaller in the mixed crystal.

(iii) Satellites may be seen above the "main" line in curve (a) of Fig. 1, which were not present in pure FeTAC.

Clues about the behavior of the mixed crystal may be obtained from the magnetic data for $[(CH_3)_3NH]CoCl_3\,2H_2O$. The moments in CoTAC lie in the ac plane, with spin canting of 22° towards the a axis.[11] Unlike FeTAC, the c axis is the easy axis for antiferromagnetic ordering, which occurs below 4.18 K. The ac susceptibility data for CoTAC were fitted to an $S = 1/2$ Ising exchange Hamiltonian, with a dominant intrachain exchange contribution given by $J_b/k_B \sim 14$ K.[12]

Difference (ii) given above may be understood qualitatively in the light of the pure CoTAC data. Since the Co^{2+} magnetic moments tend to align perpendicularly to the b axis, in contrast to the Fe^{2+} moments, the major axis of the g-tensor ellipsoid for Co^{2+} should be normal to that for Fe^{2+}. Thus the presence of Co^{2+} in a FeTAC crystal should reduce the magnetic anisotropy, and hence the demagnetization fields associated with the needle-like sample shape. Another phenomenon associated with the insertion of Co^{2+} into a FeTAC crystal is the lowering of the antiferromagnetic ordering temperature.[13] Difference (iii) may indicate the presence of a Co^{2+} spectrum in the mixed crystal. Since the g value for pure CoTAC has been measured to be 3.8 in the b direction,[12] one would expect the Co^{2+} hyperfine structure ($I = 7/2$) to appear on the high-field side of the main Fe^{2+} line. However, further experiments are needed to make a definite identification of the structure seen in Fig. 1, curve (a).

An indication of how the addition of Co^{2+} affects the FeTAC satellite structure may be obtained by modifying Eq. (1) to allow for the inclusion of a single Co^{2+} ion in a ferrous chain. Assuming Ising exchange between the Co^{2+} ion at the pth site and its Fe^{2+} neighbors, Eq. (1) requires the addition of the terms

$$\mathcal{H} = -2(J' - J)S_p^z(S_{p-1}^z + S_{p+1}^z) - (g_z' - g_z)\mu_B H_{\text{eff}} S_p^z, \quad (3)$$

where J' is the Fe-Co coupling constant and g_z' is the Co^{2+} g value.

The energies of some of the lower eigenstates of Eq. (1) relative to the ferromagnetic groundstate are shown schematically in Fig. 3 for the arbitrarily chosen values $J = 4J'$, $g_z = 2g_z'$ and $J' > g_z\mu_B H$. Ignoring excitations in which an

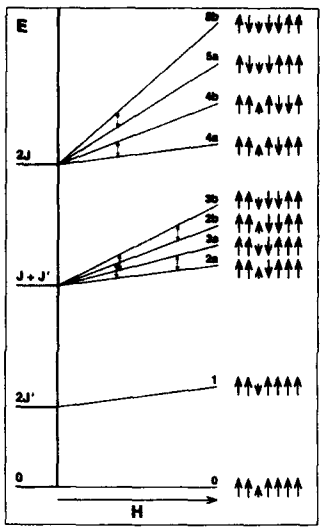

FIG. 3. A schematic representation of the Zeeman and exchange splittings of a long chain of $S=1/2$ spins containing one impurity of lower magnetic moment. The energies relative to the ferromagnetic groundstate are obtained from the spin Hamiltonian of Eqs. (1) and (3), using the arbitrarily chosen ratios $J/J'=4$ and $g_z/g_z'=2$, with the exchange splittings dominant. Only the two lowest spin cluster states in each sequence are shown. Schematic representations of the relevant spin arrangements associated with each Zeeman level are shown at the right of the diagram.

Fe^{2+} ion at the end of the chain is reversed, the first excited state corresponds to the reversal of the Co^{2+} spin alone. The two lowest sets of spin-cluster states, with a zero-field excitation of $J+J'$, contain an n-fold Fe^{2+} spin cluster neighboring the Co^{2+} ion. In Fig. 3, the Co^{2+} spin is reversed for states $3a$ and $3b$ but not for states $2a$ and $2b$. (For simplicity, only the lowest two of each set of spin-cluster states are shown in Fig. 3.) Fe^{2+} resonances are associated with the transitions $2a \leftrightarrow 2b$, etc., while the higher-field Co^{2+} resonances result from the transitions $2a \leftrightarrow 3a$ and $2b \leftrightarrow 3b$, etc. The next sets of spin-cluster states, with a zero-field excitation of $2J$ are again of two types. Those represented by states $4a$ and $4b$ are equivalent to the lowest set of spin-cluster states in pure FeTAC. The second type, in which the Co^{2+} ion is reversed and lies within the spin cluster, is represented by the states $5a$ and $5b$.

In the approximation given by Eqs. (1) and (3), the Fe^{2+} resonances would produce a single line at a frequency given by $h\nu=g_z\mu_B H_{\text{eff}}$. The addition of the ΔS_x term to the $S=1/2$ spin Hamiltonian for Fe^{2+} is needed to produce the low-field satellite structure.[10] The different satellite structure in the mixed sample could be caused by both the shorter chain length and the different magnetic dipolar interaction. Since dipolar fields in the range 10^2-10^3 Oe are produced by the n[illegible] one can visualize qualitatively a *breaku[illegible]te structure of the pure sample into a* more complicated structure, as occurs in the 36 GHz data of Fig. 2.

Further studies of such mixed crystal systems by EPR are clearly needed. In particular, the data indicate a marked dependence of the demagnetization field on the Co^{2+} concentration, and show EPR to be a sensitive and informative technique for studying systems of this type.

This work was supported in part by the National Science Foundation under Grant No. DMR9310967.

[1] R. E. Greeney, C. P. Landee, J. H. Zhang, and W. M. Reiff, Phys. Rev. B **39**, 12 200 (1989).
[2] C. P. Landee, R. Kuentzler, and J. J. M. Williams, J. Appl. Phys. **67**, 5604 (1990).
[3] See, for example, A. Abragam and B. Bleaney, *Electron Paramagnetic Resonance of Transition Ions*, 1st ed. (Oxford University, London, 1970), pp. 209–216.
[4] M. Date and M. Motokawa, J. Phys. Soc. Jpn. **24**, 41 (1968).
[5] M. Date and M. Motokawa, Phys. Rev. Lett. **16**, 1111 (1966).
[6] J. B. Torrance, Jr. and M. Tinkham, Phys. Rev. **187**, 587 (1969).
[7] K. Ravindran, Ph.D. dissertation, Montana State University, 1991, pp. 50–59.
[8] K. Ravindran, S. Waplak, T. E. Grigereit, J. E. Drumheller, and R. S. Rubins, Phys. Rev. B **47**, 14568 (1993).
[9] R. S. Rubins, T. D. Black, K. Ravindran, T. E. Gringereit, and J. E. Drumheller, J. Appl. Phys. **73**, 6977 (1993).
[10] R. S. Rubins, T. D. Black, A. Sohn, and J. E. Drumheller, Phys. Rev. B (to be published).
[11] D. B. Losee, J. N. McElearney, G. E. Shankle, R. L. Carlin, P. J. Cresswell, and W. T. Robinson, Phys. Rev. B **8**, 2185 (1973).
[12] H. A. Groenendijk and A. J. van Duyneveldt, Physica **115B**, 41 (1982).
[13] K. Ravindran and J. E. Drumheller (unpublished data).

New perspective on the Green's function dipole-exchange spin wave theory for thin films (abstract)

Ming Chen and Carl E. Patton
Department of Physics, Colorado State University, Fort Collins, Colorado 80523

In contrast with the scalar potential theory for dipole-exchange spin waves in thin films,[1] the Green's function (GF) approach in combination with perturbation methods (PM) gives simple closed form dispersion equations, analytical expressions for the dipole-exchange frequency gaps, and good intuitive physics.[2] However, in the case of in-plane magnetized films and perpendicular propagation, the GF/PM results present two major problems. (1) The multibranch dipole-exchange solutions bear little resemblance to the single dispersion curve for the well-established Damon–Eshbach magnetostatic surface modes and the nonreciprocal mode profiles predicted by the simple theory and observed experimentally. (2) The lowest order exchange branch has a curvature that is much greater than expected from either simple spin wave considerations or scalar potential theory. To resolve these problems, a simple method has been developed to solve the coupled mode equations obtained from the GF formalism without recourse to perturbation methods. The coupled mode dispersion relations obtained with this method are valid for an arbitrary field configuration and propagation direction, and are not subject to the restrictions imposed by perturbation methods. The solutions agree well with the surface mode theory for in-plane magnetized films. Good agreement is also found with the Brillouin light scattering data for iron thin films.

This work was supported in part by the National Science Foundation, Grant DMR-8921761 and by the U.S. Army Research Office, Grant DAAL03-91-G-0327.

[1] T. Wolfram and R. E. DeWames, Prog. Surf. Sci. 2, 233 (1972).
[2] B. A. Kalinikos and A. N. Slavin, J. Phys. C 19, 7013 (1986).

 0021-8979/94/75(10)/6084/1/$6.00 © 1994 American Institute of Physics

Ground state and spin dynamics in hexagonal antiferromagnet $CsCuCl_3$ (abstract)

E. P. Stefanovskii and A. L. Sukstanskii
Physico-Technical Institute, Donetsk 340114, Ukraine

Modulated magnetic structure in $CsCuCl_3$ was obtained[1] by the neutron diffraction technique and theoretically discussed in Refs. 1 and 2 by means of the model including Dzyaloshinskii–Moriya and exchange interactions as well as sixth order anisotropy in the basal plane.[2] The present abstract aims at presenting some new aspects of a magnetization distribution in the ground state of the system and more adequate theory of its dynamic properties. We described the so-called "space mutation" effect caused by an external magnetic field parallel to the hexagonal axis. Sufficiently large hexagonal anisotropy results in appearing of the soliton lattice structure and enables us to explain nonmagnetic resonance (NMR) experiments.[3] Dynamic properties of the magnet were investigated by means of the effective Lagrange function method using Cartan differential forms. The spin wave spectrum and the magnetic susceptibility tensor were obtained. If, the hexagonal anisotropy being neglected, the spectrum was shown to consist of three branches in contrast to Ref. 2 where there was a single branch only, antiferromagnetic (AFMR) frequencies dependence on an external magnetic field occurred to be in a good agreement with experimental data.[4] Taking into account the hexagonal anisotropy, the usual zone structure of the spectrum was obtained.

[1] K. Adachi, N. Achiwa, and M. Mekata, J. Phys. Soc. Jpn. **49**, 545 (1980).
[2] A. L. Alistratov, E. P. Stefanovskii, and D. A. Yablonskii, Fiz. Nizkh. Temp. **16**, 1306 (1990).
[3] K. LeDang, P. Veillet, and J. P. Renard, Solid State Commun. **24**, 313 (1977).
[4] G. A. Petrakovskii and V. N. Vasil'ev, Proceedings of the Conference on Radiospectroscopy of Crystals with Phase Transitions, Kiev, 1989, p. 71.

 0021-8979/94/75(10)/6085/1/$6.00 © 1994 American Institute of Physics

Successive Bloch line write operation in a 1-μM bubble material

K. Matsuyama, T. Ohyama, H. Asada, and K. Taniguchi
Department of Electrical Engineering, Kyushu University 36, Fukuoka 812, Japan

The successive vertical Bloch line (VBL) write operation has been performed in an as-grown 1-μm bubble material with a flank wall writing scheme. An unwinding VBL pair was nucleated by a domain expanding pulse current (200-mA amplitude, 200-ns pulse width, 8-ns rising edge) applied through a hair-pin type conductor (gap:2.6 μm, width:4 μm). The VBL position was controlled by a local in-plane magnetic field produced by a conductor current of 30 mA and a uniform in-plane magnetic field of 10 Oe. The above operating parameters were adjusted by measuring the collapse field of the stripe domain as a function of the parameters. The increase of bubble collapse field from 442 to 513 Oe in accordance with the number of write operations indicated a successful write operation.

A liquid phase epitaxial (LPE) bubble garnet film with 1-μm domain width is intended to be used as a material for a 256 Mbit/cm^2 vertical Bloch line (VBL) memory. Recently, the prototype 256 Mbit/cm^2 VBL memory chip was fabricated and the performance of basic memory operation was reported.[1] In order to realize a practical memory device, further precise understanding of each memory operation seems to be necessary. A problem in developing high bit density VBL memory is the difficulty in direct observation of VBLs. In a previous report,[2] the dependence of bubble collapse properties on the number of included VBLs was studied for a 1-μm bubble material. In the present study, this dependence was utilized to estimate the number of VBL pairs in a stripe domain subjected to constituent or whole write operations.

The LPE garnet film used is a standard as-grown 1-μm bubble material with the following material characteristics: saturation induction $4\pi M=900$ G, uniaxial anisotropy $K_u=0.95\times10^5$ erg/cm^3, characteristics length $l=1.05\times10^{-5}$ cm, gyromagnetic constant $\gamma=1.72\times10^7$ (s Oe)$^{-1}$, damping constant $\alpha=0.067$. The top view and cross section of the test chip are shown in Fig. 1. The test chip consists of two conductor layers. An isolated stripe domain was confined in the current induced magnetic potential well from the loop conductor (1). The loop conductor was also used to apply pulsed bias fields to the domain. The parallel conductor (2) was used for bubble and stripe rocking. These two conductors were patterned in the first conductor layer. Other conductors for the write operation were formed in the second conductor layer. Conductors (3), (4). and (7) were used to hold the stripe head. The stripe head was shrunk and stretched between conductors (4) and (7) by varying the bias field.

Writing of a winding VBL pair was performed by constituent operations as shown in Fig. 2. First, a successive domain contracting pulse was applied to the bubble domain to eliminate the extra VBLs and initiate the $S=0$ state, which has one winding VBL pair [Fig. 2(a)]. Through the following write operation a static in-plane field H_x was applied along the stripe length direction. The stripe was stretched by decreasing the bias field, and one of the initial VBLs was intended to be trapped by the current induced in-plane magnetic field from the dc conductor current I_{tr} [Fig. 2(b)]. During the stripe stretch motion and the following VBL nucleation processes an additional in-plane field H_y of 20 Oe was applied in the stripe width direction. This field defines the VBL position at the prescribed sidewall. An expanding pulse field was applied by conductor (6) to nucleate an unwinding VBL pair at one side of the flank wall[3] [Fig. 2(c)]. Then, the stripe head was chopped by a contracting bias pulse field from the same conductor (6) to convert the unwinding VBL pair to a winding one [Fig. 2(d)]. A winding pair can be used as the bit information carrier in a VBL memory. The chopped additional domain was collapsed by a pulse current applied through conductor (7) and the stripe was shrunk toward the initial position [Fig. 2(e)]. The above operations were repeated to accumulate winding VBL pairs with same polarity.

The preliminary test was carried out for some constituent operations. The threshold value for the in-plane field H_x to displace the VBL trapped by the conductor current I_{tr} was

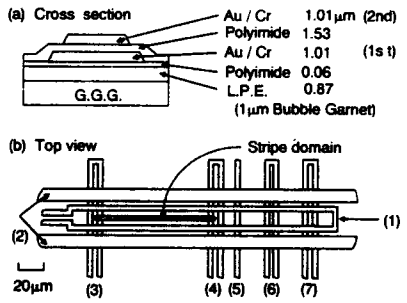

FIG. 1. Configuration of the test chip.

0021-8979/94/75(10)/6086/3/$6.00
© 1994 American Institute of Physics

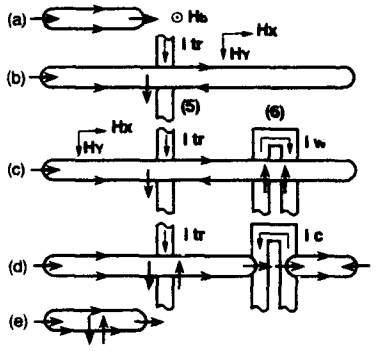

FIG. 2. VBL write operation.

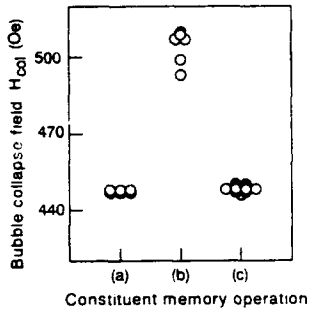

FIG. 4. Bubble collapse field H_{col} measured after constituent memory operation; stretch and shrink for (a) $S=0$ stripe, (b) hard stripe, and (c) chopping for $S=0$ stripe.

measured, as shown in Fig. 3. The trapped VBL was observed as a local constriction during stripe rocking. The rocking conductor current of 430-mA amplitude, 250-ns pulse width with 100-Hz pulse frequency enables the optical observation of constriction. From the slope of the linear plots, the effective in-plane field generated by the conductor current I_{tr} can be evaluated as 0.63 Oe/mA. The intercept of the plots with the abscissa axis corresponds to the VBL coercivity in terms of the in-plane magnetic field necessary to displace the VBL along the wall. The VBL coercivity can be estimated as 3.7 Oe, by averaging the two intercept values. The different intercept values for the two plots with different H_x polarity would be caused by the centering error of the chip position in the external coil system. The centering was carried out by moving the chip in the coil system manually so as to minimize the difference of the intercept values, however, it was difficult to center it perfectly.

The collapse field H_{col} was measured for the stripe domain subjected to the constituent operation, as shown in Fig. 4. The plots (a) and (b) present H_{col} measured after ten successive stretch and shrink operations. The $S=0$ and hard bubble was selected as initial states in plots (a) and (b), respectively. The H_{col} for the $S=0$ bubble was 442 Oe. The hard bubble was initiated by applying the successive expand ing bias pulse (produced by the loop conductor current of 120-mA amplitude and 300-ns width) to the stripe domain, and the state was checked by assuring that the domain remained after increasing the bias field up to 500 Oe. The collapse field for the most of bubbles obtained by this method was about 510 Oe, which is that for the hardest bubble. As can be seen in the figure, significant variation of H_{col} values were not observed for the $S=0$ and hard stripe. The results suggest that nucleation and annihilation of the VBL do not frequently occur during the stretch and shrink motion. The plots (c) present the H_{col} measured after ten successive stripe chopping operations on the initial $S=0$ stripe. The results reveal that the initial $S=0$ stripe retains its original wall state, that is, the chopping process does not produce an extra nucleation of VBLs.

The conductor current I_{tr} and the external in-plane field H_x are the representative operation parameters, and should be carefully optimized to realize practical operation margin. The dependence of the write performance on these parameters has been studied by measuring the collapse field H_{col}. Values of H_{col} measured after ten successive write operations

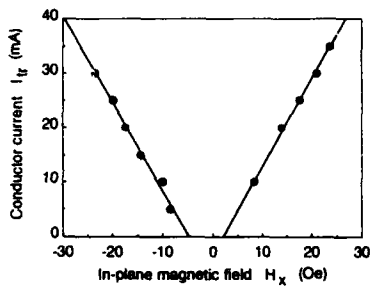

FIG. 3. In-plane magnetic field H_x necessary to displace a VBL trapped by conductor current I_{tr}.

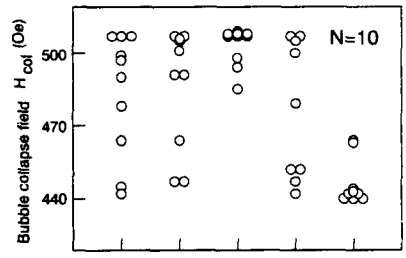

	(a)	(b)	(c)	(d)	(e)
H_x (Oe)	10	10	10	20	30
I_{tr} (mA)	10	20	30	30	30

FIG. 5. Bubble collapse field H_{col} measured after ten successive write operations with various operation parameters.

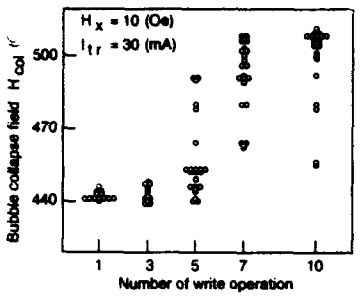

FIG. 6. Bubble collapse field H_{col} measured after various repetitions of write operation.

with various values of I_{tr} and H_x are shown in Fig. 5. A trapezoidal pulse current (200-mA amplitude, 8-ns rising edge, 200-ns pulse width) was used for VBL nucleation. If ten VBL pairs were written into the stripe successfully, the H_{col} value is expected to be 510 Oe from the bubble statics theory extended to the hard bubble.[2] As can be seen in the figure, most of results for operation parameter (c) present H_{col} of about 510 Oe, where H_x=10 Oe and I_{tr}=30 mA, respectively. The results for other parameter values reveal that further increase of H_x or the decrease of I_{tr} results in the degraded performance, which appears to be caused by a VBL trap error. The threshold values for H_x and I_{tr} for the successful write operation can be reasonably explained by the estimated value for the current induced in-plane magnetic field (0.63 Oe/cm^2).

Similar experiments were performed as a function of repetition number N of the write operation, with the parameters of H_x=10 Oe and I_{tr}=30 mA, as shown in Fig. 6. The increase of H_{col} for $N \leq 3$ is not prominent, which agrees with the theoretical prediction that the difference of H_{col} for a bubble with less than three VBL pairs is fairly small.[2] The increase of H_{col} value was found to saturate for a repetition number larger than ten, which can be also explained by the predicted maximum number of VBL pairs of 12. The increase of H_{col} in accordance with the number of write operations reveals that the VBL pairs were accumulated in the domain through the repeated write operation. The considerable scattering in the measured H_{col} values suggests the occurrence of accidental operation error. The probable causes of them appear to be the VBL trap error and the nucleation of more than one VBL pair during each operation. The difference of the spread of data in Figs. 5(c) and 6 (N=10) would be due to the stochastic aspect of the error. It should be noticed that the number of data in Fig. 6 is more than twice of those in Fig. 5.

The successive VBL write operation has been performed in an as-grown 1-μm bubble material. The flank wall write scheme was adopted in the present study. The write operation was carried out for an isolated stripe domain confined in a current induced magnetic potential well. An unwinding VBL pair was nucleated by a domain expanding pulse current (200-mA amplitude, 200-ns pulse width, 8-ns rising edge) applied through a hair-pin type write conductor (gap 2.6 μm, width 4 μm). The VBL position was controlled by a local in-plane magnetic field produced by a conductor current of 30 mA and uniform in-plane magnetic field of 10 Oe. The increase of the bubble collapse field from 442 Oe for single write operation to 511 Oe for ten successive ones indicated a successful write operation.

We would like to thank Central Research Laboratory of Hitachi Ltd. for providing LPE garnet wafers.

[1] Y. Maruyama, K. Fujimoto, and R. Imura, in Digests of the 15th Annual Conference on Magnetics, Japan, 1992, p. 283.
[2] K. Matsuyama, K. Ishizu, H. Asada, and K. Taniguchi, IEEE Trans. Magn. 29, 2575 (1993).
[3] Y. Hidaka, Jpn. J. Appl. Phys. 18, L228 (1986).

Micromagnetic computation for wall and Bloch line coercivity in thin films with perpendicular anisotropy

H. Asada, K. Matsuyama, M. Gamachi, and K. Taniguchi
Department of Electrical Engineering, Kyushu University 36, Fukuoka 812, Japan

Wall and vertical Bloch line (VBL) coercivity arising from spatial nonuniformity in the material parameters has been investigated for a typical 5-μm bubble garnet film by means of a two-dimensional micromagnetic computation. Two-dimensional sinusoidal modulations in the magnitude of the uniaxial anisotropy were assumed as a model for a compositional nonuniformity. Nonuniformities with a spatial wavelength comparable to the wall width were found to exert the largest pinning effect. The typical computed value for the wall and VBL coercivity were 0.7 and 2.2 Oe, respectively, where 10% variation and wavelength of 0.47 μm were assumed. The tendency, that the VBL coercivity is larger than that for the domain wall, agrees with the experimental results reported previously. The wall and VBL coercivity caused by a nonuniform exchange constant have also been computed and compared to the analytical solutions due to the step-like variation of wall and VBL energies, respectively. The larger VBL coercivity compared to that for the wall was observed for a local modulation with the size less than wall width and period more than 1 μm.

INTRODUCTION

Insight into the coercivity of a domain wall and vertical Bloch line (VBL) is important for a material consideration in Bloch line memory to realize the stable memory operation. VBL coercivity, defined as the minimum in-plane field along the domain wall required to displace the VBL, has been reported experimentally to be larger than wall coercivity.[1-3] Micromagnetic computation is useful to evaluate the coercivity for various physical models.[4,5] In this paper, wall and VBL coercivity have been studied by numerical integration of the Landau–Lifshits–Gilbert (LLG) equation for a typical 5-μm bubble garnet film with a spatial nonuniformity in the anisotropy and exchange material parameters.

RESULTS AND DISCUSSION

The computation was performed for a two-dimensional grid system representing the magnetization direction in a film plane. The LLG equation was integrated by using the modified Dufort–Frankel method.[6] The computation region had the free and periodic boundary condition for the wall normal and tangential direction, respectively. The spacing interval of grid elements was 300×300 Å, and the time step interval for iteration was 1 ps. The following typical parameters were used: saturation induction $4\pi M = 195$ G, uniaxial anisotropy $K = 8230$ erg/cm^3, exchange constant $A = 2.63 \times 10^{-7}$ erg/cm, gyromagnetic constant $\gamma = 1.82 \times 10^7$ (Oe s)$^{-1}$, damping parameter $\alpha = 0.5$, which yields the wall width $\delta(=\pi\Delta) = 0.18$ μm, and Bloch linewidth $\lambda(=\pi\Lambda) = 0.42$ μm. To save the computation time, the demagnetizing field from the wall normal component of magnetization was calculated by a approximate formulation of $4\pi M_x \exp\{-(x/\delta)^2\}$, where M_x is the wall normal component of magnetization at the wall center and x is the distance from the wall center to grid elements. This formulation is based on the magnetic field from the wall surface charges ($4\pi M_x$), and modified considering the decrease of the field amplitude according to the distance from the charges.

Figure 1 shows the time transient of the orthogonal component of the effective field to the magnetization, which was calculated for each grid elements and averaged over the computation region with a local pinning site, for the pinned (a) and moved (b) wall applying to the step bias field. It corresponds to the residual torque divided by the amplitude of the magnetization. The coordinate axis expresses the logarithm of the effective field. In the relaxation process, the effective field was confirmed to decrease the 10^{-13} order after 150 000 step iterations, which was limited by the numerical accuracy in the double precision calculation in the FORTRAN77 program. After the relaxation, the drive field H_p was applied to the wall. In Fig. 1(a), after increasing the drive field of 0.1 Oe in addition to the former drive field of 3.2 Oe, the effective field rapidly increases at first, but decreases continuously less than 10^{-4} Oe. This means that the wall was pinned. Furthermore, in Fig. 1(b), increasing the drive field of 0.1 Oe, then the total drive field is 3.4 Oe, the effective field increases again after 50 ns, which means that the wall passed through the pinning site. The wall coercive field was defined

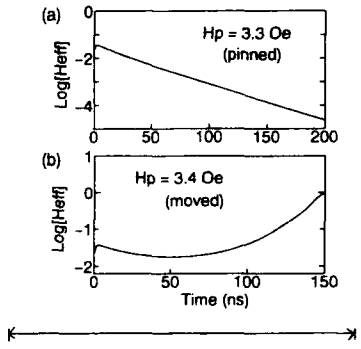

FIG. 1. Time transient of the orthogonal component of averaged effective fields for the moved (a) and pinned (b) wall applying the step bias field.

 0021-8979/94/75(10)/6089/3/$6.00 © 1994 American Institute of Physics

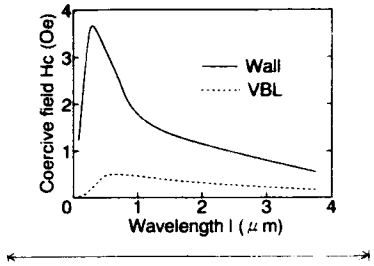

FIG. 2. Dependence of the wall and VBL coercive field H_c on wavelength l of one-dimensional sinusoidal modulation in uniaxial anisotropy. The modulation directions were taken to be normal and tangential to the wall plane in the computation of wall and VBL coercivity, respectively.

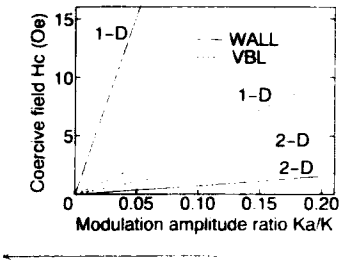

FIG. 3. Wall and VBL coercivity as a function of the modulation amplitude ratio K_a/K of one- (1D) and two-dimensional (2D) sinusoidal modulation in uniaxial anisotropy.

as this threshold value of the bias field. The VBL coercive field was also defined by the orthogonal component of the effective field as the threshold value of the in-plane field along the wall was required to displace the VBL.

Figure 2 shows the dependence of the wall and VBL coercive field H_c, resulting from a one-dimensional sinusoidal anisotropy modulation of wavelength l. The modulation amplitude K_a was 1% of the averaged value. The modulation directions were taken to be normal and tangential to the wall plane in the computation of the wall and VBL coercivity, respectively. We observed that the wall is pinned at the region where the uniaxial anisotropy is small, while VBL is pinned where the anisotropy is large. This tendency can be inferred from the dependence of wall ($4\sqrt{AK}$) and VBL ($8AQ^{-1/2}$) energies on the material parameters. Both the wall and VBL coercivity decrease remarkably when the modulation wavelength is smaller than wall and Bloch linewidth, since the spatial variation of energy caused by the modulation are smoothed away. The modulation with the wavelength comparable to the wall width was found to exert the largest pinning effect. For the one-dimensional modulation, the computed VBL coercivity was smaller than that for wall, which is incompatible with the experimental results. Then we assumed a two-dimensional sinusoidal modulation, which seems to be a more practical model for actual nonuniformity in the thin film. Figure 3 shows the coercivity as a function of the modulation amplitude ratio K_a/K. The wavelength was 0.47 μm. Both the wall and VBL coercivity increase linearly with increasing modulation amplitude. The wall coercivity for a two-dimensional modulation is 1/50th of the value found for a one-dimensional modulation. This is because wall coercivity for the two-dimensional modulation was produced by wall bending, which enables the small anisotropy region to decrease the wall energy. On the other hand, VBL coercivity for a two-dimensional modulation is reduced to one-half of the value observed for a one-dimensional modulation due to the local distribution of VBL structure. VBL coercivity becomes larger than wall coercivity for a two-dimensional modulation. This tendency agrees well with the experimental results. The wall and VBL coercivity were computed as 0.7 and 2.2 Oe, where 10% modulation of the averaged value was assumed.

The coercivity caused by the local area having different magnetic parameters was also examined. It is difficult to pin the wall containing VBL at the local anisotropy modulation due to the difference of the modulation amplitude direction mentioned before. Therefore, we estimated the coercivity caused by the local modulation in an exchange constant (size $L \times L$) located periodically along the wall. In this case, both the wall and VBL were pinned at the local modulation having a reduced exchange constant. The wall and VBL coercivity due to the wall and VBL energy variations caused by a two-dimensional step-like modulation were given by the following approximate formulations:[4]

$$\text{Wall: } H_c = \Delta\sigma/\delta_m \cdot P/L, \tag{1}$$

$$\text{VBL: } H_c = \Delta E_b/\lambda_m \cdot 1/2\delta_m M \quad (L > \delta_m)$$
$$= \Delta E_b/\lambda_m \cdot 1/2\delta_m M \cdot L/\delta_m \quad (L < \delta_m)$$
$$(\Delta\sigma = \sigma_2 - \sigma_1, \Delta E_b = E_{b2} - E_{b1}), \tag{2}$$

where P is the modulation period, and i denotes each region with the different wall energy $\sigma_i = 4\sqrt{A_i K_i}$, VBL energy $E_{bi} = 8A_i Q_i^{-1/2}$, wall width δ_i, and VBL width λ_i. δ_m is the mean wall width defined as $\delta_m = (\delta_1 + \delta_2)/2$ for $L > (\delta_1 + \delta_2)/2$ and $\delta_m = \delta_1 + (\delta_2 - \delta_1)/(\delta_2 + \delta_1) \cdot L$ for $L < (\delta_1 + \delta_2)/2$. λ_m is the mean Bloch line width defined as the same formula as the wall width. Figure 4 shows the dependence of the coercivity on the local modulation size. The exchange constant is reduced by 10% in the modulation region for a period of 0.96 μm. The wall coercivity increases with the increase of the modulation size in spite of the fact that the VBL coercivity saturates when the local modulation size becomes larger than the wall width. The dependence of both the wall and VBL coercivity on defect size agrees well with the approximation. The larger VBL coercivity compared to that for the wall was obtained with the modulation size less than the wall width. Figure 5 shows the wall and VBL coercivity as a function of the modulation period with a fixed size of 0.12×0.12 μm. The broken line indicates the coercive field defined as the threshold value of the bias field required to displace the wall containing the VBL aligned with the same period as that of

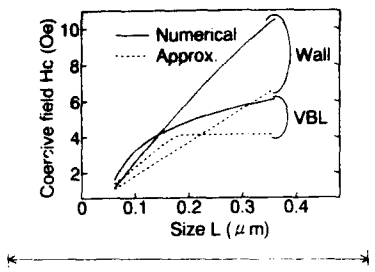

FIG. 4. Dependence of the wall and VBL coercive field H_c on the size L of a local modulation in the exchange constant. Numerical result (solid curve) and analytical approximation (dotted curve).

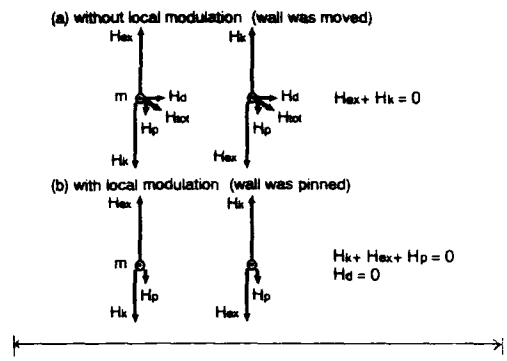

FIG. 6. Schematic diagram of equivalent fields without (a) and with (b) local exchange constant modulation under application of a step bias field of 2 Oe.

modulation. The wall coercivity decreases with increasing the period. The coercivity of wall containing the VBL is larger than the normal Bloch wall coercivity, which is attributed to the fact that the wall coercivity increases with the increase of the wall energy. In order to confirm this aspect, the wall coercivity was computed by changing the wall energy but keeping the wall width constant to eliminate the modulation size effect. It was found that the wall coercivity increases with increasing wall energy for the same modulation. This means that the wall coercivity increases in the material with the small bubble diameter.

To study the pinning mechanism precisely, we investigated each equivalent field, exchange (H_{ex}), anisotropy (H_k), and demagnetizing (H_d), which act on the magnetization. Figure 6 shows a schematic diagram of each equivalent field normal to the magnetization direction after applying the step bias field H_p of 2 Oe to the Bloch wall, without (a) and with (b) the local modulation in the exchange constant, respectively. The arrows in the figures are not drawn to scale. The total field H_{tot} of equivalent fields provides the torque, which rotates the magnetization. Two magnetizations were chosen to be neighboring grid elements of wall center position. In Fig. 6(a), since the H_{ex} and H_k also balanced after applying the H_p, the magnetization rotated around the H_{tot} composed of H_p and H_d, and the wall was moved. In Fig. 6(b), the spin structure was changed to cause the exchange field variation to cancel the H_p. Therefore, the H_d did not arise and the wall was pinned.

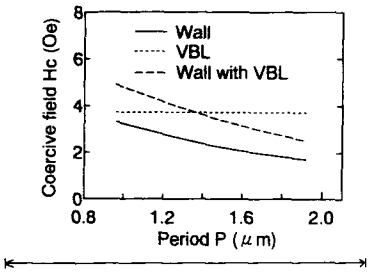

FIG. 5. Wall and VBL coercivity as a function of the local modulation period P in the exchange constant.

CONCLUSIONS

Wall and VBL coercivity resulting from spatial nonuniformity in the material parameters was investigated by micromagnetic computation. Spatial modulation of the material parameters with a wavelength comparable to the wall width was found to exert the largest pinning effect on the wall and VBL. The coercivity of the wall containing the VBL was larger than that of the normal Bloch wall for a local modulation in the exchange constant. The larger VBL coercivity compared to that for the wall was obtained for a two-dimensional sinusoidal modulation in the anisotropy constant with the wavelength of 0.47 μm and for a local modulation with the size less than wall width and a period more than 1 μm.

[1] G. Ronan, J. Theile, H. Krause, and J. Engemann, IEEE Trans. Magn. **MAG-23**, 2332 (1987).
[2] A. Thiaville, F. Boileau, and J. Miltat, IEEE Trans. Magn. **MAG-24**, 3045 (1988).
[3] H. Krause, J. Theile, R. Dahlbeck, and J. Engemann, J. Magn. Magn. Mater. **95**, 95 (1991).
[4] K. Matsuyama, Y. Hirokado, and H. Asada, J. Appl. Phys. **69**, 4853 (1991).
[5] S. W. Yuan and H. N. Bertram, IEEE Trans. Magn. **28**, 2916 (1992).
[6] G. Ronan, K. Matsuyama, E. Fujita, M. Ohbo, S. Kubota, and S. Konishi, IEEE Trans. Magn. **MAG-21**, 2680 (1985).

Phase transitions in bubble lattice under temperature lowering (abstract)

V. S. Gerasimchuk
Civil Engineering Institute of Mackeevka, 339023 Mackeevka, Ukraine

Yu. I. Gorobets
Donetsk State University, 340055 Donetsk, Ukraine

K. De Ville
University Paris XII, France

It is usually considered that bubbles forming a close-packed hexagonal bubble lattice have equal diameters.[1] It turned out[2] that bubbles of different diameters can exist in a certain temperature interval in zero bias field in bubble lattices. With temperature-lowering one of them collapses, and others exist as a lattice-like graphite-type lattice. In the present paper theoretical grounds of the experimental results are given. Energy of a lattice containing bubble of different diameters is calculated. Variations of full energy in bubble diameters give the system of equations. Joint solution of the system with appropriate conditions of stability characterize stability of a bubble lattice in respect to collapse. The conditions of loosing of stability determine critical points of (1) collapse of a lattice with bubbles of equal diameters;[1] (2) structural phase transitions under which hexagonal bubble lattice transforms into lattice with bubbles of different diameters. Diameters of bubbles situated in the center of a hexagonal cell are shown to decrease with lowering temperature, while bubble diameters situated in junctions of a cell increase. On achieving a certain critical size the former collapses and the latter increases its size by a sudden leap. Further bubble lattices such as graphite-type lattices exist. Conditions of existence and collapse of the latter lattice are reviewed.

[1] J. A. Cape and G. W. Lehman, J. Appl. Phys. **42**, 5732 (1971).
[2] Yu. Gorobets, I. Melnichuk, and Yu. Pimenov, J. Magn. Magn. Mater. **115**, 204 (1992).

 0021-8979/94/75(10)/6092/1/$6.00 © 1994 American Institute of Physics

An adaptive computational method for domain wall dynamics (abstract)

Sergey G. Osipov
Department of Computational Mathematics & Cybernetics, Moscow State University, Moscow 119899, Russia

The dynamics of magnetic domain walls is a subject of intensive computer simulation of last years. Now it is well understood, that strongly twisted structures (like horizontal Bloch lines) of domain walls can be created. In some cases this HBL can have a very small localization region. Appearance of such inconvenient objects, like HBL, states a new scale for numerical model and it required a significant increase of node number for the uniform grid model. The main idea of the new adaptive computational method for LLG equation for two-dimensional (2D) domain wall dynamics is to inject and delete additional nodes only to the HBL localization region, using a special target function, which is based on the twisting angle of the domain wall. Node injection occurs when HBL is created, and node deleting occurs when HBL is breakthrough. The conjugated gradient method was used for fast demagnetization field computation by two Dirichlet problems for Poisson equations. We show an effective application of this method for 2D computations of domain wall dynamics for bubble film with parameters: $Q=4$, $D=3(l)$, $\alpha=0.2$, $h=(0,8,-3)$, (Ms) [Here Q is the quality factor of the film, D the film thickness in characterization units, α the damping parameter, h the external magnetic field in Ms units, $8(Ms)$ the value of in-plane magnetic field via chirality, $-3(Ms)$ is the driven magnetic field.] We found that HBL has very strong localization in this case. To carry out this computation we need $\mathbf{n_x \times n_z = 65 \times 162}$ for uniform grid system, and only $\mathbf{n_x \times n_z = 33 \times 60}$ for adaptive grid system. A color computer movie was created for this case. The new mechanics of HBL generation and breakthrough is discussed. Here we can see significant asymmetry in HBL generation: two HBL created at one moment at the lower surface of the film, but upper HBL goes to the upper surface of the film and the lower goes to the opposite direction. The next pair of HBL is created at the lower surface of the film at the same place.

 0021-8979/94/75(10)/6093/1/$6.00 © 1994 American Institute of Physics

Wet-process preparation of amorphous Y-Fe oxide films ferromagnetic at room temperature

Q. Zhang, T. Itoh, M. Abe, and M. J. Zhang
Department of Physical Electronics, Tokyo Institute of Technology, Ookayama, Meguro-ku, Tokyo 152, Japan

Yttrium iron ferrite films of amorphous structure (as examined by x-ray diffraction), having ferromagnetic moment at room temperature, are successfully synthesized from an aqueous solution by a ferrite plating method in which the substrate is heated by Xe-lamp beams. The atomic ratio of Y/Fe in the films is adjusted to Y/Fe=0.6, as in $Y_3Fe_5O_{12}$, by properly choosing the atomic ratio (Y/Fe=3.5) in the reaction solution. The magnetization of the films at room temperature is 10–40 emu/cc, several times smaller than that observed for crystalline YIG. It exhibited, however, a paramagnetic Mössbauer spectrum at room temperature, suggesting that the weak magnetization is ascribed to the magnetic impurity phase whose concentration is too small to be discerned by x-ray diffraction and Mössbauer measurements. The spectrum has an isomer shift of 0.22 mm/sec at 300 K and a hyperfine field splitting of 462 kOe at 12 K, indicating that the Fe ions are in a trivalent high spin state.

I. INTRODUCTION

Amorphous oxide films ferromagnetic at room temperature so far reported have been synthesized in a vacuum process. However, we succeeded recently in synthesizing from an aqueous solution ferromagnetic (at room temperature) oxide films containing Y and Fe at an atomic ratio Y/Fe=3/5, as in $Y_3Fe_5O_{12}$ (YIG), which are amorphous as examined by x-ray diffraction. The wet-process method used for preparing the amorphous films is a modification of the so-called ferrite plating, a chemistry method which facilitates synthesis of polycrystalline ferrite films of spinel structure from aqueous solution at low temperature (<100 °C).[1–3] The polycrystalline ferrite films prepared by the conventional ferrite plating method have grain boundaries and columnar structure (perpendicular to film plane), which restricts magnetic, optical, and microwave characteristics of the films for device applications; magnetic domain mobility is suppressed and light and electromagnetic waves are scattered by such inhomogeneous structures inherent in the polycrystalline films.[4] The amorphous ferrite films are, on the other hand, free from this problem, and, therefore, are advantageous for optical and microwave device applications.

In this article we describe preparation of the amorphous Y-Fe ferrite films, and report their structural and magnetic properties.

II. EXPERIMENT

A. Film synthesis

The films were deposited on substrates of quartz (20 ×15×1 mm^3) and polyethylene terephthalate (PET) (30×15 ×0.1 mm^3), which were heated to 70–95 °C by Xe-lamp beams (6–10 mm in spot diameter and 450 W/cm^2 in intensity) and a supplementary electric heater. As given in Table I, a reaction solution of YCl_3+FeCl_2 and an oxidizing solution of $NaNO_2+CH_3COONH_4$ (*p*H buffer) were prepared by dissolving the starting chemicals into distilled water. It was not necessary to deaerate the distilled water (purge air from the water by bubbling with N_2) in this experiment, whereas deaerating the water was required in the conventional ferrite plating.[5]

B. Measurements

The chemical composition of the films was analyzed by inductively coupled plasma (ICP) spectroscopy, after dissolving the films in a 50% HCl solution. X-ray (Cu $K\alpha$) and scanning electron microscope (SEM) analysis were performed at room temperature on the films as grown and those annealed in air at 500–800 °C for 3 h. For the x-ray analysis we used a conventional diffractometer (RIGAKU, RAD-1B) and also a thin-film diffractometer (PHILIPS PW3020) for which the incident angle is fixed at $\theta=0.1°$ and 2θ is scanned. Saturation magnetization curves of the films were measured by a vibrating sample magnetometer (VSM) at room temperature. ^{57}Fe Mössbauer absorption spectra were taken at room temperature and 12 K for a sample deposited on the PET substrate (10 pieces of the sample were stacked to obtain sufficient absorption for γ rays) by a conventional constant acceleration spectrometer using a 1.11 GBq of ^{57}Co embedded in a Pd matrix as a source.

TABLE I. Aqueous solutions used for ferrite plating of Y-Fe oxide films.

	Chemical	Concentration(g/l)	*p*H
Reaction solution	$FeCl_2 \cdot 4H_2O$	0.5–1	
	$YCl_3 \cdot 6H_2O$	2.0–3.5	~5.8
Oxidizing solution	$NaNO_2$	1	
	CH_3COONH_4	4.0	~6.8–8.0

 0021-8979/94/75(10)/6094/3/$6.00 © 1994 American Institute of Physics

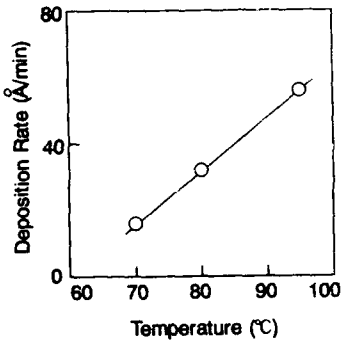

FIG. 1. Deposition rate of amorphous Y-Fe oxide film, plotted as a function of substrate temperature.

III. RESULTS AND DISCUSSION

Performing the plating for 4–5 h, we obtained films 0.5–2 μm in thickness. The rate of film deposition linearly increases with temperature, from 15 Å/min at 70 °C to 60 Å/min at 95 °C (Fig. 1). The film deposition rate is about 5–20 times smaller than that (~300 Å/min) obtained in the conventional ferrite plating of crystalline spinel films.

As Fig. 2 shows, the atomic ratio of Y/Fe in the film linearly increases with that in the reaction solution. The ratio of Y/Fe=3/5=0.6, as in YIG, is obtained in the film when Y/Fe~3.5 in the reaction solution.

Typical x-ray diffraction diagrams are shown in Fig. 3, for the film with Y/Fe=0.63. All the as-grown films do not exhibit diffraction peaks due to their crystalline structure, even when measured by the thin-film diffractometer. After annealed at above 650 °C the films exhibit diffraction peaks due to YIG, showing that the as-grown films are amorphous.

One can see in Fig. 4 that the as-grown films do not exhibit in scanning electron microscope images grain boundaries or the columnar structure, which is observed for the crystalline spinel films prepared by the conventional ferrite plating. However, grains grow after the annealing at the high temperatures.

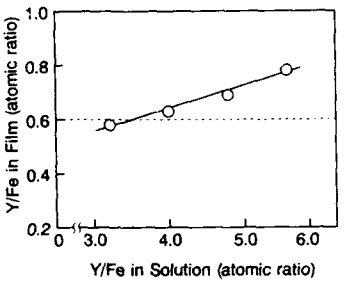

FIG. 2. Atomic ratio of Y/Fe in film, plotted as a function of that in solution.

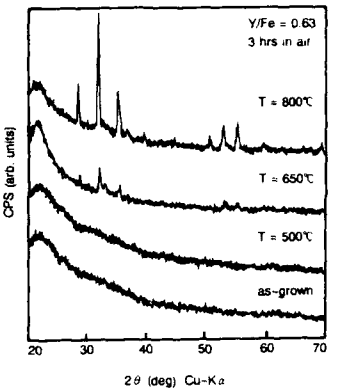

FIG. 3. X-ray diffraction diagrams for ferrite-plated Y-Fe oxide film as-grown and after annealed at various temperatures, obtained by a conventional Cu $K\alpha$ diffractometer.

Figures 5 and 6 show that the as-grown films have at room temperature a saturation magnetization of 10–40 emu/cc, smaller than that reported for the bulk YIG sample (139 emu/cc). The magnetization lies in-plane due to the demagnetizing field. All the films have a coercive force of 50–60 Oe.

^{57}Fe Mössbauer absorption spectrum taken at room temperature (Fig. 7) exhibits a paramagnetic quadrupole double with no ferromagnetic hyperfine-field absorption. At 12 K the spectrum splits into a broad sextuplet with no additional paramagnetic absorption. The average hyperfine field at 12 K

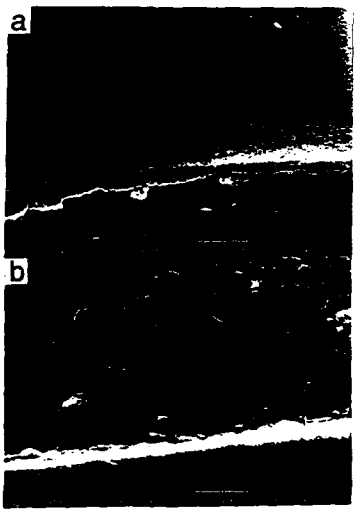

FIG. 4. SEM observation of cross section of the ferrite-plated Y-Fe oxide film. (a) As-grown and (b) after annealed at 800 °C in air for 3 h.

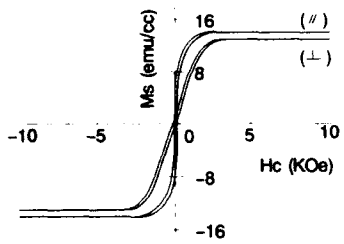

FIG. 5. A magnetization curve for the $Y_3Fe_{4.9}O_{12}$ amorphous film, measured parallel (∥) and perpendicular (⊥) to film plane.

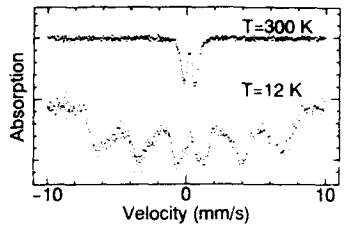

FIG. 7. ^{57}Fe Mössbauer spectra for amorphous Y-Fe oxide film with Y/Fe ≈0.63.

is 462 kOe, and the isomer shift at 300 K is 0.22 mm/s in absolute velocity. These values indicate that Fe ions in the amorphous films are in a trivalent high spin state.

Why at room temperature are the amorphous films paramagnetic as observed by VSM, while they are paramagnetic as observed by the Mössbauer effect? In some (ferro or antiferro) magnetic materials with spin fluctuation (due to amorphous structure or disordered arrangement of magnetic and nonmagnetic ions) a hyperfine field is observed by the ^{57}Fe Mössbauer effect even at a temperature higher than a critical temperature where magnetic ordering vanishes as observed by VSM. This is because the detection time for ^{57}Fe Mössbauer effect ($\tau=10^{-8}$ s) is shorter than that for VSM ($\tau=\sim10^{0}$ s). An opposite phenomenum (namely, magnetic ordering is observed by VSM at a temperature higher than a critical temperature where the hyperfine field observed by ^{57}Fe Mössbauer effect vanishes) never occurs. Therefore, the weak saturation magnetization observed at room temperature for the amorphous films cannot be ascribed to intrinsic magnetization with spin fluctuation. It may be ascribed to the magnetic impurity phase whose concentration is too small to be discerned by the x-ray and the Mössbauer experiments.

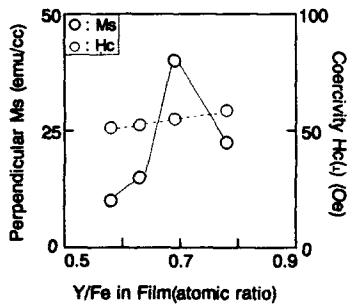

FIG. 6. Magnetization and coercivity of the amorphous Y-Fe oxide films, ploted as a function of atomic ratio of Y/Fe in film.

Since the Fe ions are in a trivalent state as mentioned above, a candidate for the impurity magnetic phase is γ-Fe_2O_3. Detailed studies are required to clarify the origin of the weak saturation magnetization in the amorphous Y-Fe films.

IV. CONCLUSIONS

Novel noncrystalline yttrium iron oxide films were prepared by a modified ferrite plating method below 100 °C. The main results are as follows:

(1) They are amorphous as examined by x-ray diffraction with a smooth surface, having no grain boundaries or columnar structure.
(2) The atomic ratio of Y/Fe in the films deviates from that in the reaction solution. The ratio is adjusted to Y/Fe=0.6, as in YIG, by choosing the ratio in the solution to an appropriate value (Y/Fe~3.5).
(3) After annealing the films at above 650 °C, x-ray diffraction peaks due to the YIG crystalline phase appear, and grains grow.
(4) The as-grown films have at room temperature saturation magnetization of 10–40 emu/cc, several times weaker than that observed for crystalline YIG samples. The films exhibit, however, a paramagnetic Mössbauer spectrum at room temperature, suggesting that the weak magnetization is ascribed to the magnetic impurity phase whose concentration is too small to be discerned by x-ray diffraction and Mössbauer measurements.

ACKNOWLEDGMENT

This study has been financially supported in part by Grant-in-Aid for Developmental Scientific Research from The Ministry of Education, Science, and Culture.

[1] M. Abe and Y. Tamaura, J. Appl. Phys. **55**, 2641 (1984).
[2] M. Abe, T. Itoh, Y. Tamaura, and M. Gomi, J. Appl. Phys. **63**, 3774 (1988).
[3] T. Itoh, M. Abe, and Y. Tamaura, Jpn. J. Appl. Phys. **27**, 839 (1988).
[4] M. Abe and M. Gomi, J. Magn. Magn. Mater. **84**, 222 (1990).
[5] M. Abe, Y. Tamaura, Y. Goto, N. Kitamura, and M. Gomi, J. Appl. Phys. **61**, 3211 (1987).

Magnetic anomalies in single crystal Fe_3O_4 thin films

D. T. Margulies, F. T. Parker, and A. E. Berkowitz
Center for Magnetic Recording Research, University of California at San Diego, La Jolla, California 92093

Fe_3O_4 thin films were reactively sputtered onto ⟨100⟩ and ⟨110⟩ MgO substrates. X-ray diffraction data indicate single crystal Fe_3O_4 films under a tensile stress. Magnetization data show good agreement with bulk Fe_3O_4 for M_s, but also show the presence of a large anisotropy component manifest in the lack of saturation in fields up to 70 kOe. Conversion electron Mössbauer spectroscopy data taken at zero field also show good agreement with bulk Fe_3O_4 for the values of the hyperfine fields and isomer shifts of the two Fe_3O_4 sites, indicate good stoichiometry, but indicate the presence of a large anisotropy component randomizing the moments. In-plane torque measurements on ⟨100⟩ oriented Fe_3O_4 are consistent with bulk Fe_3O_4 magnetocrystalline anisotropy. However, in-plane torque measurements on ⟨110⟩ oriented Fe_3O_4 show the presence of a uniaxial anisotropy superimposed on the crystalline terms. This anisotropy, modeled as being due to the stress induced by epitaxy, changes the easy axis from the ⟨111⟩ directions to the ⟨110⟩ directions in the (110) plane. Since the directional dependence of the crystal and stress anisotropy are measurable the "large anisotropy" component is considered to be random.

Several studies have examined the epitaxial growth of Fe_3O_4 on single crystal MgO,[1-4] because of the good lattice match. The distances between the oxygen atoms in the fcc lattices of MgO and Fe_3O_4 along ⟨100⟩ directions are 2.1060 Å and 2.0994 Å, respectively, corresponding to a 0.31% lattice mismatch. This article discusses the effects on the magnetic properties of single crystal Fe_3O_4 when it is grown epitaxially constrained to an MgO substrate.

All films were about 3000 Å thick and were prepared by dc magnetron reactive sputtering from an Fe target onto polished ⟨100⟩ and ⟨110⟩ MgO substrates which were preheated for 45 min at 500 °C before sputtering at 500 °C substrate temperature. The Ar pressure during sputtering was 2 mTorr and the O_2 pressure was 0.06 mTorr. The background pressure was 5×10^{-7} Torr and the deposition rate was ~60 Å/min.

Symmetric Bragg reflection x-ray diffraction (XRD) experiments (θ–2θ scans) on the ⟨100⟩ oriented Fe_3O_4 films deposited on ⟨100⟩ MgO show the 400 and 800 reflections for the Fe_3O_4 film near the 200 and 400 reflections for the MgO. Likewise, for the ⟨110⟩ oriented films deposited on ⟨110⟩ MgO the 440 reflection for the Fe_3O_4 was seen near the 220 reflection for the MgO. For the ⟨100⟩ oriented films, the $K_{\alpha1}$–$K_{\alpha2}$ splitting was plainly visible at $2\theta\cong50°$ which for our diffractometer (Co K_α radiation) was indicative of single crystal or highly oriented films. The lattice constant measured by XRD normal to the plane for the ⟨100⟩ oriented film is 8.374±0.002 Å and that for the ⟨110⟩ oriented film is 8.376±0.002 Å (for bulk Fe_3O_4 the lattice constant a_0 is 8.396 Å).[5] These lattice constants are very close to those seen by Lind *et al.*[1] and Fujii *et al.*[3] and show that these films are under a compressive stress normal to the film plane which shows an in-plane tensile stress. Also, the similarity in lattice parameters shows that the tensile stress is similar for both film directions which means this stress may be modeled as being isotropic. Furthermore, the full width at half maximum of the Fe_3O_4 800 reflection at $2\theta=117.41°$ is $\Delta2\theta=0.15°$ (where the value for bulk Fe_3O_4 occurs at $2\theta=116.91°$), while that of the MgO substrate 400 reflection at $2\theta=116.34°$ is $\Delta2\theta=0.11°$, showing essentially the instrumental broadening in both cases. This indicates that the strain is uniform throughout the film thickness.

The high field in-plane magnetization at 300 K taken with a superconducting quantum interference device (SQUID) is shown in Fig. 1. The lack of saturation of this film, even in fields of 70 kOe, is quite evident and was independent of crystallographic direction. If the approach to saturation is modeled by[6] $M=M_s(1-a/H)$, then a value of 479 emu/cc is found for the saturation magnetization. This is very close to the value for M_s in bulk materials, 471 emu/cc.[5] Films prepared with different sputtering conditions and orientations were analyzed on the vibrating sample magnetometer up to 24 kOe and none were saturated, while the high field susceptibility was qualitatively the same. This lack of saturation is similar to the results of Speriosu *et al.*[7] Thus a large anisotropy component is present in these films.

Conversion electron Mössbauer spectroscopy (CEMS) studies were performed at 296 K and zero field. Sample spectra and fits can be seen in Fig. 2. Iron in Fe_3O_4 occupies two crystallographic sites which exhibit six lines each. The tetrahedral A site contains the Fe^{3+} ions and the octahedral B site contains Fe^{2+} and Fe^{3+} ions. The hyperfine fields at the A and B sites and the isomer shifts of the A and B sites are determined from the fit. These values are, within experimental error, the same for ⟨100⟩ and ⟨110⟩ oriented films. They

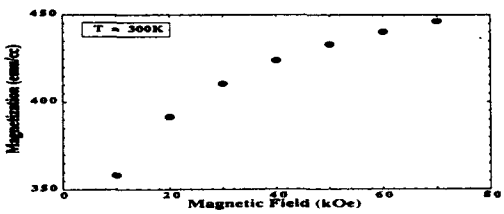

FIG. 1. In-plane magnetization vs applied field for Fe_3O_4 ⟨100⟩ MgO.

 0021 979/94/75(10)/6097/3/$6.00 © 1994 American Institute of Physics

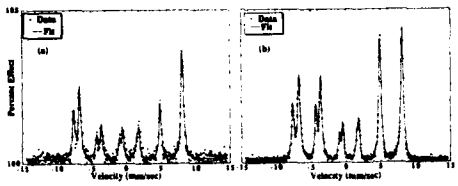

FIG. 2. CEMS data and fit for Fe_3O_4 on (a) ⟨100⟩ MgO and (b) ⟨110⟩ MgO.

are found to be 488 and 458 kOe, and 0.27 and 0.67 mm/s with respect to iron metal, respectively, which agree well with values found for bulk Fe_3O_4, 491 and 462 kOe, and 0.27 and 0.67 mm/s, respectively.[8] The relative intensity of the A to B sites is 1:2 reflecting the good stoichiometry of the film for both orientations. The relative intensity of the lines in each sextet is given as $3:2p:1:1:2p:3$, where $p=2\sin^2\theta/(1+\cos^2\theta)$, and θ is the equivalent single orientation angle between the magnetic hyperfine field and the γ-ray direction. For 3D random moment orientation, $p=1$. For the ⟨100⟩ oriented films p is found to vary around 0.8 and for the ⟨110⟩ oriented films around 1.2. For the ⟨100⟩ film this is similar to that seen by Fujii *et al.*,[3] who claim that the ratio of 3:2:1, or $p=1$, is expected because it shows that the moments are lying along the ⟨111⟩ directions, which are known to be easy for bulk Fe_3O_4. However, in a thin film there is a large shape anisotropy with an anisotropy constant of $2\pi M_s^2=139\times10^4$ ergs/cc. The existence of this shape anisotropy was confirmed by magnetization measurements with the magnetic field perpendicular to the film plane as well as by out of plane torque magnetometry. This anisotropy constant is an order of magnitude larger than the crystalline anisotropy constant $K_1=-11\times10^4$ ergs/cc. Therefore, the moments should all be lying in the plane of the film which corresponds to $\theta=90°$, $p=2$, and the ratio of relative intensities 3:4:1. This is not the case here. Therefore, it can be concluded that there is a large anisotropy component in these films, larger than the shape anisotropy, which produces nearly random moments.

The in-plane anisotropy was studied with torque magnetometry on 0.75 mm diameter discs. For the ⟨100⟩ oriented film [Fig. 3(a)] the cubic anisotropy was clearly visible from the presence of the $\sin(4\theta)$ term. From Fig. 3(a) the anisotropy constant K_1 can be determined and is shown in Fig. 4. Similar to the M-H curve, a lack of saturation is also seen for K_1. Again assuming a $1/H$ approach to saturation, a value of -10×10^4 ergs/cc is obtained which is close to the value of -11×10^4 ergs/cc known for bulk Fe_3O_4.[5] The easy axis was confirmed to correspond to the structural ⟨110⟩ direction within 5 deg by comparing reflection high-energy electron diffraction (RHEED) data to torque data. The temperature dependence on this term was also studied and can be seen in Fig. 5 along with values for bulk Fe_3O_4.[5] Although the magnitude of K_1 is lower, since the applied field was 10 kOe for the measurements, the trend of the curve agrees well with bulk Fe_3O_4. Similar to the results of Speriosu *et al.*,[7] rotational hysteresis is still present at 20 kOe for both ⟨100⟩

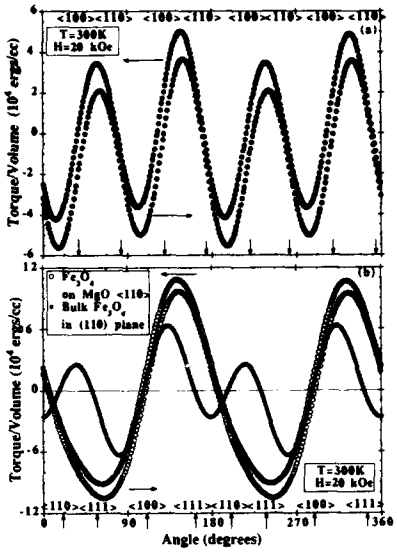

FIG. 3. In-plane torque curves for Fe_3O_4 on (a) ⟨100⟩ MgO and (b) ⟨110⟩ MgO. In (b) the Fe_3O_4 bulk torque curve was calculated from parameters given in Ref. 5 and Ref. 6.

and ⟨110⟩ films, again showing the presence of a large anisotropy.

However, the torque data for the ⟨110⟩ oriented film do not exhibit the cubic symmetry expected. In Fig. 3(b) the in-plane torque curve for the ⟨110⟩ film is compared to a theoretical curve for the (110) plane in bulk Fe_3O_4. The expected cubic symmetry is dominated by a uniaxial symmetry. The magnitude of the associated uniaxial anisotropy constant, K_u, is indicated in Fig. 4. The x-ray data show that these films are under a tensile stress in the film plane and show the stress is isotropic. The torque L_{me} arising from the magnetoelastic energy, E_{me}, is given by the relation

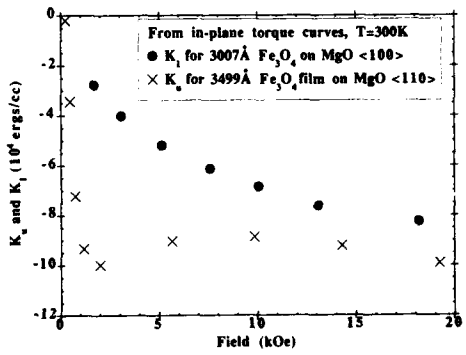

FIG. 4. (a) K_1 for Fe_3O_4 on ⟨100⟩ MgO and (b) K_u for Fe_3O_4 ⟨110⟩ MgO.

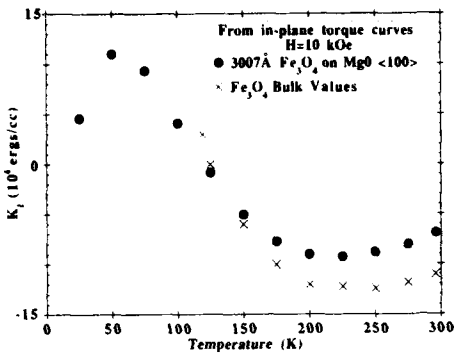

FIG. 5. K_1 for Fe_3O_4 on ⟨100⟩ MgO vs temperature. The bulk Fe_3O_4 values are from Ref. 5.

$$L_{me} = -dE_{me}/d\theta, \tag{1}$$

where θ is the angle between M_s and a reference direction in the film plane, and where

$$E_{me} = -(3/2)\lambda_{100}\sigma(\alpha_1^2\gamma_1^2 + \alpha_2^2\gamma_2^2 + \alpha_3^2\gamma_3^2) - 3\lambda_{111}\sigma(\alpha_1\alpha_2\gamma_1\gamma_2 + \alpha_2\alpha_3\gamma_2\gamma_3 + \alpha_3\alpha_1\gamma_3\gamma_1), \tag{2}$$

for a cubic crystal. Here, σ is the stress, α_i are direction cosines of M_s, γ_i are the direction cosines of σ, and λ_{hkl} are the magnetostriction coefficients.[6] Now, within the spinel {110} planes there will be directions of the form ⟨100⟩, ⟨110⟩, and ⟨111⟩. We first consider the $(1\bar{1}0)$ spinel plane for our discussion of how the torque varies as M_s rotates in the plane. This particular choice places the orthogonal [110] and [001] directions in the film plane. σ_1 and σ_2 are the respective principal stresses along these directions. The total in-plane magnetoelastic energy is given by

$$E_{me} = E_{me\sigma} + E_{me\sigma_2}. \tag{3}$$

We now define θ as the angle between the [001] direction and M_s, use the assumption of isotropic stress in the plane ($|\sigma_1| = |\sigma_2| = |\sigma|$), and combine Eqs. (1), (2), and (3), to obtain

$$L_{me} = (-3/4)\sigma(\lambda_{100} - \lambda_{111})\sin 2\theta = -K_u \sin 2\theta. \tag{4}$$

Therefore, a uniaxial term is expected from the tensile stress. From the lattice parameter normal to the film plane, $a_\perp$, a value for σ can be obtained. Using, $(a_\perp - a_0)/a_0 = -2\upsilon\sigma/E$, with E (Young's modulus) $= 1.6\times10^{12}$ dyn/cm^2 and υ (Poisson's ratio) $= 0.3$ gives $\sigma = 6.7\times10^9$ dyn/cm^2. Using[5] $\lambda_{111} = 77.6\times10^{-6}$ and $\lambda_{100} = -19.5\times10^{-6}$ gives a calculated value of -49×10^4 ergs/cc for K_u. This is a factor of 5 larger than the measured K_u, Fig. 4, but indicates that stress is the probable cause of the dominant uniaxial anisotropy in the film. Furthermore, the value of 8.421 Å for the in-plane lattice parameter, $a_\parallel$, is obtained using $(a_\parallel - a_0)/a_0 = (1-\upsilon)\sigma/E$. This is very close the effective MgO lattice parameter 8.424 Å and shows that the in-plane lattice parameter of the Fe_3O_4 is taking on that of the MgO. Therefore, the stress is modeled as being caused by an epitaxial strain. A lower deposition temperature did not decrease the anisotropy due to stress for the ⟨110⟩ oriented film. From this it can be concluded that the stress is not due to a thermal strain. Further, the crystallographic directions where the torque is equal to zero represent the easy and hard axes. Whether the axis is easy or hard is determined by the slope of the torque through those directions.[6] A positive slope defines a hard axis and a negative slope an easy axis. Therefore, it can now be seen that the ⟨110⟩ axis is the easy axis, instead of the ⟨111⟩.

It is important to see how this stress affects the anisotropy in the ⟨100⟩ oriented film. Similar calculations for the (001) plane show that $L_{me} \equiv 0$. Therefore, no anisotropy is induced by the strain in the (100) plane. This explains why the (100) plane gives bulk behavior for the magnitude and temperature dependence of the crystalline anisotropy constant K_1. Since crystalline anisotropy, shape anisotropy, and stress anisotropy are measurable, the "large anisotropy" also seen must be random.

In summary, single crystalline Fe_3O_4 thin films have been grown on ⟨100⟩ and ⟨110⟩ MgO substrates. X-ray diffraction data show highly oriented Fe_3O_4 films under a tensile stress. Magnetization data show good agreement with bulk Fe_3O_4 for M_s, but also show the presence of a large anisotropy component manifest in the lack of saturation in fields up to 70 kOe. CEMS data also show good agreement with bulk Fe_3O_4 for the values of the hyperfine fields and isomer shifts of the two sites, indicate good stoichiometry, but indicate the presence of a large anisotropy component randomizing the moments. In-plane torque measurements on ⟨100⟩ oriented Fe_3O_4 agree well with the magnitude and temperature dependence of the crystalline anisotropy constant K_1 of bulk Fe_3O_4. However, in-plane torque measurements on ⟨110⟩ oriented Fe_3O_4 show the presence of a dominant uniaxial anisotropy. This anisotropy is shown to arise from the stress induced by epitaxy.

The authors would like to thank Matt Carey for assistance with torque magnetometry and sputtering, Fred Spada for useful suggestions on x-ray diffraction, and Sihong Kim for the RHEED measurements. This research is supported by NSF Grant No. DMR-90-10908 and by a grant from the National Media Laboratory.

[1] D. M. Lind, S. D. Berry, G. Chern, H. Mathias, and L. R. Testardi, Phys. Rev. B **45**, 1838 (1992).
[2] D. M. Lind, S.-P. Tay, and S. D. Berry, J. Appl. Phys. **73**, 6886 (1993).
[3] T. Fujii, M. Takano, R. Katano, and Y. Bando, J. Cryst. Growth **99**, 606 (1990).
[4] J. Krebs, D. M. Lind, and S. D. Berry, J. Appl. Phys. **73**, 6458 (1993).
[5] *Magnetic and Other Properties of Oxides and Related Compounds*, edited by K.-H. Hellwege, A. M. Hellwege, and Landolt Börnstein (Springer, Berlin, 1970), Vol. 4, New Series.
[6] B. D. Cullity, *Introduction to Magnetic Materials* (Addison–Wesley, Reading, MA, 1972), pp. 216, 222, 270, 347.
[7] V. S. Speriosu, M. M. Chen, and T. Suzuki, IEEE Trans. Magn. **25**, 3875 (1989).
[8] B. J. Evans and S. S. Hafner, J. Appl. Phys. **40**, 1411 (1969).

An analysis of the high-temperature relaxation in polycrystalline magnetite

J. Castro, D. Martinez, and J. Rivas
Grupo de Electromagnetismo, Universidad de Santiago de Compostela, E-15706, Spain

H. J. Blythe
Department of Physics, The University Sheffield, Sheffield S3-7RH, United Kingdom

Magnetic relaxation measurements were performed in the temperature range $200<T(\mathrm{K})<800$ on vacancy-doped polycrystalline magnetite. Important relaxation peaks have been observed in the temperature ranges $250<T(\mathrm{K})<350$ (peak III) and $400<T(\mathrm{K})<600$ (peak I). Particular attention has been focused on the behavior of peak I where isothermal measurements have extended over times up to 10^5 s. It is argued that the main features of peak I are compatible with a dislocation relaxation.

I. INTRODUCTION

The magnetic relaxations occurring in magnetite have been the subject of many investigations; for a review see Ref. 1. In the temperature range $200<T(\mathrm{K})<700$, two relaxation peaks occur; in the literature these are designated as peak III $[250<T(\mathrm{K})<350]$ and peak I $[400<T(\mathrm{K})<600]$.

In a series of previous articles we have revisited the topic of magnetic relaxation in polycrystalline magnetite.[2–6]

The aim of this work is to carry out a critical review of the state of knowledge of the MAE in magnetite and to present a preliminary evaluation of our experimental data[6] on relaxation peak Ib.

II. EXPERIMENTAL TECHNIQUE

Polycrystalline magnetite samples were prepared from pure Fe_2O_3 powder (Merk p.a.). These samples were sintered for 24 h at 1500–1700 K in an appropriate atmosphere $(3\times10^{-2}< P_{O_2}(\mathrm{Pa})<10^5)$ according to the iron-oxygen phase diagram.[7] The high-temperature phase equilibrium was frozen-in by rapidly quenching the samples in air. Using this procedure, we were able to obtain a series of nonstoichiometric magnetite samples of composition $Fe_{3-\delta}O_4$.

The MAE measurements were performed using a fully automated ac technique described elsewhere.[3] The time dependence of the initial susceptibility, $\chi(t,T)$, is measured isothermally in the interval $t_1<t<t_2$ following a demagnetization of the sample. From a theoretical point of view, it is more appropriate to consider the reciprocal of the susceptibility, $r(t,T)$, the reluctivity. From measurements of $r(t,T)$ made at various temperatures, we can construct isochronal relaxation curves via the expression

$$\Delta r(t_1,t_2,T)=r(t_2,T)-r(t_1,T). \tag{1}$$

This representation has the advantage of enabling different relaxation phenomena to be separated from one another and also enables us to obtain an unambiguous interpretation of the temperature and time dependences.[8]

To prevent sample oxidation all our measurements were performed in a N_2 atmosphere.

III. EXPERIMENTAL RESULTS

Figure 1 shows the isochronal relaxation spectrum of Δr for a polycrystalline sample in the temperature range $200<T(\mathrm{K})<800$ after different treatments. Figure 1(a) displays the spectrum of the "as-quenched" sample. The estimated vacancy concentration was $\delta\approx5\times10^{-3}$.[9] We observe two well-defined relaxation processes: peak III $[250<T(\mathrm{K})<350]$ and peak I $[400<T(\mathrm{K})<600]$.

Additional information about the relaxation processes can be obtained from an annealing technique in which the maximum measuring temperature is increased in each successive pass. In Fig. 2 we present the annealing behavior of Δr at selected temperatures during such an experiment for our magnetite sample. In the present case, the maximum temperature was increased in 50 K steps starting at 400 K until a temperature of 800 K was attained. We see that the decrease of peak III (300 K isochronal) is accompanied by a reduction of the 430 K isochronal and an increase of the 530 K relaxation. Thus, we now have a clear indication that, in the temperature range of peak I, we are dealing with more than one relaxation process. We denote these as peak Ia $[400<T(\mathrm{K})<500]$ and peak Ib $[500<T(\mathrm{K})<600]$. Another important experimental fact is that, during the annealing experiment, the initial susceptibility increases by a factor of 2.

The relaxation spectrum of the sample after the annealing experiment is shown in Fig. 1(b). We see that the reduction of peak III is accompanied by a decrease of peak Ia and an increase of peak Ib.

In order to investigate the nature of the 530 K relaxation, we performed a series of long-time isothermals at this temperature. The results are presented in the Fig. 3. Each run begins with a demagnetization of the sample and the temperature is maintained constant to better than 0.5 K throughout the measurement. We can see that, after a long period of time, the initial isothermals (L_1-L_8) tend to a constant value, whereas the latter ones (L_9-L_{14}) do not show this behavior.

The isochronal spectrum for Δr of the sample after the isothermal measurements is shown in Fig. 1(c). We see that the reappearance of peak III and peak Ia is accompanied by the disappearance of peak Ib.

Another important experimental fact is the decrease of the initial susceptibility with the annealing.

IV. DISCUSSION

We start the discussion with some cautionary remarks on our interpretation of the experimental magnetite data.

 0021-8979/94/75(10)/6100/3/$6.00 © 1994 American Institute of Physics

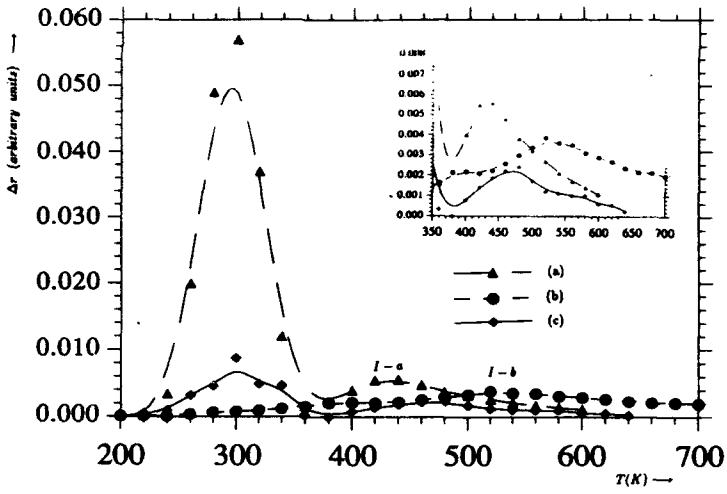

FIG. 1. Isochronal relaxation spectrum of a polycrystalline magnetite sample after different treatments. For the sake of clarity, the $400<T(K)<700$ region is shown in the inset.

We have interpreted peak III and Ia as a combined after effect due to octahedrally coordinated vacancies. The main experimental support comes from the fact that peaks III and Ia anneal out simultaneously. However, we point out that this interpretation is not completely satisfactory due to the fact that for an unambiguous determination of a combined after effect we should have the following relation between the amplitudes of the orientation and diffusion processes:[10]

$$\frac{\Delta r_{\text{orientation}}}{\Delta r_{\text{diffusion}}} \approx \text{const.} \tag{2}$$

In Fig. 2, we see that this relation is not even approximately satisfied.

The separation of peak I into two peaks, Ia and Ib, is not without controversy. Another possible interpretation, consistent with the experimental results for peak I, could be a pro-

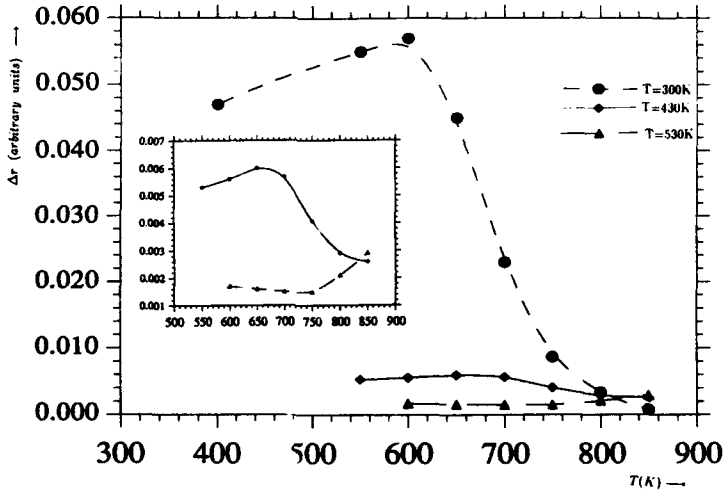

FIG. 2. Annealing behavior Δr at selected temperatures. For the sake of clarity the 430 and 530 K isochrons are shown in the inset.

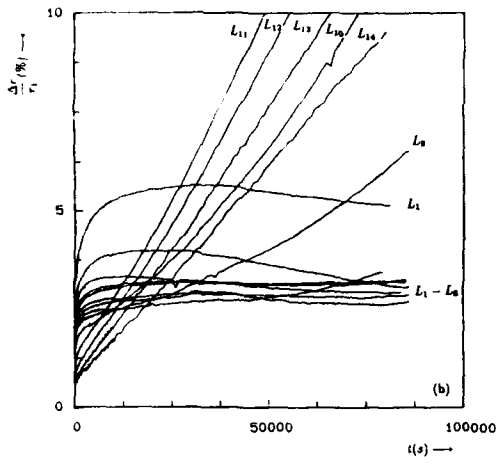

FIG. 3. Long-time isothermals at 530 K. The isothermals are numbered according to its relaxation order.

cess whose position is correlated with the inverse of the amplitude of peak III, i.e., whose relaxation time depends monotonically on the inverse of the vacancy concentration.[11] However, magnetite is only composed of iron and oxygen and it is very difficult to imagine such a process involving only point defects which moves 100 K during the annealing. A possible way out to this controversy, see below, would be to invoke dislocations in order to explain peak I. At this point, we want to point out that the MAE in magnetite is very sensitive to the presence of impurities. Impurities give rise to a magnetic after effect located at 370 K.[12] In none of our samples have we observed this relaxation process. We take this as an indication of that our samples are free of impurities.

From Fig. 3, we see that our isothermal curves present two different kinds of behaviors. Initially, the isothermal curves tend to a constant value, or show a small decrease at large times (L_1 to L_7), whereas for the isotherms (L_8 to L_{14}) we obtain, at large times, a linear time dependence. These experimental results clearly indicate that we are dealing with more than one relaxation process.

A possible interpretation can be made: In each isothermal run a magnetic relaxation phenomenon associated with a relatively rapid movement of defects is initially predominant. Due to the isothermal heating, superposed on this magnetic relaxation, we find a very slow process that we assume to be linear in the time scale of magnetic relaxation and which we describe as a microstructural relaxation. Using these assumptions, some conclusions can be drawn on the microstructural relaxation from a simple analysis of the isotherms of Fig. 3.[13]

(1) The microstructural relaxation follows a typical recrystallization kinetics with nucleation time $t_N \approx 6\times10^5$ s.

(2) Assuming that the microstructural changes correspond to a movement of defects over distances of the order of magnitude of the grain size, the estimated value for the activation energy of the microstructural relaxation is 0.94 eV. This value is comparable to the activation energy of cation diffusion in magnetite.

We can now give a tentative model for the isothermal relaxation. Before our isothermal measurements, our sample is free of vacancies, i.e., we do not observe peak III. The main expected effect of an isothermal treatment of our samples is a redistribution of dislocations. Dislocations would start first to glide and bow out until they reach those atomic valleys where sessile dissociation is possible and from which further motion is only possible by climb.[14] In this kind of material the activation energy for the climb is the activation energy of the motion of cation vacancies.[15] This would explain the activation energy previously encountered. Climb motion of dislocations would produce subgrain boundaries. Following Trauble,[16] the effect of these boundaries could be to decrease the initial susceptibility. The movement of the dislocations can generate point defects. This fact can explain the reappearance of the peak III after the isothermal annealing. Another important fact is that glide in this material needs a climb dissociation of the dislocations. This can be made possible through a migration of vacancies to dislocations giving rise to a process that is similar to the one studied by Iida for the case of Co substituted magnetite.[17] This could explain the correlation of the position of the relaxation peak with the inverse of the amplitude of peak III.

Thus, unlike previously reported models, we have explained the main features of peak I relaxation qualitatively by a simple dislocation model.

[1] S. Krupicka and P. Novak, in *Ferromagnetic Materials*, edited by E. P. Wohlfarth (North-Holland, Amsterdam, 1982), Vol. 3, Chap. 4.
[2] D. Martinez, J. I. López Cabido, and J. Castro, Phys. Status Solidi A **134**, K33 (1992).
[3] J. Castro, H. J. Blythe, and J. Rivas, J. Magn. Magn. Mater. (in press).
[4] J. Castro, J. Rivas, H. J. Blythe, J. Iñiguez, and C. de Francisco, Phys. Status Solidi A **113**, 541 (1989).
[5] J. Castro and J. Rivas, Appl. Phys. A **56**, 323 (1993).
[6] J. Castro, J Rivas, H. J. Blythe, and J. Iñiguez, Ann. Phys. (Spain) B **86**, 29 (1990).
[7] R. Dieckmann, Ber. Bunsenges, Phys. Chem. **86**, 112 (1982).
[8] H. Kronmüller, *Nachwirkung in Ferromagnetika* (Springer, Berlin, 1968).
[9] R. Schutzenauer, Diplomarbeit, Stuttgart, 1971.
[10] H. Kronmüller, in *Vacancies and Interstitials in Metals* (North-Holland, Amsterdam, 1969), p. 667.
[11] J. Castro and M. Phil, University of Sheffield, 1992.
[12] F. Waiz, V. A. M. Brabers, S. Chikazumi, H. Kronmuller, and M. O. Rigo, Phys. Status Solid B **110**, 471 (1982).
[13] J. Castro, D. Martinez, J. Rivas, and H. J. Blythe (to be published).
[14] M. G. Blanchin, J. Castaing, G. Fontaine, A. H. Heuer, L. W. Hobbs, and T. E. Mitchell, J. Phys. (France) C **42**, 3 (1981).
[15] T. Bretheau, J. Castaing, J. Rabier, and P. Veyniere, Adv. Phys. **20**, 829 (1979).
[16] Träuble in *Moderne Probleme der Metallphysik*, edited by A. Seeger (Springer, Berlin, 1966), Vol. 26.
[17] S. Iida and H. Miwa, J. Phys. Soc. Jpn. B **17**, 304 (1966).

$Dy_3Fe_5O_{12}$ garnet thin films grown from sputtering of metallic targets

J. Ostoréro, M. Escorne, and A. Pecheron-Guegan
Laboratoire de Chimie Métallurgique et Spectroscopie des Terres Rares, CNRS 92195 Meudon Cedex France

F. Soulette and H. Le Gall
Laboratoire de Magnétisme et Matériaux Magnétiques, CNRS, 92195 Meudon Cedex, France

Dysprosium iron garnet $Dy_3Fe_5O_{12}$ (DyIG) thin films have been synthesized by postoxidizing at a temperature T_{ox} (400 °C$<T_{ox}<$1100 °C) of rf sputtered amorphous Dy-Fe metallic films. The sputtering conditions strongly influence the growth, the composition and magnetic and magneto-optic properties of the oxidized films. Pure DyIG films, free of $DyFeO_3$, are synthesized at $T_{ox}\sim$1000 °C. Magnetic and Faraday rotation (FR) experiments at three wavelengths (543.5, 632.8, and 1152 nm) were performed on DyIG films in the 4–300 K temperature range, as a function of magnetic field up to 20 kOe perpendicular to the film plane. Magnetization and FR data are in good agreement with results obtained on bulk DyIG materials. Temperature dependent coercivity is observed with a discontinuity in the vicinity of the compensation temperature ($T_{comp}\sim$225 K). The temperature variations of the spontaneous FR values for the three wavelengths are interpreted on the basis of contributions proportional to the magnetization of each sublattice.

I. INTRODUCTION

For magneto-optical (MO) recording applications, sputtering methods are now widely used to grow thin films of ferrimagnetic rare earth-iron garnet from ceramic oxide targets.[1–6] On the other hand, a lot of work[7–10] has been devoted to the sputtering of amorphous rare earth-transition metal alloy thin films which are sensitive to oxidation.[11] This leads to the synthesis of garnet thin films by oxidizing of a rf sputtered metallic rare earth-iron alloy film; this method should allow one to prepare garnet films in a wide range of composition by varying the surface ratio of the different metals of the target instead of sintering large discrete ceramic oxide targets. Furthermore, synthesis of thin films from oxide targets also often requires a post-deposition heat treatment. Bi and Ga substituted Dysprosium iron garnet, $Dy_3Fe_5O_{12}$ (DyIG), have been the subject of numerous works as thin films for high density MO recording.[12] In contrast, studies performed on pure DyIG concerned essentially bulk materials. We present here the results of crystallographic, magnetic, and MO properties [Faraday rotation (FR)] of thin films of pure DyIG synthesized by this method.

II. EXPERIMENT

In a first step, metallic films of Dy–Fe alloy were deposited on fused quartz substrates by rf sputtering of a metallic target of Fe covered by a mosaic of Dy platelets. The rf power was varied between 0.6 and 2.5 W/cm^2. The deposit was performed in a pure Ar atmosphere at pressures between 6×10^{-3} and 10^{-2} mbar (base pressure of 2×10^{-7} mbar). The metallic film growth rate was between 0.25 and 1.3 μm/h. Higher power and pressures resulted in increased growth rates to the detriment of the quality of the films. The Dy/Fe ratio was varied in the vicinity of 0.6 (stoichiometric garnet). The as-deposited films were oxidized in air at a temperature T_{ox} (400 °C$<T_{ox}<$1100 °C) during several hours, then cooled in the furnace.

X-ray diffraction measurements were performed using Cu $K\alpha$ radiation to determine the structure and phase composition of the films. Magnetic properties of the films were measured using a vibrating sample magnetometer (VSM) at room temperature (oxidation experiments) and a Manics DSM8 susceptometer from 4.2 to 300 K (DyIG films). Faraday rotation (FR) measurements were performed at three wavelengths: 1152, 632.8, and 543.5 nm as a function of temperature (6 K$<T<$300 K). In both cases the magnetic field (0–20 kOe) was perpendicular to the film plane.

III. RESULTS AND DISCUSSION

The x-ray diffraction patterns of a sputtered Dy_3Fe_5 film oxidized in air at increasing temperatures, T_{ox}, are presented

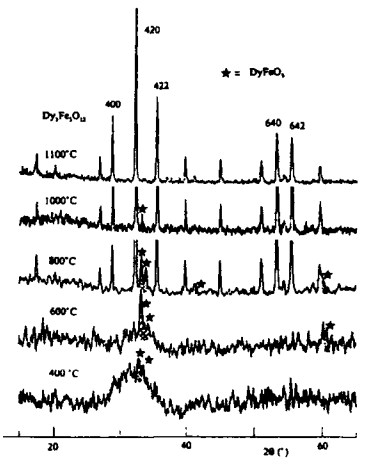

FIG. 1. X-ray diffraction spectra of a Dy-Fe thin film oxidized at different temperatures T_{ox} (annealing time=15 h). *=x-ray diffraction lines of $DyFeO_3$.

 0021-8979/94/75(10)/6103/3/$6.00 © 1994 American Institute of Physics

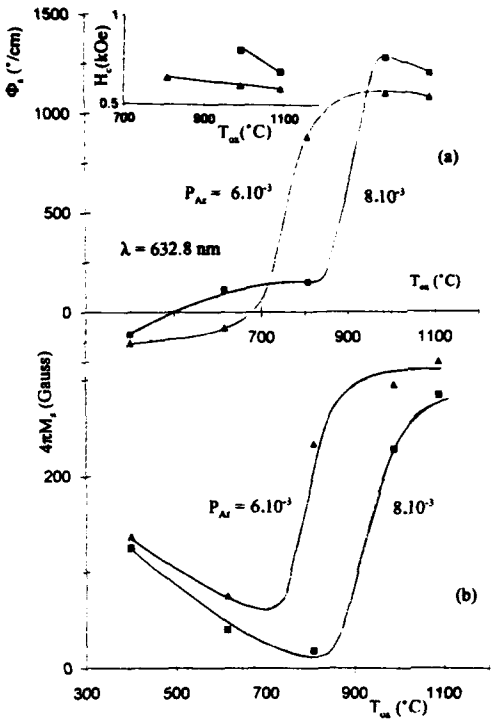

FIG. 2. (a) Spontaneous Faraday rotation Φ_s and (b) spontaneous $4\pi M_s$ of two Dy-Fe thin films sputtered at two different Ar pressures: 6×10^{-3} (▲) and 8×10^{-3} (■) mbar vs T_{ox} (Lines are only a guide to the eyes.) Insert: coercive field H_c vs T_{ox}.

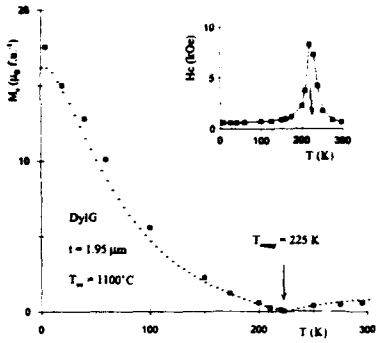

FIG. 3. Temperature dependence of the spontaneous magnetization of a DyIG thin film (T_{ox}=1100 °C, 1.95 μm thick). Broken curve: calculated results using Dionne's model (Ref. 16). Insert: temperature dependence of the coercive field.

in Fig. 1. Oxidation begins below or near 400 °C and, as T_{ox} increases, diffraction lines become clearer. These lines correspond to the two phases: $Dy_3Fe_5O_{12}$ and $DyFeO_3$.[13] DyIG is largely dominant at 800 °C but the 112 line of $DyFeO_3$ vanishes only at 1100 °C. No preferential orientation was observed which can be partly explained by the use of amorphous substrates. It is to be noted that obtaining stoichiometric DyIG films depends strongly on the sputtering conditions and composition of the metallic target. In our case, a metallic target with Dy/Fe=0.6 leads to oxidized films corresponding to a mixture of orthoferrite and garnet and, in some cases (high Ar pressure and rf power), of $DyFeO_3$ only.[13] Pure DyIG films were synthesized with a target corresponding to Dy/Fe=0.55. Within experimental accuracy, no line shift of the garnet structure could be detected as a function of T_{ox}. Only a slight decrease of the half-width of e.g., 420 line [from 0.145° (800 °C) to 0.12° (1100 °C)], was observed.

The Ar sputtering deposition pressure seems to play an important role concerning the synthesis of garnet films. This is illustrated in Fig. 2 where we plotted the magnetic and MO properties at room temperature of two films deposited at two different Ar pressures: 6×10^{-3} and 8×10^{-3} mbar (Dy/Fe=0.55 and P_{rf}=1.9 W/cm^2), as a function of T_{ox} (annealing time=15 h). When $T_{ox}<800$ °C, the magnetization of the film decreases towards 0 when T_{ox} increases. This can be attributed to the presence of residual amounts of as yet unoxidized Dy-Fe particles.[11] At higher T_{ox}, magnetic and FR properties present a jump. In both cases the observed transition corresponds to the formation of the preponderant DyIG garnet phase as confirmed by x-ray diffraction patterns (Fig. 1). However, this transition is shifted nearly 200 °C higher in the case of metallic films synthesized at the higher Ar pressure. The magnetic and, especially, MO properties of the films present a plateau for $T_{ox}>1000$ °C. The spontaneous values M_s and Φ_s are close to that of pure bulk DyIG within experimental accuracy (~10% for magnetization and 5%–10% for FR) when T_{ox}=1100 °C. The coercivity of the oxidized films seems to decrease as T_{ox} increases. This may be due to the crystallization of larger grains.

All these results show that the synthesis and the formation conditions of pure DyIG from oxidation of a metallic Dy-Fe film are very sensitive to deviations from the stoichiometric Dy/Fe=3/5 ratio in the sputtered film (particularly Dy excess), resulting either from the target composition or sputtering conditions. Nevertheless, oxidation of Dy_3Fe_5 films to pure DyIG can be achieved for $T_{ox}>1000$ °C.

The magnetic properties of a 1.95 μm thick DyIG film [Dy/Fe=0.55, P_{rf}=1.8 W/cm^2, $P_{Ar}=6\times10^{-3}$ mbar, T_{ox}=1100 °C (10 h)] are presented in Fig. 3. The results are in good agreement with data obtained on bulk DyIG,[14] particularly the compensation temperature (T_{comp}=225 K) which is very sensitive to inhomogeneities.[2] The coercive filed H_c is strongly temperature dependent only in the vicinity of T_{comp}, and has nearly the same value at 4.2 and 300 K (650 Oe). A good agreement between calculated and experimental magnetization data (Fig. 3) is obtained using the Dionne-refined Néel model of ferrimagnetic garnets.[15,16]

The temperature variations of the spontaneous FR, Φ_s, (normalized to the 6 K absolute values) at three wavelengths are presented in Fig. 4. At 300 K, Φ_s=350, 1000, and 3100°/cm for 1152, 632.8, and 543.5, respectively. Φ_s

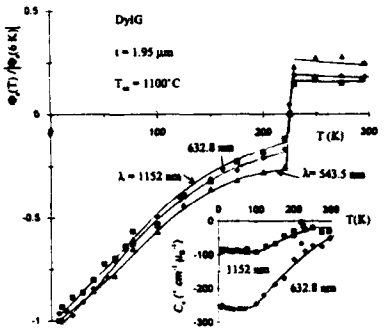

FIG. 4. Temperature dependence at three wavelengths: 1152, 632.8, and 543.5 nm, of the spontaneous Faraday rotation $\Phi_s(T)/|\Phi_s(6\ K)|$ of the same DyIG thin film. Insert: temperature dependence of the MO coefficient C_e of the Dy sublattice at 1152 and 632.8 nm.

changes sign at $T_{comp}=225$ K confirming the magnetization results. The influence of the wavelength on the FR is best evidenced for $T>150$ K: FR increases more when λ decreases at constant T. This temperature zone corresponds to preponderant contributions from the Fe^{3+} sublattices, this may be related, in the visible range, to the increasing influence of electric dipole transitions in the Fe^{3+} sublattices.[1,14] According to Crossley *et al.*[17]

$$\Phi=A|M_a|+D|M_d|+C|M_c|, \tag{1}$$

$$A=-A_e-A_m, \quad D=D_e+D_m, \quad C=-C_e-C_m, \tag{2}$$

where subscripts e and m refer, respectively, to the gyroelectric and gyromagnetic contributions. In a first approximation, A_m, D_m, and C_m are constants independent of temperature and wavelength.[14] Using Eq. (1) with A_e and D_e of Ref. 2 at 1152 and 632.8 nm (543.5 nm values as yet not determined), and the sublattice magnetizations previously obtained from the Dionne model, the temperature variation of C_e was deduced from experimental data (Fig. 4). At low temperature C_e(632.8 nm) is ~2.5 C_e(1152 nm) in comparison to the corresponding MO coefficients of Fe^{3+} (Ref. 2) which are multiplied by 10.

IV. CONCLUSION

Pure garnet $Dy_3Fe_5O_{12}$ thin films are synthesized by oxidizing at a temperature T_{ox}, between 800 and 1100 °C, of a sputtered Dy-Fe film when Dy/Fe=3/5 for the deposited film. Sputtering conditions leading to an excess of Dy result in a shift towards 1100 °C of the formation of a mixture of preponderant DyIG and orthoferrite $DyFeO_3$.

The magnetic and MO properties of pure DyIG films are close to those of bulk material, particularly the compensation temperature which is sensitive to inhomogeneities. The FR of the film in the visible range is strongly influenced by electric dipolar contributions attributed to Fe^{3+} transitions.

[1] M. Gomi, J. Ceram. Soc. Jpn. **99**, 852 (1991).
[2] P. Hansen and J.-P. Krumme, Thin *Solid Films* **114**, 69 (1984).
[3] T. Suzuki, F. Sequeda, H. Do, T. C. Huang, and G. Gorman, J. Appl. Phys. **67**, 4435 (1990).
[4] M. Gomi, T. Okazaki, and M. Abe, IEEE Trans. Magn. **MAG-23**, 2967 (1987).
[5] J.-P. Krumme, V. Doormann, and P. Willig, J. Appl. Phys. **57**, 3885 (1985).
[6] E. Sawatzky and E. Kay, J. Appl. Phys. **39**, 4700 (1968).
[7] K. Naito, T. Numata, K. Nakashima, and Y. Namba, J. Magn. Magn. Mater. **104–107**, 1025 (1992).
[8] U. W. Lee, H. P. D. Shieh, M. H. Kryder, and D. Lauphin, J. Appl. Phys. **63**, 3627 (1988).
[9] Y. Mimura, N. Imamura, and T. Kobayashi, Jpn. J. Appl. Phys. **15**, 933 (1976).
[10] P. Chaudaari, J. J. Cuomo, and R. J. Gambino, Appl. Phys. Lett. **22**, 337 (1973).
[11] E. E. Marinero, D. C. Miller, A. E. Bell, A. Gupta, R. N. Payne, and H. Notarys, IEEE Trans. Magn. **MAG-23**, 2629 (1987).
[12] S. Kuroda, K. Shono, and S. Ogawa, Jpn. J. Appl. Phys. **31**, 431 (1992).
[13] The diffraction pattern correspond to an orthorhombic phase with $a=5.309$, $b=5.583$, $c=7.631$ Å, close to those previously determined for $DyFeO_3$ [M. Eibschutz, Acta Cryst. **19**, 337 (1965); J. A. W. Daziel and A. J. E. Welch, Acta Cryst. **13**, 956 (1960)] but the intensities of the lines, particularly when $2\theta>45°$, are more in agreement with those of the isomorphous compound $DyCrO_3$ [Gallagher and McCarthy (1973), JCPDS-ICDD #25-1050].
[14] *Physics of Magnetic Garnets*, edited by A. Paoletti (North-Holland, Amsterdam, 1978).
[15] G. F. Dionne, J. Appl. Phys. **47**, 4220 (1976).
[16] G. F. Dionne and P. F. Tumelty, J. Appl. Phys. **50**, 8257 (1979). (N_{dc} was slightly changed to 5.93 mol cm^{-3} in order to adjust calculated T_{comp} to 225 K).
[17] W. A. Crossley, R. W. Cooper, J. L. Page, and R. P. Van Stapele, Phys. Rev. **181**, 89 (1969).

Enhanced coercivity due to a local anisotropy increase

J. A. Jatau, M. Pardavi-Horváth, and E. Della Torre
Institute for Magnetics Research, George Washington University, Washington, DC 20052

In most of the cases, a local wall energy decrease, usually associated with defects, leads to domain wall pinning. Another mechanism for coercivity is to create local maxima in the anisotropy energy. It is observed that in epitaxial garnet crystals, locally enhanced anisotropy due to stress arising from iridium inclusions embedded in the substrate is the source of coercivity. By modifying our previous energy barrier model, the coercivity has been calculated as a function of the size and position of the iridium inclusions in the substrate. It is shown that the coercivity varies nonlinearly with inclusion size and depth in the substrate material, in agreement with experimental observation.

INTRODUCTION

Localized stresses and inclusions in an otherwise perfect material lead to localized changes in the anisotropy and exchange energies and thus to a position dependence of the domain wall energy. One of the sources of the anisotropy in magnetic materials is connected with the existence of the magnetostriction. Depending on the sign of the magnetostriction λ_s, the same stress σ, can lead either to a local decrease or increase in the anisotropy energy

$$K_u^s = -(3/2)\sigma\lambda_s. \tag{1}$$

This was the basis for the one-dimensional energy barrier micromagnetic model that was developed to compute the coercivity of domain wall motion in magnetic media.[1] In that study, it was assumed that the local increase in the domain wall energy was due to the inclusions in the magnetic material; however, there are materials in which no inclusion is associated with the energy barrier. This is the case for the stress-induced anisotropy energy increase, when the source of the localized stress is not an inclusion inside the magnetic medium but in the substrate supporting that medium. Then, only the stress field interacts in the magnetic material. Now the theoretical treatment is simple, as only the stress field has to be taken into account rather than the additional effects of nonmagnetic inclusions.

EXPERIMENTS

The repulsion of domain walls by the stress field originating in the substrate has been observed in single crystalline epitaxial garnet crystals of substituted $Y_3Fe_5O_{12}$ (YIG) grown on nonmagnetic $Gd_3Ga_5O_{12}$ (GGG) substrates.[2] In the process of growth the bulk GGG thin iridium flakes in the form of triangular or hexagonal platelets, originating from the crucible material, are trapped in the growing crystal. The lateral size of these inclusions is typically on the order of 10–100 μm. On cooling the crystal, a strong stress field is formed around the inclusions due to the difference in thermal expansion of iridium and GGG.[3] The stress is given by

$$\sigma = \frac{E}{1-\nu}\,\Delta\alpha\Delta T \simeq 0.5\ \text{GN m}^{-2}, \tag{2}$$

where E is the Young modulus of elasticity in the YIG, ν is the Poisson ratio, $\Delta\alpha$ is the difference in thermal expansion between the GGG and iridium, and ΔT is the temperature difference between the melting point of GGG and room temperature. For this material these parameters are $\alpha_{\text{Ir}} = 7.8\times10^{-6}\ \text{K}^{-1}$, $\alpha_{\text{GGG}} = 9.03\times10^{-6}\ \text{K}^{-1}$, and $\Delta T = 1400$ K. The iridium platelet exerts a compressive stress on the GGG, i.e., $\sigma>0$. The substrate is typically 400 μm thick, and the YIG film thickness is in the range of several μm. The stress field created by iridium propagates into the epitaxial YIG film, locally influencing its properties.

YIG has negative magnetostriction that combined with the positive stress produces a stress-induced anisotropy on the order of 1.5×10^3 J/m^3, considerably increasing the original growth induced uniaxial anisotropy of 1×10^3 J/m^3 in the magnetic film. It was observed experimentally that the locally increased domain wall energy results in the repulsion of the domain walls from defects, as shown in Fig. 1. On this microphotograph, taken in a polarizing microscope using the Faraday effect with transmitted light, the iridium inclusion in the substrate can be seen, as can the stress field in the epitaxial film. When an external magnetic field is applied normal to the film plane, a few domains can be seen at an equilibrium distance from the maximum of the stress field, that is located above the iridium inclusion. These domains are repelled by the defects according to the locally enhanced domain wall energy, since there is no inclusion in the magnetic material associated with the stress, and thus no direct contribution to the coercivity through an inclusion mechanism. Only the stress field due to the inclusion in the substrate penetrates into the magnetic film.

The distribution in size and depth in the GGG of more

FIG. 1. Microphotograph in polarized light of a 5 μm thick epitaxial YIG film. Iridium inclusions in the GGG substrate and light contrast due to their stress field in the magnetic film can be seen together with magnetic domains repelled by the local increase of the wall energy at maximum stress.

 0021-8979/94/75(10)/6106/3/$6.00 © 1994 American Institute of Physics

than a hundred of iridium inclusions was measured in a polarizing microscope and a qualitative evaluation of the strength of the repulsion between the stress field and the domain walls was performed. As can be expected, the results showed that the deeper the inclusion the weaker is its effect on coercivity; and the coercivity increases with the size of the inclusion.

THE MODEL

Our previous model of enhanced coercivity due to local anisotropy increase[1] has been modified to include the stress-induced anisotropy in the magnetic garnet film, originating in the substrate at iridium inclusions. The model solves for the equilibrium magnetization distribution by minimizing the energy given by

$$E=\int_{-\infty}^{\infty}\{A(\nabla M_x)^2+K_u\sin^2\theta-\mu_0 H\cdot M\cos\theta + \mu_0 M^2\cos^2\theta\}dx, \tag{3}$$

where A is the exchange constant, K_u is the uniaxial anisotropy constant, H is the applied field, M is the magnetization, and θ is the angle the magnetization makes with the easy axis. The resulting Euler–Lagrange equation is discretized to give the following solution for the magnetization angle, which is then solved numerically:

$$\phi(k)=\frac{\phi(k+1)+\phi(k-1)}{2}-\frac{h^2\sin\phi}{2A(x)}\times\left[(K_u-\mu_0M^2)\cos\phi+\frac{\mu_0 HM}{2}\right], \tag{4}$$

where h is the lattice spacing in the discretization of the problem. The problem is then solved using the Gauss–Seidel technique. Because of the stiffness of the equations, a mode pushing technique[4] was used to accelerate the convergence of the solution.

The following equation was used to represent the variation of the anisotropy in the energy barrier:

$$K(x)=K_u^{\xi}\left[1+\xi\frac{d^3}{x^3+l^3}\right], \tag{5}$$

where K_u^{ξ} is the growth induced anisotropy, d is the size (diameter) of the iridium inclusion and l is its depth in the substrate, x is the magnitude of the distance from the inclusion in the direction of the wall motion, and ξ is a parameter chosen to represent the height of the anisotropy barrier. Figure 2 illustrates the geometry of the model. The form of Eq. (5) reflects the distribution of the dipole stress field from a localized source.[5]

RESULTS AND DISCUSSION

In order to describe the dependence of coercivity on the size of the iridium inclusion and its depth in the GGG substrate, we used our model to compute the coercivity at various depths in the substrate, and also for various sizes of the inclusion. Figure 3 shows the variation of the coercivity with the depth of the iridium inclusion in the substrate for an

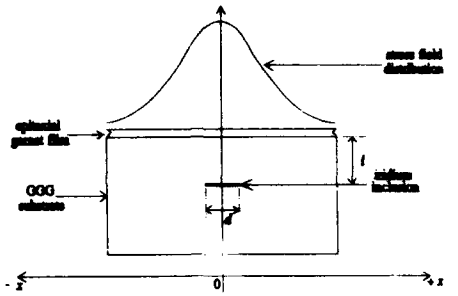

FIG. 2. A geometric model of the YIG film/GGG substrate arrangement with the iridium inclusion, showing the nature of stress field distribution.

inclusion size of 10 and 40 μm. The coercivity is found to increase with increasing size of the inclusion and with decreasing depth in the substrate. The relationship is nonlinear, and may be approximated by the cube of the reciprocal depth of the iridium inclusion in the substrate. This observation is in agreement with experimental observation, thus validating the choice of our model. When computing the coercivity as a function of the inclusion size, the classical case is observed where the coercivity increases to a maximum when the domain wall width is on the order of magnitude of the inclusion size; with further increase in the size of the inclusion the coercivity decreases. This can be seen in Fig. 4, where the dependence of the coercivity on the size of the inclusion is shown for the two cases where the inclusion is located 100 and 300 μm deep in the substrate, respectively. It is seen that the coercivity increases with decrease in the depth of the iridium inclusion in the substrate. Figure 5 illustrates a three-dimensional plot of coercivity as a function of both the size of the iridium inclusion and its depth in the substrate. It also shows the case where the iridium is almost on the surface of the substrate, corresponding to the case where l approaches zero in Eq. (5), and thus the maximum coercivity depends very strongly only on the inclusion size d. It is seen that there appears to be no significant increase in the coercivity when the depth of the iridium in the substrate is greater than 100

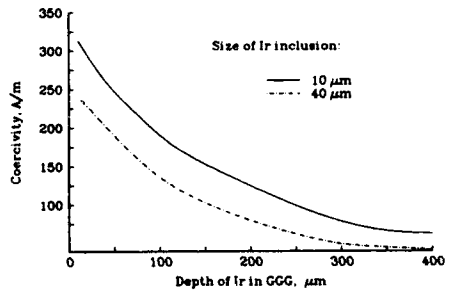

FIG. 3. A plot of coercivity vs depth of iridium inclusion in the GGG substrate.

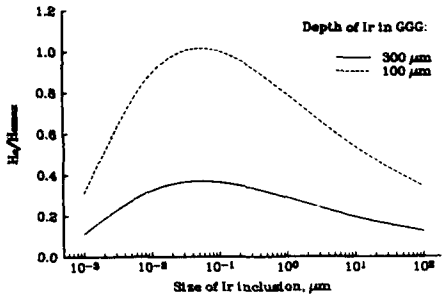

FIG. 4. A plot of coercivity vs size of iridium inclusion; H_{cmax} =356.73 A/m.

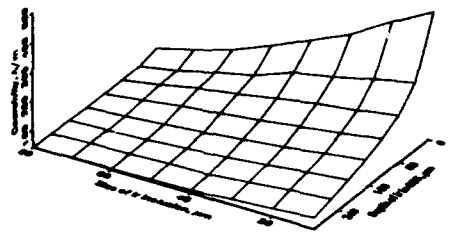

FIG. 5. A three-dimensional view of coercivity vs the size of iridium inclusion and its depth in GGG substrate.

μm. Similarly, the effect on the coercivity is more pronounced when the size of the inclusion is less than about 50 μm. As the size of the inclusion and its depth in the substrate is increased, there is gradual decrease in the coercivity.

CONCLUSIONS

Experimental evidence is given for a possible mechanism to control the coercivity through a localized increase of the domain wall energy. In the case of epitaxial substituted magnetic garnet films the origin of the effect is in the stress-induced anisotropy due to an iridium inclusion in the substrate material rather than in the magnetic film itself. The cause for the stress is in the difference in the thermal expansion of iridium and GGG. A numerical model of the energy barrier mechanism of coercivity has been applied to describe the effect. Similar stress-induced effects should be taken into account whenever a coercivity mechanism related to inclusions of foreign phases is considered.

ACKNOWLEDGMENTS

The authors would like to acknowledge the useful discussions with members of the Institute for Magnetics Research. This work was partially supported by an ATP grant through the National Storage Industries Consortium.

[1] J. A. Jatau and E. Della Torre, J. Appl. Phys. **73**, 6829 (1993).
[2] M. Pardavi-Horváth, A. Cziraki, I. Fellegvari, G. Vertesy, J. Vandlik, and B. Keszei, IEEE Trans. Magn. **20**, 1123 (1984).
[3] M. Pardavi-Horváth, Prog. Cryst. Growth Characterization **5**, 175 (1982).
[4] E. Della Torre and C. M. Perlov, J. Appl. Phys. **69**, 4596 (1991).
[5] See L. D. Landau and E. M. Lifshitz, in *Theoretical Physics VII. Theory of Elasticity* (Nauka, Moscow, 1965), Chap. 1.

The microwave absorbing and resonance phenomena of Y-type hexagonal ferrite microwave absorbers

H. J. Kwon
R&D Laboratory, Samhwa Electronics Company, Ltd., 211-1, Jangji-Ri, Dongtan-Myun, Hwasung-Gun, Kyungki-Do, Korea

J. Y. Shin and J. H. Oh
Department of Ceramic Engineering, Inha University, 253, Yonghyun-Dong, Nam-Gu, Inchon, Korea

The microwave absorbing characteristics and resonance of Y-type hexagonal ferrite–rubber composites were investigated. The complex permeability and permittivity of $Ni_{2-x}Zn_xY$ ferrite bodies were measured using a network analyzer in the frequency range of 200 MHz–14 GHz. Two types of resonance, the domain wall and the spin rotational resonance, were observed. With a ferrite particle with a diameter of about 1 μm, only spin rotational resonance was observed. The first matching frequency, found in the ferrite–rubber composites, which was higher than that of spin rotational resonance, increased with spin rotational resonance frequency. It was also found that domain wall resonance had no effects on the microwave absorbing characteristics. Based on these findings, it could be concluded that the microwave absorbing characteristics were caused by only one type of resonance, the spin rotational resonance.

I. INTRODUCTION

In developing the ferrite microwave absorber, the microwave absorbing characteristics, such as the matching frequency, matching thickness, and band width, have been evaluated during the last two decades. These microwave absorbing characteristics are influenced by the complex permeability and permittivity. Since the complex permittivity of a ferrite absorber is constant in the GHz frequency region, the microwave absorbing characteristics strongly depend on the resonance phenomena of the ferrite body.[1] The research about the resonance phenomena of ferrites has been extensively studied and described by domain wall motion, spin resonance, etc.[2] But little work has been done on the relationship between the microwave absorbing characteristics and resonance phenomena of ferrites.

The purpose of this study was to investigate the effect of the resonance phenomena on the microwave absorbing characteristics of $Ni_{2-x}Zn_xY$–rubber composites.

II. EXPERIMENTS

Y-type hexagonal ferrites, $Ni_{2-x}Zn_xY$ ($Ba_2Ni_{2-x}Zn_xFe_{12}O_{22}$), were prepared by the conventional ceramic process. The starting materials ($BaCO_3$, NiO, ZnO, and α-Fe_2O_3) were stoichiometrically weighed, ball milled in water for 10 h, dried, and then synthesized at 1150 and 1300 °C for 3 h in air to produce aggregated $Ni_{2-x}Zn_xY$ ferrite powders. $Ni_{2-x}Zn_xY$ powders were obtained by milling the aggregated $Ni_{2-x}Zn_xY$ powders. The phase and particle size of the prepared $Ni_{2-x}Zn_xY$ powders were characterized by x-ray diffraction (XRD) and scanning electron microscopy (SEM), respectively. Sintered $Ni_{2-x}Zn_xY$ ferrites and $Ni_{2-x}Zn_xY$–rubber composites were prepared. The shape of each specimen was toroidal. $Ni_{2-x}Zn_xY$–rubber composites were obtained by mixing $Ni_{2-x}Zn_xY$ powders with silicone rubber in a weight ratio (weight of ferrite/weight of rubber) of 4. This weight ratio is equivalent to 43 in the ferrite volume percent. The sintered $Ni_{1.5}Zn_{0.5}Y$ body was prepared by sintering the green compact at 1300 °C for 3 h in air.

The scattering parameters (S_{11}, S_{21}) of the toroidally shaped sintered ferrite and ferrite–rubber composites (outer diameter=7.0 mm, inner diameter=3.0 mm) were measured using a Hewlett-Packard 8720B network analyzer. The scattering parameters were measured in the frequency range of 200 MHz–14 GHz, and the complex permeability and permittivity were determined from the measured scattering parameters.[3]

III. RESULTS AND DISCUSSION

The complex permeability spectra of $Ni_{2-x}Zn_xY$ composites is shown in Fig. 1. Two types of resonance were observed in the ferrite composites. These resonance phenomena were due to the domain wall resonance (f_{r1}) at lower frequency and the spin rotational resonance (f_{r2}) at higher frequency. No effect of Zn content on variation of the domain wall resonance was found in the complex permeability spectra. It was observed, however, that the spin rotational resonance frequency was shifted toward lower frequency with increasing Zn content.

For spin rotation, general model is the Snoek one[4] which predicts the resonance frequency given by

$$f_r=(\gamma/2\pi)H_a, \tag{1}$$

where γ is a gyromagnetic ratio, H_a is the anisotropy field and f_r is the spin rotational resonance frequency of material. Equation (1) indicates that the spin rotational resonance depends on the anisctropic field. Smit and Wijn[5] reported that the anisotropy field of Ni_2Y and Zn_2Y at room temperature was 14 000 and 9000 Oe, respectively. Thus, decreasing the spin rotational resonance frequency with increasing Zn content (See Fig. 1) indicates that the anisotropy becomes smaller as the Zn content increases.

In order to investigate the effect of particle size on the complex permeability of the $Ni_{2-x}Zn_xY$-rubber composites, $Ni_{2-x}Zn_xY$ powders were synthesized at different tempera-

 0021-8979/94/75(10)/6109/3/$6.00 © 1994 American Institute of Physics

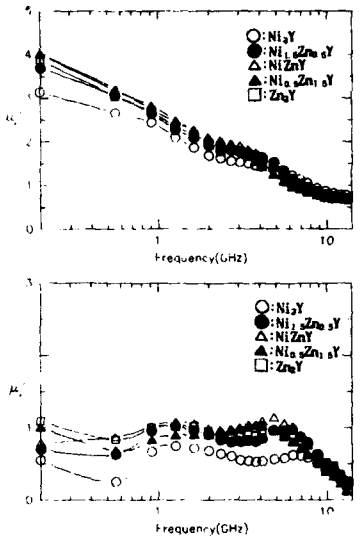

FIG. 1. Frequency dependence of the complex permeability of $Ni_{2-x}Zn_xY$–rubber composites (synthesizing temperature=1300 °C).

tures. The particle size of ferrite powder synthesized at 1300 °C was about 4–5 μm. On the other hand, a majority of the particles synthesized at 1150 °C were smaller than 1 μm. Figure 2 represents the complex permeability spectra of the

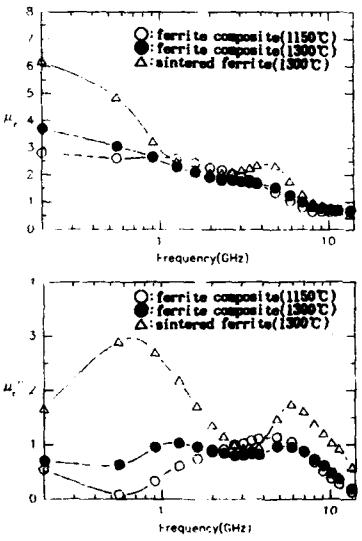

FIG. 2. Frequency dependence of the complex permeability of sintered $Ni_{1.5}Zn_{0.5}Y$ and $Ni_{1.5}Zn_{0.5}Y$–rubber composites with different synthesizing temperatures.

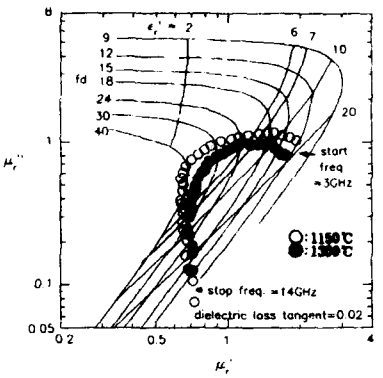

FIG. 3. The complex permeability locus of $Ni_{1.5}Zn_{0.5}Y$–rubber composites with different synthesizing temperatures on the impedance matching solution map (tan δ_ϵ=0.02).

sintered $Ni_{1.5}Zn_{0.5}Y$ body and $Ni_{1.5}Zn_{0.5}Y$–rubber composites. The complex permeability of sintered ferrite is higher than that of ferrite composite, because ferrite particles in ferrite–rubber composites are covered with a thin nonmagnetic layer of rubber. From the complex permeability spectra of the sintered $Ni_{1.5}Zn_{0.5}Y$ and $Ni_{1.5}Zn_{0.5}Y$–rubber composite containing ferrite powder synthesized at 1300 °C, one sees both domain wall resonance and spin rotational resonance. However, the composite containing ferrite powder synthesized at 1150 °C shows spin rotational resonance only. This behavior is probably due to the particles being sufficiently small to approach single domain characteristics so that only spin rotations can occur.

For a microwave absorbing layer backed by a metal plate, the normalized input impedance (Z_{in}) at the absorber surface is given by

$$Z_{in}=1=\sqrt{\mu_r/\epsilon_r}\,\tanh[j(2\pi/c)\sqrt{\mu_r\epsilon_r}\,fd], \tag{2}$$

where μ_r is the complex permeability ($\mu_r'-j\mu_r''$), ϵ_r is the complex permittivity ($\epsilon_r'-j\epsilon_r''$), c is the velocity of light, f is the frequency, and d is the thickness of the absorber. This equation is called the zero reflection condition for an absorber. Naito and Suetake[1] constructed the impedance matching solution map for zero reflection in the case of no dielectric loss (tan δ_ϵ=0). Musal and Hahn[6] extended this work to the lossy dielectric case.

To illustrate the use of the impedance matching solution map, the complex permeability of $Ni_{1.5}Zn_{0.5}Y$–rubber composites is plotted in the map as shown in Fig. 3. The impedance matching solution map for tan δ_ϵ=0.02 is applicable since the real parts of the permittivity (ϵ_r') of the specimens are constant at 7 and ϵ_r''=0.14 in the 200 MHz–14 GHz frequency range. The matching points are found along the line of ϵ_r'=7 on the map because the real parts of permittivity of these specimens are 7. For $Ni_{1.5}Zn_{0.5}Y$–rubber composite containing ferrite powder synthesized at 1150 °C, two matching points are found. One occurs at 4.7 GHz (fd=19.3

TABLE I. The resonance frequency and the microwave absorbing characteristics of $Ni_{2-x}Zn_xY$–rubber composites.

	Synthesizing temperature = 1150 °C					
	Resonance frequency (GHz)		Matching frequency (GHz)		Matching thickness (mm)	
Composition	f_{r1}	f_{r2}	f_{m1}	f_{m2}	d_{m1}	d_{m2}
Ni_2Y	···	5.0	5.9	8.8	4.0	3.3
$Ni_{1.5}Zn_{0.5}Y$	···	4.1	4.7	11.1	4.1	3.0
NiZnY	···	4.1	4.5	12.1	4.1	2.8
$Ni_{0.5}Zn_{1.5}Y$	···	3.9	4.3	12.2	4.3	2.8
Zn_2Y	···	3.0	3.6	10.9	4.9	3.1
	Synthesizing temperature = 1300 °C					
Ni_2Y	1.2	6.4	8.9	···	3.1	···
$Ni_{1.5}Zn_{0.5}Y$	1.2	5.0	5.6	12.2	3.7	2.6
NiZnY	1.2	4.8	4.9	12.7	4.0	2.6
$Ni_{0.5}Zn_{1.5}Y$	1.2	4.8	4.9	13.5	4.2	2.4
Zn_2Y	1.2	3.0	3.0	11.8	5.9	2.7

GHz mm) and the other at 11.1 GHz (fd=33.3 GHz mm). Therefore, the first and second matching thickness are predicted to be 4.1 mm (d_{m1}) and 3.0 mm (d_{m2}), respectively. It is determined that f_{m1} is 5.6 GHz and f_{m2} is 12.2 GHz for $Ni_{1.5}Zn_{0.5}Y$–rubber composite containing ferrite powder synthesized at 1300 °C. Thus, the matching thicknesses are also predicted to be 3.7 and 2.6 mm. The reflection loss (dB) is a function of Z_{in}, and the reflection loss of the microwave absorber can be calculated at given f and d using Eq. (3):

$$\text{Reflection loss(dB)} = 20 \log|(Z_{in}-1)/(Z_{in}+1)|. \quad (3)$$

The results of the resonance frequency observed from the complex permeability spectra of $Ni_{2-x}Zn_xY$–rubber composites and the matching frequencies and thicknesses calculated from Eqs. (2) and (3) are summarized in Table I. The calculated matching frequencies and thicknesses are in good agreement with the prediction values from the impedance matching solution map. As shown in Table I, the spin rotational resonance frequency (f_{r2}) and the first matching frequency (f_{m1}) decreases with Zn content. And, despite the absence of the domain wall resonance, two impedance matching phenomena were still observed.

Figure 4 represents the relation between the spin rotational resonance frequency (f_{r2}) and the first and second matching frequency of various ferrite–rubber composites. This figure shows that the first matching frequency (f_{m1}) is higher than that of the spin rotational resonance. The first matching frequency of the ferrite microwave absorber is proportional to its spin rotational resonance frequency, whereas the second matching frequency is independent of spin rotational resonance frequency. From the results of Table I and Fig. 4, it could be concluded that the domain wall resonance does not seem to affect microwave absorbing phenomena, and the impedance matching phenomena of ferrite microwave absorbers result from spin rotational resonance only.

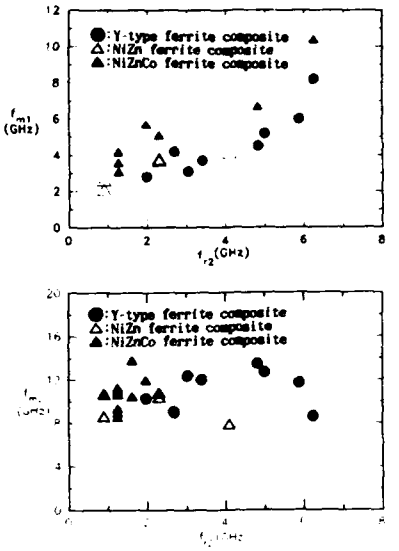

FIG. 4. The relation between the spin rotational resonance frequency (f_{r2}) and the first and second matching frequency (f_{m1} and f_{m2}) of various ferrite–rubber composites.

IV. CONCLUSION

It was found that the first matching frequency, which was always higher than that of the spin rotational resonance, increased with the spin rotational resonance frequency. It was also found that the domain wall resonance did not seem to affect the microwave absorbing phenomena, and the microwave absorbing phenomena occurred by spin rotational resonance only.

[1] Y. Naito and K. Suetake, IEEE Trans. Microwave Theory Tech. **MTT-19**, 65 (1971).
[2] G. T. Rado, Rev. Mod. Phys. **25**, 81 (1953).
[3] W. B. Weir, Proc. IEEE **62**, 33 (1974).
[4] J. L. Snoek, Physica **14**, 207 (1948).
[5] J. Smit and H. P. J. Wijn, *Ferrites* (Wiley, New York, 1959), pp. 202–211.
[6] H. M. Musal, Jr. and H. T. Hahn, IEEE Trans. Magn. **MAG-25**, 3851 (1989).

Effect of Er_2O_3 addition on microstructure and physical properties of Mn–Zn ferrites for high-power use

C. S. Liu and J. M. Wu
Department of Materials Science and Engineering, National Tsing Hua University, Hsinchu, Taiwan, Republic of China

C. J. Chen and M. J. Tung
Materials Research Laboratories, Industrial Technology Research Institute, Hsinchu 31015, Taiwan, Republic of China

The present authors found that Mn–Zn ferrites containing Er_2O_3 had improved values of σ_s (specific magnetization) and amplitude permeability. Samples with different addition amount of Er_2O_3 were sintered at 1180 °C. The results show that Er_2O_3 addition from 0.02 to 0.1 wt % causes the amplitude permeability to increase from 1070 to 2180. The magnetization can be increased from 91.6 to 92.8 emu/g within the range 0.02–0.1 wt %. Furthermore, the effect of Er_2O_3 addition was investigated in detail by power-loss analysis and scanning electron microscopy examination of microstructure. We found that samples with Er_2O_3 less than 0.04 wt % exhibit power loss [illegible] to the sample without Er_2O_3 addition and with SiO_2–CaO contents. Thus we conc[illegible] amplitude permeability and specific magnetization of Mn–Zn ferrites for high-fre[illegible] high-power use were improved by a small Er_2O_3 addition (<0.04 wt %).

I. INTRODUCTION

Recently, many efforts have been made in developing low-power-loss materials of Mn–Zn ferrites at high frequency, in accordance with the demand for miniaturization of electrical devices.[1–3] Therefore, many efforts have been made in developing fine grain Mn–Zn ferrites. The higher the frequency, the smaller the grain size. However, the amplitude permeability and saturation magnetization were lowered inevitably due to the demand of small grain size and high resistivity. Because there are few reports about the effects of rare-earth metal oxides on the Mn–Zn ferrites for high-power use, the present authors examined the addition effects of various rare-earth metal oxides on low-loss Mn–Zn ferrites in order to resolve the above-described problem. This paper is intended to present the effect of addition of Er_2O_3 on physical properties and the microstructure of low loss Mn–Zn ferrites.

Generally, the power loss P_B of ferrite materials is given by the summation of hysteresis loss P_h, eddy current loss P_e, and residual loss P_r. P_h and P_e are given as

$$P_h = W_h f,$$

$$P_e = cd^2 f^2 B_m^2/\rho,$$

where W_h is the energy equivalent to the area of the dc B-H hysteresis loop measured under the same maximum flux density as in the power-loss measurement, f the frequency, d the dimension of the circuit of eddy current, B_m the maximum flux density, ρ the electrical resistivity, and c the coefficient related to the dimension of the circuit of the eddy current. The residual loss is caused by the delay in magnetization equilibrium. In this paper, eddy current loss is interpreted as including residual loss.

II. EXPERIMENT

Samples of $Mn_{0.72}Zn_{0.22}Fe_{2.06}O_4$ are prepared by wet mixing Fe_2O_3, $MnCO_3$, ZnO, and Er_2O_3, and then drying and calcining at 900 °C in air. The resulting [illegible]wders, plus optimum CaO–SiO_2, are milled in water for 4[illegible] min. After drying, the powders are granulated through a 40-mes[illegible] sieve and pressed into toroids. A computer-controlled tube f[illegible]ace was used to regulate both firing temperature and oxygen [illegible]artial pressure. The samples were sintered at 1180 °C for 3 h and atmospheric conditions were controlled during cooling to maintain spinel phase equilibrium.

The power loss and amplitude permeability were measured by an apparatus made by the Ryowa Company. That is to say, power loss was obtained by computing the digital data of primary exciting current and secondary induced voltage detected from coils wound around a toroidal core under sinusoidal excitation. The test frequencies were from 100 kHz to 2 MHz sine waves. Specimens were placed in a oven so that its temperature could be controlled. Hysteresis loss was obtained by calculating the area surrounded by the B-H loop, which was measured using a dc B-H loop tracer.

The resistivity of the materials was measured by HP3478A. The specimen was 9 mm in diameter and 4 mm long, and both ends were indium gallium coated as an electrode. Scanning electron microscopy and EDAX were used to observe the microstructure and addition effect.

III. RESULTS AND DISCUSSION

A. Er_2O_3-added Mn–Zn ferrites

In order to investigate the effect of Er_2O_3 addition on the spinel matrix of Mn–Zn ferrites, samples with various Er_2O_3 content were prepared. Table I shows the static characteristics of the $Mn_{0.72}Zn_{0.22}Fe_{2.06}O_4$ containing 0–0.12% Er_2O_3. It is obvious that the effect of additions refers to the increase in ρ and σ_s from 0.02 to 0.1 wt %. The increment of ρ is most effective for lowering P_e. Therefore, it causes a decrease in power loss measured at 500 kHz and 50 mT. Table I also shows that the specific magnetization can be raised within this range of addition. Meanwhile, a similar effect is

 0021-8979/94/75(10)/6112/3/$6.00 © 1994 American Institute of Physics

TABLE I. Static characteristics for samples containing Er_2O_3.

Er_2O_3 (wt %)	0	0.02	0.04	0.08	0.10	0.12
Sintered density (g/cm^3)	4.91	4.90	4.89	4.85	4.84	4.80
dc ρ (Ω cm)	1.2	33.6	91	149	266	304
Power loss[a] (mW/cm^3)	3600	2030	1974	1460	953	500
σ_s (emu/g)	91.6	91.8	92.3	92.8	91.9	91.0
Amplitude permeability	1070	1150	1112	1450	2000	2180

[a]At 500 kHz, 50 mT, RT.

TABLE II. Static characteristics for samples containing SiO_2–CaO–Er_2O_3.

Er_2O_3 (wt %)	0	0.02	0.04	0.06	0.08	0.10	0.12
Sintered density (g/cm^3)	4.75	4.77	4.77	4.78	4.81	4.81	4.80
dc ρ (Ω cm)	1200	1230	1200	1130	1100	810	468
Power loss[a] (mW/cm^3)	200	200	205	250	333	368	410
σ_s (emu/g)	91.7	91.8	91.8	92.1	92.5	91.2	88.0
Amplitude permeability	1450	1478	1660	1650	1640	1605	1600

[a]At 500 kHz, 50 mT, RT.

observed for the value of amplitude permeability. It is presumed that the increase in amplitude permeability is regarded to originate from the change in the temperature dependence of k_1 or the magnitude value of k_1 itself by the addition of Er_2O_3.

The ion radius of Er is 0.88 Å. It is larger than the radius of sublattice sites in the crystal structure of Mn–Zn ferrites. Although the maximum solubility of Er_2O_3 in Mn–Zn ferrites is about 0.5–0.8 wt % according to Ref. 4, it is believed that when the content of Er_2O_3 is less than the maximum solubility limit, Er_2O_3 is thought to be not completely dissolved in the Mn–Zn ferrites. In other words, the electrical resistivity of Mn–Zn ferrites is expected to be increased by raising the electrical resistivity of the grain boundary due to the segregation of Er_2O_3. Furthermore, it is found that the influence of Er_2O_3 addition on electrical resistivity is not related to the reduction of grain size (Fig. 1). Thus, the variation of sintering density with Er_2O_3 content shown in Table I seems to be closely related to the grain boundary condition. Therefore, Fig. 1 shows that the higher the electrical resistivity, the lower the eddy current becomes and the smaller P_e becomes.

B. SiO_2–CaO–Er_2O_3 added Mn–Zn ferrites

The addition of SiO_2 and CaO is known to raise ρ of Mn–Zn ferrites for high-power use. Therefore, Table II shows the variation of static characteristics of the Mn–Zn ferrites coadded with 0.04 wt % SiO_2 and 0.08 wt % CaO and various Er_2O_3 contents. As compared with the samples with Er_2O_3 addition and without SiO_2–CaO addition, it is remarkable that ρ is further increased. But when ρ reaches a maximum value, it then decreases significantly with further increasing Er_2O_3 content. We also find that the effect of Er_2O_3 addition on specific magnetization and amplitude permeability of the spinel matrix is still positive, as shown in Table II.

In order to observe the microstructure of ferrites coadded with Er_2O_3 and SiO_2–CaO, Fig. 2 shows the scanning electron micrographs for samples containing 0, 0.04, and 0.1 wt % Er_2O_3, respectively. The average grain size becomes smaller when the Er_2O_3 content is gradually increased. Both effects of SiO_2–CaO addition and reduction of grain size increase the electrical resistivity of Mn–Zn ferrites contain-

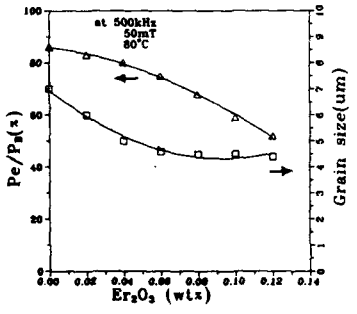

FIG. 1. Variation of grain size and P_e/P_s with Er_2O_3 content.

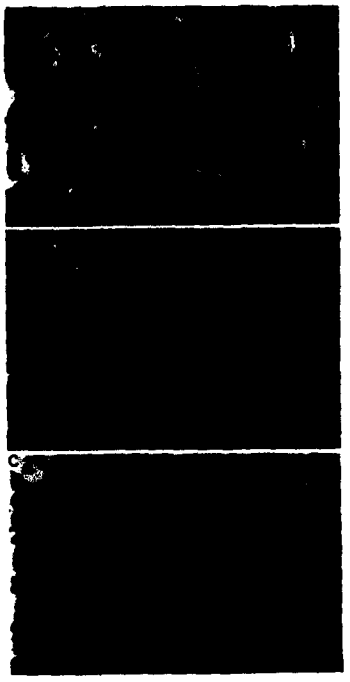

FIG. 2. Effect of Er_2O_3 content on power loss between samples with and without SiO_2–CaO.

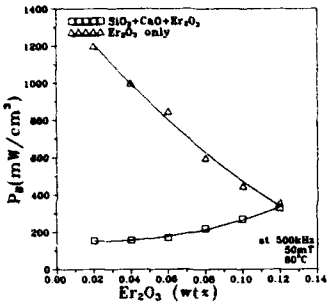

FIG. 3. Scanning electron micrograph for samples coadded with SiO_2–CaO–Er_2O_3 and sintered at 1180 °C for 3 h. (A) 0 wt %; (B) 0.04 wt %; (C) 0.1 wt % Er_2O_3.

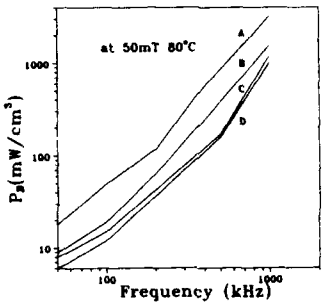

FIG. 4. Frequency dependence of power loss for samples with (A) 0.08 wt % Er_2O_3; (B) 0.12 wt % Er_2O_3; (C) SiO_2–CaO and 0.04 wt % Er_2O_3; (D) SiO_2–CaO.

ing Er_2O_3. Therefore, Fig. 3 shows that the power loss measured at 500 kHz and 50 mT is further lowered for samples coadded with SiO_2–CaO and Er_2O_3.

Figure 4 shows the effect of frequency on power loss measured at 50 mT and 80 °C. Compared with the value of ρ for Er_2O_3 contents shown in Tables I and II, the frequency dependence of power loss for samples with SiO_2–CaO is seen to be improved by enhancing ρ. In addition, we find that the sample added with little Er_2O_3 (~0.04 wt %) and SiO_2–CaO cooperatively exhibits a similar frequency dependence of power loss at high frequency compared with the sample with only a SiO_2–CaO addition. As described above, the amplitude permeability and specific magnetization of Mn–Zn ferrites for high-power use can be improved by little addition of Er_2O_3 (<0.04 wt %).

IV. CONCLUSIONS

(1) When 0.02–0.12 wt % Er_2O_3 is added to $Mn_{0.72}Zn_{0.22}Fe_{2.06}O_4$ ferrite, the power loss is gradually lowered due to the increase of electrical resistivity. In addition, the amplitude permeability and specific magnetization can be increased.

(2) For samples coadded with SiO_2–CaO and Er_2O_3, a small Er_2O_3 content can cause an increase in specific magnetization and amplitude permeability. Thus Mn–Zn ferrites with fine grain size for high-frequency and high-power use were improved by a small Er_2O_3 addition (<0.04 wt %).

(3) Microstructure with fine grain size is obtained by adding SiO_2–CaO and Er_2O_3 cooperatively.

ACKNOWLEDGMENTS

The authors would like to thank the Ministry of Economic Affairs, Republic of China, for financial support under Contract No. 3A92100 to the Industrial Research Institute.

[1] E. Otsuki, S. Yamada, T. Otsuka, K. Shoji, and T. Sato, J. Appl. Phys. **69**, 5942 (1991).
[2] T. Sano, A. Morita, and A. Matsukawa, "A New Power Ferrite for High Frequency Switching Power Supplies," Proceedings of the 3rd Annual High Frequency Power Conversion Conference, San Diego (1988).
[3] Yo. Sakaki, M. Yoshida, and T. Sato, IEEE Trans. Magn. **MAG-29**, 3517 (1993).
[4] T. Mizushima, A. Makino, and A. Inoue, "The Effect of Rare Earth Metal Oxide Addition on Magnetic Properties of Mn-Zn Ferrite," Proceedings of the Sixth International Conference on Ferrites, Tokyo, 1221 (1992).
[5] T. Mochizuki, I. Sasaki, and M. Torii, *Mn-Zn Ferrite for 400–600 kHz Switching Power Supplies*, edited by F. F. Y. Wang (The American Ceramic Society, Columbus, 1985), pp. 487–492.

Dispersion observed in electrical properties of titanium-substituted lithium ferrites

Bijoy Kumar Kuanr
Department of Physics and Electronics, Zakir Husain College, University of Delhi, Jawaharlal Nehru Marg, Delhi-110002, India

G. P. Srivastava
Department of Electronic Science, University of Delhi, India

The current-voltage characteristic of polycrystalline titanium-substituted lithium ferrites has been measured at temperatures above room temperature. At voltages below a critical value an Ohmic relationship is observed, while it obeys a power-law relationship ($i \propto V^{\alpha}$, where α is a temperature-dependent constant) above the critical voltage. At low voltages conduction is determined by the boundary layer, whereas at higher voltages, the current in the solid is mainly due to the space-charge-limited carriers. ac conductivity (σ_{ac}) and dielectric permittivity (ϵ') show a large temperature-dependent dispersion in the 5–10-MHz range. The experimental results indicate that titanium substitution suppresses all these parameters. The dielectric relaxation has a very large relaxation intensity. In the theoretical model the temperature- and frequency-dependent layer properties are inserted into Koop's model and the theoretical dispersion curves are obtained. The agreement of these data with the experimental findings is remarkable.

Lithium ferrites incorporated with titanium are very attractive for microwave applications as a low-cost substitution for garnets and other spinel ferrites. The inclusion of titanium in lithium ferrite necessitates adjustment of both monovalent lithium and trivalent iron ions. The aim of the present work is to investigate the dc and dielectric properties on a series of Ti^{4+}-substituted lithium ferrites. Ferrites may be considered to be composed of layers with different conductivities and thicknesses in series with each other.[1–4] The well-conducting grains, having thickness d_1, conductivity σ_1, and permittivity ϵ_1 are separated by a thin layer of poorly conducting grain boundaries (GB) having thickness d_2, conductivity σ_2, and permittivity ϵ_2. It is reasonable to assume that $\sigma_1 \gg \sigma_2$. If V_1 and V_2 are the dc voltage drops across the grain and the GB, respectively, then $V = V_1 + V_2$ is the externally applied dc voltage. The voltage drop will take place mainly across the grain boundary (i.e., $V \simeq V_2$). If the current (i_{Ω_1}) through the grain is only ohmic, and the current through the GB is Ohmic (i_{Ω_2}) as well as space-charge limited (i_{scl}), the total current $i = i_{\Omega_1} = i_{\Omega_2} + i_{scl}$. The total current in the solid can be approximated as $i_{\Omega_2} \ll i_{scl} \simeq i$. Thus the I-V characteristic in the nonohmic region is given by $i_{scl} \propto V_2^{\alpha}$. The space-charge-limited current is determined mainly by the number of free charge carriers available in the grain-boundary layers. At low applied dc voltages, i.e., before the non-Ohmic region, the current is purely Ohmic ($\alpha = 1$). In this region the total current through the solid is $i_{scl} \ll i_{\Omega_2} \simeq i$, and hence an ohmic relation holds. According to this theory, the I–V curve consists of three parts: (i) low-current ohmic range, (ii) scl-current range or the nonohmic range, and (iii) high-current ohmic range.

The ac conductivity and dielectric permittivity of ferrites show large dispersion at audio frequencies. This dispersion can be explained with the help of the Maxwell–Wagner two-layer model.[1] Koop's[2] phenomenological theory is generally used to describe the dielectric relaxation in ferrites. The frequency-dependent effective conductivity $\sigma(\omega)$ and permittivity $\epsilon'(\omega)$ are

$$\sigma(\omega) = [\sigma_s + \sigma_\infty(\omega\tau)^2]/[1 + (\omega\tau)^2] \tag{1}$$

and

$$\epsilon'(\omega) = [\epsilon_s + \epsilon_\infty(\omega\tau)^2]/[1 + (\omega\tau)^2], \tag{2}$$

where

$$\tau = \epsilon_0(\epsilon_s - \epsilon_\infty)/(\sigma_\infty - \sigma_s) \tag{3}$$

is the relaxation time. The subscript s corresponds to low frequency and the subscript ∞ to high frequency. Equations (1) and (2) cannot provide the interpretation for the experimental σ and ϵ' at temperatures other than room temperature. In order to study the temperature dependence of $\sigma(\omega)$ and $\epsilon'(\omega)$, the effect of temperature on σ_1, σ_2, ϵ_1, and ϵ_2 should be known. But from the experimental results only σ_s, σ_∞, ϵ_s, and ϵ_∞ can be observed. The correlation suggested[2] between the layer properties and the experimentally observed parameters are $\epsilon_1 = \epsilon_2 = \epsilon_\infty$, $x = d_2/d_1 = \epsilon_\infty/\epsilon_s$, $\sigma_1 = x\sigma_s$, and $\sigma_2 = \sigma_\infty$. The temperature variation of layer properties at high- and low-frequency levels can be obtained from the experimental results of ϵ_s, ϵ_∞, σ_s, and σ_∞. The suggestion made in the present investigation is that the temperature dependence of $\sigma(\omega)$ and $\epsilon'(\omega)$ [Eqs. (1) and (2)] can be obtained by introducing one exponential term $[\sigma_i = \sigma_{i\infty} \exp(-E_{ai}/kT), i = 1,2]$ to σ_1 and σ_2. E_{a1} and E_{a2} are the activation energies at low- and high-frequency levels.[1] The temperature- and frequency-dependent σ and ϵ' are

$$\sigma(\omega,T) = (1+x) \times \frac{x^2\sigma_s\sigma_\infty(\sigma_s+\sigma_\infty) + \omega^2\epsilon_0^2\epsilon_\infty^2(\sigma_\infty + x^2\sigma_s)}{x^2(\sigma_s+\sigma_\infty)^2 + \omega^2\epsilon_0^2\epsilon_\infty^2(1+x)^2} \tag{4}$$

and

 0021-8979/94/75(10)/6115/3/$6.00 © 1994 American Institute of Physics

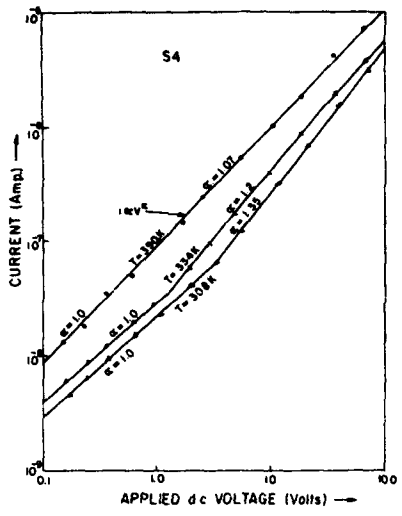

FIG. 1. dc current voltage characteristic of sample S4.

$$\epsilon'(\omega,T)=(1+x)\,\frac{x\epsilon_\infty(x\sigma_s^2+\sigma_\infty^2)+\omega^2\epsilon_0^2\epsilon_\infty^3(1+x)}{x^2(\sigma_s+\sigma_\infty)^2+\omega^2\epsilon_0^2\epsilon_\infty^2(1+x)^2}\,. \tag{5}$$

ϵ_0 is a constant and ω and T are variables in Eqs. (4) and (5). These two equations are used in the present investigation to explain the experimental results theoretically.

The samples having stoichiometry ($Li_{0.5+0.5x}Ti_xMn_{0.1}Fe_{2.4-1.5x}O_4$, $x=0$, 0.1, 0.3, 0.5, and 0.7, samples S1–S5, respectively) were prepared by the dry ceramic method. The final sintering was carried out at 1050 °C. A small amount of manganese was included in the composition to increase the resistivity of the samples. X-ray diffraction studies ensured a single spinel phase formation. All the measurements were carried out by a three-probe pressure contact technique on pellet-shaped samples coated with air-dried silver epoxy. dc electrical measurements were made employing a Keithley Electrometer, Model No. 610C, and dielectric measurements were performed using a HP 4192A LF Impedance Analyzer from 5 to 10 MHz at different temperatures.

The I-V characteristics for sample S4 is shown in Fig. 1. It is evident from this figure that at low applied dc voltages an ohmic relationship ($\alpha=1$) is obtained. This is called the low-current-ohmic range. But at higher voltages, i.e., $V>1$ V, the nonohmic relation, $i\propto V^\alpha$, holds good. The parameter α, which essentially defines the non-Ohmic nature of the material, is observed to decrease with an increase of temperature. The non-Ohmic region ($\alpha>1$), in the I-V curves, arises due to the space-charge effects and is termed as space-charge-limited current region. These observations show that the I-V characteristics provide the best understanding of the conduction mechanism in ferrites.

Figures 2 and 3 show the experimental variation of room-temperature σ_{ac} and ϵ' from 5 to 10 MHz for samples

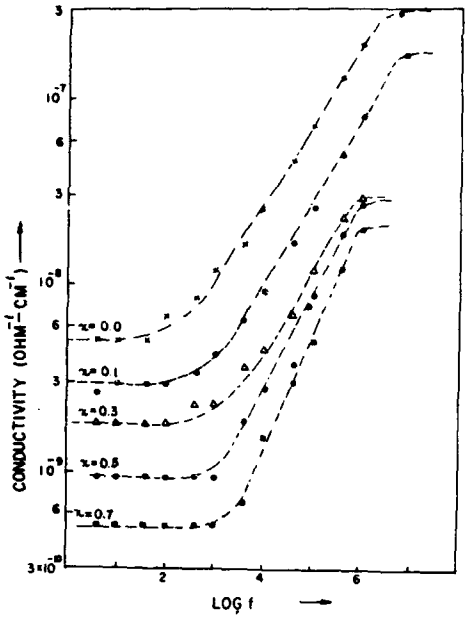

FIG. 2. ac conductivity vs frequency at room temperature for different titanium-substituted lithium ferrites.

of different titanium concentration. Figure 2 depicts that, for sample S1, σ_{ac} increases rapidly with the increase of frequency. Addition of titanium in lithium ferrite makes the σ_{ac} frequency independent at low frequencies, but after a certain frequency its value increases rapidly. Further addition of titanium makes σ_{ac} more and more frequency independent at

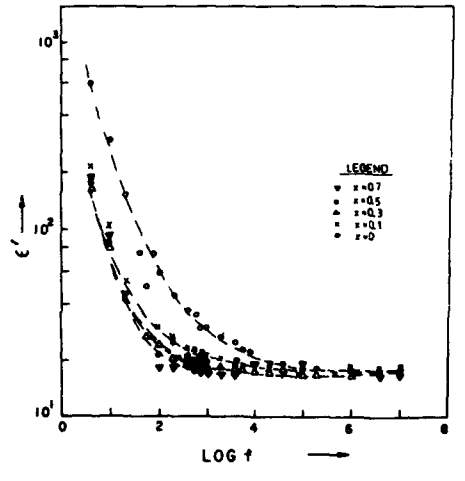

FIG. 3. Experimental variation of permittivity with frequency at room temperature for titanium-substituted lithium ferrite samples.

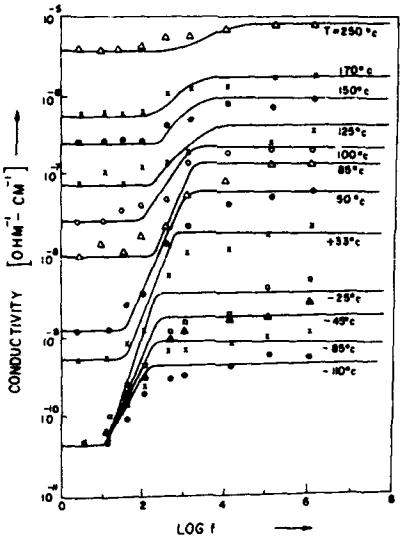

FIG. 4. Experimental variation of conductivity as a function of frequency at different temperatures for sample S5.

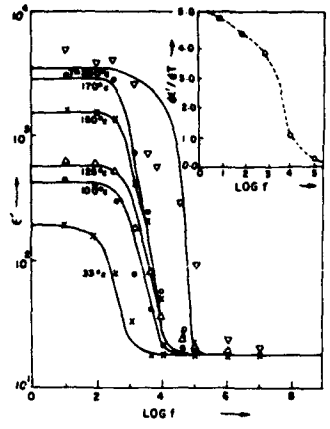

FIG. 5. ϵ' vs frequency at different temperatures for sample S5. The inset shows the variation of $d\epsilon'/dT$ as a function of frequency.

low frequencies. It is also observed that the value of conductivity decreases with the increase in titanium percentage in lithium ferrites.

Figure 3 shows that in the low-frequency region, the values of ϵ' (ϵ_s) are very high. The increase of titanium concentration, in lithium ferrites, decreases ϵ_s. The value of ϵ' decreases rapidly with an increase in frequency and attains a constant value (ϵ_∞) at higher frequencies independent of Ti^{4+} contents.

The experimentally observed room-temperature variation of σ_{ac} and ϵ' with composition and frequency are interpreted on the basis of space-charge polarization. This is governed by two factors: (i) the number of space-charge carriers and (ii) the resistivity of the sample. The polarization effect may be interpreted in the following way: A partial evaporation of Li^{1+} ions takes place at the sample surface during the sintering process in the lithium-containing ferrites. This leads to the formation of some Fe^{2+} ions from Fe^{3+} ions. The polarization of the ferrite is determined by local displacement of electrons in the direction of an applied field, which is due to the electron exchange interaction, $Fe^{2+} \rightleftarrows Fe^{3+}$. From the accepted cation distribution it is seen that the Fe^{2+} ions are maximum at the octahedral sites for the sample S1. Hence a high value of ϵ' is expected for this sample. The substitution of x amount of titanium decreases the iron ion concentration from 2.4 to $(2.4-1.5x)$, in the formula unit. Hence, there is a decrease in the number of ferrous ions on the octahedral sites which are responsible for dielectric polarization. Therefore, the dielectric permittivity decreases with an increase of Ti^{4+} in lithium ferrites.

The experimental variations of σ_{ac} and ϵ' with frequency for sample S5 are shown in Figs. 4 and 5, respectively, at different temperatures. From Fig. 4 limiting values of the low-frequency conductivity (σ_s) and high frequency conductivity (σ_∞) are observed. In the temperature range from -110 to -25 °C the value of σ_s is observed to be independent of temperature, and beyond σ_s it shows the usual trend. It may be pointed out here that other samples of this series were also found to exhibit similar behavior. Figure 5 depicts the experimental variation of permittivity with frequency at different temperatures for sample S5. However, it is observed that at 5 Hz, ϵ_s is a function of temperature. This is due to the fact that in the present investigation it was not possible to measure ϵ' below 5 Hz. But at high frequencies ($>10^4$ Hz), ϵ' is independent of frequency as well as temperature. The inset in this figure shows the variation of $d\epsilon'/dT$ as a function of frequency.

Temperature variations of σ_{ac} and ϵ' as a function of frequency cannot be reproduced theoretically by the use of the relations (1) and (2). In order to find the validity of the Koops phenomenological model[2] with the present investigation, the temperature variation of layer properties were studied. For this purpose σ_s, σ_∞, ϵ_s, and ϵ_∞ were studied experimentally as a function of temperature. The theoretical dispersion curves for σ_{ac} and ϵ' as a function of frequency and temperature are obtained from Eqs. (4) and (5). These curves are also shown in Figs. 4 and 5 for sample S5 along with the experimental data. The dispersion region in the experimentally observed curves extends from 10 Hz and above for σ_{ac} and 100 Hz to 10 kHz for ϵ', whereas the theoretical dispersion curves show a dispersion region up to 1 kHz for σ_{ac} and 10 kHz for ϵ'. These discrepancies may be due to the fact that ϵ_s is taken to be temperature dependent in the present investigation.

[1] P. K. Larsen and R. Metselaar, Phys. Rev. B 8, 2016 (1973).
[2] C. G. Koops, Phys. Rev. 83, 121 (1951).
[3] J. Krausse, Z. Angew. Phys. 27, 251 (1969).
[4] P. D. Baba et al., IEEE Trans. Magn. MAG-8, 83 (1972).

Electrical conductivity of Mn–Zn ferrites

D. Ravinder
Department of Physics, Post-Graduate College of Science, Osmania University, Saifabad, Hyderabad-500 004, A.P., India

K. Latha
Railway Junior College, Lallaguda, Secunderabad-500 017, A.P., India

The electrical conductivity of polycrystalline mixed ferrite system having the chemical formula $Mn_xZn_{1-x}Fe_2O_4$ (where $x=0.0$, 0.2, 0.4, 0.6, and 0.8) was investigated from room temperature to the neighborhood of the Curie temperature by the two-probe method. The electrical conduction in these ferrites is explained on the basis of the hopping mechanism. Plots of log (σT) versus $10^3/T$ are almost linear and show a transition near the Curie temperature. The activation energy in the ferrimagnetic region is in general less than that in the paramagnetic region.

I. INTRODUCTION

Manganese–zinc and nickel–zinc mixed ferrites are still by far the most important ferrites for high permeability and low loss applications.[1] Though several researchers have studied the magnetic properties of the mixed Mn–Zn ferrites as a function of composition and temperature, very few studies are available on various nonmagnetic properties such as electrical conductivity, thermoelectric power, and dielectric constant. With a view to understand the conduction mechanism in mixed Mn–Zn ferrites, the electrical conductivity and thermoelectric power as functions of composition and temperature were undertaken. The results of such a study are presented in this article.

II. EXPERIMENT

Polycrystalline samples of mixed Mn–Zn ferrites having the chemical formula $Mn_xZn_{1-x}Fe_2O_4$ (where $x=0.0$, 0.2, 0.4, 0.6, and 0.8) were prepared by the conventional double sintering method. The final sintering was done at 1200 °C. X-ray diffractometer of the samples using Cu$K\alpha$ radiation confirmed the spinel formation. Thermo-emf of mixed Mn–Zn ferrites was measured as a function of temperature by the hot probe method.[2] The electrical conductivity measurements were made by the two probe method[3] from room temperature to well beyond the Curie temperature.

III. RESULTS AND DISCUSSION

Experimental data for the mixed Mn–Zn are given in Table I, which includes the compositional formulae of all the ferrites and the values of the Seebeck coefficient and the electrical conductivity at room temperature.

Based on the observed Seebeck coefficients in Table I, the mixed Mn–Zn ferrites studied in this investigation can be divided into two groups. The specimens I, III, IV, and V (group 1) have negative Seebeck coefficients, indicating that they are n-type semiconductors; specimen II (group 2) is a p-type semiconductor as its Seebeck coefficient is positive. It can be seen from the Table I that the values of Seebeck coefficient continuously decreases with the increase of zinc concentration from 0.0 to unity. A similar continuous decrease of Seebeck coefficient with the increase of nickel content was observed by Reddy and Rao in the case of Li–Ni ferrites.[4] The variation of Seebeck coefficient with temperature for all the mixed Mn–Zn ferrites is shown in Fig. 1. It can be seen from the figure that the Seebeck coefficient decreases with increase of temperature. A similar behavior has been observed in several other ferrites.[5,6] It can also be seen from Fig. 1 that the Seebeck coefficient in all the cases is strongly dependent on temperature. The decrease of Seebeck coefficient from room temperature up to about 150 °C is rapid, whereas beyond 150 °C the decrease is slow. Similar rapid decrease of Seebeck coefficient from room temperature

TABLE I. Experimental data on Mn–Zn mixed ferrites at room temperature.

Specimen	Molecular formula	Electrical conductivity σ ($\Omega\,cm^{-1}$)	Seebeck coefficient Q (μV/K)	Activation energies (eV) Ferrimagnetic region E_1	Activation energies (eV) Paramagnetic region E_2	$\Delta E=E_2-E_1$ (eV)	Curie temperature (K)
			Group 1				
I	$MnFe_2O_4$	5.32×10^{-9}	−750	0.28	0.70	0.42	559
III	$Mn_{0.4}Zn_{0.4}Fe_2O_4$	4.77×10^{-8}	−692	0.24	0.64	0.40	501
IV	$Mn_{0.4}Zn_{0.6}Fe_2O_4$	5.85×10^{-7}	−598	0.21	0.55	0.34	441
V	$Mn_{0.2}Zn_{0.8}Fe_2O_4$	1.79×10^{-5}	−530	0.19	0.46	0.27	417
			Group 2				
II	$Mn_{0.8}Zn_{0.2}Fe_2O_4$	7.73×10^{-8}	710	0.25	0.68	0.43	521

 0021-8979/94/75(10)/6118/3/$6.00 © 1994 American Institute of Physics

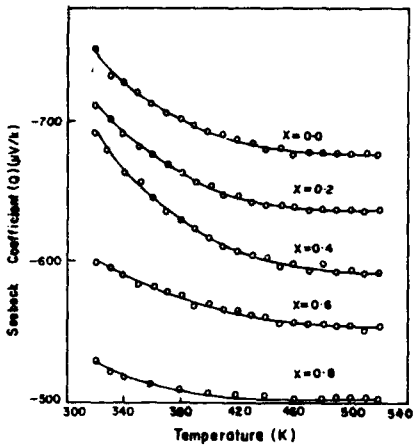

FIG. 1. Plot of Seebeck coefficient Q vs temperature for mixed Mn–Zn ferrites.

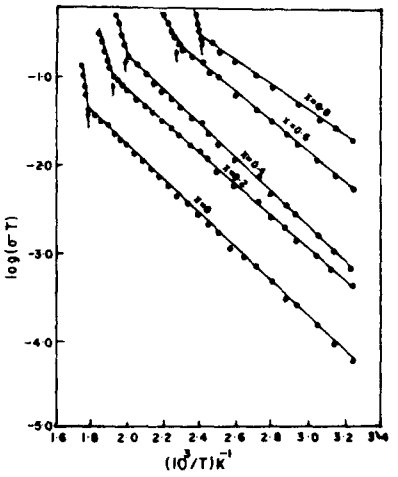

FIG. 2. Plot of log (σT) vs $10^3/T$ for mixed Mn–Zn ferrites.

up to 150 °C has also been observed by Ravinder and Seshagiri Rao in the case of mixed Li–Cd ferrites.[7] Samokhvalov and Rustmov[8] measured the Seebeck coefficient Q of mixed nickel–zinc ferrites and observed a similar variation of Q with temperature. From this observation it follows that the conduction mechanism in the n-type specimens of group 1 is predominantly due to hopping of electrons[9] from Fe^{2+} to Fe^{3+} ions, whereas the conduction mechanism in specimens of group 2 is hole transfer from Mn^{3+} to Mn^{2+} ions.

It can be seen from the table that in the case of Mn–Zn ferrites, the values of electrical conductivity vary from $5.32\times10^{-9}\ \Omega^{-1}\ cm^{-1}$ for $MnFe_2O_4$ to $1.79\times10^{-5}\ \Omega^{-1}\ cm^{-1}$ for $Mn_{0.2}Zn_{0.8}Fe_2O_4$. It is also evident from the table that the conductivity continuously increases, with the addition of the zinc. A similar continuous increase of electrical conductivity was observed by Reddy and Rao[10] in the case of Mn–Mg ferrites and also by Eatah *et al.*[11] in the case of Cu–Co ferrites. The electrical conductivity of mixed Mn–Zn ferrites of various compositions was measured over the temperature range 308–575 K. Plots of log (σT) versus temperature $(10^3/T)$ are shown in Fig. 2. It can be seen from the figure that the log (σT) increases almost linearly with increasing temperature up to a certain temperature T_1 (K) at which a change of slope has occurred. It is observed that the transition temperature T_1 (K) is in good agreement with the Curie temperature, showing that the kink in each case has occurred at the Curie point of the corresponding ferrite.

Figure 3 shows the relation between the Curie temperature T_c and the zinc concentration X. It illustrates that the Curie temperature decreases linearly due to increasing zinc content. Similar transitions in the neighborhood of the Curie point have also been observed in the mixed Co–Zn (Ref. 12) and Li–Zn (Ref. 13) ferrites. It was shown theoretically on passing through the Curie point a change must occur in the gradient of the straight line,[14] and magnitude of the effect depends on the exchange interaction between the outer and inner electrons which changes at the Curie point. The experimental observation of the transition near the Curie point in the case of Mn–Zn ferrites is thus in conformity with theory developed by Irkhin and Turov.[15]

The activation energies in the ferrimagnetic and paramagnetic regions are calculated from the slopes of log (σT) versus $10^3/T$ and are presented in the Table I. It can be seen from the table that the activation energy in the paramagnetic region is higher than that in the ferrimagnetic region. This result is in agreement with the theory developed by Irkhin and Turov.[15] Similar results have been obtained in the case of a number of mixed ferrites such as lithium–titanium[16] and nickel–zinc ferrites.[17] It may also be noted from the Table I that the high activation energy goes hand in hand with low conductivity of the ferrite. This result is in accordance with the conclusion drawn by Smit and Wijn[14] who collected the data on a number of ferrites. As already pointed out, the kink

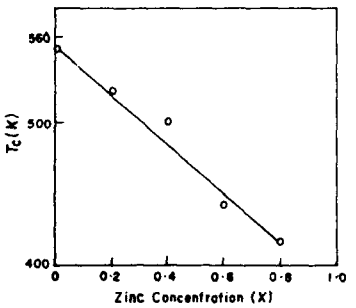

FIG. 3. Variation of transition temperature T_c with zinc concentration X.

will be larger for cases in which there is a stronger exchange interaction between the outer and inner electrons. The size of this kink can be smaller or larger in various ferrites, depending on their structural peculiarities and also on the value of electrical resistance. The earlier experiments have shown that the larger kinks are characteristic of ferrites that have small specific resistance because in these materials the activation energy is comparable with the magnitude of the energy of the spontaneous magnetization that is "released" as a result of magnetic transition.

The magnitude of the kink as determined by the difference between the activation energies in the ferrimagnetic and paramagnetic regions (ΔE) is given in the next to last column of Table I. The third column of the table gives the values of electrical conductivity for the mixed Mn–Zn ferrites under investigation. Inspection of these two columns reveals, however, that there is no correlation between the values of ΔE and the conductivity. This may perhaps be attributed to the structural peculiarities of the ferrite specimens under investigation.

ACKNOWLEDGMENTS

The authors are grateful to Professor K. Rama Reddy, Head of the Department of Physics, Osmania University, Hyderabad for his interest in this work. The authors also thank Professor T. Seshagiri Rao, Professor K. Shankaraiah, Principal, and Professor U. V. Subba Rao, Head, Department of Physics, Post-Graduate College of Science, Osmania University, Saifabad, Hyderabad for their cooperation.

[1] D. Polder, Proc. Inst. Electron Eng. **97**, 246 (1950).
[2] A. G. Rustamov, A. A. Samokhvalov, and I. G. Fakidov, Sov. Phys. Solid State **5**, 751 (1964).
[3] V. R. K. Murthy and J. Sobhanadri, Phys. Status Solidi A **38**, 647 (1976).
[4] P. V. Reddy and T. S. Rao, Phys. Status Solidi A **92**, 303 (1985).
[5] F. J. Morin and T. H. Geballe, Phys. Rev. **99**, 467 (1955).
[6] D. Ravinder, Cryst. Res. Technol. **27**, 545 (1992).
[7] D. Ravinder and T. Seshagiri Rao, Cryst. Res. Technol. **25**, 963 (1990).
[8] A. A. Samokhvalov and A. G. Rustmov, Sov. Phys. Solid State **7**, 961 (1965).
[9] L. G. Van Uitert, J. Chem. Phys. **23**, 1883 (1955).
[10] P. Venugopal Reddy and T. Seshagiri Rao, J. Less Common Met. **90**, 243 (1983).
[11] A. I. Eath, A. A. Ghani, M. F. Elshaht, and E. El-Faramay, Phys. Status Solidi A **104**, 793 (1987).
[12] R. Satyanarayana, S. Ramana Murthy, and T. Seshagiri Rao, J. Less Common Met. **86**, 115 (1982).
[13] D. Ravinder and T. Seshagiri Rao, Cryst. Res. Technol. **25**, 1079 (1990).
[14] J. Smit and H. P. J. Wijn, *Ferrites*, Philips' Tech. Library Series (Cleaver-Home, London, 1959), p. 234.
[15] Yu. P. Irkhin and E. A. Turov, Sov. Phys. JETP **33**, 673 (1957).
[16] R. Manjula, V. R. K. Murthy, and J. Sobhanadri, J. Appl. Phys. **59**, 2929 (1986).
[17] R. Satyanarayana, S. Ramana Murthy, and T. Seshagiri Rao, J. Less Comm. Met. **90**, 243 (1983).

Composition dependence of the elastic moduli of mixed lithium–cadmium ferrites

D. Ravinder
Department of Physics, Postgraduate College of Science, Osmania University, Saifabad, Hyderabad-500 004, AP, India

Mixed Li–Cd ferrites having the chemical formula $Li_{0.5-x/2}Cd_xFe_{2.5-x/2}O_4$ (where $x=0.2$, 0.4, 0.6, 0.8, and 1.0) are prepared by the well-known double sintering ceramic technique. From x-ray diffraction studies lattice parameters are calculated and their variation with composition is explained on the basis of the tetrahedral ionic radius. The bulk density of the specimens are determined by the hydrostatic method and the percentage porosity was calculated. The ultrasonic compressional (V_l) and shear (V_s) velocities of mixed Li–Cd ferrites are measured at room temperature by the ultrasonic pulse transmission technique. The values of Young's modulus, the rigidity modulus, Debye temperatures, and average sound velocities are calculated from the experimental values of V_l and V_s. The elastic moduli have been corrected to zero porosity. The variation of elastic moduli with composition is interpreted in terms of binding forces between the atoms.

I. INTRODUCTION

Ferrites are finding wide application as core materials of inductors, transformers, etc. in the electronics industry. Mixed lithium–cadmium ferrites are of much interest because of their useful applications in several microwave devices like isolators, circulators, gyrators, phase shifters, etc.[1] So a study of the elastic properties of mixed ferrites especially with reference to the composition is of importance in understanding the nature of interatomic forces existing in ferrites. As such, a study of the elastic behavior of mixed Li–Cd ferrites of different compositions has been undertaken, and the results are presented in this paper.

II. EXPERIMENT

The ferrite samples used in the present investigation have the composition formula $Li_{0.5-x/2}Cd_xFe_{2.5-x/2}O_4$ (where $x=0.2$, 0.4, 0.6, 0.8, and 1.0) were prepared by the conventional double sintering method. The final sintering was done at 1300 °C. The details of the preparation method have been given in an earlier publication.[2] The ultrasonic compressional (V_l) and shear velocities (V_s) at room temperature of all the mixed ferrites were determined by the ultrasonic pulse transmission technique[3] but modified and improved by using a digital Tectronik 2230 oscilloscope and utilizing cursor movement for travel time measurements.[4] The error in the measurement of velocities is less than ±0.5%.

III. RESULTS AND DISCUSSION

X-ray diffraction patterns for all the Li–Cd ferrites have been obtained using Cu$K\alpha$ radiation. The value of the lattice parameter for each composition has been calculated using the values of d spacings. In the case of $CdFe_2O_4$, the value of the lattice parameter obtained in the present investigation is 0.8698 nm, which is in agreement with that of 0.8700 nm reported by Globus, Pascard, and Cagan.[5] No data are available in the literature to compare the values of other Li–Cd ferrites. The variation of the lattice parameter with cadmium composition is shown in Fig 1. The lattice parameter is found to vary linearly with increasing cadmium concentration, thereby indicating that the Li–Cd ferrite system obeys Vegard's law.[6] Further, the variation of lattice parameter with composition can be explained on the basis of the variation in the tetrahedral ionic radius as outlined below.

The cation distribution of lithium ferrite having the inverse spinel structure is given by

$$(Fe^{3+})[Li^{+}_{0.5}Fe^{3+}_{1.5}]O^{-}_{4},$$

where the parentheses ( ) and brackets [ ] indicate the tetrahedral and octahedral sites, respectively. Starting from lithium ferrite, when a nonmagnetic ion Cd^{2+} is substituted it is known to occupy preferably the tetrahedral sites,[7] replacing Fe^{3+} ions. As such, the cation distribution of Li–Cd ferrites can be written as

$$(Fe^{3+}_{1-x}Cd^{2+}_{x})[Li^{1+}_{0.5-0.5x}Fe^{3+}_{1.5+0.5x}]O^{2-}_{4}.$$

The ionic radius of Fe^{3+} and Cd^{2+} is 0.049 and 0.084 nm, respectively. When Cd^{2+} with a larger ionic radius replaces Fe^{3+} on the tetrahedral site having a smaller ionic radius, the

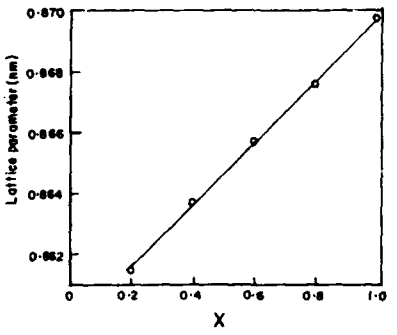

FIG. 1. Variation of the lattice parameter with cadmium content.

 0021-8979/94/75(10)/6121/3/$6.00 © 1994 American Institute of Physics

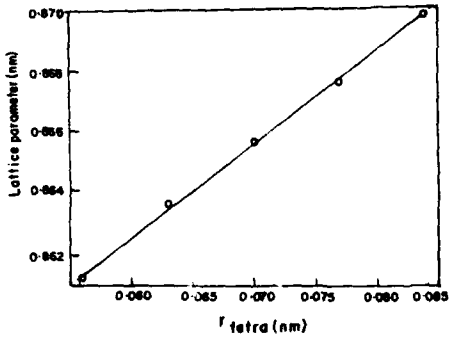

FIG. 2. Plot of the lattice parameter and tetrahedral ionic radius.

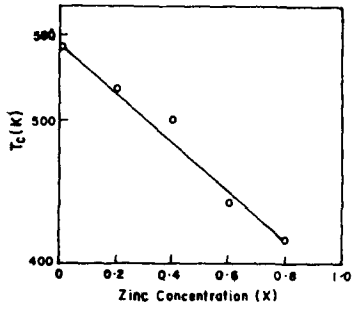

FIG. 3. Variation of bulk density with cadmium composition.

lattice parameter is expected to increase continuously. Now the relationship between tetrahedral ionic radius and the lattice parameter can be arrived at as follows.

For a given composition x, the mean ionic radius per molecule of the tetrahedral site may be defined as

$$r_{\text{tetra}}=(1-x)r_{\text{tetra}}(Fe^{3+})+xr_{\text{tetra}}(Me^{2+}),$$

where Me^{2+} denotes the substituted divalent metal. Using this formula, the mean tetrahedral ionic radius for each composition has been computed. A plot of lattice parameter versus tetraionic radius for all Li–Cd samples is shown in Fig 2. It can be seen from the figure that when Cd^{2+}, having an ionic radius of 0.084 nm, replaces the Fe^{3+} ion ($r=0.049$ nm), the mean tetrahedral ionic radius is found to increase continuously with increasing cadmium concentration. Accordingly, the lattice parameter is found to increase with increasing tetrahedral ionic radius. As such, it can be concluded that the tetrahedral site is influencing the value of lattice parameter. A similar result has been reported by Globus, Pascard, and Cagan[5] in the case of Li–Ni and Mn–Mg ferrites.[8]

The bulk density of the specimens has been determined accurately by the hydrostatic method and the percentage porosity was calculated. The values of bulk density and the percentage of porosity for Li–Cd ferrites are given in Table I. It can be seen from the table that the bulk density increases and the porosity decreases with the addition of cadmium to lithium ferrite, cadmium ferrite having the least porosity. This confirms the observation that the addition of cadmium to lithium ferrite results in the densification of the material.[9]

Figure 3 shows a plot of bulk density versus cadmium content for mixed Li–Cd ferrite specimens. It may be seen from the figure that the bulk density increases linearly with the increase of cadmium content. A similar linear variation has also been observed by West and Blankenship[10] in the case of mixed lithium–zinc ferrites sintered at 980 °C.

The experimental values of compressional (V_l) and shear (V_s) velocities, along with the computed values of the Young's modulus (E), and rigidity modulus (n), are in Table I. Since ferrites under investigation are porous (porosity ranging from 0.3% to 0.6%), the elastic moduli have been corrected to zero porosity using McKenzie's formula.[11] The corrected values of E_0, n_0, K_0, and σ_0 are in Table II (where K_0=bulk modulus of nonporous material). It can be seen from the Tables I and II that the values of E, n, E_0, n_0, and K_0 of the mixed Li–Cd ferrites are found to decrease continuously with increasing cadmium content. From Table II, it can further be seen that the Poisson's ratio remains constant. Following Wooster's work,[12] the variation of elastic moduli with composition may be interpreted in terms of binding forces between the atoms. As such, it can be understood from the experimental values of E_0 and n_0 (Table III) that the atomic binding between the ions of Li–Cd mixed ferrites decreases continuously with increasing cadmium content. This composition variation of elastic moduli in the case of Li–Cd ferrites is similar to what has been observed in several other ferrites like Li–Ti (Ref. 13) and Li–Zn (Ref. 14).

TABLE I. Elastic data (uncorrected) of mixed lithium–cadmium ferrites at room temperature.

Sample No.	Ferrite composition	Bulk density (10^3 kg m^{-3})	X-ray density (10^3 kg m^{-3})	Percentage porosity (%)	V_l (m s^{-1})	V_s (m s^{-1})	E (GN n^{-2})	n (GN m^{-2})
1	$Li_{0.4}Cd_{0.2}Fe_{2.4}O_4$	4.62	4.64	0.4	5068	3837	159.16	68.02
2	$Li_{0.3}Cd_{0.4}Fe_{2.3}O_4$	4.91	4.94	0.6	4977	3383	123.62	56.19
3	$Li_{0.2}Cd_{0.6}Fe_{2.2}O_4$	5.21	5.24	0.6	4907	2805	103.30	40.99
4	$Li_{0.1}Cd_{0.8}Fe_{2.1}O_4$	5.50	5.53	0.6	4021	2518	82.29	34.87
5	$CdFe_2O_4$	5.80	5.82	0.3	3938	2400	80.18	33.49

TABLE II. Elastic data (corrected) of mixed lithium–cadmium ferrites at room temperature.

Sample No.	Ferrite composition	E_0 (GN m^{-2})	n_0 (GN m^{-2})	K_0 (GN m^{-2})	Poisson's ratio (σ_0)
1	$Li_{0.4}Cd_{0.2}Fe_{2.4}O_4$	161.20	66.94	90.79	0.21
2	$Li_{0.3}Cd_{0.4}Fe_{2.3}O_4$	128.78	52.75	76.84	0.22
3	$Li_{0.2}Cd_{0.6}Fe_{2.2}O_4$	103.40	43.70	54.38	0.18
4	$Li_{0.1}Cd_{0.8}Fe_{2.1}O_4$	83.60	34.69	47.23	0.21
5	$CdFe_2O_4$	80.61	33.59	44.77	0.20

Debye temperatures (Θ_D) for the mixed Li–Cd ferrites have been calculated using the sample method given by Anderson,[15]

$$\Theta_D = \frac{h}{k}\left(\frac{3Nq\rho}{4\pi m}\right)^{1/3} V_m, \tag{1}$$

where h=Planck's constant, k=Boltzmann's constant, N=Avogadro's number, m=molecular weight of the specimen, q=number of atoms, ρ=density of the specimen, and V_m=average sound velocity, which is given by

$$V_m = \left[\frac{1}{3}\left(\frac{2}{V_s^3} + \frac{1}{V_l^3}\right)\right]^{-1/3}. \tag{2}$$

From the values of compressional (V_l) and shear (V_s) velocities and x-ray density, V_l/ρ and V_s/ρ are calculated and are shown in Table III. The mean weight m/q of the ferrite under investigation, calculated from the molecular weight m and the number of atoms q in the chemical formula, are also included in Table III. The values of Θ_D and V_m thus obtained are also given in Table III. The values of V_l/ρ, V_s/ρ, V_m, Θ_D also decrease continuously with increasing cadmium content. A plot of Θ_D against V_m is shown in Fig. 4. It is interesting to note from the figure that Θ_D varies linearly with V_m. A similar variation of Θ_D with V_m was reported by Narayana and Swamy[16] in the rare-earth and noble metals, and by Reddy *et al.* in the case of Li–Ti (Ref. 13) mixed ferrites.

TABLE III. Relation between atomic weights and velocities for mixed lithium–cadmium ferrites.

Sample No.	Ferrite composition	m/q	V_l/ρ	V_s/ρ	V_m (m s^{-1})	Θ_D (K)
1	$Li_{0.4}Cd_{0.2}Fe_{2.4}O_4$	31.90	1093	827	4114	543
2	$Li_{0.3}Cd_{0.4}Fe_{2.3}O_4$	34.21	1008	685	3689	485
3	$Li_{0.2}Cd_{0.6}Fe_{2.2}O_4$	36.53	937	536	3117	409
4	$Li_{0.1}Cd_{0.8}Fe_{2.1}O_4$	38.64	727	455	2773	363
5	$CdFe_2O_4$	41.16	677	413	2651	347

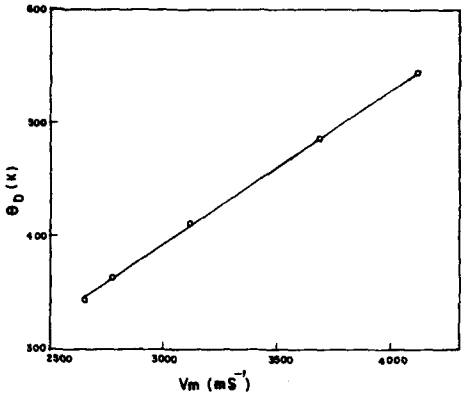

FIG. 4. Plot of the Debye temperature (Θ_D) against the average sound velocity (V_m) for the Li–Cd mixed ferrites.

ACKNOWLEDGMENTS

The author is grateful to Professor K. Rama Reddy, Head of the Department of Physics, Osmania University, Hyderabad, for his interest in this work. The author also thanks Professor T. Sheshagiri Rao, Professor K. Shankariah, Principal, and Professor U. V. Subba Rao, Head of the Department of Physics Post-Graduate College of Science (OU), Saifabad, Hyderabad for their cooperation.

[1] Alex Goldman, J. Am. Ceram. Soc. **63**, 582 (1984).
[2] D. Ravinder and T. Sheshagiri Rao, Crst. Res. Technol. **25**, 963 (1990).
[3] Y. V. Ramana, Int. J. Rock Miner. Sci. **6**, 191 (1969).
[4] Y. V. Ramana and P. V. Reddy, Acoust. Lett. **13**, 83 (1989).
[5] A. Globus, H. Pascard, and V. Cagan, J. Phys. (Paris) Colloq. **38**, C1-163 (1977).
[6] L. Vegard, Z. Phys. **5**, 17 (1921).
[7] E. J. W. Verwey and E. L. Heilmann, J. Chem. Phys. **15**, 174 (1947).
[8] P. V. Reddy and T. S. Rao, J. Less-Common Met. **75**, 225 (1980).
[9] Pran Kishan, D. R. Sagar, and Prem Swarup, J. Less-Common Met. **108**, 345 (1985).
[10] R. G. West and A. C. Blankenship, J. Am. Ceram. Soc. **50**, 343 (1967).
[11] J. K. McKenzie, Proc. Phys. Soc. London B **63**, 2 (1950).
[12] W. A. Wooster, Rep. Prog. Phys. **16**, 62 (1953).
[13] P. V. Reddy, M. B. Reddy, V. N. Mulay, K. B. Reddy, and Y. V. Ramana, J. Mater. Sci. Lett. **7**, 1243 (1988).
[14] D. Ravinder and P. K. Raju, Phys. Status Solidi A **136**, 351 (1993).
[15] O. L. Anderson, in *Physical Acoustics*, edited by W. P. Mason (Academic, New York, 1965), Vol. III, p. 43.
[16] K. L. Narayana and K. M. Swamy, Acoustica **39**, 336 (1978).

Deposition and properties of $NiFe_2O_4$ thin films (abstract)

R. B. van Dover, E. M. Gyorgy, J. M. Phillips, J. H. Marshall, R. J. Felder, R. M. Fleming, and H. O'Bryan, Jr.
AT&T Bell Labs, Murray Hill, New Jersey 07974

We have investigated the properties of $NiFe_2O_4$ thin films prepared by laser ablation of a stoichiometric $NiFe_2O_4$ target. Textured polycrystalline films were obtained on a-SiO_2 as well as on various substrates with Au, Ag, Pt, and MgF_2 buffer layers. Epitaxially oriented films were obtained on MgO, $(1\bar{1}02)$-oriented Al_2O_3, $(11\bar{2}0)$-oriented Al_2O_3, Y-stabilized ZrO_2 (YSZ), and $SrTiO_3$, although the crystalline quality of the films varied. Contamination by diffusion from the substrate and strains induced by both lattice constant mismatch and differential thermal expansion degraded the magnetic properties of the films, and in some cases decreased the electrical resistivity as well. By choosing the right substrate (YSZ), temperature (600 °C), and P_{O_2} (0.01 mT), we are able to prepare epitaxial films with bulk saturation magnetization ($M_s = 270$ G) and fairly low anisotropy ($K \sim 10^5$ erg/cm^3) as inferred by torque magnetometry. These films and bilayers are expected to be useful in a variety of fundamental investigations as well as having the potential for technological applications.

Studies of stoichiometric variations of epitaxially grown $Fe_{3-\delta}O_4$ (abstract)

E. Lochner, K. A. Shaw, R. C. DiBari, D. Hilton, D. M. Lind, and S. D. Berry
Department of Physics and Center for Materials Research and Technology (MARTECH), The Florida State University, Tallahassee, Florida 32306-3016

Using plasma-assisted molecular beam epitaxy, films of iron oxide cubic spinel phases have been prepared on single crystal MgO (100). Preparation was by deposition of Fe from an elemental e^- gun in a reactive oxygen plasma (primarily O^+) from an ECR source. Sample stoichiometry during synthesis was controlled by variation of growth parameters, including substrate temperature, oxygen flux, plasma power, and deposition rate. We present the results of structural and magnetic studies of these materials using electron and x-ray diffraction, as well as SQUID magnetometry. Lattice spacing, saturation magnetization, and magnetic anisotropy all provide strong evidence that the variation of growth parameters does indeed produce a range of "cubic" defect spinel structures ranging from Fe_3O_4 to one approximating γ-Fe_2O_3. Both structural and magnetic probes indicate that strong ordering changes occur in these systems as they are cooled through the ~119 K Verwey transition. The behavior of the Verwey transition as a function of growth parameters indicates that Fe vacancies in these defect spinels have a profound effect on the structural distortion related to the Verwey transition. Epitaxial strain due to lattice mismatch further contributes to structural distortion, and thus to the Verwey transition. The relative contributions of these stoichiometric variations and epitaxial strain on the Verwey transition will be discussed.

Aspects of the research were supported by NSF grant No. DMR-9206870 and ONR grant No. N000014-92-J-1356.

 0021-8979/94/75(10)/6124/1/$6.00 © 1994 American Institute of Physics

Cation distribution of Li-Ti mixed ferrites (abstract)

M. Bhagavantha Reddy and P. Venugopal Reddy
Department of Physics, Post-Graduate Centre, A. V. College of Arts, Science & Commerce, Gagan Mahal, Hyderabad, Andhra Pradesh, India

Lithium-titanium mixed ferrites of different compositions have been prepared by the well known ceramic technique. Thermo power studies of these samples, after usual characterization by x-ray diffraction (XRD), bulk density, porosity, etc. have been measured by the differential method. Room temperature values of the Seebeck coefficient are found to vary from 2.3 to 114 μV/K. It is an established fact that the thermo power measurement would also be used to study the cation distributions on octahedral and tetrahedral sublattices of ferro spinel. This technique was successfully used in the study of cation distribution of Fe_3O_4, Fe_3O_4-$TiFe_2O_4$, etc. As such the cation distribution of Li-Ti mixed ferrites of P.I. has been arrived at using thermo-power data by assuming that small polorans rather than electrons/holes are responsible for the process of conduction. A knowledge of cation distribution among octahedral sites of a spinel ferrite is essential to understand the mechanism responsible for electrical properties like electrical conductivity, thermo power, dielectric properties, etc. Saturation magnetization of all the samples has also been obtained by the well known oscillation method. From the cation distribution it has been observed that the concentration of Ti^{4+} on octahedral sites is found to increase while those of Fe^{3+} and Fe^{2+} are found to decrease rapidly.

 0021-8979/94/75(10)/6125/1/$6.00 © 1994 American Institute of Physics

Magnetic and microstructural properties of CoCrPt/CoCrPtSi dual-layered magnetic recording media

N. Inaba, Y. Matsuda, M. Suzuki, A. Nakamura, and M. Futamoto
Central Research Laboratory, Hitachi Ltd., Higashi-Koigakubo 1-280, Kokubunji-shi, Tokyo 180, Japan

The magnetic properties of CoCrPt/CoCrPtSi dual-magnetic-layered thin films are investigated in terms of the crystalline microstructures using a vibrating-sample magnometer, transmission electron microscope, and scanning electron microscope. The magnetic crystal grains of the films are aligned with forming chainlike clusters. Each stacked magnetic crystal grain is epitaxially grown on individually isolated columnar Cr crystals with a relationship of hcp $(10\bar{1}1)_{\text{Co-based alloy}}$ //bcc $(110)_{\text{Cr}}$. The direction of magnetic easy axes of two stacked magnetic crystals are aligned in a same direction. Single-crystalline dual-magnetic-layered thin films, which are epitaxially grown on MgO(110) single-crystal substrates, are prepared to estimate the K_u of the dual-layered magnetic grains. The K_u is determined to be 4×10^6 erg/cm^3, whose value is about 2 times as large as that of single-layered CoCrPtSi. This large anisotropy energy is presumed to lead the increase of H_c in the dual-layered magnetic films.

Recently, CoCrPt-based alloy media have been actively investigated in attempts to increase the areal density of longitudinal magnetic recording because of their high coercivities.[1–5] As the size of bit cell recorded on a medium decreases, the influence of magnetic irregularities increases.[6] These irregularities are caused by the distributions of grain size, grain morphology, crystalline orientation, microstructural composition inside a grain, and the exchange interaction between magnetic grains in a medium. Therefore, it is important to study the relationship between the microstructural features and magnetic properties in a crystal grain level. Wong *et al.* investigated the fine structures inside the magnetic grains of CoCrTa and CoNiCr media using a high-resolution transmission electron microscope (HRTEM).[7,8]

One of key components in an ultrahigh density recording is a high coercivity medium with a very thin magnetic layer. In our previous paper,[5] the CoCrPt/CoCrPtSi dual-magnetic-layered thin films possessed large coercivities at the maximum value of 2.7 kOe, which was about 1.5 times as large as that of the CoCrPt or CoCrPtSi single-layered specimens. In this work, the origin of the increase of H_c in the dual-layered films is investigated.

The structure of the dual-magnetic-layered thin films was $C/Co_{74.2}Cr_{4.7}Pt_{21.1}/Co_{74.2}Cr_{14.5}Pt_{8.4}Si_{2.9}/Cr$. The thickness of the Cr underlayer was 150 nm. The total magnetic layer thickness was 30 nm and the thickness ratio between the two magnetic layers was changed. The specimens were deposited on glass substrates using a dc magnetron sputtering system. The details of sputtering deposition are described in Ref. 5.

The magnetic properties of the samples were measured by using a vibrating-sample magnetometer (VSM). The microstructures of the films were investigated by x-ray diffraction, HRTEM and high-resolution scanning electron microscopy (HRSEM).

The CoCrPt/CoCrPtSi dual-magnetic layered specimens were deposited under the condition[5] to enhance the morphological separation between magnetic grains. Figure 1(a) shows the plan-view TEM image and the selected area electron diffraction pattern of the CoCrPt (15 nm)/CoCrPtSi(15) dual-magnetic layer. The crystal grain size of the specimen is determined to be 28 ± 8.7 nm. The magnetic crystal grains are grown to form chainlike clusters. The average separation distance between the clusters is 4.5 ± 0.4 nm. The surface morphology of the Cr underlayer deposited under the high Ar gas pressure of 28 mTorr was observed using HRSEM [Fig. 1(b)]. Some of the Cr crystal grains come in contact with each other and form chainlike clusters. The result indicates that the chainlike structure of the magnetic grains are due to the anisotropic alignment of Cr crystals, which was caused by an anisotropic crystal growth parallel to the film plane of each Cr grain. The crystal directions, of magnetic grains are randomly oriented in the plane judging from the ring-shaped diffraction pattern shown in Fig. 1. However, as the magnetic coupling between the grains is stronger along the chain, each cluster consisting of several magnetic grains tends to behave as a one unit when magnetized.[6]

In the specimens, a single magnetic grain was observed to be grown on each Cr columnar crystal, and no subgrain structure was observed.[5] It seems that only one nucleation site of magnetic grain exists on each Cr crystal grain. A cross-sectional HRTEM image of the CoCrPt(25 nm)/CoCrPtSi(5)/Cr(150) specimen is shown in Fig. 2. The crystalline orientation relationships were determined by taking into account the symmetry and the interplaner distance ratios of lattice image lines as shown in this figure. The CoCrPtSi and the CoCrPt grains are epitaxially grown on individually isolated columnar of Cr crystal with a relationship of

$$\text{hcp}(1011)_{\text{CoCrPt}}//\text{hcp}(1011)_{\text{CoCrPtSi}}//\text{bcc}(110)_{\text{Cr}}. \quad (1)$$

The lattice image lines are bent at the interface between the Cr and the CoCrPtSi layers and at the interface of the CoCrPtSi and the CoCrPt layers [Fig. 2(b)]. The dislocations are observed at the boundary between the Cr and CoCrPtSi as shown for example in Fig. 2(b) by a black arrow. These dislocations were probably introduced to accommodate the lattice misfit between both layers or the surface roughness of Cr columnar crystal. On the other hand, no clear dislocation is observed at the interface between the two magnetic layers.

 0021-8979/94/75(10)/6128/3/$6.00 © 1994 American Institute of Physics

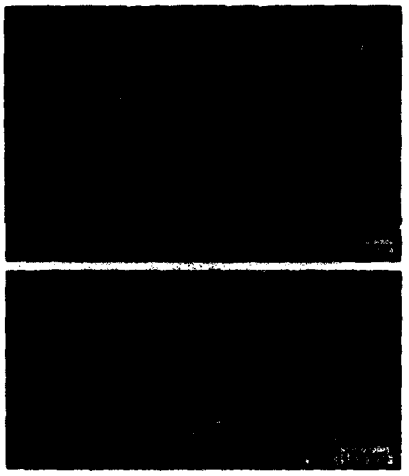

FIG. 1. (a) Plan-view TEM image and selected area electron diffraction pattern of CoCrPt (15 nm)/CoCrPtSi(15) dual-magnetic layer, (b) HRSEM image of surface morphology of Cr underlayer deposited under a high Ar gas pressure of 28 mTorr.

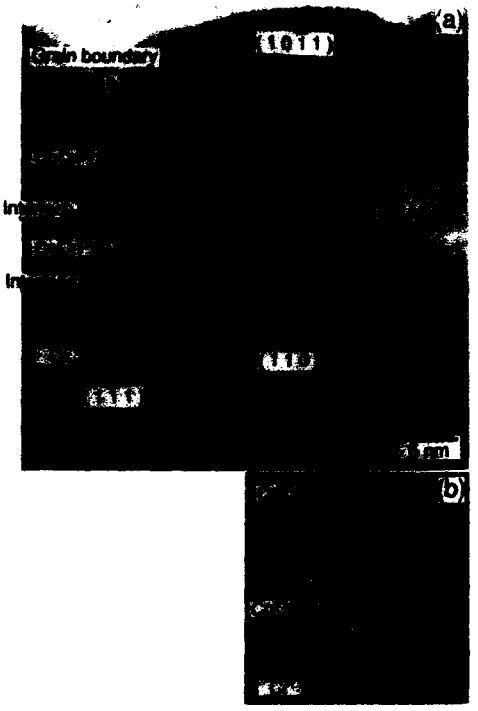

FIG. 2. Cross-sectional HRTEM image of CoCrPt(25 nm)/CoCrPtSi(5)/Cr(150) specimen.

This is probably due to the small difference in the lattice constants between the magnetic layers of less than 2%. The c axis, which is the magnetization easy axis, of hcp magnetic crystal is lying in the same direction for the epitaxially grown two magnetic crystals. The c axis of magnetic crystal grain shown in Fig. 2(a) is aligned at an angle of 28° with respect to the interface between the CoCrPtSi and the Cr layers.

The compositional microstructure of a dual-layered film was investigated using a high-spatial-resolution TEM (300 kV) equipped with an energy dispersion x-ray analyzer (EDX). The probe diameter was 2 nm in this present analysis. The local compositions were measured along a crystalline column as shown in the schematic picture inserted in Fig. 3. The variations of Co, Cr, and Pt concentrations in the CoCrPt(25 nm)/CoCrPtSi(5) specimen are shown in this figure as a function of distance from the interface between the Cr underlayer and the CoCrPtSi layer. The dotted lines in Fig. 3 give the average concentrations of Co, Cr, and Pt elements estimated from bulk sample compositions. In the Cr underlayer, only the Cr element was detected. The Co and Cr concentrations show sharp changes at the interface between the Cr underlayer and the CoCrPtSi layer as well as at the interface between the two magnetic layers. On the other hand, the variation of the Pt concentration is much broader than those of the Co and Cr in the vicinity of the stacked magnetic layers. This result indicates that some Pt atoms have diffused from the CoCrPt layer into the CoCrPtSi layer through the interface. A small peak of Si was also observed around the CoCrPtSi layer in EDX spectrum. This Si peak was overlapped with a subpeak of Pt. The Si intensity was estimated using a peak separation technique through computer processing. The Si intensity seemed to be increased near the interface between the stacked magnetic layers. These results suggest that a very thin layer whose composition is different from either of the CoCrPt and the CoCrPtSi layers may have formed near the interface between the stacked magnetic layers.

The coercivity values, H_c, of CoCrPt/CoCrPtSi dual-magnetic-layered media deposited on glass substrates showed nonlinear variation when the thickness ratio between the stacked magnetic layers was changed while keeping the total magnetic layer thickness to be constant.[5] It is not easy to clarify the origin of the nonlinear behavior of H_c in the dual-magnetic-layered films, because these specimens have polycrystalline structures, which mean random distributions in the direction of magnetization easy axis. Therefore, we prepared single-crystalline specimens of the dual-magnetic layers employing the epitaxial growth technique.[9] The Co/Cr bilayer thin film has been epitaxially grown on the MgO (110) single-crystal substrate with the crystallographic relationship of

$$(1\bar{1}00)[0001]_{Co}//(211)[011]_{Cr}//(110)[001]_{MgO}. \quad (2)$$

Here, the c axis of Co layer lies along only one direction parallel to the film plane throughout the Co layer. We deposited the CoCrPt/CoCrPtSi dual-magnetic-layered films on MgO (110) substrates. In the x-ray diffraction investigation of a CoCrPt(15 nm)/CoCrPtSi(15)/Cr(50) film, only bcc (211) peak from the Cr underlayer and peaks corresponding only to the hcp (10$\bar{1}$0) in the CoCrPt and CoCrPtSi layers were observed. The specimen was confirmed to be epitaxi-

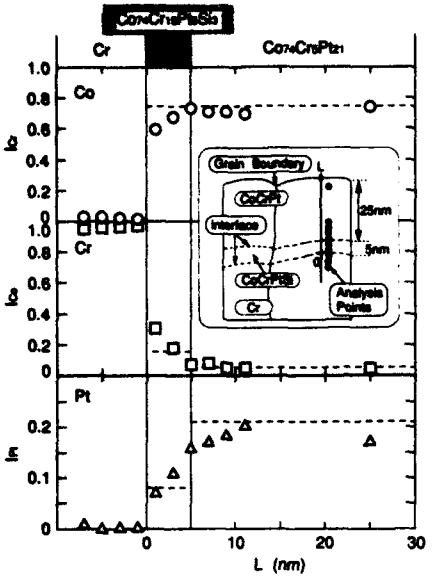

FIG. 3. Variations of Co, Cr, Pt concentrations in CoCrPt (25 nm)/CoCrPtSi(5) specimen as a function of analysis position.

ally grown on the MgO substrate with the same crystallographic relationship of Eq. (2). The magnetic properties of the specimen were measured using VSM. The [0001] and [11$\bar{2}$0] axes in the magnetic layer were determined to be the magnetization easy axis and the hard axis, respectively. The value of the magnetocrystalline anisotropy, K_u, of the dual-magnetic-layered specimen was estimated from the M-H curves to be 4×10^6 erg/cm^3. This value is equivalent to that of Co. Using the epitaxial growth technique, we also prepared a single-crystalline CoCrPtSi film of 30 nm thick. The K_u of the CoCrPtSi film was determined to be 2×10^6 erg/cm^3. The value of K_u in the dual-magnetic-layered film is twice as large as that of the CoCrPtSi. This increase of K_u in the stacked magnetic layers seems to be related somehow with the nonlinear variation of H_c of the dual-magnetic-layered medium. The origin of the increase of K_u in the dual-layered specimens has not yet been clarified. It is necessary to further extend the study to clarify the mechanism.

Since the specimens, as mentioned above, possess the morphologically isolated crystal grains with the average diameter of 28 nm, each magnetic grain is considered to be a single domain particle. Using the experimentally determined K_u values and the Stoner and Wohlfarth model,[10] the H_c values of the magnetic grains in the dual-magnetic-layered specimen and in the CoCrPtSi film are estimated to be 4.4 and 2.5 kOe, respectively. And also the dual-magnetic-layered specimens are expected to have large H_c values even with very thin magnetic layer thicknesses, since the large K_u reduces the influence of thermal fluctuation of the magnetic moments. The real coercivity value of a medium with polycrystalline structure will decrease due to the random distribution of easy magnetization axis. The coercivity value of

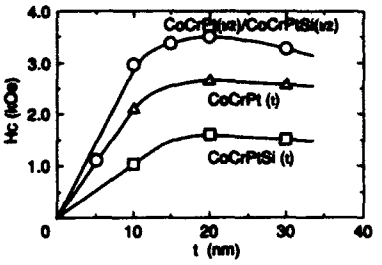

FIG. 4. Magnetic layer thickness dependences of H_c for the CoCrPtSi, CoCrPt, and CoCrPt/CoCrPtSi specimens.

the dual-magnetic-layered medium is considered to be higher than that of single-layer CoCrPtSi medium. It is interesting to investigate how the coercivity value for both the dual-layered and single-layered media changes when the total magnetic layer thickness is varied.

Figure 4 shows the magnetic layer thickness dependence of H_c measured for three types of medium structures, CoCrPt/CoCrPtSi, CoCrPtSi and CoCrPt. When the magnetic layer thickness is 20 nm, the coercivities of the CoCrPt, and CoCrPtSi and the dual-magnetic-layered media show the maximum values of 2.6, 1.6, and 3.5 kOe, respectively. This maximum value of the dual-magnetic-layered medium is smaller than the 4.4 kOe which is estimated from K_u value of 4×10^6 erg/cm^3. This is mainly due to the polycrystalline structure in the specimen. The decrease in H_c with decreasing the magnetic layer thickness below 20 nm is probably reflecting the influence of thermal fluctuation in the magnetic moments. However, the dual-magnetic-layered specimen possesses a large H_c of around 3.0 kOe at a very thin thickness of 10 nm, which is 1.5 or 3 times as large as those of single-layer specimens. The dual-magnetic-layered medium is very promising for high areal density longitudinal magnetic recording.

The authors would like to thank emeritus Professor S. Chikazumi of Tokyo University, Dr. Y. Sugita and Dr. R. Suzuki of Hitachi Central Research Laboratory for their encouragement and helpful discussions. They also thank Dr. H. Kakibayashi and Dr. H. Murakoshi of Hitachi Central Research Laboratory and Dr. M. Shimotu of Hitachi Techno-Research Center for their observation of TEM.

[1] C. Tsang, M.-M. Chen, T. Yogi, and K. Ju, IEEE Trans. Magn. 26, 1689 (1990).
[2] T. Yogi, C. Tsang, T. A. Nguyen, K. Ju, G. L. Gorman, and G. Castillo, IEEE Trans. Magn. 26, 2271 (1990).
[3] T. D. Howell, D. P. MaCown, T. A. Diola, Y. Tang, K. R. Hense, and R. L. Ge, IEEE Trans. Magn. 26, 2298 (1990).
[4] M. Futamoto, F. Kugiya, M. Suzuki, H. Takano, Y. Matsuda, N. Inaba, Y. Miyamura, K. Akagi, T. Nakao, and H. Sawaguchi, IEEE Trans. Magn. 27, 5280 (1991).
[5] Y. Matsuda, N. Inaba, M. Suzuki, H. Takano, and M. Futamoto, J. Mag. Soc. Jpn. 15, Suppl. S2, 1001 (1991).
[6] Y. Honda, N. Inaba, M. Suzuki, A. Kikugawa, and M. Futamoto, IEEE Trans. Magn. 29, 3721 (1993).
[7] B. Y. Wong and E. E. Laughlin, J. Appl. Phys. 61, 2533 (1992).
[8] B. Y. Wong, Y. Shen, and D. E. Laughlin, J. Appl. Phys. 73, 418 (1993).
[9] A. Nakamura and M. Futamoto, in Proceedings of IUMRS-ICAM-'93, Jpn. J. Appl. Phys. 32, L1410 (1993).
[10] E. C. Stoner and E. P. Wohlfarth, Philos. Trans. R. Soc. London, Ser. A 240, 599 (1948).

Bicrystal advanced thin-film media for high density recording

Tai Min and Jian-Gang Zhu
Center for Micromagnetics and Information Technology, Department of Electrical Engineering, University of Minnesota, Minneapolis, Minnesota 55455

A new type of thin-film recording media with advanced microstructure: the bicrystal film, has been studied experimentally. The easy axes of the bicrystal films are oriented along two specified orthogonal directions in the film plane. In this study, an LiF single crystal substrate with (100) orientation is utilized to obtain the Cr monocrystal underlayer with (100) orientation, and on top of the (100)Cr underlayer the CoCrTa with $(11\bar{2}0)$ texture was grown epitaxially. X-ray and transmission electron microscopy (TEM) diffraction studies confirm the fabricated thin-film media has the bicrystal microstructure. The magnetic properties of the bicrystal films have demonstrated very high coercivity ($H_C \sim 3000$ Oe) and coercive and remanent squareness ($S^* \sim 0.9$, $S \sim 0.9$), all desired for high areal density magnetic recording. The in-plane hysteresis loops of the fabricated films show fourfold symmetry which is the characteristic of the bicrystal microstructure. The effects of Cr underlayer thickness on the magnetic properties of the bicrystal film has also been studied.

INTRODUCTION

To achieve 10-Gbit/in.^{2} recording areal density, the bit length and the track width are both expected to decrease dramatically. This requires the future thin-film media to have high coercivity (H_C), coercive and remanent squareness (S^* and S), and low media noise, as well as excellent narrow track recording performance at the same time. The current thin-film media has difficulty to meet these high standard requirements, e.g., in the IBM 1 Gbit/in.^{2} demonstration,[1] S^* has to be sacrificed ($\sim$0.75) in order to lower the media noise. The micromagnetic computer modeling study[2] has shown that if the thin-film media has the bicrystal microstructure, the media with high H_C,S^*,S, low media noise along with excellent side-written behavior can be achieved at once. The easy axes of the crystallites of the bicrystal film are oriented along two specified orthogonal directions inside the film plane. This kind of special easy axis orientation can be obtained by epitaxially growing $(11\bar{2}0)$ CoCrTa on the (100) Cr monocrystal which enables the easy axes the CoCrTa crystallites to locate in the film plane and orient along the [011] or $[01\bar{1}]$ direction of (100) Cr. The modeling study has suggested that the in-plane magnetic property of the thin film with the bicrystal microstructure should have additional anisotropy, i.e., the hysteresis loop along 45° to one of the c-axis direction (effective easy axis) is a very square one while the loop along one of the c-axis direction has lower H_C, S^*, and S.[2] In addition, the H_C and S^* of the bicrystal film along the effective easy axis are higher than the planar isotropic film, while the noise power at high density is lower than both planar isotropic and well-oriented films.

To obtain the bicrystal thin-film media experimentally, successful fabrication of the (100) Cr monocrystal is the key for the epitaxy growth of the $(11\bar{2}0)$ Co alloy. The NaCl single crystal with (100) orientation has been attempted.[3] Even though the microstructure of the film deposited on the (100) NaCl substrate has been shown to have the bicrystal microstructure, the magnetic properties of the film are very poor (H_C is lower than the planar isotropic film). To fully realize the advantages of the bicrystal microstructure, a new type of substrate: LiF single crystal with (100) orientation, has been tried in this study to improve the epitaxial growth of the (100) Cr monolayer which will in turn enhance the magnetic properties of the fabricated bicrystal film.

SAMPLE PREPARATION

In this study, the Cr underlayer and $CoCr_{14}Ta_2$ magnetic films were dc and rf magnetron sputtered in a Temescal sputtering system which has a base pressure $\sim 2 \times 10^{-8}$ Torr. The argon sputtering gas pressure for both Cr and CoCrTa was 8 mTorr. The sputtering rates for Cr and CoCrTa were 400 and 560 Å/min, respectively. During the deposition of CoCrTa film the substrate was biased at -60 V. The substrate was heated by a four set of quartz lamp to 320 °C before deposition of the Cr underlayer. The crystallographic structures of the films were studied by x-ray and TEM diffractions. The thickness of the CoCrTa magnetic films is fixed at 225 Å while the Cr underlayer thickness has been varied. The LiF single crystal with (100) orientation was used as a substrate and was air cleaved before deposition. Along with the LiF substrate, a Corning No. 2 glass substrate was also used to fabricate the planar isotropic film which can be used as a comparison.

RESULTS AND DISCUSSIONS

The LiF single crystal has fcc structure with a 4.01-Å lattice constant. The atomic distances between Li^+–Li^+ and F^-–F^- are 2.84 Å, very close to the lattice constant 2.88 Å of bcc Cr. Strong epitaxy growth of (100) Cr on (100) LiF can be expected with the following orientation relationship: (100)[001]Cr//(100)[011]LiF. If the Cr film grows epitaxially on the (100) LiF substrate, it should have a strong (100) texture with the [001] direction pointed to the same direction. The obtained Cr underlayer should possess a fourfold in-plane orientation symmetry. On top of the (100) Cr monolayer, the epitaxial growth of the CoCrTa film will have the orientation relationship: $(11\bar{2}0)$[0001]CoCrTa//(100)[011]Cr. The c axis of the $(11\bar{2}0)$ CoCrTa grain orients in-plane and along either the [011] or $[01\bar{1}]$ direction of the (100) Cr, resulting in the bicrystal microstructure. The bicrystal microstructure should possess a fourfold in-plane symmetry which will characterize in-plane magnetic properties of the film.

 0021-8979/94/75(10)/6129/3/$6.00 © 1994 American Institute of Physics

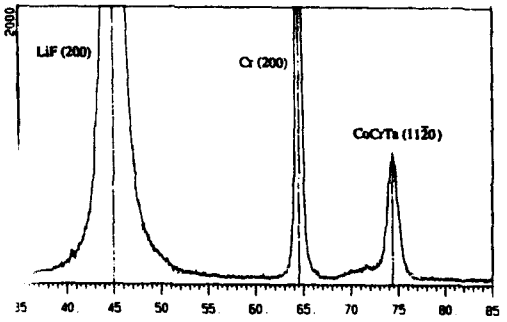

FIG. 1. X-ray diffraction spectrum of a typical CoCrTa bicrystal thin film deposited on the LiF substrate.

The x-ray diffraction spectrum of the CoCrTa/Cr film deposited in the LiF substrate is shown in Fig. 1. The CoCrTa and Cr thicknesses are 225 and 450 Å, respectively. Figure 1 shows that the Cr underlayer has strong (200) orientation and the CoCrTa has (11$\bar{2}$0) texture, different from the planar isotropic film deposited on a glass substrate in which the Cr has (110) and the CoCrTa (10$\bar{1}$0) and (10$\bar{1}$1) texture. This result indicates that by utilizing the (100) LiF single crystal substrate, the texture of the Cr underlayer can be changed from (110) to (100). As a consequence, the texture of CoCrTa can be changed from (10$\bar{1}$0) and (10$\bar{1}$1) to (11$\bar{2}$0). The in-plane crystallographic orientation of CoCrTa/Cr film deposited on LiF can be verified by the TEM diffraction pattern, as shown in Fig. 2(a), which clearly demonstrates that the microstructure of the film has a high degree in-plane orientation with fourfold symmetry. The TEM diffraction pattern can be considered as a superimposition of one (100)[001] Cr orientation and two (11$\bar{2}$0)[0001] CoCrTa orientations with the two [0001] directions perpendicular to each other, as illustrated in Fig. 2(b). The equal intensity of the diffraction spots shown in Fig. 2(a) suggests that the c axis of the CoCrTa grains has a 50% chance oriented along either [011] or [01$\bar{1}$] of the (100) Cr monolayer. The TEM diffraction pattern confirms that the CoCrTa/Cr deposited on LiF indeed has the bicrystal microstructure.

The in-plane hysteresis loops of the bicrystal film with 225-Å-thick CoCrTa on 900-Å-thick Cr underlayer are shown in Fig. 3, where θ is the angle with respect to one of the c axis. Figure 3 shows that the hysteresis loop along the θ=45° direction, denoted as an effective easy axis, exhibits very high coercivity H_C=3153 Oe, high S^*=0.93, and S=0.88. For the CoCrTa type of thin-film media, the coercivity higher than 2000 Oe has not yet been reported and the S^* is usually very low for the film deposited at the high substrate temperature on the NiP substrate.[4] This result indicates that for the film with the bicrystal substrate, significant enhancement of H_C along with high S^* and S can be obtained. The in-plane crystalline anisotropy resulting from the bicrystal microstructure can be verified by the in-plane hysteresis loops measured along different directions. Figure 4 shows the coercivity as a function of angle θ for the bicrystal

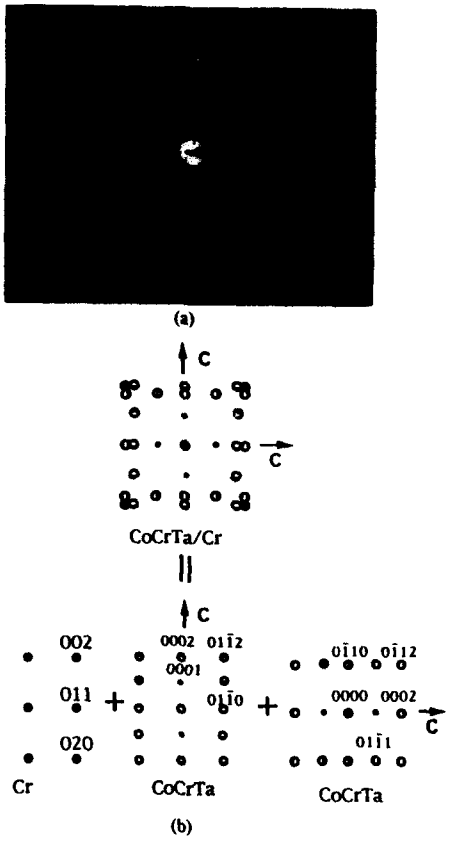

FIG. 2. (a) TEM diffraction pattern of a typical CoCrTa bicrystal thin film; (b) schematic drawing of the superimposed components of the TEM pattern.

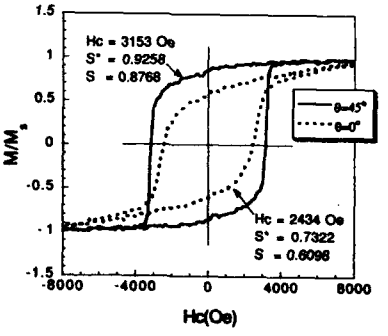

FIG. 3. Hysteresis loops along the effective easy (θ=45°) and hard (θ=0°) axes of a typical CoCrTa bicrystal film.

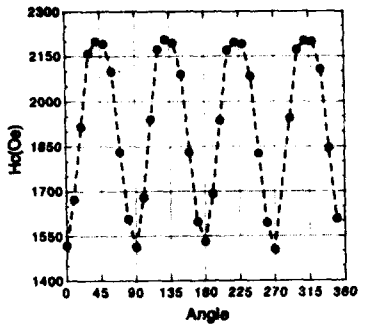

FIG. 4. In-plane H_C as a function of angle with respect to one of the c axes.

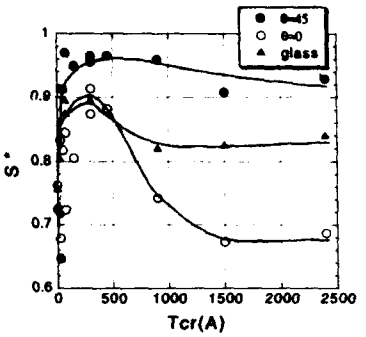

FIG. 6. The measured S^* vs Cr underlayer thickness for the bicrystal films (circles) and planar isotropic films (triangles).

film with 225-Å-thick CoCrTa and 300-Å-thick Cr underlayers which show excellent in-plane fourfold symmetry, every 90° the H_C value repeats itself. The S^* and S also show in-plane fourfold symmetry even though they are not shown in this paper.[5]

The effects of Cr underlayer thickness on the magnetic properties of bicrystal film were also studied. The CoCrTa thickness is fixed at 225 Å and the Cr underlayer thickness is varied from 0 to 2400 Å. The coercivities of the bicrystal films on various Cr underlayer thickness are shown in Fig. 5. Also included in the figure are the coercivities of the planar isotropic films deposited on a glass substrate, represented by triangles. The H_C of the isotropic films increases rapidly as the Cr underlayer increasing from 0 to 300 Å and then stays virtually constant at around 1600 Oe. For the film deposited on a LiF substrate, at zero or very thin (25 Å) Cr thickness, the H_C is low and the difference between the loops along the effective easy and hard axes is negligible. As the Cr underlayer becomes thicker than 50 Å, the difference between the hysteresis loops along effective easy and hard axes starts to appear. As shown by Fig. 5, the H_C along the effective easy

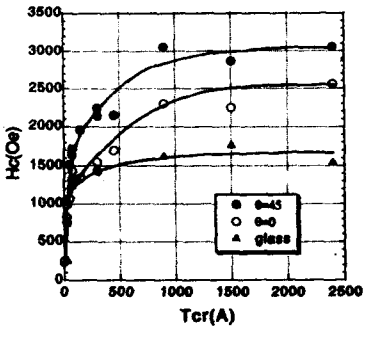

FIG. 5. The measured H_C vs Cr underlayer thickness for the bicrystal films (circles) and planar isotropic films (triangles).

axis (filled circles) increases dramatically from 1500 Oe at 50-Å-thick Cr to about 3000 Oe at 900-Å-thick Cr and remains at this high value for the thicker Cr underlayer. The H_C along the effective hard axis also increases from about 1000 to about 2500 Oe during the same range of increasing Cr thickness. Interestingly, at the thick Cr even the coercivity along the effective hard axis is much higher than the planar isotropic films. The coercive squareness (S^*) of the films deposited on the LiF and glass substrate are plotted in Fig. 6. The S^* of the bicrystal films along an effective easy axis rises rapidly from 0.65 at 0-Å-thick Cr to 0.95 at 150-Å-thick Cr and then decreases slightly to 0.92 as the Cr underlayer grows to 2400 Å. The S^* along the effective hard axis shows quite different behavior, it increases rapidly at an initial increase of Cr thickness (from 0 to 300 Å) and then decreases into a very low value for very thick Cr.

CONCLUSIONS

CoCrTa bicrystal films have been successfully fabricated on (100) LiF single crystal substrates. The in-plane hysteresis loops have demonstrated a fourfold symmetry which is the characteristic of the bicrystal microstructure. X-ray and TEM diffraction studies have been performed to confirm that the obtained films have bicrystal microstructure. It is found that the CoCrTa bicrystal films can have very high coercivity (~3000 Oe) along with high S^*(~0.9) and S(~0.9). The effects of Cr underlayer thickness on the magnetic properties of the bicrystal films have also been investigated. It shows that starting from the very thin Cr underlayer, the bicrystal film with high H_C, S^*, and S can be obtained.

[1] T. Yogi, C. Tsang, T. A. Nguyen, K. Ju, G. L. Gorman, and G. Castillo, IEEE Trans. Magn. MAG-26, 2271 (1990).
[2] J. G. Zhu, X. G. Ye, and T. Arnoldussen, IEEE Trans. Magn. MAG-29, 324 (1992).
[3] M. Mirzamaani, C. V. Jahanes, and M. A. Russak, J. Appl. Phys. 69, 5169 (1991).
[4] M. Lu, T. Min, Q. Chen, and J. Judy, IEEE Trans. Magn. MAG-28, 3224 (1992).
[5] T. Min, Ph.D. thesis (1993).

AFM structure and media noise of SmCo/Cr thin films and hard disks

E. M. T. Velu and D. N. Lambeth
Data Storage Systems Center, Electrical and Computer Engineering Department, Carnegie Mellon University, Pittsburgh, Pennsylvania 15213

J. T. Thornton and P. E. Russell
Precision Engineering Center, Department of Materials Science and Engineering, North Carolina State University, Raleigh, North Carolina 27695

Longitudinal media for ultrahigh density recording require a high coercivity and a low medium noise. While the coercivity is controlled mainly by the chemical composition of the alloy, the medium noise is influenced significantly by the microstructure of the underlayer. We used atomic force microscopy (AFM) to study the microstructure of Cr underlayers and SmCo magnetic films. The AFM study shows that the Cr grains have elongated "rice"-like granular features whereas the SmCo grains without an underlayer appear circular with nonuniform grain size. The Cr underlayer grows as well isolated columns with voids. When thin SmCo films (<20 nm) were deposited on the thin Cr (<35 nm) underlayers the SmCo grains were found to replicate the isolated, columnar structure of the underlayer. The intergranular exchange interaction and the recording media noise of SmCo/Cr thin films decreased with a decreasing thickness of the Cr underlayer. The medium noise of high coercivity SmCo/Cr hard disks prepared on thin Cr underlayers remained almost flat with no supralinear increase when tested up to 2760 fc/mm (70 kfci).

INTRODUCTION

Longitudinal thin-film metal media for ultrahigh recording densities require an extremely sharp and narrow transition width.[1,2] This requirement is achievable if the magnetic film is thin, has a high coercivity, and is composed of magnetically noninteracting grains.[3,4] Chromium thin films are commonly used as an underlayer for Co-alloy media since Cr can be grown with (110) or (200) textures which provide a close epitaxial match to the $\{10\bar{1}0\}$, $\{10\bar{1}1\}$, or $\{11\bar{2}0\}$ planes of the hcp Co-alloy films.[5] This epitaxy promotes in-plane orientation of the c axis of hexagonal Co-alloy films. Since the grain size, crystallographic texture, and morphology of the magnetic films are largely determined by the corresponding properties of the Cr underlayer, it is very important to understand the variation of the Cr grain size and morphology with its thickness and other sputtering process parameters. We reported earlier that $SmCo_4$ films grown on the Cr underlayer show a high coercivity[6] and a low medium noise at high recording densities.[7]

We report here the microstructure of Cr underlayers sputtered on glass substrates, and SmCo films grown on the Cr underlayers. The microstructure of pure Cr films with respect to the sputtering process parameters have been studied in the past by using conventional scanning electron microscopy (SEM) and transmission electron microscopy (TEM) techniques for thick (25 μm)[8] and thin (50 nm–4 μm)[9] films. AFM has the advantage of showing the surface morphological features of thin films better than SEM and TEM, since sub-angstrom lateral resolution is possible when the appropriate AFM scan probe tip is used.[10] Also, the dimensions of features in the z direction can be measured accurately which is not possible by the other two techniques. We also report the correlation of the recording noise characteristics to the AFM microstructure for media with various Cr underlayer thicknesses.

EXPERIMENTAL PROCEDURE

Chromium films were rf diode sputtered onto 7059 Corning glass substrates from pure (99.9%) Cr targets in a Leybold Heraeus Z-650 sputtering system. The films were prepared at 10-mTorr argon pressure with a sputtering rate of 35 nm per minute and with no substrate heating. The SmCo films were sputtered at 20-mTorr argon pressure at a sputtering rate of 14 nm per minute.[4] The use of these sputtering parameters in our earlier studies resulted in SmCo/Cr media with a high coercivity and a low medium noise.[6,7] The microstructure of Cr, SmCo, and SmCo/Cr films were studied with a Digital Nanoscope III scanning probe microscope in contact mode with 4-nN repulsive force using silicon nitride pyramidal tips and electron beam contamination tips. The intergranular magnetic exchange interaction in SmCo/Cr films were evaluated by obtaining delta-$M(H)$ plots from forward and reverse magnetization curves. The experimental procedures for the disk fabrication and for the recording characterization are the same as those described in our earlier publication.[7]

RESULTS AND DISCUSSION

In Fig. 1, the surface morphological features of Cr thin films as a function of their thickness are displayed in both two- and three-dimensional micrographs. In the two-dimensional view the Cr crystallites vividly appear to have a rice-like shape, while in the three-dimensional view the Cr grains appear as nodules with a rounded morphology. This is particularly true for films of smaller thicknesses (<105 nm). The grain size of Cr is seen to increase with its thickness, but the grain shape and the void structure isolating the Cr grains remain almost the same even for thick Cr films. X-ray diffraction results of these films revealed that they all had only (110) crystalline texure. In Fig. 2 the microstructure of $SmCo_4$ films of varying thickness prepared on glass substrates with no underlayer are shown. The shapes of SmCo

 0021-8979/94/75(10)/6132/3/$6.00 © 1994 American Institute of Physics

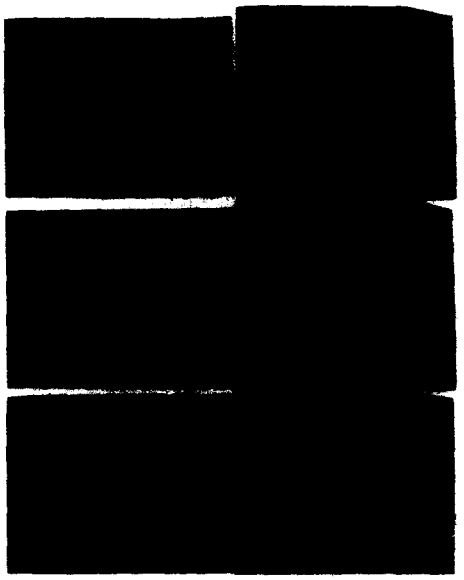

FIG. 1. Atomic force micrographs of Cr thin films on glass substrates.

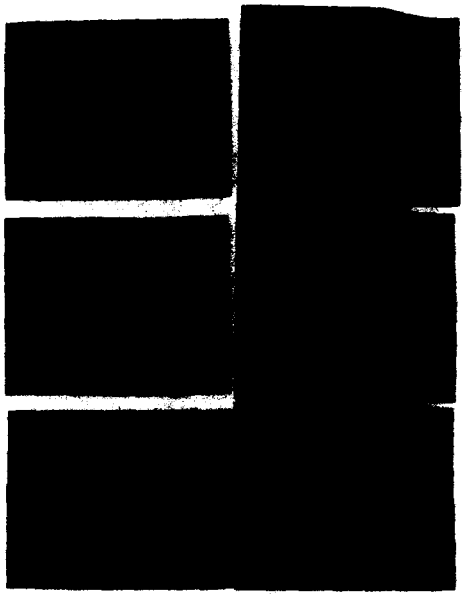

FIG. 2. Atomic force micrographs of SmCo thin films sputtered on glass substrates.

FIG. 3. Atomic force micrographs of SmCo thin films sputtered on a Cr underlayer on glass substrates.

grains are well rounded and appear distinctly different from that of pure Cr films. The SmCo grains are well isolated with voids when the film is thin (<28 nm) and a clustering of grains is seen for thicker (>42 nm) SmCo films. The two-dimensional view of SmCo films shows a more pronounced columnar growth structure even for films as thin as 14 nm. In Fig. 3 the structure of the 28-nm-thick SmCo films sputtered onto 35- and 105-nm-thick Cr underlayers are shown. The SmCo grains grown on the Cr underlayers appear nearly circular and are well isolated with voids. The grain size of the Cr underlayer increased from 15 to 75 nm as its thickness varied from 35 to 350 nm (Table I). It is interesting to note that when a 28-nm-thick SmCo film is grown on 35- and 105-nm -thick Cr underlayers, the grain size of SmCo was found to increase from 12 to 20 nm. The three-dimensional displays of SmCo/Cr films shown in Fig. 3 also reveal that the SmCo films grown on Cr underlayers are well isolated with voids. This columnar growth structure observed for Cr, SmCo, and SmCo/Cr thin films resemble the "zone 1 microstructure" reported for sputtered films[8] and evaporated films.[11] The predominantly unidirectional flow of mass in the zero bias sputtering process, coupled with substrate surface roughness, low adatom mobility (absence of surface and volume diffusion), and scattering of sputtered atoms by sputtering gas atoms, promotes the atomic shadowing effect and a growth of columnar microstructure. By controlling argon pressure, substrate temperature, deposition rate, and film thickness, one can control the columnar grain size and the width of the void space isolating the columnar grains. This is

TABLE I. Grain size and surface roughness of Cr films sputtered on glass as a function of film thickness.

Cr film thickness (nm)	Avg. Grain size (nm)	Roughness values (nm)		
		Peak to valley	rms	R_a
35	15	8.02	1.00	0.80
105	30	14.79	1.81	1.47
350	75	36.80	4.73	3.76
blank glass		2.78	0.29	0.23

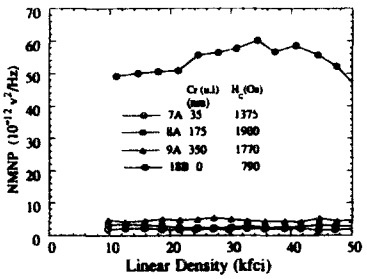

FIG. 4. Normalized medium noise power vs linear recording density for SmCo (18*B*) and SmCo/Cr (7*A*, 8*A*, and 9*A*) hard disks.

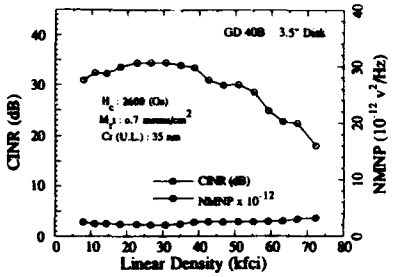

FIG. 5. Carrier to total integrated noise ratio and normalized medium noise power vs linear recording density for a high coercivity SmCo/Cr hard disk prepared on a 35-nm-thick Cr underlayer.

especially important in the designing of low noise recording media since the isolation of magnetic grains will minimize the intergranular exchange interaction effects in metallic thin films. The two and three dimensional AFM views of SmCo (Fig. 2) indicate well isolated columnar particles. However, the AFM probe tip scans only surface features and any contacts among the SmCo columns at the base will not be observed. On the contrary, SmCo films grown on well separated Cr columns result in isolated SmCo columns which replicate the Cr column size. Thus, the grains of the SmCo films grown on a Cr underlayer of separated columnar structure are effectively isolated by the nonmagnetic Cr at the base and by voids on the sides. Delta-$M(H)$ plots of SmCo films prepared with and without Cr underlayers were measured. The SmCo films prepared with no Cr underlayer show a large positive delta-M peak which is indicative of a strong interparticle exchange interaction. The decoupled films prepared on Cr films of 105 nm showed slightly negative (magnetostatic coupling) delta-M peaks, while positive delta-M peaks (exchange coupling) reappeared as the Cr films got thicker (175–350 nm) indicating that the Cr columns had grown together. Our experimental recording results are in good agreement with the delta-M and AFM microstructure observations. The normalized medium noise power versus recording density, Fig. 4, first shows a dramatic reduction in noise when a Cr underlayer is used and then increases with the Cr layer thickness. This corresponds to an increase in Cr grain size and a decrease of the void space with the increasing Cr layer thickness (see Fig. 1). Carrier signal to integrated noise ratio measurements[7] were made for the disk series of Fig. 4. There was a 22 dB improvement at 50 kfci with the use of a 350-nm-thick Cr underlayer and a further gain of 10 dB when a thinner Cr (35 nm) was used. The use of a thin Cr underlayer helps to keep the grain size of the magnetic layer small. This is essential in high density recording as it will help to reduce the sawtooth amplitude at the transition and hence is favored to obtain sharp transition boundaries. Also, the thin Cr underlayer has lower surface roughness (Table I) which facilitates the use of lower fly height in the design of high density disk drives. In Fig. 5 is shown the recording results for a high coercivity SmCo/Cr hard disk where a 14-nm-thick SmCo film was sputtered onto a 35-nm-thick Cr underlayer. The medium noise is nearly flat up to 2760 fc/mm (70 kfci) with a high carrier to integrated noise ratio of 20 dB.

CONCLUSIONS

The surface morphological features of SmCo films and Cr films sputtered on glass substrates are different. The Cr grains have an elongated rice-like shape whereas the SmCo films have a circular grain shape. Thin SmCo films when sputtered on thin Cr underlayers grow as well isolated columns with voids. This structure brings about a dramatic reduction in intergranular magnetic exchange interaction and hence in medium noise power for SmCo/Cr hard disks. The intergranular exchange interaction and medium noise power decreases with a decreasing thickness of the Cr underlayer. SmCo/Cr hard disks with superior signal-to-noise ratio are obtained when thin Cr underlayers are used.

ACKNOWLEDGMENTS

This work was supported in part by the National Science Foundation under Grant No. ECD-8907068 and the Department of Energy under Award No. DE-FG02-90ER45423. The government has certain rights in this material. Partial support for P. E. Russell and J. T. Thornton was provided by the Precision Engineering Center at North Carolina State University.

[1] E. S. Murdock, R. F. Simmons, and R. Davidson, IEEE Trans. Magn. MAG-28, 3079 (1992).
[2] J. G. Zhu and H. N. Bertram, IEEE Trans. Magn. MAG-27, 3553 (1991).
[3] M. L. Williams and R. L. Comstock, *AIP Conference Proceedings No. 5*, edited by C. D. Graham and J. J. Rhyne (AIP, New York, 1972), p. 738.
[4] T. Chen and T. Yamashita, IEEE Trans. Magn. MAG-24, 2700 (1988).
[5] D. E. Laughlin and B. Y. Wong, IEEE Trans. Magn. MAG-27, 4713 (1991).
[6] E. M. T. Velu and D. N. Lambeth, J. Appl. Phys. 69, 5175 (1991).
[7] E. M. T. Velu and D. N. Lambeth, IEEE Trans. Magn. MAG-28, 3249 (1992).
[8] J. A. Thornton, J. Vac. Sci. Technol. A 4, 3059 (1986).
[9] H. J. Lee, J. Appl. Phys. 57, 4037 (1985).
[10] E. Meyer, Prog. Surf. Sci. 41, 3 (1992).
[11] B. A. Movchan and A. V. Demchishin, Phys. Met. Metallogr. 28, 83 (1969).

Modeling of thin-film media with advanced microstructure for ultrahigh density recording

Xiao-Guang Ye and Jian-Gang Zhu
Department of Electrical Engineering, University of Minnesota, Minneapolis, Minnesota 55455

Magnetic thin films with subgrain structure, or nanocrytalline films are studied via micromagnetic modeling. The subgrain nanocrystallites form a bicrystal structure inside a normal grain, due to proper epitaxial growth. It is shown that a relatively small but nonzero exchange coupling through normal grain boundaries is critical for obtaining high coercive squareness. Maintaining low exchange coupling between subgrains in a normal grain is important for achieving low transition noise. The calculation shows that films with this microstructure can have $S^*\approx 0.95$ and a signal-to-noise ratio of 36 dB at 385 KFCI with 1-μm track width. Such film microstructure is practically achievable in principle and is suited for future high recording density applications.

I. INTRODUCTION

For high density magnetic recording, both high signal amplitude and low transition noise are critical. Thus films with more advanced microstructures are required. Previous micromagnetic modeling studies show that film with advanced microstructure, such as bicrystal film, can achieve both high squareness of hysteresis loop and low media noise at the same time, however, with difficulties to implement in the circular disk forms.[1] In this paper, a new kind of magnetic film with subgrain structure, or nanocrystalline film, is studied via micromagnetic modeling.

A recent high-resolution transmission electron microscopy (TEM) study has shown nanocrystalline subgrain structures in Co-alloy magnetic thin films grown on a (001) textured Cr underlayer.[2] The hcp Co-alloy nanocrystallites are epitaxially grown on the Cr underlayer with the $(11\bar{2}0)$ plane matching the (001) plane of Cr. The c axes of the Co-alloy subgrains within one Cr grain can be either in Cr $\langle 110\rangle$ or $\langle 1\bar{1}0\rangle$ directions, forming a bicrystal structure within each Cr grain. Clear physical separation between subgrain nanocrystallites has been observed for CoCrTa magnetic film, which could be caused by Cr segregation at subgrain boundaries inside a normal grain. A recent experimental study on Cr-rich CoCrPt magnetic film has also shown high squareness of hysteresis loops and very low media noise.[3] It is speculated that high Cr concentration causes phase segregation inside normal grains, thereby weakening the exchange interaction between subgrains and resulting in low recording noise.

In this paper, micromagnetic modeling is utilized to study the magnetic hysteresis and recording properties of films with nanoscale subgrain structure. The focus is on how to achieve high coercive squareness and low medium noise at the same time.

II. MODEL

A previously developed micromagnetic model is extended to study the modeled film.[4] A nanocrystalline magnetic film is represented by a 2D array of hexagons closely packed on a triangular lattice. Each hexagon represents a magnetic subgrain. A cluster of seven subgrains forms a single normal grain, as shown in Fig. 1. In the case of CoCrTa $(11\bar{2}0)$ epitaxially grown on the (001) plane of Cr, each normal grain corresponds to a cluster of subgrains grown on top of a Cr underlayer column. The normal grain size, which is determined by the column size of the Cr underlayer, is assumed to be 200 Å in the calculation. The medium thickness is also assumed to be 200 Å. The magnetic easy axis of the subgrains are oriented in two orthogonal directions in the film plane, forming a bicrystal structure within each normal grain. The principle orientation of normal grains is assumed to be random in the film plane, so the overall magnetic properties of the nanocrystalline films are planar isotropic. The calculation array contains 48×48 normal grains, i.e., 128×128 nanocrystallites. The exchange coupling between subgrains inside a normal grain, denoted by h_{e_in}, and the exchange coupling between subgrains on the boundary of normal grains, denoted by h_{e_out}, can be chosen independently in the model, as illustrated in Fig. 1. The magnetic parameters of the simulated films are chosen to represent a high anisotropy, low M_s medium. Assuming the saturation magnetization $M_s=375$ emu/cm^3 and the anisotropy constant $K=1.4\times10^6$ erg/cm^3, then the crystalline anisotropy field is $H_k=2K/M_s=7500$ Oe and therefore the magnetostatic interaction constant is $h_m=M_s/H_k=0.05$.

Since the Cr underlayer can yield a voided structure in the magnetic film, one may assume h_{e_out} to be relatively small. However, for some Cr-rich Co-alloy magnetic thin films, phase segregation may occur inside a normal magnetic grain, forming a Cr-rich area on the subgrain boundaries inside the grain. This can effectively weaken the exchange in-

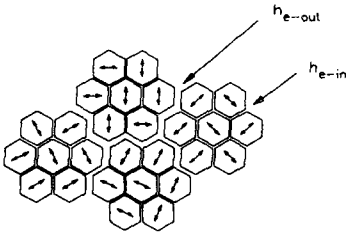

FIG. 1. Modeling of nanocrystalline films.

 0021-8979/94/75(10)/6135/3/$6.00 © 1994 American Institute of Physics

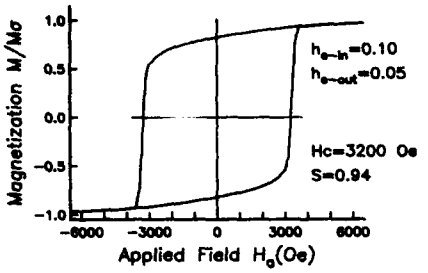

FIG. 2. Calculated hysteresis loop for nanocrystalline films with $h_{e_in} = 0.1, h_{e_out} = 0.05$.

teraction between the subgrains inside the normal grain. Thus the parameter h_{e_in} can vary over quite a wide range of values.

The hysteresis loops are calculated by decreasing the external field quasistatically from the saturation direction. Dibit magnetization transition pairs are simulated by utilizing the 2D Karlqvist head field to study the recording performance. Periodic boundary conditions are applied so that the track edge effect can be disregarded. The fast Fourier transformation method is used to calculate the long-range magnetostatic interaction. Most of the calculations are performed on a CM-200 Connection Machine.

III. HYSTERESIS PROPERTIES

The calculations show that high coercive squareness can be obtained for the nanocrystalline films when the two exchange coupling constants are appropriately selected. The hysteresis loop with $h_{e_in} = 0.1$ and $h_{e_out} = 0.05$ is shown in Fig. 2. Hysteresis coercivity is $H_c = 0.43H_k = 3200$ Oe. Coercive squareness of $S^* = 0.94$ is achieved. It is found that a small but nonzero exchange coupling through the normal grain boundaries, h_{e_out}, is critical for achieving high coercive squareness in the modeled nanocrystalline films. The effect of exchange coupling constants on coercive squareness

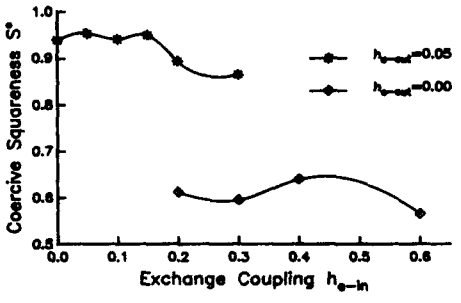

FIG. 3. Effect of exchange coupling inside the normal grain on coercive squareness of nanocrystalline films with $h_{e_out} = 0.05$ and $h_{e_out} = 0.0$.

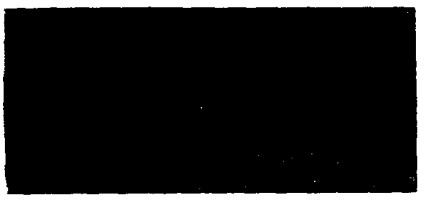

FIG. 4. Typical dibit magnetization pattern at $B = 0.13$ μm for nanocrystalline film with $h_{e_in} = 0.1, h_{e_out} = 0.05$. The horizontal width of the array is 1 μm. The gray scale represents the magnetization component along the recording direction.

S^* is demonstrated in Fig. 3. For a fixed $h_{e_out} = 0.05$, S^* remains at the level of 0.95 while h_{e_in} ranges from 0.0 to 0.15. S^* drops slightly to 0.90 with further increase in h_{e_in} to 0.3. However, if there is no exchange coupling between normal grain boundaries, i.e., $h_{e_out} = 0.0$, S^* falls dramatically into the range of 0.6, regardless of the value of h_{e_in}.

IV. RECORDING PROPERTIES

Figure 4 shows a typical simulated dibit magnetization recording pattern on a nanocrystalline film with $h_{e_in} = 0.1$ and $h_{e_out} = 0.05$. A 0.12-μm gap and a flying height of 0.02 μm is used for the recording head field. The interbit interval B is approximately 0.13 μm, and the width of the array is 1 μm. No percolation between the two transitions has occurred at this bit interval. Statistically, the size of the zig–zag magnetic domain at the transition determines the transition noise. As shown in Fig. 4, the zig–zag domain at the transition boundary has a very fine structure, indicating very low media noise of the nanocrystalline film.

Figure 5 shows the cross-track correlation function of the magnetization component along the recording direction calculated at the center of the second transition of the dibit shown in Fig. 4. The correlation length, defined here as the distance (in the cross-track direction) where the autocorrelation function drops to half of its peak value, is approximately

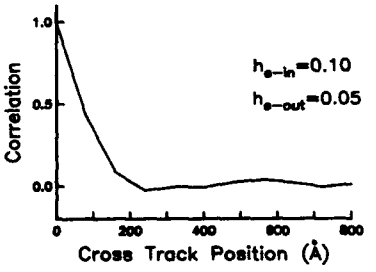

FIG. 5. Calculated cross-track correlation function of magnetization at the center of second transition.

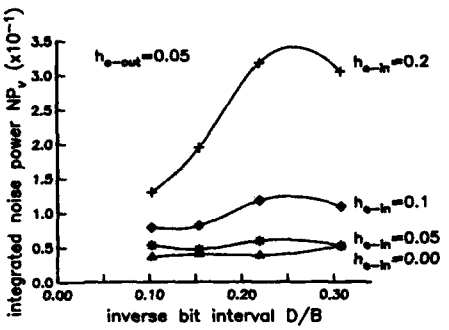

FIG. 6. Calculated integrated noise power as a function of the inverse bit interval for nanocrystalline films with different sets of exchange coupling constants (h_{e_in} and h_{e_out}).

the dimension of a subgrain. Even though there is a small exchange coupling between the normal grains and the subgrains, the effective width of the zig–zags at the transition center is smaller than the dimension of a normal grain.

To study the noise behavior of the nanocrystalline films, a recording simulation of the dibit transition pair is repeated 30 times, each time with a different set of easy axes to mimic recording at different locations in the film plane. Read back voltage waveforms are calculated by convolving the head field with the simulated recording dibit magnetization patterns. The variance of the read back waveforms of the dibit transitions is calculated. The total voltage noise power is defined as the average variance value over an interbit interval, B, centered at the second transition of the dibit.[5]

By simulating dibit transition pairs at different bit intervals, the integrated voltage noise power of the nanocrystalline films are calculated as a function of inverse bit intervals, as shown in Fig. 6. The four curves represent four nanocrystalline films with $h_{e_in} = 0.0$, $h_{e_in} = 0.05$, $h_{e_in} = 0.1$, and $h_{e_in} = 0.2$, respectively, while the exchange coupling constant between normal grain boundaries h_{e_out} is fixed at 0.05. The coercive squareness of the four films is around 0.95. The horizontal axis is normalized as D/B, where $D = 200$ Å is the diameter of a normal grain. In the cases of $h_{e_in} = 0.0$ and $h_{e_in} = 0.05$, the integrated noise power remains low and virtually unchanged as bit interval decreases. Increasing the exchange coupling between the subgrains results in higher transition noise and significantly pronounced supralinear noise increase at small bit intervals.

The read back signal amplitude is defined as the peak value of the read back waveform of an isolated transition, and therefore the signal-to-noise ratio is calculated. At the bit interval $B = 0.07$ μm, i.e., 385 KFCI recording density, a SNR = 36 dB is achieved for nanocrystalline film with $h_{e_in} = 0.0$ and $h_{e_out} = 0.05$. Increasing the exchange coupling inside the normal grain to $h_{e_in} = 0.1$, the signal-to-noise ratio decreases to 33 dB. This is still above the SNR required by system designers.

V. CONCLUSIONS

Planar isotropic nanocrystalline films with bicrystal subgrain structures are studied via micromagnetic simulation. High coercive squareness can be achieved for nanocrystalline films with weak exchange coupling between the normal grain boundary. The bicrystal structure of subgrains inside each normal grain tend to break the collective behaviors of magnetization processes, so the cross-track magnetization correlation length is small, in the range of the dimension of a subgrain. For films with relatively low exchange coupling between subgrains, the medium noise is low even at very small bit intervals. At 385-KFCI recording density, and 1-μm track-width, calculated SNR is 36 dB. It is concluded that nanocrystalline film with adequate exchange coupling can support the targeted 10-Gbits/in.[2] recording density.

ACKNOWLEDGMENTS

This research was supported in part by the NSF under Grant Nos. ECS-9110119 and ECD-8907068, the DSSC at Carnegie Mellon University, ARPA/NSIC disk program, and the Army Research Office under Contract No. DAAL03-89-C-0038 with the University of Minnesota Army High Performance Computing Research Center.

[1] J.-G. Zhu and X.-G. Ye, IEEE Trans. Magn. **MAG-29**, 324 (1993).
[2] T. P. Nolan, R. Sinclair, R. Ranjan, and T. Yamashita, J. Appl. Phys. **73**, 5566 (1993).
[3] M. F. Doerner, T. Yogi, D. S. Parker, and T. Nguyen (these proceedings).
[4] J.-G. Zhu and H. N. Bertram, J. Appl. Phys. **63**, 3248 (1988).
[5] J.-G. Zhu, IEEE Trans. Magn. **MAG-29**, 195 (1993).

Evaluation of the CoCrTaPt alloy for longitudinal magnetic recording

Yuanda Cheng, Mojtaba Sedighi, Irene Lam, and Richard A. Gardner
Advanced Technology, Akashic Memories Corp., San Jose, California 95134

ZhiJun Yang and Michael R. Scheinfein
Department of Physics, Arizona State University, Tempe, Arizona 85287

A quaternary alloy of CoCrTaPt with a composition of 80-10-4-6 (in at. %) was evaluated for its magnetic and recording properties. Samples of C/CoCrTaPt/Cr recording media were prepared by dc magnetron sputtering on circumferentially textured Al/NiP substrates. The effects on static magnetic properties and recording performance were studied for different substrate preheating times, Cr underlayer thicknesses, and Co-alloy layer thicknesses. It was found that both the coercivity H_c and remanent magnetization M_r increased with substrate preheating time. H_c also increased with Cr underlayer thickness, as expected. The $M_r\delta$ value depended linearly on the Co-alloy layer thickness. In addition, we found that the coercivity increased dramatically as the magnetic layer thickness decreased from ~800 to ~200 Å. For a sample with a 235-Å CoCrTaPt magnetic layer and ~1000-Å Cr underlayer, the coercivity was found to be >2700 Oe. Parametric evaluation showed that CoCrTaPt samples have performance similar to samples of CoCrTa and, because of the Pt addition, the CoCrTaPt alloy offers significantly higher attainable coercivities than the CoCrTa alloy. Therefore, the CoCrTaPt alloy proves to be a good candidate for use in high density recording media which require coercivity of higher than 2000 Oe.

Studies have shown that quaternary alloys of CoCrTaPt are promising candidates for high density recording in longitudinal thin-film media, where both the high coercivity H_c and the high signal-to-noise ratio are required. By adding only a few at. % Pt to CoCrTa alloys which are being used in thin-film recording media, one can significantly increase H_c without causing degradation of the recording performance.[1–3] In contrast, in order to achieve similar magnetic properties, more than 10-at. % Pt have to be used in another popular magnetic alloy of CoCrPt,[4–7] which significantly increases the cost of the sputtering target and thus limits its use in recording media production. In this study, we evaluated a CoCrTaPt alloy with the composition of 80-10-4-6 (in at. %) for its magnetic and recording properties, using different substrate preheating times, Cr underlayer thicknesses, and magnetic layer thicknesses.

The samples of this study were prepared by using an Intevac MDP-250 dc magnetron sputtering system with a separate preheating station, Cr station, Co-alloy station, and carbon stations. The base pressure of the sputtering system was about 10^{-7} Torr. The Ar pressures of both Cr and Co-alloy stations were set to 5.5 mTorr. Circumferentially textured Al disks with plated NiP layers were used as substrates. Sample sputtering was done in different stations in the sequence of substrate preheating, Cr underlayer, Co-alloy (magnetic) layer, and carbon protection layer. A −200-V dc bias was applied to both Cr and Co-alloy stations. In order to study the effects of sputter conditions on both the magnetic properties and recording performance of the CoCrTaPt alloy, the substrates were preheated before sputtering for different duration times. The substrate temperature was varied from room temperature (no preheating) to ~250 °C (8-s preheating). The thickness of the Cr underlayer was varied from 0 to 1000 Å and the Co-alloy layer thickness was changed from 200 to 1600 Å.

The samples were characterized using θ–2θ x-ray scattering on a Rigaku RU200 diffractometer with $K\alpha$ radiation of a rotating Cu anode. The thicknesses of the Cr underlayer and the Co-alloy layer were determined using x-ray fluorescence (XRF) spectrometry. The magnetic properties were measured on a vibrating sample magnetometer (VSM). The recording performance was characterized using a Guzik read–write analyzer with a thin-film head which had a 0.35-μm gap. The high frequency was 5.5 MHz (40 KFCI). The write current was 14 mA (base-to-peak) and the rotation speed was 3000 rpm. The head flying height was 3.5–4.0 μ".

X-ray scattering spectra of samples with different preheating times are shown in Fig. 1, together with the spectrum of an Al/NiP substrate. It showed that at low-temperature hcp Co (10.0), (00.2), and (10.1) grew epitaxially on bcc Cr (110) which resulted in the random orientations of the magnetocrystalline easy axis of the Co alloy (c axis). At elevated temperatures Cr (200) and hcp Co(11.0) started to grow. This led to the c axis of the Co alloy lying in the film plane, which

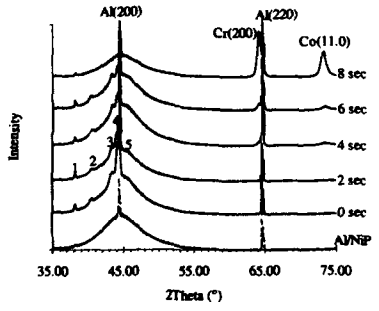

FIG. 1. X-ray diffraction spectra for the Al/NiP substrate, and for samples sputtered with different preheating times, in which peak 1 is Al (111), peak 2 Co (10.0), peak 3 Co (00.2), peak 4 Cr (110), and peak 5 Co (10.1).

 0021-8979/94/75(10)/6138/3/$6.00 © 1994 American Institute of Physics

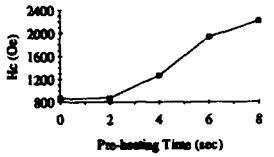

FIG. 2. Dependence of H_c of the CoCrTaPt alloy on substrate preheating time.

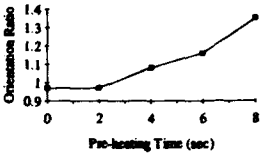

FIG. 4. Dependence of the orientation ratio of the CoCrTaPt alloy on preheating time.

is the preferred orientation to achieve higher H_c and better recording performance.[2] The lattice spacings of Co (10.0) and (00.2) were found to be 2.227 and 2.084 Å, respectively, for 0-s preheat and unchanged for preheat times up to 6 s. For samples with 8-s preheat, the crystallite sizes in the direction of film growth were found to be ~180 and ~130 Å for (200) Cr and (11.0) Co, respectively, estimated from peak widths of x-ray scattering.

In Figs. 2 to 4 we plot the variations with preheating time of H_c, remanent magnetization (M_r), and orientation ratio (OR), where the Cr underlayer and magnetic layer thicknesses were ~1000 and ~800 Å, respectively. H_c did not change for 0- and 2-s preheating times, as seen in Fig. 2. We then observed an almost linear increase of H_c as the preheating time changed from 2 to 8 s. For preheating times longer than 8 s, the NiP layer is expected to crystallize and become magnetic. The M_r was also seen to increase with preheating time as shown in Fig. 3, which is different from the conclusion of a previous study.[1] For the sample sputtered without substrate preheating, the M_r was found to be ~480 emu/cc. The M_r was seen to have increased by ~17% to ~560 emu/cc for the sample sputtered at ~250 °C. This change in M_r was caused by the increase of saturation magnetization M_s, and also by the increase in remanence squareness S, as shown in Fig. 4. A very interesting feature was observed for orientation ratio of the samples. For 0- and 2-s heat, the circumferential H_c was lower than the radial H_c which resulted in ORs smaller than 1. The squareness was also higher in the radial direction than in the circumferential direction for 0-s preheating time. It seems to indicate that there are more Co crystallites, which have a hcp structure,[1] oriented with the c axis in the radial direction than in the circumferential direction, when the temperature of the substrate is sufficiently low. At preheating time between 2 and 4 s, OR was seen to change from below 1 to above 1, and then increased linearly with preheating time, as shown in Fig. 4.

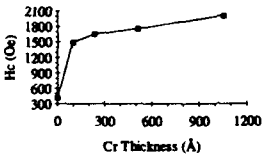

FIG. 5. Dependence of H_c of the CoCrTaPt alloy on Cr underlayer thickness.

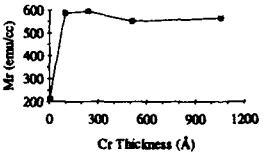

FIG. 6. Dependence of M_r of the CoCrTaPt alloy on Cr underlayer thickness.

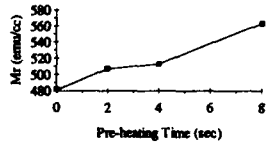

FIG. 3. Dependence of M_r of the CoCrTaPt alloy on substrate preheating time.

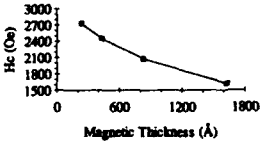

FIG. 7. Dependence of H_c of the CoCrTaPt alloy on magnetic layer thickness.

TABLE I. Comparison of parametric performance of CoCrTaPt and CoCrTa alloys.

Magnetic alloy	H_c (Oe)	$M_r\delta$ (memu/cm^2)	Amplitude (μV)	Resolution (%)	PW50 (ns)	OW (−dB)	S/N (dB)	BS (ns)
CoCrTaPt	1705	2.62	227	87.7	82.2	36.6	29.3	9.3
CoCrTa	1726	2.74	237	87.1	81.1	38.9	29.5	8.1

Underlayers such as the Cr layer, which is sputtered prior to the magnetic layer, affects the grain size and orientation of the magnetic films and thus can enhance the magnetic properties of the recording media. In this part of the experiment, the magnetic layer was fixed at ~800 Å while the Cr underlayer was changed from 0 to ~1000 Å. The substrates were preheated for 7-s duration time. Figure 5 plots the variation of H_c with Cr layer thickness. For the sample with no Cr underlayer, H_c was seen to be only ~400 Oe. H_c gained more than 1000 Oe when a Cr underlayer of only ~100 Å was sputtered. As the Cr underlayer increased further from 100 Å, the H_c increased with Cr thickness but at a much lower rate. Figure 6 shows the dependence of M_r on the Cr thickness. The value of M_r was very low (~210 emu/cc) for the sample with no Cr underlayer indicating poor crystallite orientation. This low value of M_r was related to both low M_s and low remanence squareness. However, M_r saturated for Cr thickness of about 100 Å at an average value of ~570 emu/cc. The orientation ratio showed a weak maximum value of 1.56 at 100-Å Cr. It decreased for thicker Cr underlayers. At ~1000 Å, the orientation ratio was 1.34. Both S and S^* were found to be only ~0.45 for the sample with no Cr underlayer. They were seen to be ~0.91 and independent to the Cr thickness as the Cr underlayer changed from 100 to 1000 Å.

To study the dependence of magnetic properties on Co-alloy thickness, we fixed the Cr underlayer at ~1000 Å and varied the Co-alloy layer from ~200 to ~1600 Å. Again, the substrates were preheated for 7-s duration time. In Fig. 7 we plot the H_c vs the Co-alloy layer thickness. It can be seen that the H_c became much higher for the thinner Co-alloy layer. This decrease in H_c with Co-alloy thickness is possibly due to the decrease in both the effect of the demagnetizing field, and the coherent strain of the initial grain-to-grain epitaxy.[8] The H_c was about 2100 Oe when the magnetic layer was ~800 Å. At about 200-Å magnetic layer thickness, the H_c increased to more than 2700 Oe. $M_r\delta$ was seen to increase linearly with the magnetic thickness δ. From the linear fit of the experiment data, we found the average remanent magnetization of 80-10-4-6 (in at. %) CoCrTaPt alloy was ~570 emu/cc which is ~5% lower than that of CoCrTa without Pt.

The recording performance of the CoCrTaPt alloy was evaluated for samples sputtered under different conditions, and samples of CoCrTa were also characterized for comparison. In Table I we list the results of two samples with different alloys. It shows that the CoCrTaPt alloy is similar to the CoCrTa alloy in amplitude (HFTAA), resolution, pulse width (PW50), overwrite (OW), bit shift (BS), and signal-to-noise ratio (S/N).

In summary, it was found that for the CoCrTaPt alloy, Co (11.0) started to grow epitaxially on Cr (200) at elevated temperatures, with the c axis lying in the film plan. We did not observe any increase with temperature in lattice spacings of the Co alloy. Both H_c and M_r increased with substrate temperature or preheating time. This dependence of M_r on substrate temperature has to be taken into account in recording media fabrication, where H_c is mainly adjusted by substrate preheating time. H_c also increased with Cr thickness. However, the M_r value was seen to be constant as Cr thickness varied from 100 to 1000 Å. The $M_r\delta$ was also found to depend linearly on the magnetic layer thickness. In addition, we found that H_c increased at a very fast rate (>1 Oe/Å) as the magnetic layer thickness decreased from ~800 to ~200 Å. Parametric evaluation of CoCrTaPt samples showed similar performance as the samples sputtered with CoCrTa alloys and, because of the Pt addition, the CoCrTaPt alloy offers significantly higher attainable coercivities than the CoCrTa alloy. Therefore, with very high attainable H_c (>2500 Oe), relatively high remanent magnetization (~570 emu/cc), and good recording performance, the CoCrTaPt alloy proves to be a good candidate to be used in recording media which requires coercivity of higher than 2000 Oe.

[1] B. B. Lal, H. Tsai, and A. Eltoukhy, IEEE Trans. Magn. MAG-27, 4739 (1991).
[2] H. Tsai, B. B. Lal, and A. Eltoukhy, J. Appl. Phys. 71, 3579 (1992).
[3] K. Utsumi, T. Inase, and A. Kondo, J. Appl. Phys. 73, 6680 (1993).
[4] T. Lin, J. Magn. Mater. 86, 159 (1990).
[5] M. A. Parker, J. K. Howard, R. Ahlert, and K. R. Coffey, J. Appl. Phys. 73, 5560 (1993).
[6] P. Glijer and J. M. Sivertsen, J. Appl. Phys. 73, 5563 (1993).
[7] Y. Shiroishi, Y. Hosoe, A. Ishikawa, Y. Yahisa, and Y. Sugita, J. Appl. Phys. 73, 5569 (1993).
[8] J. C. Lin, C. D. Wu, and J. M. Sivertsen, IEEE Trans. Magn. MAG-26, 39 (1990).

Analysis of the electronic properties of CoCrPt thin films using parallel electron energy loss spectroscopy (PEELS)

Pawel Glijer, John M. Sivertsen, and Jack H. Judy[a)]
Department of Chemical Engineering and Materials Science, The Center for Micromagnetics and Information Technology (MINT), University of Minnesota, Minneapolis, Minnesota 55455

The effects of the Pt content in CoCrPt thin films on the appearance of the near-edge structure of the Cr and Co $L_{2,3}$ absorption edges were studied using parallel electron energy loss spectroscopy (PEELS). These reflect local changes in the $3d$ band of the material. It was found that addition of Pt leads to local fluctuations in the $3d$ band occupancy in CoCrPt films which causes a decrease of the number of $3d$ electrons per Co atom. An increase of the L_3 to L_2 white lines intensities ratio on the $L_{2,3}$ Co edge with Pt content probably indicates an increase of the magnitude of exchange interactions in the CoCrPt thin films.

I. INTRODUCTION

CoCrPt/Cr thin films have been successfully used as magnetic media for the high density recording[1] and are considered as one of the best candidates for the gigabit density recording magnetic media. Magnetic and recording properties of the CoCrPt/Cr are structure sensitive. Effects of the addition of Pt to the CoCr films on the microstructure, texture, and magnetic properties have been reported in the past few years.[2–4] However, very little attention has been given to the role of Pt in altering electronic structure of these materials.

The purpose of this paper is to present the results of the analysis of $3d$ band properties of CoCrPt thin films using electron energy loss spectroscopy (EELS).

II. EXPERIMENTAL PROCEDURE

CoCrPt films with a thickness of ~600 Å and Pt content of 0, 13, 20, and 40 at. % were sputtered on glass using rf diode sputtering with substrate bias. The Co:Cr ratio in all the films was around 5.1:1. Magnetic properties of the films were measured using a vibrating sample magnetometer (VSM). Crystallographic texture of the films was determined using an x-ray diffractometer and electron diffraction in a transmission electron microscope (TEM).

TEM samples were prepared by chemically removing the glass substrate. Thickness of the examined samples was within a range of 0.4λ–0.7λ (λ—mean free path for inelastic scattering). Such thickness was chosen as a compromise between avoiding a significant amount of multiple scattering and obtaining sufficient signal to collect core edges of Cr and Co. Transmission electron microscopy (TEM) observations of the films as well as EELS analysis was performed in the Philips CM-30 electron microscope with a Gatan 666 parallel electron energy loss spectrometer (PEELS). PEELS spectra were collected in a diffraction mode using a camera length of 110 mm and collection aperture of 2 mm. Low loss regions of the spectra were collected using dispersion of 0.5 eV/channel. L-Cr and L-Co edges were collected using dispersion of 0.2 eV/channel. Calibration, spectra collection, thickness measurement, and background removal were performed using Gatan E1P 2.1 software. PEELS spectra of pure Co, Cr, Ni, and Cu deposited in the same sputtering system were collected and used as references. PEELS spectra were collected from the areas of ~1 μm^2 which covered an area of 10^2–10^3 grains in the polycrystalline CoCrPt films. All spectra were examined for the oxygen edges. Only in the Cr and CoCr case samples was a very weak oxygen signal detected.

The peaks appearing at the L edges of the $3d$ elements are due to transitions from the $2p_{3/2}$ (L_3 peak) and $2p_{1/2}$ (L_2 peak) states to the $3d$ band and are designated as "white lines." Normalized white lines intensities (NWLI) and ratio of the L_3:L_2 peaks were calculated using a method similar to the one described by Pearson *et al.*[5] The method is illustrated in Fig. 1. The near-edge structure of a $L_{2,3}$ spectrum is due to the excitations to the bound states as well as due to excitations to the continuum. The continuum part of the $L_{2,3}$ edge was modeled as a step function where the first step at the L_3 edge was twice as high as a step at the L_2 edge, because of the 2:1 ratio of the initial $2p$ states. The intensity of the white lines was obtained by integrating the area of the peaks above the step function. The intensity was subsequently normalized by dividing it by the area of the edge with a 50-eV width and lying 50 eV past the L_3 line. For L_3:L_2 ratio the L_3 line intensity was counted as an integral of the

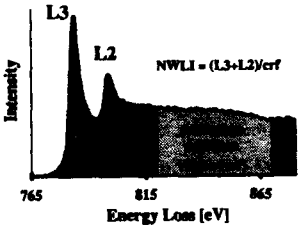

FIG. 1. Graphic illustration of the method for isolating and normalizing white lines intensities. The presented edge is an L Co edge measured for a CoCr-13% Pt thin film.

a)Department of Electrical Engineering, The Center for Micromagnetics and Information Technologies (MINT), University of Minnesota, Minneapolis, Minnesota 55455.

 0021-8979/94/75(10)/6141/3/$6.00 © 1994 American Institute of Physics

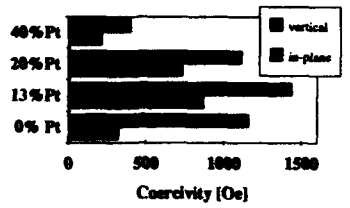

FIG. 2. In-plane and vertical coercivity of the examined CoCrPt thin films.

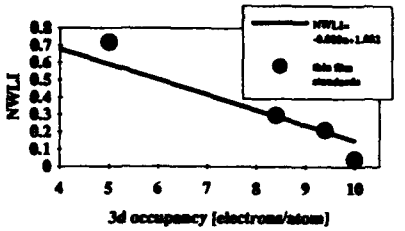

FIG. 3. NWLI values for standard pure element thin films compared to the NWLI calculated from Eq. (2).

white line above the step function up to the intensity minimum between the L_3 and L_2 lines. L_2 line intensity was integrated above the step function between this minimum and energy at which L_2 joins the continuum part of the edge.

Several thick samples ($t \sim 0.7\lambda$) were ion milled to the thickness in the range of 0.3λ–0.4λ using a liquid nitrogen-cooled stage. Spectra for the ion milled samples were analyzed using the same procedure and gave virtually the same results in almost all the cases, proving that thickness effects in the range used in the experiment were negligible. The pure Cr film intensities of the white lines were significantly larger than the case of the unmilled sample. This result can be associated with the removal of the surface oxide layer since the oxygen edge vanished from the spectrum after the ion milling.

III. RESULTS AND DISCUSSION

CoCrPt films with Pt content 0-, 13-, 20-at. % Pt exhibited (0002) texture of the hcp phase whereas CoCr 40% Pt film exhibited fcc structure with a {111} preferred orientation. The magnetic properties measured in the CoCrPt films were consistent with previously reported properties of the CoCrPt/Cr thin films[3] as shown in Fig. 2. Films with 13- and 20-at. % Pt were magnetically hardest and Pt-rich film (40-at. % Pt) was magnetically softest among samples examined.

Occupancy of $3d$ bands based on the $L_{2,3}$ absorption edges of Cr and Co has been calculated, using the method proposed by Pearson *et al.*,[5] which assumes that the normalized intensity of $L_{2,3}$ white lines (NWLI) decreases linearly with $3d$ occupancy as

$$\mathrm{NWLI} = 1.04(1 - 0.088n), \tag{1}$$

where n is the $3d$ occupancy (electrons/atom). However, in their analysis Pearson *et al.*[5] assumed that one electron occupies a $4s$ band. For elements close to Ni it is more appropriate to assume 0.6 electrons in a $4s$ band.[6] If such a correction is made for Ni, Co, and Fe Eq. (1) becomes

$$\mathrm{NWLI} = 1.032 - 0.088n. \tag{2}$$

Figure 3 shows good agreement of the NWLI experimentally obtained from pure thin films of Co, Ni, Cu, and Cr with the relation given by Eq. (2). $3d$ occupancy for Co and Cr measured for CoCrPt films (Fig. 4) show that addition of Pt changes the local electronic arrangement in the $3d$ band of the material. In particular, small additions of Pt (up to 20%) tend to decrease the number of the $3d$ electrons per Co atoms which most probably leads to the larger moment per Co atom in these alloys. Such an effect of Pt addition could be expected since Pt is known to cause a giant moment phenomenon in the Co–Pt alloys.[7] This result explains the observed very weak sensitivity of the measured M_s values to small additions of Pt in some CoCrPt films.[4] $3d$ occupancy in the CoCr 40% Pt film is back to its theoretical value of 8.4, which is associated with a change of the crystallographic structure of the material. Local $3d$ occupancy for Cr atoms in the CoCrPt films tend to decrease significantly with Pt content resulting in a large difference between the local number of $3d$ electrons per Co atom and the number of $3d$ electrons per Cr atom. This shows that alloying CoCr films with Pt produces significant local charge transfers within the band structure of the material. Such a result may also be caused by the presence of a second phase in the material or by the Cr segregation.

The theoretical ratio of the white line intensities based solely on the initial $2p$ states should be 2:1. For most of the $3d$ metals, however, an observed $L_3{:}L_2$ ratio is usually different from 2 (in most of the cases smaller) due to interactions of the $2p$ states with band electrons.[8,9] In the case of Cu the $L_3{:}L_2$ ratio is close to 2 (reported ratios range between 1.7 and 2.1).[8] But here these numbers refer more to the relative heights of the L_3 and L_2 steps, since white lines are barely observable due to the filled $3d$ band. The $L_3{:}L_2$ ratio becomes larger than 2 only in the case of ferromagnetic $3d$ metals which is a possible result of the large positive exchange integral in this material. The $L_3{:}L_2$ ratios which we measured for the pure element thin films were consistent

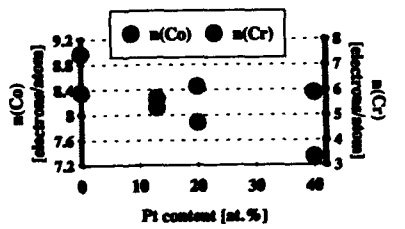

FIG. 4. $3d$ occupancy for Co–n(Co) and Cr–n(Cr) in the CoCrPt thin films as a function of Pt content.

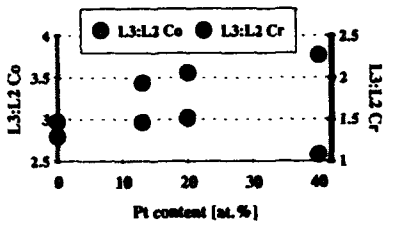

FIG. 5. L_3:L_2 white lines ratios for Co and Cr measured for CoCrPt thin films.

with those reported in the literature. The measured L_3:L_2 values were 1.50, 1.71, 2.79, and 3.08 for Cr, Cu, Ni, and Co, respectively.[10] L_3:L_2 ratios for Co measured in CoCrPt films increase monotonically with increasing Pt content (Fig. 5) which suggests that the addition of Pt induces an increase in the exchange constant of CoCrPt. Such an effect could contribute to larger intergranullar exchange interactions in the CoCrPt films with larger Pt content.

IV. CONCLUSIONS

A study of the $3d$ band properties of the CoCrPt films was performed using PEELS white line analysis of the $L_{2,3}$ edges of Co and Cr. $3d$ band occupancy was estimated by measuring the relative intensities of $L_{2,3}$ white lines. It has been shown that the addition of small amounts of Pt to CoCrPt films causes a decrease in the number of $3d$ electrons per Co atom which leads to an increased moment per Co atom of the material. Also, an addition of Pt to the material causes local fluctuations in the $3d$ occupancy. Such fluctuations may be caused by the local charge transfers within the band structure of the material or by the composition inhomogenities.

The observed increase of the L_3:L_2 white lines intensity ratio for Co in CoCrPt films with increasing platinum content suggests an increase in the magnitude of the exchange interactions in these materials. Such an effect would contribute to larger intergranullar exchange interactions in CoCrPt films with larger Pt content.

ACKNOWLEDGMENTS

The authors are grateful to Chien-Li Lin for help in the deposition of pure metal (standard) films. The research presented was supported by IBM ADSTAR, Rochester, MN.

[1] T. Yogi, C. Tsang, T. A. Nguyen, K. Ju, G. L. Gorman, and G. Castillo, IEEE Trans. Magn. MAG-26, 2271 (1990).
[2] K. E. Johnson, P. R. Ivett, D. R. Timmons, M. Mirzamani, S. E. Lambert, and T. Yogi, J. Appl. Phys. 67, 4686 (1990).
[3] P. Glijer, J. M. Sivertsen, and J. H. Judy, J. Appl. Phys. 73, 5563 (1993).
[4] M. Doerner, T. Yogi, T. Nguyen, D. Parker, S. Lambert, B. Hermsmeier, and O. C. Allegranza, IEEE Trans. Magn. 29, 3667 (1994).
[5] D. H. Pearson, B. Fultz, and C. C. Ahn, Appl. Phys. Lett. 53, 1405 (1988).
[6] B. D. Cullity, *Introduction to Magnetic Materials* (Addison-Wesley, Reading, MA, 1972), pp. 131–143.
[7] S. Foner, *Magnetism Selected Topics* (Gordon and Breach, New York, 1976), Chap. VI.
[8] R. D. Leapman, L. A. Grunes, and P. L. Fejes, Phys. Rev. B 26, 614 (1982).
[9] J. Zaanen, G. A. Sawatzky, J. Fink, W. Speier, and J. C. Fuggle, Phys. Rev. B 32, 4905 (1985).
[10] For Cu, the L_3:L_2 ratio refers to the ratio of the L_3 and L_2 steps on the $L_{2,3}$ Cu absorption edge.

Noise properties and microstructure of oriented CoCrTa/Cr media

R. Ranjan, W. R. Bennett, G. J. Tarnopolsky, and T. Yamashita
Komag, Inc., 275 South Hillview Drive, Milpitas, California 95035

T. Nolan and R. Sinclair
Department of Materials Science and Engineering, Stanford University, Stanford, California 94305

Magnetic and noise properties of oriented CoCrTa/Cr media sputtered at temperatures from ambient to 250 °C were studied and correlated with microstructural data from HRSEM and HRTEM micrographs. Coercivity increases monotonically and loop squareness decreases with substrate temperature. Transition and uniform magnetization noise power are highest for media sputtered at 150 °C. Micrographs and noise powers show that the media sputtered at 150 °C is relatively highly exchange-coupled. Media sputtered below 150 °C shows topographic isolation, and those sputtered above 150 °C exhibit increasing intergranular isolation of about 10 Å and thus lower exchange. Coercivity varies linearly but exchange drops abruptly at high temperature. Other mechanisms besides exchange contribute to the coercivity variation.

I. INTRODUCTION

Sputtered CoCrTa Cr oriented media is widely used for high density recording applications due to its low media noise and high coercivity H_c. It was shown in Ref. 1 that the noise of sputtered CoCrTa/Cr media decreases and H_c increases with substrate temperature. CoCrTa/Cr media has been also studied using remanence curves,[1–3] which show that the intergranular interaction decreases with increasing substrate temperature. Transmission electron microscopy (TEM) and scanning electron microscopy (SEM) micrographs of Duan *et al.*[4] do not reveal any intergranular isolation. Atomic force microscopy (AFM) studies by Lu *et al.*[2] show increasing grain sizes as the substrate temperature rises. Maeda *et al.*,[5] using NMR, indicated that there may also be an enhancement of Cr segregation. Microscopic evidence of grain isolation in CoCrTa media sputtered at high temperature was reported, and interpreted as an exchange breaking mechanism.[6,7] In this work we investigate the onset of grain isolation to understand the relationship between film structure, its magnetic characteristics, and micromagnetic behavior. We present, as a function of the common substrate and deposition temperature T_s, high-resolution SEM and TEM micrographs of oriented CoCrTa/Cr media, together with measurements of transition noise, uniform magnetization noise, and magnetization correlation lengths.

II. EXPERIMENTAL PROCEDURE

$CoCr_{12}Ta_4$ media were sputtered in an in-line sputtering system. The CoCrTa layer, Cr underlayer, and C overcoat thicknesses are 600, 750, and 200 Å, respectively. T_s was varied from 25 to 250 °C. The substrates were circumferentially textured NiP/Al with roughness $R_a \sim 45$ Å and peak-to-valley of ~360 Å. Magnetic properties were measured using VSM. Microstructural analysis was carried out using a Philips EM-430ST TEM operating at 300 kV, and a Hitachi S900 SEM operating at 30 kV.

A single thin-film head was used to measure media noise power for all disks. The head has pole and gap lengths $p_1/g/p_2 = 3.35/0.35/3.35$ μm, leading and trailing pole widths of 15 and 12 μm, respectively, and 30 turns. The flying height was 3.6 μ" at velocity $v = 7.52$ m/s. Transition noise (TN) and uniform magnetization noise (UMN) power spectral densities (PSD) were acquired with a spectrum analyzer. At each frequency, the total TN power was obtained by subtraction of the background noise and integration of the PSD. TN PSDs were not normalized by the transfer function of the head and channel. Thus, the TN powers given here are in arbitrary units. The UMN raw spectra were acquired and analyzed in the frequency interval $0.15 < f < 15$ MHz corresponding to a wave number $k = 2\pi f/v$ interval $0.12 < k < 12$ μm^{-1}, using techniques previously described.[8] The electronic-, head-, and saturated-media-noise background were subtracted from the UMN spectra, which were further divided by all the appropriate factors such as amplifier gain, media velocity, spacing and thickness losses, etc., and by the Fourier transform of the head surface field. For the latter, the finite-pole length-head formulas of Bertram *et al.*[11] were used. The UMN PSDs given here represent intrinsic measures of the magnetic film noise power.

III. RESULTS

Results are shown in the micrographs in Fig. 1 and in Table I. We first describe the film microstructure, then the magnetic properties, and finally the noise analysis.

A. Microstructure

Figures 1(a)–1(d) show high resolution-SEM (left), and high resolutuion-TEM with selected area diffraction (SAD) pattern (right) micrographs of CoCrTa/Cr. The sequence from Figs. 1(a) to 1(d) corresponds to $T_s = 25$, 100, 175, and 250 °C, respectively. The SAD shows that at low T_s there is no definite growth direction. As T_s increases, a prominent $\langle 11\bar{2}0 \rangle$ growth orientation develops. Low T_s samples exhibit many stacking faults, shown by radial streaks in the diffraction pattern; these disappear with increasing substrate temperature. This is likely due to better crystallographic matching between the Cr and the CoCrTa layers at higher T_s. HRSEM micrographs show that there is a definite topographic isolation between the CoCrTa grains for low *and* high T_s, but at intermediate $T_s \sim 175$ °C the grains appear to be very dense. At 250 °C, HRTEM micrographs show that

 0021-8979/94/75(10)/6144/3/$6.00 © 1994 American Institute of Physics

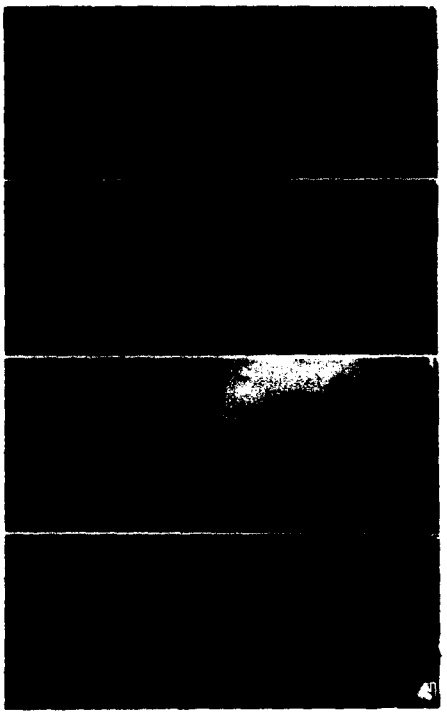

FIG. 1. HRSEM (left-hand side), HRTEM, and SAD (right-hand side) of CoCrTa/Cr media sputtered at T_s=25 (top), 100, 175, and 250 °C (bottom).

the films exhibit ~150–200 Å-diam subgrains that are visibly isolated from each other. The crystallographic orientation and growth mechanism of such subgrains have been described previously.[7] At high T_s, the isolation between the subgrains of CoCrTa is about 10 Å, which is sufficient to break the intergranular exchange interaction. In summary, with increasing temperature the film evolves from a topographically isolated film, to a very dense one, and finally to a subgrain-boundary-isolated structure.

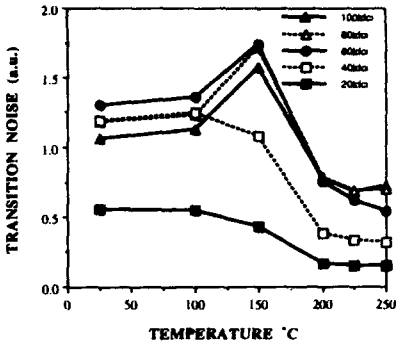

FIG. 2. Transition noise vs substrate sputtering temperature for various recording densities.

B. Magnetic properties

The H_c values in Table I show that H_c remains nearly constant up to T_s~100 °C. Then it linearly increases with T_s at a rate of ~8 Oe °C. Although it has been shown[1] that the CoCrTa deposition temperature controls H_c, in this study both the Cr and CoCrTa layers were heated to the *same* T_s. In Table I, ΔH is the magnitude of the field required to change the magnetization from $-M_r/2$ to $+M_r/2$. ΔH increases (S^* decreases) for $T_s \geq 150$ °C. High ΔH's describe skewed hysteresis loops, possibly due to a lower intergranular interaction with increasing $T_s \geq 150$ °C. The orientation ratio OR = $M_{r,\text{circumferential}}/M_{r,\text{radial}}$ also increases for $T_s \geq 150$ °C. The contrast between the linear variation of H_c vs T_s and the more complex variation of the other loop parameters points to stress or the change in crystallographic orientation as a coercivity-inducing mechanism, since thermal effects are linear with T_s. If H_c were driven by an exchange breaking mechanism, it would be expected to show a step-like behavior as the exchange is broken.

C. Transition noise and uniform magnetization noise

Figure 2 shows total TN power values, in arbitrary units, as a function of T_s at various recording densities. For recording densities of 20 and 40 kfci, the transition noise remains nearly constant up to 150 °C. Then it drops sharply for the

TABLE I. Media magnetic parameters and results.

T (°C)	$M_r t$ (memu/cm^2)	H_c (Oe)	S^*	ΔH (Oe)	OR, M_r	TN (arb. units)	UMN (nm)	CL (μm)	α (μm)
25	2.69	553	0.83	92	0.97	1.301	30	1.0	0.23
100	2.69	615	0.80	133	0.98	1.361	37	1.1	0.22
150	2.74	935	0.90	115	1.13	1.741	55	1.7	0.17
200	2.71	1450	0.89	200	1.43	0.755	29	1.7	0.15
225	2.68	1630	0.87	232	1.43	0.616	30	1.6	0.14
250	2.66	1773	0.84	340	1.34	0.54	22	1.6	0.13

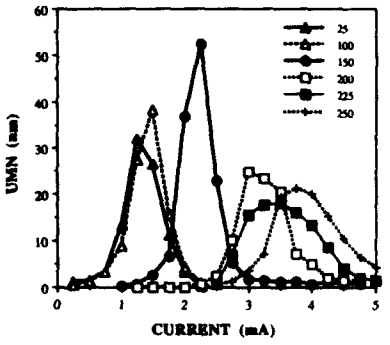

FIG. 3. Total uniform magnetization noise vs current for various substrate sputtering temperature.

200 °C media, and stays nearly constant for $T_s \geq 200$ °C. For densities >40 kfci, TN shows a maximum at $T_s \sim 150$ °C; below and above that temperature, TN~constant.

Figure 3 shows total UMN for the various T_s's as a function of the reverse dc excitation current. It can be seen that the maximum total UMN, which corresponds to $H_{applied} = H_{c,r}$, increases with T_s, peaks for the 150 °C media, and then decreases for $T_s \geq 200$ °C. The width of the UMN curves, a measure of the switching field distribution, remains nearly constant up to 150 °C and increases for $T_s \geq 200$ °C. As Table I shows, the total UMN and TN powers exhibit the same complex temperature evolution, which differentiates the 150 °C media from both the low and high T_s films.

The UMN PSD has been shown both experimentally[8,10] and theoretically[12] to reflect magnetostatic and exchange properties of the film. These PSDs were analyzed to obtain the down-track magnetization autocorrelation functions, from which a conventionally defined, $1/e$, correlation length (CL) can be obtained. For each temperature, the PSD was found to be approximately a Lorentzian function of k, although deviating from that functional form. The CLs are ~1.0 μm for $T_s < 150$ °C, and ~1.7 μm for $T_s \geq 150$ °C. This CL variation was verified to be experimentally significant.

IV. DISCUSSION

HRTEM micrographs show that the films sputtered at low temperatures have many stacking faults, while the films sputtered at ~175 °C seems highly exchanged coupled, and those sputtered at $T_s \geq 200$ °C have isolated subgrains. VSM results show that among the various loop parameters, only H_c varies linearly with T_s. The values of TN and UMN power show a nonmonotonic dependence on T_s, with the media sputtered at $T_s \sim 150$ °C exhibiting maximum noise. This behavior corresponds to the structural evolution shown by the HRSEM and HRTEM micrographs: Figure 1(c) shows highly exchange-coupled CoCrTa grains. Other work[1-3] has shown a monotonic drop in media noise and intergranular interaction with increasing deposition temperature in isotropic CoCrTa/Cr. It is likely that the nonmonotonic dependence of noise that we observe could be related to the preferred orientation of the CoCrTa/Cr film. Although increased intergranular isolation has been indirectly shown using ΔM techniques,[1-3] our HRTEM results clearly show intergranular isolation for CoCrTa/Cr media sputtered at high T_s. Results of down-track CL show no clear correlation with TN and UMN for media sputtered at high temperatures. It is possible that the stacking faults of the lower T_s films limit the size of the relaxation domains both in the down-track and cross-track directions: for these films the coercivity indicates a high degree of exchange, while the stacking faults limit the noise by creating independent, stacking-fault-isolated, noise sources. This could explain both the lower noise power of the low T_s films and their shorter CL.

The coercivity origin for these films appears to be at most partially related to the level of exchange of the film. H_c depends linearly on T_s, whereas both the grain isolation micrography data as well as the total noise powers hint at a complex evolution of the exchange with T_s. Although the evolution of exchange and coercivity seem to follow a mechanism for which increased grain isolation increases H_c and reduces the noise above 150 °C, below that temperature there is no such behavior ascribable to exchange. The absence of any deviation from linearity in the H_c vs T_s relation, Table I, above $T_s = 100$ °C seems to rule out an exchange-driven mechanism of H_c, requiring other explanations, e.g., stress-induced or crystallographic-induced H_c variation.

The dependence of CLs and total UMN power upon T_s seems to indicate that, at low temperatures, stacking faults limit both the cross-track and down-track correlation lengths, while at higher T_s the noise is limited by isolated subgrains.

[1] M. Lu, T. Min, Q. Chen, and J. H. Judy, IEEE Trans. Magn. MAG-28, 3255 (1992).
[2] M. Lu, Q. Chen, J. H. Judy, and J. M. Sivertsen, J. Magn. Soc. Jpn. 15, Suppl. No. S2, 945 (1991).
[3] Y. Shen, D. E. Laughlin, and D. N. Lambeth, IEEE Trans. Magn. MAG-28, 3261 (1992).
[4] S. Duan, M. R. Khan, and J. E. Haefele, IEEE Trans. Magn. MAG-28, 3258 (1992).
[5] Y. Maeda and K. Takei, IEEE Trans. Magn. MAG-27, 4721 (1991).
[6] R. Ranjan, J. Chang, T. Yamashita, and T. Chen, J. Appl. Phys. 73, 5542 (1993).
[7] T. Nolan, R. Sinclair, R. Ranjan, and T. Yamashita, J. Appl. Phys. 73, 5566 (1993).
[8] G. J. Tarnopolsky, H. N. Bertram, and L. T. Tran, J. Appl. Phys. 69, 4730 (1991).
[9] A. Kawamoto and F. Hikami, J. Appl. Phys. 69, 5151 (1991).
[10] H. N. Bertram and R. Arias, J. Appl. Phys. 71, 3439 (1992).
[11] G. A. Bertero, H. N. Bertram, and D. M. Barnett, IEEE Trans. Magn. MAG-29, 67 (1993).
[12] J.-G. Zhu and H. N. Bertram, J. Appl. Phys. 69, 4709 (1991).

Effects of oxide addition on magnetic and structural properties of CoNiPt alloy films

A. Murayama, S. Kondoh,[a] and M. Miyamura
R&D, ASAHI KOMAG Co., Ltd., Hachimannhara, Yonezawa 992-11, Japan

The effects of oxide addition on magnetic and structural properties of sputtered CoNiPt alloy films for high density longitudinal recording with a random c-axis orientation of hcp Co have been studied. It is found that the addition of SiO_2 up to 4.2 at. % results in a significant increase in the in-plane coercivity from 1700 to 2400 Oe and a signal to media noise ratio with a slight decrease in coercive squareness from 0.90 to 0.87, while the perpendicular magnetic anisotropy is not significantly changed. X-ray diffraction shows that the c-axis orientation normal to the film plane does not change and the hcp lattice is strained due to the addition of SiO_2. A marked decrease in the grain size is observed with the addition of 4.2-at. % SiO_2, which causes the development of grain separation and therefore enhances the coercivity. The origin of the increase in coercivity with 2.1-at. % SiO_2 is also discussed.

I. INTRODUCTION

CoPt-based alloy films have attracted much interest for use in high density longitudinal recording, because a high coercivity (H_c) of around 2000 Oe and low media noise properties can be obtained by optimizing both alloy compositions and sputtering processes.[1,2] Therefore, the relationship between the microstructure and magnetic properties in the CoPt-based alloy films are still the subject of interest.

On the other hand, ferromagnetic metal films with oxide's addition have been studied because of their potential for high H_c.[3] Magnetic anisotropy originating from the interface between the metal and the oxide is discussed.[4] Recently, the addition of oxides such as SiO_2 to CoCrPt magnetic films has been shown to cause an increase in both in-plane H_c and coercive squareness (S^*) due to the reduction of the strong hcp Co c-axis texture perpendicular to the film plane.[5]

In this paper, we report the effects of SiO_2 addition on CoNiPt alloy films which have a random hcp Co c-axis orientation and strong in-plane magnetic anisotropy.

II. EXPERIMENTAL PROCEDURE

A NiP underlayer[2] with a thickness of 420 A and a CoNiPt magnetic layer were successively deposited on NiP-plated and mechanically textured Al substrates by rf sputtering. Ar pressure during the deposition was 20 mTorr. SiO_2 was added to the CoNiPt films by placing pure SiO_2 chips on the $Co_{81}Ni_7Pt_{12}$ alloy target. The composition of the SiO_2 was controlled from 0 to 8 at. % by changing the number of the chips and the overall composition was determined by ICP and Auger electron spectroscopy (AES).

Magnetic hysteresis curves were measured by the vibrating sample magnetometer (VSM) and magnetic anisotropies were evaluated by a torque magnetometer. Media noise was measured by a recording tester using thin film head. Signal frequency was 6 MHz and media noise integrated in the range from 0 to 13 MHz was measured as a ratio to the signal intensity (STMNR). The Si–O bonding state in the sputtered alloy films were analyzed by XPS. Crystal structures, such as lattice constant, crystal orientation, and crystallinity were determined by using x-ray diffraction with Cu-$K\alpha$ radiation. Grain structure was observed by SEM and TEM.

III. RESULTS AND DISCUSSION

Figure 1 shows in-plane magnetic hysteresis properties, such as in-plane H_c, thickness saturation-magnetization product (tM_s) and S^*, measured by VSM as a function of SiO_2 content in the CoNiPt$(SiO_2)_x$ films with a constant film thickness of 525 Å. H_c rapidly increases from 1400 to 2600 Oe with increasing SiO_2 to 3.5 at. %. Saturation magnetization gradually decreases as the amount of SiO_2 increases. S^* decreases slightly from 0.90 to 0.85 in the range from 0 to 3.5-at. % SiO_2.

Magnetic properties of the CoNiPt$(SiO_2)_x$ films with constant tM_s of 4.50 ±0.15 memu/cm^2 are listed in Table I. The addition of SiO_2 results in the significant increase in H_c without a large reduction of squareness. The uniaxial anisotropy energy $K_\perp$ is measured by the field dependence of the torque for the direction at 45° from the film normal.[6] The magnetic anisotropy energy K including shape anisotropy energy is calculated by the equation, as follows:

$$K = K_\perp + 2\pi M_s^2.$$

The observed values of $K_\perp$ are positive, which indicates that the in-plane uniaxial anisotropy exists. The SiO_2 addition causes the slight increase in the $K_\perp$. However, this increase in the $K_\perp$, which means the increase in the in-plane anisotropy, is relatively small compared with the shape anisotropy. No systematic dependence of K which represents macroscopic in-plane magnetic anisotropy, with respect to the SiO_2 content, is observed and the increase of H_c with SiO_2 addition cannot be explained by the increase in $K_\perp$. Media noise is also shown as STMNR in Table I. The addition of SiO_2 is very effective for reduction of the media noise.

XPS shows the chemical shift in the binding energy of Si atoms in the sputtered films is close to that of bulk SiO_2, which indicates that the Si atoms in the sputtered film are in the form of SiO_2. The formation of SiO_2 in the sputtered

[a]Research Center, ASAHI Glass Co., Ltd., Hazawa-cho, Yokohama 221, Japan.

 0021-8979/94/75(10)/6147/3/$6.00 © 1994 American Institute of Physics

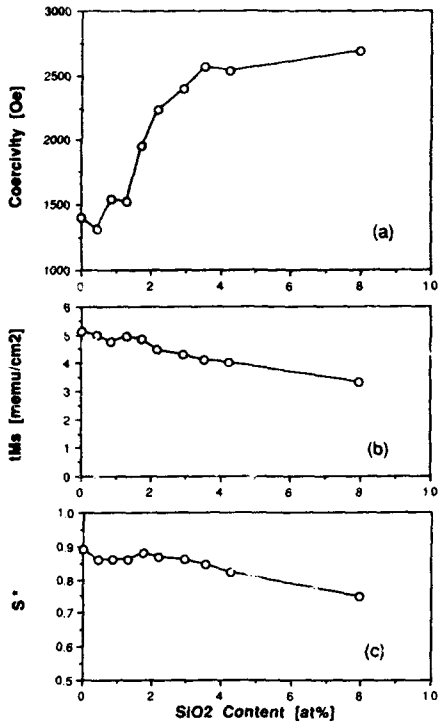

FIG. 1. Magnetic hysteresis properties, such as H_c (a), tM_s (b), and S^* (c) in CoNiPt(SiO_2) films with a constant thickness of 525 A, as a function of SiO_2 content.

films play an important role in the H_c enhancement. This result is also supported by the fact that Si addition is not effective for the H_c increase.

X-ray diffraction patterns from CoNiPt$(SiO_2)_x$ alloy films are shown in Fig. 2. Diffraction angles (2θ) of pure hcp Co as a bulk are $2\theta(100)=41.72°$, $2\theta(002)=44.80°$, and $2\theta(101)=47.61°$, respectively. Diffraction angles of a bulk CoNiPt (target piece) are measured as $2\theta(100)=40.68°$, $2\theta(002)=43.73°$, and $2\theta(101)=46.45°$, respectively. Thus diffraction peaks of the expanded hcp Co lattice due to the alloying are observed in the sputtered CoNiPt film. The ratio of integrated intensity (I) of the diffraction peak from the CoNiPt film is calculated to be $I(100)/I(101)=0.58$ and $I(002)/I(101)=0.57$. In hcp Co with a perfect random c-axis orientation, the ratio is $I(100)/I(101)=0.20$ and $I(002)/I(101)=0.60$. Hence, the c-axis orientation in the CoNiPt film is random except that the degree of the (100) plane parallel to the film plane is relatively higher, i.e., the film is of slight (100) texture, which is also confirmed by three-dimensional distribution of each planes in pole figure analysis. The diffraction peak from the (101) plane is largely broadened. The addition of SiO_2 enhances the expansion of the hcp lattice, in comparison with that in the CoNiPt film without SiO_2. This result suggests that the hcp lattice is strained by thermal induced stress due to the interface between SiO_2 and CoNiPt. Integrated intensities of each diffraction peak are not influenced by the addition of SiO_2 and the intensity ratio is the same as that in the CoNiPt film with a random c-axis orientation.

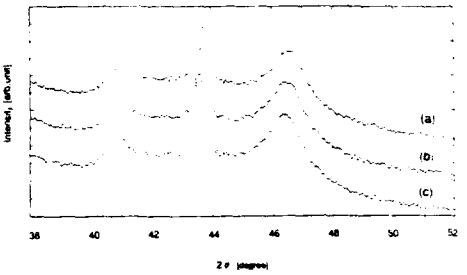

FIG. 2. X-ray diffractions from CoNiPt$(SiO_2)_x$ films, where $x=0$ (a), 2.1 (b), and 4.2 (c).

Figure 3 shows grain structure of the surface of CoNiPt$(SiO_2)_x$ films, observed by SEM. Grain size is significantly reduced by the addition of 4.2-at. % SiO_2, while that in the film with 2.1-at. % SiO_2 is not strongly influenced. It is suggested that the excess SiO_2 except that present in the grain prevents the coalescence of grains during grain growth and/or enhances the nucleation density at the initial stage of the grain growth. Well separated fine grains with a diameter from 50 to 200 A are clarified in the CoNiPt$(SiO_2)_{4.2}$ film, by TEM analysis as shown in Fig. 4. At present, it cannot be identified whether the excess SiO_2 exists at grain boundaries. By observing the grain structures, the magnetic separation among crystal grains are enhanced in the film with 4.2-at. % SiO_2. This change of grain separation can cause an increase in H_c and a decrease in S^* and media noise without the change of the c-axis orientation of the hcp lattice in those

TABLE I. Magnetic properties in CoNiPt$(SiO_2)_x$ ($x=0$, 2.1, 4.2 at. %) films with a constant tM_s of 4.5 memu/cm^2, measured by VSM and a torque magnetometer.

Alloy	DEKTAK Thickness (A)	VSM H_c (Oe)	tM_s (memu/cm^2)	tM_r (memu/cm^2)	S	S^*	Torque M_s (G)	Torque K_1 (erg/cc)	K (erg/cc)	Media noise STMNR (dB)
CoNiPt	458	1680	4.35	3.24	0.744	0.903	950	2.29×10^6	7.96×10^6	23.3
CoNiPt$(SiO_2)_{2.1}$	500	2009	4.62	3.36	0.730	0.894	924	2.65×10^6	8.01×10^6	27.3
CoNiPt$(SiO_2)_{4.2}$	550	2414	4.60	3.22	0.698	0.869	836	3.11×10^6	7.50×10^6	29.4

FIG. 3. SEM images of the surface of $CoNiPt(SiO_2)_x$ ($x=0$, 2.1, 4.2 at. %) films.

systems composed of exchange coupled crystal grains with a random c-axis orientation.[7]

Finally, we consider the origin of the H_c increase with the addition of a small amount of SiO_2. From TEM analysis, in the film with 2.1-at. % SiO_2, the degree of grain separation between crystal grains is observed to be similar to that in CoNiPt film without SiO_2. The shape and outline of the grains are observed to be more clear than those in pure CoNiPt film. It suggests that the addition of a small amount of SiO_2 influence the coalescence of the grain, possibly due to the existence of SiO_2 at the grain boundary. In addition, media noise is significantly reduced even by the addition of 2.1-at. % SiO_2, which suggests that the degree of magnetic isolation between grains is developed. In addition, the hcp lattice is expanded by the SiO_2 addition. In granular metal–oxide films, stress induced magneto-elastic anisotropy due to the lattice misfit and the dislocation at the interface between the metal and the oxide has been discussed.[4,8] Therefore, the increase in crystalline anisotropy of each grain is due to the expansion of the hcp lattice mainly originated from the difference of the thermal expansion coefficient between the CoNiPt and the SiO_2 at the grain boundary is also considered as a possible contribution to enhance H_c, in this alloy system.

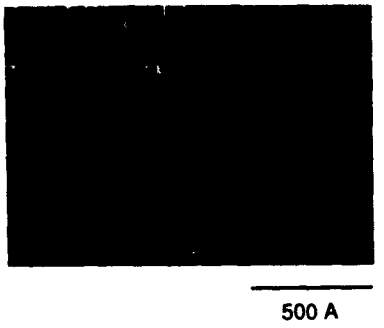

FIG. 4. TEM image of the grain structure in the $CoNiPt(SiO_2)_{4.2}$ film.

IV. CONCLUSIONS

Effects of SiO_2 addition on magnetic and structural properties have been studied in CoNiPt alloy films with a random c-axis orientation. A significant increase in H_c and signal to media noise ratio with a slight decrease in S^* are observed, while the perpendicular magnetic anisotropy decreases, slightly. The hcp lattice is expanded and the orientation of the c axis normal to the film plane is not changed by the addition of the SiO_2. A heavy doping of SiO_2 arises a marked decrease in the grain size and development of intergranular isolation, which result in the increase in H_c and the decrease in S^* and media noise. The origin of the increase in H_c with a small addition of SiO_2 is also discussed.

[1] T. Yogi, C. Tsang, T. A. Nguyen, K. Ju, G. L. Gorman, and G. Castillo, IEEE Trans. Magn. **MAG-26**, 2271 (1990).
[2] T. Yamashita, L. H. Chan, T. Fujiwara, and T. Chen, IEEE Trans. Magn. **MAG-27**, 4727 (1991).
[3] S. H. Liou and C. L. Chien, Appl. Phys. Lett. **52**, 512 (1988).
[4] G. Xiao and C. L. Chien, J. Appl. Phys. **63**, 4252 (1988).
[5] T. Shimizu, Y. Ikeda, and S. Takayama, IEEE Trans. Magn. **MAG-28**, 3102 (1992).
[6] H. Miyajima, K. Sato, and T. Mizoguchi, J. Appl. Phys. **47**, 4669 (1976).
[7] J. G. Zhu and H. N. Bertram, J. Appl. Phys. **69**, 3248 (1988).
[8] J. H. Hsu and C. Chang, J. Magn. Magn. Mater. **120**, 342 (1993).

Comparison of reproduce signal and noise of conventional and keepered CoCrTa/Cr thin film media

Kyusik Sin, Juren Ding,[a] Pawel Glijer, John M. Sivertsen, Jack H. Judy,[a] and Jian-Gang Zhu[a]
The Center for Micromagnetics and Information Technologies (MINT), Department of Chemical Engineering and Materials Science, University of Minnesota, Minneapolis, Minnesota 55455

We studied keepered high coercivity CoCrTa/Cr thin film media with a Cr isolation layer between the CoCrTa storage and an overcoating of an isotropic NiFe soft magnetic layer. The influence of the thickness of the NiFe and Cr layers, and the effects of head bias current on the signal output and noise, were studied using a thin film head. The reproduced signal increased by 7.3 dB, but the signal-to-noise ratio decreased by 4 dB at a linear density of 2100 fr/mm (53.3 kfr/in.) with a 1000 Å thick NiFe keeper layer. The medium noise increased with increasing NiFe thickness and the signal output decreased with decreasing Cr thickness. A low output signal obtained with very thin Cr may be due to magnetic interactions between the keeper layer and magnetic media layer. It is observed that signal distortion and timing asymmetry of the output signals depend on the thickness of the keeper layer and the head bias current. The signal distortion increased and the timing asymmetry decreased as the head bias current was increased. These results may be associated with different permeability of the keeper under the poles of the thin film head due to the superposition of head bias and bit fields.

I. INTRODUCTION

In recent years, the thickness of thin film media and the flying height have been reduced significantly to meet the requirements for higher recording densities. A novel method of increasing the reproduce signal by using a magnetically soft keeper overcoating to effectively reduce the spacing loss of the reproduce signal has been proposed.[1,2]

In keepered media, conventional longitudinal thin film media are coated with a low-coercivity and high-permeability magnetic thin film (NiFe). A thin carbon isolation layer between the magnetic media and the soft magnetic overcoating has been used to break the magnetic interactions.[3] The magnetically soft keeper acts as a low reluctance flux closure path between transitions. A dc bias current is applied to a read head to saturate the keeper layer in the gap area. The reproduce signal can then be obtained without spacing loss due to the coupling between the read head and soft magnetic layer. A substantial increase in signal output and reduction in the bit error rate at high bit densities has been reported.[3] However, the noise characteristics due to the soft magnetic layer have not been reported.

The purpose of this paper is to use Cr instead of C as the isolation layer material and to study the effects of the thickness of the Cr and the NiFe keeper layer on the reproduce signal and noise of keepered high-coercivity CoCrTa/Cr thin film media.

II. EXPERIMENTAL PROCEDURE

Keepered thin film media were prepared by dc magnetron and rf sputtering on textured 3.5 in. NiP/AlMg disk substrates. The CoCrTa/Cr media were prepared using a Temescal magnetron sputtering system, and then the media was overcoated with an isolation layer of Cr films (50–200 Å). A magnetically soft keeper layer of Permalloy ($Ni_{83}Fe_{17}$) was then deposited on the Cr isolation layer using a Perkin–Elmer RF sputtering system. A substrate bias of −100 V was applied during the NiFe deposition.

A vibrating sample magnetometer (VSM) was used to measure the magnetic properties of the films. A spin tester was used to characterize the output signal, medium noise, and signal-to-noise ratio (S/N). Recording properties were measured with a 12 turn thin film head with a gap length of 0.56 μm and a track width of 20 μm. The linear velocity of the head was 10.2 m/s. Small DC bias currents from 0.5 to 3 mA were applied to the head coil during measuring of the reproduce signal. The saturation write current at a recording density of 100 fr/mm was 25 mA. The medium noise was measured with a spectrum analyzer with a total bandwidth of 20 MHz.

III. RESULTS AND DISCUSSION

The hysteresis curve of a 1000 Å NiFe deposited on a 50 Å Cr film on a glass substrate is shown in Fig. 1. The coercivity of 1000 Å NiFe was 2 Oe and it decreased to 1.4 Oe for a 500 Å NiFe deposited on a 50 Å Cr film. The coercivity of the CoCrTa/Cr thin film media was 1500 Oe.

Figure 2(a) shows the influence of NiFe thickness on the reproduce signal. The thickness of a CoCrTa layer and a Cr isolation layer was kept at 500 and 100 Å, respectively. As the thickness of the NiFe film increased from 200 to 1000 Å, the output signal increased. A maximum increase of 7.3 dB at a linear density of 2100 fr/mm was obtained with a 1000 Å thick keeper layer. This result implies that when the thickness of the keeper layer is small, there is still some leakage of flux from the recorded bit that does not contribute to the reproduce signal. If the thickness of the keeper layer was thin (200 Å), the head read through the keeper layer with zero

[a]Also at the Department of Electrical Engineering.

 0021-8979/94/75(10)/6150/3/$6.00 © 1994 American Institute of Physics

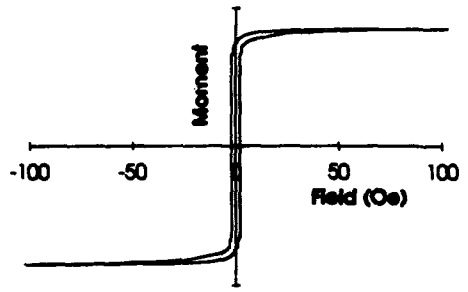

FIG. 1. The typical hysteresis curve of 1000 Å NiFe/50 Å Cr/glass sample ($Hc \approx 2$ Oe).

bias current. When the NiFe thickness was 200 and 600 Å, the increases in output signal were small and decreased as the linear density increased. However, when the NiFe thickness was 1000 Å, a maximum increase was obtained at high density, which was also reported by Kao[3] and Gooch.[4] However, there was an asymmetry with a distortion at the bottom of an isolated pulse being observed. As the thickness of the NiFe increased, the degree of distortion of the signal increased. As shown in Fig. 2(b), the noise also increased with increasing thickness of the NiFe layer. The noise level was very high at very low density. Beyond that region the noise did not change much with recording density. Therefore, even though there was an increase in output signal, the S/N ratio did not show improvement, especially for thick NiFe keepered media.

Figure 3 shows the effect of the Cr isolation layer thickness on the amplitude of the signal output. In this case, NiFe thickness was kept at 600 Å. A readable signal could not be detected without a Cr isolation layer, which is contrary to the result reported by Gooch *et al.*[4] They did not deposit an isolation layer between the thin film media storage and the NiFe keeper layer, but there might have been an oxide layer on the surface of the media. The output signal increased with an increase of the Cr isolation layer thickness up to 200 Å. The small signal at small isolation layer thickness might be due to the magnetic interaction between NiFe and CoCrTa layers. The output signal may decrease after an optimum thickness of the Cr isolation layer, because the isolation layer increases spacing between the head and CoCrTa media.

Figures 4(a) and 4(b) show the hysteresis curve of 600 Å NiFe/500 Å CoCrTa/glass and 600 Å NiFe/50 Å Cr/500 Å CoCrTa/glass samples. Without a Cr isolation layer, the coercivity of NiFe film was 93 Oe, and it decreased to 12 Oe with 50 Å of Cr isolation layer. The Cr isolation layers decouple the interactions between the high coercivity media and the soft magnetic keeper layer. With a 50 Å thick isolation layer, the signal output was smaller than for conventional media. In this case, such a very thin isolation layer might not be continuous and may have pinholes that might induce magnetic interaction between the media and the NiFe film, such that the keeper layer might not be fully saturated

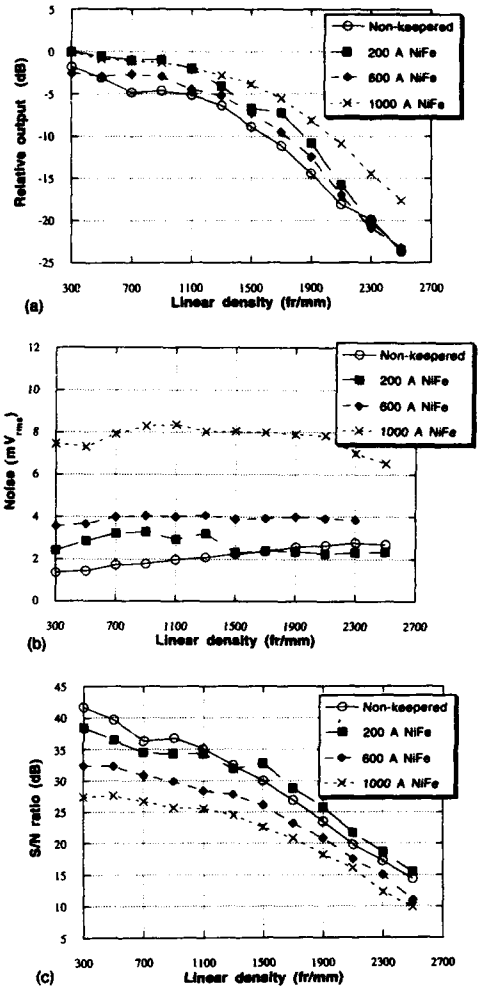

FIG. 2. (a) The effect of the thickness of NiFe on signal output. (b) The effect of the thickness of NiFe on noise. (c) The effect of the thickness of NiFe on the signal-to-noise ratio. (The thickness of the Cr isolation layer is fixed at 100 Å.)

with a small bias current. With 100 and 200 Å of the isolation layer, the signal output was improved.

Several important effects of keepered media are the timing asymmetry, the output signal shape, and the hump at the edge of an isolated signal. The influence of bias current on the signal output and timing asymmetry is shown in Fig. 5. An optimum bias current was about 1.8 mA with a 100 Å Cr isolation layer and a 600 Å keeper layer. The timing difference between the leading and trailing pulse decreased with a bias current from 115 ns at 0.8 mA to 2.3 ns at 3.0 mA. The signal distortion became smaller and eventually became flat as the bias decreased from 2.0 mA to 0.75 mA. The timing asymmetry observed in keepered media may be due to the

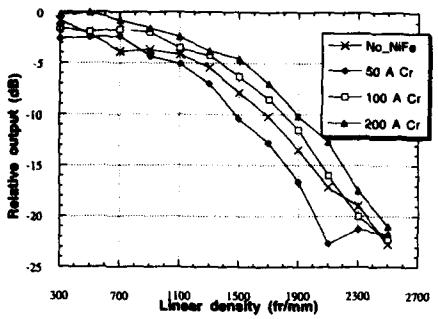

FIG. 3. The effect of the thickness of the Cr isolation layer on the output signal. (The thickness of NiFe is fixed at 600 Å.)

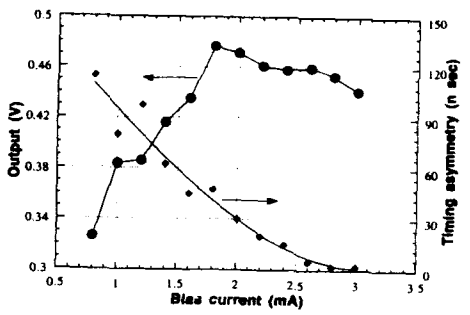

FIG. 5. The effect of bias current on the output signal. (The thickness of the Cr isolation layer and NiFe is 100 and 600 Å, respectively.)

additive and subtractive superposition of the magnetic field from the bias current and stray field from the recorded bits. This effect results in low and high permeabilities of the keeper layer under the pole tips of the thin film head.

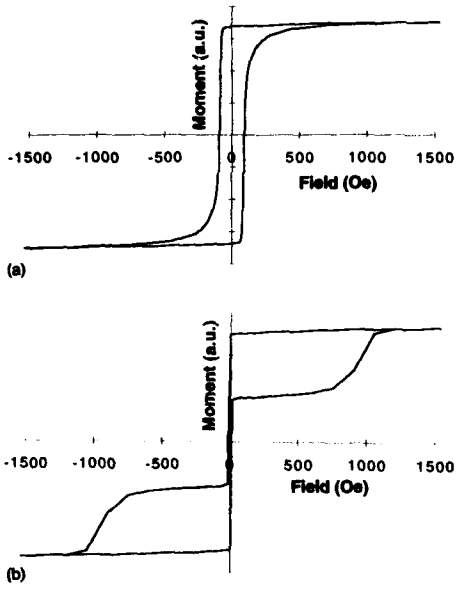

FIG. 4. Hysteresis curves of (a) 600 Å NiFe/500 Å CoCrTa/glass, and (b) 600 Å NiFe/50 Å Cr/500 Å CoCrTa/glass.

IV. CONCLUSION

Experimental research is carried out on longitudinal CoCrTa/Cr thin film media with a NiFe soft magnetic layer and a Cr isolation layer. It is studied about the effects of the thickness of a NiFe keeper layer, Cr isolation layer, and bias current on the reproduce signal and medium noise of the keepered media. The following is concluded.

(1) The signal output increases with increasing NiFe thickness. However, there was a large increase in medium noise with an increase in the thickness of the NiFe keeper layer.

(2) Without a Cr isolation layer, a readable signal could not be obtained due to magnetic interactions between NiFe and CoCrTa films. The signal output increased as the Cr thickness increased. A low output signal from the thin Cr might be due to the magnetic interaction between the keeper layer and the CoCrTa storage layer, or a reduction of the permeability of the keeper layer.

(3) A timing asymmetry of the output signal was observed, which decreased with increasing bias current. A distortion of the signal at the edge was observed.

ACKNOWLEDGMENTS

The authors would like to express their thanks to the Maxtor Corporation and Seagate Technology for the support of this work.

[1] B. R. Gooch, U.S. Patent #4,985,795.
[2] R. R. Wood and B. R. Gooch, U.S. Patent pending.
[3] A. S. Kao, W. B. Reed, R. B. Zubeck, D. R. Hollars, and K. S. Goodson, FB-06, Intermag Conference Digest, Stockholm, Sweden, 1993.
[4] B. R. Gooch, R. Niedermeyer, R. Wood, and R. Pisharody, IEEE Trans. Magn. 27, 4549 (1991).

Process temperature dependence of ∂M plots on Co alloy media on amorphous carbon substrates

Masago Kuwabara, Haydee Saffari, Mark R. Visokay, Hidetaka Hayashi, and Motoharu Sato[a)]
Kobe Steel U.S.A. Applied Electronics Center, Palo Alto, California 94304

The static magnetic properties and the film structure of Co alloy recording media made under different deposition and annealing temperatures were investigated. With increasing film coercivity an increase of the grain size and a reduction of the positive peak in the ∂M plots were observed. It is believed that reduced exchange coupling was achieved by preferential Cr segregation at the grain boundaries during high-temperature processing.

One of the important requirements for attaining higher recording density in magnetic hard disks is an increase in the film coercivity (H_c). There are various process factors which affect H_c, such as Co alloy composition, Cr underlayer thickness, deposition temperature, Ar pressure, dc bias, etc. It is known that both high-temperature deposition and post-annealing are effective in producing a high H_c in Co alloy thin films,[1–3] although the detailed mechanism of H_c is not fully understood yet. However, conventional Al/NiP substrates have a problem at high temperature due to crystallization of amorphous NiP. Recently developed ultradensified amorphous carbon (UDAC) substrates[4] have a high heat resistance which allows sputtering at higher substrate temperatures and post-annealing. In this paper the process temperature dependence of the static magnetic properties of Co alloy media was studied.

The Co alloy media were prepared on polished UDAC substrates by dc magnetron sputtering with Cr, CoCrX (X =Ni, Ta, or Pt), and carbon or Zr targets. The Zr was used for annealing experiments. The Ar pressure was 3–5 mTorr and the substrates were kept at temperatures ranging from 30 to 300 °C by heaters located behind the substrates. The post-annealing was performed at temperatures between 350 and 800 °C at a pressure of 30 mTorr.[3] The M–H loop and ∂M plots were measured with a vibrating sample magnetometer (VSM) and rotational hysteresis loss measurements were carried out with a torque magnetometer. Structural analysis was carried out by transmission electron microscopy (TEM).

Figure 1 shows the relationship between deposition temperature (T_s) and H_c for the three Co alloy media. Since polished substrates were used, no magnetic anisotropy was observed in the film plane. In all three cases, as T_s increases up to around 200 °C, H_c increases and at the same time S^* decreases. Figure 2 shows TEM images of $Co_{70}Cr_{18}Pt_{12}$ media: (a) deposited at 30 °C and (b) at 250 °C. The H_c of samples (a) and (b) are 1530 and 2670 Oe, respectively. For our sputtering conditions, the films have a heavily densified structure and no physical separation between grains was observed. By conventional x-ray and selected area electron diffraction, no significant difference in crystal orientation is observed between the samples deposited at different temperatures. In Fig. 2 it is clear that the grain size increases and surface roughness decreases as T_s increases. These phenomena were observed in all three alloy cases and are due to the shadowing effect and to the increase in mobility of sputtered atoms with temperature. The grain size and surface roughness may be related to H_c. The origin of H_c decrease at higher deposition temperature is not clear at this moment. However, it is confirmed that the temperature that gives the maximum H_c depends on the Ar pressure and the dc bias voltage.[5] Figure 3 is a high-resolution cross-sectional TEM image of $Co_{70}Cr_{18}Pt_{12}$. It is obvious that Co alloy columns have a replica structure of the Cr underlayer columns. Stacking faults were frequently observed in the Co alloy layer and its density tends to slightly increase as the deposition temperature increases. The fcc phase of the Co alloy was occasionally observed in the films.[6] However, the effect of stacking faults and fcc phase on H_c is not clear at this moment.

Figure 4 is a ∂M plot of $Co_{70}Cr_{18}Pt_{12}$ media. $\partial M(H)$ is defined as $\partial M(H)=I_d(H)/I_r(\infty)-[1-2I_r(H)/I_r(\infty)]$.[7] I_r and I_d are the isothermal remanent magnetization and the dc demagnetization remanent magnetization, respectively. Since the ∂M behavior is related to the magnetic interactions between grains in the magnetic film, ∂M plots have been used to understand the media noise.[8,9] As T_s increases, the positive peak decreases. This tendency was observed in all three alloy cases. A positive peak in a ∂M plot reveals the existence of exchange coupling between the grains in the ferromagnetic films and its height is related to the degree of coupling. Therefore, it is believed there is less exchange coupling at higher deposition temperatures, leading to a higher film coercivity. Since there is no physical separation between the grains in our films, the decoupling may be achieved by a nonmagnetic layer formed between the grains.

It is reported that under suitable annealing conditions the H_c of Co alloy media can be improved drastically.[3] Figure 5 shows ∂M plots of unannealed and annealed $Co_{75}Cr_{13}Pt_{12}$ media with H_c of 1560, 2670, and 3040 Oe, respectively. On the unannealed sample a strong positive peak was observed, which decreases and finally disappears as the annealing temperature increases. This tendency was also observed in all three Co alloy cases. Figure 6 shows TEM images of $Co_{86}Cr_{12}Ta_2$ both unannealed and annealed at 700 °C. The grain size increases slightly after high-temperature annealing and a reaction occurs at the interface between the Cr and Co alloy layers. It was confirmed by high-resolution EDS analysis that the Cr concentration both in the grains and at the

a)Kobe Steel, Ltd., Electronics Research Lab., Kobe, Japan.

 0021-8979/94/75(10)/6153/3/$6.00 © 1994 American Institute of Physics

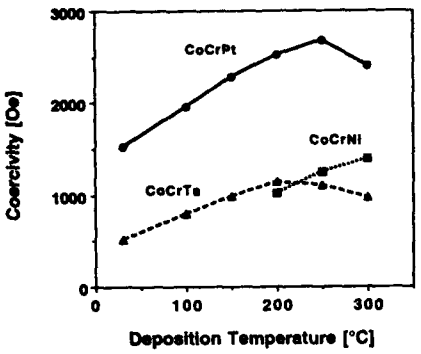

FIG. 1. The relationship between T_s and H_c of $Co_{70}Cr_{18}Pt_{12}$, $Co_{69}Cr_9Ni_{31}$, and $Co_{85}Cr_{11}Ta_4$ media.

grain boundaries increases due to annealing. However, the increase of the Cr concentration at the grain boundaries is greater than in the grains.[3] These results suggest that preferential Cr segregation from the Cr underlayer to the Co grain boundaries forms a thin nonmagnetic layer at the grain boundaries. This layer then reduces the exchange coupling between grains and improves the film coercivity. The Cr concentration of the sample deposited at high temperature has not been confirmed experimentally, but since the temperature dependence of the ∂M plots is similar, the mechanism of H_c is believed to be the same as in the annealing case. On the other hand, the negative peak in the ∂M plot reveals the presence of magnetostatic interactions. The negative peak tends to increase through high-temperature annealing. This may be related to the grain size increase during the annealing.

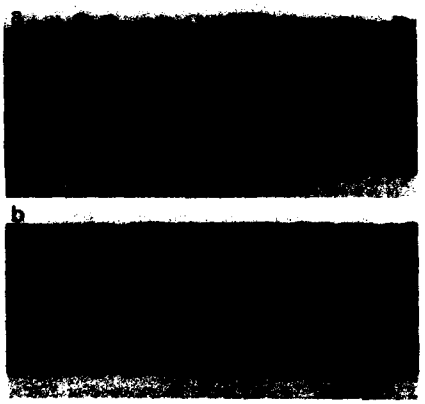

FIG. 2. Bright field cross-sectional TEM images of $Co_{70}Cr_{18}Pt_{12}$ media. (a) Deposited at 30 °C; (b) deposited at 250 °C.

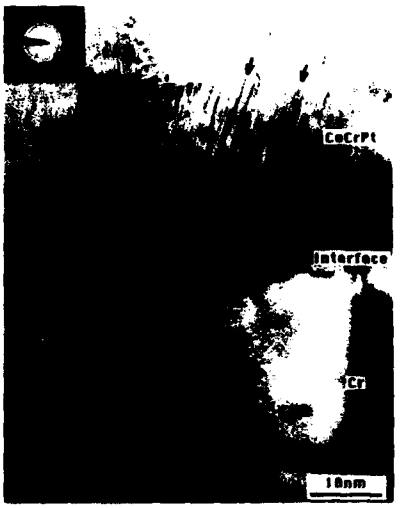

FIG. 3. HREM image of the interface of $Co_{70}Cr_{18}Pt_{12}$ and Cr underlayer. The dark lines in $Co_{70}Cr_{18}Pt_{12}$ layer whose direction is indicated by arrows are stacking faults.

It has been reported that the magnetic anisotropy field (H_k) does not depend on the film coercivity in the same alloy and H_c is strongly related to the intergranular magnetic interactions.[10] Figure 7 shows the relationship between normalized H_c and normalized H_k. The normalized H_c (H_k) was obtained by dividing $H_c(H_k)$ by the $H_c(H_k)$ of the sample deposited at 200 °C without annealing. The H_k was measured as the magnetic field at which extrapolation of the rotational hysteresis loss curve becomes zero.[10] The H_k values of CoCrTa, CoCrNi, and CoCrPt media do not change drastically within the same alloy even though the H_c

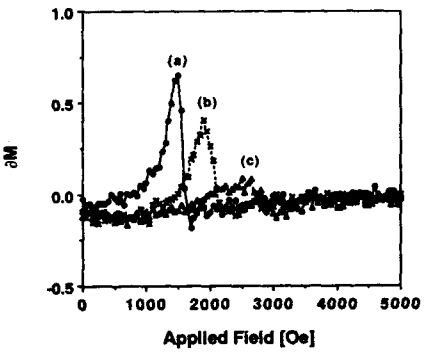

FIG. 4. ∂M plots of $Co_{70}Cr_{18}Pt_{12}$ media. The media were deposited at (a) 30, (b) 100, and (c) 200 °C. The positive peak height decreases with deposition temperature.

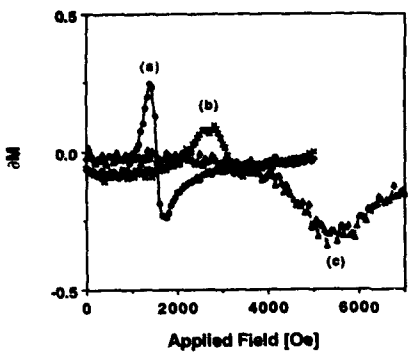

FIG. 5. ∂M plots of $Co_{75}Cr_{13}Pt_{12}$ media. (a) The unannealed media; (b) the media annealed at 500 °C and (c) at 600 °C. The positive peak height decreases with annealing temperature.

changes. There is a tendency for the H_k values of the media with lower H_c within the same alloy to be smaller than that of the media with higher H_c. The H_k measured from the rotational hysteresis loss curve is not the same as the intrinsic H_k if the interactions between the grains are too strong. The ∂M plots indicate that the lower H_c samples within the same alloy have strong exchange coupling and therefore the H_k of the lower H_c sample within the same alloy is not close

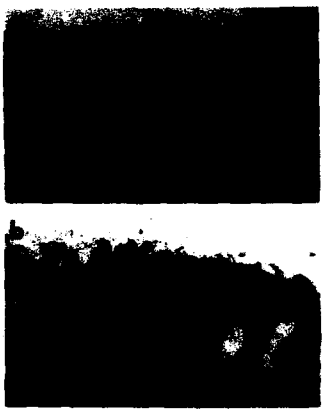

FIG. 6. Cross-sectional TEM images of $Co_{86}Cr_{12}Ta_2$ media. (a) Unannealed and (b) annealed at 700 °C.

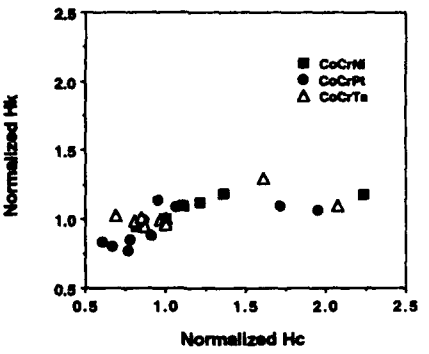

FIG. 7. The relationship between normalized H_c and normalized H_k.

to the value of the intrinsic H_k. Therefore it is believed that the intrinsic H_k is not affected significantly by the different process temperatures and it is concluded that a decrease in exchange coupling due to Cr segregation at the grain boundaries strongly improves the film coercivity both for higher temperature deposition and post-annealing. The transition noise is strongly related to the exchange coupling in the magnetic films. Therefore high-temperature processing not only helps improve the H_c but also reduces the media noise. A preliminary study indicates that the media noise of $Co_{70}Cr_{18}Pt_{12}$ media with $H_c=2500$ Oe is about half that of $Co_{70}Cr_{18}Pt_{12}$ media with $H_c=1700$ Oe.

In conclusion, it is confirmed that the improvement of H_c in CoCrNi, CoCrTa, and CoCrPt by both high-temperature deposition and annealing is mainly driven by the reduction of the exchange coupling between the grains. This is believed to be due to preferential Cr segregation at the grain boundaries.

[1] N. Tani, M. Hashimoto, M. Ishikawa, Y. Ota, K. Nakanura, and A. Itoh, IEEE Trans. Magn. MAG-26, 1282 (1990).
[2] M. Kuwabara, M. Sato, Y. Onishi, M. R. Visokay, H. Hayashi, H. Inoue, and K. Muramatsu, J. Appl. Phys. 73, 6686 (1993).
[3] M. Sato, Y. Onishi, and A. Nakaue, IEEE Trans. Magn. (to be published).
[4] K. Muramatsu, Y. Sakashita, Y. Onishi, and Y. Hara, R&D Kobe Steel Eng. Rep. 39, 35 (1989).
[5] H. Saffari and M. Kuwabara (unpublished).
[6] M. Kuwabara and M. R. Visokay, Proc. 51st MSA Ann. Conf. (1993), p. 1020.
[7] P. E. Kelly, K. O'Grady, P. I. Mayo, and R. W. Chantrell, IEEE Trans. Magn. MAG-25, 3881 (1989).
[8] K. O'Grady, IEEE Trans. Magn. MAG-26, 1870 (1990).
[9] M. El-Hillo, K. O'Grady, R. W. Chantrell, I. L. Sanders, M. M. Yang, and J. K. Howard, IEEE Trans. Magn. MAG-27, 5061 (1991).
[10] M. Takahashi, T. Shimatsu, M. Suekane, M. Miyamura, K. Yamaguchi, and H. Yamasaki, IEEE Trans. Magn. MAG-28, 3285 (1992).

Friction and wear of ion-implanted diamondlike carbon and fullerene films for thin-film rigid disks

Bharat Bhushan and B. K. Gupta
Computer Microtribology and Contamination Laboratory, Department of Mechanical Engineering, The Ohio State University, Columbus, Ohio 43210-1107

In this paper, DLC coatings on a rigid magnetic disk were ion implanted with nitrogen and carbon ions to improve their wear lives. Nitrogen and carbon ion implantation with a dose of 5×10^{15} ions cm^{-2} at 200 keV have shown significant improvements in the coefficient of friction and sliding wear life which suggests that ion-implanted DLCs may be more desirable overcoats. Microstructural examinations of implanted films show that these films are still amorphous with no long range order. Implanted DLC films also may be attractive as an overcoat for the slider surface. An approximately 20-nm-thick fullerene film, a new solid lubricant, was also deposited on the disk surface to reduce its friction and wear. Fullerene films exhibited lower friction, however, these readily formed a transfer film on the mating slider surface. Since any transfer and movement of the material at the head-disk interface is undesirable, fullerene films are not expected to be potential overcoats. Coefficient of friction of implanted DLC and fullerene films on a microscale was also measured and was found to be lower than that on macroscale. Microfriction values of unimplanted and implanted DLC films were comparable.

Metal films that are used to achieve the high recording densities have weak durability and are prone to environmental corrosion. Diamondlike carbon (DLC) coatings (20–30 nm thick) with lubricant overlays are commonly used to provide low friction, low wear, and corrosion resistance. The need for increasing higher recording densities requires that disk and head slider surfaces be as smooth as possible and flying heights (head-to-disk separation) be as low as possible. Smoother surfaces and lower flying heights lead to more intimate contact and high friction and wear.[1] There is a need for thinner overcoats with lower friction and wear than those currently used.

Liu and Cohen[2] hypothesized that a metastable carbon-based material β-C_3N_4 can be fabricated which may be superior to diamond in its mechanical properties. Since then there have been few attempts to synthesize C-N compounds. Carbon compound coatings can be produced by incorporating nitrogen either during their growth or by a post-deposition ion-beam treatment. Iwaki *et al.*[3] and Kenny *et al.*[4] reported significant improvements in the wear resistance of glassy carbon by implanting with nitrogen and carbon ions in the dose range of 5×10^{14}–5×10^{16} ions cm^{-2} at 50–150 keV. Chen *et al.*[5] reported a coefficient of friction of about 0.16 for the CN_x films deposited by dc planar magnetron sputtering. Torng *et al.*[6] reported a coefficient of friction of 0.2 for rf sputtered amorphous CN_x films. Niu *et al.*[7] have reported that they are able to produce β-C_3N_4 compound using pulsed laser ablation of graphite targets combined with an intense atomic nitrogen source.

There also have been attempts to produce potentially hard C-N coatings for magnetic disk applications. Yeh *et al.*[8] reported an increase in sliding wear life of a magnetic disk that was coated with a rf sputtered carbon-nitrogen coating. Inoue *et al.*[9] ion implanted DLC coated magnetic disk with 10^{15}–10^{18} ions cm^{-2} nitrogen ions at 5–20 keV. Based on electrochemical and atmospheric corrosion tests, they reported improvements in the corrosion resistance of the underlying Co-Ni alloy magnetic layer. In the present study, we have explored the possibility of modifying friction and wear properties of DLC coated magnetic disk by ion implantation with N_2^+ and C^+ ion species. Ion implantation is known to improve hardness, porosity, and friction and wear properties of surfaces. We have also deposited a new solid lubricant C_{60}-rich fullerene film[10] on the disk surface. Results of ion-implanted DLC and fullerene films are the subject of this paper.

The disks used in this study were commercially available thin-film magnetic rigid disks without any liquid lubricant.[1] The textured disk coupons were implanted with N_2^+ and C^+ at 2–4 μA cm^{-2} ion current densities, 200 keV accelerating voltage, and ion doses ranging from 5×10^{15} to 2×10^{17} ions cm^{-2}. The C_{60}-rich fullerene films were deposited on disk coupons by sublimation at about 450 °C and a vacuum of 10^{-6} Torr.[10]

Raman measurements were made using an argon ion laser at 514.5 nm wavelength with an output of about 100 mW and a spot size of 0.1 mm diam. The variation in the composition of ion-implanted disk with depth was measured by Auger electron spectroscopy (AES) using a Perkin–Elmer M50 ESCA/Auger spectrometer. The electron beam energy, used for Auger analysis, was 3 keV with a current density of about 1 μA cm^{-2}.

The friction and wear tests were made both on macro and microscales. Macrotests were conducted by sliding an Al_2O_3-TiC head slider (rms roughness ~1.5 nm; crown=2 nm) against a disk coupon (15 mm×15 mm) in a reciprocating mode. Typical test conditions were as follows: reciprocating amplitude—5 mm, frequency—1 Hz, normal load 0.1 N, average linear speed—10 mm/s, temperature—20 °C, and atmospheric conditions— humidity 45%–55% RH. One pass corresponds to a round trip sliding of 10 mm. These tests were repeated at least three times on identical samples and the variation in the measured friction was less than 10%. Microscale measurements were made using friction force mi-

 0021-8979/94/75(10)/6156/3/$6.00 © 1994 American Institute of Physics

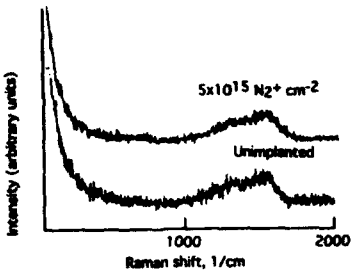

FIG. 1. Raman spectra of (a) unimplanted and (b) ion implanted disk with 5×10^{15} N_2^+ cm^{-2}. Raman spectra of disks that were ion implanted with 1×10^{16} and 5×10^{16} N_2^+ cm^{-2} were similar to that of the disk that was ion implanted with 5×10^{15} N_2^+ cm^{-2}.

croscopy. Tests were made on a 500×500 nm scan size at normal load of 15–120 nN and a scanning speed of 2 μm/s.

The microstructure of approximately 22-nm-thick DLC overcoat on the magnetic coating after ion implantation was studied using Raman spectroscopy. No significant differences were observed between the spectra of the unimplanted disk and disks implanted with 5×10^{15} N_2^+ cm^{-2} and 5×10^{15} C^+ cm^{-2}. Representative Raman spectra of unimplanted disk and an implanted disk with 5×10^{15} N_2^+ cm^{-2} at 200 keV are shown in Fig. 1. Raman spectra of disks that were ion implanted with 1×10^{16} and 5×10^{16} N_2^+ cm^{-2} were similar to that of the disk that was ion implanted with 5×10^{15} N_2^+ cm^{-2}. An increase in the dose did not affect the Raman spectra of the ion-implanted disk. The occurrence of a broad hump at 1550 cm^{-1} in the Raman spectra of unimplanted and implanted disks suggests that the coating remains amorphous after ion implantation. Slight difference in the shape of the peak is observed though. The thicknesses of the DLC coatings before and after ion implantation were estimated from ellipsometric measurements. A reduction in the thickness from 22 to 15 nm of the DLC coating was observed as a result of ion implantation.

Because of a thin DLC coating, there is a danger that ion beam mixing may occur at the DLC-magnetic coating interface which may affect magnetic properties. Composition as a function of depth of implanted samples was measured using AES, Fig. 2. An abrupt change in the compositions of C, Co, and Ni at the carbon-magnetic film interface suggests that there is no observable ion beam mixing at the interface. From this observation, we conclude that ion implantation does not cause any deterioration in the magnetic layer. If ion beam mixing is an issue, implantation at lower energy should be tried.

The friction profiles of N_2^+- and C^+-implanted disks on a macroscale with varying doses are shown in Figs. 3(a) and 3(b). Ion implantation with a lower dose of 5×10^{15} ions cm^{-2} exhibits a decrease in the coefficient of friction, from 0.20 to 0.17, while higher doses resulted in an increase. Coefficient of friction of carbon implanted (5×10^{15} ions cm^{-2}) disk on a microscale was also found to be lower (~0.03) than that of unimplanted disk (~0.05). Reduced

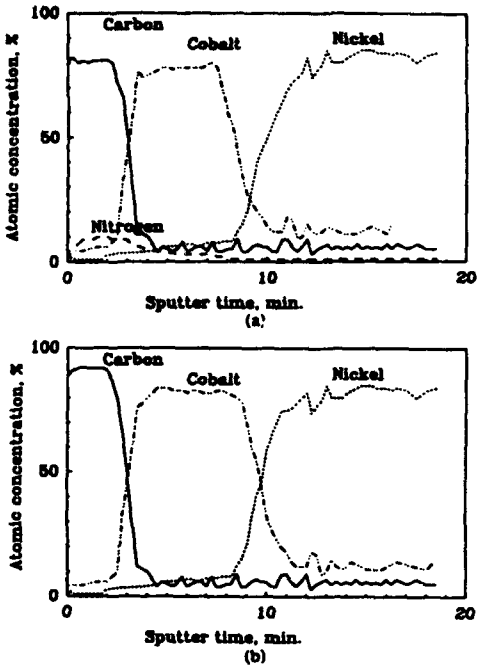

FIG. 2. AES composition (atomic concentrations) profiles of nitrogen, carbon, cobalt, and nickel of disk ion implanted with (a) 1×10^{16} N_2^+ cm^{-2}, (b) 1×10^{16} C^+ cm^{-2}.

friction is also accompanied with an increase in sliding wear life measured in the macrotests. The sliding wear life is estimated in terms of the sliding distance at which the friction is increased abruptly to a higher value. The optical micrographs of the wear track obtained on the ion implanted disk with 5×10^{15} and 1×10^{16} N_2^+ cm^{-2} are shown in Fig. 4(i). There is no evidence of wear debris in the lower dose disk, however, wear debris is observed in the higher dose disk. The carbon ion-implanted disks have also shown the similar trends of wear debris. Reduction in the coefficient of friction and increase in sliding wear life of N_2^+- and C^+-implanted disk with a low dose (5×10^{15} ions cm^{-2}) probably results from the modified chemistry of the DLC coating, such as formation of CN_x compound in the case of nitrogen ion implantation which may have higher hardness and bulk modulus. Increase in friction at a dose of 1×10^{16} ions cm^{-2} is probably due to structural damage to the DLC coating. Yeh *et al.*[8] reported an increase in the sliding wear life of rf sputtered carbon-nitrogen compound overcoated magnetic disk with nitrogen content. Higher wear life was attributed to greater sp^3 bonding and finer microstructure of C-N coatings with high nitrogen content. Inoue *et al.*[9] have shown that ion implantation with 3×10^{16} N_2^+ cm^{-2} at 20 keV resulted in the formation of amine, ammonium, and *pi–pi* binding compounds. Torng *et al.*[6] have observed a reduction in the coefficient of friction of sputtered DLC films (from 0.4 to 0.2)

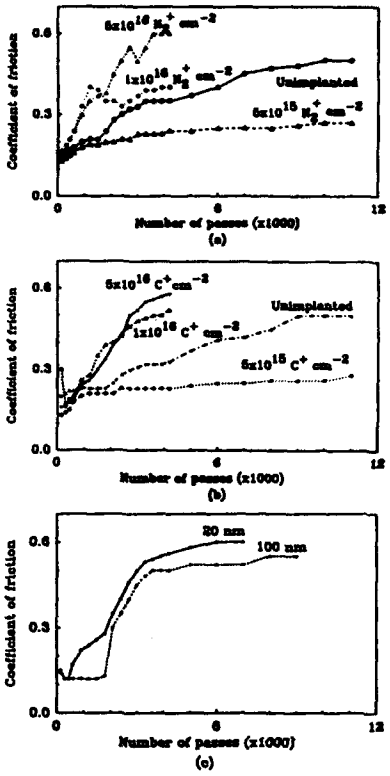

FIG. 3. Friction profiles of unimplanted and ion implanted disks with varying doses of (a) N_2^+, (b) C^+, and (c) disks coated with 20- and 100-nm-thick fullerene films. The disk coupon were slid against Al_2O_3-TiC slider.

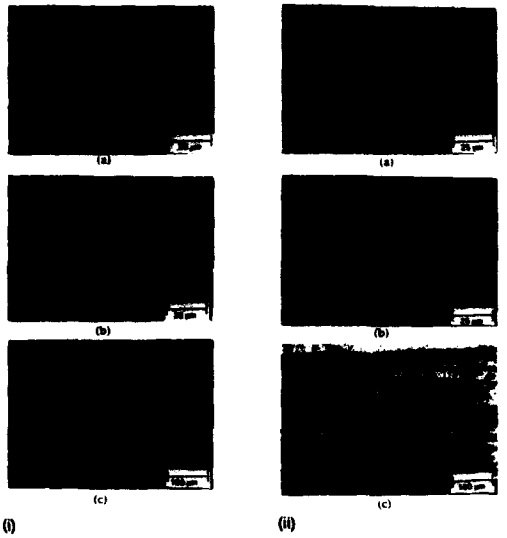

FIG. 4. (i) Optical micrographs of wear tracks obtained on the disks that slid against the Al_2O_3-TiC slider (a) disk that was ion implanted with 5×10^{15} N_2^+ cm^{-2} and tested for 10 000 passes (100 m), (b) disk that was ion implanted with 1×10^{16} N_2^+ cm^{-2} and tested for 5000 passes (50 m), (c) slider that slid against the disk identified in (b). (ii) Optical micrographs of fullerene-coated disk (a) before and (b) after the wear test, and (c) slider after the wear test.

with an increase in the pressure of nitrogen sputtering gas. They have predicted from AES, x-ray photoelectron spectroscopy, and transmission electron microscopy analyses that increased amount of nitrogen enhanced the diamond sp^3 bonding. Our observation of increased sliding wear life of DLC coatings implanted with 5×10^{15} N_2^+ or C^+ cm^{-2} is in agreement with the findings of Kenny *et al.*[4] for amorphous glassy carbon. They reported an improvement in wear resistance by two orders of magnitude as a result of ion implantation.

The friction profile of a C_{60}-rich fullerene-coated disk slid against an Al_2O_3-TiC slider is shown in Fig. 3(c). It is obvious from this figure that fullerene film (~20 nm thick) provide a lower friction initially (~0.12) compared to the DLC overcoat (~0.2), but it increased abruptly after 500 passes. However, a 100-nm-thick fullerene film survived for 1800 passes. The increase in friction is attributed to the damage to the fullerene film. Coefficient of friction of fullerene-coated disk on a microscale was also measured and was found to be lower (~0.04) than that on macroscale (~0.12). The optical micrographs of the wear track on the fullerene coated disk before and after the wear test are shown in Fig. 4(ii). We see evidence of bare spots and wear debris (redeposition of fullerene material) on disk surface and a formation of transfer film on the slider [Figs. 4(ii b) and 4(ii c)]. Filling of the roughness grooves on the disk surface [Fig. 4(ii b)] may be responsible for the increase in real area of contact which in turn increases the friction. The wear life of the fullerene film was limited possibly because of inadequate adhesion which may be improved by depositing it by a more energetic deposition process such as ion beam deposition and magnetron sputtering. Since any transfer and movement of material at the head-disk interface is undesirable, fullerene films deposited by sublimation may not be suitable.

[1] B. Bhushan, *Tribology and Mechanics of Magnetic Storage Devices* (Springer, New York, 1990).
[2] A. Y. Liu and M. L. Cohen, Science **245**, 841 (1989).
[3] M. Iwaki, K. Takahashi, and A. Sekiguchi, J. Mater. Res. **5**, 2562 (1990).
[4] M. J. Kenny, J. T. A. Pollock, and L. S. Wielunski, Nucl. Instrum. Methods Phys. Res. B **39**, 704 (1989).
[5] M. Y. Chen, V. P. Dravid, Y. W. Chung, M. S. Wong, and W. D. Sproul, Trib. Trans. **36**, 491 (1993).
[6] C. J. Torng, J. M. Sivertsen, J. H. Judy, and C. Chang, J. Mater. Res. **5**, 2490 (1990).
[7] C. Niu, Y. Z. Lu, and C. M. Lieber, Science **261**, 334 (1993).
[8] T. A. Yeh, C. L. Lin, J. M. Sivertsen, and J. H. Judy, IEEE Trans. Magn. **MAG-27**, 5163 (1991).
[9] Y. Inoue, Y. Satou, and K. Tanaka, Adv. Info. Storage System **4**, 263 (1992).
[10] B. Bhushan, B. K. Gupta, G. W. Van Cleef, C. Capp, and J. V. Coe, Appl. Phys. Lett. **62**, 3253 (1993).

Thin film disks for high density recording with textured underlayers (abstract)

Mohammad Mirzamaani
IBM Adstar, San Jose, California 95193

Michael A. Russak and Christopher V. Jahnes
IBM T. J. Watson Research Center, Yorktown Heights, New York 10598

As higher recording densities are required on thin film disks the balance between magnetic and tribological performance becomes a delicate one.[1] Optimized magnetics dictate very smooth magnetic films with small, well isolated (i.e., magnetically decoupled) grains whereas acceptable mechanical performance requires sufficient surface roughness to insure low stiction.[2] This balance may not be readily obtained by mechanical texturing but can be accomplished by nonmechanical texturing.[3] In this work AFM and conventional magnetic measurements have been used to characterize a variety of thin film disk surfaces and conditions found which permit the simultaneous attainment of excellent tribological and magnetic performance. In the case of nonmechanical texture a first layer of In was sputtered to provide the texture and then Cr and CoPtCr layers (single as well as laminated) deposited to provide the magnetics. The thickness and crystallographic orientation of the Cr interlayer have a marked effect on the macromagnetic properties of the magnetic layer and in turn disk recording performance. The optimized process produces disks with signal to noise (S/N) at 4000 fr/mm of ≈35 db, acceptable soft error rates for high density recording and CSS stiction values of <3 g. These parameters have been obtained on metallic and nonmetallic substrates.

[1] T. Reith *et al.*, Intermag '92 Conference, St. Louis, MO, paper JA-07.
[2] V. Raman *et al.*, J. Appl. Phys. **70**, 1826 (1991).
[3] M. Mirzamaani *et al.*, IEEE Trans. Mag. **28**, 3090 (1992).

 0021-8979/94/75(10)/6159/1/$6.00 © 1994 American Institute of Physics

A study of the structural properties of sputtered CoCrPt based on x-ray diffraction, small angle x-ray scattering, XAFS, and transmission electron microscopy measurements (abstract)

S. Yumoto and N. Ohshima
Functional Devices Research Laboratories, NEC Corporation, Kawasaki, Kanagawa, Japan

As a first step in trying to understand the relationship between magnetic properties and structural properties, the authors have conducted a systematic structural investigation of CoCrPt samples that have been sputtered at different levels of sputtering power, which affects magnetic properties. X-ray diffraction (XRD), small angle x-ray scattering (SAXS), and XAFS were used to examine, respectively, long, medium, and short range orderings. TEM was used to examine the structural morphology. CoCrPt was fabricated on Kapton films by dc magnetron sputtering at levels of 0.1, 0.3, 0.5, and 1 kW sputtering power. XRD indicated a *continuous* increase in the intensity of the peak corresponding to hcp (002), as sputtering power was increased. SAXS, on the other hand, in the range of 0.5–3.0 deg. at 2θ, indicated the presence of scattering for the 0.1 and 0.3 kW samples alone, not for the others. Similarly *discontinuous* were the spectrums produced by XANES of Co for the 0.3, 0.5, and 1.0 kW samples, which resembled the spectrum of sputtered Co. The spectrum of the 0.1 kW samples was quite different. TEM indicated a clear small-grain structure for the 0.1 kW sample, less clearly defined grains for the 0.3 kW sample, and no observable grains for the others. When conducted after chemical etching, it further identified the source of the grain structure as Pt segregation. This leads to speculation that Pt segregation may be responsible, to some degree, for the discontinuity observed in SAXS and XANES measurements. It is further speculated that the long range ordering (crystal orientation) is quite probably related to magnetic anisotropy, and that segregation affects wall motion, which means that, in order to understand the relationship between magnetic and structural properties, structural investigations should be systematic and include short, medium, and long range orderings.

 0021-8979/94/75(10)/6160/1/$6.00 © 1994 American Institute of Physics

Multinuclear nonmagnetic resonance studies of perfluoro poly ether lubricants (abstract)

K. V. Viswanathan
IBM AdStar Division, Rochester, Minnesota 55901

Commercial perfluoro poly ethers (PFPE) are available with different backbone structures and end groups and are being used as lubricants for particulate/thin film disks. Very little published information is available other than F-19 spectra for these polymers.[1] In this abstract a systematic study was undertaken to study the structure of these PFPE polymers using multinuclear magnetic resonance (NMR). Backbone structural differences of Z. Fomblin, Y. Fomblin, Krytox, and Demnums could be clearly seen from F-19 NMR studies. Number average molecular weight of PFPE polymers was also determined from F-19 NMR and found to be between 2000 and 10 000. C-13 NMR was used to differentiate the end group from backbone structure. Associated proton test (APT) was used to distinguish the primary, secondary, and tertiary carbons. The proton connectivity of end group (e.g., Fomblin AM2001) was studied by two dimensional (2D) proton correlation spectroscopy (COSY). The connectivity of a hydrogen containing end group to the backbone was studied by heteronuclear shift correlation spectroscopy (HCORR). Even though these PFPE polymers have low vapor pressure, a significant amount of lube loss is found over a period of time under HDA (head disk assembly) conditions. The temperature could increase from 25 to 60 °C. Additionally under certain asperity/head interaction conditions the temperature variation could be as high as 300 °C to 500 °C. It is also reported that functionalized polymeric materials (e.g., Krytox 143 AC) can be bonded to magnetic disk surface by applying heat. The effect of temperature on lubricant volatility/stability was studied for AM 2001. The molecular weight of heat treated AM 2001 (90 min at 130 °C) changed from 2100 to 4500. This could be due to preferential volatilization of low molecular weight fragments. NMR analysis showed significant conversion of piperonyl end group to $-CH_2OH$. Thus AM 2001 is not thermally stable. Precipitation was also found to occur when AM 2001 is stored over a period of time. The precipitate is found to be a derivative of 9.10 dihydroanthracene. Unlike other PFPE polymers AM 2001 is found to be sparingly soluble in dichloromethane (contrary to the claim by the manufacturer that it is soluble only in fluorinated solvents) and hence more polar than Fomblin Z-Dol.

 0021-8979/94/75(10)/6161/1/$6.00 © 1994 American Institute of Physics

The durability of new rigid disks by molded plastic substrates (abstract)

Osamu Morita, TakanobuSano, Yasuyuki Imai, Naoko Hisayama, and Hiroshi Takino
SONY Co., Atsugi, Kanagawa, Japan

Media that have discrete data tracks and servo pits for rigid disk systems have been developed.[1] Discrete data tracks and servo pits are embossed on plastic substrates by a stamping technique similar to that used in optical disk technology. The outer diameter of the substrates is 65 mm, and the thickness is 1.2 mm. To enhance the durability of contact-start-stop (CSS) environment and reduce glide height, we have developed a method of texturing the surface with a fine dispersion of SiO_2 particles, whose diameters are between 10 and 40 nm, by dipping. Thin film layers are then sputtered on the substrates, and the shapes of SiO_2 particles are reflected in the surface profile of the thin film layers. The initial friction coefficient (μi) is 0.46, and the friction coefficient after 50 000 CSS events is 0.56 for CSS tests on molded plastic substrates at a radius of 28 mm. In addition, glide height depends on surface roughness of the disks. Surface roughness of a glass template used on stampers is carried over to the molded plastic substrates. Therefore the arithmetic average (Ra) of the molded plastic substrates with SiO_2 particles is 1.5 nm. The peak-to-valley height (PV) is 20 nm, reducing the glide height to less than 65 nm. Simultaneously, with these media, a slider flying height of 0.1 μm has been achieved. Therefore, the media satisfy parameters of CSS environment, glide height, and flying height for rigid disks.

[1] K. Watanabe *et al.*, Intermag'93 Digest, April, 1993, paper FD-10.

 0021-8979/94/75(10)/6162/1/$6.00 © 1994 American Institute of Physics

Temperature-dependent non-Heisenberg exchange coupling of ferromagnetic layers (Invited)

R. P. Erickson[a)]
Department of Mathematics, City University, London EC1V 0HB, United Kingdom

We consider with temperature the exchange coupling of two identical ferromagnetic films separated by a paramagnetic metal of thickness d. The minority-spin band of the ferromagnets is matched to the band of the paramagnet. Majority-spin electrons experience a repulsive potential of maximum height equal to the exchange gap of the ferromagnets. A spin-flip current, which flows as a result of a virtual rotation of the ferromagnetic moments, is calculated at temperature T, assuming single-particle excitations only. This current, equated to the torque exerted by one ferromagnet on the other, defines the exchange energy as an infinite sum of terms with coefficients $A_{12}(d,T)$,$B_{12}(d,T)$,..., extending beyond the Heisenberg-like $A_{12}(d,T)$ term. For certain d, the biquadratic $B_{12}(d,T)$ term is of the proper magnitude and sign to cause intrinsic 90° coupling between the moments of the two ferromagnets. Additionally, we calculate the T dependence of $A_{12}(d,T)$ and $B_{12}(d,T)$ for different Fermi energy to exchange-gap ratios, showing that, in general, a nonmonotonic dependence of both $A_{12}(d,T)$ and $B_{12}(d,T)$ vs T is expected. Monotonic T dependence occurs in the asymptotic regime of large d.

I. INTRODUCTION

Extensive investigations of the ferromagnetic (FM)/antiferromagntic (AFM) oscillatory exchange coupling of transition-metal ferromagnets through non-FM spacers, in both thin-film sandwiches and multilayers of varying compositions, has led to a large and growing list of spacer metals in which this phenomenon has been seen.[1-9] In Fe/Cr/Fe[6,7] and Fe/Al/Fe,[8] strong biquadratic coupling through the spacer, which gives rise to 90° alignment of the Fe moments, is also observed. Most of the measurements of exchange coupling have been limited to room or liquid helium temperatures. The exceptions of which we are aware include the studies of Demokritov *et al.*,[3] Barthélémy *et al.*,[4] and Chaiken *et al.*,[5] in which Fe/Cr data has been presented for a range of temperatures.

With regard to the biquadratic coupling, most notably in the wedge films of Fe/Cr/Fe, the authors of Ref. 6 detected, via Kerr magneto-optic microscopy, Fe domains, on either side of the Cr spacer, with this relative 90° orientation. Similar evidence was also found by the authors of Ref. 7 in micrographs made using scanning-electron microscopy with polarization analysis. From the studies of Ref. 6, the energy of exchange coupling between the Fe layers, a function of both the Cr spacer thickness d and the temperature T, can be written in the phenomenological form

$$E_c(d,T;\theta)=A_{12}(d,T)(1-\mathbf{m}_1\cdot\mathbf{m}_2)+\tfrac{1}{2}B_{12}(d,T)[1-(\mathbf{m}_1\cdot\mathbf{m}_2)^2], \quad (1)$$

where $\mathbf{m}_1$ and $\mathbf{m}_2$ are the unit moments of the two Fe layers, which lie in the plane of the film. As an extension beyond the Heisenberg-like bilinear $A_{12}(d,T)$ coefficient, which has its origins in the oscillatory Ruderman–Kittel–Kasuya–Yosida (RKKY) interaction of ferromagnets, the biquadratic $B_{12}(d,T)$ coefficient generates a noncolinear state of $\mathbf{m}_1$ and $\mathbf{m}_2$. Specifically, with θ denoting the angle between $\mathbf{m}_1$ and $\mathbf{m}_2$, we have $\cos\theta=A_{12}(d,T)/|B_{12}(d,T)|$ if $B_{12}(d,T)<-|A_{12}(d,T)|$, a criterion that is favorable when the oscillatory $A_{12}(d,T)$ is nearly zero in magnitude. Hence, a biquadratic contribution of $B_{12}(d,T)<0$ will generate essentially 90° coupling between the Fe moments near Cr thicknesses corresponding to nodes of $A_{12}(d,T)$.

In a very elegant micromagnetic study, Slonczewski[10] has shown that such a favorable biquadratic term can arise from fluctuations of the spacer thickness, indicative of step-like terraces at the ferromagnet/spacer interfaces, with origin in an average of the induced fluctuations in $A_{12}(d,T)$ across these interfaces. From a very different perspective, a Stoner-like model with band matching applicable to a film like Fe/Cr/Fe,[11] we have shown that such a favorable biquadratic coefficient can follow from a natural expansion of the RKKY-like exchange coupling to higher powers in $\mathbf{m}_1\cdot\mathbf{m}_2$. Within the context of our exchange theory, as reported in Ref. 11 at $T=0$, the biquadratic term oscillates with spacer thickness not unlike the bilinear term, except that the biquadratic oscillations are approximately twice as rapid as those of the bilinear coefficient. Moreover, at least in the preasymptotic regime of spacer thickness, the biquadratic oscillations are incommensurate with those of the bilinear term, leading to occurrences of $B_{12}(d,0)<-|A_{12}(d,0)|$ at certain spacer thicknesses, near nodes of $A_{12}(d,0)$.

Concerning the temperature-dependent studies of exchange coupling, we turn to the work of Refs. 3–5. In particular, the Brillouin light scattering measurements of $A_{12}(d,T)+B_{12}(d,T)$ vs T of Ref. 3, Fig. 5, reproduced in different e beam treated Fe/Cr/Fe wedge samples, show a pronounced peak in the AFM exchange coupling at $T\cong 20$–

a)Present address: Department of Mathematics, Imperial College of Science, Technology, and Medicine, London SW7 2BZ, United Kingdom.

 0021-8979/94/75(10)/6163/6/$6.00 © 1994 American Institute of Physics

30 K, for a Cr thickness of $d \cong 0.6$ nm (four monolayers), while a nearly monotonic temperature dependence is measured at $d \cong 0.9$ nm (five monolayers). On the other hand, it was noted in Ref. 5 that the AFM coupling strength decreased monotonically with increasing temperature. In the face of these sometimes conflicting reports, a knowledge of predictions based on theory would be helpful.

We have since extended our $T=0$ model to finite temperatures,[12] allowing for the Stoner-like excitations that are at least partly responsible for the decrease in magnetization of the itinerant ferromagnets Fe, Ni, and Co. We have shown that, in addition to attenuating the amplitude of the oscillations in $A_{12}(d,T)$ and $B_{12}(d,T)$ vs d, the excitations also change the phase of these oscillations. In particular, the phase shift can give rise to nonmonotonic temperature dependence, and for some spacer thicknesses, even change the sign of the exchange coefficient. As the spacer thickness increases, the phase change tends to zero and the amplitude of the oscillations diminishes as $\exp(-T/T_0)$, where the effective temperature T_0 is proportional to the Fermi temperature T_F and inversely proportional to $2k_F d$, with k_F the Fermi wave number. Therefore, as $d \to \infty$, T_0 is much smaller than T_F, and the amplitude of exchange oscillations rapidly approaches zero. As $d \to 0$, the exchange energy is also found to decrease monotonically with T, but within the scale of the characteristic temperature T_F, instead of T_0.

In Sec. II, we describe our model of exchange-coupled FM layers, extended to finite temperatures. In Sec. III, we report the results of the model, illustrating the occurrences of 90° coupling for certain preasymptotic spacer thicknesses. Additionally, in Sec. III, with spacer thickness held fixed, we discuss the temperature dependence of the bilinear and biquadratic exchange coefficients, showing that, in general, the T dependence of the exchange energy is nonmonotonic. In Sec. IV, we conclude with a qualitative comparison of our model to experiment.

II. THE FINITE-TEMPERATURE MODEL

We have considered a model of exchange coupling between two ferromagnetic (Fe) layers separated by a paramagnetic (Cr) spacer of thickness d in which we represent the Fe layers by spin-split parabolic bands,[11] with exchange gap $2h_0 = \hbar^2 k_0^2/2m$. The Fermi energy $E_F = \hbar^2 k_F^2/2m$ is situated above the bottom of the minority-spin ($\downarrow$) band, which is matched in energy to the paramagnetic band of the spacer, i.e., $k_F = k_F^{(\downarrow)}$, a situation most applicable to a film like Fe/Cr/Fe. We denote the angle between the in-plane moments of the two Fe layers by θ.

Specifically, we have utilized Slonczewski's spin-flip current method,[13] equating the spin-flip current density $j(d,T;\theta)$ of the spacer to the torque exerted on one FM layer by the other, viz.,

$$\frac{\partial}{\partial \theta} E_c(d,T;\theta) = -\frac{i}{2} A_0 \hbar j(d,T;\theta). \tag{2}$$

If the current density is expanded in powers of $\cos\theta$ as

$$j(d,T;\theta) = \sum_{n=0}^{\infty} j_n(d,T) \cos^n \theta \sin \theta, \tag{3}$$

then the exchange coefficients $A_{12}(d,T)$ and $B_{12}(d,T)$ of Eq. (1) have the intrinsic definitions $A_{12}(d,T) = -(A_0\hbar/2) \times j_0(d,T)$ and $B_{12}(d,T) = -(A_0\hbar/2) j_1(d,T)$, where A_0 is the area of a Fe/Cr interface. Higher-order exchange coefficients can be realized from the model, but they will not be discussed here.

In Ref. 11, we derived the zero-temperature spin-flip current density inside the spacer of our film; we showed it to be (with $0 < \arg \alpha < \pi/2$)

$$j(d,E;\theta) = -\frac{\hbar k_0^4 \tan(\theta/2)}{2\pi^2 m} \lim_{\alpha \to 0} \mathrm{Im} \int_{\sqrt{E/2h_0}}^{\infty} dz \times \frac{z(z^2 - E/2h_0) e^{i\alpha z}}{1 - (z - \sqrt{1+z^2})^4 e^{i2k_0 d z} \cos^2(\theta/2)}, \tag{4a}$$

if one sets $E = E_F$.[14] With $E = E_F$, this current density is the sum of contributions from all majority- and minority-spin electrons of the ground state. The extension of our model to finite T requires that the sum over all electron states, of both minority and majority spin, be weighted by a Fermi factor $f(E,T)$. This results in the finite-temperature expression,

$$j(d,T;\theta) = -\int_{-\infty}^{\infty} dE \; j(d,E;\theta) \frac{\partial}{\partial E} f(E,T). \tag{4b}$$

While the double-integral expression of Eqs. (4) is most useful for the analytic approximations to be discussed below, a single-integral expression is more suitable for numerical calculations. Successive integration of Eq. (4b) by parts expresses $j(d,T;\theta)$ in terms of a single integral over the dimensionless, and complex, wave number $z = (E/2h_0)^{1/2}$, viz.,

$$j(d,T;\theta) = -\int_{-\infty}^{\infty} dE \frac{\partial^2 j(d,E;\theta)}{\partial E^2} \int_E dE' f(E',T) = -\frac{\hbar k_0^4 \tan(\theta/2)}{2\pi^2 m} \frac{k_B T}{2h_0} \times \mathrm{Im} \int_{\mathscr{C}} dz \frac{z \log(1 + e^{-2h_0(z^2 - z_F^2)/k_B T})}{1 - (z - \sqrt{1+z^2})^4 e^{i2k_0 d z} \cos^2(\theta/2)}, \tag{5}$$

where $z_F = k_F/k_0$. The contour $\mathscr{C}$ is taken from $z = i$ to $z = 0$, then $z = 0$ to $z = \infty$. We use this single-integral equation, expanded as in Eq. (3), for the numerical calculations of $A_{12}(d,T)$ and $B_{12}(d,T)$ presented in Sec. III.

III. RESULTS OF THE MODEL

In this section, we discuss the behavior of $A_{12}(d,T)$ and $B_{12}(d,T)$ of our model as a function of both spacer thickness and temperature. First, we consider these coefficients as a function of spacer thickness, for several values of the coupling strength $z_F = k_F/k_0$, illustrating the appearance of intrinsic 90° coupling for certain spacer thicknesses. For this purpose, it is sufficient to present the $T=0$ behavior. For a

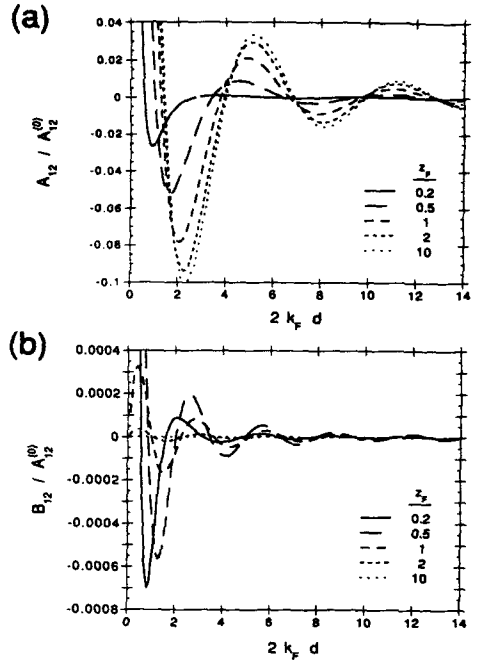

FIG. 1. The (a) bilinear and (b) biquadratic exchange coefficients of $T=0$, as calculated from the cos θ expansion of Eq. (5), vs $2k_Fd$ for several values of coupling strength $z_F=k_f/k_0$. All curves are normalized by the zero-temperature, zero-spacer-thickness FM bilinear coefficient $A_{12}^{(0)}=A_0\hbar^2k_0^4/256\pi m$, which is itself dependent on coupling strength z_F. Biquadratic curves corresponding to $z_F=0.2$ and $z_F=0.5$ have maxima that occur off the scale of the plot; these maxima are $0.0034A_{12}^{(0)}$ at $2k_Fd\cong0.2$ and $0.0015A_{12}^{(0)}$ at $2k_Fd\cong0.3$, respectively. All curves of (b) approach zero as $d\to0$.

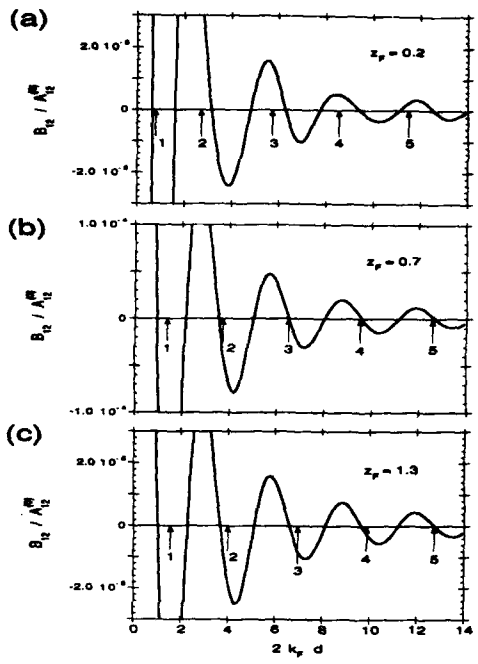

FIG. 2. Plots of the $T=0$ biquadratic exchange coefficient vs $2k_Fd$, with the zeros (nodes) of the bilinear term marked by arrows. (a), (b), and (c) illustrate the effect that the coupling strength has on the relative phase of both exchange coefficients. In (a) $z_F=0.2$, only for d close to node "1" can there be 90° coupling ($B_{12}<0$ and $A_{12}\cong0$); in (b) $z_F=0.7$, the region near node "2" exhibits 90° coupling; and in (c) $z_F=1.3$, enough slippage has occurred that regions of d near nodes "1," "2," and "3" clearly have $B_{12}<0$.

discussion of the effect of Stoner excitations, we fix the value of $2k_Fd$, focusing our attention to $A_{12}(d,T)$ and $B_{12}(d,T)$ vs T.

In Fig. 1(a), we plot the results of numerical calculations of $A_{12}(d,0)=-(A_0\hbar/2)j_0(d,0)$ as a function of $2k_Fd$ from the cos θ expansion of Eq. (5), for several z_F. Similarly, in Fig. 1(b), we plot the numerical calculations of $B_{12}(d,0)$ vs $2k_Fd$. All curves are normalized by a factor of $A_{12}^{(0)}=A_0\hbar^2k_0^4/256\pi m$, which is $A_{12}(0,0)$, the zero-spacer-thickness, zero-temperature FM bilinear coefficient. Since $A_{12}^{(0)}$ is a function of the coupling strength, care must be taken when comparing the curves of a given plot frame, since each curve is normalized differently. All curves of Fig. 1(a) rise to unity as $d\to0$, while, in this same limit, all the curves of Fig. 1(b) approach zero. Points located off the scale of the plot of Fig. 1(b) are noted in the accompanying figure caption.

While the overall amplitude of $B_{12}(d,0)$ is typically smaller than that of $A_{12}(d,0)$, the striking result upon comparing Figs. 1 is that these two coefficients oscillate incommensurately as a function of $2k_Fd$, for a given z_F. In fact, the phase slip between $A_{12}(d,0)$ and $B_{12}(d,0)$ is a function of z_F, and decreases as $2k_Fd\to\infty$.[15] We show this below.

In Figs. 2, we plot $B_{12}(d,0)$ and the nodes of $A_{12}(d,0)$, indicated by arrows and labeled with integers, for three values of z_F. The panel of figures in Fig. 2 illustrates the phase slip between the bilinear and biquadratic coefficients as the coupling strength is varied. The effect is most pronounced for small values of $2k_Fd$, where the amplitude of $B_{12}(d,0)$ is greatest. In particular, at the node of $A_{12}(d,0)$ labeled "3," we see in Fig. 2(a) that $B_{12}(d,0)$ is initially greater than zero at "3," but then slips past the node with decreasing coupling strength (increasing z_F), becoming negative, as in Fig. 2(c). Note, node "3" of $A_{12}(d,0)$ itself shifts to larger $2k_Fd$ as z_F increases.

Figures 2 depict intervals of $2k_Fd$ for which the biquadratic coupling criterion $B_{12}(d,0)<-|A_{12}(d,0)|$ is satisfied, minimizing the energy of Eq. (1). Thus, for example, Fig. 2(a) illustrates 90° coupling in the vicinity of node "1" of $A_{12}(d,0)$, at a spacer thickness $2k_Fd\cong0.8$, where $B_{12}(d,0)<0$. However, note the lack of such coupling where $B_{12}(d,0)>0$, such as at nodes "2"–"5" of this same figure. As z_F increases, Fig. 2(b) illustrates 90° coupling at node "2" while Fig. 2(c) shows the onset of 90° coupling at node "3" (and possibly node "4"), in addition to nodes "1" and "2."

Thus, as the coupling strength, the degree of exchange splitting of the ferromagnet energy bands, decreases (z_F increases), the biquadratic state of near 90° alignment of the FM moments appears, with increasing $2k_Fd$, at successive nodes of the bilinear coefficient, as depicted in Figs. 2. However, as $2k_Fd\to\infty$ for a given z_F, the nodes of the bilinear term coincide with nodes of the biquadratic term,[15] so this effect is restricted to the preasymptotic regime of $2k_Fd$.

We now turn to the evaluation of $A_{12}(d,T)$ and $B_{12}(d,T)$ with temperature. First, we consider the RKKY limit ($k_0\ll k_F$) at *finite T*, specifically *the RKKY form of* $A_{12}(d,T)$, which brings out the salient features of the nonmonotonic temperature dependence of both $A_{12}(d,T)$ and $B_{12}(d,T)$.

To begin, we can expand $j(d,E;\theta)$ of Eq. (4a) in powers of $\cos\theta$, as we have done formally for $j(d,T;\theta)$ of Eq. (3), expressing the expansion in terms of coefficients $j_n(d,E)$, analogous to $j_n(d,T)$. In this way, we integrate over $j_n(d,E)$ in the manner of Eq. (4b) to obtain the various $j_n(d,T)$, which define $A_{12}(d,T),B_{12}(d,T),\ldots$. The expansion coefficients can be written explicitly as

$$j_n(d,E)=-\frac{\hbar k_0^4}{4\pi^2 m}\lim_{\alpha\to 0}\operatorname{Im}\sum_{l=n}^{\infty}\binom{l}{n}\left(\frac{1}{2}\right)^l\int_{\sqrt{E/2k_0}}^{\infty}dz\,z\times\left(z^2-\frac{E}{2k_0}\right)(z-\sqrt{1+z^2})^{4(l+1)}e^{i[2k_0d(l+1)+\alpha]z}. \tag{6}$$

As $z_F\to\infty$ (the RKKY limit), the $l=0$ term in the sum of Eq. (6) provides the most significant contribution to the integral. This can be seen by noting that the factor $(z-\sqrt{1+z^2})^4$ tends to zero for z of large modulus. Since it is the values of $E\cong E_F$ that matter most, so that the lower bound of the integral in Eq. (6) will be nearly $z_F\gg 1$, the integrand of a given l will rapidly tend to zero as l increases. Thus, only $j_0(d,E)$ is significant in the extreme limit of large z_F, and therefore, only the $A_{12}(d,T)=-(A_0\hbar/2)j_0(d,T)$ exchange coefficient remains, hence

$$\begin{aligned}A_{12}(d,T)&=\frac{1}{2}A_0\hbar\int_{-\infty}^{\infty}dE\;j_0(d,E)\frac{\partial}{\partial E}f(E,T)\\&\cong-\frac{32}{\pi}A_{12}^{(0)}\lim_{\alpha\to 0}\operatorname{Im}\int_{-\infty}^{\infty}dE\,\frac{\partial}{\partial E}f(E,T)\times\int_{\sqrt{E/2k_0}}^{\infty}dz\,z\left(z^2-\frac{E}{2k_0}\right)\times(z-\sqrt{1+z^2})^4e^{i(2k_0d+\alpha)z},\quad k_0\ll k_F.\end{aligned} \tag{7}$$

Now, defining ϵ via $E=(1+\epsilon)E_F$, and $x=z(2k_0d)(1+\epsilon)^{-1/2}$, we change integration variables from E and z to ϵ and x, respectively. With $\phi=2k_Fd$, the approximation of Eq. (7) becomes

$$A_{12}(\phi,T)\cong A_{12}^{(0)}\lim_{\alpha\to 0}\operatorname{Im}\int_{-\infty}^{\infty}d\epsilon\;g(\phi,\epsilon)\frac{\partial}{\partial\epsilon}f(\epsilon,T), \tag{8a}$$

where

$$g(\phi,\epsilon)=-\frac{32}{\pi}(1+\epsilon)^4\left(\frac{z_F}{\phi}\right)^8\int_{\phi}^{\infty}dx\;x(x^2-\phi^2)\times[x-\sqrt{x^2+z_F^{-2}\phi^2(1+\epsilon)^{-1}}]^4e^{i(\alpha+\sqrt{1+\epsilon})x}. \tag{8b}$$

Since we are only interested in the leading term as $z_F\to\infty$, we have

$$g(\phi,\epsilon)=-\frac{2}{\pi}\int_{\phi}^{\infty}dx\,\frac{x^2-\phi^2}{x^3}\;e^{i(\alpha+\sqrt{1+\epsilon})x}, \tag{9}$$

representative of *the RKKY limit. Most of the contribution* to the integral over ϵ comes from $\epsilon\cong 0$, so we take $(1+\epsilon)^{1/2}\cong 1+\epsilon/2$ in the argument of the exponent of Eq. (9). In this way, the integral of Eq. (8a), equated to one that encloses the upper-half-plane of complex ϵ, is approximated as a sum over the second-order poles $\epsilon_p(T)=i\pi(2p+1)(k_BT/E_F)$ of $\partial f(\epsilon,T)/\partial\epsilon$, viz.,

$$\begin{aligned}A_{12}(\phi,T)&\cong A_{12}^{(0)}\operatorname{Im}2\pi i\frac{k_BT}{E_F}\sum_{p=0}^{\infty}\frac{\partial}{\partial\epsilon}\,g(\phi,\epsilon)\Big|_{\epsilon=\epsilon_p(T)}\\&\cong A_{12}^{(0)}\frac{4}{\pi}\frac{k_BT}{E_F}\operatorname{Im}\sum_{p=0}^{\infty}\int_{\phi}^{\infty}dx\,\frac{x^2-\phi^2}{x^2}\times e^{i[1+\epsilon_p(T)/2]x}.\end{aligned} \tag{10}$$

Expressing *the sum over* p in closed form, and defining $\tau=(\pi/2)(k_BT/E_F)$, then

$$A_{12}(\phi,\tau)\cong A_{12}^{(0)}\frac{2}{\pi}\int_{\phi}^{\infty}dx\,\frac{x^2-\phi^2}{x^3}\,\frac{\tau x}{\sinh\tau x}\,\sin x. \tag{11}$$

Note, as $d\to 0$, Eq. (11) has the closed form

$$A_{12}(0,T)=A_{12}^{(0)}\tanh(E_F/k_BT), \tag{12}$$

which is clearly a monotonic function of the temperature, as we alluded to in the Introduction, controlled by the ratio of k_BT to E_F. Thus, $A_{12}(0,T)$ is typically a slowly varying function of T.

In the limit of $T=0$, Eq. (11) is in exact agreement with the RKKY result of Baltensberger and Helman,[16] as can be demonstrated. Additionally, in the limit $\phi\to\infty$, an asymptotic expansion of Eq. (11) yields the leading term,

$$A_{12}(\phi,\tau)\cong-\frac{\pi}{4}A_{12}^{(0)}\frac{\tau\phi}{\sinh\tau\phi}\frac{\sin\phi}{\phi^2},\quad\text{as }\phi\to\infty, \tag{13}$$

which agrees in form with the tight-binding result of Edwards *et al.*[17] As pointed out in Ref. 17, this asymptotic form illustrates the characteristic temperature $T_0=(2/\pi)(E_F/2k_Fd)$ (i.e., $\tau\phi=T/T_0$) of the integral of Eq. (11), which indicates that the temperature dependence of $A_{12}(d,T)$ is not controlled completely by the ratio of the thermal energy to the Fermi energy, but is instead mediated by the spacer thickness d via the factor $\phi=2k_Fd$.

The role of T_0 is especially important in Eq. (11) for intermediate values of ϕ, when the function $\tau x^{-2}(x^2-\phi^2)/\sinh\tau x$, which modulates $\sin x$, has a local maximum in x. If $\sin x$ does not oscillate too rapidly, as when ϕ is of modest size, then the integral over x itself can

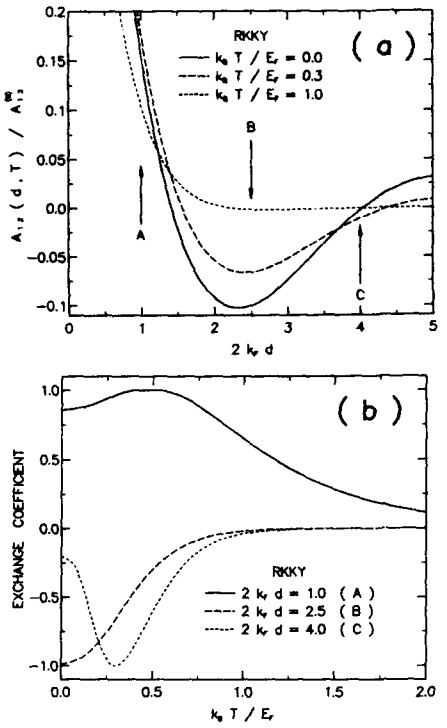

FIG. 3. Equation (11) as a function of (a) $2k_Fd$ and (b) k_BT/E_F. In (b), selected points A, B, and C of (a) are normalized via the magnitude of their most extreme values, which are, respectively, the fractions 0.182, −0.100, and −0.0107 of $A_{12}^{(0)}$.

pass through a maximum or minimum corresponding to some value of τ. We illustrate this effect for preasymptotic values of spacer thickness, plotting numerical calculations of Eq. (11) as a function of $\phi=2k_Fd$ for several values of temperature in Fig. 3(a). At first glance, it is apparent from the figure that an effect of increased T is an attenuation of the amplitude of the exchange oscillations. However, in addition to this effect, there is also an accompanying shift in the phase, which is nonmonotonic with increasing T. We can realize the consequences of this phase shift by comparing the amplitudes of the plots in Fig. 3(a) as a function of increasing $2k_Fd$.

In Fig. 3(a), we have selected three points, A, B, C, that characterize the different types of T dependence of $A_{12}(d,T)$. At A ($2k_Fd=1.0$), we see an initial increase in amplitude before an eventual decay to zero. (Note the phase transition from the AFM state to the FM state near $2k_Fd=1.5$.) At B ($2k_Fd=2.5$), near the first AFM peak, the implication of Fig. 3(a) is a monotonic T dependence. And, at C ($2k_Fd=4.0$), there is an initial decrease in amplitude of $A_{12}(d,T)$, followed by an eventual increase to zero. Figure 3(b) explicitly illustrates the T dependence at points A, B, and C. Note the large change in magnitude of $A_{12}(d,T)$ at point C, a result of its proximity to a node, where the slope of $A_{12}(d,T)$ with d is greatest. The effect of the thermally induced phase shift is thus accentuated here.

Summarizing our analysis of Eq. (11), we found that as $2k_Fd$ increases from zero, the character of $A_{12}(d,T)$ vs T alternates in a continuous fashion between regimes A and C according to the sequence "B, A, B, C,...," with transition point B occurring near each FM/AFM peak in the oscillations. As $2k_Fd\to\infty$, the regimes A and C must evolve continuously into the monotonic character of the points B, in the manner of Eq. (13). Our numerical evaluation of Eq. (5) was limited to $2k_Fd\lesssim10$, due to the rapid oscillations of the integrand; however, regime A was clearly evident, even at $2k_Fd=9.0$, for instance.

We now turn to the evaluation of $A_{12}(d,T)$ and $B_{12}(d,T)$ for finite coupling strengths $z_F=k_F/k_0$, via the numerical calculation of Eq. (5). As we do, we note in passing that the nonmonotonic behavior depicted in Figs. 3 is not particular to the RKKY limit of our model, but is, in fact, typical of RKKY coupling at finite T. For example, if we consider the simple case of two magnetic moments separated by a distance r and coupled through an electron gas, and apply an approximation scheme like that presented above, the exchange strength between these moments exhibits a T dependence, with increasing r, very similar to that described above and depicted in Figs. 3. It is for modest values of r that a nonmonotonic T dependence is realized; monotonic behavior is recovered as $r\to\infty$.[18]

We have determined numerically the exchange coupling for values of z_F in the range $0.1<z_F<\infty$, from the cos θ expansion of Eq. (5). In particular, we have found that $A_{12}(d,T)$ vs T follows trends in $2k_Fd$ similar to those depicted in Figs. 3. As an example, Fig. 4(a) depicts $A_{12}(d,T)$ as a function of k_BT/E_F for several values of $2k_Fd$, corresponding to the coupling strength $z_F=1.0$. Compare the behavior with temperature illustrated in Fig. 4(a) with that of Fig. 3(b). Note the appearance of a secondary maximum in C of Fig. 4(a).

Also of consideration for finite coupling strengths z_F is the temperature dependence of $B_{12}(d,T)$. The coefficient $B_{12}(d,T)$ also exhibits a T-dependent form similar to that illustrated in Figs. 3 and Fig. 4(a), except that the nonmonotonic regions in $2k_Fd$, A and C, are approximately half the size of the corresponding regions of $A_{12}(d,T)$. This occurs because the $B_{12}(d,T)$ coefficient oscillates, as a function of d, approximately twice as rapidly as the $A_{12}(d,T)$ coefficient. [This is easily seen from Eq. (6), noting that the leading harmonic of $j_n(d,E)$ is $l=n$.] Thus, as a function of $2k_Fd$, the switching between the regions of maximum and minimum behavior with T is essentially twice as rapid for $B_{12}(d,T)$. Figure 4(b) illustrates the T dependence of $B_{12}(d,T)$ for several values of $2k_Fd$, corresponding to the coupling strength $z_F=1.0$.

IV. CONCLUDING REMARKS

We have presented a model of mismatched majority- and minority-spin electrons, treated as a finite-barrier tunneling problem, in which oscillatory biquadratic, as well as bilinear, exchange coupling arises between FM films. Moreover, the biquadratic coupling is shown to dominate the bilinear cou-

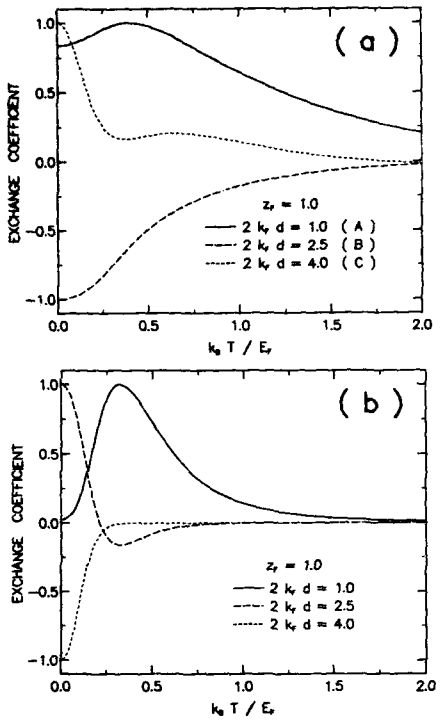

FIG. 4. (a) $A_{12}(d,T) = -(A_0\hbar/2)j_0(d,T)$ and (b) $B_{12}(d,T) = -(A_0\hbar/2)j_1(d,T)$, from the cos θ expansion of Eq. (5) vs k_BT/E_F for z_p=1.0. Curves A, B, and C are normalized again via the magnitude of their most extreme values, which are, respectively, the fractions (a) 0.103, −0.0674, and -7.29×10^{-3}; and (b) 2.69×10^{-4}, 1.11×10^{-4}, and -7.38×10^{-5}, of $A_{12}^{(0)}$.

pling for certain values of spacer thickness, over a range of coupling strengths, implying the existence of 90° relative spin orientations in the ferromagnets at these thicknesses. Our simple model of exchange coupling, being free-electron-like, fails to produce the multiple periodicities of a more realistic band-structure approach, nor has it included the interfacial effects of charge transfer, the "softening" of interfacial exchange interactions, and roughness. It is therefore not possible to make detailed quantitative comparisons between the experimental results and our model. There may be several sources of biquadratic coupling; our results nevertheless make clear that biquadratic coupling is a feature intrinsic to exchange-coupled films.

With regard to the behavior of our model with temperature, we are again limited in the extent to which quantitative comparisons of our model with experiment can be made. Indeed, and quite obviously, a fit ($k_F \sim 1.0$ Å^{-1}) of our model to the short-period oscillations observed in Fe/Cr/Fe would make for a temperature scale in Figs. 3 and 4 that is unrealistically large by two orders of magnitude. However, we speculate that a more realistic T scale might be obtained from a "pocket" of electrons originating from a portion of Fermi surface of small curvature. Such speculation is not unreasonable with regard to Cr, whose bulk form can exhibit an AFM spin-density-wave ground state. The Brillouin light scattering measurements of $A_{12}(d,T)+B_{12}(d,T)$ vs T of Ref. 3, Fig. 5, reproduced in different e-beam treated Fe/Cr/Fe wedge samples, appear to be qualitatively the same as Figs. 3(b) and 4. As mentioned in the Introduction, at a spacer thickness of four monolayers, these authors measure a pronounced peak in the AFM exchange energy, at $T \cong 20$–30 K, only to find nearly monotonic temperature dependence at a thickness of five monolayers.[19] A strong temperature dependence of $A_{12}(d,T)$, as speculated here, would also have ramifications for the temperature dependence of the extrinsic $B_{12}(d,T)$ of Ref. 10, which originates from averaging roughness-induced fluctuations of the intrinsic $A_{12}(d,T)$. We hope this paper will stimulate further temperature-dependent measurements of exchange-coupled films. More realistic band-structure calculations are clearly a necessity.

ACKNOWLEDGMENTS

The author acknowledges J. Cullen and K. Hathaway, for helpful comments and suggestions; and discussions with D. Pappas, M. Filipkowski, G. Prinz, J. Mathon, and M. Villeret. This work was supported jointly by the National Research Council and the Naval Research Laboratory, and also by the Naval Surface Warfare Center and the Office of Naval Research.

[1] P. Grünberg, R. Schreiber, Y. Pang, M. B. Brodsky, and H. Sowers, Phys. Rev. Lett. **57**, 2442 (1986).
[2] S. S. P. Parkin, Phys. Rev. Lett. **67**, 3598 (1991).
[3] S. Demokritov, J. A. Wolf, P. Grünberg, and W. Zinn, in *Magnetic Thin Films, Multilayers, and Surfaces*, edited by S. S. P. Parkin, H. Hopster, J-P. Renard, T. Shinjo, and W. Zinn, Materials Research Society Symposium Proceedings, Anaheim, 1992, Vol. 231, p. 133.
[4] A. Barthélémy, A. Fert, M. N. Baibich, S. Hadjoudj, and F. Petroff, J. Appl. Phys. **67**, 5908 (1990).
[5] A. Chaiken, T. M. Tritt, D. J. Gillespie, J. J. Krebs, P. Lubitz, M. Z. Harford, and G. A. Prinz, J. Appl. Phys. **69**, 4798 (1991).
[6] M. Rührig, R. Schäfer, A. Hubert, R. Mosler, J. A. Wolf, S. Demokritov, and P. Grünberg, Phys. Stat. Solid. A **125**, 635 (1991).
[7] J. Unguris, R. J. Celotta, and D. T. Pierce, Phys. Rev. Lett. **69**, 1125 (1992).
[8] C. J. Gutierrez, J. J. Krebs, M. E. Filipkowski, and G. A. Prinz, J. Magn. Magn. Mat. **116**, L305 (1992).
[9] Also see the articles cited in Ref. 11 below.
[10] J. C. Slonczewski, Phys. Rev. Lett. **67**, 3172 (1991).
[11] R. P. Erickson, K. B. Hathaway, and J. R. Cullen, Phys. Rev. B **47**, 2626 (1993).
[12] R. P. Erickson, submitted to Phys. Rev. B (in press).
[13] *J. C. Slonczewski, Phys. Rev. B* **39**, 6995 (1989).
[14] Note, Eq. (4a) is the $T=0$ total spin-flip current density j_T of Eq. (11) of Ref. 11 when $E=E_F$.
[15] See the asymptotic expansion of $j_n(d,0)$ of Eq. (18) in Ref. 11. A node of $A_{12}(d,0) = -(A_0\hbar/2)j_0(d,0)$, appearing at $2k_Fd=\pi l$, where $l \gg 1$ is an integer, is also a node of $B_{12}(d,0) = -(A_0\hbar/2)j_1(d,0)$, so that $A_{12}(d,0)$ and $B_{12}(d,0)$ are asymptotically commensurate.
[16] W. Baltensberger and J. S. Helman, Appl. Phys. Lett. **57**, 2954 (1990).
[17] D. M. Edwards, J. Mathon, R. B. Muniz, M. Villeret, and J. M. Ward, in *Magnetism and Structure in Systems of Reduced Dimension*, edited by R. F. C. Farrow *et al.*, NATO Advanced Study Institute, Series B: Physics, Vol. 309 (Plenum, New York, 1993), p. 401.
[18] R. P. Erickson (unpublished).
[19] It is of interest to note that if we naively fit our model to the long-period oscillations of Fe/Cr/Fe ($k_F \sim 0.08$ Å^{-1}), the temperature scale of Figs. 3(b) and 4 matches that of Ref. 3, with maxima and minima occurring on the order of tens of Kelvins.

Photo-induced antiferromagnetic interlayer coupling in Fe superlattices with iron silicide spacers (invited)

J. E. Mattson, Eric E. Fullerton, Sudha Kumar, S. R. Lee,[a] C. H. Sowers, M. Grimsditch, and S. D. Bader
Materials Science Division, Argonne National Laboratory, Argonne, Illinois 60439

F. T. Parker
Center for Magnetic Recording Research, University of California at San Diego, La Jolla, California 92093-0401

Sputtered Fe/FeSi films possessing antiferromagnetic (AF) interlayer coupling at room temperature develop ferromagnetic remanence when cooled below 100 K, but the AF coupling can be restored at low temperature by exposure to visible light of sufficient intensity (>10 mW/mm^2). We attribute these effects to charge carriers in the FeSi spacer layer, which, when thermally or photogenerated, are capable of communicating spin information between the Fe layers.

I. INTRODUCTION

Antiferromagnetic (AF) coupling of ferromagnetic layers across metallic spacers has been studied extensively.[1] Recent experimental studies have also focused on nonmetallic spacers. Fe/FeSi sputtered superlattices provide an example of such a system. At room temperature, superlattices with FeSi spacer thicknesses of ~13–17 Å exhibit AF coupling.[2–4] Upon cooling, the layers uncouple and the hysteresis loops exhibit ferromagnetic remanence. At low temperatures, the AF coupling can be restored by irradiation with visible laser light.[4] These phenomena are attributed to charge carriers in the spacer, which can be either thermally or photoinduced to mediate the magnetic coupling. Though present theories describe coupling in systems with metallic spacers,[5–8] it remains a challenge to describe magnetic coupling across nonmetallic spacers. Other systems with nonmetallic spacers include amorphous (a) spacers such as Fe/a-Si/Fe trilayers,[9] and epitaxial CoO/NiO superlattices.[10]

In this paper we provide an overview of our studies of Fe/Si and Fe/FeSi superlattices. Two different routes were taken to grow the samples. The first was to alternately sputter deposit Fe and Si layers, with the Fe layer thickness held constant at 30 Å and the Si layer thickness varied. In this case, a silicide spacer formed from the interfacial reaction of the Fe and Si during growth. This resulted in a crystalline spacer for nominal Si thicknesses ≤17 Å. The second route utilized superlattices that consist of 30-Å Fe layers separated by spacers deposited as [Fe(2 Å)/Si(3–4 Å)]$_n$ multilayers, where the index n is adjusted to change the spacer thickness. In the latter case atomic Fe and Si layers react to form crystalline FeSi spacers for all thicknesses explored (≤80 Å). All samples were grown by dc magnetron sputtering onto Si, sapphire, and Kapton substrates at ambient temperature. For simplicity, we refer to the samples as Fe/Si and Fe/FeSi superlattices to differentiate between the two growth sequences.

Structural characterizations by means of x-ray diffraction are summarized in Sec. II. Magnetic properties, probed by SQUID and Kerr magnetometry, appear in Sec. III. Mössbauer results appear in Sec. IV. The paper is concluded with a presentation and discussion of the photoinduced effects in Sec. V.

II. STRUCTURAL CHARACTERIZATIONS

The structural properties of the Fe/Si and Fe/FeSi superlattices are very similar when the nominal spacer thickness is ≤17 Å. High-angle superlattice peaks are observed, which indicate (110) growth of the Fe layers. The crystalline coherence length ξ, estimated from the full width at half-maximum (FWHM) of the main diffraction peak, is ≈150 Å for both series of samples (see Fig. 1). This indicates crystalline coherence over many bilayers. The average lattice spacing, determined from the position of the central Bragg reflection, is ≈2.015 Å. The diffraction spectra could be reproduced quantitatively[11,12] using a two-component model, where one layer has a lattice spacing of 2.03 Å and the other has 2.00 Å. The former corresponds to the Fe(110) layer and the latter to the silicide spacer. Asymmetric and transmission diffraction scans indicate coherent diffraction peaks in the expected bcc positions. This indicates that lateral coherence is maintained at the interfaces, and suggests that the silicide

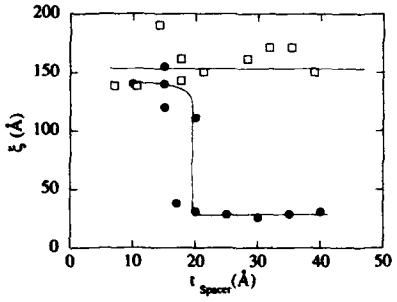

FIG. 1. Structural coherence length estimated from the FWHM of the Fe(110) Bragg peak for the Fe/Si (solid circles) and the Fe/Fe–Si (open squares) films. The solid lines serve as a guide to the eye.

[a]Permanent address: Department of Metallurgical Engineering, Korea University, Seoul, Korea, 136-701.

 0021-8979/94/75(10)/6169/5/$6.00 © 1994 American Institute of Physics

spacer shares the same cubic symmetry as the Fe layers. There are a number of silicides that can satisfy this criterion.

We identify the primary silicide species in the spacer as ϵ-FeSi. ϵ-FeSi has a simple cubic Bravais lattice with tetrahedral point symmetry,[13] and the [210] direction of ϵ-FeSi has a lattice spacing of 2.007 Å, which is consistent with that determined from fitting the data. There are four other candidate silicides that would satisfy our structural criterion, but these can be ruled out on other grounds. These include the disilicide structures and orientations: α-$FeSi_2$ (cubic),[14] β-$FeSi_2$ [004] (orthorhombic),[15] and γ-$FeSi_2$ [002] (CaF_2 structure).[16] Disilicides are not anticipated on thermodynamic grounds,[17] and can be eliminated from consideration based on the Mössbauer results discussed in Sec. IV. The other candidate, a monosilicide, has a CsCl structure.[18,19] However, this phase is metallic, while ϵ-FeSi, a small-gap semiconductor, can more plausibly explain the electronic properties of our superlattices. Thus, while structural and symmetry arguments alone are insufficient to distinguish the dominant silicide phase in our spacer layers, we nonetheless can converge on ϵ-FeSi as the species that controls the physics.

For spacer thicknesses >17Å, there are significant structural differences between the Fe/FeSi and Fe/Si samples. The crystalline coherence length versus spacer thickness for the two are shown in Fig. 1. Whereas the Fe/FeSi samples maintain crystalline coherence, a weakly textured Fe(110) peak with a FWHM that yields $\xi \sim 30$ Å is observed for the Fe/Si samples. Since $\xi \sim t_{Fe}$ for the Fe/Si samples, the Si spacer is either amorphous or sufficiently disordered to limit crystalline coherence between the Fe layers. This sets an upper limit to the crystalline silicide interfacial reaction distance of ~17 Å, in agreement with the quantitative neutron-reflectivity studies of Ankner *et al.*[20]

III. MAGNETIZATION

The in-plane magnetic hysteresis loop and saturation magnetization M_s were measured by means of both SQUID magnetometry and the longitudinal Kerr effect for magnetic fields ≤10 kOe. The room-temperature M_s value (in the Fe/Si samples) is significantly reduced (~30%) from the bulk Fe moment due to the interaction with Si. A typical hysteresis loop for an AF coupled film is shown in Fig. 2(a). The low-temperature loop of Fig. 2(b) reveals that the film develops ferromagnetic remanence upon cooling. These results are confirmed by polarized neutron reflectometry.[3] The temperature effects result from the freezing out of carriers upon cooling, as will be discussed further.

Figure 3 shows the room temperature saturation field H_s versus spacer thickness. Both series of films show large H_s values in the thickness range of 14–17 Å, characteristic of AF coupling, but no evidence of higher-order AF oscillations. The difference in H_s between the two series is largely accounted for by the reduction in the moment of the Fe layer in the Fe/Si series. The lack of higher-order AF oscillations is rather surprising, since the coupling energy observed at 15-Å spacer thickness is quite large: $J_{AF} \sim 0.5$ erg/cm^2, where $J_{AF} \sim H_s M_s t_{Fe}/4$. In an earlier publication we attributed the lack of AF oscillations to the formation of an amorphous spacer in the larger Si thickness regime.[2] However, we subsequently found that no oscillations are observed even when the crystallinity is maintained in the Fe/FeSi samples.

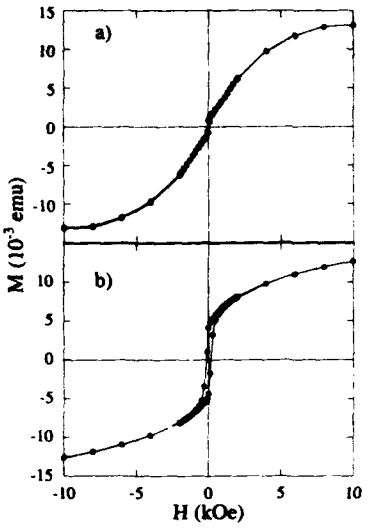

FIG. 2. Magnetic hysteresis loops for [Fe(30 Å)/Si(15 Å)]$_{50}$ at (a) 298 K and (b) 10 K.

IV. MÖSSBAUER RESULTS

Transmission and conversion-electron Mössbauer spectroscopy were used to identify the different Fe phases in the superlattices. Samples were grown on Kapton substrates for the low-temperature transmission studies. The Mössbauer results show no dependence on the choice of substrate. For all films, the spectra consist of a superposition of a magnetically split, six-line contribution and a nonmagnetic central portion, as shown in Fig. 4. The magnetically split component results from the Fe layers, and the nonmagnetic component originates from the silicide spacer. The polarization of the spins,

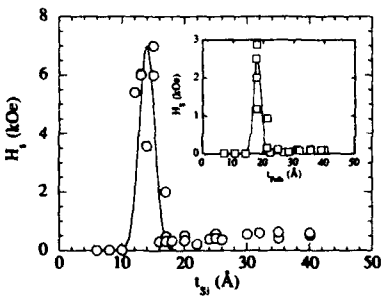

FIG. 3. The saturation field H_s at 298 K versus spacer thickness for Fe/Si and Fe/FeSi (inset) films, where the solid lines are guides to the eye.

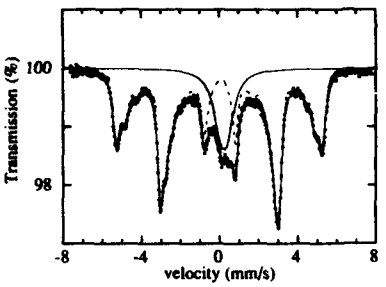

FIG. 4. Transmission Mössbauer spectrum for $[Fe(30\ Å)/Si(14\ Å)]_{200}$ at 298 K.

determined from the relative peak areas, confirms that the Fe moments are in plane with no out-of-plane components in zero applied field.

The magnetically split part of the spectrum was fitted to a distribution of six-line spectral components characterized by areas $P(H_i)$ and hyperfine fields H_i, using a standard procedure outlined elsewhere.[21] The H_i reflect the local environment of the Fe atom. For all films, H_i values between 0 and 230 kOe contributed negligibly, as anticipated. Briefly, to determine the relative amounts of magnetic phases in the films, the resulting $P(H_i)$ distribution was fitted to the known Mössbauer values for different Fe_xSi_{1-x} alloy phases.[21] The H_i were restricted to published values[22] at room temperature, and allowed to vary somewhat at low temperature, where the appropriate Mössbauer parameters are unknown. In practice, no more than two magnetic phases could be handled while still retaining statistical significance. The combination of 0 at. % Si (i.e., α-Fe) and 15 at. % Si as the two phases yields better fits than α-Fe combined with either 10 or 20 at. % Si. The 15 at. % Si phase represents the approximate solubility limit of Si in bcc-Fe, which implies Si diffusion into the Fe layers. Another possible component of the magnetically split part of the spectrum is the ordered Fe_3Si phase (Fe_3Al structure). However, examination of the H_i distribution indicates that <5% of the Fe exists in this structure. The fractional composition for some representative films is given in Table I. For the Fe/Si superlattices, little difference in the fractional composition is observed for the magnetically split part of the spectra whether the spacer is crystalline or amorphous. For the Fe/FeSi superlattices, there is a significant increase in the amount of α-Fe relative to the 15 at. % Si phase, since there is more Fe in the overall structure and the Fe in the spacer preferentially forms FeSi.

For the Fe/Si superlattices, the quadrupole splitting (Δ) and isomer shift (IS) of the nonmagnetic layer are dependent on the spacer thickness, t_{Si}, as shown in Fig. 5. For $t_{Si}>17$ Å, where the spacer is amorphous, Δ and IS are, indeed, characteristic of a-FeSi.[23,24] As t_{Si} increases, IS decreases, indicating a Si-rich a-Fe–Si composition. For the superlattices with crystalline spacers, Δ is smaller than for the a-Fe–Si alloys, as expected.

TABLE I. Mössbauer parameters for selected Fe/Si and Fe/FeSi films. Parameters in the first three columns of results are obtained by fitting the nonmagnetic component to an electric quadrupole doublet, while those in the last two columns utilize a singlet in the fitting procedure. (a) and (b) list the composition of the magnetic and nonmagnetic phases, respectively, based on the relative spectral areas. (c) lists parameters for the nonmagnetic phase. Numbers in parentheses represent statistical uncertainties.

	$[Fe(30\ Å)/Si(25\ Å)]_{10}$	$[Fe(30\ Å)/Si(20\ Å)]_{50}$	$[Fe(30\ Å)/Si(15\ Å)]_{50}$	$[Fe(30\ Å)/Si(14\ Å)]_{200}$	$[Fe(30\ Å)/FeSi(17\ Å)]_{80}$
(a) Magnetic phases					
% α-Fe					
298 K	9(5)	14(4)	16(6)	23(6)	42(6)
% $Fe_{0.85}Si_{0.15}$					
298 K	57(8)	57(6)	58(6)	48(7)	29(4)
% Fe_xSi_{1-x} ($x>0.5$)					
298 K	8(1)	8(1)	7(1)	8(1)	5(1)
(b) Nonmagnetic phase					
% FeSi					
298 K	26(1)	22(1)	19(1)	21(1)	24(1)
79 K				19(1)	22(1)
4.2 K				20(1)	21(1)
(c) FeSi parameters					
Δ (mm/s)					
298 K	0.64(2)	0.60(2)	0.41(4)		
HWHM[a] (mm/s)					
298 K				0.55(1)	0.38(1)
77 K				0.69(3)	0.49(3)
4.2 K				0.77(2)	0.57(2)
IS (mm/s)					
298 K	0.21(1)	0.23(1)	0.24(1)	0.227(5)	0.257(5)
77 K				0.333(9)	0.375(4)
4.2 K				0.365(8)	0.390(8)

[a]Half-width at half-maximum of the central, nonmagnetic feature.

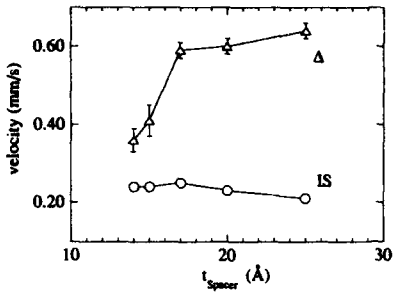

FIG. 5. Quadrupole splitting Δ (open triangles) and isomer shift IS (open circles) for selected [Fe(30 Å)/Si(x)] films, where IS is referenced to the value for bulk Fe at 296 K.

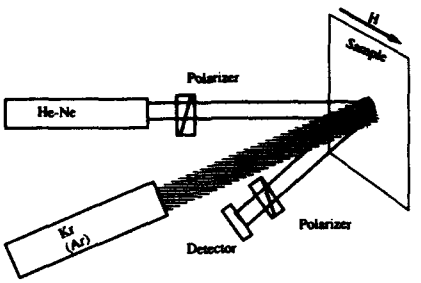

FIG. 6. Schematic of the photoinduced Kerr effect setup.

The nonmagnetic character of the spacer at all temperatures limits the possible crystalline phases to the various structural modifications of $FeSi_2$ and FeSi. α-$FeSi_2$ is metastable at room temperature and only exists with ~15% Fe vacancies.[14] It has a room temperature $\Delta \sim 0.55$ mm/s and an average IS of 0.20 mm/s. But the vacancies would lead to an *asymmetric* quadrupole doublet that is not observed in our studies. β-$FeSi_2$ can be eliminated because the average room-temperature IS for its two Fe sites (~0.10 mm/s) is much smaller than the observed value. Also, for both of the above forms of $FeSi_2$, Δ shows only a slight temperature dependence below 300 K, contrary to experiment. The Mössbauer properties of γ-$FeSi_2$ are unknown.

The most likely stoichiometry for the crystalline spacer is FeSi. A metastable, cubic CsCl structure was reported recently for $FeSi_{1+x}$ deposited on Si(111)[19,25] via molecular beam epitaxy (MBE) below 300 °C. While the Mössbauer properties of this phase are unknown, it is metallic at room temperature and is not expected to show the strong temperature dependence observed in our Mössbauer and magnetization studies. We discussed this phase previously,[3] but we now believe that its presence is inhibited due to the growth on Fe(110), and because with our sputtering conditions the impinging atoms are significantly more energetic than those in MBE.

The room-temperature Δ and IS of ϵ-FeSi are 0.48 and 0.28 mm/s, respectively.[26] These values are in reasonably good agreement with the parameters for our crystalline [Fe(30 Å)/Si(15 Å)]$_{50}$ superlattice (~0.41 and 0.24 mm/s, respectively). Most importantly, ϵ-FeSi has a very narrow semiconducting band gap estimated to be 0.05–0.06 eV experimentally[26,27] and ~0.11 eV theoretically.[28] The narrow gap causes Δ (but not IS) to vary rapidly with temperature.[26] Two films, [Fe(30 Å)/Si(14 Å)]$_{200}$ and [Fe(30 Å)/Fe–Si(14 Å)]$_{80}$, were studied as a function of temperature. Unfortunately, the nonmagnetic spectral component is not sufficiently resolved at low temperature to determine Δ accurately. But it can be fitted with a single broad line, whose width increases by nearly 50% on cooling from room temperature to 4.2 K, and whose IS exhibits the same temperature dependence as that of the magnetic layer, consistent with the known behavior of ϵ-FeSi.[26] Additionally, for both films the fractional area of the nonmagnetic phase is independent of temperature.

V. PHOTOINDUCED RESULTS

For a semiconducting spacer, exposure of the samples to visible light should produce effects similar to those of increasing the temperature. To explore this we used a two-laser pump-probe arrangement to study the effects of incident light on the magnetic coupling. A low power (25 mW) He–Ne laser (λ=6328 Å) was used as the probe to obtain magneto-optic Kerr loops, and a variable power (10–1000 mW) Kr (6471 or 5309 Å) or Ar (5145 Å) laser was used to illuminate the sample. This is shown schematically in Fig. 6. The unfocused (~2 mm diameter) laser beams were superimposed on the sample. The experiment consists of varying the power of the Kr(Ar) laser and monitoring the magnetization via the Kerr effect using the He–Ne laser. The measurements were performed as a function of temperature using an optical cryostat.

Figure 7 shows Kerr loops for a superlattice with a nominal 17-Å FeSi spacer. At room temperature the film is AF coupled and does not noticeably change when irradiated with 100 mW of pump power. Upon cooling to 53 K, the film becomes ferromagnetic; but, most strikingly, *the AF coupling is restored by irradiation with 100 mW of pump power*. Ev-

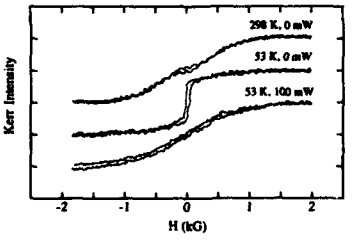

FIG. 7. Kerr loops for a [Fe(30 Å)/FeSi(17 Å)]$_{20}$ superlattice: (a) shows the loop at room temperature with no pump-laser power; (b) also shows the loop at 53 K with no pump power; and (c) shows the loop at 53 K with 100 mW of pump power.

ery one of the Fe/FeSi and Fe/Si superlattices investigated, which exhibits AF coupling at room temperature and becomes increasingly ferromagnetic (or uncoupled) upon cooling (as indicated by an increase in the remanence), recovers its AF coupling upon exposure to visible laser light of sufficient intensity (>10 mW/mm^2). However, films that are not AF coupled at room temperature do not become AF coupled after similar exposures to intense light. An additional feature of importance is that there is a time constant of ~10–60 s associated with the photoinduced change in the interlayer magnetic coupling.[4] The existence of long time scale photoexcitation effects are attributed to trapping of electrons or holes in metastable states.[29–33]

We rule out the possibility that laser heating can play a role in our results because a temperature rise of only a few degrees is typically reported in the literature for Raman experiments with similar laser power densities.[34] In addition, we find that it takes *less* pump power at 53 K than at 75 K to restore the AF alignment.[4] If laser heating were the cause of the AF coupling, one would expect that the lower-temperature experiments would require more, not less, power.

We believe that the photoinduced AF coupling described above is caused by the excitation of carriers by the radiation. If the mechanism involving conduction electrons proposed for metallic layers is applicable to the present samples, then the strength of the AF coupling should depend on the number of carriers. If the number of charge carriers changes significantly, as expected in the case of photogenerated carriers in semiconductors for very intense light, the Fermi wave vector also should change, and might alter the period of the coupling. It should then be possible either to induce or inhibit coupling, even at room temperature, an effect we did not observe. In addition, one would expect that H_s should vary continuously with laser power, however, this was not observed. The long time constants also seem to be inconsistent with lifetimes of intrinsic conduction electrons, and are more reminiscent of impurity or defect induced states. Furthermore, that lower power is necessary to restore AF coupling at lower temperatures is consistent with there being less thermal energy available to de-excite the trapped electrons (holes). However, until a theoretical model is developed to explain the phenomenon of photoinduced AF coupling, no definite conclusion can be drawn regarding the nature of the states involved.

In summary, the observations that films that are AF at room temperature become uncoupled (or ferromagnetic) upon cooling, and that the AF coupling can be restored by intense laser irradiation, indicate that the FeSi spacer is semiconducting with a small energy gap. This further implies that charge and spin carriers in the spacer are essential for the AF coupling. Mössbauer spectroscopy as well as structural and thermodynamic considerations implicate ϵ-FeSi as the spacer-medium species that controls the physics of interest.

ACKNOWLEDGMENTS

This work was supported by the U.S. Department of Energy, BES—Materials Sciences, under Contract No. W-31-109-ENG-38. F.T.P. was supported by National Science Foundation Contract No. DMR-90-10908.

[1] P. Grünberg, R. Schreiber, Y. Pang, M. B. Brodsky, and C. H. Sowers, Phys. Rev. Lett. **57**, 2442 (1986).
[2] E. E. Fullerton, J. E. Mattson, S. R. Lee, C. H. Sowers, Y. Y. Huang, G. Felcher, S. D. Bader, and F. T. Parker, J. Magn. Magn. Mat. **117**, L301 (1992).
[3] E. E. Fullerton, J. E. Mattson, S. R. Lee, C. H. Sowers, Y. Y. Huang, G. Felcher, S. D. Bader, and F. T. Parker, J. Appl. Phys. **73**, 6335 (1992).
[4] J. E. Mattson, S. Kumar, E. E. Fullerton, S. R. Lee, C. H. Sowers, M. Grimsditch, S. D. Bader, and F. T. Parker, Phys. Rev. Lett. **71**, 185 (1993).
[5] R. Coehoorn, Phys. Rev. B **44**, 9331 (1991).
[6] P. Bruno and C. Chappert, Phys. Rev. B **46**, 261 (1992).
[7] D. M. Edwards, J. Mathon, R. B. Muniz, and M. S. Phan, Phys. Rev. Lett. **67**, 493 (1991).
[8] Y. Wang, P. M. Levy, and J. L. Fry, Phys. Rev. Lett. **65**, 2732 (1990).
[9] S. Toscano, B. Briner, H. Hopster, and M. Landolt, J. Magn. Magn. Mat. **114**, L6 (1992).
[10] M. J. Carey, A. E. Berkowitz, J. A. Borchers, and R. W. Erwin, Phys. Rev. B **47**, 9952 (1993).
[11] E. E. Fullerton, I. K. Schuller, H. Vanderstraeten, and Y. Bruynseraede, Phys. Rev. B **45**, 9292 (1992).
[12] E. E. Fullerton, I. K. Schuller, and Y. Bruynseraede, MRS Bull. **XVII**, 33 (1992).
[13] H. Watanabe, H. Yamamoto, and K. Ito, J. Phys. Soc. Jpn. **18**, 995 (1963).
[14] C. Blaauw, F. van der Woude, and G. A. Sawatzky, J. Phys. C **6**, 2371 (1973).
[15] Par Y. Dusausoy, J. Protas, R. Wandji, and B. Roques, Acta Cryst. B **27**, 1209 (1971).
[16] N. Onda, J. Henz, E. Müller, K. A. Mäder, and H. von Känel, Appl. Surf. Sci. **56–58**, 421 (1992).
[17] R. Pretorius, Vacuum **41**, 1038 (1990).
[18] H. von Känel, K. A. Mäder, E. Müller, N. Onda, and H. Sirringhaus, Phys. Rev. B **45**, 13 807 (1992).
[19] J. Alvarez, A. L. Vázquez de Parga, J. J. de la Figura, E. G. Michel, C. Ocal, and R. Miranda, Appl. Surf. Sci. **70/71**, 578 (1993).
[20] J. F. Ankner, C. F. Majkrzak, and H. Homma, J. Appl. Phys. **73**, 6436 (1993).
[21] F. T. Parker, H. Oesterreicher, and E. Fullerton, J. Appl. Phys. **66**, 5988 (1989).
[22] M. B. Stearns, Phys. Rev. **129**, 1136 (1963).
[23] G. Marchal, P. Mangin, M. Piecuch, and C. Janot, J. Phys. Paris Colloq. **37**, C6-763 (1976).
[24] C. Bansal, S. J. Campbell, and A. M. Stewart, J Magn. Magn. Mat. **27**, 195 (1982).
[25] H. von Känel, N. Onda, H. Sirringhaus, E. Müller, S. Goncalves-Conto, and C. Schwarz, Appl. Surf. Sci. **70/71**, 559 (1993).
[26] G. K. Wertheim, V. Jaccarino, J. H. Wernick, J. A. Seitchik, H. J. Williams, and R. C. Sherwood. Phys. Rev. Lett. **18**, 89 (1965).
[27] Z. Schlesinger, Z. Fisk, H.-T. Zhang, M. B. Maple, J. F. DiTusa, and G. Aeppli, Phys. Rev. Lett. **71**, 1748 (1993).
[28] L. F. Mattheiss and D. R. Hamann, Phys. Rev. B **47**, 13114 (1993).
[29] P. V. Santos, N. M. Johnson, and R. A. Street, Phys. Rev. Lett. **67**, 2686 (1991).
[30] G. Nieva, E. Osuiguil, J. Guimpel, M. Maenhoudt, B. Wuyts, Y. Bruynseraede, M. B. Maple, and I. K. Schuller, Phys. Rev. B **46**, 14 249 (1992).
[31] G. Nieva, E. Osuiguil, J. Guimpel, M. Maenhoudt, B. Wuyts, Y. Bruynseraede, M. B. Maple, and I. K. Schuller, Appl. Phys. Lett. **60**, 2159 (1992).
[32] J.-H. Zhou and S. R. Elliot, Phys. Rev. B **46**, 12 402 (1992).
[33] D. L. Staebler and C. R. Wronski, J. Appl. Phys. **51**, 3262 (1980).
[34] M. Boekholt, M. Hoffmann, and G. Güntherodt. Physica C **175**, 127 (1991).

An alternate route to giant magnetoresistance in MBE-grown Co–Cu superlattices (invited)

Roy Clarke, Darryl Barlett, Frank Tsui, Baoxing Chen, and Ctirad Uher
Harrison Randall Laboratory of Physics, University of Michigan, 500 E. University, Ann Arbor, Michigan 48109-1120

Co–Cu superlattices grown by MBE in the (111) orientation show weak or nonexistent interlayer exchange coupling, yet several groups have observed large high-field magnetoresistance signals in excess of 30%. In the present work, we address some of the questions relating to GMR and the interlayer coupling by studying samples with atomically abrupt interfaces, as probed by real-time RHEED techniques, HRTEM, and spin-echo NMR. We propose that the lowered dimensionality of the structure leads to an enhancement of the scattering of conduction electrons from paramagnetic interfaces obeying a Langevin-like saturation at very high fields, well beyond the switching field of the Co layers. Scaling between the GMR and thermopower measurements suggests that a spin-dependent density of states at the Co–Cu interfaces is responsible for the observed magnetotransport behavior in these samples, rather than antiferromagnetically coupled Co layers.

I. INTRODUCTION

The magnetotransport behavior of (111)-oriented Co–Cu multilayers grown by molecular beam epitaxy (MBE) has recently generated some controversy. A much debated issue concerns the appearance of giant magnetoresistance (GMR) in samples that show little[1–4] or no[5,6] evidence of antiferromagnetic (AFM) interlayer coupling. The latter is a well-established mechanism for GMR in magnetic multilayers *via* spin-dependent scattering; it is characterized by a sharp "knee" in the resistance versus field curve at the flip field of the counteraligned spins.[7]

A number of authors have put forward sample defects as a possible explanation why AFM may be masked in the Co–Cu (111) system. For example, it has been suggested that stacking faults[8] and pinholes[9] may lead to ferromagnetic bridging across neighboring Co layers. However, ferromagnetic bridging, by definition, suppresses AFM coupling, and it should suppress spin-dependent GMR effects as well. While no definitive evidence has yet been presented for such a mechanism, the scanning tunneling micrographs of de la Figuera *et al.*,[10] showing a tendency for island nucleation, graphically illustrate the need for careful growth studies as well as atomic-scale structural characterization.

In this paper we present an alternative description of the GMR in (111) Co–Cu MBE samples. Our approach is based on a comparison of magnetotransport and magnetization measurements on a series of carefully grown superlattices with atomically smooth interfaces. We observe what appears to be a new type of GMR, one that is not dependent on AFM coupling and is operative to very high magnetic fields. In the limit of atomically smooth interfaces, our results suggest that the lowered dimensionality of the magnetic/nonmagnetic interfaces in our samples is the key factor in the observed magnetotransport behavior rather than sample defects.

II. SAMPLE GROWTH AND CHARACTERIZATION

The samples in this research were grown by MBE on Ge-buffered (110) GaAs substrates. Buffer layers of 15 Å (110) bcc Co, followed by 20 Å (111) Au, were deposited on the Ge to initiate layer-by-layer superlattice growth in the (111) orientation. The superlattice samples typically consist of 30 bilayers. The pressure during superlattice growth was $<4\times10^{-10}$ mbar, and the substrate temperature was held at 150 °C. Co was deposited from an electron beam hearth at rates between 0.15 and 0.25 Å/s, and Cu from a Knudsen cell at a rate of 0.33 Å/s. The thickness variations of individual layers of Co and Cu were controlled to about 0.5 ML. Details of the growth are described in a previous publication.[11] The growth was monitored *in situ* by reflection high energy electron diffraction (RHEED) using a CCD imaging and analysis system.[12] X-ray scattering performed after growth confirmed that the layer stacking was fcc in the (111) orientation.[11]

A crucial aspect of the interface characterization involved spin-echo NMR measurements of the local cobalt environment.[13] Only two characteristic NMR peaks were observed, one of which corresponds to bulk fcc Co with 12 Co neighbors and the other to interfacial Co having three Cu neighbors (see Fig. 1). The results will be described in more

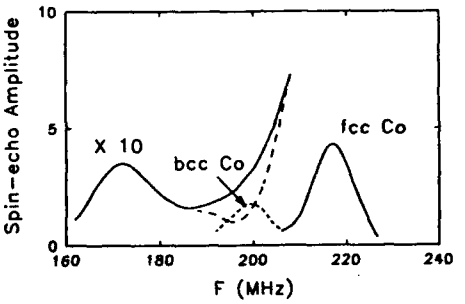

FIG. 1. Co spin-echo NMR spectra[14] at $T=2$ K in a Co–Cu superlattice $[Co(7.5\ ML)/Cu(3\ ML)]_{30}$. The interface peak has been magnified by a factor of 10. The dashed line shows the contribution of the 15 Å bcc Co buffer layer.

 0021-8979/94/75(10)/6174/4/$6.00 © 1994 American Institute of Physics

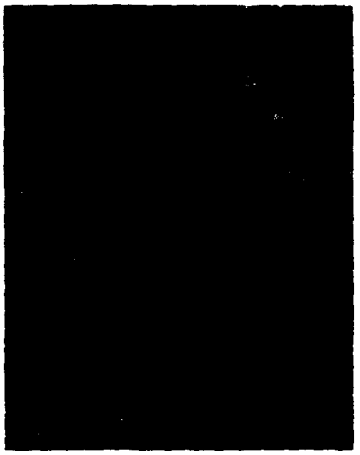

FIG. 2. Typical cross-sectional HRTEM micrograph along a [110] azimuth of $[Co(7\ ML)/Cu(3\ ML)]_{40}$. The variation in contrast along the growth direction, which is obtained by defocusing the image, corresponds to interference fringes due to the superlattice periodicity, as indicated by the arrows. Note that the defocused image shown here still exhibits atomic resolution, indicating high crystal coherence. The horizontal bar corresponds to 50 Å. Inset: the HRTEM image over a larger area. The horizontal bar corresponds to 100 Å. The straight horizontal contrast bands indicate flat superlattice layers.

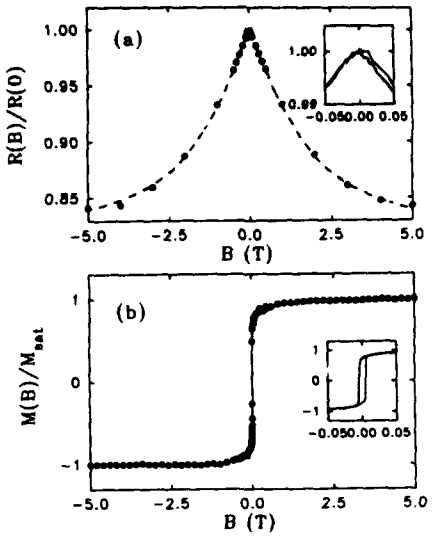

FIG. 3. (a) Ambient temperature magnetoresistance, $R(B)/R(0)$, vs field (Tesla) for a $[Co(7.5\ ML)/Cu(5.5\ ML)]_{26}$ superlattice. The dashed line is a theoretical fit to the Langevin function described in the text, where $N=480$ and $\beta=0.194$. Inset: low-field MR vs field dependence. (b) Magnetization curve for same sample. $M_{sat}=1400$ emu/cm^3. Inset: low-field magnetization curve. $T=300$ K.

detail in a separate publication.[14] They provide two important insights on the microstructure of our MBE samples. First, a comparison of the intensities of the "bulk" and "interface" NMR peaks shows that a significant area of the Co–Cu interfaces is atomically abrupt. Second, the absence of an hcp stacking "shoulder"[13] on the high frequency side of the bulk fcc peak at 217 MHz places a lower limit on the stacking coherence of our samples. Coherent fcc stacking over at least 200 Å is inferred from these measurements. The NMR results therefore indicate a low density of stacking faults. This is contrary to the island-growth mechanism presented by Gradmann *et al.*,[8] where one would expect a large concentration of stacking faults.

With reference to the STM results[10] mentioned above, where Co growth was performed at an ambient temperature on a Cu(111) single crystal surface, we note some important differences with the growth of our samples. The main difference is that in our samples the lattice mismatch (~1.8%) is shared between the (thin) Cu layers and the Co layers. Neither layer fully relaxes during growth, so that coherent layer-by-layer deposition is promoted.[15] Also, the substrate temperature in our case is elevated in order to enhance the surface diffusion of the incident atoms. We find much improved growth compared to ambient temperature conditions.

The high quality of our MBE samples is also illustrated by cross-sectional high-resolution transmission electron microscopy (HRTEM) (see Fig. 2). Note that the atomic layers are coherent over several hundred Å, which again is consistent with our x-ray diffraction and RHEED experiments. The flatness and continuity of the layers in this micrograph does not support the view that the growth of (111)-oriented samples is particularly prone to pinhole formation.

The MR measurements were made using the standard dc four-point probe technique with the field applied parallel to the current (longitudinal MR). The magnetization was measured in a commercial SQUID magnetometer and the measured saturation moments are within 10% of the bulk value for Co. Both the magnetization and MR measurements were made for fields applied in the growth plane along the [110] and $[11\bar{2}]$ directions of the superlattice.[16]

III. RESULTS AND DISCUSSION

A. Comparison of magnetization and magnetoresistance

Figure 3 compares the MR for a $[Co(7.5\ ML)/Cu(5.5\ ML)]_{26}$ superlattice with its magnetization for fields applied along the $[11\bar{2}]$ direction. Immediately it is apparent that the magnetization is largely saturated by 500 Oe, whereas the MR is still changing significantly at 50 000 Oe, the highest field we can achieve in our cryostat. Moreover, the magnetization is clearly ferromagnetic in character, with no evidence for a flip-field in the MR curve, such as is seen in the case of AFM-coupled Fe–Cr.[7] In what follows we will provide an alternative explanation that resolves the discrepancy between the different saturation behaviors of the MR and the bulk magnetization.

The field dependence of the MR shown in Fig. 3(a) can be described accurately by a Langevin-like saturation func-

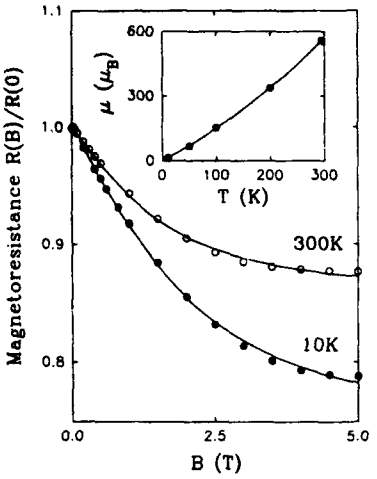

FIG. 4. Field dependence of MR at two different temperatures for [Co(7.5 ML)/Cu(5.5 ML)]$_{30}$. The solid lines are fits to the Langevin function described in the text. Inset: the number of correlated spins as a function of temperature.

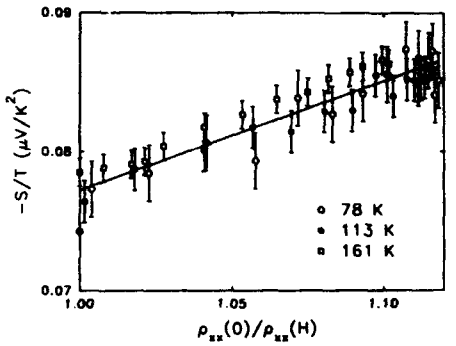

FIG. 5. Scaling behavior of magnetothermopower and magnetoresistance at various temperatures for [Co_{15} Å/Cu_{10} Å]$_{30}$.

tion, 1-β(coth $\alpha-1/\alpha$), where $\alpha=N\mu_0 B/k_B T$, β, and N are fitting parameters and μ_0 is the Bohr magneton. The dashed line in Fig. 3(a) is a fit to the experimental data using the Langevin function. This specific field dependence suggests that scattering from an assemblage of paramagnetic spins, mostly likely at the interfaces between Co and Cu layers, is responsible for the GMR in our samples. We note here that the Cu conduction electron band becomes partially polarized in proximity to the Co layers.[17] Interfacial "loose" spins have also been proposed in order to explain the origin of biquadratic coupling.[18]

It is interesting to point out here that the character of the paramagnetism is not that of isolated spins; rather, we find that there are substantial correlations, akin to a superparamagnetic layer. We envision the paramagnetic spin arrangement as forming small patches of correlated spins of size $\sqrt{N}$. The values of N returned by the Langevin fit at ambient temperature are roughly 500, falling approximately linearly toward unity at $T=0$, as shown in Fig. 4. The enhanced exchange interactions between the interfacial spins and the ferromagnetic Co spins at low temperatures perhaps give rise to the observed decrease of N. We note in passing that these findings make contact with observations of GMR in annealed granular Co–Cu films.[19] In these systems the field dependence of the GMR is also Langevin-like, presumably reflecting the important role of interface states in these systems as well.

The field-dependent MR results discussed here point to a new mechanism for GMR that depends on the scattering associated with interfacial magnetic states, not the ferromagnetic spins in the Co layers, since the Co layers are already fully saturated at low fields. The traditional spin-dependent scattering mechanism, as it has been discussed previously in the context of AFM coupling, is not present in the results discussed here, since it requires one-to-one correlation between MR and magnetization of the magnetic layer.

In light of the above discussion, what are the consequences for interlayer coupling? Due to enhanced scattering by the interfacial paramagnetic layers, the exchange interactions between the neighboring magnetic Co layers are significantly weakened. Our results also reveal that atomically "rougher" interfaces (i.e., samples showing broadened RHEED streak.. indicative of short in-plane coherence) have decreased values of the high-field MR. These studies are preliminary at this point, and a fuller account will be reported in a subsequent publication. In the context of roughness, one can envisage regions of the sample that have smooth terraces, together with regions where islands have nucleated (e.g., Stranski–Krastanov growth). This may explain the observation of mixed coupling in recent polarized neutron scattering measurements[4] on (111) Co–Cu superlattices grown on sapphire.

B. Magnetothermopower measurements

In order to shed further light on the origin of the GMR in these superlattices, we have carried out a study of the magnetothermopower as a probe of spin-dependent density of states effects.[20] While the MR shows no apparent dependence on the Co magnetization (see Fig. 3), our measurements reveal a clear scaling relationship with the thermopower at temperatures where diffusion thermopower is dominant ($T>50$ K). Figure 5 illustrates the scaling, which is of the form $S(H)/T\sim\rho_{xx}(0)/\rho_{xx}(H)$. Scattering of conduction electrons due to the spin-dependent density of states of the unfilled d bands at the Fermi level leads to precisely this form of scaling.[20] A more detailed account of this work is presented in a separate publication.[21]

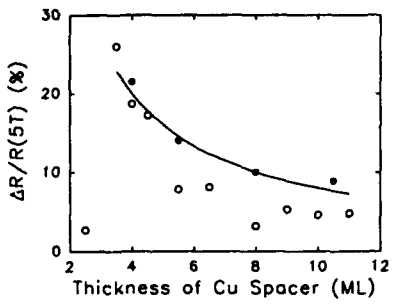

FIG. 6. Spacer layer thickness dependence of MR for Co–Cu (111) superlattices (●, this work; ○, Hall *et al.*[22]). $T=5$ K. The solid line is a fit to the $1/t_{Cu}$ dependence discussed in the text.

C. Dependence of GMR on Cu layer thickness

Oscillations in the GMR as a function of nonmagnetic spacer layer thickness are often taken as a signature of antiferromagnetic exchange coupling. In the present work we have argued that the GMR in our samples originates not from AFM coupling, but from interfacial states that are spin dependent. We should not then expect to see oscillatory GMR behavior, but rather a monotonic decrease of the spin-dependent interface scattering contribution as the spacer layer thickness increases. This is precisely what we observe. Our MR data plotted in Fig. 6, along with previously published results[22] on MBE samples also grown on (110) GaAs substrates, show a $1/t_{Cu}$ thickness dependence consistent with the dominant role of the interfaces in these samples. It is interesting that the monotonic increase of MR is truncated abruptly at a spacer layer thickness of approximately 5 Å (~2 ML). This thickness corresponds to a layer structure in which each Cu atomic layer is in atomically close proximity to Co. In this case, the MR falls to normal bulk-like values, suggesting that the spin-dependent density of states effects are quenched in the limit of very thin spacer layers.

IV. SUMMARY

We have demonstrated what we believe is a new type of high field MR mechanism, which results from scattering of conduction electrons from paramagnetic Co–Cu interfaces. Our observations call for a more thorough treatment of the band offsets at the interfaces, including $s-d$ hybridization, and for a better understanding of the interfacial scattering of the conduction electrons. We hope that our results will stimulate additional theoretical work in this area.

ACKNOWLEDGMENTS

We acknowledge useful discussions with R. Merlin. We also acknowledge the HRTEM assistance provided by T. Mandrekar, B. Demczyk, and J. Mansfield at the University of Michigan Electron Microbeam Analysis Laboratory. Funding for this work was provided by ONR Grant No. N00014-92-J-1335.

[1] D. Greig, M. J. Hall, C. Hammon, B. J. Hickey, H. P. Ho, M. A. Howson, M. J. Walker, N. Wiser, and D. G. Wright, J. Magn. Magn. Mat. **110**, L239 (1992).
[2] J. P. Renard, F. Beauvillain, C. Dupas, K. Le Dang, P. Veillet, E. Vélu, C. Marlière, and D. Renard, J. Magn. Magn. Mat. **115**, L147 (1992).
[3] J. Kohlhepp, S. Cordes, H. J. Elmers, and U. Gradmann, J. Magn. Magn. Mat. **111**, L231 (1992).
[4] A. Schreyer, K. Bröhl, J. F. Ankner, C. F. Majkrzak, T. Zeidler, P. Bödeker, N. Metoki, and H. Zabel, Phys. Rev. B **47**, 15 334 (1993).
[5] W. F. Egelhoff, Jr. and M. T. Kief, Phys. Rev. B **45**, 7795 (1992).
[6] R. F. Marks, R. F. C. Farrow, S. S. P. Parkin, C. H. Lee, B. D. Hermsmeier, C. J. Chien, and S. B. Hagstrom, Mater. Res. Soc. Symp. Proc. **221**, 15 (1991).
[7] M. N. Baibich, J. M. Broto, A. Fert, F. Nguyen Van Dau, F. Petroff, P Eitenne, G. Creuzet, A. Friederich, and J. Chazelas, Phys. Rev. Lett. **61**, 2472 (1988).
[8] U. Gradmann, H.-J. Elmer and J. Kohlhepp, Mat. Res. Soc. Symp. Proc. **313**, 107 (1993).
[9] S. S. P. Parkin, R. Bhadra and K. P. Roche, Phys. Rev. Lett. **66**, 2152 (1991).
[10] I. de la Figuera, J. E. Prieto, C. Ocal, and R. Miranda, Phys. Rev. B **47**, 13 043 (1993).
[11] F. J. Lamelas, C. H. Lee, H. He, W. Vavra, and R. Clarke, Phys. Rev. B **40**, 5837 (1989).
[12] Model KSA300, Manufactured by k-Space Associates Inc., Ann Arbor, MI 48104.
[13] K. Le Dang, P. Veillet, H. Hui, F. J. Lamelas, C. H. Lee, and R. Clarke, Phys. Rev. B **41**, 12 902 (1990); H. A. M. de Gronkel, K. Kopinga, W. J. M. de Jonge, P. Panissod, J. P. Schillé, and F. J. A. den Broeder, Phys. Rev. B **44**, 9100 (1992); J. S. Lord, H. Kubo, P. C. Riedi, and M. J. Walker, J. Appl. Phys. **73**, 6381 (1994).
[14] K. Le Dang, P. Veillet, F. Tsui, D. Barlett, and R. Clarke (unpublished).
[15] This finding is also consistent with the results reported by S. Pizzini, F. Baudelet, A. Fontaine, M. Galtier, D. Renard, and C. Marlière, Phys. Rev. B **47**, 8754 (1993).
[16] The observed MR is nearly isotropic and in-plane magnetization anisotropy is also small (<150 Oe).
[17] S. Pizzini, C. Giorgetti, A. Fontaine, E. Dartyge, G. Krill, J. F. Bobo, and M. Piecuch, Mat. Res. Soc. Symp. Proc. **313**, 625 (1993).
[18] J. C. Slonczewski, J. Appl. Phys. **73**, 5957 (1993).
[19] A. E. Berkowitz, J. R. Mitchell, M. J. Carey, A. P. Young, S. Zhang, F. E. Sapda, F. T. Parker, A. Hutten, and G. Thomas, Phys. Rev. Lett. **68**, 3745 (1992); J. Q. Xiao, J. S. Jiang, and C. L. Chien, *ibid.* **68** 3749 (1992).
[20] L. Xing, Y. C. Chang, M. B. Salamon, D. M. Frenkel, J. Shi, and J. P. Lu, Phys. Rev. B **48**, 6728 (1993).
[21] F. Tsui, B. Chen, D. Barlett, R. Clarke, and C. Uher, Phys. Rev. Lett. **72**, 740 (1994).
[22] M. J. Hall, B. J. Hickey, M. A. Howson, M. J. Walker, J. Xu, D. Greig, and N. Wiser, Phys. Rev. B **47**, 12 785 (1993).

Magnetic profile as a function of structural disorder in Fe/Cr superlattices

Michael J. Pechan
Department of Physics, Miami University, Oxford, Ohio 45056

J. F. Ankner and C. F. Majkrzak
NIST, Gaithersburg, Maryland 20899

David M. Kelly and Ivan K. Schuller
Department of Physics, UC San Diego, La Jolla, California 92093

Structural disorder has been systematically introduced in an $[Fe(30\ Å)/Cr(17\ Å)]_{10}$ superlattice to investigate its effects on the magnetization profile. Low angle x-ray and neutron scattering results indicate progressive structural degradation in samples produced with increased argon pressure (3, 6, and 12 mTorr). The x-ray spectra from the more disordered samples are characterized by a decreased intensity and increased linewidth of the superlattice Bragg peaks, along with a systematic disappearance of the finite size intensity oscillations. Elastic, polarized, low angle, neutron reflectivity data exhibit decreasing superlattice Bragg intensities and increasing linewidths, indicating increased disorder in agreement with x-ray data. Antiferromagnetic alignment of adjacent Fe layers is inferred by the appearance of magnetic peaks between the structural peaks and by the lack of magnetic contribution to the structural superlattice peaks. Interestingly, the magnetic superlattice peak does not exhibit appreciable degradation with increasing disorder in the structure, indicating a magnetic coherence length significantly greater than that of the chemical superlattice structure.

INTRODUCTION

Magnetic multilayer materials are proving fruitful in both technological and fundamental arenas. This is perhaps most readily exemplified in magnetic/nonmagnetic multilayers in which large magnetotransport effects are observed in a wide range of systems, which also exhibit magnetic interlayer coupling.[1] An understanding of the role played by superlattice structure in determining the magnetic and transport properties is essential, and is the subject of considerable theoretical and experimental investigation. Degree of epitaxy and varying crystalline orientation are examples of parameters varied in probing structural dependences. Neutron scattering has been utilized by others in structural investigations of Fe/Cr,[2] but not to probe systems wherein roughness is a controlled parameter. Recently, a significant correlation was shown between the size of magnetoresistance and structural disorder, by systematically increasing and characterizing the superlattice disorder in Fe/Cr multilayers.[3] As an extension of this approach, the present investigation characterizes the magnetization profile as a function of structural disorder in the Fe/Cr system. Results indicate a magnetic multilayer profile that is essentially independent of structural disorder over the ranges investigated.

EXPERIMENTAL DETAILS AND ANALYSIS TECHNIQUES

Fe(30 Å)/Cr(17 Å) multilayer samples were prepared on [100] Si substrates by dc sputtering in an Ar atmosphere. System base pressure was less than 2×10^{-7} Torr. First Fe, then Cr was deposited, forming a bilayer structure that was repeated ten times for each sample. Structural disorder was introduced by increasing the Ar pressure during sputtering from 3 to 12 mTorr. Both high and low angle x-ray (Cu, K_α, $\lambda=1.54$ Å) measurements were performed on each sample. Low angle diffuse scattering contributions were accounted for by repeating the specular scans with the sample rotated 0.1° away from the superlattice Bragg condition and subtracting from the specular scans. Superlattice structural information is obtained by fitting the specular low angle spectra to a classical optics model,[4] where each layer is assigned a thickness and scattering density, and has an associated interfacially mixed region. Polarized, low angle neutron ($\lambda=2.37$ Å) reflectivity measurements were also performed, providing additional structural information and characterization of the multilayer magnetic profile. Polarized neutrons have historically been used, at the atomic level (and therefore high scattering angles), to extract the magnetic contribution from a combined nuclear/magnetic scattering amplitude. Recently,[5,6] the technique has been applied to layered structures, operating in the low angle regime, to characterize the superlattice magnetization profile and chemical modulation. A small quantization field, $\mathbf{H}=14$ Oe is applied in the plane of the film, following *ex situ* application of 200 Oe in the same direction. The scattering vector is normal to the film plane. Assuming an in-plane magnetization (appropriate for Fe/Cr), one can realize two scattering processes–spin flip (SF) and non-spin flip (NSF)—each with two channels: $(-+)$ and $(+-)$ in the SF and $(++)$ and $(--)$ in the NSF, where the states refer to the spin polarization of the incoming and reflected neutrons, respectively. The SF process refers to scattering from a component of the magnetization M normal to $\mathbf{H}$, whereas NSF scattering arises from components of M along $\mathbf{H}$ and from the nuclei. The scattering intensities from the two SF channels will be identical, but the NSF $(++)$ intensity is derived from the sum of the magnetic and nuclear scattering amplitudes, whereas the $(--)$ intensity arises from their difference. Low angle neutron spectra are also analyzed according to a classical optics model, utilizing the same fitting approach as for the x rays.

RESULTS AND DISCUSSION

Low angle x-ray spectra for samples prepared with increasing Ar pressure are shown in Fig. 1. The sample sput-

 0021-8979/94/75(10)/6178/3/$6.00 © 1994 American Institute of Physics

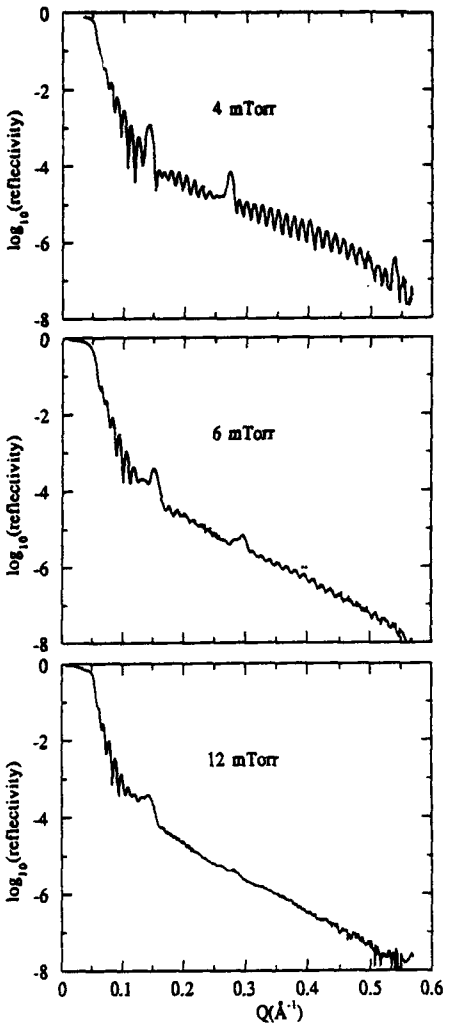

FIG. 1. Low angle x-ray spectra for $[Fe(30\ Å)/Cr(17\ Å)]_{10}$ samples prepared at various Ar sputtering pressures.

tered at 4 mTorr exhibits superlattice Bragg peaks out to fourth order (the third order is suppressed, owing to the approximate 2:1 thickness ratio of the bilayer components), indicating square wave chemical modulation. In addition, short period, finite size peaks, (interference from the top and bottom of the aggregate bilayer stack) are evident throughout the spectrum, attesting to uniform film thickness. These spectral features degrade with increasing Ar sputtering pressure. The finite size peaks become much less pronounced and less extended in Q space, indicating decreasing uniformity in the overall film thickness. The superlattice Bragg peaks exhibit progressively weaker higher-order amplitudes and increasing linewidths. One may be tempted to conclude, based upon the disappearance of higher-order amplitudes, that the samples are increasingly characterized by interfacial interdiffusion. However, interdiffusion alone will *not* increase linewidths *nor* depress the finite size peak structure. Rather, these latter effects are known to arise from cumulative random variations in layer thic[illegible] superimpose wavelike modulations on th[illegible]ucture. Such fluctuations would also give rise to *apparent* interdiffusion as they are averaged over the lateral coherence length (>1000 Å) of the low angle x rays, producing the observed broadening of the higher-order Bragg peaks. The present optic model used to extract structural information treats thickness fluctuations in the simplest sense—layers are assumed flat but their thicknesses are adjustable. In order to produce the increase in linewidth observed in going from the 4 to 12 mTorr sample, the Cr layer thicknesses went from 100% t_{Cr}=17 Å (and Fe/Cr intermixing of 4 Å) to 50% t_{Cr}=18.6 Å, 25% each of t_{Cr}=17.4 and 20.1 Å (again Fe/Cr intermixing of 4 Å). A more complex model of the layer thickness fluctuations may be useful for explaining details of the spectra, however, this simple approach reproduces the measured data adequately for the present discussion.

The *high* angle x-ray spectra are essentially indistinguishable for the samples shown in Fig. 1. All films exhibit a predominant bcc (110) orientation with linewidths, indicative of approximately 130 Å grain sizes. Owing to the similar scattering strengths of Fe and Cr, only weak superlattice satellites are observed at high angle, however, these provide some indication of the interfacial mixing on the atomic scale. The fact that the "smoothest" through the "roughest" samples show the same high angle pattern, yet differ so greatly in low angle, indicates that the roughness induced is on a length scale much greater than the interatomic spacing, but less than the coherence length of the x-ray beam.

Low angle polarized neutron spectra are shown in Fig. 2. The NSF peaks seen at approximately 0.14 $Å^{-1}$ correspond to the first-order superlattice Bragg peaks seen in the x-ray spectra. No difference is observed in these (++) and (−−) intensities, indicating no magnetic component to the scattering amplitude, and therefore ruling out ferromagnetic alignment of adjacent Fe layers. The half-order (0.07 $Å^{-1}$) NSF peaks again show no difference in the (++) and (−−) intensities. However, based upon the x-ray spectra (no Bragg peak), one assumes *only* magnetic scattering, which arises from antiferromagnetically aligned adjacent Fe layers. Half-order peaks are also observed in SF scattering, indicating that either the Fe sublattice magnetization makes an angle with respect to the applied quantizing field, **H**, or that there exist AF domains parallel and perpendicular to **H**. As with the x rays, the neutrons show a degradation of the chemical superlattice structure with increasing Ar pressure. The NSF AF peak also decreases in intensity with increasing sample roughness, however, the SF AF peak changes very little during the roughening process.

How can we understand a system where the magnetic structure persists in the face of degrading chemical superlattice structure? As evidenced by the decrease, with roughness, in NSF magnetic scattering, while the SF remains essentially

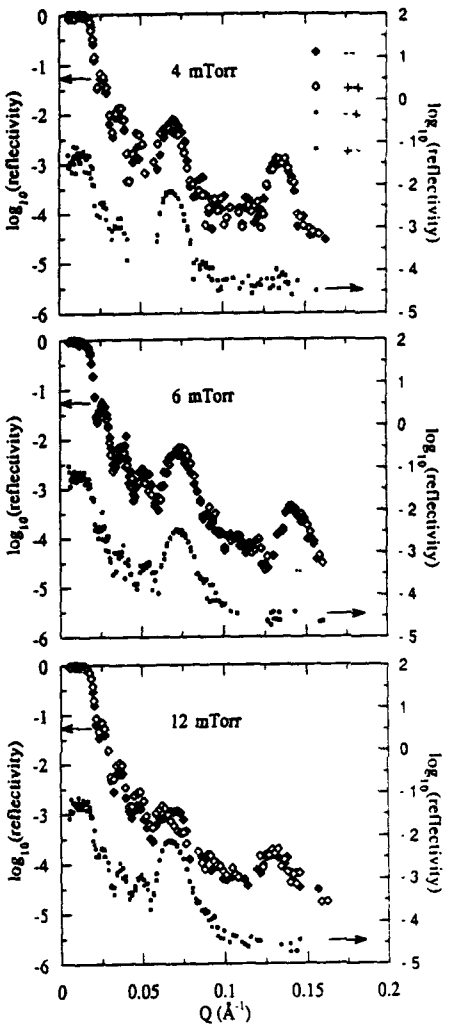

FIG. 2. Low angle polarized neutron spectra for $[Fe(30\ Å)/Cr(17\ Å)]_{10}$ samples prepared at various Ar sputtering pressures. Open diamonds and closed diamonds represent the two NSF (++) and (−−) scattering channels, respectively, whereas both SF (−+) and (+−) channels are represented by closed squares.

constant, the Fe layer superlattice becomes less ordered. This is consistent with magnetization measurements,[2] where the remnant moment is much larger in the rougher sample, indicating a decrease in the AF coupled component, but would require alignment without spatial coherence among the ferromagnetic component comprising the remnant. It is not hard to imagine random layer thickness fluctuations producing such a remnant. Why is the half-order magnetic peak retained in the SF component, but not the NSF? In the absence of in-plane anisotropy, the initial response of a simple AF structure is for each sublattice to align perpendicular to an applied field. This arrangement would give rise to half-order peaks in the SF but not the NSF spectra. Therefore one possibility here is that an in-plane ansotropy exists in the smoother sample, which disappears in the rougher. On the other hand, if the NSF and SF components in the smoother sample arise from AF domains with distributed orientations, then the coercive field must be reduced with increasing roughness. Finally, why is the SF AF peak affected so little by roughening? In the smooth samples, an AF component is pinned parallel to H, presumably by some in-plane anisotropy. With roughening, the spacially coherent AF volume fraction decreases (declining total AF scattered intensity), but this is accompanied by an apparent decrease in pinning strength (disappearance of the NSF AF scattering). Therefore the data would suggest a compensation process, wherein the AF component normal to the field is degraded by the decreasing coherent AF volume fraction, but is enhanced as a larger portion of that fraction orients normal to that field.

Addressing more precisely the relationship between the magnetic multilayer profile and structural disorder will require careful analysis of diffuse as well as specular scattering components of both x rays and neutrons.[8]

However, the most striking feature of the neutron data is the persistance of a coherent magnetic scattering in the face of greatly degraded chemical superlattice scattering. This, interestingly, implies a magnetic coherence length significantly greater than that of the chemical superlattice.

ACKNOWLEDGMENTS

This work was supported in part by the U.S. Department of Energy Contract No. DE-FG02-86ER45281 (Miami) and National Science Foundation Contract No. NSF DMR 9201698 (UCSD).

[1] A. Fert, A. Barthelemy, P. Lequien, R. Loloee, D. K. Lottis, D. H. Mosca, F. Petroff, W. P. Pratt, and P. A. Schroeder, J. Magn. Magn. Mater. **104–7**, 1712 (1992).
[2] A. Barthelemy, A. Fert, M. N. Babich, S. Hadjoudj, F. Petroff, P. Etienne, R. Cabanel, S. Lequien, F. Nguyen Van Dau, and G. Creuzet, J. Appl. Phys. **67**, 5908 (1990); N. Hosoito, S Araki, K. Mibu, and T. Shinjo, J. Phys. Soc. Jpn. **59**, 1925 (1990); S. S. Parkin, A. Mansour, and G. P. Felcher, Appl. Phys. Lett. **58**, 1473 (1991); J. A. C. Bland, A. D. Johnson, H. J. Lauter, R. D. Bateson, S. J. Blundell, C. Shackleton, and J. Penfold, J. Magn. Magn. Mater. **93**, 513 (1991). N. Hosito, K. Mibu, S. Araki, T. Shinjo, S. Itoh, and Y. Endoh, J. Phys. Soc. Jpn. **61**, 300 (1992); M. Takeda, Y. Endoh, H. Yasuda, K. Yamada, A. Kamijo, and J. Mizuki, J. Phys. Soc. Jpn. **62**, 3015 (1993). M. Lowenhaupt, W. Hahn, Y. Y. Huang, G. P. Felcher, and S. S. Parkin, to appear in Int. J. Phys. B.
[3] Eric E. Fullerton, D. M. Kelly, J. Guimpel, and I. K. Schuller, Phys. Rev. Lett. **68**, 859 (1992).
[4] J. F. Ankner and C. F. Majkrzak, in *Neutron Optical Devices and Applications*, edited by C. F. Majkrzak and J. L. Wood, Proc. SPIE, Bellingham, WA, 1992, Vol. 1738, p. 260.
[5] G. P. Felcher, R. O. Killeke, R. K. Crawford, J. Haumann, R. Kleb, and G. Ostrowski, Rev. Sci. Instrum. **58**, 609 (1987).
[6] C. F. Majkrzak, Physica B **173**, 75 (1991).
[7] E. E. Fullerton, I. K. Schuller, H. Vanderstraeten, and Y. Bruynseraede, Phys. Rev. B **45**, 9292 (1992). Also, as an example of cumulative random layer thickness fluctuations, see E. E. Fullerton, I. K. Schuller, and Y. Bruynseraede, MRS Bulletin, Dec. 1992, p. 33.
[8] S. K. Sinha, Physica B **173**, 25 (1991).

Temperature dependence of the exchange coupling in the Fe(001) whisker/11 ML Cr/20 ML Fe structure

M. From, L. X. Liao, J. F. Cochran, and B. Heinrich
Department of Physics, Simon Fraser University, Burnaby, British Columbia, V5A 1S6, Canada

The exchange coupling between iron layers separated by 11 monolayers (ML) of Cr(001) has been investigated using a structure in which the Cr(001) was grown on a bulk iron whisker Fe(001) surface at a temperature of approximately 300 °C. This temperature was selected to produce near optimum smoothness of the Cr layer. The Cr(001) deposition was followed by the deposition of 20 ML of Fe(001) at room temperature, and by the deposition of a 20 ML Au(001) protective layer. The frequencies corresponding to the magnetic excitations in this structure were measured by means of Brillouin light scattering (BLS). One of the observed frequencies corresponds to a surface mode in the bulk iron whisker. Another observed frequency corresponds to the lowest lying precessional mode of the magnetization in the 20 ML thick Fe(001) thin film. Typically, the thin film frequency exhibits a dependence on applied magnetic field that displays two cusps. The positions of the cusps are dependent on the exchange coupling between the 20 ML Fe film and the bulk iron substrate. The surface mode frequency increases monotonically with increasing field over most of the field range investigated. However, at the field corresponding to the low field cusp in the thin film frequency, the surface mode frequency undergoes an abrupt jump in magnitude. We have used the position of the cusps in the thin film data to deduce values for the bilinear, J_1, and biquadratic, J_2, coupling terms, where the coupling energy is written in the form $E_{AB}=-J_1\cos(\Delta\phi)+J_2\cos^2(\Delta\phi)$; $\Delta\phi$ is the angle between the thin film and bulk iron magnetizations. Measurements of J_1 and J_2 have been carried out at six temperatures that span the range 100–350 K. Both J_1 and J_2 are found to depend strongly on temperature. The data are well described by the quadratic expression $J_2=-0.54+1.46\times|J_1|-0.52\times J_1^2$, where J_1 and J_2 are expressed in erg/cm^2. The large nonzero intercept and the linear term probably imply a significant *intrinsic* contribution to the biquadratic exchange.

INTRODUCTION

Phenomenologically, the coupling energy between two iron layers separated by a nonferromagnetic spacer layer can be written[1-3] as

$$E_{AB}=-J_1\cos(\Delta\phi)+J_2\cos^2(\Delta\phi), \quad (1)$$

where J_1 and J_2 are the bilinear and biquadratic coupling parameters and $\Delta\phi$ is the angle between the magnetizations of the two films. It is a well-established experimental fact that both J_1 and J_2 oscillate as a function of the spacer thickness.[4] Numerous mechanisms have been proposed, which explain many of the features of these oscillations.

However, detailed tests of these theories with respect to the *temperature dependence* of the coupling parameters are still needed. Much interest was generated when Slonczewski[5] showed that J_2 might arise simply from variations, ΔJ, in J_1 due to a fluctuating thickness of the spacer layer. According to the Slonczewski theory, J_2 is proportional to $(\Delta J)^2$. If the magnitude of ΔJ scales with $|J_1|$, then one would expect J_2 to be proportional to J_1^2. We propose, in the present work, to test the origin of the observed biquadratic exchange coupling term by making measurements of the coupling parameters as a function of temperature.

We have previously reported[4] data on the dependence of the exchange coupling parameters on spacer thickness in the system Fe Whisker/Cr/Fe(001). It has been demonstrated that the Fe Whisker/Cr/Fe system exhibits a well-defined short wavelength oscillatory exchange.[6] The extremely flat surface of the whisker ensures that the effects of interface roughness are kept to a minimum. In the present work we extend our recent room temperature study of the Fe Whisker/Cr/Fe system to the temperature dependence of the Fe Whisker/11 ML Cr/Fe structure. The particular spacer thickness of 11 ML of Cr (i.e., 15.8 Å of Cr) was chosen because this corresponds to a maximum in antiferromagnetic coupling. Thus temperature effects, if present, were expected to be large.

EXPERIMENTAL DETAILS

The composition of the specimen used in our study was Fe Whisker(001)/11 ML Cr/20 ML Fe/20 ML Au; 1 ML of Cr corresponds to 1.44 Å and 1 ML of Fe corresponds to 1.43 Å. The specimen was prepared in a PHI-400 MBE system equipped with a reflection high energy electron diffraction apparatus (RHEED). Details of the whisker substrate preparation, and a description of RHEED patterns corresponding to optimum growth conditions have been given elsewhere.[4] The best of the specimens available to us exhibited RHEED patterns, which indicated a good Cr growth but a growth at slightly less than optimum conditions (see Fig. 1). The quality of the Cr growth is very sensitive to the substrate temperature. For optimum growth conditions the amplitude of the RHEED oscillations would be stronger than those shown in Fig. 1(a), and after the deposition of three monolayers the oscillations amplitudes corresponding to the maxima and minima would not change with time. The width of the specular diffraction spot, Fig. 1(b) alternates between a relatively narrow peak, corresponding to a filled layer, and a broader peak, corresponding to a half-filled layer (see Fig. 1 of Ref. 4). The specular spot width corresponding to a filled layer was observed to be broader than the specular spot observed for the bare whisker; this indicates that the Cr terraces were not as large as the substrate terraces (>1 μm).

 0021-8979/94/75(10)/6181/3/$6.00 © 1994 American Institute of Physics

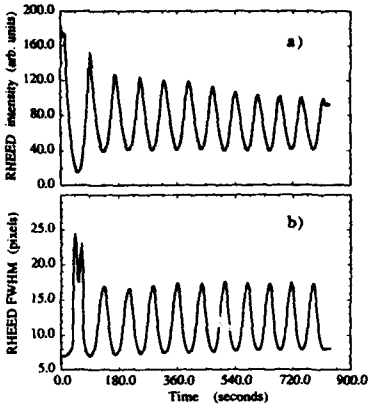

FIG. 1. (a) Reflection High Energy Electron Diffraction (RHEED) intensity oscillations measured at the specular spot during the Cr growth for an incident angle corresponding to the second anti-Bragg condition. (b) The full width at half-maximum (FWHM) obtained from line scans across the specular RHEED spot during the Cr growth. The increase of FWHM with increasing Cr thickness, as well as the decreasing peak-to-peak amplitudes of the RHEED oscillations indicate that the growth conditions for the Cr were good, but not optimal. The splitting of the first peak shown in Fig. 1(b) is an artifact introduced by the data collection system.

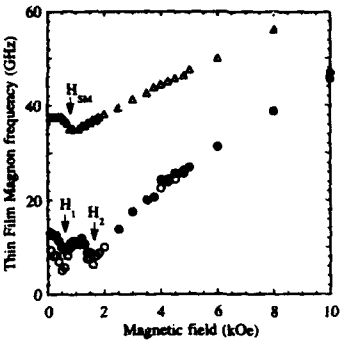

FIG. 2. The magnetic field dependence observed for the surface mode frequencies (△) and the thin film frequencies (○,●) for the Fe Whisker(001)/11 ML Cr(001)/20 ML Fe(001) specimen used to measure the temperature dependence of the bilinear and biquadratic coupling terms. The data were obtained for a free-standing specimen in air using 300 mW of 5145 Å argon ion laser light. The open circles denote downshifted frequencies. The filled circles denote upshifted frequencies. (The surface mode frequency is downshifted.) The intensity ratio of upshifted to downshifted light was found to be strongly field dependent. The cusps at H_1 and H_2 and the discontinuity at H_{SM} are a signature of antiferromagnetic coupling between the thin film and bulk.

The specimen was *loosely* clamped at a single point to a cold finger (at 77 K) inside a cryostat evacuated to a pressure of approximately 10^{-5} Torr. We chose this method of mounting to eliminate temperature-dependent stresses on the specimen. The distance between the laser spot and the clamp was large enough (about 8 mm) and the cross section of the whisker small enough (about 0.1 mm^2) that relatively modest incident light powers were sufficient to cause significant local heating of the specimen. The specimen was also measured in air at ambient temperature and pressure using a relatively small laser power (100 mW). The positions of the cusps at 300 K provided a benchmark that enabled us to deduce that 500 mW of incident power on the vacuum isolated specimen was required to raise the local temperature at the laser light spot to 300 K. To estimate the spot temperature at other powers, we used the linear interpolation:

$$T=77+(300-77)/500\times P, \tag{2}$$

where T is the temperature in K and P is the power in mW.

Brillouin light scattering (BLS) measurements were carried out using the green line from an Argon ion laser (λ =5145 Å). The light scattered by the sample was analyzed using a Sandercock[7] tandem interferometer in a 4+2 pass configuration and a free spectral range of 70 GHz. This relatively large free spectral range was convenient because it enabled the surface mode to be measured for all magnetic fields up to a maximum of 10 kOe. The free spectral range was divided into 256 channels and data were collected for a total of approximately one second per channel. The frequency of a spectral feature was calculated from the centroid of the data contained within ±5 channels of the estimated peak position. A polarizing beam cube was used to block scattered light having the same polarization as the incident light. Magnon frequencies were measured as a function of applied magnetic field at six different incident light powers. The signals were rather noisy because of stray light scattered by the cryostat windows and because of small sample vibrations caused by the boiling of the liquid nitrogen used to cool the cold finger.

RESULTS AND DISCUSSION

Figure 2 shows the dependencies of the surface mode and thin film frequencies on the applied magnetic field. As discussed in our previous paper,[4] the prominent cusp-like features are a signature of the antiferromagnetic coupling between the iron thin film and the bulk. Roughly speaking, the larger the cusp fields, H_1 and H_2, the greater is the antiferromagnetic coupling. An interesting feature of our data that has not previously been reported is the sudden change in the surface mode frequency at the field $H_{SM}\sim H_1$. This sharp drop in frequency with a slight increase in magnetic field at or near H_1 has been observed in all cases in which the thin film and the bulk substrate are antiferromagnetically coupled.

In order to deduce the coupling parameters, J_1 and J_2, from the positions of the cusps in the thin film frequency data, we used a calculation,[8] which allows for the possibility of a spatial variation in the magnetization direction in both the thin film and in the bulk. As such, it is superior to the calculation we used in our earlier study of the dependence of exchange coupling on spacer thickness.[4] In both calculations we assumed that the magnetizations rotated in the plane defined by the substrate surface; the bulk and thin film magnetizations are constrained to remain [illegible]ne by the demagnetizing field energy. The results [illegible]sent work are

TABLE I. $|J_1|$ and J_2 as a function of temperature for the specimen Fe Whisker(001)/11 ML Cr/20 ML Fe/20 ML Au. These parameters were obtained from the values of the cusp fields, H_1 and H_2, using a computer calculation (see Ref. 8). This calculation allows for a spatial variation of the magnetization direction in both the thin iron film and the bulk. It uses temperature-dependent values for the saturation magnetization and first-order cubic anisotropy constant taken from the work of Escudier.[9]

Temperature (K)	H_1 (kOe)	H_2 (kOe)	$\|J_1\|$ (erg s/cm^2)	J_2 (erg s/cm^2)	$\|J_1\|/J_2$
120	1.00±0.20	6.3±0.2	1.24±0.02	0.47±0.02	2.64
170	0.75±0.20	5.3±0.2	1.04±0.06	0.44±0.04	2.36
210	0.75±0.20	4.0±0.2	0.88±0.06	0.34±0.03	2.59
250	0.75±0.20	3.0±0.2	0.75±0.04	0.26±0.04	2.88
300	0.75±0.20	2.0±0.2	0.61±0.04	0.16±0.04	3.82
340	0.75±0.20	1.9±0.2	0.59±0.07	0.15±0.02	3.93

summarized in Table I. The analyses of Table I used temperature-dependent values for the saturation magnetization and first-order cubic anisotropy parameter of iron taken from the work of Escudier.[9]

Figure 3 presents the coupling parameter data of Table I. In Fig. 3(a), both $|J_1|$ and J_2 are seen to decrease monotonically with temperature. Figure 3(b) is a plot of J_2 against J_1. The dashed line in this figure is the best fit of a quadratic function to the data. The fitting equation is

$$J_2 = -0.54 + 1.46 \times |J_1| - 0.52 \times J_1^2, \tag{3}$$

where J_1 and J_2 are both expressed in erg/cm^2.

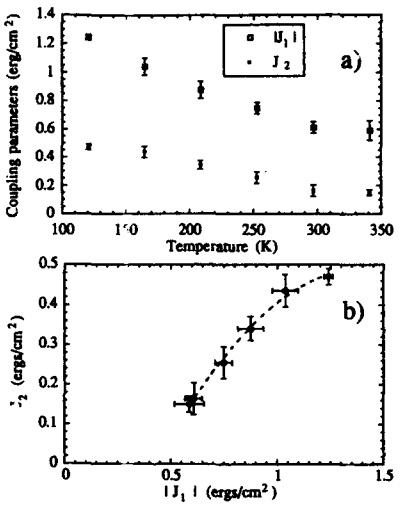

FIG. 3. Data from Table II. (a) $|J_1|$ and J_2 as a function of temperature. (b) J_2 as a function of $|J_1|$. The dashed line shows the best fit of a quadratic to the data. The fitting function is $J_2 = -0.54 + 1.46 \times |J_1| - 0.52 \times J_1^2$. A possible origin of the term in J_1^2 is the Slonczewski surface roughness mechanism. The large linear contribution to the fitting function is a signature of an *intrinsic* source of biquadratic exchange. The error bars shown have been calculated, assuming an uncertainty of ±0.2 kOe in the values of the cusp fields H_1 and H_2.

Although Eq. (3) does contain a term proportional to J_1^2, the dominant contribution to J_2 is linear in J_1. This observation is consistent with the results of measurements on the Fe/Cu/Fe(001) and the Fe/Ag/Fe(001) systems,[10] for which a linear dependence of both J_1 and J_2 on temperature has been obtained, and for which the biquadratic coupling coefficient displayed a linear dependence on the bilinear coefficient J_1. In both cases, J_1 and J_2 decreased by approximately a factor of 2 as the temperature was increased from 77 to 300 K.

The surface roughness mechanism proposed by Slonczewski[5] predicts a contribution to J_2 that is proportional to $(\Delta J)^2/A$, where ΔJ is the change in J_1 for a change in spacer layer thickness of one monolayer, and A is the bulk exchange stiffness coefficient for the ferromagnetic layers. It is reasonable to suppose that the ratio $\Delta J/A$ could have essentially no temperature dependence; for instance, both quantities could vary as $M_S(T)$. The temperature dependence for both J_1 and J_2 would then be the same, since $\Delta J \sim J_1$. However, the strength of the temperature dependence is very surprising: nearly 200% over the interval 100–300 K. This can be compared with a magnetization change for iron of approximately 3% over the interval 100–300 K. Moreover, this strong temperature dependence has been observed, both in the present system for which the interfaces are very smooth, and in systems for which the interface terraces are relatively short: Fe/Cu/Fe(001) and Fe/Ag/Fe(001).[10] It is therefore very likely that both the bilinear and biquadratic coupling terms are mainly due to an intrinsic mechanism and not due to the interlayer roughness.

[1] B. Heinrich, J. F. Cochran, M. Kowalewski, J. Kirschner, Z. Celinski, A. S. Arrott, and K. Myrtle, Phys. Rev. B **44**, 9348 (1991).
[2] M. Rührig, R. Schäfer, A. Hubert, R. Mosler, J. A. Wolf, S Demokritov, and P. Grünberg, Phys. Stat. Solid. A **125**, 635 (1991).
[3] B. Heinrich, in *Ultrathin Magnetic Structures*, edited by B. Heinrich and J. A. C. Bland (Springer, Berlin, 1993), Vol. 2.
[4] B. Heinrich, M. From, J. F. Cochran, L. X. Liao, Z. Celinski, C. M. Schneider, and K. Myrtle, *Proceedings of the 1993 Spring Meeting of the Materials Research Society Symposium Proceedings* **313**, 119 (1993).
[5] J. C. Slonczewski, Phys. Rev. Let. **67**, 3172 (1991); J. Appl. Phys. **73**, 5957 (1993).
[6] J. Unguris, R. J. Celotta, and D. T. Pierce, Phys. Rev. Lett. **67**, 140 (1991).
[7] P. Grünberg, Prog. Surf. Sci. **18**, 1 (1985).
[8] W. Folkerts and S. T. Purcell, J. Magn. Magn. Mat. **111**, 306 (1992).
[9] T. Escudier, Ann. Phys. **9**, 125 (1975).
[10] Z. Celinski, B. Heinrich, and J. F. Cochran, unpublished.

Anisotropy studies of AFM coupled MBE grown Co/Cu(001) superlattices

K. Bröhl, S. Di Nunzio, F. Schreiber, Th. Zeidler, and H. Zabel
Institut für Experimentalphysik, Ruhr-Universität Bochum, 44780 Bochum, Germany

We have studied the anisotropy behavior of antiferromagnetically (AFM) coupled fcc Co/Cu(001) sandwiches and superlattices. Magneto-optical Kerr effect measurements on samples with Cu film thicknesses in the range of the second antiferromagnetic maximum reveal characteristic shapes of the hysteresis loops in close agreement with theoretical predictions. For the AFM coupled samples we infer antiparallel spin orientations in remanence perpendicular to the originally applied magnetic field direction. Changing the magnetic layer thickness and maintaining a constant thickness of the spacer completely alters the shape of the hysteresis loops. The loops of weakly coupled AFM layers show characteristic steps, indicative for a rather unusual nonsymmetric spin state. This behavior can be explained by the competing effects of anisotropy with the exchange coupling.

The oscillation of the strength and the sign of the exchange coupling between magnetic layers as a function of the nonmagnetic spacer thickness has recently been observed in a large number of systems. Following quantitative predictions[1] about the strength and the orientational dependence of the interlayer coupling, most of the experimental interest has focused on the oscillatory coupling in model systems such as fcc Co/Cu in several crystallographic orientations.[2,3]

A thorough understanding of anisotropy properties is of equal importance. They have a pronounced impact on the magnetization behavior, in particular, for AFM coupled layers. Here we will show that the consideration of anisotropy effects advances the interpretation of complex hysteresis loops.

Phenomenological studies of the magnetization behavior of AFM coupled multilayer systems by Dieny *et al.*[4] assume that each ferromagnetic layer is single domain and that its magnetization rotates only as a rigidly coupled block of moments. The calculations of the local minima of the internal energy yield the stable states and provide magnetization curves. The volume energy density of a sample with two magnetic layers and an in-plane fourfold anisotropy appropriate for the systems discussed further can be expressed in a normalized form:

$$\frac{E\cdot t_{\mathrm{mag}}}{J} = -\cos(\Theta_1-\Theta_2)+b(\cos\Theta_1+\cos\Theta_2) -k(\cos^2\Theta_1\sin^2\Theta_1+\cos^2\Theta_2\sin^2\Theta_2). \quad (1)$$

Here Θ_1 and Θ_2 are angles between the magnetizations of the two magnetic layers with respect to the applied magnetic field, J is the exchange coupling constant, and t_{mag} is the thickness of the magnetic layers (assumed here to be equal). The normalized parameters are given by $k=-K\cdot t_{\mathrm{mag}}/2J$ and $b=-\mu_0 M_S H\cdot t_{\mathrm{mag}}/2J$, where K is the crystal volume anisotropy constant, μ_0 is the magnetic permeability, M_S is the saturation magnetization, and H is the external field. For the present work the constant k is of crucial interest. It represents the ratio between the crystal anisotropy and the exchange coupling, i.e., the competing interaction between these energy contributions. Since the exchange coupling varies strongly as a function of spacer thickness, in particular, close to the maxima for AFM coupling, strikingly different magnetization curves are expected for small changes of the spacer thickness. Co/Cu(001) is well known as a system in which anisotropy effects compete with AFM coupling, and it seems ideally suited for the investigation of these effects.[5]

We have grown Co/Cu(001) sandwich and multilayer structures on sapphire($1\bar{1}.2$) substrates by molecular beam epitaxy (MBE). A buffer layer system of Cu/Cr/Nb(001) is necessary before growing the Co to obtain a high quality of epitaxial growth. The films have been characterized *in situ* by RHEED and *ex situ* by x-ray scattering.[6] The thickness of the Cu spacer is chosen in the range around the second AFM maximum at $t_{Cu}\cong 20$ Å.

A simple system consisting of two Co layers of constant thickness seems useful to study the effect of k on the magnetization behavior and to compare it with theoretical predictions. Therefore we have grown a sandwich with two 30 Å thick Co layers separated by a wedge-shaped Cu spacer with a thickness range between 17 and 28 Å. The sandwich was covered by a 30 Å thick Cu film. The thicknesses were determined via the evaporation rates, calibrated from x-ray scattering data.

Figure 1 shows longitudinal MOKE measurements of hysteresis loops for various thicknesses. The MOKE setup is described elsewhere.[7] The field was applied in plane along the [110] easy axis. The AFM maximum was identified for $t_{Cu}=20.3$ Å from the hysteresis loop with the highest spin flip fields. The loop [Fig. 1(a)] exhibits a first-order spin-flip transition at $H_0\cong 200$ Oe from a parallel state in saturation to a state with almost zero remanence. Spin reversal is reached through a second-order spin-flip process as the field is reversed. In remanence the spins in the top and bottom Co layers are almost oppositely oriented along the [$1\bar{1}0$] and [$\bar{1}10$] direction and perpendicular to the [110] field direction. The obtained loop is in good agreement with the predicted shape corresponding to the $0.2<k<1.0$ region by Dieny *et al.*[4] Only the small hysteresis phenomenon obtained in the second-order spin-flip range does not agree with the theoretically calculated loops. As shown later, a value of $k\cong 0.6$ can be concluded from the spin-flip fields. A small change of the Cu thickness results in hysteresis loops with smaller spin-flip

 0021-8979/94/75(10)/6184/3/$6.00 © 1994 American Institute of Physics

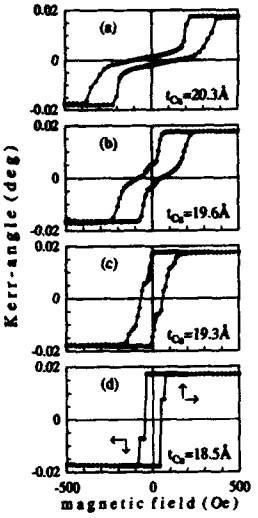

FIG. 1. MOKE hysteresis loops measured along the easy axis of a Co/Cu/Co(001) sandwich with a magnetic layer thickness of $t_{Co}=30$ Å and a wedged Cu spacer. The lines are guides to the eyes.

fields, corresponding to an increase of k moving away from the AFM maximum, but, in principle, in loops with a similar shape like those at the AFM maximum. Reaching a Cu thickness of 19.6 and 21.1 Å, respectively, the shape of the loops changes slightly [see Fig. 1(b)]. We estimate $k\cong 0.8\ldots 0.9$ in this region according to Ref. 4. The magnetization behavior in the spin-flop region is not completely in agreement with the predicted one. A small step close to the zero field leads to a constant and finite magnetization at $H=0$ and to a larger hysteresis phenomenon in this range. The step indicates a stable spin state at $H=0$ caused possibly by the shape of the interlayers.

By a further decrease or increase of the Cu thickness to 19.3 and 21.3 Å, respectively, k becomes slightly larger than 1 and the magnetization in the zero field remains just about saturated. For these values of k we have measured hysteresis loops in which two small steps are observed [Fig. 1(c)]. The first step has the same value of the magnetization, like the step at $H=0$ in the hysteresis loop shown in Fig. 1(b), and therefore it should have the same origin. The second step is in good agreement with the predicted magnetization behavior in the range $1<k<1.96$. The spins flip to a spin state that is symmetric to the applied field.

Finally, a clear jump to a nonsymmetric 90° spin configuration is observed when the Cu thickness is increased or reduced further.[8] Figure 1(d) shows a typical example of a corresponding hysteresis loop, which can be observed in the range from 17 to 19 Å and from 21.5 to 23.5 Å on either side of the AFM maximum. The characteristic shape of these loops provides us, according to the model presented in Ref. 4, with a narrow range of k values between 1.96 and 2.00 for which these loops are possible. The predicted spin structure is nicely confirmed by the quantitative value of the magnetization of the observed step of $M\cong 0.5\cdot M_S$. However, there is a problem. According to the calculated phase diagram[4] the nonsymmetric spin state should occur at much higher fields. Nevertheless, the hysteresis loops can be described qualitatively with this model rather well.

Typical ferromagnetic (FM) loops can be observed for Cu thicknesses larger than 23.5 Å. For these loops the value of k is larger than 2.

It should be noted that the local energy minima calculations assume a highly idealized single domain system. This assumption cannot be fulfilled completely in real systems, and domain wall processes could be the reason for the obtained hysteresis phenomena in the loops close to the AFM maximum. The hysteresis effects of the theoretical loops are induced in the model by different flip fields for the demagnetization process (DP) by decreasing the field from the saturated state and for the magnetization process (MP) by increasing the field after reaching the zero field. In real systems the shape of the hysteresis loops will be affected by domain wall motion as well. Neglecting these domain wall movements, the value of k in the range of $0.2<k<1$ can be estimated from the different flip fields for the demagnetization and magnetization process, as described in detail in the following.

When demagnetization is started from the saturated state, the magnetization remains constant (saturated) down to a field H_0^{DP}, or in reduced notation $b_0^{DP}=2(1-k)$. By further decreasing the magnetic field, the antiparallel spin state is reached in a second-order (spin-flop) process.

Now we start the magnetization process by increasing the field from the antiparallel spin configuration perpendicular to the applied field. First the magnetization increases gradually, and for values $0.2<k<0.5$ saturation is then reached via a first-order transition at a field $b_0^{MP}=\frac{4}{3}\sqrt{(1+k)^3/6k}$. For $k>0.5$, a rather peculiar magnetization process was predicted, with a sudden rotation into a nonsymmetric 90° spin configuration of the spins at a critical field b_{90}^{MP}. This can be seen by a narrow step in the hysteresis curve of the magnetization process [see Fig. 1(d)]. Full magnetization is reached at a slightly increased magnetic field. Nevertheless, b_0^{MP} describes the reduced field b at the small step, normalized by the field H_0^{MP}. For typical AFM hysteresis loops the value of k can be estimated from the ratio of the field H_0^{MP} of the magnetization process to the saturation field H_0^{DP} in the demagnetization process:

$$\frac{H_0^{MP}}{H_0^{DP}}=\frac{2}{3}\frac{\sqrt{(1+k)^3/6k}}{(1-k)}. \tag{2}$$

From this we have found a minimum value of $k\cong 0.6$ for the AFM maximum of the system with two 30 Å thick Co layers at a Cu thickness of 20.3 Å [Fig. 1(a)] and a value $k\cong 0.8$ for a Cu layer thickness of 19.6 Å [Fig. 1(b)].

From the hysteresis loops of the ferromagnetic part of the wedge sample we have estimated the volume anisotropy constant $2K_1/M_S\cong 1$ kG. This value is in good agreement with our FMR measurements and with values reported in the literature.[9]

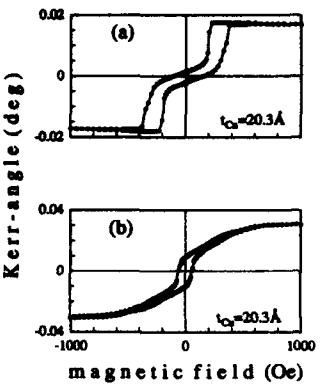

FIG. 2. MOKE hysteresis loops measured along the easy axis at the AFM maxima (a) of a Co/Cu(001) sandwich with a magnetic layer thickness of t_{Co}=30 Å; and (b) of a Co/Cu(001) superlattice with 15 periods and a magnetic layer thickness of t_{Co}=15 Å. The lines are guides to the eyes.

Completely different hysteresis loops can be observed at a wedge-shaped superlattice with 15 periods of Co/Cu(001) with a Co layer thickness of only 15 Å. The thickness of the Cu spacers was similar to its value in the sandwich. In Fig. 2 and Fig. 3 loops of the two systems are compared. The shape of the hysteresis loop at the AFM maximum of the superlattice [Fig. 2(b)] is completely different from the shape of the loop at the AFM maximum of the sandwich. It shows no spin flip, and it can be concluded that k must be smaller than 0.2. This value is expected for a second-order (spin-flop) transition from the saturated to the zero field state and the reverse. A smaller value of k can be explained without invoking a decrease of the anisotropy constant K: first the fact that every magnetic layer in superlattices has two neighbors instead of one reduces the value of k by a factor of $\frac{1}{2}$, and second, the magnetic layer thickness in the measured multilayer is much smaller than in the sandwich. At $H=0$ a finite magnetization with a value of $M \sim 0.3 \cdot M_S$ similar to that at the steps close to $H=0$ in Figs. 1(b) and 1(c) was obtained, in contradiction to the predicted shape of the calculated loops with k smaller than 0.2. This value of the magnetization is not consistent with a biquadratic coupling with a 90° spin structure.

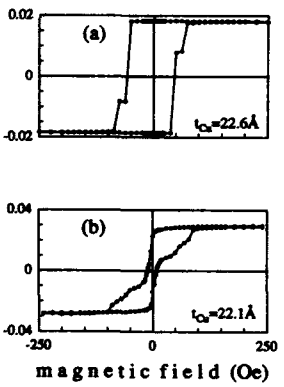

FIG. 3. MOKE hysteresis loops measured along the easy axis in a Cu thickness range with a week AFM coupling (a) of a Co/Cu(001) sandwich with a magnetic layer thickness of t_{Co}=30 Å; and (b) of a Co/Cu(001) superlattice with 15 periods and a magnetic layer thickness of t_{Co}=15 Å. The lines are guides to the eyes.

In relatively large Cu thickness ranges from 15.0 to 19.0 Å and from 21.5 to 24.6 Å on both sides of the AFM maximum hysteresis loops can be observed, which provide us a value of $k \sim 1$. For $k=1$ a hysteresis loop is expected to exhibit a spin-flip transition from the saturated state to an antiparallel spin state at an exactly zero field. Figure 3 compares a typical loop of the superlattice in these ranges with a typical loop of the sandwich obtained from 17–19 Å and from 21.5 to 23.5 Å. The behavior of the magnetization process in these Cu ranges in the superlattice is in good agreement to that predicted for a k value slightly larger than 1. The spins flip near the zero field to a symmetric spin state and possibly later to the nonsymmetric one. The step corresponding to the nonsymmetric spin state is faintly visible only.

In conclusion, we have studied hysteresis loops of AFM coupled Co/Cu(001) epitaxial layered systems with 2 and 15 magnetic layers. The thickness of the nonmagnetic spacer material with $t_{Cu} \cong 20$ Å corresponds to a range of maximum AFM coupling. Completely different hysteresis loops with a spin-flip transition in the AFM maximum for the sandwich system and a spin-flop transition for the multilayer system have been related to different values of the reduced anisotropy constant k. Its value is determined by the number of the magnetic layers and the magnetic layer thicknesses. For a constant thickness of the magnetic layers the coupling constant J varies strongly with small changes of the Cu thickness and so does the value of k. This provokes strikingly different hysteresis loops around an AFM peak.

ACKNOWLEDGMENTS

We gratefully acknowledge technical help by J. Podschwadek. The work in Bochum was supported by the DFG through SFB 166.

[1] P. Bruno and C. Chappert, Phys. Rev. Lett. **67** (1991) 1602; Phys. Rev. B **46**, 261 (1992).
[2] M. T. Johnson, S. T. Purcell, N. W. E. McGree, R. Coehorn, J. aan de Stegge, and W. Hoving, Phys. Rev. Lett. **68**, 2688 (1992); M. T. Johnson, R. Coehorn, J. J. de Vries, N. W. E. McGree, J. aan de Stegge, and P. J. H. Bloemen, *ibid.* **69**, 969 (1992).
[3] A. Schreyer, K. Bröhl, J. F. Ankner, Th. Zeidler, P. Bödeker, N. Metoki, C. F. Majkrzak, and H. Zabel, Phys. Rev. B **47**, 15 334 (1993).
[4] B. Dieny, J. P. Gavigan, and J. P. Rebouillat, J. Phys. Condensed Matter **2**, 159 (1990).
[5] Z. Q. Qiu, J. Pearson, and S. D. Bader, J. Appl. Phys. **73**, 5765 (1993).
[6] S. Di Nunzio, K. Bröhl, and H. Zabel, to be published.
[7] N. Metoki, Th. Zeidler, A. Stierle, K. Bröhl, and H. Zabel, J. Magn. Magn. Mat. **118**, 57 (1993).
[8] K. Bröhl, Th. Zeidler, F. Schreiber, A. Schreyer, and H. Zabel, J. Magn. Magn. Mater. Lett. **130**, L1 (1994).
[9] B. Heinrich, J. F. Cbochran, M. Kowalewski, J. Kirschner, Z. Celinski, A. S. Arott, and K. Myrtle, Phys. Rev. B **44**, 9348 (1991-I).

"Loose spins" in Fe/Cu/Fe(001) structures

B. Heinrich, Z. Celinski, L. X. Liao, M. From, and J. F. Cochran
Department of Physics, Simon Fraser University, Burnaby, V5A 1S6, Canada

Slonczewski recently proposed a model for the exchange coupling between ferromagnetic layers separated by a nonferromagnetic spacer based on the concept of "loose spins." "Loose spins" contribute to the total exchange energy. We have studied the role of "loose spins" in bcc Fe/Cu/Fe(001) structures. bcc Fe/Cu/Fe(001) trilayers deposited at room temperature were investigated extensively in our previous studies. In our "loose spin" studies, the Fe was added inside the Cu interlayer. Several structures were atomically engineered in order to test the behavior of "loose spins:" One additional atomic layer of an (Fe+Cu) alloy were located in appropriate positions in a Cu spacer. The bilinear and biquadratic exchange coupling in the above structures was quantitatively studied with FMR in the temperature range 77–370 K and with MOKE at RT.

INTRODUCTION

Recently, Fe/Al/Fe(001) samples have been investigated by Fuss *et al.*,[1] by Gutierrez *et al.*,[2] and by Grünberg *et al.*[3] In the above studies the measured interlayer magnetic coupling was mostly due to biquadratic exchange coupling. The biquadratic exchange coupling in these measurements exhibited a very strong temperature dependence. The growth of the Al proceeded in an obvious three-dimensional-(3-D) like manner. In such a case one could expect that Fe atoms would be dispersed within the Al interlayer. These Fe atoms are not a part of the ferromagnetic layer, but they are still subject to the RKKY interaction facilitated by the surrounding Fe layers. Slonczewski[4] recently proposed a model based on the concept of "loose spins." "Loose spins" contribute to the total exchange energy. The angular dependence of this coupling is not expected to follow a simple bilinear form of exchange coupling, and its strength should be strongly dependent on temperature because of the intrinsic nonlinearity connected with the easy saturability of the loose spin polarization.

We have found a "loose spin"-like behavior in two systems: (1) Co/Cu/Co(001)/Fe[5] and (2) Fe/Pd/Fe(001).[6] The sample 4Co/6Cu/4Co (the integers describe the number of atomic layers) was found to be coupled antiferromagnetically. With the addition of 3 ML of Fe to the second Co layer the structure developed a well-defined surface reconstruction and the exchange coupling became ferromagnetic. Moreover, the temperature dependence of the exchange coupling became strong and followed a $1/T$ dependence. We have explained this behavior by the presence of Co atoms in the Cu, which were subjected to the exchange field of the surrounding Co layers. The presence of Co atoms in the Cu interlayer was presumably promoted by the presence of lattice defects connected with the Fe lattice reconstruction. The exchange coupling through 5 ML Pd also followed a Curie–Weiss dependence in temperature. In our view, this behavior indicates the presence of a fluctuating magnetic moment in the Pd, which was subjected to the RKKY field from the surrounding Fe magnetic layers.

In this paper we present our recent studies in which a low concentration of Fe atoms was intentionally added to various parts of a nonferromagnetic spacer. Our studies were carried out using unreconstructed bcc Fe/Cu/Fe(001) trilayers. The Fe atoms in a Cu spacer can be expected to behave as "loose spins." The Fe atoms were coevaporated together with the Cu atoms during the formation of a nonferromagnetic Cu spacer. Table I lists "loose spin" ultrathin film structures, which were investigated in this paper.

Note that the thickness of the ferromagnetic layers was kept constant, and the total number of Cu atomic layers was kept equal to 10 ML. The exchange coupling between the Fe layers (5.7Fe and 10Fe) was investigated using the Ferromagnetic Resonance (FMR) and Magneto-Optical Kerr Effect (MOKE) techniques.

In the following, the exchange energy is written in the form $E=-J_1\cos(\theta)+J_2\cos^2(\theta)$, where J_1 and J_2 describe the strength of the bilinear and biquadratic exchange coupling, respectively. θ is the angle between magnetic moments.

GROWTH AND MAGNETIC PROPERTIES OF Fe/Cu/Fe TRILAYERS

The detailed growth and magnetic studies of Fe/Cu/Fe(001) trilayers were presented in our recent article.[7] Here we will summarize only those aspects that are relevant to the results presented in this work.

The structures were prepared using a PHI-400 MBE machine. All structures were grown at room temperature (RT) on a bulk Ag(001) substrate. The first Fe layer (5.7 Fe) grows in a "quasi"layer by layer mode. It means that the surface roughness is mostly confined to the last two atomic layers. For the growth carried out at RT, the average distance between Fe terraces is approximately 50–60 Å. The growth of Cu over the first Fe layer proceeds epitaxially in an almost pure bcc structure (with negligible tetragonal distortion) up

TABLE I. "Loose spin" structures used in this work. The integers describe the number of atomic layers. "Loose spins" were inserted in one atomic layer inside a Cu spacer. The Fe atoms (loose spins) were coevaporated, together with the Cu atoms. All samples were protected with a 20Au(001) capping layer.

(1) 5.7Fe/5Cu/1 ML Fe/5Cu/10Fe(001);
(2) 5.7Fe/5Cu/1 ML (50%Fe+50%Cu)/5Cu/10Fe(001);
(3) 5.7Fe/5Cu/1 ML (25%Fe+75%Cu)/5Cu/10Fe(001);
(4) 5.7Fe/8Cu/1 ML (50%Fe+50%Cu)/2Cu/10Fe(001).

 0021-8979/94/75(10)/6187/3/$6.00 © 1994 American Institute of Physics

to 11–12 atomic layers. The first 5 MLs of Cu grow also in a "quasi"layer by layer mode, but with large atomic terraces several hundred Å wide. With increasing Cu thickness and especially when approaching the critical thickness of Cu (11–12 ML), the atomic terraces on the top surface of the Cu spacer layer become progressively smaller and they eventually become comparable to those of the 5.7Fe layer. RHEED patterns and RHEED intensity oscillations exhibited no noticeable changes when a mixed (Fe+Cu) layer was grown, and therefore the above structural properties were not affected by the deposition of "loose spin" Fe atoms.

The magnetic properties of the individual Fe layers (with the same interfaces as those in an Fe/Cu/Fe trilayer) and of the 5.7Fe/Cu/10Fe trilayers were determined in our previous studies.[6] Fe/Cu/Fe trilayers with a 10 ML Cu spacer exhibit a maximum antiferromagnetic coupling, $J_{total}=J_1-2J_2=-0.2$ erg/cm^2 at room temperature (RT), and J_{total} increases linearly with temperature upon cooling to $J_{total}\sim-0.4$ erg/cm^2 at liquid N_2 temperature (LN_2).[6] For a Cu thickness greater than 10 ML, the antiferromagnetic exchange coupling decreases gradually and reaches its half-maximum value at 13 ML, and it is nearly equal to zero at 16 ML. For thicknesses less than 10 ML of Cu, the antiferromagnetic coupling decreases rapidly and crosses zero at 8 ML. For thickness less than 8 ML, there is no evidence that the exchange coupling crosses again to antiferromagnetic coupling; the experimental measurements[6–8] and the theoretical calculations[9] show that the coupling remains ferromagnetic and rapidly increases with decreasing Cu thickness. At 5 ML thick Cu, the exchange coupling is expected to be strongly ferromagnetic, $J_1>1-2$ erg/cm^2. The exchange coupling in samples grown at RT is mostly bilinear, only a small fraction of the total exchange coupling at RT is due to the biquadratic term, $J_2\sim0.01-0.02$ erg/cm^2. Recently we found that J_2 follows the same temperature dependence as J_1.[10]

RESULTS AND DISCUSSION

The FMR studies were carried out between 77–370 K, and the MOKE studies were carried out only at RT. A detailed description of FMR and MOKE studies can be found in Ref. 5. Samples 1, 2, and 3 have their "loose spin" layers inserted in the center of the Cu spacer. Sample 1 with a full atomic layer of Fe shows a strong ferromagnetic coupling, $J=0.27$ and 0.4 erg/cm^2 at RT and LN_2, respectively. Samples 2 and 3 are coupled antiferromagnetically. The MOKE measurements on samples 2 and 3 showed that the presence of a "loose spin" atomic layer significantly decreases J_1 (-0.008, -0.018 erg/cm^2) compared with that of a 10 ML Cu spacer (-0.2 erg/cm^2), but J_2 (0.02, 0.016 erg/cm^2) in samples 2 and 3 is almost unaffected by the presence of "loose spins." A large decrease in J_1 resulted in a perpendicular relative orientation of the layer magnetic moments in zero field due to the biquadratic coupling term.

It is tempting to assume that the coupling between "loose spin atoms" and the surrounding Fe layers is nearly the same as that between ferromagnetic layers separated by a Cu spacer of an equivalent thickness. Our choice of samples and our expectations were guided by this oversimplified assumption. However, a word of caution is needed. The phase and strength of the exchange coupling depend both upon the Fermi surface of the spacer material and upon the interaction between the spacer electrons and the magnetic atoms.[11] The energy levels of "loose spin atoms" are definitely not identical to those at the interface of a complete ferromagnetic layer; and therefore the strength and even the sign of the coupling could be different from those expected between two ferromagnetic layers separated by a spacer of an equivalent thickness. The coupling energy due to "loose spins" in the Slonczewski model is given by

$$U(\theta)=(U_1^2+U_2^2+2U_1^*U_2^*\cos\theta)^{0.5},$$

where U_1 and U_2 describes the exchange energy between semi-infinite ferromagnets 1 and 2 and a "loose spin atom." θ is the angle between the magnetic moments $\mathbf{m}_1$ and $\mathbf{m}_2$. The free energy of loose spins is then used to evaluate the contribution of "loose spins" to the total exchange coupling; see the details in Ref. 4.

The coupling energy U can be estimated from the measured (or extrapolated) exchange coupling in the Fe/Cu/Fe trilayer, which possesses an equivalent Cu spacer. The parameter U for a 5 ML thick Cu layer can be expected to be at least 12 K (equivalent to $J_1=1.5$ erg/cm),[7] but it is unlikely larger than 25 K. Since in these samples "loose spin" atomic layers are inserted symmetrically, one expects that the parameters $U_{1,2}$ for both Fe layers are of the same sign and are also equal. For low values of $U_{1,2}$, the Slonczewski model predicts a ferromagnetic bilinear coupling, J_{1LS}, with a negligible contribution of J_{2LS}. In that case the temperature dependence of J_{1LS} should exhibit a $1/T$ behavior. The strength of this coupling depends on the particular choice of $U_{1,2}$ and on the density of "loose spins." The exchange coupling due to the presence of "loose spins" and that caused by direct coupling through the Cu interlayer are difficult to incorporate into one single picture. Clearly, the presence of the Fe atoms in the middle of the Cu spacer will affect the direct coupling between the Fe layers in some manner that is not known at the present time. One would expect that the Fe impurity scatterers would result in some decrease of the direct exchange coupling, as was definitely found for 1 atomic layer of Ag inserted in a Cu spacer.[7] At this point it is interesting to discuss a simple model. Assume that the direct bilinear exchange coupling is decreased by a temperature-independent constant value ΔJ_1 due to the Fe scatterers, but otherwise the direct coupling has the same strength and temperature dependence, as it has in Fe/Cu/Fe trilayers. A 1 ML of Ag inserted in the Cu spacer of a Fe/Cu/Fe(001) sample resulted in $\Delta J_1\sim0.1$ erg/cm^2.[7] Further, let us assume that the direct coupling reduced by ΔJ_1 and the contribution from the "loose spins" are additive. For $\Delta J_1=0.1$ erg/cm^2, the difference between the reduced direct exchange coupling and the measured exchange coupling in samples 2 and 3 increases rapidly with decreasing temperature. The difference between the measured and the reduced direct exchange coupling should be equal to the contribution of the "loose spins", J_{1SL}. Parameters $U_1=U_2=22$ K for sample 3 explain the increase in J_{1SL} between 370 and 77 K. However, the overall temperature dependence of J_{1SL} in samples 2 and

3 does not follow well a $1/T$ term. In order to obtain a J_{1SL} proportional to $1/T$, one has to accept that the direct exchange coupling between ferromagnetic layers does not increase linearly with decreasing temperature, but that it is described by the sum of a constant, and a $1/T$ term ($-0.035-20.4/T$ erg/cm^2 in sample 3). It is interesting to note that the first (constant) term (-0.035) is very close to $-2J_2$, and therefore the second term $-20.4/T$ represents a bilinear antiferromagnetic exchange coupling. This rather unexpected conclusion is not that surprising. The loose spin atoms create a spin-dependent potential ($\sim 1/T$), which affects the spin minority and majority bands of Cu valence electrons, and consequently they should affect the direct exchange coupling between the ferromagnetic layers. The presence of a $1/T$ term could be due to an increasing loose spin moment (spin potential) with decreasing temperature. The value of the parameter $U_{1,2}$ corresponds to an equivalent exchange coupling of 2.8 erg/cm^2, and that value is in agreement with observations of very strong ferromagnetic coupling for a 5 ML Cu spacer.

The temperature dependence of the measured exchange coupling in sample 4 is very weak; see Fig. 1. In this sample the "loose spin" atomic layer is located close to the 10Fe ferromagnetic layer, and it is 8 ML removed from the 5.7Fe layer. One could expect that in this case U_1 (describing the strength of the coupling through 2 ML Cu) is very large and ferromagnetic. The parameter U_2 is expected to be small, since the 8 ML thick Cu interlayer corresponds to the crossover of the exchange coupling from the ferromagnetic to the antiferromagnetic region. The measured exchange coupling in sample 4 was found to be ferromagnetic. This implies that U_2 was positive. The measured temperature dependence in this sample can be described by taking the Slonczewski model without direct exchange. Using $U_1=800$ K, $U_2=2$ K leads to good agreement between the measured and calculated values of the exchange coupling. The absence of the direct exchange coupling in this sample can be expected. The proximity of the "loose spins" to the ferromagnetic layer very likely results in a large magnetic moment per loose spin. In this case the "loose spins" would be magnetically ordered and would be chiefly responsible for the coupling between ferromagnetic layers. The value $U_1=800$ K is, however, very large: nearly as large as the exchange coupling in pure iron. It is interesting to note that the ferromagnetic coupling between "loose spins," by adding self-consistently the molecular field $\lambda\langle m\rangle$ to their coupling energy results in a decreased dependence of J_{1LS} on temperature. Here $\langle m\rangle$ is the average moment per "loose spin" in units of the Bohr magneton and λ is the "loose spin" molecular field parameter. A much lower value of U_1 could be used to obtain a small increase with decreasing temperature. For sample 4, a choice of $U_1=200$ K, $U_2=2.8$ K, and $\lambda=300$ describes the observed data well; see Fig. 1. In fact the inclusion of the molecular field $\lambda\langle m\rangle$ produces a convex temperature dependence that is very consistent with the experimental data; see the solid line in Fig. 1. The Slonczewski model without the molecular field $\lambda\langle m\rangle$ actually produces a concave curvature in J_1 vs T; that means J_{1LS} increases with decreasing temperature more rapidly at lower temperatures and becomes almost flat at higher temperatures.

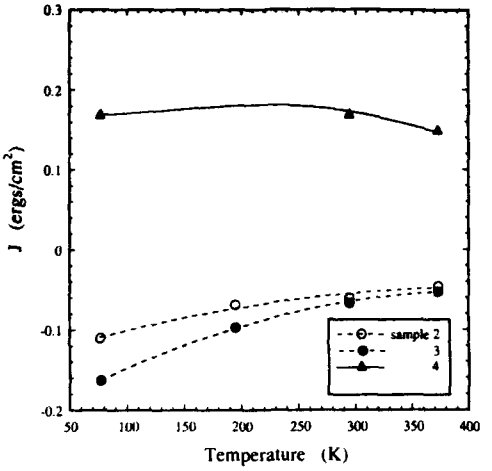

FIG. 1. The temperature dependence of the total exchange coupling, J_1-2J_2, for samples indicated in Table I. Positive J_1 corresponds to ferromagnetic coupling. The exchange coupling was measued using FMR. The dashed lines are second-order polynomial fits to help the reader's eye. The solid line is a theoretical fit using the following parameters: $U_1=200$ K, $U_2=2.8$ K, $\lambda=300$, and the density of "loose spins" $=6.0\times10.^{14}$ The magnetic properties of the 5.7 and 10 ML Fe layers at all measured temperatures were determined separately by measurements on the individual Fe layers, which had the same interfaces as the Fe/Cu/Fe trilayers. The strength of exchange coupling in the studied trilayers was determined by using the measured positions of the acoustic and optical resonance peaks; it was double-checked by comparing the measured and calculated intensities of the acoustic and optical peaks.

[1] A. Fuss, S. Demokritov, P. Grunberg, and W. Zinn, J. Magn. Magn. Mat. **103**, L221 (1992).
[2] C. J. Gutierrez, J. J. Krebs, M. E. Filipkowski, and G. A. Prinz, J. Magn. Magn. Mat. **116**, L305 (1992).
[3] P. Grunberg, V. Cross, A. Fuss, Q. Leng, M. Schaefer, J. Wolf, and W. Zinn, MRS Spring Meeting, San Francisco, CA (1993).
[4] J. C. Slonczewski, J. Appl. Phys. **73**, 5957 (1993).
[5] B. Heinrich, J. F. Cochran, M. Kowalewski, J. Kirschner, Z. Celinski, A. S. Arrott, and K. Myrtle, Phys. Rev. B **44**, 9348 (1991).
[6] Z. Celinski and B. Heinrich, J. Magn. Magn. Mat. **99**, L25 (1991).
[7] B. Heinrich, Z. Celinski, J. F. Cochran, A. S. Arrott, K. Myrtle, and S. T. Purcell, Phys. Rev. B **47**, 5077 (1993).
[8] M. T. Johnson, S. T. Purcell, N. W. E. McGee, R. Coehoorn, J aan de Stege, and W. Hoving, Phys. Rev. Lett. **68**, 2688 (1992).
[9] F. Herman, J. Sticht, and M. van Schilfgaard, Mat. Res. Soc. Proc. **231**, 195 (1992).
[10] Z. Celinski, B. Heinrich, and J. F. Cochran, to be published.
[11] Zhu-Pei Shi, P. Levy, and J. L. Fry, J. Appl. Phys. **73**, 5975 (1993).

Interlayer coupling and spin polarization of the nonmagnetic layers in Fe/Cu and Fe/Ag CMFs

Y. B. Xu, M. Lu, Q. Y. Jin,[a] C. Hu, Y. Z. Miao, Y. Zhai,[b] Q. S. Bie, and H. R. Zhai
National Laboratory of Solid State Microstructure, Center of Materials Analysis, and Department of Physics, Nanjing University, Nanjing 210008, China

G. L. Dunifer, R. Naik, and M. Ahmad
Department of Physics, Wayne State University, Detroit, Michigan 48202

Compositionally modulated films (CMFs) of Fe/Cu and Fe/Ag, made by RF sputtering, were investigated with ferromagnetic resonance (FMR), nuclear magnetic resonance (NMR), and magneto-optical (MO) spectroscopy. Evidence of spin polarization of the nonmagnetic layers, related to the interlayer coupling, was obtained. Direct evidence of the penetration of an exchange field and the spin polarization of the conduction electrons in the nonmagnetic Cu layers was obtained in Fe/Cu CMFs by NMR. Spin-wave resonances were observed in Fe/Cu CMFs in FMR experiments, and the spin wave was found to be sustained by both the Fe and Cu sublayers. The MO spectra of Fe/Ag CMFs indicated that the conduction electrons of Ag are spin polarized and give an additional MO activity.

INTRODUCTION

Interlayer exchange coupling in magnetic/nonmagnetic multilayers has attracted much attention recently.[1,2] One interesting and important question, related to interlayer coupling, is the possible spin polarization of the nonmagnetic layers and its effects. We have investigated Fe/Cu, Fe/Ag, Co/Cu, and Co/Al multilayers with nuclear magnetic resonance (NMR), spin wave resonance (SWR), and magneto-optical (MO) spectroscopy, trying to get some insight into this question. Some results are reported in this paper.

EXPERIMENTS

The samples were prepared by RF sputtering onto water-cooled glass substrates. Details are given in Ref. 3. The low-angle x-ray diffraction pattern of a $[Fe(22\ Å)/Cu(17\ Å)]_{50}$ CMF showed that the multilayers are well periodically layered. Taking into account the correction due to the refractive index, the period determined by x-ray diffraction agrees with the designed value, with deviations less than 5%. Large-angle x-ray diffraction showed a small FCC (111) peak, indicating a slight (111) texture in the Fe/Cu multilayers. The microstructure of the interfaces has not been analyzed at this time.

The NMR measurements were performed on a Bruker MSL-300 NMR spectrometer. High sensitivity was achieved by using a pulsed-echo and Fourier-transformation method. The applied magnetic field was 7 T, oriented parallel to the film plane. For the FMR experiments, the samples were mounted inside the X-band cavity (9.7 GHz) of a Bruker EPR spectrometer. The orientation of the film plane can be rotated through the range 0°–90°. The magneto-optical Kerr effect (MOKE) was measured with a Faraday-modulated MO spectrometer.[3]

NMR OF Fe/Cu CMFs

Nuclear magnetic resonance (NMR) provides a direct way to investigate the spin polarization of conduction electrons. Lang *et al.*[4] and Boyce *et al.*[5] used a spin-echo technique to study the electron-spin density in Cu for CuCo and CuFe dilute alloys. Both of them found several resonant "satellite" peaks corresponding to Cu atoms, which were the first, second, and farther nearest neighbors of the Co or Fe atoms, and the extra Knight shift $\Delta K/K$, due to the induced spin polarization of the conduction electrons in the Cu, showed an oscillation between positive and negative values.

Figure 1 shows the NMR spin-echo spectrum of ^{63}Cu nuclei in a $[Fe(22\ Å)/Cu(17\ Å)]_{50}$ CMF, in which the resonant frequency of a pure copper film is taken as the zero point. For pure copper films only one peak was observed, which gave the standard Knight shift of 0.233% compared with $CuCl_2$ powder. Differing from that of a pure Cu film, the NMR spectra of ^{63}Cu in the Fe/Cu multilayers is composed of a group of peaks, as shown in Fig. 1.

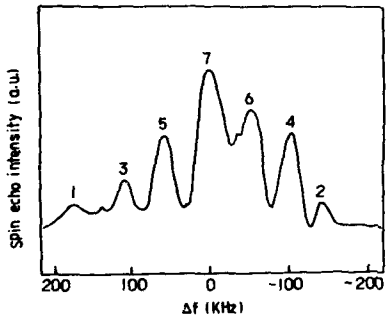

FIG. 1. Spin-echo spectrum of ^{63}Cu nuclei in a $[Fe(22\ Å)/Cu(17\ Å)]_{50}$ CMF.

[a]Permanent address: Fudan-T. D. Lee Physics Laboratory, Department of Physics, Fudan University, Shanghai 200433, China.
[b]Department of Physics, Southeast University, Nanjing, China.

 0021-8979/94/75(10)/6190/3/$6.00 © 1994 American Institute of Physics

TABLE I. The exchange fields (in kOe) of the samples with $d_{Cu} \approx 17$ and 25 Å.

d_{Cu} (Å)	H_1	H_2	H_3	H_4	H_5	H_6	H_7	H_8	H_9	H_{10}	H_{11}	H_{12}
17	67	−55	42	−37	24	−18	0.4					
25	72	−62	58	−50	43	−38	36	−30	21	−15	14	−5

The NMR resonance frequency in metals can be expressed as

$$f_0 = \gamma H_0(1+K) = \gamma H_0(1+\Delta H/H_0), \tag{1}$$

where γ is the gyromagnetic ratio of the nuclei under study ($\gamma = 11.285$ MHz/T for ^{63}Cu), K is the Knight shift of the metal, and ΔH is the Fermi contact field experienced by the nuclei due to the spin polarization of the conduction electrons caused by the external magnetic field H_0. In multilayers, the additional spin polarization within the nonmagnetic Cu layers, caused by the exchange field H_{ex} due to the interlayer coupling, leads to a modified expression for the resonant frequency with an additional Knight shift:

$$f = f_0 + \Delta f = \gamma H_0(1+K+\Delta K) = \gamma H_0[1+\Delta H/H_0 + (\Delta H/H_0)(H_{ex}/H_0)]. \tag{2}$$

Thus, the exchange field in the Cu layers, associated with any particular NMR peak, is

$$H_{ex} = \Delta f/\gamma K, \tag{3}$$

where Δf is the additional Knight shift frequency, which can be obtained from the NMR spectrum, as shown in Fig. 1.

Table I gives calculated values of H_{ex} for Fe(22 Å)/Cu(17 Å) and Fe(60 Å)/Cu(25 Å) CMFs. It is interesting that with the decrease of the absolute value of the exchange field, positive and negative values appear alternately, as shown in the table. This can be explained as due to a spatially damped oscillation of the exchange field and spin polarization of the conduction electrons in the Cu sublayers. Trying to determine the oscillation period of H_{ex} and the spin polarization within the Cu layers, we find from the presently limited NMR data that there is no way to localize the regions in the layers that contribute to the various NMR peaks. If we assume that the peaks of the spin-echo signal result from an equally-spaced oscillation along the normal to the plane of the Cu layer, the total number of oscillations is about 3.5 and 6 for $d_{Cu} \approx 17$ and 25 Å, respectively. This gives an average period for the oscillation of about 4–5 Å for the (111) orientation, which seems to be somewhat less than expected from an RKKY model.

SWR IN Fe/Cu CMFs

The thickness of the magnetic layers in the multilayers is usually less than 50 Å. Thus, for standing spin waves localized within the individual magnetic layers, the wavelength is of the order of tens of angstroms, and the exchange field is so high that the microwave frequency needed to excite the spin-wave modes is much higher than the microwave frequency usually used for FMR, say 10 GHz. However, when interlayer coupling occurs, and the multilayers becomes a single coupled system, the spin waves may propagate through the nonmagnetic layers, and the standing spin-wave modes are sustained by the whole film. Thus, the wavelength of the spin wave can be increased by one or two orders of magnitude, and the SWR may be excited and observed. Wigen *et al.*[6] observed SWR in Fe/Pt multilayer films by FMR measurements and found that there is a significant phase change occurring within the Pt layers.

In Fe/Cu multilayers, we found that when the external field is parallel to the plane of the film, only one resonance peak was observed in the FMR measurements. However, when the magnetic field is perpendicular to the surface, the FMR spectra consist of at least two peaks for $d < 28$ Å. Figure 2 shows the FMR spectra of a [Fe(22 Å)/Cu(17 Å)]$_{50}$ CMF for the external field perpendicular to the film plane. For the multilayers, it is reasonable to assume that both odd and even numbers of the spin-wave modes can be excited due to the inhomogeneity across the thickness of the film or different pinning conditions on both surfaces. The inset in Fig. 2 shows the relation of the nth resonance field to n^2 for samples having Cu thickness $d = 8$, 12, and 17 Å. The separation, $H_n - H_1$, between the positions of the nth and the first peak is approximately proportional to (n^2-1), that is, the n^2 law.

The magnetic-field separations between the modes are much too small to be accounted for by spin-wave modes confined to the individual magnetic layers, but they can be fitted if we assume that the Fe layers are coupled together by an interlayer exchange coupling, and that the spin waves extend across the whole multilayer sample. The propagation

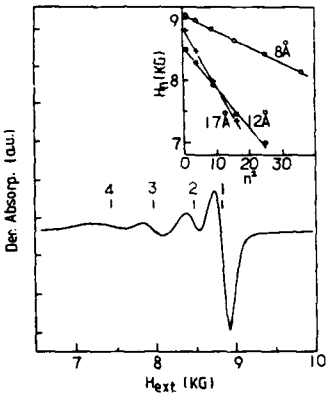

FIG. 2. FMR spectrum of a [Fe(22 Å)/Cu(17 Å)]$_{50}$ CMF. Inset: The relation of the nth resonance field H_n vs n^2 for [Fe(22 Å)/Cu(d_{Cu})]$_{50}$ CMFs with $d_{Cu} \approx 8$, 12, and 17 Å.

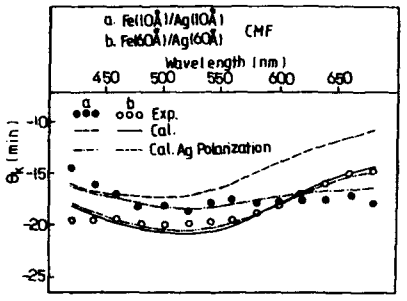

FIG. 3. θ_k spectra of Fe/Ag CMFs. Dots are experimental results. Lines are calculated results with and without the spin polarization of the Ag included.

of spin waves through the Cu layers inplies the existence of spin polarization within the Cu.

MOKE OF Fe/Ag CMFs

If the nonmagnetic layers in multilayers are spin polarized, this should give an additional MO activity. Our theoretical study of the MO spectra of Fe/Ag demonstrated that the conduction electrons of Ag are spin polarized, and give an additional MO activity.[7]

Figure 3 shows the experimental and theoretical MO spectra of Fe/Ag CMFs. The dots are experimental values and the lines are calculated results. An interesting feature, as we can see from the experimental dots, is that with a reduction of the modulation length, θ_k increases for longer wavelengths and decreases for shorter wavelengths. For comparison with theory, first, a numerical calculation of the θ_k spectra is made based on Fresnel's formula by assuming that the Ag layers have no spin polarization and no additional MO activity. As seen from the figure, the change of the calculated θ_k spectra with a variation of the modulation length differs from that of the experiment. θ_k decreases with decreasing modulation length over the whole wavelength range. This disagreement with experiment can be corrected if an additional MO activity, caused by the spin polarization of the Ag layers, is assumed as follows.

If the spin-up and spin-down conduction electrons of Ag are split in energy by $\hbar\omega_0$, they will give rise to an additional wavelength-dependent MO effect, which can be described by the Drude model.[7] This gives a dielectric constant of the form

$$\epsilon_{xy}=\frac{\omega_0\omega_p^2}{\omega[(\omega-i\gamma)^2-\omega_0^2]}, \tag{4}$$

where for the plasma frequency $\hbar\omega_p=4$ eV, and for the relaxation frequency $\hbar\gamma=0.02$ eV for Ag. This is the formula used by Krinchik[8] in his discussion of the MOKE of Fe, Co, and Ni with $\hbar\omega_0=eH_i/m_{\text{eff}}c$. H_i is the internal effective magnetic field due to spin polarization, which is responsible for the splitting of the plasma edge for right and left circularly polarized light.

According to Moodera *et al.*,[9] the exchange splitting of the conduction band of a paramagnetic metal adjacent to a ferromagnet is given by

$$\Delta E_{\text{para}}=\frac{a}{d+a}\ \Delta E_{\text{Fe}}; \tag{5}$$

ΔE_{Fe} is the exchange splitting of the conduction bands of Fe, $\Delta E_{\text{Fe}}=0.90$ eV.[9] a is the cube root of the atomic volume of iron, $a=2.28$ Å, and d is taken as the thickness of each individual Ag layer in the CMF. For our calculation, we use Eq. (4), assuming an *average* magnetization within the Ag layers, where ω_0 is obtained by setting $\hbar\omega_0=\Delta E_{\text{para}}$ from Eq. (5). This gives $\omega_0=185$ and 33 meV for the Fe(10 Å)/Ag(10 Å) and Fe(60 Å)/Ag(60 Å) CMFs, respectively. As seen from the figure, the calculated spectra fit the experimental data surprisingly well. The calculation cannot be rigorously justified at this stage, and further theoretical study is warranted. Also, for samples this thin, one needs to consider the contributions from any Fe/Ag interdiffusion.

The value of the spin polarization of Ag is estimated from the band splitting in Eq. (5) to be 1.4% for the Fe(10 Å)/Ag(10 Å) CMF. In our numerical calculations, a positive ω_0 was assumed, opposite to that in Fe, Co, and Ni, in order to fit the experimental results. This suggests that the average direction of the magnetization of Ag is opposite to that of Fe.

Here, we would like to point out that in Co/Cu and Co/Au CMFs,[10,11] no additional MO activities of the Au and Cu were observed. Nevertheless, our preliminary studies of FeSi/Cu CMFs suggest an additional magneto-optical activity of Cu with a Cu thickness of about 10 Å.[12] Further experimental and theoretical studies in this area are needed.

This work in China is supported by the NNSFC, SEC, and the State Key Laboratory of Magnetism. In the USA the work is supported in part by National Science Foundation Grant No. DMR-9120274.

[1] P. Grunberg, R. Schreiber, Y. Pang, M. B. Brodsky, and H. Sowers, Phys. Rev. Lett. **57**, 2442 (1986).
[2] S. S. P. Parkin, R. Bhadra, and K. P. Roche, Phys. Rev. Lett. **66**, 2152 (1991).
[3] Y. B. Xu, Q. Y. Jin, Y. Zhai, M. Lu, Y. Z. Miao, Q. S. Bie, and H. R. Zhai, J. Appl. Phys. **74**, 3470 (1993).
[4] D. V. Lang, J. B. Boyce, C. Lo, and C. P. Slichter, Phys. Rev. Lett. **29**, 776 (1972).
[5] J. B. Boyce and C. P. Slichter, Phys. Rev. Lett. **32**, 61 (1974).
[6] P. E. Wigen, Z. Zhang, S. Iwata, and T. Suzuki, J. Magn. Soc. Jpn. **15**, Supplement No. S1, 33 (1991).
[7] Y. B. Xu, H. R. Zhai, M. Lu, Q. Y. Jin, and Y. Z. Miao, Phys. Lett. A **168**, 213 (1992).
[8] G. S. Krinchik, J. Appl. Phys. **35**, 1089 (1964).
[9] J. S. Moodera, M. E. Taylor, and R. Meservey, Phys. Rev. B **40**, 11 980 (1989).
[10] D. Weller, W. Reim, and K. Sporl, J. Magn. Magn. Mat. **93**, 183 (1991).
[11] E. R. Moog, J. Zak, and S. D. Bader, J. Appl. Phys. **69**, 4559 (1991).
[12] H. R. Zhai, Y. B. Xu, M. Lu, Y. Z. Miao, H. Wang, S. M. Zhou, B. X. Gu, and Q. R. Jin, (invited paper), Proceedings of ISPMM '92, Beijing, July, 1992.

Growth temperature dependence of biquadratic coupling in Fe/Cr(100) superlattices studied by polarized neutron reflectivity and x-ray diffraction (abstract)

M. Schäfer, J. A. Wolf, and P. Grünberg
NIST, Reactor Radiation Division, Gaithersburg Maryland 20899

J. F. Ankner, A. Schreyer, and H. Zabel
Fakultät für Physik und Astronomie, Ruhr Universität Bochum, D-4630 Bochum, Germany

C. F. Majkrzak
NIST, Reactor Radiation Division, Gaithersburg, Maryland 20899

We have measured the polarized neutron specular reflectivity of superlattices of nominal composition (5.0 nm Fe/1.7 nm Cr) grown by molecular-beam epitaxy. This chromium thickness lies at a minimum of the oscillatory bilinear (180°) coupling parameter, so these films are especially sensitive to biquadratic (90°) terms. One set of films was grown at a substrate temperature of 293 K and another at 593 K. Using neutron reflection, we find that the films grown at 523 K exhibit a 90° magnetic moment rotation between successive Fe layers, while the 293 K films are remanently ferromagnetically ordered in small applied fields ($H = 1.7$ mT). Furthermore, we have observed that films grown at elevated temperature exhibit a larger amount of diffuse x-ray scattering due to conformal roughness than those grown at room temperature. These results suggest that the biquadratic coupling could be induced by the structure of the interfaces. We will also present the field and temperature dependence of the neutron reflectivity from the biquadratic films.

 0021-8979/94/75(10)/6193/1/$5.00 © 1994 American Institute of Physics

Symposium: Novel Time-Resolved Probes of Dynamical Magnetism

David Awschalom, Chairman

Picosecond pulsed-field probes of magnetic systems (invited)

M. R. Freeman
IBM Research Division, T. J. Watson Research Center, P.O. Box 218, Yorktown Heights, New York 10598

Time-resolved methods using picosecond scale transient magnetic fields have been developed for investigations of ultrafast magnetic phenomena in a broad variety of systems. When combined with synchronous magneto-optic detection, the approach yields stroboscopic observations of magnetic dynamics with a time resolution of order 1 ps, and a corresponding spatial resolution down to the diffraction limit of optics. Results are presented from experiments on europium chalcogenide films at low temperatures. A continuum of behavior from paramagnetic relaxation to ferromagnetic resonance is observed. Electron-beam deposited EuS films are found to have surprisingly fast spin-lattice relaxation rates, of order $(100\ \text{ps})^{-1}$, and the influence of spin-orbit interactions on the spin dynamics is studied through rare-earth alloying. Results are presented from experiments utilizing the magneto-optic sampling method for direct time-resolved screening measurements of normal and superconducting metal films.

I. INTRODUCTION

A growing trend in magnetism research in recent years has been towards studies of high speed phenomena, driven by both scientific[1] and technological[2] interest in smaller and faster structures. Among the most significant developments in this area has been the realization that it is possible, in magnetics, to take advantage of some of the advances in optics that have enabled the effectively "real-time" observation of transient phenomena on unprecedented scales, corresponding to femtosecond times or terahertz frequencies.[1] The primary goal of these efforts is an improved understanding of nonequilibrium behavior, which often requires detailed physical information not reflected in equilibrium properties. Time-resolved experiments are designed to directly measure the dynamical evolution (away from or towards equilibrium) of systems in response to sudden perturbations. The earliest work of this nature on an explicitly magnetic problem concerned spin dynamics in dilute magnetic semiconductors, and utilized the fact that an optically induced magnetization can be generated in these materials.[3] However, many systems of interest are not amenable to such excitation, creating motivation to develop alternative means of driving systems away from equilibrium quickly on the time scale of the dynamical processes to be investigated. Fortunately, it is possible to import a widely exploited tool used to generate electromagnetic transients in time-resolved studies of electronic phenomena[4] —namely, the photoconductive (or Auston) switch.[5] Specifically, picosecond pulsed *magnetic* fields can be generated and applied to the study of magnetic dynamics, including relaxation and resonance in regimes which extend beyond the scope of conventional microwave techniques.[6] In such experiments, an optically triggered magnetic field transient is propagated past the sample under study, perturbing the spin system, and the subsequent evolution of the spin system is monitored through its interaction with a time-delayed optical probe beam. The detection schemes themselves are nonresonant, and are therefore very useful for field-dependent and nonlinear phenomena. In addition, optical detection makes it possible to probe microscopic specimens without incurring a penalty of poor coupling to the sample. Beyond studies of purely magnetic systems, the methods also lend themselves to the monitoring of time-dependent magnetic behavior in many other instances, as illustrated by the case of magnetic flux dynamics in nonequilibrium superconductors.[7]

II. PICOSECOND MAGNETO-OPTIC SAMPLING

A. Experimental details

The measurements are performed in a conventional stroboscopic optical "pump-probe" fashion, in which the sample is first driven from equilibrium by an excitation pulse (here the transient magnetic field) and subsequently interrogated in a narrow time window, after a controllable delay, by a picosecond probe. Essential features of the experimental configuration are illustrated schematically in Fig. 1. An above-bandgap optical pulse from a picosecond dye laser strikes a biased coplanar transmission line structure, fabricated on a semi-insulating semiconductor substrate, to create a transient photoconductivity and launch a current pulse down the transmission line. Associated with this current is a transient magnetic field normal to the plane, in the gap between the wires. Illuminating the transmission line at an open end takes advantage of the instantaneous reflection to double the current. Lithographic coil structures may be used to obtain somewhat larger or more homogeneous fields when longer transition times are acceptable. The devices are mounted on a chip carrier and electrically connected to an external bias source through wire bonds. The magnetic response of a sample subject to this transient field is probed optically by a second laser pulse, produced by beam-splitting (or, in the case of two-color experiments, by a second synchronously-pumped dye laser), and time-delayed with respect to the first. In a

 0021-8979/94/75(10)/6194/5/$6.00 © 1994 American Institute of Physics

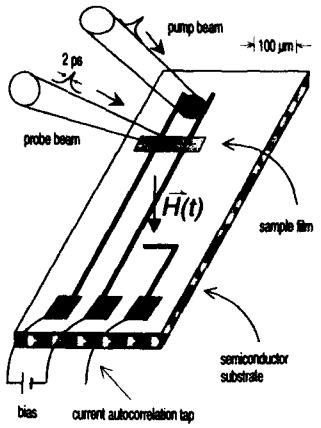

FIG. 1. Schematic of the picosecond magneto-optic sampling chip, showing the coplanar transmission line and the arrangement of pump beam, probe beam, and sample.

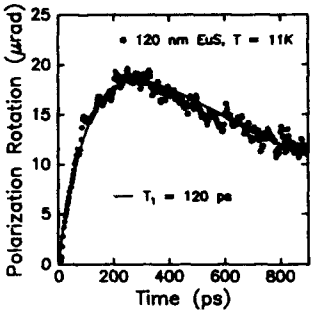

FIG. 2. Magnetic relaxation of a 120 nm thick undoped EuS film, measured in response to field pulses generated on an InP device with a current decay time-constant of 920 ps.

wide variety of materials the component of magnetization along the k-vector of the probe light can be measured via a polarization (Faraday or Kerr) rotation or magneto-absorption.[8] Such resonant optical effects are ideal as they allow the magnetization to be sampled in an interval as narrow as the optical pulse. By scanning the relative arrival time of the two laser pulses with an optical delay line, the complete time-dependent magnetic response of the sample is recorded. In common with other stroboscopic optical measurements, a bandwidth of order 1 THz is obtained in a system for which electrical signals no faster than 1 kHz need be manipulated, making adaptations to cryogenic, UHV, and other specialized environments straightforward. Related magnetic methods employing cw microwave excitation and optical detection have been reported.[9,10]

The propagating current pulse itself can be characterized by a correlation measurement at a tap point along the transmission line. When the optical probe strikes the gap between the tap electrode and the transmission line conductor, a portion of the current pulse is diverted into the sense line. One of the strengths of the photoconductive switch approach derives from the great flexibility in tuning the pulse profile through the choice and preparation of the semiconductor material. The rise-time of the current pulse is limited by a combination of the laser pulse width and the (nonequilibrium) photocarrier mobility. The decay time constant is generally determined for direct-bandgap semiconductors by the carrier lifetime (dominated by surface recombination), and for indirect-gap materials by the bias-dependent carrier sweep-out time (which leads to a more rectangular than exponentially decaying tail). The carrier lifetime may be adjusted over a wide range to suit the application, employing surface passivation schemes or ion implantation, respectively, to increase or decrease the time constant. In the present work we are usually interested in the response to step-function like excitations, with typical pulsed field amplitudes of order 30 G produced using transmission line structures with lateral dimensions of order 100 μm.

B. Results for EuS-based thin films

The availability of fast pulsed fields, combined with the ability to optically detect a specific component of the magnetization, lends itself naturally to detailed measurements of magnetic relaxation and resonance on short time scales. The europium chalcogenides represent an ideal model system for such studies, as they allow the systematic exploration of problems of interest such as the effect of spin-orbit interactions on the spin dynamics. Furthermore these materials have convenient Curie temperatures for studies of dynamical effects at the ferromagnetic phase transition, and display strong magneto-optic activity.

For the determination of longitudinal spin relaxation times, a step-function-like magnetic field change is applied, and the component of magnetization parallel to that field is measured. The method is capable of determining much shorter T_1's than can be measured by other means. In the case of longitudinal paramagnetic relaxation according to a single exponential time constant T_1, the magnetization, M, follows a time-varying magnetic field, $H(t)$, according to

$$M(t)=\chi \frac{e^{-t/T_1}}{T_1}\int_0^t H(t')e^{t'/T_1}\,dt',$$

where χ is the magnetic susceptibility.

Figure 2 shows such a relaxation measurement for a thin EuS film at low temperatures. This time-resolved measurement is performed using an InP photoconductive device having a carrier lifetime close to 1 ns, and the data can be fit to determine the T_1 of the EuS, in this case 120 ps. The material is grown by electron beam deposition,[11] and standard characterizations indicate the quality to be high, finding a bulk-like Curie temperature, T_c= 16 K, a high resistivity (0.2 Ω cm at room temperature), and, from x-ray diffraction, the EuS lattice constant. However, the measured T_1 is several orders of magnitude shorter than expected for the Eu^{2+}, an S-state ion with negligible spin-orbit coupling. The mechanism responsible for this rapid relaxation has not been

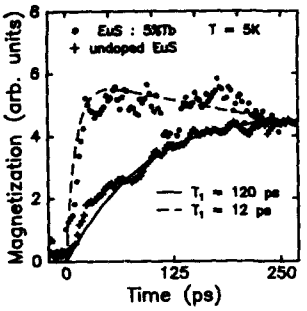

FIG. 3. Modification of the spin dynamics due to spin-orbit interactions illustrated by a comparison of the response of an undoped EuS film to one containing 5% Tb.

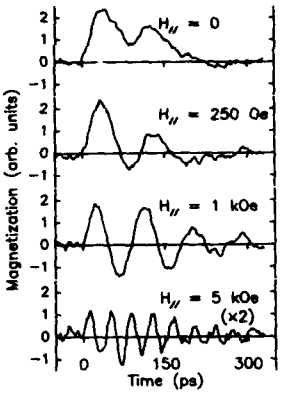

FIG. 4. The evolution of the resonant response of a 120 nm thick EuS film at $T = 2.1$ K as a function of the in-plane applied magnetic field.

identified, although impurity-mediated relaxation seems the most likely candidate. Unexpectedly short T_1's have also been indicated in another Eu^{2+} system.[12] The low frequency magnetic susceptibility is measured simultaneously through the modulation of the optical signal produced by a low frequency ac magnetic field, which is particularly useful in studies of magnetic field and temperature dependence. We find that the time-resolved signal at fixed delay is nearly proportional to the low frequency susceptibility as a function of temperature, directly indicating that the relaxation time is not strongly temperature dependent. Another implication of this finding is that no sharp indication of T_c is reflected in the temporal response (which allows us to reasonably model the data of Fig. 2 by the simple form despite the fact that the sample temperature is less than T_c). The nonequilibrium behavior of the spontaneous magnetization, M_s, contributes an additional component, growing continuously with M_s, and dependent on the magnetic history of the sample as reflected in the domain structure. At short delay times such a response appears as additional signal clearly not due to simple spin relaxation.

When Tb is doped into the EuS films to deliberately introduce a spin-orbit coupling, the spin dynamics are dramatically altered, as anticipated. The spin-lattice relaxation times become much shorter, as illustrated in Fig. 3. An unanticipated consequence of the Tb doping is a very large elevation of T_c,[11] which in the present context makes the spontaneous magnetization effects significant over a broader temperature range. In order to explore these effects we control the domain structure with an in-plane static magnetic field, and observe the evolution of the domain modes into well-defined ferromagnetic resonances in fields strong enough to uniformly magnetize the samples.

With the sample magnetization aligned along an in-plane magnetic field, the time-resolved magneto-optic sampling probe acts as a very-high bandwidth probe of magnetic resonance, featuring the advantages of time-domain or pulse magnetic resonance spectroscopy over its continuous wave counterpart. For example, nonequilibrium spin populations may be prepared to generate echoes revealing intrinsic spin relaxation rates, and signals covering a broad frequency range are collected simultaneously. The high bandwidth of the optical technique has been used to directly detect free induction decays up to 200 GHz, and optical detection furthermore permits efficient coupling to very small sample dimensions. Under optimum conditions the *flux* sensitivity of this method can approach that of an rf superconducting quantum interference device (although for most practical applications this is too generous a comparison, as the *energy* sensitivity of the magneto-optic material is far less owing to its high permeability). Another major advantage of the optical readout comes in the form of perfect isolation from the tipping pulse, as the immunity of the optical probe to stray pick-up from the pump pulse eliminates the "dead-time" between when the tipping of the spins and when signal recording may commence.

In this configuration, the transient magnetic field pulses apply a torque to the sample magnetization vector to cause it to rotate in the plane, away from the static field. Each current pulse is effectively a half cycle of radiation over a broad range of frequencies. For a given magnetic field, the tipping angle is proportional to the spectral density in the pulse on resonance, where the spectral function is the Fourier transform of the temporal pulse profile. Following the tipping pulse, the transverse component of the magnetization, freely precessing about the static magnetic field, is detected optically, and the entire free induction decay mapped out by scanning the relative arrival time of pump and probe pulses.

Field dependent measurements of the ferromagnetic resonance in a thin EuS film at $T = 2.1$ K by this technique are shown in Fig. 4, and illustrate the ability of this method to track the resonant frequency and spin relaxation continuously with applied magnetic field with picosecond resolution. Again we emphasize that this nonresonant method is capable of measuring arbitrarily damped resonances, including those having much broader linewidths than can be measured by frequency- or field-sweep techniques. In applied magnetic fields greater than ~ 1 kOe the EuS films are

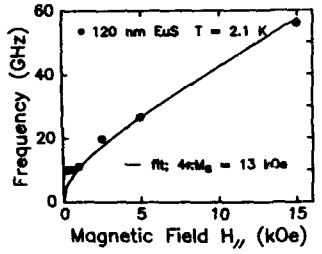

FIG. 5. The ferromagnetic resonance frequency of the EuS film of Fig. 4 as a function of the magnetic field.

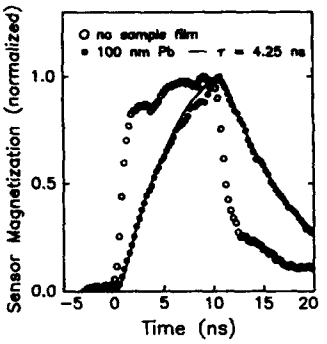

FIG. 6. A time-domain screening measurement. The open circles show the sensor (100 nm EuS/10% BaF_2) calibration, while the filled circles indicate how the field pulse is screened by the eddy currents in a 100 nm thick normal state Pb film.

uniformly magnetized, and the observed resonant frequency, f, is in accordance with the Kittel relation,[13]

$$f^2=\left(\frac{g\mu_B}{\hbar}\right)^2[H(H+4\pi M_s)],$$

with the static field, H, in the plane. This is shown in Fig. 5 The g-factor, g, is 2 for EuS, and μ_B,$\hbar$ respectively are the Bohr magneton and Planck's constant. The solid line in the plot is a fit yielding $4\pi M_s=13$ kOe, the saturation magnetization of the EuS film well below T_c.

The zero-field signal in Fig. 4 is a superposition of longitudinally relaxed magnetization and precessing spontaneous magnetization. The low-field domain behavior can be separated out more cleanly in systems with much longer relaxation times. The ability to probe areas smaller than the domain size in this case brings a unique advantage to the study of the inhomogeneously broadened resonance of the nonuniformly magnetized state, in contrast to more conventional magnetic resonance techniques which lack the spatial resolution of this approach. We have studied resonance within single domains of demagnetized yttrium-iron-garnet films,[14] and are currently employing near-field techniques[15] to record spatial maps of single-domain particles when they are driven out of equilibrium.[16]

III. NONEQUILIBRIUM SUPERCONDUCTIVITY STUDIED BY A FAST MAGNETIC PROBE

Additional motivation for developing the methods described above stems from their applicability to a wide range of magnetically active systems in which a detailed understanding of the dynamics requires direct investigation using probes which simultaneously combine sufficient temporal and spatial resolution. It would be of great interest, for example, to directly observe on a local scale the intrinsic dynamics of magnetic flux threading superconductors to help elucidate such long-standing and complex issues as pattern formation in the type I intermediate state.[17,18] As a significant step in this direction, the flux dynamics of nonequilibrium superconductors has been studied through a simple adaptation of the time-resolved magnetic relaxation experiments.[7] Specifically, a transient nonequilibrium state is driven by heating the electron gas at optical frequencies by picosecond laser pulses, and flux motion in this regime is recorded by magneto-optic sampling. Magneto-optic sensors have long been used for the imaging of flux structures in superconductors;[19] what is novel here is their use on fast enough time scales to observe nonequilibrium phenomena. Previously this regime has been accessible only through transport measurements,[20] which constitute a qualitatively different probe yielding complementary information, and are for example insensitive to nonequilibrium phenomena involving changes in the magnetic flux distribution threading a superconductor.

Our experimental geometry consists of a superconducting sample film sandwiched between a lithographic field coil and a thin-film EuS-based magneto-optic sensor. This stack is cooled in a 0–7 T split-coil magneto-optic dewar. Local changes in flux density are recorded by the Faraday rotation on reflection from the back of the sensor (here EuS diluted with 10% BaF_2 to reduce T_c) of a weak (average power $< 100\ \mu$W) focused optical probe beam consisting of 3 ps wide pulses delivered by a dye laser cavity dumped at 19 kHz. The open symbols in Fig. 6 show a system calibration taken before the superconducting film is put in place, for a 10 ns duration, 30 Oe amplitude magnetic field pulse, plotted as a function of the optical probe delay relative to the rising edge of the field pulse. Characterization of the sample films comes in part from the dynamic screening response of the normal metal. This is shown by the solid symbols in Fig. 6 for a 100 nm thick Pb film held in the normal state by a perpendicular applied magnetic field ($H_\perp=1$ kOe, $T\approx 1.5$ K) exceeding the critical field, $H_{c\perp}$, and measured using the same 10 ns duration field pulse. An eddy-current decay time of 4.25 ns is found, from which the normal state conductivity, $\sigma_n\sim 1\times 10^8\,\mathrm{S\cdot cm^{-1}}$, is determined to be much higher than the measured dc conductivity, a manifestation of the inhomogeneous spatial distribution of scattering sites which gives rise to a frequency-dependent conductivity. Within the accuracy of the measurements, the screening response is independent of field for $H_\perp > H_{c\perp}$. As the measurements require a nonzero differential susceptibility of the sensor, the applied magnetic field range is limited by the saturation field

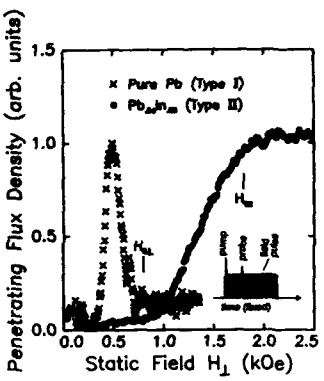

FIG. 7. Comparison of nonequilibrium flux dynamics for 500 nm thick films at $T=1.5$ K, type I (pure Pb) vs type II ($Pb_{0.94}In_{0.06}$) material. The extent of flux penetration from the transient field pulse is plotted as a function of the perpendicular applied field. The inset illustrates the fixed relative timing of the optical pump, optical probe (delay = 5 ns), and magnetic field pulses.

for the magnetization normal to the plane, $H_{sat} \geq 6$ kOe for the diluted EuS films.

By configuring the pulsed measurement to record the dynamics for a fixed timing sequence, environmental parameters such as the temperature or magnetic field may be scanned in order to map out the response of the superconducting state. For static magnetic fields below $H_{c\perp}$, and in the absence of optical electron heating, the penetrating flux signal vanishes, indicating the expected slow decay of the screening currents (because of the unit demagnetizing factor of the geometry, all of the flux will eventually penetrate, but we simply cannot wait long enough in this measurement, by many orders of magnitude). However, when the superconductivity is weakened or destroyed by electron heating from an optical pump pulse (derived from the same beam and focused to the same spot as the probe) it is found that there is another time constant governing the rate of flux penetration in the nonequilibrium regime. The motion of the normal/superconducting interfaces defining the large multivortex structures characteristic of the intermediate state facilitates rapid transport of flux, effectively allowing the flux density in the nonequilibrium state to follow changes in the applied field even more quickly than in the normal metal film. This phenomenon manifests itself in the pure Pb data of Fig. 7 as the peak in the response seen below $H_{c\perp}$; for these signals measured at fixed time-delay, the amplitude of the signal is correlated with the time-constant. It is also to be expected that this behavior would depend sensitively on the type of equilibrium flux structure that exists in the film. The Pb system is ideally suited to studies of this point because it is easily converted into a type II material (characterized by flux penetration in individual, isolated vortex lines) by alloying. The very different response of the type II film is also shown in Fig. 7. The critical field H_{c2} is substantially higher than $H_{c\perp}$ of the pure film, as in bulk material, but in addition the peaked response is not seen owing to the absence of large domains of flux which are easily rearranged.

IV. CONCLUSION

In summary, we have described how spin dynamics in thin films can be examined with a combination of picosecond-scale temporal and micrometer-scale spatial resolution, using photoconductively generated picosecond pulsed magnetic fields. In analogy with pulsed laser studies of electronic and electro-optic phenomena,[4] there is a "parallel universe" of ultrafast magnetic and magneto-optic effects amenable to similar investigation. Results from experiments on europium chalcogenide films have been presented to illustrate measurements of magnetic resonance and relaxation. Direct observations of the very fast spin dynamics arising from spin orbit interactions are possible in this case. Time-resolved studies of magnetic flux dynamics in nonequilibrium superconductors, using a simple adaptation of the method, have also been presented. Our current efforts are directed toward simultaneously observing fine-scale spatially dependent details, for example within single-domain particles driven far from equilibrium, with the aid of scanned probe techniques. Detection by nonoptical means, such as through transport properties, is also being pursued in applications to other magnetic systems. An exciting evolution of these methods may be anticipated, as each advance in spatial resolution, temporal resolution, or sensitivity creates new opportunities to studying magnetic dynamics in detail.

ACKNOWLEDGMENTS

It is a pleasure to thank R. Gambino and R. Ruf for magneto-optic materials, and to acknowledge helpful discussions with those gentlemen as well as D. Awschalom, T. Penney, and J. Smyth.

[1] D. D. Awschalom, M. R. Freeman, N. Samarth, H. Luo, and J. K. Furdyna, Phys. Rev. Lett. **66**, 1212 (1991).
[2] H. Shinada, H. Suzuki, S. Sasaki, H. Todokoro, H. Takano, and K. Shiiki, IEEE Trans. Mag. (USA) **28**, 3117 (1992).
[3] D. D. Awschalom, J.-M. Halbout, S. von Molnár, T. Siegrist, and F. Holtzberg, Phys. Rev. Lett. **55**, 1128 (1985).
[4] See, for example, part I of *Picosecond Electronics and Optoelectronics II*, edited by F. J. Leonberger, C. H. Lee, F. Capasso, and H. Morkoc (Springer, Berlin, 1987).
[5] D. H. Auston, Appl. Phys. Lett. **26**, 101 (1975)
[6] M. R. Freeman, R. R. Ruf, and R. J. Gambino, IEEE Trans. Magn. **27**, 4840 (1991).
[7] M. R. Freeman, Phys. Rev. Lett. **69**, 1691 (1992).
[8] W. A. Crossley, R. W. Cooper, J. L. Page, and R. P. van Stapele, Phys. Rev. **181**, 896 (1969).
[9] J. T. Hanlon and J. F. Dillon, Jr., J. Appl. Phys. **36**, 1269 (1965).
[10] M. A. Butler, S. J. Martin, and R. J. Baughman, Appl. Phys. Lett. **49**, 1053 (1986).
[11] R. J. Gambino, R. R. Ruf, T. R. McGuire, and P. Fumagalli, J. Appl. Phys. **70**, 6386 (1991).
[12] I. Sarda, G. Ablart, J. Pescia, P. LeBail, and P. Colombet, Solid State Commun. **74**, 1071 (1990).
[13] C. Kittel, Phys. Rev. **73**, 155 (1948).
[14] *M. R. Freeman, M. J. Brady, and J. Smyth, Appl. Phys. Lett.* **60**, 2555 (1992).
[15] E. Betzig and J. K. Trautman, Science **257**, 189 (1992).
[16] M. R. Freeman *et al.* (to be published).
[17] L. D. Landau, Phys. Z. Sov. **11**, 129 (1937).
[18] D. J. E. Callaway, Ann. Phys. (NY) **213**, 166 (1991).
[19] H. Kirchner, Phys. Status Solidi A **4**, 531 (1971).
[20] C. C. Chi, M. M. T. Loy, and D. C. Cronemeyer, Phys. Rev. B **23**, 124 (1981); C. C. Chi (private communication).

Femtosecond Faraday rotation in spin-engineered heterostructures (invited)

J. J. Baumberg and D. D. Awschalom
Department of Physics, University of California, Santa Barbara, California 93106

N. Samarth
Department of Physics, The Pennsylvania State University, University Park, Pennsylvania 16802

We have developed a new femtosecond-resolved optical technique with which one may examine magnetic spin dynamics in near-atomic scale structures by employing a highly sensitive, ultrafast measurement of the Faraday rotation. We apply this spectroscopy to novel band-gap-engineered II–VI diluted magnetic semiconductor heterostructures of two types to demonstrate the ability to simultaneously monitor electronic and magnetic interactions in a quantum geometry. The experiments show that these dynamics evolve on widely different time scales, and reveal the onset and decay of magnetization due to carrier spin scattering with femtosecond temporal resolution (300 fs). Although photoexcited carriers recombine within several hundred picoseconds, they leave behind a magnetic "footprint" that persists considerably longer and relaxes through an entirely different spin-lattice mechanism. Time-resolved magnetic measurements reveal the unusual dynamical properties of low-dimensional systems incorporating magnetic spins as compared to traditional semiconductor heterostructures.

I. INTRODUCTION

The interaction between charged carriers and magnetic species is an important issue in solid state science and a subject of considerable theoretical and experimental interest.[1] This problem continues to be actively investigated in diluted magnetic semiconductors (DMS) systems which have proved to be excellent hosts in which to explore this physics.[2] Despite several recent measurements of carrier spin polarization,[3] the microscopic interaction between embedded magnetic and electronic spins remains poorly understood. Recent advances in the molecular beam epitaxy of DMS alloys have made it possible to fabricate layers of these materials with near-atomic thickness. Employing such quantum geometries enhances the spin interactions and makes possible the tailoring of specific magnetic environments for detailed investigation of dynamical behavior. Moreover, careful placement of the magnetic species allows one to separate electronic and magnetic behavior in a single structure.[3] In addition to these questions, the influence of scaling and dimensionality on the *magnetic* behavior of ultrathin layers has also been contentious,[4] and may be studied in these geometries. To address many of these issues, we require an experimental tool that will selectively measure magnetization in structures as thin as a single magnetic monolayer on the timescale of individual spin reorientation events.

Here we describe a new technique that uses an *optical* probe of magnetization to reveal spin dynamics on the femtosecond and picosecond timescales. This is coupled with epitaxially grown II–VI DMS heterostructures which enable nanometer-scale engineering of both electronic band-gap and magnetic environment. Such high-quality "spin-engineered" samples provide an ideal laboratory for exploring in detail the interaction of electrons with magnetic ions, and of the magnetic interactions themselves, as the magnetic thicknesses is reduced to the order of a single monolayer. In addition, a judicious combination of magnetic and nonmagnetic species may be employed to construct novel heterostructures whose properties can be tuned with an applied magnetic field, for example by fabricating magnetic quantum wells or alternatively magnetic barriers.

We concentrate first on sensitive static measurements that characterize the magnetically doped thin films (Sec. II) and proceed to examine their dynamical behavior directly (Sec. III). Incorporating optical methods allows a powerful range of tools developed for short-pulse laser measurements to be focused on magnetic behavior. Time-resolved Faraday rotation is well-suited to address questions about the dynamical effects of reduced dimensionality in magnetic layers, as well as examining the spin interactions in low-dimensional electronic and magnetic systems. We believe this work can be further extended to metallic systems where electronic and magnetic interactions are also relevant such as giant magnetoresistance and spin switching.[5] One further application we note in conjunction with these spin-engineered structures is ultrafast magneto-optic thermometry with millikelvin, femtosecond resolution at 4 K.

In the II–VI alloys considered here, the dopant magnetic Mn^{2+} ions behave for the most part as independent paramagnetic spins of magnitude $S=5/2$.[2] The total magnetization induced in an applied magnetic field depends on the thermal population of the five Zeeman-split states which results in its Brillouin functional dependence on $\mu B/kT$. An extremely strong exchange interaction between delocalized band-edge carriers and the localized electrons on each magnetic ion leads to huge Zeeman splittings of the band-edge exciton at low temperature. In addition to opportunities for scientific research, this has led to the strong interest in such materials for use in magneto-optic applications. Here we show results on two different types of II–VI magnetic heterostructures based on the Zn(Cd,Mn)Se alloy system. We choose ZnMnSe in particular for its large magnetic interaction strength and unusual band-gap dependence on Mn concentration. The first structure, termed the "spin superlattice"[6]

 0021-8979/94/75(10)/6199/6/$6.00 © 1994 American Institute of Physics

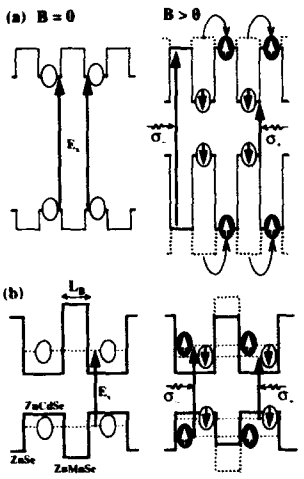

FIG. 1. Schematic band diagram along the growth axis for electrons and heavy holes at magnetic field $B=0$ (left), and $B>0$ (right) which Zeeman splits the band gaps (dashed) in the magnetic regions (shaded). (a) ZnSe/ZnMnSe spin superlattice structure: The spin-up carriers spatially relocate to the ZnSe barriers if $B>0.5$ T. (b) ZnCdSe/ZnMnSe/ZnCdSe DMS coupled double quantum well.

(SSL) consists of alternating 100-Å layers of $Zn_{1-x}Mn_xSe$ magnetic quantum wells ($x=8\%$ or 14%) and ZnSe barriers [Fig. 1(a)]. Initially the confinement potentials in the magnetic quantum wells are weak (depending on the exact concentration x), but they can be tuned as a magnetic field is applied, resulting in greater (less) confinement for the spin-down (up) carriers. Above about 0.5 T, the spin-up carriers favor a spatial transfer into the ZnSe barrier layers, and a periodic spin modulation results. In the second sequence of structures, a pair of 40-Å nonmagnetic $Zn_{0.77}Cd_{0.23}Se$/ZnSe double quantum wells are coupled by a thin "field-tunable" $Zn_{0.76}Mn_{0.24}Se$ magnetic barrier [Fig. 1(b)]. These allow us to explore both spin scattering as carriers tunnel and the dynamics of magnetization in reduced dimensionalities. All these samples are MBE grown on (100) GaAs substrates with a 6000-Å-thick buffer and 2000-Å cap of ZnSe. Layer thicknesses and magnetic concentrations are determined by standard methods and their quality confirmed by subsequent absorption and photoluminescence spectroscopy (PL).[7] We use a standard etching technique to remove the opaque GaAs substrates[8] and confirm that this PL remains unaffected.

II. STATIC MEASUREMENTS

To resolve the minute magnetizations from thin magnetic layers, we adopt an extremely sensitive and powerful extension of the Faraday rotation measurements commonly applied to bulk samples.[8] Using a modulation coil technique, we can clearly see the magnetization from a few atomic layers of magnetic material. The true spectroscopic nature of this measurement allows isolation of the specific magnetic interaction of interest over a wide range of temperatures and applied fields, in contrast with low noise, low-field SQUID experiments previously used to characterize related magnetic heterostructures.[9]

We use a modelocked Ti:Sapphire laser to produce high power, tunable infrared pulses which are subsequently frequency doubled, using a 1-mm-thick β-barium borate (BBO) crystal, into the 350–520-nm wavelength range to match the II–VI heterostructure energy levels of interest. The probe light is attenuated below 100 μW, linearly polarized and focused through a ~100-μm spot on the etched sample after which it is collected and analyzed in an optical bridge arrangement. This bridge consists of a Glan–Laser polarization separator whose optical outputs are separately directed onto two matched, low-noise PIN Si-photodiodes, the amplified signals of which are electronically subtracted and further amplified. The bridge is balanced when fed with linearly polarized light at 45° to the axes of the Glan–Laser prism. Any rotation changes induced in the probe polarization produce an output signal which, to first order, is uncontaminated by noise on the laser beam (this being subtracted out in the balancing arrangement). Hence even in the presence of typically 5% intensity noise on the laser, millidegree rotations can be isolated, limited only by the photodiode dark currents. Our samples are placed in a magneto-optical cryostat capable of $B=9$ T and $T=1.7$–300 K with the incoming probe beam parallel to the magnetic field (Faraday geometry) and to the heterostructure growth axis. In order to separate out the small Faraday rotation of the sample from the relatively larger rotations of the cryostat windows and other field-sensitive optical components, we utilize a coil modulation technique.[8] A 5-mm-long, 440 turn coil, fabricated from 60-μm-diam superconducting $Nb_{0.52}Ti_{0.48}$ or 100-μm Cu wire, is mounted horizontally on the cryostat insert and the sample cemented to one end of the aperture in a strain-free configuration. This coil is calibrated by comparing the Faraday signal produced from a dc current flowing through it, to that from the cryostat superconducting solenoid. Using this coil, the magnetic field at the sample is weakly modulated by 5 mT at 105 Hz. In addition, the probe beam is mechanically chopped at 1.1 kHz and by measuring the induced Faraday rotation in a phase-sensitive fashion at the sum of these frequencies, we select solely that rotation induced by the sample. The lock-in difference signal, S, from the optical bridge is proportional to the derivative of the sample Faraday rotation, θ_F, with applied field, B.[8] We simultaneously record the individual detector intensities (I_a and I_b) so that the difference signal can be scaled to yield the normalized differential rotation (NDR):

$$\mathrm{NDR}=\frac{S}{I_a+I_b}\approx\frac{\partial\theta_F}{\partial B}. \tag{1}$$

If this signal is measured as a function of applied field, the total Faraday rotation can be reconstituted by integration. Figure 2 shows typical results at two detection energies close to the exciton absorption peak in a $Zn_{0.92}Mn_{0.08}Se$/ZnSe SSL sample ($E_x=2.80$ eV), demonstrating both the sensitivity and spectroscopic nature of the measurement. The signal arises from just 1000 Å net total of magnetic material and reveals several features not found in corresponding magnetoabsorption data. The low-field Verdet coefficient is found to be

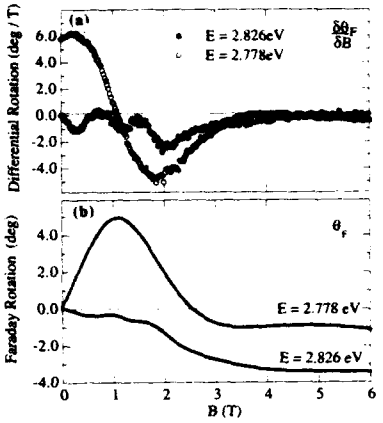

FIG. 2. (a) Differential Faraday rotation measured on a 100 Å/100 Å $Zn_{0.92}Mn_{0.08}Se/ZnSe$ SSL sample at probe energies, E, above and below the zero-field heavy-hole exciton (E_x=2.803 eV) at 4.5 K. (b) Integration of (a) yields the total sample Faraday rotation and clearly shows the spin down state shift into view on the low energy side of the zero-field exciton at B=1.2 T.

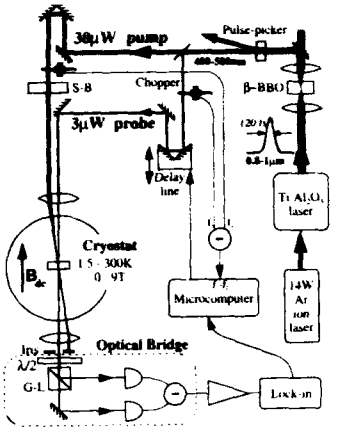

FIG. 4. Experimental layout for dynamic measurements. The output of the tunable Ti:sapphire laser is focused through a BBO crystal and the resulting blue pulses selected by dichroic filters which discard the infrared. The beam is focused through a pulse-picker which selects 1 of every N pulses at 35% efficiency, before being split into a strong pump and weak probe beam at a dielectric beamsplitter and delayed relative to each other by a computer controlled delay stage. The probe polarization is linear and the Soleil–Babinet variable retarder (S–B) allows the pump to be linearly or circularly polarized.

greater than 5×10^5 deg/T cm for certain detection energies, corresponding to the huge enhancement in g-factor in these systems.[2] The experimental sensitivity of 10^{-5} deg/G allows us to clearly resolve rotations of 1 arc s. In conjunction with the quantum structures, we achieve a magnetic sensitivity difficult to obtain in a dc SQUID magnetometer.[9] We also show the zero-field differential Faraday spectrum of the 12-Å-thick magnetic barrier DQW sample which clearly displays the lowest excitonic resonance (E_x=2.53 eV) from a few atomic layers of magnetic alloy (Fig. 3). This result is compared favorably to that derived from a Kramers–Krönig analysis of the magnetoabsorption.

Since we operate at a wide range of applied fields and temperatures we can follow the temperature dependence of the magnetization. We utilize this in susceptibility measurements (equivalent to zero-field NDR) at low temperature to investigate the magnetic behavior of low-dimensional magnetic structures. In contrast to the bulk $Zn_{0.75}Mn_{0.25}Se$ alloy which exhibits a spin-glass phase transition around 7 K,[10] even the largest DQW barrier thickness we examined (32 Å) showed no clear signature of a phase transition down to 1.7 K. This suggests that the phase transition is suppressed by the reduced dimensionality as has been discussed elsewhere.[4]

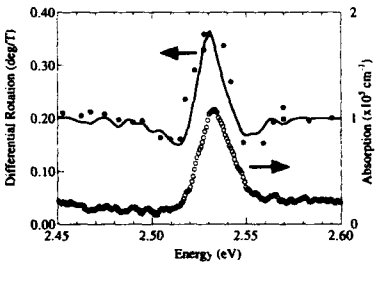

FIG. 3. Differential Faraday spectrum (solid circles) and absorption (open circles) of the 12-Å magnetic DQW sample at B=0 T and T=4.5 K. The solid line is the differential Faraday rotation calculated from a Kramers–Krönig analysis of the magnetoabsorption, suitably scaled and offset.

III. DYNAMIC MEASUREMENTS

Having characterized the static magnetic behavior of these samples, we now demonstrate a new extension of the technique to time-resolved studies of quantum systems. We use the power of ultrafast pump-probe spectroscopy to excite electronic states of the DMS samples and subsequently probe their Faraday rotation some arbitrary time delay later. By scanning this time delay, τ, between pump and probe pulses we are able to map out the electronic and magnetic dynamics and show they follow completely different physical relaxations.

The same laser system is used to produce 120-fs pump and probe pulses of identical wavelength which can be delayed relative to each other by up to 1 ns using a retroreflector mounted on a compressed-air delay stage (Fig. 4). Each beam is separately mechanically chopped before passing through polarization optics, and then focused through the same lens into the cryostat. The two foci are overlapped optimally at the sample and the transmitted pump beam blocked while the probe passes through an iris into the optical bridge outlined above. Because the pulses interact only at the sample we can discard the previous coil technique and

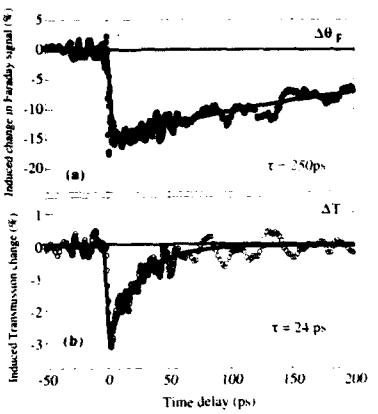

FIG. 5. Time-resolved (a) Faraday rotation, $\Delta\theta_F$, and (b) transmission, ΔT, induced by the pump pulse and taken simultaneously on the $Zn_{0.92}Mn_{0.08}Se/ZnSe$ SSL sample. The pump and probe are collinearly polarized, $T=1.7$ K, $B=1$ T and $E=2.810$ eV. The solid lines are exponential fits with the lifetimes shown.

measure pump-induced changes to the Faraday rotation at the difference frequency of probe (1.1 kHz) and pump (397 Hz) modulations. While the pump polarization can be varied from linear to circular using a Soleil–Babinet variable retarder in the pump arm, the probe remains linear, balanced at 45° to the Glan–Laser prism, and always <10% of the pump intensity.

As discussed below, the sample magnetizations appear extremely sensitive to the average light intensity so we further reduce this while retaining the high peak powers by externally pulse picking the output of the Ti:sapphire laser using a $LiNbO_3$ crystal. This acousto-optic crystal is driven by 380 MHz rf wave packets which diffract every Nth pulse from the $T_{rep}=13$ ns repeating train, where N can be varied from 8 to 518, resulting in interpulse delays from 100 ns to 7 μs. This is necessary to reduce the heating of the spin system which is measured as a background (time-delay independent) component to the induced Faraday rotation. Interference between the two beams near zero delay allows calibration of the system temporal resolution as 350 fs. The subsequent time-resolved Faraday rotation signals, $\Delta\theta_F$, were confirmed to originate only from the sample, reverse their sign when the applied field was oppositely directed, and depend on the presence of both pump and probe beams. In addition to monitoring the Faraday rotation, the sum of the diode photocurrents (I_a+I_b) was directed into a second lock-in referenced to the same $f_{probe}-f_{pump}$ difference frequency. This records the pump-induced change in sample transmission, ΔT, and *simultaneously* identifies the carrier lifetime.

Initial experiments were performed on a $Zn_{0.92}Mn_{0.08}Se/ZnSe$ SSL sample using collinearly polarized pump and probe beams. The pump excites different spin-down and spin-up carrier concentrations at nonzero field since the states are considerably Zeeman-split in energy ($\Delta E_{\pm}=10$ meV/T). As seen in Fig. 5, on longer time scales it is apparent that there is a completely different relaxation process for the absorption and Faraday rotation. The pump-induced absorption changes are produced when sufficient carriers are optically injected to fill a substantial fraction of the exciton density of states and, by Pauli exclusion, block further absorption of probe photons into these same states. Thus the decay of the induced transmission reflects the recombination of carriers, within 100 ps in this sample. This deduction is supported by time-resolved photoluminescence performed on a sample from the same wafer.[11]

After the carriers have recombined, it is traditionally believed that the sample has reattained equilibrium. The simultaneously recorded time-resolved Faraday signal shows that this is clearly *not* the case. Injecting carriers instantaneously changes the magnetization, presumably through spin-scattering events as the carriers cool so that the effective spin temperature of the Mn^{2+} spin system increases.[3] This spin system cools as the Mn^{2+} spins slowly reorient through a spin-lattice relaxation over a time scale at least an order of magnitude longer than the carrier lifetime. Although the carriers have decayed, they impart a "magnetic footprint" which persists far longer than their lifetime in the structure. Hence we are able to resolve the magnetization dynamics completely independently of the electronic dynamics, both of which may be separately modified by field, geometry, and heterostructure type.

The above SSL data, taken without pulse picking, was performed at 1.8 K in superfluid helium to reduce the background heating signal. The improvement in signal to noise when the pulse separation is increased by a factor of 50 is apparent in Fig. 6 for the 32-Å magnetic-barrier DQW. Circular pump polarizations are now used to excite particular carrier spin orientations and at zero field the signals originate from populating these specific spin states. The Faraday rotation is a function of both the magnetization, manifest as the energy splitting ($\Delta E_{\pm}$) between the two spin states, and their individual oscillator strengths ($f_{\pm}$) which in this case are bleached by the influx of excitons. These exciton spin states are resonantly excited as apparent from the ultrafast (<200 fs) rise time of the Faraday rotation. Examining the subsequent relaxation in zero field, we find it consists of two exponential components of very different time scales. The initial fast decay (~5 ps) reflects carrier spin scattering to the initially unoccupied spin state, driven entropically in zero field and thermodynamically if $B\neq 0$. However after 10 ps, spin scattering appears to cease and the longer decay timescale (~70 ps) takes over, this corresponding well with the carrier lifetime as measured by time-resolved transmission and independently measured time-resolved photoluminescence.[11] As a check, injecting carriers of opposite spin orientation only reverses the sign of the measured rotation change. However if a magnetic field is now applied, this symmetry disappears since the energies of the spin states are split. The results are also shown in Fig. 6 with the zero field data for comparison. Although little change is measured in the carrier lifetime by time-resolved transmission and PL, a residual Faraday signal remains at very long time delays (τ >500 ps) as also found in the SSL sample (Fig. 5). We interpret this long-lived signal as a net magnetization change

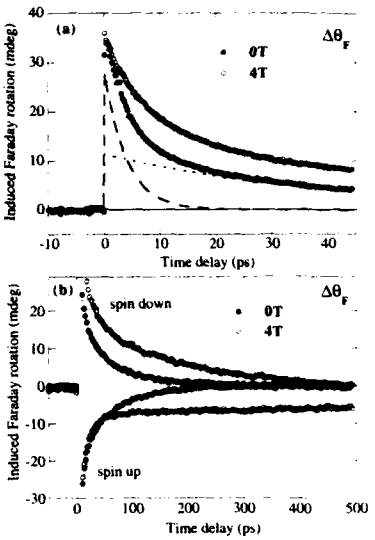

FIG. 6. Time-resolved Faraday rotation on the 32-Å magnetically coupled DQW at $T=4.5$ K and $E=E_x=2.542$ eV. (a) The initial 50 ps at zero applied field and $B=4$ T when injected with spin-down excitons from the circularly polarized pump. At $B=0$ T, the fast transient component (dashed curve) is due to spin scattering and the slower component (dotted curve) from carrier recombination. (b) Longer time scale comparison of spin-up and spin-down pumped excitons at $B=0$, 4 T. The magnetic signature is a spin-dependent signal remaining beyond 500 ps, long after the carriers have decayed.

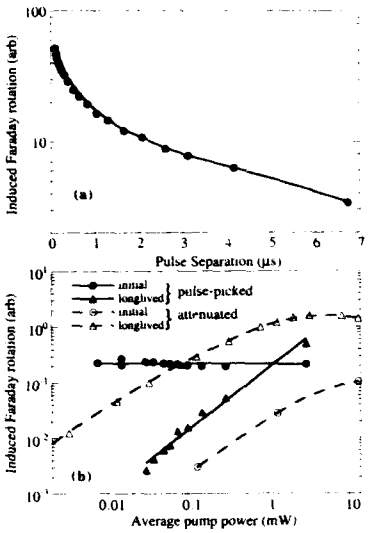

FIG. 7. Time-resolved Faraday rotation of ultra-long-lived component measured just before the arrival of the next pump pulse. (a) DQW sample with 24-Å barrier at $B=4$ T, $T=4.5$ K, and $E=E_x=2.546$ eV. The pulse separation is varied using the pulse picker while the peak power in the pulses is kept fixed. Solid line is to guide the eye. (b) Long lived ($\tau=NT_{rep}-5$ ps) and initial ($\tau=+1$ ps) signals from the 32 Å DQW sample at 2 T and 4.5 K as a function of average pump power, measured by changing either the interpulse separation (solid lines) or pump attenuation (dashed lines). The signals are scaled to the same average probe intensity. The pulse-picked experiments reported here operate at average pump powers below 80 μW where the signal substantially exceeds the background.

reflected in $\Delta E_{\pm}$ and hence Faraday rotation. Further work is underway to understand the exact form of the induced magnetization dynamics for the different initial spin distributions.[12] Similar results are obtained for three different magnetic tunneling barrier widths (12,24,32 Å) while no magnetically active decay component is identified in a sample containing a nonmagnetic ZnSe tunneling barrier. Ongoing work shows that the time scales also change radically as a function of temperature and applied field. In addition, we report elsewhere the observation of refractive-index beats between coherently excited spin states.[12]

To demonstrate the sensitivity of the Mn^{2+} spin system to carrier heating we look at very long time delays, keeping the peak power fixed but changing the interpulse separation, NT_{rep} [Fig. 7(a)]. Measuring the induced Faraday signal at time delay $\tau=-5$ ps corresponds to measuring the signal remaining after $\tau=NT_{rep}-5$ ps, and this falls exponentially at large N ($\tau_{relax}\approx 5$ μs). At closer pulse separations this cumulative background builds up because the signal has not decayed before the arrival of the next pulse. This background signal is independent of the initial carrier spin, so it appears that acoustic phonons emitted by the cooling carriers remain to heat the Mn^{2+} spin system long after carrier recombination. We also note that $S=\frac{3}{2}$ excited states of the Mn^{2+} ions, previously identified with 2 eV PL emission[13] (observed weakly in these heterostructures), are similarly long lived and may be an alternative reservoir for this residual excitation of the spin system. In contrast to the microsecond behavior, at one nanosecond the magnetic signature *is* spin dependent and so arises from the initial spin scattering between excitons and magnetic ions. Additionally we show in Fig. 7(b), the scaling with average pump power of the initial transient signal ($\tau=+1$ ps) and the longlived background component ($\tau=-5$ ps) taken either by attenuating the pump beam or reducing the pulse repetition rate. This shows that the immediate response is linearly proportional to the initial carrier density ($\propto I_{pump}^{peak}$) as expected from the previous discussion. The dominant dependence of the background on average power confirms that it originates from a very long-lived component and demonstrates the necessity of pulse picking to suppress the background below the signal level.

This behavior also suggests one possible application for optically sensed, ultrathin paramagnetic layers as an ultrafast probe of temperature. Any heating of the spin system is measured on optical time scales and provides the lattice temperature at one particular spatial depth and time in the sample. The resolution of such a thermometer would depend critically on the temperature range of interest in relation to the temperature dependence of the susceptibility. It should be noted that thermal effects from optical injection as reported here are visible at carrier densities $<10^8$ cm^{-2}, significantly below those normally associated with such parasitic effects.

IV. CONCLUSION

We have demonstrated a powerful new technique for using Faraday rotation to follow the static and dynamic magnetization in near-monolayer magnetic systems with a high degree of energy and temporal resolution. These allow sensitive measurements of the magnetization and carrier spin-scattering in spin-engineered II–VI quantum structures and provide additional time-resolved spectroscopic information to conventional magnetoabsorption studies. Initial results demonstrate the entirely separate dynamics of magnetic and electronic relaxation in such systems, and in contrast to all other optical probes, allows the measurement of magnetization dynamics long after carriers have decayed. The power of ultrafast Faraday spectroscopy can be applied to a host of available material systems and promises to elucidate theoretical predictions of the magnetic behavior in reduced dimensionality.

ACKNOWLEDGMENTS

We would like to thank J. K. Furdyna and H. Luo for the sample fabrication and materials expertise, and David Tulchinsky and Scott Crooker for making results available and experimental assistance. JJB gratefully acknowledges the support of IBM. This work was supported by grants NSF DMR-92-07567, NSF DMR-92-08400, and AFOSR F49620-93-1-0117.

[1] M. Z. Maialle, E. A. de Andrada e Silva, and L. J. Sham, Phys. Rev. B **47**, 15776 (1993); G. Bastard, Phys. Rev. B **46**, 4253 (1992); M. R. Freeman, D. D. Awschalom, J. M. Hong, and L. L. Chang, Phys. Rev. Lett. **64**, 2430 (1990); S. Bar-Ad and I. Bar-Joseph, Phys. Rev. Lett. **68**, 349 (1992).

[2] *Diluted Magnetic Semiconductors*, edited by J. K. Furdyna and J. Kossut, Semiconductors and Semimetals, **25** (Academic, San Diego, 1988).

[3] J. F. Smyth, D. A. Tulchinsky, D. D. Awschalom, N. Samarth, H. Luo, and J. K. Furdyna, Phys. Rev. Lett. **71**, 601 (1993).

[4] G. G. Kenning, J. Bass, W. P. Pratt, Jr., D. Leslie-Pelecky, L. Hoines, W. Leach, M. L. Wilson, R. Stubi, and J. A. Cowen, Phys. Rev. B **42**, 2393 (1990).

[5] M. Johnson, Phys. Rev. Lett. **67**, 3594 (1991).

[6] N. Dai, H. Luo, F. C. Zhang, N. Samarth, M. Dobrowolska, and J. K. Furdyna, Phys. Rev. Lett. **67**, 3824 (1991); W. C. Chou, A. Petrou, J. Warnock, and B. T. Jonker, Phys. Rev. Lett. **67**, 3820 (1991).

[7] J. F. Smyth, D. D. Awschalom, N. Samarth, H. Luo, and J. K. Furdyna, Phys. Rev. B **46**, 4340 (1992).

[8] M. Kohl, M. R. Freeman, J. M. Hong, and D. D. Awschalom, Phys. Rev. B **43**, 2431 (1991).

[9] D. D. Awschalom, J. R. Rozen, M. B. Ketchen, W. J. Gallagher, A. W. Kleinsasser, R. L. Sandstrom, and B. Bumble, Appl. Phys. Lett. **53**, 2108 (1988).

[10] A. Twardowski, C. J. M. Denissen, W. J. M. de Jonge, A. T. de Waele, M. Demianiuk, and R. Triboulet, Solid State Commun. **59**, 199 (1986).

[11] D. A. Tulchinsky, J. J. Baumberg, D. D. Awschalom, N. Samarth, H. Luo, and J. K. Furdyna (to be published).

[12] J. J. Baumberg, D. D. Awschalom, N. Samarth, H. Luo, and J. K. Furdyna, Phys. Rev. Lett. **72**, 717 (1994).

[13] Y. R. Lee, A. K. Ramdas, and R. L. Aggarwal, Phys. Rev. B **33**, 7383 (1986).

Time-resolved scanning probe microscopy: Investigations and applications of dynamic magnetostriction (invited)

G. Nunes, Jr.
Department of Physics and Astronomy, Dartmouth College, Hanover, New Hampshire 03755

M. R. Freeman
IBM T. J. Watson Research Center, Yorktown Heights, New York 10598

We have measured the magnetostrictive response of small nickel and $Tb_{0.3}Dy_{0.7}Fe_{1.95}$ cylinders to sudden step changes in applied magnetic field with a time-resolved scanning fiber interferometer. Spatially resolved measurements reveal the nonuniform distortion of the face of the rod as the induced magnetization propagates in toward the center. A crossover is observed, as a function of decreasing cylinder diameter, from eddy current- to longitudinal phonon-limited response times. The ability to characterize dynamic magnetostriction in small samples has also enabled us to perform time-resolved measurements of fast transient signals with a scanning tunneling microscope. Modulation of the tip-sample separation on short time scales is provided by the use of a nickel magnetostrictive tip driven by a local magnetic field coil. The technique offers a broadly applicable means of obtaining fast dynamical information in tunneling microscopy, and is demonstrated here on nanosecond time scales. These experiments illustrate, in the context of magnetics, the general promise of time-resolved scanning probe methods.

I. INTRODUCTION

The success of the scanning tunneling microscope (STM)[1] has inspired the development of a variety of very powerful scanned probe techniques.[2] To date, however, a significant limitation of these methods has been an inability to measure fast signals, such as would arise from dynamic phenomena at the atomic level or in the operation of nanometer scale electronic and mechanical devices. Efforts to surpass this "speed limit" have recently become the focus of increasing interest.[3–5] These efforts are driven by the scientific and technological applications for which high temporal resolution is as essential as the extreme spatial resolution offered by the scanned probes. Scanned fiber-optic probes, including near-field instruments,[6] offer the possibility of attaining a high spatial resolution while retaining much of the flexibility inherent in optical techniques, and are natural candidates for ultrafast time resolution. In this paper we describe a scanned fiber probe that is not only capable of measuring subangstrom displacements, but can also follow the time dependence of these displacements with picosecond resolution.[7] We have used this probe to characterize the dynamic magnetostrictive response of small cylinders of $Tb_{0.3}Dy_{0.7}Fe_{1.95}$ (Terfenol D) and nickel. In the case of nickel, these measurements have enabled us to develop an STM which incorporates a magnetostrictive tip, and which is capable of detecting fast transient signals on nanosecond time scales.[8] Taken together, these new techniques represent substantial progress towards the development of methods which offer simultaneously high spatial *and* time resolution.

II. TIME-RESOLVED FIBER INTERFEROMETRY

While magnetostriction has been thoroughly investigated in "bulk" systems[9] (pure and alloyed, metallic and insulating), very little is known about the magneto-mechanical properties of small (mono- or even few-domain) particles, owing to the difficulty of measuring the small dimensional changes involved. A scanned probe with the ability to both spatially and temporally resolve extremely small displacements would enable important measurements in this regime, including dynamical studies of magnetization reversal and other nonequilibrium phenomena in small magnetic systems. The time-resolved scanning fiber interferometry technique described here was developed to address some of these issues, but should also prove widely useful in characterizing micromechanical phenomena of all kinds.

The essence of our approach is to use a picosecond-pulsed laser as the optical source for a fiber interferometer of the sort which has recently been popularized in the context of scanning force microscopy.[10] A schematic illustration of our experimental set up is shown in Fig. 1. The output of a cavity-dumped, mode-locked dye laser (pulse width ~ 2 ps) operating at 633 nm is fed into one arm of a 2×2 fiber-optic directional coupler. The cleaved end of one of the output fibers from the coupler is mounted on a piezo-tube scanner with quartered electrodes, and moved to within ~ 30 μm of the reflective sample surface (prepared here by a mechanical polish) using a mechanical flexure stage. Fine adjustment of the length of the resulting Fabry–Perot interference cavity is made by using a dc voltage to control the length of the piezo tube. A small ac modulation is added to this dc voltage, and is used both to calibrate the sensitivity of the interferometer and to provide a feedback signal with which a constant fiber-sample separation is maintained. The sensitivity of this apparatus, as limited by external vibrations, is ~ 0.1 Å$/\sqrt{\text{Hz}}$. The directional coupler's two remaining outputs are fed, using index matching gel to minimize back reflections, to a pair of photodiodes, one of which is used to monitor the laser pulse amplitude. The signal from the other photodiode is dominated by the reflected light from the interference cavity and shows a very high degree of modulation ($>50\%$) as a function of cavity spacing.

A small ferrite core electromagnet allows us to apply static magnetic field biases of up to 250 Oe along the axis of

 0021-8979/94/75(10)/6205/6/$6.00 © 1994 American Institute of Physics

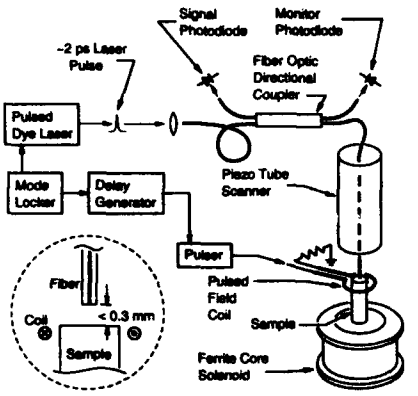

FIG. 1. Schematic of the time-resolved fiber interferometry apparatus. The inset in the lower left shows a detail of the Fabry–Perot interference cavity formed between the fiber and sample.

the cylindrical samples. The field from this solenoid is used to characterize the static magnetostrictive response of the samples using fiber interferometry, as shown in Fig. 2 for a 125 μm diameter nickel rod undergoing cyclic magnetization. Magnetic field transients are introduced using a simple one-turn coil which produces field strengths on the order of 20 Oe/A over an effective length of 0.5 mm. A "free-standing" arrangement allows the vertical position of the coil to be adjusted with respect to the top of the sample. This coil is driven by a current pulser with a minimum rise time of 45 ps, and whose output is chopped at an audio frequency to allow heterodyne detection of the sample response. The individual current pulses are triggered synchronously with the dye laser's optical pulses by the electronic signal from the laser's mode locker and cavity dumper (19 kHz). An electronic delay unit between the laser and the current pulser allows the relative arrival time (at the sample) of the magnetic field pulse and the optical pulse to be precisely controlled. The complete time-dependent response of the sample

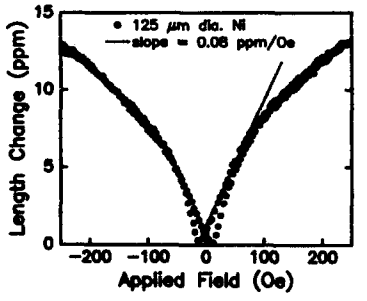

FIG. 2. Static magnetostriction of a 125 μm diameter nickel rod as measured with the apparatus illustrated in Fig. 1, but using a continuous wave He-Ne laser as the light source. The straight line gives the slope in the region where the dynamic measurements were made.

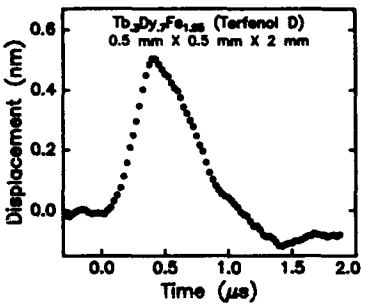

FIG. 3. Dynamic magnetostriction of a 0.5 mm×0.5 mm×2 mm rod shaped sample of $Tb_{0.3}Dy_{0.7}Fe_{1.95}$ (Terfenol D) excited by a 200 ns wide 5 Oe magnetic field pulse. The sample was biased with a 100 Oe static field.

is obtained by incrementing the electronic delay in a series of discrete steps so as to sweep the arrival time of the optical pulse through that of the field pulse. The ultimate time resolution of this boxcar method is limited by a combination of trigger jitter and optical pulse length. In our present implementation, the resolution is jitter limited to ~50 ps, which is more than adequate for the current experiment, although extension to resolutions of order 3 ps would be straightforward.[11]

Figure 3 illustrates the application of this technique to the measurement of the dynamic magnetostrictive response of a 0.5 mm×0.5 mm×2 mm rod shaped sample of $Tb_{0.3}Dy_{0.7}Fe_{1.95}$ (Terfenol D). The magnetic field pulse was 200 ns long with an amplitude of 5 Oe, while the sample was biased with a static field of 100 Oe. The total displacement of the end of the rod in this case is 0.5 nm. Because the pulse is so short compared to the response time of this relatively large sample, the measured displacement is much less than the ~5 nm we would expect from the large saturation magnetostriction $\lambda_s \sim 500$ ppm in (unstressed) Terfenol D.[12]

Although the saturation magnetostriction in nickel ($\lambda_s \simeq -40$ ppm) is much smaller than that in Terfenol D, the sensitivity of this interferometric technique is sufficient to allow us to characterize the response in this case as well. Figure 4(a) shows a measurement of the dynamic magnetostrictive response of the nickel sample characterized in Fig. 2 to a 430 ns duration, 46 Oe amplitude magnetic field pulse (indicated by the dotted line). The sample was prepared from 99.98% nickel wire[13] and was biased with a 26 Oe static field. The measurement was made with the 4 μm core of the fiber over the center of the rod face, so the interferometer recorded the response of that point in the sample to the time dependent magnetization. As can be seen from the figure, as soon as the pulsed field is applied, the rod begins to magnetostrict with a characteristic time of 300 ns. After the field pulse shuts off, the magnetization begins to decay, and the end of the rod moves back to its intitial position with the same characteristic time constant. The total excursion in this case is about 6 Å, from which we determine the reversible component of the longitudinal magnetostriction under these low field bias conditions to be $-0.08 \pm 0.01 \times 10^{-6}$/Oe.

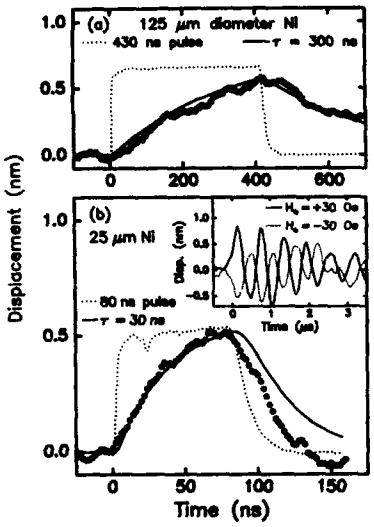

FIG. 4. (a) Magnetostriction of a 125 μm diameter Ni cylinder (●) excited by a 430 ns wide 46 Oe magnetic field pulse (dotted line). The fitted response time (solid line) is limited by eddy current screening in the wire. (b) Response of 25 μm diameter cylinder (●) to an 80 ns duration 30 Oe rectangular field pulse (dotted line). Solid line shows fit for 30 ns time constant. The vertical scale for the magnetic field pulses is arbitrary. Inset: Longer time scan illustrates acoustic ringdown of a long wire and reversal of the response when the direction of the static bias field H_0 is reversed.

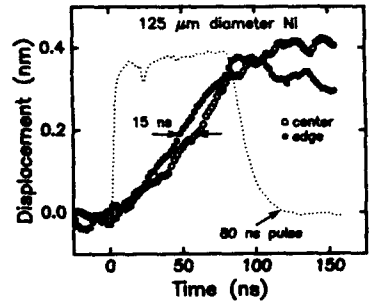

FIG. 5. Comparison of the time-dependent displacement of the edge (●) and center (○) of 125 μm rod face when the duration of the excitation pulse is short compared to eddy current damping time. The vertical scale for the magnetic field pulse is arbitrary.

This is in good agreement with the fit to our static measurements, as indicated in Fig. 2. The largest contribution to the quoted uncertainty arises not in measuring the displacement (since the interferometer is self-calibrating, given the optical wavelength), but in measuring the geometry and placement of the pulsed field coil in order to accurately estimate the field pulse amplitude. Note that both the static bias field and transient pulsed field are much smaller the the $\simeq 1$ kOe field necessary to saturate the magnetization of the sample.

For large enough metallic samples, the response will be limited by eddy current damping, i.e., the rate at which the transient field can penetrate the sample, and will have a time constant $\tau \simeq \mu_r \sigma d^2/8$ where d is the rod diameter, σ is its conductivity, and μ_r is the reversible permeability. Our data indicate this 125 μm diameter sample to be in that limit. From the measured τ, d, and σ, we find $\mu_r \simeq 10$, which is consistent with the results from conventional magnetometry measurements.

Since the eddy current damping time varies as the square of the sample diameter, it is straightforward to enter a regime where the field penetrates quickly and the sample response is instead limited by the longitudinal phonon velocity, i.e., the time required for displacements to propagate along the length of the sample at the speed of sound. Figure 4(b) shows the response of a 25 μm diameter nickel rod to an 80 ns, 30 Oe field pulse. In this case, the field completely penetrates the sample in about 10 ns. As can be seen from the figure, however, the time constant for the sample response is a somewhat longer 30 ns, so that we have, in this case, entered the phonon limited regime. For the arrangement of coil and sample used in this particular case (400 μm diameter coil centered 100 μm *above* the top of the sample), the field falls by a factor of 2/3 over the top 150 μm of rod. If we take this length as the "active" region of the rod, and assume that the magnetostrictive response is limited by the longitudinal sound velocity in nickel (4900 m/s[14]), we find a characteristic time of 31 ns, in good agreement with the data.

In this regime, the sample is acting as a lossy acoustic transmission line, where the loss has been introduced by plotting the line in epoxy to within 50 μm of it's free end. In the absence of this lossy medium, however, it is possible to observe acoustic resonances in the rod. The solid line in the inset to Fig. 4(b) shows the response of a 25 μm diameter, 1.5 mm long sample to a 230 ns, 44 Oe field pulse. As can be seen from the figure, the sample continues to ring for several microseconds after the pulse has shut off. The dotted line shows the response of the sample to an identical pulse, but with the direction of the 30 Oe static bias field reversed. The fact that the sign of the displacement depends on whether the transient field opposes or augments the static field H_0 provides confirmation that the observed signals arise from magnetostriction.

In fitting the response time to the data shown in Fig. 4(a), we assumed that the displacement of the 125 μm rod could be characterized by a single exponential, and that the face of the rod was displaced uniformly. The spatial and temporal resolution of our technique, however, is such that we can easily observe the breakdown of the second of these two assumptions. Eddy current screening of the magnetic field pulse causes a nonuniform magnetization profile along the sample radius. The nonuniform stresses accompanying this magnetization profile are large enough that, despite the large shear modulus of nickel, the outer edge of the rod face begins to displace before the center.

Figure 5 shows a comparison of the magnetostrictive response at the center of the 125 μm diameter rod with that obtained by positioning the fiber core at the edge of the rod. The field pulses used in this case were 80 ns long and had an

amplitude of 92 Oe. It is clear from the figure that the displacement of the edge does in fact lead that of the center over the entire duration of the field pulse. At a displacement of 0.2 nm, for example, the center lags behind the edge by 15 ns. It is also clearly observed that while the direction of travel at the edge immediately reverses when the field pulse is shut off, the center of the rod continues to rise as magnetization deep in the sample continues to diffuse towards the center.

III. TIME-RESOLVED TUNNELING MICROSCOPY

The optical scanned probe technique demonstrated above offers very high temporal resolution, and a spatial resolution perpendicular to the sample surface sufficient to resolve magnetostriction in samples on the order of 100 nm tall or less, which has important implications in the context of magnetometry. Moreover, this ability to characterize and control small, rapid physical displacements can be exploited in such other contexts as nanomechanics and scanning tunneling microscopy. In particular, we have applied dynamic magnetostriction in small systems to the development of a time-resolved scanning tunneling microscope. The combination of the extraordinarily high spatial resolution of tunneling microscopy with a comparably high time resolution would provide a powerful tool for the investigation of dynamic phenomena on surfaces, and thereby help to overcome one of the remaining limitations of the STM.

The useful bandwidth of conventional scanning tunneling devices is limited by two major obstacles: the difficulty of measuring high frequency signals from the very high source impedance tunnel junction, and the relatively slow speeds at which the traditional piezoelectric actuators used in the STM are able to move. The first of these obstacles may be overcome (for repetitive signals) by performing a demodulation at the tunnel junction itself in order to bring a fast signal into the bandwidth of the conventional electronics. Transient phenomena can then be recorded through a boxcar averaging technique in which the signal is sampled during a short interval, and that interval is scanned through time. A particularly appealing approach, because of its generality, would be to modulate the tunneling distance itself, thereby changing the tunneling impedance and "gating" the signal in a straightforward way. Such an approach could be used to time-resolve changes in topography, electronic structure, or any other surface property accessible to the STM and which can be driven repetitively over the course of a measurement. To achieve such a direct modulation of the tunnel junction, however, one must also overcome the second obstacle posed by the slow response of the piezoelectric actuator which controls the tunneling distance. Our experiments on dynamic magnetostriction have led us to an approach in which, through the use of an etched nickel wire, the tip itself acts as a fast actuator.

Our straightforward experimental arrangement is shown schematically in Fig. 6. The magnetostrictive tip is fitted onto a conventional STM (operating in air at room temperature), and is threaded through a $\sim 400\,\mu$m diameter, single-turn coil of fine copper wire suspended just above the sample, which is an evaporated Au film in the form of a transmission line. The tip itself must be made from a material which satisfies two requirements: it must have adequate dynamic magnetostrictive response, and it must be amenable to forming a sharp tip for tunneling. Unfortunately, rare-earth alloys such as Terfenol D, which are particularly attractive from the point of view of this first requirement, respond poorly to standard tip-forming techniques: they preferentially etch along grain boundaries and ultimately disintegrate. Consequently, we have chosen here to work with nickel, which is easily etched to form very sharp tips, and which, as shown in our time-resolved interferometry measurements, has sufficient dynamic response. This wire was formed into tunneling tips using standard electrochemical methods.[15] Roughly 10 nm of gold was evaporated onto the ends of the freshly etched tips to prevent oxide formation.

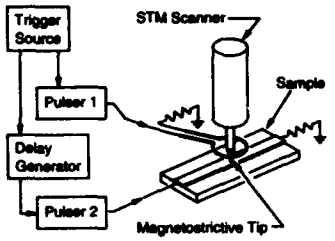

FIG. 6. A schematic diagram of the time-resolved STM apparatus which illustrates how the tip is threaded through a local magnetic field coil. Pulser 1 delivers current pulses to the field coil, and pulser 2 applies voltage pulses to the gold stripline sample. The resistive (50 Ω) terminations eliminate electronic reflections.

The quantum mechanical tunneling interaction on which the STM is based has a characteristic range $(2\kappa)^{-1}$, where $\kappa = \sqrt{2m\phi/\hbar}$ (m is the mass of the electron and $\hbar$ is Planck's constant). For typical effective work functions ϕ, this range is extremely short, so that reversible tip motions on the 0.1 nm level are sufficient for useful tunnel gap modulation. Figure 7 shows the measured tunnel current vs. tunneling distance characteristic of our gold-coated nickel/gold STM junction at a constant bias voltage of 50 mV. As the tip is extended toward the surface, the current increases exponentially with a characteristic length scale $(2\kappa)^{-1} = 0.145$ nm,

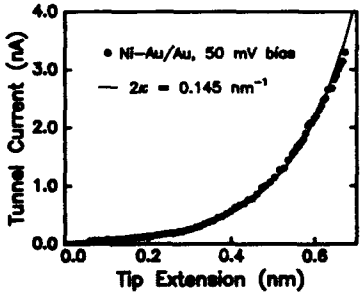

FIG. 7. Tunnel current as a function of tip extension (at fixed bias voltage) for the Au-coated Ni tip tunneling into the Au sample.

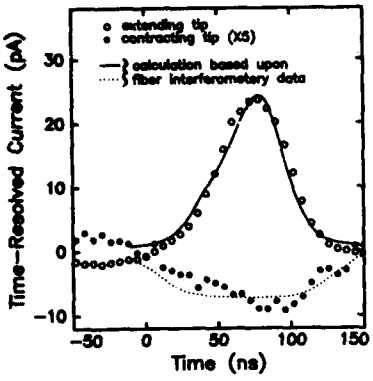

FIG. 8. Measured time-resolved tunneling current obtained via the tunnel distance modulation technique using large amplitude (0.5 nm) tip excursions to sample the presence of a voltage pulse on the transmission line sample. Data are shown for both magnetic field pulse orientations, and are compared with a model calculation based on the data of Fig. 7 and a measurement similar to that shown in Fig. 4(b). Note that the vertical scale for the lower curve has been expanded by a factor of 5.

from which we find an effective work function $\bar{\phi} = 0.45$ eV.

At this extremely small level of displacement, it is of course unnecessary to accelerate the entire mass of the tip as a rigid body in order to perform gated measurements. Higher speeds can be obtained by launching a longitudinal acoustic pulse down the tip towards the etched end. In the present work such a pulse is launched by applying a fast rise-time magnetic field pulse to the nickel wire close to the tip—exactly as in our time-resolved fiber interferometry experiments. These interferometry measurements allow us to quantitatively characterize the dynamic tip response which results from this excitation.

We have used this technique to perform time-resolved tunneling measurements in which the moving tip is used to sample for the presence of a high-speed voltage pulse propagating along an Au transmission line. The time-resolved current signal arises from the simultaneous arrival at the tunnel junction of the acoustic displacement pulse on the tip and the voltage pulse on the sample. An example of such a measurement is illustrated in Fig. 8 in which the entire time dependent signal was constructed by varying the relative time delay between an 80 ns, 20 Oe field pulse applied to the magnetostrictive tip and a 10 ns duration, 160 mV amplitude voltage pulse applied to the sample. In practice, these pulses were applied at a repetition rate of 631.7 kHz, and the resulting signal was averaged with a 3 s time constant. The time-resolved tunnel current was discriminated from the substantially larger dc tunnel current (which is fed back to stabilize the quiescent position of the tip) by a phase-sensitive detection scheme analogous to optical chopping.

A critical indication that the time-resolved current shown in Fig. 8 arises from the magnetostrictive behavior of the tip, and which distinguishes it from such artifacts as thermal displacements, is the "bipolar" dependence of the signal on the direction of propagation of the current around the pulse coil. When this current is arranged so that the field pulse causes the tip to move toward the sample, there is a corresponding increase in the tunnel current. On the other hand, when the field pulse is reversed and the tip pulls away from the sample, there is a small net decrease (below the level of the dc quiescent signal used for feedback) in the tunnel current. The disparity in the amplitude of the time-resolved current in the two cases arises from the fact that the tip excursions (0.5 nm) are large compared to the ~ 0.15 nm characteristic length scale for tunneling. Note that the vertical scale for the measurement in the case where the tip is pulled back has been expanded by a factor of five. As a check that these signals were associated with tunneling, we pulled the STM tip back to reduce the quiescent dc tunnel current to a negligible value, and observed that the time-resolved signal disappeared.

In order for this instrument to be genuinely useful, it is important to characterize the time dependent response of the microscope itself. By combining a characterization of the magnetostrictive behavior of the tip by time-resolved fiber interferometry [essentially the same response as illustrated in part (b) of Fig. 4] with the measured distance dependence of the tunnel current illustrated in Fig. 7, we are able to calculate the expected time dependence of the tunneling signal. This calculation is shown as the solid and dotted lines superimposed on the data in Fig. 8. As can be seen from the figure, the predicted response is in good agreement with what is actually observed.

It is worth noting that the zero of time in Fig. 8 is not arbitrary, and was chosen to correspond to the simultaneous arrival of the leading edges of the voltage and current pulses at the tunnel junction. This "time-zero" measurement was made through an alternative time-resolved response in which the nonlinear current-voltage characteristic of the tunnel junction itself demodulates the signal.[5] The measurements presented here, however were taken under conditions in which these nonlinear mixing effects were negligible. Given this determination of time-zero, the 75 ns temporal offset observed in Fig. 8 can be seen to be the consequence of the propagation delay for the magnetostrictively launched acoustic pulse to reach the very end of the tip.

IV. CONCLUSION

In summary, we have demonstrated the feasibility of studying magnetostriction in micrometer-scale structures and on fast time scales (such that intrinsic relaxation times may be observed). The measurements have been accomplished using a scanning fiber interferometer which is characterized by picosecond time resolution, picometer displacement resolution, and micrometer lateral resolution. We have been able to observe a cross-over, as a function of sample size, from a regime in which the magnetostrictive response is limited by eddy current damping, to one in which it limited by the longitudinal phonon velocity. In smaller particles we expect to observe a cross-over to a third regime in which the sample response is limited not by acoustic processes, but by the spin-lattice relaxation time. Our technique has sufficient resolution to observe the spatial and temporal non-

uniformities induced in response to a nonuniform penetrating magnetization. We have used our fiber-interferometry characterization of the dynamic magnetostriction in nickel to develop a novel technique for obtaining time resolution in scanning tunneling microscopy. The method, which is particularly suited to the study of phenomena which may be repetitively triggered, uses a magnetostrictive tip to modulate the tunneling distance between the sample surface and the tip. The most appealing feature of this approach is its generality: it is independent of specific sample properties, and is applicable to the time-resolved measurement of any information which can be obtained with the STM, including surface electronic, magnetic, and topographic effects, as well as the high speed characteristics of nanometer scale devices. In the present implementation, this technique has been demonstrated to provide temporal resolution in the nanosecond regime, and there is every indication that it will be straightforward to extend the method to significantly higher speeds. The ability to acquire information in the time domain adds unprecedented capabilities to the STM and offers a genuinely interesting technique for scientific and technological applications which require a localized probe having high resolution simultaneously in all *four* dimensions. Taken together, these experiments not only illustrate particular methods for both the investigation, and application, of micro-magnetic phenomena, but also demonstrate the more general promise of time-resolved scanning probe techniques.

ACKNOWLEDGMENT

We thank R. J. Gambino for static magnetization measurements.

[1] G. Binnig and H. Rohrer, IBM J. Res. Develop. **30**, 355 (1986) and references therein.
[2] See, for example, *AIP Conference Proceedings*, Vol. 241, edited by H. K. Wickramasinghe (American Institute of Physics, New York, 1991).
[3] R. J. Hamers and D. G. Cahill, J. Vac. Sci. Technol. B **9**, 514 (1991).
[4] A. S. Hou, F. Ho, and D. M. Bloom, Electron. Lett. **28**, 2302 (1992)
[5] G. Nunes, Jr. and M. R. Freeman, Science **262**, 1029 (1993).
[6] E. Betzig and J. K. Trautman, Science **257**, 189 (1992).
[7] M. R. Freeman and G. Nunes, Jr., Appl. Phys. Lett. **63**, 1200 (1993).
[8] M.R. Freeman and G. Nunes, Jr., Appl. Phys. Lett. **63**, 2633 (1993).
[9] E. W. Lee, Rep. Prog. Phys. **18**, 184 (1955).
[10] D. Rugar, H. J. Mamin, and P. Güthner, Appl. Phys. Lett. **55**, 2588 (1989).
[11] M. R. Freeman, R. R. Ruf, and R. J. Gambino, IEEE Trans. Magn. **27**, 4840 (1991).
[12] See, for example, A. E. Clark, in *Ferromagnetic Materials* (North-Holland, Amsterdam, 1980), Vol. 1, pp. 531–589.
[13] Nickel 270, annealed, from California Fine Wire, Grover City, CA. Used as received.
[14] *CRC Handbook* (Chemical Rubber, Cleveland, OH, 1975).
[15] C. Schönenberger and S. F. Alvarado, Z. Phys. B **80**, 373 (1990).

Magnetic resonance detection and imaging using force microscope techniques (invited)

O. Züger and D. Rugar
IBM Research Division, Almaden Research Center, 650 Harry Road, San Jose, California 95120-6099

We describe the principles and imaging characteristics of a new type of high resolution magnetic resonance microscopy. Magnetic resonance is detected by measuring a small oscillating magnetic force acting between the spins in a sample and a nearby ferromagnetic particle. The oscillating magnetic force is generated by polarizing the spins in the magnetic field and then modulating the sample magnetization using magnetic resonance techniques. The oscillating magnetic force is detected by sensing the angstrom-scale vibration of a micromechanical cantilever on which the sample is mounted. High spatial resolution is achieved as a result of the narrowness of the magnetic resonance spectral response and the large magnetic field gradient generated by the ferromagnetic particle. Electron paramagnetic resonance images are presented that demonstrate axial resolution on the order of 1 μm and lateral resolution on the order of 5 μm. Submicron resolution can be expected with straightforward technical improvements.

INTRODUCTION

Magnetic force microscopy[1–3] was originally developed to visualize the fields emanating from ferromagnetic samples. The technique has found numerous applications, including the mapping of bit patterns on magnetic and magneto-optical disks,[3–5] observing domain walls in soft magnetic materials,[6,7] measuring field distributions from recording heads,[1] and measuring the switching behavior of individual submicron magnetic particles.[8] One of the strengths of magnetic force microscopy is its great versatility. For example, magnetic force detection need not be restricted to the measurement of ferromagnetic phenomena. In principle, the technique is sensitive enough to detect much weaker magnetic effects, such as those due to electron or nuclear paramagnetism.

One particularly exciting possibility is the combination of magnetic force detection with magnetic resonance. Sidles[9,10] recently made the intriguing proposal that force detection of nuclear magnetic resonance (NMR) could be made sufficiently sensitive that signals from individual nuclear magnetic moments might be detectable. If this could be realized in practice, then molecules could be imaged in a chemically specific way with three-dimensional, subangstrom resolution. In the first experimental demonstration of magnetic force detection of magnetic resonance, Rugar *et al.*[11] detected an oscillating 10^{-14} N force while exciting and modulating electron spin resonance (ESR) in micrometer-size crystallites of diphenylpicrylhydrazil (DPPH).

The adaptation of magnetic resonance force detection for the purposes of electron spin resonance imaging was described in a previous paper.[12] We will refer to this technique as "magnetic resonance force microscopy" (MRFM). In the present paper, we discuss in a more complete manner the imaging principles and experimental methods. In contrast to other scanning probe microscopes, the magnetic resonance force microscope exhibits an unusual shell-like spatial response. In order to form an image that corresponds to the spin density of the sample, some type of image reconstruction technique must be applied to the measured data. High spatial resolution is achieved by virtue of the narrowness of the magnetic resonance spectral response and the large field gradient generated by a ferromagnetic tip. Even though this work is still in its early stages, the achieved 1-μm resolution is already superior to that previously achieved using the best conventional ESR imaging techniques.[13,14]

EXPERIMENT

The experimental apparatus of the magnetic resonance force microscope is shown schematically in Fig. 1. The paramagnetic test sample consisted of micrometer-size DPPH particles glued to the end of a micromechanical silicon nitride cantilever. The cantilever was approximately 200 μm in length with spring constant $k=0.05$ N/m.[15] The electron spins in the sample are polarized by the magnetic field B_t from the tip. In addition, the tip also produces the field gra-

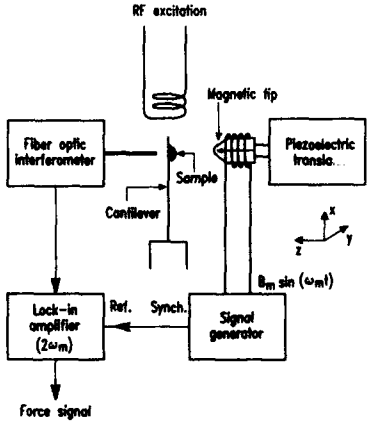

FIG. 1. Block diagram of the magnetic resonance force microscope.

 0021-8979/94/75(10)/6211/6/$6.00 © 1994 American Institute of Physics

dient needed to generate a measurable magnetic force and to provide spatial resolution for imaging. The magnetic tip consisted of a conical NdFeB permanent magnet magnetized along the axis of the cone. The size of the tip was typically 1 mm in length and 0.5 mm in diameter. The tip is mounted on a piezoelectric translator to allow mechanical scanning in any of three dimensions. The electron spins in the sample are resonantly excited by the radiofrequency (800–1610 MHz) magnetic field B_1 which is generated by a small coil (diameter 0.7 mm, 2.5 turns) located about 0.5 mm from the sample. A photograph of the key elements of the experimental apparatus is shown in Fig. 2.

Because the electron spin relaxation times at room temperature are very short compared to the time scale of the magnetic force detection, the cantilever responds only to the steady-state magnetization of the sample. In the presence of the rf field B_1, the steady state longitudinal magnetization in the sample is given by[16]

$$M_z=\chi_0 B_t-\frac{\chi_0 B_t\gamma^2\omega^2\tau^4 B_1^2}{[1+(\gamma B_t-\omega)^2\tau^2][1+(\gamma B_t+\omega)^2\tau^2]+\frac{1}{2}\gamma^2 B_1^2\tau^2(1+\omega^2\tau^2+\gamma^2 B_t^2\tau^2)}, \tag{1}$$

where χ_0 is the paramagnetic susceptibility, B_1 and ω are the amplitude and frequency of the rf field, γ is the gyromagnetic ratio (1.76×10^7 G^{-1} s^{-1} for electrons) and τ is the relaxation time. At room temperature, the susceptibility and the relaxation time for DPPH are $\chi_0=4.3\times10^{-6}$ (cgs units) and $\tau=6.2\times10^{-8}$ s, respectively.[17,18] The first term in Eq. (1) reflects the standard relation for a paramagnet in an external field. The second term is significant only in vicinity of the resonance field $B_t=B_0=\omega/\gamma$ and causes the magnetization M_z to be sharply suppressed at $B_t=B_0$. By supplementing the polarizing field B_t with a modulation field $B_m \sin\omega_m t$, a time varying magnetization $M_z(t)$ is created that has a substantial second harmonic component ($2\omega_m$) due to the nonlinearity of $M_z(B)$ in vicinity of the resonance field B_0. The modulation field is generated by an additional coil mounted concentric with the magnetic tip.

In the presence of the field gradient $\partial B_t/\partial z$, the z component of the magnetic force on the sample is given by

$$F_z=M_z(B_t)\frac{\partial B_t}{\partial z}V_s, \tag{2}$$

FIG. 2. Photograph of the key elements of the experimental apparatus. The labels denote: f: optical fiber of the interferometer, c: rf coil, t: permanent magnet tip, s: DPPH sample glued on the cantilever.

where V_s denotes the sample volume. Because the force F_z is linear in M_z, the second harmonic component of $M_z(t)$ induces a corresponding second harmonic force acting on the cantilever. For small modulation fields B_m, Eq. (2) can be expanded into a Taylor series and the resulting amplitude of the $2\omega_m$ component of the force per spin can be written as

$$f_z^{(2)}(B_t)=\frac{1}{4N}\frac{\partial^2 M_z}{\partial B^2}B_m^2\frac{\partial B_t}{\partial z}, \tag{3}$$

where N is the number of spins per unit volume ($N=2.3\times10^{21}$ spins/cm^3 for DPPH).

For a cantilever with a resonance frequency ω_c (~10 kHz), maximum force sensitivity is achieved by choosing $\omega_m=\omega_c/2$, so that the cantilever vibration is excited at resonance. The vibration amplitude is given by $A=(Q/k)F_z$, where Q is the quality factor and k is the spring constant. The cantilever vibration amplitude A was typically a few angstroms and was detected by a sensitive fiber-optic interferometer.[19] A high Q value is desirable in order to achieve good force sensitivity. By operating in vacuum ($p\simeq10^{-3}$ Torr) so as to eliminate air damping, Q values on the order of 2000 were obtained.

A theoretical second harmonic force response $f_z^{(2)}(B_t)$ is shown in Fig. 3(a). The force per spin was calculated from Eqs. (1) and (2) by using the second harmonic component of $M_z[B_t+B_m\sin(\omega_c t/2)]$ and the typical experimental conditions $\omega=2\pi\times822$ MHz, $B_1\simeq2$ G, $B_m=4$ G, and $\partial B_t/\partial z=-0.9$ G/μm. The force signal has a sharp peak at $B_t=B_0$ with a width ΔB of approximately 5 G, corresponding to the linewidth of the resonance. A measured force response curve for these experimental parameters is shown in Fig. 3(b). The sample consisted of a single DPPH particle with a diameter of $\simeq20$ μm and a thickness of $\simeq5$ μm. The polarizing field B_t at the sample was varied by scanning the magnetic tip in z direction. The range of the B field was calculated by multiplying the z scan range with the field gradient $\partial B_t/\partial z=-0.9$ G/μm.[20]

In the presence of the large field gradients $\partial B_t/\partial z$, the sharply peaked force response $f_z^{(2)}(B_t)$ confines the region where $B_t\simeq B_0$ to a thin layer of thickness $\Delta z\simeq\Delta B/|\partial B_t/\partial z|$. For a spatially extended sample, only those parts within this

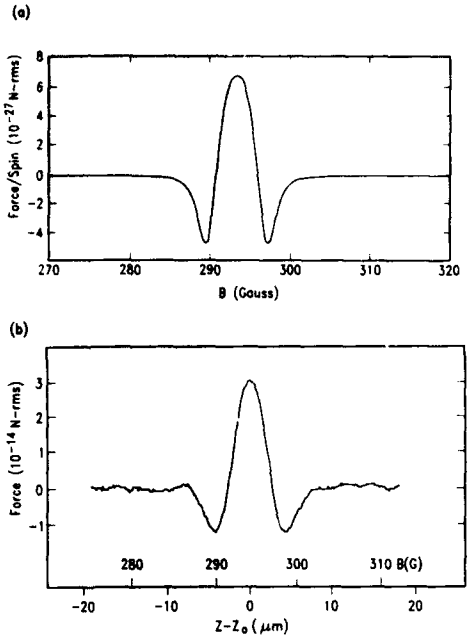

FIG. 3. (a) Calculated magnetic resonance force response $f_z^{(2)}(B_1)$. The curve shows the second harmonic amplitude of the force generated while exciting and modulating electron spin resonance in DPPH. The curve has been normalized to show root-mean-square force per unpaired electron spin. Assumed parameters are $\partial B_1/\partial z = -0.9$ G/μm, $B_1 = 2$ G, $B_m = 4$ G, $\omega = 2\pi \times 822$ MHz, relaxation times $\tau = 6.2\times10^{-8}$ s and temperature $T = 300$ K. Further details of the calculation may be found in Refs. 11 and 16. (b) Measured second harmonic force response F_z using the experimental parameters of (a). The magnetic field at the sample was varied by scanning the magnetic tip in z direction. The magnetic field range was obtained by multiplying the z scan range with the gradient $\partial B_1/\partial z = -0.9$ G/μm.

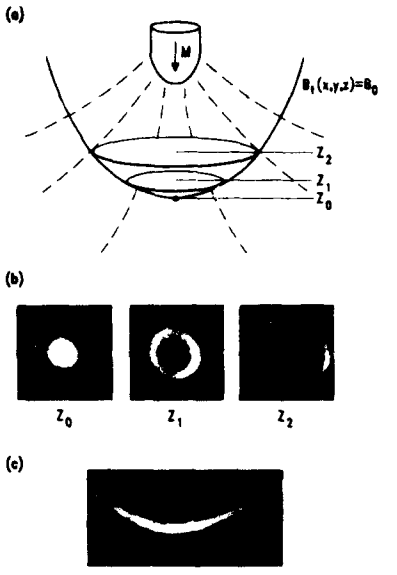

FIG. 4. (a) Dashed lines show magnetic field lines emanating from magnetic tip. Near the axis of the tip, the surface of constant magnetic field strength, $B_1(x,y,z) = B_0$, has a paraboloidal shape. In a scan plane at fixed distance z from the tip, the spins are resonantly excited only when the sample is located on the ringlike intersection between the plane and the paraboloid of constant field. The ring diameter depends on the z position of the plane. (b) Measured force maps for a small DPPH particle with the magnetic tip scanned in the x-y plane at three different z spacings: $z_0 \approx 200$ μm, $z_1 = z_0 - 4$ μm and $z_2 = z_0 - 12$ μm. Gray scale represents cantilever vibration amplitude, with white representing maximum amplitude. The image size is 200×200 μm^2. (c) Measured force map for the magnetic tip scanned in the x-z plane. The parabolic character of the tip field is clearly evident. The image size is 200×50 μm^2.

layer contribute to the force signal. Thus the sharpness of the response peak directly transforms into a spatial resolution determined by the linewidth ΔB and the spatial gradients of the magnetic field. This behavior allows spatial resolution to be considerably better than what one might otherwise expect based on the size and spacing of the magnetic tip.

MAGNETIC RESONANCE FORCE IMAGING

We now consider the imaging characteristics of the MRFM for a pointlike sample as it is scanned in the x-y plane at a fixed distance z relative to the tip. The pointlike sample will generate a significant oscillating magnetic force only when it is located in a region where the tip field is approximately B_0 (i.e., when the spins of the sample are resonantly excited). This condition is met on a surface of constant tip field defined by $B_1(x,y,z) = B_0$. For our tip geometry, the surface can be approximately described by a paraboloid whose apex is located along the axis of the tip at a distance from the tip that we define to be z_0 [see Fig. 4(a)]. The x-y scan plane will intersect the paraboloid in a circular ring if the scan plane is sufficiently close to the tip ($z \leq z_0$). We thus expect the response of the pointlike sample in the x-y plane to have a corresponding ringlike characteristic. The radius of the intersection decreases as the scan plane is moved away from the tip until, at a distance $z = z_0$, the intersection is only a single point at the apex of the paraboloid.

The above imaging behavior has been verified experimentally. Figure 4(b) shows force maps measured by scanning the magnetic tip in the x-y plane relative to the 20-μm size DPPH sample. Three different tip-sample distances were used: $z_0 \approx 200$ μm, $z_1 = z_0 - 4$ μm, and $z_2 = z_0 - 12$ μm. The size of the scanned area was 200×200 μm^2. The force maps show that for distances z_1 and z_2 the cantilever response signal is indeed confined to a circular ring, as expected. At the distance $z = z_0$, the ring collapses to a disk whose center corresponds to the apex of the paraboloid.

The paraboloidal shape of the constant field contours $B_1(x,y,z) = B_0$ from the magnetic tip can be directly imaged by scanning the tip in a plane perpendicular to the x-y plane. Figure 4(c) shows a x-z scan with a size of 200×50 μm^2.

The force maps of Figs. 4(b) and 4(c) can be used to quantitatively characterize the shape of the magnetic field from the tip. The tip field can be expanded in the vicinity of

the coordinate $(0,0,z_0)$ using the lowest order terms of the Taylor series. Because the ring shaped responses in Fig. 4(b) are almost circular, we assume rotational symmetry about the z axis and the expansion in cylindrical coordinates can be written as

$$B_z(z,r)=B_0+\frac{\partial B_z}{\partial z}\,(z-z_0)+\frac{1}{2}\frac{\partial^2 B_z}{\partial r^2}\,r^2, \tag{4a}$$

$$B_r(z,r)=\frac{\partial B_r}{\partial r}\,r. \tag{4b}$$

The expansion coefficients in these equations can be obtained as follows: The axial field gradient $\partial B_z/\partial z$ was determined by slightly shifting the rf frequency by $\delta\omega$ and measuring the change of the tip position δz required to maintain spin resonance. For the parameters used in Figs. 4(b) and 4(c), the axial gradient was $\partial B_z/\partial z=-1.7$ G/μm. The radial gradient $\partial B_r/\partial r$ in Eq. (4b) is related to $\partial B_z/\partial z$ through $\nabla\cdot\mathbf{B}_t=0$, yielding $\partial B_r/\partial r=-\frac{1}{2}\partial B_z/\partial z$. Finally, the second derivative $\partial^2 B_z/\partial r^2$ can be obtained from the shape of the paraboloid of constant field B_0 defined by the equation $\sqrt{B_z^2+B_r^2}=B_0$. With the expansions (4a) and (4b) for the field components B_z and B_r in this equation, the second derivative can be written (to lowest order) as

$$\frac{\partial^2 B_z}{\partial r^2}=-\frac{\partial B_z}{\partial z}\left(\frac{1}{4B_0}\frac{\partial B_z}{\partial z}+\kappa\right), \tag{5}$$

where κ is the curvature (inverse of the radius of curvature R) at the apex of the paraboloid. This parameter can be obtained from the parabolic shape of the response in the x-z plane of a pointlike sample. In Fig. 4(c), the curvature is $\kappa=-4.6\times10^{-3}$ μm^{-1} and, with the axial gradient $\partial B_z/\partial z=-1.7$ G/μm, we obtain then $\partial^2 B_z/\partial r^2=-1.0\times10^{-2}$ G/μm^2. This detailed knowledge of the tip field will prove to be useful for calculating the point-response function and the spatial resolution of the microscope.

To further illustrate the imaging characteristics of the MRFM, a more "complex" sample consisting of two 20-μm size DPPH particles separated by 35 μm was investigated. An optical micrograph of the sample is shown in Fig. 5(a). In order to achieve better spatial resolution and higher sensitivity, the rf frequency was increased to 1610 MHz, which corresponds to a spin resonance field of $B_0=575$ G. To achieve this field, the separation between the magnetic tip and sample was reduced to $z_0\approx130$ μm, resulting in the increased field gradients $\partial B_z/\partial z=-4.3$ G/μm and $\partial^2 B_z/\partial r^2=-2.5\times10^{-2}$ G/μm^2.

Figure 5(b) shows the force map measured at the distance $z=z_0-6$ μm. Two rings are evident, one from each particle. The distance between the centers of the rings is equal to the lateral spacing between the particles. The slightly different diameter of the rings arises from a small difference in the z position of the particles. The rings also exhibit different radial thicknesses, indicating that the two particles have slightly different lateral size.

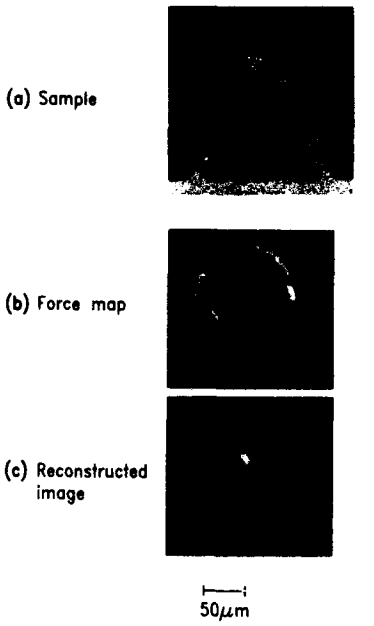

FIG. 5. (a) Optical micrograph showing two DPPH particles (~20 μm wide) attached to a silicon nitride cantilever. The distance between the particles is about 35 μm. (b) Magnetic resonance force map of the sample measured at a distance $z=z_0-6$ μm$\approx$124 μm. The data shown consists of a 128×128 pixel array which was acquired during a 90-min scan. (c) Reconstructed spin density image obtained by deconvolving the data in (b) using Wiener filtering technique. The two bright features correspond to the two DPPH particles. The large rings slightly visible in the image are artifacts of the deconvolution procedure.

IMAGE RECONSTRUCTION

To convert the ringlike force map into a real-space representation of spin density, we have developed a simple image reconstruction procedure using inverse filtering. The technique is based on the fact that the measured force map is essentially a superposition of the force responses from each volume element of the sample. For an extended sample described by the spin density distribution $N(x,y,z)$, the total magnetic force amplitude $F_z(x,y,z)$ for the magnetic tip located at (x,y,z) can be expressed by the convolution integral

$$F_z(x,y,z)=\int\int\int N(x',y',z')h(x-x',y-y',z-z')dx'\,dy'\,dz', \tag{6}$$

where $h(x,y,z)$ denotes the force response of a pointlike sample. Using the detailed knowledge of the tip field, the point response can be calculated from Eqs. (3) and (4), giving $h(x,y,z)=f_2^{(2)}[B_t(x,y,z)]$. From the measured force $F_z(x,y,z)$, the spin density $N(x,y,z)$ can then be reconstructed by using a deconvolution technique.

We demonstrate the reconstruction in two dimensions using the force map $F_z(x,y)$ of Fig. 5(b) and the point-response $h(x,y,z)$ calculated for the fixed distance z at which the force map was measured. For ease of implementation, we use a Wiener filtering technique.[21] The Fourier transform of the reconstructed spin density $N_R(x,y)$ can be calculated according to

$$\hat{N}_R = \frac{\hat{h}\hat{F}}{|\hat{h}|^2 + C}, \tag{7}$$

where $\hat{N}_R$, $\hat{F}_z$, and $\hat{h}$ are the complex-valued two-dimensional Fourier transforms of N_R, F_z, and h, respectively, and C is a constant that is adjusted according to the signal-to-noise ratio of the data.[21] The real space reconstructed image $N_R(x,y)$ is then found by the inverse Fourier transform of $\hat{N}_R$.

The result of the image reconstruction is shown in Fig. 5(c). Two spin density maxima are obtained with a separation of 35 μm, in agreement with the separation of the two DPPH particles in Fig. 5(a). Even the slight triangular shape of the lower particle in Fig. 5(a) is reproduced in the reconstructed image. Although the reconstruction presented here is confined to two dimensions, the extension to three dimensions is straightforward using a set of force maps measured at different z positions.

SPATIAL RESOLUTION

The spatial resolution of the microscope can be estimated from knowledge of the magnetic resonance linewidth ΔB and the gradient of the tip field. The resolution in the z direction is given by $\Delta z = \Delta B/|\partial B_t/\partial z|$, where the gradient $\partial B_t/\partial z$ is calculated on the paraboloid of constant field B_0. With Eqs. (4a) and (4b), the gradient on the paraboloid can be written as

$$\left|\frac{\partial B_t}{\partial z}\right|_{B_0} = \left(1 + \frac{(\partial B_z/\partial z)^3 (z - z_0)}{(\partial B_z/\partial z)^2 B_0 + 4B_0^2(\partial^2 B_z/\partial r^2)}\right)\left|\frac{\partial B_z}{\partial z}\right|. \tag{8}$$

For the parameters used in the experiment, the variation of the gradient $|\partial B_t/\partial z|_{B_0}$ for different z values is only minor. For the imaging conditions of Fig. 5(b) for example ($|z - z_0| = 6$ μm), the gradient is reduced by only $\simeq 2\%$ from the value of 4.3 G/μm at $z = z_0$. Thus the spatial resolution in z direction is almost constant on the paraboloid of constant field. For $\Delta B = 5$ G, the theoretical resolution $\Delta z = \Delta B/|\partial B_t/\partial z|_{B_0}$ in Fig. 5(b) is then 1.2 μm.

Experimental data supporting this theoretical estimate is shown in Fig. 6. The figure shows the force signal measured as the tip was scanned in the z direction. Two distinct resonance peaks are observed, corresponding to the two particles in Fig. 5(a). The width of each peak is approximately 2 μm. Since at least 1 μm of the observed width is due to the particle thickness, it is reasonable to conclude that the resolution in the z direction is approximately 1 μm. We believe that this resolution is at least five times better than has been achieved previously using conventional ESR imaging techniques.[13,14] Our higher resolution is a direct consequence of the large field gradient generated by the magnetic tip.

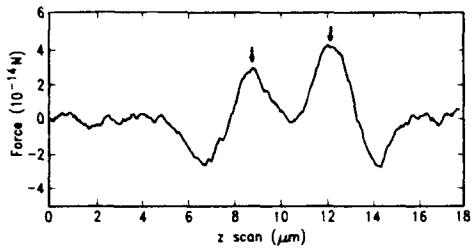

FIG. 6. Force measured as the tip was scanned in the z direction. The two positive peaks marked by arrows correspond to the two DPPH particles in Fig. 5. Spatial resolution can be estimated by the width of the observed features. Since the peaks are ~ 2 μm wide and the particles are at least 1 μm thick, the spatial resolution is 1 μm or better.

For the lateral resolution, two regimes have to be distinguished. In vicinity of the apex of the paraboloid ($z \simeq z_0$), the lateral field gradient $\partial B_t/\partial r$ vanishes and the resolution is determined by the curvature κ of the paraboloid. In this case, the resolution defined as the halfwidth of the spatial response of a point size sample is given by $\Delta x = \sqrt{4\Delta B/(\kappa \partial B_z/\partial z)}$. For the tip used in this experiment, the curvature was $\kappa = -4.0 \times 10^{-3}$ μm^{-1} and the lateral resolution for the linewidth $\Delta B = 5$ G would be $\Delta x \simeq 35$ μm. In the second regime, the sample intersects the paraboloid away from the apex (i.e., $z < z_0$) and the resolution is determined by the lateral field gradient $\partial B_t/\partial r$. The lateral resolution is then given by $\Delta x = \Delta B/|\partial B_t/\partial r|$, where $\partial B_t/\partial r$ is calculated on the paraboloid $B_t(x,y,z) = B_0$. With Eqs. (4a) and (4b), the lateral gradient on the paraboloid is given by

$$\left|\frac{\partial B_t}{\partial r}\right|_{B_0} = \sqrt{2\frac{\partial B_z}{\partial z}\left[\frac{\partial^2 B_z}{\partial r^2} + \frac{1}{4B_0}\left(\frac{\partial B_z}{\partial z}\right)^2\right]}\,|z - z_0|^{1/2}. \tag{9}$$

The lateral gradient increases for smaller z (i.e., larger ring diameter) and, as a consequence, the lateral resolution improves.

For the force map of Fig. 5(b) measured at $|z - z_0| = 6$ μm, the lateral field gradient calculated from Eq. (9) is $|\partial B_t/\partial r|_{B_0} = 0.95$ G/μm, giving a lateral resolution of $\Delta x = 5.3$ μm. The maximum achievable lateral resolution can be estimated by choosing $z = 0$ μm, i.e., when the tip is close to touching the sample during the x-y scan. For the experimental parameters used in Fig. 5(b), the limiting lateral resolution would be $\Delta x \simeq 1$ μm.

SENSITIVITY

The spin number sensitivity achieved in our experiment is limited only by the thermal vibration noise of the cantilever. The in-phase root-mean-square (rms) noise force detected with the lock-in amplifier is given by[10,22,23]

$$F_{\rm rms} = \sqrt{\frac{4k}{Q\omega_c}\, k_B T \Delta f}, \tag{10}$$

where k_B is the Bolzmann's constant, T is the temperature and Δf is the bandwidth of the measurement. For the 10 Hz detection bandwidth of the lock-in amplifier, the equivalent noise force for our cantilever was 3×10^{-15} N rms. For the experimental conditions used in Fig. 5, the signal contribution per spin was approximately 9×10^{-26} N rms, obtained from an equivalent calculation as in Fig. 3(a). Thus the number of spins required for unity signal-to-noise ratio is about 3×10^{10}. We note, however, that during the acquisition of the force map, each volume element in the sample is measured many times in the process of forming the final ring-shaped image pattern. In Fig. 5(b), for example, each volume element was sampled approximately 200 times (equal to the number of pixels on the circumference of the rings). Thus the signal-to-noise ratio in the reconstructed image was improved by $\sqrt{200}$ since each reconstructed data point is essentially the average of 200 independent measurements. The sensitivity achieved in Fig. 5(c) is, therefore, about $3 \times 10^{10}/\sqrt{200} \simeq 2 \times 10^9$ spins, equivalent to a 1 μm^3 volume of DPPH. Comparable spin number sensitivity has been achieved at a two order of magnitude higher polarizing field using a special microwave cavity detector.[14]

The force detection principle has one important advantage over conventional detection techniques, namely, the force signal per spin *increases* with higher spatial resolution. The reason for this unique behavior can be seen from Eq. (3): The magnetic force per spin $f_z^{(2)}$ is proportional to the field gradient $\partial B_t/\partial z$, which also determines the axial resolution by $\Delta z = \Delta B/|\partial B_t/\partial z|$. Thus Eq. (3) implies $f_z^{(2)} \propto \Delta z^{-1}$. This fact has an important consequence for microscopic applications: the detected magnetic force signal of the MRFM does not degrade in proportion to the cube of the spatial resolution, as in conventional magnetic resonance imaging, but only proportional to the square of the lateral resolution. This fact will be especially important in improving the spatial resolution of the instrument by using higher field gradients.

OUTLOOK

In the future, we expect that straightforward engineering improvements can dramatically enhance the performance of magnetic resonance force microscopy. Cantilevers with orders of magnitude lower stiffness can be readily fabricated with current micromechanical technology,[24] yielding significant improvement in spin sensitivity. Higher field gradients can be generated easily using smaller magnetic tips,[3,25] thus improving both spin sensitivity and spatial resolution. Lower temperatures and higher polarizing fields are additional parameters that can provide considerable performance enhancement. Although we don't yet know what resolution and sensitivity can ultimately be achieved, it is clear that we are still far from the theoretical and technological limits of this new technique.

ACKNOWLEDGMENTS

We thank C. S. Yannoni, J. A. Sidles, and H. M. Vieth for many stimulating discussions. One of us (O.Z.) gratefully acknowledges financial support by the Swiss National Science Foundation.

[1] Y. Martin and H. K. Wickramasinghe, Appl. Phys. Lett. **50**, 1455 (1987).
[2] J. J. Saenz, N. Garcia, P. Grütter, E. Meyer, H. Heinzelmann, R. Wiesendanger, L. Rosenthaler, H. R. Hidber, and H. J. Güntherodt, J. Appl. Phys. **62**, 4293 (1987).
[3] D. Rugar, H. J. Mamin, P. Guethner, S. E. Lambert, J. E. Stern, I. McFadyen, and T. Yogi, J. Appl. Phys. **68**, 1169 (1990).
[4] Y. Martin, D. Rugar, and H. K. Wickramasinghe, Appl. Phys. Lett. **52**, 244 (1988).
[5] H. J. Mamin, D. Rugar, J. E. Stern, B. D. Terris, and S. E. Lambert, Appl. Phys. Lett. **53**, 1563 (1988).
[6] H. J. Mamin, D. Rugar, J. E. Stern, R. E. Fontana, Jr., and P. Kasiraj, Appl. Phys. Lett. **53**, 318 (1989).
[7] U. Hartmann and C. Heiden, J. Microsc. **152**, 281 (1988).
[8] G. A. Gibson, J. F. Smyth, S. Schultz, and D. P. Kern, IEEE Trans. Magn. **27**, 5187 (1991).
[9] J. A. Sidles, Phys. Rev. Lett. **68**, 1124 (1992).
[10] J. A. Sidles, J. L. Garbini, and G. P. Drobny, Rev. Sci. Instrum. **63**, 3881 (1992).
[11] D. Rugar, C. S. Yannoni, and J. A. Sidles, Nature **360**, 563 (1992).
[12] O. Züger and D. Rugar, Appl. Phys. Lett. **63**, 2496 (1993).
[13] M. Ikeya, in *Magnetic Resonance Microscopy*, edited by B. Blümich and W. Kuhn (Plenum, Weinheim, 1992), pp. 133–149.
[14] A. I. Smirnov, O. G. Poluectov, and Y. S. Lebedev, J. Magn. Reson. **97**, 1 (1992).
[15] The cantilevers are commercially available from Park Scientific Instruments, Sunnyvale, California, or Digital Instruments Inc., Santa Barbara, California.
[16] M. A. Garstens and J. I. Kaplan, Phys. Rev. **99**, 459 (1955).
[17] A. van Itterbeek and M. Labro, Physica **30**, 157 (1964).
[18] G. Whitfield and A. G. Redfield, Phys. Rev. **106**, 918 (1957).
[19] D. Rugar, H. J. Mamin, and P. Guethner, Appl. Phys. Lett. **55**, 2588 (1989).
[20] The local field gradient from the magnetic tip was determined by slightly shifting the rf frequency by $\delta\omega$ and measuring the change of tip position δz required to maintain spin resonance.
[21] E. L. Hall, *Computer Image Processing and Recognition* (Academic, New York, 1979), pp. 214–239.
[22] U. Dürig, O. Züger, and A. Stalder, J. Appl. Phys. **72**, 1778 (1992).
[23] J. A. Sidles and D. Rugar, Phys. Rev. Lett. **70**, 3506 (1993).
[24] K. E. Petersen, Proc. IEEE **70**, 420 (1982).
[25] P. Grütter, D. Rugar, H. J. Mamin, G. Castillo, C.-J. Lin, I. R. McFadyen, R. M. Valetta, O. Wolter, T. Bayer, and J. Greschner, J. Appl. Phys. **69**, 5883 (1991).

Measurement of thermal switching of the magnetization of single domain particles (invited)

M. Lederman, D. R. Fredkin, R. O'Barr, and S. Schultz
Center for Magnetic Recording Research and Department of Physics, University of California, San Diego, 9500 Gilman Drive, La Jolla, California 92093-0319

M. Ozaki
Department of Chemistry, Yokohama City University, 22-2 Seto, Kanazawa-Ku, Yokohama 236, Japan

We present an experimental study of the thermally activated switching of the magnetization of individual isolated γ-Fe_2O_3 particles. These particles are prolate ellipsoids ~3000 Å long and 650 Å wide. The measured angular dependence of the switching field, $H_s(\theta)$, is consistent at large angles with a uniform rotation, but as θ approaches zero, other modes of reversal appear possible, and most likely the mode of reversal is curling. By measuring the probability of reversal of the moment as a function of time and applied magnetic field at $T \sim 300$ K, we found that the switching was thermally assisted, but couldn't be described by hopping over a single energy barrier. Our results indicate that the dynamics of switching are described by a complex path in the energy landscape.

INTRODUCTION

The problem of how a single domain ferromagnetic particle reverses its magnetization has interested scientists for over 40 years.[1] In addition to its scientific interest, a complete understanding of this phenomenon is now of considerable technological importance, in particular, for the magnetic recording industry. As recording densities increase, bit sizes decrease and, therefore, the individual grains (ferromagnetic particles) that form each bit have to be smaller. The question of their thermal stability (spontaneous switching) is now more relevant than ever before.

The first theory explaining the mechanism for reversal was proposed by Néel in 1949.[2] Since then, other theories have emerged,[3] but all contain similar physics. Namely, the idea that in $H=0$, a single domain particle has two equivalent ground states of opposite magnetization and separated by an energy barrier. If a magnetic field H is applied, the barrier decreases in height and, when H is larger than a threshold field H_s (switching field), thermal fluctuations are sufficient to overcome the barrier and the magnetization is reversed. Testing these ideas will be the main aspect of the work presented here.

I. MAGNETIC FORCE MICROSCOPY

This work was made possible by the development of magnetic force microscopy (MFM),[4] an instrument that is capable of detecting magnetic moments as low as 10^{-13} emu,[5] the typical moment of a single domain ferromagnetic particle. This instrument has also the spatial resolution to resolve such a small particle, typically, a fraction of a micron long. Therefore, this instrument with an *in situ* electromagnet is the ideal one for studying the physics of switching of the magnetization in the presence of a magnetic field.[6] A schematic diagram of the MFM is presented in Fig. 1. In our setup, the sample holder rotates around the z axis allowing measurements as a function of the angle between the magnetization easy axis and the direction of the field (see Sec. II). It also has a heater and a temperature control element that allows for temperature-dependent measurements above room temperature (see Secs. III and IV).

The MFM does not measure the magnetization, but instead detects the magnetic poles of the sample.[4] Thus, the MFM image of a single domain particle will correspond to both a North and a South pole. In a scale of gray plot, they appear as a white and a black dot respectively.[7] In Fig. 2(a), we present a MFM scan of 55 single domain permalloy particles[8] following the application of a field $H=650$ Oe in the $(-x)$ direction (see Fig. 1).[6] The position of one particle is highlighted. If the particle corresponding to the pair of black and white dots in the lower left corner is labeled (1,1), the highlighted particle is in position (2,4). Note that to its right, two particles are absent. That is how we unequivocally

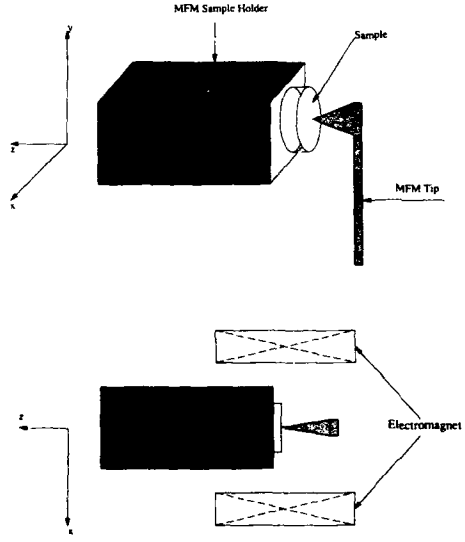

FIG. 1. Schematic diagram of the magnetic force microscope with an *in situ* electromagnet.

 0021-8979/94/75(10)/6217/6/$6.00 © 1994 American Institute of Physics

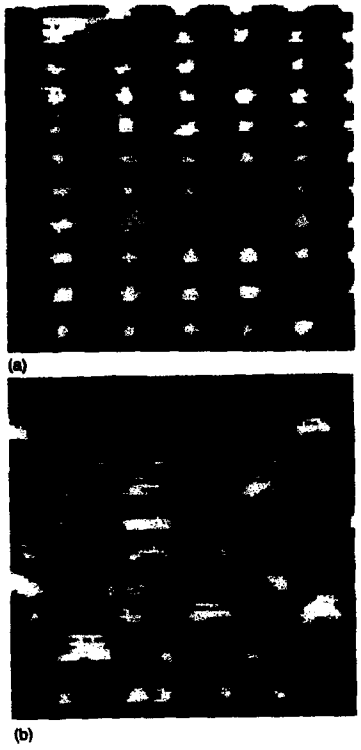

FIG. 2. (a) A 12 by 12 μm MFM scan of 55 single domain permalloy particles following the application of a field $H=-650$ Oe. The particle in position (2,4) is highlighted. (b) MFM scan of the same 55 particles as in (a) after applying a field $H=+425$ Oe. See text for discussion.

determine when a pair of dots correspond to the magnetic poles of a given particle. Note also that the South pole of all the particles is on their left-hand side. This means that the magnetic moment of all the particles points in the same direction.

In Fig. 2(b), we present a MFM scan of the same 55 particles after applying a field $H=425$ Oe in the $(+x)$ direction. Note that some particles have their South pole on the left and others on the right. Therefore, a field $H=650$ Oe is sufficient to polarize all the moments in the same direction, but a field $H=425$ Oe is not. This is an example of how the MFM can be used to measure the switching field H_s of a given particle. We will use this capability of the instrument in the next two sections

II. MODE OF REVERSAL OF THE MAGNETIZATION

In this section, we present a study of the mode of reversal of the magnetization of a single isolated particle of γ-Fe_2O_3. The particle is very close to a prolate ellipsoid 3000 Å long and 650 Å wide (see Fig. 3). A γ-Fe_2O_3 particle having these dimensions is in a single domain state and the magnetization is along its long axis. The particles were made by Ozaki *et al.* using a technique described in Ref. 9. We

FIG. 3. Transmission electron micrograph of the γ-Fe_2O_3 particle whose study is presented in this paper. Note that it is very close to a prolate ellipsoid 3000 Å long and 650 Å wide. The white dots correspond to voids in the volume.

separated them using the procedure of Salling *et al.*[10] and deposited them on a transmission electron microscope (TEM) grid. We used a TEM to fully characterize the shape of the particle as well as to position it in the grid. We then mounted the TEM grid with the particle attached to it (the particle "sits" on the plane of the grid) to a MFM sample holder. The holder is such that it can rotate around an axis (z axis) perpendicular to the plane of the TEM grid, refereed to as the $\{x,y\}$ plane (see Fig. 1). By rotating the holder, we effectively change the angle θ between the anisotropy axis of the particle and the direction of the applied magnetic field which is always along the x direction.

In this experiment, we used the MFM to determine the angular dependence of the switching field $H_s(\theta)$ of the particle shown in Fig. 3. By drawing a line through the two poles of the particle, we established the angle between the anisotropy axis of the particle and the direction of the magnetic field (see Fig. 4). The error in θ is $\pm 2°$, a relatively large one due to the relatively big size of the magnetic poles compared to their separation. The experiments were done at room temperature, $T\sim 23$ °C.

In order to determine $H_s(\theta)$, we used the following experimental procedure. Once the particle was unequivocally located in the grid, we moved the magnetic sensing tip (an electrochemically etched nickel wire) 12.5 μm away from the sample, so that the stray magnetic field it generates at the particle location is negligible (less than 10^{-2} Oe). We then applied a field of 1.5 kOe in the negative x direction (see Fig. 4), followed by a test field H applied for a time $t=1$ s in the positive x direction. The tip was then approached to the sample and a scan was made to determine whether the magnetization of the particle had reversed its direction or not.

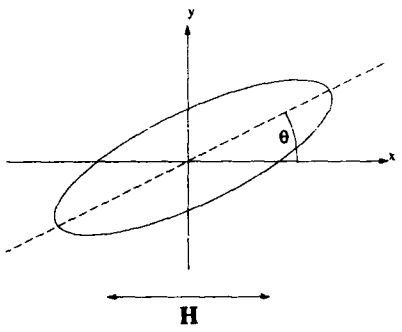

FIG. 4. Schematic representation of the angle between the magnetization easy axis and the direction of the applied field.

This was determined by establishing whether the magnetic poles of the particle had traded places or not. If the moment had not reversed, the applied test field H was raised by 8 Oe and the previous procedure was repeated (without applying the negative 1.5 kOe) until the strength of H was enough to reverse the direction of magnetization. The switching field was taken to be the mean value of the minimum field that would reverse the moment and the largest field that would not. The experiment was done only once per angle θ (the statistics of switching will be described later).

The experimental results of $H_s(\theta)$ for the particle shown in Fig. 3 are presented in Fig. 5. Our electromagnet is capable of applying fields up to 1634 Oe. When $\theta \sim 90°$, we could not reverse the moment of the particle, so $H_s(\theta \sim 90°) > 1634$ Oe. The solid line corresponds to the prediction by the Stoner–Wohlfart model of uniform rotation[11] for a particle having the same shape as ours and a saturation magnetization $M_s = 350$ emu/cm^3, a typical value of M_s for γ-Fe_2O_3. The experimental data shows excellent agreement with the uniform rotation prediction except perhaps around

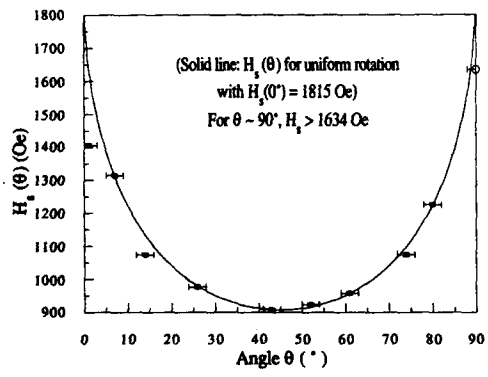

FIG. 5. Angular dependence of the switching field $H_s(\theta)$ of the γ-Fe_2O_3 particle shown in Fig. 3. The solid curve represents $H_s(\theta)$ predicted by Stoner–Wohlfart with the parameters given in the text.

$\theta \sim 0°$, a particularly difficult angle to obtain because excellent alignment is necessary[12] since the slope of H_s versus θ is very steep. Work in that regard is in progress.[13] This work confirms that at large angles, the switching occurs via uniform rotation of the magnetization, but as θ approaches 0°, the reversal may occur via curling.[14] Other recent theories also indicate that as θ tends to 0°, for the particular size of this particle, modes of reversal other than coherent rotation are very likely.[15] Besides the particle shown in Fig. 3, we did an identical study for another particle of the same batch and same dimension. Its $H_s(\theta)$ shows the same qualitative features, namely a minimum around $\theta \sim 45°$ and a maximum at $\theta = 0$ and 90° but $H_s(\theta)$ is not symmetrical around $\theta \sim 45°$, and it only fits well the prediction of Stoner–Wohlfart in an angle interval around 45°.[16] This indicates that the exact morphology of an individual particle may play a crucial role in the reversal process.

III. DYNAMICS OF THE REVERSAL PROCESS

Time-dependent effects have long been known to exist in a collection of single domain ferromagnetic particles.[1] The dynamics have been attributed to thermal activation,[2,17] which predicts that the probability $P(t)$ of the magnetization of the particle *not* to switch spontaneously due to thermal excitations decays exponentially with time,

$$P(t) = e^{-t/\tau} \tag{1}$$

with a characteristic time

$$\tau = \tau_0 e^{\Delta/k_B T}. \tag{2}$$

In Eq. (2), k_B is Boltzmann constant, T is the absolute temperature, τ_0 is a microscopic spin flipping time typically taken to be $\tau_0 = 10^{-10}$–10^{-9} s,[2,17] although it may strongly change with field H,[18] and Δ is the height of the energy barrier associated with the switching process. Δ is in particular a function of the characteristics of the particle (dimensions, anisotropy constants, etc.) and the external applied field H. In this study, we have changed H so as to reduce the height of Δ and make τ in Eq. (2) to fall in our experimentally available time frame, $0.1 \leq t \leq 100$ s.

Exponential time dependence has never been observed in collections of ferromagnetic particles.[1] Instead, the time dependence of, say, the magnetization (magnetic viscosity) follows a logarithmic decay over typically 2 decades in time.[1] This nonexponential behavior has been linked to the distribution of τ due to the distribution of particle sizes and shapes. Having a single isolated particle, we can now determine whether Eq. (1) is valid. In order to establish this experimentally, we carried out the following protocol at constant temperature $T = (30.0 \pm 0.05)$ °C:

(1) Move the tip away from the sample and apply 1.5 kOe in the negative x direction for 0.5 s so as to insure that the magnetization points in the direction of that large field. One second later a test field H is applied in the positive x direction for an amount of time t. The tip is then brought close to the sample and a scan is made to determine if the moment has NOT switched.

(2) The above procedure is repeated N times so as to collect statistics.

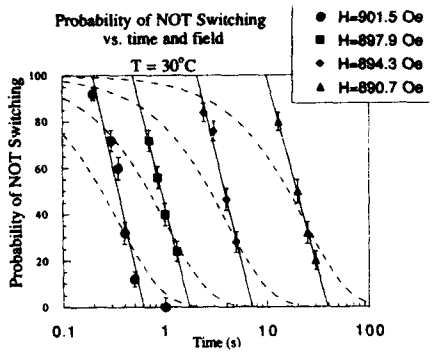

FIG. 6. Probability that the magnetization direction of the γ-Fe_2O_3 particle of Fig. 3 does *not* switch when a field H is applied for a time t. The field makes an angle $\theta \sim 45°$ with respect to the long axis of the particle. Four fields $H = 890.7$, 894.3, 897.9, and 901.5 Oe show finite $P(t)$ in the experimental time window $0.1 \leq t \leq 100$ s. The measurements were made at $T = (30.0 \pm .05)$ °C. The solid lines are guides to the eye for the four fields considered. The dashed lines correspond to $f(t) = e^{-t/\tau}$ where the τ are chosen to best fit the data. See text for a full discussion.

(3) The test field H is changed and the above two steps are repeated.

(4) The temperature T is changed and the above three steps are repeated.

In this experiment the angle between the field and the long axis of the particle is $\theta = 45°$. This angle was chosen because H_s is weakly angle dependent around $\theta = 45°$, and because the mode of reversal may be coherent rotation[11] (see Sec. II). The probability for the particle NOT to switch when a field H is applied for a time t, $P(H,t)$, is defined to be the number of times the particle did not switch divided by N. The number N in step 2 varied from 25 to 36 when $P(t,H)$ was around 50% to $N = 100$ when $P(t,H)$ was close to 0 or 100%. The results for $P(t)$ taken at four different fields $H = 890.7$, 894.3, 897.9, and 901.5 Oe, are shown in Fig. 6. They are plotted in semilog form where the time axis is the logarithmic one. Our results indicate the following:

(α) In the intermediate region, $20 \leq P(t) \leq 80\%$, the variation is linear i.e. logarithmic in time. In a previous report,[16] we show that as $P(t)$ approaches 0 and 100%, there is deviation from logarithmic behavior.

(β) The slope of the decay is constant as a function of magnetic field H. It has already been observed that, when $\theta \sim 7°$, the slope increases with increasing field. A similar result was obtained with a collection of particles were the magnetic viscosity is largest at coercivity;[20]

(γ) The magnetic field plays a very strong role in the dynamics. When the field is changed from 890.7 to 901.5 Oe, the time τ that corresponds to $P(t = \tau_{50\%}) = 50\%$ varies from $\tau \sim 18$ to 0.32 s, respectively. Thus a ~10.8-Oe change in applied field, that is a 1.2% change in H, causes the characteristic time for switching to change by ~5600%!

In order to check whether Eq. (1) is verified by our data, we draw in Fig. 6 a series of solid straight lines which should be considered as a guide to the eye. We superimpose in broken lines a best choice of $e^{-t/\tau}$ by adjusting τ. We remark that a good fit is not possible. Moreover, we note that:

$$\text{for } t \ll \tau, \quad P(t) > e^{-t/\tau}, \tag{3a}$$

$$\text{for } t \gg \tau, \quad P(t) < e^{-t/\tau}. \tag{3b}$$

As indicated previously, nonexponential time dependences are observed in a collection of ferromagnetic particles. The time dependence of, say the magnetization $M(t)$, has been described by

$$M(t) \propto \int_0^\infty P'(\tau) e^{-t/\tau} d\tau, \tag{4}$$

where $P'(\tau)$ is the normalized distribution of characteristic times τ associated with the distribution of particles. Eq. (4) simply represents the time dependence of the magnetization of particles relaxing independently due thermal activation. If the distribution $P'(\tau)$ is a continuous function of τ which has a mean $\tau = \tau_0$, then (see appendix)

$$\text{for } t \ll \tau_0, \quad M(t) < e^{-t/\tau_0}, \tag{5a}$$

$$\text{for } t \gg \tau_0, \quad M(t) > e^{-t/\tau_0}. \tag{5b}$$

This result is just the opposite of Eq. (3) which indicates that our data, not only cannot be represented by a simple exponential of the type $e^{-t/\tau}$ but, furthermore, cannot be described by the integral form $\int_0^\infty P'(\tau) e^{-t/\tau} d\tau$. The implication of this result is that for an ellipsoidal single domain particle of γ-Fe_2O_3 with some surface roughness and voids in the volume (see Fig. 3), the reversal of the magnetization is governed by a complex energy landscape and not by the naive picture of thermally hopping over a single energy barrier.[2,17] In that complex energy landscape, we envision the existence of many intermediate states such that the paths in configuration space to go from the initial to the final state are not independent of one another. Those intermediate states may be the consequence of many nucleation sites either on the surface or close to the voids present in the volume, but the true origin of the complexity of the dynamics is not clear at the present moment.

IV. TEMPERATURE DEPENDENT EFFECTS

In Section III, we show that the dynamics of the reversal process are not well described by a simple exponential $e^{-t/\tau}$. Therefore, from the data we cannot extract a true characteristic time τ. Therefore, we cannot test the validity of Eq. (2). Nevertheless, that equation should give a good idea of how the dynamics should slow down or speed up as the temperature is decreased or increased, respectively. So for example, if the characteristic time $\tau = 1$ s in that equation (that is a typical value in our experimentally accessible time interval), then Eq. (2) indicates that the height of the barrier is $\Delta \sim 23 k_B T$. Therefore, if a temperature change of 10 K at 300 K is made, one expects the characteristic time for reversal to vary from $\tau = 1$ s to $\tau = 0.46$ s. That is a change of approximately a factor of 2.

We tested this prediction by repeating the experiment of Sec. III at these two other temperatures, 40.0° and 50.0 °C. The results are presented in Figs. 7 and 8, respectively. At

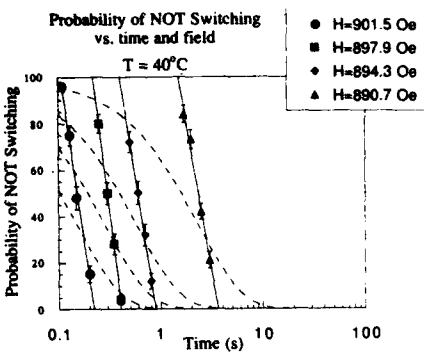

FIG. 7. Probability of the magnetization not switching when a field H is applied for a time t (same as Fig. 6) at a temperature $T=(40.0\pm.05)$ °C. The horizontal scale is the same as in Fig. 6 so as to better appreciate the effect of changing the temperature.

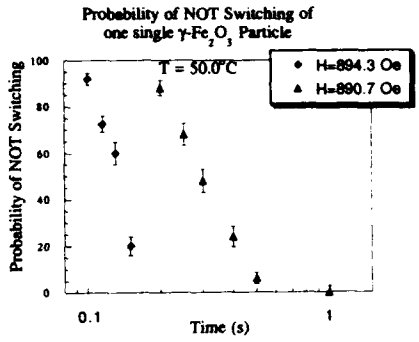

FIG. 8. Same plot as in Figs. 6 and 7 but at $T=(50.0\pm.05)$ °C. Only $H=890.7$ and 894.3 were considered. For $H=897.9$ and 901.5 Oe, the switching was to fast (faster than 0.1 s) for us to detect.

this two higher temperatures, the results of Sec. III are still valid. But the main result is that temperature variation of $\tau_{50\%}$, the time such that $P(t=\tau_{50\%})=50\%$, is much stronger than suggested by Eq. (2). For example, when $H=890.7$ Oe,

$$\tau_{50\%}(T=30.0\ ^\circ\text{C})\sim 18.5\ \text{s},$$

$$\tau_{50\%}(T=40.0\ ^\circ\text{C})\sim 2.3\ \text{s},$$

$$\tau_{50\%}(T=50.0\ ^\circ\text{C})\sim 0.3\ \text{s}.$$

That corresponds to a change of a factor of ~ 8 with a $\Delta T=10.0$ °C. This is four times more than what was suggested above. This is a further indication that the dynamics, although clearly thermally activated, are complex and not described by hopping over a single energy barrier.

V. CONCLUSION

The work presented here describes the reversal mechanism of an individual, isolated, single domain particle having an ellipsoidal shape. Its magnetic moment lies along the long axis of the prolate ellipsoid. Experimentally, it is an ideal candidate to determine whether the reversal of the magnetization occurs by thermally hopping over a single energy barrier, and whether that barrier corresponds to the one predicted by the Stoner–Wohlfart model (uniform rotation)[11] for reversal. This is important because those two ideas have been widely used in the past 40 years[3] to explain what is observed experimentally in a collection of particles. Further more, recently, those same ideas appear to be the starting point for analyzing the relaxation of very small magnetic particles at very low temperatures to try to establish the validity of macroscopic quantum tunneling (MQT) and macroscopic quantum coherence (MQC) in magnetic systems.[21]

Our results indicate that the switching of the magnetization of a single particle is not as simple as suggested above. In particular, the dynamics appear to be quite complex and, certainly, not described by thermal activation over a single energy barrier. Instead, a complex path in configuration space to go from the initial to the final state is most likely although the reason for this complexity is not clear at the present time. Although these experiments were performed at room temperature, we believe that as low temperatures are approached and MQT/MQC phenomena may take place, it is important to remember when designing an experiment that may look for MQT/MQC that the switching of the magnetization may not be described by tunneling through a single barrier.

ACKNOWLEDGMENTS

We would like to thank Dr. W. Chen for very stimulating conversations, Dr. G. A. Gibson for building the MFM, and G. Kassabian for building the excellent electronics necessary to do this study. This work was sponsored by the Center for Magnetic Recording Research, and by NSF grant DMR-90-10908.

APPENDIX

Let $M(t)=\int_0^\infty P'(\tau)e^{-t/\tau}\,d\tau=\int_0^\infty P'(\tau)f_t(\tau)\,d\tau$, with $f_t(\tau)=e^{-t/\tau}$, and $P'(\tau)$ is the distribution of τ with mean τ_0,

$$\int_0^\infty P'(\tau)d\tau=1, \tag{A1}$$

and

$$\int_0^\infty P'(\tau)\tau d\tau=\tau_0=\langle\tau\rangle. \tag{A2}$$

Therefore,

$$\langle f_t(\tau)\rangle=M(t) \tag{A3}$$

and

$$f_t(\langle\tau\rangle)=e^{-t/\tau_0}. \tag{A4}$$

If $f_t(\tau)$ is a *concave* function of $\tau[[\partial^2 f_t(\tau)/\partial^2\tau]>0]$ for any τ where $P(\tau)\neq 0$, then $\langle f_t(\tau)\rangle>f_t(\langle\tau\rangle)$. If $f_t(\tau)$ is a *convex* function of $\tau[[\partial^2 f_t(\tau)/\partial^2\tau]<0]$ for any τ where $P(\tau)\neq 0$, then $\langle f_t(\tau)\rangle<f_t(\langle\tau\rangle)$.

Since $f_t(\tau)$ is concave for $\tau < t/2$ and it is convex for $\tau > t/2$, then if the distribution $P(\tau)$ has a width small compared to t,

$$\text{for } t \ll \tau_0, \quad M(t) < e^{-t/\tau_0} \tag{A5}$$

and

$$\text{for } t \gg \tau_0, \quad M(t) > e^{-t/\tau_0}, \tag{A6}$$

which corresponds to Eq. (5a) and (5b) in the text.

[1] Recent reviews on the dynamics can be found in A. Aharoni, in *Studies of Magnetic Properties of Fine Particles and their Relevance to Materials Science*, edited by J. L. Dormann and D. Fiorani (Elsevier, New York, 1992); R. W. Chantrell, J. Magn. Magn. Mater. **95**, 365 (1991); P. Hänggi, P. Talkner, and M. Borkovec, Rev. Mod. Phys. **62**, 251 (1990).

[2] L. Néel, Ann. Géophys. **5**, 99 (1949).

[3] Recent research in the subject is presented in *Studies of Magnetic Properties of Fine Particles and their Relevance to Materials Science*, edited by J. L. Dormann and D. Fiorani (Elsevier, New York, 1992).

[4] Y. Martin and H. K. Wickramasinghe, Appl. Phys. Lett. **50**, 1455 (1987).

[5] G. A. Gibson and S. Schultz, J. Appl. Phys. **69**, 5877 (1991).

[6] M. Lederman, G. A. Gibson, and Schultz, J. Appl. Phys. **73**, 6961 (1993).

[7] G. A. Gibson, S. Schultz, J. F. Smyth, and D. P. Kern, IEEE Trans. Magn. **27**, 5000 (1991).

[8] J. F. Smyth, S. Schultz, D. R. Fredkin, T. R. Koehler, I. R. McFayden, D. P. Kern, and S. A. Rishton, J. Appl. Phys. **69**, 5262 (1991).

[9] M. Ozaki and E. Matijevic, J. Coll. Int. Sci. **107**, 199 (1985).

[10] C. Salling, S. Schultz, I. McFadyen, and M. Ozaki, IEEE Trans. Magn. **27**(6), (1991).

[11] E. C. Stoner and E. P. Wohlfart, Philos. Trans. Soc. London Ser. A **240**, 599 (1948).

[12] C. Salling, R. O'Barr, S. Schultz, and I. R. McFayden, J. Appl. Phys. (to be published).

[13] D. R. Fredkin, M. Lederman, and S. Schultz (in preparation).

[14] S. Shtrikman and D. Treves, J. Phys. (Paris) **20**, 286 (1959); and E. H. Frei, S. Shtrikman, and D. Treves, Phys. Rev. **106**, 446 (1957).

[15] H. B. Braun (private communication).

[16] M. Lederman and S. Schultz (submitted to Phys. Rev. Lett.).

[17] W. F. Brown, Phys. Rev. **130**, 1677 (1963).

[18] H. B. Braun, Phys. Rev. Lett. **71**, 3557 (1993).

[19] R. Street and J. C. Wooley, Proc. Phys. Soc. A **62**, 562 (1949).

[20] S. B. Oseroff, D. Franks, V. M. Tobin, and S. Schultz, IEEE Trans. Magn. **23**, 2871 (1987).

[21] P. C. E. Stamp, E. M. Chudnovsky, and B. Barbara, Int. J. Mod. Phys. B **6**, 1355 (1992).

AUTHOR INDEX

aan de Stegge, J.–(10) 6424, 6440
aan de Stegge, J. B. F.–(10) 6709
Abad, H.–(10) 5725
Abd-Elmeguid, M. M.–(10) 6741
Abdul-Razzaq, W.–(10) 6567
Abe, M.–(10) 6094, 6804, 7171
Abele, M. G.–(10) 6993
Abele, Manlio G.–(10) 6990
Abell, J. S.–(10) 5850
Abraham, M. M.–(10) 7030
Acet, M.–(10) 6069, 7012, 7015
Adams, C. P.–(10) 6318
Adly, A. A.–(10) 5502
Aguilar-Sahagun, G.–(10) 7000
Aharoni, Amikam–(10) 5891
Ahmad, M.–(10) 6190
Ahmed, M. Ramadan–(10) 6030
Akioka, K.–(10) 6631
Aktas, B.–(10) 6819
Alba, M.–(10) 5826
Alberts, H. L.–(10) 5665, 7149
Albrecht, A. S.–(10) 5535
Alexander, Chester, Jr.–(10) 6754
Algarabel, P. A.–(10) 6223
Ali, K. F.–(10) 6030
Ali, Naushad–(10) 7128, 7161
Allen, Gary A.–(10) 6372
Allibert, C. H.–(10) 6277
Allibert, Colette H.–(10) 6658
Almeida, B.–(10) 6551
Alper, M.–(10) 6543
Al-Sharif, A.-L.–(10) 6673
Altounian, Z.–(10) 5997, 6012, 6560, 7064
Amano, E.–(10) 6940, 7000
Amaral, V. S.–(10) 6513
Anders, A. G.–(10) 7186
Anker, J. F.–(10) 6178, 6193, 6498, 6692
Antropov, V. P.–(10) 6366
Aoi, H.–(10) 6400, 6890
Araga, K.–(10) 6918
Aragoneses, P.–(10) 6315
Arai, A.–(10) 6631
Araki, S.–(10) 6379
Argyle, B. E.–(10) 6782
Arnold, Z.–(10) 5662, 7158
Arnoldussen, T. C.–(10) 6773
Arnoldussen, Thomas C.–(10) 5762
Arons, R. R.–(10) 6602, 7050
Arrott, A. S.–(10) 5695, 5713, 7006
Arroyo, J. Carlos–(10) 5568
Artigas, M.–(10) 6577
Artman, J. O.–(10) 5879, 5882
Asada, H.–(10) 6086, 6089
Asano, H.–(10) 6283
Atkinson, R.–(10) 6783, 6861
Atkinson, Ron–(10) 6786
Attenborough, K.–(10) 6543
Atwater, H. A.–(10) 6516
Aulock, S.–(10) 6298, 6301
Avgin, I.–(10) 5517
Awano, Hiroyuki–(10) 6852, 6893
Awschalom, D. D.–(10) 6199
Ayers, J. D.–(10) 5801
Azevedo, A.–(10) 5613, 6763
Babanin, Vyacheslav F.–(10) 7182, 7183, 7184
Bach, H.–(10) 6069, 6072
Bacman, M.–(10) 6577
Bader, S. D.–(10) 6169, 6461, 7080
Baggio-Saitovitch, E.–(10) 6483, 6741, 6766
Bak, J.–(10) 5719
Balchin, M. J.–(10) 6987
Balentine, C. A.–(10) 6430
Ballantyne, Catherine C.–(10) 6959
Ballentine, C. A.–(10) 6427, 6429
Ballou, R.–(10) 6277
Banerjee, Subir K.–(10) 5925
Bao, Xiaohua–(10) 5870
Barandiarán, J. M.–(10) 6952
Barariu, Firuta–(10) 6949
Barbara, B.–(10) 5634, 6513
Barbara, Bernard–(10) 5642
Barlett, Darryl–(10) 6174
Barnard, J. A.–(10) 6930, 6934, 7067
Barnas, Jozef–(10) 6693
Barrom, Stacy–(10) 5578
Barrué, R.–(10) 6946
Barthélémy, A.–(10) 6412, 6623
Baryshev, V.–(10) 6543
Bass, J.–(10) 6699
Basso, V.–(10) 5677
Bauer, Gerrit E. W.–(10) 6704
Baumberg, J. J.–(10) 6199
Bayreuther, G.–(10) 6849
Beach, R. S.–(10) 6933
Beacom, T.–(10) 6723
Beauchamp, K. M.–(10) 6343
Bedrosian, G.–(10) 6027
Beers, K. L.–(10) 5940
Bellamy, B.–(10) 6623
Bellesis, George H.–(10) 6884
Bellouard, C.–(10) 5900
Belmans, Ronnie–(10) 6048, 6050
Belt, Roger F.–(10) 6363
Ben-Dor, L.–(10) 6720
Bennett, L. H.–(10) 5493
Bennett, W. R.–(10) 6144
Berger, A.–(10) 5598
Bergqvist, A.–(10) 5484, 5496
Berkowitz, A. E.–(10) 5562, 5639, 6097, 6613, 6622, 6912, 6933
Berry, S. D.–(10) 6124, 6688, 6691, 6692
Bertora, Franco–(10) 6990
Bertotti, G.–(10) 5490, 5677
Bertram, H. Neal–(10) 5765, 6385, 6779
Beyer, Adalbert–(10) 6049
Bhat, Sushma–(10) 7185
Bhushan, Bharat–(10) 5741, 5771, 6156
Bi, Y. J.–(10) 5850
Bian, X.–(10) 6534, 6554, 6560, 7064
Bie, Q. S.–(10) 6190
Bilic, D.–(10) 7073
Binek, C.–(10) 5856
Black, T. D.–(10) 6081
Blanco, J. M.–(10) 6315
Bland, J. A. C.–(10) 5586, 6458, 6501, 6508, 6528
Blevennec, Gilles Le–(10) 5647
Blumenfeld, L. A.–(10) 7183
Blunason, Cherie R.–(10) 5538
Blythe, H. J.–(10) 6100
Boardman, A. D.–(10) 5630, 5631, 6804, 6804
Boatner, L. A.–(10) 7030
Bochi, G.–(10) 6430
Bödeker, P.–(10) 6492
Bødker, F.–(10) 6583
Boer, F. R. de–(10) 6522
Bogomolov, S. S.–(10) 6430
Bojarczuk, Nestor–(10) 6871
Booth, J. G.–(10) 5630
Booth, K. M.–(10) 5630
Borchers, J. A.–(10) 6477, 6498, 6592, 6691, 6692
Bornfreund, R. E.–(10) 5740
Borsa, F.–(10) 7146
Bortz, E.–(10) 5882
Bounds, C. O.–(10) 6628
Boursier, D.–(10) 6577, 6682
Bouterfas, N.–(10) 6476
Bowden, G. J.–(10) 7120, 7122
Bowen, Arlen–(10) 5750
Boyle, J.–(10) 5630
Braga, M. E.–(10) 6551
Bramwell, S. T.–(10) 5523, 5955
Brandisky, Kostadin–(10) 6050
Brard, Isabelle–(10) 5647
Brataas, Arne–(10) 6704
Bray, Ashley–(10) 5578
Breuer, M.–(10) 6741
Brewer, E. G.–(10) 6637
Bröhl, K.–(10) 6184, 6492
Brooks, M. S. S.–(10) 6298, 6301
Broussard, P. R.–(10) 5595, 6679
Brown, L. M.–(10) 6501
Brown, P. J.–(10) 6816
Browning, V.–(10) 6610
Brubaker, W. W.–(10) 5529, 5940
Brück, E.–(10) 6522
Brunett, B.–(10) 5879
Brunsman, E. M.–(10) 5882
Bruyneraede, Y.–(10) 7079
Bunn, J.–(10) 6344
Buchholz, B.–(10) 7012
Büchner, B.–(10) 6741
Buckley, M. E.–(10) 6508
Bue, M. Lo–(10) 5677
Burke, E. R.–(10) 5756, 5759, 5910, 6891
Burkhardt, G. L.–(10) 5673
Buschow, K. H. J.–(10) 5994, 6247, 7117
Cable, J. W.–(10) 6601
Cabral, Cyril, Jr.–(10) 6909
Cadieu, F. J.–(10) 6006, 6009, 6286, 6640
Cadogan, J. M.–(10) 7114, 7120, 7122
Callaby, D. Roy–(10) 6843
Callaway, J.–(10) 7024, 7041
Cambliong, Horacio E.–(10) 6906, 7076
Cammarano, R.–(10) 5481
Cannell, P. Y.–(10) 5673
Cao, G.–(10) 6328, 6595
Cao, Lei–(10) 6250, 6253, 6256, 6259, 7111
Capehart, T. W.–(10) 7018
Carbucicchio, Massimo–(10) 5870
Cardoso, L. P.–(10) 6003
Carey, M. J.–(10) 6933
Carey, R.–(10) 6789, 7081, 7087
Cash, Andrew–(10) 6066
Castro, J.–(10) 6100
Cates, James C.–(10) 6754
Cava, R. J.–(10) 6603
Cavalleri, A.–(10) 5634
Cedell, T.–(10) 5656
Celinski, Z.–(10) 5583, 6187, 6473
Celotta, R. J.–(10) 6437, 6452
Cerdonio, M.–(10) 5634, 6996
Chaiken, A.–(10) 5808, 7073
Chandarlapaty, S.–(10) 5940
Chang, C. R.–(10) 5794
Chang, Ching-Ray–(10) 5487, 5499, 5505, 5897
Chang, Chung-Hee–(10) 6864
Chang, J. W.–(10) 5923
Chang, Thomas–(10) 5553
Chang, W. C.–(10) 6244
Chantrell, R. W.–(10) 5574
Chao, B. L.–(10) 5667
Chappert, C.–(10) 5807
Charap, Stanley H.–(10) 5768
Chardarlapaty, S.–(10) 5529
Charles, S. W.–(10) 6583
Charriere, F.–(10) 6623
Châtel, P. F. de–(10) 6522
Chattopadhyay, T.–(10) 6072, 6816
Che, Xiaodong–(10) 6779
Cheeks, T. L.–(10) 6665
Chen, Baoxing–(10) 6174
Chen, C. J.–(10) 5897, 6112
Chen, C. T.–(10) 5808, 5810, 6378
Chen, Christina H.–(10) 6760
Chen, F. R.–(10) 5888
Chen, Guan-mian–(10) 6293
Chen, H.–(10) 7041
Chen, J.–(10) 6828
Chen, J. P.–(10) 5876
Chen, L. H.–(10) 6915, 7052
Chen, M.–(10) 5628, 5629
Chen, Ming–(10) 6084
Chen, S. C.–(10) 5577
Chen, Shoan Chung–(10) 5797
Chen, X.–(10) 5997, 6012
Chen, Z. J.–(10) 5922, 6975
Cheney, S.–(10) 6828
Cheng, Song–(10) 5578
Cheng, Yuanda–(10) 6138, 6894
Cheong, B. K.–(10) 7093
Cheong, S.-W.–(10) 6723
Cheong, S-W.–(10) 6819
Cherenkov, Valery A.–(10) 6746
Cherepanov, V. B.–(10) 5610
Chernakova, Ana K.–(10) 6066

Chien, C. L.–(10) 5800
Chien, C.-L.–(10) 6489
Childress, J. R.–(10) 6412, 6623, 7061
Chin, Tsung-Shune–(10) 5888
Ching, W. Y.–(10) 6834, 7034
Chiriac, Horia–(10) 6949
Choi, Hyoung J.–(10) 5579
Choi, J. O.–(10) 5785
Choi, S. D.–(10) 6274, 6655
Choi, Y. S.–(10) 6937
Chou, T.–(10) 6379
Chow, Y. M.–(10) 5779
Chrisey, D. B.–(10) 5595, 6622
Chu, F.–(10) 6397
Chuang, D. S.–(10) 6427
Chuang, Y. C.–(10) 7117
Chubukov, Andrey V.–(10) 6345
Cinbis, C.–(10) 6763
Čingoski, Vlatko–(10) 6042
Cinquina, C. C.–(10) 5529
Cisneros, P.–(10) 6397
Clark, A. E.–(10) 5656
Clarke, Roy–(10) 6174
Clemens, Bruce M.–(10) 5644
Cochran, J. F.–(10) 6181, 6187, 6473
Cochrane, R.–(10) 6546
Cochrane, R. W.–(10) 6534, 6554, 6560, 7064
Cockcroft, J. K.–(10) 7050
Coehoorn, R.–(10) 6659
Coey, J. M. D.–(10) 6235, 6921
Coffey, G. A.–(10) 5940
Coffey, K. R.–(10) 5960, 6382, 7058
Cohenca, C. H.–(10) 6720
Coles, P. C.–(10) 6987
Collocott, S. J.–(10) 7114
Colucci, C. C.–(10) 6003
Conover, M. J.–(10) 6461, 7080
Continentino, M. A.–(10) 6734
Continenza, Alessandra–(10) 7027
Cooper, Bernard R.–(10) 7035
Cordone, S. S.–(10) 5610
Correia, Vanessa M.–(10) 5838
Corti, M.–(10) 7143, 7146
Costa, U. M. S.–(10) 5811
Cottam, M. G.–(10) 5823, 6443
Coverdale, G. N.–(10) 5574
Cowen, J. A.–(10) 6489
Cox, T. J.–(10) 5562
Cressoni, J. C.–(10) 5820, 5841
Cresswell, A.–(10) 6619
Crook, Elizabeth M.–(10) 5565
Crooker, B. C.–(10) 5731
Cross, R. W.–(10) 6400
Crow, J. E.–(10) 6328, 6595, 6748, 6812
Cuccoli, Alessandro–(10) 5814
Cullen, James R.–(10) 6475
Cunha, S. F.–(10) 6766

Daboo, C.–(10) 5586, 6458, 6528
Dagotto, Elbio–(10) 6340
Dahlberg, E. Dan–(10) 5475, 5776, 6567, 7073
Dahmen, Karin–(10) 5946
Daniel, D.–(10) 6921
Das, B. N.–(10) 6924
Das, Badri–(10) 6622
da Silva, B. L.–(10) 6563
da Silva, F. C. S.–(10) 5616
Dautais, M.–(10) 5707
Davies, K.–(10) 6583
Davis, R. L.–(10) 7114
Dawson, A. LeR.–(10) 6837
de Aguiar, F. M.–(10) 5613, 5616
de Albuquerque, Douglas F.–(10) 5832
de Boer, F. R.–(10) 6247, 7117
DeFotis, G. C.–(10) 5529, 5940
Defoug, S.–(10) 5707
De Graef, M.–(10) 5882
de Haan, S.–(10) 5508
de Jesus, J. C. O.–(10) 5520, 5862
de Jonge, W. J. M.–(10) 5728, 6440, 6709
Della Torre, E.–(10) 6106
Della Torre, Edward–(10) 5689, 5692, 5710, 6770
del Moral, A.–(10) 5662, 7158
del Moral, M. Ciria, A.–(10) 5850
den Broeder, F. J. A.–(10) 6424
Deng, Ming-Cheng–(10) 5888
de Oliveira, N. A.–(10) 6296
de Sousa, J. Ricardo–(10) 5835
De Ville, K.–(10) 6092
de Vries, J. J.–(10) 6440
Dewar, G.–(10) 5919
DeWeerdt, Robrecht–(10) 6050
Deymier, P. A.–(10) 5571
DiBari, R. C.–(10) 6124
Dieter Storzer, Hans–(10) 6049
Diggs, B.–(10) 5879
Ding, Juren–(10) 6150
Dingley, D.–(10) 6782
Dinia, A.–(10) 6548
Dionne, Gerald F.–(10) 6372
Di Pietro, C.–(10) 6039
Dissanayake, A.–(10) 5734
Djurberg, C.–(10) 5541
Dodge, J. S.–(10) 6872
Doi, T.–(10) 5907
Domański, Z.–(10) 5847
Dombrowski, R.–(10) 6054
Donner, W.–(10) 6421
Dormann, J. L.–(10) 5900
Dosanjh, P.–(10) 6334
dos Santos, R. J. V.–(10) 5820
dos Santos, Roberto J. V.–(10) 5838
Dou, S. X.–(10) 7120
Doyle, W. D.–(10) 5547, 5550, 5577, 6446
Driouch, L.–(10) 6309
Drucker, J. S.–(10) 5589, 5592
Drumheller, John E.–(10) 5952, 6081
Dube, D. C.–(10) 6744
Dufour, C.–(10) 6477
Duijn, V. H. M.–(10) 7117
Dumesnil, K.–(10) 6477
Dunham, D.–(10) 6890
Dunifer, G. L.–(10) 6190
Dunlop, J. B.–(10) 7114
Durand, O.–(10) 6412, 7061
Durin, G.–(10) 5490
Duvail, J. L.–(10) 6412, 7070

Eastham, J. F.–(10) 6987
Echer, C.–(10) 6900
Eckert, D.–(10) 6018
Edelstein, A. S.–(10) 6610
Edwards, G.–(10) 5873
Eggenkamp, P. J. T.–(10) 5728
Eibschutz, M.–(10) 6915
Elam, W. T.–(10) 5801, 6610
Eley, D. E. P.–(10) 5586
Elike, John–(10) 5578
Elkousabgy, N. M.–(10) 6039
Ellison, A. J. G.–(10) 6825
Elstner, N.–(10) 5943
Emerson, K.–(10) 5952
Engdahl, G.–(10) 5484, 5496
Engel, B. N.–(10) 6498
Engel, Brad N.–(10) 6401
Eppler, W. R.–(10) 7093
Epstein, A. J.–(10) 5782
Erata, Tomoki–(10) 5903
Erdös, P.–(10) 5847
Eremenko, V.–(10) 6744, 6805
Erickson, R. P.–(10) 6163
Ervin, A. M.–(10) 6610
Erwin, R. W.–(10) 6477, 6592, 6691, 6692
Escobar, M. A.–(10) 6946
Escorne, M.–(10) 6103
Evans, B. J.–(10) 5538, 6643
Everett, R. K.–(10) 6610
Everitt, B. A.–(10) 6592

Fagan, A.–(10) 6921
Fahlander, M.–(10) 5656
Falco, C. M.–(10) 6498
Falco, Charles M.–(10) 6401
Fan, Hong–(10) 5578
Farle, M.–(10) 5601, 5604
Farle, Michael–(10) 5644
Farrell, G. P.–(10) 6997
Farrow, R. F. C.–(10) 6900
Fauth, F.–(10) 6334
Favorski, I. A.–(10) 5823
Fawcett, E.–(10) 6321
Fedoseev, B.–(10) 6743
Fejer, M. M.–(10) 6872
Felder, R. J.–(10) 6124, 6603
Fernandez-Baca, J. A.–(10) 6060, 6603
Fernando, A. S.–(10) 6303
Fert, A.–(10) 6412, 6623, 7070
Fert, Albert–(10) 6693
Feutrill, E. H.–(10) 5701
Filippi, J.–(10) 6513
Filoti, G.–(10) 6586, 6813
Fisch, Ronald–(10) 5544
Fischer, P.–(10) 6331, 6337, 6743
Fishman, R. S.–(10) 6290
Fisk, Z.–(10) 6723, 6819
Fittipaldi, I. P.–(10) 5829, 5832, 5835
Flanders, P. J.–(10) 5547
Flanders, Philip J.–(10) 5931
Fleming, R. M.–(10) 6124, 7052
Flynn, C. P.–(10) 6592
Folks, L.–(10) 6271, 6634
Fomin, V.–(10) 6744
Fondado, A.–(10) 6723, 6819
Foss, S.–(10) 6892
Foss, Sheryl–(10) 5776
Fraga, E.–(10) 6952
Frattini, Paul L.–(10) 5579
Fredkin, D. R.–(10) 6217
Freeland, J. W.–(10) 6464
Freeman, A. J.–(10) 5802, 6409
Freeman, M. R.–(10) 6194, 6205
Freitas, P. P.–(10) 6449, 6480, 6551
Friedberg, S. A.–(10) 5529
Friedman, G.–(10) 5683
From, M.–(10) 6181, 6187
Fruchart, D.–(10) 5988, 6577
Fruchart, R.–(10) 6577
Fu, L. P.–(10) 5714, 5725
Fu, Y. W.–(10) 7152
Fuerst, C. D.–(10) 6015, 6625, 6637
Fujii, H.–(10) 6522
Fujimoto, T.–(10) 6528
Fujiwara, H.–(10) 7067
Fujiwara, Hideo–(10) 6446
Fujiwara, Y.–(10) 6415, 7102
Fullerton, Eric E.–(10) 6169, 6461, 7080
Furrer, A.–(10) 6331, 6334, 6337, 6743
Furuya, T.–(10) 6658
Futamoto, M.–(10) 6126

Gago-Sandoval, P. A.–(10) 6789
Galam, Serge–(10) 5526
Galtier, P.–(10) 6412
Gama, S.–(10) 6003
Gamachi, M.–(10) 6089
Gambino, R. J.–(10) 6909
Gambino, Richard J.–(10) 6871
Gandra, F. G.–(10) 7125
Ganguly, B.–(10) 5873
Gao, Y. H.–(10) 6238
Garanin, D.–(10) 5958
Garcia, N.–(10) 6580
Garcia-Orza, L.–(10) 5662
Garcia-Orza, L.–(10) 7158
Gardner, Richard A.–(10) 6138
Garifullin, I. A.–(10) 6492
Garshelis, I. J.–(10) 5670
Gautier, F.–(10) 6467
Gavrin, A.–(10) 6489
Gebel, B.–(10) 6018
Geerts, W.–(10) 6360
Gehring, P. M.–(10) 5959
Genoa, A.–(10) 6036
Genova, D. J.–(10) 6858
George, J.-M.–(10) 7061
Georges, Roland–(10) 5647
Geramimchuk, V. S.–(10) 6092
Geri, A.–(10) 6024, 6033
Gester, M.–(10) 5586, 6458, 6501
Giesbers, J. B.–(10) 6709
Gijs, M. A. M.–(10) 6709
Gillespie, D. J.–(10) 6610
Gingras, M. J. P.–(10) 5523
Girt, Er.–(10) 5997
Givord, D.–(10) 6682
Glebova, Irina N.–(10) 7182
Glijer, Pawel–(10) 6141, 6150
Godart, C.–(10) 7155
Goldman, A. I.–(10) 6366
Goldman, A. M.–(10) 6343, 6344
Goltsev, A. V.–(10) 6742, 6747
Gomes, A. A.–(10) 6296, 7125
Gomez, R. D.–(10) 5756, 5759, 5910, 6891
Gómez Polo, C.–(10) 5791
Gomi, M.–(10) 6804
Gong, Wei–(10) 6649
Gonzalez, A. C.–(10) 7137
González, J.–(10) 6315
Görlitz, D.–(10) 6054
Gorobets, Yu. I.–(10) 6092
Govindaraju, M. R.–(10) 6981
Grasso, Enzo–(10) 6960
Grandjean, F.–(10) 5994
Gratz, E.–(10) 6602
Gray, S. J.–(10) 5586, 6458
Greaves, S. J.–(10) 6849
Green, M. A.–(10) 6811
Gregg, J. F.–(10) 6921
Greig, D.–(10) 7055
Grieves, S.–(10) 6921
Grigereit, T. E.–(10) 5952
Grimes, Craig A.–(10) 6959
Grimsditch, M.–(10) 6169
Grosu, J.–(10) 6723
Grünberg, P.–(10) 6193
Grundy, P. J.–(10) 6861
Gu, B. X.–(10) 6955, 7099, 7103
Gu, E.–(10) 6501, 6528
Guillaume, M.–(10) 6331, 6334
Guillot, M.–(10) 5988, 6577, 6792
Galyaev, Yu. V.–(10) 5619
Gunther, Leon–(10) 5642
Guo, Hui-qun–(10) 6250, 6312
Guo, Yimin–(10) 6388
Guo, Zhenzhou–(10) 5710, 6770
Gupta, B. K.–(10) 6156
Gupta, L. C.–(10) 7155
Gurney, Bruce A.–(10) 7079
Guruswamy, Sivaraman–(10) 6607
Guthmiller, G.–(10) 6397
Gutierrez, C.–(10) 7073
Gutierrez, C. J.–(10) 6286, 7021

Gwan, P. B.–(10) 7114
Gyorgy, E. M.–(10) 6124, 6603, 7052

Ha, Min Yong–(10) 6078
Haas, S.–(10) 6748
Haas, Stephan–(10) 6340
Hadjipanayis, G. C.–(10) 5876, 5885, 6000, 6507, 6623, 6624, 6646, 6649, 6676
Hahn, C.–(10) 5782
Hahn, Song-yop–(10) 6045
Han, S. H.–(10) 5785
Hanna, S. M.–(10) 5625
Hanratty, C. M.–(10) 6861
Harbison, J. P.–(10) 6665
Hardner, H. T.–(10) 6531
Harford, M. Z.–(10) 7073
Harlioe, Peter S., III–(10) 6884
Harmon, B. N.–(10) 6366
Harp, G.–(10) 6890
Harper, J. M. E.–(10) 6909
Harrell, J. W.–(10) 5550
Harris, V. G.–(10) 5801, 6610, 6924
Hart, A.–(10) 5574
Hart, R.–(10) 6543
Hartl, M.–(10) 5958
Hasan, M. K.–(10) 6343
Hashim, I.–(10) 6516
Hastings, J. B.–(10) 5810
Hathaway, Kristi B.–(10) 6475
Hattori, K.–(10) 6415
Hatwar, T. K.–(10) 6858
Haushalter, Robert C.–(10) 5859
Havela, L.–(10) 6522
Hayano, S.–(10) 5904, 5907, 6887
Hayashi, Hidetaka–(10) 6153
Hayashi, K.–(10) 6540
Hayashi, M.–(10) 6360
He, Huahui–(10) 6795
He, L.–(10) 5547, 5577
He, P.–(10) 6495
He, Y.-L.–(10) 5580
Healy, S. D.–(10) 5589, 5592
Hedge, H.–(10) 6286
Hegde, H.–(10) 6006, 6009, 6640
Heim, K. R.–(10) 5589, 5592
Heinrich, B.–(10) 5583, 6181, 6187, 6473
Heitbrink, Axel–(10) 6049
Held, G.–(10) 5807
Hellman, F.–(10) 6870
Hembree, G. G.–(10) 5589, 5592
Hempel, K. A.–(10) 5981
Hendren, W. R.–(10) 6783
Hendriksen, P. V.–(10) 6583
Hennion, M.–(10) 5900
Henry, Y.–(10) 5601
Herbst, J. F.–(10) 6015, 6625
Hermsmeier, B.–(10) 6890
Hermsmeier, B. D.–(10) 5807
Hernando, A.–(10) 5791, 6952
Herr, A.–(10) 6921
Heuer, L. A.–(10) 5779
Hickox, R. J.–(10) 5586, 6458
Hickey, B. J.–(10) 6546, 7055
Hikosaka, Takashi–(10) 5774
Hill, E. W.–(10) 6997
Hilton, D.–(10) 6124
Hintz, M. B.–(10) 7084
Hirama, Y.–(10) 5904
Hirano, H.–(10) 5788
Hirayama, Yukihiro–(10) 5903
Hirota, K.–(10) 5959
Hisatake, K.–(10) 6321
Hisayama, Naoko–(10) 6162
Ho, G.–(10) 5808, 6378
Höchst, H.–(10) 6811
Hoff, C. N.–(10) 6489
Hofer, R.–(10) 6268
Holden, T. M.–(10) 6318
Holdsworth, P. C. W.–(10) 5955
Holody, P.–(10) 6699
Honda, Naoki–(10) 5984
Honda, Y.–(10) 6379
Honda, Yukio–(10) 6893
Horwitz, J.–(10) 6622
Horwitz, J. S.–(10) 5595
Hosaka, Sumio–(10) 6893
Hosoe, Y.–(10) 5978
Hossain, S.–(10) 7067
Hota, R. L.–(10) 5737
Howard, J. K.–(10) 5960, 6382, 7058
Howson, M. A.–(10) 6546
Hsieh, W. T.–(10) 6598
Hsih, C. S.–(10) 5577
Hsu, J. H.–(10) 6616
Hsu, Jen Hwa–(10) 7152
Hsu, T. C.–(10) 6063
Hu, B. P.–(10) 6226
Hu, Bo-Ping–(10) 6235
Hu, C.–(10) 6190
Hu, Ming–(10) 6256, 7111
Hu, Xiao–(10) 6486
Hu, Z.–(10) 6000
Huai, Y.–(10) 6534, 6554, 6560, 7064
Huang, C. C.–(10) 6344
Huang, D.–(10) 6351
Huang, F.–(10) 6406
Huang, H. B.–(10) 7099, 7103
Huang, H. L.–(10) 5794
Huang, Huei Li–(10) 5499, 5797, 7003
Huang, M. Q.–(10) 6280, 6574
Huang, Ming-Zhu–(10) 7034
Huang, Y. H.–(10) 6616
Huber, D. L.–(10) 5517
Huber, W. H.–(10) 6343
Huffman, G. P.–(10) 5873
Humphrey, F. B.–(10) 6958
Hurdequint, H.–(10) 6476
Hwang, D. M.–(10) 6665
Hylton, T. L.–(10) 5960, 6382, 7058

Ibarra, M. R.–(10) 5662, 6223, 7158
Ibrahim, M. M.–(10) 5873, 6822
Ido, H.–(10) 6283, 7140
Idzerda, Y. U.–(10) 5808, 5810, 6378, 6679
Il'yashenko, E. I.–(10) 7104
Imai, Yasuyuki–(10) 6162
Imura, Ryo–(10) 6893
Inaba, N.–(10) 6126
Indeck, R. S.–(10) 5753
Ingersent, Kevin–(10) 7051
Inglefield, H. E.–(10) 6430
Ings, John B.–(10) 6363
Inoue, A.–(10) 6306
Iramina, K.–(10) 7168
Irurieta, E.–(10) 6315
Irvine, J. T. S.–(10) 6940, 7000
Ishida, N.–(10) 5904, 5907
Ishikawa, A.–(10) 5978, 6890
Ishikawa, C.–(10) 6400
Ishikawa, Tomohiro–(10) 6446
Ismail, O.–(10) 5988
Israeloff, N. E.–(10) 6344
Itakura, A.–(10) 6769
Ito, T.–(10) 6283
Itoh, A.–(10) 6415
Itoh, Akiyoshi–(10) 7096
Itoh, Ikuo–(10) 6966
Itoh, N.–(10) 6801
Itoh, T.–(10) 6094, 7171
Ivanov, Alexander V.–(10) 7184
Ivanov, Alexandr V.–(10) 7183
Ivanov, Valery A.–(10) 6729
Ives, A. J. R.–(10) 5586, 6458
Iwasaka, M.–(10) 7162, 7165, 7174, 7177, 7181
Iwasaki, Shun-ichi–(10) 5984
Iwata, S.–(10) 6769, 7090, 7102

Jahnes, C. V.–(10) 5923
Jahnes, Christopher V.–(10) 6159
Jakubovics, J. P.–(10) 7009
Jankowska, J.–(10) 6321
Janssen, H. H. J. M.–(10) 6709
Janstrom, Thomas J.–(10) 5747
Japiassu, G. M.–(10) 6734
Jardim, R. F.–(10) 6720
Jarlborg, T.–(10) 6571, 7034
Jarratt, J.–(10) 7067
Jasmin, S.–(10) 6412
Jaswal, D. Welipitiya, S. S.–(10) 6303
Jaswal, S. S.–(10) 6346
Jatau, J. A.–(10) 6106
Jatau, James A.–(10) 6846
Jen, S. U.–(10) 5667
Jenniches, H.–(10) 7081
Jhon, Myung S.–(10) 5579, 5747, 6867
Jiang, H. X.–(10) 5734
Jiles, D. C.–(10) 5511, 5676, 5922, 6975, 6981
Jin, Q. Y.–(10) 6190
Jin, S.–(10) 6915, 7052
Jinfang, Liu–(10) 6289
Johnson, E. D.–(10) 5810
Johnson, M. T.–(10) 6424, 6440, 6659, 6709
Johnson, Mark–(10) 6714
Johnston, D. C.–(10) 6603
Jones, Barbara A.–(10) 7051
Jones, T. E.–(10) 6723, 6757
Jonker, B. T.–(10) 5714, 5719, 5725
Judy, Jack H.–(10) 5972, 6141, 6150
Jung, C.–(10) 5571
Jungblut, R.–(10) 6424, 6659

Kaatz, F. H.–(10) 6610
Kabos, P.–(10) 5632
Kachur, I.–(10) 6744, 6805
Kaczmarek, R.–(10) 5707
Kagawa, K.–(10) 6540
Kaiser, H.–(10) 6477
Kamada, O.–(10) 6801
Kameda, J.–(10) 6975
Kamijima, A.–(10) 6379
Kane, S. N.–(10) 6952
Kanematsu, Kazuo–(10) 7105
Kang, I. K.–(10) 5785, 6937, 6943
Kang, T.–(10) 6943
Kashere, D. G.–(10) 7024
Kano, H.–(10) 6540
Kao, C. C.–(10) 5810
Kapitulnik, A.–(10) 6872
Karis, Thomas E.–(10) 6867
Kartha, Sivan–(10) 5946
Karube, Hiro–(10) 6855
Kasai, Y.–(10) 6658
Kashyap, A.–(10) 6298
Kashyap, Arti–(10) 6301
Kästner, J.–(10) 6072
Katayama, T.–(10) 6360
Kawano, S.–(10) 6060
Kawazoe, Yoshiyuki–(10) 6486
Keavney, D. J.–(10) 6464
Kelly, David M.–(10) 6178, 7079
Kelly, Paul J.–(10) 6704
Kemmler-Sack, S.–(10) 6813
Kennedy, R. J.–(10) 6328
Keramidas, V. G.–(10) 6665
Kerch, H. M.–(10) 6840
Kido, G.–(10) 6283
Kikukawa, Atsushi–(10) 6893
Kim, Chul Sung–(10) 6078
Kim, H. J.–(10) 5785
Kim, Jun-o–(10) 6045
Kim, K. Y.–(10) 6943
Kiranmai, V.–(10) 7181
Kirby, R. D.–(10) 6346, 6348, 6418, 6495, 6670
Kirby, Roger D.–(10) 6507
Kirkpatrick, S.–(10) 5879, 588.
Kishio, K.–(10) 6322
Kita, E.–(10) 6455, 6531, 6918
Kita, Eiji–(10) 5903
Kitajima, T.–(10) 7174
Klabunde, K. J.–(10) 5876, 5885
Kleemann, W.–(10) 5856
Klein, L.–(10) 6322
Klein, V.–(10) 6813
Kleinefeld, Th.–(10) 7102
Klik, I.–(10) 5794, 5897
Klik, Ivo–(10) 5487, 5499, 5505
Klin, V. P.–(10) 7104
Knappmann, S.–(10) 5598
Ko, Heung Moon–(10) 6078
Kobayashi, O.–(10) 6631
Kodama, R. H.–(10) 5639
Koetzler, J.–(10) 5958, 6566
Koga, F.–(10) 5916
Koh, Chang Seop–(10) 6045
Koide, T.–(10) 5809
Koike, K.–(10) 6890
Koinkar, Vilas N.–(10) 5741
Kojuharoff, Victor I.–(10) 6972
Kolchin, A.–(10) 7024
Komai, Tomoko–(10) 5774
Kondoh, S.–(10) 6147
Kong, Lin-Shu–(10) 6250, 7111
Kong, Lin-shu–(10) 6253, 6256, 6259
Kono, Raymond-Noel–(10) 6867
Koon, N. C.–(10) 6622, 6924
Kopeć, T. K.–(10) 5847
Koranda, S.–(10) 6890
Korman, Can E.–(10) 5478
Kos, A. B.–(10) 6400
Kotru, P. N.–(10) 7185
Kötzler, J.–(10) 6054
Kouvel, J. S.–(10) 5683, 6343
Koyama, N.–(10) 6400
Krajewski, J. E.–(10) 6603
Kraus, L.–(10) 6952
Krause, R. F.–(10) 6646, 6649
Krebs, J. J.–(10) 6688, 7073
Krishnan, Kannan M.–(10) 6900
Krishnan, R.–(10) 6309, 6607
Krumhansl, James A.–(10) 5946
Kryder, M. H.–(10) 5966, 6391, 6394, 6763, 7093
Kryder, Mark H.–(10) 6864
Ktitorov, Sergey A.–(10) 6745
Kumar, Bijoy Kumar–(10) 6115
Kübler, J.–(10) 7033
Kubrakov, Nikolai F.–(10) 6786
Kuga, Kiyoshi–(10) 5987
Kulakowski, K.–(10) 6315
Kumar, Binod–(10) 6760
Kumar, Sudha–(10) 6169
Kunkel, H. P.–(10) 6510, 7108
Kuo, P. C.–(10) 5577, 6244
Kurashina, Seiji–(10) 7096
Kusheuer, J.–(10) 5856
Kuwabara, Masago–(10) 6153
Kuznietz, Moshe–(10) 7134
Kwon, H. J.–(10) 6109
Kwun, H.–(10) 5673

Lacerda, F.–(10) 5829
Lai, W. Y.–(10) 6226
Lai, Wuyan–(10) 6504
Lam, Irene–(10) 6138

Lambeth, D. N.–(10) 6132
Lambeth, David N.–(10) 6884
Landee, C. P.–(10) 5535
Lane, Alan M.–(10) 5578
Lane, L.–(10) 6397
Lang, J. C.–(10) 6366
Langman, R. A.–(10) 5673
Larica, C.–(10) 6766
Larionov, M.–(10) 6741
La Rosa, M.–(10) 6033
Lascialfari, A.–(10) 7143
Lashmore, D. S.–(10) 6543
Lassri, H.–(10) 6309, 6607
Latha, K.–(10) 6118
Laughlin, D. E.–(10) 5966, 7093
Laulicht, I.–(10) 5607
Lawson, A. C.–(10) 6589
Leal, C. E.–(10) 6737
Leal, J. L.–(10) 6449, 6480
Lectard, E.–(10) 6277
Lectard, Eric–(10) 6658
Lederman, M.–(10) 6217
Lee, Heung Soo–(10) 6078
Lee, J.–(10) 5487, 5505
Lee, J. -G.–(10) 7006
Lee, J.-G.–(10) 5713
Lee, J. J.–(10) 5785
Lee, J. S.–(10) 6943
Lee, K. C.–(10) 6598
Lee, K. H.–(10) 5913
Lee, K. M.–(10) 5876
Lee, R. E.–(10) 6397
Lee, S. F.–(10) 6699
Lee, S. R.–(10) 6169
Lee, S. T.–(10) 5714
Lee, Sang Youl–(10) 6078
Lee, W. T.–(10) 6477
Lee, W. Y.–(10) 6274, 6655
Lee, Y. H.–(10) 5913
Lefakis, Harry–(10) 7079
Le Gall, H.–(10) 6103
Legros, W.–(10) 6036
Lenczowski, S. K. J.–(10) 6709
Leslie-Pelecky, D. L.–(10) 6489
Levy, M.–(10) 6286
Levy, Peter M.–(10) 6906, 7076
Lewis, V. G.–(10) 6927
Lewis, W. A.–(10) 5604
Lewis, William A.–(10) 5644
Li, D.–(10) 5844
Li, Hong-Shuo–(10) 7114, 7120, 7122
Li, L. X.–(10) 5734
Li, Shuxiang–(10) 6504
Li, W. Z.–(10) 6238
Li, W-H.–(10) 6598
Li, Yuet–(10) 6394
Li, Z. G.–(10) 6624
Lian, F. Z.–(10) 6289
Liang, Y. L.–(10) 6628
Liao, L. X.–(10) 6181, 6187
Liao, Simon H.–(10) 5800
Licci, F.–(10) 7143, 7185
Liew, Y.-F.–(10) 5580
Lim, S. H.–(10) 6937
Lin, C. H.–(10) 5577
Lin, Gang Herbert–(10) 5765
Lin, H.-J.–(10) 5808, 6378
Lin, H. Q.–(10) 7041
Lin, Jiang-Ching–(10) 5897
Lin, Ming-xi–(10) 6293
Lin, W. G.–(10) 6238, 6241
Lin, X.–(10) 6676
Lind, D. M.–(10) 6124, 6688, 6691, 6692
Linderoth, S.–(10) 6583
Linderoth, Sørea–(10) 5867
Ling, Ji-wu–(10) 6293
Liu, C. J.–(10) 6244
Liu, C. S.–(10) 6112
Liu, F. H.–(10) 6391, 6394
Liu, G. C.–(10) 6226
Liu, G. K.–(10) 7030
Liu, H. K.–(10) 7120
Liu, J.–(10) 6624
Liu, J. P.–(10) 6247
Liu, J. Z.–(10) 6344
Liu, Jian-Min–(10) 6751
Liu, L.–(10) 5683
Liu, S. H.–(10) 6290
Liu, W. L.–(10) 6628
Liu, X.–(10) 7021
Lo, C. C. H.–(10) 7009
Lo, J.–(10) 6397
Lochner, E.–(10) 6124, 6688, 6691, 6692
Lodder, J. C.–(10) 5508
Loewenhaupt, M.–(10) 6602
Loloee, R.–(10) 6699
Long, Gary J.–(10) 5994
Loong, C.-K.–(10) 6825, 7030
López-Quintela, M. A.–(10) 6757
Lorentz, Robert D.–(10) 6843
Lottis, D. K.–(10) 5475, 7070
Lu, Jing Ju–(10) 5499
Lu, M.–(10) 6190, 7099, 7103
Lu, Pu-Ling–(10) 5768
Lubitz, P.–(10) 5595, 7073
Lukin, J. A.–(10) 5529
Luo, C. P.–(10) 6351
Lussier, J-G.–(10) 6063
Lyberatos, A.–(10) 5704
Lynn, J. W.–(10) 6069, 6072, 6589, 6598, 6806

Ma, B. M.–(10) 6628
Ma, H.–(10) 6510
Maccio, M.–(10) 6431
Machado, F. L. A.–(10) 5862, 6563
MacLaren, J. M.–(10) 6428
Madabhushi, R.–(10) 5759
Maeda, K.–(10) 6321
Maekawa, M.–(10) 5559
Magni, A.–(10) 5490
Mahia, J.–(10) 6757
Majetich, S. A.–(10) 5879, 5882
Majkrzak, C. F.–(10) 6178
Majkrzak, C. F.–(10) 5959, 6193, 6498
Mak, Chee-leung–(10) 5719
Maley, C.–(10) 6723
Mangin, Ph.–(10) 6477
Mankey, G. J.–(10) 6406
Mao, Ming–(10) 6534
Maple, M. B.–(10) 5639, 6720
Marchal, G.–(10) 6477
Margarian, A.–(10) 7114
Margulies, D. T.–(10) 6097
Marinova, I.–(10) 5904, 5907, 6887
Marks, R. F.–(10) 6900
Marquina, C.–(10) 5662, 7158
Marshall, J. H.–(10) 6124
Martinez, D.–(10) 6100
Martins, C. S.–(10) 6563
Maruti, Sanchit–(10) 5949
Marx, Chr.–(10) 6054
Maslennikov, Yu. V.–(10) 6996
Masson, A.–(10) 6623
Mather, S. C.–(10) 6744
Matson, M. E.–(10) 5475
Matsubara, I.–(10) 6321
Matsuda, Y.–(10) 6126
Matsumoto, Mitsunori–(10) 5969
Matsumura, Kunihiko–(10) 6855
Matsushita, N.–(10) 5975, 7131
Matsuyama, H.–(10) 6890
Matsuyama, K.–(10) 6086, 6089
Mattson, J. E.–(10) 6169, 6461, 7080
Mattsson, J.–(10) 5541
Mauger, Alain–(10) 5526
Maury, Claire–(10) 6658
Mayergoyz, I. D.–(10) 5686, 5756, 5759, 5910, 6027, 6891, 6963
Mayergoyz, Isaak D.–(10) 5478
Mazumdar, Chandan–(10) 7155
McCormick, P. G.–(10) 5481, 5701, 6634
McGuire, T. R.–(10) 6537, 6909
McHenry, M. E.–(10) 5879, 5882
McMichael, R. D.–(10) 5493, 5650, 5689, 5692
Meckenstock, R.–(10) 6492, 6508
Medina, A. N.–(10) 7125
Meigs, G.–(10) 5808, 6378
Melamud, Mordechai–(10) 7134
Melo, L. V.–(10) 6480, 6551
Merlin, Roberto–(10) 6340
Mesot, J.–(10) 6334
Messer, M. T.–(10) 6870
Metoki, N.–(10) 6421
Metzger, Robert M.–(10) 5870
Meys, B.–(10) 6036
Miao, Y. Z.–(10) 6190, 7099, 7103
Mibu, K.–(10) 6483
Micklitz, H.–(10) 6741
Micski, Anders–(10) 6265
Midelfort, K.–(10) 5882
Migliori, A.–(10) 6625
Milham, Clive D.–(10) 5659
Miller, B. H.–(10) 6567
Miller, Joel S.–(10) 5782
Miller, L. L.–(10) 7146
Miller, M. S.–(10) 5779
Min, Tai–(10) 6129
Minemoto, H.–(10) 6801
Miotkowski, I.–(10) 5731
Mira, J.–(10) 6757
Miraglia, S.–(10) 5988
Mirebeau, I.–(10) 5900
Mirzamaani, Mohammad–(10) 6159
Mishra, R. K.–(10) 7018
Mishra, Raja K.–(10) 6652
Mishra, S.–(10) 5994
Misra, P. K.–(10) 5737
Mitchell, J. R.–(10) 6912
Miyajima, Hideki–(10) 5903, 7161
Miyamoto, Yasuyoshi–(10) 6525
Miyamura, M.–(10) 6147
Miyauchi, D.–(10) 6379
Moghadam, A.–(10) 5630
Mohammed, Osama A.–(10) 6045
Monachesi, Patrizia–(10) 7027
Montarroyos, E.–(10) 5862
Montenegro, F. C.–(10) 5520, 5862
Moorthy, V. N.–(10) 6740
Moreira, J. M.–(10) 6513
Morel, R.–(10) 6623
Moreland, John–(10) 6878
Mori, T.–(10) 6769
Morin, B. G.–(10) 5782
Morisako, Akimitsu–(10) 5969
Morisue, T.–(10) 6969
Morita, Osamu–(10) 6162
Moroni, E. G.–(10) 6571, 7034
Morrish, A. H.–(10) 5556
Mørup, S.–(10) 6583
Moskowitz, B.–(10) 6892
Moskowitz, Bruce–(10) 5894
Moustafa, Ibrahim–(10) 6030
Muir, W. B.–(10) 6534
Müller, Gerhard–(10) 5937, 6057, 6751
Müller, K.-H.–(10) 6018
Muller, M. W.–(10) 5753
Muñoz, M. C.–(10) 6470
Murayama, A.–(10) 6147
Musa, S. O.–(10) 6546
Nagai, N.–(10) 5559
Nagamine, L. C. C. M.–(10) 6223
Nagarajan, R.–(10) 7155
Naik, R.–(10) 6190
Nakada, Masafumi–(10) 6855
Nakagawa, K.–(10) 6415
Nakagawa, Katsuji–(10) 7096
Nakagawa, S.–(10) 5975, 7131
Nakagawa, Shigeki–(10) 6525, 6568
Nakamura, A.–(10) 6126
Nakamura, Yoshihisa–(10) 6776
Nakanishi, Hiroaki–(10) 5969
Nakotte, H.–(10) 6522, 6589
Nanjo, M.–(10) 7140
Naoe, M.–(10) 5975, 7131
Naoe, Masahiko–(10) 5969, 5987, 6357, 6509, 6525, 6568
Narlikar, Anant V.–(10) 6740
Narumiya, Y.–(10) 6379
Nash, J. M.–(10) 5629
Nautiyal, T.–(10) 6298
Navarathna, A.–(10) 6006, 6009
Navas, C.–(10) 5535
Nedkov, I.–(10) 6726
Need, Omar U.–(10) 7079
Newman, D. M.–(10) 6789, 7081, 7087
Ng, D. H. L.–(10) 7009
Niarchos, D.–(10) 5853, 6232
Nichols, D. H.–(10) 6328
Nicklow, R. M.–(10) 6060
Nickolsky, A. D.–(10) 7104
Nicolaides, G. K.–(10) 5853, 6306
Nicolet, A.–(10) 6036
Nikitov, S. A.–(10) 5630, 5631
Nikles, David E.–(10) 5565, 5578
Ning, Tai-shan–(10) 6250, 6256
Nishio, T.–(10) 6658
Noakes, D. R.–(10) 6321
Noguchi, K.–(10) 6379
Nogués, J.–(10) 5862
Nogues, M.–(10) 5826
Noh, T. H.–(10) 6937, 6943
Nolan, T.–(10) 6144
Noma, K.–(10) 5975, 7131
Nordblad, P.–(10) 5541
Nori, Franco–(10) 6340
Nuhfer, N. T.–(10) 5879
Numazawa, Junji–(10) 5987
Nunes, Jr., G.–(10) 6205
Nunzio, S. Di–(10) 6184
Nývlt, M.–(10) 6783

O'Barr, R.–(10) 6217
Ober, R.–(10) 5900
Obermyer, R. T.–(10) 6262, 6574
O'Brien, W.–(10) 6811
O'Bryan, H., Jr.–(10) 6124
O'Connor, Charles J.–(10) 5859
Oepen, H. P.–(10) 5598
O'Grady, K.–(10) 6921, 6927
O'Grady, K.–(10) 6849
Oh, J. H.–(10) 6109
Oh, Young Jei–(10) 6078
O'Handley, R. C.–(10) 6427, 6429, 6430
Ohnuki, Satoru–(10) 6852
Ohshima, N.–(10) 6160
Ohta, Norio–(10) 6852
Ohyama, T.–(10) 6086
Ojima, Masahiro–(10) 6852
Okabe, A.–(10) 6540
Okada, Osamu–(10) 6855
Oliveira, V. S.–(10) 7125
Oonaka, Y.–(10) 6984
O'Reilly, J. W.–(10) 6328, 6595
Orme, C.–(10) 6892
Oseroff, S.–(10) 6723, 6819

Oseroff, S. B.–(10) 6757
Osgood, R. M., Jr.–(10) 6286
O'Shea, M. J.–(10) 5643, 6673
Osipov, Sergey G.–(10) 6093
Osofsky, M. S.–(10) 6679
Ostorero, J.–(10) 6103, 6792
Ostovic, Vlado–(10) 6048
Ostrovskii, V. S.–(10) 5622
O'Sullivan, J. A.–(10) 5753
Otani, Yoshichika–(10) 5903, 7161
Oti, John O.–(10) 6519, 6881
Otsuka, Hiroaki–(10) 6966
Ouchi, Kazuhiro–(10) 5984
Ounadjela, K.–(10) 5601, 6434, 6467, 6548, 6921
Ouyang, Jia–(10) 6795
Ozaki, M.–(10) 6217

Padalia, B. D.–(10) 6740, 7155
Pahner, Uwe–(10) 6048, 6050
Panagiotopoulos, I.–(10) 6232
Panchanathan, V.–(10) 6652
Papaefthymiou, V.–(10) 6000
Pardavi-Horvath, M.–(10) 6106
Pardavi-Horvath, Martha–(10) 5864
Parent, J. L.–(10) 5535
Park, B. J.–(10) 6592
Park, Jae Yun–(10) 6078
Park, S. J.–(10) 6343
Park, Yoon D.–(10) 5579
Parker, D.–(10) 5574
Parker, F. T.–(10) 5562, 6097, 6169, 6613, 6622, 6933
Parker, M. A.–(10) 5960, 6382, 7058
Parker, M. R.–(10) 6930, 7067
Parker, Martin R.–(10) 5565
Parkin, D. M.–(10) 6812
Parkin, S. S. P.–(10) 6455, 6531, 6900
Parra, R. E.–(10) 7137
Pashkevich, Yu.–(10) 6741
Passamani, E. C.–(10) 6483
Patel, M.–(10) 6528
Patterson, B. M.–(10) 6303
Patton, C. E.–(10) 5628, 5629, 5632
Patton, Carl E.–(10) 6084
Patton, Steven T.–(10) 5771
Paul, D. I.–(10) 6619
Pázmándi, F.–(10) 5847
Pechan, Michael J.–(10) 6178
Pecheron-Guegan, A.–(10) 6103
Peck, Paul R.–(10) 5747
Peck, W. F., Jr.–(10) 6603
Pedersen, Michael S.–(10) 5867
Pedziwiatr, A. T.–(10) 6574
Pelzl, J.–(10) 6492, 6508
Pepperhoff, W.–(10) 7012, 7015
Pereira, L. G.–(10) 7061, 7070
Perera, P.–(10) 5643
Pérez-Díaz, J. L.–(10) 6470
Perlov, A. Ya.–(10) 5922
Perron, J. C.–(10) 6946
Peruyero, Jose–(10) 6066
Petasis, D.–(10) 5879
Petrakovskii, G.–(10) 6743
Petrou, A.–(10) 5714, 5725
Pettit, Kevin–(10) 6918
Pfeiffer, Alfred–(10) 6996
Phillips, J. M.–(10) 6124
Pierce, D. T.–(10) 6437, 6452
Pini, M. G.–(10) 6431, 6464
Pinkerton, F. E.–(10) 6015, 7018
Pinto, Haim–(10) 7134
Pinto, R. P.–(10) 6551
Piryatinskaya, V.–(10) 6744, 6805
Pissas, M.–(10) 5853
Planès, J.–(10) 5698
Plaskett, T. S.–(10) 6480, 6537
Podlesnyak, A.–(10) 6331
Poinsot, R.–(10) 6921
Politi, P.–(10) 6431, 6464
Pollard, R. J.–(10) 6861
Polstra, P. A.–(10) 5731
Pomyalov, A. V.–(10) 5607
Ponce, M.–(10) 6397
Pop, Gheorghe–(10) 6949
Popma, Th. J. A.–(10) 5508
Porter, D. G.–(10) 5753
Portwine, W.–(10) 6688
Potter, M.–(10) 7079
Pouget, S.–(10) 5826
Pourarian, F.–(10) 6262, 6289
Praino, A. P.–(10) 6782
Prakash, Om–(10) 6740
Pratt, W. P., Jr.–(10) 6699
Préjean, J. J.–(10) 6682
Price, Edward–(10) 6903
Prikhod'ko, O.–(10) 6744
Pringle, O. A.–(10) 5994
Prinz, G. A.–(10) 5808, 6286, 7021, 7073
Prinz, Gary–(10) 5776
Prodi, G. A.–(10) 6996
Prokeš, K.–(10) 6522
Proksch, R.–(10) 6892
Proksch, Roger–(10) 5776, 5894
Prosser, V.–(10) 6783

Qi, Qi-Nian–(10) 6235
Qiu, G.–(10) 7067
Qiu, Gan–(10) 6934
Quandt, E.–(10) 5653
Quintana, P.–(10) 6940, 7000

Rabenberg, Lew–(10) 6658
Radhakrishna, P.–(10) 6601
Raffo, L.–(10) 7143
Raghavan, P. K. N.–(10) 6744
Raghavan, S.–(10) 5571
Raina, Urvashi–(10) 7185
Ramesh, R.–(10) 6915
Rani, R.–(10) 6006, 6009
Ranjan, R.–(10) 6144
Rao, D.–(10) 6622, 6933
Rao, K. V.–(10) 5853, 5862, 6306
Rao, X. L.–(10) 6226
Rastelli, E.–(10) 5817, 6051
Ratnam, A.–(10) 5634
Ravinder, D.–(10) 6118, 6121
Ravindran, K.–(10) 6081
Re, M. E.–(10) 6782
Rechenberg, H. R.–(10) 6223
Reddy, M. Bhagavantha–(10) 6125
Reddy, P. Venugopal–(10) 6125
Reimers, J. N.–(10) 5523
Reinders, A.–(10) 6424, 6440, 6659
Reininger, R.–(10) 6811
Remacle, J.-F.–(10) 6036
Ressouche, E.–(10) 7050
Restorff, J. B.–(10) 5656
Rettori, A.–(10) 6431, 6464
Rezende, S. M.–(10) 5613, 5616, 5862, 6563
Rhee, J. R.–(10) 5913
Rhyne, J. J.–(10) 6477
Ribeiro, C. A.–(10) 6003
Ricardo de Sousa, J.–(10) 5829
Rice, Paul–(10) 6878, 6881
Riera, Jose–(10) 6340
Rigamonti, A.–(10) 7143, 7146
Riley, L. A.–(10) 5673
Ritter, J. J.–(10) 6840
Rivas, J.–(10) 6100, 6757
Rivero, G.–(10) 6952
Roberts, Bruce W.–(10) 5946
Robertson, N.–(10) 6397
Robinson, R. A.–(10) 6589
Robson, M. C.–(10) 6870
Roesler, G. M., Jr.–(10) 6679
Roessli, B.–(10) 6331, 6337, 6743, 6816
Rojdestvenski, I. V.–(10) 5811, 5823, 6443
Roky, K.–(10) 6831
Romaniuk, Anatoly V.–(10) 7182
Rook, K.–(10) 5779
Rosales-Rivera, A.–(10) 5862
Rosales-Rivera, A.–(10) 5520
Rosenberg, M.–(10) 6586, 6813
Roshko, R. M.–(10) 5844
Rosov, N.–(10) 6069, 6072
Rubins, R. S.–(10) 6081
Rubinstein, M.–(10) 5595, 6924
Rubinstein, Mark–(10) 6557, 6622
Ruf, Ralph R.–(10) 6871
Rugar, D.–(10) 6211
Runge, A. P.–(10) 6354
Rusinek, Henry–(10) 6990
Russak, M. A.–(10) 5923
Russak, Michael A.–(10) 6159
Russek, Stephen E.–(10) 6519, 6881
Russell, P. E.–(10) 6132
Ryan, D. H.–(10) 6837

Sablik, M. J.–(10) 5673, 6769
Sablina, K.–(10) 6743
Sachdev, Subir–(10) 6345
Sadamura, H.–(10) 5559
Saenger, Dirk Uwe–(10) 6746
Saffari, Haydee–(10) 6153
Saffarian, Hassan M.–(10) 5568
Safonov, Vladimir L.–(10) 6745
Sahay, Satyam–(10) 6607
Sahu, S.–(10) 6892
Saito, Y.–(10) 5904, 5907, 6887
Salamon, M. B.–(10) 6455, 6531, 6592, 6918
Salter, I. W.–(10) 6783, 6861
Salvini, A.–(10) 6024
Samant, M.–(10) 6890
Samant, M. G.–(10) 5807
Samarasekara, P.–(10) 6640
Samarth, N.–(10) 6199
Sanders, Steven C.–(10) 6519
Sandlund, L.–(10) 5656
Sandratskii, L.–(10) 7033
Sands, T.–(10) 6665
Sankar, S. G.–(10) 6262, 6289, 6574
Sano, Takanobu–(10) 6162
Santini, H.–(10) 6397
Sarkissian, B. V. B.–(10) 6766
Sarmento, E. F.–(10) 5820, 5841
Sarrao, J. L.–(10) 6625
Sasada, I.–(10) 5916, 6984
Sato, Motoharu–(10) 6153
Sato, T.–(10) 5788
Saylor, C.–(10) 6723
Scarmozzino, R.–(10) 6286
Schad, R.–(10) 7079
Schäfer, M.–(10) 6193
Schäfer, R.–(10) 6782
Schefer, J.–(10) 6331
Scheinfein, M. R.–(10) 5589, 5592
Scheinfein, Michael R.–(10) 6138
Schep, Kees M.–(10) 6704
Schiebener, Peter–(10) 6996
Schlottmann, P.–(10) 5532, 6731, 7044
Schneider, T.–(10) 7015
Schneider-Muntau, H. J.–(10) 6812
Schreiber, F.–(10) 6184, 6421, 6492, 6508
Schrey, P.–(10) 6586
Schreyer, A.–(10) 6193
Schroeder, P. A.–(10) 6699
Schuhl, A.–(10) 6412, 7061
Schuller, Ivan K.–(10) 6178, 7079
Schultz, S.–(10) 6217
Schultz, T.–(10) 6723
Schumann, F. O.–(10) 6508
Schurer, P. J.–(10) 5583
Schwarzacher, W.–(10) 6543
Scorzelli, R. B.–(10) 6741
Scott, D. W.–(10) 6628
Seale, D.–(10) 7067
Seaman, C. L.–(10) 5639
Sechovsky, V.–(10) 6522
Sedazzari, S.–(10) 5817
Seddat, M.–(10) 6607
Sedighi, Mojtaba–(10) 6138
Seehra, M. S.–(10) 5873, 6822
Self, Terry M.–(10) 5565
Sellmyer, D. J.–(10) 6232, 6303, 6346, 6348, 6354, 6418, 6495, 6507, 6670
Serena, P. A.–(10) 6580
Sethna, James P.–(10) 5946
Shah, S. I.–(10) 6676
Shaheen, S. A.–(10) 6021, 6229
Shalaev, Boris N.–(10) 6745
Shan, Z. S.–(10) 6354, 6418
Shand, P. M.–(10) 5731
Shapiro, V.–(10) 6805
Shaw, K. A.–(10) 6124, 6688, 6691, 6692
Shelton, R. N.–(10) 6344
Shen, B. G.–(10) 6955
Shen, Bao-Gen–(10) 7111
Shen, Bao-gen–(10) 6250, 6253, 6256, 6259, 6312
Shen, J. X.–(10) 6346, 6348, 6418, 6495, 6507, 6670
Sheng, Q. G.–(10) 7035
Shi, Jing–(10) 6455
Shi, X.–(10) 6394
Shimazaki, Katsusuke–(10) 6852
Shimoda, T.–(10) 6631
Shin, J. Y.–(10) 6109
Shin, Y. D.–(10) 5913
Shinjo, T.–(10) 6483
Shinoura, Ø.–(10) 6379
Shiokawa, K.–(10) 7165
Shirane, G.–(10) 5959, 6321
Shiroishi, Y.–(10) 5978, 6890
Shoba, Sergei A.–(10) 7184
Shore, Joel D.–(10) 5946
Shpilkina, Irina V.–(10) 7182, 7183
Shpilkina, Irina V.–(10) 7184
Shu, Xiao Zhou–(10) 6375
Shull, R. D.–(10) 6840
Shuming, Pan–(10) 6289
Silva, C.–(10) 5879
Simizu, S.–(10) 6289, 6574
Simmons, Ralph–(10) 5765
Simmons, Ralph F., Jr.–(10) 5747
Sin, Kyusik–(10) 5972, 6150
Sinclair, R.–(10) 6144
Singh, Bharat–(10) 7187
Singh, Okram G.–(10) 6740
Singh, R. R. P.–(10) 5943
Singleton, E. W.–(10) 6000
Sinha, Urvija–(10) 6744
Sipahi, L. B.–(10) 6978, 6981
Sivertsen, John M.–(10) 5972, 6141, 6150
Sivron, N.–(10) 5952
Slade, S. B.–(10) 6613
Slavin, A. N.–(10) 5610, 6443
Slonczewski, J. C.–(10) 6474
Smirra, Karl–(10) 6996
Smit, P.–(10) 7149
Smith, M.–(10) 5734
Smith, N. V.–(10) 6378
Smith, P.–(10) 5882

Smith, R.–(10) 6723
Snelling, J. P.–(10) 7087
Snigirev, O.–(10) 6996
Soares, J. C.–(10) 6480
Sobolev, V. L.–(10) 5794
Sobolev, Vladimir L.–(10) 5797, 7003
Soderholm, L.–(10) 6740
Soghomonian, Victoria–(10) 5859
Sokoloff, J. B.–(10) 6075
Solanki, A. K.–(10) 6301
Soliman, A.–(10) 6492
Solovjov, A. G.–(10) 7104
Song, Kibong–(10) 6357
Song, L.–(10) 6226
Song, Oh Sung–(10) 6429
Song, Y. J.–(10) 5740
Sooryakumar, R.–(10) 5719, 7021
Sorensen, C. M.–(10) 5876, 5885
Souletie, J.–(10) 5512
Soulette, F.–(10) 6103
Sousa, J. B.–(10) 6513, 6551
Souza Azevedo, I.–(10) 6741
Sowers, C. H.–(10) 6169, 6461, 7080
Spada, E. J.–(10) 5923
Spada, F. E.–(10) 5562
Spalding, G. C.–(10) 6343
Speriosu, Virgil S.–(10) 7079
Sprague, J. A.–(10) 5801
Srinivasan, G.–(10) 5610, 6822, 6828
Srivastava, G. P.–(10) 6115
Srivastava, Niraj–(10) 6751
Staddon, C. R.–(10) 6921
Stageberg, F. E.–(10) 5779
Staley, S. W.–(10) 5879, 5882
Stampe, P. A.–(10) 6510
Stancil, Daniel D.–(10) 6066
Staub, U.–(10) 6334, 6337
Stearns, Mary Beth–(10) 6894
Stefanovskii, E. P.–(10) 6085
Stegge, J. aan de–(10) 6659
Steiner, M. M.–(10) 5719
Steinitz, M. O.–(10) 6318
Stelmaszyk, P.–(10) 6813
Sternlieb, B. J.–(10) 6321
Stevens, R.–(10) 6546
Sticht, J.–(10) 6467
Stoeffler, D.–(10) 6467
Stöhr, J.–(10) 5807, 6890
Stolze, Joachim–(10) 5937, 6057
Stöm-Olsen, J. O.–(10) 6560
Storm, D. F.–(10) 6464
Story, T.–(10) 5728
Street, R.–(10) 5481, 5701, 6271, 6634
Ström-Olsen, J. O.–(10) 7064
Su, J. L.–(10) 6397
Suganuma, T.–(10) 7090
Sugita, N.–(10) 5559
Suharyana–(10) 7120
Suhasaria, –(10) 7122
Sui, X.–(10) 5966
Suits, F.–(10) 5923
Sukstanskii, A. L.–(10) 5633, 6085
Sullivan, N.–(10) 6812
Sur, Jung Chul–(10) 6078
Suran, G.–(10) 6831
Sörig, C.–(10) 5981
Sutton, M.–(10) 6554
Sutton, R.–(10) 5882
Suzuki, A.–(10) 6540
Suzuki, M.–(10) 6126
Suzuki, Y.–(10) 6360, 6400
Swagten, H. J. M.–(10) 5728
Swarup, R.–(10) 7187
Swüste, C. H. W.–(10) 5728

Tabak, F.–(10) 7143
Tagawa, Ikuya–(10) 6776
Takacs, Laszlo–(10) 5864
Takagi, F.–(10) 6631
Takahashi, H.–(10) 6769
Takahashi, Takakazu–(10) 6509
Takajo, M.–(10) 6958
Takayama, S.–(10) 6782
Takeo, Akihiko–(10) 6776
Takeshita, H.–(10) 6415
Takino, Hiroshi–(10) 6162
Tanahashi, K.–(10) 5978
Tanaka, M.–(10) 6665
Tanaka, N.–(10) 5788
Tanaka, Yoichiro–(10) 5774
Tang, D. D.–(10) 6397
Tang, H. C.–(10) 5493
Tang, N.–(10) 6238, 6241, 6247
Tang, T.–(10) 7103
Tanigawa, K.–(10) 5788
Taniguchi, K.–(10) 6086, 6089
Tarasenko, S. V.–(10) 5633
Tarasov, O. Ju.–(10) 7186
Tarnopolsky, G. J.–(10) 6144
Tasaki, A.–(10) 6918
Tasaki, Akira–(10) 5903
Tassi, A.–(10) 5817, 6051
Taylor, R. D.–(10) 5853
Teh, Chai Tak–(10) 7003
Tejada, J.–(10) 5637, 5642, 6557
Temiryazev, A. G.–(10) 5619
Templeton, T. L.–(10) 5695
ter Haar, Leonard W.–(10) 5949
Tessier, M.–(10) 6607
Testardi, L. R.–(10) 6595
Thangaraj, N.–(10) 6900
Thole, Bernard Theodoor–(10) 5807
Tholence, J. L.–(10) 6766
Thomas, B. W. J.–(10) 6789, 7081, 7087
Thompson, C. V.–(10) 6430
Thompson, G. K.–(10) 6643
Thompson, S. M.–(10) 6921
Thomson, T.–(10) 6849
Thornton, J. T.–(10) 6132
Thummes, G.–(10) 6566
Tiefel, T. H.–(10) 6915, 7052
Tikhomirova, M. P.–(10) 5619
Tindall, D. A.–(10) 6318
Ting, S. T.–(10) 6748
Tinklenberg, P.–(10) 6723
Tobin, J. G.–(10) 6369
Tognetti, Valerio–(10) 5814
Tomi-ita, K.–(10) 6769
Tomiyama, F.–(10) 6890
Tondra, Mark–(10) 6567
Tonner, B. P.–(10) 6890
Tonner, Brian–(10) 6811
Toporov, A. Yu.–(10) 6804, 6804
Torng, Terry–(10) 5800
Torre, Edward Della–(10) 5775, 6846
Trequattrini, Alessandro–(10) 6990
Trindade, I. G.–(10) 6551
Tripathi, G. S.–(10) 5737
Troper, A.–(10) 6296, 6734, 6737
Trouilloud, P. L.–(10) 5923, 6782
Trouw, F.–(10) 7030
Tsameret, A.–(10) 6322
Tsankov, M. A.–(10) 5628, 5629
Tsapin, Alexandre I.–(10) 7183
Tsoukatos, A.–(10) 6507, 6623
Tsoukatos, T.–(10) 6624
Tsuda, H.–(10) 7162
Tsui, F.–(10) 6592
Tsui, Frank–(10) 6174
Tsunashima, S.–(10) 6769, 7090, 7102
Tucker, J. W.–(10) 5841
Tucker, Roy–(10) 6021, 6229
Tun, Z.–(10) 6063
Tung, M. J.–(10) 6112
Turnbull, M. M.–(10) 5535
Turpin, G. B.–(10) 5740

Uchiyama, S.–(10) 6769, 7090, 7102
Ueno, K.–(10) 7168
Ueno, S.–(10) 7162, 7165, 7168, 7174, 7177, 7181
Uher, Ctirad–(10) 6174
Uhl, M.–(10) 7033
Uhrenius, Bjorn–(10) 6265
Ullah, M.–(10) 5960
Umphress, R.–(10) 5960
Unguris, J.–(10) 6437, 6452
Utochkin, Sergey N.–(10) 6786

Vaia, Ruggero–(10) 5814
Vajda, Ferenc–(10) 5689, 5692, 5775
Vaknin, D.–(10) 6603
Valentin, J.–(10) 7102
Valenzuela, R.–(10) 6940, 7000
Valet, Thierry–(10) 6693
Val'kov, V.–(10) 6743
van de Veerdonk, R. J. M.–(10) 6709
Van Dover, R. B.–(10) 7052
van Dover, R. B.–(10) 6124, 6603
van Kooten, M.–(10) 5508
Van Leeuwen, R. A.–(10) 6498
VanWijland, F.–(10) 6489
Varga, L.–(10) 5547
Vasilyev, V. M.–(10) 5924
Vaurés, A.–(10) 6476
Vázquez, M.–(10) 5791, 6952
Vázquez, Manuel–(10) 6949
Vázquez-Vázquez, C.–(10) 6757
Veca, G. M.–(10) 6024, 6033
Vekhter, Benjamin G.–(10) 5863
Velázquez, J.–(10) 5791
Velicescu, M.–(10) 6586
Velu, E. M. T.–(10) 6132
Veneva, A.–(10) 6726
Vennegues, P.–(10) 5601
Vennix, C. W. H. M.–(10) 5728
Verkhovceva, Nadezda V.–(10) 7182
Verkhovtseva, Nadezda V.–(10) 7182
Verrucchi, Paola–(10) 5814
Vetoshko, P. M.–(10) 5922, 6804, 6804
Victora, R. H.–(10) 6428, 6858
Vijayaraghavan, R.–(10) 7155
Vinogradov, A. G.–(10) 7186
Višňovský, S.–(10) 6783
Visokay, Mark R.–(10) 6153
Viswanath, V. S.–(10) 5937, 6057, 6751
Viswanathan, K. V.–(10) 6161
Vitale, S.–(10) 5634, 6996
Voiron, J.–(10) 6682
Volkovoy, V. B.–(10) 5922, 6804, 6804
Volotskii, S. V.–(10) 7186
von Geisau, O.–(10) 6508
Vorderwisch, P.–(10) 6334
Voronko, A. J.–(10) 5922, 6804, 6804
Vumni, G. B.–(10) 5535

Waby, N. A.–(10) 5631
Wadas, Andrzej–(10) 6878
Waddill, G. D.–(10) 6369
Wadewitz, Scott–(10) 5919
Wagner, J.–(10) 6825
Wakabayashi, N.–(10) 6601
Waknis, A.–(10) 6930
Waldfried, Carlo–(10) 5919
Walker, J. C.–(10) 6464
Walker, M. J.–(10) 6546, 6783, 7055
Wallace, W. E.–(10) 6280, 6574
Wallance, W. E.–(10) 6289
Wan, H.–(10) 6623, 6624
Wan, Hong–(10) 6507
Wang, D.–(10) 6232
Wang, Ding-sheng–(10) 6409
Wang, Dingsheng–(10) 5802
Wang, Fang-Wei–(10) 7111
Wang, Fang-wei–(10) 6250, 6253, 6259
Wang, G.-C.–(10) 5580
Wang, Haiyun–(10) 5762
Wang, J. L.–(10) 6238, 6241
Wang, Jian-Qiang–(10) 6604, 6903
Wang, Xindong–(10) 6366
Wang, Xun-Li–(10) 6603
Wang, Y. G.–(10) 6268
Wang, Y. J.–(10) 6351, 6418
Wang, Y. Z.–(10) 6226
Wang, Z.–(10) 7108
Wang, Z. R.–(10) 6603
Wang, Zhanwen–(10) 5859
Warnock, J.–(10) 5714, 5725
Warren, Garry W.–(10) 5568
Wassermann, E. F.–(10) 6072, 7012, 7015
Watabe, H.–(10) 7090, 7102
Watson, M. L.–(10) 6927
Watson, R. E.–(10) 5493
Watts, K. T.–(10) 5673
Weissman, M. B.–(10) 6531
Weller, D.–(10) 5807, 7102
Wellock, K. P.–(10) 7055
Wells, S.–(10) 6583
Wendhausen, P. A. P.–(10) 6018
Westphal, C. H.–(10) 6720
White, Robert L.–(10) 5644
Whitlock, Jonathan B.–(10) 6363
Wiedmann, M. H.–(10) 6498
Wiedmann, Michael H.–(10) 6401
Wierman, K. W.–(10) 6348, 6670
Wiese, G.–(10) 5632
Wigen, P. E.–(10) 5740, 6434
Wilhoit, Dennis R.–(10) 7079
Willett, R. D.–(10) 5952
Williams, C. W.–(10) 6740
Williams, G.–(10) 6510
Williams, Gwyn–(10) 7108
Williams, J.–(10) 5882
Willis, R. F.–(10) 6406
Winkelman, A. J. M.–(10) 6247
Wiser, N.–(10) 7055
Withanawasam, L.–(10) 6646
Wolf, J. A.–(10) 6193
Wolfe, R.–(10) 6286
Wong, B. Y.–(10) 5966
Woods, J. P.–(10) 6303
Woodward, R.–(10) 6271, 6634
Woollam, J. A.–(10) 6495, 6670
Wu, J. M.–(10) 6112
Wu, Ruqian–(10) 5802, 6409
Wu, S. Y.–(10) 6598
Wu, Y.–(10) 5807, 6890
Wüchner, S.–(10) 6682
Wun-Fogle, M.–(10) 5656
Wynn, C. M.–(10) 5535

Xia, S. K.–(10) 6766
Xiao, Gang–(10) 6604, 6903
Xiao, John Q.–(10) 5800
Xu, J.–(10) 7055
Xu, Jian-Min–(10) 7120
Xu, Xie–(10) 6021, 6229
Xu, Y. B.–(10) 6190
Xu, You–(10) 6798
Xue, J. Simon–(10) 6740

Yacoby, E. R.–(10) 6322
Yagi, H.–(10) 6658
Yahisa, Y.–(10) 5978
Yajima, T.–(10) 6969
Yamada, M.–(10) 7140

Yamaguchi, Makoto–(10) 5903
Yamamoto, M.–(10) 5904
Yamasaki, J.–(10) 6958
Yamashita, Hideo–(10) 6042
Yamashita, T.–(10) 6144
Yan, Mingliang–(10) 6504
Yang, C. J.–(10) 6274, 6655
Yang, F. M.–(10) 6238, 6241
Yang, G.–(10) 5844
Yang, H. D.–(10) 6598
Yang, H. S.–(10) 6351
Yang, Jie Hui–(10) 6798
Yang, Lin-yuan–(10) 6312
Yang, Ningjiang–(10) 7180
Yang, Q.–(10) 6699
Yang, Z. J.–(10) 5589, 5592
Yang, Zheng–(10) 5556
Yang, ZhiJun–(10) 6138
Yao, Y. D.–(10) 6244
Yatsuya, S.–(10) 7084
Yatsuya, Shigeki–(10) 6843
Yavari, A. R.–(10) 6946
Ye, Xiao-Guang–(10) 6135
Yelon, W. B.–(10) 6000
Yeshurun, Y.–(10) 6322
Yin, L.–(10) 6226
Yinfan, Xu–(10) 6289
Yiping, L.–(10) 5885
Yoneda, Yoshiro–(10) 5987
Yoshida, K.–(10) 6400
Yoshida, Y.–(10) 5695
Yoshimoto, Hideaki–(10) 5987
Yoshino, S.–(10) 6769
Young, A. P.–(10) 5943
Yu, Chengtao–(10) 6504
Yu, W. Y.–(10) 5714, 5725
Yu, X. Y.–(10) 7090, 7102
Yu, Yongmin–(10) 5937
Yu, Yuwu–(10) 5550
Yuan, J.–(10) 6501
Yuan, Samuel W.–(10) 6385
Yuan, Sui hua–(10) 6375
Yuasa, Shinji–(10) 7161
Yumoto, S.–(10) 6160

Zabel, H.–(10) 6184, 6193, 6421
Zähres, H.–(10) 7015
Zaluska, A.–(10) 6560
Zeidler, T.–(10) 6421
Zeidler, Th.–(10) 6184
Zeng, D. C.–(10) 6247
Zeng, Hua-Xian–(10) 5556
Zhai, H. R.–(10) 6190, 6955, 7099, 7103
Zhai, Y.–(10) 6190
Zhan, Wen-shan–(10) 6253
Zhang, Bo–(10) 6259
Zhang, Changmin–(10) 7180
Zhang, Guibus–(10) 6685
Zhang, Guo Ying–(10) 6798
Zhang, H.–(10) 6534
Zhang, H. Y.–(10) 7099, 7103
Zhang, M. J.–(10) 6094
Zhang, Q.–(10) 6094, 7171
Zhang, S. Y.–(10) 7099
Zhang, Shu–(10) 5937
Zhang, Shufeng–(10) 6685, 6906, 7076
Zhang, W.–(10) 5535
Zhang, X. W.–(10) 6351
Zhang, X. X.–(10) 5637, 5642, 6557
Zhang, Xianfeng–(10) 7128, 7161
Zhang, Y.–(10) 6354
Zhang, Y. B.–(10) 6495, 6670
Zhang, Ying–(10) 6795
Zhang, Z.–(10) 6434
Zhao, Jian-Gao–(10) 7111
Zhao, Jian-gao–(10) 6259, 6312
Zhao, R. W.–(10) 6241
Zhao, Y. J.–(10) 5502
Zhao, Z. G.–(10) 7117
Zheng, Y.–(10) 6280
Zhong, X. P.–(10) 6241
Zhong, Xue-Fu–(10) 6834
Zhou, A.–(10) 5879
Zhou, H.–(10) 6334
Zhou, L.–(10) 6434
Zhou, R. J.–(10) 6586
Zhou, S. X.–(10) 6268
Zhou, X. Z.–(10) 5556
Zhu, J. G.–(10) 6773
Zhu, Jian Gang–(10) 5553
Zhu, Jian-Gang–(10) 5762, 6129, 6135, 6150, 6388
Zhuravlev, Michail Ye.–(10) 6729
Zil'berman, P. E.–(10) 5619
Zimmermann, G.–(10) 5981
Zoll, S.–(10) 6548
Zolliker, M.–(10) 6337
Zubieta, Jon–(10) 5859
Z'ubin, Pavel B.–(10) 6729
Zuekov, O. E.–(10) 7186
Züger, O.–(10) 6211
Zvezdin, Anatoley K.–(10) 6786

AMERICAN INSTITUTE OF PHYSICS

500 Sunnyside Boulevard, Woodbury, NY 11797

The American Institute of Physics is a not-for-profit membership corporation chartered in New York State in 1931 for the purpose of promoting the advancement and diffusion of the knowledge of physics and its application to human welfare. Leading societies in the fields of physics, astronomy, and related sciences are its members.

The Institute publishes its own scientific journals as well as those of its member societies; publishes both technical and general *interest* books; provides abstracting and indexing services; provides on-line database and e-mail services; disseminates reliable information on physics to the public; collects and analyzes statistics on the profession and on physics education; encourages and assists in the documentation and study of the history and philosophy of physics; cooperates with other organizations on educational projects at all levels; and collects and analyzes information on Federal programs and budgets.

Member Societies

The American Physical Society
Harry Lustig, Acting Executive Secretary
One Physics Ellipse
College Park, MD 20740-3844

Optical Society of America
David W. Hennage, Executive Director
2010 Massachusetts Avenue, N.W.
Washington, DC 20036

Acoustical Society of America
Charles Schmid, Executive Director
500 Sunnyside Blvd., Woodbury, NY 11797-2999

The Society of Rheology
Andrew M. Kraynik, Secretary
Department 1512
Sandia National Labs.
Albuquerque, NM 87185

American Association of Physics Teachers
Bernard V. Khoury, Executive Officer
One Physics Ellipse
College Park, MD 20740-3845

American Crystallographic Association
William L. Duax, Exec. Officer
PO Box 96, Ellicott Station
Buffalo, NY 14205-0096

American Astronomical Society
Peter B. Boyce, Executive Officer
1630 Connecticut Avenue, N.W.
Washington, DC 20009

American Association of Physicists in Medicine
Sal Trofi, Executive Director
One Physics Ellipse
College Park, MD 20740-3846

American Vacuum Society
William D. Westwood, Secretary
Bell-Northern Research, Ltd.
PO Box 3511, Station C
Ottawa, Ontario K1Y 4H7, Canada

American Geophysical Union
A. F. Spilhaus, Jr., Executive Director
1630 Connecticut Avenue, N.W.
Washington, DC 20009

Affiliated Societies

American Institute of Aeronautics and Astronautics, American Meteorological Society, American Nuclear Society, ASM International, Astronomical Society of the Pacific, Division of Physical Chemistry of ACS, Engineering Information, Inc., The Geological Society of America, Instrument Society of America, International Association of Mathematical Physicists, International Centre for Diffraction Data, Materials Research Society, Microscopy Society of America, Nuclear and Plasma Sciences Society of IEEE, Physics/Astronomy Section of *the Council on Undergraduate Research*, Physics Section of AAAS, Society for Applied Spectroscopy, SPIE—The International Society for Optical Engineering.

Corporate Associates: Approximately 175 leading corporations *by their membership, participate in and contribute to the support of AIP.*

Publications

Physical Review A · Bernd Crasemann, *Editor*, Physics Dept., University of Oregon, Eugene, OR 97403
Physical Review B · P.D. Adams, *Editor*, The American Physical Society, 1 Research Rd., Box 1000, Ridge, NY 11961
Physical Review C · Sam Austin, *Editor*, Cyclotron Labs., Michigan State University, E. Lansing, MI 48824
Physical Review D · Lowell S. Brown and D.L. Nordstrom, *Editors*, APS, 1 Research Rd., Box 1000, Ridge, NY 11961
Physical Review E · Irwin Oppenheim, *Editor*, Dept. of Chemistry, Massachusetts Institute of Technology, Cambridge, MA 02139
Physical Review Abstracts · *Reid Terwilliger, Editor*, APS, One Physics Ellipse, College Park, MD 20740-3844
Physical Review Letters · J. Sandweiss, G. Basbas, S.G. Brown, and G.I. Wells, *Editors*, APS
APS News · Brian Schwartz, *Editor*, APS, One Physics Ellipse, College Park, MD 20740-3844
Bulletin of The American Physical Society · Brian Schwartz, *Editor*, APS, One Physics Ellipse, College Park, MD 20740-3844
Reviews of Modern Physics · David Pines, *Editor*, Loomis Lab. of Physics, 1110 W. Green St., Urbana, IL 61801
The Journal of the Acoustical Society of America · Daniel W. Martin, *Editor-in-Chief*, 7349 Clough Pike, Cincinnati, OH 45244
American Journal of Physics · Robert H. Romer, *Editor*, 222 Merrill Science Bldg., Box 2262, *Amherst College*, Amherst, MA 01002
The Astronomical Journal · Paul W. Hodge, *Editor*, Astronomy Dept.FM-20, University of Washington, Seattle, WA 98195
Publications of the Astronomical Society of the Pacific · Howard E. Bond, *Editor*, Space Telescope Science Institute, Baltimore, MD 21218
Bulletin of the American Astronomical Society · Peter B. Boyce, *Editor*, AAS
The Astrophysical Journal · Helmut A. Abt, *Managing Editor*, Kitt Peak National Observatory, Box 26732, Tucson, AZ 85726
The Journal of Chemical Physics · J.C. Light, *Editor*, James Franck Institute, The University of Chicago, Chicago, IL 60637
Journal of Mathematical Physics · Roger G. Newton, *Editor*, Indiana Univ., The Poplars, Rm. 324, Bloomington, IN 47405
Physics of Fluids · A. Acrivos, *Editor*, The Levich Institute, Steinman 202, CCNY, Convent Ave. at 140 St., New York, NY 10031
Physics of Plasmas · Ronald C. Davidson, *Editor*, Plasma Phys. Lab., Princeton Univ., PO Box 451, Princeton, NJ 08543
Journal of Applied Physics · Steven J. Rothman, *Editor*, Argonne Natl. Lab., Box 8296, Argonne, IL 60439-8296
Applied Physics Letters · Hartmut Weidersich, *Editor*, Argonne Natl. Lab., Box 8296, Argonne, IL 60439-8296
Review of Scientific Instruments · Thomas H. Braid, *Editor*, Argonne Natl. Lab., Box 8293, Argonne, IL 60439-8293
Journal of Physical and Chemical Reference Data · Jean W. Gallagher, *Editor*, NIST, MS221/A3223, Gaithersburg, MD 20899
Physics Today · Gloria B. Lubkin, *Editor*, AIP, One Physics Ellipse, College Park, MD 20740-3843
Computers in Physics · Lewis Holmes, *Editor*, One Physics Ellipse, College Park, MD 20740-3843
Chaos · David K. Campbell, *Editor*, Dept. of Physics, University of Illinois–UC, Urbana, IL 61891
Journal of Vacuum Science and Technology A · Gerald Lucovsky, *Editor*, Dept. of Physics, N. Carolina State Univ., Raleigh, NC 27650
Journal of Vacuum Science and Technology B · Gary E. McGuire, *Editor*, MCNC, Research Triangle Park, NC 27709
Medical Physics · J.S. Laughlin, *Editor*, Memorial Sloan-Kettering Cancer Center, 1275 York Ave., New York, NY 10021
Noise Control Engineering Journal · Alan H. Marsh, *Editor-in-Chief*, DyTec Engineering, Inc., 5092 Tasman Dr., Huntington Beach, CA 92649
Powder Diffraction · Deane K. Smith, *Editor-in-Chief*, Dept. of Geosci. and Mineralogy, Penn State Univ., University Park, PA 16802
AAPT Announcer · Bernard V. Khoury, *Editor*, AAPT, One Physics Ellipse, College Park, MD 20740-3845
The Physics Teacher · Clifford E. Swartz, *Editor*, Phys. Dept., State University of New York, Stony Brook, NY 11794
Journal of Rheology · Arthur B. Metzner, *Editor*, Dept. of Chemical Engineering, University of Delaware, Newark, DE 19716
Journal of the Optical Society of America A · Bahaa E. A. Saleh, *Editor*, 2010 Massachusetts Ave., N.W., Washington, DC 20036
Journal of the Optical Society of America B · Paul F. Liao, *Editor*, 2010 Massachusetts Ave., N.W., Washington, DC 20036
Applied Optics · William T. Rhodes, *Editor-in-Chief*, Dept. of Electr. & Computer Eng., Univ. of Colorado, Boulder, CO 80309-0425
Optics Letters · Peter W. E. Smith, *Editor*, Bellcore, 331 Newman Springs Rd., Red Bank, NJ 07701
Optics and Photonics News · Andrea Pendleton, *Editor*, 2010 Massachusetts Ave., N.W., Washington, DC 20036
Journal of Lightwave Technology · Donald B. Keck, *Editor*, Corning Glass Works, Sullivan Park FR29, Corning, NY 14830
The Journal of Undergraduate Research in Physics · R.E. Adelberger, *Editor*, Physics Dept., Guilford College, Greensboro, NC 27410

AIP Conference Proceedings

Acoustical Physics
Astronomy Reports
Astronomy Letters
Crystallography Reports
JETP
JETP Letters
Low Temperature Physics
Optics and Spectroscopy
Physics-Doklady
Physics of Atomic Nuclei
Physics of the Solid State
Plasma Physics Reports
Physics of Particles and Nuclei
Semiconductors
Journal of Optical Technology
Technical Physics
Technical Physics Letters

Current Physics Index (CPI), quarterly and annual subject index with abstracts to all the above journals.
General Physics Advance Abstracts (GPAA), semimonthly advance abstracts of AIP-published physics literature.
Searchable Physics Information Notices (SPIN), monthly computer-readable tape of abstracts.
Current Physics Microform (CPM), monthly microfilm edition of all the above journals.
Current Physics Reprints (CPR), on-demand copies of any article in any of the above journals.
Physics Briefs (PB), semimonthly comprehensive index with abstracts to the world literature of physics.
PINET, an online physics information network.

Governing Board 1994–1995

Roland W. Schmitt, *Chair**
Reuben E. Alley
Benjamin Bederson
Roger A. Bell
Marc H. Brodsky (*ex officio*)*
Robert L. Byer*
Patricia E. Cladis
Charles Counselman, III
G. Brent Dalrymple*
Robert L. Dixon
William L. Duax
Judy R. Franz
Roderick M. Grant (*ex officio*)*
Joseph E. Greene
David Hennage
David W. Hoffman*
Karen L. Johnston
Frank J. Kerr
Bernard V. Khoury*
Carl Kisslinger
Patricia K. Kuhl
Donald N. Langenberg
Tingye Li
Harry Lustig*
Christopher H. Marshall
Gregory B. McKenna
Duncan T. Moore
Norman F. Ness
C. Robert O'Dell
C. Kumar N. Patel
Burton Richter
Barrett H. Ripin
J. William Rogers, Jr.
Charles E. Schmid*
Benjamin Snavely
A. F. Spilhaus, Jr.
Hugo Steinfink
Richard Stern
Howard G. Voss*
Martin Walt
* executive committee

AIP Officers

Marc H. Brodsky, *Executive Director and CEO*
Rodcrick M. Grant, *Secretary*
Arthur T. Bent, *Treasurer and CFO*
Theresa C. Braun, *Director of Human Resources*
Darlene Carlin, *Director of Publishing*
John S. Rigden, *Director of Physics Programs*

Publishing Services

James J. Donohue, *Director Publishing Services*
Edward P. Greeley, *Director Advertising and Exhibits*
Douglas LaFrenier, *Director of Marketing*
Peggy Judd, *Director of Information Technology*
Maria Taylor, *Publisher AIP Press*
Carol Fleming, *Manager Publishing II Branch*
Doreene A. Berger, *Manager Journal Production I Division*
Maya Flikop, *Manager Translation Program Division*
John T. Scott, *Manager Editorial Operations Division*
Cheryl Taub, *Manager Composition I Division*
Denise Weiss, *Manager Books/Special Projects*
Janice Wilmot, *Manager Production II Division*

APPLIED PHYSICS LETTERS: Current Table of Contents

Applied Physics Letters, a companion publication to the *Journal of Applied Physics*, is published weekly by the American Institute of Physics. Its letters are timely, short reports devoted to important new findings in applied physics. The contents list below is from a recent issue.

APPLIED PHYSICS LETTERS

Vol. 64, No. 18, 2 May 1994

CODEN: APPLAB ISSN: 0003-6951

OPTICS

2329 Cr^{4+}:$Gd_3Sc_2Ga_3O_{12}$ passive Q-switch for the Cr^{3+}:LiCaAlF$_6$ laser — Yen-Kuang Kuo, Yang Yang, Milton Birnbaum

2332 Noise suppression for photorefractive image amplification in the $LiNbO_3$:Fe crystal sheet — Jingjun Xu, Guangyin Zhang, Simin Liu, Junmin Liu, Liqiu Men

2335 Polarization-independent wavelength filter using a grating-assisted vertical directional coupler in InP — *F. Heismann, L. L. Buhl, B. I. Miller,* M. Newkirk, U. Koren, M. G. Young, R. C. Alferness

2338 Optical near-field imaging with a semiconductor probe tip — J. Mertz, M. Hipp, J. Mlynek, O. Marti

2341 Phase conjugation of $BaTiO_3$:Ce by backward stimulated photorefractive scattering — Yong Zhu, Changxi Yang, Mengjun Hui, Xiaojuan Niu, Jinfeng Zhang, Tang Zhou, Xing Wu

CONDENSED MATTER: STRUCTURE, MECHANICAL AND THERMAL PROPERTIES

2344 Transmission electron microscopy characterization of $In_xGa_{1-x}As$ substrates grown by heteroepitaxial lateral overgrowth — J. P. McCaffrey, B. Bryskiewicz, T. Bryskiewicz, E. Jinin

2347 Anomalous laser-induced voltages in $YBa_2Cu_3O_x$ and "off-diagonal" thermoelectricity — Louis R. Testardi

2350 Raman scattering and x-ray diffraction investigations of highly textured $(Pb_{1-x}La_x)TiO_3$ thin films — *Z. C. Feng, B. S. Kwak, A. Erbil,* L. A. Boatner

2353 Thermal expansion of polycrystalline diamond produced by chemical vapor deposition — D. J. Pickrell, K. A. Kline, R. E. Taylor

2356 Kinetic suppression of islanding in impurity-mediated heteroepitaxial growth of germanium on silicon — H. J. Osten

2359 Absence of solute drag in solidification — J. A. Iqbl, M. J. Aziz, D. P. Bruno, M. O. Thompson

SEMICONDUCTORS

2362 Threshold voltage shift of amorphous silicon thin film transistors with atmospheric pressure chemical vapor deposition silicon dioxide — Jeong Hyun Kim, Eui Yeol Oh, Jung Kee Yoon, Yong Suk Park, Chan Hee Hong

2364 Blue electroluminescent devices with high quantum efficiency from alkoxy-substituted poly(para-phenylene vinylene)-trimers in a polystyrene matrix — W. Tachelet, S. Jacobs, H. Ndayikengurukiye, H. J. Geise, J. Grüner

2367 Optical properties of porous silicon superlattices — G. Vincent

2370 Long-wavelength stacked SiGe/Si heterojunction internal photoemission infrared detectors using multiple SiGe/Si layers — J. S. Park, T. L. Lin, E. W. Jones, H. M. Del Castillo, S. D. Gunapala

2373 Photoluminescence of Si/SiGe/Si quantum wells on sapphire by oxygen implantation substrate — D. K. Nayak, N. Usami, S. Fukatsu, Y. Shiraki

2376 Photoluminescence of chemically vapor deposited Si on silica aerogels — Wenqing Cao, Arlon J. Hunt

2379 Single electron transport and current quantization in a novel quantum dot structure — Y. Nagamune, H. Sakaki, L. P. Kouwenhoven, L. C. Mur, C. J. P. M. Harmans, J. Motohisa, H. Noge

2382 Temperature dependence of cathodoluminescence from thin GaAs-AlGaAs multiple quantum wells — U. Jahn, J. Menniger, R. Hey, H. T. Grahn

2385 Ultrafast carrier trapping and slow recombination in ion-bombarded silicon on sapphire measured via THz spectroscopy — Stuart D. Brorson, Jucheng Zhang, Søren R. Keiding

2388 Ultraviolet photoexfoliation of III-V compound semiconductors: A new approach to surface passivation — Carol I. H. Ashby, Kevin R. Zavadil, Arnold J. Howard, *B. E. (Gene)* Hammons

2391 Laser-induced sputtered neutral mass spectrometry study of arsenic concentration profiles in a polycrystalline silicon/single-crystal silicon system — Yasuhiro Higashi, Tetsuya Maruo, Yoshikazu Homma, Jun'ichi Kodate, Masayasu Miyake

2394 Electroluminescence from porous silicon with conducting polymer film contacts — Kun-hai Li, Dennis C. Diaz, Yuesong He, Joe C. Campbell, Chaochieh Tsai

2397 Low-temperature growth of high resistivity GaAs by photoassisted metalorganic chemical vapor deposition — J. C. Roberts, K. S. Boutros, *S. M. Bedair,* D. C. Look

2400 Evidence for population inversion in excited electron states of a double barrier resonant tunneling structure — J. W. Cockburn, M. S. Skolnick, D. M. Whittaker, P. D. Buckle, A. R. K. Willcox, G. W. Smith

2403 Observation of resonant tunneling through localized continuum states in electron wave interference diodes — R. E. Carnahan, M. A. Maldonado, K. P. Martin, R. J. Higgins, *J. P. A. van der Wagt,* J. S. Harris, Jr.

2406 Back side Raman measurements on Ge/Pd/n-GaAs ohmic contact structures — K. Wuyts, J. Watté, R. E. Silverans, M. Van Hove, G. Borghs, C. J. Palmstrøm, L. T. Florez, H. Munder

2409 New interface structure for *A*-type $CoSi_2$/Si(111) — M. F. Chisholm, S. J. Pennycook, R. Jebasinski, S. Mantl

2412 Threshold dose for ion-induced intermixing in InGaAs/GaAs quantum wells — L. B. Allard, G. C. Aers, P. G. Piva, P. J. Poole, M. Buchanan, I. M. Templeton, T. E. Jackman, S. Charbonneau, U. Akano, I. V. Mitchell

2415 High efficiency indium gallium arsenide photovoltaic devices for thermophotovoltaic power systems — David M. Wilt, Navid S. Fatemi, Richard W. Hoffman, Jr., Phillip P. Jenkins, David J. Brinker, David Scheiman, Roland Lowe, Maria Fatemi, Raj K. Jain

2418 Dimerization induced incorporation nonlinearities in GaAsP — J. E. Cunningham, M. B. Santos, K. W. Goossen, M. D. Williams, W. Jan

2421 Full band structure calculation of the linear electro-optic susceptibility — *Ed Ghahramani, J. E. Sipe*

2424 Observation of voids induced by mechanical stress and electromigration in passivated Al lines deposited at different purity levels — T. Marieb, J. C. Bravman, P. Flinn, D. S. Gardner, M. Madden

2427 Dry etching and implantation characteristics of $Al_{0.5}In_{0.5}P$ — S. J. Pearton, C. R. Abernathy, F. Ren

2430 Photoluminescence lifetime of GaP/AlP superlattices grown by gas-source molecular-beam epitaxy — Kumiko Asami, Hajime Asahi, Song Gang Kim, Joon Hong Kim, Akito Ishida, Setsuo Takamuku, Shun-ichi Gonda

2433 Uncooled InSb/$In_{1-x}Al_xSb$ mid-infrared emitter — T. Ashley, C. T. Elliott, N. T. Gordon, R. S. Hall, A. D. Johnson, G. J. Pryce

2436 Asymmetric dark current in quantum well infrared photodetectors — K. L. Tsai, C. P. Lee, K. H. Chang, D. C. Liu, H. R. Chen, J. S. Tsang

2439 Excitonic properties of ZnSe/ZnSeS superlattices — *R. Cingolani, M. Lomascolo,* N. Lovergine, M. Dabbicco, M. Ferrara, I. Suemune

SUPERCONDUCTORS

2442 Superconducting readout of semiconductor memory at liquid nitrogen temperature — Claude Hilbert, Uttam Ghoshal, Harry Kroger, Jon S. Martens, V. M. Hietala, T. A. Plut

2445 Influence of inductance induced noise in an $YBa_2Cu_3O_x$ dc-SQUID at high operation temperatures — P. Å. Nilsson, T. Claeson, J. B. Hansen, A. Kühle

Subscription information may be obtained by writing Marketing Services at the American Institute of Physics.